

189,87

Cuk-H01760-16-P0244

AJR

16

American
Journal of
Roentgenology



January 1987

© M.C. Escher Heirs c/o Gordon Art-Barn, Holland



SELECTION

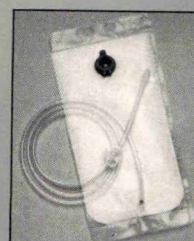
Through selection we exercise our individuality, letting our choices reflect our unique identities.

E-Z-EM has always sought to give the medical profession the widest range of products to choose from. E-Z-EM is the leading supplier of barium products because, in addition to quality, we offer the most complete selection of products through one of the most efficient distribution networks in the industry.

The scope of products we supply has grown. Now a full-line supplier of imaging products, E-Z-EM offers a range of choices within each product line. Our Pinnacle™ protective garments include Adjust-A-Weight™ aprons, as well as gloves and eyeglasses. The modular design of our PercuSet™ disposable procedure trays permits a wide range of options. Our PercuCut™ biopsy needles are available in a variety of gauges and lengths. Our E-Z-EM Prep kits can accommodate the use of either suppositories or enemas in the bowel prepping regimen.

E-Z-EM

**More than barium—
much more**



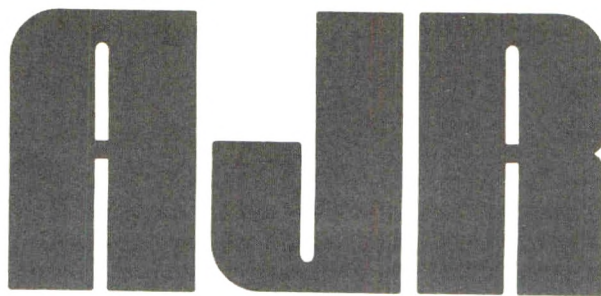
Protective Products
Colon Prepping Products
Interventional Products
Barium Products



E-Z-EM, Inc., 7 Portland Ave., Westbury, N.Y. 11590, Toll Free 800-645-3052, In New York 516-333-8230

CIRCLE 5 ON READER SERVICE CARD

© E-Z-EM, Inc. 1986



American Journal of Roentgenology
Diagnostic Imaging and Related Sciences

Editor-In-Chief Robert N. Berk, *San Diego, California*

Editor Emeritus Melvin M. Figley, *Seattle, Washington*

Associate Editors Alan J. Davidson, *Washington, District of Columbia*
Saskia von Waldenburg Hilton, *San Diego, California*
Juan M. Taveras, *Boston, Massachusetts*

Assistant Editors William L. Ashburn, *San Diego, California*
Charles C. Berry, *San Diego, California*
William G. Bradley Jr., *Pasadena, California*
Edward Buonocore, *Knoxville, Tennessee*
Peter L. Cooperberg, *Vancouver, British Columbia*
Peter Doubilet, *Boston, Massachusetts*
N. Reed Dunnick, *Durham, North Carolina*
Ronald G. Evens, *St. Louis, Missouri*
Henry I. Goldberg, *San Francisco, California*
William R. Hendee, *Chicago, Illinois*
John R. Hesselink, *San Diego, California*
Charles B. Higgins, *San Francisco, California*
Helen C. Redman, *Dallas, Texas*
Donald L. Resnick, *San Diego, California*
Stewart R. Reuter, *San Antonio, Texas*
Stuart S. Sagel, *St. Louis, Missouri*
Edward A. Sickles, *San Francisco, California*
Eric vanSonnenberg, *San Diego, California*

Editorial Staff: Gita S. Braude, *managing editor*; Elizabeth A. Whalen, *senior editor*; Linda Wood and Barbara Rose, *manuscript editors*; Nancy Rydbeck, *administrative assistant*; Sandra Wood, *administrative secretary*.

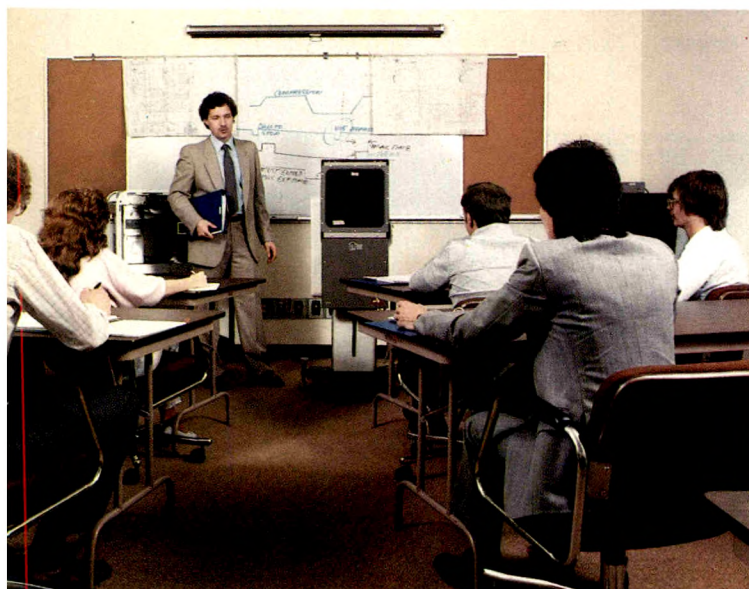
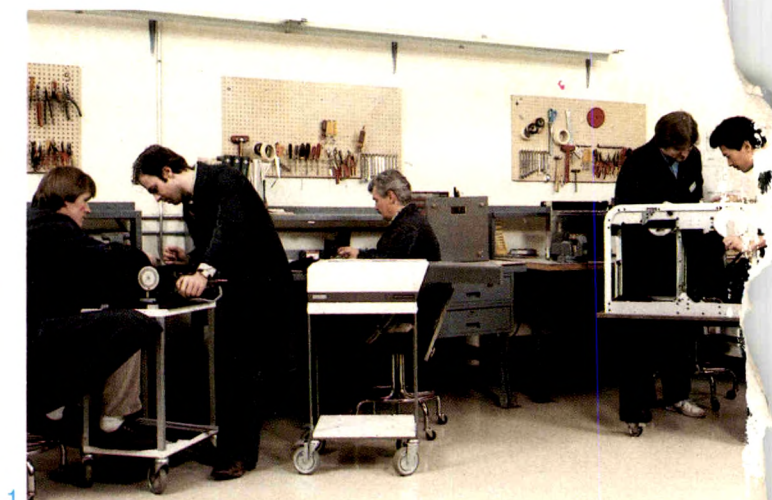
All business correspondence, including display (not classified) advertising, subscriptions, address changes, reprints, and permission requests should be addressed to Williams & Wilkins, 428 East Preston Street, Baltimore, MD 21202. Correspondence regarding editorial matters and classified advertising should be addressed to the editorial office, AJR, 2223 Avenida de la Playa, Suite 200, La Jolla, CA 92037. For manuscript submission, see Guidelines for Authors, next page. Undelivered or damaged copies replaced within 60 days of publication; 90 days for foreign subscribers. Allow 90 days for address changes.

AJR AMERICAN JOURNAL OF ROENTGENOLOGY (ISSN 0361-803X) is published monthly by American Roentgen Ray Society, 428 E. Preston Street, Baltimore, MD 21202. Annual dues include \$50 for journal subscription. Second class postage paid at Baltimore, MD and at additional mailing offices. Postmaster send address changes (Form 3579) to Williams & Wilkins, 428 East Preston St., Baltimore, MD 21202. Subscription rates \$90 (\$120 foreign); institutions \$100 (\$130 foreign); in training \$25; single copy \$16 (\$19). Japanese Yen price is available from our sole agent USACO Corporation, 13-12, Shimbashi 1-Chome, Minato-Ku, Tokyo 105, Japan, telephone 03-502-6471. Airmail rates furnished on request. Indexed by *Current Contents* and *Index Medicus*. Copyright © 1986 by American Roentgen Ray Society. 0361-803X/86\$2.00

ELEMA-SCHONANDER

PUCK Angiographic Filmchanger Systems

Trained, experienced
SERVICE network...nationwide



1 Headquarters shop service for major refurbishing.

2 On-site hospital field service by trained distributor service engineers, backed by Elema-Schonander's technical staff.

3 Headquarters technical training for distributor service organizations.

PUCK Filmchangers have a reputation for reliability. When service is needed, distributor service technicians, trained by Elema-Schonander, are locally available for immediate assistance. They are supported in the field by our own staff of filmchanger specialists, operating out of our Schaumburg, IL (Chicago) headquarters and from several major cities across the country.

A comprehensive inventory of factory spare parts is always on hand and urgent needs can usually be filled within hours.

We operate a year-round training school at our headquarters for distributor service engineers, as well as for the continuing education of our own service force.

85224



Elema-Schonander, Inc.
2360 North Palmer Drive
P.O. Box 94517
Schaumburg, IL 60195
Telephone (312) 397-5900

CIRCLE 4 ON READER SERVICE CARD

AJR Guidelines for Authors

Address new and revised manuscripts, correspondence, and classified ads to the Editor:

AJR Editorial Office

2223 Avenida de la Playa, Suite 200

La Jolla, CA 92037 Telephone: (619) 459-2229

Inquiries regarding subscriptions, display advertising, reprints, or permission to republish AJR material should be addressed to the publisher:

The Williams & Wilkins Co.

428 E. Preston St.

Baltimore, MD 21202 Telephone: (301) 528-4133

The AJR publishes original contributions to the advancement of medical diagnosis and treatment. Submitted manuscripts should not contain previously published material and should not be under consideration for publication elsewhere. Papers dealing with neuroradiology should be addressed to: American Journal of Neuroradiology, Dept. of Radiology, Massachusetts General Hospital, Boston, MA 02114. At the discretion of the AJR Editor, AJNR articles that are of interest to the general reader may be republished in the AJR. Neuroradiologic papers sent to the AJR will be forwarded to the Editorial Office of the AJNR.

Manuscript decisions are based on peer review. Reviewers receive manuscripts without title pages to ensure an unbiased review. All accepted manuscripts are subject to editing. Statements made in the article, including changes made by the Editor or manuscript editor, are the responsibility of the author and not of the AJR or its publisher. Authors will be sent the edited manuscript, galley proof, and proofs of illustrations. If the corresponding author will be unavailable to review galleys, arrangements should be made for a coauthor or colleague to read and return the proof.

General Guidelines for Major Papers

Abstract. Clearly state (in 150 words or less) the purpose, methods, results, and conclusions of the study. Include actual data.

Introduction. Briefly describe the purpose of the investigation, including relevant background information.

Methods. Describe the research plan, the materials (or subjects), and the methods used, in that order. State in detail the confirmation of disease and control of subjectivity in observations.

Results. Present results in a clear, logical sequence. If tables are used, do not duplicate tabular data in text, but do describe important trends and points.

Discussion. Describe the limitations of the research plan, materials (or subjects), and methods, considering both the purpose and the outcome of the study. When results differ from those of previous investigators, explain the discrepancy.

AUTHOR'S CHECKLIST

For priority handling, please complete the following checklist, sign the copyright form on the reverse side of this page, and send in both with your manuscript.

_____ Two copies of the manuscript (the original and a photocopy) and two complete sets of figures are submitted.

_____ If appropriate, AJR Guidelines for case reports, technical notes, pictorial essays, or letters to the Editor have been followed.

_____ The manuscript, including references, figure legends, and tables, is typed double-spaced throughout on 8½ × 11 in. (21.6 × 27.9 cm) nonerasable paper. Right-hand margins are not justified.

_____ All manuscript pages are numbered consecutively without author identification.

_____ The manuscript is organized as follows: title page, blind title page (title only), abstract, introduction, methods, results, discussion, acknowledgments, references, tables, figure legends, and figures.

_____ Use of unfamiliar acronyms and abbreviations is kept to a minimum. When abbreviations are used they are written out at first mention, with the abbreviation following in parentheses.

_____ Metric measurements are used throughout, or the metric equivalent is given in parentheses.

_____ Names and locations (city and state only) of manufacturers are given for equipment and nongeneric drugs.

Title Page

_____ The following information is given: title of article; names and complete addresses (including zip code) of all authors; current addresses of authors who have moved since study; acknowledgment of grant or other assistance; and a current phone number for the corresponding author.

_____ Two copies of a blind title page are included giving only the title (omitting the authors' names) for use in the review process.

Abstract

_____ An abstract of approximately 150 words concisely states the purpose, methods, results, and conclusions of the study. Actual data are not included.

_____ No abbreviations or reference citations are used in the abstract.

References

References (not to exceed 35) are typed double-spaced starting on a separate page and are numbered consecutively in the order in which they appear in the text.

All references are cited in the text and are enclosed in brackets and typed on line with the text (not superscript).

Unpublished data are not cited in the reference list, but are cited parenthetically in the text, for example, (Smith DJ, personal communication), (Smith DJ, unpublished data). This includes papers submitted, but not yet accepted, for publication.

Inclusive page numbers (e.g., 333–335) are given for all references.

Journal names are abbreviated according to *Index Medicus*.

Style and punctuation of references follow the format illustrated in the following examples (all authors are listed when six or less; when seven or more authors, the first three are listed, followed by "et al."):

Journal article

1. Long RS, Roe EW, Wu EU, et al. Membrane oxygenation: radiographic appearance. *AJR* 1986;146:1257–1260

Book

2. Smith LW, Cohen AR. *Pathology of tumors*, 6th ed. Baltimore: Williams & Wilkins, 1977:100–109

Chapter in a book

3. Breon AJ. Serum monitors of bone metastasis. In: Clark SA, ed. *Bone metastases*. Baltimore: Williams & Wilkins, 1983:165–180

Published paper presented at a meeting

4. Lau FS, Kirk AN, Beck RA. MR imaging of the spine. Presented at the annual meeting of the American Roentgen Ray Society, Washington DC, April 1986

Tables

Each table is typed double-spaced on a separate page without vertical or horizontal rules; each has a short, descriptive title. Tables do not exceed two pages in length and contain at least four lines of data.

Tables are numbered in the order in which they are cited in the text.

Abbreviations are defined in an explanatory note below each table.

Tables are self-explanatory and do not duplicate data given in the text or figures.

All arithmetic (percentages, totals, differences) has been double checked for accuracy, and tabular data agree with data given in the text.

Figures and Legends

Two complete sets of original figures are submitted unmounted in labeled envelopes.

Figures are clean, unscratched, 5 × 7 in. (13 × 18 cm) glossy prints with white borders. A separate print is submitted for each figure part.

Each figure is labeled on the back with the figure number and an arrow indicating "top." Labeling is done on a gummed label and then affixed to the back of the print. (Never use ink on front or back of figures.)

Author's names are not written on the backs of figures.

Only removable (rub-on) arrows and letters are used on the figures themselves. Symbols are not broken or cracked.

Images are uniform in size and magnification.

Line drawings are done in black ink on a white background and are of professional quality. (Only glossy prints, not originals or photocopies, are acceptable.)

Written permission has been obtained for use of all previously published illustrations (and copies of permission letters are included), and an appropriate credit line is given in the legends.

Legends are typed double-spaced, and figure numbers correspond with the order in which the figures are cited in the text.

Author's signature

Date

Transfer of Copyright Agreement and Exclusive Publication Statement

Complete copyright to the article entitled: _____

is hereby transferred to the American Roentgen Ray Society (for United States government employees to the extent transferable), effective if and when the article is accepted for publication in the *American Journal of Roentgenology*. In the case of the authors who are officers or employees of the United States government, the American Roentgen Ray Society recognizes that works prepared by officers or employees of the United States government as part of their official government duties are in the public domain.

Authors reserve all proprietary rights other than copyright, such as patent rights and the right to use all or part of this article in future works of their own. The authors retain the right of replication, subject only to crediting the original source of publication and receiving written permission from the publisher.

Authors guarantee that this manuscript contains no matter that is libelous or otherwise unlawful, invades individual privacy, or infringes any proprietary rights.

Authors understand that they will receive no royalty or other compensation from the American Roentgen Ray Society.

Finally, the authors certify that none of the material in this manuscript has been published previously or is currently under consideration for publication elsewhere.

First author/date

Second author

Third author

This agreement must be signed by all authors in order for the manuscript to be published.

Guidelines for Case Reports

A case report is a brief description of a special case that provides a message that transcends the individual patient.

Format. There is no abstract. The introduction should be a short paragraph giving the general background and the specific interest of the case. No more than one case should be described in detail (similar ones can be mentioned briefly in the discussion). Emphasis should be on the radiologic aspects; clinical information must be limited to that necessary to provide a background for the radiology. The discussion should be succinct and should focus on the specific message and relevance of radiologic methods. A review of the literature is not appropriate.

Length. Maximum of five double-spaced, typewritten pages, including the references but not the title page or figure legends.

References. Maximum of eight.

Figures. Maximum of three or four, unless the text is shortened accordingly. Legends must not repeat the text.

Tables and Acknowledgments. Not appropriate in case reports.

Author's Checklist and Copyright Agreement. Submit both with the manuscript.

Guidelines for Technical Notes

A technical note is a brief description of a specific technique or procedure, modification of a technique, or equipment of interest to radiologists.

Format. No abstract, headings, or subheadings are required. If headings are used, they should be a combination of "Case Report," "Materials and Methods," "Results," and "Discussion." A brief one-paragraph introduction should be included to give the general background. Discussion should be limited to the specific message, including the uses of the technique or equipment. Literature reviews and lengthy case reports are not appropriate.

Length. Maximum of five double-spaced, typewritten pages, including the references but not the title page or figure legends.

References. Maximum of eight.

Figures. Maximum of two, unless the text is shortened accordingly.

Tables and Acknowledgments. Not appropriate in technical notes.

Author's Checklist and Copyright Agreement. Submit both with the manuscript.

Guidelines for Pictorial Essays

A "pictorial essay" is an article that conveys its message through illustrations and their legends. Unlike other *AJR* articles, which are based on original research, pictorial essays serve primarily as teaching tools, like exhibits at a scientific meeting. They are not encyclopedic book chapters. No abstract is necessary.

Length. Maximum of four double-spaced, typewritten pages, including the references but not the title page or figure legends.

References. Maximum of four.

Figures. Maximum of 30 figure parts. Number should be as few as necessary to convey the message of the paper.

Tables and Acknowledgments. Not appropriate in pictorial essays.

Author's Checklist and Copyright Agreement. Submit both with the manuscript.

Guidelines for Letters to the Editor and Replies

Letters to the Editor and Replies should offer objective and constructive criticism of published articles. Letters may also discuss matters of general interest to radiologists. Letters and replies are subject to editing and condensation. Authors will receive galley proof for correction and approval.

Format. All letters should be typed double-spaced on nonletterhead paper, with no greeting or salutation. Signature and affiliation should appear at the end of the letter. Titles for letters should be short and pertinent. The title for a reply is simply "Reply."

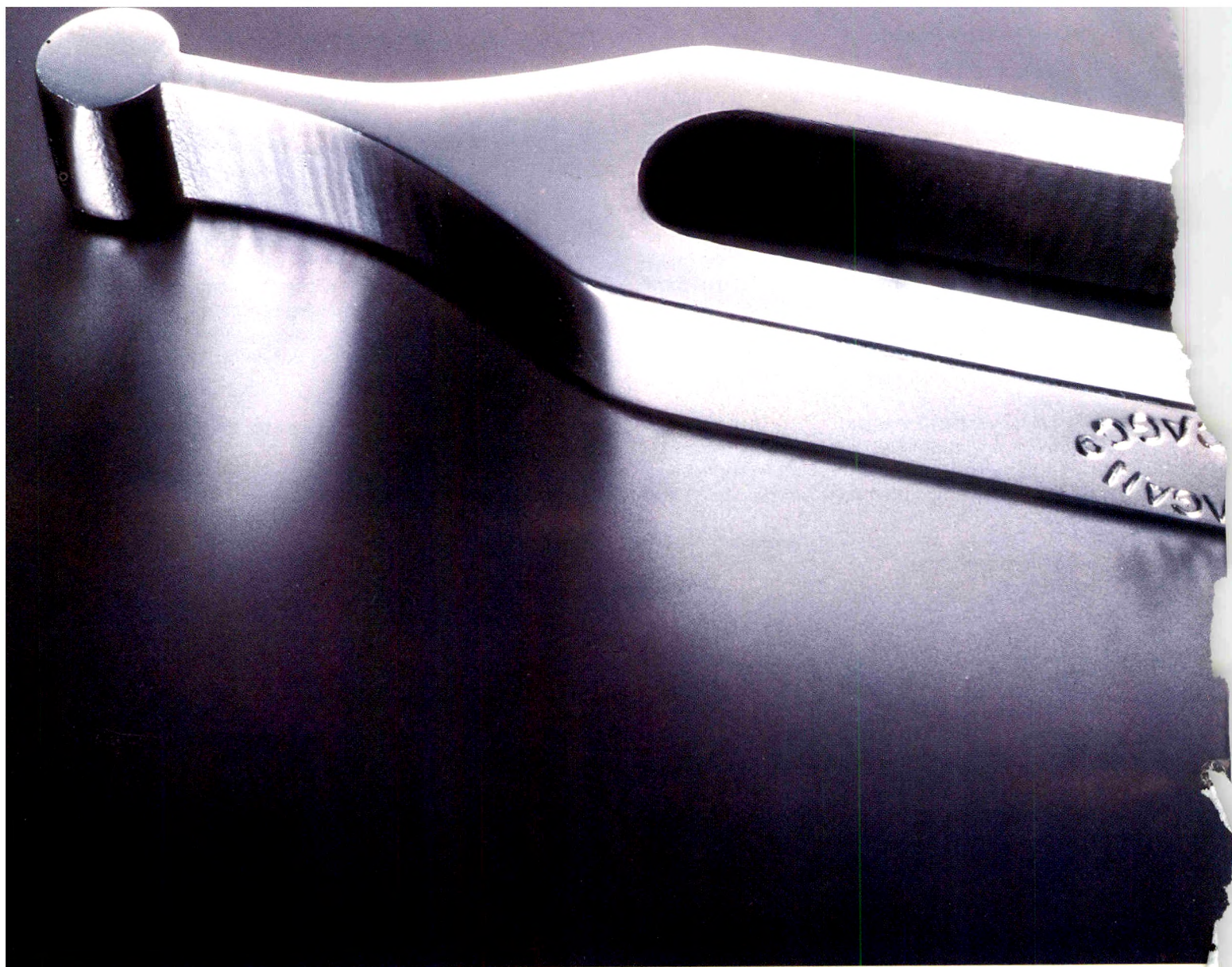
Length. Maximum of two double-spaced, typewritten pages, including references and figure legends.

References. Maximum of four.

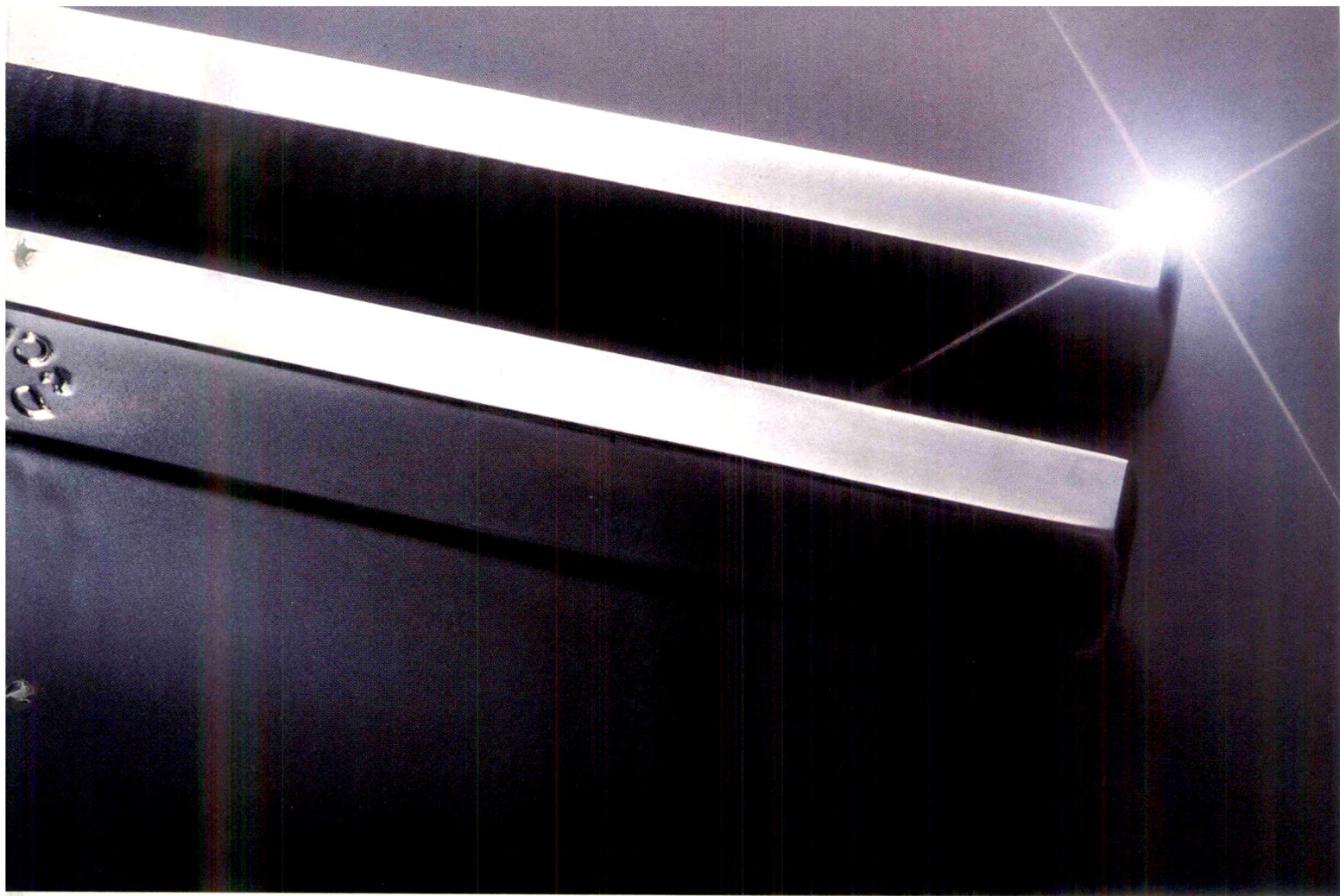
Figures. Maximum of two.

Tables and Acknowledgments. Not appropriate in Letters to the Editor and Replies.

Author's Checklist and Copyright Release Form. Submit both with the manuscript.



**The art of fine-tuning.
At Kodak, we use it to give you
the video image you like.**



Your ideal video image is probably unlike any other. Subtly lighter or darker. A little more contrast. Or a little less. Perhaps your eyes are accustomed to a blue base. Perhaps not. Kodak has the means to *fine-tune* your video images to your personal preferences.

First step: Your Kodak representative adjusts your multiformat cameras to your "look." And measures that look precisely with our exclusive Kodak video display analyzer. And then matches that look to one of Kodak's five video imaging

films. More options than anyone else can offer.

Then, to make sure everything works with everything else, there's a complete line of video imaging products from Kodak. Ranging from Kodaflex roomlight film-handling products for speed and efficiency to reliable, proven Kodak X-Omat processors.

For details, ask your Kodak representative, or write Eastman Kodak Company, Dept. 412L-HS, 343 State Street, Rochester, NY 14650.

Can you afford anything less?



CIRCLE 3 ON READER SERVICE CARD

Tecnomed USA

Mamex DC

**MAMMOGRAPHIC
SYSTEM**

**In the beginning ...
The original MAMEX DC**

The Mamex DC is a complete mammographic system, consisting of a modern, efficient DC generator which virtually eliminates "ripple" and gives a higher resolution image with consistently higher subject contrast; a molybdenum anode x-ray tube; and a motorized compression system with floor remote control.

Standard features:

- ★ Compact DC generator with automatic exposure control.
Exposures can be made once every 30 seconds.
- ★ Stand designed for x-ray examination of the breast.
- ★ Hardened glass screen protects technician during exposure.
- ★ Floor remote compression control.
- ★ Phototiming detector position selector.
- ★ Field light.
- ★ Breast compression plate;
Biopsy compression plate;
Spot cone compression plate.
- ★ 18x24cm Kodak Min-R cassette with screen.
- ★ Film identification markers.
- ★ Automatic line voltage compensation.
- ★ .6x.6 stationary anode molybdenum x-ray tube with beryllium window.

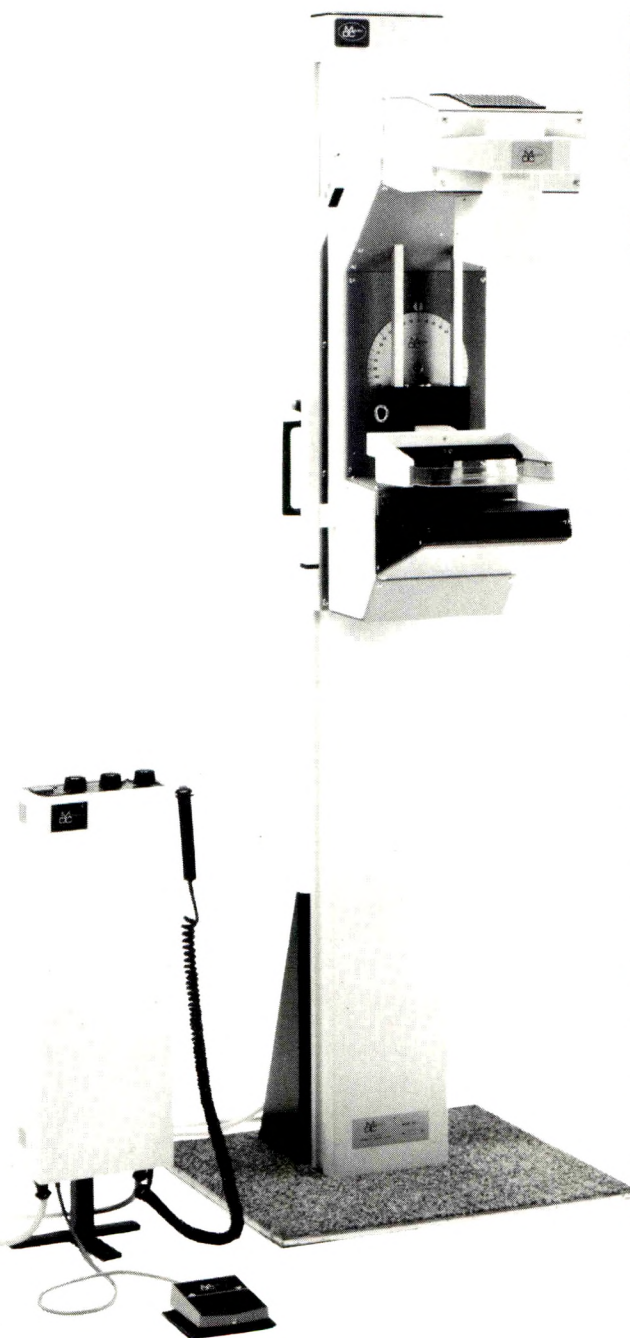
Options:

- ★ 200L 3.5:1 grid.
- ★ Carbon fiber cassette tunnel with grid pocket.
- ★ In-hospital wheel assembly (shown).
- ★ Van wheel assembly.

Mamex DC . . .

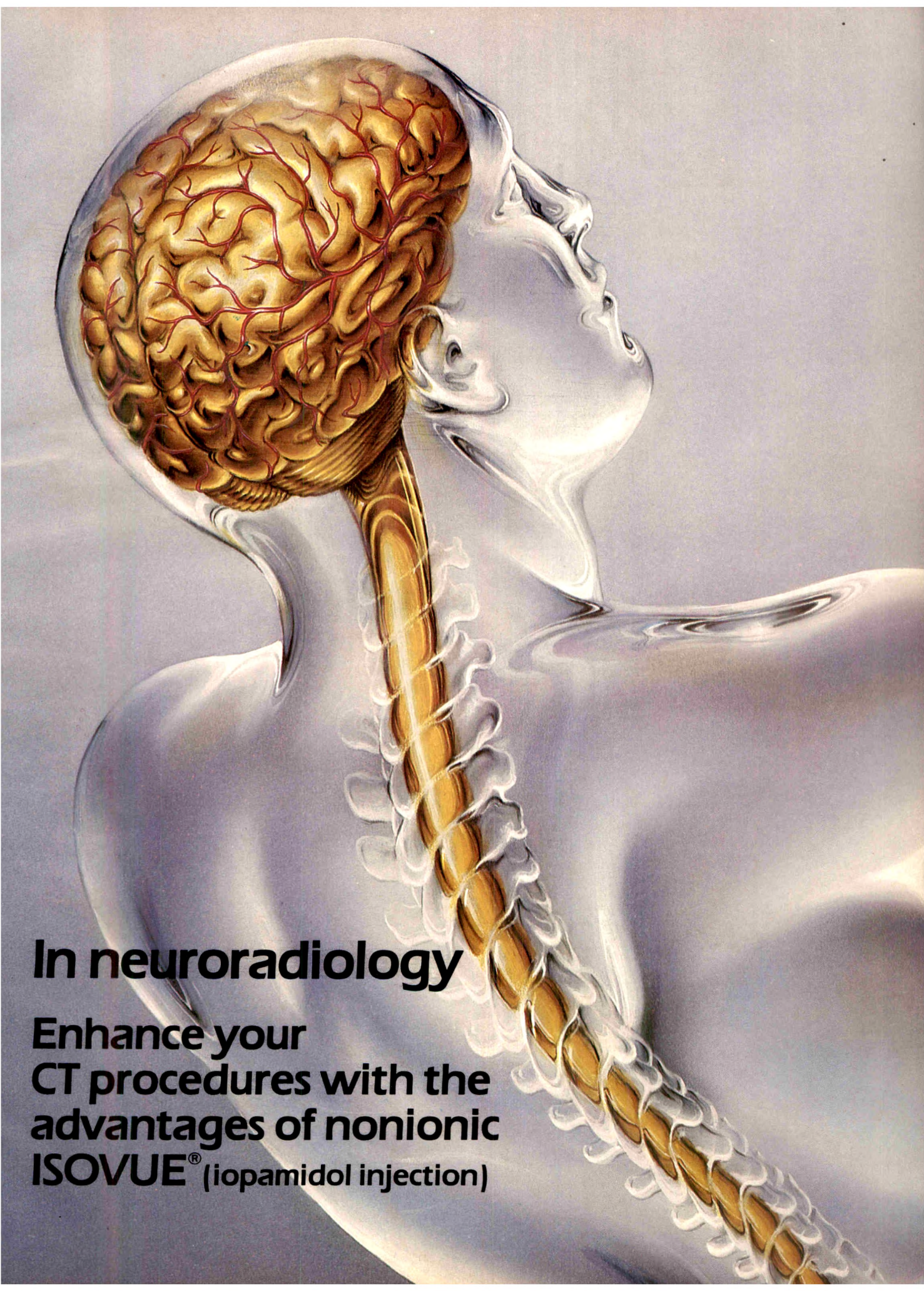
- ★ Five-year proven track record of performance and reliability;
- ★ Hundreds of satisfied physicians, clinics, and hospitals throughout the United States and internationally;
- ★ Full 12-month non-prorated warranty on the x-ray tube;
- ★ Average midbreast dosages, on a 2-film exam of a 6cm compressed breast, of .07R or less (as documented by the University of Michigan Breast Cancer Detection Center – Ingvar Andersson, M.D.)

. . . offers your facility the very best in diagnostic equipment available in today's marketplace.

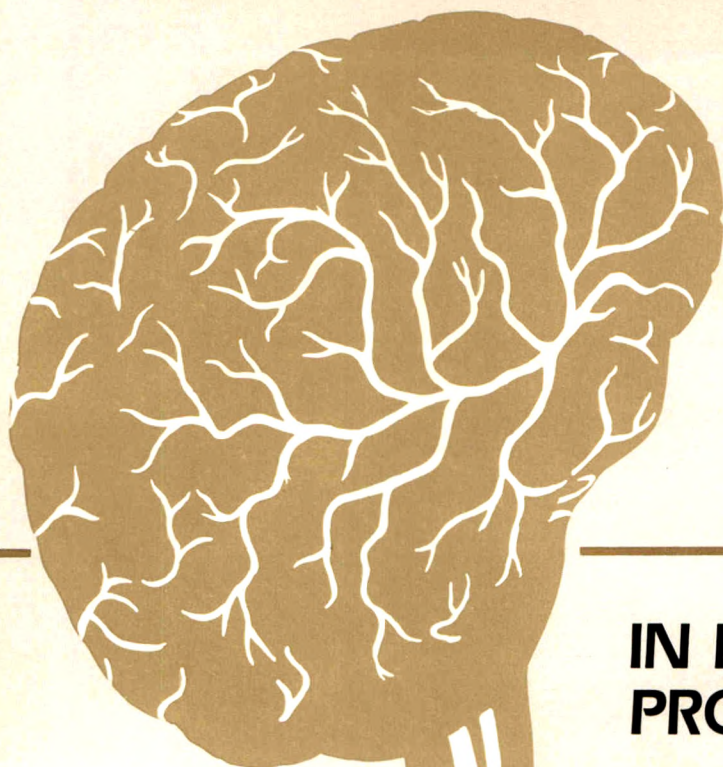


Original MAMEX DC

CIRCLE 10 ON READER SERVICE CARD



In neuroradiology
Enhance your
CT procedures with the
advantages of nonionic
ISOVUE[®] (iopamidol injection)



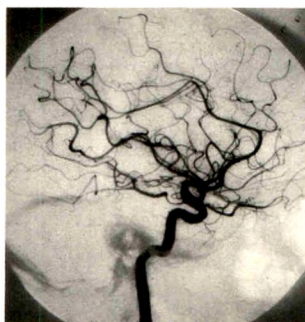
**IN NEURORADIOLOGY
PROCEDURES:**

**Use with
confidence
on both sides of
the blood-brain
barrier**

ISOVUE[®]
iopamidol injection

ISOVUE-M[®]
iopamidol injection

OUTSIDE
Intravascular
use

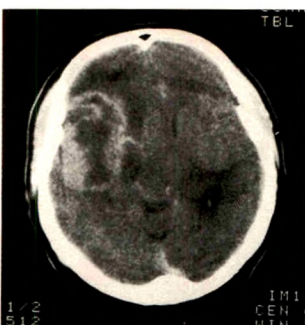


In clinical trials involving 1099 Isovue patients: approximately half the incidence of mild to moderate adverse reactions (e.g., pain, nausea, vomiting) seen with the ionic control agent* in all intravascular procedures combined.¹

INSIDE
Intrathecal
use



When Isovue-M was compared in a double-blind study to metrizamide in lumbar, thoracic, cervical, and total columnar myelography, the 370 patients given Isovue-M experienced less neurotoxicity (psycho-organic manifestations) and approximately half the incidence of observed adverse reactions.¹



An excellent choice
when contrast media
may cross the blood-brain
barrier unexpectedly

**The first "nonionic" indicated in
intravenous contrast enhanced CT.
Also indicated in CT cisternography
and ventriculography.**

As with all injectable contrast agents, the possibility of severe reactions should be borne in mind. See brief summary of prescribing information on last pages of this advertisement for CONTRAINDICATIONS, WARNINGS, PRECAUTIONS, and ADVERSE REACTIONS.

*Diatrizoate meglumine/diatrizoate sodium for most intravascular procedures; iothalamate meglumine for cerebral arteriography.

Enhance your CT procedures with the advantages of nonionic ISOVUE

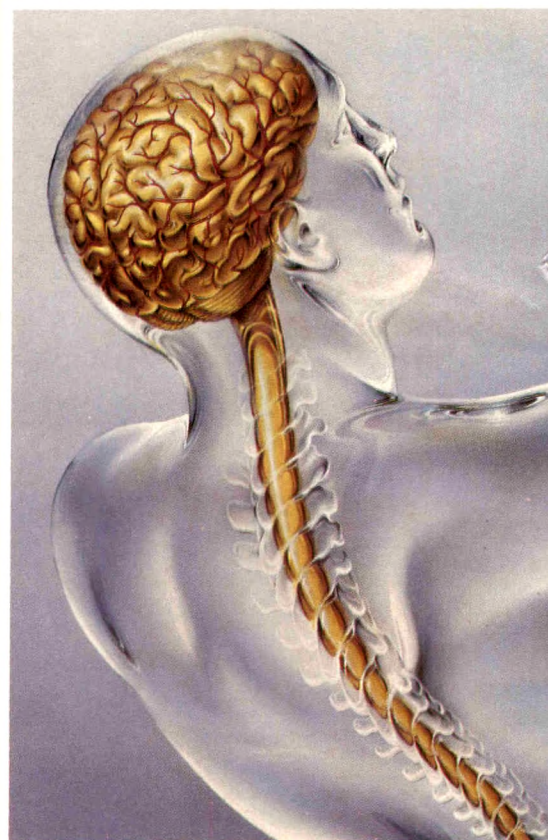
ISOVUE[®]-300
iopamidol injection 61%

For cerebral arteriography
and head and body CT

ISOVUE[®]-M 200
iopamidol injection 41%

ISOVUE[®]-M 300
iopamidol injection 61%

For myelography and CT cistern-
ography and ventriculography



Compared to conventional, ionic contrast media

- Nonionic and low osmolality.
- Increased confidence for the radiologist.
 - Improved patient comfort and cooperation.
 - Fewer mild to moderate adverse reactions: less pain, less nausea, less vomiting.
- Procedures go more efficiently with fewer disruptions.

As with all injectable contrast agents, the possibility of severe reactions should be borne in mind. See brief summary of prescribing information on next page for CONTRAINDICATIONS, WARNINGS, PRECAUTIONS, and ADVERSE REACTIONS.

References: 1. Data on file, Squibb Institute for Medical Research.

This product is under license from Bracco Industria Chimica, S.p.A.
U.S. Patent #4,001,323.



SQUIBB[™]
Diagnostics

646-507

ISOVUE®-300
Iopamidol Injection 61%
ISOVUE®-370
Iopamidol Injection 76%
ISOVUE-M® 200
Iopamidol Injection 41%
ISOVUE-M® 300
Iopamidol Injection 61%

DESCRIPTION—ISOVUE and ISOVUE-M (iopamidol injection) are nonionic radiopaque contrast media for diagnostic use. The formulations are stable, aqueous, sterile, and nonpyrogenic solutions for intravascular and intrathecal administration, respectively. Each mL of ISOVUE-300 (iopamidol injection 61%) provides 612 mg iopamidol with 1 mg tromethamine and 0.39 mg edetate calcium disodium. The solution contains approximately 0.037 mg (0.002 mEq) sodium and 300 mg organically bound iodine per mL. Each mL of ISOVUE-370 (iopamidol injection 76%) provides 755 mg iopamidol with 1 mg tromethamine and 0.48 mg edetate calcium disodium. The solution contains approximately 0.046 mg (0.002 mEq) sodium and 370 mg organically bound iodine per mL. Each mL of ISOVUE-M 200 (iopamidol injection 41%) provides 408 mg iopamidol with 1 mg tromethamine and 0.26 mg edetate calcium disodium. The solution contains approximately 0.025 mg (0.001 mEq) sodium and 200 mg organically bound iodine per mL. Each mL of ISOVUE-M 300 (iopamidol injection 61%) provides 612 mg iopamidol with 1 mg tromethamine and 0.39 mg edetate calcium disodium. The solution contains approximately 0.037 mg (0.002 mEq) sodium and 300 mg organically bound iodine per mL. The pH of each solution has been adjusted to 6.5 to 7.5 with hydrochloric acid.

CONTRAINDICATIONS: ISOVUE (iopamidol injection)—None.

ISOVUE-M (iopamidol injection)—Intrathecal administration of corticosteroids with iopamidol is contraindicated. Because of overdosage considerations, immediate repeat myelography in the event of technical failure is contraindicated (see interval recommendation under DOSAGE AND ADMINISTRATION in the product package insert). Myelography should not be performed in the presence of significant local or systemic infection where bacteremia is likely.

WARNINGS: ISOVUE (iopamidol injection)—Use caution in patients with severely impaired renal function, combined renal and hepatic disease, or anuria, particularly when larger doses are administered. Radiopaque diagnostic contrast agents are potentially hazardous in patients with multiple myeloma or other paraproteinemia, particularly in those with therapeutically resistant anuria. It has been speculated that the combination of the contrast agent and dehydration may be causative of anuria in myelomatous patients. This risk is not a contraindication; however, special precautions are required. Contrast media may promote sickling in individuals who are homozygous for sickle cell disease when injected intravenously or intraarterially. Administration to patients known or suspected of having pheochromocytoma should be performed with extreme caution. If the possible benefits outweigh the considered risks, the procedures may be performed; however, the amount of the medium injected should be kept to an absolute minimum. Assess blood pressure throughout the procedure and measures for treatment of a hypertensive crisis should be available. Monitor such patients very closely. Use caution in patients with hyperthyroidism or with an autonomously functioning thyroid nodule because of risk of thyroid storm.

ISOVUE-M (iopamidol injection)—Carefully evaluate the need for myelographic examination. Administer with caution in patients with increased intracranial pressure or suspicion of intracranial tumor, abscess or hematoma, those with a history of convulsive disorder, severe cardiovascular disease, chronic alcoholism, or multiple sclerosis, and elderly patients. Particular attention must be given to state of hydration, concentration of medium, dose, and technique used in these patients. If frankly bloody cerebrospinal fluid is observed, the possible benefits of the examination should be considered in terms of risk to the patient. Patients on anticonvulsant medication should be maintained on this therapy. Direct intracisternal or ventricular administration for standard radiography (without computerized tomographic enhancement) is not recommended. Inadvertent intracranial entry of a large or concentrated bolus of agent, which increases the risk of neurotoxicity, can be prevented by careful patient management. Avoid rapid dispersion of the medium causing inadvertent rise to intracranial levels. If such entry of the medium occurs, prophylactic anticonvulsant treatment with diazepam or barbiturates orally for 24 to 48 hours should be considered. Use of medications that may lower the seizure threshold should be carefully evaluated. While the contributory role of such medications has not been established, these agents are often discontinued at least 48 hours before and for at least 24 hours following intrathecal use. Motor seizures have been reported after intrathecal use, however in several of the cases, higher than recommended doses were employed. Therefore avoid: deviations from recommended neuroradiologic procedure or patient management; use in patients with a history of epilepsy; overdosage; intracranial entry of a bolus or premature diffusion of a high concentration of the medium; failure to maintain head elevation during procedure, on stretcher, and in bed; excessive and active patient movement or staining.

PRECAUTIONS: General—Diagnostic procedures should be carried out under the direction of personnel with the prerequisite training and a thorough knowledge of the particular procedure to be performed. Appropriate facilities should be available for coping with any complications for emergency treatment of severe reaction to the agent itself. After parenteral administration, competent personnel and emergency facilities should be available for at least 30 to 60 minutes since severe delayed reactions may occur. Preparatory dehydration is dangerous and may contribute to acute renal failure in susceptible patients. *Patients should be well hydrated prior to and following administration.* Reactions to the medium, including serious, life-threatening, fatal, anaphylactoid or cardiovascular reactions, should always be considered (see ADVERSE REACTIONS in the product package insert). Patients at increased risk include those with a history of a previous reaction to a contrast medium, a known sensitivity to iodine per se, and those with a known clinical hypersensitivity (bronchial asthma, hay fever, and food allergies). Pretesting cannot be relied upon to predict severe reactions and may itself be hazardous for the patient. A thorough medical his-

tory with emphasis on allergy and hypersensitivity prior to the injection of any contrast medium may be more predictive and accurate than pretesting. Premedication with antihistamines or corticosteroids to avoid or minimize possible allergic reactions in such patients should be considered (see CONTRAINDICATIONS). If nondisposable equipment is used, scrupulous care should be taken to prevent residual contamination.

ISOVUE (iopamidol injection)—General anesthesia may be indicated in some procedures in selected patients; however, a higher incidence of adverse reactions has been reported in anesthetized patients, which may be attributable to the inability of the patient to identify untoward symptoms, or to the hypotensive effect of anesthesia which can reduce cardiac output and increase the duration of exposure to the agent. Even though the osmolality is low compared to diatrizoate or iohalamate based ionic agents of comparable iodine concentration, the potential transitory increase in the circulatory osmotic load in patients with congestive heart failure requires caution during injection. Observe these patients for several hours following the procedure. In angiographic procedures, be aware of the possibility of dislodging plaques or damaging or perforating the vessel wall during catheter manipulations and contrast medium injection. Test injections to ensure proper catheter placement are suggested.

The inhibitory effects of nonionic contrast media on mechanisms of hemostasis have been shown, *in vitro*, to be less than ionic contrast media at comparable concentrations. For this reason, standard angiographic procedures should always be followed: angiographic catheters should be flushed frequently, and prolonged contact of blood with contrast in syringes and catheters should be avoided.

Perform *selective coronary arteriography* only in those in whom the expected benefits outweigh the procedural risk. The inherent risks of *angiocardiography* in patients with chronic pulmonary emphysema must be weighed against the necessity for performing this procedure. *Angiography* should be avoided whenever possible in patients with homocystinuria, because of the risk of inducing thrombosis and embolism.

Drug Interactions: General—Other drugs should not be admixed with iopamidol (see CONTRAINDICATIONS, and DOSAGE AND ADMINISTRATION, Drug Incompatibilities).

ISOVUE (iopamidol injection)—Renal toxicity has been reported in a few patients with liver dysfunction who were given oral cholecystographic agents followed by intravascular contrast agents. Administration of intravascular agents should therefore be postponed in any patient with a known or suspected hepatic or biliary disorder who has recently received a cholecystographic contrast agent.

Drug/Laboratory Test Interactions—PBI and radioactive iodine uptake studies will not accurately reflect thyroid function for up to 16 days following administration, however T3 resin uptake and total or free thyroxine (T4) assays are not affected.

Carcinogenesis, Mutagenesis, Impairment of Fertility—In animal reproduction studies performed on rats, intravenously administered iopamidol did not induce adverse effects on fertility or general reproductive performance. In studies to determine mutagenic activity, iopamidol did not cause any increase in mutation rates.

Pregnancy Category B—No teratogenic effects attributable to iopamidol have been observed in teratology studies performed in animals. There are, however, no adequate and well controlled studies in pregnant women. It is not known whether iopamidol crosses the placental barrier or reaches fetal tissues. Because animal studies are not always predictive of human response, this drug should be used during pregnancy only if clearly needed. Radiologic procedures involve a certain risk related to the exposure of the fetus to ionizing radiation.

Labor and Delivery: ISOVUE (iopamidol injection)—It is not known whether use during labor or delivery has immediate or delayed adverse effects on the labor, the delivery or the newborn.

Nursing Mothers—It is not known whether iopamidol is excreted in human milk. Use caution when contrast media are administered to nursing women because of potential adverse reactions; consideration should be given to temporarily discontinuing nursing.

Pediatric Use—Safety and effectiveness in children have not been established.

ADVERSE REACTIONS: ISOVUE (iopamidol injection)—Usually mild to moderate, self-limited and transient. In angiocardiography (597 patients), the adverse reactions with an estimated incidence of one percent or higher are: hot flashes 3.4%; angina pectoris 3.0%; flushing 1.8%; bradycardia 1.3%; hypotension 1.0%; hives 1.0%. Intravascular injection is frequently associated with the sensation of warmth and pain, especially in peripheral arteriography; pain and warmth are less frequent and less severe with ISOVUE than with diatrizoate meglumine and diatrizoate sodium injection. The following table of incidence of reactions is based on clinical studies with ISOVUE in about 1835 patients:

System	Adverse Reactions Estimated Overall Incidence	
	>1%	≤ 1%
Cardiovascular	none	tachycardia
		hypotension
		hypertension
		myocardial ischemia
		circulatory collapse
		S-T segment depression
		bigeminy
		extrasystoles
		ventricular fibrillation
		angina pectoris
		bradycardia
		transient ischemic attack
		thrombophlebitis

(continued on next page)

Adverse Reactions (continued from previous page)		
System	>1%	Estimated Overall Incidence ≤ 1%
Nervous	pain (1.7%) burning sensation (1.4%)	vasovagal reaction tingling in arms grimace faintness
Digestive	nausea (1.2%)	vomiting anorexia
Respiratory	none	throat constriction dyspnea pulmonary edema
Skin and Appendages	none	rash urticaria pruritus flushing
Body as a Whole	hot flashes (1.5%)	headache fever chills excessive sweating back spasm
Special Senses	warmth (1.1%)	taste alterations warmth in throat/ arms/chest nasal congestion visual disturbances
Urogenital	none	urinary retention

Regardless of the agent employed, overall estimated incidence of serious adverse reactions is higher with *coronary arteriography* than with other procedures. Cardiac decompensation, serious arrhythmias, or myocardial ischemia or infarction may occur during *coronary arteriography and left ventriculography*. Following coronary and ventricular injections, certain electrocardiographic changes (increased QTc, increased R-R, T-wave amplitude) and certain hemodynamic changes (decreased systolic pressure) occurred less frequently with ISOVUE (iopamidol injection) than with diatrizoate meglumine and diatrizoate sodium injection; increased LVEDP occurred less frequently after ventricular iopamidol injections. In *aortography*, the risks of procedures also include injury to the aorta and neighboring organs, pleural puncture, renal damage including infarction and acute tubular necrosis with oliguria and anuria, accidental selective filling of the right renal artery during the translumbar procedure in the presence of preexisting renal disease, retroperitoneal hemorrhage from the translumbar approach, and spinal cord injury and pathology associated with the syndrome of transverse myelitis. Adverse effects reported in literature include arrhythmia, arterial spasms, hematuria, periorbital edema, involuntary leg movement, malaise, and triggering of deglutition; some of these may be procedural. Other reactions due to procedural hazards include hemorrhage or pseudoaneurysms at the puncture site, brachial plexus palsy following axillary artery injections, chest pain, myocardial infarction, and transient changes in hepatorenal chemistry tests; and rarely arterial thrombosis, displacement of arterial plaques, venous thrombosis, dissection of the coronary vessels and transient sinus arrest.

ISOVUE-M (iopamidol injection)—The most frequently reported following intrathecal administration are headache, nausea, vomiting, usually mild to moderate, and musculoskeletal pain. These usually occur 1 to 10 hours after injection, almost all occurring and ending within 24 hours. Backache, neck stiffness, numbness and paresthesias, leg or sciatic-type pain occurred less frequently. Transient alterations in vital signs may occur and should be assessed on an individual basis. The following table of incidence of reactions is based on clinical studies with ISOVUE-M in about 615 patients:

Adverse Reactions		
System	>1%	Estimated Overall Incidence ≤ 1%
Body as a Whole	headache (18.1%)	pyrexia muscle weakness hot flashes malaise fatigue weakness
Digestive	nausea (7.3%) vomiting (3.7%)	diarrhea heartburn
Musculoskeletal	back pain (2.3%) leg pain (1.4%) neck pain (1.1%)	leg cramps sciatica cervicobrachial irritation meningeal irritation radicular irritation, lumbosacral other musculoskeletal pain involuntary movement burning sensation
Cardiovascular	hypotension (1.1%)	tachycardia hypertension chest pain <i>(continued on next column)</i>

Nervous	none	emotional stress dizziness paresthesia confusion hallucinations lightheadedness syncope numbness cold extremities
Urogenital	none	urinary retention
Respiratory	none	dyspnea
Skin and Appendages	none	rash
Miscellaneous	none	injection site pain

Other adverse effects reported in literature include facial neuralgia, tinnitus, and sweating. Major motor seizures have been reported in the clinical literature and since market introduction in the United States. Transitory EEG changes occur and usually take the form of slow wave activity. The following adverse reactions may occur because they have been reported with other nonionic contrast agents: cardiovascular (arrhythmias); aseptic meningitis syndrome; allergy or idiosyncrasy (chills, pruritus, nasal congestion, Guillain-Barre syndrome); CNS irritation (psycho-organic syndrome: mild and transitory perceptual aberrations such as depersonalization, anxiety, depression, hyperesthesia, disturbances in speech, sight, or hearing, and disorientation; in addition, hyperreflexia or areflexia, hypertonia or flaccidity, restlessness, tremor, echoacousia, echolalia, asterixis or dysphasia have occurred). Profound mental disturbances have rarely been reported (various forms and degrees of aphasia, mental confusion or disorientation); the onset is usually 8 to 10 hours and lasts for about 24 hours without aftereffects. However, occasionally they have been manifest as apprehension, agitation, or progressive withdrawal to the point of stupor, rarely accompanied by transitory hearing loss or other auditory symptoms and visual disturbances. Also reported: persistent cortical loss of vision in association with convulsions, and ventricular block, transitory weakness in the leg or ocular muscles, *peripheral neuropathies*, including sensory and/or motor or nerve root disturbances, myelitis, persistent leg muscle pain or weakness, or sixth nerve palsy, or cauda equina syndrome, muscle cramps, fasciculation or myoclonia, spinal convulsion, or spasticity.

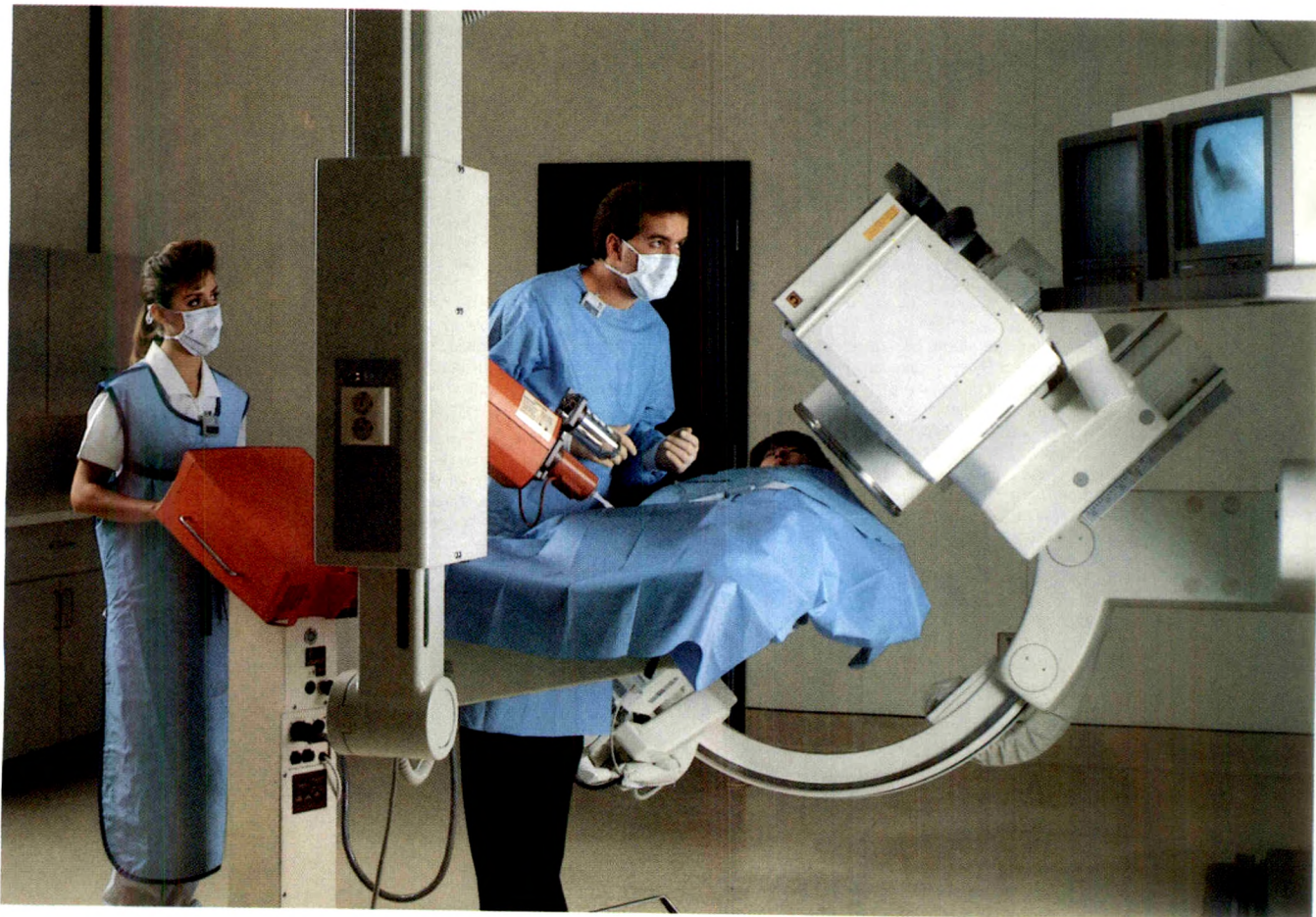
General Adverse Reactions To Contrast Media—Reactions known to occur (mostly mild—moderate in degree) with parenteral administration of iodinated ionic contrast agents (see the listing below) are possible with any nonionic agent. Life-threatening reactions and fatalities, mostly of cardiovascular origin, have occurred. Reported incidences of death from administration of other iodinated contrast media range from 6.6 per 1 million (0.00066%) to 1 in 10,000 patients (0.01%). Most deaths occur during injection or 5 to 10 minutes later, the main feature being cardiac arrest with cardiovascular disease as the main aggravating factor with isolated reports of hypotensive collapse and shock (est. 0.005%). Experience with iopamidol suggests less discomfort (e.g., pain and/or warmth) with peripheral arteriography. Fever changes are noted in ventricular function after ventriculography and coronary arteriography. During intrathecal use, there is a lower incidence of electroencephalographic changes as well as neurotoxicity by virtue of the intrinsic properties of the iopamidol molecule. The reported incidence of adverse reactions to contrast media in patients with a history of allergy is twice that for the general population; patients with a history of previous reactions to a contrast medium are three times more susceptible. Although most reactions to intravascular contrast agents appear within 1-3 minutes after start of injection, delayed reactions may occur (see PRECAUTIONS, General). Adverse reactions reported with other intravascular contrast agents and therefore theoretically possible with iopamidol include: *Cardiovascular*: vasodilation, cerebral hematomas, petechiae, hemodynamic disturbances, sinus bradycardia, transient electrocardiographic abnormalities, ventricular fibrillation; *Nervous*: paresthesia, dizziness, convulsions, paralysis, coma; *Digestive*: nausea, vomiting, severe unilateral or bilateral swelling of the parotid and subparotid glands; *Respiratory*: increased cough, asthma, laryngeal edema, pulmonary edema, bronchospasm, rhinitis; *Skin and Appendages*: injection site pain usually due to extravasation and/or erythematous swelling, skin necrosis, urticaria; *Urogenital*: osmotic nephrosis of proximal tubular cells, renal failure, pain; *Special Senses*: bilateral ocular irritation; lacrimation; conjunctival chemosis, infection, and conjunctivitis, perversion of taste; *Other*: neutropenia, thrombophlebitis, flushing, pallor, weakness, severe retching and choking, wheezing, cramps, tremors, and sneezing.

OVERDOSAGE—Treatment is directed toward the support of all vital functions, and prompt institution of symptomatic therapy. In myelography, even use of a recommended dose can produce mental aberrations tantamount to overdosage, if incorrect management of the patient during or immediately following the procedure permits inadvertent early intracranial entry of a large portion of the medium. Treatment is directed toward the support of all vital functions, and prompt institution of symptomatic therapy.

HOW SUPPLIED—ISOVUE-300 (iopamidol injection 61%) and ISOVUE-370 (iopamidol injection 76%) are available in cartons of ten single dose vials, and ten 100 mL single dose bottles. ISOVUE-370 is also available in cartons of ten 150 mL and ten 200 mL single dose bottles. ISOVUE-M 200 (iopamidol injection 41%) and ISOVUE-M 300 (iopamidol injection 61%) are available in cartons of ten 20 mL and ten 15 mL single dose vials, respectively.

For full prescribing information consult package insert. (J3-652D/J3-653E)

SIEMENS



Siemens vascular imaging. Experience you can trust.

At Siemens we have the experience you're looking for. In facilities planning, equipment installation, staff training, lease financing...and thoroughly proven c-arm imaging systems installed in over 1,000 clinical sites.

Vascular imaging specialists know that Siemens BICOR® and ANGIOSKOP® systems represent the widest choice in imaging systems available anywhere. Plus they can select from a complete line of support products including X-ray generators, film changers, DSA equipment, and computerized data management systems.

Siemens equipment is compatible in engineering and design so that all room components perform as they should. And because we manufacture it, we control the quality. There's no better way to assure investment protection and long-term dependable performance.

A Siemens partnership also provides security for the future. We'll help you stay efficient and up to date with new enhancements like our 40cm II...DSA mass storage device...highload image tubes...and rapid pulse generators.

Siemens has the products and the services to support your cardiac, angiographic, and interventional studies. Talk to us and share the experience.

Siemens Medical Systems, Inc.

186 Wood Avenue South
Iselin, NJ 08830

In Canada:

Siemens Electric Ltd.
1180 Courtney Park Drive
Mississauga, Ontario L5T 1P2

CIRCLE 8 ON READER SERVICE CARD

**Siemens...
technology with integrity.**

MG/5000-106 WLM 489

Structured for Sharpness!

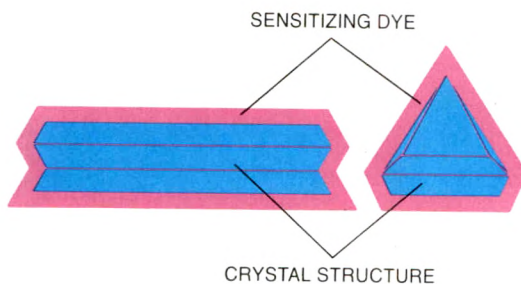


CURIX® Ortho ST (Structured Twin) Crystal emulsions improve sharpness and sensitivity, plus provide greater dynamic range.

CURIX® Ortho ST Films achieve superior image quality and noise suppression through fundamental innovations in crystal and emulsion technology.

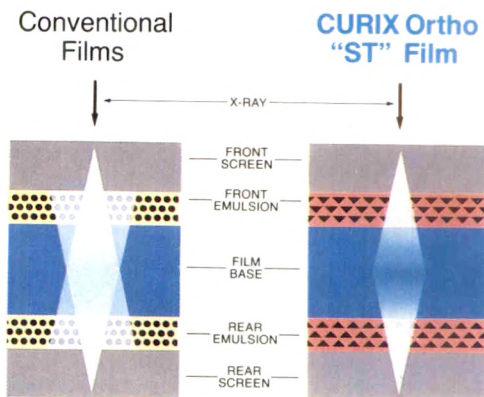
First: AGFA's twin tabular and compact silver halide crystals provide both *increased surface area* for improved sensitivity, and *compact size* for increased sharpness and reduced graininess.

Second: The unique silver bromo-iodide crystal structure of CURIX Ortho ST Films enhances image perception and suppresses noise, because of improved adherence of the sensitizing dye upon the crystal surfaces. Thus, the dye is better utilized in image formation than with other tabular grain films, resulting in a cleaner, brighter, sharper image.



CURIX Ortho ST emulsions reduce Crossover Exposure

Screen-emitted light is absorbed in the layers adjacent to the screens, resulting in increased sharpness.



You can see the increased sharpness.

CURIX Ortho ST Films are compatible with standard CURIX Ortho Screens, require no change in technique, and provide the same high speed with greater sharpness and less grain.

AGFA is setting new standards...with innovations in imaging technology, equipment, and service.

CURIX Ortho ST Films provide improvement in sharpness that you can actually see!

Let us prove it to you. Call 914-682-5650 for a demonstration.

Agfa-Gevaert Rex, Inc.
A Subsidiary of Agfa-Gevaert, Inc.
P.O. Box 190, White Plains, NY 10602
914-682-5650

CIRCLE 12 ON READER SERVICE CARD

AGFA



Advancing the Science
of Medical Imaging

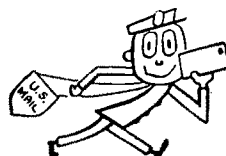


PROFESSOR AND CHAIRMAN DEPARTMENT OF RADIOLOGY

New Jersey Medical School seeks professor and chairperson, department of Radiology. Candidates must be board-certified and have had experience in diagnostic radiology with a major interest in teaching and research as well as expertise in advanced imaging modalities. Send curriculum vitae to: Stuart D. Cook, M.D., Chairman, Radiology Search Committee, (AJR), UMDNJ-NJMS, Department of Neurosciences, H-506, 185 South Orange Avenue, Newark, New Jersey, 07103-2757. An Equal Opportunity/Affirmative Action Employer m/f/h/v.



Help us to serve you better.....



**USE
YOUR
ZIP
CODE**

**Remember, your zip code
provides faster, more direct
delivery of your journals.
Use it on all correspondence,
too.**

*for prompt
subscription
service...*

attach label here

Please use this coupon and attach a *recent* label in the space provided when writing to us about:

- change of address
- renewal
- questions regarding your subscription

Please use the space below to indicate your *new* address.

Name of Journal _____

Name _____

Address _____

City/State/Zip _____

THE WILLIAMS & WILKINS COMPANY

428 East Preston Street/Baltimore, Maryland 21202

How to reduce the costs of bowel preparation before and after the X-ray



Before

Evac-Q-Kwik® helps keep hospital costs down by eliminating the staff time and labor involved in giving enemas. And everything needed for effective bowel evacuation is contained in one cost-effective kit.



Nurses appreciate Evac-Q-Kwik because it can be administered during a single shift and completed during one

6-hour period. Patients prefer the simple, comfortable Evac-Q-Kwik procedure, too. Evac-Q-Kwik contains no sugar, no alcohol, and is low in sodium.

After

Evac-Q-Kwik is the ideal bowel prep for today's cost-conscious climate. It effectively cleans the colon for clear X-rays *the first time*, to reduce the need for expensive, time-consuming retakes that escalate hospital costs.



Evac-Q-Kwik®



Adria®

Adria Laboratories
Columbus, OH 43215

CIRCLE 1 ON READER SERVICE CARD
078508

15 LP/CM. WHY SETTLE FOR LESS?

Spatial resolution.

Accurate diagnoses depend on it.
Referring physicians demand it.
Your images can never get enough of it.
And now you don't have to settle for less.

Introducing the 1200 EXPERT™

The new 1200 EXPERT delivers the spatial resolution needed to give your CT Service a competitive edge. At more than 15 Lp/cm, the 1200 EXPERT has 50% greater resolution than the 9800 QUICK. More resolution than any major CT in the market. Having the best image quality available helps increase referrals and accelerate return-on-investment.

The Referral Builder

EXPERT has 32 referral-building case-oriented scan protocols each optimized for such special studies as 3-D display, xenon blood-flow, cardiac assessment, bone mineral QCT, real-time reformatting of neuro and orthopedic cases, and much more.

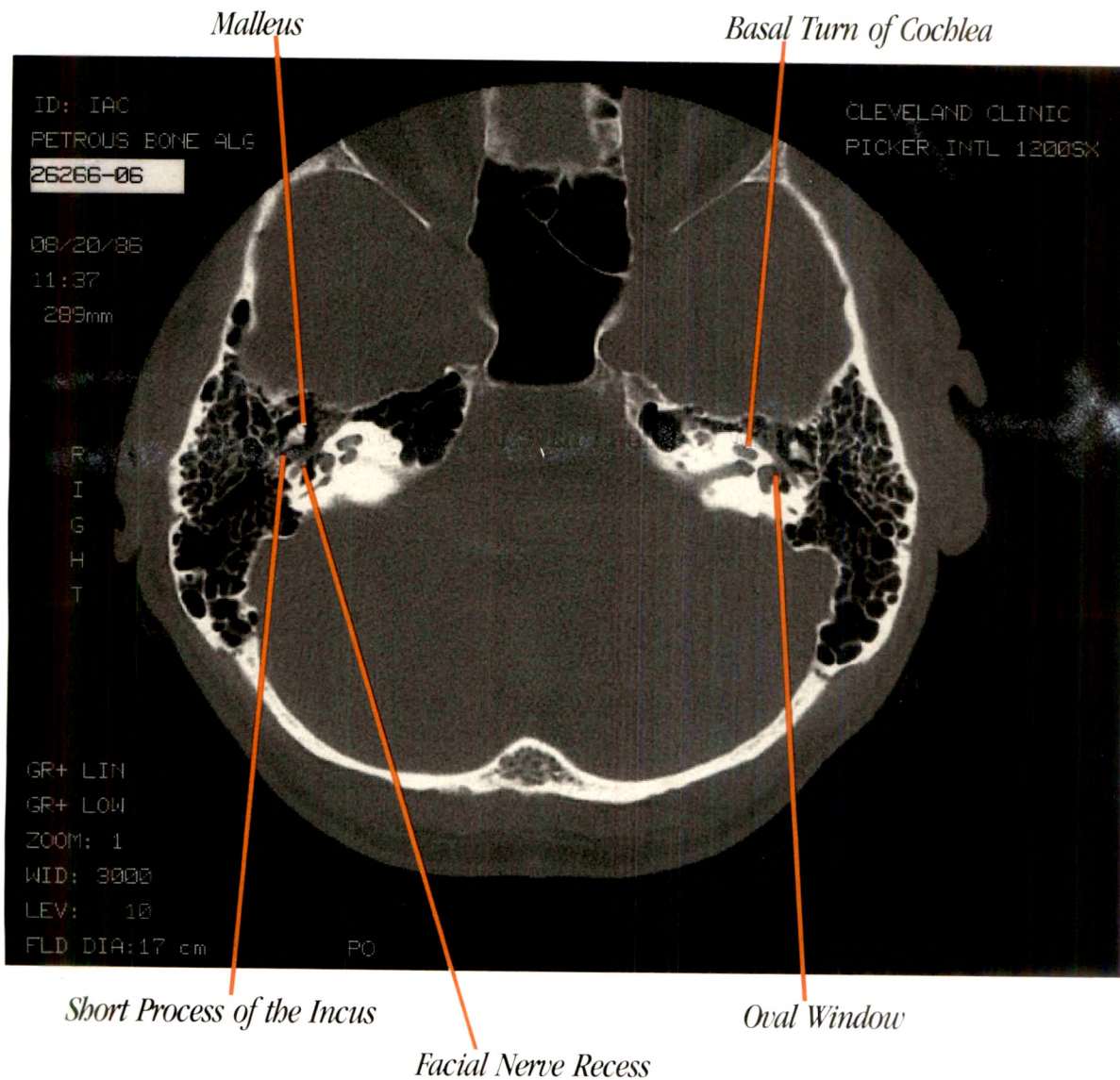
The Technology Leader

The EXPERT's 2,000,000 H.U. X-ray tube, 85% dose efficient solid state detectors, new Level II Imaging Software, and Rapid Scan Mode make this the system of choice for high volume routine scanning *and* special studies.

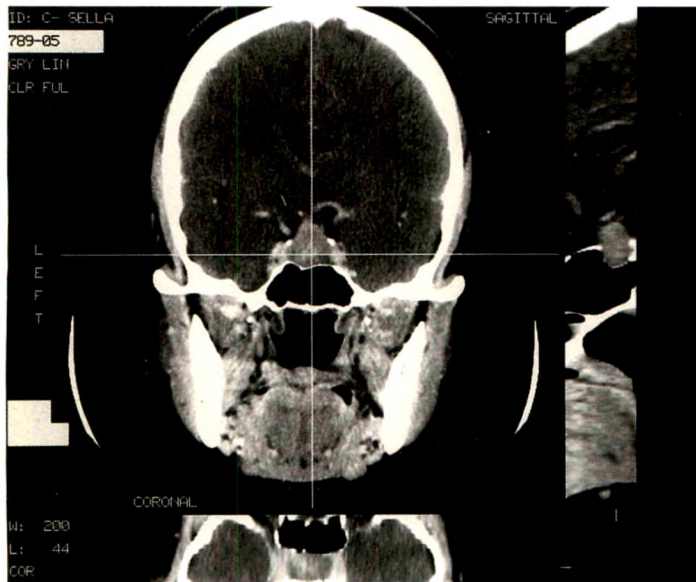
1200 EXPERT...Why Settle for Less?

CIRCLE 13 ON READER SERVICE CARD

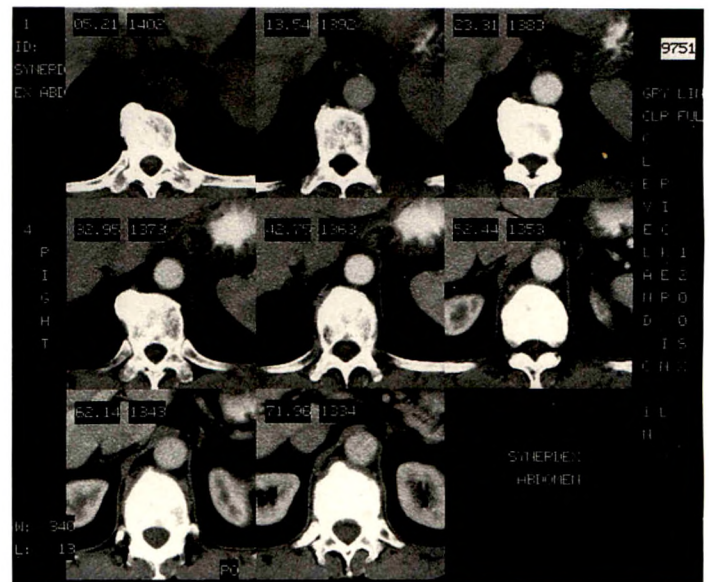
Anatomy of EXPERT Image Quality.



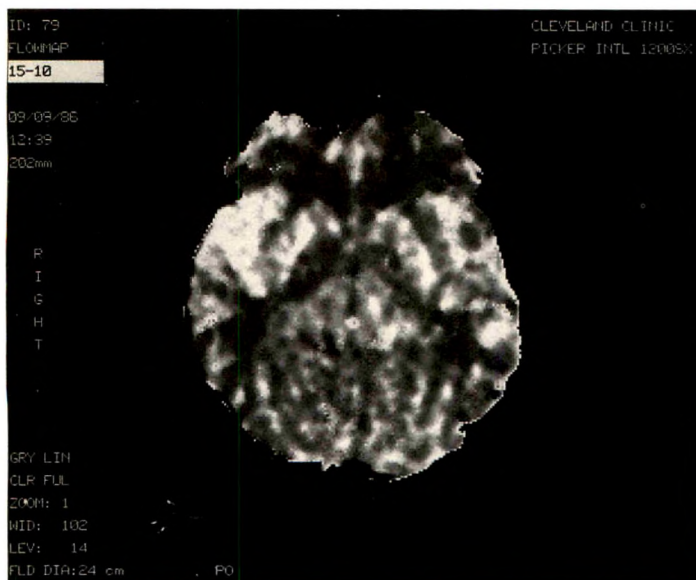
EXPERT Image Quality for Your Special Studies.



Direct 3mm coronal sections of the sella turcica demonstrate superior image quality. The sagittal/coronal display provides fast, easy reference of the pituitary lesion in three different planes.



Dynamic abdominal study with high contrast enhancement and superb spatial resolution provides excellent visualization of the aorta and best assessment of blood flow. Imaging completed in 72 seconds with 10mm couch index.



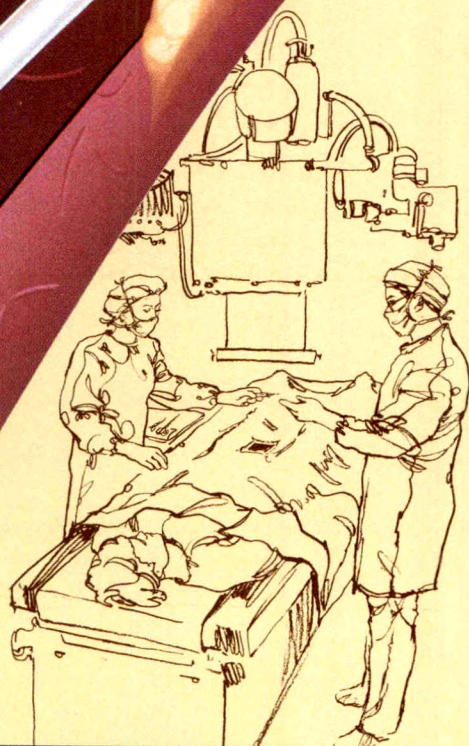
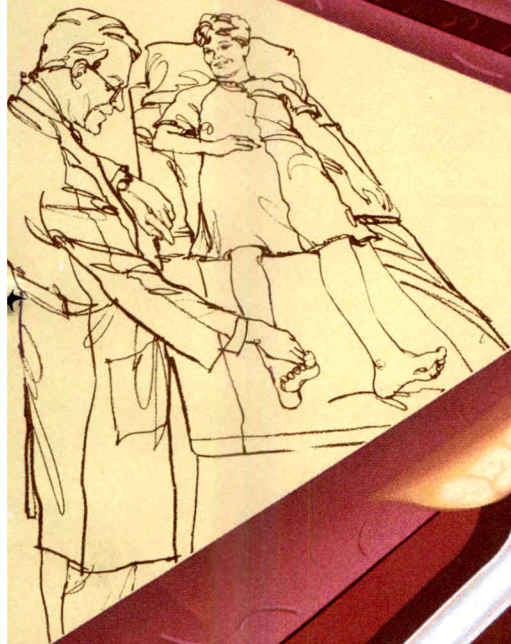
This is a xenon enhanced CT image, often referred to as a flow map, with each shade of grey representing a blood flow rate. The white areas represent increased flow and conversely the darker areas represent less flow.



THE IMAGE OF EXCELLENCE

The perfect profile for narrow navigation.

The New Schwarten™ LP Catheter



How narrow can you get? As narrow as the new Schwarten™ LP Balloon Dilatation Catheter from ACS. The new Schwarten Low Profile Catheter gives you smooth, simple and confident performance in fragile tibial, peroneal and renal vasculature.

Experience easy entry and passage in some of the tightest situations a patient's peripheral circulation can present. In addition, flexible but firm coaxial design can provide you with excellent tracking over a guide wire to get where you want to be during positioning. Radiopaque balloon and tip markers allow for vivid visualization and more exact balloon placement.

For additional information on the new Schwarten LP Balloon Dilatation Catheter, call toll-free: 800 227-9902.



Where Innovation continues.



ACS is a wholly owned subsidiary of Eli Lilly and Company.

Advanced Cardiovascular Systems, Inc.

1395 Charleston Road
Mountain View, CA 94039
415 965-7360

Toll free: 800 227-9902

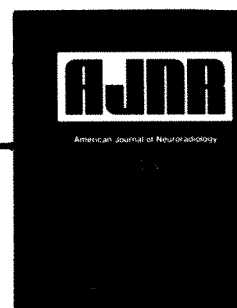
TWX (Telex II) 23-289-720

CIRCLE 2 ON READER SERVICE CARD

© 1986 Advanced Cardiovascular Systems, Inc.

Increase your expertise in evaluating CNS lesions

AJNR American Journal of Neuroradiology



Editor: **Juan M. Taveras, MD**, Harvard Medical School; MGH

Outstanding clinical papers on every aspect of CNS imaging, including spinal diagnosis...informed coverage of head and neck radiology...clear, readable CTs, angiographs, MR imaging and ultrasound studies. These are the features you demand of a quality professional journal. You'll find them in every issue of **AJNR: American Journal of Neuroradiology**.

As you are called upon to perform and interpret more and more sophisticated diagnostic tests — from myelography to CT to newborn ultrasound studies — you need a comprehensive, reliable journal that can keep you abreast of all the latest developments. Each bimonthly issue of **AJNR** brings you timely, clinically pertinent information, as well as important clinical research presented with an eye toward immediate practical application.

Here are just a few of the many excellent articles from the November/December 1985 issue:

Contrast-Enhanced MR Imaging of Malignant Brain Tumors
by Moshe Graif, et al.

MR Imaging of Cerebral Vascular Malformations
by Benjamin C. P. Lee, et al.

Cranial Computed Tomography in the Abused Child with Head Injury
by Ronald A. Cohen, et al.

Cavernous Sinus Invasion by Pituitary Adenomas
by Jamshid Ahmadi, et al.

Sonography of the Internal Capsule and Basal Ganglia in Infants: 1. Coronal Sections
by Thomas P. Naidich, et al.


Iohexol vs. Metrizamide: Study of Efficacy and Morbidity in Cervical Myelography
by Richard E. Latchaw, et al.

Superselective Injection of Polyvinyl Alcohol Microemboli for the Treatment of Cerebral Arteriovenous Malformations
by Giuseppe Scialfa and Giuseppe Scott.

If you can benefit from articles like these, then you should be a regular reader of **AJNR**. Use the attached coupon to subscribe today.

Bimonthly
Personal \$95/yr Institutions \$115/yr In-training \$65/yr
(add \$15.00 outside the US)

ORDER FREE BY PHONE. Just call

 1-800-638-6423 from anywhere in the US except AK and HI. MD residents, call 528-4105 collect.

Williams & Wilkins

P.O. Box 1496 Baltimore, Maryland 21203

266 Fulham Road London SW10 9EL England



Subscribe to AJNR for 3 years and SAVE

Avoid future rate increases and ensure uninterrupted service by placing a multi-year subscription at current rates.

☐ New subscription ☐ Renewal

☐ 3 yrs ☐ 2 yrs ☐ 1 yr

☐ **Personal \$95** ☐ **Institutions \$115** ☐ **In-training \$65**
(add \$15.00 outside the US)

☐ Also send me the **1986 Bound Volume** at \$45.00 (\$50.00 outside the US). \$2.00 discount for orders placed before October 1, 1985, and for pre-paid orders. I understand that the bound volume is *in addition to* my regular subscription and is available only to subscribers. (To be shipped in early 1987. Sorry, bound volumes for years prior to 1986 are not available.) All bound volume orders must be received by December 31, 1986.

☐ Check enclosed ☐ Bill me
☐ VISA ☐ MasterCard ☐ American Express

card # _____ exp. _____

signature/P.O. # _____

printed in USA

Name _____

Address _____

City/State/Zip _____

MD residents, please add 5% sales tax. Subscription orders from outside the US must be prepaid in US dollars only.

Residents, Fellows, Interns, and Students: when applying for the in-training rate, available for 3 years, please specify name of institution and training status. Rates valid through October 31, 1986.

Please allow 8 weeks for order processing and delivery of your first issue. Surface mail delivery to countries outside the US may take up to 16 weeks. Airmail rates available upon request.

Williams & Wilkins

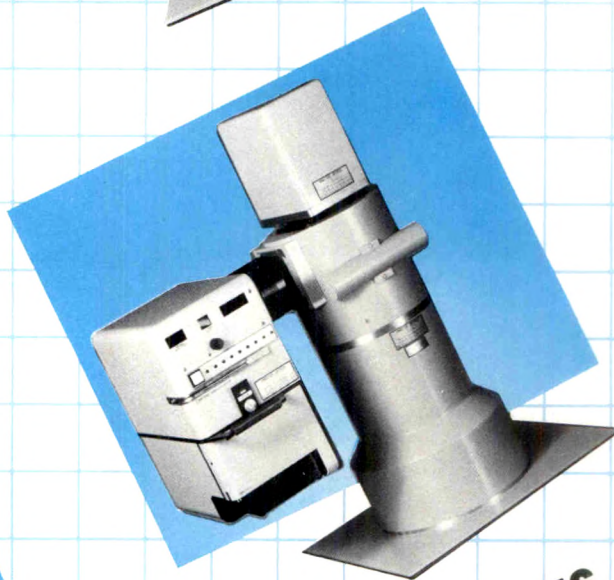
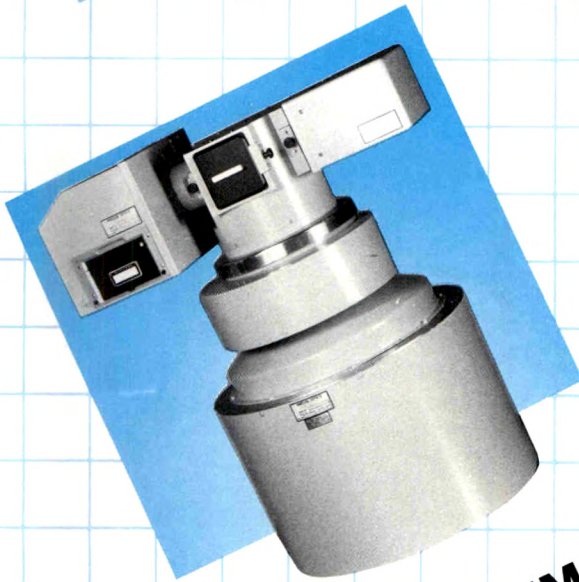
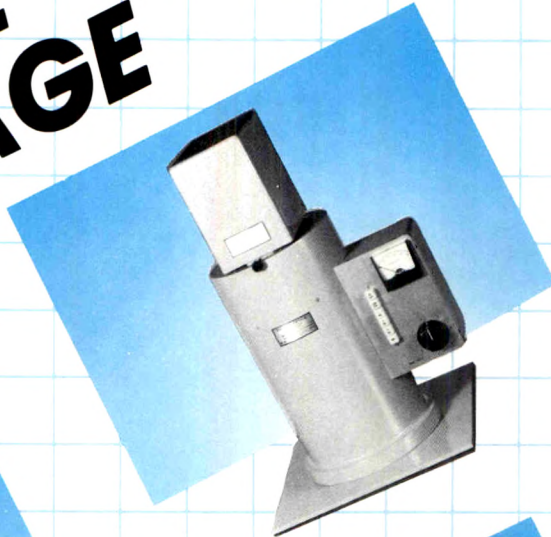
P.O. Box 1496
Baltimore, Maryland 21203

266 Fulham Road
London SW10 9EL
England



AJNRAD 94625 86

IMPROVE YOUR IMAGE



WITH PRECISE OPTICS IMAGE INTENSIFIER SYSTEMS

- The world's largest independent manufacturer of Image Intensifier Systems and components
- Over 30 years of experience in design and manufacture
- 6, 9, 12, and 16-Inch latest series image tubes for optimum performance
- 525/875/1023 line CCTV's, 6fps 100mm/105mm cameras
- Cost effective, versatile, reliable
- Compatible with new or existing x-ray equipment
- Extend the life of existing apparatus
- Worldwide dealer network

239 South Fehr Way
Bay Shore, New York 11706
Tel.: 516-242-6600
TWX: 510-227-9837
CIRCLE 6 ON READER SERVICE CARD

**precise
optics®**
PHOTO MEDIC
EQUIPMENT, INC.

Signa magnetic resonance system

Reference point



When physicians refer to clinically superior MR, they're referring to Signa

The Signa® system has always attracted physicians' attention. It's also attracting their referrals.

The reason? Image quality. Images of stunning definition and detail that provide diagnostic accuracy from thin slice to thick, from routine to the most demanding studies. Also, access to a dynamic range of MR applications that only the high field Signa system can perform... and to the leading-edge MR research and development that only General Electric can offer.

Spine imaging

MR is rapidly becoming the imaging modality of choice for spine evaluations,¹ and Signa the preferred system. Diagnosticians count on Signa images to provide the edge definition, contrast detail and superior signal-to-noise ratio needed for accurate cervical, thoracic and lumbar studies. This confidence is being reflected in the bottom line at Signa sites: many of our sites are now receiving spine



First and second echo images of a L5/S1 herniated disc in a 32 year old female. Note the visualization of the nerve roots (arrows) and the loss of signal intensity in the degenerated disc on the T2 weighted image.

cases that used to be referred routinely to other institutions—ones with low field systems.

High resolution imaging of minute structures

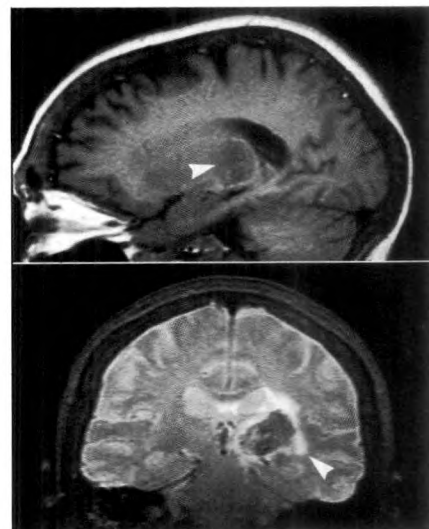
With the high signal-to-noise ratio of the Signa system, fine details of anatomy and pathology are revealed with exceptional clarity. For example, pituitary microadenomas are detected routinely in clinical settings with the Signa system.² Such thin section, high resolution imaging is simply not possible with most other MR systems.



T1 weighted image of a pituitary microadenoma (arrow) in a 27 year old female.

Imaging of iron

One of the breakthrough applications of the 1.5T Signa system is the ability to image iron distribution. This high field advantage enables clinicians to detect intracranial hematomas, and to determine their age and characteristics as well.³ It also is providing new insights into many neurodegenerative disorders, including Huntington's, Parkinson's, and Alzheimer's diseases.⁴



T1 weighted image (top) of a 66 year old female with elevated blood pressure and a 24-hour-old intracerebral hematoma in the basal ganglion. T2 weighted image (bottom) of same patient demonstrates hypointensity caused by deoxyhemoglobin in intact red blood cells.

The future, built-in

The Signa system is your direct link to the future of MR. Tomorrow's protocols and applications are being developed today at leading research sites using Signa technology.

With Signa you get more than an MR system that accommodates the future. You get the system that's determining it.

To discover how Signa can make your site the reference point for MR, call us.

800-433-5566.

¹D. Norman, T.H. Newton. "MRI of the spine and cord: a present perspective." *ASNR* 1986.

²Image courtesy of St. Joseph's Hospital, Phoenix, AZ.

³J.M. Gomori, R.I. Grossman, et al. "Intracranial hematomas: imaging by high-field MR." *Radiology* 157(2), 87-93, Oct. 1985.

⁴B. Drayer, et al. "Magnetic resonance imaging of brain iron." *AJNR*, May, 1986.

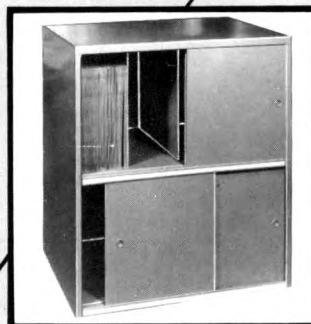
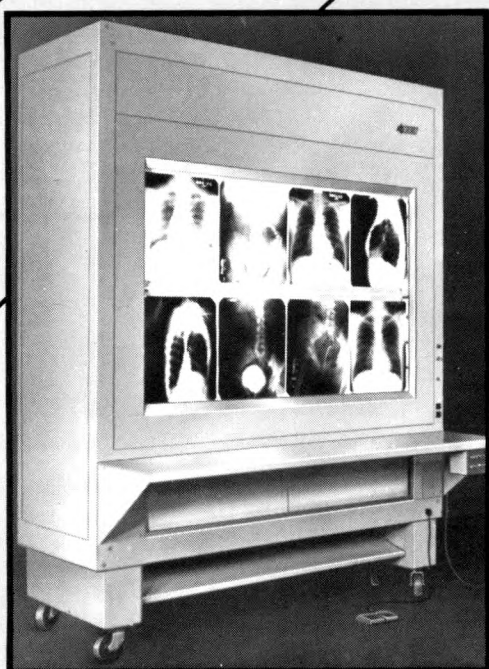
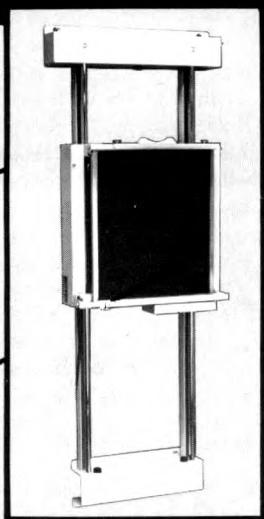
CIRCLE 15 ON READER SERVICE CARD

GENERAL  ELECTRIC

There are reasons S.&S. X-RAY ACCESSORIES are preferred...



PROVEN the best in X-Ray Departments throughout the world
UNEQUALLED in design, construction and—quality
REPUTATION unmatched for RELIABILITY and PERFORMANCE



- Motorized Viewers
- Illuminators
- Transfer Cabinets
- File Cabinets
- Protective Panels
- Protective Aprons
- Wall Cassette Holders
- Dryers
- Safelights
- Dark Room Cabinets
- Storage Chests
- Loading Bins
- X-Ray Accessories

For more than 30 years, S. & S. has been meeting Radiologists' needs with a complete line of illuminators and accessories.

Contact S. & S. or your local x-ray dealer for additional information.

CIRCLE 9 ON READER SERVICE CARD

MANUFACTURED BY

S. & S. X-RAY PRODUCTS INC.



*The Complete Line of
X-Ray Accessories*
(800)221-6634

Telephone: (212) 852-6900

87-93 JAY STREET, BROOKLYN, N.Y. 11201

Comparison of CT and Fiberoptic Bronchoscopy in the Evaluation of Bronchial Disease

David P. Naidich¹
 Jen-Jyh Lee²
 Stuart M. Garay²
 Dorothy I. McCauley¹
 Conrado P. Aranda²
 Arthur D. Boyd³

CT was compared to fiberoptic bronchoscopy in a large series of patients to study the value of CT for visualizing bronchial disease. CT scans were available for review in 64 cases in which focal airway disease was identified with fiberoptic bronchoscopy and in 38 patients in whom the airways appeared normal at bronchoscopy. CT was positive in 59 of 64 cases in which lesions were detected endoscopically. If the results are analyzed according to the extent of involvement of individual bronchi, CT successfully identified 88 (90%) of 98 lesions. CT correctly excluded disease in 35 (92%) of 38 cases that were subsequently verified to be normal by fiberoptic bronchoscopy. In no case was the diagnosis of malignancy missed by CT. While extremely accurate in detecting focal lesions, CT was inaccurate in predicting whether a given abnormality was endobronchial, submucosal, or extrinsic (peribronchial). In three cases CT failed to detect submucosal extension into the left mainstream bronchus, which has important implications concerning the value of CT in staging bronchial malignancy. It is concluded that CT is helpful when bronchoscopy is contraindicated or refused. CT may also be used in selected cases when there is low clinical suspicion of endobronchial disease and as a complementary procedure to fiberoptic bronchoscopy for outlining the exact location of major mediastinal and hilar vessels, lymph nodes, and tumor in relation to adjacent airways.

While cross-sectional bronchial anatomy has been described in detail, the use of CT as a noninvasive technique for evaluating the airways has yet to be determined (Fig. 1). Because of the importance of fiberoptic bronchoscopy (FOB) in the clinical management of patients, a meaningful assessment of the potential role of CT is possible only by comparison of these two techniques in a large series of patients, both normal patients and those with a wide spectrum of disease. The purpose of this report is to undertake such an evaluation in order to gain insight into the specific clinical contexts in which CT should be used.

Materials and Methods

Between November 1983 and September 1985, a total of 716 patients underwent bronchoscopic examination. In all cases, descriptions of the airways recorded at the time of FOB were available for review. From this total two separate populations were identified.

Group 1 consisted of 78 patients reported at FOB as having focal bronchial abnormalities. CT examinations were obtained before bronchoscopy in 64 of these cases. In order to facilitate comparison between CT and FOB, the following definitions were used. Lesions were classified endoscopically as either (1) endobronchial, characterized by involvement of the bronchial mucosa, usually in the form of an exophytic mass or nodularity with resultant narrowing and/or obstruction of the airways; (2) submucosal, characterized endoscopically by a loss of normal bronchial markings, erythema, and apparent thickening of an otherwise intact mucosa, generally associated with diffuse narrowing of the involved airway; or (3) peribronchial (extrinsic), in which endoscopic findings were limited to bronchial narrowing or compression, frequently asymmetric. Whenever findings were equivocal, cases were classified by the predominant finding at bronchoscopy. CT scans were classified only according to their

Received June 9, 1986; accepted after revision August 22, 1986.

¹ Department of Radiology, New York University Medical Center-Bellevue Hospital, 27th St. and 1st Ave., New York, NY 10016. Address reprint requests to D. P. Naidich.

² Department of Pulmonary Medicine, New York University Medical Center-Bellevue Hospital, 27th St. and 1st Ave., New York, NY 10016.

³ Department of Thoracic Surgery, New York University Medical Center-Bellevue Hospital, 27th St. and 1st Ave., New York, NY 10016.

AJR 148:1-7, January 1987
 0361-803X/87/1481-0001

© American Roentgen Ray Society

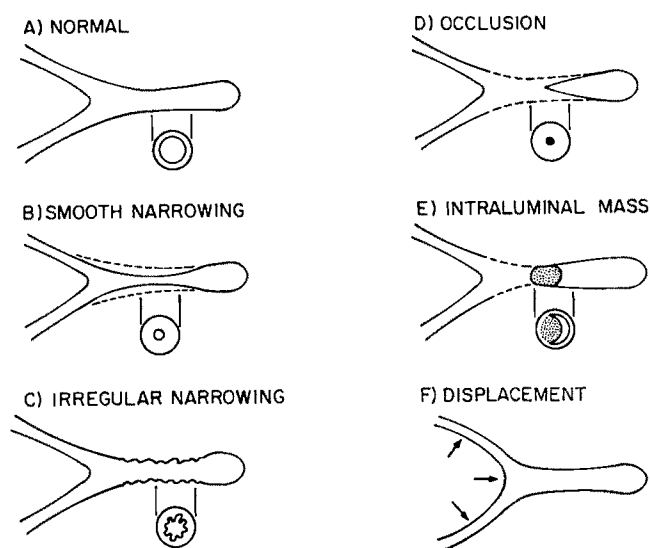


Fig. 1.—Proposed radiographic classification of bronchial abnormalities detected by CT.

radiographic appearance (Table 1). No presumptions were made as to the precise endoscopic appearance of a lesion solely on the basis of its cross-sectional configuration.

Group 2 consisted of 130 patients examined between January and September 1985 for whom FOB was reported as either normal or only as showing mild diffuse erythema compatible with the clinical diagnosis of bronchitis. Thirty-eight cases from this group had CT examinations before FOB and were chosen for inclusion specifically to allow some assessment of the negative predictive value of CT in the absence of a large, prospectively studied population.

All cases were evaluated with a GE 8800 scanner by using 4.8-sec scan times. Patients were usually scanned at end-expiratory lung volumes in order to maximize reproducibility of airway position. In select cases scans were obtained at end-inspiration, especially when patients experienced difficulty with breath holding. Patients initially were evaluated with consecutive 10-mm-thick sections, reviewed during the course of scanning. Additional sections (1.5- and/or 5-mm thick) were obtained in most patients either through bronchi that were believed to be abnormal or through lobar or segmental bronchi not visualized on the initial sequence, particularly in the presence of segmental lung disease. Bolus injections of IV contrast material were obtained as indicated to clarify hilar vascular anatomy. Scan quality was interpreted as either excellent, good, or poor for all cases.

Results

The range of diagnoses encountered among the 64 cases with abnormal bronchoscopic examinations is shown in Table 1. The spectrum of abnormalities noted on corresponding chest radiographs is presented in Table 2. All cases with bronchial disease (group 1) had abnormal chest radiographs, which constituted a major indication for bronchoscopy. Verification of all diagnoses was based on a combination of clinical, bronchoscopic, bacteriologic, and surgical data.

Group 1

The results of comparison between CT and FOB analyzed by case for group 1 are shown in Table 3. Five patients with

TABLE 1: Pathologic Diagnoses Encountered Among 64 Cases with Abnormal Bronchoscopy

Diagnosis	No. of Cases
Malignant diseases	
Lung cancer (45)	
Adenocarcinoma	10
Large cell	6
Squamous	16
Small cell	13
Metastatic cancer (4)	
Renal cell	3
Colon	1
Lymphoma	1
Bronchial adenoma	1
Tracheal granular cell tumor	1
Subtotal	52
Inflammatory diseases	
Tuberculosis	6
Mucous plug	2
Sarcoidosis	1
Inflammatory adenopathy (3)	
Pneumonia	2
Lung abscess	1
Subtotal	12
Total	64

TABLE 2: Radiographic Findings in 64 Cases with Positive Bronchoscopy

Radiographic Finding	No. of Cases
Parenchymal disease	
Pulmonary masses	16
Pulmonary consolidation (segmental/subsegmental)	15
Lobar collapse (18)	
RUL	4
RML	1
RML/RLL (combined)	1
LUL	4
Lingular	1
LLL	7
Subtotal	49
Mediastinal and hilar disease	
Unilateral hilar disease	9
Mediastinal/subcarinal disease	6
Subtotal	15
Total	64

Note.—RUL = right upper lobe; RML = right middle lobe; LUL = left upper lobe; LLL = left lower lobe; RLL = right lower lobe.

TABLE 3: CT/Bronchoscopic Correlation in 64 Patients (Group 1): Results by Case

CT Finding	Positive FOB Finding		
	Endobronchial Disease	Submucosal Disease	Peribronchial (Extrinsic) Disease
Positive			
59/64 (92%)	41	9	9
Negative			
5/64 (8%)	2	2	1
Subtotal	43	11	10

Note.—FOB = fiberoptic bronchoscopy.

focal bronchial disease detected by FOB were interpreted as having completely normal airways at CT. In two cases the abnormality was endobronchial, including total occlusion of the posterior subsegment of the inferior lingular bronchus in a patient with a 2-cm lingular mass and a focal endobronchial lesion in the left lower lobe bronchus in a patient with extensive adenopathy due to sarcoidosis. In two cases submucosal abnormalities were evident bronchoscopically, including (1) diffuse narrowing of the anterior segmental bronchus of the left upper lobe in a patient with a large, left upper lobe tumor mass and (2) a contralateral metastasis to the basilar segmental bronchi in a patient with a large, cavitary neoplasm in the left upper lobe (Fig. 2). In one case, FOB detected focal extrinsic compression of the left lower lobe bronchus in a patient with massive left-sided adenopathy resulting from small-cell carcinoma.

For analysis of these results in greater detail, this same group of patients was recategorized according to the extent of involvement of individual bronchi. As pathologic changes in a given case often involved more than one airway, classification in this manner allowed significantly more precise CT/FOB correlation. Altogether, there were 98 lesions visualized bronchoscopically; 88 (90%) were identified with CT. Lesions were further subdivided by location according to involvement of either the trachea, main-stem, lobar, or segmental bronchi. These data are illustrated schematically in Figure 3. Seventy-seven (93%) of 83 lesions involving main-stem and lobar bronchi were identified with CT; 11 (73%) of 15 lesions involving segmental bronchi were detected.

Of the 10 lesions missed by CT, six were located in main-stem or lobar bronchi; significantly all of these involved the left bronchial tree. Four segmental lesions were missed; these

Fig. 2.—CT localization: false negative examination.

A. Section at level of aortic arch. A thin-walled cavity in left upper lobe was subsequently proven to be a primary adenocarcinoma.

B. Section through lower lobes. Compared with left side there is considerable soft-tissue density surrounding right lower lobe basilar bronchi (arrows). Biopsy-proven contralateral metastatic disease causing extrinsic compression of anterior and lateral basilar segmental bronchi at bronchoscopy.

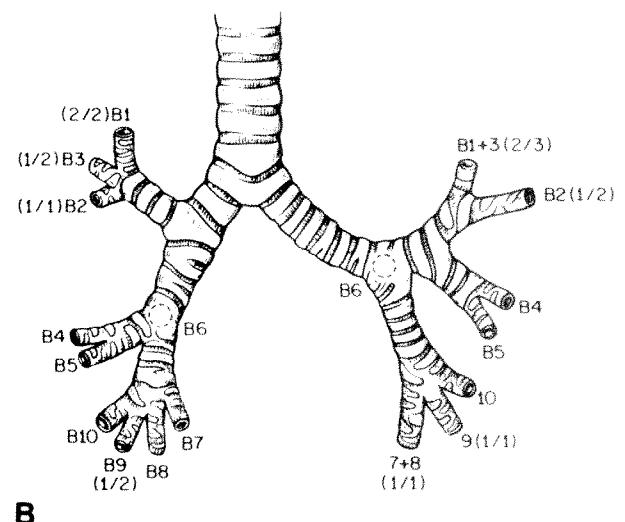
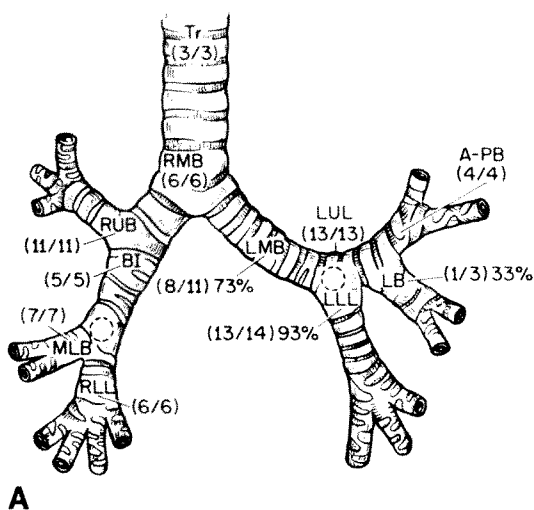
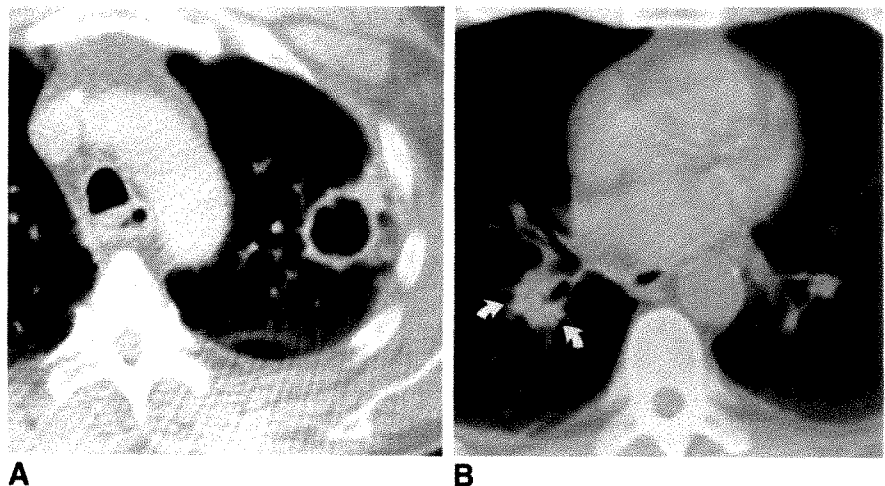


Fig. 3.—Diagrams showing the distribution of individual bronchial lesions according to their location. Numbers in parentheses indicate the number of lesions identified by CT (first number) and the number of lesions confirmed by bronchoscopy (second number).

A. Main-stem and lobar bronchi. CT identified a total of 77 (93%) of 83 lesions. Tr = trachea; RMB = right main-stem bronchus; RUB = right upper

bronchus; BI = bronchus intermedius; MLB = middle lobe bronchus; RLL = right lower lobe; LMB = left main-stem bronchus; LUL = left upper lobe; A-PB = apical-posterior bronchus; LLL = left lower lobe; LB = lingular bronchus.

B. Segmental bronchi. CT identified a total of 11 (73%) of 15 lesions.

were evenly divided between the right and left sides. Two of these lesions appeared endobronchial at endoscopy, two were described as extrinsic, and six represented contiguous submucosal extension from adjacent lesions detected by CT (Fig. 4). Only one of 10 false-negative CT scans could be attributed to a poor-quality study; three studies were rated as excellent. Two scans were interpreted incorrectly as abnormal despite contiguous 5-mm-thick sections. In only one case was a bronchoscopic abnormality missed because of nonvisualization of the involved airway at CT. In two cases retrospective analysis clearly showed that the scans had been improperly analyzed; these were still interpreted as false negatives (Fig. 2).

In five cases (three on the left side, two on the right side), CT identified bronchial abnormalities not recorded at FOB. In each case the findings were distal to proximally abnormal airways in patients subsequently proven to have carcinoma. In all cases bolus injections of contrast material confirmed the presence of massive hilar lymphadenopathy.

The accuracy of CT in predicting whether an abnormality was primarily endobronchial, submucosal, or extrinsic at FOB is shown in Table 4. By using the criteria illustrated schematically in Figure 1, it is apparent that overall CT is imprecise in making an accurate distinction. Smooth narrowing was the primary finding in 29 (52%) of 56 cases subsequently shown to be caused by endobronchial disease and in seven (78%) of nine cases resulting from submucosal disease. However,

this same finding was present in 21 (91%) of 23 cases defined bronchoscopically as having extrinsic abnormalities, a statistically greater percentage of cases than those seen with endobronchial or submucosal disease. Only two observations, (1) irregular narrowing, a finding that can be accurately defined only for airways that course in the horizontal plane, and (2) the presence of a definable intraluminal mass (soft-tissue or calcified), proved to be specific signs in both cases of endobronchial disease (Fig. 5).

Group 2

Thirty-eight patients were evaluated in whom there was no bronchoscopic evidence of focal disease. In these cases, FOB

TABLE 4: CT/Bronchoscopic Correlation in 88 Lesions

Bronchoscopic Finding	CT Finding				
	Smooth Narrowing	Irregular Narrowing	Occlusion	Mass	Displacement
Endobronchial (56)	29	7	12	8	None
Submucosal (9)	7	None	2	None	None
Peribronchial (extrinsic) (23)	21	None	None	None	2

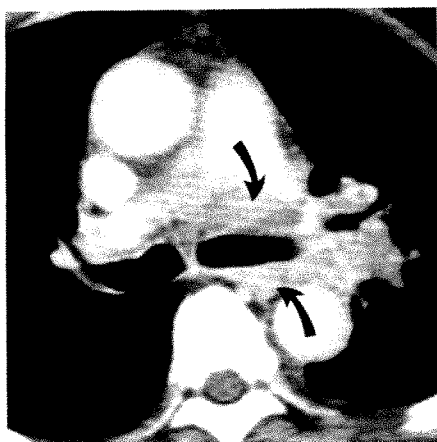
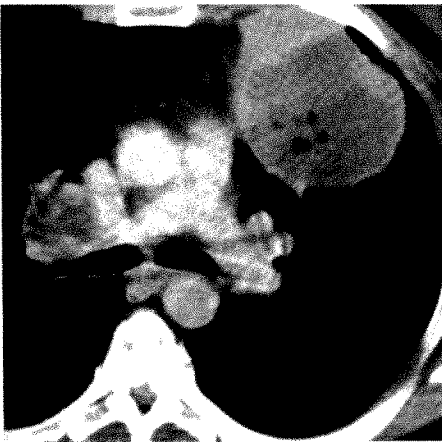


Fig. 4.—Submucosal extension, left main stem bronchus. Section through portions of both left main stem and apical-posterior bronchus after a bolus of IV contrast medium. There is extensive tumor throughout left hilum extending into mediastinum lying adjacent to left main stem bronchus both anteriorly and posteriorly (arrows). This is the only finding to suggest submucosal involvement, which was subsequently confirmed bronchoscopically. Note that overall configuration of left main stem bronchus is within range of normal, also true when viewed with wide windows (not illustrated).



A



B

Fig. 5.—CT localization: intrinsic vs extrinsic disease.

A and B, Sections through right upper lobe bronchus imaged with wide and narrow windows, respectively, after a bolus of IV contrast medium. In addition to necrotic left upper lobe tumor, there is a large, contralateral, right hilar mass that is causing slight posterior displacement of entire right upper lobe bronchus, with apparent obstruction of anterior segmental bronchus (curved arrow in A). At bronchoscopy, although anterior segmental bronchus was extrinsically compressed to a slit, there was no evidence of endobronchial disease.

was reported as either normal (26 patients) or as showing changes compatible with diffuse, usually mild bronchitis (12 patients). In three cases (8%) CT scans were interpreted as showing focal abnormalities. In one case, transbronchial biopsy obtained at the site of the CT abnormality proved negative (Fig. 6). In two other cases, focal narrowing was observed that could not be verified bronchoscopically. In these two cases, peripheral transbronchial biopsies resulted in the diagnosis of lymphangitic carcinomatosis and diffuse alveolar cell carcinoma, respectively. Among the 12 cases in which FOB showed diffuse bronchitis, CTs were normal in all except one, which was interpreted as showing mild, diffuse bronchial wall-thickening.

In three cases interpreted as normal at FOB, CT disclosed unsuspected evidence of bronchiectasis. In one case this was attributable to tuberculosis and in another to cystic fibrosis. One case had no documented cause, despite bronchographic confirmation of the presence of disease.

Discussion

Fiberoptic bronchoscopy is the procedure of choice for evaluating patients with suspected bronchial disease because it is relatively safe and frequently leads to a precise histologic diagnosis [1-3]. Accurate determination of the role of CT is therefore meaningful only by comparison. The purpose of this report has been to retrospectively investigate the potential of

CT in a large series of patients with both normal and abnormal airways who were examined endoscopically.

Previous reports have been contradictory concerning the role of CT. Webb et al. [4] analyzed CT scans in 30 patients with histologically proven carcinoma and abnormal chest radiographs, and concluded that there was close correlation between bronchial abnormalities identified with CT and FOB. Among 24 patients who had FOB, a total of 40 abnormalities were detected either by CT or bronchoscopy. In 25 of 40 cases there was general agreement between CT and FOB. In three, CT failed to detect lesions identified at FOB, including one case in which tumor involved the middle lobe bronchus in a patient with distal atelectasis. In 12 cases, CT detected abnormalities not seen at FOB. This included three cases in which the lesion was distal to a proximally abnormal bronchus verified by FOB and two cases in which the CT abnormality was confirmed by bronchial washings obtained at the site of the specified airway. Unfortunately, in seven cases there was no pathologic confirmation, making an accurate determination of sensitivity difficult.

Colice et al. [5] studied the potential role of CT by retrospectively comparing scans with bronchoscopic findings in 53 patients with known or suspected lung cancer. The authors reported considerable interobserver variation with sensitivities ranging from 63% to 85% and negative predictive values ranging from 67% to 80%. These authors concluded that CT was only moderately accurate in predicting the presence of airway disease and consequently should not be relied



Fig. 6.—CT localization: false-positive examination. Enlargement of a section obtained through origin of right lower lobe bronchus, imaged with wide windows, after a bolus of IV contrast material. There is apparent circumferential thickening of origin of right lower lobe bronchus (straight arrow), especially when compared with lateral segmental bronchus (curved arrow). Bronchoscopically, the mucosa at this level appeared slightly erythematous. Although biopsy revealed mild inflammation compatible with bronchitis, extent of disease histologically was interpreted as insignificant compared with the apparent extent of disease identified at CT.

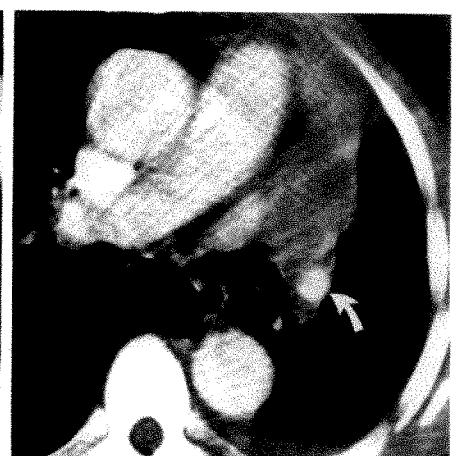


Fig. 7. CT localization, left upper lobe collapse.

A and B, Enlargement of a section through secondary carina imaged with wide and narrow windows, respectively, after a bolus of IV contrast material. Left upper lobe is collapsed due to endobronchial obstruction (arrow in A). In addition, tumor has infiltrated into left hilum causing thickening of left upper lobe spur and lateral displacement of left interlobar pulmonary artery (arrow in B). In this case, CT served as a roadmap for the bronchoscopist by documenting the extent of tumor and its relation to adjacent hilar vessels.

on for the identification of endobronchial abnormalities in patients with known or suspected lung cancer. Unfortunately, scans were interpreted according to the likelihood that abnormalities seen on CT could be correlated directly with specific endobronchial abnormalities without reference to a predefined radiographic classification (Fig. 1). Furthermore, no attempt was made in this study to use thin sections to assess airway disease, nor was the role of IV contrast material evaluated.

On the basis of the data presented in this report, we think that the following conclusions are justified.

1. There is good overall statistical correlation between CT and bronchoscopy in the identification of focal bronchial abnormalities. CT detected 59 of 64 cases confirmed to be abnormal by FOB. For individual airways, CT identified 88 (90%) of 98 lesions visualized bronchoscopically. CT incorrectly predicted the presence of focal airway disease in only three of 38 cases subsequently confirmed as normal at FOB.

2. On the basis of radiographic findings, CT is inaccurate in predicting whether a given focal abnormality documented at FOB will be endobronchial, submucosal, or extrinsic (Table 4). Only bronchial irregularity or the presence of a discrete intraluminal filling defect are specific indicators of endobronchial disease, and even these findings do not imply histologic specificity. Of particular concern is the finding that CT may be inaccurate in detecting submucosal extension of tumors. Of four cases in which submucosal extension went undetected by CT, three cases involved the left main-stem bronchus, recognition of which generally precludes attempts at surgical resection. While the accuracy of CT in detecting submucosal extension can be augmented by use of a bolus contrast injection, the subtle nature of this type of involvement makes it unlikely that CT will attain sufficient sensitivity to be of reliable use in staging (Fig. 4).

3. CT is inaccurate in detecting diffuse mucosal disease. Only one of 12 patients with bronchoscopic evidence of bronchitis had an abnormal CT scan, in this case probably secondary to unrelated peribronchial fibrosis.

4. Despite inaccuracy in predicting specific bronchoscopic findings, CT should be considered complementary to bronchoscopy, especially in detecting and delineating the presence and extent of extraluminal disease (Fig. 7). This has obvious significance in cases for which either transthoracic or, more particularly, transbronchial needle aspiration biopsy (TBNA) is planned [6-10]. As shown independently by Shure and Fedullo [11], Wang and Terry [12], and Wang [6], the addition of TBNA with a 20-gauge \times 1-cm needle significantly improved the diagnostic accuracy of bronchoscopy when compared with traditional bronchoscopic techniques. By providing a detailed outline of the exact location of major mediastinal and hilar vessels, lymph nodes, and tumor in relation to adjacent airways (especially when abnormal), CT may allow more confident and widespread use of these techniques [7, 8]. It is significant that in this series, of nine patients with submucosal abnormalities identified both with FOB and CT (Table 3), three required surgery to establish the final diagnosis; and in one other patient, transbronchial biopsy was positive only on a second attempt. In none of these was TBNA attempted

despite clear evidence of extensive peribronchial disease on the CT scan.

5. Only limited conclusions can be drawn concerning the potential of CT as a screening procedure. As discussed previously, in this series all cases with positive FOB had correspondingly abnormal chest radiographs (Table 2). From this select population it can be concluded that CT may be of value as a screening technique. The airways were interpreted as normal in only five of 64 cases in which focal disease was identified at FOB. This suggests that CT may provide adequate screening in patients for whom bronchoscopy is either contraindicated or refused.

In our opinion these results also support selective use of CT in screening patients for whom there is a low clinical suspicion of endobronchial disease, especially in young patients presenting with either infection or hemoptysis [9, 10]. In this series CT disclosed bronchiectasis in three patients presenting with hemoptysis in whom the correct diagnosis would otherwise have been overlooked.

Unfortunately, a negative CT scan cannot be assumed definitive in patients for whom there is a strong clinical suspicion of endobronchial disease. While the diagnosis of cancer was never missed in this series, it is obvious that focal bronchial lesions may not be identified, even when the quality of the scan is excellent. Of particular concern is the relative inaccuracy of CT in evaluating the left bronchial tree (Fig. 3). This is probably a consequence of the oblique orientation of both the left main-stem and lingular bronchi, a limitation that is only in part resolved by the use of thin sections. Also, detection of focal lesions within small, peripheral segmental bronchi may be problematic, although these reservations actually apply to a small subset of the total number of patients presenting with endobronchial disease. Definitive evaluation of CT as a screening procedure must await a large, prospective study. This will require examination of a large, carefully defined population, including individuals with negative chest radiographs, in order to more fully assess the relative contributions of both bronchoscopy and CT to overall patient evaluation and management.

In summary, our findings endorse selective use of CT as a noninvasive technique for assessing the airways, provided that care is exercised to obtain technically adequate studies, including the use of thin sections and IV contrast material whenever indicated, and that there is thorough familiarity with the specific limitations of CT.

ACKNOWLEDGMENT

We wish to acknowledge the invaluable contribution of Jane Crafts in the preparation and review of this manuscript.

REFERENCES

1. Suratt PM, Smiddy JF, Gruber B. Deaths and complications associated with fiberoptic bronchoscopy. *Chest* 1976;69:747-751
2. Pereira W, Kovnat DM, Snider GL. A prospective cooperative study of complications following flexible fiberoptic bronchoscopy. *Chest* 1978; 73:813-816

3. Kvale PA, Bode FR, Kini S. Diagnostic accuracy in lung cancer. Comparison of techniques used in association with flexible fiberoptic bronchoscopy. *Chest* 1976;69:752-757
4. Webb WR, Gamsu G, Speckman JM. Computed tomography of the pulmonary hilum in patients with bronchogenic carcinoma. *J Comput Assist Tomogr* 1983;7:219-225
5. Colice GL, Chappel GJ, Frenchman SM, Solomon DA. Comparison of computerized tomography with fiberoptic bronchoscopy in identifying endobronchial abnormalities in patients with known or suspected lung cancer. *Am Rev Respir Dis* 1985;131:397-400
6. Wang KP. Flexible transbronchial needle aspiration biopsy for histologic specimens. *Chest* 1985;88:860-864
7. Cropp AJ, Dimarco AF, Lankerani M. False-positive transbronchial needle aspiration in bronchogenic carcinoma. *Chest* 1984;85:696-697
8. Schenk DA, Bower JH, Bryan CL, et al. Transbronchial needle aspiration staging of bronchogenic carcinoma. *Am Rev Respir Dis* 1986;134:146-148
9. Jackson CV, Savage PJ, Quinn DL. Role of fiberoptic bronchoscopy in patients with hemoptysis and a normal chest roentgenogram. *Chest* 1985;87:142-144
10. Sosenko A, Glassroth J. Fiberoptic bronchoscopy in the evaluation of lung abscesses. *Chest* 1985;87:489-493
11. Shure D, Fedullo PF. Transbronchial needle aspiration in the diagnosis of submucosal and peribronchial bronchogenic carcinoma. *Chest* 1985;88:49-51
12. Wang KP, Terry PB. Transbronchial needle aspiration in the diagnosis and staging of bronchogenic carcinoma. *Am Rev Respir Dis* 1983;127:344-347

Book Review

Computed Tomography of the Pituitary Gland. By J.-F. Bonneville, F. Cattin, and J.-L. Dietemann. Berlin: Springer-Verlag, 235 pp., 1986. \$113

Computed Tomography of the Pituitary Gland has been written to raise the reliability of diagnostic radiologic studies of the pituitary gland to the same level as that of other available studies. The goal is to provide accurate guidelines for physicians treating patients with these disorders. This book is divided into 19 chapters. The first three chapters cover technique and anatomy and the next 11 chapters discuss specific clinical problems involving the pituitary gland. The last five chapters include discussions of the pituitary stalk, suprasellar and parasellar disease, and picture problems that may be encountered in CT studies of the pituitary region. The final chapter of the text provides a brief review of the use of MR imaging in the study of sellar and juxtasellar diagnostic problems.

This book reflects the extensive experience of these authors, as well as the thoroughness and exact attention to detail that is necessary for a study of the pituitary region. The design of the protocols for pituitary scans is more complex than those performed by the usual physician but has provided the authors with material and a degree of accuracy not achieved by other investigators in this field. The use of dynamic scanning is strongly encouraged, and careful guidelines are provided for the reader to enable a thorough study on each patient regardless of technical problems that may be encountered. Each chapter is succinct and well organized into a brief discussion of the clinical problems and the differential features of the diagnosis by CT. Generally a reference to the authors' experience of the accuracy of CT in the diagnosis of the particular clinical problem.

The tables are appropriate in number, and the illustrations are universally of high quality, again reflecting the authors' care and thoroughness in their study. The content of the text flows well, and the illustrations are well labeled. Some readers would prefer to have had illustrations interspersed throughout the text of a chapter rather than all grouped at the end of the chapter as in this presentation, but this is an individual preference. The chapter on picture problems is well done and is a useful adjunct.

I have no significant criticisms of this book and believe that the authors have generally achieved their goals. Some readers might prefer more discussion of some of the controversies in the clinical and radiologic study of patients with pituitary disorders. This includes the problems of the natural history of pituitary microadenomas, of diagnosis of cavernous sinus displacement vs invasion, and of recurrent neoplasm vs scarring in the postoperative patient. Others may not be able to reconcile the differences in diagnostic accuracy achieved by the authors vs other published reports. I believe this, again, represents the thoroughness with which the authors have studied their patients and provides a goal for other investigators.

I recommend *Computed Tomography of the Pituitary Gland* highly, as a reference text for Radiology and Endocrinology Departments and for physicians specializing in this area.

Frederick Vines
University Hospital of Jacksonville
Jacksonville, FL 32209

CT of Interstitial Lung Disease: A Diagnostic Approach

Colleen J. Bergin¹
Nestor L. Müller¹

Weibel divided the pulmonary interstitium into three compartments: axial, parenchymal, and peripheral. Heitzman and others have shown that certain interstitial diseases selectively involve these compartments. A model is proposed of the CT appearances in interstitial lung disease based on Weibel's divisions. To assess the validity of this model, the distribution of disease was studied in 44 patients with proven interstitial lung disease. Lymphangitic carcinomatosis ($n = 5$), lymphoma ($n = 2$), and sarcoid in two of three patients typically involved the axial compartment. The middle (or parenchymal) compartment was abnormal in advanced stages of many interstitial diseases, particularly granulomatous diseases and drug toxicity ($n = 2$) in this series, but diffuse changes were seen early in extrinsic allergic alveolitis ($n = 4$). The peripheral compartment was predominantly affected in idiopathic pulmonary fibrosis ($n = 9$), rheumatoid lung ($n = 3$), and scleroderma ($n = 1$). Prominent nodularity was a feature of lymphangitic carcinomatosis and of the granulomatous diseases, silicosis and sarcoid. The presence or absence of nodules coupled with CT demonstration of differential involvement of the three interstitial compartments is useful in limiting diagnostic possibilities in interstitial disease. By more accurately showing disease distribution, a more reasonable approach to lung biopsy options may be developed.

Despite the controversy surrounding limitations of pattern recognition in chest radiograph-pathology correlation [1, 2], the categories "air space" and "interstitial" persist in chest radiograph descriptions and are proving useful in early investigations with CT [3, 4]. Naidich et al. [4] have delineated the CT characteristics of interstitial disease that reflect changes seen on the chest radiograph. The CT appearances of many interstitial lung diseases have been described [4-7], but a systematic approach to the diagnosis of interstitial disease with CT has not been reported. Therefore, we propose a model with which to view the CT appearances in interstitial lung disease based on the three-compartment model of Weibel and Gil [8].

Materials and Methods

All patients with proven interstitial disease in whom CT scans were obtained between May 1984 and August 1985 were included in this study (44 patients). The spectrum of interstitial diseases studied is summarized in Table 1.

The CT scans in all 44 patients were assessed for disease distribution in the three compartments of our model (Fig. 1). In this model, the pulmonary interstitium is divided into axial, middle, and peripheral compartments. The axial compartment is contiguous with the mediastinum; it extends as a sheath around the bronchovascular structures and includes the lymphatics. The middle compartment is formed by alveolar walls. The peripheral compartment includes the pleura, subpleural connective tissue, interlobular septa enclosing pulmonary veins and lymphatics, and the walls of cortical alveoli. The presence or absence of nodules, pleural effusions, associated parenchymal abnormalities, and upper- or lower-lobe distribution were also assessed. In each patient, the CT appearance was correlated with the disease process as defined by pathology. The scans were reviewed by two observers and conclusions were reached by consensus.

Received March 3, 1986; accepted after revision August 4, 1986.

Presented at the annual meeting of the American Roentgen Ray Society, Washington, DC, April 1986.

¹ Department of Radiology, University of British Columbia, and Vancouver General Hospital, 855 W. 12th Ave., Vancouver, B.C., Canada V5Z 1M9. Address reprint requests to N. L. Müller.

AJR 148:8-15, January 1987
0361-803X/87/1481-0008
© American Roentgen Ray Society

TABLE 1: Spectrum of Interstitial Lung Disease in Patients Scanned by CT

Diagnosis (No. of Patients)	Interval from Onset of Chest Symptoms to CT	CT Distribution	Method of Diagnosis
Lymphangitic carcinomatosis (5):			
Breast (2)	<1 yr	Axial, middle, & peripheral	Sputum cytology & transbronchial biopsy
Bowel (1)	<1 yr	Axial, peripheral	Sputum cytology
Unknown primary (2)	<1 yr	Axial	Pleural fluid cytology & transbronchial biopsy
Lymphoma (non-Hodgkin's) (2)	3 yr	Axial	Pleural fluid cytology
	5 yr	Axial, middle	Open-lung biopsy
Sarcoid (3)	3 mo	Axial, middle, & peripheral	Transbronchial biopsy
	1 yr	Axial, middle, & peripheral	Mediastinoscopy
	3 yr	Middle	Mediastinoscopy
Extrinsic allergic alveolitis (4):			
Farmer's lung (2)	<1 yr	Middle	Open-lung biopsy
Farmer's lung (1)	3 yr	Middle	Open-lung biopsy
Unknown allergen (1)	<6 mo	Middle	Open-lung biopsy
Neurofibromatosis (1)	2 yr	Middle	Open-lung biopsy
Busulfan toxicity (2)	<1 yr	Middle	Open-lung biopsy
Silicosis (13)	5-20 yr	Middle	History
Fibrosing alveolitis (13):			
Idiopathic pulmonary fibrosis (9)	6 mo-3 yr	Peripheral & middle	Open-lung biopsy
Rheumatoid lung (3)	1 yr	Peripheral	Open-lung biopsy
Scleroderma (1)	3 yr	Peripheral	Open-lung biopsy

Note.—yr = year; mo = month.

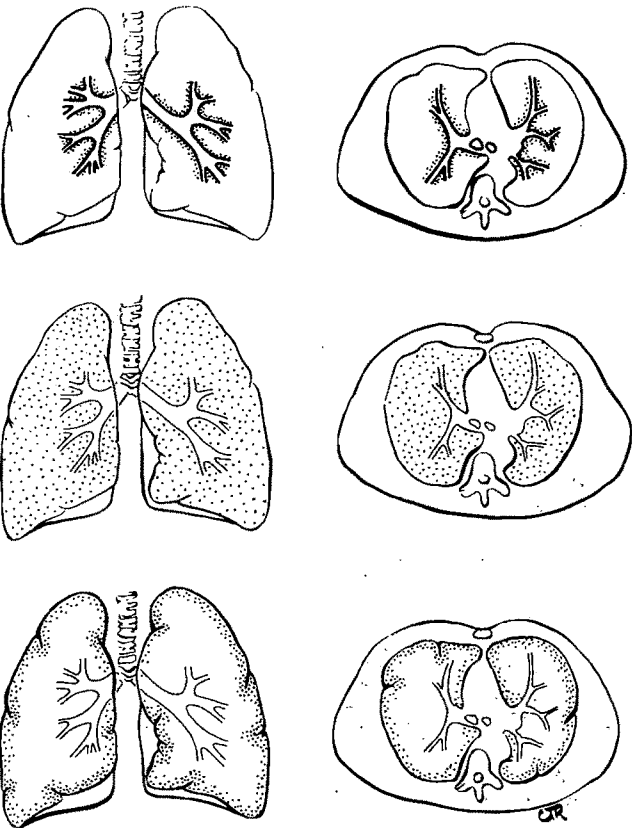


Fig. 1.—Three-compartment model for viewing disease in pulmonary interstitium with CT: axial, middle, and peripheral (top to bottom, respectively).

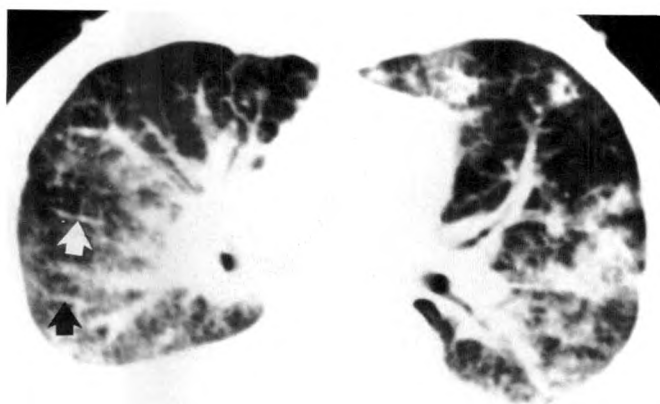
TABLE 2: CT Distribution of Interstitial Diseases

Axial:
Lymphangitic carcinomatosis
Sarcoid
Lymphoma
Middle:
Lymphangitic carcinomatosis
Sarcoid
Silicosis
Extrinsic allergic alveolitis
Neurofibromatosis
Drugs
Vasculitis
Peripheral:
Lymphangitic carcinomatosis
Sarcoid
Fibrosing alveolitis
Rheumatoid lung
Scleroderma

CT scans were obtained by using either a GE 8800 or a GE 9800 scanner at 1-cm intervals, with 10-mm collimation from the apex of the lungs to the base of the diaphragm during breath-holding after deep inspiration in all patients. Lung settings appropriate to viewing the pulmonary parenchyma were used (window width 1000-1500 H, level -500 to -700 H).

Results

Disease distribution in the three compartments is summarized in Table 2.

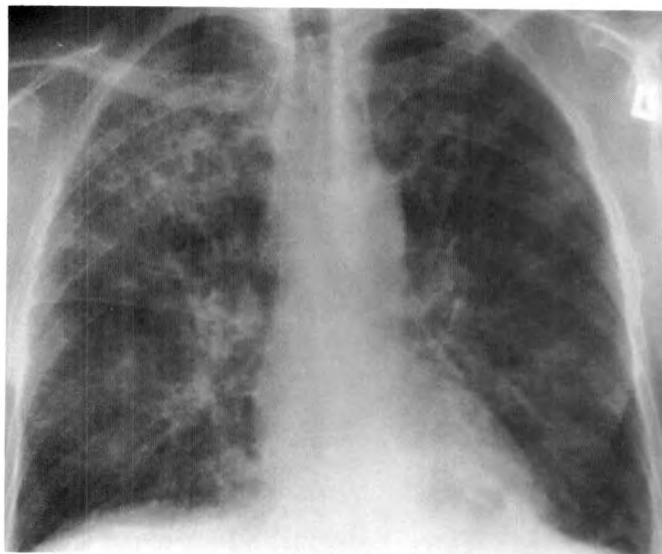


A

Fig. 2.—Lymphangitic carcinomatosis.

A, CT scan through lower lobes. Thickening along length of bronchovascular bundles in axial distribution. Bilateral pleural effusions are seen together with thickened interlobular septa (arrows) and network of parenchymal reticular densities.

B, Chest radiograph. Lung parenchyma appears diffusely abnormal with little evidence of markedly abnormal axial interstitium.



B

Axial Compartment

The axial compartment was abnormal in all patients with lymphangitic carcinomatosis (five) and pulmonary lymphoma (two) and in two of the three patients with sarcoid. In lymphangitic carcinomatosis, CT showed thickening along the bronchovascular bundles radiating from the hili. In longitudinal section, the increased thickness of the bronchovascular bundles was more pronounced closer to the hilum with distal tapering, but peripheral branches were also more prominent than is usually seen in normal bronchi (Fig. 2A). In cross section, the bronchovascular bundles infiltrated by tumor appeared circumferentially thickened. Other features of the patients with lymphangitic carcinomatosis were multiple linear densities seen throughout the parenchyma, presumably representing metastatic involvement of interlobular septa. In places, these lines formed a reticular network. Fine nodularity was evident along the bronchovascular bundles and throughout the parenchymal "lattice." Lower-lobe predominance of interstitial changes was present in only two patients. Mediastinal adenopathy was seen in all cases and pleural effusions were present in three of the patients with lymphangitic carcinomatosis. Although diffuse parenchymal abnormality was readily apparent on chest radiographs in all patients, prominent involvement of the bronchovascular bundles was obscured by overlying parenchymal abnormality (Fig. 2B). Abnormality in the axial interstitium was detected more readily on the CT images in all patients with lymphangitic carcinomatosis.

In two of the three patients with sarcoid, small nodules were again seen scattered throughout the pulmonary parenchyma. Again, the axial interstitium was accentuated with some clustering of nodules along the bronchovascular bundles (Fig. 3A). Clumps of nodules were seen in a subpleural location in two of the patients with sarcoid but there was no evidence of the reticular lattice formed by thickened interlob-

ular septa seen in lymphangitic carcinomatosis. Again, because of overlying parenchymal abnormality, the nodular clustering along the bronchovascular bundles was not readily apparent on the chest radiographs (Fig. 3B). In the patient with a 3-year history of sarcoid, interstitial thickening was more prominent than nodules and axial predominance was not seen. In all three patients, nodules and interstitial changes were more prominent in the apices.

In two patients with lymphoma, isolated bronchovascular bundles were involved without diffuse parenchymal abnormality. In contrast to the patients with lymphangitic carcinomatosis and sarcoid, lymphoma resulted in fusiform swellings around patent bronchi and extended as discrete masses into the pulmonary parenchyma (Fig. 4). The chest radiograph showed opacities in the pulmonary parenchyma, and in some of the masses air bronchograms were seen suggesting the relationship between tumor and bronchovascular bundles.

Middle Compartment

The middle compartment was diffusely abnormal in extrinsic allergic alveolitis ($n = 4$), in pulmonary vasculitis secondary to cryoglobulinemia ($n = 1$), in busulfan toxicity ($n = 2$), and in neurofibromatosis ($n = 1$). In the patient with the shortest history of allergen exposure (3 months), there was a fine granular appearance to the lung parenchyma not easily classified as distinctly air space or interstitial. The CT images showed features of both with areas of poorly marginated opacities, coalescent densities, and poorly defined air bronchograms, as well as thickening of parenchymal vascular and bronchial markings (Fig. 5). In three patients with longer histories of antigen exposure, however, linear densities were more prominent and air-space densities were less obvious.

In patients with vasculitis, busulfan toxicity, and neurofibromatosis, the middle compartment of the interstitium was abnormal with predominantly linear and reticular densities in

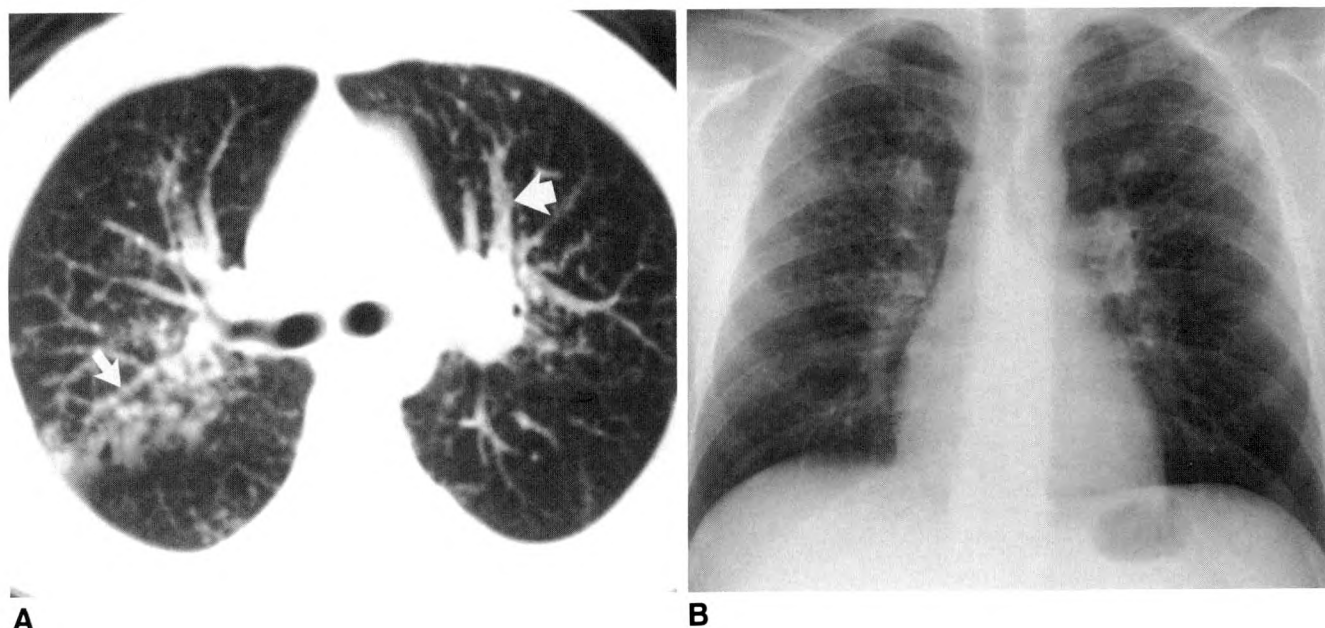


Fig. 3.—Sarcoid.

A, CT scan below carina. Nodules are scattered through parenchyma but concentrated along bronchovascular bundles in axial distribution (arrows). B, Chest radiograph. Bilateral upper-lobe nodules with no evidence of bronchovascular predominance.

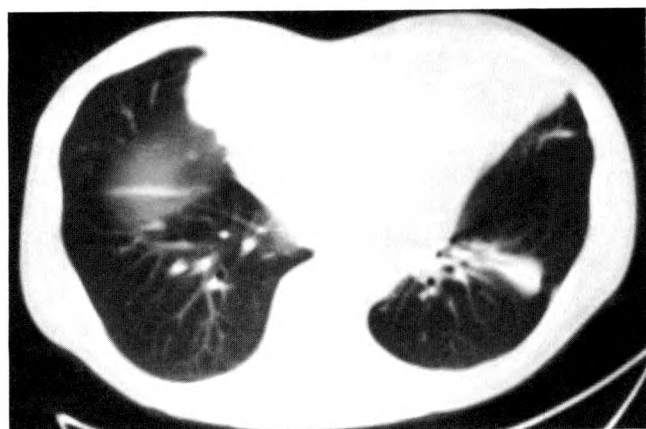


Fig. 4.—CT scan through lower lobes in patient with non-Hodgkin's lymphoma. In the left lower lobe, fusiform mass of lymphoma surrounds bronchovascular bundle leaving bronchus patent. At autopsy, epicardial masses also proved to be lymphoma.

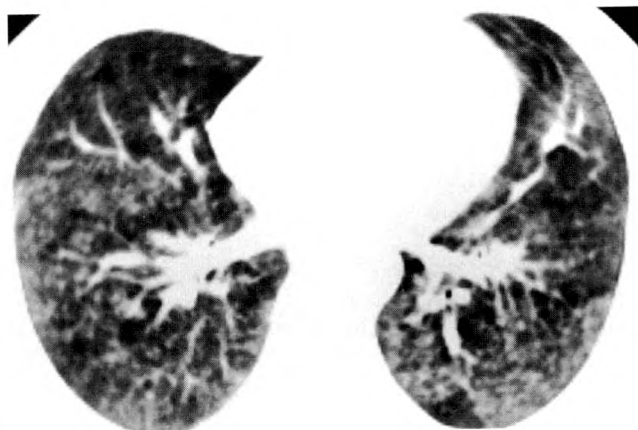


Fig. 5.—CT scan through lower lobes in patient with extrinsic allergic alveolitis and 6-month history of symptoms. Features of both air-space and interstitial abnormality are present with coalescent finely nodular opacities and thickened linear densities throughout parenchyma.

all patients, most prominent in the lower lobes. Nodularity was not a feature of these diseases. The CT images in each case reflected the chest radiograph findings.

In 13 patients with silicosis, nodularity was the prominent abnormality in the middle compartment (Fig. 6). The size of the nodules varied from barely discernible up to confluent masses 5 cm in width consistent with the diagnosis of progressive massive fibrosis. The distribution of nodules was markedly different from that in sarcoid and lymphangitic car-

cinomatosis in that they bore no relationship to the bronchovascular bundles and showed a predominantly posterior distribution in the upper and middle lung zones on CT. This characteristic posterior distribution was not evident from the chest radiographs. Reticular and linear densities were much less prominent than nodules. In all cases of silicosis, the nodules were readily apparent on the chest radiographs, although the posterior distribution of nodules was identified only on the CT scans.

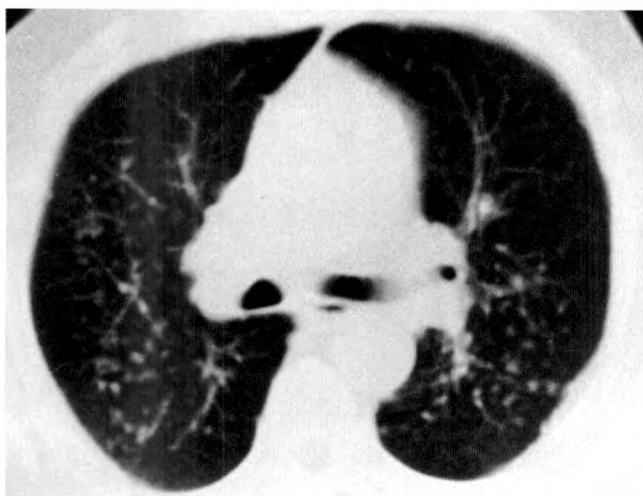


Fig. 6.—CT scan below carina in patient with silicosis shows nodules in middle interstitium with posterior predominance. Axial and peripheral interstitial compartments are normal.

Peripheral Compartment

An abnormal peripheral compartment was shown by CT in 13 patients with fibrosing alveolitis resulting from idiopathic pulmonary fibrosis ($n = 9$), rheumatoid lung ($n = 3$), and scleroderma ($n = 1$). This group was characterized by a peripheral rim of reticular densities and honeycomb cysts, together with peripheral linear densities suggestive of thickened interlobar septa. Fine irregularity and thickening of the pleural surface was prominent in this group, and these changes along the mediastinal interfaces echoed the "shaggy-heart" appearance seen on the chest radiographs (Figs. 7A and 7B). In patients with long-standing fibrosing alveolitis, more of the middle interstitium was abnormal, but the peripheral predominance of fibrosis and cystic spaces was still evident on CT in patients with a symptomatic history as short as 6 months and as long as 3 years (Figs. 7C and 7D). The peripheral distribution was easily distinguishable from the previously described axial- and middle-compartment CT patterns. On the chest radiograph, the peripheral predominance was obvious in eight of the 13 patients.

Discussion

We have presented a CT model with which to view the pulmonary interstitium and have shown the CT appearance of interstitial diseases involving each of the three compartments: axial, middle, and peripheral. Weibel and Gil [8] divided the normal interstitium into three compartments. Our model has extended this concept to potentially incorporate the distribution of all interstitial diseases as they are shown on CT. We recognize that these divisions are somewhat artificial as the compartments do freely communicate with one another, but others [9–12] have shown selective involvement of the compartments in a variety of interstitial diseases. We consider

that the transverse sections of CT enhance our ability to identify differential involvement of the three interstitial compartments, particularly when diffuse parenchymal abnormality obscures good demonstration of the axial and peripheral compartments on the chest radiograph.

Recent descriptions of the CT appearances in interstitial disease have suggested that CT may complement chest radiography in the diagnosis of interstitial disease [3, 5, 13, 14]. It is not yet known if the use of patterns to recognize specific pathologic processes from CT images will prove more or less accurate than the chest radiograph in predicting disease as these investigations are still in the early stages. Disease distribution between the upper and lower lobes and in the lung periphery has long been used as a feature of the chest radiograph in identifying certain groups of interstitial diseases, but differential pathologic involvement has also been shown between the axial and peripheral compartments [9–12]. These divisions are not always so readily identified on the chest radiograph. In our study, involvement of the bronchovascular bundles in most cases was not readily determined from the chest radiograph because of overlying parenchymal disease. CT offers the advantage of decreased superimposition of parenchymal opacities, and in this group, CT clearly showed abnormality of the axial interstitium. CT also showed the network of thickened interlobular septa described by Naidich et al. [4] in the pulmonary parenchyma of patients with lymphangitic carcinomatosis but not in sarcoid. Fine nodularity was evident in both of these diseases, but unfortunately our CT images were 1 cm thick and therefore did not provide as much detail of nodular features as might have been obtained by using thin sections. In contrast to the spread of lymphangitic carcinomatosis and sarcoid along the length of bronchovascular bundles, lymphomatous involvement of the bronchovascular bundles was more mass-like in nature. This relationship of lymphoma masses to the bronchovascular bundles was appreciated on the chest radiograph when air bronchograms were seen [9, 12]. An abnormal peripheral compartment is characteristic pathologically and has been identified on the chest radiograph as a feature of fibrosing alveolitis [15, 16]. Early peripheral opacities may be difficult to distinguish from pleural abnormality on the chest radiograph, however, and in later stages of the disease, the peripheral predominance may be obscured by increased parenchymal densities. In situations where the peripheral distribution is not evident from the chest radiograph, CT may show this distribution.

Our small group of patients suggests that CT demonstration of diseases involving the axial and peripheral compartments may have diagnostic potential. With an abnormal middle compartment, however, CT as yet offers little as a diagnostic tool compared with the chest radiograph, on which the changing patterns of parenchymal diseases can be followed inexpensively. Apart from diagnostic potential, however, we suggest that CT demonstration of disease distribution may help to plan the next diagnostic procedure. If the axial pattern is seen on CT, a transbronchial approach may be adequate to provide a diagnostic lung biopsy. In interstitial diseases

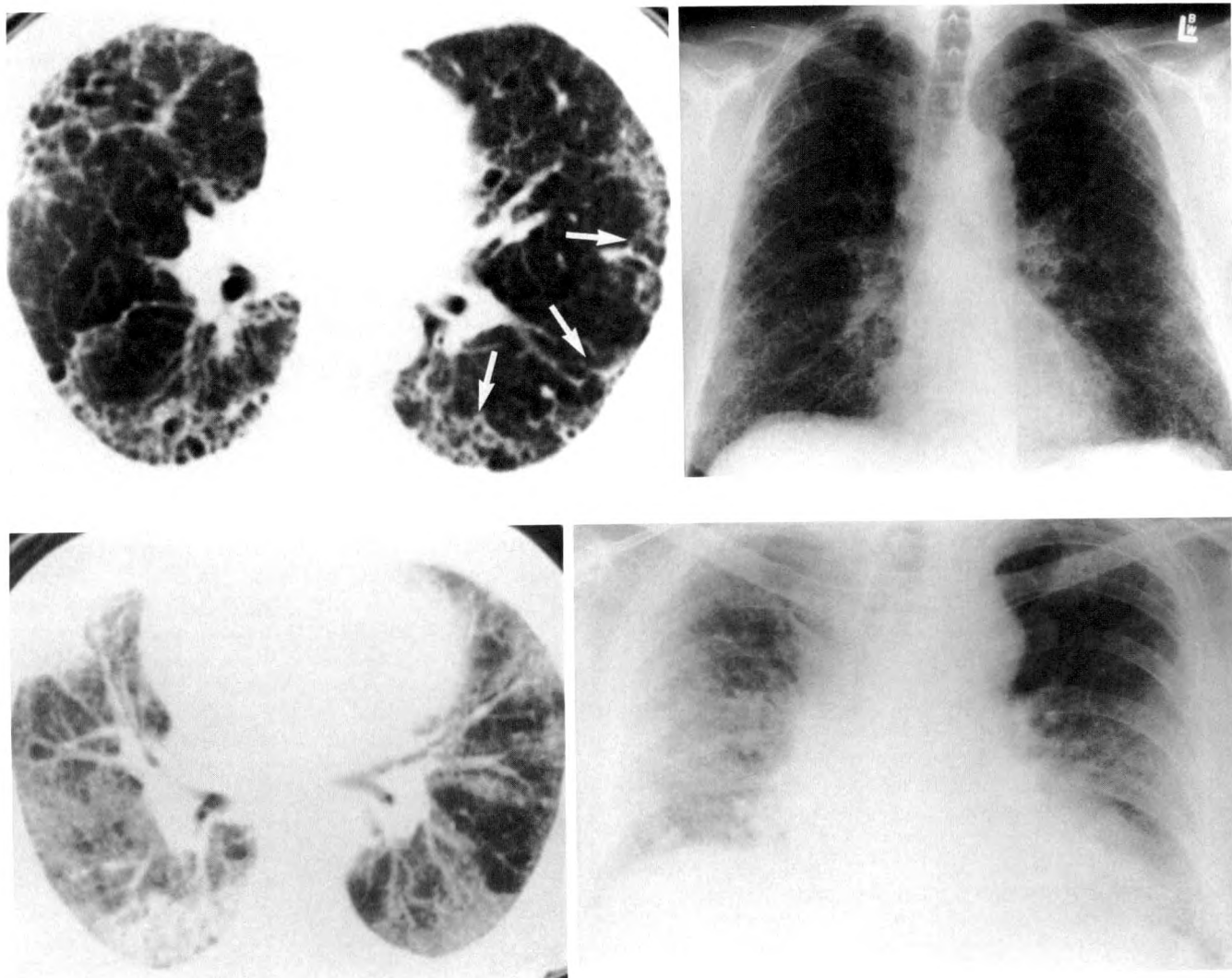


Fig. 7.—A and B, Fibrosing alveolitis associated with rheumatoid arthritis.

A, CT scan through lower lobes. Increased reticular densities and cysts in peripheral distribution (arrows) together with "shaggy-heart" appearance from irregularly thickened mediastinal pleura.

B, Chest radiograph. Lower lobe and peripheral increased interstitial markings.

C and D, Patient with a 3-year history of idiopathic pulmonary fibrosis. C, CT scan through lower lobes. Abnormal interstitial markings are prominent throughout pulmonary parenchyma, but peripheral predominance is still evident.

D, Chest radiograph. Peripheral predominance is partly obscured by diffuse parenchymal abnormality.

involving the pulmonary parenchyma diffusely, however, an open-lung biopsy is usually indicated to obtain adequate tissue for diagnosis. In many diseases with peripheral fibrosis, the diagnosis is frequently suggested by clinical presentation. In the appropriate clinical setting, CT confirmation of the characteristic peripheral fibrotic pattern may obviate lung biopsy in this group, thereby preventing an invasive procedure.

The number of patients in our study was small. We used this group to evaluate the ability of CT to demonstrate selective involvement of the three compartments in our model, which as an aid to diagnosis has yet to be fully explored. In many cases of interstitial lung disease, the chest radiograph combined with clinical history is adequate for diagnosis; but in doubtful situations, CT may provide useful information on

disease distribution, particularly in the axial and peripheral compartments. As other distinguishing features of interstitial diseases, such as nodularity, are explored more fully with the detail obtained by using thin slice sections, it is hoped that CT will further supplement chest-radiograph information by providing a more complete picture of disease in the pulmonary parenchyma and thereby help the radiologist in more accurately predicting disease.

ACKNOWLEDGMENTS

We thank R. Miller and Andrew Churg for pathology; M. Chan-Yeung, Paul Champion, and David Ostrow for supplying patients; R. K. Elwood for advice; and Betty Fowler for secretarial assistance.

REFERENCES

1. Fraser RG. The radiology of interstitial lung disease. *Clin Chest Med* 1982;3(3):475-484
2. McLoud TC, Gaensler EA, Carrington CB. Chronic diffuse infiltrative lung disease: newer approaches. *Clin Chest Med* 1984;5:332-344
3. Zerhouni EA, Naidich DP, Stitik FP, Khouri NF, Siegelman SS. Computed tomography of the pulmonary parenchyma. Part 2. Interstitial disease. *J Thorac Imaging* 1985;1:54-64
4. Naidich DP, Zerhouni EA, Hutchins GM, Genieser NB, McCauley DI, Siegelman SS. Computed tomography of the pulmonary parenchyma. Part 1. Distal airspace disease. *J Thorac Imaging* 1985;1:39-53
5. Bergin CJ, Müller NL. CT in the diagnosis of interstitial lung disease. *AJR* 1985;145:505-510
6. Coddington R, Mera SL, Goddard PR, Bradfield JWB. Pathological evaluation of computed tomography images of lungs. *J Clin Pathol* 1982;35:536-540
7. Kreel L. Computed tomography of interstitial pulmonary disease. *J Comput Assist Tomogr* 1982;6:181-199
8. Weibel ER, Gil J. Structure-function relationships at the alveolar level. In: West JB, ed. *Bioengineering aspect of the lung*. New York: Marcel Dekker, 1977:1-81
9. Heitzman ER. *The lung. Radiologic-pathologic correlations*. Toronto: Mosby, 1984:48-105
10. Staub NC, Nagaro H, Pearce ML. Pulmonary edema in dogs, especially the sequence of fluid accumulation in the lungs. *J Appl Physiol* 1967;22:227-240
11. Stolberg HO, Patt NL, MacEwen KF, Warwick OH, Brown TC. Hodgkin's disease of the lung. *AJR* 1964;92:96-115
12. Spencer H. *Pathology of the lung*, 4th ed. Oxford: Pergamon, 1985:788-802
13. Steinberg DL, Webb WR. CT appearances of rheumatoid lung disease. *J Comput Assist Tomogr* 1984;8:881-884
14. Yoshimura H, Hatakeyama M, Otsuji H, et al. Pulmonary asbestosis: CT study of subpleural curvilinear shadow. Work in progress. *Radiology* 1986;158:653-658
15. Fraser RG, Paré JAP. *Diagnosis of diseases of the chest*. Philadelphia: Saunders, 1977:410-434
16. Forrest JV, Feigin DS, eds. *Essentials of chest radiology*. Philadelphia: Saunders, 1982:25-29

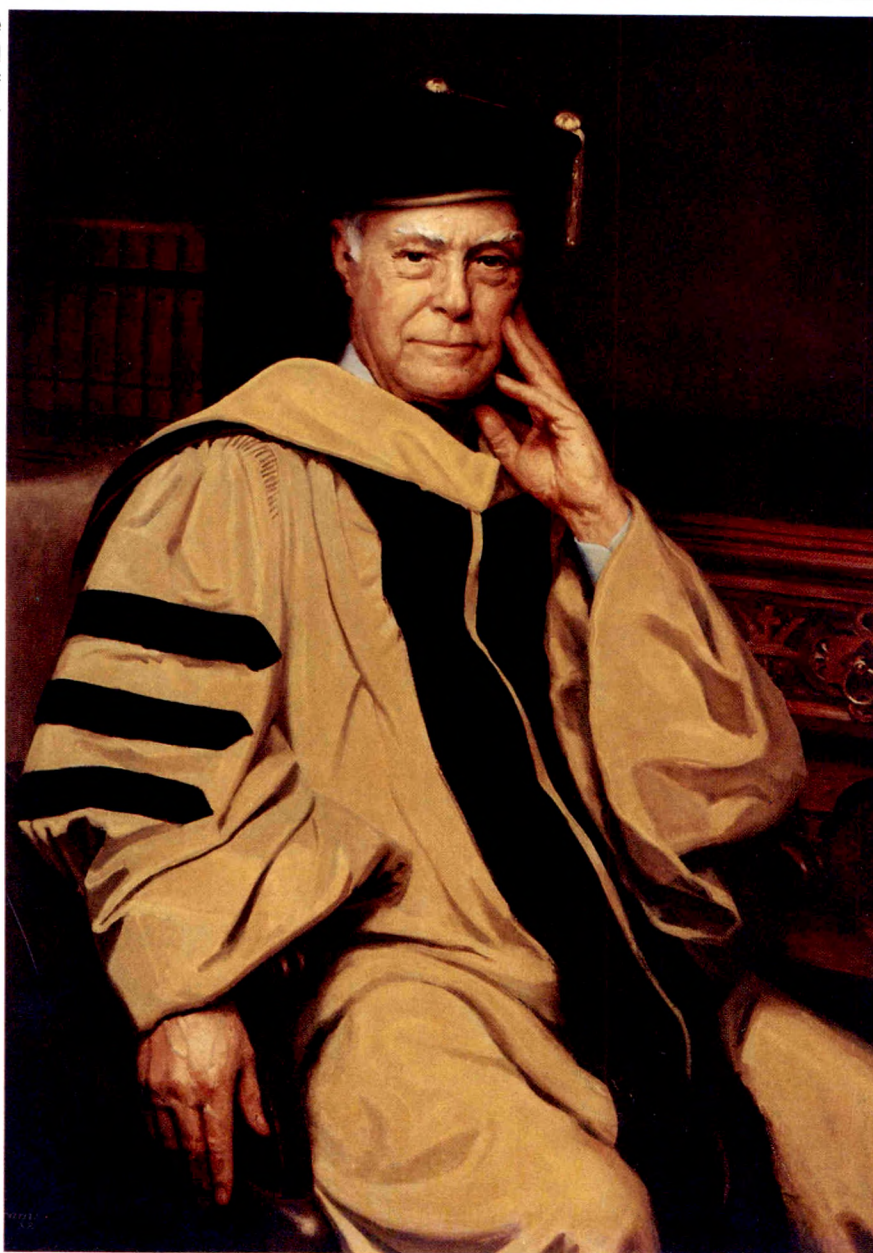
Memorial Tribute to Russell H. Morgan, 1911–1986

Russell H. Morgan, Dean Emeritus of the medical faculty and former Chairman and Radiologist-in-Chief of the Department of Radiology of The Johns Hopkins University School of Medicine and The Johns Hopkins Hospital died February 24, 1986, after a long illness. He was 75 years old.

Dr. Morgan was born in London, Ontario, Canada. He graduated from the University of Western Ontario School of Medicine. After internship and a residency in pathology, he completed his residency training in radiology at the University of Chicago. His performance during and after his residency was stellar, and his contributions to radiology were milestones.

His knowledge of physics, mathematics, and engineering and his use of engineering methods to investigate medical problems (long before the present-day discipline of biomedical engineering) stemmed from an understanding of the needs of clinical radiology and resulted in the research and development of some of the most important technological advances in radiology. They include the photoelectric timer for automatic control of radiographic exposures, the perfection of image intensification, and the application of television techniques in clinical fluoroscopy and cinefluorography. His studies of image formation, visual perception, and physiologic optics related to radiographic and fluoroscopic systems were landmarks, and his application of computer methods and data-processing systems in medicine have had a profound and lasting impact on radiology.

Dr. Morgan's career at Johns Hopkins began in 1946, when at age 35 he was appointed Professor and Chairman of the Department of Radiology at the School of Medicine and the first Radiologist-in-Chief at the hospital. As a physician and radiologist, teacher and scientist, mentor and friend, he provided the atmosphere that



Russell H. Morgan—portrait by Herbert E. Abrams, Warren, CT 06754.

trained and nurtured physicians for academic careers at Hopkins and at other institutions both here and abroad. His appointment in 1960 to the professorship of Radiological Science in the School of Hygiene and Public Health led to the development of a vigorous multidisciplinary program in radiologic medicine.

His untiring work with the U. S. Public Health Service began during World War II, when he served as Commander. This association developed into a long and active participation with the Division of Radiological Health and led to the design and application of public health measures in radiologic health for the control of radiation hazards. He chaired and was a member of many national and international commissions and committees related to radiation health, safety, and regulation.

In 1971, Dr. Morgan was appointed Dean of the Medical Faculty of The Johns Hopkins School of Medicine. He held that position for 4 years, during which he developed the Medical Faculty Practice Plan and balanced the school budget in a period of increasingly scarce federal resources. Also during that interval, he was named Vice President for the Health Division and University Professor of Medicine. In 1980, the department that he had served so well for 23 years was named in his honor: "The Russell H. Morgan Department of Radiology and Radiological Science."

After 1975, in so-called retirement, Dr. Morgan remained extremely active as University Professor Emeritus. He continued to serve as director of several industrial corporations, medical institutions, and philanthropic foundations. He was chairman of the board of the Picker Foundation for 28 years and a member of the Editorial Board of the *American Journal of Roentgenology* for 41 years. He was first Vice President of the American Roentgen Ray Society and Founder and First President of the Association of University Radiologists.

Numerous honors, awards, and accolades were bestowed on him. They include honorary Doctor of Science degrees

from the University of Western Ontario and the University of Chicago; Gold Medals from the American Roentgen Ray Society and the Radiological Society of North America; and Gold Medals of the American College of Radiology, the Association of University Radiologists, and the American Society of Radiologic Technologists. In 1979, he was awarded the prestigious German Roentgen Plakette for outstanding advances in radiology.

Quiet, kind, and sensitive, Dr. Morgan was very well liked. He was devoted to his family: his wife, Stella; his daughters, Monica and Mary; and his grandson, Oliver Morgan. He was a brilliant and articulate man with a good sense of humor, a subtle and gentle wit, and unbounded understanding and tolerance. He was a prolific reader, an untiring writer, a financial scholar, and an accomplished pianist. He was a truly modest person, although his influence was global; he was a great man who brought honor and glory to his profession. In addition to his great legacy of achievement and honor, he also leaves the enduring affection of all those who were fortunate to have known him, as well as the admiration, respect, and gratitude of the great institution that was so fortunate to benefit from his expertise and that he, in turn, so proudly served.

Transcripts and programs of the Hopkins Memorial Tribute (held at The Johns Hopkins Medical Institutions on May 15, 1986) are available upon request. Memorial contributions may be made to the Russell H. Morgan Memorial Fund, 600 N. Wolfe St., Baltimore, MD 21205.

Martin W. Donner
Olga M. B. Gatewood
*Department of Radiology and
Radiological Science
The Johns Hopkins Hospital
Baltimore, MD 21205*

Book Review

Notes on Radiological Diagnosis. 2nd ed. By Lawrence S.W. Lau and John F. DeCampo. Philadelphia: Saunders, 204 pp., 1985. \$24.95

This book, written specifically as a guide for preparation for the final Diploma of the Royal Australasian College of Radiologists, contains much that is relevant for the American resident who is preparing for the oral section of the American Board of Radiology. It consists principally of gamuts; this book differs from the classic by Reeder and Felson in that the list for each abnormality is less exhaustive and is conveniently arranged in an approximate order of frequency. The book includes gamuts for CT and sonography, yet it is small enough to be carried in one's pocket.

Six organ-system sections are supplemented by separate sections on obstetrics and gynecology, and pediatrics. A few selected flow-charts provide the resident with a rational approach to common problems, such as jaundice, suspected liver metastasis, and first trimester bleeding. The guide also improves on a simple gamut list in that it provides a brief discussion on the pathophysiology of a disease process if that explanation can help one understand the cause and promote recall. Supplemental subsections are inserted on such subjects as the polyposis syndromes, bone tumors according to age group, and cranial CT findings of inflammatory disorders.

Among the limitations of this type of book are the necessary lack of illustrations and a limited bibliography. The absence of explanation

in some instances (e.g., sonography is recommended for evaluation of the acutely traumatized testicle without indicating why the study may be of value to the surgeon) is unfortunate. A mild but vexing problem for the American reader is the use of colloquial abbreviations without definitions. For example, "P/H D.X.R.T. to head and neck" is listed as a risk factor associated with thyroid carcinoma. Presumably the letters stand for "past history of (direct?) X-ray therapy." Finally, the authors imply that memorization of gamut lists is necessary. Although in some instances this will be necessary, I hope that the authors will, in their next edition, include suggestions for recall, such as tissues and organs in an area for the differential diagnosis of a tumor mass, and categories of disease (e.g., congenital, infectious, traumatic, neoplastic) for others.

These minor criticisms aside, this is an excellent little book. It has been well thought out, and it is well indexed and easy to use. I recommend it for radiology residents as a stimulus to supplemental reading during the training period and as a handy last-minute review.

J. H. Arndt
Baylor University Medical Center
Dallas, TX 75246

Dual-Energy Digital Radiographic Quantification of Calcium in Simulated Pulmonary Nodules

Nancy M. Hickey^{1,2}
Loren T. Niklason¹
Eduardo Sabbagh¹
Robert G. Fraser¹
Gary T. Barnes¹

The presence or absence of calcium in solitary pulmonary nodules may indicate whether a nodule is benign or malignant. Because current techniques for measuring the amount of calcium in these nodules are unsatisfactory, a study was carried out to assess the capability of dual-energy digital chest radiography to identify and quantify the calcium content of simulated pulmonary nodules of known calcium content. Measurements were carried out on 280 nodules of various sizes and calcium content that were placed within the lungs of a frozen human-chest phantom. A new calcium quantification technique that uses a parallelogram was developed to eliminate the problem of nodule superimposition over ribs. Nodules containing more than 35 mg of calcium per square centimeter (i.e., 7, 30, 60, and 110 mg of calcium for spherical nodules 0.5, 1.0, 1.5, and 2.0 cm in diameter) were measured with a high degree of accuracy and reasonable precision. Dual-energy digital radiography is a simple and accurate method of measuring the calcium content of solitary pulmonary nodules in humans.

Methods for the detection of calcium in solitary pulmonary nodules have received much attention recently. Many of these nodules are found in asymptomatic patients, and an appreciable percentage are primary carcinomas [1]. In an analysis of 887 resected solitary pulmonary nodules from asymptomatic patients, Steele [2] found prevalences of 60% and 40% for benignancy and malignancy, respectively. In a compilation of five large series consisting of 1711 resected solitary pulmonary nodules, Siegelman et al. [3] reported prevalences of 62% and 38% for benignancy and malignancy, respectively. Noncalcified solitary pulmonary nodules can be either benign or malignant; with rare exceptions, nodules containing calcium are benign. Identification of calcium is therefore an important clinical goal.

Conventional tomograms show calcium within solitary pulmonary nodules more frequently than chest radiographs [4] but may be difficult to interpret, especially when calcium is diffusely distributed. CT is generally accepted as superior to conventional tomography in the identification and analysis of these nodules [5]. However, single-energy CT has inherent problems that limit its usefulness in estimating the calcium content [6]. Zerhouni et al. [7] have developed a phantom technique that minimizes some of these problems, but their approach is still compromised by partial-volume and patient-motion problems; in addition, it does not permit quantification of the calcium content of solitary nodules and is time-consuming. We have investigated the potential of dual-energy digital radiography as a simpler, more accurate technique to quantify calcium content.

Materials and Methods

Apparatus

The study was performed on a prototype scanning slit dual-energy chest unit. Geometric and image parameters are listed in Tables 1 and 2. With the exception of the detector, the geometry and configuration of the unit are essentially identical to those of a previous single-

Received April 17, 1986; accepted after revision July 16, 1986.

Presented at the annual meeting of the American Roentgen Ray Society, Washington, DC, April 1986.

¹ Department of Radiology, University of Alabama at Birmingham, School of Medicine, 619 S. 19th St., Birmingham, AL 35233. Address reprint requests to R. G. Fraser.

² Present address: Department of Radiological Sciences, Ottawa Civic Hospital, 1053 Carling Ave., Ottawa, Ontario, K1Y 4E9, Canada.

AJR 148:19-24, January 1987
0361-803X/87/1481-0019
© American Roentgen Ray Society

TABLE 1: Geometric and System Parameters of Dual-Energy Unit

Parameter	Setting
Source-to-foreslit distance	62.5 cm
Source-to-detector distance	130.8 cm
Foreslit width	0.38 mm
Aftslit width	2.5 mm
Focal spot size (horizontal and vertical)	1.7 × 0.9 mm
Beam width—FWHM per detector	0.77 mm
Front detector	107 mg/cm ² ; Y ₂ O ₂ S
Rear detector	110 mg/cm ² ; Gd ₂ O ₂ S
Scan technique	140 kVp, 110 mA
Scan time	4.9 sec
Effective exposure time	8.8 msec
Entrance skin exposure	17 mR

Note.—FWHM = full width at half-maximum intensity.

TABLE 2: Image Parameters of Dual-Energy Unit

Parameter	Setting
Field size	46 × 46 cm
Matrix	1024 × 1024
Pixel size	0.45 mm
Matrix resolution	1.1 lp/mm
Gray scale	4096 shades (12 bits)
Images per scan	3
Patient magnification	1.1–1.4×
Midplane resolution (1.2×	1.4 lp/mm

energy unit [8]. The linear detector array used is based on a concept described by Barnes et al. [9] and consists of a low-atomic-number/high-atomic-number phosphor (and photodiode) sandwich of 1024 front and 1024 back elements (Fig. 1). The X-ray beam emerging from the patient passes through the front and back sections sequentially: The low-atomic-number front section preferentially absorbs the lower energy X-rays and in so doing hardens the X-ray beam incident on and absorbed by the high-atomic-number back section. The low- and high-energy images thus obtained are processed by using the approach described by Lehmann et al. [10] to obtain soft-tissue (bone cancelled) and bone (soft-tissue cancelled) images. The advantage of the sandwich-detector approach to dual-energy imaging is that simultaneous acquisition of the two images eliminates misregistration due to patient motion.

Image Acquisition and Viewing

To determine the accuracy of dual-energy subtraction in predicting calcium content of pulmonary nodules, we designed a phantom study that permitted comparison of predicted vs known amounts of calcium in simulated nodules. A frozen, unembalmed human-chest phantom (Fig. 2), prepared according to the method of Littleton [11], was used to create a realistic radiation environment. The phantom was bivalved along a coronal plane, and 20 hemispheric excavations (0.5, 1.0, and 1.5 cm in diameter) were cut in the frozen lung surface to avoid compression of adjacent lung tissue. When the two halves of the phantom were brought together, the two hemispheric excavations produced a spherical hole of the same diameter. The phantom could be opened and securely closed by using three fiberglass rods, one placed in each shoulder and one placed in the lower abdomen above the umbilicus.

The simulated pulmonary nodules consisted of wax spheres measuring 0.5, 1.0 and 1.6 cm in diameter. Each contained a known and

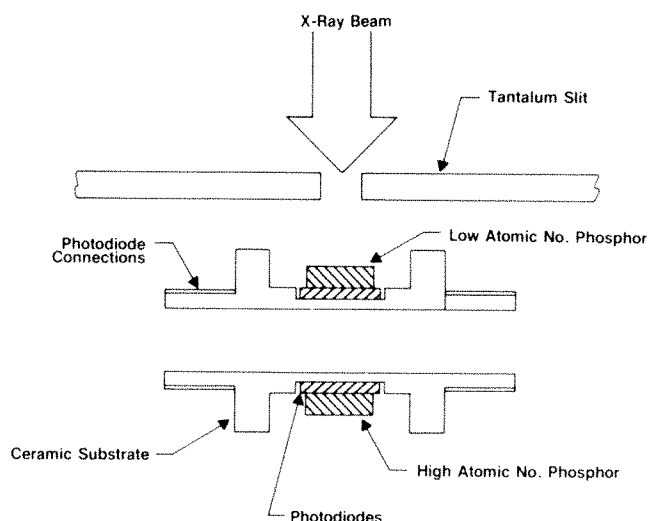


Fig. 1.—Detector scheme. Each detector element consists of a low- and a high-atomic-number detector sandwich that permits simultaneous detection of low- and high-energy information.

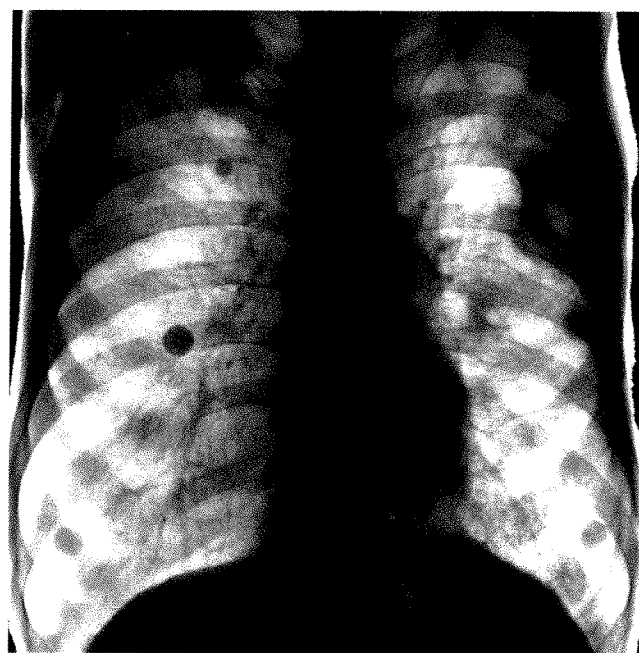


Fig. 2.—Conventional digital image of frozen human chest phantom with wax nodules of various calcium content placed in lungs.

uniformly distributed amount of calcium hydroxide. The calcium content (as calcium hydroxide) ranged from 0 to 658 mg; seven levels were used for the 1.0- and 1.6-cm nodules and two levels for the 5-mm nodules. The nodules were placed in the lungs of the human-chest phantom by one of the authors not involved in interpreting the images, and 15 images were obtained with normal dual-energy operating techniques (see Table 1). In each image, approximately 10 of the 20 nodule locations were used, and the calcium content and location of nodules were changed from image to image. Nodule locations and calcium content were noted on a drawing of the lung outline and no nodules projected over the mediastinum.

Three viewers interpreted the images independently. Each scan

(or phantom exposure) produced three images (a conventional digital image, a bone image, and a soft-tissue image), and the viewers were allowed to view all three on the console simultaneously or separately, along with bone and soft-tissue hard copies made with a laser imager (3M Co., Minneapolis, MN). In each case the nodule locations were known, and, as described in the following, zoomed bone images (i.e., ¼ of the image displayed at full pixel resolution) were used to quantify calcium content.

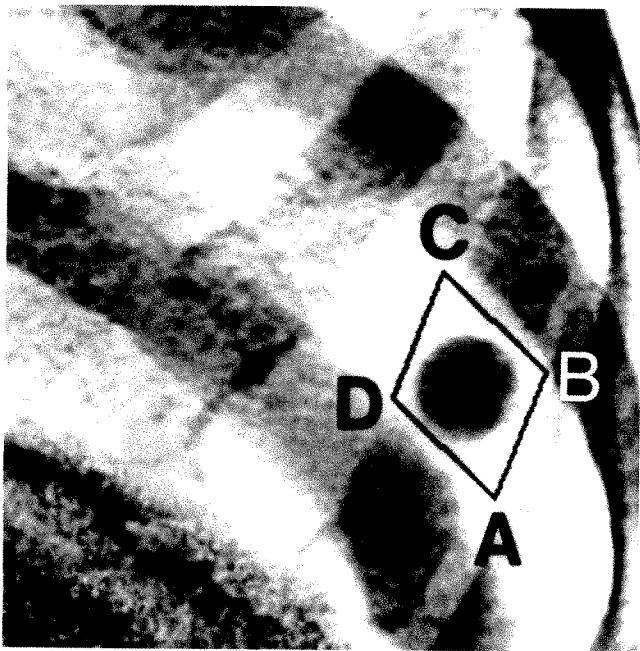


Fig. 3.—Bone image of human chest phantom's left lower zone with parallelogram used for calcium quantification positioned around a nodule. Three corners of the parallelogram (A, B, C) are selected by viewer; fourth corner (D) and sides are completed by computer. Points A and B determine base of parallelogram. For each pixel position along the base, computer determines and sums values of a row of pixels parallel to sides AD and BC.

Calcium Quantification

Calibration of the bone image's pixel values was necessary before the calcium content of the nodules could be assessed. This was accomplished with a calcium step wedge fabricated by machining six square holes (32 × 32 mm) of different depths (2.11, 3.17, 4.75, 7.13, 10.7, and 16.1 mm) in a 2.8-cm thick Lucite block. The holes were filled with a mixture of calcium hydroxide and paraffin wax (calcium hydroxide concentration, 350 mg/cm³) to obtain the calcium steps. Lucite, calcium hydroxide, and paraffin wax were selected as wedge materials so that the only high-atomic-number (bone-equivalent) component of each step was a known amount of calcium.

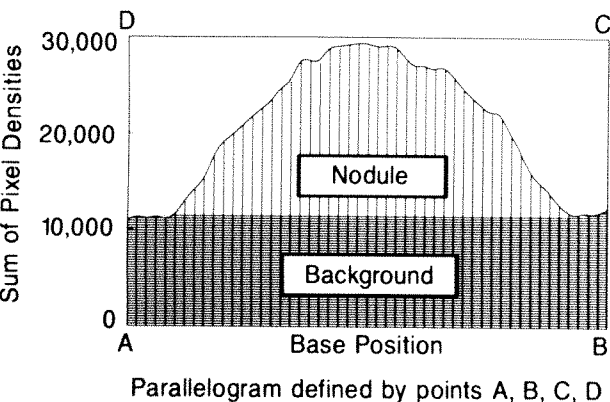
To simulate the attenuation effects of the lung, we imaged the calcium calibration wedge along with a 7.6-cm thickness of Lucite. Linear regression analysis was applied to the mean bone-image pixel number vs the known amount (mg/cm²) of calcium in the six steps to determine a value for the amount of calcium (mg/cm²) per unit pixel count (K_{cal}). By using K_{cal} , the calcium mass of an imaged nodule (M_{Ca}) can be determined from the expressions

$$M_{Ca} = P_{av} \times K_{cal} \times A_{obj} \tag{1}$$

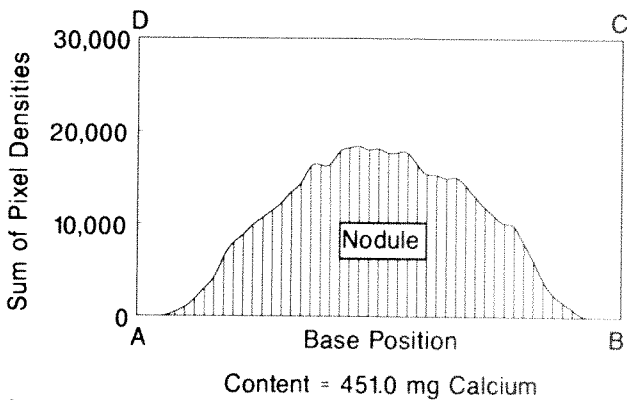
$$= P_{av} \times K_{cal} \times (A_{im}/M^2) \tag{2}$$

where P_{av} is the average pixel value of the imaged nodule, A_{obj} and A_{im} are the projected areas of the nodule in the object and image planes, respectively, and M is the magnification factor with which the nodule is imaged. In clinical situations, A_{obj} is not known, and it is necessary to use equation 2. For this reason, equation 2 was used in this study, and values for P_{av} and A_{im} were obtained from the image data. M was estimated from our knowledge of the imaging geometry.

On images of the human-chest phantom, nodules usually were projected over ribs, thus creating difficulties in quantifying calcium content of nodules because of superimposition. To address this problem, an algorithm was developed by Sones et al. in which a parallelogram is placed around the nodule (Fig. 3). (Sones RA, Lauro KL, Tesic MM, Barnes GT. Substance quantification in animal bodies. U.S. patent application filed November 15, 1985.) Three corners of the parallelogram (A, B, and C) are selected by the viewer; the fourth corner (D) and sides are completed by the computer. A two-dimensional array (matrix) of pixel values are defined by the parallelogram: Pixels A and B define the rows, and pixels B and C define the columns. Each column is summed, and a histogram of the resultant



A



B

Fig. 4.—Plot of computer printout of row sums for pixel locations along base of a parallelogram. Parallelogram is selected to obtain a uniform background across the nodule so that on either side summed values correspond to background only. Subtracting background results in a value that represents nodule contribution only.

- A, Background plus nodule.
- 3, Background subtracted.

P 24,443

values is plotted (Fig. 4A). If the parallelogram is larger than the nodule and selected so that sides AD and BC are parallel to the rib, the plotted values have contributions both from the chest phantom alone and from the chest phantom plus the nodule. The background associated with the chest phantom alone is selected by the viewer and subtracted, leaving only the contribution for the nodule (Fig. 4B). Using the number of pixels in a column, the average value of the pixels, and the background pixel value, the computer determines the number of pixels in the column that have a nodule contribution. This is repeated for each column to determine the total number of pixels (A_{im}) associated with the imaged nodule. P_{av} is also determined, and equation 2 is used to determine the amount of calcium in the nodule.

Difficulties arose when a nodule was projected in a location unsuitable for uniform background subtraction, such as over two crossing ribs. In this event, a split-cursor technique was used that permitted quantification of individual parts of a nodule. The two measurements were then added to estimate the total calcium content of the nodule. This problem could be eliminated in a clinical setting by obtaining additional oblique views on which a nodule would be projected in a more favorable location (e.g., in an interspace or over a single rib).

Results

Calibration data for the calcium step wedge are plotted in Fig. 5 along with the linear regression line fit. This figure demonstrates an impressive, almost perfect, linear correlation between calcium concentration and mean pixel value: The correlation coefficient for the fit is .9985, and the value for K_{cal} is 0.498 mg/cm² per pixel count. The results of the quantification of 280 nodules are summarized in Table 3, including the average and standard deviation for each size and calcium content of each nodule. Each of the 16 different nodules was quantified by the three readers 12 to 22 times (mean, 17.5). The two major sources of variability in the measured values were nodule location and differences in background; inter- and intraobserver standard deviations were typically 1/3 of the standard deviations listed in Table 3.

The data are presented somewhat differently in Fig. 6, in which the average measured and known amount of nodule calcium per unit area is plotted along with the standard deviation of the measurements. The differences between the

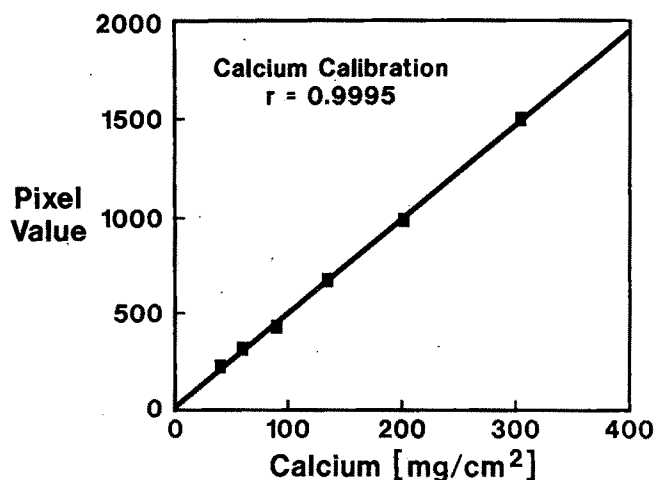


Fig. 5.—Plot of calibration data for calcium step wedge.

TABLE 3: Dual-Energy Digital Radiographic Quantification of Calcium in Simulated Pulmonary Nodules

0.5-cm Nodules		1.0-cm Nodules		1.6-cm Nodules	
Actual	Measured (Mean ± SD)	Actual	Measured (Mean ± SD)	Actual	Measured (Mean ± SD)
		0	3.7 ± 11	0	0 ± 0
		17.8	8.7 ± 13	78	47.1 ± 31
		29.6	31.0 ± 36	138	128 ± 38
		40.2	26.6 ± 14	191	161 ± 34
		67.7	65.2 ± 21	294	294 ± 51
11.0	12.6 ± 30	102	99.0 ± 20	448	448 ± 34
16.3	18.3 ± 5.3	142	142 ± 37	658	671 ± 124

Note.—Numbers = milligrams of calcium. $n = 16$ nodules. Each row corresponds to simulated nodules made from the same mixture of calcium hydroxide and paraffin. SD = standard deviation.

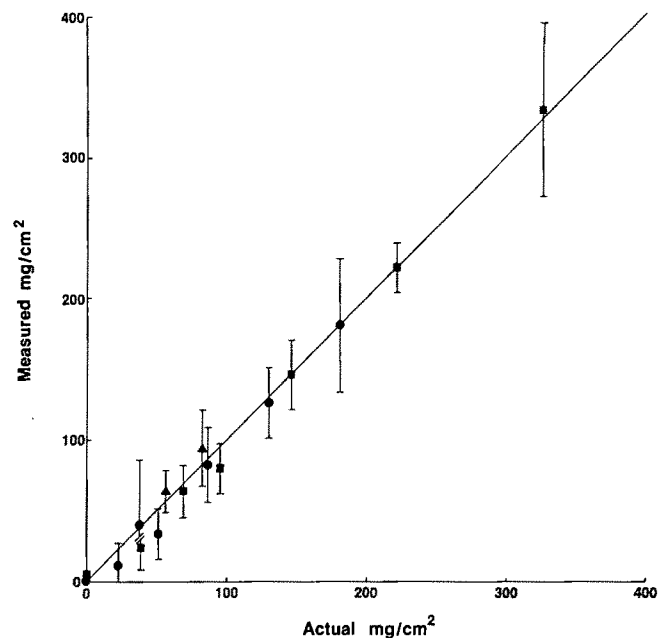


Fig. 6.—Plot of the measured vs known calcium concentration of projected nodules. Bars show standard deviations. Triangles = 0.5-cm diameter nodules; circles = 1.0-cm diameter nodules; squares = 1.6-cm diameter nodules.

averages of measured and known projected calcium concentrations range from -17.3 to 10.2, with a root mean square difference of 8.3 mg/cm². As expected, the differences are larger at the lower concentrations when expressed relative to the known concentrations. Also, the relative standard deviations of the measurements are larger at the lower concentrations, ranging from 150% to 50% for calcium concentrations from 23 to 51 mg/cm². For calcium concentrations of 56 mg/cm² or greater, the relative standard deviations are 30% or less; for concentrations greater than 100 mg/cm², the measured precision is typically 20% or less.

Discussion

Inspection of Table 3 and Fig. 6 shows that quantification of the calcium content of 280 pulmonary nodules by three

readers resulted in a measured calcium content that correlated extremely well with actual calcium content. Fig. 6 also indicates that the measurement accuracy (percentage difference between the measured and known calcium content) and precision (percentage standard deviation of the measurements) were not dependent on the size of the nodules but on the projected calcium concentration (i.e., mg/cm²).

All nodules containing calcium concentrations higher than 35 mg/cm² were identifiable on the bone images. Their appearance ranged from very opaque (high levels of calcium) to faintly opaque (low levels of calcium). A discrepancy arose in our measurement of the calcium content (3.7 mg) of 1.0-cm nodules that actually contained no calcium. These nodules were not visible on the bone image, and an attempt was made to quantify calcium content by positioning a cursor on the bone image by using landmarks from the soft-tissue image (on which the nodules were clearly seen). This was done to discover whether quantification was more sensitive than the human eye in detecting the presence of calcification. We found that a variation in the background of the chest phantom produced a "pseudonodule" computer printout, and we concluded that if calcification was definitely not visible on the bone image, an attempt at quantification was futile.

What is the minimal detectable quantity of calcium within a pulmonary nodule? Inspection of Fig. 6 shows that the measurement accuracy and precision is poor for projected calcium concentrations of 35 mg/cm² or less, a lower limit that corresponds to a calcium content of 7, 30, 60, and 110 mg for spherical nodules that are 0.6, 1.0, 1.5, and 2.0 cm in diameter, respectively. Our results also suggest that the clinical determination of whether a nodule is calcified depends on the projected concentration rather than on the actual amount of calcium in the nodule. For example, a 0.5-cm nodule containing 20 mg of calcium would be called calcified, whereas a 1.5-cm nodule containing the same amount of calcium would

not. Also, on the soft-tissue images, calcified nodules were less visible than noncalcified nodules of the same size.

For a clinical perspective of these data, a study of 61 patients with pulmonary nodules [6] compared the dual-energy technique to other currently available techniques (CT, linear tomography, and conventional chest radiography). Two of the 61 patients had nodules that were questionably calcified on conventional radiographs and tomograms but contained 346 mg and 266 mg of calcium by dual-energy quantification (one of these two had a CT that showed that the lesion was definitely calcified). At the insistence of both patients, these two nodules were resected and on chemical analysis were shown to contain 328 mg and 275 mg of calcium, respectively. Conversely, the calcium content of resected carcinomas was very low, approximating the calcium content of each patient's normal lung parenchyma in milligrams per gram and ranging on average from 1.1 to 6.4 mg, depending on tumor weight. In no instance was calcium detected within a neoplasm by the dual-energy technique. However, rarely a bronchogenic carcinoma contains sufficient calcium to be radiographically demonstrable, at least with CT. In this instance, visual assessment of the pattern of calcification rather than actual calcium content might distinguish a benign from a malignant nodule, but this theory has not been tested.

Current single-energy CT methods use Hounsfield units to determine the density of nodules, hence inferring the presence or absence of calcium. This necessitates the development of a range of values with a specified threshold above which a lesion is considered calcified. This method of assessment is quite different from that of dual-energy subtraction in which calcium is either present or not present as determined visually on a cathode ray tube monitor (Fig. 7). If calcium is identified, it can be quantified; if calcium is not evident, quantification is not necessary. In a clinical setting, it is not yet known whether quantification will be necessary to confirm benignity once

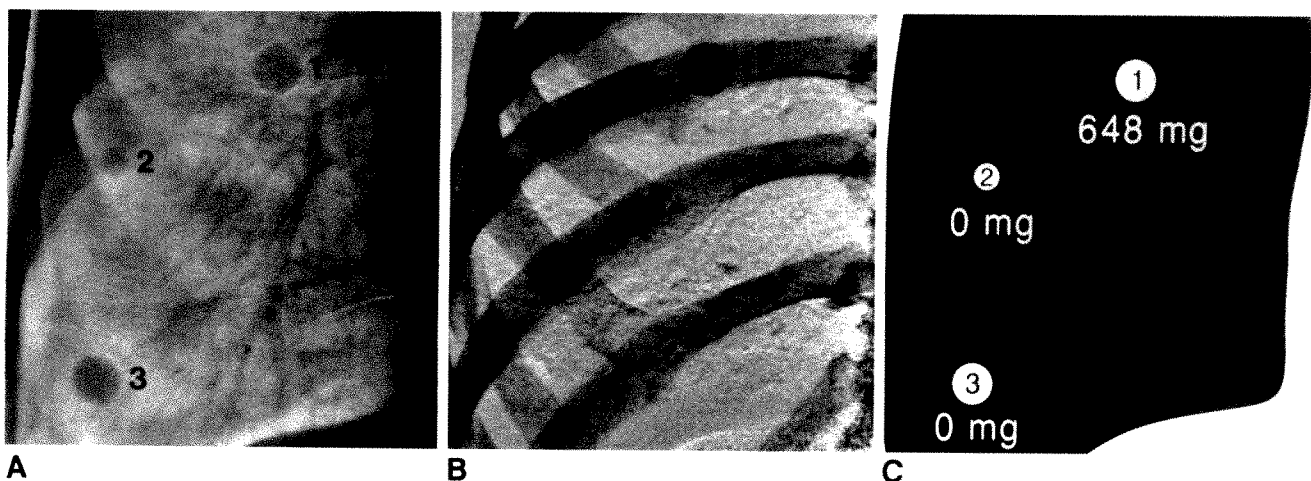


Fig. 7.—Demonstration of visual method of assessing calcium content of pulmonary nodules.

A, Soft-tissue image of the chest phantom's right lower zone shows three nodules. Although nodules 1 and 3 are the same size, the latter is denser because it contains more wax per unit volume, suggesting that

nodule 1 must contain calcium.

B, Bone image of same section of chest phantom's right lower lung shows nodule 1 clearly because nodule contains calcium. Nodules 2 and 3 cannot be identified and thus contain no calcium.

C, Diagram shows calcium content of simulated nodules.

calcification has been shown within a lesion. However, initial results from the clinical study [6] suggested that visual assessment alone was sufficient in most instances. It remains to be shown whether low levels of calcium within neoplasms are detectable by the dual-energy technique; if so, it may be necessary to quantify calcium content of many nodules to establish a threshold value above which a nodule is considered benign and below which a nodule must be regarded as indeterminate.

The most difficult aspect of accurate calcium quantification is subtraction of background. We have found the parallelogram technique more accurate than an alternative technique that used two square cursors, one to measure calcium content of a similar area of background nearby (enabling background to be subtracted). The variability of the human chest makes it difficult to find two locations with perfectly matched backgrounds.

The results of this study indicate that dual-energy digital chest radiography is a sensitive and accurate method of identifying and quantifying the calcium content of pulmonary nodules and thus provides a useful criterion for distinguishing benign from malignant lesions. Although CT is accurate in detecting the presence of calcium, particularly if the phantom technique [7] is used, the comparative accuracy of CT and dual-energy digital radiography for this purpose has not been tested and needs to be established. Of practical importance, accuracy of the dual-energy technique is achieved with one

modest radiation exposure (10–20 mR—or 2.58–5.16 $\mu\text{C/kg}$) and takes no more time than that required to perform a routine examination on a dedicated chest unit.

REFERENCES

1. Good CA. The solitary pulmonary nodule: a problem of management. *Radiol Clin North Am* 1963;1:429–438
2. Steele JD. The solitary pulmonary nodule: report of a cooperative study of resected asymptomatic solitary pulmonary nodules in males. *J Thorac Cardiovasc Surg* 1963;46:21–39
3. Siegelman SS, Khouri NF, Scott WW, Leo FP, Zerhouni EA. Computed tomography of the solitary pulmonary nodule. *Semin Roentgenol* 1984;19:165–172
4. Rigler LG, Heitzman ER. Plainigraphy in the differential diagnosis of the pulmonary nodule. *Radiology* 1955;65:692–702
5. Muhm JR, Brown LR, Crowe JK. Use of computed tomography in the detection of pulmonary nodules. *Mayo Clin Proc* 1977;52:345–348
6. Fraser RG, Hickey NM, Niklason LT, Sabbagh EA, Luna RF, Barnes GT. Dual-energy digital radiography in the detection of calcification in pulmonary nodules. *Radiology*, in press
7. Zerhouni EA, Boukadoom M, Siddiky MA, et al. A standard phantom for quantitative CT analysis of pulmonary nodules. *Radiology* 1983;149:767–773
8. Tesic MM, Mattson RA, Barnes GT, Sones RA, Stickney JB. Digital radiography of the chest: design features and considerations for a prototype unit. *Radiology* 1983;148:259–264
9. Barnes GT, Sones RA, Tesic MM, Morgan DR, Sanders JN. Detector for dual-energy digital radiography. *Radiology* 1985;156:537–540
10. Lehmann LA, Alvarez RE, Macovski A, Brody WR. Generalized image constructions in dual kVp digital radiography. *Med Phys* 1981;5:659–667
11. Littleton J. The human chest phantom. *Radiology* 1982;145:829–831

Kaposi's Sarcoma of the Lung in AIDS: Radiologic-Pathologic Analysis

Carlos J. Sivit¹
 Arnold M. Schwartz²
 S. David Rockoff¹

Kaposi's sarcoma in patients with AIDS involves the lung more often than it does in the African form of the neoplasm. This article describes the radiographic and histologic features in nine cases of pulmonary Kaposi's sarcoma, uncomplicated by infection, and reviews the radiographic descriptions of 22 similar cases from the literature. Pulmonary parenchymal disease in reported cases and in this series was usually diffuse. Three cases had localized disease. In one of these cases, the localized disease was segmental while in the other two cases, the disease involved a single entire lobe. Hilar adenopathy was noted in three of 22 cases in the literature and in three of nine cases in this series. Pleural effusion was noted in eight of 22 cases in the literature and in three of the nine cases in the current series. Histologic examination of the lung from patients whose radiographs showed predominantly nodular lesions revealed a prevalence of nodules composed of prominent spindle cells with atypical mitotic figures in the nuclei. However, patients having a linear pattern on radiographs showed predominantly thickened interstitium characterized by invasive angiomatous proliferation of irregular slitlike vessels with atypical endothelial cells. The results of this study indicate that in AIDS patients with Kaposi's sarcoma of the lungs, uncomplicated by infection, two distinctive radiographic appearances of the lesions occur and that these two apparently different lesions can be explained by two types of histologic findings that correspond well with the radiographic features.

Kaposi's sarcoma occurs in 35% of patients with AIDS [1]. The tumor is an aggressive, multicentric lesion that usually involves the skin, lymph nodes, and abdominal viscera. The radiographic appearance of Kaposi's sarcoma of the lung, uncomplicated by opportunistic infections, has previously been reported in 22 cases [1-9]. The frequency of pulmonary involvement with Kaposi's sarcoma is uncertain, because definitive diagnosis requires lung biopsy. In addition, other pulmonary complications of AIDS, such as opportunistic infections, often mask the findings of pulmonary Kaposi's sarcoma.

We studied the radiologic features in nine cases of biopsy-proven pulmonary Kaposi's sarcoma that occurred in the absence of a concurrent infection and compared the findings with similar cases reported in the literature. Also, we studied the pathologic material derived from the lungs to determine the histologic basis for the radiographic patterns observed.

Materials and Methods

A retrospective examination of the surgical pathology records of all AIDS patients, as defined by the Centers for Disease Control [10, 11], with Kaposi's sarcoma of the lung seen at The George Washington University Hospital between September 1981 and July 1985 was performed. The pathologic specimens had been obtained either by transbronchial biopsy or by open-lung biopsy. Bacterial, fungal, mycobacterial, and viral stains and cultures were obtained on all specimens. Patients with evidence of a concurrent bacterial or opportunistic infection at the time of the diagnostic biopsy were excluded. Patients who had been previously

Received February 11, 1986; accepted after revision August 13, 1986.

¹ Department of Radiology, The George Washington University Hospital, 901 23rd St. N.W., Washington, DC 20037. Address reprint requests to S. D. Rockoff.

² Department of Pathology, The George Washington University Medical Center, 901 23rd St. N.W., Washington, DC 20037.

AJR 148:25-28, January 1987
 0361-803X/87/1481-0025
 © American Roentgen Ray Society

diagnosed to have Kaposi's sarcoma of the lung at an outside institution were also excluded from the study.

The histologic material was reviewed and the predominant radiographic and histologic findings were compared on a case-by-case basis. Kaposi's sarcoma without infection was found in 13 biopsies (two transbronchial and 11 open lung) in nine patients. Attempts were made to take the biopsies from the areas of maximum radiographically evident disease. Seven of the nine patients had involvement of other organs at the time of lung biopsy, while the other two subsequently developed extrapulmonary involvement during the course of their illness.

The chest radiographs made immediately before the first lung-biopsy procedure were analyzed in each case. Although some of the patients required more than one biopsy for diagnosis, only the radiograph preceding the first biopsy was used in order to exclude the effect the biopsies might have on the subsequent radiographic appearance. Patterns of parenchymal involvement were characterized and the presence of hilar adenopathy and pleural effusions were noted.

We also tabulated all AIDS patients with Kaposi's sarcoma of the lung, described as being uncomplicated by infection, reported in the literature between 1981 and 1985. This review yielded descriptions of the chest radiographic features in 22 cases contained in nine reports [1-9].

Results

An analysis of the radiographic findings in 31 patients, nine from our institution and 22 reported in the literature presented the following findings.

Pulmonary Parenchymal Disease

The lung disease present was categorized as "localized," meaning a single focus in one lobe or less, or as "diffuse," defined as pulmonary involvement in excess of that designated as localized. In six of the nine cases, parenchymal

disease was considered to be diffuse. In the analysis of the radiographic patterns, it was noted that two types of patterns were evident; predominantly *linear* densities and predominantly *nodular* densities. Diffuse *linear* densities were noted in four patients (Fig. 1). Three of these had a patchy, nonhomogenous pattern with localized lobar or segmental areas of consolidation. In one, the densities were more prominent in the perihilar region. Diffuse *nodular* lesions were noted in two of our patients (Fig. 2). In both, poorly margined nodular densities of varying sizes, with a tendency to coalesce, were noted. In no cases were both nodular and linear lesions prominent in the same patient.

Two patients presented initially with localized disease. One had sparse, bilateral, lower-lobe, nodular densities with localized segmental right-lower-lobe consolidation. The other had localized, segmental, right-lower-lobe consolidation alone. In four of the five cases with lobar or segmental disease, additional parenchymal disease was noted and no evidence of volume loss was seen. One patient had no parenchymal abnormalities, although Kaposi's sarcoma was shown on biopsy.

Of the cases reviewed from the literature and in the present series, parenchymal involvement was noted in 30 of the 31 patients. The extent of the parenchymal disease was considered diffuse or multifocal in 28 of the 30 patients—all 22 cases reported in the literature and six of our nine cases. Lesions were considered to be "diffuse" in our patients if they were bilateral and involved more than one lobe on each side. For the cases from the literature, the term diffuse was accepted descriptively but was never defined explicitly. In 14 of the 22 from the literature, a specific radiographic pattern was not characterized [1, 9]. In the remaining eight cases, nodular densities were noted in seven [3-8] and linear interstitial

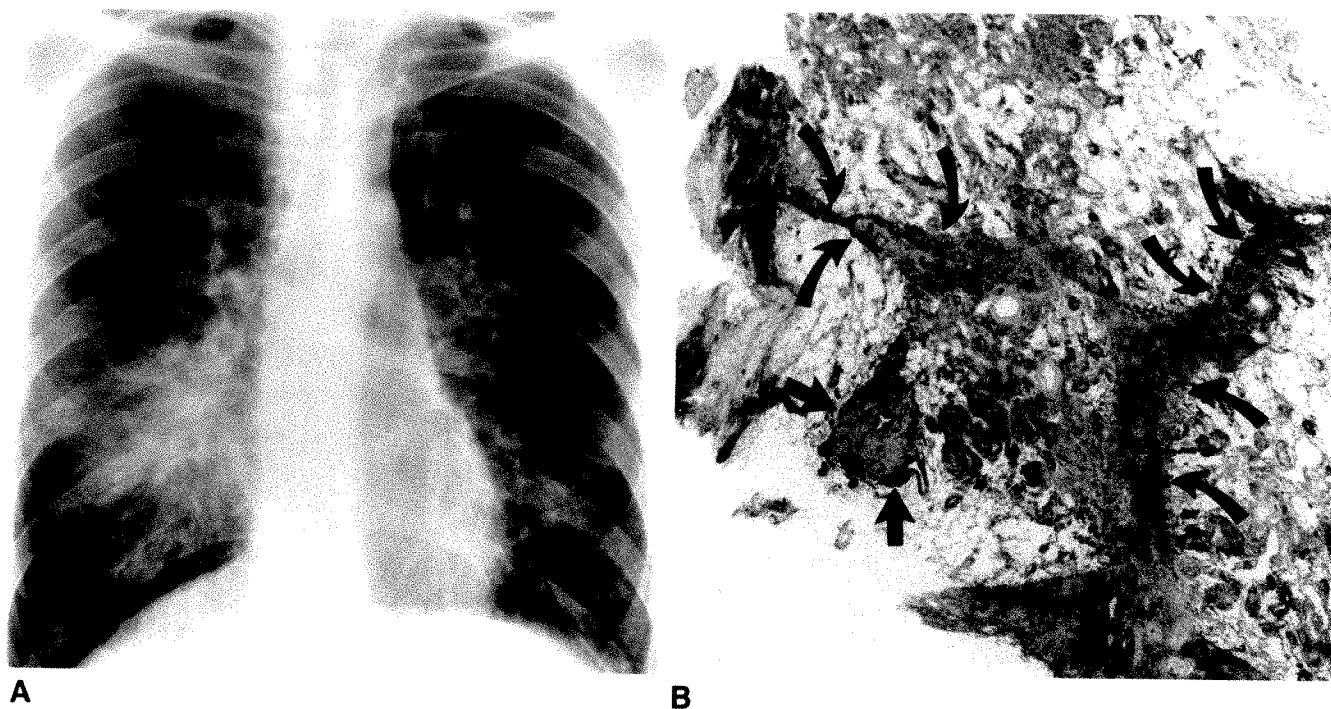


Fig. 1.—Radiographic-pathologic correlation in AIDS patients with Kaposi's sarcoma, uncomplicated by infection, showing linear pattern.

A, Radiograph showing diffuse linear interstitial parenchymal disease in Kaposi's sarcoma including right-middle-lobe coalescence.

B, Histologic section shows nodular infiltration of Kaposi's sarcoma (straight arrows) with adjacent interstitial and alveolar pneumonitis (curved arrows). Note slitlike angiomatous and dense fibroblastic stromal patterns within interstitium (H and E $\times 25$).

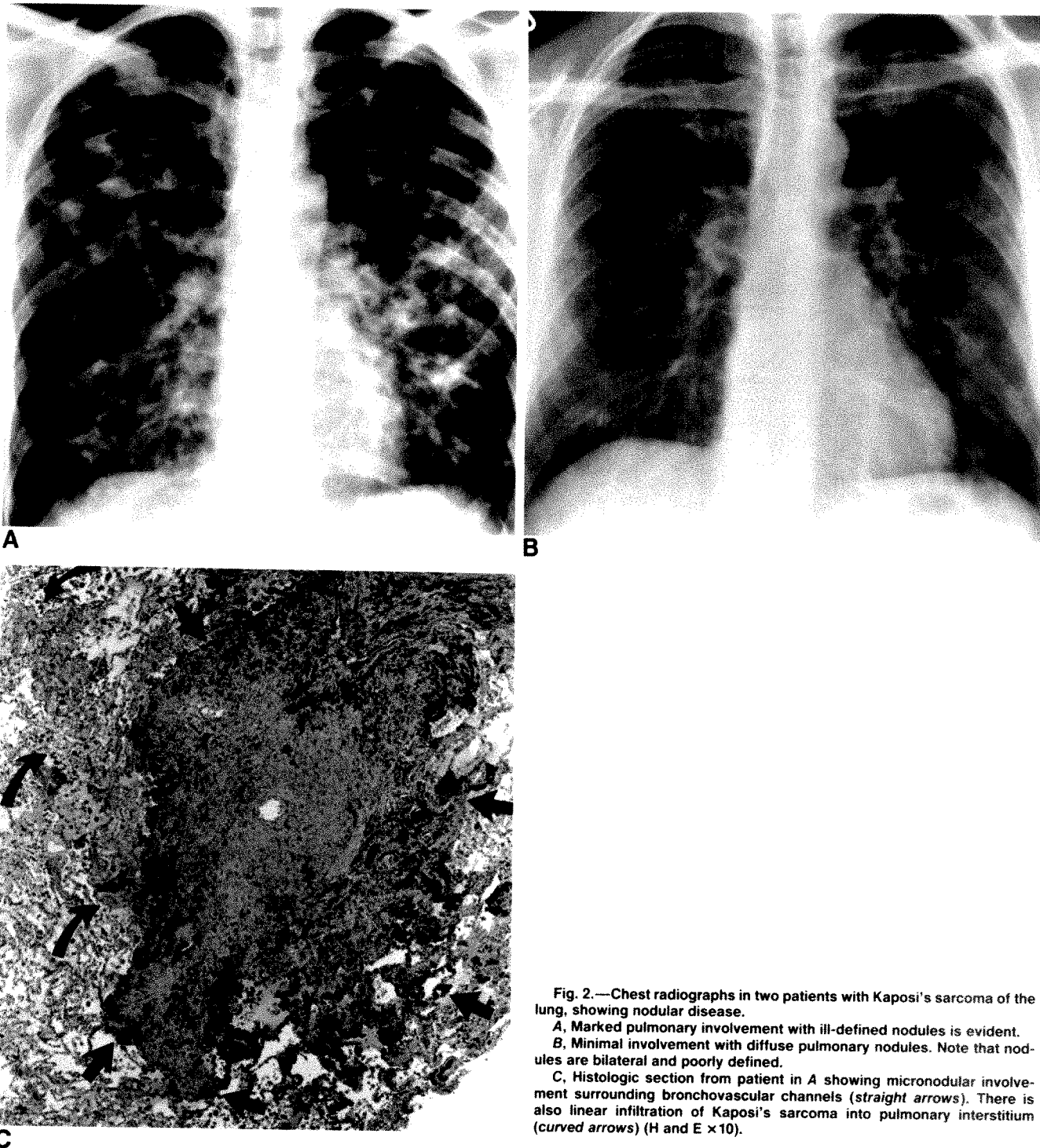


Fig. 2.—Chest radiographs in two patients with Kaposi's sarcoma of the lung, showing nodular disease.
 A, Marked pulmonary involvement with ill-defined nodules is evident.
 B, Minimal involvement with diffuse pulmonary nodules. Note that nodules are bilateral and poorly defined.
 C, Histologic section from patient in A showing micronodular involvement surrounding bronchovascular channels (straight arrows). There is also linear infiltration of Kaposi's sarcoma into pulmonary interstitium (curved arrows) (H and E $\times 10$).

densities were described in one [2]. Lobar or segmental consolidations were not described in the literature.

Pleural Effusions

Pleural effusions were described in eight cases from the literature [1, 9] and were observed in three current patients, always in association with parenchymal disease. In two of our cases, small unilateral collections were noted. Thoracentesis was not performed on these patients. In the third case a large, rapidly developing, unilateral effusion was seen. Thor-

acentesis in this case revealed hemorrhagic fluid. In one report of four patients with pleural effusions, thoracentesis revealed hemorrhagic fluid in all [1].

Hilar Adenopathy

Hilar adenopathy was described in three of the 22 cases from the literature [2, 5] and in three of our nine patients (always in association with pulmonary parenchymal disease) (Fig. 2B). Of the three cases of hilar adenopathy in our series, two were bilateral and one was unilateral. The degree of

adenopathy was considered marked in all three. All of our cases of adenopathy had lung disease, and one had a pleural effusion on the same side as the unilateral adenopathy (i.e., the right side). Follow-up in these three patients ranged from 6 to 15 months without evidence of lymphoma.

Pathology and Radiographic Comparison

The gross and microscopic patterns consisted of linear or nodular infiltration. The linear infiltration was characterized by an expansion of the pulmonary interstitium caused by an invasive angiomatous proliferation of irregular slitlike vessels with atypical endothelial cells. The nodular lesions were composed of prominent fascicles of spindle cells with atypical nuclei mitotic figures and pleomorphism. Comparison of the histologic findings and the radiographic observations showed that the patients with radiographic findings of nodular lesions had histologic findings of nodular lesions with characteristic spindle-cell features (Fig. 2), while those patients whose radiographic pulmonary lesions were mainly of the linear type had histologic patterns characterized by invasive angiomatous interstitial infiltrations (Fig. 1).

Discussion

Kaposi's sarcoma in patients with AIDS is an aggressive, multicentric neoplasm that frequently involves the visceral organs. The incidence of thoracic involvement is uncertain, but it appears to be far more common than in the African form of the neoplasm [10]. In those cases the chest radiographs are normal and even when systemic involvement occurs, the most common pulmonary abnormality in adults is hilar and mediastinal adenopathy [11].

In cases of AIDS-related Kaposi's sarcoma reported in the literature and in our nine cases, two patterns of diffuse disease are seen; poorly marginated nodular-appearing densities and linear interstitial densities [12, 13]. Although parenchymal disease is usually diffuse, in our patients the densities were often patchy and irregular in their distribution, and lobar or segmental areas of consolidation were often noted. In two of our patients, only localized parenchymal disease was noted. We could find no cases reported in the literature with this appearance.

One of our patients with biopsy-proven Kaposi's sarcoma of the lung had a normal chest radiograph. A biopsy had been performed because of the diagnosis of AIDS and because of pulmonary symptoms suggesting the possibility of a pulmonary infection. In this case, the interstitial involvement with Kaposi's sarcoma was shown to be still microscopic.

The hilar adenopathy that was seen was unilateral or bilateral. Its presence is not surprising since lymphatic involvement in Kaposi's sarcoma is common [13, 14]. Pleural effusions also were fairly common and explainable by the fact that pleural involvement has been noted postmortem. Hemorrhagic effusions are consistent with the observation that areas

of pulmonary hemorrhage are commonly seen on histopathologic examination [12].

Follow-up was available in five of the nine patients over a period of 3–15 months after the first diagnosis of Kaposi's sarcoma. Four of the five patients subsequently developed opportunistic infections as documented by diagnostic lung biopsy or postmortem examination. All of these had *Pneumocystis carinii* pneumonia and one had, in addition, infection with *Mycobacterium intracellulare-avium*. The interval between the first diagnosis of Kaposi's sarcoma involving the lung and documentation of opportunistic infection ranged from 2 to 15 months.

Pathologic assessment of lung tissue in patients with AIDS and Kaposi's sarcoma involving the lung reveals characteristic findings that explain the various pulmonary abnormalities seen radiographically. Interstitial linear and nodular accumulations of spindle cells that form vascular slits containing erythrocytes are noted and areas of fresh pulmonary hemorrhage are common [12, 13]. The pattern of involvement varies from multifocal interstitial infiltrates involving the pulmonary interstitium, bronchovascular sheaths, interlobular septa, and pleura to nodular masses obliterating the underlying pulmonary tissue. The predominant distribution of Kaposi's sarcoma is along a lymphatic route. Pathologically, lymph-node involvement is common and pleural-space involvement causing lymphatic obstruction has also been reported [9, 13, 14].

REFERENCES

- Ognibene FP, Steis RG, Macher AM. Kaposi's sarcoma causing pulmonary infiltrates and respiratory failure in the acquired immunodeficiency syndrome. *Ann Intern Med* 1985;102:471–475
- Brown KJ, Huberman RP, Vanley G. Pulmonary features of Kaposi's sarcoma. *AJR* 1982;139:659–660
- Hill CA, Harle TS, Mansell PW. The prodrome, Kaposi sarcoma, and infections associated with acquired immunodeficiency syndrome: radiographic findings in 39 patients. *Radiology* 1983;149:393–399
- Epstein DM, Geffer WB, Conrad K, Kelley MA, Miller WT. Lung disease in homosexual men. *Radiology* 1982;143:7–10
- McCauley DI, Naidich DP, Leitman BS, Reed DL, Laubenstein L. Radiographic patterns of opportunistic lung infections and Kaposi sarcoma in homosexual men. *AJR* 1982;139:653–658
- Misra DP, Sunderrajan EV, Hurst DJ, Maltby JD. Kaposi's sarcoma of the lung: radiography and pathology. *Thorax* 1982;37:155–156
- Kornfeld H, Axelrod JL. Pulmonary presentation of Kaposi's sarcoma in a homosexual patient. *Am Rev Respir Dis* 1983;127:248–249
- Friedman-Kien AE, Laubenstein LJ, Rubinstein P, et al. Disseminated Kaposi's sarcoma in homosexual men. *Ann Intern Med* 1982;96:693–700
- Stovber DE, White DA, Romano PA, Gellene RA, Robeson WA. Spectrum of pulmonary diseases associated with the acquired immunodeficiency syndrome. *Am J Med* 1985;78:429–437
- Mann SG. Kaposi's sarcoma. *AJR* 1974;121:793–800
- Palmer PES. The radiological changes of Kaposi's sarcoma. *Int J Cancer* 1962;18:87–91
- Nash G, Fligiel S. Pathologic features of the lung in the acquired immunodeficiency syndrome: an autopsy study of seventeen homosexual males. *Am J Clin Pathol* 1984;81:6–12
- Millar PR. AIDS: Histopathological aspects. *J Pathol* 1984;143:223–239
- Guarda LA, Luna MA, Smith JL, Mansell PWA. Acquired immunodeficiency syndrome: postmortem findings. *Am J Clin Pathol* 1984;81:549–557

Case Report

Dystrophic Calcification in Carcinoma of the Lung: Demonstration by CT

James G. Stewart,¹ Heber MacMahon,¹ Carl J. Vyborny,¹ and Elizabeth R. Pollak²

The ability of CT to detect diffuse or microscopic calcification not visible on plain radiographs can help distinguish indeterminate pulmonary nodules from benign granulomas [1]. Recently, however, Goldstein et al. [2] described an extensively calcified adenocarcinoma of the lung with high average density on CT scan. We describe two cases of lung carcinoma in which CT revealed a diffuse, stippled pattern of calcification throughout the tumor. Although these lesions did not exhibit an average CT number as high as that of the adenocarcinoma reported by Goldstein et al. [2], they did show patterns of calcification on CT that are probably representative of dystrophic calcifications occasionally seen in carcinoma of the lung.

Case Report

A 47-year-old female smoker had a history of several months of vague chest discomfort. A chest radiograph revealed a 3.5-cm mass in the right upper lobe without apparent calcification. A CT examination was performed with a Siemens Somatom 2 unit by using 125-kV tube potential and contiguous 8-mm sections. A 50-ml bolus of contrast material followed by a drip infusion at a rate of approximately 10 ml/min was used.

Several small areas of high density were seen throughout the nodule (Fig. 1A). The average CT number was 120 H, with a maximum of 240 H. Because of these extensive calcifications, we thought that the lesion might be benign, but the level of clinical suspicion for carcinoma was high, and a right upper lobectomy was done.

A radiograph of the resected specimen (Fig. 1B) showed finely stippled calcifications uniformly distributed throughout the lesion.

Histologic examination revealed poorly differentiated squamous carcinoma. The centers of many cell nests were necrotic and contained foci of calcification that were positive on von Kossa stain and thought to be dystrophic in origin.

We encountered a second similar case shortly after the first. An asymptomatic 41-year-old woman had a radiographically noncalcified 2.5-cm mass in the left upper lobe. A CT examination performed on a GE 9800 scanner and without IV contrast material showed irregular calcifications throughout the lesion (Fig. 2). Because of our earlier experience, the question of dystrophic calcification in a carcinoma was raised. A thoracotomy was performed, and histologic examination revealed adenocarcinoma with several areas of dystrophic calcification.

Discussion

The presence or absence of calcification is an important factor in assessing the significance of a solitary pulmonary nodule [3]. Certain patterns of calcification, when identified on plain radiographs, strongly suggest benignancy. However, calcification within malignant pulmonary lesions has been documented also [4-6]. Its prevalence, as detected by plain radiography or conventional tomography, has been reported to range from 0.5% to 4% [4-6]. Specimen radiographs of resected lung cancers revealed calcification in a higher proportion of cases, with a prevalence of 14% in one series [4]. Calcification in malignant lesions can result from several processes: (1) calcified scar tissue or cartilage engulfed by tumor, (2) dystrophic calcification in necrotic tumor, and (3) primary tumor calcification [4]. The latter two mechanisms can pro-

Received May 1, 1986; accepted after revision August 7, 1986.

C. J. Vyborny is supported in part by a fellowship from the Andrew W. Mellon Foundation.

¹ Department of Radiology, University of Chicago Medical Center, Chicago, IL 60637. Address reprint requests to H. MacMahon, Department of Radiology, The University of Chicago, 5841 S. Maryland Ave., Chicago, IL 60637.

² Department of Pathology, West Suburban Hospital Medical Center, Oak Park, IL 60302.

AJR 148:29-30, January 1987 0361-803X/87/1481-0029 © American Roentgen Ray Society

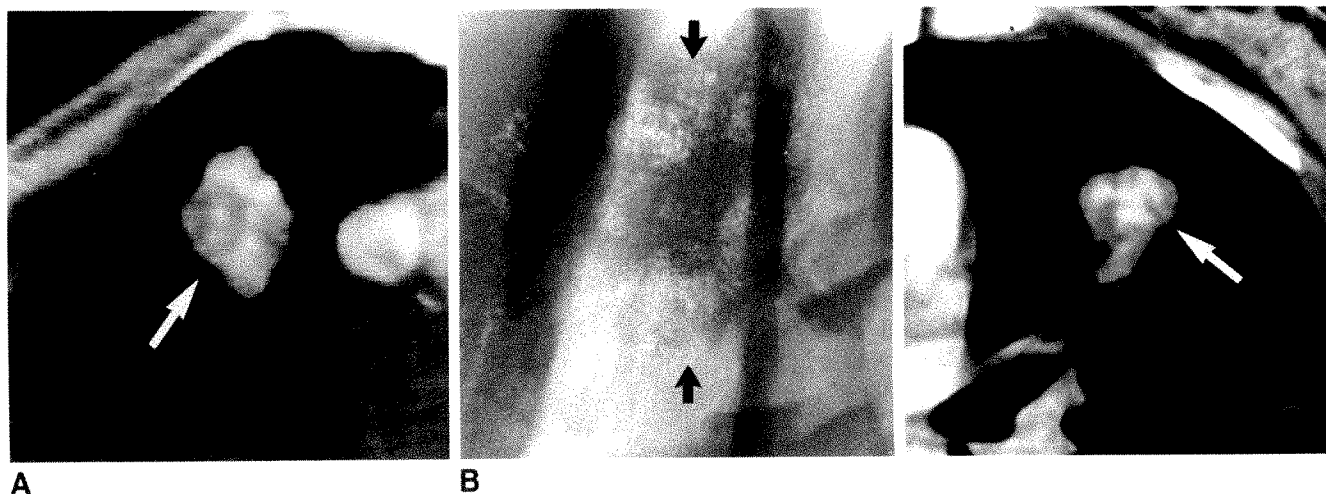


Fig. 1.—A, CT scan of 47-year-old woman shows multiple foci of high density throughout a lobulated right upper lobe mass (arrow). Although a contrast drip infusion was used, intensity of these foci (maximum CT number: 240 H) was thought to be far in excess of that which might be produced by contrast enhancement with this technique.

B, Contact radiograph performed on a cut specimen of resected mass shows minute punctate areas of calcification (arrows) throughout lesion.

Fig. 2.—CT scan of 41-year-old woman without IV contrast material shows multiple foci of calcification throughout a left upper lobe mass (arrow). Histologic examination after resection revealed adenocarcinoma with extensive dystrophic calcification.

duce diffuse calcification that, although not detectable on plain radiographs, may be readily shown by CT.

In the first case reported here, the specimen radiograph showed diffusely distributed flecks of calcification due to minute foci of calcium within areas of tumor necrosis. The appearance on CT suggested a coarser pattern of calcification, presumably due to volume averaging. We think it is unlikely that this pattern was caused by inhomogeneous contrast enhancement: A slow rate of contrast infusion was used, and abundant calcification was seen on subsequent specimen radiography. Although the average CT number of the tumor was not in the range that Siegelman et al. [7] found indicative of benignancy, the presence of diffusely distributed foci of calcification within the mass initially suggested a benign cause. On closer inspection, however, the findings did not correspond to any of the classic patterns of benign disease, such as uniformly high density and central, laminar, or "pop-corn" calcification. Neither did the findings suggest a preexisting calcified granuloma engulfed by a cancer. The pattern of calcification in the second case was similar to the first, except that the calcium was located preponderantly within the central portion of the tumor.

This CT pattern of dystrophic calcification in lung cancer has not been reported before. Goldstein et al. [2] described an adenocarcinoma of the lung with high density throughout that was due to dystrophic calcification. Similar to our cases, their specimen radiograph showed flecks of calcium in the tumor. The CT appearance was different, however, probably due to volume averaging of the relatively large amounts of calcium present.

Because CT allows quantification of X-ray attenuation more precisely than plain radiography, it has provided an additional

factor for diagnosis of benign pulmonary nodules (i.e., the average CT number). However, the possible significance of the pattern of calcification observed on CT has not been emphasized. Because CT is more sensitive in identifying small amounts of calcification in pulmonary nodules, such "subradiographic" foci of calcification, even if diffuse, do not necessarily have the same diagnostic implications as calcification that is visible on a conventional radiograph.

Scattered calcifications within a granuloma might simulate the findings shown here. However, these cases emphasize that criteria developed over many years in conventional radiography may not be applicable to CT scans. Dystrophic calcification is rarely demonstrable on a chest radiograph, but it will be identified more frequently by using CT. Though uncommon, the pattern of calcification reported here should be regarded with suspicion, especially when conventional radiography suggests carcinoma.

REFERENCES

1. Aronberg DJ, Sagel SS. High CT attenuation values of a benign pulmonary nodule. *J Comput Assist Tomogr* 1981;5(4):563-564
2. Goldstein MS, Rush M, Johnson P, Sprung CL. A calcified adenocarcinoma of the lung with very high CT numbers. *Radiology* 1984;150:785-786
3. Good CA. The solitary pulmonary nodule: a problem of management. *Radiol Clin North Am* 1963;1:429-438
4. O'Keefe ME, Good CA, McDonald JR. Calcification in solitary nodules of the lung. *AJR* 1957;77:1023-1033
5. Steele JD. The solitary pulmonary nodule: report of a cooperative study of resected asymptomatic solitary pulmonary nodules in males. *J Thorac Cardiovasc Surg* 1963;46:21-39
6. Theros EG. Varying manifestations of peripheral pulmonary neoplasms: a radiologic-pathologic correlative study. *AJR* 1977;128:893-914
7. Siegelman SS, Zerhouni EA, Leo FP, Khouri NF, Stitik FP. CT of the solitary pulmonary nodule. *AJR* 1980;135:1-13

Case Report

Extension of Ascites into the Chest with Hiatal Hernia: Visualization on CT

J. David Godwin^{1,2} and John M. MacGregor^{1,3}

Ascites can extend from the abdomen into the posterior mediastinum through the esophageal hiatus. On CT, this mediastinal fluid may simulate the appearance of a foregut cyst, mediastinal abscess, necrotic tumor, or pancreatic fluid collection. The following two cases illustrate the CT appearance and the anatomic basis for this abnormality.

Case Reports

Case 1

A 79-year-old woman had a stage-III papillary serous cystadenocarcinoma of the ovary treated by surgery 4 years before and by several courses of chemotherapy. At time of presentation, she was experiencing nausea, vomiting, and abdominal discomfort. Examination revealed a tense, distended abdomen and a pelvic mass.

An upper gastrointestinal study with barium showed hiatal hernia with gastroesophageal reflux; a study 4 years before had also shown the hiatal hernia. CT showed ascites, bilateral pleural effusion, small peritoneal nodules, and hepatic lesions thought to be metastases; there was no visible pelvic mass. Malignant cells were found in the pleural effusion and the ascites.

Of special interest was the extension of the ascites into the chest (Fig. 1), anteriorly and to the left of the esophagus. The fluid collection displaced the esophagus to the right and posteriorly and flattened the posterior contour of the inferior vena cava.

Case 2

A 76-year-old man had metastatic carcinoma of the prostate. He had been treated 15 years earlier by radical prostatectomy and 8 years after that by pelvic and perineal radiation for metastases.

He now suffered cachexia, abdominal pain, and intermittent diarrhea and constipation. Examination revealed no abdominal mass, organomegaly, or distension. A CT examination showed bilateral

pleural effusions, ascites, hiatal hernia, and cholelithiasis. The ascitic fluid extended into the chest and surrounded the esophagus (Fig. 2). A CT scan made 8 months earlier had shown a normal distal esophagus and no associated fluid collection; at that time there had been no visible hiatal hernia or ascites.

Discussion

These cases illustrate that ascites can extend into the chest in the presence of a hiatal hernia. This occurrence implies that the peritoneum enters the chest, since ascites is an intraperitoneal process. The relevant anatomic structures are the phrenoesophageal ligament (also known as the phrenoesophageal membrane or membrane of Laimer Bertelli) and the peritoneal reflections near the esophageal hiatus; these structures are altered by hiatal hernia (Fig. 3).

The phrenoesophageal ligament attaches the esophagus to the diaphragm, thereby closing the potential space between the diaphragm and esophagus [1] and separating the thoracic and abdominal cavities at the esophageal hiatus. The ligament arises primarily from the fascia on the undersurface of the diaphragm with a lesser contribution from the diaphragmatic reflection of the endothoracic fascia [2]. It splits into two main layers that attach to the wall of the esophagus at different levels [3]. It contains abundant elastic fibers, and it serves both to permit and to limit the sliding motion of the esophagus relative to the diaphragm during swallowing and breathing [4, 5]. In older persons, the ligament thins and loses its elasticity. Fat and areolar tissue are deposited between its layers, and the esophagus becomes more mobile. In the presence of hiatal hernia, the ligament is greatly thinned and stretched, and its elasticity is further reduced. The phrenoesophageal

Received July 28, 1986; accepted after revision August 28, 1986.

¹ Department of Radiology, Duke University Medical Center, Durham, NC 27710.

² Present address: Department of Radiology, SB-05, University of Washington, Seattle, WA 98195. Address reprint requests to J. D. Godwin.

³ Present address: Department of Diagnostic Radiology, Victoria General Hospital, 1278 Tower Rd., Halifax, Nova Scotia B3H 2Y9, Canada.

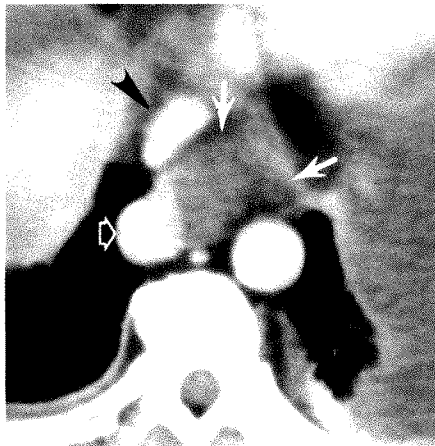
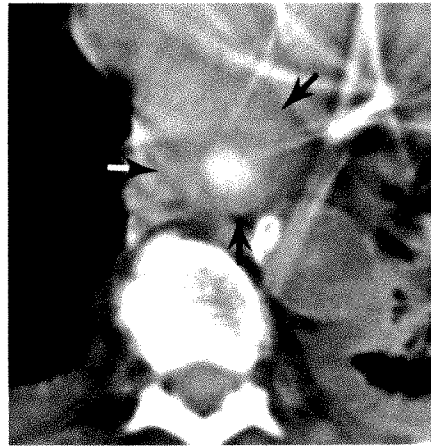
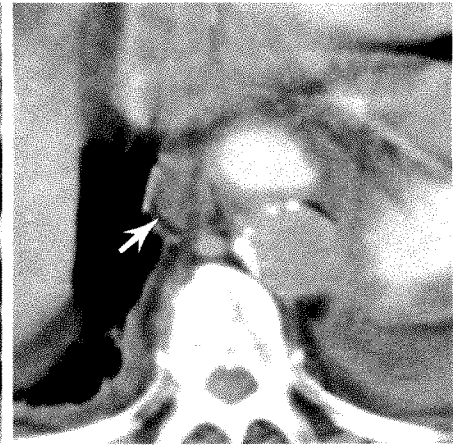


Fig. 1.—Case 1: Metastatic ovarian carcinoma. Contrast-enhanced CT scan shows extension of ascitic fluid (white arrows) into mediastinum with displacement of contrast-filled esophagus (open arrow) to right and indentation on posterior wall of inferior vena cava (black arrow-head). Ascites is visible below diaphragm bilaterally. Lower sections showed hiatal hernia and continuity of mediastinal fluid with ascites in abdomen.



A



B

Fig. 2.—Case 2: Metastatic prostatic carcinoma.

A, Contrast-filled esophagus is surrounded by low-density (4 H) fluid collection (arrows). B, Section 2 cm lower shows elevation of gastroesophageal junction into chest (indicating hiatal hernia), abdominal ascites, and fluid to right of esophagus (arrow). Lower sections showed continuity of mediastinal fluid with ascites in abdomen.

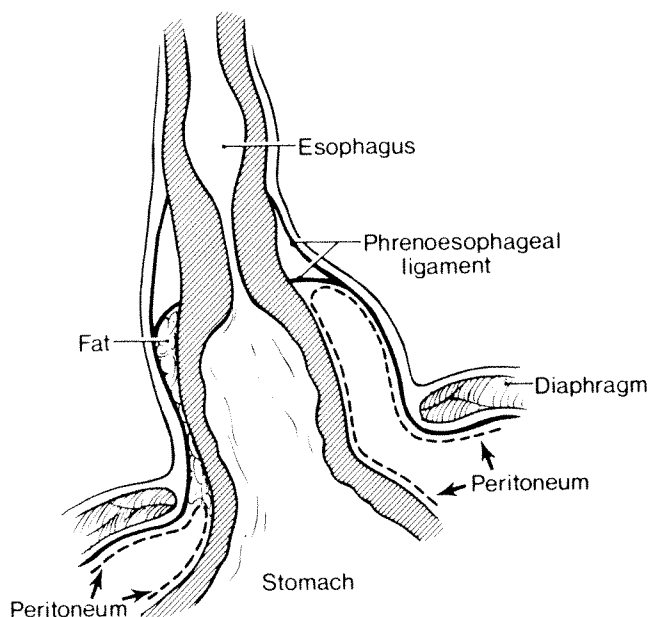


Fig. 3.—Small sliding hiatal hernia. Diagram in coronal plane through gastroesophageal junction clarifies peritoneal relationships that permit ascites to enter chest. In hiatal hernia, stretching of phrenoesophageal ligament permits esophagogastric junction to rise, accompanied on left and anterior surfaces by anterior layer of lesser omentum. Only when hernia is large does peritoneum posterior and to right of the hiatus also enter chest. Ascites can extend into chest along with peritoneum.

ligament probably affects the proper function of the lower esophageal sphincter in preventing reflux [6].

The peritoneum in the vicinity of the esophageal hiatus is contributed by the lesser omentum. The anterior layer of the lesser omentum covers the anterior and left lateral parts of the hiatus [7]. This part of the peritoneum most readily enters the chest with a hiatal hernia and forms the hernial sac [7]. Peritoneum is not in contact with the posterior and right parts of the hiatus. Instead, the peritoneum reflects off the stomach in a manner that leaves extraperitoneal the part of the pos-

terior gastric wall near the esophagogastric junction. The space between the peritoneum and esophagogastric junction is filled by a variable amount of fat, which may enter the chest in the presence of a large hiatal hernia [8].

The peritoneal relationships determine the CT appearance of the ascitic fluid extending into the chest. With a small hiatal hernia, only the peritoneum that lies to the left of and anterior to the esophagus enters the chest; therefore, the fluid collection will lie to the left of and anterior to the esophagus. With a larger hernia, either sliding or paraesophageal, the posterior peritoneal reflection may also enter the chest, and fluid may then surround the esophagus (case 2). In both of our cases the fluid could be traced on contiguous slices from the abdomen into the thorax.

Ascites can be the cause of a posterior mediastinal fluid collection, particularly in a patient with evidence of hiatal hernia. Our cases suggest that continuity of the thoracic with the intraabdominal fluid helps in making the correct diagnosis. If continuity is not apparent, then other causes of low-density posterior mediastinal abnormalities must be considered, such as foregut cyst, abscess, necrotic tumor, and pancreatic fluid collection.

REFERENCES

1. Zaino C, Poppel MH, Jacobson HG, Lepow H. *The lower esophageal vestibular complex*. Springfield, IL: Thomas, 1963
2. Carey JM, Hollinshead WH. An anatomic study of the esophageal hiatus. *Surg Gynecol Obstet* 1965;100:196-200
3. Bombeck CT, Dillard DH, Nyhus LM. Muscular anatomy of the gastroesophageal junction and role of phrenoesophageal ligament. *Ann Surg* 1966;164:643-654
4. Friedland GW. Historical review of the changing concepts of lower esophageal anatomy: 430 B.C.-1977. *AJR* 1978;131:373-388
5. Govoni AF, Whalen JP, Kazam E. Hiatal hernia: a relook. *Radiographics* 1983;3:612-644
6. Michelson E, Siegel CI. The role of the phrenicoesophageal ligament in the lower esophageal sphincter. *Surg Gynecol Obstet* 1964;118:1291-1294
7. Nyhus LM, Harkins HN. *Hernia*. Philadelphia: Lippincott, 1964
8. Geffen N, Maisel B. Artificial pneumoperitoneum in the diagnosis and treatment of hiatus hernia. *Postgrad Med J* 1966;42:765-769

Measurement of Canine Left Ventricular Mass by Using MR Imaging

Gary R. Caputo^{1,2}
 Dimiter Tscholakoff^{1,3}
 Udo Sechtem¹
 Charles B. Higgins¹

This study assessed the capability of ECG-gated MR imaging for quantitating left ventricular mass by means of signal intensity-based and geometric methods for measuring left ventricular mass of normal dogs and dogs with left ventricular hypertrophy. Mass was measured on transverse images encompassing the left ventricle during both diastole and late systole. Partial-volume errors were minimized by measuring the length of the left ventricle on a sagittal image and weighting the mass of end slices accordingly. The range of postmortem left ventricular mass was 61–100 g. The linear relationship between postmortem left ventricular mass and mass measured via MR images correlated closely when MR imaging measurements were done at either end diastole ($r = .94$) or late systole ($r = .94$). The standard errors of the estimate were 13.7 and 14.7 g for images gated to end diastole and late systole, respectively. Inter- and intraobserver reproducibility showed excellent agreement ($r = .93$ and $r = .89$ for end diastole and $r = .99$ and $r = .93$ for late systole, respectively). Thus, left ventricular mass can be quantified accurately and reproducibly over a wide range of masses by using ECG-gated MR imaging.

Various techniques have been used to determine left ventricular mass, including ECG [1], biplane left ventricular angiography [2, 3], M-mode and two-dimensional echocardiography [4–9], transmission CT [10–13], and single-photon emission CT [14–16]. Because they are invasive, use ionizing radiation, or give equivocal definition of the myocardial edge, none of these techniques has been completely satisfactory for monitoring myocardial mass and changes in mass after therapeutic intervention. Some techniques are less accurate in the presence of regional left ventricular abnormalities [17, 18].

MR imaging is a new noninvasive technique [19–21] that does not require the use of ionizing radiation or contrast media. MR imaging of the heart offers the advantages of the natural contrast between the blood pool and cardiac structures (flowing blood produces minimal MR signal [20, 22]) and high soft-tissue contrast, enabling direct visualization of the myocardium and sharp delineation of the myocardium from the blood pool and pericardium [19, 21, 23]. MR of the heart requires ECG gating, and this is accomplished with relative ease [24, 25].

The purpose of this study was to examine signal intensity-based and geometric methods for measurement of left ventricular mass over a wide range of masses. Mass was assessed in normal dogs and in dogs with left ventricular hypertrophy.

Methods

Animal Preparation and Experimental Protocol

Seven adult mongrel dogs weighing 14–23 kg and six adult Rottweiler dogs weighing 27–38 kg were premedicated intramuscularly with droperidol and ^Nfentanyl citrate (Innovar, 0.1 ml/kg), intubated, and anesthetized with IV sodium pentobarbital (20–25 mg/kg). The Rottweiler dogs were from the same litter and had congenital subaortic stenosis with accompanying left ventricular hypertrophy.

Received May 5, 1986; accepted after revision August 11, 1986.

G. R. Caputo and D. Tscholakoff were research fellows in MR imaging. G. R. Caputo was supported by NRSA Grant 5T32 HL 07278-08; D. Tscholakoff, by NIH Fogarty International Center Grant FOSTW03437.

¹ Department of Radiology, University of California School of Medicine, San Francisco, CA 94143. Address reprint requests to C. B. Higgins.

² Present address: Advanced Cardiac Imaging, LDS Hospital, 8th Ave. and C St., Salt Lake City, UT 84143.

³ Present address: Zentrales Institut sur Radio-diagnostik der Universitat, 4 Alser Str., Vienna, Austria.

AJR 148:33–38, January 1987
 0361–803X/87/1481–0033
 © American Roentgen Ray Society

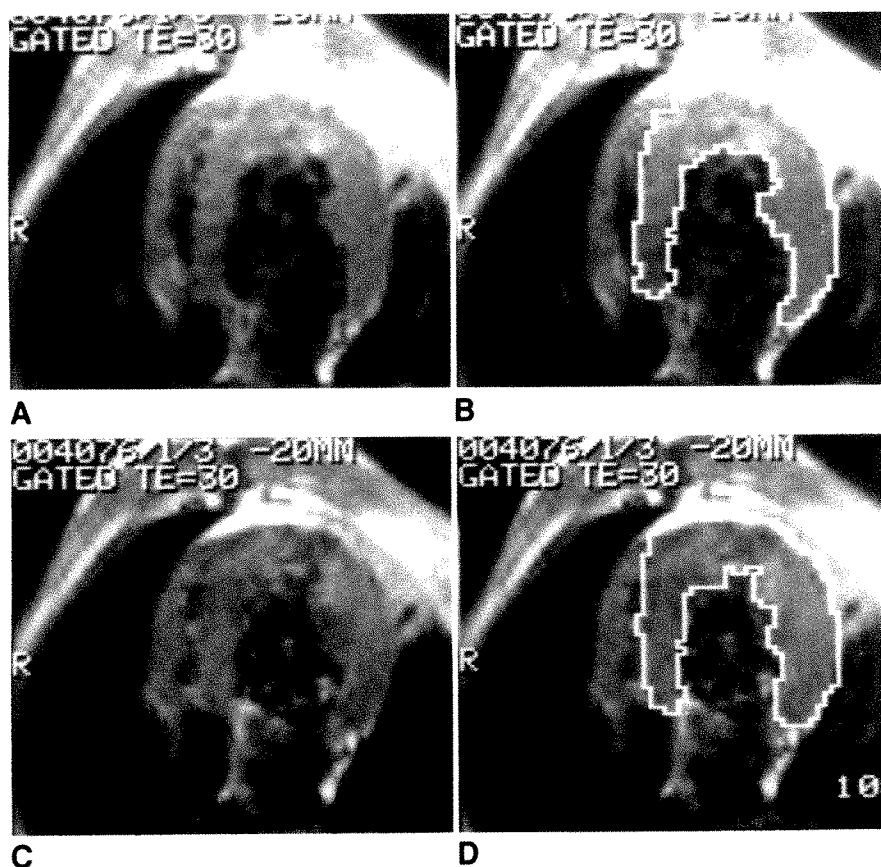


Fig. 1.—Transaxial midventricular MR images.

- A, Acquired at end diastole.
- B, Region of interest drawn for end-diastolic image.
- C, Acquired during systole.
- D, Region of interest drawn for late systolic image.

The imaging protocol was designed to obtain multiple slices through the entire left ventricle at the same phase of the cardiac cycle. The dogs were sacrificed after completion of MR imaging. At autopsy the right ventricle, both atria, and the semilunar and atrio-ventricular valves were removed. The left ventricle was weighed five times on a Mettler balance, and an average mass was calculated.

MR Imaging

Imaging was performed with a superconducting magnet operating at 0.35 T (Diasonics MT/S) with a corresponding resonance frequency of 15 MHz [26]. ECG-gated single spin-echo sequences with multislice acquisition were used to image the left ventricle from apex to base with 10 contiguous slices of 10-mm thickness, starting with the most cranial section synchronous with the R wave of the ECG. A 44-cm field of view was used. The image matrix was 256×256 pixels, and two excitations were averaged. The pulse repetition time was determined by the dogs' heart rates and varied from 600 to 1000 msec, corresponding to heart rates of 60–100 beats/min. Transaxial, multisection imaging was implemented to allow the imaging of each section several times during the cardiac cycle. This cycled, gated sequence obtained each of the 10 anatomic sections at five phases of the cardiac cycle [25]. Each of the 10 sections was imaged at end diastole and then at four 100-msec intervals, extending into the cardiac cycle. The total imaging time required to achieve this multi-phase, multisectional imaging was approximately 35–40 min.

After completion of the transaxial cycled sequences, a standard 10-slice, single-echo, sagittal imaging sequence lasting between 7 and 10 min was used to measure the height of the left ventricle.

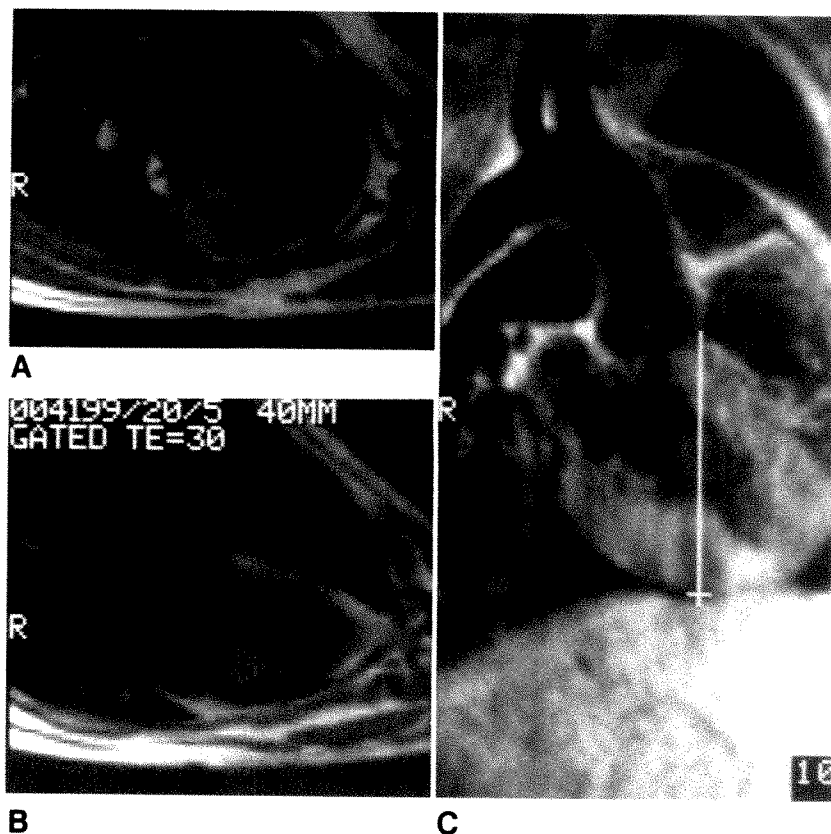
Because of such factors as respiratory motion artifacts and coil filling factor, the signal-to-noise ratio varied from animal to animal. Although fixed image-display window-settings for all animals seemed theoretically desirable, in practice, because of the aforementioned limiting factors, each observer found it necessary to vary the intensity and background settings independently. In each case the observer selected intensity settings between 60 and 70% of the maximum pixel intensity with 4 to 8% background subtraction.

Regions of interest were constructed that encompassed the endocardial and epicardial borders of the left ventricle for each transaxial level acquired at end diastole and late systole. Late systole was chosen as the slices acquired at 305 msec after the R wave. The end-diastolic images were all acquired at 10 msec after the R wave (Fig. 1). A midventricular sagittal slice was used to measure the height of the left ventricle to correct for partial-volume effects (Fig. 2). This was used to define the height of the left ventricle, and this measurement was used for partial-volume corrections of the slice at the caudal end of the ventricle. Each of these regions was drawn twice on two separate occasions by two independent observers to investigate observer variability.

Spatial Calibration

An oil-filled, Lucite phantom of known dimensions was used for spatial calibration. The phantom was imaged in the transaxial and sagittal planes by using a 256×256 pixel matrix. The transaxial image was displayed in a pixelated format, and the number of pixels in the x and y directions along each edge was determined. Dividing the known edge dimension by the number of pixels yielded the

Fig. 2.—Transaxial and sagittal MR images.
A, At the most cranial extent of the left ventricle (transaxial).
B, At the most caudal extent of the left ventricle (transaxial).
C, Through the left ventricle (sagittal) showing the height measurement used to correct the most caudal slices for partial volume effects.



centimeters per pixel in the x and y dimensions. Subjecting the sagittal image to the same analysis yielded the slice thickness in the z direction as there was 1 voxel per slice. The product of the x, y, and z calibrations (1.88 mm × 1.88 mm × 94.5 mm) yielded 0.0334 cm³/voxel. This calibration was done each month during the 4 months of the study; it varied less than 1% throughout the course of the study.

Geometric Approach

For end diastole and late systole the total number of left ventricular myocardial voxels was determined by using regions of interest encompassing the left ventricle. The total number of left ventricular myocardial voxels was multiplied by 0.0334 cm³/voxel to determine myocardial volume. The specific gravity of myocardium (1.05 g/cm³) was then multiplied by the myocardial volume to yield myocardial mass. Because the most inferior transaxial slice was most affected by partial-volume problems, its number of voxels was adjusted by using the length of the left ventricle (Fig. 2). If the length of the ventricle was measured as a number of centimeters and a fraction of a centimeter, then the caudal boundary section was multiplied by this fraction to minimize partial volume errors.

Signal-Intensity Approach

Several emission tomographic studies have shown that the accurate in vivo measurement of left ventricular volume can be accomplished by using the principle that the total counts contained within the left ventricle divided by the counts per voxel, multiplied by the cubic centimeters per voxel yields volume [27, 28]. The MR imaging

spin-echo signal is determined from the following standard equation:

$$I = N(H) F(V) \exp(-TE/T2)[1 - \exp(-TR/T1)]$$

where I = MR imaging signal intensity, N(H) = mobile hydrogen spin density, F(V) = function of both the speed with which hydrogen nuclei move through the imaged region and the fraction of the moving nuclei, TE = time to reception of spin-echo signal (30 or 60 msec after 90° radiofrequency pulse), T2 = spin-spin or transverse relaxation time, TR = radiofrequency pulse sequence repetition time, and T1 = spin-lattice or longitudinal relaxation time.

Variations in heart rate lead to variability in the TR and consequent inaccuracies in the measurement of myocardial T1 and spin density. Therefore, if two assumptions are made, namely that MR imaging signal intensity is relatively homogeneous and that this intensity is proportional to spin density, then myocardial volume can be approximated by dividing the total myocardial signal intensity by the intensity per voxel and multiplying by the cubic centimeters per voxel. At least one of these assumptions does not hold completely, as signal intensity across the myocardium likely varies because of respiratory and some cardiac motion occurring during the acquisition of imaging data.

For each end-diastolic and late systolic slice, the mean intensity per voxel was multiplied by the number of voxels in that slice to obtain total myocardial signal intensity. Regions of interest were constructed centrally within the septum and free wall of the left ventricle to determine the signal intensity per voxel, thereby avoiding the voxels at the endocardial and epicardial interfaces. The summed total left ventricular myocardial signal intensity was divided by the intensity per voxel to obtain total myocardial voxels. The same region of interest was outlined for the geometric and intensity methods. This measurement was multiplied by the cm³/voxel and 1.05 g/cm³ to

obtain left ventricular mass. Again, the number of voxels in the most caudal transaxial slice was adjusted for the height of the heart to minimize partial volume effects.

Statistical Analysis

Two determinations of end-diastolic and late systolic left ventricular mass were averaged and compared with autopsy mass by means of linear regression with calculations of the standard error of the estimate (SEE). Inter- and intraobserver variability were evaluated by using linear regression. Statistically significant differences between calculated and autopsy mass and between end-diastolic and late systolic mass were tested by using a paired t test.

Results

Table 1 contains the correlation coefficients and the standard errors of the estimate for mass determined by the geometric and signal-intensity methods compared with mass measured at autopsy. In comparing the two methods for end-diastolic left ventricular mass (Figs. 3 and 4), the geometric method had a higher correlation coefficient than that found for the signal-intensity method (.94 vs .89) and a smaller SEE (13.7 vs 22.1 g). The geometric method also was more accurate than the intensity method for late systolic left ven-

tricular mass (Figs. 5 and 6): $r = .94$ vs $.90$, and $SEE = 14.7$ vs 16.6 g. There was no statistically significant difference between the relationship of postmortem mass compared with the mass measured by the two MRI imaging methods. Likewise, there was no significant difference between end-diastolic and late systolic mass measured by MR imaging.

Comparisons of intraobserver reproducibility for the geometric vs the signal-intensity method showed few differences whether mass was determined from end-diastolic ($r = .93$ vs $.97$) or late systolic images ($r = .99$ vs $.95$). The geometric method as compared with the signal-intensity method showed slightly better interobserver reproducibility for end diastolic ($r = .89$ vs $.83$) and was decidedly less variable for late systolic left ventricular mass ($r = .93$ vs $.68$).

Discussion

This study shows the capability of gated MR imaging for measuring left ventricular mass in normal dogs and in dogs with left ventricular hypertrophy. Equally accurate measurements were obtained by using MR tomograms gated at end diastole or late systole. In spite of correction for partial volume error, MR imaging underestimated the true left ventricular mass.

Besides MR imaging, five in vivo techniques have been used to measure left ventricular mass: ECG, contrast ventriculography, echocardiography, transmission CT, and single-photon emission CT. Although ECG is easy to use, its sensitivity in detecting left ventricular hypertrophy is poor [1]. Contrast angiography has relatively good correlation with autopsy mass [3]; however, its invasive methodology is poorly suited to serial determinations of left ventricular mass.

Two-dimensional echocardiographic studies give an accurate determination of left ventricular mass [6]. However, the quality of the images obtained in a given patient becomes the limiting factor, such as in patients with chronic obstructive lung disease.

TABLE 1: Comparison of Geometric and Intensity Methods for Determining Left Ventricular Mass

Method	Diastole		Systole	
	r	SEE	r	SEE
Geometric	.94	13.7	.94	14.7
Intensity	.89	22.1	.90	16.6

Note.—Values are for the relationship of each MR method plotted against the mass determined at autopsy. r = correlation coefficient, SEE = standard error of the estimate.

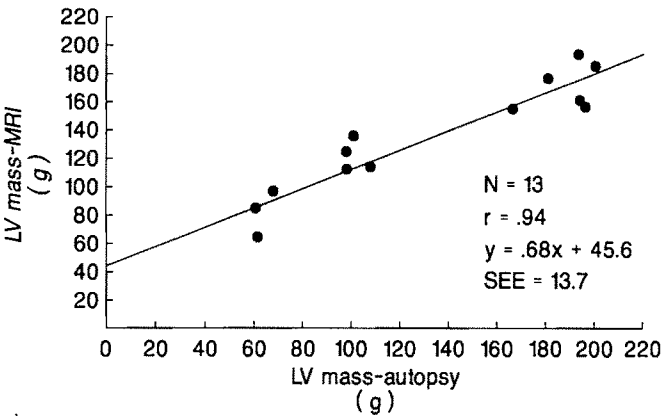


Fig. 3.—Comparison of left ventricular masses determined by MR imaging (LV mass-MRI) at end diastole by using the geometric method with those obtained at autopsy. N = number of dogs; r = correlation coefficient; equation represents linear regression line; SEE = standard error of the estimate.

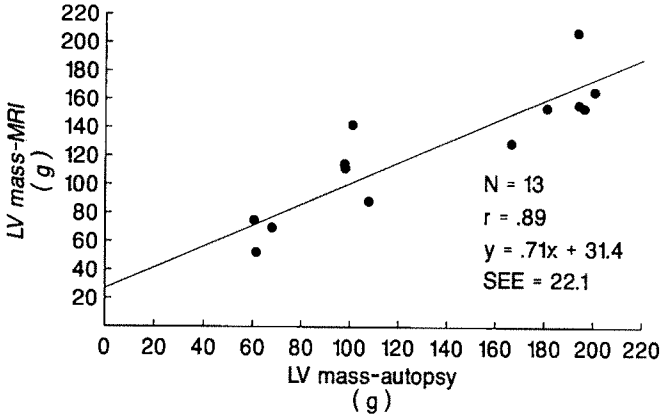


Fig. 4.—Comparison of left ventricular masses determined by MR imaging (LV mass-MRI) at end diastole by using the intensity method with those obtained at autopsy. N = number of dogs; r = correlation coefficient; SEE = standard error of the estimate.

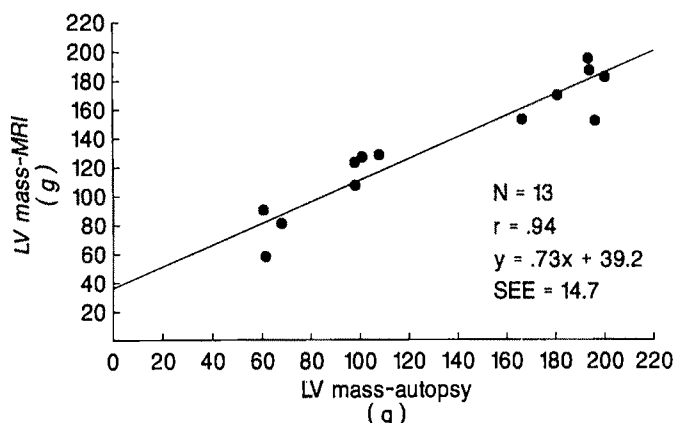


Fig. 5.—Comparison of left ventricular masses determined by MR imaging (LV mass-MRI) during late systole by using the geometric method with those obtained at autopsy. N = number of dogs; r = correlation coefficient; SEE = standard error of the estimate.

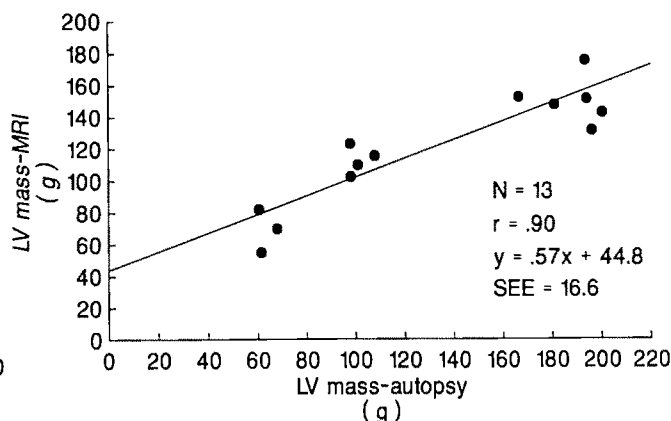


Fig. 6.—Comparison of left ventricular masses determined by MR imaging (LV mass-MRI) during late systole by using the intensity method with those obtained at autopsy. N = number of dogs; r = correlation coefficient; SEE = standard error of the estimate.

Single-photon emission CT with thallium-201 has been used to quantitate left ventricular mass in man [16] and has an accuracy comparable to contrast angiography and two-dimensional echocardiography. This technique suffers from inherent, limited spatial resolution and the necessity for attenuation correction because of the low-energy, low-count-rate radiopharmaceutical used. Because this technique measures perfused tissue mass, its precision in estimating left ventricular mass in patients with severe coronary artery disease or prior myocardial infarction would be limited.

Transmission CT with conventional scanners has been used to measure left ventricular mass [10, 11], but these methods are not multislice and require that the patient endure a large IV contrast load and sustain prolonged breath holding. Subsecond CT scanners have provided very precise accurate estimates of left ventricular mass in dogs [12, 13]. However, these scanners also require the use of IV contrast and ionizing radiation. Automated edge-detection techniques applied to the chamber-wall interface do make this an objective and reproducible technique for monitoring left ventricular mass. Mass determination by either MR imaging or the subsecond CT scanner offer a new measurement for monitoring the left ventricular response to a variety of diseases.

An earlier study from our laboratory [29] showed that the transaxial MR imaging plane can be used to accurately quantitate the left ventricular mass of ex vivo human hearts; the mean deviation from autopsy mass was 3.3%. In vivo ECG-gated MR imaging had approximately a 10% error for both end-diastolic and late systolic left ventricular mass determined by the geometric method. The limitations of this technique stem from the in-plane spatial resolution of 1.7 mm currently available for MR imaging, partial-volume problems contributed to by in-plane left ventricular curvature, and some imprecision in determinations of the upper and lower extent of the left ventricle. The use of a higher in-plane spatial resolution should provide greater accuracy in the future.

The signal-intensity approach to the measurement of left ventricular mass was somewhat less accurate and less repro-

ducible. Although this approach should be less subject to partial-volume effects, a recent report [30] has shown a $2 \pm 15\%$ variation in regional signal intensity in normal volunteers at end diastole and $10 \pm 18\%$ variation at late systole. Therefore, the original assumptions of signal homogeneity and approximation of spin density may not be valid. This variation in signal intensity in the left ventricular myocardium is probably caused by respiratory motion and some residual effects of cardiac motion, even though gating is used. Quantitation of organ mass via this approach may be more accurate for stationary organs such as the kidney and spleen. Less rigorous construction of regions of interest should be sufficient for this technique as compared with the geometric technique, possibly allowing automation in the future.

A noninvasive technique for quantitating left ventricular mass may have important clinical implications because it can be used to monitor the progression or regression of left ventricular mass in diseases in which this measurement has prognostic significance. There may be a critical left ventricular mass above which the hypertrophied left ventricle can no longer be maintained by its blood supply, resulting in decreased left ventricular function [31]. Previous studies [32, 33] have shown that significantly more left ventricular hypertrophy was present in patients with aortic stenosis who had depressed systolic left ventricular function than in those with normal function. This technique also can be used to monitor regression of hypertrophy after treatment of hypertension and aortic stenosis. Moreover, measurement of left ventricular mass and wall thickness at end diastole and end systole provides insight into the level of left ventricular wall stress in compensated and decompensated stages of diseases that cause elevated afterload.

In summary, we have accurately measured left ventricular mass in seven normal dogs and in six dogs with left ventricular hypertrophy by using a commercially available MR scanner. ECG-gated MR imaging is a reasonably accurate and noninvasive approach to determining left ventricular mass that should be applicable to virtually all patients.

REFERENCES

- Romhilt DW, Bove KE, Norris RJ, et al. A critical appraisal of the electrocardiographic criteria for the diagnosis of left ventricular hypertrophy. *Circulation* 1969;40:185-195
- Rackley CE, Dodge HT, Coble YD, Hay RE. A method for determining left ventricular mass in man. *Circulation* 1964;19:666-671
- Kennedy JW, Reichenbach DD, Baxley WA, Dodge HT. Left ventricular mass: a comparison of angiographic measurements with autopsy weight. *Am J Cardiol* 1967;19:221-223
- Schiller NB, Skioldebrand CG, Schiller EJ, et al. Canine left ventricular mass estimation by two-dimensional echocardiography. *Circulation* 1983;68:210-216
- Devereaux RB, Reichek N. Echocardiographic determination of left ventricular mass in man. *Circulation* 1976;55:613-618
- Reichek N, Helak J, Plappert T, Sutton MSJ, Weber KT. Anatomic validation of left ventricular mass estimates from clinical two-dimensional echocardiography: initial results. *Circulation* 1983;348-352
- Troy BL, Pombo J, Rackley CE. Measurement of left ventricular wall thickness and mass by echocardiography. *Circulation* 1972;45:602-611
- Ditchey RV, Schuler G, Peterson KL. Reliability of echocardiographic and electrocardiographic parameters in assessing serial changes in left ventricular mass. *Am J Med* 1981;70:1042-1050
- Helak JW, Reichek N. Quantitation of human left ventricular mass and volume by two-dimensional echocardiography: in vitro anatomic validation. *Circulation* 1981;63:1398-1407
- Skioldebrand CG, Lipton MJ, Mavroudis C, Hayashi TT. Determination of left ventricular mass by computed tomography. *Am J Cardiol* 1982;49:63-70
- Peck WW, Mancini GBJ, Slutsky RA, Mathey RF, Higgins CB. In vivo assessment by computed tomography of the natural progression of infarct size, left ventricular muscle mass and function after acute myocardial infarction in the dog. *Am J Cardiol* 1984;53:929-935
- Iwasaki T, Sinak LJ, Hoffman EA, et al. Mass of left ventricular myocardium estimated with dynamic spatial reconstruction. *Am J Physiol* 1984;H138-H142
- Feiring AJ, Rumberger JA, Reiter SJ, et al. Determination of left ventricular mass in dogs with rapid acquisition cardiac CT scanning. *Circulation* 1985;72:1355-1364
- Keyes JW, Brady TJ, Leonard PF, et al. Calculations of viable and infarcted myocardial mass from thallium-201 tomograms. *J Nucl Med* 1981;22:339-343
- Wolfe CL, Corbett JR, Lewis SE, Buja LM, Willerson JT. Determination of left ventricular mass by single-photon emission computed tomography with thallium-201. *Am J Cardiol* 1984;53:1365-1368
- Wolfe CL, Jansen DE, Corbett JR, et al. Determination of left ventricular mass using single-photon emission computed tomography. *Am J Cardiol* 1985;56:761-764
- Teichholz LE, Kreulin T, Herman MV, Gorlin R. Problems in echocardiographic volume determinations: echocardiographic-angiographic correlations in the presence or absence of asynergy. *Am J Cardiol* 1976;37:7-11
- Linhardt JW, Mintz GS, Segal BL, Kawai N, Kotler MN. Left ventricular volume measurement by echocardiography: fact or fiction? *Am J Cardiol* 1975;36:114-118
- Herfkens RJ, Higgins CB, Hricak H, et al. Nuclear magnetic resonance imaging of the cardiovascular system: normal and pathological findings. *Radiology* 1983;147:749-759
- Kaufman L, Crooks L, Sheldon P, Hricak H, Herfkens R, Bank W. The potential impact of nuclear magnetic resonance imaging on cardiovascular diagnosis. *Circulation* 1983;67:251-257
- Hawkes RC, Holland GN, Moore WS, Roebuck EJ, Worthington BS. Nuclear magnetic resonance (NMR) tomography of the normal heart. *J Comput Assist Tomogr* 1981;5:605-612
- Crooks LE, Sheldon P, Kaufman L, Rowan W. Quantitation of obstructions on vessels by nuclear magnetic resonance. *IEEE Trans Nucl Sci* 1982;29:1181-1185
- Stark DD, Higgins CB, Lanzer P. Magnetic resonance imaging of the pericardium: normal and pathologic findings. *Radiology* 1984;150:469-474
- Lanzer P, Banta C, Botvinick EH, Wisendanger HU, Modin G, Higgins CB. ECG-synchronized cardiac MR imaging: method and evaluation. *Radiology* 1985;155:681-686
- Crooks LE, Banker B, Chang H, et al. Magnetic resonance imaging strategies of heart studies. *Radiology* 1984;153:459-465
- Crooks LE, Arakawa M, Hoenninger J, et al. Nuclear magnetic resonance whole-body imager operating at 3.5 KGauss. *Radiology* 1982;143:169-174
- Caputo GR, Graham MM, Brust KD, Kennedy JW, Welp WB. Measurement of left ventricular volume using single-photon emission computed tomography. *Am J Cardiol* 1985;56:781-786
- Bunker SR, Hartshorne MF, Schmidt WP, et al. Left ventricular volume determination from single-photon emission computed tomography. *AJR* 1985;144:295-298
- Lanzer P, Botvinick E, Finkbinder W, Byrd B, Schiller N, Higgins CB. Left ventricular mass assessment by magnetic resonance imaging of ex vivo human hearts (abstr). Presented at the annual meeting of the Society of Magnetic Resonance in Medicine 1984;3:445
- Caputo GR, Fisher MR, McNamara M, Lipton M, Higgins CB. Myocardial tissue characterization with the use of magnetic resonance imaging (abstr). *Circulation [Suppl]* 1985;72:III-23
- Linzbach AJ. Heart failure from the point of view of quantitative anatomy. *Am J Cardiol* 1960;5:370-382
- Gunther S, Grossman W. Determinants of ventricular function in pressure-overload hypertrophy in man. *Circulation* 1979;59:679-688
- Spann JF, Bove AA, Natarajan G, Kreulen T. Ventricular performance, pump function, and compensatory mechanisms in patients with aortic stenosis. *Circulation* 1980;62:576-582

Mammographic Detection of Recurrent Cancer in the Irradiated Breast

Paul C. Stomper¹
 Abram Recht²
 Arnold L. Berenberg³
 Maxine S. Jochelson¹
 Jay R. Harris²

Recurrence of cancer in the irradiated breast is an uncommon but potentially curable problem. Posttreatment mammograms were studied in 45 patients who had biopsies of an irradiated breast for suspected local recurrence to evaluate the usefulness of mammography in detecting such recurrences. Of 23 biopsy-proven recurrences, eight (35%) were detected by mammography only, nine (39%) were detected by physical examination only, and six (26%) were detected by both. Mammographic findings in recurrent malignancy included microcalcifications in six, microcalcifications associated with a mass in four, soft-tissue masses in three, and inflammatory changes in one. The results show that mammographic follow-up is complementary to physical examination in the detection of local recurrence in women who have undergone radiation therapy for early breast cancer.

Resection of the primary tumor with subsequent radiation therapy is now an acceptable option to mastectomy in the treatment of patients with early-stage breast cancer. Three recent prospective studies showed no significant difference in freedom from distant relapse or survival when these two treatments were compared [1-3]. Although both offer good local tumor control, primary radiation therapy has the advantage of breast conservation with good cosmetic results [4-8].

The chief cause of treatment failure after both mastectomy and conservative surgery followed by radiation is metastatic involvement, and both treatments are associated with a small risk of local recurrence. Unlike local recurrence after mastectomy, which is associated with an extremely poor prognosis, recurrence after breast-conserving treatment appears to be associated with a significant salvage rate (freedom from distant relapse). The salvage rate of recurrences after conservative treatment was 58% at 5 years and 50% at 10 years [9], whereas a group of 215 postmastectomy patients with isolated local recurrences treated by radiation therapy had a 5-year survival rate of 21% and a 10-year survival rate of 5% [10].

Improved methods of detection and earlier diagnosis of recurrent cancers in the irradiated breast may further improve the salvage rate for these patients. Meanwhile, little information is available on the clinical usefulness of mammography in the detection of such recurrences. In order to determine the value of this technique, we evaluated the mammographic findings in a group of patients treated by conservative surgery and radiation therapy who later had biopsies of suspected local recurrences.

Materials and Methods

From 1968 through 1984, more than 1600 women with clinical stage I or II invasive breast cancer, as determined by the guidelines of the International Union Against Cancer (UICC), were treated with primary radiation treatment at the Joint Center for Radiation Therapy.

Received April 28, 1986; accepted after revision August 12, 1986.

¹Department of Radiology, Harvard Medical School, Dana-Farber Cancer Institute, Brigham and Women's Hospital, 44 Binney St., Boston, MA 02115. Address reprint requests to P. C. Stomper.

²Joint Center for Radiation Therapy, Department of Radiation Therapy, Harvard Medical School, Boston, MA 02115.

³Department of Radiology, Harvard Medical School, Beth Israel Hospital, Boston, MA 02115.

AJR 148:39-43, January 1987

0361-803X/87/1481-0039

© American Roentgen Ray Society

During that time, 50 biopsies were performed in 50 patients within 4 months of a mammogram for suspected recurrent cancer in the irradiated breast. The biopsies were prompted by suspicious findings on physical examination alone, on mammography alone, or on both physical examination and mammography. The study group in this analysis consisted of 45 of the 50 patients who had mammograms available for review. Twenty-eight other patients who had biopsies did not undergo mammography; they were seen early in the study period before mammography was routinely employed after radiation treatment.

The details of treatment have been described [11]. The median age of the patients at the time of biopsy for suspected recurrence was 48 years (range, 30–77). Most (94%) had excisional biopsies, defined as resection of gross or palpable tumor without regard to whether the margins were later found to be microscopically involved. Six percent had less than excisional biopsies. All were treated with tangential radiation fields to the breast, lower axillary nodes, and adjacent chest wall. The ipsilateral internal mammary nodes were usually included within the tangential fields in patients who had central or inner quadrant lesions or positive axillary nodes. The upper axillary lymph nodes, supraclavicular nodes, and internal mammary nodes in the first and second interspace usually were treated with a separate anterior field. The dose to the tangential fields was prescribed at 1 cm from the deep intersection of the treatment fields and was usually 4500–5000 cGy. The dose to the anterior field was usually 4600 cGy prescribed at a depth of 5 cm. A supplemental dose of radiation to the tumor site, a “boost,” was given to 90% of the patients. Boosts were given either via an external beam (photons or electrons) or, more commonly, via interstitial iridium-192 implantation. Boost doses varied but were typically 2000 cGy.

After therapy, physical examinations were performed at 3- to 4-month intervals by a radiation therapist or surgeon who was familiar with the patient and experienced in the examination of the biopsied and irradiated breast. The follow-up protocol also included mammograms at yearly intervals, most of which were performed on film screen units. The compliance rate for obtaining mammograms during follow-up in the entire population of patients treated was not determined. Of the 45 patients included in the study group, 73% had yearly mammograms and 27% had mammograms at 2- to 3-year intervals. These mammographic studies were obtained with dedicated low-dose film screen units and consisted of a minimum of craniocaudal and oblique medial-lateral projections.

Each mammogram in the study was reviewed retrospectively by two mammographers without knowledge of the pathologic results or initial mammographic interpretation. Suspicious findings were defined as development of microcalcifications or a soft-tissue change (mass, architectural distortion) not attributable to the local excision or to radiation effects as determined on a posttreatment baseline study. Location of recurrences in the breast was designated the same if at the initial tumor and biopsy site, elsewhere if distinctly separate from the biopsy site, and multifocal if at several distinctly separate sites.

Excisional biopsies were performed on each patient; mammographically guided needle localization was performed for clinically occult lesions. Clinical records and surgical pathology reports were reviewed for all patients. A review of sections stained with hematoxylin and eosin also distinguished whether microcalcifications were observed within the recurrent tumor or within adjacent benign tissue. Recurrent cancer was defined as the appearance of carcinoma anywhere in the treated breast.

Results

Recurrent cancer was found in 51% (23/45) of the biopsies. Median time to recurrence after the start of radiation therapy

was 39 months (range, 6–95). Thirty-five percent (8/23) of all recurrences were detected by mammography alone. Overall, 61% of all recurrences were visualized by mammography (Table 1). In each case, the reviewers' findings agreed completely with the original mammographic interpretation.

The results of biopsies for microcalcifications only, microcalcifications associated with a mass, and soft-tissue masses or architectural distortion are shown in Table 2 (see also Figs. 1–3). One other patient developed severe inflammatory changes that were obvious on clinical examination and mammography. All tumors manifested by microcalcifications only and two manifested by microcalcifications and associated masses were clinically occult. Overall, the positive predictive value of a suspicious mammographic finding in this series was 61%. (Positive predictive value is defined as the percentage of biopsies performed for a specific mammographic finding that showed malignancy on pathologic examination.) The positive predictive value was 40% (4/10) in patients with soft-tissue abnormalities without microcalcifications and 77% (10/13) in patients with new microcalcifications.

The median diameter of recurrences was 2 cm (range, 1–6) for those detected by mammography only and 3 cm (range 2–3.5) for those detected by mammography and physical examination. Sixty-five percent recurred at the primary site, 22% recurred in different sites, and 13% were multifocal. This distribution was the same for the recurrences detected either by physical examination or by mammography. Nine tumors recurring at the primary site were evident mammographically; of these, 78% (7/9) contained microcalcifications, and 22% (2/9) were manifested by soft-tissue abnormalities.

On pathologic review, seven of the recurrent cancers were noninvasive intraductal cancers, and 16 were infiltrating ductal cancers. Six of the seven noninvasive cancers (89%) were detected by mammography only and had microcalcifications. In five of these patients, calcifications were shown histologi-

TABLE 1: Results of Biopsies for Suspected Recurrent Breast Cancer

Suspicious Finding on:	No. Malignant (%)	No. Benign (%)
Mammogram only	8 (35)	5 (23)
Physical examination only	9 (39)	13 (59)
Both	6 (26)	4 (18)
Total	23 (100)	22 (100)

Note.— $n = 45$.

TABLE 2: Results of Biopsies for Suspicious Mammographic Findings in Suspected Recurrent Breast Cancer

Suspicious Finding	No. Malignant (%)	No. Benign (%)
Calcifications	6 (43)	3 (33)
Calcifications with a mass	4 (29)	0 (0)
Mass or architectural distortion	3 (21)	6 (67)
Inflammatory changes	1 (7)	0 (0)
Total	14 (100)	9 (100)

Fig. 1.—Mammograms show microcalcifications that developed after radiation treatment.

A, Microcalcification cluster (arrows) that appeared on a follow-up examination 2 years after radiation treatment. Biopsy results showed infiltrating ductal and intraductal cancer containing calcifications at primary tumor site.

B, Microcalcification cluster (arrows) that appeared 1 year after treatment. Biopsy results showed benign calcifications in a region of sclerosis at primary tumor site.

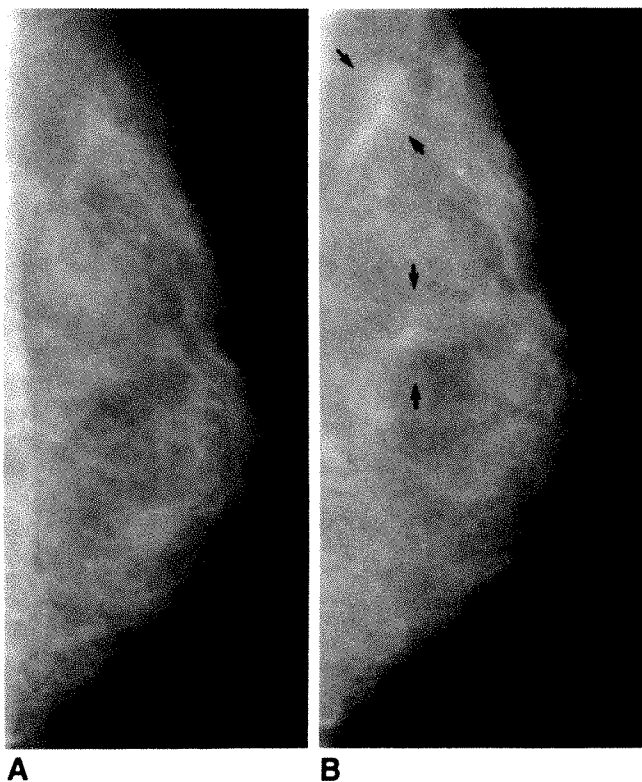
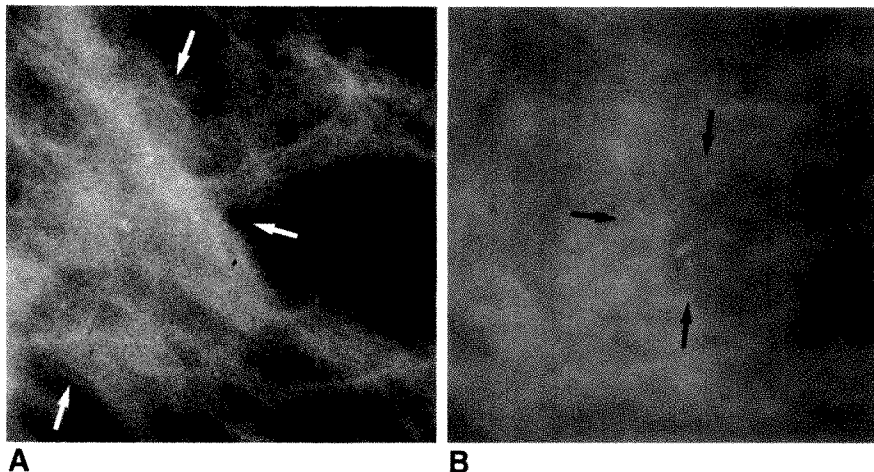


Fig. 2.—Mammograms show serial development of soft-tissue abnormalities after radiation treatment.

A, Medial-lateral view obtained 3 years after treatment showed a stable appearance relative to earlier post-treatment films.

B, One year later, two new areas of architectural distortion (arrows) appeared; the uppermost was associated with a palpable abnormality. Pathologic examination showed multifocal infiltrating ductal cancers in both lesions.

cally within the intraductal tumor. In one patient, calcifications were shown histologically in adjacent benign tissue. One other noninvasive recurrent cancer was found in tissue from a biopsy that was prompted by an abnormality on physical examination only. The proportion of noninvasive cancers (6/8) detected by mammography only was greater than the

proportion (1/15) detected by clinical examination ($p = .002$ by Fisher exact test).

Eighteen of the 23 patients with recurrences underwent mastectomy. Mastectomy was contraindicated in five patients for surgical or medical reasons. Of the eight patients with recurrences detected by mammography only, three had axillary dissections that showed no evidence of lymph-node involvement. These eight patients were alive and free of disease at a median follow-up of 37 months (range, 24–85). Six of 15 patients with clinically palpable recurrences had axillary dissections. Lymph-node involvement was present in three. Two of these patients developed systemic metastases in 4 and 22 months, respectively, and subsequently died. The remainder were free of disease at a median follow-up of 59 months (range, 14–78).

Discussion

This study shows the importance of mammography in the detection of recurrent cancer in the irradiated breast. Thirty-five percent of the recurrent cancers in this series were clinically inapparent and were detected by mammography only. Overall, 61% of the recurrences were visualized by mammography. Furthermore, recurrences detected by mammography only were more likely to be purely noninvasive than those detected by physical examination.

The frequency and time course of local recurrence over a long period has been described in a multi-institutional study of 152 patients treated before 1967 and followed for a minimum of 15 years [9]. The actuarial risk of local recurrence after primary radiation therapy was shown to be fairly constant (approximately 2% per year) over the first 14 years after treatment. Another study of 366 patients treated at the Joint Center for Radiation Therapy before 1980 and followed for a median interval of 52 months (range, 16–150) showed an actuarial 5-year local recurrence rate of $9 \pm 2\%$ [12]. With improved methods of patient selection and treatment, a decrease in the local recurrence rate may occur. However, these studies indicate that long-term follow-up is necessary to detect curable local recurrences.

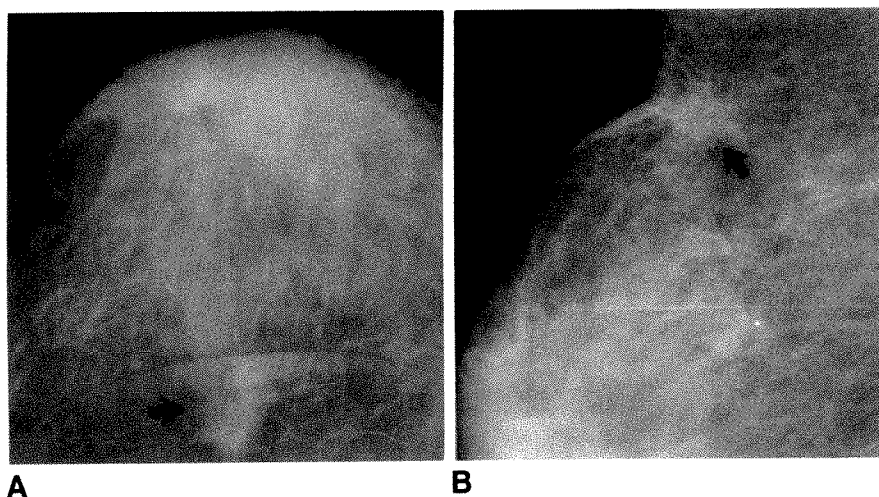


Fig. 3.—Mammogram shows a spiculated mass at primary tumor excision site (arrows) on initial posttreatment examination. A biopsy performed because of a suspicious palpable abnormality showed fibrosis only.

A, Craniocaudal view.

B, Medial-lateral view, upper half of breast.

Differentiation of recurrent cancer from benign changes attributable to surgical excision and radiation treatment has been a dilemma for both clinical examiners and mammographers. Benign physical findings after treatment include defects, ridges, and induration at the excision site; distortions caused by surgical approximation; and pectoral muscle fibrosis [13]. Similarly, benign mammographic changes after surgical excision and radiation include breast retraction, increased parenchymal density; skin thickening; development of coarse, dystrophic calcifications; and the presence of a mass (pseudotumor) or architectural distortion at the biopsy or hematoma site [14–20]. Aside from skin thickening and the development of calcifications, most of these changes stabilize by 3–6 months after treatment. We believe that comparison with a posttreatment study performed after stabilization is helpful in differentiating benign changes from recurrent malignancy. Our current follow-up protocol includes a detailed physical examination and mammography at both 6 months and 1 year after treatment to establish a baseline for future comparison.

The overlap between the appearance of benign and malignant microcalcification clusters in the irradiated breast has not been well described. Although the frequency of specific mammographic findings in this study is too small to be conclusive, the high positive predictive values of suspicious microcalcifications, masses, or architectural distortion seen during follow-up in this series (61% overall) strongly support biopsy of these abnormalities. As in other clinical settings, suspicious physical findings without associated mammographic abnormality (39% of recurrences in this series) always warrant biopsy.

Analysis of the location of recurrences in this study—65% at the primary tumor site and 35% at different or multifocal sites—has two practical implications. First, it suggests whether the recurrences represent a failure to control the primary tumor or a failure to eradicate multicentric disease, which has a reported frequency of 13–74% [21–23]. Further improvements in the effectiveness of radiation therapy will depend on a clearer understanding of the cause for failure

[12]. Second, as most recurrences are at the primary site, adequate imaging of this area of the breast is important. We have found that localization of the primary tumor site is aided by (1) placement of a wire marker over the biopsy scar during the initial posttreatment mammogram and (2) correlation with prebiopsy films that show the primary tumor.

The optimal frequency for obtaining mammograms after treatment has not been determined. We currently obtain craniocaudal, medial-lateral, and oblique medial-lateral views at 6 and 12 months after the completion of radiation therapy. Subsequently, mammography is performed at yearly intervals. For later studies, the choice of additional projections or the deletion of one of the medial-lateral projections is tailored to each individual's posttreatment mammographic appearance.

ACKNOWLEDGMENT

We thank Marybeth Lamb and Barbara Silver for their assistance in the preparation of this manuscript.

REFERENCES

1. Fisher B, Bauer M, Margolese R, et al. Five-year results of a randomized clinical trial comparing total mastectomy and segmental mastectomy with or without radiation in the treatment of breast cancer. *N Engl J Med* 1985;312(11):665–673
2. Veronesi U, Saccozzi R, Del Vecchio M, et al. Comparing radical mastectomy with quadrantectomy, axillary dissection, and radiotherapy in patients with small cancers of the breast. *N Engl J Med* 1981;305:6–11
3. Sarrazin D, Le M, Rouesse J, et al. Conservative treatment versus mastectomy in breast cancer with macroscopic diameter of 20 millimeters or less. The experience of the Institut Gustave-Roussy. *Cancer* 1984;53:1209–1213
4. Beadle GF, Silver B, Botnick L, Hellman S, Harris JR. Cosmetic results following primary radiation therapy for early breast cancer. *Cancer* 1984;54:2911–2918
5. Harris JR, Beadle GF, Hellman S. Clinical studies on the use of radiation therapy as primary treatment of early breast cancer. *Cancer* 1984;53:705–711
6. Amalric R, Santamaria F, Robert F, et al. Radiation therapy with or without primary limited surgery for operable breast cancer: a 20-year experience at the Marseilles Cancer Institute. *Cancer* 1982;49:30–34
7. Osborne MP, Ormiston N, Harmer CL, McKinna JA, Baker J, Greening

- WP. Breast conservation in the treatment of early breast cancer: a 20-year follow-up. *Cancer* 1984;53:349-355
8. Romsdahl MM, Montague ED, Ames FC, Richards PC, Schell SR. Conservation surgery and irradiation as treatment for early breast cancer. *Arch Surg* 1983;118:521-528
 9. Harris JR, Recht A, Amalric R, et al. Time course and prognosis of local recurrence following primary radiation therapy for early breast cancer. *J Clin Oncol* 1984;2(1):37-41
 10. Chu F, Lin F, Kim J, Huh SH, Garmatis CJ. Locally recurrent carcinoma of the breast: results of radiation therapy. *Cancer* 1976;37:2677-2681
 11. Harris JR, Botnick LE, Bloomer WD, Chaffey JT, Hellman S. Primary radiation therapy for early breast cancer: the experience at the Joint Center for Radiation Therapy. *Int J Radiat Oncol Biol Phys* 1981;7:1549-1552
 12. Recht A, Silver B, Schnitt S, Connolly J, Hellman S, Harris JR. Breast relapse following primary radiation therapy for early breast cancer. I. Classification, frequency and salvage. *Int J Radiat Oncol Biol Phys* 1985;11:1271-1276
 13. Silen W, Botnick LE. Physical examination of the treated breast. In: Harris JR, Hellman S, Silen W, eds. *Conservative management of breast cancer*. Philadelphia: Lippincott, 1983:261-264
 14. Bloomer WD, Berenberg AL, Weissman BN. Mammography of the definitively irradiated breast. *Radiology* 1976;118:425-428
 15. Paulus DD. Conservative treatment of breast cancer: mammography in patient selection and follow-up. *AJR* 1984;143:483-487
 16. Libshitz HI, Montague ED, Paulus DD. Calcifications and the therapeutically irradiated breast. *AJR* 1977;128:1021-1025
 17. Libshitz HI, Montague ED, Paulus DD. Skin thickness in the therapeutically irradiated breast. *AJR* 1978;130:345-347
 18. Montague ED, Paulus DD, Schell SR. Selection and follow-up of patients for conservation surgery and irradiation. *Front Radiat Ther Oncol* 1983;17:124-130
 19. Geffer WB, Friedman AK, Goodman RL. The role of mammography in evaluating patients with early carcinoma of the breast for tylectomy and radiation therapy. *Radiology* 1982;142:77-80
 20. Berenberg AL, Levene MB, Tonnesen GL. Mammographic evaluation of the postirradiated breast. In: Harris JR, Hellman S, Silen W, eds. *Conservative management of breast cancer*. Philadelphia: Lippincott, 1983:265-272
 21. Fisher ER, Gregorio R, Redmond C, Vellios F, Sommers SC, Fisher B. Pathologic findings from the National Surgical Adjuvant Breast Project (Protocol No. 4). I. Observations concerning the multicentricity of mammary cancer. *Cancer* 1975;35:247-254
 22. Gallager HS. Multicentricity in breast cancer. In: Harris JR, Hellman S, Silen W, eds. *Conservative management of breast cancer*. Philadelphia: Lippincott, 1983:117-122
 23. Rosen PP, Fracchia AA, Urban JA, Schottenfeld D, Robbins GF. "Residual" mammary carcinoma following simulated partial mastectomy. *Cancer* 1975;35:739-747

Book Review

Diagnostic Paediatric Imaging. By Christine M. Hall and Sundara Lingam. New York: Springer-Verlag, 206 pp., 1986. \$43

The subtitle of this book, "A case study teaching manual," is more descriptive than the title. The authors' objective was to create a text on pediatric radiology for clinicians and radiologists in training who are preparing for fellowship, membership, and diploma examinations of various colleges. This book consists of the radiographs and other imaging studies of 100 cases from the radiology teaching collection at the Hospital for Sick Children at Great Ormond Street in London, England. Each case has a short clinical history with a series of questions. Answers and additional illustrations are on the following page. The cases are grouped according to specialty: the gastrointestinal tract, the genitourinary system, the respiratory and cardiovascular systems, the central nervous system, the endocrine system, or the skeletal system.

Many of the illustrations are of excellent quality, but some are so poor that the abnormalities presented are difficult to see. Most of the imaging studies shown are of plain radiographs. Some sonographic images, nuclear medicine studies, and CT studies are illustrated when

appropriate.

Occasional typographic errors are present, such as on page 8 where "Gastrogratin is hypotonic," when it should be "hypertonic." Some of the text is written in British jargon, which may be difficult for American readers to understand. Little discussion of the cases is offered and occasionally the statements are controversial. No references are cited.

While this text may be of value to students in the United Kingdom, most major medical centers in the United States have teaching collections either of their own or from the American College of Radiology that contain much of the same case material in this book. Also the "Radiologic Case of the Month" from the *American Journal of Diseases of Childhood* provides similar material but with more discussion and with references.

Melvin Becker
New York University Medical Center
New York, NY 10016

Sonography in the Follow-up of 100 Patients with Thyroid Carcinoma

Joseph F. Simeone¹
 Gilbert H. Daniels²
 Deborah A. Hall¹
 Kathleen McCarthy¹
 Daniel B. Kopans¹
 Rodney J. Butch¹
 Peter R. Mueller¹
 David D. Stark¹
 Joseph T. Ferrucci, Jr.¹
 Chiu An Wang³

High-frequency, high-resolution sonography was used to detect recurrent thyroid carcinoma in 73 patients with papillary carcinoma, 16 with medullary carcinoma, 10 with follicular carcinoma, and one with small-cell carcinoma. Of the 36 patients with negative sonograms, 35 had no other evidence of recurrence, while one had surgical proof of recurrence. Of 25 patients with positive sonograms, confirmed with surgery or radioactive iodine (¹³¹I) scanning (sonographic sensitivity 96%, specificity 83%), palpation was negative in 17 (palpation sensitivity 32%, specificity 100%). Thirty-two patients with positive sonographic findings had no objective clinical proof of recurrence. There were seven false-positive studies. This study suggests that sonography may be the method of choice for earliest detection and localization of recurrent carcinoma of the thyroid.

Papillary, follicular, and medullary carcinoma of the thyroid gland comprise about 90% of all thyroid cancers [1]. Papillary and medullary carcinomas frequently metastasize to regional nodes in the neck, while follicular carcinomas have more distant metastases. High-frequency, high-resolution sonography is ideally suited to detect recurrent carcinomas that are too small to palpate [2, 3]. This paper reviews the sonographic findings in the follow-up studies of 100 patients with thyroid cancer.

Methods and Materials

We reviewed the records of patients with possible recurrent thyroid cancer who had one or more postoperative sonograms and who were followed at Massachusetts General Hospital. Seventy-three patients had papillary carcinoma, 16 had medullary carcinoma, 10 had follicular carcinoma (six with the Hurthle-cell variants), and one had nonlymphomatous small-cell carcinoma. Two patients developed a second, pathologically distinct, thyroid carcinoma; one patient with a well-documented papillary carcinoma developed medullary carcinoma of the thyroid; a second patient with a clear-cell papillary carcinoma developed a Hurthle-cell follicular carcinoma in the opposite lobe. Patients with disseminated metastases were not studied.

Patients were categorized by the findings on the most recent sonogram or on the last sonogram before a repeat surgical exploration. If follow-up to a positive sonogram resulted in a negative sonogram without surgery, the original positive results were recorded as well.

The following variables were examined: results of palpation; serum thyroglobulin or calcitonin; radioactive iodine (¹³¹I) therapy, and the results of ¹³¹I scanning. Palpation of the neck was performed in all cases. ¹³¹I scanning was performed by using gamma cameras with pinhole collimation in all cases and with rectilinear scanners as well in some patients.

All patients were scanned with a real-time sonographic scanner with a 10-MHz transducer [4]. Scanning was performed over the entire neck and included visualization of the submandibular gland, the thyroid bed, the area deep to the clavicle, and the superior mediastinum. With the small footprint of the 10-MHz transducers (1.5–2.5 cm), the superior mediastinum, including the innominate artery, was visualized well in most patients. The anatomic area lateral to the carotid artery and jugular vein was also examined for lymphadenopathy.

Sonographically, the normal postoperative neck shows an absence of thyroid tissue, close apposition of the carotid artery to the trachea, and a group of highly reflective echoes in the

Received July 14, 1986; accepted after revision August 22, 1986.

¹ Department of Radiology, Massachusetts General Hospital and Harvard Medical School, Boston, MA 02114. Address reprint requests to J. F. Simeone.

² Department of Medicine, Massachusetts General Hospital and Harvard Medical School, Boston, MA 02114.

³ Department of Surgery, Massachusetts General Hospital and Harvard Medical School, Boston, MA 02114.

AJR 148:45–49, January 1987
 0361–803X/87/1481–0045
 © American Roentgen Ray Society

thyroid bed that probably represent postoperative scar (Fig. 1). In all cases in this series, the sonographic appearance of recurrent carcinoma was that of small hypoechoic masses that were easy to detect in the midst of echogenic fibrous tissue (Fig. 2). The shape of the recurrences varied from spherical nodules to oval nodules (Fig. 3).

Results

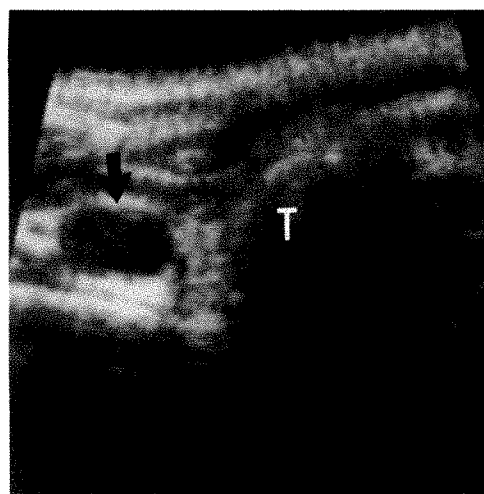
Patients with Negative Sonograms

Thirty-six patients had negative sonograms at the end of the period of observation. Thirty patients had papillary carcinoma, four had follicular, one had medullary, and one had small-cell carcinoma (one patient had two distinct carcinoma types). The mean age at diagnosis was 36 years (range, 17–70), with a mean follow-up period after surgery of 4 years (range, 0.5–18). Nodal metastases were present at the original operation in 14 patients, and three had surgically detect-

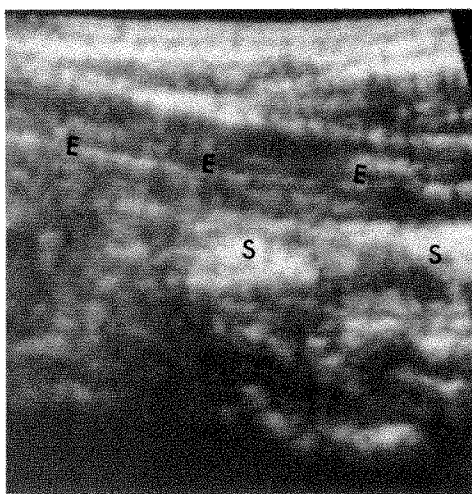
able invasive disease. I^{131} ablative therapy was given to nine patients.

Six patients with negative sonograms had previous recurrences treated surgically. Five of these patients had a positive sonogram at some time after the last surgical procedure; the sonogram spontaneously reverted to normal. The one patient with a false-negative examination had a lymph node palpable in the left posterior cervical region. This node was removed surgically and proved to be metastatic papillary carcinoma. No other patient had a palpable abnormality at the time of a negative sonogram.

Serum thyroglobulin (normal = 5–20 ng/ml) was measured in 34 patients with papillary and follicular carcinoma: 13 patients had antibodies to thyroglobulin that precluded measurement, 16 had thyroglobulin of less than 5, four had thyroglobulin in the range of 5–20, and one had thyroglobulin between 20 and 40. The one patient with medullary carcinoma had an elevated serum calcitonin. Fourteen patients had I^{131}



A

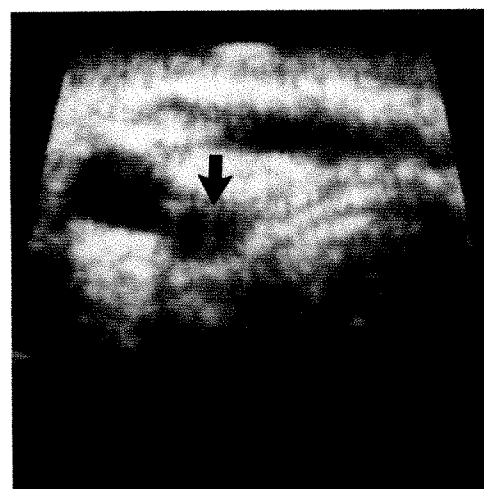


B

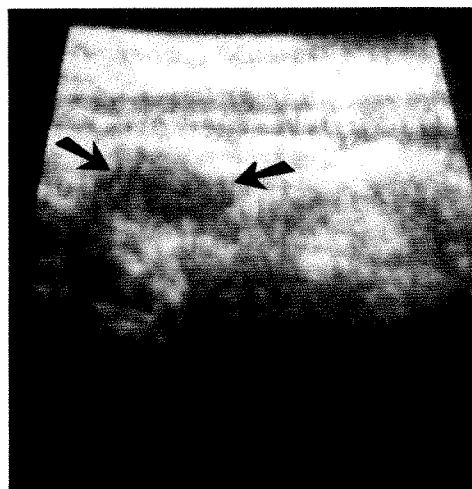
Fig. 1.—Sonograms showing the normal postthyroidectomy neck.

A, Transverse section on right side. Carotid artery (arrow) and trachea (T) are easily distinguished. Highly echogenic fibrous tissue interposed between these two landmarks.

B, Sagittal section on left side. Esophagus (E) and fibrous tissue (S) in thyroid bed.



A



B

Fig. 2.—Sonograms showing post-operative recurrence of thyroid carcinoma.

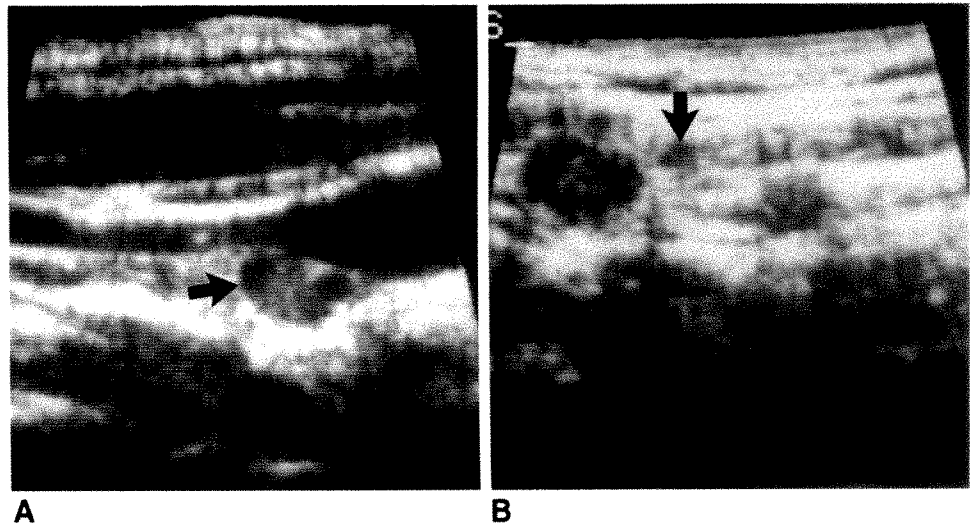
A, Transverse sections on right side. Just medial to carotid artery is hypoechoic nodule (arrow) due to recurrent papillary carcinoma.

B, Sagittal section on right side. Nodule (arrows) is easily detected in echogenic fibrous tissue.

Fig. 3.—Sonograms of other examples of recurrent thyroid carcinoma.

A, Longitudinal section. Solitary nodule (arrow) posterior to jugular vein.

B, Sagittal section. Two definite and one possible (arrow) recurrences of different sizes.



scans, all of which were negative in the area of the original tumor.

Patients with Confirmed Positive Sonograms

Twenty-five patients had positive sonograms that were confirmed by surgery (21) or I^{131} scanning (four). Disease was palpable in eight at the time of the sonogram and in two more at the time of surgery. Papillary carcinoma was present in 12, medullary carcinoma in nine, and follicular carcinoma in four. The mean age at diagnosis was 49 years (range, 17–73), with a mean follow-up of 3 years (range, 0.1–13). Seven of these patients had positive nodes at the time of original surgery, and two had invasive disease. Four patients had received I^{131} therapy.

All nine patients with medullary carcinoma had elevated basal or stimulated calcitonin concentrations. Serum thyroglobulin was performed in 11 patients, with three having antibodies precluding detection. Serum thyroglobulin was less than 5 in two, between 5 and 20 in two, between 20 and 40 in two, and between 41 and 100 in two.

Tumor recurrences were on the same side as the primary tumor in 20 patients and on the opposite side in five. Of those occurring in the contralateral lobe, two appeared to be new primary tumors that differed pathologically from the original tumor.

Patients with Unconfirmed Positive Sonograms

Thirty-two patients had positive sonograms classified as indeterminate because objective confirmatory data were not available. None of these patients has had exploratory surgery. Papillary carcinoma was present in 26, medullary carcinoma in four, and Hürthle-cell follicular in two. The mean age at diagnosis was 41 years (range, 17–79), with a mean follow-up period of 3.9 years (range, 0.1–12). Eight of these patients had nodal involvement at the time of original surgery, and

four had locally invasive disease. Seven patients had received I^{131} ablative therapy.

Four patients in this group had I^{131} scans. Two were positive in areas remote from the residual disease, one showed no uptake in a tumor too aggressive to take up I^{131} , and one was positive in the area of recurrence expected from sonography. This lesion, which was not palpable, may have been normal residual thyroid tissue.

All four patients with medullary carcinoma had persistent calcitonin elevation. Twenty-six patients had serum thyroglobulin measured: antibodies were present in seven, thyroglobulin was less than 5 in 10, between 5 and 20 in five, between 20 and 40 in two, and between 41 and 100 in two. Two patients had negative I^{131} scans at the time of the abnormal sonogram. One later developed distant metastases that were not detected by I^{131} scanning, either.

Patients with Confirmed False-Positive Sonograms

Seven patients had sonographic abnormalities that must be considered false positives, although many of these were indeterminate. Papillary carcinoma was present in five and medullary carcinoma in two. Five patients had sonographic abnormalities that later disappeared (one had an elevated calcitonin, three had thyroglobulin antibodies, and one had thyroglobulin of 22). In two patients, the abnormalities appeared (and disappeared) in the contralateral lobe, and in three patients ipsilateral nodes seemed to disappear. In one patient the abnormality seemed palpable at the time of the abnormal sonogram and not when the sonogram was repeated 2 months later. Two patients had sonographic abnormalities that were proved benign at surgical exploration. One patient had bilateral abnormalities that proved to be benign lymph-node hyperplasia at surgical exploration. The last patient had a stitch granuloma removed, although the "nodes" seen at the time of the preoperative sonogram, also present on the postoperative study, were not found by the surgeon.

Discussion

Imaging studies available for detecting recurrent thyroid carcinoma include I^{131} scintigraphy, sonography with high-frequency transducers, CT, and recently, MR of the neck [5–7]. I^{131} is accurate in detecting residual papillary or follicular thyroid carcinoma, provided the lesions take up the isotope. Scans are useful only after total thyroidectomy or I^{131} ablation of residual tissues, practices that are not routine in our institution. Furthermore, patients need to be hypothyroid for 2 weeks after cytomele (L-triiodothyronine) therapy or 5 weeks after L-thyroxine. I^{131} activity in the thyroid bed may represent residual normal tissue or carcinoma.

Nodal metastases do not appear to influence the survival in patients with papillary [8–11] or medullary carcinoma [2] of the thyroid gland, and the early detection of nodal recurrences by sonography may be only of theoretical interest. However, local, nonnodal recurrence, usually in patients with locally invasive disease, does lead to shortened life expectancy [1]. The potential for early detection of nonnodal soft-tissue recurrences in patients with invasive disease is of great clinical importance because it might lead to more successful surgery or radiation therapy. It is not yet clear whether sonography can distinguish nodal disease from nonnodal neck recurrence.

Sensitivity and Specificity

If the 32 patients with abnormal sonograms but without surgical confirmation are eliminated from the statistical analysis, the sensitivity of sonography is 96% and the specificity is 83%. The I^{131} studies in 18 patients had a sensitivity of 100% and specificity of 100%. Patient eligibility for I^{131} is limited in our practice because total thyroidectomy or total I^{131} ablation are not routinely performed. Of the 25 patients with true-positive sonograms, recurrence was not palpable in 17 at the time of the sonogram. Palpation had a sensitivity of 32% (many false negatives) and a specificity of 100% (no false positives).

The high sensitivity of sonography is further evident when it is compared with the high sensitivity of serum calcitonin in recurrent medullary carcinoma. Patients with medullary carcinoma with nodal metastases almost always have persistent basal or stimulated calcitonin elevation after surgery [2]. Such calcitonin persistence is thought to represent residual disease, but surgical confirmation is rarely available [10, 11]. Ten of 11 patients with persistent calcitonin elevation had abnormal sonograms. On nine occasions, these patients underwent repeated surgery, at which nodal metastases were found.

In the 32 patients without surgical confirmation of their abnormal sonograms, the validity of the sonographic findings is supported by the data from the thyroglobulin studies and from the localization of the lesions.

Laboratory data.—In the papillary carcinoma group, only one of nine patients with serum thyroglobulin greater than 20 had a negative sonogram. Only four of 11 patients with thyroglobulin between 5 and 20 had a negative sonogram. Of 28 patients with undetectable thyroglobulin, 12 had positive sonograms (two surgically proven), consistent with the ob-

servation that thyroglobulin may be undetectable with residual disease while the patient is on suppressive therapy [12, 13].

Localization data.—Of those patients with indeterminate (positive) sonograms, 24 (83%) of 29 with unilateral surgical disease had soft-tissue or nodal metastases that appeared on the same side as the primary lesion. This proportion is comparable to our findings in the 25 patients with documented true-positive sonograms—20 recurrences (80%) on the same side as the original lesion.

High Frequency of Abnormal Sonograms

Palpable nodal recurrences occur in 10–15% of patients, mostly on the side of the original lesion. In most surgical series, 30–70% of patients with papillary carcinoma have nodal metastases at the time of surgery [8–10]. The sonographic data in this series support the surgical data: 43 (59%) of 73 patients had abnormal sonograms. We are probably seeing the subclinical nodal disease that persists or develops in most patients with papillary carcinoma. This study suggests that residual or recurrent nodal disease, although commonly undetected in patients with papillary carcinoma, may not be of clinical significance.

False-Positive and False-Negative Studies

One patient had a false-negative sonogram that failed to detect a clinically palpable posterior cervical node. This false negative was caused by failure to examine this area of the neck, which occurred early in the series. A more thorough examination is now performed, including all soft-tissue areas. Seven patients seemed to have false-positive sonograms, but we are uncertain about the final diagnosis in several of these patients. We have chosen to designate these as false positive because the results were considered clinically significant and they affected alternative patient care. When a sonogram is found to be abnormal without clinically palpable disease, repeated evaluation in 6–12 months is indicated to determine and confirm the presence and growth potential of the recurrence.

"Disappearing" Nodules

The appearance and subsequent disappearance of hypoechoic nodules in the soft tissues were probably caused by inflamed lymph nodes. All the patients with disappearing soft-tissue masses had had surgery and may have had reactive inflammatory lymphadenopathy. The lesions seen in the contralateral lobes may simply represent normally occurring dilated thyroid follicles that later reabsorbed [2].

Conclusion

In detecting recurrent thyroid carcinoma, sonography had a sensitivity of 96% and a specificity of 83%. Although the use of I^{131} was limited to 18 patients in this study, it had a sensitivity and specificity of 100%. Both sonography and

serum-calcitonin determinations had a sensitivity of 100% in detecting surgically proven medullary carcinoma. Palpation had a sensitivity of 32% and a specificity of 100%.

These findings suggest the following protocol: In patients with locally invasive disease a sonogram should be performed 6 months after surgery and then yearly thereafter. A suspected recurrence may be confirmed with I^{131} or palpation.

REFERENCES

1. Schimpff SC. Well differentiated thyroid cancer. *Am J Med Sci* 1979;278:100-106
2. Katz JF, Kane RA, Reyes J, Clarke MP, Hill TC. Thyroid nodules: sonographic-pathologic correlation. *Radiology* 1984;151:741-744
3. Schwarrock R, Muller ST, Schober O, et al. Ultrasonography in malignant thyroid disease. *Aktuel Endokr Stoffw* 1983;4:107-120
4. Simeone JF, Daniels GH, Mueller PR, et al. High-resolution real-time sonography of the thyroid. *Radiology* 1982;145:431-435
5. Solbiati L, Volterrani L, Rizzato G, et al. Thyroid gland with low uptake lesions: evaluation by ultrasound. *Radiology* 1985;155:187-190
6. Radecki PD, Arger PH, Arenson RL, et al. Thyroid imaging: comparison of high-resolution real-time ultrasound and computed tomography. *Radiology* 1984;153:145-148
7. James EM, Charboneau JW. High frequency (10 MHz) thyroid ultrasonography. *Semin Ultrasound* 1985;6:294-298
8. Frazell EL, Foote FW Jr. Papillary thyroid carcinoma. Pathological findings in cases with and without clinical evidence of cervical node involvement. *Cancer* 1955;8:1164-1166
9. Cady B, Sedgwick CE, Meissner WA. Changing clinical, pathologic, therapeutic, and survival patterns in differentiated thyroid carcinoma. *Ann Surg* 1976;184:541-553
10. Mazzaferri EL, Young RL, Oetzel JE. Papillary thyroid carcinoma: the impact of therapy in 576 patients. *Medicine* 1977;56:171-196
11. Mazzaferri EL, Young RL. Papillary thyroid carcinoma: a 10 year follow-up report of the impact of therapy in 576 patients. *Am J Med* 1981;70:511-521
12. Refetoff S, Lever EG. The value of serum thyroglobulin measurement in clinical practice. *JAMA* 1983;250:2352-2357
13. Schneider AB, Line BR, Goldman JM, Robbins J. Sequential serum thyroglobulin determinations, ^{131}I scans, and ^{131}I uptakes after triiodothyronine withdrawal in patients with thyroid cancer. *J Clin Endocrinol Metab* 1981;53:1199-1206

Forthcoming Articles

CARDIOVASCULAR RADIOLOGY

- Acute myocardial infarction: MR evaluation in 29 patients.** *Fisher MR, McNamara MT, Higgins CB*
- Aberrant right subclavian artery: further observations.** *Proto AV, Cuthbert NW, Raider L*
- Superior vena cava obstruction: a classification based on venocavography findings.** *Stanford W, Jolles H, Ell S, Chiu LC*
- Occult pulmonary embolism: common occurrence in deep venous thrombosis.** *Dorfman GS, Cronan JJ, Tupper TB, Messersmith RN, Denny DF, Lee CH*
- Case report. Primary angiosarcoma of the heart: CT characteristics.** *Shin MS, Kirklin JK, Cain JB, Ho K-J*

GASTROINTESTINAL RADIOLOGY

- Pictorial essay. Contrast pharyngography: the importance of phonation.** *Rubenstein SE, Jones B, Donner MW*
- Patterns of recurrence of esophageal carcinoma after transhiatal esophagectomy and gastric interposition.** *Becker CD, Barbier PA, Terrier F, Porcellini B*
- Case report. Acute gastric dilatation: a rare cause of portal venous gas.** *Radin DR, Rosen RS, Halls JM*
- Natural history of the obstructed rabbit appendix: observations with radiography, sonography, and CT.** *Dachman AH, Nichols JB, Patrick DH, Lichtenstein JE*
- Case report. Ringlike rectal ulcers after biopsy or polypectomy.** *Lev-toaff AS, Levine MS, Laufer I, Herlinger H*

GENITOURINARY RADIOLOGY

- MR evaluation of uterine anomalies.** *Mintz MC, Thickman DJ, Gussman D, Kressel HY*
- Sonography in the diagnosis of acute renal allograft rejection and cyclosporine nephrotoxicity.** *Linkowski GD, Warvariv V, Filly RA, Vincenti F*
- Needle puncture of cystic renal masses: a survey of the Society of Uro-radiology.** *Amis ES Jr, Cronan JJ, Pfister RC*
- Interstitial emphysema associated with epidural anesthesia for extracorporeal shock-wave lithotripsy.** *Roberts MC, Pollack HM, Banner MP, Castro AD, VanArsdalen KN*
- Case report. Polyorchidism: evaluation by MR.** *Baker LL, Hajek PC, Burkhard TK, Mattrey RF*

MUSCULOSKELETAL RADIOLOGY

- MR imaging of the carpal tunnel: normal anatomy and preliminary findings in the carpal tunnel syndrome.** *Middleton WD, Kneeland JB, Kellman GM, et al.*
- MR imaging of osteogenic and Ewing's sarcoma.** *Boyko OB, Cory DA, Cohen MD, Provisor A, Mirkin D, DeRosa GP*
- Parosteal osteosarcoma: radiologic-pathologic correlation with emphasis on CT.** *Lindell MM, Shirkhoda A, Raymond AK, Murray JA, Harle TS*
- Pictorial essay. Cystic masses of the knee: arthrographic and CT evaluation.** *Lee KR, Cox GG, Neff JR, Arnett GR, Murphey MD*
- Technical note. Digital subtraction arthrography of the temporomandibular joint.** *Jacobs JM, Manaster BJ*
- Diagnostic oncology case study. Bone scan-positive and radiograph- and CT-negative vertebral lesion in a woman with locally advanced breast cancer.** *Kagan RA, Steckel RJ, Mink JH, Weitz I*

PEDIATRIC AND FETAL RADIOLOGY

- Evaluation of chronic pediatric airway obstruction with cine-CT.** *Frey EE, Smith WL, Grandgeorge S, et al.*
- The radiologic findings in children and young adults with Barrett's esophagus.** *Yulish BS, Rothstein FC, Halpin TC Jr*
- Sonographic detection of neonatal umbilical artery thrombosis: clinical correlation.** *Seibert JJ, Taylor BJ, Williamson SL, Williams BJ, Szabo JS, Corbitt SL*
- Sonographic analysis of the fetus with ureteropelvic junction obstruction.** *Kleiner B, Callen PW, Filly RA*
- Main stem bronchial atresia: intrauterine sonographic diagnosis.** *McAlister WH, Wright JR Jr, Crane JP*

INTERVENTIONAL RADIOLOGY

- The risks of percutaneous transhepatic drainage in patients with cholangitis.** *Lois JF, Gomes AS, Grace PA, Deutsch L-S, Pitt HA*
- Case report. Common bile duct stone dissolution with methyl tertiary butyl ether: experience with three patients.** *Teplick SK, Haskin PH, Goldstein RC, et al.*
- Case report. Transcatheter recanalization of a chronically occluded saphenous aortocoronary bypass graft.** *Marx M, Armstrong WT, Brent BN, Wack JP, Bernstein RM, Gregoratos G*
- Case report. Transcatheter intracavitary fibrinolysis of infected extravascular hematomas.** *Vogelzang RL, Tobin RS, Burstein S, Anschuetz SL, Marzano M, Kozlowski JM*

NEURORADIOLOGY

- The MR appearance of syringomyelia: new observations.** *Sherman JL, Barkovich AJ, Citrin CM*
- CT patterns of facet fracture dislocations in the thoracolumbar region.** *Manaster BJ, Osborn AG*
- Spontaneous dissection of the cervical internal carotid artery: correlation of arteriography, CT, and pathology.** *Petro GR, Witwer GA, Cacayorin ED, et al.*

MAGNETIC RESONANCE

- Magnetite albumin microspheres: a new MR contrast material.** *Widder DJ, Greif WL, Widder KJ, et al.*
- Quantitative phase-flow imaging by MR with standard sequences: comparison with in vivo flow meter measurements.** *Pettigrew RI, Dannels W, Galloway JR, et al.*
- Use of standard gradients with compound oblique angulation for optimal quantitative MR flow imaging in oblique vessels.** *Pettigrew RI, Dannels W*
- Effects of MR imaging on murine natural killer cell cytotoxicity.** *Prasad N, Lotzova E, Thornby JI, Madewell JE, Ford JJ, Bushong SC*
- Intensity correction in surface coil MR imaging.** *Axel L, Costantini J, Listerud J*

DIGITAL RADIOLOGY

- Total digital radiology department: spatial resolution requirements.** *Seeley GW, Fisher HD, Stempki MA, Borgstrom M, Bjelland J, Capp MP*
- Commentary. Picture archiving and communication systems in Japan.** *Huang HK, Mankovich NJ, Cho PS, Taira R, Stewart BK, Ho BK*

MR Imaging of the Prostate Gland: Normal Anatomy

Hedvig Hricak¹
 Georges C. Dooms²
 John E. McNeal³
 Alexander S. Mark¹
 Miljenko Marotti¹
 Anthony Avallone⁴
 Mark Pelzer¹
 Evelyn C. Proctor¹
 Emil A. Tanagho⁴

MR images of the male pelvis in 55 subjects were analyzed retrospectively for depiction of the zonal anatomy of the prostate gland as related to different repetition (TR) and echo (TE) times, slice thickness, plane of imaging, chronologic age of the patient, and different magnetic field strengths. With imagers operating at 0.35 and 1.5 T, T2-based tissue-contrast images were needed for the demonstration of the internal anatomy of the prostate gland. The display of zonal anatomy was improved when continuous 0.5-cm slices were used. Evaluating sequential sections, the peripheral, central, and transition zones could be differentiated. The peripheral zone showed higher signal intensity than either the central or transition zone and was discerned in the coronal, sagittal, and transverse planes. The central zone was of low signal intensity and was well displayed in the coronal and sagittal planes. The central zone was seen in 31 of the 32 young men (aged 25–35 years) but in only eight of the 23 older men (aged 40 years and older). The transition zone had intrinsic MR parameters similar to the central zone, and the two could be distinguished from each other only by the knowledge of their respective anatomic location. The low-intensity transition zone blended with the periurethral glands and the preprostatic sphincter. The transition zone was of homogeneous low signal intensity in young men but varied in size and signal intensity in older men. Such a detailed display of the prostate zonal anatomy offers a unique potential for the evaluation of prostatic physiology and disease.

The introduction of sonography and CT has improved the diagnostic evaluation of the prostate gland [1–5]. While CT can accurately display prostatic size, contour, and periprostatic disease, it is limited in delineating the internal anatomy of the gland [1–4]. Transrectal sonography, with the use of high-frequency (5 MHz or more) transducers, allows excellent display of the prostatic parenchyma [5], but demonstration of prostatic zonal anatomy by sonography has not been reported. The value of MR imaging with a low magnetic field strength for the evaluation of the male pelvis has been described [6–9]. A detailed description of the normal zonal anatomy of the prostate as seen with MR with imagers of either low or high magnetic field strength has not been provided.

Our study was undertaken to analyze the MR appearance of the prostate and the periprostatic anatomy with special emphasis on the demonstration of anatomic zones according to the architectural system proposed by McNeal [10]. The appearance of the zonal anatomy was analyzed in relation to repetition (TR) and echo (TE) times, slice thickness, plane of imaging, age of the patient, and magnetic field strength.

Materials and Methods

The MR examinations of 55 subjects were reviewed retrospectively. All 55 subjects were normal volunteers or patients imaged for reasons other than prostatic disorders. None of the subjects had a history of lower urinary tract disease. The subjects were divided into two groups according to age: group 1 (32 subjects aged 22–35 years) and group 2 (23 subjects aged 40–75 years).

Received June 6, 1986; accepted after revision August 14, 1986.

¹ Department of Radiology, University of California School of Medicine, San Francisco, CA 94143. Reprints are not available.

² Department of Radiology, Université Catholique de Louvain, UCL Saint-Luc, Brussels, Belgium.

³ Department of Surgery, Division of Urology, Stanford University Medical Center, Stanford, CA 94305.

⁴ Department of Urology, University of California School of Medicine, San Francisco, CA 94143.

AJR 148:51–58, January 1987
 0361–803X/87/1481–0051
 © American Roentgen Ray Society

Technical Considerations

Proton MR imaging was performed either with a 0.35-T Diasonics MT/S or 1.5-T General Electric (Signa) system. The specifications of both 0.35 and 1.5 T have been described [11, 12].

On the 0.35-T unit, a multislice, double-spin-echo (SE) imaging technique was used in 45 subjects with a TR of 2000 msec (two acquisitions) and a TR of 500 msec (four acquisitions). TE times were 28 and 56 msec (30 subjects), 30 and 60 msec (10 subjects), and 40 and 80 msec (five subjects). The MR examinations were performed with two different TRs in all subjects in at least one imaging plane. Images with two different TRs allowed calculations of T1 relaxation times and spin density. T2 was measured on the image obtained with TR = 2000 msec and TE = 28–30 and 56–60 msec. Section thickness was 7 mm with a 3-mm gap (30 subjects), 10 mm without gap (10 subjects), or 5 mm without gap (five subjects). Images were obtained with the elliptical body coil, aperture 55 × 40 cm, in 35 subjects; and with the quadrate body coil, aperture 55 cm in diameter, in 10 subjects. Matrix size of 256 × 256 and pixel size of 1.7 × 1.7 were used in all subjects. All subjects were scanned in the transverse plane. Thirty-nine were scanned in an additional sagittal and 30 subjects in an additional coronal plane. In 24 patients all three imaging planes were used.

Ten subjects were imaged on a 1.5-T unit. An SE sequence with a TR 600 msec, TE 25 msec (two excitations) was used in all 10 subjects; TR 2000 msec, TE 40 and 80 msec (two excitations) in three subjects; or TR 2000 msec, TE 20, 40, and 60 msec (two excitations) in seven subjects. Imaging was done with a quadrate-system body coil, aperture 55 cm. Matrix size was 256 × 128. The slice thickness (5 mm) and imaging section were contiguous in all 10 patients. The imaging plane was transverse (10 subjects), coronal (10 patients), and sagittal (five patients). In five subjects all three imaging planes were used.

Image Analysis

The MR examinations were reviewed retrospectively in conference by five observers. The appearance of the normal zonal anatomy of the prostate gland was analyzed in relation to (1) various TR and TE parameters, (2) slice thickness, (3) plane of imaging, (4) age of the patient, and (5) magnetic field strength. The zonal anatomy of the prostate gland was based on the McNeal guidelines [10]. An attempt was made to identify the peripheral, central, and transition zones in all imaging planes. As advocated by McNeal [10], the urethra and verumontanum were used as key reference points (Figs. 1 and 2).

On images obtained with the 0.35-T unit the signal intensity was obtained in absolute numbers (mean intensity value). This was performed by circumscribing a region of interest with a cursor on the displayed image. The equation used to calculate the spin density and the T1 and T2 relaxation times for a particular tissue has been reported [13]. The T1 and T2 relaxation times were determined for the central and peripheral zones of the normal prostate gland and for three pelvic tissues: fat (subcutaneous or pelvic), striated muscle (internal obturator muscle), and urine. T1 and T2 relaxation times of the transition zone were not calculated. The internal obturator muscle was chosen as muscle-tissue reference because it was not possible to obtain a region of interest in the levator ani muscle of sufficient size to permit reliable intensity measurements.

The MR spin-density number in a particular tissue is not to be regarded as an absolute measurement but should be interpreted as a relative value (ratio) compared with another reference tissue. Therefore, the values determined in the different tissues described above are relative. The relative spin density was calculated by dividing the

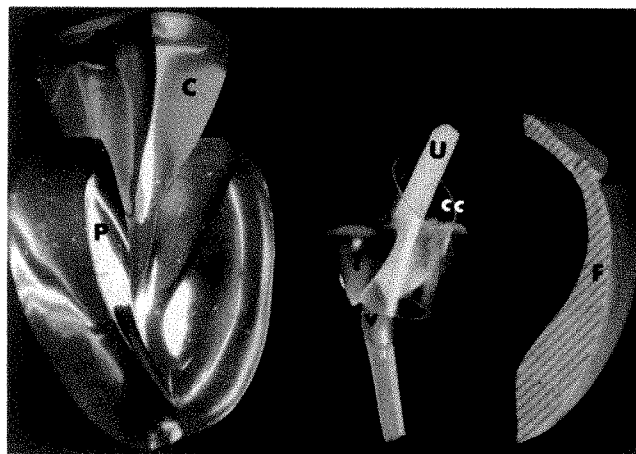


Fig. 1.—Three-dimensional model of prostate gland. Anterior fibromuscular stroma (F) is cut sagittally. Transition zone contacts central (C) and peripheral (P) zones but lies anterior to their coronal plane. At level of verumontanum (V), urethra (U) forms anterior angle. Distal urethra is in contact with peripheral zone. Urethra above verumontanum is in contact with transition zone. CC = preprostatic sphincter (clear cylinder associated with urethra); T = transition zone glands. (Reprinted from [10].)

spin density of tissue of interest by the spin density of the reference tissue.

The difference in signal intensity between two tissues is of greater significance than the absolute intensity of a tissue. Therefore, the values for absolute intensity were used to calculate percentage contrast of the intensity of tissue of interest (I_i) versus reference tissue intensity (I_r) with the equation, $\% \text{Contrast} = [(I_i - I_r) / (I_i + I_r)] 100$.

The calculations of T1, T2, and tissue intensity were not done for the studies obtained on the 1.5-T device because, at the time this study was undertaken, the capability to calculate T1 and T2 was not available.

Results

Prostate Anatomy

TR, TE parameters.—With a short TR (500 msec) and TE (28 or 30 msec) on the 0.35-T unit (T1-weighted image), the prostate gland was imaged with homogeneous intermediate signal intensity, and differentiation between the three zones was not possible (Table 1, Fig. 3A). At 1.5-T magnetic field strength the zones could be seen on the image obtained with TR 600 msec, TE 25 msec (T1-weighted image) (Fig. 4A). However, the contrast between the zones was considerably less than with longer TR, TE parameters (Figs. 4B–4D). The zonal anatomy was well delineated by using the T2-weighted image. On the 0.35-T device, an image with SE 2000/60 or greater and on the 1.5-T device an image with SE 1500/40 or greater were considered T2-weighted images. On the T2-weighted image, the peripheral zone showed higher signal intensity than either the central or transition zone (Figs. 3B and 4C). In each subject the intrinsic tissue parameters (T1 relaxation time, T2 relaxation time, and relative spin density) of the peripheral zone were greater than those of the central zone (Table 2). Regardless of the TR and TE used, the

Fig. 2.—Schematic drawing of prostatic anatomy in coronal (A) and sagittal (B) planes shows central (C) and peripheral (P) zones of prostate gland. Bulbous urethra (arrows) in corpora spongiosa. R = rectum; F = fibromuscular band; L = levator ani muscle; O = internal obturator muscle; T = transversalis perinei; SV = seminal vesicle; B = urinary bladder.

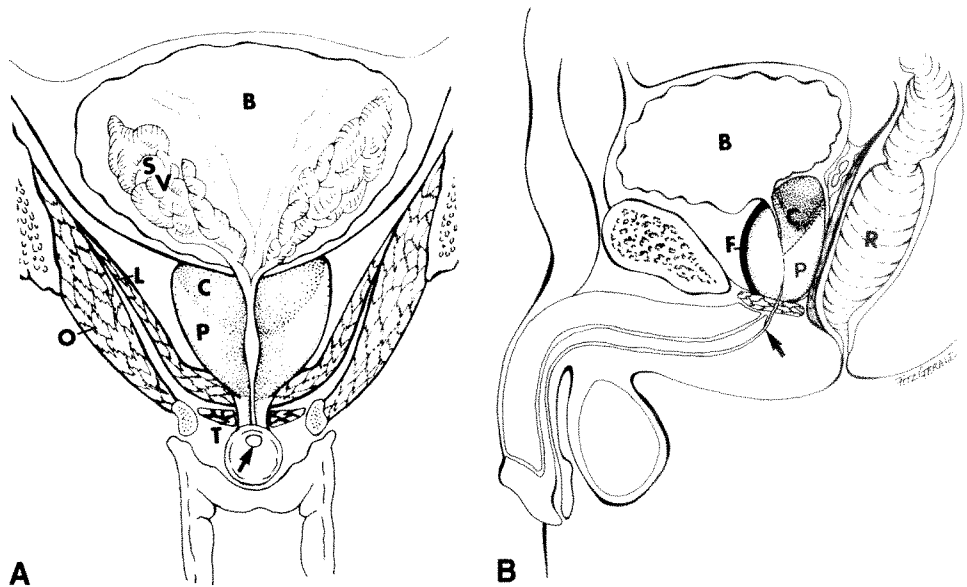


TABLE 1: Contrast Between Peripheral Zone of Prostate and Adjacent Tissue in Relation to Imaging Parameters

Peripheral zone vs:	% Contrast \pm SD at:			
	TR = 500 msec; TE = 28 or 30 msec	TR = 500 msec; TE = 56 or 60 msec	TR = 2000 msec; TE = 28 or 30 msec	TR = 2000 msec; TE = 56 or 60 msec
Central zone	1 \pm 4	3 \pm 3	3 \pm 3	7 \pm 4
Fat	-45 \pm 6	-41 \pm 8	-15 \pm 2	-17 \pm 4
Striated muscle	14 \pm 5	21 \pm 7	24 \pm 5	42 \pm 6
Urine	43 \pm 2	26 \pm 4	24 \pm 11	10 \pm 8

Note.—TR = repetition time; TE = echo time.

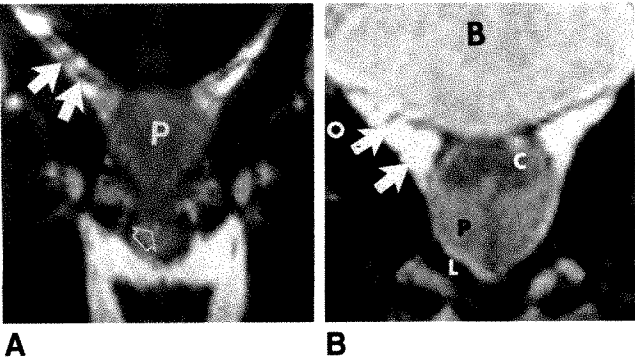


Fig. 3.—25-year-old man. Coronal image at 0.35 T; 5-mm-thick contiguous sections. Quadrate body coil, 55-cm aperture.
A, TR 500 msec, TE 40 msec. Prostate (P) is imaged with homogeneous medium signal intensity. Prostate veins (solid arrows) are superolateral to gland. Bulbous urethra (open arrow) is within corpora spongiosa.
B, TR 2000 msec, TE 80 msec. On this T2-weighted image, peripheral (P) and central (C) zones of prostate can be differentiated. Periprostatic veins (arrows) emit high signal intensity due to second-echo rephasing phenomenon [14]. B = urinary bladder; L = levator ani muscle; O = internal obturator muscle.

transition zone had a signal intensity similar to that of the central zone and the two could be separated only by the knowledge of anatomic location (Figs. 4C, 4D, and 5). The urethra was recognized on the T2-weighted image because it had a high-signal-intensity center surrounded by the lower-signal-intensity urethral muscle wall and periurethral tissue (Figs. 4F, 5B, 6, and 7A). The signal intensity of the center of the urethra was greater than of urine in the bladder, indicating that it did not represent residual urine, but most likely was a reflection of abundant vascularity in the urethral mucosa. The verumontanum in 60% of the patients emitted high signal intensity on T2-weighted images (Figs. 4B and 4C). The ejaculatory ducts were seen with either a low- (40%) (Fig. 4E) or high- (60%) signal-intensity center. A rim of low intensity surrounding the prostate was seen on the T2-weighted image in 31% of the patients. Although the location of this line corresponds to the location of the prostate capsule, its width was greater than 1 mm, which is the reported width of the normal prostate capsule [10]. The low-intensity line is probably related to a combination of the capsule and periprostatic tissue (Fig. 8). Segmental demonstration of the low-intensity

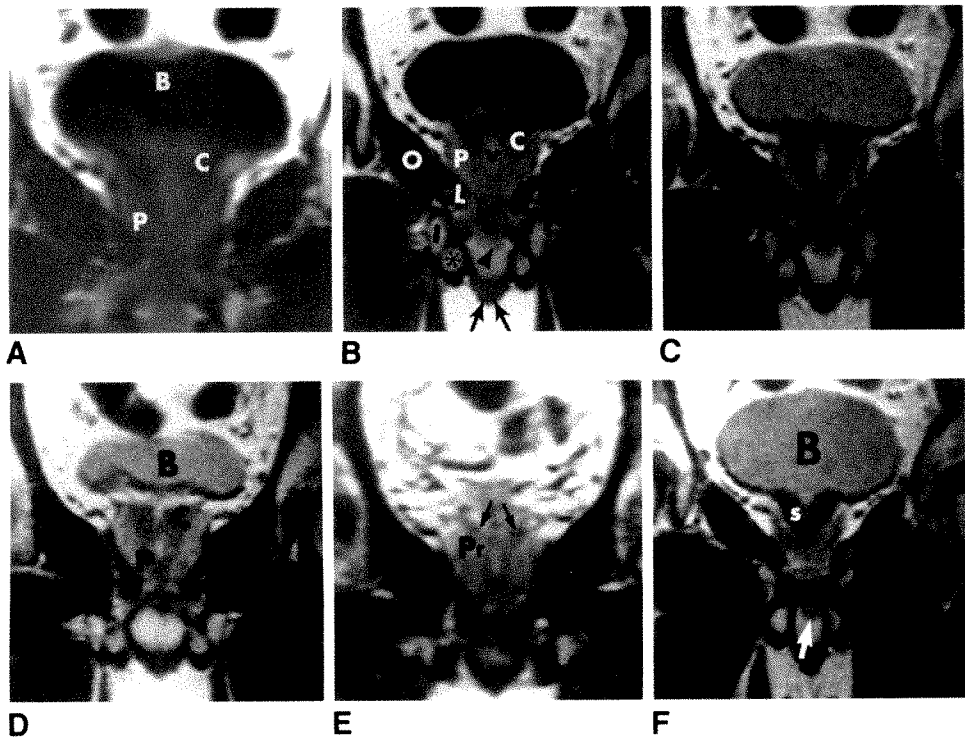


Fig. 4.—35-year-old man. Coronal image at 1.5 T, 5-mm-thick contiguous sections. Body coil, quadrate system, 55-cm aperture. C = central zone; P = peripheral zone; O = internal obturator muscle; B = urinary bladder; L = levator ani muscle; Pr = prostate gland; s = preprostatic sphincter.

A, TR 600 msec, TE 20 msec. T1-weighted image. Differentiation between central and peripheral zones is indistinct.

B and C, TR 2000 msec, TE 20 msec (one of four echoes) for B; TR 2000 msec, TE 60 msec (three of four echoes) for C. With prolongation of TR and TE parameters, differentiation between central and peripheral zones becomes more distinct. In this imaging plane, low-intensity transition zone blends with central zone, periurethral glands, and preprostatic sphincter. Corpora cavernosa (asterisk) are attached to ischium. Urethra (arrowhead) is identified within the corpora spongiosa. Arrows show bulbo spongiosus muscle.

D, TR 2000 msec, TE 60 msec (three of four echoes). 5 mm posterior to C. Central and peripheral zones clearly shown.

E, TR 2000 msec, TE 60 msec (three of four echoes) (scan obtained 2 days after D). Most posterior plane through prostate gland. Ejaculatory ducts (arrows).

F, TR 2000 msec, TE 60 msec (three of four echoes). Through most anterior plane. Low signal intensity in area of preprostatic sphincter. Bulbous urethra (arrow) within corpora spongiosa.

TABLE 2: Intrinsic Parameters of Prostatic Zones and Adjacent Normal Tissue

	Mean \pm SD in msec		Relative Spin Density ^a
	T1	T2	
Peripheral zone ^b	872 \pm 129	62 \pm 8	1.06 \pm 0.04 ^c 0.93 \pm 0.11
Central zone ^b	783 \pm 95	53 \pm 5	0.88 \pm 0.12
Pelvic or subcutaneous fat	266 \pm 35	61 \pm 10	1.0
Striated muscle	570 \pm 112	31 \pm 7	0.67 \pm 0.18
Urine	2435 \pm 699	130 \pm 42	1.22 \pm 0.72

^a Fat used as reference tissue.

^b These intrinsic relaxation parameters were calculated from normal subjects in whom differentiation between central and peripheral zones was possible.

^c vs central zone.

rim at the margin of the prostate gland was related to the chemical-shift artifact (Fig. 7B). The anterior fibromuscular band covering the anterolateral surface of the prostate gland was identified with low signal intensity, especially when long TR/TE parameters were used (Figs. 5B and 9). The peripros-

tatic venous plexus was identified as a round, tubular structure with low signal intensity on the first echo (Figs. 3A, 5A, and 7B). On the long TR and the second echo, the veins emitted high signal intensity due to the even-echo rephasing phenomenon [14] (Figs. 3B, 5B, and 9). The veins were seen lateral and anterior to the prostate and their distribution changed from the apex to the base of the gland. The surrounding levator ani muscle had lower signal intensity than the prostate gland no matter which TR or TE was used (Table 1) or which magnetic field was used. The best contrast between the levator ani muscle and peripheral zone of the prostate gland was obtained using a long TR/TE parameter.

Slice thickness.—Contrast between the zones was increased by the use of thin (5-mm) continuous slices that diminished the partial-volume effect. The proximal prostatic urethra was identified in the transverse plane in 85% of the subjects in whom 5-mm slices were used (Fig. 5B). When the slice thickness was 1 cm, the prostatic urethra was seen in 60% of the subjects. The distal urethra was identified in 90% when 5-mm slices were used (Fig. 9A) and in 80% when 1-cm slices were used (Fig. 6). The membranous (Fig. 7A) and bulbous (Figs. 4B and 4D) urethra were identified in all patients regardless of slice thickness.

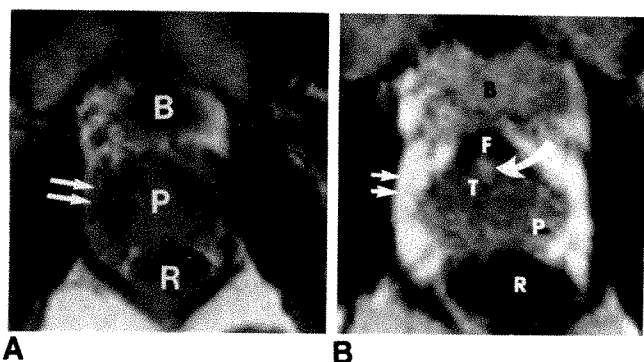


Fig. 5.—25-year-old man. Transverse image at 0.35 T, 5-mm continuous slices. Quadrate body coil, 55-cm aperture.

A, TR 500 msec, TE 40 msec. Prostate (P) has homogeneous medium signal intensity. Periprostatic veins (arrows) are imaged with medium signal intensity. B = urinary bladder; R = rectum.

B, TR 2000 msec, TE 80 msec. With prolongation of TR and TE parameters, separation between transition (T) and peripheral (P) zones is possible. High signal intensity of periprostatic veins (straight arrows) is from second-echo rephasing phenomenon [14]. Proximal prostatic urethra (curved arrow). F = anterior fibromuscular band; R = rectum; B = urinary bladder.

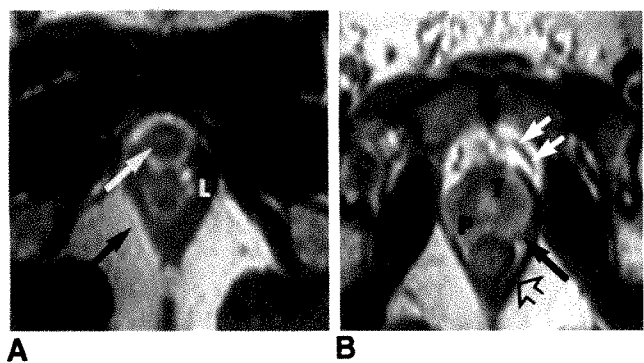


Fig. 7.—35-year-old man imaged on 1.5-T unit; 5-mm continuous slices, body coil, quadrate system, 55-cm aperture. TR 2000 msec, TE 40 msec.

A, Transverse scan. Membranous urethra (white arrow) shows high-intensity center and thick, lower-intensity wall. Chemical-shift artifact causes asymmetric thickening of levator ani muscle (L) and high-intensity stripe of right levator ani muscle (black arrow).

B, More craniad section. Clear differentiation between transition (T) and peripheral (P) zones. Periuethral glandular region and preprostatic sphincter cannot be separated from transition zone. Chemical-shift artifact is responsible for thicker appearance of levator ani on left (open arrow) as compared with right side. In addition, adjacent to right levator ani muscle there is a high-signal-intensity stripe. Low-intensity line at left posterior part of prostate (solid black arrow) is also from chemical-shift artifact. Periprostatic veins (white arrows).

Plane of imaging.—The bulk of the true glandular tissue of the prostate gland is a flat disk oriented in the coronal plane. The peripheral and central zones were well differentiated in the coronal plane of imaging on the section located posterior to the level of the verumontanum (Figs. 3B and 4B). At the level of the urethra and verumontanum, the peripheral zone could be separated from the central or transition zone (Figs. 4C and 4D), while the central zone, transition zone, and periuethral tissue blended together (Fig. 4C). Periprostatic veins were seen lateral and superior to the gland (Fig. 3).

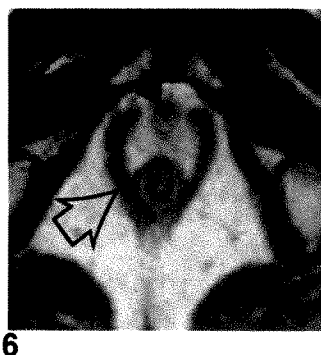


Fig. 6.—34-year-old man. TR 2000 msec, TE 56 msec. Transverse image on 0.35-T unit, elliptical body coil 55 × 40 cm, 7-mm-thick slices with 3-mm gap. Distal prostatic urethra (solid arrow) is in apex of prostate gland. Levator ani muscle (open arrow) appears thicker on right than on left side because of chemical-shift artifact.

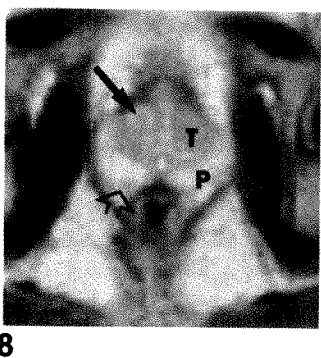


Fig. 8.—56-year-old man. Image obtained on 0.35-T unit; 7-mm-thick sections with 3-mm gap. Elliptical body coil, aperture 55 × 40 cm (TR 2000 msec, TE 56 msec). Transition zone (T) is inhomogeneous with localized high signal intensity anteriorly (solid arrow). Low-intensity stripe at periphery of gland (open arrow) is in region of prostatic capsule. P = peripheral zone.

On the sagittal plane of imaging on sections 1 cm from the midline and farther lateral, the central and peripheral zones could be differentiated (Fig. 9B). The anterior fibromuscular band was clearly seen in the sagittal plane (Fig. 9B). The relation between the prostate and rectum was well shown in the midsagittal projection because of the depiction of the Denonvillier's fascia, which had a lower signal intensity than either the rectal wall or peripheral zone of the prostate gland when long TR/TE imaging was used (Fig. 9A). Periprostatic veins were seen anterior to the prostate (Fig. 9).

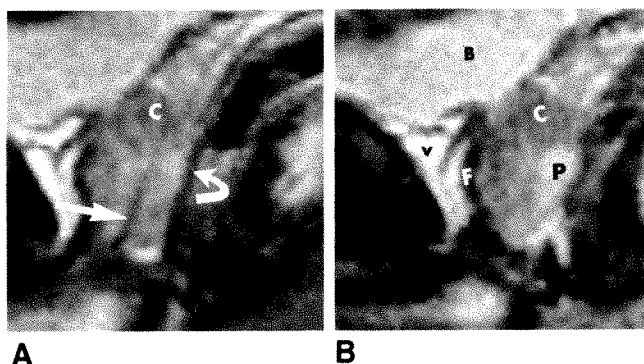


Fig. 9.—25-year-old man imaged on 0.35-T unit with quadrate coil, aperture 55 cm, section thickness 5 mm, continuous slices (TR 2000 msec, TE 80 msec). Sagittal scans at midline (A) and 5 mm to the right (B).

A, Distal prostatic urethra (straight arrow). C = central zone. Dennonviller's fascia (curved arrow).

B, Differentiation between central (C) and peripheral (P) zones is clear. F = anterior fibromuscular band; v = preprostatic veins; B = urinary bladder.

The transverse section was optimal for differentiation between the urethra, transition zone, and peripheral zone (Fig. 7B). Depiction of the urethra and verumontanum were enhanced on the transverse scan, as was depiction of the membranous urethra, which had a thicker wall than the prostatic urethra (Fig. 7A). The periprostatic veins and levator ani could be easily displayed in this imaging plane (Figs. 5 and 7).

Age of the patient.—On the T2-weighted image, differentiation between the central and peripheral zones was possible in 31 of the 32 young subjects (less than 35 years old) (Figs. 3, 4, and 9) but in only eight of the 23 older subjects (Figs. 10 and 11). Furthermore, the size of the central zone was smaller in the older subjects (Figs. 3 and 10). The transition zone was seen in all subjects (Figs. 5 and 7). While in young subjects the transition zone was of homogeneous low signal intensity (Figs. 5B and 7B), in older subjects it was larger and had various signal intensities. In 10 of 23 older subjects the low-intensity stripe, representing the surgical pseudocapsule, was interposed between the transition and peripheral zones (Fig. 8). The thin rim of low intensity surrounding the prostate on the T2-weighted image was seen in five of the 32 young patients and in 12 of the 23 older subjects. The periprostatic venous plexus anterior and lateral to the gland was identified in 30 of 32 young subjects. In older subjects, anterior venous plexus were seen in 23 of 23, but lateral plexus were seen in only 10 of 23 older subjects.

Magnetic field strength.—Zonal anatomy can be delineated on the T2-weighted image on either the 0.35-T or 1.5-T magnets. The intensity relation between the peripheral, central, and transition zones on T1- and T2-weighted images was similar on both magnets. Depiction of the urethra, verumontanum, and ejaculatory ducts was similar with both magnets when 5-mm slices were used. While the intensity relations between the zones of the prostate gland were similar on both units, the contrast between fat and prostate gland varied. On 0.35-T unit, the surrounding fat had high signal

intensity regardless of the TR or TE used (Table 1). The best contrast between fat and prostate gland was obtained by using a short TR (500 msec) and either a short or long TE (Table 1). With the 1.5-T device, the fat was of higher signal intensity than the prostate on the T1-weighted image, and of similar or lower signal intensity than the peripheral zone of the prostate on the T2-weighted image. The chemical-shift artifact represented a problem on both units. It was most noticeable in the area of the levator ani muscle. In the transverse plane, demonstration of the anterior portion of one side of the levator ani muscle was difficult in 69% of the subjects on the 0.35-T device and in seven of 10 subjects on the 1.5-T. Chemical-shift artifact appeared as a thick, low-intensity stripe on one side of the gland and as a corresponding high-intensity stripe on the opposite side [15] (Figs. 6–8). The position of the low-intensity band changed when the direction of the readout gradient changed. Our study was performed on two different 0.35-T Disonics MT/S units. One unit had the readout gradient from right to left and the low-intensity stripe was located along the right side of the prostate (Fig. 6). The other unit had a readout gradient from left to right, and the low-intensity band was seen along the left side (Fig. 12). On the 1.5-T imager the chemical-shift artifact had a similar appearance on the transverse scan. It was seen as a low-intensity line along the left side and was present in all 10 patients (Fig. 7).

Discussion

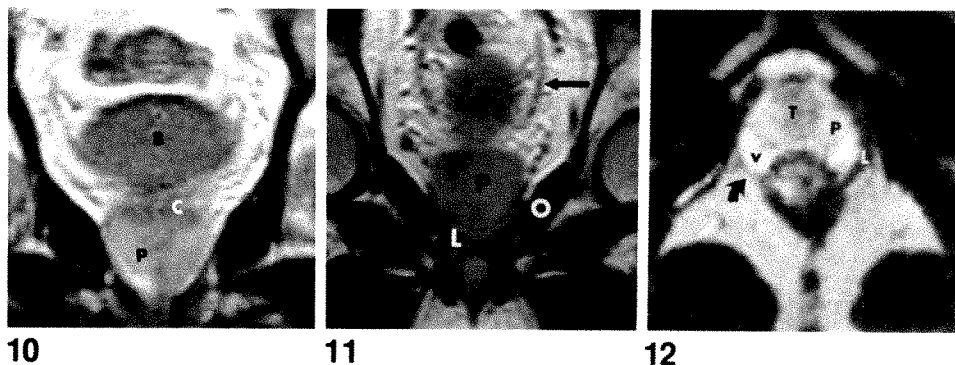
Demonstration of the zonal anatomy of the prostate gland and distinction between the gland and the periprostatic tissue are readily effected by MR imaging. Differentiation between the peripheral, central, and transition zones and observation of zonal changes with age is a unique contribution of MR imaging. Because changes occur in the prostate after age 35 years [10], the subjects were divided into two groups: group 1 (less than 35 years old) and group 2 (40–75 years old).

There are two main glandular regions of the prostate gland: central and peripheral. The peripheral zone occupies nearly 75% and the central zone 25% of the volume of the glandular tissue [10]. As the bulk of glandular tissue is a flat disk oriented in the coronal plane, depiction of the peripheral and central zone was best in the coronal section, extending along the long axis of the distal portion of the prostatic urethra. The peripheral and central zones markedly differ in morphology. The distinction between the peripheral and the central zones by MR is possible on the T2-weighted image, mainly because of the shorter T2 relaxation time of the central zone. This may be explained by the presence of stroma consisting of compact muscle fiber bundles, which have a very short T2 relaxation time [10]. In the peripheral zone, the muscle bundles are loosely interwoven and the glandular components are more abundant. The distinction between the two zones was consistently seen in the younger group and was seen in 35% of the older group. This correlates with the reported morphologic and histologic changes associated with increasing age [10]. The volume of the central zone is greatest in young subjects. With advancing age, there is progressive atrophy of the

Fig. 10.—65-year-old man imaged on 0.35-T unit, coronal scan, TR 1500 msec, TE 60 msec, 1-cm-thick continuous slices. Quadrant coil, 55-cm aperture. Central zone (C) is small (atrophic). P = peripheral zone; B = urinary bladder.

Fig. 11.—59-year-old man imaged on 1.5-T body-coil unit, TR 2000 msec, TE 40 msec. Prostate gland (P) is enlarged. Central zone is not visible. The patient was given glucagon, and distal ureters (arrow) were seen. L = levator ani; O = internal obturator muscle; B = urinary bladder.

Fig. 12.—25-year-old man imaged on 0.35-T unit, 5-mm continuous slices, quadrate coil, 55-cm aperture, TR 2000 msec, TE 80 msec. Chemical-shift artifact on 0.35 T. Left levator ani (L) is well seen, but levator ani on right side (arrow) is indistinct because of chemical-shift artifact. T = transition zone; P = peripheral zone; v = periprostatic veins.



central zone, leading to reduction of the total mass [10]. The anatomic distinction between the central and the peripheral zones is clinically important. The peripheral zone is almost exclusively the site of origin of carcinoma [10]. The function of the central zone is still unclear. A third zone of the prostate gland, which occupies about 5% of the volume of the gland, is the transition zone. The transition zone is the origin of benign nodular hyperplasia. On MR in young subjects, the transition zone is imaged with low signal intensity and blends with the periurethral glands and the preprostatic sphincter. In older subjects, the peripheral zone shows variation in size and signal intensity.

For easier mapping of the prostatic zonal anatomy, the urethra can be used as a key anatomic reference point (Fig. 1). There is a 35° anterior angulation in the prostatic urethra at about half the distance between the apex and the base of the prostate gland, which divides the urethra into proximal and distal segments. The proximal segment is related to the transition zone, periurethral glands, and preprostatic sphincter. The preprostatic sphincter is composed of striate muscle and surrounds the proximal segment of the prostatic urethra between the base of the verumontanum and the bladder neck. The verumontanum lies entirely in the distal segment of the urethra. The base of the verumontanum at the level of angulation of the urethra lies at the geometric center of the disk. The distal urethral segment is surrounded by a sphincter composed of striated muscle fibers, which blends distally beyond the apex of the gland with the external sphincter. The proximal and distal urethra are easily displayed on transverse MR images. On the coronal image, because of urethral angulation, the segment of proximal and distal urethra are seen at different imaging planes. The bulbous urethra is best seen in the coronal plane.

The stroma of the anterior fibromuscular band, composed of smooth muscle, blends with the muscle fibers surrounding

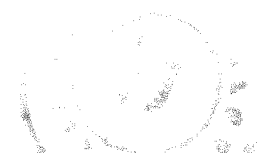
the urethra at the bladder neck. The fibers of the anterior fibromuscular stroma extend from the bladder neck and fan out laterally, covering the entire anterior and anterolateral surface of the glandular prostate. Because of its muscle and fiber composition, the anterior fibromuscular stroma is imaged with low signal intensity regardless of TR/TE used.

It is uncertain if the prostatic capsule was shown. The periprostatic venous plexus was consistently seen in young subjects. As described by Reiner and Walsh [16], the periprostatic veins are present anterior and lateral and their distribution changes from the apex to the base. This distribution can be seen on MR images. In older subjects in whom the prostate was enlarged, periprostatic veins along the side of the gland were not always imaged. This may be because of the mechanical effect of the vein stretching and thus becoming smaller.

All three imaging planes clearly display the prostate gland and periprostatic tissue. Each has its own merit. The coronal plane clearly delineates the peripheral and central zones, allows the display of the urethra and verumontanum along its long axis, and best displays the relationship between the prostate and the levator ani muscle and prostate and pelvic sidewalls. The sagittal plane is useful for evaluating the relationship between the prostate and the bladder base, prostate, and rectum and for showing the anterior fibromuscular band that separates the prostate from the preprostatic space. The peripheral and central zones can also be differentiated. The transverse plane allows assessment of the relation between the prostate and the levator ani muscle, preprostatic space, and rectum. The transverse plane also depicts the peripheral zone, transition zone, and urethra.

ACKNOWLEDGMENT

We thank Gloria Riggs for editorial assistance.



REFERENCES

1. Morgan CL, Calkins RF, Cavalcanti EJ. Computed tomography in the evaluation, staging, and therapy of carcinoma of the bladder and prostate. *Radiology* **1981**;140:751-761
2. Price JM, Davidson AJ. Computed tomography in the evaluation of the suspected carcinomatous prostate. *Urol Radiol* **1979**;1:38-42
3. Sukov RJ, Scardino PT, Sample WF, Winter J, Confer DJ. Computed tomography and transabdominal ultrasound in the evaluation of the prostate. *J Comput Assist Tomogr* **1977**;1:281-289
4. Denkhaus H, Dierpke W, Grabbe E. Comparative study of suprapubic sonography and computed tomography for staging of prostatic carcinoma. *Urol Radiol* **1983**;5:1-9
5. Lee F, Gray JM, McLeary RD, et al. Transrectal ultrasound in the diagnosis of prostate cancer: location, echogenicity, histopathology and staging. *Prostate* **1985**;7:117-129
6. Hricak H, Williams RD, Spring DB. Anatomy and pathology of the male pelvis by magnetic resonance imaging. *AJR* **1983**;141:1101-1110
7. Bryan PJ, Butler HE, Lipuma JP, et al. NMR scanning of the pelvis: initial experience with a 0.3T system. *AJR* **1983**;141:1111-1118
8. Buonocore E, Hesemann C, Pavlicek W. Clinical and in vitro magnetic resonance imaging of prostatic carcinoma. *AJR* **1984**;143:1267-1272
9. Poon PY, McCallum RW, Henkelman MM, et al. Magnetic resonance imaging of the prostate. *Radiology* **1985**;154:143-149
10. McNeal JE. The prostate gland. Morphology and pathobiology. *Monogr Urol* **1983**;4(1):5-13
11. Crooks L, Arakawa M, Hoenninger J, Watts J, McRee R, Kaufman L. Nuclear magnetic resonance whole-body imager operating at 3.5 Kgauss. *Radiology* **1982**;143:169-174
12. General Electric. *NMR—a perspective in imaging*. Milwaukee: General Electric, **1984**;5485:5-20
13. Ehman RL, Kjos BO, Hricak H, Higgins CB. Relative intensity of abdominal organs in MR images. *J Comput Assist Tomogr* **1985**;9:315-319
14. Von Schulthess GK, Higgins CB. Blood flow imaging with MR: spin-phase phenomena. *Radiology* **1985**;157:687-695
15. Babcock EE, Brateman L, Weinreb JC, Hroner DS, Nunnally RL. Edge artifacts in MR images: chemical shift effect. *J Comput Assist Tomogr* **1985**;9:252-257
16. Reiner WG, Walsh PC. An anatomical approach to the surgical management of the dorsal vein and Santorini's plexus during radical retropubic surgery. *J Urol* **1979**;121:198-200

Renal Adenocarcinoma: CT Staging of 100 Tumors

G. Daniel Johnson^{1,2}
N. Reed Dunnick¹
Richard H. Cohan¹
Fernando F. Illescas^{1,3}

The preoperative CT scans of 100 pathologically proven renal adenocarcinomas were retrospectively reviewed to assess the accuracy of CT for staging the tumor. Regardless of tumor stage, perinephric extension was assessed with a sensitivity of 46% and a specificity of 98%. The sensitivity of CT in detecting venous invasion (either venous enlargement or thrombus) was 78%, with a specificity of 96%. For detection of metastatic adenopathy, CT had a sensitivity of 83% and specificity of 88%. Adjacent organ invasion was correctly identified in 60% of patients, with a specificity of 100%. Overall, CT correctly staged 91% of patients. If errors associated with perinephric invasion were excluded, CT staging accuracy improved to 96%. CT is useful in staging renal adenocarcinoma. If the renal vein is not well seen, angiography or sonography may be necessary to determine the presence of venous tumor extension.

CT of the abdomen is widely used for the preoperative staging of renal adenocarcinoma. Early reports on the use of CT to stage renal cancer suggested a high accuracy rate but limited value in showing venous invasion [1-7]. This is the largest study yet that evaluates the accuracy of CT in staging renal adenocarcinoma.

Materials and Methods

All patients with pathologically proven renal adenocarcinoma who had a CT examination between October 1980 and October 1985 were included in the study. A total of 100 tumors were present in 97 patients. There were 60 men and 37 women, ranging in age from 24 to 81 years. Final diagnosis was established at surgery (79 tumors) or by biopsy of distant metastases (21 cases). The medical records and pathology reports of all patients were reviewed and compared to the CT examination.

All CT examinations were performed on a GE 8800 (71 tumors) or GE 9800 (29 tumors) scanner. Scan sections were performed by using 10-mm slice thickness at 10-mm intervals, with additional images obtained when judged necessary by the supervising radiologist. IV contrast was given to evaluate all but 18 tumors. Noncontrast studies were performed in patients with a contrast allergy or an elevated creatinine. A 100 ml IV bolus of contrast medium was routinely given, followed by a rapid drip of an additional 100 ml during the course of the CT examination.

The CT examinations were retrospectively reviewed to assess tumor extension into the perinephric tissues; involvement of the renal vein and inferior vena cava; and the presence of regional lymphadenopathy, adjacent organ invasion, and distant metastases. These findings were compared with actual pathologic staging.

Criteria for perinephric invasion required a soft-tissue mass at least 1 cm in diameter in the perinephric space. Perinephric soft-tissue stranding was not considered evidence of tumor invasion. Venous invasion was considered to be present if there was either enlargement (based on the reviewer's estimation rather than on actual measurement) or identifiable thrombus in the renal vein or inferior vena cava. Regional lymph nodes were considered to be involved with tumor if they were at least 1 cm in diameter. Adjacent organ invasion was diagnosed only if there was enlargement and/or a density change in the adjacent structure. The loss of a fat plane between the tumor and adjacent organ was not considered tumor invasion.

Received May 30, 1986; accepted after revision August 26, 1986.

¹ Department of Radiology, Duke University Medical Center, Durham, NC 27710.

² Present address: Department of Diagnostic Radiology, Mayo Clinic, Rochester, MN 55905. Address reprint requests to C. D. Johnson.

³ Present address: Department of Radiology, Montreal General Hospital, Montreal, Quebec, Canada H3G 1A4.

Presented at the annual meeting of the American Roentgen Ray Society, Washington DC, April 1986.

AJR 148:59-63, January 1987

0361-803X/87/1481-0059

© American Roentgen Ray Society

Staging of renal tumors was done according to the Robson classification [8]. Stage I consists of tumor confined within the renal capsule, stage II of perinephric extension (yet contained by Gerota's fascia), stage IIIA of venous invasion (renal vein that may extend into the inferior vena cava), and stage IIIB of regional lymph node metastases. Stage IV tumors have either adjacent organ involvement (excluding ipsilateral adrenal invasion) or distant metastases.

Results

Seventy-nine tumors were removed surgically, providing the basis for pathologic comparison to CT scans for each staging category. Adequate information from the pathology reports was available for analysis of perinephric extension in 71 tumors, venous extension in 74 tumors, regional lymph nodes in 63 tumors, and adjacent organ invasion in 58 tumors. The remaining 21 tumors had pathologic confirmation of distant metastases by percutaneous biopsy. Since a large number of these advanced tumors were not surgically removed, selection bias may be present. We have therefore included a percentage range (best case–worst case) for the sensitivity and specificity in each of the following areas.

Perinephric Extension

Perinephric extension was correctly identified, regardless of overall tumor staging, in 11 (46%) of 24 tumors (range,

58–23%) by a soft-tissue mass at least 1 cm in diameter. The remaining 13 tumors had perinephric soft-tissue stranding or normal fat at CT.

Forty-six (98%) of 47 tumors (range, 98–83%) with proven normal perinephric tissues were correctly evaluated by CT. In one patient an enlarged perinephric vessel supplying the tumor was misdiagnosed as representing tumor extension (Table 1). Seventeen (50%) of 34 stage I tumors also had identifiable soft-tissue stranding at CT (Fig. 1).

Venous Extension

Venous extension, defined as either enlargement of and/or thrombus within the renal vein or inferior vena cava, was correctly identified in 14 (78%) of 18 tumors (range, 86–42%) regardless of tumor stage. In eight (44%) of 18 tumors only venous enlargement was seen, while the remaining six tumors (33%) had identifiable tumor thrombus. The four false negatives were due to motion artifact (one), poor visualization of the right renal vein owing to a large right renal tumor (two), and a tumor thrombus that occurred in only a branch renal vein (one).

Normal renal veins were correctly identified in 54 (96%) of 56 tumors (range, 97–80%). The two false-positive studies were due to enlarged renal veins from increased blood flow through the hypervascular tumor, which did not contain thrombus (Fig. 2).

Table 1: Proven Renal Adenocarcinoma^a

	Sensitivity (%)	Specificity (%)
Perinephric extension	11/24 (46)	46/47 (98)
Venous invasion	14/18 (78)	54/56 (96)
Metastatic adenopathy	10/12 (83)	45/51 (88)
Adjacent organ invasion	3/5 (60)	53/53 (100)

^a All stages included.

Adenopathy

Lymph nodes at least 1 cm in diameter containing tumor were correctly identified in 10 (83%) of 12 tumors (range, 93–32%). Four (33%) of 12 nodes were 1–2 cm in diameter, while six (50%) of 12 nodes were larger than 2 cm. Two patients had tumor within normal-sized lymph nodes.

Forty-five (88%) of 51 tumors (range, 91–65%) had normal-sized lymph nodes that did not contain tumor. Three false-

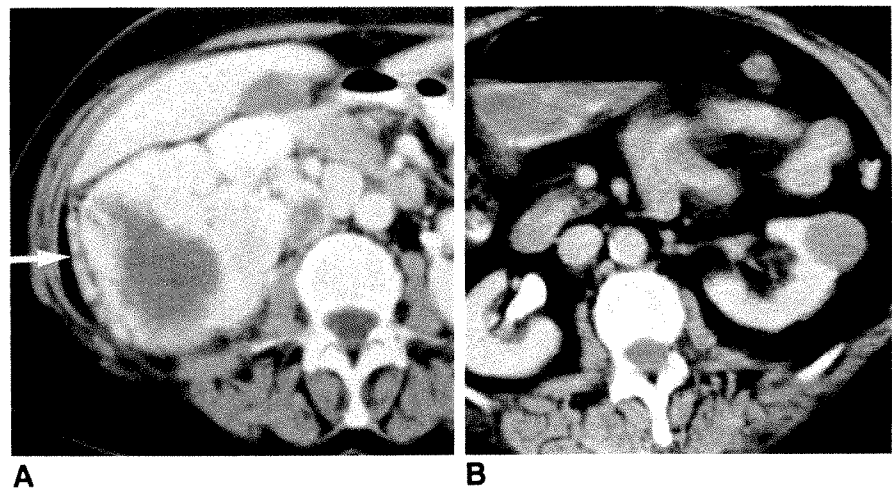


Fig. 1.—Perinephric extension.
A, Large right-sided renal adenocarcinoma with enhancing surgically proven tumor in perinephric tissues (arrow). Also note paracaval lymphadenopathy.
B, Small left-sided renal adenocarcinoma with normal-appearing perirenal fat (CT stage I). Pathologically, microscopic perinephric invasion had occurred (pathologic stage II).

positive studies occurred in nodes 1–2 cm in diameter that were histologically hyperplastic, but did not contain tumor (Fig. 3).

Adjacent Organ Invasion

Adjacent organ invasion was correctly identified in three (60%) of five proven tumors (range, 77–7%), with either enlargement and/or a density change in the affected organ. Two false-negative studies showed obliteration of the fat plane between tumor and adjacent organ, but no other sign of invasion.

All 53 tumors (100%) (range, 100–93%) without adjacent organ invasion showed either a preserved fat plane between tumor and adjacent organ or a lost fat plane without other signs of invasion (increased adjacent organ size or density change). Forty-five (85%) of these 53 tumors without adjacent organ invasion showed a preserved fat plane, while the other eight (15%) had loss of the intervening fat plane (Fig. 4).

Overall Staging

Overall staging results were better than the sensitivity reported for each separate category. Thirty-four (97%) of 35 stage I, four (44%) of nine stage II, 14 (88%) of 16 stage III, and 39 (98%) of 40 stage IV tumors were correctly staged by CT when compared with pathologic staging (Table 2).

Nine CT staging errors occurred, for an overall accuracy of 91%. Only one error was an overstaging error. This patient had an enlarged lymph node identified by CT (CT stage IIIB) not commented on at pathologic examination (surgical stage I). The remaining eight errors were understaged by CT. Five errors were due to microscopic perinephric extension that did not appear as a discrete 1-cm mass on CT. Two stage III errors were due to large right-sided tumors in which the involved renal vein could not be identified by CT. Motion artifact and a poor bolus of contrast material also contributed to these errors. The ninth error was due to posterior body-wall invasion, not identified by CT because enlargement or density change of the affected body wall was not present.

Fig. 2.—Venous extension.

A, Large right-sided renal adenocarcinoma with proven renal vein and inferior vena caval extension.

B, Enlarged left renal vein (arrow) arising from left-sided renal adenocarcinoma (seen on lower section). No tumor thrombus found pathologically. Venous enlargement secondary to high-volume blood flow through hypervascular tumor.

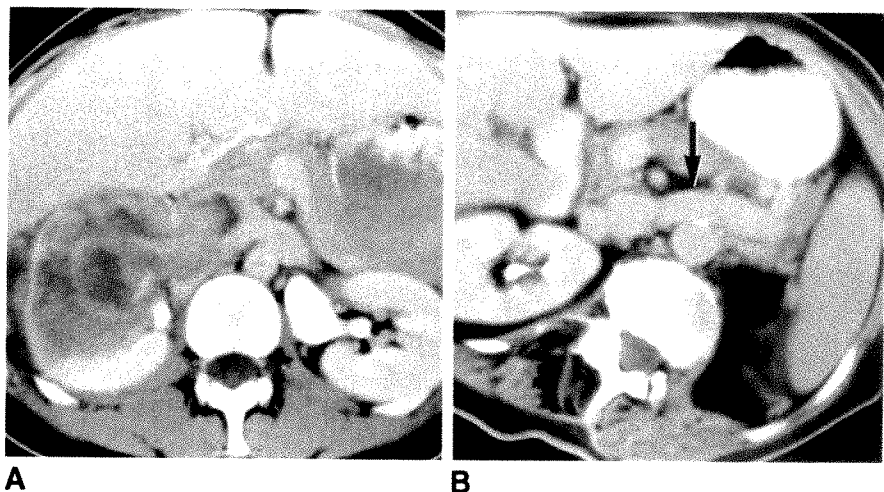
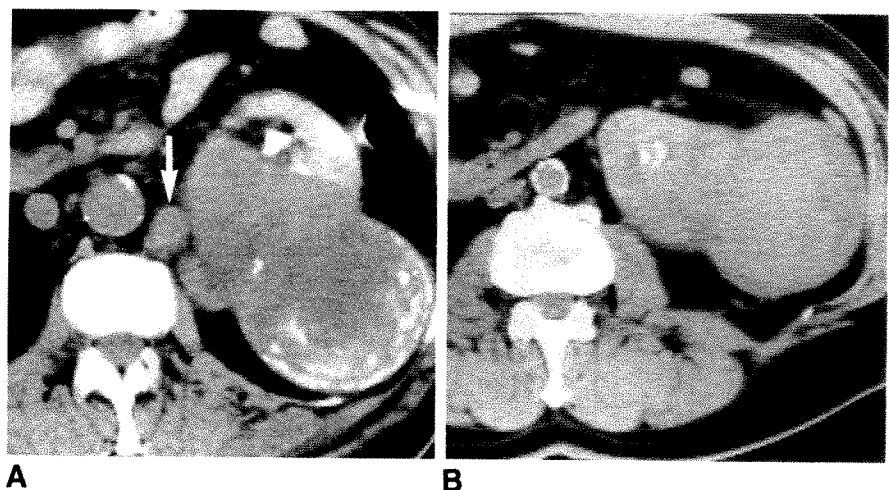


Fig. 3.—Regional lymphadenopathy.

A, Large, calcified left-sided renal adenocarcinoma with enlarged paraaortic lymph nodes (arrow). Pathologically metastatic regional lymphadenopathy was present.

B, Left-sided renal adenocarcinoma with several normal-sized paraaortic lymph nodes. Pathologically, these lymph nodes contained metastatic tumor.



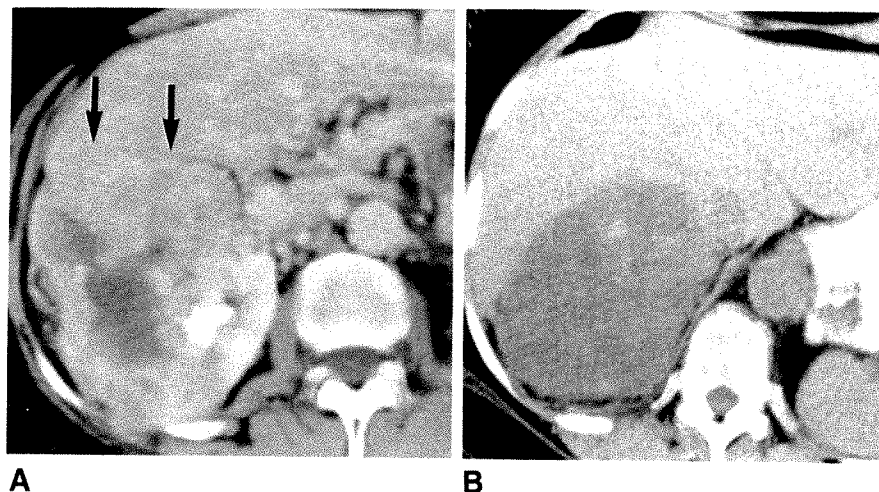


Fig. 4.—Adjacent organ invasion.

A, Large right-sided renal adenocarcinoma with loss of fat plane between the tumor and adjacent liver (arrows). No other signs of liver invasion visible, but at surgery hepatic invasion was present.

B, Large right-sided renal adenocarcinoma with obliteration of fat plane between tumor and liver. No hepatic invasion was present at surgery.

Table 2: Renal Adenocarcinoma, Overall Staging

CT Staging	Pathological Staging				Total
	I	II	III	IV	
I	34	5	1	0	40
II	0	4	1	0	5
III	1	0	14 ^a	1	16
IV	0	0	0	39 ^b	39
Total	35	9	16	40	100

^a Includes two patients with distant metastases identified by CT but not confirmed pathologically.

^b Includes six patients with proven distant metastases that were outside the region scanned by CT.

Discussion

CT is a reliable and accurate means of preoperatively staging renal adenocarcinoma, with an overall staging accuracy of 91%. These results are comparable to the 90–95% accuracy reported in previous smaller series [3, 6, 7]. Results from CT are important, for nearly all surgeons perform a partial or radical nephrectomy for stage I or stage II disease. Venous thrombus is important information preoperatively, because a more extensive surgical procedure may be required in attempting to clamp distal to intravascular tumor. Debulking of enlarged lymph nodes can also be planned if nodal metastases are identified. Treatment of stage IV disease differs from center to center; some perform a radical nephrectomy in nearly all patients while others do so only in symptomatic patients. In advanced disease, percutaneous biopsy to document a distant metastases is all that may be required before start of chemotherapy.

Perinephric invasion is the most troublesome CT area, accounting for more than half of the staging errors. Perinephric soft-tissue masses at least 1 cm in diameter were seen in only 46% of patients with proven tumor, accounting for this low sensitivity. Perinephric stranding is also very nonspecific, for it was seen in half of patients with stage I tumors. If errors associated with perinephric invasion were excluded, the CT accuracy improved to 98%. This is a legitimate consideration,

for both stage I and stage II tumors are usually treated similarly with radical nephrectomy. Of course, perinephric invasion would be important if partial nephrectomy was considered.

The difficulties of detecting venous extension with CT have been previously reported [2, 9]. Half of our false-negative studies were in patients with large right-sided tumors in which the involved renal vein could not be identified. False-positive studies were seen in patients with enlarged renal veins that did not contain tumor. These enlarged renal veins were most likely caused by increased blood flow from a hypervascular tumor. These results may be improved by using bolus, dynamic, and thin-section collimation scanning. A larger contrast bolus with dynamic scanning should eliminate the false-positive studies. Thin sections during a bolus injection may make identification of short, distorted right renal veins easier. Equivocal cases should undergo angiography (either conventional or digital) [10, 11], sonography [12], or MR imaging to more carefully examine for venous thrombus.

Metastatic adenopathy was identified by CT with a sensitivity of 83% and a specificity of 88%. CT was successful in identifying nodal size and location. Errors were due to an inability to differentiate between normal hyperplastic nodes and cancerous nodes. Seven tumors had regional lymph nodes 1–2 cm in diameter, four (57%) contained cancer, and three (43%) were hyperplastic histologically. All nodes greater than 2 cm in diameter contained tumor. Therefore, nodes greater than 2 cm in diameter are highly suspicious for metastases. Nodes 1–2 cm in size are worrisome, but nondiagnostic.

Adjacent organ invasion was assessed in only a small number of tumors, because these patients typically had distant metastases that were more easily biopsied percutaneously without radical nephrectomy. By using the criteria for adjacent organ invasion of enlargement or density change, the sensitivity of CT was 60% with a specificity of 100%. Caution must be exercised when obliteration of the fat plane is observed between tumor and adjacent organ; this was observed in 15% of patients without adjacent organ invasion. Sonography and/or MR might be helpful in some patients

because of their capability to image sagittally and coronally and to provide a different means of tissue characterization.

Conclusion

Preoperative CT staging of renal adenocarcinoma is highly accurate. Perinephric invasion is the most difficult to detect but is of minor importance if radical nephrectomy is planned. Accurate assessment of renal vein invasion may require bolus, dynamic, and thin-collimation scanning, especially in large right-sided tumors in which identification of the short renal vein is most difficult. Lymph nodes larger than 2 cm in diameter were always associated with metastases in our series. Nodes 1–2 cm in diameter are worrisome but not diagnostic of metastases. Identification of a fat plane between tumor and adjacent organs excludes local invasion, but loss of the fat plane can be seen in 15% of patients without local invasion.

REFERENCES

1. Weyman PJ, McClennan BL, Stanley RJ, Levitt RG, Sagel SS. Comparison of computed tomography and angiography in the evaluation of renal cell carcinoma. *Radiology* 1980;137:417–424
2. Levine E, Lee KR, Weigel J. Preoperative determination of abdominal extent of renal cell carcinoma by computed tomography. *Radiology* 1979;132:395–398
3. Love L, Churchill R, Reynes C, Schuster GA, Moncada R, Berhow A. Computed tomography staging of renal carcinoma. *Urol Radiol* 1979;1:3–10
4. Steele JR, Sones PJ, Heffner LT. The detection of inferior vena caval thrombosis with computed tomography. *Radiology* 1978;128:385–386
5. Marks WM, Korobkin M, Callen PW, Kaiser JA. CT diagnosis of tumor thrombosis of the renal vein and inferior vena cava. *AJR* 1978;131:843–846
6. Levine E, Madlad NF, Rosenthal SJ, Lee KR, Weigel J. Comparison of computed tomography and ultrasound in abdominal staging of renal cancer. *Urology* 1980;16:317–322
7. Cronan JJ, Zeman RK, Rosenfield AT. Comparison of computed tomography, ultrasound and angiography in staging renal cell carcinoma. *J Urol* 1982;127:712–714
8. Robson CJ, Churchill BM, Anderson W. The results of radical nephrectomy for renal cell carcinoma. *J Urol* 1969;101:297–301
9. Marks WM, Korobkin M, Callen PW, Kaiser JA. CT diagnosis of tumor thrombosis of the renal vein and inferior vena cava. *AJR* 1978;131:843–846
10. Ford KK, Braun SD, Miller GA, Newman GE, Dunnick NR. Intravenous digital subtraction angiography in the preoperative evaluation of renal masses. *AJR* 1985;145:323–326
11. Mauro MA, Wadsworth DE, Stanley RJ, McClennan BL. Renal cell carcinoma: angiography in the CT era. *AJR* 1982;139:1135–1138
12. Schwert WB, Schwert WN, Rodeck G. Venous renal tumor extension: a prospective US evaluation. *Radiology* 1985;156:491–495

Book Review

Percutaneous and Interventional Urology and Radiology. Edited by Eric K. Lang. New York: Springer-Verlag, 355 pp., 1986. \$95

Edited by an author well known in many of these fields, the book is written by the editor and 18 contributing authors, representing 17 well-known institutions in the United States and Europe. As with most Springer-Verlag publications, the book is well produced and nicely illustrated.

The first chapter on percutaneous nephrostomy initiates the discussion of interventional procedures. The dynamics of the collecting system (Whitaker test; ureter physiology) are covered in the second chapter. Two chapters review the procedure of percutaneous stone removal and these reflect both the European and American experiences, although the book was written before extracorporeal shock-wave lithotripsy could be included. The chapter on antegrade and retrograde ureteral stenting is superbly done and excellently illustrated with many helpful diagrams. Complementary to the chapter on stenting is a brief chapter summarizing the experience with dilation of ureteral strictures. A chapter on percutaneous drainage of abscesses, urinomas, and hematomas is well done, and the illustrations depict clearly the entities and techniques. Similarly, the chapter on fine-needle aspiration biopsy specifically addresses the techniques and results in various organs.

Four chapters (two by the editor) discuss and review various aspects of embolotherapy: a chapter on embolization of malignant and benign disease of the kidney; embolization for pelvic organ hemorrhage; embolization for primary varicocele; and a chapter on embolization with radioactive particles for renal cell carcinoma. These procedures are placed in appropriate perspective compared with other available therapies, and the chapters are well referenced. A subsequent chapter discusses regional perfusion for chemotherapy.

The technique of percutaneous dilation of renal artery stenosis is thoroughly discussed. However, the selection of patients for dilation (for example, atherosclerosis of the main renal artery vs an aortic plaque-causing orifice narrowing) is only superficially addressed; follow-up results are similarly sparse.

In addition to the interventional and urologic techniques, there are three good chapters discussing the evaluation of renal masses. A chapter by the editor nicely discusses the diagnosis and management of renal cysts, exhibiting his extensive experience with these lesions. The chapter on imaging of renal neoplasms is well done, except for a paucity of sonographic images. Also, at the time that this book was written, the authors thought that it was too early to assess the role of MR imaging. The chapter on benign renal tumors particularly reviews the characteristic images of the more common entities. A final chapter summarizes the diagnosis and assessment of inflammatory renal disease. Although these last four chapters are not directed particularly toward percutaneous or interventional urology or radiology, by their nature and quality they complement the contents of the book.

The book is well written, very readable, well illustrated, and nicely produced. For the radiologist and the urologist, especially those not heavily involved with interventional procedures, this book succinctly illustrates and summarizes interventional techniques. The chapters on the integrated evaluation of renal disease are a nice bonus.

William H. Bush
The Mason Clinic
Seattle, WA 98111.

CT and Sonography of Advanced Urinary Tract Tuberculosis

Ahalya Premkumar¹
John Lattimer²
Jeffrey H. Newhouse¹

Sonographic and CT examinations were performed prospectively on 14 patients with advanced urinary tract tuberculosis who had undergone serial urography. Sonography and CT showed abnormalities in the affected kidney in each patient. Detailed morphologic information (patterns of calcification and hydronephrosis) and functional status (nephrogram and urogram) were better shown by CT than by urography; sonography showed the fewest morphologic details. CT is probably at least as accurate as urography in detecting advanced urinary tuberculosis; sonography appears to be less accurate than either CT or urography.

The gross pathologic and urographic abnormalities produced by advanced urinary tract tuberculosis are well known [1-4]. The CT manifestations, however, have been described only in a small number of patients and in a retrospective fashion [5, 6]. Sonography of renal tuberculosis has also been only rarely described in the literature [7, 8]. Therefore, we undertook to examine prospectively with urography, sonography, and CT a group of patients with known urinary tract tuberculosis in order to see if there were additional findings on sonography and CT that were not evident on urography and to provide a detailed analysis of the sonographic and CT findings in this disease.

Materials and Methods

Fourteen patients (six men, eight women) ranging in age from 30 to 60 years were examined. They constituted a group with known renal tuberculosis seen by one of the authors over a period of several years. No attempt was made to choose patients with a particular stage of disease, but all had advanced changes and had been known to have urinary tract tuberculosis for at least 10 years. The diagnosis had been established by urine culture in each patient. Each had had a series of urograms prior to the current investigation, and each had another urogram within a few days of the sonographic and CT examinations.

Urography was performed according to a standard protocol: A plain film of the abdomen was obtained, after which a 75-ml bolus of 60% sodium/meglumine diatrizoate was administered intravenously. Tomograms at 1-cm intervals were obtained through the kidneys immediately after contrast administration. Fifteen minutes after contrast administration, an anteroposterior and both posterior oblique views of the abdomen were obtained. The patient was asked to void and then another film of the abdomen was obtained. Additional films were obtained in some patients as needed.

Real-time gray-scale sonography was performed on an ATL scanner (MK 300 series) that uses a 3.5-MHz transducer. In some patients, a 5-MHz transducer was also used in order to search for relatively superficial small regions of calcification. Real-time views in the coronal and transverse planes were obtained through the entirety of both kidneys. The retroperitoneum was examined as the bowel gas permitted, and transverse and sagittal views were obtained through the bladder. Hard-copy images were generated for review to demonstrate any observed abnormality and to reveal visualized normal urinary structures.

A Siemens DR-3 Somatom scanner was used for the CT scans. In each patient, the entire abdomen was scanned from the dome of the diaphragm to the floor of the pelvis by using

Received June 2, 1986; accepted after revision August 26, 1986.

Presented at the annual meeting of the American Roentgen Ray Society, Washington, DC, April 1986.

¹ Department of Radiology, Columbia-Presbyterian Medical Center, 622 W. 168th St., New York, NY 10032. Address reprint requests to A. Premkumar.

² Department of Urology, Columbia-Presbyterian Medical Center, 622 W. 168th St., New York, NY 10032.

AJR 148:65-69, January 1987
0361-803X/87/1481-0065

© American Roentgen Ray Society

8-mm-thick slices separated by 2-mm gaps. Bowel was opacified before the scans, and the scans were then repeated by using the same protocol but adding the infusion of 300 ml of 30% contrast material.

All of the abnormalities noted at any one examination were listed at the time of the examination. A list was then compiled containing all the abnormalities seen on any patient in any examination; the examinations were then all reinterpreted by two of the authors without reference to the original readings or to the other examinations. The investigators recorded the presence or absence of each finding; the independent assessments agreed with each other.

Specific criteria were used to establish the presence of each finding. A nephrogram was said to be present if the renal parenchyma underwent a detectable increase in attenuation after the administration of contrast material. Calyceal opacification was present if there was any increased density of calyceal urine after injection. Generalized hydronephrosis was diagnosed if all of the calyces and the renal pelvis were dilated; total calyceal hydronephrosis was diagnosed if all the calyces were dilated but the renal pelvis was obliterated; and focal hydronephrosis was diagnosed if some, but not all, of the calyces in a kidney were dilated. Focal scars consisted of local thinning in the renal parenchyma. Calcification of the entire kidney was present when all of the visible portions of the kidney were seen to be calcified on any examination; any other pattern was called partial calcification. "Puttylike" calcification constituted any region greater than 1 cm in diameter in which the calcification was faint and uniform in density.

Results

Virtually all the examinations revealed numerous abnormalities. The results are shown in Table 1.

The nephrogram effect—an increase in the density of the renal parenchyma after contrast administration—was much more frequently seen on CT than on urography, although there was no difference between the two examinations in the frequency of observation of calyceal opacification (Fig. 1). Urography and CT were identical in their capacity to show focal scars; sonography showed fewer. Urography and CT were also identical in their capacity to show hydronephrosis when the calyces and pelvis were dilated (Fig. 1); CT was most sensitive in showing caliectasis without renal pelvic dilatation (Fig. 2) and focal caliectasis (Fig. 3). CT was also most sensitive in detecting any renal calcification (Fig. 4), calcification of part of the kidney (Fig. 5), and calcification of the ureter. Sonography and urography each showed one more case of calcification of the entire kidney than did CT, but CT revealed that the two cases were really only partially calcified; sonography and urography had not visualized the noncalcified portions of the kidney (Fig. 5). CT and urography were equally able to show "puttylike" or homogeneous calcification (Figs. 5 and 6). CT was as sensitive as urography in detecting ureteral calcification; sonography detected none. Urography was the most sensitive and sonography the least sensitive in showing bladder abnormalities. Neither sonography nor CT revealed abnormalities in the contralateral kidney that were due to direct tuberculous involvement.

Discussion

Overall, the results of this investigation show that CT and sonography both reveal findings in patients with advanced

TABLE 1: Imaging Findings in 14 Patients with Advanced Urinary Tuberculosis

Findings	EU	S	CT
Functional features			
Nephrogram effect	4	None	10
Calyceal opacification	4	None	5
Calcification			
Entire kidney	3 ^a	3 ^a	2
Part of kidney	9	10	12
Homogeneous ("puttylike")	8	None	8
Ureteral calcification	2	None	2
Morphologic changes			
Focal scars	4	3	4
Generalized hydronephrosis	5	5	6
Caliectasis without pelvic dilatation	3	3	4
Focal hydronephrosis	0	3	4
Hydroureter	2	0	3
Bladder scarring	4	1	2

Note.—EU = excretory urogram; S = sonography.

^aOne case shown by CT to be only partially calcified.

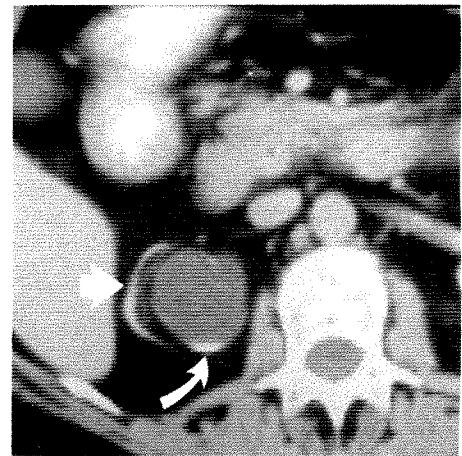


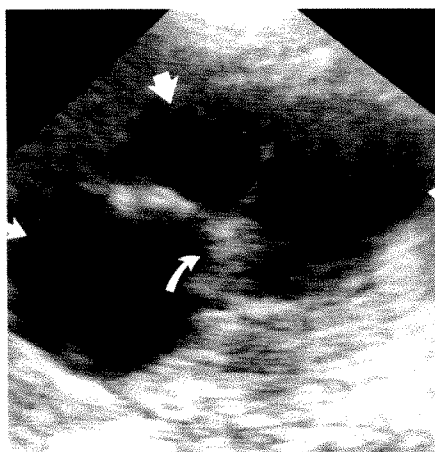
Fig. 1.—Right renal tuberculosis. Contrast-enhanced CT reveals dilated right renal pelvis with small amount of contrast layered posteriorly (curved arrow). Parenchyma (arrow) is very thin.

urinary tract tuberculosis similar to those of the more classic IV urogram. There were small differences between the techniques: CT, in general, showed more details of pathologic anatomy than did the other techniques, and sonography failed to find certain details of calcification.

CT best showed renal morphologic abnormalities, including scars and various patterns of hydronephrosis and extraurinary abnormalities. It showed the greatest detail in the kidneys' excretion of contrast media and was the best at demonstrating the extent and nature of calcification and its distribution within the abnormal kidney. Sonography was slightly less accurate overall in detecting certain abnormalities; it could not, of course, detect any contrast-related abnormalities; it failed to detect ureteral calcifications, and it was unable to distinguish between puttylike calcification, which is characteristic of renal tuberculosis, and other kinds of calcification. However, all the techniques exhibited 100% sensitivity in that



A



B

Fig. 2.—Tuberculous left renal pelvic stricture. CT (A) and sonography (B) show dilated calyces (arrows). Pelvis is not seen on CT but presumably resides within echogenic region (curved arrow) on sonogram.

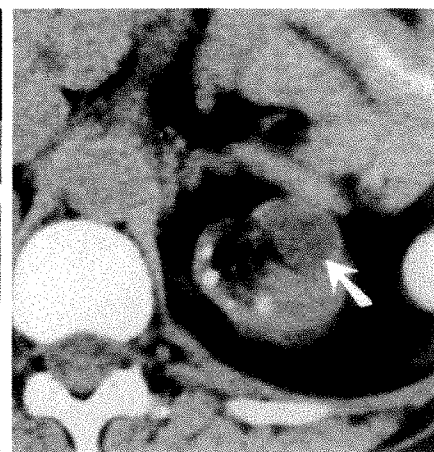
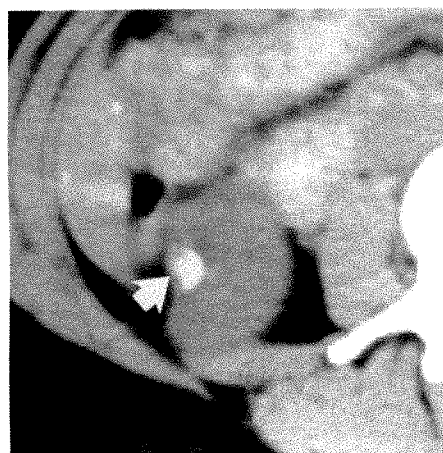
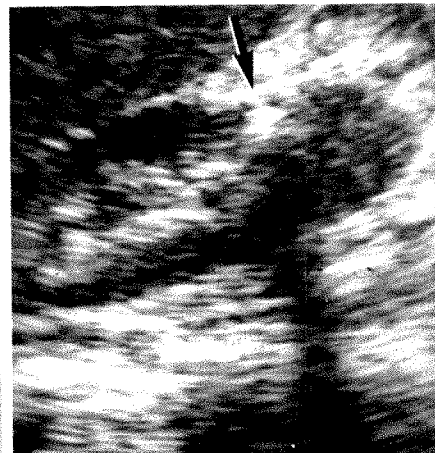


Fig. 3.—Left renal tuberculosis. CT reveals a shrunken kidney with scattered parenchymal calcification and one region of either caseous necrosis or hydrocalyx (arrow).



A



B

Fig. 4.—Tuberculous right kidney. A, CT reveals a focal scar (arrow) in small region of homogeneous calcification. B, Sonogram also reveals focal parenchymal thinning (arrow). Calcification is very echogenic and casts a shadow.



Fig. 5.—Right renal tuberculosis. CT reveals several patterns of calcification, including a homogeneous region and linear and punctate foci. Region of diminished attenuation (arrow) represents focal caseous necrosis, focal hydronephrosis, or cyst.

they all displayed some combination of abnormalities. In view of the marked morphologic abnormalities seen in advanced urinary tract tuberculosis, we suspect that this sensitivity would also be obtained in much larger series; we also suspect, however, that the minor papillary and urothelial abnormalities that constitute the findings in early renal tuberculosis would not be reliably shown by sonography or CT.

It is not clear from this investigation what the efficacy of sonography or CT might be in making the specific diagnosis of urinary tract tuberculosis in a patient in whom the diagnosis was not previously known. Because in advanced disease

standard urographic findings can lead one to suspect the diagnosis in most cases, because urographic findings are almost always also visible on CT, and because CT seems to be better at showing the gross morphology of the affected kidney and ureter, CT probably is at least as accurate in making the diagnosis as urography. Conversely, since the diagnosis is sometimes suggested by the particular configuration of the calcification and by bladder changes that are often not recognized on sonography, sonography will probably be less effective than urography in diagnosing urinary tract tuberculosis. But these conclusions must remain spec-

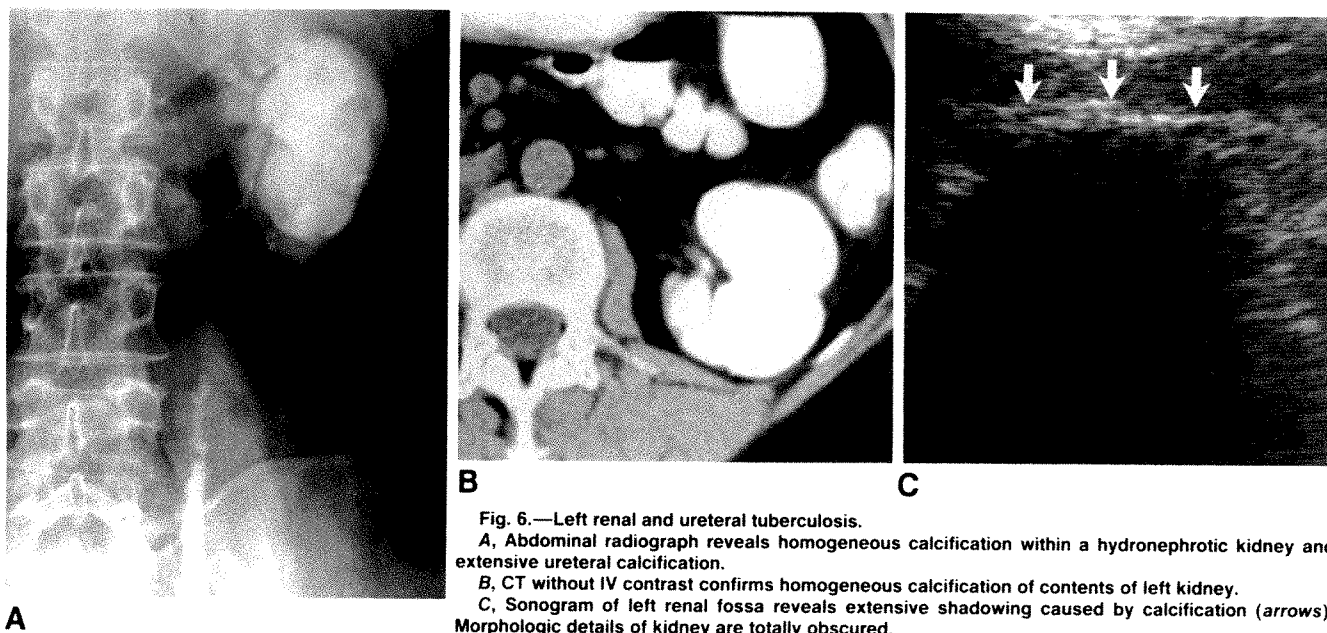


Fig. 6.—Left renal and ureteral tuberculosis.

A, Abdominal radiograph reveals homogeneous calcification within a hydronephrotic kidney and extensive ureteral calcification.

B, CT without IV contrast confirms homogeneous calcification of contents of left kidney.

C, Sonogram of left renal fossa reveals extensive shadowing caused by calcification (arrows). Morphologic details of kidney are totally obscured.

ulative: The current investigation did not test whether a radiologist who did not know the diagnosis could reach one from the results of a sonographic or CT examination. Nor did this investigation consider the differential diagnosis of urinary tract tuberculosis; xanthogranulomatous pyelonephritis, obstructive pyonephrosis, congenital multicystic dysplastic kidney, and calyceal or diverticular stones with scarring all share imaging features that are also seen in various stages of urinary tract tuberculosis. A direct comparison of the CT and sonographic features in these diseases was not possible with the available patients.

The current view of the pathogenesis of urinary tuberculosis [9–16] holds that the bacilli first reached the kidney by hematogenous “seeding” from an extrarenal source, and that multiple small granulomata then form throughout the cortices of both kidneys. Yet in more advanced disease, studies have shown that the macroscopic morphologic renal abnormalities visible at urography are almost always unilateral; if the contralateral kidney is abnormal, the abnormality is usually due to ureteral reflux or obstruction produced by bladder changes caused by the disease, not by progress of the primary hematogenous infection. In our series, we carefully inspected (with sonography and CT) the parenchyma of the contralateral kidney for any evidence of calcification, granulomata, or areas of necrosis that were not visible at urography; none was seen. The reasons for asymmetry of the gross findings in a disease whose early stages are symmetric remain unclear.

Although this study concerns the sonographic and CT findings in advanced urinary tract tuberculosis, the role of these imaging techniques in the diagnosis or follow-up of this disease will require further investigation. CT undoubtedly reveals greater anatomic detail than the other imaging techniques, but neither this investigation nor previous ones have

studied the impact of this improvement on differential diagnosis. We speculate that the lesser information that sonography provides regarding the distribution in detailed morphology of calcification, together with its presumed inability to detect the earlier stages of the disease, would not make sonography attractive as a first-line diagnostic maneuver. We were not able to show that either sonography or CT caused any change in the therapy of our patients, but with further study, serial CT exams may be shown to provide more detailed information concerning the progression of individual cases of urinary tuberculosis, and thus contribute to therapeutic decisions.

REFERENCES

1. Tonkin AK, Witten DM. Genitourinary tuberculosis. *Semin Roentgenol* 1979;14(4):305–318
2. Friedenber RM. Tuberculosis of the genitourinary system *Semin Roentgenol* 1971;6(3):310–322
3. Kollins SA, Hartman GW, Carr DT, Segura JW, Hattery RR. Roentgenographic findings in urinary tract tuberculosis. *Proc Mayo Clin* 1974;121(3):487–494
4. Friedenber RM, Ney C, Stachenfeld RA. Roentgenographic manifestations of tuberculosis of ureter. *J Urol* 1968;99:25–29
5. Goldman SM, Fishman EK, Hartman DS, Kim YC, Siegelman SS. Computed tomography of renal tuberculosis and its pathological correlates. *J Comput Assist Tomogr* 1985;9(4):771–776
6. Planker M, Schoppe W-D, Jungblut RM, Fischer J-Th. Stellenwert der Computertomographie bei extrapulmonaler tuberkulose. *Dtsch Med Wochenschr* 1985;110:1841–1848
7. Schaffer R, Becker JA, Goodman J. Sonography of tuberculous kidney. *Urology* 1983;22(2):209–211
8. Angelelli G, Mossa A, Garriba P, Pagliarulo A. L'Echographie dans l'étude de la tuberculose renale. *J Radiol* 1983;64(2):99–102
9. Narayana AS. Overview of renal tuberculosis. *Urology* 1982;19(3):231–237

10. Teklu B, Ortrow JM. Urinary tuberculosis: a review of 44 cases treated since 1963. *J Urol* **1975**;115:507-509
11. Lattimer J, Wechsler M. Genitourinary tuberculosis. In: Harrison JH, Grittes RF, Perlmutter AD, Stamey TA, Walsh PC (eds.) *Campbell's urology*, 4th ed. Philadelphia: Saunders, **1978**:559-575
12. Wechsler H, Westfall M, Lattimer JK. The earliest signs and symptoms in 127 male patients with genitourinary tuberculosis. *J Urol* **1960**;83(6):801-803
13. Barrie HJ, Kerr WK, Gale AL. The incidence and pathogenesis of tuberculosis strictures of the renal pelvis. *J Urol* **1967**;98:584-589
14. Rees RWM, Rollands FG. The ureter in renal tuberculosis. *Br J Urol* **1970**;42:693-696
15. Claridge M. Ureteric obstruction in tuberculosis. *Br J Urol* **1970**;42:688-692
16. Ross JC. Calcification in genito-urinary tuberculosis. *Br J Urol* **1970**;42:656-660

Book Review

1986 Yearbook of Nuclear Medicine. Edited by Paul B. Hoffer. Chicago: Year Book Medical, 411 pp., 1986. \$46.75

It is a pleasure each year to look forward to receiving a copy of the *Yearbook of Nuclear Medicine*. The 1986 edition is no exception. The editors regularly compile an excellent selection of reviews of key articles related to nuclear medicine imaging. The articles are compiled from a list of 63 national and international journals. To help the reader focus on a particular area of interest the book is divided into sections on each of the major organ systems as well as radiochemistry and radiopharmacology, health physics and radiation biology, oncology, infection, and MR imaging. The brief summaries by the editors that accompany the articles consistently bring out the most significant aspect of each article. They add to the enjoyment of reading this book in that one looks forward to the brief editorial comments that attempt to place the material into a broader perspective. The 1986

book also contains a nice review article on quantitative analysis of thallium imaging. It is unclear why the editors include such a review article since it appears out of place but it is well done and worth reading. Overall the editors have maintained the high quality that has characterized the nuclear medicine yearbooks. The *Yearbook of Nuclear Medicine* serves as an excellent resource for those primarily interested in nuclear medicine imaging and who want to keep abreast of a wide range of topics.

Alan H. Maurer
Temple University Hospital
Philadelphia, PA 19140

Diagnosis of Subclinical Varicocele in Infertility

Roger L. Gonda, Jr.¹
James J. Karo¹
Robert A. Forte²
Kevin T. O'Donnell²

The clinically obvious varicocele is perhaps the most common identifiable and correctable cause of male infertility. However, less is known about the subclinical (not palpable) varicocele and its relationship to infertility. We undertook this study to compare the ability of high-resolution sonography and radionuclide scrotal scanning to detect subclinical varicocele. Fifty patients who were referred to our department with a diagnosis of infertility, an abnormal semen analysis, and a normal physical examination of the scrotum underwent both sonography and nuclear scanning. The final study group included 20 men who agreed to surgical ligation of the spermatic vein(s) after a positive sonographic and/or radionuclide study. Sonography was considered positive for subclinical varicocele in 95% of patients, while nuclear scanning was considered positive in only 55%. Postoperatively, all patients showed improvement in their semen and 40% (eight patients) became fertile. Subclinical varicocele seems to be an important causal factor in infertility and, in our experience, high-resolution sonography is superior to radionuclide scanning in its diagnosis.

A varicocele is an abnormal dilatation of the pampiniform plexus resulting from absence or incompetence of the valves of the internal spermatic vein [1-3]. The clinically palpable varicocele is the most common identifiable and correctable cause of male infertility. It occurs in 15-20% of the general population and in 21-39% of men attending infertility clinics [4, 5]. The subclinical varicocele (SCV) is one that is so small it is not clinically palpable. The incidence of SCV is not known, but its importance in male infertility may be significant. A number of techniques have been used to diagnose SCV: (1) thermography [6, 7], which is not widely available and may be unreliable in some cases; (2) Doppler sonography [8, 9], which requires an experienced operator and cannot always be objectively documented; (3) gonadal venography [6, 10-12], which is invasive, carries some risk, is uncomfortable, and may not be physiologic in all cases; and (4) the radionuclide scrotal scan. Several authors have studied the ability of the nuclear scan to detect clinical and subclinical varicocele, [13-18] and although it is a simple and sensitive test, it can be fraught with difficulties in bilateral lesions.

High-resolution sonography has been used to diagnose a number of scrotal abnormalities including varicocele [19-22]. However, since infertile men without palpable scrotal lesions are not usually referred for sonographic study, little has been written on the use of sonography to detect SCV. We undertook this study in order to compare the ability of high-resolution sonography and radionuclide scanning to diagnose SCV and to comment on the possible significance of SCV as it relates to infertility.

Subjects and Methods

Over a period of 3 years 50 patients were referred to our department with a diagnosis of infertility and a "stress pattern" on semen analysis. This "stress pattern" is defined as oligospermia, abnormal motility of the sperm, and increased percentages of tapered and

Received May 5, 1986; accepted after revision August 4, 1986.

Presented at the annual meeting of the American Institute of Ultrasound in Medicine, Dallas, TX, October 1985.

¹ Department of Diagnostic Imaging and Interventional Radiology, Providence Hospital, 16001 W. Nine Mile Rd., Southfield, MI 48075. Address reprint requests to J. J. Karo.

² Department of Surgery, Providence Hospital, 16001 W. Nine Mile Rd., Southfield, MI 48075.

AJR 148:71-75, January 1987

0361-803X/87/1481-0071

© American Roentgen Ray Society

immature sperm forms in the semen [1, 2]. This pattern has been described as a characteristic response of the testes when varicocele is present [2]. At our institution the normal range of values for sperm count is 60–150 million/ml with a motility at 1–2 hr of greater than 80%. At least 70% of visible sperm forms should be of normal, mature morphology. All of the referred patients had received a careful physical examination of the scrotum by an experienced urologist, and none were found to have clinical evidence of varicocele. All 50 patients had been unable to achieve pregnancy despite at least 1 year of unprotected intercourse. All of these patients underwent a radionuclide scan and sonogram of the scrotum.

In the Nuclear Medicine Department each patient was injected intravenously (in the antecubital vein) with 15 mg of stannous pyrophosphate ("cold PYP") to tag the RBC pool. The patient was placed in the supine position and a midline marker was placed on the median raphe of the scrotum. The penis was taped to the anterior abdominal wall. After a 20-min delay (required for the stannous ions to diffuse into the red cells), 20 mCi of ^{99m}Tc pertechnetate was injected as a bolus into the antecubital vein. The pertechnetate diffuses into the red cells and becomes reduced by the intracellular stannous ions, preventing elution from the red cells.

Dynamic and static images were obtained by using high-sensitivity parallel-hole collimation. Additional static images were obtained with the patient in the upright position with and without Valsalva maneuver.

Regions of interest were outlined on representative scans and radioactivity count ratios were tabulated by the computer. The radionuclide scan was interpreted as positive if any combination of one or all of the following was present: (1) there was asymmetry of activity on the flow study; (2) on static images there was a small area of focal activity in either hemiscrotum; (3) a difference of over 10% on the computerized count ratios was seen when right and left sides were compared. The static images were most helpful in making the diagnosis. An example of a positive scan is seen in Figure 1.

In the Sonography Department each patient was placed in the supine position. By using a Biosound (Biodynamics, Indianapolis, IN) high-resolution (real-time), small-parts scanner equipped with an 8-MHz focused annular-array transducer, the scrotum was scanned in the longitudinal and transverse planes. Static scans were obtained with the patient at rest and during Valsalva maneuver. In a few cases, patients were asked to stand for 30–60 min and the scans were repeated in the upright position. This technique did not seem to add to our diagnostic accuracy and was therefore not done routinely. Neither blood flow through the varicose veins nor direction of flow was documented.

The sonographic study was interpreted as positive if the veins of the pampiniform plexus were prominent (exceeding 2 mm in diameter) and if some increase in the caliber of the vessels was observed on Valsalva maneuver. Rifkin et al. [19] and Wolverson et al. [20] have

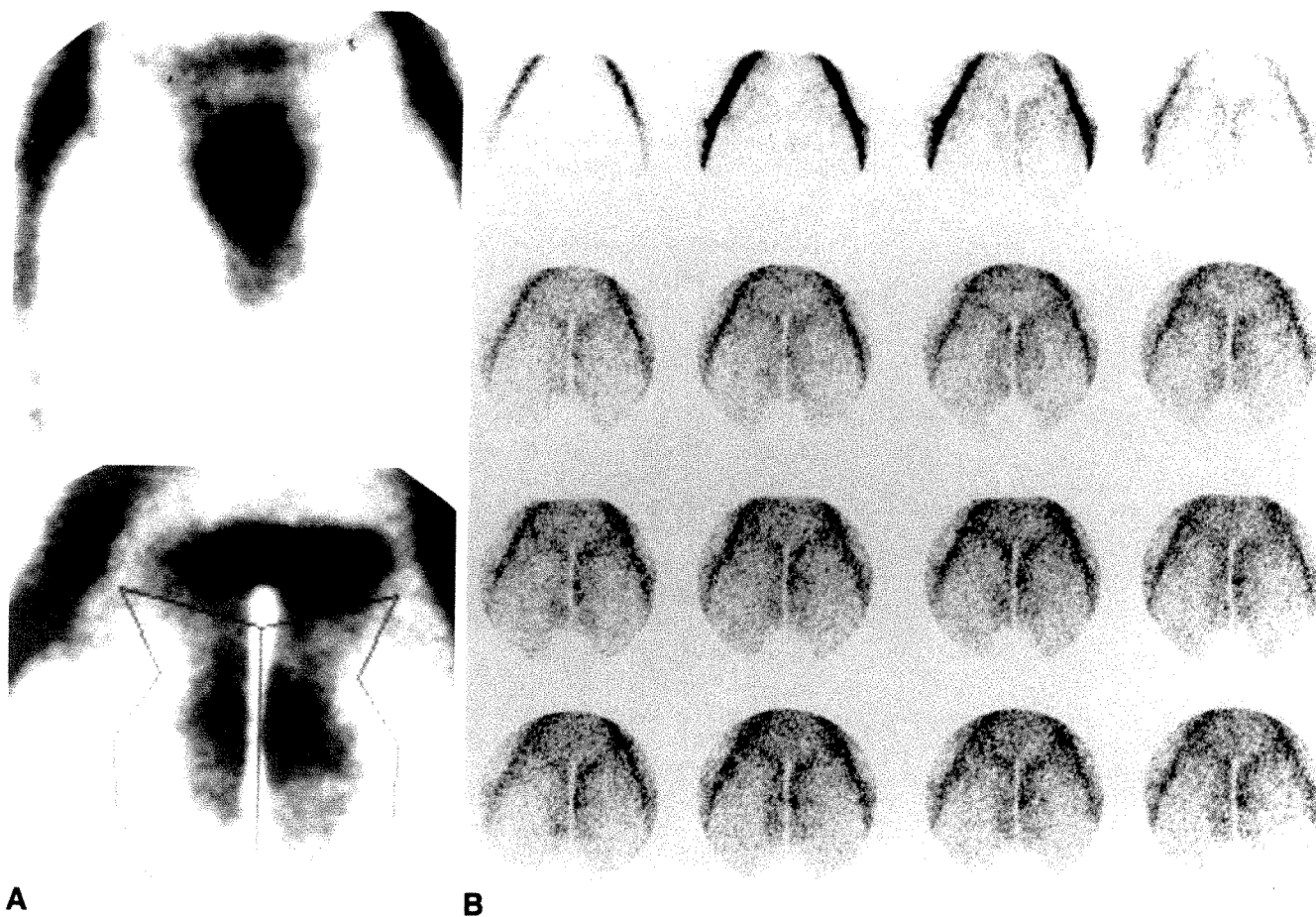


Fig. 1.—A, Subclinical left varicocele. Top: radionuclide scan showing asymmetry of uptake in scrotum on static imaging. Bottom: computerized count ratios show 17% greater activity on left. Sonographic study on this

patient was also positive.

B, Flow study from same patient as A. Activity appears in left hemiscrotum. Images were acquired every 7 sec.

described normal veins in the pampiniform plexus up to 2 mm in diameter. Examples of normal and positive sonograms are seen in Figures 2 and 3.

Results

Of the 50 patients studied, 10 were found to have normal sonographic and radionuclide studies. Because these men were excluded from the study, the incidence of false-negative studies could not be determined. Any patient who had a positive sonographic or nuclear exam was offered surgery to correct the varicocele. Of the 40 remaining men in the referral group, 20 elected not to have surgery or were lost to follow-up. Thus, the true incidence of false-positive studies could not be obtained. The study group consisted of the remaining 20 patients, all of whom had surgical correction.

The subclinical varicoceles were repaired with high ligation of the spermatic vein(s). Postoperative semen analysis was performed in all but one patient and all showed improvement. Eight of the 20 patients achieved fertility after surgery. Details of the actual sperm counts and motility and their improvement postoperatively are seen in Table 1. Mean improvement in sperm count postoperatively was 17 million/ml. Mean improvement in sperm motility postoperatively was 19%.

Table 2 outlines the ages of patients, radionuclide and sonographic results, and success at achieving pregnancy. The 20 patients ranged in age from 26 to 35 years.

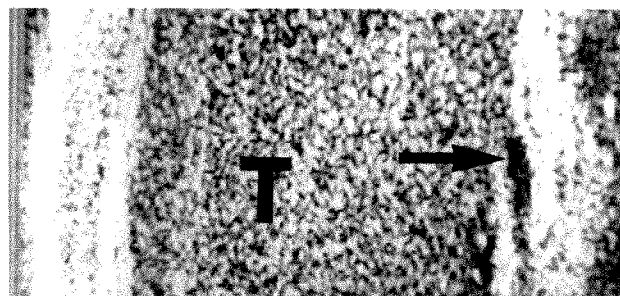
Table 3 compares the results of the nuclear and sonographic procedures. Of the 20 patients who had left subclinical varicocele, the nine patients with negative radionuclide studies had positive sonographic results. One sonographic study

was interpreted as negative, but this patient had a positive radionuclide scan. There were eight patients with bilateral varicoceles. Of these the radionuclide scan was able to diagnose only one, while sonography correctly diagnosed all

TABLE 1: Semen Analysis Comparison

Case No.	Preoperative		Postoperative	
	Count (millions/ml)	Motility (%)	Count (millions/ml)	Motility (%)
1	35	40	75	62
2	7	30	28	54
3	30	30	40	70
4	3	10	29	50
5	1	20	46	80
6	1	10	4	25
7	7	40	18	55
8	11	65	20	50
9	1	30	7	30
10	8	30	20	35
11	40	40	93	30
12	6	30	25	50
13	11	50	25	80
14	7	50	20	54
15	7	50	30	65
16	1	20	5	40
17	30	50	22	70
18	1	50	25	75
19	1	60	—	—
20	9	20	11	50

Note.—Case 19 did not have postoperative semen analysis performed. Those patients who did not show improvement in motility showed improvement in sperm count. One patient (no. 17) with a decreased sperm count postoperatively showed improvement in sperm motility.



2



3

Figure 2.—Normal scrotal sonogram. Longitudinal (top) and transverse (bottom) high-resolution scans of scrotum showing normal testis (T) and normal pampiniform plexus (arrows).

Fig. 3.—Subclinical left varicocele. Sonographic scan shows a dilated, serpiginous pampiniform plexus (arrows).

TABLE 2: Varicocele Data Summary

Case No.	Age	RNS	S	Pregnancy
1	29	Neg	Small bilat	No
2	28	+L	+L	No
3	27	Neg	+L	No
4	31	+L	+L	No
5	27	Possible bilat	Small bilat	No
6	32	Neg	Small bilat	No
7	29	Neg	Bilat	No
8	29	+L	+L	No
9	29	+L	+L	No
10	31	Neg	Bilat	No
11	31	+L	Bilat	No
12	27	+L	+L	Yes
13	26	+L	+L	Yes
14	28	+L	Neg	Yes
15	32	+L	Bilat	Yes
16	30	Neg	+L	Yes
17	35	Neg	Bilat	Yes
18	30	+L	+L	Yes
19	31	Neg	+L	Yes
20	26	Neg	+L	No

Note.—RNS = radionuclide scrotal scan result; S = high-resolution scrotal sonography result; +L = a study was positive for left-sided varicocele; Bilat = a study was positive for left and right varicocele; Neg = a negative interpretation was given for varicocele.

TABLE 3: Comparison of Results of Sonography and Scintigraphy in 20 Patients with 28 Surgically Proven Varicoceles

	Left Varicocele (20)			Bilateral Varicocele (8)			Total (28)	
	+	—	%	+	—	%	No.	%
RNS	11	9	55	1	7	13	12	43
S	19	1	95	8	8	100	27	96

Note.—+ denotes a positive interpretation; — denotes a negative interpretation. RNS = radionuclide scan; S = sonography.

eight. None of the patients in this study group had unilateral right-sided varicoceles.

Discussion

The pampiniform plexus is the main group of veins draining the testes. It flows into the cremasteric and internal spermatic veins with eventual drainage into the renal vein on the left and the inferior vena cava on the right. Varicoceles may result from extrinsic obstruction to any of these veins. Most varicoceles occur as a result of incompetent internal spermatic venous valves or collateral bypass of competent valves with resultant free reflux of venous blood into the pampiniform plexus [2]. The prevalence of left-sided varicocele is due to the fact that the left internal spermatic vein usually drains into the left renal vein at right angles [2]. Also the left varicocele may be the result of compression of the left renal vein as it courses between the abdominal aorta and the superior mesenteric artery [4].

Numerous theories have been proposed to explain the apparent effect of varicocele on spermatogenesis. Elevation of scrotal temperature, hormonal disturbances, and reflux of toxic metabolites from renal or adrenal sources have all been implicated as responsible for the infertility associated with varicocele [2, 4, 5]. None of these theories has been definitely proven.

Surgical ligation of the spermatic vein in men with clinically obvious varicocele and a "stress pattern" seminal analysis improves semen quality in 60–81% and results in pregnancy rates of 30–55% [1, 3, 4, 23]. The implications of ligation of the same veins in men with similar seminal abnormalities but with subclinical varicocele are not as clear in the literature, probably because it has been difficult to definitely diagnose SCV. Our work compares the efficacy of high-resolution sonography and radionuclide scanning in the diagnosis of SCV in patients with documented infertility.

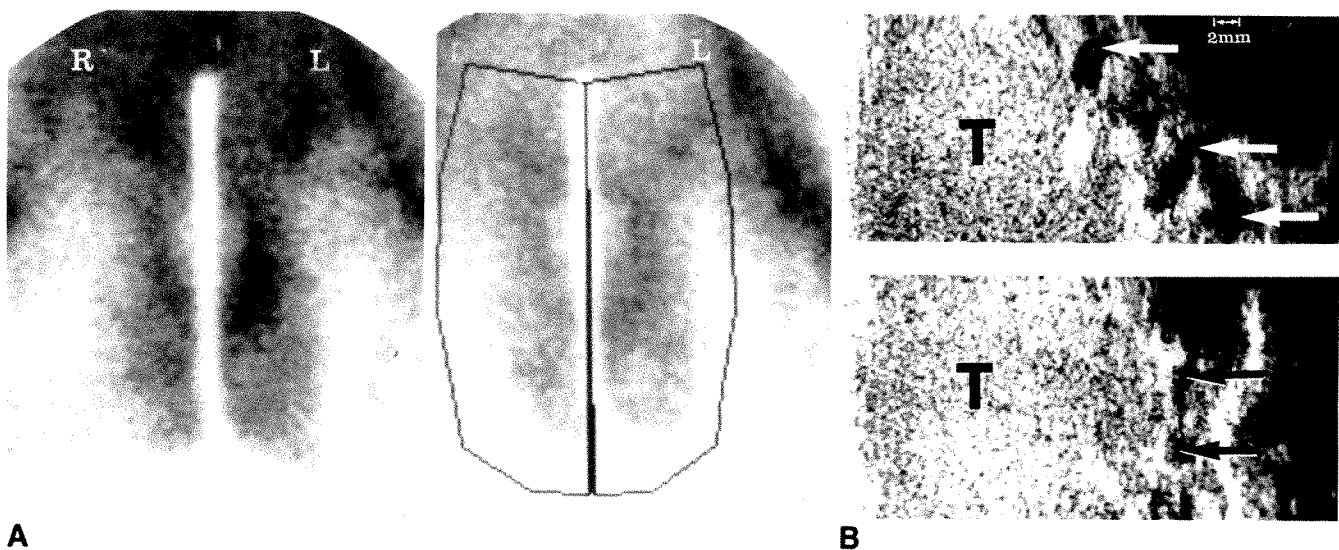


Fig. 4—A, Bilateral subclinical varicoceles. Radionuclide scan shows no asymmetry on static images (left). Computerized count ratios (right) did not differ by more than 10% (R = 183,779 counts, L = 195,669 counts).

B, Bilateral subclinical varicoceles. Sonographic scans of left scrotum (top) and right scrotum (bottom) performed during Valsalva maneuver reveal dilated pampiniform plexus of veins bilaterally (arrows). T = testis.

Our data (Table 3) suggest that diagnosing bilateral SCV with radionuclide scanning is difficult. Of the eight patients with bilateral lesions, seven were not detected. Three of the seven patients were interpreted as having only a left-sided lesion on the basis of focal activity on that side. The radionuclide scans of the remaining four patients with bilateral disease were interpreted as negative since there was no asymmetry of radioactivity. Bilaterality, then, appears to be a source of difficulty in the radionuclide diagnosis of SCV. An example of a patient with a negative radionuclide scan in the presence of bilateral varicoceles detected by sonography is seen in Figure 4.

All of our patients who underwent postoperative semen analysis improved, and in our series pregnancy was achieved in 40%. These results are comparable with those of several reports dealing with the diagnosis, treatment, and subsequent postoperative improvement in semen quality and fertility rates in patients with clinically obvious varicoceles [1, 3, 4, 23].

Several reports of the diagnosis of SCV by venography show reflux into the internal spermatic vein(s) and pampiniform plexus in patients without palpable varicoceles [7, 11–13, 24]. To our knowledge, no study has been performed comparing sonography and venography in the diagnosis of SCV. Dubin and Amelar [1] concluded that there was no relationship between the size of the varicocele and the postoperative results in their series. Our work would support this impression since our patients all had nonpalpable subclinical varicoceles and the postoperative semen analysis and pregnancy-rate statistics are comparable to the results of their work [1] in clinically obvious varicoceles.

Many questions remain unanswered about the causal relationship between SCV and infertility. In addition, there does not appear to be a consensus on an actual "gold standard" for the diagnosis of SCV. We were unable to determine the actual incidence of false-negative and false-positive diagnoses in our series. Nonetheless, we believe that the favorable pregnancy rates achieved in our patients who were treated on the basis of positive studies emphasizes the importance of making this diagnosis. In our experience sonography is superior to radionuclide scanning for the diagnosis of SCV.

Conclusions

The conclusions drawn from this study may be summarized as follows: (1) There appears to be a strong correlation between infertility and the presence of a SCV. (2) High-resolution sonography is a noninvasive, relatively inexpensive technique that uses no ionizing radiation, requires no IV contrast injection, and appears to be very sensitive in the diagnosis of SCV. (3) In our experience, sonography is superior to radionuclide scanning in the diagnosis of SCV. (4) We believe that all patients who present with infertility and an abnormal seminal analysis should undergo high-resolution sonography to determine the presence of varicocele, especially those men with a normal physical examination of the scrotum.

ACKNOWLEDGMENTS

Special thanks to Deborah A. Lach and May L. Birkett for secretarial assistance and to Phillip E. Perkins for his help with the nuclear imaging.

REFERENCES

- Dubin L, Amelar RD. Varicocele size and results in varicocelectomy in selected subfertile men with varicocele. *Fertil Steril* 1970;21:606–609
- Belker AM. The varicocele and male infertility. *Urol Clin North Am* 1981;8(1):41–51
- Charny CW, Baum S. Varicocele and infertility. *JAMA* 1968;204(13):75–78
- Dubin L, Amelar RD. Varicocele. *Urol Clin North Am* 1978;5(3):563–572
- Greenberg SH. Varicocele and male fertility. *Fertil Steril* 1977;28(7):699–706
- Comhaire F, Monteyne R, Kunnen M. The value of scrotal thermography as compared with selective retrograde venography of the internal spermatic vein for the diagnosis of "subclinical" varicocele. *Fertil Steril* 1976;27(6):694–698
- Nicolaiji D, Steeno OP, Couck W, et al. Comparison of scrotal scintigraphy and thermography for the diagnosis of varicocele. *Eur J Nucl Med* 1983;8:123–126
- Hirsh AV, Cameron KM, Tyler JP, Simpson J, Pryor JP. The Doppler assessment of varicoceles and internal spermatic vein reflux in infertile men. *Br J Urol* 1980;52:50–56
- Greenberg SH, Lipschultz LI, Wein AJ. A preliminary report on "subclinical varicocele": diagnosis by Doppler ultrasonic stethoscope. *J Rep Med* 1979;22(2):77–81
- Delaere KPJ, Debruyne FMJ, Mattelaer JJ. Renal and gonadal venography in male infertility. *Eur Urol* 1981;7:340–342
- Bigot JM, Chatel A. The value of retrograde spermatic phlebography in varicocele. *Eur Urol* 1980;6:301–306
- Narayan P, Amplatz K, Gonzalez R. Varicocele and male subfertility. *Fertil Steril* 1981;36:92–97
- Freund J, Handelsman DJ, Bautovich GJ, Conway AJ, Morris JG. Detection of varicocele by radionuclide blood-pool scanning. *Radiology* 1980;137:227–230
- Wheatley JK, Fajman WA, Witten FR. Clinical experience with the radionuclide varicocele scan as a screening method for the detection of subclinical varicoceles. *Urology* 1982;128:57–59
- Van Der Vis-Melsen MJE, Baert RJM, Van Der Beek FJ, Dewringer THPJ. Sensitivity of scrotal scintigraphy in the diagnosis of varicocele. *Clin Nucl Med* 1982;7(6):287–291
- Harris JD, Lipshultz LI, Conoley PH, McConnell BJ, McConnell RW. Radioisotope angiography in diagnosis of varicocele. *Urology* 1980;16(1):69–72
- Fajman WA, Berkman WA, Wheatley JK, McClees EC, Berger HJ. Correlation of varicocele scintigraphy with venography. *Radiographics* 1984;4(3):465–477
- Marmar JL, Zeiger TJ, DeBenedictis TJ, Praiss DE. Comprehensive scrotal flow and scan technique for detection of varicoceles. *Urology* 1985;25:505–510
- Rifkin MD, Foy PM, Kurtz AB, Pasto MD, Goldberg B. The role of diagnostic ultrasonography in varicocele evaluation. *J Ultrasound Med* 1983;2:271–275
- Wolverson MD, Houttuin E, Heiberg E, Sundaram M, Gregory J. High-resolution real-time sonography of scrotal varicocele. *AJR* 1983;141:775–779
- Carroll BA, Gross DM. High-frequency scrotal sonography. *AJR* 1983;140:511–515
- Hricak H, Filly RA. Sonography of the scrotum. *Invest Radiol* 1983;18:112–121
- Dubin L, Amelar RD. Varicocelectomy as therapy in male infertility: a study of 504 cases. *J Urol* 1975;113:640–641
- Pieter Marsman JW. Clinical versus subclinical varicocele: venographic findings and improvement of fertility after embolization. *Radiology* 1985;155:635–638

Book Review

Orthopedic Radiology. By Barbara N. W. Weissman and Clement B. Sledge. Philadelphia: Saunders, 679 pp., 1986. \$75

This textbook constitutes an extremely important contribution to both diagnostic imaging and orthopedic surgery. The two coauthors are well-respected academicians from the two areas, and the book provides an appropriate combination of image interpretation, clinical information, and concepts of surgical management regarding a broad spectrum of bone and joint disease. An introductory chapter deals with general principles of orthopedic radiology (including technical aspects of imaging methods; fracture terminology and healing; and surgical management via internal fixation, bone grafting, electrical stimulation, osteotomy, and arthroplasty). In subsequent chapters, these concepts are applied to specific sites including the hand, wrist, elbow, shoulder, lumbar spine, pelvis, hip, knee, ankle, and foot. A comprehensive index and an introductory outline for each chapter facilitate access to desired information.

Positive aspects of the book include superb organization of the text and extensive up-to-date reference lists at the end of each chapter, which are arranged according to specific topics. The quality of the radiographic images, which include conventional, arthrographic, CT, and scintigraphic studies, is exquisite. Illustrative material is highlighted by numerous high-quality line drawings, photographs of specimens and orthopedic hardware, and informative tables and charts. Line drawings are also employed to enhance the chapter and page headings, and the pleasant typeface as well as the authors' concise writing style renders the book easily readable.

The only major drawback of the book lies in its sparse consideration of MR imaging, an omission that is related to expected publication

schedules and numerous recent advances in the application of this technique to musculoskeletal disorders. As compared to the well-known text by Resnick and Niwayama, the book is more manageable in size and includes greater emphasis on clinical and surgical concepts as opposed to imaging-pathologic correlation. The scope of the work is broader than that of Roger's book on the radiology of skeletal trauma, which is limited to the latter topic and includes less information on management and postoperative evaluation. In many respects, the book resembles the well-known text by Ozonoff on pediatric orthopedic radiology, but is applicable chiefly to bone and joint disorders in adults.

The authors have successfully filled a significant void in the medical literature by creating a text with an optimal balance of information concerning the clinical, surgical, and diagnostic imaging aspects of musculoskeletal disease. I highly recommend this book to radiologists as well as to orthopedic surgeons in both academic and private-practice settings, and it will be a valuable contribution to any department library. Physicians-in-training within both the orthopedic and the diagnostic imaging disciplines will also find the text useful as a learning aid. The book is well worth its moderate cost and constitutes one of the foremost publications on bone and joint disease that has been written in recent years.

David J. Sartoris
UCSD Medical Center
San Diego, CA 92103

Pictorial Essay

MR Imaging of the Supraclavicular Region: Normal Anatomy

Gary M. Kellman,^{1,2} J. Bruce Kneeland,¹ William D. Middleton,¹ James D. Cates,^{1,3} Peter Pech,^{1,4} Thomas M. Grist,¹ W. Dennis Foley,¹ A. Jesmanowicz,¹ W. Froncisz,¹ and James S. Hyde¹

The supraclavicular fossa including the brachial plexus have traditionally been difficult to evaluate, both clinically and from an imaging standpoint. Conventional radiographs only depict indirect changes in the adjacent lung apex and skeletal structures. CT is currently the best technique for assessing the supraclavicular region [1–5], but CT has several significant limitations, including a restriction to the axial imaging plane and streak artifacts from the shoulders. MR provides better soft-tissue contrast than CT, permits direct multiplanar imaging, and is not associated with streak artifacts. In addition, the superficial location of this area makes it accessible to local (surface) coils. Thus, MR has great potential in the evaluation of this region, and a detailed understanding of the normal anatomy of the supraclavicular fossa as seen on MR is important. We present a correlative study between high-resolution MR images obtained with local coils and anatomic sections obtained with a cryomicrotome.

Materials and Methods

MR imaging was performed on a General Electric Signa MR system (Milwaukee, WI) operating at 1.5 T; one of a variety of counterrotating current loop-gap resonators was used as the local receiver coil with the body coil as the transmitter. The properties of these coils have been investigated at length [6, 7]. The coil was placed directly on the

surface of the patient's anterior upper thorax with the patient in the supine position as shown in Fig. 1.

Three normal volunteers were imaged. The volunteers were all men (ages 30–33 years) and had no signs or symptoms of disease in the supraclavicular region. Imaging data were acquired by using a 2D Fourier transform, spin-echo, multisection technique with either 128×256 or 256×256 matrices, a 16- or 20-cm field-of-view, and 3- or 5-mm-thick sections obtained either contiguously or with 1–1.5 mm gaps. Images were obtained in axial, sagittal, and coronal planes in all subjects. Relatively T1-weighted (TR = 500–600 msec, TE = 20–25 msec), proton density-weighted (TR = 2000–2500 msec, TE = 20–25 msec), and T2-weighted (TR = 2000–2500 msec, TE = 60–80 msec) spin-echo pulse sequences were performed for one of the planes of section in each subject. We employed respiratory motion compensation, using a reordering of the phase-encoding gradient (ExorCist, General Electric), for all of the subjects. Cardiac gating was used for one of the volunteers.

Anatomic sections of four supraclavicular regions were obtained (two in the coronal plane and one each in the axial and sagittal planes) with a cryomicrotome (LKB 2250, Gaithersburg, MD). Blocks of tissue were harvested from frozen cadavers and placed on the stage of the cryomicrotome. As each millimeter of tissue was removed, a photograph was taken of the surface. The photographs and MR images were compared [8]. CT and MR images of one of the cadaver specimens were also obtained in three planes prior to cryosectioning for correlation purposes. MR was performed on only one cadaver specimen, since the quality of the cryomicrotome sections suffered

Received June 12, 1986; accepted after revision August 26, 1986.

Presented at the annual meeting of the American Roentgen Ray Society, Washington, DC, April 1986.

This work was supported in part by NIH Grants CA41464, RR01008, and AM33667.

¹ Department of Radiology, Medical College of Wisconsin, Milwaukee, WI 53226. Address reprint requests to J. B. Kneeland, Dept. of Radiology, Milwaukee County Medical Complex, 8700 W. Wisconsin Ave., Box 137, Milwaukee, WI 53226.

² Department of Radiology, Western Pennsylvania Hospital, 4800 Friendship Ave., Pittsburgh, PA 15224.

³ Department of Radiology, Tampa General Hospital, Tampa, FL 33606.

⁴ Department of Radiology, University Hospital, SA 750 14 Uppsala, Sweden.

AJR 148:77–82, January 1987 0361–803X/87/1481–0077 © American Roentgen Ray Society



Fig. 1.—Photograph showing position of surface coil used for MR imaging of supraclavicular region.

owing to the need to thaw the specimens for MR imaging and then to refreeze them for sectioning. Standard references were used to study the anatomy of the anatomic sections and MR images [9–11]. The axial cryomicrotome sections are not presented since similar work has been presented in detail [1].

Observations

The supraclavicular fossa is a complex anatomic region that is contiguous with the neck above and axilla below (Fig. 2). Many of the structures in this region, such as the scalene and omohyoid muscles, subclavian vessels, and brachial plexus, course from one of these compartments to another. Other contents of the supraclavicular fossa include small branches of the subclavian vessels, fat, lymph nodes, and the posterior lung apex. A diagram of this region is shown in Figure 2 [12].

The supraclavicular fossa and axilla are filled with fat, which typically has high signal intensity on all pulse sequences (Figs. 3–6). It is the abundant fat that gives excellent contrast with the other structures in this region, allowing their delineation even in the thinnest of subjects.

Understanding this complex area is made easier by knowing the anatomy of the scalene muscles and their relationship with other supraclavicular structures. The scalenus anticus is a cone-shaped muscle that arises from the transverse processes of vertebrae C3 through C7, extending inferolaterally to insert by a narrow flat tendon on the upper inner aspect of the first rib (Figs. 2, 3A, and 3B). The middle scalene is the largest and longest of the scalene muscles. It arises from the transverse processes of vertebrae C2 through C7 and inserts onto the upper surface of the first rib by a broad attachment posterior to the insertion of the anterior scalene (Figs. 2, 3C, and 4C). The posterior scalene is the smallest of these muscles and often is not identified as a separate structure from the middle scalene muscle on CT or MR images. It arises

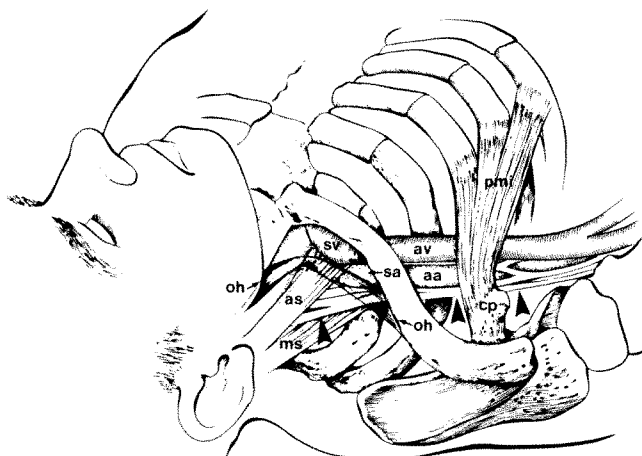


Fig. 2.—Normal anatomy of supraclavicular region. Copyright 1971, CIBA Pharmaceutical Co., a division of CIBA-GEIGY. Adapted with permission from *Clinical Symposia*—by F. H. Netter [12]. All rights reserved. Omohyoid muscle drawn as if transparent. Arrowheads = brachial plexus. See key for abbreviations.

Key to Abbreviations Used in Figures

aa	axillary artery
ANT	anterior aspect
ap	acromion process
apex	lung apex
as	anterior scalene muscle
av	axillary vein
cca	common carotid artery
cb-shb	coracobrachialis/short head of biceps muscles
cl	clavicle
cp	coracoid process
del	deltoid
es	esophagus
gp	glenoid process
hum	humerus
ijv	internal jugular vein
ms	middle scalene muscle
oh	omohyoid muscle
pma	pectoralis major muscle
pmi	pectoralis minor muscle
R1	first rib
sa	subclavian artery
sc	subclavius muscle
ser	serratus anterior muscle
ss	subscapularis muscle
su	supraspinatus muscle
sv	subclavian vein
thy	thyroid gland
tr	trachea
trp	trapezius muscle

from the transverse processes of C5 through C7 and inserts by a thin tendon onto the outer surface of the second rib. These muscles possess a medium-level signal intensity on all pulse sequences, higher than that of blood vessels or lung and lower than that of fat.

The subclavian artery and vein have parallel courses from

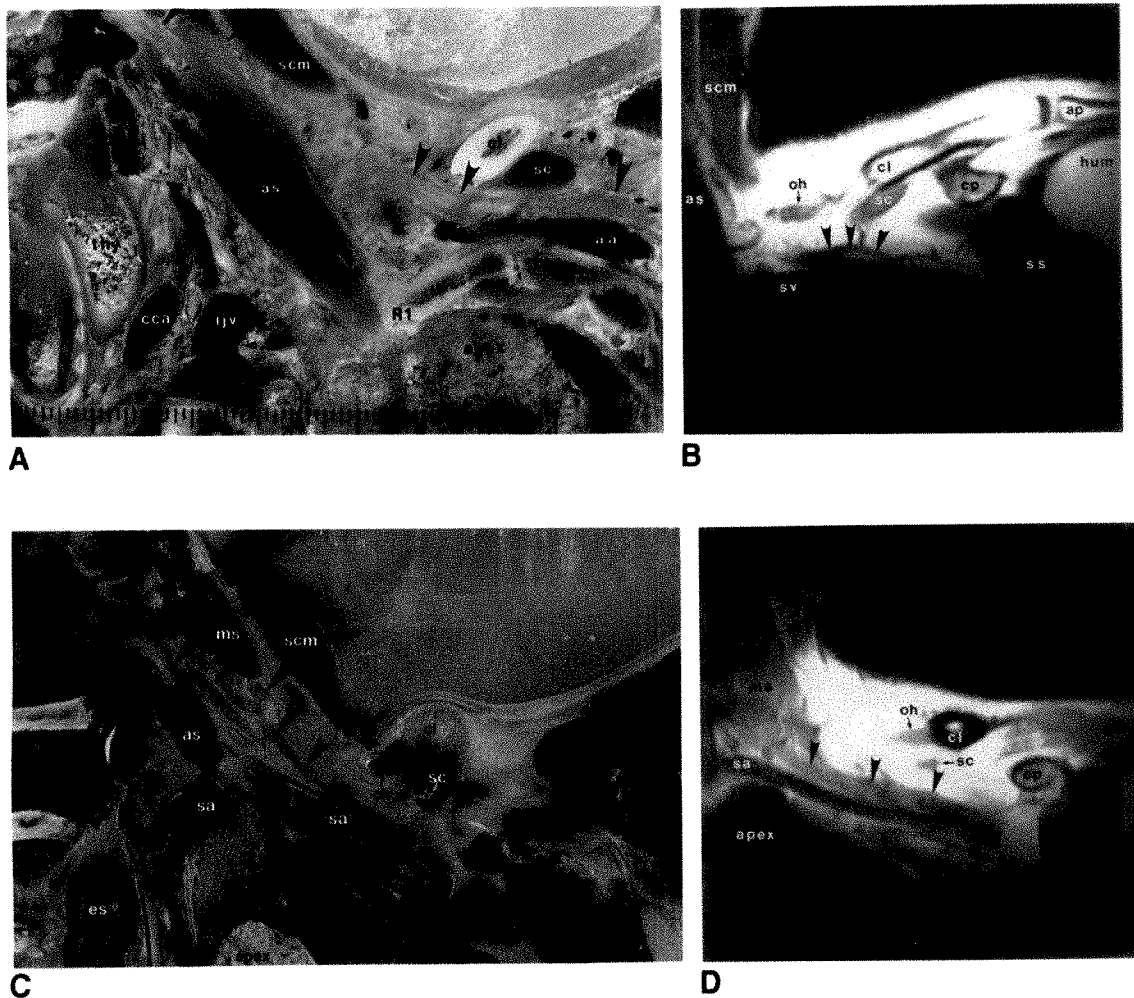


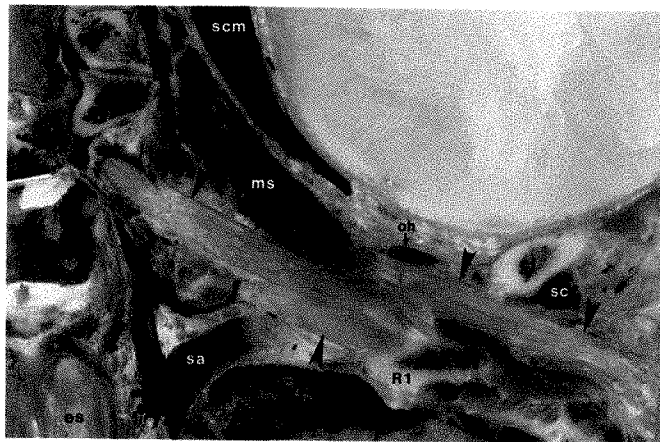
Fig. 3.—Coronal sections and MR images of left supraclavicular fossa. See key for abbreviations.
 A, B, Coronal sections at the level of the anterior scalene muscle. TR = 2000 msec, TE = 20 msec, arrowheads = brachial plexus.
 C, D, Coronal sections between anterior and middle scalene muscles. TR = cardiac gated, TE = 20 msec, arrowheads = brachial plexus.

the thoracic inlet, over the first rib, under the clavicle and subclavius muscle, and into the axilla as the axillary artery and vein. The subclavian vein courses between the clavicle anteriorly and the anterior scalene muscle posteriorly, while the subclavian artery courses between the anterior and middle scalene muscles (Fig. 2). The subclavian artery is usually smaller in diameter than the corresponding vein and possesses a thicker wall. The vein is consistently located anterior and slightly inferior to the artery (Figs. 2, 5A, and 5B).

The subclavian and axillary vessels and their branches are easily recognized on MR by their low or absent signal intensity on all pulse sequences. As with MR in other parts of the body, varying amounts of signal can sometimes be seen within vessels due to flow-related enhancement, even echo rephasing or diastolic pseudogating [13]. An example of this is seen in Fig. 5E where the subclavian vein contains a moderate amount of signal.

The nerve roots that form the brachial plexus emerge between the anterior and middle scalene muscles, just superior and slightly posterior to the subclavian artery (Figs. 2, 3C, and 5E). Occasionally, nerve roots course through the substance of the anterior or middle scalene muscles. The brachial plexus parallels the course of the subclavian/axillary artery into the axilla, remaining immediately superoposterior to it (Figs. 2, 3A–D, 5A, and 5B). The cords of the brachial plexus eventually surround the axillary artery as the neurovascular bundle courses posterior to the pectoralis minor muscle and inferior to the coracoid process (Figs. 2, 4B, 5C, and 5D). It is the relative position of the cords with respect to the axillary artery that gives rise to their respective names (for example, the posterior cord is located posterior to the artery).

Gebarski et al. [1] pointed out that, in general, CT could only show certain elements of the brachial plexus, specifically the nerve roots as they exited from the neural foramina and

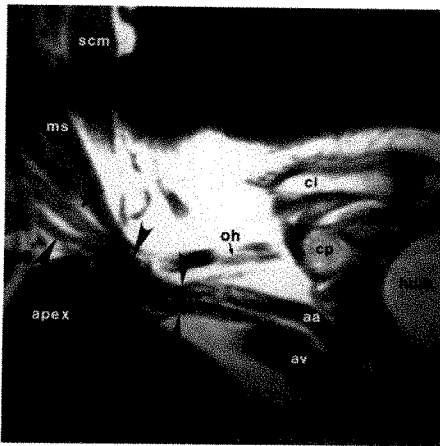


A

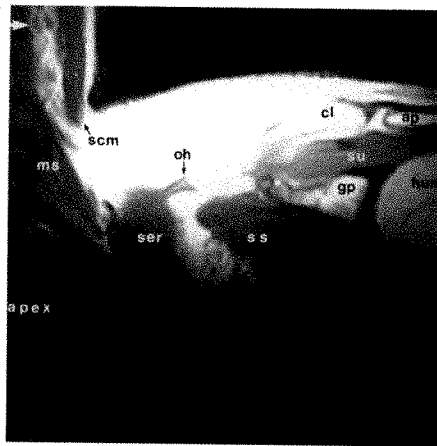
Fig. 4.—Coronal sections and MR images of left supraclavicular fossa. See key for abbreviations.

A, B, Coronal sections posterior to anterior scalene and at level of middle scalene. TR = 2000 msec, TE = 20 msec. Arrowheads = brachial plexus.

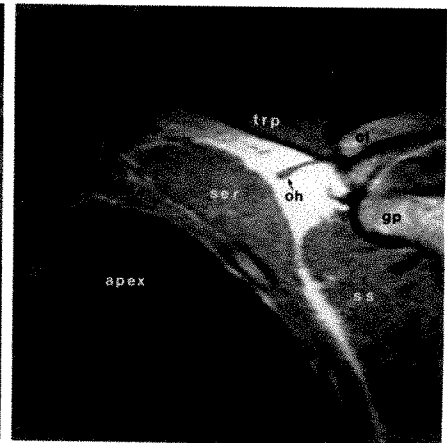
C, D, Coronal sections posterior to neurovascular bundle. TR = 2500 msec, TE = 20 msec. White arrow = small lymph nodes deep to the sternocleidomastoid.



B



C



D

the terminal branches in the lower axilla. They also noted that the neurovascular bundle of axillary artery and brachial plexus generally appears as a single structure on CT sections. With MR, it is possible to identify all the components of the brachial plexus as structures distinct from the adjacent artery (Figs. 3D, 4B, 5B, and 5E). Some of the individual plexal elements can be distinguished from one another as well (Figs. 3B, 3D, 4B, 5B, 5D, 5E, and 6B), although it has not yet been possible to specifically identify these structures as trunks, divisions, or cords. The normal nerve elements have a medium-level signal intensity similar to that of muscle on all pulse sequences.

The scalene lymph nodes represent the most inferior group in the deep cervical chain and are located anterior to the anterior scalene muscle. These have been identified in all three normal volunteers in this study (Fig. 5E). They have medium-level signal intensity similar to that of adjacent muscle. The largest of these was 8 mm in the shortest diameter of the lymph node.

Several muscles of minor importance deserve mention only because knowledge of their anatomy can avoid confusing

them with masses. These include the subclavius, omohyoid, pectoralis minor, and serratus anterior muscles. Their signal intensity characteristics are identical to those already described for the scalene muscles.

The subclavius muscle parallels the clavicle along its inferior aspect (Figs. 3A, 3B, 3C, 5A, 5B, and 6). It originates from the first rib and costal cartilage and inserts into the undersurface of the clavicle. Its medial portion can be separated from the clavicle (Fig. 3D).

The omohyoid muscle has two bellies united by a central tendon, which is anchored by a slip of the deep cervical fascia anterior to the internal jugular vein and deep to the sternocleidomastoid muscle (Fig. 2). The superior belly, which represents one of the strap muscles, is not normally imaged when evaluating the supraclavicular region because it is superior and medial to the region of interest, usually out of the range of sensitivity of the local coil. It originates from the hyoid bone and extends inferiorly to join the central tendon. The inferior belly extends from the central tendon to the superior border of the scapula where it inserts just medial to

Fig. 5.—Sagittal cryomicrotome sections and MR images (TR = 600 msec, TE = 25 msec). See key for abbreviations.

A, B, Alternating light and dark lines such as those denoted by large arrow represent ghosting artifact caused by respiratory motion. **Asterisk** = transverse cervical vein. **Arrowheads** = brachial plexus.

C, D, Sagittal sections at level of coracoid process. Arrowheads = brachial plexus; white arrows = neurovascular bundle.

E, Sagittal section through sternocleidomastoid muscle. **Large black arrows** = normal scalene lymph nodes; **white arrowheads** = brachial plexus.

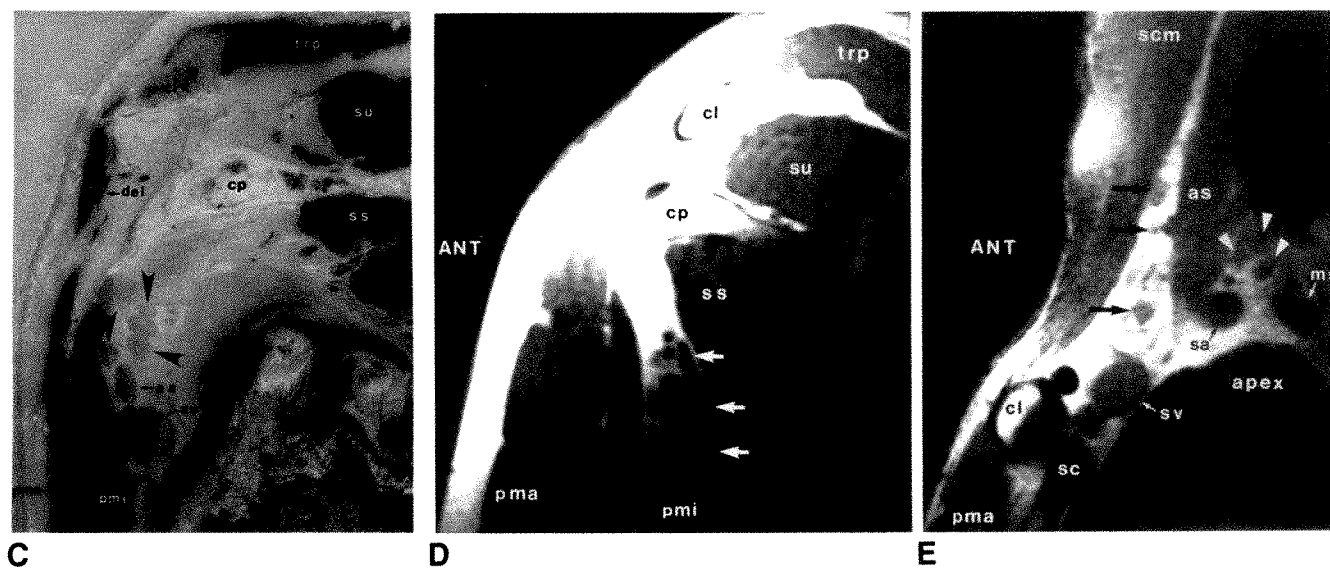
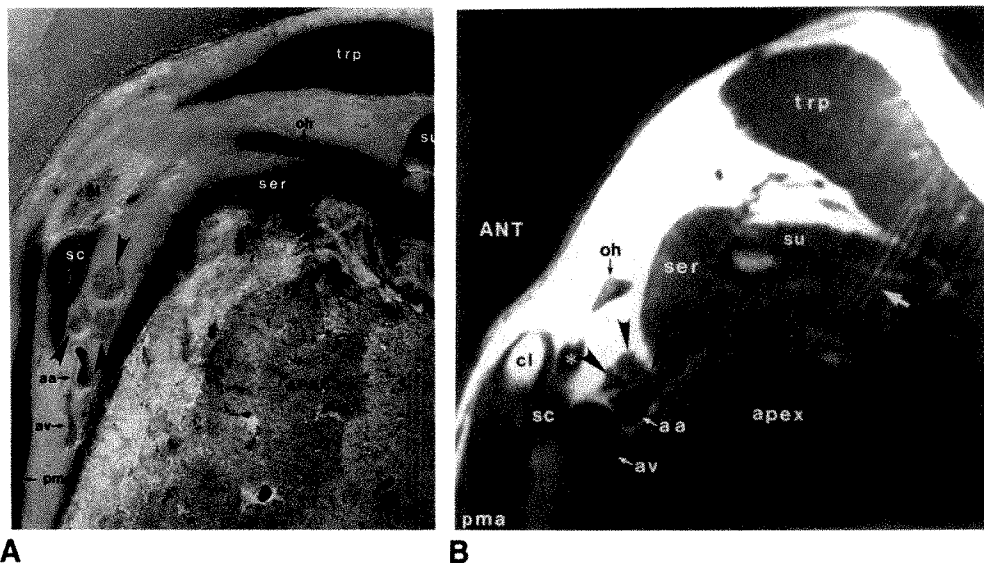


Fig. 6.—Axial MR images (TR = 600 msec, TE = 25 msec) through medial (superior, A) and lateral (inferior, B) portions of the brachial plexus. Arrowheads = brachial plexus; curved black arrows = small lymph nodes; large white arrow = ghosting artifact caused by blood flow in a vein. See key for abbreviations.

the coracoid process. The inferior belly is routinely seen as it courses through the supraclavicular fossa from anteromedial to posterolateral (Figs. 3, 5A, 5B, and 6A).

The pectoralis minor muscle arises as separate digitations from ribs three to five and inserts onto the coracoid process of the scapula. The neurovascular bundle passes directly posterior to this muscle and inferior to the coracoid process (Figs. 2, 5C, 5D, and 6B).

The serratus anterior muscle arises as separate digitations from the eight upper ribs and inserts by a broad thin attachment onto the ventral medial border of the scapula. It is located adjacent to the chest wall where it forms the medial border of the axilla. Its bulbous superior portion can be confused with a mass (Figs. 4C and 4D). The brachial plexus passes directly anterior to this muscle (Figs. 5A, 5B, and 6B).

ACKNOWLEDGMENTS

We wish to thank Shirley Laszewski for her assistance in manuscript preparation and Bruce Nowicki for his assistance in the preparation of cryomicrotome sections.

REFERENCES

1. Gebarski KS, Glazer GM, Gebarski SS. Brachial plexus: anatomic, radiologic and pathologic correlation using computed tomography. *J Comput Assist Tomogr* **1981**;6:1058-1063
2. Usselman J, Vint V, Waltz T. CT demonstration of a brachial plexus neuroma. *AJNR* **1980**;1:346-347
3. Cascino TL, Kori S, Krol G, Foley KM. CT of the brachial plexus in patients with cancer. *Neurology* **1983**;33:1553-1557
4. Powers SK, Norman D, Edwards MSB. Computerized tomography of peripheral nerve lesions. *J Neurosurg* **1983**;59:131-136
5. Webb WR, Jeffery RB, Godwin JD. Thoracic computed tomography in superior sulcus tumors. *J Comput Assist Tomogr* **1981**;5:361-365
6. Froncisz W, Jesmanowicz A, Kneeland JB, Hyde JS. Counter rotating current local coils for high resolution magnetic resonance imaging. *Magnetic Resonance Med* **1986**;3:590-603
7. Kneeland JB, Carrera GF, Middleton WD, et al. High resolution magnetic resonance imaging with counter rotating current loop-gap resonators: preliminary application to the imaging of rotator cuff tears. *Radiology* **1986**;160:695-699
8. Rauschnig W. Popliteal cysts, and their relation to the gastrocnemiosemimembranosus bursa. Studies on the surgical and functional anatomy. *Acta Orthop Scand [Suppl]* **1979**;179:1-43
9. Williams PL, Warwick R, eds. *Gray's anatomy*, 36th British ed. Philadelphia: Saunders, **1980**;536-542, 692-702, 1094-1095
10. Clemente CD. *Anatomy: a regional atlas of the human body*. Philadelphia: Lea & Febiger, **1975**;426-443
11. Wagner M, Lawson TL. *Segmental anatomy: applications to clinical medicine*. New York: Macmillan, **1982**;91-176
12. Lord JW, Rosati LM. Thoracic outlet syndromes. *Ciba Clin Symp* **1971**;23(2):1-32
13. Bradley WG, Waluch V. Blood flow: magnetic resonance imaging. *Radiology* **1985**;154:443-450

MR Imaging of the Normal Shoulder: Anatomic Correlation

Leanne L. Seeger¹
 June T. Ruszkowski²
 Lawrence W. Bassett¹
 Stephen P. Kay^{3,4}
 Richard D. Kahmann³
 Harvard Ellman⁵

The complex anatomy and the requirement to image in the peripheral magnetic field have made the shoulder difficult to examine with MR. However, the use of high-resolution scanning techniques and specialized surface coils has improved the quality of MR images obtained. Seventy-five scans of the shoulders of normal volunteers were correlated with multiplanar cryomicrosections of six cadaver shoulders to study the MR appearance of normal structures. MR was shown to provide excellent depiction of shoulder anatomy.

MR is a useful tool for imaging the musculoskeletal system. Exquisite depiction of the bone marrow rivals or surpasses other imaging techniques [1, 2]. Soft tissues are clearly delineated because normal fat, muscle, hyaline cartilage, and fibrous tissue have different individual signal intensities [3, 4]. Radiation exposure is avoided and arthrography may be unnecessary.

However, the shoulder poses several unique difficulties for imaging with MR. Because of space limitations in the magnet, the shoulder cannot be positioned in the center of the magnetic field. This necessitates shifting laterally for image centering and scanning in a region where the signal-to-noise ratio is low. Also, because diseases of the shoulder usually involve small soft-tissue structures, high-resolution scans are needed to provide diagnostic information. This requires steep magnetic gradients, which decrease the MR signal. These problems can be overcome by combining high-resolution scanning with the use of a surface coil [5, 6]. Finally, the bony and soft tissues of the shoulder are oriented along multiple nonorthogonal axes, necessitating oblique scanning [7, 8].

The goal of this study is to determine if MR allows detailed evaluation of the anatomic structures comprising the normal shoulder joint and to correlate the MR images with cadaver cryomicrosections.

Materials and Methods

Scan and Cryomicrosection Planes

The MR images and anatomic sections were made in the orthogonal planes and a frontal oblique plane along the course of the supraspinatus muscle. The oblique axis was required to visualize both the continuity of the supraspinatus muscle-tendon unit and the relationship of this tendon to the acromion and acromioclavicular joint above.

Scanning Technique

Seventy-five scans of 20 shoulders were obtained in healthy young adults. Scanning was performed on a Fonar Beta-3000 0.3-T permanent-magnet imaging system by using a spin-echo pulse sequence with TR = 500 msec, TE = 28 msec. A 256 × 256 imaging matrix was used and was interpolated to 512 × 512 for display. Pixel size was 0.75 mm². Slice thickness was 5 mm, obtained at 7-mm intervals. With four excitations, scan time was 8.33 min for a

Received February 7, 1986; accepted after revision August 20, 1986.

Presented at the annual meeting of the American Roentgen Ray Society, Washington, DC, April 1986.

Recipient of the 1986 ARRS President's Resident Award.

This work was supported in part by a grant from the James T. Case Foundation, UCLA Department of Radiological Sciences.

¹ Department of Radiological Sciences, UCLA School of Medicine, Los Angeles, CA 90024. Address reprint requests to L. L. Seeger.

² 30-64 34th St., Astoria, NY 11103.

³ Department of Surgery, Division of Orthopedic Surgery, UCLA School of Medicine, Los Angeles, CA 90024.

⁴ Present address: Department of Orthopedic Surgery, University of Texas Medical School, San Antonio, TX 78284.

⁵ 2080 Century Park E., Ste. 1500, Los Angeles, CA 90067.

AJR 148:83-91, January 1987

0361-803X/87/1481-0083

© American Roentgen Ray Society

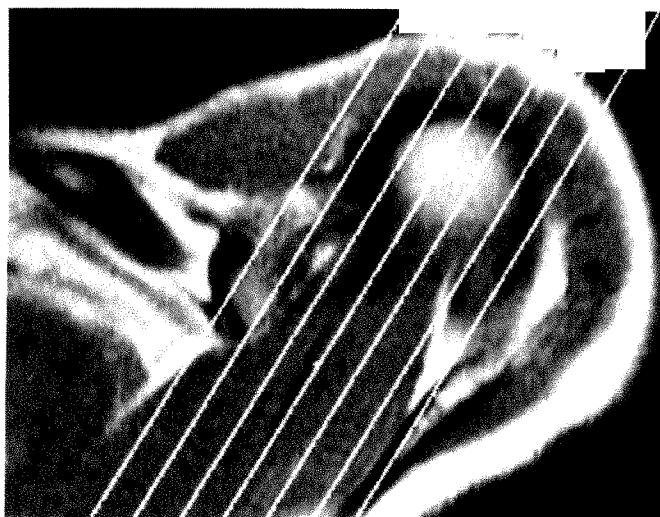


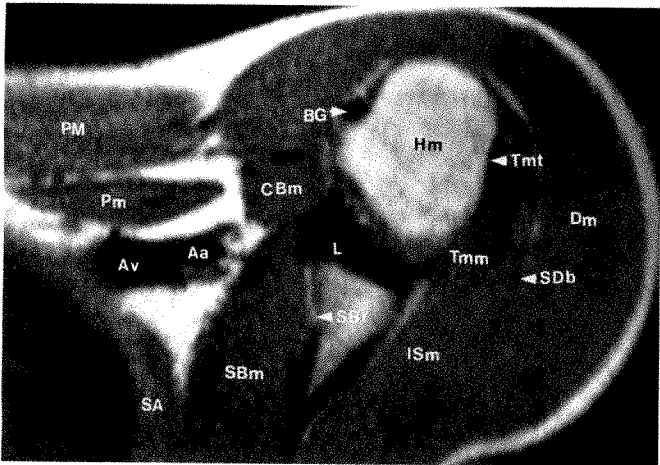
Fig. 1.—Axial scout scan showing cursor alignment through the long axis of the supraspinatus belly for oblique imaging.

multislice series of seven images. The amount of lateral shift required for image centering depended on patient size, varying from 80 to 120 mm from center toward the shoulder to be scanned. This was accomplished by manipulation of the radiofrequency to allow the imaging plane to be moved in any desired direction.

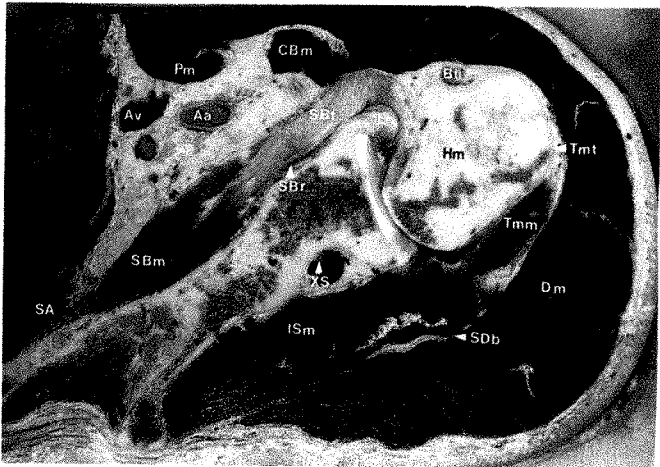
An 18-cm or 22.5-cm diameter planar surface coil was used, with the size determined by the body build of the subject. The coil was positioned obliquely over the shoulder such that its axis was perpendicular to the magnetic field. Foam wedges placed between the inner surface of the coil and the patient assisted in maintaining coil alignment and allowed for signal uniformity over the entire area to be imaged.

A standard position was chosen to provide consistency in anatomic relationships while maximizing comfort. The arm was placed across the abdomen (therefore internally rotated), and the elbow was elevated to parallel the humeral head.

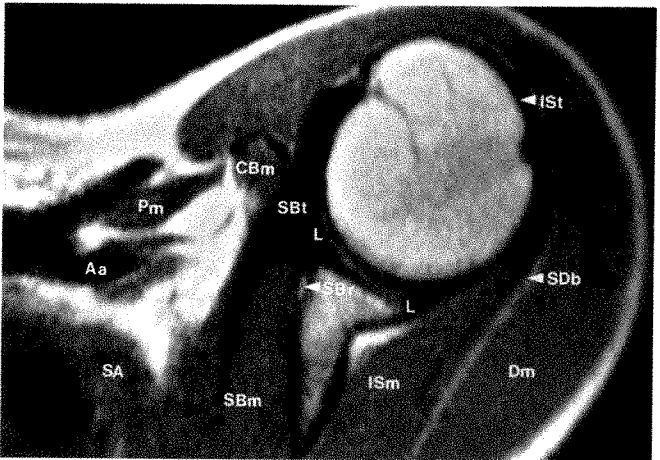
An axial scan was used as a scout for the frontal oblique plane, which allowed precise sagittal-to-coronal alignment along the long axis of the supraspinatus belly (Fig. 1).



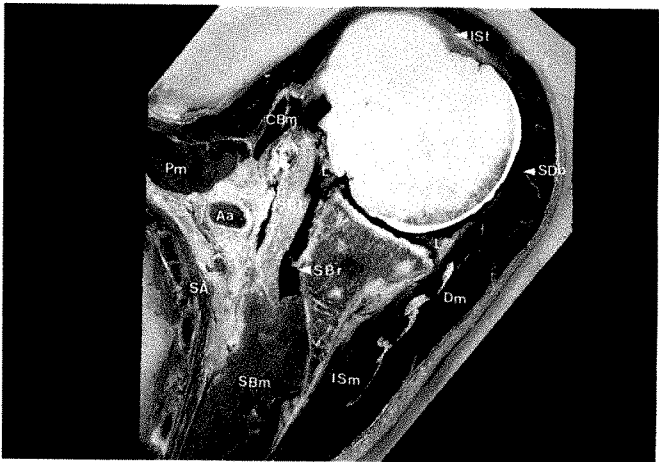
A



B



C



D

Fig. 2.—A–H, MR images and photographs of cadaver specimens made in the axial plane. Serial images from inferior to superior are shown. See Key to Abbreviations on page 86.

Cadaver Preparation and Sectioning

Six fresh cadaver shoulders were used for anatomic study. Available cadavers were elderly and had degenerative changes. Specimens with major shoulder abnormalities were excluded after evaluation with fluoroscopy and, when necessary, limited arthrography. Aortic injection of plaster mixed with red dye forced deoxygenated blood into the venous system. Blue dye mixed with dilute radiographic contrast material was injected under fluoroscopic control into two shoulders to define the joint space. Care was taken to avoid excessive joint distension that would distort anatomic relationships.

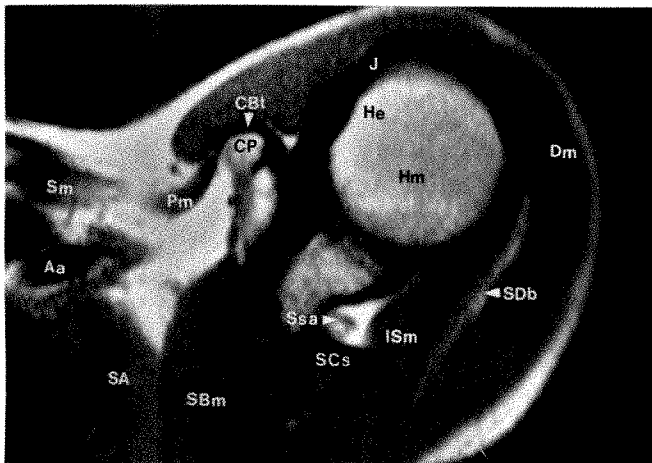
After injection, the cadavers were frozen with the lower arm across the abdomen, causing internal rotation of the shoulder similar to the position used for scanning. The shoulders were then block resected, cryomicrosectioned (LKB 2250, Bromma, Sweden), and photographed at 0.5-mm intervals [9]. One shoulder was sectioned in each of the axial, coronal, sagittal, and frontal oblique planes. Because of the superior depiction of several structures in the axial and oblique

projections, sectioning in these two planes was repeated on the shoulders that had been injected with blue intraarticular dye.

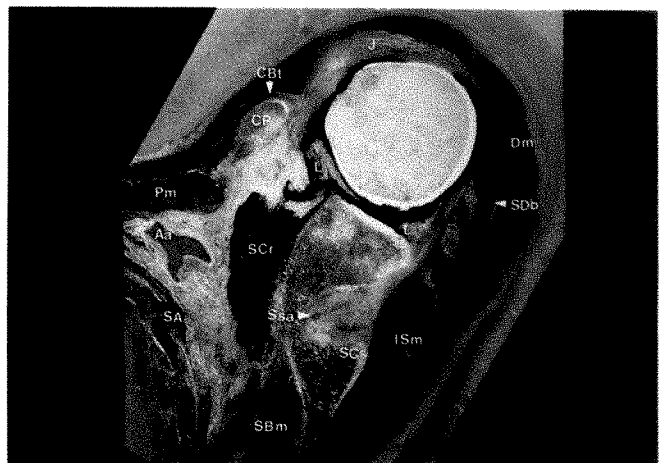
Results

Although the plane of optimal visualization varied, MR depicted the humeral head, acromion, distal clavicle, acromioclavicular joint, hyaline cartilage of the glenohumeral joint, glenoid labrum, rotator cuff muscles and tendons, joint capsule, and the coracoclavicular ligament. Identification of nerves and vascular structures was enhanced either by surrounding fat or flow through the vessels.

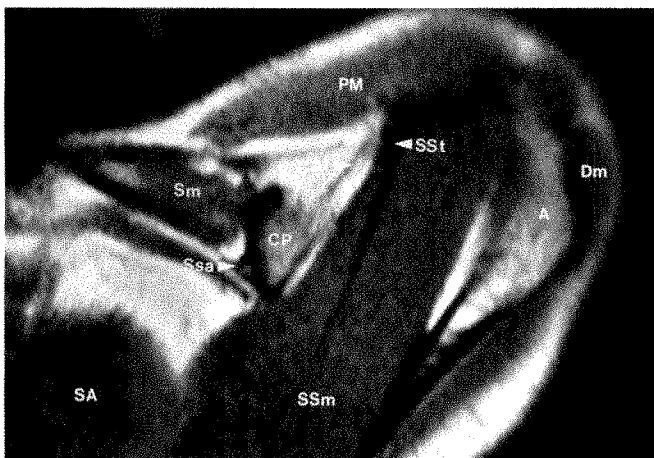
With this T1-weighted sequence, the MR appearance of the osseous structures is as expected: cortical bone has no signal, and a bright signal originates from the marrow cavity. The humeral head epiphysis can be differentiated from the



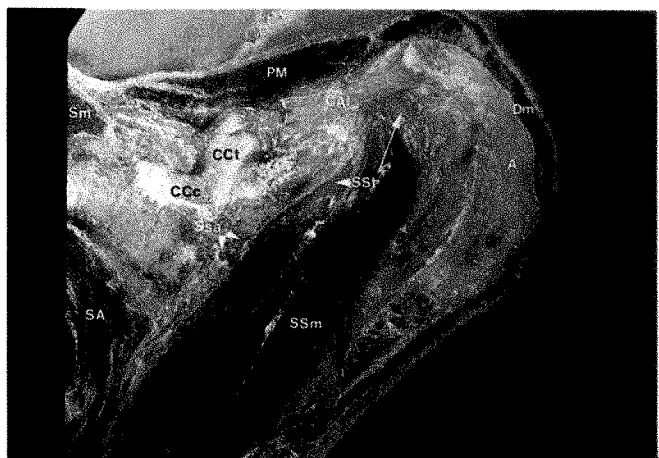
E



F



G



H

metaphysis in normal young adults because the epiphyseal signal is brighter. Ligaments and tendons have a very low signal intensity, which allows differentiation from the adjacent brighter muscle. Precise sites of bony attachment cannot be seen because of the similar signal-void associated with cortical bone. Likewise, the low signal intensity of the fibrous joint capsule cannot be differentiated from the glenohumeral ligaments or the cuff tendons that lie adjacent to and are incorporated into the capsule [10-12]. The glenoid labrum is a redundant fold of the joint capsule [10]; accordingly, this

structure appears homogeneously black, typical of fibrous tissue. The signal of the articular hyaline cartilage of the humeral head and glenoid is bright, which contrasts well against the low-signal cortical bone and labrum. The two surfaces of hyaline cartilage cannot be seen as separate at the site of coaptation. The subacromial-subdeltoid bursa is not distended with fluid in the normal state [11, 13]. This flat but expansive potential space is represented by a thin band of high signal intensity, corresponding to abundant fat both within and beneath the synovial lining [10, 11, 14].

Axial scans (Fig. 2) clearly show the anteroposterior alignment of the glenohumeral articulation. The inferior humeral head is oblong, and the posterolateral aspect is noticeably flat. Continuous with this surface is an indentation on the posterolateral aspect of the midhumeral head. Both of these regions lack hyaline cartilage and serve as sites of attachment for some fibers of the teres minor and infraspinatus tendons. The head becomes progressively rounder superiorly. Marrow within the humeral head is inhomogeneous because of the oblique anterior-to-posterior axis of the physis. This appearance is especially evident at the level of the mid-head but may extend quite far superiorly. Axial scans provide good depiction of the low-signal glenoid labrum. The shape of this structure is significantly influenced by the position of the humeral head [10]. With internal rotation, the anterior labrum is larger than the posterior at all levels, and its apex is pointed. The contour of the posterior labrum is smooth throughout. A thin rim of medium to high signal intensity allows the labrum to be seen as separate from the adjacent capsule and cuff tendons. This corresponds to synovial folds that extend into the joint cavity [11, 14, 15]. As with the labrum, the appearance of these folds is influenced by humeral-head rotation [10, 14, 15]. The bicipital groove can be readily identified; however, the tendon within it cannot be distinguished from surrounding cortical bone or the transverse humeral ligament. A small region of bright signal is occasionally seen within the intertubercular sulcus, either adjacent to or surrounding the biceps tendon. The tendons of the subscapularis, infraspinatus, and teres minor muscles are visible over their entire lengths. The variable development of the three glenohumeral ligaments is indirectly evident by the extent of the subscapularis recess [10, 12].

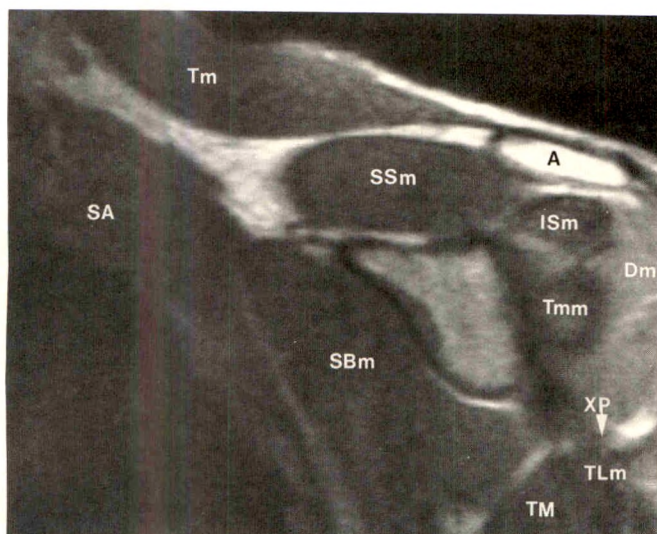
In the coronal plane (Fig. 3), the coracoclavicular ligament, acromioclavicular joint, and superior humeral-head articular cartilage are well seen. The transition from supraspinatus muscle to tendon is gradual [12]. Because the coronal plane traverses this junction obliquely, inhomogeneous medium signal intensity is seen above the humeral head, and the expected signal-void of the tendon is only evident at its most lateral extent.

In the sagittal plane (Fig. 4), the oblique alignment of the physis is easily identified, and possible confusion arising from the inhomogeneity on axial scans is avoided. This plane also reveals the horizontal axis of the acromion and its relationship to the supraspinatus tendon.

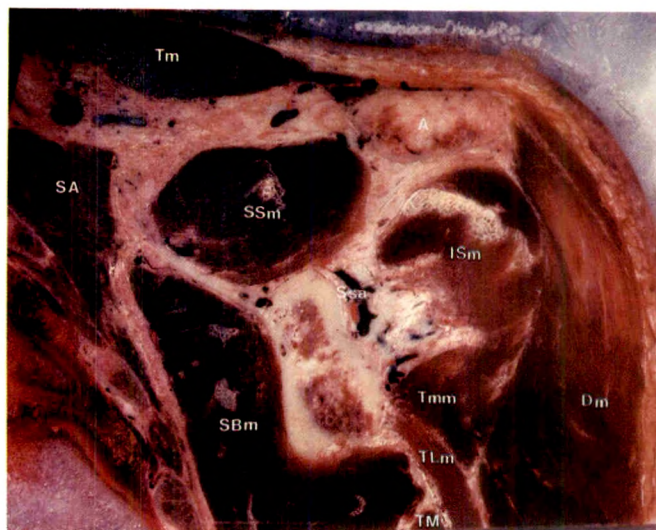
The oblique plane (Fig. 5) shows the supraspinatus muscle and tendon in continuity. The relationship of the inferior acromion and acromioclavicular joint to the supraspinatus ten-

Key to Abbreviations Used in Figures

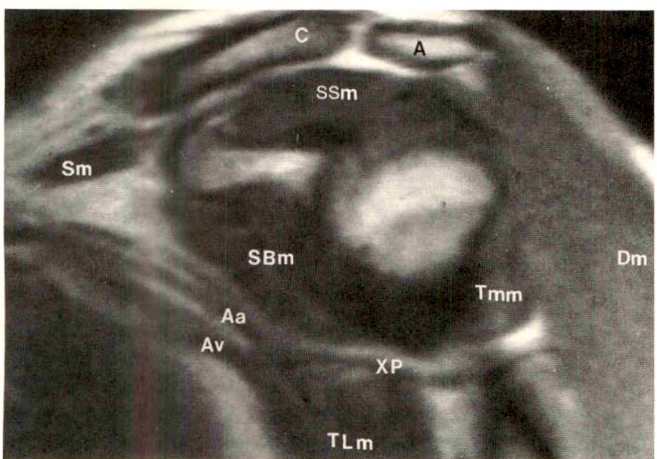
A	acromion
Aa	axillary artery
ACj	acromioclavicular joint
AHl	acromiohumeral ligament
Ar	axillary recess
Av	axillary vein
Ba	brachial artery
BG	bicipital groove
Bm	biceps (long head) muscle
Bt	biceps (long head) tendon
C	clavicle
CAI	coracoacromial ligament
CBm	coracobrachialis/biceps (short head) muscle
CBt	coracobrachialis/biceps (short head) tendon
CCc	coracoclavicular ligament, conoid
CCt	coracoclavicular ligament, trapezoid
CHl	coracohumeral ligament
CP	coracoid process
Cv	cephalic vein
Dm	deltoid muscle
Dt	deltoid tendon
He	humeral head epiphysis
HC	hyaline cartilage
Hm	humeral head metaphysis
ISm	infraspinatus muscle
ISt	infraspinatus tendon
J	joint capsule
L	glenoid labrum
PM	pectoralis major muscle
Pm	pectoralis minor muscle
SA	serratus anterior muscle
Sba	subscapular artery and branches
SBm	subscapularis muscle
SBr	subscapularis recess
SBt	subscapularis tendon
SCb	scapula body
SCr	subcoracoid recess
SCs	scapula spine
SCu	scapula upper (superomedial) aspect
SDB	subdeltoid bursa
Sm	subclavis muscle
Ssa	suprascapular artery and branches
SSm	supraspinatus muscle
SSt	supraspinatus tendon
Tm	trapezius muscle
TLm	triceps (long head) muscle
TLt	triceps (long head) tendon
TM	teres major muscle
Tmm	teres minor muscle
Tmt	teres minor tendon
XA	anterior circumflex humeral artery
XP	posterior circumflex humeral artery
XS	circumflex scapular artery and branches



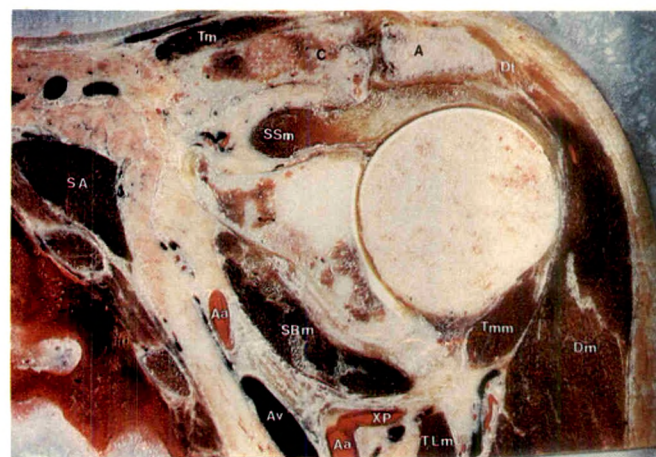
A



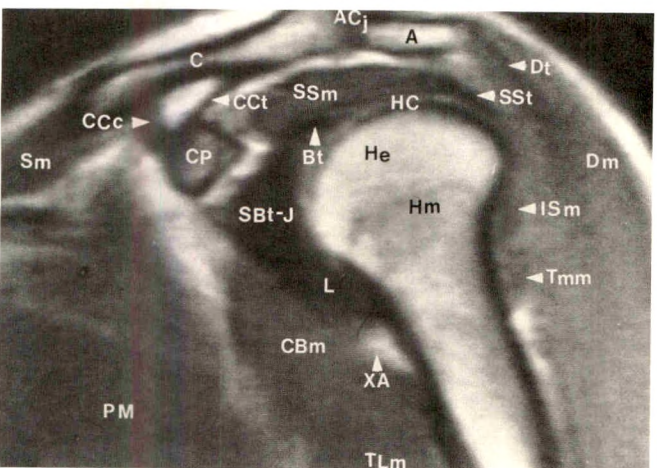
B



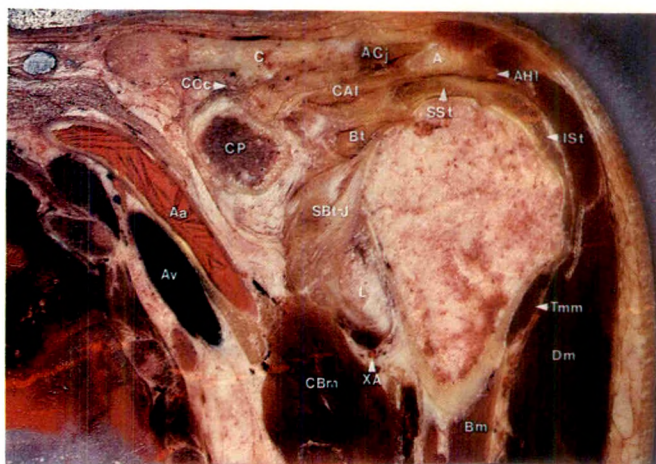
C



D

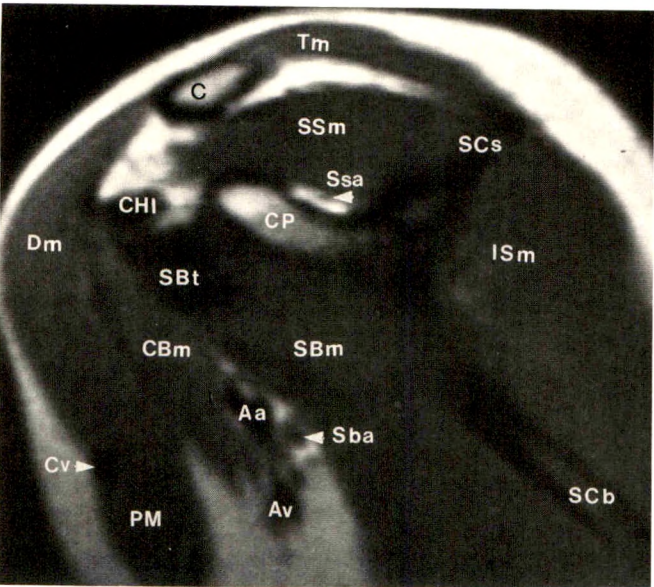


E

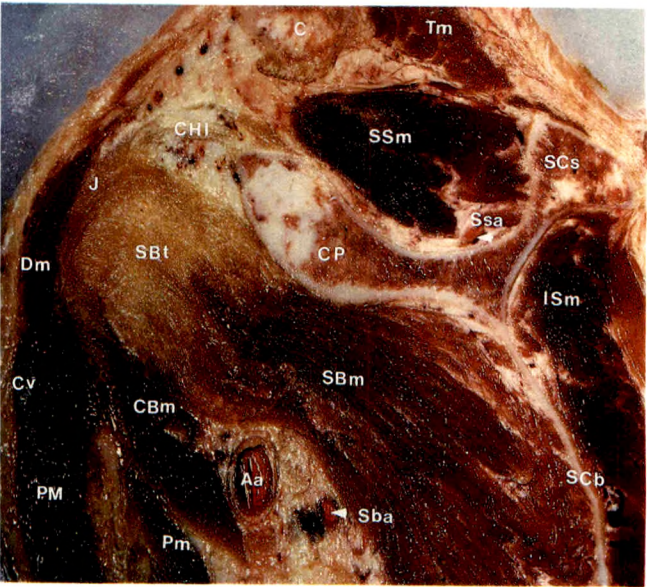


F

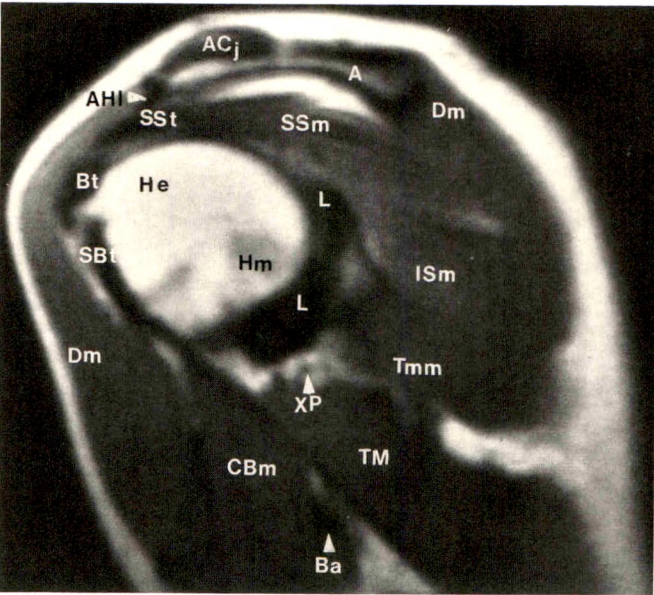
Fig. 3.—A–F, MR images and photographs of cadaver specimens made in the coronal plane. Serial images from posterior to anterior are shown. See Key to Abbreviations on page 86.



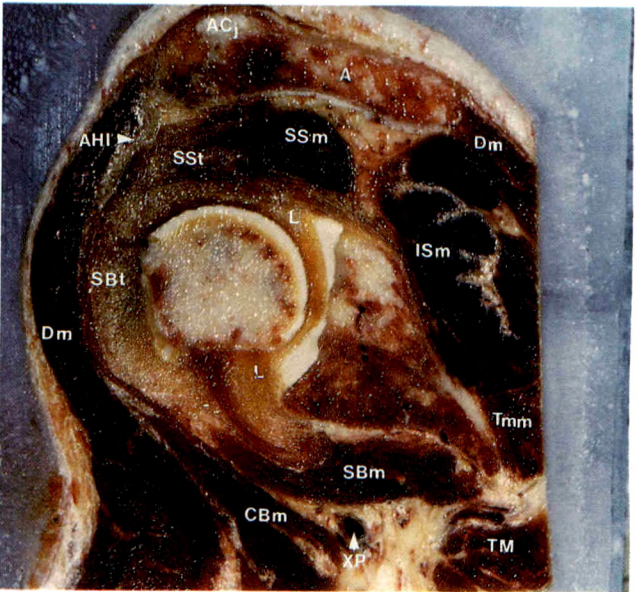
A



B

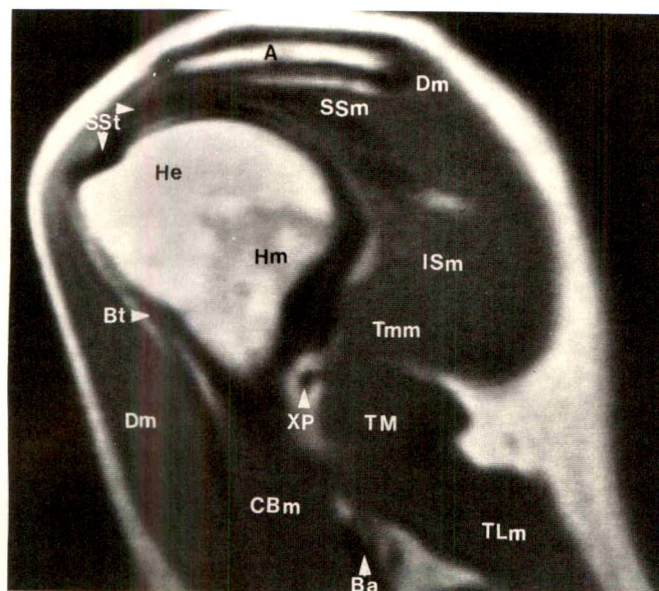


C

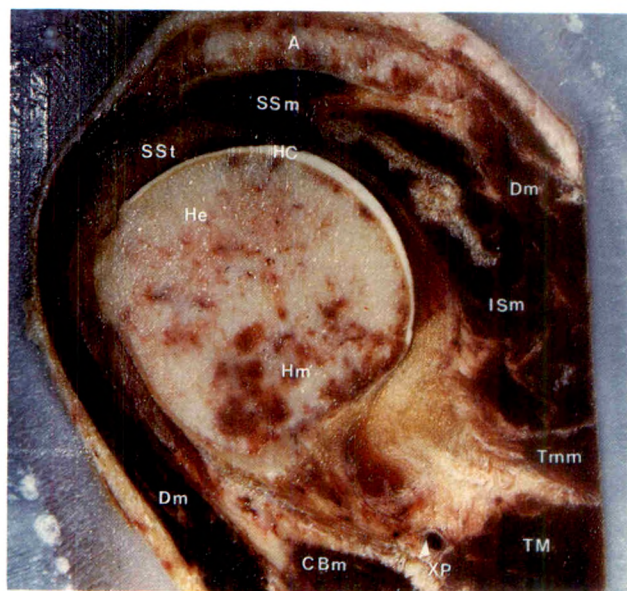


D

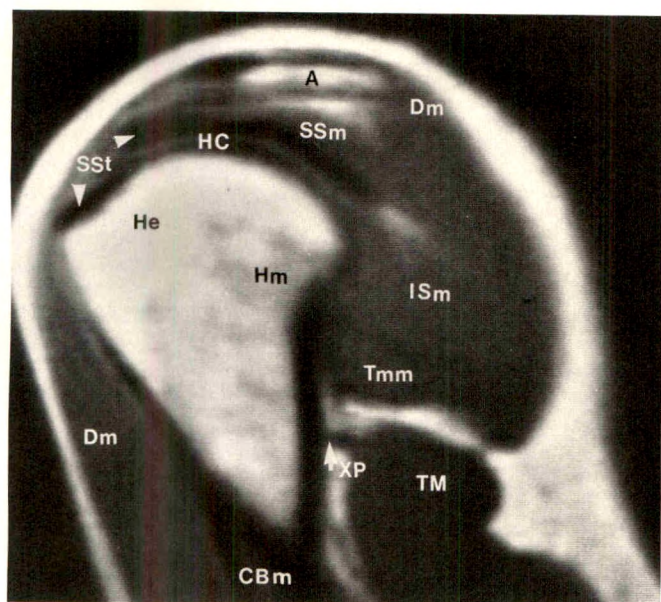
Fig. 4.—A–H, MR images and photographs of cadaver specimens made in the sagittal plane. Serial images from medial to lateral are shown. See Key to Abbreviations on page 86.



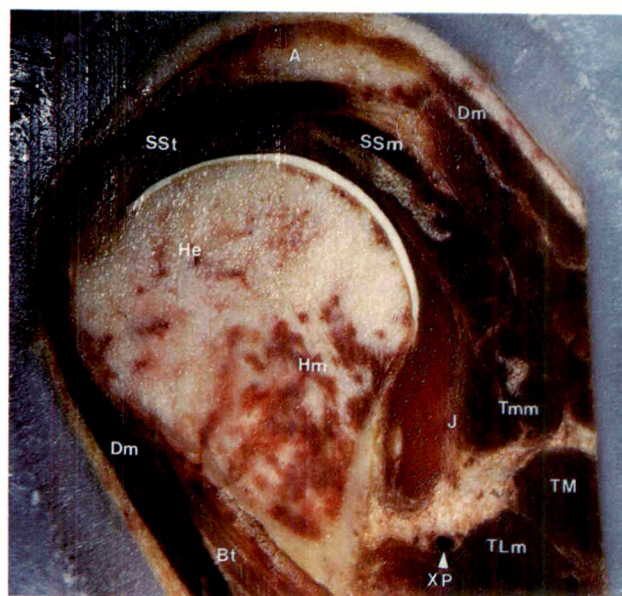
E



F



G



H

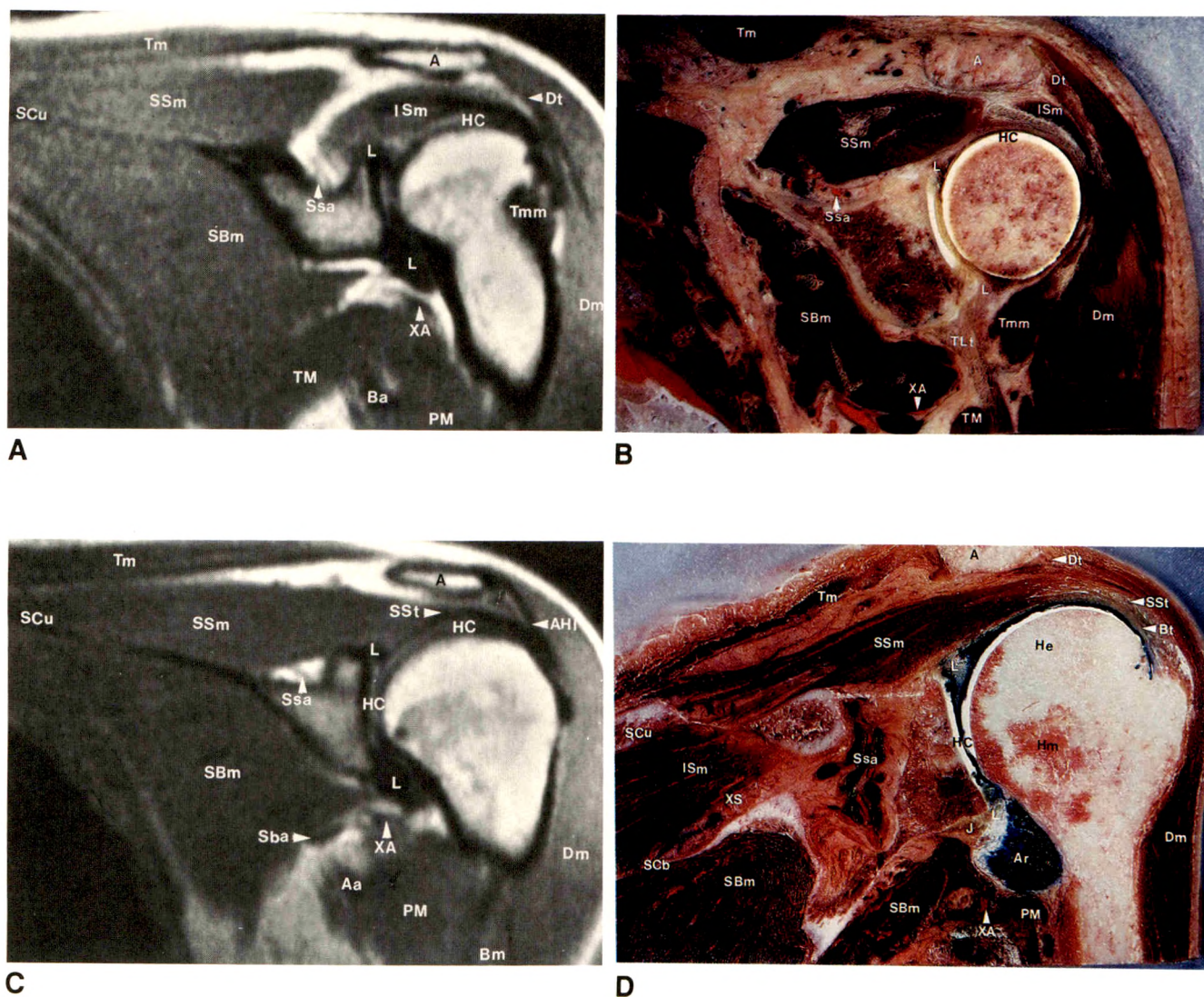


Fig. 5.—A–H, MR images and photographs of cadaver specimens made in the oblique plane. Serial images from posterior to anterior are shown. See Key to Abbreviations on page 86.

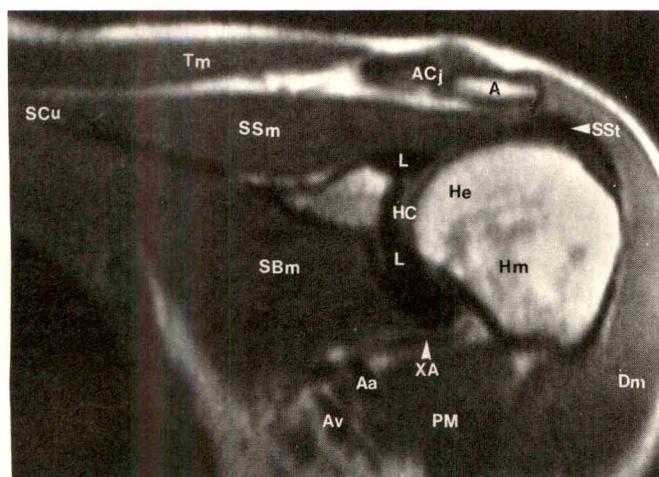
don is also evident. Because the coronal-to-sagittal angulation of the scapula is usually similar to the course of the supraspinatus muscle [11], this orientation is superior to the coronal plane for imaging the superior and larger inferior glenoid labra. The articular cartilage and coracoclavicular ligament are well seen.

ACKNOWLEDGMENTS

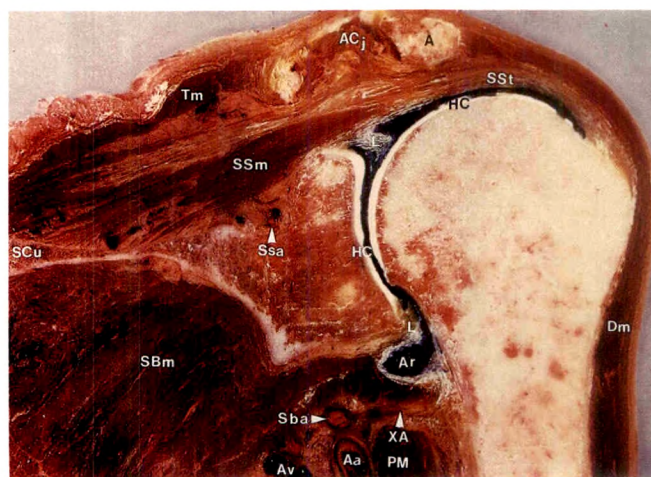
We thank the following people for their assistance with this project: John Robert (cadaver preparation), Val Gausche and Bobby Keen (technical assistance with scanning), Jerry Spellman (technical advice for development of scanning technique), and Jan Votruba, James Genova, and Neil Schaknowski (surface-coil development and production).

REFERENCES

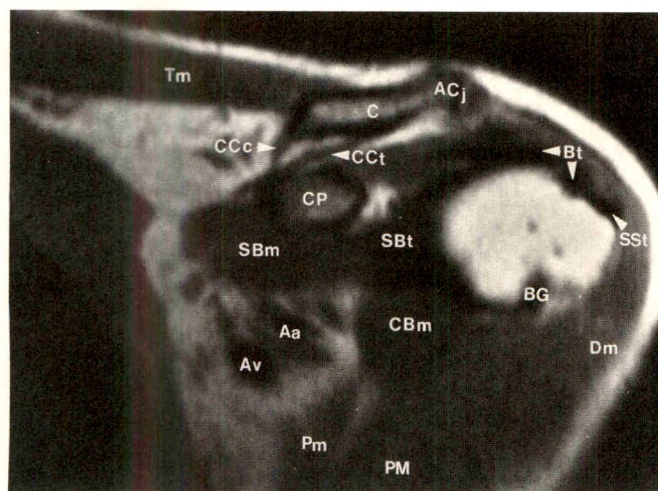
1. Daffner RH, Lupetin AR, Dash N, Deeb ZL, Sefczek RJ, Schapiro RL. MRI in the detection of malignant infiltration of bone marrow. *AJR* 1986;146:353–358
2. Aisen AM, Martel W, Braunstein EM, McMillin KI, Phillips WA, Kling TF. MRI and CT evaluation of primary bone and soft-tissue tumors. *AJR* 1986;146:749–756
3. Moon KL, Genant HK, Davis PL, et al. Nuclear magnetic resonance imaging in orthopaedics: principles and applications. *J Orthop Res* 1983;1:101–114
4. Li KC, Henkelman RM, Poon PY, Rubenstein J. MR imaging of the normal knee. *J Comput Assist Tomogr* 1984;8:1147–1154
5. Fisher MR, Barker B, Amparo EG, et al. MR imaging using specialized coils. *Radiology* 1985;157:443–447
6. Ehman RL. MR imaging with surface coils. *Radiology* 1985;157:549–550
7. Huber DJ, Mueller E, Heubes P. Oblique magnetic resonance imaging of normal structures. *AJR* 1985;145:843–846
8. Edelman RR, Stark DD, Saini S, et al. Oblique planes of section in MR imaging. *Radiology* 1986;159:807–810
9. Rauschnig W. Computed tomography and cryomicrotomy of lumbar spine specimens: a new technique for multiplanar anatomic correlation. *Spine* 1983;8:170–180



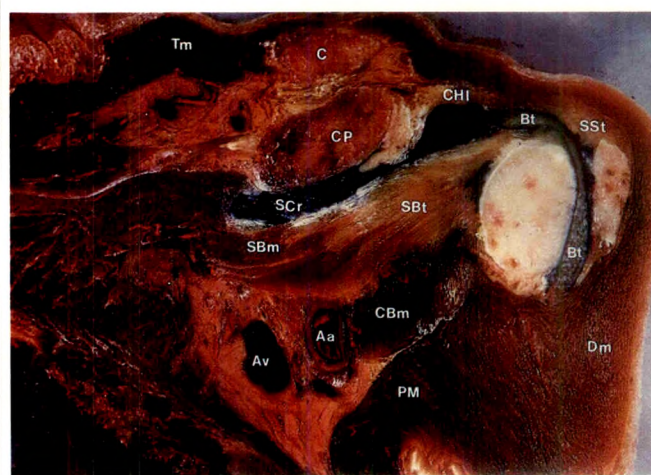
E



F



G



H

10. Moseley HF, Övergaard B. The anterior capsular mechanism in recurrent anterior dislocation of the shoulder: morphological and clinical studies with special reference to the glenoid labrum and the gleno-humeral ligaments. *J Bone Joint Surg [Br]* 1962;44:913-927
11. Williams PL, Warwick R, eds. *Gray's anatomy*, 36th Br ed. Philadelphia: Saunders, 1980:425-428, 489
12. Bateman JE. *The shoulder and environs*. St. Louis: Mosby,

1955:62-63

13. Codman EA. *The shoulder: rupture of the supraspinatus tendon and other lesions in or about the subacromial bursa*. Malabar, FL: Kreiger, 1984:22
14. Bloom W, Fawcett DW. *A textbook of histology*, 9th ed. Philadelphia: Saunders, 1968:255-260
15. Boileau Grant JC. Interarticular synovial folds. *Br J Surg* 1931;18:636-640

Books Received

Receipt of books is acknowledged as a courtesy to the sender. Books that appear of sufficient interest will be reviewed as space permits.

- Differential Diagnosis of Soft Tissue and Bone Tumors.** By Steven I. Hajdu. Philadelphia: Lea & Febiger, 478 pp., 1985. \$110
- Thyroid and Parathyroid.** By Martin P. Sandler, James A. Patton, and C. Leon Partain. East Norwalk, CT: Appleton-Century-Crofts, 379 pp., 1986.
- The Skin in Diabetes.** By J. E. Jelinek. Philadelphia: Lea & Febiger, 237 pp., 1986.
- The Selection and Performance of Radiologic Equipment.** Edited by W. R. Hendee. Baltimore: Williams & Wilkins, 263 pp., 1986. \$48.50
- SI Units in Radiation Protection and Measurements.** NCRP report no. 82. 64 pp., 1985. \$10
- Some Issues Important in Developing Basic Radiation Protection Recommendations.** NCRP Proceedings No. 6 (20th annual meeting). 325 pp., 1985. \$19
- Cardiac Imaging and Image Processing.** By Steve M. Collins and David J. Skorton. New York: McGraw-Hill, 451 pp., 1986.
- Roentgen Signs in Diagnostic Imaging Vol. 3: Spine and Central Nervous System, 2nd ed.** By Isadore Meschan and R. M. Farrer-Meschan. Philadelphia: Saunders, 672 pp., 1985. \$80
- Ultrasound Physics and Instrumentation.** By D. Hykes, W. R. Hedrick, and D. E. Starchman. New York: Churchill Livingstone, 241 pp., 1985. \$36
- The Fundamentals of X-Ray and Radium Physics, 7th ed.** By J. Selman. Springfield, IL: Thomas, 632 pp., 1985. \$29.75
- Angioplasty.** Edited by G. D. Jang. New York: McGraw-Hill, 451 pp., 1986. \$70
- Oncologic Imaging.** By D. G. Bragg, P. Rubin, and J. E. Youker. New York: Pergamon Press.
- Practice of Coronary Angioplasty.** Edited by Thomas Ischinger. Berlin: Springer-Verlag, 325 pp., 1986. \$79
- Dimethyl Sulfate** (environmental health criteria 48). Geneva: World Health Organization, 55 pp., 1985. Swiss Fr/55
- Clinical Radiology of the Spine and the Spinal Cord.** By Mohamed Banna. Rockville, MD: Aspen, 449 pp., 1985. \$78
- Guide to Prosthetic Cardiac Valves.** Edited by Dryden Morse, Robert M. Steiner, and Javier Fernandez. New York: Springer-Verlag, 362 pp., 1985. \$89.50
- Radiology of the Spine Tumors.** Edited by L. Jeanmart. New York: Springer-Verlag, 118 pp., 1986. \$49.50
- The Radiologic Clinics of North America.** Symposium on Advances in Cardiac Imaging. Guest editor: Stephen W. Miller. Philadelphia: Saunders, 1985: 244 pp. By subscription, 4 issues annually, \$60
- Practice of Coronary Angioplasty.** By T. Ischinger. New York: Springer-Verlag, 325 pp., 1985. \$79
- Atlas for Maxillofacial Pantomographic Interpretation.** By A. Chomlenko. Chicago: Quintessence Books, 296 pp., 1985.
- Medical Effects of Ionizing Radiation.** By Fred A. Mettler, Jr., and Robert D. Moseley, Jr. Orlando, FL: Grune and Stratton, 288 pp., 1985.
- Radiology Today 3.** Edited by M. W. Donner and F. H. W. Heuck. Berlin: Springer-Verlag, 203 pp., 1985. \$55
- Bone Marrow Disorders.** The Biological Basis of Clinical Problems. By M. Y. Gordon and A. J. Barrett. Oxford: Blackwell, 422 pp., 1985.
- Echocardiography, 4th ed.** By Harvey Feigenbaum. Philadelphia: Lea & Febiger, 662 pp., 1986. \$60
- Nuclear Imaging in Pediatrics.** By Aslam R. Siddiqui. Chicago: Year Book Medical, 306 pp., 1985.
- The Computer in Radiology.** Edited by Tim B. Hunter. Rockville, MD: Aspen, 355 pp., 1986. \$39.95
- Consultation in Diagnostic Imaging.** Medical Consultation Series. By William W. Scott, Jr., and Penelope P. Scott. Philadelphia: Decker, 229 pp., 1985. \$16, soft cover
- Radionuclide Imaging Technique.** Medical Physics Series. By Peter F. Sharp, Phillip P. Dendy, and W. Ian Keyes. London: Academic, 271 pp., 1985. \$63.50
- Ultrasound Annual 1985.** Edited by Roger C. Sanders and Michael C. Hill. New York: Raven, 371 pp., 1985. \$69.50
- Radioisotope Studies in Cardiology.** Developments in Nuclear Medicine Series. Edited by H. J. Biersack and P. H. Cox. The Hague: Nijhoff, 404 pp., 1985. \$59.50
- Radiolabeled Cellular Blood Elements.** Pathophysiology, Techniques & Scintigraphic Applications. Nato Advanced Science Inst. Series. Edited by M. L. Thakur, M. D. Ezikowitz, and M. R. Hardeman. New York: Plenum, 434 pp., 1985.
- Lymphatic Imaging.** Lymphography, Computed Tomography and Scintigraphy, 2nd ed. Golden's Diagnostic Radiology. Edited by Melvin E. Clouse and Sidney Wallace. Baltimore: Williams & Wilkins, 526 pp., 1985. \$87.50
- Double Contrast Examination of the Colon.** Principles and Practice. By A. Weissman, M. Clot, and J. Grellet. Berlin: Springer-Verlag, 165 pp., 1985. \$39.50
- Radiology of Liver Circulation.** Series in Radiology. By Claude L'Hermine. The Hague: Nijhoff, 174 pp., 1985. \$60
- Atlas of Positron Emission Tomography of the Brain.** By W. E. Heiss, C. Ceil, K. Herholz, G. Pawlik, R. Wagner, and K. Weinhard. Berlin: Springer-Verlag, 130 pp., 1985. \$52
- The Radiologic Clinics of North America.** Symposium on New Imaging Technology Pitfalls and Controversies. Guest editor: Robert K. Zeman. Philadelphia: Saunders, 1985: 207 pp. By subscription, 4 issues annually, \$60
- Guidelines for the Study of Genetic Effects in Human Populations** (environmental health criteria 46). Geneva: World Health Organization, 126 pp., 1985. Swiss Fr/12
- Summary Report on the Evaluation of Short-Term Tests for Carcinogens** (environmental health criteria 47). Geneva: World Health Organization. 77 pp., 1985. Swiss Fr/9
- Pediatric Ultrasonography.** Edited by G. Kalifa. New York: Springer-Verlag, 241 pp., 1985. \$52
- Diagnostic Imaging in Ophthalmology.** Edited by G. Gonzalez. New York: Springer-Verlag, 366 pp., 1985. \$129
- Pocket Atlas of Cranial Magnetic Resonance Imaging.** By V. M. Haughton and D. Daniels. New York: Raven, 61 pp., 1986. \$12.50
- Doppler Echocardiography.** By A. Labovitz and G. A. Williams. Philadelphia: Lea & Febiger, 136 pp., 1985. \$19.95
- Tumors of the Brain.** Edited by Norman M. Bleehen. New York: Springer-Verlag, 221 pp., 1986. \$69
- Cancer Treatment Symposia.** Proceedings of the Workshop on Radiotherapy for Lung Cancer, vol. 2. Edited by Robert E. Wittes. Bethesda, MD: U. S. Dept. of Health and Human Services, 149 pp., 1985. \$8.50
- Liver Cancer.** Series: Developments in Oncology. Edited by Joseph C. Bottino. Boston: Nijhoff, 391 pp., 1985. \$82.50
- Gastro-Intestinal Radiology.** Series: Self-Assessment in Radiology and Imaging. By Michael Berger. New York: Wiley, 174 pp., 1985. \$18.50
- Aortitis.** Clinical, Pathologic and Radiologic Aspects. Edited by Adam Lande, Yahya M. Berkmen, and Hugh A. McAllister, Jr. New York: Raven, 278 pp., 1986. \$57.50
- Ear, Nose and Throat.** Series: Self-Assessment in Radiology 1. By Maurice Hawthorne and Richard Num. New York: Wiley, 223 pp., 1984. \$19.50
- Progress in Radiopharmacology 1985.** Series: Developments in Nuclear Medicine. Edited by Peter H. Cox, George Limouris, and Martin G. Woldring. The Hague: Nijhoff, 287 pp., 1985. \$54
- Hand-Held and Automated Breast Ultrasound.** By Lawrence W. Bassett, Richard H. Gold, and Carolyn Kimme-Smith. Thorofare, NJ: Slack, 204 pp., 1986. \$49.50
- Cervico-Occipital Joint.** 158 Radiological Exercises for Students and Practitioners. By Auguste Wackenheim. Berlin: Springer-Verlag, 192 pp., 1985. \$39.50
- Musculoskeletal Magnetic Resonance Imaging.** By Edward J. Easton, Jr., and John A. Powers. Thorofare, NJ: Slack, 168 pp., 1985. \$39.50
- Radiology Review Cards.** Abdominal Imaging. Chest Imaging. Head and Spine Imaging. Skeletal Imaging. By Andrew H. Cragg and Gunnar Lund. Thorofare, NJ: Slack, 1985. \$34.50 (all four \$99)

The Posterior Vertebral Body Line: Importance in the Detection of Burst Fractures

Richard H. Daffner¹
Ziad L. Deeb
William E. Rothfus

A review of the lateral radiographs and CT studies of 114 patients with burst fractures, 46 patients with combined injuries in whom bursting was a major component, and 82 patients with simple anterior compression fractures was performed to evaluate the integrity of the posterior vertebral body margin. This structure normally produces a single or bifid vertical line on the lateral radiograph. Disruption, displacement, or rotation of this line was found in all 114 patients with "pure" burst fractures. These abnormalities were also present in 36 of the 46 patients with combined burst injuries. In all patients with simple compression fracture, flexion, distraction or dislocation, and extension injuries, the line was normal. CT studies showed these abnormalities to be the result of retropulsion of one or more bone fragments from the posterior margin of the vertebral body. Disruptive abnormalities of the posterior vertebral body line are reliable plain-film signs that a burst fracture has occurred and that compromise of the vertebral canal and subarachnoid space is present.

The radiographic evaluation of vertebral injury begins with a careful analysis of plain films, and many authors have emphasized the subtle findings on plain radiographs of the vertebral column [1-3]. We recently observed a subtle finding on lateral radiographs involving disruption of the normal thin dense line caused by the posterior aspect of the vertebral body and have found it to be a reliable indicator of a burst fracture (Fig. 1). We report our experience of this finding in a group of 491 patients with injuries of the vertebral column.

Materials and Methods

Between 1981 and 1985, 160 patients with bursting vertebral injuries were evaluated and treated at our medical center. One hundred fourteen of these were considered "pure" burst fractures; 46 occurred in combination with shearing or rotary mechanisms where axial load was a factor. Of the pure burst fractures, 36 were cervical, 11 were upper thoracic (T1-T6), three were lower thoracic (T7-T10), and 64 were thoracolumbar (T11-L2). All 46 of the mixed injuries were thoracolumbar. In addition, 82 patients with simple flexion injuries (defined by involvement solely of the superior and anterior aspect of the vertebral body with intact posterior structures), 23 with pure flexion-distraction injuries, 142 with pure flexion-dislocation injuries, 78 with extension injuries, and six with seat-belt injuries of the thoracolumbar region were studied. All patients were evaluated by plain films and CT. Plain films were evaluated for disruption, displacement, rotation, or obliteration of the posterior vertebral body line. CT studies were used to determine the presence of canal encroachment in these fractures and to explain the plain-film findings.

Results

All of the 114 patients with pure burst fractures had abnormalities of the posterior vertebral line. The most common pattern was posterior displacement of a segment of this line, which represented the posteriorly displaced fragment (Fig. 2). Most

Received June 5, 1986; accepted after revision August 26, 1986.

¹ All authors: Department of Diagnostic Radiology, Allegheny General Hospital, 320 E. North Ave., Pittsburgh, PA 15212. Address reprint requests to R. H. Daffner.

AJR 148:93-96, January 1987
0361-803X/87/1481-0093
© American Roentgen Ray Society

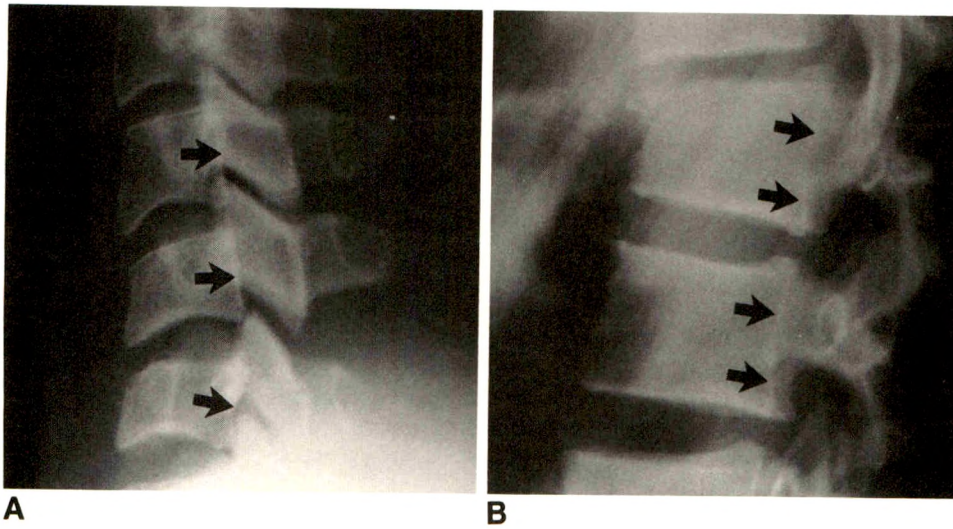


Fig. 1.—Normal appearance of posterior vertebral body line (arrows).
A, Patient with hyperflexion sprain at C5–C6.
B, Patient with simple compression fracture of L1.

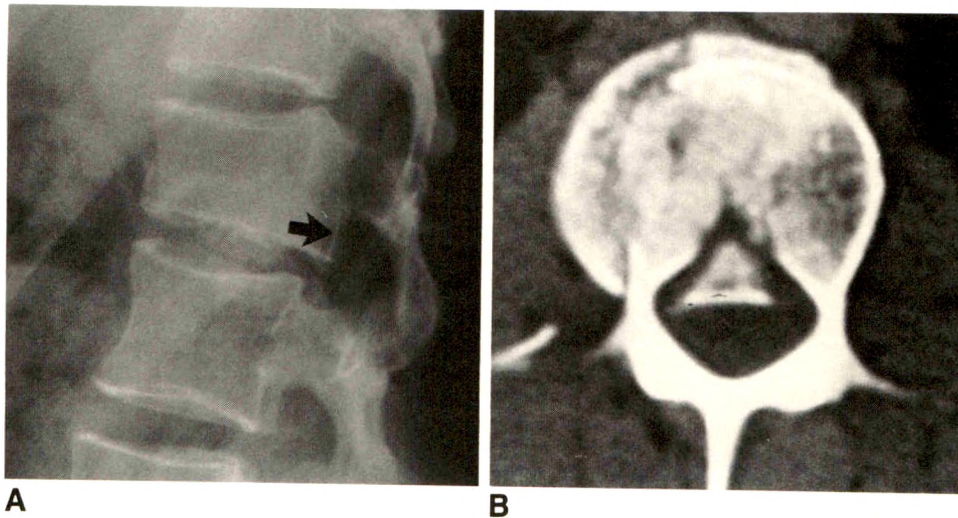


Fig. 2.—Burst fracture of L1 with posterior displacement of posterior vertebral line.
A, Lateral radiograph shows retropulsion of bone fragment (arrow) inferiorly.
B, CT scan shows canal encroachment by retropulsed fragment.

often this was from the superior aspect of the vertebral body, but in three instances the disruption resulted from inferior fracture. Posterior displacement occurred in 77 patients. The second most common pattern (26 patients) was rotation of a portion of the posterior vertebral line (Fig. 3). A third pattern, obliteration of all or a portion of the posterior vertebral body line, was encountered in 11 patients (Fig. 4).

Of the 46 patients with combined injuries in whom burst was a major component, abnormalities of the posterior vertebral body line occurred in 36. Posterior-fragment displacement occurred in 24 patients, rotation of the fragment in nine, and obliteration of the line in three. All of the 10 patients who had no posterior abnormality had lateral flexion burst injuries.

Of the six patients with seat-belt injuries, the posterior vertebral body line was preserved. However, in all of these cases widening of the vascular cleft indicated the point of traverse of the injury. No abnormalities of the posterior vertebral body line were present in the 82 patients with simple fractures. Patients with flexion-distraction, flexion-dislocation,

or extension injuries likewise had no abnormalities of the posterior vertebral body line.

Discussion

Burst fractures are the most disruptive type of injury to the vertebral column. These relatively common fractures usually produce one or more large fragments from the posterior aspect of the vertebral body. Most often, these are displaced into the vertebral canal [4–8], and this displacement is apparent on a lateral radiograph of the involved vertebrae (Figs. 2–4). Plain-film analysis, when performed in a careful manner, should predict findings that will be encountered on CT, MR, or myelography.

The posterior aspect of the vertebral body should be clearly visible on all lateral radiographs. In the cervical region this consists of a single dense line. In the thoracolumbar region, the entry of a nutrient vessel interrupts this line centrally [1]. Any interruption of this line elsewhere, or displacement or

Fig. 3.—Rotation of posterior vertebral line in burst fracture of L1.

A, Lateral radiograph shows rotation of superior aspect of posterior vertebral line (straight arrow). Bone fragment lies within vertebral canal (curved arrow).

B, CT scan confirms findings and shows marked compromise of vertebral canal by retropulsed fragment.

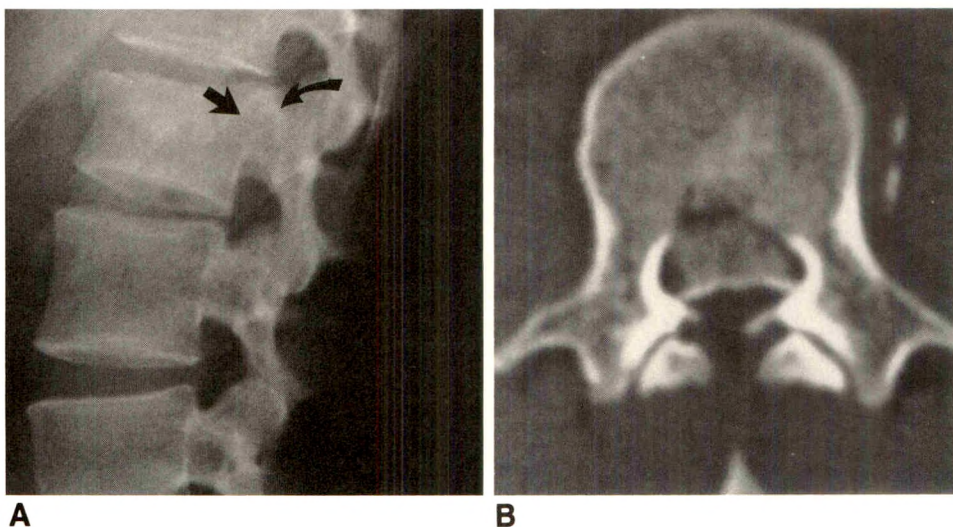
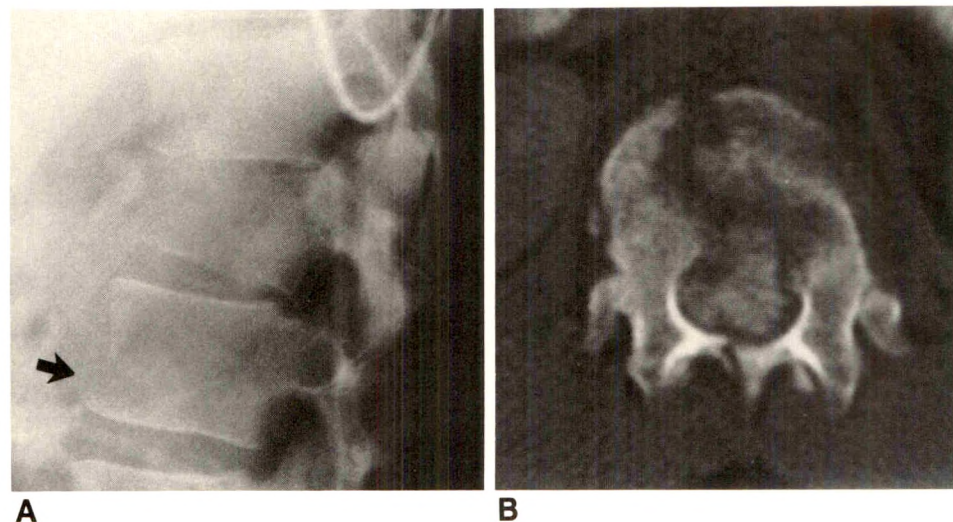


Fig. 4.—Obliteration of posterior vertebral line in patient with burst fractures of T12 and L1.

A, Lateral radiograph shows absence of upper posterior vertebral line of T12. Note absence of line of L1, which is also fractured anteriorly (arrow).

B, CT scan at T12 shows bone fragment that completely occupies vertebral canal. Large fragment was also present at L1.



angulation of the line, should be considered an abnormal finding. We have not observed any of these findings in patients who did not have a burst fracture. Thus, in an individual who has suffered a flexion-type injury, the presence of any of these findings should be considered evidence that a burst fracture has occurred, and an immediate CT or MR examination should be performed to locate the displaced fragment(s).

Obliteration of the posterior vertebral body line is not a specific finding in burst injuries, occurring in only 14 of our patients. We have observed this finding in neoplastic destruction of a vertebra and also, on occasion, as the result of minor degrees of rotation. However, in the clinical setting where flexion injury has occurred, this finding should be viewed with suspicion, and additional studies should be performed to confirm the diagnosis.

The significance of disruptive abnormalities of the posterior vertebral body line may best be understood in light of the biomechanics of burst fractures. In a flexion injury with axial loading the following sequence of events occurs: The initial

force compresses the anterior superior portion of the vertebral body. As the force continues, the posterior ligaments rupture. Further application of force causes the vertebral body to burst, separating fragments posteriorly in the direction of least resistance [1, 7, 9]. For a burst fracture to occur, sufficient skeletal and ligamentous damage must be present posteriorly. All burst injuries are therefore considered unstable by most surgeons.

Denis [9, 10] defined three anatomic portions of the vertebral column. The anterior column extends from the anterior longitudinal ligament to the middle of the vertebral body. The middle column extends from the middle of the vertebral body to the posterior longitudinal ligament. The posterior column extends from the posterior longitudinal ligament to the supraspinous ligament. Furthermore, he defined instability as any disruption that involved the middle and posterior columns since the major posterior skeletal and ligamentous structures would be disrupted. Gehweiler et al. [2] defined four radiographic features that would indicate instability: (1) displace-

ment of vertebrae, (2) widening of the interspinous space, (3) widening of an apophyseal joint, and (4) widening of the vertebral canal (interpedicular distance). Of these findings, all but displacement indicate disruption of the posterior column. Displacement, by definition, indicates disruption in the middle column. If there is no displacement, however, the assessment of middle-column integrity is difficult. We believe that disruption of the posterior vertebral body line as described above constitutes a valid sign that a disruption has occurred within the middle column. This finding is, therefore, useful for predicting the presence of a burst fracture as well as in aiding the surgeon in the evaluation of spinal stability.

REFERENCES

1. Gehweiler JA, Osborne RL Jr, Becker RF. *The radiology of vertebral trauma*. Philadelphia: Saunders, 1980;91-130
2. Gehweiler JA Jr, Daffner RH, Osborne RL Jr. Relevant signs of stable and unstable thoracolumbar vertebral column trauma. *Skeletal Radiol* 1981;7:179-183
3. Clark WM, Gehweiler JA Jr, Laib R. Twelve significant signs of cervical spine trauma. *Skeletal Radiol* 1979;3:201-205
4. Kilcoyne RF, Mack LA, King HA, et al. Thoracolumbar spine injuries associated with vertical plunges: reappraisal with computed tomography. *Radiology* 1983;146:137-140
5. Shuman WP, Rogers JV, Sickler ME, et al. Thoracolumbar burst fractures: CT dimensions of the spinal canal relative to postsurgical improvement. *AJNR* 1985;6:337-341
6. Guerra J Jr, Garfin SR, Resnick D. Vertebral burst fractures: CT analysis of the retropulsed fragment. *Radiology* 1984;153:769-772
7. Atlas SW, Regenbogen V, Rogers LF, et al. The radiographic characterization of burst fractures of the spine. *AJNR* 1986;7:675-682
8. Daffner RH, Deeb ZL, Rothfus WE. Fingerprints of vertebral trauma—a unifying concept based on mechanisms. *Skeletal Radiol* 1986;15:518-525
9. Denis F. The three column spine and its significance in the classification of acute thoracolumbar spinal injuries. *Spine* 1983;8:817-831
10. Denis F. Spinal instability as defined by the three-column spine concept in acute spinal trauma. *Clin Orthop* 1984;189:65-76

Spinal Deformities and Pseudofractures

M. Ines Boechat¹

Nine children with spinal deformities had CT examinations after sustaining blunt abdominal trauma. Partial-volume averaging of two lumbar vertebrae suggested a spinal fracture in four children. All four pseudofractures were oriented in a plane perpendicular to the deformity. In two children the spinal deformity could be recognized easily on the scout view. In the other two, the scout view was obtained in a plane different from that of the curvature and concealed the vertebral deformity. Scoliosis resulted in pseudofractures running from front to back of the vertebral body, whereas kyphosis resulted in pseudofractures seen in the coronal plane. The pseudofractures lacked associated soft-tissue swelling and had poorly defined, irregular borders that were widely separated by disk material.

CT has had a marked impact on the evaluation of abdominal abnormalities in traumatized children. It has reduced the need for scintigraphy, angiography, and even surgical intervention. Nevertheless, despite its accuracy, there are circumstances in which misleading appearances may lead to erroneous diagnoses. CT images of a child with a spinal deformity may suggest a fracture of a vertebral body and lead to incorrect diagnoses in children with trauma.

Materials and Methods

Six girls and three boys (9 to 16 years old) with thoracolumbar or lumbar vertebral curvature had CT after blunt trauma to the abdomen. Three patients (two boys and one girl) had kyphosis either secondary to Scheuermann's disease or previous infection; six patients (one boy and five girls) had scoliosis of 20° or more. Four of the scoliotic curves were idiopathic, one was secondary to neuromuscular disease, and another was the result of radiation therapy. All studies were done with 10-mm sections at 10-mm intervals on a 9800 GE scanner. Scout views were obtained in the coronal plane for six children and in the lateral projection for the other three.

Results

Four children had CT images that suggested a lumbar vertebral body fracture. Two had scoliosis and a pseudofracture oriented in the sagittal plane (Fig. 1); two suffered from kyphosis and had a pseudofracture in the coronal plane (Fig. 2). The pseudofractures were related not only to the CT section but also to the degree of the spinal deformity; all four children had curvatures of 40° or more. The spinal deformities of two children could be recognized on the initial scout view of the CT study. In the other two children, the scout views had been obtained in a different plane from the curvature, and the deformity was not evident (Fig. 2).

Discussion

Although spinal curvatures may prevent accurate interpretation of axial CT

Received June 20, 1986; accepted after revision August 12, 1986.

¹ Department of Radiological Sciences, Section of Pediatric Radiology, University of California, Los Angeles, School of Medicine, Los Angeles, CA 90024. Address reprint requests to M. I. Boechat.

AJR 148:97-98, January 1987
0361-803X/87/1481-0097
© American Roentgen Ray Society

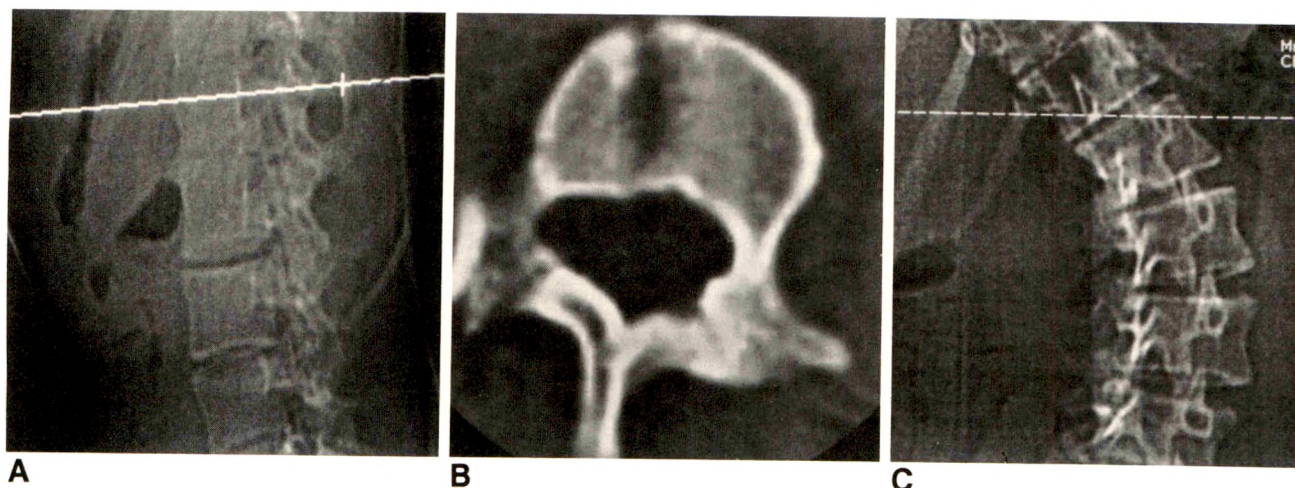


Fig. 1.—Pseudofracture caused by scoliosis.

A, Lateral scout view of abdomen indicates level of B.

B, CT suggests a vertebral fracture oriented in sagittal plane.

C, Anteroposterior scout view shows that abnormality is pseudofracture due to scoliosis and partial-volume averaging of T12 and L1.

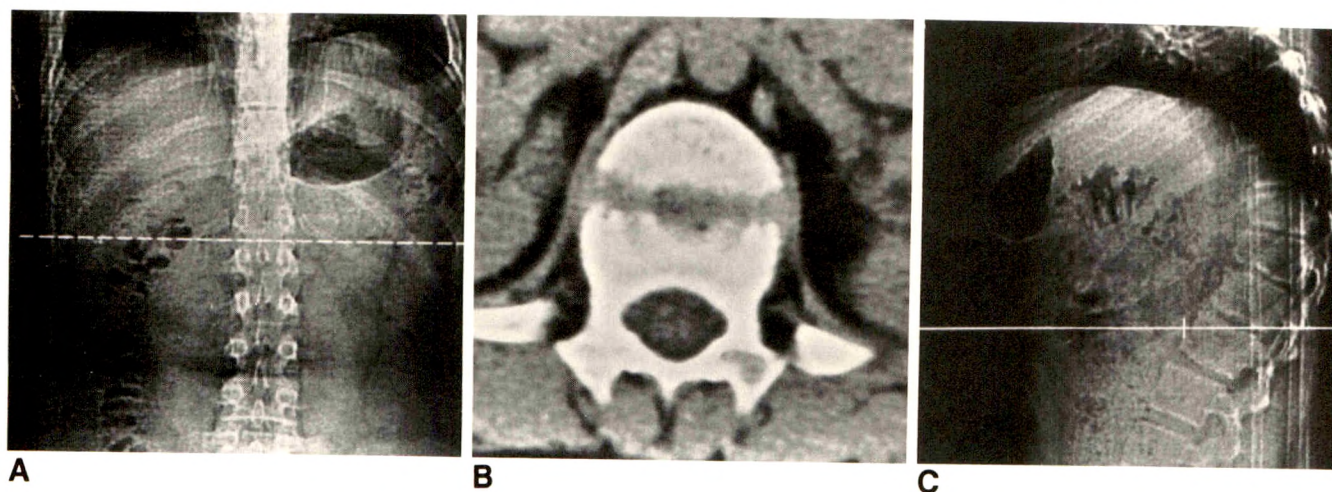


Fig. 2.—Pseudofracture caused by kyphosis.

A, Normal anteroposterior view of abdomen shows level of B.

B, CT suggests vertebral fracture oriented in coronal plane.

C, Lateral scout view shows that pseudofracture is secondary to kyphosis and partial-volume averaging of T12 and L1.

studies [1, 2], scoliosis and kyphosis can produce CT images that simulate a spinal fracture [3]. The fictitious fractures always appear in a plane perpendicular to the plane of the spinal deformity: the coronal plane in patients with kyphosis and the sagittal plane in patients with scoliosis. The fictitious fractures are not associated with soft-tissue swelling and have poorly defined, irregular borders that are widely separated by intervertebral disk material. There is no evidence of displacement of fragments, impingement on nerve roots, or involvement of posterior elements—findings that are typical of spinal fractures [2].

Although it is advisable to obtain anteroposterior and lateral scout views before CT studies in all spinal cases, to adjust patient position and provide precise anatomic location [4], such a routine frequently is not followed in daily practice. Nevertheless, because recognition of the deformity will help to avoid misinterpretations, CT examinations in children with

scoliosis or kyphosis should include at least a scout view in the same plane as the deformity.

ACKNOWLEDGMENTS

I wish to acknowledge Vicente Gilsanz for lending cases to this study and Judy Jonas for secretarial assistance.

REFERENCES

1. Braun IF, Lin JP, George AE, Kricheff II, Hoffman JC. Pitfalls in the computed tomographic evaluation of the lumbar spine in disc disease. *Neuroradiology* 1984;26:15-20
2. Cacayorin ED, Kieffer SA. Applications and limitations of computed tomography of the spine. *Radiol Clin North Am* 1982;20:185-206
3. Handel SF, Lee YY. Computed tomography of spinal fractures. *Radiol Clin North Am* 1981;19:69-90
4. Genant HK. Computed tomography of the lumbar spine: technical considerations. In: Genant HK, Chafetz N, Helms CA, eds. *Computed tomography of the lumbar spine: diagnostic and therapeutic implications for the radiologist, orthopedist, and neurosurgeon*. San Francisco: University of California, Dept. of Radiology, 1982:23-52

Technical Note

Prosthetic Fit in Below-Knee Amputation: Evaluation with Xeroradiography

Gerald A. L. Irwin,¹ Lawrence Friedman,² and Daniel Shapiro²

Xeroradiography for evaluating prosthetic devices in patients with below-knee amputations has been used by the Departments of Radiology and of Physical Medicine and Rehabilitation at Nassau County Medical Center for 7 years. The procedure has been excellent for imaging skin, muscle, bone, and the prosthetic device with minimal radiation dose.

Jing et al. [1] described using xeroradiographs for this purpose, but they did not discuss the indications or interpretations. Baumgartner and Langlotz [2] discussed stump radiography in general for low kilovolt techniques but did not discuss xeroradiographs. Haslam et al. [3] stated "An x-ray of the patients' residual limb should not be a luxury, but a necessity." They mentioned xeroradiographs, but did not indicate the value of radiographs taken with the artificial limb in place.

Methods

Physicians in the Department of Physical Medicine and Rehabilitation see 175 amputees annually for evaluation of the amputees' stumps and prostheses. Those patients who because of faulty prosthetic fit have pain or skin irritations over bony prominences that cannot be resolved by routine modification of the prosthesis are referred for radiographic study. Most of these patients have below-knee amputations because above-knee amputees have much more mobile and voluminous soft tissues that prevent a prosthesis from causing irritation of a stump at the bone/socket interface. Occasionally, pressure-sensitive materials may be useful in evaluating poor contact fit, but xeroradiography of the stump and prosthesis is the best method of determining the cause of the problem.

Anteroposterior and lateral xeroradiographs should be taken with

the patient erect and the prosthetic device in place, with and without weight bearing. The non-weight-bearing views must be taken with the patient erect, knee extended, and the prosthetic foot touching the ground. Typical factors used are 120 kV, 40 mAs, and nonbucky technique with the negative xerographic mode to decrease radiation dosage as much as possible. Oblique views may be needed if metallic parts overlap the image. The following should be evaluated: (1) the position of the patellar tendon bar of the prosthesis relative to the patella and the tibial tubercle; (2) the popliteal bulge, medial and lateral tibial flare, and general contour of the prosthesis; (3) the presence of lining material (e.g., foam, socks) in the prosthesis; and (4) the relationship between the stump tissues and the socket of the prosthesis, especially the extent of contact during weight bearing.

Results and Discussion

Typical cases and observations are illustrated in Figures 1 through 4.

The anteroposterior and lateral weight-bearing and non-weight-bearing radiographs should be studied for motion of the stump tissues within the prosthesis (piston action). Two measurements are important. The first is the difference in the distance between the bone end and the end of the stump with and without weight bearing. The second is the distance between the soft-tissue stump end and the liner of the prosthesis (or socket if no liner is used). In each instance the distance should not be more than 1 cm (Fig. 1).

The fibular and tibial relationship with weight bearing should be evaluated by measuring the distance between the two bones on both the anteroposterior and lateral views. Upon weight bearing, motion between the ends of the tibia and

Received February 10, 1986; accepted after revision August 26, 1986.

¹ Department of Radiology, Nassau County Medical Center, State University of New York, Stony Brook, 2201 Hempstead Turnpike, East Meadow, NY 11554. Address reprint requests to G. A. L. Irwin.

² Physical Medicine and Rehabilitation, Nassau County Medical Center, State University of New York, Stony Brook, 2201 Hempstead Turnpike, East Meadow, NY 11554.

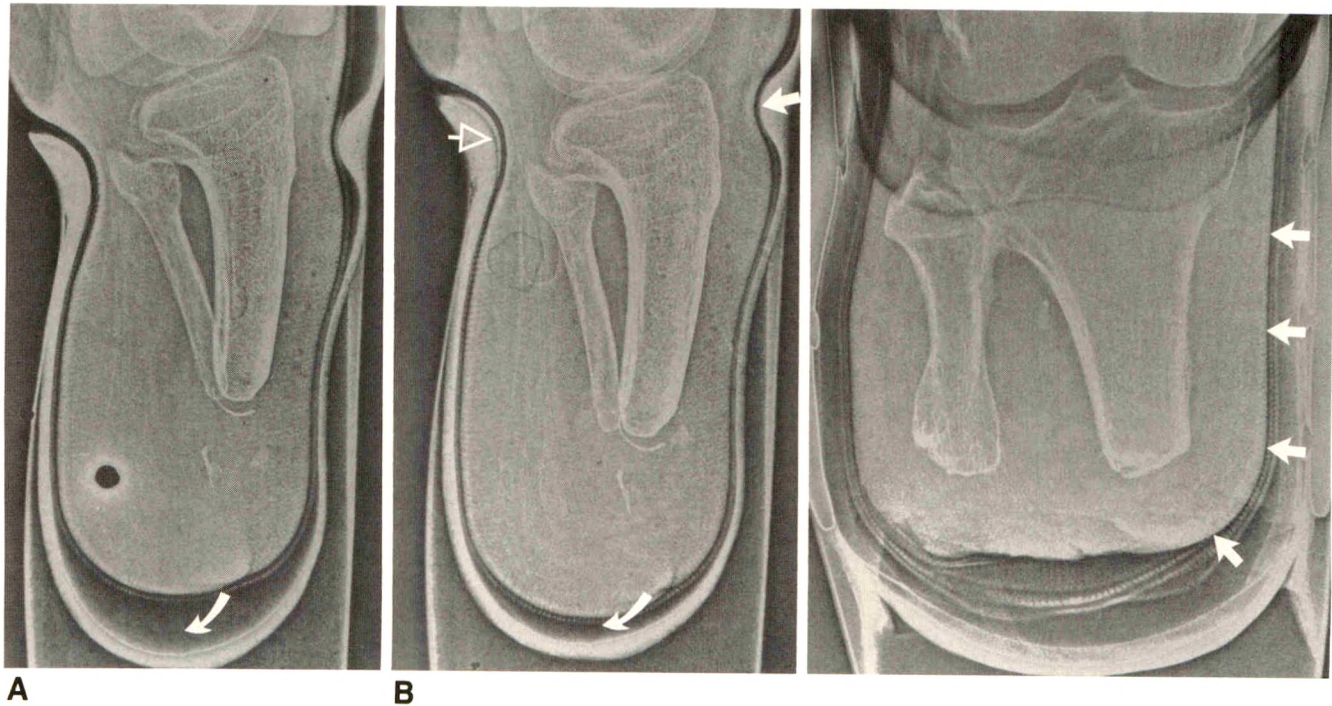


Fig. 1—Lateral xeroradiographs of knee and leg of a 44-year-old amputee with prosthesis in place. A, Non-weight-bearing view shows excessive piston motion (*curved arrow*). B, Weight-bearing view shows excessive piston motion (*curved arrow*) and correct positioning of patellar tendon bar (*straight white arrow*) and popliteal bulge (*open arrow*).

Fig. 2.—Anteroposterior weight-bearing xeroradiograph of knee in a 39-year-old amputee shows separation of ends of tibia and fibula, indicating a disrupted interosseous membrane, which can cause pain on weight bearing. Shelf in prosthesis (medial tibial flare) (*arrows*), necessary to support stump medially, is not present.

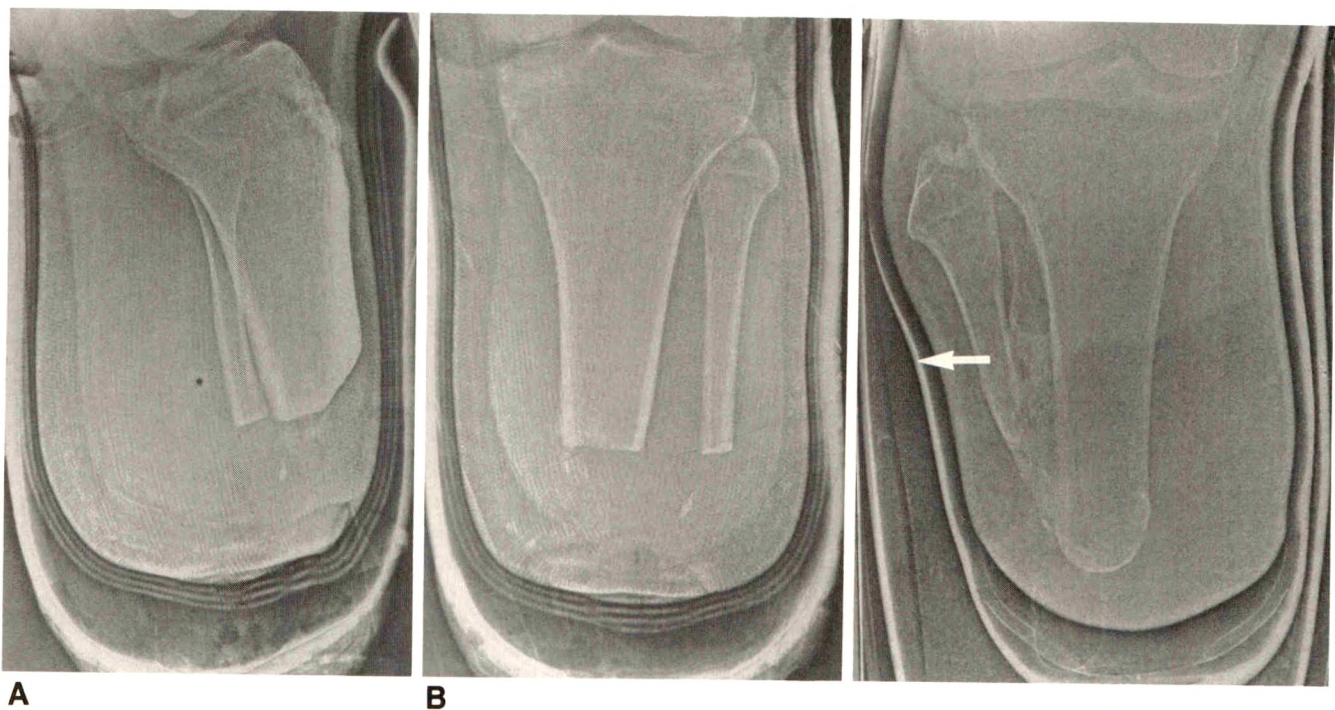


Fig. 3—Xeroradiographs of 23-year-old with painful prosthesis show lack of beveling of sharp corners of tibia. Fibula should be transected at a higher level. Bone fragments are seen in soft tissues. Stump stocking fits poorly. A, Lateral. B, Anteroposterior.

Fig. 4.—Anteroposterior xeroradiograph shows good sculpting of tibia and cone shape with fibula resected at least 1 cm above end of tibia. Extensive bony bridging between tibia and fibula leads to nerve entrapment and pain. Good support of lateral tibial flare (*arrow*) is evident.

fibula may occur (Fig. 2). Separation implies that the interosseous septum is not intact.

The patellar tendon-bar relationship is best evaluated on the lateral view. This area bears most of the weight in a below-knee amputation, with the inferior patellar tendon in firm opposition to the anterior curved ridge of the prosthesis (the patellar tendon bar) (Fig. 1). The bar should lie midway between the tibial tubercle and the inferior aspect of the patella.

The posterior aspect of the prosthesis (the popliteal bulge) must be in close opposition to soft tissues so as to push the stump anteriorly to fit snugly against the patellar tendon bar (Fig. 1). A loose fit will cause problems by allowing the stump to drop down too far into the socket. The prosthesis also should have a smoothly angled shelf medially and laterally to support the tibia beneath the plateau (medial and lateral tibial flare) (Fig. 3).

Patients usually wear a protective sock on the skin before putting on the prosthesis. Images should be carefully examined for excess folds of sock and for skin areas devoid of the foam-pad support (Fig. 3).

When performing a below-knee amputation, most surgeons suture a flap of muscle and soft tissue forward over the ends of the bone (myoplasty) to act as a natural cushion for weight

bearing and to give a better fit in the prosthesis. The radiographs should be evaluated for the presence or absence of this soft-tissue flap (Fig. 3).

Bones should be evaluated for sharp ends rather than proper "sculpting." Current surgical amputation technique consists of transecting the tibia and then beveling it from anterior to posterior (i.e., sculpting).

The fibula should be transected at a level at least 1 cm proximal to the tibia, giving a cone shape to the stump. Sharp bony corners, spicules of bone, foreign bodies, wire sutures, and early osteomyelitis or inflammatory soft-tissue changes should be reported. Bony bridging between the fibula and tibia may lead to nerve entrapment with subsequent pain (Fig. 4). The inner margins of the plastic shell should not have localized bulges that may impact soft tissue or bone and cause patient discomfort.

REFERENCES

1. Jing B, Villanueva R, Dodd G. A new radiological technique in evaluation of prosthetic fitting. *Radiology* **1977**;122:534-535
2. Baumgartner R, Langlotz M. Amputee stump radiology. *Prosthet Orthot Int* **1980**;4:97-100
3. Haslam TP, Wilson MT, Urlaub MJ, Borrell RM. The use of X-rays and xerograms in prosthetics. *Orthot Prosthet* **1983**;37:32-35

American Roentgen Ray Society:

Officers, Committees, and Meeting Information

Officers

President: Jerome F. Wiot

President-elect: Raymond A. Gagliardi

1st Vice-president: Lee F. Rogers

2nd Vice-president: Gerald D. Dodd

Secretary: Glen W. Hartman

Treasurer: Ronald G. Evens

Executive Council: E. Gedgaudas, J. F. Wiot, L. F. Rogers, R. A. Gagliardi, R. G. Evens, R. N. Berk, F. L. Angell, J. E. Madewell, M. P. Capp, G. W. Hartman, B. G. Brogdon, G. A. Kling, H. C. Carlson, A. K. Poznanski, A. E. James, Jr., J. A. Kirkpatrick, Jr., G. R. Leopold, G. D. Dodd, J. T. Ferrucci, Jr., R. H. Troupin, chairman

Committees 1986-1987

Editorial Policy: S. S. Sagel, W. J. Casarella, J. T. Ferrucci, Jr., N. C. Whitley, S. Hilton, A. J. Davidson, J. M. Taveras, R. N. Berk, M. P. Capp, chairman

Education and Research: C. E. Putman, A. R. Margulis, J. R. Thornbury, R. A. McLeod, J. T. Ferrucci, Jr., ex officio, B. G. Brogdon, chairman

Finance and Budget: B. P. Wood, L. R. James, J. A. Kirkpatrick, Jr., A. E. James, F. L. Angell, chairman

Instruction Courses: R. A. McLeod, associate chairman, J. T. Ferrucci, Jr., chairman

Program: J. Wiot, G. W. Hartman, J. A. Kirkpatrick, Jr., R. H. Troupin, M. P. Capp, J. E. Madewell, B. G. Brogdon, J. T. Ferrucci, Jr., G. A. Kling, G. G. Ghahremani, M. Viamonte, R. A. Gagliardi, chairman

Publications: W. J. Casarella, J. T. Ferrucci, Jr., S. S. Sagel, N. C. Whitley, M. P. Capp, chairman

Scientific Exhibits: S. G. Kirchner, A. V. Proto, S. M. Goldman, J. E. Madewell, chairman

Nominating: W. J. Casarella, H. C. Carlson, A. E. James, chairman.

Representatives to Other Organizations

American Board of Radiology: E. C. Klatte, R. W. McConnell, L. F. Rogers

American College of Radiology: J. L. Gwinn, G. A. Kling, G. W. Hartman, J. M. Dennis, E. J. Ferris, J. E. Madewell

American Medical Association House of Delegates: S. F. Ochsner, K. C. Krabbenhoft, alternate

American National Standards Institute: M. Haskin

National Council on Radiation Protection and Measurements: E. L. Saenger, H. L. Friedell

Meetings, Membership, Business Information

Annual Meetings: April 26-May 1, 1987, Fontainebleau-Hilton, Miami Beach; May 8-13, 1988, Hilton, San Francisco; May 7-13, 1989, Hilton, New Orleans.

Director Annual Meeting: George A. Kling, Harper Hospital, Detroit, MI 48201; (313) 745-8401.

ARRS Membership: Rosalind H. Troupin, Dept. of Radiology, Hospital of University of Pennsylvania, 3400 Spruce St., Philadelphia, PA 19104. The ARRS has two membership categories: active and in-training. For active membership, applicants must practice radiology in the U.S. or Canada. Each must have graduated in good standing from an approved medical school or hold an advanced degree in a physical, chemical, or biological science and be certified by the American Board of Radiology, the Royal College of Physicians and Surgeons of Canada, or otherwise adequately document training and credentials. A member-in-training must be in a radiology residency, a postresidency fellowship program, or a postgraduate student in an allied science. Status must be verified by the program director. For consideration during the 1987 ARRS meeting, completed applications must be received by Dr. Troupin no later than Feb. 1, 1987.

Business Office: Paul Fullagar, administrative director, George J. O'Hop, controller, American Roentgen Ray Society, 1891 Preston White Dr., Reston, VA 22091; (703) 648-8900.

Pseudobursae: A Useful Finding in Patients with Painful Hip Arthroplasty

Thomas H. Berquist¹
 Claire E. Bender¹
 Timothy P. Maus¹
 Ellen M. Ward¹
 James A. Rand²

A retrospective review of 178 consecutive subtraction hip arthrograms (175 patients) was performed to evaluate the significance of cavities or bursal communications (or both) with the pseudocapsule in patients with painful hip arthroplasty. Bursae and/or communicating cavities were shown in 75 (43%) of the 175 patients. Communicating irregular cavities were noted in 12 patients (nine infected), and smooth bursae or bursalike structures were noted in 63 patients. The most frequent bursal locations were the greater trochanteric region (32/63), supraacetabular region (18/63), and iliopsoas (12/63). Three patients had multiple bursae. Six of the 18 acetabular bursae were associated with previous dislocations. Twenty-seven patients with bursae had no radiographic findings of loosening or infection. Of these 27, 12 (44%) responded to local injection of anesthetic into the bursa and were judged clinically to have bursitis. Arthrography, with aspiration from the bursae or cavities and injection of anesthetic, provides additional information regarding painful hip arthroplasty and may prevent unnecessary surgery.

Evaluation of patients with hip pain after total hip arthroplasty can be difficult. Plain films, isotope scans, and arthrography are all useful. Arthrography is usually performed to confirm suspected loosening or infection. However, a significant number of patients present with pain and yet do not have characteristic radiographic or isotope findings that suggest loosening or infection. Subtraction arthrography is more sensitive than conventional arthrography after arthroplasty and is valuable for defining the anatomy. In addition, arthrography allows aspiration of fluid for study and injection of anesthetic for diagnosis and therapy. A review of 178 subtraction arthrograms in 175 consecutive patients indicated that significant findings other than loosening or infection could be detected.

Materials and Methods

A total of 178 subtraction arthrograms in 175 patients were retrospectively reviewed to determine the clinical significance of cavities or bursae (or both) noted on arthrograms. Bursae and cavities were noted in 75 of 175 patients. The ages of the patients ranged from 17 to 82 years (mean, 58). Ninety-seven of the 175 patients underwent surgical revision after the arthrogram. In the remaining 78 patients, surgery was not performed because of lack of evidence of loosening or infection, the patient's weight, or other arthrographic findings suggesting bursitis or some other cause for the pain. Aspiration and injection of the pseudocapsule and any communicating structures by using 0.25% bupivacaine was routinely performed along with arthrography to provide additional information. Typically, the pseudocapsule was aspirated before arthrography. If fluid was not obtained, the pseudocapsule was flushed with nonbacteriostatic normal saline and reaspirated. If little fluid was obtained, or if a narrow communication was shown during arthrography, a second aspiration of the bursae or cavity was performed. Anesthetic alone was used in patients with arthroplasty. Steroids should not be used in this category of patient.

Arthrographic findings, including response to injections, were correlated with the surgical findings or the clinical response to conservative therapy. The location of the bursa, pseudo-

Received June 12, 1986; accepted after revision August 26, 1986.

¹Department of Diagnostic Radiology, Mayo Clinic and Mayo Foundation, Rochester, MN 55905. Address reprint requests to T. H. Berquist.

²Department of Orthopedics, Mayo Clinic and Mayo Foundation, Rochester, MN 55905.

AJR 148:103-106, January 1987
 0361-803X/87/1481-0103
 © American Roentgen Ray Society

TABLE 1: Bursae Associated With Total Hip Arthroplasty

	Location				Total
	Greater Trochanter	Acetabulum	Iliopsoas	Multiple Sites	
No. bursae	32	18	12	3	65 ^a
Capsule size ^b					
Small	12	3	3	0	18
Medium	13	10	3	2	28
Large	7	5	6	1	19
Previous revision	6	4	3	0	13
Surgically proved					
Loosening	18	5	9	1	33
Loosening plus infection	2	0	2	0	4
No loosening or infection					
Total	12	8	3	2	25
Responded to injection	8	3	0	1	12

^a Three patients had more than one bursa noted, so that numbers total more than 63.

^b Small, ≤ 10 cm³; medium, 11–25 cm³; large, >25 cm³.

capsule size, associated loosening or infection, presence of previous revision, and dislocations were tabulated. Pseudocapsule size was calculated by noting the volume of injected medium that either resulted in lymphatic filling or caused patient discomfort. Pseudocapsules were classified as small (≤ 10 cm³), medium (11–25 cm³), and large (>25 cm³) [1], on the basis of the volume accepted by the pseudocapsule after aspiration.

Results

Bursae were noted in 63 (36%) of the 175 patients presenting with painful hip arthroplasty (Table 1). The most common location was adjacent to the greater trochanter. Other sites included the supraacetabular region, the iliopsoas, and the lesser trochanteric region. More than one bursa was present in three patients. The radiographic appearance of the uninfected bursae differed from that of the infected pockets and cavities. The noninfected bursae were generally large, smooth-walled capsular extensions, in contrast to the infected cavities, which were more irregular, with synovial proliferation and frequently a narrow, irregular neck. Fluoroscopically guided aspiration of the cavities and pseudobursae of the latter group is required to exclude infection and to allow anesthetic injection. Reinjection with aspiration of large extensions is generally not required (see Fig. 2).

Greater Trochanteric Bursae

The bursae in the greater trochanter could not be correlated with capsule size because small capsules were present in 12 patients, moderate in 13, and large in seven. Six patients had previous revisions, and five had had nonunion of the greater trochanter. In these 11 patients, both factors undoubtedly contributed to bursa formation. Of the 32 patients with bursae of the greater trochanter, 20 underwent surgery: 18 had

component loosening and two had infection plus loosening. When infected, the bursae were more irregular and usually had multiple filling defects (Fig. 1).

Twelve patients with bursae of the greater trochanter did not have radiographic or clinical evidence of loosening. Aspirations showed no evidence of infection. These patients were believed to have bursal inflammation or extraarticular hip pain. Eight of the 12 patients responded to local injection of bupivacaine into the bursae, thus confirming the clinical diagnosis of greater trochanteric bursitis.

Acetabular Bursae

Eighteen patients had bursal communications at the superior lateral margin of the acetabulum (Fig. 2). Generally, this extension is not noted on routine arthrograms. Capsule size here did not seem related to the presence of a bursa (Table 1). Four patients had previous revisions, and five had associated loosening. Of the eight patients given local anesthetic injection, only three responded. Six patients experienced recurrent dislocation of the femoral component from the acetabular cup (Fig. 2). The location of the bursae (anterosuperior or posterosuperior) in relation to the previous dislocations could not be confirmed. However, the size and location of the bursa should indicate previous dislocations.

Iliopsoas Bursae

Of 12 patients with filling of the iliopsoas bursae, nine had associated loosening or infection, or both. The iliopsoas bursa is oblique in orientation, similar to the course of the tendon. Communication with this bursa has been noted on 20% of routine arthrograms and in patients with rheumatoid and other inflammatory arthropathies. If the bursa is sufficiently enlarged, adjacent neurovascular structures and the bladder may be compressed [2, 3]. In three patients with secure implants, there was no response to injection of bupivacaine.

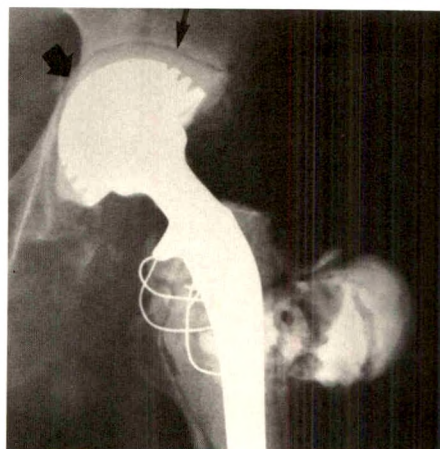
Multiple Sites

Three patients had multiple bursae (Fig. 3). Loosening of the components was evident in one of the three patients. The symptoms in one of the remaining two patients responded to injection of bupivacaine into the bursae. In certain cases, injection of the pseudocapsule may be sufficient (wide neck), but if more than one bursa is present, separate injections may be required.

Cavities

Multiple or single irregular cavities were noted in 12 patients (Fig. 4). This finding was more frequently noted with infection. Arthrography allowed the demonstration and, if a narrow neck of difficult filling was noted, direct aspiration of the cavity. Aspiration fluid and surgical confirmation were positive in nine of the 12 cases. In the remaining three cases, aspiration fluid was negative and surgical confirmation was not obtained.

Fig. 1.—Anteroposterior arthrogram of hip shows large bursa in region of greater trochanter, along with several lucent filling defects. Bursa was infected. Lucency due to loosening seen at bone/cement interface in zones I (*thin arrow*) and II (*thick arrow*) of acetabular component. When bursae are present, filling these areas with contrast medium may be difficult because of decompression of pseudocapsule by large bursa.



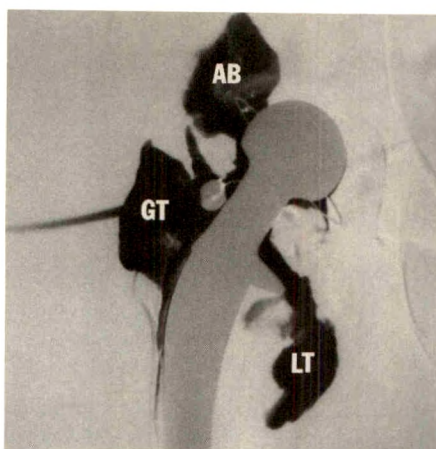
1

Fig. 2.—Anteroposterior subtraction hip arthrogram shows large bursa at acetabular margin. No evidence of loosening, but dislocation had previously occurred.



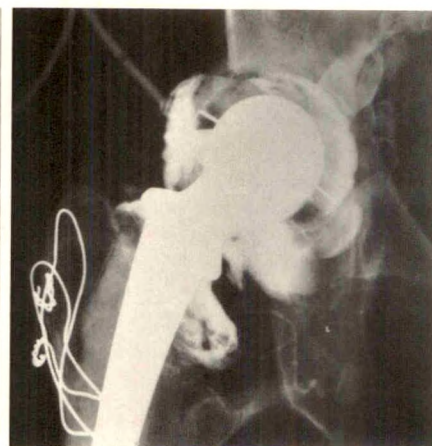
2

Fig. 3.—Anteroposterior view of subtraction arthrogram shows lesser trochanteric (LT), greater trochanteric (GT), and acetabular (AB) bursae. Both components loose.



3

Fig. 4.—Arthrogram showing loose acetabular component with a "shaggy-appearing" capsular lining and several irregular pockets due to infection.



4

Discussion

Subtraction arthrography, with aspiration and anesthetic injection technique, provides a valuable tool for evaluating painful hip arthroplasty. Arthrography is particularly accurate in identifying loosening of the femoral component [1, 4, 5]. Accuracy rates as high as 96% have been reported [1, 5] (Maus TP, Berquist TH, Bender CE, Rand JA, unpublished data). Detection of loosening of the acetabular component can be more difficult. Sensitivity and specificity of 97% and 68–75%, respectively, have been reported [1] (Maus T, Berquist TH, Bender CE, Rand JA, unpublished data).

Although pain is often due to loosening with or without associated infection, other abnormalities may also cause pain. In a first review, our group [1] noted bursae that communicated with the pseudocapsule. We also found that an injection of bupivacaine is useful in localizing the site of the pain. That experience initiated the present review of 178 arthrograms to determine the significance of bursae and cavities shown on arthrograms.

Steinbach et al. [6] noted communicating bursae or cavities in 40 patients when they reviewed 158 arthrograms—some

associated with arthroplasty. They postulated that bursae resulted from elevated pseudocapsule pressure, chronic trauma, or friction in a region of the capsule near a bursa.

In our present series, 75 bursae or cavities were detected. The bursae were associated with small pseudocapsules in 18 (24%) of the 75 cases. Thus, the increased pressure of an inflamed small capsule may not be a major factor. Thirteen patients had previous revision, which should be a significant factor. In addition, 39 patients had loosening, infection, and nonunion of the greater trochanter, which definitely contribute to pseudocapsule changes. Another important feature, recurrent dislocation, was noted in six of the 18 patients with acetabular bursae.

Defining the cause of the symptoms, in addition to considering loosening or infection, can have a significant role in patient management. Unnecessary surgery can be avoided, and the patient can be reassured about the status of the arthroplasty.

Bursae of the greater trochanter were most commonly noted. These bursae were extensions of the pseudocapsule, having broad communications, except when there was nonunion of the greater trochanter—a situation in which the

communication may be narrow and extend between the site of the nonunion. Two patients had associated infection, and both had bursae that were more irregular, with large, lucent filling defects due to synovial proliferation. Although this appearance is not a specific one, it is useful when considered along with the aspiration of fluid. Twelve patients with greater trochanteric bursae did not have evidence of loosening or infection. Eight of these patients responded to local injection of bupivacaine and were treated conservatively. The arthrogram was useful in confirming the clinical diagnosis of bursitis. Thus, in all but one of the 12 patients, an operation was avoided. The bursa of one patient was resected. The decision to resect the bursae can be made on the basis of the clinical symptoms and arthrographic criteria (size and configuration of the bursa, no infection by culture aspirate, no evidence of loosening).

Bursae near the lateral margin of the acetabulum were noted in 18 patients. These patients did not respond well to local anesthetic injection (symptoms improved in three of the eight). However, six had had recurrent dislocations. Coventry [7] and Woo and Morrey [8] reviewed dislocations after total hip arthroplasty. The prevalence of dislocation was 3.2–3.9% in 10,833 cases [8, 9]. In his review of 32 late dislocations (5–10 years after surgery), Coventry [7] noted increased range of motion and enlarged pseudocapsules with extensions near the acetabulum. He postulated that the dislocations resulted from these factors. In addition, he found an increased incidence of acetabular loosening. Other factors that may lead to late dislocation include leg-length discrepancy, retroversion of the acetabular cup, and increased acetabular tilt [7]. These features, along with an acetabular bursa or extension, indicate recurrent dislocation.

Communication with the iliopsoas bursa was noted in 12 patients. Three patients had previous revision of their arthroplasty, nine had component loosening, and two had associated infection. Communication with the iliopsoas bursa can be seen on 15% or more of routine arthrograms [10, 11]. If this bursa becomes large enough, it may be seen as an inguinal mass and can compress vascular structures and the bladder [11]. Except for patients with associated infection, fluid aspiration and injection of anesthetic into the iliopsoas bursa did not change the course of patient care. However, one must keep in mind that revision because of loosening and/or infection was needed in nine of 12 cases.

Although the radiographic features are not specific, infected

cavities often have a radiographic appearance different from that of bursae. The cavities arise from irregular pseudocapsules. Also, these cavities are generally more irregular and filling defects are noted more consistently (8/9 with proven infection) (Fig. 4). Accurate identification of infection requires aspiration. Aspiration of the cavity in addition to the pseudocapsule is especially important if the communicating cavity has a narrow neck and is difficult to fill during arthrography, or if little fluid can be obtained from the pseudocapsule.

Conclusion

Arthrography is valuable for evaluating patients who have undergone total hip arthroplasty. Pain from causes other than loosening and infection can be identified. The ability to identify the capsular anatomy (including cavities and bursae), to aspirate fluid, and to perform diagnostic injections gives this technique added versatility that is not available with isotope scans and routine radiographic studies. In addition, unnecessary surgery often can be avoided.

REFERENCES

1. Lyons CW, Berquist TH, Lyons JC, Rand JA, Brown ML. Evaluation of radiographic findings in painful hip arthroplasties. *Clin Orthop* 1985; 195:239–251
2. Sartoris DJ, Danzig L, Gilula L, Greenway G, Resnick D. Synovial cysts of the hip joint and iliopsoas bursitis: a spectrum of imaging abnormalities. *Skeletal Radiol* 1985;14:85–94
3. Staple TW. Arthrographic demonstration of iliopsoas bursa extension of the hip joint. *Radiology* 1972;102:515–516
4. Hendrix RW, Wixson RL, Rana NA, Rogers LF. Arthrography after total hip arthroplasty: a modified technique used in the diagnosis of pain. *Radiology* 1983;148:647–652
5. Phillips WC, Kattapuram SV. Prosthetic hip replacements: plain films and arthrography for component loosening. *AJR* 1982;138:677–682
6. Steinbach LS, Schneider R, Goldman AB, Kazam E, Ranawat CS, Ghelman B. Bursae and abscess cavities communicating with the hip: diagnosis using arthrography and CT. *Radiology* 1985;156:303–307
7. Coventry MB. Late dislocations in patients with Charnley total hip arthroplasty. *J Bone Joint Surg [Am]* 1985;67:832–841
8. Woo RYG, Morrey BF. Dislocations after total hip arthroplasty. *J Bone Joint Surg [Am]* 1982;64:1295–1306
9. Beckenbaugh RD, Ilstrup DM. Total hip arthroplasty: a review of three hundred and thirty-three cases with long follow-up. *J Bone Joint Surg [Am]* 1978;60:306–313
10. Penkava RR. Iliopsoas bursitis demonstrated by computed tomography. *AJR* 1980;135:175–176
11. Warren R, Kaye JJ, Salvati EA. Arthrographic demonstration of an enlarged iliopsoas bursa complicating osteoarthritis of the hip: a case report. *J Bone Joint Surg [Am]* 1975;57:413–415

Radiation Dose in Radiography, CT, and Arthrography of the Temporomandibular Joint

E. L. Christiansen¹
 R. J. Moore²
 J. R. Thompson³
 A. N. Hasso³
 D. B. Hinshaw, Jr.⁴

Thermoluminescent dosimetry studies were performed on a Rando Humanoid head phantom to compare radiation dosages used in temporomandibular joint examinations. Studies included transaxial and direct sagittal high-resolution CT, reduced milliamperage dynamic CT, tomoarthrography, pluridirectional and linear tomography, pantomography, transcranial plain films, and fluoroscopy. Radiation doses were determined for the brain, lens, pituitary gland, condylar marrow, and thyroid gland. Condylar marrow received doses of 64 and 52 mGy, respectively, for the GE 9800 and 8800 high-resolution scans; 21 and 17 mGy, respectively, for the dynamically sequenced scans; and 26 mGy for the GE 9800 direct sagittal sections. Tomoarthrography yielded 31 mGy and fluoroscopy 12 mGy. Other lower doses showed 5 mGy for polytomography, 3 mGy for ipsilateral joint linear tomography, 1.9 mGy for the GE 9800 slow ScoutView, 1.8 mGy for xeroradiography, 0.9 mGy for contralateral joint linear tomography, 0.3–0.4 mGy for transcranial plain films and pantomography, and 0.2 mGy for the GE 8800 ScoutView. The estimated error in this study was calculated to be $\pm 15\%$. On a relative scale, the radiation doses from high-resolution CT and tomoarthrography are high, dynamic CT yields a medium dose, and all other tomographic and plain-film techniques yield low doses.

The demand for temporomandibular joint (TMJ) radiography has increased because of greater awareness among physicians and dentists of TMJ pain and dysfunction. While emphasis should be given to the sensitivity and diagnostic accuracy of the various techniques, a knowledge of the resulting radiation doses is important in the selection of the appropriate TMJ study.

A review of the recent literature disclosed interest in TMJ dosimetry dating back to 1964 [1]. Two articles dealt with radiation dose from mandibular radiography [2, 3]. Another discussed TMJ microfocal spot magnification radiography in which dosimetry was also discussed [4]. Two recent articles compared X-ray doses to the TMJ (among other sites) from various plain-film and tomographic procedures, but CT was not included [5, 6].

This investigation was designed to compare the radiation doses from the complete spectrum of X-ray examinations used for the TMJ, including tomoarthrography and CT. We believe that information on X-ray dose is important in considering which examination to use for a particular patient. Our purpose was also to discover how CT and tomoarthrography doses compare with more conventional plain-film and tomographic studies.

Materials and Methods

Lithium fluoride (LiF-100) thermoluminescent dosimeter (TLD) chips were used to measure the radiation exposure in a Rando Humanoid skull phantom. TLD chips were exposed to an estimated 280 mR (72 $\mu\text{C/kg}$) for calibration. The mean value for the chips was determined on an Eberline TLR-5 reader, after which the chips were binned according to $\pm 1\%$ variations from the mean. Those chips varying more than 5% from the mean were discarded from the sample.

Received June 6, 1986; accepted after revision August 27, 1986.

¹ Department of Endodontics, Section of TMJ/Orofacial Pain, School of Dentistry, Loma Linda University, Loma Linda, CA 92350. Address reprint requests to E. L. Christiansen.

² Department of Radiation Sciences, School of Medicine, Loma Linda University, Loma Linda, CA 92350.

³ Department of Radiation Sciences, Section of Neuroradiology, School of Medicine, Loma Linda University, Loma Linda, CA 92350.

⁴ Department of Radiation Sciences, Section of Magnetic Resonance Imaging, School of Medicine, Loma Linda University, Loma Linda, CA 92350.

AJR 148:107–109, January 1987

0361–803X/87/1481–0107

© American Roentgen Ray Society

Triples of TLD chips were placed in the sella turcica, condylar marrow spaces, and over the lens of the eyes. Single chips were used for readings taken in the cortex of the frontal lobes and in the thyroid gland. Readings from the three chips at any given site were averaged to give a single value. The same chips were assigned the identical location for each study to minimize variation in sensitivities. Kodak Lanex regular intensifying screens were loaded with Kodak OG-1 X-ray film (system speed of 400). Film images of the phantom's TMJs were made for all examinations to verify proper exposure and positioning.

Whenever the beam hardness changed significantly, as from plane tomography to CT, TLD chips were calibrated because chip sensitivity decreases with increasing beam hardness. Sensitivity averaged 3.4 counts/mR.

The minimum TLD chip reading (usually in a chip from the superiormost level of the head phantom) was chosen as the background level unless the reading exceeded 10 counts, in which case 10 was chosen to be the background level. Each "raw" TLD reading was then converted into an exposure reading according to the formula, $\text{exposure reading} = (\text{raw TLD reading} - \text{background}) / \text{sensitivity}$.

The estimated sources of error in the surface TLD chips are $\pm 10\%$ from chamber calibration, $\pm 3\%$ from orientation effect [7], and $\pm 2\%$ inherent in the chips. The estimated sources of error from the internal chips are $\pm 10\%$ from chamber calibration, $\pm 3\%$ beam hardening, and $\pm 2\%$ inherent in the chips. For both external and internal chips the total estimated error is $\pm 15\%$. For soft tissue (including marrow), exposure readings were converted to dose readings by multiplying by a Roentgen-to-rad factor of 0.90. The results are expressed in milliGrays (1 mGy = 100 mrad).

Linearity of the TLD chips was also investigated. Exposures were made of the target condyle with a Siemens Multiplanograph II and a Quint Sectograph over a period of 6 months. The number of exposures ranged from one to 24.

Results

Linearity of the TLD chips is within acceptable limits for the two tomographic methods tested, and there is no evidence to suggest significant drift in chip sensitivity during the study (Fig. 1).

The target condylar marrow received doses of 64 and 52 mGy, respectively, for the General Electric 9800 and 8800 series scanners with high-resolution overlapping axial images through the joint; 21 and 17 mGy, respectively, for the dynamically sequenced axial overlapping projections; and 26 mGy for the GE 9800 overlapping direct sagittal scans. Tomoarthography yielded 31 mGy and fluoroscopy 12 mGy for a total of 43 mGy. All other studies showed lower doses, with 5 mGy for polytomography, 3 mGy for linear tomography of the target joint ipsilateral to the beam, 1.9 mGy for the GE 9800 slow ScoutView, 1.8 mGy for xeroradiography, 0.9 mGy for linear tomography of the target joint contralateral to the beam, 0.3–0.4 mGy for transcranial plain films and pantomography, and 0.2 mGy for the GE 8800 ScoutView.

Discussion

The radiation dose to the condylar marrow, the target tissue, fell into relative categories of high, medium, and low; high-resolution CT was highest relative to the other techniques studied. The high-resolution CT dose was also greater

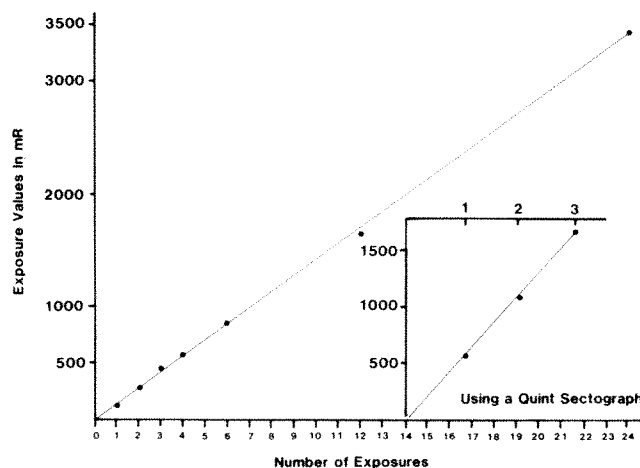


Fig. 1.—Thermoluminescent-dosimeter (TLD) linearity tested with several exposures with same TLD chips in same locations for Siemens Multiplanograph II and Quint Sectograph (inset) over 6-month period.

in all locations other than the condyle, and we attributed this to radiation scatter. Some investigators use high-resolution CT techniques in direct sagittal scanning of the TMJ [8, 9]. We find that usually fewer sections are used in direct sagittal imaging than in axial plane scanning: in the range of six or seven sections as compared with 20 overlapping transaxial sections. We found that direct sagittal scanning did not significantly increase the dose to the lens and thyroid when compared with high-resolution axial CT. Section for section, high-resolution CT exposes the patients to about three times the dose than does lower-milliamperage dynamic CT. Of interest, the GE 9800 dose was higher than the GE 8800 in both the high-resolution and dynamic scanning modes. This is probably because of the continuous rather than pulsed output of the X-ray tube of the GE 9800 scanner.

Unilateral TMJ tomoarthography, a relatively high-dose study, involves fluoroscopic guidance with videofluoroscopic and tomographic records of the dual compartment injections. The dose from the 24 linear tomographic sections (30.8 mGy) must be added to the 2-min dose from fluoroscopy (11.6 mGy) for a total dose of 42.4 mGy. Unquestionably, plain films rather than tomography and/or single-compartment arthrographic studies would yield reduced radiation doses. Polytomography, linear tomography, pantomography, and all transcranial plain-film techniques (with the exception of xeroradiography) rank as relatively low-dose studies in this investigation.

The radiation risk from radiographic examinations of the TMJ with the techniques discussed is minute. The threshold dose for the induction of a vision-impairing cataract is in the thousands of mGy range [10]. The greatest eye dose in this study was 4.6 mGy for high-resolution CT, indicating a minute risk for this somatic effect.

With respect to carcinogenesis, of the tissues exposed for which risk factors exist (marrow, thyroid, brain, salivary gland, and skin), the thyroid gland has the highest radiosensitivity. The probabilities for radiation-induced cancer, based on a straight-line dose-effect curve with no threshold, are 0.15 and

0.05 chances per million per year per mGy for adult females and males, respectively [11]. The risk factor for children is three times greater than for adults [11]. Assuming the worst theoretical risk for high-resolution-CT-based cancer induction gives a maximum risk of 0.45 chances per million per year. Comparing this with the probability of spontaneous occurrence of 400 thyroid cancers per million per year yields a theoretical worst-case increase in the chance of getting thyroid cancer of no more than 0.1% [12]. This small added risk could be further reduced through thyroid shielding during TMJ radiographic studies, especially in children.

The absolute radiation dose values of this study are only valid for our institution since radiation dose is a complex function of a number of variables. The radiographic technique may vary from one institution to another, but it is reasonable to expect that the relative grouping of these studies as high-, medium-, or low-dose would be maintained.

REFERENCES

- Hollender L, Lysell G. Radiation doses during roentgenography of the head. *Odontol Rev* 1964;15:15-22
- White SC, Rose TC. Absorbed bone marrow dose in certain dental radiographic techniques. *J Am Dent Assoc* 1979;98(4):553-558
- Schwartz HC, Wollin M, Leake DL, Kagan AR. Interface radiation dosimetry in mandibular reconstruction. *Arch Otolaryngol* 1979;105(5):293-295
- Murphy WA, Adams RJ, Gilula LA, Barbier JY. Magnification radiography of the temporomandibular joint: technical considerations. *Radiology* 1979;133:424-440
- Borglin K, Petersson A, Rohlin M, Thapper K. Radiation dosimetry in radiology of the temporomandibular joint. *Br J Radiol* 1984;57:997-1007
- Brooks SL, Lanzetta ML. Absorbed doses from temporomandibular joint radiography. *Oral Surg Oral Med Oral Pathol* 1985;59:647-652
- Archer BR, Bushong SC, Thornby JL. Multivariate analysis of TLD orientation effects. *Med Phys* 1980;5(4):352-354
- Manzione JV, Seltzer SE, Katzberg RW, Hammerschlag SB, Chiango BF. Direct sagittal computed tomography of the temporomandibular joint. *AJNR* 1982;3:677-679
- Manzione JV, Katzberg RW, Brodsky GL, Seltzer SE, Mellins HZ. Internal derangements of the temporomandibular joint: diagnosis by direct sagittal computed tomography. *Radiology* 1984;150:111-115
- Hall EJ. Radiation cataractogenesis. In: *Radiobiology for the radiologist*. New York: Harper & Row, 1978:349-356
- Committee on Radiological Units, Standards and Protection. *Medical radiation: a guide to good practice*. Chicago: American College of Radiology, 1985
- Gregg EC. Radiation risks with diagnostic x-rays. *Radiology* 1977;123:447-453

American Roentgen Ray Society 87th Annual Meeting April 26–May 1, 1987, Miami Beach, FL Fontainebleau-Hilton Hotel

Registration and Hotel Reservations

Forms for advance registration and hotel reservations will be in the February and March 1987 issues of the *AJR*.

Refresher Course Program

A summary of the refresher courses will appear in the *AJR* in January along with advance registration forms. Early registration is an advantage in assuring preferred courses in this popular program. Dr. J. T. Ferruci, Jr. is program director.

Local Program

A program of sightseeing, shopping, and entertainment will be developed by the Local Arrangements Chairman. Information and advance registration forms will be in the January and February issues of the *AJR*.

President's Award Papers

The society offers several cash awards for the best scientific papers prepared by residents in radiology. The President's Award has a \$1000 prize. There are two Executive Council awards of \$500 each. All are presented at the annual meeting. Papers should be submitted by Jan. 31 for consideration in this competition. Send entries to:

B. G. Brogdon, M.D.
Dept. of Radiology
University of South Alabama Medical Center
2451 Fillingim Street
Mobile, AL 36617

ARRS Membership Requirements

The American Roentgen Ray Society (ARRS) has two membership categories: active and in-training. For active membership, applicants must practice radiology in the U.S. or Canada. Each must have graduated in good standing from an approved medical school or hold an advanced degree in physical, chemical, or biological science and be certified by the American Board of Radiology, the Royal College of Physicians and Surgeons of Canada, or otherwise adequately document training and credentials.

A member-in-training must be in a radiology residency or postresidency fellowship program or be a postgraduate student in an allied science. Status must be verified by the program director.

For consideration during the 1987 ARRS meeting, completed applications must be received no later than Feb. 1. Obtain forms and details from:

Rosalind H. Troupin, M.D.
Department of Radiology
Hospital of University of Pennsylvania
3400 Spruce St.
Philadelphia, PA 19104

Associated Society Meetings

Society for Pediatric Radiology and European Society of Pediatric Radiology

The inaugural conjoint International Pediatric Radiology '87 meeting will meet May 30–June 4, 1987 at the Westin Hotel, Toronto, Ontario, Canada. Deadline for receipt of abstracts is February 1, 1987. For details contact: Donald R. Kirks, M.D., Secretary, Society for Pediatric Radiology, c/o Dept. of Radiology, Childrens Hospital Medical Center, Elland and Bethesda Aves., Cincinnati, OH 45229, (513) 559-4880

Deadlines

President's Award papers: January 31
Membership applications February 1

Scintigraphic Diagnosis of Sacral Fractures

Jesse Balseiro¹
Anne C. Brower
Harvey A. Ziessman

The H- or butterfly-pattern of uptake in the sacrum on Tc-99m-methylene diphosphonate bone scintigraphy is typical of fractures of the body of the sacrum that involve the sacral alae. This report describes four patients with a focal linear or curvilinear pattern of uptake in sacral fractures without alae involvement. This pattern differs from that associated with metastases in the sacrum, which typically has a random pattern. Recognition of this scintigraphic linear dot pattern of uptake in horizontal fractures in the inferior body of the sacrum is useful for detecting fractures without alae involvement that are not readily apparent on radiographs.

Fractures of the sacrum in persons who fall onto their buttocks are not uncommon [1, 2], especially when predisposing conditions that cause osteoporosis are present. Radiographic diagnosis is difficult because of the anatomic location, overlying soft tissues, and osteoporosis [1, 2]. Bone scans have been more useful in making this diagnosis [3-5].

The H- or butterfly-pattern of radionuclide uptake on bone scans has been described for fractures through the sacrum and sacral alae [3-5]. We have recognized another pattern: a series of focal areas of uptake (linear dot pattern) in horizontal fractures in the inferior part of the body of the sacrum without sacral alae involvement.

Materials and Methods

Three men and one woman were referred for whole-body bone scans to determine the cause of low-back pain. All four had sustained a recent fall. Their ages were 52, 75, 80, and 88 years. Three had a known primary malignancy. Two had had vertebral compression fractures before.

Bone scintigraphy was performed after an IV injection of 20 mCi (740 MBq) of Tc-99m-methylene diphosphonate. Beginning 3 hours after injection, an anterior chest image was acquired for 500,000 counts. A large-field-of-view gamma camera with a low-energy, parallel-hole collimator was used. Whole-body spot images of the head, chest, abdomen, pelvis, and extremities were then acquired for equal amounts of time. An inferior pelvic view also was obtained when indicated. Two patients had anteroposterior and lateral radiographs of the pelvis obtained before the bone scan; two had radiographs made after the bone scan.

Results

All four patients had abnormal uptake of Tc-99m-methylene diphosphonate in the inferior portion of the sacrum that appeared as a horizontal series of three to four focal dots of increased uptake distributed in a linear or curvilinear configuration (linear dot pattern) (Figs. 1A, 2A, and 3A).

In two patients radiographs taken before the bone scan were interpreted as normal. Review of these radiographs revealed subtle fractures of the sacrum corresponding to the abnormal uptake on the technetium scans. In the other two

Received April 21, 1986; accepted after revision August 26, 1986.

¹ All authors: Division of Nuclear Medicine, Department of Radiology, Georgetown University Hospital, 3800 Reservoir Rd., N.W., Washington, DC 20007. Address reprint requests to J. Balseiro.

AJR 148:111-113, January 1987
0361-803X/87/1481-0111
© American Roentgen Ray Society

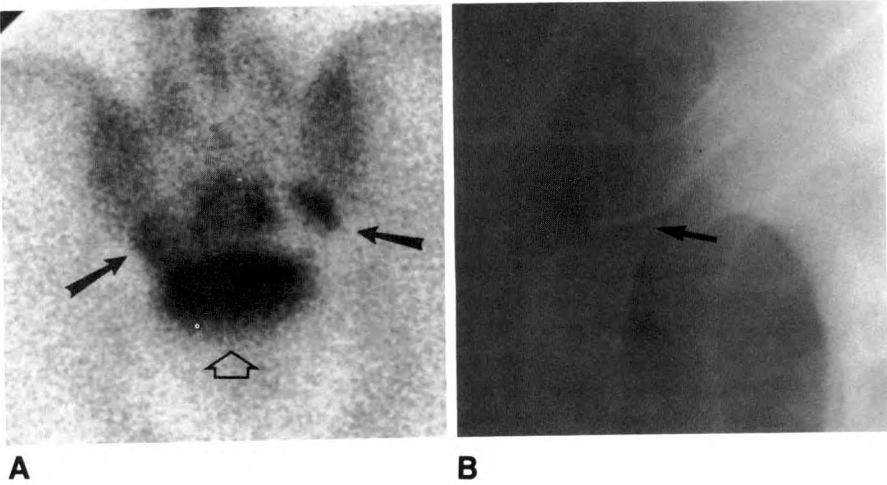


Fig. 1.—A, Tc-99m-methylene diphosphonate bone scan. Posterior view of pelvis shows bladder (open arrow) and four foci of increased activity linearly and horizontally in inferior sacral area (linear dot pattern [arrows]).
B, Lateral radiograph shows a fracture of inferior part of sacral body (arrow).

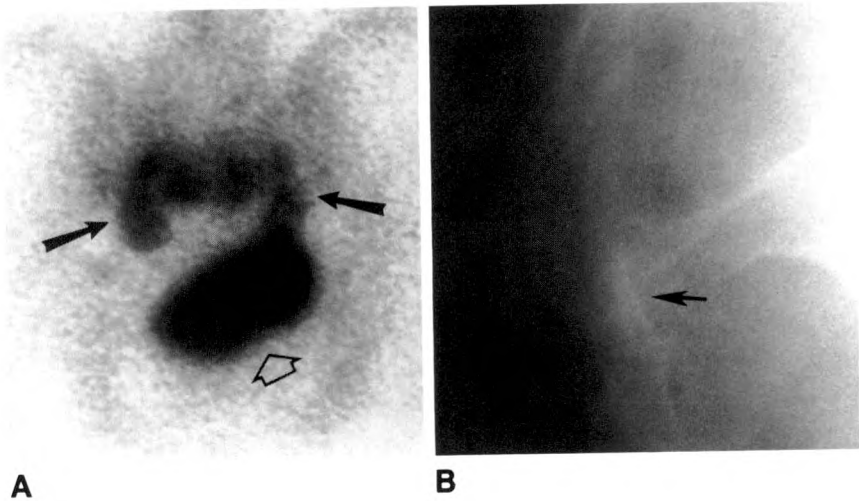


Fig. 2.—A, Tc-99m-methylene diphosphonate bone scan. Posterior view of pelvis shows bladder (open arrow) and four foci of increased activity in a curvilinear distribution in inferior sacrum (linear dot pattern [arrows]).
B, Lateral radiograph shows a fracture of inferior part of sacral body (arrow).

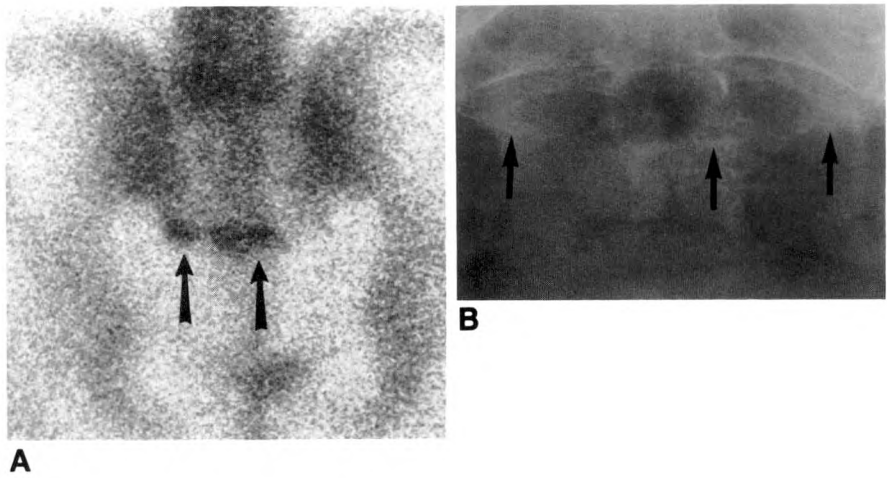


Fig. 3.—A, Tc-99m-methylene diphosphonate bone scan. Posterior view of pelvis shows three foci of increased activity distributed in a horizontal linear fashion in inferior part of sacrum (linear dot pattern [arrows]).
B, Anteroposterior radiograph shows a horizontal fracture in body of sacrum (arrows).

patients, review of radiographs made after the bone scans failed to show the fractures; however, coned-down radiographs were then obtained, and they showed horizontal sacral fractures that did not extend to the sacral alae.

Discussion

Isolated fractures of the sacrum apparently are more common than previously realized [6]. A history of trauma may be absent, or the injury may be minimal, especially when the patient falls in a sitting position. Various conditions, including osteopenia, radiation therapy, steroid therapy, and rheumatoid arthritis, may lead to sacral fractures without a history of trauma. In the absence of point tenderness, symptoms associated with sacral fractures are nonspecific (back pain is the most common complaint) [6].

Radiographic diagnosis of sacral fractures is often difficult, even with special oblique views. The curvature of the sacrum, overlying bowel gas, and osteoporosis often obscure the findings [1, 2]. The radionuclide bone scan is more sensitive because the area of abnormal uptake is easily recognized [7]. Once the bone scan has shown an abnormal area, special coned-down radiographs can usually corroborate the pres-

ence of a fracture.

The H- or butterfly-pattern of uptake in the sacrum on bone scintigraphy has been described as typical of fractures of the body of the sacrum involving the sacral alae [3-5]. This report demonstrates another characteristic scintigraphic pattern of sacral fracture that occurs when the sacral alae are not involved. This linear or curvilinear pattern differs from that associated with metastases in the sacrum, which typically has a random distribution of uptake.

REFERENCES

1. Bonnin JG. Sacral fractures and injuries to the cauda equina. *J Bone Joint Surg [Am]* **1945**;28:113-127
2. Laasonen EM. Missed sacral fractures. *Ann Clin Res* **1977**;9:84-87
3. Ries T. Detection of osteoporotic sacral fracture with radionuclides. *Radiology* **1983**;146:783-785
4. DeSmet AA, Neff JR. Pubic and sacral insufficiency fractures: clinical course and radiologic findings. *AJR* **1985**;145:601-606
5. Schneider R, Yacovone J, Ghelman B. Unsuspected sacral fractures: detection by radionuclide bone scanning. *AJR* **1985**;144:337-341
6. Cooper KL, Beabout JW, Swee RG. Insufficiency fractures of the sacrum. *Radiology* **1985**;156:15-20
7. Charkes ND, Young I, Sklaroff DM. The pathologic basis of the strontium bone scan. *JAMA* **1968**;206:2482-2488.

Categorical Course in Gastrointestinal Radiology
American Roentgen Ray Society 87th Annual Meeting

April 26–May 1, 1987, Miami Beach, FL, Fontainebleau Hilton Hotel

Program Chairman: *Gary G. Ghahremani, Evanston, IL; (312) 492-6556*

Program Co-Chairman: *Richard M. Gore, Chicago, IL; (312) 908-5138*

Sunday, April 26

- 10:00–10:45 a.m. Mucosal lesions of the esophagus: evaluation by double-contrast radiography (*Levine*)
- 10:45–11:15 a.m. Motility disorders of the esophagus (*Ott*)
- 11:15–Noon Radiological evaluation of the gastric mucosa (*Gelfand*)
- Break
- 1:30–2:00 p.m. Mucosal abnormalities of the duodenum (*Glick*)
- 2:00–3:00 p.m. Complications of pancreatitis: radiological diagnosis and management (*Freeny*)
- Break
- 3:30–4:00 p.m. Sonography of the hepatobiliary tract: an update (*Laing*)
- 4:00–4:30 p.m. CT of the hepatobiliary tract: current concepts (*Moss*)
- 4:30–5:00 p.m. MRI of the hepatobiliary tract (*Ferrucci*)

Monday, April 27

- 1:30–2:15 p.m. Interventional techniques in the gastrointestinal tract (*vanSonnenberg*)
- 2:15–3:00 p.m. Interventional techniques in the diagnosis and management of abdominal fluid collections, abscesses, and tumors (*Mueller*)
- 3:00–3:30 p.m. Gastrointestinal manifestations of AIDS (*Berk*)
- Break
- 4:00–4:30 p.m. MRI of retroperitoneum, pancreas, and gut (*Goldberg*)
- 4:30–5:30 p.m. Current concepts in small-bowel radiography (*Maglinte*)

Tuesday, April 28

- 4:00–4:45 p.m. CT of acute gastrointestinal disorders (*Federle*)
- 4:45–5:30 p.m. CT staging and follow-up of gastrointestinal malignancies (*Megibow*)

Wednesday, April 29

- 4:00–4:40 p.m. Radiological diagnosis of colorectal neoplasms (*Goldstein*)
- 4:40–5:10 p.m. Inflammatory bowel disease: initial radiographic manifestations (*Laufer*)
- 5:10–5:30 p.m. CT features of inflammatory bowel disease (*Gore*)

Thursday, April 30

- 4:00–4:45 p.m. Functional evaluation of the gastrointestinal tract by scintigraphy (*Malmud*)
- 4:45–5:30 p.m. Gastrointestinal complications of diagnostic and therapeutic procedures (*Ghahremani*)

Intraabdominal Hematoma: The Concentric-Ring Sign in MR Imaging



Peter F. Hahn¹
Sanjay Saini
David D. Stark
Nicholas Papanicolaou
Joseph T. Ferrucci, Jr.

Extracranial hematomas have variable CT appearances and may be confused with other entities. MR imaging of 12 patients with intraabdominal or intrapelvic hemorrhages showed that intraabdominal hematomas develop a unique MR appearance after 3 weeks. Nine hematomas imaged after this time all showed a characteristic concentric-ring configuration, with a thin, dark peripheral rim on all pulse sequences and a bright inner ring most distinctive on T1-weighted images. Six hematomas imaged during the first 3 weeks failed to show this architecture. The concentric rings in MR images of chronic hematomas allowed a tissue-specific diagnosis.

CT has become the preferred imaging technique for evaluation of hemorrhage. Increased X-ray attenuation relative to other soft tissues (hyperdensity) allows a specific diagnosis of recent hemorrhage in many cases. However, hematomas in extracranial sites are quite variable in CT appearance and may be confused with tumors or nonhemorrhagic fluid collections, particularly in patients without a suggestive history of trauma or coagulopathy. Acutely hyperdense hematomas become isodense or hypodense as sedimented blood and fibrinous clot are reabsorbed; after 2 or 3 weeks a specific diagnosis of abdominal hematoma by CT may be impossible [1].

A characteristic MR feature of subacute intracranial hematoma has been described: a dark peripheral rim and a more central bright ring that fills in towards the center as the lesion matures [2]. Early reports of hematoma in extraaxial locations also noted occasional annular architecture and a variable halo of either long T1 or long T2 [3, 4]. However, no consistent relationship between the age of the hematoma and its structure was shown.

Recently we reported two patients whose duodenal hematomas had a highly characteristic MR appearance [5]. The findings suggested that MR might help to diagnose hematomas that appear as chronic mass lesions within the abdomen and motivated a review of MR and CT images of 14 well-documented abdominal hematomas. We attempted to determine the effect of location, cause, and age on the appearance of the hematoma with various pulse sequences. Architectural features of abdominal hematomas were correlated with the previously described MR appearance of hematomas in the nervous system.

Materials and Methods

Twelve patients with intraabdominal or intrapelvic hemorrhage underwent MR imaging for clinical indications. One patient had three hematomas. Two patients were imaged serially. Eight hematomas were proven by surgery or percutaneous aspiration. In the other six cases, the diagnosis was based on compelling clinical evidence and CT findings. In each case, the cause and time of onset of hemorrhage were known. Hemorrhage into or adjacent to a tumor was excluded from consideration. Table 1 summarizes the cases by location, cause, time elapsed after hemorrhage, and method of verification.

MR imaging was performed by using a whole-body Technicare imager (Solon, OH) operated at 0.6 T with a corresponding proton resonance frequency of 25.4 MHz. This system has

Received April 28, 1986; accepted after revision July 21, 1986.

Presented in part at the annual meeting of the Society for Magnetic Resonance Imaging, Philadelphia, March 1986.

¹ All authors: Department of Radiology, Massachusetts General Hospital, Boston, MA 02114. Address reprint requests to P. F. Hahn.

AJR 148:115-119, January 1987
0361-803X/87/1481-0115

© American Roentgen Ray Society

TABLE 1: MR Imaging of Intraabdominal Hematomas

Age (yr)	Gender	Location	Cause	Time Elapsed until Imaging	Verification Method	Appearance on MR
65	M	Perirenal	Shock lithotripsy	1, 5, 10, and 40 days	CT, Hct	Developed ring at 40 days
70	F	Rectus sheath	Anticoagulation	1, 4, 21, and 72 days	CT, aspiration	Level, then ring at 21 days
30	F	Spleen	Trauma	3 days	CT	Invisible by MR
13	M	Spleen (subcapsular)	Trauma	3 days	CT	Long T2
75	F	Iliacus	Anticoagulation	3-5 days	CT, Hct	Fluid level
40	M	Iliopsoas	Exertion	18 days	Surgery	Streaks of short T1
71	M	Duodenal wall	Idiopathic	3 weeks	Clinical onset, CT f/u	Ring
58	M	Duodenal wall	Surgery	3 weeks	Reexploration	Ring
60	F	Rectus sheath	Anticoagulation	6 weeks	Aspiration	Ring
83	M	Iliac aneurysm (2)	Surgical isolation	7 weeks	Surgery	Rings in both
		Psoas	Surgery	7 weeks	Aspiration	Ring
19	F	Liver	Biopsy	10 weeks	Repeat biopsy	Irregular ring
65	M	Adrenal	Spontaneous	11 months	Clinical onset, CT f/u	Ring (punctate center)

Note.—Hct = hematocrit; f/u = follow-up.

been described in detail previously [6]. Patients were imaged in a saddle-shaped body coil with a useful aperture of 65 cm. Multislice images with relative T1 weighting were obtained by using both spin-echo (TR 250–500 msec, TE 18–30 msec) and (in most cases) inversion recovery (TR 1500, TI 450 msec, TE 30) techniques (TR = recovery time; TE = echo time; TI = inversion time). Images with T2 weighting were obtained by using a multiecho pulse sequence (TR 1650–2350, TE 60–180). The term *SE 2000/60/2* is used to indicate a spin-echo sequence with repetition rate of 2000 msec and echo time of 60 msec, averaging two excitations.

Contemporary CT scans or sonograms were available for all patients. CT scans were performed by using late-generation whole-body scanners.

Results

Hematomas with Rings (Chronic Hematomas)

Nine hematomas in seven patients were imaged between 3 and 10 weeks after hemorrhage. All nine hematomas exhibited a characteristic concentric ring (Figs. 1 and 2). Rings developed after 3 weeks in two patients first imaged during the acute period (Figs. 3 and 4). At the periphery was a 2- to 4-mm rim with a low signal on all images. This peripheral rim did not always extend around the entire circumference. The rim appeared to coincide with the pseudocapsule sometimes visible on the CT scans. Immediately within this peripheral rim was a ring of high signal intensity visible with all pulse sequences. On T1-weighted images, this high-intensity ring was sharply demarcated peripherally but sometimes ill defined centrally. On T2-weighted images, the bright ring faded gradually towards the center.

In all of these chronic hematomas, the central core occupied most of the volume. On T1-weighted images, the center appeared homogeneous, with intensity slightly greater than muscle. On T2-weighted images, the intensity of the central

region was higher than muscle but less intense than the surrounding ring. With narrow window settings, a gradient of intensity lowest at the center could be perceived on the T2-weighted acquisitions.

Once established, the concentric-ring pattern tended to persist over time. The rings in a large rectus hematoma were stable upon reimaging at 9 weeks despite a 50% decrease in the size of the lesion. A small adrenal hemorrhage was intensely bright on both T1- and T2-weighted images 11 months after onset of adrenal apoplexy; a punctate center of lower signal remained.

Hematomas without Rings (Acute Hematomas)

MR imaging of six patients with intraabdominal hemorrhage was performed between 1 and 20 days after the hemorrhagic event. In five cases, the lesion was discernible on both T1- and T2-weighted images as a space-occupying mass. A splenic laceration readily visible on noncontrast CT was not detected with MR. Unlike the chronic hematomas, none of the lesions imaged during the first 3 weeks had a ring pattern.

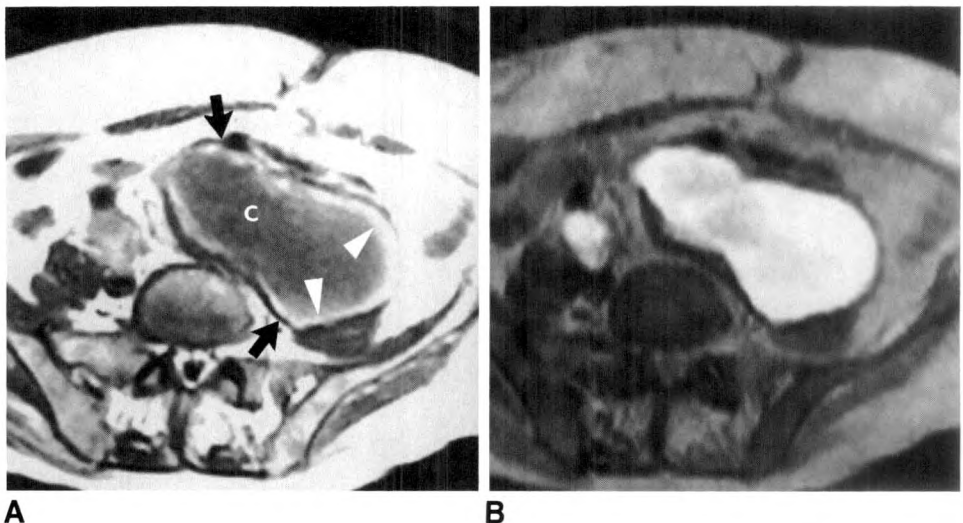
T1-weighted images showed that acute hematomas had a signal intensity slightly higher than adjacent muscle. After the first few days, bright streaks became visible (Fig. 3). Large, acute hematomas with a fluid-fluid ("hematocrit") level on CT also had a level on T1-weighted MR images, with greater signal in the dependent layer (Fig. 4).

On T2-weighted pulse sequences, the smaller acute hematomas showed increased intensity similar to other fluids. Fluid levels in the larger hematomas were visible on strongly T2-weighted pulse sequences. Compared with the T1-weighted images, the relationship of signal intensities on T2-weighted images was reversed; the superior layer had the higher intensity. This suggested that the dependent layer had shorter T1 and T2 relaxation times than the supernatant fluid.

Fig. 1.—MR images of hematoma associated with left iliac artery aneurysm surgically isolated 7 weeks earlier.

A, SE 310/20/12 (T1-weighted) shows a dark rim (arrows) surrounding a bright ring (arrowheads). Central core (C) is of intermediate intensity.

B, On SE 2000/60/2 (T2-weighted) image, inner bright ring merges imperceptibly with central core.



Discussion

In MR diagnosis of hematoma, both the internal architecture and the temporal evolution of the lesion are important. Our series shows a characteristic MR appearance of abdominal hematomas, the concentric-ring sign, that develops as early as 3 weeks after hemorrhage. The concentric-ring sign is best recognized on T1-weighted images. Surrounding a central core of intermediate signal are two discrete concentric rings. The inner ring is bright, indicating short T1. The outer rim is dark on all pulse sequences, consistent with a short T2. In one case in which the surgical specimen was made available, the hematoma consisted of a gelatinous clot surrounded by fluid. Analysis of the fluid *in vitro* showed a relatively short T1 of 650 msec [5]. Our findings are consistent with studies of intracranial hematoma, in which the short T1 has been attributed to paramagnetic effects of hemoglobin degradation products such as methemoglobin [7]. Hemosiderin digested by phagocytic cells surrounding the hematoma may account for the dark rim of short T2 [2].

The concentric-ring sign in our series was a sensitive indicator of the maturing abdominal hematoma. The sign developed reliably about 3 weeks after hemorrhage and was not present earlier. We did not see concentric rings in nearly 300 patients who had nonhemorrhagic abdominal masses or fluid collections imaged by MR. The concentric-ring sign therefore may be a tissue-specific MR characteristic of hematomas.

Large abdominal hematomas that develop the concentric-ring configuration continue to exhibit it for several months; gradually the central area of low signal intensity may fill in from the periphery with higher signal intensity [4]. The timing of this phenomenon is thus more indolent than in the brain, where the ring appears and then fills in completely within a few weeks of hemorrhage [2]. Both the rate of cell lysis and the local oxygen tension affect the formation of methemoglobin within a hematoma. Oxygen partial pressures both above and below 20 torr retard the reaction [2]. The smaller size of most intracranial lesions, presence of the blood-brain barrier, and absence of fibrous tissue in the gliotic response to hemorrhage are differences between intracranial hematomas and extracranial ones. Any of these differences could affect the redox potential within a hematoma and so modify the evolution of the bright methemoglobin ring.

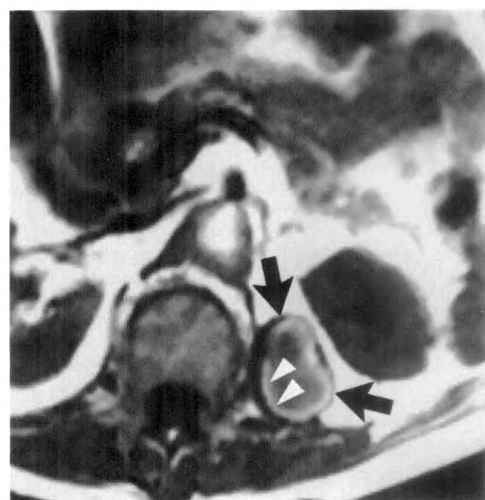


Fig. 2.—SE 310/20/12 MR image of left psoas hematoma after 7 weeks (same patient as in Fig. 1) shows bright ring (arrowheads) immediately central to dark rim (arrows).

Some pitfalls and limitations exist in using MR to detect and diagnose abdominal hematomas. Early in the acute period hematomas may be isointense with adjacent tissue on T1-weighted images. By using T2-weighted pulse sequences, all of the hematomas presenting as space-occupying masses were readily detected in our series. Hemorrhage into a tissue plane or potential space is detected more easily than intraparenchymal hemorrhage by MR and is probably more likely to develop the ring sign.

The MR appearance of hematomas changes progressively during the acute period. Hematomas are initially isointense with muscle on T1-weighted pulse sequences and become more intense as the T1 falls; inhomogeneous streaks are present by the end of the first week. Although bright streaks in a mass on T1-weighted images may suggest the presence of blood, the MR appearance of acute hematomas is nonspecific. Both abscesses and solid tumors can mimic hematomas at this stage. Fluid-fluid levels due to settling of debris within

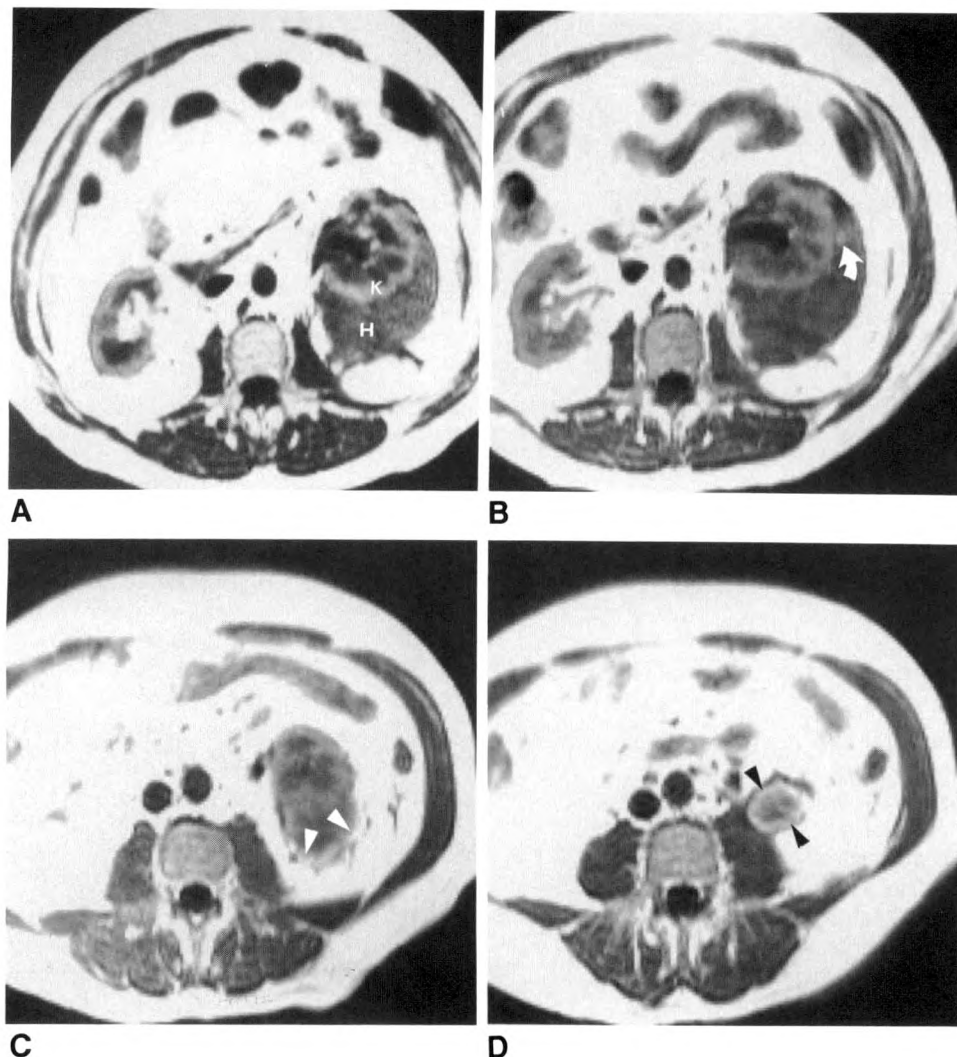


Fig. 3.—SE 310/20/14 (T1-weighted) serial MR images of perinephric hematoma after extracorporeal shockwave lithotripsy.

A, At 1 day, hematoma (H) is isointense with medulla of kidney (K).

B, 9 days later, bright streaks (arrow) have appeared within the hematoma.

C, After 40 days, peripheral bright ring has formed (arrowheads).

D, Ring in C (arrowheads) is better seen in this section caudad to lower renal pole.

an abscess can simulate the appearance of sedimented blood. The dependent portion of both abscesses and acute hematomas often will have a higher protein content and therefore have shorter T1 and T2 relaxation times than the supernatant fluid. Such diamagnetic relaxation [8] due to cells, debris, and proteins is nonspecific and cannot be distinguished from paramagnetic effects of sedimented erythrocytes. These imaging findings agree with previous *in vitro* work that showed that acute hematomas and nonhemorrhagic fluid collections have overlapping distributions of relaxation parameters [9].

A solid mass or fluid collection occasionally may be surrounded by fat, giving a very bright ring on T1-weighted images (Fig. 5). In this situation, the outer dark rim is absent, and the bright ring will be the same intensity as subcutaneous fat on all pulse sequences, whereas hematomas are brighter than fat on T2-weighted images. These features should permit distinction from the ring sign of hematoma described here.

Chemical shifts can produce a dark crescent along one edge of a mass and a bright crescent along the opposite edge. These artifacts never overlap each other and attain maximal width in the frequency encoded dimension. In the rare situation in which chemical-shift artifacts present a prob-

lem in differential diagnosis, turning the patient or reversing the gradient axes will differentiate artifact from hematoma.

Hemorrhage into large necrotic tumors or hemorrhage after tumor biopsy may appear as bright globules or streaks on T1-weighted images. We have not observed the ring sign in such cases. However, until more information is available, patients with an unexplained hematoma exhibiting the concentric-ring sign should be followed carefully. Similarly, recognition of the ring sign should not delay aspiration and culture of any hematoma thought to be infected.

A chronic extracranial hematoma may appear as a mass of uncertain cause. The ring sign appears in abdominal hematomas at the time when the CT appearance often becomes nonspecific. Our series includes two cases in which the presence of a ringed mass on the MR permitted a diagnosis of hematoma when the conventional evaluation had left the issue in doubt. We have seen another example, in the mediastinum, of a hematoma that was first recognized by its ring on MR imaging and that was followed to resolution without intervention. Use of the ring sign thus may extend beyond the abdomen to the diagnosis of occult hematoma in other extracranial locations.

Fig. 4.—Rectus sheath hematoma. CT (A) and SE 500/30/4 (T1-weighted) MR image (B) show fluid-fluid gravity level first day after hemorrhage.

C, On sagittal SE 2000/120/2 (T2-weighted) MR image, relative intensity of two components is reversed; superior component is brighter.

D, T1-weighted MR image 3 weeks after hemorrhage shows development of concentric-ring appearance with dark rim (arrows), bright ring (arrowheads), and intermediate central core (C).

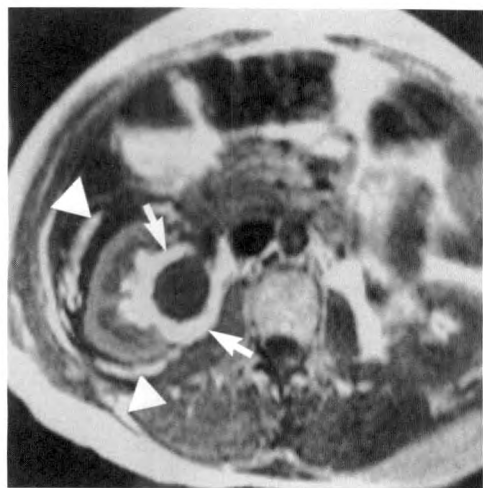
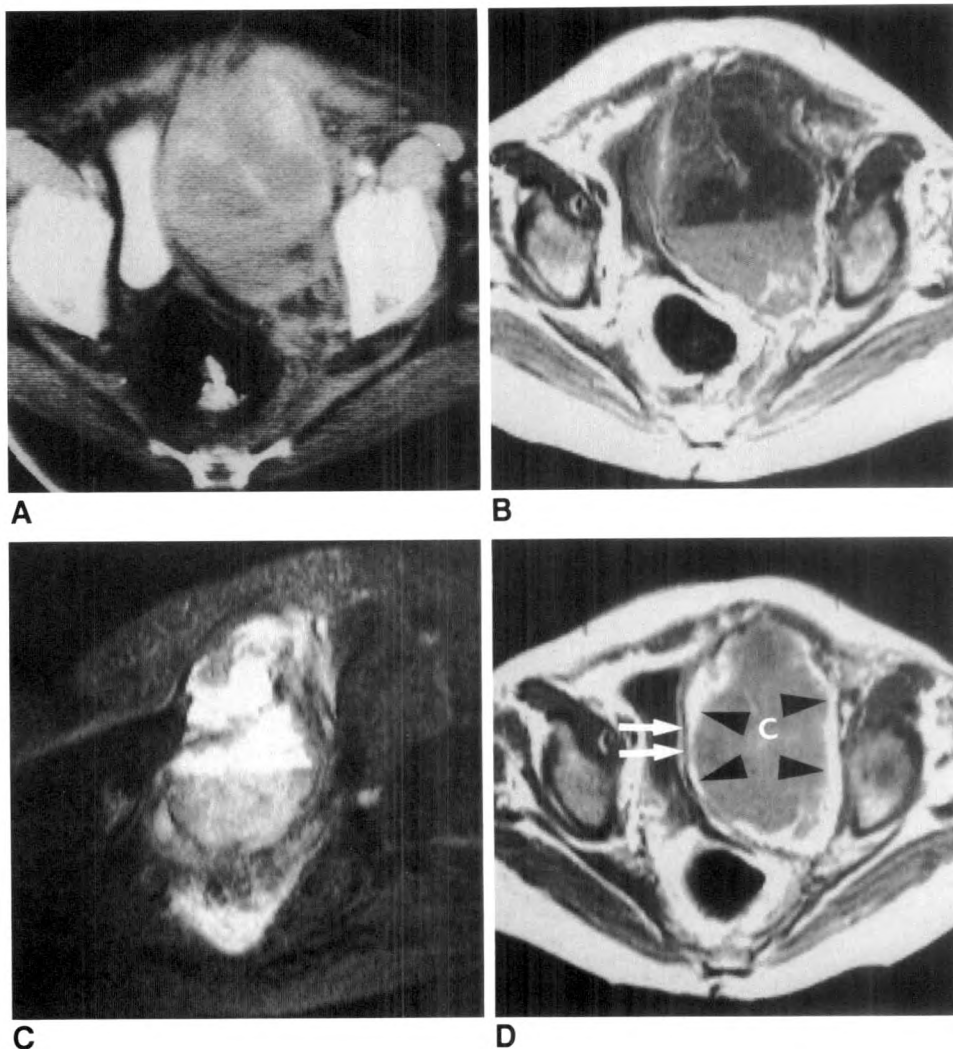


Fig. 5.—Hydronephrosis and urinoma, illustrating a diagnostic pitfall. SE 300/32/8 (T1-weighted) MR image shows bright ring of perinephric fat (arrowheads) displaced from kidney by extravasated urine. Parapelvic fat (arrows) surrounds dilated renal pelvis. Appearance is similar morphologically to hematomas demonstrating the ring sign.

REFERENCES

- Swensen SJ, McLeod RA, Stephens DH. CT of extracranial hemorrhage and hematomas. *AJR* 1984;143:907-912
- Gomori JM, Grossman RI, Goldberg HI, Zimmerman RA, Bilaniuk LT. Intracranial hematomas: imaging by high-field MR. *Radiology* 1985;157:87-93
- Swensen SJ, Keller PL, Berquist TH, McLeod RA, Stephens DH. Magnetic resonance imaging of hemorrhage. *AJR* 1985;145:921-927
- Unger EC, Glazer HS, Lee JKT, Ling D. MRI of extracranial hematomas: preliminary observations. *AJR* 1986;146:403-407
- Hahn PF, Stark DD, Vici L-G, Ferrucci JT, Jr. The ring sign in MR imaging of duodenal hematoma. *Radiology* 1986;159:379-382
- Stark DD, Felder RC, Wittenberg J, et al. Magnetic resonance imaging of cavernous hemangioma of the liver. *AJR* 1985;145:213-222
- Bradley WG, Jr, Schmid PG. Effect of methemoglobin formation on the MR appearance of subarachnoid hemorrhage. *Radiology* 1985;156:99-103
- Gadian DG. *Nuclear magnetic resonance and its applications to living systems*. New York: Oxford Univ. Press, 1982
- Brown JJ, vanSonnenberg E, Gerber KH, Stritch G, Wittich GR, Slutsky RA. Magnetic resonance relaxation times of percutaneously obtained normal and abnormal body fluids. *Radiology* 1985;154:727-731

Forthcoming ARRS Meeting Information

Details of the American Roentgen Ray Society Meeting in Miami Beach, FL, April 26–May 1, 1987, will appear in the **February** and **March** 1987 issues of the *AJR*. The complete scientific program, abstracts of the instructional courses, information about social events, and hotel and travel forms will be published in the Journal.

Sonographic Localization of Hematomas in Hemophilic Patients with Positive Iliopsoas Sign

M. Graif¹
U. Martinovitz
S. Strauss
M. Heim
Y. Itzhak

Sonography was performed on 23 hemophilic patients presenting with positive iliopsoas sign. In 21 of these patients sonography confirmed the presence of hematomas. Comparison of the presumed clinical location and the sonographic location, however, revealed a significant discrepancy. Only seven of 15 hematomas that were clinically suspected to be in the iliopsoas muscle were confirmed by sonography at that location. Of the remaining cases, three were localized in the hip joint, one in the proximal thigh, one in the abdominal wall, and one in the iliac fossa. Hemorrhage was not found in two cases. This study indicates that sonography provides valuable information about the site of hematoma in these patients.

Eighty percent of bleeding episodes in hemophilic patients occur within the musculoskeletal system [1]. The muscles of the retroperitoneum, abdominal wall, and extremities, as well as joints, are usually involved [2]. Nonspecific signs such as positive iliopsoas test, regional tenderness, irradiating pain, and muscular spasm are not sufficiently accurate to confirm and assess the presence, extent, and exact location of hemorrhaging in these areas [3-5].

The use of sonography for the detection of hematoma in the groin and adjacent areas was evaluated. The sonographic findings were correlated with the initial clinical diagnosis in order to assess the contribution of this imaging technique in localizing the hematoma. A possible regimen for the sonographic approach to the hemophilic patient presenting with a positive iliopsoas sign is recommended.

Materials and Methods

A total of 350 hemophilic patients underwent follow-up examinations at the Israel Hemophilic Center. During the past 3 years, 23 of these patients (mean age, 19 years) were referred for sonographic evaluation of the groin and adjacent areas for suspected bleeding. All 23 patients presented with a positive iliopsoas sign and pain in the groin. The iliopsoas test was considered positive if pain was elicited when the supine patient tried to flex the thigh against the resistance of the examiner's hand. Associated flexion contracture of the hip was present in six patients, four patients complained of back pain, and three had signs of femoral neuropathy. One patient had diffuse swelling of the upper thigh, and another had a localized mass palpable in the groin.

Sonography was performed within 6 to 24 hr after the onset of the symptoms. Commercially available static and real-time sonographic equipment was used, with transducer frequencies ranging from 3.5 to 10 MHz. In children and thin subjects, a Picker Microview (Picker Corp., Northford, CT) high-resolution small-parts scanner with a 10-MHz transducer was used for the study of joints and superficial muscles.

An intramuscular hematoma was considered loculated when seen as a focal anechoic or hypoechoic area with relative posterior acoustic enhancement. Additional features for identification of loculated hematomas included displacement of muscular fibers and fascial planes. The hemorrhage was considered to be diffuse (interstitial) when the involved muscle was increased in thickness and differed in echogenicity in comparison with the contralateral muscle, but internal striations representing muscle fibers and fasciculi were preserved [6].

Received January 6, 1986; accepted after revision June 30, 1986.

¹ All authors: Chaim Sheba Medical Center and Sackler School of Medicine, Tel Aviv University, Tel-Hashomer 52621, Israel. Address reprint requests to M. Graif.

AJR 148:121-123, January 1987
0361-803X/87/1481-0121
© American Roentgen Ray Society

The hip joint was evaluated in both transverse and longitudinal planes, and the extraarticular portion of the capsule was imaged to its insertion into the femur at the peritrochanteric level. The width of the intracapsular space, its contents, and the configuration of the capsule were assessed and compared with the contralateral joint.

Results

The results of clinical tests and sonography are compared in Table 1. The location of the hemorrhage was suspected clinically to be iliopsoas in 15 patients, within the muscles of the thigh in five cases, within the hip joint in three cases, and retroperitoneal (extramuscular) in two patients. In one additional patient, subperiosteal hemorrhage was suggested on a radiograph of the femur after trauma to the thigh. In three of these patients hemorrhage was suspected in more than one site.

Twenty-four structures with sonographic findings consistent with hematomas were detected. Their anatomic site was correlated with the suspected clinical location. Of 15 clinically suspected lesions in the iliopsoas muscle, only seven were confirmed by sonography in this location (Fig. 1). Of the remaining eight, three were located sonographically in the hip

joint (Fig. 2), one intraperitoneally in the iliac fossa, one in the proximal thigh musculature, and one in the low-anterior abdominal wall (Fig. 3). Two examinations were negative.

Intraarticular hemorrhage in the hip joint was suspected clinically in three patients. Sonography demonstrated all of these, in addition to three others that were suspected to be in the iliopsoas muscle (Fig. 2). Articular puncture was performed in two of the patients, and fresh blood was aspirated with consequent relief of pain.

Five hematomas were clinically suspected to be in the thigh musculature. Of these, sonography showed four to be intramuscular (Fig. 4) and showed one beneath the periosteum of the femur. Subperiosteal bleeding was found in two patients. Its location was correctly predicted in one patient in whom a radiograph showed periosteal elevation. In the other case it was suspected to be in the thigh musculature. Extramuscular retroperitoneal hemorrhage was suspected in two cases, both of which were confirmed by sonography.

Analysis of the pattern in 11 intramuscular hematomas (extremities and iliopsoas muscles) showed a completely anechoic lesion in three cases and mixed-type lesions (basically anechoic with irregular internal echogenic foci, possibly blood clots) in four cases. All seven cases were suggestive of loculated intramuscular hematomas. The internal muscular pattern was conserved in four cases, suggesting a diffuse (interstitial) hemorrhage.

TABLE 1: Comparison of the Clinical and Sonographic Location of the Hemorrhage

Anatomic Area	Suspected Clinical Location	Sonographic Location
Iliopsoas muscle	15	7
Extremity muscles (thigh)	5	5
Hip joint	3	6
Retroperitoneum (extramuscular)	2	2
Subperiosteal	1	2
Anterior abdominal wall	0	1
Iliac fossa (intraperitoneal)	0	1
Total	26	24

Discussion

Pathologic processes in the inguinal region and adjacent areas of the body may present a difficult diagnostic problem. Hip flexion contracture and a positive iliopsoas sign may indicate hemorrhage into the hip joint, the rectus femoral muscle, the iliopsoas muscle, or even the anterior abdominal wall [1, 3, 5]. Accurate localization of the hematoma is important in the management of these cases. Hemarthrosis, in which the hemorrhage is self-limiting, does not usually require

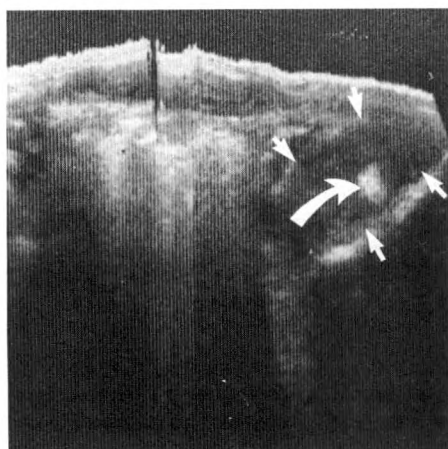


Fig. 1.—Iliopsoas hematoma. Transverse sonogram of pelvis shows thickening of left iliopsoas muscle (short arrows) and lateral displacement of femoral nerve complex (curved arrow).

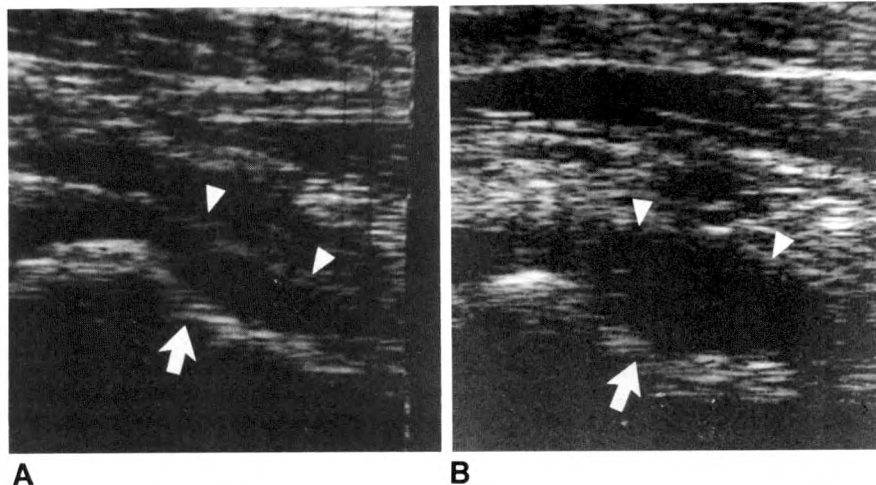
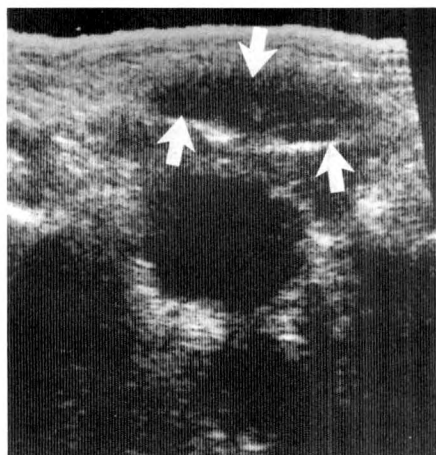


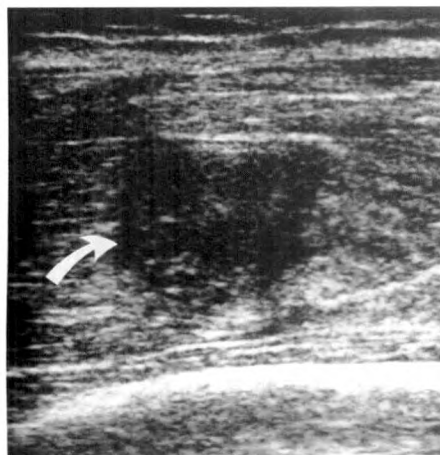
Fig. 2.—Hemarthrosis of the hip.
A, Sagittal high-resolution sonogram (10 MHz) of normal hip joint. Note bone (arrow) and joint capsule (arrowheads).
B, Sonogram of contralateral, painful hip joint. Capsule has a convex configuration (arrowheads), with increased width of intracapsular space. Arrow = bone.

Fig. 3.—Abdominal-wall hematoma. Transverse sonogram of pelvis showing a hypoechoic fusiform mass (arrows) within anterior abdominal wall.



3

Fig. 4.—Intramuscular hematoma of thigh. A well-defined hypoechoic mass (arrow) is seen, with disruption of normal muscular structure.



4

prolonged systemic treatment. In order to prevent aseptic necrosis of the femur epiphysis or hip dislocation, however, joint aspiration is recommended. Intramuscular hematomas, however, tend to be much larger in volume and often recur, and the prolonged use of factor VIII is required to maintain hemostasis [7–11].

Sonographic experience in the evaluation of hemophilic patients was first reported in 1977 by McVerry et al. [2]. Several later reports analyzed the sonographic features of soft-tissue and muscular hematomas [5, 6, 11, 12]. Thickening of the muscle with conservation of the internal muscular pattern was described in cases with interstitial intramuscular hematomas, whereas anechoic lesions with posterior acoustic enhancement were considered to be loculated hematomas [6]. Echogenic structures within the latter type of hemorrhage were attributed to clot formation [6, 12]. A recent report describes expansion of the hip-joint space in cases of hemarthrosis [12].

In our study, we compared the suspected clinical diagnosis with the sonographic findings. In most cases (21 of 23), sonography demonstrated the presence of a hematoma. There was a significant discrepancy between the clinical and sonographic localization of the hemorrhage, however, which was most obvious in the group of patients with suspected iliopsoas bleeding. The presumed clinical localization within the iliopsoas muscle was confirmed by sonography in only seven of 15 cases. In the remaining eight cases sonography showed evidence of bleed into the hip joint (three cases), anterior abdominal wall (one case), iliac fossa (one case), and thigh muscle (one case). Two examinations were negative.

In addition to the anatomic localization of the hemorrhage, the sonographic examination provided information about the nature of the hematoma. Seven of the 11 intramuscular hematomas were considered loculated and the other four were considered to be diffuse (interstitial). Differentiation between these two types of intramuscular hemorrhage may be useful because aspiration of a loculated hematoma can be performed to relieve severe pain caused by compression of adjacent tissues and nerves. The extent of the hemorrhage was grossly assessed by measurement of the dimensions and degree of displacement of adjacent anatomic structures. An accurate volumetry was not considered feasible owing to the imperfect geometric configuration of most of the hematomas, but an early posthemorrhagic sonogram was found

very useful in follow-up for the establishment of a baseline image of size.

The results of this study indicate that sonography provides valuable information regarding the site of the hematoma in the hemophilic patient. It is recommended that sonographic examinations of these patients include—in addition to the iliopsoas muscle—the retroperitoneal space, iliac fossa, anterior abdominal wall, hip joint, and thigh musculature and osseous components. The possibility of a hemorrhage occurring simultaneously in more than one site should not be overlooked.

REFERENCES

1. Duthie RB, Matthews JM, Rizza CR, Steel WM. *The management of musculo-skeletal problems in the hemophilias*. Oxford: Blackwell Scientific Publ., 1972:65–68
2. McVerry BA, Voke J, Vicary FR, Dormandy KM. Ultrasonography in the management of hemophilia. *Lancet* 1977;1:872–874
3. Duthie RB, Matthews JM, Rizza CR, Steel WM. *The management of musculo-skeletal problems in the hemophilias*. Oxford: Blackwell Scientific Publ., 1972:36, 56, 58
4. Goodfellow J, Fiearm CB, Matthews JM. Iliacus hematoma, a common complication of hemophilia. *J Bone Joint Surg [Br]* 1967;49:748–756
5. Shirkhoda A, Mauro MA, Staab EV, Blatt PM. Soft tissue hemorrhage in hemophilic patients. *Radiology* 1983;147:811–814
6. Aspelin P, Pettersson H, Sigurjonsson S, Nilsson IM. Ultrasonographic examination in muscle hematomas in hemophiliacs. *Acta Radiol [Diagn] (Stockh)* 1984;25:513–516
7. Heim M, Horoszowski H, Seligsohn U, Martinovitz U, Strauss S. Iliopsoas hematoma—its detection and treatment with special reference to hemophilia. *Arch Orthop Trauma Surg* 1982;99:195–197
8. Floman Y, Aiska M. Dislocation of the hip joint complicating repeated hemarthrosis in hemophilia. *J Pediatr Orthop* 1983;3:99–100
9. Winston ME. Hemophilic arthropathy of the hip. *J Bone Joint Surg [Br]* 1952;34:412–420
10. Tietjens BR, Gray DH, Berry EW. Avascular necrosis of the femoral head in a mild hemophilic. *J Bone Joint Surg [Br]* 1985;67:675
11. Kumari S, Fulco JD, Karayalcin G, Lipton R. Gray scale ultrasound: evaluation of iliopsoas hematomas in hemophiliacs. *AJR* 1979;133:103–106
12. Kinnas PA, Woodham CH, MacLarnon. Ultrasonic measurements of hematomata in joints and soft tissues in the hemophilic. *Scand J Haematol [Suppl]* 1984;33[Suppl. 40]:225–235

Genitourinary Imaging Update

American Roentgen Ray Society Annual Meeting Friday Symposium

May 1, 1987, Fontainebleau Hilton, Miami Beach, FL

Introduction

8:00 a.m.

Moderator: David S. Hartman

Moderator: Harry Z. Mellins

Contrast Media—The New Agents

8:05 a.m.

When and where? (*McClennan*)

8:25 a.m.

Why? (*Lalli*)

Interventional

8:45 a.m.

Stone disease (*Pfister*)

Pediatrics

9:05 a.m.

Imaging the child's urinary tract in 1987 (*Lebowitz*)

Ultrasonography

9:25 a.m.

Update in obstetrical ultrasound (*Pretorius*)

9:45 a.m.

Ultrasound evaluation of fetal GI and GU tract (*Manco-Johnson*)

10:05 a.m.

Prostate (*Rifkin*)

10:25 a.m.

Coffee break

Nuclear Medicine

10:50 a.m.

State-of-the-art (*Thrall*)

CT/MR Imaging

11:10 a.m.

Trauma (*Federle*)

11:30 a.m.

Bladder, prostate, and cervix (*Thornbury*)

11:55 a.m.

Adrenal (*Dunnick*)

12:15 a.m.

Renal lesions (*Newhouse*)

Hepatic Cavernous Hemangioma: Diagnosis With ^{99m}Tc -Labeled Red Cells and Single-Photon Emission CT

Randall I. Brodsky¹
 Arnold C. Friedman
 Alan H. Maurer
 Paul D. Radecki
 Dina F. Caroline

During the performance of high-resolution real-time abdominal sonography, small echogenic hepatic masses are frequently discovered. A second imaging test to confirm the suspected diagnosis of hemangioma is often required. Planar labeled red-cell imaging will often not detect hemangiomas smaller than 3 cm. We studied 14 patients with labeled red-cell scintigraphy and single-photon emission CT (SPECT). Six hemangiomas were diagnosed by SPECT that would have been missed by planar imaging alone. All six were smaller than 2.5 cm. With the addition of SPECT, labeled red-cell scintigraphy has specificity and sensitivity that make it at least as reliable as dynamic CT for the noninvasive diagnosis of hepatic cavernous hemangioma.

Cavernous hemangioma is the most common benign liver tumor [1]. Small (1–2 cm) echogenic masses presumed to be hemangiomas are commonly encountered incidentally during high-resolution real-time abdominal sonography. Discovery of these masses often causes referral for dynamic CT since the demonstration of peripheral enhancement followed by progressive centripetal central enhancement is considered diagnostic for hemangioma [2]. We have found CT evaluation of these small lesions difficult because of respiratory motion, which causes the lesion to move in and out of the scanning plane, often resulting in the absence of the classic hemangioma pattern.

Planar labeled red cell scintigraphy is specific for the diagnosis of hepatic cavernous hemangioma when a perfusion blood-pool mismatch (cold on the angiographic phase, hot on delayed blood-pool images) occurs [3–5]. However, planar scintigraphy frequently will not detect hemangiomas 3 cm or smaller.

This study was undertaken to see whether single-photon emission CT (SPECT) could improve the sensitivity of labeled red-cell scintigraphy for detecting small hepatic hemangiomas.

Materials and Methods

Fourteen patients had more than 17 masses (one patient had masses too numerous to count) that were considered probable or possible hepatic hemangiomas sonographically. The patients were referred for ^{99m}Tc -labeled red-cell scintigraphy. The age and sex of the population is given in Table 1.

All patients had abdominal real-time sonography using either a 3.5- or 5-MHz transducer. Seven patients had correlation with third-generation CT. All had a noncontrast scan. Four of these patients had a single-level dynamic scan through the lesion(s) after hand bolus injection of 100 ml of 60% contrast material. The remainder were scanned after an air-injection-augmented (75–100 ml of air injected into an infusion bottle) rapid infusion of 150 ml of 60% contrast material. One patient had MR imaging performed with a 0.3-T nonsuperconducting magnet and both T1- and T2-weighted sequences.

All patients had ^{99m}Tc -labeled red-cell scintigraphy performed using the in vivo labeling technique [5]. After the IV administration of 1.34 mg of stannous pyrophosphate, 20 mCi (740 Bq) of ^{99m}Tc pertechnetate was given intravenously as a bolus in a separate location.

Received April 18, 1986; accepted after revision July 7, 1986.

Presented at the annual meeting of the American Roentgen Ray Society, Washington, DC, April 1986.

¹ All authors: Department of Diagnostic Imaging, Temple University Hospital, Broad and Ontario Sts., Philadelphia, PA 19140. Address reprint requests to A. C. Friedman.

AJR 148:125–129, January 1987
 0361–803X/87/1481–0125
 © American Roentgen Ray Society

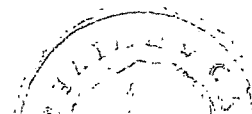


TABLE 1: Results of Studies of 14 Patients with Labeled Red-Cell Scintigraphy and Single-Photon Emission CT (SPECT)

Case No.	Age (years)	Gender	Diagnosis (Proof)	Size (cm), Location (Lobe)	Sonography	Unenhanced CT	Enhanced CT	RN Angio	Planar Scintigram	SPECT	Mode of Discovery
1	19	F	Hemangioma (F/U)	2, left	Echogenic	Hypodense	Peripheral enhancement A/B	—	—	+	S
2	28	F	Metastatic chorio (Bx)	3, right	Echogenic	Hypodense	Peripheral enhancement, size diminution A/B	—	—	—	CT
3	30	F	Hemangioma (F/U)	2, right	—	Hypodense	Dynamic, classic	—	—	+	CT
4	50	F	Hemangioma (F/U)	5, right 1.5, right	Echogenic —	Hypodense —	Dynamic, peripheral enhancement	— —	+ +	+ +	S
5	57	F	Hemangioma (Bx)	TNTC	Echogenic	—	—	—	+	+	S
6	58	F	Hemangioma (F/U)	3, right	Echogenic	—	—	—	+	+	SC
7	62	F	Hemangioma (F/U)	4, right	Echogenic	—	—	—	+	+	S
8	63	F	Hemangioma (F/U)	1.5, right	Echogenic	—	—	—	—	+	S
9	67	F	Hemangioma (F/U and MRI)	0.5, right 0.5, right 0.8, right 2.3, left 2.5, right	— — Echogenic Echogenic Echogenic	— — — Hypodense Hypodense	— — — — Dynamic, classic	— — — — —	— — — — +	— — — + +	CT
10	68	F	Hemangioma (F/U)	4, right	Inhomogeneous, moderately echogenic	Hypodense	Dynamic, classic	+	+	+	S
11	48	M	Hemangioma (Bx)	0.8, right 1.0, right 2.0, right	Echogenic — Echogenic	Hypodense Hypodense Hypodense	Dynamic, diffuse Dynamic, diffuse Dynamic, diffuse	— — —	— — —	— + +	S
12	58	M	Hemangioma (F/U)	1, right	Hypoechoic	Hypodense	Central enhancement, A/B	—	+	+	S
13	75	M	Adenoma (Bx)	5, right	Echogenic inhomogeneous	—	—	+	—	—	S
14	79	M	Hemangioma (F/U)	1, right	Echogenic	—	—	—	—	+	S

Note.—RN = radionuclide; angio = angiography; F/U = follow-up; — = not seen or cold; + = hot; S = sonography; chorio = choriocarcinoma; A/B = air bolus; classic = peripheral enhancement followed by centripetal central enhancement; TNTC = too numerous to count; SC = sulfur-colloid scan.

The patient was positioned under the gamma camera with a low-energy all-purpose parallel hole collimator in an optimal position based on sonography or CT. Dynamic images of the liver were obtained every 3 sec for the first 60 sec. Static images were acquired for 500,000 counts in the same projection at 1, 2, 5, and 10 min. Additional lateral and oblique projections were obtained when imaging at 15, 30, and 120 min. SPECT imaging was performed in a 360° rotation at 2 hr using 128 stops with 20 sec per stop. Computerized reconstructions were obtained at 1 pixel width per slice in the transaxial, sagittal, and coronal planes.

Results

The final clinical diagnosis of the hepatic mass lesions was hemangioma(s) in 12 patients, solitary liver metastasis in one patient, and hepatic adenoma in one patient. Two of the patients with hemangioma(s) had biopsy proof. The remaining 10 patients with hemangioma(s) had no clinical or laboratory

evidence of liver disease and have had at least 6 months follow-up without signs of malignancy. The patient with the liver metastasis (choriocarcinoma) had an open biopsy, and the diagnosis of hepatic adenoma was made by sonography-guided core biopsy.

In 11 of the 12 patients with a final diagnosis of hemangioma(s) after all imaging studies, 18 lesions were present (one new hemangioma was discovered on scintigraphy and two previously undetected hemangiomas were discovered by MR). The 12th patient had too many hemangiomas to count throughout the liver; these were detected on sonography and confirmed by scintigraphy (case 5). Twelve of the 18 tumors were smaller than 2 cm, three were between 2 and 3 cm, and three were larger than 3 cm.

Sonography detected 14 of the hemangiomas. Eleven were typical (round, homogeneous, well-defined, and echogenic) (Figs. 1A and 1B, case 11). A 1-cm and a 2-cm mass were not visualized sonographically; both were very superficial and

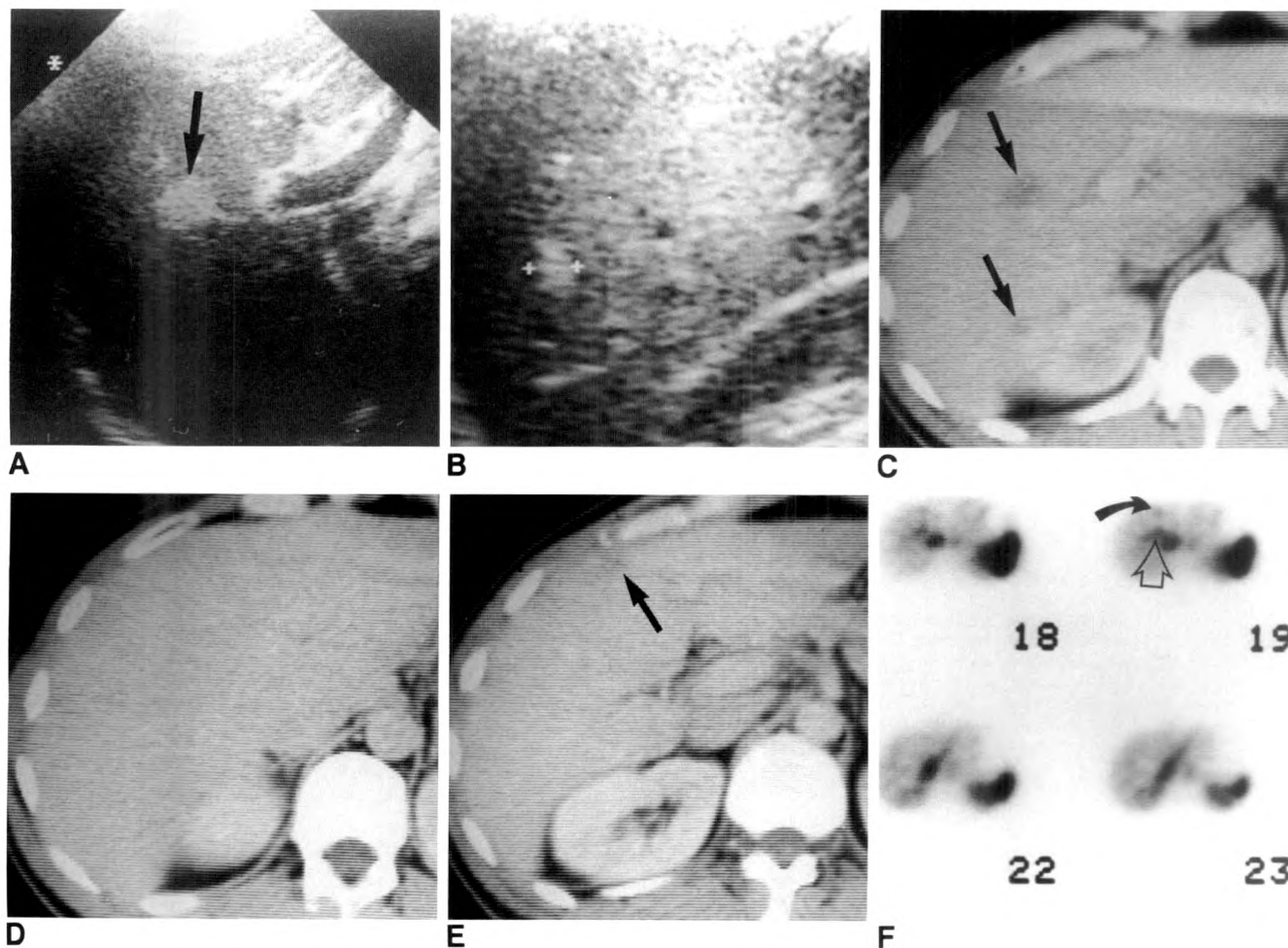


Fig. 1.—Case 11. Multiple hemangiomas of liver in a 48-year-old man with weight loss but normal liver-function tests.

A, Oblique transverse sonogram. 2-cm echogenic mass (arrow) medial to portal vein.

B, Magnified parasagittal sonogram through posterior right lobe of liver. 0.8-cm echogenic mass (cursors).

C, Initial phase of dynamic CT. The two hemangiomas are still hypodense (arrows).

D, 19 min later the two hemangiomas are isodense.

E, A third small hemangioma (not seen on sonography) was detected on CT (arrow) but could not be proven to enhance.

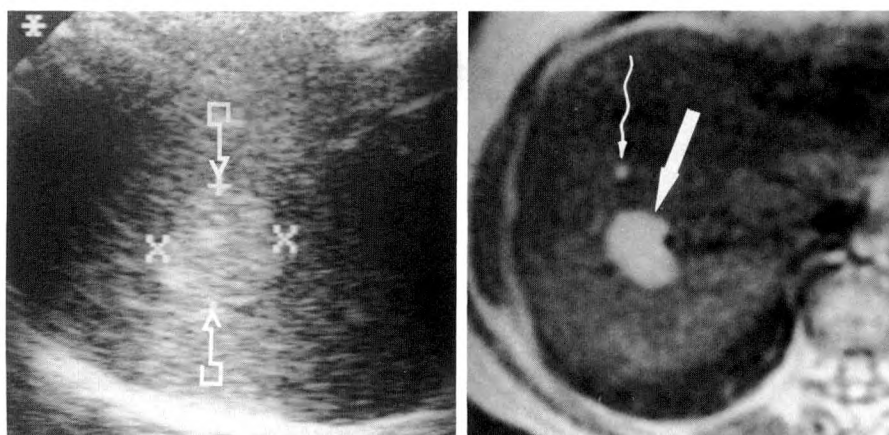
F, Axial single-photon emission CT 2-hr labeled red-cell scintigram. Definite hemangioma anteriorly (closed arrow) corresponding to E. After comparison with sonogram, avid region near portal vein (open arrow) was thought to represent the hemangioma in A. Planar images were negative for hemangioma. Because of persistent clinical concern, an aspiration biopsy of this mass was performed under sonographic control and yielded endothelial cells and blood.

adjacent to ribs. In a patient in whom sonography detected three masses, two additional 0.5-cm masses were seen only with MR (Fig. 2, case 9).

CT detected 10 out of 14 possible hemangiomas in eight patients scanned. All of the masses appeared hypodense on unenhanced CT. Contrast CT showed a classic hemangioma pattern (peripheral enhancement followed by progressive centripetal central enhancement) in only three patients. In another patient, three masses smaller than 1 cm were missed by CT but were seen on SE 2000/56 MR; one of them was also present on sonography (Fig. 2B, case 9). One hemangioma (case 4) was hidden on CT by beam hardening from an adjacent rib.

Red-cell-labeled scintigraphy showed increased arterial flow in only one hemangioma. This mass did show increased

activity on delayed images but nevertheless had to be considered indeterminate for hemangioma because of the increased flow. The remaining flow studies of hemangiomas were either normal or showed hypoperfusion. Eight of the 18 hemangiomas were seen on delayed planar images as an active focus within the hepatic parenchyma (Fig. 2C, case 9). Six additional hemangiomas were identified on the SPECT images (Figs. 1F, 2C, and 2D). Five of these lesions were smaller than 2 cm while the other was 2.5 cm. The four hemangiomas that were missed by scintigraphy were found in two patients and were smaller than 1 cm. The metastasis (Fig. 3, case 2) did not have increased activity on either flow, planar, or SPECT-labeled red-cell images. The adenoma (case 13) had increased arterial flow but no delayed increased activity. Data are summarized in Table 1.



A

B

C

Fig. 2.—Case 9. 68-year-old woman referred for biopsy of a "liver metastasis." A hemangioma had been discovered and was proven to be in right lobe by CT. A follow-up noncontrast CT 3 months later revealed a "new" mass in left lobe. Sonography and labeled red-cell scans were consistent with hemangiomas, as was MR.

A, Transverse sonography shows a 2.5-cm echogenic mass with acoustic enhancement in right lobe (arrows and cursors) and a 2.3-cm echogenic mass in left lobe (not shown).

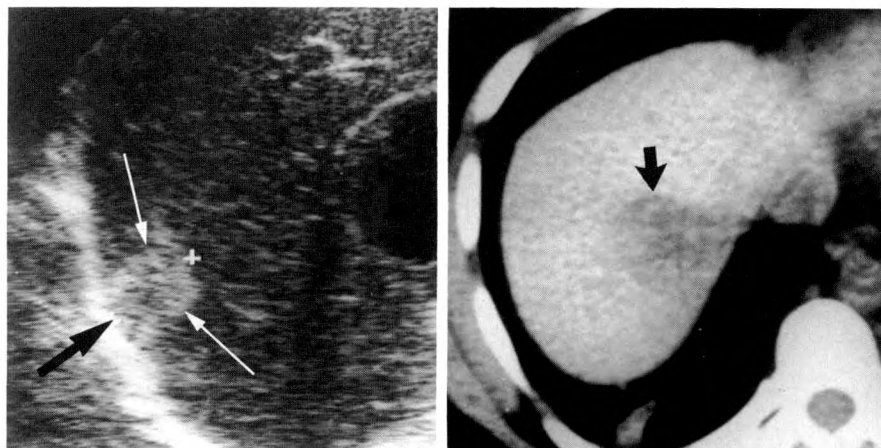
B, Axial SE 2000/56 MRI. Both left lobe (not shown) and right lobe (straight arrow) mass are homogeneously hyperintense, consistent with hemangioma. A second, smaller hemangioma is seen (wavy arrow); this mass was detected on sonography. Two other small hemangiomas were seen at other levels only on SE 56/2000 MR. The two large hemangiomas were hypointense on inversion recovery.

C, 2-hr planar, labeled red-cell scintigram. Only right-sided hemangioma is seen (arrow).

D, Axial single-photon emission CT shows both large hemangiomas (arrows).

C

D



A

B

Fig. 3.—Case 2. Metastatic choriocarcinoma, 26-year-old woman.

A, Sagittal sonogram. 2.6-cm echogenic mass consistent with a hemangioma (arrows, cursor). Inferior to liver is a large adrenal hemorrhage.

B, Noncontrast CT shows a hypodense mass (arrow). Because of an equivocal contrast-enhanced CT and presence of known primary, a labeled red-cell scan was performed and showed no avidity in liver mass, and correct diagnosis of metastasis was made.

Discussion

Sonography is sensitive but not specific for evaluating hepatic hemangiomas [6–11]. A characteristic dynamic CT enhancement pattern has been described: early peripheral enhancement with subsequent centripetal central enhancement [2, 8, 9, 12–14]. The typical enhancement pattern is generally considered reliable for diagnosis. However, in one large series [13], the typical dynamic CT pattern of hemangioma incorrectly suggested hemangioma (the correct diagnosis was metastasis) 20–30% of the time when the patient had a known primary malignancy. Smaller (less than 2 cm) hemangiomas, which can be easily detected by sonography,

may be hard to scan dynamically or even missed completely by CT owing to nonreproducible respiration and/or volume averaging [8, 14]. When successfully scanned these smaller lesions may only show a diffuse contrast enhancement towards iso- or hyperdensity [2, 8, 12]. When many lesions are present, the process becomes tedious, and safe dosages of contrast material may be exceeded.

Labeled red-cell scintigraphic findings specific for hemangioma have been described [3–5, 15]. Radionuclide angiography is either normal or shows relative arterial hypoperfusion. Uncommonly, hemangiomas have increased arterial flow. Delayed images performed up to 2 hr after injection show increasing relative activity within the hemangioma with re-

spect to the adjacent liver. This perfusion blood-pool mismatch is specific for hemangiomas and can be used to diagnose most hemangiomas 3 cm or larger on planar images [4]. Placing the patient in an optimal position based on sonography or CT yielded the best results for planar images in our cases. Additional projections supplied no other information.

In this study we acquired 500,000 counts/planar image, as others have [5], and acknowledge that, theoretically, increasing the total counts per image to one million might improve resolution and detection of small lesions. However, the detection of "hot spots" in nuclear imaging is more a function of image contrast (which is improved by SPECT) than a function of intrinsic camera resolution. We employed routine in vivo labeling of the patients' red blood cells [5]. A theoretical argument could be made for using the modified in vitro technique, which reportedly increases the RBC labeling efficiency from 90 to 95% [5]. The resulting decrease in free pertechnetate in the extracellular fluid could enhance image contrast and thus increase the sensitivity of both planar and SPECT imaging for the detection of hemangioma.

False-negative labeled red-cell scans for hemangioma have been reported due to fibrosis of the lesion [14]. When there is increased arterial flow as well as activity on delayed images, as in one of our cases, hepatocellular carcinoma cannot be excluded [4]. The only large hepatic malignancy likely to have a perfusion blood-pool mismatch is the rare angiosarcoma [16]. A small hepatocellular carcinoma or hypervascular metastasis could be red-cell avid on SPECT yet small enough so that its hypervascularity could not be appreciated on the flow study, causing misdiagnosis. Further experience will be necessary to determine the likelihood of this occurrence.

Since most of our patients had cavernous hemangiomas, information with respect to specificity is limited, but important conclusions can be drawn regarding the relative sensitivity of planar scintigraphy and SPECT. The improved contrast and size/shape definition afforded by the tomographic removal of superimposed structures increased our sensitivity as compared with planar imaging by enabling us to detect hemangiomas 1–2 cm in size. It is important to correlate SPECT images with sonography and/or CT to distinguish central hemangiomas from adjacent normal vascular structures. Peripheral hemangiomas are obvious.

When small (<3.0 cm), homogeneous, intrahepatic, highly echogenic masses are detected sonographically as incidental findings, we believe that they can be assumed to be hemangiomas (or, less likely, angiomyolipomas). If either metastasis or primary liver cancer is a clinical consideration, other studies are needed to confirm the benign nature of these lesions. Compared with dynamic single-level CT, labeled red-cell scintigraphy with SPECT is cheaper, easier to perform (especially when several masses are present), and more specific. A scintigram not diagnostic of hemangioma should prompt other tests to confirm malignancy. The exact role of MR imaging remains to be established, and although highly sensitive, it may not be sufficiently specific [17–19].

When clinical index of suspicion for malignancy is high, despite a labeled red-cell study positive for hemangioma, a

guided fine-needle-aspiration biopsy can be safely performed [20], and cytologic findings of no malignancy and abundant endothelial cells, although not pathognomonic for hemangioma, can be reassuring.

REFERENCES

1. Ishak KG, Rabin L. Benign tumors of the liver. *Med Clin North Am* 1975;59:995–996
2. Barnett PH, Zérhouni EA, White RI, Siegelman SS. Computed tomography in the diagnosis of cavernous hemangioma of the liver. *AJR* 1980;134:439–447
3. Engel MA, Marks DS, Sandler MA, Shetty P. Differentiation of focal intrahepatic lesions with 99m Tc red blood cell imaging. *Radiology* 1983;146:777–782
4. Rabinowitz SA, McKusick KA, Stravas HW. 99mTc red blood cell scintigraphy in evaluating focal liver lesions. *AJR* 1984;142:63–65
5. Front D, Israel O, Groshar O, Weininger J. Tc 99m labeled red blood cell imaging. *Semin Nucl Med* 1984;14:226–249
6. Sandler MA, Marks DS, Hricak H, Madrazo BL, Petrocelli RD. Benign focal diseases of the liver. *Semin Ultrasound* 1981;2:202–211
7. Mirk P, Rubaltelli L, Bazzocchi M, et al. Ultrasonic patterns in hepatic hemangiomas. *J Clin Ultrasound* 1982;10:272–278
8. Itai Y, Furui S, Araki T, Yashiro N, Tasaka A. Computed tomography of the cavernous hemangioma of the liver. *Radiology* 1980;137:149–155
9. Bree RL, Schwab RE, Neiman L. Solitary echogenic spot in the liver: is it diagnostic of a hemangioma? *AJR* 1983;140:41–45
10. Taborny J, Porcel A, Tubiana J, Monnier J. Cavernous hemangiomas of the liver studied by ultrasound. *Radiology* 1983;149:781–785
11. Sheu JC, Chen DS, Sung JL, et al. Hepatocellular carcinoma: ultrasound evolution in the early stage. *Radiology* 1985;155:463–467
12. Burgener FA, Hamlin DT. Contrast enhancement of focal hepatic lesions in CT. *AJR* 1983;140:297–301
13. Freeny PC. Patterns of contrast enhancement of benign and malignant hepatic neoplasms during bolus dynamic CT scanning. *Radiology* 1984;153(P):78
14. Itai Y, Ohtomo K, Araki T, Furui S, Iio M, Atomi Y. Computed tomography and sonography of cavernous hemangioma of the liver. *AJR* 1983;141:315–320
15. Moinuddin M, Allison JR, Montgomery JH, Rockett JF, McMurray JM. Scintigraphic diagnosis of hepatic hemangioma: its role in the management of hepatic mass lesions. *AJR* 1985;145:223–228
16. Whelan JG, Creech JL, Tamburns CL. Angiographic and radionuclide characteristics of hepatic angiosarcoma found in vinyl chloride workers. *Radiology* 1976;118:549–557
17. Ohtomo K, Itai Y, Furui S, Yashiro N, Yoshikawa K, Iio M. Hepatic tumors: differentiation by transverse relaxation time (T2) of magnetic resonance imaging. *Radiology* 1985;155:421–423
18. Stark DD, Felder RC, Wittenberg J, et al. Magnetic resonance imaging of cavernous hemangioma of the liver and tissue: specific characterization. *AJR* 1985;145:213–222
19. Glazer GM, Aisen AM, Francis IR, Gyves JW, Lande I, Adler DD. Hepatic cavernous hemangioma: magnetic resonance imaging. *Radiology* 1985;155:417–420
20. Solbiati L, Livraghi T, De Pra L, Ierace T, Masciadri N, Ravetto C. Fine needle biopsy of hepatic hemangioma with sonographic guidance. *AJR* 1985;144:471–474

Airline Discounts to 1987 ARRS Meeting

Eastern airlines is offering a 60% discount off normal round-trip coach airfare to the 1987 American Roentgen Ray Society meeting, April 26–May 1, Fontainebleau Hilton, Miami Beach, FL. To make reservations, registrants should call (800) 468-7022 outside Florida and (800) 282-0244 within Florida. The identification number for this meeting discount is EZ4P5.

United airlines is also offering discount fares for the ARRS meeting. Travel must take place between April 22nd and May 5th. A 5% discount is available for any United available applicable fare (UltraSavers included); A 40% discount is offered off standard coach fare (all restrictions waived). To obtain these fares you must call (800) 521-4041. (48 contiguous states) or (800) 722-5243 ext 6608 (Alaska, Hawaii), 8:30 a.m. to 8:00 p.m. est. Immediately refer to the ARRS number 7092H.

CT Evaluation of Esophageal Varices

Emil J. Balthazar^{1,2}
David P. Naidich¹
Alec J. Megibow¹
Richard S. Lefleur¹

CT findings in 20 consecutive patients with proven esophageal varices are reviewed and analyzed. In 85% of patients, abnormalities were seen involving the esophageal wall and/or periesophageal region. In 65%, findings specific to varices were present: thickening of esophageal wall, a scalloped contour, and intraluminal protrusions enhancing after a contrast bolus injection. These findings were seen alone or in association with periesophageal varices, which were seen in 45% of patients; evidence of portal hypertension with varices in the lesser omentum was present in 95%. CT has a sensitivity similar to barium esophagram but evaluates better the presence and extent of periesophageal varices and portal hypertension. Normal CT does not rule out esophageal varices because small varices may escape detection, particularly in scans done without a contrast bolus injection.

During routine abdominal examinations the distal esophagus and the esophagogastric junction are easily shown by CT [1, 2]. CT abnormalities of the esophagus, such as carcinoma or esophagitis consisting mainly of esophageal-wall thickening, have been previously reported [3-5]. A few publications describing abdominal venous collaterals in patients with portal hypertension have mentioned the occasional CT demonstration of esophageal varices [6-9]. To the best of our knowledge, however, the spectrum of CT findings and potential role of CT in diagnosing and evaluating esophageal varices has not been described.

Normal Esophagus

CT visualization of the distal esophagus is facilitated by air in the lumen and paraesophageal fat in the lower mediastinum. Since the amount of intraluminal air varies, the appearance of the esophagus on cross-section will differ slightly among normal persons. If the esophagus is distended, its wall is clearly visualized with a sharp outer and inner contour, a smooth surface, and a thickness of about 1-1.5 mm (Fig. 1). If it is partly or totally collapsed, the wall thickness is greater but does not exceed 3 mm. Its outer contour remains perfectly symmetric and sharp, but its inner contour is somewhat irregular, reflecting the more redundant mucosal surface. After an IV bolus injection, the wall of the esophagus remains homogeneous in appearance and its density enhances greatly. In our experience, enhancement values twice as high as the base values of the unenhanced scans (from 30-40 to 60-80 H) are not unusual (Fig. 1). Therefore, significant enhancement of the wall of the esophagus without associated abnormalities does not indicate esophageal disease.

Material and Methods

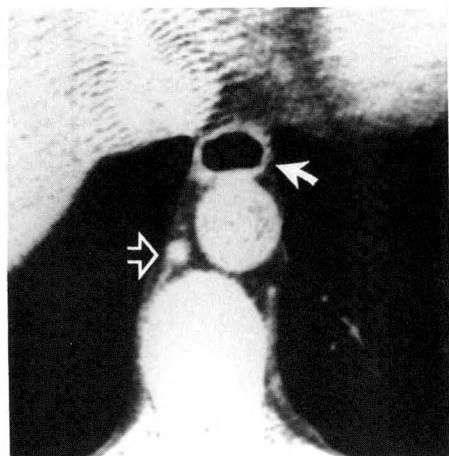
Twenty consecutive CT scans performed in patients with proven esophageal varices were retrospectively evaluated for esophageal abnormalities and associated findings. This series

Received July 15, 1986; accepted after revision August 27, 1986.

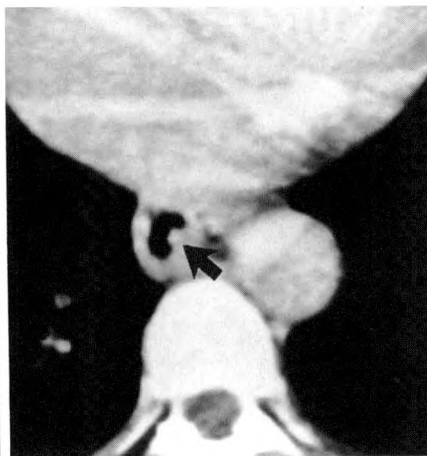
¹ Department of Radiology, NYU Medical Center, 560 First Ave., New York, NY 10016.

² Present address: Department of Radiology, Bellevue Hospital, New York, NY 10016. Address reprint requests to E. J. Balthazar.

AJR 148:131-135, January 1987
0361-803X/87/1481-0131
© American Roentgen Ray Society



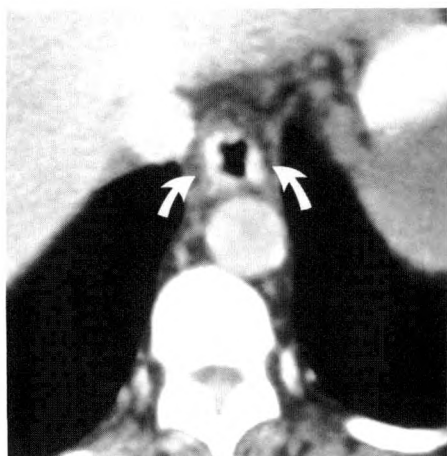
1



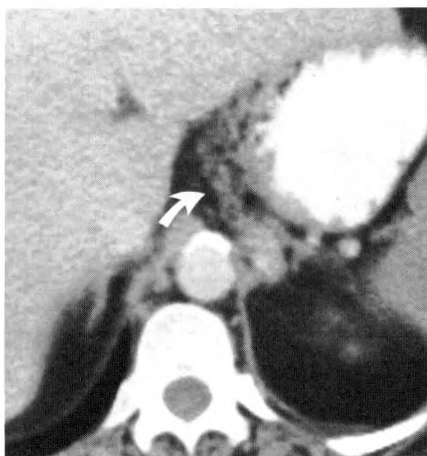
2

Fig. 1.—Normal esophagus, IV bolus technique, magnified view. Esophagus is distended with air, has a thin and sharply contoured wall, and shows enhancement from 40 H before contrast injection to 80 H afterward (white arrow). Azygous vein (open arrow) posterior and to right of aorta.

Fig. 2.—Varices confined to wall of esophagus. Lower esophagus has thick wall and shows protruding luminal defect (arrow). Marked enhancement (33–140 H) after contrast bolus injection.



A



B

Fig. 3.—Varices confined to wall of esophagus.

A, After bolus injection, lower esophagus shows thick wall, scalloped inner contour, and slightly lobulated outer contour (arrows). Marked enhancement similar to aorta and inferior vena cava.

B, Venous collaterals adjacent to wall of proximal stomach within lesser omentum (arrow).

is composed of 14 men and six women, ranging in age from 30 to 71 years old (mean, 51 years). All patients had cirrhotic livers, and in most patients the diagnosis of esophageal varices was made before the CT evaluation. The diagnosis was made in all patients by endoscopy; 14 patients had upper-gastrointestinal studies including esophagrams, and in nine patients angiographic examinations were done to evaluate the type and degree of portal hypertension. Abdominal CT examinations were requested for a variety of reasons, including pain, fever, palpable mass, and suspected hepatocellular carcinoma. CT studies of the entire abdomen were performed on a GE 8800 or Picker 1200 unit. Transaxial images 10 × 10 mm over the lower mediastinum and upper abdomen were obtained before and after the administration of IV iodinated contrast material. The lower abdomen and pelvis were subsequently examined by 10-mm sections every 20 mm. In 15 patients, an IV bolus injection of 60 ml of 60% iodinated diatrizoate was followed by a rapid drip-infusion of 300 ml of 30% iodinated solution. In five patients, only a rapid drip-infusion was administered. No special effort was made to visualize the esophageal lumen. All patients however, received 700–800 ml of 2% diluted peroral barium solution 45–60 min before scanning.

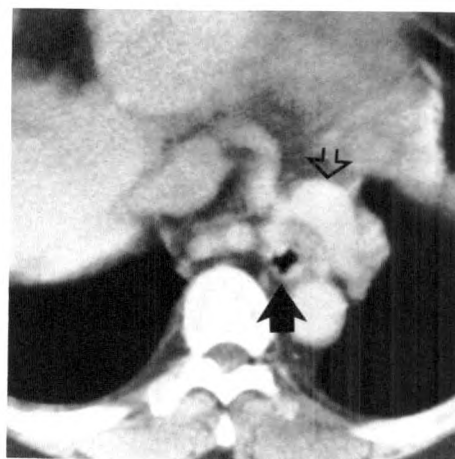
Results

CT abnormalities specific of esophageal and/or periesophageal varices were shown in 13 cases (65%). In four patients, varices involved only the wall of the esophagus, producing a thickened wall with a slightly lobulated contour (Figs. 2 and 3). After a bolus injection the esophageal wall increased in density about three times over its base value, showing an enhancement similar to the aorta and inferior vena cava. The varices projected into the esophageal lumen, appearing as a single filling defect (Fig. 2), or circumferentially involving the wall and changing the shape of the esophageal lumen from a round or oval to a scalloped contour (Fig. 3). In five patients, in addition to the esophageal-wall abnormalities, CT showed varices in the lower mediastinum adjacent to the esophagus (Figs. 4 and 5). The number, size, and distribution of the periesophageal varices varied greatly: Some cases showed a dominant large vein in the left mediastinum (Fig. 4), while

Fig. 4.—Esophageal varices with large periesophageal venous collaterals.

A, Esophageal wall is thick with scalloped lumen indicative of submucosal varices (*black arrow*). Numerous periesophageal enhancing varices and dominant large vein in left lower mediastinum (*open arrow*).

B, Barium swallow in same patient shows large esophageal varices.



A



B

others showed a plexus of varices, mostly in the right mediastinum (Fig. 5). In the remaining four cases, large mediastinal periesophageal varices were shown. However, the esophagus was collapsed and could not be evaluated because it was not adequately visualized (Fig. 6).

In seven patients, the CT diagnosis of esophageal varices could not be confidently made. The esophagus was adequately visualized in these patients. It had a normal CT appearance in three patients while showing a symmetric circumferential wall thickening with moderate enhancement in four cases (Fig. 7). Although abnormal, this pattern was not specific enough for a definite diagnosis. Periesophageal varices were seen in a total of nine cases (45%), and esophageal and/or periesophageal abnormalities were present in 17 cases (sensitivity of 85%). In addition to the lower-mediastinal abnormalities, all patients had shown abdominal CT abnormalities consistent with portal hypertension. In 19 patients (95%) varices were seen in the lesser omentum within the distribution of the left coronary vein (Fig. 3). Typical CT findings of liver cirrhosis, such as shrunken liver, nodular contour, hypertrophy of the left lobe, and/or caudate lobe, were found in 15 patients. Splenomegaly was present in 12 and ascites was seen in two patients.

Barium esophagrams consisting of double-contrast and single-contrast studies were available for review in 14 patients. Varices were visualized in 12 patients (Figs. 4–6) (sensitivity of 86%) and were not recognized in two cases. In these two patients, CT showed no varices in one case but showed large periesophageal varices in the other. No correlation was established between the degree of esophageal involvement on barium swallow and the presence, type, and extent of involvement on CT examination (Figs. 4 and 5). In three patients, radiographs showed a lower mediastinal mass compressing and, in one instance, displacing the lower esoph-

agus (Fig. 6). CT showed large periesophageal venous collaterals, promptly establishing the nature of the lower mediastinal mass.

Discussion

Although CT is not considered a primary imaging technique to diagnose esophageal varices, it can be important in assessing the presence and extent of venous collaterals in patients with portal hypertension [6–9]. CT has been positive in 18 (72%) of 25 patients with proven esophageal varices in one series [6] and has shown periesophageal varices in seven (39%) of 18 patients with portal hypertension in another series [7].

Circumferential thickening of the esophageal wall and enhancement after IV contrast administration were the only criteria previously described for the CT diagnosis of esophageal varices [5, 6]. While these findings are suspicious, they should not be considered specific because wall thickening and moderate enhancement may be present in inflammatory or neoplastic disease. In fact, significant enhancement of the esophageal wall may be seen in normal persons after a bolus injection (Fig. 1). The association of esophageal-wall thickening and contrast enhancement with CT evidence of portal hypertension, particularly with large veins in the lesser omentum, is more consistent with esophageal varices (Fig. 3), a presentation seen in four cases in this series (Fig. 7). In 13 of our patients, findings that we consider characteristic of esophageal varices were shown: thickening of the esophageal wall, slightly lobulated outer contour (Fig. 3), scalloped esophageal lumen with protruding luminal masses (Figs. 2–4), and enhancement of esophageal wall similar to aorta, better appreciated with a bolus technique (Fig. 3). These findings may be seen alone or associated with periesophageal venous collat-

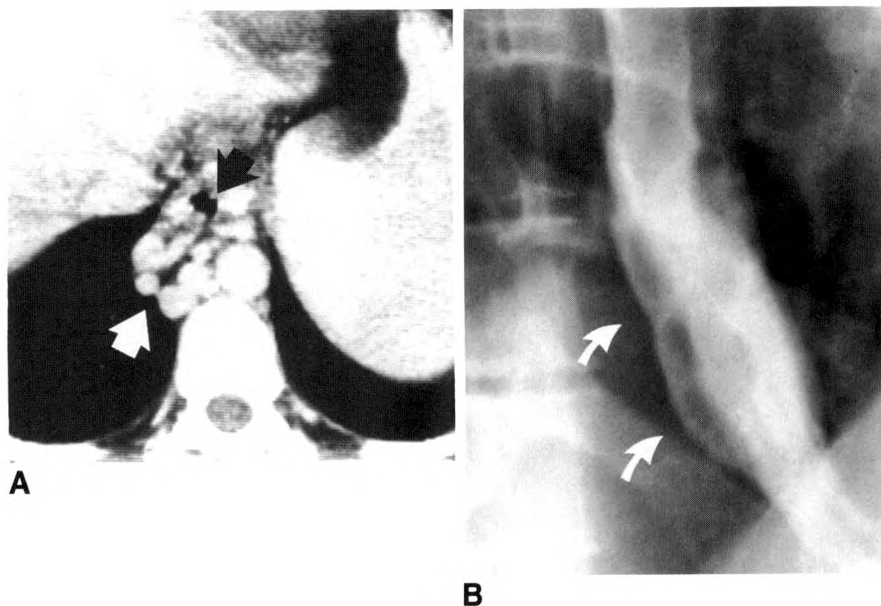


Fig. 5.—Esophageal and periesophageal varices.

A, Esophagus has a scalloped configuration (black arrow); many small enhancing veins seen mainly in right posterior mediastinum (white arrow).

B, Barium esophagram shows only intrinsic esophageal varices (arrows).

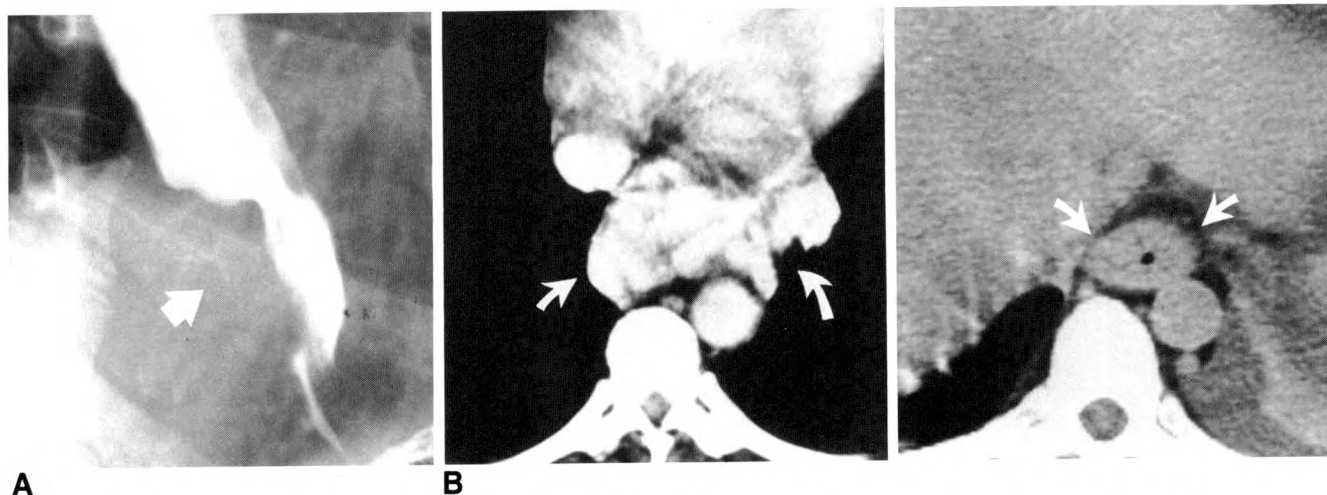


Fig. 6.—Periesophageal varices.

A, Barium swallow shows esophageal varices and mediastinal mass compressing and displacing lower esophagus anteriorly (arrow).

B, Large enhancing collateral veins in lower mediastinum (arrows). Esophagus compressed by large periesophageal veins and not adequately visualized.

Fig. 7.—Esophageal varices presenting as circumferential wall thickening (arrows). Drip-infusion technique was employed; although abnormal, pattern was considered nonspecific.

erals, which were present in 45% of our patients with proven esophageal varices. On the basis of our experience and the literature [7], it is reasonable to assume that esophageal varices are present in all patients with periesophageal venous collaterals. However, no correlation has been established between degree of involvement of these structures: In one patient in this series large periesophageal collaterals were associated with rather small submucosal varices seen on endoscopy and missed on barium esophagram.

In this series CT had a sensitivity of 85% in visualizing esophageal varices and showed characteristic findings in 65%

of cases. These numbers should be expected to vary depending on the size of varices, type of equipment, and technique employed. The barium esophagram, which shows a similar sensitivity (86% in this series), is less expensive, faster, and easier to perform, should be used as the primary imaging technique to diagnose esophageal varices. On routine examinations performed with IV contrast media, however, CT can diagnose esophageal varices in most patients. It may occasionally show varices in patients with normal esophagrams. It can also show the extent of periesophageal venous collaterals and the associated abdominal findings of liver

cirrhosis and portal hypertension (Fig. 3). In patients known to have esophageal varices and a lower mediastinal mass, CT can promptly establish the nature of the mass (Fig. 6). As with the barium esophagram, small varices cannot be ruled out in patients with normal CT examinations, particularly if the examinations are done without a bolus technique.

REFERENCES

1. Halber MD, Daffner RH, Thompson WH. CT of the esophagus. 1. Normal appearance. *AJR* 1979;133:1047-1050
2. Thompson WM, Halvorsen RA, Williford ME, Foster WL, Korobkin M. Computed tomography of the gastroesophageal junction. *Radiographics* 1982;2:179-193
3. Daffner RH, Halber MD, Postlethwait RW, Korobkin M, Thompson WM. CT of the esophagus. II. Carcinoma. *AJR* 1979;133:1051-1055
4. Moss AA, Schnyder P, Thoeni RF, Margulis AR. Esophageal carcinoma: pretherapy staging by computed tomography. *AJR* 1981;136:1051-1056
5. Reinig JW, Stanley JH, Schabel SI. CT evaluation of thickened esophageal walls. *AJR* 1983;140:931-934
6. Ishikawa T, Tsukune Y, Ohyama Y, Fujikawa M, Sakuyama K, (1F-2565)Fujii M. Venous abnormalities in portal hypertension demonstrated by CT. *AJR* 1980;134:271-276
7. Clark KE, Foley WD, Lawson TL, Berland LL, Maddison FE. CT evaluation of esophageal and upper abdominal varices. *J Comput Assist Tomogr* 1980;4:510-515
8. Pagani JJ, Thomas JL, Bernardino ME. Computed tomographic manifestations of abdominal and pelvic venous collaterals. *Radiology* 1982;142:415-419
9. Balthazar EJ, Megibow A, Naidich D, Lefleur RS. Computed tomographic recognition of gastric varices. *AJR* 1984;142:1121-1125

Technical Note

Radiolucency in the Common Bile Duct Simulating a Gallstone

John S. Train,¹ Andrew Novick,¹ Sol J. Dan,¹ Stavros Efremidis,^{1,2} and Harold A. Mitty¹

Filling defects seen on transhepatic or T-tube cholangiograms can be created by clots, air bubbles, and adjacent vessels [1]. Thick, inspissated bile also can cause large, lucent, common-duct filling defects termed admixture defects [2]. Recently, we have observed a radiolucency at the mouth of the dilated cystic duct in six patients with long-standing obstruction of the distal common bile duct. We think this radiolucent filling defect is the result of the physical interaction of two fluids (bile and contrast material) that vary in viscosity, surface tension, and density. A simple experiment was performed to test this hypothesis.

Materials, Methods, and Results

A round radiolucent defect was seen in the region of the junction of the cystic duct with the common bile duct during cholangiography in six patients with obstruction of the distal common bile duct (Fig. 1). Thirty percent meglumine diatrizoate was used in all cases. On delayed films the radiolucency disappeared, and the cystic duct filled with contrast material.

A study was performed using a T-shaped plastic model of the biliary tree to determine the interaction of bile and flowing contrast material (Figs. 2 and 3). The model was filled with cadaver gallbladder bile. Then, to simulate filling of the common bile duct during cholangiography, a 22-gauge Chiba needle was used to slowly inject 30% meglumine diatrizoate into one end of the horizontal limb while serial films were

taken. The injection was performed at a rate similar to that used during cholangiography.

It was shown that the heavier contrast material layered on the bottom of the horizontal limb of the tube. When the contrast material reached the vertical limb, simulating the origin of the cystic duct, it flowed around the bile column between the wall of the limb and the bile rather than mixing with the bile. A film taken 5 min later showed that the lucency was no longer present, indicating complete mixing of contrast material and bile.

Discussion

Kriss [3] observed in 1971 that a transient filling defect could occur in the region of the cystic and common duct. He described "a dot surrounded by a fine rim of opacity," which he believed was caused by flow-density differences. The results of our experiment support his conclusion.

The viscosity of normal bile is greater than that of diluted contrast material. In long-standing obstruction the viscosity of bile increases greatly, accentuating the difference. Sobotka [4] reported values of bile viscosity in excess of 80 times the viscosity of water and 20 times that of 30% meglumine diatrizoate in obstructed systems.

Contrast material, however, is denser than bile no matter how viscous bile becomes. The specific gravity of bile can range from 1.026–1.063 mg/ml, whereas the specific gravity

Received March 17, 1986; accepted after revision August 18, 1986.

¹ Department of Radiology, The Mount Sinai Hospital, The Mount Sinai School of Medicine of the City University of New York, One Gustave L. Levy Pl., New York, NY 10029. Address reprint requests to J. S. Train.

² Present address: Department of Radiology, St. Sophia Hospital, Thessaloniki, Greece.

AJR 148:136–138, January 1987 0361–803X/87/1481–0136 © American Roentgen Ray Society

Fig. 1.—A, Case 1: Transhepatic cholangiogram shows a radiolucency in midportion of common bile duct (arrows).

B, Case 2: Transhepatic cholangiogram shows a radiolucency in cystic duct. Contrast media surrounding radiolucencies within cystic duct can be seen also (arrow).

C, Case 3: Cholangiogram performed via an external drainage catheter immediately after placement shows a radiolucent defect in region of cystic duct's origin (arrow).

D, Case 3: Later film made during cholangiogram shows filling of cystic duct and gallbladder and demonstrates relationship of radiolucency to mouth of cystic duct (arrow).

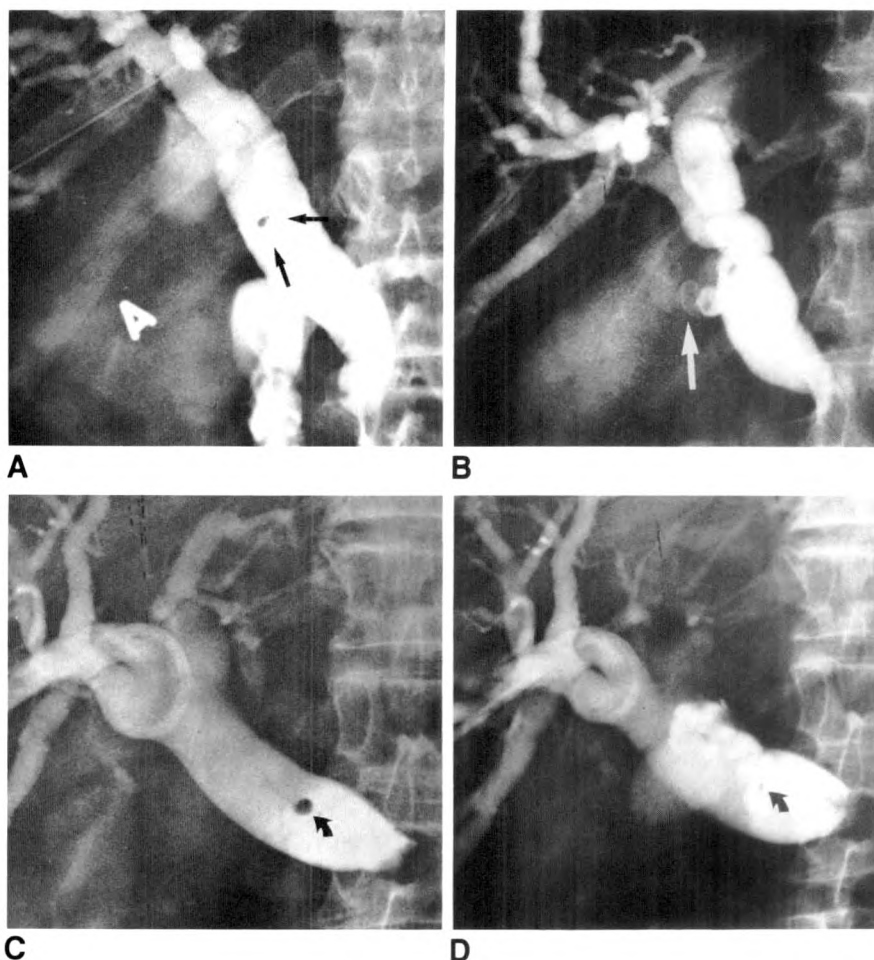
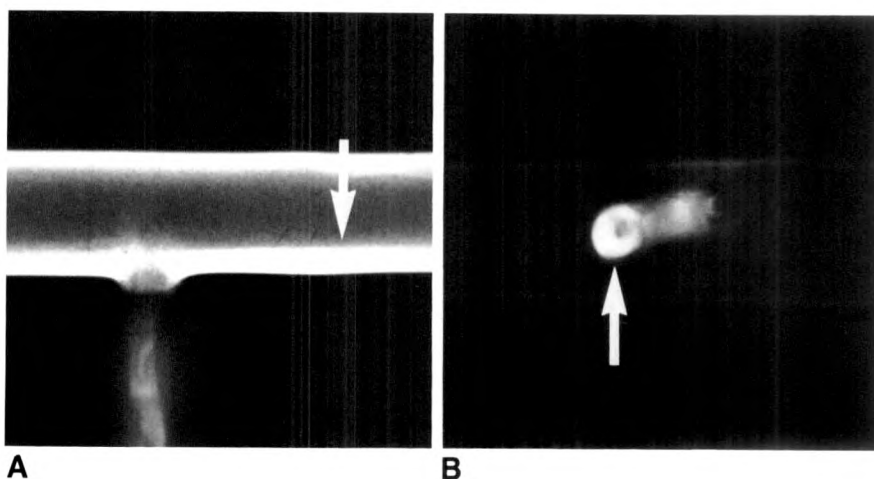


Fig. 2.—Radiograph of a T-shaped plastic model of common bile duct filled with gallbladder bile. Contrast material was injected into right end of horizontal limb.

A, View from side shows contrast material flowing beneath bile (arrow) and into vertical portion of model designed to simulate cystic duct.

B, View from the top shows radiolucency at mouth of vertical limb that simulates lucency seen in Fig. 1 (arrow). Apparent lack of contrast material in horizontal limb in B occurs because heavy contrast forms a layer on dependent side of tube. Because this layer is thin, contrast material is not visible when viewed from above.



of contrast material (diatrizoate meglumine 30%) is 1.162 mg/ml [5]. Thus, although bile, especially in an obstructed system, is more viscous, it is less dense than contrast material.

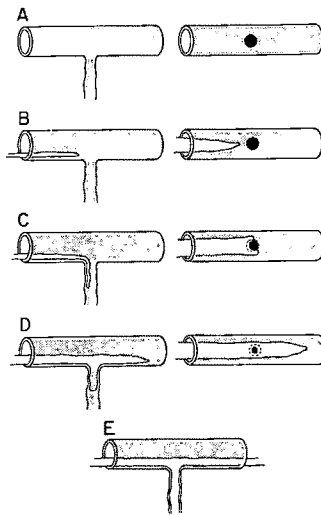
When two fluids of different viscosities first come in contact with each other, they will displace each other even though

the two liquids are miscible. The greater the difference in viscosity, the more obvious is the displacement [6]. This physical phenomenon explains, in part, why contrast material does not mix initially with the bile in the cystic duct orifice.

The differences in the surface tensions of the two fluids

Fig. 3.—Diagram of plastic model seen from side (left) and from above (right).

A, Model is filled with bile.
 B, Contrast material flows along bottom of horizontal limb.
 C, Contrast material in horizontal limb abuts vertical column.
 D, Contrast material flows around bile in vertical column, creating radiolucency seen in Fig. 2.
 E, Subsequently, bile and contrast material mix completely in vertical limb.



also may contribute to the observed radiographic findings. Water, the major constituent of water-soluble contrast material, has a higher surface tension than most oils or detergents [6]. Conversely, bile has a low surface tension because of the

presence of bile salts and lecithin, which are known to have lower surface tension [7].

Fluids with high surface tension tend to stick to a surface just as a drop of water on glass remains spherical rather than spreading out [8]. It follows then that contrast material will stick initially to the walls of the cystic duct and displace the bile rather than mixing with it.

REFERENCES

1. Kittredge RD, Baer JW. Percutaneous transhepatic cholangiography: problems in interpretation. *AJR* 1975;125:35-46
2. Ferrucci JT, Wittenberg J. Refinements in Chiba needle transhepatic cholangiogram. *AJR* 1977;129:11-16
3. Kriss N. False filling defects in neck of gallbladder. *NY State J Med* 1971;71:1079-1082
4. Sobotka H. *Physiological chemistry of bile*. Baltimore: Williams & Wilkins, 1937:44
5. Weast RC. *CRC handbook of chemistry and physics*. Cleveland: CRC, 1975:210
6. Sears F, Zemansky M. *Young university physics*. Reading, MA: Addison-Wesley, 1985:248-258
7. Fraser RG, Pare JAP. *Diagnosis of diseases of the chest*. Philadelphia: Saunders, 1977:35-40
8. Adamson A. *Physical chemistry of surfaces*, 4th ed. New York: Wiley, 1982:106

CT Diagnosis of Occult Incisional Hernias

Gary G. Ghahremani¹
Miguel A. Jimenez
Mark Rosenfeld
David Rochester

CT of the abdomen was performed on 14 adult patients 2–25 months after laparotomy in order to evaluate intraabdominal processes. Clinically unsuspected incisional hernias were detected in all cases. These herniations were not disclosed by previous physical examination because of the patients' obesity, abdominal pain, distension, or various other factors. However, CT scans showed the exact size, location, and content of each incisional hernia. The evaluation of postsurgical abdomen by CT should include a careful assessment of previous laparotomy sites in search of occult incisional hernias that may be the source of the patient's abdominal symptoms.

Incisional hernias are delayed complications of abdominal surgery and occur in 0.5–13.9% of patients according to various reported series [1–3]. The average frequency is currently about 4%, but these iatrogenic hernias constitute a significant problem, given that almost 2 million abdominal operations are performed in the United States each year [4, 5].

Most incisional hernias are easily recognized by careful inspection and palpation. However, there are several situations whereby an accurate clinical diagnosis may be difficult or impossible. In obese patients, for example, the abundant subcutaneous fat can prevent the palpation of a deeply seated peritoneal defect and the protruding intestinal loop or greater omentum. The detection of an incisional hernia by physical examination alone may also be difficult in patients with abdominal pain and distension or in the presence of keloid or thick panniculus. Furthermore, the herniated segments occasionally dissect and hide between muscular, aponeurotic, and fascial layers of the abdominal wall. These interparietal or interstitial hernias often present with localized swelling and tenderness adjacent to the surgical scar, but their actual content and internal orifice are seldom palpable [6]. Under these circumstances, evaluation of the abdominal wall by sonography or CT can provide the correct diagnosis as illustrated in a few case reports [5, 7–10]. This article describes our experience with 14 adult patients whose postoperative CT of the abdomen showed clinically occult incisional hernias of various size, location, and content.

Received July 10, 1986; accepted after revision August 21, 1986.

Presented at the annual meeting of the American Roentgen Ray Society, Washington DC, April 1986.

¹ All authors: Department of Diagnostic Radiology, Evanston Hospital–Northwestern University McGaw Medical Center, 2650 Ridge Ave., Evanston, IL 60201. Address reprint requests to G. G. Ghahremani.

AJR 148:139–142, January 1987
0361–803X/87/1481–0139
© American Roentgen Ray Society

Materials and Methods

This series includes four men and 10 women, ranging in age from 25 to 86 years (average, 57 years). They were evaluated at our institution over a 7½-year period between August 1978 and February 1986. All had nonpalpable incisional hernias that were first recognized on postoperative CT of the abdomen and pelvis. These scans were obtained primarily for follow-up of gynecologic malignancies (five cases) or colon carcinoma (three cases). Six others were examined because of abdominal symptoms after laparotomy for ulcerative colitis, lymphoma, diverticulitis of the colon, cholecystitis, aortic aneurysm, and internal injuries due to numerous stab wounds (one case of each). Two of our patients had undergone surgery twice and one had had three laparotomies.

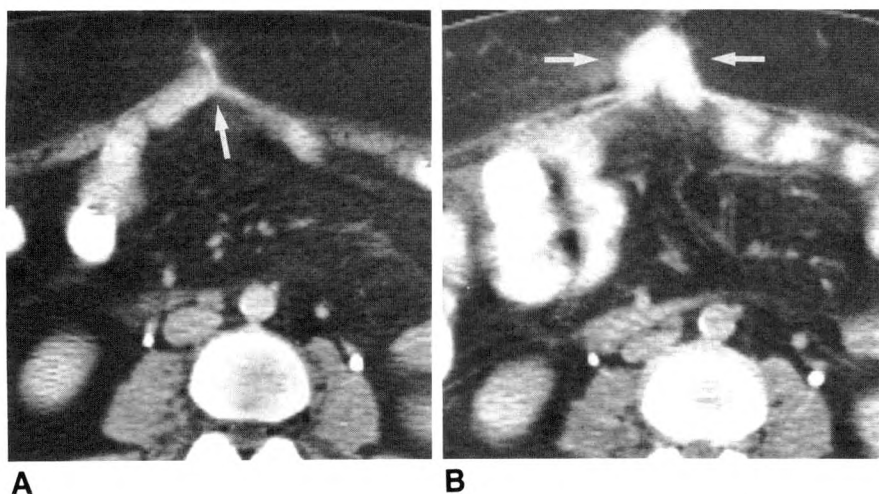


Fig. 1.—Development and progression of an occult midline incisional hernia after total abdominal hysterectomy for endometrial carcinoma.

A, CT examination 4 months after laparotomy shows healing incision with slight tenting of its peritoneal aspect (arrow).

B, Reexamination 1 year postoperatively shows a knuckle of small bowel protruding into subcutaneous fat (arrows). Patient had midline scar tenderness, but developed bowel obstruction 2 months later when a loop of distal jejunum became incarcerated in the anterior abdominal wall.

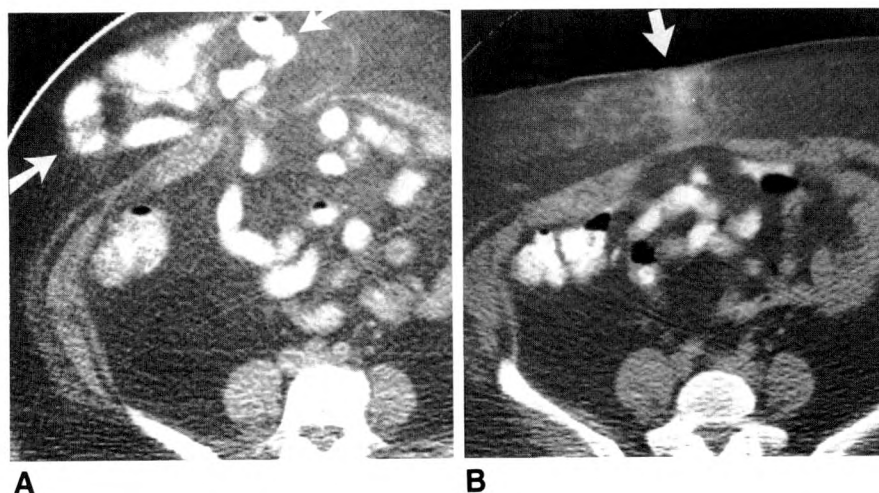


Fig. 2.—Large, nonpalpable hernia complicating right paramedian incision. This obese woman (340 lb.-154 kg) presented with postprandial cramps in the periumbilical region.

A, CT section at level of iliac crest shows several small-bowel loops deeply embedded within the subcutaneous fat (arrows).

B, Another section 4 cm caudad after abdominal compression with sponge shows that rest of paramedian incision has healed completely (arrow).

All patients had undergone repeated physical examinations, but their incisional hernias were not diagnosed because they were nonpalpable even after being detected by CT. Nevertheless, 10 of the 14 patients experienced abdominal symptoms that were directly related to these herniations. Three had suffered from episodes of bowel obstruction that were previously attributed to either recurrent tumor or adhesions, while seven others had recurrent periumbilical pain and localized tenderness of their laparotomy scars.

The first two cases were examined with an EMI-5005 scanner (Northbrook, IL) and the remaining 12 with a General Electric CT/T 8800 unit (Milwaukee, WI). A series of 1-cm-thick sections of the abdomen and pelvis were obtained after gastrointestinal opacification with diluted contrast material. All but two patients had also received an IV bolus of 100–150 ml of Conray-60 (Mallinckrodt, St. Louis, MO).

Results

The existence of an incisional hernia was first disclosed by CT performed at variable postoperative intervals: at 2–6 months (4 cases); at 6–12 months (8 cases); and at 16 and

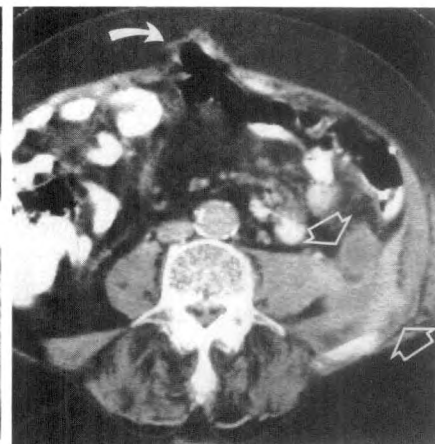
25 months (one case each). The herniation occurred along the midline or paramedian incision in eight of our 14 cases. CT typically showed a defect in the peritoneal and fascial layers of the anterior abdominal wall, through which a knuckle of small bowel protruded into the subcutaneous fat (Fig. 1). In a very obese woman, several loops of small bowel were embedded in the 7-cm-thick subcutaneous fat by extending far laterally beyond the limits of her midline incision (Fig. 2). She had frequent periumbilical cramps, but neither the hernia content nor its underlying wall defect could be palpated. CT of another patient showed two separate small-bowel herniations involving the superior and inferior aspects of a long paramedian incision, while the middle segment had remained intact. There were also two cases in which midline incisional hernias contained properitoneal fat and edge of greater omentum (Fig. 3), or an outpouching of the transverse colon causing a Richter's hernia (Fig. 4).

CT in the remaining six patients revealed occult incisional hernias at various other locations. Two were in the left lower quadrant, involving the sites of a previous colostomy (Fig. 5)

Fig. 3.—CT of pelvis 8 months after laparotomy for ovarian carcinoma reveals an incisional hernia (arrows) containing properitoneal fat and edge of greater omentum. Hernia accounted for this patient's lower abdominal pain and obstructive symptoms.

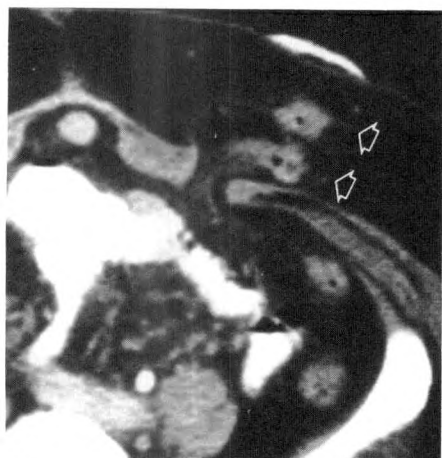


3

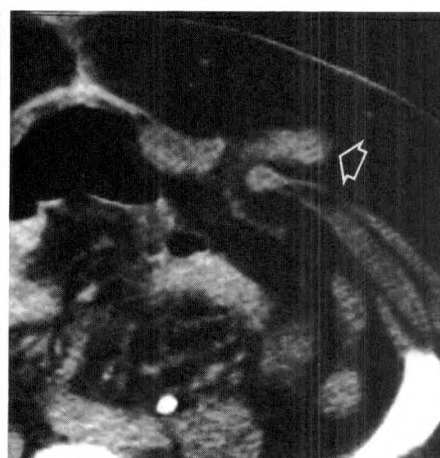


4

Fig. 4.—CT of abdomen 2 months after segmental resection of a rectosigmoid carcinoma shows an abscess involving left iliac fossa and psoas muscle (open arrows). Incidentally noted is a localized outpouching of transverse colon into midline incision (curved arrow), representing a Richter's hernia that was confirmed by barium enema a few weeks later.



A



B

Fig. 5.—Occult incisional hernia at site of a previous colostomy.
A, CT 3 months after emergency laparotomy for perforated sigmoid diverticulitis shows a double-barrel colostomy (arrows).
B, CT at same level 10 months after colostomy closure reveals a hernia through residual defect in peritoneal and muscular layers (arrow). Note fibrotic scar along healed midline incision.

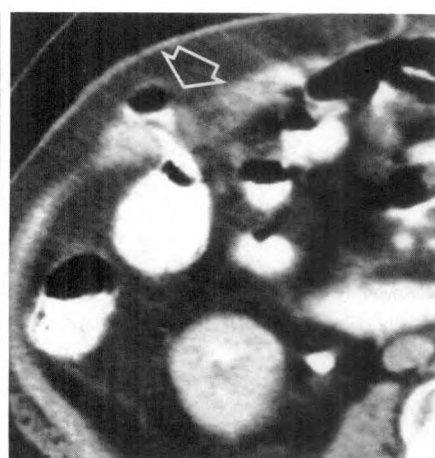


Fig. 6.—Occult incisional hernia after cholecystectomy. CT shows an intestinal loop protruding through a defect in muscular layers under right subcostal incision (arrow). Subsequent barium enema confirmed intermittent herniation of proximal transverse colon into subcutaneous fat 2 cm beneath intact skin.

and an abscess drainage. One occurred along the transverse incision of the lower abdomen. CT of two postcholecystectomy patients showed protrusion of a small-bowel loop or transverse colon beneath their right subcostal incisions (Fig. 6). CT of another patient after total colectomy for ulcerative colitis disclosed a paraileostomy hernia in the right lower abdomen as well as a separate herniation through the midline incision.

Eight patients have had surgical repair of an incisional hernia. This was performed either shortly after the CT diagnosis (three cases) or 3–14 months later (five cases) when follow-up CT or gastrointestinal barium studies showed pro-

gressive enlargement of the hernia with obstructive symptoms caused by incarceration.

Discussion

Most incisional hernias develop during the first 4 months after surgery, a critical period for the healing of transected muscular and fibrous layers of the abdominal wall [2, 11]. Progressive enlargement of these hernias will usually manifest signs and symptoms within the first year. However, 5–10% may remain clinically silent for up to 5 years until their detection [3, 12].

The correct diagnosis of an incisional hernia is usually based on careful inspection and palpation. Radiologic studies may then be used to visualize the herniated segments and to evaluate associated complications such as intestinal obstruction [5]. Approximately 5–10% of incisional hernias and recurrences after ventral or inguinal herniorrhaphy are not detectable by physical examination alone. This may be due to marked obesity of the patient; easily reducible hernia content; excessive scar formation over a small, deep peritoneal defect; or the interstitial nature of the herniation whereby the bowel loops or greater omentum protrude between various muscular and fascial layers of the abdominal wall [3–9]. In such cases the existence of a clinically occult incisional hernia can be documented by gastrointestinal barium studies [5, 13], peritoneography [14], or sonography [7–9]. Several authors have also described the CT findings of hernias that were inaccessible to physical examination [15–20]. To our knowledge, however, the value of CT in the detection of occult incisional hernia has not been previously assessed.

The postoperative CT examinations of our 14 patients were done to evaluate the extent of their malignancy or other intraabdominal processes. Their healed laparotomy sites appeared unremarkable on repeated physical examinations despite a slight tenderness on palpation in seven cases. Therefore, the detection of 16 incisional hernias (two separate sites in two patients) was an unexpected but relevant finding. The incisional hernia represented the source of intermittent abdominal pain and obstructive symptoms in 10 patients, eight of whom later had incisional hernias repaired.

In all but two patients the incisional hernias were recognized on CT done within the first postoperative year, and the majority were located beneath the midline incisions. Several other types were also encountered, including paraileostomy hernia and bowel protrusion at the sites of previous colostomy, cholecystectomy, and abscess drainage. In each instance the CT sections provided a clear definition of the underlying peritoneal defect as well as the size and content of the hernia. The herniated segment most often was a small-bowel loop and occasionally parts of the colon, properitoneal fat, or the greater omentum (Figs. 1–6).

Our experience indicates that CT is an accurate method for the detection of nonpalpable incisional hernias; it is just as valuable as its already proven application in the diagnosis of other hernias that are not accessible to physical examination [15–20]. Almost 2 million abdominal operations of various types are performed annually in the United States, and inci-

sional hernias are among the most frequent complications [3–5]. Many of these patients later undergo CT primarily to evaluate intraabdominal processes. However, radiologists should also carefully assess the CT appearance of the abdominal wall in search of a clinically occult incisional hernia that may be the unsuspected source of a patient's abdominal pain or intestinal obstruction.

REFERENCES

1. Fischer JD, Turner FW. Abdominal incisional hernias—a 10 year review. *Can J Surg* 1974;17:202–204
2. Bucknall TE, Cox PJ, Ellis H. Burst abdomen and incisional hernia: a prospective study of 1129 major laparotomies. *Br Med J* 1982;284:931–933
3. Baker RJ. Incisional hernia. In: Nyhus LM, Condon RE, eds. *Hernia*. Philadelphia: Lippincott, 1978:329–341
4. Larson GM, Vandertoll DJ. Approaches to repair of ventral hernia and full-thickness losses of the abdominal wall. *Surg Clin North Am* 1984;64:335–349
5. Ghahremani GG, Meyers MA. Iatrogenic abdominal hernias. In: Meyers MA, Ghahremani GG. *Iatrogenic gastrointestinal complications*. New York: Springer-Verlag, 1981:269–278
6. Altman B. Interparietal hernia. In: Nyhus LM, Condon RE, eds. *Hernia*. Philadelphia: Lippincott, 1978:387–394
7. Thomas JL, Cunningham JJ. Ultrasonic evaluation of ventral hernias disguised as intraabdominal neoplasms. *Arch Surg* 1978;113:589–590
8. Deitch EA, Engel JM. Ultrasonic diagnosis of surgical diseases of the anterior abdominal wall. *Surg Gynecol Obstet* 1980;151:484–486
9. Spangen L. Ultrasound as a diagnostic aid in ventral abdominal hernia. *JCU* 1975;3:211–213
10. Fisch AE, Brodey PA. Computed tomography of the anterior abdominal wall: normal anatomy and pathology. *J Comput Assist Tomogr* 1981;5:728–733
11. Douglas DM. The healing of aponeurotic incisions. *Br J Surg* 1952;40:79–82
12. Ellis H, Gajraj H, George CD. Incisional hernias: when do they occur? *Br J Surg* 1983;70:290–291
13. Maglinte DDT, Miller RE, Lappas JC. Radiologic diagnosis of occult incisional hernias of the small intestine. *AJR* 1984;142:931–932
14. Ekberg O, Fork FT, Aspelin P. Herniography in anterior abdominal wall hernia. *ROFO* 1985;143:562–568
15. Meziene MA, Fishman EK, Siegelman SS. Computed tomographic diagnosis of obturator foramen hernia. *Gastrointest Radiol* 1983;8:375–377
16. Balthazar EJ, Subramanyan BR, Megibow A. Spigelian hernia: CT and ultrasonography diagnosis. *Gastrointest Radiol* 1984;9:81–84
17. Kane VG, Silverstein GS. CT demonstration of hernia through an iliac crest defect. *J Comput Assist Tomogr* 1986;10:432–434
18. Passas V, Karavias D, Grilias D, Birbas A. Computed tomography of left paraduodenal hernia. *J Comput Assist Tomogr* 1986;10:542–543
19. Fagelman D, Caridi JG. CT diagnosis of hernia of Morgagni. *Gastrointest Radiol* 1984;9:153–155
20. Gale ME. Bochdalek hernia: prevalence and CT characteristics. *Radiology* 1985;156:449–452

Case Report

MR Imaging of Gallbladder Carcinoma

Michelle D. Rossmann,¹ Arnold C. Friedman, Paul D. Radecki, and Dina F. Caroline

Carcinoma of the gallbladder is the most common malignant tumor of the biliary tract [1, 2]. The symptoms and physical findings are often indistinguishable from those of cholelithiasis and cholecystitis. The latter are present in 80–90% of cases [3, 4]. Because the clinical presentation is nonspecific, the radiologist is often the first to suggest the correct diagnosis. Others have reviewed the appearance of adenocarcinoma of the gallbladder on sonography [1–3, 5, 6] and CT [4–7]. This is a report of a case of gallbladder carcinoma in which MR was performed and compared with sonography and CT.

Case Report

A 61-year-old woman had a painless jaundice of 1-week duration. Serum alkaline phosphatase was 955 IU/l (normal, 15–85), SGOT was 221 mU/ml (normal, 10–50), and total bilirubin was 19.5 mg/dl (normal, 0.2–1.0). Sonography revealed marked extrahepatic biliary duct dilation (12 mm) and mild intrahepatic duct dilation (Fig. 1). The gallbladder was not identified as a fluid-filled structure. A large crescentic echogenic focus with posterior shadowing consistent with a large gallstone was seen in the gallbladder fossa. A poorly defined hypoechoic mass (2–3 cm thick) surrounded the gallstone and obstructed the common duct. It could not be separated from the liver.

A contrast-enhanced CT scan showed a faintly calcified gallstone surrounded by a small amount of fluid. Dilated intrahepatic bile ducts could be followed down to the porta hepatis just below the bifurcation. A mass in the hepatoduodenal ligament extending into the liver was barely perceptible just cephalad to the gallstone (Fig. 2).

MR images revealed a large area of low signal intensity within the gallbladder, consistent with a gallstone (Fig. 3). Surrounding the stone was a poorly marginated mass of approximately 7 cm. The mass was of medium signal intensity on the relatively T1-weighted image

and of higher intensity on the more T2-weighted image. The absence of a clear interface between normal liver and the mass on MR suggested liver invasion. Biliary duct dilation was far less obvious than on sonography or CT.

At surgery, a neoplasm (approximately 8 × 7 cm) was found in the hepatoduodenal ligament; it arose from the gallbladder, encased the common bile duct, and invaded the right lobe of the liver. A biopsy and pathologic examination of the tumor mass revealed adenosquamous carcinoma. The extent of the neoplasm was best depicted by MR imaging.

Discussion

The MR findings in this case of gallbladder carcinoma showed a gallstone surrounded by a poorly marginated hypointense mass within the gallbladder fossa on the relatively T1-weighted spin-echo images. On the more T2-weighted spin-echo images, the mass became hyperintense compared to the liver. The gallstone appeared as a filling defect of low signal intensity on all MR images. The extent of the neoplastic process was best depicted by MR, although the dilated biliary tree was shown better by sonography and CT.

When not degraded by motion artifact, MR may depict the extent of gallbladder carcinoma better than sonography or CT. However, dilated biliary ducts may be depicted better by CT or sonography than by MR. MR may be useful in differential diagnosis in selected cases when sonography shows marked gallbladder-wall thickening in the absence of clinical signs of acute cholecystitis or other causes of gallbladder-wall thickening. If MR shows invasion of the liver, gallbladder carcinoma is more likely than either chronic cholecystitis or hyperplastic cholecystosis.

Received June 9, 1986; accepted after revision August 7, 1986.

¹ All authors: Department of Diagnostic Imaging, Temple University Hospital, Broad and Ontario Streets, Philadelphia, PA 19140. Address reprint requests to A. C. Friedman.

AJR 148:143–144, January 1987 0361–803X/87/1481–0143 © American Roentgen Ray Society

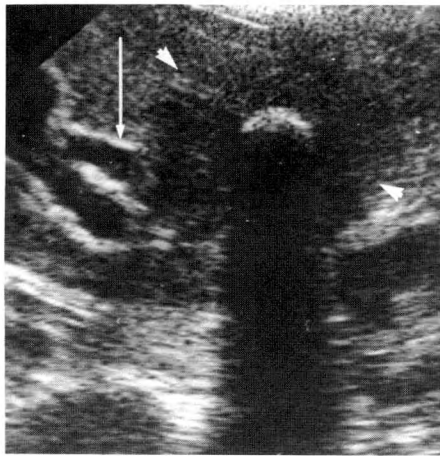
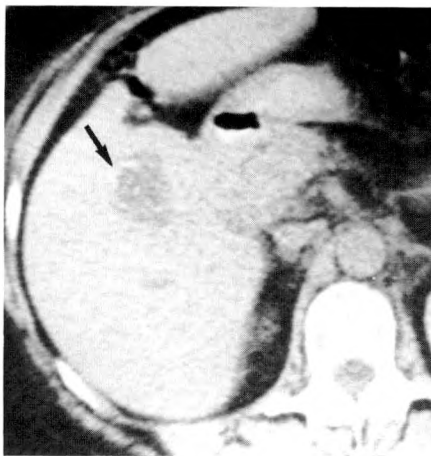
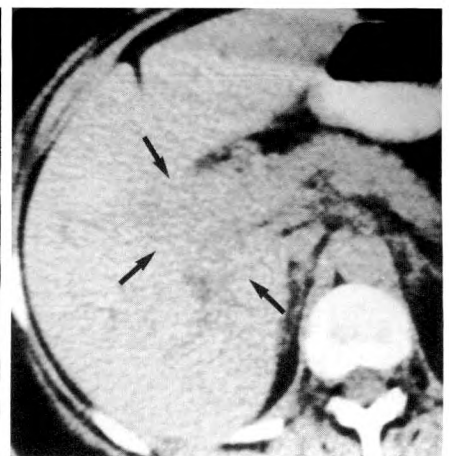


Fig. 1.—Parasagittal right anterior oblique sonogram shows large crescentic echogenic focus with posterior shadowing, consistent with a gallstone, in gallbladder fossa. Poorly defined hypoechoic mass (arrowhead) surrounds gallstone and obstructs common duct (arrow).



A

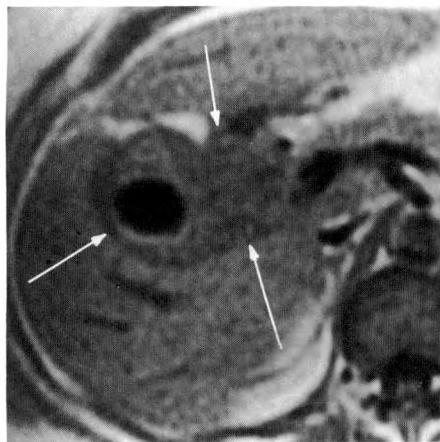


B

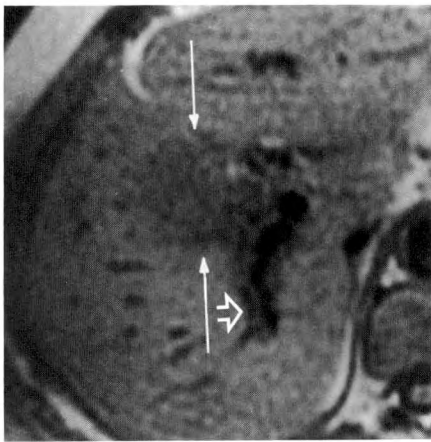
Fig. 2.—CT scan after IV and oral contrast administration.

A, Faintly calcified gallstone (arrow) is surrounded by small amount of fluid.

B, Hypodense mass (arrows) 14 cm cephalad to A involves hepatoduodenal ligament and liver. Dilated intrahepatic ducts are evident.



A

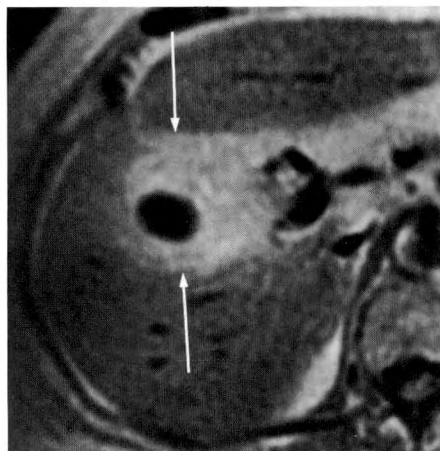


B

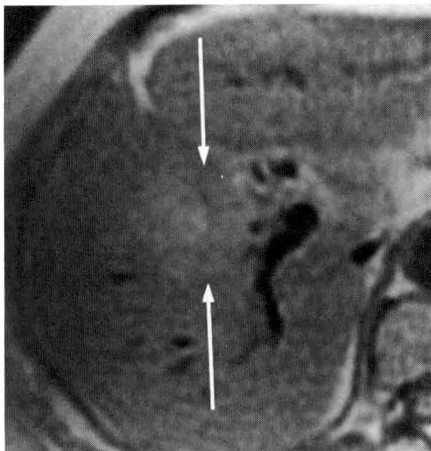
Fig. 3.—Axial MR images.

A, B, SE 500/28 images. Ovoid region of absent signal represents gallstone, which is surrounded by high-intensity bile and low-intensity mass (arrows, A). Mass is infiltrating liver (closed arrows, B), and dilated intrahepatic duct is anterolateral to a portal vein (open arrow, B).

C, D, Mass increases in intensity (arrows) at SE 2000/28.



C



D

REFERENCES

1. Ruiz R, Teyssou H, Fernandez N, et al. Ultrasonic diagnosis of primary carcinoma of the gallbladder: review of 16 cases. *JCU* 1980;8:489-495
2. Raghavendra BN. Ultrasonographic features of primary carcinoma of the gallbladder: report of five cases. *Gastrointest Radiol* 1980;5:239-244
3. Yum HY, Fink AH. Sonographic findings in primary carcinoma of the gallbladder. *Radiology* 1980;134:693-696
4. Smathers RL, Lee JKT, Heiken JP. Differentiation of complicated cholecystitis from gallbladder carcinoma by computed tomography. *AJR* 1984;143:255-259
5. Yeh HC. Ultrasonography and computed tomography of carcinoma of the gallbladder. *Radiology* 1979;133:167-173
6. Weiner SN, Koenigsberg M, Morehouse H, Hoffman J. Sonography and computed tomography in the diagnosis of carcinoma of the gallbladder. *AJR* 1984;142:735-739
7. Itai Y, Araki T, Yoshikawa K, Furui S, Tasaka A. Computed tomography of gallbladder cancer. *Radiology* 1980;137:713-718

Case Report

Voice Change After Barium Enema: A Clinical Sign of Extraperitoneal Colon Perforation

David N. Rabin,¹ Claire Smith,¹ Thomas R. Witt,² and Lauren D. Holinger³

Colonic perforation is an infrequent complication of barium enema examinations and is reported to occur with a frequency of one in 2250 to one in 12,000 procedures [1, 2]. Nevertheless, radiologists must be aware of the clinical presentation of this problem since they can expect to see at least one colonic perforation during their career [1]. Delayed diagnosis increases patient morbidity and mortality due to infection and peritonitis [3, 4]. Prompt recognition may be difficult, since these patients are usually initially asymptomatic and perforation may be difficult to recognize during fluoroscopy [3, 4]. We report a case in which a change in the patient's voice (pitch) caused by subcutaneous emphysema was a sign of the presence of an extraperitoneal colonic perforation.

Case Report

Double-contrast barium enema examination was performed on a 51-year-old white man for the evaluation of rectal bleeding. The procedure was performed 24 hr after an uncomplicated complete colonoscopy without biopsy. Because the patient was initially unable to retain the enema, a retention balloon catheter was inflated without difficulty under fluoroscopic observation. The procedure was performed in the usual fashion without difficulty. However, the patient complained of a high-pitched quality to his voice when he returned from the bathroom after the study. There were no other signs or symptoms. Radiographs obtained during the study showed gas in the retroperitoneum and in the peritoneal cavity (Fig. 1). There was

minimal contrast-material extravasation (Fig. 1, arrow) near the medial aspect of the proximal descending colon, but the colon was otherwise normal. Further fluoroscopic studies of the chest and neck showed pneumomediastinum and gas in the soft tissues of the neck (Fig. 2).

The patient returned to his room in stable condition without shortness of breath, pain, or abdominal tenderness. Within 1 hr, he developed mild dysphagia. A surgical consultation was obtained, and the patient was given nothing by mouth and started on IV fluids. He underwent a thorough head and neck examination including mirror examination of the larynx and hypopharynx. Aside from crepitance in the soft tissues of the neck, there were no abnormalities noted. The airway was widely patent.

The patient remained afebrile without local or systemic signs of infection, and his dysphagia cleared rapidly, although his voice remained unusually high pitched. Radiographs demonstrated gradual resolution of the intraperitoneal and extraperitoneal gas. The patient was discharged with near-normal voice quality after 5 days of observation. On a follow-up outpatient visit a few weeks later, his voice was normal.

Discussion

Extraperitoneal (retroperitoneal) rupture of the colon during double-contrast barium enema can result in parapharyngeal emphysema. Gas ascends into the mediastinum from the retroperitoneum through the diaphragmatic hiatus traveling along the trachea and esophagus [5].

Received May 13, 1986; accepted after revision July 25, 1986.

¹ Department of Diagnostic Radiology and Nuclear Medicine, Rush-Presbyterian-St. Luke's Medical Center, 1753 W. Congress Pkwy., Chicago, IL 60612. Address reprint requests to D. N. Rabin. After July 1, 1987, address reprint requests to D. N. Rabin, Mallinckrodt Institute of Radiology, 510 S. Kingshighway Blvd., St. Louis, MO 63110.

² Department of General Surgery, Rush-Presbyterian-St. Luke's Medical Center, Chicago, IL 60612.

³ Department of Otolaryngology/Bronchoesophagology, Rush-Presbyterian-St. Luke's Medical Center, Chicago, IL 60612.

AJR 148:145-146, January 1987 0361-803X/87/1481-0145 © American Roentgen Ray Society

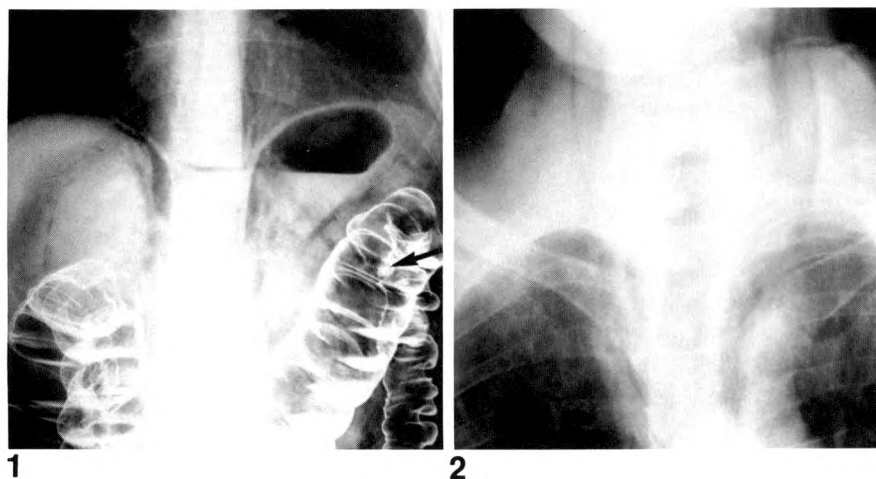


Fig. 1.—Upright radiograph made during air-contrast barium enema shows pneumoperitoneum and gas in retroperitoneum tracking into mediastinum. Arrow indicates site of extravasation of contrast material.

Fig. 2.—Radiograph of neck shows pneumomediastinum and parapharyngeal emphysema.

Parapharyngeal emphysema can occur during the examination or it may be delayed for several hours, while gas dissects from the site of perforation to the larynx and hypopharynx [6]. Signs and symptoms of mediastinal and retropharyngeal emphysema include chest pain, dyspnea, a puffy face and neck, and "crackles" in the skin [5]. A search of the literature yielded only one report of vocal signs, a "husky, whispering, 'hot potato' voice," occurring because of parapharyngeal emphysema [5]. The emphysema was not related to a barium enema.

It seems likely that the gas that dissected into our patient's neck caused a slight alteration of the contours and dimensions of the laryngeal and hypopharyngeal structures, which changed the quality of his voice. Vocal frequency is determined by the shape and length of the supralaryngeal vocal tract (nose, mouth, and pharynx), which acts as a variable acoustic filter that lets more energy through at different frequencies as the speaker changes the shape of the tract [7]. Narrowing of the pharynx can have a major effect on voice resonance [8], as this case illustrates.

On the basis of our experience, we suggest that any report of a peculiar change in the patient's voice, even hours after a "normal" barium enema examination, be investigated promptly

since the underlying cause may be extraperitoneal colonic perforation.

REFERENCES

1. Gelfand DW. Complications of gastrointestinal radiologic procedures. I. Complications of routine fluoroscopic studies. *Gastrointest Radiol* **1980**;5:293-315
2. Seaman WB, Wells J. Complications of the barium enema. *Gastroenterol* **1965**;48:728-737
3. Han SY, Tishler JM. Perforation of the colon above the peritoneal reflection during the barium-enema examination. *Radiology* **1982**;144:253-255
4. Peterson N, Rohrmann CA Jr, Lennard ES. Diagnosis and treatment of retroperitoneal perforation complicating the double-contrast barium-enema examination. *Radiology* **1982**;144:249-252
5. Maunder RJ, Pierson DJ, Hudson LD. Subcutaneous and mediastinal emphysema: pathophysiology, diagnosis, and management. *Arch Intern Med* **1984**;144:1447-1453
6. Brown S, Fine A. Diffuse emphysema following a double contrast enema. *Radiology* **1941**;37:228-229
7. Lieberman P. *Speech physiology and acoustic phonetics: an introduction*. New York: MacMillan, **1977**:3-96
8. Hardcastle WJ. *Physiology of speech production: an introduction for speech scientists*. London: Academic Press, **1976**:125

Case Report

Symptomatic Congenital Ectopic Gastric Mucosa in the Upper Esophagus

Susan M. Williams,¹ Clarence May, Duane W. Krause, and Roger K. Harned

Endoscopic diagnosis of congenital ectopic gastric mucosa in the upper esophagus has been described recently [1, 2]. This condition is more common than generally realized; careful endoscopy shows a prevalence of 4%. Because of its strong emphasis in the literature, a radiologist might erroneously assume that all gastric mucosa in the esophagus represents acquired Barrett's esophagus. However, when isolated patches or rings of gastric mucosa are seen in the upper esophagus and the distal esophagus is normal, congenital rests are usually the cause. This report describes a case in which isolated rests of gastric mucosa formed a symptomatic ring in the upper esophagus that was demonstrated on barium esophagram.

Case Report

A 40-year-old white man complained of intermittent episodes of dysphagia with temporary lodging of food in his upper esophagus. After a few minutes, the food would pass, and he could continue eating. Barium esophagram showed a ringlike narrowing in the upper esophagus at the thoracic inlet (Fig. 1). At endoscopy, a narrowed area 3 mm long was encountered 18 cm from the incisors. The mucosa had a red-orange coloration distinct from the remainder of the esophagus. No evidence of ulceration was seen in the distal esophagus. The gastroesophageal junction was normal and located below the diaphragm at 40 cm.

The ring of reddened mucosa was biopsied, and histologic examination of the specimen showed columnar epithelium and gastric glands containing parietal cells. Examination of specimens taken distal to the ring showed normal squamous esophageal mucosa.

Discussion

The presence of congenital aberrant gastric mucosa in the upper esophagus has been recognized since the 1800s. Extensive study of the developmental changes in the esophageal epithelium by Johns [3] suggested a possible embryologic explanation for this phenomenon. At first, the embryonic esophagus is lined entirely by stratified columnar epithelium. This is replaced sequentially by ciliated columnar epithelium and then stratified squamous epithelium. Replacement begins in the midesophagus and extends proximally and distally. The last part of the esophagus to lose its columnar lining is the upper end, and rests of columnar epithelium occasionally may persist. Superficial glands develop in the embryonic esophagus from residual columnar epithelium and may persist into adult life.

The reported incidence of this condition varies widely. Schridde [4] found a prevalence of 70% when serial sections of the upper esophagus were examined microscopically. Most of these were microscopic rests and would not be expected to cause symptoms or be demonstrable radiographically.

Grossly visible ectopic rests are less common. Taylor [5] reported six cases in a series of 900 autopsies. The ectopic patches were $\frac{1}{8}$ – $\frac{3}{4}$ in. in diameter, reddish, frequently paired on each side of the lumen, and consistently found near the upper end of the esophagus.

A careful endoscopic survey by Jabbari et al. [1] found a prevalence of 4% (16 cases) in 420 sequential endoscopies. The gastric mucosa appeared as a velvety red area varying

Received June 2, 1986; accepted after revision August 12, 1986.

¹ All authors: Department of Radiology, University of Nebraska Medical Center, 42nd and Dewey Ave., Omaha, NE 68105. Address reprint requests to S. M. Williams.

AJR 148:147–148, January 1987 0361–803X/87/1481–0147 © American Roentgen Ray Society



Fig. 1.—Barium esophagram shows a persistent ringlike narrowing in upper esophagus at level of thoracic inlet (arrows).

in size from a few millimeters to a ring completely encircling the esophagus. In all instances, the ectopic mucosa was found at or just below the level of the cricopharyngeus. Histologically, the lesions consisted of gastric-type columnar epithelium and contained parietal and chief cells. In only one of the 16 cases was Barrett's epithelium noted in the lower esophagus; in the other 15, the lower esophageal mucosa was endoscopically normal.

Recently, Hamilton et al. [2] used Congo red dye and found evidence of acid production in four cases of ectopic gastric epithelium in the cervical esophagus. The capacity for acid production may explain vague symptoms or cricopharyngeal spasm associated with some reported cases. Specific search

for ectopic gastric mucosa is warranted in patients with upper dysphagia or fluoroscopic evidence of cricopharyngeal spasm.

In summary, congenital ectopic gastric mucosal rests in the upper esophagus are not rare and are recognized endoscopically and pathologically. This lesion is distinct from Barrett's esophagus, which represents acquired columnar metaplasia extending proximally from the distal esophagus secondary to reflux esophagitis. Observations supporting the conclusion that this lesion is distinct from Barrett's esophagus include the following: the consistent location of the lesions in the uppermost portion of the esophagus, the consistent finding of normal squamous mucosa distal to the ectopic patches, the absence of symptoms or a definite history of reflux esophagitis in most cases, and the steady incidence of the lesion from embryonic life through adulthood. Radiologists should be aware that this condition exists and can be shown radiographically. Radiographic and endoscopic examination of the upper esophagus for ectopic mucosa is indicated in patients with upper esophageal dysphagia and may result in more frequent radiographic diagnosis of this condition.

REFERENCES

1. Jabbari M, Goresky CA, Lough J, Yaffe C, Daly D, Cote C. The inlet patch: heterotopic gastric mucosa in the upper esophagus. *Gastroenterology* 1985;89:352-356
2. Hamilton JW, Thune RG, Morrissey JF. Symptomatic ectopic gastric epithelium of the cervical esophagus: demonstration of acid production with congo red. *Dig Dis Sci* 1986;31:337-342
3. Johns BAE. Developmental changes in the oesophageal epithelium in man. *J Anat* 1952;86:431-442
4. Schridde H. Über Manenschleimhaut-inseln vom bau der Cardialdrusenzone und Fundusdrusenregion und den untern, oesophagealen cardialdrusen gleichende Drusen im obersten Oesophagusabschnitt. *Virchows Arch [Pathol Anat]* 1904;175:1-16
5. Taylor AL. The epithelial heterotopias of the alimentary tract. *J Pathol* 1927;30:415-449

Case Report

Pneumoretroperitoneum Secondary to Hydrogen Peroxide Wound Irrigations

Lawrence C. Swayne,¹ Hal N. Ginsberg,¹ and Arthur Ginsburg²

Gas in the retroperitoneum may occur secondary to perforation of the gastrointestinal tract, trauma, pneumomediastinum, pneumatosis intestinalis, abscess, or iatrogenic causes such as surgery and endoscopy [1]. We report a patient with retroperitoneal gas caused by wound irrigation with hydrogen peroxide. CT showed bilateral psoas air-fluid levels. After the irrigations were stopped, serial CT showed gradual complete resolution. The dissection of molecular oxygen and water [2, 3] through the retroperitoneal fascial planes in this case illustrates several potential anatomic pathways for spread of infection.

Case Report

An 84-year-old woman presented to the emergency room with fever (102° F), chills, and an elevated WBC count (16,000). One month before admission, she had undergone a right nephrectomy for sepsis, pyonephrosis, and a perirenal abscess secondary to multiple renal calculi. The patient's condition rapidly improved after oral treatment with cephalosporin and wound irrigations with 3% hydrogen peroxide performed through Penrose drains (Davol, Inc., Cranston, RI) left in the operative site.

A CT scan, performed 3 days after admission to rule out a recurrent abscess, revealed multiple gas collections extending from the right flank incision to involve the right perirenal space, the adjacent right psoas muscle, the third lumbar vertebral body, and the left psoas muscle (Fig. 1). Because of the patient's clinical improvement, gas formation from the hydrogen peroxide therapy was suspected. Hydrogen peroxide is unstable when applied to tissues and rapidly decomposes into molecular oxygen and water [2, 3]. Because an

abscess could not be excluded, the irrigations were discontinued and a second CT scan was performed 3 days later. This scan showed a decrease in the amount of gas, suggesting that the peroxide therapy was indeed the most likely cause. The patient continued to improve clinically without further therapy, and a third CT scan done 3 weeks later showed complete resolution of the gas collections. The patient remained asymptomatic and was well at a 7-month clinical follow-up.

Discussion

Hydrogen peroxide solution is commonly employed for cleansing and irrigations of wounds. When hydrogen peroxide is applied to tissues, the enzyme (catalase) causes its rapid decomposition, releasing nascent molecular oxygen (1 ml of hydrogen peroxide 3% releases 10 ml of oxygen) [2]. This effervescence has slight germicidal effects and may result in mechanical removal of particulate debris as well. Forced irrigation into a closed body cavity, however, may have certain dangerous consequences [2, 3]. Soft-tissue emphysema and embolization to the mesenteric and portal veins (from colonic irrigations) and to pulmonary arteries have been reported [2, 3]. Also, animal studies and one case report have shown that the oxygen bubbles may traverse the pulmonary bed and cause cerebral, coronary, and other systemic embolizations [3].

In this case, the dissection of molecular oxygen apparently proceeded from the surgical wound in the right perirenal space to successively involve the right psoas muscle, the intervertebral disk space, the adjacent vertebral body, and the left

Received July 10, 1986; accepted after revision August 28, 1986.

¹ Department of Radiology, Morristown Memorial Hospital, 100 Madison Ave., Morristown, NJ 07960. Address reprint requests to L. C. Swayne.

² Department of Surgery, Morristown Memorial Hospital, 100 Madison Ave., Morristown, NJ 07960.

AJR 148:149-150, January 1987 0361-803X/87/1481-0149 © American Roentgen Ray Society

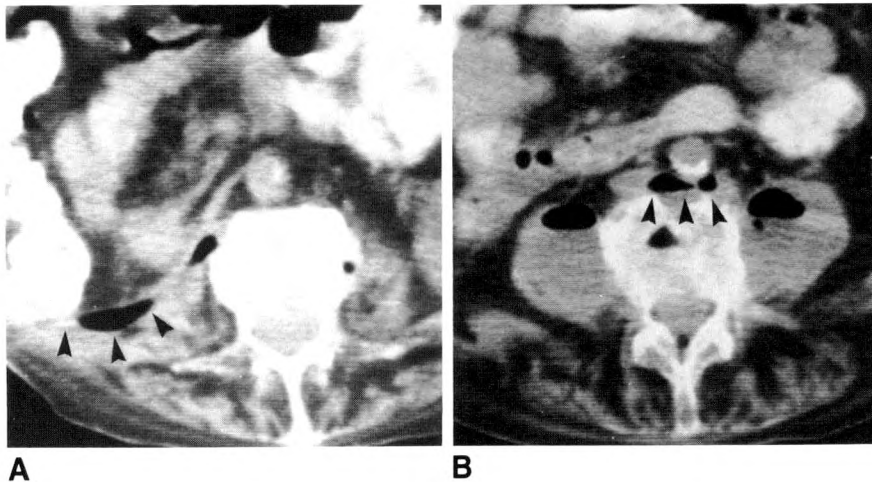


Fig. 1.—A, CT at level of renal hilus shows gas (arrowheads) extending from nephrectomy incision into right renal fossa and both psoas muscles.

B, CT obtained more caudally shows more extensive gas collections (arrowheads) involving both psoas compartments, the vertebral body, and the prevertebral space.

psoas muscle. Intercommunications between anatomic compartments of the retroperitoneum may occur because of incomplete fascial coverings, thus providing potential pathways for infectious spread. Primary infection of the psoas muscle is unusual and more commonly is secondary to extension from the adjacent spine, kidney, pancreas, or bowel [4, 5]. Spinal osteomyelitis or diskitis is often a precipitating cause of psoas abscesses, and bilateral involvement has been reported in association with both pyogenic and tuberculous organisms [4, 6]. Conversely, a paravertebral abscess may directly invade the spine and, along with the vertebral osteomyelitis, represent the most frequent cause of diskitis in patients older than 30 years old [7]. CT may show the presence of gas collections in both diskitis [8] and in up to 50% of patients with psoas abscesses [4].

The differential diagnosis in this case included: air from the indwelling Penrose drains, abscess formation, and dissection of molecular oxygen from the hydrogen peroxide irrigations. The extensive soft-tissue emphysema, lack of soft-tissue inflammation, and improvement in the patient's symptoms indicated the hydrogen peroxide irrigations as the probable cause. In the appropriate clinical setting, gas formation sec-

ondary to hydrogen peroxide wound irrigations should be included in the differential diagnosis of pneumoretroperitoneum.

REFERENCES

1. Calenoff L, Poticha SM. Combined occurrence of retroperitoneum and pneumoperitoneum. *AJR* 1973;117:366-372
2. Sleigh JW, Linter SPK. Hazards of hydrogen peroxide. *Br Med J* 1985;291:1706
3. Bassan MM, Dudai M, Shalev O. Near-fatal systemic oxygen embolism due to wound irrigation with hydrogen peroxide. *Postgrad Med J* 1982;58:448-451
4. Feldberg MAM, Koehler PR, van Waes PFGM. Psoas compartment disease studied by computed tomography. *Radiology* 1983;148:505-512
5. Mendez G Jr, Isikoff MB, Hill MC. Retroperitoneal processes involving the psoas demonstrated by computed tomography. *J Comput Assist Tomogr* 1980;4:78-82
6. de Roos A, van Persijn van Meerten EL, Bloem JL, Bluemmer RG. MRI of tuberculous spondylitis. *AJR* 1986;146:79-82
7. Boston HC Jr, Bianco AJ Jr, Rhodes KH. Disk space infections in children. *Orthop Clin North Am* 1975;6:953-964
8. Bielecki DK, Sartoris D, Resnick D, Lom KV, Fierer J, Haghighi P. Intraosseous and intradiscal gas in association with spinal infection: report of three cases. *AJR* 1986;147:83-86

Significance of Membrane Thickness in the Sonographic Evaluation of Twin Gestations

Barbara S. Hertzberg^{1,2}
 Alfred B. Kurtz¹
 Hong Y. Choi³
 Joseph M. Kaczmarczyk⁴
 Wendy Warren⁵
 Ronald J. Wapner⁵
 Laurence Needleman¹
 Oksana H. Baltarowich¹
 Matthew E. Pasto¹
 Matthew D. Rifkin¹
 Rebecca G. Pennell¹
 Barry B. Goldberg¹

A retrospective study of 55 twin pregnancies was performed to determine the role of sonography in distinguishing between dichorionic and monochorionic diamniotic gestations solely by evaluating the thickness of the membrane between the fetuses. The presence of a thick dividing membrane indicated a dichorionic diamniotic gestation in 38 (90%) of 42 cases in which it was identified. Inability to identify a membrane between dichorionic diamniotic twins occurred most commonly during the third trimester. A thin membrane indicated monochorionic diamniotic twinning and was seen in three (25%) of 12 cases. Membrane thickness was indeterminate in one case. Therefore, on the basis of the thickness of the dividing membrane imaged by sonography, dichorionic diamniotic gestations can be distinguished from monochorionic diamniotic gestations. Inability to show a separating membrane by sonography, however, can occur with any form of twin gestation, particularly in the third trimester. Membrane thickness should be used in conjunction with other sonographic criteria to predict the amnionicity and chorionicity of twin gestations.

Twin pregnancies are subdivided into the following three groups on the basis of the number of membranes surrounding the fetuses: dichorionic diamniotic (DC-DA), monochorionic diamniotic (MC-DA), and monochorionic monoamniotic (MC-MA). Prenatal sonographic determination of amnionicity and chorionicity is important in clinical management because the prevalence of complications depends on membrane composition; DC-DA gestations have the best prognosis and MC-MA the poorest [1-7].

Sonographic criteria for diagnosing DC-DA and MC-MA twinning have been described [1, 2]. Demonstration of two separate placental sites or of male and female fetal gender indicates a DC-DA gestation. Intertwining of the umbilical cords, conjoined twins, or more than three vessels in the umbilical cord occur only with MC-MA twinning. However, sonographic demonstration of only a single placental site or inability to show a membrane between the fetuses may occur with any of the three types of twinning; these two sonographic findings do not aid in classification of the pregnancy [1].

Sonographic criteria for diagnosing MC-DA twinning are not well established. Although sonographic identification of a membrane separating the fetuses indicates diamniotic twinning [1], it is important to differentiate DC-DA from MC-DA gestations. The dividing septum in DC-DA pregnancies is composed of two layers of amnion and two layers of chorion and thus is thicker than the membrane in MC-DA gestations, which contains only two layers of amnion [1, 5, 8, 9]. The goal of this study was to determine if DC-DA and MC-DA twin gestations could be distinguished from each other by analyzing the thickness of the membrane between the fetuses as seen on sonograms.

Material and Methods

Between January 1982 and December 1984, 124 sets of twins were delivered at Thomas Jefferson University Hospital. Prenatal sonography was performed in 72 of these pregnancies.

Received June 9, 1986; accepted after revision August 14, 1986.

¹ Department of Radiology, Division of Diagnostic Ultrasound, Thomas Jefferson University Hospital, Philadelphia, PA 19107.

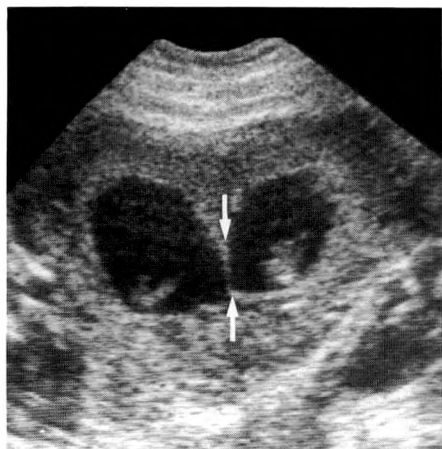
² Present address: Department of Radiology, Box 3808, Duke University Medical Center, Durham, NC 27710. Address reprint requests to B. S. Hertzberg.

³ Department of Pathology, Thomas Jefferson University Hospital, Philadelphia, PA 19107.

⁴ Department of Obstetrics and Gynecology, The Osteopathic Medical Center of Philadelphia, Philadelphia, PA 19131.

⁵ Department of Obstetrics and Gynecology, Division of Maternal-Fetal Medicine, Thomas Jefferson University Hospital, Philadelphia, PA 19107.

AJR 148:151-153, January 1987
 0361-803X/87/1481-0151
 © American Roentgen Ray Society



1

Fig. 1.—Transverse sonogram of a dichorionic diamniotic twin pregnancy during first trimester shows thick dividing membrane (arrows).



2

Fig. 2.—Oblique sonogram of a dichorionic diamniotic twin pregnancy during second trimester shows a thick septum separating the fetuses (arrows).



3

Fig. 3.—Oblique sonogram of a monochorionic diamniotic twin pregnancy during second trimester shows a short segment of a thin, wispy dividing membrane (arrows).

Sonograms were obtained by using a variety of commercially available machines with 3.5- and 5.0-MHz transducers. Real-time scanning was performed during most examinations, and static images were also available in many cases.

Amnionity and chorionity could be determined with certainty, on the basis of clinical or pathologic information, in 55 of these twin sets, and these 55 are the basis for this report. Twin gestations were classified as DC-DA if they satisfied at least one of the following clinical or pathologic criteria: male and female gender of the neonates, presence of two separate placentas at delivery, and determination of the DC-DA form of twinning by pathologic examination of the placenta (18 cases). MC-MA or MC-DA twinnings were diagnosed only if pathologic analysis of placental specimens indicated these types of twins.

All prenatal sonograms were reviewed without previous knowledge of the amnionity and chorionity to determine the presence or absence of a membrane separating the fetuses and, when imaged, membrane thickness. This analysis was performed independently of ancillary findings such as fetal gender and number of placental sites. Membranes were classified as thick if they were well-defined discrete linear or curvilinear hyperechoic structures, of finite measurable width usually greater than 1 mm, and frequently imaged over a long segment (Figs. 1 and 2). Conversely, membranes were classified as thin if they were wispy or hairlike and generally visualized in short segments (Fig. 3), and if it was difficult to assign finite measurements of thickness.

Results

Of the 55 twin pregnancies in which amnionity and chorionity could be determined, 42 (76%) were DC-DA, 12 (22%) were MC-DA, and one (2%) was MC-MA. A total of 121 sonograms were performed during the course of these 55 pregnancies, for an average of 2.2 for each gestation.

One hundred one sonograms were obtained on the 42 DC-DA pregnancies, and a separating membrane was identified on at least one sonogram in 38 of these gestations (91% sensitivity) (Figs. 1 and 2). The visualized membrane was categorized as thick in all these cases. All gestations in which a thick membrane was identified were DC-DA (100% predictive value). The identification of a thick membrane was related

to the age of the gestation. A thick separating membrane was accurately seen in 100% of examinations performed in the first trimester, 89% in the second trimester, and 36% in the third trimester (Table 1).

Twenty sonograms were obtained on the monochorionic pregnancies. A total of 19 examinations were performed on the 12 MC-DA pregnancies, and a thin membrane was identified in three (25%) of these 12 (Fig. 3). In one additional MC-DA pregnancy, the visualized membrane displayed some characteristics of both membrane types and could not be categorized as thick or thin. No membrane was visualized in the remaining eight MC-DA gestations. One sonogram was obtained during the course of the single MC-MA gestation, and no membrane was visualized. The data for the MC-DA gestations as a function of stage of gestation are summarized in Table 2. Although the numbers are small, visualization of a membrane during the third trimester was particularly unsuccessful.

Discussion

Although all twin pregnancies are at increased risk for perinatal morbidity and mortality, the prevalence of complications is related to amnionity and chorionity. DC-DA twins fare the best; they are at risk mainly for preterm labor, intrauterine growth retardation, maternal complications such as hypertension, and difficult delivery [4, 7]. MC-DA and MC-MA gestations are at risk for these aforementioned complications and for the twin-to-twin transfusion syndrome due to vascular connections that occur between the fetal circulations in monochorionic placentas [4, 5]. The worst prognosis occurs with MC-MA twin pregnancies and is due to hazards related to the absence of a dividing membrane; these include entanglement of fetal parts, knotting or entanglement of the umbilical cords, and a high prevalence of congenital anomalies. Conjoined twinning occurs only in this form of gestation [3-6].

Because complications vary according to the type of twin gestation, prenatal sonographic determination of amnionity

TABLE 1: Sonographic Identification of a Thick Membrane in Dichorionic Diamniotic Twin Pregnancies as a Function of Stage of Gestation

Trimester	No. of Examinations	No. Revealing a Thick Membrane (%)
First (through 12 weeks)	10	10 (100)
Second (13–26 weeks)	44	39 (89)
Third (27 weeks to term)	47	17 (36)

TABLE 2: Sonographic Identification of a Thin Membrane in Monochorionic Diamniotic Twin Pregnancies as a Function of Stage of Gestation

Trimester	No. of Examinations	No. Revealing a Thin Membrane (%)
First (through 12 weeks)	1	0 (0)
Second (13–26 weeks)	12	3 (25)
Third (27 weeks to term)	6	1 (17)

and chorionicity can be instrumental in the management of these pregnancies. When sonography reveals the presence of two separate placental sites or male and female fetal gender, a DC-DA gestation is reliably diagnosed [1]. However, two placental sites were identified in only 33% of DC-DA gestations in a recent sonographic study on twins [1]. The presence of a membrane separating the fetuses in a twin pregnancy implies a diamniotic gestation [1]. Although a separating membrane was identified in 55 of 65 diamniotic pregnancies in the same study [1], no attempt was made to differentiate dichorionic from monochorionic twins by analyzing the thickness of the membrane. This distinction should be possible because the chorionic membrane is considerably thicker than the amnion and because the membrane in a DC-DA gestation is composed of two layers of chorion and two layers of amnion, whereas MC-DA septae contain only two layers of amnion [5, 8, 9].

We found that the thickness of the membrane separating the fetuses was a good discriminator of chorion type in diamniotic twin gestations. The thick membrane of a DC-DA twin pregnancy is a well-defined, discrete, linear or curvilinear hyperechoic structure of finite thickness (Figs. 1 and 2). Its presence indicated DC-DA twinning in all 38 cases (91% of DC-DA gestations) in which it was shown. The thinner membrane associated with MC-DA twins was wispy or hairlike and often visualized over only short segments (Fig. 3). It was more difficult to image but was seen in four of 12 cases of MC-DA twin gestations. In only three of these cases (25% of MC-DA gestations) could we be certain that the characteristics were those of a diamniotic membrane. Histologic sections of membranes from DC-DA and MC-DA gestations (Fig. 4) show the greater thickness of the DC-DA membrane.

Visualization of the membranes is related to gestational age. As pregnancy proceeds, even thick membranes become more difficult to image. Our success rate on any given examination in the DC-DA gestations decreased sharply from 100% in the first trimester and 89% in the second trimester to 36% in the third trimester. The normal decrease in the relative quantity of amniotic fluid and crowding of fetal parts in the third trimester undoubtedly contributed to the decline in membrane visualization. In cases of thin membranes of MC-DA gestations, success of membrane visualization was

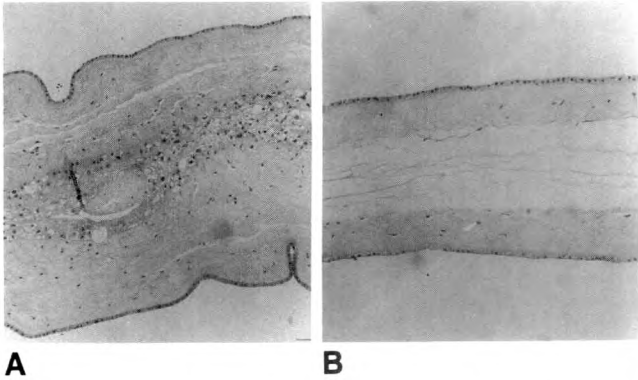


Fig. 4.—Histologic sections of dividing membranes in twin pregnancies. A, Dichorionic diamniotic. Note greater thickness of membrane from dichorionic diamniotic gestation compared with B. B, Monochorionic diamniotic.

poor throughout gestation, particularly in the third trimester. The frequency of visualization of either type of membrane would be greater if the uterine contents were prospectively scanned for a septum. Although the thick membrane separating DC-DA twins is more readily shown than the thin MC-DA membrane, a higher percentage of the thin MC-DA membranes can probably be imaged if specifically sought. Demonstration of a thin membrane in a monochorionic gestation excludes MC-MA twinning and its extremely poor prognosis, so careful scanning for such membranes should be considered an integral component in the sonographic evaluation of twins. Uterine synechiae and congenital septations are other sources of intrauterine membranes in pregnancy. Sonographic characteristics that aid in distinguishing such intrauterine septations from the normal amniotic and chorionic membranes dividing twins include aberrant location (not separating the fetuses), disproportionately wide base, and presence of a free edge [10]. In conclusion, membrane characteristics should be used in conjunction with other sonographic criteria such as number of placental sites and fetal gender to predict the amnionicity and chorionicity of twin gestations prenatally.

REFERENCES

1. Mahony BS, Filly RA, Callen PW. Amnionicity and chorionicity in twin pregnancies: prediction using ultrasound. *Radiology* 1985;155:205–209
2. Nyberg DA, Filly RA, Golbus MS, et al. Entangled umbilical cords: a sign of monoamniotic twins. *J Ultrasound Med* 1984;3:29–32
3. Brzezinski A, Mor-Yosef S, Granat M. Antepartum diagnosis of twin pregnancy. *Int J Gynecol Obstet* 1985;23:335–337
4. Benirschke K, Kim CK. Multiple pregnancy (1st of 2 parts). *N Engl J Med* 1973;288:1276–1284
5. Potter K, Craig JM. *Pathology of the fetus and the infant*, 3rd ed. Chicago: Year Book Medical, 1975:209–210
6. Salerno LJ. Monamniotic twinning: a survey of the American literature since 1935 with a report of four new cases. *Obstet Gynecol* 1959;14:205–213
7. Levi CS, Lyons EA. The sonographic evaluation of multiple gestation pregnancy. In: Sanders RC, James AE, eds. *The principles and practice of ultrasonography in obstetrics and gynecology*, 3rd ed. E. Norwalk, CT: Appleton-Century-Crofts, 1985:321–332
8. Jeanty P, Renoy P, Vankerkem J, et al. Ultrasonic demonstration of the amnion. *J Ultrasound Med* 1982;1:243–247
9. Benirschke K, Driscoll SG. *The pathology of the human placenta*. New York: Springer-Verlag, 1967:39–55
10. Mahony BS, Filly RA, Callen PW, Golbus MS. The amniotic band syndrome: antenatal sonographic diagnosis and potential pitfalls. *Am J Obstet Gynecol* 1985;152:63–68

**American Roentgen Ray Society
Resident Award Papers, 1987**

The ARRS announces competition for the 1987 President's Award and two Executive Council's Awards for the best papers concerning the clinical application of the radiological sciences.

Awards

The winner of the President's Award will receive a certificate and a \$1000 prize. The winners of the two Executive Council Awards will each be given a certificate and a prize of \$500. The winners will be announced March 1, 1987.

Regulations

Papers written and submitted by residents in radiology are eligible. The resident must be the sole or senior author and be responsible for all or most of the project.

Submitted manuscripts must not exceed 5000 words and have no more than 15 illustrations. Four copies of the manuscript and the illustrations are required.

Winning papers will be presented at the annual meeting of the American Roentgen Ray Society, Fontainebleau Hilton Hotel, Miami Beach, FL, April 26–May 1, 1987.

Winning papers will be submitted for early publication in the *American Journal of Roentgenology*. All other manuscripts will be returned to the authors.

Deadline for submissions is January 31, 1987. Send papers to

Byron G. Brogdon, M.D.
Department of Radiology
University of South Alabama Medical Center
2451 Fillingim Street
Mobile, AL 30617

Severe Polyhydramnios: Incidence of Anomalies

Suzanne Z. Barkin¹
Dolores H. Pretorius^{1,2}
Mary Katherine Beckett¹
David K. Manchester³
Thomas R. Nelson^{1,2}
Michael L. Manco-Johnson¹

The sonograms of 195 singleton pregnancies complicated by polyhydramnios were reviewed, and follow-up information was obtained on 191 patients. A grading system was developed that differentiated mild from severe polyhydramnios using real-time or static sonographic equipment. Mild polyhydramnios was present in 138 (71%), and severe polyhydramnios was present in 57 (29%). Previously it has been reported that 60% of cases of polyhydramnios are idiopathic and the pregnancies have a normal outcome. Twenty percent are associated with maternal abnormalities and 20% are associated with fetal anomalies. In this study, pregnancies with severe polyhydramnios had a much greater prevalence of fetal anomalies (75%) than pregnancies with mild polyhydramnios (29%). The 57 singleton pregnancies with severe polyhydramnios were analyzed in depth. Fourteen (25%) of the fetuses were normal; 43 (75%) had significant congenital abnormalities that predominantly involved the CNS, gastrointestinal tract, heart, and genitourinary tract. In all fetuses with primary CNS abnormalities, polyhydramnios was diagnosed at or before 30 weeks of gestation, while in most of the fetuses (83%) with gastrointestinal abnormalities it was diagnosed after 30 weeks. Sonographic findings correlated closely with the findings noted at birth or autopsy. In patients with severe polyhydramnios, normal sonograms were sensitive in excluding major congenital anomalies and, thus, were helpful in providing the parents with favorable prognoses. Sonograms should be performed in patients with polyhydramnios to identify congenital anomalies and to provide information regarding prognosis for fetal outcome.

Sonography has become increasingly important in fetal diagnosis, specifically in defining abnormalities that require counseling and possible intervention in utero. Approximately 1% of all pregnancies are complicated by polyhydramnios, which occurs when more than 2 l of amniotic fluid are present at term [1] or when the amount of fluid exceeds the norm expected for the gestational age. Most studies [2-6] have found that fetal abnormalities occur in approximately 20% of pregnancies complicated by polyhydramnios. Chamberlain et al. [6] found that the incidence of major congenital anomalies was significantly related to increased amniotic-fluid volume. Anomalies are primarily associated with the CNS and the gastrointestinal tract [2-6]. The findings vary widely, partly reflecting variability in the sensitivity of equipment, training of personnel, and populations studied.

The severity of polyhydramnios with fetal anomalies has not previously been correlated with an assessment of fetal outcome. We evaluated patients with severe polyhydramnios to determine whether sonography could accurately predict the presence of anomalies and, thus, assist in determining the prognosis for fetuses with a "normal" fetal sonogram but with severe polyhydramnios.

Methods

Polyhydramnios was diagnosed by sonography in 195 women with singleton pregnancies who were examined between 1977 and 1985 at University Hospital, Denver. The population represented patients seen for primary obstetric care as well as those referred for second-

Received June 23, 1986; accepted after revision August 21, 1986.

¹ Department of Radiology, University of Colorado Health Sciences Center, 4200 E. Ninth Ave., Denver, CO 80262. Address reprint requests to M. L. Manco-Johnson.

² Present address: Department of Radiology, University Hospital, UCSD, 225 Dickinson St., San Diego, CA 92103.

³ Department of Pediatrics, University of Colorado Health Sciences Center, 4200 E. Ninth Ave., Denver, CO 80262.

AJR 148:155-159, January 1987
0361-803X/87/1481-0155

© American Roentgen Ray Society

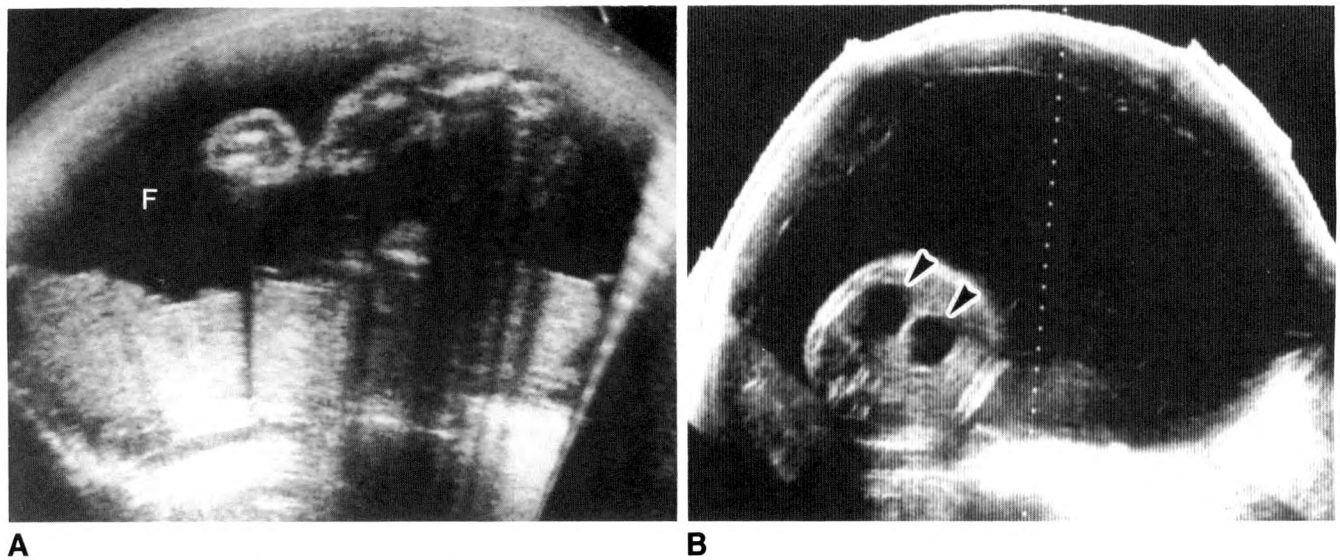


Fig. 1.—Categories of polyhydramnios.

A, Mild. Transverse static scan of 26-week fetus. Note large pocket of amniotic fluid (F).

B, Severe. Transverse static scan of 36-week fetus. Fetal abdomen in dependent position in uterus shows “double bubble” (arrowheads) associated with duodenal atresia.

opinion sonograms. The three senior authors retrospectively reviewed static sonograms from these patients concurrently and assigned them to one of two predefined classes of polyhydramnios (mild and severe) without knowing the interpretation of the original sonograms or the pregnancy outcomes.

The gestational age (determined by sonography) of the fetus was considered when classifying each examination because the amount of amniotic fluid varies with age. The distinction between mild and severe polyhydramnios was subjective. Mild polyhydramnios (Fig. 1A) had only a few large pockets of fluid seen in the uterus, whereas severe (Fig. 1B) polyhydramnios had many pockets of fluid seen throughout the uterus, including the space between the fetus and the anterior uterine wall.

Initial-sonogram reports were also reviewed to obtain fetal measurements for age determination and to identify fetal anomalies. In the patients with severe polyhydramnios, abnormalities were divided into three categories according to primary involvement of (1) the CNS, (2) the gastrointestinal tract, or (3) several organ systems or systems other than the first two.

Patients were considered to have severe polyhydramnios if any of the serial sonograms were categorized as such. Medical records (including autopsy reports) of each neonate were reviewed. Additional follow-up information was obtained by telephone interviews with primary physicians. Data collected included fetal age at diagnosis of polyhydramnios, physical examination and status at birth, autopsy findings, age and cause of fetal death, and status of live infants.

Results

Of the 195 patients with polyhydramnios, 138 (71%) were classified as mild and 57 (29%) as severe. Follow-up data were unavailable in four patients in the mild category, and so these patients were not included in the subsequent analysis.

Analysis of Mild Polyhydramnios

Mild polyhydramnios was observed in 134 singleton pregnancies with available follow-up. Ninety-five (71%) delivered normal infants. Thirty-nine babies were abnormal: 16 were stillborn or died in the neonatal period, 14 pregnancies were terminated because of fetal anomalies, and nine infants survived with major defects (Table 1).

Abnormalities other than polyhydramnios were noted on sonography in all but one of the abnormal fetuses. Truncus arteriosus was missed in one fetus. In addition, one fetus, diagnosed by sonography as having hydronephrosis, was normal at birth.

Analysis of Severe Polyhydramnios

Severe polyhydramnios was noted in 57 singleton pregnancies. The average maternal age was 27 years (range, 18–41 years), and the mean fetal age at delivery (excluding therapeutic abortions) was 33 weeks (range, 16–43 weeks). Fourteen infants (25%) were normal at follow-up. Forty-three babies (75%) were abnormal: 22 were stillborn or died in the neonatal period, 2 pregnancies were terminated for fetal anomalies, and 19 infants survived with major defects (Table 1). Analysis of the sonographic diagnoses and neonatal outcome showed a substantial relationship between findings at birth and autopsy and those diagnosed by sonography (Table 2). Of the 14 pregnancies complicated by severe polyhydramnios without abnormalities found on sonography, 13 were normal at birth. One fetus with a normal sonogram was found to have a tracheoesophageal fistula at birth. A single fetus,

TABLE 1: Severity of Polyhydramnios and Fetal Outcome (n = 191)

Sonographic Classification	Total Number (%)	Fetal Outcome						
		Number Living (%)			Number Dead (%)			
		Normal	Abnormal ^a	Total	Normal	Abnormal ^a	TAB	Total
Mild	134 (71)	95 (71)	9 (7)	104 (78)	0 (0)	16 (12)	14 (10)	30 (22)
Severe	57 (29)	10 (18)	19 (33)	29 (51)	4 ^b (7)	22 (39)	2 (4)	28 (49)

Note.—Follow-up was unavailable on four of the original 195 patients reviewed. TAB = therapeutic abortion.

^a Includes fetuses with congenital anomalies, abnormal chromosomes, or infection.

^b Four children died, despite absence of anatomic lesions; (1) Stillborn at 37 weeks; (2), stillborn at 39 weeks with umbilical cord twisted; (3), neonatal death at 3 days from complications of prematurity (28-week fetus); (4), neonatal death at 1 hr due to hypoxia in 37-week fetus.

TABLE 2: Diagnoses in Infants with Severe Polyhydramnios (n = 57)

Diagnostic Category	Number with Sonographic Diagnosis (%)	Number with Neonatal Diagnosis (%)
Normal (Polyhydramnios only)	14 (25)	14 (25)
Primarily CNS abnormality	7 (12)	7 (12)
Primarily GI abnormality	12 (21)	13 (23) ^a
Multisystem or other abnormalities	24 (42) ^b	23 (40)

Note.—GI = gastrointestinal system.

^a One infant with tracheoesophageal fistula not diagnosed by sonography.

^b One normal infant diagnosed as having hydronephrosis by sonography.

diagnosed in utero with hydronephrosis, was born with normal kidneys. The time at which polyhydramnios was identified in each category is presented in Figure 2.

Abnormalities noted at birth in patients with severe polyhydramnios were diverse, primarily affecting the CNS (30 patients) and gastrointestinal tract (27 patients). Abnormalities were also frequently noted in the cardiovascular system (17 patients), the genitourinary tract (nine patients), and the musculoskeletal system (11 patients). Six fetuses had abnormal chromosomes (five with associated abnormalities and one with ascites only).

Discussion

Amniotic fluid arises from various sources throughout pregnancy. Fluid is probably secreted by the amnion up to approximately 10 weeks of gestation [7]. During this time, amniotic fluid is comparable in composition to a dialysate of maternal and fetal serum [5, 7]. Fluid is produced by expulsion of water across the fetal skin from approximately 10–20 weeks gestation on. The fetal kidneys begin excreting urine into the amniotic cavity some time between 10 and 20 weeks; they become increasingly important in amniotic-fluid production throughout pregnancy. In the third trimester, the fetal lungs take on a major role in amniotic-fluid production and absorption. The placenta also contributes to regulation of fluid volume throughout pregnancy [7, 8]. Water moves across the placental membrane in response to hydrostatic osmotic

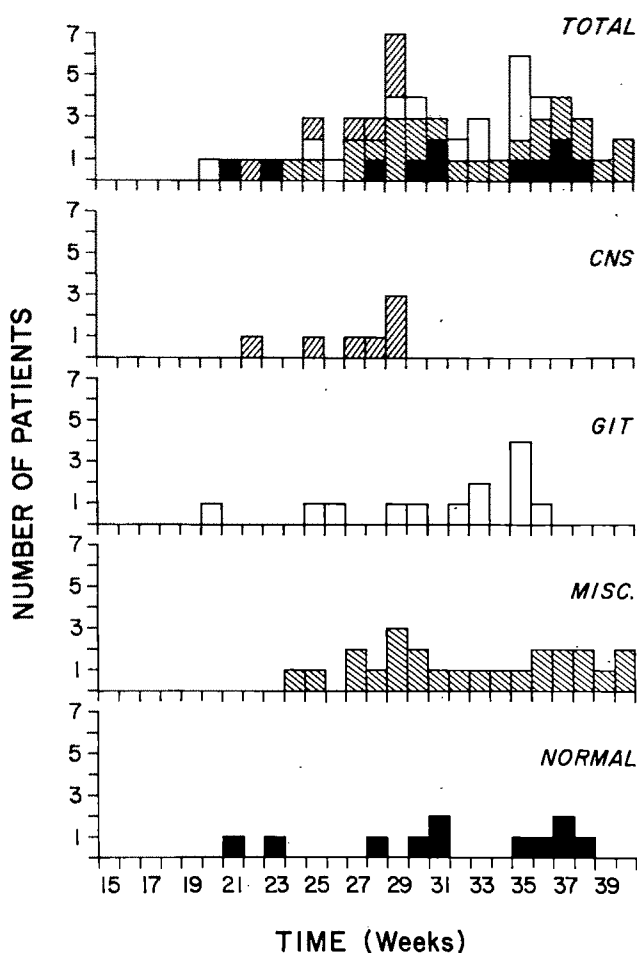


Fig. 2.—Gestational age of first recognition of polyhydramnios in patients who develop severe polyhydramnios during pregnancy. Primary abnormality noted at birth or autopsy is indicated by CNS, GIT (gastrointestinal tract), MISC. (multisystem or other abnormalities), or NORMAL.

gradients, particularly important in women with poorly controlled diabetes mellitus. Amniotic fluid constantly changes and moves within the fetus and amniotic cavity, its normal volume gradually increasing during pregnancy from 35 ml at

12 weeks gestational age, to 250 ml at 17–18 weeks, to 800 ml at term. After 38 weeks, the quantity of fluid decreases to about 250 ml by 43 weeks [5, 8–10]. The ratio of amniotic fluid to total uterine volume also varies throughout pregnancy, gradually rising until 26 weeks and then decreasing, so that at term the fetus accounts for most of total intrauterine volume.

Polyhydramnios is an excessive amount of amniotic fluid at any gestational age, generally a manifestation of disruption of normal development. The association of polyhydramnios with defined anomalies may be obvious in some cases and unexplained in others. Polyhydramnios may also result from a biological variation of normal.

Previous attempts at quantifying the uterine volume have not been consistently successful. One approach estimated total intrauterine volume with sonographic measurements [11]; various mathematical models have also been suggested [12]. Difficulty in obtaining reproducible results and in identifying a minimal amount of polyhydramnios or oligohydramnios has affected the utility of these methods. Jones et al. [12], Geirsson et al. [13], and Morrison and Brunello [14] developed more accurate methods of estimating amniotic-fluid volume using planimetric techniques, but these methods are tedious and rarely used clinically. Chamberlain et al. [6] found that amniotic-fluid volume, determined by measuring the depth of the largest pocket of amniotic fluid (if ≥ 8.0 cm), should increase the suspicion of an associated congenital anomaly or fetal macrosomia. The classification adopted in the present study is easy to use in the clinical setting and is adequate to assess the severity of polyhydramnios. Although the distinction between mild and severe polyhydramnios is subjective, the differentiation can generally be made without difficulty. Furthermore, although static sonograms were used in this study, real-time studies in our department are also used to categorize the severity of polyhydramnios.

Polyhydramnios is associated with several maternal and fetal problems. Up to 60% of cases of polyhydramnios are idiopathic, with the pregnancy resulting in a normal baby at delivery [1–6]. Alexander et al. [3] found that polyhydramnios in 132 patients was idiopathic (62%), secondary to maternal disease (20%), and associated with fetal anomalies (18%). Queenan's review of 358 patients [15] noted that 63% of the cases of polyhydramnios were idiopathic and 37% were associated with fetal anomalies. Multiple fetal anomalies are often noted [2–6, 16, 17].

We correlated the severity of polyhydramnios with the prevalence of fetal anomalies. In patients with mild polyhydramnios, fetal anomalies were present in only 30% of the cases. In those with severe polyhydramnios, fetal anomalies were present in 75% of the cases. Thus, the severity of polyhydramnios should be taken into account when counseling patients about fetal prognosis.

The relationship between anomalies and polyhydramnios is readily explainable for some conditions: CNS abnormalities affect swallowing, and gastrointestinal anomalies obstruct the flow of fluid through the bowel. The cause of polyhydramnios associated with other fetal anomalies is less clear. One hypothesis is that congestive heart failure due to congenital

heart disease, chorioangiomas, or pulmonary tumors may lead to fetal water imbalance [1]. Another hypothesis is that renal tubular defects may lead to excessive urine production.

This report confirms the preponderance of CNS and gastrointestinal anomalies in patients with severe polyhydramnios. In addition, we also found a high frequency of cardiac, pulmonary, and genitourinary anomalies. Cardiac anomalies were present in 17 (30%) of the patients with severe polyhydramnios. These anomalies can be diagnosed in utero with current high-resolution sonography. Although genitourinary anomalies are classically associated with oligohydramnios, isolated cases of bilateral renal agenesis and ureteropelvic junction obstruction have been reported with polyhydramnios [1, 17]. In 57 patients with severe polyhydramnios, nine fetuses had genitourinary anomalies, including bladder malformation, renal agenesis, renal tubular defect, cryptorchidism, and genital abnormalities. Because of similarities in the morphogenic time scale, all organ systems must be evaluated when one congenital abnormality is found.

The time of onset of polyhydramnios was helpful in predicting outcome and suggesting the type of fetal anomaly likely to be present. Ninety-three percent of neonates who were normal at birth but who had developed severe polyhydramnios had done so after 30 weeks of gestation. Primary CNS abnormalities were diagnosed at or before 30 weeks of gestation in all cases. Primary gastrointestinal abnormalities had polyhydramnios diagnosed after 30 weeks gestational age in 83% of the patients. Patients with other anomalies or no anomalies were diagnosed throughout pregnancy without any time-period predilection (Fig. 2).

The relationship was excellent between sonographic diagnosis and the neonatal findings and outcome. In 14 patients with severe polyhydramnios but without sonographically detected abnormalities, 13 were normal at birth. A tracheoesophageal fistula was shown at birth in one fetus who had been diagnosed as normal by sonography. Clinically, it is valuable to provide the patient and primary physician with a favorable prognosis when there is severe polyhydramnios and an otherwise normal sonogram. However, when a fetal anomaly is identified sonographically, the prognosis will be based on the abnormality detected.

The accuracy of sonography increases its importance in the diagnosis and management of polyhydramnios and concurrent anomalies. Knowledge of fetal abnormalities and the potential risks is the basis for counseling parents about the pregnancy. Early intervention is frequently essential in the management of anomalies that are amenable to correction or palliation. Knowledge of potential risks is also helpful in making decisions and planning for maternal transport, understanding the likelihood of neonatal survival and handicaps, and anticipating difficulties during labor.

In conclusion, sonography accurately evaluates pregnancies complicated by polyhydramnios. Differentiating severe from mild polyhydramnios has prognostic implications. Fetuses with severe polyhydramnios have a greater risk of having fetal anomalies (75%) than fetuses with mild polyhydramnios (29%). Severe polyhydramnios detected before 30 weeks gestation should alert the physician to possible CNS

anomalies, whereas polyhydramnios that develops after 30 weeks suggests gastrointestinal anomalies, other anomalies, or a normal perinatal outcome.

REFERENCES

- Wallenburg HCS, Wladimiroff JW. The amniotic fluid. II. Polyhydramnios and oligohydramnios. *J Perinat Med* 1977;5:233-243
- Hobbins JC, Grannum PAT, Berkowitz RL, Silverman R, Mahoney MJ. Ultrasound in the diagnosis of congenital abnormalities. *Am J Obstet Gynecol* 1979;134:331-345
- Alexander ES, Spitz HB, Clark RA. Sonography of polyhydramnios. *AJR* 1982;138:343-346
- Horger EO, Pai GS. Ultrasound in the diagnosis of fetal malformations. Implications for obstetric management. *Am J Obstet Gynecol* 1983;147:163-170
- Graham D, Sanders RC. Amniotic fluid. *Semin Reontgenol* 1982;27:210-218
- Chamberlain PF, Manning FA, Morrison I, et al. Ultrasound evaluation of amniotic fluid volume. II. The relationship of increased amniotic fluid volume to perinatal outcome. *Am J Obstet Gynecol* 1984;150:250-254
- Good W. Water relations of fetal development. *Med Hypotheses* 1979;5:859-879
- Wallenburg HCS. The amniotic fluid. I. Water and electrolyte homeostasis. *J Perinat Med* 1977;5:193-201
- Gadd RL. The volume of liquor amnii in normal and abnormal pregnancies. *J Obstet Gynecol Br Commonw* 1966;73:11-22
- Queenan JT, Thompson W, Whitefield CR, Shah SI. Amniotic fluid volumes in normal pregnancies. *Am J Obstet Gynecol* 1972;114:34-38
- Gohari P, Berkowitz RL, Hobbins JC. Prediction of intrauterine growth retardation by determination of total intrauterine volume. *Am J Obstet Gynecol* 1977;127:255-260
- Jones TB, Price RR, Gibbs SJ. Volumetric determination of placental and uterine growth relationships from B-mode ultrasound by serial area-volume determinations. *Invest Radiol* 1981;16:101-106
- Geirsson RT, Christie AD, Patel N. Ultrasound volume measurements comparing a prolate ellipsoid method with a parallel planimetric area method against a known volume. *J Clin Ultrasound* 1982;10:329-332
- Morrison J, Brunello LB. The antenatal diagnosis of hyperplacentosis, hydramnios and fetal ascites. *J Clin Ultrasound* 1977;5:338-340
- Queenan JT, Gadow EC. Polyhydramnios: chronic versus acute. *Am J Obstet Gynecol* 1970;108:349-355
- Quinlan RW, Cruz AC, Martin M. Hydramnios: ultrasound diagnosis and its impact on perinatal management and pregnancy outcome. *Am J Obstet Gynecol* 1983;145:306-311
- Sanders R, Graham D. Twelve cases of hydronephrosis in utero diagnosed by ultrasonography. *J Ultrasound Med* 1982;1:341-348

Letter from the Editor

New Guidelines and Checklist for Authors

Beginning with this issue, simplified author guidelines and a new manuscript checklist will be published monthly in the Journal. These are designed to facilitate preparation of manuscripts for publication in the *AJR*.

The guidelines include a description of specific format requirements for each type of article published in the Journal. The checklist provides a convenient way for the author to confirm that no important detail is overlooked.

The editorial staff works diligently to expedite the review process. We are pleased that the average time between receiving a manuscript and informing the author of the editorial decision is now less than 4 weeks. Our goal is to reduce the total time for publication from an average of 7 to 6 months. Careful use of the guidelines and the checklist by authors will help to achieve this end by reducing the need for revisions.

We encourage authors to use the guidelines and the checklist and hope that they find them helpful in preparing manuscripts that can then be published in the shortest time possible.

Robert N. Berk
Editor-in-Chief

Sonographic Spectrum of Placental Abruption

David A. Nyberg¹
 Dale R. Cyr
 Laurence A. Mack
 Doreen A. Wilson
 William P. Shuman

Fifty-seven cases of placental abruption detected by sonography were retrospectively reviewed. The location of hemorrhage was subchorionic in 46 cases (81%), retroplacental in nine cases (16%), and preplacental in two cases (4%). Subchorionic hematomas were more frequently shown in the 33 patients presenting before 20 menstrual weeks (91%) than in the 24 patients presenting after 20 weeks (67%). The echogenicity of hemorrhage depended on the time the sonogram was performed relative to the onset of symptoms: Acute hemorrhage was hyperechoic to isoechoic compared with the placenta, while resolving hematomas became hypoechoic within 1 week and sonolucent within 2 weeks. Acute hemorrhage was occasionally difficult to distinguish from the adjacent placenta. This occurred in five retroplacental hematomas that showed only an abnormally thick and heterogeneous placenta. Nine cases of placental abruption were initially confused with other mass lesions. Placental abruption causes a wide spectrum of sonographic findings that may be overlooked or misdiagnosed.

Placental abruption is recognized as one of the most serious complications of pregnancy. It is commonly associated with premature labor and delivery, and has been implicated in 15–25% of all perinatal deaths [1, 2]. Symptoms of third-trimester abruption, seen in approximately 0.49–1.29% of gestations, include maternal hemorrhage, a tense and painful uterus, fetal distress, and coagulopathy [3]. Less dramatic, but more common, manifestations of placental abruption have been recently recognized throughout pregnancy [4–9], including “idiopathic” premature labor [4], painless vaginal bleeding, and threatened abortion in the first and second trimesters [7–9]. As the signs and symptoms are highly variable, the diagnosis of placental abruption requires a high index of clinical suspicion [10].

Previously published reports suggest that the sonographic findings of placental abruption are also variable [7–9, 11–12]. While most sonographers recognize a retroplacental hematoma as evidence of placental abruption, other findings are less well known. In order to further evaluate the sonographic appearances of placental abruption, we reviewed our experience with 57 cases.

Materials and Methods

The study group included 57 consecutive women who had evidence of a placental abruption on sonograms performed during a 4-year period (1981–1985) at a university hospital. The sonograms, clinical history, and gestational outcome were retrospectively reviewed in each case. Thirty-three patients first presented before 20 menstrual weeks, and 24 patients presented after 20 weeks. All but two women were referred for sonographic evaluation because of vaginal bleeding. Most women also experienced uterine cramps or contractions. Placental abruption was clinically suspected in 14 cases; placenta previa or some other source of vaginal bleeding was suspected in the remaining cases.

Sonograms were performed with commercially available real-time and static equipment by using a 3.5-MHz transducer. Thirty-nine women had two or more sonograms performed. When more than one examination was performed, only the initial sonogram was used for data analysis.

Received June 30, 1986; accepted after revision August 21, 1986.

¹ All authors: Department of Radiology, University of Washington Hospital, SB-05, Seattle, WA 98195. Address reprint requests to D. A. Nyberg.

AJR 148:161–164, January 1987
 0361–803X/87/1481–0161
 © American Roentgen Ray Society

The size, location, and echogenicity of hemorrhage were noted in each case. The volume of hemorrhage was estimated from a measurement of three perpendicular diameters (D) by the formula for an ellipsoid: $0.52 \times (D_1 D_2 D_3)$. The location of hemorrhage was defined by its predominant location and categorized as one of the following: subchorionic (between the myometrium and the placental membranes), retroplacental (between the placenta and the myometrium), and preplacental (between the placenta and the amniotic fluid). In cases of subchorionic hematomas, a determination was also made as to whether the hematoma extended beneath the margin of the placenta. The echogenicity of hemorrhage was compared with adjacent structures and was defined as hyperechoic when it was equal to or greater than that of the adjacent placenta; hypoechoic when it was less than that of placenta and similar to that of myometrium; and sonolucent when it was similar to that of the amniotic fluid.

Of the 57 cases of placental abruptions in this series, 21 were confirmed by inspection of the placenta after delivery; seven had a subsequent amniocentesis that yielded brownish fluid and were consistent with previous hemorrhage; seven resolved on serial sonograms; and four underwent uterine curettage because of a clinical diagnosis of inevitable abortion. The remaining 17 patients were all seen before 20 menstrual weeks, including six who had a spontaneous abortion, eight whose symptoms resolved and who had a normal term delivery, and four who were lost to clinical follow-up.

Results

The estimated volume of hematoma for the 57 cases ranged from 4.3 to 343 cm³, with a mean of 69 cm³. The size

of hematoma did not vary significantly with its location or menstrual age. However, small hematomas were more easily detected during early pregnancy when they were relatively large in comparison with the gestational sac.

The predominant locations of hematomas are shown in Table 1. Of the 57 hematomas visualized, 46 (81%) were subchorionic (Fig. 1), nine (16%) were retroplacental (Fig. 2), and two (4%) were preplacental (Fig. 3) in location. Compared with women seen before 20 menstrual weeks, women presenting after 20 weeks demonstrated a higher frequency of retroplacental hematomas (29% vs 6%) and fewer subchorionic hematomas (67% vs 91%).

All 46 subchorionic hematomas were contiguous with the placental margin, including 26 cases (57%) that extended beneath the margin of the placenta (Fig. 1). However, the majority of blood was often separate from the placenta, and in six cases, the predominant hemorrhage was located on the myometrial surface opposite the placenta (Fig. 4).

Hematomas were hyperechoic in 17 cases, hypoechoic in 21 cases, and sonolucent in 19 cases. The echogenicity of hematomas varied with the time of the sonogram relative to the initial symptoms. Hematomas identified on sonograms performed at the time of the initial symptoms were hyperechoic to isoechoic compared with the placenta, while resolving hematomas became hypoechoic within 1 week and sonolucent within 2 weeks (Figs. 2 and 4).

Because acute hemorrhage was similar in echogenicity to the adjacent placenta, the extent of hemorrhage was occasionally difficult to appreciate on the initial sonogram. Five retroplacental hematomas were seen only as an abnormally thick and heterogeneous placenta (Fig. 5B). In some cases, a previous sonogram for comparison (Fig. 5A) or a follow-up sonogram that showed a resolving hematoma were useful for confirming the diagnosis of placental abruption.

Nine cases (16%) of placental abruptions were prospectively misdiagnosed on the initial sonogram. Primary diagnoses that were initially considered included succenturiate lobe

TABLE 1: Comparison of the Location of Hematoma with Menstrual Age for 57 Placental Abruptions

Menstrual Age	Hematoma Location			Total
	Subchorionic (%)	Retroplacental (%)	Preplacental (%)	
<20 weeks	30 (91)	2 (6)	1 (3)	33
>20 weeks	16 (67)	7 (29)	1 (4)	24
Total	46 (81)	9 (16)	2 (4)	57

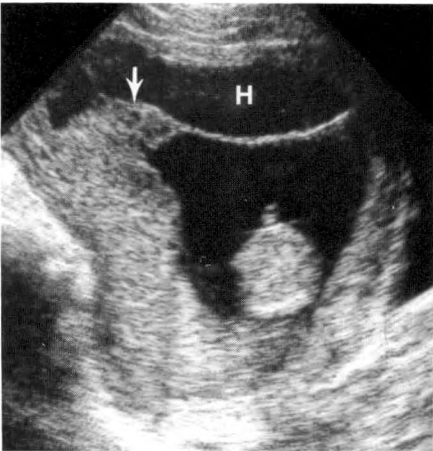
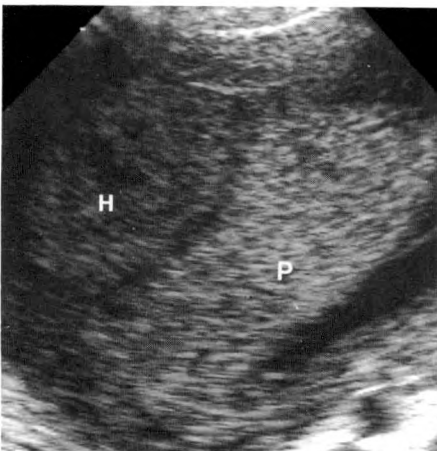


Fig. 1.—A sonogram made at 13 menstrual weeks shows a large, sonolucent hematoma (H) that is predominantly subchorionic in location. Hematoma extends beneath margin of placenta (arrow), detaching it from adjacent myometrium.



A



B

Fig. 2.—A, A sonogram made at 25 menstrual weeks shows a hyperechoic hematoma (arrowheads) in a retroplacental location, beneath placenta (P).
B, Repeat sonogram made 1 week later shows hematoma (H) to be hypoechoic compared with adjacent placenta (P).

of the placenta (three cases, Fig. 5), uterine myoma (three cases), chorioangioma (two cases, Fig. 6), and coexisting molar pregnancy (one case). In each of these cases, a repeat sonogram that showed a resolving hematoma helped to establish the correct diagnosis (Fig. 5).

Discussion

Placental abruption is defined as premature separation of the placenta from the myometrium, although some authorities reserve this term only for its occurrence in symptomatic patients [5]. The primary sonographic evidence for placental abruption is demonstration of a hemorrhage produced by the placental detachment [11]. Sonographic examination has been reported to be negative in most cases of clinically suspected abruption [10], presumably owing to the free pas-

sage of blood through the cervical os, which prevents the formation of a contained hemorrhage large enough to be visualized [11]. Despite the limitations of sonography, however, demonstration of a hematoma is clinically important since these pregnancies may have a worse prognosis than placental abruptions that do not show a hematoma. Fetal demise and premature labor have been correlated with the size of the hematoma in several clinical studies [13, 14] as well as in a recent sonographic study [9].

The reported sensitivity of sonography for detecting placental abruption varies considerably. In one series of 56 pathologically confirmed third-trimester abruptions, only one (2%) was detected by sonography [10]. Similarly, Mantoni [7] detected subchorionic hematomas in six (4%) of 148 women. In comparison, Goldstein et al. [8] detected subchorionic hematomas in 10 (20%) of 50 women with vaginal bleeding at 8–20 menstrual weeks.

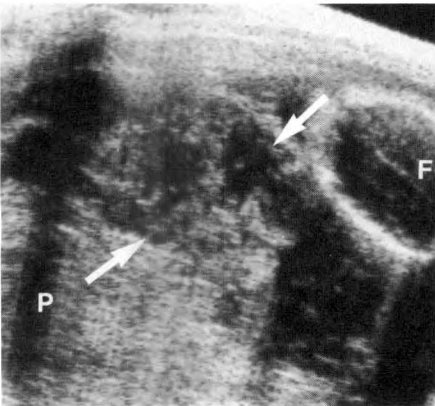
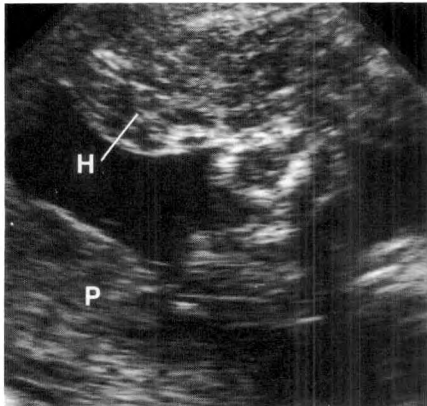
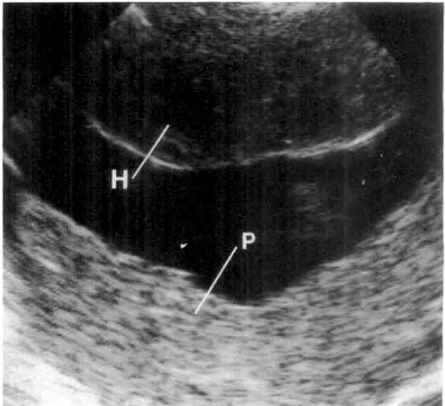


Fig. 3.—Sonogram made at 18 weeks gestation shows a large hematoma (arrows) in a pre-placental location, between placenta (P) and fetus (F). An old hematoma was found at delivery.

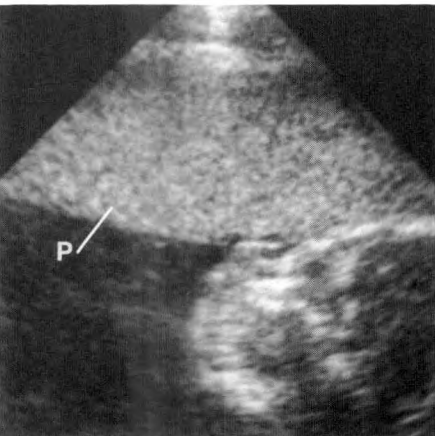


A



B

Fig. 4.—A, Sonogram made at 31 weeks shows a large subchorionic hematoma (H) located on myometrial surface opposite posterior placenta (P). This hemorrhage, which is similar in echogenicity to that of placenta, was initially confused for a succincurate lobe. B, Repeat sonogram made 2 weeks later shows that hematoma has become nearly sonolucent in appearance.



A



B

Fig. 5.—A, Sonogram made of a woman who presented with vaginal bleeding at 26 menstrual weeks shows a normal-appearing, anterior placenta (P). B, Repeat sonogram made 5 days later, after acute worsening of vaginal bleeding and onset of uterine contractions, shows a markedly thick and heterogeneous placenta (P). A large retroplacental hematoma was found after spontaneous abortion.

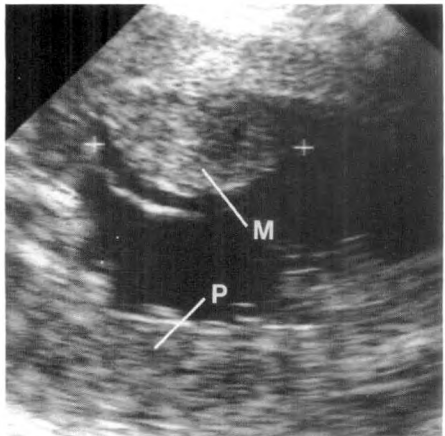


Fig. 6.—Sonogram made at 31 weeks shows a solid-appearing mass (M) on anterior myometrial surface, adjacent to margin of placenta (P). This mass, which was initially confused for a chorioangioma, proved to be a marginal placental abruption at delivery.

The wide range of sonographic appearances undoubtedly contributes to the range of sensitivities reported for detecting placental abruption. In the present study, sonographic findings varied with the size and location of the hematoma as well as with the time of the sonogram. These are important factors in evaluation of suspected placental abruption.

The most common location of hemorrhage was subchorionic, observed in 81% of cases (Fig. 1). A higher frequency of subchorionic hematomas was shown in women presenting before 20 menstrual weeks (91%) than in those presenting after 20 weeks (67%). These results are consistent with those of other authors [7-9] who have frequently observed subchorionic hematomas in women who experience vaginal bleeding before 20 weeks.

Subchorionic hematomas appear to result from abruptions of the placental margin, a common site of placental detachment that has been frequently recognized in clinical and pathologic studies [4-6]. The marginal detachment itself was observed in 57% of subchorionic hematomas in this study (Fig. 1), a finding that agrees with the 60% of marginal detachments observed by Sauerbrei and Pham [9]. Presumably, hemorrhage produced by a marginal abruption accumulates in a subchorionic location because the placental membranes are more easily stripped from the myometrium than from the more firmly attached placenta. All subchorionic hemorrhages in this study were contiguous with the edge of the placenta, although the predominant hemorrhage was frequently separate from the placenta. In six cases, the hematoma actually accumulated on the myometrial surface opposite the placenta itself (Fig. 4).

Retroplacental hematomas (Figs. 2 and 5) were detected in only 16% of abruptions in this study, although they were observed more frequently in women presenting after 20 weeks (29%) than in those presenting before 20 weeks (6%). This difference, although statistically significant ($p < .05$), may simply reflect the difficulty in detecting smaller marginal abruptions later in pregnancy. Alternatively, it may reflect the severity of clinical symptoms in the two patient groups. In one clinical study, marginal abruptions were five times more common than retroplacental abruptions in women with mild clinical symptoms, but only twice as common in women with more severe symptoms [5].

Preplacental hematomas are unusual in placental abruptions, seen in two cases (4%) in this series (Fig. 3). Previously described in the pathologic literature as a "subchorial" hemorrhage [15, 16], we have adopted the descriptive term "preplacental" hematoma to indicate its location between the placenta and amniotic fluid and to distinguish it from a subchorionic hematoma. Although the origin and significance of a preplacental hematoma has been debated [15], its association with vaginal bleeding, spontaneous abortion, premature labor, and hypertension [16] leaves little doubt that it represents an unusual site of hemorrhage from placental abruption.

The time at which the sonogram is performed relative to the onset of clinical symptoms significantly affects the appearance of placental abruption, although this point has not been previously emphasized. Acute hemorrhage was hyper-echoic to isoechoic relative to the placenta and gradually became sonolucent in the following 1-2 weeks (Figs. 2 and 4). Acute hemorrhage was particularly difficult to detect on the initial sonogram because its echo texture was similar to

that of the adjacent placenta. In five cases, acute retroplacental hemorrhage was seen as an abnormally thick and heterogeneous placenta, an observation that has also been noted by others [17]. In these cases, a recent sonogram for comparison (Fig. 5A) or a follow-up sonogram that shows a resolving hematoma can confirm the diagnosis and determine the extent of hemorrhage. Because this study included only patients in whom a hematoma was recognized, many acute hematomas may have been overlooked.

Hematomas may occasionally have a confusing sonographic appearance that may be mistaken for other mass lesions. Spirt et al. [11] previously noted that a resolving hematoma may be confused for a myoma, and in the present study nine placental abruptions were initially misdiagnosed. In each of these cases, a repeat sonogram helped to establish the correct diagnosis by showing a resolving hematoma.

We conclude that placental abruptions result in a wide variety of sonographic findings. In women who present with otherwise unexplained vaginal bleeding and/or premature labor, placental abruption should be strongly suspected and specifically searched for. An awareness of the various sonographic findings that may be seen with placental abruption should improve its sonographic detection.

ACKNOWLEDGMENTS

The authors wish to thank Lorri Froid for technical assistance.

REFERENCES

1. Douglas RG, Buchman MI, MacDonald PF. Premature separation of the normally implanted placenta. *Br J Obstet Gynaecol* 1955;62:710-736
2. Knab DR. Abruptio placentae. An assessment of the time and method of delivery. *Obstet Gynecol* 1978;52:625-629
3. Sexton LI, Hertig AT, Reid DE, et al. Premature separation of the normally implanted placenta: a clinicopathologic study of 476 cases. *Am J Obstet Gynecol* 1950;59:13-24
4. Harris BA Jr, Gore H, Flowers CE. Peripheral placental separation: a possible relationship to premature labor. *Obstet Gynecol* 1985;6:774-778
5. Gruenewald P, Levin H, Yousem H. Abruptio and premature separation of the placenta. *Am J Obstet Gynecol* 1968;102:604-610
6. Harris BA. Marginal placental bleeding. *Am J Obstet Gynecol* 1952;64:53-61
7. Mantoni M. Ultrasound signs in threatened abortion and their prognostic significance. *Obstet Gynecol* 1985;65:471-475
8. Goldstein SR, Subramanyan BR, Raghavendra BN, Horii SC, Hilton S. Subchorionic bleeding in threatened abortion: sonographic findings and significance. *AJR* 1983;141:975-978
9. Sauerbrei EE, Pham DH. Placental abruption and subchorionic hemorrhage in the first half of pregnancy: ultrasound appearance and clinical outcome. *Radiology* 1986;160:109-112
10. Hurd WW, Miodovnik M, Hertzberg V. Selective management of abruptio placentae: a prospective study. *Obstet Gynecol* 1983;61:467-472
11. Spirt BA, Kagan EH, Rozanski RM. Abruptio placentae: sonographic and pathologic correlation. *AJR* 1979;133:877-881
12. Mantoni M, Pedersen JF. Intrauterine hematoma. An ultrasound study of threatened abortion. *Br J Obstet Gynaecol* 1981;88:47-51
13. Sher G. A rational basis for the management of abruptio placentae. *J Reprod Med* 1978;21:123-129
14. Lunan CB. The management of abruptio placentae. *Br J Obstet Gynaecol* 1973;80:120-124
15. Fox H. *Pathology of the placenta*. London: Saunders, 1978, 107-157
16. Shanklin DR, Scott JS. Massive subchorial thrombohaematoma (Breus' mole). *Br J Obstet Gynaecol* 1975;82:476-487
17. Mintz MC, Kurtz AB, Arenson R, et al. Abruptio placentae: apparent thickening of the placenta caused by hyperechoic retroplacental clot. *J Ultrasound Med* 1986;5:411-413

Malignant Gestational Trophoblastic Disease: CT Findings

Colleen Sanders¹
Eva Rubin

Eight patients with malignant gestational trophoblastic disease had CT of the pelvis as part of their staging before chemotherapy. CT appearance of the uterus fell into three major types: (1) normal size with irregular areas of hypodensity, (2) uniform enlargement with areas of hypodensity, and (3) focal areas of enlargement with or without areas of hypodensity. Patients with the second and third types were much more likely to have distant metastases and to require hysterectomy for successful treatment. CT findings of tumor nodules in the parametrium or myometrium were confirmed in three of the four surgical specimens of the uterus available for correlation. Myometrial tumor nodules were seen as areas of focal enlargement or as irregular eccentric areas of hypodensity. In one patient, parametrial extension was seen as an enhancing mass adjacent to the uterus. CT may be accurate in defining the extent of myometrial and adnexal disease and may have prognostic and therapeutic value.

Little information is available on pelvic CT in women with malignant gestational trophoblastic disease (MTD) despite the technique's widespread use in evaluation of pulmonary, cerebral, and hepatic metastases [1]. MTD, defined as choriocarcinoma, invasive mole (chorioadenoma destruens), or persistently elevated levels of β -human chorionic gonadotropin (β -HCG) after evacuation of a hydatidiform mole, requires accurate initial assessment of local and distant disease for optimal therapy [1-3]. The purpose of this report is to analyze the CT appearances of the uterus in eight cases of MTD and to correlate the CT and pathologic findings.

Materials and Methods

Between January 1980 and April 1986, eight women had CT of the abdomen and pelvis as part of their initial evaluation of MTD before chemotherapy. Examinations were performed on a GE 8800 or 9800 CT/T or on a Philips Tomoscan 310 by using 10-mm sections at 1 to 2-cm intervals through the pelvis. All patients received oral and IV contrast material, and six also received rectal contrast material (five received water-soluble iodinated contrast material, one received air). The CT criteria for a normal uterus, as defined by Lee et al. [4], were used as the basis for evaluating the uterine appearance. Two radiologists reviewed the CT examinations separately without knowledge of the clinical or surgical findings. Subsequently, findings were reviewed jointly. No significant differences occurred between the two readers. Sonography was not performed at the time of staging. The CT appearance was correlated with clinical records and available pathologic specimens.

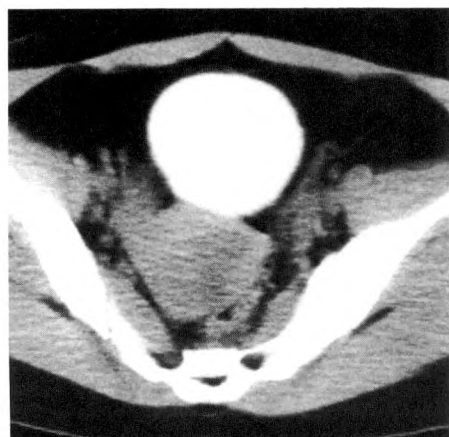
MTD followed molar pregnancy in five patients, elective abortion in one, and full-term delivery in one. The antecedent pregnancy was unknown in one woman whose last live birth had occurred 25 years before but who was sexually active without contraception. In the five women with molar pregnancies, MTD was diagnosed by rising titers of β -HCG after surgical or spontaneous evacuation. CT was performed an average of 11 weeks (range, 6-20) after evacuation of the mole. Two patients had vaginal bleeding and one was admitted with shortness of breath and hemoptysis due to pulmonary metastases. The average age was 30 years (range, 17-49), and average parity was 2.5 (range, 0-12). One patient had had a molar pregnancy that did not require chemotherapy several years before the current hydatidiform

Received July 9, 1986; accepted after revision September 2, 1986.

¹ Both authors: Department of Radiology, University of Alabama at Birmingham, 619 S. 19th St., Birmingham, AL 35233. Address reprint requests to C. Sanders.

AJR 148:165-168, January 1987
0361-803X/87/1481-0165

© American Roentgen Ray Society



1

Fig. 1.—CT of 17-year-old woman with rising β -HCG after evacuation of mole shows normal-sized uterus with an irregular central hypodense area, probably due to tumor and hemorrhage.

mole. Three patients had pulmonary metastases at the time of staging.

The decision to perform hysterectomy was based on persistent elevation or increase in β -HCG levels during chemotherapy in three patients. Hysterectomy was an elective procedure in one patient who did not desire more children. The average time from start of therapy to hysterectomy was 7.5 weeks (range, 4–11).

At the end of the follow-up period (4 months–5.5 years), two patients were considered cured, defined as "complete absence of clinical or humoral evidence of disease for 5 years" [1]. At the time this paper was written, five patients were in remission with normal β -HCG levels (<5 mIU/ml) on no chemotherapy for a period of 13–54 months. One patient was still receiving chemotherapy.

Results

CT Appearance

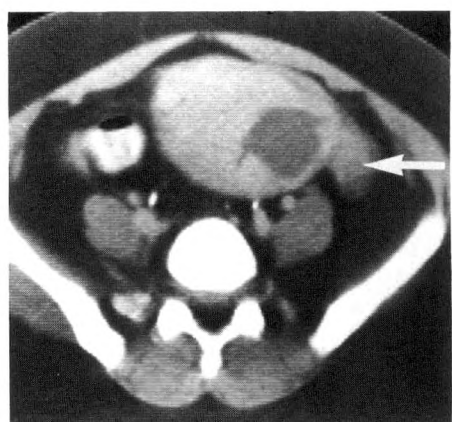
The CT appearance fell into three types: (1) uterus of normal size containing irregular central or eccentric areas of hypodensity (Fig. 1), (2) uniformly enlarged uterus with areas of hypodensity (Fig. 2), and (3) lobular uterus with focal uterine or cervical enlargement (Fig. 3). Fifty percent of the third type had irregular areas of hypodensity.

Clinicopathologic Correlation

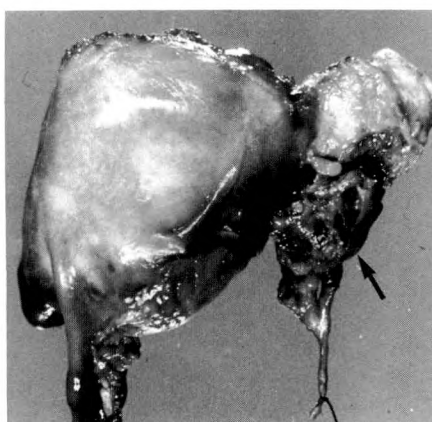
The three patients with normal uterine size had no evidence of distant metastases. Two were cured with chemotherapy without hysterectomy; one was responding to chemotherapy without evidence of distant metastases 4 months after diagnosis. The one patient with a uniformly enlarged uterus had evidence of parametrial extension diagnosed by CT and confirmed at the time of surgery (Fig. 2). This patient had three tumor nodules in the myometrium that did not deform the uterine contour and were shown on CT as an irregular eccentric hypodense area.

Of the four patients with a lobular uterine contour, one was in remission after chemotherapy alone. The other three required hysterectomy for successful treatment. Two had residual tumor in the uterine body or cervix confirmed by pathology. No viable tumor was identified in the third surgical specimen although there was evidence of necrosis. This patient had bilateral cystic adnexal masses on CT that were palpable on physical examination and were thought to represent theca-lutein cysts (Fig. 3).

Uterine size by CT varied from $5 \times 5 \times 4$ cm to $10 \times 7 \times 10$ cm (length \times maximum transverse diameter \times maximum anteroposterior diameter). Serum β -HCG levels at the time of



A



B



C

Fig. 2.—49-year-old multigravida woman with elevated β -HCG after evacuation of mole

A, CT scan shows slightly enlarged uterus with an eccentric low-density area in left myometrium without focal uterine enlargement. Enhancing soft-tissue mass (arrow) contiguous with left uterine wall is due to extension of tumor through uterine wall into parametrium.

B, Surgical specimen shows hemorrhagic tumor in left parametrium (arrow).

C, Cut surgical specimen shows myometrial tumor nodule in area of eccentric hypodensity.

Fig. 3.—CT of nulliparous 19-year-old woman with elevated β -HCG after evacuation of mole shows uterine enlargement with a lobular uterine contour and bilateral cystic adnexal masses (C) consistent with theca-lutein cysts.

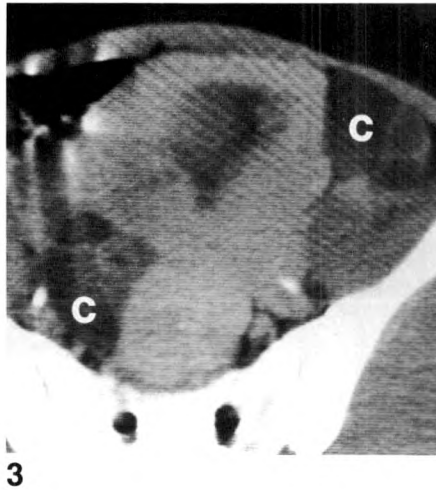


Fig. 4.—CT of 46-year-old woman with a 2-month history of vaginal bleeding and passage of tissue shows focal cervical enlargement due to residual tumor in endocervix and lower uterine segment that was documented by pathology. Vaginal tampon in place.



the CT ranged from 84 to 128,000 mIU/ml. There was no apparent correlation between the size of the uterus and the serum β -HCG concentration.

Discussion

This series of patients illustrates many of the pathologic characteristics of gestational trophoblastic disease. Uterine enlargement, focal uterine masses, and areas of hemorrhage within the highly vascular tumor are common. These features were also noted by Amendola et al. [5] in a case report of CT in persistent molar disease. Overall, the extent and severity of the disease seemed to correlate with the CT appearance. The three patients with a normal uterine size have not developed metastatic disease or required hysterectomy for cure. Patients with an enlarged uterus, whether smooth or lobular, were more likely to have distant metastases (4/5) and to require hysterectomy (4/5).

Myometrial tumor nodules on CT may appear as hypodense or isodense areas of focal enlargement in the uterus or cervix (Fig. 4) or as irregular eccentric areas of hypodensity that are not large enough to create focal masses. Although classically hypervascular by angiography [6], the frequent hypodensity of tumor nodules by CT may be due to associated hemorrhage or to delayed imaging of the uterus after IV contrast material. Pathologically, these low-density areas were tumor nodules associated with areas of hemorrhage and necrosis.

Adnexal abnormalities also may be identified by CT. Parametrial extension, which may cause life-threatening hemorrhage [1, 7], was seen in one patient as an enhancing mass adjacent to the uterus (Fig. 2). Theca-lutein cysts, described in up to 30% of all patients and associated with an increased incidence of malignant disease [8], were clearly identified by CT in one patient.

Of the four hysterectomy specimens, CT findings were confirmed pathologically in three. In the fourth patient, hysterectomy was performed 2 months after the CT exam. During this time, physical examination showed that the uterus de-

creased in size, and concentrations of serum β -HCG declined, though not to normal levels. Although no tumor was found, necrosis was seen microscopically, and no other uterine abnormality was identified to explain the CT findings. The absence of tumor in this patient may be due to chemotherapy and may explain the apparent false-positive results.

Although current therapy is highly effective, with cure rates greater than 80% [9, 10], resistance to chemotherapy is more common when the tumor involves the uterine wall [11]. In a large series reported by Hammond et al. [12], hysterectomy was performed in 26% of patients with MTD. Hysterectomy at the time of initial treatment decreases the amount of chemotherapy required to obtain a remission [12] and is often considered in patients of high parity, in women more than 40 years old, and in those who have completed childbearing [1]. Delayed hysterectomy is often necessary to control residual tumor foci in the pelvis when resistance to chemotherapy develops, and it may be curative [12]. Therefore, identification of tumor nodules in the myometrium and parametrium may have therapeutic implications.

Sonography has been the major imaging technique in hydatidiform mole for many years [13, 14], but experience in MTD is somewhat more limited. Several authors [8, 15–17] noted areas of high-amplitude echoes within the myometrium that were thought to represent tumor nodules, but this was not found by Requard and Mettler [18]. Of the 38 combined cases of MTD [12, 15–18], pathologic confirmation of sonographic findings was given in only two cases, although regression of myometrial masses with chemotherapy has been described. Although we cannot directly compare sonography and CT in this study because no patient had sonography at the time of staging, our preliminary report with pathologic confirmation in three of eight cases suggests that CT may be at least as accurate as sonography. Further investigation, ideally a prospective study that uses both sonography and CT, is necessary to accurately assess the relative sensitivity and specificity of these two techniques.

We have shown that CT imaging of the pelvis in MTD may be accurate in depicting the extent of tumor within the pelvis.

Penetration through the uterine wall into the parametrium and foci of tumor in the uterine wall can be recognized from their CT appearance. The size and contour of the uterus appear to correlate well with the severity of the disease and may predict the need for future hysterectomy. Patients with an enlarged uterus at the time of staging are at high risk for residual pelvic tumor as well as metastatic disease and may require hysterectomy for successful treatment. Because residual tumor in the myometrium appears to be relatively resistant to chemotherapy, these patients may benefit from early hysterectomy if preservation of their fertility is not desired [1, 12].

REFERENCES

- Hilgers RD, Lewis JL. Gestational trophoblastic disease. In: Danforth DN, ed. *Obstetrics and gynecology*. Philadelphia: Harper & Row, 1982:393-406
- Bagshawe KD. Risk and prognostic factors in trophoblastic neoplasia. *Cancer* 1976;38:1373-1385
- Stone M, Bagshawe KD. An analysis of the influences of maternal age, gestational age, contraceptive method and the mode of primary treatment of patients with hydatidiform moles on the incidence of subsequent chemotherapy. *Br J Obstet Gynaecol* 1979;86:782-792
- Lee JKT, Sagel SS, Stanley RJ. *Computed body tomography*. New York: Raven, 1982
- Amendola MA, Jaffe MH, Amendola BE, Hoffman JS. Gestational trophoblastic neoplasia: computed tomographic appearance. *Comput Radiol* 1983;7:103-106
- Cockshott WP, Evans KT, Hendrickse JP. Arteriography of trophoblastic tumours. *Clin Radiol* 1964;15:1-8
- Magrath T, Golding PR, Bagshawe KD. Medical presentations of chorio-carcinoma. *Br Med J* 1971;2:633-637
- Fleischer AC, James AE, Krause DA, Millis JB. Sonographic patterns in trophoblastic disease. *Radiology* 1978;126:215-220
- Morrow CP, Kletzky OA, Disaia PJ, Townsend DE, Mishell DR, Nakamura RM. Clinical and laboratory correlates of molar pregnancy and trophoblastic disease. *Am J Obstet Gynecol* 1977;128:424-429
- Jones WB. Trophoblastic tumors: prognostic factors. *Cancer* 1981;48:602-607
- Hertz R. Biological aspects of gestational neoplasms derived from trophoblast. *Ann NY Acad Sci* 1971;172:279-287
- Hammond GB, Weed JC, Currie JL. The role of operation in the current therapy of gestational trophoblastic disease. *Am J Obstet Gynecol* 1980;136:844-856
- Reuter K, Michlewitz H, Kahn PC. Early appearance of hydatidiform mole by ultrasound. *AJR* 1980;134:588-589
- Baird AM, Beckly DE, Ross FGM. The ultrasound diagnosis of hydatidiform mole. *Clin Radiol* 1977;28:637-645
- Reid MH, McGahan JP, Oi R. Sonographic evaluation of hydatidiform mole and its look-alikes. *AJR* 1983;140:307-311
- Munyer TP, Callen PW, Filly RA, Braga CA, Jones HW. Further observations on the sonographic spectrum of gestational trophoblastic disease. *JCU* 1981;9:349-358
- Santos-Ramos R, Forney JP, Schwartz BE. Sonographic findings and clinical correlations in molar pregnancy. *Obstet Gynecol* 1980;56:186-192
- Requard CK, Mettler FA. The use of ultrasound in the evaluation of trophoblastic disease and its response to therapy. *Radiology* 1980;135:419-422

Technical Note

CT of Children's Feet: An Immobilization Technique

James S. Donaldson,¹ Andrew K. Poznanski, and Arthur Nieves

Many uses of CT for evaluation of the tarsals, subtalar joints, and ankles are well established [1-4]. Proper positioning and immobilization of the feet in children are important to prevent motion, ensure symmetry of the feet, obtain proper alignment for direct axial and coronal imaging, and provide reproducibility for future studies. Patient comfort, particularly in children, is essential since "squirming" can easily move the feet several millimeters. Most methods of taping the feet still allow some motion. The technical approach described by Smith and Staple [5] (resting the feet on a slightly angled table extension) may work well in older cooperative patients, but more secure immobilization is necessary in children. A simple and effective immobilization technique that uses tennis shoes (Figs. 1 and 2) in CT scanning of children's feet is described.

Materials and Methods

Ten pairs of rubber and canvas tennis shoes of various sizes containing no metal parts were purchased. The total cost of the shoes was small (\$98) since inexpensive shoes can be easily used for this purpose. The child uses the pair of shoes that fit most closely. If children come in wearing shoes without metal parts, these shoes can be used. However, metal is commonly used in the vents along the instep and in the eyelets or hooks for the shoelaces.

For the direct axial scanning the knees are taped to the table with the legs straight. The feet in the tennis shoes are taped together and then directly to a 12 × 12 × ½" piece of plywood, the base of which is cut to the same curve as the CT cradle in order to rest on the scanning table (Fig. 1). Right-angle shelf brackets are screwed to the back of the plywood holding it at a 90° angle to the table and are then anchored with sandbags.

The direct coronal scans are obtained with the knees flexed (Fig. 2), the shoes (and feet) flat on the tabletop to which they are directly taped. The lateral scout radiograph (Fig. 3A) is used to prescribe both coronal and axial scans.

Thirty-one patients, 18 months to 20 years old, have been scanned with this method during the past 14 months. All patients were examined with a GE 9800 scanner. Each position took approximately 15 min, allowing for reconstruction time.

Results

The canvas and rubber tennis shoes cause no degradation or artifact on the scout or computed images (Fig. 3B). They provide good immobilization of the feet for the entire time of the scan series. Optimal studies have been achieved in most patients (only slight motion has been noted with some of the younger children).

Discussion

With children younger than 2 years old, secure immobilization is essential, particularly if the examination is attempted without sedation. Older, cooperative children and adolescents also find it easier to keep from wiggling when the feet are fixed in snugly fitting tennis shoes. This technique is particularly important for accurate positioning for images in the axial plane: the long axis of the feet should be directly parallel to the scanning plane in order to ensure optimal visualization of the bony relationships. Severe congenital deformities, fractures, or acute inflammatory processes of the feet or ankles may prevent the use of this type of immobilization.

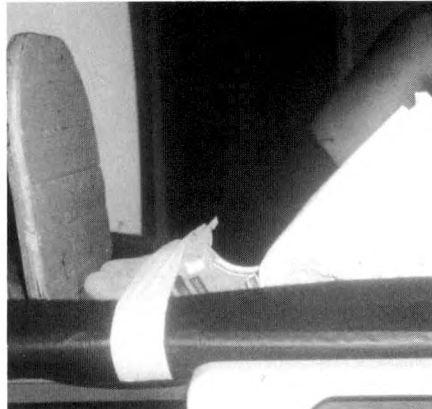
Received May 30, 1986; accepted after revision August 12, 1986.

¹ All authors: Department of Radiology, Northwestern University Medical School, The Children's Memorial Hospital, 2300 Children's Plaza, Chicago, IL 60614. Address reprint requests to J. S. Donaldson.

AJR 148:169-170, January 1987 0361-803X/87/1481-0169 © American Roentgen Ray Society



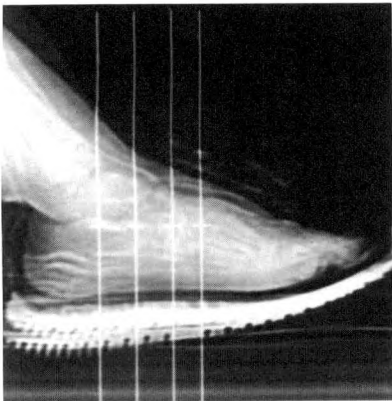
1



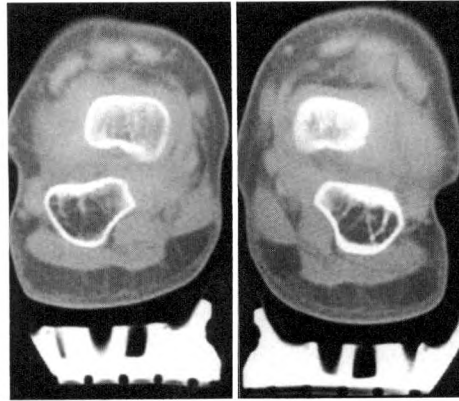
2

Fig. 1.—Positioning for axial scanning.

Fig. 2.—Positioning for coronal scanning.



A



B

Fig. 3.—Lateral scout (A) and CT (B) images of feet positioned for scanning show optimal positioning with no degradation of images from tennis shoes.

REFERENCES

1. Deutsch AL, Resnick D, Campbell G. Computed tomography and bone scintigraphy in the evaluation of tarsal coalition. *Radiology* **1982**;144:137-140
2. Heger L, Wulff K, Seddiqi MSA. Computed tomography of calcaneal fractures. *AJR* **1985**;145:131-137
3. Heger L, Wulff K. Computed tomography of the calcaneus: normal anatomy. *AJR* **1985**;145:123-129
4. Stoskopf CA, Hernandez RJ, Kelikian A, Tachdjian MO, Dias LS. Evaluation of tarsal coalition by computed tomography. *J Pediatr Surg* **1984**;4:365-369
5. Smith RW, Staple TW. Computerized tomography (CT) scanning technique for the hindfoot. *Clin Orthop* **1983**;177:34-38

Normalized Pediatric Organ-Absorbed Doses from CT Examinations

Thomas Fearon¹
James Vucich²

Absorbed doses to the bone marrow, gonads, thyroid, eyes, breast, and skin from CT examinations of the head, chest, abdomen, and torso were measured in a phantom mimicking an average 6-year-old child. The doses were normalized to the CT dose index measured at the central position of a standardized cylindrical phantom, to allow approximation of organ-absorbed doses for similar scanners for which the CT dose index has been measured. Estimating organ-absorbed doses associated with CT examinations of children is necessary to evaluate the relative risks of carcinogenesis associated with radiation exposure of a particular organ. The risks from a particular CT examination depends on the patient's age because the geometric configuration of the organs (e.g., marrow distribution) changes over time and will, therefore, affect the scatter dose to the organs.

One of the most difficult problems encountered in the science of radiation protection is estimating absorbed dose delivered to various organs [1, 2]. Review of available human and animal radiobiological data over the past decade reveals that for both internal and external irradiation, carcinogenesis is the dominant biological effect of concern and that all tissues of the body must be considered at cancer risk. The risk of developing radiation-induced leukemia and breast cancer may be greater in the child [3-4]. To evaluate the risk-benefit ratio of diagnostic radiologic examinations, particularly those with the potential of delivering significant radiation exposure, such as CT and angiography, accurate knowledge of the absorbed dose to specific organs resulting from these procedures is necessary.

Radiation doses associated with CT examinations for various scanners have been reported [5, 6]; however, only sparse data exist concerning organ-absorbed dose from out-of-plane scatter radiation [7-10]. The Food and Drug Administration (FDA) amended its regulations [11] to require manufacturers to report dose information by using the CT dose index concept defined by Shope et al. [12]. The CT dose index takes into account the scattered penumbral dose and describes the absorbed dose delivered from CT procedures that use a series of adjacent slices under prescribed geometry in a specialized cylindrical phantom. The dose descriptor is the average dose at specified locations in the phantom (e.g., central axis, 1 cm from the outer surface) in the central scan of a series of slices and is equal to the integral of the dose profile perpendicular to the scan plane at these same locations for a single scan, divided by the nominal slice thickness. The CT dose index is equal to the multiple-scan average dose resulting from a series of adjacent scans separated by the nominal slice width [12]. A comparison of the entrance-skin dose for children with the CT dose index measured for points near the surface in the standardized FDA phantoms showed that the CT dose index does not predict patient doses in clinical practice [13]. The FDA cylindrical head phantom more closely predicted typical entrance-skin absorbed doses for children, while the body phantom underestimated the entrance-skin absorbed dose. The CT dose index concept does offer the advantage of being a consistent means of comparing the

Received June 9, 1986; accepted after revision August 28, 1986.

This work was supported in part by grants from the National Cancer Institute (1 R01CA42421-01) and the Research Foundation of Children's Hospital National Medical Center, Washington, DC 20013.

¹ Departments of Radiology and of Child and Health Development, Children's Hospital National Medical Center, George Washington Medical Center, George Washington University School of Medicine, Washington, DC. Address reprint requests to T. Fearon, Department of Radiology, Children's Hospital National Medical Center, 111 Michigan Ave. NW, Washington, DC 20010.

² Department of Radiology, National Institutes of Health, Bethesda, MD 20892.

AJR 148:171-174, January 1987

0361-803X/87/1481-0171

© American Roentgen Ray Society

dose efficiency of various CT scanners. We measured the absorbed doses to the testes, ovaries, thyroid, eyes, breast, and bone marrow in a phantom to simulate an average 6-year-old patient undergoing CT examination of the head, chest, abdomen, and torso. The doses were also normalized to the CT dose index measured in the center position of the FDA cylindrical head phantom [11].

Materials and Methods

All dosimetry measurements were conducted on a General Electric CT/T 9800 scanner by using typical clinical technique factors for pediatric patients.

Anthropomorphic Phantom Measurements

An anthropomorphic pediatric phantom (Humanoid System; Carson, CA) representing an average 6-year-old child (height, 120 cm; weight, 20 kg) was used in conjunction with thermoluminescent dosimetry to measure pediatric organ doses for CT examinations of the head, chest, abdomen, and torso. The phantom consists of a human skeleton, lungs, and airway (Fig. 1). The skeleton is impregnated with tissue-equivalent material (density, 1.002 g/cm³; average effective attenuation coefficient at 120 kVp, 0.191 cm⁻¹) and is encased in tissue-equivalent material molded to model an average 6-year-old patient. Lungs are molded of lung-equivalent material (density, 0.433 g/cm³). The molded phantom is sliced into 20 2.5-cm transaxial sections, each of which contains a matrix of 5-mm holes at 1.5-cm spacing. Tissue- and lung-equivalent plugs with internal cavities to accommodate CaF₂ thermoluminescent dosimeter chips are inserted in the grid holes at positions corresponding to organs of interest. This arrangement keeps the chips at the center of each slice, away from the gap between slices where the radiation field might be perturbed by X-rays passing between the gap and, thus, be unable to provide adequate attenuation. All other grid holes were filled with solid tissue or lung-equivalent inserts. Five CaF₂ thermoluminescent dosimeter chips were used at each of the measurement points. Absorbed dose to the testes, ovaries, thyroid, eyes, breast, and bone marrow was measured for CT scans of the head, chest, abdomen, and torso by using typical pediatric technique factors. Organ locations are defined in Table 1.

Organ-absorbed doses were determined from the average of the five thermoluminescent dosimeter readings at each position; paired organs were averaged. The absorbed dose to bone marrow was determined from the sum of weighted sampled measurements of 20 bone marrow sites (Table 2). Weighting factors, equal to the ratio of the bone marrow at a given site [14] to the total bone marrow of all the sites sampled, were assigned to the sampled sites.

Approximately 1000 TLD-200 CaF₂ chips (Harshaw Chemical Co., Solon, OH) with dimensions of 0.32 × 0.32 × 0.69 cm, in five batches, were used in this study. The standard deviation of the response of the chips in each batch was about 3% for a uniform exposure of 1 R (0.258 mC/kg). After standard annealing, the response of the chips was calibrated with the response to about 200 mR (0.052 mC/kg) of a scattered-energy spectrum of X-rays generated at 120 kVp (3.5 mm Al half-value layer, 0.96 homogeneity factor). The scattered-energy spectrum was generated by means of a water-filled lucite tank (30 × 30 × 20 cm). The distance from the X-ray target to the front surface of the tank was 80 cm, and the entrance beam was 10 × 10 cm. The chips were positioned 90° to the primary X-ray beam and outside of the primary X-ray beam in a 10 × 10 cm area. Calibration exposures were monitored with a secondary ionization chamber



Fig. 1.—Assembled anthropomorphic phantom representing an average 6-year-old child.

TABLE 1: Phantom Organ Locations Used for TLD Absorbed Dose Measurements

Organ	Slice No.	Distance From Top of Head (cm)	Distance (cm) From Midline	Depth (cm) (anterior surface)
Eyes	4	11.5	3.0	0.5
Thyroid	8	21.5	0.0	2.0
Breast	12	31.5	4.5	1.0
Ovaries	19	48.5	6.0	3.0
Testes	21	54.0	0.0	1.0

(MDH 1050 X-ray monitor with ± 5% calibration uncertainty; Radcal Corp., Monrovia, CA). The chips were read out on a thermoluminescent analyzer (Model 200B; Harshaw Chemical Co.). The thermoluminescent response was converted to absorbed dose in tissue by using the calibration factor for each batch and the f-factor; $f = 0.92 \text{ rad/R} = 35.7 \text{ (Gy-kg)/C}$.

CT Dose Index

The organ-absorbed doses were normalized to the CT dose index measured in a specialized lucite head phantom [11]. This normalization allows for the estimation of organ-absorbed dose if the CT dose index for a given scanner is known. The phantom was 14 cm long and 16 cm in diameter, with holes drilled at locations lying along eight radii of 0, 4.95, and 7.0 cm. The maximum average dose was measured at the center position by using an MDH 1050 radiation exposure monitor with model 10 × 5 – 10.3 CT pencil ionization chamber (Radcal Corp.). The chamber exposure readings were converted to absorbed dose in tissue.

TABLE 2: Bone Marrow Dose Weighting Factors

Location	Slice (No. Points)	Fraction of Active Bone Marrow ^a	Weighting Factor ^b
Cranium	2 (2)	0.159	0.176
Mandible	6 (1)	0.016	0.018
Scapulae	9 (1)	0.027	0.030
Clavicles	8 (1)	0.009	0.010
Sternum	11 (1)	0.017	0.019
Ribs	11 (1)	0.086	0.098
Cervical spine	6 (1)	0.022	0.024
Thoracic spine	10, 11		
	13, 13 (4)	0.089	0.099
Lumbar spine	16 (2)	0.068	0.075
Sacrum	18 (1)	0.055	0.061
Pelvis	18, 19 (4)	0.131	0.145
Femur, tibiae, fibulae, and patella	20 (2)	0.221	0.245
Totals		0.902	1.020

^a From Cristy [14], a 5-year-old child.

^b The following regions of the skeleton with their associated fraction of active bone marrow are not included in the normalized weighting factor: ankle and foot (0.025), humeri (0.046), ulnae and radii (0.02), wrist and hand bones (0.009).

Results

Table 3 presents the pediatric organ-absorbed doses to bone marrow, eyes, thyroid, breast, ovaries, and testes for CT examinations of the head, chest, abdomen, and torso with typical pediatric techniques. Table 4 lists the organ-absorbed dose normalized to the central axis CT dose index measured in the head phantom for the same technique factors. The CT dose index per unit mAs was 12.9 ± 0.2 mrad/mAs ($129 \mu\text{Gy}/\text{mAs}$), which corresponds to a CT dose index for the head technique of 4.1 ± 0.06 rad and 2.1 ± 0.03 rad (cGy) for the body technique. Absorbed dose as a function of milliampere-seconds (mAs) was shown to be linear, thus allowing direct comparison of absorbed-dose measurements for different mAs values [13]. A comparison of the entrance-skin absorbed dose measured with the phantom and actual entrance-skin absorbed dose for children [13] is presented in Table 5.

Discussion

The radiation dose to the bone marrow in children depends on the body part scanned and the age-dependent bone-marrow distribution. In the neonate, approximately 30% of the marrow is in the skull and 30% in the extremities, with the remaining 40% uniformly distributed among the remaining bone-marrow cavities [14]. By the age of 15, the major distribution sites have gradually shifted from the skull (10%) and extremities (15%) to the pelvis (19%), vertebrae (28%), and ribs (14%). As a result of the bone-marrow distribution, the absorbed dose to a neonate's bone marrow from a head scan would be higher than for an older child, and the risk factor would be higher for the neonate. Therefore, high priority should be given to dose-reduction measures for head scans in infants. Conversely, as the marrow distribution shifts to the

TABLE 3: Organ-Absorbed Dose for CT Examinations in a 6-Year-Old Patient Phantom

Organ Examined	Dose Absorbed in mrad (10^{-5} Gy) During Examination			
	Head	Chest	Abdomen	Torso
Bone marrow	530 ± 60	386 ± 60	322 ± 76	1096 ± 64
Eyes	480 ± 60	30 ± 3	8 ± 1	32 ± 3
Thyroid	70 ± 8	550 ± 60	16 ± 5	506 ± 38
Breast	14 ± 1	1480 ± 90	189 ± 22	1600 ± 140
Ovaries	3 ± 2	56 ± 9	239 ± 21	1410 ± 50
Testes	2 ± 1	20 ± 3	77 ± 10	540 ± 38

Note: All CT examinations were done with the following specifications: 120 kVp, 140 mA, 2 sec, 10-mm slices. Number of slices for each examination were as follows: head = 11 slices, chest = 14 slices, abdomen = 12 slices, torso = 30 slices.

TABLE 4: Organ-Absorbed Dose Normalized to the CTDI Measured at the Central Position of the Recommended Head Phantom

Organ Examined	Organ-Absorbed Dose/CTDI Ratio ^a During Examination			
	Head	Chest	Abdomen	Torso
Bone marrow	0.147	0.214	0.178	0.607
Eyes	0.133	0.017	0.004	0.018
Thyroid	0.019	0.304	0.009	0.280
Breast	0.004	0.819	0.104	0.886
Ovaries	0.001	0.031	0.132	0.781
Testes	0.001	0.011	0.043	0.299

Note.—CTDI = CT dose index.

^a The ratio is normalized to the CTDI derived for the mAs used in each examination.

TABLE 5: Comparison of Entrance Skin-Absorbed Dose Measured on the Phantom to That Measured on Pediatric Patients and at the Anterior Position of the FDA Head Phantom [11]

Organ Examined	Patient Average Absorbed Dose (Range)	Phantom Average Absorbed Dose	CTDI ^a Anterior
Head	2.6 ± 0.3 (2.0–3.4)	3.0 ± 0.3	4.1 ± 0.06
Chest	1.8 ± 0.6 (1.1–2.4)	2.2 ± 0.2	2.1 ± 0.03
Abdomen	1.6 ± 0.4 (1.1–2.4)	2.1 ± 0.2	2.1 ± 0.03

Note.—FDA = Food and Drug Administration. Observed doses are given in rad (cGy).

^a CTDI = CT dose index. Anterior position of FDA phantom.

torso with increasing age, the higher risk associated with increased bone-marrow exposure must be taken into consideration.

Organ-absorbed doses for children who are 5–6 years old may be approximated by measuring the CT dose index at the central position of the head phantom recommended in 21 CFR 1020 [11] and then multiplying by the organ-dose: CT-dose-index ratio for the organ of interest. Alternatively, if the dose index is not available for the mAs used for patient scans, then its value can be scaled linearly because the CT dose index is a linear function of the mAs, given a properly functioning scanner. The estimated organ dose will be a reason-

ably good estimate for similar scanners because the ratio of scattered to incident dose should be the same for similar units. The estimated organ dose will be less accurate for scanners having external-scatter and tube-leakage characteristics that are different from those of the GE CT/T 9800 used in this study. This variation will be particularly important for organ sites remote from the scan plane, where external scatter predominates over internal scatter. The CT dose index measured at the anterior position of the FDA head phantom agrees with the entrance-skin exposure to children and the phantom for chest and abdomen scans, but overestimates the dose for the head (Table 5). The phantom and patient data agree. The CT dose index measured at the anterior position of the FDA head phantom can, therefore, be used as a reasonable estimate for entrance-skin absorbed dose measurements in children undergoing CT examination of the body, when corrected to the mAs used in the study.

ACKNOWLEDGMENTS

We thank Joel Gray of the Department of Radiology, Mayo Clinic, for his helpful discussions regarding this project and Debra Souders and Dianne Lyles for typing the manuscript.

REFERENCES

1. International Commission on Radiological Protection. *Recommendations of the International Commission on Radiological Protection*. ICRP publication 26. New York: Pergamon Press, 1977
2. National Council on Radiation Protection and Measurements. *Influence of dose and its distribution in time on dose-response relationships for low-LET radiations*. NCRP report 64. Washington, DC: National Council on Radiation Protection and Measurements 1980
3. Beebe GW, Kato H, Land CE. Studies of the mortality of A-bomb survivors. 6. Mortality and radiation dose, 1950-1974. *Radiat Res* 1978;75:138-201
4. National Council on Radiation Protection and Measurements. *Mammography*. NCRP report 66. Washington, DC: National Council on Radiation Protection and Measurements, 1980
5. Brasch RC, Cann CE. Computed tomographic scanning in children. II. An updated comparison of radiation dose and resolving power of commercial scanners. *AJR* 1982;138:127-133
6. Shope TB, Morgan TJ, Showalter CK, et al. Radiation dosimetry survey of computed tomography systems from ten manufacturers. *Br J Radiol* 1982;55:60-69
7. Brasch RC, Boyd DP, Gooding CA. Computed tomography scanning in children: comparison of radiation dose and resolving power of commercial CT scanners. *AJR* 1978;131:95-101
8. Burgess AE. Scatter radiation from abdominal CT examinations. *J Comput Assist Tomogr* 1985;9:926-930
9. Chopp M, Ewald L, Hartson M. The contribution of internal scatter to radiation dose during CT scan of the head. *Neuroradiology* 1981;22:145-150
10. Yalcintas MG, Nalcioğlu O. A method for dose determination in computerized tomography. *Health Phys* 1979;37:543-548
11. Food and Drug Administration. *Diagnostic x-ray systems and their major components; amendments to performance standard: final rule*. Fed Reg 21 CFR Part 1020, 1984;49:34,698-34,714
12. Shope TB, Gagne RM, Johnson GC. A method of describing the doses delivered by transmission x-ray computed tomography. *Med Phys* 1981;8:488-495
13. Fearon T, Vucich J. Pediatric patient exposures from CT examinations: GE CT/T 9800 scanner. *AJR* 1985;144:805-809
14. Cristy M. Active bone marrow distribution as a function of age in humans. *Phys Med Biol* 1985;26:389-400

Case Report

Spontaneous Resolution of Neonatal Ovarian Cysts

A. R. Nussbaum,¹ R. C. Sanders,¹ R. M. Benator,² J. A. Haller, Jr.,³ and D. L. Dudgeon³

Ovarian cysts in the neonate vary considerably in size, with the largest reported to be 19 cm in diameter [1]. Most of these cysts are asymptomatic, but occasionally complications occur, such as torsion or rupture [1-5]. Large cysts may cause intestinal obstruction and respiratory compromise [1-3]. Surgery has been advocated by most authors [5-6]. Even in the absence of ovarian torsion, however, an oophorectomy is usually required because the cyst is closely adherent to residual ovarian tissue [1, 2, 6]. We sonographically studied three infants with medium-sized (3-5 cm in diameter) lower abdominal cysts, presumed to be ovarian in origin (Figs. 1 and 2). All cysts disappeared within 4 months of discovery. Our experience indicates that the natural history of some ovarian cysts is spontaneous resolution.

Representative Case Report

A 4-month-old girl was referred to Johns Hopkins Hospital for surgical removal of a presumed ovarian cyst that had been discovered on a fetal sonogram at 26 weeks gestation. A postnatal sonogram at 1 day of age confirmed the presence of a 4.2 × 4 × 2.3 cm left pelvic cyst (Fig. 1). A repeat sonogram at 2 weeks showed a decrease in the size of the cyst (2.9 × 3.2 × 2.5 cm), which was now seen on the right side. Surgical therapy was delayed to allow interval growth of the baby, who was asymptomatic. A third sonogram, performed at 4 months, just before planned surgical resection, showed no pelvic or abdominal mass. The infant has remained asymptomatic and a sonogram at 22 months showed a normal prepubertal uterus and ovaries.

Discussion

Ovarian cysts in neonates and young infants have been considered uncommon in the past, with only 71 cases re-

ported in the literature through 1976 [6]. Ovarian cysts were discovered only if they were palpable, caused symptoms because of torsion or rupture, or were associated with intestinal obstruction [1-3]. With the increased use of sonography, asymptomatic cystic ovarian masses are being discovered more often [4, 5]. Autopsy studies show similar data. DeSa [7] reviewed 332 stillbirths and neonatal deaths within 28 days of birth and discovered that 34% (113) had small follicular cysts.

Currently, ovarian cysts discovered in early infancy are surgically removed. Although cystectomy has been used with bilateral cysts, oophorectomy has been the standard procedure for a unilateral cyst because of concerns about ovarian torsion, replacement of the entire ovary by the cyst, and the inability to separate the cyst from any remaining histologically normal but distorted ovarian tissue [1, 5, 6]. Cystectomy alone has been recently employed, however, leaving the remainder of the ovary or ovaries intact [5]. It is unknown if ovarian function and morphology are preserved.

Neonatal ovaries show functional and anatomic similarities to pubertal and adult ovaries [7]. In the third-trimester fetus and the neonate, the ovaries may be enlarged with prominent cystic follicles and luteinized theca interna. These small cysts, which measure 1-7 mm in diameter, are thought to be the result of excessive stimulation from maternal placental chorionic gonadotropin, and to regress spontaneously [7].

Presumably maternal hormones also stimulate the development of larger ovarian cysts, because there is a higher incidence of theca lutein ovarian cysts in babies of mothers with diabetes, toxemia, or rhesus isoimmunization, all of which result in a greater release of placental chorionic gonadotropins [1, 7, 8]. Theoretically, when the baby is removed

Received May 27, 1986; accepted after revision September 23, 1986.

¹ Russell H. Morgan Department of Radiology and Radiological Science, The Johns Hopkins Medical Institutions, 600 N. Wolfe St., Baltimore, MD 21205. Address reprint requests to A. R. Nussbaum.

² Department of Radiology, Medical College of Virginia, Richmond, VA 23298.

³ Department of Surgery and Pediatrics, The Johns Hopkins University School of Medicine, Baltimore, MD 21205

AJR 148:175-176, January 1987 0361-803X/87/1481-0175 © American Roentgen Ray Society

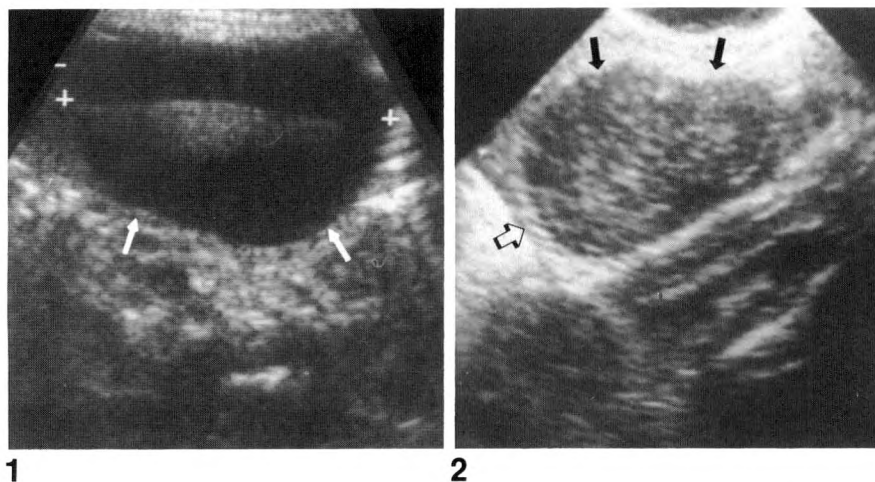


Fig. 1.—Transverse sonogram, left pelvis. Female neonate with cystic mass (arrows). Few internal echoes are artifacts related to gain setting. Repeat sonograms showed a decrease in size of presumed ovarian cyst and complete resolution at 4 months of age.

Fig. 2.—Five-month-old premature girl. Longitudinal sonogram of lower right abdomen. Eight days earlier, this echogenic mass (black arrows) with thin, highly echogenic rim (open arrow) was completely cystic. This presumed hemorrhagic ovarian cyst decreased in size and resolved in 2 months. Possibility of ovarian torsion was considered, but infant remained asymptomatic.

from the maternal influence, spontaneous resolution of ovarian cysts should occur.

A search of the literature revealed three cases of documented resolution of neonatal cysts that were 2.5 cm or less in diameter. Resolution has also been reported in four premature infants with estradiol-producing cysts discovered in early infancy (2–4 months) [9]. These infants had ovarian hyperstimulation caused by markedly elevated follicle-stimulating-hormone and luteinizing-hormone levels, a common finding in premature babies with an immature negative-feedback system. Two of the infants were treated with medroxy-progesterone, which inhibited the release of gonadotropins. One of the infants in our study was also premature and had clinical evidence of estrogenic hyperstimulation (Fig. 2).

One of the potential risks in conservative management is that the cystic lesion under observation is not an ovarian cyst. Whereas most ovarian lesions in early infancy are ovarian cysts, lesions such as cystadenomas and cystic granulosa cell tumors have been reported [2]. Malignancy is extremely rare, and is usually not a fluid-filled mass [2]. Mesenteric and duplication cysts may be sonographically indistinguishable from ovarian cysts [5]; because these cystic masses are benign, conservative management should not be hazardous. Surgery could be delayed and performed only if the mass either failed to decrease in size or caused mechanical bowel obstruction.

It is unclear whether there is a potential risk in leaving a twisted, infarcted ovarian cyst untreated (Fig. 2). Torsion has been reported in approximately 13% of ovarian cysts [1, 2, 4, 5]. In most but not all cases, abnormal clinical parameters such as pain, fever, vomiting, intestinal obstruction, leukocytosis, and peritonitis were present and served as warning signals for this complication [1, 2]. Twisted cysts are solid or complex on sonograms and may have a fluid-debris level or fluid in the cul-de-sac, unlike the purely cystic appearance of an uncomplicated cyst [4, 5].

Another risk is the potential for an uncomplicated cyst to undergo torsion during the period of observation. This occurred in two reported cases, one in a 3-cm cyst and the other in a 4-cm cyst [4, 5]. In both infants, sonography was able to detect the complication; the cysts, which were initially

purely cystic, developed a fluid-debris level. Even though both infants were asymptomatic, their cysts were surgically removed when the sonographic character of the masses changed.

Rupture of the cyst is a rare complication. The few cases reported have all occurred in the period immediately after birth. In each instance, the cyst was large (10–12 cm) and there was evidence of an acute abdomen [3]. Each infant had marked abdominal distension due to hemoperitoneum and a low or dropping hematocrit.

Our experience and a review of the literature suggest that conservative management with sonographic reevaluation is an acceptable alternative to surgical therapy in uncomplicated cysts that are less than 5 cm in diameter. To date, larger cysts have not been treated conservatively. Percutaneous aspiration of a large ovarian cyst is yet another potential therapeutic approach.

ACKNOWLEDGMENT

We thank Elizabeth Schriock and Claude Migeon for their assistance in the clinical evaluation of our cases.

REFERENCES

1. Carlson DH, Griscom NT. Ovarian cysts in the newborn. *AJR* 1972;116:664–672
2. Marshall JR. Ovarian enlargements in the first year of life: review of 45 cases. *Ann Surg* 1965;161:372–377
3. Monson R, Rodgers BM, Nelson RM, Young TK. Ruptured ovarian cyst in a newborn infant. *J Pediatr* 1978;73:324–325
4. Avni EF, Godart S, Israel C, Schmitz C. Ovarian torsion cyst presenting as a wandering tumor in a newborn: antenatal diagnosis and postnatal assessment. *Pediatr Radiol* 1983;13:169–171
5. Montagne JPH, Neuenschwander S, Prot D, Cordier MD. Solitary intraperitoneal cystic lesions in newborn girls: ten cases studied by ultrasound. *Ann Radiol (Paris)* 1982;25:131–135
6. Alvear DT, Rayfield MM. Bilateral ovarian cysts in early infancy. *J Pediatr Surg* 1976;11:993–995
7. DeSa DJ. Follicular ovarian cysts in stillbirths and neonates. *Arch Dis Child* 1975;50:45–50
8. Ahlvin RC, Bauer WC. Luteinized cysts in ovaries of infants born of diabetic mothers. *Am J Dis Child* 1957;93:107–109
9. Sedin G, Bergquist C, Lindgren PG. Ovarian hyperstimulation syndrome in preterm infants. *Pediatr Res* 1985;19:548–552

Complications of Percutaneous Nephrolithotomy

Won J. Lee^{1,3}
 Arthur D. Smith^{2,4}
 Vincent Cubelli²
 Gopal H. Badlani^{2,4}
 Bernard Lewin^{1,5}
 Frances Vernace^{1,3}
 Eric Cantos¹

Of 582 patients who underwent percutaneous nephrolithotomy, 4% had complications. The most common complications were fever (23%) and bleeding necessitating transfusion (12%). Extravasation was seen in 7% of patients and transient ureteral obstruction in 6%. Other complications included pneumothorax or hydrothorax, pneumonia/atelectasis, paralytic ileus, nephrostomy-tube dislodgment or urine drainage from the flank lasting more than 1 week, significant infection, urinoma formation, renal pelvic laceration, ureteral avulsion, ureteropelvic or ureteral stricture, bowel injury, or escape of stone fragments into the retroperitoneum. Seven patients (1%) required immediate surgery: four to repair renal pelvic lacerations, one to repair a ureteral avulsion, and two to control bleeding after nephrostomy-tube removal when embolization failed. Four patients required delayed surgery for ureteral or ureteropelvic junction strictures, which may have been caused by a tissue reaction to the stones rather than by the procedure itself. There were two deaths—one from respiratory failure in a patient with severe interstitial pulmonary fibrosis and chronic renal failure and the other from myocardial infarction in an obese diabetic patient with hypertension.

Since its introduction in the late 1970s, when it was primarily used to treat kidney-stone patients who were poor operative risks, percutaneous nephrolithotomy (nephrostolithotomy) has virtually replaced open-stone operations in patients of all ages and for nearly all types of stones. The advantages of the percutaneous method include lower rates of mortality and morbidity, a faster convalescence, greater ease of repeat procedures, and greater cost effectiveness. Nevertheless, the recent approval by the Food and Drug Administration of extracorporeal shock-wave lithotripsy (ESWL) mandates a critical new look at the percutaneous methods. While ESWL is neither free of morbidity nor suitable for all cases [1], it does create a new standard by which percutaneous nephrolithotomy and its complications must be judged. In this article, we examine the complications in one of the largest series of percutaneous nephrolithotomy cases reported to date (582 patients) and offer several recommendations for minimizing these problems. Previous reports based on this series were concerned with techniques and results rather than with complications [2-4].

Materials and Methods

Since April 1982, all stones in the renal pelvis, calyces, and middle-to-upper ureter have been initially treated by percutaneous means. Thus, the indications for percutaneous nephrolithotomy are the same as those for open surgery. This report includes 582 consecutive patients—312 men and 270 women—aged 18-96 years (average, 57 years) seen from April 1982 through September 1985. Seventy-five of these patients had staghorn calculi, including one in an ectopic pelvic kidney and one in a solitary allograft kidney. Nine patients had bilateral stones and 14 had associated ureteropelvic junction obstruction necessitating endopyelotomy [5]. All patients in whom a percutaneous nephrostomy (PCN) was attempted for extraction of upper urinary stones are included in this study.

Received March 17, 1986; accepted after revision July 8, 1986.

¹ Department of Radiology, Long Island Jewish Medical Center, New Hyde Park, NY 11042. Address reprint requests to W. J. Lee.

² Division of Urology, Department of Surgery, Long Island Jewish Medical Center, New Hyde Park, NY 11042.

³ Department of Radiology, State University of New York at Stony Brook, Stony Brook, NY 11794.

⁴ Department of Urology, State University of New York at Stony Brook, Stony Brook, NY 11794.

⁵ Present address: Radiology Affiliates of Central New Jersey, Trenton, NJ 08618.

AJR 148:177-180, January 1987
 0361-803X/87/1481-0177
 © American Roentgen Ray Society

Our methods for visualization of the collecting system, tract dilatation, and stone removal, and our technique of PCN access route have been described previously [2, 4]. Briefly, we inject contrast material, usually through a cystoscopically placed retrograde ureteral catheter, to outline the collecting system. The PCN is performed in the radiology suite by using local anesthesia supplemented with IV analgesics. We prefer direct entry into the calyx for calyceal stones and puncture of middle or lower calyces for stones in the pelvis or upper ureter. A 7-French angiogram catheter is passed down the ureter over a guidewire and is sutured to the skin. Tract dilatation and stone removal generally are performed the next day in the operating room with the patient under general anesthesia. A safety guidewire is routinely placed into the distal ureter. Over the working wire, the tract is dilated (usually to 34 French) with Amplatz renal dilators (Cook Inc., Bloomington, IN). The stones are removed under direct nephroscopic vision by using various grasping forceps, baskets, and ultrasonic lithotripsy, depending on their size and location. Normal saline is used as the irrigant. When the stone has been removed, a 14-French Malecot nephrostomy tube is inserted, unless urinary-tract perforation or extravasation is apparent, in which case a 24-French reentry nephrostomy tube (Van Tec Inc., Spencer, IN) is inserted to tamponade, stent, and preserve the tract. Within 48 hr after stone removal, a plain abdominal radiograph, a nephrotomogram, and a nephrostogram are obtained in order to verify that the stone has been completely removed and that the collecting system has remained intact. The nephrostomy tube is clamped overnight and subsequently is removed. A follow-up IV urogram is obtained 3–6 months later.

Results

Gross hematuria occurred in all 582 patients, but only bleeding that required transfusion was considered a complication. Bleeding occurred in only one patient after PCN alone but in 64 patients after stone extraction (Table 1). An additional seven patients had bleeding either immediately or 1 day after nephrostomy-tube removal. This was the result of pseudoaneurysm or arteriovenous fistula formation in six patients, as shown angiographically. In the remaining patient, a large perinephric hematoma occurred as a result of intermittent bleeding. Percutaneous embolization stopped the bleeding in four patients and failed in two patients who underwent nephrectomy or segmental nephrectomy. One patient who had a retroperitoneal hematoma responded to conservative therapy.

Temperature elevation above 38.5°C was considered a febrile complication and occurred in almost one-fourth of the patients (Table 2). In most cases, the fever began during the

procedure or within 4–6 hr afterward, suggesting retrograde flow of urine, irrigant, or both as a significant factor [3]. Antipyretics were rarely needed. Fever was clearly associated with significant infection in only five patients. In two of these patients, pyelonephritis caused by an organism not previously isolated from the patient occurred after PCN puncture; in another patient, a previous infection was reactivated by the puncture. The other two patients suffered septic shock 4–6 hr after stone removal. All of these patients recovered with appropriate antibiotic treatment. Approximately 6% of the remaining patients had urinary infections that responded to antibiotics.

Extravasation was visible radiographically in 42 patients (7%) after stone removal, but urinomas formed in only three patients and were drained percutaneously. Thirteen patients had renal pelvic lacerations, but only four required open repair. Ureteral and ureteropelvic junction strictures generally followed extraction of an embedded stone. Transient urinary obstruction occurred in 35 patients (6%) as a result of ureteral edema and was easily managed by nephrostomy drainage.

Pneumothorax or hydrothorax occurred in 18 patients (3%), most often in those who had nephrostomy tracts created above the 12th rib to facilitate access to the stones. In 13 cases, a chest tube was inserted for 2–3 days; in the other cases, the fluid was aspirated. There have been no sequelae.

Prolonged (>1 week) drainage of urine from the flank was seen in nine patients (2%). Ureteral-catheter insertion or continued nephrostomy drainage led to an uneventful recovery in all cases.

There were two deaths in this series. The first patient, a 59-year-old man who had systemic sarcoidosis with severe interstitial pulmonary fibrosis and chronic renal failure, presented with bilateral kidney stones, which were extracted with the patient under general anesthesia. On the fourth postoperative day, his respiratory function began to deteriorate and he died. An autopsy revealed a large right-sided retroperitoneal hematoma and some bloody ascites. The second patient, a 67-year-old obese woman with hypertension and diabetes mellitus, presented with an enormous staghorn calculus. Two sessions of lithotripsy and fragment extraction were completed without problems, but after the third session, the patient died of myocardial infarction in the postanesthesia recovery room. Preoperative ECGs showed mild ischemic changes. Neither of these patients would have been a candidate for ESWL.

TABLE 1: Major Complications of Percutaneous Nephrolithotomy in 582 Patients

Complication	PCN (%)	NLT (%)	Late (%)	Total (%)
Death		2 (0.3)		2 (0.3)
Bleeding necessitating intervention	None	6 (1.0)	1 (0.2)	7 (1.2)
Significant infection	3 (0.5)	2 (0.3)	None	5 (0.8)
Urinary tract injury				
Urinoma formation	1 (0.2)	2 (0.3)	None	3 (0.5)
Pelvic laceration	None	5 (0.9)	None	5 (0.9)
Ureteral avulsion	None	1 (0.2)	None	1 (0.2)
Ureteropelvic junction or ureteral stricture	None	None	5 (0.9)	5 (0.9)
Injury to adjacent organs:				
Pneumothorax/hemothorax	1 (0.2)	17 (2.9)	None	18 (3.1)
Bowel	1 (0.2)	None	None	1 (0.2)

Note.—Some patients had more than one complication; overall, 4% of the patients had significant complications. PCN = percutaneous nephrostomy; NLT = nephrolithotomy; late = delayed complications.

TABLE 2: Minor Complications of Percutaneous Nephrolithotomy in 582 Patients

Complication	PCN (%)	NLT (%)	Total (%)
Low fever (38.5°C)	18 (3.0)	113 (19.4)	131 (22.4)
Bleeding necessitating transfusion	1 (0.2)	64 (11.0)	65 (11.2)
Extravasation	None	42 (7.2)	42 (7.2)
Tube dislodgment	2 (0.3)	32 (5.5)	34 (5.8)
Pneumonia/atelectasis	None	16 (2.7)	16 (2.7)
Transient urinary obstruction	None	35 (6.0)	35 (6.0)
Paralytic ileus	None	15 (2.6)	15 (2.6)
Urine drainage from flank for >1 week	None	9	9 (1.5)
Stone fragments escaping into retroperitoneum	None	6 (1.0)	6 (1.0)

Note.—PCN = percutaneous nephrostomy; NLT = nephrolithotomy.

Discussion

Urinary Tract Injury

Two questions arise in connection with urinary-tract injury by PCN and stone removal: How many accidental injuries occur during the manipulations, and how much damage attends the creation of a PCN tract?

Extravasation of contrast medium during or immediately after the procedure may or may not indicate a complication. For example, 26% of the patients described by Clayman et al. [6] had extravasation, but many of these patients were seen early in the Minnesota study, when opacification of the renal pelvis for PCN puncture was often achieved by instilling contrast medium through a Chiba needle—the “2-stick” PCN method. This method increases the risk of contrast loss through a deliberately created hole. Later in the series, contrast medium was instilled through a ureteral catheter that was inserted retrograde, thereby reducing the risk of extravasation (while permitting distension of the renal pelvis for easier manipulation) and preventing the escape of stones into the ureter, a method we use routinely. Of greater interest are the unquestionable injuries such as lacerations, avulsions, and perforations. We observed five significant renal-pelvic lacerations, one ureteral avulsion, three instances of urine leakage sufficient to form urinomas, and six escapes of stones into the retroperitoneum, suggesting perforation. Four of the significant pelvic lacerations occurred early in our series and were explored immediately; the other healed with nephrostomy drainage. Indeed, most small leaks and tears will seal quickly without assistance if the urinary tract is adequately drained. The avulsion was surgically managed. The urinomas and escaped stones were managed conservatively. Segura et al. [7] reported one case of ureteral separation necessitating operation, one case of ureteral perforation with stone escape into the retroperitoneum, and two cases of renal parenchymal laceration by dilators that necessitated open operation.

The formation of strictures may be a response to the stone rather than an effect of stone removal. In our series, most of the strictures formed at sites where stones had been embedded, and one of our patients with stones at the ureteropelvic junction already had strictures that had to be incised before the stones could be removed. It is not possible to test this hypothesis of stone-induced stricture by comparison with

the results of ESWL, since embedded stones or obstructed urinary tracts are not treated with ESWL.

Bleeding

Approximately 1% of patients who undergo PCN puncture will bleed enough to require transfusion [8, 9]. The higher frequency of transfusions in our series as compared with other reports [6–8] may be due to the frequency of staghorn calculi (and hence of more extensive manipulation) or to the performance of intrarenal surgery, such as an endopyelotomy in several cases. If formation of a subcapsular or perirenal hematoma visible by CT is the criterion, presumably the frequency would be higher, although there are few data on this point. Clayman et al. [6] found perirenal hematomas not requiring treatment in two of their 100 patients without using CT, and we found one large and two small collections in three of the 20 patients we studied by CT.

Delayed bleeding from an arteriovenous fistula or a ruptured pseudoaneurysm occurs in less than 1% of patients undergoing PCN with or without stone removal [7, 8, 10–12]. In these patients, gross hematuria may be followed by hypertension and anuria, and embolization or nephrectomy may be needed to control the bleeding. Both Segura et al. [7] and Reddy et al. [8] reported one patient with delayed serious bleeding necessitating partial or total nephrectomy; we had two such cases.

Several steps can be taken to minimize the frequency of serious blood loss after PCN puncture and stone removal: (1) a clotting profile should be obtained and any abnormalities corrected before the procedures; (2) the operator should have a clear mental image of the renal vasculature when choosing the puncture site and try to puncture through Brodel’s avascular line; (3) if any intrarenal surgery is to be done to free trapped stones or correct anomalies that encourage stone formation, the area to be incised should first be examined under direct vision to be certain there are no arterial pulsations [13]; (4) through (two-wall) punctures of the renal pelvis, which can injure the anterior segmental renal artery, should be avoided—biplane or C-arm fluoroscopy is invaluable; and (5) punctures close to a rib also should be avoided, because they may damage the intercostal vessels. Because significant bleeding may occur despite these precautions, equipment, cross-matched blood, and surgical back-up must be readily available.

Bleeding is much less common after stone removal by ESWL. Chaussy et al. [14] found only six subcapsular hematomas by routine sonography of more than 1000 patients, and only two of these patients required transfusions.

Injuries to Other Organs

The organs most often injured during PCN and stone removal are the lungs and pleura, with possible pneumothorax or hydrothorax. These problems are especially likely with PCN puncture above the 12th rib, yet experienced operators do not hesitate to make such a puncture when it provides the best access to a stone [8, 15]. In these cases, it is especially important to use a working sheath in the PCN tract to prevent the escape of fluid. A chest tube or percutaneous drainage will be necessary in a few cases.

Bowel perforation can be a serious complication of PCN puncture. In a series of 250 patients reported from France

[16], perforation of the left side of the colon led to rectal hemorrhage and shock in one patient and passage of gas through the PCN tract in another. Both patients required operative repair. The authors of that report suggest that bowel perforation is most likely in patients with mobile kidneys (a condition found in both cases) and when the PCN tract is placed far laterally. Surveillance is the appropriate treatment only when the perforation is extraperitoneal and no predisposition to complication is present.

Puncture of the spleen has occurred in several patients undergoing PCN with or without stone removal. In some cases, no treatment was required; in a few, splenectomy was necessary. Liver injuries are less common and seldom require treatment. Indeed, we are aware of one instance in which a transhepatic PCN tract was inadvertently created, dilated, and used to extract a stone without sequelae.

Infection

A PCN puncture and stone removal may reactivate infection, as in two of our patients. Bacteriuria is common in patients with large stones subjected to lithotripsy; it occurred in one-fourth of our patients with staghorn stones. In many cases, the bacteria probably are released from infected stones as they disintegrate, a contention supported by the fact that reactivated infection and the appearance of bacteriuria in patients with previously sterile urine have occurred in several patients receiving ESWL [14]. A few cases of septic shock have been reported, generally in association with extravasation and absorption of irrigating fluid [7]. The occurrence of this potentially fatal complication even when broad-spectrum antibiotics are being given reinforces the long-standing admonition that antibiotics cannot be expected to replace good technique, especially when, as in the case of infected stones, the operating field will inevitably become contaminated.

Deaths

Early in the use of PCN punctures in endourology, bleeding was the usual cause of the few deaths that were reported. This is no longer the case. One of the deaths in our series was caused by respiratory failure in a patient with previous pulmonary disease and the other by myocardial infarction. The single fatality in the Mayo Clinic series resulted from acute myocardial infarction and refractory arrhythmia in a 64-year-old quadriplegic woman who had undergone removal of staghorn calculi bilaterally. Autopsy revealed two previous myocardial infarctions. None of these patients would have been considered a good operative risk, and percutaneous nephrolithotomy was the only option available at the time. A single death from acute cardiac decompensation has been associated with ESWL; the autopsy revealed several areas of old infarcts, and the pathologist found no evidence of a direct relation between the death and ESWL. The shock-wave-dependent arrhythmias seen in 80% of the early patients treated by ESWL have since been minimized by synchronizing the shock wave with the R wave of the ECG [14].

Conclusion

Some of the early comparisons of percutaneous nephrolithotomy (PNL) and ESWL had the effect of making PNL look less effective and the ESWL more effective; this has been the

case in large series. That is, the earliest percutaneous stone removals were done in patients for whom that procedure (highly experimental at that time) was the only option; whereas during the development of ESWL, the first patients were, of necessity, those with small uncomplicated stones who were in better physical condition than those subjected to percutaneous methods [14]. Moreover, some of the instruments that have been most useful in percutaneous stone removal (such as the flexible nephroscope) were not available for the early cases. Therefore, only in the last few years has it become possible to compare the results of the two methods in similar populations.

It is becoming clear that ESWL will not supplant PNL. Chaussy et al. [14] estimate that 15% of patients will need percutaneous manipulation in addition to ESWL and that another 15% will not be candidates for ESWL. At present, a far higher percentage of patients are not candidates because of lack of availability of ESWL. Thus, continued study of the complications of PNL is mandatory.

REFERENCES

1. Chaussy C, Fuchs GJ. World experience with extracorporeal shock-wave lithotripsy (ESWL) for the treatment of urinary stones: an assessment of its role after 5 years of clinical use. *Endourol Newsletter* 1986;1(1):7-8
2. Lee WJ, Loh G, Smith AD, et al. Percutaneous extraction of renal stones: experience in 100 patients. *AJR* 1985;144:457-462
3. Snyder JA, Smith AD. Staghorn calculi: percutaneous stone extraction versus anatomic nephrolithotomy. *J Urol*, in press
4. Lee WJ, Smith AD, Cubelli V, Vernace FM. Percutaneous nephrolithotomy: analysis of 500 consecutive cases. *Urol Radiol* 1986;8:61-66
5. Badlani G, Eshghi M, Smith AD. Percutaneous surgery for ureteropelvic junction obstruction (endopyelotomy): technique and early results. *J Urol* 1986;135:26-28
6. Clayman RV, Surya V, Miller RP, et al. Percutaneous nephrolithotomy: extraction of renal and ureteral calculi from 100 patients. *J Urol* 1984;131:868-871
7. Segura JW, Patterson DE, LeRoy AJ, et al. Percutaneous removal of kidney stones: review of 1,000 cases. *J Urol* 1985;134:1077-1081
8. Reddy PK, Hulbert JC, Lange PH, et al. Percutaneous removal of renal and ureteral calculi: experience with 400 cases. *J Urol* 1985;134:662-665
9. Stable DP. Percutaneous nephrostomy: technique, indications and results. *Urol Clin North Am* 1982;9:15-29
10. Savant ML, Gold RE, Church JC. Delayed rupture of renal pseudoaneurysms: complication of percutaneous nephrostomy. *AJR* 1982;138:948-949
11. Cope C, Zeit RM. Pseudoaneurysms after nephrostomy. *AJR* 1982;139:255-261
12. Clayman RV, Surya V, Hunter D, et al. Renal vascular complications associated with the percutaneous removal of renal calculi. *J Urol* 1984;132:228-230
13. Clayman RV, Hunter D, Surya V, Castaneda-Zuniga WR, Amplatz K, Lange PH. Percutaneous intrarenal electrosurgery. *J Urol* 1984;131:864-867
14. Chaussy C, Schmidt E, Jocham D, Schuller J, Brandt H, Liedl B. Extracorporeal shock-wave lithotripsy (ESWL) for treatment of urolithiasis. *Urology* 1984;23(May Suppl):59-66
15. Young AT, Hunter DW, Castaneda-Zuniga WR, et al. Percutaneous extraction of urinary calculi: use of the intercostal approach. *Radiology* 1985;154:633-638
16. Vallanien G, Capdeville R, Viellon B, Charton M, Brissel JM. Colonic perforation during percutaneous nephrostomy. *J Urol* 1985;134:1185-1187

Percutaneous Balloon Dilatation of Ureteral Strictures



C. Daniel Johnson^{1,2}
 Edward J. Oke^{1,3}
 N. Reed Dunnick¹
 Ari Van Moore⁴
 Simon D. Braun¹
 Glenn E. Newman¹
 Louis Perlmutter¹
 Lowell R. King⁵

Percutaneous balloon dilatation of ureteral strictures has not gained widespread acceptance, despite proven success with the techniques for dilating stenotic blood vessels. Thirty-one ureteral strictures (in 30 patients) that were dilated during a 42-month period were reviewed to assess the results and to determine which patients are most likely to benefit from the procedure. Eighteen (58%) of 31 strictures were successfully dilated and remained patent for at least 6 months. Thirteen (42%) of 31 strictures resulted in failed patency either immediately (two patients) or within 3 months (seven patients), 6 months (three patients), or 21 months (one patient). Fourteen (64%) of 22 strictures less than 7 months of age were successfully dilated. All dilations for strictures more than 7 months of age failed. Four strictures were of unknown age. Nine (69%) of 13 strictures located in the proximal or midureter remained patent, and three (60%) of five dilations at a ureteroileal anastomosis were successful. Neither of two strictures at a ureterocolic anastomosis was treated successfully. We conclude that percutaneous balloon dilatation is an effective treatment of ureteral strictures in some patients, especially when the strictures are less than 7 months of age.

Transluminal angioplasty has been valuable for dilating stenotic blood vessels. The development of the balloon angioplasty catheter has expanded the indications and increased the safety of the technique. More recently this technology has been applied to stenotic lesions in nonvascular tubular structures such as the bile ducts [1], gastrointestinal tract [2], urethra [3], and ureter [4-11]. Although successful ureteral dilation has been reported [4-13], further experience is needed to determine the value of the procedure. We analyzed 30 patients who had percutaneous ureteral dilation followed for 6 months to 3 years to determine the results of the technique and to define those patients most likely to benefit from the procedure.

Materials and Methods

A retrospective review was performed of 31 ureteral strictures in 30 patients that were dilated over a 42-month period. There were 21 males and nine females ranging in age from 5 weeks to 81 years. Seven patients were 11 years old or younger, three of these were younger than 2 years old. The strictures were secondary to surgery in 21, ureteral calculi in four, and infection in one, and from unknown causes in five. All patients had a ureteral stricture with dilation of the ureter and collecting system proximal to the stenosis identified radiologically before dilation. Dilations were performed with standard polyethylene angioplasty balloon catheters in 26 patients, van Andel catheters in one patient, and both types in three patients. Postdilation ureteral stenting was used in all but three strictures. All strictures except one were dilated in an antegrade fashion after placement of a percutaneous nephrostomy tube. A single patient was dilated via a retrograde approach at surgery.

Dilatation was performed by initially passing a 0.035- or 0.038-in. (0.89- or 0.97-cm) guidewire across the stenosis. The angioplasty catheter was passed over the guidewire until the balloon was centered across the stricture. Balloon size was selected to approximate normal ureteral diameter, as measured from a radiograph. Balloon diameters ranged from 4 to 10 mm. The balloons were inflated for 30-60 sec, by using at least 5 atm of pressure (or

Received September 24, 1985; accepted after revision August 19, 1986.

¹ Department of Radiology, Duke University Medical Center, Durham, NC 27710.

² Present address: Department of Diagnostic Radiology, Mayo Clinic, Rochester, MN 55905. Address reprint requests to C. D. Johnson.

³ Present address: Department of Radiology, Presbyterian Hospital, Charlotte, NC 28233.

⁴ Department of Radiology, Charlotte Memorial Hospital, Charlotte, NC 28232.

⁵ Department of Urologic Surgery, Duke University Medical Center, Durham, NC 27710.

AJR 148:181-184, January 1987
 0361-803X/87/1481-0181
 © American Roentgen Ray Society

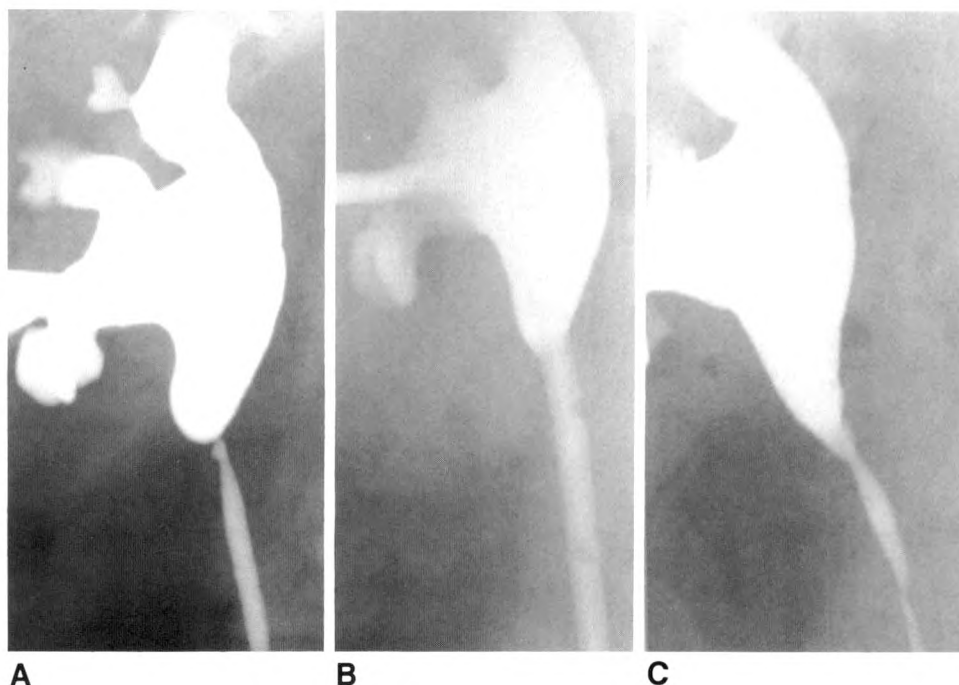


Fig. 1.—Nephrostograms show successful dilation of ureteropelvic junction stricture.

A, High-grade upper ureteral stricture from numerous attempts at trans-renal stone extraction.

B, After balloon dilation, 16-French stent was left across stenosis for 4 months.

C, After removal of stent, there is good antegrade flow of contrast material down ureter with improved appearance of stricture.

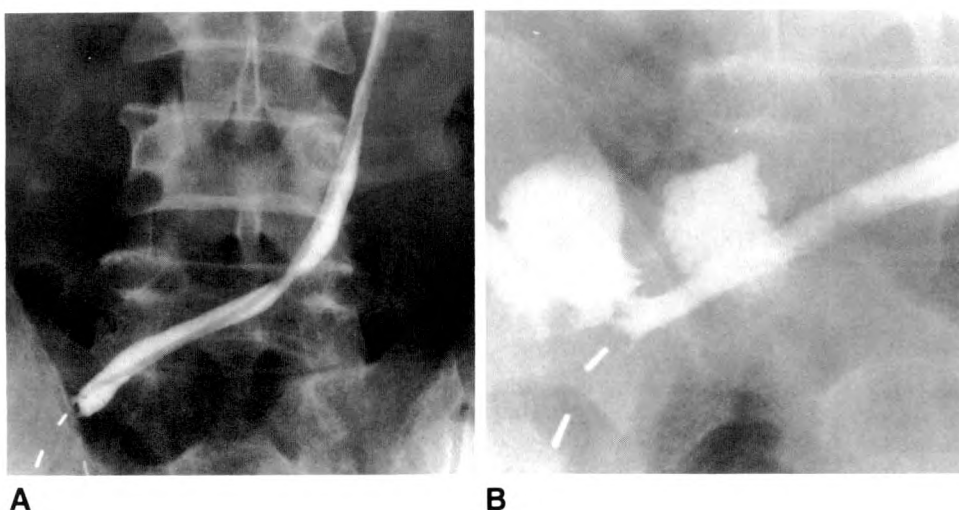


Fig. 2.—Ureterograms show successful dilation of stricture at uretero-ileal anastomosis.

A, Complete obstruction at anastomosis before dilation.

B, After dilation. Free flow of contrast material via irregular-appearing anastomosis into ileal loop. Follow-up 9 months after dilation showed no obstruction.

until balloon waisting disappeared). Usually, three separate inflations were carried out across the stenosis. When the balloon ruptured, contrast material was instilled down the ureter to judge the effectiveness of dilatation and to exclude ureteral rupture. If a residual significant stricture was identified, another balloon was inserted and the procedure repeated. Most stenoses were stented with a 5- to 14-French polyethylene catheter for a minimum of 2 days. Success was judged by one or usually a combination of the following: improved radiographic appearance of the stricture, stable or improved hydronephrosis, and stable or improved renal function (as judged by serum creatinine or radionuclide renogram). Criteria for failure included a persistent stenosis radiographically, persistent balloon waisting at the time of dilatation, advancing hydronephrosis or hydroureter, rising creatinine, or unchanged hydronephrosis with recurrent pyelonephrosis.

Results

Dilatation was attempted on 31 strictures in 30 patients. Eighteen (58%) of 31 strictures were successfully dilated (Figs. 1 and 2). All of these 18 strictures remained patent during the available follow-up interval, ranging from 6 months to 3 years. Thirteen (42%) of 31 strictures were not dilated successfully, with either initial failure (two cases) or with restenosis within 3 months (seven cases), 6 months (three cases), or 21 months (one case) (Figs. 3 and 4). No significant complications occurred in any of the patients.

Twenty-two strictures were 7 months of age or less. Fourteen (64%) of these 22 dilatations were classified as successful. Eight dilatations in the newest strictures were deemed

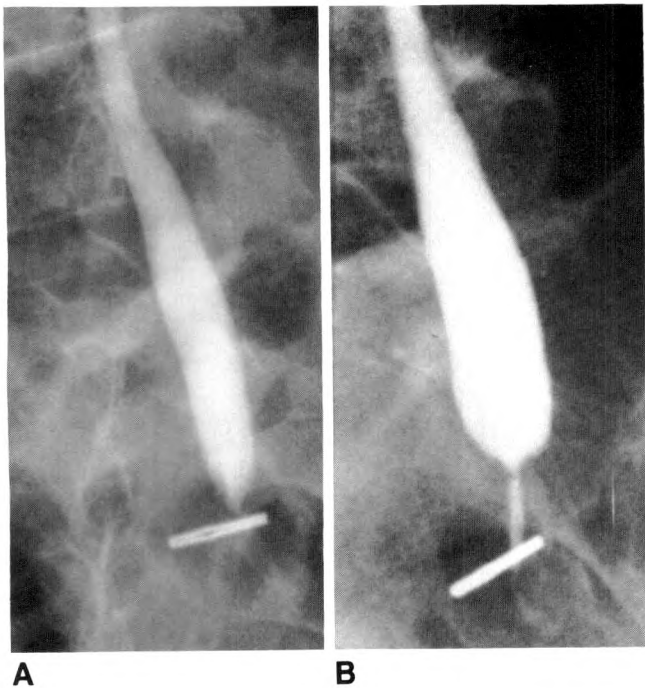


Fig. 3.—Ureterograms show unsuccessful dilation of ureteral stricture.
 A, High-grade distal ureteral stricture after Boari flap (pedicle tube graft from bladder to bridge ureteral defect) and left ureteral reimplantation 2 months before.
 B, No improvement after dilation with 5-mm balloon and 8.3-French stent.

failures, two within a few days after dilatation, five within 3 months, and one after 21 months. None of the five strictures more than 7 months of age were successfully dilated. Four strictures of unknown age were successfully dilated (Table 1).

Thirteen strictures were located in the proximal or midureter. Nine (69%) of these 13 were successfully dilated, while four failed within 3 months. Dilation of nine (50%) of 18 strictures at either the ureterovesical junction, lower ureter, or ureteroileal anastomosis was successful. Three (60%) of five of the dilations at a ureteroileal anastomosis were dilated successfully. Nine (50%) of 18 strictures in the lower ureter, ureterovesical junction, or at a ureteroenteric anastomosis were unsuccessfully dilated. Both dilations at the ureterocolic junction failed.

Ureteral stenting was performed after dilation in all but three patients. In those patients deemed to have a successful dilatation, a 5-French catheter was used in two patients, 6- to 8.3-French in five patients, 10-French in six patients, 14-French in one patient, and 16-French in two patients. Of the 12 patients with stents that failed dilatation, a 5-French stent was used in two patients, 6- to 8.3-French in three patients, and 10-French in seven patients. The duration of stenting was variable in both groups, from only a few days to several months. Three patients did not receive a stent, two patients having successful results and one patient developing a restenosis within 3 months.

Six patients were dilated on several occasions. Three of these patients had successful results after two dilations. Two patients had failed results and another successful results after three dilations.

Extravasation of contrast material outside the ureter was identified after three successful dilations and in two unsuccessful dilations. There were no significant complications related to the dilation procedure.

Discussion

Ureteral stricture dilation via the retrograde approach has been used by urologists for many years. Its use lost favor probably because of difficulty in using large-caliber catheters safely. Interventional radiologists revised and modified the procedure, using balloon catheters and techniques that proved successful in dilating stenotic blood vessels. Balloon dilatation has been expanded to treat stenoses in nonvascular structures, including the ureter [1-4]. Its successful use has been shown in surgically produced ureteral strictures in dogs [12]. Only a few early reports have been published, with an overall success rate of about 50% [4, 5, 13].

Percutaneous dilatation of ureteral strictures was successful in slightly more than half of the cases in our series, having at least 6 months of follow-up. This overall success rate is comparable to other reported results [4, 5].

No criteria could be identified that would definitely indicate that a stricture dilation would result in either success or failure. However, the age of the stricture seemed an important variable determining long-range success. Sixty-four percent of all strictures less than 7 months of age were successfully dilated. No strictures more than 7 months of age were dilated successfully; however, four were of indeterminate age. This is presumably related to the fibrotic nature of more chronic lesions.

The location of a stricture is also helpful in predicting outcome. Proximal ureteral strictures, either at the ureteropelvic junction or in the proximal two-thirds of the ureter, were successfully dilated in nearly 70% of patients. Neither of two strictures at a ureterocolic anastomosis was successfully dilated. Strictures dilated at the ureterovesical junction may be prone to failure (four of seven cases), but the small numbers in this series do not yet justify a conclusion.

Frequent follow-up can help identify failures early; more than half of our failures were recognized either at the time of dilation or within a few weeks after the procedure. Nearly 80% of failures were recognized within 3 months after dilatation. It is uncertain if repeat dilations would have been helpful in cases that failed, because only eight patients received more than one dilatation on separate occasions. New high-pressure balloons were routinely used over the past year (eight successfully and three unsuccessfully), but their overall effectiveness is unknown. Possibly, early stenoses resistant to dilation may have been treated successfully if these newer balloons had been used.

The use of ureteral stents after dilation has been advocated to maintain an adequate luminal diameter during ureteral healing [5]. Others have disputed stent use, claiming that

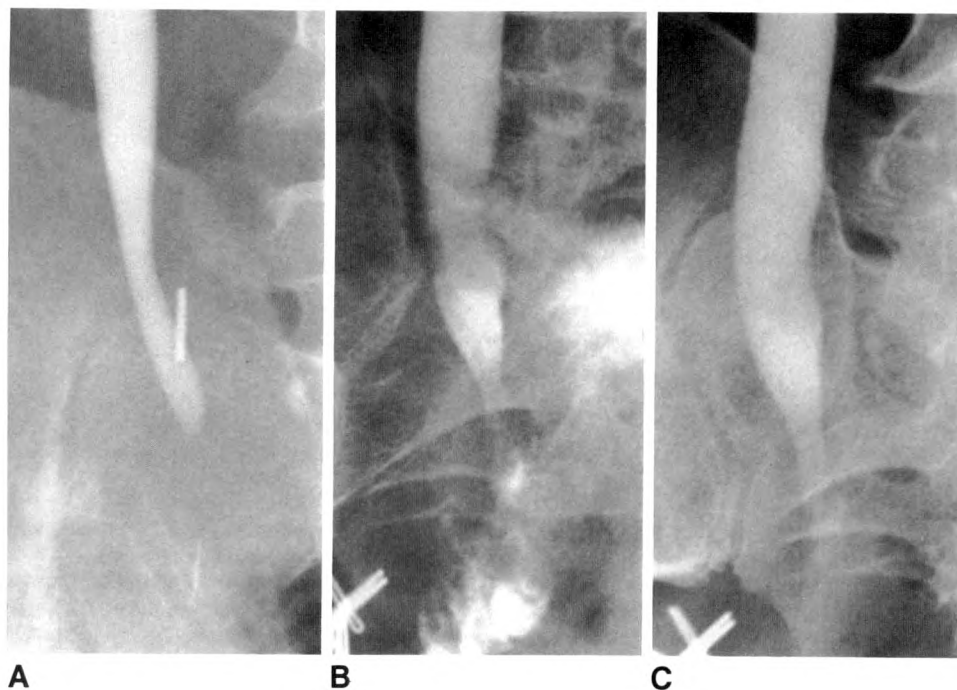


Fig. 4.—Ureterograms show restenoses of ureteroileal anastomosis.

A, Complete obstruction before dilation at ureteroileal junction, 16 months after urinary diversion with ureteroileal anastomosis.

B, 1 week after dilation with van Arden catheters and 10-mm balloon, contrast material flows freely into ileal conduit.

C, 10 days after dilation. Restenoses with complete obstruction. Surgical revision was required. Ureteral edema usually substantially resolves within 1 week after uncomplicated dilation.

TABLE 1: Ureteral Stricture Dilatation

	No. of Successes	No. of Failures
Stricture Age:		
<7 months	14	8
>7 months	0	5
Unknown	4	0
Total	18	13
Location:		
Proximal two-thirds	9	4
Distal one-third	6	5
Ileal or colic anastomosis	3	4
Total	18	13

large-diameter stents may cause ureteral ischemia that can contribute to additional unwanted fibrosis and eventual restenosis [4]. This issue has not been resolved and warrants further study. All but three strictures in our series were stented for a variable interval. There does not seem to be a difference in success rate between the use of larger (≥ 10 -French) vs smaller stents. We do not have enough experience to comment on results when ureteral stenting is not used. In addition, the ideal duration of ureteral stenting is unknown.

Dilation of ureteral strictures is often effective, especially in strictures of recent origin. Little harm is done in attempting to dilate a stricture of any age or location, for despite documented extravasation in five cases in our series, no significant complications occurred. Postdilation stenting was not nec-

essarily associated with a successful outcome. Most failures become apparent within 3 months after dilation.

REFERENCES

1. Teplick SK. Balloon dilatation of bile duct strictures. *Gastrointest Radiol* 1982;7:92
2. McLean GK, Rosen RJ, Ring EJ. Miscellaneous interventional procedures. In: Ring EJ, McLean GK, eds. *Interventional radiology. Principles and techniques*. Boston: Little, Brown, 1981:442-450
3. Russinovich NAE, Lloyd LK, Griggs WP, Jander HP. Balloon dilatation of ureteral strictures. *Urol Radiol* 1980;2:33-37
4. Banner MP, Pollack HM, Ring EJ, Wein AJ. Catheter dilatation of benign ureteral strictures. *Radiology* 1983;147:427-433
5. Glanz G, Gordon DH, Butt K, Rufin B, Hong J, Sclafani SJA. Percutaneous transrenal balloon dilatation of the ureter. *Radiology* 1983;149:101-104
6. Martin EC, Fankuchen EI, Casarella WJ. Percutaneous dilatation of ureteroenteric strictures or occlusions in ileal conduits. *Urol Radiol* 1982;4:19-21
7. Dixon GD, Moore JD, Stockton R. Successful dilatation of ureteroileal anastomotic stenosis using Gruntzig catheter. *Urology* 1982;19:555-558
8. Reimer DE, Oswald GC. Iatrogenic ureteral obstruction treated with balloon dilatation. *J Urol* 1981;126:689-690
9. Kadir S, White RI, Engel R. Balloon dilatation of a ureteropelvic junction obstruction. *Radiology* 1982;143:263-264
10. Lieberman SF, Keller FS, Barry JM, Rosch J. Percutaneous antegrade transluminal ureteroplasty for renal allograft ureteral stenosis. *J Urol* 1981;128:122-124
11. Kaplan JO, Winslow OP, Sneider SE, Pryor TH, Caplan LH, Messinger NH. Dilatation of a surgically ligated ureter through a percutaneous nephrostomy. *AJR* 1982;139:188-189
12. El-Mahronky A, Ford KK, Moore AV, Shore M, King LR. Balloon dilatation of ureteral strictures in dogs. *J Urol* 1984;131:582-586
13. King LR, Conghlin PWF, Ford KK, Brown MW, Moore AV. Initial experiences with percutaneous and transurethral ablation of postoperative ureteral strictures in children. *J Urol* 1984;131:1167-1170

Monoctanoin Infusion and Stone Removal Through the Transparenchymal Tract: Use in 17 Patients

Pamela H. Haskin¹
 Steven K. Teplick¹
 John K. Sammon¹
 Richard A. Gambescia²
 Norman Zitomer²
 Constantinos A. Pavlides³

Seventeen patients underwent monoctanoin infusion and biliary stone removal through the percutaneous transhepatic biliary drainage tract. In the first five patients, monoctanoin was infused until the stone(s) became smaller or disappeared; basket extraction was not attempted until this reduction was observed. An average of 22 hospital days was required for the procedure. In the next 12 patients, basket extraction was attempted after as few as 3 days of infusion, without waiting for a reduction in stone size. After infusion, these stones became extremely friable, fragmented easily, and were atraumatically removed through the fresh liver tract. The average hospital stay for these patients was 7 days, with no complications. The ability of monoctanoin to soften some stones allows an earlier, more aggressive approach to stone removal through the transparenchymal tract without risk of soft-tissue laceration; use of the infusion significantly decreases the hospital stay.

In the several reports [1-6] describing the use of monoctanoin (Mocetanin, Ascot Pharmaceuticals, Skokie, IL) infusion through the transparenchymal liver tract, the compound was used until stone dissolution occurred, until stones could be crushed and delivered antegrade into the duodenum, or after crushing of stones with the Dormia basket to dissolve residual fragments in the common duct. Reported instances of retrograde stone removal through the fresh liver tract after monoctanoin therapy are few [7, 8].

During the past 4 years we have infused monoctanoin through a transhepatic catheter in 17 persons, 13 of whom subsequently had stone(s) removed in a retrograde fashion through the liver tract. Over the last 2 years, stones have been fragmented and removed at increasingly shorter intervals after tract creation and monoctanoin infusion, even though fluoroscopic evidence of dissolution was questionable. There have been no complications, and hospital stay has been reduced. Immature parenchymal tracts do not preclude monoctanoin infusion or retrograde stone extraction. Moreover, a lack of visual evidence of the effect of monoctanoin, such as a decrease in stone size, does not imply that monoctanoin has been ineffective.

Subjects and Methods

Seventeen patients between the ages of 33 and 89 years (mean, 69 years) underwent percutaneous transhepatic biliary drainage because of biliary colic, jaundice, or cholangitis. All were poor risks for surgical stone removal because of advanced age (six patients), hemorrhagic pancreatitis (one patient), cardiac disease (two patients), carcinoma (two patients), chronic obstructive pulmonary disease (one patient), or more than one previous biliary surgical procedure (five patients). Two patients had successful ERCP, but the common duct stone was too large for papillotomy and removal. One patient had hemorrhagic pancreatitis, contraindicating endoscopic manipulation. Previous choledochenteric anastomoses precluded ERCP in six patients. In one patient ERCP was unsuccessful. In the remaining seven patients, endoscopic visualization of the biliary system was not attempted. Ten patients had

Received April 25, 1986; accepted after revision August 11, 1986.

¹Department of Diagnostic Radiology, Hahnemann University Hospital, Broad and Vine Sts., Philadelphia, PA 19102. Address reprint requests to P. H. Haskin.

²Department of Medicine, Hahnemann University Hospital, Broad and Vine Sts., Philadelphia, PA 19102.

³Department of Surgery, Hahnemann University Hospital, Broad and Vine Sts., Philadelphia, PA 19102.

AJR 148:185-188, January 1987
 0361-803X/87/1481-0185
 © American Roentgen Ray Society

undergone cholecystectomy 1–40 years earlier; seven had intact gallbladders at the time of percutaneous transhepatic biliary drainage.

Standard percutaneous transhepatic cholangiography with a 22-gauge Chiba needle was performed in all patients to identify the bile ducts and the number, size, and location of biliary calculi. Sixteen of the 17 patients had stone(s) in the common duct; the remaining patient had a stone in a left main intrahepatic duct. Stone number ranged from 1 to 9, and stone size from 1 to 3.7 cm. In the 16 patients with common duct stones, an 8- or 10-French Ring biliary drainage tube was placed, using a mid or anterior axillary line approach, with the standard Seldinger technique. The left intrahepatic duct was drained in a similar manner, using a midline epigastric approach with sonographic guidance. Internal drainage was achieved in all patients without difficulty. All received IV broad-spectrum antibiotics throughout the biliary drainage procedure and subsequent monooctanoin administration period.

After dilatation of the tract to 16 or 18 French, a second and sometimes a third catheter for monooctanoin infusion was placed around the stone(s) by a method described previously [8]. We elected to use a multicatheter system because the pigtail of the infusion catheter can be snugly wrapped around the stone to provide maximum drug-stone contact, while the drainage catheter simultaneously provides continuous decompression of the entire biliary tree. The time between biliary drainage and second catheter placement varied from 0 days to 6 months; patients whose drainage tubes were placed at other institutions accounted for the longer time intervals. If no cholangitis was present and if the referring service decided to institute monooctanoin therapy during or shortly after the biliary drainage procedure, the monooctanoin delivery catheter was placed either at the same time as the drainage catheter or 24–48 hr afterward. Monooctanoin infusion, which began within 12–24 hr, was delivered through a Harvard infusion pump at a rate of 5 cc/hr or less, continuously, with the exception of 1 hr three times a day at mealtimes and 1 hr at bedtime. The biliary drainage catheter was left to straight drainage. Cholangiograms with iohalamate meglumine 43% (Conray-43) were performed every 3–5 days, by using a constant source-image distance, and were phototimed at 70 kVp, 400 mA.

In the first five patients, extraction was not attempted until there was fluoroscopic evidence of a reduction in stone size; in subsequent patients a steerable catheter and Dormia basket were inserted into the biliary tree, the stone(s) crushed, and the fragments extracted after 3–7 days of infusion, even when there was no definite fluoroscopic evidence of size reduction. In all cases a safety guidewire [9] was left in the biliary tree during the extraction to ensure reentry into the immature tract. If obvious large fragments remained after an extraction session, monooctanoin was continued for an additional 2–3 days. If none remained, a 16- or 18-French feeding tube with enlarged side holes was inserted into the biliary tree and its distal end placed through the ampulla. The tube was clamped and the patient was discharged. An outpatient cholangiogram was obtained before the biliary tube was removed. Placement through the ampulla of a large-bore tube with enlarged side holes not only dilated the ampulla, but also allowed any small fragments to pass through the tube into the small bowel without risk of recurrent obstruction and cholangitis.

Results

Stones dissolved completely in three patients, two of whom had solitary stones (largest, 1.3 cm), and one of whom had three stones (largest, 1 cm). In 13 patients, the stones were removed through the parenchymal tract with a Dormia basket; nine of these patients had solitary stones (largest, 2.8 cm),

and four had more than one stone (largest, 3 cm). In one patient, a 3.7-cm stone changed in configuration but could not be removed even though it could be snared. At surgery it was found embedded in the common duct mucosa. In the 13 patients who underwent basket extraction, six had stones that showed a definite (4 mm or more) decrease in mean diameter or that fragmented spontaneously after monooctanoin and before basket manipulation. Seven of these 13 patients had a questionable change in stone size (less than 4 mm). In these seven, however, the stones had an irregular hazy outline not present on radiographs made before monooctanoin therapy. All of these stones, when snared by the basket, crumbled during the extraction procedure without the use of crushing pressure.

Fifty percent of patients who had had a previous cholecystectomy and 43% of patients with an intact gallbladder had stones that unequivocally responded to monooctanoin. Three stones retrieved from patients who had had cholecystectomies 5, 10, and 40 years previously were chemically analyzed. Their ratios of cholesterol to calcium bilirubinate were 58/40, 86/2, and 60/37, respectively.

In comparing our first two years of monooctanoin experience with the last two, we found that the average time from tract creation to the first stone extraction decreased from 18 days to 9 days. The time of monooctanoin infusion before extraction decreased from 11 days to 5 days, and the time for the entire monooctanoin procedure, from the second (infusion) catheter placement to cessation of infusion, decreased by 68%, from 22 days to 7 days.

No serious side effects occurred that could be directly attributed to monooctanoin infusion through the immature liver tract or to retrograde removal of stones from it. One patient, reported previously [8], developed right subdiaphragmatic and intrahepatic abscesses from the severe cholangitis present before biliary drainage. All patients experienced diarrhea and varying degrees of nausea and vomiting and were treated with Lomotil (diphenoxylate hydrochloride/atropine sulfate) and Reglan (metoclopramide hydrochloride), respectively. All noted some anorexia, which promptly resolved with completion of infusion. All, predictably, had a transient rise in alkaline phosphatase after basket extraction of the stones.

Patients treated during the last two years required, at most, one trip to the interventional suite for correction of tube displacement, whereas the earlier patients often required up to five tube repositionings. Patients treated during the last two years required an average of two cholangiograms to remove residual fragments after infusion tube placement, as compared with the earlier group of patients who required an average of 5 cholangiograms after tube placement. Overall, patients who received short periods of chemolysis therapy and early stone removal had a less debilitating course of stone management than did the patients who received long-term chemolysis.

Discussion

Although endoscopic papillotomy and stone removal is an optimal method of biliary stone management, this procedure

is not available at all institutions and is precluded in some patients by surgical distortion of the biliary-enteric anatomy. Monooctanoin infusion through the transparenchymal tract, followed by early retrograde extraction, is a safe and therapeutic alternative regimen for managing biliary stones found during transhepatic biliary decompression in patients who are a poor surgical risk. No complications of transparenchymal infusion have been encountered in any of our 17 patients. Retrograde extraction was atraumatic and successful in all but one patient, and in this patient the stone was embedded in ductal mucosa.

The physical and chemical properties, efficacy, and use of monooctanoin are well documented [8, 10–13], although there has been some concern about the toxicity of the drug when infused through transhepatic catheters. Injection of monooctanoin directly into liver parenchyma can produce lethal hepatic and systemic toxicity in laboratory animals [14]. In the several clinical reports of systemic toxicity of monooctanoin [2, 14–16], it appears that toxicity is not a function of route of administration, but rather of infusion rate, an inadequate overflow mechanism, or the presence of cholangitis, all of which can damage duct epithelium and result in systemic absorption of monooctanoin. We encountered no such episodes of toxicity, but we were careful to use low infusion rates, to use a second drainage catheter to avoid generalized biliary distention, and to delay infusion until symptoms of cholangitis subsided. The use of a two-catheter system and low rate of infusion does not compromise the effect of monooctanoin [12, 17]. Our series, as well as those of several other investigators [1, 3–8], suggests that this is a safe route of administration when appropriate technique is used.

Standard teaching has been to delay retrograde basket extraction until tract maturation occurs to avoid tract laceration during basket insertion and stone extraction. We did not encounter this complication. Use of a second, safety guidewire [9] assures unlimited and certain entry into the ductal system, and the softened stones after perfusion are easily crumbled into small fragments that will not lacerate the tract during retrograde removal.

Early in our experience with monooctanoin, we continued perfusion of biliary stones until they diminished or disappeared so that we could show a true dissolution effect by documenting reduction in stone size. Long hospital stay was a major disadvantage of this protocol. The ability of monooctanoin to dissolve cholesterol stones has now been unequivocally proved [8, 11, 12, 13, 17–20], so that long perfusion periods are no longer required for either investigational purposes or successful therapy. Cholesterol stones in contact with monooctanoin do become softer both in vitro [21] and in vivo [8]. Lee and McGahan [22] report that stones in contact with monooctanoin had an 18% weight reduction after 9 hr and a 28% weight reduction after 12 hr. Gadacz [19] documented a 60% weight decrease after 2 days and an 87% weight decrease after 4 days. Therefore, dissolution occurs when cholesterol stones are placed in contact with monooctanoin for short periods of time. In vivo, change in stone size is gauged by measuring mean diameter on radiographs taken at a constant source-image distance. It is difficult to obtain

identical images on sequential cholangiograms because of changes in stone position and axis, as well as variations in the volume of contrast material used. Even if these variables could be held constant, fluoroscopy provides a two-dimensional image of a three-dimensional object. Volume or weight changes cannot be inferred from this two-dimensional image. Consequently, the effect of monooctanoin cannot always be judged by viewing the fluoroscopic spot film. In several patients we noted poorly defined borders and an apparent decrease in the density of stones after monooctanoin, without a reduction in mean diameter. Because mere snaring of these stones resulted in immediate crumbling, a dissolution effect may have occurred that did not affect the size of the stones but that may have reduced their volume, rendering them extremely friable.

We had no control group to document that monooctanoin does produce increased stone friability. In the past, however, we have encountered several large common duct stones that could not be fragmented; in one case T-tube tract dissection was required to remove a snared stone lodged at the junction of the common duct and the T-tube tract. We found that infusion of monooctanoin to render large stones more friable was a more certain, less traumatic method of transparenchymal stone extraction. After several days of infusion a trial basket extraction is warranted, even without definite visual evidence of decreased stone size. This approach is cost effective because it allows inpatient monitoring to ensure optimal infusion technique, yet requires shorter hospitalization. Patients accept this approach better than long-term monooctanoin infusion because it avoids the debilitation of lengthy hospital stays, the discomfort of repeated interventions, or the inconvenience of protracted use of external biliary drainage devices.

REFERENCES

1. Mack E, Crummy AB, Babayan VK. Percutaneous transhepatic dissolution of common bile duct stones. *Surgery* 1981;90:584–587
2. Minuk GY, Hoeffnagle JH, Jones EA. Systemic side effects from the intrabiliary infusion of monooctanoin for the dissolution of gallstones. *J Clin Gastroenterol* 1982;4:133–135
3. Clouse ME, Falchuk KR. Percutaneous transhepatic removal of common duct stones: report of ten patients. *Gastroenterology* 1983;85:815–819
4. Steinhagen RM, Pertsemidis D. Monooctanoin dissolution of retained biliary stones in high risk patients. *Am J Gastroenterol* 1983;78:756–760
5. Train JS, Dan SJ, Cohen LB, Mitty HA. Duodenal ulceration associated with monooctanoin infusion. *AJR* 1983;141:577–558
6. Butch RJ, MacCarty RL, Mueller PR, et al. Treatment of intrahepatic calculi with monooctanoin infusion. *Radiology* 1984;153:375–377
7. Haskin PH, Teplick SK, Gambescia RA, Zitomer N, Pavlides CA. Percutaneous transhepatic removal of a common duct stone after monooctanoin infusion. *Radiology* 1984;151:247–248
8. Teplick SK, Haskin PH. Monooctanoin perfusion for *in vivo* dissolution of biliary stones: a series of 11 patients. *Radiology* 1984;153:379–383
9. Hublitz UF, Cogliano FD, Arena PJ. Early extraction of residual biliary tract stones: a two guidewire technique. *AJR* 1984;143:1090–1092
10. Allen BL, Deveney CW, Way LW. Chemical dissolution of bile duct stones. *World J. Surg* 1978;2:429–436
11. Thistle JL, Carlson GL, Hofmann AF, et al. Monooctanoin. A dissolution agent for retained cholesterol bile duct stones: physical properties and clinical application. *Gastroenterology* 1980;78:1016–1022
12. Jarrett LN, Bell GD, Balfour TW, Knapp DR, Rose DH. Intraductal infusion of monooctanoin: experience in 24 patients with retained common-duct

- stones. *Lancet* **1981**;i:68-70
13. Witzel L, Wiederholt J, Wolbergs E, Krankenhaus DRK. Dissolution of gallstones by perfusion with Capmul via a catheter introduced endoscopically into the bile duct (letter). *N Engl J Med* **1980**;303:465
 14. Sharp KW, Gadacz TR, Sampliner RE. Hepatic response to parenchymal injection of sodium cholate and monooctanoin. *Surg Forum* **1981**;32:176-177
 15. Crabtree TS, Dykstra R, Kelly J, Preshaw RM. Necrotizing choledochomalacia after use of monooctanoin to dissolve bile-duct stones. *Can J Surg* **1982**;25:644-646
 16. Uribe M, Uscanga L, Farca S, Sanjurjo JL, Lagarriga J, Ortiz JH. Dissolution of cholesterol ductal stones in the biliary tree with medium-chain glycerides. *Dig Dis Sci* **1981**;26:636-640
 17. Mack E, Patzer EM, Crummy AB, Hofmann AF, Babayan VK. Retained biliary tract stones. *Arch Surg* **1981**;116:341-344
 18. Thistle JL, Carlson GL, LaRusso NF, Hofmann AF. Effective dissolution of biliary duct stones by intraductal infusion of mono-octanoin (abstr). *Gastroenterology* **1978**;74:1103
 19. Gadacz TR. Efficacy of Capmul and the dissolution of biliary stones. *J Surg Res* **1979**;26:378-380
 20. Hofmann AF, Schmack B, Thistle JL, Babayan VK. Clinical experience with monooctanoin for dissolution of bile duct stones. An uncontrolled multicenter trial. *Dig Dis Sci* **1981**;26:954-955
 21. Teplick SK, Pavlides CA, Goodman LR, Babayan VK. In vitro dissolution of gallstones: comparison of monooctanoin, sodium dehydrocholate, heparin, and saline. *AJR* **1982**;138:271-273
 22. Lee LL, McGahan JP. Dissolution of cholesterol gallstones: comparison of solvents. *Gastrointest Radiol* **1986**;11:169-171

Percutaneous Nephrostomy for Endopyelotomy

Won J. Lee^{1,2}
Gopal H. Badlani^{3,4}
Arthur D. Smith^{3,4}

Percutaneous full-thickness incision and stenting of the ureteropelvic junction (endopyelotomy) relieved obstruction in 33 (87%) of 38 patients treated over a 2-year period. Proper placement of the percutaneous nephrostomy tract through a posterior middle calyx and of a guidewire across the ureteropelvic junction is necessary in order to gain access to the narrowed area with a rigid cutting instrument. Except in patients with long lesions, high insertion of the ureter, or an enormously redundant renal pelvis, endopyelotomy gives excellent results with less morbidity and a shorter recovery time than open pyeloplasty.

Ureteropelvic junction (UPJ) obstruction has long been managed by open pyeloplasty, an operation with a failure rate of 10% [1]. Thus, when percutaneous nephrostomy, originally used only for drainage [2], was found to provide valuable access to the urinary tract for various diagnostic and therapeutic maneuvers, attempts were made to use nephrostomy to relieve UPJ obstruction with less morbidity. The first attempts at percutaneous (endourological) relief of UPJ obstruction were made with balloon catheters, which met with mixed results here as elsewhere in ureter [3–5]. It appeared that only fresh (i.e., immediately postoperative) strictures could be reversed permanently by this method.

Encouraged by the success of Clayman et al. [6] with percutaneous intrarenal electrosurgery, we used a cold-knife pyelotome via a percutaneous nephrostomy to incise the UPJ. Afterward, the area was held open by several weeks of stenting until it healed in its larger-caliber form [7]. This procedure, called endopyelotomy, is a closed version of the Davis intubated ureterotomy [8] and is successful in properly selected patients provided that there is close cooperation between radiologist and urologist. The morbidity is low, and in the few patients in which it fails, open pyeloplasty is not precluded.

Materials and Methods

Between July 1983 and August 1985, 38 patients (aged 7 to 79 years) underwent endopyelotomy for UPJ obstruction. Of these patients, 14 had strictures associated with stones, nine had undergone unsuccessful open pyeloplasty, eight had primary UPJ obstruction, and seven had postpyelolithotomy strictures.

In our technique, the collecting system is opacified with dilute contrast medium, usually via a ureteral catheter inserted transcystoscopically. The nephrostomy puncture is made with an 18-gauge trocar needle and a Teflon-coated curved J wire (TSCH 0.038-inch [0.097 cm], 145-cm; Cook Inc., Bloomington, IN) or a torque wire is inserted and used with a cobra visceral angiographic catheter to negotiate the UPJ. Cannulation of the UPJ can be accomplished under fluoroscopy or direct nephroscopic vision. In a few cases, a retrograde approach may be necessary. We have employed a safety wire in the renal collecting system or down the ureter in all cases. The nephrostomy tract is dilated to admit a 26-French rigid nephroscope. For this, we prefer the Amplatz renal dilators [9], which include a 34-French sheath (30-French inner diameter) that is left in the tract as a working sheath to facilitate instrument

Received June 30, 1986; accepted after revision August 26, 1986.

¹ Department of Radiology, Long Island Jewish Medical Center, New Hyde Park, NY 11042. Address reprint requests to W. J. Lee.

² Department of Radiology, School of Medicine, State University of New York at Stony Brook, Stony Brook, NY 11794.

³ Division of Urology, Long Island Jewish Medical Center, New Hyde Park, NY 11042.

⁴ Department of Urology, School of Medicine, State University of New York at Stony Brook, Stony Brook, NY 11794.

AJR 148:189–192, January 1987

0361-803X/87/1481-0189

© American Roentgen Ray Society

passage and to keep the intrapelvic pressure within a safe range during the irrigation needed to maintain a clear view of the operating field. Normal saline is used as irrigant. Telescopic metal dilators are used in scarred flanks.

The posterolateral wall of the UPJ is incised with the cold-knife pyelotome until the periureteral fat is visible through the instrument (Fig. 1). Such an incision avoids aberrant anterior ureteral blood vessels and those that may have been transposed posteriorly during earlier ureteral operations; it also spares the blood supply of the ureter [10]. An 8- or 12-French universal (Smith) stent (Heyer-Schulte, Mentor, Goleta, CA) [11] is inserted through a peel-away stent introducer (CPLVW, Cook, Bloomington, IN) [12]. The safety guide-wire is then used for the insertion of a 14-French Malecot nephrostomy catheter (Cook Urological, Spencer, IN), which serves as a temporary nephrostomy before being removed. The position of the universal stent is checked to ensure that (1) the proximal opaque marker is in the renal collecting system, (2) the second marker is just above the UPJ, and (3) the distal marker is in the lower ureter. If a nephrostogram performed 72 hr later is satisfactory, the nephrostomy tube is clamped for 12 hr and removed if no symptoms ensue (Fig. 2). Some extravasation will be seen at the site of the incision. If the nephrostogram is abnormal, the nephrostomy tube is left open until abnormality is corrected. The patient is discharged with the universal stent clamped at the nephrostomy site and returns 4–6 weeks later. During this interval, if pain, fever, or urine leakage indicates obstruction, the stent can be irrigated with saline or reamed with a guidewire. When the patient returns, the universal stent is pulled back until its distal tip is in the renal pelvis and a nephrostogram is obtained to ensure that urine drains freely into the bladder. If so, the stent is removed. If urine does not drain freely, the stent is converted to a nephrostomy tube. The patient is then observed for a period of 1 week. If at the end of the week obstruction of the ureter is still present, the procedure is considered a failure. For those cases considered a success, an IV urogram is performed 3–6 months later to assess the results.

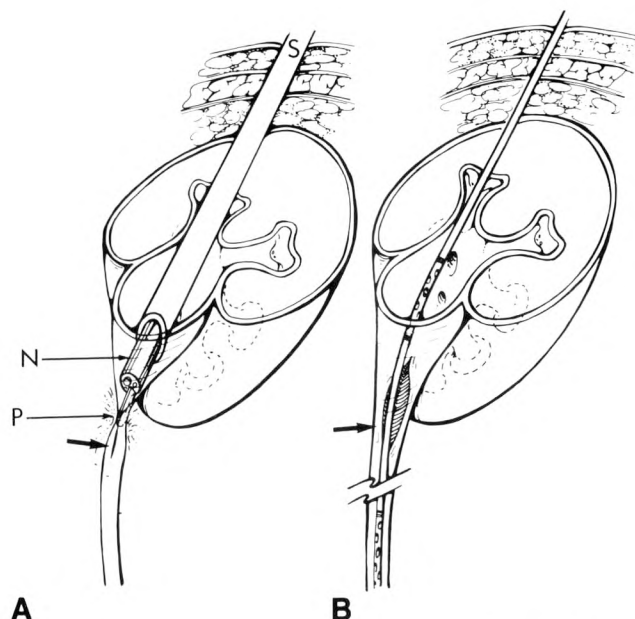


Fig. 1.—Diagram of techniques for percutaneous endopyelotomy.
A, Bold arrow indicates ureteric division (incision) in stricture site. Posterolateral wall of ureteropelvic junction is incised until periureteral fat is visible through nephroscope. P = pyelotome; N = nephroscope; S = working sheath.
B, A universal stent has been passed to maintain ureteral lumen. No drainage holes overlie the incision (bold arrow). 14-French Malecot nephrostomy has been removed.

Results

In 33 of the 38 patients, 14 of whom underwent ancillary percutaneous stone extraction, endopyelotomy relieved UPJ



Fig. 2.—48-year-old man with ureteropelvic junction obstruction due to pyelolithotomy. Nephrostogram 72 hr after percutaneous endopyelotomy shows no evidence of complications such as obstruction, clot retention, or extravasation. Small leak of contrast material from pyelotomy site (arrow) is normal. Stent is adjusted (pulled back) until its distal marker (arrowhead) is in renal pelvis.

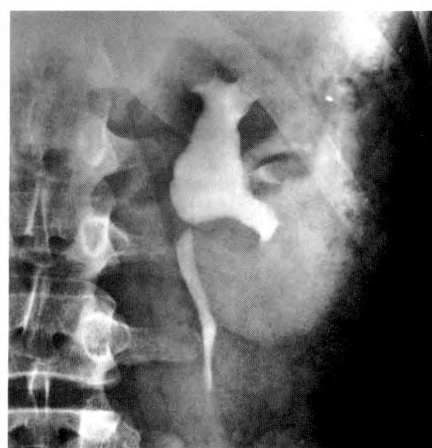
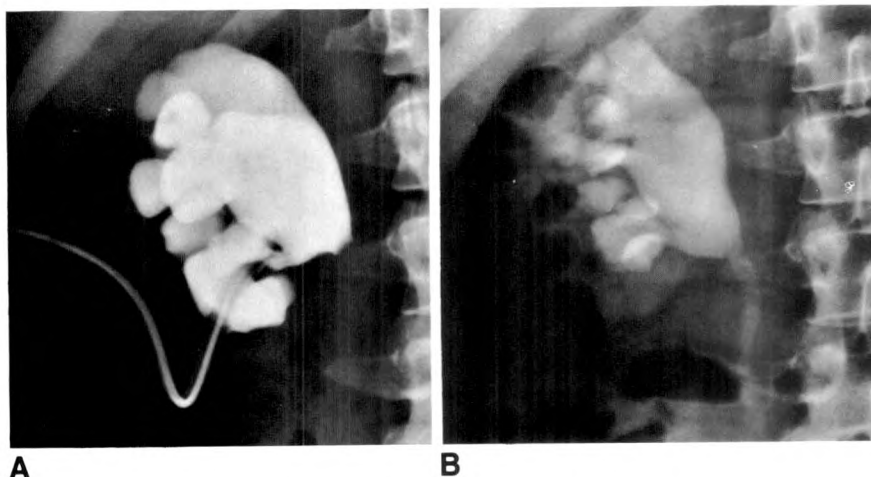


Fig. 3.—45-year-old white man with idiopathic ureteropelvic junction (UPJ) obstruction.
A, Preoperative IV urogram shows partial UPJ obstruction.
B, 4-month follow-up excretory urogram after endopyelotomy shows patency of UPJ. Patient has been symptom free for 8 months after procedure.

Fig. 4.—39-year-old white woman with failed pyeloplasty.

A, Nephrostogram 7 weeks after pyeloplasty shows complete obstruction at the ureteropelvic junction, indicating initial failure.

B, Excretory urogram 3 months after endopyelotomy shows patency of ureteropelvic junction.



obstruction (Figs. 3 and 4). No correlation was apparent between success and cause of UPJ obstruction (Table 1). Gross hematuria was seen for a few days in all patients, as expected, and two patients required transfusions for a hematocrit less than 30%, but there were no serious complications. The absence of infection is attributable to coverage by broad-spectrum antibiotics and to preoperative urine culture to ensure sterility. The average hospital stay was 7 days (range, 6–18 days). The occluded stent had to be replaced in three patients after the flushing and guidewire manipulation had failed to reopen the stent. Premature dislodgment of a stent, which occurred in two patients, is considered an emergency.

The five failures were due to a stricture too long to be incised percutaneously (three patients), technical difficulties in an enormously redundant renal pelvis (one patient), or inability to catheterize the UPJ (one patient). Postprocedure failure was usually evident shortly after stent removal. When a failure occurs after 6 weeks of conservative therapy, we then use a standard procedure. Open surgery (three ureterocalicostomy and one pyeloplasty) was performed on four patients without difficulties, and one patient had a double-J stent for an additional 3 months and on follow-up at the time of this writing was asymptomatic. A satisfactory excretory urogram at 3–6 months is a good predictor of long-term success.

Discussion

Percutaneous management of UPJ obstruction is a logical addition to the list of endourological procedures. Compared with open operation, endopyelotomy is far less traumatic and has a low incidence of complications. For endopyelotomy to succeed, the operator must have easy access to the UPJ with a rigid cutting instrument. Therefore, proper siting of the nephrostomy is critical (Fig. 5). A common mistake is to make the puncture low in the kidney in the erroneous belief that this facilitates access to the ureter. The puncture *should* be

TABLE 1: Results of Endopyelotomy

Cause of Obstruction	No. of Cases	No. of Failures	Success (%)
UPJ + stone disease	14	2	86
Postpyelolithotomy	7	1	86
Failed open pyeloplasty	9	1	89
Primary UPJ	8	1	88
Total	38	5	87

Note.—UPJ = ureteropelvic junction.

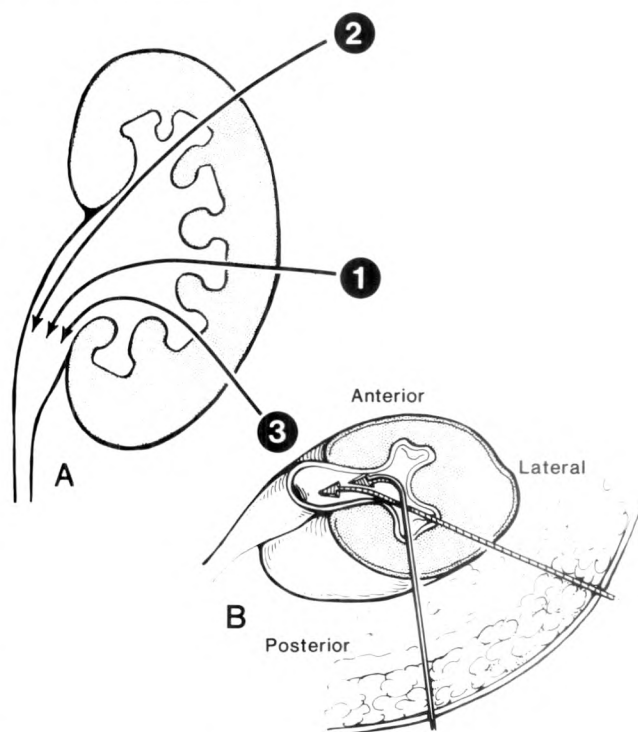


Fig. 5.—Diagram illustrating (A) access to ureteropelvic junction (UPJ) and (B) importance of posterolateral approach. (1) There is minimal chance of pleural perforation and good access to UPJ. (2) This route is best access to UPJ, but there is a significant chance of pleural perforation. (3) There is no chance of pleural perforation, but very poor access to UPJ. Use of this route is only possible in mobile kidney with no previous surgery.

in the central region through a posterior middle calyx; this creates a gently curved route to the ureter that a guidewire will often follow spontaneously [13]. Endopyelotomy is ideal for obstruction associated with stones, because the stone can be removed and the stricture incised in one session. Further, endopyelotomy can be repeated and can be performed in bifid collecting systems to improve drainage [14]. Although at first some thought that endopyelotomy might be insufficient because it does not remove redundant renal pelvis, our experience and that of Wickham (Wickham JEA, personal communication) shows that reconstruction of the renal pelvis is not always necessary. We now consider endopyelotomy the preferred approach to UPJ obstruction except when there is an enormously redundant renal pelvis, high insertion of the ureter, or a long postoperative stenosis.

The endourological management of UPJ obstruction involves both diagnostic and interventional radiology. The diagnostic aspect is the verification of the significance of a lesion when neither excretory urography nor retrograde pyelography has been able to determine the significance. For this purpose, we have used antegrade pyelography (with Whitaker test) [15] and diuretic (Lasix) renal scanning. The interventional aspect is the proper establishment of a percutaneous nephrostomy tract through a posterior middle calyx and the passage of a guidewire across the obstructed UPJ to allow the urologist to pass the direct-vision pyelotome easily to the UPJ.

Besides decreased morbidity, endopyelotomy also offers the advantages of shorter hospital stay, shorter total recovery time, and smaller incisional scar than conventional surgery.

REFERENCES

1. Cherrie RJ, Kaufman JJ. Pyeloplasty for ureteropelvic junction obstruction in adults: correlation of radiographic and clinical results. *J Urol* 1983;129:711-714
2. Goodwin WE, Casey WC, Woolf W. Percutaneous trocar (needle) nephrostomy. *JAMA* 1955;157:891-894
3. Dixon GD, Moore JD, Stockton R. Successful dilatation of ureteroileal anastomatic stenosis using Grüntzig catheter. *Urology* 1982;19:555-558
4. Kadir S, White RI, Engel R. Balloon dilatation of a ureteropelvic junction obstruction. *Radiology* 1982;143:263-264
5. Banner MP, Pollack HM, Ring EJ, Wein AJ. Catheter dilatation of benign ureteral strictures. *Radiology* 1983;147:427-433
6. Clayman RV, Hunter D, Surya V, Castaneda-Zuniga WR, Amplatz K, Lange PH. Percutaneous intrarenal electrosurgery. *J Urol* 1984;131:866-867
7. Badlani GH, Eshghi M, Smith AD. Percutaneous surgery for ureteropelvic junction obstruction (endopyelotomy): technique and early results. *J Urol* 1986;135:26-28
8. Davis DM. Intubated ureterotomy: new operation for ureteral and ureteropelvic stricture. *Surg Gynecol Obstet* 1943;76:513-518
9. Rusnak B, Castaneda-Zuniga WR, Katula F, Herrara M, Amplatz K. An improved dilator system for percutaneous nephrostomies. *Radiology* 1982;144:174
10. Snyder JA, Smith AD. Anatomy of ureter. In: Smith AD, Castaneda-Zuniga W, Bronson J, eds. *Endourology: principles and practice*. New York: Thieme, 1986:250-251
11. Smith AD, Lee WJ. Characteristics and uses of the universal (Smith) ureteric stent. *Brit J Urol* 1983;55[Suppl]:79-81
12. Lee WJ, Rich M. The Universal stent introducer; a simplified approach to antegrade ureteral stent insertion. *AJR* 1986;147:830-831
13. Miller RP, Reinke DB, Clayman RV, Lange PH. Percutaneous approach to the ureter. *Urol Clin North Am* 1982;9:31-40
14. Smith AD, Badlani GH. Percutaneous endopyelotomy: endourological management of a bifid renal pelvis with ureteropelvic junction obstruction. *J Urol* 1985;134:327-329
15. Whitaker RH. Upper-tract urodynamics. In: Kaye KW, ed. *Outpatient urologic surgery*. Philadelphia: Lea & Febiger, 1985:85-91

The MR Appearance of CSF Flow in Patients with Ventriculomegaly

John L. Sherman¹⁻³
Charles M. Citrin^{1,3}
Raymond E. Gangarosa⁴
Bruce J. Bowen¹

The purpose of this study was to investigate the MR imaging appearance of mobile CSF in the ventricular system in patients with ventriculomegaly caused by brain atrophy and extraventricular obstructive hydrocephalus. Pulsatile CSF often has decreased intensity relative to less mobile areas of CSF, particularly on T2-weighted scans. At times, the flow-related signal dropout causes striking heterogeneity in the appearance of CSF. This has been termed the *CSF flow-void sign* (CFVS) and is most likely caused by spin-phase shifts and time-of-flight effects created as a result of CSF turbulence and increased velocity of CSF pulsatile flow. The effect is most pronounced in areas where a larger volume of CSF moves through a small channel or foramen, such as the aqueduct of Sylvius or foramen of Magendie. The scans of 40 patients with ventriculomegaly caused by brain atrophy or extraventricular obstructive hydrocephalus were reviewed for the presence of the CFVS. All patients had the CFVS in the aqueduct of Sylvius on T2-weighted spin-echo sequences. The sign was present in the fourth ventricle in 96%, in the third ventricle in 70%, in the foramen of Magendie in 65-77%, and in the foramina of Monro in 33%. The sign was more pronounced in patients with larger ventricles but could not be used to differentiate patients with brain atrophy from those with extraventricular obstructive hydrocephalus.

This article appears in the November/December 1986 issue of AJNR and the January 1987 issue of AJR.

Received March 3, 1986; accepted after revision May 28, 1986.

Presented in part at the annual meeting of the Radiological Society of North America, Chicago, November 1985.

¹ Magnetic Imaging of Washington, 5550 Friendship Blvd., Chevy Chase, MD 20815. Address reprint requests to J. L. Sherman.

² Department of Radiology, Uniformed Services University of the Health Sciences, Bethesda, MD 20814.

³ Department of Radiology, George Washington University School of Medicine, Washington, DC 20037.

⁴ Clinical Science Center, Picker International, Highland Heights, OH 44143.

AJR 148:193-199, January 1987

0361-803X/87/1481-0193

© American Roentgen Ray Society

MR imaging has proven superior to CT in the evaluation of intracranial disease primarily because of its superior contrast resolution [1-3]. Cerebral vasculature and vascular malformations are clearly delineated by hypointensity resulting from the lack of signal caused by rapidly flowing blood [4, 5]. Rapidly flowing or turbulent CSF in the third ventricle, the aqueduct of Sylvius, and the fourth ventricle may also be delineated as a hypointense area because of the lack of signal (Fig. 1). This has been termed the *CSF flow-void sign* (CFVS) [6, 7]. We investigated the incidence and variations of the CFVS in patients with ventriculomegaly caused by brain atrophy and extraventricular obstructive hydrocephalus (EVOH) [8].

Materials and Methods

The MR examinations of 40 patients with enlarged ventricles were reviewed and divided into two groups on the basis of clinical evaluations and results of other imaging studies. Patients with evidence of obstruction or mass effect involving the third ventricle, fourth ventricle, or aqueduct of Sylvius were excluded.

Group 1 included 29 patients with enlarged ventricles caused by brain atrophy, normal aging, or congenital anomalies. There were 19 men and 10 women aged 17-83 years (average age, 57 years). Two patients were 17 years old: between them, one had vermian dysgenesis and the other had olivopontocerebellar degeneration.

Group 2 included 11 patients with EVOH. The five males and six females were 2-77 years old (average age, 56 years). One patient (a 36-year-old man) had presumed inferior vermian dysgenesis but also had EVOH from previous head trauma.

All examinations were evaluated for the presence of the CFVS [6] on T2-weighted images and on T1-weighted images or balanced T2/T1 images. The CFVS was differentiated from the low signal intensity of arteries and veins by comparing the size and location of the sign

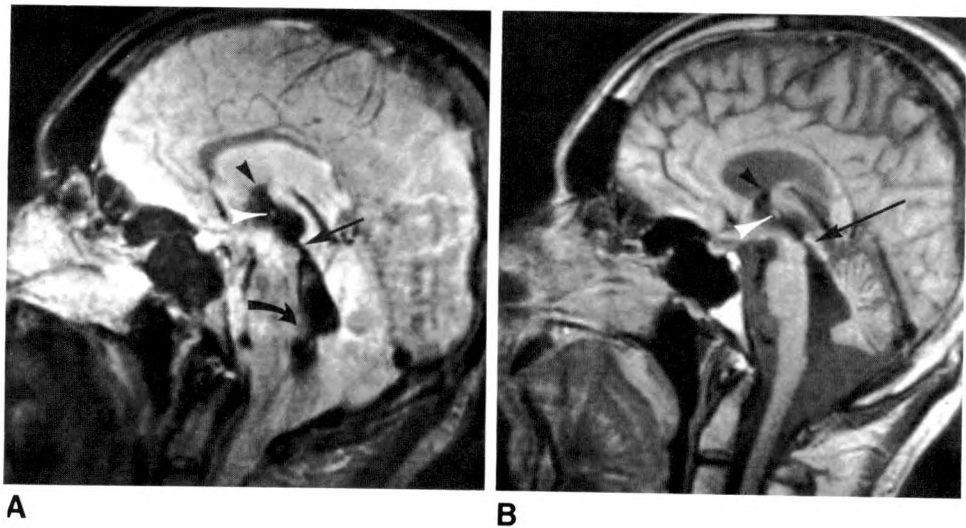


Fig. 1.—37-year-old man with inferior vermian dysgenesis and posttraumatic EVOH. Basilar subarachnoid spaces are enlarged. Midsagittal MR scans are 5 mm thick. **A**, T2-weighted scan (SE 2200/80). CSF in lateral ventricles is bright. Striking CFVS in foramina of Monro (black arrowhead), third ventricle, aqueduct of Sylvius (straight arrow), fourth ventricle, and foramen of Magendie (curved arrow). CFVS surrounds massa intermedia (white arrowhead). **B**, T1-weighted scan (SE 750/40). CFVS is less well seen but is present in foramina of Monro (black arrowhead), posterior third ventricle, aqueduct of Sylvius (arrow), and proximal fourth ventricle. Massa intermedia (white arrowhead).

with known vascular anatomy. Its location was identified at the foramen of Magendie, the fourth ventricle, the aqueduct of Sylvius, the third ventricle, or at the foramina of Monro. The severity of the ventriculomegaly was measured using the ventricular size index [9], which is the ratio of the distance between the lateral margins of the frontal horns to the distance between the inner tables of the skull at the same level. Using this index, normal ventricular size is present when the ratio is 30% or less, mild ventriculomegaly is present with a ratio of 30–39%, moderate ventriculomegaly is present with a ratio of 40–46%, and severe ventriculomegaly is present with a ratio of 47% or more. (The same criteria were used in the “normal” group included in Table 2 reported by Sherman and Citrin [6].) The presence or absence of interstitial edema was also noted. The length of the longest unbroken CFVS was measured on the T2-weighted images.

MR examinations were performed with a Picker Vista MR superconductive 0.5-T imager with standard pulse sequences, software, and hardware. Read gradient magnetic field amplitudes used in these sequences were 3×10^{-3} T/m. Data were typically acquired with 256 complex samples/view, 256 views, and two excitations using the standard 2DFT method and spin-echo (SE) pulse sequences [10]. Magnitude reconstruction was used in all cases. The resultant 256×256 image was then interpolated to a 512-element display matrix. Field of view for these examinations was 30 cm, resulting in a pixel size before interpolation of 1.17 mm. Sampling times were 24 msec, and sampling bandwidth 5 kHz. The phase-encoding gradient was in the horizontal plane for all cases. Single-echo 8- or 16-multisection SE sequences were performed with selective excitation in staggered slice order by exciting odd-numbered slices sequentially followed by even-numbered slices sequentially. Slices were contiguous and either 5 or 10 mm thick. Slice profiles were approximately trapezoidal, with 1 mm transitional zones on either side of a flat region of the nominal thickness [11]. T2- and T1-weighted sequences were used in all cases.

T2-weighted sequences were obtained with a TE of 60, 80, or 100 msec and a TR of 1500–4000 msec. T1-weighted sequences used a TE of 30 or 40 msec, with a TR of 500–600 msec. The CSF in the lateral ventricles appears hyperintense relative to cerebral cortex on the T2-weighted sequences and hypointense on the T1-weighted sequences. In some cases additional sequences were added to the basic examination. Slice-to-slice variability in contrast was not significant in any pulse sequences.

Results

Sixteen patients (40%) had mild ventriculomegaly, 15 (37%) had moderate ventriculomegaly, and nine (23%) had severe ventriculomegaly. The occurrence of the CFVS in patients with brain atrophy or EVOH is given in Table 1. The CFVS was more difficult to identify specifically in the foramen of Magendie in five patients because of the proximity of the posterior inferior cerebellar arteries.

Group 1: Ventriculomegaly from Atrophy or Congenital Anomaly

Fifteen of these 29 patients had mild ventriculomegaly, 10 had moderate enlargement, and four had severe enlargement of the ventricles. Two patients had a periventricular rim of slightly increased intensity that was believed to represent deep white-matter disease, probably caused by ischemia.

TABLE 1: CFVS Occurrence in Atrophy and Extraventricular Obstructive Hydrocephalus (EVOH)

Location of CFVS	No. of Patients (%)		
	Cerebral Atrophy (n = 29)	EVOH (n = 11)	Total (n = 40)
Foramen of Monro	8 (28)	5 (45)	13 (33)
Third ventricle	19 (66)	9 (82)	28 (70)
Aqueduct	29 (100)	11 (100)	40 (100)
Fourth ventricle	27 (93)	11 (100)	38 (95)
Foramen of Magendie*	17–21 (59–72)	9–10 (82–91)	26–31 (65–78)
CFVS length (average)	37 mm	47 mm	40 mm

Note.—CSF flow-void sign (CFVS) was analyzed on MR images obtained with T2-weighted spin-echo pulse sequences (TR = 1500–4000 msec, TE = 60–100 msec). * Range of observations reflects the difficulty in separating the CFVS from arterial structures.

TABLE 2: CFVS Occurrence According to Ventricular Size

Location of CFVS	Degree of Ventriculomegaly and No. of Patients (%)			
	Normal (n = 46)	Mild (n = 16)	Moderate (n = 15)	Severe (n = 9)
Foramen of Monro	0	4 (24)	5 (27)	5 (56)
Third ventricle	2 (4)	10 (63)	11 (73)	7 (78)
Aqueduct	31 (67)	16 (100)	15 (100)	9 (100)
Fourth ventricle	15 (32)	15 (94)	14 (93)	9 (100)
Foramen of Magendie*	18 (39)	8-11 (50-67)	11-13 (73-87)	7 (78)

Note.—Data were compiled on the visualization of the CSF flow-void sign (CFVS) on T2-weighted spin-echo pulse sequence (TR = 1500–4000 msec, TE = 60–100 msec). Data on normal patients from [6]. Categorization of ventricular size was made during the ventricular size index. Note the increasing likelihood of observing the CFVS as ventricular size increases.

* Range of observations reflects the difficulty in separating the CFVS from arterial structures.

All 29 patients had the CFVS in the aqueduct of Sylvius on T2-weighted images. One patient with severe ventriculomegaly had a narrow CFVS in the aqueduct and mild periventricular hyperintensity. Before the MR examination, this patient was suspected of having aqueductal stenosis; however, a limited pneumoencephalogram showed free passage of air into the third ventricle. A radionuclide cisternogram was normal. Nineteen patients (66%) had the sign in the third ventricle and 27 (93%) had the sign in the fourth ventricle. Of the 27 patients with CFVS in the fourth ventricle, 17 to 21 (59–72%) had the sign in the foramen of Magendie. Eight patients (28%) had the CFVS in or near the foramina of Monro. Twenty-six patients (90%) had the CFVS on T1-weighted images. In these cases it was seen only in areas that were positive for the CFVS on the T2-weighted images. The average length of the CFVS was 3.7 cm.

Group 2: EVOH

One of these 11 patients had mild hydrocephalus, while five had moderate hydrocephalus and five had severe hydrocephalus. Three of the patients with moderate and two with severe hydrocephalus had a smooth periventricular rim of increased intensity on T2-weighted images that was interpreted as interstitial edema. The CFVS was most marked in the patient with inferior vermian dysgenesis and moderate hydrocephalus (Fig. 1).

All patients had the CFVS in the aqueduct of Sylvius and fourth ventricle on T2-weighted scans. Nine or 10 (82–91%) of these patients had the sign clearly in the foramen of Magendie, while it was absent in this location in two others. Nine patients (82%) had the CFVS in the third ventricle and five (45%) had the CFVS in or near the foramina of Monro. Ten patients (91%) had evidence of the CFVS on T1-weighted images in areas also positive for the CFVS on T2-weighted images. The average length of the CFVS was 4.7 cm.

The data are summarized in Table 1. An analysis of the data according to ventricular size has been combined with previously reported observations of the CFVS in normal patients [6] and is presented in Table 2.

Discussion

The forces driving CSF throughout the subarachnoid space are not completely understood. The rate of continuous formation (0.4 ml/min) and absorption of CSF is inadequate to produce flow velocities detectable by MR. However, turbulence and localized areas of high-velocity CSF flow are created by pulsatile shifts of CSF. These CSF pulsations have been commonly observed during Pantopaque myelography or cisternography. In 1943, O'Connell [12] suggested that intracranial arterial pulsations were the main source of CSF pulsations. In 1955, Bering [13] maintained that the main impetus to CSF pulsations was pulsations within the choroid plexus. In 1966, Du Boulay [14] confirmed O'Connell's theoretical concepts, showing that forceful CSF pulsations occur in the basilar subarachnoid space and third ventricle in synchrony with arterial systole and diastole. He referred to the forceful thalamic compression of the third ventricle as the "third ventricular pump" and discounted the contribution of choroid plexus pulsation. Du Boulay believed that pulsation in the basal cisterns stemmed from displacement of CSF from the brain as well as expansion of the main arteries in the basilar cisterns.

Flow-dependent effects in the presence of magnetic field gradients have been described in conventional [15], specialized [16], and zeugmatographic [17, 18] MR devices. Flow-dependent MR images have been shown in both conventional [19] and specialized pulse sequences [20]. These effects can be manifested as time-of-flight or phase-shift effects, or as a combination of both, as is the case in conventional 2DFT SE sequences [16, 21]. Time-of-flight effects include flow-related enhancement (as seen in slow venous flow) and high-velocity signal loss, which occurs with rapid flow (10 cm/sec or more) caused by movement of spins out of the imaged volume before the refocusing pulses occur [22]. As von Schulthess and Higgins [21] pointed out, this effect may explain the loss of signal for flow of spins perpendicular to the plane, but it cannot explain loss of signal for flowing spins coursing within the imaged plane. Spin-phase shifts occur whenever spins move in gradient fields regardless of whether the movement is in the imaged plane. In the case of spins flowing along a magnetic gradient, the magnetic field experienced by those spins varies during the evolution of the pulse sequence. Thus, the magnetic history of the spins will be more complex in the case of flowing spins. The signal intensity is critically dependent on the spatial distribution of velocities and accelerations of spins within a voxel. The larger the spatial variation of the velocity or accelerations across a voxel, the greater the loss in signal amplitude [18]. Turbulence, whether from high velocity or intrinsic physiologic movements, results in large spatial variations of the velocities of the fluid within the imaging plane that then translate into spin-phase changes and loss of signal

amplitude. We have anecdotally noted that the CFVS is present in the aqueduct on both odd and even echoes, in keeping with von Schulthess and Higgins' observations on spin-phase changes in blood vessels. Changes in the phase-encoding plane have not been noted to change the CFVS, although associated artifacts are moved from one plane to the other. Based on the above observations, most of the aqueductal signal loss known as the aqueductal CFVS is most likely caused by spin-phase changes. These observations do not necessarily apply to the loss of signal in other subarachnoid spaces. For example, we have noted more uniform signal intensity in the spinal CSF on the second echo of a multiecho chain. Theoretically, the time-of-flight effects could be calculated by determining the differences in intensity between images of identical TR and TE on single-echo images versus dual-echo images. We recently presented material confirming the relation of the CFVS to the cardiac cycle, specifically showing more marked loss of signal (CFVS) during cardiac systole [23], apparently because of accentuation of the time-of-flight effects. Similar effects may be seen from fortuitous synchronization of the cardiac cycle and the MR acquisition sequence. This has been termed "pseudogating" [22] and could be a factor in some instances [24].

A comparison of the reported incidence of the CFVS in patients with normal ventricles [6] with those of our series indicates that it is seen much more often in patients with ventriculomegaly (Table 2). Our results indicate that the CFVS is present in the aqueduct of Sylvius in all patients with enlarged ventricles caused by brain atrophy or EVOH (Figs. 1, 2, and 4). On T2-weighted images the CFVS stands out as an area of decreased intensity in contrast to the bright appearance of the CSF in other areas of the ventricular system (Figs. 1 and 2A). It was seen in the fourth ventricle in 96% of patients (Figs. 1-3), in the third ventricle in 70% (Figs. 1, 2, 4, and 5), in the foramina of Monro in 33% (Figs. 1, 2, and 5), and in the foramen of Magendie in 65-77% (Figs. 1-4). It was present in at least one area on T1-weighted scans in 90% of patients (Fig. 1B).

Subtle differences in CSF velocity or turbulence in different

areas of the ventricle can be appreciated by comparing midsagittal T1-weighted images with midsagittal T2-weighted images in the same patient.

There is no difficulty in differentiating the CFVS in the aqueduct of Sylvius, third ventricle, or fourth ventricle from arteries or veins. However, care must be taken to differentiate the posterior inferior cerebellar arteries from the foramen of Magendie and the internal cerebral veins from the foramina of Monro (Figs. 2, 3, and 5). In these areas we relied on the size of the CFVS and close observations of the anatomy on contiguous sections. The CFVS probably occurs frequently in basilar cisterns but is more difficult to differentiate from vessels [7]. In one patient with brain atrophy and multiple sclerosis we observed large areas of decreased intensity that we believe represented the CFVS in the ambient cisterns (Fig. 6).

The CFVS was seen more often and was more prominent in the group of patients with EVOH (Table 1), but this is believed to be a reflection of the more marked ventricular enlargement in this group of patients. The data in Table 2 reflect the relatively frequent occurrence of the CFVS in the foramina of Monro, the third ventricle, the fourth ventricle, and the foramen of Magendie in moderate or severe ventricular enlargement when compared with only mild ventriculomegaly. The CFVS alone cannot be used to differentiate patients with brain atrophy from those with EVOH.

The increased frequency and prominence of the CFVS in patients with large ventricles is probably related to several factors. Decreased compliance of periventricular tissues may allow increased transmission of pulsations to the ventricular system [25]. The expansion of the CSF spaces alone in a turbulent system may simply allow more mixing of spins with differing constant velocities and accelerations, resulting in more signal loss from spin-phase changes [21]. Signal loss from time-of-flight effects may also be increased in patients with large ventricles. These effects are most likely to be seen in areas where the cross-sectional area of the CSF space narrows abruptly, such as the aqueduct of Sylvius and the various ventricular foramina. Although the net production of CSF does not change, the velocity of CSF flow through these



2



3

Fig. 2.—65-year-old man with mild cerebral atrophy. T2-weighted (SE 2200/80) midsagittal scan is 5 mm thick. CFVS in foramina of Monro (large arrowhead), third ventricle (short straight arrow), aqueduct of Sylvius (small arrowheads), fourth ventricle, and foramen of Magendie (curved arrow). Note proximity of internal cerebral veins to foramina of Monro (long straight arrows).

Fig. 3.—55-year-old man with mild cerebral atrophy. T2-weighted (SE 2400/80) coronal scan through plane of floor of fourth ventricle is 5 mm thick. Aqueduct of Sylvius (straight solid arrow), foramen of Magendie (curved arrow), internal cerebral veins (open arrows).

Fig. 4.—61-year-old man with EVOH. Fourth ventricle is small. Coronal scans through plane of aqueduct and fourth ventricle are 10 mm thick. **A**, T2-weighted scan (SE 1600/100). CSF in enlarged lateral ventricles is isointense with brain (arrowheads). CFVS in posterior third ventricle (short straight arrows), aqueduct of Sylvius (long straight arrow), rostral fourth ventricle, and foramen of Magendie (curved arrow), indicating patency of these areas. **B**, Balanced T2/T1 scan (SE 1500/40). Aqueduct of Sylvius (arrowheads) appears to be laterally compressed.

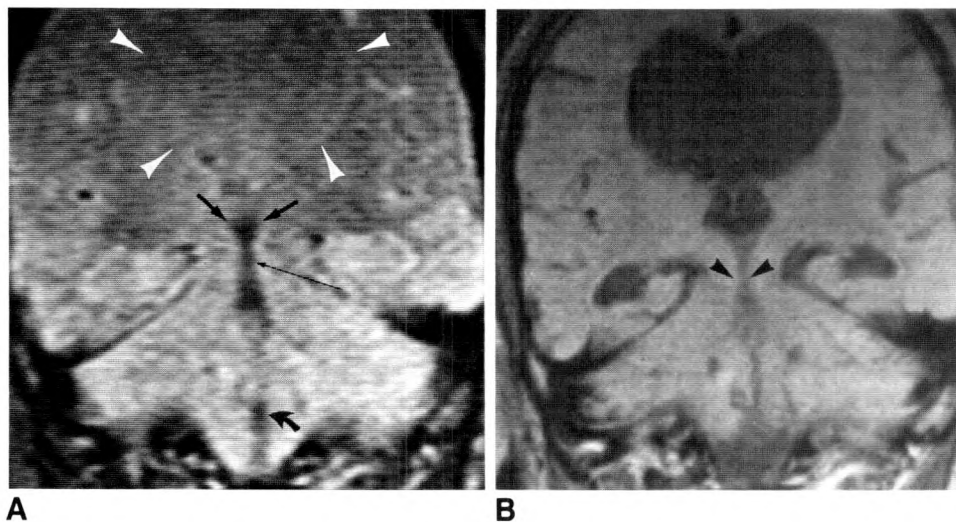


Fig. 5.—2-year-old girl with EVOH. T2-weighted (SE 2400/80) axial scan is 10 mm thick. CFVS is seen well in foramina of Monro (solid arrows) and in third ventricle (open arrow). Artifact from shunt tube is seen posteriorly on right side.

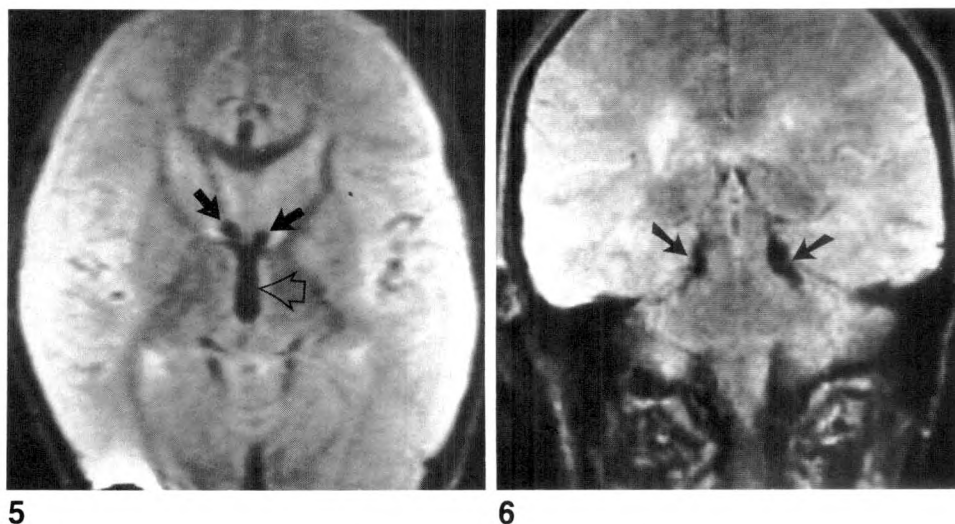


Fig. 6.—35-year-old woman with multiple sclerosis. T2-weighted (SE 2400/80) coronal scan through posterior brainstem is 5 mm thick. Prominent areas of decreased intensity in ambient cisterns (arrows) probably represent summation of CFVS and cerebral vasculature.



areas will be increased. This can be explained by applying the concept of the continuity equation [26], which states that for a steady-stream tube with a narrow end (section 1) and a wide end (section 2), the product of density (d), velocity (v), and cross-sectional area (A) is the same at both ends, or $d_1 v_1 A_1 = d_2 v_2 A_2$. The actual description of the flow through a structure such as the aqueduct of Sylvius is much more complex, but the concept is valid. In patients with hydrocephalus, the change in the cross-sectional area of the ventricles relative to the normal state is much greater than the change in the size of the aqueduct of Sylvius or the ventricular foramina relative to their normal state. Thus, applying the continuity equation, the velocity of the CSF flow must increase. This in turn could lead to high-velocity signal loss as well as spin-phase shift signal loss.

We cannot explain the smaller-than-expected aqueductal CFVS in one patient with severe hydrocephalus, but we were able to corroborate the pneumoencephalographic finding of

aqueductal patency by using a 5-mm T2-weighted (SE 2300/80) MR imaging pulse sequence (Fig. 7). Mild stenosis of the caudal segment of the aqueduct may be present. This case is important since it illustrated the utility of the CFVS in the aqueduct. In future cases the observation of the CFVS in the aqueduct may obviate invasive techniques to evaluate the aqueduct. This case also illustrates the need to use meticulous technique. The narrow CFVS might not have been seen if there had been patient motion or if other factors decreased spatial and/or contrast resolution.

One patient had a marked CFVS extending from the foramina of Monro to the foramen of Magendie, virtually filling the fourth ventricle (Fig. 1). As in all cases, the CFVS was best seen on the T2-weighted sequence. This patient had inferior vermian dysgenesis and probable posttraumatic EVOH. The caudal aqueduct of Sylvius was dilated. The foramen of Magendie was voluminous and may have allowed more vigorous transmission of CSF pulsations into the fourth ventricle

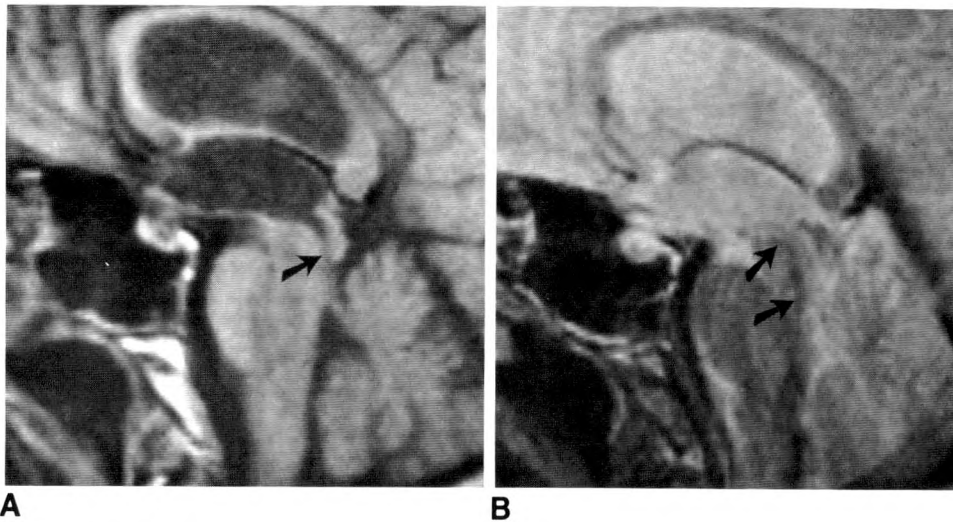


Fig. 7.—77-year-old man with cerebral atrophy. Midsagittal scans are 5 mm thick. **A**, T1-weighted (SE 750/40). Dilated lateral and third ventricles. Caudal segment of aqueduct of Sylvius is poorly seen (arrow). **B**, T2-weighted (SE 2300/80). CFVS is present (arrows), indicating patency of aqueduct of Sylvius. Limited pneumoencephalogram confirmed patency of aqueduct of Sylvius.

and aqueduct. It has been stated that the pulsatile displacement of CSF through the basal cisterns is 10 to 25 times as great as the ventricular displacement, even in normal patients [24, 27, 28].

The CFVS is a useful direct indicator of the patency of the channel or foramen in which it is seen. In 25–35% of patients with EVOH, the fourth ventricle is normal or minimally enlarged [29]. We encountered two such patients in our series (Fig. 4). The observation of the aqueductal CFVS avoids the consideration of aqueductal obstruction in those patients. The CFVS should prove to be more useful than the traditional criterion for determining the site of obstruction by observation of the point of transition from dilated to nondilated CSF spaces.

Magnetic field strength does not appear to be an important factor. The CFVS has been observed on a variety of systems at different field strengths including 0.35 T, 0.5 T, 0.6 T, and 1.5 T [6, 7, 24, 30]. We have also anecdotally observed the sign on images from a 0.3 T permanent magnet system. Von Schulthess and Higgins [21] suggested that the loss of signal from movements of spins in gradient fields (spin-phase changes) may vary between the different MR imager systems. This is because of the variability in gradient fields used for spatial position encoding. We are not aware of examples of such machine differences at this time.

We have noted a markedly higher incidence of the CFVS when comparing scans obtained with T2-weighted versus T1-weighted SE pulse sequences. Since the loss of signal is probably primarily from spin-phase changes, the phenomenon should not depend on the TE or TR. However, the decreased intensity will not be easily observed unless the intensity of the CSF is increased. The longer TE/TR sequences provide better contrast and thus allow easier detection of the CFVS. Time-of-flight effects are dependent on the TE and are more likely to be demonstrated as the TE increases [4].

The CFVS may prove to be useful in the follow-up examination of patients with treated (shunted) hydrocephalus. There have been reports of the development of shunt independence with spontaneous nonsurgical restoration of normal CSF cir-

culatory patterns in 9–20% of patients treated for hydrocephalus [31–33]. The appearance of the CFVS in areas where it was previously absent would indicate restoration of normal CSF flow through the area. The disappearance of the CFVS in patients with hydrocephalus who are being followed should be of great value. It would be an indication that previously intact CSF flow pathways had been altered. For instance, some patients with EVOH have been shown to develop secondary aqueductal stenosis from depression of the third ventricle and lateral compression of the aqueduct by the enlarged lateral ventricle [34, 35]. This superimposes an obstructive component on an advanced EVOH and accelerates neurologic deterioration.

It is important to recognize the CFVS because it explains otherwise confusing areas of heterogeneous intensity in CSF spaces and it provides information about CSF dynamics. While it promises to be a useful sign in the evaluation of patients with ventriculomegaly, further investigations of the sensitivity and specificity of the sign are needed. Although our results indicate that the CFVS is present in the aqueduct of Sylvius in all patients with hydrocephalus, we must add a note of caution since this series is limited to only 40 patients. It does appear clear that the presence of the CFVS in and of itself does not indicate the presence of EVOH. The application of the CFVS is leading us to a deeper understanding of CSF circulatory system dynamics, and this in turn may lead to improved diagnosis and treatment of patients with CSF circulatory disorders.

ACKNOWLEDGMENTS

We thank Mary Anne Thomas, Arlene Kisiuk, and Bari Weiner for help in image preparation and manuscript review.

REFERENCES

1. Bradley WG, Waluch V, Yadley RA, Wyckoff RR. Comparison of CT and MR in 400 patients with suspected disease of the brain

- and cervical spinal cord. *Radiology* 1984;152:695-702
2. Brant-Zawadzki M, David PL, Crooks LE, et al. NMR demonstration of cerebral abnormalities: comparison with CT. *AJNR* 1983;4:117-124, *AJR* 1983;140:847-854
 3. Bydder GM, Steiner RE, Young IR, et al. Clinical NMR imaging of the brain: 140 cases. *AJNR* 1982;3:459-480, *AJR* 1982;139:215-236
 4. Bradley WG, Waluch V, Laie K, Fernandez EJ, Spalter C. The appearance of rapidly flowing blood on magnetic resonance images. *AJR* 1984;143:1167-1174
 5. Kucharczyk W, Lemme-Plegos L, Uske A, Brant-Zawadzki M, Dooms G, Norman D. Intracranial vascular malformations: MR and CT imaging. *Radiology* 1985;156:383-389
 6. Sherman JL, Citrin CM. Magnetic resonance demonstration of normal CSF flow. *AJNR* 1986;7:3-6
 7. DeLaPaz RL, Davis DO, Norman D, O'Donohue J, Enzmann DR. Cerebrospinal fluid motion effects in cerebral MR imaging. Presented at the annual meeting of the Radiological Society of North America, Chicago, November 1985
 8. Naidich TP, Schott LH, Baron RL. Computed tomography in the evaluation of hydrocephalus. *Radiol Clin North Am* 1982;20:143-167
 9. TerBrugge KG, Rao KC. Hydrocephalus and atrophy. In: Lee SH, Rao KC, eds. *Cranial computed tomography*. New York: McGraw-Hill, 1983:171-200
 10. Haacke EM, Bearden FH, Clayton JR, Linga NR. Reduction of MR imaging time by the hybrid fast-scan technique. *Radiology* 1986;158:521-529
 11. Chui KM, Blakesley DM, Mohapatra SN. Test method for MR image slice profile. *J Comput Assist Tomogr* 1985;9:1150-1152
 12. O'Connell JEA. The vascular factor in intracranial pressure and the maintenance of the cerebrospinal fluid circulation. *Brain* 1943;66:204-228
 13. Bering EA. Choroid plexus and arterial pulsation of the choroid plexuses as a cerebrospinal fluid pump. *Arch Neurol Psychiatry* 1955;73:165-172
 14. Du Boulay GH. Pulsatile movements in the CSF pathways. *Br J Radiol* 1966;39:255-262
 15. Singer JR. Blood flow rates by nuclear magnetic resonance measurements. *Science* 1985;130:1652-1653
 16. Battocletti JH, Linehan JH, Larsen SJ, et al. Analysis of a nuclear magnetic resonance blood flow for pulsatile flow. *IEEE Trans Biomed Eng* 1972;19:403-407
 17. Moran PR. A flow velocity zeugmatographic interlace for NMR imaging in humans. *Magnetic Resonance Imaging* 1982;1:197-203
 18. Waluch V, Bradley WG. NMR even echo rephasing in slow laminar flow. *J Comput Assist Tomogr* 1984;8:594-598
 19. Wedeen VJ, Meuli RA, Edelman RR, et al. Projective imaging of pulsatile flow with magnetic resonance. *Science* 1985;230:946-948
 20. Le Bihan D, Breton E, Lallemand D, Grenier P, Cabanis E. Diffusion MR imaging: neurological results. Presented at the annual meeting of the Radiological Society of North America, Chicago, November 1985
 21. von Schulthess GK, Higgins CR. Blood flow imaging with MR: spin-phase phenomena. *Radiology* 1985;157:687-695
 22. Bradley WG, Waluch VW. Blood flow: magnetic resonance imaging. *Radiology* 1985;154:443-450
 23. Citrin CM, Sherman JL. Alteration of the MRI appearance of CSF flow by cardiac gating. Presented at the annual meeting of the American Society of Neuroradiology, San Diego, January 1986
 24. Bradley WG, Kortman KE. Use of aqueductal flow void phenomenon in the diagnosis of normal pressure hydrocephalus. Presented at the annual meeting of the American Society of Neuroradiology, San Diego January 1986
 25. Bradley WG, Kortman KE. Use of the aqueductal flow void phenomenon in the diagnosis of normal pressure hydrocephalus. Presented at the annual meeting of the American Society of Neuroradiology, San Diego, January 1986
 26. Streeter VL. *Fluid mechanics*. 6th ed. New York: McGraw-Hill, 1975:134-144
 27. Du Boulay GH. Specialization broadens the view. The significance of a C.S.F. pulse. *Clin Radiol* 1972;23:401-409
 28. Du Boulay GH, Shah SH, Currie JC, Logue V. The mechanism of hydromyelia in Chiari type 1 malformations. *Br J Radiol* 1974;47:579-587
 29. Naidich TP, Schott LH, Baron BL. Computed tomography in the evaluation of hydrocephalus. *Radiol Clin North Am* 1982;20:143-167
 30. Mills CM, Posin JP, McCreary J, Kleiner BC. MRI of the spine: effect of flow on CSF intensity. Presented at the annual meeting of the American Society of Neuroradiology, San Diego, January 1986
 31. Johnston IH, Howman-Giles R, Whittle IR. The arrest of treated hydrocephalus in children. *J Neurosurg* 1984;61:752-756
 32. Hemmer R, Bohm B. Once a shunt, always a shunt? *Med Child Neurol* 1976;18[suppl 37]:69-73
 33. Holtzer GJ, de Lange SA. Shunt-independent arrest of hydrocephalus. *Neurosurgery* 1972;39:698-701
 34. Nugent GR, Al-Mefty O, Chou S. Communicating hydrocephalus as a cause of aqueductal stenosis. *J Neurosurg* 1979;51:812-818
 35. McMillan JJ, Williams B. Aqueduct stenosis: case review and discussion. *J Neurol Neurosurg Psychiatry* 1977;40:521-532

Memorials

Kathryn Sue Edwards Jacobi, 1953–1986



Kathryn Sue Edwards Jacobi died suddenly and unexpectedly July 8, 1986, at

the age of 33. She was born February 4, 1953, and grew up in Galveston, TX, where she graduated from high school in 1970. Sue graduated summa cum laude from Texas A & M University in 1974. She moved to San Antonio, TX, to attend medical school at the University of Texas Health and Science Center and graduated in 1978. She and her husband, Rick Jacobi, then returned to Galveston while she completed her residency in Diagnostic Radiology at the University of Texas Medical Branch. It was during her residency that she gave birth to a daughter and a son.

The death of Sue Jacobi is a terrible loss, not only to all of us who loved and respected her, but also to Radiology. She was a dedicated and caring physician with seemingly infinite patience. She was kind and considerate of patients and always willing to lend a hand to those of us who worked with

her. It was important to Sue that she practice the best radiology possible, and she maintained high standards.

After completing her residency, Sue entered private practice with Radiology Consultants of Austin, TX. It is a tragedy that she had been in practice barely 4 years at the time of her death.

She was a dedicated physician, a loving wife and mother, and a delightful friend. She earned respect and genuine affection from all of those who knew her: her family, neighbors, church members, colleagues, and patients.

She is survived by her husband and their two children, 6-year-old Leslie and 3-year-old Brian, and by her parents, Mr. and Mrs. L. D. Edwards of Galveston, TX.

Deborah K. Ahrendt
Humble, TX 77338

MR Imaging of Paragangliomas

Walter L. Olsen¹
 William P. Dillon
 William M. Kelly
 David Norman
 Michael Brant-Zawadzki
 T. Hans Newton

MR imaging of 15 paragangliomas in 10 patients was compared with CT of 13 of the lesions in eight patients. All lesions were confirmed with angiography. All lesions were detected by MR and CT with the exception of one small glomus tympanicum tumor that was seen only in retrospect with MR. CT better demonstrated subtle osseous changes of the skull base and the relation of the tumor to the middle ear structures. MR better demonstrated the relation of the tumor to the adjacent internal jugular vein and carotid artery. The paragangliomas had a characteristic MR appearance based on their vascularity. Serpiginous areas of signal void representing high vascular flow were interspersed among areas of high signal intensity caused by slowly flowing blood and tumor cells. This "salt-and-pepper" pattern was seen in all lesions greater than 2 cm in maximal dimension. MR was therefore able to accurately characterize the tumors as highly vascular. Multiplanar imaging and good tissue contrast and anatomic detail permitted display of the relations of these neoplasms to surrounding carotid sheath vessels and to intracranial structures better than did CT. In this experience, the MR appearance of paragangliomas was quite characteristic and differed markedly from meningiomas, neuromas, and metastatic disease of the skull base.

Paragangliomas are slowly growing hypervascular tumors arising from neural crest cell derivatives throughout the body. In the head and neck region, the major paraganglial cells are located at the carotid bifurcation (carotid body), along the nodose ganglia of the vagus nerve, and along the nerves supplying the middle ear and jugular bulb. In recent years, CT and angiography have been the primary radiologic tools used to investigate the paragangliomas. Contrast-enhanced CT studies demonstrate an enhancing mass either at the carotid bifurcation or in the region of the jugular foramen. The vascular nature of paragangliomas can be detected by dynamic CT scanning during a rapid bolus of intravenous contrast material [1-3] or by angiography, which demonstrates the typical hypervascular mass supplied by the external carotid artery. Bolus dynamic CT scanning has not gained wide acceptance, as this technique involves a second rapid infusion of contrast material after the initial diagnostic study. Angiography demonstrates the highly vascular nature of the tumor and permits either palliative or preoperative embolization, if appropriate.

The role of MR imaging in the evaluation of patients with paragangliomas has not been established. Therefore, we reviewed retrospectively 15 proven examples of paragangliomas of the head and neck imaged with MR, angiography, and, in most cases, CT. The ability of MR to identify the nature and extent of paragangliomas and their relation to adjacent structures was assessed.

Materials and Methods

Ten patients with 15 paragangliomas were studied with MR imaging. One patient had bilateral carotid body tumors. Two patients had a carotid body tumor on one side and a contralateral glomus jugulare tumor. One patient had bilateral carotid body tumors with a

This article appears in the November/December 1986 issue of *AJNR* and the January 1987 issue of *AJR*.

Received March 31, 1986; accepted after revision May 28, 1986.

Presented at the annual meeting of the American Society of Neuroradiology, San Diego, January 1986.

¹ All authors: Department of Radiology, University of California, San Francisco, CA 94143. Address reprint requests to W. L. Olsen, San Francisco General Hospital, San Francisco, CA 94110.

AJR 148:201-204, January 1987
 0361-803X/87/1481-0201

© American Roentgen Ray Society

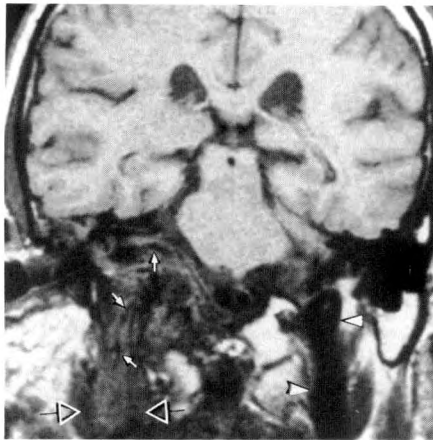
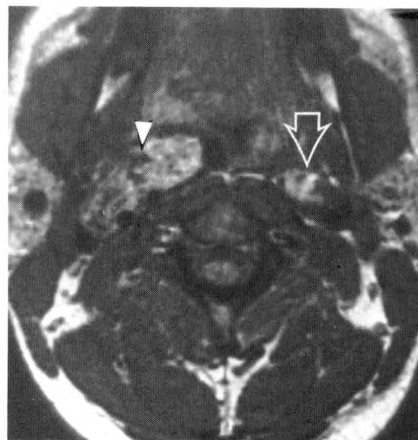
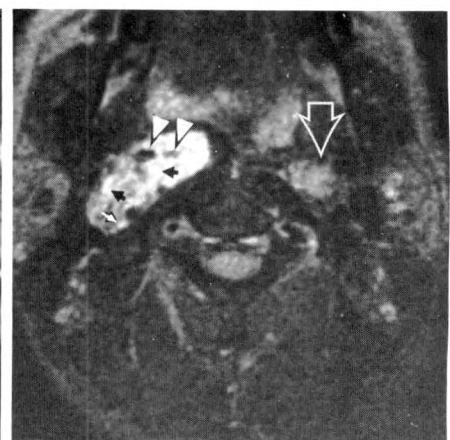


Fig. 1.—Right jugulotympanic paraganglioma. TR 600 msec, TE 25 msec, 1.5 T. Coronal section shows serpiginous areas of signal void reflecting hypervascularity typical of paragangliomas (solid arrows). Tumor extends intracranially and down lumen of right internal jugular vein (open arrows). Normal left internal jugular vein has signal void characteristic of blood flow (arrowheads). (Courtesy of Bent Kjos.)



A



B

Fig. 2.—Bilateral carotid body paragangliomas. A, TR 2000 msec, TE 40 msec, 1.5 T. B, TR 2000 msec, TE 80 msec, 1.5 T. Even-echo rephasing phenomena characteristic of slow blood flow are suggested by punctate areas of high signal intensity that have increased markedly between first- and second-echo images (solid arrows). Punctate areas of signal loss reflect regions of high-blood-flow velocity (arrowheads). Small left carotid body tumor (open arrows).

small separate glomus tympanicum tumor. In total, there were seven carotid body tumors, six jugulotympanic tumors, one vagal paraganglioma, and one glomus tympanicum tumor. Selective angiography was performed in all patients. Contrast-enhanced CT using a rapid drip infusion was performed in eight patients. Pathology was available in seven patients. In the other three patients, the clinical features and radiographic appearance were considered to be typical of paragangliomas. They were treated with radiation therapy without histologic confirmation.

MR examinations were performed with a 0.35 T unit (Diasonics MT/S) in six patients (nine tumors) and with a 1.5 T unit (GE Signa) in four patients (six tumors). Multisection, spin-echo (SE) T1- and T2-weighted images were obtained. MR imaging parameters were repetition time (TR) 500–600 msec, echo time (TE) 25–40 msec (T1-weighted) and TR 1500–2000 msec, TE 25–80 msec (T2-weighted). T2-weighted images were obtained using a multiecho SE technique. In almost all cases, section thickness was 5 mm with an acquisition matrix of 256×256 . There were no interslice gaps with the Diasonics images. On the GE studies, a 20% gap was used with T1-weighted images and a 50% gap was used with T2-weighted images. CT scans were obtained on either a GE 8800 or 9800 scanner.

Results

Thirteen paragangliomas in eight patients were detected by CT and MR. In two other patients imaged with MR alone, two paragangliomas were seen. A small glomus tympanicum tumor, well visualized by angiography and CT, was less conspicuous on MR because of partial-volume averaging with adjacent middle ear inflammation. It was seen only in retrospect. This patient also had bilateral carotid body tumors.

In 12 of the 15 tumors, there were multiple punctate and serpiginous areas of signal void due to high-velocity flow in tumor vessels seen on both T1- and T2-weighted images

(Figs. 1 and 2). In three patients the tumors demonstrated foci of even-echo rephasing indicating relatively slow blood flow (Fig. 2). These even-echo rephasing phenomena appeared on T2-weighted images as punctate areas of increased signal intensity on the second echo, particularly in regions where there was little or no signal present on the first echo [4, 5]. Three tumors demonstrated neither high-velocity signal loss nor even-echo rephasing phenomena. Two of these lesions were less than 2 cm in maximum dimension (Fig. 3). The third lesion was studied by MR after angiographic embolization.

The relation of the paraganglioma to the adjacent carotid artery and/or jugular vein was well demonstrated by MR in all cases (Fig. 4). Focal obliteration and invasion of the jugular vein was demonstrated by MR in six cases and was confirmed by angiography (Figs. 1 and 3). CT scans were available in four of these cases. Since both tumor and vein enhanced, invasion was seen less easily on CT than on MR.

The T1 and T2 characteristics of the paragangliomas showed regional variation when compared visually with nearby muscle or brain. In general, the tumors exhibited relatively prolonged T1 and T2 relaxation times. On T1-weighted images (TR \leq 600 msec, TE \leq 40 msec), 11 tumors were of approximately equal signal intensity to adjacent muscle, while four tumors were slightly higher in intensity than surrounding muscle (Fig. 1). On T2-weighted images (TR \geq 1500 msec, TE \geq 56 msec), all tumors showed a variable but greater signal intensity than muscle (Fig. 2). The appearance of high-signal and low-signal regions resulted in a "salt-and-pepper" heterogeneity on T2-weighted images that has not been seen by us in any other mass lesion imaged with MR. T2-weighted images were better for identifying the two small lesions. T1-weighted images gave the better spatial resolution

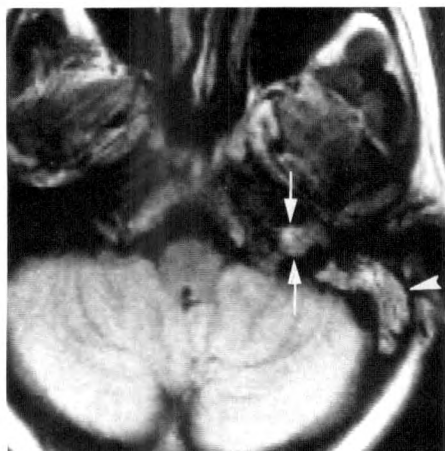
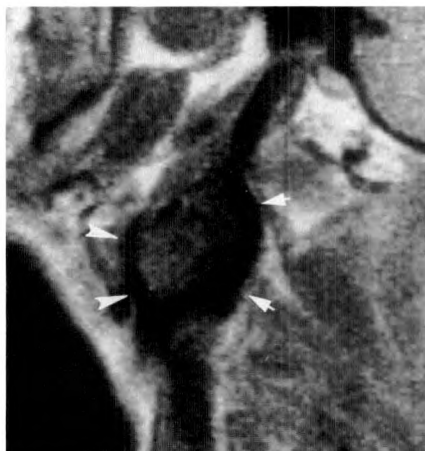
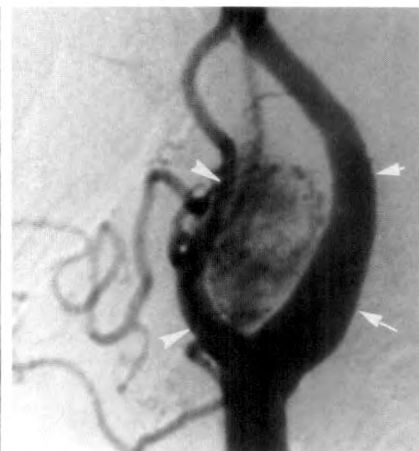


Fig. 3.—Left jugular bulb paraganglioma. TR 2000 msec, TE 35 msec, 0.35 T. Small mass within jugular bulb (arrows) does not show evidence of hypervascularity characteristic of larger paragangliomas. Mastoid air cell signal (arrowhead) secondary to obstruction of eustachian tube.

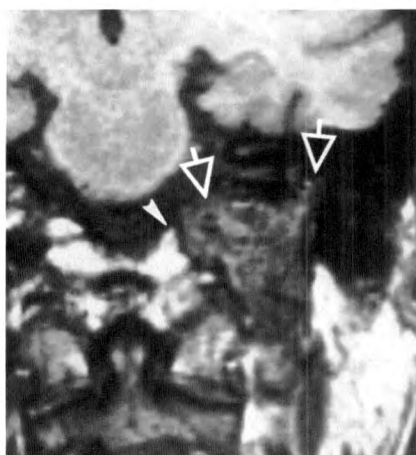


A



B

Fig. 4.—Carotid body paraganglioma. **A**, TR 500 msec, TE 30 msec, 0.35 T. **B**, Lateral common carotid arteriogram. Posterior displacement of internal carotid artery (arrows) and anterior displacement of external carotid artery (arrowheads) are well demonstrated by both studies. MR image was obtained using a 128×256 image matrix, accounting for less than optimal spatial resolution.



A



B

Fig. 5.—Jugulotympanic paraganglioma. **A**, TR 600 msec, TE 25 msec, 1.5 T. **B**, Coronal CT section using prospective bone review algorithm. Bony detail of destructive process at skull base is optimally demonstrated by CT (solid arrows). Invasion of jugular tubercle is also shown by MR (arrowhead), as is intracranial extent of tumor and its relation to brainstem (open arrows).

of the internal matrix of the paragangliomas. T1-weighted images in the coronal and sagittal planes were best for judging the relation of the tumor to nearby vessels and intracranial contents.

Skull-base erosion was present in all six jugulotympanic tumors (Figs. 1 and 5). MR and CT demonstrated the skull-base erosion in each case. Subtle areas of bone destruction were more easily identified on CT. The relation of the tumor to intracranial structures was better seen on MR. Coronal images were optimal for demonstrating skull-base destruction and intracranial extension (Figs. 1 and 5). Unilateral denervation atrophy of the tongue caused by hypoglossal nerve damage was present in two patients. The atrophy was more striking on MR than on CT because of the greater signal contrast between fat and muscle, especially on T1-weighted images.

Discussion

MR imaging provides a unique tool to assess the patient with suspected paragangliomas. MR detects the vascular nature of these lesions, and in our experience is highly characteristic for the diagnosis of paraganglioma. Indeed, in 12 of our 15 cases, multiple areas of low signal resulting from high-velocity signal loss characteristic of rapid arterial and venous blood flow were present in the matrix of these tumors on both T1- and T2-weighted images. In our experience, other tumors involving the carotid space and skull base—such as neurofibromas, schwannomas, and nasopharyngeal malignancies—have a less vascular appearance to their internal matrix (Fig. 6). This appearance was also noted with very small paragangliomas (Fig. 3). Calcification can also produce signal void on MR images; however, serpiginous calcification

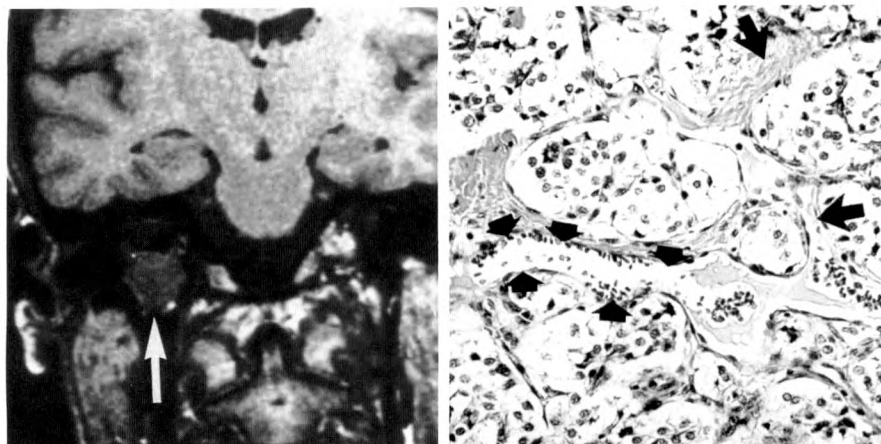


Fig. 6.—Schwannoma of vagus nerve in jugular foramen (proven). TR 600 msec, TE 25 msec, 1.5 T. Homogeneous signal intensity of mass in jugular foramen (arrow).

Fig. 7.—Carotid body tumor. Pathologic slide, H and E stain. Prominent vascular channels (small arrows) and lobules of cells separated by thick fibrous septae (large arrows) are typical of paragangliomas.

in neck masses is rare and was not a feature in any of our CT studies.

Paragangliomas in the head and neck occur most often in the carotid body and have a multicentric origin in about 3% of all patients, increasing to 26% in patients with familial tendencies [6]. Pathologically, the paragangliomas are composed of nests of cells separated by numerous vascular channels in a fibrous matrix (Fig. 7). In the past, angiography has been the primary radiographic tool in the preoperative assessment of head and neck paragangliomas. Angiography demonstrates the vascular supply and pattern of these lesions as well as the extent of the tumor and its relation to the carotid artery and internal jugular vein (Fig. 4A). Angiography also detects occlusion of the internal jugular vein, a common finding with larger lesions. Bilateral carotid arteriography is helpful in assessing the rare bilateral lesion. CT demonstrates the extent of these lesions, including skull-base and intracranial invasion [7, 8]. The vascularity of paragangliomas is reflected by their intense enhancement on CT. However, since other tumors, most notably schwannomas, also enhance on CT after drip infusion of contrast material, the profusely vascular nature of paragangliomas is not reliably detected without bolus-enhanced dynamic CT [1–3].

The advantages of MR over CT include the ability to characterize the vascularity of a lesion without the use of intravenous contrast material as well as demonstration of the tumor extension into the posterior fossa without the high-spatial-frequency artifact from the petrous bone that frequently diminishes the quality of CT examination. Additional information regarding the relation of the tumor to the surrounding important vascular structures such as the carotid artery and jugular vein was also more easily evaluated by MR than CT (Figs. 1–4). We recommend obtaining both T1- and T2-weighted images. T1-weighted images give better spatial resolution and better show the highly vascular internal matrix of the tumor. T2-weighted images give better tissue contrast, making smaller lesions more conspicuous. In larger lesions, the "salt-and-pepper" appearance on T2-weighted images was characteristic of paragangliomas. T1-weighted coronal images are best for evaluating intracranial extension.

MR certainly has limitations, as evidenced by the single lesion that was less conspicuous on MR because of its small size and apparent partial-volume averaging. Thin sections displayed on a 256×256 matrix will optimize detection of these smaller lesions and in our experience are necessary imaging parameters. The ability to detect the relation of the tumor to the important structures of the middle ear, such as the ossicles and the semicircular canals, is better with CT than MR.

In conclusion, angiography will still be necessary to outline the vascular supply of these lesions before surgical resection and for embolization therapy. However, MR can identify large paragangliomas with great specificity, obviating angiography before radiation therapy. Fine-needle aspiration biopsy techniques may be performed once MR has characterized the lesion as a paraganglioma.

REFERENCES

1. Shugar MA, Mafee MF. Diagnosis of carotid body tumors by dynamic computed tomography. *Head Neck Surg* **1982**;4:518–521
2. Mafee MF. Dynamic CT and its application to otolaryngology-head and neck surgery. *J Otolaryngol* **1982**;11:307–318
3. Som PM, Biller HF, Lawson W, Sacher M, Lanzieri CF. Parapharyngeal space masses: an updated protocol based upon 104 cases. *Radiology* **1984**;153:149–156
4. Waluch V, Bradley WG. NMR even echo rephasing in slow laminar flow. *J Comput Assist Tomogr* **1984**;8:594–598
5. Bradley WG, Waluch V. Blood flow: magnetic resonance imaging. *Radiology* **1985**;154:443–450
6. Batsakis JG. *Tumors of the head and neck: clinical and pathological considerations*. Baltimore: Williams & Wilkins, **1979**:369–379
7. Duncan AW, Lade EE, Deck MF. Radiologic evaluation of paragangliomas of the head and neck. *Radiology* **1979**;132:99–105
8. Som PM, Biller HF, Lawson W. Tumors of the parapharyngeal space: preoperative evaluation, diagnosis and surgical approaches. *Ann Otolaryngol [Suppl]* **1981**;90:3–15

Physiology of the CSF Flow-Void Sign: Modification by Cardiac Gating

Charles M. Citrin^{1,2}
 John L. Sherman^{1,3}
 Raymond E. Gangarosa⁴
 Diana Scanlon⁴

Low-intensity signal seen within areas of narrowing within the ventricular system has been termed the *CSF flow-void sign*. This decreased signal is related to CSF flow and turbulence. Seven normal volunteers were examined, and the changes that occurred in the appearance of the CFVS were noted when data acquisition was modified by cardiac gating. Flow-void patterns within the internal cerebral veins and basilar artery were also examined. The results of this study confirm that CSF flow is related to cardiac systole and diastole. An increase in hypointensity is seen in the areas of the aqueduct of Sylvius and the foramen of Magendie during the time at which the systemic arterial pulse wave is transmitted into the brain. The physiology of this observation is related either to a direct hydraulic effect of the venous system on the CSF or to filling and expansion of the thin-walled cerebral venous system. Hypointensity or an increase in the width of the basilar artery and internal cerebral veins during systolic data acquisition was also noted. The mechanism of this phenomenon is related to propagation of the systemic arterial pulse wave.

Recent publications and presentations [1–3] have addressed the significance of decreased signal intensity identified within the ventricular system and usually best seen at levels at which the ventricular system narrows (aqueduct of Sylvius, foramen of Magendie, and foramina of Monro). This area of decreased signal related to CSF flow and turbulence has been termed the *CSF flow-void sign* (CFVS). We have investigated the presence of the CFVS within the brains of normal volunteers and have referenced the presence and intensity of the sign as it relates to the cardiac cycle. Changes in the appearance of the CFVS have also been compared with changes observed in a major intracerebral artery and major intracerebral vein.

This article appears in the November/December 1986 issue of *AJNR* and the January 1987 issue of *AJR*.

Received February 13, 1986; accepted after revision May 28, 1986.

Presented at the annual meeting of the American Society of Neuroradiology, San Diego, January 1986.

¹ Magnetic Imaging of Washington, 5550 Friendship Blvd., Chevy Chase, MD 20815. Address reprint requests to C. M. Citrin.

² Department of Radiology, George Washington University School of Medicine, Washington, DC 20037.

³ Department of Radiology, Uniformed Services University of the Health Sciences, Bethesda, MD 20814.

⁴ Picker International, Inc., Highland Heights, OH 44143.

AJR 148:205–208, January 1987
 0361–803X/87/1481–0205
 © American Roentgen Ray Society

Subjects and Methods

Multislice MR imaging examinations were obtained using a Picker Vista MR superconductive imager operating at 0.5 T. Data were acquired with 256 views and two excitations using the 2DFT method. Scans were reconstructed and interpolated to a 512×512 image matrix.

Six-slice spin-echo pulse sequences were performed, with excitation of selected slices in a staggered order, exciting odd-numbered slices sequentially, followed by even-numbered slices sequentially. Slices were contiguous and were 5 mm thick in all cases. Only sagittal scans were obtained in this study because of the ease of identifying anatomic structures. An echo time (TE) value of 60 msec was used in all cases. RF stimulation and all scan data acquisitions were gated to the QRS complex; therefore, repetition time (TR) was determined by the patient's R-R interval, which varied between 710 and 1000 msec. This corresponds to a heart rate of 60–84 beats/min. Seven normal volunteers were examined. Each normal volunteer was monitored with ECG leads in place. No arrhythmias were noted. Cardiac gating was performed using a fiberoptic transmitter-receiver pair and appropriate blanking circuitry to prevent cross talk between the imager and monitoring equipment. Gating was performed on every other cardiac cycle, which resulted in the TR varying from 1420 msec to 2000 msec. Each scan was obtained with a variable delay t_d . The time delays t_d in milliseconds between

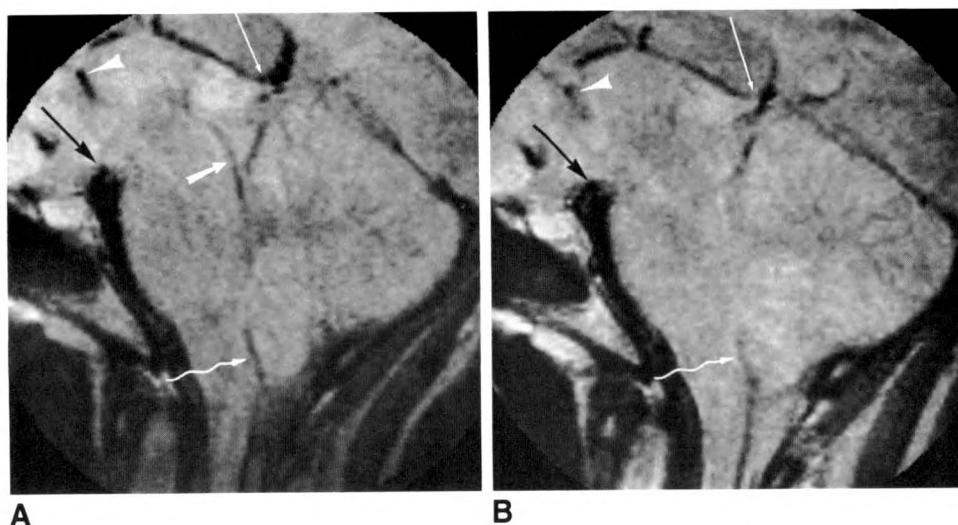


Fig. 1.—Images generated during SDA (A) and DDA (B). CFVS is seen well within aqueduct of Sylvius during SDA (A, short white arrow) and is not seen during DDA. There is diminution of CFVS within foramina of Monro during DDA (arrow-heads). CFVS within foramen of Magendie (wavy arrows). Mild diminution in degree of hypointensity during DDA. Diminution in vascular flow-void sign (VFVS) within internal cerebral vein, especially at level of its junction with vein of Galen (long white arrows) during diastolic data acquisition, and minimal change in VFVS at tip of basilar artery (black arrows), with diminution in sign during DDA.

the peak of the R wave and data sampling were given approximately by $t_d = t + (k - 1)(T_{ss}/2) + TE$ for k odd and $t_d = t + (n + k - 2)(T_{ss}/2) + TE$ for k even, where t = selected time delay in msec for the first slice, k = slice number, n = number of slices = 6, T_{ss} = time between successively excited slices = 120 msec, and TE = echo time in msec.

Since the slice used was always number 3, this indicates a data acquisition delay after the R wave of 120 msec + the selected delay + TE . To obtain a CFVS that related to cardiac systole, each normal volunteer had a scan with a selected delay of 50 msec. Therefore, in all subjects a 5-mm sagittal scan was obtained with variable TR depending on the patient's cardiac rate, a TE of 60 msec, and a data acquisition delay equal to 120 msec + 50 msec + 60 msec, representing, in order, the time between successively excited slices, the selected delay, and the TE . This equals a total delay of 230 msec between the R wave and data acquisition. An additional delay was applied to the timing mechanism of the scanner so that a delay after data acquisition equal to the R-R interval would occur before initiation of any additional data acquisition. This resulted in data being acquired on every other cardiac contraction. This allowed for T2-weighting of the images, which resulted in accentuation of the CFVS and permitted easier interpretation.

A second sequence was also obtained in each subject that related to cardiac diastole. The selected time delay varied in these patients according to the patient's R-R interval. Volunteers with a slower cardiac rate had scans obtained with a selected delay as long as 750 msec, which resulted in data acquisition being obtained at a total of 930 msec after cardiac contraction; volunteers with faster rates had scans obtained with a selected delay of only 500 msec, so that data acquisition occurred at 680 msec after the R wave. The delay (t_d) was always shorter than the R-R interval. As in the systolic series, information was acquired on every other R wave.

All scans from an individual patient were imaged at the same window width and window level. The scans were then rated as to the intensity of the CFVS at the levels of the foramina of Monro, the aqueduct of Sylvius, and the foramen of Magendie. The length and width of the CFVS were also measured, using calipers to give a point-to-point length rather than following the course of curved structures such as the aqueduct of Sylvius. Comparison was also made in the degree of hypointensity and the length and width of the basilar artery and internal cerebral veins. These vascular structures were selected for comparison with the CFVS because of their midline sagittal position and simultaneous visualization of the midline CSF-containing ventricular structures.

Results

Using the parameters established above, the CFVS was noted to vary with cardiac gating. At the level of the aqueduct of Sylvius, the CFVS became much more prominent during systolic data acquisition (SDA) in six of seven volunteers (Figs. 1–3) when compared with images generated during diastolic data acquisition (DDA). At the aqueduct, the CFVS was unchanged in one volunteer. The length or width of the CFVS at the aqueduct increased in seven of seven volunteers during SDA. This resulted in demonstration of the posterior third ventricle in six volunteers and demonstration of the proximal fourth ventricle in one volunteer during SDA (Fig. 2); findings not apparent during DDA. At the foramina of Monro, the CFVS was observed in two subjects during SDA (Fig. 1) and was not present during DDA. Enhancement of the CFVS was noted in one volunteer during SDA in the mid-fourth ventricle (not shown). The other area of striking change occurred at the level of the foramen of Magendie. In six of seven subjects the CFVS became more prominent during SDA than DDA, and it was unchanged in one subject. The length and width of the CFVS were increased at the level of the foramen of Magendie in five subjects during SDA and were unchanged in two subjects.

Evaluation of the basilar artery and internal cerebral vein revealed an increase in the vascular flow-void sign (VFVS) in five of seven individuals within the basilar artery during SDA. In three of seven individuals the VFVS in the basilar artery was of greater length or width during SDA. The other subjects were unchanged when SDA was compared with DDA. Similar results occurred at the internal cerebral vein, where in four of seven individuals the VFVS was more prominent during SDA and was seen to be of either greater length or greater width in two of seven individuals (Figs. 1 and 2). The other subjects were unchanged in this category when SDA was compared with DDA.

Discussion

CSF, a plasma ultrafiltrate, is continuously formed at a rate of about 25 ml/hr. Choroidal and ependymal CSF production

Fig. 2.—During SDA (A) CFVS is prominent in posterior third ventricle and aqueduct of Sylvius (*short white arrow*) and is not seen during DDA (B). Hypointensity within foramen of Magendie (*long white arrows*) during SDA is much wider and more hypointense than during DDA. Internal cerebral vein is seen well during SDA as a negative signal (*short black arrows*) and is barely visible during DDA. Basilar artery is much more hypointense during SDA than during DDA (*long black arrows*). Flow-void sign is not present at either foramen of Monro.

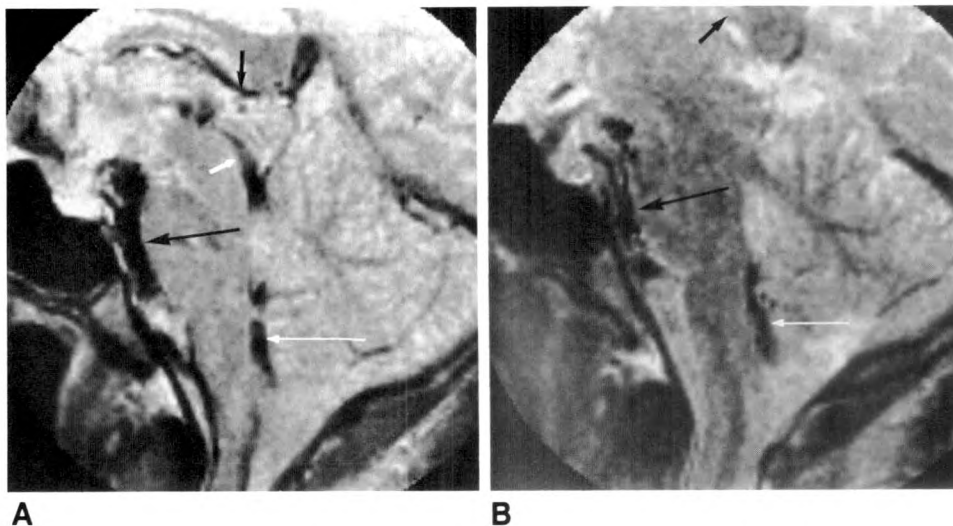
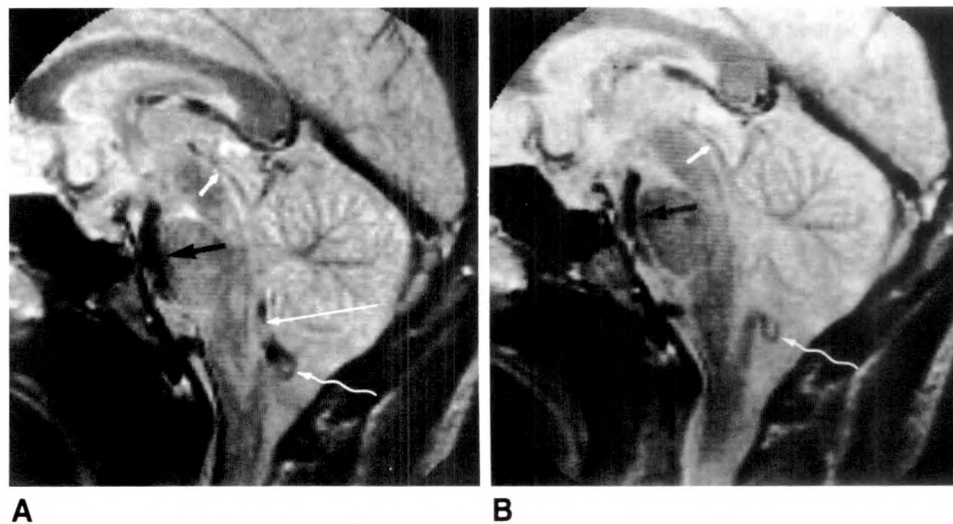


Fig. 3.—Greater hypointensity within aqueduct of Sylvius during SDA (A) than during DDA (B), and length of CFVS in aqueduct is increased during SDA (*short white arrows*). VFVS within basilar artery is increased during SDA when compared with DDA (*black arrows*). At level of foramen of Magendie, CFVS is quite prominent during SDA (*long straight white arrow*) and is not apparent during DDA. Curvilinear signal during SDA beneath foramen of Magendie (*wavy arrows*) is diminished in both width and hypointensity during DDA; this is thought to represent a loop of posterior inferior cerebellar artery.



within the ventricular system and CSF resorption by the arachnoid villi over the convexities result in a bulk CSF flow from within the ventricular system to outside the ventricular system [4, 5]. The rate of this flow is insufficient to cause signal dropout. However, vigorous pulsations of the CSF result from the action of the systolic arterial pressure pulse wave that is transmitted from the aortic root into the cerebral vasculature. The pulse wave is transmitted intact through the arteriolar and capillary arborization into the cerebral venous system and can be detected within the superior sagittal sinus [6]. This pulse wave is transmitted into the CSF. Marmarou et al. [7] contend that there is a direct hydraulic coupling of the craniospinal venous system to the CSF system. Pressure wave variations within the CSF are therefore linked by a fluid/fluid interface. Portnoy et al. [6] hypothesize that transmission of the arterial pulse wave through the capillaries into the venous system results in expansion of the thin-walled venous system. This expansion results in a pressure effect upon the brain and subsequent propagation of this pressure wave into the CSF. This is further contributed to by arteriolar and

capillary filling.

After the R wave of the QRS complex, there is a delay of about 90 msec during which isometric ventricular contraction occurs [8]. After opening of the aortic valve, maximum pressure within the aorta is realized about 150 msec after the R wave. This results in dilatation of this vessel. It is the distensibility of the aorta and other arterial structures that allows for rapid propagation of the pressure pulse wave into the arterial system. The transmission of the pressure pulse wave into the carotid arteries and brain is much more rapid than that of the actual motion of blood. The pulse wave within the aorta progresses at a rate of about 5–6 m/sec, while blood flow is traveling at a rate of only 0.5 m/sec. In smaller vessels, due to a decrease in distensibility, the rate of pulse propagation may rise to 40 m/sec [9]. Concomitant with a decrease in distensibility and a rise in the rate of pulse propagation is a diminution in the amplitude of the pulse. However, there is ultimate transmission of this pulse into the arteriolar and capillary system of the brain, as well as into the cerebral venous system. The phenomenon of pulse propagation, as

opposed to actual blood flow, requires about 240 msec to be transmitted from the initiation of isometric contraction of the heart to observation at the capillary venous junction of the brain [10].

Transmission of the arterial pulse pressure wave to the brain has already occurred by the time ventricular systole has ended, about 280 msec after the R wave. Diastole follows immediately afterward and results in a prompt drop-off in pulse pressure within the carotid arteries and brain. The rate of drop-off of arterial pressure is less than that of the rapid rise during systole, but by 550 msec after the R wave in an individual with a pulse of 75 beats/min, pulse pressure has returned to presystolic levels. It remains at this lower level until the next ventricular contraction.

Comparison of systolic and diastolic gated images obtained in this study demonstrates a definite change in the CFVS. There is a clear increased presence of the degree and size of the CFVS during systole. The change is most marked in the areas of maximal narrowing of the CSF pathways, the aqueduct of Sylvius, and the foramen of Magendie, and is noted to be less prominent in areas of lesser narrowing, such as the foramina of Monro and proximal fourth ventricle. The VFVS seen within the basilar artery and internal cerebral vein also varies with systole and diastole, and is statistically almost as striking as the changes in the CFVS observed within the narrowest portions of the CSF pathways.

The effects of flow on MR images have been described [11-13]. Changes in the MR images secondary to flow have been related to both time-of-flight effects as well as spin-phase shift effects. Signal dropout perceived as the CFVS is probably related to a combination of both these effects. The spin-phase effects occur either in the imaging plane or through the imaging plane and may be perceived on transverse, coronal, or sagittal images. Pulsatile, turbulent flow will result in spin-phase effect change due to spatial variation of the spins. The appearance of the CFVS is probably not related to the phase-encoding gradient because of the strength of that gradient, which for most views is weaker than the read-out gradients. Others have offered more technical explanations of time-of-flight and spin-phase effects [14].

Regardless of the physical etiology of the CFVS, we have demonstrated that there is a clear relation between cardiac systole and the presence and enhancement of the CFVS. We

attribute this to transmission of the systemic artery pulse wave into the cerebral arterial system, with propagation of that pulse wave into the cerebral venous network. The CFVS is a normal physiologic phenomenon that should not be construed as representative of pathology. Its absence, however, may be indicative of an obstructive lesion and in some instances, as a later report will demonstrate, can be pathognomonic of an obstructive lesion within the ventricular system.

REFERENCES

1. Sherman JL, Citrin CM. Magnetic resonance demonstration of normal CSF flow. *AJNR* 1986;7:3-6
2. Citrin CM, Sherman JL. Alteration of the MRI appearance of CSF flow by cardiac gating. Presented at the annual meeting of the American Society of Neuroradiology, San Diego, January 1986
3. Bergstrand G, Berstrom M, Nordell B, et al. Cardiac gated MR imaging of cerebrospinal fluid flow. *J Comput Assist Tomogr* 1985;9:1003-1006
4. Milhorat TH. The third circulation revisited. *J Neurosurg* 1975;42:628-645
5. Cutler RW, Page L, Galicich J, Waters GV. Formation and absorption of cerebrospinal fluid in man. *Brain* 1968;91:707-719
6. Portnoy HD, Chopp M, Branch C, Shannon MB. Cerebrospinal fluid pulse waveform as an indicator of cerebral autoregulation. *J Neurosurg* 1982;56:666-678
7. Marmarou A, Shulman K, Rosende RM. A nonlinear analysis of the cerebrospinal fluid system and intracranial pressure dynamics. *J Neurosurg* 1978;48:332-344
8. Ganong WF. *Review of medical physiology*, Los Altos, CA: Lange Medical, 1973
9. McDonald DA. *Blood flow in arteries*. Baltimore: Williams & Wilkins, 1974
10. Wright S. *Applied physiology*, 11th ed. New York: Oxford University, 1965
11. Bradley WG, Waluch V. Blood flow: magnetic resonance imaging. *Radiology* 1985;154:554-560
12. Bradley WG, Waluch V, Laie K, Fernandez EJ, Spalter C. The appearance of rapidly flowing blood on magnetic resonance images. *AJR* 1984;143:1167-1174
13. Mills CM, Brant-Zawadzki M, Crooks LE, et al. Nuclear magnetic resonance: principles of blood flow imaging. *AJNR* 1983;4:1161-1166, *AJR* 1984;142:165-170
14. Von Schultheis GK, Higgins CB. Blood flow imaging with MR: spin-phase phenomenon. *Radiology* 1985;157:687-695

Embolization of Epistaxis and Juvenile Nasopharyngeal Angiofibromas

Kenneth R. Davis¹

This article reviews arterial embolization of epistaxis and juvenile nasopharyngeal angiofibromas. A protocol for the complete and rapid exploration of epistaxis is suggested that is based upon which arteries providing blood to the nasal fossa may be responsible for the bleeding and the most optimal way for their demonstration and evaluation. The relevant anatomy of the major arteries, their branches, and important anastomoses are described. The goals of embolization are to control severe or recurrent epistaxis, prevent recurrence if possible, and avoid occlusion of any vessels not responsible for the hemorrhage. The most appropriate embolic material is chosen, realizing that recurrence can be caused by the use of resorbable embolic material or by a very proximal or too complete embolization. Embolization may be used for specific causes of epistaxis including idiopathic, hereditary hemorrhagic telangiectasia, hemorrhagic tumors, vascular malformations, trauma, disorders of hemostasis, and postsurgical problems. Juvenile nasopharyngeal angiofibromas are discussed with respect to their clinical presentation, classification, computed tomographic, MR imaging, and angiographic evaluation, treatment, future trends in treatment, and precautions and complications.

The purpose of the review of embolization of epistaxis is to describe a method for the investigation of the patient with epistaxis. This will enable the neuroradiologist to formulate an arterial map of the nasal fossa in order to choose the most appropriate site and material for embolization. The anatomy, goals of embolization, embolic materials, uses in specific diseases, postoperative cases, and overall considerations and precautions are covered.

The purpose of the review of embolization of juvenile nasopharyngeal angiofibromas (JNAs) is to emphasize the usefulness of presurgical embolization and to describe a complete and safe method of investigation. The clinical presentations; classifications; computed tomographic (CT), magnetic resonance imaging (MRI), and angiographic evaluations; treatments; future trends; precautions; and complications are covered.

Epistaxis

Anatomy

Protocols that have been established for the investigation of epistaxis require awareness of the presumed approximate site and etiology of the hemorrhage, which arteries may be responsible for the bleeding, the most convenient means of demonstrating the arteries, and knowledge of the blood supply to the territory in question [1-3]. An arterial map of the nasal fossa for any given case is then generated and evaluated to make the best choice for the most appropriate site and material for embolization [3]. The vessels studied are those that arise from the internal carotid, maxillary, facial, and ascending pharyngeal arteries (Table 1). Even if there has been a previous ligation of the ethmoidal and maxillary arteries, an

This article appears in the September/October 1986 issue of *AJNR* and the January 1987 issue of *AJR*.

Received March 13, 1986; accepted after revision May 20, 1986.

Presented at the annual meeting of the American Society of Neuroradiology, New Orleans, February 1985.

¹ Department of Radiology, Neuroradiology Section, Massachusetts General Hospital, Harvard Medical School, Boston, MA 02114.

AJR 148:209-218, January 1987
0361-803X/87/1481-0209

© American Roentgen Ray Society

TABLE 1: Major Vascular Supply and Branches in Epistaxis Evaluation

Major Artery: Branch	Area of Interest Supplied	Important Anastomotic Branches
Internal carotid:		
Ophthalmic:		
Anterior and posterior ethmoidal	Ethmoid sinuses and adjacent meninges; nasal septum and conchae by anastomoses	Facial, maxillary, transverse facial
Nasoangular, nasoorbital	Malar region around ala of nose via anastomoses	Facial, maxillary, transverse facial
Capsular	Sphenoid sinus	...
Artery of foramen rotundum from inferolateral trunk	Distal maxillary territory	Pathway for revascularization if proximal maxillary occluded
Persistent mandibular (mandibulovidian):		
Mandibular	Nasopharynx	Inferomedial eustachian branch of accessory meningeal, eustachian branch of ascending pharyngeal, pterygovaginal
Vidian	Sphenoid sinus	Petrous internal carotid, sphenopalatine
Maxillary:		
Sphenopalatine:		
Medial nasal	Septum	Ophthalmic anterior and posterior ethmoidal, septal branch of superior labial of facial, alar branch of facial
Lateral nasal	Conchae	...
Pterygovaginal	Eustachian meatus (via pterygovaginal canal)	Inferomedial branch of accessory meningeal, eustachian branch of ascending pharyngeal, mandibular branch of internal carotid
Anterior branch of descending palatine	Posterior septum, conchae, and palate	Ophthalmic posterior and anterior ethmoidal
Infraorbital	Maxillary antrum	Facial, transverse facial, ophthalmic nasoangular, nasoorbital hemodynamic balance
Alveoloantral	Maxillary antrum roof	Same as for infraorbital
Accessory meningeal	Nasopharynx, eustachian meatus	Posterior: mandibular branch of internal carotid, superior pharyngeal eustachian branch of ascending pharyngeal; anteromedial: eustachian branch of ascending pharyngeal; anterior: pterygovaginal; inferior: palatine branch to ascending and descending palatine
Pterygopalatine	Palate, nasopharynx	...
Facial:	Distal maxillary territory	Pathway for revascularization if proximal occlusion of maxillary
Alar	Ala and external nose structures	Maxillary (infraorbital and alveoloantral), transverse facial, ophthalmic nasoangular or nasoorbital hemodynamic balance
Ascending palatine	Soft palate and nasopharynx	Descending palatine
Septal branch of superior labial	Inferior nasal septum	...
Transverse facial	Malar region around ala of the nose	Facial, maxillary (infraorbital and alveoloantral), ophthalmic nasoangular, nasoorbital hemodynamic balance
Ascending pharyngeal:		
Ascending palatine from middle pharyngeal	Soft palate	Descending palatine, accessory meningeal
Superior pharyngeal (eustachian)	Medial and paramedial nasopharynx	Accessory meningeal, mandibular, pterygovaginal, carotid branch to inferolateral trunk and recurrent artery of lacerum from carotid siphon
Ascending palatine:		
May arise from facial, external carotid, accessory meningeal, or middle pharyngeal branch of ascending pharyngeal arteries	Palate	...

evaluation of the collateral supply, which is usually from the ipsilateral side, is required.

Branches of the internal carotid artery. Branches of the internal carotid artery may be divided into two groups depending on whether the epistaxis arises primarily in the sphenoid sinus or in the ethmoid cells. The anterior and posterior ethmoidal arteries arise from the third portion of the intraorbital course of the ophthalmic artery and sometimes as a common trunk with the supraorbital artery. They run medially through the anterior and posterior ethmoid canals to reach the ipsilateral ethmoid cells. Most of their supply is to the sinuses and adjacent meninges, but through anastomoses contribute supply to the conchae and nasal septum. The nasoangular or nasoorbital branches of the ophthalmic artery may provide supply to the malar region around the ala of the nose through anastomoses with the facial, maxillary, and transverse facial arteries [1, 3].

The capsular arteries arise from the horizontal cavernous segment of the internal carotid artery to supply the sphenoid sinus and are not usually seen on angiography.

The artery of the foramen rotundum from the inferolateral trunk of the internal carotid artery is a potential collateral pathway for revascularization of the distal maxillary territory when there has been a proximal maxillary occlusion.

The persistent mandibular (mandibulovidian) artery, when present, arises from the petrosal segment of the internal carotid artery and usually divides into two branches in the foramen lacerum. The horizontal branch passes into the pterygoid canal and anastomoses with the vidian artery (not usually visible at angiography), giving supply to the sphenoid sinus. The inferior branch, or mandibular artery, anastomoses with the inferomedial eustachian branch of the accessory meningeal, the eustachian branch of the ascending pharyngeal, and the pterygovaginal arteries to provide nasopharyngeal supply [1, 3].

The carotid siphon and cavernous sinus are next to the sphenoid sinus, and massive hemorrhage can result if a communication is created by trauma or rupture of an aneurysm [3].

Branches of the maxillary artery. The maxillary artery supplies the conchae and nasal septum by the medial and lateral nasal branches from the sphenopalatine segment, whereas an anterior branch from the descending palatine artery may also supply the posterior portion of the septum and conchae. The supply to the maxillary sinus is from the alveoloantral and infraorbital artery branches [1-5], and the pterygovaginal and accessory meningeal branches provide supply to the eustachian meatus, nasopharynx, and soft palate.

Branches of the facial artery. The facial artery supplies the ala and external nose. It has a more important role as a pathway for recanalization of an incompletely or completely occluded maxillary artery than as a primary source of hemorrhage and is often responsible for recurrent epistaxis since it carries blood flow to the distal portion of the maxillary artery. Therefore, postembolization studies should be made by injection of the ipsilateral facial artery rather than of the distal external carotid artery [3]. The alar branch supplies the ala and structures of the external nose, and the ascending

palatine branch may originate from the proximal facial artery and provides supply to the palate. The lowest part of the nasal septum is supplied by a branch of the superior labial artery, which is not ordinarily visible at angiography and has a questionable role in the production of epistaxis [3]. There is a hemodynamic balance between the facial artery and three other systems in the malar region and around the ala of the nose, which includes the infraorbital and alveoloantral branches of the maxillary artery, the transverse facial artery, and the nasoangular or nasoorbital branch of the ophthalmic artery [1, 3].

Depending on this balance, the supply of the nasal ala may come from the facial, ophthalmic, or transverse facial/internal maxillary systems. It is only when the malar region and ala are predominantly supplied by the facial artery that embolization of this vessel is required, either for treatment of an anterior bleeding point or to prevent early revascularization of a more posterior site that is fed by sphenopalatine artery branches [3].

Branches of the ascending pharyngeal artery. The ascending pharyngeal artery anterior branch gives origin to superior, middle, and inferior pharyngeal branches that supply the medial and paramedial nasopharynx. The middle pharyngeal branch may supply the soft palate by giving origin to the ascending palatine artery, which has anastomoses with the descending palatine and accessory meningeal arteries.

The superior pharyngeal (or eustachian) branch reaches the foramen of the eustachian tube and anastomoses with the corresponding branches of the accessory meningeal and pterygovaginal arteries, as well as with the mandibular artery vestige from the internal carotid artery, when present. The carotid branch originates from the superior pharyngeal branch and anastomoses with the inferolateral trunk and the recurrent artery of the foramen lacerum from the carotid siphon [1, 3]. The vessels of the ascending pharyngeal system usually only require embolization for epistaxis caused by juvenile nasopharyngeal angiofibromas or angiomatosis, as in Rendu-Osler disease [1, 2, 3, 5].

Goals of Embolization

The goal of embolization is palliative [3, 6-11] for control of severe or recurrent epistaxis, whether idiopathic or caused by hypertension, angiomatous diseases, tumors, vascular malformations, trauma, disorders of hemostasis, or postsurgical problems, when the epistaxis is resistant to the usual treatment of packing and/or surgery. Embolization may also be used along with other techniques to reduce blood supply to hemorrhagic tumors or vascular malformations. As an emergency procedure, it can be lifesaving in cases of catastrophic bleeding [3].

Epistaxis can be classified as arterial, venous, or arteriolized venous depending on the source of bleeding. Venous bleeding is usually well controlled by manual compression or simple anterior nasal packing; venous epistaxis sometimes stops spontaneously. Arterial or arteriolized venous hemorrhages are life-threatening unless immediate control is accomplished. This type of bleeding may occur from the venous

drainage of arteriovenous malformations or arteriovenous fistulas, including carotid cavernous fistulas. The primary treatment should be nasal packing, anterior and/or posterior. If the bleeding persists or recurs, then either ligation of the maxillary and possibly the ethmoidal arteries or angiography is indicated. If angiography is chosen, then embolization may be performed at that time. Alternatively, after diagnostic angiography, the maxillary and possibly the ethmoidal arteries may be ligated. If embolization is chosen and fails to control the epistaxis, operative ligation of the maxillary and possibly the ethmoidal arteries may then be performed (Choi IS, personal communication).

Techniques

Nonresorbable embolic materials such as polyvinyl alcohol (PVA) foam or dura mater (available in Europe) should result in fewer recurrences [2, 3, 6]. The endovascular occlusion, however, must be regarded as a potentially repeatable procedure; therefore, it should be located as distal as possible so as not to compromise subsequent treatment [3]. Recurrence from revascularization is normally from vessels ipsilateral to the midline, particularly if the embolization was distal enough to occlude the territory in question [3].

The embolization technique uses superselective catheterization with 4 French and sometimes 5 French catheters. Coaxial use of an open-ended guidewire or a 2 or 3 French inner catheter may be necessary to insert through the 5 French catheter in order to enter a small vessel, such as a branch of the ascending pharyngeal artery. The small lumen, however, only permits passage of small particles or liquid embolic agents. A 4 French catheter will enter small branches that are not possible to catheterize with the 5 French catheter and permits injection of larger particles than through the open-ended guidewire. The internal carotid, maxillary, and facial arteries of the presumed noninvolved side are usually injected first (in that order) so that most of the diagnostic evaluation will be completed before the main feeding vessels to be embolized are entered. The internal carotid artery is studied best on the lateral view and the distal maxillary artery on Water's view—and on the lateral view if the catheter is placed proximal to the origin of the maxillary artery in order to see the transverse facial artery and to assess the facial artery (and therefore possibly obviate injection of the facial artery). The facial artery is then studied selectively, and the lateral view is optimal to examine the supply of this vessel. The side of the hemorrhage is studied next. The internal carotid artery is examined first and evaluated best on the lateral view. The maxillary artery is then studied, and a decision is made as to whether embolization is indicated. A piece of Gelfoam may be used to temporarily occlude the superficial temporal artery if embolization is performed from proximal to the origin of the maxillary artery. The facial artery is then studied after embolization of the maxillary artery to determine whether the embolization was distal and effective, as well as to evaluate for ascending palatine artery supply. Examination of the ascending pharyngeal artery may be required if a posterior source of bleeding is suspected and to check for residual

abnormal supply from the ascending or descending palatine, accessory meningeal, pterygovaginal, or mandibular artery.

Embolic Materials

Different embolic agents should be chosen according to the etiology of an individual case. Although Gelfoam particles, which are resorbable, and PVA particles, which are not resorbable, are both commonly used in the United States for endovascular occlusion of idiopathic epistaxis, nonresorbable embolic materials such as PVA should reduce recurrence rates. Some recanalization, however, can be seen several months after PVA embolization. PVA particles have been available in various size ranges including 149–250, 250–590, and 590–1000 μm . They are prepared by washing them with sterile distilled water or saline in a blender to eliminate clumped particles. The fluid is then decanted to remove the formalin. The blender may produce a larger percentage of smaller particles than planned, so extra caution must be exercised during embolization. Contrast material is added to the PVA to provide opacification. Albumin may be mixed with the PVA to prevent clumping and achieve a more distal embolization. Gelfoam powder (40–60 μm) has also been combined with the PVA. Small Gelfoam particles, which are cut from Gelfoam strips and are considerably larger than the Gelfoam powder, generally provide a 2–4 day period of reliable, temporary occlusion. Strips of Gelfoam are usually adequate to stop posttraumatic hemorrhage or bleeding caused by a necrotic tumor from the maxillary artery territory. This permits sparing of the parent vessel and allows for the possibility of more definitive subsequent embolization therapy, if necessary. The use of a fluid embolic agent such as isobutyl-2-cyanoacrylate (IBCA) or alcohol into these arteries is not usually indicated because of the risk of complications from possible embolization of dangerous external carotid to ophthalmic and intracranial anastomoses as well as possible embolization of dangerous external carotid supply to cranial nerves [3]. Very small particles should also be used very cautiously where there are such dangerous communications. Arteriovenous fistulas, however, are often treated best by IBCA or detachable balloons, and the best form of treatment for a false aneurysm may be the detachable balloon. The choice of embolic material, therefore, depends on the type of primary lesion, the severity and site of hemorrhage, and the presence of dangerous anastomoses [6].

Uses for Specific Causes

The causes of epistaxis in which embolization can be considered include idiopathic (spontaneous or hypertensive); hereditary hemorrhagic telangiectasia (HHT) [12–16]; hemorrhagic tumors of the benign type, which include juvenile angiofibroma, hemangioma, and angiomatous polyp, or of the malignant type, which includes ulcerating primary carcinoma (Fig. 1), and hypervascular metastatic tumors such as hypernephromas and melanomas; arteriovenous malformations; trauma with rupture of an artery by direct injury or from an incomplete tear and formation of a pseudoaneurysm; disor-

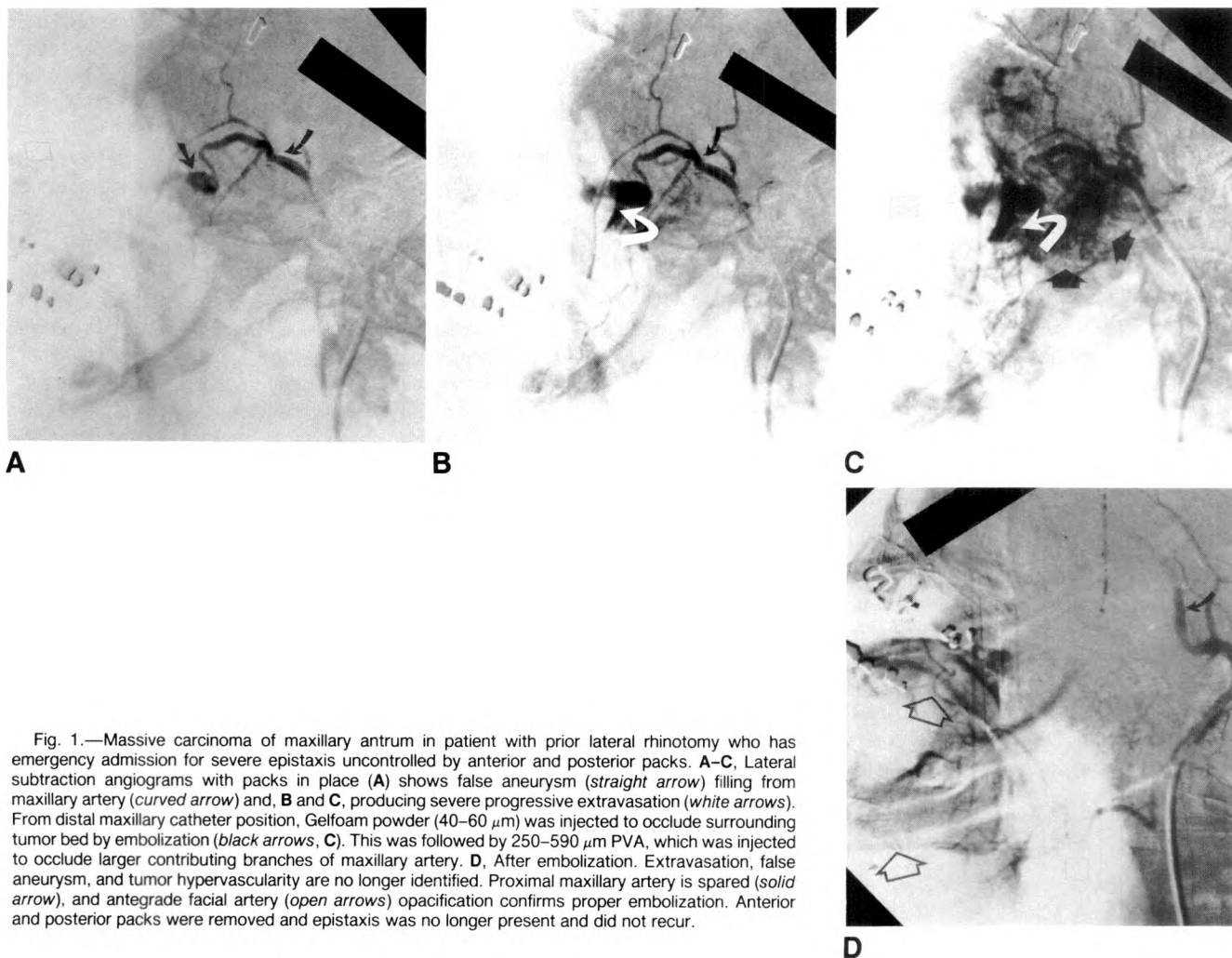


Fig. 1.—Massive carcinoma of maxillary antrum in patient with prior lateral rhinotomy who has emergency admission for severe epistaxis uncontrolled by anterior and posterior packs. **A–C**, Lateral subtraction angiograms with packs in place (**A**) shows false aneurysm (straight arrow) filling from maxillary artery (curved arrow) and, **B** and **C**, producing severe progressive extravasation (white arrows). From distal maxillary catheter position, Gelfoam powder (40–60 μ m) was injected to occlude surrounding tumor bed by embolization (black arrows, **C**). This was followed by 250–590 μ m PVA, which was injected to occlude larger contributing branches of maxillary artery. **D**, After embolization. Extravasation, false aneurysm, and tumor hypervascularity are no longer identified. Proximal maxillary artery is spared (solid arrow), and antegrade facial artery (open arrows) opacification confirms proper embolization. Anterior and posterior packs were removed and epistaxis was no longer present and did not recur.

ders of hemostasis; and postsurgical problems from instrumentation or poor clip position.

Idiopathic. Angiographic demonstration of the bleeding point is particularly rare in the idiopathic, spontaneous, or hypertensive type of epistaxis, and, therefore, the referring clinician should indicate the approximate presumed site of bleeding. It may be dangerous to remove the nasal packing for the angiographic injection in order to attempt to demonstrate the bleeding point since it may be difficult to immediately replace it while the patient is on the angiographic table. It is, however, reasonable to remove the packing upon completion of the embolization to check the effectiveness of the occlusion. Patients with severe idiopathic (arteriosclerotic, hypertensive) epistaxis can be treated very effectively with embolization of PVA particles when there has been recurrent bleeding after anterior and/or posterior nasal packing.

HTT. Global or selective injection may not show the angiomatous tufts of HHT; however, the maxillary artery is usually the source of the epistaxis. Bilateral facial arterial supply may

also be present in certain cases. When estrogen treatment has failed, palliative endovascular occlusive treatment is necessary to control bleeding. Embolization may be performed, first with small PVA particles followed by larger particles [12, 16]. Only the distal symptomatic area should be embolized, and the proximal segment of the main feeder should be left open for possible reembolization.

Hemorrhagic tumors are discussed under Embolic Materials and Juvenile Nasopharyngeal Angiofibromas and are illustrated in Figure 1.

Vascular malformations. Epistaxis from extensive angiomatosis should probably be treated, when feasible, by operative ligation of the feeding ethmoidal branches of the ophthalmic artery prior to embolization of the branches of the external carotid artery, since external carotid embolization may only increase the internal carotid supply [6]. A considerable part of the blood supply in Wyburn-Mason syndrome, however, comes from the ethmoidal arteries, which are often inaccessible to both embolization and clipping and represent

a continuous source of danger to the patient. Embolization should always be only palliative. In these extensive nonoperative lesions, the main vessels should be left open for possible future embolizations, since subsequent and possibly emergency embolizations may be the only means to ensure survival of these patients [6]. Bilateral angiographic evaluation of a vascular malformation is performed even though there may be clinical evidence of a unilateral lesion [1, 3], because vascular malformations of the nasal fold and alar area are sometimes supplied by contralateral arteries.

Trauma. Traumatic epistaxis may occur in association with facial fractures and penetrating injuries as well as with carotid cavernous fistulas. Hemorrhage from a traumatic aneurysm in the region of the cavernous sinus or carotid siphon may occur in the acute stages of injury. Treatment of a traumatic aneurysm of the cavernous carotid performed to prevent a fatal hemorrhage into the nasopharynx (Fig. 2) is an emergency.

Balloon occlusion of the internal carotid artery is performed in acute traumatic injuries, whereas in older traumatic aneurysms fibrotic changes develop in the wall. This permits sparing occlusion of the internal carotid artery since the balloon may be detached within the aneurysm if the neck of the aneurysm is not very wide.

Postoperative cases. With poor surgical clip position, the maxillary artery is sometimes found to be patent at the site of presumed adequate ligation, and embolization may then be accomplished without difficulty. In other cases after ligation, even though direct internal maxillary artery puncture distal to the surgical ligature may be possible [3], an under-

standing of the collateral supply to the maxillary artery distal to the occlusion may permit these channels to be used effectively for embolization via femoral artery catheterization.

Considerations and Precautions

Occlusion of vessels not responsible for the hemorrhage is to be avoided. Recurrence is prevented by avoiding use of resorbable material, proximal embolization, and excessive embolization. Since embolization for epistaxis is palliative, proper analysis of the angiographic findings and prediction of the collateral circulation are necessary [1-3, 5]. Proximal maxillary artery occlusion should be avoided, since revascularization by other vessels such as the facial, ascending palatine, and foramen rotundum arteries may occur. In spontaneous epistaxis only the vessels responsible for bleeding are embolized to prevent local ischemia and further bleeding. Epistaxis caused by certain blood disorders may require embolization; however, if a low platelet count is present, it must be corrected with prior platelet transfusion to avoid a problem at the puncture site during and on completion of the procedure [3].

Juvenile Nasopharyngeal Angiofibromas (JNAs)

Clinical Presentation

Incidence. JNAs constitute 0.5% of head and neck tumors and are found almost exclusively in adolescent males [17-19]. Only five cases have been reported in females, and

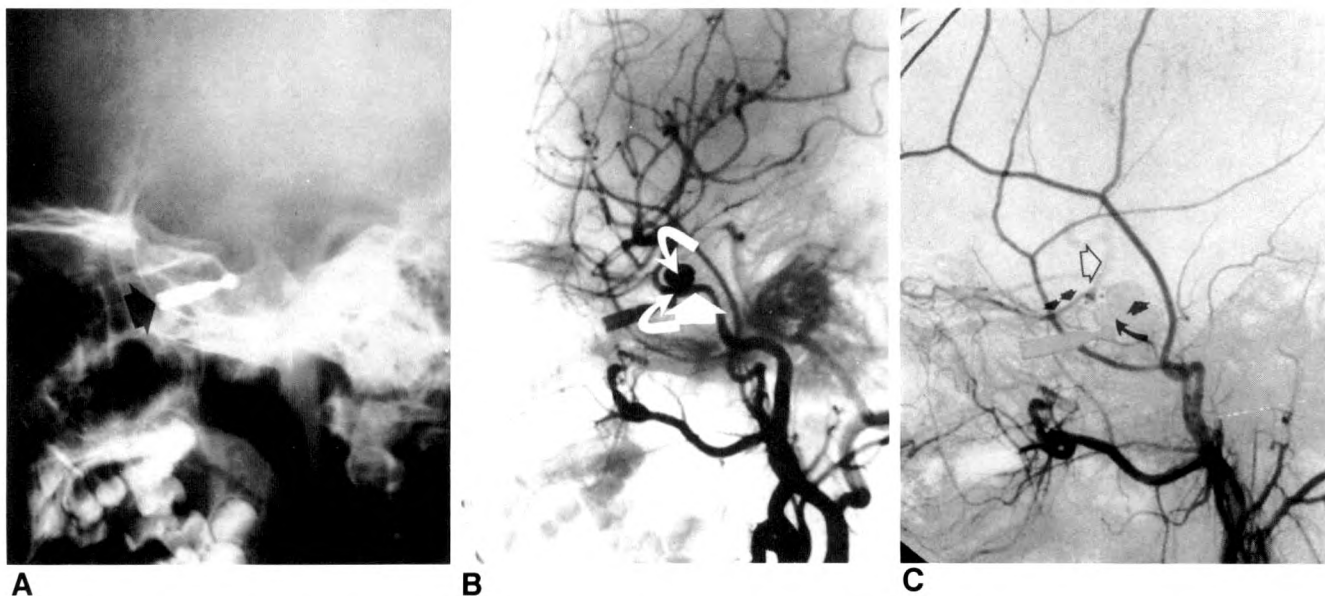


Fig. 2.—9-year-old boy just after puncture by umbrella tip through right orbit. **A**, Lateral skull film. Retained umbrella tip (arrow). **B**, Right carotid angiogram. False aneurysm (curved arrows) from cavernous internal carotid artery with narrowing and elevation of internal carotid (straight arrow). **C**, To prevent severe epistaxis into nasopharynx before or after removing umbrella tip, internal carotid artery was occluded by balloons. First balloon was detached within aneurysm (single solid straight arrow) to occupy some of dead space in

order to permit tip of second balloon (curved arrow) to pass distal to neck of false aneurysm near ophthalmic artery origin. Second balloon was inflated across cavernous carotid artery and detached. This post-balloon detachment film shows ophthalmic artery (double arrows) filling retrograde to supra-ophthalmic internal carotid artery (open arrow). Umbrella tip was removed without any hemorrhagic difficulty related to internal carotid artery.

therefore chromosome analysis might be considered in the evaluation of such patients [19].

Symptoms and signs. The symptoms and signs are related to extension of the tumor into the nose, orbit, and skull base [20–22]. There is usually nasal obstruction and/or epistaxis. Other findings include nasal discharge, facial deformity, exophthalmos, anosmia, hearing loss, and a grayish red-colored mass in the nose or nasopharynx. Recurrent epistaxis has been found to result from vascular fragility and a rise in circulating estrogens. Endogenous estrogens reduce smooth muscle and elastic fibers in the vessel wall, whereas exogenous estrogens have an opposite effect [19].

Classification

The JNA is a benign, highly vascular, fibromatous or angiofibromatous hamartoma that is locally invasive, arises from the nasopharynx, and has a marked tendency to recur [13, 23]. Prepubertal adolescent tumors are comparatively less aggressive than are young adult tumors. Several surgical classifications have been proposed to stage the various patterns of tumor extension and predict the surgical resectability. Other incomplete therapeutic approaches based on morphologic classifications are not very useful since the therapeutic goal for JNAs should be complete and permanent eradication of the tumor.

Histology

The JNA has a fibrovascular stroma with the myofibroblast as the principal cell [19]. The myofibroblast interferes with synthesis of collagen fibers and elastin and can transform itself into smooth muscle cells. The stroma is invaded by fine vessels producing pseudolymphatic endothelialized spaces. The general appearance varies from cavernouslike with fibrovascular stroma to being cellular or purely fibrous. Fibrous change reduces the incidence of local invasion and the frequency of epistaxis.

CT, MRI, and Angiography

Axial and coronal CT depicts the probable nature and anatomic extent of the lesion [24, 25]. Findings may include nasopharyngeal mass, anterior bowing of the posterior wall of the maxillary antrum with a mass in the pterygopalatine fossa, opacity of one or more of the paranasal sinuses, erosion of the sphenoid bone with mass in the sinus, erosion of the hard palate, erosion of the medial wall of the maxillary sinus, deviation of the nasal septum, and intracranial extension. CT provides better demonstration of bone involvement than does MRI, but MRI has the advantage of being able to differentiate between sinus extension of tumor and sinus obstructive changes. MRI usually produces a brighter signal on T2-weighted images of the mucosal thickening and fluid within the sinus as compared with tumor. Intracranial and extracranial extension boundaries are also well shown on MRI using transverse, coronal, and sagittal planes with T1- and T2-weighted pulse sequences. Biopsy is hazardous because

of the danger of massive hemorrhage. Fortunately, the characteristic CT and angiographic appearances obviate biopsies.

Combined or separate diagnostic and therapeutic sessions may be undertaken. A 4- or 5-French catheter tip is used, and an excellent fluoroscopic image, digital and conventional subtraction, and direct magnification should be available. A characteristic reticulated pattern is usually seen in the early arterial phase (Fig. 3), with a dense, homogeneous blush persisting into the venous phase [5, 19, 26–28]. The presence of early draining veins is rare. A similar angiographic appearance, however, has been reported with fibrous dysplasia and with lymphoepithelioma, which produces a dense blush as well as occasional anterior bowing of the posterior wall of the antrum [29–31].

An angiographic protocol has been developed to show the blood supply of the lesion and anatomic variations, to confirm the diagnosis when clinical findings and CT are in doubt, and to permit safe embolization [1, 2]. This involves examination of the ipsilateral internal carotid, maxillary, ascending pharyngeal, and ascending palatine arteries in that order on the lateral view. The internal carotid injection will show whether or not any abnormal vascularity indicates invasion of the base of the skull. Embolizing the maxillary artery first affords the best chance of devascularizing the tumor. Embolization of the pharyngeal branch of the accessory meningeal artery may be accomplished by selective catheterization of the accessory meningeal artery or with a proximal maxillary artery catheter position. Residual vascularity in this territory may be reached indirectly by the eustachian branch of the ascending pharyngeal artery. A facial artery injection is finally used to opacify the collateral to the maxillary artery as a check for completeness of maxillary embolization. If the JNA reaches or crosses the midline, the contralateral internal carotid artery is filmed on an anteroposterior (AP) view during temporary compression of the ipsilateral internal carotid artery. AP views are best for examining the contralateral distal maxillary and ascending pharyngeal arteries, whereas lateral images are optimal for the ascending palatine artery. The use of this sequence of branches for injection and embolization permits assessment of the branches that have just been embolized (Fig. 3). Superselective catheterization of vessels should be in the correct sequence with use of the optimal projection to prevent complications. A tumor stain seen on the internal carotid injection may correspond to intracranial or intraorbital extension but might also be due to transcranial supply and opacification of extracranial vascular territories of an exocranial lesion as an indirect rather than true tumor supply [19, 32–34]. There then may be no residual internal carotid artery opacification of the lesion after distal external carotid branch embolization. However, if the occlusion after embolization is too proximal (similar to surgical ligation), then the internal carotid artery–external carotid branch anastomotic channels may become true arterial feeders. Then, embolization of the ascending pharyngeal or ascending palatine branches becomes more critical, but may not reach the lesion [2, 19].

Extension of the lesion may be intrasphenoidal with capsular branches from both internal carotid arteries, intraethmoidal on each side with posterior ethmoidal artery supply from the ophthalmic arteries, intraorbital with supply from the

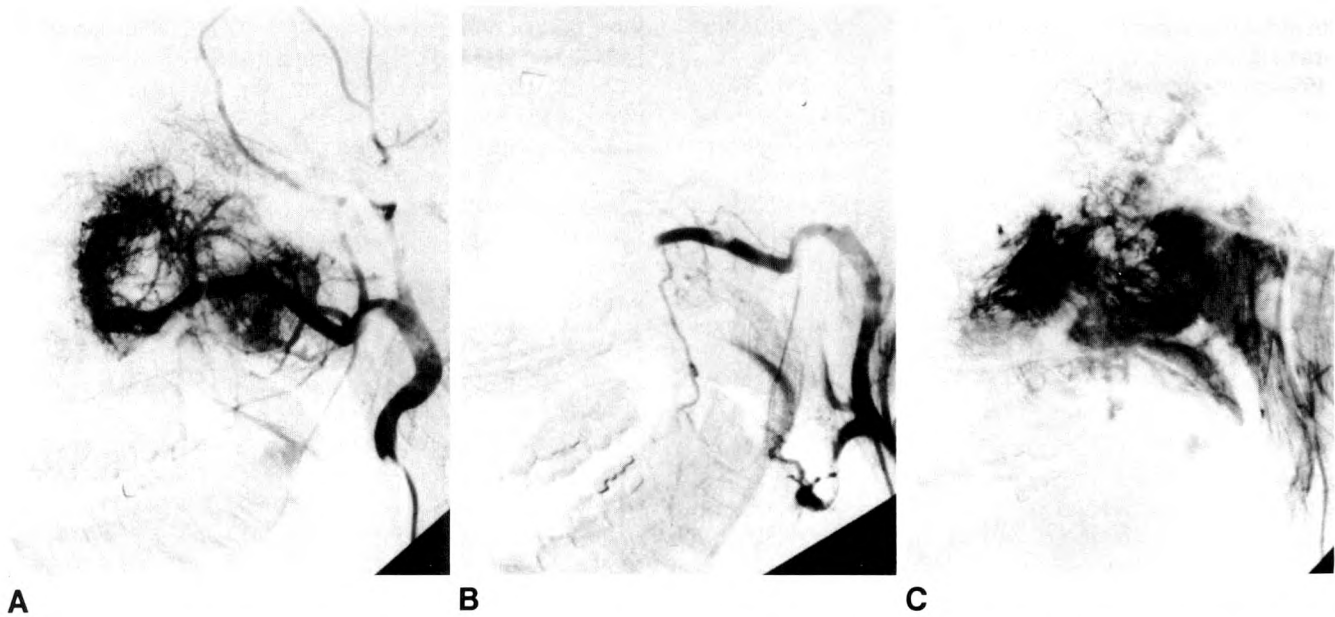


Fig. 3.—**A**, Early arterial phase of maxillary angiogram, lateral view. Reticulated hypervascular stain without early draining veins consistent with JNA. **B**, After maxillary PVA embolization. Minimal residual hypervascularity. **C**, As-

cending pharyngeal angiogram after maxillary embolization reveals marked hypervascularity in ascending pharyngeal and collateral to some of the incompletely embolized distal maxillary artery.



Fig. 4.—Left internal carotid angiogram after ascending pharyngeal artery eustachian branch embolization. Persistent mandibular (mandibulovidian) artery (arrow) supply to tumor is seen.

inferior muscular branch of the ipsilateral ophthalmic artery, or intracavernous with vascular supply shown by internal carotid, as well as middle and accessory meningeal, distal maxillary, and ascending pharyngeal artery injections [1, 19, 32, 34, 35].

The persistent mandibular (mandibulovidian) artery may arise from the petrous internal carotid artery (Fig. 4), and the

surgeon should be apprised of this so that it may be ligated at the time of operative intervention [19].

Treatment

Various types of treatment have been reported [36, 37]. Surgery alone has a 25%–60% recurrence rate [19]. Radiation alone has a 25% recurrence rate and is rarely indicated because of the possibility of long-term induction of sarcomatous changes [19, 36]. Cryotherapy, electrocoagulation, hormonal therapy to reduce the size and vascularity, or injection of sclerosing agents, respectively, have also been used. Observation in the hope of unusual spontaneous regression has also been tried [19].

Surgical removal is the best and most widely accepted mode of therapy, but resection alone may be limited by significant intraoperative hemorrhage and tumor size. After embolization for devascularization, total excision may be possible with insignificant blood loss.

A therapeutic protocol [2, 19] has been designed, the objectives of which include preoperative identification of possible sources of bleeding and preoperative devascularization by embolization. Since intraoperative hemorrhage may not be controlled by packing, embolization may prevent a fatal outcome. A drier surgical field may also permit a more complete removal of the lesion, and embolization probably also reduces the incidence of recurrence regardless of the type of surgery. Because of the underlying hormonal abnormality, embolization is only effective locally, and often the tumor has extended beyond the apparent boundaries. Therefore, an intentional, more extensive embolization beyond the boundaries of the vascularity seen on the angiogram may be of value.

Superselective distal catheterization is performed, and if this is not possible, a proximal properly directed flow-con-

trolled particle injection is performed [2, 19]. A Gelfoam plug may be used to protect dangerous anastomotic vessels [2, 19]. The presence of dangerous anatomically located vessels along the course of the vessels to be embolized does not contraindicate embolization, but argues for the use of certain types of embolic material such as PVA or Gelfoam particles with a larger diameter than the lumen of the dangerous communicating vessel [19]. PVA and Gelfoam particulate agents are commonly used in the United States, whereas dura has been commonly used in Europe. The goal of post-embolization tumor necrosis may be achieved by using particles [19]. Surgery is performed 2–5 days after embolization.

Liquid embolization with IBCA is dangerous because of the nearby skull base branches to the cranial nerves and external-to-internal carotid artery anastomoses. It would only be indicated if a very aggressive embolization approach is necessary for invasion into the base of the skull. This would follow placement of a permanent balloon occlusion distal to the inferior lateral trunk of the internal carotid artery (after good circle of Willis collateral has been demonstrated) with slow IBCA injection into the internal carotid artery feeders proximal to the distal balloon occlusion. Flow of the glue can reach the tumor with sparing of the nerves (Berenstein A, personal communication). There is no role for the use of this agent in the external carotid artery branches for these tumors.

Future Trends

An alternative method of treatment has been used where, after a radial arterial line has been inserted to monitor the blood pressure and with the patient under general anesthesia, nitroprusside is used to produce vasodilatation and reduce the effect of any minimal vasospasm during a reduction in blood pressure (Moret J, Picard L, personal communication). The internal carotid artery is examined first, and then the catheter tip is placed just below the internal maxillary–superficial temporal artery junction so that flow is not disturbed. Embolization is made from this point using flow control, and steroids may be used for any later discomfort caused by particles in the superficial temporal artery area. This is followed by catheter placement in the proximal ascending pharyngeal artery and flow-controlled embolization. About 100 μ m dura particles are used, and no cranial nerve palsies or ocular complications have occurred thus far.

Estrogen spheres may be available for embolization procedures within the next few years (Moret J, Picard L, personal communication). Estrogens may have an effect on the bleeding complications of these tumors. However, the problems produced by the required dose for a significant clinical effect are important in this population of adolescent males (Lasjaunias P, personal communication).

Dextran microspheres have been experimentally used in animals and may prove useful in humans. Particles of 50–150 μ m or 100–300 μ m can be injected through a 2-French calibrated-leak balloon catheter into the feeding vessel. These are suspended in contrast material and are more permanent and flow is better controlled than with PVA particles. However, the dextran microspheres tend to reflux more easily at

the end of the procedure and, therefore, monitoring is required [38].

Precautions and Complications

Complications of ischemic cranial nerve palsies from very small particles and intracranial or ocular embolization via external carotid-to-internal carotid or ophthalmic (rarely vertebral artery from this territory) artery anastomoses may often be avoided by identifying the largest potentially dangerous vessel and placing the catheter distal to its orifice. When this is not possible, particles larger than the lumen of the dangerous vessel can be used, as well as careful flow control techniques. If the dangerous vessel is too large, occlusion of its origin by a large piece of Gelfoam may permit small particles to be injected from a more proximal position of the catheter tip.

The vascular supply to the transcranial nerves is mainly from three branches of the maxillary artery [1, 2, 5, 19, 33, 34]. These include the cavernous branch of the middle meningeal, which supplies the gasserian ganglion; the intracranial branch of the middle meningeal artery or accessory meningeal artery, which supplies the third division of the fifth nerve; and the artery of the foramen rotundum, which supplies the second division of the fifth nerve. Anatomic variants of the artery of the foramen rotundum may result in supply to the third, fourth, first division of the fifth, and sixth nerves. Other vessels that may be at possible risk include the petrosal branch of the middle meningeal artery supplying the intrapetrous segment of the seventh nerve, the recurrent meningeal or meningoophthalmic branch connecting the intraorbital ophthalmic artery with the middle meningeal artery through the superior orbital fissure, the meningolacrimal artery communication with the middle meningeal artery, and the accessory meningeal artery, which may supply the petrosal branch territory of the middle meningeal artery to the seventh nerve. To assess the middle meningeal artery supply to the seventh nerve, a lidocaine test has been suggested [39]. Even though the vascular territories are not terminal, capillary occlusion may nonetheless produce ischemic palsy. In addition, edema of the nerve within a constrictive bone foramen may result in a palsy. Important branches of the ascending pharyngeal include the neuromeningeal branch, which supplies the ninth, tenth, eleventh, twelfth, and part of the sixth cranial nerves, and the lacerum branch, which communicates with the internal carotid artery.

Minor complications such as fever and local pain may occur 12–24 hr after embolization and are treated with steroids. Transient bradycardia may occur during the injection of the maxillary artery or rarely during injection of the ascending pharyngeal artery. This is treated with intravenous atropine. Pain in the upper and/or lower teeth and analgesia without anesthesia in the skin around the mouth and distribution of the second division of the fifth nerve may be found up to 1 week after the embolization.

Major complications usually result from the use of improper embolic material, reflux of embolic material (secondary to vascular spasm, insufficient selective catheterization, or rapid injection of too many particles), or failure to recognize poten-

tially dangerous external carotid-to-internal carotid artery anastomoses because of incomplete angiographic delineation or inadequate anatomic analysis. Safe and successful embolization depends on detailed demonstration and analysis of vascular supply to the lesion and the surrounding area, knowledge of the vascular supply to the transcranial nerves, knowledge of the various external carotid-internal carotid artery anastomoses, and meticulous technique [40-42].

ACKNOWLEDGMENTS

I thank Drs. Berenstein, Lasjaunias, Moret, Picard, Kerber, and Debrun for substantive contributions in this area, personal assistance, and general support.

REFERENCES

- Lasjaunias PL, Berenstein A. *Craniofacial and upper cervical arteries. Functional, clinical and angiographic aspects*. Baltimore: Williams & Wilkins, 1981
- Lasjaunias PL, Berenstein A. *Craniofacial and upper cervical arteries. Collateral circulation and angiographic protocols*. Baltimore: Williams & Wilkins, 1983
- Lasjaunias P, Marsot-Dupuch K, Doyon D. The radio-anatomical basis of arterial embolization for epistaxis. *J Neuroradiol* 1979;6:45-53
- Djindjian R, Merland JJ. *Superselective arteriography of the external carotid artery*. New York: Springer-Verlag, 1978
- Lasjaunias P, Moret J. The superselective arteriography of the cavum. *J Neuroradiol* 1978;5:103-112
- Riche MC, Chiras J, Melki JP, Merland JJ. The role of embolization in the treatment of severe epistaxis. *J Neuroradiol* 1979;6:207-220
- Coel MN, Janon EA. Angiography in patients with intractable epistaxis. *AJR* 1972;116:37-40
- Sokoloff J, Wickbom I, McDonald D, Brahme F, Goergen TG, Goldberger LE. Therapeutic percutaneous embolization in intractable epistaxis. *Radiology* 1974;111:285-287
- Duggan CA, Brylski JR. Angiographic demonstration of bleeding and intractable traumatic epistaxis. *Radiology* 1970;97:605-606
- Merland JJ, Djindjian R. Embolization of angiomas of the external carotid territory. Techniques and results. *J Neuroradiol* 1975;2:201-232
- Pletcher JD, Newton TH, Dedo Y, Norman D. Preoperative embolization of juvenile angiofibromas of the nasopharynx. *Ann Otol* 1975;84:740-746
- Merland JJ, Djindjian R. Cerebral manifestations of Rendu-Osler disease. *J Neuroradiol* 1974;1:257-285
- Roman G, Fisher M, Perl DP, Poser CM. Neurological manifestations of hereditary hemorrhagic telangiectasia. (Rendu-Osler-Weber disease): report of 2 cases and review of the literature. *Ann Neurol* 1978;4:130-144
- Sobel D, Norman D. CNS manifestations of hereditary hemorrhagic telangiectasia. *AJNR* 1984;5:569-573
- Hieshima GB, Cahan LD, Berlin MS, Pribram HW. Calvarial, orbital and dural vascular anomalies in hereditary hemorrhagic telangiectasia. *Surg Neurol* 1977;8:263-267
- Kendall BE, Joyner M, Grant H. Hereditary haemorrhagic telangiectasia: microembolization in the management of epistaxis. *Clin Otolaryngol* 1977;2:249-261
- Christiansen TA, Duvall AJ III, Rosenberg Z, et al. Juvenile nasopharyngeal angiofibroma. *Trans Am Acad Ophth Otolaryngol* 1974;78:140-147
- Jereb B, Anggard A, Baryd I. Juvenile nasopharyngeal angiofibroma: a clinical study of 69 cases. *Acta Radiol [Ther]* (Stockh) 1970;9:320-310
- Lasjaunias P, Picard L, Manelfe C, Moret J, Doyon D. Angiofibroma of the nasopharynx. *J Neuroradiol* 1980;7:73-95
- Sinaha PP, Aziz HI. Juvenile nasopharyngeal angiofibroma. *Radiology* 1978;127:501-505
- Bahtia ML, Mishra SC. Intracranial extension of juvenile angiofibroma of the nasopharynx. *J Laryngol Otol* 1967;81:1395-1402
- Changani DL, Sharma SD, Popli SP. Intracranial extensions in nasopharyngeal fibroma. *J Laryngol Otol* 1969;82:1137-1144
- Bryan RN, Sessions RB, Horowitz BL. Radiographic management of juvenile angiofibromas. *AJNR* 1981;2:157-166
- Duckert LG, Carley RB, Hilger JA. Computerized axial tomography in the preoperative evaluation of an angiofibroma. *Laryngoscope* 1978;88:613-618
- Weinstein MA, Levine H, Duchesneau PM, Tucker H. Diagnosis of juvenile angiofibroma by computed tomography. *Radiology* 1978;126:703-705
- Allen WE, Kier EL, Rothman SLG. The maxillary artery: normal arteriographic anatomy. *AJR* 1973;118:517-527
- Hilal SK, Michelsen JW. Therapeutic percutaneous embolization for extra-axial vascular lesions of the head, neck and spine. *J Neurosurg* 1975;43:275-287
- Rosen L, Hanafee W, Nahum A. Nasopharyngeal angiofibroma, and angiographic evaluation. *Radiology* 1966;86:103-107
- Schaffer K, Haughton V, Farley G, Friedman J. Pitfalls in the radiographic diagnosis of angiofibroma. *Radiology* 1978;127:425-428
- Wilson GH, Hanafee WN. Angiographic findings in 16 patients with juvenile nasopharyngeal angiofibroma. *Radiology* 1969;92:279-284
- Wilson GH, Hanafee WN. Angiographic findings in juvenile nasopharyngeal hemangiofibroma. *Clin Radiol* 1970;21:279-284
- Lasjaunias P, Moret J, Mink J. The anatomy of the inferolateral trunk (ILT) of the internal carotid artery. *Neuroradiology* 1977;13:215-220
- Lasjaunias P, Moret J. Normal and non-pathological variations in the angiographic aspects of the arteries of the middle ear. *Neuroradiology* 1978;15:213-219
- Lasjaunias P, Doyon D. The ascending pharyngeal artery and the blood supply of the lower cranial nerves. *J Neuroradiol* 1978;5:287-301
- Lasjaunias P. Nasopharyngeal angiofibromas: hazards of embolization. *Radiology* 1980;136:119-123
- Kadin MR, Thompson RW, Bentson JR, Ward PH, Calcatera TC. Angiographic evaluation of the regression of an extensive juvenile nasopharyngeal angiofibroma after radiation therapy: a case report with therapeutic implications. *Br J Radiol* 1974;47:902-905
- Katsiotis P, Tzortzis G, Karaminis CH. Transcatheter arterial embolization in nasopharyngeal angiofibroma. *Acta Radiol [Diagn]* (Stockh) 1979;20:fasc 3
- Dion J, Rankin R, Vinuela F, Fox AJ. Radiopathological correlation of experimental canine renal dextran microsphere embolization. Presented at the annual meeting of the American Society of Neuroradiology, New Orleans, February, 1985
- Horton JA, Kerber CW. Lidocaine injection into external carotid branches: provocative test to preserve cranial nerve function in therapeutic embolization. *AJNR* 1986;7:105-108
- Roberson G, Biller H, Sessions DG, Ogura JH. Presurgical internal maxillary artery embolization in juvenile angiofibroma. *Laryngoscope* 1972;82:1524-1532
- Roberson GH, Price AC, Davis JM, Gulati A. Therapeutic embolization of juvenile angiofibroma. *AJR* 1979;133:657-663
- Sessions RB, Wills PI, Alford BR, Harrel JE, Evans RE. Juvenile nasopharyngeal angiofibroma: radiographic aspects. *Laryngoscope* 1976;86:2-18

An Overview of Informed Consent for Radiologists

Stewart R. Reuter¹

Because of the procedure-oriented nature of their specialty, radiologists obtain informed consent from patients daily. This paper attempts to help the radiologist obtain informed consent without incurring malpractice liability by discussing (1) the important legal concept of simple consent as distinguished from informed consent, (2) the elements a patient must prove to succeed in court with an allegation of lack of informed consent, (3) the varying state requirements about the amount of information the patient must be given, (4) the persons who must obtain consent from the patient, and (5) the persons who can give consent for the patient. Consent for IV injections of contrast medium and consent forms are discussed because of the current controversy on these subjects. Courts and state legislatures have usually addressed only specific aspects of informed consent. However, except for the amount of information that must be given the patient, the courts have been relatively uniform in their requirements. Therefore, it is likely that a state court faced with issues of informed consent about which no law exists in their own state will use the existing law in other states as a precedent and adopt similar rules. However, each radiologist must be familiar with the specific rules for informed consent that have been developed by the courts and legislatures in the state in which he or she practices.

Informed consent is important in radiologic practice, partly because consent has become one of the major focuses of the discussion about patients' rights, but also because procedural technicalities in many jurisdictions allow a plaintiff alleging lack of informed consent to get his or her case before a jury without expert testimony. Therefore, every radiologist must understand the rules for informed consent for his or her own state. The legal requirements for obtaining informed consent are not complicated, but they vary slightly from state to state.

Informed consent should grow naturally out of the patient-physician relationship. Unfortunately, the patient-radiologist relationship tends to be brief and episodic, so that radiologists may not feel comfortable discussing the risks and complications of their procedures with the patient. Many radiologists have considered that obtaining consent is a chore imposed by lawyers or a legal trap that should be approached defensively. This attitude is unfortunate. An inadequately informed consent for a radiologic procedure may weaken an otherwise defensible medical malpractice suit. Moreover, the time spent obtaining consent before the patient comes to the radiology department may allow enough patient-radiologist communication to be of significant help if something goes wrong during a procedure. The radiologist should approach informed consent as an opportunity to discuss the proposed procedure with the patient in detail, learn the patient's fears, and give the patient an opportunity to gain some confidence in the radiologist who will perform the procedure.

Legal Basis of Informed Consent

Informed consent has two bases of development. The first is the patient's right

Received May 9, 1986; accepted after revision August 4, 1986.

¹ Department of Radiology, The University of Texas, Health Science Center, San Antonio, TX 78284. Address reprint requests to S. R. Reuter.

AJR 148:219-227, January 1987
0361-803X/87/1481-0219
© American Roentgen Ray Society



to self-determination, perhaps best enunciated by Justice Cardozo in 1914: "Every human being of adult years and sound mind has a right to determine what shall be done with his own body; and the surgeon who performs an operation without his patient's consent commits an assault for which he is liable in damages" [1]. Although it seems obvious to us today that patients have a right to determine the course of their medical care, the thought was almost revolutionary in 1914. Meaningful discussions of informed consent are not found in appellate court decisions until the 1970s.

The other basis for informed consent is the fiduciary relationship between the patient and physician. A fiduciary duty is one owed by a party who is handling the affairs of another. Generally, the person having the duty has superior knowledge or bargaining power compared with the person who is placing trust in him or her. A range of fiduciary obligations exists at law. Perhaps the highest duty is that owed by a person who is guardian for an incompetent parent's financial transactions, whereas the duty owed by an employer to an employee is at the low end of the range. In many fiduciary relationships the duty is measured by the standard of full and fair disclosure. For example, a corporate director who wants to buy land in which the corporation has a potential interest must disclose that fact and get approval. This duty is not dissimilar from the one that grows out of the physician-patient relationship. Physicians should provide adequate information about the risks and complications of the proposed procedure, about alternative procedures, and about the risk of not having the procedure at all, so that patients can balance these factors against the benefits to be derived and can make a reasoned and intelligent decision about their course of treatment.

Simple Consent

We frequently become so involved with the details of informed consent that we overlook the baseline requirement of simple consent, which means merely obtaining permission from the patient to carry out the procedure. A patient can give simple consent without knowing anything about the procedure to be performed. When a physician carries out a treatment without the patient's consent, he or she has committed the tort of civil battery and will be liable for all of the injuries that flow from the unwanted touching. In some egregious circumstances, the physician may even be subject to punitive damages.

Simple consent may be either express or implied [2]. Thus, patients may give a radiologist consent verbally or in writing to perform an excretory urography, or they may climb onto the X-ray table and hold out their arms for an injection, implying through their actions that they have given consent. Patients give implied consent to most radiologic procedures.

Slightly different is the legal doctrine of implied consent. Most states have such a doctrine either in the form of a statute or as common law. Although the doctrine varies slightly from state to state, if the patient is in an emergency setting and requires immediate treatment, and if a reasonable person in the same or similar circumstances would have given

consent, consent will be implied [3]. Thus, if the patient is facing an emergency, whether unconscious on the street or oversedated in the angiography suite, courts will assume implied consent if a procedure or treatment would prevent loss of life or a vital function, or if a delay in treatment would cause deterioration of the patient's condition. In fact, courts will interpret the doctrine liberally because they do not want to discourage physicians from acting in emergency situations. However, this doctrine does not apply to elective procedures, no matter how badly needed.

The radiologist is probably at risk for failing to obtain simple consent in three different situations. The first occurs when a valid consent by the patient is withdrawn. For example, during an angiogram, myelogram, or any other procedure, the patient may say, "Please, Doctor, stop. I cannot take any more pain," or words to this effect. Radiologists, being goal-oriented, may be very close to finishing the study and have a strong desire to complete the examination. However, the patient has withdrawn consent for the procedure, and the radiologist must back off. The consequences of proceeding after consent has been withdrawn are the same as for proceeding with no consent at all: civil battery. When the patient withdraws consent, the radiologist must stop and attempt to explain the value of finishing the procedure, perhaps with the assistance of the referring physician. If the patient then agrees to continue, a note should be placed on the chart to this effect, and the procedure can be completed. If the patient refuses to give a new consent, then the procedure must be terminated.

The problem with withdrawn consent becomes more complex when the patient withdrawing consent is confused, overmedicated, or lacking the mental capacity to give an informed consent to the procedure in the first place. I know of no case law arising in such a situation; I assume, however, that the radiologist should make the decision either to terminate the procedure or to administer additional analgesic agents and proceed on the basis of the individual situation.

Exceeded consent occurs when a procedure is done or a treatment given beyond that to which the patient has consented. It happens occasionally in the surgical setting [4], but may occur in radiology as well. For example, a patient may give consent for a femoral arteriogram to evaluate a stenotic lesion. At the time of the procedure, the stenotic lesion is found to be ideal for angioplasty and, without obtaining additional permission, the angioplasty is performed. No matter how successful the angioplasty, a civil battery has been committed if the procedure was done without the patient's consent. In this situation, one of two procedures may be followed. First, the examination may be terminated and the angioplasty performed later. Or the patient, if not too sedated to understand the consent process, may be asked to give consent for the angioplasty before the physician continues. In this case, a separate observation by an independent observer probably should be made in the chart that the patient had sufficient mental capacity to give the additional consent.

The final trap in the consent process for the unwary radiologist can be termed the "curbstone consult," illustrated in a recent Georgia Court of Appeals opinion, *Gragg v. Neurological Assoc* [5]. In this case, a neurologist was performing a

carotid arteriogram in the radiology department. Having successfully catheterized the left carotid artery, he encountered some difficulty in catheterizing the right. Rather than continue, he requested the assistance of a neuroradiologist who was in the department. The neuroradiologist placed the catheter into the right carotid artery and left the room. The neurologist then made an injection and the patient had a stroke. The patient sued both the neurologist and the neuroradiologist, the former for negligence and the latter for absence of consent. At the trial of the case, both defendants moved for summary judgment. The court granted both their motions; for the neurologist because the plaintiff could produce no expert testimony on the issue of negligence and for the neuroradiologist because it accepted the radiologist's defense of Georgia's Good Samaritan statute.

The plaintiff appealed to the Georgia Court of Appeals; arguing that the trial court's use of the Good Samaritan statute to release the radiologist from liability was in error. The Court of Appeals agreed, holding that the hardship by an experienced physician encountered during the angiogram did not constitute the type of accident or emergency that would invoke the provisions of the Good Samaritan statute, and reversed the trial court judgment.

After the Court of Appeals decision, Mr. Gragg refiled his suit against the neuroradiologist, again alleging lack of informed consent and adding an allegation that he was negligent in catheterizing the right carotid artery. The neuroradiologist again moved for summary judgment, and this time the trial court entered a partial judgment in his favor, dismissing the claim of negligence against him but again denying his motion on the issue of consent. Dissatisfied at having his allegation of negligence dismissed by the trial court, Mr. Gragg again appealed to the Court of Appeals. Confining their opinion to the issue of negligence, the appeals court agreed with Mr. Gragg, finding that several questions of fact about negligence were raised in the appeal. They reversed the trial court judgment as to negligence and remanded the case for a new trial. This case illustrates the potential legal problems facing a radiologist who gives a curbside consult. It is ironic that this case occurred in Georgia, the only state that has expressly rejected informed consent. Simple consent would have been sufficient.

Although the decision may seem outrageous to many radiologists, it is legally correct. It is common for radiologists to assist other physicians in the performance of procedures that involve radiologic facilities. However, when radiologists approach a patient as part of a consultative process, they should introduce themselves to the patient, get consent to participate in the procedure, and make a note in the chart that consent was given. Alternatively, the original consent that the patient signs may indicate that the procedure will be done by the radiologist and his or her associates. This extends the consent to others beyond the person who is primarily responsible for the procedure. However, patients have the right to choose the physicians who perform procedures, operations, and treatments on them. When physicians other than the one they have chosen perform the procedure, a civil battery has been committed [6].

Required Elements of Proof in an Action Based on Lack of Informed Consent

In many states absence of simple consent (i.e., no consent at all) is considered civil battery. Similarly, withdrawn consent and exceeded consent are likely to be brought as battery suits because withdrawn or exceeded consent is equivalent to no consent at all.

The tort of civil battery was also used at first to cover lack of informed consent as well as lack of simple consent, because an inadequately informed consent was considered to be absence of consent. However, courts trying to grapple with the problem soon became aware that civil battery was not a useful legal theory for this problem. In most instances, the physician had actually obtained simple consent. Therefore, courts have tended progressively toward use of the tort of negligence. Today, in almost all states, patients alleging inadequately informed consent must sue for negligence.

The legal theory of negligence has four elements. First, the physician must have a duty to the patient. As mentioned previously, this duty grows out of the fiduciary aspects of the patient-physician relationship, and if a radiologist is performing a procedure that carries a material (or significant) risk, he or she has the duty to obtain an informed consent. Second, breach of the duty is the failure to give adequate information so that the patient can make an informed decision to accept or reject the procedure. Third, "injury" is rather broadly defined and may range from the pain associated with the procedure or treatment to a severe complication. The patient's monetary compensation in a successful action for lack of informed consent is proportional to the severity of the injury. Good lawyers do not take cases for which they do not expect significant compensation; therefore, suits alleging lack of informed consent usually are not filed unless the patient has had a severe injury. Fourth, in the informed consent context, causal relationship between breach of duty and the injury means that if the patient had known the risks and the alternative procedures available, he or she would have rejected the procedure or would have chosen an alternative procedure. In summary, successful suits for lack of informed consent require that patients undergo a procedure or treatment with significant risks, have an injury, and show that if they had known the risks and complications they would have rejected the procedure and therefore would not have sustained the injury.

Situations in Which Informed Consent May Not be Necessary

Informed consent may not be necessary in two situations. First, if patients state that they do not want to know the complications of the procedure, they do not have to be informed. They have waived their legal right to be informed, the physician can make a note in the chart to this effect (ideally, also signed by the patient), and no further information need be given. The second exception to the need for consent, recognized in almost all states, is the therapeutic privilege. If the physician feels that the information about the procedure

or treatment will harm the patient, he or she can withhold that information. This exception is relatively narrow, however, and probably should be limited to the type of information that would cause the patient extreme mental anguish. At the time of trial, the patient can allege that he or she would have wanted the withheld information and, therefore, the use of the therapeutic privilege as a defense will sound self-serving.

Standards Used by Various Jurisdictions to Determine the Adequacy of Informed Consent

Different jurisdictions have moved to different legal standards to determine the adequacy of the consent. In increasing order of required disclosure of information the three standards used are the reasonable-physician standard, the reasonable-patient standard, and the subjective-patient standard.

The reasonable-physician standard, the first to be used, was almost the only standard used from the middle 1930s through the middle 1970s. In jurisdictions that use this standard, courts judge the adequacy of the information given the patient by comparing it with the information that a reasonable physician would have revealed under similar circumstances. The plaintiff must obtain an expert witness to testify about the amount of information a reasonable physician would disclose to the patient, and this requirement for expert testimony is an advantage to the defendant physician. Expert witnesses, particularly experts from the adjacent geographic area, are difficult for plaintiffs to obtain. Without an expert witness, the standard of care and the deviation from that standard cannot be established. In fact, the requirement for expert testimony and the difficulty plaintiffs have in obtaining physicians as expert witnesses are some of the reasons courts moved away from the reasonable-physician standard to the reasonable-patient standard. The reasonable-physician standard, still the most frequently used, is followed in Arizona, Arkansas, Colorado, Delaware, Idaho, Illinois, Indiana, Kansas, Kentucky, Maine, Michigan, Mississippi, Missouri, Montana, Nebraska, New Jersey, New York, North Carolina, South Carolina, Tennessee, Vermont, Virginia, and Wyoming [7]. Recent Colorado Court of Appeals decisions, however, have begun to lean toward a reasonable-patient standard [8]. The legislators in Florida, New York, and Vermont passed statutes returning these states to the reasonable-physician standard after the courts had moved to the reasonable-patient standard. However, a Florida Court of Appeals recently declared their consent statute unconstitutional on grounds other than the standard of disclosure [9].

In states that have moved to the reasonable-patient standard, courts have recognized the importance of the patient's role in the decision-making process. If the appropriate person to accept or reject a proposed procedure is the patient, then the information the physician needs to disclose should be measured by what a reasonable patient would need to know rather than what a reasonable physician would choose to disclose. The primary problem for physicians is knowing how much information a reasonable patient would want. In making this determination, it is important to recognize that courts and juries try to decide what an abstract, average, reasonable

patient would want to know, as opposed to what the specific patient-plaintiff in the case would want to know. Jurisdictions that use the reasonable-patient standard are California, Connecticut, District of Columbia, Iowa, Maryland, Massachusetts, Minnesota, New Mexico, North Dakota, Oregon, Pennsylvania, Rhode Island, Utah, Washington, West Virginia, and Wisconsin [10].

The rules were perhaps best articulated in two early cases in 1972, *Canterbury v. Spence* [11], and *Cobbs v. Grant* [12]. In these cases the courts held that a reasonable patient would want to know the material risks and complications, the alternative procedures available, and the risks of not having the procedure at all. Unfortunately, courts have defined "material risks" to be what a reasonable patient would want to know under similar circumstances, a rather circular definition. In various opinions, however, appellate courts have considered both severe and common risks to be material. If a complication is severe, such as death, a reasonable patient would want to know its incidence. Similarly, if a complication is common but not particularly severe, a reasonable patient would want to know about that as well. In general, materiality equals severity \times incidence, with the emphasis on severity. The California Supreme Court observed that a minicourse in medicine is not necessary [13].

Recently, the Washington State Supreme Court was faced with a case in which the patient-plaintiff, who developed thrombophlebitis after injection of contrast medium for IV urography, claimed that a reasonable patient would want to know about that risk because it was one of the potential complications listed in the *Physicians' Desk Reference* [14]. The court held that thrombophlebitis was neither a particularly severe nor particularly common complication of IV urography and that physicians are not bound by the contents of the *Physicians' Desk Reference* in deciding what risks a patient would want to know.

As noted previously, the main procedural advantage to the patient in a reasonable-patient jurisdiction is the absence of a need for expert testimony by physicians in the area. Because the jurors are all reasonable people, they don't need physicians to tell them what a reasonable patient would want to know. Therefore, plaintiffs may get their case before the jury even though they cannot find an expert witness, and even though they face summary dismissal on the issue of negligence. A recent Rand Corporation study found that one of the primary factors increasing malpractice litigation in California during the middle 1970s was the change by the California Supreme Court from a standard for informed consent that required expert testimony to one that allowed the jury to decide whether the consent was adequately informed without expert testimony [15].

Some jurisdictions that use the reasonable-patient standard still require expert testimony, but only to describe the relationship between the procedure and the nature, the severity, and occurrence of the risk. Once this information is given by the expert, the jury then makes its own determination as to the materiality of the risk. Moreover, expert testimony of this type may not necessarily require a physician if another expert is familiar with the procedures and the risks and complications of the procedures [16].

Physicians in reasonable-patient jurisdictions were somewhat alarmed by the recent California decision in *Truman v. Thomas* [17]. In this case, the patient refused a Papanicolaou smear despite the encouragement of the gynecologist to have the examination done. A year later, the patient died of carcinoma of the cervix and her surviving husband sued the physician, stating that if the patient had known that the risk of not having the procedure was cervical carcinoma, she would have accepted the procedure. The California Supreme Court agreed and found the consent to have been inadequate. In fact, to most lawyers following the development of the law of informed consent in states that use the reasonable-patient standard, this was not a surprising decision. Other cases antedating this decision had stated that knowledge of the risk of not having a procedure done is a material part of making the choice to accept it or not.

In Oklahoma [18], the only state that currently uses the subjective-patient standard, the court asks what risks and complications each specific patient-plaintiff would want to know. In effect, this is an unworkable standard and should be abandoned. At the time of trial, of course, patients in Oklahoma will testify that if they had known about the existence of whatever complication happened to occur, they would have rejected the procedure. Physicians, therefore, must inform the patients of virtually all risks and complications.

About 23 states have passed statutes that regulate consent for medical procedures. In 14 (Arkansas, Delaware, Idaho, Kentucky, Maine, Nebraska, New York, North Carolina, Oregon, Pennsylvania, Tennessee, Utah, Vermont, and Washington) [8, 10], the statutes simply codify the reasonable-physician or reasonable-patient standard. However, in Louisiana, Ohio, Hawaii, and Texas, the statutes specify the information that should be given to the patient. In Louisiana and Ohio [19], the statutes set out a list of risks that must be revealed to the patient if the proposed procedure entails one of those risks. In Hawaii and Texas [20], the statutes authorize an administrative body to develop a list of risks about which a reasonable patient would want to know for each type of procedure. If the physician has informed the patient of the risks on the list, the consent is presumed to be adequate. In Texas the reasonable-patient standard of disclosure is used for procedures that have not yet been placed on the list by the designated administrative body [21].

The standards of disclosure required in Alaska, South Dakota, and Nevada are not clear. Although informed consent was addressed by the Alaska Supreme Court in one case, the court declined to reach the issue of duty and scope of disclosure [22]. The South Dakota Supreme Court, in a case involving informed consent, used language suggesting that it might adopt the reasonable-patient standard but failed to decide whether or not expert testimony was required [23]. Nevada has a statute that seems to use the reasonable-physician standard but does not mention whether expert testimony is needed, and Nevada has no common law on the issue [24]. Alabama has no statute or case law on informed consent, and Georgia courts have declined to recognize the doctrine of informed consent [25]. Simple consent is enough in Georgia.

Finally, the state of the law in New Hampshire is not clear. The legislature had passed N.H. Rev. Stat. Ann. §507-C:1, subd. 3, §507-C:2, as part of a comprehensive medical malpractice act. These sections established the reasonable-physician standard for informed consent and required expert testimony. In 1980, the New Hampshire Supreme Court held the entire malpractice act to be unconstitutional in *Carson v. Maurer* [26], including the informed-consent sections. However, the Court earlier had had the opportunity to review the informed-consent sections separately from the rest of the malpractice act, in *Folger v. Corbett* [27], and had found these sections to be constitutional. Therefore, New Hampshire will probably retain the reasonable-physician standard despite *Carson*.

Consent for IV Injections of Contrast Agents

An issue recently raised in the radiologic literature is whether radiologists should obtain informed consent from patients receiving IV urograms, contrast injections for CT, venograms, and so on, and if so, which risks and complications should be disclosed [28]. This problem has no simple answer. The information that must be given to the patient depends primarily on the state in which the radiologist practices. If the IV injection is being done in a state that uses the reasonable-physician standard, the radiologist can inquire of colleagues whether they obtain informed consent for IV injection of contrast agent and, if so, what risks and complications are disclosed. In these jurisdictions the physicians, within reason, set their own standard of disclosure. Since the logistics of obtaining informed consent from patients for IV injections of contrast agent are frequently difficult, it is unlikely that many radiologists in reasonable-physician jurisdictions obtain an informed consent. At a trial for lack of informed consent, several local expert witnesses could be obtained to testify that they do not use informed consent for IV contrast injections. The plaintiff would probably have difficulty finding physicians from the same state willing to testify against colleagues, and the judge would probably exclude the testimony of expert witnesses from jurisdictions that use a more patient-oriented standard.

On the other hand, if the radiologist practices in a reasonable-patient jurisdiction, informed consent should probably be obtained for IV injections. It is commonly recognized that the risk of death from IV injections of contrast medium is about 1/40,000 patients. Is a 1/40,000 risk of death "material" (i.e., a risk about which a reasonable person would want to know)? In my opinion, any procedure that has a risk of death for which a numeric prevalence can be placed probably becomes a material risk. The patient can then consider the prevalence and decide whether he or she wants to accept the procedure. Because of the logistic problems and the low prevalence of risk, the radiologist might want to use a consent form of the type described later in this paper. In this case, the consent form might be used by an agent, such as a technician. Any questions that the patient has after reading the consent form can be answered by the radiologist who injects the contrast agent.

In Oklahoma, with the subjective-patient standard, radiologists should inform patients about all the potential risks accompanying an IV contrast injection. In this state, the list in the *Physicians' Desk Reference* might be a good guide. If a patient has a reaction to contrast medium, the plaintiff will certainly claim at trial that he or she would not have accepted the procedure knowing the possibility of the complication. Then the jury must decide whether that particular patient would have accepted the injection.

If a patient has previously reacted to a contrast medium, the radiologist must be especially careful to inform the patient of the greater risk of a severe reaction compared with patients who have not had contrast-medium reactions and of a higher risk of death.

Who Has the Legal Responsibility for Obtaining Consent from the Patient?

Courts are beginning to address the issue of responsibility for obtaining consent and are responding in a uniform manner. Responsibility for obtaining consent from a patient lies with the physician or surgeon who is to perform the procedure or carry out the treatment [29]. Most physicians would come to this same conclusion. However, physicians and surgeons who have failed to obtain consent and who have then been sued because of that failure have attempted to place responsibility either on a referring physician or on the hospital. The courts have rejected both approaches. The question of who should obtain consent usually does not arise in the context of primary patient care, in which the patient's personal physician is the one who will perform the procedure. A discussion of the usual factors that make up informed consent evolves naturally from their patient-physician relationship. The problem arises when the patient is referred to a consultant for a diagnostic procedure or treatment. The consultant's contact with the patient may be brief. The extreme situation occurs frequently in the radiologic setting, in which a patient may be referred to a radiologist for an arteriogram or other invasive procedure. The radiologist can certainly explain the procedure to the patient and enumerate the material risks and complications, which may even include the risk of death. However, many of the alternative procedures may not be radiologic, and the radiologist may not have adequate information about the risks of not having the procedure. Thus, the radiologist, seeing the patient for the first time, might prefer that the patient's primary physician obtain a consent. However, the legal responsibility clearly belongs to the radiologist.

Under the ordinary rules of agency law, the radiologist may delegate the process of obtaining consent to an agent, such as a nurse or even a referring physician, if the agent accepts the responsibility. Except for obtaining consent for standard IV injections, this is a dangerous practice. The radiologist, as principal, is bound by any defects in the consent obtained by the agent, frequently without even knowing what defect occurred until the suit is filed [30]. In some cases reaching the appellate courts, a consultant thought the referring physician had obtained consent and vice versa. Confusion about who should have gotten a consent had resulted in no consent

being obtained at all. Radiologists who rely on the referring physician or a hospital employee to obtain consent for a procedure more complex than an IV injection of contrast medium do so at their own risk.

Moreover, for many consultations, the time spent with the patient obtaining an informed consent before the procedure may be the only opportunity for the consultant and patient to get to know one another. If problems occur during the procedure, even a small amount of respect and trust developed for a consultant may deter patients from filing later malpractice actions.

Who Has the Legal Capacity to Consent?

The question of legal capacity to give informed consent is more complex than who should obtain the consent, and the answer varies from state to state. It also varies significantly depending on whether the patient is a minor, a competent adult, an incompetent adult who has had a guardian or conservator appointed by the courts, or an adult who has inadequate mental capacity to understand the nature of the consent and yet has no court-appointed guardian.

Minors

Almost every state has a statute giving parents the legal power to consent to procedures on their minor children. In addition to the parents, most statutes give a substituted power of consent to adult brothers and sisters and other near relatives if the parents are unavailable. Also, most states have statutes that give emancipated minors (married minors, minors serving in the armed forces, minors living apart from their parents, or minors who are self-supporting) the right to consent to procedures on themselves. Most states also allow minors to give consent for diagnostic procedures and treatments related to reportable infectious diseases, venereal diseases, and pregnancy. Because these statutes are detailed and broad in most states, physicians rarely have a problem obtaining a legally valid consent when a minor needs an elective procedure.

The Mentally Competent Patient or Patient Who Has a Court-appointed Guardian or Conservator

In many states with common law or statutes governing consent to medical procedures, the general wording is that consent can be given by a competent adult patient or, if the patient is incompetent, by a person who is legally authorized to consent for the patient [31]. Although competency is relative and the level of mental capacity required for different legal acts varies with the type of act, the level of competency required to give informed consent to medical procedures should be high. The patient must be able to understand the nature of the proposed procedure or treatment and balance the risks against the benefits in deciding whether to accept treatment, forego it, or accept an alternative procedure. Moreover, the level of mentation necessary varies with the complexity of the procedure proposed. Finally, mental capacity

may vary during the course of a patient's illness. Therefore, each radiologist approaching a patient must make an individual judgment about the patient's ability to understand and to balance the factors necessary for a rational decision at the time.

"Legal representative," a term with which physicians usually do not deal, means a person who has the legal power to make decisions on behalf of someone else. This power must be granted either by a court or by an individual in a legally recognized manner. Certainly, court-appointed guardians or conservators are legal representatives. Similarly, in states with a durable-power-of-attorney statute, the person with the power of attorney may consent to needed elective procedures on behalf of the person who granted the power of attorney. Physicians should, however, know their state law regarding powers of attorney. In general, to be valid, all powers of attorney must be granted while the patient is mentally competent to make such a decision. If the state statute grants a durable power of attorney, it remains valid even though the patient later becomes mentally incompetent. If the state's power of attorney is not durable, the power terminates if the patient becomes incompetent.

The Mentally Incompetent Patient Who Has No Legal Representative

Radiologists are faced daily with patients who need elective procedures but who do not have the mental capacity to give an informed consent, particularly in public hospitals and nursing homes. Although senility is perhaps the most common problem leading to inadequate mental capacity, the issue also arises when physicians deal with inebriated patients, with patients who are on drugs that decrease mental capacity, and with patients whose primary disease processes have diminished their mental capacity.

Radiologists faced with such patients need to obtain a substituted consent, and the question always arises from whom it should be obtained. A few states, including Arkansas, Idaho, Maine, Maryland, Mississippi, North Carolina, and Utah [32] have specific statutes that allow substituted consent for elective procedures and treatments to be given by spouses or specified near relatives. In some of these states the designated relatives must be approached in the order they are ranked in the statute; in others, the physician may pick the spouse or any relative on the list. Georgia and Louisiana have statutes allowing substituted consent by spouses [33]. Nebraska includes spouses and near relatives in its definition of legal representative [34]. In California and Florida, appellate courts have held that a parent's duty to make decisions and to give consent for medical treatment for incompetent children continues into the child's adulthood [35]. In other jurisdictions, including the District of Columbia, California, Kentucky, Massachusetts, Missouri, Oklahoma, Tennessee, and Washington [36], appellate courts have stated in legal opinions that the consent of a spouse or near relative may be substituted for that of an incompetent patient.

In states without a statute or common law precedent allowing substituted consent for treatment of incompetent

patients, radiologists may question the appropriate approach to take. One approach, if the patient is marginally competent, is to have the patient consent to his or her own treatment. One of the basic maxims of law is that a person is considered to be competent until shown to be incompetent [37]. In marginal situations, the radiologist can probably rely on the court's adherence to this maxim. However, radiologists must remember that informed consent does not become a legal issue until a law suit is filed. At that time, they will face a patient or patient's relative who claims that the patient did not have the mental capacity to make the decision. Therefore, in determining the competency of the patient, the radiologist should err on the side of requiring a greater, rather than a lesser, level of mental capacity.

Alternatively, the radiologist can obtain consent from a spouse or near relative. Most attorneys would accept this approach, and in fact, little litigation has arisen to challenge such substituted consent. However, in a few cases, courts have held that such consent was not valid. Specifically, Texas, Louisiana, and North Carolina have cases that state that one spouse is not the other's authorized agent simply because of the marital relationship; a Hawaii decision has language, which was not essential to the central holding of the case, that suggests the same [38]. However, the decision in the Louisiana case (*Beck v. Lovell*) is in direct conflict with Louisiana's consent statute [19] and seems to overturn the statute without mentioning it. In the North Carolina decision (*Ipoc v. Gilmore*), the court seems to restrict North Carolina's consent statute to emergency situations. In New Mexico, the consent of an adult daughter to the treatment of an incompetent parent was held to be invalid [39]. Although these specific decisions represent exceptions to the generally stated rule that substituted consent for elective procedures on incompetent patients may be obtained from spouses and near relatives, the rule is probably more in tune with contemporary ideas about interfamily relationships. In 1982, the President's Commission for the Study of Ethical Problems in Medicine and Biomedical and Behavioral Research determined that the family is the entity best suited to give substituted consent because family members are generally concerned about the good of the patient; because they are usually most knowledgeable about the patient's goals, purposes, and values; and because they deserve recognition as an important social unit in matters that immediately affect family members [40].

If the radiologist faces an incompetent patient who has no spouse or near relative available, he or she must petition the local court with appropriate legal authority to make a health-care decision or to appoint a representative for the purpose of giving consent for the procedure. Most localities have legal procedures to expedite such decisions, and hospital lawyers are generally familiar with the procedures necessary to obtain consent in this manner.

It is probably worthwhile to restate that this discussion applies only to patients who need elective procedures. If a patient is in an emergency situation and cannot give consent for any reason, incompetence or any other, the implied consent doctrine may be invoked, consent will be implied by the courts, and the physician may proceed without consent.

Finally, this discussion only covers consent for needed elective procedures; it has nothing to do with withholding treatment, for which the consent process is much more complex.

Consent Forms

Some type of consent form is generally used for all medical procedures. These forms range from general statements with blank spaces to be completed at the time consent is obtained, to detailed forms that list all potential risks and complications. These forms have proliferated partly because of the requirements of many state statutes that consent for medical procedures be in writing, be signed by the patient, and be witnessed. They have also proliferated because radiologists have a general feeling that a consent form that details the risks and complications affords greater legal protection.

Detailed consent forms may be a two-edged sword. They certainly document the risks and complications that were explained to the patient. However, if the patient has a complication not on the list, the consent form may be equally good evidence that that risk was not explained to the patient. For this reason, some defense attorneys would prefer not to use detailed consent forms but would rather have the radiologist place a note in the chart that the risks and complications were explained to the patient. Except for obvious fraud, jurors tend to believe what is written in charts.

In my opinion, whether detailed consent forms should be used depends on the rules for informed consent in the state in which the radiologist practices. For example, if the radiologist practices in a state that uses the reasonable-physician standard, the adequacy of the disclosure will be judged by comparing it with the practice of other physicians in the community. In such jurisdictions the amount of information generally disclosed by physicians is less than that required by reasonable-patient jurisdictions. Therefore, a detailed consent form is not necessary, and a note by the radiologist in the chart that he or she has explained the usual risks, complications, and alternative procedures to the patient is probably preferable.

In states that use the reasonable-patient standard, and certainly in Oklahoma (with the subjective-patient standard), a detailed list of the risks and complications of which the patient has been advised may have greater value. In a reasonable-patient jurisdiction, the consent form should list the severe and common risks and complications; in a subjective-patient jurisdiction the form should probably list all of the known risks and complications.

The blanket consent forms signed by the patient on admission to the hospital give the radiologist no protection. The boiler-plate language of these forms—for example, that the patient agrees to any procedures the physician feels necessary—has little legal value, and most blanket consent forms have been abandoned.

Detailed consent forms should have additional clauses to protect the radiologist. One clause should state that the patient has read and understood the information provided on

the form. Another clause should give the patient the opportunity to ask any questions of the physician about information that is not understood. Finally, to protect against the type of nonconsent that occurred in *Gragg v. Neurological Assoc.* [5], a clause should allow associates to assist the radiologist in performing the procedure.

REFERENCES

1. *Schloendorff v. The Society of the New York Hosp.* 105 N.E. 92, 93 (N.Y. 1914)
2. Am Jur.2d §§182, 183 (1981)
3. Am. Jur.2d §185 (1981)
4. *Lipscomb v. Memorial Hosp.* 733 F.2d 332, 336, 337 (4th Cir. 1984); *Pizzalotto v. Wilson*, 437 So.2d 859, 863 (La. 1983)
5. *Gragg v. Neurological Assoc.*, 263 S.E.2d 496 (Ga. App. 1979); *Gragg v. Spenser*, 284 S.E.2d 40 (Ga. App. 1981)
6. *Perna v. Pirozzi*, 457 A.2d 431 (N.J. 1983)
7. *Riedisser v. Nelson*, 534 P.2d 1052, 1054 (Ariz. 1975); Ark. Stat. Ann. §34-2614(B)(1), *Fuller v. Starnes*, 597 S.W.2d 88, 90 (Ark. 1980); *Mallet v. Pirkey*, 466 P.2d 466, 473 (Colo. 1970); Del. Code Ann. tit. 18 §6852(a)(2), *Wagner v. Olmedo*, 365 A.2d 643, 644, 645 (Del. 1976); Idaho Code §39-4304, *Le Pelley v. Grefenson*, 614 P.2d 962, 969 note 1 (Idaho 1980); *Guebard v. Jabaay*, 452 N.E.2d 751, 757 (Ill. App. 1983); *Revord v. Russell*, 401 N.E.2d 763, 766, 767 (Ind. App. 1980); *Charley v. Cameron*, 528 P.2d 1205, 1210 (Kan. 1974); Ky. Rev. Stat. Ann. §304.40-320(1) (Baldwin), *Holton v. Pfingst*, 534 S.W.2d 786, 789 (Ky. App. 1976); Me. Rev. Stat. Ann. tit. 24 §2905(1)(A), (B) (Baldwin), *Woolley v. Henderson*, 418 A.2d 1123, 1131 (Me. 1980); *Rice v. Jaskolski*, 313 N.W.2d 893, 895 (Mich. 1981); *Ross v. Hodges*, 234 So.2d 905, 909 (Miss. 1970); *Aiken v. Clary*, 396 S.W.2d 668, 674 (Mo. 1965); *Llera v. Wisner*, 557 P.2d 805, 810 (Mont. 1976); Nebr. Rev. Stat. §44-2816, *Calabrese v. Trenton State College*, 413 A.2d 315, 316 (N.J. 1978); N.Y. Public Health Law §2805-d(1) (McKinney), overturning previous common law reasonable-patient standard; N.C. Gen. Stat. §90-21.13(a)(1), *McPherson v. Ellis*, 287 S.E.2d 892, 897 note 2 (N.C. 1983); *Dixon v. Peters*, 306 S.E.2d 477, 480 (N.C. App. 1983); *Hook v. Rothstein*, 316 S.E.2d 690, 698 (S.C. App. 1984); Tenn. Code Ann. §29-26-118, *Rush v. Miller*, 648 F.2d 1075, 1076 (6th Cir. 1981); Vt. Stat. Ann., tit. 12 §1909(a)(1), overturning previous common-law reasonable-patient standard, *Bly v. Rhoads*, 222 S.E.2d 783, 787 (Va. 1976); *Stundon v. Stadnik*, 469 P.2d 16, 21 (Wyo. 1970)
8. *Hamilton v. Hardy*, 549 P.2d 1099, 1105 (Colo. App. 1976); *Greenwell v. Gill*, 660 P.2d 1305, 1307 (Colo. App. 1982)
9. *Cunningham v. Parikh*, 472 So.2d 746 (Fla. App. 1985)
10. *Cobbs v. Grant*, 502 P.2d 1, 11 (Cal. 1972); *Logan v. Greenwich Hosp. Assn.*, 465 A.2d 294, 300, 301 (Conn. 1983); *Canterbury v. Spence*, 464 F.2d 772, 786 (D.C. Cir. 1972); *Cowman v. Hornady*, 329 N.W.2d 422, 424, 425 (Iowa 1983); *Sard v. Hardy*, 379 A.2d 1014, 1022 (Md. 1977); *Harnish v. Children's Hosp. Med. Center*, 439 N.E.2d 240, 242 (Mass. 1982); *Cornfeldt v. Tongen*, 262 N.W.2d 684, 702 (Minn. 1977); *Gerety v. Demers*, 589 P.2d 180, 195 (N.M. 1978); *Winkjer v. Herr*, 277 N.W.2d 579, 588 (N.D. 1979); Ore. Rev. Stat. Ann. §677.097, *Getchell v. Mansfield*, 489 P.2d 953, 956 (Ore. 1971); Pa. Stat. Ann., tit. §40 1301.103, *Defulvio v. Holst*, 414 A.2d 1087, 1089 (Pa. Super. 1979); *Wilkinson v. Vesey*, 295 A.2d 676, 688 (R.I. 1972); Utah Code Ann. §78-14-5(1)(f), *Nixdorf v. Hicken*, 612 P.2d 348, 354 (Utah 1980); Wash. Rev. Code §7.70.050(1)(c)(2), *Smith v. Shannon*, 666 P.2d 351, 355 (Wash. 1983); *Cross v. Trapp*, 294 S.E.2d 446, 455 (W.Va. 1982); *Trogun v. Fruchtmann*, 207 N.W.2d 297, 315 (Wisc. 1973)
11. *Canterbury v. Spence*, 464 F.2d 772 (D.C. Cir. 1972)
12. *Cobbs v. Grant*, 502 P.2d 1 (Cal. 1972)
13. *Cobbs v. Grant*, 502 P.2d 1, 11 (Cal. 1972)
14. *Smith v. Shannon*, 666 P.2d 351 (Wash. 1983)
15. Danzon P. *The frequency and severity of medical malpractice claims*. Santa Monica, CA: Rand Corporation, 1982:28
16. *Harris v. Groth*, 645 P.2d 1104 (Wash. App. 1982)
17. *Truman v. Thomas*, 611 P.2d 902 (Cal. 1980)

18. *Scott v. Bradford*, 606 P.2d 554 (Okla. 1979)
19. La. Rev. Stat. Ann. §40:1299.40 (West); Ohio Rev. Code Ann. §2317.54(A) (Baldwin)
20. Hawaii Rev. Stat. §671-3; Tex. Rev. Stat. Ann., tit. 71, art. 4590 §603(a) (Vernon)
21. *Peterson v. Shields*, 652 S.W.2d 929, 931 (Tex. 1983)
22. *Poulin v. Zartman*, 542 P.2d 251 (Alaska 1975)
23. *Cunningham v. Yankton Clinic, P.A.*, 262 N.W.2d 508, 511 (S.D. 1978)
24. Nev. Rev. Stat. §41A.110
25. *Simpson v. Dickson*, 306 S.E.2d 404 (Ga. App. 1983), relying on Ga. Code Ann. §31-9-6(d), *Holbrook v. Schatten*, 229 S.E.2d 128 (Ga. App. 1983)
26. 424 A.2d 825 (N.H. 1980)
27. 394 A.2d 63, 64 (N.H. 1978)
28. Spring DB, Akin JR, Margulis AR. Informed consent for intravenous contrast-enhanced radiography: a national survey of practice and opinion *Radiology* 1984;152:609-613
29. *Halley v. Birbiglia*, 458 N.E.2d 710, 716 (Mass. 1983); *Nelson v. Patrick*, 293 S.E.2d 829, 832 (N.C. App. 1982)
30. *Hill v. Steward*, 470 N.Y.S.2d 971 (N.Y. Super. 1983)
31. Am. Jur.2d §175 (1981)
32. Ark. Stat. §82-363(h), (i), (j), (k); Idaho Code, §39-4303; Me. Rev. Stat. Ann., tit. 24, §2905(a); Md. Ann. Code Health-General §20-107(d), (e); Miss. Code Ann. §41-41-3; N.C. Gen. Stat. §90-21.13(a); Utah Code Ann. §78-14-5(4)(b)(d)
33. Ga. Code Ann. §31-9-2(a)(3); La. Stat. Ann. §40.129.53(c)
34. Nebr. Rev. Stat. §44-2808
35. *Farber v. Olkon*, 254 P.2d 520, 524 (Cal. 1953); *Ritz v. Fla. Patient's Comp. Fund*, 434 So.2d 987, 989 (Fla. App. 1983)
36. *Canterbury v. Spence*, 464 F.2d 772, 789 n. 92 (D.C. Cir. 1972); *Cobbs v. Grant*, 502 P.2d 1, 10 (Cal. 1972); *Wilson v. Lehman*, 379 S.W.2d 478, 480 (Ky. 1964); *In the Matter of Spring*, 399 N.E.2d 493, 497 n. 5 (Mass. 1979); *Steele v. Woods*, 327 S.W.2d 187, 198 (Mo. 1959); *Murray v. Van Devander*, 522 P.2d 302, 304 (Okla. App. 1974); *Campbell v. Oliva*, 424 F.2d 1244, 1251 (6th Cir. Tenn. 1970); *Grannum v. Berard*, 422 P.2d 812, 814 (Wash. 1967)
37. Am. Jur.2d §176 (1981)
38. *Gravis v. Physicians and Surgeons Hosp. of Alice*, 427 S.W.2d 310, 311 (Tex. 1968); *Beck v. Lovell*, 361 So.2d 245, 250 (La. App. 1978); *Ipoc v. Gilmore*, 326 S.E.2d 271, 279 (N.C. App. 1985); *Nishi v. Hartwell*, 473 P.2d 116, 122 (Hawaii 1970)
39. *Eis v. Chestnut*, 627 P.2d 1244, 1247 (N.M. App. 1981)
40. President's Commission for the Study of Ethical Problems in Medicine and Biomedical and Behavioral Research. *Making health care decisions*. Washington, DC: U. S. Government Printing Office, 1982:182-183

ARRS Meeting Section

Invitation to the 1987 American Roentgen Ray Society Meeting in Miami Beach, FL, April 26–May 1, 1987

The entire radiologic community is invited to attend the 87th annual meeting of the American Roentgen Ray Society in Miami Beach, FL, April 26–May 1, 1987. There are numerous exciting attractions.

First is the site. The Fontainebleau Hilton has undergone total modernization and redecoration and provides a plush facility at the time when Florida weather is at its best. The opportunity for the busy radiologist to attend a major national meeting while enjoying such weather is ideal.

Second, the scientific program, instructional courses, and

categorical course (see Table 1 for schedule) are certain to be interesting and educational. Third, participants will enjoy the exhibits, Caldwell Lecture, and planned social events.

Scientific Program

Almost 600 scientific papers have been submitted. From these, 190 have been selected for presentation. Special emphasis has been placed on discussion of new developments

TABLE 1 Summary of 1987 American Roentgen Ray Society Meeting

Sunday April 26	Monday April 27	Tuesday April 28	Wednesday April 29	Thursday April 30	Friday May 1
	8–9:30 Instructional courses	8–9:30 Instructional courses	8–9:30 Instructional courses	8–9:30 Instructional courses	8–1 Symposium. Genitouri- nary imaging update
10–noon Categorical course. GI radiol- ogy	10–10:30 Opening cere- mony 10:30–12:30 Scientific pro- gram	10–12:30 Scientific program	10–12:30 Awards session/ Caldwell lecture	10–12:30 Scientific program	
Noon Lunch	12:30 Lunch	12:30 Lunch	12:30 Lunch	12:30 Lunch	
1:30–5:30 Categorical course. GI radiol- ogy	1:30–5:30 Categorical course. GI radiology	1:30–3:30 Scientific program 4–5:30 Categorical course. GI ra- diology	1:30–3:30 Scientific program 4–5:30 Categorical course. GI ra- diology	1:30–3:30 Scientific program 4–5:30 Categorical course. GI ra- diology	

as well as reinforcement of established areas. One entire scientific session will be devoted to breast diseases.

The Friday morning scientific sessions will be replaced by one major session entitled "Genitourinary imaging update." Glen Hartman has assembled an outstanding faculty to cover all facets of urology from contrast materials to MR imaging.

Instructional Courses

The Instructional Courses have been revised and updated by the new Chairman of the Instructional Course Committee, Joseph Ferrucci. Advance registration is recommended.

Categorical Course

The Categorical Course returns this year to the subject of gastrointestinal radiology. With the emphasis shifting from traditional barium studies to newer techniques, Chairman Gary Ghahremani has structured a course of special utility for the practicing radiologist.

Exhibits

The Scientific Exhibits coordinated by John Madewell will cover a wider range of topics than ever before. Some of the space usually allotted to technical exhibits will be used for the scientific exhibits, enhancing the total learning experience available.

The Technical Exhibit area will be compact and permit convenient review of new technologic developments.

Caldwell Lecture

The Caldwell Lecture for 1987 will be given by M. Paul Capp, Professor and Chairman, Department of Radiology, University of Arizona. Dr. Capp will discuss current imaging research studies and their applicability and availability, both short and long term.

Social Events

South Florida in the spring offers a myriad of diversions, and Manuel Viamonte, Chairman of Local Arrangements Committee, has assembled a group of activities, including golf and tennis tournaments, for attendees and their accompanying persons. The traditional cocktail party given by the Society for all registrants in the exhibit area on Tuesday evening will provide a convenient meeting place before an evening on the town.

Let me repeat my invitation to everyone. The idea of a meaningful "spring break" for radiologists is one whose time has come. Don't miss it!

Raymond A. Gagliardi
President Elect, ARRS

Forthcoming ARRS Meeting Information

Details of the American Roentgen Ray Society Meeting in Miami Beach, FL, April 26-May 1, 1987, will appear in the **February** and **March** 1987 issues of the *AJR*. The complete scientific program, abstracts of the instructional courses, information about social events, and hotel and travel forms will be published in the Journal.

See pages 110, 114, 124, and 130 of this issue for more information concerning the meeting.

Letters

Anomalous Drainage of the Common Bile Duct: Demonstration of Hepatobiliary Imaging

The common bile duct normally empties into the second portion of the duodenum. Drainage into the horizontal or third portion of the duodenum is a rare finding, which was previously observed only in autopsies and intraoperative radiologic procedures. The appearance of this anatomic curiosity in a nuclear medicine study is reported here.

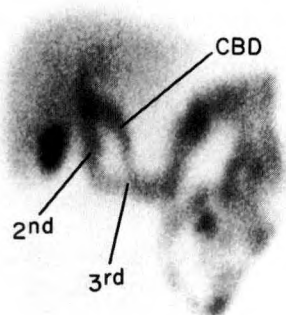
A 64-year-old man with end-stage renal disease and non-insulin-dependent diabetes mellitus presented at the hospital with epigastric pain of sudden onset associated with severe vomiting. The serum amylase was 1600 U/l (normal: 25–115 U/l), and the serum lipase was 90 U/l (normal: 4–24 U/l). The working diagnosis was acute pancreatitis, and appropriate therapy was started.

Scintigraphy, performed with 7 mCi of ^{99m}Tc Disofenin, revealed adequate tracer uptake by the liver and rapid visualization of the gallbladder and common bile duct. Although the presence of acute cholecystitis was excluded, an anomalous drainage of the common bile duct into the third portion of the duodenum was seen (Fig. 1). An endoscopic examination confirmed the presence of the Papilla of Vater in the third portion of the duodenum. The patient recovered with conservative treatment.

The junction of the bile duct and the duodenum in most people occurs in the second portion, about 7.5 to 10 cm below the pylorus. However, the junction can occur in the gastric antrum, duodenal bulb, third portion of the duodenum, or even the fourth portion.

The true prevalence of drainage into the horizontal portion is unknown. Puente and Bannura [1] reported eight cases in a series of operative cholangiograms (0.2%), but Lurje [2] found a prevalence of 8% in 194 autopsies performed in Moscow. An ethnic explanation has been proposed for this high prevalence.

Fig. 1.—Scintigram showing common bile duct entering horizontal portion of duodenum. CBD = common bile duct; 2nd = second portion of duodenum; 3rd = third portion of duodenum.



With the widespread use of hepatobiliary imaging, this variant will undoubtedly be encountered and must be recognized. Although the anomalous drainage can be considered a normal variant with no known clinical implications, its recognition may help guide the endoscopist attempting an ERCP or the surgeon contemplating biliary tree surgery.

Carlos A. Encarnacion
Samuel Sostre

Veterans Administration Medical and Regional Office Center
San Juan, Puerto Rico 00936

REFERENCES

1. Puente SG, Bannura G. Radiological anatomy of the biliary tract: variations and congenital abnormalities. *World J Surg* 1983;7(2):271–276
2. Lurje A. The topography of extrahepatic biliary passages. *Ann Surg* 1937;105:161–168

High Tech Days—Low Tech Reports

Few radiology departments will escape the rapid deployment of computers [2]. Radiology reports are often structured via word processors and handled further by the data bases of dedicated departmental computers or hospital main frames. However, the radiologist who enters a suboptimal report into the computer becomes the bottleneck in an expensive system. The word processor can be no better than the thought processor, and the technology will be improperly used.

Today reporting is so fundamental to the radiologist that the radiology report merits high priority in the literature and residency programs. The ideal report, like any medical consultation, should be the concise and accurate transfer of information regarding patient diagnosis and management [3]. The elements of such a report include pertinent observations; reasonable and logical development of implications, conclusions, and perhaps suggestions for further investigation. Just as the report must be accurate, the information must have appropriate context. With progressive subspecialization in radiology there is a lamentable problem in integrating the results of various diagnostic studies. Too often subspecialized radiologists do not reconcile their results with those of other diagnostic procedures [1]. Formulation of a report may require review of that patient's previous studies with appropriate comment.

When that report has been assembled and has reached the computer's data bank, the radiologist should consider if there is need for a more pedestrian form of technology—the telephone. Telephone

communication with the clinician is rapid and provides a safety net for an important report that may be overlooked, delayed, or misplaced. Such direct communication satisfies concerns for expedience, ethics, and malpractice, not to mention the educational value in discussing a particular disease process. Whether a radiologist issues 20 or 100 reports a day, several key telephone calls would represent a small amount of time well spent.

Radiologists should ask themselves more often if they are using the high technology available today optimally.

L. F. W. Martin
St. Joseph's Hospital
Hamilton, Ontario
L8N 4A6 Canada

REFERENCES

1. Heilman RS. What's wrong with radiology? *N Engl J Med* 1982;306:477-479
2. Lodwick GS. Pictorial information systems and radiology: improving communications. *Appl Radiol* 1986;May/June:18-32
3. Martin LFW. Opinion. Is this your report? *J Can Assoc Radiol* 1982;33:255-256

An Alternative Method to Identify Location of Catheter Entrance

In response to two articles recently published in *AJR* [1,2], we want to mention an alternative method to identify the exact location of the catheter entrance into the arterial lumen during percutaneous catheterization techniques, particularly during percutaneous transluminal angioplasty (PTA). This is of great importance during PTA to avoid inflating the balloon at the site of the catheter's entrance into the artery when a lesion close to the puncture site is to be dilated. Inflation of the balloon at the entrance site could be disastrous.

Dorne et al. [1] described a method that uses a radiolucent catheter outlined by contrast material in the arterial lumen (outside of the catheter lumen). Bakal and Sprayregen [2] suggested an alternative method that uses a spot film of the needle and guidewire at the puncture site. The change in caliber from the needle to the guidewire is the indicator of the site of arterial entrance.

For many years we have used another and perhaps simpler method. After the artery has been punctured, the needle has been withdrawn, and the arterial blood has spurted from the hub of the needle, the stylet of the needle is reintroduced and a lead bead is taped to the skin to mark exactly the entry site of the needle into the

artery. Then a spot film is taken. Care should be taken to center the spot film to avoid parallax (Fig. 1). This simple method allows rapid and exact location of the catheter entrance into the common femoral artery.

Jaime Tisnado
Diran Bezirdjian
Shao-Ru Cho
Medical College of Virginia
Richmond, VA 23298

REFERENCES

1. Dorne HL, Satin R, Palayew MJ. Method for determining arterial entry site for catheter. *AJR* 1986;146:175
2. Bakal CW, Sprayregen S. Determining arterial entry site for catheter. *AJR* 1986;147:438

Reply

Tisnado et al. have described an interesting method for localization of the arterial puncture site during percutaneous transluminal angioplasty. However, we think that it is neither as simple, rapid, or efficacious as the methods described by Dorne et al. and by ourselves.

Both previously described methods require only analysis of needle and guidewire or of catheter position as they have been placed during normal conduct of the case; they demand no extra manipulation. The technique described by Tisnado et al., however, requires replacement of the stylet after arterial puncture, followed by fluoroscopic localization of the needle tip with a lead skin marker. These extra steps not only prolong the procedure, but they also could result in dislodgment of the puncture needle. An added advantage of the previously described techniques over that of Tisnado et al. is that the marker is within the artery, rather than on the soft tissues spatially removed from the artery, and therefore not subject to changes due to displacement of the soft tissues. Also, placement of the lead bead on the skin over the needle tip may involve additional radiation to the operator's fingers.

We thus fail to see how this method is simpler than those that have been described previously.

Curtis W. Bakal
Seymour Sprayregen
Montefiore Medical Center
Department of Radiology
Albert Einstein College of Medicine
Bronx, New York 10467

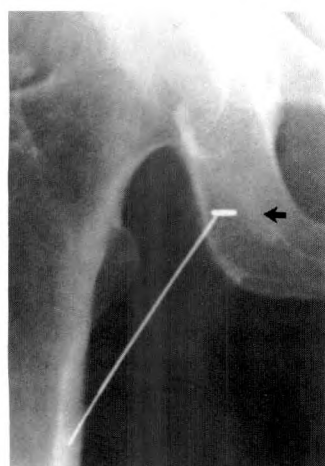


Fig. 1.—Radiograph shows lead marker (arrow) taped to skin, marking entry site of the needle into artery.

Is Fine-Needle Biopsy of Liver Hemangioma Hazardous?

In the June issue of *AJR*, Takayasu et al. [1] described the radiologic features of liver hemangioma in three atypical cases.

The authors mention that the danger of percutaneous needle biopsy is well documented and refer to two articles [2, 3]. In 1970, Adam et al. [2] described one fatal hemorrhage after an incisional operative biopsy of a hemangioma. Adam et al. also referred to two other articles that indicated that aspiration or biopsy of a liver hemangioma was hazardous. One of them was published in 1903 and the other in 1912. Kato et al. [3] referred to four fatalities after exploratory paracentesis or external needle biopsy of a liver hemangioma.

In recent years, the technique of aspiration biopsy for cytologic diagnosis has radically changed. Disposable fine needles have surpassed other instruments, and guided aspirations have replaced blind biopsies. Hemorrhage has not been a problem in guided transhepatic

fine-needle biopsies of liver hemangiomas [4]. This is important information for anyone who performs diagnostic aspirations of focal changes of the liver. The spectrum of radiologic features of a liver hemangioma is so wide [5, 6] that it is hardly possible to exclude it, and an inadvertent biopsy of a hemangioma may be performed when focal liver lesions are aspirated.

In our clinic we do not hesitate to aspirate a suspected hemangioma when malignant disease cannot be excluded. We have had no complications. In most cases we have obtained a specific diagnosis from the aspirated mesenchymal cells.

There is no proof that fine-needle aspiration biopsy of a liver hemangioma is hazardous with the present technique and instruments. We encourage use of it for the differential diagnosis of hemangioma and other focal liver diseases.

Matti Taavitsainen
Leena Kivisaari
Meilahti Hospital
Helsinki University Central Hospital
SF 00290 Helsinki
Finland

REFERENCES

1. Takayasu K, Moriyama N, Shima Y, et al. Atypical radiographic findings in hepatic hemangioma: correlation with histologic features. *AJR* 1986; 146:1149-1153
2. Adam YG, Huvois AG, Fortner JG. Giant hemangiomas of the liver. *Ann Surg* 1970;172:239-245
3. Kato M, Sugawara I, Okada A, et al. Hemangioma of the liver. Diagnosis with combined use of laparoscopy and hepatic arteriography. *Am J Surg* 1975;129:689-703
4. Solbiati L, Livraghi T, De Pra L, et al. Fine-needle biopsy of hepatic hemangioma with sonographic guidance. *AJR* 1985;144:471-475
5. Cosgrove D, McCready R. *Ultrasound imaging. Liver, spleen and pancreas*. Chichester: Wiley, 1982
6. Baert AL, Marchal GJ, Wilms GE, et al. A comparative study of angiography and dynamic computed tomography in liver angioma. *CT* 1982;6:245-255

Reply

We believe that fine-needle biopsy is contraindicated in an operable patient in whom the diagnosis of hemangioma cannot be established even with the currently available imaging techniques.

With real-time sonography, asymptomatic small lesions are frequently and incidentally detected in the liver. It is not always easy to differentiate hemangioma from malignant lesions (such as hepatocellular carcinoma and metastatic cancer) by sonography alone [1]. If dynamic CT is carried out, most hemangiomas are correctly diagnosed because of the characteristic findings [2], except for a small number of cases in which fibrosis, thrombosis, or fluid collection is present in the mass as described in our paper. In Japan, CT is routinely carried out when sonography has shown a lesion that appears to be hemangioma. Even though angiography is performed in patients in whom CT has failed to make a definitive diagnosis, the diagnostic capability of angiography for hemangioma is the same as that of CT (89%, unpublished data). Thus, there are occasional difficulties with the diagnosis of hemangioma.

In our hospital, sonography- or CT-guided (fine) needle biopsy is not commonly done because of possible complications (e.g., hemorrhage [3], pneumothorax, and needle-tract seeding [4]). One of our patients had advanced liver cirrhosis, and sonography detected a small, low-echo lesion (about 1 cm) in the immediate subcapsular region (Fig. 1). CT failed to detect the lesion. Finally, 21-gauge needle aspiration was carried out, but only blood was obtained. Two hours

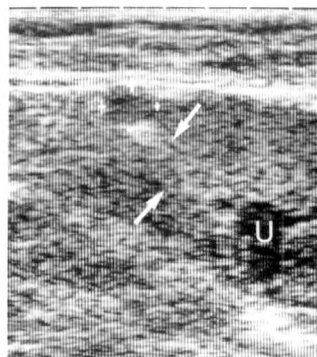


Fig. 1.—Sonogram shows solitary low-echo lesion (cursors) in the subcapsular area of the liver. Small hepatocellular carcinoma was strongly suspected and fine-needle aspiration was carried out three times. Even though an echogenic structure suggesting fibrotic changes (arrows) of umbilical vein was recognized, vessel communication between the umbilical portion of the left portal vein (U) and this lesion was not shown.

later the patient underwent laparotomy because of hypotension and suspected hemorrhage. The bleeding lesion was a locally dilated paraumbilical vein.

Needle-tract seeding was experienced in at least two patients with hepatocellular carcinoma who were referred to our hospital after fine-needle biopsy. Sakurai et al. [5] also reported needle-tract implantation of hepatocellular carcinoma in the skin, after biopsy with a thin Trucut needle. Even though the frequency of these complications is low [6], the sequelae are serious. Therefore, we believe that even fine-needle biopsy should not be done before hepatectomy in patients who have a suspected malignancy and are operable, or in patients in whom the diagnosis of hemangioma cannot be established, even though imaging techniques have been fully used. There is a relative indication for fine-needle biopsy in inoperable patients who have multiple lesions strongly suspected to be malignancies.

Another reason to avoid fine-needle biopsy is the difficulty in interpretation when blood alone instead of epithelial cells is aspirated from the lesion. Solbiati et al. reported the same aspiration finding in 24 of 33 hemangiomas. We also had the same result in one patient in whom enhanced CT could not be done because of severe allergic reactions to contrast medium; blood alone was aspirated by fine-needle biopsy.

For these reasons, in our hospital, surgery is performed for patients who have a suspicious malignancy and whose diagnosis remains uncertain despite various diagnostic procedures.

Kenichi Takayasu
Katsuhiko Uesaka
Department of Diagnostic Radiology
National Cancer Center Hospital
Chuo-ku Tokyo 104
Japan

REFERENCES

1. Bree RL, Schwab RE, Neiman HL. Solitary echogenic spot in the liver: is it diagnostic of a hemangioma? *AJR* 1983;140:41-45
2. Itai Y, Frui S, Araki T, Yashiro N, Tasaka A. Computed tomography of cavernous hemangioma of the liver. *Radiology* 1980;137:149-155
3. Riska H, Friman C. Fatality after fine-needle aspiration biopsy of liver (letter). *Br Med J* 1975;1:517
4. Ferrucci JT, Wittenberg J, Margolies MN, Carey RW. Malignant seeding of the tract after thin-needle aspiration biopsy. *Radiology* 1979;130:345-346
5. Sakurai M, Seki K, Okamura J, Kuroda C. Needle tract implantation of hepatocellular carcinoma after percutaneous liver biopsy. *Am J Surg Pathol* 1983;7:191-195
6. Smith EH. The hazards of fine-needle aspiration biopsy. *Ultrasound Med Biol* 1984;10:629-634

News

Addendum on International Symposium on MR Imaging-'87

Details concerning the second International Symposium on MR Imaging-'87 (Jan. 29-Feb. 1, 1987) were published in August 1986 *AJR*. Information: Sekretariat Prof. Dr., J. Lissner, Radiologische Klinikum Grobhadern, Marchioninstr. 15, 8000 Munchen 70, West Germany; (089) 7095-2750.

AFIP Neuroradiology Review Course

The Armed Forces Institute of Pathology, the American College of Radiology, and the American Registry of Pathology will sponsor a course to review the basics of neuroradiology with an emphasis on pathologic correlation and pathophysiology, Feb. 23, 1987, at the Hyatt Regency Bethesda, Bethesda, MD. Course director: James G. Smirniotopoulos. Information: James G. Smirniotopoulos, M.D., Chief, Section of Neuroradiology, Dept. of Radiologic Pathology, American Registry of Pathology, AFIP, Washington, DC 20306-6000; (202) 576-2973.

Aspen Uroradiology Seminar

The School of Medicine in New Orleans of Louisiana State University will sponsor the Aspen Uroradiology Seminar March 1-4, 1987, at the Inn at Aspen, Aspen, CO. The seminar will focus on interventional radiology with discussions of new contrast media for MR, CT, and sonography. A special session on oncologic diagnostic radiology and interface of diagnostic oncoradiology and radiation therapy, as well as a mini-symposium on current concepts of management of urinary tract calculi will be included. Information: Erich K. Lang, M.D., Professor and Chairman, Program Coordinator, Dept. of Radiology, Louisiana State University Medical Center, 1542 Tulane Ave., New Orleans, LA 70112-2822; (504) 568-4646.

Sierra Radiology Conference

The Sacramento Radiology Research and Education Foundation will sponsor a conference on March 2-6, 1987, at the Hyatt Lake Tahoe Hotel in Incline Village, NV. The emphasis of this year's course will be on imaging and invasive techniques. It is designed for practicing diagnostic radiologists with a particular interest in clinical radiology. Guest faculty: E. vanSonnenberg, R. B. Lufkin, H. Goldberg, and B. Klein. Category 1 credit: 20 hr. Fee: \$385; \$285; fellows, residents. Information: John P. McGahan, M.D., or John P. Walter, Ph.D., M.D., Sacramento Research and Education Foundation, P.O. Box 19184, Sacramento, CA 95819.

Skeletal Symposium

The Department of Radiology, Hospital of the University of Pennsylvania, will sponsor its 10th annual Skeletal Symposium on March 9-13, 1987, at Sun Valley, ID. Guest faculty: H. K. Dunn, D. M. Forrester, M. I. Gelman, J. J. Kaye, J. C. Mall, M. J. Pitt, D. Resnick, and R. G. Volz. Category 1 credit: 23 hr. Fee: \$445; \$325: residents. Information: Janice Ford, CME Coordinator, Dept. of Radiology, Hospital of the University of Pennsylvania, 3400 Spruce St., Philadelphia, PA 19104.

Breast Disease Update IV Seminar

Mount Sinai Medical Center of Greater Miami will sponsor a Breast Disease Update seminar March 18-22, 1987, at the Hilton in Walt Disney Village at Lake Buena Vista, FL. A comprehensive review of current and new advances in the diagnosis and management of breast disease will be presented with emphasis on the state-of-the-art film mammography and breast sonography as complementary techniques. Special attention will be given to clinical mammography, sonography, and pathology correlations. Category 1 credit: 18 hr. Fee: \$375; \$185: residents, fellows, technicians. Information: Dept. of Continuing Medical Education, 4300 Alton Rd., Miami Beach, FL 33140; (305) 674-2311.

Pediatric Radiology 1987

The Department of Radiology, The Children's Hospital of Philadelphia, will present Pediatric Radiology 1987 on March 19-21, 1987, at The Children's Hospital of Philadelphia. In-depth presentation of state-of-the-art imaging in infants and children, lectures, workshops, and refresher courses will be offered to cover a wide gamut of pediatric diseases and the appropriate applications for sonography, MR, CT, scintigraphy, and Doppler sonography. Category 1 credit. Fee: \$300; \$200: residents, technologists. Information: Henrietta Rosenberg, M.D., Dept. of Radiology, The Children's Hospital of Philadelphia, 34th St. and Civic Center Blvd., Philadelphia, PA 19104; (215) 596-9308.

Neuroradiology at Vail

The Department of Radiology at the Hospital of the University of Pennsylvania will sponsor Neuroradiology at Vail on March 23-27, 1987, at the Westin Hotel, Vail, CO. Category 1 credit: 23 hr. Fee: \$495; \$350: residents. Course director: Herbert I. Goldberg. Information: Janice Ford, CME Coordinator, Dept. of Radiology, Hospital

of the University of Pennsylvania, 3400 Spruce St., Philadelphia, PA 19104; (215) 662-2904 or (215) 662-6982.

Differential Diagnosis in Radiology

The University of Michigan will present its 4th annual course Differential Diagnosis in Radiology: Review Course for Residents on April 3-5, 1987, in Ann Arbor, MI. The course will emphasize a case-solving approach to the unknown radiograph. Differential diagnostic features on common radiographic abnormalities will be stressed in lecture and workshop settings. Category 1 credit: 18 hr. Fee: \$125. Information: B. H. Gross, M.D., Dept. of Radiology, Box 0030, University of Michigan Medical School, University Hospital B1D502/0030, 1500 E. Medical Center Dr., Ann Arbor, MI 48109-0030; (313) 936-4477.

Mammography Course

The Department of Radiology, Tufts-New England Medical Center, will sponsor the 1987 tutorials, Mammography for the General Radiologist, on April 6-9, May 18-21, Oct. 5-8, and Nov. 2-5, 1987, in Boston, MA. This intensive course is designed to teach a practical approach to mammography to the general radiologist. Enrollment in each session is limited to 25. Category 1 credit: 28 hr. Fee: \$700. Information: Dr. M. J. Homer, Box 388, Dept. of Radiology, New England Medical Center Hospital, 750 Washington St., Boston, MA 02111.

The Profession of Medical Physics

The Southern California Chapter of the American Association of Physicists in Medicine will hold the 1987 spring seminar April 29-May 1, 1987, at Caesars Tahoe, Lake Tahoe, CA. The purpose of this seminar will be to assess the present and future professional status of physicists in medicine. Topics will be the current and future aspects or roles of the rival colleges and boards, professional fees, licensure, continuing education, and professional interactions with physicians and administrators. Presentations will be made by students chosen to receive the Norman A. Baily awards. Information: Dr. Norman A. Baily, Dept. of Radiology, M-010, University of California, San Diego, La Jolla, CA 92093.

Surgical Neuroangiography

New York University Medical Center will sponsor a surgical neuroangiography course May 4-8, 1987, at NYU Medical Center, New York, NY. This course is divided into didactic lectures on anatomy, nursing, techniques of embolization surgery of vascular lesions, and embolization and the clinical presentation of the various disease entities that can be treated transvascularly. Direct participation of registrants will be accomplished by workshops on materials and anatomy. Guest faculty: J. Eskridge, G. Hieshima, J. Folkman, C. Kerber, J. Pile-Spellman, and A. G. Valavanis. Category 1 credit: 28 hr. Fee: \$600. Information: NYU Medical Center Post-Graduate Medical School, 550 First Ave., New York, NY 10016; (212) 340-5295.

Echocardiography 1987

Tufts University School of Medicine will sponsor its 3rd annual echocardiography symposium on May 14-16, 1987, with a basic workshop on May 13, 1987, at the Hyatt Regency Hotel, Cambridge, MA. The course is designed for cardiologists, radiologists, and ech-

ocardiography technicians. Topics covered include: 2-dimensional echocardiography, Doppler echocardiography, color flow Doppler imaging, technical aspects, interpretative approaches, and clinical implications. Course director: Natesa G. Pandian. Guest faculty: A. DeMaria, R. DeSanctis, H. Feigenbaum, J. Gardin, R. Kerber, R. Martin, N. Nanda, A. Parisi, W. Roberts, D. Sahn, Pravin Shah, and Samuel Wann. Category 1 credit available. Information: Tufts University School of Medicine, Office of Continuing Education, 136 Harrison Ave., Box 36, Boston, MA 02111.

Delaware Valley MRI Society Meetings

A new society, the Delaware Valley MRI Society, will offer monthly meetings on Thursday evenings throughout the academic year at the Philadelphia County Medical Society, 2100 Spring Garden St., from 7-9 p.m. Information: David P. Mayer, M.D., Radiology Associates, Albert Einstein Medical Center, York and Tabor Rd., Philadelphia, PA 19141.

Clinical Ultrasound Fellowships

The Ultrasound Department at Vancouver General Hospital, Vancouver, BC, offers year-round fellowships for 1 to 12 weeks at the University of British Columbia, under Dr. Peter L. Cooperberg. Heavy ultrasound caseload with Doppler and real-time techniques are emphasized. Information: Gail Hourigan, Ultrasound Dept., Vancouver General Hospital, 855 W. 12th Ave., Vancouver, BC V5Z 1M9, Canada.

Pfizer \$50,000 Award for Innovation in Medical Devices

Pfizer Hospital Products Group has posted a \$50,000 "Award for Innovation" in medical devices. The Award will recognize an individual or research team for excellence in medical device innovation and encourages further research and development of medical devices to manage and treat diseases. Any person in a health care-related field is eligible to submit an entry. The deadline for applications is January 30, 1987, and the Award recipient will be announced in May 1987. Application information: George Flouty, MD, Pfizer Hospital Products Group, 235 E. 42nd St., New York, NY 10017; Attn: Award for Innovation.

Meeting and Course Review

For reader convenience, a summary of upcoming meetings and courses is provided. Detailed listings in the *AJR* issues are noted in parentheses.

UC San Diego Courses: Physicians Imaging Courses 1987, times arranged, San Diego, CA (Nov)

International Symposium on Breast Cancer, Jan. 1-4, New Delhi, India (Aug)

University of Texas Continuing Medical Education, Radiation Safety Officer's Course, Jan. 5-9 or May 18-22; **Radiotherapy Treatment Planning Anatomy**, Jan. 26-30; **Basic Radiologic Health**, Feb. 9-13; **Review of Radiation Calculations**, Feb. 16-18; **Advanced Radiologic Health**, May 11-15, San Antonio, TX (all Sept)

International Continuing Medical Education Series: Controversies in Medicine & Surgery, Jan. 16-23, St. Moritz, Switzerland; **Clinical Update in Medicine & Surgery**, Feb. 10-17; Feb. 17-24, Maui, HI; **Topic to be announced**, March 14-21, Banff, Canada; **Topic to be**

announced, May 20–26, Japan; **Topic to be announced**, May 20–26, Bermuda; **Topic to be announced**, June, Ireland; **Topic to be announced**, July 24–30, Pebble Beach, CA; **Topic to be announced**, Aug., Gstaad, Switzerland (all Oct)

Uroradiology Course, Jan. 19–20, Bethesda, MD (Dec)

Nuclear Medicine Update: 1987, Jan. 19–22, Philadelphia, PA (Nov)

UC San Francisco Courses; Diagnostic Radiology Seminars, Jan. 19–23, Ixtapa, Mexico; Feb. 1–6, Aspen, CO; Feb. 22–27, Park City, UT; **Diagnostic Imaging: 1987**, March 16–21, Waiohai, Kauai, HI (all Oct)

Interventional Radiology and Didactic Imaging, Jan. 24–30, St. Thomas, U. S. Virgin Islands (Nov)

International Symposium on MR 1987, Jan. 29–Feb. 1, Garmisch-Partenkirchen, Bavaria (Aug)

Los Angeles Radiological Conference, Jan. 30–Feb. 1, Los Angeles (Oct)

The Pacific Radiological Institute Courses, Honolulu, HI (weekly courses) Feb.–April (Dec)

Perspectives on Imaging Modalities, Feb. 2–6, Cancun, Mexico (Sept)

Palm Beach Magnetic Resonance Imaging Update, Feb. 8–11, West Palm Beach, FL (Dec)

Big Sky Radiology Conference, Feb. 8–13, Great Falls, MT (Oct)

Advanced Course in Diagnostic Imaging, Feb. 8–13, Singapore (Nov)

Gastrointestinal Radiologists Meeting and Course, Feb. 8–13, Scottsdale, AZ (Aug)

Sun Valley Imaging, Feb. 14–21, Sun Valley, ID (Nov)

Intermountain Imaging Conference, Feb. 14–21, Snowmass, CO (Nov)

Postgraduate Course in Diagnostic Imaging, Feb. 14–21, Cancun, Mexico (Nov)

Thoracic Imaging 1987, Feb. 16–19, Orlando, FL (May)

University of Arizona Postgraduate Practical Radiology Course, Feb. 16–19, Loews Ventana Canyon Resort, AZ (Nov)

Mammography: A Practical Approach, Feb. 16–20, Aspen, CO (Nov)

Sonomammography, Feb. 16–20, Thomas Jefferson Hospital, Philadelphia, PA (Nov)

Radiologic-Pathologic Concepts in Diagnosis, Feb. 19–23, Lake Buena Vista, FL (Nov)

Diagnostic Radiology and Nuclear Medicine, Feb. 21–28, St. Thomas, U. S. Virgin Islands (Oct)

Vail Winter Imaging Seminar III, Feb. 21–28, Vail, CO (Dec)

Radiation Research Society Meeting, Feb. 22–26, Atlanta, GA (July)

Medical Imaging Conference in the High Sierras, Feb. 22–27, Lake Tahoe, NV (Nov)

Masters Diagnostic Radiology Conference, Feb. 22–27, 1987, Maui, HI (Nov)

Advanced Perinatal Ultrasound Seminar, Feb. 26–28, Lake Buena Vista, FL (Aug)

Society for Magnetic Resonance Imaging, Feb. 28–March 4, San Antonio, TX (Oct)

George Simon Award—The Fleischner Society, deadline March 1 (Dec)

Practical Radiology 1987, March 1–6, Vancouver, BC, Canada (Nov)

Intermountain Imaging Conference—Extension, March 1–7, Snowbird, UT (Nov)

Winter Imaging at Stowe, VT, March 2–6, Stowe, VT (Dec)

Computed Body Tomography 1987—The Cutting Edge, March 5–8, Orlando, FL (Nov)

Diagnostic Imaging and Interventional Radiology, March 8–13, Park City, UT (Dec)

Positron Emission Tomography and the Chemistry of Mental Illness, March 12–13, Baltimore, MD (Dec)

London Course in Whole Body CT, March 15–19, Auchterarder, Perthshire, Scotland, UK (Nov)

Diagnostic Radiology Conference on Imaging Modalities in Chest and Abdomen, March 16–20, Maui, HI (Dec)

Ultrasound at Vail, March 22–28, Vail, CO (Nov)

Diagnostic Angiography and Interventional Radiology, March 23–26, San Diego, CA (Nov)

Radiology and Early Colon Cancer Workshop, March 30, Denver, CO (Nov)

Federation of Western Societies of Neurological Science Meeting, March 30–April 1, Coronado, CA (Dec)

Society of Computed Tomography Meeting/Course, March 30–April 3, San Diego, CA (Dec)

Alexandria International Conference on Laryngeal Cancer, April 1–2, Alexandria, Egypt (Sept)

Intrauterine Diagnosis and Treatment: the New Frontier, April 2–4, San Diego, CA (Nov)

American Radium Society Meeting, April 6–10, London (Aug)

Annual Meeting, National Council on Radiation Protection and Measurements, April 8–9, Bethesda, MD (Sept)

Radiation Therapy Clinical Research Seminar, April 23–25, Gainesville, FL (Dec)

Fleischner Society Annual Symposium, May 21–23, San Francisco, CA (July)

1987 Radiology Congress, Lisbon, May 31–June 6 (Aug)

Society of Nuclear Medicine Annual Meeting, June 2–5, Toronto, Ontario, Canada (Dec)

American Board of Radiology Examinations. Oral examinations: June 8–12, 1987; May 23–27, 1988; June 5–9, 1989, all at Louisville, KY. Written examinations: Oct. 8–9, 1987; Oct. 6–7, 1988; Oct. 5–6, 1989 (Dec)

Euroson '87, June 14–18, Helsinki, Finland (Sept)

International Conference on Computer Assisted Radiology, July 1–4, West Berlin (Feb)

Sarcoidosis and Granulomatous Disorders, congress, Sept. 6–11, Milan (June)

The Asian-Oceanian Congress of Radiology, Sept. 21–25, Seoul, South Korea (Nov)

AJR carries announcements of courses, symposia, and meetings of interest to its readers if received a minimum of 5 months before the event. There is no charge; receipt of items by the AJR Editorial Office is not acknowledged. Submit items for publication typed double spaced. Provide title, date, location, brief description, sponsor, course directors, fees, category I credit, and address and telephone number for additional information. Faculty from the host institution will not be listed. Guest faculty names will appear **only** if initials are provided. Mail news items to AJR Editorial Office, 2223 Avenida de la Playa, Suite 200, La Jolla, CA 92037.

Classified Advertising

Positions Available

ISRAEL, DIAGNOSTIC RADIOLOGY. Opportunities for 3-4 week or longer working vacations in a number of Israeli medical centers, on a volunteer basis. Positions varied, arrangements flexible. For information contact: Jonathan H. Fish, M.D., 1844 San Miguel Dr., #302, Walnut Creek, CA 94596; (415) 947-0560. 8xa

IMMEDIATE OPENING—BC/BE RADIOLOGIST to join 8-man group in South Bay area of northern CA. Hospital and private office practice. All diagnostic modalities including MRI. Send CV to Box M3, A/JR (see address this section). 1-3ap

ULTRASOUND/CT/MRI. Opportunity for board-certified radiologist specializing in ultrasound, body CT, and body MRI to pursue academic career at The New York Hospital-Cornell Medical Center. Dept. provides state-of-the-art equipment, including Acuson ultrasound, GE 9800 CT, and GE Signa 1.5 Tesla MR. Wide variety of ultrasound examinations include abdominal, doppler, Ob-Gyn, small parts, and neonatal head. Prefer candidate with prior fellowship in sectional imaging or ultrasound. Responsibilities include clinical practice, teaching, and research. Please send CV to Elias Kazam, M.D., Dept. of Radiology, The New York Hospital-Cornell Medical Center, 525 East 68th St., New York, NY 10021. 1-2a

RADIOLOGIST—ST. LUKE'S-ROOSEVELT HOSPITAL CENTER, NYC is searching for a radiologist with broad experience in general radiology and with expertise in ultrasound, CT, and mammography. The Hospital is a 1315-bed voluntary university hospital of Columbia University, College of Physicians and Surgeons. Candidates should meet the requirements for faculty appointment. Excellent remuneration. Please send inquiries with a CV to Ronald C. Ablow, M.D., Dept. of Radiology, St. Luke's-Roosevelt Hospital, Amsterdam Ave. & 114th St., New York, NY 10025. An equal opportunity employer. 1a

GENERAL DIAGNOSTIC RADIOLOGIST with expertise in skeletal and/or mammographic radiology is being sought for St. Luke's-Roosevelt Hospital Center, 1315-bed voluntary university hospital of Columbia University, College of Physicians and Surgeons, New York City. Fellowship or practice experience, together with interest in teaching, is desirable. Excellent remuneration. Please send inquiries with a CV to Ronald C. Ablow, M.D., Dept. of Radiology, St. Luke's-Roosevelt Hospital, Amsterdam Ave. & 114th St., New York, NY 10025. An equal opportunity employer. 1a

RADIOLOGY—GROUP HEALTH ASSOCIATES is a 45-member multi-specialty group practice searching for a full-time board-eligible/board-certified radiologist to complement our existing radiology staff. We operate an entirely ambulatory service to include IVP, fluoroscopy, ultrasound, mammography, etc. We project continued aggressive expansion and growth of the group as a whole and of the radiology dept. in particular. Please send CV to Search Committee, Group Health Associates, Inc., 2915 Clifton Ave., Cincinnati, OH 45220. 1a

TWO YOUNG RADIOLOGISTS seek a third radiologist in expanding hospital-based practice near Canadian border in northern New York. All modalities available. Write P. Berman, HC 61 Box 454, Massena, NY 13662. 8-7a

BOARD CERTIFIED diagnostic radiologist. All diagnostic modalities except MR. MR installation planned in 1½ years. Busy in-patient and out-patient practice. Salary negotiable and early partnership available. Send CV to Box C23, A/JR (see address this section). 6xa

THE DEPT. OF RADIOLOGY AT THE UNIVERSITY OF MINNESOTA has a 1-yr, full-time, temporary, nontenured position in the Div. of Nuclear Medicine available at the rank of Instructor beginning July 1, 1987. Minimum requirements include board certification in radiology by beginning date of appointment, and an accredited radiology residency. Responsibilities will include graduate and undergraduate medical instruction and assisting with related dept. research projects. Responsibilities will also include providing both in-patient and out-patient clinical services. Equipment is state-of-the-art within new 500-bed medical center, providing 6,000 in-patient and 3,000 out-patient nuclear medicine exams each year. Salary is negotiable, competitive, and is dependent upon past scholarly productivity and post-M.D. experience. Successful candidates must be licensed or able to obtain license to practice medicine in the State of Minnesota before appointment date. Applications will be accepted through May 15, 1987. Send letters and resumes to Robert Boudreau, M.D., Div. of Nuclear Medicine, Dept. of Radiology, Box 362 UMHC, University of Minnesota Hospital, 420 Delaware St., S.E., Minneapolis, MN 55455. The University of Minnesota is an equal opportunity educator and employer and specifically invites and encourages applications from women and minorities. 1a

UNIVERSITY HOSPITALS OF CLEVELAND is seeking a board-certified radiologist for an assistant professor position in nuclear medicine. Position entails work in both conventional nuclear medicine and in the PET facility. Teaching experience and demonstrated interest in research are desirable. Salary commensurate with experience. University Hospitals of Cleveland is a 900-bed hospital associated with Case Western Reserve University. Interested candidates should forward CV and approximate date of availability to Floro Miraldi, M.D., Director, Division of Nuclear Radiology, University Hospitals of Cleveland, 2074 Abington Rd., Cleveland, OH 44106. AA/EOE. 12-1a

DIRECTOR, NUCLEAR MEDICINE—Fully-equipped nuclear imaging facility being integrated with Diagnostic Radiology Dept. Access to other imaging modalities including CT, ultrasound, and MR, if desired. Nuclear medicine board certification required; research and scholarly endeavor essential aspects of position. Nuclear cardiology shared with Cardiology Division. Associate Professor or Professor, dependent on experience. Income from salary and private practice. Contact John Howieson, M.D., Chairman, Radiology L-340, Oregon Health Sciences University, Portland, OR 97201 (503) 225-7660. 1a

NEURORADIOLOGIST. Applications are being sought for an academically oriented neuroradiologist for a 612-bed teaching hospital. Position to start July 1987. Candidate should be board certified preferably with 2 yr of neuroradiology fellowship. Training in MR, CT, angiography, and myelography necessary. Individual will be the second neuroradiologist in an active, aggressive section. Private practice. Send current CV to Harvey L. Neiman, M.D., Chairman, Dept. of Radiology, The Western Pennsylvania Hospital, 4800 Friendship Ave., Pittsburgh, PA 15224. 12-2a

RADIOLOGY INSTRUCTOR to assist candidate in preparation for Oral Radiology Boards. Candidate needs practice in formally discussing cases and answering board-type questions. Would like to meet on a weekly basis beginning early 1987. Fee negotiable. Please call (215) 342-4110 or (615) 359-7092 eves. 12-2a

THE DEPT. OF RADIOLOGY AT THE UNIVERSITY OF MINNESOTA has 3 temporary, 2-yr fellowship trainee positions in cardiovascular radiology available at the rank of Instructor beginning July 1, 1987. Minimum requirements include board certification in radiology by beginning date of appointment and an accredited radiology residency. Successful candidates will be responsible for performance of all clinical procedures in specialty setting. Responsibilities also include graduate and undergraduate medical instruction and assisting with related dept. research projects. Salary is negotiable, competitive, and is dependent upon past scholarly productivity and post-M.D. experience. Successful candidates must be licensed or able to obtain license to practice medicine in the State of Minnesota before appointment date. Applications will be accepted through May 15, 1987 for all positions. Send letters to William M. Thompson, M.D., Professor and Chairman, Dept. of Radiology, Box 292 UMHC, University of Minnesota Hospital, 420 Delaware St., S.E., Minneapolis, MN 55455. The University of Minnesota is an equal opportunity educator and employer and specifically invites and encourages applications from women and minorities. 1a

THE DEPT. OF RADIOLOGY AT THE UNIVERSITY OF MINNESOTA has 8 tenure-track positions available at the rank of Assistant, Associate, or Full Professor. At the Assistant Professor level, minimum requirements are board certification in radiology and a minimum of 1-yr post-residency specialty training or experience in radiology. Appointment at the rank of Associate Professor requires a minimum of 4-yr post-residency experience and a demonstrated record of research, publication, and teaching in addition to the other qualifications listed for Assistant Professor status. Appointment at the rank of Professor requires a minimum of 6-yr post-residency experience and a demonstrated strong record of research, publication, and teaching in addition to the other qualifications listed for Assistant Professor status. Positions available are 1 pediatrics, 2 neuroradiology, 1 skeletal radiology, 1 chest, 1 ultrasound, and 2 abdominal/thoracic imaging. All but one of the neuroradiology positions begin February 1, 1987. The other neuroradiology position will begin July 1, 1987. Successful candidates will be responsible for performance of all clinical procedures in specialty setting. Responsibilities also include graduate and undergraduate medical instruction. Research performance will be strongly encouraged and evaluated. Salary is negotiable, competitive, and is dependent upon past scholarly productivity and post-M.D. experience. Applications will be accepted through January 31, 1987 for all positions with the exception of the 1 neuroradiology position beginning July 1, 1987. Applications for the July 1 neuroradiology position will be accepted through March 31, 1987. Send letters to William M. Thompson, M.D., Professor and Chairman, Dept. of Radiology, Box 292 UMHC, University of Minnesota Hospital, 420 Delaware St., S.E., Minneapolis, MN 55455. The University of Minnesota is an equal opportunity educator and employer and specifically invites and encourages applications from women and minorities. 1a

PEDIATRIC RADIOLOGIST. Large hospital-based group seeks associate with recent pediatric radiology fellowship training. Busy private practice group needs second pediatric radiologist for coverage of small pediatric hospital. Practice would include 25% pediatric and 75% adult work. All modalities including MRI. Board certification mandatory. Opportunity for partnership in well-established western Washington practice. Reply Box H74, A/JR (see address this section). 11-6a

RADIOLOGICAL PHYSICISTS. The Dept. of Radiology at Thomas Jefferson University Hospital/Jefferson Medical College wishes to recruit two highly qualified radiologic physicists. The first position is for an MRI physicist to work with our GE 1.5T MRI system currently being installed. He/she will work closely with radiologists in our MRI division on applied and basic research. The second position is for a physicist with particular interests in image processing. The Dept. has a broad range of interests in digital radiography, DSA, PACS, and other methods of improving information content of radiologic images. Candidates for both positions should have strong academic records and current research interests. Hard money support is available for both positions. Contact David C. Levin, M.D., Chairman, Dept. of Radiology, Thomas Jefferson University Hospital, Philadelphia, PA 19107. 11-1a

MRI/ULTRASOUND RADIOLOGISTS. The Dept. of Radiology at Thomas Jefferson University Hospital/Jefferson Medical College is seeking two academically oriented radiologists to join its MRI and Ultrasound divisions. Both divisions are housed in modern, spacious facilities with state-of-the-art technology. A GE 1.5 T MRI unit is now being installed. Candidates will have the option of working in either of these divisions or both, according to their interests. The Dept. is currently under new leadership, and is expanding in both size and academic scope. Generous salaries and benefits are offered. Contact David C. Levin, M.D., Chairman, Dept. of Radiology, Thomas Jefferson University Hospital, Philadelphia, PA 19107. 11-1a

THE DEPT. OF RADIOLOGY AT THE UNIVERSITY OF MINNESOTA has 9 temporary, 1-yr fellowship trainee positions available at the rank of Instructor beginning July 1, 1987. Minimum requirements include board certification in radiology by beginning date of appointment and an accredited radiology residency. Positions available are 1 pediatrics, 2 neuroradiology, 1 skeletal radiology, 1 chest, 1 ultrasound, 1 MRI, and 2 abdominal/thoracic imaging. Successful candidates will be responsible for performance of all clinical procedures in specialty setting. Responsibilities also include graduate and undergraduate medical instruction and assisting with related dept. research projects. Salary is negotiable, competitive, and is dependent upon past scholarly productivity and post-M.D. experience. Successful candidates must be licensed or able to obtain license to practice medicine in the State of Minnesota before appointment date. Applications will be accepted through May 15, 1987 for all positions. Send letters to William M. Thompson, M.D., Professor and Chairman, Dept. of Radiology, Box 292 UMHC, University of Minnesota Hospital, 420 Delaware St., S.E., Minneapolis, MN 55455. The University of Minnesota is an equal opportunity educator and employer and specifically invites and encourages applications from women and minorities. 1a

A 400-BED COMMUNITY HOSPITAL staffed by private practice group seeks a second neuroradiologist preferably with MR experience. Ongoing neuroradiologic service includes state-of-the-art CT, angiography with digital, and myelography. MR unit on order. Must be capable and willing to do general radiology also. Contact Ben R. Mayes, Jr., M.D., Radiology Dept., St. Luke's Hospital, 232 So. Woods Mill Rd., St. Louis, MO 63017, (314) 434-1500, ext. 4250. 11-1a

DIAGNOSTIC RADIOLOGIST. Need aggressive associate to perform all aspects of diagnostic radiology in well-equipped hospital with large outpatient component in South Texas. MR training a plus but not essential. Excellent salary and early partnership available. For confidential consideration please submit CV to Box H70, AJR (see address this section). 11-1a

BOARD-CERTIFIED DIAGNOSTIC RADIOLOGIST to join multispecialty private corporation, with a well-equipped X-ray area, dedicated mammography, nuclear medicine, high-resolution real-time ultrasound, and whole-body CT scanner. Send CV and reply to Raymond Kuntz, Administrator, Johnson Clinic, P.D., P.O. Box 315, Rugby, ND 58368. 12-1a

Positions Desired

PGY II RADIOLOGY POSITION sought for July 1, 1987 by quality American grad now engaged in medical internship at a major medical school affiliated with a New England teaching hospital. Reply Box M1, AJR (see address this section). 1-4bp

BOARD-CERTIFIED INTERVENTIONAL RADIOLOGIST, university background, some general radiology, seeking permanent position in moderate-size hospital. Reply Box 15414, Pittsburgh, PA 15237. 1b

BOARD-CERTIFIED RADIOLOGIST, currently angiography and interventional fellow at major university center, seeks hospital or private practice position beginning July 1987. Reply Box M5, AJR (see address this section) 1-2b

PGY-2 OR PGY-3 DIAGNOSTIC RADIOLOGY POSITION sought by resident with 16 months' training at midwest university program. Currently involved in MR and contrast research. Affable and committed. Available January 1987. Reply Box I90, AJR (see address this section). 12-1b

Fellowship and Residencies

INTERVENTIONAL RADIOLOGY FELLOWSHIP—JULY 1, 1987. One-year fellowship in interventional radiology available at George Washington University Medical Center. Training in all aspects of the field are covered including vascular, biliary, and genitourinary. Applicants must have completed an approved residency program in diagnostic radiology and be board eligible/board certified. Send letter of inquiry with CV to Edward M. Druy, M.D., George Washington University Hospital, Radiology Dept., 901 23rd St., N.W., Washington, DC 20037. Affirmative action/equal opportunity employer. 1c

CARDIOVASCULAR/INTERVENTIONAL RADIOLOGY FELLOWSHIP—Thomas Jefferson University Hospital announces a new fellowship program combining training in cardiac, vascular, and interventional radiology. One- and two-year positions are available beginning July 1, 1987. The 1-yr program offers intensive clinical experience in general angiography, coronary angiography, and interventional procedures. The 2-yr program emphasizes additional experience in interventional techniques and cardiac imaging, and provides time for research. Applicants should be board certified or in the certification process. Contact David C. Levin, M.D., or Geoffrey A. Gardiner, Jr., M.D. at Dept. of Radiology, Thomas Jefferson University Hospital, Philadelphia, PA 19107. 1-3c

TMJ MINI-RESIDENCY. University of Rochester School of Medicine and Dentistry offers 1- to 5-day periods designed for radiologists and dental clinicians involved in the diagnosis and treatment of TMJ internal derangements. Special emphasis placed on MR imaging, conservative and nonconservative treatment modalities. Offered 6 times per yr with limited registrations. Director, Richard W. Katzberg, M.D. Contact Judy Olevnik, University of Rochester Medical Center, Dept. of Radiology, P.O. Box 648, Rochester, NY 14642. (716) 275-8800. 1a

CARDIOPULMONARY RADIOLOGY FELLOWSHIP—The Dept. of Radiology of Thomas Jefferson University Hospital offers a fellowship in cardiopulmonary radiology. This innovative program provides intense training in pulmonary radiology under the guidance of a highly motivated staff in an academic university setting. It also includes experience in thoracic CT, percutaneous thoracic interventional procedures, cardiovascular MRI, cardiac angiography, and echocardiography. In close cooperation with the division of pulmonary medicine, an excellent background in the clinical and physiologic aspects of pulmonary disease will be provided. Applicants should be board certified or eligible. Contact Robert M. Steiner, M.D., Chief of Thoracic Radiology, Thomas Jefferson University Hospital, Philadelphia, PA 19107. 1-2c

FELLOWSHIP—THE COLLEGE OF PHYSICIANS AND SURGEONS at Columbia University is offering a 1-yr appointment in cardiac imaging at the Instructor level to begin July 1, 1988. The program involves extensive exposure to MRI, echocardiography, nuclear cardiology, and digital imaging in addition to participation in conventional angiocardiology and coronary arteriography. The cardiac catheterization laboratories perform 1500 adult and 400 pediatric procedures per year. Requirements include board eligibility or certification in diagnostic radiology and a New York State medical license. Narcotics license desirable. The Program Directors will be Kent Ellis, M.D. and Eric Martin, M.D. For further information enclose a CV and write to Eric C. Martin, M.D., Dept. of Radiology, Columbia-Presbyterian Medical Center, 622 West 168th St., New York, NY 10032. Columbia University is an affirmative action/equal opportunity employer. 1c

FELLOW IN MRI - BUFFALO, NY. Available Jan. 1, 1987 a fellowship position is open in a 313-bed pediatric teaching hospital. Eight radiologists associated in practice; CT, nuclear medicine, 2 Acuson units, angiography, and Diconics 0.5 Tesla Superconductive magnet in our department. Write to J.P. Kuhn, M.D., 219 Bryant St., Buffalo, NY 14222. 11-1a

Tutorials/Courses

LONDON, ENGLAND—MAY 2-10, 1987. CME I Accred. International Faculty. Topics: CT, MR, and other imaging modalities. Fees: To Feb. 28, US\$395. After Mar. 1, US\$435. Information: Medical Seminars, 21915 Roscoe Blvd., Suite 222, Canoga Park, CA 91304. (818) 340-0580 X280. 1-4d

Other

MRI OVER-READING SERVICE. Backup interpretation of MR scans now available using state-of-the-art Raytel teleradiology equipment and regular phone lines. Service available from across-the-street to across-the-country from 1-month to 1-year. Competitive rates. Contact Murray A. Solomon, M.D., San Jose MRI Center, 361 South Monroe, San Jose, CA 95128. 1-6ep

REALIZE THE VALUE of your practice. A group of successful and well-qualified radiologists is interested in acquiring established radiology practices. Hospital contracts, clinics, and private office settings are desired. Opportunity for radiologists considering retirement or reduction in practice activities to capitalize on the value of the practice they have built up during their careers. Alleviate the problems of professional recruitment or administrative pressures. Practices considered throughout the country. Flexible purchase options with opportunity for continuing relationship arrangements. Write Box C49, AJR (see address this section). 11-1a

RAD/TOMO ROOM FOR SALE. Fischer 660 ma, single phase, automatic exposure control, wall bucky. Still under warranty. 80% of cost. Contact Margaret M. Sanders, M.D., Dallas, TX (214) 661-7575. 1-2ep

AJR Classified Advertising Information

Box Responses and Address for Ad Placement

Write Box _____, AJR, Suite 200, 2223 Avenida de la Playa, La Jolla, CA 92037; (619) 459-2229.

How to Place an Ad

AJR accepts classified advertising for Positions Available, Positions Desired, Fellowships and Residencies, and Tutorials/Courses. Ads are accepted by mail or telephone. Institutions should supply purchase orders.

Rates: \$6.00/line with a \$30 minimum charge. Box service is \$10 additional for each month the ad appears. There are discounts for multiple insertions: 10% for 2-3 insertions; 20% for 4 or more. To estimate lines, count all words and divide by 5.5.

Billing: Ads may be prepaid or invoices will be sent after the ad appears.

Deadlines. About 3 weeks before the issue mails. AJR issues mail in the middle of the month preceding the cover date (e.g., July mails June 17). For specific deadlines, write or telephone the AJR editorial office.

Estimating Ad Charges

Line charge: divide total words by 5.5 and multiply by \$6.00	\$ _____
Multiple insertions? If so, multiply by number	x _____
Subtotal	\$ _____
Box response requested? If so, multiply number of months by \$10.00	+ _____
Subtotal	\$ _____
Discount applies to two or more insertions. Subtract 10% if ad appears 2-3 months, 20% if 4 months or more	- _____
Approximate advertising charge	\$ _____

All the benefits without all the bulk—Williams & Wilkins journals in MICROEDITIONS

AAC: Augmentative and Alternative Communication
(Vol. 1-current)

Advances in Orthopaedic Surgery (Vol. 1-current)

Alcoholism: Clinical and Experimental Research
(Vol. 5-current)

AJNR: American Journal of Neuroradiology
(Vol. 1-current)

AJR: American Journal of Roentgenology (Vol. 132-current)

The American Journal of Gastroenterology
(Vol. 77-current)

American Journal of Optometry and Physiological
Optics (Vol. 53-current)

American Journal of Physical Medicine (Vol. 1-current)

The American Journal of Sports Medicine
(Vol. 1-current)

Critical Care Medicine (Vol. 1-current)

Drug Metabolism and Disposition (Vol. 1-current)

Ear and Hearing (Vol. 1-current)
as Journal of the American Auditory Society
(Vol. 1-5)

Endocrine Reviews (Vol. 1-current)

Endocrinology (Vol. 102-current)

Foot & Ankle (Vol. 1-current)

Gastrointestinal Endoscopy (Vol. 1-current)

Hepatology (Vol. 1-current)

Journal of the American Academy of Child Psychiatry
(Vol. 10-current)

The Journal of Clinical Endocrinology & Metabolism
(Vol. 46-current)

Journal of Clinical Psychopharmacology (Vol. 1-current)

Journal of Developmental and Behavioral Pediatrics
(Vol. 1-current)

Journal of Endodontics (Vol. 9-current)

Journal of Foot Surgery (Vol. 7-current)

The Journal of Investigative Dermatology (Vol. 1-current)

Journal of Medical Practice Management (Vol. 1-current)

The Journal of Nervous and Mental Disease
(Vol. 1-current)

The Journal of Neuroscience (Vol. 1-current)

The Journal of Orthopaedic and Sports Physical
Therapy (Vol. 1-current)

The Journal of Pharmacology and Experimental
Therapeutics (Vol. 1-current)

The Journal of Trauma (Vol. 1-current)

The Journal of Urology (Vol. 1-current)

JPEN: Journal of Parenteral and Enteral Nutrition
(Vol. 1-current)

Laboratory Investigation (Vol. 1-current)

Medicine (Vol. 1-current)

Medicine and Science in Sports and Exercise
(Vol. 17-current)

Molecular Pharmacology (Vol. 19-current)

Neurosurgery (Vol. 1-current)

Nutrition Today (Vol. 20-current)

Obstetrical & Gynecological Survey (Vol. 1-current)

Pediatric Emergency Care (Vol. 1-current)

Pediatric Infectious Disease (Vol. 1-current)

Pediatric Research (Vol. 1-current)

Pharmacological Reviews (Vol. 1-current)

Plastic and Reconstructive Surgery (Vol. 1-current)

SGA Journal (Vol. 7, #3-current)

Soil Science (Vol. 1-current)

Stain Technology (Vol. 1-current)

Survey of Anesthesiology (Vol. 1-current)

Transplantation (Vol. 1-current)

These journals are available in microfilm only—no longer published by Williams & Wilkins (call for availability)

Acta Cytologica • Behavioral Medicine Abstracts •
Cytometry • Gastroenterology • Investigative Urology •
Journal of Criminal Law and Criminology • Journal of
Histochemistry and Cytochemistry • The Journal of
Immunology • Urological Survey

MICROFILM FORMATS:

16 mm reel	35mm reel
16 mm cartridges	positive or negative film
(3M or KODAK)	

\$55/reel (price subject to change without notice)

MICROFICHE:

contact KRAUSE MICROFORM

ORDERING INFORMATION

MICROFICHE

KRAUSE MICROFORM
Route 100, Millwood, NJ 10546

MICROFILM

WILLIAMS & WILKINS
Microfilm Sales
attn: Yvonne Hahn
428 East Preston Street
Baltimore, MD 21202
(301) 528-4144



Williams & Wilkins

printed in USA JRNLAB 94627 85

AJNR: AMERICAN JOURNAL OF NEURORADIOLOGY
Bound Volume Offer

A trouble-free way
to keep your
reference library
up to date

As an **AJNR: American Journal of Neuroradiology** subscriber, you know how much useful information is packed into each issue. But you also probably know how frustrating and time-consuming it can be to try and locate one particular article from a back issue.

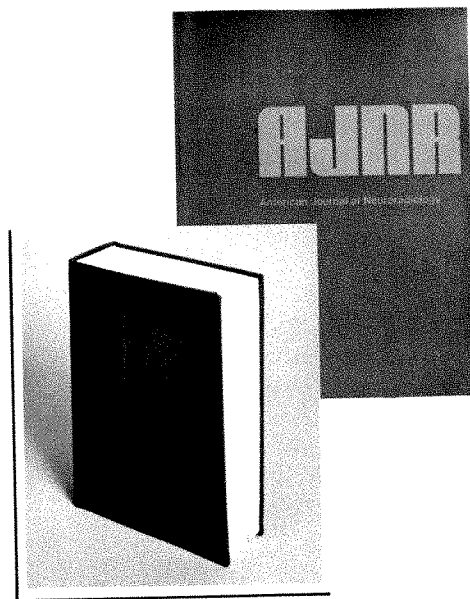
Find that back issue quickly and easily

Now you can get a year's worth of articles in bound volume form—a special offer available only to subscribers. So the information you need will be at your fingertips, handsomely preserved and ready for years of future reference.

You get the timely coverage only a journal can provide— penetrating discussions of the topics that interest you most, by the brightest names in your field—with all the durability and convenience of a hard-cover edition. With a bound volume, you'll never again spend frustrating hours sifting through dog-eared back issues, only to discover that the article you need has been torn out. You'll have a year's worth of vital information all arranged and indexed in one sturdy source. And each carefully crafted volume will make a handsome addition to your permanent library.

Send in your paid order by October 31, 1986
and SAVE

Act now and receive the **1986 Bound Volume** for only \$43.00 for all prepaid orders, \$2.00 off the regular price of



\$45.00. (Please add \$5.00 to all orders outside the US.) Bound volumes are available for the current year only, and are in addition to the regular subscription price.

We'll help you keep your reference library up to date

Once a year, we'll send you a reminder so you can order the latest bound volume. When you send in your paid order, a volume will be reserved for you, to be sent as soon as available on 30-day approval. If you do not want the bound volume for any reason, simply return it to us within 30 days for a courteous refund. It's that easy.



Williams & Wilkins

P.O. Box 23291 Baltimore, Maryland 21203
266 Fulham Road London SW10 9EL England

EASY ORDERING

Please send me the **AJNR: American Journal of Neuroradiology 1986 Bound Volume** at \$45.00 (\$50.00 outside the US). I understand that I can save \$2.00 by sending in my prepaid order (check or charge) by October 31, 1986. I also understand that this offer is in addition to my regular subscription, that it is available only to subscribers, and that I will have the option of ordering bound volumes for subsequent years as long as I remain a subscriber. I will receive my 1986 bound volume in early 1987.

- ☐ Check enclosed ☐ Bill me
☐ VISA ☐ MasterCard ☐ American Express

Card #

Exp. date

Signature P.O. #

Please pay in US dollars. MD residents, please add 5% sales tax. Orders outside the US and Canada must be prepaid. Rates subject to change without notice. All orders must be received by December 31, 1986.

Name

Address

City State Zip

Date of order

ORDER FREE BY PHONE. Call 1-800-638-6423 from anywhere in the US except AK. MD residents, call 528-4105 collect.



Williams & Wilkins

P.O. Box 23291 Baltimore, Maryland 21203
266 Fulham Road London SW10 9EL England

**Vital new
references on
30-day FREE trial**

EMERGENCY RADIOLOGY OF THE ACUTELY ILL OR INJURED CHILD

Second Edition

By **Leonard E. Swischuk, MD**

"Only Len Swischuk could produce a book quite like this....The reproductions, particularly of soft tissues, are superb....A true teacher, [Swischuk] stresses the basic facts, the simple, the obvious, the variations, and the pitfalls....This book should be in the library of even the smallest radiology department." — **J Can Assoc Radiol** (of the First Edition)

1986/622 pages/685 illustrations/#8049-0/\$75.00

COMPUTED TOMOGRAPHY AND MAGNETIC RESONANCE IMAGING OF THE HEAD AND NECK

Second Edition

By **Anthony A. Mancuso, MD** and **William N. Hanafec, MD**

with a special contribution from **John A. Kirchner, MD**

The leading guide to head and neck imaging now includes the first comprehensive discussion of otolaryngologic MRI, an extensively revised chapter on temporal bone, extraordinary images generated by state-of-the-art equipment, and more.

1985/504 pages/155 illustrations/#5476-7/\$84.75

LYMPHATIC IMAGING

**Lymphography, Computed Tomography
and Scintigraphy**

Second Edition

Edited by **Melvin E. Clouse, MD** and **Sidney Wallace, MD**

For assistance in selecting, performing and interpreting lymphatic images using state-of-the-art equipment and techniques, turn to the new **Second Edition** of the only book-length exploration of lymphatic evaluation.

1985/526 pages/352 illustrations/#1651-2/\$87.50

COMPUTED TOMOGRAPHY IN THE EVALUATION OF TRAUMA

Second Edition

Edited by **Michael P. Federle, MD** and **Michael Brant-Zawadzki, MD**

In this new edition you'll find a thorough and up-to-date discussion of the clinical indications for CT scanning in different types of trauma to virtually all areas of the body, keys to techniques of scanning and to accurate interpretation, and comparisons of CT to other radiographic procedures and laboratory tests.

1986/about 300 pages/about 370 illustrations/
#3102-3/about \$58.95

CLINICAL ARTHROGRAPHY

Second Edition

By **Rolf-D. Arndt, MD**, **John W. Horns, MD**, and **Richard H. Gold, MD**

with a special contribution by **Donald D. Blaschke, DDS**

Including inflammatory diseases and other joint abnormalities, the **Second Edition** retains the emphasis on orthopedic disorders as it expands the basic principles of arthrography and adds new, recently published concepts, such as double-contrast CT arthrography.

1985/282 pages/147 illustrations/#0256-2/\$62.50



Williams & Wilkins

428 E. Preston Street Baltimore, MD 21202

— YES! Please rush my copy of —

If not completely satisfied, I may return the books within 30 days at no further obligation. (US & Canada only).

PAYMENT OPTIONS

(Enclose payment or charge your order and Williams & Wilkins will pay all postage and handling costs.)

☐ Check enclosed ☐ Bill me

☐ VISA ☐ MasterCard ☐ American Express

card # exp.

signature/p.o. #

For fastest service... call 1-800-638-0672 toll free anywhere in the US except AK and HI; MD residents call 528-4221 collect.

Full Name

Address

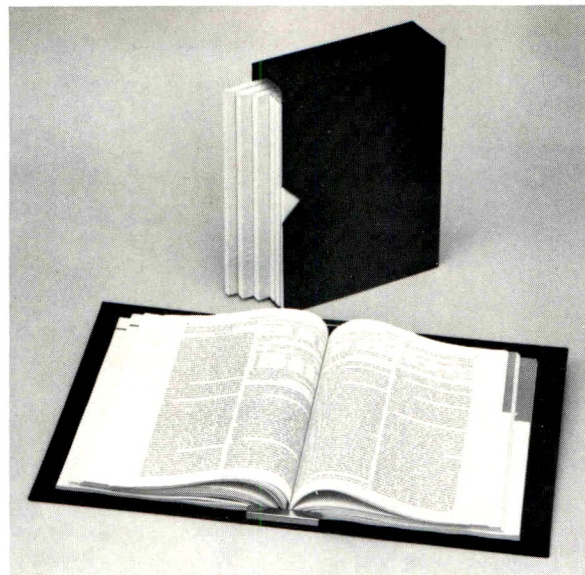
City State Zip

SWISAD 95401

INDEX TO ADVERTISERS

Adria Laboratories	A19
Advanced Cardiovascular Systems	A23
AGFA-Gevaert-Rex	A16, A17
Eastman Kodak	A6, A7
Elema Schonander, Inc.	A2
E-Z-EM	Cover 2
General Electric	A26, A27
Picker International	A20, A21, A22
Precise Optics/PME, Inc.	A25
Pyne Corporation	Cover 3
Siemens Corporation	A15
E. R. Squibb & Sons, Inc.	A9, A10, A11, A12, A13, A14
S & S X-Ray	A28
Tecnomed	A8
Tobias Associates	A18
University of Medicine and Dentistry	A18

We try to present an accurate index. Occasionally this may not be possible because of a last-minute change or an omission.



Protect your copies of

AJNR: AMERICAN JOURNAL OF NEURORADIOLOGY

with Jesse Jones Binders or Files

Keep your journals clean, orderly, and readily accessible with Jesse Jones Binders or Files. One Binder or one box style File is all you need to accommodate a full year's worth of issues. Both Binders and Files are handsomely made with rich dark blue leatherette covers and gold leaf embossed lettering.

Jesse Jones Binders open flat for easy reading and reference and are economically priced at only \$9.95 each; 3 for \$27.95, or 6 for \$52.95 postpaid. The rugged, compact box Files are only \$7.95 each; 3 for \$21.95, or 6 for \$39.95. Add \$1.00/unit postage and handling. (Outside the U.S. add \$2.50/unit.)

For charge orders call toll free 1-800-972-5858. (\$15.00 minimum).

Free gold transfer slips included for indexing volume and year.

Please allow four to five weeks for delivery.

TO: Jesse Jones Industries
499 E. Erie Avenue, DEPT. AJNR
Philadelphia, PA 19134

I enclose my check or money order for \$ _____
(PA residents add 6% sales tax)

Send me ☐ Files ☐ Binders for my journals

Name _____

Address (will not ship to P.O. Box) _____

City/State/Zip _____

Satisfaction guaranteed.



From the beginning of Fuji's effort to manufacture the highest quality medical x-ray films in the world, one thing was apparent. Quality that can't be reproduced with every sheet is no quality at all.

That's why Fuji designed and constructed what remains today the most modern and sophisticated medical x-ray film factory in the world. Other exclusive Fuji technologies—such as non-contact, helical emulsion drying—have elevated standards for the consistent performance of photographic emulsions to a new plateau. The result: From sheet-to-sheet, box-to-box, no manufacturer produces a *more consistent medical x-ray film* than FUJI. NO ONE!

The point is—If you're not getting this kind of consistency from your current film, you are wasting hundreds of dollars.

Let Fuji show your radiology department the difference between consistent and **UNCOMMONLY CONSISTENT**. Call your local Pyne Representative, or 800-431-1850.



**FUJI QUALITY...
UNCOMMONLY
CONSISTENT.**



PYNE CORPORATION

90 Viaduct Road, P.O. Box 4960, Stamford, CT 06907

CIRCLE 7 ON READER SERVICE CARD



PULMONARY RADIOLOGY

- 1 Comparison of CT and fiberoptic bronchoscopy in the evaluation of bronchial disease. Naidich DP, Lee J-J, Garay SM, McCauley DI, Aranda CP, Boyd AD
- 9 CT of interstitial lung disease: a diagnostic approach. Bergin CJ, Müller NL
- 19 Dual-energy digital radiographic quantification of calcium in simulated pulmonary nodules. Hickey NM, Nicklasen LT, Sabagh E, Fraser RG, Barnes GT
- 25 Kaposi's sarcoma of the lung in AIDS: radiologic-pathologic analysis. Sivit CJ, Schwartz AM, Rockoff SD
- 29 Case report. Dystrophic calcification in carcinoma of the lung: demonstration by CT. Stewart JG, MacMahon H, Vyborny CJ, Pollak ER
- 31 Case report. Extension of ascites into the chest with hiatal hernia: visualization on CT. Godwin JD, MacGregor JM

CARDIAC RADIOLOGY

- 33 Measurement of canine left ventricular mass by using MR imaging. Caputo GR, Tscholakoff D, Sechtem U, Higgins CB

BREAST RADIOLOGY

- 39 Mammographic detection of recurrent cancer in the irradiated breast. Stomper PC, Recht A, Berenberg AL, Jochelson MS, Harris JR

ENDOCRINE RADIOLOGY

- 45 Sonography in follow-up of 100 patients with thyroid carcinoma. Simeone JF, Daniels GH, Hall DA, et al.

GENITOURINARY RADIOLOGY

- 51 MR imaging of the prostate gland: normal anatomy. Hricak H, Doores GC, McNeal JE, et al.
- 59 Renal adenocarcinoma: CT staging of 100 tumors. Johnson CD, Dunnick NR, Cohan RH, Illescas FF
- 65 CT and sonography of advanced urinary tract tuberculosis. Premkumar A, Lattimer J, Newhouse JH
- 71 Diagnosis of subclinical varicocele in infertility. Gonda RL Jr, Karo JJ, Forte RA, O'Donnell KT

MUSCULOSKELETAL RADIOLOGY

- 77 Pictorial essay. MR imaging of the supraclavicular region: normal anatomy. Kellman GM, Kneeland JB, Middleton WD, et al.
- 83 MR imaging of the normal shoulder: anatomic correlation. Seeger LL, Ruszkowski JT, Bassett LW, Kay SP, Kahmann RD, Ellman H
- 93 The posterior vertebral body line: importance in the detection of burst fractures. Daffner RH, Deeb ZL, Rothfus WE
- 97 Spinal deformities and pseudofractures. Boechat MI
- 99 Technical note. Prosthetic fit in below-knee amputation: evaluation with xeroradiography. Irwin GAL, Friedman L, Shapiro D
- 103 Pseudobursae: a useful finding in patients with painful hip arthroplasty. Berquist TH, Bender CE, Maus TP, Ward EM, Rand JA
- 107 Radiation dose in radiography, CT, and arthrography of the temporomandibular joint. Christiansen EL, Moore RJ, Thompson JR, Hasso AN, Hinshaw DB Jr
- 111 Scintigraphic diagnosis of sacral fractures. Balseiro J, Brower AC, Ziessman HA

GASTROINTESTINAL RADIOLOGY

- 115 Intraabdominal hematoma: the concentric-ring sign in MR imaging. Hahn PF, Saini S, Stark DD, Papanicolaou N, Ferrucci JT Jr
- 121 Sonographic localization of hematomas in hemophilic patients with positive iliopsoas sign. Graif M, Martinovitz U, Strauss S, Heim M, Itzhak Y
- 125 Hepatic cavernous hemangioma: diagnosis with ^{99m}Tc-labeled red cells and single-photon emission CT. Brodsky RI, Friedman AC, Maurer AH, Radecki PD, Caroline DF
- 131 CT evaluation of esophageal varices. Balthazar EJ, Naidich DP, Megibow AJ, Lefleur RS
- 136 Technical note. Radiolucency in the common bile duct simulating a gallstone. Train JS, Novick A, Dan SJ, Efremidis S, Mitty HA

- 139 CT diagnosis of occult incisional hernias. Ghahremani GG, Jimenez MA, Rosenfeld M, Rochester D
- 143 Case report. MR imaging of gallbladder carcinoma. Rossmann MD, Friedman AC, Radecki PD, Caroline DF
- 145 Case report. Voice change after barium enema: a clinical sign of extraperitoneal colon perforation. Rabin DN, Smith C, Witt TR, Holinger LD
- 147 Case report. Symptomatic congenital ectopic gastric mucosa in the upper esophagus. Williams SM, May C, Krause DW, Harned RK
- 149 Case report. Pneumoretroperitoneum secondary to hydrogen peroxide wound irrigations. Swayne LC, Ginsberg HN, Ginsburg A

FETAL AND OBSTETRIC RADIOLOGY

- 151 Significance of membrane thickness in the sonographic evaluation of twin gestations. Hertzberg BS, Kurtz AB, Choi HY, et al.
- 155 Severe polyhydramnios: incidence of anomalies. Barkin SZ, Pretorius DH, Beckett MK, Manchester DK, Nelson TR, Manco-Johnson ML
- 161 Sonographic spectrum of placental abruption. Nyberg DA, Cyr DR, Mack LA, Wilson DA, Shuman WP
- 165 Malignant gestational trophoblastic disease: CT findings. Sanders C, Rubin E

PEDIATRIC RADIOLOGY

- 169 Technical note. CT of children's feet: an immobilization technique. Donaldson JS, Poznanski AK, Nieves A
- 171 Normalized pediatric organ-absorbed doses from CT examinations. Fearon T, Vucich J
- 175 Case report. Spontaneous resolution of neonatal ovarian cysts. Nussbaum AR, Sanders RC, Benator RM, Haller JA Jr, Dudgeon DL

INTERVENTIONAL RADIOLOGY

- 177 Complications of percutaneous nephrolithotomy. Lee WJ, Smith AD, Cubelli V, et al.
- 181 Percutaneous balloon dilatation of ureteral strictures. Johnson CD, Oke EJ, Dunnick NR, et al.
- 185 Monooctanoic infusion and stone removal through the transparenchymal tract: use in 17 patients. Haskin PH, Teplick SK, Sammon JK, Gambescia RA, Zitomer N, Pavlides CA
- 189 Percutaneous nephrostomy for endopyelotomy. Lee WJ, Badlani GH, Smith AD

NEURORADIOLOGY

- 193 The MR appearance of CSF flow in patients with ventriculomegaly. Sherman JL, Citrin CM, Gangarosa RE, Bowen BJ
- 201 MR imaging of paragangliomas. Olsen WL, Dillon WP, Kelly WM, Norman D, Brant-Zawadzki M, Newton TH
- 205 Physiology of the CSF flow-void sign: modification by cardiac gating. Citrin CM, Sherman JL, Gangarosa RE, Scanlon D
- 209 Embolization of epistaxis and juvenile nasopharyngeal angiofibromas. Davis KR

MEDICOLEGAL RADIOLOGY

- 219 An overview of informed consent for radiologists. Reuter SR

OTHER CONTENT

- 50 Forthcoming articles
- 92 Books received
- 102 American Roentgen Ray Society officers
- 154 ARRS 1987 resident award papers
- 160 Letter from the editor. New guidelines and checklist for authors. Berk RN
- 228 Invitation to the 1987 ARRS meeting. Gagliardi RA
- ARRS 1987 meeting information 110, 114, 120, 124, 130
- Book Reviews 8, 18, 44, 64, 70, 76
- Memorials Russell H. Morgan 16
Kathryn Sue Edwards Jacobi 200
- 230 Letters
- 233 News
- 236 Classified ads
- A3 Guidelines for authors

Rec.
18.9.87

This issue: ARRS Meeting Section

AJR

American
Journal of
Roentgenology



February 1987

Procedure trays to control costs ...new from E-Z-EM

The objective:

Respond to the demand for a set of disposable trays to help hospitals and private practices control biopsy costs on a per-procedure basis.

The result:

E-Z-EM's new PercuSet line of disposable biopsy trays creating a system of procedure trays—a system of trays which offers the doctor progressive degrees of procedure capability.

The PercuSet Skin Prep Tray includes every implement and agent needed to cleanse, aseptisize, and anesthetize the procedure area—for biopsy, or for any percutaneous procedure.

The PercuSet Basic Biopsy Tray includes all the elements of the Prep Tray, plus a needle stop, and a ruler/protractor, and the option of an E-Z-EM biopsy needle.

The PercuSet Expanded Biopsy Tray adds a specimen-handling section, for complete biopsy procedure capability, also with the option of an E-Z-EM biopsy needle.

PercuSet Biopsy Trays assure absolute sterility, minimize component handling, eliminate cross-contamination, and are laid out in a logical procedural sequence.

They provide effective cost control, and reduce inventory management of components.

For additional information and a color brochure that details the PercuSet System, contact your local representative, or call E-Z-EM toll-free at 800-645-3052. In New York call 516-333-8230.

E-Z-EM

More than barium—
much more

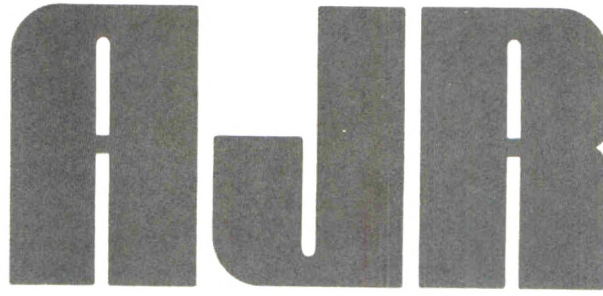


CIRCLE 5 ON READER SERVICE CARD

E-Z-EM, Inc.
7 Portland Avenue
Westbury, N.Y. 11590

© 1986 E-Z-EM, Inc.





American Journal of Roentgenology
Diagnostic Imaging and Related Sciences

Editor-In-Chief Robert N. Berk, *San Diego, California*

Editor Emeritus Melvin M. Figley, *Seattle, Washington*

Associate Editors Alan J. Davidson, *Washington, District of Columbia*
Saskia von Waldenburg Hilton, *San Diego, California*
Juan M. Taveras, *Boston, Massachusetts*

Assistant Editors William L. Ashburn, *San Diego, California*
Charles C. Berry, *San Diego, California*
William G. Bradley Jr., *Pasadena, California*
Edward Buonocore, *Knoxville, Tennessee*
Peter L. Cooperberg, *Vancouver, British Columbia*
Peter Doubilet, *Boston, Massachusetts*
N. Reed Dunnick, *Durham, North Carolina*
Ronald G. Evens, *St. Louis, Missouri*
Henry I. Goldberg, *San Francisco, California*
William R. Hendee, *Chicago, Illinois*
John R. Hesselink, *San Diego, California*
Charles B. Higgins, *San Francisco, California*
Helen C. Redman, *Dallas, Texas*
Donald L. Resnick, *San Diego, California*
Stewart R. Reuter, *San Antonio, Texas*
Stuart S. Sagel, *St. Louis, Missouri*
Edward A. Sickles, *San Francisco, California*
Eric vanSonnenberg, *San Diego, California*

Editorial Staff: Gita S. Braude, *managing editor*; Elizabeth A. Whalen, *senior editor*; Linda Wood and Barbara Rose, *manuscript editors*; Nancy Rydbeck, *administrative assistant*; Sandra Wood, *administrative secretary*.

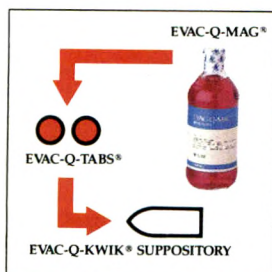
All business correspondence, including display (not classified) advertising, subscriptions, address changes, reprints, and permission requests should be addressed to Williams & Wilkins, 428 East Preston Street, Baltimore, MD 21202. Correspondence regarding editorial matters and classified advertising should be addressed to the editorial office, AJR, 2223 Avenida de la Playa, Suite 200, La Jolla, CA 92037. For manuscript submission, see Guidelines for Authors, next page. Undelivered or damaged copies replaced within 60 days of publication; 90 days for foreign subscribers. Allow 90 days for address changes. AJR AMERICAN JOURNAL OF ROENTGENOLOGY (ISSN 0361 803X) is published monthly by American Roentgen Ray Society, 428 E. Preston Street, Baltimore, MD 21202. Annual dues include \$50 for journal subscription. Second class postage paid at Baltimore, MD and at additional mailing offices. Postmaster send address changes (Form 3579) to Williams & Wilkins, 428 East Preston St., Baltimore, MD 21202. Subscription rates \$90 (\$120 foreign); institutions \$100 (\$130 foreign); in training \$25; single copy \$16 (\$19). Japanese Yen price is available from our sole agent USACO Corporation, 13-12, Shimbashi 1-Chome, Minato-Ku, Tokyo 105, Japan, telephone 03-502-6471. Airmail rates furnished on request. Indexed by *Current Contents* and *Index Medicus*. Copyright © 1987 by American Roentgen Ray Society. 0361-803X/87\$2.00

How to reduce the costs of bowel preparation before and after the X-ray



Before

Evac-Q-Kwik® helps keep hospital costs down by eliminating the staff time and labor involved in giving enemas. And everything needed for effective bowel evacuation is contained in one cost-effective kit.



Nurses appreciate Evac-Q-Kwik because it can be administered during a single shift and completed during one

6-hour period. Patients prefer the simple, comfortable Evac-Q-Kwik procedure, too. Evac-Q-Kwik contains no sugar, no alcohol, and is low in sodium.

After

Evac-Q-Kwik is the ideal bowel prep for today's cost-conscious climate. It effectively cleans the colon for clear X-rays *the first time*, to reduce the need for expensive, time-consuming retakes that escalate hospital costs.



Evac-Q-Kwik®



Adria®

Adria Laboratories
Columbus, OH 43215

CIRCLE 1 ON READER SERVICE CARD

AJR Guidelines for Authors

Address new and revised manuscripts, correspondence, and classified ads to the Editor:

AJR Editorial Office

2223 Avenida de la Playa, Suite 200

La Jolla, CA 92037 Telephone: (619) 459-2229

Inquiries regarding subscriptions, display advertising, reprints, or permission to republish *AJR* material should be addressed to the publisher:

The Williams & Wilkins Co.

428 E. Preston St.

Baltimore, MD 21202 Telephone: (301) 528-4133

The *AJR* publishes original contributions to the advancement of medical diagnosis and treatment. Submitted manuscripts should not contain previously published material and should not be under consideration for publication elsewhere. Papers dealing with neuroradiology should be addressed to: American Journal of Neuroradiology, Dept. of Radiology, Massachusetts General Hospital, Boston, MA 02114. At the discretion of the *AJR* Editor, *AJNR* articles that are of interest to the general reader may be republished in the *AJR*. Neuroradiologic papers sent to the *AJR* will be forwarded to the Editorial Office of the *AJNR*.

Manuscript decisions are based on peer review. Reviewers receive manuscripts without title pages to ensure an unbiased review. All accepted manuscripts are subject to editing. Statements made in the article, including changes made by the Editor or manuscript editor, are the responsibility of the author and not of the *AJR* or its publisher. Authors will be sent the edited manuscript, galley proof, and proofs of illustrations. If the corresponding author will be unavailable to review galleys, arrangements should be made for a coauthor or colleague to read and return the proof.

General Guidelines for Major Papers

Abstract. Clearly state (in 150 words or less) the purpose, methods, results, and conclusions of the study. Include actual data.

Introduction. Briefly describe the purpose of the investigation, including relevant background information.

Methods. Describe the research plan, the materials (or subjects), and the methods used, in that order. State in detail the confirmation of disease and control of subjectivity in observations.

Results. Present results in a clear, logical sequence. If tables are used, do not duplicate tabular data in text, but do describe important trends and points.

Discussion. Describe the limitations of the research plan, materials (or subjects), and methods, considering both the purpose and the outcome of the study. When results differ from those of previous investigators, explain the discrepancy.

AUTHOR'S CHECKLIST

For priority handling, please complete the following checklist, sign the copyright form on the reverse side of this page, and send in both with your manuscript.

_____ Two copies of the manuscript (the original and a photocopy) and two complete sets of figures are submitted.

_____ If appropriate, *AJR* Guidelines for case reports, technical notes, pictorial essays, or letters to the Editor have been followed.

_____ The manuscript, including references, figure legends, and tables, is typed double-spaced throughout on 8½ × 11 in. (21.6 × 27.9 cm) nonerasable paper. Right-hand margins are not justified.

_____ All manuscript pages are numbered consecutively without author identification.

_____ The manuscript is organized as follows: title page, blind title page (title only), abstract, introduction, methods, results, discussion, acknowledgments, references, tables, figure legends, and figures.

_____ Use of unfamiliar acronyms and abbreviations is kept to a minimum. When abbreviations are used they are written out at first mention, with the abbreviation following in parentheses.

_____ Metric measurements are used throughout, or the metric equivalent is given in parentheses.

_____ Names and locations (city and state only) of manufacturers are given for equipment and nongeneric drugs.

Title Page

_____ The following information is given: title of article; names and complete addresses (including zip code) of all authors; current addresses of authors who have moved since study; acknowledgment of grant or other assistance; and a current phone number for the corresponding author.

_____ Two copies of a blind title page are included giving only the title (omitting the authors' names) for use in the review process.

Abstract

_____ An abstract of approximately 150 words concisely states the purpose, methods, results, and conclusions of the study. Actual data are not included.

_____ No abbreviations or reference citations are used in the abstract.

References

References (not to exceed 35) are typed double-spaced starting on a separate page and are numbered consecutively in the order in which they appear in the text.

All references are cited in the text and are enclosed in brackets and typed on line with the text (not superscript).

Unpublished data are not cited in the reference list, but are cited parenthetically in the text, for example, (Smith DJ, personal communication), (Smith DJ, unpublished data). This includes papers submitted, but not yet accepted, for publication.

Inclusive page numbers (e.g., 333–335) are given for all references.

Journal names are abbreviated according to *Index Medicus*.

Style and punctuation of references follow the format illustrated in the following examples (all authors are listed when six or less; when seven or more authors, the first three are listed, followed by "et al."):

Journal article

1. Long RS, Roe EW, Wu EU, et al. Membrane oxygenation: radiographic appearance. *AJR* 1986;146:1257–1260

Book

2. Smith LW, Cohen AR. *Pathology of tumors*, 6th ed. Baltimore: Williams & Wilkins, 1977:100–109

Chapter in a book

3. Breon AJ. Serum monitors of bone metastasis. In: Clark SA, ed. *Bone metastases*. Baltimore: Williams & Wilkins, 1983:165–180

Published paper presented at a meeting

4. Lau FS, Kirk AN, Beck RA. MR imaging of the spine. Presented at the annual meeting of the American Roentgen Ray Society, Washington DC, April 1986

Tables

Each table is typed double-spaced on a separate page without vertical or horizontal rules; each has a short, descriptive title. Tables do not exceed two pages in length and contain at least four lines of data.

Tables are numbered in the order in which they are cited in the text.

Abbreviations are defined in an explanatory note below each table.

Tables are self-explanatory and do not duplicate data given in the text or figures.

All arithmetic (percentages, totals, differences) has been double checked for accuracy, and tabular data agree with data given in the text.

Figures and Legends

Two complete sets of original figures are submitted unmounted in labeled envelopes.

Figures are clean, unscratched, 5 × 7 in. (13 × 18 cm) glossy prints with white borders. A separate print is submitted for each figure part.

Each figure is labeled on the back with the figure number and an arrow indicating "top." Labeling is done on a gummed label and then affixed to the back of the print. (Never use ink on front or back of figures.)

Author's names are *not* written on the backs of figures.

Only removable (rub-on) arrows and letters are used on the figures themselves. Symbols are not broken or cracked.

Images are uniform in size and magnification.

Line drawings are done in black ink on a white background and are of professional quality. (Only glossy prints, not originals or photocopies, are acceptable.)

Written permission has been obtained for use of all previously published illustrations (and copies of permission letters are included), and an appropriate credit line is given in the legends.

Legends are typed double-spaced, and figure numbers correspond with the order in which the figures are cited in the text.

Transfer of Copyright Agreement and Exclusive Publication Statement

Complete copyright to the article entitled: _____

is hereby transferred to the American Roentgen Ray Society (for United States government employees to the extent transferable), effective if and when the article is accepted for publication in the *American Journal of Roentgenology*. In the case of the authors who are officers or employees of the United States government, the American Roentgen Ray Society recognizes that works prepared by officers or employees of the United States government as part of their official government duties are in the public domain.

Authors reserve all proprietary rights other than copyright, such as patent rights and the right to use all or part of this article in future works of their own. The authors retain the right of replication, subject only to crediting the original source of publication and receiving written permission from the publisher.

Authors guarantee that this manuscript contains no matter that is libelous or otherwise unlawful, invades individual privacy, or infringes any proprietary rights.

Authors understand that they will receive no royalty or other compensation from the American Roentgen Ray Society.

Finally, the authors certify that none of the material in this manuscript has been published previously or is currently under consideration for publication elsewhere.

First author/date

Second author

Third author

This agreement must be signed by all authors in order for the manuscript to be published.

Guidelines for Case Reports

A case report is a brief description of a special case that provides a message that transcends the individual patient.

Format. There is no abstract. The introduction should be a short paragraph giving the general background and the specific interest of the case. No more than one case should be described in detail (similar ones can be mentioned briefly in the discussion). Emphasis should be on the radiologic aspects; clinical information must be limited to that necessary to provide a background for the radiology. The discussion should be succinct and should focus on the specific message and relevance of radiologic methods. A review of the literature is not appropriate.

Length. Maximum of five double-spaced, typewritten pages, including the references but not the title page or figure legends.

References. Maximum of eight.

Figures. Maximum of three or four, unless the text is shortened accordingly. Legends must not repeat the text.

Tables and Acknowledgments. Not appropriate in case reports.

Author's Checklist and Copyright Agreement. Submit both with the manuscript.

Guidelines for Technical Notes

A technical note is a brief description of a specific technique or procedure, modification of a technique, or equipment of interest to radiologists.

Format. No abstract, headings, or subheadings are required. If headings are used, they should be a combination of "Case Report," "Materials and Methods," "Results," and "Discussion." A brief one-paragraph introduction should be included to give the general background. Discussion should be limited to the specific message, including the uses of the technique or equipment. Literature reviews and lengthy case reports are not appropriate.

Length. Maximum of five double-spaced, typewritten pages, including the references but not the title page or figure legends.

References. Maximum of eight.

Figures. Maximum of two, unless the text is shortened accordingly.

Tables and Acknowledgments. Not appropriate in technical notes.

Author's Checklist and Copyright Agreement. Submit both with the manuscript.

Guidelines for Pictorial Essays

A "pictorial essay" is an article that conveys its message through illustrations and their legends. Unlike other *AJR* articles, which are based on original research, pictorial essays serve primarily as teaching tools, like exhibits at a scientific meeting. They are not encyclopedic book chapters. No abstract is necessary.

Length. Maximum of four double-spaced, typewritten pages, including the references but not the title page or figure legends.

References. Maximum of four.

Figures. Maximum of 30 figure parts. Number should be as few as necessary to convey the message of the paper.

Tables and Acknowledgments. Not appropriate in pictorial essays.

Author's Checklist and Copyright Agreement. Submit both with the manuscript.

Guidelines for Letters to the Editor and Replies

Letters to the Editor and Replies should offer objective and constructive criticism of published articles. Letters may also discuss matters of general interest to radiologists. Letters and replies are subject to editing and condensation. Authors will receive galley proof for correction and approval.

Format. All letters should be typed double-spaced on nonletterhead paper, with no greeting or salutation. Signature and affiliation should appear at the end of the letter. Titles for letters should be short and pertinent. The title for a reply is simply "Reply."

Length. Maximum of two double-spaced, typewritten pages, including references and figure legends.

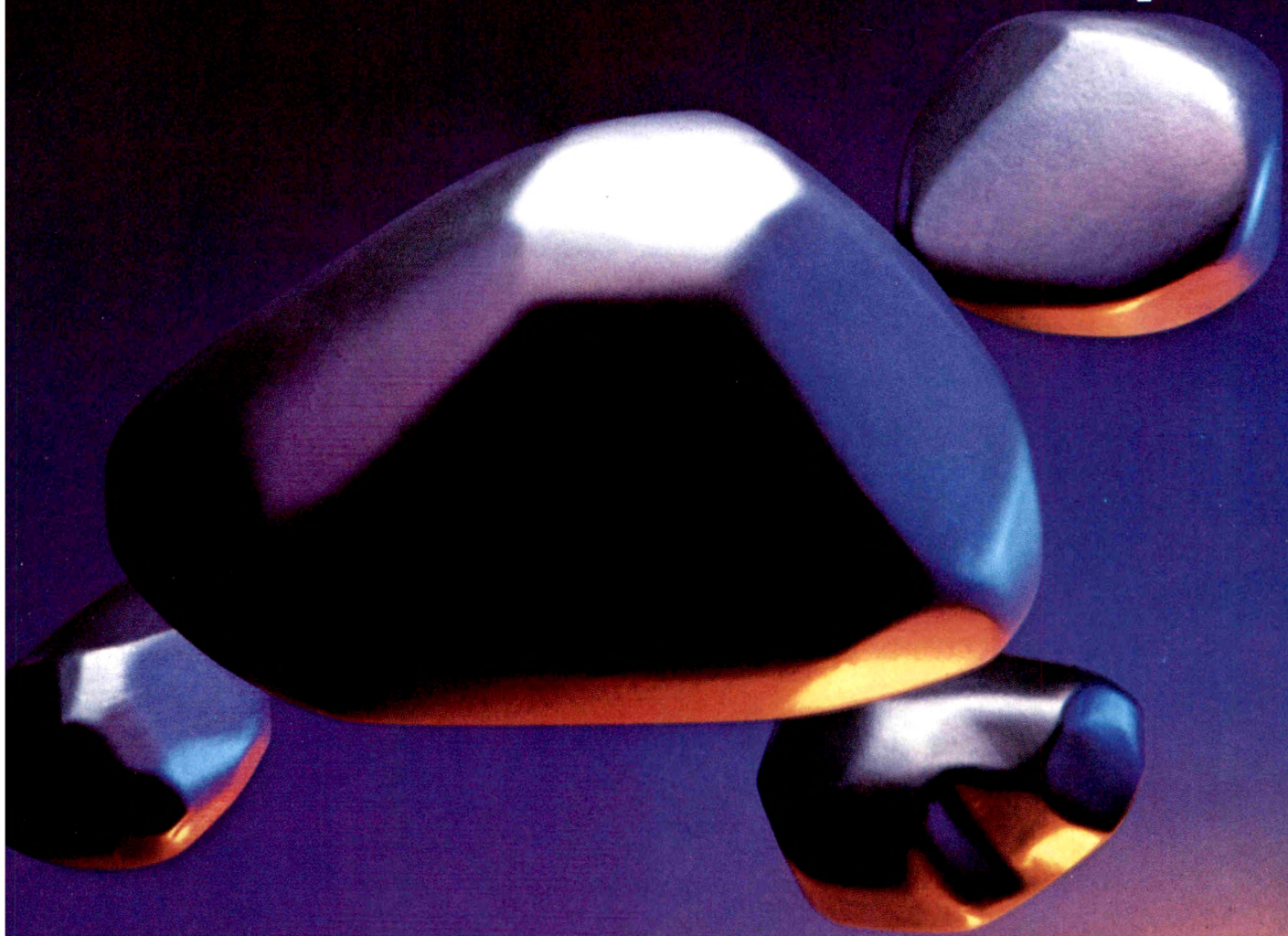
References. Maximum of four.

Figures. Maximum of two.

Tables and Acknowledgments. Not appropriate in Letters to the Editor and Replies.

Author's Checklist and Copyright Release Form. Submit both with the manuscript.

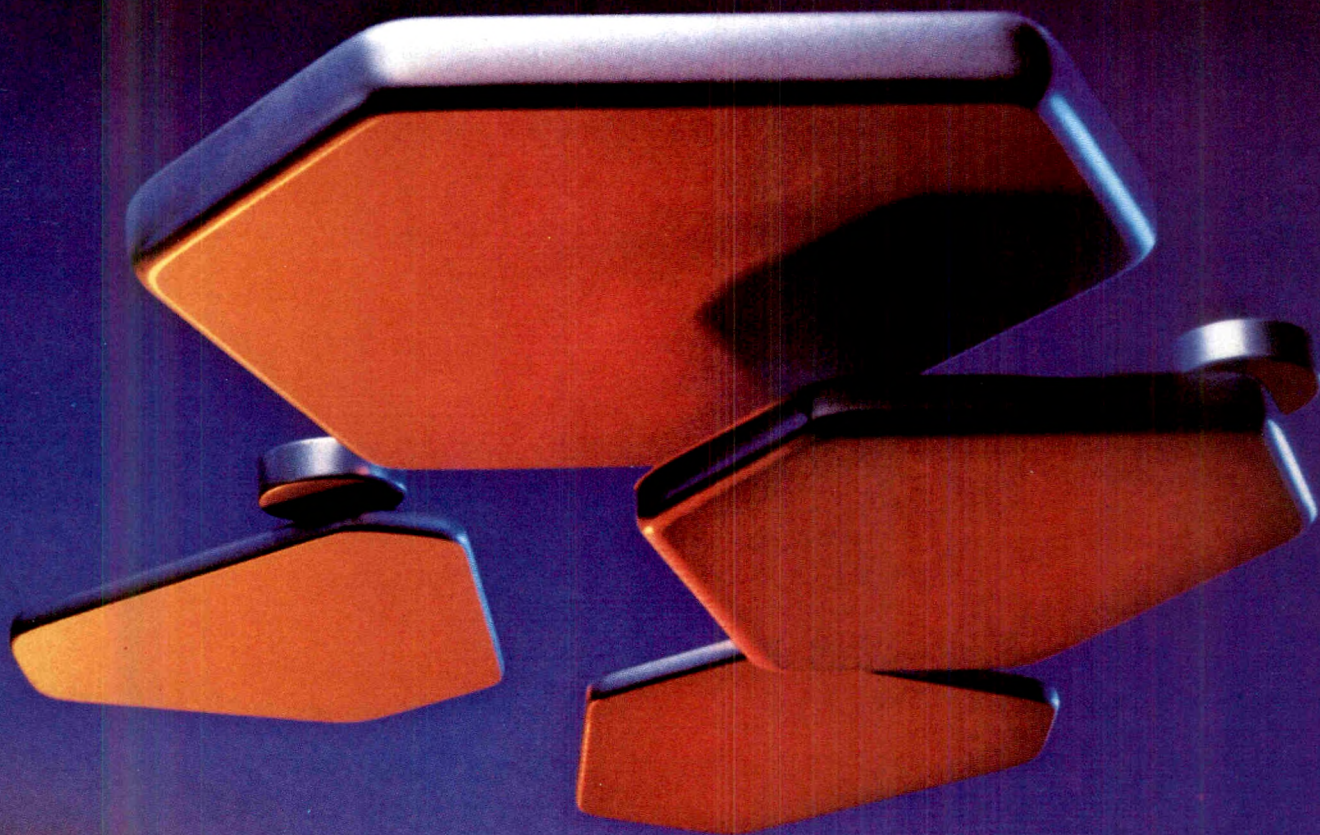
The difference between sharp



Conventional silver halide grains are pebble-shaped, like these.

See for yourself the difference between sharp and sharper. Ask your Kodak representative for a view box comparison of your current film and Kodak T-Mat films.

...and sharper.



Kodak T-Grain emulsion technology results in "tabular" grains.

The difference between conventional silver grains and tabular grains can be seen in the sharpness of the images. And only in Kodak T-Mat films do you get the sharpness produced by T-Grain emulsions. Best of all, there aren't any tradeoffs. You get increased detail, yet techniques are the same as with Kodak ortho films and Kodak Lanex screens, including the same high, motion-stopping, exposure-reducing speeds.

The only other difference is noticeably less processing sensitivity! Ask your Kodak representative for a head-to-head demonstration of Kodak T-Mat films. And about all the extra support that comes with any Kodak product. Or write for details. Eastman Kodak Company, Dept. 412-LMI, 343 State Street, Rochester, New York 14650.

Can you afford anything less?



15 LP/CM. WHY SETTLE FOR LESS?

Spatial resolution.

Accurate diagnoses depend on it.
Referring physicians demand it.
Your images can never get enough of it.
And now you don't have to settle for less.

Introducing the 1200 EXPERT™

The new 1200 EXPERT delivers the spatial resolution needed to give your CT Service a competitive edge. At more than 15 Lp/cm, the 1200 EXPERT has 50% greater resolution than the 9800 QUICK. More resolution than any major CT in the market. Having the best image quality available helps increase referrals and accelerate return-on-investment.

The Referral Builder

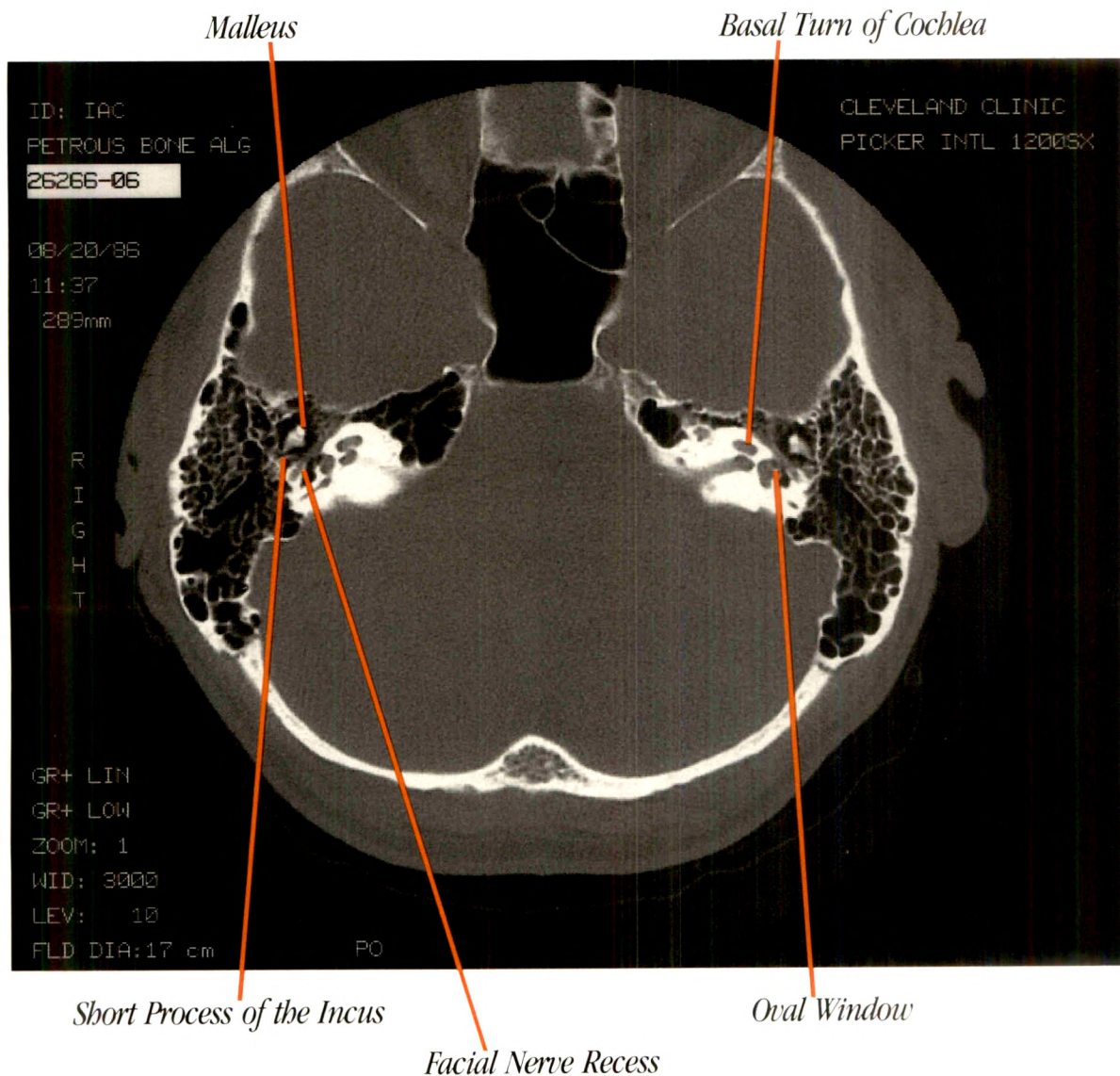
EXPERT has 32 referral-building case-oriented scan protocols each optimized for such special studies as 3-D display, xenon blood-flow, cardiac assessment, bone mineral QCT, real-time reformatting of neuro and orthopedic cases, and much more.

The Technology Leader

The EXPERT's 2,000,000 H.U. X-ray tube, 85% dose efficient solid state detectors, new Level II Imaging Software, and Rapid Scan Mode make this the system of choice for high volume routine scanning *and* special studies.

1200 EXPERT...Why Settle for Less?

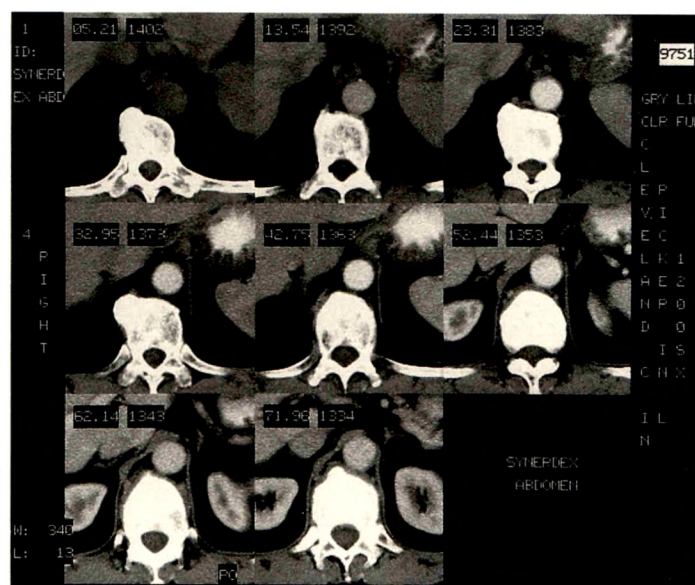
Anatomy of EXPERT Image Quality.



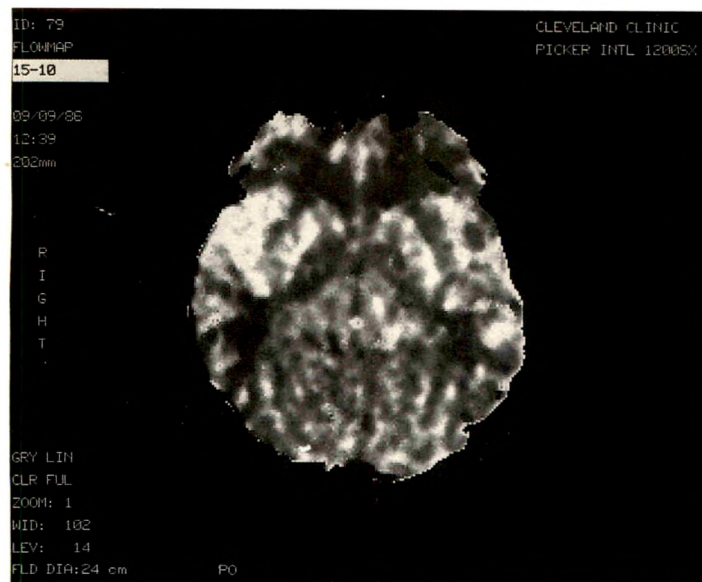
EXPERT Image Quality for Your Special Studies.



Direct 3mm coronal sections of the sella turcica demonstrate superior image quality. The sagittal/coronal display provides fast, easy reference of the pituitary lesion in three different planes.



Dynamic abdominal study with high contrast enhancement and superb spatial resolution provides excellent visualization of the aorta and best assessment of blood flow. Imaging completed in 72 seconds with 10mm couch index.



This is a xenon enhanced CT image, often referred to as a flow map, with each shade of grey representing a blood flow rate. The white areas represent increased flow and conversely the darker areas represent less flow.

 **PICKER**
THE IMAGE OF EXCELLENCE

CIRCLE 17 ON READER SERVICE CARD

The NEW Ackrad H/S Catheter Set for Hysterosalpingography



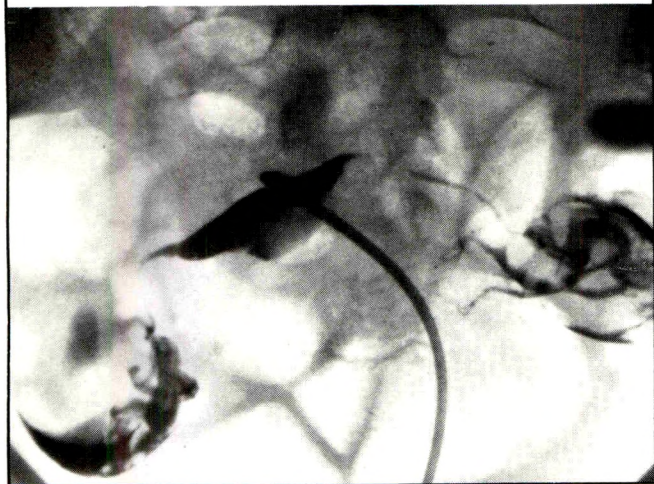
*Now: Easier on the Patient . . .
Better for the Physician*

The unique small sizes (5 and 7F) of the flexible balloon-bearing catheter provide previously unavailable freedom from trauma for the patient. A placement sheath and inflation syringe are included in the set for a rapid and efficient procedure.

Sample furnished on request.



ACKRAD LABORATORIES, Inc.
70 Jackson Drive, P.O. Box 1085, Cranford, NJ 07016
(201) 276-6390



This publication is available in microform.



University Microfilms

International reproduces this publication in microform: microfiche and 16mm or 35mm film. For information about this publication or any of the more than 13,000 titles

we offer, complete and mail the coupon to: University Microfilms International, 300 N. Zeeb Road, Ann Arbor, MI 48106. Call us toll-free for an immediate response: 800-521-3044. Or call collect in Michigan, Alaska and Hawaii: 313-761-4700.

☐ Please send information about these titles:

Name _____
Company/Institution _____
Address _____
City _____
State _____ Zip _____
Phone (____) _____

**University
Microfilms
International**

People Serving People.

Part of an International Fortune 500 Company with over \$1 billion in sales, Konica Medical Corporation, has an important resource no other company can claim. Our people. Konica people. We've earned our reputation worldwide as quality imaging professionals. And serving you is what we do best, with a higher ratio of technical service and support personnel to customers than anyone else in the industry. We realize that having the best value in medical imaging products alone isn't enough in today's market. You also need the best value in service and support. That's why we're dedicated to supporting you in all phases of medical imaging. Promptly. Professionally. Comprehensively. We're Konica. We work harder for you.

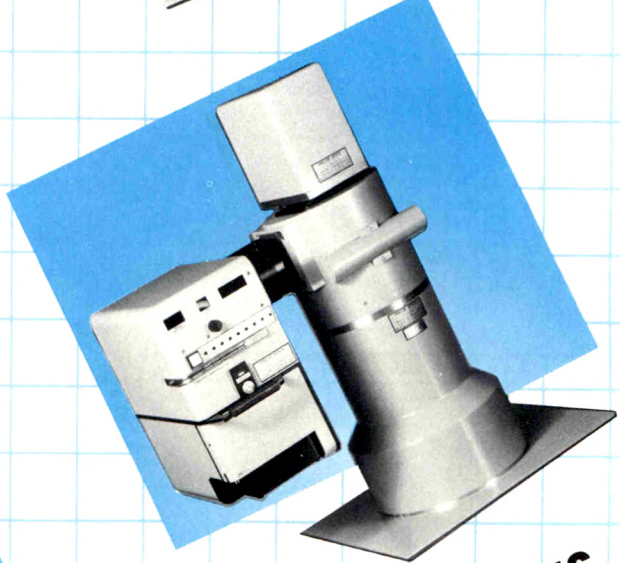
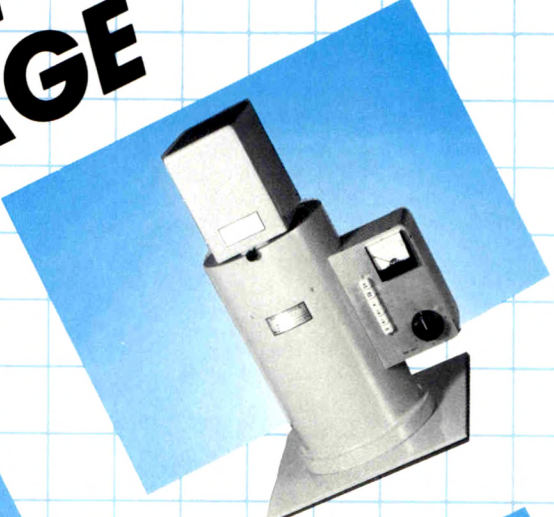
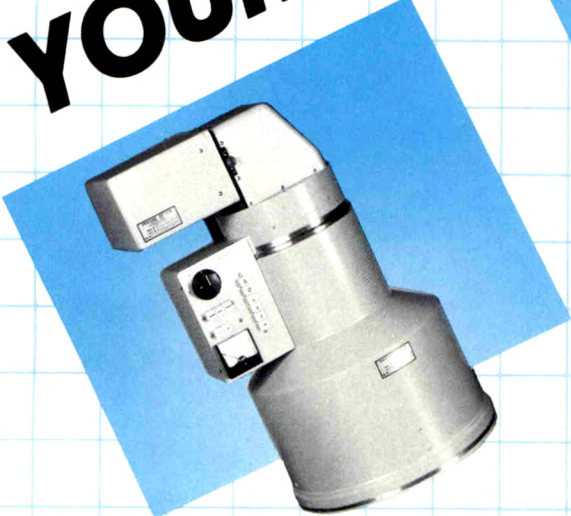
**Konica...
The Image of
Perfection,
Since 1873.**



Konica Medical Corporation
411 Newark Pompton Turnpike, Wayne, NJ 07470 (201) 633-1500

CIRCLE 18 ON READER SERVICE CARD

IMPROVE YOUR IMAGE



WITH PRECISE OPTICS IMAGE INTENSIFIER SYSTEMS

- The world's largest independent manufacturer of Image Intensifier Systems and components
- Over 30 years of experience in design and manufacture
- 6, 9, 12, and 16-Inch latest series image tubes for optimum performance
- 525/875/1023 line CCTV's, 6fps 100mm/105mm cameras

- Cost effective, versatile, reliable
- Compatible with new or existing x-ray equipment
- Extend the life of existing apparatus
- Worldwide dealer network

239 South Fehr Way
Bay Shore, New York 11706
Tel.: 516 242-6600
TWX: 510-227-9837
CIRCLE 6 ON READER SERVICE CARD



LOCUM TENENS and PERMANENT INTERVENTIONAL RADIOLOGIST

Aramco's Dhahran Health Center in Saudi Arabia needs Interventional Radiologists to join a staff of seven doing general diagnostic radiology, specialty diagnostic procedures including ultrasound nuclear medicine, computed tomography and interventional medicine. **Locum assignments** are available for 1-3 months and Board Certification is required. A **full-time position** is also available. American Board Certification and a minimum of 2 years experience after residency required.

Our modern 483-bed hospital, JCAH accredited since 1956, has all major specialty services as well as most subspecialties and functions as a referral center for a patient population of approximately 200,000. The medical services organization includes four district clinics, one with a new 80-bed hospital.

These positions offer state-of-the-art health care facilities in a multi-national environment. The locum contractor, in addition to daily compensation rate, receives a living allowance, housing, 4 paid travel days and transportation from and to contractors point of origin. Permanent positions offer a comprehensive benefits package.

For immediate consideration, call **Velma Guy** at 1-800-231-7577, ext. 8060 or 713-432-8060. Or send resume to **Velma Guy, Aramco Services Company, Dept. 07G-012-7, P.O. Box 4530, Houston, Texas 77210-4530.**

ARAMCO

prn, ltd. locum tenens

*the U.S.A.'s "temporary" solution
specializing in
family practice, radiology,
and anesthesiology*

1-800-531-1122
1000 N. Walnut (Suite A)
New Braunfels, Texas 78130

Nationwide Service and Support by Dedicated Professionals

Our imaging specialists and technical representatives are dedicated professionals. They stand behind every box of film. Through Radiology Support Programs and National Accounts Programs for Materials Management, they give you the right support for your specific imaging needs. And they'll keep you abreast of the latest developments and breakthroughs in medical imaging ... as well as administer our E.C.E. Approved Educational Programs, which provide excellent training for your staff personnel, radiology managers and technologists. From cost control and technique guidance to on-site computer generated reports for your information needs, helping you get the most out of your radiology departments is what we're all about. We're Konica. We work harder for you.

Konica...
The Image of
Perfection,
Since 1873.



Konica Medical Corporation
411 Newark Pompton Turnpike, Wayne, NJ 07470 (201) 633-1500

CIRCLE 18 ON READER SERVICE CARD



illumination

E X C E L L E N C E

S&S X-Ray medical film reading illumination excellence has provided radiologists with unequalled quality and reliability for over 30 years.

The S&S commitment to quality and R&D has earned the reputation for excellence we enjoy, and has made S&S the world's largest manufacturer of Motorized Viewers.

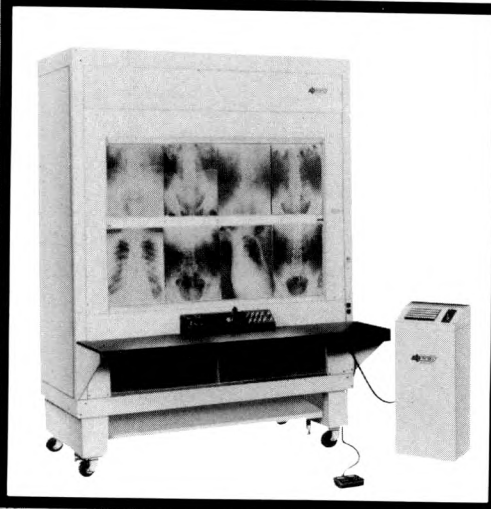
Models' film capacity range from 48 14"x17" radiographs to 400 (4 over 4).

Whether stationary or motorized, S&S viewers together with our complete line of x-ray accessories are designed and engineered to fit every need, every budget.

Catalog available upon request.



Modular Mobile Illuminator



Model MV200A with optional MV 200C and MV200T

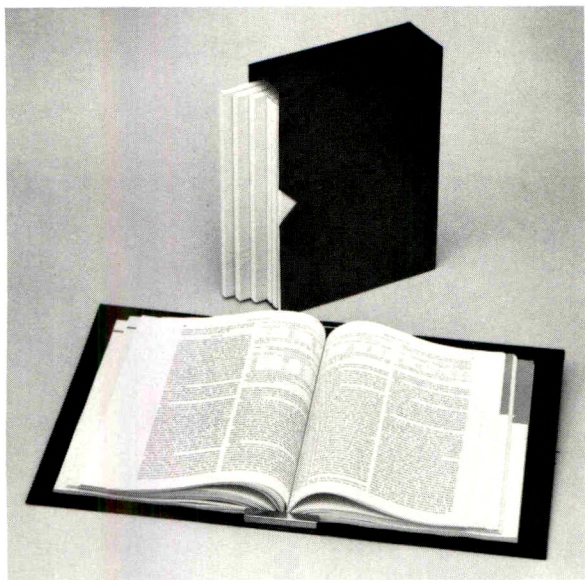
Engineered and produced by the world's leading manufacturer of X-Ray Accessories



S&S X-RAY PRODUCTS, INC.

87-93 Jay Street, Brooklyn, NY 11201
Telex: 219262 TLX UR
Tel: In NY State: (718) 852-6900
Toll Free: (800) 221-6634

CIRCLE 9 ON READER SERVICE CARD



Protect your copies of

AJR: AMERICAN JOURNAL OF ROENTGENOLOGY

with Jesse Jones Binders or Files

Keep your journals clean, orderly, and readily accessible with Jesse Jones Binders or Files. Two Binders or two box style Files are all you need to accommodate a full year's worth of issues. Both Binders and Files are handsomely made with rich black leatherette covers and gold leaf embossed lettering.

Jesse Jones Binders open flat for easy reading and reference and are economically priced at only \$9.95 each; 3 for \$27.95, or 6 for \$52.95 postpaid. The rugged, compact box Files are only \$7.95 each; 3 for \$21.95, or 6 for \$39.95. Add \$1.00/unit postage and handling. (Outside the U.S. add \$2.50/unit.)

For charge orders call toll free 1-800-972-5858. (\$15.00 minimum).

Free gold transfer slips included for indexing volume and year.

Please allow four to five weeks for delivery.

TO: Jesse Jones Industries
499 E. Erie Avenue, DEPT. AJR
Philadelphia, PA 19134

I enclose my check or money order for \$ _____
(PA residents add 6% sales tax)

Send me ☐ Files ☐ Binders for my journals

Name _____

Address (will not ship to P.O. Box) _____

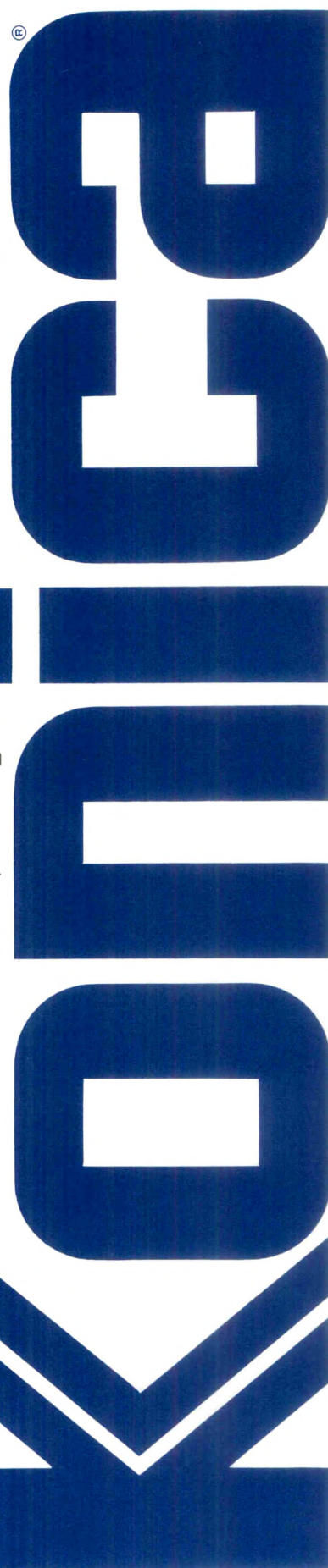
City/State/Zip _____

Satisfaction guaranteed.

Technology & Products for State-Of-The-Art Imaging.

Since 1873, we've been a leader in advanced imaging research and technology. Today, we continue to meet your medical imaging needs by combining state-of-the-art computerized manufacturing with a strong commitment to research and development, and stringent quality control to create new, advanced medical imaging products. You can rely on us to provide sophisticated technologies in electronic imaging, automatic film processing, digital radiography systems, and the latest breakthrough in imaging film, New High Ortho Mono-Dispersed Grain Technology. At Konica we never stop working on new ideas for better imaging products. And we never will. We're Konica. We work harder for you.

**Konica...
The Image of
Perfection,
Since 1873.**



Konica Medical Corporation
411 Newark Pompton Turnpike, Wayne, NJ 07470 (201) 633-1500

CIRCLE 18 ON READER SERVICE CARD

Toshiba's TCT-900S..



one giant leap for CT!

CT beyond the fourth generation.

Toshiba's TCT900S scanner is indisputably unique to the CT imaging industry. In fact, Toshiba's leading edge technology actually takes CT beyond the fourth generation into another dimension with these technological features found in no other comparable system:

1. Consistently superior image quality: just what you expect from Toshiba.
2. Nutate/Rotate geometry with continuous scan: thirty scans in thirty seconds.
3. True dynamic scan: no inter-scan delay.
4. Sub-second scanning: quality images in 0.6 seconds.

Let the competition tell you that CT technology can go no further. But you owe it to yourself to see just how far Toshiba can really go...

Call or write: Toshiba Medical Systems,
2441 Michelle Drive, Tustin, CA 92680.
In California, call (714) 669-5419. Outside
California, call toll-free (800) 421-1968.
In Canada, call (416) 298-6100.

CIRCLE 19 ON READER SERVICE CARD

In Touch with Tomorrow



TOSHIBA
GLOBAL IMAGING SPECIALISTS

Tecnomed USA

Mamex DC

In the beginning ... The original MAMEX D

The Mamex DC is a complete system, consisting of a generator which virtually gives a higher resolution, higher subject contrast x-ray tube; and a motor with floor remote control.

Standard features:

- ★ Compact DC generator exposure control. Exposures can be made.
- ★ Stand designed for x-ray breast.
- ★ Hardened glass screen during exposure.
- ★ Floor remote control.
- ★ Phototiming detector.
- ★ Field light.
- ★ Breast compression. Biopsy compression. Spot cone compression.
- ★ 18x24cm Kodak Min.
- ★ Film identification mark.
- ★ Automatic line voltage.
- ★ .6x.6 stationary anode with beryllium window.

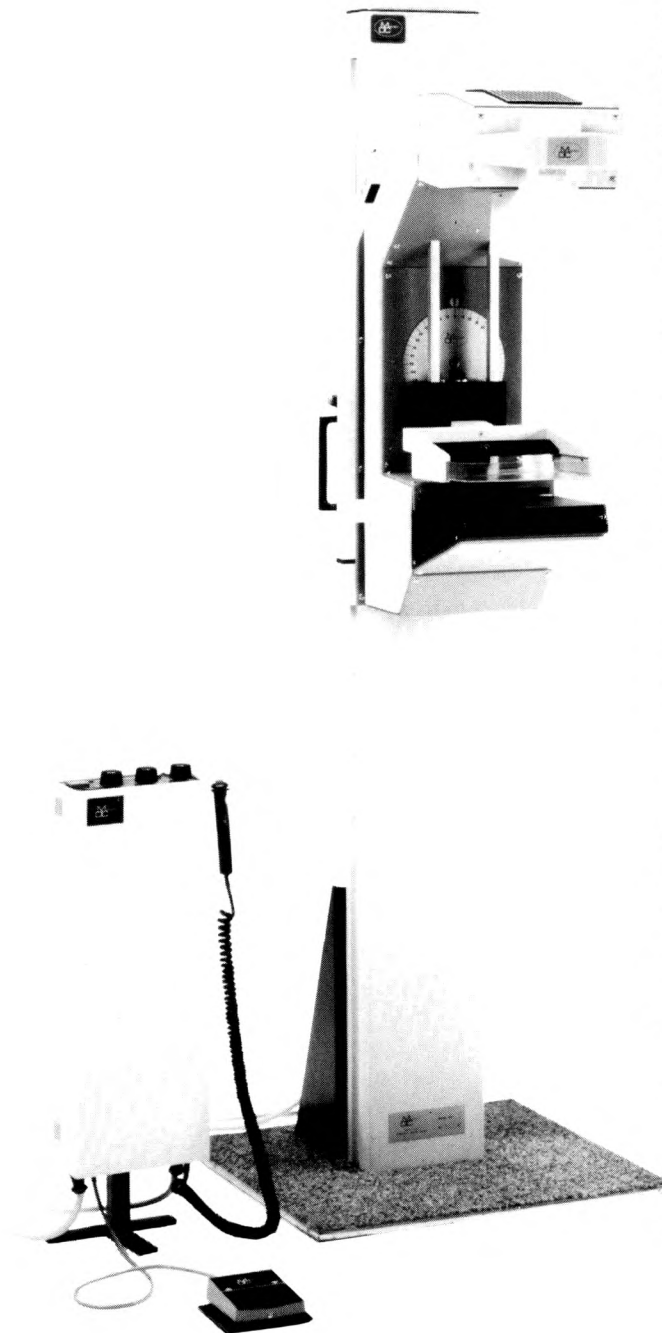
Options:

- ★ 200L 3.5:1 grid.
- ★ Carbon fiber cassette.
- ★ In-hospital wheel assembly.
- ★ Van wheel assembly.

Mamex DC ...

- ★ Five-year proven track record and reliability;
- ★ Hundreds of satisfied hospitals throughout the world;
- ★ Full 12-month non-payable x-ray tube;
- ★ Average midbreast density of a 6cm compressed breast documented by the Breast Cancer Detection Andersson, M.D.)

... offers your facility the best equipment available in

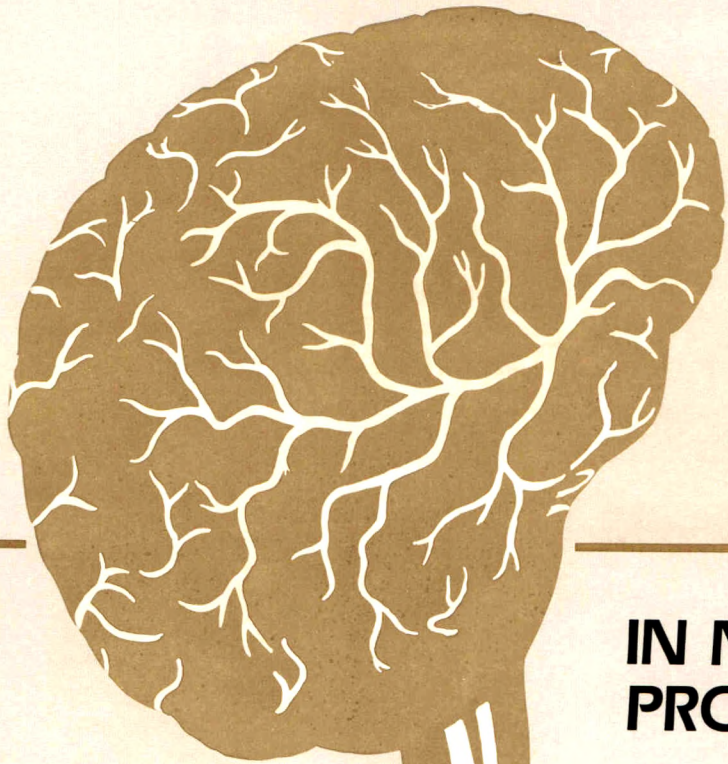


Original MAMEX DC



in neuroradiology

**enhance your
CT procedures with the
advantages of nonionic
SOVUE® (iopamidol injection)**



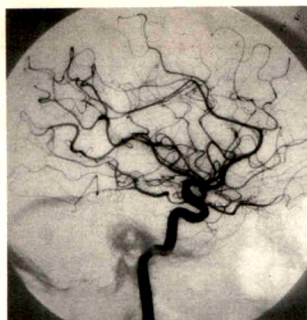
**IN NEURORADIOLOGY
PROCEDURES:**

**Use with
confidence
on both sides of
the blood-brain
barrier**

ISOVUE
iopamidol injection

ISOVUE-M
iopamidol injection

OUTSIDE
Intravascular
use

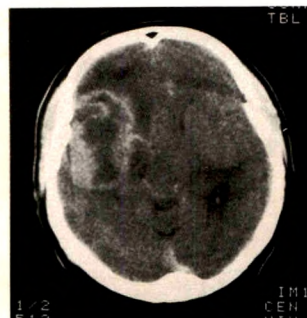


In clinical trials involving 1099 Isovue patients: approximately half the incidence of mild to moderate adverse reactions (e.g., pain, nausea, vomiting) seen with the ionic control agent* in all intravascular procedures combined.¹

INSIDE
Intrathecal
use



When Isovue-M was compared in a double-blind study to metrizamide in lumbar, thoracic, cervical, and total columnar myelography, the 370 patients given Isovue-M experienced less neurotoxicity (psycho-organic manifestations) and approximately half the incidence of observed adverse reactions.¹



An excellent choice
when contrast media
may cross the blood-brain
barrier unexpectedly

**The first "nonionic" indicated in
intravenous contrast enhanced CT.
Also indicated in CT cisternography
and ventriculography.**



As with all injectable contrast agents, the possibility of severe reactions should be borne in mind. See brief summary of prescribing information on last pages of this advertisement for CONTRAINDICATIONS, WARNINGS, PRECAUTIONS, and ADVERSE REACTIONS.

*Diatrizoate meglumine/diatrizoate sodium for most intravascular procedures; iothalamate meglumine for cerebral arteriography.

Enhance your CT procedures with the advantages of nonionic ISOVUE

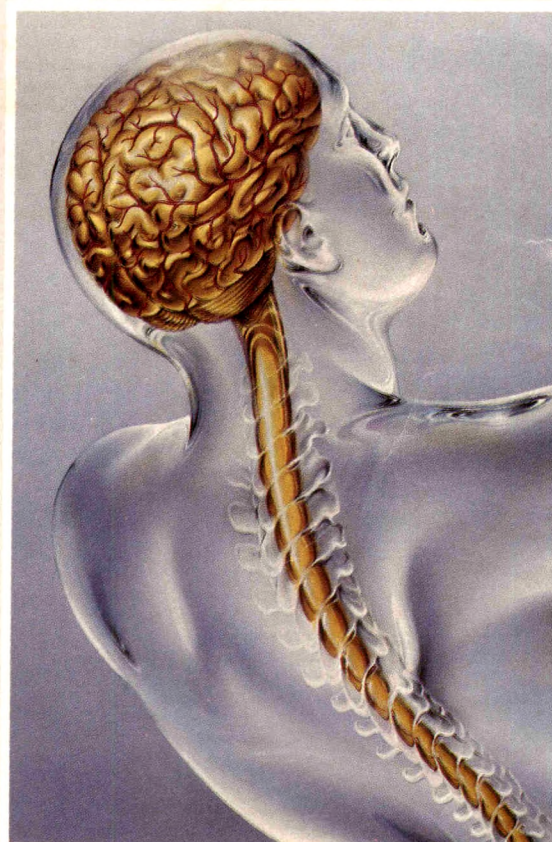
ISOVUE[®]-300
iopamidol injection 61%

**For cerebral arteriography
and head and body CT**

ISOVUE[®]-M[®] 200
iopamidol injection 41%

ISOVUE[®]-M[®] 300
iopamidol injection 61%

For myelography and CT cisternography and ventriculography



Compared to conventional, ionic contrast media

- Nonionic and low osmolality.
- Increased confidence for the radiologist.
 - Improved patient comfort and cooperation.
 - Fewer mild to moderate adverse reactions: less pain, less nausea, less vomiting.
- Procedures go more efficiently with fewer disruptions.

As with all injectable contrast agents, the possibility of severe reactions should be borne in mind. See brief summary of prescribing information on next page for CONTRAINDICATIONS, WARNINGS, PRECAUTIONS, and ADVERSE REACTIONS.

References: 1. Data on file, Squibb Institute for Medical Research.

This product is under license from Bracco Industria Chimica, S.p.A.
U.S. Patent #4,001,323.

 **SQUIBB**[™]
Diagnostics 646-507

ISOVUE®-300
Iopamidol Injection 61%
ISOVUE®-370
Iopamidol Injection 76%
ISOVUE-M® 200
Iopamidol Injection 41%
ISOVUE-M® 300
Iopamidol Injection 61%

DESCRIPTION—ISOVUE and ISOVUE-M (iopamidol injection) are nonionic radiopaque contrast media for diagnostic use. The formulations are stable, aqueous, sterile, and nonpyrogenic solutions for intravascular and intrathecal administration, respectively. Each mL of ISOVUE-300 (iopamidol injection 61%) provides 612 mg iopamidol with 1 mg tromethamine and 0.39 mg edetate calcium disodium. The solution contains approximately 0.037 mg (0.002 mEq) sodium and 300 mg organically bound iodine per mL. Each mL of ISOVUE-370 (iopamidol injection 76%) provides 755 mg iopamidol with 1 mg tromethamine and 0.48 mg edetate calcium disodium. The solution contains approximately 0.046 mg (0.002 mEq) sodium and 370 mg organically bound iodine per mL. Each mL of ISOVUE-M 200 (iopamidol injection 41%) provides 408 mg iopamidol with 1 mg tromethamine and 0.26 mg edetate calcium disodium. The solution contains approximately 0.025 mg (0.001 mEq) sodium and 200 mg organically bound iodine per mL. Each mL of ISOVUE-M 300 (iopamidol injection 61%) provides 612 mg iopamidol with 1 mg tromethamine and 0.39 mg edetate calcium disodium. The solution contains approximately 0.037 mg (0.002 mEq) sodium and 300 mg organically bound iodine per mL. The pH of each solution has been adjusted to 6.5 to 7.5 with hydrochloric acid.

CONTRAINDICATIONS: ISOVUE (iopamidol injection)—None.

ISOVUE-M (iopamidol injection)—Intrathecal administration of corticosteroids with iopamidol is contraindicated. Because of overdosage considerations, immediate repeat myelography in the event of technical failure is contraindicated (see interval recommendation under DOSAGE AND ADMINISTRATION in the product package insert). Myelography should not be performed in the presence of significant local or systemic infection where bacteremia is likely.

WARNINGS: ISOVUE (iopamidol injection)—Use caution in patients with severely impaired renal function, combined renal and hepatic disease, or anuria, particularly when larger doses are administered. Radiopaque diagnostic contrast agents are potentially hazardous in patients with multiple myeloma or other paraproteinemia, particularly in those with therapeutically resistant anuria. It has been speculated that the combination of the contrast agent and dehydration may be causative of anuria in myelomatous patients. This risk is not a contraindication; however, special precautions are required. Contrast media may promote sickling in individuals who are homozygous for sickle cell disease when injected intravenously or intraarterially. Administration to patients known or suspected of having pheochromocytoma should be performed with extreme caution. If the possible benefits outweigh the considered risks, the procedures may be performed; however, the amount of the medium injected should be kept to an absolute minimum. Assess blood pressure throughout the procedure and measures for treatment of a hypertensive crisis should be available. Monitor such patients very closely. Use caution in patients with hyperthyroidism or with an autonomously functioning thyroid nodule because of risk of thyroid storm.

ISOVUE-M (iopamidol injection)—Carefully evaluate the need for myelographic examination. Administer with caution in patients with increased intracranial pressure or suspicion of intracranial tumor, abscess or hematoma, those with a history of convulsive disorder, severe cardiovascular disease, chronic alcoholism, or multiple sclerosis, and elderly patients. Particular attention must be given to state of hydration, concentration of medium, dose, and technique used in these patients. If frankly bloody cerebrospinal fluid is observed, the possible benefits of the examination should be considered in terms of risk to the patient. Patients on anticonvulsant medication should be maintained on this therapy. Direct intracisternal or ventricular administration for standard radiography (without computerized tomographic enhancement) is not recommended. Inadvertent intracranial entry of a large or concentrated bolus of agent, which increases the risk of neurotoxicity, can be prevented by careful patient management. Avoid rapid dispersion of the medium causing inadvertent rise to intracranial levels. If such entry of the medium occurs, prophylactic anticonvulsant treatment with diazepam or barbiturates orally for 24 to 48 hours should be considered. Use of medications that may lower the seizure threshold should be carefully evaluated. While the contributory role of such medications has not been established, these agents are often discontinued at least 48 hours before and for at least 24 hours following intrathecal use. Motor seizures have been reported after intrathecal use, however in several of the cases, higher than recommended doses were employed. Therefore avoid: deviations from recommended neuroradiologic procedure or patient management; use in patients with a history of epilepsy; overdosage; intracranial entry of a bolus or premature diffusion of a high concentration of the medium; failure to maintain head elevation during procedure, on stretcher, and in bed; excessive and active patient movement or staining.

PRECAUTIONS: General—Diagnostic procedures should be carried out under the direction of personnel with the prerequisite training and a thorough knowledge of the particular procedure to be performed. Appropriate facilities should be available for coping with any complications for emergency treatment of severe reaction to the agent itself. After parenteral administration, competent personnel and emergency facilities should be available for at least 30 to 60 minutes since severe delayed reactions may occur. Preparatory dehydration is dangerous and may contribute to acute renal failure in susceptible patients. *Patients should be well hydrated prior to and following administration.* Reactions to the medium, including serious, life-threatening, fatal, anaphylactoid or cardiovascular reactions, should always be considered (see ADVERSE REACTIONS in the product package insert). Patients at increased risk include those with a history of a previous reaction to a contrast medium, a known sensitivity to iodine per se, and those with a known clinical hypersensitivity (bronchial asthma, hay fever, and food allergies). Pretesting cannot be relied upon to predict severe reactions and may itself be hazardous for the patient. A thorough medical his-

tory with emphasis on allergy and hypersensitivity prior to the injection of any contrast medium may be more predictive and accurate than pretesting. Premedication with antihistamines or corticosteroids to avoid or minimize possible allergic reactions in such patients should be considered (see CONTRAINDICATIONS). If nondisposable equipment is used, scrupulous care should be taken to prevent residual contamination.

ISOVUE (iopamidol injection)—General anesthesia may be indicated in some procedures in selected patients; however, a higher incidence of adverse reactions has been reported in anesthetized patients, which may be attributable to the inability of the patient to identify untoward symptoms, or to the hypotensive effect of anesthesia which can reduce cardiac output and increase the duration of exposure to the agent. Even though the osmolality is low compared to diatrizoate or iohalamate based ionic agents of comparable iodine concentration, the potential transitory increase in the circulatory osmotic load in patients with congestive heart failure requires caution during injection. Observe these patients for several hours following the procedure. In angiographic procedures, be aware of the possibility of dislodging plaques or damaging or perforating the vessel wall during catheter manipulations and contrast medium injection. Test injections to ensure proper catheter placement are suggested.

The inhibitory effects of nonionic contrast media on mechanisms of hemostasis have been shown, in vitro, to be less than ionic contrast media at comparable concentrations. For this reason, standard angiographic procedures should always be followed: angiographic catheters should be flushed frequently, and prolonged contact of blood with contrast in syringes and catheters should be avoided.

Perform *selective coronary arteriography* only in those in whom the expected benefits outweigh the procedural risk. The inherent risks of *angiocardiology* in patients with chronic pulmonary emphysema must be weighed against the necessity for performing this procedure. *Angiography* should be avoided whenever possible in patients with homocystinuria, because of the risk of inducing thrombosis and embolism.

Drug Interactions: General—Other drugs should not be admixed with iopamidol (see CONTRAINDICATIONS, and DOSAGE AND ADMINISTRATION, Drug Incompatibilities).

ISOVUE (iopamidol injection)—Renal toxicity has been reported in a few patients with liver dysfunction who were given oral cholecystographic agents followed by intravascular contrast agents. Administration of intravascular agents should therefore be postponed in any patient with a known or suspected hepatic or biliary disorder who has recently received a cholecystographic contrast agent.

Drug/Laboratory Test Interactions—PBI and radioactive iodine uptake studies will not accurately reflect thyroid function for up to 16 days following administration, however T3 resin uptake and total or free thyroxine (T4) assays are not affected.

Carcinogenesis, Mutagenesis, Impairment of Fertility—In animal reproduction studies performed on rats, intravenously administered iopamidol did not induce adverse effects on fertility or general reproductive performance. In studies to determine mutagenic activity, iopamidol did not cause any increase in mutation rates.

Pregnancy Category B—No teratogenic effects attributable to iopamidol have been observed in teratology studies performed in animals. There are, however, no adequate and well controlled studies in pregnant women. It is not known whether iopamidol crosses the placental barrier or reaches fetal tissues. Because animal studies are not always predictive of human response, this drug should be used during pregnancy only if clearly needed. Radiologic procedures involve a certain risk related to the exposure of the fetus to ionizing radiation.

Labor and Delivery: ISOVUE (iopamidol injection)—It is not known whether use during labor or delivery has immediate or delayed adverse effects on the labor, the delivery or the newborn.

Nursing Mothers—It is not known whether iopamidol is excreted in human milk. Use caution when contrast media are administered to nursing women because of potential adverse reactions; consideration should be given to temporarily discontinuing nursing.

Pediatric Use—Safety and effectiveness in children have not been established.

ADVERSE REACTIONS: ISOVUE (iopamidol injection)—Usually mild to moderate, self-limited and transient. In angiocardiology (597 patients), the adverse reactions with an estimated incidence of one percent or higher are: hot flashes 3.4%; angina pectoris 3.0%; flushing 1.8%; bradycardia 1.3%; hypotension 1.0%; hives 1.0%. Intravascular injection is frequently associated with the sensation of warmth and pain, especially in peripheral arteriography; pain and warmth are less frequent and less severe with ISOVUE than with diatrizoate meglumine and diatrizoate sodium injection. The following table of incidence of reactions is based on clinical studies with ISOVUE in about 1835 patients:

Adverse Reactions		
Estimated Overall Incidence		
System	>1%	≤1%
Cardiovascular	none	tachycardia
		hypotension
		hypertension
		myocardial ischemia
		circulatory collapse
		S-T segment depression
		bigeminy
		extrasystoles
		ventricular fibrillation
		angina pectoris
		bradycardia
		transient ischemic attack
		thrombophlebitis

(continued on next page)

Adverse Reactions (continued from previous page)		
System	>1%	Estimated Overall Incidence
		≤ 1%
Nervous	pain (1.7%) burning sensation (1.4%)	vasovagal reaction tingling in arms grimace faintness
Digestive	nausea (1.2%)	vomiting anorexia
Respiratory	none	throat constriction dyspnea pulmonary edema
Skin and Appendages	none	rash urticaria pruritus flushing
Body as a Whole	hot flashes (1.5%)	headache fever chills excessive sweating back spasm
Special Senses	warmth (1.1%)	taste alterations warmth in throat/ arms/chest nasal congestion visual disturbances
Urogenital	none	urinary retention

Regardless of the agent employed, overall estimated incidence of serious adverse reactions is higher with *coronary arteriography* than with other procedures. Cardiac decompensation, serious arrhythmias, or myocardial ischemia or infarction may occur during *coronary arteriography* and *left ventriculography*. Following coronary and ventricular injections, certain electrocardiographic changes (increased QTc, increased R-R, T-wave amplitude) and certain hemodynamic changes (decreased systolic pressure) occurred less frequently with ISOVUE (iopamidol injection) than with diatrizoate meglumine and diatrizoate sodium injection; increased LVEDP occurred less frequently after ventricular iopamidol injections. In *aortography*, the risks of procedures also include injury to the aorta and neighboring organs, pleural puncture, renal damage including infarction and acute tubular necrosis with oliguria and anuria, accidental selective filling of the right renal artery during the translumbar procedure in the presence of preexisting renal disease, retroperitoneal hemorrhage from the translumbar approach, and spinal cord injury and pathology associated with the syndrome of transverse myelitis. Adverse effects reported in literature include arrhythmia, arterial spasms, hematuria, periorbital edema, involuntary leg movement, malaise, and triggering of deglutition; some of these may be procedural. Other reactions due to procedural hazards include hemorrhage or pseudoaneurysms at the puncture site, brachial plexus palsy following axillary artery injections, chest pain, myocardial infarction, and transient changes in hepatorenal chemistry tests; and rarely arterial thrombosis, displacement of arterial plaques, venous thrombosis, dissection of the coronary vessels and transient sinus arrest.

ISOVUE-M (iopamidol injection)—The most frequently reported following intrathecal administration are headache, nausea, vomiting, usually mild to moderate, and musculoskeletal pain. These usually occur 1 to 10 hours after injection, almost all occurring and ending within 24 hours. Backache, neck stiffness, numbness and paresthesias, leg or sciatic-type pain occurred less frequently. Transient alterations in vital signs may occur and should be assessed on an individual basis. The following table of incidence of reactions is based on clinical studies with ISOVUE-M in about 615 patients:

Adverse Reactions		
System	>1%	Estimated Overall Incidence
		≤ 1%
Body as a Whole	headache (18.1%)	pyrexia muscle weakness hot flashes malaise fatigue weakness
Digestive	nausea (7.3%) vomiting (3.7%)	diarrhea heartburn
Musculoskeletal	back pain (2.3%) leg pain (1.4%) neck pain (1.1%)	leg cramps sciatica cervicobrachial irritation meningeal irritation radicular irritation, lumbosacral other musculoskeletal pain involuntary movement burning sensation
Cardiovascular	hypotension (1.1%)	tachycardia hypertension chest pain

(continued on next column)

Nervous	none	emotional stress dizziness paresthesia confusion hallucinations lightheadedness syncope numbness cold extremities
Urogenital	none	urinary retention
Respiratory	none	dyspnea
Skin and Appendages	none	rash
Miscellaneous	none	injection site pain

Other adverse effects reported in literature include facial neuralgia, tinnitus, and sweating. Major motor seizures have been reported in the clinical literature and since market introduction in the United States. Transitory EEG changes occur and usually take the form of slow wave activity. The following adverse reactions may occur because they have been reported with other nonionic contrast agents: cardiovascular (arrhythmias); aseptic meningitis syndrome; allergy or idiosyncrasy (chills, pruritus, nasal congestion, Guillain-Barre syndrome); CNS irritation (psycho-organic syndrome: mild and transitory perceptual aberrations such as depersonalization, anxiety, depression, hyperesthesia, disturbances in speech, sight, or hearing, and disorientation; in addition, hyperreflexia or areflexia, hypertonia or flaccidity, restlessness, tremor, echocousia, echolalia, asterixis or dysphasia have occurred). Profound mental disturbances have rarely been reported (various forms and degrees of aphasia, mental confusion or disorientation); the onset is usually 8 to 10 hours and lasts for about 24 hours without aftereffects. However, occasionally they have been manifest as apprehension, agitation, or progressive withdrawal to the point of stupor, rarely accompanied by transitory hearing loss or other auditory symptoms and visual disturbances. Also reported: persistent cortical loss of vision in association with convulsions, and ventricular block, transitory weakness in the leg or ocular muscles, *peripheral neuropathies*, including sensory and/or motor or nerve root disturbances, myelitis, persistent leg muscle pain or weakness, or sixth nerve palsy, or cauda equina syndrome, muscle cramps, fasciculation or myoclonia, spinal convulsion, or spasticity.

General Adverse Reactions To Contrast Media—Reactions known to occur (mostly mild—moderate in degree) with parenteral administration of iodinated ionic contrast agents (see the listing below) are possible with any nonionic agent. Life-threatening reactions and fatalities, mostly of cardiovascular origin, have occurred. Reported incidences of death from administration of other iodinated contrast media range from 6.6 per 1 million (0.00066%) to 1 in 10,000 patients (0.01%). Most deaths occur during injection or 5 to 10 minutes later, the main feature being cardiac arrest with cardiovascular disease as the main aggravating factor with isolated reports of hypotensive collapse and shock (est. 0.005%). Experience with iopamidol suggests less discomfort (e.g., pain and/or warmth) with peripheral arteriography. Fever changes are noted in ventricular function after ventriculography and coronary arteriography. During intrathecal use, there is a lower incidence of electroencephalographic changes as well as neurotoxicity by virtue of the intrinsic properties of the iopamidol molecule. The reported incidence of adverse reactions to contrast media in patients with a history of allergy is twice that for the general population; patients with a history of previous reactions to a contrast medium are three times more susceptible. Although most reactions to intravascular contrast agents appear within 1-3 minutes after start of injection, delayed reactions may occur (see PRECAUTIONS, General). Adverse reactions reported with other intravascular contrast agents and therefore theoretically possible with iopamidol include: *Cardiovascular*: vasodilation, cerebral hematomas, petechiae, hemodynamic disturbances, sinus bradycardia, transient electrocardiographic abnormalities, ventricular fibrillation; *Nervous*: paresthesia, dizziness, convulsions, paralysis, coma; *Digestive*: nausea, vomiting, severe unilateral or bilateral swelling of the parotid and subparotid glands; *Respiratory*: increased cough, asthma, laryngeal edema, pulmonary edema, bronchospasm, rhinitis; *Skin and Appendages*: injection site pain usually due to extravasation and/or erythematous swelling, skin necrosis, urticaria; *Urogenital*: osmotic nephrosis of proximal tubular cells, renal failure, pain; *Special Senses*: bilateral ocular irritation; lacrimation; conjunctival chemosis, infection, and conjunctivitis, perversion of taste; *Other*: neutropenia, thrombophlebitis, flushing, pallor, weakness, severe retching and choking, wheezing, cramps, tremors, and sneezing.

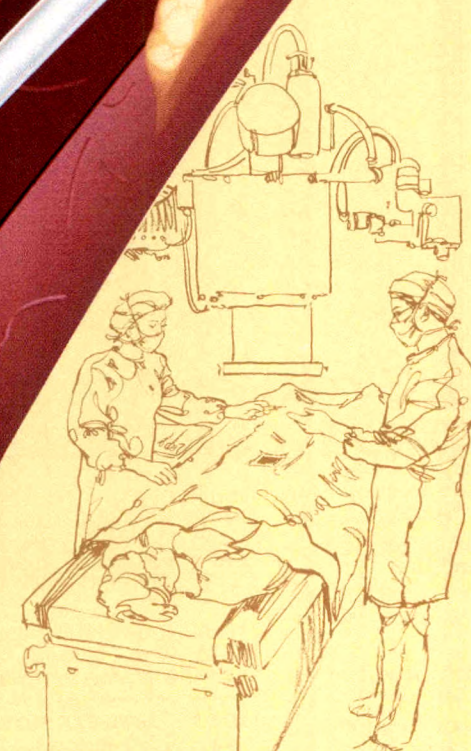
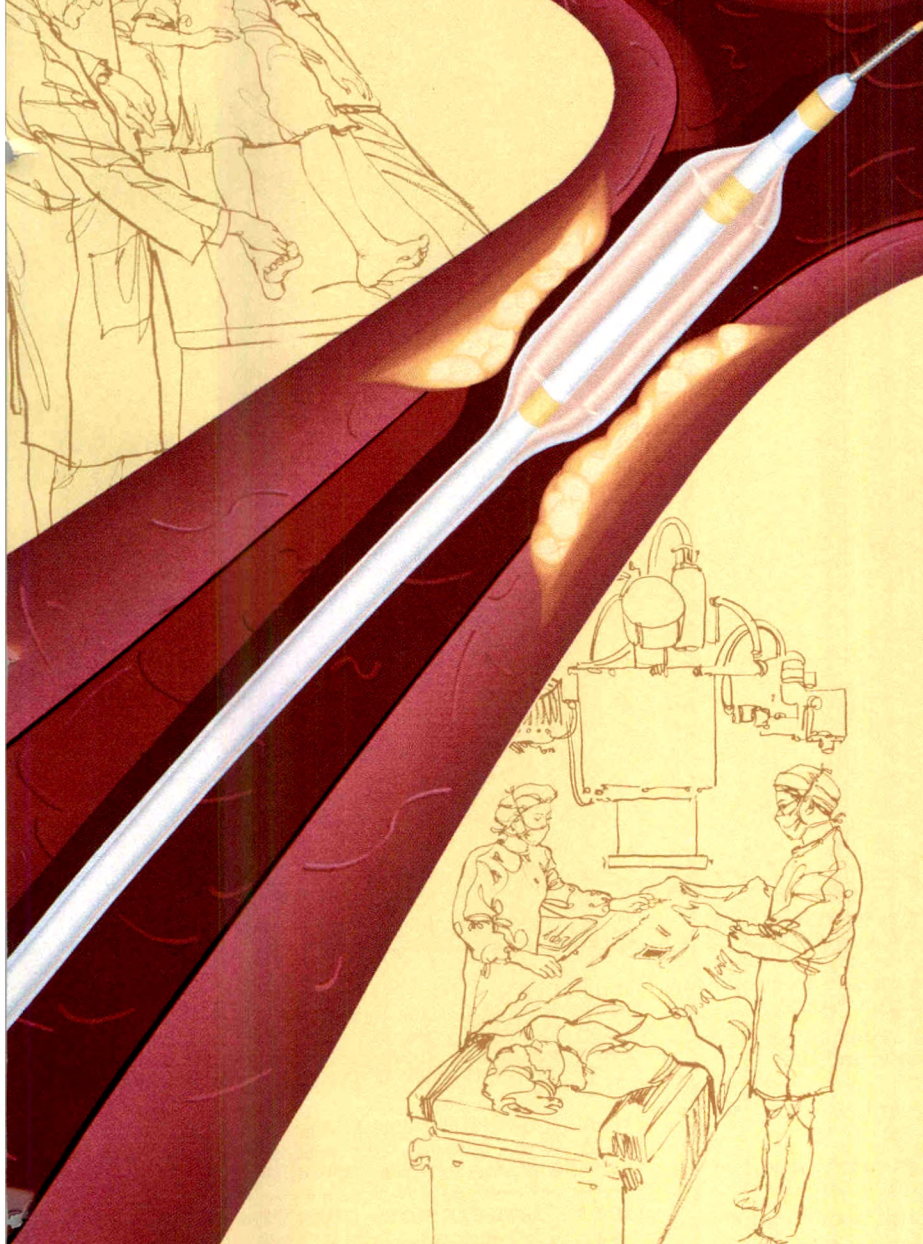
OVERDOSAGE—Treatment is directed toward the support of all vital functions, and prompt institution of symptomatic therapy. In myelography, even use of a recommended dose can produce mental aberrations tantamount to overdosage, if incorrect management of the patient during or immediately following the procedure permits inadvertent early intracranial entry of a large portion of the medium. Treatment is directed toward the support of all vital functions, and prompt institution of symptomatic therapy.

HOW SUPPLIED—ISOVUE-300 (iopamidol injection 61%) and ISOVUE-370 (iopamidol injection 76%) are available in cartons of ten single dose vials, and ten 100 mL single dose bottles. ISOVUE-370 is also available in cartons of ten 150 mL and ten 200 mL single dose bottles. ISOVUE-M 200 (iopamidol injection 41%) and ISOVUE-M 300 (iopamidol injection 61%) are available in cartons of ten 20 mL and ten 15 mL single dose vials, respectively.

For full prescribing information consult package insert. (J3-652D/J3-653E)

The perfect profile for narrow navigation.

The New Schwarten™ LP Catheter



How narrow can you get? As narrow as the new Schwarten™ LP Balloon Dilatation Catheter from ACS. The new Schwarten Low Profile Catheter gives you smooth, simple and confident performance in fragile tibial, peroneal and renal vasculature.

Experience easy entry and passage in some of the tightest situations a patient's peripheral circulation can present. In addition, flexible but firm coaxial design can provide you with excellent tracking over a guide wire to get where you want to be during positioning. Radiopaque balloon and tip markers allow for vivid visualization and more exact balloon placement.

For additional information on the new Schwarten LP Balloon Dilatation Catheter, call toll-free: 800 227-9902.



Where Innovation continues.



ACS is a wholly owned subsidiary of Eli Lilly and Company.

Advanced Cardiovascular Systems, Inc.

1395 Charleston Road
Mountain View, CA 94039
415 965-7360

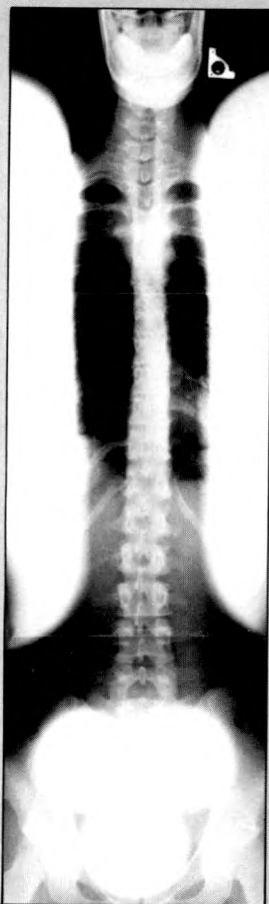
Toll free: 800 227-9902

TWX (Telex II) 23-289-720

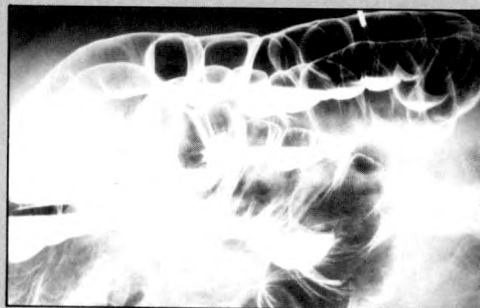
CIRCLE 2 ON READER SERVICE CARD

© 1986 Advanced Cardiovascular Systems, Inc.

MORE DIAGNOSTIC DETAIL... LESS RADIATION EXPOSURE



FULL-SPINE. Full-spine scoliosis exam using compensation filters (as recommended by the FDA to reduce exposure). Note ideal density throughout the spinal column.



DECUBITUS. Right lateral decubitus radiograph with double contrast (barium and air). CLEAR-Pb Filter ends "image burn-out."

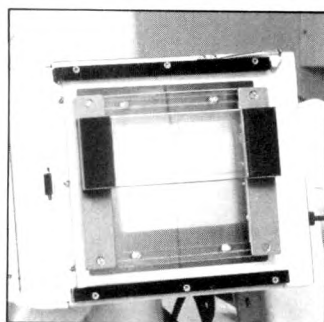


CHEST. Chest radiograph taken with CLEAR-Pb Chest Filter. Reveals all details of lungs and mediastinum.



LONG-LEG. Long-leg radiograph (weight-bearing) obtained with uniform-speed screens and a CLEAR-Pb Long-Leg filter. Note the even film density from hips to ankles.

Radiography Takes a Giant Step Forward with CLEAR-Pb® TRANSPARENT X-RAY COMPENSATION FILTERS



Magnetic mounting system allows instant adjustment of lightweight filter.

- Improve image quality by providing a more uniform film density.
- Reduce patient exposure by selectively attenuating the x-ray beam.
- Reduce the need for multiple exposures.
- Transparent lead-plastic filters never block the collimator light field.
- Easy to use, mount to any collimator.

Finally, there's an easy way to solve your imaging problems. With a CLEAR-Pb Filter you are assured of top-quality images the first time...every time. Over and under-penetration of the patient are eliminated, and important details are improved dramatically.

Try a CLEAR-Pb Filter. You will find one available for most routine exams. There's no easier or better way to obtain superb images... **GUARANTEED!***

***100% SATISFACTION GUARANTEED!** Buy a CLEAR-Pb Filter and use it for 30 days. If it doesn't meet your expectations, return it for full credit.

For details on our full line of
Image Compensators,
request Bulletin 361-C.

CIRCLE 16 ON READER SERVICE CARD

NUCLEAR ASSOCIATES



A Division of VICTOREEN, INC.
100 VOICE ROAD
CARLE PLACE, NY 11514-1593
(516) 741-6360
A Subsidiary of Sheller-Globe **SG**

© Victoreen, Inc.

THE BREAKTHROUGH IN IMAGE COMPENSATORS

Cine MR Imaging: Potential for the Evaluation of Cardiovascular Function

Udo Sechtem¹
 Peter W. Pflugfelder
 Richard D. White
 Robert G. Gould
 William Holt
 Martin J. Lipton
 Charles B. Higgins

MR imaging is valuable in defining cardiac anatomy in a variety of cardiac abnormalities. However, evaluation of cardiac function by this technique has been limited by long imaging times and low temporal resolution. New, recently described pulse sequences shorten imaging time considerably and improve temporal resolution. This paper reports our early experience with cine MR imaging of the heart, a technique of gradient-recalled acquisition in the steady state (GRASS) that uses low flip angles and gradient-recalled echoes. Images were obtained in 36 subjects (14 normal volunteers and 22 patients with coronary artery or valvular heart disease) and displayed in a cinegraphic mode for assessment of cardiac function. The acquisition of 10 to 12 levels, covering the whole heart with up to 24 time frames per level, required a maximum imaging time of only 30 min. Because systole and diastole were readily identified, and the contrast between blood and surrounding structures was excellent, systolic wall thickening, wall motion, and motion of the cardiac valves were visualized easily. Regions of myocardial infarcts were clearly visible and characterized by lack of systolic wall thickening and/or diastolic wall thinning. Turbulence caused signal loss within the flowing blood, which usually had higher signal intensity than myocardium. Therefore, turbulent blood flow in valvular regurgitation and in valvular and subvalvular stenosis could be detected. Cine MR imaging is a promising new technique for the evaluation of myocardial and valvular function.

MR imaging clearly depicts cardiac anatomy in congenital [1-3] and acquired heart disease [4, 5]. Although this technique may have advantages over other noninvasive procedures [6, 7] and can provide functional information [6, 8, 9], it currently is limited by long imaging times and low temporal resolution. Recently, rapid MR imaging techniques that use low flip angles and gradient-refocused echoes have been described [10-12]. When referenced to a simultaneously acquired ECG, this technique should augment the capability of MR imaging for evaluating cardiovascular function.

This paper reports our early experience with a rapid MR imaging sequence applied specifically to assess the dynamics of the normal and diseased heart. It is intended to provide insight into the potential clinical applications of cine MR imaging when this technique is used to simulate real-time cardiac imaging.

Subjects and Methods

Study Population

The study group included 14 normal volunteers (age range, 20-39 years) and 22 patients (age range, 19-72 years) with various types of heart disease previously documented by contrast angiography and/or combined two-dimensional and Doppler echocardiography. Primary cardiac diagnoses were remote myocardial infarction (nine), aortic insufficiency (four), mitral regurgitation (two), tricuspid regurgitation (three), pulmonic regurgitation (one), atrial septal defect (two), and aortic stenosis (one). All normal subjects and 17 patients were in sinus rhythm. Three patients were in atrial fibrillation, and five had frequent premature

Received September 15, 1986; accepted October 21, 1986.

U. Sechtem and P. W. Pflugfelder are research fellows in MR imaging. U. Sechtem is supported by grant SE 441-2 from Deutsche Forschungsgemeinschaft, Bonn, West Germany; P. W. Pflugfelder, by a grant from the Canadian Heart Foundation.

¹ All authors: Department of Radiology, C-309, University of California School of Medicine, San Francisco, CA 94143. Address reprint requests to C. B. Higgins.

AJR 148:239-246, February 1987
 0361-803X/87/1482-0239
 © American Roentgen Ray Society

ventricular contractions (>5/min). The study was approved by the Human Research Committee at the University of California, San Francisco, and patients gave informed consent.

Imaging Technique

MR imaging was done in a commercially available 1.5-T superconducting magnet (General Electric). Images were obtained by using the technique of gradient-recalled acquisition in steady state (GRASS), which employs low flip angles of 30° and gradient-refocused echoes with an echo time (TE) of 12 msec. Repetition time (TR) was 21 msec. The acquisition matrix was 128 × 256 interpolated to 256 × 256 for display. Pixel size was 1.25 × 1.25 mm. Pulse repetition was independent of the ECG signal, which was recorded simultaneously and stored on a microcomputer that controlled advancement of the phase-encoding gradient with each R wave. The number of time frames per cardiac cycle corresponded to the number of 30° pulses delivered within one RR interval. Thus, in a subject with a heart rate of 60 beats/min, the RR interval contained 1000/21 = 48 time frames. If two or more slices were acquired simultaneously in this subject, excitations would alternate between the respective slices, resulting in 24 time frames for a two-slice series with a time resolution of 42 msec, or 12 time frames in a four-slice series with a time resolution of 84 msec. The number of time frames acquired for each RR interval was not constant because of variations of the heart rate. Before image reconstruction, we corrected for these differences by changing time intervals slightly by means of linear interpolation. Images were reconstructed by means of two-dimensional Fourier transformation. Reconstruction time was 5 min for each cine series.

A multislice, coronal, ECG-gated localizing sequence (imaging time, 2 min) was used to identify the inferior extent of the heart. The first transverse cine series was started at this anatomic level. Two levels with a slice thickness of 10 mm and an interslice gap of 10 mm to avoid level interaction [13], were scanned at the same time. The interslice gap between the two levels obtained with this first cine series was covered by the inferior level of the second two-level cine series. Thus, two interleaved series covered 40 mm or four contiguous levels of the heart. The whole heart was covered with 10 or 12 levels, corresponding to five or six cine series. Imaging was completed after the bifurcation of the pulmonary artery was visualized. Total imaging time was determined by the subject's heart rate and the number of series required. This ranged from 15 to 31 min (imaging time = 128 phase-encoding steps × 2 excitations × number of series × [60 sec/heart rate]). Fourteen of 22 patients were repositioned in the magnet and had additional cine series in the sagittal or coronal planes.

Image Analysis

For analysis, images were displayed on the computer monitor in a cinematic mode, facilitating the observation of changes in cardiac configuration and blood intensity during the cardiac cycle. The shape, extension, and timing of areas of altered-blood signal intensity and the appearance and dynamic changes of anatomic structures such as heart chambers, myocardium, and cardiac valves were noted. Measurements of wall thickness or cross-sectional areas were made on still frames by using a track-ball cursor and existing computer software. Volumes were calculated for each time frame by adding chamber cross-sectional areas in each anatomic section multiplied by slice thickness.

Results

Normal Subjects

On images obtained in the cine mode, blood had higher signal intensity than myocardium and appeared white (Fig. 1). The contrast between blood and myocardium was slightly less than that seen on conventional MR images. However, edge detection at the endocardial and epicardial border was facilitated by the cinematic display of images. Myocardial wall thickening during systole was visualized in all normal subjects. The time course of right and left ventricular volumes calculated from cine MR images of a normal subject is shown in Fig. 2. The improved time resolution allowed identification of the late increase in diastolic volume due to atrial contraction. The atrioventricular valves could be identified in systole and diastole in all cases.

In early systole, nine normal subjects had a small area of signal loss in the right atrium that was confined to the area immediately posterior to the tricuspid valve (see Fig. 1). This signal loss usually was seen in the first two to three systolic time frames, corresponding to a time interval of 84–126 msec. It was attributed to momentary reversal of blood flow in the tricuspid valve cone when the tricuspid valve closed. A smaller circumscribed area of signal loss was observed in early diastole within the left ventricle close to the mitral valve (see Fig. 1). A layer of signal loss was regularly seen on the ventricular aspects of atrioventricular valve leaflets during diastole. This effect was most pronounced in early diastole and after atrial contraction. Although the area of the aortic valve was imaged tangentially in the transverse plane, opening of the valve could be seen on cine images at the level of the aortic root because of a characteristic loss of signal in early systole as the valve opened. Motion of the pulmonic valve could be identified in six subjects.

Regional Wall-Motion Abnormalities

Regions of absent or decreased left ventricular systolic wall thickening could be identified readily in patients with previously documented myocardial infarction (Fig. 3). Passive systolic inward motion of infarcted areas without wall thickening was noted in some patients. As in conventional MR images, areas of diastolic wall thinning and aneurysms were sharply demarcated from myocardium with normal diastolic thickness.

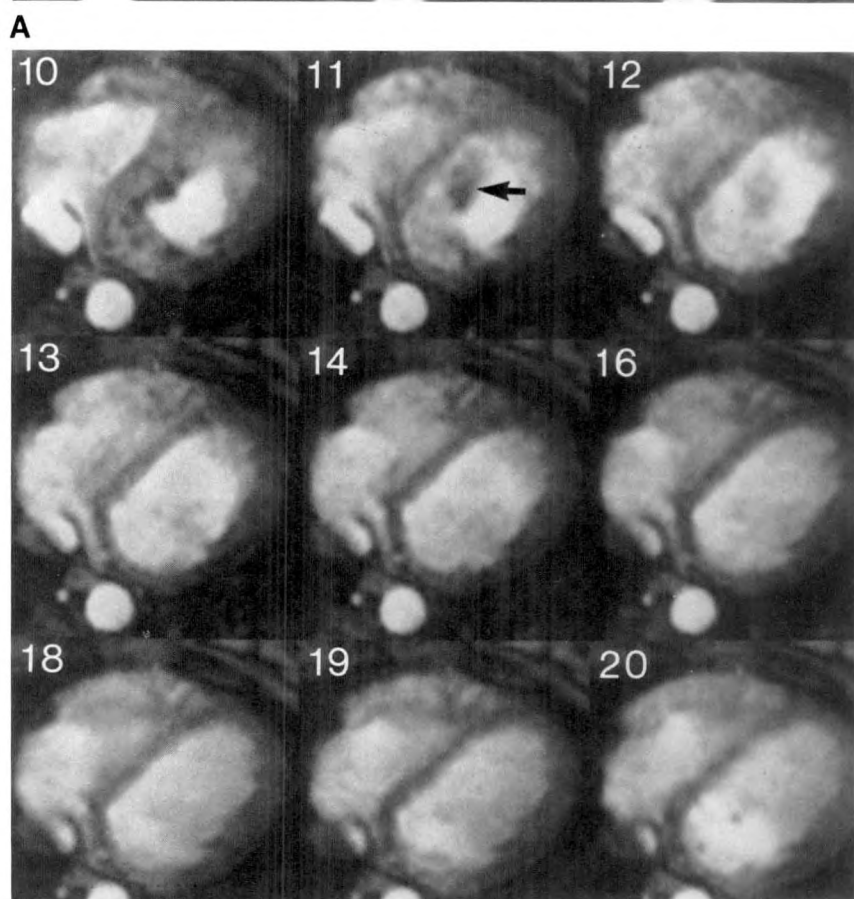
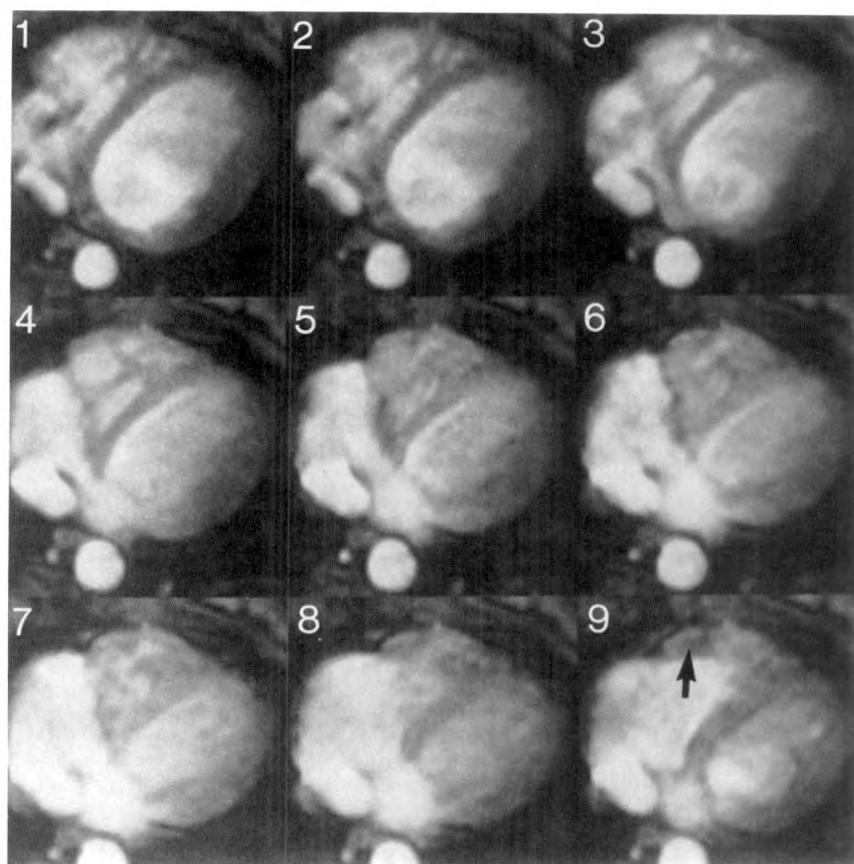
Valvular Disease

In patients with documented valvular regurgitation, the regurgitant jet was visible as a discrete area of low signal intensity extending from the incompetent valve into the respective cardiac chamber (Fig. 4). Unlike the early systolic signal dropout observed in normal subjects, the time course of the jet in mitral or tricuspid regurgitation was pansystolic, and the area of signal loss extended farther towards the posterior wall of the atria. The morphology of abnormal tricuspid and mitral valves was clearly seen in a patient with

Fig. 1.—Transverse cine MR images in a normal subject with a heart rate of 60 beats/min. Time resolution was 42 msec. Eighteen of 20 time frames acquired at the same level are shown in A and B.

A, Midventricular level of left ventricle. *Image 1* was obtained 20 msec after the R wave and subsequent images at 42-msec intervals thereafter. Note area of low signal intensity within right atrium close to tricuspid valve in first three systolic frames. Wall thickening at end systole (*image 8*) is uniform over circumference of left ventricle. Areas of low signal intensity on ventricular aspect of opened valve leaflet (arrow, *image 9*) likely are related to turbulence caused by rapid diastolic influx of atrial blood.

B, Diastolic frames at same level as A. During early diastole, there is some low-intensity signal within left ventricle, possibly related to ventricular filling (arrow, *image 11*). Note closing of tricuspid valve in middiastole (*image 16*) and reopening with atrial contraction at end diastole (*images 18 and 19*).



B

mitral and tricuspid valve prolapse and previous repair of the mitral valve. Images of good or at least diagnostic quality were obtained in patients with atrial fibrillation and/or premature ventricular beats. In aortic incompetence, a pandiastolic jet was seen at several anatomic levels, beginning at the level

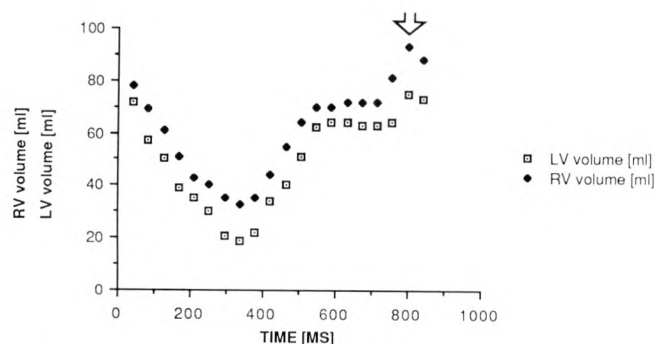


Fig. 2.—Right and left ventricular (RV, LV) volumes over time in normal subject. Right and left ventricular stroke volumes can be obtained by subtraction of end-diastolic and end-systolic volumes. Both are virtually identical in this subject (RV stroke volume = 66 ml, LV stroke volume = 61 ml). End-diastolic filling due to atrial contraction can be seen in both ventricles (open arrow). MS = msec.

of the aortic valve (Fig. 5) and extending back to the lateral and inferior walls of the left ventricle. Pulmonic regurgitation appeared as an area of signal loss within the right ventricular outflow tract during diastole.

A method for quantitating the severity of valvular regurgitation on cine MR imaging is to compare right and left ventricular stroke volumes [14]. In the normal subject, right ventricular stroke volume is equivalent to left ventricular stroke volume (Fig. 2). Right ventricular and left ventricular stroke volumes were clearly different in a patient with isolated moderate aortic incompetence (Fig. 6).

Cine MR images showed a jet of blood of low signal intensity through the immobile cusps of the aortic valve (Fig. 7) in a patient with valvular aortic stenosis. In addition, apposition of the anterior papillary muscle to the hypertrophied interventricular septum was seen. The presence of a subaortic gradient was suggested by the abrupt appearance of low signal intensity of blood in the left ventricular outflow tract (Fig. 7) and was confirmed at cardiac catheterization.

Intracardiac Shunts

In a patient with primum atrial septal defect, blood shunting from the left to the right atrium appeared as a fan of low signal intensity at the level of the attachments of the atrioven-

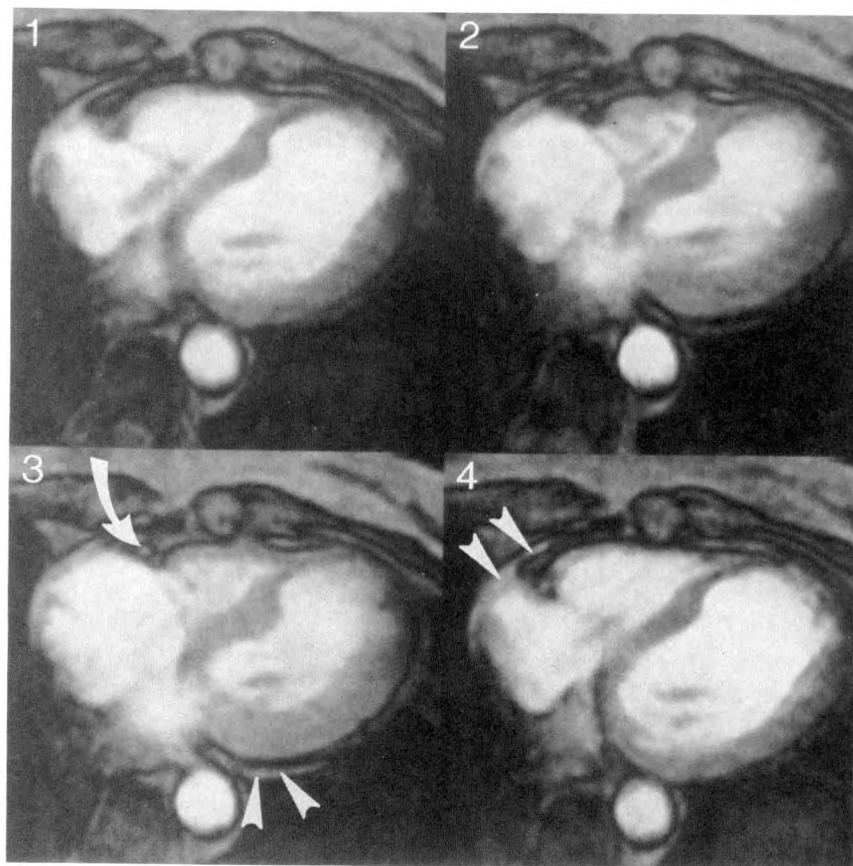


Fig. 3.—Transverse cine MR images through heart of patient with 3-month-old anteroseptal myocardial infarction. Image 1 was obtained in early systole, image 2 further into systole, and image 3 at end systole. Image 4 represents late diastole. Note absence of wall thickening in anteroseptal region and localized hypertrophy of mid-septal area. Damaged myocardium is sharply demarcated from normal myocardium. A small pericardial effusion with high signal intensity is visible over right atrium and behind left ventricle (arrowheads, images 3 and 4). Note right coronary artery within right atrioventricular groove (curved arrow).

Fig. 4.—Systolic transverse cine MR images (time resolution, 42 msec) through heart of a patient with moderate mitral regurgitation as assessed by Doppler echocardiography. During systole, a fan-shaped area of signal loss extending into left atrium represents mitral regurgitation.

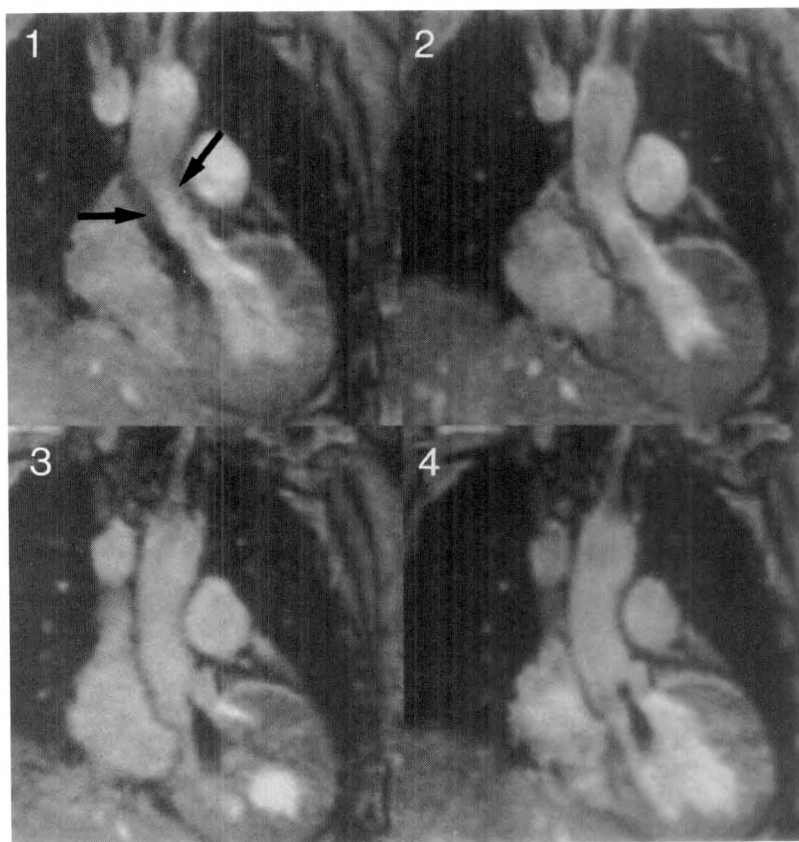
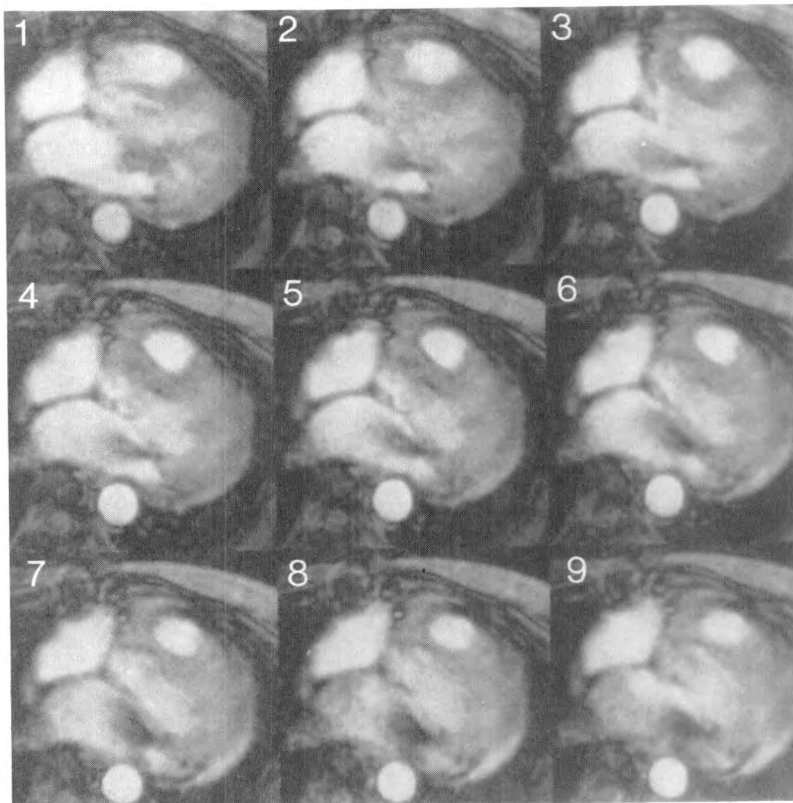


Fig. 5.—Coronal cine MR images in a patient with moderate aortic regurgitation by Doppler echocardiography. *Image 1* obtained in early systole shows increased thickness of left ventricular wall and areas of signal loss at lateral walls of ascending aorta (arrows). Blood flowing centrally through aortic valve has high signal intensity. *Image 2* was obtained at end systole. At early diastole (*image 3*), a fan-shaped area of signal loss originating between aortic valve cusps extends into left ventricle, indicating aortic regurgitation. At end diastole (*image 4*), regurgitant turbulent blood flow is still visible.

tricular valves. Abnormal movement of the interventricular septum was seen in a patient with an echocardiograph-documented 5:1 shunt and paradoxical septal motion. The size of the right atrium and the right ventricle and the thickness of the right ventricular wall could be measured throughout the cardiac cycle.

Other Abnormalities

Cine MR imaging showed pericardial effusions as areas of high signal intensity adjacent to the epicardium. Changes in the three-dimensional distribution of the fluid were visible during the cardiac cycle. Calcifications within the myocardium were seen as areas of low signal intensity in a patient with documented calcification of the mitral annulus (Fig. 7).

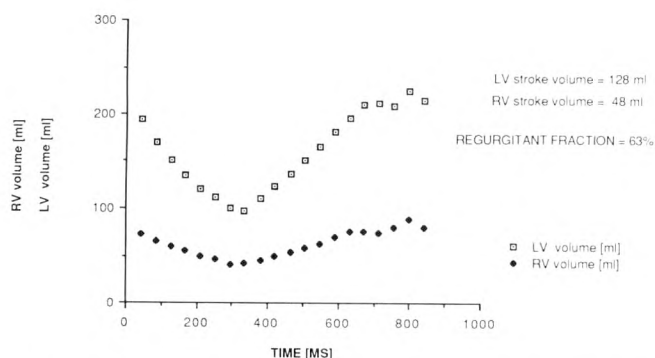


Fig. 6.—Determination of regurgitant fraction in a patient with moderate to severe aortic incompetence. Left ventricle was markedly dilated, and left and right ventricular (LV, RV) stroke volumes determined from end-systolic and end-diastolic volumes differed considerably. Regurgitant fraction = (LV stroke volume – RV stroke volume)/LV stroke volume. MS = msec.

Discussion

Cine MR imaging, a new pulse sequence with partial flip angles and gradient-refocused echoes, was used to acquire high-quality MR images of the heart within a fraction of the time currently needed by conventional gated MR imaging. A complete study with 240 images covering the whole heart in 12 levels and 20 time frames at each level did not require more than 30 min of imaging time. However, because of the limitations of computer hardware, an additional 30 min were needed to reconstruct the images. The time resolution was 42 msec. Higher temporal resolution can be obtained at the cost of longer imaging times. Temporal resolution of cine MR imaging is comparable to techniques such as angiography and two-dimensional echocardiography, commonly used for evaluation of cardiac function.

Unlike its appearance on conventional gated MR images, blood has higher signal intensity relative to myocardium on cine images. The high intensity of flowing blood apparently is caused by the continuous entry of unsaturated spins into the sensitive slice. At a TR of 21 msec, complete washout of saturated spins occurs at a blood velocity of 23 cm/sec [15]. However, the stationary spins of the myocardium are partially saturated when they see the next pulse, leading to diminished signal intensity relative to the flowing blood. The high proton density of blood may be an additional enhancing factor because the pulse sequence used is most sensitive to hydrogen density [10]. Moreover, signal loss from phase-cancellation effects due to blood movement possibly decreases when echo time is very short (TE = 12 msec). Another possible factor leading to greater signal intensity on cine images is the absence of the 180°-section selection pulse used in conventional gated spin-echo sequences. Instead, the echo is caused by reversal of the readout gradient, which does not affect the signal phase of flowing blood [16].

Pericardial fluid in patients with congestive heart failure had

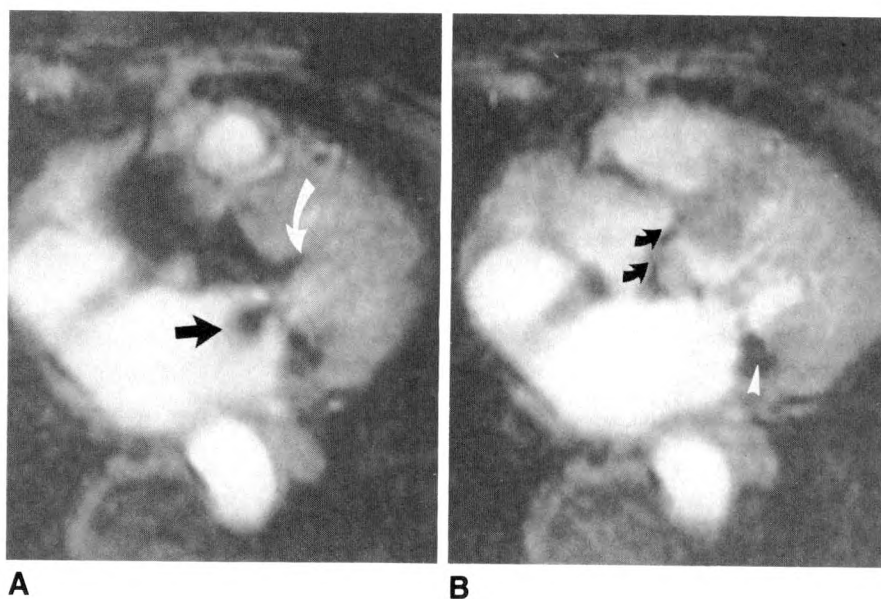


Fig. 7.—Systolic (A) and diastolic (B) transverse cine MR images through left ventricular outflow region of a patient with subaortic and aortic stenosis and accompanying mitral incompetence.

A, In systole, an area of signal loss is visible within left ventricular outflow tract distal to site of outflow tract obstruction (curved white arrow). There is clear narrowing of area of turbulent flow at level of aortic valve cusps. Signal loss is again evident distal to aortic valve. Note fan-shaped area of signal loss within left atrium due to mitral regurgitation (straight black arrow).

B, In diastole, aortic cusps appear thickened and have low signal intensity because of calcification (curved black arrows). Calcification is seen also adjacent to posterior mitral valve leaflet (arrowhead).

high signal intensity on cine images. This appearance might be caused by the same factors that alter blood intensity. If confirmed by further investigation, differentiation of pericardial fluid from pericardial calcification, which is sometimes difficult on conventional MR images, may become possible.

In certain circumstances, the alteration of the signal intensity of blood was useful for assessing the functional integrity of cardiac valves. Low signal intensity of the blood was seen posterior to the tricuspid valve in early systole in normal subjects. Pansystolic right atrial signal loss of varying spatial extent was observed in patients with tricuspid regurgitation. Both findings may be related to observations made with Doppler echocardiography [17]. A short negative Doppler signal often detected in normal subjects is ascribed to the closing movement of the tricuspid valve and the resulting movement of the blood adjacent to the valve. On conventional MR images, signal loss of moving blood is due to a combination of time-of-flight and spin-phase-cancellation effects [18–20]. The reason for the signal loss of blood in systole in normal subjects and in regurgitant lesions on cine images is not entirely clear. Transverse cine MR images transect the tricuspid valve plane almost perpendicularly in a fashion similar to the echocardiographic four-chamber view, so some of the regurgitant blood flow is probably in-plane flow. Thus, time-of-flight effects probably are not the major factor causing signal dropout. However, turbulent flow is expected when blood emerges from a narrowing and decelerates into a low-pressure chamber [21]. The presence of turbulent flow in tricuspid regurgitation also is indicated by the clear widening of the band of frequencies of the time-interval histogram in Doppler echocardiography [22].

In conventional MR imaging, signal loss caused by turbulence is due to the cancellation of the different phase angles of spins that experience different velocities and acceleration [18]. The same should hold true with the pulse sequence used in cine MR imaging. A similar fan- or spindle-shaped appearance of the regurgitant jet observed on cine MR images has been seen with pulsed Doppler echocardiography [17]. Therefore, turbulent flow seems to be a major factor leading to the observed signal loss in valvular lesions. Comparison of cine MR imaging and color Doppler echocardiography might provide a better understanding of the flow phenomena produced by regurgitant blood.

The cine display of the images enhances visual assessment of important parameters of cardiac function such as wall thickening and wall motion. Analysis of left ventricular wall thickening may result in a more accurate determination of infarct size than the assessment of wall motion only [23]. Also, quantitation of cardiac function may be facilitated by the improved time resolution of this new technique. With the three-dimensional information contained in a stack of images encompassing the whole heart, volume calculations of all heart chambers can be made without the need for any geometric assumptions. Like conventional gated MR imaging [7], cine MR imaging clearly depicts anatomic details of the right side of the heart, including right ventricular wall thickness, and therefore may become an important technique for assessing right ventricular function.

The use of cine MR imaging for assessing cardiac function may be limited because images are not acquired in real time, as in angiography or two-dimensional echocardiography, but are compiled from the cumulative information from 128 heart beats. However, like radionuclide angiography, this technique sufficiently simulates real-time cardiac imaging, and functional abnormalities can be viewed as with angiography and two-dimensional echocardiography. Surprisingly, even the combination of atrial fibrillation and frequent premature ventricular contractions did not result in poor-quality images.

In conclusion, our early experience indicates that cine MR imaging surpasses major limitations of conventional gated MR imaging of the heart, such as long imaging times and low temporal resolution. It provides images of the heart within a three-dimensional frame of reference and with good contrast between blood and myocardium without the need for contrast material. These advantages make cine MR imaging a potentially useful tool for the evaluation of cardiac function in patients with heart disease.

ACKNOWLEDGMENTS

This imaging technique was developed by Gary Glover and Norbert Pelc, General Electric, Medical Division, Milwaukee, WI. We also are grateful to Ann Shimakawa of General Electric and Robert Herfkens of Duke University for early advice on the implementation of the technique.

REFERENCES

- Higgins CB, Byrd BF, Farmer DW, Osaki L, Silverman N, Cheitlin M. Magnetic resonance imaging in patients with congenital heart disease. *Circulation* 1984;70:851–860
- Didier D, Higgins CB, Fisher M, Osaki L, Silverman NH, Cheitlin MD. Congenital heart disease: gated MR imaging in 72 patients. *Radiology* 1986;158:227–235
- Dinsmore RE, Wismer GL, Guyer D, et al. Magnetic resonance imaging of the interatrial septum and atrial septal defects. *AJR* 1985;145:697–703
- McNamara M, Higgins CB. Magnetic resonance imaging of chronic myocardial infarcts in man. *AJR* 1986;146:315–320
- Higgins CB, Byrd BF, Stark D, et al. Magnetic resonance imaging in hypertrophic cardiomyopathy. *Am J Cardiol* 1985;55:1121–1126
- Fisher MR, von Schulthess GK, Higgins CB. Multiphasic cardiac magnetic resonance imaging: normal regional left ventricular wall thickening. *AJR* 1985;145:27–30
- Markiewicz W, Sechtem U, Higgins CB. Evaluation of the right ventricle by MRI. *Am Heart J* 1986 (in press)
- Stratemeier EJ, Thompson R, Brady TJ, et al. Ejection fraction determination by MR imaging: comparison with left ventricular angiography. *Radiology* 1986;158:775–777
- Buckwalter KA, Aisen AM, Dilworth LR, Mancini GJB, Buda AJ. Gated cardiac MRI: ejection fraction determination using right anterior oblique view. *AJR* 1986;147:33–38
- Haase A, Matthaei D, Hänicke W, Merboldt KD. FLASH imaging: rapid NMR imaging using low flip-angle pulses. *J Magnetic Resonance* 1986;67:258–266
- Frahm J, Haase A, Matthaei D. Rapid three-dimensional MR imaging using the FLASH technique. *Comput Assist Tomogr* 1986;10:363–368
- van Dijk P, van der Meulen P, Pettigrew RI, Bluemm R, Dannels W, Doornbos J. Dynamic studies of cardiac motion and flow with a fast multiphase MRI technique (abstr). *J Am Coll Cardiol* 1986;7:197A
- Kneeland JB, Shimakawa A, Wehrli FW. Effect of intersection spacing on MR image contrast and study time. *Radiology* 1986;158:819–822

14. Rigo P, Alderson PO, Robertson RM, Becker LC, Wagner HN. Measurement of aortic and mitral regurgitation by gated cardiac blood pool scans. *Circulation* 1979;60:306-312
15. Schmalbrock P, Cornhill JF, Hunter WW, Stiving S. Quantitative flow measurement using gradient recalled acquisition into the steady state (GRASS). Presented at the annual meeting of the Society of Magnetic Resonance in Medicine, Montreal, Canada, August 1986
16. Wehrli FW, Shimakawa A, Gullberg GT, MacFall JR. Time-of-flight MR flow imaging: selective saturation recovery with gradient refocusing. *Radiology* 1986;160:781-785
17. Miyatake K, Okamoto M, Kinoshita N, et al. Evaluation of tricuspid regurgitation by pulsed Doppler and two-dimensional echocardiography. *Circulation* 1982;66:777-784
18. von Schulthess GK, Higgins CB. Blood flow imaging with MR: spin-phase phenomena. *Radiology* 1985;157:687-695
19. Axel L. Blood flow effects in magnetic resonance imaging. *AJR* 1984;143:1157-1166
20. Bradley WG, Waluch V, Lai KS, Fernandez EJ, Spalter C. The appearance of rapidly flowing blood on magnetic resonance images. *AJR* 1984;143:1167-1174
21. Wong W, Kirkeeide RL, Gould KL. Computer applications in angiography. In: Collins SM, Skorton DJ, eds. *Cardiac imaging and image processing*. New York: McGraw-Hill, 1986:223
22. Garcia-Dorado D, Falzgraf S, Almazan A, Delcan JI, Lopez-Bescos L, Menarguez L. Diagnosis of functional tricuspid insufficiency by pulsed-wave Doppler ultrasound. *Circulation* 1982;66:1315-1321
23. Liebermann AN, Weiss JL, Jugdutt BI, et al. Two-dimensional echocardiography and infarct size: relationship of regional wall motion and thickening to the extent of myocardial infarction in the dog. *Circulation* 1981;63:739-746

Acute Myocardial Infarction: MR Evaluation in 29 Patients

Madeline R. Fisher^{1,2}
Michael T. McNamara¹
Charles B. Higgins¹

This study evaluated the ability of MR to identify and characterize the region of myocardial infarction in humans. Twenty-nine patients, all with ECG and enzyme rises consistent with an acute myocardial infarction, were studied by MR 3–17 days from the onset of acute chest pain. Four patients were excluded because of inability to acquire adequate MR studies. For comparison, 20 normal subjects were studied who also had gated MR examinations. The site of infarction was visualized in 23 patients as an area of high signal intensity in relation to the normal myocardium, a contrast that increased on the second-echo image. The regions of abnormal signal intensity corresponded to the anatomic site of infarction as defined by the ECG changes. The mean T2 relaxation time of the infarcted myocardium (79 ± 22 msec) was significantly prolonged in comparison with the mean T2 (43.9 ± 9 msec) of normal myocardium ($p < .01$). The mean percentage of contrast (intensity difference) between normal and infarcted myocardium was much greater on the second-echo images ($65.6 \pm 34.0\%$) than the first-echo images ($27.5 \pm 18.7\%$). In the normal subjects there was no difference in T2 between the anterolateral (40.3 ± 5.7 msec) and septal (39.5 ± 7.4 msec) regions, and percentages of contrast between these two regions of myocardium on the first-echo ($9.1 \pm 7.4\%$) and second-echo ($15.0 \pm 13.3\%$) images were similar. Thus, MR can be used to directly visualize acute infarcts. However, it has several pitfalls, including the necessity to differentiate signal from slowly flowing blood in the ventricle, from increased signal from a region of infarction and artifactual variation of signal intensity in the myocardium due to respiratory motion or residual cardiac motion.

MR offers several advantages for the study of cardiovascular system and myocardial disease [1, 2]. The high velocity of protons in flowing blood generates little or no MR signal [1–3], providing natural contrast between the lumen and walls of blood vessels and cardiac chambers without the need for contrast material. MR also offers the potential for characterizing myocardial tissues by T1 and T2 relaxation times and spin (hydrogen) density [4].

Several early spectrometric studies [5, 6] suggested that relaxation times were altered during the early stages of acute myocardial infarction. MR imaging of ex situ canine hearts with 24-hour-old infarcts showed increased signal intensity on spin-echo images and prolongation of relaxation times of the infarcted region [7]. The increase in relaxation times showed a linear relationship to the increase in water content of the myocardium [5–7]. ECG-gated MR in dogs with acute infarcts also showed high signal intensity in the infarcted myocardium and improved contrast between infarcted and normal myocardium with increased T2 weighting of the spin-echo images [8]. Subsequently, experimental studies in animals imaged immediately and at frequent intervals during the first hours after coronary occlusion indicated that significant increases in intensity and T2 relaxation times occur within 4 hr after coronary occlusion [9, 10]. An initial report in seven patients with acute myocardial infarctions studied by spin-echo MR within 5–12 days after the confirmed time of infarction showed increased signal intensity and T2 relaxation time in the infarcted region [11]. While this report was encouraging, the consistency of

Received March 21, 1986; accepted after revision September 10, 1986.

¹ Department of Radiology, C-309, University of California School of Medicine, San Francisco, CA 94143. Address reprint requests to C. B. Higgins.

² Present address: Department of Radiology, Northwest University Medical School, Chicago, IL 60611.

AJR 148:247–251, February 1987
0361–803X/87/1482-0247
© American Roentgen Ray Society

these findings in a larger number of patients should be determined. Moreover, the determination of the diagnostic significance of regional increase in myocardial signal intensity is important; the frequency and degree of variation in MR signal intensity and T2 relaxation time across the normal myocardium have not been evaluated. Accordingly, the purposes of the current study were to (1) evaluate the ability of MR to detect and locate acute myocardial infarctions in a large group of patients with acute infarcts in various segments of the left ventricle, (2) determine the variation in signal intensity and T2 in different sites of the left ventricular myocardium in normal subjects, (3) compare T2 relaxation times between infarcted and normal myocardium, and (4) assess variation in contrast between infarcted and normal myocardium on first- and second-echo images.

Subjects and Methods

Subjects

Twenty-nine consecutive patients, 21 men and eight women, ranging in age from 43 to 83 years, were studied with ECG-gated proton MR. Technically adequate gated MR studies were obtained in 25 of these patients; the other four patients were excluded from the study because the images of their hearts were too poor to analyze. There was evidence of severe motion artifacts resulting in complete absence of signal from large portions of the heart. Documentation of acute myocardial infarction in the remaining 25 patients was based on acute ECG abnormalities and abnormal elevation of serum levels of creatine kinase isoenzymes, specifically, the myocardial band. Twenty of the 25 patients had Q waves, and 24 had ST elevations. Creatine kinase was elevated in 23. Patients were imaged 3–17 days after the onset of acute chest pain. The sites of infarctions defined by ECG abnormalities were located in the anterior (four patients), anteroseptal (five patients), anterolateral (three patients), anterolateral and anteroseptal (seven patients), posterolateral (one patient), inferolateral (three patients), inferior (one patient), and septal (one patient).

The intention of this study was to detect a region of abnormal signal intensity in patients with acute myocardial infarctions. No attempt was made to determine sensitivity and specificity of MR for diagnosing myocardial infarction. However, for the determination of the frequency and degree of variation in signal intensity of the normal myocardium, gated images were also obtained in 20 normal adult volunteers with no known cardiac abnormalities (16 men, four women; ranging from 24–35 years old).

Imaging Technique

Imaging was performed with a superconducting magnet operating at 0.35 T with a corresponding hydrogen resonance frequency of 15 MHz. Gating was performed by use of nonferromagnetic ECG leads placed on the right and left subclavian and right abdominal regions. A gating device designed for use in high electromagnetic fields and rapidly changing switched-field gradients was used to obtain the ECG signal [12]. The gating signal was initiated by the R wave with a 5-msec trigger delay. A suppression circuit was used to prevent activation of the RF and gradient pulse sequence for approximately 500 msec after the R wave trigger.

The spin-echo technique was used with an echo delay (TE) of 28 and 56 msec or 30 and 60 msec. The pulse-sequence repetition time (TR) was determined by each subject's heart rate. A multiple-plane selective irradiation technique was used for data acquisition. Sectional

images were reconstructed by using the two-dimensional Fourier transformation technique. The matrix was 256×256 , the spatial resolution 1.9 mm, and slice thickness was 10 mm without a gap. With the multisection technique, five adjacent sections were obtained with a delay of 100 msec between adjacent sections. As a result, each section was 100 msec out of phase with the preceding one. The time required to obtain five transverse sections depended on the patient's heart rate, the number of lines along the y axis (256 in our technique), and the number of excitations done for each line (two in our technique). The time required to obtain five sections was approximately 5.5 to 8.5 min.

Data Analysis

Infarct patients.—MR images in each patient with acute infarction were assessed for (1) presence of a focal region of increased signal intensity depicting the site of infarction, (2) the spin-echo signal intensity for normal and infarcted myocardium on first and second spin-echo images, (3) the T2 relaxation time for the normal and infarcted regions of the myocardium, and (4) the percentage of contrast between normal and infarcted myocardium on first and second spin-echo images. In patients with regions of high signal intensity, one region of interest was constructed circumscribing that region, and another was constructed circumscribing a region of similar dimension in the opposite wall of the left ventricle (presumably normal myocardium). Epicardial fat and flow signal were carefully excluded from the left ventricular chamber in the region of interest, which contained at least 20 pixels in both infarcted and normal myocardium. These measurements were done three times for each region of interest, on one occasion by one observer.

T2 relaxation values were calculated from the two Fourier-transformed spin-echo intensities (I_1 and I_2) obtained from the first- and second-echo images, by using the following formula:

$$T2 = \frac{TE_2 - TE_1}{\ln I_1/I_2}$$

T1 could not be calculated because gated MR studies were performed with only one TR: Images in this study were only gated to every heart beat.

The percentage of difference in signal intensity (I) of normal myocardium and infarcted myocardium was calculated in the following manner:

$$\% \text{ difference} = \frac{I(\text{infarct}) - I(\text{normal})}{I(\text{normal})} \times 100\%$$

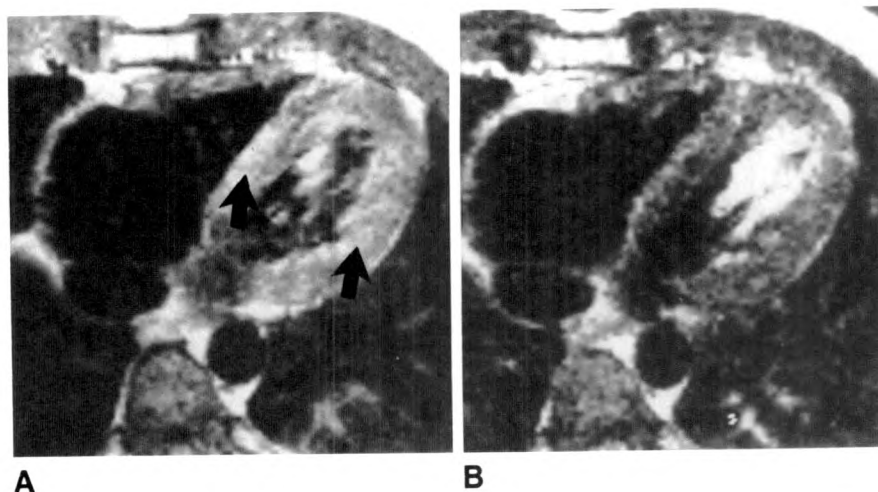
Normalization ratios were calculated to standardize the intensity values for both the first- and second-echo images and among patients because the intensity value is a relative quantity. Myocardial intensity values were normalized to fat by dividing the intensity of the infarcted or normal myocardium by the intensity of fat.

Normal subjects.—For the normal volunteers, regions of interest were constructed in the septum and anterolateral myocardium and subcutaneous fat to obtain intensity and T2 relaxation times for each region. The percentage of difference in intensity between the two segments of myocardium was calculated as follows:

$$\% \text{ difference} = \frac{I(\text{anterolateral}) - I(\text{septum})}{I(\text{septum})} \times 100\%$$

Intensity values for the volunteers were standardized by dividing the intensity of the anterolateral or septal portions of the myocardium by the intensity of fat for both first- and second-echo images.

Fig. 1.—Normal volunteer.
A, Focal regions of high signal intensity on first-echo image (TE = 30 msec).
B, Regions show decreased intensity on second-echo image (TE = 60 msec), as well as decreased contrast between focal regions and adjacent myocardium. Myocardium becomes more homogeneous in signal intensity.



Differentiation of flow signal from infarction.—Differentiation of flow signal from an infarct was accomplished by calculation of the T2 value for each region. Flow signal had a negative T2 (absolute increase in intensity on the second echo) value, while the T2 in the region of infarction had a positive T2 value, always less than 100 msec. Negative T2 is an artifactual value that results when T2 is calculated from the spin-echo formula under the circumstances of an absolute increase in intensity of the first compared to the second spin-echo formula. The Diasonics MR software sets voxels with such value to the highest gray-scale level (white). A higher intensity on the second-echo image results from second-echo rephasing of spins in motion (flowing blood).

Statistical Analysis

Data are given as mean \pm SD. A Student's two-tailed *t* test was used to evaluate the significance of differences in signal intensity and T2 in infarcted and normal myocardium. A *p* value smaller than .05 was considered statistically significant.

Results

Normal Subjects

The gated MR images of the 20 volunteers were characterized by generally homogeneous signal intensity, but regions of higher signal intensity were observed in some persons (Fig. 1). In the normal subjects such regions were usually only seen on one or the other spin-echo image. The percentage of difference in intensity between the septal and anterolateral segments of myocardium on first and second spin-echo images were $9.2 \pm 7.5\%$ and $15.0 \pm 13.3\%$, respectively. The mean ratios between the anterolateral myocardium and fat for 28- and 56-msec images were 0.43 ± 0.08 and 0.38 ± 0.07 , respectively, and the mean ratios between the intensity of the septum and fat for the first- and second-echo images were 0.42 ± 0.09 and 0.37 ± 0.12 , respectively.

The mean T2 relaxation times for these regions of interest were 40.3 ± 5.7 msec and 39.5 ± 7.4 msec, respectively.

The T2 value was less than 50 msec in 38 (95%) of 40 regions of interest in this group of volunteers.

Infarct Patients

Gated MR images at the level of the left ventricle showed focal areas of high signal intensity that corresponded to the location of the myocardial infarction as defined by the ECG abnormalities in 23 of the 25 patients. These regions were clearly discriminated from the surrounding normal myocardium, which was visualized as homogeneous signal intensity. The areas of high signal intensity at the sites of the infarction were visible on both the first- and second-echo images and were more intense in relation to adjacent myocardium on the second-echo image (Figs. 2 and 3). The MR images in two patients did not disclose definite regions of high signal intensity. One of these patients was treated early with streptokinase, and the other patient, one of the five without a Q wave on the ECG, had ECG features that suggested a subendocardial infarction.

The mean percentage of difference in signal intensity between the abnormal and normal myocardium was greater on the second-echo images ($66 \pm 34\%$) than on the first-echo images ($28 \pm 19\%$). The ratios of intensity of the infarcts standardized to fat were 0.49 ± 0.17 for the first echo and 0.60 ± 0.28 for the second echo. Ratios of the intensity of normal myocardium standardized to fat were 0.40 ± 0.18 for the first echo and 0.40 and 0.23 for the second echo, by use of the normal region of the infarct patients.

The T2 of the infarct (79.0 ± 22.1 msec) was significantly longer ($p < .01$) than that of normal myocardium (43.9 ± 9.0 msec). The T2 value was less than 50 msec in 23 of the 25 normal regions in these patients, while T2 was greater than 50 msec in 24 (96%) of 25 infarct regions.

Intracavitary flow signal was observed within the left ventricle, particularly on the second-echo image (Figs. 2 and 3). It was visualized as regions of high signal intensity, either immediately adjacent to the left ventricular wall or filling the entire cavity in most patients with acute infarctions.

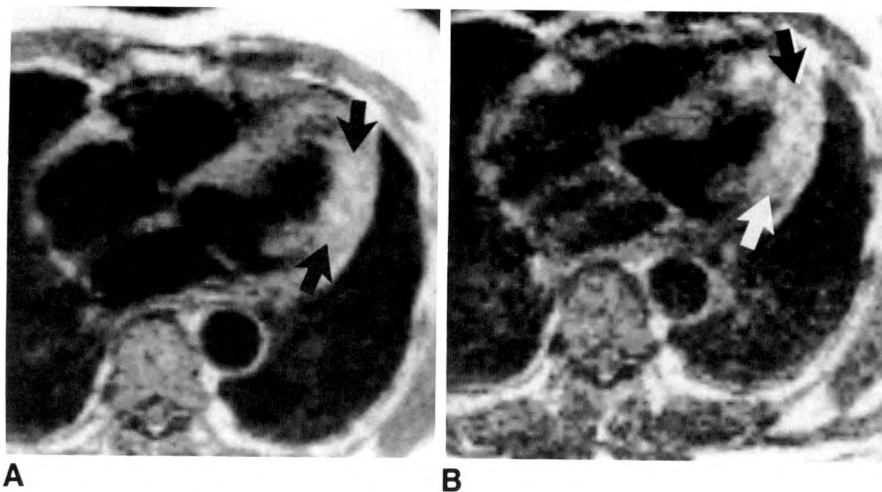


Fig. 2.—Transaxial ECG-gated spin-echo images of patient with recent myocardial infarction (A, TE = 30 msec; B, TE = 60 msec). High signal intensity within anteroseptal walls of left ventricle (arrows). Contrast between normal and infarcted myocardium improved on B because of prolonged T2 of infarct.

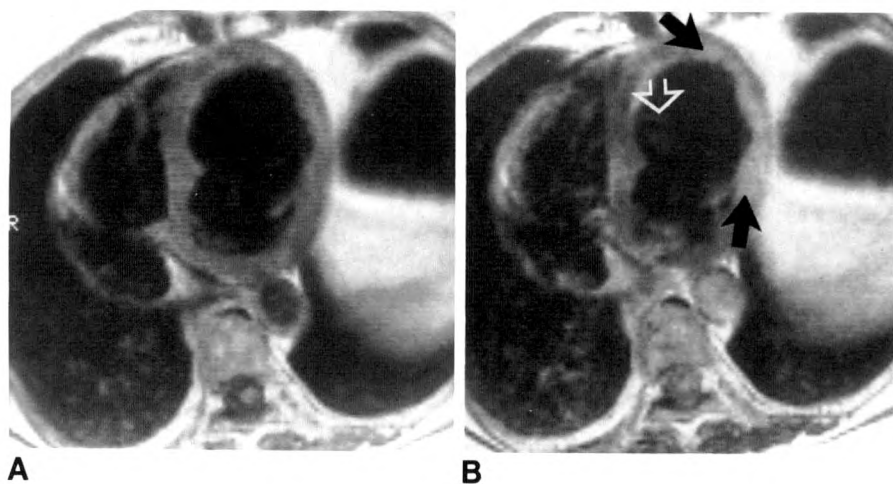


Fig. 3.—Spin-echo MR images of patient with acute anterolateral wall myocardial infarction. Images are from patient examined after completion of study.

A, TE = 28 msec.

B, TE = 56 msec. High intensity of infarct (arrows) best seen on this image. Slowly moving blood characterized by high intensity on second-echo image (arrowhead) because of even echo rephasing.

Discussion

MR imaging of acute myocardial infarctions in experimental models [7–10] and in humans [11] has shown the area of acute infarct as a region of discrete increased signal intensity compared with the normal myocardium. When the spin-echo technique was used in a previous study [11] evaluating myocardial infarcts in humans, the abnormal region was delineated best on the second-echo images. Measurement of relative T2 relaxation time for these images showed a prolongation of this MR parameter in the infarcted region [11]. Although more difficult to measure from in vivo gated studies, the T1 time also increased on in vitro studies [5–7]. The prolongation of T1 and T2 has been related to focal changes in tissue water at the infarct site. A linear relationship has been found between myocardial relaxation times and water content of myocardial tissue samples [5, 7]. These changes may also be related to (1) loss of cellular membrane integrity, which decreases the distinction between intra- and extracellular water distinction; (2) changes in motion of blood in the myocardium; (3) motion of the myocardial wall; and (4) paramagnetic substances in the infarcted tissue.

This study has shown the ability of MR, with a spin-echo,

ECG-gated technique, to detect acute myocardial infarction in a large group of patients. Human myocardial infarctions were identified as regions of increased signal intensity compared with normal myocardium in 23 of 25 patients. The high signal intensity at the site of infarction on spin-echo images was associated with prolongation of the T2 relaxation time of the infarcted myocardium. However, the increase in T1 shown to occur in the infarcted myocardium [5–7] is not responsible for increase in intensity: This factor tends to offset the increase in signal intensity. On the basis of a cut-off T2 value of 50 msec with our imager, MR could characterize myocardial infarction accurately in 96% of patients. Likewise, MR accurately predicted normal myocardium in 95% of the normal volunteers.

The percentage of contrast in intensity between normal and infarcted myocardium on first- and second-echo images reflected variable effects on signal intensity in each region with the increase in TE. The signal intensity was greater for the infarcted than the normal myocardium on images generated by both the first- and second-echo images. Signal intensity decreased from the first to second echo for both normal and abnormal myocardium, but this decline was much less for the infarcted myocardium. Because intensity decreased

less in the infarcted than the normal myocardium with lengthening of the TE parameter, the percentage of contrast was greater on the second-echo image. This effect was also shown by the intensity values for myocardial infarction/fat and normal myocardium/fat. The ratio for the myocardial infarction/fat increased on the second-echo image, while there was no difference between first- and second-echo images for normal myocardium/fat. This pattern of intensity values reflected the prolonged T2 relaxation at the infarct site.

Several pitfalls were identified in evaluating myocardial infarcts. High signal intensity within the left ventricular cavity results from flow signal and may be observed at sites of wall-motion abnormalities [11, 13, 14] but has also been seen in normal persons [15]. Differentiation of flow signal in the ventricle from an acute infarct may be possible if there is awareness of this phenomenon. Calculation of T2 results in a negative value for an area of slow flow, and partial averaging of flow with a region of infarct results in a T2 value more prolonged (T2 > 100 msec) than that observed for myocardial infarction in this and other studies [7-11]. Variation of signal intensity across the myocardium is not specific for infarcted myocardium; we observed it occasionally in our normal subjects. This variation in signal intensity in normal subjects probably results from respiratory motion or the effect of residual cardiac wall motion, even with gating. This artifactual increase in regional myocardial intensity usually can be differentiated from the increase due to prolonged T2 in the infarcted myocardium by comparing first and second spin-echo images. The percentage of contrast increased significantly from first- to second-echo images in the infarcted patients, while the percentage of contrast between the regions of variable intensity in the normal volunteers decreased from first- to second-echo images (Fig. 3).

Another pitfall observed was flow signal appearing within the myocardium, probably a result of spatial misregistration of flow signal as a consequence of the time disparity between the phase encoding and readout gradient [13]. Because of the difference in timing of the two gradients, signal arising from intracavitary flow may be displaced into voxels representing the myocardium on the images; this phenomenon has been described previously [13]. Consequently, bright signal from stagnant blood lying against the endocardium could produce high signal in the myocardial wall. Consistent with even-echo rephasing, such high signal would appear on the second-echo image and could be recognized if the T2 value in such a region were greater than 100 msec or were calculated as a negative value from the dual spin-echo formula.

Measurements were performed at the level of the middle left ventricle to avoid partial volume averaging with epicardial fat. Moreover, when circumscribing the region of interest, we always left a rim between the abnormal myocardium and pericardial fat.

In our study, a myocardial infarction was not shown in two infarct patients (besides the four patients in whom diagnostic images could not be obtained because of inadequate gating). One of these two patients apparently had a small subendocardial infarction, suggested by ECG. The other had received thrombolytic therapy early in the course of the infarct and may have also had a small infarct. Neither of these patients

had Q waves pathognomic for infarction. Therefore, gated MR will probably not be completely sensitive for the detection of acute myocardial infarctions.

Few of the infarctions in our study were located in the inferior wall of the left ventricle, which is poorly evaluated by the standard transverse imaging plane. This site can be evaluated by using other imaging planes but we did not routinely use them. Our study does not indicate the possible sensitivity and specificity of MR for detecting infarcts because measurements were done in consecutive subjects who were known to be normal at the time of analysis, and selection of patients was guided toward anterior and lateral infarctions.

In summary, gated MR can be used to identify acute myocardial infarctions, which are characterized on MR images as focal regions of increased signal intensity compared with normal myocardium. Contrast between infarcted and normal myocardium varies with TE because of prolonged T2 relaxation time of the infarct. This technique may prove useful for measuring myocardial infarctions in humans. Future studies are needed to define the sensitivity and specificity of MR for identifying acute myocardial infarctions, so that the technique can be used to exclude infarcted myocardium in patients with undiagnosed chest pain and in patients with preinfarctional angina.

REFERENCES

- McNamara MT, Higgins CB. Cardiovascular applications of magnetic resonance imaging. *Magnetic Resonance Imaging* 1984;2:167-186
- Higgins CB, Byrd BF III, McNamara MT, et al. Magnetic resonance imaging of the heart: a review of the mitral experience in 172 subjects. *Cardiology* 1985;155:671-679
- Bradley WG, Waluch V. Blood flow: magnetic resonance imaging. *Radiology* 1985;154:443-450
- Herfkens R, Davis PL, Crooks LE, et al. Nuclear magnetic resonance imaging of the abnormal live rat and correlation with tissue characteristics. *Radiology* 1981;141:211-218
- Frank JA, Feller MA, House WV, Lauterbur PC, Jacobson MJ. Measurement of proton nuclear magnetic longitudinal relaxation times and water content in infarcted canine myocardium and induced pulmonary injury. *Clin Res* 1976;24:217A
- Williams ES, Kaplan JL, Thatcher F, Zimmerman G, Knoebel SB. Prolongation of proton spin lattice relaxation times in regionally ischemic tissue from dog hearts. *J Nucl Med* 1980;21:449-453
- Higgins CB, Herfkens R, Lipton MJ, et al. Nuclear magnetic resonance imaging of acute myocardial infarction in dogs: alterations in magnetic relaxation times. *Am J Cardiol* 1983;52:184-188
- Wesbey G, Higgins CB, Lanzer P, Botvinick E, Lipton MJ. Imaging and characterization of acute myocardial infarction. *Circulation* 84:69:125-130
- Pflugfelder PW, Wisenberg G, Prato FS, Carroll E, Turner KL. Early detection of canine myocardial infarction by magnetic resonance imaging in vivo. *Circulation* 1985;71:587-594
- Tscholakoff D, McNamara MT, Derugin N, Higgins CB. Evaluation of early myocardial ischemia by magnetic resonance imaging. *Radiology* 1986 (in press)
- McNamara MT, Higgins CB, Schechtman N, et al. Detection and characterization of acute myocardial infarction in man with the use of gated magnetic resonance. *Circulation* 1985;71:717-724
- Lanzer P, Botvinick E, Kaufman L, et al. Cardiac imaging using gated NMR. *Radiology* 1984;150:121-129
- von Schulthess GD, Higgins CB. Magnetic resonance of flow. *Radiology* 1986;157:687-695
- Higgins CB, Lanzer P, Stark D, et al. Imaging by nuclear magnetic resonance in patients with chronic ischemic heart disease. *Circulation* 1984;69:523-530
- von Schulthess GK, Fisher MR, Crooks LE, Higgins CB. The nature of intracardiac signal on gated MRI images in normals and patients with abnormal left ventricular function. *Radiology* 1985;156:125-132

American Roentgen Ray Society: Officers, Committees, and Meeting Information

Officers

President: Jerome F. Wiot
President-elect: Raymond A. Gagliardi
1st Vice-president: Lee F. Rogers
2nd Vice-president: Gerald D. Dodd
Secretary: Glen W. Hartman
Treasurer: Ronald G. Evens

Executive Council: E. Gedgudas, J. F. Wiot, L. F. Rogers, R. A. Gagliardi, R. G. Evens, R. N. Berk, F. L. Angell, J. E. Madewell, M. P. Capp, G. W. Hartman, B. G. Brogdon, G. A. Kling, H. C. Carlson, A. K. Poznanski, A. E. James, Jr., J. A. Kirkpatrick, Jr., G. R. Leopold, G. D. Dodd, J. T. Ferrucci, Jr., R. H. Troupin, chairman

Committees 1986-1987

Editorial Policy: S. S. Sagel, W. J. Casarella, J. T. Ferrucci, Jr., N. C. Whitley, S. Hilton, A. J. Davidson, J. M. Taveras, R. N. Berk, M. P. Capp, chairman

Education and Research: C. E. Putman, A. R. Margulis, J. R. Thornbury, R. A. McLeod, J. T. Ferrucci, Jr., ex officio, B. G. Brogdon, chairman

Finance and Budget: B. P. Wood, L. R. James, J. A. Kirkpatrick, Jr., A. E. James, F. L. Angell, chairman

Instruction Courses: R. A. McLeod, associate chairman, J. T. Ferrucci, Jr., chairman

Program: J. Wiot, G. W. Hartman, J. A. Kirkpatrick, Jr., R. H. Troupin, M. P. Capp, J. E. Madewell, B. G. Brogdon, J. T. Ferrucci, Jr., G. A. Kling, G. G. Ghahremani, M. Viamonte, R. A. Gagliardi, chairman

Publications: W. J. Casarella, J. T. Ferrucci, Jr., S. S. Sagel, N. C. Whitley, M. P. Capp, chairman

Scientific Exhibits: S. G. Kirchner, A. V. Proto, S. M. Goldman, J. E. Madewell, chairman

Nominating: W. J. Casarella, H. C. Carlson, A. E. James, chairman

Representatives to Other Organizations

American Board of Radiology: E. C. Klatte, R. W. McConnell, L. F. Rogers

American College of Radiology: J. L. Gwinn, G. A. Kling, G. W. Hartman, J. M. Dennis, E. J. Ferris, J. E. Madewell

American Medical Association House of Delegates: S. F. Ochsner, K. C. Krabbenhoft, alternate

American National Standards Institute: M. Haskin

National Council on Radiation Protection and Measurements: E. L. Saenger, H. L. Friedell

Meetings, Membership, Business Information

Annual Meetings: April 26-May 1, 1987, Fontainebleau-Hilton, Miami Beach; May 8-13, 1988, Hilton, San Francisco; May 7-13, 1989, Hilton, New Orleans.

Director Annual Meeting: George A. Kling, Harper Hospital, Detroit, MI 48201; (313) 745-8401.

ARRS Membership: Rosalind H. Troupin, Dept. of Radiology, Hospital of University of Pennsylvania, 3400 Spruce St., Philadelphia, PA 19104. The ARRS has two membership categories: active and in-training. For active membership, applicants must practice radiology in the U.S. or Canada. Each must have graduated in good standing from an approved medical school or hold an advanced degree in a physical, chemical, or biological science and be certified by the American Board of Radiology, the Royal College of Physicians and Surgeons of Canada, or otherwise adequately document training and credentials. A member-in-training must be in a radiology residency, a postresidency fellowship program, or a postgraduate student in an allied science. Status must be verified by the program director. For consideration during the 1987 ARRS meeting, completed applications must be received by Dr. Troupin no later than Feb. 1, 1987.

Business Office: Paul Fullagar, administrative director, George J. O'Hop, controller, American Roentgen Ray Society, 1891 Preston White Dr., Reston, VA 22091; (703) 648-8900.

Aberrant Right Subclavian Artery: Further Observations

Anthony V. Proto¹
Nathaniel W. Cuthbert¹
Louis Raider²

One hundred one posteroanterior and 89 lateral chest radiographs were reviewed of patients with proven aberrant right subclavian artery. The patients were 17–96 years old. Three findings were noted on the posteroanterior radiograph: an oblique edge extending to the right from the aortic knob (60%); demonstration of the vessel through the lucency of the tracheal air column (43%) with sharp margins (29%) or as a tubular opacity without sharp margins (14%); and a “mass” effect at the medial right clavicular area (32%). Three findings were noted on the lateral radiograph: retrotracheal opacity (79%), aortic arch obscuration (62%), and posterior tracheal imprint (49%). Two of these findings (tubular opacity and mass effect) are reported as new observations in patients with aberrant right subclavian artery.

The aberrant right subclavian artery (ARSCA) is a well-known vascular anomaly [1–3]. Having observed two additional findings indicating its presence on conventional posteroanterior and lateral radiographs, we undertook a systematic review of patients with proven ARSCA to determine the frequency of these findings as well as of those previously reported.

Materials and Methods

We retrospectively reviewed the posteroanterior and lateral chest radiographs in 101 patients with proven ARSCA—65 women (aged 17–96 years) and 36 men (aged 30–84 years). The ARSCA had been verified by esophagram (91), angiography (eight), or CT (six) [4–8]. Four patients had more than one type of proof.

Posteroanterior radiographs were available in all 101 patients, while lateral radiographs were available in 89.

Results

The ARSCA arises from the aortic arch or proximal descending aorta distal to the left subclavian artery [1, 4, 5]. It courses through the mediastinum from left to right behind the esophagus and then ascends toward the apex of the chest en route to the axilla (Fig. 1).

Posteroanterior Radiograph

Three findings indicating ARSCA are visible on the posteroanterior radiograph, two of which are new (tubular opacity and “mass” effect).

Oblique edge.—In 60% of patients (61/101), an oblique edge extended to the right from the aortic knob area (Fig. 2), the edge produced by left lung contact with the upper surface of the vessel as it originates from the aortic arch (Fig. 1). In 12 patients, the oblique edge was the only finding on the posteroanterior radiograph indicating the ARSCA.

Received June 16, 1986; accepted after revision, September 19, 1986.

Presented at the annual meeting of the American Roentgen Ray Society, Washington, DC, April 1986.

¹ Department of Radiology, Medical College of Virginia, Box 615 MCV Station, Richmond, VA 23298. Address reprint requests to A. V. Proto.

² Department of Radiology, Providence Hospital, Mobile, AL 36652.

AJR 148:253–257, February 1987
0361–803X/87/1482–0253
© American Roentgen Ray Society

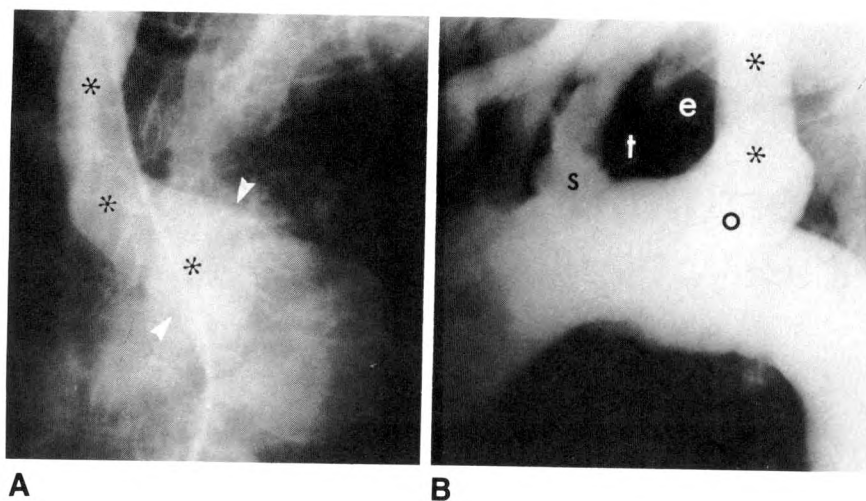


Fig. 1.—Angiogram. Anteroposterior (left) and lateral (right) angiograms show aberrant right subclavian artery (asterisks) originating (o) distal to left subclavian artery (s) and coursing through mediastinum behind trachea (t) and esophagus (e). Note wide origin of vessel (arrowheads).

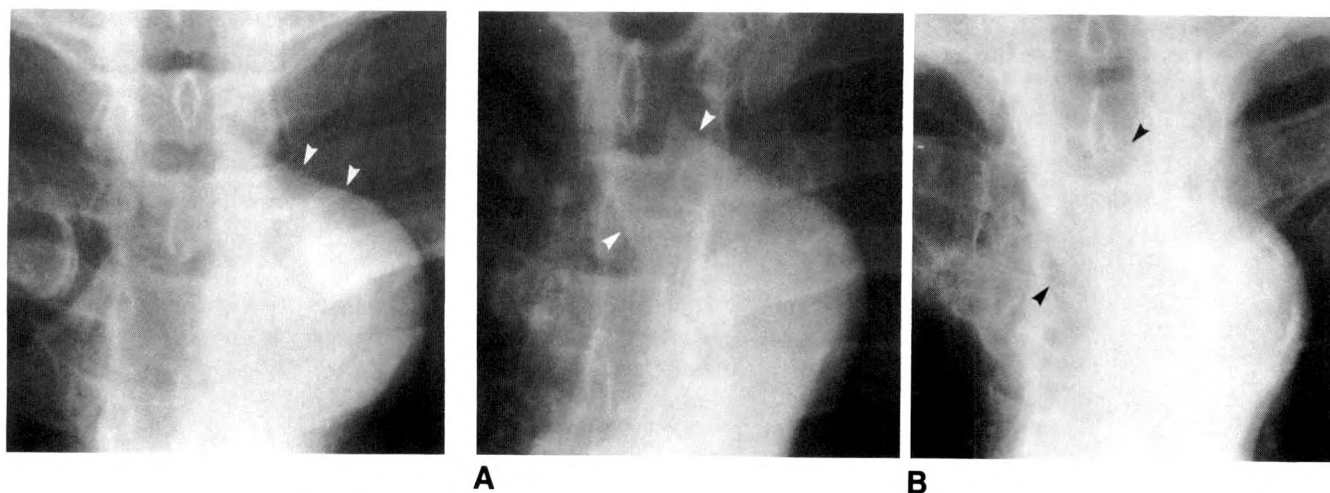


Fig. 2.—Oblique edge. Posteroanterior radiograph shows oblique edge of aberrant right subclavian artery (arrowheads) extending to right from aortic knob.

Fig. 3.—Vessel through trachea. Posteroanterior radiographs show aberrant right subclavian artery (arrowheads) with sharp margins in one patient (A) and as subtle tubular opacity with greater lucency above and below in another (B).

Vessel through trachea.—In 43% of patients (43/101), the vessel was demonstrated through the lucent tracheal air column, with a sharp upper or upper-and-lower margin in 29 or as a tubular opacity without sharp margins in 14 (Figs. 1 and 3). Recognition as a subtle tubular opacity is facilitated by identification of the slightly greater lucency above and below the area of tubular opacity that represents the vessel.

In all of the 29 patients in whom the ARSCA was seen through the trachea with sharp margination, the oblique edge extending to the right from the aortic knob was also noted. In three of the 14 patients in whom the ARSCA was seen as a subtle tubular opacity, this was the only finding noted on the posteroanterior radiograph.

"Mass" effect.—In 32% of patients (32/101), a mass projected at the right clavicle medially, sometimes slightly above or below (Fig. 4). The mass is produced by contact of the ARSCA with the right lung as the vessel "turns" to proceed

upward toward the apex of the chest (Fig. 5). In five patients, the mass effect was the only finding on the posteroanterior radiograph indicating the ARSCA.

Lateral Radiograph

Three findings indicating ARSCA are visible on the lateral radiograph.

Retrotracheal opacity.—In 79% of patients (70/89), retrotracheal opacity, rather than lucency, was noted above the aortic arch (Fig. 6A). The opacity is produced by the ARSCA, which is present in, and excludes lung from, the retrotracheal area (Figs. 6B and 6C).

The retrotracheal opacity, measured from the inner posterior tracheal wall to the posterior extent of the opacity, showed an anteroposterior dimension of 1.0–4.0 cm (mean, 2.6 cm). Some of the opacity immediately behind the tracheal

Fig. 4.—Mass effect.

A, Posteroanterior radiograph shows mass effect of aberrant right subclavian artery (arrowheads) projected at right clavicle (c) medially.

B, CT scan shows margin of contact of right lung with vessel (arrowhead) to explain mass. Note right clavicle (c) medially.

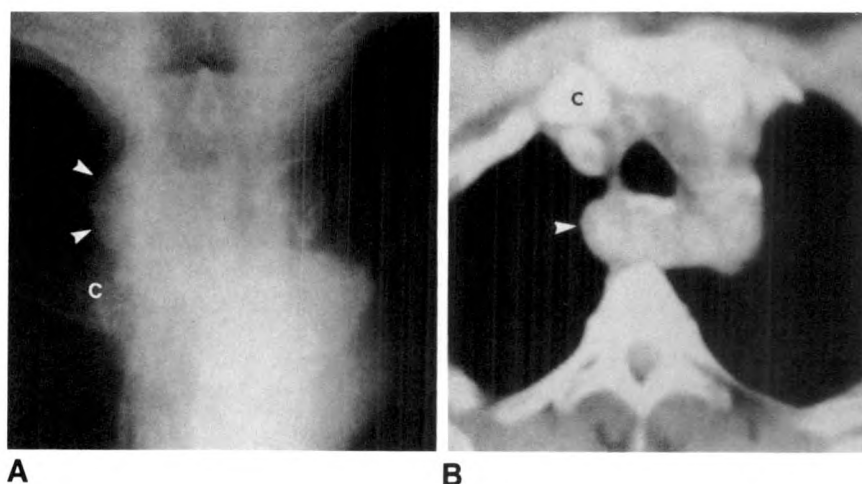
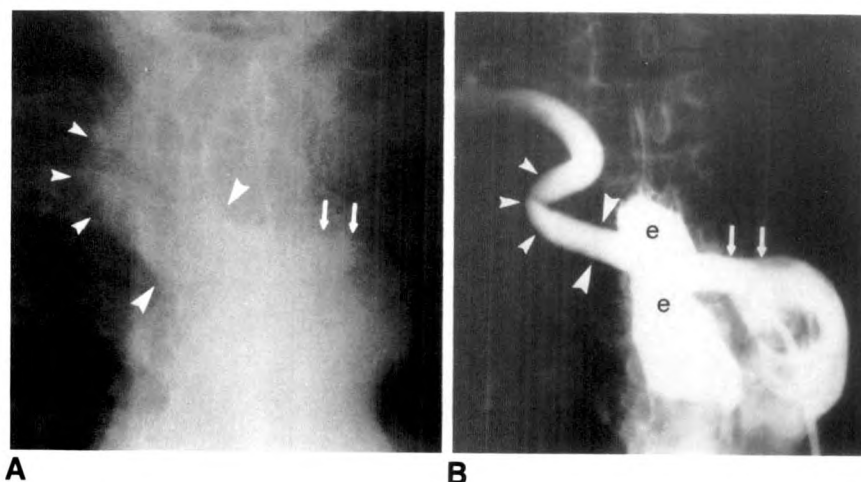


Fig. 5.—Three findings. In aberrant right subclavian artery, oblique edge (arrows), margins of vessel (large arrowheads) through tracheal air column, and mass effect (small arrowheads) projected at right clavicle medially are seen on posteroanterior radiograph (A) in correlation with anteroposterior angiogram (B). High density of contrast material in esophagus (e) obliterates some margins of vessel in B.



air column is accounted for by the posterior tracheal wall and the esophagus [1, 9]. In 11 patients, the retrotracheal opacity was the only finding on the lateral radiograph indicating the ARSCA.

Aortic arch obstruction.—In 62% of patients (55/89), obscuration of the aortic arch by the retrotracheal opacity above it was noted (Fig. 6A). This is explained by the origin of the vessel preventing the left lung from outlining the upper surface of the aortic arch (Fig. 1).

In 15 patients who showed retrotracheal opacity, the aortic arch was not obscured. This happens when the origin of the vessel from the arch lies slightly inferior to the upper surface of the arch, thereby not preventing lung from contacting the uppermost surface of the arch. In no patient was obscuration of the arch the only indication of the ARSCA on the lateral radiograph.

Posterior tracheal imprint.—In 49% of patients (44/89), a focal imprint along the posterior tracheal air column was noted (Fig. 7). This may occur when the retroesophageal ARSCA pushes the esophagus forward, and the esophagus in turn impinges on the pliable noncartilaginous posterior tracheal

wall (Fig. 6B). In no patient was a posterior tracheal imprint the only finding indicating the ARSCA on the lateral radiograph.

Posteroanterior and Lateral Radiographs

The frequencies of the number of findings indicating ARSCA in posteroanterior, lateral, and both posteroanterior and lateral radiographs are given in Table 1.

Discussion

ARSCA is said to occur in 0.4–2.3% of patients [1, 2, 4, 8]. Up to 60% of the time it has a diverticular origin (diverticulum of Kommerell), a remnant of the right dorsal aortic arch (Fig. 1) [1, 4]. Currently, the vessel is thought to course solely in a retroesophageal position [1, 4, 6], although previously a preesophageal or pretracheal course had also been considered.

Perhaps the two most well-known conventional radi-

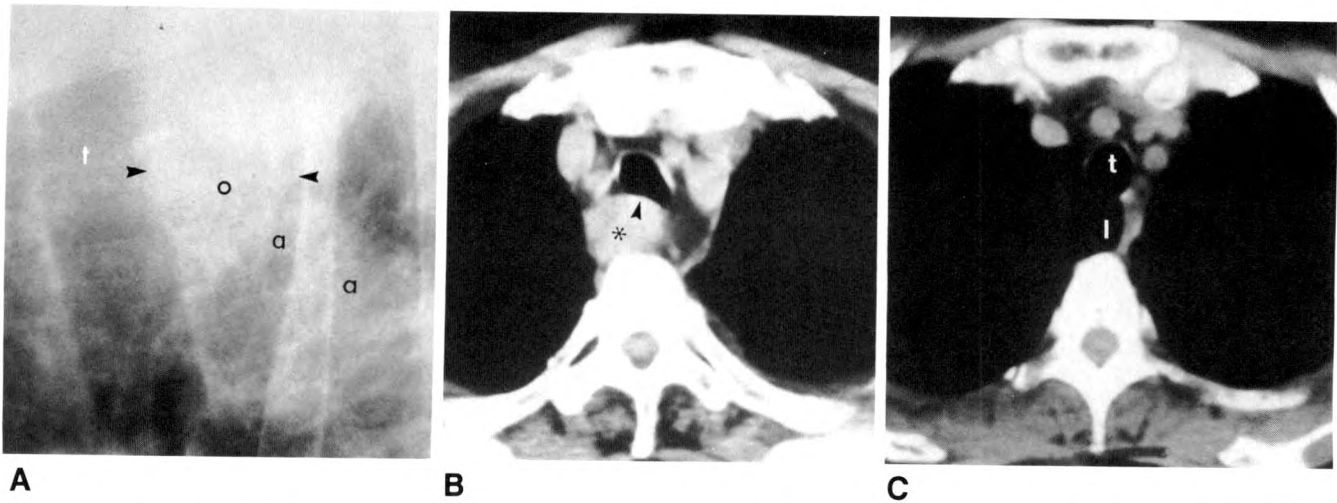


Fig. 6.—Retrotracheal opacity.

A, Lateral radiograph in aberrant right subclavian artery shows opacity (arrowheads) behind trachea (t) with obscuration of upper margin of aortic arch (a) at origin (o) of vessel from arch. Opacity does not imprint posterior tracheal wall.

B, In CT scan in another patient with aberrant right subclavian artery

(asterisk), vessel excluding lung from retrotracheal area explains retrotracheal opacity on lateral radiograph. Note posterior tracheal imprint (arrowhead).

C, In CT scan in a patient without aberrant right subclavian artery, lung (l) behind trachea (t) explains usual retrotracheal lucency on lateral radiograph.

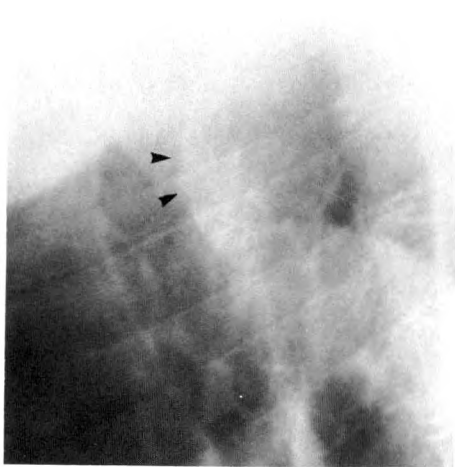


Fig. 7.—Posterior tracheal imprint. Lateral radiograph shows retrotracheal opacity of aberrant right subclavian artery associated with imprint (arrowheads) along posterior tracheal wall. (Compare with Fig. 6A.)

ographic findings of ARSCA are the oblique edge and the retrotracheal opacity [1–3, 10]. Demonstration of the sharp margins of the vessel through the tracheal air column, the posterior tracheal imprint, and obscuration of the aortic arch have received less attention in the literature [1, 2, 8]. We emphasize two additional findings also indicative of ARSCA: a subtle tubular opacity and a mass effect, the latter easily being confused with significant mediastinal abnormality. In addition, we have tabulated the frequencies with which each of the conventional radiographic findings were seen in our study group. One lateral radiographic finding noted by Branscom and Austin [3], a bulge along the superior surface of

TABLE 1 Frequency of Aberrant Right Subclavian Artery Findings on Posteroanterior and Lateral Chest Radiographs

No. of Findings Possible	Posteroanterior	Lateral	Posteroanterior and Lateral
None	29	17	6
One of three	20	11	NA
Two of three	34	27	NA
Three of three	18	34	NA
One of six	NA	NA	8
Two of six	NA	NA	19
Three of six	NA	NA	14
Four of six	NA	NA	16
Five of six	NA	NA	19
Six of six	NA	NA	7
Total	101	89	89

Note.—Three possible findings on posteroanterior radiograph: oblique edge, vessel through trachea, “mass” effect; three possible findings on lateral radiograph: retrotracheal opacity, aortic arch obscuration, posterior tracheal imprint; six possible findings on posteroanterior and lateral radiographs: combination of above. NA = not applicable.

the aortic arch representing the origin of the vessel, was not seen in our series.

Aneurysm and dissection of the ARSCA have been reported [11, 12]. Our experience with a patient developing an aneurysm of the vessel points out the utility of understanding the conventional radiographic findings so that an abnormality of this vessel can be considered in the differential diagnosis (Fig. 8).

Recognition of the ARSCA has clinical significance. First, dysphagia has been associated with this vascular anomaly, although it is now thought to be an infrequent, if not a rare, occurrence [4, 6]. Recently, however, a 27-year-old woman was reported whose dysphagia was relieved by division of her ARSCA [13]. Second, Raider [1] emphasized the importance of recognition by the vascular surgeon and the angiog-

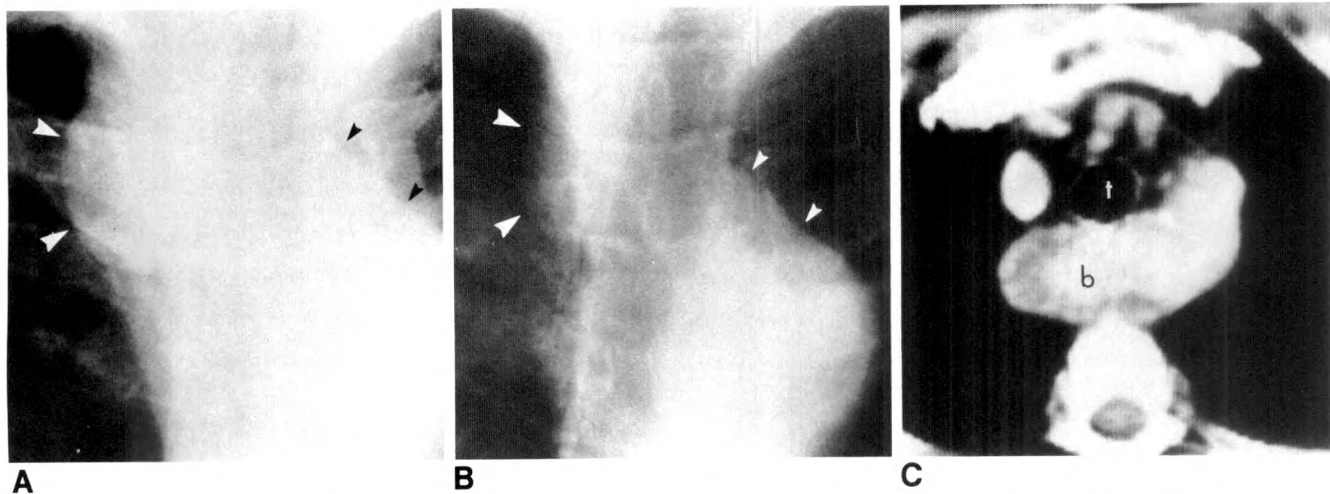


Fig. 8.—Aneurysm of aberrant right subclavian artery.
A, Posteroanterior radiograph in a patient with widened upper mediastinum shows two features of aberrant artery: oblique edge (small arrowheads) and mass effect (large arrowheads), both seen to lesser degree on

posteroanterior radiograph 4 years before (B).

C, Contrast-enhanced CT scan obtained at time of mediastinal widening shows aneurysmal artery behind trachea (t), with central, higher-density flowing blood (b) and peripheral, lower-density thrombus.

rapher. Third, variance in position of the recurrent laryngeal nerve and the thoracic duct has been reported [1]. Fourth, ARSCA may explain unilateral left rib notching in a patient with coarctation of the aorta [1]. Fifth, aortic dissection with extension into the ARSCA has been associated with exsanguination (perforation into the esophagus) and brainstem infarction (at surgery for aortic dissection, the aorta was clamped proximal to the left subclavian artery to compromise blood supply to both subclavian, and thus both vertebral, arteries) [12]. Sixth, ARSCA has been found in approximately 37% of children with Down syndrome who have congenital heart disease [14]. Thus, the presence of ARSCA may suggest the need for further cardiac evaluation in such patients.

We do not imply that these findings are never mimicked by other entities. Previous authors have offered lists of differential diagnoses of various vascular anomalies and other anatomic structures with which ARSCA may be confused [4–6, 11, 15]. Since our study was not a prospective one, we cannot tell how often one or more of the findings described indicated an ARSCA that was not subsequently proven by an esophagram. A tortuous innominate artery or a true mediastinal mass might produce similar findings. However, ARSCA should be considered in the differential diagnosis when any of these radiographic findings are noted: oblique edge, vessel through trachea, or mass effect on posteroanterior radiograph; retrotracheal opacity, aortic arch obscuration, or posterior tracheal imprint on lateral radiograph; or any combination of the preceding findings.

REFERENCES

1. Raider L. Aberrant right subclavian artery. *South Med J* 1967;60:145–151
2. Raider L. The retrotracheal triangle. *Chest* 1973;63:835–838
3. Branscom JJ, Austin JHM. Aberrant right subclavian artery: findings seen on plain chest roentgenograms. *AJR* 1973;119:539–542
4. Salomonowitz E, Edwards JE, Hunter DW, et al. The three types of aortic diverticula. *AJR* 1984;142:673–679
5. Felson B, Cohen S, Courter SR, McGuire J. Anomalous right subclavian artery. *Radiology* 1950;54:340–349
6. Beabout JW, Stewart JR, Kincaid OW. Aberrant right subclavian artery: dispute of commonly accepted concepts. *AJR* 1964;92:855–864
7. Webb WR, Gamsu G, Speckman JM, Kaiser JA, Federle MP, Lipton MJ. CT demonstration of mediastinal aortic arch anomalies. *J Comput Assist Tomogr* 1982;6:445–451
8. Nguyen KT, Vas W, Zylak CJ. Diagnosis of an aberrant right subclavian artery on CT. *J Comput Tomogr* 1981;5:38–40
9. Proto AV, Speckman JM. The left lateral radiograph of the chest. Part I. *Kodak Med Radiogr Photogr* 1979;55:29–74
10. Heitzman ER. *The mediastinum: radiologic correlations with anatomy and pathology*. St. Louis: Mosby, 1977:139
11. Austin EH, Wolfe WG. Aneurysm of aberrant subclavian artery with a review of the literature. *J Vasc Surg* 1985;2:571–577
12. Weinberger G, Randall PA, Parker FB, Kieffer SA. Involvement of an aberrant right subclavian artery in dissection of the thoracic aorta: diagnostic and therapeutic implications. *AJR* 1977;129:653–655
13. Karlson KJ, Heiss FW, Ellis FH. Adult dysphagia lusoria: treatment by arterial division and reestablishment of vascular continuity. *Chest* 1985;87:684–686
14. Goldstein WB. Aberrant right subclavian artery in mongolism. *AJR* 1965;95:131–134
15. Ball JB, Proto AV. The variable appearance of the left superior intercostal vein. *Radiology* 1982;144:445–452

Forthcoming Articles

SPECIAL ARTICLE

Aubrey O. Hampton lecture. Subspecialization in radiology: response to a need. *Taveras JM*

PEDIATRIC URORADIOLOGY

Imaging in acute renal infection in children. *Sty JR, Wells RG, Starshak RJ, Schroeder BA*

Urography and voiding cystourethrography: findings in girls with urinary tract infection. *Bisset GS, Strife JL, Dunbar JS*

Ureteral dilatation in children with febrile urinary tract infection or screening bacteriuria. *Hellström M, Jodal U, Mårild S, Wettergren B*

Posttransplant renal artery stenosis in children. *Stanley P, Malekzadeh M, Diamant MJ*

Stones in the urinary bladder in children and young adults. *Vargas B, Lebowitz RL*

The duplex collecting system in girls with urinary tract infection. *Bissett GS III, Strife JL*

CHEST RADIOLOGY

CT assessment of silicosis in exposed workers. *Bégin R, Bergeron D, Samson L, Bector M, Cantin A*

Case report. Mediastinal paraganglioma: radiologic evaluation of an unusual vascular tumor. *Drucker EA, McLoud TC, Dedrick CG, Hilgenberg AD, Geller SC, Shepard JO*

Case report. Pleuroperitoneal endometriosis with diaphragmatic defects: CT and sonographic findings. *Im J-G, Kang HS, Choi BI, Park JH, Han MC, Kim C-W*

BREAST RADIOLOGY

The relationship between mammographic density and physical assessment of the breast. *Swann CA, Kopans DB, McCarthy KA, White G, Hall DA*

ENDOCRINE RADIOLOGY

Efficacy of thyroid scintigraphy in the diagnosis of intrathoracic goiter. *Park H-M, Tarver RD, Siddiqui AR, Schauwecker DS, Wellman HN*

Primary adrenocortical carcinoma: CT evaluation with clinical correlation. *Fishman EK, Deutch BM, Hartman DS, Goldman SM, Zerhouni EA, Siegelman SS*

GASTROINTESTINAL RADIOLOGY

CT evaluation of Crohn's disease: effect on patient management. *Fishman EK, Wolf EJ, Jones B, Bayless TM, Siegelman SS*

Diagnosis of acute colonic diverticulitis: comparison of barium enema and CT. *Johnson CD, Baker ME, Rice RP, Silverman P, Thompson WM*

Efficacy of an intracassette filter for improved pneumocolon decubitus radiographs. *Olson DL, Dodds WJ, Stewart ET, Unger GF*

Pictorial essay. Sonography in patients with a possible pancreatic mass on CT. *Ormson MJ, Charboneau JW, Stephens DH*

Technical note. Daytime constancy of bile duct diameter. *Raptopoulos V, Smith EH, Karellas A, Miranda DK, Tefft CA*

Technical note. Stereoscopic digital subtraction angiography of hepatic artery and vein. *Yamauchi T, Furui S, Ohtomo K, Itai Y*

MUSCULOSKELETAL RADIOLOGY

High-resolution MR imaging of the normal rotator cuff. *Middleton WD, Kneeland JB, Carrera GF, et al*

Lumbar hernia: diagnosis by CT. *Baker ME, Weinerth JL, Andriani RT, Cohan RH, Dunnick NR*

Direct radiographic magnification by using CT. *Nakano Y, Hiraoka T, Togashi K, et al*

Case report. Synovial chondromatosis of the temporomandibular joint: diagnosis by CT. *Manco LG, DeLuca DM*

Case report. Superficial fascial calcification in epidermolysis bullosa. *Panicek DM, Leeson SH*

NEURORADIOLOGY

MR imaging and spectroscopy in clinical and experimental cerebral ischemia: a review. *Brant-Zawadzki M, Weinstein P, Bartowski H, Moseley M*

MR imaging of the intratemporal facial nerve using surface coils. *Teresi L, Lufkin R, Wortham D, et al*

The utility of MR in planning the radiation therapy of oligodendroglioma. *Shuman WP, Griffin BR, Haynor DR, et al*

Direct oblique sagittal CT of orbital wall fractures. *Ball JB Jr*

The "fat" C2: a sign of fracture. *Smoker WRK, Dolan KD*

Case report. Traumatic pneumorrhachis. *Newbold RG, Wiener MD, Vogler JB III, Martinez S*

INTERVENTIONAL RADIOLOGY

Technical note. Direct percutaneous ureterolithotomy. *Smith TP, Hunter DW, Hulbert JC, Darcy MD, Castaneda-Zuniga WR, Amplatz K*

Technical note. Translumbar inferior vena cava Hickman catheter placement for total parenteral nutrition. *Denny DF Jr, Dorfman GS, Greenwood LH, Horowitz NR, Morse SS*

Technical note. Fine needle aspiration biopsy of superficially located lesions under sonographic guidance: the use of a linear array biopsy probe. *Rizzatto G, Solbiati L, Croce F, Derchi LE*

Technical note. Hepatic embolization through periportal collaterals by using balloon occlusion technique. *Nakamura H, Hashimoto T, Oi H, Sawada S*

MAGNETIC RESONANCE

Technical note. Phase offset technique to distinguish slow blood flow and thrombus on MR images. *Dinsmore RE, Wedeen V, Rosen B, Wismer GL, Miller SW, Brady TJ*

Two-second MR images: initial experience. *Utz JA, Herfkens RJ, Johnson D, et al*

ARRS ANNUAL MEETING CASE OF THE DAY

Chest case of the day. *Crass JR, Letourneau JG, Day DL, Goldberg ME*

Abdominal case of the day. *Letourneau JG, Day DL, Crass JR, Goldberg ME, Drake G*

Musculoskeletal case of the day. *Day DL, Letourneau JG, Crass JR, Goldberg ME, Drake G*

Neuroradiologic case of the day. *McGeachie RE, Ford WJ*

Superior Vena Cava Obstruction: A Venographic Classification

William Stanford¹
Howard Jolles²
Stephen Eli³
Lee C. Chiu⁴

Analysis of venacavograms in 27 patients with superior vena caval obstruction revealed the following four patterns of venous collateral return: type I, partial obstruction (up to 90% stenosis) of the superior vena cava with patency of the azygos vein; type II, near-complete to complete obstruction (90–100%) of the superior vena cava with patency and antegrade flow through the azygos vein and into the right atrium; type III, near-complete to complete obstruction (90–100%) of the superior vena cava with reversal of azygos blood flow; type IV, complete obstruction of the superior vena cava and one or more of the major caval tributaries, including the azygos system. These patterns correlate well with the patients' clinical courses and can be used to identify patients who are at risk of developing cerebral and airway compromise and therefore would benefit from superior vena cava bypass surgery.

An increasing number of spiral-vein-bypass grafts of the superior vena cava (SVC) are being done for malignant obstructive lesions [1–6]. In this operation a saphenous vein is harvested from the leg, split longitudinally, and spirally wrapped around a 10–15 mm mandrel. The vein edges are then sewn together creating a vein conduit approximately the size of the mandrel. The proximal end of the conduit is anastomosed to a large vein above the obstruction (usually the left brachiocephalic), and the distal end is anastomosed to the right atrium, thus bypassing the obstruction. The operation is done primarily in patients who are becoming mentally confused or developing symptoms of airway obstruction. Its purpose is to relieve the increased pressure in the head and neck veins in order to make the patient more comfortable while radiation or chemotherapy is carried out. Because the types of venous collateral return vary in cases of SVC obstruction, an attempt was made to classify the patterns into subgroups that identify patients at risk of developing cerebral or airway compromise and make them candidates for spiral-vein bypass.

Received March 11, 1986; accepted after revision September 19, 1986.

Presented in part at the meeting of the Society of Thoracic Radiology, Orlando, FL, March 1984.

¹ Department of Radiology, Rm. 7006, Roy Carver Pavilion, The University of Iowa Hospitals and Clinics, Iowa City, IA 52242. Address reprint requests to W. Stanford.

² Department of Radiology, Medical College of Virginia, Richmond, VA 23219.

³ Department of Radiology, University of Chicago, 5841 S. Maryland Ave., Chicago, IL 60637.

⁴ Department of Radiology, Harbor-UCLA Medical Center, 1000 W. Carson St., Torrance, CA 90509.

AJR 148:259–262, February 1987
0361–803X/87/1482–0259

© American Roentgen Ray Society

Subjects and Methods

We reviewed the records of 67 patients with SVC obstruction who were examined and treated at University of Iowa Hospitals and Clinics between 1977 and 1982. Satisfactory venograms were available for 27 of these patients (21 men, 6 women; 39–72 years old, median age 60 years). All patients had proven primary carcinoma of the lung. The presenting symptoms, duration of onset, and degree of disability were evaluated in each patient. Special note was made of those patients with mental confusion and airway obstruction.

Superior venacavograms made after bilateral antecubital-vein injections of 60 ml diatrizoate meglumine (60%) were studied to locate the obstruction and determine its extent. Stenosis was expressed as the percentage of narrowing of the diameter of the SVC. Collateral venous channels were identified, classified, and evaluated for the degree of their development (on a scale of 1–4+ with 4+ being the most extensive). Competence of the valves of the veins of the neck and upper thorax was noted along with evaluation of the degree of venous dilatation, irregularity of vein walls, and presence of thrombi. The examination included the right superior

intercostal, left accessory hemiazygos, azygos, hemiazygos, para-vertebral, and internal mammary veins. Composite, spiral, saphenous-vein grafts to bypass the obstructed cava were made in six patients. All patients were studied from the onset of symptoms until death or through 37 months of survival.

Results

Studies of the superior venacavograms revealed that the cavograms could be classified into four types (Fig. 1): *type I*, partial obstruction (up to 90% stenosis) of the SVC with

patency of the azygos vein (three patients); *type II*, near-complete to complete obstruction (90–100%) of the SVC with patency and blood flow through the azygos vein into the right atrium (seven patients); *type III*, near-complete to complete obstruction (90–100%) of the SVC with reversal of azygos blood flow (seven patients); *type IV*, complete obstruction of the SVC and one or more of the major caval tributaries, including the azygos system (10 patients).

We grouped the patients according to the type of obstruction, extent of collateral flow, venous-valve incompetence, and presence of cerebral or airway compromise. Symptoms

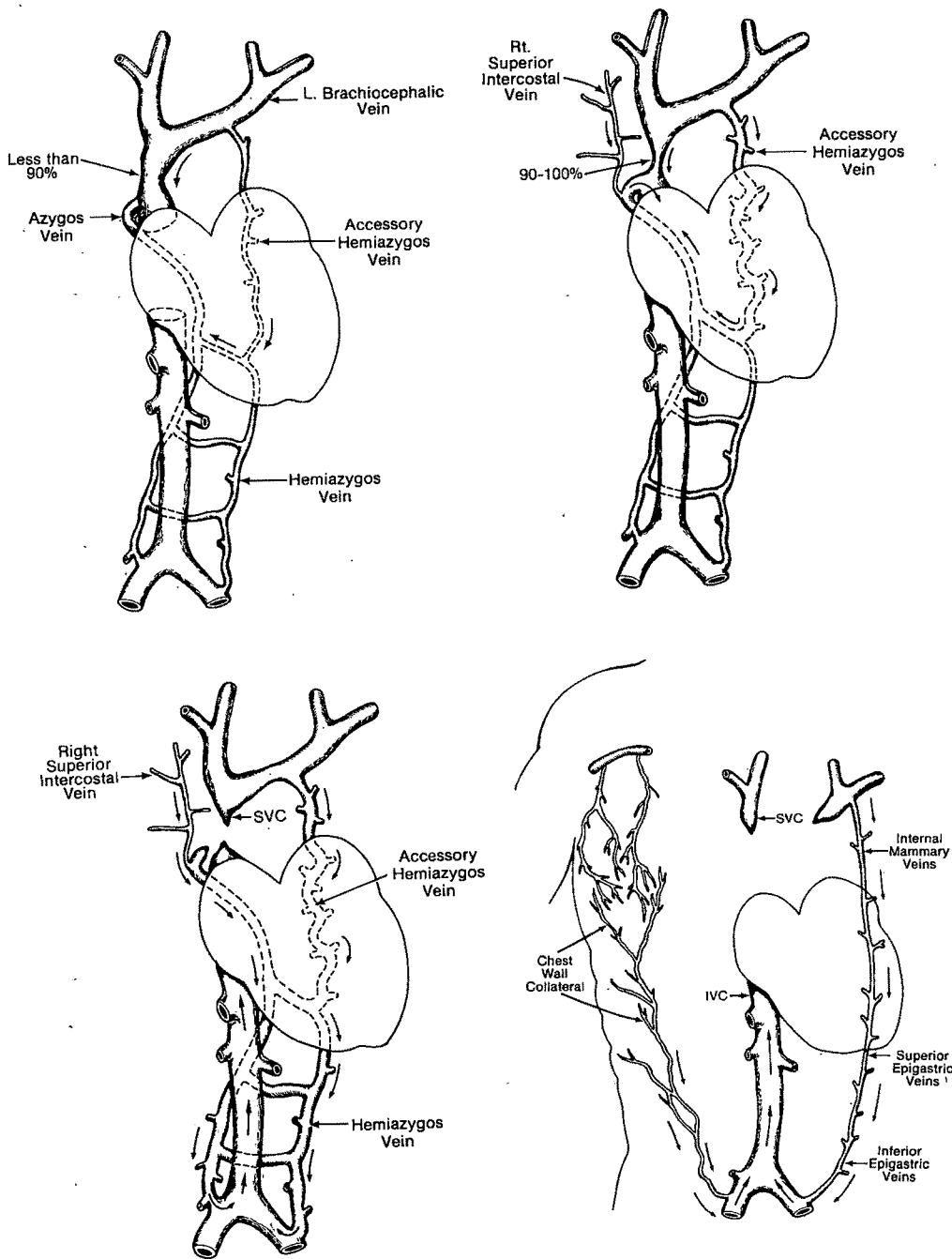


Fig. 1.—Diagrams of four patterns of collateral blood flow in superior vena cava (SVC) obstruction (reprinted with permission from Stanford and Doty [6]).
A, Type I. Partial obstruction of SVC with patency and antegrade flow in azygos vein.
B, Type II. Near-complete obstruction of SVC with patency and antegrade flow in azygos vein.
C, Type III. Complete obstruction of SVC with reversal of azygos blood flow.
D, Type IV. Complete obstruction of SVC and azygos system with development of chest-wall and internal mammary collaterals. IVC = inferior vena cava.

of cerebral or airway compromise were present in 10 patients. The symptoms were absent in type I patients and present in two (29%) of 7 type-II patients, four (57%) of 7 type-III patients, and four (40%) of 10 type-IV patients.

All 10 patients with cerebral or airway compromise had shortened length of survival—a 1.4-month average vs a 10.3-month average in patients without compromise ($p < .003$).

Collateral vein development was absent or minimal in type

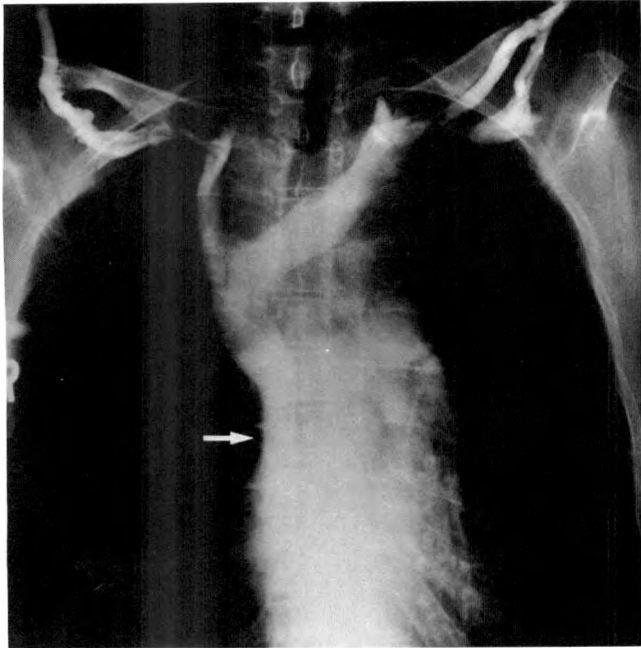


Fig. 2.—Superior venacavograms showing minimal narrowing of SVC (arrow) with antegrade flow, representative of type I obstruction.

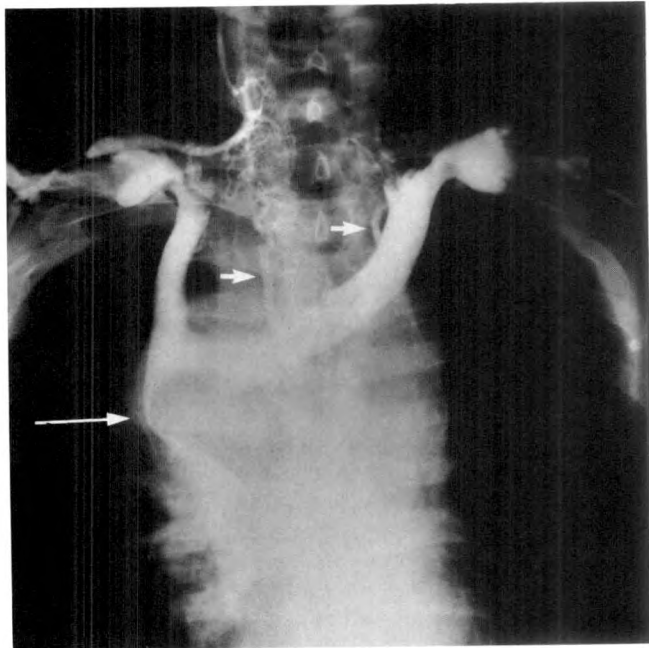


Fig. 3.—Superior venacavogram representative of type II showing 90% obstruction of SVC with antegrade flow into atrium (long arrow). Internal mammary vein collaterals are evident (small arrows).

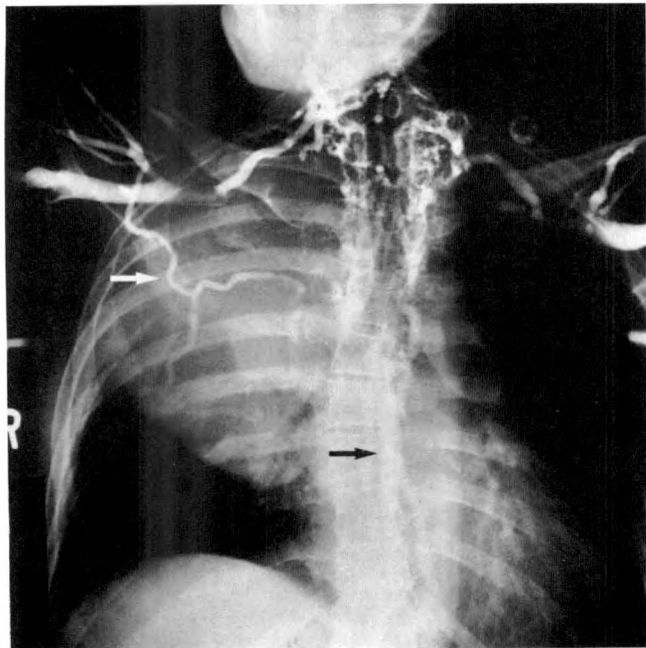


Fig. 4.—Superior venacavogram representative of type III showing complete obstruction of SVC with reversible flow in azygos vein (black arrow). Right superior intercostal vein is present (white arrow).

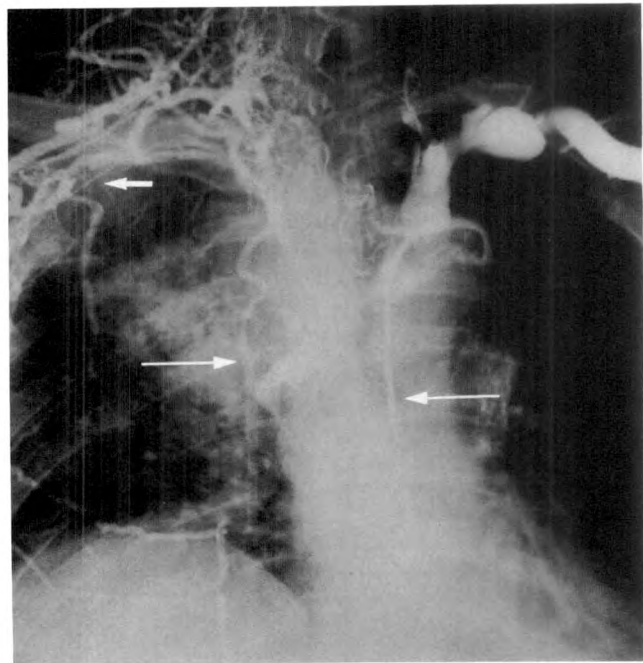


Fig. 5.—Superior venacavogram representative of type IV showing complete obstruction of SVC, brachiocephalic, and azygos veins. Patent chest-wall (short arrow) and internal mammary veins (long arrows) are evident.

I and moderate in types II and IV. Collateral development was most pronounced in type III patients, where there was near-complete to complete obstruction of the cava and reversal of flow in the azygos system. Overall, 80% of the patients with cerebral or airway compromise were in type III or IV categories, but no correlations could be made with the extent of collateral development or with venous valve competence. A higher frequency of cerebral or airway compromise was found in type IV patients when the visualized collaterals lay in central rather than peripheral locations.

All but one of the six patients who had spiral-vein-bypass grafts were of type III or IV and all but one had symptoms of cerebral or airway compromise. Survival in the operated group was 10.8 months as compared with 1.4 months in the group with cerebral or airway compromise and no operation ($p < .001$). In addition, all patients in the group with surgery had immediate relief of symptoms lasting from 2 to 21 months; however, all eventually died.

Discussion

SVC obstruction occurs from direct tumor invasion, extrinsic compression, or thrombosis secondary to the slowing and stagnating of blood as a result of a partial obstruction [7]. Caval obstructions can occur at different levels and therefore the patterns of venous return vary; however, we were able to classify the return patterns into four types (see Figs. 2-5 for representative radiographs). When the blockage is in the midsuperior vena cava, blood drains via the right superior intercostal and left accessory hemiazygos veins from the right and left sides of the neck, respectively, into the azygos and hemiazygos systems where it flows antegrade into the right atrium. When the blockage is at the caval atrial junction, blood flows retrograde in the azygos system into the iliac veins and inferior vena cava. Other important pathways are the internal mammary veins and the more indirect paravertebral and chest-wall channels.

It was anticipated that cerebral or airway compromise would be greatest in the type-IV patients who had extensive occlusions of the SVC and azygos systems. One could speculate that in those patients where the venous return became more circuitous, the back pressure would be greatest and

clinically the patients would do less well. This did not seem to be the case because more patients with type-III than type-IV obstructions developed compromise. It may be that high central pressure rather than high peripheral pressure is responsible for the development of edema; because there are fewer central collaterals and more chest-wall collaterals in type-IV patients, the development of cerebral and airway compromise is less frequent. We did not do pressure measurements to determine if this is the case. It may also be true that the chest-wall collaterals, while sufficient to decompress the upper compartment, do not visualize well with our current angiographic techniques. This may explain why the overall collateral development is less visible in type-IV patients. Type-IV patients with central collaterals predominating had a higher frequency of cerebral and airway compromise. These are ominous signs and portend a significant decrease in survival (10.3 vs 1.4 months) ($p < .003$).

The venacavogram was also helpful in identifying veins available for a proximal anastomosis should spiral-vein-bypass grafting be selected. In type-III obstructions, the left brachiocephalic vein was generally large enough to accept the proximal end of the vein graft, whereas in type-IV patients, the veins were often smaller and would require thrombectomy or extension of the vein graft outside the thorax.

REFERENCES

1. Lochridge SK, Knibbe WP, Doty DB. Obstruction of the superior vena cava. *Surgery* 1979;85:14-24
2. Effeney DJ, Windsor HM, Shanahan MX. Superior vena cava obstruction: resection and bypass for malignant lesions. *Aust NZ J Surg* 1973;42:231-237
3. Dyet JF, Moghissi K. Role of venography in assessing patients with superior caval obstruction caused by bronchial carcinoma for bypass operations. *Thorax* 1980;35:628-630
4. Avasthi RB, Moghissi K. Malignant obstruction of the superior vena cava and its palliation: report of four cases. *J Thorac Cardiovasc Surg* 1977;74:244-248
5. Smith ER, Brantigan CO. Bypass of superior vena cava obstruction using spiral vein graft. *J Cardiovasc Surg (Torino)* 1983;24:259-261
6. Stanford W, Doty DB. The role of venography and surgery in the management of patients with superior vena cava obstruction. *Ann Thorac Surg* 1986;41:158-163
7. Parish JM, Marschke RF Jr, Dines D, Lee RF. Etiologic considerations in superior vena cava syndrome. *Mayo Clin Proc* 1981;56:407-413

Occult Pulmonary Embolism: A Common Occurrence in Deep Venous Thrombosis

Gary S. Dorfman¹
John J. Cronan¹
Thomas B. Tupper¹
Richard N. Messersmith^{1,2}
Donald F. Denny^{1,3}
Carol H. Lee^{1,3}

Ventilation-perfusion scans were used in a prospective study to determine the prevalence of occult pulmonary embolus in proven deep venous thrombosis. Fifty-eight patients without symptoms of pulmonary embolism, but with venographically proven deep venous thrombosis, were subjected to chest radiographs, ^{99m}Tc macroaggregated-albumin perfusion scans, and ¹³³Xe ventilation scans. Of the 49 patients with deep venous thrombosis proximal to the calf veins, 17 (35%) had high-probability scans. Of all 58 patients, only 12 (21%) had normal scans. When the study population was compared with a group of 430 patients described in reports of pulmonary perfusion in asymptomatic persons, a significantly higher percentage of high-probability scans was found in the study population with deep venous thrombosis. Baseline ventilation-perfusion lung scanning is valuable for patients with proven above-knee deep venous thrombosis.

It has been estimated that 20 million new cases of lower extremity, deep venous thrombosis and 600,000 new cases of pulmonary embolism occur in the United States each year [1]. However, truly accurate statements regarding the frequency of embolism and the exact site of origin of the embolic material are difficult because of the unreliability of clinical diagnosis. Yearly deaths from pulmonary embolism have been estimated between 47,000 and 200,000 by various authors [1-4]. Yet Alpert et al. [2] reported a mortality rate of only 3% in a group of 144 patients with properly diagnosed and treated embolism.

In patients who escape early death from massive pulmonary embolism, delayed mortality often occurs from recurrent, often unsuspected, pulmonary embolism [2, 5]. Comparisons of autopsy and clinical series show that silent embolism must be a frequent antecedent of more serious and clinically obvious pulmonary embolism [6]. It is, therefore, important to identify patients at risk for silent embolism.

Treatment regimens for venous thrombosis and pulmonary embolism vary. However, in no therapeutic protocol is progression of disease tolerated [5]. Authors have advocated caval interruption either for recurrent embolism [2] or for failure of anticoagulation to prevent recurrent thromboembolic disease [7]. While caval interruption can be performed easily [8], it is not to be undertaken lightly. It would be unfortunate to treat a patient erroneously for progression of disease if embolism had actually occurred before therapy rather than during it. Knowledge of the extent of disease before starting therapy is critical.

We undertook this prospective study to (1) identify a population at risk for silent pulmonary embolism, and (2) assess the extent of thromboembolic disease when patients are diagnosed with lower-extremity thrombosis. Therefore, we sought to show the prevalence of pulmonary embolism in a patient population presenting with venographically proven venous thrombosis but without symptoms of pulmonary embolism.

Subjects and Methods

Over a 24-month period beginning in January 1983, we selected our study population in a

Received April 9, 1986; accepted after revision August 4, 1986.

¹ Department of Diagnostic Radiology, Rhode Island Hospital, Brown University Program in Medicine, 593 Eddy St., Providence, RI 02902. Address reprint requests to G. S. Dorfman.

² Present address: Department of Radiology, Mitchell Hospital—University of Chicago, 5841 Maryland Ave., P.O. Box 427, Chicago, IL 60637.

³ Present address: Department of Diagnostic Imaging, Yale University School of Medicine, 333 Cedar St., New Haven, CT 06504.

AJR 148:263-266, February 1987

0361-803X/87/1482-0263

© American Roentgen Ray Society

Table 1: Analysis of Patient Data (Ventilation-Perfusion Scans)

Location of Thrombus	No. of Patients	Normal Scans (%)	Abnormal Scans			
			Total (%)	Low (%)	Moderate or Indeterminate (%)	High (%)
Above knee	49	12 (24)	37 (76)	17 (35)	3 (6)	17 (35)
Below knee	9	0	9 (100)	9 (100)	0	0
Total	58	12 (21)	46 (79)	26 (45)	3 (5)	17 (29)

prospective and consecutive manner. All patients in this study had venographically proven deep-venous thrombosis of a lower extremity. Venograms were performed by a modification of the technique described by Rabinov and Paulin [9]. Hypaque (60%) (Winthrop-Breon New York, NY), 100 ml diluted by normal saline to a volume of 150 ml and a concentration of 40%, was injected into a dorsal pedal vein while the patient was examined on a moving-tabletop fluoroscopic-radiographic unit. For the purposes of this study, a positive venographic examination was defined as the presence of intraluminal thrombus seen on at least two views. All patients with venographic examinations positive for intraluminal thrombus were considered for our study. Specifically, chart review, interview, physical examination, and primary physician's evaluations were used to ascertain the suspicion of pulmonary embolus. Any patients with findings that suggested pulmonary embolism were excluded. Similarly, patients with recent pelvic or orthopedic surgical procedures were excluded. The patients who were appropriate for our study and who gave informed consent were subjected to ventilation-perfusion scanning within 12 hr of the venogram, in conjunction with posteroanterior and lateral chest radiographs.

The 58 patients ranged in age from 18 to 93 years old (mean, 55 years). The group was composed of 31 women (18–89 years old; mean, 56 years) and 27 men (19–93 years old; mean, 54 years). Nine patients with thrombus limited to the calf veins, muscular veins below the knee joint, or the distal popliteal vein below the knee joint composed the below-knee group. Forty-nine patients with thrombus extending proximal to the knee joint in the popliteal vein, superficial femoral vein, common femoral vein, or the iliac vein made up the above-knee group. No patients had thrombus extension into the inferior vena cava.

The perfusion scans were routinely performed before the ventilation scans. ^{99m}Tc macroaggregated albumin (3–4 mCi [111–148 MBq]) was injected intravenously into each patient. Perfusion images were obtained in six projections: anterior, posterior, both laterals, and both posterior obliques. Ventilation scans were not performed on patients with normal perfusion images or on those with such small defects that the ventilation study would not significantly change the interpretation. In the cases in which ventilation studies were performed, the projection that best showed the defect(s) was chosen. Patients inhaled 15–20 mCi (555–740 MBq) ^{133}Xe , and images were obtained during first inhalation, equilibrium, and washout phases. All scans were interpreted by using current chest radiographs according to the criteria of Neumann et al. [10], without knowledge of the results of venography. Scans were assigned one of five categories: (1) normal perfusion, (2) low probability, (3) moderate probability, (4) high probability, and (5) indeterminate.

To ensure consistency, at the close of the study all venograms and lung scans were reread in a blinded fashion by two separate pairs of radiologists. No discrepancies in interpretation were found. Concomitantly, when the lung scans were reinterpreted by using the

postperfusion ventilation criteria of McNeil et al. [11], all normal and high-probability scans remained interpreted as such.

To assess the significance of our results, we established a comparison group from the literature. We could locate only six previously published studies [12–17] that report the results of ventilation-perfusion scanning in various patient populations without symptoms of pulmonary embolism. Combining the populations of these studies provided a comparison group of 430 patients without symptoms of either deep venous thrombosis or pulmonary embolus.

Results

During the 24-months of our study, 288 ascending venograms were performed at Rhode Island Hospital for deep venous thrombosis. Of these examinations, 116 were positive for intraluminal thrombus, and of these, 62 patients had no signs or symptoms suggesting pulmonary embolism by chart review, interview, physical examination, or the primary physician's evaluations. All patients were ambulatory, and none had had recent pelvic or orthopedic surgery. On retrospective chart analysis, none of the patients had underlying illnesses associated with false-positive or false-negative lung scans, nor had they any history of pulmonary emboli. Shortly after venography but before ventilation-perfusion scanning, one patient developed symptoms that could have been due to pulmonary embolism and he was, therefore, excluded from the study. (His scan was performed and was interpreted as a high-probability scan by our criteria.) Two patients refused to participate, and one patient's referring physician refused to allow his patient to participate. Hence, 58 consecutive patients with venographically proven deep venous thrombosis, but without clinical evidence of pulmonary embolism, were properly informed of the risks and benefits of lung scanning, and consented to participate.

All patients in the below-knee group had low-probability, abnormal scans. In the above-knee group, 12 patients had normal scans, 17 patients had low-probability scans, three patients had moderate or indeterminate scans, and 17 patients had high-probability scans (Table 1).

Only 12 (21%) of our 58 patients had normal scans. Seventeen (35%) of 49 patients with above-knee thrombosis had high-probability scans.

Table 2 summarizes the results collected from the literature. The first three studies [12–14] used techniques similar to ours, but the techniques of lung scanning in the latter three studies [15–17] varied. While 92% of the 430 patients re-

Table 2: Lung Scanning in Patients Without Symptoms of Pulmonary Embolism

Authors [Reference No.]	No. of Patients	Normal Scans (%)	Abnormal Scans			
			Total (%)	Low (%)	Indeterminate (%)	High (%)
Wallace et al. [12]	80	79 (99)	1 (1)	1 (1)	0	0
Wallace et al. [13]	40	40 (100)	0	0	0	0
Fedullo et al. [14]	40	40 (100) ^a	0	0	0	0
Tetalman et al. [15] ^b	61	58 (95)	3 (5) ^c	2 (3)	1 (2)	0
Walker et al. [16] ^d	169	144 (85)	25 (15)	20 (12)	5 (3)	0
Browse et al. [17] ^e	40	33 (83)	7 (18) ^f	1 (2)	6 (15)	0
Total	430 ^g	394 (92)	36 (8)	24 (6)	12 (3)	0

^a One patient had subsegmental defect corresponding to tortuous aorta with scoliosis.

^b Four view perfusion scans without ventilation studies.

^c Personal communication: A. Gottschalk to assign probabilities to three abnormal scans.

^d Four view perfusion scans with 127 xenon ventilation studies.

^e Four view perfusion scans with preperfusion ventilation studies.

^f All may really be low probability; They are described as subsegmental matched defects.

^g Total of all studies tabulated as worst case.

ported without venous thrombosis had normal scans, only 21% of our 58 patients with deep venous thrombosis had normal scans ($p < .0001$, chi-square analysis). There was a 35% prevalence of high-probability scans in our above-knee group, while no high-probability scans are reported in the group from the literature ($p < .0001$).

Discussion

The risks of either over- or undertreating patients with thromboembolic disease are well recognized [1-6, 18]. Our goal in this study was to identify a patient population at risk for undertreatment of silent embolism or for overtreatment of erroneously presumed disease progression. Undertreatment would occur in patients who might have several episodes of "silent" embolism in conjunction with recurrent venous thrombosis. Overtreatment would result from a patient's becoming symptomatic from an embolus while on adequate therapy for deep venous thrombosis, when in reality that embolus had occurred before the treatment began. Proper staging of thromboembolic disease and identification of "silent" embolism at presentation would eliminate these possibilities.

Other investigators have attempted to ferret out the occurrence of pulmonary embolus in patients with deep-venous thrombosis. Browse et al. [17] in 1972 and Walker et al. [16] in 1981 found "silent" emboli in 6 (55%) of 11 and in 5 (45%) of 11 patients with postoperative thrombosis, respectively. In 1983, Hull et al. [19] found that 51% of patients with proximal venous thrombosis had "large mismatched perfusion deficits." All patients in his series, however, were clinically suspected of having pulmonary emboli.

Kistner et al. [6] reported that in patients presenting with deep venous thrombosis, 24 (52%) of 46 developed "positive" lung scans at some point in the course of their illnesses. Some were symptomatic for emboli, others were not. More recently, Moser and Lemoine [20] investigated 36 patients with lower-extremity thrombosis. Of 21 patients with below-knee clot, none had "positive" lung scans. Yet, 8 (53%) of 15

of the above-knee group had scans reported as "positive," with one patient symptomatic for emboli. Kistner et al. [6] never defined degree of "positivity" of lung scanning, and Moser and Lemoine [20] required at least a one-lobe mismatch for a positive scan.

On the basis of our own work and a review of the pertinent literature, we have reached several conclusions. The prevalence of abnormal ventilation-perfusion scans is significantly greater in a population with deep venous thrombosis than in one without. Specifically, in patients with above-knee thrombosis, high-probability scans are inordinately prevalent despite lack of clinical suspicion of pulmonary embolism.

Therefore, we strongly suggest ventilation-perfusion scans in patients with thrombus extension above the knee joint. Patients who have abnormal lung scans should be rescanned if symptoms that suggest emboli develop, or at a proper interval to document a posttreatment baseline for future use. The initial scan obtained after the positive venogram may be considered a baseline study. Should the patient develop signs or symptoms suggestive of embolus while undergoing adequate therapy for venous thrombosis, a repeat scan could be obtained. If no new significant ventilation-perfusion mismatch is noted, one would not classify the treatment as a failure. Alternatively, should new significant defects become apparent, then further diagnostic and therapeutic action may be indicated because treatment would be considered to have failed. Without the baseline scan, theoretically up to 35% of patients with above-knee clot might be erroneously overtreated if clinical suspicion of embolism should develop. This protocol also identifies a group of patients who may be at risk for long-term morbidity or mortality from silent pulmonary embolism. Further long-term prospective study is necessary to evaluate the outcome of this group.

ACKNOWLEDGMENT

The authors would like to acknowledge the clerical and secretarial assistance of Carolyn Elderkin, Susan St. Sauveur, and Gayle Pascetta in the preparation of this paper.

REFERENCES

1. Roberts HJ. Controversies and enigmas in thrombophlebitis and pulmonary embolism: perspectives on alleged overdiagnosis. *Angiology* 1980; 31:686-699
2. Alpert JS, Smith R, Carlson J, Ockene IS, Dexter L, Dalen JE. Mortality in patients treated for pulmonary embolism. *JAMA* 1976;236:1477-1480
3. Wright IS. Pulmonary embolism: a most underdiagnosed and untreated disorder. *J Am Geriatr Soc* 1974;22:433-439
4. Kakkar VV. Deep vein thrombosis: detection and prevention. *Circulation* 1975;51:8-19
5. Goldhaber SZ. Strategies for management. In: Goldhaber SZ, ed. *Pulmonary embolism and deep venous thrombosis*. Philadelphia: Saunders, 1985:121-133
6. Kistner RL, Ball JS, Nordyke RA, Freeman GC. Incidence of pulmonary embolism in the course of thrombophlebitis of the lower extremities. *Am J Surg* 1972;124:169-176
7. Hoagland PM. Massive pulmonary embolism. In: Goldhaber SZ, ed. *Pulmonary embolism and deep venous thrombosis*. Philadelphia: Saunders, 1985:179-208
8. Denny DF, Cronan JJ, Dorfman GS, Esplin C. Percutaneous Kimray-Greenfield filter placement by femoral vein puncture. *AJR* 1985;145:827-829
9. Rabinov K, Paulin S. Roentgen diagnosis of venous thrombosis in the leg. *Arch Surg* 1972;104:134-144
10. Neumann RD, Sostman HD, Gottschalk A. Current status of ventilation-perfusion imaging. *Semin Nucl Med* 1980;10:198-217
11. McNeil BJ, Holman BL, Adelstein SJ. The scintigraphic definition of pulmonary embolism. *JAMA* 1974;227:753-756
12. Wallace JM, Moser KM, Hartman MT, Ashburn WL. Patterns of pulmonary perfusion scans in normal subjects. *Am Rev Respir Dis* 1981;124:480-483
13. Wallace J, Moser KM, Hartman MT, Ashburn WL. Patterns of pulmonary perfusion scans in normal subjects. II. The prevalence of abnormal scans in young smokers. *Am Rev Respir Dis* 1982;125:465-467
14. Fedullo PF, Moser KM, Hartman MT, Ashburn WL. Concise clinical study: patterns of pulmonary perfusion scans in normal subjects. III. The prevalence of abnormal scans in non-smokers 30 to 49 years of age. *Am Rev Respir Dis* 1983;127:776-779
15. Tetelman MR, Hoffer PB, Heck LL, Kunzmann A, Gottschalk A. Perfusion lung scan in normal volunteers. *Radiology* 1973;106:593-594
16. Walker I, Aukland P, Hirsh J, et al. The low specificity of postoperative perfusion lung scan defects. *Can Med Assoc J* 1981;124:153-157
17. Browse NL, Clemenson G, Croft DN. Fibrinogen-detectable thrombosis in the legs and pulmonary embolism. *Br Med J* 1972;1:603-604
18. Robin ED. Overdiagnosis and overtreatment of pulmonary embolism: the emperor may have no clothes. *Ann Intern Med* 1977;87:775-781
19. Hull RD, Hirsh J, Carter CJ, et al. Pulmonary angiography, ventilation lung scanning, and venography for clinically suspected pulmonary embolism with abnormal perfusion lung scan. *Ann Intern Med* 1983;98:891-899
20. Moser KM, LeMoine JR. Is embolic risk conditioned by location of deep venous thrombosis? *Ann Intern Med* 1981;94:439-444

Case Report

Primary Angiosarcoma of the Heart: CT Characteristics

Myung S. Shin,^{1,2} James K. Kirklin,^{2,3} Joan B. Cain,^{2,4} and Kang-Jey Ho^{2,5}

Primary angiosarcoma of the heart is a rare tumor [1]. Although in most of the reported cases the diagnoses were made either at autopsy or shortly before the patient's death, long-term survival after early diagnosis followed by surgical removal and postoperative radiotherapy has been reported [2]. The premortem diagnoses usually have been made by angiocardiology and echocardiography [2]. The findings are, however, nonspecific and can be confused with atrial myxoma [2] or pericardial effusion [3]. Reported here is a case of angiosarcoma arising from the right atrium with direct extension to the pericardial cavity. The case was studied with CT and the diagnosis confirmed by biopsy. The case shows the usefulness of CT in evaluating such a unique tumor.

Case Report

A 74-year-old man with a history of hypertension for many years was first treated at a local hospital for congestive heart failure and atrial fibrillation of recent onset. Four months later he was again admitted for upper respiratory infection and worsening of congestive heart failure. One year after his first admission he returned a third time with complaints of chronic cough, exertional dyspnea, regurgitation of liquids, and decreased appetite with a 14-kg weight loss over a period of several months. A chest radiograph revealed marked enlargement of the cardiac silhouette that had occurred since the last admission. A thoracic CT showed a grapefruit-sized mediastinal mass associated with a large amount of pericardial fluid. The patient underwent a right thoracotomy at the local hospital with partial pericardiectomy and evacuation of a large hematoma. Palpation inside

the pericardium revealed a large firm mass adherent to the right atrium. Biopsy of the pericardium, however, showed only organizing blood clot and inflammatory debris without malignant cells. After being discharged, the patient continued to have cough and dyspnea. Two days before his transfer to University Hospital he developed prolonged paroxysmal nocturnal dyspnea associated with sharp pain over the entire chest.

Physical examination on admission revealed a cachectic elderly man in mild respiratory distress. Other pertinent physical findings included a jugular venous distension to 9 cm of water with positive hepatojugular reflex, moist rales in both lung bases, cardiomegaly with friction rubs, and moderate pitting edema in the lower legs. A chest radiograph revealed massive cardiomegaly with bilateral pleural effusion. Electrocardiography showed normal sinus rhythm with first-degree atrioventricular block. A thoracic CT showed enlargement of all four cardiac chambers and a large tumor mass apparently arising from the free wall of the right atrium, protruding into the pericardial cavity, and encasing the aortic root (Fig. 1). The tumor measured 14 cm in its greatest dimension and contained irregular low-density areas. Massive bilateral pleural effusion and atelectasis of a portion of the right lung were noted. A 1-cm low-attenuation area was found in the right lobe of the liver by abdominal CT.

The CT findings were confirmed at exploratory pericardiectomy. In addition to the highly vascular tumor adherent to the right atrium, the pericardial cavity also contained organizing blood clots and loculated serosanguinous fluids. Biopsy of the tumor revealed an angiosarcoma characterized by proliferation of neoplastic endothelial cells, and the tumor stained positive for factor VIII-related antigen by immunohistochemical technique (Fig. 2). Because of its large size and critical location, the tumor was considered unresectable. The patient died 1 month after the surgery during a course of radiotherapy. No autopsy was performed.

Received June 30, 1986; accepted after revision September 2, 1986.

¹ Department of Radiology, University of Alabama at Birmingham, University Station, Birmingham, AL 35233. Address reprint requests to M. S. Shin.

² Veterans Administration Medical Center, Birmingham, AL 35233.

³ Department of Surgery (Cardiovascular Section), University of Alabama at Birmingham, Birmingham, AL 35233.

⁴ Department of Medicine, University of Alabama at Birmingham, Birmingham, AL 35233.

⁵ Department of Pathology, University of Alabama at Birmingham, Birmingham, AL 35233.

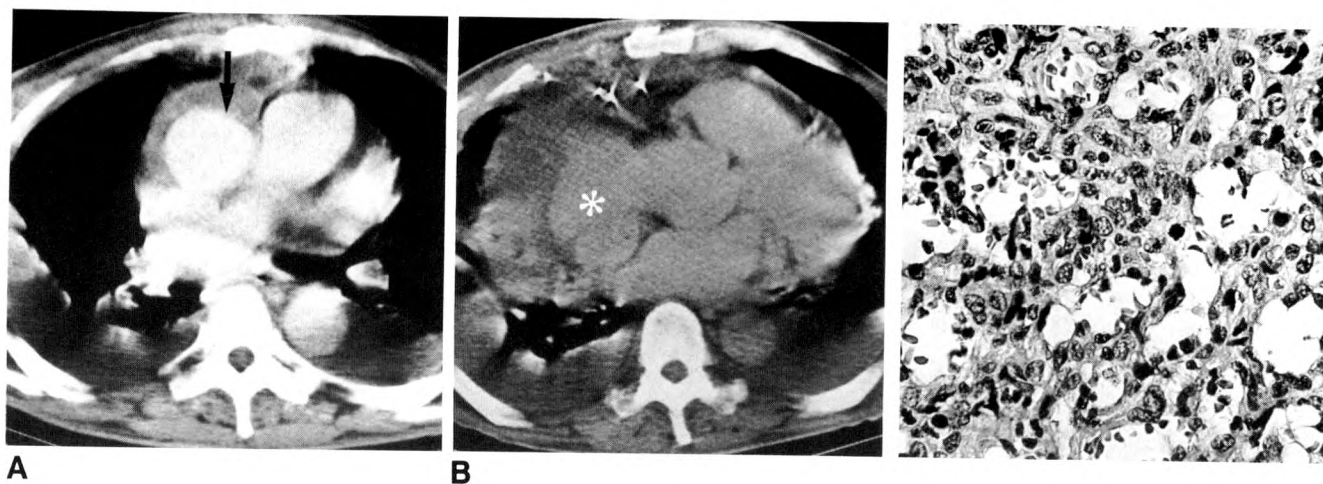


Fig. 1.—A and B, CT scans through the heart (A more cephalad than B) after IV administration of 150 ml of contrast media shows a large mass in direct connection with the right atrium (white asterisk in B) protruding into the pericardium (B) and encasing the aortic root (arrow) (A). Note also pericardial thickening and effusion and bilateral pleural effusion.

Fig. 2.—Light micrograph of tumor showing irregular vascular spaces lined by neoplastic endothelial cells typical of angiosarcoma (H and E, original magnification $\times 350$).

Discussion

Primary sarcomas of the heart are rare, and angiosarcoma is among the least common of them [1]. Only 76 cases of cardiac angiosarcomas have been reported in the literature [2–4]. The tumor occurs predominantly in adults with a mean age of 40 years, varying from 12 to 69 years. Our patient was 74 years old, older than any of the reported cases. Most cardiac angiosarcomas arise from the right atrium, as did the tumor in the present case. Since the patient's hypertension was under control with medication, his initial symptoms and signs of congestive heart failure and cardiac arrhythmia were most likely related to the early intramural growth of the tumor. The tumor can grow into a cardiac chamber and/or extend to the pericardial cavity. When growing into the right atrium the tumor often becomes pedunculated with a broad-based stalk embedded in the atrial wall, mimicking an atrial myxoma [2]. The primary manifestations of the intrachamber growth are obstructive symptoms, mechanical hemolysis, and tumor embolization. Such symptoms were minimal or absent in our case because the intrachamber growth was limited.

The tumor in this case grew mainly into the pericardial cavity accompanied by pericardial effusion and later by hemorrhage. The patient's congestive heart failure was likely caused by the combined effects of intramural tumor, cardiac arrhythmia, and pericardial constriction. In some reported cases extensive pericardial spread of the angiosarcoma has simulated pericardial effusion, mesothelioma, or pericarditis [2]. Metastases occur most commonly to the lungs, regional lymph nodes, and liver. In this case some enlarged pretracheal lymph nodes and a low-density area in the liver could represent the metastatic lesions.

Most of the recently reported cases of the cardiac angiosarcoma were detected by angiocardiology and/or echocardiography [2–4]. Echocardiography is extremely useful in the evaluation of pericardial effusion but is less helpful in the evaluation of focal disease such as pericardial thickening or mass lesions [5]. CT has been useful in the investigation of pericardial diseases such as effusion, hematoma, thickening, congenital defects, and mass lesions [6–8]. Glazer et al. [8] reported that CT prospectively identified pericardial pheo-

chromocytomas in all eight patients whereas echocardiography identified the tumor in only one of seven patients.

In our patient the anatomic relationship of the tumor to the right atrium and pericardium and the associated pericardial thickening, effusion, and hematoma were well shown (Fig. 1). Although a definite diagnosis can only be made with histologic examination, a cardiac angiosarcoma should be considered when characteristic clinical symptoms and signs of congestive heart failure secondary to blood-flow obstruction or pericardial restriction are combined with the CT demonstration of a mass lesion directly related to the right atrium with intrachamber or pericardial extension.

On CT, cardiac angiosarcoma differs from atrial myxoma, the most common primary tumor of the heart, in that the latter is usually a pedunculated mass occurring in the left atrium in the region of the fossa ovalis. The right atrial location and rapid growth of the cardiac angiosarcoma are distinct from other cardiac tumors, such as mesothelioma, rhabdomyoma, fibroma, lipoma, angioma, and other sarcomas, which grow slowly and have no predilection for the right atrium.

REFERENCES

1. Rosman HS, Goodwin JF, Cleland WP, Bentall HH. Two decades of atrial tumour. *Eur Heart J* 1982;3:100–106
2. Sorlie D, Myhre ESP, Stalsberg H. Angiosarcoma of the heart: unusual presentation and survival after treatment. *Br Heart J* 1984;51:94–97
3. Lin TK, Stech JM, Eckert WG, Lin JJ, Farha SJ, Hagan CT. Pericardial angiosarcoma simulating pericardial effusion by echocardiography. *Chest* 1978;73:881–883
4. Rossi NP, Kioschos JM, Aschenbrener CA, Ehrenhaft JL. Primary angiosarcoma of the heart. *Cancer* 1976;37:891–894
5. Schiller NB. Echocardiography in pericardial disease. *Med Clin North Am* 1980;64:253–282
6. Isner JM, Carter BL, Bankoff MS, Konstam MA, Salem DN. Computed tomography in the diagnosis of pericardial heart disease. *Ann Intern Med* 1982;97:473–479
7. Tomoda H, Hoshiai M, Furuya H. Evaluation of pericardial effusion with computed tomography. *Am Heart J* 1980;99:701–706
8. Glazer GM, Gross BH, Orringer MB, Buda AJ, Francis IR, Shapiro B. Computed tomography of pericardial masses: further observations and comparison with echocardiography. *J Comput Assist Tomogr* 1984;8:895–899

Pictorial Essay

Contrast Pharyngography: The Importance of Phonation

Stephen E. Rubesin,^{1,2} Bronwyn Jones,¹ and Martin W. Donner¹

Examination of the pharynx should include dynamic imaging to assess motility and double-contrast spot films to study anatomic detail [1-3]. The morphology of the pharynx can be better shown when the barium-coated, air-filled pharynx is distended. This is most easily accomplished by having the

patient say "Eee. . . ." This pictorial essay shows that distension of the pharynx allows better visualization of the tonsillar fossa, base of the tongue, epiglottic tip and aryepiglottic folds, and pharyngeal mucosa from the inferior surface of the soft palate to the superior border of the cricoid cartilage.

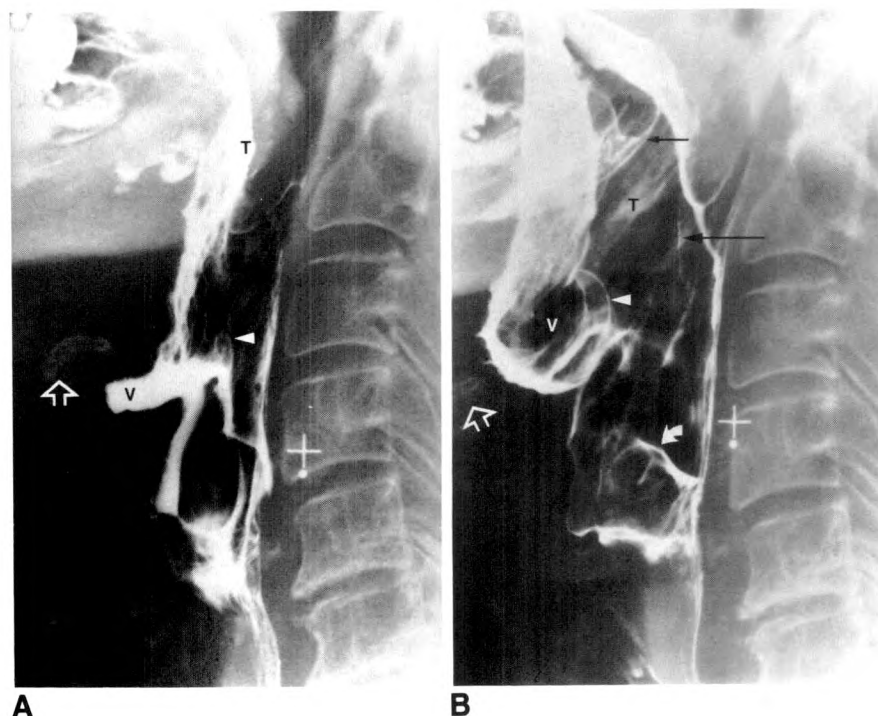


Fig. 1.—Double-contrast lateral spot films of pharynx made at rest (A) and with phonation (B). Pharynx is expanded during phonation, causing tonsillar fossa (T) and valleculae (V) to distend. Paired palatoglossal (short black arrow in B) and palatopharyngeal (long black arrow in B) folds are seen only with phonation. Epiglottis (arrowheads) and mucosa over arytenoid cartilages (curved arrow in B) are much better shown during phonation. Hyoid moves anteriorly and slightly inferiorly during phonation (open arrow).

Received June 16, 1986; accepted after revision September 19, 1986.

Presented at the annual meeting of the American Roentgen Ray Society, Washington, DC, April 1986.

¹ Russell H. Morgan Department of Radiology and Radiologic Science, Johns Hopkins Medical Institutions, Baltimore, MD 21205.

² Present address: Department of Radiology, Hospital of the University of Pennsylvania, 3400 Spruce St., Philadelphia, PA 19104. Address reprint requests to S. E. Rubesin.

AJR 148:269-272, February 1987 0361-803X/87/1482-0269 © American Roentgen Ray Society

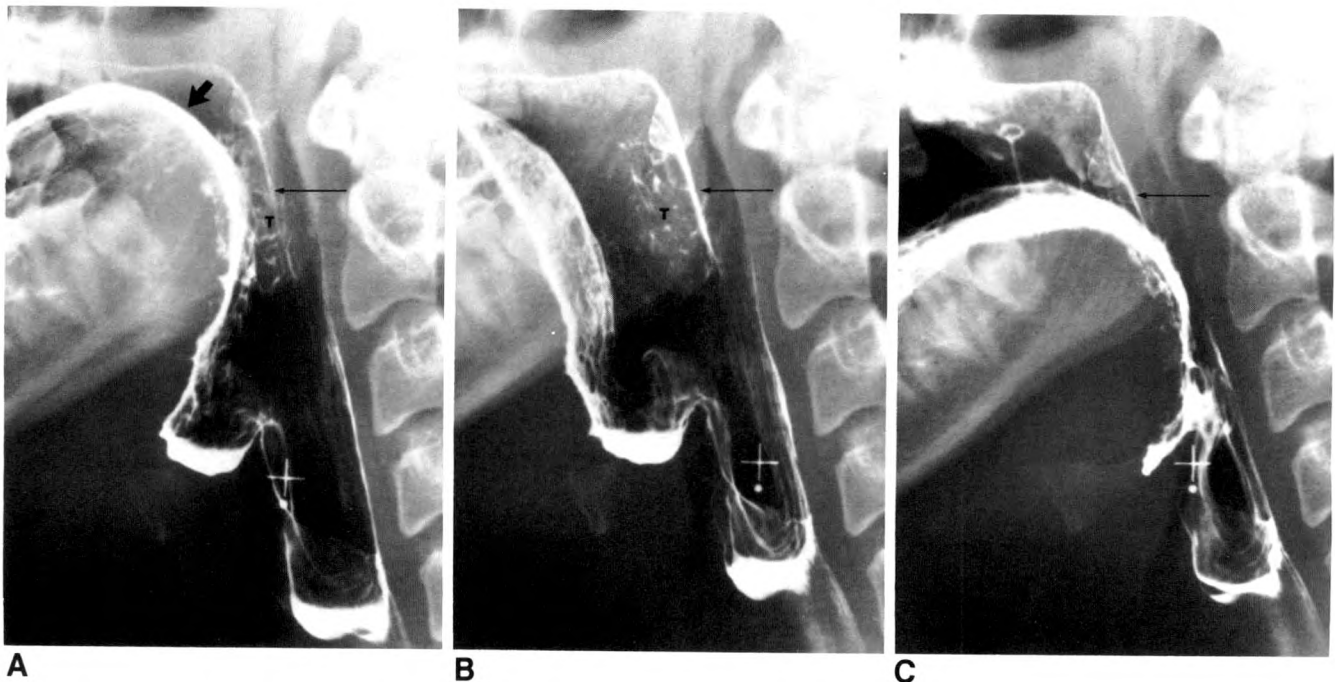


Fig. 2.—Position and shape of tongue changes markedly with prolonged phonation of vowel sounds “Ooo” (A), “Eee” (B), and “Ah” (C).

A, with “Ooo,” middle one-third of tongue is pulled superiorly and tongue moves slightly anteriorly (*short arrow*), partially obscuring tonsillar fossa (T).

B, With “Eee,” tongue is pulled farther forward, expanding mesopharynx and opening tonsillar fossa. Nodularity of normal palatine tonsil is appreciated.

C, With “Ah,” pharynx is collapsed. Palatopharyngeal fold is visible (*long arrows*).

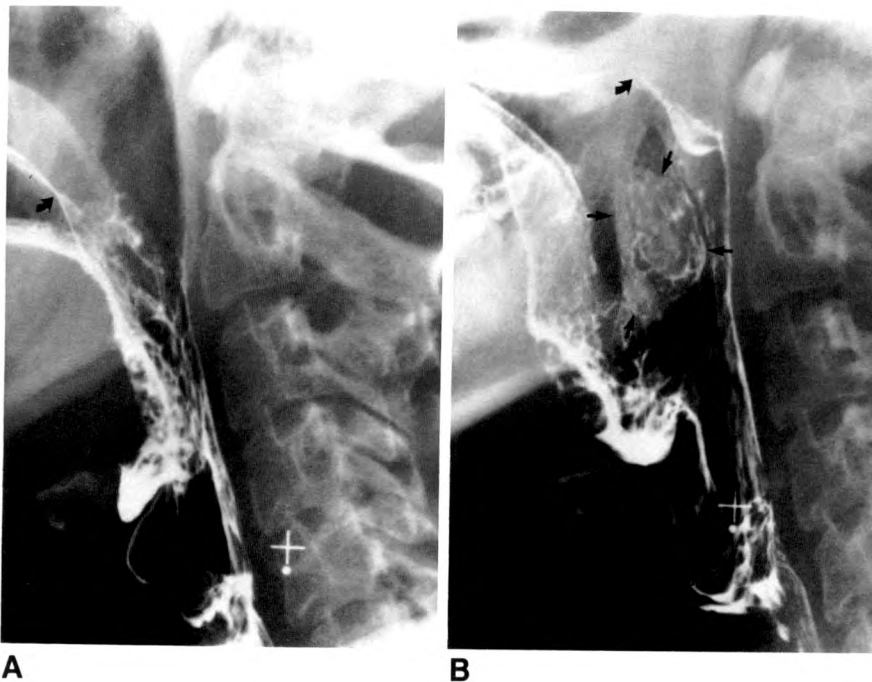


Fig. 3.—Radiographs in 23-year-old man recently recovered from pharyngitis and presumed to have lymphoid hyperplasia of palatine tonsil.

A, At rest, soft palate (*arrow*) is superimposed on tonsillar fossa.

B, When soft palate (*curved arrow*) elevates during phonation, tonsillar fossa is visible. Large palatine tonsil is evident (*arrows*).

The anatomy of the pharynx on the lateral view is seen much more clearly during phonation than at rest, when the pharynx is relatively collapsed (Fig. 1). At rest, the inferior surface of the soft palate contacts the tongue; the epiglottic tip is closely situated or apposed to the vertical surface of the tongue, and the mesopharynx and hypopharynx are collapsed (Fig. 1A). With phonation of the long vowel sound “Eee” (as pronounced in “see”), there is distension of the tonsillar fossa, valleculae, mesopharynx, and hypopharynx to the level of the

upper part of the cricoid cartilage (Fig. 1B). The soft palate rises to appose Passavant’s cushion, a forward converging segment of the posterior pharyngeal wall. Anterior movement of the tongue expands the valleculae and separates the epiglottis from the base of the tongue. The aryepiglottic folds become straightened and come to lie in an oblique plane. The pharyngoesophageal segment, however, is not affected by phonation and remains closed, opening only during swallowing or during esophageal speech.

Fig. 4.—Lateral radiographs in 67-year-old smoker with squamous cell cancer of tongue base.

A, At rest, nodularity (arrow) in base of tongue is apparent. Tip of epiglottis is obscured.

B, With phonation, tongue base moves anteriorly. Valleculae are expanded and round nodular mass is revealed (black arrows). Epiglottic tip (straight white arrow) and uvula (curved arrow) are now well seen.

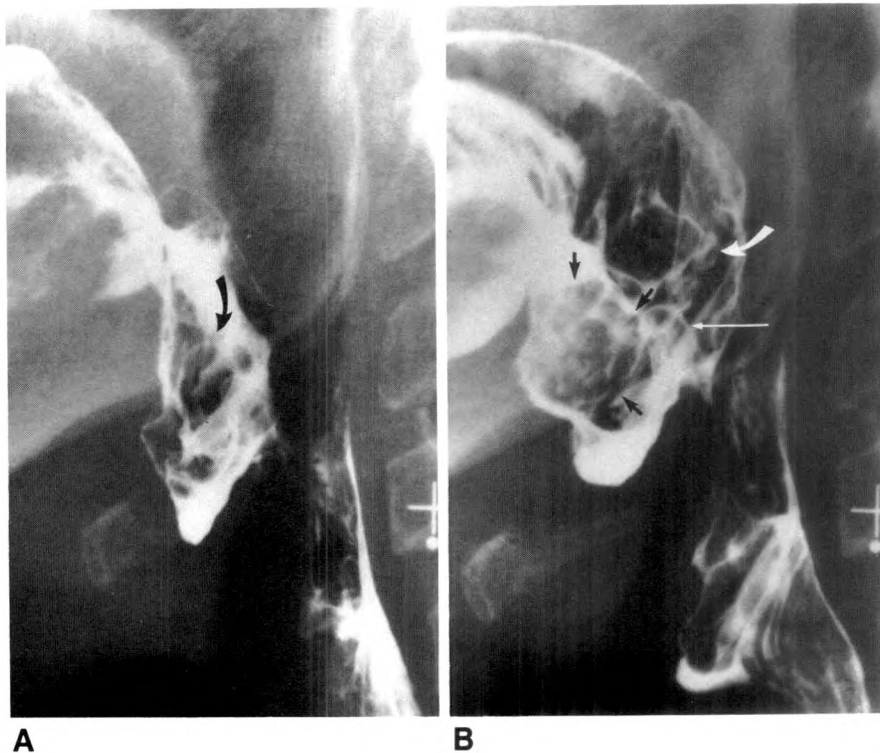
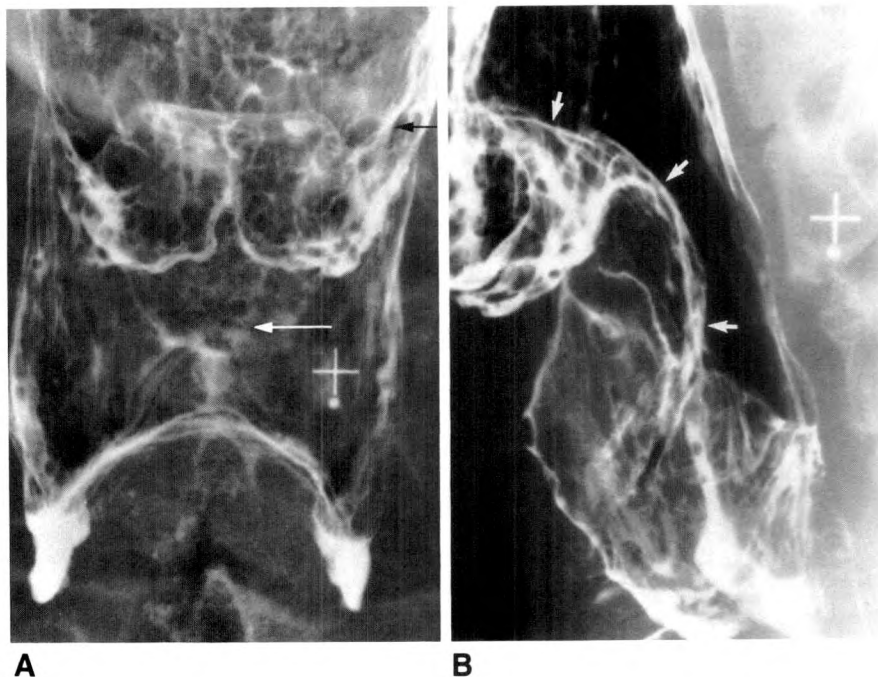


Fig. 5.—Frontal and lateral radiographs in 64-year-old man with squamous carcinoma of epiglottis.

A, Frontal view of pharynx shows mild nodularity of tongue base and valleculae. Nodularity extends inferiorly onto surface of epiglottis (white arrow). Epiglottis has smooth contour but appears mildly enlarged. Left pharyngoepiglottic fold is elevated (black arrow) indicating tumor extension laterally.

B, Lateral view during phonation shows markedly enlarged epiglottis and aryepiglottic folds (arrows).



Phonation with other prolonged vowel sounds also results in changes in pharyngeal configuration [4] (Fig. 2). With the sound "Ooo" (as pronounced in "too") (Fig. 2A), the pharynx also expands but in a slightly different configuration than with "Eee" (Fig. 2B). The tongue is again pulled anteriorly, widening the pharynx, and also superiorly toward the soft palate. At the same time, the anterior portion of the soft palate moves toward the raised tongue [4]. These tongue and palate movements result in constriction of the faucal isthmus of the

pharynx. The vowel sound "Ah" (pronounced as in "father") (Fig. 2C) causes not expansion but constriction of the pharynx. The vertical portion of the tongue moves backward parallel to the pharyngeal wall, and the space between the tongue and epiglottis is obliterated. The resultant narrowing of the pharynx does not improve the radiographic image. Because of its overall superiority, phonation with "Eee" is routinely performed when the lateral radiograph is obtained. "Ooo" and "Ah" are not used.

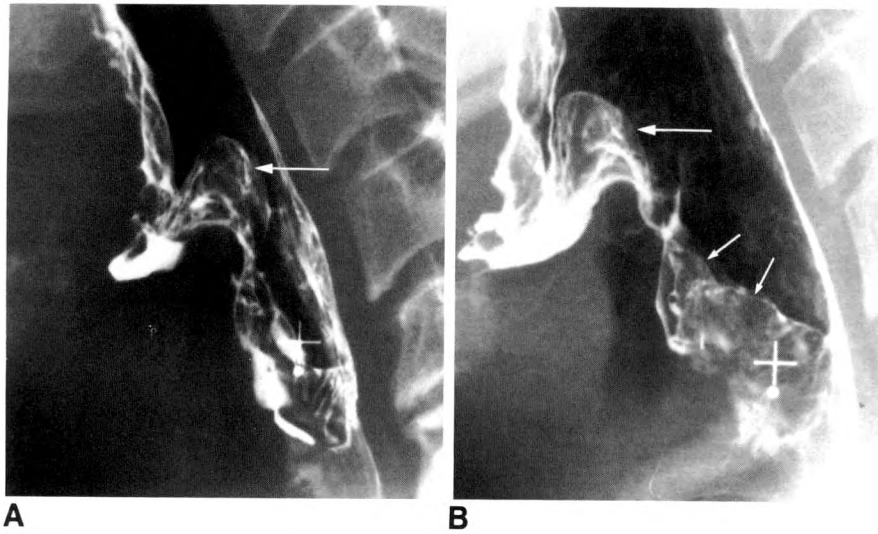


Fig. 6.—Lateral radiographs in 59-year-old man with squamous carcinoma of epiglottis.

A, At rest, tumor is evident (arrow).

B, With phonation, nodularity of one aryepiglottic fold indicates tumor (long arrow) extension into aryepiglottic fold (short arrows) not seen in A.

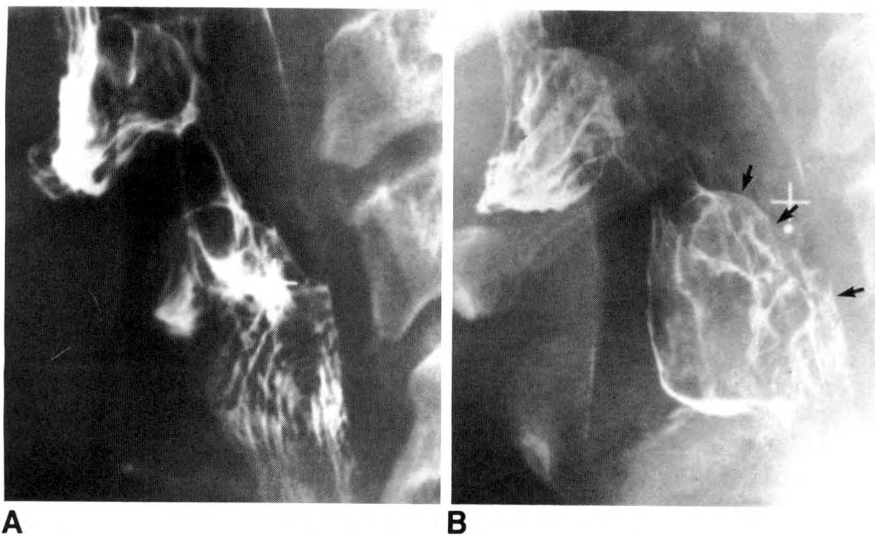


Fig. 7.—Lateral radiographs in 53-year-old man with squamous carcinoma of anterior hypopharyngeal wall.

A, At rest, mid and lower hypopharynx are collapsed, obscuring tumor.

B, With phonation, nodularity of lower portion of aryepiglottic folds and anterior hypopharyngeal wall caused by tumor is evident (arrows).

Distension by phonation is critical in evaluation of the tonsillar fossa, an area often poorly seen on lateral radiographs made at rest. Many tonsillar masses are well seen only when the tonsillar fossa is expanded and the soft palate is elevated during phonation (Fig. 3).

Anterior movement of the tongue and widening of the space between the tongue and epiglottis with phonation improves the lateral view of the tongue base. Phonation views are imperative in the evaluation of masses in this area (Fig. 4).

The aryepiglottic folds are anatomically oriented so that they are poorly seen on frontal projections, but are well seen on lateral or oblique views. Obvious abnormalities of the epiglottis and aryepiglottic folds on the lateral projection may be subtle or even invisible on the frontal view (Fig. 5). With phonation, the aryepiglottic folds are straightened so that a full en face view is possible in the lateral projection. Lateral views in phonation show tumor spread along the aryepiglottic

folds much better than do views obtained at rest (Fig. 6).

The midhypopharynx is collapsed at rest but distends during phonation, allowing evaluation to the level of the interarytenoid fossa (Fig. 7). The inferior 2 cm of hypopharynx above and surrounded by the cricopharyngeus muscle are not seen at rest or during phonation, because the pharyngoesophageal segment remains closed; this area is difficult to distend except during swallowing.

REFERENCES

1. Jing B. The pharynx and larynx: roentgenographic technique. *Semin Roentgenol* 1974;9:259-265
2. Ekberg O, Nylander G. Double contrast examination of the pharynx. *Gastrointest Radiol* 1985;10:263-271
3. Donner MW, Bosma JF, Robertson DL. Anatomy and physiology of the pharynx. *Gastrointest Radiol* 1985;10:196-212
4. DuBrul EL: *Sicher's oral anatomy*, 7th ed. St. Louis: Mosby, 1980:319-350

Patterns of Recurrence of Esophageal Carcinoma After Transhiatal Esophagectomy and Gastric Interposition

Christoph D. Becker^{1,2}
 Peter A. Barbier³
 François Terrier¹
 Beat Porcellini⁴

Serial barium and CT studies were performed for follow-up of 35 patients who had undergone transhiatal esophagectomy with gastric interposition for esophageal carcinoma. The results were compared with the clinical and pathologic findings. Thirteen patients (37%) were clinically and radiologically free of tumor recurrence after a mean observation period of 18 months. Twenty-one patients (60%) developed recurrent carcinoma within 12 months and one patient (3%) within 14 months. Thirteen patients were clinically asymptomatic when recurrence was detected radiologically. Recurrence was initially confined to the mediastinum in one-half of the patients, whereas the others already had distant metastases when recurrence first became evident. Because most of the recurrent lesions originated outside the interposed stomach, CT was more useful than barium studies in showing early recurrence. Radiologic follow-up including CT allows earlier detection of limited recurrent carcinoma after surgery and, thus, offers the possibility of appropriate additional palliative radiotherapy or chemotherapy.

Carcinoma of the esophagus and gastroesophageal junction are usually diagnosed after the onset of obstructive symptoms that imply advanced disease with a poor prognosis [1]. In most of these patients, surgery is thus performed for palliation rather than for cure. Transhiatal esophagectomy without thoracotomy carries a lower surgical risk than the standard transpleural procedure, but it does not allow radical lymphadenectomy [2]. Therefore, a high risk of mediastinal tumor recurrence might be associated with transhiatal esophagectomy. Little information is available in the literature about the site and time at which recurrence develops after transhiatal esophagectomy and gastric interposition [3, 4]. We evaluated the radiographic patterns of tumor recurrence after this surgical procedure.

Subjects and Methods

Our study was based on the clinical, radiologic, and histologic findings of 35 patients who had undergone transhiatal esophagectomy with gastric interposition for cancer at the Inselspital, Bern, between 1982 and 1985. There were 30 men and five women, 41–76 years old (mean, 61 years). In all patients, resection of the complete thoracic and lower esophagus was performed through a combined abdominal and left cervical approach. The esophagus was usually dissected bluntly; sharp dissection was necessary only in large tumors that had infiltrated the surrounding structures. Abdominal exploration always included excision of all lymph nodes suspected to be involved by metastases. The lesser gastric curvature was resected and a gastric tube formed using metallic stapling sutures. The resulting tube was pulled up within the posterior or anterior mediastinum, and the gastric fundus was anastomosed with the cervical esophagus. In two patients, the gastric interposition was performed in the anterior mediastinum, and in 33 patients, in the posterior mediastinum. Eighteen of the resected specimens were squamous-cell carcinomas, 14 adenocarcinomas, two undifferentiated carcinomas, and one a verrucous carcinoma. On the basis of the International Union Against Cancer Classification [5], one lesion was stage I, eight were stage II, 12 were stage III, and 14 were stage IV. Nine primary lesions were located in the upper thoracic esophagus, 12 in the middle thoracic esophagus, and 14 in the lower esophagus. Adjuvant chemotherapy

Received July 1, 1986; accepted after revision September 5, 1986.

¹Department of Diagnostic Radiology, University of Bern, Inselspital, 3010 Bern, Switzerland.

²Present address: Department of Radiology, University of British Columbia and Vancouver General Hospital, 855 W. 12th Ave., Vancouver, BC, Canada V5Z 1M9. Address reprint requests to C. D. Becker.

³Department of Visceral and Transplantation Surgery, University of Bern, Inselspital, 3010 Bern, Switzerland.

⁴Department of Radiology, Klinik Beau-Site, 3000 Bern, Switzerland.

AJR 148:273–277, February 1987
 0361–803X/87/1482–0273
 © American Roentgen Ray Society

was used in two patients; radiotherapy was used in two patients; and surgery alone was used in the remaining 31.

In all patients, clinical and radiologic follow-up was performed at intervals of 3 months during the first year, 6 months during the 2nd and 3rd years, and at annual intervals later. When there was suspicion or evidence of recurrence, shorter intervals or additional tests, such as endoscopy, were used. Each examination consisted of clinical and laboratory studies, posteroanterior and lateral chest radiographs, barium examination of the esophagus and interposed stomach, and CT. Usually all three radiologic procedures were performed on the same day. CT scans were obtained from the thoracic inlet to the midabdomen at sectional intervals of usually 8 mm (sometimes 16 mm), by using a Somatom SF or DR scanner (Siemens, Erlangen, West Germany). Oral contrast material was administered in all cases before and during the CT examination in order to distend and delineate the interposed stomach and the small bowel. A bolus injection of 60–100 ml of sodium-meglumine-ioxithalamate (Telebrix r) was given whenever considered necessary by the radiologist.

Evaluation was based on (1) the prospective clinical and radiologic records from a total of 91 complete follow-up examinations, and (2) a retrospective analysis of all radiographs and CT scans. Preoperative CT scans were available for comparison in all cases.

On chest radiographs, a progressive mediastinal or pleural mass or pulmonary nodules were considered signs of recurrence, whereas pleural effusions alone were considered nonspecific. On barium examinations, (1) progressive extrinsic indentation or narrowing of the interposed stomach or (2) mucosal destruction or ulceration were considered signs of recurrence. On CT, the diagnosis of recurrence was made when there was evidence of a new or progressive mediastinal, pleural, or abdominal soft-tissue mass; progressive thickening of the wall of the interposed stomach; and pulmonary nodules or focal hepatic hypodensities that had been absent on preoperative CT scans.

Recurrence was confirmed by autopsy in three cases, surgical biopsy in four, endoscopic biopsy in six, and percutaneous biopsy in two. In seven patients, the diagnosis of recurrence was made by serial radiologic examination together with the clinical course—significant weight loss and a progressive soft-tissue mass on CT in comparison with previous scans. The diagnosis of “no recurrence” was made when there was neither clinical nor radiologic evidence of neoplastic changes on serial follow-up.

Results

Postoperative Radiologic Features

After the first 3 months, pleural effusions were seen on chest films and aspirated for cytology in seven patients who had been free of recurrence earlier. In one of these patients, the effusion was proven to be neoplastic in origin; the other six were due to cardiac failure or were of unknown cause. Other postoperative findings on chest radiographs included iatrogenic transhiatal visceral hernias containing intestinal structures in four patients and mediastinal gas-containing abscess in one patient. Pulmonary lymphangitic spread was erroneously suspected in a patient who later proved to have reversible interstitial pulmonary edema owing to cardiac decompensation during adriamycin therapy.

On barium studies, the esophagogastric anastomosis in the upright position was observed at the level of the T1–T2 vertebra (range C6–T3). Asymmetric narrowing of the esophagogastric anastomosis was a common finding depending on the degree of gastric distension. Although the benign cause

of anastomotic stenoses was usually obvious because there were no mucosal destructions, endoscopy was performed to rule out malignancy in all equivocal cases. When the stomach was positioned in the posterior mediastinum, it followed a straight course in the midline from the thoracic inlet through the hiatus. In five cases, the stomach shifted to a right posterior paravertebral position below the tracheal bifurcation, returning to the midline just above the hiatus. In three patients, the stomach shifted to the left of the midline to be situated in front of the descending aorta.

On CT, outpouchings of the gastric fundus just below the anastomosis were frequently seen and could be mistaken for a mass unless filled with air or contrast material. Misinterpretation was avoided by simultaneous evaluation of the CT and barium examinations. In two patients, the density of the mediastinal fat was increased on CT because of inflammation and scar formation. In one of these, a large mediastinal abscess was drained under CT guidance; in another, the radiodensity of the abdominal fat was increased after adjuvant radiotherapy of the paraaortic region. In the remaining 33 patients, no relevant scar formation was observed on CT, and all other soft-tissue masses originating in the postoperative period progressively increased in size and were thus considered to be neoplastic in origin. In one patient, the arch of the azygos vein led to the erroneous suspicion of recurrence on prospective CT evaluation because of its close relationship to the right dorsolateral wall of the interposed stomach, mimicking wall thickening (Fig. 1). This potential pitfall was later observed but correctly recognized in six additional patients. The underdistended interposed stomach in patients unable to swallow sufficient contrast material in the supine position was difficult to distinguish from recurrent neoplasm, particularly in the subcarinal region. A few CT images were impaired in their quality because of metal clips or respiration artifacts in a patient suffering from chronic aspiration. Benign focal hepatic hypodense lesions, such as cysts or hemangiomas, caused no diagnostic problems because they were readily distinguishable from metastases by comparison with the preoperative scans.

Recurrence

The results of the clinical and radiologic follow-up are given in Table 1. Twenty-one of the 22 patients developing recurrence had advanced primary esophageal carcinoma (stage III or IV). Distant metastases at the time of the diagnosis of recurrence involved the abdominal or cervical lymph nodes, liver, lung, pleura, peritoneum, skin, adrenals, or other sites. Fourteen patients died from recurrent carcinoma during the period of observation; one patient died from liver cirrhosis without evidence of neoplastic disease.

On retrospective evaluation, recurrence was detectable initially on conventional chest radiographs in two (9%) of 22 patients because of a mediastinal mass. Barium studies were initially positive in seven patients (32%), showing indentation of the interposed stomach in five (23%) and mucosal destruction in four (18%), the latter being proven by endoscopy in all cases. In two of the four cases with mucosal destruction, a major soft-tissue mass was shown on CT adjacent to the

Fig. 1.—No recurrence.

A, Interposed stomach poorly distended. Azygos vein, closely adjacent to stomach on right, mimics thickening of gastric wall (arrowheads).

B, After additional administration of contrast material, interposed stomach is distended completely, and azygous vein (arrowheads) can be identified more clearly.

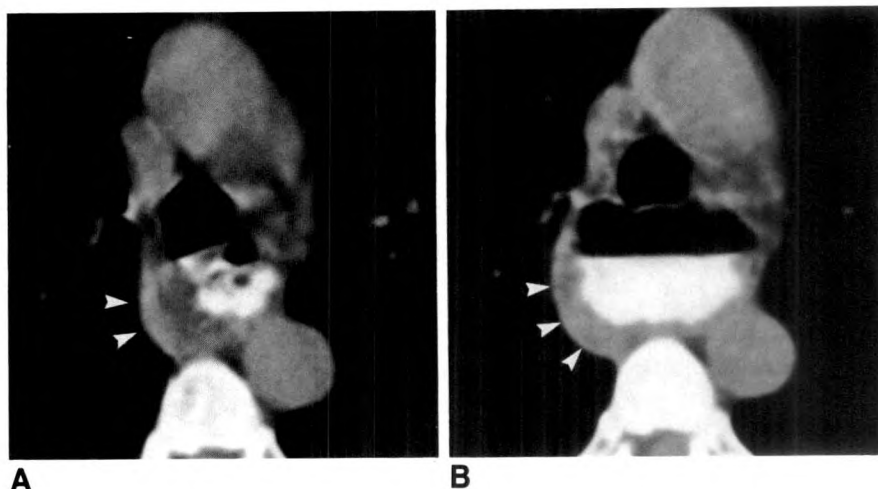


Table 1 Results of Clinical and Radiologic Follow-up

Neoplastic Manifestations	No. of Patients (%)
None ^a	13 (37)
First recurrence ^b	22 (63)
Local alone	11 (31)
Local with DM	8 (23)
DM alone	3 (9)
Total	35 (100)

Note. DM = distant metastases.

^a Mean observation time: 18 months (range, 9–48 months).

^b Mean observation time: 11 months (range, 3–36 months).

corresponding mucosal lesion that indicated secondary neoplastic involvement of the mucosa rather than recurrence originating from the gastric mucosa (Fig. 2). In the other two cases, CT showed focal thickening of the gastric wall without a major extrinsic mass, and recurrence was then considered to arise in the interposed stomach. CT was the most useful test in detecting neoplastic recurrence, and mediastinal soft-tissue masses were the most common initial manifestations of recurrence on CT. In 11 cases, these masses were situated at the level of the primary tumor, whereas in three patients, no mass was seen at the level of the primary tumor but nodular lesions were present above (two patients) or below (one patient) (Figs. 3 and 4). In three patients, nodular thickening of the gastric wall was observed. Liver metastases were found in six (27%) of 22 patients, abdominal lymph node metastases in three (14%), pleural masses in two (9%), and peritoneal carcinomatosis and adrenal masses in two (9%).

Prospectively, recurrence was missed on CT in five patients. One of these presented with distal small-bowel obstruction. Enteroclysis showed an extrinsic compression of the terminal ileum, and exploratory laparotomy revealed extensive peritoneal carcinomatosis. A large mass compressing the terminal ileum had remained undetected on CT because the pelvis had not been examined. In one patient, recurrence first appeared as a mucosal ulcer within the interposed stomach; this lesion was detected on barium examination but not

on CT. A large mediastinal abscess in another patient precluded CT detection of adjacent recurrent tumor that was proven later at autopsy. In two patients, neoplastic masses were missed because of poor CT image quality owing to respiration and motion artifacts.

Recurrence was detected in 13 patients without clinical symptoms or evidence of neoplastic disease. The mean duration of the tumor-free postoperative interval in the 22 patients with recurrence was 9 months at clinical evaluation and 6 months at prospective radiologic evaluation. On retrospective evaluation, the first signs of recurrence were detectable after 3 months in nine patients, after 6 months in 7 patients, and after 12 months in 5 patients.

Detection of recurrence prompted the start of palliative chemotherapy in four and palliative radiotherapy in seven patients.

Discussion

The normal postoperative changes and the appearance of surgical complications on barium studies after transhiatal esophagectomy with gastric interposition have been analyzed by Agha et al. [3]. The early postoperative abnormalities, such as anastomotic leakage with mediastinal or cutaneous fistula, are entirely different from the changes observed on later follow-up; our study considered only the radiologic findings after 3 months and later. Serial follow-up with esophagram is well suited to detect mucosal destruction, stenosis, leaks, perforation, and gross invasion of the interposed stomach. Neoplastic recurrence after transhiatal esophagectomy with gastric interposition is, however, unlikely to originate within the gastric mucosa, and penetration of the gastric wall by an extrinsic mediastinal mass is a late manifestation of recurrence. Anastomotic stenosis is usually due to fibrosis; in none of the cases of our present series was the cervical anastomosis the initial site of neoplastic recurrence. Agha et al. [3] reported neoplastic recurrence at the esophagogastric anastomosis in only one case. Another study [4] from the same institution compared barium studies and CT in 17 patients

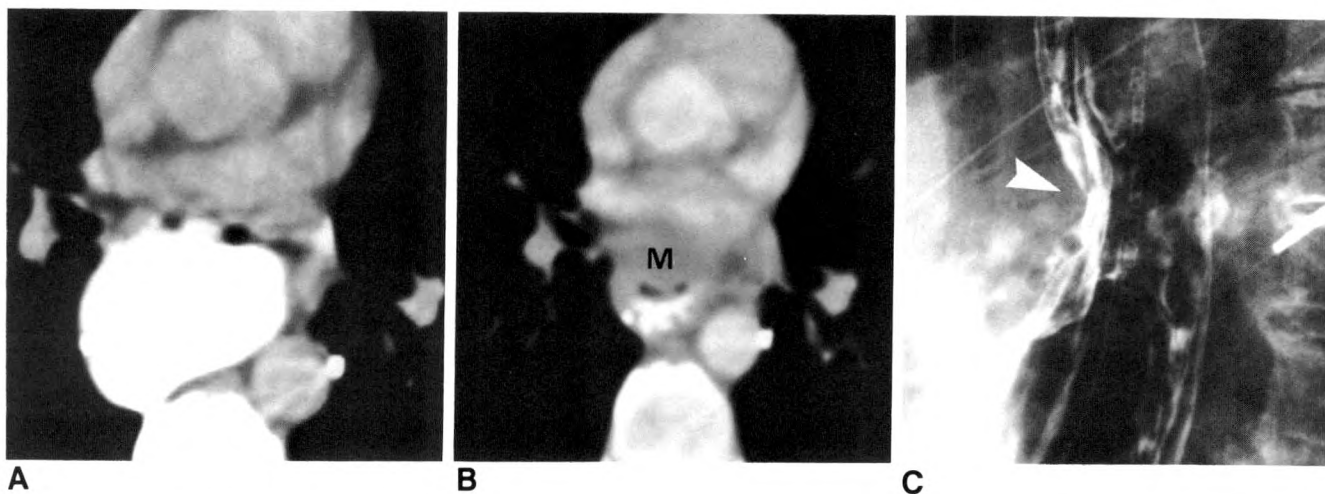


Fig. 2.—Recurrence below level of primary tumor with infiltration of gastric mucosa (proven by endoscopic biopsy).

A, Normal baseline study done 3 months after transhiatal esophagectomy with gastric interposition for advanced squamous-cell carcinoma of upper thoracic esophagus. At level of left atrium, interposed stomach is distended.

B, Follow-up 6 months after surgery reveals mediastinal soft-tissue mass (M) between heart and undistended interposed stomach.

C, Barium study 6 months after surgery shows involvement of anterior aspect of interposed stomach (arrowhead).

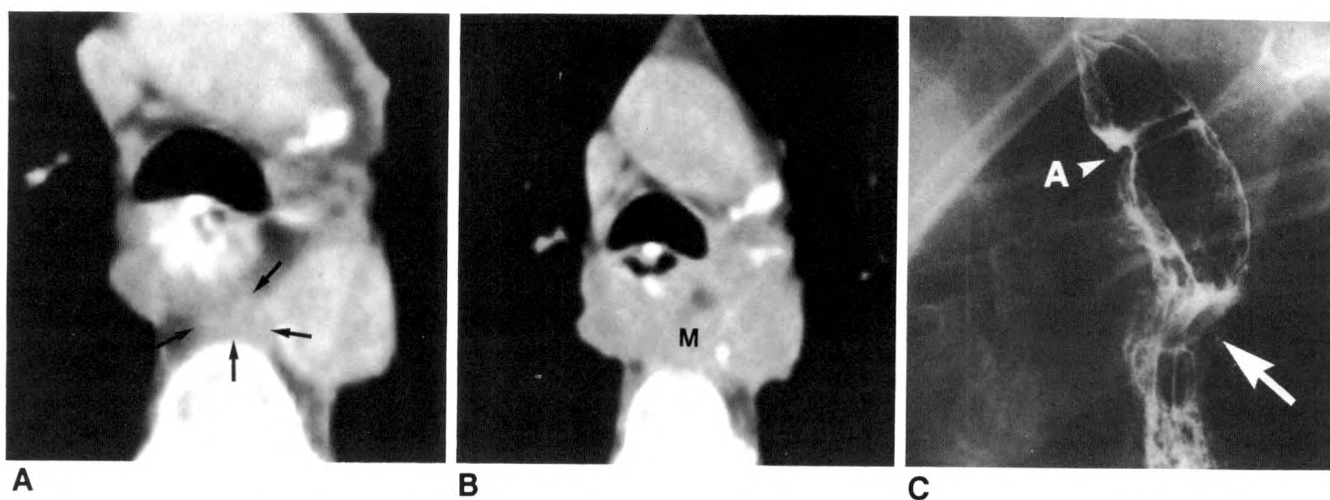


Fig. 3.—Local recurrence at primary site of esophageal carcinoma causing extrinsic impression of interposed stomach without mucosal infiltration. A, 3 months after transhiatal esophagectomy with gastric interposition for squamous-cell carcinoma of the upper thoracic esophagus, density of paraaortic fat is increased on CT (arrows). Because there are no other signs of inflammatory complications, recurrent carcinoma must be suspected.

B, 6 months after surgery, a large mass (M) due to neoplastic recurrence has developed.

C, Barium study corresponding to CT scan (B) shows extrinsic impression of the interposed stomach (arrow). A = esophagogastric anastomosis.

who had undergone transhiatal esophagectomy with gastric interposition for cancer; this study concluded that CT was superior in detecting recurrent neoplasm.

Familiarity with the postoperative anatomy is essential to avoid potential pitfalls in CT interpretation. The azygos vein may evoke the impression of gastric wall thickening, and the nondistended interposed stomach, particularly just below the esophagogastric anastomosis and the tracheal bifurcation, may be mistaken for a neoplastic mass. Increased attenuation of the mediastinal fat adjacent to the interposed stomach has

been observed in the early postoperative period and has sometimes been difficult to distinguish from neoplastic recurrence [4]. In our series, no such postoperative changes were seen except in two patients with known inflammatory post-surgical complications that persisted until 3 months after transhiatal esophagectomy. It may thus be concluded that (1) 3 months after transhiatal esophagectomy, no relevant scar formation is characteristically visible on CT unless there are major active postsurgical complications with corresponding clinical symptoms, and (2) mediastinal soft-tissue masses

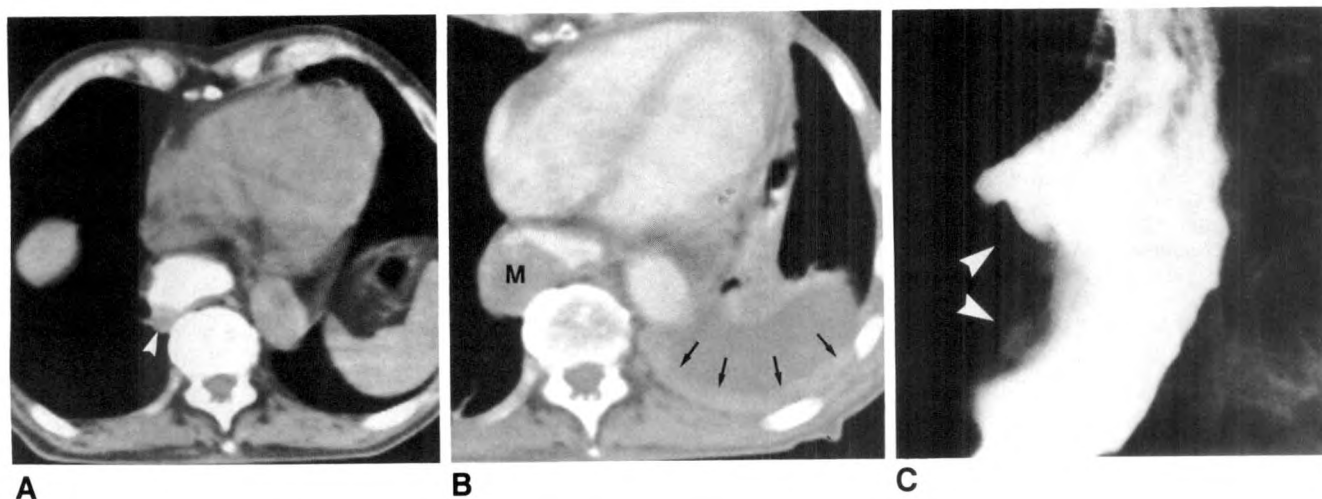


Fig. 4.—Recurrent esophageal carcinoma resulting in pleural carcinomatosis.
 A, 6 months after transhiatal esophagectomy with gastric interposition for squamous-cell carcinoma of middle thoracic esophagus, CT shows small soft-tissue mass adjacent to interposed stomach (arrowhead). No neoplastic changes seen on corresponding barium study.
 B, 9 months after surgery, CT reveals large mass (M) and pleural effusion on left with thickening of left dorsal pleura (arrows) due to carcinomatosis.
 C, Barium study 9 months after surgery shows extrinsic impression of gastric lumen (arrowheads).

shown on CT after transhiatal esophagectomy are likely to represent recurrent carcinoma.

The clinical long-term follow-up of 94 patients after transhiatal esophagectomy for cancer has been reported by Orringer [2] with actuarial survival rates at 12, 24, and 36 months of 52%, 32%, and 22%, respectively. In their terminal stage, all but three of his patients had widespread metastatic esophageal carcinoma. In our present serial radiologic follow-up study, neoplastic lesions due to recurrence were initially found to be limited to the mediastinum in 50% of patients, whereas the other 50% already had distant metastases when recurrence was first detected. A progressive extramucosal mediastinal soft-tissue mass was the most common initial manifestation of neoplastic recurrence, and CT was the most useful test for its detection. In most cases, lesions first appeared at the level of the primary tumor and were thus considered recurrent growth either from residual esophageal tumor or from adjacent lymph node metastases; three patients first developed recurrence in mediastinal lymph nodes above or below the primary tumor level.

On prospective evaluation, 13 of 22 patients were clinically asymptomatic when recurrence was detected by either barium or CT studies. Radiologic diagnosis of recurrence pre-

ceded the clinical symptoms by an average of 3 months. Serial radiologic follow-up including CT thus offers the possibility of detecting asymptomatic neoplastic recurrence after transhiatal esophagectomy. Although there is currently no general agreement regarding treatment of patients with recurrent esophageal carcinoma after surgery, early radiologic detection of limited disease may warrant appropriate radiotherapy or chemotherapy that offers an additional palliative effect.

REFERENCES

1. Skinner DB. Surgical treatment for esophageal carcinoma. *Semin Oncol* 1984;11:136-143
2. Orringer MB. Transhiatal esophagectomy without thoracotomy for carcinoma of the thoracic esophagus. *Ann Surg* 1984;200:282-288
3. Agha FP, Orringer MB, Amendola MA. Gastric interposition following transhiatal esophagectomy: radiologic evaluation. *Gastrointest Radiol* 1985;10:17-24
4. Gross BH, Agha FP, Glazer GM, Orringer MB. Gastric interposition following transhiatal esophagectomy: CT evaluation. *Radiology* 1985;155:177-179
5. Harmer MH, ed. *TNM classification of malignant tumours*, 3rd ed. Geneva, Switzerland: UICC (International Union Against Cancer), 1982

Books Received

Receipt of books is acknowledged as a courtesy to the sender. Books that appear of sufficient interest will be reviewed as space permits.

- Diagnostic Imaging in Ophthalmology.** Edited by Carlos F. Gonzalez, Melvin H. Becker, and Joseph C. Flanagan. New York: Springer-Verlag, 366 pp., 1986. \$129
- Emergency Radiology of the Acutely Ill or Injured Child**, 2nd ed. By Leonard E. Swischuk. Baltimore: Williams & Wilkins, 622 pp., 1986. \$75
- Pediatric Magnetic Resonance Imaging.** By Mervyn D. Cohen. Philadelphia: Saunders, 162 pp., 1986. \$49.50
- Brigham and Women's Hospital Handbook of Diagnostic Imaging.** Edited by Barbara J. McNeil and Herbert L. Abrams. Boston: Little, Brown, 342 pp., 1986. \$18, soft cover
- Atlas of Pediatric Orthopedic Radiology.** By Alan E. Oestreich. New York: Thieme-Stratton, 334 pp., 1985. \$80
- Digital Subtraction Angiography. Practical Aspects.** By Arina Van Breda and Barry T. Katzen. Thorofare, NJ: Slack, 230 pp., 1986.
- Radiology of the Hand: A Diagnostic Synopsis of many General Diseases.** By Cornelis J. P. Thijn. New York: Springer-Verlag, 302 pp., 1985. \$90
- The Cerebral Infarct.** Pathology, Pathogenesis and Computed Tomography. New York: Springer-Verlag, 104 pp., 1985. \$29.50
- Tumors of Unknown Origin.** Orlando, FL: Grune & Stratton, 1985. \$69.50
- Cerebral Blood Flow Metabolism Measurement.** New York: Springer-Verlag, 1985. \$69.50
- Radiation Oncology.** A Handbook for Residents and the Allied Health Professions. By Stewart M. Jackson. St. Louis: Green, 249 pp., 1985.
- Sectional Human Anatomy.** By Man-Chung Han and Chu-Wan Kim. Seoul: Ilchokak, 224 pp., 1985. \$40
- Diagnostic Imaging of the Acute Injured Patient.** By T. H. Berquist. Baltimore: Urban and Schwarzenberg, 1985. \$47.50
- Radiation Protection.** Medical Physics Handbooks 16. By R. L. Kathren. Boston: Adam Hilger Ltd., 197 pp., 1985. \$29.50
- Joints and Vertebral Connections.** By Wolfgang Dihlmann. New York: Thieme, 580 pp., 1985. \$75
- Osteology for Radiographers.** By Christina Shillingford. Boston: Blackwell Scientific Publ., 133 pp., 1985.
- Ultrasound Exam Review.** Sonographer's Self-Assessment Guide. By Marveen Craig. Philadelphia: Lippincott, 267 pp., 1985. \$24.50
- Radiology of the Spine. Tumors.** Edited by J. Jeanmart. New York: Springer-Verlag, 116 pp., 1986. \$49.50
- Manual of Darkroom Technique: WHO Basic Radiological System.** Geneva: World Health Organization, 25 pp., 1985. Swiss Fr/8
- Imaging of Orthopedic Trauma and Surgery.** By Thomas H. Berquist. Philadelphia: Saunders, 816 pp., 1985. \$125
- Functional Mapping of the Brain in Vascular Disorders.** Edited by Wolf Dieter Heiss. Berlin: Springer-Verlag, 126 pp., 1985. \$19.50
- Learning to Heal.** The Development of American Medical Education. By Kenneth M. Ludmerer. New York: Basic Books, 346 pp., 1985. \$21.95
- Cardiac Catheterization and Angiography**, 3rd ed. Edited by William Grossman. Philadelphia: Lea & Febiger, 562 pp., 1986. \$49.50
- Computed Tomography of Trauma.** Edited by Martin Heller, Hans-Holger Jend, and Harry K. Genant. New York: Thieme, 128 pp., 1986. \$45
- Essentials of Nuclear Medicine Imaging**, 2nd ed. By Fred A. Mettler, Jr., and Milton J. Guiberteau. Orlando, FL: Grune & Stratton, 391 pp., 1986.
- Handbook of Radiologic Orthopedic Terminology.** By R. F. Kilcoyne and Edward Farrar. Chicago: Year Book Medical, 152 pp., 1986.
- Single-Photon Emission Computed Tomography.** By Barbara Y. Croft. Chicago: Year Book Medical, 306 pp., 1986.
- Brain CT.** An introduction. By John R. Bradshaw. England: Wright, 208 pp., 1985. \$20
- Nuclear Pharmacy.** An Introduction to the Clinical Application of Radiopharmaceuticals. By Henry M. Chilton and Richard L. Witcofski. Philadelphia: Lea & Febiger, 190 pp., 1986.
- Echographie de la Prostate.** By Bruno Fornage. Paris: Vigot, 336 pp., 1985.
- Clinical Diagnostic Ultrasound.** Edited by E. Barnett and P. Morley. Boston: Blackwell Scientific Publ., 617 pp., 1986.
- Radiology of Lymphomas.** Edited by Jean-Noel Bruneton and Maurice Schneider. Berlin: Springer-Verlag, 144 pp., 1986. \$56.50
- Ostomy Care and the Cancer Patient: Surgical and Clinical Considerations.** Edited by Dorothy B. Smith and Douglas E. Johnson. Orlando, FL: Grune & Stratton, 179 pp., 1986. \$35
- Magnetic Resonance Imaging: Principles and Applications.** By David Kean and Michael Smith. Baltimore: Williams & Wilkins, 164 pp., 1986. \$43.95
- Radiology of Adverse Reactions to Drugs and Toxic Hazards.** By George Ansell. Rockville, MD: Aspen, 357 pp., 1985. \$40
- The Radiologic Clinics of North America.** Use of Computers in Radiology. Edited by Ronald L. Arenson. Philadelphia: Saunders, 133 pp., 1986.
- Biological Effects and Dosimetry of Static and ELF Electromagnetic Fields.** Edited by M. Grandolfo, S. M. Michaelson, and A. Rindi. New York: Plenum Press, 697 pp., 1985. \$97.50
- Cranial Computed Tomography: A Comprehensive Text.** Edited by Alan L. Williams and Victor M. Haughton. St. Louis: Mosby, 655 pp., 1985.
- Introduction to Vascular Ultrasonography**, 2nd ed. Edited by William J. Zwiebel. Orlando, FL: Grune & Stratton, 503 pp., 1986. \$57
- Color Atlas of Anatomy.** By Johannes W. Rohen and Chihiro Yokochi. Tokyo: Igaku-Shoin, 417 pp., 1983. \$85
- Stapfne's Oral Radiographic Diagnosis**, 5th ed. Edited by Joseph A. Bibilisco and Eastwood G. Turlington. Philadelphia: Saunders, 560 pp., 1985. \$37.95
- Mammography—A User's Guide: Recommendations of the National Council on Radiation Protection and Measurements.** Bethesda, MD: NCRP, 178 pp., 1986.
- Multiple Choice Questions in Radiology.** By P. R. Patel. London: Arnold, 71 pp., 1986.
- Radiologic Diagnosis of Renal Transplant Complications.** Edited by W. R. Castaneda-Zuniga. Minneapolis: Univ. of Minnesota Press, 298 pp., 1986.
- Digital Subtraction Angiography: Practical Aspects.** By Arina van Breda and Barry T. Katzen. New Jersey: Slack, 230 pp., 1986.
- Computed Tomography in the Evaluation of Trauma**, 2nd ed. Edited by Michael P. Federle and Michael Brant-Zawadzki. Baltimore: Williams & Wilkins, 305 pp., 1986. \$58.95
- Diagnostic Patient Studies in Surgery.** Edited by Bernard Sigel. Philadelphia: Lea & Febiger, 449 pp., 1986. \$60
- Differential Diagnosis in Pediatric Radiology.** By Michael Grunebaum. Switzerland: Karger, 139 pp., 1986. \$27.25, soft cover
- Atlas of Two-Dimensional Echocardiography in Congenital Cardiac Defects.** By G. J. Van Mill, A. J. Moulart, and E. Harinck. The Hague, The Netherlands: Nijhoff, 143 pp., 1985. \$29.50, soft cover
- Environmental Health Criteria 51: Guide to Short Term Tests for Detecting Mutagenic and Carcinogenic Chemicals.** Geneva: WHO, 208 pp., 1985. Swiss Fr/16, soft cover
- A Guide to Cardiac Pacemakers: Supplement 1986–1987.** By Dryden Morse, Robert M. Steiner, and Victor Parsonnet. Philadelphia: Davis, 219 pp., 1986. \$50
- Computed Tomography of the Gastrointestinal Tract Including the Peritoneal Cavity and Mesentery.** Edited by Morton A. Meyers. New York: Springer-Verlag, 279 pp., 1986. \$98
- Information Processing in Medical Imaging.** Edited by Stephen L. Bacharach. The Hague, The Netherlands: Nijhoff, 555 pp., 1986. \$99.50

Case Report

Acute Gastric Dilatation: A Rare Cause of Portal Venous Gas

D. Randall Radin,¹ Robert S. Rosen, and James M. Halls

Although a large number of pathologic conditions have been reported to accompany the visualization of portal venous gas, most cases are associated with bowel necrosis. Urgent surgical exploration has been recommended in all patients except those in whom portal venous gas is associated with ulcerative colitis [1]. We report a patient in whom portal venous gas was associated with acute gastric dilatation, another condition that does not require surgical intervention if it is recognized early [2].

Case Report

A 28-year-old woman with a 10-year history of drug abuse and numerous previous admissions for coma due to drug overdose was admitted for treatment of decubitus ulcers. Hypoxic brain damage had been diagnosed. She underwent repeated debridement of her decubitus ulcers and was given supportive and rehabilitative therapy. On her 85th day in the hospital, she had the acute onset of abdominal distension. Bowel sounds were absent. Serum levels of electrolytes and calcium were normal. A massively dilated, air-filled stomach with streaks of air in the stomach wall was observed on an abdominal radiograph. An arborized gas pattern in the right upper quadrant, representing air either in the biliary tree or in the portal venous system, was also observed (Fig. 1A). On a second radiograph taken 1 hr later, after placement of a nasogastric tube and aspiration of gastric contents, the stomach remained dilated, although to a lesser degree (Fig. 1B). Air was now seen in a normal-sized duodenal bulb. Six hours later, after nasogastric suction, an upper gastrointestinal series was performed with water-soluble contrast material (Fig. 1C). The stomach and duodenum appeared normal. The gastric emphysema

and the extraintestinal gas in the right upper quadrant were no longer visible. With careful monitoring and adjustment of her fluid and electrolyte status, the patient improved. Three weeks later, however, the patient died after developing status epilepticus and extensive aspiration pneumonia. A postmortem examination was not performed.

Discussion

When branching lucencies are seen in the right upper quadrant on an abdominal radiograph, portal venous gas must be distinguished from pneumobilia. In this patient, gas was observed in both a central and a peripheral distribution. Because of the presence of gastric emphysema, the rapid resolution of the extraintestinal gas, and the absence of a fistula on upper gastrointestinal series, it was concluded that this patient had portal venous gas.

Although a central distribution of gas is more common with pneumobilia than with portal venous gas, it is not a reliable distinguishing feature. The radiographic appearance of gas in the extrahepatic main portal vein is difficult to differentiate from air in the common bile duct. Reliable evidence that a branching gas pattern overlying the liver is within the portal venous system rather than the biliary tree is visualization of gas in small peripheral radicles within 2 cm of the liver capsule [3], as observed in this patient (Fig. 1A).

In our patient, the diagnosis of acute gastric dilatation, with gastric emphysema as the cause of portal venous gas, was made by excluding other entities associated with gas in the

Received July 22, 1986; accepted after revision September 4, 1986.

¹All authors: Department of Radiology, University of Southern California School of Medicine, Los Angeles County-USC Medical Center, 1200 N. State St., Los Angeles, CA 90033. No reprints available.

AJR 148:279-280, February 1987 0361-803X/87/1482-0279 © American Roentgen Ray Society

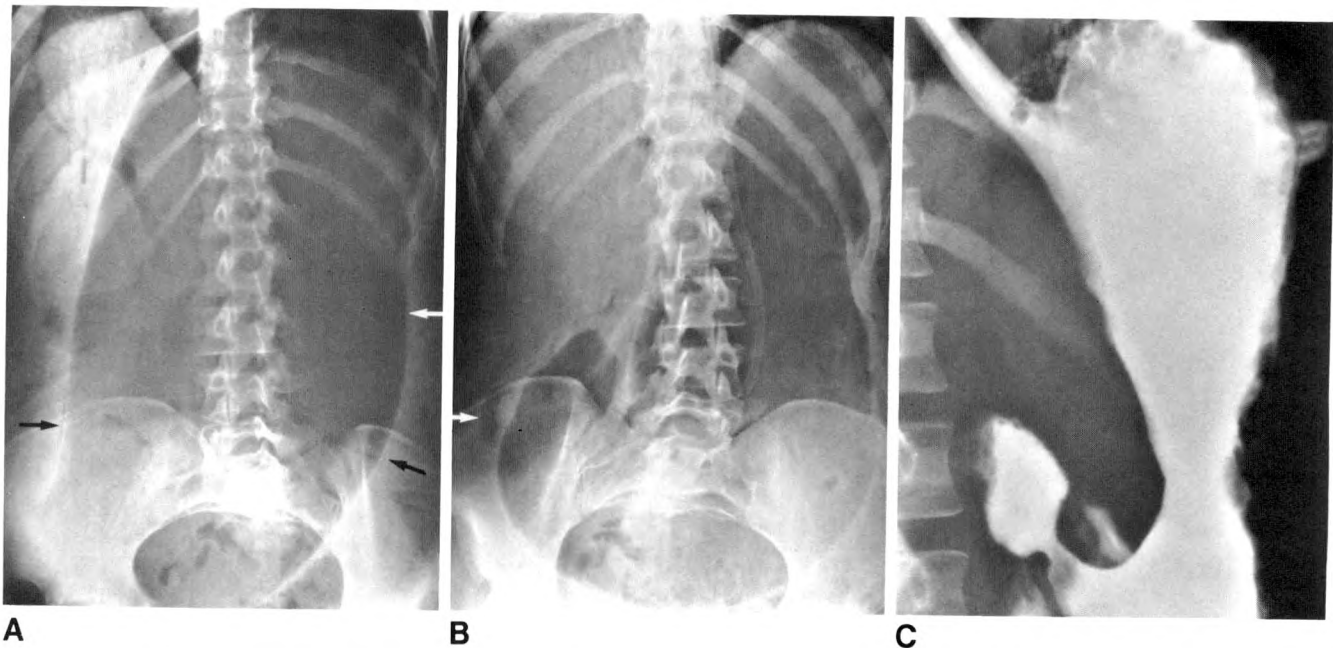


Fig. 1.—A, Abdominal radiograph. Massive gastric dilatation with lucent streaks in stomach wall (arrows). Branching lucencies in right upper quadrant extend to within 2 cm of liver capsule.

B, 1 hr later, after partial gastric decompression by nasogastric tube, nondilated duodenal bulb is seen (arrow). Branching lucencies are still present in right upper quadrant.

C, Upper GI series, after nasogastric suction. No evidence of obstruction.

wall of the stomach. Emphysematous gastritis, an infectious gastritis caused by gas-forming bacteria, is manifested by a "bubbly" appearance of intramural gas rather than the linear streaks of radiolucency seen in interstitial gastric emphysema [4]. The causes of gastric emphysema can be classified as traumatic, pulmonary, and obstructive [4]. This patient had no history of instrumentation or caustic ingestion that might have damaged the gastric mucosa. She also had no evidence of pulmonary emphysema. The upper gastrointestinal series excluded obstructive causes such as neoplasm, ulcer, and volvulus. In some patients with bowel necrosis, gas-forming organisms may be the source of portal venous gas. In this patient, the clinical and radiographic findings indicate that the source of the portal venous gas was dissection of luminal gas through breaches in the gastric mucosa caused by severe distension.

This patient and three previously reported patients with portal venous gas due to acute gastric dilatation were all bedridden young people, aged 13 to 28 years [3, 5, 6]. Two of the patients recovered completely after decompression of the stomach with a nasogastric tube [5, 6], as did this patient who also improved with conservative management but died 3 weeks later from causes not directly related to gastric dilatation. The single patient who died as a direct result of

gastric dilatation had bloody fluid recovered from the stomach when a nasogastric tube was passed, which suggested that ischemic necrosis of the gastric mucosa had already begun [3].

Most patients with radiographic evidence of portal venous gas require surgical resection of necrotic bowel, although many are poor surgical candidates. However, the presence of portal venous gas only is not an indication for surgery. With prompt recognition, acute gastric dilatation, a rare cause of portal venous gas, can be treated conservatively.

REFERENCES

1. Liebman PR, Patten MT, Manny J, Benfield JR, Hechtman HB. Hepatic-portal venous gas in adults: etiology, pathophysiology and clinical significance. *Ann Surg* 1978;187:281-287
2. Clearfield HR, Stahlgren LH. Acute dilatation, volvulus, and torsion of the stomach. In: Berk JE, ed. *Bockus gastroenterology*, 4th ed. Philadelphia: Saunders, 1985:1373-1380
3. Sisk PB. Gas in the portal venous system. *Radiology* 1961;77:103-106
4. Kussin SZ, Henry C, Navarro C, Stenson W, Clain DJ. Gas within the wall of the stomach: report of a case and review of the literature. *Dig Dis Sci* 1982;27:949-954
5. Dell JM Jr. Gas in the portal vein. *AJR* 1967;100:424-425
6. Benson MD. Adult survival with intrahepatic portal venous gas secondary to acute gastric dilatation, with a review of portal venous gas. *Clin Radiol* 1985;36:441-443

Natural History of the Obstructed Rabbit Appendix: Observations with Radiography, Sonography, and CT

Abraham H. Dachman¹
James B. Nichols²
Darryl H. Patrick²
Joel E. Lichtenstein^{1,3}

Received July 15, 1986; accepted after revision September 4, 1986.

This work was supported by the Uniformed Services University of the Health Sciences Protocol #C08902. The opinions or assertions contained herein are the private ones of the authors and are not to be construed as official or reflecting the views of the Department of Defense or the Uniformed Services University of the Health Sciences. The experiments reported herein were conducted according to the principles set forth in the "Guide for the Care and Use of Laboratory Animals," Institute of Animal Resources, National Research Council, DHEW Pub. No. (NIH) 78-23.

Winner of Memorial Award, 1986, Society of Gastrointestinal Radiology.

Presented at the annual meeting of the Society of Gastrointestinal Radiology, Acapulco, Mexico, January 1986, and at the annual meeting of the American Roentgen Ray Society, Washington, DC, April 1986.

¹ Department of Radiology and Nuclear Medicine, Uniformed Services University of the Health Sciences, F. Edward Hébert School of Medicine, 4301 Jones Bridge Rd., Bethesda, MD 20814-4799. Address reprint requests to A. H. Dachman.

² Department of Laboratory Animal Medicine, Uniformed Services University of the Health Sciences, F. Edward Hébert School of Medicine, 4301 Jones Bridge Rd., Bethesda, MD 20814-4799.

³ Present address: Department of Radiology, Cincinnati General Hospital, 234 Goodman St., Cincinnati, OH 45267.

AJR 148:281-284, February 1987
0361-803X/87/1482-0281

Chronic (1-3 months' duration) appendiceal obstruction was induced in 11 rabbits to assess the pathologic consequences and to study the associated radiologic, sonographic, and CT findings. Three pathologic/radiologic groups resulted with approximately equal frequency. In group A, the abscess was characterized by inflammatory cells in the lumen and wall of the appendix without mucin production. Calcification was shown radiographically, and sonography showed an anechoic or complex pattern. Group B, the "mixed response," was characterized by an intact hyperplastic mucosa, mucin secretion, and inflammatory debris in the lumen. Occasional calcification was present radiographically, and sonography showed a complex or hypoechoic pattern. In group C, true mucocoeles had an intact hyperplastic mucosa, a mucin-filled lumen, and minimal inflammation. These were anechoic on sonography except for mobile foci of inflammatory debris. Chronic obstruction of the appendix results in a spectrum of pathologic responses with varying degrees of either inflammation and mucosal destruction or mucosal hyperplasia and mucin secretion. An abscess results when infection overwhelms the host's inflammatory responses. If the bacteria are destroyed by these defenses, a mucocoele forms. An intermediate situation occurs when there is a mixed response with chronic inflammatory changes and an intact mucosa. This finding supports the existence of chronic appendicitis in humans.

The natural history of chronic appendiceal obstruction is uncertain. In studies performed before 1950, chronic appendiceal obstruction induced in rabbits was used to study the formation of mucocoeles and pseudomyxoma peritonei [1-3]. Although the conclusion of these experiments was that mucocoeles can be produced experimentally with relative ease, the gross and histologic descriptions provided do not support this conclusion.

Chronic appendiceal obstruction may lead to chronic appendicitis [1-8]. Whereas acute appendicitis and recurrent appendicitis are recognized diseases [9-19], chronic appendicitis remains controversial [4, 20, 21] despite recent data that support its existence [4-8].

This study was designed to assess pathologic consequences of chronic appendiceal obstruction induced in rabbits and evaluate their radiologic appearance.

Materials and Methods

Twelve adult male and female New Zealand white rabbits (lagomorphs) weighing 2.6-4.1 kg were used. Systemic gentamicin was given 48 hr before surgery. The anesthesia used was 8.8 mg/kg of intramuscular xylazine, followed by 50 mg/kg of intramuscular ketamine hydrochloride, with additional doses of ketamine given as needed. Through a midline abdominal incision, the appendix was isolated leaving its vasculature intact; an incision was made near its base. A catheter was inserted and used to empty the appendiceal contents with instillation of 1 l of saline. This was followed by a 10% iodine flush and 1 ml of gentamicin (50 mg/ml). The appendiceal incision was closed and, distal to the incision, the appendix was doubly ligated with umbilical tape. The abdomen was closed and systemic gentamicin was continued for 1 week postoperatively. Surgery was performed again after 1-3 months

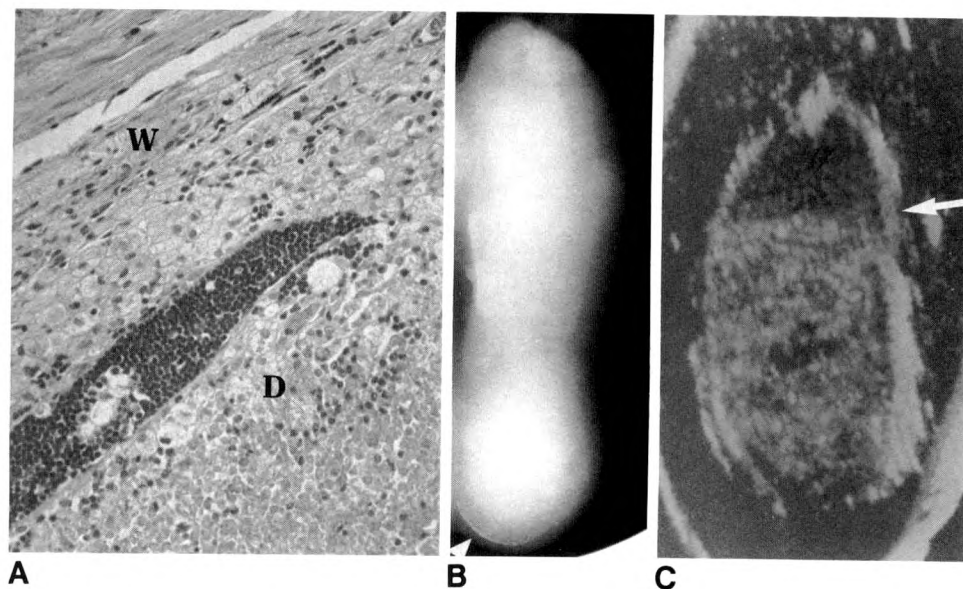


Fig. 1.—Group A (abscess).

A, Microscopy of appendix (H and E $\times 250$) shows cellular debris in lumen and infiltrate in appendix wall. No mucosal hyperplasia or mucin production is seen. D = debris, W = appendiceal wall.

B, Radiograph of appendix shows calcification at tip (arrowhead).

C, Sonogram of appendix suspended from its tied end, in water-filled glove. Echoes in water represent bubbles. Fluid level is seen in specimen (arrow), representing layering of cellular debris. Relatively hypoechoic areas represent debris and possibly collections of mucin.

(average, 2.2 months) and the appendix was removed intact.

The fresh specimen was transilluminated. Radiographs, sonograms, and CT scans were made and the specimen was then fixed in formalin. The cut, fixed specimen was studied in order to correlate the pathologic findings with the radiographs. Several sections from all parts of the appendix were stained with H and E and mucin stains to study the wall and luminal contents.

Radiographs of the fresh specimen were obtained by using 35–40 kVp, 25 mAs, and 0.3-mm focal spot, with $1.5\times$ magnification in frontal and horizontal beam projections, to look for fluid levels or dependent calcifications. For sonography, the specimen was either in a water bath or in a water-filled glove. Bubbles in the water bath were carefully distinguished from true echoes within the specimen. The appendix was examined in two positions (flat and suspended on end) to look for fluid levels or mobile contents. Static and real-time sonography was used with 7.5- and 10-MHz transducers to minimize the possibility of false echoes due to gain setting or beam averaging. CT was done with a 512×512 matrix at 100 kV, 50 mAs, and a small focal spot. A 3- to 5-mm slice thickness was used with a 12- to 24-cm field size and a soft-tissue algorithm setting. All studies were performed and assessed by the same individual without knowledge of the microscopic findings.

Results

Pathology

One rabbit was excluded because of early postoperative death. The 11 remaining specimens were grouped into three pathologic categories.

Group A (three cases) showed abscess formation (Fig. 1). The specimen did not transilluminate. The lumen was filled with white suppurative material, and the wall was replaced by fibrosis and was often calcified. Mucin stains were negative, except for rare microscopic foci.

Group B (five cases) was characterized by a mixed response with white inflammatory exudate in the lumen separated from the wall by a thin layer of mucin with some

collection of mucin present in the exudate (Fig. 2). The mucosa was intact with goblet-cell hyperplasia and prominent mucin secretion. The specimen did not transilluminate.

Group C (three cases) comprised true mucoceles (Fig. 3). The fresh gross specimens transilluminated. In one case, small, mobile, white flecks floated throughout the mucin and could be seen through the thinned appendiceal wall. The lumen was filled with clear mucin with virtually no inflammatory debris. The wall was intact with a hyperplastic epithelial lining, hyperplastic goblet cells, obliteration of most submucosal lymphoid follicles, and little, if any, inflammatory infiltrate.

Radiology

Group A (abscess, three cases) showed peripheral wall calcification in otherwise homogeneous soft tissue in two of three cases (Fig. 1B). On sonography, the contents of the appendectomy specimen were anechoic in one case and complex in two cases, with a possible fluid level in one of these (Fig. 1C). CT showed a homogeneous soft-tissue lesion with peripheral calcific foci in two of three cases and a possible fluid level in one (not the same as the case with possible fluid level on sonogram).

Group B (mixed response, five cases) showed foci of predominantly central with some peripheral calcification in two cases. On sonography, two were complex and three were hypoechoic. There was suggestion of a fluid level in one, though to represent layering of the inflammatory infiltrate with a collection of mucin at one end (Fig. 2C). CT showed foci of calcification in two (Fig. 2D), and one had a possible fluid level. One had an average density of -18 H.

Group C (true mucocoele, three cases) showed no calcification on radiography. All were anechoic on sonography. A single, small, mobile echogenic focus was seen in one case (Fig. 3B). All were homogeneous on CT. One had an average

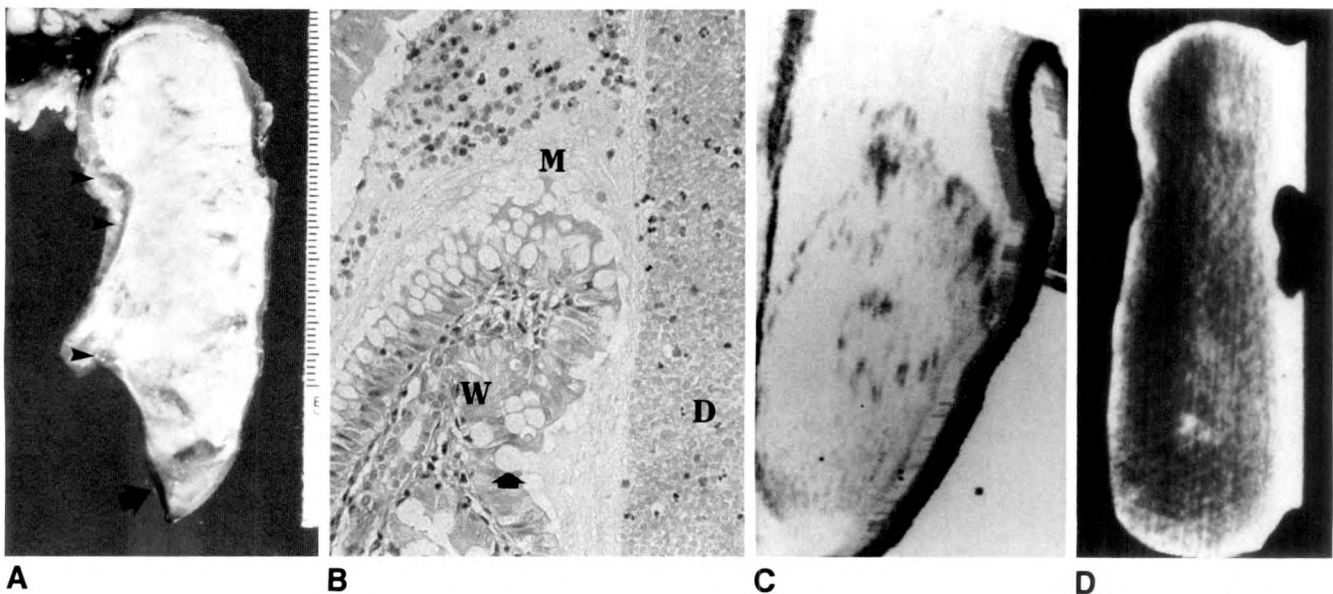


Fig. 2.—Group B (mixed response).

A, Photograph of cut surface of fixed appendix shows thick inflammatory debris in lumen. Collection of mucin is present at tip (arrow) and along wall (arrowheads).

B, Microscopy (H and E stain $\times 250$) shows inflammatory debris in lumen separated from wall by layer of mucin. Hyperplastic goblet cells with

abundant mucin (arrow) are in mucosa. D = debris, W = appendix wall, M = mucin.

C, Sonogram of appendix in water-filled glove. Anechoic areas represent collections of mucin, and echogenic areas represent debris in lumen.

D, CT scan of appendix shows calcific foci in lumen and in wall.

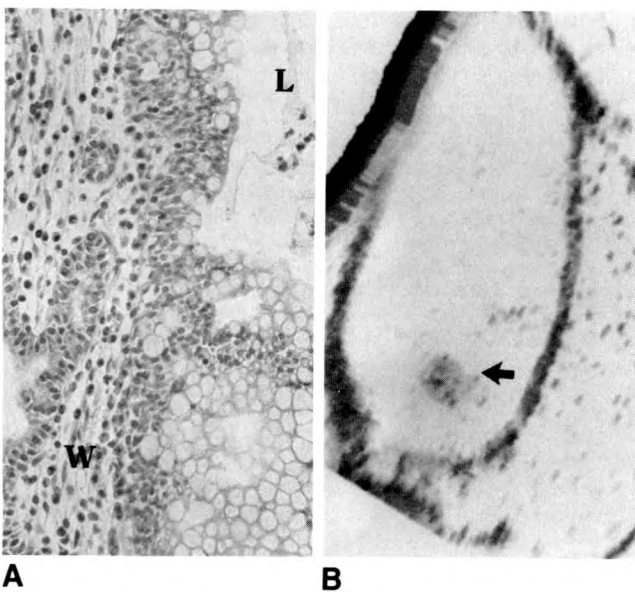


Fig. 3.—Group C (mucocoele).

A, Microscopy (H and E stain $\times 250$) of appendix. Wall is similar to group B, but no inflammatory debris is present in lumen. W = appendix wall, L = lumen.

B, Sonogram of appendix suspended from its tied end, in water-filled glove. Echoes in water represent bubbles. Mucocoele is anechoic with single echogenic focus observed in dependent portion (arrow).

density measurement of -50 H. The density ranged from 0 to $+40$ H in the other two mucocoeles (as well as in groups A and B, except in the areas of calcification, which measured 56 – 100 H).

Discussion

The results indicate that there is a spectrum of responses to chronic obstruction of the appendix. All cases show a combination of inflammation and mucosal hyperplasia with mucin production; in group A inflammation predominates with abscess formation, in group B there is a mixed response of inflammatory cells and debris distending the lumen with an intact hyperplastic mucosa secreting mucin, and in group C the inflammation is minimal with abundant mucin production resulting in mucocoele formation. We hypothesize that the factors determining which response predominates include the number and pathogenicity of the bacteria remaining in the appendix and the host's inflammatory response to them. If infection overwhelms the host's response, abscess results. When the reverse occurs, mucocoele results. The mixed response represents an intermediate between these two situations.

Grodinsky and Rubnitz [1] used chronic appendiceal obstruction to produce mucocoeles in 10 of 12 rabbits and described an intact mucosa with decreased lymphoid tissue as typical of a mucocoele. The mucocoele contents varied from opaque and thick to clear and thin and they contained inflammatory cells in the wall. Cheng [3] reported similar results. These authors concluded that mucocoeles could be produced experimentally with relative ease.

Differences between mucocoeles in humans [22–24] and those produced experimentally in animals include the prominent inflammatory debris that occurs in many experimentally produced mucocoeles and the varying degrees of fibrosis and residual epithelium in the appendiceal wall.

Calcification is characteristic of groups A and B, whereas

the mucocoeles produced in this study had none, possibly because of their short duration. Increased intraluminal pressure in a mucocoele may cause mucosal atrophy and later stages may show a calcified fibrotic wall similar to that described in many mucocoeles in humans [22].

While low-level echoes in mucocoeles in humans may be due to mucin [25, 26], dependent echoes or excrescences seen on sonography or CT are unexplained [22]. Our results suggest that minimal inflammatory debris is present within a mucocoele and that its quantity may depend on the nature and rapidity of the mucosal response to appendiceal obstruction. When little inflammation or sloughed mucosa is present, the mucocoele will be homogeneous and anechoic. If appendiceal obstruction produces a mixed response initially, one would expect some inflammatory debris and sloughed mucosa to persist in the mucocoele. This debris may be mobile or adherent to the wall, explaining the presence of dependent echoes or excrescences.

Clinicopathologic evidence for the existence of chronic appendicitis in humans comes from a number of sources [4–8, 27]. Butler [8] reviewed 276 appendectomies and found 12 cases with subacute or chronic symptoms that correlated with histologic evidence of acute and chronic inflammation, and one case with only chronic inflammation. Savrin et al. [4] found a similar correlation between a clinical history of chronic, right-lower-quadrant pain and histologic evidence of chronic inflammation in four cases. Additionally, one patient with chronic pain had plasma cells and foreign-body giant cells in his appendiceal wall. This description resembles the appendiceal inflammatory pseudotumor reported in a child with chronic, right-lower-quadrant pain [28], and we surmise that both of these cases represent a chronic appendicitis. Additional support for the concept of chronic appendicitis is found in patients treated with "delayed" or "interval" appendectomy [3, 29–32]. Janik et al. [7] reviewed histologic material from appendectomies of 36 children treated with interval appendectomy and found a spectrum of fibrosis, subacute inflammation, or acute inflammation. He concluded that the appendix is potentially able to "sustain a low-grade infection even up to five months after initial clinical symptoms resolved" [7].

The finding of a mixed response in our experimental model corresponds histologically to a subacute or chronic appendicitis and supports the existence of chronic appendicitis as a clinicopathologic entity [4–8, 27].

ACKNOWLEDGMENTS

The authors thank Martha Ross and Shirley Zabrek for manuscript preparation and George Hummel for assistance in pathology.

REFERENCES

- Grodinsky M, Rubnitz AS. Mucocoele of the appendix and pseudomyxoma peritonei. *Surg Gynecol Obstet* 1941;73:345–354
- Rubnitz AS, Herman HT. Experimental appendical (sic) mucocoele, myxoglobulosis and peritoneal pseudomyxoma. *Arch Pathol* 1943;36:297–310
- Cheng KK. An experimental study of mucocoele of the appendix and pseudomyxoma peritonei. *J Pathol Bacteriol* 1949;61:217–225
- Savrin RA, Clausen K, Martin EW Jr, Cooperman M. Chronic and recurrent appendicitis. *Am J Surg* 1979;137:355–357
- Grossman EB Jr. Chronic appendicitis. *Surg Gynecol Obstet* 1978;146:596–598
- Bonzanigo C, Scheidegger S. Zum Krankheitsbild der sogenannten "chronischen Appendizitis" (Diagnostic features of so-called "chronic appendicitis"). *Schweiz Rundschau Med Prax* 1981;70:953–961
- Janik JS, Ein SH, Shandling B, Simpson JS, Stephens CA. Nonsurgical management of appendiceal mass in late presenting children. *J Pediatr Surg* 1980;15:574–576
- Butler C. Surgical pathology of acute appendicitis. *Hum Pathol* 1981;12:870–878
- Wangensteen OH, Dennis C. Experimental proof of the obstructive origin of appendicitis in man. *Ann Surg* 1939;110:629–633
- Wangensteen OH, Dennis C. The production of experimental appendicitis (with rupture) in higher apes by luminal obstruction. *Surg Gynecol Obstet* 1940;70:799–808
- Pieper R, Kager L, Tidefeldt U. Obstruction of appendix veriformis causing acute appendicitis. *Acta Chir Scand* 1982;148:63–72
- Buirge RE, Dennis C, Vargo RL, Wangenstein OH. Histology of experimental appendiceal obstruction (rabbit, ape and man). *Arch Pathol* 1940;30:481–492
- Befeler D. Recurrent appendicitis, incidence and prophylaxis. *Arch Surg* 1964;89:666–668
- Goldman M. The radiological investigation of recurrent appendicitis. *Clin Radiol* 1966;17:289–294
- Sack DM, Carle G, Shama SK. Recurrent acute appendicitis with erythema annulare centrifugum. *Arch Intern Med* 1984;144:2090–2092
- Ferrier PK. Acute appendicitis in university students: a twenty-year study of 1,028 cases. *J Am Coll Health Assoc* 1972;20:287–290
- Homer MJ, Braver JM. Recurrent appendicitis: re-examination of a controversial disease. *Gastrointest Radiol* 1979;4:295–301
- McLennan I, Kennedy J. Justification for appendectomy in chronic appendicitis. *Br Med J* 1954;2:736–738
- Arnbjornsson E. Some factors affecting perforation in acute appendicitis. *Ann Chir Gynaecol* 1963;72:50–52
- Talbert JL, Zuidema GD. Appendicitis—a reappraisal of an old problem. *Surg Clin North Am* 1966;46:1101–1112
- Bellina PV, Morock J. Chronic appendicitis: approaches by x-ray, ultrasound, nuclear medicine. *J La State Med Soc* 1984;79:32–34
- Dachman AH, Lichtenstein JE, Friedman AC. Mucocoele of the appendix and pseudomyxoma peritonei. *AJR* 1985;144:923–929
- Wackym PA, Gray GF Jr. Tumors of the appendix. I. Neoplastic and nonneoplastic mucocoeles. *South Med J* 1984;77:283–287
- Woodruff R, McDonald JR. Benign and malignant cystic tumors of the appendix. *Surg Gynecol Obstet* 1940;71:750–755
- Horgan JG, Chow PP, Richter JO, Rosenfeld AT, Taylor KJW. CT and sonography in the recognition of mucocoele of the appendix. *AJR* 1984;143:959–962
- Cunningham JJ, Wooten W, Cunningham MH. Gray scale echography of soluble protein and protein aggregate fluid collections (in vitro study). *JCU* 1976;4:417–419
- Martin-Gomez R, Loscertales-Abril J. Nueva contribución al esclarecimiento de la etiopatogenia de las llamadas appendicopatías crónicas. *Rev Esp Enferm Apar Dig* 1984;66:217–225
- Narasimharao KL, Malik AK, Mitra SK, Pathak IC. Inflammatory pseudotumor of the appendix. *Am J Gastroenterol* 1984;79:32–34
- Mosegaard A, Nielsen OS. Interval appendectomy, a retrospective study. *Acta Chir Scand* 1979;145:109–111
- Skoubo-Kristensen E, Hvid I. The appendiceal mass, results of conservative management. *Ann Surg* 1982;196:584–587
- Thomas DR. Conservative management of the appendix mass. *Surgery* 1973;73:677–680
- Hoffman J, Lindhard A, Jensen HE. Appendix mass: conservative management without interval appendectomy. *Am J Surg* 1984;148:379–382

Case Report

Ringlike Rectal Ulcers After Biopsy or Polypectomy

Anna S. Lev-Toaff,^{1,2} Marc S. Levine,¹ Igor Laufer,¹ and Hans Herlinger¹

Barium enemas are often performed after colorectal biopsy or polypectomy. There is evidence that these barium enema examinations may be safely performed immediately after a superficial mucosal biopsy with a flexible sigmoidoscopic or colonoscopic forceps [1-3]. The biopsy sites can sometimes be identified on double-contrast barium studies [4]. However, they can be mistaken for pathologic conditions in the rectum. We report three cases in which postbiopsy or postpolypectomy lesions appeared radiographically as ringlike ulcers in the rectum.

Case Reports

Case 1

A 32-year-old woman with a history of Crohn's disease underwent a double-contrast barium enema that revealed an 8-cm area of narrowing in the terminal ileum as well as four ringlike ulcers in the rectum and sigmoid colon (Fig. 1). The latter findings were thought to indicate rectosigmoid involvement by Crohn's disease. However, it was subsequently learned that the patient underwent flexible sigmoidoscopy 4 days earlier and that four rectal biopsies were taken from normal-appearing mucosa. The pathology report revealed no evidence of inflammation or granulomas.

Case 2

A 66-year-old woman was referred for follow-up barium enema 6 months after sigmoid resection for a colonic carcinoma. Two tiny ringlike ulcers were identified 7 and 10 cm from the anal verge (Fig.

2). Further inquiry revealed that colonoscopy had been performed 3 days before the barium study with removal of two tiny polyps that corresponded in location to the ulcers.

Case 3

A 77-year-old man had a double-contrast barium enema that revealed a single ringlike ulcer in the rectum 5 cm proximal to the anal verge (Fig. 3). Because of our experience with previous cases, a biopsy-related lesion was suspected, and it was later confirmed that a 0.5 × 1.0 cm rectal polyp had been removed during sigmoidoscopy 2 days earlier.

Discussion

We have presented three cases of postbiopsy or postpolypectomy lesions that appeared radiographically as ringlike ulcers in the rectum. Millward et al. [5] also reported three cases of rectal biopsy causing discrete ringlike ulcers. In all of our cases, the lesions were recognized as shallow, punched-out, ringlike ulcers surrounded by a radiolucent elevation (Figs. 1-3). The latter finding was presumably caused by a zone of edematous mucosa or the reepithelializing margin of the mucosal defect. In one case, the patient had documented Crohn's disease of the terminal ileum, and the findings led to an erroneous impression of rectosigmoid involvement (Fig. 1). However, the aphthous ulcers of Crohn's disease typically appear as tiny central collections of barium surrounded by a radiolucent halo [6]. Thus, these ringlike ulcers in the rectum after biopsy or polypectomy have a somewhat

Received July 7, 1986; accepted after revision September 5, 1986.

¹ Department of Radiology, Hospital of the University of Pennsylvania, 3400 Spruce St., Philadelphia, PA 19104. Address reprint requests to M. S. Levine.

² Present address: Department of Radiology, Temple University Hospital, Philadelphia, PA 19140.

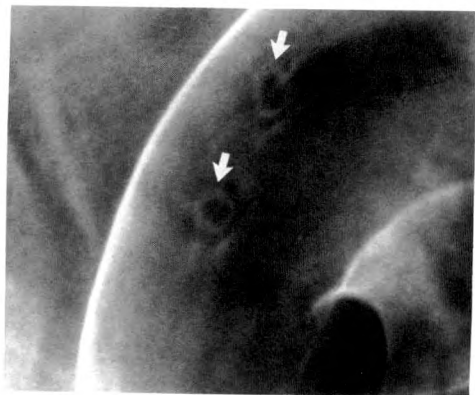


Fig. 1.—Closeup of rectosigmoid shows two shallow, ringlike ulcers (arrows) with surrounding radiolucent halos. Two other ringlike ulcers were identified more distally in rectum. These findings were the sites of four rectal biopsies taken from normal-appearing mucosa 4 days earlier.



Fig. 2.—Double-contrast radiograph shows a tiny ringlike ulcer (arrow) in proximal rectum with a faint halo surrounding ulcer. A second ulcer was identified more proximally in rectosigmoid. Ulcers corresponded in location to two small polyps removed colonoscopically 3 days earlier.



Fig. 3.—Solitary ringlike ulcer (arrow) in rectum 2 days after sigmoidoscopic removal of a polyp from this location.

different appearance from the classic aphthous ulcers of Crohn's disease.

It is important that the radiologist know whether a biopsy or polypectomy has been performed on any patient referred for a barium enema examination. In our department, there is a well-established protocol for questioning patients about previous endoscopic procedures before performing the examination. Nevertheless, the radiologist occasionally remains unaware of a recent endoscopic procedure. As a result, unexpected postbiopsy lesions may be encountered on barium studies. However, the presence of one or more ringlike ulcers in the rectum should suggest the possibility of a recent biopsy or polypectomy in these patients.

REFERENCES

1. Harned RK, Consigny PM, Cooper NB, Williams SM, Woltjen AJ. Barium enema examination following biopsy of the rectum or colon. *Radiology* 1982;145:11-16
2. Maglinte DDT, Strong RC, Strate RW, et al. Barium enema after colorectal biopsies: experimental data. *AJR* 1982;139:693-697
3. Harned RK, Williams SM, Maglinte DDT, Hayes JM, Paustian FF, Consigny PM. Clinical application of in vitro studies for barium-enema examination following colorectal biopsy. *Radiology* 1985;154:319-321
4. Caroline DF, Creteur V, Kressel HY, Rhoads JE. Verification of superficial biopsy sites by barium enema. *AJR* 1983;140:945-946
5. Millward SF, Chapman A, Somers S, Stevenson GW. Rectal biopsy as a cause of rectal ulceration. *Radiology* 1985;156:42
6. Laufer I, Costopoulos L. Early lesions of Crohn's disease. *AJR* 1978;130:307-311

MR Evaluation of Uterine Anomalies

Marshall C. Mintz¹
David I. Thickman²
Debra Gussman³
Herbert Y. Kressel¹

The MR features of uterine anomalies were analyzed in eight women. Scans were done on a 1.5-T magnet with T1-weighted (TR 600 msec, TE 25 msec) and T2-weighted (TR 2000–2500 msec, TE 35–80 msec) spin-echo images obtained in several planes. The anomalies consisted of bicornuate uterus (three cases), septate uterus (one case), bicornuate uterus with septation (two cases), unicornuate uterus (one case), and uterus didelphys with vaginal septum (one case). These diagnoses were confirmed by hysterosalpingography with laparoscopy (five cases), dilation and curettage with laparoscopy (one case), or cesarean section (two cases). In six of the eight cases, MR correctly identified and accurately classified the type of anomaly. In the other two cases, the MR diagnosis was a bicornuate uterus with septation. One case proved to be a uterus didelphys with vaginal septum, and the other a bicornuate uterus without septation. The study shows that MR is a valuable tool for the diagnosis of uterine anomalies.

The prevalence of congenital uterine anomalies is approximately 0.1–0.5% [1–3]. Although many patients are asymptomatic, others suffer from repeated spontaneous abortion and premature labor [4]. Currently, evaluation of patients with suspected uterine anomalies includes physical examination and imaging studies such as sonography, hysterosalpingography, and hysteroscopy. Because these studies are often inconclusive, diagnostic laparoscopy is often necessary for definitive evaluation. This procedure has the disadvantage of being invasive.

Several authors [5–9] report that MR can successfully define the anatomy and pathology of the uterus. MR can distinguish the endometrium from the myometrium, image the uterus in several planes, and define uterine contour. We, therefore, evaluated the use of MR to detect various uterine anomalies.

Materials and Methods

Eight patients with high clinical suspicion of uterine anomaly underwent MR imaging of the pelvis. These patients were referred for the procedure on the basis of repeated pregnancy loss, a suspicious physical examination, positive results from another imaging test, or an anomaly discovered during previous surgery.

Imaging was performed on a whole-body General Electric unit operating at 1.5 T. Patients had no preparation for the examination and no contrast agents were used. Images with T1 weighting were obtained by using a repetition time (TR) of 600 msec and a time to echo (TE) of 25 msec. Varying amounts of T2 weighting were obtained by using pulse sequences with TR of 2000–2500 msec and TE of 35–80 msec. Because of time limitations, not all pulse sequences were performed in all planes in all patients. Each patient had both axial and coronal images of the pelvis, and many underwent imaging in the sagittal plane, as well. The slice thickness was 8 mm, and two excitations were obtained for data collection of a 128 × 256 matrix.

The MR images were reviewed simultaneously by two radiologists without knowledge of the patients' history, physical findings, or results of other diagnostic procedures. The MR findings were then correlated with the surgical diagnosis to look for a characteristic pattern for each type of anomaly. The final diagnoses were confirmed by hysterosalpingography with

Received July 21, 1986; accepted after revision September 10, 1986.

¹ Department of Radiology, Hospital of the University of Pennsylvania, 3400 Spruce St., Philadelphia, PA 19104. Address reprint requests to M. C. Mintz.

² Presbyterian University of Pennsylvania Medical Center, 51 N. 39th St., Philadelphia, PA 19104.

³ Department of Obstetrics and Gynecology, Hospital of the University of Pennsylvania, 3400 Spruce St., Philadelphia, PA 19104.

AJR 148:287–290, February 1987

0361–803X/87/1482–0287

© American Roentgen Ray Society

laparoscopy in five cases, dilation and curettage with laparoscopy in one case, and cesarean section in two cases.

Results

In six of the eight cases, MR findings predicted the surgical diagnosis: two cases of bicornuate uterus, one case of septate uterus, one case of unicornuate uterus, and two cases of bicornuate uterus with septation. In the remaining two cases, the MR diagnosis was a bicornuate uterus with septation. One case was found to be a uterus didelphys with vaginal septum, and the other a bicornuate uterus without septum.

Just as long-TR, long-TE sequences delineate normal uterine anatomy best [5], the morphology of bicornuate uteri and external contour of the uterus were most clearly seen with these sequences. Axial and coronal planes were complementary for visualizing the configuration of the endometrial canal, but sagittal images were not helpful. Because all of the cases had anteverted uteri, axial scans through the pelvis showed fundal contour best.

When the MR findings were retrospectively reviewed and compared with the surgical results, two basic patterns were seen that correlated with bicornuate and septate uteri (Fig. 1). In cases of bicornuate uterus, two high-signal areas (endometrium) were seen, each of which was surrounded by a low-signal junctional zone. In addition, a band of medium-

signal myometrium separated the two endometrial-junctional zone complexes (Fig. 2). The separation between the endometrial cavities increased as the fundus was approached. One patient with a bicornuate uterus also had multiple fibroids (Fig. 3). In one case of septate uterus, only a low-intensity zone (the septum) separated the cavities (Fig. 4). Although the septum was seen on both long-TR, long-TE and long-TR, intermediate-TE images, it was best seen as a distinct low-intensity zone on long-TR, intermediate-TE pulse sequences. Each of two patients with a bicornuate uterus containing a septum had a combination of the features seen in a bicornuate uterus and a septate uterus: In the fundal area the cavities were separated by medium-signal myometrium, but only a low-signal area separated the cavities in the lower uterine-cervical area (Fig. 5). The case of unicornuate uterus was diagnosed by visualization of one uterine horn with failure of the endometrial canal to widen as the imaging plane moved toward the fundus.

Visualization of uterine fundal contour aids in differentiating septate from bicornuate uteri. In cases of bicornuate uteri and uterus didelphys, a fundal cleft is seen that is not visualized with septate uteri. In our cases, however, MR evaluation of fundal contour was not helpful, perhaps because optimal pulse sequences and imaging planes were not obtained in all cases. Four of six uteri with expected clefts were imaged with T2 weighting in the axial plane. Two had definite clefts, one had a possible cleft, and one a small dimple. In two cases with only T1-weighted axial images, clefts were not seen. In the unicornuate uterus, a normal uterine fundal contour was seen, and a small dimple was seen in the septate uterus.

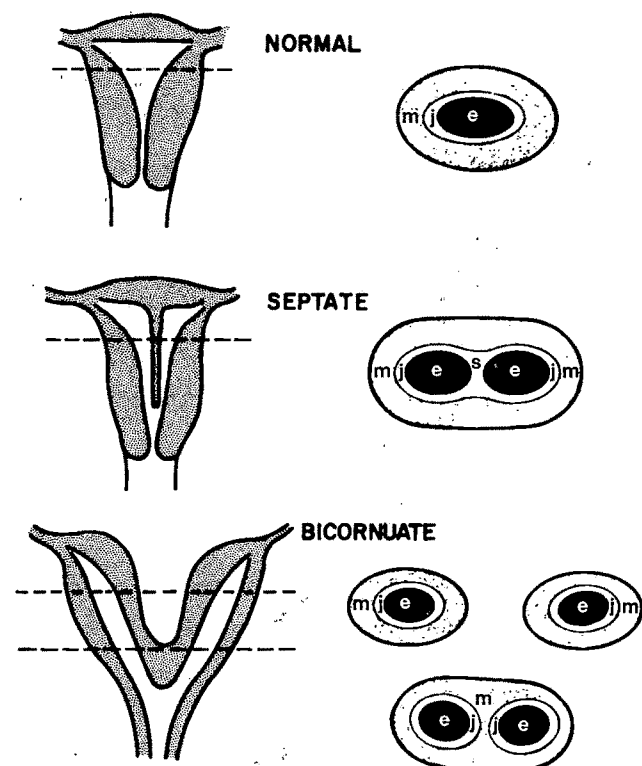


Fig. 1.—Cross sections of normal, septate, and bicornuate uteri. e = endometrium. j = junctional zone, m = myometrium, s = septum.

Discussion

Patients with uterine anomalies may suffer from repeated abortion, premature labor, and increased incidence of breech presentation and transverse lie. Recognizing that a uterine anomaly is indeed the cause of a patient's symptoms, as well as identifying the type of anomaly, are important in management. Septate uteri cause more frequent reproductive problems and are repaired with different surgical procedures than bicornuate uteri [3, 4, 10].

Sonography and hysterosalpingography have been used with some success in identifying uterine anomalies [3, 10–14]. However, neither technique can reliably differentiate a bicornuate from a septate uterus, and since each anomaly is associated with a different prognosis and treatment, this differentiation is important. Also, hysterosalpingography involves ionizing radiation, and use of contrast material may cause an allergic reaction. In addition, genital instrumentation imposes risks of uterine perforation and infection, and entails patient discomfort.

In our series of eight cases, MR was effective in identifying various types of uterine anomalies. Bicornuate uteri were differentiated from septate. In cases of bicornuate uteri, a medium-intensity band of myometrium separates the endometrial-junctional zone complexes. Septations were seen as low-intensity bands separating the high-signal endometrium.

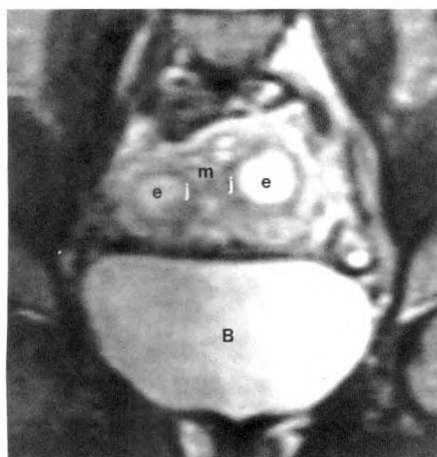


Fig. 2.—Coronal MR section (TR 2500 msec, TE 80 msec) showing bicornuate uterus. e = endometrium, j = junctional zone, m = myometrium, B = bladder.

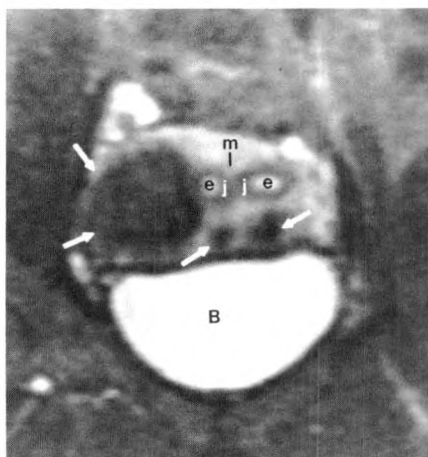


Fig. 3.—Coronal MR view (TR 2500, TE 80 msec) showing several fibroids (arrows) within bicornuate uterus. Small portion of myometrium separates endometrial cavities. e = endometrium, j = junctional zone, m = myometrium, B = bladder.

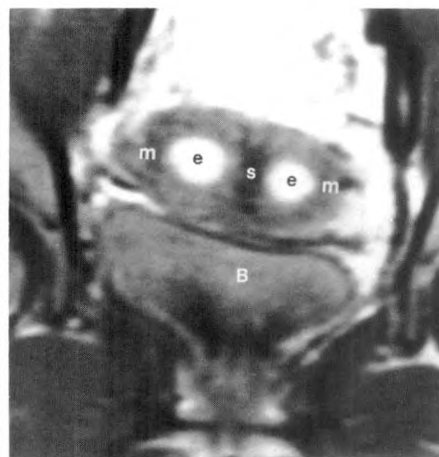
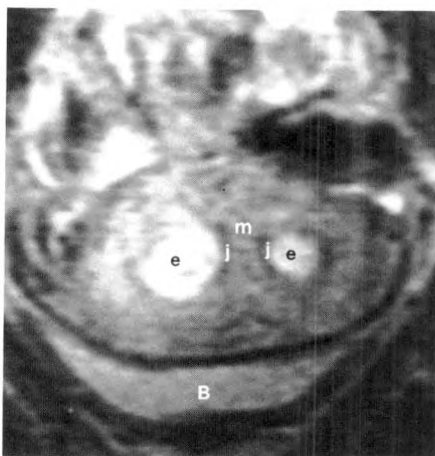


Fig. 4.—Coronal MR image (TR 2000 msec, TE 35 msec) showing septate uterus. e = endometrium, m = myometrium, s = septum, B = bladder.

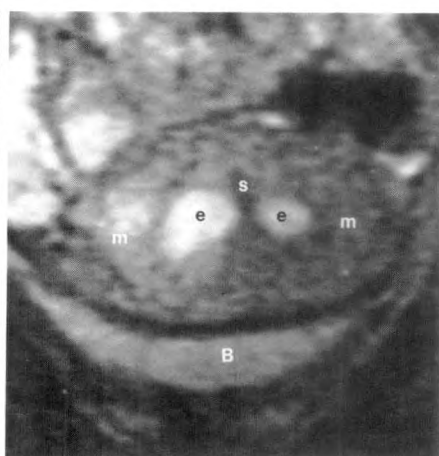
Fig. 5.—Coronal MR section illustrating bicornuate uterus with lower uterine septation. e = endometrium, j = junctional zone, m = myometrium, s = septum, B = bladder.

A, (TR 2000, TE 80 msec) images uterine body.

B, (TR 2000 msec, TE 80 msec) shows lower uterine segment.



A



B

The composition of the septum is the primary factor contributing to its low signal. Typically, fibrous tissue produces little signal on MR images.

In our series, MR evaluation of uterine fundal contour was not helpful in classifying uterine anomalies, perhaps because optimal pulse sequences and imaging planes were not obtained in many cases. However, in MR imaging, determination of fundal anatomy does not appear necessary in order to reliably distinguish septate from bicornuate uteri.

Although MR was effective in distinguishing bicornuate from septate and unicornuate uteri, in two cases MR findings did not exactly agree with surgical findings. In one case, the

MR diagnosis of a bicornuate uterus with inferior septum proved to be a uterus didelphys with vaginal septum. Comparison of physical examination findings with the MR study probably would have led to the correct diagnosis. In the other case, a small lower uterine-cervical septum was thought to be present in a bicornuate uterus. The bicornuate uterus was proven by hysterosalpingography and laparoscopy, but the cervical septum was not. The MR appearance may have been caused by the convergence of the two junctional zones. However, the primary diagnosis of bicornuate uterus was made. These two cases illustrate possible pitfalls in the use of MR to diagnose duplication anomalies and small septations.

REFERENCES

1. Woolf RB, Allen WM. Concomitant malformations: the frequent, simultaneous occurrence of congenital malformations of the reproductive and urinary tracts. *Obstet Gynecol* 1953;2:236-265
2. Wiersma AF, Peterson LF, Justema EJ. Uterine anomalies associated with unilateral renal agenesis. *Obstet Gynecol* 1976;47:654-657
3. Sharp HC. Reproductive tract disorders. In: Danforth DN, Scott JR, eds. *Obstetrics and gynecology*. Philadelphia: Lippincott, 1986:561-576
4. Valle RF, Sciarra JJ. Hysteroscopic treatment of the septate uterus. *Obstet Gynecol* 1986;67:253-257
5. Hricak H. MRI of the female pelvis: a review. *AJR* 1986;146:1115-1122
6. Hricak H, Tscholakoff D, Heinrichs L, et al. Uterine leiomyomas: correlation of MR, histopathologic findings, and symptoms. *Radiology* 1986;158:385-391
7. Bryan PJ, Butler HE, LiPuma JP, et al. NMR scanning of the pelvis: initial experience with a 0.3T system. *AJR* 1983;141:1111-1118
8. Hricak H, Alpérs C, Crooks LE, Sheldon PE. Magnetic resonance of the female pelvis: initial experience. *AJR* 1983;141:1119-1128
9. Lee JKT, Gersell DJ, Balfe DM, Worthington JL, Picus D, Gapp G. The uterus: in vitro MR-anatomic correlation of normal and abnormal specimens. *Radiology* 1985;157:175-179
10. Buttram VC, Gibbons WE. Mullerian anomalies: a proposed classification (an analysis of 144 cases). *Fertil Steril* 1979;32:40-46
11. Malini S, Valdes C, Malinak LR. Sonographic diagnosis and classification of anomalies of the female genital tract. *J Ultrasound Med* 1984;3:397-404
12. McArdle CR, Berezin AF. Ultrasound demonstration of uterus subseptus. *JCU* 1980;8:139-141
13. Kurtz AB, Wapner RJ, Rubin CS, Cole-Beuglet C, Kendall B. Bicornuate uterus: unilateral pregnancy and pelvic kidney. *JCU* 1980;8:353-355
14. Jones TB, Fleischer AC, Daniell JF, Lindsay AM, James AEJ. Sonographic characteristics of congenital uterine abnormalities and associated pregnancy. *JCU* 1980;8:435-437

Sonography in the Diagnosis of Acute Renal Allograft Rejection and Cyclosporine Nephrotoxicity

Gregory D. Linkowski¹
 Vasyi Warvariv²
 Roy A. Filly¹
 Flavio Vincenti²

High-resolution real-time sonography was used at the time an allograft biopsy was performed on 58 renal transplant recipients to elucidate the cause of posttransplantation decline in renal function. These procedures were performed within 3 months of transplantation. Fifty-four out of 58 patients were on a cyclosporine-steroid regimen. Acute rejection was diagnosed if one or more of the following findings was present on sonogram: transplant swelling, increased conspicuity of the medullary pyramids, medullary pyramid enlargement, decreased renal-sinus fat, and pelvi-infundibular thickening. Correlation of sonography and histopathologic findings showed that sonography cannot be used independently to diagnose rejection or to distinguish between cyclosporine nephrotoxicity and rejection. A creatinine level of 2.5 mg/dl was then randomly selected as a threshold level to possibly improve the sonographic results, anticipating that above this threshold an abnormal sonogram would invariably be recorded in the presence of rejection. This threshold was not found to be discriminatory. Only at a higher threshold level of creatinine (6.9 mg/dl or more) was there 100% correlation between acute rejection and the presence of abnormal sonographic findings. Furthermore, whereas most patients with four or five abnormal sonographic criteria tended to have acute rejection, this group of patients constituted a minority and, even within this group, sonography was not entirely reliable in detecting transplant rejection.

Since the first successful transplant between identical twins was performed in 1956, renal transplantation has become the most effective therapeutic technique for patients with end-stage renal disease [1]. Acute rejection often endangers the transplant, and immunosuppressive agents such as cyclosporine-a are being used with increasing frequency to overcome this problem. Unfortunately, this may lead to cyclosporine-a nephrotoxicity [2, 3].

Various diagnostic techniques have been used to evaluate posttransplantation renal failure including sonography [4-10], radionuclide scintigraphy [11], dynamic CT [12], angiography and digital-subtraction angiography, excretory urography, pulsed Doppler duplex sonography [13] and, most recently, MR imaging [14-16].

Until recently, there was a general consensus that sonography was valuable in the diagnosis of acute rejection. Sonographic features characteristic of rejection have been delineated in clinical and animal experiments [17, 18]. In a recent study at our institution, however, sonography was not helpful in segregating the various causes of posttransplantation allograft hypofunction [19]. However, this study suffered because there was a long time interval between transplantation and biopsy and because few patients were evaluated for cyclosporine-a nephrotoxicity, a now-common clinical problem [19]. Differences among individual physician thresholds for biopsying transplants with rising serum creatinine may also have been an important variable that was not considered.

The purpose of the current study is to determine if sonography can help to discriminate between cyclosporine-a nephrotoxicity and acute rejection [20]. Furthermore, in the absence of clear-cut discrimination between rejection and cyclosporine-a nephrotoxicity, attempts were made to discover if there was a threshold

Received July 25, 1986; accepted after revision September 19, 1986.

¹ Department of Radiology, University of California School of Medicine, San Francisco, CA 94143. Address reprint requests to R. A. Filly.

² UCSF Transplant Service, University of California School of Medicine, San Francisco, CA 94143.

AJR 148:291-295, February 1987
 0361-803X/87/1482-0291

© American Roentgen Ray Society

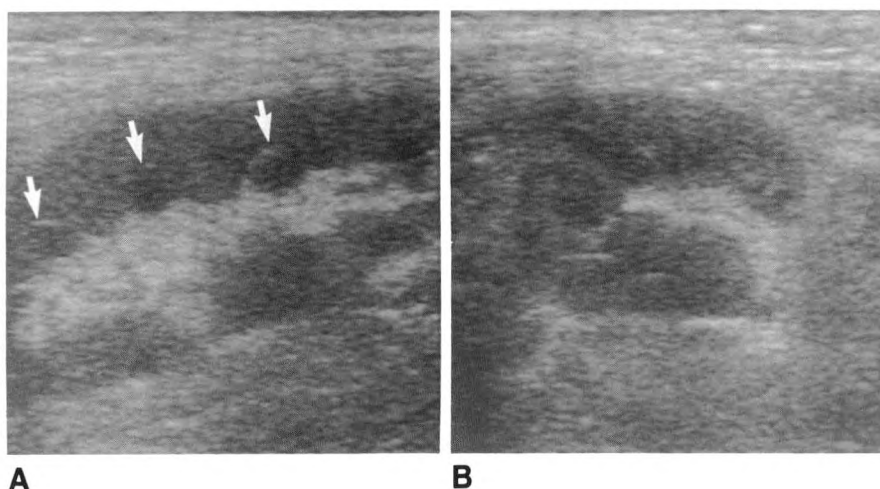


Fig. 1.—Longitudinal (A) and transverse (B) normal sonograms in a patient with a renal allograft and a normal renal biopsy. Arrows show normal medullary pyramids.

creatinine level at which one would always anticipate the sonogram to be abnormal in a patient with rejection. Individual and group sonographic features suggestive of rejection were examined, and correlations with histopathologic and clinical diagnoses were statistically analyzed.

Materials and Methods

A total of 67 sonography-guided biopsies were performed on 58 patients (37 men and 21 women) experiencing posttransplantation deterioration in renal function (seven patients had two biopsies and one patient had three biopsies). The patients studied were limited to those who had biopsies within 3 months of transplantation. At the time of biopsy, 53 patients undergoing 61 biopsies were on a cyclosporine-a-steroid regimen, and four were on an azathioprine-steroid regimen. One patient who underwent two biopsies had an interval change in immunosuppressive regimen. The serum creatinine at the time of biopsy ranged between 1.0 and 15.4 mg/dl. There were 43 cadaver renal transplants and 15 living, related transplants.

All patients were studied with high-resolution, electronically focused linear-array, real-time units (GE RT 3000, Picker LS 5000, Acuson 128). The sonograms were graded by one author. Each criterion useful in the discrimination of normal allografts (Fig. 1) from those with rejection or other causes of posttransplantation hypofunction were graded as present or absent. These features included swelling of the allograft, increased medullary pyramid conspicuity, medullary pyramid enlargement, decreased renal-sinus fat, and pelvi-infundibular thickening (Fig. 2). If at least one feature was present, the diagnosis of rejection was made without knowledge of the biopsy results. Sonograms from 10 patients randomly selected from the group were reinterpreted after 3 weeks had passed to assess intraobserver variation.

Transplant swelling was diagnosed if the anteroposterior diameter of the allograft was equal to the transverse diameter (compare Fig. 1B with Fig. 2). The medullary pyramid was judged to be enlarged if it was greater than the height of the overlying cortex (compare Fig. 1 with Figs. 2 and 3). Pelvi-infundibular thickening was judged to be present if the walls of these structures were perceptible (i.e., other than a thin echogenic margin to pelvis or infundibular fluid) (Fig. 3A). Medullary conspicuity (compare Fig. 1 with Figs. 2 and 3A) and diminution in renal-sinus fat echogenicity (compare Fig. 1 with Fig. 2) were more subjective judgments based on an experiential comparison to a normal, native kidney.

The biopsy specimens were evaluated by light microscopy, as well as immunofluorescent and electron microscopy when deemed necessary. The biopsy results were judged as normal, mild rejection, or moderate-to-severe rejection. The type of rejection was judged as either interstitial (mononuclear cells in the interstitium), or mixed (interstitial plus vascular). The specimens were also evaluated for acute tubular necrosis and recurrent or de novo glomerular disease. Cyclosporine-a nephrotoxicity was diagnosed by using the histopathologic results (absence of rejection or mild rejection) and the clinical course (improvement in renal function after decreasing the cyclosporine-a dose). Subsequently, a creatinine level of 2.5 mg/dl was randomly selected as a possible threshold level in an attempt to improve the diagnostic accuracy of sonography in distinguishing between rejection and cyclosporine-a nephrotoxicity.

Results

The pathologic diagnoses for the 67 biopsies were available for comparison with the sonographic analyses. The efficiency of sonography in the diagnosis of acute rejection was analyzed. Nine patients were excluded from the acute rejection category: five had chronic rejection, one had de novo membranous glomerulonephritis, one had recurrent focal glomerulosclerosis, and two had ureteropelvic junction obstruction. Of the remaining 58 biopsies, 51 (88%) showed histopathologic features of acute rejection. Of these, six showed mild rejection (five interstitial and one mixed rejection). Forty-five showed moderate-to-severe rejection (31 interstitial and 14 mixed rejection).

The sonographic results for diagnosing acute rejection were as follows: the accuracy of a positive prediction for rejection was 88% and the accuracy of a normal prediction was 13%. The sensitivity and specificity were 73% and 29%, respectively, and the accuracy was 72%. Because mild rejection may be clinically insignificant, patients with clinically significant histologic moderate-to-severe acute rejection were compared with patients with normal histology or mild rejection with little change in overall performance of sonography: sensitivity was 71%, specificity was 23%, and accuracy was 60%. The accuracy of a positive prediction for rejection and accuracy of a normal prediction were 76% and 19%, respectively.

Fig. 2.—Transverse sonograms of two different allografts showing virtually identical sonographic features of rejection immediately before biopsies that showed mild acute interstitial rejection in A and moderate-to-severe acute interstitial rejection in B.

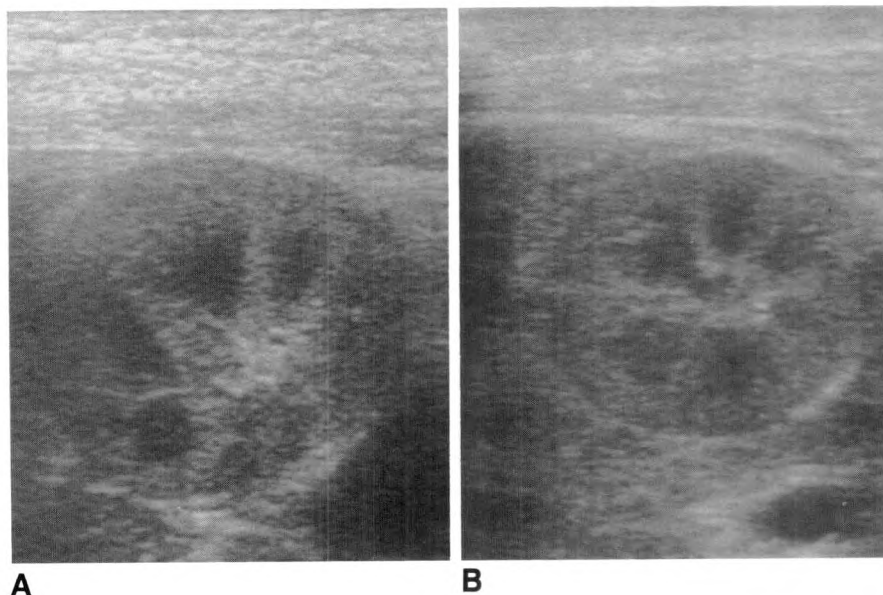
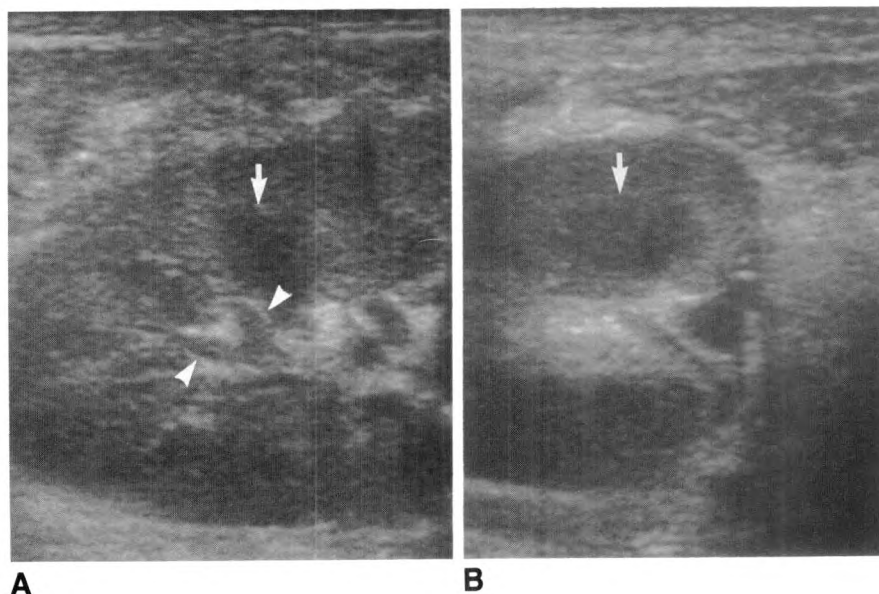


Fig. 3.—Longitudinal (A) and transverse (B) sonograms showing a renal allograft erroneously diagnosed as undergoing acute rejection. Mild swelling was observed. Infundibular walls appear thickened (arrowheads). Medullary pyramids (arrows) appear large and conspicuous.



Results of intraobserver variation performed on 10 randomly selected patients for a total of 55 judgments found that 50 judgments were consistent (91%).

In 21 patients with no sonographic findings of rejection, 14 (67%) had acute rejection. Ten of these patients had moderate rejection and three had severe rejection (Fig. 4). Sixteen patients showed multiple sonographic abnormalities (totals of 4–5 abnormalities). Twelve of these patients had moderate-to-severe acute rejection, but one patient had no rejection, and another had chronic rejection. Two patients had mild rejection.

Of seven patients with pure cyclosporine-a nephrotoxicity, five (71%) had sonographic abnormalities (Fig. 3). The creatinine values in these patients ranged from 2.2 to 3.9 mg/dl.

Fifty-one patients with acute rejection were further cate-

gorized by their creatinine level (greater or less than 2.5 mg/dl). Nine of these 51 patients (18%) were sonographically normal despite the simultaneous occurrence of acute rejection and a creatinine greater than or equal to 2.5 mg/dl. Our data did confirm that all seven patients with a creatinine level of 6.9 mg/dl or greater and acute rejection had an abnormal sonogram.

Discussion

Posttransplantation renal failure is a difficult clinical problem for which prompt and appropriate therapy is mandatory. Causes include acute or chronic rejection, cyclosporine-a nephrotoxicity, acute tubular necrosis, acute obstruction of the vascular or urinary collecting systems, de novo or recur-

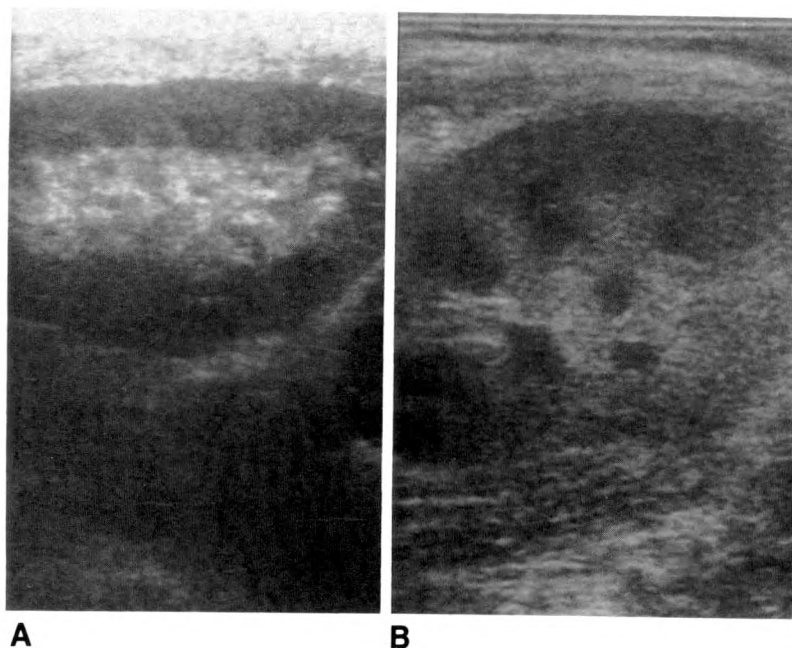


Fig. 4.—A, Longitudinal sonogram of patient interpreted as having a normal allograft but in whom biopsy showed severe rejection.

B, Another patient with features interpreted as acute rejection but in whom chronic rejection was seen histologically.

rent disease, and infection [21]. Sonography has been used extensively to predict rejection and has been considered helpful in this regard. A recent prospective study at our institution, however, examined a larger number of patients than previous studies and used immediate correlation with biopsy material [19]. This study indicated that sonography alone could not accurately exclude rejection or discriminate between the various causes of posttransplantation hypofunction with the accuracy needed to guide critical decisions. Sonography is a desirable test because it is easy to perform, results are known immediately, and it is inexpensive. The present study sought to reassess the value of sonography in a more specifically defined patient group. The previous study included a long time interval between transplantation and biopsy; furthermore, the contribution of cyclosporine-a nephrotoxicity could not be determined on the basis of data that were collected. The current study reassessed the use of sonography in the evaluation of patients a short time after transplantation and concentrated on those individuals taking cyclosporine-a.

The present study was restricted to patients who had biopsies within 3 months from transplantation. Fifty-four of the 58 patients considered were taking cyclosporine-a-steroid regimen at the time of biopsy. In this patient group, the accuracy of a positive prediction for the presence of acute rejection was 88%, if at least one abnormal sonographic feature was visible. Unfortunately, this seemingly favorable result was biased by the high prevalence of acute rejection in this group of patients, also 88%. Sensitivity was modestly high at 73%, but specificity was only 29% and the accuracy of a negative prediction was 13%. A normal sonogram did not exclude moderate-to-severe acute rejection (Fig. 4). Thirteen out of 22 patients who had negative sonography showed a positive histologic diagnosis of rejection. Five separate

sonographic features were judged. When four or five abnormal sonographic findings were present, this usually indicated the presence of acute rejection (Fig. 2) although all five sonographic findings were present in one patient without histologic evidence of rejection and in one patient with chronic rejection.

In a subgroup of seven patients with "pure" cyclosporine-a nephrotoxicity, five (71%) had sonographic abnormalities (Fig. 3). Creatinine values in these patients ranged from 2.2 to 3.9 mg/dl. An arbitrary threshold creatinine level of 2.5 mg/dl was set, but nine sonographically normal patients with acute rejection had attained this level of creatinine or more. Only at a higher threshold level for creatinine (6.9 mg/dl) was there 100% correlation between acute rejection and the presence of abnormal sonographic findings (seven of seven patients).

We speculate that there may be a lag between clinical deterioration or improvement and the sonographic findings. Posttransplantation renal biopsies may be performed at our institution at an earlier stage than at others. This could help explain discrepancies between sonographic and histopathologic findings at our institution compared to results found elsewhere.

Sonographic interpretation of some of the described features of rejection is subjective. We assessed intraobserver variation but did not address interobserver variation. However, others [22] have recently noted similar interpretations between observers in 80% of cases. We noted similar interpretations from a single observer at two different times in 90% of cases. Thus, both inter- and intraobserver interpretational variations are relatively low among experienced examiners, but still add to the potential for an erroneous or varying diagnosis in these clinically difficult patients.

Baseline and serial sonography have been advocated [22]. While we did not test this in our series, it is difficult to

agree that these additional examinations would substantially improve our results. A sonographic diagnosis of rejection in this study was based on the demonstration of any abnormal finding. Employing this concept, sensitivity was relatively good. The major failing of sonography was in specificity and accuracy of a normal prediction. Increasing sonographic surveillance may improve sensitivity but would be unlikely to alter specificity significantly.

The current study discloses that sonography cannot reliably distinguish cyclosporine-a nephrotoxicity from acute rejection. Sonography can accurately predict the presence of acute rejection in two limited circumstances. These include patients with multiple sonographic findings of rejection (16 of 61) and those with a markedly elevated creatinine (greater than 6.9 mg/dl). Unfortunately, most of our patients with cyclosporine-a nephrotoxicity had abnormal sonographic findings that could be misinterpreted as rejection. Sonography remains a valuable tool to detect obstruction or peritransplant fluid collections and can precisely localize an allograft biopsy site. However, caution should be taken when using sonography alone in the evaluation of posttransplantation hypofunction, especially when attempting to distinguish between acute rejection and cyclosporine-a nephrotoxicity.

REFERENCES

- Merrill JP, Murray JE, Harrison JR, Guild WR. Successful homotransplantation of the human kidney between identical twins. *JAMA* 1956;160:277-282
- Feduska NJ, Melzer J, Amend WJC, Vincente F, Tomlanovich S, Salvatierra O Jr. Clinical management of immunosuppressive therapy for cyclosporine-treated recipients of cadaver kidney transplants at one to six months. Presented at the clinical management of the renal transplant recipient with cyclosporine conference, Palm Beach, FL, November 1985
- Feduska NJ, Melzer J, Amend WJC, Vincente F, Salvatierra O Jr. Analysis of some factors which might affect the outcome for cadaveric kidney transplants in cyclosporine-treated patients. Presented at the international symposium on organ procurement, Detroit, MI, October 1985
- Koehler PR, Kanemoto HH, Maxwell JG. Ultrasonic "B" scanning in the diagnosis of complications in renal transplant patients. *Radiology* 1976;119:661-664
- Bartrum RJ Jr, Smith EH, D'Orsi CJ, Tilney NL, Dantonio J. Evaluation of renal transplants with ultrasound. *Radiology* 1976;118:405-410
- Maklad NF, Wright CH, Rosenthal SJ. Gray scale ultrasonic appearances of renal transplant rejection. *Radiology* 1979;131:711-717
- Hricak H, Cruz C, Eyler WR, Madrazo BL, Romanski R, Sandler MA. Acute post-transplantation renal failure: differential diagnosis by ultrasound. *Radiology* 1981;139:441-449
- Hricak H, Romanski RN, Eyler WR. The renal sinus during allograft rejection: sonographic and histopathologic findings. *Radiology* 1982;142:693-699
- Fried AM, Woodring JH, Loh FK, Lucas BA, Kryscio RJ. The medullary pyramid index: an objective assessment of prominence in renal transplant rejection. *Radiology* 1983;149:787-791
- Slovic TL, Babcock DS, Hricak H, et al. Renal transplant rejection: sonographic evaluation in children. *Radiology* 1984;153:659-665
- Singh A, Cohen WN. Renal allograft rejection: sonography and scintigraphy. *AJR* 1980;135:73-77
- Fuld IL, Matalon TA, Vogelzang RL, et al. Dynamic CT in the evaluation of physiologic status of renal transplants. *AJR* 1984;142:1157-1160
- Berland LL, Lawson TL, Adams MB, Melrose BL, Foley WD. Evaluation of renal transplants with pulsed Doppler duplex sonography. *J Ultrasound Med* 1982;1:215-222
- Hricak H, Englestad B, Feduska NJ, et al. Imaging of acute post-transplant renal failure: comparison of quantitative scintigraphy, ultrasonography and magnetic resonance. *Radiology* (in press)
- Feduska NJ, Terrier F, Vincente F, et al. Evaluation of acute renal transplant rejection and cyclosporine nephrotoxicity by magnetic resonance imaging. *Transplant Proc* 1985;XVII(6):2597-2599
- Hricak H, Terrier F, Demas B. Magnetic resonance imaging in the evaluation of renal allografts. Presented at the scientific assembly and annual meeting of the Radiological Society of North America, Washington, DC, November 1984
- Hricak H, Cruz C, Eyler WR, Madrazo BL, Sandler MA. Post-transplant renal failure: differential diagnosis by ultrasound: experimental and clinical observations. *Medical Ultrasound* 1982;6:1-10
- Hricak H, Toledo-Pereyra LH, Eyler WR, Madrazo BL, Zammit M. The role of ultrasound in the diagnosis of kidney allograft rejection. *Radiology* 1979;132:667-672
- Hoddick W, Backman U, Filly RA, et al. Ultrasound evaluation of renal allograft rejection. *Radiology* (in press)
- Klintmalm G, Bergstrand O, Ringden O, et al. Graft biopsy for the differentiation between nephrotoxicity and rejection in cyclosporin-a-treated renal transplant recipients. *Transplant Proc* 1983;XV(1):493-496
- Potter JL, Sullivan BM, Flournoy JG, Gerza C. Emphysema in the renal allograft. *Radiology* 1985;155:51-52
- Raiss GH, Bree FL, Schwab RE, et al. Further observations in the ultrasound evaluation of renal allograft rejection. *J Ultrasound Med* 1986;5:439-444

Book Review

Abdominal Imaging: An Introduction. By Mathis Frick and Samuel Feinberg. Chicago: Year Book Medical, 233 pp., 1986

Some books are a delight to read; the sentences flow smoothly and thoughts merge gently together. Other books are turgid and slow; thoughts are jumbled and unclear. The mind balks at reading such leaden prose. Unfortunately, *Abdominal Imaging* falls into the latter category. In the space of 233 pages, its authors attempt to examine the abdomen with sonography, CT, nuclear medicine, and conventional barium studies. Urography is not included, although imaging of the retroperitoneum is discussed in chapters on CT and sonography.

The book begins with the obligatory chapter on the physics of imaging, but the writing is so incomprehensible that one soon skips over to the second chapter, looking for relief. This section, "Selecting an Imaging Modality," along with further sections on plain radiography, CT, and abdominal sonography are difficult to read because the writing is choppy and the author spews out facts as though he were presenting an outline in paragraph form. This style does not lend itself to clarity. Important topics are covered only cursorily. For example, hepatomas get only two sentences: one states that the appearance of hepatomas varies and the other says that they sometimes calcify. Also, the illustrations are too few for the amount of

material covered, and those that are present need arrows to point out salient features.

A long cookbook chapter discusses contrast studies of the gut, and another (the longest chapter in the book, 62 pages) concerns interpretation of them. In contrast, the chapter on nuclear radiology is well written, concise, and informative. The last chapter, on interventional radiology, is too brief to be of any use. As if for a gift, however, this chapter also throws in some vascular interventional radiology, interventional urology, and transluminal angioplasty of peripheral vascular disease.

It's difficult to find anything to praise in this mercifully short book. Practicing radiologists will consider it too brief to be useful, as will radiology residents. Medical students and physicians in fields other than radiology will have neither the time nor the inclination to plod through this melange of facts.

Peter C. Meyers
LSU Medical Center
Shreveport, LA 71130-3932

Needle Puncture of Cystic Renal Masses: A Survey of the Society of Uroradiology

Edward S. Amis, Jr.¹
John J. Cronan²
Richard C. Pfister³

A survey of 114 members of the Society of Uroradiology provided data on the results of needle punctures of cystic renal masses in approximately 16,000 cases. The 73 respondents reported that cyst puncture is currently performed only for specific indications, that opacification is only occasionally performed after puncture, and that cytology is the laboratory procedure of choice for aspirated fluid. While all respondents accepted sonographic confirmation of cysts seen on nephrotomography, only 92% accepted sonography alone as diagnostic, compared to 100% for CT alone. Aspiration of clear fluid (usually an indicator of benignity) with positive or negative cytology, occurred in 19 cystic renal malignancies. Thus, gross and laboratory characteristics of aspirated fluid are not conclusive in diagnosing cystic lesions. CT should be the final arbiter in suspicious lesions.

Renal cyst puncture, once considered necessary to establish the diagnosis of simple renal cyst, has in recent years been used less frequently because of the availability of more sophisticated imaging techniques. Recently, Bosniak [1] reported that the procedure is performed less than 10 times per year in many uroradiologic practices. Specific indications include diagnosis of an infected cyst, diagnosis of lesions that might be malignant in poor-risk patients, therapy of painful or obstructing cysts, and lesions considered indeterminate on CT and sonography. Nonetheless, differences of opinion remain about the indications for the procedure, opacification of the punctured cyst, the significance of clear cyst fluid, and the laboratory studies that should be performed on the aspirate.

Subjects and Methods

A questionnaire was mailed to the 114 members of the Society of Uroradiology. These radiologists spend most of their professional time in the practice of this subspecialty. Seventy-three (64%) responded, providing data on the use of needle cyst puncture in approximately 16,000 cases.

Results

Results of the survey (Table 1) indicate that renal cyst puncture is no longer a routine diagnostic procedure. Most respondents do, however, occasionally use needle aspiration to resolve conflicting imaging results. Of the common imaging techniques used in evaluating cystic renal lesions, only CT is considered by all respondents to provide unquestionable evidence for diagnosing a simple cyst. One-fifth of respondents confidently diagnose a simple renal cyst by nephrotomography alone, although most noted that the nephrotomography must be of high quality and all criteria for simple cyst must be met. All respondents, however, accept nephrotomographic findings confirmed by sonography as diagnostic of simple cyst. With reference to cyst fluid, almost one-fourth of respondents claimed to dispose

Received July 7, 1986; accepted after revision September 4, 1986.

The opinions and assertions expressed are the private ones of the authors and are not to be construed as official or reflecting the views of the Navy Department, the Naval Service at large, or the Department of Defense.

Presented at the Society of Uroradiology scientific session, The Hague, Holland, May 1986.

¹ Department of Radiology, Naval Hospital, Bethesda, MD 20814. Address reprint requests to E. S. Amis, Jr.

² Department of Radiology, Rhode Island Hospital, Providence, RI 02902.

³ Department of Radiology, Massachusetts General Hospital, Boston, MA 02114.

AJR 148:297-299, February 1987
0361-803X/87/1482-0297

Table 1: Responses to Questionnaire

1.	Given current state-of-the-art imaging, for what reasons would you perform renal cyst puncture?	
	Conflicting results on two or more techniques	92%
	Symptomatic patient (e.g., pain, hematuria)	58%
	Ablation or drainage of obstructive cyst	78%
	Routine	0%
2.	Are you comfortable diagnosing a simple renal cyst if it meets all the criteria for a cyst on:	
	Nephrotomography alone?	20%
	Sonography alone?	92%
	CT alone?	100%
3.	If nephrotomography reveals a classic renal cyst, and sonography is confirmatory, do you still perform diagnostic cyst puncture?	
	Yes	0%
	No	100%
4.	If you performed a cyst puncture that yielded completely clear fluid (colorless or straw color), do you feel comfortable in disposing of the fluid rather than sending it for laboratory tests?	
	Yes	23%
	No	77%
5.	Do you routinely inject contrast material and perform a radiographic evaluation of the cyst wall? ^a	
	Always	32%
	Sometimes	42%
	If there is cloudy or bloody fluid	23%
	Never	12%
6.	For what laboratory tests (if any) do you routinely submit the cyst fluid?	
	Cytology	92%
	Culture	23%
	Lipid	22%
	Lactate dehydrogenase (LDH)	23%
	Glucose	10%
7.	Have you ever submitted completely clear fluid for laboratory studies in which the results of any or all of the studies were positive?	
	Cytology	11 cases
	Lactate dehydrogenase (LDH)	1 case
	Lipid	1 case
	Protein	1 case
8.	Have you ever aspirated completely clear fluid from a renal-cell carcinoma (cystic or necrotic)?	
	Yes	19 cases
9.	Have positive laboratory test results performed on completely clear aspirated fluid been the deciding factor in diagnosing as malignant a renal mass that was by IV urogram/sonogram criteria a simple cyst?	
	Yes	3 cases ^b

Note.—73 of 114 members of the Society of Uroradiology responded to this questionnaire.

^a Some overlap occurred in answers to this question.

^b CT was not reported as having been performed in these cases.

of completely clear fluid rather than sending it for laboratory tests.

Only one-third of respondents routinely opacify a cystic lesion with contrast medium (cystography) after aspiration of fluid. Most respondents indicated that this study is performed only when other factors are involved, such as cloudy or bloody fluid. In cases when aspirated fluid was submitted to the laboratory for evaluation, most (92%) respondents routinely ordered cytology, while less than one-fourth ordered any other studies such as culture, lipids, lactate dehydrogenase, glucose, or protein.

Aspiration of completely clear fluid (colorless or straw color) from a lesion has generally been thought to argue for benignity. Yet 14 cases were reported as having positive laboratory results on clear fluid (Table 1). Of these, seven had imaging

evidence of their malignancy, including a mural nodule on cystography, calcification in the wall, or inconclusive CT or sonogram studies. Of the remaining seven cases, four were benign and three malignant. In the three malignant lesions, respondents reported no positive imaging evidence, although CT was not performed in these cases. In the 19 reported cases (Table 1) in which clear fluid (with or without positive laboratory findings) was aspirated from a cystic or necrotic renal-cell carcinoma, or in which renal-cell carcinoma was found in the wall of the cyst, 16 cases had suspicious imaging results. The three remaining cases are the same as those previously mentioned, in which positive aspirates were the only indicator of the malignant nature of the lesion (CT had not been performed). Had CT been obtained, it probably would have suggested malignancy.

Discussion

A review of the literature confirms the survey results, indicating that clear fluid may occasionally be found in cases of cystic or necrotic renal-cell carcinomas, as well as when renal-cell carcinoma occurs in the wall of a cyst [2-11]. Some of these reports [6-11] indicate that not only may the fluid be clear, but cytologic studies on the aspirate may be negative. Sufrin et al. [12] reported the cytopathologic study of cyst aspirate to be normal in 50% of cysts containing wall tumors. Conversely, false-positive cytologies have been found in benign renal cystic lesions [7, 10]. Moreover, bloody renal-cyst aspirate may yield negative cytologies in cases of cystic renal malignancies [13]. It can, therefore, be concluded that, although the gross and laboratory characteristics of fluid aspirated from cystic renal masses can suggest the nature of the lesion, they are not conclusively diagnostic.

The results of this study and the current literature [14] support CT as the gold standard in evaluating cystic masses in the kidney. Novetsky et al. [15] reported a case in which CT diagnosed a renal-cell carcinoma in the wall of the cyst. They concluded that CT should be mandatory in all cases in which there is any clinical or radiologic suspicion of the malignancy of an apparent renal cyst. Another caveat is early infection developing in an existing renal cyst. In such a case, all CT criteria for simple cyst may be met, and yet the clinical presentation of fever and/or flank pain should lead to the correct diagnosis. Confusion also surrounds the issue of a hyperdense renal cyst, for which all criteria for simple cyst are met except for a high attenuation value. Cyst puncture is recommended as an integral part of the workup in hyperdense cysts if the internal contents are fluid and, thus, subject to aspiration [16].

In summary, CT should be the final arbiter in establishing the diagnosis of cystic lesions of the kidney. Abnormalities other than hyperdensity of the cyst contents are probably an indication for surgery. Cyst puncture and aspiration are indicated in the obstructing cyst, in the hyperdense cyst seen on CT, and in cases of suspicion of an early infection within an existing renal cyst. Cyst puncture is also frequently used to resolve conflict between two imaging techniques, although suspicious CT findings should weigh heavily in favor of sur-

gical exploration. Cystography should be performed if warranted by a positive clinical history or aspiration of cloudy or bloody fluid. Further, cytology is the laboratory test of choice for fluid aspirated during puncture, even if the fluid is totally clear, remembering that false positives and false negatives may occasionally occur.

Cyst puncture does have an accuracy in excess of 99%. Rather than exclude it entirely, recognition of its indications and shortcomings should allow it to remain in the diagnostic repertoire of the radiologist.

REFERENCES

1. Bosniak MA. The current radiological approach to renal cysts. *Radiology* 1986;158:1-10
2. Brannan W, Miller W, Crisler M. Coexistence of renal neoplasms and renal cyst. *South Med J* 1962;55:749-752
3. Khorsand D. Carcinoma within solitary cysts. *J Urol* 1965;93:440-444
4. Kleist H, Jonsson O, Lundstam S, Naucler J, Nilsson AE, Pettersson S. Quantitative lipid analysis in the differential diagnosis of cystic renal lesions. *Br J Urol* 1982;54:441-445
5. Parienty RA, Pradel J, Parienty I. Cystic renal cancers: CT characteristics. *Radiology* 1985;157:741-744
6. Ambrose SS, Lewis EL, O'Brien DP III, Walton KN, Ross JR. Unsuspected renal tumors associated with renal cysts. *J Urol* 1977;117:704-707
7. Curry NS, Reinig J, Schabel SI, Ross P, Vujic I, Gobien RP. An evaluation of the effectiveness of CT vs. other imaging modalities in the diagnosis of atypical renal masses. *Invest Radiol* 1984;19:447-452
8. Curry NS, Schabel SI, Betsill WL Jr. Small renal neoplasms: diagnostic imaging, pathologic features, and clinical course. *Radiology* 1984;158:113-117
9. Ekelund L, Karp W. Evaluation of solitary renal cystic lesions. *Acta Radiol [Diagn] (Stockh)* 1978;19(fasc 2):321-328
10. Marshall FF. The role of selective exploration in ambiguous renal cystic lesions. *Urol Clin North Am* 1980;7:689-695
11. Murphy JB, Marshall FF. Renal cyst versus tumor: a continuing dilemma. *J Urol* 1980;123:566-569
12. Sufrin G, Etra W, Gaeta J, Merrin CE. Hypernephroma arising in wall of simple renal cyst. *Urology* 1975;6:507-510
13. Harris RD, Goergen TG, Talner LB. The bloody renal cyst aspirate: a diagnostic dilemma. *J Urol* 1975;114:832-835
14. McClennan BL, Stanley RJ, Melson GL, Levitt RG, Sagel SS. CT of the renal cyst: is cyst aspiration necessary? *AJR* 1979;133:671-675
15. Novetsky GJ, Berlin L, Epstein AJ, Lobo N, Miller SH. CT diagnosis of renal cyst wall tumor. *J Comput Assist Tomogr* 1983;7:539-540
16. Coleman BG, Arger PH, Mintz MC, Pollack HM, Banner MP. Hyper-dense renal masses: a computed tomographic dilemma. *AJR* 1984;143:291-294

Book Review



Cardiac Imaging. New Techniques and Clinical Applications Edited by Morris N. Kotler and Robert M. Steiner. Philadelphia: F. A. Davis, 454 pp., 1986. \$85

Many new imaging technologies developed over the past few years now have become incorporated into the daily practice of cardiac diagnosis. While previous reviews have focused on the engineering aspects of these machines, this book is one of the first to review the burgeoning literature of clinical application in humans. In general, the writing is succinct, and the pictures and graphs are excellent. There are also six color figures in the chapters concerning single-photon emission CT, thallium techniques, scintigraphic quantitation of ejection fraction, and Doppler color-coded flow mapping.

In tune with the current controversies between functional and anatomic assessment of cardiac lesions, the first half of the book compares each imaging technique with its physiologic counterpart and not only gives an extensive literature review but also supplies practical indications and limitations of each technique. Several chapters on Doppler sonography discuss the detection and quantitation of stenotic and regurgitant valvular lesions, methods for calculating cardiac output and shunts, and the correlation with nonimaging techniques. A fascinating chapter on the application of Doppler technology to the coronary circulation points out the limitations of the "gold-standard" coronary arteriogram in the determination of the hemodynamic significance of the moderate coronary stenosis. The

functional assessment section ends with chapters on MR imaging and spectroscopy, emission tomography as contrasted with planar imaging, and the use of a computer for imaging analysis.

The last half of the book describes the clinical assessment of a number of cardiac diseases with emphasis on the multiple-imaging technique approach to cardiac diagnosis. Topics include the value of two-dimensional echocardiography in evaluating valvular heart lesions and valve prostheses, nuclear techniques in patient with angina, Doppler echocardiography for the diagnosis of congenital heart disease, high-speed CT, and digital vascular imaging. Multitechnique approaches to aortic dissection and the pericardium conclude this volume.

As is evident from the list of topics, this book is not an introduction to cardiac imaging and is not meant to be comprehensive, as it excludes the plain chest film and angiography. However, for the radiologist or cardiologist with some experience in imaging, this book is one of the best current reviews, particularly in the application of two-dimensional and Doppler echocardiography.

Stephen W. Miller
Massachusetts General Hospital
Boston, MA 02114

Interstitial Emphysema Associated with Epidural Anesthesia for Extracorporeal Shock-Wave Lithotripsy

Michael C. Roberts¹
Howard M. Pollack¹
Marc P. Banner¹
Angelina D. Castro²
Keith N. VanArsdalen³

Interstitial emphysema was noted on abdominal radiographs in 38 (15%) of the first 150 patients treated by extracorporeal shock-wave lithotripsy at our hospital. All 38 patients had undergone successful or attempted epidural anesthesia for the lithotripsy. This finding was not seen in any patient who had not undergone epidural puncture. The emphysema is the result of the introduction of air into the paraspinal and back muscles or subcutaneous tissues during attempted or actual puncture of the epidural space. This air was apparent on abdominal radiographs taken after lumbar puncture in 38 (23%) of 167 patients who underwent attempted or actual puncture of the epidural space. The emphysema decreases over the ensuing days, is of no clinical significance, and bears no direct relationship to extracorporeal shock-wave lithotripsy. This finding should not be mistaken for emphysema caused by gas-producing or gas-containing retroperitoneal diseases.

Extracorporeal shock-wave lithotripsy (ESWL) is becoming widely available as the preferred method of treating most renal and upper ureteral calculi [1]. Patients so treated are monitored radiologically with a series of abdominal radiographs taken 1 or more days after treatment. The presence of interstitial emphysema in the paravertebral soft tissues on the plain films of several patients treated with ESWL at our hospital prompted us to do a retrospective review of the first 260 patients undergoing the procedure. We attempted to determine the cause of the emphysema and its clinical significance.

Materials and Methods

Two hundred fifty patients were hospitalized and had either epidural (149), spinal (45), or general (56) anesthesia for ESWL. Eighteen of the 101 patients in the latter two groups had undergone prior unsuccessful puncture of the epidural space before receiving either spinal or general anesthesia. Thus, 167 of 250 patients underwent successful or attempted epidural puncture. Ten other patients in whom all of the abdominal radiographs obtained before and after ESWL could not be located and were excluded from the study. The abdominal films in the 250 patients were analyzed retrospectively.

Each patient had an abdominal radiograph within 18 hr before induction of anesthesia to ascertain the location of the stone or stones to be treated. Additional abdominal films were obtained 1 and 2 days after ESWL to determine the adequacy of stone disintegration and to monitor the passage of stone fragments.

Pre- and post-ESWL abdominal radiographs were reviewed retrospectively without knowledge of the type of anesthesia received by the patient. Clinical and anesthetic records and subsequent radiographs were reviewed in those patients whose initial radiographs after ESWL displayed paravertebral interstitial emphysema. Excretory urograms performed 4–6 weeks later to evaluate the status of the urinary tract were available for review in 23 of the 38 patients with interstitial emphysema. CT scans obtained as part of an independent investigation were also available for review in 22 patients.

Received June 6, 1986; accepted after revision September 19, 1986.

Presented at the annual meeting of the American Roentgen Ray Society, Washington, DC, April 1986.

¹ Department of Radiology, University of Pennsylvania School of Medicine and Hospital, 3400 Spruce St., Philadelphia, PA 19104. Address reprint requests to H. M. Pollack.

² Department of Anesthesia, University of Pennsylvania School of Medicine and Hospital, 3400 Spruce St., Philadelphia, PA 19104.

³ Division of Urology, University of Pennsylvania School of Medicine and Hospital, 3400 Spruce St., Philadelphia, PA 19104.

AJR 148:301–304, February 1987
0361–803X/87/1482–0301
© American Roentgen Ray Society

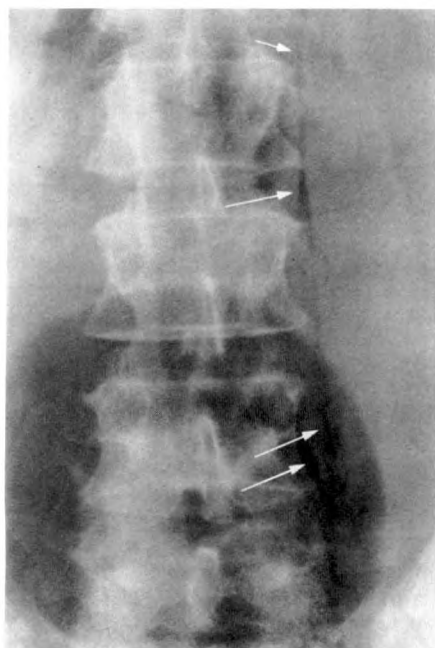
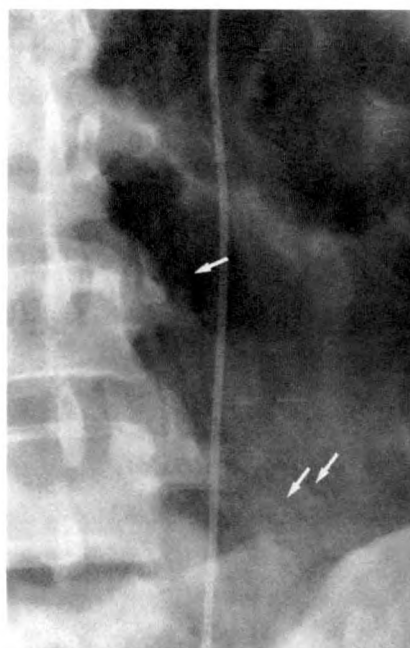
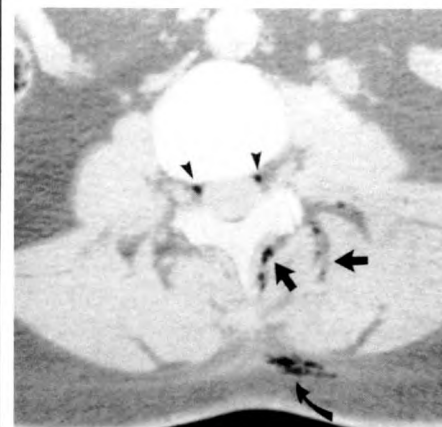


Fig. 1.—Plain abdominal radiograph 1 day after extracorporeal shock-wave lithotripsy with epidural anesthesia shows paraspinal emphysema (arrows) on left side of spine. This was no longer present at excretory urography 1 month later.



A



B

Fig. 2.—A, Plain abdominal radiograph of obese middle-aged woman 1 day after extracorporeal shock-wave lithotripsy with epidural anesthesia. Interstitial air is evident (arrows). Left ureteral catheter is in place.

B, CT scan later the same day shows gas in subcutaneous tissues (curved arrow), in fat planes between paraspinal muscles (straight arrows), and in epidural space itself (arrowheads). No gas is seen in retroperitoneum. Scan has been windowed to clearly distinguish gas from fat and soft-tissue density. The patient was discharged 1 day later and had an uneventful clinical course.

Results

Thirty-eight patients (15% of 250; 22 men and 16 women) exhibited abnormal gas collections on abdominal films obtained the day after ESWL (Fig. 1). The abnormality consisted of linear or crescentic radiolucencies adjacent to the spine or paraspinal muscles. These radiolucencies extended from as high as the first lumbar vertebral body to as low as the first sacral segment. The gas collections ranged in appearance from a single, distinct, unilateral radiolucent line to multiple bilateral asymmetric streaks with the predominant appearance that of several unilateral streaks. Thirty-one cases were unilateral, and seven were bilateral. There was no predilection for the right or left side, nor was there any correlation between the side of the gas collection and the location of the stone being treated with ESWL. In three patients the emphysema was noted only directly over the lumbar spine.

The emphysema decreased or disappeared rapidly. Gas was no longer apparent in seven patients by the second day after ESWL and had diminished in amount in almost all 38 during this period. It never increased in extent. Subsequent abdominal radiography in four patients 3, 5, 6, and 7 days after ESWL, respectively, failed to show the gas. A fifth patient who had minimal residual gas on a radiograph 9 days after ESWL had no emphysema by the time a subsequent urogram was obtained 5 weeks later. No abnormal gas collections

were evident at the time of follow-up excretory urography 4–6 weeks after ESWL.

CT scans 24–36 hr after ESWL clearly showed in four patients that the abnormal gas collections were located in subcutaneous fat and paraspinal muscles (interstitial emphysema) but not in the peritoneal or extraperitoneal spaces (Figs. 2 and 3). Gas collections overlying the vertebral column were more easily identified on CT than on plain radiographs.

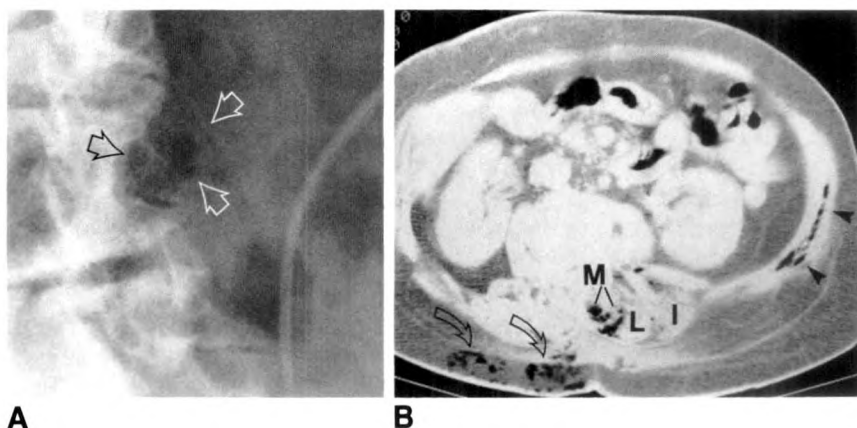
All 38 patients who had emphysema had undergone successful or attempted puncture of the epidural space as part of their anesthesia for ESWL. They represented 15% (38/250) of the treated population and 23% (38/167) of the group who had undergone successful or attempted epidural puncture. Epidural anesthesia was successfully completed in 149 of 167 patients in whom it was attempted. The other 18 patients in whom localization of the epidural space was unsuccessful subsequently received spinal or general anesthesia. The gas collections herein described were not seen in patients who had received spinal or general anesthesia, unless the epidural route had been attempted first.

In five patients who had ureteral catheterization under epidural anesthesia before ESWL, the emphysema was evident on abdominal films exposed before ESWL, thereby confirming that ESWL did not contribute to the abnormal gas collections.

The presence of interstitial emphysema appeared to be

Fig. 3.—A, Plain abdominal radiograph after extracorporeal shock-wave lithotripsy with epidural anesthesia shows unilateral paraspinal streaks of gas (arrows) adjacent to second and third lumbar vertebrae in obese patient in whom localization of epidural space was difficult. Left ureteral catheter is in place.

B, CT scan shows air in subcutaneous tissues (arrows) as well as within and in between multifidus (M), longissimus thoracis (L), and iliocostalis lumborum (I) muscles. Air has dissected laterally into muscles of abdominal wall (arrowheads).



unrelated to the patient's clinical course and was asymptomatic. Thirty-two of the 38 patients had an uneventful hospital course and were discharged on the second or third day after the procedure. In six patients whose ureters were obstructed by stone fragments, symptoms were relieved either with spontaneous passage of fragments or with treatment.

Discussion

ESWL as performed by the Dornier lithotripter uses focused hydrodynamic pressure waves to pulverize renal and proximal ureteral calculi [1]. The shock waves, transmitted through a water bath in which the patient is immersed, produce a painful slapping sensation at the skin entry site and, to a lesser degree, at the exit site. As the number of shock waves needed to achieve in situ calculus pulverization usually ranges from 1000 to 2000, some form of anesthesia is necessary to minimize patient motion, thereby keeping the calculus within the area of maximal shock-wave impact. Epidural anesthesia is currently the preferred method of achieving these goals and was successful in 149 (60%) of our first 250 patients. Spinal or general anesthesia, used in the other 40% of patients, was used when the epidural route was not possible, if patients preferred to be asleep during ESWL, or if rigid control of cardiac output was necessary because of preexisting medical conditions.

The findings in the patients studied establish the association between gas in the subcutaneous tissues of the back and back muscles with attempted or actual puncture of the epidural space. All 38 patients who exhibited this form of emphysema had undergone prior epidural puncture. None of the patients who received only spinal or general anesthesia for ESWL exhibited emphysema on subsequent abdominal radiographs. The presence of emphysema on radiographs obtained after administration of epidural anesthesia and before ESWL (as in those patients who underwent pretreatment cystoscopic placement of a ureteral catheter under epidural anesthesia) further validates its relationship to epidural puncture and precludes any association with ESWL itself. Similarly, the lack of correlation between the side of the stone treated with ESWL and the location of the gas further nullifies any causal relationship between the two.

An appreciation of the technique of epidural puncture fur-

ther clarifies this association. In contrast to spinal anesthesia where the appearance of CSF at the hub of the lumbar puncture needle attests to proper needle placement in the subarachnoid space, entry into the epidural space is detected by a sudden loss of resistance. This is facilitated by applying constant or intermittent positive pressure on the plunger of an air-filled glass syringe attached to the puncture needle. There is resistance to the injection of air until the tip of the needle enters the epidural space, at which time air is either pulled into the epidural space by the negative pressure in that space or pushed in with almost no resistance, thus signifying proper needle placement. The pressure placed on the syringe during needle insertion may deposit air in the paraspinal or back muscles or subcutaneous tissues of the back. In patients in whom localization is difficult, such as in those who are uncooperative, as much as 20 cm³ of air may be injected into the subcutaneous tissues and muscles during the search for the epidural space. In patients in whom localization is not difficult, less than 1 cm³ of air may be injected.

If of sufficient quantity, the injected air is apparent on abdominal films as streaky, linear, or crescentic gas lucencies overlying or, more often, paralleling either the spine or the paraspinal muscles. It is most often apparent on kidney/urinary/bladder films obtained 1 day after epidural anesthesia for ESWL, diminishes over a period of days, and is often not apparent by the second or third postanesthesia day. Follow-up urograms 4–6 weeks after ESWL failed to show residual interstitial emphysema in the 23 patients who returned for urography.

Retroperitoneal gas usually appears either mottled and bubbly or linear and crescentic [2]. The bubbly pattern is seen most often in the anterior paranephric or perinephric spaces and is most often related to necrotizing pancreatitis or perforation of retroperitoneal portions of the alimentary tract. Perinephric gas originates either from a gas-producing infection, often involving the kidneys, or from perforation of a hollow viscus with secondary involvement of the perinephric space caused by rupture of fascial planes. Posterior paranephric-space gas usually appears linear or curvilinear and most often originates from alimentary tract perforation (including the rectum) or from the mediastinum and pleural space, as in patients with extraalveolar air secondary to positive-

pressure ventilation. Most of these causes result in gas on both sides of the spine, often extending to the flank and, in many cases, on both sides of the diaphragm. Unilateral gas in the posterior paranephric space is most often due to perforation of the duodenum or ascending colon on the right and descending or sigmoid colon on the left [2]. The latter are the diseases that most closely simulate the form of interstitial emphysema reported herein.

Differentiation between air in the subcutaneous tissues and back muscles and retroperitoneal gas requires clinical correlation. Patients with retroperitoneal gas are more likely to be acutely ill than those who had recently undergone ESWL. The latter are either asymptomatic or have ureteral colic as they pass stone fragments. Interstitial emphysema associated with epidural anesthesia diminishes in extent over a short period of time (usually 1 or 2 days) without treatment, whereas other forms of emphysema either increase in amount over time if the underlying cause of the gas is inadequately or not treated, or diminish more slowly (e.g., the air that remains for up to 12 days after retroperitoneal surgery such as nephrectomy [3]).

Heretofore, abdominal radiographs were seldom obtained

in patients shortly after epidural anesthesia. Therefore, radiologists may be unfamiliar with the appearance of interstitial emphysema in this location and may attribute it to more ominous disease. Weissman et al. [4] reported three cases of "factitious retroperitoneal gas" after epidural anesthesia and suggested use of oblique and lateral projections to confirm the interstitial location of the gas. Although the precise distribution and extent of the gas can be better characterized by CT, plain abdominal radiographs and the knowledge that the patient has recently undergone epidural anesthesia usually permit confident diagnosis of this interstitial emphysema.

REFERENCES

1. Chaussy C, Schmiedt E. Extracorporeal shock wave lithotripsy (ESWL) for kidney stones. An alternative to surgery? *Urol Radiol* 1984;6:80-87
2. Han SY, Tishler JM, Aldrete JS. Extraperitoneal gas: compartmental localization and identification of source. *J Can Assoc Radiol* 1985;36:17-21
3. Older RA, Rice RP, Kelvin FM, Thompson WM, Weinerth JL. Extraperitoneal gas following nephrectomy: patterns and duration. *J Urol* 1978;120:24-27
4. Weissman B, Van Houten FX, Smith EH. Factitious retroperitoneal emphysema due to attempted epidural anesthesia. *Radiology* 1973;107:345-347

Case Report

Polyorchidism: Evaluation by MR

Lori L. Baker,¹ Paul C. Hajek,¹ Thomas K. Burkhard,² and Robert F. Mattrey¹

Polyorchidism (testicular duplication) is a rare congenital anomaly of the genitourinary tract. Ahlfeld [1] is credited with the first histologically confirmed description in 1880, and Lane [2] reported the first case found at surgery in 1895. Subsequent reports of supernumerary testicles have involved cases of triorchidism [3], with the exception of one patient with bilateral duplication [4].

With the advent of high-resolution sonography, accurate assessment of polyorchidism before surgery is possible in certain cases [5]. We report a case in which MR imaging was successfully used to detect bilateral polyorchidism.

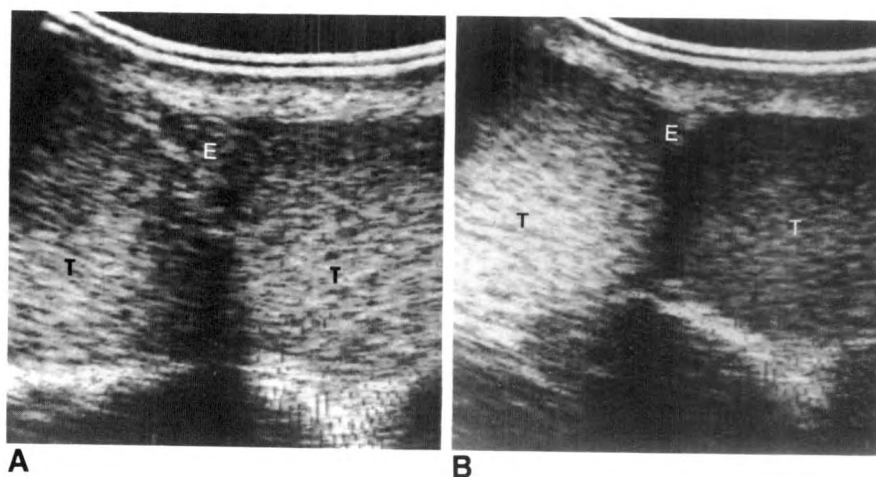
Case Report

A 41-year-old man, father of two children, presented with a mass of long-standing duration in each hemiscrotum. He was otherwise asymptomatic and denied any history of trauma or scrotal disease.

Physical examination confirmed the presence of oval-shaped masses in each hemiscrotum that were loosely connected to the two normal testes. One epididymis could be palpated on each side. Transillumination excluded cystic lesions. On thermography, the temperature of the masses was similar to that of the testes.

Sonography showed two smoothly margined, oval-shaped homogeneous structures in each hemiscrotum (Fig. 1) with patterns

Fig. 1.—Longitudinal sonograms of left (A) and right (B) hemiscrotum showing two testicles (T) on each side and a single epididymis (E). One of the testicles on the right is hypoechoic for an unknown reason.



Received June 26, 1986; accepted after revision September 4, 1986.

P. C. Hajek is a recipient of Erwin Schroedinger Stipendium Fellowship award J0062, Austria. R. F. Mattrey is a recipient of Physician-Investigator award K08-CA00940 from the National Cancer Institute.

¹ Department of Radiology, University of California, San Diego, Medical Center, San Diego, CA 92103 and The Magnetic Resonance Imaging Institute, 410 Dickinson St., San Diego, CA 92103. Address reprint requests to R. F. Mattrey at the Magnetic Resonance Imaging Institute.

² Department of Radiology, Naval Hospital, San Diego, CA 92134.

AJR 148:305-306, February 1987 0361-803X/87/1482-0305 © American Roentgen Ray Society

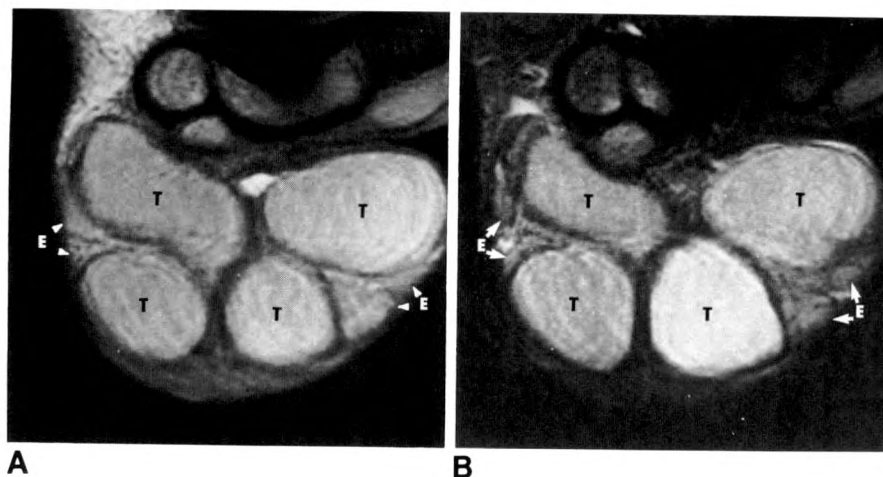


Fig. 2.—MR scan (coronal section) made at slightly different levels. (A), TR = 2000, TE = 25; (B), TR = 2000, TE = 70. Four testicles (T) are present. A separate epididymis (E) is seen for each testis. Higher signal intensity of left lower testis is due to more optimal positioning relative to surface coil.

that were similar to those of normal testes. The lower right testis was less echogenic than the upper testis. This finding decreased the confidence in the diagnosis of bilateral duplication. A single epididymis could be seen on each side.

MR was performed on a 1.5-T system with a 12.5-cm circular surface coil (General Electric, Milwaukee, WI). The imaging parameters used were TR = 2000 msec, TE = 25 and 70 msec, 256 × 256 data acquisition matrix, 16-cm field of view, two excitations, 3-mm slice thickness and a 1.5-mm interslice gap. Images were made in the coronal plane and required 17 min for acquisition.

MR showed four well-delineated, oval-shaped structures within the scrotum. The homogeneous signal intensity that was intermediate on T1-weighted images and high on T2-weighted images was characteristic of normal testicular tissue (Fig. 2). Each mass was surrounded by a thin continuous band of low signal intensity on both T1- and T2-weighted images, consistent with the tunica albuginea. There was increased signal intensity of the lower left testis on the T2-weighted image owing to better positioning relative to the coil. A separate epididymis was present for all four testicles.

A diagnosis of polyorchidism with bilateral duplication of the testes was made and no further diagnostic evaluation or treatment was deemed necessary. The patient has been well for 10 months.

Discussion

Scrotal polyorchidism is an unusual anomaly that does not have added risk except for torsion in rare cases [6–7]. Ac-

curate preoperative assessment of this benign condition is required to avoid surgery to exclude tumor or abscess. High-resolution sonography has been used in this regard, although the findings may be inclusive [8].

The testis, tunica albuginea, epididymis, fluid, and fat can be clearly identified by MR. Testicular disease is easily recognized on T2-weighted images, since diseased tissues are less intense than the normal testis. The finding of bilateral polyorchidism was clear on MR in the case reported here, making further diagnostic evaluation unnecessary.

REFERENCES

1. Ahlfeld F. *Die Missbildungen des Menschen*. Leipzig: Grunow, 1880
2. Lane A. A case of supernumerary testes. *Trans Clin Soc Lond* 1895;28:59
3. Al-Habbal Z, Izzidian AY. Polyorchidism: case report and review of the literature. *J Ped Surg* 1984;19:212
4. Snow BW, Tarry WF, Duckett JW. Polyorchidism: an unusual case. *J Urol* 1985;133:483
5. Rifkin MD, Kurtz AB, Pasto ME, Goldberg BB. Polyorchidism diagnosed preoperatively by ultrasonography. *J Ultrasound Med* 1983;2:93–94
6. Wilson WA, Littler J. Polyorchidism: report of two cases with torsion. *Br J Surg* 1953;41:302
7. Feldman S, Drach GW. Polyorchidism discovered as testicular torsion. *J Urol* 1983;130:976–977
8. Butz RE, Croushore JH. Polyorchidism. *J Urol* 1978;119:289

MR Imaging of the Carpal Tunnel: Normal Anatomy and Preliminary Findings in the Carpal Tunnel Syndrome

William D. Middleton¹
 J. Bruce Kneeland¹
 Gary M. Kellman^{1,2}
 James D. Cates^{1,3}
 James R. Sanger⁴
 Andrzej Jesmanowicz¹
 Wojciech Froncisz^{1,5}
 James S. Hyde¹

MR imaging was performed through the carpal tunnel in 18 wrists of nine normal volunteers and compared with cryomicrotome sections from cadaver wrists. MR reliably imaged the flexor retinaculum and carpal bones and thus defined the borders of the carpal tunnel. In all cases the median nerve was seen as an ovoid structure of moderate signal intensity and was easily distinguished from the flexor tendons of the hands running in the carpal tunnel. The tendons were separated from each other by their tendon sheaths, and this allowed for identification of the various tendons. Anatomic variations encountered in the normal volunteers included anomalous positioning of the origin of the lumbrical muscles within the carpal tunnel in two, persistent median arteries in two, and interposition of the median nerve between the flexor pollicis longus and the superficial flexor tendon to the index finger in one. Preliminary observations in 10 wrists of patients with carpal tunnel syndrome include segmental and diffuse swelling of the median nerve in six, distortion of the nerve in one, and thickening of the tendon sheaths in one. We conclude that MR imaging accurately and reliably displays the normal anatomy of the carpal tunnel and can detect morphologic changes in patients with carpal tunnel syndrome.

Received August 4, 1986; accepted after revision September 19, 1986.

Presented at the annual meeting of the American Roentgen Ray Society, Washington, DC, April 1986.

This work was supported in part by National Institutes of Health grants RR 01008, CA 41464-01, and AM 33667 and a grant from General Electric Medical Systems.

¹Department of Radiology, Medical College of Wisconsin, Milwaukee County Medical Complex, 8700 W. Wisconsin Ave., Milwaukee, WI 53226. Address reprint requests to W. D. Middleton.

²Present address: Department of Radiology, Western Pennsylvania Hospital, Pittsburgh, PA 15224.

³Present address: Department of Radiology, Tampa General Hospital, Tampa, FL 33606.

⁴Department of Surgery, Medical College of Wisconsin, Milwaukee, WI 53226.

⁵On leave from the Department of Biophysics, Jagiellonian University, Krakow 31-120, Poland.

AJR 148:307-316, February 1987

0361-803X/87/1482-0307

© American Roentgen Ray Society

MR imaging is rapidly gaining acceptance as a valuable noninvasive means of imaging the extremities. Lack of respiratory or cardiac motion allows for imaging without the artifacts that frequently degrade image quality in the abdomen and chest. Use of local coils improves image quality even further by increasing the signal-to-noise ratio and hence the resolution. These factors, coupled with the inherently high contrast of MR imaging, have allowed depiction of soft-tissue anatomy of the extremities that has not been possible by other means. This study was performed to determine the ability of MR to image the carpal tunnel and its contents. Scans from asymptomatic volunteers were analyzed to determine the MR appearance of the normal carpal tunnel. These were then contrasted with scans from a limited number of patients with carpal tunnel syndrome to determine if commonly described surgical findings could be detected with MR.

Subjects and Methods

All imaging was done on a General Electric Signa system operating at 1.5 T. Several different local coils were used. All belong to a family of coils known as loop-gap resonators. The properties of these coils have been investigated at length and the results presented in previous publications [1, 2]. Data were acquired with a two-dimensional Fourier transform multisection technique by using either 128 × 256 or 256 × 256 matrices, 8- or 12-cm field of view, and 3-mm-thick sections obtained with a 1.5-mm gap. Spin-echo pulse sequences were obtained and were relatively T1 weighted with a 500-600 msec repetition time (TR) and 20-30 msec echo time (TE); proton-density weighted (TR = 2000-2500 msec, TE = 20-30 msec); or T2-weighted (TR = 2000-2500 msec, TE = 60-80 msec). Two excitations were used in all cases. Imaging time varied with the pulse sequence with the maximum 10 min and 18 sec. All measurements of median nerve dimensions were done at the viewing console with built-in computer software.

All the subjects were scanned in the prone position with the arm extended overhead. The palm was placed on the surface coil, and the proximal palmar crease was used as a landmark of the most proximal portion of the carpal tunnel. Sandbags were used to stabilize the wrist. The coil was elevated about 10 cm off the tabletop to ensure positioning in the center of the field of view.

Eighteen normal wrists were scanned in nine volunteers: six women and three men aged 24–35 years (mean, 29). In addition, seven patients with carpal tunnel syndrome were scanned. In three patients the symptoms were bilateral, so altogether 10 symptomatic wrists were analyzed. Ages of the patients ranged from 29 to 59 (mean, 43).

Anatomic sections of three wrists were obtained in axial, coronal, and sagittal planes with a cryomicrotome (LKB 2250, Gaithersburg, MD). Blocks of tissue were frozen and placed on the stage of the cryomicrotome. As each millimeter of tissue was removed, a photograph was taken of the surface. The photographs and MR images were compared.

Results

Anatomic Review

The anatomy of the carpal tunnel is shown in Figure 1. The deep border of the carpal tunnel is formed by the carpal bones, and the superficial border is formed by a thick ligamentous band known as the flexor retinaculum. The attachments of the flexor retinaculum are to the hook of the hamate and pisiform bone medially and the tubercle of the trapezium and scaphoid laterally. The ligament is thickest distally where it attaches to the hook of the hamate and tubercle of the trapezium. Radially, the flexor retinaculum is pierced by the tendon of the flexor carpi radialis. This forms a superficial and

deep layer of the retinaculum that, along with the vertical groove of the trapezium, forms a fibroosseous tunnel for the flexor carpi radialis. Because the flexor carpi radialis has its own fibroosseous tunnel, it is technically separate from the carpal tunnel.

The bulk of the space in the carpal tunnel is occupied by the tendons of the flexor muscles of the hand. These muscles originate from the medial epicondyle of the humerus and the anterior aspect of the radius, ulna, and interosseous membrane. The muscles become tendinous before entering the carpal tunnel. The most superficial of the muscles is the flexor carpi radialis. Although its tendon is not strictly considered within the carpal tunnel, it is included here because it does travel within the space surrounded by the carpal bones and the flexor retinaculum. Distally, it inserts at the base of the second and third metacarpals. Deep to the flexor carpi radialis is the flexor digitorum superficialis. This muscle divides into four separate tendons that pass through the carpal tunnel just deep to the flexor retinaculum and insert onto the middle phalanges of the fingers. Deep to the flexor digitorum superficialis are the deep flexors of the digits. The flexor pollicis longus originates from the midradius and inserts onto the proximal phalanx of the thumb. The flexor digitorum profundus arises from the proximal ulna and divides into four tendons that insert separately onto the distal phalanges of the fingers. These four tendons rest along the floor of the carpal tunnel. The lumbrical muscles take their origin from the tendons of the flexor digitorum profundus beyond the level of the carpal tunnel (Fig. 1).

All of the tendons in the carpal tunnel are surrounded by synovial tissue, which allows for a smooth gliding motion. The arrangement is variable, but generally there is an ulnar bursa that surrounds the superficial and deep flexors of the fingers and a separate radial bursa that surrounds the flexor pollicis longus. These bursae separate the tendons and allow for their identification on MR (Fig. 1).

The final structure in the carpal tunnel is the median nerve. The median nerve is composed of branches from C5 through

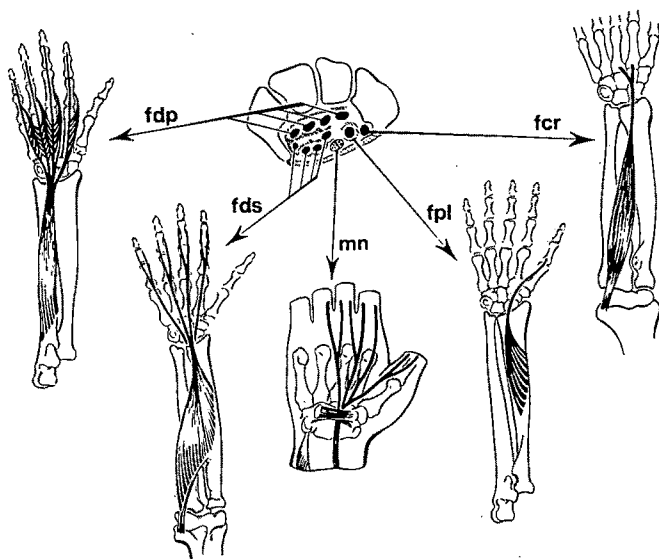


Fig. 1.—Schematic diagram of cross-sectional appearance of carpal tunnel at level of hook of hamate. Overall anatomy of various structures in carpal tunnel is displayed. Radial bursa is seen surrounding flexor pollicis longus, and ulnar bursa is seen surrounding flexor digitorum superficialis and flexor digitorum profundus on cross-sectional view. Lumbrical muscles are seen attaching to tendons of flexor digitorum profundus. See key for abbreviations.

Key to Abbreviations Used in Figures 1–7

c	capitate bone
fcr	flexor carpi radialis
fdp	flexor digitorum profundus
fds	flexor digitorum superficialis
fpl	flexor pollicis longus
h	hook of the hamate
ha	hamate
L	lumbrical muscles
lu	lunate
m	metacarpal
mn	median nerve
p	pisiform bone
pl	palmaris longus tendon
r	radius
s	scaphoid
t	tubercle of the trapezium
td	trapezoid
tm	trapezium
tr	triquetrum

T1. In the forearm it innervates all of the muscles previously mentioned. Before entering the carpal tunnel it gives off a small superficial palmar cutaneous branch that courses superficial to the flexor retinaculum. After exiting the carpal tunnel it divides into three terminal branches that supply muscle innervation to the thenar and first two lumbrical muscles and sensory innervation to the radial half of the hand (Fig. 1).

MR Appearance of the Normal Carpal Tunnel

Figures 2–5 are sequential axial images through the right wrist viewed as if looking from the fingers toward the elbow. Palmar is inferior, radial is to the right, and ulnar to the left. Corresponding anatomic sections are also shown in Figures 2–4.

The borders of the carpal tunnel were easily identified on MR. The attachments of the flexor retinaculum to the hook of the hamate and the tubercle of the trapezium were seen in all cases, while the attachments to the pisiform and tubercle of the scaphoid were occasionally shown. This corresponds with anatomic dissections, which show the thickest portion of the retinaculum occurring distally at the level of the hook of the hamate and the tubercle of the trapezium. Attachments

to the pisiform and scaphoid are thin and attenuated. In all of the normal volunteers the flexor retinaculum could be seen on axial sections to the level of the base of the metacarpals.

Because of a lack of mobile protons, tendons generate an extremely weak signal and appear black on MR. In all cases the tendon of the flexor carpi radialis was identified and was separate from the other tendons in the carpal tunnel. On more proximal sections it was seen as an ovoid structure coursing superficial to the scaphoid bone (Fig. 2). As it extended distally it was seen within the vertical groove of the trapezium (Fig. 3). Distally it thinned as it inserted onto the base of the second and third metacarpals. In no normal wrist was contact established between the tendon of the flexor carpi radialis and the median nerve.

The tendon of the flexor pollicis longus was also identified in all normals as a structure separate from the other flexor tendons. On more proximal sections it was located deep to the median nerve (Fig. 2). As the tendon extended distally, it began to assume a position lateral to the median nerve (Figs. 3 and 4). On the most distal sections it could be seen extending toward the thumb between the adductor pollicis muscle and the thenar muscles (Fig. 5).

In most normal volunteers the four tendons of the flexor digitorum superficialis were seen as separate structures. Occasionally, the superficial flexor tendon to the fifth finger was

Fig. 2.—Axial MR image (TR 600, TE 25) (A) and anatomic section (B) at level of pisiform bone. Right wrist viewed toward elbow with palm down. (See key for abbreviations.)

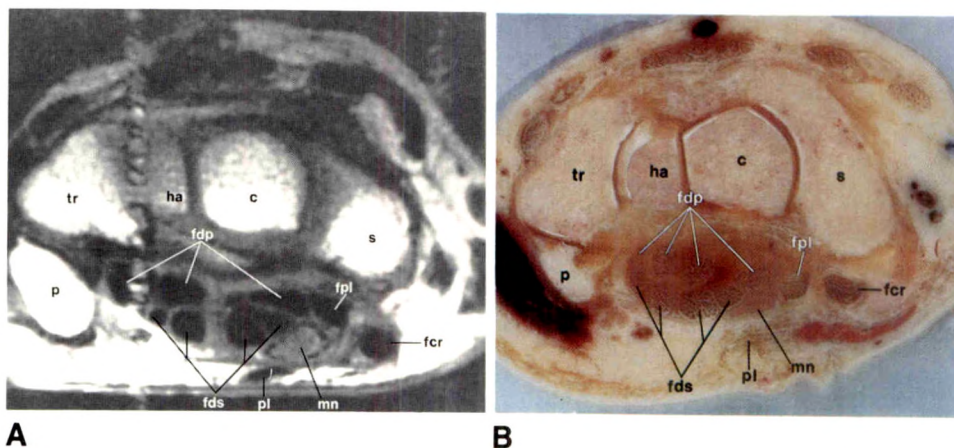
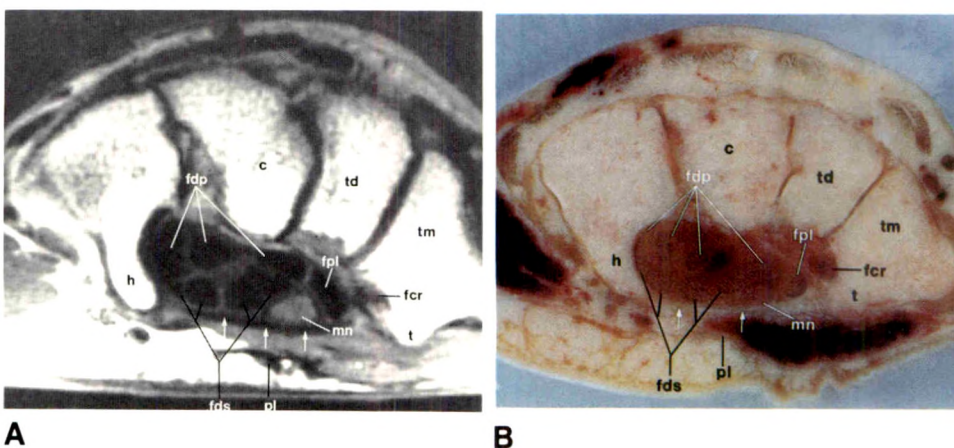


Fig. 3.—Axial MR image (TR 600, TE 25) (A) and anatomic section (B) at level of hook of hamate. Right wrist viewed toward elbow with palm down. Flexor retinaculum (arrows). (See key for abbreviations.)



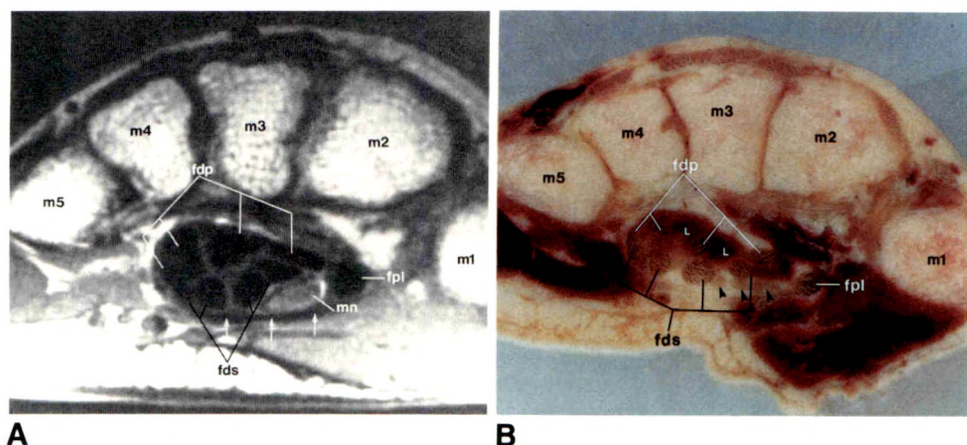


Fig. 4.—Axial MR image (TR 600, TE 25) (A) and anatomic section (B) at level of metacarpal bases. Right wrist viewed toward elbow with palm down. On MR image, median nerve has begun to thin but has not yet branched. On anatomic section, median nerve has divided into its three terminal divisions (arrowheads). Note origins of lumbrical muscles on anatomic section (arrows). Flexor retinaculum (arrows). (See key for abbreviations.)

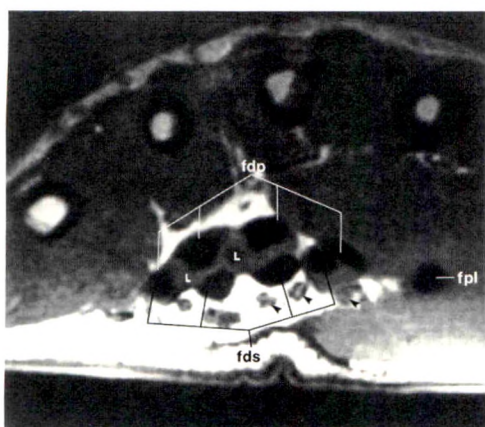


Fig. 5.—Axial MR image (TR 600, TE 25) at level of proximal metacarpals. Right wrist viewed toward elbow with palm down. Note three terminal divisions of median nerve (arrowheads) and origin of lumbrical muscles. (See key for abbreviations.)

not identified as a structure separate from the deep flexor tendon to this digit. This was because of an extremely close contact between these two tendons as seen on the cryomicrotome sections (Figs. 2B, 3B, and 4B). In all cases the superficial flexor tendon to the index finger was juxtaposed to the deep surface of the median nerve. The superficial flexor tendon to the long finger was contiguous to the medial aspect of the median nerve in all cases. In some instances it also formed a portion of the deep border of the median nerve. Within the carpal tunnel, the two central superficial flexor tendons (to the third and fourth digits) were slightly more superficial than were the peripheral superficial flexor tendons (to the first and fifth digits). Because of this arrangement, the superficial flexor tendons formed a gentle arc just deep to the flexor retinaculum. On more distal sections the superficial flexor tendons began to separate as they extended toward their respective insertions (Fig. 5).

The four tendons of the flexor digitorum profundus were generally not imaged as four separate structures within the

carpal tunnel. Most often, only three tendons were identified. On more distal sections beyond the carpal tunnel, the deep flexor tendons separated, and at these levels, they could be identified as four discrete structures. In addition, on more distal sections the origins of the lumbrical muscles could be identified adjacent to the deep flexor tendons. The muscles appeared as tissue of moderate signal intensity similar to the other muscles in the hand. Although the lumbricals are attached to the deep flexor tendons of the finger, on MR they often appeared contiguous to both the deep and superficial flexor tendons to the fingers.

The median nerve had a signal intensity similar to that of muscle and was therefore easy to separate from the black tendons within the carpal tunnel. In all but one volunteer it rested against the flexor retinaculum with its longest dimension oriented parallel to the retinaculum. Just before branching, the median nerve consistently flattened slightly (Fig. 4A). In all cases, the three terminal branches of the median nerve could be identified at their origin (Fig. 5). Slightly more distally, the branches became difficult to separate from the palmar vessels. In no case was the palmar cutaneous branch of the median nerve identified.

The average thickness of the median nerve at the level of the pisiform bone was 2 mm (range, 1.6–2.8 mm). The average width at this level was 4.5 mm (range, 3.4–6.0 mm). Assuming an elliptical shape, we calculate the average area of the median nerve at this level to be 7.0 mm² (range, 5.3–9.7 mm²; 1.4 mm² SD). At the level of the hook of the hamate the average thickness of the median nerve was 2.1 mm (range, 1.4–2.6 mm). The average width at this level was 4.9 mm (range, 3.4–6.3 mm). Again, assuming an elliptical shape, we calculate the average area of the median nerve at this level to be 8.0 mm² (range, 4.2–10.8 mm²; 1.9 mm² SD). The average difference in area between the proximal and distal portions of the median nerve (proximal minus distal) was –0.9 mm² (range, –3.4 to +1.1 mm²; 1.3 mm² SD).

Figure 6 is a T1-weighted sagittal image through the wrist. The deep and superficial flexor tendons of the fingers can be identified, as can the flexor retinaculum. The flexor retinaculum is identified distally to the level of the metacarpal bases. The sagittal anatomy of the carpal bones is well displayed;

Fig. 6.—Sagittal MR image (TR 600, TE 25) (A) and anatomic section (B) through lunate and capitate. Flexor retinaculum (arrows). (See key for abbreviations.)

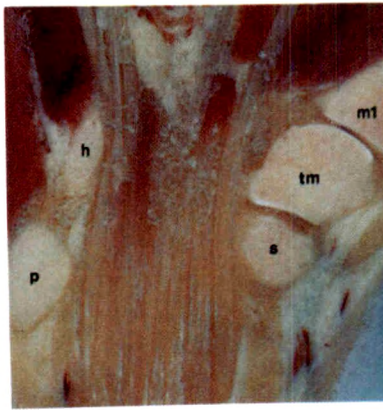
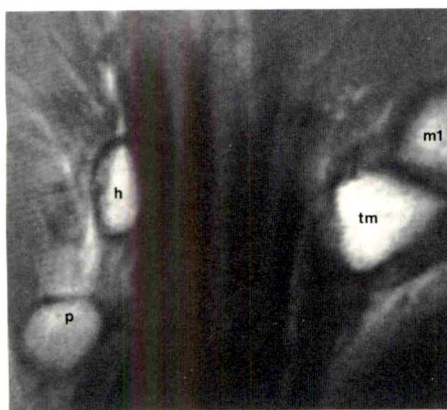
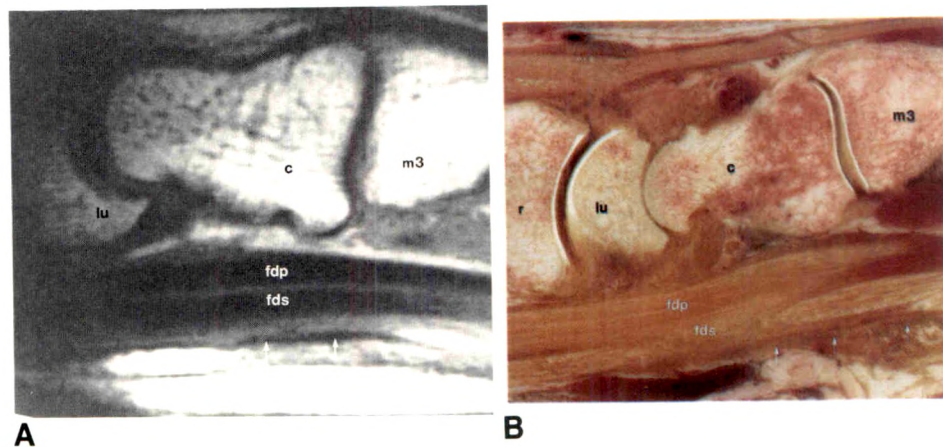


Fig. 7.—Coronal MR image (TR 600, TE 25) (A) and anatomic section (B) through hook of hamate, pisiform, and tubercle of trapezium. (See key for abbreviations.)

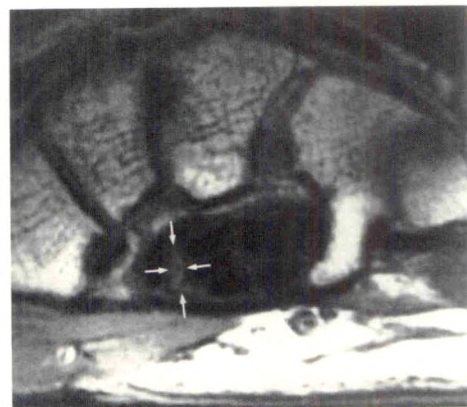


Fig. 8.—Interposition of median nerve. Axial MR image (TR 600, TE 25) in normal volunteer. Left wrist viewed toward elbow with palm down. Note that long axis of median nerve (arrows) is perpendicular to flexor retinaculum at this level and that median nerve has migrated deeper into carpal tunnel between flexor pollicis longus and superficial and deep flexors of fingers.

however, identification of the various tendons is much more difficult than in the axial plane and demonstration of the median nerve is poor. Figure 7 is a coronal view through the carpal tunnel. Again the tendons within the carpal tunnel can be identified and can be seen to diverge distally. However, as in the sagittal plane, determination of the identity of each individual tendon is difficult when compared with the ease of determination in the axial plane. Therefore, in our experience, these views were not as helpful as the axial views in analyzing normal or pathologic anatomy in the carpal tunnel.

T2-weighted images obtained from the normal volunteers in an axial plane showed no change in the relative intensities of the various structures in the carpal tunnel. In particular, the median nerve maintained a signal intensity similar to that of the thenar muscles.

Normal Variations

In one normal volunteer the median nerve had migrated away from the flexor retinaculum and become interposed between the flexor pollicis longus and the superficial flexor tendon of the first finger (Fig. 8). In this case the longest cross-sectional dimension of the median nerve had shifted from an axis parallel to the flexor retinaculum to an axis perpendicular to the retinaculum. On proximal and distal sections the median nerve assumed a more normal configuration.

In two normal volunteers, tissue of moderate signal intensity was identified between the deep flexor tendons within the carpal tunnel (Fig. 9). Scans at more distal levels proved that this tissue was contiguous with the lumbrical muscles and represented the most proximal portion of the lumbrical mus-

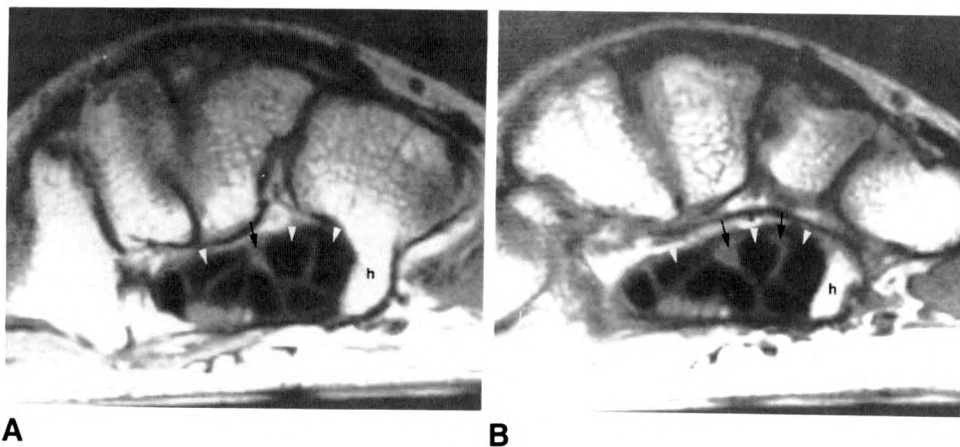


Fig. 9.—Anomalous proximal origin of lumbrical muscles. Proximal (A) and distal (B) axial MR images (TR 600, TE 25) through hook of hamate (h) show lumbrical muscle tissue (arrows) originating in carpal tunnel of normal volunteer as far proximally as hook of hamate. Deep flexor tendons (arrow-heads). Left wrist viewed toward elbow with palm down.

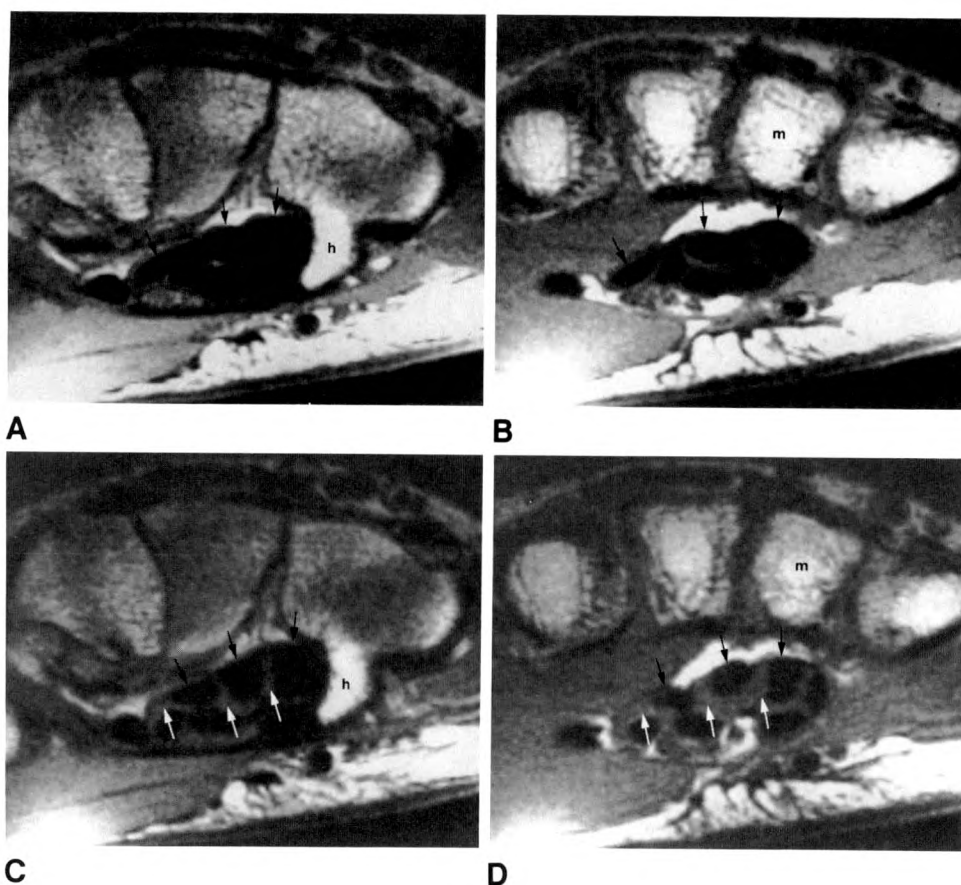


Fig. 10.—Proximal migration of lumbricals with finger flexion. Left wrist viewed toward elbow with palm down. Axial MR images (TR 600, TE 25) at level of hook of hamate (h) and metacarpal bases (m). White arrows indicate lumbrical muscles; black arrows show deep flexor tendons.

A and B, Fingers extended. No lumbrical tissue can be seen between deep flexor tendons at either level of hook of hamate or base of metacarpals.

C and D, Fingers flexed. Lumbrical muscles (white arrows) have been pulled proximally to level of hook of hamate.

cles. Both of these wrists were scanned with the fingers extended. Images in a third normal volunteer showed that flexion of the fingers could pull the most proximal portion of the lumbricals within the carpal tunnel despite normal positioning of the muscles with the fingers extended (Fig. 10).

Finally, in two wrists a well-described arterial anomaly, the persistent median artery, was identified. In both of these images, flow artifact generated along the axis of the phase-encoding gradient was identified originating from a vessel adjacent to the median nerve (Fig. 11). In one subject it was

a small vessel; in the other it was a moderate-sized vessel only slightly smaller than the radial and ulnar arteries. In both subjects it was a unilateral finding.

Pathologic Anatomy

Various abnormalities were seen in the seven patients with symptomatic carpal tunnel syndrome. In six wrists, enlargement of the median nerve was detected. In three, the swelling was segmental and located at the level of the pisiform bone (Fig. 12). In all three of these patients, the computed areas of

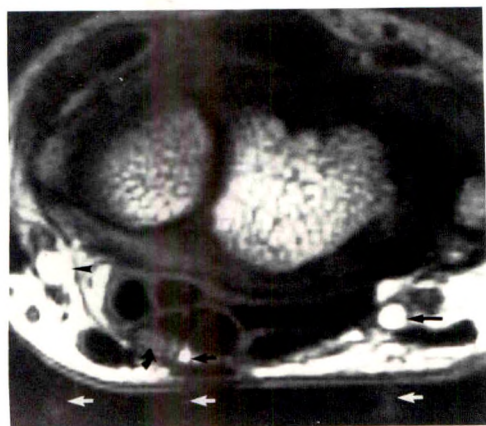


Fig. 11.—Persistent median artery. Axial MR image (TR 600, TE 25) in normal volunteer. Left wrist viewed toward elbow with palm down. Persistent median artery (short straight black arrow), median nerve (curved arrow), radial artery (arrowhead), ulnar artery (long straight black arrow), and flow artifact from three arteries (white arrows).

the median nerve at the level of the pisiform were 2 SD above the mean, while the areas at the level of the hook of the hamate were normal.

In three other wrists, the enlargement of the median nerve was diffuse and the areas were greater than 2 SD above the mean at both the proximal and distal carpal tunnel (Fig. 13). In one patient with bilateral postpartum carpal tunnel syndrome, the median nerves were diffusely enlarged and displayed a marked increase in signal intensity on T2-weighted images (Fig. 13B). This markedly increased signal intensity was not detected in other patients or in normal volunteers examined with T2-weighted pulse sequences.

Distortion of the median nerve was detected in one patient. In this case the nerve was flattened and angulated over a small excrescence of tissue originating from the superficial border of the carpal tunnel (Fig. 14). This patient had undergone surgery for carpal tunnel syndrome, as evidenced by

the lack of continuity of the flexor retinaculum. The abnormal tissue most likely represented fibrous proliferation.

In the final patient with unilateral symptoms, scans through the symptomatic wrist were initially interpreted as normal. However, careful comparison with the asymptomatic contralateral side showed mild but definite thickening of the synovial tendon sheaths, resulting in increased separation of the tendons on the symptomatic side (Fig. 15).

Discussion

Attempts at imaging normal structures in the carpal tunnel have been made. CT has been successful in defining the borders of the carpal tunnel and identifying the flexor tendons within the carpal tunnel [3–5]. However, differences in attenuation values of the various structures in the carpal tunnel are small and contrast resolution is limited. Therefore, CT has not gained acceptance as a means of studying the carpal tunnel. Sonography has also been used to image the carpal tunnel and has an advantage over CT in that motion of the tendons can be detected on real-time examination [6]. However, differentiation of the structures in the carpal tunnel is poor, and sonography has not become a valuable means of imaging the carpal tunnel.

Mesgarzede et al. [7] documented the ability of MR to image the normal wrist and carpal tunnel by using a low-field-strength system. Weiss et al. [8, 9] and Koenig et al. [10] described normal and pathologic anatomy of the hand and wrist in general on a high-field system but did not present a detailed description of the normal or pathologic anatomy of the carpal tunnel. In this study we investigated the normal and abnormal carpal tunnel using MR and showed the ability of MR to define normal and pathologic anatomy. While operative proof was not available on the pathologic cases, the MR findings did correspond to carpal tunnel abnormalities that have been well described in the surgical literature.

In the normal volunteers, the borders of the carpal tunnel and the contents of the carpal tunnel were well defined. The contrast between the median nerve and the flexor tendons

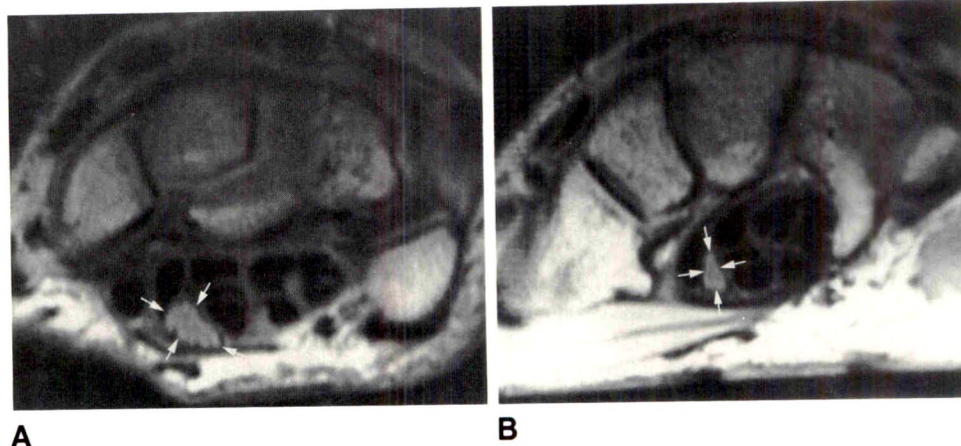


Fig. 12.—Segmental swelling of median nerve (arrows). Axial MR images (TR 2000, TE 20) at levels of pisiform (A) and hook of hamate (B). Left wrist viewed toward elbow with palm down. Note enlargement of nerve proximally (A) compared with normal caliber of nerve distally (B).

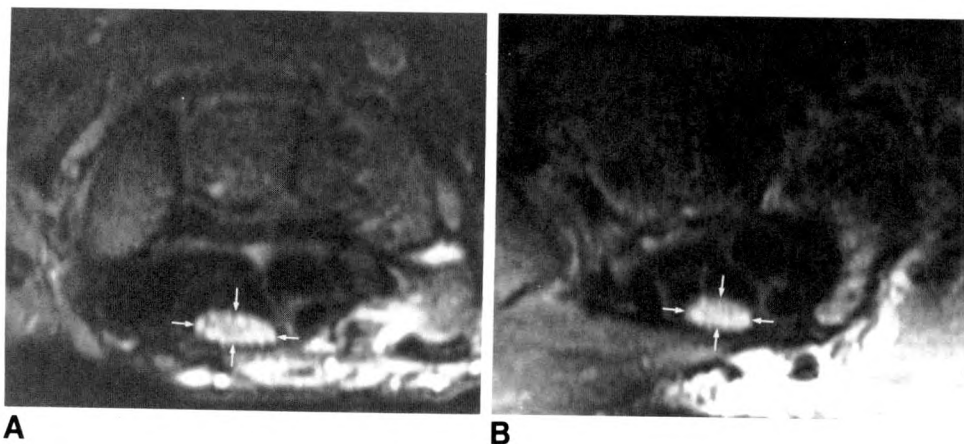


Fig. 13.—Diffuse swelling of median nerve (arrows). Axial MR images (TR 2000, TE 60) of left wrist viewed toward elbow with palm down in patient with bilateral postpartum carpal tunnel syndrome. Note enlargement as well as markedly increased signal intensity at both level of pisiform (A) and level of hook of hamate (B). Right wrist had similar appearance.

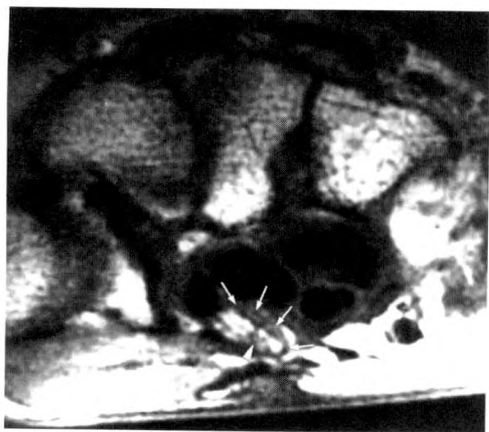


Fig. 14.—Distortion of median nerve in patient with recurrent carpal tunnel syndrome after flexor retinaculum release. Axial MR image (TR 500, TE 25) showing flattened median nerve (arrows), which is distorted by small soft-tissue mass (arrowhead). Note absence of normal flexor retinaculum secondary to prior surgery. Left wrist viewed toward elbow with palm down.

was striking and allowed for easy distinction of these structures. In general, the individual tendons could also be separated from each other. Because of this, a relatively constant arrangement of the tendons with respect to the median nerve was discovered. Knowledge of this arrangement made possible the identification of the various tendons on the basis of a single image.

The caliber of the median nerve was relatively constant through the level of the pisiform bone and the hook of the hamate. At the proximal level the average dimensions were 4.5×2.0 mm and at distal level were $4.9 \text{ mm} \times 2.1$ mm. In a previous autopsy study [11], the average dimensions of the median nerve at the proximal and distal portions of the carpal tunnel were 6.0×3.2 mm and 8.0×3.4 mm, respectively. The increased dimensions of the median nerve in this study may be related to swelling of the median nerve in the cadaver wrist or to the use of slightly oblique planes of sections. The smaller dimensions obtained in the current study may have

been related to nonoptimal window and level settings or lack of inclusion of the epineurium. In both studies, the average dimensions of the median nerve were slightly greater at the distal level than at the proximal level.

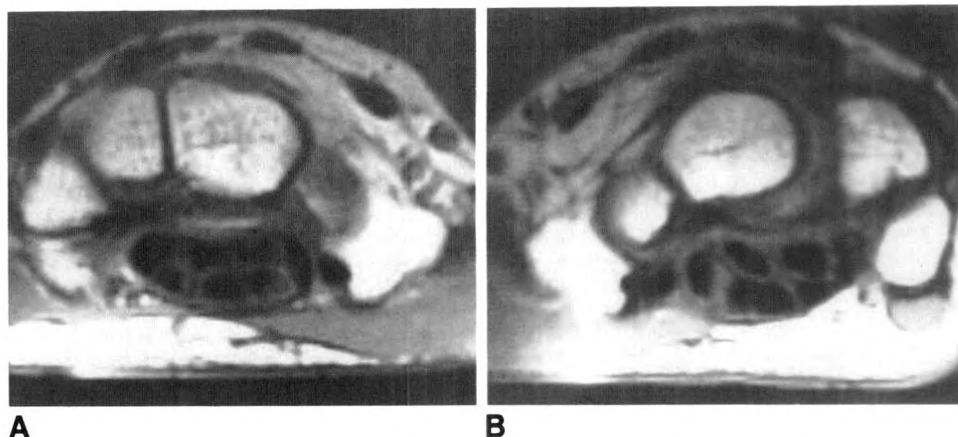
Several anatomic variations were identified in the normal population. Perhaps the most interesting was detection of portions of lumbrical muscles within the carpal tunnel. Because the muscle tissue can act as a space-occupying lesion within the carpal tunnel, it is believed that this condition may predispose to the development of carpal tunnel syndrome [12]. Therefore, when identified in a symptomatic wrist, this finding may be significant; however, since other pathologic changes are generally present, anomalous lumbricals should not be assumed to be the sole cause of the carpal tunnel syndrome. Also, imaging with the fingers flexed may result in the false impression of anomalous lumbrical muscles because the lumbricals originate from the deep flexor tendons of the fingers. When the flexor muscles contract, the tendons are pulled proximally and the lumbricals are pulled with them. If the lumbricals move enough, their most proximal portion may migrate into the carpal tunnel. For this reason all imaging should be done with the fingers in the neutral anatomic position.

Another normal variation that may predispose to the development of carpal tunnel syndrome is a persistent median artery [13], a generally small vessel that normally obliterates in the perinatal period but may persist into adulthood. This vessel may be the major source of blood flow to the hand. A persistent median artery was detected in two normal volunteers and in none of the symptomatic patients. As with the anomalous lumbrical muscles, its presence may be significant when detected in a symptomatic wrist; however, it will probably not be the only factor in the cause of symptoms.

A final normal variation detected was interposition of the median nerve. This normal variation alters the arrangement of the median nerve with respect to the flexor tendons and flexor retinaculum. It has no known pathologic significance, and its identification is important only to avoid misinterpretation as a pathologic condition.

A number of morphologic changes have been detected surgically in patients with carpal tunnel syndrome. The most

Fig. 15.—Swelling of tendon sheaths in patient with left-sided carpal tunnel syndrome. Axial MR images (TR 600, TE 25) of the right (A) and left (B) wrists viewed toward elbow with palm down. Note increased separation of deep flexor tendons by thickened tendon sheaths on left compared with their close apposition on right.



common finding at surgery is thickening or fibrosis of the tendon sheath, which Phalen [14] detected in 203 of 212 cases. When this occurs within the restricted space of the carpal tunnel, pressure is exerted on the median nerve and the carpal tunnel syndrome results. In our study, abnormally thickened tendon sheaths were detected in one wrist by noting asymmetry with the opposite side. In this case comparison with the opposite side was essential, and because of this, bilateral scanning is recommended in all patients with carpal tunnel syndrome.

A discrepancy in the frequency of tendon-sheath thickening detected by MR and the incidence reported in the surgical literature is expected for two reasons. First, in approximately two-thirds of hands with carpal tunnel syndrome, the contralateral side is also affected [13, 14]. In these instances, detection of tendon-sheath thickening would be difficult because of lack of asymmetry between the two wrists. Perhaps with more experience, a range of normal thicknesses will be discovered that may aid in detection of bilateral thickening. Second, mild degrees of thickening may be sufficient to exert enough pressure on the median nerve to result in carpal tunnel syndrome. Phalen [13] described mild thickening in 38%, moderate thickening in 41%, and severe thickening in only 6% of operated cases. Mild or moderate degrees of thickening may not be detected on MR.

Another common surgical observation is swelling of the median nerve proximal to the level of the carpal tunnel. Commonly referred to as a pseudoneuroma, this was detected in 43 of 65 patients in one series [15]. In some instances it was associated with constriction of the median nerve within the carpal tunnel. In our limited series of patients, enlargement of the median nerve was detected in six wrists. In three cases the swelling was segmental at the level of the pisiform bone and fell into the category of a pseudoneuroma. In all three of these cases the caliber of the nerve at the level of the hook of the hamate was within 1 SD of the mean when compared with the normal volunteers. However, there was a marked discrepancy in the caliber of the nerve at the level of the pisiform and at the level of the hook of the hamate. In the three other wrists the enlargement of the median nerve was diffuse and detected at both the level of the pisiform bone

and the level of the hook of the hamate. The increased signal intensity of the median nerve bilaterally on T2-weighted sequences in a patient with postpartum carpal tunnel syndrome suggests that in this patient the enlargement was secondary to swelling and edema of the median nerve. This finding was reported previously by Weiss et al. [9].

A third observation made at surgery is thinning and indentation of the median nerve [12]. This occurs in the most advanced cases of carpal tunnel syndrome. We detected this type of change in one patient with persistent carpal tunnel syndrome after surgical release of the flexor retinaculum. In this patient a small soft-tissue mass appeared to be causing the indentation of the nerve. This most likely represented scar tissue, which is a well-described cause of recurrent carpal tunnel syndrome in postoperative patients. In a series of 34 wrists explored for recurrent carpal tunnel syndrome, fibrous proliferation was a contributing cause in 22 and represented the most frequent surgical finding [16].

In summary, MR imaging seems to be an adequate means of displaying the normal anatomy of the carpal tunnel. Normal variations and morphologic changes in patients with carpal tunnel syndrome can be differentiated from the normal anatomy. The exact role of MR in evaluating patients with carpal tunnel syndrome is uncertain and requires further evaluation.

ACKNOWLEDGMENTS

We thank Debbie Bauer for manuscript preparation; Bruce Nowicki for preparation of the cryomicrotomes; and Steve Censky, Beth Beck, Lisa Klotz, and Marie Bye for assistance in scanning the normal volunteers and patients.

REFERENCES

1. Kneeland JB, Jesmanowicz A, Froncisz W, Grist TM, Hyde JS. High resolution localized MRI using loop-gap resonators. *Radiology* 1986; 158:247-250
2. Kneeland JB, Carrera GF, Middleton WD, et al. Rotator cuff tears: preliminary application of high resolution MRI with counter rotating current loop-gap resonators. *Radiology* 1986;160:695-699
3. Zucker-Pinchoff B, Hermann G, Srinivasan R. Computed tomography of the carpal tunnel: a radioanatomical study. *J Comput Assist Tomogr* 1982;5:525-528

4. John V, Nau HE, Nahsen HC, Reinhardt V, Venjakob K. CT of carpal tunnel syndrome. *AJNR* 1983;4:770-772
5. Marhar GL, Clark RA, Schneider HJ. High resolution CT scans of the wrist in patients with carpal tunnel syndrome (abstr). *Radiology* 1985;157(P):30
6. Fornage BD, Schemberg FL, Rifken MD. Ultrasound examination of the hand. *Radiology* 1985;155:785-788
7. Mesgarzadeh M, Schenck CD, Bonakdarpour A. MR imaging of the wrist and carpal tunnel: correlation with normal anatomy (abstr). *Radiology* 1985;157(P):30
8. Weiss KL, Beltran J, Shamam OM, Stilla RF, Levey ML. High field MR surface-coil imaging of the hand and wrist. Part I. Normal anatomy. *Radiology* 1986;160:143-146
9. Weiss KL, Beltran J, Lubbers LM. High field MR surface-coil imaging of the hand and wrist. Part II. Pathologic correlations and clinical relevance. *Radiology* 1986;160:147-152
10. Koenig H, Dietrich L, Meissner R. The wrist: a preliminary report on high resolution MR imaging. *Radiology* 1986;160:463-467
11. Tanzer RC. The carpal tunnel syndrome: a clinical and anatomic study. *J Bone Joint Surg [Am]* 1959;41:626-634
12. Tanzer RC. Compression neuropathies. In: Flynn JE, ed. *Hand surgery*. Baltimore: Williams & Wilkins, 1975:317-321
13. Phalen GS. The carpal tunnel syndrome—clinical evaluation of 598 hands. *Clin Orthop* 1972;83:29-40
14. Phalen GS. The carpal tunnel syndrome—seventeen years' experience in diagnosis and treatment of six hundred fifty-four hands. *J Bone Joint Surg [Am]* 1966;48:211-228
15. Rietz KA, Omne L. Analysis of 65 operated cases of carpal tunnel syndrome. *Acta Chir Scand* 1967;133:443-447
16. Langlois ND, Tinscheid RL. Recurrent and unrelieved carpal tunnel syndrome. *Clin Orthop* 1972;83:41-47

MR Imaging of Osteogenic and Ewing's Sarcoma

Orest B. Boyko¹
David A. Cory¹
Mervyn D. Cohen¹
Arthur Provisor²
David Mirkin³
G. Paul DeRosa⁴

Twenty patients with biopsy-proven osteogenic (11 cases) or Ewing's (nine cases) sarcoma were evaluated by MR imaging on a 0.15-T resistive unit to determine the value of MR in the diagnosis and treatment of these two neoplasms and to develop the best protocol for MR imaging. In all 20 cases, MR identified tumor spread into bone marrow, and it was superior to CT in five cases. Extension of tumor into the soft tissues adjacent to bone was shown better by MR than CT in six cases. Improved anatomic information from MR is the result of the ability to image in the axial, coronal, and sagittal planes. Compared with CT, MR identifies cortical disease but has inferior spatial resolution and defines calcium poorly. MR can be used to monitor tumor response to chemotherapy, and the relationship of tumor to adjacent vasculature can be determined without the use of contrast agents. Two pulse sequences are necessary for maximum display of disease, since, in general, tumor involvement of the bone marrow is best assessed on T1-weighted sequences, and tumor involvement of the soft tissue is best seen on T2-weighted sequences. Additional information about bone-marrow involvement, soft-tissue tumor extent, and the relationship of tumor to blood vessels makes MR a valuable adjunct to CT in the evaluation of these neoplasms.

Clinical experience with MR imaging of primary bone tumors is accumulating [1-11]. MR is also becoming increasingly important in the imaging of bone-marrow disease [11-16]. MR provides multiplanar images, identifies bone-marrow and soft-tissue extension of tumor, and holds promise as a means of monitoring tumor response to therapy [5-8]. We reviewed the MR findings in 11 cases of osteogenic sarcoma and nine cases of Ewing's sarcoma to evaluate the clinical usefulness of the technique and to determine the best MR imaging strategy for these two tumors.

Received February 27, 1986; accepted after revision September 10, 1986

Presented at the annual meeting of the American Roentgen Ray Society, Boston, April 1985.

¹ Department of Radiology, Indiana University School of Medicine, and Regenstrief Institute, Indianapolis, IN 46223. Address reprint requests to O. B. Boyko, Department of Radiology, Indiana University School of Medicine, 926 W. Michigan St., Indianapolis, IN 46223.

² Department of Hematology and Oncology, Indiana University School of Medicine, and Regenstrief Institute, Indianapolis, IN 46223.

³ Department of Pathology, Indiana University School of Medicine, and Regenstrief Institute, Indianapolis, IN 46223.

⁴ Department of Orthopaedic Surgery, Indiana University School of Medicine, and Regenstrief Institute, Indianapolis, IN 46223.

AJR 148:317-322, February 1987
0361-803X/87/1482-0317

© American Roentgen Ray Society

Materials and Methods

Twenty patients aged 9-21 years with either osteogenic sarcoma (11 cases) or Ewing's sarcoma (nine cases) had MR scans before chemotherapy or radiation therapy. A 0.15-T resistive scanner (Technicare Teslacon) was used. All patients were examined with at least one T1- and one T2-weighted spin-echo (SE) pulse sequence, and three patients were examined with inversion-recovery (IR) pulse sequences. The echo-delay time (TE) was 30, 32, 60, or 120 msec; the repetition time (TR) was 250, 500, 550, 1000, or 2000 msec. (SE 250/32, 550/32, and 500/30 are T1 weighted; SE 1000/30, 1000/60, 2000/60, and 2000/120 are more T2 weighted.) For the IR sequence, a 90°-180° signal-reading pulse pair followed the initial 180° inverting pulse. The inversion time (TI) was 450 msec. The 90° and 180° refocusing pulses were separated by 15 msec. The TR was 1500 msec. IR images are heavily T1 weighted. In one case, multiecho images were obtained with a TR of 2000 msec and a TE ranging from 30 to 240 msec.

Contiguous slices of either 10 or 15 mm were obtained in the coronal, axial, or sagittal plane. Images were reconstructed into a 256 × 128 matrix and interpolated to 256 × 256 for display. No contrast agents were used.

The distribution of the 11 cases of osteogenic sarcoma were femur (seven), pelvis (two), humerus (one), and tibia (one). The nine cases of Ewing's sarcoma were located in the femur

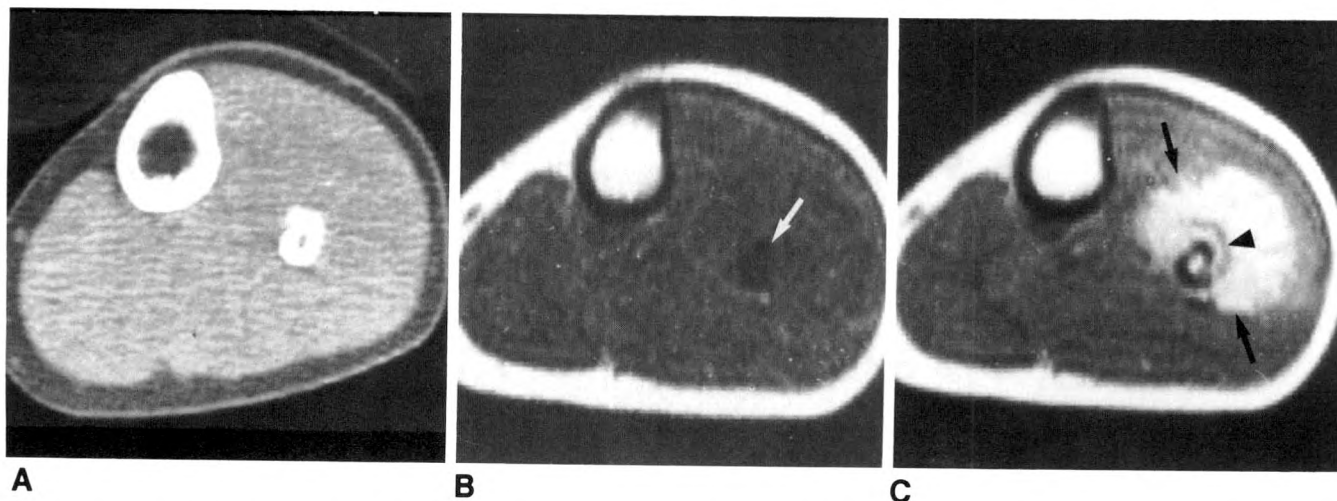


Fig. 1.—Ewing's sarcoma of the left fibula.

A, Soft-tissue-window CT shows no soft-tissue mass or marrow abnormality.

B, IR 1500/450 image shows marrow replacement by tumor (arrow).

C, SE 1000/60 image shows soft-tissue mass (arrows) and periosteal elevation (arrowhead), but fails to show difference between normal tibia and abnormal fibula marrow as was seen in B.

(two), pelvis (five), spine (one), and fibula (one). All patients had plain-film examinations, and 19 patients had CT scans before MR imaging. CT was performed on either a Philips Tomoscan 310 or Technicare 2060Q scanner. Follow-up MR studies were performed in nine patients to monitor response to therapy. Diagnoses in all 20 cases were proven by biopsy. Two resected osteogenic sarcoma specimens were studied for pathologic correlation of MR findings.

MR studies were reviewed retrospectively by two of the authors; their observations were correlated with plain films and CT scans simultaneously, and a consensus impression was reached. Presence of tumor in the soft tissues and bone marrow was confirmed at the time of open biopsy and/or amputation.

Results

MR identified soft-tissue masses in all 20 cases. In the 19 cases in which CT was performed, MR showed better the soft-tissue mass in six, including one case of Ewing's where the mass was isodense with muscle on CT (Fig. 1A). Marrow involvement was evident in all cases imaged by MR and CT, but the extent was better shown by MR in five cases. CT showed marrow abnormalities better than MR in one case. Both T1- and T2-weighted images were required in the evaluation of tumor in soft tissue and bone marrow, since on T1-weighted images tumor that infiltrates muscle can have a signal isointense with muscle (Fig. 1B). The signal becomes more intense on T2-weighted images (Fig. 1C). Conversely, the T2 pulse sequence chosen can cause tumor that is infiltrating bone marrow to have a bright signal similar to normal marrow (Fig. 1C).

In one case of a pelvic osteogenic sarcoma, the extensive marrow involvement shown by MR changed the surgical approach to a hemipelvectomy. MR can also show metastatic sites of osteogenic sarcoma even when there is calcified tumor matrix (Fig. 2).

The soft-tissue component of both osteogenic and Ewing's sarcoma had an inhomogeneous signal intensity, and these two tumors could not be distinguished based on T1 or T2 signal intensity.

MR showed cortical thickening and tumor infiltration of the cortex by both types of tumors. In four cases where cortical disease was seen on plain film and/or CT, no cortical disease was evident on MR. Cortical involvement by Ewing's or osteogenic sarcoma is identified on MR by the replacement of the dark signal of the cortex with the comparatively increased signal intensity of the invading tumor.

Both CT and plain radiographs provided better definition and localization of calcifications in all cases. On MR large foci of calcification produced discrete areas of signal void (Fig. 2A). Small calcifications resulted in an inhomogeneous appearance in some cases (Figs. 3 and 4). The areas of lowest signal in tumors on MR did not always correspond to areas of calcification (Fig. 4). Fourteen cases had periosteal reaction seen on plain films or CT, and this could be identified by MR in eight cases (Fig. 1C).

Pathologic-radiologic correlation in two cases of osteogenic sarcoma showed the reliability of MR to display the true extent of tumor in bone marrow and soft tissue. In one case, a lateral plain film of the distal femur showed an osteoblastic lesion with a wide zone of transition, periosteal reaction, and soft-tissue mass (Fig. 5). Comparison of a sagittal MR image with the gross specimen showed that MR predicted the proximal extent of marrow disease within several millimeters. Histologically no tumor was present in the epiphysis. A large amount of tumor necrosis was present, with the greatest amount of viable tumor adjacent to the epiphyseal line. Chondroid as well as osteoid matrix were present, but their distribution did not correlate directly with the inhomogeneous signal of infiltrated marrow. Soft-tissue extension and periosteal reaction were seen on MR. In this case CT provided

Fig. 2.—Osteogenic sarcoma of the right humerus.

A, Coronal SE 2000/60 image shows primary tumor (arrows). Calcified axillary node metastases (arrowheads) appear as areas of decreased signal.

B, Chest radiograph confirms densely calcified axillary node metastases (arrowheads).

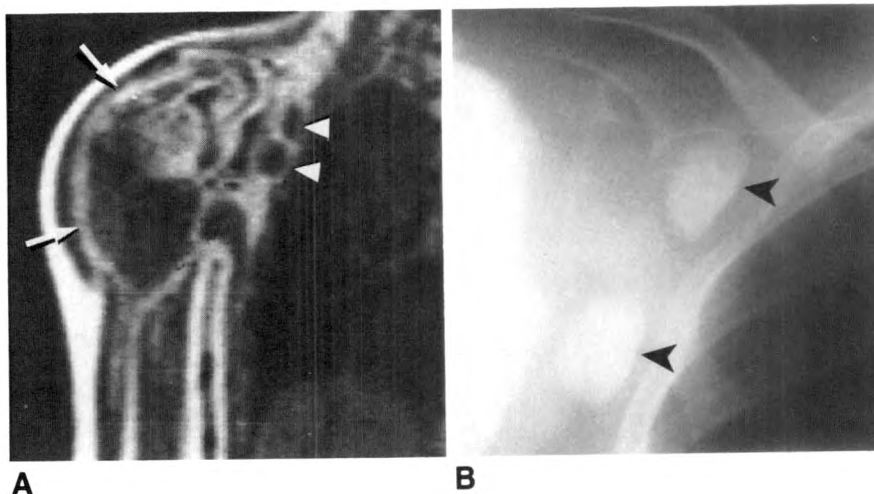
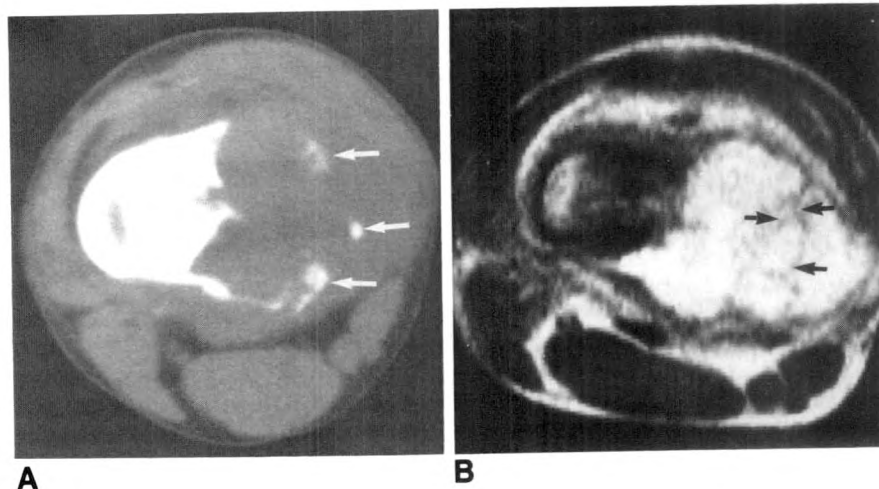


Fig. 3.—Osteogenic sarcoma of the femur.

A, Bone-window CT scan shows several small areas of calcification (arrows), and tumor extension into marrow and surrounding soft tissue.

B, Axial SE 1000/60 image shows inhomogeneous signal from tumor (arrows) that cannot be correlated with CT as being areas of calcification, which shows limitation of MR in the evaluation of calcium. Tumor replacement of normal marrow signal is seen.



better definition than MR of calcium deposition in the tumor matrix.

Examination of a coronal specimen section in another case of osteogenic sarcoma showed tumor extension into the epiphysis (Fig. 6). The extent of tumor involvement of the marrow and soft tissue in the gross specimen directly correlated with the abnormal signal shown by MR.

Flowing blood emitted no signal and appeared black on all pulse sequences. In 12 cases, MR showed the relationship of tumor to blood vessels more easily than CT did. Scanning in the sagittal plane was often useful for demonstration of the superficial femoral and popliteal arteries. The coronal plane provided excellent demonstration of major pelvic vessels and displacement of pelvic structures (Fig. 7).

Improved anatomic information can be derived from MR by the opportunity to image in several planes. In Figure 8 a coronal MR image showed extension of a spinal Ewing's sarcoma behind the diaphragmatic crus. The CT scan was initially interpreted as an adrenal mass that was invading bone.

Response to therapy could be monitored for both Ewing's (Fig. 8) and osteogenic sarcomas. In three cases of osteogenic sarcoma, tumor enlargement documented by MR allowed for the early cessation of methotrexate chemotherapy, followed by amputation.

Discussion

We found infiltration of the bone marrow by osteogenic and Ewing's sarcoma to be clearly shown by MR; in five cases it was superior to CT. Tumor has a long T1 relaxation time and thus has a signal intensity lower than that of marrow fat on T1-weighted images [16]. Pathologic correlation of marrow involvement by two osteogenic sarcomas (Figs. 5 and 6) showed the marrow involvement demonstrated by MR to be within several millimeters of that documented on the pathologic specimen. This supports the findings by other investigators of the reliability of MR in showing the true marrow extent of neoplasm [10, 16].

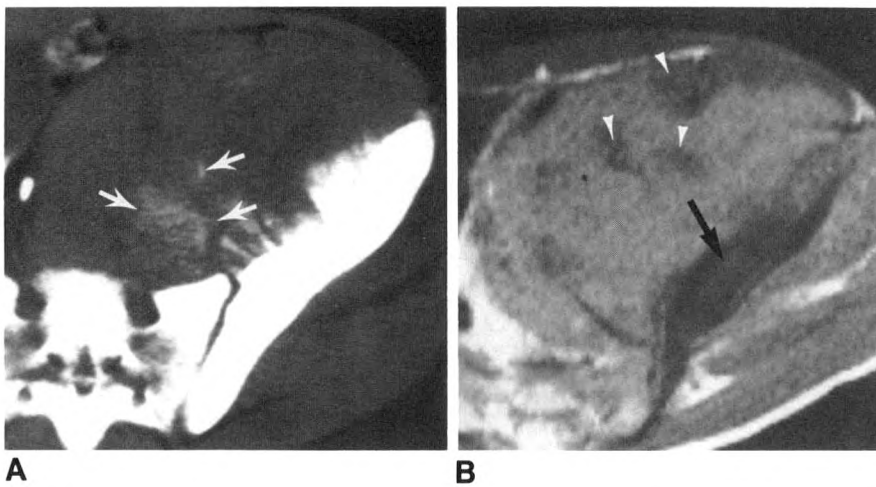


Fig. 4.—Ewing's sarcoma of the left ilium.
A, CT shows areas of calcification (*arrows*) within tumor with periosteal reaction and soft-tissue mass.

B, Axial SE 500/30 image shows inhomogeneous signal in tumor, but areas of lowest signal (*arrowheads*) do not correspond to calcifications seen on CT. There is marrow replacement by tumor (*arrow*).

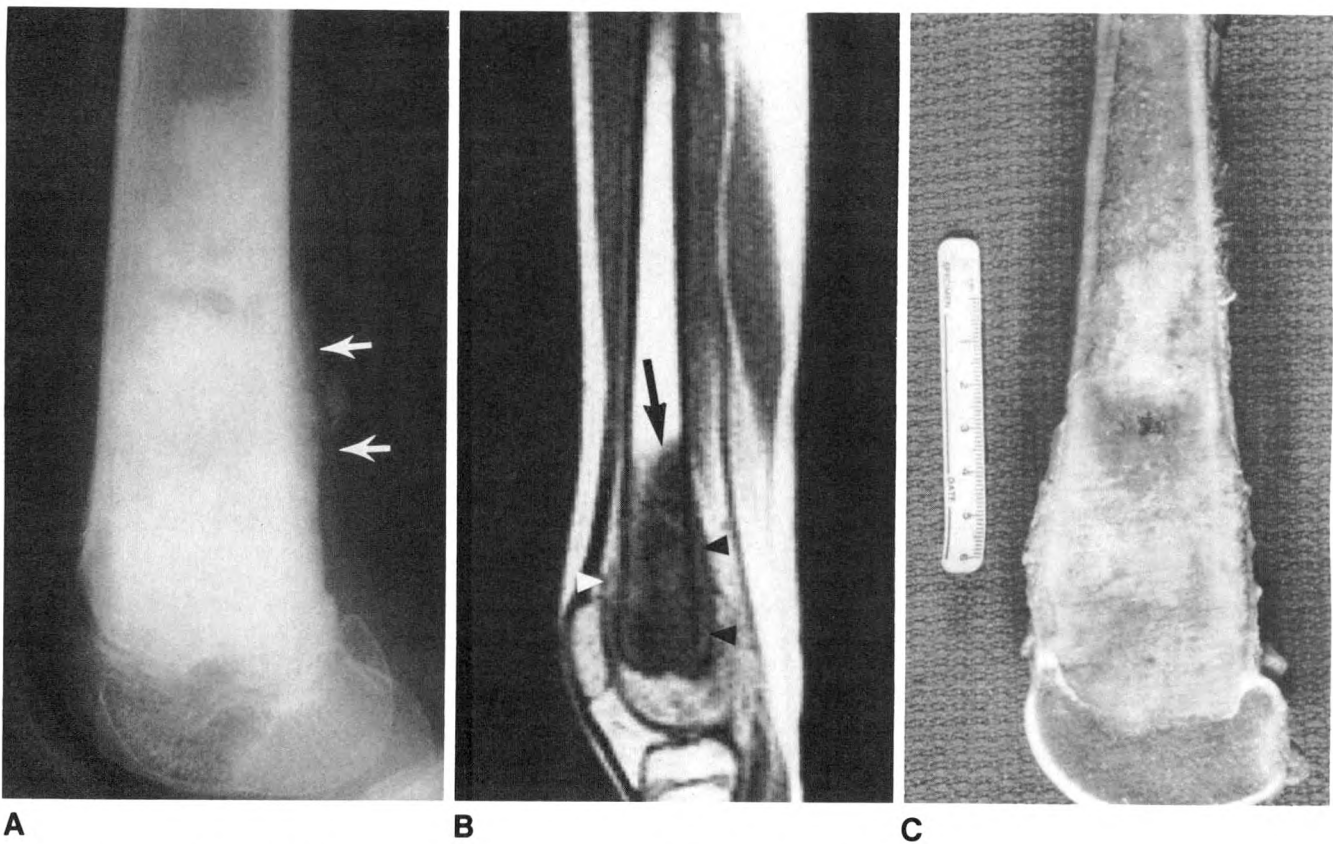


Fig. 5.—Osteogenic sarcoma of the femur.
A, Preoperative radiograph shows osteoblastic marrow lesion with periosteal reaction and a soft-tissue mass (*arrows*).
B, Sagittal SE 500/30 image shows proximal tumor extent in marrow

(*arrow*) and soft-tissue mass (*arrowheads*).

C, Gross specimen. Tumor extends proximally into marrow 12 cm and does not involve epiphysis as predicted by MR (B).

The inhomogeneous MR signal of osteogenic sarcoma did not correlate with the histologic distribution of chondroid or osteoid tumor matrix. We did find on MR that tumor spread into the bone marrow can extend beyond the cortical or soft-tissue component of both of these neoplasms. Decreased

signal in bone marrow on T1-weighted images, however, is not specific for tumor since avascular necrosis or any marrow-replacing process can produce the same signal decrease [14, 16].

In six cases MR was superior to CT in defining soft-tissue

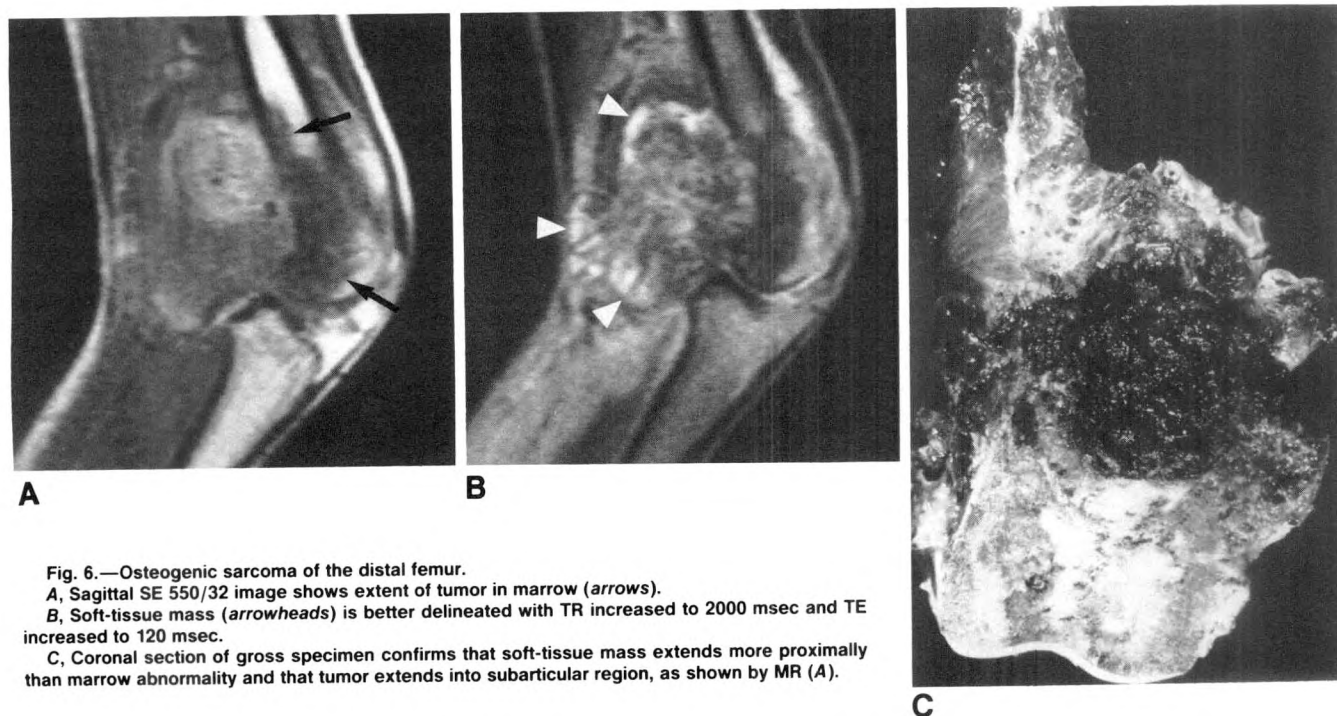


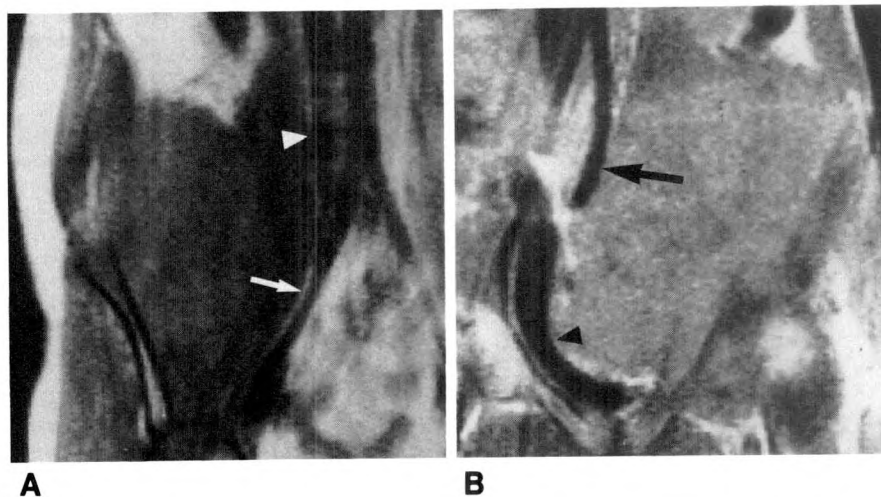
Fig. 6.—Osteogenic sarcoma of the distal femur.

A, Sagittal SE 550/32 image shows extent of tumor in marrow (arrows).

B, Soft-tissue mass (arrowheads) is better delineated with TR increased to 2000 msec and TE increased to 120 msec.

C, Coronal section of gross specimen confirms that soft-tissue mass extends more proximally than marrow abnormality and that tumor extends into subarticular region, as shown by MR (A).

Fig. 7.—Ewing's sarcoma arising from iliac wings in two different patients shows displacement of right (A) and left (B) iliac arteries (arrows), inferior vena cava (A, arrowhead), and bladder (B, arrowhead).



contrast and tumor extension. T2-weighted images enhanced soft-tissue contrast between tumor and muscle better than T1-weighted images.

MR was found to be inferior to CT in showing soft-tissue calcification and tumor matrix mineralization in all 16 cases in which calcium was shown by either CT or plain films. This was more of a problem in the interpretation of osteogenic sarcomas.

MR can show thickening, infiltration, and destruction of the cortex by both osteogenic sarcoma and Ewing's sarcoma. Bone cortex lacks mobile protons and thus has dark signal on all pulse sequences. Tumor invasion of bone cortex can be identified because of its prolonged T1 and T2 relaxation

times. Although Zimmer et al. [5] believed that cortical disease was more obviously shown on longer SE sequences (TE = 60 msec, TR = 2,000 msec), in 15 cases with evident cortical disease on MR this was seen as well on T1- as on T2-weighted MR pulse sequences. Cortical disease was appreciated more consistently on axial images since problems arose with partial voluming of signal intensity on coronal and sagittal images; and cortical outline was not as sharply defined when the long axis of the bone took a more angled or oblique course, as has been reported by other workers [14]. Periosteal reaction could be identified in eight cases by MR.

In both osteogenic and Ewing's sarcoma, MR can show the relationship of tumor to vasculature without the use of

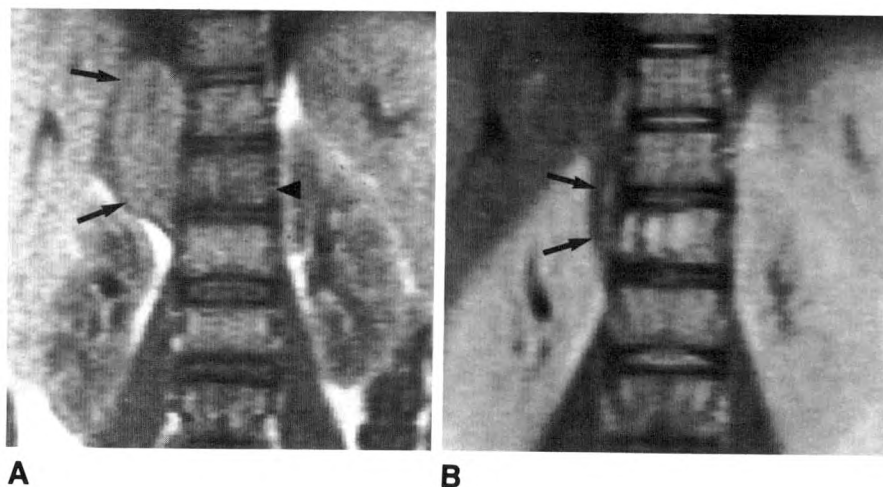


Fig. 8.—Ewing's sarcoma arising from spine.
A, Coronal SE 500/30 image shows soft-tissue mass (arrows) and decreased marrow signal of involved vertebral body (arrowhead).
B, Coronal SE 2000/30 image after therapy shows decrease in size of soft-tissue mass (arrows).

contrast agents. Part of this advantage rests with the ability of MR to image in the coronal and sagittal planes. Pettersson et al. [10] have also commented on the advantage of MR in providing information on tumor relationship to major vessels.

Although CT can be used in follow-up to monitor the response to therapy of osteogenic sarcoma [17], we found MR to be a suitable alternative. Interval growth of tumor shown by MR allowed cessation of chemotherapy and early amputation in three cases of osteogenic sarcoma. MR was useful as a follow-up to monitor therapy response of three cases of Ewing's sarcoma.

In summary, we have found MR to provide adjunct information in the preoperative planning and posttherapy follow-up in cases of Ewing's and osteogenic sarcoma. Images obtained in multiple planes and with both T1- and T2-weighted pulse sequences are necessary to evaluate the bone-marrow and soft-tissue extent of these two tumors. The axial plane allows best assessment of bone cortex without partial-volume artifacts. Sagittal and coronal planes provide an excellent display of the relationship of tumor to major vessels and provide images of the entire length of a bone for evaluation of proximal bone-marrow or epiphyseal extent of tumor and skip lesions. In general, T1-weighted images provide the greatest contrast between tumor and marrow, T2-weighted images show the most contrast between tumor and muscles, and tumor-infiltrating-bone cortex may be seen with either. One limitation of MR, compared with CT, is the inability of MR to definitively identify tumor matrix calcification and periosteal reaction in all cases.

REFERENCES

1. Brady TJ, Gebhardt MC, Pykett IL, et al. NMR imaging of forearms in healthy volunteers and patients with giant-cell tumor of bone. *Radiology* 1982;144:549-552
2. Moon KL Jr, Genant HK, Helms CA, Chafetz NI, Crooks LE, Kaufman L. Musculoskeletal applications of nuclear magnetic resonance. *Radiology* 1983;147:161-171
3. Brady TJ, Rosen BR, Pykett IL, McGuire MH, Mankin HJ, Rosenthal DI. NMR imaging of leg tumors. *Radiology* 1983;149:181-187
4. Berquist TH. Magnetic resonance imaging: preliminary experience in orthopedic radiology. *Magnetic Resonance Imag* 1984;2:41-52
5. Zimmer WD, Berquist TH, McLeod RA, et al. Bone tumors: magnetic resonance imaging versus computed tomography. *Radiology* 1985;155:709-718
6. Bloem JL, Falke THM, Taminiau AHM, et al. Magnetic resonance imaging of primary malignant bone tumors. *Radiographics* 1985;5:853-886
7. Baker HL Jr, Berquist TH, Kispert DB, et al. Magnetic resonance imaging in a routine clinical setting. *Mayo Clin Proc* 1985;60:75-90
8. Hudson TM, Hamlin DJ, Enneking WF, Pettersson H. Magnetic resonance imaging of bone and soft tissue tumors: early experience in 31 patients compared with computed tomography. *Skeletal Radiol* 1985;13:134-146
9. Pettersson H, Hudson T, Hamlin D, et al. Magnetic resonance imaging of sacrococcygeal tumors. *Acta Radiol [Diagn]* (Stockh) 1985;26:161-165
10. Pettersson H, Hamlin DJ, Mancuso A, Scott KN. Magnetic resonance imaging of the musculoskeletal system. *Acta Radiol [Diagn]* (Stockh) 1985;26:225-234
11. McMillin KI, Pennes DR, Aisen A, Braunstein, Martel W. MRI and CT evaluation of primary bone and soft tissue tumors. Presented at the annual meeting of the American Roentgen Ray Society, Boston, April 1985
12. Cohen MD, Klatte EC, Baehner R, et al. Magnetic resonance imaging of bone marrow disease in children. *Radiology* 1984;151:715-718
13. Fletcher BD, Scoles PV, Nelson AD. Osteomyelitis in children: detection by magnetic resonance. *Radiology* 1984;150:57-60
14. Totty WG, Murphy WA, Ganz WY, Kumar B, Daum WJ, Siegel BA. Magnetic resonance imaging of the normal and ischemic femoral head. *AJR* 1984;143:1273-1280
15. Tjon-A-Tham RT, Bloem JL, Falke THM, et al. Magnetic resonance imaging in Paget disease of the skull. *AJNR* 1985;6:879-881
16. Daffner RH, Lupetin AR, Dash N, Deeb ZL, Sefczek RJ, Schapiro RL. MRI in the detection of malignant infiltration of bone marrow. *AJR* 1986;146:353-358
17. Mail JT, Cohen MD, Mirkin D, Provisor AJ. Response of osteosarcoma to preoperative intravenous high-dose methotrexate chemotherapy: CT evaluation. *AJR* 1985;144:89-93

Parosteal Osteosarcoma: Radiologic-Pathologic Correlation with Emphasis on CT

Marvin M. Lindell, Jr.¹
Ali Shirkhoda¹
A. Kevin Raymond²
John A. Murray³
Thomas S. Harle¹

Parosteal osteosarcoma, a distinct entity in which the neoplasm arises on the bone surface, presents characteristic features. Thorough radiologic and histologic evaluation and early definitive surgery usually result in a favorable prognosis and make limb salvage feasible in many adult patients. Twenty-six patients with proven parosteal osteosarcoma were seen at The University of Texas M. D. Anderson Hospital and Tumor Institute at Houston. All were examined by conventional radiography, 16 by CT, and one by both CT and MR. CT is valuable for the evaluation of tumor invasion of the medullary canal, involvement of the cortex, and extension into the soft tissues, findings frequently not demonstrable by other noninvasive techniques. Additional information is obtained regarding the presence and location of satellite lesions and intralesional radiolucent areas and the relationship of the vascular bundle to the tumor mass. These findings are important for planning both percutaneous biopsy and surgery.

The radiographic and pathologic features of conventional parosteal osteosarcoma (POS) have been well documented [1-15]. POS is a relatively rare primary neoplasm of bone. In some series it constitutes about 1.7% of all benign and malignant tumors of bone [12]. The tubular long bones of the appendicular skeleton are usually involved, most often the popliteal surface of the femur (79%).

Recently, a subset or variant of conventional POS has been recognized: dedifferentiated POS. In most cases dedifferentiated POS occurs as a result of recurrence of a previously treated conventional POS; however, dedifferentiated POS may also occur as the primary manifestation. In either case, this neoplasm is a high-grade malignant tumor with full capacity for systemic metastasis and death in more than 50% of affected patients. The behavior of dedifferentiated POS, therefore, is more akin to conventional high-grade intramedullary osteosarcoma than to conventional POS.

Conventional POS is a tumor of indolent behavior in which the potential morbidity and mortality of contemporary chemotherapy are unjustified and unwarranted. Treatment is aimed at the primary lesion and is surgical. However, considering the mortality in dedifferentiated POS (>50%), chemotherapy may affect it significantly. At M. D. Anderson Hospital the diagnosis of dedifferentiated POS indicates the use of preoperative chemotherapy: intraarterial cis-platinum and systemic adriamycin. Therefore, accurate evaluation of these patients before definitive surgery is essential in order to identify those who might benefit from preoperative chemotherapy. Twenty-six cases of conventional and dedifferentiated POS, (16 had CT and one MR) are reviewed to determine the radiographic spectrum of conventional POS and which features might suggest the diagnosis of dedifferentiated POS.

Materials and Methods

The clinical, radiographic, and histologic materials of 26 patients with either conventional POS (23) or dedifferentiated POS (three) seen at The University of Texas M. D. Anderson

Received February 28, 1986; accepted after revision September 19, 1986.

Presented at the annual meeting of the American Roentgen Ray Society, Washington, DC, April 1986.

¹ Department of Diagnostic Radiology, The University of Texas M. D. Anderson Hospital and Tumor Institute, 6723 Bertner Ave., Houston, TX 77030. Address reprint requests to M. M. Lindell.

² Department of Pathology, The University of Texas M. D. Anderson Hospital and Tumor Institute, 6723 Bertner Ave., Houston, TX 77030.

³ Department of Orthopedic Surgery, The University of Texas M. D. Anderson Hospital and Tumor Institute, 6723 Bertner Ave., Houston, TX 77030.

AJR 148:323-328, February 1987
0361-803X/87/1482-0323
© American Roentgen Ray Society

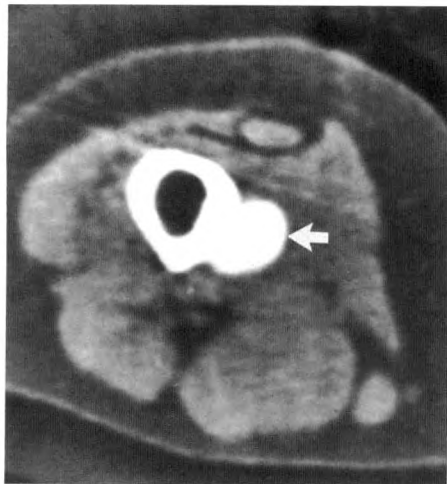


Fig. 1.—CT shows parosteal osteosarcoma of distal femur with localized and homogeneous calcification (arrow).



Fig. 2.—CT shows parosteal osteosarcoma of distal femur with amorphous and irregular calcification.

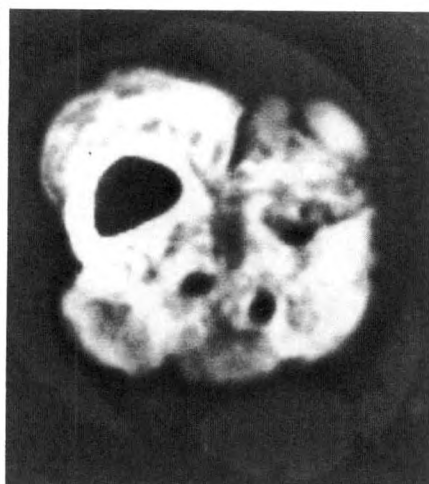


Fig. 3.—CT shows parosteal osteosarcoma of distal femur with equivocal findings of cortical bone invasion.

Hospital and Tumor Institute at Houston between 1976 and 1986 were reviewed. Of the 26 patients, 16 (seven men and nine women, ranging in age from 16 to 47 years) were examined by CT and one (a woman) was studied by CT and MR. The neoplasm was located in the distal femur in 13 patients and in the proximal tibia in three patients. All tumors were treated surgically and histologically documented as either conventional or dedifferentiated POS. In six cases, percutaneous biopsy was done before resection of the neoplasm.

The surgical specimens were first correlated with the preoperative radiographs and then sectioned for further correlation with the CT images. Specimens from patients receiving preoperative chemotherapy were sectioned according to protocol to ensure that qualitative and quantitative evaluation of tumor necrosis could be determined. This also provided three-dimensional specimen preoperative radiographic comparison and precise spatial localization of viable tumor.

The CT scans were obtained on Siemens Somatom II, GE 8800, and EMI 5005 scanners. Depending on the scanning device used, scans were obtained by using an 8- to 10-mm slice interval and table increment. Window widths and levels were selected for optimal image display. The one MR study was done on a Diasonics superconductive 0.35-T unit, and the images were obtained in axial, coronal, and sagittal planes.

Results

The size of the neoplasms ranged from 2 to 12 cm by measurement of the greatest transverse dimension on the CT images. In nine patients, significant intralesional components of the tumor were nonossified. In three of these, the area of lucency was large, well defined, and located deep within the main portion of the tumor. In six they tended to be small, poorly defined, and peripherally located at the interface of tumor and normal tissue. In seven patients, the tissue plane surrounding the neoplasm was obliterated, probably secondary to edema. As shown by CT, three patterns of calcification within the tumor masses were recognized: amorphous and irregular in five patients, localized and homogeneous in seven, and a mixture of both in four (Figs. 1–3).

By using proper window and center settings, the CT images obtained were reviewed for evaluation of the size and extent of the tumor mass. There was excellent demonstration of radiolucent areas within the tumors as well as visualization of satellite nodules. Of the six cases with radiolucent areas shown on CT, only two were seen on conventional radiographs. In two cases, the radiolucent areas were shown to be hypervascular angiographically and corresponded to histologically documented foci of high-grade sarcoma, thereby establishing the diagnosis of dedifferentiated POS (Fig. 4). Satellite lesions were present in seven cases; all were seen on CT and six were visible on radiographs. In two cases, CT showed the satellite lesion to a much better extent than conventional radiographs did (Fig. 5).

The cortical bone was evaluated in all patients who had CT or MR. In 12 patients (71%), the cortex appeared definitely invaded, and in two there was no demonstrable abnormality of the cortical bone. In two patients, the judgment was equivocal and no firm diagnostic conclusion could be made (Fig. 3). In one patient, the cortical involvement was better seen on the sagittal MR images than on axial CT or MR (Fig. 5D). Furthermore, by using the same CT setting, the density of the medullary cavity was compared with the contralateral limb at the same level. Eleven patients having CT did not have evidence of medullary involvement, while in five cases the marrow cavity was invaded by the neoplasm (Fig. 4). There was no tumor in the marrow cavity of the patient examined by both CT and MR.

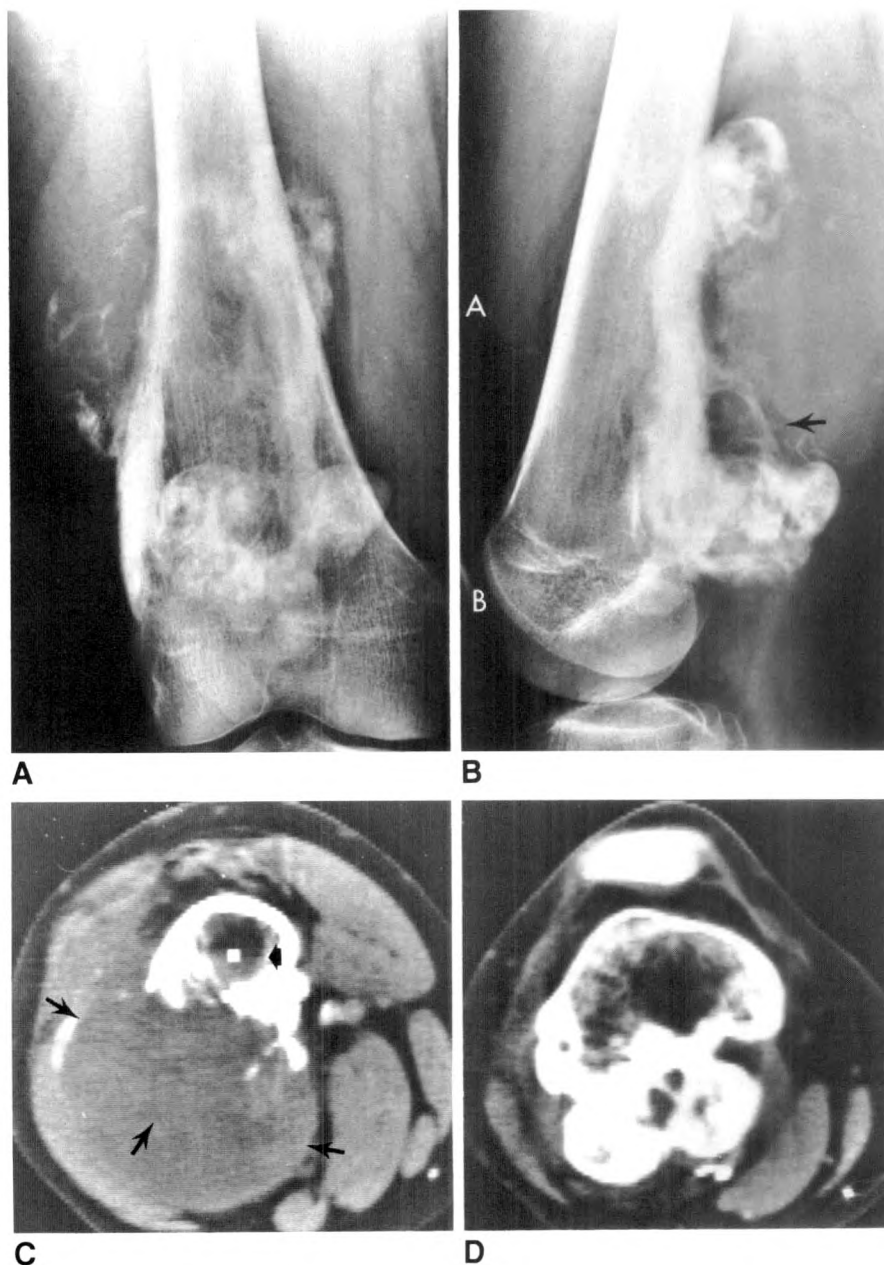
Histologically, all cases of conventional POS were composed of relatively bland spindle cells, which produce well-formed bone. The peripheral areas of radiolucency corresponded to either normal or neoplastic elements. The normal structures in these areas included foci of entrapped fibrous connective tissue, tendon, adipose tissue, vessels, and skeletal muscle. Radiolucent neoplastic elements in conventional POS corresponded to foci of nonmineralized low-grade carti-

Fig. 4.—A, Anteroposterior radiograph shows large dedifferentiated parosteal osteosarcoma of distal femur.

B, Lateral radiograph shows dedifferentiated parosteal osteosarcoma of distal femur having large radiolucent area (arrow). (Levels A and B correspond to CT levels in C and D).

C, CT at level A shows dedifferentiated parosteal osteosarcoma of distal femur (long arrows) with cortical erosion. Soft-tissue plane is obliterated. Cursor shows tumor within medullary canal (short arrow).

D, CT at level B shows calcified tumor matrix in lower area of mass.



lage (i.e., cartilage cap or satellite lesions) or areas of otherwise typical low-grade tumor that did not produce bone matrix.

The three cases of dedifferentiated POS presented a consistent pattern. In each, large areas were similar to conventional POS: low-grade bland spindle cells producing well-formed bone. These areas corresponded to those parts of the tumor that were radiopaque and radiographically indistinguishable from conventional POS. However, superimposed on otherwise typical conventional POS were areas of high-grade sarcoma. These high-grade components corresponded to the large, well-defined radiolucent areas deep within the lesions. In the two cases in which the high-grade component

was identified before surgery (i.e., at preoperative needle biopsy), each patient underwent preoperative chemotherapy. Histologic examination of the subsequent resection specimens showed a consistent phenomenon: the low-grade component showed minimal or no tumor necrosis and was left virtually unaltered by the chemotherapy. However, the high-grade component showed changes similar to those observed in conventional high-grade intramedullary osteosarcoma. These latter changes consisted of massive tumor necrosis, with reparative changes and an ingrowth of granulation tissue [16].

Four patients with conventional POS have had local recurrence only. These have been managed successfully with

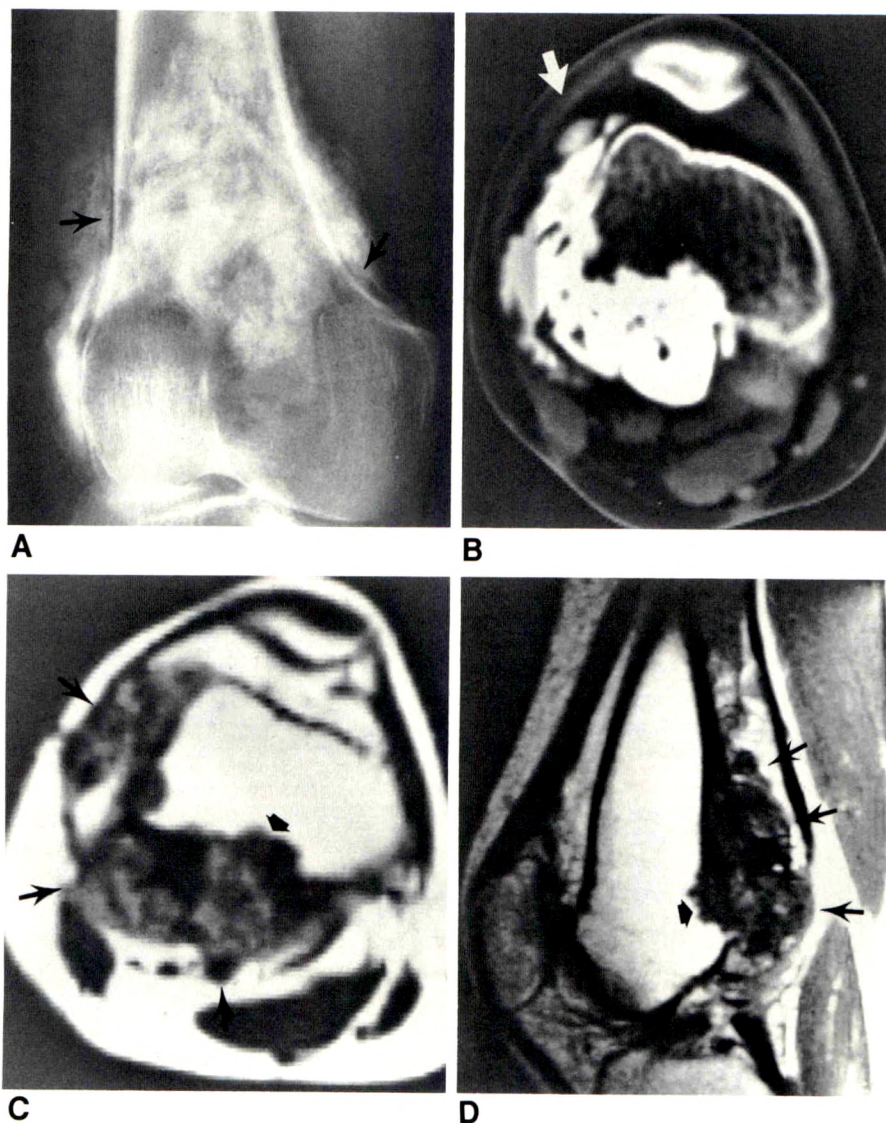


Fig. 5.—A, Anteroposterior radiograph shows parosteal osteosarcoma of distal femur to be ossified and enveloping bone. Radiolucent cleavage planes (arrows) between normal cortex and neoplasm.

B, CT shows parosteal osteosarcoma of distal femur eroding cortex posterolaterally. Satellite lesion anteriorly (arrow).

C, Transaxial MR image (TR 2 sec, TE 60 msec) shows parosteal osteosarcoma of distal femur as tumor with mixture of intermediate- and low-intensity signals (long arrows). Level corresponds to CT image. Note erosion of posterior cortex in same area as on CT (short arrow).

D, Parasagittal MR image (TR 0.5 sec, TE 40 msec) of parosteal osteosarcoma of distal femur shows craniocaudal extent of tumor (long arrows) and erosion of posterior cortex (short arrow).

localized therapy. Reresection was performed in three patients and an elective amputation in one patient who believed that she could not tolerate the attendant postoperative training required for a new prosthesis. One patient with dedifferentiated POS had pulmonary metastases at presentation and died of systemic disease within 6 months of surgery. The other patients are alive and well without evidence of local or systemic recurrence.

Discussion

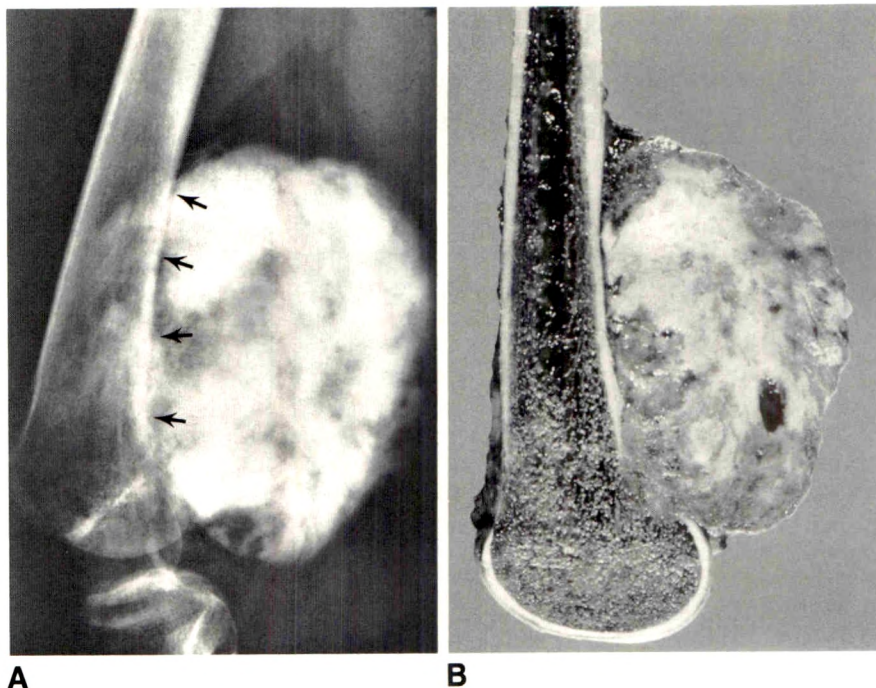
Since its original description, parosteal osteosarcoma has been traditionally regarded as the single manifestation of osteosarcoma arising on the periosteal aspect of bone. However, it has become progressively more apparent that conventional POS represents only one form of a heterogeneous group of osteosarcomas that arise on the cortical surface; the other members of this group are periosteal osteosarcoma

[17], dedifferentiated POS [18], and high-grade surface osteosarcoma [19].

Conventional POS remains a distinct pathologic/biologic entity. Conventional POS is seen most often in the third and fourth decades, affects women more often than men, and has a marked predilection for the long bones of the appendicular skeleton, in particular the posterior aspect of the distal femur [4, 20, 21]. Histologically, conventional POS is a low-grade form of osteosarcoma in which bland spindle cells produce well-formed bone. Biologically, it is a slowly progressive disease. Pulmonary metastases tend to appear late in the course of the disease, frequently following one or more local recurrences. Therefore, therapy is directed toward control of the primary tumor and is surgical. Early diagnosis (which depends on clinical suspicion, thorough radiologic evaluation, and accurate histologic interpretation followed by appropriate therapy) usually presages a favorable prognosis. Within technical limitations, adult patients may qualify as

Fig. 6.—A, Lateral radiograph shows large parosteal osteosarcoma of distal femur demonstrating radiolucent cleavage plane between tumor and cortex (arrows).

B, Specimen photograph shows large parosteal osteosarcoma of distal femur. Note erosion of cortex by lower aspect of tumor.



candidates for limb salvage. Long-term survival is in excess of 80–90% in patients receiving appropriate therapy after the onset of the disease.

Dedifferentiated POS is a rare and unusual bone tumor. Most cases have originated as typical examples of conventional POS that, after multiple local recurrences, have undergone “transformation” into a histologically high-grade sarcoma. However, dedifferentiated POS as a primary manifestation of an osteosarcoma arising on a cortical surface is also well described by Wold et al. [18] (Case 11). In this primary form the radiographic, gross, and histologic features of the neoplasm closely mimic conventional POS. However, superimposed on the low-grade tumor are areas of high-grade sarcoma. In either case, primary or secondary, the ultimate prognosis is a function of the high-grade component and survival is <50% at 5 years.

Several parameters were investigated to help define more fully the spectrum of the radiographic features of conventional POS and attempt to identify those unique features of dedifferentiated POS. These included the presence or absence of cortical or medullary cavity invasion, the nature of tumor soft-tissue interfaces, and the evaluation of areas of intralesional radiolucency.

Radiographically, conventional POS is dense and lobular with a broad base at the level of attachment to the cortical bone. Early tumors may have only a small sessile attachment to the bone surface [4]. The presence of a radiolucent cleavage plane between portions of the tumor and cortex is helpful for diagnosis (Fig. 6). These slow-growing, bone-producing malignant neoplasms tend to grow circumferentially along the cortical surface and may eventually envelop the bone shaft. If left untreated, they may eventually attain considerable size. The cases in our series follow this pattern well.

The differential diagnoses of POS are well known, having been the subject of a number of excellent studies. Included are osteochondroma, myositis ossificans, extraosseous osteosarcoma, osteosarcoma, ossifying or calcifying hematoma, and exuberant callus [7, 9, 12, 15, 21, 22].

Many investigators believe that the medullary cavity is usually spared, except in cases of previous treatment or a history of long duration of growth. The precise biologic significance of medullary involvement in conventional POS is unclear. Some authors [20, 23] have interpreted the presence of tumor within the marrow cavity as indicative of a more aggressive lesion, which is invariably associated with pulmonary metastases and has a poorer prognosis. However, others [5, 9, 12, 15] have submitted data that the prognosis is not significantly affected by medullary extension. Although the present attitude seems to indicate that the ultimate prognosis may be related to the degree of medullary involvement [24], our experience has been that medullary disease does not exclude successful limb salvage or significantly alter prognosis. Furthermore, none of the three cases in our series with pulmonary metastases had marrow invasion. Others [25–33] have reported malignant bone and soft-tissue sarcomas that have been examined by CT for evaluation of tumor invasion into the medullary canal.

Identification of satellite nodules, which are so well shown on CT, provides further valuable information for treatment planning. If the patient is having a limb-salvage procedure and these nodules are not totally removed, the frequency of recurrent tumor would undoubtedly be higher.

Although the density of the calcific tumor is often homogeneous, the next most common pattern is amorphous and irregular. These findings are best appreciated on CT and do not correlate with the degree of malignancy of the tumors.

With rare exceptions, a notable feature of POS is the absence of periosteal reaction [4, 10–12, 21].

The CT images may exhibit intralesional lucent defects that can be either superficial or deep within the substance of the tumor, and may be hypervascular at angiography (Fig. 4); if so, they often constitute high-grade sarcoma. If biopsy confirms this, the tumor may then be diagnosed as dedifferentiated POS [18–20] (Fig. 4). The ability of CT to localize these radiolucent areas is important in the evaluation of the grade of malignancy. Needle biopsies are performed in our institution on all suspected malignant bone tumors that exhibit areas of hypervascularity on angiography. CT is used in guiding the interventional radiologist to the areas within the tumor most likely to yield useful pathologic material. A biopsy that reveals the presence of dedifferentiated POS changes our treatment regimen. These patients are taken from the conventional POS protocol (surgery only) and treated as other osteosarcoma cases (preoperative chemotherapy followed by surgery and adjuvant chemotherapy).

CT scanning is extremely useful in the determination of the precise size of the lesion, which is of prime prognostic significance in a complex composite that includes the anatomic setting, growth rate, and time of physician intervention [23]. The extent of the soft-tissue component of the POS, which is well seen on CT, is most important because the size and location of a soft-tissue component may preclude a limb salvage procedure. Cortical and medullary involvement continue to be important considerations in planning the proper surgical approach.

MR is valuable in the investigation of the musculoskeletal system [34, 35], but in the one case in this series in which it was done, MR did not add any new information beyond that seen on CT images. However, in this case MR imaging in the sagittal plane better illustrated cortical bone invasion and neoplastic bulk (Fig. 5).

REFERENCES

- Geschlechter CF, Copeland MM. Parosteal osteoma in bone: a new entity. *Ann Surg* 1951;133:790–807
- Jaffe HL, Selin G. Golden: tumors of bones and joints. In: Ashford M, ed. *New York Academy of Medicine: the musculoskeletal system. A Symposium*. New York: MacMillan, 1952:338–339
- Dwinell LA, Dahlin DC, Ghormley RK. Parosteal (juxtacortical) osteogenic sarcoma. *J Bone Joint Surg [Am]* 1954;36:732–744
- Stevens GM, Pugh DG, Dahlin DC. Roentgenographic recognition and differentiation of parosteal osteogenic sarcoma. *AJR* 1957;78:1–12
- Jaffe HL. *Tumors and tumorous conditions of the bone and joints*. Philadelphia: Lea & Febiger, 1958
- Jacobson SA. Early juxtacortical osteosarcoma (parosteal osteoma). *J Bone Joint Surg [Am]* 1958;40:1310–1328
- Scaglietti O, Calandriello B. Ossifying parosteal sarcoma. Parosteal osteoma or juxtacortical osteogenic sarcoma. *J Bone Joint Surg [Am]* 1962;44:635–647
- Dahlin DC. Parosteal osteogenic sarcoma (juxtacortical osteogenic sarcoma). In: *Bone tumors*, 2nd ed. Springfield, IL: Thomas, 1967:176–185
- Wolfe DA, Carter PR. Parosteal osteosarcoma. *AJR* 1969;105:142–146
- Van der Heul RO, Von Ronnen JR. Juxtacortical osteosarcoma. *J Bone Joint Surg [Am]* 1967;49:415–439
- Edeiken J, Farrell C, Ackerman LV, Spjut HJ. Parosteal sarcoma. *AJR* 1971;111:579–583
- Spjut HJ, Dorfman HD, Fechner RE, Ackerman LA. Tumors of bone and cartilage. In: *Atlas of tumor pathology*, fasc 5. Washington, DC: Armed Forces Institute of Pathology, 1971:166–174
- Farr GH, Huvo AG. Juxtacortical osteogenic sarcoma. *J Bone Joint Surg [Am]* 1972;54:1205–1216
- Aegerter E, Kirkpatrick JA. Orthopedic diseases. In: *Physiology, pathology, radiology*, 4th ed. Philadelphia: Saunders, 1975:530–537
- Unni KK, Dahlin DC, Beabout JW, Ivins JC. Parosteal osteogenic sarcoma. *Cancer* 1976;37:2466–2475
- Shirkhoda A, Jaffe N, Wallace S, Ayala A, Lindell MM, Zornoza J. Computed tomography of osteosarcoma after intraarterial chemotherapy. *AJR* 1985;144:95–99
- Spjut HJ, Ayala AG, deSantos LA, Murray JA. Periosteal osteosarcoma. In: *Management of primary bone and soft tissue tumors*. Chicago: Year Book Medical, 1977:79–95
- Wold LE, Unni KK, Beabout JW, Sim FH, Dahlin DC. Dedifferentiated parosteal osteosarcoma. *J Bone Joint Surg [Am]* 1984;66:53–59
- Wold LE, Unni KK, Beabout JW, Pritchard DJ. High-grade surface osteosarcomas. *Am J Surg Pathol* 1984;8:181–186
- Campanacci M, Picci P, Gherlinzoni F, Guerra A, Bertoni F, James RN. Parosteal osteosarcoma. *J Bone Joint Surg [Br]* 1984;66:313–321
- Smith J, Ahuya SC, Huvo AG, Bullough PG. Parosteal (juxtacortical) osteogenic sarcoma. A roentgenological study of 30 patients. *J Can Assoc Radiol* 1978;29:167–175
- Amendola MA, Glazer GM, Adha FP, Francis IR, Weatherbee L, Martel W. Myositis ossificans circumscripta: computed tomographic diagnosis. *Radiology* 1983;149:775–779
- Enneking WF, Spanier SS, Goodman MA. A system for the surgical staging of musculoskeletal sarcoma. *Clin Orthop* 1980;153:106–120
- Hudson TM, Springfield DS, Benjamin M, Bertoni F, Present DA. Computed tomography of parosteal osteosarcoma. *AJR* 1985;144:961–965
- Wilson JS, Korobkin M, Genant HK, Bovill EG Jr. Computed tomography of musculoskeletal disorders. *AJR* 1978;131:55–61
- Levine E, Lee KR, Neff JR, Maklad NF, Robinson RG, Preston DF. Comparison of computed tomography and other imaging modalities in the evaluation of musculoskeletal tumors. *Radiology* 1979;131:431–437
- Schumacher TM, Genant HK, Korobkin M, Bovill EG Jr. Computed tomography. Its use in space-occupying lesions of the musculoskeletal system. *J Bone Joint Surg [Am]* 1978;60:600–607
- Weinberger G, Levinsohn EM. Computed tomography in the evaluation of sarcomatous tumors of the thigh. *AJR* 1978;130:115–118
- McLeod RA, Stephens DH, Beabout JW, Sheedy PF II, Hattery RR. Computed tomography of the skeletal system. *Semin Roentgenol* 1978;13:235–247
- Destouet JM, Gilula LA, Murphy WA. Computed tomography of long-bone osteosarcoma. *Radiology* 1979;131:439–445
- Weis L, Heelan RT, Watson RC. Computed tomography of orthopedic tumors of the pelvis and lower extremities. *Clin Orthop* 1978;130:254–259
- deSantos LA, Murray JA, Finkelstein JF, et al. The radiographic spectrum of periosteal osteosarcoma. *Radiology* 1978;127:123–129
- Orcutt J, Ragsdale BD, Curtis DJ, Levine MI. Misleading CT in parosteal osteosarcoma. *AJR* 1981;136:1233–1235
- Murphy WA, Totty WG, Carroll JE. MRI of normal and pathologic skeletal muscle. *AJR* 1986;146:565–574
- Hudson TM, Hamlin DJ, Enneking WF, Petersson H. Magnetic resonance imaging of bone and soft tissue tumors. Early experience in 31 patients compared with computed tomography. *Skeletal Radiol* 1985;13:134–146

Pictorial Essay

Cystic Masses of the Knee: Arthrographic and CT Evaluation

Kyo Rak Lee,¹ Glendon G. Cox,¹ James R. Neff,² Gwen R. Arnett,¹ and Mark D. Murphey¹

The knee, which has the largest synovial membrane of any joint, is the most common site for the formation of synovial cysts or other cystic lesions related to the synovium. Knee arthrography has been widely used for the diagnosis of popliteal cysts, but the findings on arthrography for other juxtaarticular cystic masses (such as antefemoral, anteromedial, and tibiofibular cysts; ganglionic cysts; and synovial hemangiomas) have been infrequently reported. Also, CT findings in these cystic lesions are not well known.

During the past 8 years, 43 patients with suspected juxtaarticular soft-tissue masses of the knees have had CT as part of the routine tumor workup at our institution. The scans were obtained by using a General Electric CT/T 7800, 8800, or 9800 scanner. Contiguous 10-mm-thick slices were obtained in the region of interest before and/or after IV infusion of 300 ml of 30% meglumine diatrizoate. If necessary, 5-mm-thick slices and/or dynamic scans with bolus injection of the contrast material were obtained. Double-contrast arthrography was performed in 29 patients. Eight patients had immediate postarthrography CT. There were 23 cystic masses: 12 popliteal cysts, three antefemoral cysts, one tibiofibular cyst, one ganglionic cyst, two synovial hemangiomas, two hematomas, one popliteal aneurysm, and one malignant fibrous histiocytoma.

Synovial Cysts

Accumulation of fluid within one of the bursae around the knee is called a synovial cyst. Any of the bursae can be

involved (Fig. 1), but we have found the following synovial cysts in the literature [1-3] or in our own series.

Popliteal cysts.—Popliteal cysts are the most common synovial cysts and involve the gastrocnemio-semimembranosus (G-S) bursa. The location and extension of the cysts depend on the anatomic variations of the G-S bursa (Figs. 2-5). Thus, a thorough understanding of the variations is important in the arthrographic and CT diagnosis of popliteal cysts. The G-S bursa is a composite of two bursae: the gastrocnemius and semimembranosus [2]. The bursa is located between the medial femoral condyle, medial head of the gastrocnemius, and semimembranosus tendon at the level of the upper portion of the medial femoral condyle. The semimembranosus bursa is larger and located medial to the gastrocnemius portion. Each compartment is subdivided into two segments (anterior and posterior horn) (Figs. 1 and 2). There is frequently a central septum in the G-S bursa that apparently reflects its composite origin. Depending on complete or incomplete division of the two compartments by the central septum, one or both compartments of the G-S bursa may be distended (Fig. 3). There are additional septa in the semimembranosus bursa, and either of the segments can be distended separately (Fig. 4). Popliteal cysts may rupture proximally or distally. A distal rupture is more common and may become a giant calf cyst (Fig. 5). While arthrography is accurate for diagnosing popliteal cysts and underlying joint diseases, it may fail to show the extent of cysts containing gelatinous fluid or the cysts not communicating with the joint. In these instances, CT is a complementary study that may accurately

Received July 15, 1986; accepted after revision September 22, 1986.

Presented as an exhibit at the annual meeting of the American Roentgen Ray Society, Washington DC, April 1986.

¹ Department of Diagnostic Radiology, The University of Kansas Medical Center, Rainbow Blvd. at 39th St., Kansas City, KS 66103. Address reprint requests to K. R. Lee.

² Department of Orthopedic Surgery, The University of Kansas Medical Center, Rainbow Blvd. at 39th St., Kansas City, KS 66103.

AJR 148:329-334, February 1987 0361-803X/87/1482-0329 © American Roentgen Ray Society

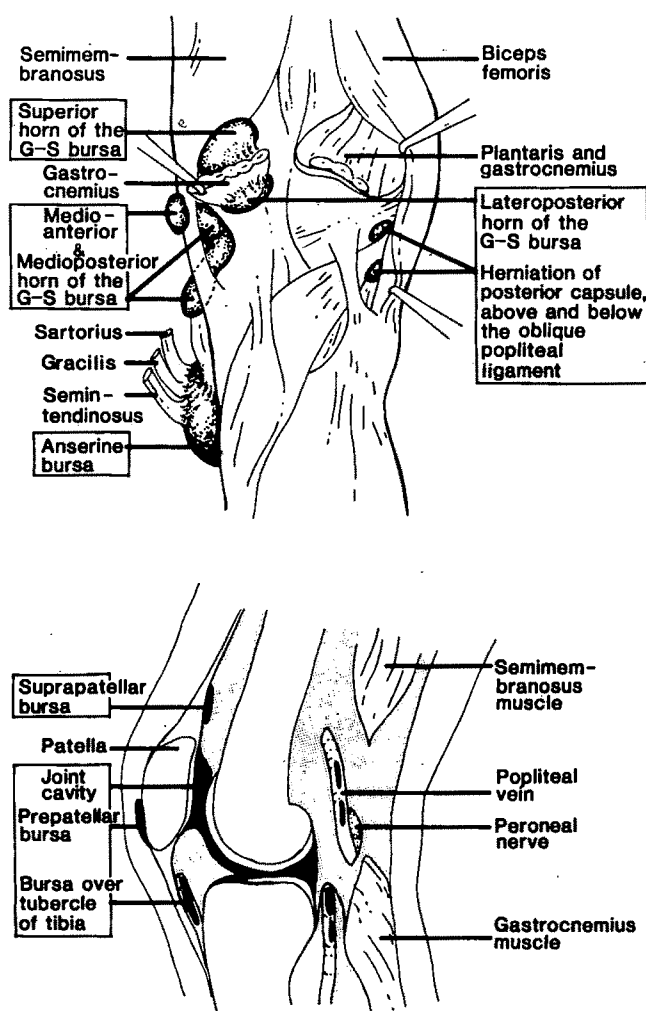


Fig. 1.—Bursae of knee in relation to formation of synovial cysts. G-S = gastrocnemio-semimembranosus.

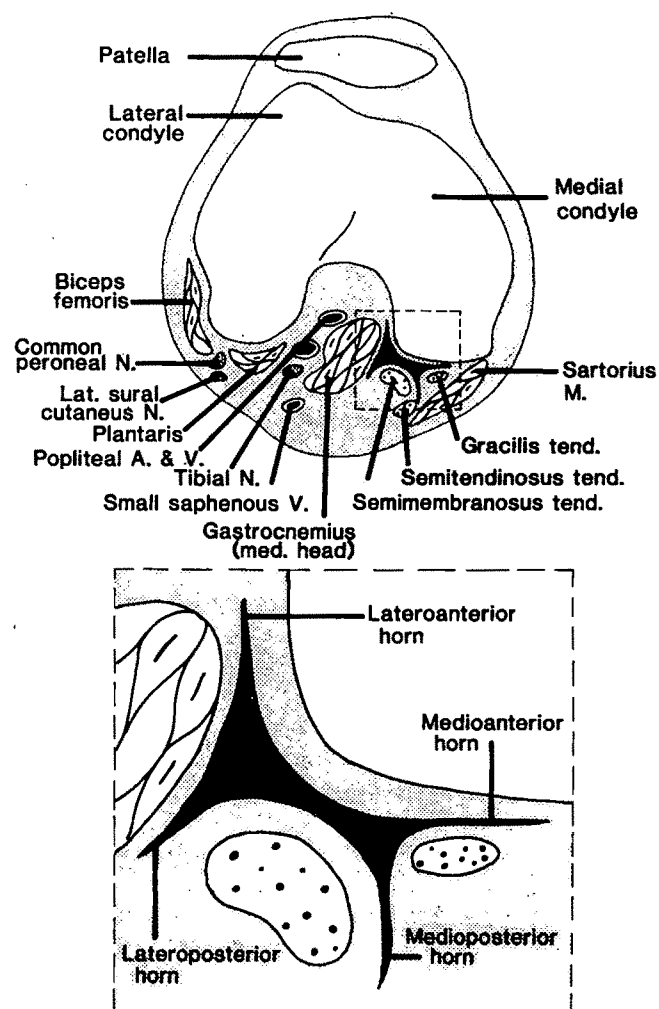


Fig. 2.—Anatomy of gastrocnemio-semimembranosus bursa. N = nerve; M = muscle, A = artery, V = vein.

diagnose the cysts and identify their extent (Fig. 4). The CT diagnosis is helpful for surgical planning and may eliminate the need for any additional examinations, including arteriography. The CT findings, however, may vary owing to rupture of the synovial membrane, gelatinous cyst contents, or metaplastic changes of the cyst wall (Fig. 6). Ganglionic cyst, popliteal aneurysm, hematoma, abscess, liposarcoma, or other soft-tissue tumors should be included in the differential diagnosis.

Antefemoral cysts.—Antefemoral cysts are the second most common synovial cysts and involve the suprapatellar (S-P) bursa [3]. The S-P plica is present in approximately 20% of adult knees and can be seen on double-contrast arthrography and postarthrography CT. It can range from a minor synovial fold to a valvelike orifice (central porta) to a complete membrane separating the S-P bursa from the joint cavity [1]. In the latter two instances, the S-P bursa becomes a potential site for cyst formation. A noncommunicating S-P cyst mimics a soft-tissue tumor and is difficult to diagnose by arthrogra-

phy. CT accurately diagnoses the cysts and identifies their extent (Fig. 7).

Anteromedial cysts.—Anteromedial cysts involve the anserine bursa (Fig. 1). Since the bursa lies in the tight space beneath the fascia, the cysts present clinically as firm, tender, cystic masses immediately below the joint line on the anteromedial aspect of the medial tibial condyle and frequently erode the bone.

Tibiofibular cysts.—The proximal tibiofibular joint communicates with the knee in 10% of adults, thereby becoming a potential site of cyst formation. Because of the anatomic location, the cyst frequently erodes the adjacent bone, mimicking a malignant tumor (Fig. 8).

Ganglionic Cysts

Ganglions are benign cystic lesions most commonly affecting the soft tissues adjacent to tendon sheaths and joint capsules [4]. Other sites of involvement include the meniscus,

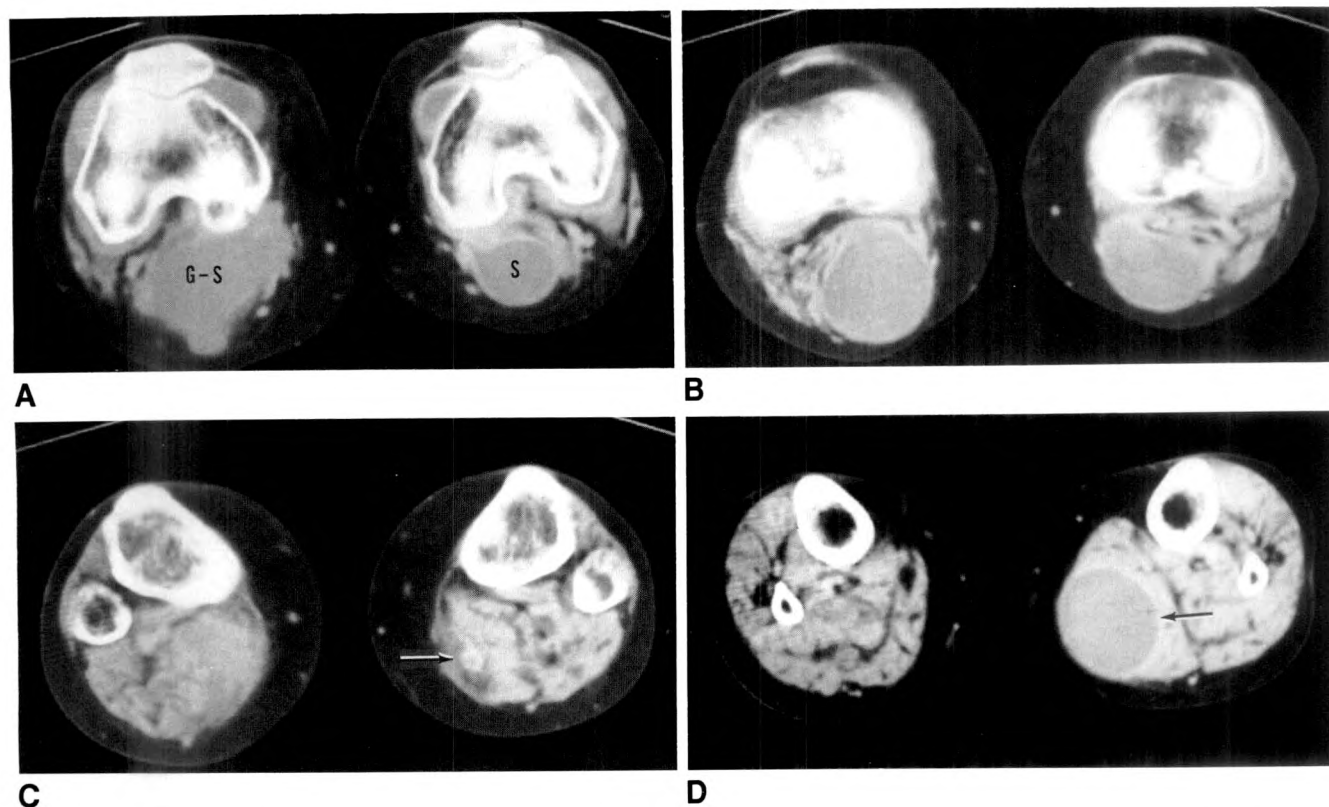


Fig. 3.—Bilateral popliteal cysts in rheumatoid arthritis. A–D, Sequential CT scans clearly show that cyst on right (G-S) involves both compartments of the gastrocnemio-semimembranosus bursa and that cyst on patient's left (S) involves only posterior segment of semimembra-

nosus bursa. Latter cyst shows rupture at distal portion (arrow, C) with large pseudocyst (arrow, D) encapsulated in medial calf beneath fascia of gastrocnemius muscle.



Fig. 4.—Noncommunicating semimembranosus bursa cyst. Double-contrast arthrogram (not shown) demonstrated noncommunicating soft-tissue mass in popliteal fossa. CT scan shows mass to be noncommunicating cyst selectively involving anterior segment of semimembranosus bursa. Septum is present within cyst (open arrow). The gastrocnemius bursa (arrowhead) and posterior segment of semimembranosus bursa (solid arrow) communicate with joint.

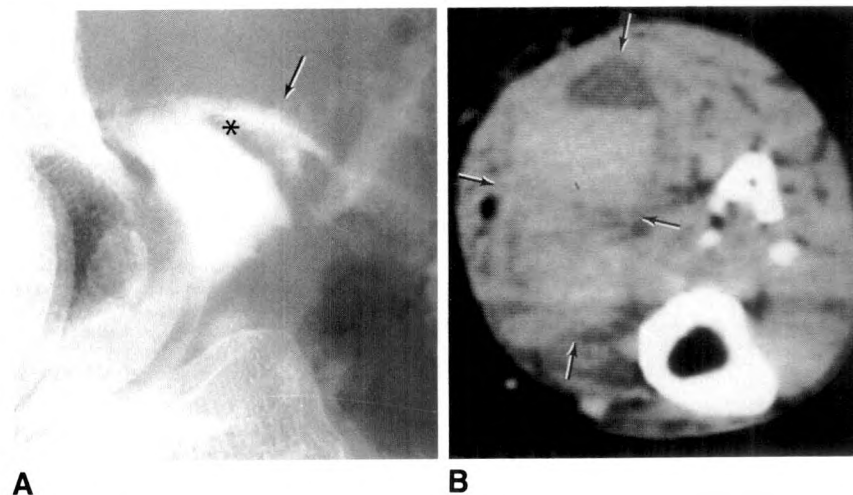


Fig. 5.—Ruptured popliteal cyst. A, Double-contrast arthrogram shows large popliteal cyst that ruptured into distal calf. Communication between joint and gastrocnemio-semimembranosus bursa (arrow) is well shown. Notice transverse slit (asterisk), which may act as a valve. B, Immediate postarthrography CT scan shows extravasated contrast material and air (arrows) that dissect into gastrocnemius and soleus muscles.



Fig. 6.—Calcified popliteal cyst. Posteromedial wall of semimembranosus bursa shows thickening and calcification (*open arrow*). Remaining portions of gastrocnemius-semimembranosus bursa also show diffuse wall thickening (*solid arrows*).

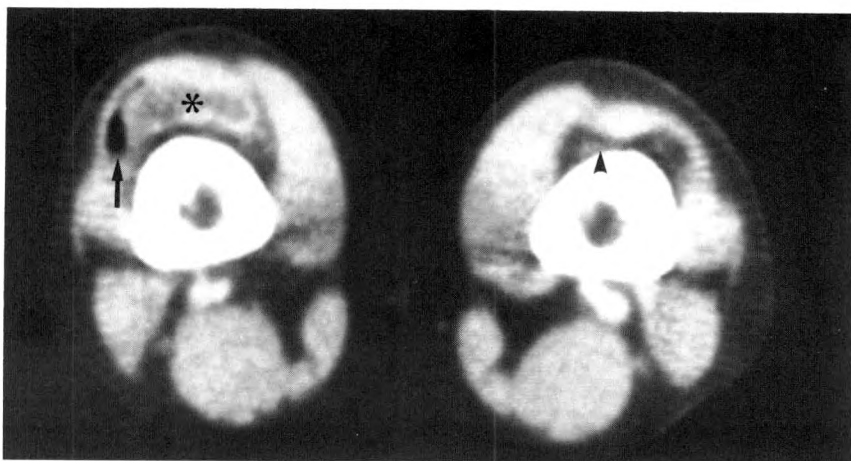


Fig. 7.—Noncommunicating antefemoral cyst. Postarthrography CT scan shows noncommunicating cystic lesion (*asterisk*) anteromedial to air-filled joint (*arrow*). Lesion shows semilunar shape with irregular, thick wall. Normal suprapatellar bursa is seen on patient's left side (*arrowhead*).



A



B



C

Fig. 8.—Tibiofibular cyst.
A, Radiograph of proximal fibula shows bony erosion with sclerotic margin along medial side of proximal fibula. No soft-tissue mass is apparent.
B and C, CT scans show two cysts, one located on lateral side and one on medial side of proximal fibula (*arrows*). Cyst arising from proximal tibiofibular joint and containing mucoid material was surgically excised and proved pathologically to be synovial cyst.

bone, and external popliteal nerve. The lesion is a result of primary cellular hyperplasia with associated mucin secretion and secondary cystic degeneration of the connective tissue. Ganglions around the knee are more often multilocular without synovial lining and contain gelatinous high-viscosity fluid. Arthrography may show that the cysts communicate with the joint or that they are noncommunicating soft-tissue masses.

CT shows multiloculated cysts that can be differentiated from synovial cysts by their locations and extent (Fig. 9).

Synovial Hemangiomas

Synovial hemangiomas most frequently involve the knee. Young women are most often affected. Pain, swelling, and

Fig. 9.—Ganglionic cyst.

A and B, CT scans show large, multiloculated cyst (arrows) surrounding lateral half of distal femur. Location, extent, and multiloculation of lesion suggest that cyst did not originate from any of the bursae.

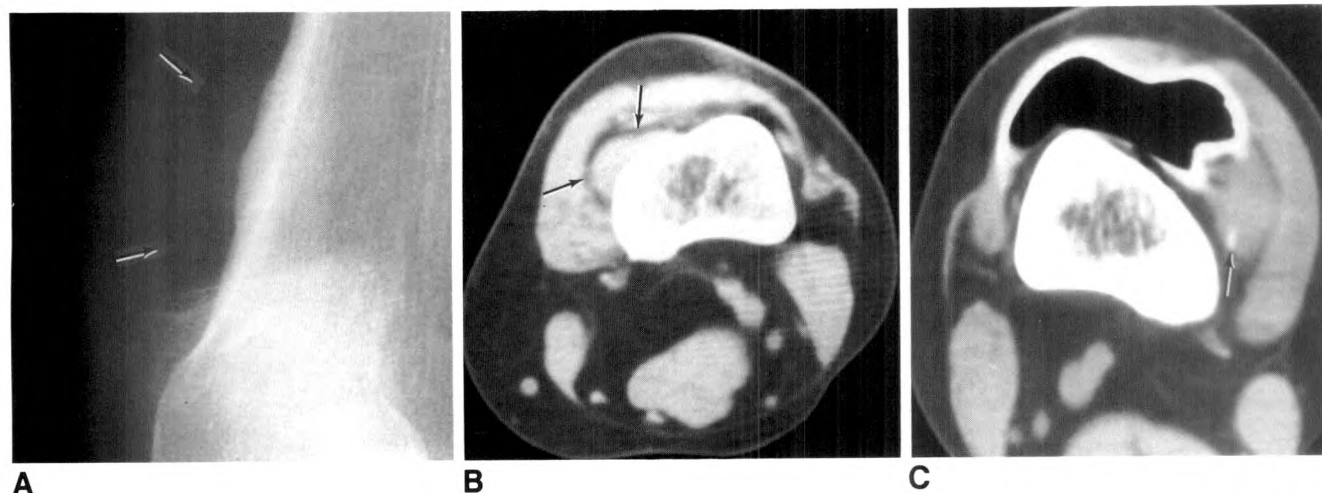
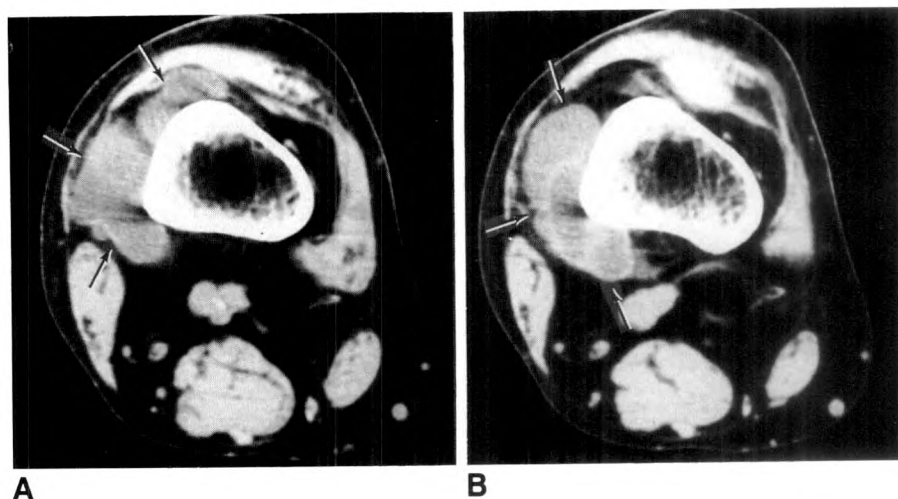


Fig. 10.—Synovial hemangiomas.

A, Oblique view of knee shows soft-tissue mass (arrows) in suprapatellar region and irregular cortical thickening of underlying bone.

B, Dynamic CT scan identifies contrast-enhancing soft-tissue mass (arrows) in suprapatellar region. CT findings suggest vascular nature of

mass. Cavernous hemangioma involving synovial and subsynovial tissues (localized type) primarily fed by superior genicular arteries was surgically excised.

C, CT scan in another patient shows hemangioma as extraarticular mass containing small calcification (arrow).

decreased range of motion are the common clinical manifestations [4]. Generally, localized sessile or pedunculated hemangiomas are excised easily with good results (Fig. 10). Diffuse, infiltrating hemangiomas may be associated with visceral and cutaneous vascular lesions and are more difficult to manage.

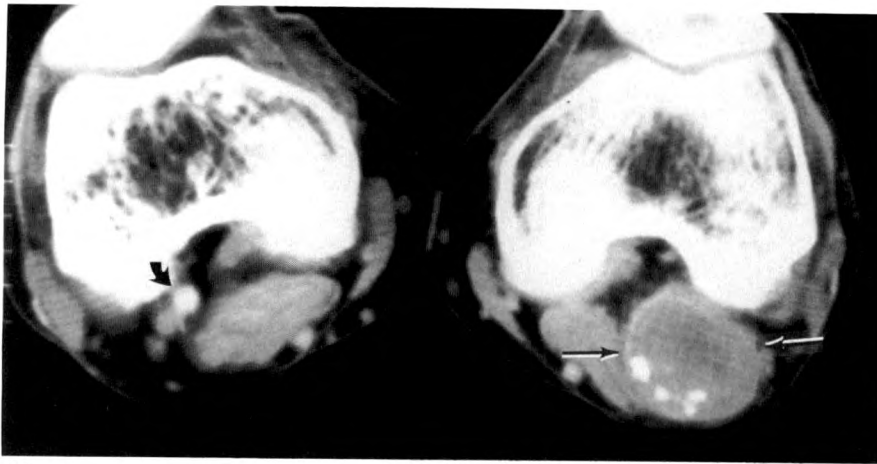
Popliteal Artery Aneurysms

Popliteal artery aneurysms are usually caused by atherosclerosis. Other causes include trauma, surgical grafting, or

infection. Bilateral involvement occurs in 25–50% of patients. The aneurysms are generally 3–4 cm in size, and most are partially calcified in a rimlike or amorphous pattern. Both CT and sonography have been used for diagnosing the aneurysms (Fig. 11). Arteriography most frequently shows occlusion of the popliteal artery.

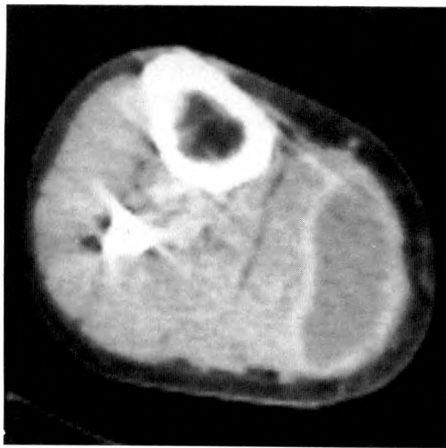
Hematomas

Because of their various causes and presentations, clinical diagnosis of soft-tissue hematomas is often delayed. CT is



11

Fig. 11.—Popliteal artery aneurysm. Dynamic CT scan shows saccular aneurysm filled with thrombus (straight arrows). Irregular calcifications are seen in posterior wall of aneurysm. Popliteal artery on right side is well opacified with contrast material (curved arrow). Intraarterial digital subtraction angiogram (not shown) showed occlusion of popliteal artery with distal reconstitution via collateral circulation.



12

Fig. 12.—Hematoma in 47-year-old man with persistent swelling of 6-weeks duration in right proximal calf. Swelling developed after sudden onset of pain without apparent precipitating trauma. CT scan shows well-encapsulated cystic mass beneath fascia of gastrocnemius muscle. Lesion has thick wall with contrast enhancement. An old hematoma was surgically evacuated.



13

Fig. 13.—Malignant fibrous histiocytoma. CT scan shows large, inhomogeneous mass arising from gastrocnemius muscle. Tumor shows large, central, low-density area and irregular anterior wall enhanced with contrast material. Tumor extends to subcutaneous fat and skin posteriorly.

an accurate method of confirming the presence of a hemorrhage and localizing its extent. The CT findings, however, vary according to the age of the hemorrhage. When a hemorrhage is encapsulated with a fibrous wall, it becomes a pseudotumor, which may be difficult to differentiate from abscess or other cystic tumors by CT findings alone (Fig. 12).

Malignant Fibrous Histiocytomas

Malignant fibrous histiocytomas are aggressive, mesenchymal tumors of histiocytic origin that may occur at any age, but most commonly in the fifth and sixth decades. The tumor shows a male predominance of 2:1. It is the most common malignant soft-tissue tumor in the adult. The lower extremity, chest wall, upper extremity, and retroperitoneum are most often involved. The tumor is locally invasive and frequently shows central necrosis (Fig. 13).

Discussion

Arthrography is an accurate method for diagnosing communicating synovial cysts and detecting their causative joint

diseases. CT complements arthrography in the diagnosis of noncommunicating synovial cysts, ganglionic cysts, or other less common cystic masses (hematoma, abscess, popliteal aneurysm, varices, hemangioma, and necrotic malignant soft-tissue tumors). Dynamic CT may be useful in evaluating the vascular nature of lesions. The location in relation to the bursae, shape, septum, calcification, attenuation number of cyst contents, contrast enhancement, and extent of the lesions should be analyzed carefully in the CT differential diagnosis of cystic masses around the knee. Postarthrography CT has little advantage over conventional CT in the evaluation of the lesions.

REFERENCES

1. Fullerton A. The surgical anatomy of the synovial membrane of the knee-joint. *Br J Surg* 1916;4:191-192
2. Wilson PD, Eyre-Brook AL, Francis JD. A clinical and anatomical study of the semimembranosus bursa in relation to popliteal cyst. *J Bone Joint Surg [Am]* 1938;20:963-984
3. Seidl G, Scherak O, Hofner W. Antefemoral dissecting cysts in rheumatoid arthritis. *Radiology* 1979;133:343-347
4. Resnick D, Madewell JE, Sweet DE. Tumors and tumor-like lesions of bone, in or about joints. In: Resnick D, Niwayama G, eds. *Diagnosis of bone and joint disorders*. Philadelphia: Saunders, 1981:2638-2751

CT Patterns of Facet Fracture Dislocations in the Thoracolumbar Region

B. J. Manaster¹
Anne G. Osborn

Thoracolumbar facets are not as commonly dislocated as are those of the cervical spine. It is, however, crucial to make an early and accurate diagnosis of thoracolumbar facet dislocation since the injury may be unstable and require reduction and internal fixation. This paper presents three major CT patterns of thoracolumbar facet fracture dislocation. The first represents anterior subluxation of the vertebral body with anteriorly locked facets. The second is a lateral vertebral body subluxation with laterally locked facets. The third is an acute kyphosis with little vertebral body subluxation but superiorly dislocated facets.

Since the vertebral body subluxation may be missed on axial CT images, these facet-dislocation patterns should be recognized by identifying the paired superior and inferior facets and establishing their congruency. Identification of the facets is accomplished by their orientation with respect to the vertebral body (superior facets are directed posteromedially and inferior facets are directed anterolaterally) as well as by the shape of the articular surface (superior facet articular surface is concave, inferior facet articular surface is flat or convex).

Flexion injury of the thoracolumbar spine most commonly results in simple anterior compression of the vertebral body. The Chance fracture is seen less commonly. With the use of lap-type seat belts, a third pattern has been described [1] in which there is minimal vertebral body compression but extensive disruption of the ligamentous framework of the posterior elements, resulting in articular facet fracture dislocation. This pattern is also seen in vertical falls. Smith et al. [2] found by plain film and plain tomography that of 38 vertical-jump thoracolumbar injuries, four had one or more locked facets and nine had varying degrees of partially dislocated, perched, or completely dislocated facets.

Facet dislocations are usually unstable injuries that require internal reduction, fixation, and fusion. Early, detailed, and accurate diagnosis is essential to allow a well-planned surgical approach and the proper choice of an internal fixation device. CT is routinely used in the preoperative workup. A complete description of CT findings in the more common cervical facet fracture dislocations is found in the literature [3], but only occasionally can cases of thoracolumbar facet dislocations be found [1, 4]. We have collected a spectrum of such cases. Three major patterns of thoracolumbar facet dislocation have become apparent in this study. These patterns are (a) anterior subluxation of the vertebral body with anteriorly locked facets, (b) lateral subluxation of the vertebral body with laterally locked facets, and (c) an acute kyphosis with superiorly dislocated facets. CT is often obtained early in the diagnostic workup of these patients, but the CT appearance of these various facet dislocations may be confusing. The purpose of this paper is to present a simple and practical method of assessing the CT appearance of thoracolumbar facet dislocations.

This article appears in the November/December 1986 issue of *AJNR* and the February 1987 issue of *AJR*.

Received October 2, 1985; accepted after revision May 28, 1986.

¹ All authors: Department of Radiology, University of Utah School of Medicine, 50 North Medical Drive, Salt Lake City, UT 84132. Address reprint requests to B. J. Manaster.

AJR 148:335-340, February 1987
0361-803X/87/1482-0335
© American Roentgen Ray Society

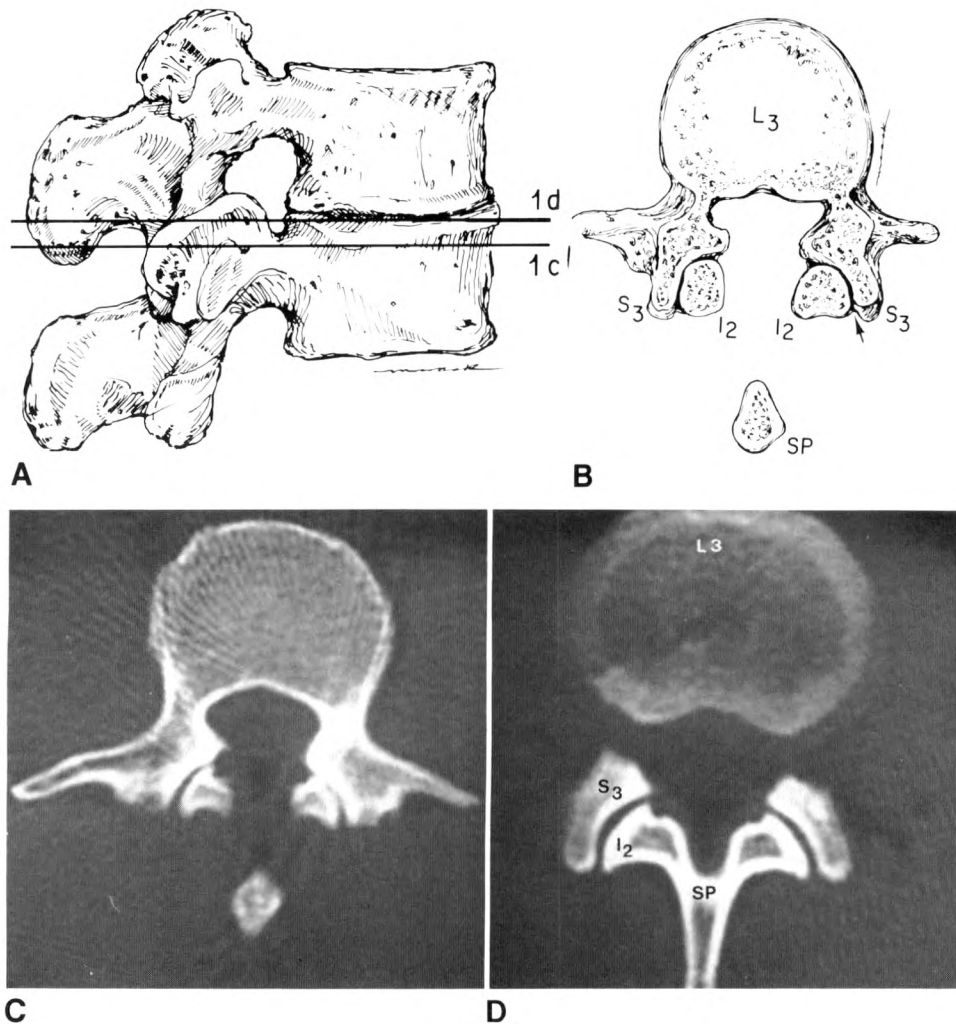


Fig. 1.—Normal lumbar facet joints. **A**, Line drawing of L2 and L3 in the lateral position, showing vertically and sagittally oriented articular facets. Lines 1c and 1d represent the levels of the axial cuts seen in parts **C** and **D**. **B**, Line drawing of axial cut at the level labeled 1c in part **A**. S = superior facet; I = inferior facet; SP = spinous process. Note that at this level, the pedicles extend into the superior facets. Just a tip of the spinous process of the adjacent body is seen. The articular facets fit concentrically together (arrow). The superior facet articular surface is concave and directed posteromedially. The inferior facet articular surface is flat or convex and is directed anterolaterally. **C**, CT at same level as line drawings in parts **A** and **B**. **D**, CT section slightly superior to that in part **C** (depicted in part **A** as level 1d), through superior endplate of L3. The pedicles are not seen attached to the superior facets of L3 at this level, while the inferior facets of L2 are seen to join the spinous process of L2. Despite those differences, the shapes and relationships of the articular facets remain constant (compare to part **C**).

Cases

Ten cases of facet dislocation, all the result of flexion injury, were examined. Examples are included with the discussion. Four cases demonstrated anterior subluxation of the vertebral bodies with anteriorly locked facets. Two of these were at the L4–L5 level, one at L5–S1, and one at T11–T12. Two cases demonstrated lateral subluxation of the bodies with laterally locked facets, one at the L3–L4 level and one at L4–L5. Finally, four cases demonstrated an acute kyphosis with superiorly locked facets. All were at the T12–L1 vertebral body levels.

Discussion

In the cervical region, the articular facets are small, flat, and angled approximately 45° from the horizontal plane. This orientation explains the great degree of motion allowed, as well as the relative ease with which cervical facets sublux, dislocate, and lock. Thoracolumbar facets, on the other hand, are large, curved, and much more vertically oriented [5]. The shape and orientation of the thoracolumbar facets act to limit flexion-extension and provide additional stability in a flexion

injury. An additional consideration is that the thoracic facets are coronally as well as vertically oriented. At L1, the orientation of the facet articular surface changes from a coronal plane to one closer to a sagittal plane [4]. This allows more flexion-extension than in the thoracic spine but is still very limited compared to the cervical spine. Thus, lumbar flexion-rotation injury rarely results in pure facet dislocation. Fracture of the facets occurs much more frequently; thus, a flexion-rotation injury of the lumbar spine not uncommonly yields a rotational fracture dislocation of the posterior elements.

Thoracolumbar fracture dislocations often are extremely unstable [5] and may be quite complex; therefore, early diagnosis is essential. If there are few fractured elements in this injury, spontaneous fusion may not occur. One cannot rely on restoration of stability by healing of posterior ligaments; such injuries often must be reduced and internally fixed.

In a trauma situation, the clinician is often first alerted to a potentially unstable lumbar spine fracture by widened interpediculate distance on the anteroposterior film, which may be indicative of a burst-type fracture. Lateral lumbar spine films

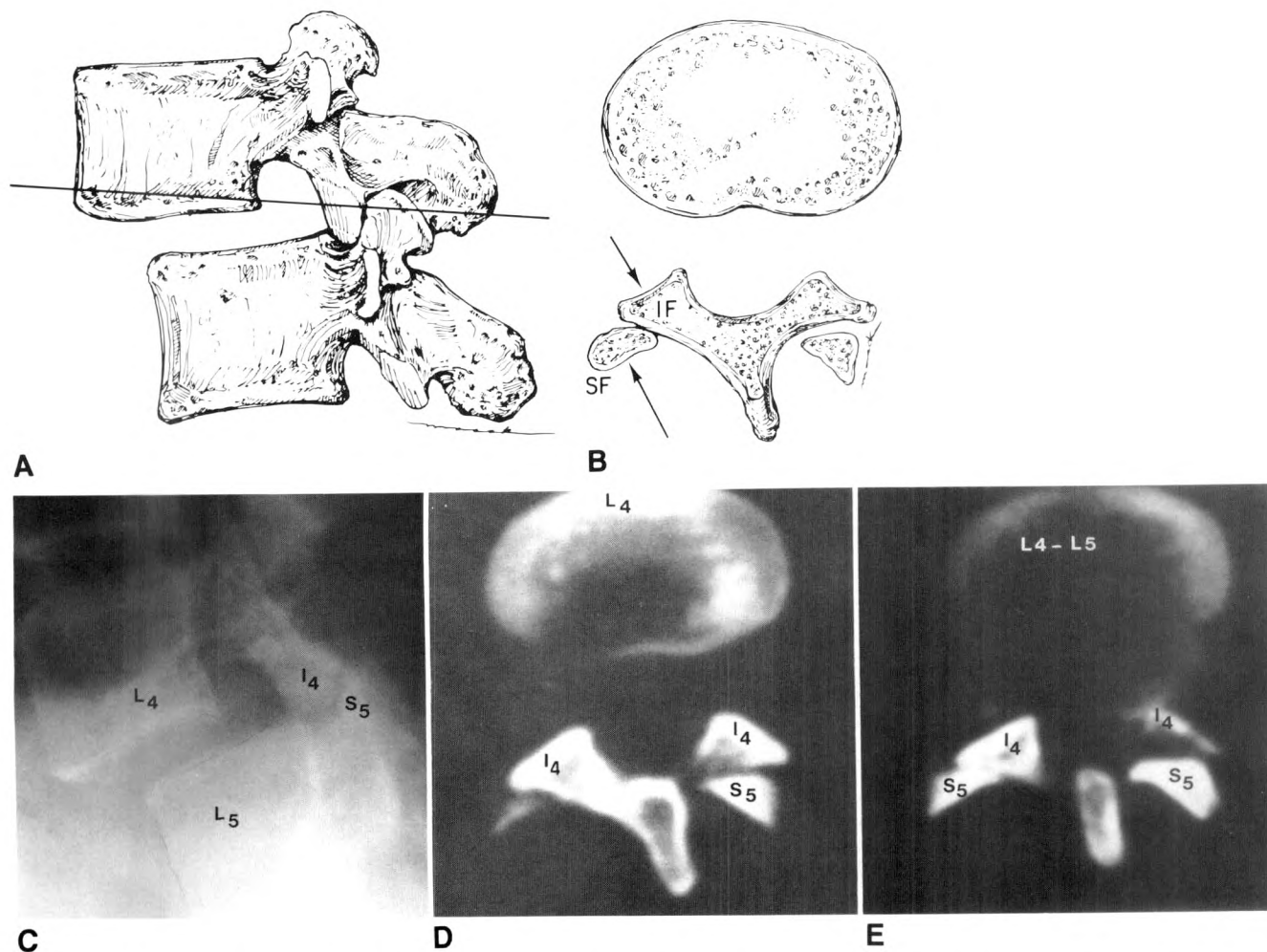


Fig. 2.—**A**, Line drawing of anterior vertebral body subluxation with anteriorly locked facets. The line corresponds to the line drawing depicted in part **B**. **B**, Line drawing of CT appearance typical of this facet dislocation pattern. SF = superior facet; IF = inferior facet. Arrows show their respective articular surfaces. **C**, **D**, and **E**, Anterior dislocation L4 on L5 with anteriorly locked facets. Lateral film, demonstrating lock (**C**); CT at inferior endplate of L4, demonstrating spinous process and inferior facets of L4 (labeled I4) with

superior facets of L5 (labeled S5) locked posteriorly (**D**). Notice that the shape and orientation of the facets make them easily identifiable. CT through L4–L5 disk space (4 mm caudal to part **D**) shows both superior L5 facets better (**E**). Notice that in this series of films, the superior subluxation and spondylolisthesis of the bodies is not easily recognized in the axial CT scans; it must be inferred from the locked facet position.

of good quality are difficult to obtain; cross-table lateral films are usually attempted, since rolling the patient into a decubitus position could cause neurologic damage. CT is now universally accepted as the next step in evaluation of a thoracolumbar fracture [1, 4, 6, 7]. The advantages of CT include superb visualization of the posterior elements and of the relation of bone fragments to the spinal canal; visualization of soft-tissue abnormalities, such as disk herniation or hematoma; improved speed of diagnosis; smaller radiation dose than with plain tomography; less patient manipulation (especially into decubitus positions); and the availability of multiplanar reconstruction.

There are, however, pitfalls in CT evaluation of spine fracture dislocations [8]. With axial sections, an increase in intervertebral distance can be missed. Furthermore, it may be difficult to correlate the alignment of adjacent vertebral bodies,

so either anteroposterior or lateral subluxation may be missed. Both sagittal and coronal reconstructions help eliminate these problems. It is also crucial to be aware of other subtle signs of subluxation/dislocation of the posterior elements demonstrated by CT.

One must be familiar with the normal appearance of facets on CT in order to recognize abnormal relationships. First, one must be able to reliably differentiate superior from inferior articular facets in the axial plane. The parameters used for this differentiation include the orientation of the facet in relation to the vertebral body, as well as the shape of the articular surface of the facet. A normal scan is illustrated in Figure 1. An axial scan at the level indicated in the line drawing shows the pedicles extending into the superior articular facets. Those superior facets are oriented medially and posteriorly with respect to the vertebral body. Note also that the articular

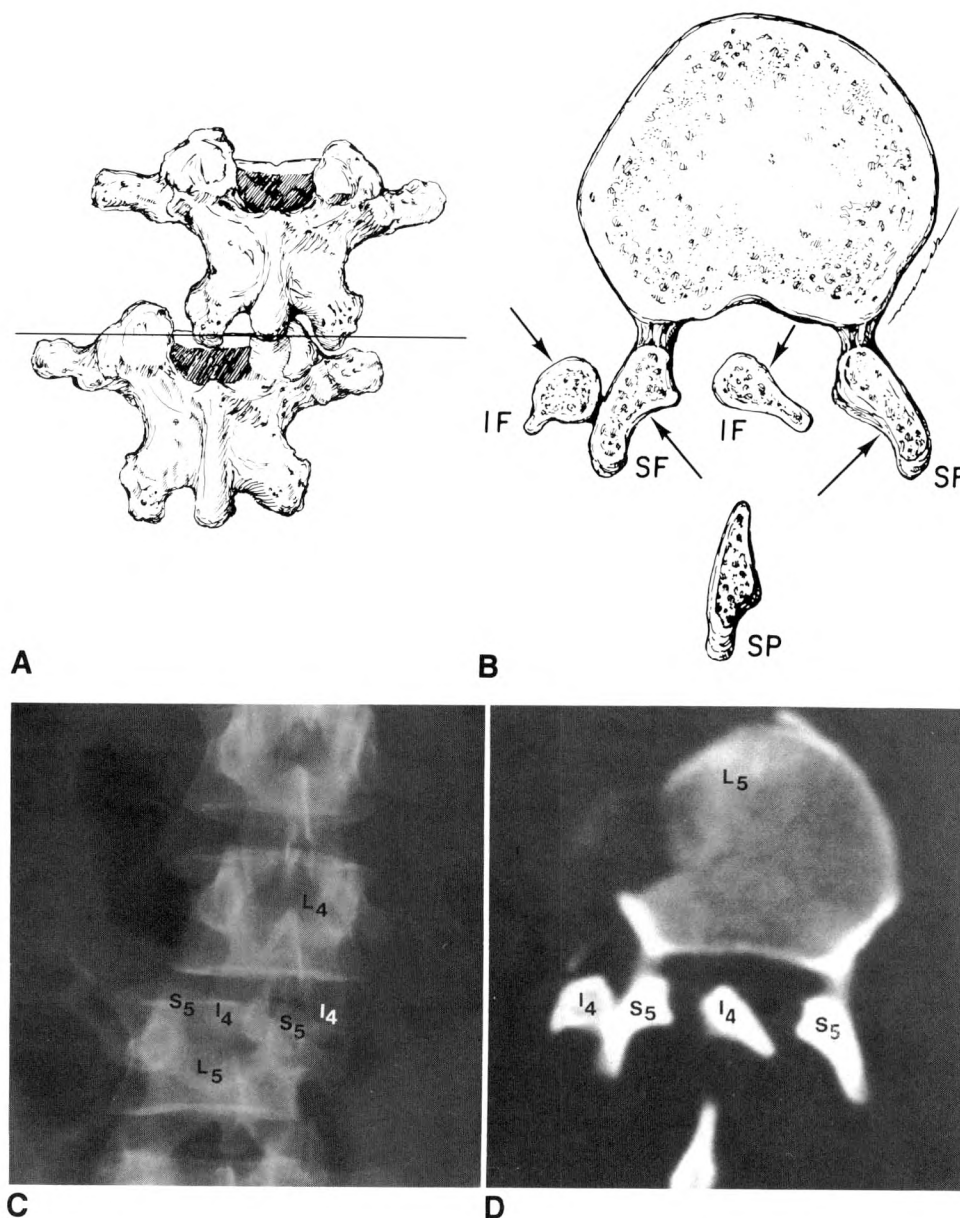


Fig. 3.—**A**, Line drawing of lateral vertebral body subluxation with laterally locked facets. The line corresponds to the axial CT cut shown in part **B**. **B**, Line drawing of the CT typical of this facet dislocation pattern. This corresponds to the CT scan shown in part **C**. SF = superior facet; IF = inferior facet. Arrows indicate the respective articular surfaces. **C**, Anteroposterior view demonstrates lateral subluxation of L4 on L5 in this patient with six non-rib-bearing vertebrae. The laterally locked facets are seen, as are multiple-fractured transverse processes. **D**, CT through superior endplate of L5 demonstrates laterally locked facets as well as compromised spinal canal diameter. Again, the facets are identified by the contour and position of the articular surfaces. S5 = superior facet L5; I4 = inferior facet L4.

surface of the superior facet is concave. Unlike the concave superior facet, the inferior facet is either flat or slightly convex at the articular surface. The orientation is also different, the inferior facets being directed anterolateral with respect to the vertebral body.

After the superior and inferior facets have been properly identified, their relationship to one another is assessed. They are normally concentrically applied over several axial scans. The shapes and relationships of the facets to one another remain constant with axial scans either superior or inferior to the one demonstrated in Figure 1A and 1B. This is illustrated by a slightly superior scan (Fig. 1D) in which the pedicles are no longer seen attached to the superior articular facets but the laminae and spinous process of the higher vertebral body

are seen extending from its inferior articular facets. Notice that the facets have an identical appearance and relationship to one another, as in the lower axial scan (Fig. 1C).

With flexion injury, the facets may momentarily sublux and return to their normal position, resulting in a normal CT. With more significant flexion force, the inferior facets may dislocate superiorly. They may then either settle back into a normal position or become perched or locked. We have observed three patterns of locked facets. Figure 2 is a line drawing with clinical examples of the first, demonstrating severe anterior subluxation of the superior vertebral body on the inferior one, and dislocation with anterior locking of the inferior articular facets on the superior facets. Although the CT may appear confusing initially, when the facets are properly identified, the

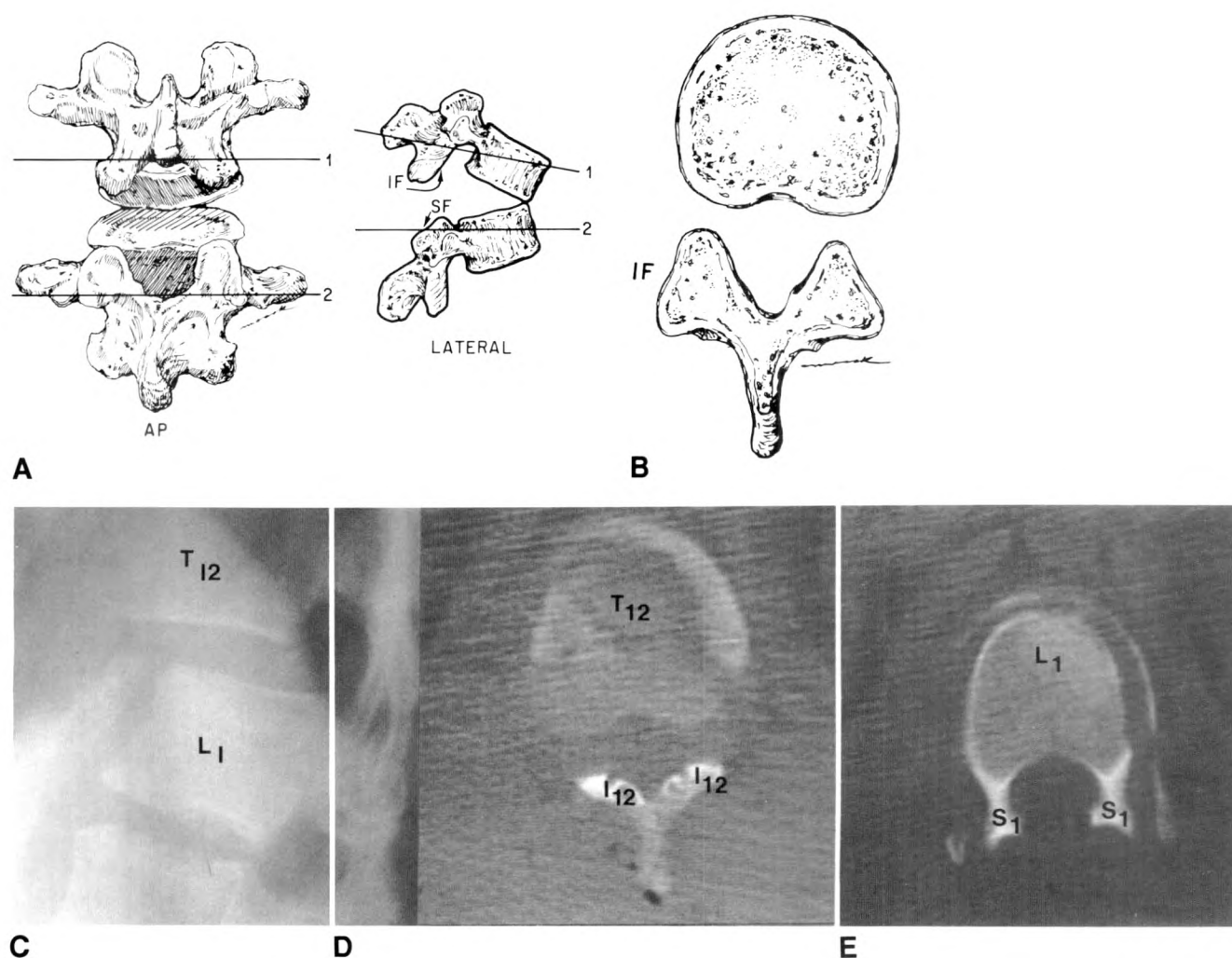


Fig. 4.—**A**, Line drawing of the third pattern of locked facets. Here, there is superior dislocation of the inferior facets from the superior facets. Line 1 corresponds to the CT drawing in part **B** and to the example in part **D**, which show "naked" inferior facets. Line 2 corresponds to the CT scan in part **E** and shows "naked" superior facets. **B**, Line drawing of a CT scan corresponding to line 1 in part **A**. Here, the inferior facets are "naked"; i.e., they are seen without the corresponding superior facets. SF = superior facets; IF = inferior facets.

C, Superior dislocation of T12 inferior facets from superior L1 facets. Lateral film shows increased intervertebral space, anterior subluxation of the body to T12 on L1, and presumed dislocation of facets. **D**, CT through inferior endplate of T12. Inferior facets (labeled I12) are seen, without evidence of superior articulating facets. **E**, CT through superior endplate of L1, showing superior facets (labeled S1) without articulating inferior facets. This is a demonstration of "naked" facets. (Case is courtesy of Dr. David Giles, Boise, Idaho.)

bilateral facet dislocation and locking become obvious.

The second pattern is shown in Figure 3. Here there is severe lateral subluxation of the superior vertebral body on the inferior one as seen in the line drawing. The CT demonstrates associated lateral dislocation and locking of the facets. Again, the diagnosis becomes obvious once the facets are identified. The third pattern is shown in Figure 4. In this instance, only slight to no anterior subluxation of the superior vertebral body is present, but there is complete superior dislocation of the inferior facets from the superior facets. The resultant CT shows inferior facets without accompanying superior facets; a more inferior scan shows superior facets without accompanying inferior facets. The number of intervening scans between the two sets of facets depends on the

degree of distraction. This appearance has been described before and termed "naked facets" [1].

Conclusions

Three major patterns of thoracolumbar facet dislocations are described. These can be accompanied by various vertebral body and posterior element fractures. The diagnosis of facet dislocation by CT may be subtle and depends largely on identification of the superior and inferior facets by means of the articular surface shape and alignment, as well as congruency at the articular surface. Timely diagnosis is essential, as these are usually unstable fractures requiring internal fixation and fusion.

REFERENCES

1. O'Callaghan JP, Ulbrich CG, Yuan HA, Kieffer SA. CT of facet distraction in flexion injuries of the thoracolumbar spine: the "naked" facet. *AJNR* **1980**;1:97-102, *AJR* **1980**;134:563-568
2. Smith GR, Northrop CH, Loop JW. Jumpers' fracture: patterns of thoracolumbar spine injuries associated with vertical plunges. *Radiology* **1977**;122:657-663
3. Yetkin Z, Osborn AG, Giles DS, Houghton VM. CT evaluation of cervical articular pillar fractures. *AJNR* **1985**;6:633-637
4. Brant-Zawadzki M, Jeffrey RB Jr., Minagi H, Pitts LH. High resolution CT of thoracolumbar fractures. *AJNR* **1982**;3:69-74, *AJR* **1982**;138:699-704
5. Holdsworth FW. Review article. Fracture, dislocations, and fracture dislocations of the spine. *J Bone Joint Surg* **1970**;52:1534-1551
6. Brant-Zawadzki M, Miller EM, Federle MP. CT in the evaluation of spine trauma. *AJR* **1981**;136:369-375
7. Kilcoyne RF, Mack LA, King HA, Ratcliffe SS, Loop JW. Thoracolumbar spine injuries associated with vertical plunges: reappraisal with computed tomography. *Radiology* **1983**;146:137-140
8. Handel SF, Lee YY. Computed tomography of spinal fractures. *Radiol Clin North Am* **1981**;19:68-89

Diagnostic Oncology Case Study

Bone Scan-Positive and Radiograph- and CT-Negative Vertebral Lesion in a Woman with Locally Advanced Breast Cancer

Jerrold H. Mink,¹ Ilene Weitz,¹ A. Robert Kagan,² and Richard J. Steckel³

Case History

This 35-year-old woman had a history of slow enlargement of the right breast over a 2-year period. Two months before she first sought clinical attention, she noted a sanguineous discharge from the nipple. She was otherwise in good health.

On physical examination there was a hard 6-cm mass occupying much of the lateral hemisphere of the right breast. No axillary or supraclavicular nodes were palpable. A complete blood count and serum alkaline phosphatase were both normal, and a preoperative mammogram showed a large noncalcified mass in the right breast, with no other abnormalities. A percutaneous needle biopsy in the surgeon's office revealed intraductal carcinoma, and the biopsied tissue was negative for estrogen receptors. A subsequent liver-spleen scan was normal, but a technetium-99m phosphonate bone scan showed a single "hot spot" in the T6 vertebral body (Fig. 1). A metastatic bone survey (including coned-down radiographs of T6) was then obtained and revealed no visible bone lesions or degenerative changes. On repeated questioning and physical examination, the patient had no symptoms or signs related to the thoracic spine. She subsequently underwent a modified radical mastectomy, and all (15/15) of the excised axillary nodes contained microscopic tumor.

After surgery, because of the positive bone scan and the

surgical findings, a limited CT scan of the midthoracic spine was performed, with overlapping sections at 2-mm intervals through the T6 vertebral body; no abnormality was shown. The patient then underwent a fluoroscopically guided percutaneous needle biopsy of T6, and two specimens were obtained. The first consisted of normal medullary bone, but the second contained nests of tumor cells within the centrum of the vertebra that were identical with the primary lesion in the breast. The patient is currently receiving combination chemotherapy.

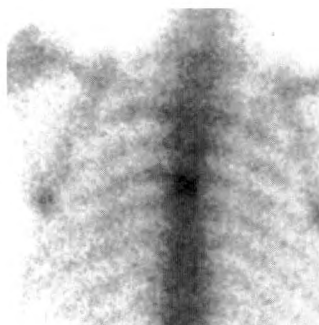


Fig. 1.—The technetium-99m phosphonate bone scan revealed a single abnormal area of uptake in the T6 vertebral body. Plain radiographs and a CT scan of the same area were negative.

This is another in a series of case studies edited by Robert A. Kagan and Richard J. Steckel to present and discuss contemporary problems and procedures in the identification and staging of neoplasms.

¹ Cedars-Sinai Medical Center, Los Angeles, CA 90048.

² Southern California Permanente Medical Group, 1510 N. Edgemont, Los Angeles, CA 90027.

³ Jonsson Comprehensive Cancer Center at UCLA, 10833 LeConte Ave., Los Angeles, CA 90024. Address reprint requests to R. J. Steckel.

Discussion

Approximately 80% of newly diagnosed patients with cancer of the breast are classified clinically as stage I or II (tumor apparently localized to the breast and/or limited axillary node involvement), while 20% are classified as stage III or IV (advanced regional node involvement or distant metastatic disease). While 50% of patients with clinical stage I-II breast cancers will eventually succumb to their disease, screening for distant metastases at the time of diagnosis (in the absence of signs or symptoms suggesting metastases) usually does not affect their clinical management [1]. This may be because the hematogenous metastases that are present in at least some of these patients are too small (and their growth rates too slow) to be detected by currently available diagnostic imaging or serologic techniques. In clinical stage III or IV patients, survival rates at 5 and 10 years remain much lower (15–20%) [2]. Furthermore, even locally advanced breast cancers may sometimes have detectable metastases at distant sites in the absence of symptoms (as in the present case). Therefore, the following specific findings should encourage the clinician and the radiologist to consider additional preoperative diagnostic studies: (1) a primary tumor greater than 5 cm in diameter (as in the present patient); (2) breast tumor fixed to the chest wall; (3) skin edema over the breast, ulceration of the primary tumor, or mammographically visible or palpable satellite nodules; (4) multiple fixed axillary nodes; (5) supraclavicular or infraclavicular node enlargement; or (6) edema of the arm prior to treatment.

Noncurable cancers of the breast commonly metastasize to bone at some point in their courses, and therefore a bone scan and a serum alkaline phosphatase should be the primary screening tests when metastases are suspected. Liver metastases (as detected by laboratory test abnormalities, a radionuclide scan, CT, and/or sonography) or a malignant effusion or evidence of mediastinal node metastases including the internal mammary nodes (as seen on lateral chest radiographs or a CT scan) occur somewhat less frequently; asymptomatic metastases to the abdominal viscera or the lung parenchyma may also occur, but are even less common at the time of initial clinical presentation.

Bone scans are exquisitely sensitive for detecting osseous lesions, whether they are neoplastic or inflammatory, and scan-positive metastatic bone lesions with negative radiographs are not unusual in some of the more common neoplasms (e.g., breast, prostate, lung). On the other hand, bone-scan-negative and radiograph-positive metastases are relatively unusual, particularly with breast cancers [3]. A "positive" bone scan signifies *only* a focal increase in bone turnover, and it is not possible to distinguish (through the bone scan alone) between benign and malignant abnormalities. Virtually any active skeletal lesion, including degenerative arthritis or a herniated disc, an acute or healing fracture, osteomyelitis, or Paget's disease, can produce a focally abnormal scan. To avoid interpretive errors, many centers now obtain spot radiographs of areas that are abnormal on the radionuclide scans [3]. Unnecessary radiographic "surveys" can be eliminated in

this way, and a single radiologic report that correlates the information from the scan with the appropriate radiograph(s) can be issued.

A focal abnormality on a radionuclide bone scan often precedes radiographic evidence of a metastasis by 2–6 months, and even by as much as 15 months [4]. Therefore, any scan-positive and radiograph-negative lesion in a patient with a tumor that may metastasize to bone should be regarded as suspicious for malignancy. On the other hand, significant numbers of patients (30–90%, depending on the primary tumor site and the series) with solitary abnormalities on a bone scan may eventually prove to have a nonmalignant lesion, and therefore additional imaging studies are usually warranted [5, 6]. CT, by virtue of its improved tissue contrast as well as its cross-sectional imaging capability, might be expected to pick up skeletal metastases earlier than conventional radiographs, and Helms et al. [7] have shown that subtle right-left differences in the densities of the medullary canals on CT scans of paired long bones may indicate the presence of medullary tumor on the side with the denser marrow cavity. In each of four reported cancer patients who had a positive bone scan involving an extremity and negative plain radiographs, subsequent CT scans revealed a difference in medullary density of more than 20 H between the normal and the abnormal limbs; all four patients were subsequently proved by surgery to have tumor in the medullary cavity on the abnormal (more dense) side. Differences in medullary canal density may not be specific for cancer, however, because hemorrhage, inflammation, or previous irradiation can produce similar increases in CT density. We have recently observed occasional cases of bone lesions that were either CT negative and MR positive or bone-scan negative and MR positive, but the final role of MR imaging in detecting skeletal metastases has not yet been established.

Many patients who have primary malignancies with a propensity to metastasize to bone and radiologically detectable bone lesions that are distant from the primary tumor site (as shown on radiographs, bone scans, CT and/or MR) may eventually require bone biopsies for histologic confirmation and treatment planning. Many reports [8–11] have now documented the efficacy and safety of percutaneous needle biopsies in the diagnosis of benign as well as malignant bone lesions. When positive, a needle bone biopsy may be sufficient; when the needle biopsy is negative, however, an open biopsy of a focal lesion that has been depicted on a bone scan may be necessary.

Percutaneous needle puncture for bone biopsy was introduced 35 years ago in the surgical literature, but advances in image intensification and biplane fluoroscopy, and more recently in CT, have placed this procedure firmly within the purview of the radiologist. While most peripheral bone lesions can be biopsied on an outpatient basis with local anesthesia, vertebral lesions are biopsied in our institutions under general anesthesia: in our experience, local anesthesia has not reliably controlled the pain or patient anxiety associated with a vertebral biopsy, during which any involuntary movement could result in neural or vascular injury or a hemopneumothorax.

Reported success rates in the literature for needle bone biopsies vary, probably depending on the skill and experience of individual examiners, but accuracy rates of between 80% and 92% can be expected [8, 10]. However, most of the reported data have been obtained with radiographically visible bone lesions, and relatively little information is available on the success of biopsies with scan-positive and radiograph-negative lesions. Collins et al. [12] performed percutaneous biopsies on 58 such patients with focally positive bone scans and no radiographic abnormalities; 24 were proved by needle biopsy to have metastatic carcinoma and 23 to have infection, but the final true- and false-negative rates were not reported. Debnam and Staple [9] reported a 33% accuracy rate in needle biopsies of lesions of this type. We have done needle biopsies on 10 patients who had suspected metastatic lesions that were visible only on radionuclide scans and not on correlative radiographs (two were also CT negative). Pathologic examination showed eight true positives (for malignancy), one true negative, and one false negative from the needle biopsies in this series. Thus, the yield from needle biopsies of scan-positive and radiograph-negative focal abnormalities in bone may be relatively good in patients who have malignancies that have a propensity to metastasize to bone. In these cases the radionuclide-scan abnormality must be precisely located before needle biopsy, and bone scans with good spatial resolution are essential. "Marking" the observed bone-scan abnormalities externally on the skin at the time of the study can increase the yield from a subsequent percutaneous biopsy. For this reason, after an initial bone scan has been reviewed and found to be positive the patient may be asked to return to the department to be reinjected for a limited scan of the area that contains the identified "hot spot." A radioactive cobalt point source marker is then placed on the skin over the lesion, and another localized scan is performed to confirm that the position of the marker coincides with the lesion. The skin over the bone lesion is then marked with indelible ink, and the patient is biopsied percutaneously on the same day or the next morning.

In summary, a focally abnormal bone scan in a patient with a malignancy that may metastasize to bone is not always

diagnostic of metastatic disease, particularly when carefully performed radiographs of the same area are negative. However, unless a benign cause for the scan abnormality can be established, a metastasis should be suspected even in the absence of symptoms, and a percutaneous needle biopsy should be considered. The level of clinical suspicion should be particularly high for patients with breast cancer who have locally or regionally advanced tumors. In the patient reported here with a focal abnormality on her bone scan and no symptoms of metastatic disease, neither plain radiographs nor carefully performed CT scans indicated the presence of a vertebral metastasis. However, a percutaneous needle biopsy established the diagnosis of metastatic bone disease, and appropriate multiagent chemotherapy was begun.

REFERENCES

1. Harris JR, Canellos GP, Hellman S, Fishkin B. Cancer of the breast. In: de Vita VT, Hellman S, Rosenberg SA, eds., *Cancer principles and practice of oncology*. Philadelphia: Lippincott, 1985:7, 11
2. Bonnadonna G, Carbone PP. Neoplasms of the breast. In: Calabresi P, Schein PS, Rosenberg SA, eds., *Medical oncology*. New York: Macmillan, 1985:996
3. Mall JC, Bekerman C, Hoffer PB, et al. A unified radiological approach to the detection of skeletal metastases. *Radiology* 1976;118:323-328
4. Hoffman HC, Marty R. Bone scanning: its value in preoperative evaluation of patients with suspicious breast masses. *Am J Surg* 1972;125:194-199
5. Corcoran RJ, Thrall JH, Kyle RW, et al. Solitary abnormalities in bone scans of patients with extrasosseous malignancies. *Radiology* 1976;121:663-667
6. Turmeh SS, Beadle G, Kaplan WD. Clinical significance of solitary rib lesions in patients with extraskkeletal malignancy. *J Nucl Med* 1985;26:1140-1143
7. Helms CA, Cann CE, Brunelle FO, et al. Detection of bone marrow metastases using quantitative computed tomography. *Radiology* 1980;140:745-750
8. deSantos LA, Lukeman JM, Wallace S, et al. Percutaneous needle biopsy in bone in the cancer patient. *AJR* 1978;130:641-649
9. Debnam JW, Staple TW. Trephine bone biopsy by radiologists. *Radiology* 1975;116:607-609
10. Ottolenghi C. Aspiration biopsy of the spine. *J Bone Joint Surg [Am]* 1969;51:1531-1544
11. Schagowicz F, Derqui JC. Puncture biopsy in lesions of the locomotor system. *Cancer* 1968;21:531-548
12. Collins JD, Bassett L, Main GD, et al. Percutaneous biopsy following positive bone scans. *Radiology* 1979;132:438-442

Technical Note

Digital Subtraction Arthrography of the Temporomandibular Joint

J. M. Jacobs¹ and B. J. Manaster

Internal derangements of the temporomandibular joint (TMJ) have been recognized as a significant cause of painful TMJ dysfunction [1–10]. Some of these disorders are amenable to surgical treatment while others respond to more conservative, nonsurgical management.

Recently developed noninvasive tests such as direct sagittal CT and MR are no doubt useful as an initial investigation of TMJ abnormalities [2, 3, 5]. However, TMJ arthrography will probably remain important for definitive diagnosis, evaluation of suspicious findings, and planning of surgical management of TMJ complex disease.

TMJ arthrography may be technically difficult in inexperienced hands, resulting in contrast extravasation and/or joint overdistension. More importantly, standard TMJ arthrography often results in the artifactual appearance of meniscal perforation [7].

Materials and Methods

Digital subtraction arthrography was performed on 13 joints in 10 successive patients referred with symptoms of TMJ dysfunction.

Each patient was placed in a lateral recumbent position on the fluoroscopic table with the head tilted slightly toward the tabletop. As in standard TMJ arthrography, fluoroscopic guidance was used for placement of a 25-gauge, 1½-in. (3.85-cm) needle into the posterior portion of the inferior recess of the TMJ space.

Digital subtraction was used only during contrast injection. Initially, 0.1 ml (approximately one drop) of contrast mixture (60% iothalamate meglumine in a 10:1 mixture with 1:1000 epinephrine) was injected to confirm needle position. If the initial drop of contrast material flowed easily away from the needle tip into the joint space, the full

volume (0.5 ml) of contrast material was immediately injected (under digital subtraction) followed by routine filming. This initial drop of contrast material may normally flow in the capsule medially or laterally rather than immediately "capping" the condyle. If the initial contrast material pools around the needle tip, indicating extravasation, the needle can be repositioned. The digital injection is then resumed with the extravasated contrast material digitally subtracted. Occasionally, it is difficult to determine if the initial drop of contrast is intraarticular; in this case, a frame-by-frame review of the subtracted image is performed to determine whether the needle should be repositioned.

The digital portion of the examination does not allow dynamic evaluation of the joint; videotaping and spot filming are required, as in conventional arthrography. Arthrotomography at 2-mm intervals was optionally obtained in the closed- and opened-mouth position.

Particular care was taken that: (1) The patient remained motionless during the injection and filming. (2) The needle and extension tubing were positioned out of the area of interest. Taping the tubing posterior and inferior to the joint was adequate. (3) Only 0.1 ml of contrast mixture was injected with a tuberculin syringe initially, followed by a maximum volume of 0.5 ml (and up to 1.5 ml if meniscal perforation was noted). (4) Frame-by-frame review of the injection localized the perforations.

The digital system, IDIS by Quantel (Palo Alto, CA), allows up to 30 sec of continuous data acquisition at up to 3 frames/sec. We found that 1.8 frames/sec and generally only 15 sec of acquisition were adequate for the examination. A small focal spot (0.2 mm) and a 6-in. (15-cm) field-of-view were used.

Results

Four of the examinations performed were normal. Three had anterior displacement of the meniscus with reduction,

Received July 22, 1986; accepted after revision September 22, 1986.

¹ Both authors: Department of Radiology, University of Utah School of Medicine, 50 N. Medical Dr., Salt Lake City, UT 84132. Address reprint requests to B. J. Manaster.

AJR 148:344–346, February 1987 0361–803X/87/1482–0344 © American Roentgen Ray Society

while six showed anterior meniscal displacement without reduction. Two perforations of the meniscus were found: one with anterior displacement with reduction, while the other was without reduction.

The images in Figure 1 show the normal appearance of contrast material in the joint space on the digital subtraction arthrogram. In two cases, both of which were normal, inadequate placement of the needle was observed on the digital arthrogram with an initial injection of 0.1 ml of contrast mixture. The needle was repositioned, and a second injection confirmed appropriate needle placement. There were no cases of contrast extravasation, and repeat examinations were unnecessary.

The precise site of meniscal perforation was revealed by sequential frame review of the digital subtraction arthrogram, but was obscured in the standard arthrogram filming (Fig. 2). In no instance did the digital subtraction technique miss a perforation detected by spot films or arthrotomography.

The exposure from 15 sec of digital acquisition was compared with that from 15 sec of fluoroscopy by using kV and mAs appropriate to the examination. An MDH ion chamber (Radcal Corp., Monrovia, CA) and a monitor with an accuracy of $\pm 2\%$ show exposure at the TMJ by using digital equipment to be 1.46 rad, while exposure with standard fluoroscopy is 0.67 rad. No measurable radiation was detected in either 15-sec examination at the lens or thyroid. Thus, the digital examination increases the radiation dose at the TMJ by only 0.79 rad.

Discussion

Internal derangements of the TMJ are rapidly becoming a well-recognized and common clinical condition warranting evaluation. Recent studies have shown that direct sagittal CT or MR imaging of the TMJ are effective tests for internal

derangements [2, 4, 5]. However, both CT and MR are limited in that they cannot show the dynamics of a meniscal displacement nor can they diagnose a meniscal perforation. Thus, TMJ arthrography will continue to be the diagnostic imaging technique of choice in many communities.

TMJ arthrography may be technically difficult in inexperienced hands because of the unique intraarticular anatomy of the TMJ. The combined volume of the superior and inferior compartments of the joint space is approximately 1.5 ml [7]. Most authors with experience in TMJ arthrography recommend injecting only 0.5 ml of contrast mixture into the inferior joint space. This small volume leaves little room for error in needle placement and injection of contrast material. The most common technical errors resulting in patient discomfort are joint overdistension and contrast extravasation [8]. Joint overdistension occurs because the small amount of contrast material required is difficult to see fluoroscopically owing to the density of overlapping bony structures. With routine fluoroscopy, 0.5 ml of contrast material may be injected while establishing correct positioning of the needle; unfortunately, if that amount of contrast material is extravasated, the joint is obscured, which means that the patient will have to return at another time for the arthrogram. By eliminating the overlying osseous structures, digital subtraction assures proper needle placement with only a single drop of contrast material. Conversely, extravasation is clearly identified as a focal collection of the contrast material remaining at the tip of the needle. Since the mask image can subtract small amounts of extravasated contrast, the joint space is clearly seen on the second injection. The contrast material is shown so well that it tends to minimize overdistension. With digital subtraction arthrography, the level of confidence in examination interpretation is also enhanced and "failed" examinations are virtually eliminated. The technique adds no time and little radiation

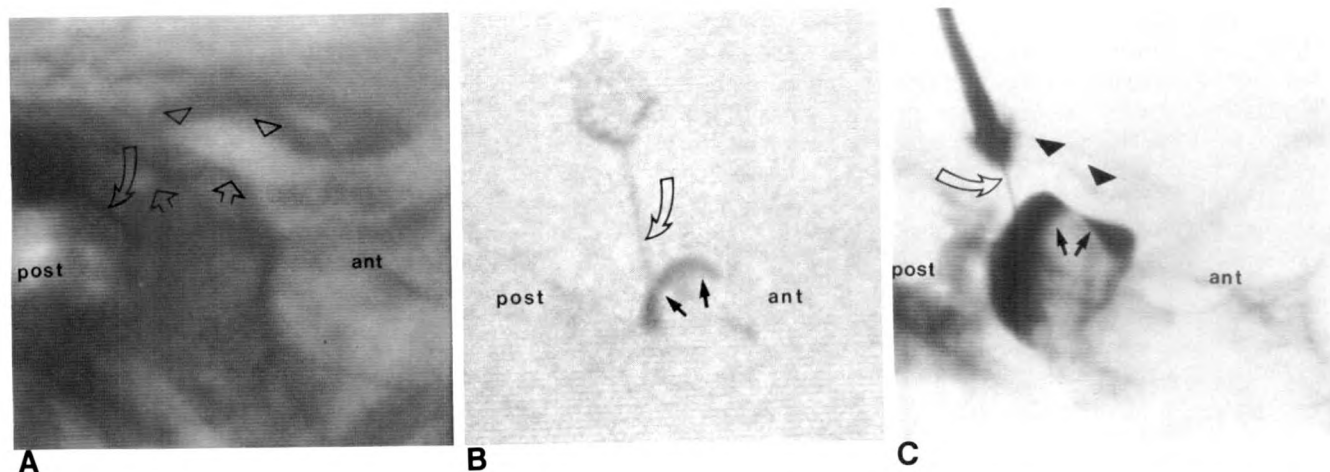


Fig. 1.—Normal appearance of temporomandibular joint. post = posterior; ant = anterior.

A, Radiograph made before injection of contrast medium. Needle (curved open arrow) is located in posterior portion of inferior recess. Condyle (short open arrows) and glenoid (arrowheads) are seen, but superimposed bony structures might obscure small amounts of radiographic contrast material.

B, Digital subtraction arthrogram after one drop (approximately 0.1 ml)

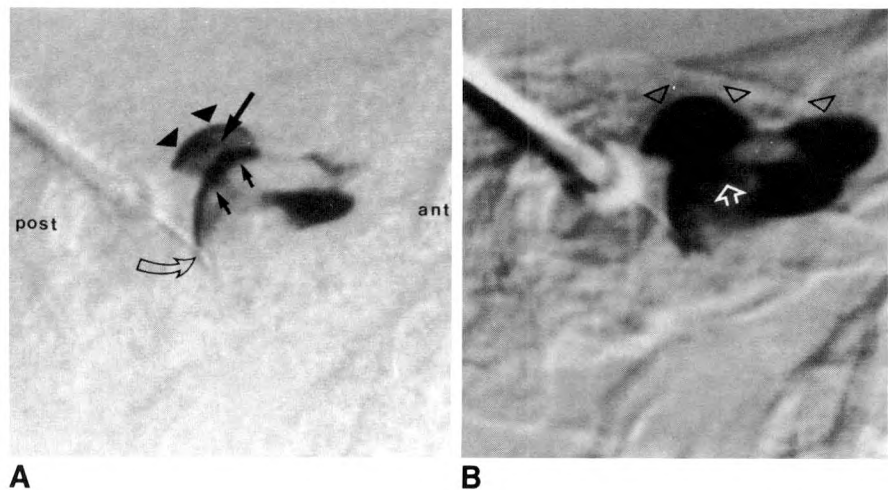
of contrast material was injected. Needle (curved open arrow) is in same position as in A. Note that contrast material (black arrows) flows easily away from tip of needle.

C, Digital subtraction arthrogram done after 0.5 ml of contrast material was injected. Needle (curved open arrow) is in same position as in A; condyle (short arrows) is outlined by contrast material. Glenoid (arrowheads) is barely seen. (It is often obscured in digital arthrography.)

Fig. 2.—Meniscal perforation.

A, Digital subtraction arthrogram (one of the first frames) shows perforation in meniscus (long arrow). Needle tip (curved arrow) is remote from site of meniscal perforation, which therefore is not iatrogenic. Inferior recesses (short arrows) and superior recesses (arrowheads) are well seen. post = posterior; ant = anterior.

B, Digital subtraction arthrogram made 10 sec later shows that site of perforation is obscured by contrast media. Both superior recesses (open arrowheads) and inferior recesses (open arrow) are filled with contrast material.



and may allow more radiologists to perform TMJ arthrography expertly.

Digital subtraction has been shown to be a useful addition to wrist arthrography by more reliably showing sites of ligamentous perforation [11, 12]. The technique assures that TMJ meniscal perforations are due to true disease rather than to iatrogenic causes resulting from the contrast injection itself [2]. Helms et al. [7] found approximately 15% false-positive cases of perforation by arthrography. This error is thought to occur as a result of the straddling of the needle between the superior and inferior compartment of the joint space. As a result, the two compartments fill simultaneously, a finding attributed to perforation of the meniscus. Because of the high incidence of this artifactual phenomenon, patients with arthrographic findings of a meniscal perforation are routinely asked to return for a second arthrogram to confirm the findings. Digital subtraction arthrography obviates this second procedure; a frame-by-frame review of the digital images shows the flow of contrast material and the exact site of leakage from the inferior to the superior recess. If the site of leakage is distant from the needle (as in Fig. 2), it represents a true perforation; if the flow of contrast material into both compartments is from the needle tip, it represents artifactual perforation. The only potential source of confusion is if the site of perforation is posterior at the site of needle placement.

REFERENCES

1. Miller TL, Katzberg RW, Tallents RH, Bessette RW, Katsumi H. Temporomandibular joint clicking with nonreducing anterior displacement of the meniscus. *Radiology* **1985**;154:121-124
2. Manzione JV, Katzberg RW, Brodsky GL, Seltzer SE, Mellins HZ. Internal derangements of the temporomandibular joint: diagnosis by direct sagittal computed tomography. *Radiology* **1984**;150:111-115
3. Katzberg RW, Tallents RH, Katsumi H, Miller TL, Goske MJ, Wood BP. Internal derangements of the temporomandibular joint: findings in the pediatric age group. *Radiology* **1985**;154:125-127
4. Thompson JR, Christiansen E, Hasso AN, Hinshaw DB Jr. Temporomandibular joints: high-resolution computed tomographic evaluation. *Radiology* **1984**;150:105-110
5. Harms SE, Wil RM, Wolford LM, Chiles DG, Milam SB. The temporomandibular joint: magnetic resonance imaging using surface coils. *Radiology* **1985**;157:133-136
6. Kaplan PA, Tu HK, Sleder PP, Lydiatt DD, Laney TJ. Inferior joint space arthrography of normal temporomandibular joints: reassessment of diagnostic criteria. *Radiology* **1986**;159:585-589
7. Helms CA, Katzberg RW, Dolwick MF. *Internal derangements of the temporomandibular joint*. San Francisco Radiology Research and Education Foundation, **1983**
8. Katzberg RW, Miller TL, Hayakawa K, Manzione JF, Tallents RH. Temporomandibular joint arthrography: comparison of morbidity with ionic and low osmolality contrast media. *Radiology* **1985**;155:245-246
9. Pettigrew J, Robert D, Riddle R, Udupa J, Collier D, Ram C. Identification of an anteriorly displaced meniscus in vitro by means of three-dimensional image reconstruction. *Oral Surg Oral Med Oral Pathol* **1985**;59:535-542
10. Roberts CA, Tallents RH, Espeland MA, Handelman SL, Katzberg RW. Mandibular range of motion vs arthrographic diagnosis of the temporomandibular joint. *Oral Surg Oral Med Oral Pathol* **1985**;60:244-251
11. Resnick D, Andre M, Kerr R, Pineda C, Guerva J, Atkinson D. Digital arthrography of the wrist: a radiographic-pathologic investigation. *AJR* **1984**;142:1187-1190
12. Manaster BJ. Digital arthrography of the wrist. *AJR* **1986**;147:563-566

Chronic Airway Obstruction in Children: Evaluation with Cine-CT

Edward E. Frey¹
 Wilbur L. Smith¹
 Steve Grandgeorge²
 Paul McCray²
 Jeff Wagener¹
 Edmund A. Franken, Jr.²
 Yutaka Sato¹

The radiographic diagnosis of airway lesions, especially laryngomalacia and tracheomalacia, often is imprecise. Endoscopy, which allows detailed examination of the upper airway, is an invasive procedure requiring sedation or anesthesia. A prospective study was undertaken to show the value of cine-CT (Imatron) scanning in diagnosing airway lesions in children. Eleven patients, aged 10 days to 4 years old, with a history of stridor were evaluated by both cine-CT and flexible fiberoptic endoscopy. Cine-CT studies of 12 children imaged for other reasons and without clinical evidence of airway disease served as controls to assess normal airway motion. Endoscopy identified 13 abnormalities, 11 of which were identified by cine-CT. Cine-CT has the capacity to image common causes of chronic stridor in children. It is rapid, noninvasive, and requires no sedation in most children. Although additional work is needed to clarify the role of cine-CT, this study suggests that cine-CT is a sensitive and specific imaging technique for evaluation of chronic stridor in infants and children.

Causes of chronic stridor in children range from benign conditions to potentially life-threatening disorders. Laryngoscopy and bronchoscopy are considered the gold standard for diagnosing airway obstruction in children and are used for definitive diagnosis [1-3]. Endoscopy is, however, an invasive procedure usually requiring sedation or anesthesia. Endoscopy introduces a highly nonphysiologic state and may alter the structures being observed. A sensitive, noninvasive imaging method would be advantageous in evaluating patients with chronic stridor. For this reason we conducted a prospective study to compare cine-CT (Imatron) scanning with flexible fiberoptic endoscopy in diagnosing airway lesions in children.

Subjects and Methods

All scans were obtained on an Imatron C-100 scanner. The "flow" mode was used in which up to eight levels are scanned in 224 msec and then repeated at fixed time intervals. Patients were scanned during quiet breathing in the supine position, except for one infant who could only lie prone because of severe respiratory distress. Sedation was not necessary in most instances. After localization scans, images were obtained depicting the airway from the level of the pharynx to several centimeters distal to the carina. Each study consisted of eight contiguous 8-mm CT slices with all eight levels being scanned repeatedly at 0.7-sec intervals. Ten images were obtained at each level. Thus, sample segments were obtained from three or four consecutive breaths. Skin radiation dosage was 300 mR (77.4 μ C/kg) per scan. This technique is similar to that described by Brasch et al. [4]. As the slice thickness is currently fixed at 8 mm, two imaging sequences were performed in each patient with the second being offset by 5 mm so that small focal abnormalities were imaged. Images were displayed in the movie mode allowing assessment of normal and abnormal airway motion.

Eleven patients, aged 10 days to 4 years, presenting with a history of chronic stridor were evaluated by both cine-CT and endoscopy. Cine-CT studies of 12 children who were examined for mediastinal mass lesions or vascular abnormalities and who had no clinical evidence of airway disease served as controls to assess normal airway motion. The ages of the controls ranged from 3 weeks to 16 years (mean, 6.5 years). Endoscopy was not performed on the control groups.

Received July 29, 1986; accepted after revision September 23, 1986.

¹ Department of Radiology, University of Iowa Hospitals and Clinics, Iowa City, IA 52242. Address reprint requests to E. E. Frey.

² Department of Pediatrics, University of Iowa Hospitals and Clinics, Iowa City, IA 52242.

AJR 148:347-352, February 1987
 0361-803X/87/1482-0347
 © American Roentgen Ray Society

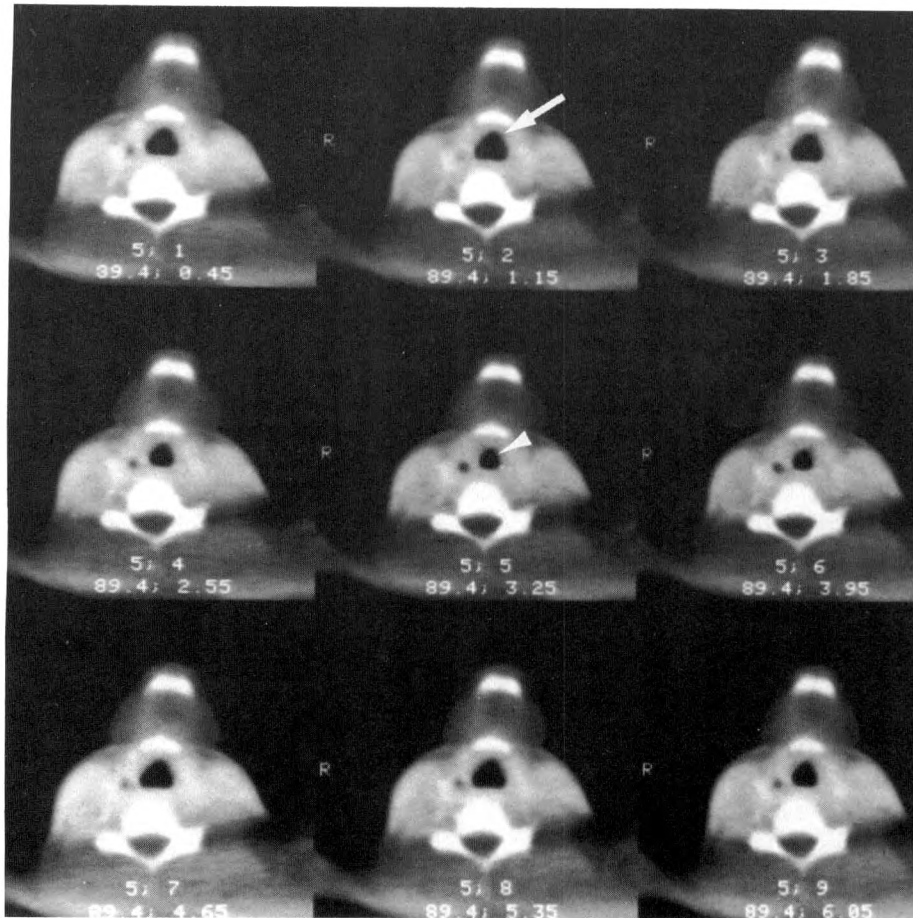


Fig. 1.—Normal larynx. Images obtained every 0.7 sec show normal movement of laryngeal airway. Read images from left to right. Airway is widely patent during inspiration (arrow) and becomes smaller in expiration (arrowhead).

Maximum recorded change in the cross-sectional area of the airway during the respiratory cycle was calculated at three levels in a control population. These levels included the area of maximum change in cross-sectional areas at the larynx, cervical trachea just cephalad to the lung apices, and midthoracic trachea. All areas of dynamic collapse in the 11 abnormal patients were also evaluated. Images with maximum and minimum airway diameter at each of these levels were selected, and regions of interest were drawn by using a semiautomated blink-mode technique with subsequent computation of percentage change in the cross-sectional area. Cine-CT and endoscopy were interpreted without knowledge of the other examination.

Results

Normal Airway

Evaluation of cine-CT studies of 12 children without clinical evidence of airway disease showed moderate change in the caliber of the airway at the level of the vocal cords (Fig. 1). Expiratory narrowing of the laryngeal airway varied from 49% to 73% (mean, 64%). The trachea showed only a small change in cross-sectional area in most patients (Fig. 2). Measurements at the cervical level exhibited a change in the cross-sectional area of 4–38% (mean, 19%). In the thoracic trachea

measurements varied from 1% to 42% (mean, 15%). Only two controls exhibited a change greater than 20% anywhere within the trachea. Slight superior and inferior movement of the airway was sometimes apparent. Tracheal buckling at the thoracic inlet was seen in several patients.

Laryngeal and Paralaryngeal Lesions

Laryngomalacia is a condition caused by a lax epiglottis and redundant arytenoepiglottic folds that are drawn into the glottis during inspiration. Laryngomalacia was correctly identified by cine-CT in five of six affected patients (Table 1). The primary manifestation of laryngomalacia was symmetric narrowing of the laryngeal airway during inspiration. Change in cross-sectional area was 81–100%, with complete collapse of the airway in two cases. Persistent distension of the hypopharynx was observed in two instances. One patient was scanned in the prone position because of severe respiratory distress when supine. For this reason the larynx was scanned obliquely, and meaningful measurements could not be obtained. Abnormally increased airway motion pointed to the correct diagnosis. One false-negative examination was made in a patient who had both laryngomalacia and tracheo-

Fig. 2.—Normal trachea. Sequential images (left to right) of cervical trachea in 14-year-old boy are representative of control group. No appreciable change in cross-sectional area of trachea during several respiratory cycles.

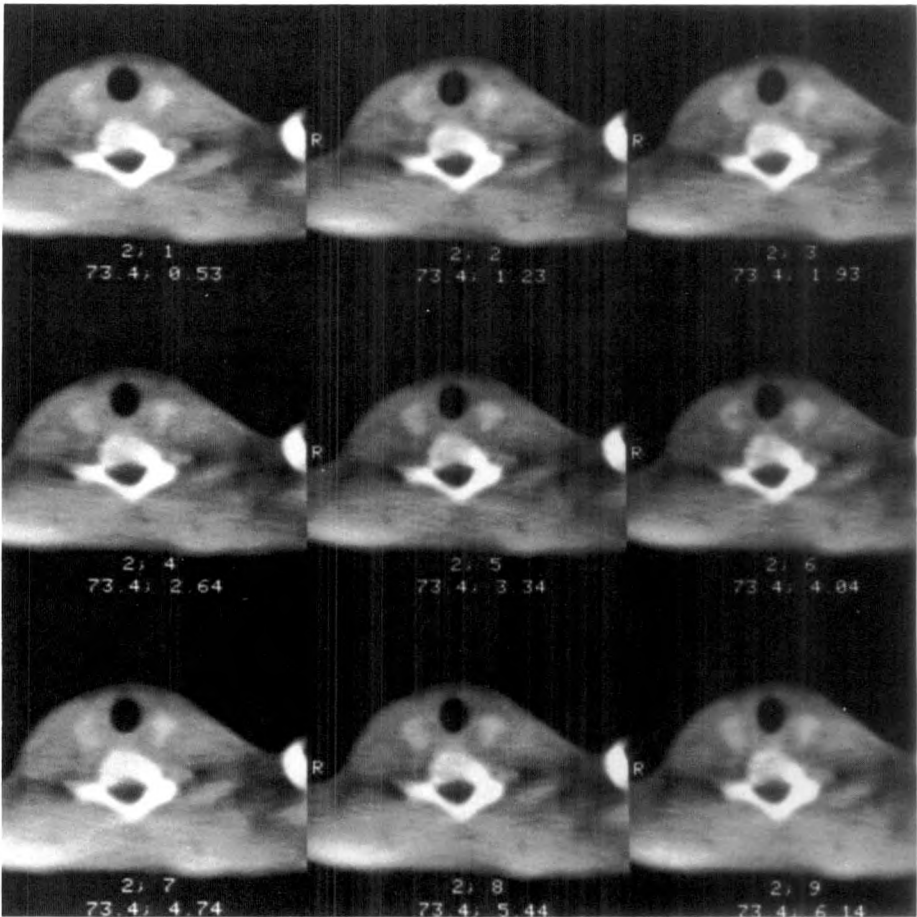


TABLE 1: Comparison of Cine-CT and Endoscopic Findings

Case No.	Age	Cine-CT	Endoscopy
1	5 m	Laryngomalacia	Laryngomalacia
2	6 m	Laryngomalacia	Laryngomalacia
3	4 y	Right vocal cord paralysis	Right vocal cord paralysis
4	6 m	Tracheomalacia	Tracheomalacia
5	2 m	Tracheomalacia	Tracheomalacia, laryngomalacia
6	3 m	Laryngomalacia	Laryngomalacia
7	2 m	Subglottic stenosis	Subglottic stenosis
8	2 m	Laryngomalacia	Laryngomalacia
9	6 m	Left vocal cord paralysis	Bilateral vocal cord paralysis
10	10 d	Laryngomalacia	Laryngomalacia, subglottic web
11	16 m	Tracheomalacia	Tracheomalacia

Note.—m = months; y = years; d = days.

malacia documented by endoscopy. Cine-CT correctly diagnosed tracheomalacia, but laryngomalacia was not recognized because of patient motion.

Vocal cord paralysis was correctly diagnosed in each of two patients. In one, cine-CT showed a persistently narrowed

glottis on both inspiration and expiration. Because of slight asymmetry, CT diagnosis of unilateral vocal cord paralysis was made. Endoscopy revealed bilateral vocal cord paralysis. Cine-CT showed asymmetric movement of the vocal cords in a second patient with failure of the right vocal cord to fully abduct. Unilateral vocal cord paralysis was confirmed by endoscopy.

Subglottic stenosis was correctly identified in one patient. A thin subglottic web was not found by cine-CT in another patient who also had laryngomalacia. The web was judged to be clinically insignificant.

Tracheal Lesions

Tracheomalacia is characterized by abnormal tracheal collapse secondary to deficient tracheal cartilage. Tracheomalacia was correctly diagnosed by cine-CT in all three affected patients. Dynamic studies showed increased collapsibility of the tracheal airway with expiratory collapse. The degree of narrowing ranged from 55% to 100%, with total expiratory collapse of the airway in two patients. Two patients had focal areas of abnormality and one had diffuse involvement of the trachea. One focal lesion would have been missed had overlapping studies not been performed.

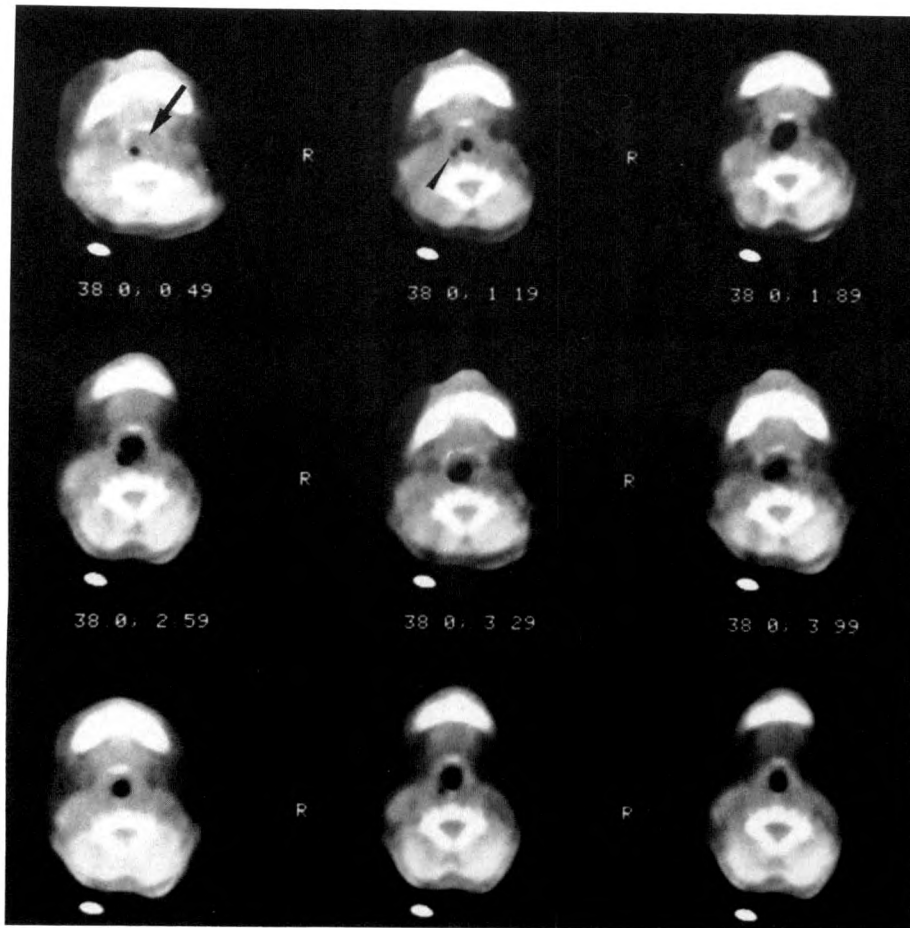


Fig. 3.—Laryngomalacia. Cine-CT examination of 6-month-old child with stridor shows complete collapse of laryngeal airway during quiet breathing (arrow). Air is seen within right pyriform sinus (arrowhead). Laryngomalacia was confirmed by endoscopy. (Read images from left to right.)

Overall, cine-CT correctly diagnosed 11 of 13 abnormalities identified by flexible fiberoptic endoscopy (Table 1).

Discussion

There are numerous conditions that may produce chronic stridor in children. Laryngomalacia is the most common cause, accounting for up to 75% of cases [5, 6]. Other frequent laryngeal and paralaryngeal causes of persistent stridor include vocal cord paralysis and subglottic stenosis [1]. Tracheomalacia, extrinsic compression by vascular rings, and tracheal stenosis are the usual reported tracheal causes of stridor [2]. We have demonstrated that many of these conditions can be diagnosed with cine-CT.

Several investigators indicate conventional radiographic procedures to be insensitive in diagnosing the cause of chronic airway obstruction. In a series of 219 patients Holinger [2] found 26.5% were being treated for an erroneous diagnosis before endoscopic examination. Gyepes and Nussbaum [3] found flexible fiberoptic endoscopy to be more accurate than radiography in the diagnosis of laryngomalacia and tracheal abnormalities. In that study only two of 13 cases of laryngomalacia were correctly diagnosed by radiographic means. While plain films of the airway remain the initial pro-

cedure of choice in evaluating chronic stridor, these studies underscore the necessity of further evaluation in patients where the diagnosis remains unclear.

Conventional CT has an established role in evaluating the larynx and trachea. However, its use has been limited primarily to the evaluation of benign and malignant neoplasms, trauma, and fixed stenosis [7, 8]. Dynamic obstructive lesions, which are much more prevalent in children, cannot be imaged because of relatively long scanning times. Cine-CT can image up to eight levels in 224 msec and repeat these scans at short time intervals. Thus, dynamic obstructive lesions of the airway are readily identified.

Cine-CT shows markedly abnormal motion of the airway in symptomatic patients with obstructive lesions. Severe symmetric narrowing of the airway during inspiration is seen in laryngomalacia with complete obliteration of the lumen in some cases (Fig. 3). Cine-CT also shows marked narrowing or complete obstruction of the trachea during expiration in tracheomalacia (Fig. 4). Vocal cord paralysis is documented by failure of the vocal cords to abduct with the glottis, remaining persistently narrowed throughout the respiratory cycle (Fig. 5). Asymmetric motion suggests unilateral paralysis. Persistent reflex pharyngeal distension, which is a secondary sign of airway obstruction, was present in several

Fig 4.—Tracheomalacia. Cine-CT airway examination of 16-month-old patient with previously repaired tracheoesophageal fistula and esophageal atresia shows complete expiratory collapse of trachea (arrow) several centimeters above carina. Trachea remains widely patent during inspiration (arrowhead). Air is present within esophagus on several images. Endoscopy confirmed complete tracheal collapse during expiration at site of previously ligated tracheoesophageal fistula. (Read images from left to right.)

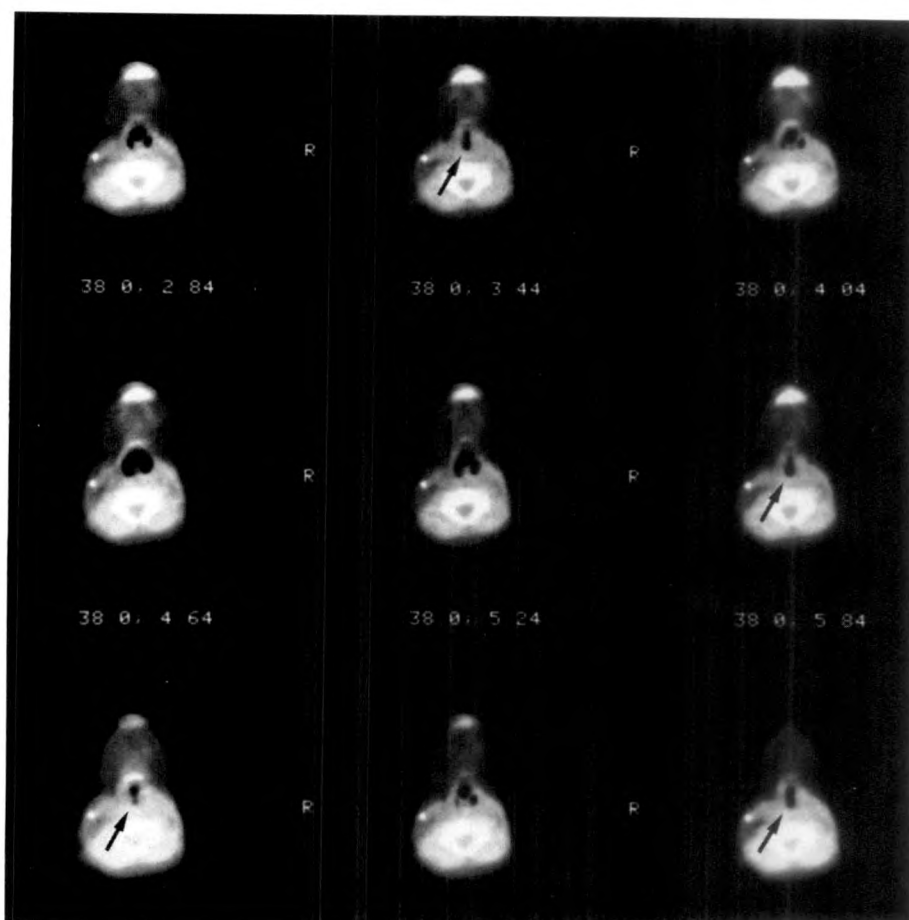
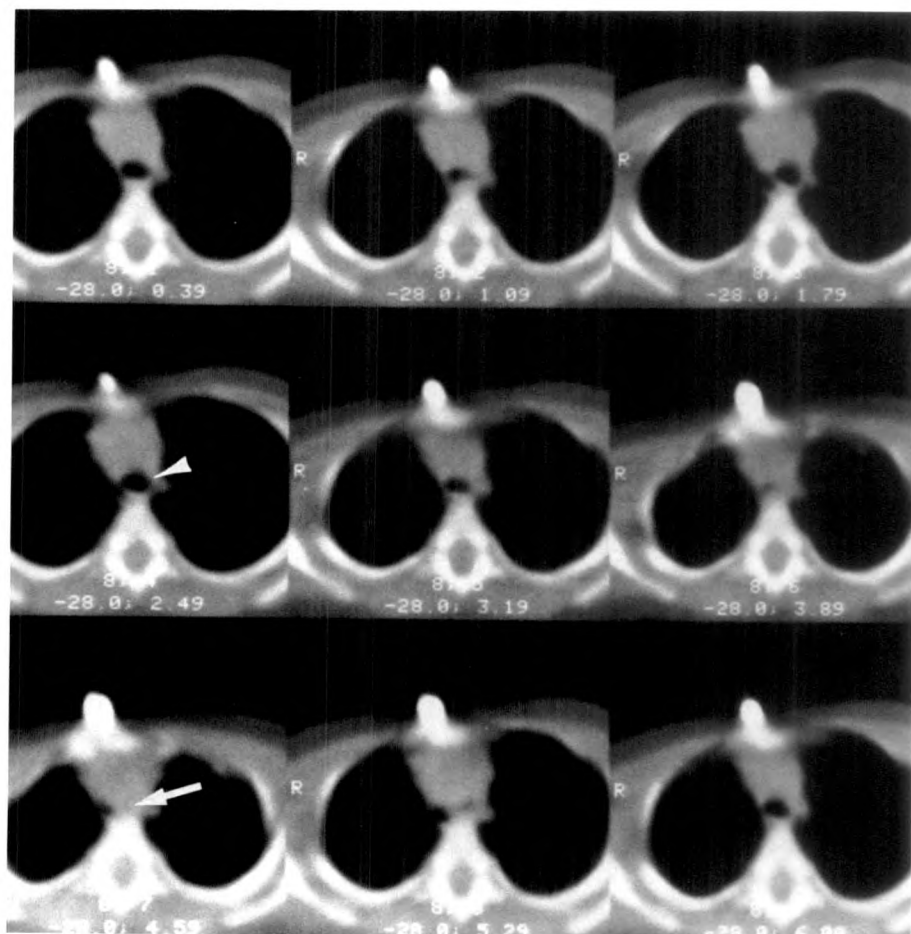


Fig. 5.—Vocal cord paralysis in 6-month-old child with history of stridor and moderate respiratory distress. Scans through larynx show some cephalad-caudad movement with hypopharynx and laryngeal vestibule being intermittently imaged. All images at level of vocal cords (arrows), however, show airway to be persistently narrowed. This finding is readily appreciated in movie mode. Laryngoscopy confirmed bilateral vocal cord paralysis. (Read images from left to right.)

patients [9].

In summary, cine-CT has the capacity to image common causes of chronic stridor in children. It is rapid and noninvasive, and it requires no sedation in most children. Although additional work is needed to clarify the role of cine-CT, this study indicates cine-CT is a highly sensitive and specific imaging method for evaluation of chronic stridor in infants and children.

REFERENCES

1. Holinger PH, Brown WT. Congenital webs, cysts, laryngoceles and other anomalies of the larynx. *Ann Otol Rhinol Laryngol* 1967;76:744-752
2. Holinger LD. Etiology of stridor in the neonate, infant, and child. *Ann Otol Rhinol Laryngol* 1980;89:397-400
3. Gyepes MT, Nussbaum E. Radiographic-endoscopic correlations in the examination of airway disease in children. *Pediatr Radiol* 1985;15:291-296
4. Brasch RC, Newth CJ, Gould RG, Gooding CA, Lipton MJ. Cine-CT diagnosis of airway obstruction in children. *Radiology* 1985;157(P):292
5. Loughlin GM, Taussig LM. Upper airway obstruction. *Semin Respir Med* 1979;1:131-146
6. Smith RJH, Catlin FI. Congenital anomalies of the larynx. *Am J Dis Child* 1984;138:35-39
7. Gamsu G. Computed tomography of the larynx and pyriform sinuses. In: Moss AA, Gamsu G, Genant HK, eds. *Computed tomography of the body*. Philadelphia: Saunders, 1983:65-144
8. Gamsu G. Computed tomography of the trachea and central bronchi. In: Moss AA, Gamsu G, Genant HK, eds. *Computed tomography of the body*. Philadelphia: Saunders, 1983:145-194
9. Meine FJ, Lorenzo RL, Lynch PF, Capitanio MA, Kirkpatrick JA. Pharyngeal distension associated with upper airway obstruction. *Radiology* 1974;111:395-398

Radiographic Findings in Children and Young Adults with Barrett's Esophagus

Barry S. Yulish¹
 Fred C. Rothstein^{2,3}
 Thomas C. Halpin, Jr.³

The upper-gastrointestinal examinations of 32 patients (mean age, 11 years) with histologically proven Barrett's esophagus were reviewed to evaluate the radiologic findings in children. All patients had symptoms of chronic gastroesophageal reflux and/or esophagitis, including atypical findings such as aspiration pneumonia, seizures, and failure to thrive. Fourteen patients had other diseases that might predispose them to abnormal esophageal motility and gastroesophageal reflux. Twenty-five patients had single-contrast and seven patients had double-contrast examinations. Four patients had normal single-contrast studies; 24 had gastroesophageal reflux; 12 had strictures; 10 had esophageal ulcers; and only four had hiatal hernias. The most notable difference between the results of endoscopy and the upper-gastrointestinal studies was the rate of detection of esophageal ulcers. Ten of the patients with single-contrast studies had ulcers seen at endoscopy but not shown radiologically. No specific radiologic signs of Barrett's esophagus were found, although most of our patients had abnormal upper gastrointestinal studies.

Chronic gastroesophageal reflux in infants and children can lead to serious sequelae, such as esophagitis, stricture, gastrointestinal bleeding, failure to thrive, seizure-like activity, aspiration pneumonia, and possibly apnea and sudden-infant-death syndrome [1-7]. The development of Barrett's esophagus in children as a result of chronic gastroesophageal reflux has not been properly appreciated until recently [6]. It occurs when the squamous epithelial lining of the lower esophagus is injured by chronic reflux of acid and pepsin and then replaced by heterotopic columnar epithelium [6, 7]. This report presents radiographic findings in 32 children and young adults with histologically proven Barrett's esophagus.

Materials and Methods

We retrospectively reviewed the upper-gastrointestinal series of 30 children and young adults referred to the pediatric gastroenterology service at Rainbow Babies and Childrens Hospital between 1978 and 1986, all of whom had symptomatic gastroesophageal reflux and histologic evidence of esophagitis and Barrett's esophagus. These patients represented 9% of those with endoscopically proven reflux esophagitis. Two additional patients had upper-gastrointestinal studies at our institution, with endoscopy and biopsy performed elsewhere. Gender distribution was equal, and the ages ranged from 6 months to 21 years old (mean, 11 years).

Most patients had chronic complaints (at least 3 months' duration and as long as several years). Twenty-two patients presented with complaints suggestive of esophagitis, including epigastric pain, dysphagia for solids, and chest discomfort. Eighteen patients had chronic vomiting; nine had protracted vomiting during infancy. Nine had gastrointestinal bleeding (usually occult blood in stool), seven had heartburn, and seven had water brash. Five patients had failure to thrive, irritability, or posturing especially with feeding. Eight patients had pulmonary problems, including night cough, pneumonia, or chronic asthma. Fourteen patients had diseases that can predispose to gastroesophageal reflux. These patients included five who had repaired esophageal atresia, five with psychomotor retardation, three with asthma

Received June 10, 1986; accepted after revision September 4, 1986.

¹ Department of Radiology, University Hospitals of Cleveland, 2074 Abington Rd., Cleveland, OH 44106. Address reprint requests to B. S. Yulish.

² Department of Pediatrics, Rainbow Babies and Childrens Hospital, 2101 Adelbert Rd., Cleveland, OH 44106.

³ Department of Pediatrics, The Mount Sinai Medical Center, University Circle, Cleveland, OH 44106.

AJR 148:353-357, February 1987
 0361-803X/87/1482-0353
 © American Roentgen Ray Society

being treated with theophylline, and one with familial dysautonomia. One child with previous esophageal atresia and one with psychomotor retardation also had asthma. Patients with other underlying diseases included two patients with cystic fibrosis, one with Down syndrome and duodenal atresia, one with acute lymphoblastic leukemia in relapse, one with isolated congenital heart disease, and one with repaired omphalocele and malrotation.

Each patient had flexible fiberoptic esophagogastroscope and biopsy performed by a pediatric gastroenterologist. All biopsies were taken under direct endoscopic visualization at least 2 cm proximal to the lower esophageal sphincter. Biopsies were considered positive for Barrett's esophagus if abnormal columnar epithelium was shown: (1) gastric fundic type mucosa, (2) junctional epithelium reminiscent of gastric cardia, and/or (3) specialized columnar epithelium with villiform surface and goblet cells [6]. Junctional epithelium was insufficient by itself unless macroscopic evidence of Barrett's mucosa was also present [6]. Columnar epithelium at endoscopy was not always apparent; its salmon-pink color in children is difficult to distinguish from the appearance of inflamed squamous epithelium [6, 7]. Esophagitis was suspected at endoscopy (edema, erythema, friability, ulcers, exudate) and confirmed by biopsy.

Contrast studies were performed by pediatric radiologists and by radiology residents with varying degrees of experience. All studies done by residents were supervised by staff radiologists who reviewed all films and who were either present during fluoroscopy or had access to the videotape for review of fluoroscopy. Seven patients had double-contrast examinations, while 25 infants and children unable to cooperate were examined by single-contrast technique. Barium was given by cup, baby bottle, feeding tube, or occasionally through gastrostomy tube. All patients had evaluation of the stomach and duodenum to rule out obstructing gastric lesions and malrotation.

Gastroesophageal reflux was evaluated by delivering a volume of barium approaching a normal feeding, removing a feeding tube if present, burping the child where appropriate, and observing the patient, usually in the supine right posterior oblique position, for spontaneous gastroesophageal reflux. If it was not readily apparent, the child was given water to drink (if he/she would) and observed while drinking water (water-siphon test). The water-siphon test was considered positive if barium reached the carina with esophageal distension [8]. We made no effort to induce reflux except for positional change.

Evaluation for esophagitis included assessment of peristalsis and a search for other esophageal abnormalities such as ulcers and strictures. Abnormal peristalsis includes absent peristalsis and uncoordinated nonpropulsive contractions with to-and-fro motion of barium in the esophagus, frequently with incomplete emptying of the esophagus. All studies were reviewed retrospectively by a radiologist who knew that each patient had Barrett's esophagus.

Results

Thirty-two upper-gastrointestinal studies were reviewed. Seven patients had double-contrast examinations, while 25 infants and children unable to cooperate were examined by single-contrast technique. No patient had gastric-outlet obstruction; however, two children had had surgically corrected malrotation in infancy.

Twenty-four patients had gastroesophageal reflux. Twelve of these patients had ulcers and/or strictures, and nine had abnormal peristalsis (Figs. 1 and 2). Eight patients had no gastroesophageal reflux, but two of these did have radiologic signs of severe esophagitis with several ulcers and strictures

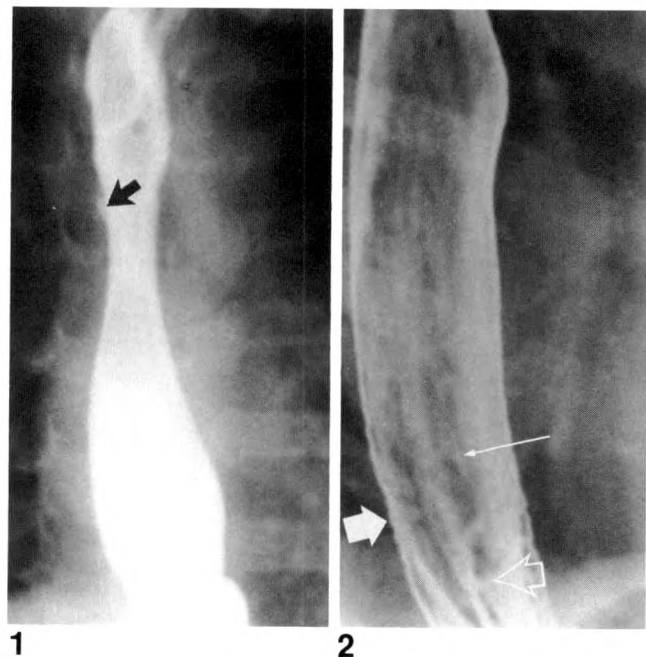


Fig. 1.—Esophagram in 1-year-old girl with repaired esophageal atresia, showing an anastomotic stricture and ulcer (arrow). Columnar epithelium was distant from stricture, in distal 3 cm of esophagus.

Fig. 2.—Esophagram in 10-year-old boy showing mild contour deformity of distal esophagus (broad closed arrow), ulcers (thin arrow), and fixed transverse folds (open arrow points to barium trapped between transverse folds). Columnar epithelium lined distal 3 cm of esophagus.

and two had abnormal peristalsis. Four patients had normal single-contrast upper-gastrointestinal studies. Two of these patients had esophageal ulcers visible at endoscopy.

Ten patients had radiologically demonstrable esophageal ulcers, usually two or more ulcers that were small and in the distal esophagus (Figs. 3 and 4). Three of these patients had single-contrast studies, and seven had double-contrast upper-gastrointestinal studies. One patient had a deep ulcer in columnar epithelium with hiatal hernia and reflux. Ten more patients had endoscopically visible ulcers not appreciated on single-contrast study. Three patients with radiologically demonstrated esophageal ulcerations had additional ulcers detected endoscopically. One of these patients had had a single-contrast upper-gastrointestinal study, while two had had double-contrast studies. For the detection of esophageal ulcers, double-contrast examinations predicted endoscopic findings better than single-contrast examinations did.

Twelve patients had strictures; seven of these were in the midesophagus, and five were in the distal esophagus. Of the seven midesophageal strictures, three were at the site of anastomosis of previous esophageal atresia repairs, and two of these patients had a single ulcer at the site of the anastomotic stricture. Two patients did not have strictures confirmed at endoscopy, and two others had strictures suspected at endoscopy but not demonstrated on upper-gastrointestinal studies.

Hiatal hernias were detected in four patients, who were 12,

15, 19, and 21 years old, respectively. Eleven patients had abnormal esophageal peristalsis with delayed esophageal emptying; four of these had had esophageal atresia. One additional patient with previous esophageal atresia had no notation of peristaltic activity in her radiographic report. Ad-

ditional patients with abnormal esophageal peristalsis included two with psychomotor retardation, one with Down syndrome and duodenal atresia, and one with familial dysautonomia. Less common manifestations of reflux esophagitis included one case each of intramural pseudodiverticulae of the esophagus [9] associated with stricture and ulcers, fixed transverse distal esophageal folds [10], and an inflammatory esophagogastric polyp and fold [11, 12]. Esophagitis was present under endoscopic visualization in all patients, but columnar epithelium could not always be appreciated macroscopically.

Discussion

Barrett [13] described the first cases of columnar-lined lower esophagus in 1950. In 1953, Allison and Johnstone [14] coined the term "Barrett's ulcer" to describe a deep ulceration occurring in the columnar epithelium. They were the first to report the association of a midesophageal stricture with ulcer in the presence of a hiatal hernia and gastroesophageal reflux. Like Barrett, they thought that the columnar lining was congenital, although they questioned the possible significance of chronic gastroesophageal reflux in the development of the lesion. More recently, reports [6, 7, 15, 16] have appeared supporting the relationship between chronic gastroesophageal reflux and the development of Barrett's esophagus. There also appears to be an increased prevalence of adenocarcinoma of the esophagus in patients with Barrett's esophagus. Chronic gastroesophageal reflux of acid, pepsin, and possibly bile may cause specific histologic changes that lead eventually to adenocarcinoma through a spectrum of multifocal dysplasia and carcinoma in situ [15-26].

Because of the premalignant nature of Barrett's mucosa,

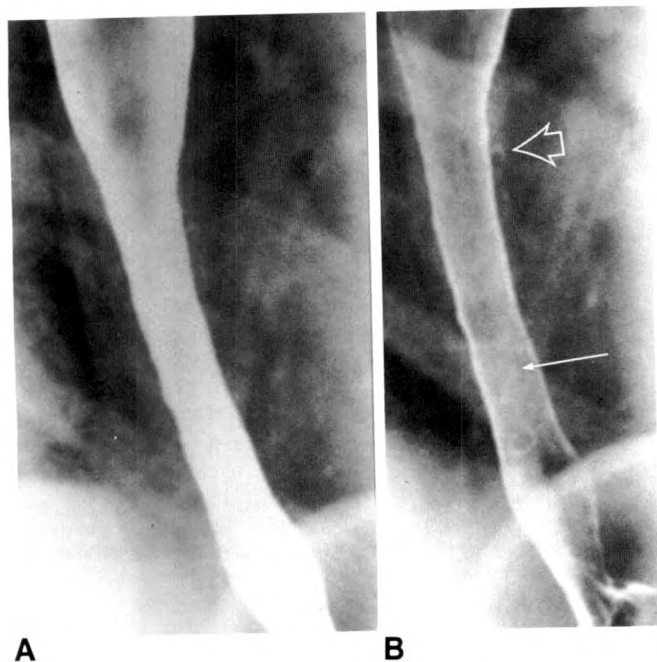


Fig. 3.—Esophagram in 16-year-old boy showing distal esophageal stricture, ulcers (*thin arrow*), and intramural pseudodiverticulae of esophagus (*open arrow*). Columnar epithelium involved entire length of stricture.

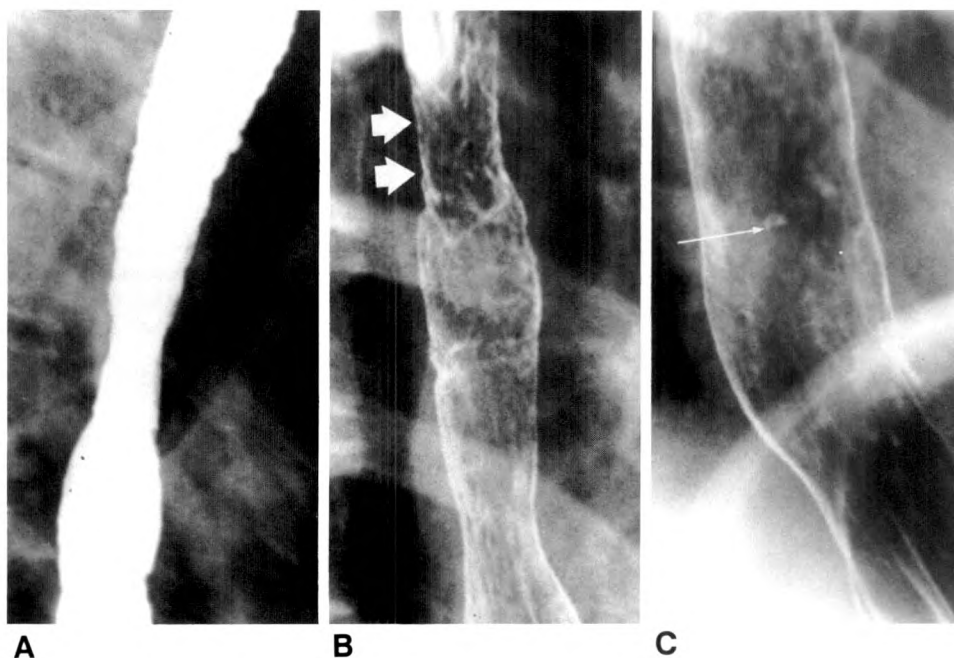


Fig. 4.—Esophagram in 19-year-old man shows diffuse esophageal ulcers (*thin arrow*), high esophageal stricture (*broad arrows*), and patulous lower esophagus. At esophagoscopy, a circular ulcer was seen at stricture site, not visible on radiographs. Columnar epithelium lined esophagus distal to stricture.

many authors [9, 27–29] have attempted to define criteria for its radiologic diagnosis. In adults, the complex of midesophageal stricture, ulcer, hiatal hernia, and gastroesophageal reflux once thought specific for Barrett's esophagus was found to be rare [9, 27–29]. Instead, these authors found that the radiologic features are nonspecific. Hiatus hernia, gastroesophageal reflux, and esophagitis, including stricture, may be present individually or in combination in persons with Barrett's esophagus. Levine et al. [28] thought that a reticular mucosal pattern on double-contrast upper-gastrointestinal studies might be more specific for Barrett's esophagus, but most of their patients did not have this finding, and Vincent et al. [29] thought that this pattern was not specific.

Gastroesophageal reflux occurs commonly in infancy and is a result of immaturity of esophageal function. Most children develop normal function within the first year of life [7]. In those with persistent symptomatic reflux, esophagitis, stricture, and Barrett's esophagus may develop [6, 7].

The radiographic features of Barrett's esophagus in infants, children, and young adults are in many respects similar to those in the older adult, but there are important differences. For example, only four of our patients had hiatal hernias, and the youngest was 12 years old. Ten patients had esophageal ulcers shown radiologically, but an additional 10 patients with single-contrast studies had ulcers seen only at esophagoscopy. Two patients with double-contrast studies had additional or different ulcers detected at endoscopy. Of these, one could not cooperate because of severe cystic fibrosis, and a good examination could not be obtained. Adequate double-contrast examinations in our patients agreed better with endoscopy for detection of esophageal ulcers than single-contrast studies did. Unlike adults, infants and young children do not cooperate for double-contrast examinations. Because only single-contrast studies are done in this age group, ulcers may not be detected.

Twelve of the 32 patients had radiographically demonstrated strictures, a lower percentage than that previously reported in adults and children [9, 27–30], and an even lower percentage when one considers that three of the midesophageal strictures were at the sites of esophageal atresia repairs. The lower rate probably results from the time it takes to develop this type of injury. If children's gastroesophageal reflux is left untreated, they could develop more significant narrowing as they progress into adulthood.

Eight of 11 patients with abnormal peristalsis and poor esophageal emptying had underlying diseases associated with abnormal esophageal motility. In these patients, refluxed gastric contents are poorly cleared, prolonging contact time with the esophageal mucosa. Abnormal peristalsis and aperistalsis have been described in conjunction with reflux esophagitis [31, 32]. The presence of abnormal esophageal peristalsis and poor esophageal emptying may be a significant finding and should alert the radiologist to look for other radiographic evidence of esophagitis.

The most common radiographic finding in our patients with Barrett's esophagus was gastroesophageal reflux, a nonspecific finding that may be associated with reflux esophagitis or Barrett's esophagus. However, its demonstration may be

fortuitous; it occurs intermittently [8]. If gastroesophageal reflux is not readily apparent, the water-siphon test may be used to permit reduction in fluoroscopy time and, hence, reduce radiation exposure. This test has a low false-negative rate, which means that a negative test is evidence against the presence of gastroesophageal reflux, but its high false-positive rate means that the presence of gastroesophageal reflux must be determined by correlation with clinical symptoms [8].

Our patients did not show any specific radiographic signs for specific diagnosis of Barrett's esophagus. Because the radiologic demonstration of reflux esophagitis can be more difficult in infants, children, and adolescents, the presence of Barrett's esophagus may be suspected less often. Therefore, one must maintain a high index of suspicion for Barrett's esophagus if there is radiographic evidence of strictures, ulcers, or other signs of reflux esophagitis (Figs. 1–4).

ACKNOWLEDGMENT

We thank Beverly Barrett Dahms for her assistance.

REFERENCES

1. Bray PF, Herbst JJ, Johnson DG, Book LS, Ziter FA, Condon VR. Childhood gastroesophageal reflux. Neurologic and psychiatric syndromes mimicked. *JAMA* 1977;237:1342–1345
2. Arasu TS, Wyllie R, Fitzgerald JF, et al. Gastroesophageal reflux in infants and children—comparative accuracy of diagnostic methods. *J Pediatr* 1980;96:798–803
3. Rothstein FC, Halpin TC. High incidence of pulmonary symptoms in infants evaluated for esophageal disease. *Ann Otol Rhinol Laryngol* 1980;89:450–453
4. Berquist WE, Rachelefsky GS, Kadden M, et al. Gastroesophageal reflux—associated recurrent pneumonia and chronic asthma in children. *Pediatrics* 1981;68:29–35
5. Allen CJ, Newhouse MT. Gastroesophageal reflux and chronic respiratory disease. *Am Rev Respir Dis* 1984;129:645–647
6. Dahms BB, Rothstein FC. Barrett's esophagus in children: a consequence of chronic gastroesophageal reflux. *Gastroenterology* 1984;86:318–323
7. Rothstein FC, Dahms BB. Barrett's esophagus in children. In: Spechler SJ and Goyal RK, eds. *Barrett's esophagus: pathophysiology, diagnosis and management*. Amsterdam: Elsevier, 1985:129–141
8. Blumhagen JD, Christie DL. Gastroesophageal reflux in children: evaluation of the water siphon test. *Radiology* 1979;131:345–349
9. Chen YM, Gelfand DW, Ott DJ, Wu WC. Barrett esophagus as an extension of severe esophagitis: analysis of radiologic signs in 29 cases. *AJR* 1985;145:275–281
10. Levine MS, Goldstein HM. Fixed transverse folds in the esophagus: a sign of reflux esophagitis. *AJR* 1984;143:275–278
11. Bleshman MH, Banner MP, Johnson RC, DeFord JW. The inflammatory esophagogastric polyp and fold. *Radiology* 1978;128:589–593
12. Styles RA, Gibb SP, Tarshis A, Silverman ML, Scholz FJ. Esophagogastric polyps: radiographic and endoscopic findings. *Radiology* 1985;154:307–311
13. Barrett NR. Chronic peptic ulcer of the oesophagus and "oesophagitis." *Br J Surg* 1950;38:175–182
14. Allison PR, Johnstone AS. The oesophagus lined with gastric mucous membrane. *Thorax* 1953;8:87–101
15. Adler RH. The lower esophagus lined by columnar epithelium. Its association with hiatal hernia, ulcer, stricture, and tumor. *J Thorac Cardiovasc Surg* 1963;45:13–34
16. Burgess JN, Payne WS, Andersen HA, Weiland LH, Carlson HC. Barrett esophagus. The columnar-epithelial-lined lower esophagus. *Mayo Clin Proc* 1971;46:728–734

17. Hawe A, Payne WS, Weiland LH, Fontana RS. Adenocarcinoma in the columnar epithelial lined lower (Barrett) oesophagus. *Thorax* **1973**;28:511-514
18. Cho KJ, Hunter TB, Whitehouse WM. The columnar epithelial-lined lower esophagus and its association with adenocarcinoma of the esophagus. *Radiology* **1975**;115:563-568
19. Naef AP, Savary M, Ozzello L, Pearson FG. Columnar-lined lower esophagus: an acquired lesion with malignant predisposition. Report on 140 cases of Barrett's esophagus with 12 adenocarcinomas. *J Thorac Cardiovasc Surg* **1975**;70:826-835
20. Radigan LR, Glover JL, Shipley FE, Shoemaker RE. Barrett esophagus. *Arch Surg* **1977**;112:486-491
21. Haggitt RC, Tryzelaar J, Ellis FH, Colcher H. Adenocarcinoma complicating columnar epithelium-lined (Barrett's) esophagus. *Am J Clin Pathol* **1978**;70:1-5
22. Berenson MM, Riddell RH, Skinner DB, Freston JW. Malignant transformation of esophageal columnar epithelium. *Cancer* **1978**;41:554-561
23. Poleyndard GD, Marty AT, Birnbaum WB, Nelson LE, O'Reilly RR. Adenocarcinoma in the columnar-lined (Barrett) esophagus. *Arch Surg* **1977**;112:997-1000
24. Cameron AJ, Payne WS. Barrett's esophagus occurring as a complication of scleroderma. *Mayo Clin Proc* **1978**;53:612-615
25. Walpert RD, Laufer I, Thompson JJ, Feczko PJ. Adenocarcinoma of the esophagus in patients with scleroderma. *AJR* **1983**;140:927-930
26. Levine MS, Caroline D, Thompson JJ, Kressel HY, Laufer I, Herlinger H. Adenocarcinoma of the esophagus: relationship to Barrett mucosa. *Radiology* **1984**;150:305-309
27. Robbins AH, Hermos JA, Schimmel EM, Friedlander DM, Messian RA. The columnar-lined esophagus—analysis of 26 cases. *Radiology* **1977**;123:1-7
28. Levine MS, Kressel HY, Caroline DF, Laufer I, Herlinger H, Thompson JJ. Barrett esophagus: reticular pattern of the mucosa. *Radiology* **1983**;147:663-667
29. Vincent ME, Robbins AH, Spechler SJ, Schwartz R, Doos WG, Schimmel EM. The reticular pattern as a radiographic sign of the Barrett esophagus: an assessment. *Radiology* **1984**;153:333-335
30. Hassall E, Weinstein WM, Ament ME. Barrett's esophagus in childhood. *Gastroenterology* **1985**;89:1331-1337
31. Simeone JF, Burrell M, Toffler R, Walker Smith GJ. Aperistalsis and esophagitis. *Radiology* **1977**;123:9-14
32. Cohen S. Motor disorders of the esophagus. *N Engl J Med* **1979**;301:184-192

Book Review

Mammography—A User's Guide. Recommendations of the National Council on Radiation Protection and Measurements. Bethesda, MD: NCRP, 178 pp., 1986. \$16, soft cover

This concise paperback (less than 200 pages) was prepared by the National Council of Radiation Protection and Measurements as a practical guide for mammographers, technologists, physicists, and engineers who calibrate and maintain mammographic equipment. Serving on the committee for the preparation of this manual were several prominent mammographers who ensured that its contents would be useful to the practicing mammographer.

Important physiologic and technical factors in state-of-the-art mammography are addressed in the first chapters, and then an unbiased discussion of the advantages and disadvantages of mammography and xerography is presented. Clear explanations of focal spot, phototiming, grids, focal spot-to-film distance, and guidelines for selection of screen-film combination make this book exceptionally useful not only for the performance of mammography but also in understanding the important factors to consider when purchasing new equipment.

A chapter on dose evaluation and image quality discusses ways to evaluate the performance of one's equipment and, more importantly, how to keep it functioning optimally. Other breast imaging techniques are mentioned briefly and the benefits and risks of mam-

mography are discussed in view of mammographic screening.

The book is slightly hampered by its multiauthor format, both in the text and graphics as well as in the discussions, which range from overly simple to very complex. These minor disadvantages are more than overcome by the unbiased presentation of many controversial issues in mammography. Most importantly, it provides a basic understanding of mammographic equipment by someone other than a salesperson. *Mammography—A User's Guide* also represents an excellent investment for the radiology resident hoping to pass the board examination.

As a practicing mammographer, I highly recommend this book to anyone involved in breast imaging. Its cost is a nominal \$16 and it can be obtained by writing to: NCRP Publications, 7910 Woodmont Ave., Suite 1016, Bethesda, MD 20814.

Saskia von W. Hilton
University of California, San Diego,
Medical Center
San Diego, CA 92103

Sonographic Analysis of the Fetus with Ureteropelvic Junction Obstruction

Beth Kleiner¹
 Peter W. Callen²
 Roy A. Filly²

Twenty-five fetuses with ureteropelvic junction obstruction were evaluated to determine the likelihood of progression of hydronephrosis in utero, and the outcome for the neonate. Such information may alter prenatal as well as perinatal management. These observations showed that (1) the degree of dilatation in utero is likely to be greater than that observed postnatally; (2) the degree of dilatation does not necessarily correlate with renal functional impairment measured postnatally; (3) significant progression of dilatation in utero is relatively uncommon, especially in unilateral cases; and (4) ureteropelvic junction obstruction, even when bilateral, is unlikely to be fatal. Of 21 live newborn infants with follow-up, 14 required surgery and seven were placed under observation.

Hydronephrosis is the most common cause of a neonatal abdominal mass and most often results from ureteropelvic junction (UPJ) obstruction [1]. Hydronephrosis of varying degrees is readily identified by antenatal sonography. The development of renal dysplasia is probably dependent on the severity of the obstruction and its time of onset during gestation [2].

The incidence of contralateral renal anomalies associated with UPJ obstruction, the extent of progression of UPJ obstruction after birth, and the correlation between degree of dilatation and renal functional impairment have been studied in the pediatric and adult populations [3-6]. The factors of progression of dilatation and relationship of dilatation to functional impairment are also relevant to fetal management, but are not as well documented in the literature [7-11]. This study was undertaken to evaluate the frequency and spectrum of contralateral renal disease associated with fetal UPJ obstruction, to determine the likelihood of progression of hydronephrosis in utero, and to compare differences in prenatal and postnatal sonographic appearance with laboratory and surgical follow-up.

Materials and Methods

Obstetric sonographic reports from January 1982 through June 1985 were retrospectively reviewed to identify cases of fetal hydronephrosis. All examinations were performed with commercially available digital gray-scale static and linear-array or sector real-time scanners equipped with 3.5-MHz-transducers.

The fetal sonograms in 25 cases were assessed for the following parameters: fetal size and interval growth (when applicable), amniotic fluid volume, and associated fetal anomalies. The fetal urinary tract was evaluated for evidence of hydronephrosis, ureterectasis, and other renal malformations (e.g., multicystic dysplasia and agenesis). Hydronephrosis was considered present if the ratio of the anteroposterior diameter of the renal pelvis to the anteroposterior diameter of the kidney was greater than 0.5 [8]. Hydronephrosis was also judged to be present if caliectasis was identified regardless of the ratio (Fig. 1). Kidneys without caliectasis and a ratio less than 0.5 were placed in a category termed "mild fetal pyelectasis" [9] (Fig. 2). An in utero diagnosis of UPJ obstruction was made in 25 fetuses who fulfilled the above criteria for significant pelvicaliectasis but showed no evidence of ureterectasis, ectopic ureterocele, or posterior urethral dilatation. The sonograms were available for review in 22

Received June 11, 1986; accepted after revision September 19, 1986.

¹ Department of Radiology, University of California, School of Medicine, San Francisco, CA 94143. Address reprint requests to R. A. Filly.

² Oakland Magnetic Imaging, 300 Hawthorne Ave., Oakland, CA 94609.

AJR 148:359-363, February 1987
 0361-803X/87/1482-0359
 © American Roentgen Ray Society

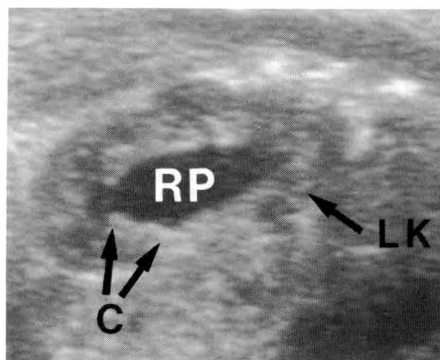


Fig. 1.—In utero sonogram of left fetal kidney (LK) shows pelvis/kidney ratio of 0.45, which is within normal range. However, dilated calices (C) are present. Such cases were considered to be hydronephrotic kidneys. RP = renal pelvis.

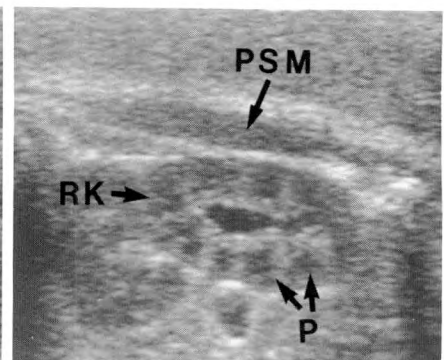
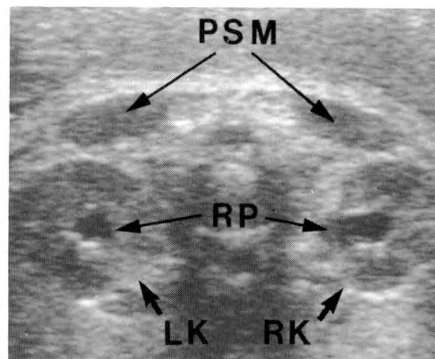


Fig. 2.—Transverse (A) and longitudinal (B) sonograms of fetus with bilateral mild pyelectasis (pelvis/kidney ratio of right kidney = 0.22). No caliceal dilatation is seen on longitudinal image. PSM = paraspinal muscles; RP = renal pelvis; LK = left kidney; RK = right kidney; P = medullary pyramids.

cases. In the other three cases the reports generated at the time of examination were used.

Serial antenatal examinations were performed in 17 fetuses in whom progression of hydronephrosis, change in amniotic fluid volume, and fetal growth were assessed. Postnatal follow-up was obtained in 24 fetuses for pregnancy outcome, progression of disease, and need for surgery. No follow-up information was available in the remaining fetus. Postnatal sonographic, excretory urographic, and technetium-99m diethyltriaminepentacetic acid (Tc DTPA) renographic results were obtained when available. Three pregnancies were therapeutically aborted and autopsy information was available in each.

Results

Of the 25 fetuses with an in utero sonographic diagnosis of UPJ obstruction, 15 had bilateral hydronephrosis. Among the 10 fetuses with unilateral UPJ obstruction, the contralateral kidney was normal in six cases. Findings in the four abnormal fetuses were mild fetal pyelectasis without caliectasis in three and multicystic dysplastic kidney in one. The upper tract dilation ranged in severity from mild with only caliceal blunting to severe obstructions resulting in rupture of the renal collection system and development of paranephric urinomas.

Sixteen fetuses were in amniotic sacs with normal fluid volume, which became significantly decreased in three fetuses during the third trimester. Seven fetuses were in polyhydramniotic sacs, four with bilateral hydronephrosis and three with unilateral hydronephrosis. One of these fetuses had an associated congenital diaphragmatic hernia. Two fetuses were in oligohydramniotic sacs, one of whom had bilateral paranephric urinomas.

Associated extrarenal anomalies included one case each of a skull and CNS malformation, trisomy 18, congenital diaphragmatic hernia, and cystic adenomatoid malformation of the lung.

Among 17 fetuses studied serially, progression of UPJ

obstruction, identified by interval increase in the pelvis/kidney ratio, was shown in four fetuses, each of which had bilateral obstructions. In three fetuses the progression was unilateral, occurring between 35 and 38 weeks in two fetuses and between 28 and 32 weeks in one. In the fourth fetus, mild fetal pyelectasis was present at 35 weeks. A sonogram at 38 weeks showed bilateral hydronephrosis with a bilateral pelvis/kidney ratio greater than 0.5. None of the fetuses with unilateral UPJ obstruction and serial sonograms showed progressive hydronephrosis.

Three fetuses were therapeutically aborted and postmortem examinations were performed. The parental decision to abort one fetus was based on a highly unfavorable prognosis based on the following sonographic findings: profound oligohydramnios; an empty fetal bladder that failed to fill with urine on serial examinations; and identification of large, bilateral paranephric urinomas (one of which was partially confirmed by in utero percutaneous antegrade pyelography) (Fig. 3). Postmortem examination confirmed the sonographic findings and also documented severe bilateral renal dysplasia and pulmonary hypoplasia. Conversely, the parental decisions to abort the two other pregnancies were not based on the suspected diagnosis of UPJ obstruction. In one, the fetus had trisomy 18; in the other a twin had severe anomalies. Autopsy, again, confirmed the suspected UPJ obstructions.

All 21 uninterrupted pregnancies resulted in live neonates. There were no neonatal deaths due to renal complications. One infant died after surgery to repair a concomitant congenital diaphragmatic hernia. Among the 21 live-born neonates with an in utero diagnosis of UPJ obstruction, there were no cases of unsuspected uterovesical or posterior urethral obstruction.

However, the postpartum diagnostic renal evaluation was performed by a variety of pediatricians, neonatologists, pediatric urologic surgeons, and general pediatric surgeons both within our hospital and in other hospitals. Thus, diagnostic procedures to confirm the prenatal diagnosis varied as did

Fig. 3.—A, Coronal sector real-time sonogram of fetus with right and left paranephric urinomas (RPU and LPU). Left has septation (arrow) in location inconsistent with dilated infundibuli or dilated renal pelvis and infundibulum. Right flank fluid collection could be either paranephric urinoma or dilated renal collecting system. R = ribs.

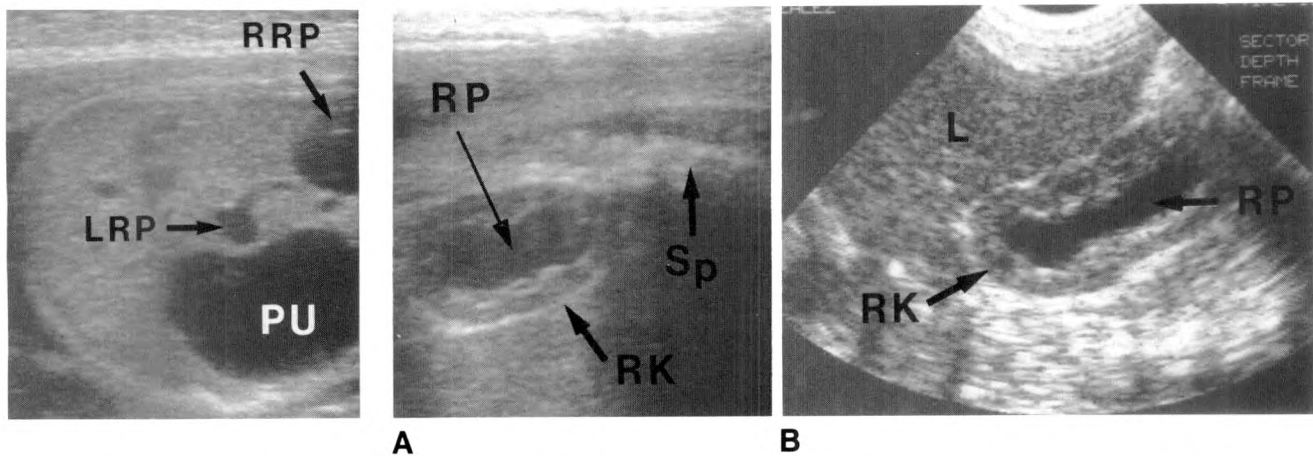
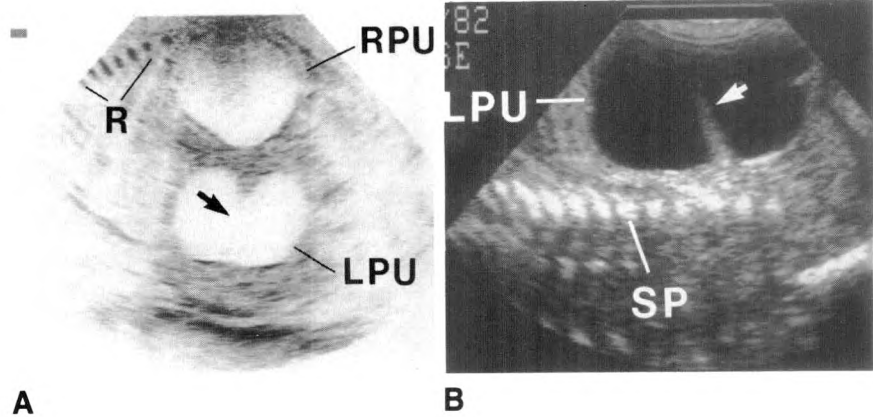


Fig. 4.—Transverse sonogram of fetal abdomen shows decompressed left renal pelvis (LRP) and large paranephric urinoma (PU). Right renal pelvis (RRP) and calices were also dilated. This fetus underwent a right pyeloplasty and left nephrectomy after birth.

Fig. 5.—A, Longitudinal sonogram of right kidney (RK) in utero at 30 menstrual weeks shows moderately severe dilatation of pelvis (RP) and effacement of calices. Sp = spine.

B, Supine longitudinal sonogram of right kidney 4 days after birth shows persistent, but reduced, dilation of intrarenal collecting structures. L = liver; RP = right pelvis; RK = right kidney.

indications for surgery. The need for surgery was generally based on the outcome of Tc DTPA diuresis studies. Those obstructed kidneys showing delayed washout of the radionuclide after furosemide injection were judged as anatomic obstructions requiring surgical intervention. Those that showed pelvicaliectasis but prompt washout of radionuclide were considered "functional" obstructions and placed under surveillance.

The prenatal diagnosis was confirmed surgically in 14 infants, eight of whom had bilateral hydronephrosis. Pyeloplasties were performed in 12 infants, unilateral in 11 and bilateral in one. A contralateral nephrectomy was performed at the time of pyeloplasty in three instances. The resected kidneys had the following pathologic diagnoses: multicystic dysplasia (Potter type II); UPJ obstruction complicated by paranephric urinoma (Fig. 4); and lastly, UPJ obstruction with renal parenchymal dysplasia (Potter type IV). One child had a nephrectomy only for a UPJ obstruction complicated by a paranephric urinoma; the contralateral kidney was normal.

Seven neonates were placed under observation and one was lost to follow-up. Among the seven managed nonoperatively, the in utero diagnosis was confirmed by excretory urography in one, Tc DTPA furosemide renogram in two, and postnatal sonography in four.

Neonatal sonograms were obtained at our institution and thus available for direct comparison with prenatal sonograms in only nine infants. In each instance (15 hydronephrotic kidneys), the degree of pelvicaliceal dilatation was less severe on postpartum sonograms (Fig. 5). Four infants had their postpartum sonograms at 24 hr; all required immediate pyeloplasties. The other five neonates were scanned between 48 hr and 5 months; two of these infants had pyeloplasties.

Tc DTPA radionuclide studies were available for direct comparison in seven of the nine infants who had postnatal sonograms. In two infants with bilateral UPJ obstructions, the kidney with the least amount of caliceal dilatation on sonography showed the poorest function on the radionuclide scan. In five neonates, the renal radionuclide scans showed bilateral

renal uptake and excretion corresponding to the relative degree of obstruction noted on the sonographic studies.

Discussion

UPJ obstruction is the most common cause of neonatal hydronephrosis [1]. The pathogenesis of this condition is unknown. When obstruction is incomplete and occurs after the 36th week, varying degrees of pelvicaliectasis are present without histologic evidence of renal dysplasia. Incomplete obstruction between the 10th and 36th week may result in dysplastic parenchymal changes with or without cyst formation in addition to pelvicaliceal dilatation. Multicystic dysplastic kidney is thought to result from complete obstruction before 8–10 weeks [2].

The sonographic criteria for diagnosis of hydronephrosis in a fetus are less clearly defined than in children or adults. This is based on the observation that pelviectasis is relatively common in normal fetuses [8, 9]. Hoddick et al. [9] found pelvic distension ranging in anteroposterior diameter from 3 to 11 mm in 18% of normal fetuses studied after 24 menstrual weeks. Another 41% of fetal kidneys showed detectable renal pelvic fluid. Arger et al. [8] refined the criteria for recognizing abnormal renal pelvic distension in fetuses and suggested that an anteroposterior renal pelvic diameter of 10 mm or more or a ratio of the pelvic diameter to the anteroposterior renal diameter greater than 50% that persists identifies significant fetal hydronephrosis. Our current study modified the above criteria of Arger et al. by considering caliectasis as evidence of hydronephrosis even when the pelvis/kidney ratio was less than 0.5 (Fig. 1). Among the 10 fetuses with unilateral UPJ obstruction, three had contralateral pyelectasis that did not meet the criteria for hydronephrosis (mild fetal pyelectasis). None of these kidneys required postnatal surgical intervention. By contrast, three fetal kidneys with caliectasis had ratios less than 0.5; two of these required postnatal pyeloplasties.

In utero progression of hydronephrosis was identified unilaterally in three fetuses with bilateral hydronephrosis. Two of these fetuses required postnatal surgical intervention in the kidney that showed progressive dilatation in utero. The fetus described previously with bilateral hydronephrosis progressing from bilateral mild pyelectasis has not required surgery at the time of this report.

Seven of 25 fetuses with UPJ obstruction (four bilateral, three unilateral) were in polyhydramniotic sacs. Polyhydramnios has been described in association with impaired renal function [10–12]. This finding is somewhat paradoxical since fetal urination is the primary source of amniotic fluid after the second trimester. One hypothesis is that obstruction impairs renal concentrating ability and results in a state of high urine output.

Two fetuses were in oligohydramniotic sacs. Oligohydramnios was detected at 32 weeks associated with a fetus with unilateral UPJ obstruction. This fetus was born live at 37 weeks without evidence for pulmonary hypoplasia. No cause for the oligohydramnios was discovered. The parents elected to terminate the pregnancy involving the second fetus with

oligohydramnios. Autopsy confirmed the presence of bilateral UPJ obstructions, bilateral renal dysplasia, bilateral paranephric urinomas, and pulmonary hypoplasia (Fig. 3). We judge the autopsy findings in this latter case to be incompatible with postnatal survival. This fetus represents the only case of UPJ obstruction resulting in a fatal renal anomaly.

We noted that pelvicaliceal dilation appeared less prominent on postnatal sonograms (Fig. 5). We believe that this resulted from the removal of the fetus from exposure to high levels of circulating progesterone-like maternal hormones. These maternal hormones cause smooth-muscle relaxation of the ureteral walls (analogous to smooth-muscle relaxation of the uterus) in the maternal urinary-collecting systems and likely cause a similar relaxation in the fetal collecting systems. The maternal urinary-collecting structures undergo dilation and develop decreased peristaltic activity as early as 3 months of pregnancy; this becomes maximal in the third trimester [13, 14].

The relative degree of hydronephrosis in utero did not always correlate with renal parenchymal function shown by Tc DTPA radionuclide imaging. Radionuclide studies can quantitate relative renal function in obstructed kidneys [15]. Radionuclide studies can also help determine operability by documenting the percentage contribution by the affected kidney to total renal function. Two of the seven fetuses with postnatal diuretic Tc DTPA renal scans showed lack of correlation with pre- and postnatal renal sonographic findings. Both fetuses had asymmetric bilateral UPJ obstructions with poorer renal function associated with the kidney with the less distended renal collecting structures. Neither of the two kidneys with diminished function and less marked caliectasis had sonographic evidence for dysplasia, such as cysts or increased echogenicity. Possibly the diminished caliceal distension is the result of poorer renal function, presumably from renal damage secondary to obstruction. Glazer et al. [16] observed that obstructed fetal pelvicaliceal systems may not distend in the manner commonly observed in the adult kidney. Although anatomic severity of hydronephrosis can be detected in utero by sonography, relative functional renal impairment, important for surgical planning, cannot be determined without postnatal renal radionuclide scans.

Although sonography is limited in its ability to predict both renal functional loss as well as the differences between "functional" vs "anatomic" UPJ obstruction, our data indicate that it has the capacity to recognize the level of obstruction accurately. There were no cases of unsuspected ureterovesical or posterior urethral obstructions in this group. However, a cautious approach still appears warranted since assignment of the level of obstruction to the ureteropelvic junction is based on "negative" observations: failure to observe a dilated ureter, ectopic ureterocele, dilated or thickened urinary bladder, or dilated posterior urethra. Furthermore, sonography was used postnatally in four instances to confirm a prenatal diagnosis made by the sonography. This could have spuriously improved our results.

Our experience has been that kidneys with severe enough obstruction to result in rupture of the collecting system and paranephric urinoma formation are unlikely to have residual renal function (Fig. 4). The three neonates with unilateral

urinomas showed no evidence of function in the involved kidney. One infant who had resection of the urinoma showed no contrast excretion in the associated kidney on a follow-up excretory urogram. The only fetus with apparently lethal renal disease caused by UPJ obstruction had bilateral paranephric urinomas. Thus, of five kidneys with UPJ obstruction complicated by paranephric urinomas, none were salvaged.

In our series of 25 cases, there was a greater frequency of bilateral than unilateral UPJ obstruction by a factor of 1.5 to 1. Bilateral UPJ obstruction in the pediatric and adult population has been reported to occur in only 10% of cases [15]. The substantially higher frequency of bilateral UPJ obstruction in our series may be due to (1) higher frequency of bilateral obstruction in the fetal population, (2) greater recognition of disease due to examination of fetuses not suspected of urinary tract obstruction, or (3) referral bias. Since our medical center serves as a fetal treatment referral center, there is a greater likelihood of evaluating fetuses with bilateral renal abnormalities who may require prenatal or perinatal intervention. Referral bias probably accounts for the higher frequency of bilateral UPJ obstruction in our study group.

REFERENCES

1. Leibowitz RL, Griscom NT. Neonatal hydronephrosis—146 cases. *Radiol Clin North Am* 1980;7:273-289
2. Sanders RC, Hartman DS. The sonographic distinction between neonatal multicystic kidney and hydronephrosis. *Radiology* 1984;151:621-625
3. Snyder NM, Leibowitz RL, Colodny AH, Bauer SB, Retik AB. Ureteropelvic junction obstruction in children. *Urol Clin North Am* 1980;7:273-290
4. Bejjani B, Belman AB. Ureteropelvic junction obstruction in newborns and infants. *J Urol* 1982;128:770-773
5. Johnston JH, Evans JP, Glassberg KI, Shapiro SR. Pelvic hydronephrosis in children—a review of 219 cases. *J Urol* 1977;117:97-101
6. Hellstrom WJG, Kogan BA, Jeffrey RB Jr, McAninch J. The natural history of prenatal hydronephrosis with normal amounts of amniotic fluid. *Urology* 1984;132:947-950
7. Callen PW, Bolding DB, Filly RA, Harrison MR. Ultrasonographic evaluation of fetal paranephric pseudocysts. *J Ultrasound Med* 1983;2:309-312
8. Arger PH, Coleman BG, Mintz MC, et al. Routine fetal genitourinary tract screening. *Radiology* 1985;156:485-489
9. Hoddick WK, Filly RA, Mahony BS, Callen PW. Minimal fetal renal pyelectasis. *J Ultrasound Med* 1985;4:85-89
10. Hadlock RP, Deter RL, Carpenter R, Gonzalez ET, Park SK. Review. Sonography of fetal urinary tract anomalies. *AJR* 1981;137:261-267
11. Henderson SC, Van Kolken RJ, Rahatzad M. Multicystic kidney with hydramnios. *JCU* 1980;8:249-250
12. Laing FC, Burke VC, Wing VW, Jeffrey RB, Hashimoto B. Postpartum evaluation of hydronephrosis: optimal timing for follow-up sonography. *Radiology* 1984;152:423-424
13. Berman LB. The pregnant kidney. *JAMA* 1975;230:111-112
14. Waltzer WC. The urinary tract in pregnancy. *J Urol* 1981;125:271-276
15. Parker RM, Rudd TG, Wonderly RK, Ansell JS. Ureteropelvic junction obstruction in infants and children: functional evaluation of the obstructed kidney preoperatively and postoperatively. *J Urol* 1981;126:509-512
16. Glazer GM, Filly RA, Callen PW. The varied sonographic appearance of the urinary tract in the fetus and newborn with urethral obstruction. *Radiology* 1982;144:563-568

Case Report

Main-Stem Bronchial Atresia: Intrauterine Sonographic Diagnosis

William H. McAlister,¹ James R. Wright, Jr.,² and James P. Crane³

Bronchial atresia probably results from a vascular insult either after the 15th menstrual week when the bronchial branching is complete or between the fifth and 15th menstrual weeks with distal branching dissociated from the atretic segment. We wish to present a patient with atresia of the right main-stem bronchus and tracheal stenosis whose serial intrauterine sonography documented an enlarged echogenic right lung with both mediastinal shift and anechoic, mucus-filled, dilated bronchi noted at 24.4 weeks after normal scans at 15.6 and 20.3 weeks. The right lung became relatively smaller during further intrauterine development while the anechoic bronchi became larger. The sonographic findings suggest that atresia occurred after the bronchial branching was completed.

Case Report

A 38-year-old insulin-dependent diabetic woman had an initial sonographic examination at 15.6 weeks menstrual age revealing a normal fetus. Diagnostic studies after that sonogram included elevated maternal serum and amniotic fluid alpha-fetoprotein (>3 SD). Because of these unexplained elevations, serial sonographic studies were performed.

Normal interval growth and fetal anatomy were noted on repeat sonographic examination at 20.3 weeks. However, the third examination at 24.4 weeks revealed in the right hemithorax a large, hyperechoic mass occupying two-thirds of the thoracic cavity, depressing the diaphragm, and producing a marked left mediastinal shift (Figs. 1A and 1B). Two small anechoic areas were noted in the mass. The

mass was unchanged at 27 weeks except that the anechoic areas were slightly larger. By 31 weeks, there was less mediastinal shift and lung echogenicity (Fig. 1C). The mass remained unchanged thereafter except for enlargement of the anechoic areas at 36 weeks.

A 38-week, 2040-g boy delivered by cesarean section developed severe respiratory distress, and multiple attempts at intubation were unsuccessful. A chest radiograph showed opacification of the right hemithorax, mediastinal shift to the right, a left pneumothorax, and a narrow trachea. Chest sonography showed multiple tubular and round anechoic areas throughout the nonaerated right lung (Fig. 2). The infant died at 4 hr.

Autopsy revealed tracheal stenosis with circumferentially continuous cartilaginous rings ("napkin rings"). The left main-stem bronchus and left pulmonary artery were normal. The right main-stem bronchus was an atretic cord. The left lung was multifocally hemorrhagic but otherwise unremarkable. The right lung was firm, rubbery, abnormally smooth, and had multiple mucus-filled cystic dilatations extending outward from the hilus on cut sections (Fig. 3). Histologically, the right lung showed marked atelectasis with abundant terminal bronchioles. The cystic spaces were filled with mucus and lined by respiratory epithelium. Additional findings included bicuspid truncus arteriosus and a membranous ventricular septal defect.

Discussion

The chronologic events surrounding lung development allow speculation about when bronchial atresia occurred. At the fourth week of gestation, the trachea arises from the foregut as a diverticulum and is invested with splanchnic

Received July 10, 1986; accepted after revision September 19, 1986.

¹ Department of Pediatric Radiology, Mallinckrodt Institute of Radiology, Washington University School of Medicine, 510 S. Kingshighway Blvd., St. Louis, MO 63110. Address reprint requests to W. H. McAlister.

² Department of Pathology, Washington University School of Medicine, 510 S. Kingshighway Blvd., St. Louis, MO 63110.

³ Department of Obstetrics and Gynecology, Washington University School of Medicine, 510 S. Kingshighway Blvd., St. Louis, MO 63110.

AJR 148:364-366, February 1987 0361-803X/87/1482-0364 © American Roentgen Ray Society

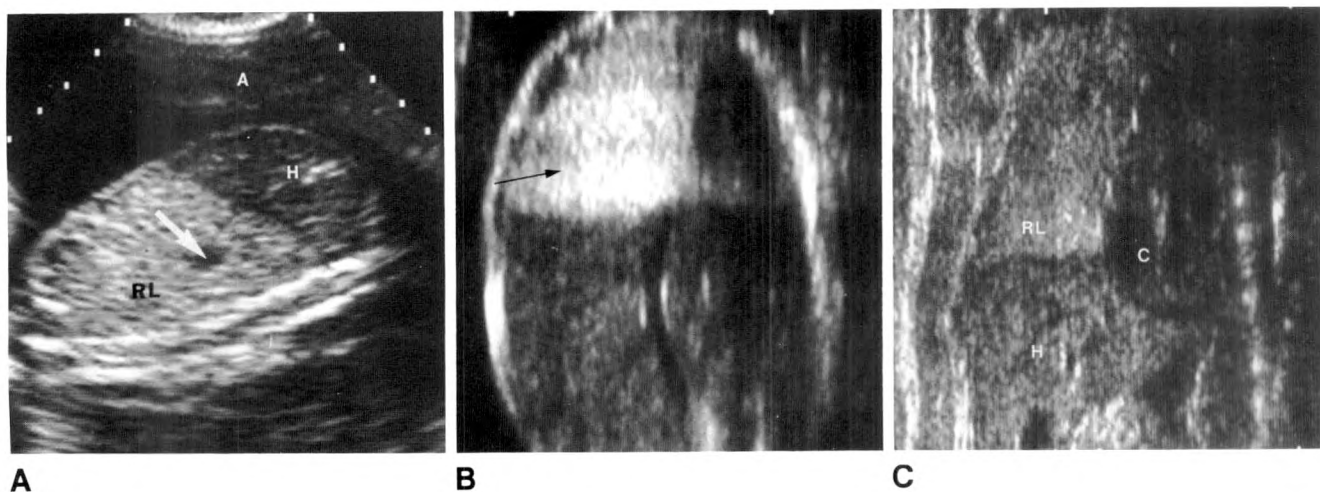


Fig. 1.—Sonograms.

A, 24.4 weeks. Sagittal scan of chest and abdomen shows an expanded echogenic right lung with small anechoic area (arrow) in lower lobe. (H = liver; A = anterior surface of fetus; RL = right lung.)
 B, 24.4 weeks. Coronal scan of chest and abdomen showing expanded echogenic right lung (arrow) with shift to mediastinum to left.
 C, 31 weeks. Coronal scan of chest and abdomen showing a decrease in echogenicity to right lung (RL) with return of mediastinum including heart (C) to midline. (H = liver.)

Fig. 2.—Postnatal sagittal sonogram of chest and upper abdomen (turned 90°). Multiple branching and dilated bronchi (arrows) are seen in right lung (RL), which is less echogenic than liver (H). (C = heart; K = kidney.)

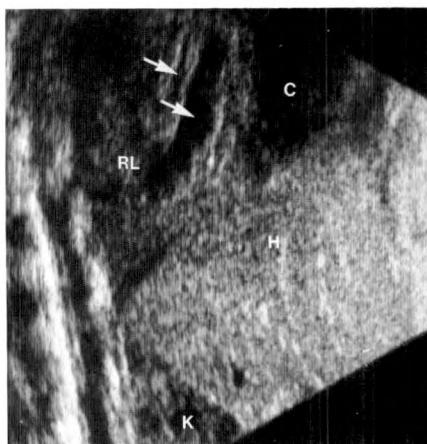
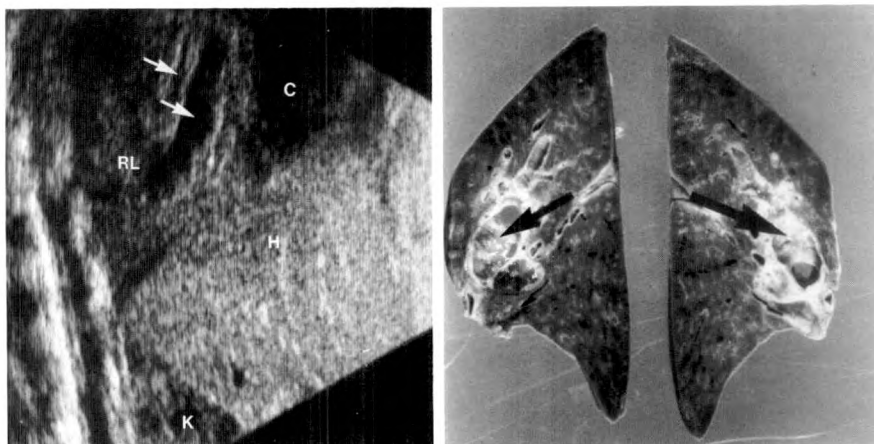


Fig. 3.—Sectioned right lung showing several massively dilated bronchi containing mucus (arrows).



mesoderm. Between the fourth and 15th weeks of fetal life, the stem bronchi arise and progressively branch to form the lungs. The lobar bronchi are present at the fifth week of gestation, and all segmental bronchi are present by 6 weeks. After the 15th week, the bronchial development is complete [1]. Alveolar development is largely postnatal.

In bronchial atresia, the bronchi distal to the atresia are normal in number. Some insult, possibly vascular, causes obliteration of the segmental, lobar, or main-stem bronchus after the more distal portions of the bronchial tree have developed—that is, after the 15th week [1], or alternatively, the insult occurs between the fifth and 15th weeks and distal bronchial development and branching continue dissociated from the proximal atresia [2]. Williams and Schuster [3] described a patient with bronchial atresia and a hilar broncho-

genic cyst and suggested that both malformations arose simultaneously at 5–6 gestational weeks, thus supporting the latter theory. In our patient, the sonographic evidence of a thoracic abnormality at 24.4 weeks after normal appearances at 15.6 and 20.3 weeks suggests that bronchial atresia can develop after the 15th week of gestation. Sonography may not be able to detect bronchial atresia until after 20 weeks even if it arose before 15 weeks.

Bronchial atresia usually occurs in segmental or lobar bronchi and is rare but not fatal. The severe tracheal stenosis and main-stem bronchial atresia (especially the former) was probably the reason for our patient's death. The usual radiographic finding in neonates with bronchial atresia is a fluid-filled chest mass. This pulmonary mass is soon replaced by a lucent area as the portions of lung distal to the atresia are aerated by

collateral ventilation. The branching, dilated, mucus-filled bronchi in the more distal atresias can be seen either on plain radiographs or CT. Congenital lobar emphysema has been associated with bronchial atresia [4].

Generally, the echogenicity of the fetal lung is similar to that of the fetal liver, but roughly one-third of normal fetuses have lungs that are more echogenic than liver [5]. The progressive fall in echogenicity of the right lung was perhaps due to changes in the soft-tissue mucous interfaces, with a greater mucous accumulation in the obstructed distal airways.

There are many causes of elevated maternal and amniotic alpha-fetoprotein levels in addition to neural-tube defects. We are unaware of elevations associated with bronchial atresia, and the explanation is unclear.

In the differential diagnosis, sonography cannot distinguish a congenital cystic adenomatous malformation from bronchial atresia since both may be characterized by echogenic lungs with anechoic areas [6]. Cystic adenomatoid malformations have been associated with atresia of the main-stem bronchus [7] or of the segmental bronchus [8] and may represent multifocal bronchial atresia [8]. Other conditions with cystic masses and variable lung echogenicity include congenital

diaphragmatic hernias, bronchopulmonary foregut malformations, and lobar emphysema.

REFERENCES

1. Reid L. The lung: its growth and remodeling in health and disease. *AJR* 1977;129:777-788
2. Simon G, Reid L. Atresia of an apical bronchus of the left upper lobe: report of 3 cases. *Br J Dis Chest* 1963;57:126-132
3. Williams AJ, Schuster SR. Bronchial atresia associated with a bronchogenic cyst. Evidence of early appearance of atretic segments. *Chest* 1985;87:396-398
4. Warner JO, Rubin S, Heard BE. Congenital lobar emphysema: a case with bronchial atresia and abnormal bronchial cartilages. *Br J Dis Chest* 1982;76:177-184
5. Fried AM, Loh RK, Umer MA, Dillon KP, Kryscio R. Echogenicity of fetal lung: relation to fetal age and maturity. *AJR* 1985;145:591-594
6. Johnson JA, Rumack CM, Johnson ML, Shikes R, Appareti K, Rees G. Cystic adenomatoid malformation: antenatal demonstration. *AJR* 1984;142:483-484
7. Mendoza A, Wolf P, Edwards DK, Leopold GR, Volland JR, Benirschke K. Prenatal ultrasonographic diagnosis of congenital adenomatoid malformation of the lung. *Arch Pathol Lab Med* 1986;110:402-404
8. Cachia R, Sobonya RE. Congenital cystic adenomatoid malformation of the lung with bronchial atresia. *Hum Pathol* 1981;12:947-950

Risks of Percutaneous Transhepatic Drainage in Patients with Cholangitis

Juan F. Lois¹
 Antoinette S. Gomes¹
 Pierce A. Grace²
 Larry-Stuart Deutsch¹
 Henry A. Pitt²

Percutaneous transhepatic biliary drainage (PTD) has been advocated as a method of achieving biliary decompression in patients with cholangitis. However, the risk of PTD in these patients has not been determined. Therefore, we reviewed the records of 95 consecutive PTD patients, 30 (32%) of whom had cholangitis. Forty-four (46%) of the 95 patients underwent PTD as a preoperative measure; the remaining 51 (54%) had PTD for palliation of end-stage malignancies. Thirty-day mortality and overall morbidity were 17% and 30%, respectively, in the patients with cholangitis and 15% and 28% in the patients without cholangitis. These differences were not statistically significant. However, patients with cholangitis had a significantly higher ($p < .05$) incidence of post-PTD bacteremia. In patients undergoing PTD for palliation, both mortality (25%, $p < .01$) and morbidity (35%) were higher than in those being drained preoperatively. This analysis suggests that PTD can be performed safely in patients with cholangitis and that the patient's underlying disease process is more important than the presence of cholangitis in determining the outcome.

In 1877 Charcot [1] published his observations on cholangitis and described the triad of fever and chills, jaundice, and abdominal pain that now bears his name. More than 100 years later cholangitis still poses a serious problem, and surgical mortality rates of 12–20% continue to be reported [2–6]. Percutaneous transhepatic biliary drainage (PTD) has been suggested as a method of achieving biliary decompression that would alleviate sepsis without the additional risks of laparotomy and general anesthesia [7, 8]. However, several reports have cautioned that in some patients PTD may be associated with significant morbidity [9–12], and the role of PTD in patients who have cholangitis has not been adequately studied. Therefore, we reviewed our experience with PTD to determine whether this procedure can be performed safely in patients who have cholangitis.

Methods

Patient Population

During a 4-year period from 1980 to 1984, PTD was attempted in 95 patients and was successful in 87 (92%). The 95 patients ranged in age from 11 to 89 years (average, 61). Patients with jaundice and/or known biliary disease, a predrainage temperature of 38.0° C or more, and no other explanation for their fever were considered to have cholangitis. On this basis, 30 (32%) of the 95 patients undergoing PTD had cholangitis. Of these, nine had positive blood cultures on admission, one had liver abscesses, and two had septic shock.

PTD was performed preoperatively in 44 patients (46%) and for palliation, usually of an advanced malignancy, in 51 (54%). Eleven (25%) of those in the preoperative group and 19 (37%) in the palliative group had cholangitis before PTD. Of the 30 patients who had cholangitis, 11 (37%) had PTD performed preoperatively, and 19 (63%) underwent palliative drainage. Of the 65 patients who did not have predrainage cholangitis, 33 (51%) had preoperative PTD, and 32 (49%) underwent PTD for palliation.

Laboratory data were similar in all groups. The underlying diseases that caused biliary obstruction are presented in Table 1.

Received July 21, 1986; accepted after revision September 19, 1986.

¹ Department of Radiological Sciences, University of California, Los Angeles, School of Medicine, Center for the Health Sciences, BL423, Los Angeles, CA 90024. Address reprint requests to J. F. Lois.

² Department of Surgery, University of California, Los Angeles, School of Medicine, Los Angeles, CA 90024.

AJR 148:367–371, February 1987
 0361–803X/87/1482–0367
 © American Roentgen Ray Society

TABLE 1. Underlying Disease in Patients Undergoing Percutaneous Transhepatic Biliary Drainage

	Number of Patients				
	Cholangitis <i>n</i> = 30	No Cholangitis <i>n</i> = 65	Preoperative PTD <i>n</i> = 44	Palliative PTD <i>n</i> = 51	Total <i>n</i> = 95
Malignancy					
Pancreatic	8	16	14	10	24
Biliary	5	16	11	10	21
Metastatic ^a	7	14	2	19	21
Ampullary	1	4	4	1	5
Miscellaneous ^b	2	2	0	4	4
Hepatocellular	1	2	1	2	3
Total	24 (80)	54 (83)	32 (73)	46 (90) ^c	78 (82)
Benign disease					
Biliary stricture	4	6	5	5	10
Choledocholithiasis	2	2	4	0	4
Sclerosing cholangitis	0	2	2	0	2
Pancreatitis	0	1	1	0	1
Total	6 (20)	11 (17)	12 (27)	5 (10)	17 (18)

Note.—Numbers in parentheses are percentages. PTD = percutaneous transhepatic biliary drainage.

^a Colon 13, gastric 4, breast 1, uterus 1, unknown 2.

^b Gallbladder 2, retroperitoneal sarcoma 1, duodenum 1.

^c $p < .025$ vs preoperative.

PTD Technique

Each patient received parenteral antibiotics for variable periods before and after PTD until the patient was afebrile for at least 24 hr. Sixty-nine patients received an aminoglycoside, usually in combination with a penicillin; 26 were given antibiotics other than an aminoglycoside. Topical anesthesia and parenteral sedation were used for most procedures. A few drainage procedures were performed under general anesthesia. Transhepatic cholangiography was performed first via a 21- or 22-gauge Chiba needle; just enough contrast medium to opacify the main hepatic radicles was injected. Biliary drainage was then achieved by using a right lateral or anterior approach with either the Cope catheter system or Hawkins needle set (both Cook, Inc., Bloomington, IN). In most patients an 8.3-French Ring catheter (Cook, Inc.) was then inserted; occasionally a 6.5-French pigtail catheter was inserted first. In six patients (6%), drainage was not accomplished at the first sitting but was achieved at a second attempt 2 to 5 days later.

Internal drainage was established by passing the biliary drainage catheter through the obstructing lesion in 39 patients (41%). Internal drainage was achieved in 23% of the preoperative group and in 57% of the palliative group. The percentage is lower for the preoperative group because for most of these patients, once satisfactory external drainage was achieved, no further attempts were made to establish internal drainage. In the palliative group, however, a more concerted effort was made to pass the catheter through the obstructing lesion. In general, patients who had cholangitis had external drainage, and attempts to achieve internal drainage were made only after sepsis had cleared in those patients considered unsuitable candidates for surgery. Patients undergoing long-term drainage had catheters exchanged every 3 months or sooner if indicated by the presence of fever, jaundice, or catheter occlusion.

PTD Complications

Complications were divided into those occurring early (within 30 days of the first drainage procedure) and those occurring later. Significant complications were defined as (1) hemorrhage sufficient to cause a fall in hematocrit of at least 5% and requiring transfusion,

(2) bacteremia caused by an organism also present in the patient's bile, (3) an increase of at least 1.0 mg/dl in a previously normal serum creatinine level, and (4) one or more liver abscesses proved by cholangiography, sonography, CT, or autopsy. Minor complications included pancreatitis (an increase in serum amylase of more than 300% of normal associated with abdominal pain and/or ileus after the procedure) and ascitic leak.

Results

Mortality

Fifteen patients died within 30 days of the procedure, an overall mortality rate of 16%. However, mortality was not significantly greater among patients who had cholangitis before PTD (17%) than among patients who were afebrile (15%) (Fig. 1). The 30-day mortality rate, however, appeared to be more related to the underlying disease process; significantly more patients in the palliative group (25%) died than in the preoperative group (5%) ($p < .01$). Of the nine patients who had positive blood cultures before PTD, two, including one with predrainage liver abscesses, died within 30 days of the procedure. This mortality rate (22%) was not significantly different from that observed (15%) among the 86 patients without predrainage bacteremia.

Two of the 15 deaths may have resulted from the procedure itself. One of these patients, a 73-year-old woman with metastatic cholangiocarcinoma, died from hemorrhage after an unsuccessful attempt at PTD of the left ductal system in the postoperative period. At autopsy, massive intra- and retroperitoneal bleeding from a vascular laceration was found. The other procedure-related death occurred in a patient who had a ruptured subcapsular hematoma 11 days after successful PTD. The two deaths in the preoperative group occurred after laparotomy in patients with unresectable, metastatic malignancies. The other early deaths were attributable to the underlying disease process. The one patient with predrainage

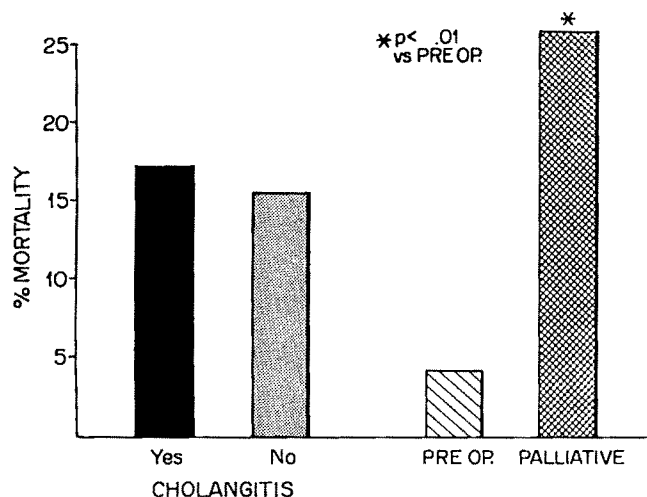


Fig. 1.—30-day mortality after percutaneous transhepatic biliary drainage (PTD) in cholangitis, no cholangitis, preoperative PTD, and palliative PTD subgroups. Mortality was significantly higher ($p < .01$) in the palliative than in the preoperative (PREOP.) group.

liver abscesses also had metastatic adenocarcinoma of the pancreas and died 28 days following PTD after apparent resolution of her septic process.

Morbidity

Table 2 shows the 30-day morbidity and late morbidity for patients with and without cholangitis. Twenty-four patients (25%) developed a complication or a significant problem within 30 days of the initial drainage procedure. The overall morbidity was 30% in the patients with cholangitis and 28% in the patients without cholangitis. The small group of nine patients who had positive blood cultures before PTD had a slightly, but not significantly, higher overall morbidity (44%) than those patients who did not have positive blood cultures (22%).

Analysis of the individual complications in the four major subgroups are presented in Table 3. The most frequently observed problem was bacteremia, which occurred shortly after PTD in eight patients (8%) and after catheter obstruction and subsequent manipulation but within 30 days of PTD in three patients (3%). Seven patients (23%) in the group with cholangitis and four (6%) in the group without cholangitis had bacteremia after PTD ($p < .02$). Of the nine patients who had positive blood cultures before PTD, three had postprocedural bacteremia. In two of these patients the same organism was isolated before and after PTD. The organisms most commonly retrieved from the blood were *Escherichia coli* (five patients) and *Klebsiella pneumoniae* (three patients). These two organisms were also present in the bloodstream of seven of the nine patients with predrainage bacteremia. *Bacteroides fragilis*, *Serratia marcescens*, *Enterobacter cloacae*, and *Citrobacter freundii* were each recovered from the blood after PTD on one occasion. Septic shock accompanying bacteremia developed in two patients in the cholangitis group and was treated successfully.

Significant hemorrhage after PTD was observed in eight

TABLE 2. Morbidity After Percutaneous Transhepatic Biliary Drainage in Patients with or without Cholangitis

	Percentage of Patients		
	Cholangitis <i>n</i> = 30	No Cholangitis <i>n</i> = 65	Total <i>n</i> = 95
30-day morbidity			
Preoperative PTD	7	9	8
Palliative PTD	23	14	17
Total	30	23	25
Late morbidity			
Preoperative PTD	0	2	1
Palliative PTD	3	3	3
Total	3	5	4
Overall morbidity ^a	30	28	28

Note.—PTD = percutaneous transhepatic biliary drainage.

^a Four patients had more than one complication.

TABLE 3. Analysis of Significant Complications and Overall Morbidity After Percutaneous Transhepatic Biliary Drainage

	Percentage of Patients				
	Cholan- gitis <i>n</i> = 30	No Cholan- gitis <i>n</i> = 65	Pre- opera- tive PTD <i>n</i> = 44	Pallia- tive PTD <i>n</i> = 51	Total <i>n</i> = 95
30-day morbidity					
Bacteremia	23 ^a	6	7	8	12
Hemorrhage	3	11	7	10	8
Creatinine >1.0 mg/dl	7	13	7	14	11
Subtotal ^b	30	23	18	31	25
Late morbidity					
Liver abscess	3	5	2	6	4
Overall morbidity ^b	30	28	21	35	28

Note.—PTD = percutaneous transhepatic biliary drainage.

^a $p < .02$ vs no cholangitis.

^b Four patients had more than one complication.

patients (8%); it occurred more frequently, but not significantly more often, in patients who did not have cholangitis before the procedure. Hemorrhagic shock developed in four patients, and three of them subsequently died. Hemorrhaging occurred in one patient 6 days after the first procedure and was managed by repositioning the drainage tube.

Elevations of serum creatinine of at least 1.0 mg/dl, which were thought possibly to be related to PTD, occurred in 10 patients (11%). In seven of these patients the increase in creatinine occurred shortly after PTD or catheter obstruction. In two patients renal dysfunction developed within 10 days after PTD after severe dehydration and hypovolemia. One patient had preexisting renal dysfunction, which worsened after PTD. Three additional patients with rising creatinine levels both before and after PTD were not included in the post-PTD morbidity data.

Sixty-nine (73%) of the 95 patients received aminoglycosides for a mean of seven days. An analysis of the effect of

aminoglycosides on renal function included all 13 patients who had increased creatinine levels after PTD. Eleven (16%) of the 69 patients who received aminoglycosides had elevated serum creatinine levels after PTD. In the 26 patients who did not receive aminoglycosides, two (8%) also had a rising creatinine after PTD. This difference was not statistically significant.

Liver abscesses developed in four patients (4%) after PTD. However, only one of these patients had predrainage cholangitis (Table 3). In two patients, the abscesses resolved with antibiotic therapy and change to a larger catheter. The other two patients died 30 and 55 days after PTD, respectively. One of these with widespread cholangiocarcinoma had a small abscess along the catheter tract when she died. The other had a similar problem and died from metastatic carcinoma and intrahepatic abscesses. Minor complications occurred in three patients (3%). These problems included subclinical pancreatitis in two and ascitic leak in one. None of these patients had cholangitis.

Discussion

In the present study, 30-day mortality and morbidity were 17% and 30%, respectively, among 30 patients with cholangitis who underwent PTD. In comparison, mortality and morbidity were 15% and 23%, respectively, among 65 patients who did not have cholangitis. These differences were not statistically significant. As might be expected, however, patients who had cholangitis had a significantly higher frequency of bacteremia after PTD. Even when the nine patients with predrainage bacteremia were analyzed separately, mortality and morbidity increased slightly, but not significantly, to 22% and 44%, respectively. However, in patients undergoing PTD for palliation, the mortality (25%) was significantly higher than in those who had preoperative PTD ($p < .01$). The overall morbidity (35%) was also higher, but not significantly different, than in the preoperative patients. This analysis suggests that the patient's underlying disease process may be more important than the presence of cholangitis in determining the outcome of PTD.

Concurrent biliary infection and obstruction give rise to cholangitis, a potentially life-threatening disorder. For many years, surgical decompression has been the standard method for dealing with this problem; however, surgery is associated with a significant mortality and morbidity [2-6]. Several authors [7, 8, 13] have suggested PTD as an alternative approach. However, to our knowledge, comparison of the risk of PTD in a relatively large group of patients with and without cholangitis has not been reported. Nakayama et al. [8] observed a 9% mortality rate after PTD in 11 septic patients with multiple liver abscesses who were considered unfit for laparotomy. Similarly, Ferrucci et al. [14] noted dramatic clinical responses in nine patients with acute toxic cholangitis or liver abscesses who were initially managed with PTD and antibiotics. Kadir et al. [7] reported 17% mortality and 33% morbidity rates in 18 patients who had cholangitis and underwent PTD as part of their treatment. Our results, 17% overall

mortality and 30% morbidity after PTD in 30 patients with cholangitis, are similar.

Mortality and morbidity did increase, to 22% and 44%, respectively, among the nine patients who had bacteremia before they underwent PTD. However, when compared with either the 86 nonbacteremic patients or the 65 patients without cholangitis, the slight increases in overall morbidity and mortality observed in bacteremic patients were not statistically significant.

An association between the severity of cholangitis and outcome has been noted in earlier reports on the surgical management of cholangitis. Pitt and Longmire [15] reported a 55% mortality rate in patients with suppurative cholangitis who presented in shock compared with a 15% mortality rate in those without shock. The mortality rate increased, however, to 85% among patients who never came to surgery. This analysis suggested that biliary decompression was a cornerstone of treatment and that presentation in shock was a significant determinant of outcome. Our study included only two patients in septic shock who were managed with PTD, and both survived.

Others [2, 16] also noted higher postoperative mortality rates when patients with suppurative cholangitis (pus in the bile ducts) were compared with those with nonsuppurative cholangitis. However, the differentiation between suppurative and nonsuppurative cholangitis is arbitrary and may be impossible to determine before biliary decompression. Also, it does not always correlate with bacteremia or septic shock. In the present analysis, all of the deaths among septic patients undergoing PTD occurred in patients having PTD for palliation of an advanced malignancy. This suggests that the patient's underlying disease process and, perhaps, immune status may be more important determinants of outcome than the degree of infection.

The overall 30-day mortality rate of 16% after PTD in this series is similar to the mortality rates of 12% to 19% reported by other groups [7, 13, 14, 17]. Moreover, in patients with advanced malignant disease, 30-day hospital mortality rates of 26% and 31%, respectively, have been noted [14, 17]. Thus, our mortality rate of 25% for patients undergoing palliative PTD concurs with these observations.

Others have reported deaths as a direct result of PTD [11, 12, 17, 18]. The usual causes are intraperitoneal hemorrhage or septic shock, but pneumothorax and biliopleural fistula with resultant empyema have been reported also [11]. Although some investigators [8, 10, 19] have not seen procedure-related deaths, recently published procedure-related mortality rates range from 1.5% to 2.7%. Our experience is similar; two (2%) of 95 patients died as a direct consequence of PTD. Both of these patients had advanced malignancies and died from hemorrhagic complications.

Increased risk of postoperative renal insufficiency in patients with obstructive jaundice has been reported [20, 21]. This problem has been linked to endotoxemia caused by intestinal bacterial overgrowth, which, in turn, may result from a lack of bile salts in the intestine [22, 23]. Few reports, however, contain details of renal status after PTD. Hatfield et al. [9] reported renal insufficiency in two (7%) of 29 patients

undergoing PTD for preoperative preparation. They attributed these renal problems to excessive biliary drainage leading to a negative fluid balance. Others [24] observed improved creatinine clearance after drainage in 14 of 17 preoperative patients whose creatinine clearance rates were less than 60 ml/min before PTD. However, similar results were achieved by simple rehydration in 14 jaundiced patients who went to surgery without preoperative PTD.

Renal dysfunction after PTD was observed in 10% of the patients in this study. Several factors may have contributed to this condition, including preexisting renal disease, aminoglycoside therapy, jaundice, and sepsis. Sixteen patients (17%) had serum creatinine levels greater than 1.3 mg/dl before PTD, and all but three of the 95 patients had jaundice. These two factors along with sepsis may account for much of the renal dysfunction observed in these patients.

Aminoglycoside therapy also has been implicated as a possible contributor to the high frequency of renal problems in patients with cholangitis who had surgery for choledocholithiasis [25]. In the present series 73% of the patients received aminoglycoside therapy. Although a higher percentage of patients on aminoglycoside developed renal problems, no statistically significant correlation was found.

The present analysis and a previous study [26] suggest that morbidity and mortality are higher when PTD is performed for palliation of patients with end-stage malignancies.

When performed to manage cholangitis, PTD can be done relatively safely in patients with cholangitis, but it does have a higher frequency of post-procedure bacteremia. PTD, therefore, can be used as a means of decompression in the subgroup of patients with severe cholangitis. If sepsis can be ameliorated before surgery, a more definitive operation may be possible when the patient's condition is more stable. Most patients with mild cholangitis respond to antibiotics, however, and do not require urgent biliary decompression.

REFERENCES

1. Charcot JM. *Leçon sur les maladies du foie des voies biliaires et des reins*. Paris: Faculté de Médecine de Paris 1877;1-102
2. Boey JH, Way L. Acute cholangitis. *Ann Surg* 1980;191:264-270
3. Saharia PC, Cameron JL. Clinical management of acute cholangitis. *Surg Gynecol Obstet* 1976;142:369-372
4. Saik RP, Greenburg AG, Farris JM, Peskin GW. Spectrum of cholangitis. *Am J Surg* 1975;130:143-150
5. Thompson JE, Tompkins RK, Longmire WP. Factors in management of acute cholangitis. *Ann Surg* 1982;195:137-145
6. Welch JP, Donaldson GA. The urgency of diagnosis and surgical treatment of acute suppurative cholangitis. *Am J Surg* 1976;131:527-532
7. Kadir S, Baassiri A, Barth KH, Kaufman SL, Cameron JL, White RI. Percutaneous biliary drainage in the management of biliary sepsis. *AJR* 1982;138:25-29
8. Nakayama T, Ideka A, Okuda K. Percutaneous transhepatic drainage of the biliary tract. *Gastroenterology* 1978;74:554-559
9. Hatfield ARW, Terblanche J, Fataar S, et al. Preoperative external biliary drainage in obstructive jaundice. *Lancet* 1982;2:896-899
10. McPherson GAD, Benjamin IS, Habib NA, Bowley NB, Blumgart LH. Percutaneous transhepatic drainage in obstructive jaundice: advantages and problems. *Br J Surg* 1982;69:277-278
11. Mueller PR, vanSonnenberg E, Ferrucci JT. Percutaneous biliary drainage: technical and catheter-related problems in 200 procedures. *AJR* 1982;138:17-23
12. Norlander A, Kalin B, Sundblad R. Effect of percutaneous transhepatic drainage upon liver function and postoperative mortality. *Surg Gynecol Obstet* 1982;155:161-166
13. Gould RJ, Vogelzang RL, Neiman HL, Pearl GI, Poticha SM. Percutaneous biliary drainage as an initial therapy in sepsis of the biliary tract. *Surg Gynecol Obstet* 1985;180:523-527
14. Ferrucci JT, Mueller PR, Harbin WP. Percutaneous transhepatic biliary drainage. *Diagn Radiol* 1980;135:1-13
15. Pitt HA, Longmire WP Jr. Suppurative cholangitis. In: Hardy JD, ed. *Critical surgical illness*, 2nd ed. Philadelphia: Saunders, 1980:380-408
16. O'Connor MJ, Schwartz ML, McQuarrie DG, Sumner HW. Acute bacterial cholangitis: an analysis of clinical manifestation. *Arch Surg* 1982;117:437-441
17. Clark RA, Mitchell SE, Colley DP, Alexander E. Percutaneous catheter biliary decompression. *AJR* 1981;137:503-509
18. Berquist TH, May GR, Johnson CM, Adson MA, Thistle JL. Percutaneous biliary decompression: internal and external drainage in 50 patients. *AJR* 1981;136:901-906
19. Smale BF, Ring EJ, Freiman DB, et al. Successful long-term percutaneous decompression of the biliary tract. *Am J Surg* 1981;141:73-76
20. Dawson J. Acute postoperative renal failure in obstructive jaundice. *Ann R Coll Surg Engl* 1968;42:163-172
21. Ozawa K, Yamada T, Tanaka J, Ukikusa M, Tobe T. The mechanism of suppression of renal function in patients and rabbits with jaundice. *Surg Gynecol Obstet* 1979;149:54-60
22. Cahill CJ. Prevention of postoperative renal failure in patients with obstructive jaundice: the role of bile salts. *Br J Surg* 1983;70:590-595
23. Evans HJR, Torrealbe V, Hudd C, Knight M. The effect of preoperative bile salt administration on postoperative renal function in patients with obstructive jaundice. *Br J Surg* 1982;69:706-708
24. McPherson GAD, Benjamin IS, Jodgson JHF, Bowley NB, Allison DJ, Blumgart LH. Pre-operative percutaneous transhepatic biliary drainage: the results of a controlled trial. *Br J Surg* 1984;71:371-375
25. Pitt HA, Postier RG, Cameron JL. Consequences of preoperative cholangitis and its treatment on the outcome of operation for choledocholithiasis. *Surgery* 1983;94:447-452
26. Stambuk EC, Pitt HA, Pais OS, Mann LL, Lois JF, Gomes AS. Percutaneous transhepatic drainage: risks and benefits. *Arch Surg* 1983;118:1388-1394

Case Report

Common Bile Duct Stone Dissolution with Methyl Tertiary Butyl Ether: Experience with Three Patients

Steven K. Teplick,¹ Pamela H. Haskin,¹ Robert C. Goldstein,² Joseph M. Corvasce,² Elliott B. Frank,² John K. Sammon,¹ and Alan F. Hofman³

Currently, monooctanoin is the preferred method of dissolving biliary stones. Monooctanoin is administered directly into the biliary system and is effective only when there is adequate drug-stone contact [1]. It is a safe and relatively effective cholesterol solvent. The main disadvantage of monooctanoin is its relatively slow action. Stone dissolution often requires 2 to 4 weeks of infusion [2].

Other agents that have been used for stone dissolution include oral agents as chenodiol or ursodeoxycholic acid and agents given directly into the bile ducts such as diethyl ether and heparin. These solutions are either ineffective, toxic, or require an even longer administration time for stone dissolution [3-6].

Methyl tertiary butyl ether (MTBE), a drug approved for investigational use only, is an aliphatic ether that has been shown to be capable of dissolving cholesterol stones 50 times faster than monooctanoin [2]. MTBE is structurally related to diethyl ether, an anesthetic, but remains a liquid at body temperature [7] and consequently can be used for instillation into the biliary system.

We present our experience infusing MTBE directly into the common bile duct in three patients with ductal stones who were considered poor surgical risks.

Case Reports

Case 1

An 85-year-old man with multiple medical problems presented with signs of biliary obstruction. He had had a cholecystectomy 20 years earlier. A sonogram showed dilated bile ducts with no indication of the cause. Transhepatic cholangiography showed a 1-cm common

bile duct stone causing partial obstruction (Fig. 1). An 8-French polyethylene biliary drainage catheter was inserted. Since the patient was considered a poor surgical risk, an attempt was made to dissolve the stone. Two days later, the tract was dilated and a second catheter (8-French polyethylene pigtail) was inserted with the curl of the pigtail wrapped around the calculus.

MTBE was injected through the pigtail catheter in 5- to 10-ml aliquots, left in the ductal system for 1 to 3 min, then aspirated through the drainage catheter. This procedure was repeated for 20 min with a total volume of 30 ml. A repeat cholangiogram showed the stone to be about 45% smaller (Fig. 2). Because the odor of MTBE on the patient's breath was becoming stronger, and because the patient had been previously sedated with narcotics, a decision was made to basket the stone rather than risk heavy sedation by continuing ether infusion. The stone was easily crushed and most of the fragments extracted. An 18-French drainage catheter was left in place.

A cholangiogram the next day showed no residual fragments. The catheter was removed and the patient was discharged 2 days later.

Case 2

A 67-year-old diabetic woman with known chronic pancreatitis was admitted to a neighboring hospital for recurrent right-upper-quadrant pain, fever, and possible obstructive jaundice. She had had a cholecystectomy, partial pancreatectomy, and sphincterotomy about 20 years previously. ERCP showed a large 3 × 2 cm common bile duct stone and a stricture of the common bile duct distal to the stone. Because of severe diabetes and cardiac disease, the patient was not considered a candidate for surgery and was referred to us for percutaneous stone dissolution and stricture dilatation.

A transhepatic cholangiogram confirmed the ERCP findings (Fig. 3). A biliary drainage procedure was performed through the liver. The tract was dilated by using a balloon catheter. A 10-French polyethyl-

Received July 15, 1986; accepted after revision September 10, 1986.

¹ Department of Diagnostic Radiology, Hahnemann University, Broad and Vine Sts., Philadelphia, PA 19102. Address reprint requests to S. K. Teplick.

² Department of Medicine, Hahnemann University, Philadelphia, PA 19102.

³ Department of Medicine, University of California Medical Center, 225 Dickinson St., San Diego, CA 92103.

Fig. 1.—Cholangiogram shows a 1-cm common bile duct stone (arrows). A biliary drainage catheter is in place.

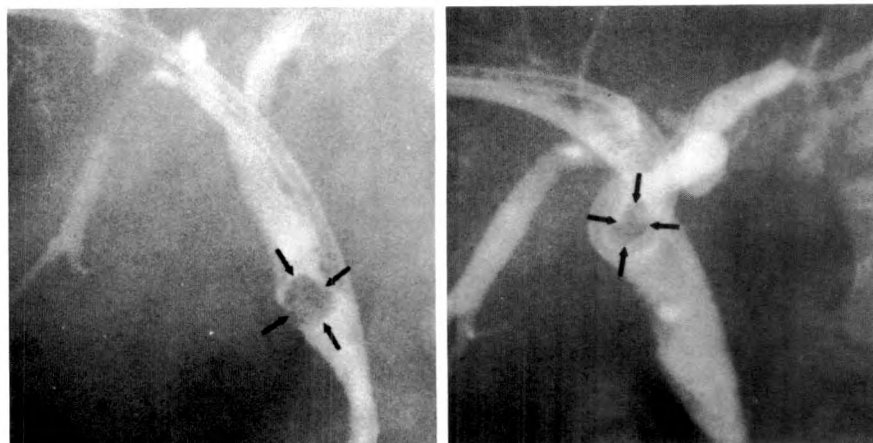


Fig. 2.—After 20 min of methyl tertiary butyl ether infusion, stone (arrows) is about 45% smaller. Methyl tertiary butyl ether was injected through pigtail catheter curled around stone.

ene drainage catheter and an 8-French polyethylene pigtail catheter were inserted. Because of mild hemobilia (no treatment was required), dissolution was postponed for 3 days.

MTBE was injected through the pigtail catheter in 10-ml aliquots, left in for 2 min, then extracted via the drainage catheter. After 35 min a cholangiogram showed no change in the stone. However, the patient became sedated, and MTBE was discontinued. The procedure was repeated the next day, again with no success.

The patient was reluctant to undergo further MTBE therapy. The stone was crushed with a Dormia basket and most of the fragments were removed. During the next 2 days the residual fragments were basketed and the stricture dilated. No internal/external stent to maintain patency of the stricture was inserted, and the patient was discharged.

Case 3

A 78-year-old woman presented with sudden onset of upper abdominal pain and jaundice without fever or chills. There was a history of a cholecystectomy, a recent stroke with hemiplegia, and a 70-pound weight loss. The serum bilirubin and alkaline phosphatase were elevated. A sonogram and CT showed an abdominal aortic aneurysm but no biliary ductal dilatation, gallstone, or pancreatic mass. The Papilla of Vater was normal on endoscopy.

A transhepatic cholangiogram showed a 1.2 × 1.1-cm common bile-duct stone without ductal dilatation (Fig. 4). An 8-French polyethylene biliary drainage catheter was inserted without complications. The following day the tract was dilated with a balloon catheter, and a second catheter (8-French polyethylene pigtail) was inserted with the top positioned around the stone.

Twenty-four hours later MTBE was started. A balloon catheter was inserted in the distal common bile duct to decrease the amount of ether entering the duodenum. Seventy milliliters of MTBE were injected in 10-ml aliquots for 60 min. The ether was left in the ductal system for 2 to 5 min and then removed. After 60 min the stone completely dissolved (Fig. 5). No MTBE was detected on the patient's breath, and she did not become sedated. A follow-up cholangiogram was normal, and the patient was discharged.

Results

The bile-duct calculus was successfully removed in all three patients. In patient 1, MTBE reduced the size of the calculus by 45% in 20 min with a total volume of 30 ml. In patient 2, the stone was not affected after 65 min with a total volume of 140 ml. Fragments of the extracted stone were placed in MTBE for 3 days without any evidence of dissolution. Chem-

ical analysis of the fragments showed it to be composed of 60% cholesterol, 35% calcium bilirubinate, and 5% mixed bile pigments. In patient 3, the calculus completely dissolved in 60 min by using 70 ml of ether.

The detection of MTBE on the patients' breath was significant with patients 1 and 2. The odor was first noted within 10 min after starting the injection and became stronger as the procedure continued. Patient 1 was sedated with narcotics before the procedure, and no perceptible change in the level of consciousness was noted. Patient 2 definitely became sedated. Patient 3 had no odor of ether throughout the procedure and did not become sedated, possibly because the balloon blocked egress of ether into the duodenum. All patients had continuous monitoring of their blood pressure, pulse, and respirations. None had any significant changes. Injection of MTBE did not cause any pain or discomfort.

The total length of the procedure, from the insertion of the initial biliary drainage catheter to the final cholangiogram, was 7 days in two patients, and 4 days in the third. MTBE infusion was not started on the day of the percutaneous transhepatic biliary drainage in any of the patients. In patient 1 the delay was 4 days because of his tenuous health. Hemobilia in patient 2 made cholangiographic evaluation difficult and resulted in a 3-day delay between the biliary drainage procedure and the start of the ether infusion. Patient 3 had no delays and the procedure was completed in 4 days.

MTBE had no adverse effects on either the polyethylene catheters or the tubing used to draw up the ether. Plastic syringes, however, could not be used because they rapidly softened. Glass syringes were not affected.

Discussion

MTBE has been used to dissolve cholesterol stones rapidly in vitro and in dogs without damage to the gallbladder, common bile duct, or duodenum [2]. Dissolution time has varied from 1 to 16 hr. MTBE has been successfully infused into the gallbladder in two patients and into the bile ducts in one patient through a nasobiliary catheter [8, 9]. Stone dissolution took from 4 to 15 hr.

In our series MTBE infusion was employed from 20 to 65 min under fluoroscopic monitoring. One stone completely dissolved, one was unaffected, and one was reduced in size by 45%. Since the calculus in patient 2 was composed

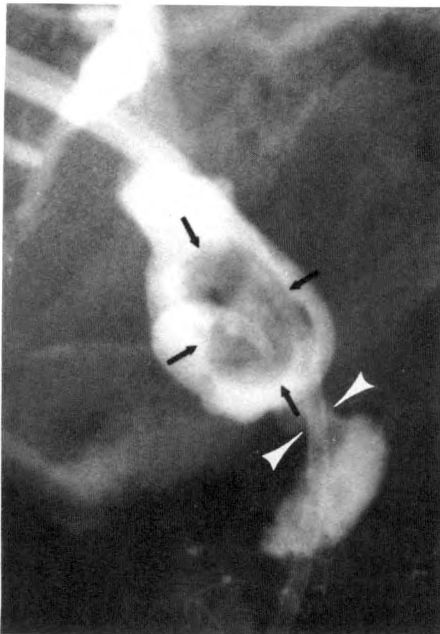


Fig. 3.—There is a 2 × 3 cm common bile duct stone (black arrows) causing partial obstruction. Common bile duct is narrowed (white arrowheads) just distal to stone.

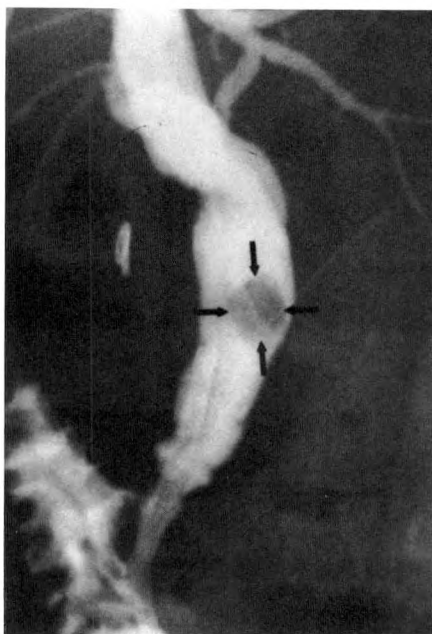


Fig. 4.—Cholangiogram showing a 1.1 × 1.2 cm common bile duct stone (arrows) and a biliary drainage catheter into the duodenum.

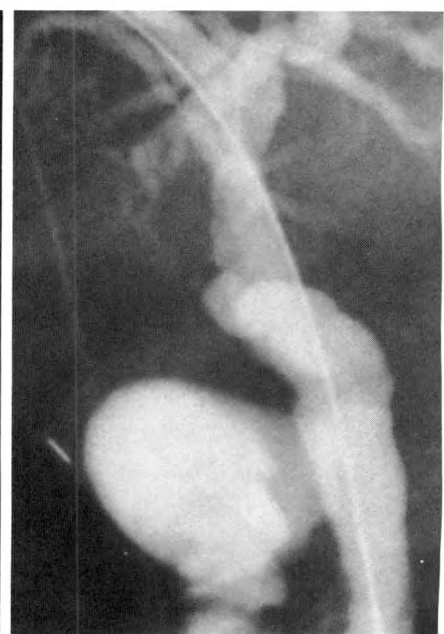


Fig. 5.—Stone completely dissolved after 1 hr of methyl tertiary butyl ether infusion.

predominantly of cholesterol, the reason it did not dissolve, even in vitro, is not clear. Possibly the outer shell was composed of calcium bilirubinate, and the ether could not penetrate to the cholesterol portion of the stone. The procedure was discontinued in two of the patients because of the possibility of excessive sedation. Consequently, instilling MTBE by continuous infusion at the bedside without constant supervision by a physician would seem dangerous. Alternatively, constant instillation and withdrawal of MTBE every few minutes in the radiology department can be labor intensive and can result in considerable radiation exposure to the personnel involved. One potential method to avoid this situation is to insert a balloon in the common bile duct distal to the calculus. This should decrease the amount of ether that enters the duodenum, where most of the systemic absorption occurs. This balloon occlusion technique seemed successful in our third patient, but more experience is needed.

The two-catheter system that has been successfully employed for mono-octanol [1] was probably not necessary in our MTBE patients. However, infusion and drainage catheters would be useful if the common bile duct were occluded by a balloon and MTBE given by continuous infusion. Although the exact timing for the instillation and withdrawal of the ether has not been determined in vivo, it probably should be exchanged frequently (every few minutes) to promote adequate mixing.

MTBE had no adverse effect on the polyethylene catheters that were used for infusion and withdrawal. It did, however, render plastic syringes useless before a single dose could be injected. Glass syringes were not affected. As reported by vanSonnenberg et al. [8], a catheter made of Percuflex macerated when exposed to MTBE and bile, but in vitro no effect was observed. We have put segments of polyethylene cath-

eters, Teflon sheaths, and IV tubing material in MTBE without detecting any damage, but none except polyethylene catheters have been used in vivo.

Although the system used for drawing up and injecting the ether was as closed as possible, a moderately strong odor was present in the room air even before it was detected on the patient's breath. Good air circulation and ventilation in the room will considerably improve the working conditions. Although MTBE is not as flammable as diethyl ether, sources of sparks should be minimized and the room should be inspected by the hospital's fire and safety department. Also, smoking must be strictly prohibited.

REFERENCES

1. Teplick SK, Haskin PH. Mono-octanol perfusion for in vivo dissolution of biliary stones: a series of 11 patients. *Radiology* 1984;153:379-383
2. Allen MJ, Borody TJ, Bugliosi TF, May GR, LaRusso NF, Thistle JL. Cholelitholysis using methyl tertiary butyl ether. *Gastroenterology* 1985;88:122-125
3. Bouchier IAD. Gallstones. *Proc Roy Soc Med* 1977;70:592-599
4. Mack E, Patzer EM, Crummy AB, et al. Retained biliary tract stones. Nonsurgical treatment with capmul 8210: a new cholesterol gallstone dissolution agent. *Arch Surg* 1981;116:341-344
5. Motson RW. Dissolution of common bile duct stones. *Br J Surg* 1981;68:203-208
6. Mack E, Saito C, Goldfarb S, et al. Local toxicity of T-tube infused cholate in the rhesus monkey. *Surg Forum* 1977;28:408-409
7. Little CJ, Dale AD, Whatley JA, Wickings JA. Methyl tertbutyl ether: a new chromatographic eluent. *J Chromatography* 1979;169:381-385
8. vanSonnenberg E, Hofmann AF, Neoptolemus J, Wittich GR, Princenthal RA, Wilson SW. Gallstone dissolution with methyl-tert-butyl ether via percutaneous cholecystostomy: success and caveats. *AJR* 1986;146:865-867
9. Allen MJ, Borody TJ, Bugliosi TF, May GR, LaRusso NF, Thistle JL. Rapid dissolution of gallstones by methyl tert butyl ether. *N Engl J Med* 1985;312:217-220

Case Report

Transcatheter Recanalization of a Chronically Occluded Saphenous Aortocoronary Bypass Graft

Myron Marx,¹ William T. Armstrong,² Bruce N. Brent,² Jon P. Wack,¹ Robert M. Bernstein,¹ and Gabriel Gregoratos²

Aortocoronary bypass surgery has become a mainstay in the surgical treatment of ischemic cardiovascular disease with an estimated 530,000 individual saphenous aortocoronary bypass grafts having been placed in 1984 [1, 2]. In the first year after surgery, 15–20% of saphenous grafts fail [1]. With graft failure, the clinical indications for myocardial reperfusion usually have not changed and are often more pressing than before surgery. In these high-risk patients, reperfusion has often meant reoperation. We document a case of recanalization of a chronically occluded aortocoronary saphenous bypass graft by using a combination of selective urokinase administration and percutaneous transluminal angioplasty.

Case Report

A 64-year-old man presented in early March 1986 with an acute myocardial infarction. Cardiac catheterization revealed a severe stenosis of the distal left main coronary artery extending into the origins of the left anterior descending and circumflex coronary arteries. Significant stenoses were also present in the proximal aspect of a large obtuse marginal branch 3 and in the posterior descending branch of the dominant right coronary artery. Shortly after catheterization the patient underwent quadruple coronary artery bypass surgery. Saphenous vein grafts were placed to the large obtuse marginal branches 2 and 3 and to the posterior descending coronary artery. The left internal mammary artery was grafted to the mid-left anterior descending coronary artery. The postoperative course was unremarkable and the patient was asymptomatic when discharged.

One month after surgery the patient developed angina with mild

exertion. He was admitted for catheterization approximately 1 month after the onset of recurrent symptoms. Arteriography showed occlusion of the three saphenous aortocoronary bypass grafts and patency of the left internal mammary artery graft. Clinical indications for cardiac reperfusion were present, but in an effort to avoid a second open-chest procedure, the patient was returned to the catheterization laboratory for attempted recanalization of the thrombosed aortocoronary bypass graft to the obtuse marginal branch 3, the most important of the occluded grafts.

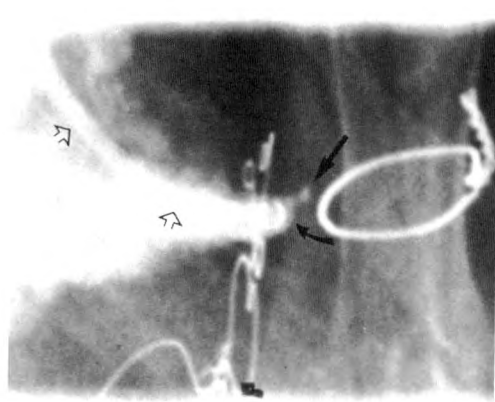
By using a right femoral arterial approach, an 8-French left-bypass-graft guiding catheter (Interventional Medical, Danvers, MA) was positioned at the orifice of the most cephalic of the three failed bypass grafts. A 0.035-in. (0.09 cm) straight guidewire was advanced 3–5 mm into the aortic end of the thrombosed graft and then removed (Fig. 1). A urokinase infusion (2000 units/ml) was begun at a rate of 6000 units/min. Angiography was performed at 15-min intervals. Partial clot lysis in the proximal one-third of the graft was initially documented at 30 min. At 30 min a 0.016-in. (0.04 cm) USCI (Bard, Billerica, MA) steerable guidewire was gently advanced into the proximal one-third of the graft and then withdrawn. Angiography at 60 min revealed continued clot lysis and a critical stenosis in the most proximal aspect of the graft (Fig. 2). After an additional 15 min of infusion, a 3.0-mm Hartzler angioplasty balloon (ACS, Temecula, CA) was positioned across the stenosis and multiple inflations were made.

Postangioplasty arteriography showed marked anatomic improvement at the site of stenosis (Fig. 3). Urokinase was continued, and angiography 15 min later (90 min into the infusion) showed continued clot lysis and minimal antegrade flow of blood into the obtuse marginal branch 3. Next, the deflated Hartzler balloon was advanced through the graft to the distal anastomosis and then withdrawn. Brisk antegrade blood flow was observed. The urokinase infusion was contin-

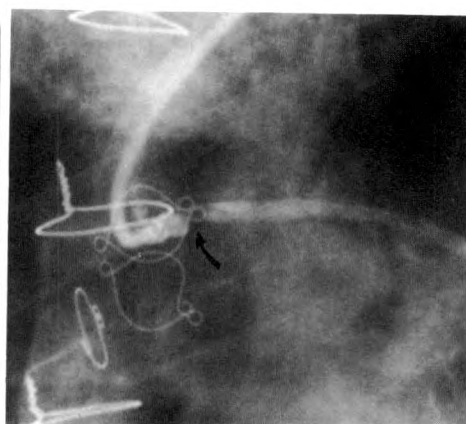
Received July 16, 1986; accepted after revision September 10, 1986.

¹ Department of Radiology, Pacific Presbyterian Medical Center, P.O. Box 7999, San Francisco, CA 94120. Address reprint requests to M. Marx.

² Division of Cardiology, Department of Medicine, Pacific Presbyterian Medical Center, P.O. Box 7999, San Francisco, CA 94120.



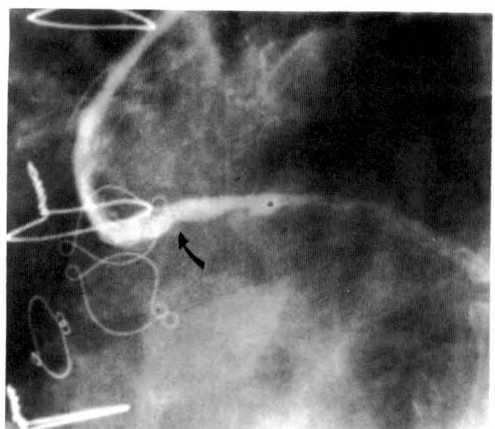
1



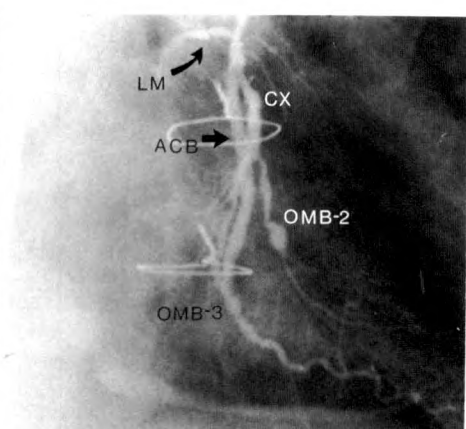
2

Fig. 1.—Angiographic catheter (open arrows) with terminal radiopaque ring marker seen in stump of proximally occluded saphenous aortocoronary bypass graft to obtuse marginal branch 3 immediately after puncture of thrombosed graft with straight guidewire. Guidewire has been removed and contrast material is opacifying occluded stump of graft (curved arrow) and excavation in proximal graft that was created by guidewire passage (straight arrow).

Fig. 2.—At 60 min into infusion of urokinase, significant clot lysis in proximal one-third of graft is noted in addition to critical proximal graft stenosis (arrow).



3



4

Fig. 3.—After percutaneous transluminal angioplasty there is significant anatomic reduction of stenosis (arrow).

Fig. 4.—After graft thrombolysis, arteriography of saphenous aortocoronary bypass graft to obtuse marginal branch 3 with imaging over distal graft anastomosis in right anterior oblique projection shows good antegrade flow of contrast material through graft (ACB), with filling of obtuse marginal branch 3 (OMB-3). Through retrograde flow there is also filling of obtuse marginal branch 2 (OMB-2), native circumflex (CX), and left main (LM) coronary arteries.

ued for an additional 30 min. At the conclusion of the study, the bypass graft was widely patent with good antegrade flow of contrast material not only into the obtuse marginal branch 3, but in a retrograde fashion into the obtuse marginal branch 2, the circumflex artery, and left main coronary artery (Fig. 4). There was no angiographic evidence of distal embolization of thrombotic material. The patient tolerated the procedure well without cardiac, neurologic, or hemorrhagic complications. During the course of the 2-hr infusion, 14,000 units of heparin were delivered intravenously in divided doses and a total dose of 720,000 units of urokinase was administered. The patient was kept fully heparinized until just before discharge, at which point he was converted to oral agents (warfarin).

Two days after this procedure, angiography showed continued patency of the recanalized bypass graft. At that time, the patient underwent successful angioplasty of the diseased left main coronary artery and of the critical stenosis at the origin of the circumflex coronary artery. After an uneventful recovery, the patient was discharged; he is currently free of chest pain.

Discussion

Coronary thrombolytic therapy has been used primarily to limit the amount of myocardial damage that occurs either in

acute myocardial infarction or as an adjunct to percutaneous transluminal coronary angioplasty that has been complicated by acute vessel occlusion [3–5]. Although thrombolytic recanalization of chronically occluded visceral and peripheral bypass grafts has been well documented [6, 7], this technique has not been applied to coronary bypass grafts.

The major difference between recanalization of an occluded aortocoronary bypass graft and other types of occluded grafts relates to the danger of reflux of organized thrombotic material from the graft into the ascending thoracic aorta, with the attendant risk of a cerebrovascular accident. Because of this risk, urokinase was only instilled in the orifice of the graft and manipulation of material within the graft itself was kept to a minimum until antegrade flow had been restored. Also, in chronic visceral and peripheral graft occlusions a thin layer of thrombus occurs at the proximal aspect of the column of thrombotic material that is more organized than most thrombus within the graft itself. This thin layer of more organized thrombotic material often needs to be broken so that the thrombolytic agent can gain access to the "softer" thrombus. This was the rationale for the initial advance of the 0.035-in. straight guidewire 3–5 mm into the thrombotic material itself. Angioplasty was only attempted once the stenosis became

clearly defined, after angiography had shown significant clot lysis in the proximal one-third of the graft, and after it had been determined that the critical nature of this stenosis would impede further access of urokinase into the middle and distal segments of the graft. Although distal embolization of thrombotic material and subsequent myocardial infarction is a theoretical risk, this did not occur in our patient.

Transcatheter recanalization of chronically occluded saphenous aortocoronary bypass grafts is an attractive alternative in certain high-risk patients who require cardiac reperfusion. It provides the opportunity to correct in a nonoperative fashion possible underlying anatomic abnormalities that may have contributed to graft failure. If the patient requires surgical intervention after aortocoronary bypass graft thrombolytic therapy, it may pinpoint the nature of the underlying abnormality so that graft repair may become an alternative to graft replacement. Increasing cardiac perfusion before surgery may also decrease operative morbidity and mortality. Additional work is needed to define the appropriate patient population, the time interval between bypass surgery and the safe appli-

cation of this technique, and the incidence of complications, most notably cerebrovascular accident.

REFERENCES

1. Bourassa MG, Fisher LD, Campeau L, et al. Long-term fate of bypass grafts: the Coronary Artery Surgery Study (CASS) and Montreal Heart Institute experiences. *Circulation* 1985;72[suppl V]:V71-V78
2. Braunwald E, Hollingsworth C, Passamani E. Surgery in the treatment of coronary artery disease. *Circulation* 1985;72[suppl V]:V1-V2
3. Marx M, Levin DC. Coronary thrombolytic therapy: state of the art. *AJR* 1986;147:1-8
4. Schofer J, Krebber H-J, Bleifeld W, et al. Acute coronary artery occlusion during percutaneous transluminal coronary angioplasty: reopening by intracoronary streptokinase before emergency coronary artery surgery to prevent myocardial infarction (abstr). *Radiology* 1983;148:592
5. Tennant SN, Dixon J, Venable TC, et al. Intracoronary thrombolysis in patients with acute myocardial infarctions: comparison of the efficacy of urokinase with streptokinase. *Circulation* 1984;69(4):756-760
6. Katzen GT, van Breda A. Low-dose streptokinase in the treatment of arterial occlusions. *AJR* 1981;136:1171-1178
7. McNamara TO, Fisher JR. Thrombolysis of peripheral arterial and graft occlusions: improved results using high dose urokinase. *AJR* 1985;144:769-775

Case Report

Transcatheter Intracavitary Fibrinolysis of Infected Extravascular Hematomas

Robert L. Vogelzang,¹ Richard S. Tobin,¹ Scott Burstein,¹ Sara L. Anschuetz,¹ Mark Marzano,^{1,2} and James M. Kozlowski³

Transcatheter thrombolysis of embolic and thrombotic vascular occlusion has been successfully used in the past several years in a wide variety of applications [1-3]. Both streptokinase and urokinase are effective in this regard, although urokinase has recently become the agent of choice in many centers, including our own. Fibrinolytic agents have also been used successfully outside the vascular system (in the pleural space) for treatment of hemothorax and empyema [4-8]. This therapy was used primarily in the 1950s, although there have been sporadic reports of intrapleural fibrinolytic therapy in the recent literature [9-11]. There is, however, little reference to this body of work in the radiologic literature and we are not aware of the application of fibrinolytic therapy to infected hematomas in the abdomen. We report here the successful use of transcatheter fibrinolysis in the treatment of infected intraabdominal postsurgical hematomas in two patients.

Case Reports

Case 1

A 66-year-old man underwent a radical prostatectomy and pelvic lymph node dissection for stage C carcinoma of the prostate. There was moderate blood loss at surgery and a Penrose drain was left in place. On the first postoperative day the patient experienced increased heart rate, decreased blood pressure, and a three-point decrease in hemoglobin. The patient received transfusions of seven

units of packed red cells over the next 2 days. Sonography showed a pelvic fluid collection, and a cystogram revealed a bladder leak at the anastomotic site that communicated with the pelvic fluid collection. The patient experienced intermittent fever to 103.4°F and elevation of the WBC to 12,400 despite antibiotic therapy and placement of a red rubber catheter through the wound into the collection. The patient continued to be febrile, and a CT scan ordered 3 weeks postoperatively revealed a large mixed-attenuation pelvic collection displacing the bladder to the right (Fig. 1). Because of continued lack of adequate drainage in the face of an obvious infection, surgical evacuation was considered; however, the patient refused further surgery. Interventional Radiology was consulted, and two 14-French sump catheters were placed in the collection. A contrast study revealed a complex collection with multiple septations and filling defects. There was spontaneous bladder filling at the bladder neck via the leak at the anastomotic site (Fig. 2). Clot lysis was attempted via infusion of urokinase. Urokinase (250,000 units dissolved in 250 ml normal saline) was instilled in three aliquots. Each aliquot was allowed to remain in contact with the hematoma for 30 min and then withdrawn. Upon withdrawal, about 30 to 50 ml of partially lysed foul-smelling, currant-jelly clot was obtained. Contrast injection revealed the filling defects to be substantially smaller. The therapy was repeated twice over the next 48 hr with elimination of all clots and a decrease in cavity size (Fig. 3). There was immediate symptomatic relief the evening after the first irrigation, and the patient became afebrile 12 hr after the procedure and remained so until discharge. A culture of the aspirated material yielded multiple gram-negative organisms. Saline irrigation was continued for 6 days with gradual reduction and disappearance of the cavity. The cavity was completely

Received May 27, 1986; accepted after revision August 5, 1986.

¹ Department of Diagnostic Radiology, Northwestern University Medical School and Northwestern Memorial Hospital, Chicago, IL 60611. Address reprint requests to R. L. Vogelzang, Northwestern Memorial Hospital, Dept. of Radiology/Olson Pavilion, 710 N. Fairbanks Ct., Chicago, IL 60611.

² Swedish Covenant Hospital, 5145 N. California Ave., Chicago, IL 60625.

³ Department of Urology, Northwestern University Medical School and Northwestern Memorial Hospital, Chicago, IL 60611.

Fig. 1.—CT scan of the pelvis shows a large, mixed-attenuation pelvic hematoma (*straight arrows*) containing gas, which displaces contrast-filled bladder. Note surgical drain (*curved arrow*).

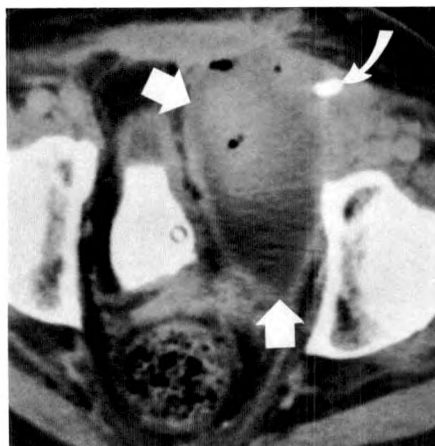
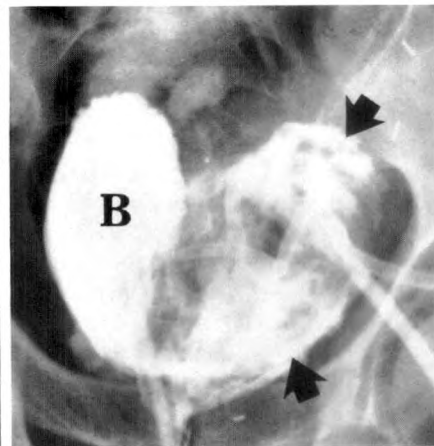


Fig. 2.—Radiograph of the pelvis made immediately after drainage with two sump catheters. Multiple large clots fill cavity (*arrows*). Communication with bladder (B) occurs at bladder neck.



1

2

Fig. 3.—Radiograph of the pelvis made 48 hr after start of urokinase therapy. Cavity is free of clot, but communication with bladder persists. One sump drain has been removed.

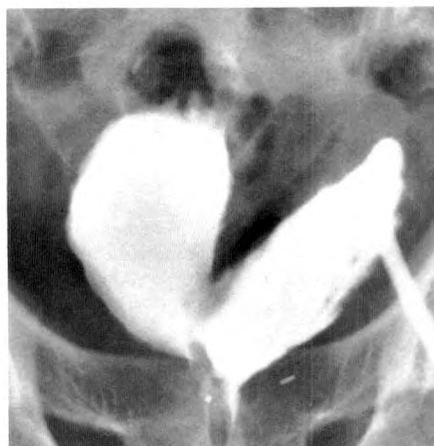
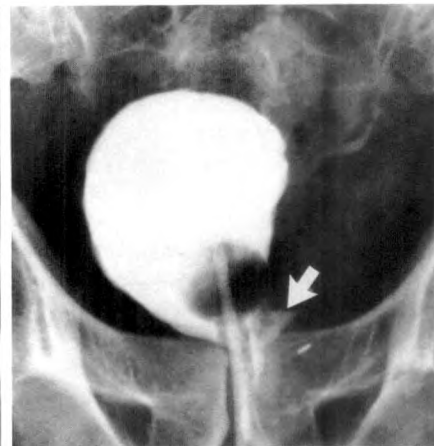


Fig. 4.—Cystogram performed 2 weeks after start of therapy. Complete closure of anastomotic leak and obliteration of cavity. A small diverticulum (*arrow*) remains.



3

4

obliterated by the sixth day after drainage, and the catheters were advanced and removed. A cystogram performed on the 16th post-procedural day revealed a small residual diverticulum at the base of the bladder (Fig. 4). After the withdrawal of the Foley catheter, the patient was able to void normally, and he was discharged with uneventful follow-up.

Case 2

A 67-year-old diabetic white man with severe chronic obstructive-airway disease underwent a radical nephrectomy for stage II renal cell carcinoma. Postoperatively, the patient had a temperature to 102°F. An abdominal CT scan was obtained on postoperative day 6 and showed a mass in the renal bed that was thought to represent an abscess. Drainage was started with a 12-French sump catheter. Small amounts of tenacious chocolate-colored viscous material were aspirated and a diagnosis of infected hematoma was made. Intermittent suction drainage over the next 18 hr yielded only 10 ml of drainage. A repeat CT scan showed adequate positioning of the drainage catheter with considerable residual hematoma. Streptokinase (50,000 units) was injected into the cavity, and the tube was clamped. Eight hours later 150 ml of bloody fluid was aspirated. The collection continued to drain well, but the patient died of respiratory

arrest the following day before further therapy or radiographs could be obtained. An autopsy was not performed.

Discussion

In the 1950s Tillett and Sherry [4] and others [5–8] accumulated significant experience in intrapleural fibrinolytic therapy of hemothorax and empyema with solutions of streptokinase and streptodornase. The therapy was quite effective, particularly if used early. Large quantities (200,000 units) were used routinely without significant hemorrhagic complications, but febrile reactions and leukocytosis were often observed. Apparently, the use of intrapleural fibrinolytic therapy became much less common; there is no referenced mention of its use from 1959 to 1976 and only sporadic indications of its use since then [9–11].

Streptokinase and urokinase lyse thrombus by activation of plasminogen to plasmin, with clot lysis probably resulting from activation of intrathrombotic plasminogen. The degree of clot dissolution is correlated with the amount of plasminogen in the clot. Failures of fibrinolytic therapy have been related to a deficiency of plasminogen within the thrombus

[12-15]. Intravascular clot may become rapidly depleted of plasminogen, accounting for failures of urokinase and streptokinase as well as of new agents such as tissue plasminogen activator in chronic thrombosis [16]. Indeed, Sherry et al. [5] refer to failures of intrapleural therapy as being secondary to inadequate levels of plasmin as early as 1950.

We believe that the extravascular location of these hematomas prevented deactivation or depletion of clot-bound plasminogen. Activation of that plasminogen thus allowed rapid fibrinolysis to take place. The therapy was safe, effective, and well tolerated in both cases. In patient 1, there was no elevation in fibrin-split products or decrease in fibrinogen either before or after therapy. Levels were not measured in patient 2. These findings are consistent with data reported by Berglin et al. [10] who showed only minimal insignificant changes in plasminogen and fibrin-split products after intrapleural instillation of 250,000 units of streptokinase.

Most postsurgical hematomas are not infected or symptomatic and therefore do not require drainage. We are, however, frequently asked to provide transcatheter drainage of these collections if they are symptomatic or infected, and we have been somewhat frustrated in our inability to provide adequate drainage. Many of these are large, well-developed clots with solid material and septations and are difficult if not impossible to effectively aspirate. The use of intracavitary urokinase or streptokinase should allow rapid and effective drainage in these difficult cases, as earlier surgical experience has shown. On the basis of reports of improved efficacy and safety of urokinase over streptokinase in intravascular fibrinolysis, as well as our own experience, we believe that urokinase should be the agent of first choice. Finally, reports of successful treatment of tenacious empyema collections with streptokinase should stimulate new interest in the use of this and similar agents in difficult abscesses.

Addendum

Since the acceptance of this manuscript we have successfully treated a third infected postoperative hematoma with

intracavitary urokinase. A large left perinephric hematoma that occurred after adrenalectomy was completely lysed within 48 hr after the start of therapy. No hemorrhagic complications occurred, and both fibrin-split products and fibrinogen remained normal during and after therapy.

REFERENCES

1. Katzen BE, van Breda A. Low dose streptokinase in the treatment of arterial occlusions. *AJR* 1981;136:1171-1178
2. Mori KW, Bookstein JJ, Heeney DJ, et al. Selective streptokinase infusion: clinical and laboratory correlates. *Radiology* 1983;148:677-682
3. Wolfson RH, Kumpe DA, Rutherford RB. Role of intraarterial streptokinase in treatment of arterial thromboembolism. *Arch Surg* 1984;119:697-702
4. Tillett WS, Sherry S. The effect in patients of streptococcal fibrinolysin (streptokinase) and streptococcal desoxyribo-nuclease on fibrinous, purulent, and sanguinous pleural exudations. *J Clin Invest* 1949;28:173-179
5. Sherry S, Tillett WS, Read T. The use of streptokinase-streptodornase in the treatment of hemothorax. *J Thorac Surg* 1950;20:393-419
6. Read CT, Berry FB. The utilization of streptokinase-streptodornase. *J Thorac Surg* 1950;20:384-393
7. Tillett WS, Sherry S, Read CT. The use of streptokinase-streptodornase in the treatment of chronic empyema. *J Thorac Surg* 1951;21:325-341
8. Streete BG, Thomas DE. Streptokinase and streptodornase in thoracic surgery for pulmonary tuberculosis. *J Thorac Surg* 1957;34:49-52
9. Bergh NP, Ekroth R, Larsson S, Nagy P. Intrapleural streptokinase in the treatment of haemothorax and empyema. *Scand J Thorac Cardiovasc Surg* 1977;11:265-268
10. Berglin E, Ekroth R, Teger-Nilsson AC, William-Olsson G. Intrapleural instillation of streptokinase: effects on systemic fibrinolysis. *Thorac Cardiovasc Surg* 1981;29:124-126
11. Mitchell ME, Alberts WM, Chandler KW. Intrapleural streptokinase to promote drainage of loculated pleural effusions. *Am Rev Respir Dis* 1986;133:A331
12. Saldinger E, Bookstein JJ. Mechanisms of fibrinolysis: native and exogenous systems. *Semin Intervent Radiol* 1985;2:321-330
13. Alkjearisig N, Fletcher A, Sherry S. The mechanism of clot dissolution by plasmin. *J Clin Invest* 1958;38:1086-1095
14. Gottlob R. Mechanisms of intravascular thrombus dissolution as induced by streptokinase. In: Martin M, Schoop W, Hirsch J, eds., *Concepts in streptokinase dosimetry*. Bern: Hans-Huber, 1978:129-137
15. Browse NL, Thomas ML, Pim HP. Streptokinase and deep vein thrombosis. *Br Med J* 1968;3:707-720
16. Mattson C, Nyberg-Arrhenius V, Wallen P. Dissolution of thrombi by tissue plasminogen activator. In: Paoletti R, Sherry S, eds., *Thrombosis and urokinase*. London: Academic Press, 1977:91-102

The MR Appearance of Syringomyelia: New Observations



John L. Sherman^{1,2,3}
A. J. Barkovich^{2,4}
Charles M. Citrin^{1,2,3}

Fifty-eight patients with spinal cord cavities were studied with MR imaging. Patients were separated into four groups, and the appearance of the cavities were compared. There were 24 patients (41.4%) with communicating syringomyelia (associated with the Chiari I malformation). Sixteen patients (27.6%) had posttraumatic syringomyelia, nine patients (15.5%) had associated tumors, and nine patients (15.5%) had idiopathic syringomyelia. The characteristics of each syrinx, the spinal cord, and the appearance of the cerebellar tonsils were analyzed on T2- and T1-weighted images. There is a striking similarity in the appearance of many syrinx cavities regardless of the cause. Characteristics that were found in some patients in every group included areas of increased intensity on T2-weighted images, the presence of the CSF flow-void sign (CFVS) in the syrinx cavity, eccentric cavities, "beaded" cavities, and cord enlargement. Tonsillar ectopia alone does not indicate that a syrinx is of the "communicating" type, since it was present in two of 16 patients (13%) with trauma and in two of five patients (40%) with tumors. T1-weighted images were most useful in evaluating the anatomic characteristics of the syrinx and the cerebellar tonsils. Most syrinx cavities involved the cervicothoracic junction. The average length was between five and nine vertebral segments (depending on category) but varied between one and 20 vertebral segments. T2-weighted images revealed areas of increased intensity in the spinal cord in 13 patients without tumors. Two of these cases were shown to represent gliosis on histopathologic review. The CFVS was present in the syrinx cavities of 23 patients (40%), probably reflecting pulsatile movements of the syrinx fluid. It has been proposed that such movements are a cause of syrinx propagation, and the observation of the CFVS may have prognostic significance. The development and progression of the CFVS was documented in serial MR examinations in one patient over an 18-month period. The theories of syrinx development and propagation are reviewed.

This article appears in the November/December 1986 issue of *AJNR* and the February 1987 issue of *AJR*.

Received May 6, 1986; accepted after revision July 14, 1986.

¹ Magnetic Imaging of Washington, 5550 Friendship Blvd., Chevy Chase, MD 20815. Address reprint requests to J. L. Sherman.

² Department of Radiology, Uniformed Services University of the Health Sciences, Bethesda, MD 20814.

³ Department of Radiology, George Washington University School of Medicine, Washington, DC 20037.

⁴ Department of Radiology, Walter Reed Army Medical Center, Washington, DC 20307-5001.

AJR 148:381-391, February 1987
0361-803X/87/1482-0381

© American Roentgen Ray Society

Syringomyelia is a chronic disorder involving the spinal cord. Pathologically, it is characterized by the presence of longitudinally oriented cavities and gliosis. The term "hydromyelia" has been used to describe the appearance of dilatation of the central canal of the spinal cord while the term "syringomyelia" has been reserved for cavities independent of the central canal [1]. From a practical viewpoint, it is impossible to differentiate most cases of true hydromyelia from those of true syringomyelia. Consequently, recent literature tends to unite the two terms (syringohydromyelia) [2, 3] or to use the terms "syringomyelia" or "syrinx," [4-6] in a generic sense to refer to the spectrum of disease that is involved without implying endorsement of a specific pathogenetic hypothesis. We will follow that trend in this report.

Previous reports have emphasized the usefulness of MR imaging in evaluating patients with suspected syringomyelia [7-9]. In this paper we report our observations of the syrinx cavities and cerebellar tonsils in patients with uncomplicated syringomyelia (communicating syringomyelia), traumatic syringomyelia, idiopathic syringomyelia, and syringomyelia associated with tumors.

Subjects and Methods

Eighty MR examinations of 58 patients with cavities within the spinal cord were evaluated retrospectively. All but two cases were selected from our combined files of approximately 5000 MR examinations. There were 33 men and 25 women ranging in age from 8 to 68 years, with an average age of 38 years. The spinal cord cavities were classified into four groups on the basis of clinical and radiologic criteria. The groups included: syringomyelia with tumor, traumatic syringomyelia, "communicating" syringomyelia (associated with Chiari I malformation), and idiopathic syringomyelia. Patients with the Chiari type I malformation who did not have a history of trauma and did not have a spinal neoplasm were placed in the "communicating" syringomyelia group.

The characteristics of the spinal cord, syrinx, and cerebellar tonsils were recorded. The selected syrinx characteristics included length (in vertebral segments), diameter of the cavity (in millimeters), intensity (specifically, presence of increased intensity on T2-weighted sequences when compared with normal spinal cord tissue), and presence of the CSF flow-void sign (CFVS) [10] in the syrinx cavity. The presence of spinal cord atrophy or enlargement was determined by inspection, and determination of central or eccentric position of cavities was made when possible. All measurements were made from the hard-copy images using calipers and the relative MR scale generated on each image. Measurements were made to the nearest millimeter. The shortest distance between the tip of the tonsil and the foramen magnum line was measured to find the extent of tonsillar ectopia [11].

MR examinations of 51 patients were performed on a 0.5-T whole-body superconductive magnet (Vista-MR, Picker International Corp.). Seven patients were studied on a 1.5-T, whole-body, superconductive unit (Toshiba, Technicare) operating initially at 0.6 T (three patients) and subsequently at 1.5 T (four patients). Standard, manufacturer-provided, single-echo spin-echo (SE) sequences were performed. Data was typically acquired with either 256 or 128 complex samples/views, 256 views, and four excitations using the 2-dimensional Fourier transform method. A 256 × 256 or 128 × 256 matrix was used. The field of view for these examinations was 30 cm for at least one sagittal sequence in all cases, although variable field diameters were also used during many examinations. T2-weighted sequences were done with a TE of 60, 80, 100, or 120 msec and a TR of 1500–3000 msec. T1-weighted sequences employed a TE of 26–40 msec with a TR of 500–800 msec. Intermediate sequences were occasionally used if time permitted. Sagittal T1-weighted images were obtained in all patients; sagittal T2-weighted images were obtained in 49 patients. The section thickness was 5 mm for all T1-weighted examinations. T2-weighted and intermediate sequences were obtained using either 5-mm or 10-mm section thicknesses. The patients

were supine during the examination. Surface coils were used in the evaluation of 40 patients, frequently in conjunction with the head coil or body coil.

Results

The results are presented by category. A comparative summary of the findings in each category is provided in Table 1. The table also gives the number of cases in which areas of cord enlargement or atrophy were present, the number of cases in which eccentric cavities were identified at least at one level, and the presence of a "beaded" shape (these latter features are not specifically detailed in the text). A stacked bar graph showing the number of cases involving each vertebral level appears in Figure 1. Figures 2, 3, 4, and 5 portray the length and location of each syrinx according to category. Most syrinx cavities involved the cervical and upper thoracic spine. Certain observations could not be made in some cases because the necessary images had not been obtained or because surgery had distorted the normal landmarks.

Communicating Syringomyelia

This group contained 24 patients (41%), including 13 women and 11 men, ranging in age from 16 to 68 years. The average age was 39 years. In six of 24 cases, surgical treatment of the syrinx cavity had been performed before MR imaging.

The syrinx cavity varied in length from one to 17 vertebral segments. The average known length was seven to eight vertebral segments. The length and locations of the cavities are depicted in Figure 2. The incidence of cord enlargement, atrophy, and eccentric cavitations is given in Table 1. In five of 24 patients, the syrinx involved the cervical segments but the lower extent was not determined because the remainder of the spine was not examined. The diameter of the syrinx cavities varied from 2 to 15 mm with an average of 5.5 mm.

T2-weighted images showed areas of abnormally increased intensity in the spinal cord at the rostral end of the syrinx in six patients. One patient (44, F) had a very prominent area of increased intensity in the cervical spinal cord around the upper margin of the syrinx cavity and extending rostrally farther than the cavity (Fig. 6). There were 12 mm of tonsillar hernia-

TABLE 1: Comparison of Characteristics of Syringomyelia by Classification Type

	Communicating (n = 24)	Trauma (n = 16)	Tumor (n = 9)	Idiopathic (n = 9)
Areas of increased T2	6/18 (33%)	4/16 (25%)	9 (100%)	3/6 (50%)
CFVS in syrinx	13/16 (81%)	4/14 (29%)	2/9 (22%)	4/6 (67%)
Cord enlargement	12/24 (50%)	12/16 (75%)	8/9 (89%)	2/8 (25%)
Cord atrophy	4/24 (16%)	4/16 (25%)	1/9 (11%)	0
Eccentric cavity	11/16 (69%)	3/3 (100%)	2/4 (50%)	2/6 (33%)
Lobulated cavity shape	9/24 (38%)	3/16 (19%)	1/9 (11%)	2/8 (25%)
Cavity length (spinal segments)	1–17 (avg = 7.5)	1–19 (avg = 8.5)	1–20 (avg = 5.7)	2–16 (avg = 6.1)
Maximum cavity diameter	2–15 mm (avg = 5.5 mm)	3–15 mm (avg = 6.6 mm)	2–12 mm (avg = 7.3 mm)	2–9 mm (avg = 5.7 mm)
Tonsillar ectopia	23/23 (100%)	2/16 (13%)	2/5 (40%)	0

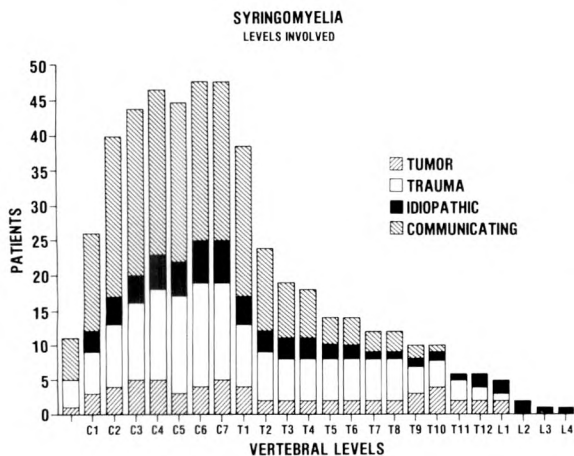


Fig. 1.—Stacked bar graph showing number of cases involving each vertebral level. Note greater number of cases involving cervicothoracic area. Length of each syrinx is shown in Figures 2–5.

Fig. 2.—Length and extent of involvement is shown for patients with “communicating” syringomyelia. Dotted lines indicate that full extent of syrinx was not determined.

Fig. 3.—Length and extent of involvement is shown for patients with traumatic syringomyelia. Dotted lines indicate that full extent of syrinx was not determined.

Fig. 4.—Length and extent of involvement is shown for patients with syringomyelia associated with tumors. Dotted lines indicate that full extent of syrinx was not determined.

Fig. 5.—Length and extent of involvement is shown for patients with idiopathic syringomyelia. Dotted lines indicate that full extent of syrinx was not determined. Two patients with spinal cord tethering had abnormally low cord positions.

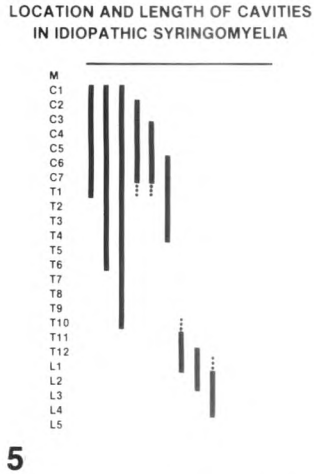
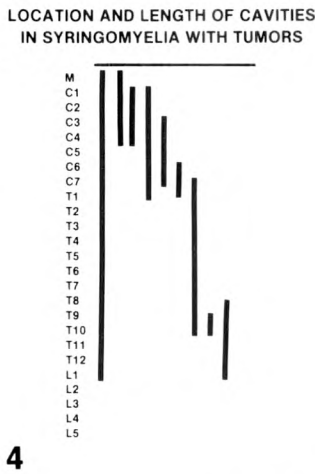
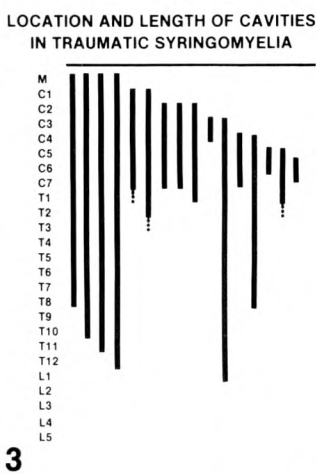
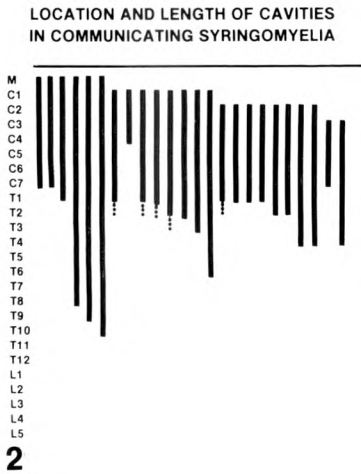
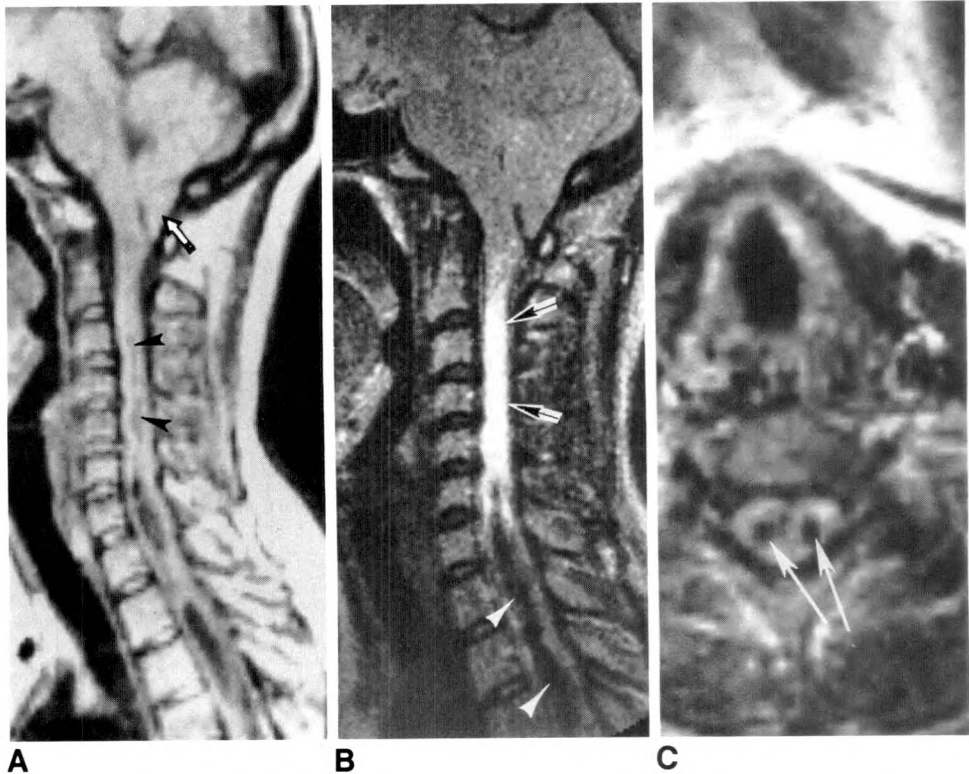


Fig. 6.—44-year-old woman with Chiari I malformation and syringomyelia. **A**, SE 800/40. Note “pointed” cerebellar tonsils 12 mm below foramen magnum (arrow). Syrinx cavity tapers rostrally (arrowheads). **B**, SE 2000/80. Prominent area of increased intensity (arrows) represents gliosis (pathologically proven). Area of decreased intensity in syrinx is CFVS (arrowheads). **C**, SE 1000/40. Transaxial image at C6 level. Note eccentric cavities (arrows).



tion. This study came early in our experience and because of the prominent increased intensity, a spinal cord neoplasm was suspected. A biopsy was performed and officially interpreted as a grade II astrocytoma. Later, at our request, the tissue was reviewed by the Armed Forces Institute of Pathology and interpreted as gliotic tissue without evidence of astrocytoma.

In 16 of 24 patients, T2-weighted SE sequences were available for evaluation of the CFVS in the syrinx cavity. The CFVS was present in 13 of these 16 patients (Figs. 6 and 7). In these 13 patients, the syrinx cavities extended an average of nine to 10 vertebral segments, and the average cavity diameter was 7.4 mm (range, 2–15 mm). In five of the 13 patients with the syrinx CFVS, the sign was seen throughout the entire length of the syrinx (average, eight segments). In the other eight of 13 patients the CFVS was seen better in the thoracic portion of the cavity, or the CFVS was discontinuous. Three patients with adequate T2-weighted examinations had no evidence of the CFVS in the syrinx cavity. In two of these patients the syrinx involved the entire cervical canal but the cavity diameter was only 3 mm. In the other patient the syrinx extended only two segments and was only 2 mm in diameter. Eight patients were evaluated with T1-weighted or proton-density SE sequences only and the presence of the syrinx CFVS could not be reliably determined.

The position of the cerebellar tonsils could be determined in all but one patient. Tonsillar position varied from 1 to 27

mm below the foramen magnum. The average position was 8–9 mm below the foramen magnum. The tonsils appeared variably compressed or pointed (Figs. 6 and 7) in all cases and also varied markedly in size in different patients.

Traumatic Syringomyelia

Sixteen patients (28%) had syringomyelic cavities that were clinically determined to be posttraumatic in origin. The group was composed of 12 men and four women, ranging in age from 19 to 58 years with an average age of 41 years.

Surgery was performed before our evaluation in 12 of 16 patients. Nine patients had cervicothoracic syrinx cavities, and seven patients had cavities apparently limited to the cervical cord; however, full thoracic MR was not performed in five of these seven patients. The lengths of the cavities ranged from one vertebral segment to total spinal cord involvement. The average known length was eight to nine vertebral segments. (The length and location of the cavities are given in Figure 3.) The diameter of the syrinx cavities varied from 3 to 15 mm, averaging 6 mm.

T2-weighted images were available in 14 of 16 patients. In four patients these images showed an adjacent area of increased intensity within the spinal cord. These areas were thought to represent gliosis, edema, or myelomalacia. In one of the patients with a focal ovoid cyst, the cyst contents had a higher intensity signal than did CSF in the basilar subarach-

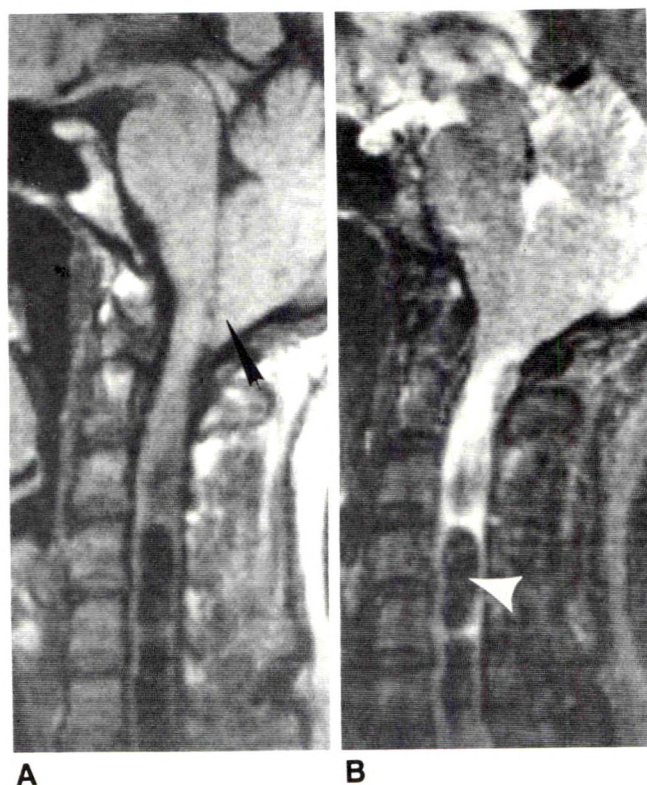


Fig. 7.—46-year-old woman with Chiari I malformation and syringomyelia. Note "beaded" shape of syrinx cavity. A, SE 500/40. "Pointed" tonsil below foramen magnum (arrow). B, SE 3000/120. "Beaded" shape is more noticeable on this T2-weighted image. Note CFVS in cavity (arrowhead). Increased intensity present at rostral end of syrinx may represent gliosis.

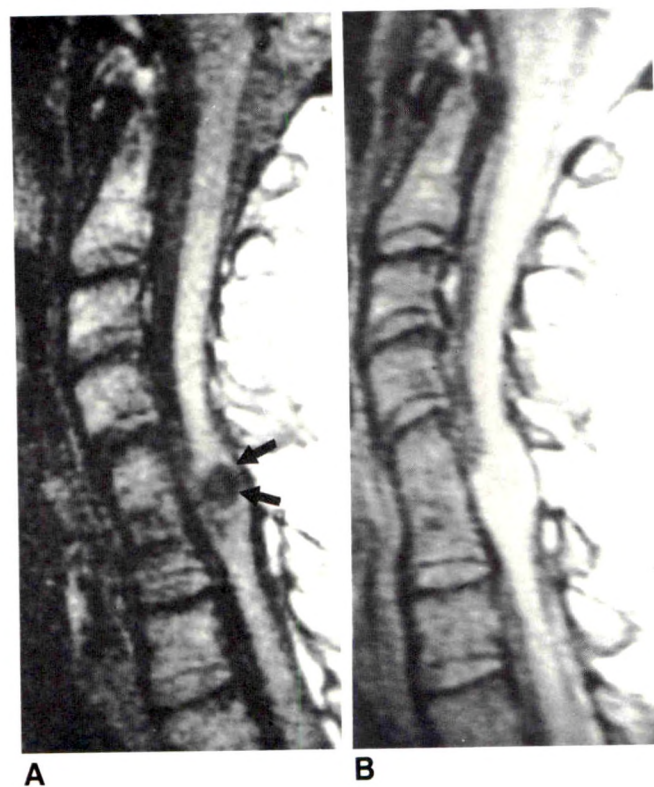


Fig. 8.—42-year-old man. Posttraumatic focal syrinx. Fusion at C5–C6. A, SE 600/30. Cyst enlarges cord (arrows). B, SE 2500/60. Diffuse increased intensity in syrinx and cord.

noid cisterns (Fig. 8). The CFVS was identified in the syrinx cavity in four of the 14 patients with adequate T2-weighted images (Fig. 9). Ten patients had no evidence of the CFVS. In one patient, multiple cysts were present in the thoracic

cord, causing marked cord enlargement (Fig. 9). Multiple drainage procedures over an 18-month period failed to halt the development of progressive cavitations and cord enlargement. The CFVS was initially seen only in a small area of the

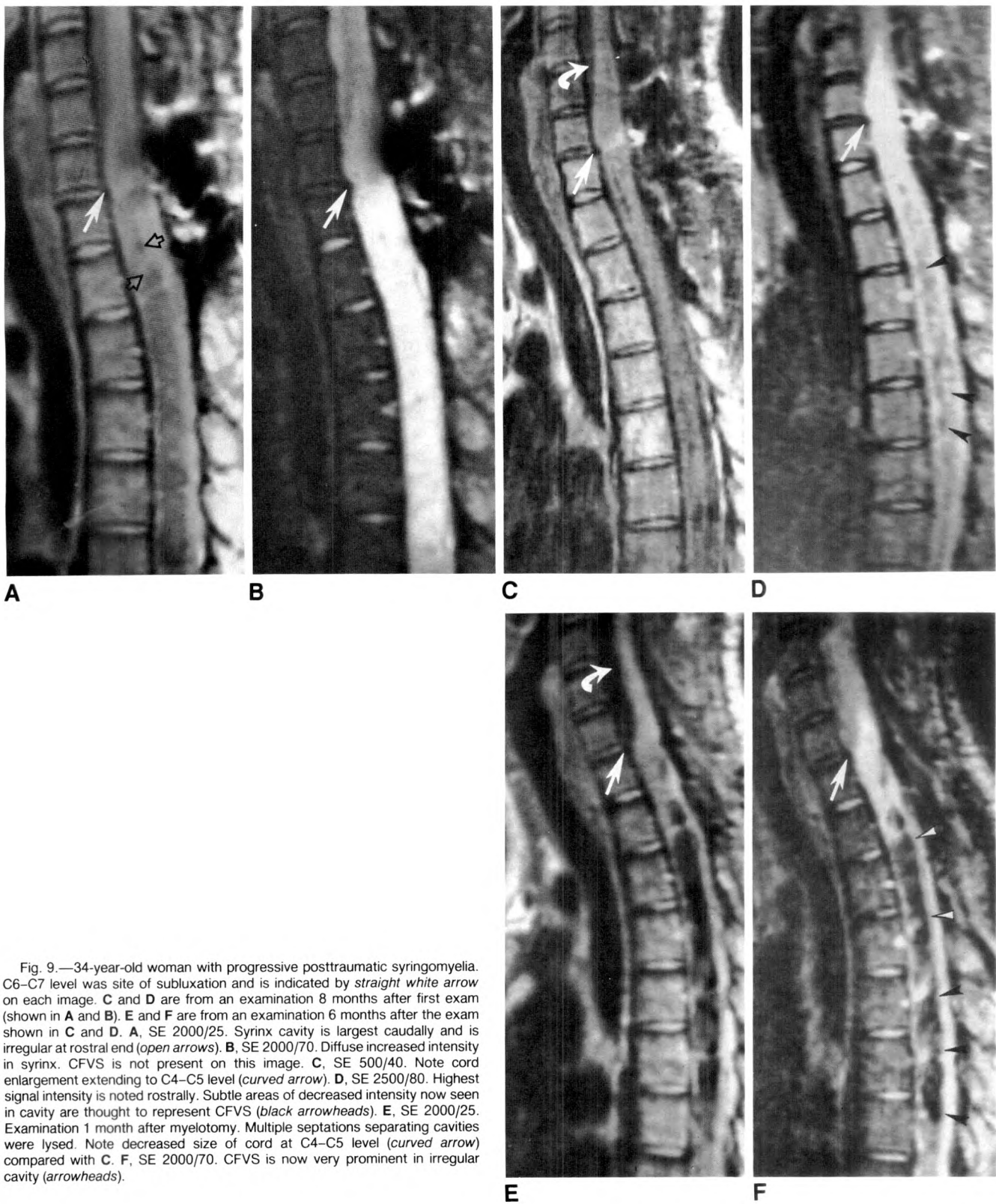


Fig. 9.—34-year-old woman with progressive posttraumatic syringomyelia. C6–C7 level was site of subluxation and is indicated by *straight white arrow* on each image. **C** and **D** are from an examination 8 months after first exam (shown in **A** and **B**). **E** and **F** are from an examination 6 months after the exam shown in **C** and **D**. **A**, SE 2000/25. Syrinx cavity is largest caudally and is irregular at rostral end (*open arrows*). **B**, SE 2000/70. Diffuse increased intensity in syrinx. CFVS is not present on this image. **C**, SE 500/40. Note cord enlargement extending to C4–C5 level (*curved arrow*). **D**, SE 2500/80. Highest signal intensity is noted rostrally. Subtle areas of decreased intensity now seen in cavity are thought to represent CFVS (*black arrowheads*). **E**, SE 2000/25. Examination 1 month after myelotomy. Multiple septations separating cavities were lysed. Note decreased size of cord at C4–C5 level (*curved arrow*) compared with **C**. **F**, SE 2000/70. CFVS is now very prominent in irregular cavity (*arrowheads*).

syrinx but subsequently developed to a much greater degree in an area that had previously appeared bright on a T2-weighted image. Finally, the patient underwent an extensive myelotomy and syrinx shunt revision, which disclosed multiple discontinuous cysts of various sizes and multiple septations. Repeat MR examination revealed that the multiloculated, discontinuous syrinx had been converted to a tubular syrinx with a single dominant cavity. The syrinx had a beaded appearance and the CFVS was present throughout most of the length of the syrinx. The length of the syrinx was reduced by two vertebral segments and the diameter was reduced by 1–2 mm. The patient reported symptomatic improvement.

The cerebellar tonsils ranged from 4 mm below to 10 mm above the foramen magnum, with an average position of 2 mm above. The two patients with mild tonsillar ectopia had a convincing history of trauma. The cerebellar tonsils appeared normally shaped in all cases.

Syringomyelia Associated with Tumors

Nine of the 58 patients (16%) had syrinx cavities associated with tumors. This group consisted of five men and four women, ranging in age from 13 to 64 years, with an average age of 33 years. Four patients were examined before surgical intervention, the other six were examined postoperatively. All cases have been pathologically proven.

Four patients had astrocytomas (three cervical, one thoracic) (Figs. 10 and 11) while four patients had ependymomas (three cervicothoracic, one in the fourth ventricle) (Fig. 12). One patient had a meningioma at the T4 level that had been resected. The length of the syrinx cavities ranged from one vertebral segment to total spinal cord involvement. The average length was five to six segments. The location and length of the cavities are depicted in Figure 4. The total spinal cord syrinx was found in the patient with a meningioma at the T4 level. The shortest cavity was found in a patient with an astrocytoma. The patient with the fourth ventricular ependymoma had a syrinx cavity limited to the cervical spinal cord. The diameter of the syrinx cavities varied from 2 to 12 mm with an average of 7.3 mm. Intratumoral cystic areas, separate from the syrinx cavities, were seen in two patients (Fig. 10). All patients had T2-weighted scans that permitted evaluation of the CFVS. The CFVS was present in the syrinx cavities in two of nine patients. The CFVS was not seen in areas known to represent intratumoral cysts. All patients had variable areas of increased intensity in the spinal cord. These areas correlated with locations of the tumor tissue in the eight patients with intramedullary tumors, but could not be differentiated from adjacent edema, gliosis, or demyelination. All patients with intramedullary tumors had either focal (Figs. 10 and 12) or diffuse (Fig. 11) spinal cord enlargement. The patient with the meningioma also had areas of increased intensity at the site of surgery, but these were interpreted by us as representative of gliosis.

The location of the cerebellar tonsils could be determined in six patients. Tonsillar position ranged from 4 mm above the foramen magnum to 18 mm below, averaging 5 mm below. Three patients had significant tonsillar herniation (7 mm, 10 mm, 18 mm herniation) (Fig. 10). The tonsils appeared



Fig. 10.—46-year-old woman with astrocytoma of cervical spinal cord. Laminectomies have enlarged spinal canal. **A**, SE 500/40. Focal ovate cyst enlarges cord (straight white arrow). Small spindle-shaped cavities above and below cyst (open arrows). Note tonsillar ectopia of 10 mm below foramen magnum (curved arrow). **B**, SE 2400/80. Diffuse increased intensity in cyst and in cavities above and below cyst. There is no evidence of CFVS.

normal in one patient with an ependymoma and in the patient with a meningioma. In four patients (including one with normal tonsillar position), the tonsils appeared pointed or compressed.

Idiopathic Syringomyelia

This group contained nine patients, four women and five men, ranging in age from 8 to 60 years; average age, 39 years.

Two of these patients (ages 8 and 46) had lumbar lipomeningoceles with spinal cord tethering. The central canal of the spinal cord was enlarged to 2 mm in both patients. There was no evidence of the CFVS in the hydromyelic cavities. Evaluation was limited to the lumbar area in the 46-year-old patient. In the younger patient there was no evidence of cervical or upper thoracic syringomyelia. The location and length of the cavities are shown in Figure 5. The cerebellar tonsils were at the level of the foramen magnum.

Six patients had syringomyelic cavities that resembled the cavities of the communicating syringomyelic group except that there was no evidence of craniocervical anomaly or hindbrain deformity. The average diameter of the cavities was 5.7 mm but ranged from 2 to 9 mm. Three patients had areas

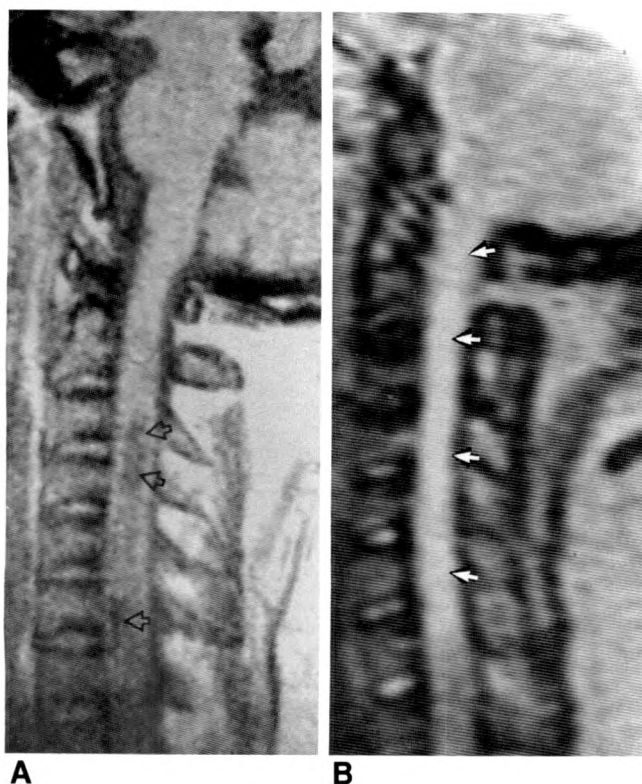


Fig. 11.—46-year-old man with diffuse cervical spinal cord astrocytoma. **A**, SE 800/30. Irregular cysts in diffusely enlarged cord (arrows). **B**, SE 2000/80. Diffuse increased intensity (arrows) represents tumor (pathologically proven at autopsy).



Fig. 12.—44-year-old man with recurrent ependymoma. **A**, SE 800/30. Syrinx cavity (arrowheads) in spinal cord below mass (arrow). Radiation changes noted in vertebral bodies. **B**, SE 2000/80. Increased intensity in tumor and spinal cord (arrows). CFVS is present in caudal aspect of syrinx (arrowheads).

of increased intensity in the spinal cord adjacent to the syrinx cavity on T2-weighted images. At surgery, these three patients had no evidence of spinal cord neoplasm. A biopsy in one case revealed gliosis. In four of six patients with sufficiently T2-weighted images, the CFVS was present in the syrinx cavity, extending most of the length of the cavity. The cerebellar tonsils and cisterna magna appeared normal in the seven patients whose cervical-cranial junction was evaluated, including one patient with a lumbar lipomeningocele.

Review of the Pathogenesis of Syringomyelia

Syringomyelia has many causes, just as cystic spaces in the brain may be of diverse origins. The shape and structure of the spinal cord and spinal canal have a strong influence on the appearance of the spinal cord cystic spaces, which makes the cavities and the clinical signs similar, regardless of the etiology.

Williams [12], Barnett [13], and others [14, 5] have adopted a classification system based on the way the syrinx communicates with the central canal. Thus, in "communicating" syringomyelia, the cavity contains fluid indistinguishable from CSF. This fluid is transmitted to the syrinx cavity via communication of the central canal with the fourth ventricle (Fig. 13). The cavitation in these cases should be centrally located.

This type is associated with the Chiari malformations. Gardner [6, 15] states that continuing communication between the fourth ventricle and the central canal is the result of a failure of the foramina of the fourth ventricle to open at the 29th week of fetal life. He describes a "water hammer effect" caused by CSF pulsations that is transmitted to the central canal. This causes the central canal to dilate, and, if the ependymal lining ruptures, causes cyst extension within the substance of the spinal cord (Fig. 13B). This theory was modified by Williams [16] to favor intracranial and spinal, venous, and CSF pressure differentials (Fig. 13C). Coughing and other maneuvers produce increased intrathoracic and intraabdominal pressure, which result in spinal epidural venous distention. Venous distention in the confined space of the spinal canal is accompanied by rapid displacement of spinal fluid into the head. In a patient with the Chiari I malformation or other obstruction, the initial surge forces CSF into the intracranial space but does not drain out immediately due to a ball-valve effect. Thus, there is craniospinal pressure dissociation. The higher intracranial pressure forces fluid into the central canal. A similar phenomenon is found in the spine in conditions that produce partial blockage [17]. Williams also theorizes that fluid shifts within the syrinx cavity lead to extension of cavities (Fig. 13C). Pulsation in the subarachnoid space may be transmitted to the fluid in the syrinx by gener-

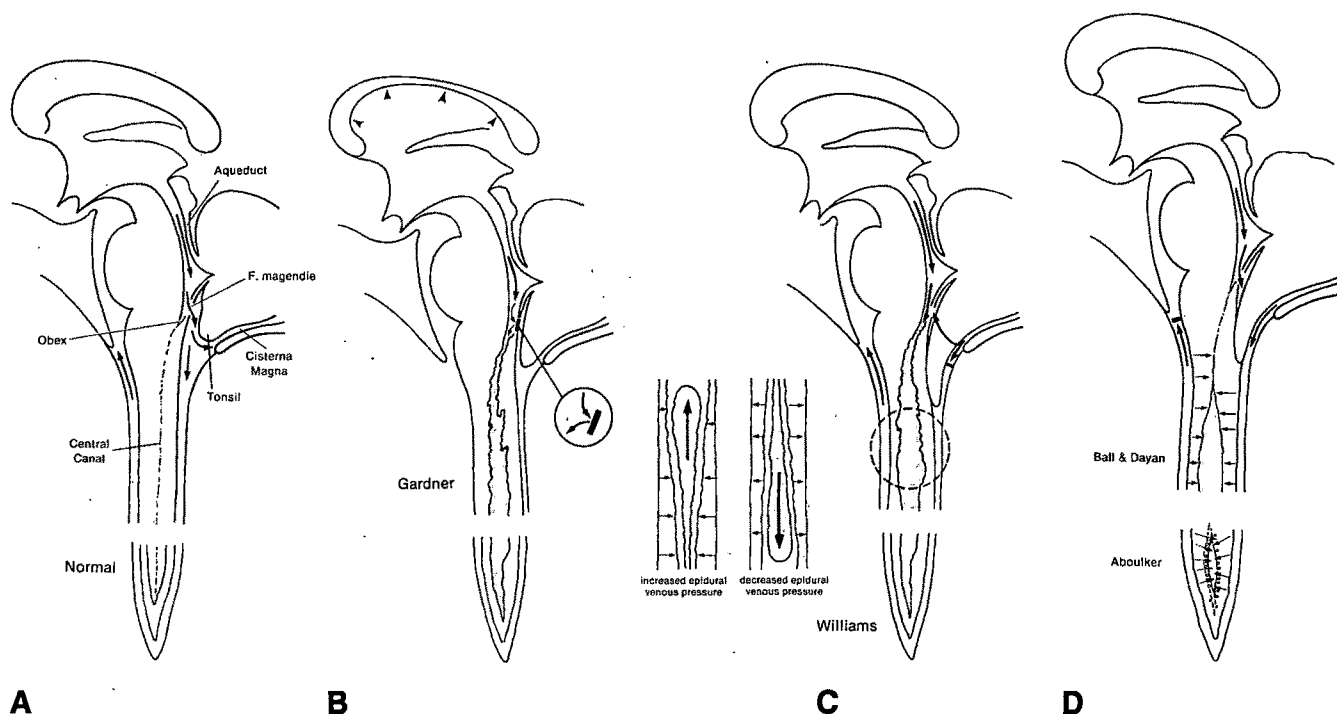


Fig. 13.—Diagrammatic representations of pathophysiological theories in syringomyelia. Refer to text for full explanation. A, Normal representation of CSF flow (arrows). Note incomplete central canal of spinal cord. B, Gardner's theory [6, 15] emphasizing imperforate foramen of Magendie (blocked arrow, inset). Hydrocephalus (arrowheads). C, Williams' theories [12, 16, 17] empha-

sizing "ball-valve" effect of foramen magnum obstruction. Movement of intracranial CSF into spinal canal is impeded (blocked arrow) and redirected into central canal. CSF movements in syrinx cavities depicted (inset). D, Theories of Ball and Dayan [20] and of Aboulker [21]. CSF movement from spinal canal into cranial space is impeded (blocked arrow). CSF passes into cord.

ating waves in the walls. These pulsations are thought to be caused by engorgement of the epidural venous plexus and are most marked in coughing and other Valsalva-like maneuvers [17–19]. As the veins fill, the increased pressure causes the fluid in the syrinx to be displaced. When the veins empty, the pressure is decreased and the displaced fluid returns to its original position. The gradual effect of these fluid shifts is to cause the cavity to extend into the part of the cord offering the least resistance.

In "noncommunicating" syringomyelia there is thought to be no direct communication with the subarachnoid space. The cavitations should be eccentric although they may appear centrally located on gross examination. Noncommunicating syringomyelia is said to be associated with trauma, tumor, or arachnoiditis.

These theories have helped the development of surgical procedures designed to correct the hypothesized etiologic abnormalities, but they are not universally accepted and there is conflicting evidence about the importance of the communication of the syrinx with the central canal [17, 20, 21]. Persistence of the syrinx in cases where the proposed communication via the calamus scriptorius [22] (at the obex) has been occluded are well known [20]. In addition, fluid within the syrinx in cases of trauma or arachnoiditis is identical to CSF in many instances.

Other theories have attempted to explain the origin of CSF in the cavity of a syrinx. Fluid may be secreted directly into

the syrinx by glial cells or ependyma lining the cavity [23].

Aboulker [21] and Aubin et al. [24] believe that obstruction at the foramen magnum causes increased spinal CSF pressure by inhibiting upward movement of CSF to sites of absorption (Fig. 13D). This is in contradistinction to Williams, who believes that foramen magnum obstruction prevents the downward passage of CSF. Aboulker theorizes that increased pressure drives CSF through the spinal parenchyma or via a pathway along the posterior roots into the spinal cord, where chronic edema gradually undergoes cavitation. The same basic mechanism is invoked by Ball and Dayan [20] except that they propose that the CSF passes into the central canal by tracking under pressure into the spinal cord along perivascular (Virchow-Robin) spaces (Fig. 13D). These latter two theories have been invoked to explain the mechanism of metrizamide passage into noncommunicating syrinx cavities [25]. Hemorrhage into the syrinx (Gowers' syringal hemorrhage) is a rare cause of acute syrinx extension [13, 26].

Discussion

We noted many similarities in the appearance of the syrinx cavities despite the different origins (Table 1). Most cases involved the cervicothoracic junction (Fig. 1). Some patients with eccentric cord cavities were seen in every category, thereby eliminating this observation as a means of differen-

tiating "true" syringomyelia from "true" hydromyelia. Areas of cord enlargement or of cord atrophy were also noted in some patients in each category.

MR Intensity Differences in Syringomyelia

One of our most important observations in this series was the range of MR intensities that could be seen in the syrinx and the surrounding spinal cord. We noted areas of increased signal intensity on T2-weighted images in the spinal cord surrounding the syrinx cavities in 13 of 40 patients (33%) without tumors (nine patients did not have T2-weighted examinations) (Figs. 6, 7, 9). Gebarski et al. [27] noted similar areas on MR examinations in traumatic syringomyelia and hypothesized that these areas represented gliosis and/or edema. In two of our cases biopsies of the abnormal areas showed gliosis (Fig. 6). Gliosis is regarded as a reaction on the part of astrocytes to adjacent tissue damage and is composed of both hypertrophic and hyperplastic changes. Gliosis is commonly associated with syringomyelia [1, 2, 28, 29] and therefore its appearance on MR images is not surprising. Gliosis is proportional not only to the age of the lesion but to the severity of the forces acting upon the walls [29]. Thus, gliosis is found in a circumferential orientation to withstand a distending force and at the top of the cavity to withstand the upward pulsations of the syrinx fluid [8]. Circumferential gliotic bands produce the frequently seen "beaded" syrinx [1, 17, 28] (Fig. 7). Gliosis at the leading edge of the cavitation is also likely to occur because the leading edge of the cavity dissects along longitudinal tissue planes, separating the tissues from their intimate blood supply [28]. Greenfield [1] noted that where there is a recent extension the wall is irregular and consists of degenerated neuroglial and neural elements. In one patient with a traumatic syrinx (Fig. 9), the cavity was noted to extend in a rostral direction into an area that had previously been identified as having increased intensity on T2-weighted images. The surgeon subsequently reported his observation of gliosis and multiple small septated cavities in this area. In this same patient, the most recent rostral extension of the cavity was associated with an area of adjacent tissue of prolonged T2, but this area returned to normal after an extensive myelotomy and shunt revision. The return of an area of increased intensity to normal is most compatible with resolution of interstitial edema after successful cyst drainage [30]. Areas of prolonged T2 may also represent microcystic changes and demyelination, as Cohen et al. [31] have shown experimentally.

Prominent loss of signal intensity was seen in the syrinx cavity in many instances (Figs. 6, 7, 9, 12). We believe this represents pulsatile fluid shifts within the syrinx cavity. The MR appearance of CSF motion in the brain [10, 32-34] and in the spine [35-37] has been described. CSF motion appears as an area of decreased signal intensity compared with the CSF in the lateral ventricles or other CSF spaces not subject to marked pulsations. The loss of signal due to motion within CSF spaces such as the aqueduct of Sylvius has been referred to as the CSF flow-void sign (CFVS) [10, 32]. The signal loss represented by the CFVS is probably caused by a

combination of phase shift and time-of-flight effects [38, 39]. We hypothesize that the CFVS in the syrinx is caused by the fluid shifts that have been proposed by Williams [40].

It is important to note that although the syrinx CFVS was more frequently seen in the communicating syringomyelia group (81%), it was also present in some cavities of other types (Table 1). Although the CFVS can be seen on T1-weighted images, it is best seen on T2-weighted images. We found that the syrinx CFVS often prevented accurate assessment of the "true" intensity of the fluid in the syrinx cavity; that is, we were unable to determine differences in protein content in the syrinx fluid because of the CFVS [41]. The largest syrinx cavities were most likely to have the CFVS. The CFVS was seen in only one of four patients with cavities that were 2 or 3 mm in diameter. It was not present in tumor cysts (Figs. 10, 11) and was not seen in two ovoid traumatic cysts (Fig. 8). In the patient with an enlarging posttraumatic syrinx, the CFVS was initially present only in a small area (Fig. 9). Subsequent exams documented extension of the syrinx and increased visualization of the CFVS as multiple loculated cavities were converted into one dominant cavity. We theorized that the CFVS became more apparent as the separate syrinx cavities developed communications, thereby allowing greater mobility of fluid within the syrinx. We infer that the absence of the CFVS may indicate the presence of septations. These septations are probably fibrous or glial scars [42]. This is important information, since it may indicate the need for multiple syrinx drainage tubes or syringotomies to adequately shunt the syrinx. Intraoperative sonography is also useful in the detection of septations within syrinx cavities [27, 42].

Syringomyelia Associated with Tumor

Previous reports have noted that in cases of syrinx associated with spinal cord tumor, the tumor enlarged the spinal cord and often had an abnormal signal on T2-weighted images while the appearance of the cystic cavity was indistinguishable from other syringes [8]. Our series confirms this observation (Figs. 10, 11, 12). Spinal cord enlargement was present in eight patients (89%). It was not present in the patient with the posterior fossa ependymoma. In the presence of spinal cord cavitation cord enlargement alone is not specific for tumor (Table 1). Some reports have suggested that the presence of increased signal intensity around a syrinx was an indication of tumor [43]. As explained above, we have found that such areas are not infrequently seen in nonneoplastic conditions and that they represent gliosis in some cases (Figs. 6, 7, 9). Barnett [3] has stated that the syringes associated with tumors are most often lined by glial tissue and are secondary to CSF flow obstruction during periods of raised intraspinal pressure. He thus questions previous authors who have suggested that the cavitation occurs within the tumor mass.

Seven patients had intramedullary spinal tumors. In these cases the tumors could be detected by the presence of solid or mixed solid and cystic tissues at the site of cord enlargement (Fig. 11). The cystic areas within the tumors had higher intensity on T2-weighted sequences than the fluid in the syrinx

cavities. The CFVS was present in the associated syrinx cavities in two patients (Fig. 12) but was not present in the cystic portions of the tumors. However, we must caution that not all such cystic cavities are neoplastic. One patient had a traumatic focal syrinx (Fig. 8) that was very similar in appearance to a patient with a cystic astrocytoma of the cord (Fig. 10). Of course, the history of trauma and the related changes in the vertebral column allow differentiation on clinical grounds.

We cannot differentiate tumor in nonenlarged areas of the spinal cord from areas of gliosis, edema, myelomalacia, or demyelination (Fig. 12). The use of paramagnetic contrast agents such as Gd-DTPA has been advocated as a means of differentiating spinal cord neoplasms from edema and may prove useful in the differentiation of neoplasm from gliosis or myelomalacia [44].

The observation of the typical findings of the Chiari I malformation makes the consideration of tumor less likely, especially if a focal solid mass is not present. One such patient in our series was thought to have a tumor clinically and the initial pathologic diagnosis was Grade II fibrillary astrocytoma. The upper cervical spinal cord appeared hyperintense relative to all other tissues on a T2-weighted exam but the Chiari I malformation was also present (Fig. 6). At our urging, the tissue was reviewed at the Armed Forces Institute of Pathology and reclassified as gliosis without evidence of neoplasm. This case points out the importance of recognizing the typical features of the Chiari I malformation as well as recognizing that diagnostic difficulties are occasionally encountered on surgical biopsy specimens in distinguishing a poorly cellular diffuse fibrillary astrocytoma from reactive gliosis [45]. However, we must also recognize that tonsillar ectopia can coexist with spinal cord neoplasm. In fact, our series has a surprisingly high incidence of tonsillar ectopia in association with cervical spinal cord neoplasm and syringomyelia (Table 1). In these cases, the tumors were easily differentiated from the associated syringes on the basis of the anatomic characteristics.

Summary

We have shown that the appearance of syringomyelia is quite similar, regardless of the origin. The diagnosis of spinal cord neoplasm cannot be made on the basis of increased signal intensity alone.

Observation of the CFVS within the syrinx may have prognostic significance, since pulsatile fluid shifts appear to play a role in the extension of syrinx cavities. We cannot differentiate "communicating" from "noncommunicating" syringomyelia on the basis of the CFVS alone. However, the frequent observation of the CFVS in syrinx cavities supports Williams' theory that the cause of syrinx progression is related to fluid shifts in the cavity and is independent of the initial factors that lead to the development of the syrinx [17].

ACKNOWLEDGMENTS

Our thanks to William Radcliffe of MR Imaging of PG County and Louis Wener of MRI Associates, Clinton, MD, for their case contri-

butions. Special thanks to Eileen Weisman for her help as patient liaison and for records management and to Arlene Kisliuk.

REFERENCES

1. Greenfield JG. Syringomyelia and syringobulbia. In: Blackwood W, McMenemey WH, Mayer A, Norman RM, Russell DS, eds. *Greenfield's neuropathology*. Baltimore: Williams & Wilkins, 1963:331-337
2. Harwood-Nash DC, Fitz CR. Myelography and syringohydromyelia in infancy and childhood. *Radiology* 1974;113:661-669
3. Barnett MJM, Rewcastle NB. Syringomyelia and tumours of the nervous system. In: Barnett MJM, Foster JB, Hudgson P, eds. *Syringomyelia*. London: Saunders, 1973:261-301
4. Yeates A, Brant-Zawadzki M, Norman D, Kaufman L, Crooks LE, Newton TH. Nuclear magnetic resonance imaging of syringomyelia. *AJNR* 1983;4:234-237
5. Peerless SJ, Durward QJ. Management of syringomyelia: a pathophysiological approach. *Clin Neurosurg* 1983;30:531-576
6. Gardner WJ. Hydrodynamic mechanism of syringomyelia: its relationship to myelocoele. *J Neurol Neurosurg Psychiatr* 1965;28:247-259
7. Pojunas K, Williams AL, Daniels DL, Haughton VM. Syringomyelia and hydromyelia: magnetic resonance evaluation. *Radiology* 1984;153:679-683
8. Lee BCP, Zimmerman RD, Manning JJ, Deck MDF. MR imaging of syringomyelia and hydromyelia. *AJNR* 1985;6:221-228, *AJR* 1985;144:1149-1156
9. Kokmen E, Marsh WR, Baker HI. Magnetic resonance imaging in syringomyelia. *Neurosurg* 1985;17:267-270
10. Sherman JL, Citrin CM. Magnetic resonance demonstration of normal CSF flow. *AJNR* 1986;7:3-6
11. Barkovich AJ, Wippold FJ, Sherman JL, Citrin CM. Significance of cerebellar tonsillar position on MR. *AJNR* 1986;7:795-799
12. Williams B. Current concepts in syringomyelia. *Br J Hosp Med* 1970;4:331-342
13. Barnett HJM. The epilogue. In: Barnett MJM, Foster JB, Hudgson P, eds., *Syringomyelia*. London: Saunders, 1973:302-313
14. Austin GM, ed. Communicating syringomyelia. In: *The spinal cord*. New York: Igaku-Shoin, 1983
15. Gardner W, Angel J. The mechanism of syringomyelia and its surgical correction. *Clin Neurosurg* 1975;6:131-140
16. Williams B. The distending force in the production of "communicating syringomyelia." *Lancet* 1969; ii:189-193
17. Williams B. On the pathogenesis of syringomyelia: a review. *J Royal Soc Med* 1980;73:798-806
18. Barnett HJM, Jousse AT, Ball MJ. Pathology and pathogenesis of progressive cystic myelopathy as a late sequel to spinal cord injury. In: Barnett HJM, Foster JB, Hudgson P, eds. *Syringomyelia*. London: Saunders, 1973:179-219
19. Du Boulay G, Shah SH, Currie JC, Logue V. The mechanism of hydromyelia in Chiari type I malformation. *Br J Radiol* 1974;47:579-587
20. Ball MJ, Dayan AD. Pathogenesis of syringomyelia. *Lancet* 1972;2:799-801
21. Aboulker J. La syringomyelie et les liquides intra rachidiens. *Neurochirurgie* 1979;25:suppl 1:9-144
22. Crosby EC, Humphrey T, Lauer EW, eds. *Correlative anatomy of the nervous system*. New York: Macmillan, 1962:114
23. Barnett HJM, Jousse AT, Ball MJ. Pathology and pathogenesis of progressive cystic myelopathy as a late sequel to spinal cord injury. In: Barnett HJM, Foster JB, Hudgson P, eds. *Syringomyelia*. London: Saunders, 1973:179-219

24. Aubin ML, Vignaud J, Jardin Bar D. Computed tomography in 75 clinical cases of syringomyelia. *AJNR* 1981;2:199-204
25. Kan S, Fox AJ, Vinuela F, Barnett HJM, Peerless SJ. Delayed CT metrizamide enhancement of syringomyelia secondary to tumor. *AJNR* 1983;4:73-78
26. Perot P, Feindel W, Lloyd-Smith D. Hematomyelia as a complication syringomyelia: Gowers' syringal hemorrhage. *J Neurosurg* 1966;25:447-451
27. Gebarski SS, Maynard FW, Gabrielsen TO, Knake JE, Latack JT, Hoff PT. Posttraumatic progressive myelopathy. *Radiology* 1985;157:379-385
28. Escourolle R, Poirier J, eds. *Manual of basic neuropathology*. Philadelphia: Saunders, 1973:19-34
29. Williams B, Timperley WR. Three cases of communicating syringomyelia secondary to midbrain gliomas. *J Neurol Neurosurg Psychiatr* 1976;40:80-88
30. Rossier AB, Foo D, Shillito J, Dyro FM. Posttraumatic cervical syringomyelia. *Brain* 1985;108:439-461
31. Cohen WA, Young W, DeCrescito V, Horii S, Kricheff II. Post-traumatic syrinx formation: experimental study. *AJNR* 1985;6:823-827
32. DeLaPaz RL, Davis DO, Norman D, O'Donohue J, Enzmann DR. Cerebrospinal fluid motion effects in cerebral MR imaging. Presented at the 71st annual meeting of the Radiological Society of North America, Chicago, 1985
33. Sherman JL, Citrin CM, Bowen BJ. The magnetic resonance appearance of CSF flow in ventriculomegaly. Presented at the 71st annual meeting of the Radiological Society of North America, Chicago, 1985
34. Bradley WG, Kortman KE, Burgoyne B. The effect of pulsatile flow on CSF intensity in MR imaging of the brain. Presented at the 71st annual meeting of the Radiological Society of North America, Chicago, 1985
35. Sherman JL, Citrin CM, Gangarosa RE, Bowen BJ. The MR appearance of CSF pulsations in the spinal canal. *AJNR* 1986;7:879-884
36. Rubin JB, Enzmann DR. Imaging spinal CSF pulsation by 2DFT magnetic resonance: significance during clinical imaging. Presented at the 24th annual meeting of the American Society of Neuroradiology, San Diego, 1986
37. Mills CM, Posin JP, McCreary J, Kleiner BC. MRI of the spine: effect of flow on CSF intensity. Presented at the 24th annual meeting of the American Society of Neuroradiology, San Diego, 1986
38. von Schulthess GK, Higgins CB. Blood flow imaging with MR: spin-phase phenomena. *Radiology* 1985;157:687-695
39. Bradley WG, Waluch VW. Blood flow: magnetic resonance imaging. *Radiology* 1985;154:443-450
40. Williams B. Cerebrospinal fluid pressure changes in response to coughing. *Brain* 1976;99:331-346
41. Brant-Zawadzki M, Kelly W, Kjos B, et al. Magnetic resonance imaging and characterization of normal and abnormal intracranial cerebrospinal fluid (CSF) spaces. *Neuroradiol* 1985;27:3-8
42. Quencer RM, Morse BMM, Green BA, Eismont FJ, Brost P. Intraoperative spinal sonography: adjunct to metrizamide CT in the assessment and surgical decompression of posttraumatic spinal cord cysts. *AJNR* 1984;5:71-79
43. Di Chiro G, Doppman JL, Dwyer AJ, et al. Tumors and arteriovenous malformations of the spinal cord: assessment using MR. *Radiology* 1985;156:689-697
44. Bydder GM, Brown J, Niendorf HP, Young IR. Enhancement of cervical intraspinal tumors with intravenous Gadolinium-DTPA. *J Comput Assist Tomogr*, 1985;9:847-851
45. Rubinstein LJ. *Tumors of the central nervous system. Fascicle 6, Atlas of tumor pathology*. Washington, DC: Armed Forces Institute of Pathology, 1972;46-47

Book Reviews

Multiplanar CT of the Spine. By Stephen L. G. Rothman and William V. Glenn, Jr. Baltimore: Univ. Park Press. 520 pp., 1985. \$125

This book, based on 14,000 CT examinations of the spine, deals exclusively with images produced by multiplanar reconstruction of axial CT scans according to the technique pioneered and refined by William V. Glenn and his associates. The introductory chapters describe the examination technique in detail, including the highly structured order in which the images are placed on the films and the equally regimented but efficient reporting system. A richly illustrated anatomic chapter by W. Rauschnig, based on beautiful photographs of large-scale cryomicrotome slices of the spine, is included for correlation with the multiplanar radiographs, but this chapter suffers from a dissociation between the text and the figures: references from text to images are sparse, which may make the chapter awkward to read for the neophyte.

Most of the book is devoted to the lumbar spine, an area to which multiplanar CT is particularly well suited, and it is amply illustrated by large, well-reproduced, and convincing images. Joint and disk diseases, pars defects, and related conditions (as well as important postoperative observations) are discussed extensively.

Modifications of surgical techniques, inspired by multiplanar CT of the spine, are discussed by the contributing neurologic surgeon, Perry Camp. Cervical and thoracic spine diseases are treated somewhat more sparingly, although craniocervical abnormalities are described in useful detail.

The book concludes with a thorough discussion of technical aspects of multiplanar reconstruction as well as of the networking

system by which raw scan data are collected from remote scanners and whereby the final product—the array of multiplanar images—is redistributed to the end users.

Throughout, the book is richly illustrated and easy to read. The authors do not hide their opinion that multiplanar CT of the spine supersedes and supplants all other radiologic techniques—including contrast studies—for examination of the spine, particularly the lumbar spine; some readers may disagree with this point of view. The book assumes that many practitioners of multiplanar CT will be working in imaging centers and similar settings in which the radiologist will have little or no contact with patients and mainly postal communication with referring physicians; it may be argued that this is not the best environment for patient evaluation. References are, except in the technical chapters, fairly sparse, but do include major works and landmark papers.

Despite these drawbacks, I recommend *Multiplanar CT of the Spine* because it is the first major work on this highly useful and thought-provoking technique. The book will be of particular interest to neuroradiologists and osteoradiologists as well as to surgeons involved in treatment of disorders of the spine.

Folke J. Brahme
University of California, San Diego
Veterans Administration Medical Center
San Diego, CA 92161

Normal Variants and Pitfalls in Imaging. By James B. Bogler III, Clyde A. Helms, and Peter W. Callen. Philadelphia: Saunders, 683 pp., 1986. \$95

The acknowledgments section of this book states its purpose succinctly: to examine the normal variants that can simulate disease from an imaging point of view. It accomplishes this goal superbly. The book is organized both by organ and by imaging technique, which makes it easy to use as a reference.

The authors represent a talented group. Usually, when there are so many authors, the quality of the chapters varies significantly, but uniformity of style and presentation is one of the strongest points of this book. Moreover, the quality of the illustrations is good throughout. They are well labeled and have appropriate captions.

This book fills an important need. I learned a great deal from reviewing the book and plan to use it as a reference in my practice. I am sure that it would be a significant addition to the library of either a beginning or experienced imager. Also, I think that residents would find this book extremely attractive since it answers many of the questions that they might be reluctant to ask.

M. E. Bernardino
Emory University School of Medicine
Atlanta, GA 30322

Spontaneous Dissection of the Cervical Internal Carotid Artery: Correlation of Arteriography, CT, and Pathology

George R. Petro¹
 Gordon A. Witwer¹
 Edwin D. Cacayorin¹
 Charles J. Hodge²
 Carl E. Bredenberg³
 Michael S. Jastremski⁴
 Stephen A. Kieffer¹

Spontaneous dissection of the internal carotid artery is being recognized as a more frequent cause of acute neurologic deficit, particularly in young persons. Saccular pseudoaneurysm formation may be an associated finding, especially in the presence of tortuosity (coiling) of the cervical internal carotid artery. Of eight patients with nine vessels demonstrating internal carotid artery dissection on arteriography, pseudoaneurysms were found in five arteries. Four of the five pseudoaneurysms occurred in tortuous (coiled) arterial segments. Thin-section contrast-enhanced dynamic incremental CT showed close agreement with the findings on selective arteriography and provided additional information on the presence and configuration of arterial wall thickening as well as the extent of the pseudoaneurysm. Our experience indicates that CT may play an important role in the diagnosis, management, and follow-up of this lesion.

Spontaneous hemorrhagic dissection of the internal carotid artery (ICA) is becoming more widely appreciated as a cause of transient ischemic attack (TIA), or stroke, particularly in relatively young patients [1-4]. Diagnosis is usually based on demonstration by arteriography of a long, tapered, eccentric narrowing of the cervical ICA beginning above the common carotid bifurcation and extending superiorly to the level of the base of the skull [2] or occasionally into the carotid canal [4]. Saccular pseudoaneurysm formation may occur as a result of dissection [4], and sequential arteriograms often demonstrate rapidly changing patterns as the process proceeds to resolution, pseudoaneurysm formation, or further stenosis and occlusion [1, 2].

CT of the neck has recently been suggested as an accurate and relatively noninvasive method for diagnosis and sequential assessment of occlusive changes affecting the common carotid bifurcation and the proximal ICA [5, 6]. We have studied eight patients with spontaneous ICA dissection using sequential arteriography; dynamic thin-section CT of the neck was obtained in five individuals in order to more completely assess both luminal and mural changes in this still incompletely understood lesion.

Materials and Methods

Eight patients with spontaneous cervical ICA dissection were diagnosed on arteriography, including four women and four men, aged 23 to 54 years. Clinical presentations included initial head and neck pain followed by TIAs in two patients, TIAs in two (one with a remote history of severe neck pain), and acute hemispheric stroke in three. Two patients also manifested an ipsilateral incomplete Horner's syndrome. In one patient who suffered a single focal seizure and was being evaluated for possible intracranial mass, contralateral dissection with pseudoaneurysm was an incidental finding on arteriography.

All eight patients underwent percutaneous transfemoral selective common carotid arteriography. Arteriography was performed promptly after clinical presentation in five patients, after 5 weeks of intermittent symptoms in one, and 2 years after the likely initial event in another. Follow-up arteriograms were obtained in five patients at 2 weeks to 14 months after the initial study.

This article appears in the November/December 1986 issue of *AJNR* and the February 1987 issue of *AJR*.

Received January 15, 1986; accepted after revision May 2, 1986.

Presented at the annual meeting of the American Society of Neuroradiology, Boston, June 1984.

¹ Department of Radiology, SUNY Health Science Center of Syracuse, 750 E. Adams St., Syracuse, NY 13210. Address reprint requests to G. R. Petro.

² Department of Neurosurgery, SUNY Health Science Center of Syracuse, Syracuse, NY 13210.

³ Department of Surgery, SUNY Health Science Center of Syracuse, Syracuse, NY 13210.

⁴ Department of Critical Care and Emergency Medicine, SUNY Health Science Center of Syracuse, Syracuse, NY 13210.

AJR 148:393-398, February 1987
 0361-803X/87/1482-0393
 © American Roentgen Ray Society

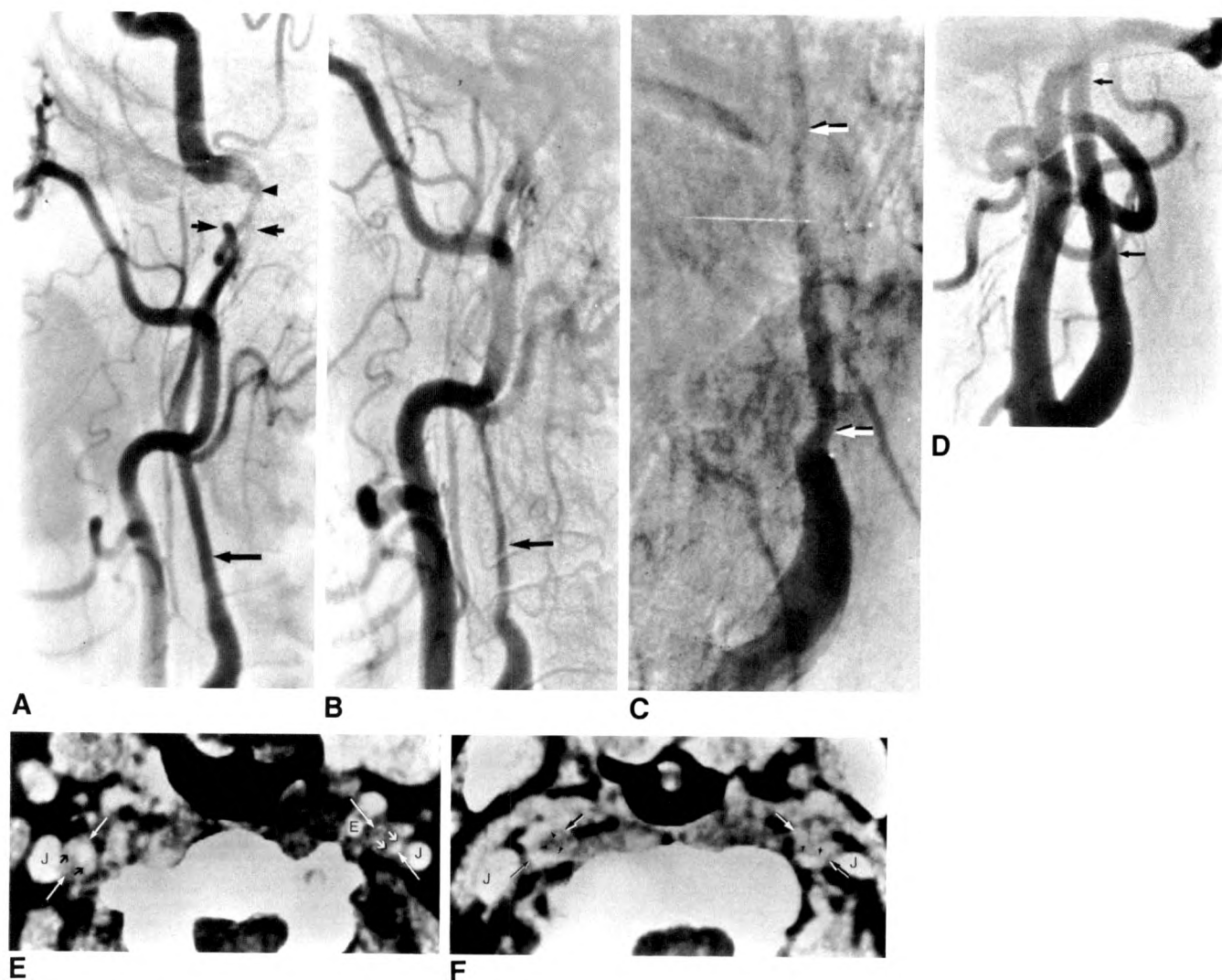


Fig. 1.—39-year-old man with left hemispheric ischemia and left incomplete Horner's syndrome after sneezing. **A**, Initial left common carotid arteriogram (lateral view) several hours after onset of symptoms demonstrates diffuse, smoothly tapering stenosis (*long arrow*) of cervical internal carotid artery with sparing of its most proximal segment. Maximal narrowing is noted in distal cervical segment (*short arrows*) with abrupt return to normal caliber within proximal carotid canal (*arrowhead*). **B** and **C**, Follow-up left common carotid arteriogram at 2 weeks. Lateral (**B**) and late arterial phase anteroposterior (**C**) views show more severe flow limiting narrowing of left cervical internal carotid artery (*arrows*). **D**, Another follow-up left common carotid arteriogram (anteroposterior projection) after 10 days of further anticoagulation demonstrates marked improvement in lumen diameter (*arrows*). **E**, On day of presentation,

axial CT with intravenous contrast at a level 2 cm above common carotid bifurcation displays eccentric luminal narrowing of internal carotid artery bilaterally, more pronounced on left side. *Long arrows* define external margins of both internal carotid arteries. Luminal compromise is due to mural thickening posterolaterally on right and anteromedially on left. (*Short arrows* indicate interface between opacified lumen and mural thickening; **E** = external carotid artery, **J** = internal jugular vein.) **F**, At level of C2 body, CT shows that intramural hematoma has spiraled medially on right side and anteriorly on left. Intramural hematoma has caused both luminal compromise (*arrowheads*) and enlargement of external dimension of vessels (*arrows*) as compared with lower level (**E**).

CT of the neck was obtained in five of the eight patients. In two patients, rapid-sequence, contiguous, 1.5-mm-thick axial images were obtained from C1 through C4 using a 100-ml rapid intravenous bolus injection with subsequent drip infusion of meglumine iothalamate 60% (Conray 60, Mallinckrodt). Three patients were scanned using overlapping 5-mm-thick sections (3-mm table incrementation) during a prolonged intravenous bolus injection of 150 ml of Conray 60. Reformatting of axial scan data was carried out in various paraxial and oblique planes. The thickness of the arterial wall (not discernible on axial CT images of the neck in normal individuals) and the size of the opacified lumen were evaluated on the axial CT images.

Four patients subsequently underwent segmental resection of a

saccular pseudoaneurysm of the high cervical ICA; gross and histologic analyses of the resected specimens were correlated with CT and arteriographic findings. No patient with internal carotid stenosis alone was treated surgically.

Results

Arteriography

Initial selective arteriograms demonstrated findings consistent with spontaneous dissection in one ICA in seven patients and in both ICAs in one patient. In seven of the nine

involved vessels, the arterial lumen was narrowed, and in two of these the narrowing was associated with an adjacent pseudoaneurysm. In two vessels, no luminal narrowing was evident but saccular pseudoaneurysms were demonstrated in the high cervical region.

Six of the seven ICAs with luminal narrowing demonstrated long stenotic segments extending to or beyond the skull base. The luminal narrowing in four vessels was smoothly tapered, becoming progressively more stenotic distally; the narrowing was relatively uniform and symmetric in two arteries and was

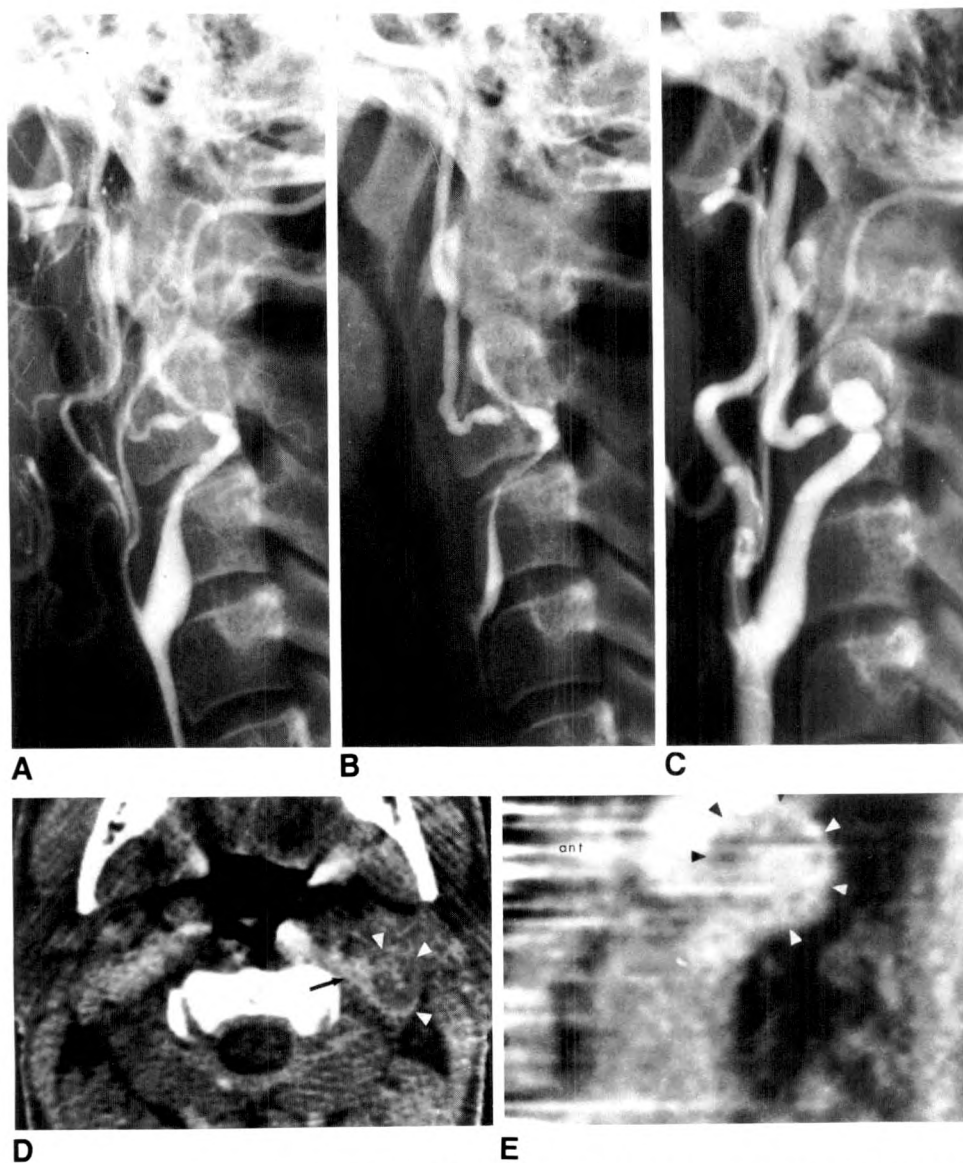


Fig. 2.—46-year-old man studied after 5 weeks of left supraorbital pain and left incomplete Horner's syndrome. **A** and **B**, Left common carotid arteriogram, mid (**A**) and late (**B**) arterial phases (lateral views), demonstrating irregular stenosis of coiled left cervical internal carotid artery. Similar coiling but without narrowing was present on right side. **C**, Left common carotid arteriogram (lateral view) 8 weeks after onset of symptoms. There has been considerable resolution of luminal narrowing, but a pseudoaneurysm is now identified in coiled segment. **D**, At 7 weeks (1 week before follow-up arteriogram), axial CT with intravenous contrast at level of C2 demonstrates a mass inseparable from left carotid sheath structures containing contrast medially (arrow) with a lucent region laterally (arrowheads). **E**, Sagittal reconstruction obtained from consecutive 1.5-mm-thick axial slice data demonstrates, despite artifacts from dental amalgam, true extent of partially thrombosed pseudoaneurysm (arrowheads), which projects superiorly and posteriorly off coiled internal carotid artery. Superior portion of mass contains lucent clot. **F**, Photomicrograph of surgical specimen. Portion of dissection (**D**) is seen within arterial wall contained by a thin layer of contrast medium (arrows) and overlying adventitia (L = true lumen).

eccentric in two vessels (Fig. 1A). In two arteries, the stenosis was not progressively tapering but rather varied in degree with focal areas of irregularity, which, in one patient, were located within a tortuous (coiled) segment of the cervical ICA (Figs. 2A and 2B). Luminal stenosis extended in continuity from the cervical through the intracranial and cavernous segments of the ICA in one patient in whom the supraclinoid ICA was completely occluded, presumably by an embolus. Stenosis of the seventh ICA began 3 cm above the common carotid bifurcation and extended to the midportion of the cervical ICA, which was severely coiled.

Follow-up angiography was performed in five patients at 2, 3, 3 1/2, 20, and 60 weeks after initial evaluation and institution of anticoagulant therapy. In all three patients reevaluated within 4 weeks of clinical presentation, residual narrowing was still present but was much reduced in severity, with the configuration being similar to that seen on initial arteriography. However, the single patient with bilateral involvement initially showed a unilateral increase in stenosis on the symptomatic side at 2 weeks with subsequent improvement after 10 days of further anticoagulation (Figs. 1B–1D). The 20-week follow-up arteriogram in a patient with severe tapered narrowing and pseudoaneurysm formation revealed minimal residual stenosis. Although follow-up arteriography demonstrated improvement or complete resolution of luminal narrowing in all five patients so studied, concomitant enlargement of a pseudoaneurysm was noted in one individual, evolution of an apparent fusiform dilatation into a large saccular pseudoaneurysm was demonstrated in another, and a new pseudoaneurysm was identified in a third patient (Fig. 2C).

Saccular pseudoaneurysms were encountered in five of the nine involved arteries, three on the initial arteriogram and two on follow-up studies. Four of the five pseudoaneurysms arose on coiled arterial segments (Fig. 2).

Arteriography also revealed occlusion of the supraclinoid ICA in one patient and of branches of the middle or anterior cerebral arteries in four, all likely embolic in origin.

Computed Tomography

Dynamic incremental CT examinations were obtained in five patients (six vessels). The diameters and configurations of the opacified arterial lumina on CT were in close agreement with the findings on arteriography in all six. Thickness and configuration of the arterial wall, findings not appreciable on arteriography, were clearly depicted on CT (Figs. 1E and 1F). Mural thickening was demonstrated on CT in all five vessels exhibiting narrowing on arteriography. The mural thickening was eccentric in distribution and was noted to spiral around the vessel from level to level with attenuation values comparable to adjacent muscles. In a normal ICA, the arterial wall is not identifiable on CT.

Mural thickening causing enlargement of total vessel dimension was demonstrated on CT in three of six involved arteries with total external diameter (lumen and walls) increased from 1.5 to 3 times that of adjacent ipsilateral or similar contralateral ICA segments. The greatest degree of external widening was recorded in association with a pseudoaneurysm that was not evident on the initial arteriogram 2

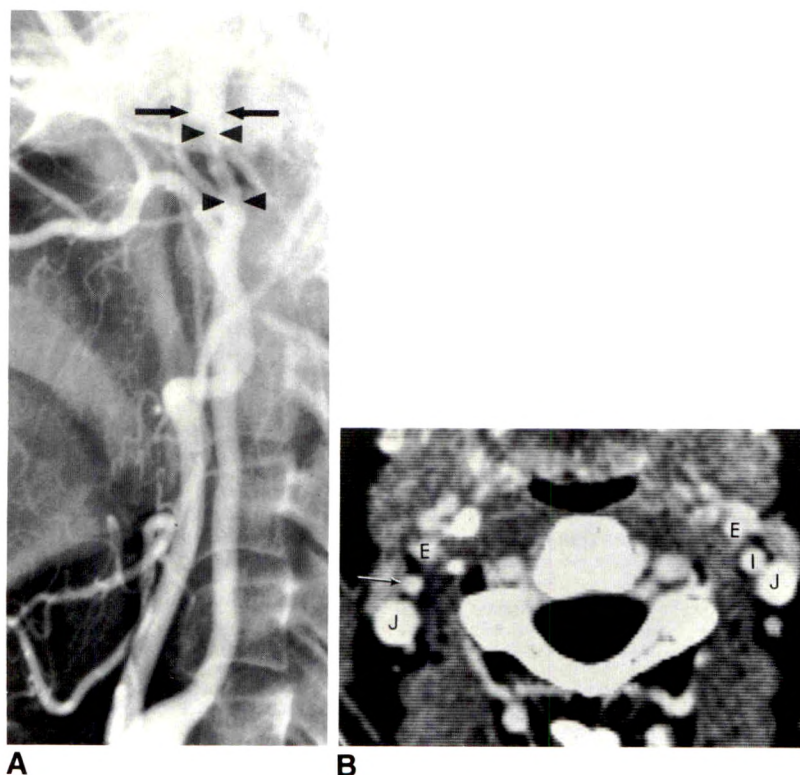


Fig. 3.—Overestimation of longitudinal extent of internal carotid artery dissection by angiography in a 39-year-old woman with right-sided headache, neck soreness, and intermittent transient ischemic attacks. **A**, Three days after initial symptoms, right common carotid arteriogram (lateral projection) shows diffusely narrowed cervical internal carotid artery with irregular, more severe narrowing distally (arrowheads) and abrupt reconstitution of lumen at its entrance into carotid canal (arrows). **B**, Proximally, axial CT image reveals relatively small lumen of right internal carotid artery (arrow) but without mural thickening to indicate dissection at this level (I = internal carotid artery, E = external carotid artery, J = internal jugular vein).

weeks earlier; axial CT images revealed an ill-defined, partially opacified, 2-cm-thick carotid sheath mass (Fig. 2D), but paraxial reformatted images better depicted the partially thrombosed pseudoaneurysm on a coiled ICA (Fig. 2E). Follow-up arteriography 1 week after the CT study confirmed the evolving pseudoaneurysm but underestimated its true extent (Fig. 2C).

In two dissected vessels, CT demonstrated mural thickening resulting in luminal compromise but without significant overall external enlargement. In one of these, CT not only confirmed the diffusely small lumen but also revealed mural thickening of only the distal half, indicating only distal dissection (Fig. 3). In another patient, CT confirmed the angiographic finding of a 3-mm saccular pseudoaneurysm on a tightly coiled ICA in which there was no luminal narrowing.

Clinical Course

Of the seven symptomatic patients in this series, four underwent successful surgical resection of their saccular pseudoaneurysms with reanastomosis, and three were treated with intravenous heparin. All seven initially symptomatic patients were either clinically improved or normal after surgery or heparinization, and none experienced recurrent neurologic deficits after therapy. One of the eight patients was asymptomatic from dissection, and no treatment was instituted.

Pathology

Gross and histologic examination of the four resected saccular pseudoaneurysms demonstrated intimal tears at the level of the proximal aspect of the pseudoaneurysm in all four. In each case, dissection occurred into the outer media (Fig. 2F) and, in two cases, extended into the plane between the media and the adventitia of the arterial wall. No identifiable predisposing atherosclerotic or other underlying pathologic changes were identified within the resected specimens.

Discussion

The cause of spontaneous hemorrhagic dissection of the ICA remains unknown. Affected individuals most typically present in the second through fifth decades of life with acute ischemic neurologic deficits [1-4]. If this is concurrent with or preceded by head or neck pain or occurs in association with an incomplete Horner's syndrome (as was the case in two of our patients) or with a subjective bruit, cervical internal carotid dissection must be strongly suspected [7].

Cervical ICA dissections have been reported after vigorous nose blowing [8], and a possible association with repeated coughing has been suggested [2]. One patient in our series experienced the onset of symptoms after an episode of repeated forceful sneezing, while another patient gave a history of recent chiropractic manipulation. In such instances, a causal versus a coincident association with apparently minor trauma can be suspected but not proven.

Occlusions of the intracranial ICA or its branches consistent

with an embolic origin were identified on arteriography in five of our seven symptomatic patients. This suggests that the cause of the ischemic neurologic symptoms is often embolic in nature rather than purely hemodynamic. In their report of 42 patients with spontaneous ICA dissection, Houser et al. [4] noted a 15% incidence of intracranial arterial occlusions likely secondary to emboli on angiography.

Most stenoses (up to 80% of reported case series) due to cervical ICA dissection appear on follow-up angiography to partially or completely resolve with time [1, 4, 9, 10]. Follow-up angiography in six stenotic cervical ICA dissections in this series showed significant improvement or complete resolution in all six involved vessels after 2 to 20 weeks of anticoagulant therapy (Figs. 1 and 2). In one of these cases, however, the stenosis progressed to near occlusion before delayed resolution with further anticoagulation (Figs. 1A-1D). Progression to complete occlusion was reported by Ehrenfeld and Wylie [1] in one of six stenoses and by Houser et al. [4] in three of 15 stenoses at repeat angiography.

Saccular pseudoaneurysms were identified in five of nine internal carotid dissections (56%) in this series. The formation of a pseudoaneurysm as a sequela of arterial dissection and the subsequent course of this lesion is a dynamic and variable phenomenon. Fisher et al. [2] and Houser et al. [4] followed a total of 13 pseudoaneurysms with sequential arteriograms showing four to be unchanged, six to have decreased in size, three to have essentially resolved, but none to have enlarged. In two of our patients and in a case reported by Bostrom and Liliequist [11], enlargement of a pseudoaneurysm was documented on serial studies, and late development of a saccular pseudoaneurysm not evident on initial examination occurred in another patient in this series (Fig. 2). Delayed appearance of a pseudoaneurysm has been reported in approximately 5% of internal carotid dissections in larger series [2, 4, 12].

Marked tortuosity (coiling) of the cervical ICAs has been reported in 3% of a large series of carotid arteriograms [13]. Four of the five pseudoaneurysms in this series occurred on such coils, while none of the four dissected vessels with narrowing alone were coiled. While an association of tortuosity of the cervical portion of the ICA with dissection has been previously noted [1, 3], the association of pseudoaneurysm and ICA coiling apparent in this small series has not been previously stressed. It is our impression that demonstration of an aneurysm-like outpouching of the arterial lumen on a coiled midcervical ICA makes dissection a preferred diagnosis. When dissection occurs in an area of coiling, the likelihood of subsequent pseudoaneurysm formation may be significantly increased, and follow-up sequential imaging (arteriography or CT) would assume greater importance.

Thin-section dynamic incremental CT with contrast enhancement demonstrated in all six vessels so studied that CT accurately assessed lumen size. Mural thickening was demonstrated in the five vessels showing narrowing on arteriography. In one case, CT established the initial diagnosis of a partially thrombosed pseudoaneurysm, characterizing its true extent, which was underestimated on subsequent arteriography (Fig. 2).

Thin-section CT with intravenous contrast infusion has

demonstrated the occurrence and extent of intraplaque hemorrhage in patients with atherosclerotic involvement at the common carotid bifurcation [6]. Our experience indicates that CT may also play an important role in the diagnosis and management of hemorrhagic dissection of the ICA. The longitudinal extent of the dissection and the full extent of an associated pseudoaneurysm can be accurately discerned, a prerequisite in those cases requiring surgical intervention. CT may prove more accurate than arteriography in differentiating luminal narrowing secondary to dissection from luminal collapse due to spasm or marked diminution in flow (Fig. 3). In patients in whom the diagnosis of cervical ICA dissection remains in doubt after arteriography, CT can be supportive if enlargement of the external dimension of the stenotic vessel is demonstrated. CT may also be useful as an alternative to arteriography in the follow-up of an arterial dissection.

ACKNOWLEDGMENTS

The authors gratefully acknowledge the contributions of George H. Collins, for histologic evaluation of the surgical specimens, and Maria Pembroke, for manuscript preparation.

REFERENCES

1. Ehrenfeld WK, Wylie EJ. Spontaneous dissection of the internal carotid artery. *Arch Surg* 1976;111:1294-1300
2. Fisher CM, Ojemann RG, Roberson GH. Spontaneous dissection of cervicocerebral arteries. *Can J Neurol Sci* 1978;5:9-19
3. Luken MG, Ascherl GF, Correll JW, Hilal SK. Spontaneous dissecting aneurysms of the extracranial internal carotid artery. *Clin Neurosurg* 1979;26:353-375
4. Houser OW, Mokri B, Sundt TM Jr, Baker HL, Reese DF. Spontaneous cervical cephalic arterial dissection and its residuum: angiographic spectrum. *AJNR* 1984;5:27-34
5. Heinz ER, Pizer SM, Fuchs H, et al. Examination of the extracranial bifurcation by thin-section dynamic CT: direct visualization of intimal atheroma in man (Part I). *AJNR* 1984;5:355-359
6. Leeson MD, Cacayorin ED, Iliya AR, et al. Atheromatous extracranial carotid arteries: assessment using CT compared with arteriography and pathologic examination. *Radiology* 1985;156:397-402
7. Mokri B, Sundt TM Jr, Houser OW. Spontaneous internal carotid dissection, hemiparesis, and Horner's syndrome. *Arch Neurol* 1979;36:677-680
8. Roome NS, Aberfeld DC. Spontaneous dissecting aneurysm of the internal carotid artery. *Arch Neurol* 1977;34:251-252
9. Quisling RG, Friedman WA, Rhoton AL. High cervical carotid artery dissection: spontaneous resolution. *AJNR* 1980;1:463-468
10. Deramond H, Remond A, Rosat P, Froissart M, Dobbelaere P, Trinez G. Spontaneous evolution of non-traumatic dissecting aneurysms of the cervical portion of the internal carotid artery. *J Neuroradiol* 1980;7:167-182
11. Bostrom K, Liliequist B. Primary dissecting aneurysm of the extracranial part of the internal carotid and vertebral arteries: a report of three cases. *Neurology (NY)* 1967;17:179-186
12. O'Dwyer JA, Moscow N, Trevor R, Ehrenfeld WK, Newton TH. Spontaneous dissection of the carotid artery. *Radiology* 1980;137:379-385
13. Weibel J, Fields WS. Tortuosity, coiling and kinking of the internal carotid. I. Etiology and radiographic anatomy. *Neurology (Minneapolis)* 1965;15:7-18

Magnetite Albumin Microspheres: A New MR Contrast Material

Donald J. Widder^{1,2}
W. Lawrence Greif¹
Kenneth J. Widder³
Robert R. Edelman¹
Thomas J. Brady^{1,4}

A superparamagnetic MR contrast agent was synthesized by incorporating 150–250-Å particles of magnetite (Fe_3O_4 , Fe_2O_3) in 1–5 μm human serum albumin microspheres. Magnetite albumin microspheres (MAM) target almost exclusively to the reticuloendothelial system after IV administration, are stable in vitro and in vivo, and possess a long shelf life. The agent has a large magnetic susceptibility effect that selectively reduces T2 with little effect on T1. Biodistribution studies that use a dose of 20 mg MAM/kg show prompt clearance from the blood pool with marked decrease in T2 for rat liver (40%) and spleen (45%) with a small decrease in liver (5%) and spleen (10%) T1 values. Pulmonary T1 and T2 decrease transiently over the first 24 hr, while no significant changes were observed in other tissues. Imaging of a rabbit VX2 tumor model resulted in a 200% increase in the contrast ratio of VX2 tumor to normal liver on T2-weighted and mixed T1-/T2-weighted pulse sequences after administration of contrast agent. The extreme potency, excellent targeting, and apparent lack of toxicity of this agent suggest that MAM probably will have a clinical application in detecting focal hepatic and splenic lesions.

Despite excellent soft-tissue contrast, MR imaging to date has shown no clear superiority over CT, sonography, or nuclear scintigraphy for the evaluation of focal liver disease [1]. Gadolinium DTPA (Gd-DTPA) contrast-enhanced MR studies of the brain have been shown to be helpful in characterizing CNS disease [2]. However, Gd-DTPA distributes randomly in the interstitial space, often obscuring rather than enhancing hepatic lesions by decreasing T1 differences of normal liver and tumor [2]. Chelates of paramagnetic ions shorten both T1 and T2, but their image contrast effect in the dose range studied is predominantly the result of reduction in T1. This study describes a new class of superparamagnetic contrast material that selectively enhances contrast between normal and pathologic tissue by augmenting T2 differences.

A reliable, safe reticuloendothelial-system (RES) MR contrast material that aids in differentiating normal and pathologic tissue has not been described. Tumor involvement of the liver consistently increases T1 and T2 relaxation but to a variable degree, resulting in false-negative MR studies if the chosen pulse sequences do not maximize contrast between tumor and normal tissue. Conditions resulting in abnormally high levels of parenchymal iron (such as transfusional hemosiderosis in liver, spleen, and pancreas or in the brain with chronic hemorrhage) result in decreased tissue signal on T1- and T2-weighted images [3–5], which suggests the potential use of particulate or aggregate nonsoluble iron compounds as T2 MR contrast material. This study evaluates subcapillary size magnetite albumin microspheres (MAM) as a liver/spleen MR contrast agent. MAM rapidly distributes to the RES and closely mimics the decrease in hepatic T2 seen in iron-storage disease states. The desired benefits of such an agent include (1) improved sensitivity in detecting and characterizing hepatic lesions, (2) shortening imaging time by using a predictable optimal pulse sequence, and (3) labeling RES function and turnover.

Received February 7, 1986; accepted after revision September 19, 1986.

Presented at the annual meeting of the American Roentgen Ray Society, Washington, DC, April 1986, where it received the Executive Council Award, second place for papers by radiology residents.

This work was supported by the Research Laboratories of Molecular Biosystems, Inc., San Diego. T. J. Brady is supported by U. S. Public Health Service grant 1 KO4 CA00848–03, awarded by the National Cancer Institute, Department of Health and Human Services; by American Cancer Society grant PDT–145; and by Technicare Corp., Solon, OH.

¹Department of Radiology, Massachusetts General Hospital, Boston, MA 02114.

²Present address: Department of Radiology, Santa Barbara Cottage Hospital, P. O. Box 689, Santa Barbara, CA 93102. Address reprint requests to D. J. Widder.

³Molecular Biosystems, Inc., San Diego, CA 92121.

⁴Medical Service, Massachusetts General Hospital, Boston, MA 02114.

AJR 148:399–404, February 1987
0361–803X/87/1482–0399
© American Roentgen Ray Society

Materials and Methods

Magnetite Albumin Microspheres: Preparation and Characterization

A modified water in oil emulsion polymerization method is used to prepare microspheres measuring approximately 1–5 μm in diameter and consisting of denatured human serum albumin matrix in which magnetite particles 150–250 Å in size are embedded (Fig. 1). In the experiments described, the following preparation was used [6]. An aqueous solution of human serum albumin (Sigma, St. Louis) and magnetite (Fe_3O_4) in the form of aqueous suspension (Ferrofluidics Corp., Nashua, NH) was made in distilled water. Aliquots of this suspension were homogenized in cottonseed oil (Sargent Welch, Skokie, IL) by sonication for 1 min. The homogenate was then added dropwise to stirred cottonseed oil kept at a constant temperature of 135°C. After 10 min, the emulsion was removed from the heat and stirred until cooled. Microspheres were washed free of the oil by centrifugation in anhydrous ether; they were washed free of ether and resuspended in 0.1% Tween 80 in 0.15 N saline. Microspheres were stored in a 10 mg/ml suspension. Before use, the microsphere suspension was vigorously agitated without sonication. The uniformity of size of the microspheres was checked with light microscopy.

Rat Biodistribution and Dose-Response Studies

Biodistribution and dose-response studies were obtained in male Sprague-Dawley rats weighing 300–400 g. The rats were anesthetized with intraperitoneal pentobarbital (35 mg/kg). Through a tail vein, injections were made of a serial concentration of 5–50 mg/kg MAM, 10% magnetite by weight. At 30 min, the animals were sacrificed by cervical dislocation, and tissues were obtained for T1 and T2 analysis. Samples included blood (obtained by cardiac puncture), liver, spleen, kidney, lung, and thigh muscle (obtained by excision). In all samples, T1 and T2 measurements were obtained within 45 min of death, and three samples were obtained at each dose and time point.

All T1 and T2 relaxation measurements were performed with an IBM PC-20 Minispec pulse MR spectrometer (IBM, Danbury, CT) at 0.47 T. Values of T1 and T2 represent an average of three consecutive measurements.

Normal Rat Imaging Studies

MR imaging of rats and rabbits was performed with a horizontal-bore (8 cm) superconducting magnet system (Technicare Corp., Solon, OH) at a magnetic field strength of 1.4 T. Images were acquired by using a two-dimensional Fourier transform technique with a 3-mm slice thickness and a 256×128 acquisition matrix. Various T1- and

T2-weighted pulse sequences were used. Signal-to-noise (S/N) ratios were calculated as *tissue signal/background deviation*. S/N measurements were normalized for time (6 min/image) where $\text{S/N normalized} = \text{S/N} \div \sqrt{\text{acquisition time}}$.

Male Sprague-Dawley rats (approximately 400 g) were anesthetized, securely placed on a calibrated carrier, and inserted into the magnet. Tubes containing paramagnetically doped water or agar gels of known T1 and T2 were placed alongside the animal. Baseline images were obtained to optimize liver position within the imaging plane. After baseline images, animals were removed from the magnet, and IV MAM saline suspension was injected at a dose of 20 mg/kg animal weight. The position of the animal was not altered during the injection of MAM and the reinsertion of the animal into the magnet. Sequential imaging was performed at 2 and 4 months after infusion.

Rabbit VX2 Tumor Model

VX2, a transplantable carcinoma, was implanted by direct laparoscopic intrahepatic implantation into the liver of a New Zealand white rabbit weighing 800 g [7]. This tumor reaches approximately 1 cm in size and creates nodular metastases within the liver during the first 3 weeks after implantation. Serial images of the liver were obtained with various T1- and T2-weighted pulse sequences before and within 10 min after IV infusion of 20 mg MAM/kg into the rabbit ear. The change in contrast-to-noise (C/N) after MAM administration was calculated as $\text{preinfusion C/N} - \text{postinfusion C/N}$, determined by measuring C/N between normal tissue and tumor with T1, mixed T1/T2, and T2-weighted pulse sequences before and after MAM administration. C/N is defined as $\text{liver signal} - \text{tumor signal/background deviation}$ [8].

Toxicity Studies.

Serial concentrations of MAM (100, 200, and 300 mg/kg) were injected in nine Sprague-Dawley rats (three rats/dose), and toxicity was assessed immediately and over the course of 1 week after injection.

Histologic Studies

Iron stain and collagen stains were obtained on liver histologic samples at 2 weeks and 2 months after MAM administration.

Results

The concentration of the agent in various tissues over time (biodistribution) is indicated by T1 and T2 changes caused by the agent.

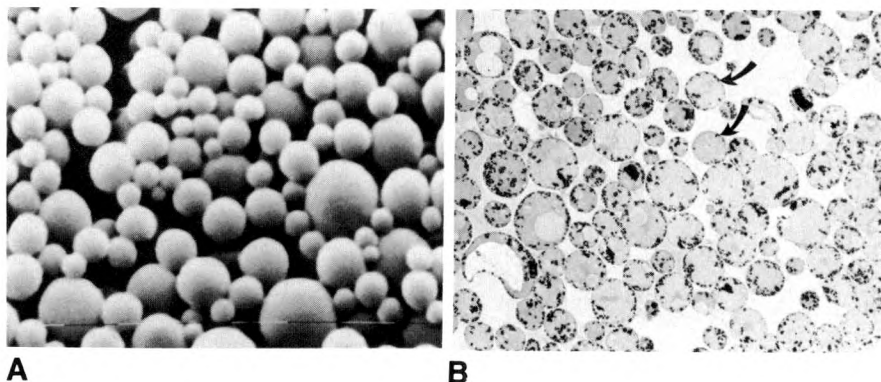


Fig. 1.—A, Scanning electron micrograph of MAM shows relative uniformity of spheres, which are subcapillary in size. Range of microsphere size used in this study is approximately 1–5 μm . Micrometer bar indicates size for both A and B. B, Transmission electron micrograph of microspheres, which consist of shell of denatured human serum albumin in which 150- to 250-Å magnetite particles, dark spots (arrows), are embedded.

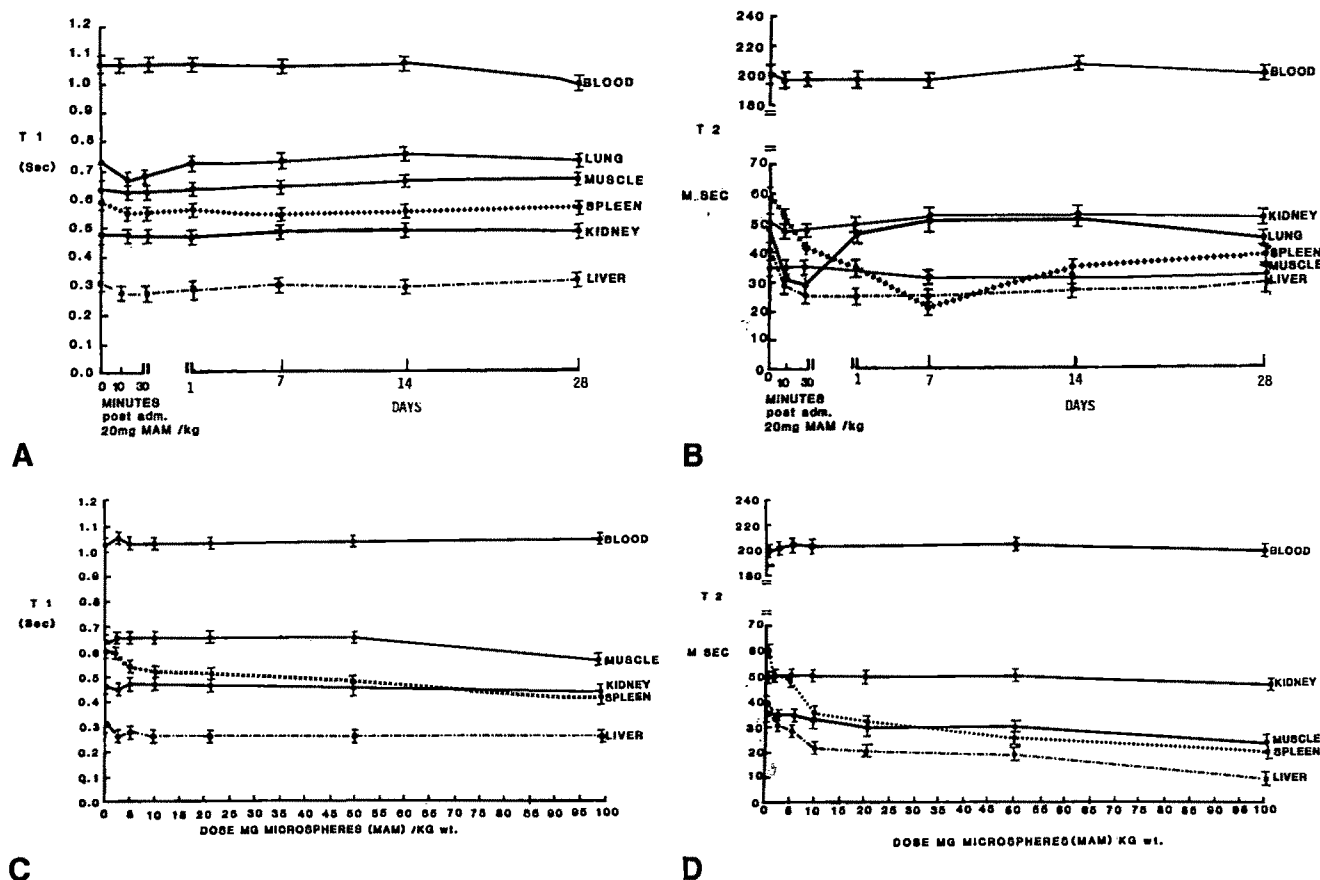


Fig. 2.—A and B, Longitudinal biodistribution. C and D, Dose/response data.

Results of biodistribution studies are summarized in Figure 2. The longitudinal biodistribution study (Figs. 2A and 2B) after administration of 20 mg MAM/kg shows no change in blood and renal T1 and T2 relaxation compared with precontrast control values, within 10 min after infusion. This indicates rapid clearance in the microspheres from the blood pool. There is a small decrease in hepatic and splenic T1 over 4 weeks. However, there is a dramatic 40% drop in hepatic and 45% drop in splenic T2 after microsphere administration. Hepatic T2 reduction persists for 4 weeks after infusion, but there is partial return to normal precontrast splenic T2 values, particularly at 2–4 weeks after infusion.

Dose-response data (Figs. 2C and 2D) show only a 10% decrease in splenic T1 and 5% decrease in hepatic T1 with increasing doses up to 100 mg/kg. There is a near-logarithmic decrease in hepatic and splenic T2 with increasing dose that is most pronounced in the low dose range. Blood, kidney, and muscle T1 and T2 are unchanged even with doses of 100 mg/kg.

Peak hepatic effect is observed within 10 min after infusion, with decrease in signal or blackening of the liver from decreased T2 in both strongly T1- and T2-weighted pulse sequences (Fig. 3). With all pulse sequences, hepatic signal decreases persistently at 2 and 4 months after infusion (Fig. 4). Liver histology specimens ($n = 2$) submitted for iron stain (obtained within 30 min after infusion of 20 mg MAM/kg) show exclusive uptake of microspheres by hepatic Kupffer cells (Fig. 5). Electron microscopy shows intracellular localization in phagosomes of resting monocytes or Kupffer cells (Fig. 6).

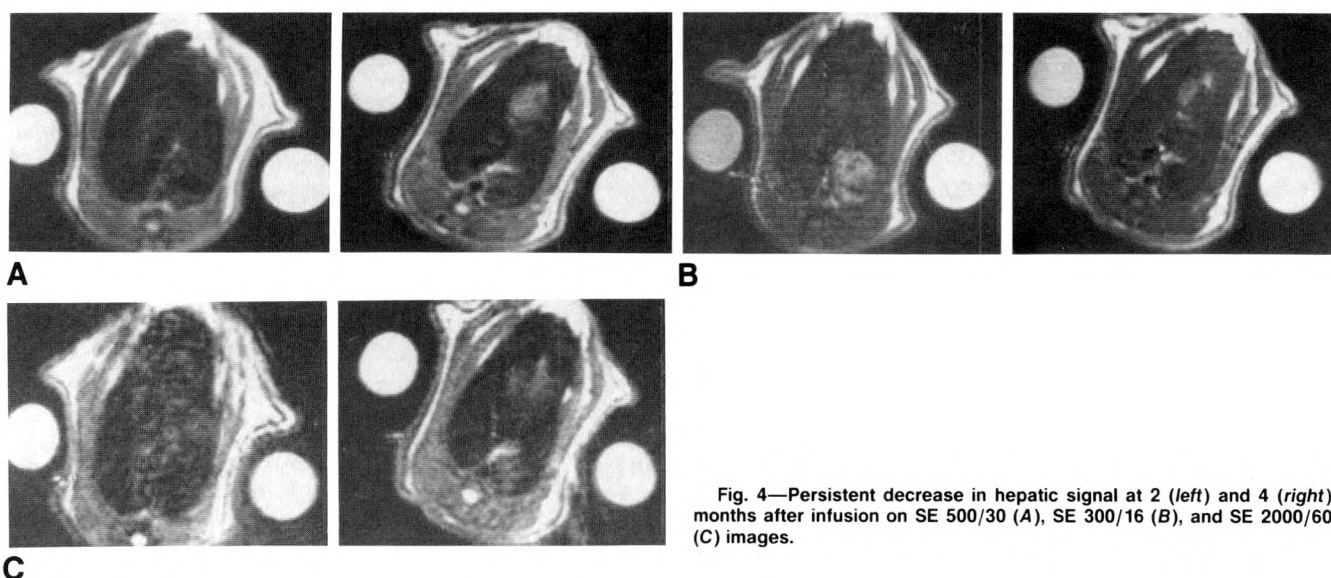
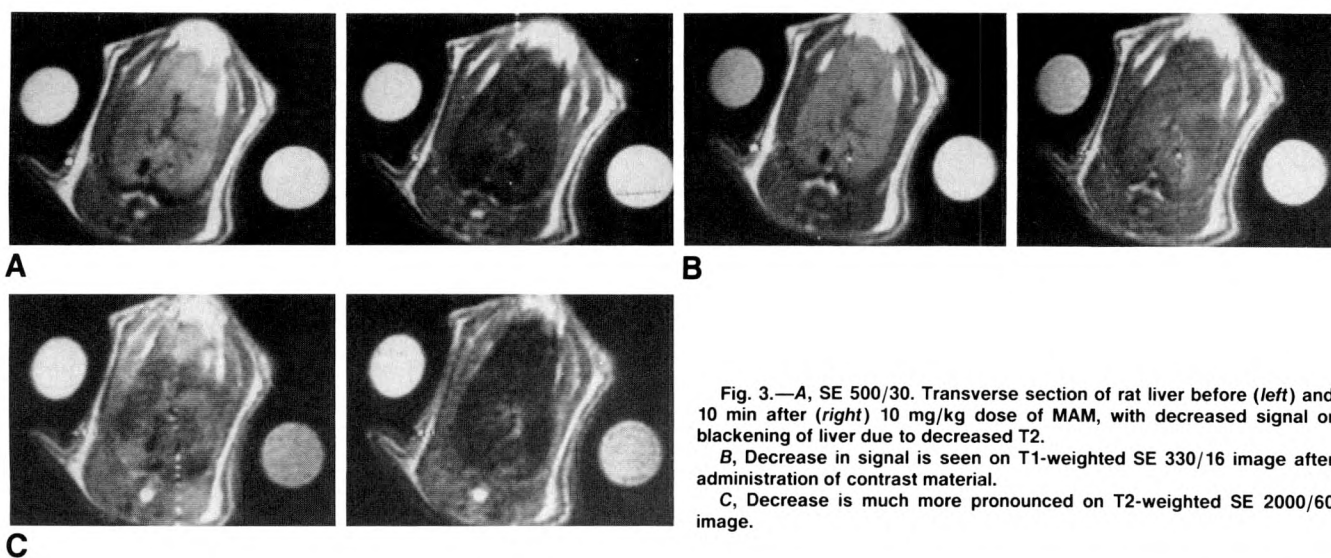
Within 20 min after a 20 mg/kg dose of microspheres in rabbits implanted with VX2 hepatic carcinoma, a marked reduction of signal

occurs in normal liver. Tumor that replaces RES and has a long T2 appears bright because the dropout in signal of adjacent normal tissue and tumor margins is well defined (Fig. 7). The tumor appears as an area of increased signal with T2-weighted, mixed T1/T2 weighted, and even strongly T1-weighted pulse sequences. Tumor is most apparent on mixed T1/T2- and strongly T2-weighted pulse sequences with a 200% increase in the C/N after MAM infusion. Spectroscopy shows a 53% increase in T2 contrast ($T2_{\text{tumor}} - T2_{\text{normal}}$) between tumor and liver after MAM. The appearance of the tumor correlates well with gross pathology and histology of the liver tumor specimen.

A limited toxicity study with injection of 100, 200, and 300 mg MAM/kg (three rats/dose) in nine Sprague-Dawley rats (300-g males) resulted in no acute or subacute (1 week) deaths or apparent morbidity. At 2 months after administration of 20 mg MAM/kg, no hepatocellular damage or evidence of fibrosis was seen.

Discussion

Paramagnetic materials, which have one or more unpaired electrons, have been extensively evaluated as MR contrast agents. Enhancement results predominantly from T1 reduction. While iron in its ionic form is paramagnetic, clusters of iron ions create a collective domain, with a magnetic moment much greater than the sum of the paramagnetic ions. In this clustered or particulate form, iron is superparamagnetic or ferromagnetic. Particulate iron less than 300 Å in size, such



as magnetite, is superparamagnetic; larger particles are ferromagnetic. Both have a much larger magnetic susceptibility than paramagnetic material [9]. The use of ferromagnetic particles as an MR contrast material has been evaluated concurrently with this study [10].

Magnetization of MAM increases in a nonlinear manner with increased applied external field of 0.3–0.9 T, with minimal increase above 0.9 T [11]. Magnetization is rapidly lost when the superparamagnetic species is removed from the external field, unlike ferromagnetic materials, in which magnetization persists. This low remanence or residual magnetization prevents clumping or aggregation of microspheres because of attraction between magnetized particles that would adversely

affect its biodistribution. The large magnetic moment of superparamagnetic material generates local field inhomogeneities and presumably promotes dephasing of proton spins and acceleration of transverse relaxation [12, 13]. Magnetite therefore exhibits a different relaxation mechanism than soluble paramagnetic contrast agents such as Gd-DTPA, which show equal enhancement of T1 and T2 relaxation, obeying the Solomon-Bloembergen equations [14]. The exact mechanism for promoting T2 relaxation is, however, not known and may be a combination of accelerated dephasing of proton spins from microfield inhomogeneity and local diffusion.

The marked enhancement of T2 relaxation with negligible T1 effects seen with magnetite is probably independent of

Fig. 5.—Liver histology specimen (iron stain) 30 min after infusion of 20 mg MAM/kg shows exclusive uptake of microspheres by hepatic Kupffer cells.

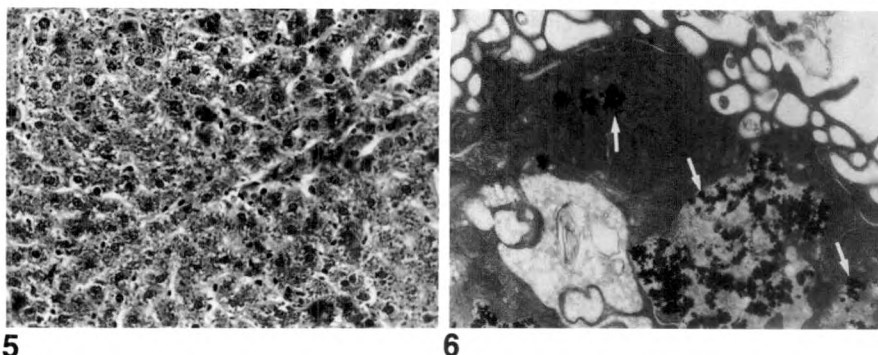


Fig. 6.—Intracellular localization of MAM in phagosomes of resting monocytes seen with electron microscopy (arrows).

5

6

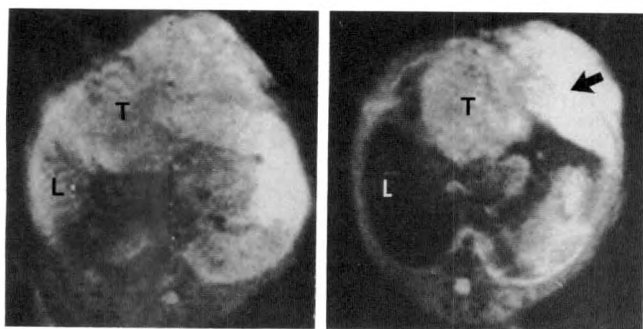


Fig. 7.—Rabbit with implanted VX2 hepatic carcinoma. Transverse section of liver shows essentially isosignal mass (T) distorting hepatic architecture (L) on SE 500/30 pulse sequence. At 10 min postcontrast there is marked reduction of signal in normal liver. Tumor that replaces reticuloendothelial system has long T2, appears bright, and has well-defined margins. Extrahepatic component of tumor (arrow) is now apparent. Increase in tumor-liver contrast/noise is 200% after MAM.

direct contact with free mobile protons. Therefore, the coupling of the superparamagnetic species to a carrier should be achieved with minimal or no loss of magnetic susceptibility, unlike the adverse effects of chelation on paramagnetic species. The acquired magnetic moment depends on microsphere diameter, fraction of magnetite, and density, and it is expressed by the Langevin equation [10]. T2 effects may be observed with ferromagnetic materials. These materials are probably less desirable, however, because the long-term biologic effects of local remanent fields after magnetization in vivo are unknown.

Targeting of MAM is superior to that of previously described MR contrast materials. Water-soluble chelates such as Gd-DTPA distribute randomly in the vascular and interstitial space and can decrease T1 contrast between normal and pathologic hepatic lesions [2]. Our results confirm the rapid clearance of MAM by the RES, particularly hepatic, after IV injection. The RES, which has been the mainstay of radiosciintigraphic study of liver and spleen disease, is the optimal target tissue for evaluating focal lesions, which are largely devoid of RES tissue. Hepatocytes appear protected from potential toxicity of MAM, which is sequestered in the RES, while they experience the local field inhomogeneities generated by the superparamagnetic agent. Significant tissue damage has not been

seen even with iron-overload states where the RES is exclusively involved [3]. The long-term retention of MAM allows follow-up examination in patients being screened for metastatic disease without readministration of contrast material.

The main proposed use of MAM is for the improved detection of hepatic and splenic focal lesions that displace reticuloendothelial tissue. By shortening T2, MAM markedly reduces the signal from normal parenchyma, which contains phagocytic Kupffer cells. Because MAM can only enter target cells by phagocytosis [15], its localization is restricted primarily to intracellular phagosomes (Fig. 5). Uptake is excluded from most primary and metastatic neoplasms, since they are nonphagocytic. Our initial experience indicates that this agent should improve sensitivity in detection of focal liver lesions because of the markedly improved T2 contrast between tumor and normal parenchyma.

Previous toxicity studies in a large series of rats and mice have been encouraging; they show an LD₅₀ of approximately 350 mg/kg (Widder KJ, unpublished data). Published toxicity studies in mice of MAM 1–1.5 μ m in size reveal negligible adverse effects both in acute and chronic studies, even at 400 mg MAM/kg [16]. In our limited study in rats, no deaths or toxic effects were noted at doses up to 300 mg MAM/kg.

No immunogenicity has yet been noted in animal studies. No reports have indicated that microspheres or microaggregates promote intravascular coagulation, a theoretical problem with large albumin microspheres that are embolic in size, as well as with liposomes that provide a lipid surface for initiating the coagulation process.

We calculated a 20- to 250-fold margin of safety between the effective dose for imaging in rats and the extrapolated effective dose of MAM in humans vs the toxic dose seen in iron-overload states. The iron content of normal human liver has been reported as 0.15–0.20 mg iron/g liver wet weight. The iron content in symptomatic transfusional hemosiderosis is 1–10 mg iron/g liver wet weight [3]. The extrapolated effective dosage for a 70-kg adult, based on a dose of 15 mg MAM/kg (or 3 mg magnetite/kg) is 210 mg iron. With an average liver weight of 2200 g (range, approximately 1700–2800 g) and a 70% deposition in liver RES, a single dose of MAM would transiently increase total hepatic iron by 147 mg or 0.07 mg/g liver. The discrepancy in iron levels and T2 changes seen with MAM points out the potency of superpar-

amagnetic magnetite as compared with hemosiderin and other iron species seen in transfusional hemosiderosis. This reflects a much greater magnetic susceptibility of MAM as compared with hemosiderin (approximately 1000-fold) [17]. On histologic specimens obtained at 2 weeks and 2 months after MAM infusion, there was no evidence of hepatocellular uptake of iron, apparent hepatocellular damage, or hepatic fibrosis.

In conclusion, MAM is a new class of superparamagnetic MR contrast material that targets rapidly and predictably to the RES and exhibits superior targeting to paramagnetic chelates. This material strongly promotes T2 relaxation with minimal T1 effect, allowing for accentuation of T2 differences between normal and pathologic lesions (particularly tumors) with prolonged T2. It also allows for acquisition of T2-weighted images of the target organ by using shorter TR and TE pulse sequences. MAM are stable, relatively uniform in size, and appear nontoxic and nonallergenic in small animals. The iron levels delivered for effective imaging appear well below toxic levels seen in iron-overload states. We believe this type of agent offers considerable promise of improved and more efficient MR liver and spleen imaging.

ACKNOWLEDGMENTS

We thank David Stark, Jack Wittenberg, Sanjay Saini, and Alfred Cohen for providing the rabbit VX2 tumor model; David Stark for reviewing; and Jane Muir for preparing the manuscript.

REFERENCES

1. Moss AA, Goldberg HI, Stark DD, et al. Nuclear magnetic resonance imaging of hepatic tumors. *Radiology* 1984;150:140-147
2. Carr DH, Brown J, Bydder GM, et al. Gadolinium DTPA as a contrast agent in MRI: initial clinical experience in 20 patients. *AJR* 1984;143:215-244
3. Stark DD, Mosely M, Bacon BR, et al. Magnetic resonance imaging and spectroscopy of hepatic iron overload. *Radiology* 1985;154:137-142
4. Stark DD, Moss A, Goldberg HI, et al. Magnetic resonance and CT of the normal and diseased pancreas: a comparative study. *Radiology* 1984;150:153-162
5. Gomori JM, Grossman RI, Goldberg HI, et al. Intracranial hematomas: imaging by high field MR. *Radiology* 1985;157:87-93
6. Widder KJ, Flouret G, Senyei AE, et al. Magnetic microspheres: synthesis of a novel parenteral drug carrier. *J Pharm Sci* 1979;68:79-82
7. Burgner FA. Peripheral hepatic artery embolization in rabbits with VX2 carcinoma of the liver. *Cancer* 1980;46:56-63
8. Greif WL, Buxton RB, Lauffer RB, et al. Pulse sequence optimization for MR imaging using a paramagnetic hepatobiliary contrast agent. *Radiology* 1985;157:461-466
9. Bean CP, Livingston JD. Superparamagnetism. *J Appl Physiol* 1968;30:1205-1298
10. Wolf GL, Burnett K, Goldstein E, Joseph P. Contrast agents for magnetic resonance imaging. In Kressel H, ed. *Magnetic resonance annual*. New York: Raven, 1985; 231-266.
11. Driscoll CF, Morris PM, Senyei AE, et al. Magnetic targeting of microspheres in blood flow. *Microvasc Res* 1984;17(3):353-369
12. Koenig SH. How to be relaxed about relaxation. *SMRM Newsletter* 1985;pp. 8-10
13. Mendoca-Dias MH, Bernado ML, Muller RN, et al. Ferromagnetic particles as contrast agents for magnetic resonance imaging (abstr). Presented at the annual meeting of the Society of Magnetic Resonance in Medicine, London, August 1985
14. Bloembergen N, Purcell EM, Pound RV. Relaxation effects in nuclear magnetic resonance absorption. *Physiol Rev* 1948;73:679-712
15. Olsson M, Persson BRB, Salford LF. Ferromagnetic particles as contrast agent in T2 NMR imaging (abstr). Presented at the annual meeting of the Society of Magnetic Resonance in Medicine, London, August 1985
16. Wagner HN, Rhodes BA, Sasaki Y, et al. Studies of the circulation of radioactive microspheres. *Invest Radiol* 1969;48:374-379
17. Widder KJ, Senyei AE, Scarpelli DG. Magnetic microspheres: a model system for site specific delivery in vivo. *Proc Soc Exp Biol Med* 1978;178:141-146

Use of Standard Gradients with Compound Oblique Angulation for Optimal Quantitative MR Flow Imaging in Oblique Vessels

Roderic I. Pettigrew¹
Wayne Dannels

The earliest described phase-modulation techniques for flow quantification by MR imaging require a phase image obtained by modifying one of the imaging gradients and a reference phase image obtained without the modified gradient. However, by using the same gradients that are used for routine two-dimensional Fourier transform imaging, both anatomic and velocity-encoded images can be obtained in one scan. Although convenient, this technique is sensitive to flow both within and perpendicular to the imaging plane. Consequently, significant errors occur in the measurement of flow in vessels oblique to the image plane. To determine the relative accuracy and practicality of quantitatively measuring flow in oblique vessels, we used standard sequence gradients with (1) routine orthogonal plane imaging and (2) direct compound oblique plane imaging. Phantom studies of flow in a vessel aligned along the z axis showed a significant linear correlation ($r = .999$; $p < .05$) between the spin phase and spin velocity. However, studies of flow at relatively low physiologic rates (12–17 cm/sec) in vessels angled 0–30° off axis showed that obliquities of as little as 10° result in significant quantification errors. This is due to a larger phase shift per unit velocity along the frequency-encoding direction vs along the slice-select direction and to a mixture of velocities within a voxel that is oblique to the flow direction. In most instances, resolution of these errors can be achieved satisfactorily only by electronic plane rotation with compound oblique angulation so that the image plane and vessel are perpendicular. When so used, this technique potentially might provide important adjunctive quantitative flow data in oblique vessels during routine clinical imaging.

Several reports [1–4] have presented quantitative methods of flow-velocity imaging that use phase modulation techniques that require gradient modifications. With these techniques, images typically are made with and without the addition of gradient pulses along the direction of flow. Subtraction of these two images allows accurate determination of the phase difference acquired by the flowing spins. Because this phase shift is directly proportional to the flow velocity [5–7], these dual-scan methods can be used to quantitatively image flow along the direction of the gradient pulses. However, one previously reported technique [8] does not require either gradient modifications or two scans for flow quantification. This technique uses the same gradients as those used routinely for conventional two-dimensional Fourier transform imaging and thus allows both anatomic (modulus) and flow-velocity-encoded (phase) images to be obtained in one scan. Although convenient, this method is sensitive to flow both within and perpendicular to the imaging plane. Hence, quantitative imaging of flow in vessels oblique to the routine planes is a challenge because the phase shift observed represents a vector sum of flow in two directions. This difficulty might be resolved by direct oblique-angle imaging so that the imaging plane is perpendicular to the vessel in which a flow measurement is sought.

The purpose of this work was to determine the relative accuracy and potential practicality of flow quantification in obliquely lying vessels by using standard sequence gradients with (1) routine orthogonal-plane imaging and (2) direct com-

Received July 16, 1986; accepted after revision September 23, 1986.

R. I. Pettigrew is the recipient of a Robert Wood Johnson Foundation Career Development Grant.

Presented in part at the annual meeting of the Society of Magnetic Resonance in Medicine, London, August 1985.

¹ Both authors: Department of Radiology, Emory University School of Medicine, Atlanta, GA 30322. Address reprint requests to R. I. Pettigrew, Department of Radiology, Emory University Hospital, 1364 Clifton Rd., N. E., Atlanta, GA 30322.

AJR 148:405–409, February 1987
0361–803X/87/1482–0405
© American Roentgen Ray Society

pound oblique-plane imaging. Phase-flow images obtained in standard axial planes were compared to those obtained in planes electronically rotated to be perpendicular to a flow phantom vessel. In the companion paper to this report [9], the technique that was successful in these studies was used in vivo, and the results were compared to direct flow-meter measurements.

Materials and Methods

Experiments were performed with a Philips 1.5-T superconducting imager operating at 0.5 T. The gradient waveforms used in routine imaging with this system have been described by van Dijk [8]. The flow phantom was a plastic tube with an inside diameter of 0.9 cm through which distilled water doped with copper sulfate (0.7 g/l) was gravity driven at variable rates. The flow rates were determined from timed collections in a graduated cylinder. A stationary vial of the same fluid and two bags of normal saline were positioned around the flow tube as reference markers. To ensure complete magnetization of the flowing fluid, a 5-ft (1.5 m) section of the tubing upstream from the imaged section was loosely coiled in the magnet.

A phase vs velocity calibration of the system was done by imaging continuous flow in the phantom tube. In all experiments, a spin-echo sequence with an echo time (TE) of 30 msec was used to obtain 25-mm slices. The short TE and relatively thick slices were used to minimize the amount of induced phase shift per unit velocity and thus extend the range of flow velocities that can be imaged unambiguously. Data were acquired and reconstructed in a 256×256 matrix with two signal excitations per line of phase-encoded data. For the oblique flow experiments, the phantom tube was oriented from 0° to 30° about y from the z axis or 0° to 20° about the x and y axes simultaneously. Phase images were obtained in both the routine orthogonal planes and in planes electronically rotated about either one or two axes, so that the latter planes were perpendicular to the flow tube. Imaging was performed with the flow rates in the phantom varied from 0 to approximately 800 ml/min (0–20 cm/sec). The phase images obtained at known flow rates were analyzed by placing a region of interest in the cross-sectional image of the tube. Peak phase values were then measured and plotted against the corresponding measured velocities. In the phase images, phase shifts are in the range of $-\pi$ to π radians (-180° to 180°). Zero radians correspond to midgray, $-\pi$ radians (-180°) are black, and π radians (180°) are white. A positive phase shift (shown as midgray to white) occurs with flow in the positive z direction, or into the scanner. Flow in the opposite direction has a negative phase shift (shown as midgray to black). In instances of phase-angle redundancy or "wraparound" (i.e., phase shifts greater than π radians), the phase shifts are depicted as motion in the reverse direction. This typically can be recognized as a predictable sharp change in the image intensity from white to black and usually can be corrected for if the total range of phase angles represented does not exceed 2π radians (360°).

From the plot of phase values vs flow velocity, a calibration factor was determined for flow along both the z (slice sheet) and x (frequency encoding) axes. Computed velocities were then compared with the actual measured flow velocities for the phantom tube placed at various degrees of obliquity and imaged with (1) routine orthogonal planes and (2) oblique planes that were perpendicular to the flow direction.

Results

Linear relationships between the spin-phase shift and the flow velocity were observed for flow along the z axis (slice-

select direction) and along the x axis (frequency-encoding direction). For flow along the z direction, a phase shift of 8.4° per unit flow velocity of 1 cm/sec was measured, whereas a phase shift of $19^\circ/1$ cm/sec was measured for flow along the x direction (see Table 1). For flow along the y direction, no measurable phase shift was observed in the phase image because any phase shift that occurred in this direction would result in displaced registration of the image data, and typically this displacement was less than the dimensions of 1 pixel. The calibration factors obtained indicated that the range of flow velocities that could be measured along the z direction was 0–40 cm/sec, whereas for velocities along the x direction, the dynamic range extended to only about 18 cm/sec.

Figure 1 shows the phase-velocity profile obtained for laminar flow within the phantom tube, and Figure 2 shows the observed linear relationship between the phase shift and flow velocity along the z axis. Applying linear regression analysis to the six data pairs in this graph yielded a slope of 0.00346 and a y-intercept of 0.049. The correlation coefficient of the data was .999, with a p value of $<.05$. The standard deviation of the slope, determined from a series of repeated measurements, was $\pm 8\%$. Thus, for flow along the z axis, velocity (cm/sec) = 6.8 ± 0.5 (cm/sec/radians) \times phase (radians).

For the phantom studies in which the flow tube was positioned at oblique angles to the routine orthogonal axis, the computed velocities vs the actual velocities are shown as a function of the degree of the obliquity about one axis in Table 2 and about two axes simultaneously in Table 3. Also shown in each instance is the computed velocity when the imaging plane was electronically rotated to be perpendicular to the tube. As indicated, the computed flow velocities in vessels with single obliquities as small as 10° (into the frequency-encoding direction) contained significant errors. The images suggested higher velocities than actually existed when obtained in a routine axial plane, and this error increased as the degree of obliquity increased. In addition, when the vessel was rotated obliquely 30° , and the flow rate increased from 13 cm/sec to only 17 cm/sec (while maintaining the same tube obliquity), a velocity could not be computed from the MR image of the higher flow rate. This occurred principally because the resultant phase changes per pixel were so large that they appeared to be discontinuous from one pixel to the next. An accurate computation could be made, however, in

TABLE 1: Flow Calibration Factors (Velocity = K \times Phase)

	Flow Direction		
	z	x	y
K (cm/sec/radian)	6.8 ± 0.5	3.0 ± 0.5	—
Phase shift (per velocity of 1 cm/sec)	$8.4^\circ \pm 0.7^\circ$	$19.0^\circ \pm 2.8^\circ$	—

Note.—K = flow velocity — phase calibration factor; gives the spin velocity (cm/sec) that induces a unit phase shift (1 radian) for flow along a specific gradient direction. z = direction along which slice-select gradient is applied. x = direction along which frequency-encoding ("measurement") gradient is applied. y = direction along which phase-encoding gradient is applied.

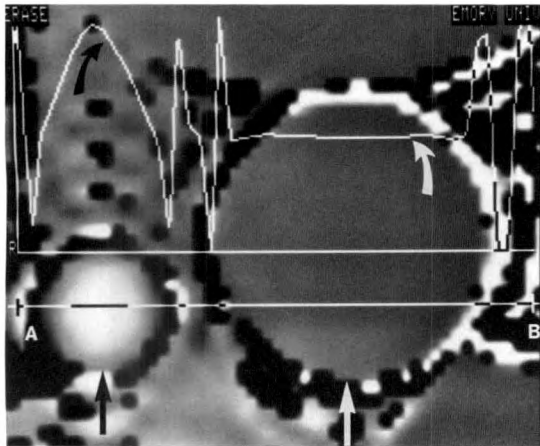


Fig. 1.—Transverse-plane phase image of flowing fluid in a phantom tube (straight black arrow) and stationary fluid in an adjacent larger vial (straight white arrow). Phase-velocity profile across tube (curved black arrow) and vial (curved white arrow) shows a laminar flow profile within the tube and a flat, zero-phase profile across the stationary fluid. Profiles are from along line between points A and B.

TABLE 2: Effect of Tube Obliquity on Computed Flow Velocity

Tube Rotation About y from z Axis (degrees)	Image Plane	Computed V (cm/sec)	Actual V (cm/sec)
Along z axis (0)	Transverse	12	13
10	Transverse	20	13
10	Perpendicular to tube	14	13
20	Transverse	25	13
20	Perpendicular to tube	15	13
30	Transverse	48	13
30	Perpendicular to tube	16	13
30	Transverse	—	17
30	Perpendicular to tube	20	17

Note.—V = flow velocity; dash indicates value could not be computed. z = direction along which slice-select gradient is applied. y = direction along which phase-encoding gradient is applied.

the obliquely rotated image plane that was perpendicular to the vessel. In each case in which vessels were turned obliquely about both the y and z axes, electronic rotation of the imaging plane to acquire image data perpendicular to the vessel also allowed significantly more accurate determination of the flow velocity.

Also, as indicated in Table 3, when the phantom tube was rotated only 20° from the z axis about both the y and x axes, the phase image could not be interpreted because of large discontinuities in the phase image. Again, these apparently resulted from the component of phase shifts occurring from flow in the x direction where the phase shift per unit velocity was more than twice that produced for flow in the z direction. Consequently, large resultant phase shifts per unit velocity

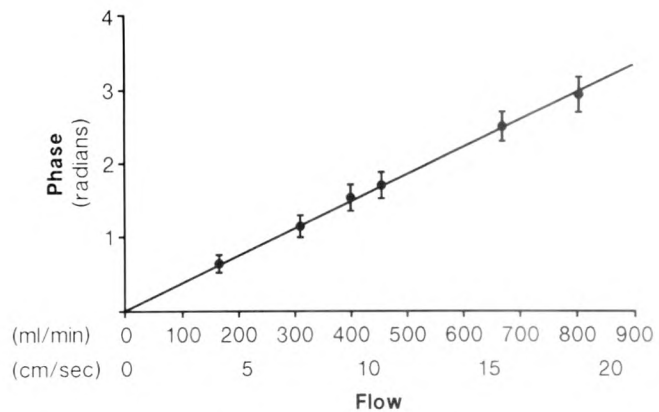


Fig. 2.—Phase-flow calibration graph shows linear relationship between spin phase and spin velocity ($r = .999$, $p < .05$). Flow rates and velocity are shown for the 0.9-cm diameter phantom tube.

were produced, yielding rapid changes in signal intensity and an uninterpretable phase image. In addition, a mixture of velocities within a voxel can result in partial to complete phase cancellation and signal "dropout" [10, 11], and this is more likely to occur when the voxel is oblique to the direction of flow.

An example of this problem, and the resultant improvement obtained when the image plane is rotated perpendicular to the vessel, is shown in Figure 3, which makes a comparison between the phantom tube lying along the z axis (Fig. 3, upper left), and the tube rotated 10° (Fig. 3, upper right) and 20° (Fig. 3, lower left) about both the y and x axes. The flow velocity (13 cm/sec) was the same for each geometric orientation. The effects of imaging perpendicular to the z axis vs imaging perpendicular to the rotated tube are shown. When the image plane was rotated to be perpendicular to the tube, which was turned obliquely 20° about x and y (Fig. 3, lower right), the phase image was clearly more interpretable and nearly identical to that of the transverse-plane image of the tube along the z axis.

Phase-velocity profiles across the vessels rotated obliquely 10° (Fig. 4A) and 20° (Fig. 4B) about both axes showed significant deviations from a parabolic profile that would be typical of the laminar flow in the vessel. When the vessel had an obliquity of 10°, the image on first inspection looked interpretable, showing no effects of phase redundancy (wrap-around). However, the phase profile showed something that was not visually apparent. The phase distribution across the obliquely rotated tube was irregular, skewed, and inconsistent with the laminar flow that was present. Thus, calculation of flow from this image was in error as listed in Table 3. The observed phase profile reflected the effects of both the component of flow in the frequency-encoding direction and the summation of various velocities within a voxel. When the vessel had an obliquity of 20°, the phase image was more strikingly irregular, as is graphically depicted by the phase profile. Here, the effects of in-plane flow contributions and intravoxel phase variations were more significant, yielding a phase image from which neither the perpendicular nor the in-plane flow compo-

TABLE 3: Effect of Compound Obliquity on Computed Flow Velocity

Tube Orientation	Image Plane	Phase Maximum (radians)	Computed V (cm/sec)	Actual V (cm/sec)
Along z axis (0°)	Transverse	1.950	13.0	12
Rotated 10° ^{aa}	Transverse	2.700	18.0	12
Rotated 20° ^{aa}	Transverse	—	None	12
Rotated 20° ^{aa}	Rotated perpendicular to tube	2.005	13.3	12

Note.—Dash indicates that value could not be interpreted. V = flow velocity. z = direction along which slice-select gradient is applied.
^a Simultaneous rotation about both x and y axes.

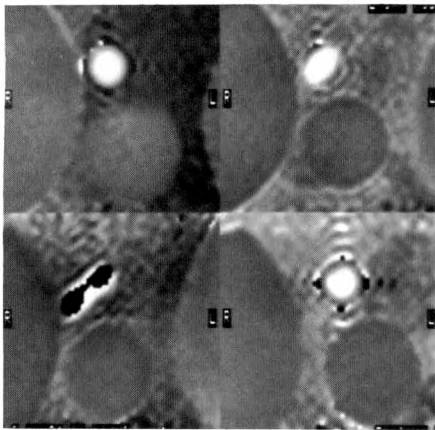


Fig. 3.—Upper left, Transverse-plane phase image of tube along z axis.
Upper right, Transverse-plane phase image of tube turned obliquely 10° about both x and y axes.
Lower left, Transverse-plane phase image of tube turned obliquely 20° about both x and y axes.
Lower right, Phase image in oblique plane perpendicular to tube turned obliquely 20° about x and y axes.
Upper left panel image accurately reflects velocity distribution. Note differences in phase images with progressive tube obliquities (upper right, lower left). These differences result in inaccuracies in velocity calculation. An accurate phase image of tube turned obliquely 20° is obtained (lower right) by electronic rotation of image plane so that it is perpendicular to tube.

nents could be retrieved. These problems were eliminated by oblique-angle imaging.

Discussion

The strong correlation between the phase-shift values and flow velocities obtained in the calibration experiments in which the tube was placed along the z axis and imaging was performed perpendicular to this axis shows a definite linear relationship between spin phase and spin velocity in the ideal situation. However, when standard imaging gradients are used, phase shifts are induced in two directions: along the slice-select direction and along the frequency-encoding direc-

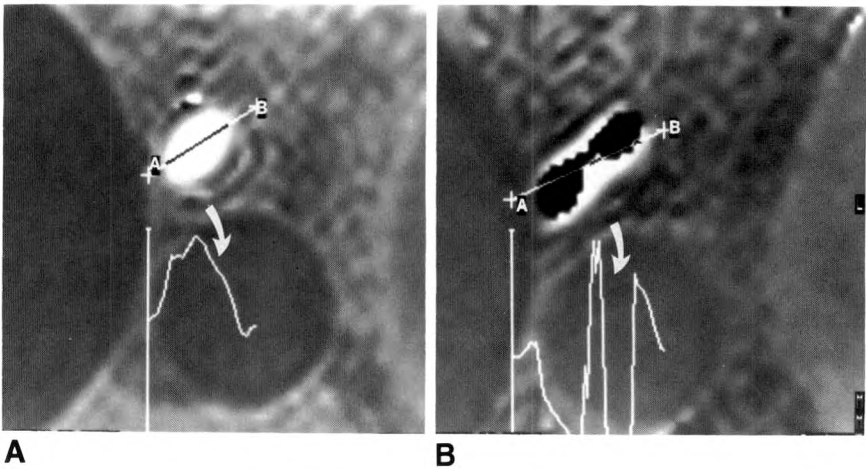


Fig. 4.—A, Transverse-plane phase-image profile for tube turned obliquely 10° about both x and y axes. Despite lack of readily apparent discontinuities in phase image, profile (arrow) from along line between points A and B shows phase distribution is irregular, skewed, and inconsistent with laminar flow that is present. Error in calculation of flow velocity from this image is 50% (Table 3).
B, Transverse-plane phase-image profile for tube turned obliquely 20° about both x and y axes. Velocity is same as in Figs. 3 and 4A. Prominent phase-image irregularities are readily apparent and graphically depicted by phase profile (arrow). With this degree of tube obliquity, effects of in-plane flow and intravoxel phase variation are more significant, yielding a phase image from which neither in-plane nor through-plane flow components can be retrieved. This problem is eliminated by oblique-plane imaging as shown in Fig. 3.

tion. With our imaging sequences and technique, this effect is observed most strongly for flow along the frequency-encoding direction, and thus the dynamic range of flow velocities that can be unambiguously measured in this direction is much smaller than the range for the slice-select direction. Consequently, a significant component of flow along the frequency-encoding direction will heavily influence the resultant phase shift. These experiments suggest that vessels that are angled from the z axis by as little as 10° will result in erroneously measured quantitative flow velocities if the phase value is extracted from an image obtained in a routine plane, transverse to the z axis.

It might be possible to correct the influence due to the component of flow along the frequency-encoding direction, but this would require precise knowledge of the angulation of the vessel. However, for faster flow rates or larger angles, even knowledge of the precise three-dimensional angle of the vessel may be insufficient to allow accurate determination of

the flow velocity. The resultant composite phase shifts per pixel may be so large that they cause an uninterpretable phase image due to rapid changes in spatial signal intensity. In such instances, it may be not only most convenient but also necessary to electronically rotate the imaging plane to achieve orthogonality to the vessel.

Other problems can arise if flow is not perpendicular to the slice. In most conventional images, the slice thickness determines the largest dimension of any voxel. Unless the longest dimension is aligned with the vessel and the direction of flow, the voxel will cut across the vessel and will contain several components with different velocities. Voxels containing different velocities will have overall phases that do not meaningfully correspond to any single velocity. For example, when high and low velocities are combined, the signal intensity from higher velocity regions will be much less, and therefore the overall phase of the entire voxel will be skewed towards the phase of the low-velocity, high-intensity components. In addition, the summation of spins with opposing phases may result in signal cancellation. Similar problems can occur in almost any quantitative imaging method, forcing, once again, consideration of the use of obliquely rotated images.

The data further suggest that the problems of sensitivity to in-plane motion and intravoxel phase variations can be overcome satisfactorily by also using compound oblique-angle imaging to define planes that are perpendicular to the vessel. Otherwise, these problems would not allow accurate flow quantification in obliquely lying vessels. In each case with a tube obliquity of 0° to 30° , the flow velocity could be determined to within approximately 15% of the actual velocity by using this improved technique. Thus, standard imaging gradients applied with compound oblique angulations might be used to obtain anatomic and quantitative flow information conveniently in one scan. The major limitations indicated by this study are (1) a dynamic range limited to less than 40 cm/sec and (2) the necessity for thick slices of 25 mm to achieve this range. In the future, this dynamic range may be extended by using a shorter TE, and a narrower RF bandwidth would yield thinner slices.

A different phase-sensitive technique described by Wedeen et al. [12] has an intrinsically larger dynamic range than the method we used, although it is more restricted by the problem of spin-phase variations within a voxel. This novel method also uses a single acquisition with conventional imaging gradients, but it is used instead to quantify in-plane flow in the frequency-encoding direction by using a phase-offset tech-

nique. Although the dynamic range of this method is greater for comparable imaging parameters, thin slices relative to the diameter of the vessel are needed for optimal results. If the slice thickness is comparable to the vessel diameter, the voxel will be large enough to contain a spectrum of spin velocities. Because the flow profile within the voxel will be parabolic (for laminar flow), a significant mixture of velocities will result, yielding an averaged phase value of uncertain meaning, or possibly signal dropout from spin-phase cancellation.

Both approaches to obtaining quantitative flow data from routine imaging sequences are relatively new and are yet to be optimized for clinical applications. At this juncture, a complementary use of these techniques might be anticipated. The phase-display approach of Wedeen et al. might be best used for measuring high flow rates in larger vessels [12], whereas the approach described in this paper may be preferable for slower flow rates and smaller vessels. Our first effort to apply this technique to vessels in vivo and a comparison of the results with flow-meter measurements are described in the following article [9].

REFERENCES

1. Moran PR. A flow velocity zeugmatographic interlace for NMR imaging in humans. *Magnetic Resonance Imaging* 1983;1:197-203
2. Moran PR, Moran RA, Karstaedt N. Verification and evaluation of internal flow and motion. *Radiology* 1985;154:433-441
3. Bryant DJ, Payne JA, Firmin DN, Longmore DB. Measurement of flow with NMR imaging using a gradient pulse and phase difference technique. *J Comput Assist Tomogr* 1984;8:588-593
4. Pattany PM, Nayler GL. High velocity flow imaging by even echo rephasing. Presented at the annual meeting of the Society of Magnetic Resonance, London, August 1985
5. Carr HY, Purcell EM. Effects of diffusion on free precession in nuclear magnetic resonance experiments. *Phys Rev* 1954;94:630-638
6. Hahn EL. Detection of sea-water motion by nuclear precession. *J Geophys Res* 1960;65:776-777
7. Singer JR. NMR diffusion and flow measurements and an introduction to spin phase graphing. *J Phys [E]* 1978;11:281-291
8. van Dijk P. Direct cardiac NMR imaging of heart wall and blood flow velocity. *J Comput Assist Tomogr* 1984;8:429-436
9. Pettigrew RI, Dannels W, Galloway JR, et al. Quantitative phase-flow MR imaging in dogs by using standard sequences: comparison with in vivo flow-meter measurements. *AJR* 1987;148:411-414
10. Axel L. Blood flow effects in magnetic resonance (MR) imaging. *AJR* 1984;143:1157-1166
11. von Schulthess GV, Higgins CB. Blood flow imaging with MR: spin-phase phenomena. *Radiology* 1985;157:687-695
12. Wedeen VJ, Rosen BR, Chester D, Brady TJ. MR velocity imaging by phase display. *J Comput Assist Tomogr* 1985;9:530-536

Memorial

John Hamilton Gilmore, 1907–1986



The many friends of John and Rae Gilmore will be saddened to learn that he died on June 2, 1986, and that she passed away on

August 13, 1986. They had married in 1934. A daughter, Mary Ramona Glaser of Appleton, WI; a son, John Richard of Seattle, WA; and five grandchildren survive them. John and Rae (nee' Ramona Mae Brockman) left the Chicago area for Port Angeles, WA, about 11 years ago.

John's mother and father were physicians, as were a large number of his close relatives. Born in downstate Benton, IL, he always retained a love of the open country. As a youth, he set a record on the town's nine-hole golf course. As an adult, he was an avid trout fisherman, making many trips to Colorado streams. A 1930 (B.S.) and 1932 (M.D.) graduate of the University of Illinois, John interned and then trained in radiology at the Illinois Masonic Hospital in Chicago. His mentor was his father, W. H. Gilmore, radiologist at that hospital and a charter member of the Radiological Society of North America (RSNA). After his father's death in 1935, John succeeded him as Director of Radiology at

the hospital. He also joined Harold E. Davis in private practice and was radiologist at the Illinois Eye and Ear Infirmary. In 1961, he was appointed radiologist at the West Suburban Hospital, in Oak Park, IL. Dr. Gilmore joined the faculty of the Northwestern University Medical School in 1936 and held the rank of Associate Professor when he retired.

John served during World War II as the Chief of the X-ray Service at the William Beaumont General Hospital in El Paso, TX. He was a member of many medical and lay societies. He was president of the Chicago Roentgen Society in 1950 and of the RSNA in 1969, and he was Delegate of the RSNA to the 12th International Congress of Radiology in Tokyo, Japan, in 1969.

All of us who knew, admired, and loved Rae and John are bereaved at their deaths.

Theodore J. Wachowski
Wheaton, IL 60187

Quantitative Phase-Flow MR Imaging in Dogs by Using Standard Sequences:

Comparison with In Vivo Flow-Meter Measurements

Roderic I. Pettigrew¹
 Wayne Dannels¹
 John R. Galloway²
 Thomas Pearson²
 William Millikan²
 J. Michael Henderson²
 Jack Peterson¹
 Michael E. Bernardino¹

For evaluation of the feasibility and clinical potential of using the phase data from standard MR imaging sequences to measure blood flow, 11 vessels with diameters of 4 to 7 mm were imaged in seven dogs. The flow in either the superior mesenteric vein or the inferior vena cava was measured first at laparotomy (in ml/min) with electromagnetic flow meters. Immediately thereafter, these vessels were imaged by MR in 25-mm thick sections by using a standard spin echo (SE) 750/30 sequence with a Philips 0.5-T imager. Previous phase-flow calibration of the imager and sequence allowed calculation of the blood flow rates from the phase images that were used to measure the vessels' cross-sectional areas and blood phase values. Comparison of the measurements obtained with each technique showed a significant correlation ($r = .977$, $p < .05$) between MR-imaging values and flow-meter measurements when the blood velocity was less than approximately 40 cm/sec, the known upper limit of the flow dynamic range for the MR hardware and sequence used. There was no correlation for blood velocities greater than 40 cm/sec. However, the range of blood flow velocities in dogs and man extends to more than 100 cm/sec. Thus, these results suggest that this technique might yield valuable adjunctive flow data in routine clinical imaging provided that improvements in hardware and software permit a larger dynamic range.

Since the advent of various schemes for phase-modulated imaging of blood flow, several investigators [1-5] have described these techniques and have assessed their potential accuracies by using flow phantoms. Bryant et al. [3] used a modification of the standard gradients for MR imaging and compared flow measurements of the carotid arteries obtained by MR imaging to those obtained by Doppler sonography. Since then, the idea of using the phase data from standard imaging sequences to measure flow quantitatively has been proposed [5] and, on the basis of experiments with phantoms, has potential clinical application.

In the preceding paper [5], this technique was shown to have promise also for quantitative imaging of flow in oblique vessels, but only if the vessels are imaged in planes perpendicular to the direction of flow. This approach is appealing because of its convenience. It requires no gradient modifications, and both the anatomic images (from the modulus data) and the velocity-encoded images (from the phase data) can be obtained with a single acquisition.

The purpose of this study was to (1) determine the feasibility of using this approach for quantitative blood-flow imaging and (2) assess its accuracy and limitations by comparing the results to those obtained from flow-meter studies of dog venous blood flow in vivo.

Materials and Methods

Laparotomies were performed on seven dogs weighing 12-18 kg that were anesthetized with sodium pentobarbital (35 mg/kg) and ventilated mechanically with a Harvard respirator (Harvard Apparatus, South Natick, MA). In each dog, the superior mesenteric vein and the inferior vena cava were isolated, and measurements of blood flow in these vessels were

Received July 16, 1986; accepted after revision September 30, 1986.

R. I. Pettigrew is the recipient of a Robert Wood Johnson Foundation Career Development Grant.

Presented at the annual meeting of the American Roentgen Ray Society, Washington, DC, April 1986.

¹ Department of Radiology, Emory University School of Medicine, Atlanta, GA 30322. Address reprint requests to R. I. Pettigrew, Department of Radiology, Emory University Hospital, 1364 Clifton Rd., N. E., Atlanta, GA 30322.

² Department of Surgery, Emory University School of Medicine, Atlanta, GA 30322.

AJR 148:411-414, February 1987
 0361-803X/87/1482-0411

© American Roentgen Ray Society

obtained by using Gould electromagnetic flow meters (Gould Inc., Oxnard, CA) temporarily placed around each vessel. In five of the dogs, a plastic vial containing air was placed in the abdomen to mark the anatomic level at which the flow in these vessels had been measured. The wounds were closed surgically, and the dogs were placed in the MR scanner. Care was taken to maintain the dogs, as closely as possible, in the same physical positioning and physiologic status during both the surgical and the MR-imaging flow measurements.

MR imaging was performed with a Philips 1.5-T magnet operating at 0.5 T. All imaging was performed by using the head coil (30-cm diameter) with an echo time (TE) of 30 msec and a repetition time (TR) of 750 msec. Data were acquired in a 256×256 matrix with two signal excitations averaged per line of phase-encoding data. The slice thickness was 25 mm. The relatively large slice thickness and the minimum available TE of 30 msec were used to minimize the induced spin phase shift per unit velocity.

In each case, initial scans were obtained first to determine the angles of the superior mesenteric vein and the inferior vena cava in the coronal and/or sagittal planes. Subsequent transverse images were then obtained with appropriate electronic angulation to ensure that the slice was perpendicular to the vessel of interest.

Blood-flow rates were calculated from the phase images, which are described and explained in further detail in the following sections. All phase images were obtained in planes perpendicular to the vessel and were reconstructed by using the two-dimensional linear-phase correction algorithm offered as part of the standard (Philips) software package. A region of interest was placed over the vessel, and the mean phase shift within the vessel cross section was recorded with the cross-sectional area. The mean phase shift was determined by summing the phase shifts of all pixels within the vessel and dividing by the number of pixels. Previous phantom experiments [5] have shown that the velocity per unit phase shift is 6.8 cm/sec/radian. This calibration factor was used to determine the mean velocity and the corresponding flow rate of the blood in the vessel. The results were computed and recorded without knowledge of the flow rates measured with the electromagnetic flow meters.

In each case in which a flow measurement was desired, both the conventional modulus image and the phase image were generated from the same acquisition data. The modulus image is simply the conventional magnitude image produced by all standard MR imagers in which the image intensity is directly proportional to the magnitude of the measured MR signal (i.e., the magnitude of the transverse magnetization). In the phase image, the pixel intensity is proportional to the shift in phase that the spins acquire as a result of moving along a magnetic field gradient. Movement into a magnetic field of higher or lower strength produces a proportional increase or decrease in spin frequency with a resultant proportional change in the spin phase. The change in the moving spin phase relative to stationary spins (phase shift) is reflected in the sinusoidal and cosinusoidal components of the detected MR signal. Both the sinusoidal component (called the imaginary data) and the cosinusoidal component (called the real data) can be extracted electronically from the detected composite signal. These components are then mathematically analyzed to determine the phase of the spins in each pixel, which are assigned a gray-scale intensity proportional to the size of the phase shift.

The gray scale is divided into opposite halves to depict motion or flow in both of two opposite directions. Stationary spins have zero phase shift and are assigned a midgray intensity. Spins that move into the magnet acquire positive phase shifts. Phase shifts from 0° to 180° are depicted in proportional intensities from midgray to white (i.e., $+180^\circ = \text{white}$). Spins that move in the opposite direction acquire negative phase shifts. Those from 0° to -180° are assigned a

proportional intensity from midgray to black (i.e., $-180^\circ = \text{black}$). Thus, there are, in effect, two display cycles: one from 0° to $+180^\circ$ and one from 0° to -180° .

The phase shifts of $+180^\circ$ and -180° , which correspond to the gray-scale end points of white and black, respectively, occur because the total range of angles that can be measured unambiguously is 360° . Because this has been divided into a positive half (0° to 180°) and a negative half (-180° to 0°), a display problem results for flow that is so fast in either direction that a phase angle greater than $\pm 180^\circ$ is acquired. For example, if the flow velocity results in a $+190^\circ$ phase shift (fast flow into the magnet), this will actually be read as an angle that is 10° beyond $+180^\circ$, or one that has "wrapped around" 10° into the -180° to 0° range, which is -170° . Thus, a $+190^\circ$ phase shift will be displayed as a -170° phase shift, appearing as flow in the negative direction would, even though it is actually fast flow in the positive direction.

This redundancy in the phase-angle display, where two or more velocities have the same displayed phase angle (also called aliasing) is unavoidable. As explained, this is inherent in measurements of cyclic phenomena because angles repeat after 360° , and thus $360^\circ + \beta^\circ$ is indistinguishable from β° . Usually, however, corrections can be made for this wraparound effect if the peak phase shift in a vessel's cross section does not exceed approximately 360° . This allows wraparound of the phase angle to occur for one display cycle, but less than two display cycles. For peak phase shifts larger than approximately 360° , the change in the corresponding signal intensity per pixel is typically too great to allow the cyclic patterns to be clearly resolved. This effect is responsible for the dynamic range limits of this and other phase-modulation techniques.

Results

A typical anatomic (modulus) image of the superior mesenteric vein and inferior vena cava and the corresponding velocity-encoded (phase) image obtained with this technique are shown in Figure 1. The phase-flow velocity profile across the superior mesenteric vein was parabolic, as expected for laminar flow. The phase image of the inferior vena cava had a dark center because of rapid flow and the consequent phase-angle redundancy and because this vessel was oriented obliquely to the imaging plane, which is perpendicular to the superior mesenteric vein. (The problems associated with this are the subject of the preceding paper [5].)

In Figure 2, the MR-imaging flow measurements are plotted vs the flow-meter measurements for the vessel in each dog. In four of the seven dogs, flow measurements were obtained for both the superior mesenteric vein and the inferior vena cava. In the remaining three dogs, flow measurements for only the superior mesenteric vein or the inferior vena cava could be obtained by MR imaging because of compression by the tube marker or kinking of the remaining vessel. In one dog not included in the study, the flow rates were so fast that there was insufficient signal in both the superior mesenteric vein and the inferior vena cava to allow determination of the phase shifts.

As shown in Figure 2, there was a significant linear correlation between the two types of measurements for flow rates that were less than approximately 500 ml/min. The linear regression equation for this portion of the graph was MR imaging = $-50.98 + (0.89 \times \text{flow meter measurement})$. The

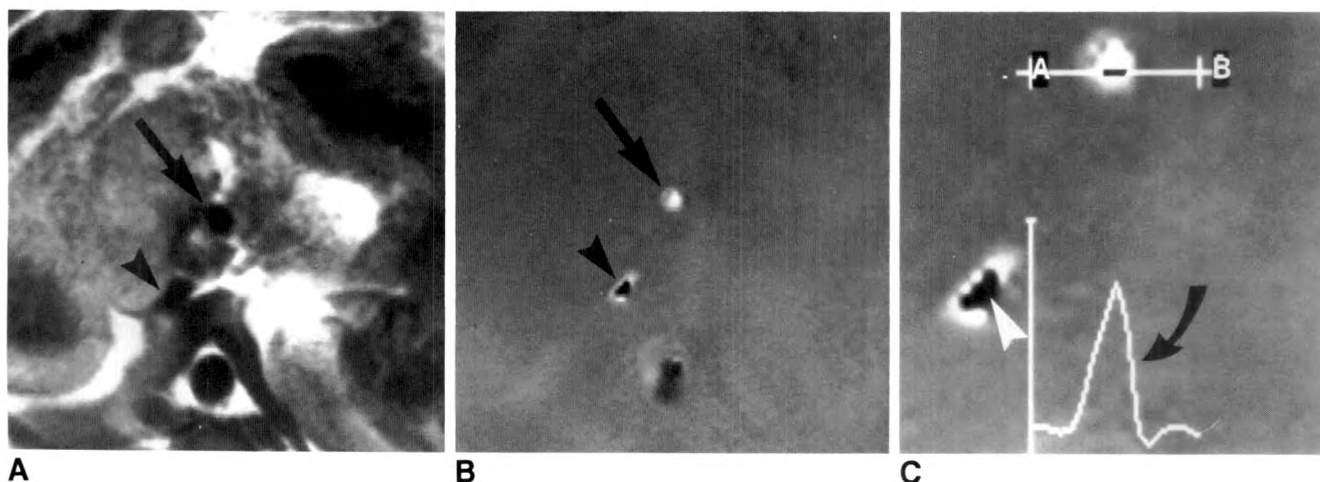


Fig. 1.—A, Modulus image of a dog's abdomen shows superior mesenteric vein (arrow) and inferior vena cava (arrowhead). Image plane is perpendicular to superior mesenteric vein.

B, Corresponding phase image of section shown in A. Image intensity is proportional to spin phase, which is proportional to velocity. Note difference in signal intensity for superior mesenteric vein (arrow) and inferior vena cava (arrowhead) vs surrounding stationary tissues. Both images (A and B) were generated from data obtained with the same acquisition.

C, Magnified view of B. Phase profile (curved arrow) from along line between points A and B shows a parabolic phase-velocity profile. Velocity can be determined from the phase-velocity calibration factor. Dark center of inferior vena cava (arrowhead) is due to phase-angle redundancy (see text) in which phase angles corresponding to the faster blood velocities in this vessel have exceeded positive range that can be displayed at a bright intensity level and have "wrapped around" into range displayed at a dark intensity level.

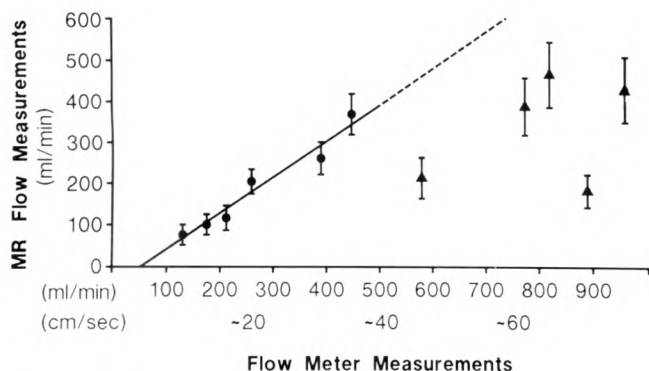


Fig. 2.—MR imaging measurements vs electromagnetic flow-meter measurements for venous blood flow in a dog. Flow-meter measurements were obtained in ml/min. Corresponding scale in cm/sec is approximate, based on a typical vessel diameter of 5 mm. Flow-meter measurements of less than 500 ml/min (approximately 40 cm/sec) are shown as closed circles and those greater than 500 ml/min as closed triangles. A linear correlation ($r = .977$, $p < .05$) is shown for velocities within the dynamic range of the MR imaging technique (<40 cm/sec), which corresponds to a phase shift of approximately 360° . Phase shifts beyond this value cannot be measured accurately because of repeated phase-angle wraparound.

product-moment correlation coefficient of the data was 0.977. With six data pairs, a correlation coefficient of 0.977 could have occurred by chance fewer than five times in 100 ($p < .05$). For flow rates greater than approximately 500 ml/min, there was no correlation. The size of the vessels ranged from 4 to 7 mm in diameter, with a typical diameter of 5 mm for the 11 vessels. For a vessel of this size, the flow rate of 500 ml/min corresponds to a velocity of approximately 40 cm/sec, and this is indicated on the lower scale, which was calculated on the basis of this mean vessel diameter.

Discussion

The most striking aspect of the results, as shown in Figure 1, is the dichotomous pattern of the MR-imaging vs flow-meter measurements. The results clearly indicate a strong correlation between the two measurements for flow rates that are less than 500 ml/min (approximately 40 cm/sec), which corresponds to the known dynamic range limit as determined from prior phantom studies [5]. As was shown with the flow phantom, imaging velocities beyond 40 cm/sec are not possible with the software and hardware used because phase-angle redundancy occurs once this velocity is exceeded.

The absolute extent to which the measurements do correlate within the established dynamic range must, however, be interpreted with some caution because of the unavoidable lack of simultaneous flow measurements in vivo. Nonetheless, one important conclusion is that despite this experimental limitation, these results appear to indicate that this technique does work in vivo. However, it is not yet suitable for routine measurement of physiologic rates in vivo, primarily because of the limited dynamic range and the large slice thickness needed to obtain it.

In three instances, flow measurements determined by MR imaging could not be obtained even though the vessel could be imaged clearly. In one instance, kinking or postsurgical compression of the vessel made it impossible to obtain a 25-mm thick section that was straight. In two vessels, the presence of vascular tributaries with associated inflow non-perpendicular to the imaging plane was a significant complication that prevented accurate phase determinations.

Improvements in software and hardware for MR imaging may circumvent some of the problems encountered in this study. For example, a shorter echo time would reduce further

the phase shift per unit velocity, and a narrower RF bandwidth would allow reducing the slice thickness while maintaining a small gradient and the corresponding small phase shift per unit velocity. Because the phase shift is proportional to the square of the TE and the gradient pulse times [6-9], simply reducing the TE (while keeping the other parameters constant) could greatly extend the dynamic range of this system. With advances of this nature, the use of the phase data from standard sequences might provide valuable adjunctive data in routine imaging studies in which quantitative blood-flow measurements would be clinically valuable. Other phase-modulation techniques in which two scans are needed to obtain a quantitative measurement might provide a greater dynamic range and thus might be used selectively in instances in which the flow rates of interest are beyond the limits of this standard technique.

In this initial study, only venous flow rates were measured. Venous flow velocities are generally slower, and it is relatively easy to measure steady, nonpulsatile flow. With system improvements that would allow higher velocities to be measured, this technique also might be applied to arterial flow if ECG gating were used. With ECG gating, measurement of arterial velocity would be made at a specific point in the cardiac cycle. If these measurements were obtained at a number of points throughout the cardiac cycle, a velocity-time

curve could be generated from which the total flow in a specific arterial vessel could be computed. With the ability to make this type of measurement, renal blood flow, hepatic arterial vs portal venous flow, forward cardiac output, and other clinically useful flow rates might be determined.

REFERENCES

1. Moran PR. A flow velocity zeugmatographic interlace for NMR imaging in humans. *Magnetic Resonance Imaging* 1983;1:197-203
2. Moran PR, Moran RA, Karstaedt N. Verification and evaluation of internal flow and motion. *Radiology* 1985;154:433-441
3. Bryant DJ, Payne JA, Firmin DN, Longmore DB. Measurement of flow with NMR imaging using a gradient pulse and phase difference technique. *J Comput Assist Tomogr* 1984;8:588-593
4. O'Donnell M. NMR blood flow imaging using multiecho, phase contrast sequences. *Med Phys* 1985;12(1):59-64
5. Pettigrew RI, Dannels W. Use of standard gradients with compound oblique angulation for optimal quantitative MR flow imaging in oblique vessels. *AJR* 1987;148:405-409
6. van Dijk P. Direct cardiac NMR imaging of heart wall and blood flow velocity. *J Comput Assist Tomogr* 1984;8:429-436
7. Hahn EL. Detection of sea-water motion by nuclear precession. *J Geophys Res* 1960;65:776-777
8. Carr HY, Purcell EM. Effects of diffusion on free precession in nuclear magnetic resonance experiments. *Phys Rev* 1954;94:630-638
9. Axel L. Blood flow effects in magnetic resonance (MR) imaging. *AJR* 1984;143:1157-1166

Effects of MR Imaging on Murine Natural Killer Cell Cytotoxicity

Naresh Prasad^{1,2}
 Eva Lotzová³
 John I. Thornby²
 John E. Madewell¹
 Joseph J. Ford⁴
 Stewart C. Bushong¹

To determine the effect of MR imaging on the immune system, 21 male C57BL/6 × DBA/2 F₁ mice were exposed to MR imaging at a field strength of 0.15 T for 2 hr. Another nine mice (controls) were sham exposed for the same amount of time. Mice were sacrificed and their spleens removed 24, 72, and 144 hr after the exposure (MR or sham). Spleen cell suspensions were passed over nylon wool columns and then used as effector cells in a short-term natural killer cell cytotoxicity assay with ⁵¹Cr-labeled YAC-1 cells as target cells. The results showed no evidence of decreased cytotoxicity due to exposure to MR. On the contrary, at all three times after exposure and for all target-to-effector cell ratios, mean cytotoxicity was greater for MR-exposed groups than for sham-exposed groups. The results show that MR exposure has no adverse effect on the immune system, as evidenced by natural killer cell activity.

MR imaging provides qualitative information in the form of images and quantitative information in the form of physiologic characteristics of tissues. Although the use of MR imaging as a diagnostic technique is increasing at a rapid rate [1, 2], no adverse effects have been reported from the use of MR imaging with a magnetic field strength of less than 2 T [3-7].

Natural killer cells are lymphocytes that can kill tumor cells without any previous antigenic exposure to the tumor. They are important both in immunosurveillance against malignancies and in resistance to metastasis [8-12]. In the present study we selected splenic natural killer cell activity as the indicator of immune status after exposure to diagnostic MR imaging. To our knowledge, no previous studies on the effects of MR imaging on the immune system have been reported.

Materials and Methods

Five-week-old male C57BL/6 × DBA/2 F₁ mice were purchased from TIMCO-HARLAN (Houston, TX) and acclimated in our colony for 2 weeks before being used in the experiments. A total of 30 mice were used: 21 were exposed to MR imaging; nine were unexposed and served as controls.

Exposure to MR imaging was performed by using a Bruker CXP-200 Nuclear Magnetic Resonance Spectrometer and whole-body imaging magnet. Characteristics of the MR imaging apparatus were as follows: 30-cm diameter magnetic imaging volume, 0.15-T static magnetic field, and 6-MHz RF. The RF pulses were 600 V peak-to-peak and were applied for 20 μsec (90 pulse) and 40 μsec (180 pulse). The duty cycle did not exceed one part per 1000 or 1 msec RF application per second of experimental time. The strongest gradient was 25 μT/cm, used with a 98% duty cycle. These exposure conditions are representative of those used clinically for head proton MR images.

Mice were exposed in a specially fabricated clear Plexiglas ventilated chamber that permitted whole-body exposure of several mice at one time. The mice were exposed for 2 hr and marked with an ear punch. Similarly, unexposed mice were placed in this chamber (to provide comparable physical stress), and the chamber was placed in a covered cardboard box on the laboratory bench to simulate the environmental conditions of the exposed mice. These control mice were always in an environment separated from the MR imaging apparatus.

Received August 11, 1986; accepted after revision September 26, 1986.

This work was supported in part by Grant CA-39632 from the National Cancer Institute, U.S. Department of Health and Human Services.

¹Department of Radiology, Baylor College of Medicine, Houston, TX 77030. Address reprint requests to N. Prasad.

²Research Service, Veterans Administration Medical Center, Houston, TX 77211.

³Laboratory of Immunogenetics, Department of General Surgery, The University of Texas M. D. Anderson Hospital and Tumor Institute, Houston, TX 77030.

⁴Center for Imaging Research, Baylor College of Medicine, 9450 Grogan's Mill Rd., The Woodlands, TX 77380.

AJR 148:415-417, February 1987

0361-803X/87/1482-0415

© American Roentgen Ray Society

Mice were sacrificed by cervical dislocation at 24, 72, and 144 hr after MR or sham exposure (control).

YAC-1 cells, a murine T-cell lymphoma of A strain origin, were used as targets in these studies. Target cells were grown as continuous cultures in RPMI 1640 medium (Grand Island Biological Co., Grand Island, NY) supplemented with 10% fetal calf serum, antibiotics (500 U/ml penicillin and 50 µg/ml streptomycin), and HEPES buffer (S-RPMI 1640).

Spleens were removed aseptically, placed in Hank's balanced salt solution, and teased apart by means of dissecting forceps. The resulting cell suspensions were filtered through a 200-mesh stainless steel screen and diluted to required concentrations. These spleen cell suspensions were passed over nylon wool columns as described in detail elsewhere [13]. Briefly, 150×10^6 splenocytes were placed on columns consisting of 0.8-g nylon wool in the barrel of a 10-ml syringe and incubated for 45 min at 37°C. After incubation, cells not adhering to the nylon wool were eluted by washing with 20 ml of warm S-RPMI 1640 and were diluted to the required concentrations. These splenocytes served as standard effector-cell populations.

The chromium release assay for natural killer cell cytolytic activity of effector splenocytes for YAC-1 target cells was performed as described in detail previously [8]. Briefly, 50 µl containing 10^4 ^{51}Cr -labeled target cells were mixed with 100 µl containing various concentrations of effector cells (1:12.5, 1:25, 1:50, and 1:100 target-to-effector-cell ratios) and incubated in quadruplicate in the wells of round-bottomed microtiter plates for 4 hr at 37°C in a 5% CO_2 , humidified atmosphere. After incubation, the plates were centrifuged at 250 g for 10 min, and then an aliquot of supernatant was removed from each well. The amount of radioactivity in the aliquot was measured in an Autogamma Scintillation Spectrometer (Packard Instrument Co., Inc., Downers Grove, IL). Spontaneous release of ^{51}Cr was determined by incubating the target cells with medium alone and ranged from 5% to 7%. The percentage of cytotoxicity was computed from specific ^{51}Cr release by the following formula:

$$\% \text{ cytotoxicity} = \frac{\text{CPM experimental release} - \text{CPM spontaneous release}}{\text{total CPM incorporated into the cells}} \times 100$$

Results

Approximately two-thirds of the animals received MR exposure or sham exposure on one day (experiment 1). The remaining animals were treated 1 week later (experiment 2). The cytotoxicity at 24, 72, and 144 hr after MR exposure (or sham exposure) was comparable for both experiments, and the data were combined for statistical analysis and presentation in this paper.

Mean values and standard errors of the percentage of cytotoxicity for all experimental groups (Fig. 1) show no evidence of decreased cytotoxicity due to exposure to MR. In fact, in all cases (i.e., at all three times after exposure and for all target-to-effector-cell ratios) the mean cytotoxicity was greater for MR-exposed groups than for sham-exposed groups. However, possibly because of the relatively small sample sizes (tissues from seven exposed or three control animals, respectively, for each mean value), analysis of variance and t-test comparisons failed to detect any significant differences between exposed and control groups.

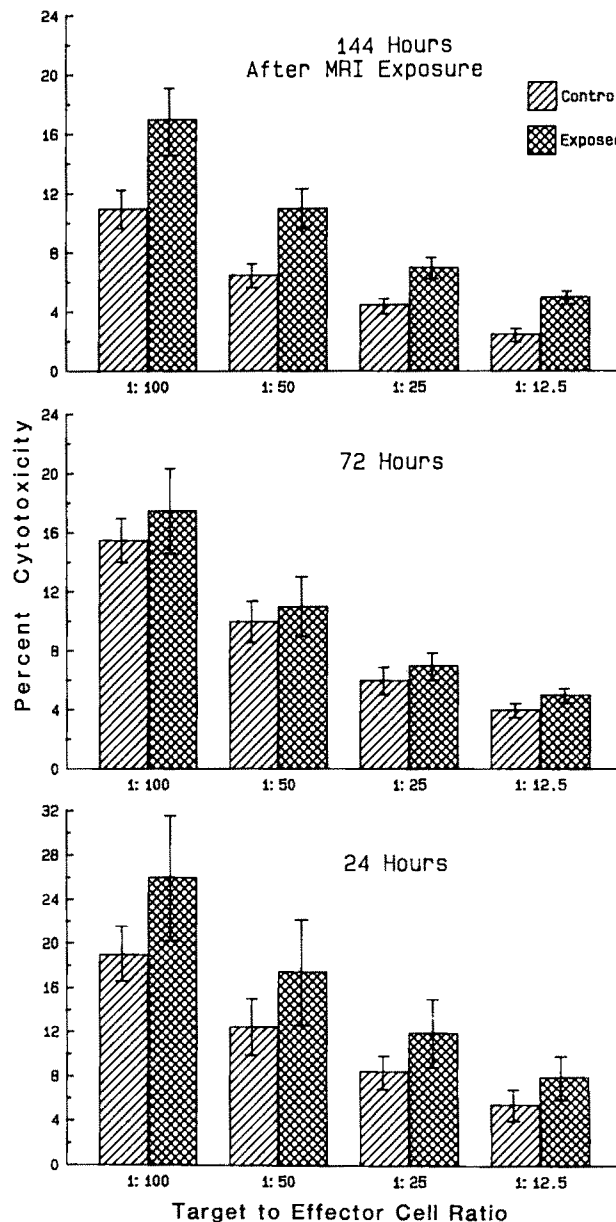


Fig. 1.—Natural killer cell cytotoxicity of spleen cells from C57BL/6 × DBA/2 F₁ male mice 24 hr, 72 hr, and 144 hr after in vivo exposure to MR imaging. Cytotoxicity was determined by the short-term ^{51}Cr -release assay with labeled YAC-1 lymphoma cells as targets. Assays were run in quadruplicate. Seven MR-exposed and three sham-exposed, control mice were used for each time period. Vertical bars show mean ± standard error.

Discussion

Recently, MR imaging systems have been approved by the U. S. Food and Drug Administration for routine clinical use in patient diagnosis. To date, thousands of patients around the world have been scanned by MR imaging. Although no adverse effect has been found, it is too early to conclude that MR exposure is completely safe.

The results of this study indicate that MR exposure has no adverse effect on the immune system as evidenced by natural killer cell activity. If anything, MR imaging may have potentiated the cytotoxic activity of natural killer cells. These cells are thought to be involved in immunosurveillance against tumors [9, 11, 12] and to provide resistance to various types of infection [10, 14]. If natural killer cell cytotoxicity is enhanced by exposure to MR, as suggested by the results of our study, then MR exposure may have a positive effect against tumors and infections. Additional research is needed to substantiate this preliminary finding and to determine the mechanism of such action.

REFERENCES

1. Steiner RE. Magnetic resonance imaging: its impact on diagnostic radiology. *AJR* **1985**;145:883-893
2. Margulis AR, Fisher MR. Present clinical status of magnetic resonance imaging. *Magnetic Resonance Med* **1985**;2:309-327
3. Budinger TF. Nuclear magnetic resonance (NMR) *in-vivo* studies: known thresholds for health effects. *J Comput Assist Tomogr* **1981**;5:800-811
4. Prasad N, Bushong SC, Thornby JI, Bryan NR, Hazlewood CF, Harrell JE. Effects of NMR on chromosomes of mouse bone marrow cells. *Magnetic Resonance Imaging* **1984**;2:37-39
5. Prasad N, Wright DA, Forster JD. Effect of nuclear magnetic resonance on early stages of amphibian development. *Magnetic Resonance Imaging* **1982**;1:35-38
6. Schwartz JL, Crooks LE. NMR imaging produces no observable mutations or cytotoxicity in mammalian cells. *AJR* **1982**;139:583-585
7. Wolff S, James TL, Young GB, Margulis AR, Bodycote J, Afzal V. Magnetic resonance imaging: absence of *in-vitro* cytogenetic damage. *Radiology* **1985**;155:163-165
8. Lotzová E, Savary CA, Stringfellow DA. 5-Halo-6-phenyl pyrimidinones: new molecules with cancer therapeutic potential and interferon-inducing capacity are strong inducers of murine natural killer cells. *J Immunol* **1983**;130:965-969
9. Herberman RB, Holden HT. Natural cell-mediated immunity. *Adv Cancer Res* **1978**;27:305-377
10. Herberman RB, Ortaldo JR. Natural killer cells: their role in defences against disease. *Science* **1981**;214:24-30
11. Hanna N, Fidler IJ. Role of natural killer cells in the destruction of circulating tumor emboli. *JNCI* **1980**;65:801-809
12. Talmadge JE, Meyers KM, Prieur DJ, Starkey JR. Role of NK cells in tumor growth and metastasis in beige mice. *Nature* **1980**;284:622-623
13. Lotzová E, Savary CA, Hersh EM, Khan AA, Rosenblum M. Depression of murine natural killer cell cytotoxicity by isobutyl nitrite. *Cancer Immunol Immunother* **1984**;17:130-134
14. Welsh RM. Mouse natural killer cells: induction, specificity, and function. *J Immunol* **1978**;121:1631-1635

Technical Note

Intensity Correction in Surface-Coil MR Imaging

Leon Axel,¹ Jay Costantini,² and John Listerud³

The use of surface coils in MR imaging has made it possible to obtain images of superficial structures with improved signal-to-noise ratio relative to conventional circumferential receiver coils [1-4]. However, the signal intensity distribution in surface-coil images is inherently nonuniform; the decreased sensitivity to signal from more distant regions implies a corresponding decreased sensitivity to noise from those regions. As the total noise detected is uniformly distributed over the image, there is a net increase in the signal-to-noise ratio in the image of regions closer to the coil as compared with the conventional receiver coil [1, 5]. The resulting range of relative intensity over surface-coil images makes it difficult to display them properly or to analyze them quantitatively. In addition, the local image contrast will decrease proportionally to the average local intensity. We report a method for correcting such surface-coil images so as to produce a uniform relative intensity over the region being imaged.

Methods

Surface-coil images are obtained both of the desired object and of a uniform phantom placed in the same position on the coil. The image of the phantom is normalized (so as to serve as a calibration of the surface-coil response pattern) and divided into the image of the object. Thresholding can be used to mask out the background. Conventional two-dimensional Fourier transform MR images have uniformly distributed noise [6]. Although the relative intensities will be made uniform in the resulting corrected image, the local noise in the corrected image will now be nonuniform, owing to the relative boost in the region of lower-coil sensitivity in proportion to the amount the signal has been boosted. If the calibration phantom image is relatively

low in noise, the actual local signal-to-noise ratio will be essentially unchanged from the original image.

An alternative method can be used to approximately correct a surface-coil image of an object for the pattern of nonuniform coil response without acquiring an additional image of a uniform phantom. The original image of the object is blurred to suppress the details of the object and thus to serve as an approximation of the image of a uniform phantom. This blurred image of the object can then be divided into the original image, as above, to produce an approximately corrected image. For the white noise typical of an MR image, the blurring process will produce a low-noise correction image.

This technique was implemented on images obtained with a simple 3-cm-wide rectangular surface coil used as a receiver coil, magnetically orthogonal to a circumferential exciting coil in a 1.4-T small-bore MR imaging system. The image processing was carried out with a Data General S-140 imaging system computer (Woodbury, MA).

Results

An image of the wrist obtained with the surface coil, with TR = 500 msec, TE = 16 msec, four signals averaged, 256 × 256 data acquisition matrix, 8-cm field of view, and 5-mm slice thickness, is shown in Figure 1. An image of a bag of normal saline, containing 2 mM CuSO₄, obtained with the same coil in the same position, is shown in Figure 2. The result of dividing the first image by the second (masking out the background) is shown in Figure 3.

As an approximation to the phantom image, the original image was blurred by repeatedly convolving the image with a 9 × 9 pixel kernel, as shown in Figure 4. The result of dividing this image into the original image is shown in Figure 5.

Received June 9, 1986; accepted after revision September 10, 1986.

Presented at the annual meeting of the American Roentgen Ray Society, Washington, DC, April 1986.

This work was supported in part by funds from the Pennsylvania chapter of the American Heart Association.

¹ Department of Radiology, Hospital of the University of Pennsylvania, 3400 Spruce St., Philadelphia, PA 19104. Address reprint requests to L. Axel.

² School of Medicine, University of Pennsylvania, Philadelphia, PA 19104.

³ School of Medicine, University of Washington, Seattle, WA 98105.

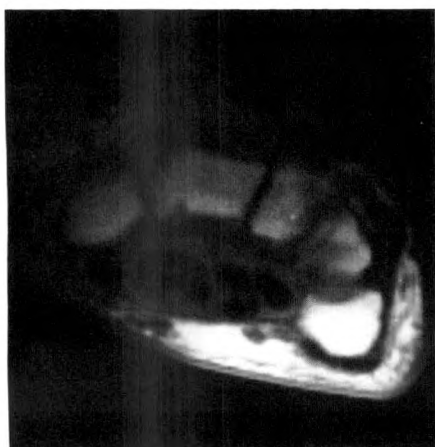


Fig. 1.—Surface-coil image of wrist; surface coil under volar aspect of wrist. Relatively small size of surface coil produces a rapid falloff of sensitivity and a corresponding rapid decrease in image intensity.



Fig. 2.—Surface-coil image of uniform phantom in same position as wrist in Fig. 1.

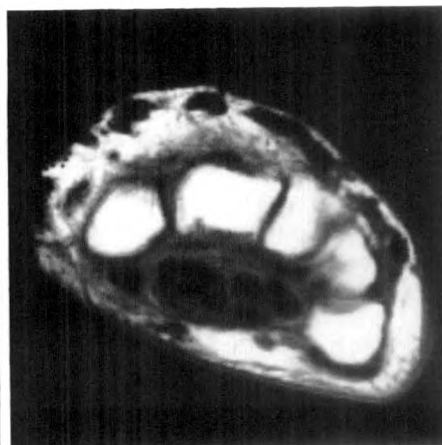


Fig. 3.—Corrected version of image in Fig. 1, produced by dividing by image in Fig. 2.

Fig. 4.—Blurred version of Fig. 1.

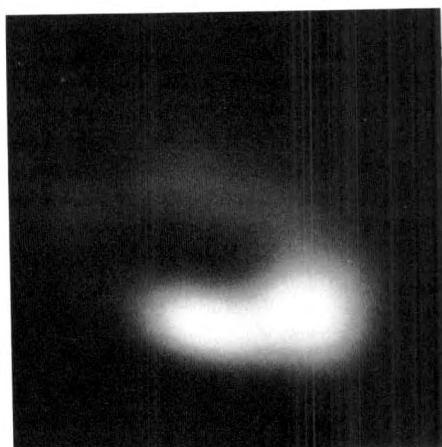
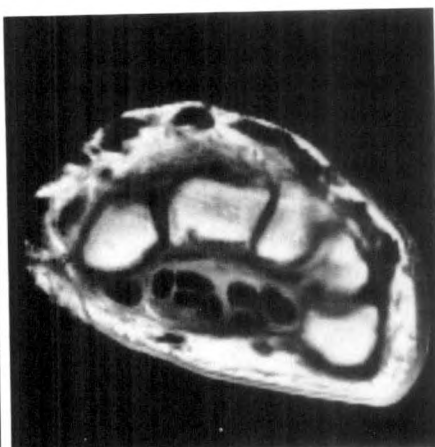


Fig. 5.—Approximately corrected version of Fig. 1 produced by dividing by blurred version in Fig. 4.

4



5

Discussion

This technique of surface-coil image intensity correction can produce good-quality corrected images, as in this example. Although it “flattens out” the overall effective sensitivity, it cannot improve the local signal-to-noise ratio (for a low-noise calibration, it also will not harm signal-to-noise ratio). Thus, the relative noisiness of the image of regions distant from the coil may be apparent in the corrected image. If this is objectionable, these regions can be easily masked out in the image correction process, just as the background was here. If the background in the calibration image is not masked out of the final image, the noisiness of these regions may be objectionable. Thus, the uniform phantom used to make the calibration image should cover at least the region likely to be of interest in the object imaged with the surface coil.

In making the overall intensity more uniform, this technique also corrects the relative contrast in different regions. In

approximately correcting the surface-coil image by dividing the image by a blurred version of itself, the overall intensity variations of the original object will be flattened and the intensity profiles of edges somewhat distorted, although local contrast will be approximately corrected. This sort of nonlinear image processing is equivalent to homomorphic filtering [7, 8]. Conventional unsharp masking, equivalent to subtracting a blurred version of the surface-coil image from the original, will produce a flattening of large-scale intensity variations in the object and will not correct the relative decrease of local contrast in regions more distant from the surface coil.

With reproducible surface-coil positioning, the pattern of response of the coil can be stored and used to correct subsequent surface-coil images without repeated phantom calibration images. Alternatively, a simplified form of the coil response can be stored and used to approximately correct the images in a similar manner with less attention to precise positioning. Because the surface-coil response pattern is

usually a relatively slowly changing function of position, small amounts of misregistration will generally not be a problem.

In this system, with uniform excitation and use of the surface coil only as a receiver, the image of a uniform phantom can be used to fully correct the image of the object. However, in systems that use the surface coil for both excitation and receiving, the variation of flip angle with distance from the coil will result in a corresponding variation of saturation that will depend on the local T1 relaxation time. This cannot be fully corrected for with the image of the uniform phantom, even if the T1 relaxation time of the phantom is adjusted to match the average value in the object. The simple approximate correction produced by dividing the image of the object by a blurred version of itself will still be useful for reducing the overall range of intensities in the image while approximately correcting local contrast.

Although the procedure of correcting surface-coil images with a calibration obtained by imaging a uniform phantom gives the best corrected image, for many imaging applications the approximation produced by simply using a blurred version of the original image instead of such a phantom image will be useful and will have the advantages of not requiring any

additional imaging time or care in reproducibly positioning the coil.

REFERENCES

1. Bernardo ML, Cohen AJ, Lauterbur PC. Radiofrequency coil designs for nuclear magnetic resonance zeugmatographic imaging. In: Nalcioglu O, Prewitt JMS, eds. *Institute of Electrical and Electronic Proceedings Engineers Proc International Workshop Physics and Engineering in Medical Imaging* Asilomar, CA, March 1982;277-287
2. EL Yousef SJ, Alfidi RJ, Duchesneau RH, et al. Initial experience with nuclear magnetic resonance (NMR) imaging of the human breast. *J Comput Assist Tomogr* 1983;7:215-218
3. Axel L. Surface coil magnetic resonance imaging. *J Comput Assist Tomogr* 1984;8:381-384
4. Edelstein WA, Schenck JF, Hart HR, Hardy CJ, Foster TH, Bottomley PA. Surface coil magnetic resonance imaging. *JAMA* 1985;253:828
5. Hayes CE, Axel L. Noise performance of surface coils for magnetic resonance imaging at 1.5 T. *Med Phys* 1985;12:604-607
6. Edelstein WA, Glover GH, Hardy CJ, Redington RW. The intrinsic signal-to-noise ratio in NMR imaging. *Magn Reson Med* 1986;3:604-618
7. Oppenheim AV, Schaffer RW. *Digital signal processing*. Englewood Cliffs, NJ: Prentice-Hall, 1975
8. Lufkin RG, Sharpless T, Flannigan B, Hanafey W. Dynamic-range compression in surface-coil MRI. *AJR* 1986;147:379-382

Total Digital Radiology Department: Spatial Resolution Requirements

G. W. Seeley^{1,2}
H. D. Fisher³
M. O. Stempski¹
M. Borgstrom¹
J. Bjelland¹
M. P. Capp¹

The minimum spatial resolution required for a total digital radiology department has yet to be defined. A pilot study designed to provide this information was performed. Abnormal and normal radiographic images of children were digitized and redisplayed on film at spatial resolutions of 5.0, 2.5, 1.25, and 0.625 lp/mm. These resolutions are comparable to a digital display of a 14 × 14 in. chest image having pixel elements of 4096 × 4096, 2048 × 2048, 1024 × 1024, and 512 × 512, respectively. Contrast resolution was maintained at 12 bits or 4096 gray levels. The three phases of data acquisition were (1) the standard analysis of receiver operating characteristics, (2) a checklist evaluation of the "seeability" of important structures, and (3) a comparison of all resolutions and a discernment of usability. Fifteen radiologists participated in the study. On the basis of the pediatric cases used, the results showed that the needed spatial resolution for a total digital radiology department may be around 2.5 lp/mm (2048 × 2048). Checklist data on seeability of structures and comparisons of all resolutions give information on specific changes that are occurring as the resolution is decreased, and, when included with the receiver-operating-characteristic data, they become a major component in developing a resolution standard. The finding that 2.5 lp/mm is the required spatial resolution makes construction of a total digital radiology department possible with present state-of-the-art technology.

The total electronic or digital radiology department becomes more possible every year because of the electronic revolution and the consequent increase in computer power and capabilities [1-3]. One major requirement is that performance proficiency must be equal to or better than that permitted by the existing film-based system. Therefore, establishing the spatial- and contrast-resolution needs for such a department is imperative.

Contrast resolution has the greatest effect on general diagnostic accuracy. However, in terms of engineering design requirements for a total digital radiology department, spatial resolution has the greatest impact on design costs, transmission-speed requirements, and storage needs. For example, assume that a 1024 × 1024 pixel spatial resolution with a 10-bit gray-scale contrast resolution is not sufficient to give the radiologist equivalent diagnostic information on a digital display as compared to a 14 × 14 in. (35.6 × 35.6 cm) chest film. Doubling the spatial resolution will increase the amount of information to be manipulated in each image by 300%, whereas doubling the contrast resolution from 10 bits to 11 bits will increase the amount of information to be manipulated by only 10%.

This pilot study used clinical images to investigate spatial-resolution requirements for a total digital radiology department.

Materials and Methods

Original clinical film images were digitized and written back to film at spatial resolutions of 5.0, 2.5, 1.25, and 0.625 lp/mm. These resolutions are comparable to a digital display of a 14 × 14 in. chest image having pixel elements of 4096 × 4096, 2048 × 2048, 1024 × 1024,

Received June 2, 1986; accepted after revision September 10, 1986.

This work was supported by a grant from the Toshiba Corporation.

¹ Radiology Department, University of Arizona Health Sciences Center, Tucson, AZ 85724. Address reprint requests to G. W. Seeley.

² Optical Sciences Center, University of Arizona, Tucson, AZ 85721.

³ Science Applications Inc., 5151 E. Broadway, Tucson, AZ, 85711.

AJR 148:421-426, February 1987
0361-803X/87/1482-0421
© American Roentgen Ray Society

and 512×512 , respectively. Contrast resolution was maintained at 12 bits. For this study, the display medium was always film.

Eight pediatric cases (four with interstitial lung disease and four normals) were selected. The abnormal radiographic findings accepted as correct for the four disease cases were (1) diffuse interstitial infiltrates, especially in the right and lower lung—possible pulmonary edema; (2) bilateral rib notching, diminished pulmonary vascularity, increased interstitial markings, and diminished bilateral pulmonary vascularity associated with abnormal cardiac configuration; (3) peribronchial thickening, increased interstitial markings, and possible cystic fibrosis or asthma; and (4) diffuse bilateral infiltrates and wet lung/edema. Truth of diagnosis was based on follow-up radiographs. For the normal cases, subsequent normal radiographs were required.

Normal cases were matched to the disease cases for film type, density range, age, and sex. Each case was digitized by using a $100\text{-}\mu\text{m}$ aperture on a Boller and Chivans flatbed microdensitometer (Applied Science Division, Perkin-Elmer, Garden Grove, CA). The number of points per line and the number of lines were set to 2048×2048 and covered an area of approximately 8×8 in. (20.3×20.3 cm) which was sufficient to include all the necessary information. This sampling procedure gave a resolution of 5 lp/mm without concern that we were introducing sampling error. The resulting digital images were then stored in a VAX 11/780 computer (Digital Equipment Corp., Maynard, MA), and a Gaussian blur function was applied to the original images. For creation of different spatial resolutions, the Gaussian blur's full width at half maximum was increased, thereby increasing the diameter of the blurring function so that it averaged more of the data as the resolution was decreased. The values used were 2, 4, and 8 for 2.5 lp/mm, 1.25 lp/mm, and 0.625 lp/mm, respectively. Tests were run on the blurred images to ensure that any changes introduced would be within acceptable tolerances. The mean and standard deviation of the pixels were calculated for the original and all the blurred images. If the blurred images were being produced properly, the means should have been the same and the standard deviations should have decreased as blur increased. This was the case for all images.

The flatbed microdensitometer was then used to write the four sets of 2048×2048 image matrices (differing only in their spatial resolution) on Kodak OM-1 film (Eastman Kodak Co., Rochester, NY). Each image took 4 hr to write. The total time for digitization and writing was 160 hr. A look-up table was incorporated to increase or decrease the light in the light-emitting diode in order to achieve the same contrast levels as those measured in the original images. The look-up table was created by digitizing a conventional radiograph of a step wedge, writing it back to film, developing the film, and then comparing the resulting densities measured with a densitometer to the original step wedge. A corrective look-up table was then incorporated to adjust the light-emitting diode's intensity as it wrote back to film. The process was continued until the difference between the original and the copy deviated by no more than 2%. This same step wedge was written to film many times and was used to standardize the radiographic film developer. Each time a batch of films was ready to be processed, the step wedges were put through the processor first, and adjustments were made until the densities measured were the same as those of the original step wedge. Once that was accomplished, the films were processed. This pilot study used not only the four sets of digital images written to film but also the original analog images. The original images provided a basis of comparison for the digitized images.

Three phases of data acquisition were used in this study. In the first phase, each of the 15 participating radiologists was shown images from only one resolution level. Because there were five sets of resolution images (four digital and one analog), the results discussed in the following sections represent the answers from three

radiologists per resolution level. To counter any bias due to this experimental design, the radiologists in all groups were matched on background, experience, and familiarity with pediatric chest images. The observers were a mix of fourth-year residents and junior and senior staff members. During each session, four types of data were acquired. First, the images were shown one at a time in random order to the participating radiologists. Their task was to decide whether the findings were abnormal. They used a six-point certainty scale as described in Seeley et al. [4] when giving their diagnoses so that an analysis of standard receiver operating characteristics could be performed [5–7]. If the finding was abnormal, the radiologist was required to state the type of abnormality and location of the disease. In the second phase, the case images were displayed again one at a time, but this time the radiologists were asked to rate the "seeability" of different structures. The checklist used for the thorax images and most of the scale used to define the perceptibility of the structures are described fully in Seeley and Newell [8]. The third type of data acquired was the subjective evaluation of each radiologist concerning the usability of different levels of spatial resolution. In this phase, all the resolutions for selected cases were put on the light box, and the radiologist assessed each spatial resolution level. Finally, eight radiologists were given images of the same case in random order and had to place the images in order of highest to lowest resolution. These eight radiologists fully represented the cross section of observers used in the study. Only eight were used because of time constraints.

Results

Analysis of Receiver Operating Characteristics

Figure 1 shows the receiver-operating-characteristic curves and the areas under the curves for all of the five resolutions studied. In general, the results were very clear. The 0.625 lp/mm spatial resolution was not acceptable. The information

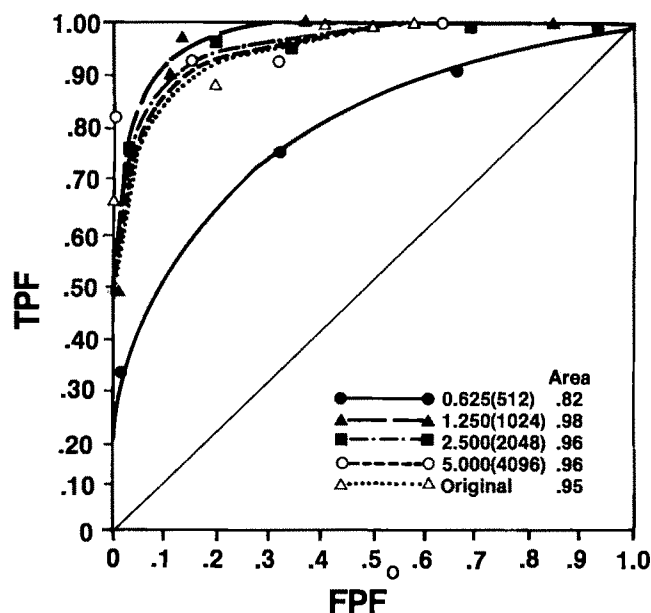


Fig. 1.—Receiver-operating-characteristic curves and areas under the curves for the five resolutions studied. TPF = true positive fraction; FPF = false positive fraction.

content from the 1.25 lp/mm resolution was virtually equivalent to that of the original films. A detailed analysis of the responses showed that the radiologists viewing the 0.625 lp/mm resolution reported 70% false-positives, therefore overcalling these images. This result was also verified anecdotally in conversation with the radiologists.

Checklist Analysis

The findings in the receiver-operating-characteristic analysis were further substantiated by the results of the data analysis of the seeability checklist. Table 1 shows the type of structures that disappeared. The ratio X/Y means that at the lowest resolution, the structure was seen only X times out of the Y total for all resolutions (i.e., Y maximum = 75, 15 radiologists at 5 resolutions). Frequently, structures were not imaged at all at the low-resolution. What disappeared was the fine detail or the sharpness of the edge resolution.

Comparison of Resolutions

The next set of data was consistent with the previous two. When the radiologists viewed all the different resolution levels at one time, they unanimously agreed that (1) they would not want to work with the 0.625 lp/mm resolution; (2) although they could see everything necessary on the 1.25 lp/mm resolution images, they did not feel comfortable with these images; and (3) they would be satisfied to work with the 2.5 lp/mm images and did not think that the 5.0 lp/mm level was necessary. This last point was supported by the data from the eight radiologists who were asked to put the images in order of resolution from low to high. All eight correctly ordered the 0.625 and the 1.25 lp/mm images. However, in comparing the 2.5 and the 5.0 lp/mm images, two of the radiologists were unable to differentiate between the two.

TABLE 1: Type of Structures That Disappeared in the Lowest Resolution

Structure	Ratio of Structure Seen (X/Y)
Peripheral structures	
Interstitial structures	4/55
Pulmonary vascular structures	7/62
Edge resolution	
Hilar bronchial structures	2/55
Hilar vasculature	7/62
Osseous erosions	
Ribs	0/41
Clavicles	0/30
Cortical structures	
Ribs	5/64
Clavicles	6/56
Trabecular structures	
Ribs	0/35
Clavicles	0/27

Note.—Ratio X/Y: the structure was seen X times at the 0.625 lp/mm resolution out of Y total sightings at all five resolutions. In many cases the structure was not seen at all at the lowest resolution.

Discussion

Experiments dealing with the evaluation of clinical images must be carefully controlled. Several choices and solutions went into the planning and implementation of this experiment.

For the experimental phase, we needed to ensure that the images and experimental situation were as close as possible to the radiologists' accustomed clinical conditions. Film was selected as the display medium for this study because (1) film is what the radiologist is used to, and it has been shown that introducing a new system can greatly affect the sensitivity of the radiologist [4]; and (2) no other type of medium can display all of the different resolution levels. Once it was decided to use film, Kodak OM-1 film was chosen because it had the same type of blue background that the radiologist was expecting (we would not be introducing bias due to an unfamiliar background), and it was one of the few films sufficiently sensitive to the light-emitting diode that we were using.

The upper limit of 5 lp/mm was chosen because this is the point for standard film-screen systems at which the modulation-transfer function levels off, and it is the standard spatial resolution in clinical practice. Because this study was concerned with spatial resolution only, contrast resolution was taken at 12 bits to ensure that any effects due to contrast or contrast-spatial resolution interactions would be virtually eliminated. We used a Gaussian blur function to reduce resolution. It best simulated what would occur with imaging systems of different spatial-resolution acquisition capabilities, and it allowed us to maintain the same number of scan lines in each of the resolution levels, thus avoiding problems or bias due to the images not being equal in every aspect except spatial resolution (i.e., artifact introduction through the reduction of the number of lines and pixels in each line whether through averaging or subsampling). The objective was to ensure that the resultant images would be truly representative of images from acquisition systems of different spatial capabilities.

Figure 2 shows all four resolutions for one of the cases used in the study. Fine-detail resolution is degraded as resolution decreases. To show how much information was lost at the different resolution levels, a 512×512 section was taken from the 2048×2048 digital matrix and displayed on the monitor. Figure 3 is a composite of these images. Each part is the upper left-hand corner of the corresponding image in Figure 2. Once the 512×512 sections were extracted, the 2.5, 1.25, and 0.625 lp/mm resolutions were subtracted from the 5 lp/mm section. Figure 4 shows the type and amount of information that are lost as the spatial resolution decreases. As can be seen from the increase in fine detail, when lower and lower resolutions are subtracted from the 5 lp/mm image, there is a definite loss of high-frequency information as spatial resolution decreases. Thus, there is a marked decrease in information content for the radiologist to use for diagnosis. However, smaller losses in high-frequency information seem to give acceptable diagnostic accuracy as was described for the analysis of receiver operating characteristics.

The results of the study show that, on the basis of the pediatric cases used, the needed spatial resolution for a total

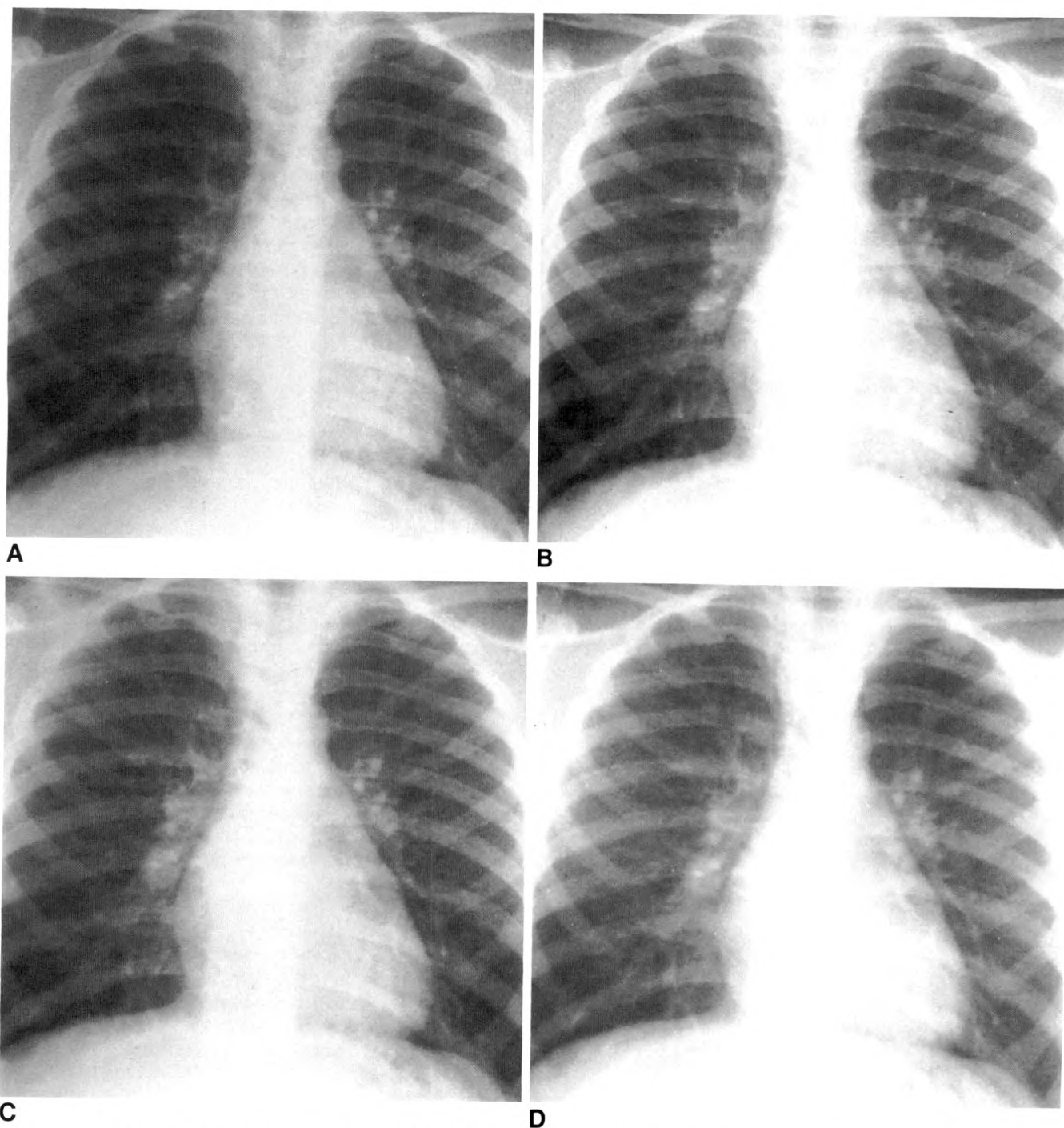


Fig. 2.—Chest radiographs showing images at four resolutions for one case in the study. A, 5 lp/mm. B, 2.5 lp/mm. C, 1.25 lp/mm. D, 0.625 lp/mm.

digital radiology department may be around 2.5 lp/mm (2048 × 2048). Checklist data on seeability of structures and comparisons of all resolutions give information on specific changes that are occurring as the resolution is decreased, and, when included with the receiver-operating-characteristic data, they become a major component in development of a resolution

standard.

Although the results of this study are intriguing, a statement on the resolution requirements for a total digital radiology department must be tempered. The results are based on a small number of images and a small number of radiologists, with a relative paucity of data for constructing the receiver-

Fig. 3.—512 × 512 section taken from 2048 × 2048 matrix that made up digital images. Each shows upper left-hand corner of corresponding image in Fig. 2. A, 5 lp/mm. B, 2.5 lp/mm. C, 1.25 lp/mm. D, 0.625 lp/mm.

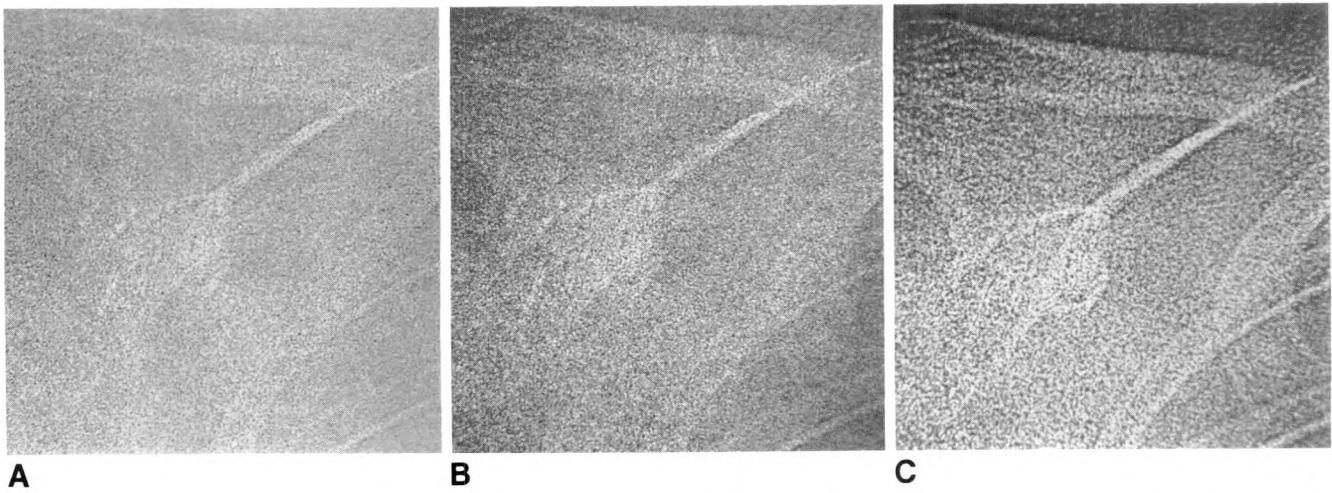
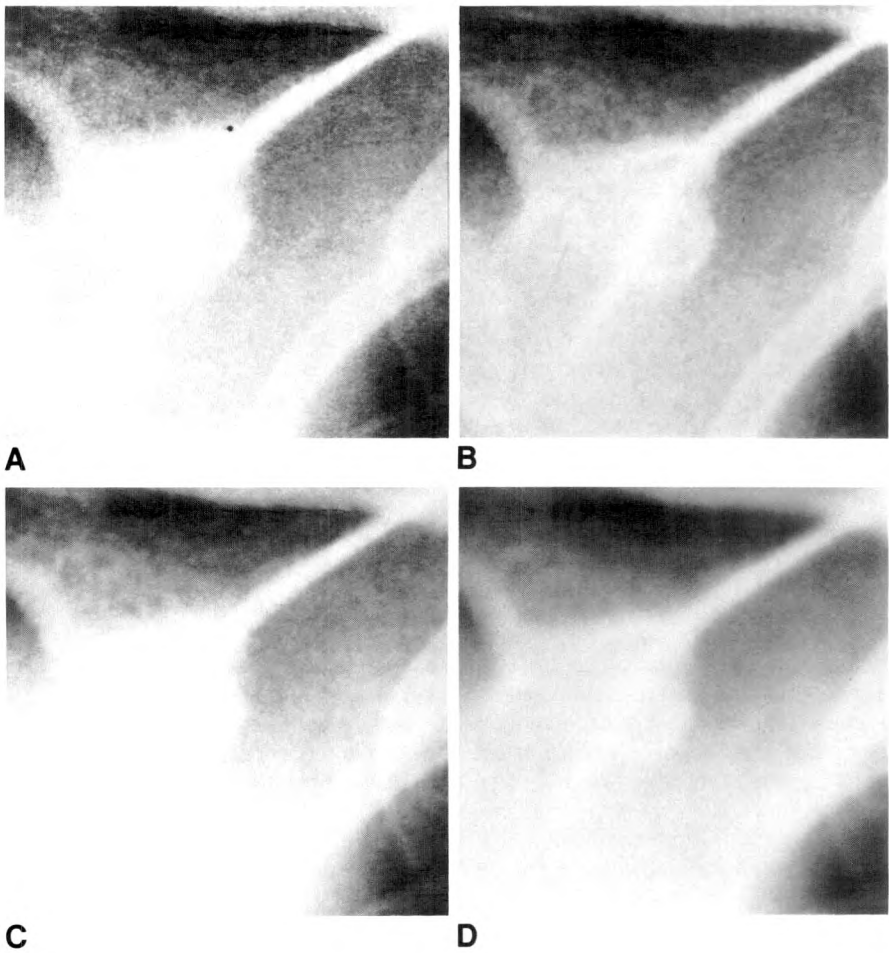


Fig. 4.—Resulting images from a subtraction of all lower resolution sections from 5.0 lp/mm image in Fig. 3A. Amount of structure lost as resolution is decreased can now be seen. A, Subtraction of 2.5 lp/mm section. B, Subtraction of 1.25 lp/mm section. C, Subtraction of 0.625 lp/mm section.

operating-characteristic curves. However, the images selected were the most demanding in terms of spatial-resolution requirements. In addition, even in the first phase of this pilot study [8, 9] when only two radiologists were being analyzed per resolution level, the same results were found.

The findings of similar results with as few as two observers per resolution level and the demonstrable loss of adequately visualized structures lead us to anticipate similar results in the larger scale studies that we have planned. If this occurs, then the problems of building a total digital radiology department may not be insurmountable.

In the resolution-comparison phase of this study, many of the radiologists were surprised that resolutions such as 1.25 lp/mm compared so favorably to the original in the quality of diagnostic information. They pointed out that this was the first time they were able to see, at one time, all the resolutions that are referred to in the literature. All of them suggested that although 1.25 lp/mm images might be adequate for most cases, they favored 2.5 lp/mm as a standard.

This study also shows that with proper care, all aspects of the experimental situation—from the selection of the images, through the generation of the experimental images, to the actual data-taking—can be controlled well enough to provide consistent and useful data. In addition, taking three different types of data during the experiment gives a much broader picture of what happens when spatial resolution is reduced than using only receiver operating characteristics. This type of research can never find “the answer” because all the possibilities can never be tested with the finite time and resources available. However, having three different types of

data that correspond so consistently increases the certainty that the results actually reflect true phenomena.

A more comprehensive study is now in progress with more cases (50) and more radiologists (20). The results from that study will be reported subsequently.

REFERENCES

1. Seeley GW, Ovitt T, Capp MP. The total digital radiology department: an alternative view. *AJR* 1985;144:421–422
2. Capp MP, Roehrig H, Seeley GW, Fisher HD, Ovitt T. The digital radiology department of the future. *Radiol Clin North Am* 1985;23:349–355
3. Capp MP, Seeley GW, Fisher HD, Roehrig H, Ovitt TW. Computerized electronic radiology department. In: Hunter T, ed. *The computer in radiology*. Rockville, MD: Aspen, 1986;235–254
4. Seeley GW, Stempki M, Roehrig H, Nudelman S, Capp MP. Psychophysical comparison of a video display system to film by using bone fracture images. Presented at the First Institute of Electrical and Electronic Engineers Computer Society International Symposium of Medical Imaging and Image Interpretation. Berlin, West Germany, October 1982
5. Green DM, Swets JA. *Signal detection theory in psychophysics*. New York: Wiley, 1966
6. Swets JA. The relative operating characteristic in psychology. *Science* 1973;182:990–1000
7. Swets JA, Pickett RM. *Evaluation of diagnostic systems: methods from signal detection theory*. New York: Academic Press, 1982
8. Seeley GW, Newell J II. The use of psychophysical principles in the design of a total digital radiology department. *Radiol Clin North Am* 1985;23:341–348
9. Fisher HD, Seeley GW, Bjelland J, Ovitt TW, Capp MP. Psychophysical evaluation of the necessary spatial and contrast resolution for a picture archiving and communication system: works in progress. Presented at the meeting of the Institute of Electrical and Electronic Engineers Computer Society Medical Images and Icons. Arlington, VA, July 1984

Commentary

Picture Archiving and Communication Systems in Japan

H. K. Huang,¹ Nicholas J. Mankovich, Paul S. Cho, Rick Taira, Brent K. Stewart, and Bruce K. Ho

Our department has been involved in the research and development of picture archiving and communication systems (PACS) for the past 4 years. Two PACS modules, one in pediatric radiology and the other in the coronary care unit, are now under clinical evaluation. We have established close contact with many hospitals and the medical imaging industry, not only in the United States but also in Japan, and are impressed by the dedication and commitment of our Japanese colleagues and the advances in their PACS-related industry.

Approximately 4 years ago Japan launched a national project to manage medical images and personal health data. Subsequently, two projects were defined—Picture Archiving and Communication Systems (PACS) for Medical Imaging and Personal Health Data Recording System (PHD)—and the Japan Society of PACS was formed. The members of the Society include academic scholars as well as technical and administrative staff from major medical imaging manufacturers. The first International Symposium on PACS and PHD was convened in the summer of 1984 under the sponsorship of the Japan Association of Medical Imaging Technology (JAMIT), and the meeting has since become an annual event.

In order to further study the Japanese technological developments in PACS we decided to attend the third annual meeting, and at the same time visit manufacturers involved in PACS research and development, as well as visit hospitals that are implementing PACS modules.

The Japanese PACS Meeting

The third International Symposium on PACS/PHD in conjunction with the Fifth Symposium on Medical Imaging and

Technology was held in July 1986 at the National Cancer Center, Tokyo.

The official language of the meeting was English for the first 2 days; then on the third and fourth days it was Japanese or English. The published proceedings were available during the meeting and can be ordered by writing to Japan Association of Medical Imaging Technology, Omuro Building, (6F) 6-2, Yushima-1-Chome, Bunkyo-ku, Tokyo, 113 Japan. The highlights of the meeting related to PACS were: (1) "System description and implementation of PACS at UCLA," by the Medical Imaging Division, Department of Radiological Sciences, UCLA, which described how PACS is being implemented at UCLA [1]; (2) "Facets of PACS," by Dr. Morio Onoe, Professor Emeritus, University of Tokyo, Tokyo, who emphasized the importance of the availability of optical storage devices for medical image storage; and (3) the system descriptions and preliminary clinical results of different PACS modules as presented by researchers in both the Japanese hospitals and medical manufacturers. We believe that the meeting was very informative and were surprised at the number of Japanese hospitals actually implementing PACS modules.

Manufacturer Visits

We spent 8 days visiting the PACS research and development laboratories of four major imaging manufacturers, including Fuji Photo Film Company, Ltd., Hitachi Medical Corporation, Konishiroku Photo Inc. Co., Ltd., and Mitsubishi Electric Corporation; we also visited Abe Sekkei, Inc., a laser scanner/printer manufacturer. In addition, we had detailed

Received August 14, 1986; accepted after revision September 5, 1986.

¹ All authors: Medical Imaging Division, Department of Radiological Sciences, University of California, Los Angeles, Los Angeles, CA 90024. Address reprint requests to H. K. Huang.

discussions with the chief engineers responsible for PACS design at both Nippon Electronic Corporation (NEC) and Toshiba Corporation. During the visits and discussions we paid particular attention to their research and development efforts in the scanning-laser-stimulated-luminescence plate system, X-ray film digitizer, image compression, image storage, and image display stations.

The scanning-laser-stimulated-luminescence plate system (computed radiography, or CR, system) was originally announced at the 1981 Brussels International Congress of Radiology. More than 40 systems are now in operation in Japan, four in the United States, and one in Europe. The CR has gained general acceptance in the Japanese radiologic community. There are three types of CR systems: (1) the general purpose system, which is used as a replacement for the conventional film/screen cassette system, (2) the upright chest system, and (3) the table system. Both the second and the third types are dedicated systems, which require no cassettes, and the operation is entirely automated after the X-ray exposure.

The basic components of a CR system include the imaging plate, the laser reader, and the laser film printer. These components are manufactured by Fuji Photo Film Company, Ltd., Tokyo, Japan. Similar systems based on the same technologies are also manufactured by Philips Medical Systems, Shelton, CT, and Toshiba Corporation, Japan. The CR input device, which can potentially be used by all conventional radiologic procedures in a department, is one of the most important components in a PACS.

In the development of the X-ray film laser scanner, five companies have delivered scanners to their customers: Abe Sekkei, Inc., Hitachi Medical Corporation, Mitsubishi Electric Corp., Konishiroku Photo Ind. Co., Ltd., and Toshiba Corporation. All the laser scanners now in use have spatial resolution in excess of 2048×2048 with density resolution from 10 to 12 bits.

Image compression is a major research topic at most universities and manufacturers implementing PACS. Extensive research and development efforts are in progress. A few manufacturers are in the hardware implementation stage using error-free and transform coding techniques. Reconstructed images from compressed data by using the transform coding technique with compression ratios as high as 20:1 on a 2048×2048 image show excellent quality.

Digital optical storage devices have become a common technology in the Japanese medical imaging industry. Optical disks with 2.6 to 3.6 gigabytes image storage are being used by manufacturers and hospitals. Some manufacturers are also using the optical disk library (jukebox) in their research and development laboratories for long-term image archiving.

In contrast to the United States, the image display station in Japan is not developed for display of CT and MR images; instead, it is developed for viewing conventional radiographs. The components in an image display station are the laser film scanner, optical disk storage, display monitors, and laser film

printer. All the major manufacturers described earlier have delivered image display stations for clinical evaluation.

The standard format of image display stations is two 1024×1024 monitors with easy-to-use retrieval and review operations. The first 2048×2048 display station with two monitors designed by Mitsubishi Electric Corporation became available at UCLA in October 1986. The system was also displayed at the 1986 RSNA meeting.

Hospital Visits

We visited two hospitals that are using the computed radiography (CR) system for routine clinical diagnosis; these hospitals are also in the process of implementing other PACS modules.

The first hospital was Kanagawa Cancer Center in Yokohama. The radiologist in charge is Dr. Kunio Odagiri, who trained at the University of Pittsburgh for 6 years. The floor plan of the hospital's radiology department is based on a three-layer architecture system with an outer corridor as the patient waiting area; the middle layer contains all of the procedure rooms and the inner layer contains the processing and reading area. The hospital is quite new and the department performs about 120,000 procedures per year. It is equipped with one general purpose CR and one upright chest CR system. About 45% of the general procedures use the CR; mammography, angiography, chest, and tomography use the CR system exclusively. However, they still use light boxes to view the films produced by the CR. The operation of the department is efficient and clean. The quality control of the imaging equipment is excellent.

The department also uses a Toshiba optical storage system connecting a CT scanner and an MR scanner together for image storage and review. The storage includes a Toshiba 3.6-gigabyte optical disk drive.

Our next visit was to Kitazato University (East) Hospital in Sagami Ono, Yokohama, opened in April 1986. The hospital is built like a hotel for long-term inpatient stays. Professor Kusano was the radiologist in charge of the department. He visited many U. S. hospitals before finalizing the plans for his department. The department has one general-purpose, one upright-chest, and one table CR system. The image readers of the upright-chest and the table CR are in two different procedure rooms, and the image recorders of all three systems are centrally located in a processing area. The department has two Toshiba Total Digital Imaging Systems (TDIS) for digitizing films, storing images, and displaying images. The department also uses a computer system for case dictation. The residents actually key in the diagnosis by using a standardized pretext format through terminals. They seem to have no problems in doing so.

At least three new hospitals are just completing construction that will use CR systems as a replacement for all conventional film/screen systems.

Collaboration Between University Hospitals and Manufacturers

The PACS/PHD project is a national project in Japan. We observed that most major manufacturers in medical imaging are investing substantially in this project. The execution of this research and development venture follows the same course in each company: the manufacturer first develops the concept, then implements the system, and finally places prototypes in selected hospitals. The selected hospitals are subsidized by national research funds to perform clinical evaluation with the system. In general, the manufacturer delivers a turnkey system to the hospital, and the physicians in the hospital then provide the clinical evaluation. It is rare that basic science staff in Japanese hospitals are involved in the implementation and development of the PACS system. Table 1 summarizes, to the best of our knowledge, the collaboration effort between university hospitals and manufacturers in Japan.

Discussion

Implementation of PACS requires two ingredients: its acceptance by the radiologic community and a commitment from the manufacturers.

The Japanese radiologic community has accepted the concept of digital radiology. In fact, it is a national goal of Japan to introduce PACS into the country's radiology departments as soon as possible. Japanese manufacturers are strongly committed to placing PACS into full clinical operation. Substantial research and development efforts have been made by the government and the manufacturers in the past few years. The only drawback at this point is that we do not see evidence of support from basic science staff within the radiology departments. PACS is not an imaging technique and requires on-site iterative modification before a system can function properly in a department. Its implementation requires the support of both the research staff and the clinical staff.

In the United States, electronic imaging research was started in the early 1970s [2], and the first International Conference on PACS was held in California in 1982 [3]. During the past 4 years PACS projects have shown some progress in University hospitals through the dedication of research and clinical staff [4]. However, up to this point the importance of

TABLE 1: Hospital and Manufacturer Collaboration on Picture Archiving and Communication Systems in Japan

Hospital	Manufacturer	Systems
Hokkaido University Hospital	NEC ^a	Image filing system
Kanagawa Cancer Center	Fuji, Toshiba	CR ^b , display station
Keio University Hospital	Fuji	CR
Kitazato University East Hospital	Fuji, Toshiba	CR, display station
Kochi Medical School	Toshiba	Display station
Kyoto University Hospital	Fuji, Hitachi	CR, display station
Nagasaki National Hospital and Izuhara Hospital	NEC	Teleradiology
National Institute of Radiological Sciences, Chiba	NEC	Communication system
Osaka University	Konishiroku	Display station
Tominaga Memorial Hospital	Fuji	CR, display station

^a See text for the complete names of manufacturers.
^b CR = Computed radiography.

PACS to the future practice of radiology has not been fully realized. There is no evidence that U. S. medical imaging manufacturers are devoting the necessary research and development effort to PACS. We do see the Japanese medical industry as gradually overtaking the United States in PACS development.

ACKNOWLEDGMENTS

We thank M. Matsui, M. Takano, H. Kato, T. Okabe, K. Ono, T. Kitahara for arranging our attendance at the JPACS meeting, as well as our visits to various manufacturers and hospitals. We would also like to thank our Japanese colleagues for their hospitality during our visits to their facilities.

REFERENCES

1. Huang HK, Mankovich NJ, Cho PS, et al. PACS at UCLA. *J Med Imaging Tech* 1986;4(2):69-93.
2. Capp MP, Nudelman S, Fisher D, et al. Photoelectronic radiology department. *Proc SPIE* 1981;314:2-8
3. Duerinckx AJ, ed. PACS for medical applications. *Proc SPIE* 1982;318:399-490
4. Schneider RH, Dwyer SJ III, eds. PACS for medical applications. *Proc SPIE* 1986;626:409-785

Memorial

Walter Leroy Kilby, 1905–1986



Dr. Walter L. Kilby died June 15, 1986, in Woodstock, VA, at the age of 81 after a long illness. He had practiced radiology in Baltimore from 1936 to 1975, except for time

served in the Armed Services during World War II.

He was born in Rappahannock County, VA, where he received his early education. After graduating from the University of Virginia with a B.S. degree, he devoted 3 years to teaching. He then entered the University of Virginia Medical School in 1929 and received his M.D. in 1933. He was elected to Alpha Omega Alpha and Iota Sigma, honorary medical fraternities.

After 1 year interning at the Cincinnati General Hospital, he returned to the University of Virginia Hospital for training in radiology.

Dr. Kilby came to Baltimore in 1936 to become associated with Henry J. Walton both in the Department of Radiology at the University of Maryland Hospital and in private practice. He became Director of the Department of Radiology and Professor of Radiology at the University of Maryland Medical School when Dr. Walton resigned in 1940. He held this position, except for Armed Serv-

ices duty, until 1953 when he resigned to devote his time to private practice in association with Dr. Walton and Dr. Charles N. Davidson.

In 1940, Dr. Kilby was commissioned as a Lieutenant in the U. S. Naval Reserve. Subsequently, he was transferred to the Army where he received a commission as a Major. He served 27 months as the Chief of Radiology in the Fiji Islands and Calcutta, India, and returned to the states in 1945 as a Lieutenant Colonel.

He was a member of the Medical and Chirurgical Faculty of Maryland, the Baltimore City Medical Society, the Maryland Radiological Society, the American Medical Association, the Radiological Society of North America, and the American Roentgen Ray Society.

Dr. Kilby is survived by his wife, the former Janet Sollenberg, and two daughters, Janet O. Kilby and Margaret Kilby.

Charles N. Davidson
Baltimore, MD 21210

ARRS Meeting Section

Invitation to the 1987 American Roentgen Ray Society Meeting in Miami Beach, FL, April 26–May 1, 1987

The entire radiologic community is invited to attend the 87th annual meeting of the American Roentgen Ray Society in Miami Beach, FL, April 26–May 1, 1987. There are numerous exciting attractions.

First is the site. The Fontainebleau Hilton has undergone total modernization and redecoration and provides a plush facility at the time when Florida weather is at its best. The opportunity for the busy radiologist to attend a major national meeting while enjoying such weather is ideal.

Second, the scientific program, instructional courses, and categorical course (see Table 1 for schedule) are certain to be interesting and educational. Third, participants will enjoy the exhibits, Caldwell Lecture, and planned social events.

Scientific Program

Almost 600 scientific papers have been submitted. From these, 189 have been selected for presentation. Special emphasis has been placed on discussion of new developments as well as reinforcement of established areas. One entire scientific session will be devoted to breast diseases.

The Friday morning scientific sessions will be replaced by one major session entitled "Genitourinary imaging update." Glen Hartman has assembled an outstanding faculty to cover all facets of urology from contrast materials to MR imaging.

Instructional Courses

The Instructional Courses have been revised and updated by the new Chairman of the Instructional Course Committee, Joseph Ferrucci. Advance registration is recommended.

Categorical Course

The Categorical Course returns this year to the subject of gastrointestinal radiology. With the emphasis shifting from

traditional barium studies to newer techniques, Chairman Gary Ghahremani has structured a course of special utility for the practicing radiologist.

Exhibits

The Scientific Exhibits coordinated by John Madewell will cover a wider range of topics than ever before. Some of the space usually allotted to technical exhibits will be used for the scientific exhibits, enhancing the total learning experience available.

The Technical Exhibit area will be compact and permit convenient review of new technologic developments.

Caldwell Lecture

The Caldwell Lecture for 1987 will be given by M. Paul Capp, Professor and Chairman, Department of Radiology, University of Arizona. Dr. Capp will discuss current imaging research studies and their applicability and availability, both short and long term.

Social Events

South Florida in the spring offers a myriad of diversions, and Manuel Viamonte, Chairman of Local Arrangements Committee, has assembled a group of activities, including golf and tennis tournaments, for attendees and their accompanying persons. The traditional cocktail party given by the Society for all registrants in the exhibit area on Tuesday evening will provide a convenient meeting place before an evening on the town.

Let me repeat my invitation to everyone. The idea of a meaningful "spring break" for radiologists is one whose time has come. Don't miss it!

Raymond A. Gagliardi
President Elect, ARRS

TABLE 1 Summary of 1987 American Roentgen Ray Society Meeting

Sunday April 26	Monday April 27	Tuesday April 28	Wednesday April 29	Thursday April 30	Friday May 1
	8-9:30 Instructional courses	8-9:30 Instructional courses	8-9:30 Instructional courses	8-9:30 Instructional courses	8-1 Symposium. Genitouri- nary imaging update
10-noon Categorical course. GI radiology	10-10:30 Opening cere- mony 10:30-12:30 Scientific pro- gram	10-12:30 Scientific program	10-12:30 Awards session/ Caldwell lecture	10-12:30 Scientific program	
Noon Lunch	12:30 Lunch	12:30 Lunch	12:30 Lunch	12:30 Lunch	
1:30-5:30 Categorical course. GI radiology	1:30-5:30 Categorical course. GI radiology	1:30-3:30 Scientific program	1:30-3:30 Scientific program	1:30-3:30 Scientific program	
		4-5:30 Categorical course. GI radiology	4-5:30 Categorical course. GI radiology	4-5:30 Categorical course. GI radiology	

1987 American Roentgen Ray Society Section on Instruction: Courses and Symposium

Joseph T. Ferrucci, director, and Richard A. McLeod, associate director

Forty-eight instructional courses will be presented during the 87th annual meeting of the American Roentgen Ray Society (ARRS) beginning Monday, April 27, and continuing through Thursday, April 30. In addition, there will be a series of courses on gastrointestinal radiology and a symposium on genitourinary imaging. The courses are arranged so that there is no overlap. Each of the 48 courses will be 90 min long; no other activities are scheduled simultaneously.

The Categorical Course in Gastrointestinal Radiology will have 14 hr of instruction and will begin on Sunday, April 26, and conclude on Thursday, April 30. The Symposium on Genitourinary Imaging Update will be on Friday, May 1, from 8 a.m. to 1 p.m. All courses carry Category 1 credit on an hour-to-hour basis.

Registration Information

To register for courses, complete the meeting registration form in this section and mail promptly. Tickets will be available at the Instruction Course Registration Desk, Fontainebleau Hilton Hotel, for courses that have not been sold out. All courses will take place in the headquarter's hotel.

After reviewing the course abstracts, select three for each day. List the course number and name of the first instructor on the registration form.

All who register for the Categorical Course in Gastrointestinal Radiology (including ARRS members) must pay a fee of \$75 and must take the entire series of classes. The categorical course totals 14 hr of instruction and includes a syllabus.

Course Schedule

Sunday, April 26, through Thursday, April 30

The Categorical Course in Gastrointestinal Radiology will have 14 hr of instruction over 5 days. Table 1 lists topics and instructors.

Monday, April 27, through Friday, May 1

A total of 48 courses will be offered (Table 2) plus a Symposium on Genitourinary Imaging Update. Course abstracts and a list of faculty follow.

Table 1: Categorical Course in Gastrointestinal Radiology, April 26-30

Day/Time	Topic/Presenter
Sunday, April 26	
10:00-10:45 a.m.	Mucosal lesions of the esophagus: evaluation by double-contrast radiography (<i>Levine</i>)
10:45-11:15 a.m.	Motility disorders of the esophagus (<i>Ott</i>)
11:15-Noon	Radiological evaluation of the gastric mucosa (<i>Gelfand</i>)
1:30-2:00 p.m.	Mucosal abnormalities of the duodenum (<i>Glick</i>)
2:00-3:00 p.m.	Complications of pancreatitis: radiological diagnosis and management (<i>Freeny</i>)
3:30-4:00 p.m.	Sonography of the hepatobiliary tract: an update (<i>Laing</i>)
4:00-4:30 p.m.	CT of the hepatobiliary tract: current concepts (<i>Moss</i>)
4:30-5:00 p.m.	MRI of the hepatobiliary tract (<i>Ferrucci</i>)
Monday, April 27	
1:30-2:15 p.m.	Interventional techniques in the gastrointestinal tract (<i>vanSonnenberg</i>)
2:15-3:00 p.m.	Interventional techniques in the diagnosis and management of abdominal fluid collections, abscesses, and tumors (<i>Mueller</i>)
3:00-3:30 p.m.	Gastrointestinal manifestations of AIDS (<i>Berk</i>)
4:00-4:30 p.m.	MRI of retroperitoneum, pancreas, and gut (<i>Goldberg</i>)
4:30-5:30 p.m.	Current concepts in small-bowel radiography (<i>Maglinte</i>)
Tuesday, April 28	
4:00-4:45 p.m.	CT of acute gastrointestinal disorders (<i>Federle</i>)
4:45-5:30 p.m.	CT staging and follow-up of gastrointestinal malignancies (<i>Megibow</i>)
Wednesday, April 29	
4:00-4:40 p.m.	Radiological diagnosis of colorectal neoplasms (<i>Goldstein</i>)
4:40-5:10 p.m.	Inflammatory bowel disease: initial radiographic manifestations (<i>Laufer</i>)
5:10-5:30 p.m.	CT features of inflammatory bowel disease (<i>Gore</i>)
Thursday, April 30	
4:00-4:45 p.m.	Functional evaluation of the gastrointestinal tract by scintigraphy (<i>Malmud</i>)
4:45-5:30 p.m.	Gastrointestinal complications of diagnostic and therapeutic procedures (<i>Ghahremani</i>)

Table 2: American Roentgen Ray Society Instructional Courses: April 27–30, 1987

Topic	Monday	Tuesday	Wednesday	Thursday
Sonography	101. Deep abdominal Doppler and venous sonography. <i>Taylor, Raghavendra</i>	201. Obstetrical ultrasound. <i>Leopold</i>	301. Correlative imaging in biliary obstruction. <i>Zeman</i>	401. Duplex Doppler ultrasound in evaluation of arteriosclerotic extracranial vascular disease. <i>Carroll</i>
Neuroradiology—Head	102. Intracranial neoplasms: Part I. <i>Sackett, Naidich</i>	202. Intracranial neoplasms: Part II. <i>Sackett, Naidich</i>	302. Neuroimaging of sellar region including MRI. <i>Davis</i>	402. Orbital and petrous bone radiology. <i>Forbes</i>
Pediatric Radiology	103. Pediatric emergencies: plain film observations and diagnostic methods. <i>Wood</i>	203. Disorders of pelvis and hips in children. <i>Poznanski</i>	303. Cysts and cystic diseases of the thorax. <i>Kirkpatrick</i>	403. Sonography in pediatric radiology: overview and recent advances. <i>Hayden, Swischuk</i>
Breast/Thorax	104. Interventional radiology of the thorax. <i>Westcott, Barth</i>	204. Mediastinal anatomy: an overview. <i>Proto</i>	304. Coordinated breast imaging. <i>Kopans</i>	404. Film-screen mammography. <i>Gisvold</i>
Body Imaging	105. CT of the gastrointestinal tract. <i>Wittenberg</i>	205. Dilemmas in abdominal tumor imaging. <i>Charboneau</i>	305. Acute gastrointestinal hemorrhage. <i>Staab, Mauro, Jacques</i>	405. Technical advances in MR of the abdomen. <i>Stark</i>
Neuroradiology—Spine	106. Advanced radiologic assessment of osteoporosis. <i>Genant</i>	206. MR imaging of the spine. <i>Ramsey</i>	306. Neuroradiology for general radiologists: trauma to head and spine. <i>Rogers, Weinberg</i>	406. Imaging (high resolution CT and MR) in degenerative disk disease of the lumbar spine—1987 update. <i>Lukin</i>
Magnetic Resonance	107. Fundamentals of MR image interpretation. <i>Bradley</i>	207. Practical MR: guide to technique and body applications. <i>Harms</i>	307. Cardiovascular and abdominal MR. <i>Alfidi, Haaga</i>	407. MRI of the pelvis: urinary tract, and retroperitoneum. <i>Kressel</i>
Chest	108. Pulmonary infection in the immunocompromised host. <i>McLoud</i>	208. Pulmonary scintigraphy: current applications and future trends. <i>Alderson</i>	308. Current concepts in chest CT. <i>Siegelman, Naidich, Zerhouni</i>	408. The post-operative chest: X-ray and CT evaluation. <i>Goodman</i>
Vascular/Interventional	109. Interventional uro-radiology. <i>Banner</i>	209. The changing role of digital subtraction angiography (DSA). <i>Buonocore</i>	309. Biliary interventional techniques: overview. <i>Russell, Yrizarry, Mendez, Nunez</i>	409. Angioplasty and fibrinolysis. <i>Katzen</i>
Cardiac radiology	110. Cardiovascular imaging: state-of-the art. <i>Viamonte</i>	210. Acquired heart disease—imaging modalities and interventions. <i>Lipton</i>	310. Roentgenologic approach and teaching tips in major forms of heart disease. <i>Elliott</i>	410. Nuclear cardiology in clinical practice. <i>Thrall</i>
Skeletal radiology	111. The diagnostic approach and new imaging techniques for staging bone and soft tissue tumors. <i>Norman, Rosenthal</i>	211. Principles in differential diagnosis of selected arthropathies. <i>Martel</i>	311. Diagnosis of battered child syndrome and conditions with which it might be confused. <i>Graham</i>	411. Advanced imaging of the musculoskeletal system: CT, MR, and densitometry techniques. <i>Resnick, Sartoris</i>
Special topics	112. Screening mammography. <i>Sickles</i>	212. Ethical, societal, and legal concerns in attempts to preserve the biomedical research enterprise: medical imaging technology. <i>James, Greeson</i>	312. How to get your manuscript published without a hassle. <i>Berk, Figley, Davidson, Hilton, Braude</i>	412. Modern pancreatic imaging. <i>Silver, Glazer</i>

Monday, April 27

101. Deep abdominal Doppler and venous sonography. Taylor KJW, Raghavendra BN. (1) Abdomen/pelvis—Duplex equipment allows detection of vascular signals derived from deep arteries or veins

within the abdomen and pelvis and allows exclusion of thrombosis or occlusion. The normal signals will be reviewed. Blood flow characteristics aid in tissue characterization. Physiologic changes in blood flow can easily be demonstrated, for example, in the functioning ovary or gravid uterus. Abnormal signals are found in pathologic conditions: high impedance signals identify vascular rejection in the renal allograft

or growth retardation in the fetus. High velocity shifts allow diagnosis of renal artery stenosis. High velocity, low impedance signals are found in neovascularization. (2) Lower extremity—The diagnosis of deep venous thrombosis (DVT) of the lower extremity can be achieved rapidly and noninvasively by venous sonography. The sonographic findings of venous thrombi are the presence of soft-tissue mass within the lumen of the vein and/or the inability to totally obliterate the lumen of the vein by probe compression. The optimal method, for the diagnosis of DVT appears to be B-scan imaging used in conjunction with Doppler.

102. Intracranial neoplasms: part I. Sackett JF, Naidich TP. Neuroradiology workup of intracranial neoplasms has been modified because of the increased sensitivity of MR imaging and new methods of neurosurgical management. MR imaging appears to be more sensitive but less specific than CT. Biopsy is still required for proper selection of therapeutic regimen of all tumors except those in which biopsy itself poses unacceptable morbidity and mortality. Angiography is now used to plan surgery or interventional vascular tumor modification. Sonography has an increasing role in surgical localization, biopsy, or drainage of cystic neoplasm and shunt placement. CT scanning for stereotactic biopsy assists the neurosurgeon in finding a small or deep neoplasm. Special techniques to improve sensitivity include air cisternography and nonionic water-soluble contrast cisternography. An approach tailored to the neuroradiologic evaluation of intracranial neoplasms provides the proper basis for therapy of intraaxial and extraaxial neoplasms in adults and children. Pathologic correlation of neuroimages and cost-effective management of tumors will be stressed.

103. Pediatric emergencies—plain film observations and diagnostic methods. Wood BP. Emergency presentations of infants and children require accurate observation and interpretation of plain films accompanied by appropriate decisions concerning the most expeditious diagnostic procedures. The life-threatening nature and unexpected arrival of emergencies require that all radiologists maintain facilities for their proper handling. Frequently the urgent nature of the patient's affliction is more grave than is clinically suspected; thus, the pathogenesis and clinical implications of the diagnosis should be understood. Airway and thoracic emergencies and acute abdominal situations in neonates and older children will be considered. Trauma suffered by children—plain film evaluation and appropriate workup, and diagnostic approaches to children with limps—are included.

104. Interventional radiology of the thorax. Westcott JL, Barth K. (1) **Biopsy and drainage procedures.** *Trans thoracic needle biopsy:* When properly performed, this technique has a reported accuracy of 90–98% for differentiating benign from malignant pulmonary lesions. It is also useful for diagnosing hilar mediastinal masses and for staging lung cancer. *Percutaneous catheter drainage (PCD):* With fluoroscopic and/or sonographic guidance, PCD is a useful procedure for drainage of parapneumonic effusions and loculated fluid collections. It can also be used as definitive treatment of empyema and in selected patients with lung abscesses. This portion of the course will emphasize technical aspects, results, and clinical indications for these procedures. (2) **Vascular procedures.** *Embolotherapy for massive hemoptysis:* Localization of bleeding site (right or left lung) by bronchoscopy is desirable but not always successful. Angiographic exploration with intent to occlude arterial feeders to the site of bleeding is the next logical step. With few exceptions, bleeding originates from bronchial arteries. The technique of bronchial arteriography in embolization will be illustrated. Rarely, massive hemoptysis originates from pulmonary arteries, as in some cases of cavitary tuberculosis, lung abscesses, or pulmonary arteriovenous malformation (AVM).

Embolotherapy of pulmonary AVM (PAVM): An infrequent but technically challenging indication for embolotherapy is suggested if patients present with single or multiple PAVM with incapacitating cyanosis due to right or left shunt and very rarely with hemoptysis. PAVMs most frequently originate from pulmonary arteries with one or few feeder vessels. Embolization with detachable balloons has proven safe and effective.

105. CT of the gastrointestinal tract. Wittenberg J. Since the advent of rapid CT scanning, examination of the gastrointestinal tract has become an increasingly important application. This presentation will encompass CT of the alimentary tract and mesentery emphasizing the more efficacious examinations. In those areas where appropriate, use of supplemental CT-guided interventional techniques will be illustrated. Staging of gastrointestinal tract malignancies is one common indication for examination. The accuracy, utility, and pitfalls of staging a variety of neoplasms will be reviewed. CT is often unique in detecting and staging recurrent tumor and, for certain lesions, is the screening procedure of choice. CT has become increasingly critical in the assessment of seriously ill patients with gastrointestinal tract inflammatory disease. The ability to specifically characterize complications in the adjacent mesentery will often dictate the advisability of conservative, interventional, or surgical therapy. The diagnostic criteria for such decisions will be discussed as well as indications for and results of percutaneous intervention.

106. Advanced radiologic assessment of osteoporosis. Genant HK. Numerous techniques have been used to quantitatively assess the skeleton in patients with osteoporosis with variable precision, accuracy, and sensitivity. The purposes of this presentation are to (1) examine the associations among various methods for noninvasive measurement of bone mineral content in both healthy and osteoporotic subjects, (2) assess the discrimination by which these techniques detect bone loss and spinal fracture, and (3) provide a basis for understanding disparity of results when comparing bone mineral measurements from different bone compartments (cortical and trabecular bone), from different anatomic sites (axial and appendicular skeleton), and from different measuring techniques (linear scanning with single-photon absorptiometry or dual-photon absorptiometry and direct volume-density measurements with quantitative CT).

107. Fundamentals of MR image interpretation. Bradley WG. This course is intended to be a practical summary of MR image interpretation: if you are already interpreting CT, what else do you need to know to be able to read MR? The effect of the magnetic relaxation times and the programmable sequence parameter times on image contrast is discussed. The variable appearance of flowing blood and CSF is noted. Attention is directed to flow-related causes of increased intraluminal signal that may be mistaken for tumor or thrombus. The concept of paramagnetism is discussed in the context of the dipole-dipole interaction (the short T1 appearance of methemoglobin in subacute hemorrhage and of gadolinium-DTPA, the new MR contrast agent.) Paramagnetism is also discussed in the context of nonuniform magnetic susceptibility, which causes T2 shortening of iron-containing substances, such as deoxyhemoglobin (in an acute hematoma) and hemosiderin within macrophages (around a chronic hematoma). Examples are shown that demonstrate the utility of these principles in the clinical setting. Specifying the numerous parameters that constitute the MR imaging sequence is an exercise in assigning multiple interrelated variables in a milieu of shifting clinical priorities and imager capabilities. A single parameter (e.g., the repetition time [TR]) may have several effects on the pulsing sequence unrelated to its primary function of providing image contrast. TR affects the acquisition time and determines the maximum number of slices that

can be obtained in a single acquisition. Often as one variable is improved, another is worsened (improving the spatial resolution by increasing the number of phase-encoded projections increases the acquisition time and decreases the signal-to-noise per pixel). The various interactions among these parameters are considered and an algorithmic approach is proposed by which they may be specified.

108. Pulmonary infection in the immunocompromised host.

McLoud TC. A compromised host may be defined as an individual with altered defense mechanisms or immunity. The lung is the organ that is specifically susceptible to infection in the immunocompromised host, with mortalities ranging from 40% to 50%. The clinical presentation of fever and an abnormal chest radiograph in such an individual poses an urgent clinical problem and demands prompt diagnosis and specific treatment. The role of the radiologist in this setting involves both detection of the abnormality on the chest radiograph and analysis of radiographic features with regard to diagnosis and choice of appropriate interventional techniques, and performance of percutaneous needle biopsy of focal lesions when appropriate. The radiographic appearance of pneumonias in this population can be classified in three patterns: (1) lobar or segmental consolidation; (2) nodules with rapid growth and cavitation; and (3) diffuse lung disease. Examples of pulmonary infection by both usual and unusual organisms will be presented and discussed. Treatment and the role of percutaneous needle aspiration biopsy of the lung will be presented.

109. Interventional urology.

Banner MP. This course will overview several nonvascular interventional genitourinary procedures that are usually performed in percutaneous fashion by radiologists, including nephrostomy, ureteral stenting, dilatation of ureteral strictures, and stone manipulation. Fluoroscopically controlled retrograde pyeloureteral manipulative procedures performed in conjunction with urologists will also be considered. For each procedure, indications and contraindications will be reviewed and both techniques and potential complications will be discussed. The current status of upper urinary tract stone management (percutaneous and ureteroscopic extraction and disintegration, chemolysis, and extracorporeal shock-wave lithotripsy) will be presented, and the role of the radiologist in each of these technologies will be discussed.

110. Cardiovascular imaging: state-of-the-art.

Viamonte M. Standard two-view chest radiograph with high KV technique, echocardiography (M-mode), two-dimensional and duplex scanning, radionuclide angiography and myocardial scintigraphy, CT techniques (including cine-CT), MR imaging and angiography (nonselective and selective) are the imaging techniques available for cardiac evaluation. For anatomic information, cine-CT and MR imaging appear to be the preferred techniques that complement chest radiography and echocardiography. For functional information, positron emission tomography and single-photon emission CT appear to be the nonimaging techniques of choice.

111. The diagnostic approach and new imaging techniques for staging bone and soft-tissue tumors.

Norman A, Rosenthal D. This course will begin with a review of the pertinent clinical and radiologic features of bone and soft-tissue tumors. The clinical history is often nonspecific and of little help. However, the location of a tumor in the skeleton and the predilection for a certain age group are as essential to the diagnosis as are the radiographic characteristics of the lesion. Such pertinent features as the extent and speed of bone destruction will be illustrated as signs of aggressiveness and whether the lesion is potentially benign or malignant. Similarly, the reparative response to the lesion will be discussed, and its indication of the behavior of the tumor will be shown. Also discussed will be how the nature of

the periosteal reaction and the soft-tissue extent of the lesion are the critical signs of the analytic process. After the discussion of the diagnostic analysis of a bone tumor, the imaging and staging of bone and soft-tissue neoplasms will be presented. Recent technologic advances in imaging equipment have enhanced the workup, the clinical management, and the posttherapy follow-up of bone neoplasms. The information provided by the combination of imaging procedures (CT and MR) has assisted in the development of limb-salvage procedures and contributed to the improved disease-free survival rate after chemotherapy with several drugs for treatment of bone tumors. CT has added immensely to the diagnosis and extent of musculoskeletal tumors. CT demonstrates more extensive disease than is suspected clinically or on the conventional radiographs. With the advent of MR imaging, we have a new mode for tumor investigation and particularly for staging of the soft-tissue extent of a lesion. Although traditional radiographic studies remain the initial study in the workup of a bone tumor, CT and MR are important in evaluating the extent and staging of these skeletal lesions.

112. Screening mammography.

Sickles EA. Mammography is capable of identifying most breast cancers before they grow large enough to be palpable. Randomized clinical trials with screening mammography have demonstrated a clear-cut reduction in mortality from breast cancer for women aged 50 years and over, and indirect evidence that there is similar mortality reduction in the 40- to 49-year age range. As a result, the use of mammography to screen asymptomatic women has been advocated by many national medical organizations, and radiologists are examining increasing numbers of screening mammograms. This course will review (1) the benefits and risks of mammography screening; (2) the equipment, techniques, and procedures most appropriate for screening (as distinguished from diagnostic) examinations; (3) the radiographic features of the small nonpalpable breast cancers usually detected by screening; (4) the methods to reduce the cost of operation so that screening can be offered at a price affordable to most women, and (5) miscellaneous screening-related topics (acceptance of self-referred patients, marketing strategy, and third-party payment).

Tuesday, April 28

201. Obstetrical ultrasound.

Leopold GR. Technologic improvements in sonographic equipment have greatly enhanced the ability of sonographers to evaluate the developing fetus at all stages of gestation. This evaluation includes an assessment of growth and development, as well as a search for the more common fetal anomalies. With every obstetric examination, several measurements need to be recorded to allow an accurate prediction of fetal age. The simplest of these include the biparietal diameter, transverse diameter of the fetal abdomen at its widest point, and the femur length. Knowledge of where to make these measurements and their clinical significance is most important. Similarly, appreciation of the changes in measurement that occur in intrauterine growth retardation is critical in making that diagnosis. In the fetal head, hydrocephalus and other cysts (porencephaly, arachnoid, vein of Galen aneurysm) all have fairly typical appearance and may be diagnosed reliably after the 18th week of gestation. In the fetal thorax, masses thus far described include cystic hygroma (often associated with Turner's syndrome), cervical meningocele, and hemangioma. Pleural effusion and masses (cystadenomatoid malformation and diaphragmatic hernia) are now being commonly reported. Pericardial effusion is easily noted in cases of fetal heart failure. Many of the structural anomalies of the heart can now be identified prenatally. In some cases, dysrhythmias rec-

ognized in utero have been successfully treated. In the abdomen, omphalocele, gastroschisis, and bowel obstruction at varying levels have already been reported. The presence of fetal ascites is readily diagnosed and should prompt a search for its cause. Heart failure (any cause) and low urinary tract obstruction are the two most common underlying factors. Routine visualization of the fetal kidneys is possible and most of the structural anomalies of the newborn period are diagnosable in utero. Examination of the fetal spine is a critical part of the examination. It should be possible to recognize dysraphism, even if a protruding mass is not present. More recently, better equipment has allowed study of the fetal extremities. Major ray deficits are now detectable. Homozygous forms of dwarfism may be recognized in the first half of pregnancy, but the heterozygous forms (the usual achondroplastic dwarf) cannot be identified until the third trimester by measurements of femur length.

202. See 102.

203. Disorders of the pelvis and hips in children. Poznanski AK.

This course will describe the various congenital and acquired disorders of the hips and pelvis in children with both plain films and the newer techniques. Radiologic evaluation is important in decisions on diagnosis and management of these problems. One of the difficulties in evaluating the hip in children has been that a large part of the proximal part of the femur is composed largely of cartilage. The new radiologic methods have made a major impact on our ability to diagnose disorders of the hip by allowing us to evaluate this cartilaginous unossified head. CT has been invaluable in the diagnosis and management of children with complex congenital dislocation of the hips, particularly before and after surgical treatment. CT has also been useful in Perthes' disease. Sonography has given us a new window to look at the hip and is becoming more useful in the evaluation of congenital dislocation, hip effusion, and other disorders. MR imaging allows us to see the unossified head clearly and is sensitive in showing abnormalities. Dislocation, aseptic necrosis, and discongruity can be seen easily. Nuclear medicine, of course, remains an important tool in the evaluation of hip disorders.

204. Mediastinal anatomy: an overview. Proto AV. Cross-sectional imaging has made clear the importance of understanding normal anatomy for adequate diagnostic interpretation. The importance of this applies equally to conventional images. In this refresher course, we will review, as time allows, the many reflections formed by contact of the lung with the mediastinum. To promote understanding and retention of this information, we have organized the material to show: (1) how a reflection may compare or contrast with another, (2) how a reflection on one side of the mediastinum may have a counterpart on the other side of the mediastinum, and (3) how a reflection relates to a specific coronal plane or structure of the mediastinum. Conventional images will be emphasized, with use of CT as needed for clarification of the conventional images.

205. Dilemmas in abdominal tumor imaging. Charboneau JW. A major goal in abdominal imaging with CT, sonography, and MR is exclusion, detection, and differentiation of solid mass lesions. This course will emphasize practical approaches to the dilemmas encountered in imaging of masses of the liver, pancreas, and kidney. *Liver:* Liver masses can be divided into two general categories: (1) insignificant and often incidentally discovered lesions that can be ignored (cavernous hemangioma, focal nodular hyperplasia); and (2) life-threatening masses that require surgical or medical therapy (metastasis, hepatoma, and adenoma). With the increasingly widespread use of abdominal sonography, CT, and MR, many solid liver masses are detected incidentally. It is the radiologist's responsibility to differ-

entiate between clinically significant and insignificant lesions. *Pancreas:* The primary and secondary CT/sonographic signs of adenocarcinoma will be reviewed. Differentiation of adenocarcinoma from other pancreatic masses, including islet cell carcinoma, cystic neoplasms, and chronic focal pancreatitis, will be discussed. The complementary roles of CT and sonography in the exclusion or detection of pancreatic lesions will be emphasized. *Kidney:* The spectrum of CT/sonographic appearances and pitfalls of diagnosis of renal cell carcinoma will be presented. Emphasis will be on approaches to differentiating renal carcinoma from other masses, including pseudotumor, oncocytoma, angiomyolipoma, transitional cell carcinoma, and lymphoma.

206. MR imaging of the spine. Ramsey RG. MR of the spine provides direct visualization of the spinal cord without degradation of the images by bone artifact. MR is sensitive, accurate, and well tolerated by patients. The multiplanar capability of MR, ready reproducibility, and accuracy allow MR to evaluate spinal-cord and vertebral abnormalities as well as other more invasive methods do, and better than most other methods. Development of hardware and software techniques such as surface imaging has made MR competitive with CT even for the evaluation of disk disease, and better than CT or myelography for evaluation of spinal-cord tumors, syringohydromyelia, and vertebral metastases. With MR, the cerebrospinal fluid acts as a contrast agent; the low signal intensity of the CSF provides contrast with the spinal cord and reflects changes similar to those seen with myelography. While initial impact of MR was with the increased sensitivity of detection of cerebral abnormalities, with increased experience the ultimate clinically significant impact of MR may well be with spine imaging. The initial discussion will address the topic of lumbar and cervical disk disease. The development of thin slices, angle slices, and magnified views allows excellent demonstration of both lumbar and cervical discs. Herniated cervical discs are sometimes easily identified by MR, and axial images identify the laterality. MR studies of disks are also frequently diagnostic, compete with CT in many cases, and preclude the need for other examinations in many cases. The MR demonstration of the decreased signal of a degenerated disk provides physiologic/pathologic data not possible with other methods. MR features of other disorders will be covered, time permitting. The presentation will include discussion of the technique of scanning, various pitfalls, and the practical usefulness of MR for diagnosis and clinical evaluation.

207. Practical MRI: guide to technique and body applications.

Harms SE. MR is rapidly emerging as a major diagnostic method for many clinical applications in the body. MR is fundamentally different from other widely used body imaging techniques. The numbers of technique choices available in MR are varied. Proper selection of technique allows the tailoring of the examination for improved diagnostic information. MR technique options can be divided into the following categories: (1) RF coil, (2) acquisition method, (3) pulse sequence, and (4) timing parameters and tip angles. Technique selection begins with the analysis of the clinical problem. The MR tissue parameters of the area to be studied are identified. Machine parameters are then selected to demonstrate best the disease condition. For example, liver-imaging techniques should reflect the need for the highly T1-weighted images necessary for liver contrast and respiratory compensation. For temporomandibular joint imaging, on the other hand, T1-weighting and respiratory compensation are not essential and the primary objective is thin-slice, high-resolution images, which are needed for visualizing small structures. The use of MR as a diagnostic technique is depicted with a number of clinical examples, including bone and soft-tissue neoplasms, joints, liver, and pelvic neoplasms. MR techniques are expected to improve further in

the near future. The radiologist's role is to analyze the clinical setting, plan the examination, and render an interpretation. A high-quality diagnostic MR study requires an understanding of the technology and its limitations. Because of the complexity of MR, the rigorous training of radiologists in imaging technology is expected to provide a substantial competitive advantage over specialists from other disciplines in the management of MR cases.

208. Pulmonary scintigraphy: current applications and future trends. Alderson PO. For many years pulmonary scintigraphy has been applied primarily for the detection of pulmonary embolism by using combined ventilation-perfusion (VP) imaging. Improvements have come via the reorganization of diagnostic schemes to provide reliable determination of the probability of pulmonary embolism in a given patient, and by development of multiprojection ventilation imaging techniques with Xe-133, Kr-81m, or Tc-99m DTPA aerosols. Current controversies surrounding the scintigraphic detection of pulmonary embolism will be addressed in the context of these new approaches, and their relationships to angiographic diagnosis of pulmonary embolism and clinical outcomes will be explored. In addition, new approaches to pulmonary scintigraphy, such as soluble aerosol clearance studies in pulmonary injury syndromes, Ga-67 imaging in AIDS, studies of pulmonary metabolism with conventional radiotracers, and imaging of tumors and emboli by radiolabeled antibodies, will be discussed as a means for developing predictions about the future directions of the field.

209. The changing role of digital subtraction angiography (DSA). Buonocore E. Since its inception in the early 1980s, DSA has gradually emerged as a complementary tool in the angiographic laboratory. Whereas DSA was first heralded as a means of "noncatheter" angiography by using the IV route, it is now an adjunct technique to intraarterial studies. With increasing operator familiarity, angiographic techniques have been modified. Smaller catheters, lower doses of contrast medium and less reliance on film-screen techniques and film processing have resulted. Understanding the basic process of digital subtraction is essential for proper purchase, technique, post-processing adjustments, and quality control. With these ends in mind, physical principles and clinical applications of digital subtraction angiography in the general radiologic practice will be discussed.

210. Acquired heart disease—imaging modalities and interventions. Lipton MJ. It is estimated that over 40 million Americans have one or more forms of heart or blood vessel disease. Cardiovascular disease is the cause of 55% of all adult deaths; it is therefore responsible for as many deaths as all other disorders combined, including cancer and trauma. The identification and evaluation of heart disease depends on an understanding and knowledge of a wide spectrum of diagnostic techniques, ranging from routine chest radiography to invasive selective coronary arteriography. This field has become even more complex with the new therapeutic interventions. Basic techniques will be reviewed together with more recently developed digital imaging techniques, notably DSA, MR, and CT. These exciting radiologic imaging techniques are rapidly evolving and have the potential to become sensitive screening and diagnostic tools. These three-dimensional imaging techniques provide unique clinical diagnostic information and have the capacity to quantitate cardiac function.

211. Principles in the differential diagnosis of selected arthropathies. Martel W. The radiologist plays a key role in the diagnosis of joint diseases. Clinical and laboratory findings in many conditions often overlap. Histologic material is usually unavailable and microscopic features on biopsy are usually nonspecific. Although many

radiologic features have low specificity, certain findings have "high predictive value" in the context of particular diseases. Even when a specific diagnosis cannot be made, it is often possible to exclude some diseases that are being considered in the clinical differential diagnosis. A definite diagnosis is possible more often than is realized and generally depends on a combination of findings, typical distribution of affected joints, tendency to involve certain anatomic sites, and characteristic manner of evolution. This course deals with principles that are helpful in distinguishing certain common arthropathies. The discussion will focus on selected diseases of both spine and appendicular joints that are commonly confused with one another.

212. Ethical, societal, and legal concerns in attempts to preserve the biomedical research enterprise: medical imaging technology. James AE, Greeson T. The tradition of success in medical imaging research is threatened by a myriad of legislative initiatives, changing economic conditions, and reimbursement policies. This set of circumstances has altered the historic relationships under which research and training have been conducted. In the United States, the federal contribution to biomedical imaging research through the National Institutes of Health, the National Academy of Science, and ADAMHA has represented a substantial public investment in the pursuit of excellence in health care. Investigator-initiated proposals with a peer review of scientific merit have proven the most efficacious method for developing and exploring original opportunities in imaging. More recently the private sector, mostly through industry, has made substantial contributions, especially in the manner of instrumentation grants.

Wednesday, April 29

301. Correlative imaging in biliary obstruction. Zeman RK. Biliary obstruction has many faces and is caused by a wide variety of diseases. This course will focus on three questions that the radiologist should be prepared to answer after examining a patient with suspected biliary obstruction: (1) Is the patient obstructed? (2) Why is the patient obstructed? (3) How should the obstruction be treated? Entities such as anicteric obstruction, obstruction without dilatation, and dilatation without obstruction will be put into proper perspective. The relationship between noninvasive imaging and cholangiography will be highlighted.

302. Neuroimaging of the sellar region including MRI. Davis KR. Normal anatomy of the sellar region will be reviewed and correlated with images in order to provide a framework to recognize abnormal findings. This may be divided into the (1) intra-, (2) para-, (3) supra-, (4) infra-, and (5) retrosellar areas. A variety of common abnormalities encountered in this region will be illustrated with emphasis upon (1) MR features and its role in evaluation, (2) pattern and sequence of neuroimaging evaluation with MR, and (3) neuroimaging approach if MR is unavailable. Emphasis will be given to the diagnostic strength and importance and to the limitations of each neuroimaging type of procedure.

303. Cysts and cystic diseases of the thorax. Kirkpatrick JA. This presentation will be concerned with those lesions that are encountered within the thorax that are cystic in nature (e.g., neuroenteric remnants, neuroblastoma, bronchogenic cysts, enteric cysts, thymic cysts, and teratoma). Plain film findings and those found by CT will be included. Cysts and cystic lesions of the lungs, such as acquired air-block phenomena and pulmonary dysplasia, will be included.

Finally, cystic lesions of the chest wall, such as mesenchymal hamartoma and cystic hygroma, will be covered. Radiologic evaluation of any one of these lesions can result in an accurate diagnosis and permit appropriate therapy.

304. Coordinated breast imaging. Kopans D. This course will detail the use of mammography (film/screen and xeroradiography), sonography, and CT for breast evaluation. These methods, plus the efficacy of transillumination, thermography, and MR imaging will be discussed along with the future potential of immunoinaging and digital mammography. The differences between detection and diagnosis will be stressed. An approach to breast lesion analysis will be presented plus a detailed discussion of the uses of mammography, sonography, and CT to localize clinically occult lesions.

305. Acute gastrointestinal hemorrhage. Staab EV, Mauro M, Jacques PF. The course is divided into three sections. (1) Noninvasive imaging will address the problems associated with triage of patients with gastrointestinal bleeding and attempt to identify the appropriate role for noninvasive methods. The advantages and limitations of widely available radionuclide techniques and their role with respect to subsequent invasive studies will be stressed. (2) Angiography and intervention in upper gastrointestinal hemorrhage will provide the attendee with a balanced overview of the diagnostic role of angiography in acute upper gastrointestinal hemorrhage. The angiographic features of the more frequently encountered causes of upper gastrointestinal tract bleeding will be presented together with certain diagnostic pitfalls. Technical advice on achieving satisfactory selective catheter position and the role of embolo- or pharmacotherapy in particular clinical contexts will be presented. (3) Angiography and intervention in lower gastrointestinal hemorrhage will cover the role of invasive radiology in acute lower gastrointestinal hemorrhage, including angiographic diagnosis of tumors, angiodysplasia, diverticulosis, and less common causes. The value of provocative angiography and therapeutic approaches will be discussed. A selected, annotated bibliography will be available.

306. Neuroradiology for general radiologists: trauma to the head and spine. Rogers LF, Weinberg PE. This course will acquaint the general radiologist with present neuroradiologic techniques in the evaluation of injuries of the CNS, spine, and skull. The CT findings in intra- and extracerebral hemorrhage, fractures of the base of the skull, sinuses, and temporal bone will be presented. The proper plain film evaluation of spinal trauma will be discussed and the indications for standard tomography, myelography, and CT in the evaluation of spinal injury will be reviewed.

307. Cardiovascular and abdominal MR imaging. Alfidi RJ, Haaga JR. The newly emerging techniques in MR imaging are making it possible to obtain rapid data acquisition with improved spatial resolution in organ systems normally characterized by respiratory, cardiovascular, or other motion artifacts. The purpose of this course is to present the latest information available in MR imaging of the cardiovascular system, pulmonary parenchyma, liver, pancreas, and retroperitoneum. Changes in tissue contrast resolution as a result of faster imaging sequence will also be discussed.

308. Current concepts in chest CT. Siegelman SS, Naidich DP, Zerhouni EA. The course will cover general principles, CT of the airways, high-resolution CT of the lung parenchyma, and CT-MR correlations in the hilum and mediastinum.

309. Biliary interventional techniques: overview. Russell E, Yrizarry JM, Mendez G Jr, Nunez D Jr. This overview of biliary interven-

tional radiology will trace a 10-year evolution of traditional techniques that led the interventionalist to the present state-of-the-art in the therapy of stone disease and biliary obstruction. The course will stress the importance of anatomy, procedural and postprocedural complications, radiation safety, and patient care.

310. Roentgenologic approach and teaching tips in major forms of heart disease. Elliott LP. Myocardial ischemia, systemic hypertension, aortic valve stenosis, rheumatic valve disease, and their attendant complications and associations make up over 90% of the cardiac entities in adults. This course will develop a systematic approach for the radiologist to enable recognition of these problems with a high degree of confidence. Emphasis will be on the approach of using physiology via the pulmonary vascularity followed by logical use of cardiac anatomy. Areas of learning strictures traditionally experienced by residents will be discussed.

311. Diagnosis of battered-child syndrome and conditions with which it might be confused. Graham CB. When suspicions of this potentially lethal situation are raised, indicated imaging studies must be obtained. Musculoskeletal abnormalities are so common that a complete bone survey is most useful. Radiographic findings of fractures and displacements include: unexplained old bone and joint deformities, soft-tissue swelling, subperiosteal hemorrhage, metaphyseal corner fractures ("bucket handle"), other avulsions, cartilage separations, long bone spiral and transverse fractures, multiple rib fractures, periosteal new bone and callus (dating the injuries), and complex skull fractures with spread sutures. The following should be considered in the skeletal differential diagnosis: normal periosteal new bone formation; innocent trauma, neuromuscular abnormality; pain insensitivity; nutritional deficiency (prematurity, scurvy); metabolic bone disease (rickets); leukemia; neuroblastoma; infection (syphilis); infantile cortical hyperostosis (Caffey); kinky-hair syndrome (Menkes); osteogenesis imperfecta; hypophosphatasia; osteopetrosis; mucopolipidosis; vitamin A toxicity; and drug effects.

312. How to get your manuscript published without a hassle. Berk RN, Figley MM, Davidson AJ, Hilton SVW, Braude G. The disposition of manuscripts in an editorial office is often perceived as mysterious, capricious, autocratic, and unnecessarily prolonged when authors are unfamiliar with the editorial process. This course will explain how manuscripts are handled when they arrive in the editorial office. It will show authors how to reduce their chance of rejection and how to avoid the frustration of multiple revisions. Understanding the process helps to expedite the flow of manuscripts as they proceed from reviewers, scientific editors, copy editors, and the publisher. The *AJR* editors will discuss the content that is required in papers, describe the logical manner in which the information should be organized, and review the guidelines for preparing manuscripts recommended by both the *AJR* and *Radiology*. Those who follow these regulations should find that their manuscripts have a better chance to be accepted and, when accepted, are more likely to be published expeditiously.

Thursday, April 30

401. Duplex Doppler ultrasound in the evaluation of arteriosclerotic extracranial vascular disease. Carroll BA. In recent decades, a relationship between thromboembolic stroke and atherosclerotic changes of the carotid and vertebral arteries has been established. Simultaneously, extensive efforts have been directed toward the development of noninvasive, accurate techniques for evaluating dis-

ease in extracranial vessels. Optimal patient management is directly related to the proper use of these recently developed techniques. One of the most accurate and least invasive techniques for evaluating extracranial vasculature is duplex sonography, which combines high frequency, real-time imaging with Doppler flow data. This course will discuss the capabilities and limitations of duplex sonography in the evaluation of patients with suspected atherosclerotic occlusive disease of extracranial vessels. Sonographic features of plaque histology will be discussed. A variety of spectral analytic techniques that can be used for analyzing Doppler flow information will be presented and discussed in detail. Indications for duplex sonographic examinations of extracranial vasculature will be discussed and diagnostic algorithms for evaluating patients with suspected extracranial carotid or vertebral disease will be presented.

402. Orbital and petrous bone radiology: Forbes GS. An overview of orbital and petrous bone imaging will be presented that is directed toward the needs of the general radiologist. Discussion will follow a practical clinical approach so that categories of clinical problems will be related to choice of imaging method and technique. Anatomy and pathology review will lead into discussion of the radiologic appearance. Scanning techniques are emphasized, although other methods (such as MR, plain film tomography, and angiography) are included. The course is intended to review the common orbital and petrous lesions and the current radiologic methods used in their diagnostic evaluation.

403. Sonography in pediatric radiology: overview and recent advances. Hayden CK Jr, Swischuk LE. Sonography has created a great impact on the investigation of pediatric disease and this course will review its current status. There will be a resumé of its use in abdominal masses, but there will be more detail on its newer uses in pediatric neurosonography and urinary tract disease, in which, in essence, it has replaced the excretory urogram. In addition, newer and previously unsuspected uses in the gastrointestinal tract will be presented in detail (e.g., pyloric stenosis, gastric ulcer disease in infants, intussusception, volvulus, imperforate anus). Finally, the use of sonography in the evaluation of the acute abdomen, soft-tissue extremity problems, thoracic abnormalities, and miscellaneous abnormalities in other parts of the body will be reviewed.

404. Film-screen mammography. Gisvold JJ. Several techniques have potential roles in breast evaluation. The cornerstone of breast imaging procedures has been and remains mammography. This course will deal strictly with film-screen mammography. Because of a resurgence of interest in film mammography, a review of this subject is considered important. Radiographic technique is critical if films of diagnostic quality are to be obtained; thus, technique will be covered. Knowledge of basic breast disease is important and a brief review will be presented. Interpretation of mammograms will be the main topic. The importance of calcifications and the wide variety of soft-tissue changes will be reviewed in detail, and the use of special views and techniques, including magnification, will be covered. The wording of interpretations is important and some clues for most effectively reporting mammograms will be offered. Many clinically occult breast lesions are being discovered and these must be localized preoperatively. The important features of this technique will be reviewed.

405. Technical advances in MRI of the abdomen. Stark DD. Clinical applications of MR imaging in the diagnosis of abdominal disorders are now established. Efficacy of MR is determined with respect to the performance and expense of alternative imaging techniques. In this course both theoretical and practical topics are reviewed: (1) Pulse-sequence optimization for detecting liver metastases: T1- and

T2-weighted spin-echo (SE), inversion-recovery, chemical-shift, and fast low-angle shot (FLASH) techniques will be compared with contrast-enhanced CT. (2) Tissue characterization of liver lesions: characteristic MR features of hepatic hemangiomas and cysts allow differentiation from metastases with 90% accuracy on T2-weighted SE images. (3) Chemical shift imaging of the liver: discrimination of water and fat hydrogen by in vivo phase-contrast imaging allows recognition of fatty infiltration, identification of focal fat deposition, and improved detection of liver metastases. Applications of the Dixon method will be emphasized. (4) Motion artifact reduction: experience with short-TR/short-TE SE techniques and extensive signal averaging suggest that respiratory gating, COPE, respiratory-ordered phase encoding, and EXORCIST may be inefficient and unnecessary. Rapid patient throughput, improved image quality, and diagnostic results are shown with new short-TR/short-TE T1-weighted techniques compared with the older T2-weighted techniques. Applications of fast scanning (FLASH or "gradient echo") techniques will be demonstrated. Multislice-imaging techniques with examination times shorter than 20 sec now allow anatomic surveys during a single breath-hold.

406. Imaging (high-resolution CT and MR) in degenerative disk disease of the lumbar spine—1987. Lukin R. High-resolution CT of the spine has dramatically altered the diagnostic evaluation of patients with degenerative disk disease. Similarly, MR scanning has had major impact on the diagnostic workup of such patients. In the lumbar area, high-resolution CT will be the primary emphasis of discussion while the evolving role of MR will also be reviewed. A major segment of this course will be devoted to so-called bulging and herniated lumbar disks and their differentiation. Differential diagnostic considerations and potential traps will be emphasized. The problem of the diagnostic evaluation of the postoperative back will be covered. There will be a discussion devoted to the analysis of so-called "spinal stenosis." In the cervical area, the role of MR scanning, plain cervical CT, water-soluble contrast CT, and myelography will be reviewed. Different approaches for the clinical presentation of radiculopathy and myelopathy will be emphasized.

407. MR imaging of the pelvis: urinary tract and retroperitoneum. Kressel HY. The application of MR imaging to pelvis and retroperitoneum presents a variety of challenges. Both the choice of pulse sequences and the plane of data acquisition must be appropriate for the question to be answered. In this course, we will review the normal MR anatomy of the pelvis and retroperitoneum and define an approach for imaging these regions. Because the composition of a lesion determines its MR appearance, understanding the MR appearance of various disease processes is important. A simple approach for characterizing lesions will be presented, and a range of inflammatory and neoplastic conditions involving the pelvis and retroperitoneum will be surveyed. In addition, the role of MR imaging in staging and monitoring response to therapy of renal, prostatic, uterine, ovarian, and cervical carcinoma will be reviewed.

408. The postoperative chest: radiographic and CT evaluation. Goodman LR. The postoperative radiograph reflects both the normal changes after thoracic surgery and the postoperative complications. Armed with a thorough knowledge of the expected changes, the radiologist is often in a position to identify potential complications before they become manifested clinically. In other situations, the chest radiograph often indicates the need for other imaging evaluation, especially CT. This lecture will concentrate on the most efficacious imaging strategies after thoracotomy for lung resection and mediastinotomy for mediastinal, cardiac, and esophageal surgery.

409. Angioplasty and fibrinolysis. Katzen BT. The purpose of this refresher course is to present an overview of the current status of

transluminal angioplasty in the treatment of peripheral vascular disease, renovascular hypertension, and upper extremity vasculature and great vessels. Emphasis on accepted technique, indications for therapy, and diagnosis and treatment of complications will be emphasized. Recent developments in balloon catheter and guidewire technology have further improved techniques and results in transluminal angioplasty. These will be discussed in detail. In addition, the current status of catheter-directed fibrinolytic techniques will be presented, particularly as they relate to concomitant use of transluminal angioplasty. Long-term results and complication rates will be discussed in detail by anatomic distribution.

410. Nuclear cardiology in clinical practice. Thrall JH. Nuclear cardiology embraces multiple imaging procedures aimed at diagnosing cardiac diseases and monitoring heart function. In current practice, three major procedures encompass most clinical applications. These are the technetium-99m, pyrophosphate infarct avid scan, the thallium-201 myocardial perfusion scan, and the radionuclide ventriculogram or radioangiogram. In this session, the rationale, basic technique, clinical application, and accuracy of the respective procedures will be presented. Applications in the evaluation of patients with coronary heart disease will be emphasized. A strategy for patient selection for each of the respective procedures will be presented within the framework of an analysis of the efficacy of the procedures. In addition to the clinically well-established techniques, a number of newer methods of imaging the heart will be briefly presented with emphasis on rationale, information available, and potential for clinical use in the near future.

411. Advanced imaging of the musculoskeletal system: CT, MR, and densitometry techniques. Resnick D, Sartoris DJ. An overview will be presented of the application of newer imaging methods to the assessment of musculoskeletal disorders. Standard, reformatted, and three-dimensional analyses of CT and MR data in the evaluation of

traumatic, infectious, neoplastic, articular, and miscellaneous disorders will be discussed. The use of CT- and MR- arthrography will be illustrated. Accepted methods (single-photon absorptiometry of the radius, dual-photon absorptiometry of the spine and femur, and quantitative CT of the spine) and investigative techniques (three-dimensional volumetric CT, dual-energy projection radiography, Compton scattering, and neutron activation analysis) used in the detection and serial monitoring of metabolic bone disorders will be contrasted in terms of indications, advantages, and disadvantages.

412. Modern pancreatic imaging. Silver TM, Glazer G. The goal of this refresher course is to present the current state-of-the-art in pancreatic imaging with CT, sonography, and MR. After a brief introduction and review of normal anatomy and imaging principles, the roles of these techniques in neoplastic, inflammatory, and metabolic disease states will be discussed. The techniques, indications, and limitations of each will be stressed and our recommendations concerning appropriate use will be presented. Newer applications, such as the role of intraoperative sonography and dynamic CT in the evaluation of pancreatic endocrine tumors will be presented. Also, the use of these methods to guide interventional procedures, such as biopsy or abscess drainage, will be considered.

Friday, May 1

Symposium on Genitourinary Imaging Update. See Table 3 for topics and instructors. Register on registration form for this complimentary program.

Table 3: Genitourinary Imaging Update

Topic/Time	Presenter
Introduction	
8:00 a.m.	Moderator: David S. Hartman Moderator: Harry Z. Mellins
Contrast Media—The New Agents	
8:05 a.m.	When and where? (McClennan)
8:25 a.m.	Why? (Lalli)
Interventional	
8:45 a.m.	Stone disease (Pfister)
Pediatrics	
9:05 a.m.	Imaging the child's urinary tract in 1987 (Lebowitz)
Sonography	
9:25 a.m.	Update in obstetrical ultrasound (Pretorius)
9:45 a.m.	Ultrasound evaluation of fetal GI and GU tract (Maklad)
10:05 a.m.	Prostate (Rifkin)
10:25 a.m.	Coffee break
Nuclear Medicine	
10:50 a.m.	State-of-the-art (Thrall)
CT/MR Imaging	
11:10 a.m.	Trauma (Federle)
11:30 a.m.	Bladder, prostate and cervix (Thornbury)
11:55 a.m.	Adrenal (Dunnick)
12:15 a.m.	Renal lesions (Newhouse)

Note.—There is no fee for this symposium. However, to facilitate planning, please register on the meeting registration form.

ACR Luncheon Presentations on Socioeconomics of Radiology

A series of luncheon presentations on the socioeconomics of radiology will be arranged by the American College of Radiology (ACR). A box lunch will be provided. The presentations do not conflict with other elements of the program. Advance registration is required. Cost per session: \$10.

Date, Topic, Speaker

Monday, April 27: The 100th Congress; What It Will Do to Radiology. Otha W. Linton, associate executive director, ACR

Tuesday, April 28: Resource-Based Relative Value Scales—The Harvard/AMA Study, Franklin L. Angell, Baltimore, MD

Wednesday, April 29: Alternative Health Delivery Systems: Problems for Radiology, Thomas G. Dehn, Milwaukee, WI

Thursday, April 30: Malpractice/Risk Management Issues for Radiologists, Jerome H. Shapiro, Boston, MA, and Harold Schwinger, New York, NY

Faculty List

- Alderson, Philip O.**, Columbia-Presbyterian Medical Center
Alfidi, Ralph J., University Hospital of Cleveland
Banner, Marc P., Hospital of the University of Pennsylvania
Barth, Klemens H., Georgetown University Hospital
Berk, Robert N., University of California, San Diego
Bradley, William G. Jr., Huntington Medical Research Institute
Braude, Gita, *American Journal of Roentgenology*
Buonocore, Edward, University of Tennessee Hospital
Carroll, Barbara A., Duke University Medical Center
Charboneau, J. William, Mayo Clinic Foundation
Davidson, Alan A., Armed Forces Institute of Pathology
Davis, Kenneth R., Massachusetts General Hospital
Dunnick, N. Reed, Duke University Medical Center
Elliott, Larry P., Georgetown University Hospital
Federle, Michael P., University of California, San Francisco
Ferrucci, Joseph T., Massachusetts General Hospital
Figley, Melvin M., University of Washington
Forbes, Glenn S., Mayo Clinic Foundation
Freeny, Patrick C., The Mason Clinic
Gelfand, David W., Bowman Gray School of Medicine
Genant, Harry K., University of California, San Francisco
Ghahremani, Gary C., Evanston Hospital-Northwestern University
Gisvold, John J., Mayo Clinic Foundation
Glazer, Gary M., University of Michigan Medical School
Glick, Seth N., Hahnemann University Hospital
Goldberg, Henry I., University of California, San Francisco
Goldstein, Harvey M., University of Texas, San Antonio
Goodman, Lawrence R., Medical College of Wisconsin
Gore, Richard M., Northwestern Memorial Hospital
Graham, C. Benjamin, Children's Orthopedic Hospital
Greenson, Thomas, American College of Radiology
Haaga, John R., University Hospital of Cleveland
Harms, Steven E., Baylor University Medical Center
Hartman, David S., Uniformed Services University of the Health Sciences, Bethesda, MD
Hayden, C. Keith Jr., University of Texas Medical Branch, Galveston
Hilton, S. v. W., University of California, San Diego
James, A. Everette, Vanderbilt University
Jaques, Paul, North Carolina Memorial Hospital
Katzen, Barry T., The Alexandra Hospital, VA
Kirkpatrick, John A., The Children's Hospital, Boston
Kopans, Daniel B., Massachusetts General Hospital
Kressel, Herbert Y., Hospital of the University of Pennsylvania
Laing, Faye C., San Francisco General Hospital
Lalli, Anthony F., Hillcrest Hospital, Ohio
Laufer, Igor, Hospital of the University of Pennsylvania
Lebowitz, Robert L., Children's Hospital Medical Center, Boston
Leopold, George R., University of California, San Diego
Levine, Marc S., Hospital of the University of Pennsylvania
Lipton, Martin, University of California, San Francisco
Lukin, Robert, University of Cincinnati Medical Center
Maglinte, Dean D. T., Methodist Hospital of Indiana
Maklad, Nabil F., University of Texas, Houston
Malmud, Leon S., Temple University Hospital Center
Martel, William, University of Michigan Medical Center
Mauro, Matthew, North Carolina Memorial Hospital
McClennan, Bruce L., Washington University Medical Center
McLoud, Theresa C., Massachusetts General Hospital
Megibow, Alec J., New York University Medical Center
Mellins, Harry Z., Harvard Medical School
Mendez, Gaston Jr., Jackson Memorial Hospital
Moss, Albert A., University of Washington Medical Center
Mueller, Peter R., Massachusetts General Hospital
Naidich, David, Johns Hopkins Medical Institution
Naidich, Thomas P., Children's Memorial Hospital, Chicago
Newhouse, Jeffrey H., Columbia-Presbyterian Medical Center
Norman, Alex, Hospital for Joint Diseases, New York
Nunez, Diego Jr., Jackson Memorial Hospital
Ott, David J., Bowman Gray School of Medicine
Pfister, Richard C., Massachusetts General Hospital
Poznanski, Andrew K., Children's Memorial Hospital, Chicago
Pretorius, Dolores H., University of California, San Diego
Proto, Anthony V., Medical College of Virginia
Raghavendra, B. Nagesh, New York University Medical Center
Ramsey, Ruth G., Rush-Presbyterian-St. Luke's Medical Center
Resnick, Donald L., VA Medical Center, San Diego
Rifkin, Matthew D., Thomas Jefferson University Hospital
Rogers, Lee F., Northwestern University Medical School
Rosenthal, Daniel I., Massachusetts General Hospital
Russell, Edward, Jackson Memorial Hospital
Sackett, Joseph F., University of Wisconsin
Sartoris, David J., University of California, San Diego
Sickles, Edward, University of California, San Francisco
Siegelman, Stanley S., Johns Hopkins Medical Institution
Silver, Terry M., University of Michigan Medical School
Staab, Edward V., North Carolina Memorial Hospital
Stark, David D., Massachusetts General Hospital
Swischuk, Leonard E., University of Texas Medical Branch
Taylor, Kenneth J. W., Yale University School of Medicine
Thornbury, John R., University of Rochester Medical Center
Thrall, James H., Henry Ford Hospital
vanSonnenberg, Eric, University of California, San Diego
Viamonte, Manuel Jr., University of Miami School of Medicine
Weinberg, Peter E., Northwestern University Medical School
Westcott, Jack L., Hospital of Saint Raphael, New Haven
Wittenberg, J., Massachusetts General Hospital
Wood, Beverly P., University of Rochester Medical Center
Yrizarry, Jose M., Jackson Memorial Hospital
Zeman, Robert K., Georgetown University Hospital
Zerhouni, Elias, Johns Hopkins Medical Institution

American Roentgen Ray Society 1987 Scientific Program

The scientific program is divided into parallel sessions so that registrants may choose topics related to their interests. A total of 189 papers will be presented Monday–Thursday, April 27–May 1. In addition, on Wednesday morning, April 29, a special session will be devoted to award-winning papers and the Caldwell Lecture, which will be delivered by M. Paul Capp of the University of Arizona. On Friday, May 1, there will be a special symposium on genitourinary imaging update.

Monday, April 27, 10:30 a.m.–12:30 p.m.

I. Chest Radiology: I

- 10:30 1. Small cell bronchogenic carcinoma: lymphadenopathy and other thoracic involvement on initial presentation. Pearlberg J, Sandler M, Lewis J, Beute G
- 10:42 2. Pulmonary pseudonodule: a normal finding in the lateral chest radiograph. Caceres J, Mata J, Rams A
- 10:54 3. Pulmonary Kaposi's sarcoma in AIDS patients: radiographic-pathologic correlation. Davis S, Henschke C, Chamides B, Westcott J
- 11:06 4. Distinction from pleural to parenchymal lung disease: value of bolus contrast enhancement. Francis I, Bressler E, Glazer M, Gross H
- 11:18 5. The anterior junction line as an indicator of chronic obstructive pulmonary disease. McMurdo K, Faria M, Gamsu G
- 11:30 6. Value of thoracic CT in detecting "occult" pathology in critically ill patients. Mirvis S, Tobin K, Kostrubiak I, Belzberg H
- 11:42 7. Torsion of the upper lobe in pneumothorax: a normal phenomenon. Berkman Y, Yankelevitz D, Zanzonico P
- 11:54 8. Clinical results with advanced multiple beam equalization radiography (AMBER) in chest radiology. Busscher D, Algra P, Schultze-Kool L, Hermans J
- 12:06 9. Pulmonary density changes by computed tomography during the development of pulmonary edema. Altin R, Flicker S, Naidech H, Eldredge J

II. Uroradiology Imaging: I

- 10:30 10. The renal fascial network in retroperitoneal extension of pathologic processes. Raptopoulos V, Kleinman P, Marks S, Davidoff A
- 10:42 11. Proximal and distal sclerotherapy of varicoceles—a comparative study. Fobbe F, Sorensen R, Hamm B, Berger T
- 10:54 12. Magnetic resonance imaging of renal carcinomas. Barbaric Z, Wegenius G, Ritchies A, DeKernion J
- 11:06 13. Interventional uroradiology: experiences with the

retrograde approach to the kidney and ureter. Amendola M, Banner M, Pollack H, Gordon R, VanArsdalen K

- 11:18 14. Cystourethrosonography: application in prostatic hyperplasia. Peetrans P, Weiser M, Lemone M, Gossart P
- 11:30 15. Validity of ethanol embolization of renal tumors. Cramer B, Schlegel E
- 11:42 16. Percutaneous management of stenotic dialysis access fistulas. Saeed M, Newman G, McCann R, Sussman S, Dunnick N
- 11:54 17. Management of urinomas by percutaneous drainage techniques. Lang E
- 12:06 18. Ultrasound guided renal biopsy in patients with diffuse renal parenchymal disease. Elyaderani M, Frick M

III. Neuroradiology: I

- 10:30 19. Radiologic-pathologic correlation of gliosarcomas. Chespak L, Smirniotopoulos J, Parisi J
- 10:42 20. Cerebral hemispheric pilocytic astrocytoma: radiologic-pathologic correlation. Smirniotopoulos J, Parisi J, Murphy F
- 10:54 21. Computed tomography manifestations of subdural hygromas. Haas R, Moon A, Knuckey N, Epstein M
- 11:06 22. Hemangioblastoma: radiologic-pathologic correlation. Murphy F, Smirniotopoulos J, Parisi J
- 11:18 23. Increased accuracy of CT diagnosis of lumbar HNP. Teplick J, Haskin M, Laffey P
- 11:30 24. Vertebral artery trauma—transcatheter embolization. Ben-Menachem Y, Fields W, Cadavid G, Gomez L, Anderson E, Fisher R
- 11:42 25. Sonography of nerve tumors. Fornage B, Schernberg F
- 11:54 26. "The pituitary high signal"—What does it represent? Shapiro M, Sostman D, Peyster R, Gore J, Milbauer D, Kier E, Kim J
- 12:06 27. Holoprosencephaly: prenatal diagnosis and clinical significance. Nyberg D, Bronstein A, Mack L, Hirsch J

Tuesday, April 28, 10:00 a.m.–12:30 p.m.

IV. Gastrointestinal Imaging: I

10:00 28. Ano-rectal atresia: accuracy of prenatal diagnosis by ultrasound and clinical significance. Harris R, Nyberg D, Mack L, Weinberger E

10:12 29. Hirschsprung's disease, Ondine's curse and the neurocristopathy syndrome. Roshkow J, Haller J, Berdon W, Shashikant M

10:24 30. Gastroesophageal reflux in infants: how much imaging is necessary? Swischuk L, Fawcett H, Hayden C

10:36 31. Balloon dilatation of esophageal strictures in children. Sato Y, Smith W, Frey E, Franken E, Soper R, Pringle K

10:48 32. New prognostic CT findings in severe acute pancreatitis. Andreu J, Perez C, Llauger J, Caceres J

11:00 33. Iatrogenic bile duct injuries: radiological diagnosis and clinical significance. Ghahremani G, Bernstein J, Crampton A, Caprini J

11:12 34. Sonographic and radiologic diagnosis and management of inadvertent ligation of bile ducts following cholecystectomy. Christensen R, vanSonnenberg E, Casola G, Orloff M, Hoyt D, Leopold G, Amberg J

11:24 35. Diffuse hepatic vascular abnormalities in focal nodular hyperplasia and adenoma: radiologic-pathologic correlation. Dorfman G, Cronan J, Jauregui H, Glickman M

11:36 36. Computed tomography in giant cavernous hemangioma of the liver. Kenny J, Scatarige J, Fishman E, Herlong F, Zerhouni E, Siegelman S

11:48 37. First clinical use of gadolinium-DTPA for gastrointestinal contrast enhancement in man. Kornmesser W, Laniado M, Hamm B, Claub W, Felix R

12:00 38. Computed tomography and interventional radiology: a safe and effective alternative to laparotomy for splenic trauma in hemodynamically stabilized patients. Sclafani S, Weisberg A, Phillips T, Goldstein A, Scalea T, Gordon D, Glanz S, Duncan A, Shaftan G

12:12 39. Magnetic resonance imaging of the Budd-Chiari syndrome. Stark D, Hahn P, Trey C, Clouse M, Ferrucci J

V. Mammography

10:00 40. Effect of community interventions on screening mammograms. Destouet J, Monsees B, Vannier M

10:12 41. Mammographic and sonographic mimics of breast carcinoma. Mendelson E, Bohm-Velez M, Neiman H, Joseph N, Bhagwanani D, Rishi U

10:24 42. Paget's disease of the nipple: is it a contraindication to breast conservation? Krause B, Willan B

10:36 43. Compression spot views in the evaluation of questionably suspicious mammographic findings. Berkowitz J, Gatewood O, Gayler B

10:48 44. Breast ultrasound: prospective comparison of 7.5 MHz automated and 7.5 MHz hand held examinations. Hansen J, Cole-Beuglet C, Cyrak D

11:00 45. Two view specimen radiography: a potential aid for radiographic confirmation in surgical biopsy of non-palpable breast lesions. Rebner M, Pennes D, Baker D, Adler D

11:12 46. The emerging role of ultrasound guided percutaneous needle aspiration in breast diagnosis. Hogg J, Skolnick M, Harris K

11:24 47. Development of breast localizing needle with a retractable wire bar. Meacham M, Akins W, Urrutia E, Hawkins M, Hawkins I

11:36 48. Fine needle aspiration breast biopsies: review of 1036 cases. Williams K

11:48 49. Advanced imaging processing: MRI of breast masses. Abbitt P, Paling M, Merickel M, Adams A

12:00 50. Evaluation of indeterminate occult breast lesions on mammography by MRI. El Yousef S, Duchesneau R, Crowe J, Lie S

12:12 51. Can physicians' assistants interpret screening mammograms? A prospective study. Hillman B, Fajardo L, Hunter T, Mockbee B, Bjelland J, Cook C, Frey C, Harris C

VI. Skeletal Radiology: I

10:00 52. Radiographic evaluation of hallux valgus: preoperative and postoperative findings. Richardson M, Hansen S, Kilkoyne R

10:12 53. Brucellosis of bone and joints excluding the spine: radiologic features. Madkour M, Sharif H, Abed M, Al Fayed M

10:24 54. Diaphyseal bone disease: scintigraphic-radiographic correlation. Shier C, Thrall J, Kottamasu S, Krasicky G, Ellis B

10:36 55. Ewing's sarcoma of rib. Moser R, Ros P, McCarthy M, Smirniotopoulos J, Buck J

10:48 56. The measurement of the mineral content of rib on dual-energy digital images of the chest: an assessment of osteoporosis. Friedman S, Sabbagh E, Dubovsky Barnes G, Fraser R

11:00 57. Neuroarthropathy associated with chronic alcoholism in non-diabetic patients. Bjorkengren A, Resnick D, Zlatkin M, Pate D, Danzig L, Sartoris D

11:12 58. Base of metatarsal V fractures. Bohrer S

11:24 59. Pyogenic sacroiliitis in intravenous drug abusers. Guyot D, Kling G, Manoli A

11:36 60. Rigid subtalar joint—an anatomic spectrum. Bower B, Keyser C, Gilula L

11:48 61. Stress fractures of the distal tibia and calcaneus subsequent to acute fractures of the tibia and fibula. Zlatkin M, Bjorkengren A, Resnick D, Sartoris D

12:00 62. Retinoid-induced hyperostoses. Pennes D, Martel W, Ellis C, Voorhees J

12:12 63. Osteonecrosis of the knee associated with corticosteroids. Schneider R, Bohn W, Johanson N, Goldman A

Tuesday, April 28, 1:30–3:30 p.m.

VII. Cardiovascular Radiology

1:30 64. Percutaneous femoral insertion of the Greenfield vena cava filter: the fate of the femoral vein. Glanz S, Gordon D, Kantor A

1:42 65. Superiority of radionuclide ventriculography (RNV) over 2-dimensional echocardiography (2-D echo) and chest radiography (CXR) in the detection of myocardial contusion. Smith R, Hulsey J

1:54 66. Transluminal angioplasty in the treatment of subclavian artery stenosis and associated subclavian steal syndromes. Smoot S, Wholey M, Jarmolowski C

2:06 67. Experimental evaluation of a new instrument designed for the percutaneous retrieval of peripheral emboli. Wholey M, Smoot S, Jarmolowski C

2:18 68. Chest radiographic findings and complications of the temporary implantation of the Jarvik-7 artificial heart while awaiting orthotopic heart transplantation—experience with 6 cases. Sadler L, Fuhrman C, Hardesty R, Griffith B

2:30 69. Metastatic calcification of the heart in end-stage renal disease: detection by dual-energy digital chest radiography. Sanders C, Frank M, Rostand S, Rutsky E, Barnes G, Fraser R

2:42 70. The application of MR phase imaging in the evaluation of cardiovascular disease. Rumancik W, Naidich D, Chandra R, Kowalski H, McCauley D, Megibow A, Genieser N

2:54 71. Four dimensional assessment of the highly conditioned athletic heart by MRI. Brunner M, Burnett O, Baron M, Fajman W, Flower S, Apple D, Allman F, Pettigrew R

3:06 72. Improved ventricular function after bypass grafting in patients with progressive angina. Newman G, Rankin J, Dunnick N, Putman C

3:18 73. Cardiac and non-cardiac gated magnetic resonance imaging in the arrhythmia patient—assessment of cardiac anatomy. Feiglin D, MacIntyre W, Moodie D, O'Donnell J, Go R

VIII. Ultrasonography: I

1:30 74. Standardized endosonography of prostate carcinoma. Baran G, Golin A, Bergsma C, Stone T, Holly L II

1:42 75. Factors affecting the false negative diagnosis of prostate carcinoma with transrectal ultrasound. Hamer M, Madrazo B

1:54 76. Ultrasound of the non-gravid uterus: correlation with gross and histopathology. Platt J, Bree R, Saylor M, Schwab R, Santilli S, Davidson D

2:06 77. Preliminary experience with endovaginal sonography. McSweeney M, Kruse B, Carson G

2:18 78. Transvaginal ultrasound of early pregnancy and its complications. Bree R, Edwards M, Chan K

2:30 79. Transvaginal sonography in the evaluation of endometrial abnormalities. Mendelson E, Joseph N, Kellman G, Neiman H, Levy E, Bohm-Velez M

2:42 80. Transvaginal sonography in the evaluation of ectopic pregnancy: comparison with transabdominal ultrasound. Mack L, Nyberg D, Harris R, Laing F, Jeffrey R

2:54 81. Ovarian torsion: sonographic evaluation. Helvie M, Silver T

3:06 82. Ultrasonography of the rotator cuff: a review of 400 cases. Crass J, Craig E, Feinberg S

3:18 83. Sonographic evaluation of the postoperative rotator cuff. Mack L, Harris R, Nyberg D, Harvey D, Gannon M, Matsen R

IX. Magnetic Resonance: I

1:30 84. Hemangioma of the liver: magnetic resonance—gross morphologic correlation. Ros P, Lubbers P, Olmsted W, Morillo G

1:42 85. Signal-to-noise and contrast-to-noise advantages of optimized flash imaging. Stark D, Hendrick R

1:54 86. MR-guided stereotactic biopsy and surgery: preliminary experience. Lund G, Mollman H, Maxwell R, Matri A

2:06 87. Magnetic resonance imaging of the hand and wrist. Steinbach L, Richardson M, Stoller D, Gillespy T, Kilcoyne R, Shuman W, Genant H

2:18 88. MR phase imaging in the evaluation of neurovascular disease. Kowalski H, Rumancik W, Chandra R, Kricheff I

2:30 89. Clinical application of a new technique for eliminating flow artifacts and improving the rendition of vascular anatomy in MRI. Ehman R, Felmlee J, Julsrud P, Berquist T, Gray J

2:42 90. Fast low angle MR sequences in the evaluation of brain pathology. Steinberg P, Masaryk T, Modic M, Ross J, Haacke E, Tkach J, Kaufman B, Deimling M, Bachus R

2:54 91. MR imaging in children—spine and spinal cord. Lund G, Duthoy M

3:06 92. Magnetic resonance in the evaluation of the adnexae. Kleiner B, Callen P, Filly R, Gordon P, Mills G

3:18 93. Reliability and reproducibility of T1 and T2 relaxation times as determined by MRI scanners. Prasad S, Bassano D, Szevenyi N

Wednesday, April 29, 1:30–3:30 p.m.

X. Interventional Radiology: I

- 1:30 94. Alternatives in percutaneous nutritional support.** Lambiase R, Dorfman G, Cronan J, Haas R, Paoletta L
- 1:42 95. PTRAs in azotemic patients.** Martin L, Gaylord G, Alspaugh J, Chuang V, Casarella W
- 1:54 96. Hepatic cysts treated with alcohol: review of recurrence.** Bean W, Mullin D, Porter R, Hawkins I, McLean G
- 2:06 97. Angiographic correction of unsatisfactory hepatic perfusion after surgical catheter placement for hepatic arterial chemotherapy.** Andrews J, Williams D, Knol J, Cho KY, Ensinger W
- 2:18 98. Percutaneous transhepatic embolization of esophageal varices results in 400 patients.** L'Hermine C, Chastanet P, Delemauzure O, Bonniere PH, Cussac J, Paris J
- 2:30 99. Percutaneous gastrostomy: comparison of radiologic versus endoscopic techniques.** Mueller P, Brown A, Saini S, Hahn P, Steiner D, Ferrucci J
- 2:42 100. MTBE dissolution of common duct calculi.** Muhr W, Brandon J, Teplick S, Haskin P, Sammon J
- 2:54 101. Percutaneous management of infected and noninfected pancreatic pseudocysts.** vanSonnenberg E, Casola G, Wittich G, Brannigan T, Christensen R, Withers C, Keightley A
- 3:06 102. Sclerosis of noninfected fluid collections via percutaneous catheters.** vanSonnenberg E, Casola G, Wittich G, Christensen R, Halasz N, Cohen M, Keightley A
- 3:18 103. Percutaneous catheter drainage of superinfected neoplasms.** Glass-Royal M, White E, Grant E, Zeman R, Choyke P, Mueller P

XI. Neuroradiology: II

- 1:30 104. Norms for the upper cervical spine: measurements of the predens space, dens tilt and "interspinous" distances with motion.** Monu J, Bohrer S
- 1:42 105. Plain film assessment of congenital cervical spinal stenosis: the canal/body ratio.** Silverstein G, Kohn M, Teplick J
- 1:54 106. MR imaging in cervical spondylosis.** Crofford M, McArdle C, Guinto F, Waggenspack G, Amparo E
- 2:06 107. Significance of sampling-related phenomena in MR spine imaging.** Levy L, Di Chiro G

- 2:18 108. The utility of MR in suspect brachial plexus pathology.** Castagno A, Shuman W, Nyberg D, Mack L, Moss A
- 2:30 109. Acquired spinal subarachnoid cysts: evaluation with MR, metrizamide CT, and intraoperative sonography.** Sklar E, Quencer R, Green B, Montalvo B, Post M
- 2:42 110. MR of arachnoiditis.** Ross J, Modic M, Masaryk T, Delamater R, Bohlman H, Kaufman B, Wilder G
- 2:54 111. Intraoperative sonography in lumbar disc herniation and canal stenosis.** Montalvo B, Quencer R, Brown M, Sklar E, Post M, Eismont F, Green B
- 3:06 112. Untreated cervical and lumbar disc herniations: can they regress?** Teplick J, Haskin M, Laffey P
- 3:18 113. MRI evaluation of paraspinal neurogenic tumors.** Lupetin A, Rothfus W, Deeb Z, Daffner R, Dash N, Schapiro R

XII. Magnetic Resonance: II

- 1:30 114. MRI of head and neck masses in children.** Swischuk L, Amparo E, Hayden C
- 1:42 115. MR of traumatic injury to the corpus callosum.** Gentry L, Godersky J, Crawford S, Strother C, Turski P, Sackett J
- 1:54 116. MR imaging of liver metastasis: pulse sequence optimization.** Paling M, Abbitt P
- 2:06 117. Otolaryngological neoplasms: prospective evaluation with MR and CT.** Waggenspack G, Guinto F, Crofford M, Bailey B, Amparo E
- 2:18 118. Comparison of S/N ratio at 0.5 and 1.5 T in human subjects.** Kowalski H, Chandra R, Rumancik W, Kricheff I
- 2:30 119. MRI with surface coils for preoperative evaluation in primary hyperparathyroidism.** Kier R, Blinder R, Herfkens R, Leight G, Spritzer C, Carroll B
- 2:42 120. Signal-two-noise and contrast-two-noise advantages of optimized flash imaging.** Hendrick R, Kneeland J, Stark D
- 2:54 121. The evaluation of vascular tumors of the head and neck.** Wilson G, Lufkin R, Teresi L, Moffit B, Dietrich R, Anselmo M, Bentson J
- 3:06 122. Magnetic resonance imaging of the knee using rotating oblique planes to produce radial cross-sections of menisci.** Drace J, Smathers R, Enzmann D
- 3:18 123. Magnetic resonance imaging of the cervical spine in rheumatoid arthritis.** Aisen A, Martel W, McCune W, Ellis J

Thursday, April 30, 10:00 a.m.–12:30 p.m.

XIII. Gastrointestinal Radiology: II

- 10:00 124. Evaluation of the mediastinum on chest radiographs in patients with esophageal cancer.** McCarroll K, Cawthon L, Roszler M, Donovan K, Guyot D, Kling G

- 10:12 125. Comparison of magnetic resonance to computed tomography for staging esophageal carcinoma.** Halvorsen R, Herfkens R, Wolfe W, Thompson W
- 10:24 126. Mesenteric fibromatosis: radiologic-pathologic correlation in 24 cases.** Ros P, Buck J, Dachman A, Federspiel B, Moser R

10:36 127. The validity of the radiological diagnosis of gastritis. Halpert R, Shier C, Waslawski S, Feczko P

10:48 128. Heterotopic gastric mucosa in the duodenum: its radiographic pathology and clinical significance. Agha F, Ghahremani G, Tsang T, Victor T

11:00 129. Computed sonography of acute appendicitis. Abu-Yousef M, Maher J, Urdaneta L, Franken E

11:12 130. Sensitivity of barium enema in colonic neoplasia relative to type of examination and age and symptoms of 128 patients. Scharling E, Chen Y, Ott D, Gelfand D, Wu W

11:24 131. Radiographic versus endoscopic detection of carcinoma complicating chronic ulcerative colitis. Hooyman J, MacCarthy R, Carlson H

11:36 132. Gallbladder lithotripsy: what will be the issue? Ferrucci J, Mueller P, Simeone J, Brink J

11:48 133. Biliary lithotripsy using a mechanical lithotripter. Ho C, Yee A

12:00 134. Gallstone solvents: considerations in the use of mono-octanoin, methyl tert-butyl ether and cheno or ursodeoxycholic acid. Mueller P, Simeone J, Ferrucci J

12:12 135. Increased sensitivity with lateral views in ⁶⁷gallium citrate scintigraphy of the thorax with esophageal carcinoma. Romero I, Sostre S, Rivera J

XIV. Ultrasonography: II

10:00 136. Sonography of normal and abnormal laryngeal anatomy. Rao B

10:12 137. Comparison of pulsed Doppler ultrasound and angiography in the portal hypertension patient. Nelson R, Lovett K, Chezmar J, Moyers J, Torres W, Murphy F, Chuang V, Bernardino M

10:24 138. Quantitative analysis of the Doppler waveform in acute renal transplant rejection using the pulsatility index. Murphy F, Gilarsky B, Steinberg H, Nelson R, Chezmar J, Bernardino M

10:36 139. The mistaken CT diagnosis of hepatic metastases: the role of sonography. Brick S, Hill M, Lande I

10:48 140. Duplex ultrasonography in chronic liver disease. White E, Grant E, Choyke P, Zeman R, Rosenbach D, Treem W, Colon A, Sarcone A

11:00 141. Sonography of breast fluid collection in lumpectomy and radiation patients. Mendelson E, Neiman H, Joseph N, Bohm-Velez M, Figura J, Leen R

11:12 142. High resolution compression ultrasound: a proven diagnosis tool for deep venous thrombosis. Cronan J, Dorfman G, Schepps B, Ridlin M, Scola F

11:24 143. Ultrasound differentiation of pseudoaneurysms

and hematomas resulting from femoral puncture and surgery. Rossman M, Haskin P, Laffey P

11:36 144. The three lines: observations regarding a mislabeled sonographic landmark in the fetal head. Hertzberg B, Bowie J, Marshburn P

11:48 145. Ultrasound-guided biopsy of small (less than or equal to 3 cm) masses: a review of 126 cases. Reading C, Charboneau J, James E, Hurt M

12:00 146. Thrombosis of upper extremity thoracic inlet veins: diagnosis using duplex Doppler sonography. Falk R, Smith D

12:12 147. Groin masses: the use of duplex Doppler sonography in distinguishing femoral artery pseudoaneurysm from other causes. Helvie M, Silver T, Rubin J, Kresowik T

XV. Skeletal Radiology: II

10:00 148. Coralline hydroxyapatite bone graft substitutes in canine diaphyseal defect model: radiographic-histometric correlation. Sartoris D, Holmes R, Bucholz R, Mooney V, Resnick D

10:12 149. Fracture nonunion: CT assessment with multiplanar reconstruction. Its role in suspected and difficult cases. Kuhlman J, Fishman E, Magid D, Scott W, Brooker A, Siegelman S

10:24 150. Cross-sectional appearance of the capsular mechanism of the shoulder: radiologic, anatomic and pathologic correlation. Zlatkin M, Bjorkengren A, Resnick D, Sartoris D

10:36 151. Evaluation of Neer total shoulder prosthesis. Aliabadi P, Weissman B, Thornhill T, Sosman J

10:48 152. The utility of surface coil imaging in avascular necrosis of the femoral head. Shuman W, Castagno A, Richardson M, Kilcoyne R

11:00 153. The role of angiography in the evaluation of penetrating injuries of the extremities. Shetty P, Spickler E, Sharma R, Burke M

11:12 154. Radiologic features of brucella spondylitis. Madkour M, Sharif H, Abed M, Al Fayed M

11:24 155. Radionuclide planar and SPECT imaging of the knee in suspected meniscal injury: correlation with arthroscopy. Fajman W, Stephenson R, Macha R, Flower S, Eisner R, Fleming L

11:36 156. MRI detection of knee fractures. Stoller D, Mink J, Crues J

11:48 157. CT guidance for skeletal biopsy and diagnosis. Frager D, Goldman M, Elkin C, Seimon L, Deitchman B

12:00 158. Magnetic resonance imaging evaluation of primary soft tissue sarcomas. Demas R, Heelan R, Marcove R, Lane J, Hajdu S, Brennan M

12:12 159. Musculoskeletal manifestations of the acquired immune deficiency syndrome. Meagher S, Tehranzadeh J

Thursday, April 30, 1:30–3:30 p.m.

XVI. Uroradiology: II

1:30 160. Evaluation of erectile dysfunctions: a proposed screening algorithm for noninvasive and invasive procedures. Schwartz A, Friedenberg D, Graham M

1:42 161. Intravascular application of a new nonionic contrast agent, iopromide—results of an open clinical trial. Langer M, Felix R, Behrends B

1:54 162. A controlled study of steroid pretreatment in intravenous contrast material reactions. Lasser E, Berry C, Santini L, Stolberg H, Holly L II, Dunnick N, Lang E

2:06 163. Percutaneous nephrostomy drainage as adjunct management of urinary septicemia. Lang E

2:18 164. Primary and adjunct applications of percutaneous urologic procedures in the era of extracorporeal lithotripsy. Stafford S, Papanicolaou N, Pfister R, Dretler S

2:30 165. Percutaneous urologic procedures and their role in the age of extracorporeal shock wave lithotripsy. Ainge G, Dyer R, Auringer S, McCullough D, Assimios D, Boyce W, Harrison L, Kroovand L

2:42 166. Staghorn calculus treatment by extracorporeal shockwave lithotripsy: the radiologists' role. Cochran S, Barbaric Z, Chaussy C, Fuchs G

2:54 167. Extracorporeal shock wave lithotripsy (ESWL) using a non-water bath system (Lithostar[®]). McClennan B, Clayman R

3:06 168. Percutaneous nephrostomy in conjunction with extracorporeal shockwave lithotripsy for treatment of nephrolithiasis. Cochran S, Barbaric Z

3:18 169. The role of the radiologist in the management of post-ESWL steinstrasse. Fedullo L, Banner M, Pollack H, Amendola M, VanArsdalen K

XVII. Interventional Radiology: II

1:30 170. New developments in balloon and wire technology for peripheral and visceral angioplasty. Smoot S, Wholey M, Jarmolowski C

1:42 171. The Blue Toe Syndrome management by anticoagulation and delayed percutaneous transluminal angioplasty. Brewer M, Kinnison M, Perler B, White R

1:54 172. Reposition of misplaced central venous catheters: a radiologic approach. Charnsangavej C, Carrasco C, Richli W, Sidney W

2:06 173. Fibrinolysis by minute intrathrombal application of urokinase in acute and chronic arterial occlusive disease with a new steerable delivery system. Cramer B

2:18 174. The percutaneous management of vascular abscesses. Lambiase R, Cronan J, Dorfman G, Haas R, Paoletta L

2:30 175. Results of intraarterial fibrinolytic therapy for the popliteal artery and trifurcation vessels. Traugher P, Cook P,

Micklos T, Wojtowycz M, Miller F

2:42 176. Percutaneous transfemoral Greenfield filter placement. Shetty P, Sharma R, Burke M, Bok L, Rollins N

2:54 177. Percutaneous Greenfield IVC filter: caveats in patient selection and placement technique. Dorfman G, Cronan J, Haas R, Lambiase R, Paoletta L

3:06 178. Technical modifications of percutaneous Kimray-Greenfield IVC filter placement. Porter D, Kim D, Crivello M, Kay D

3:18 179. Percutaneous dilatation of axillary and subclavian vein stenoses. Glanz S, Gordon D

XVIII. Chest Radiology: II

1:30 180. Pulmonary artery catheter-induced pulmonary artery false aneurysms. Dieden J, Friloux L, Renner J

1:42 181. Metastatic calcification of the lungs in end-stage renal disease: detection and quantitation by dual-energy digital chest radiography. Sanders C, Frank M, Rostand S, Rutsky E, Barnes G, Fraser R

1:54 182. CT evaluation of the mediastinum in lung cancer: influence of primary location on staging accuracy. Platt J, Glazer G, Quint L, Francis I, Gross B, Orringer M

2:06 183. CT diagnosis and nonsurgical management of mediastinal cysts of enteric and bronchogenic origin. Kuhlman J, Fishman E, Wang K, Zerhouni E, Siegelman S

2:18 184. MR of obscure pulmonary mass lesions. Naidich D, Rumancik W, McCauley D, Ettenger N, Genieser N

2:30 185. MRI in the evaluation of superior sulcus carcinomas. Filion R, McLoud T, Edelman R, Shepard J, Zancanaro A

2:42 186. Contrast enhancement of pulmonary masses. Littleton J

2:54 187. Transthoracic needle aspiration biopsy of lung lesions: a study of 1000 consecutive cases. Meziene M, Khouri N

3:06 188. Transthoracic needle aspiration: treatment of complications with a small chest tube. Dunnick N, Perlmutt L, Braun S, Newman G, Cohan R, Saeed M, Sussman S

3:18 189. Role of transthoracic needle biopsy after negative bronchoscopy. Nath H, Vaid Y, Breatnach E, Holley H

1987 ARRS Meeting: Local Activities and Tennis and Golf Tournaments

The 87th annual meeting of the American Roentgen Ray Society (ARRS) in Miami Beach, FL, April 26–May 1, will feature activities for members, guests, spouses, and friends. Manual Viamonte heads the Local Arrangements Committee. Lucy R. Kelley, Conference Coordinator, has planned the local programs. The tennis tournament will be arranged and supervised by Reuven Porgis; the golf tournament will be arranged and supervised by Neil Messinger. To register for these events please complete the registration form in this issue.

Golf Tournament

The annual golf tournament will be held at the Turnberry Isle Country Club, North Miami Beach, FL, on Monday, April 27. Buses will leave the Fontainebleau Hilton at 11 a.m. and will return to the hotel in the early evening at the completion of play. There will be a buffet lunch from 11:45 a.m. to 12:45 p.m. and a shotgun start at 1 p.m. Participants must bring golf clubs. No rental equipment will be available. Fee for the golf tournament is \$65 including transportation, luncheon, greens fee, cart, and prizes.

Men's and Women's Tennis Tournaments

The annual Men's and Women's Tennis Tournaments will be at the Turnberry Isle Country Club, North Miami Beach, FL, on Monday, April 27. Buses will leave the Fontainebleau Hilton at 11 a.m. and will return to the hotel in the early evening at the completion of play. There will be a buffet lunch from 11:45 a.m. to 12:45 p.m. Matches will begin at 1 p.m. Register early so that arrangements can be made to accommodate all who wish to play. Court space may be limited. Appropriate dress is required. \$50 fee includes transportation, luncheon, court fees, and prizes.

Local Program

All local activities have minimum enrollments and may be cancelled if there are not enough registrants. Transportation from the Fontainebleau Hilton Hotel will be provided for the

events listed below. With the exception of the trip on Tuesday, April 28, which is an all-day event, the day tours will depart from the hotel at 9:00 a.m. and return to the hotel at about 1:00 p.m., where the group can enjoy lunch on their own and a free afternoon of "sun and fun." Deadlines for registration are March 20 for the Sunday dinner cruise and April 15 for the other events. For further details, contact Lucy R. Kelley, Mt. Sinai Medical Center, Radiology, 4300 Alton Rd., Miami Beach, FL 33140; (305) 674-2681.

Sunday, April 26

Dinner Cruise and Show Aboard the Yacht THE SPIRIT, 6:00–10:00 p.m. Cruise south Florida's beautiful intercoastal waterway and enjoy all the elements of an ocean-going cruise for the price of a meal in a fine restaurant. All meals are prepared fresh daily on board in the ship's complete galley, and THE SPIRIT's entertainment features live bands playing songs from the '40s through the '80s, plus the rousing "Salute to Broadway" performed by talented waiters and waitresses. Before and after the show, you can dance under the stars to your favorite tunes. Fee: \$30.

Monday, April 27

Tour of Greater Miami and Shopping Tour to Bal Harbour, 9:00 a.m.–1:00 p.m. This tour will include a view of Greater Miami—a pleasing contrast of new and old landmarks: downtown Miami; the stately Royal palms along Biscayne Boulevard; Brickwell Avenue, the business district with its splendid and varied architecture; Coconut Grove, Miami's tropical village, both old-fashioned and avant garde; beautiful Coral Gables, one of the first planned communities in the nation, a hub of Mediterranean architecture; Calle Ocho (Eighth Street), the main street of Miami's Latin World; a view of the causeway spanning the bright blue Bay of Biscayne that artist Christo wrapped in pink; island homes; and more. The tour will end at Bal Harbour Shops, one of the finest and most exclusive shopping malls featuring Saks Fifth Avenue, Neiman Marcus, Bonwit Teller, Gucci, and Cartier. The chartered bus will return to the hotel at about 1:00 p.m. Members of the group will be free to return to the hotel at that time or remain at the mall for lunch and an afternoon of shopping (transportation information will be provided for those who choose to remain at the mall). Fee: \$12.

Tuesday, April 28

Parrot Jungle and Miami Seaquarium, 9:00 a.m.–4:00 p.m. This attraction is in a natural Florida hammock and has the world's most colorful collection of tropical birds. The birds are uncaged and fly freely down to eat seed from the hands of visitors.

The Seaquarium is situated on 60 acres. The world's largest oceanarium houses Lolita, the killer whale; TV star Flipper; sea lions; sharks; and hundreds of exotic sea creatures in glass tanks. Fee: \$40. Along the way to the Seaquarium, a box lunch, prepared by "Poppi's in the Grove," will be served.

Wednesday, April 29

Villa Vizcaya Boat Tour, 9:00 a.m.–1:00 p.m. A great Italian villa on Biscayne Bay, Villa Vizcaya has often been called the finest private house ever built in America. James Deering of the International Harvester Company searched the world for the perfect climate and location for his winter home. He picked the then-small town of Miami. The house was begun in 1914, and as many as 1000 artisans worked on it during the following years to create a masterpiece of architectural, interior, and garden design. Fee: \$30.

Thursday, April 30

Metro Zoo, 9:00 a.m.–1:00 p.m. At Metro Zoo, the animals are uncaged. Only moats separate the people from the wild life. You can enjoy a guided monorail tour, a free-flight bird show, the ecology theater, the Malaysian village, the puppet theater, and even an elephant ride. A recent addition to the zoo is a pure white African tiger cub. Refreshments will be served on the way back to the hotel. Fee: \$15.

Dinner and Show at Les Violins Supper Club, 6:30 p.m.–

11:30 p.m. For over 20 years, the Cachaldora-Currais family has been offering fine entertainment and cuisine at Les Violins. The unique combination of strolling violinists, singing waiters, and award-winning floor shows have made this the longest-running nightclub in Florida. Their million-dollar productions evoke the legendary Tropicana shows, with spectacular costumes, runways that rise out of the floors, and dancers that descend from the second level as stairways are lowered to the main stage. The shows are a melange of music, color excitement, and superb showmanship. Fee: \$30.

Friday, May 1

Tour of Miami Beach, 9:00 a.m.–11:00 a.m. The tour will include some of the most colorful places in South Miami Beach: 600–1000 Lincoln Road, containing the galleries of the South Florida Art Center; the Colony Theatre, the new home of the South Florida Shakespeare Company, the South of Broadway theater ensemble, and the Miami City Ballet; the Historic Preservation District, 1 square mile and 20 blocks of the nation's largest collection of art deco architecture, the style of the 1920s and 1930s; the Bass Museum (which features the fine and applied arts of the early 20th century), a keystone building designed by Russell Pancoast. Fee: \$11.

Postconvention Tours to the Islands

Estimated prices for cruises are as follows: 1-day cruise to the Bahamas, \$98; 1-day tours of Nassau and Freeport, \$88; weekend tours of Jamaica or Grand Cayman, \$190 and up. Contact Lucy R. Kelley, Conference Coordinator, for additional information.

Meeting and Local Activities Registration Form: ARRS 87th Annual Meeting, April 26–May 1, Miami Beach, FL

If you plan to attend, please complete this form. Official badges and program booklets will be available at the ARRS Registration Desk, Fontainebleau Hilton. **There will be no confirmations before the meeting.** Preregistration by mail will be accepted until March 26. On site registration will be available.

Make all checks payable to: American Roentgen Ray Society

Mail to: American Roentgen Ray Society
1891 Preston White Drive
Reston, VA 22091

Please type or print:

Last Name First Name or Initials

Street

City State ZIP Code

☐ Check here if you wish a program of events for accompanying persons. Indicate the address to which this is to be sent.

Name (Accompanying person's name to be printed on badge)

Street

City State ZIP Code

Check those desired:	Registration fee:
<input type="checkbox"/> Member ARRS	None
<input type="checkbox"/> Guest	\$100
<input type="checkbox"/> Physician in training (please fill where indicated below)	\$25
<input type="checkbox"/> Course faculty, scientific paper author, scientific exhibitor	None
<input type="checkbox"/> ACR luncheon course, Monday, April 27	\$10
<input type="checkbox"/> ACR luncheon course, Tuesday, April 28	\$10
<input type="checkbox"/> ACR luncheon course, Wednesday, April 29	\$10
<input type="checkbox"/> ACR luncheon course, Thursday, April 30	\$10
<input type="checkbox"/> Categorical course on gastrointestinal radiology. Categorical course registrants may also register for other instructional courses.	\$75
Total enclosed	_____

Section on Instruction

Please register early for Instruction Courses. Attendance is limited. List first, second, and third choices for each period by course number. Ticket orders are filled according to postmark. ARRS members, nonmembers, and those in radiology training may take all courses without charge except the Categorical Course on Gastrointestinal Radiology. **For the categorical course, all must pay \$75. All who wish to attend courses must complete this section. Residents and nonmembers must pay the meeting registration fee.**

Course tickets will be available at the ARRS Registration Desk of the Section on Instruction at the Fontainebleau Hilton on and after Saturday, April 25, at 1 p.m.

Complete section at right for courses other than the categorical course. Be sure to fill out second and third choices for each period.

	First Choice	Second Choice	Third Choice
Monday			
Tuesday			
Wednesday			
Thursday			
Friday	Check if you wish to attend the Genitourinary Symposium (only course offered this day)		
For Physicians in Training:			
_____ is in training in my department			
Department Chief _____			
Institution _____ Date _____			

(OVER)

Local Activities

No refunds after April 15
Exception: Dinner Cruise on Sunday: no refunds after March 20

- Sunday, April 26, 6:00–10:00 p.m., Dinner Cruise and Show aboard the Yacht THE SPIRIT (cruises up the Intracoastal Waterway to Fort Lauderdale; bus departs from Hotel at 6:00 p.m. No refunds on this tour after March 20.

_____ tickets @ \$30 \$ _____
- Monday, April 27, 9:00 a.m.–1:00 p.m., Tour of Miami and shopping tour to Bal Harbour

_____ tickets @ \$12 \$ _____
- Tuesday, April 28, 9:00 a.m.–4:00 p.m., Parrot Jungle and Seaquarium (Box lunch will be served.)

_____ tickets @ \$40 \$ _____
- Wednesday, April 29, 9:00 a.m.–1:00 p.m., Villa Vizcaya Boat Tour (Deering Estate)

_____ tickets @ \$30 \$ _____
- Thursday, April 30, 9:00 a.m.–1:00 p.m., Metro Zoo

_____ tickets @ \$15 \$ _____
- Thursday, April 30, 6:30–11:30 p.m., Dinner and Show at Les Violins Supper Club (Latin Extravaganza)

_____ tickets @ \$30 \$ _____
- Friday, May 1, 9:00 a.m.–11:00 a.m., Tour of Miami Beach

_____ tickets @ \$11 \$ _____

Preregistration is required.

Annual ARRS Golf Tournament, Monday, April 27, 11 a.m.

The tournament will be at the Turnberry Isle Country Club, North Miami Beach, FL. Transportation, luncheon, greens fee, cart, and prizes are included in the \$65 fee. Preregistration is important.

Name: _____

Telephone: _____

Address: _____

Hotel: _____

Handicap (if any): _____

My foursome includes (list handicaps): _____

_____ tickets @ \$65 \$ _____

Men’s and Women’s Tennis Tournaments, Monday, April 27, 11 a.m.

The tournaments will be at the Turnberry Isle Country Club, North Miami Beach, FL. Tennis attire is required. Fee of \$50 includes transportation, luncheon, court fees, and prizes.

Name: _____

Telephone: _____

Address: _____

_____ tickets @ \$50 \$ _____

May be photocopied

Deadline: March 26

Hotel Registration Form: ARRS 87th Annual Meeting, April 26–May 1, 1987, Fontainebleau Hilton, Miami Beach, FL

Mail to:

ARRS Housing Bureau
Fontainebleau Hilton
Attention: Reservations
4441 Collins Ave.
Miami Beach, FL 33140

(PLEASE MAKE CHECKS PAYABLE TO THE FONTAINEBLEAU HILTON HOTEL—NOT TO THE ARRS)

Individual guest name _____

Address _____

City & State _____ ZIP _____

Arrival date/time _____ Departure date/time _____

Individual requesting reservation _____

Address _____

City & State _____ ZIP _____

Deposit amount: _____

Please forward with your reservation a deposit of one night's room rate to be applied to the last night of your scheduled stay, or provide credit card information to guarantee your reservation. The hotel accepts American Express, Diners Club, Carte Blanche, and Hilton credit cards. The deposit will hold your room until 6 a.m. of the morning following your scheduled arrival date. In the event of an early departure, the deposit is nonrefundable unless the hotel is notified prior to or at the time of check-in. Cancellation notice of 14 days is required for a deposit refund.

Check accommodations desired

Room Category	Rate
Single	_____ \$115
Double	_____ \$115
1-bedroom suite	_____ \$325–450
2-bedroom suite	_____ \$450–600

Important Information:

1. Reservations must be received by the Fontainebleau Hilton/ARRS Housing Bureau no later than March 26 to be assured of written confirmed accommodation. Reservations after that time are subject to availability. We urge you to make your reservations promptly.
2. Written confirmation of your reservation will be sent to you by the hotel.
3. To change or cancel reservations, please call either Hilton Reservations Service at 1-800-HILTONS or the hotel directly at (305) 538-2000.
4. If you plan to share a room, please send in only one housing form. Be sure to list all names of occupants of rooms. Assignment is delayed until complete information is received.
5. Check-in is after 3 p.m., or earlier if the room is available. Check-out time is 11 a.m.

Airline Discount to 1987 ARRS Meeting

Eastern Airlines is offering a 60% discount off normal round-trip coach airfare to the 1987 American Roentgen Ray Society meeting, April 26–May 1, Fontainebleau Hilton, Miami Beach, FL. To make reservations, registrants should call (800) 468-7022 outside Florida and (800) 282-0244 within Florida. The identification number for this meeting discount is EZ4P5.

United Airlines is also offering special airfares to the ARRS 1987 meeting for travel to and from Miami Beach between April 22 and May 4 inclusive. To obtain a 5% discount from any United available/applicable fare (Ultra Savers included) or a 40% discount off standard coach fares (all restrictions waived), follow these steps: (1) phone toll-free (800) 521-4041 (48 contiguous states) or (800) 722-5243, ext. 6608 (Alaska, Hawaii), daily between 8:30 a.m. and 8:00 p.m. EST; and (2) immediately reference special ARRS account number 7092H. In addition, ARRS attendees who fly on United (as outlined above) will be eligible for a special drawing. The prize is one complimentary round-trip continental U.S. ticket good for travel before December 15, 1987 (holiday periods excluded).

1987 ARRS Meeting Summary, April 26–May 1, Miami Beach, FL

A comprehensive description of the meeting, including the scientific program, Categorical Course in Gastrointestinal Radiology, and instructional courses, appears in this issue of the *AJR*. A special loose insert on the meeting also accompanies this issue. Meeting and registration forms will be found in the February and March issues. These may be photocopied.

Accreditation

All courses and scientific sessions carry AMA Category I credit on an hour-for-hour basis.

Meeting Format

Scientific Program. Sessions will be grouped in parallel sessions, Monday–Thursday. A total of 189 scientific papers will be presented in 18 sessions. In addition, on Wednesday, April 29, the morning session will feature award papers and the Caldwell Lecture, which will be delivered by M. Paul Capp of the Arizona Health Sciences Center, Tucson, AZ. On Friday, there will be a special symposium on genitourinary imaging.

Categorical Course in Gastrointestinal Radiology. This 14-hr course will be Sunday–Thursday. Registrants may enroll in other courses as well.

Luncheon Sessions. Registrants may enroll in special luncheon sessions, Monday–Thursday. A box lunch will be provided.

Exhibits

Scientific Exhibits and Case of the Day Presentations will be Monday–Thursday, April 27–30.

Commercial Exhibits will be open daily, Monday–Thursday.

Local Activities

General Reception. Tuesday evening, April 28, for all registrants.

Golf Tournament. Monday, April 27, Turnberry Isle Country Club, North Miami Beach, FL. Transportation leaves the hotel at 11 a.m.; shotgun start at 1 p.m.

Men's and Women's Tennis Tournaments. Monday, April 27, Turnberry Isle Country Club, North Miami Beach, FL. Transportation leaves the hotel at 11 a.m.

Local Tours. Sunday, April 26, 6–10 p.m., Dinner Cruise and Show Aboard the Yacht THE SPIRIT; Monday, April 27, 9 a.m.–1 p.m., Tour of Miami and Bal Harbour Shopping Tour; Tuesday, April 28, 9 a.m.–4 p.m., Parrott Jungle and Seaquarium; Wednesday, April 29, 9 a.m.–1 p.m., Villa Vizcaya Tour; Thursday, April 30, 9 a.m.–1 p.m., Metro Zoo; 6:30–11:30 p.m., Les Violins Supper Club; Friday, May 1, 9–11 a.m., Tour of Miami Beach. No refunds after April 15 (March 20 for SPIRIT cruise).

Meeting Registration

Preregistration will be accepted until March 26. There will be on-site registration. Official badges and program books will be available

at the registration desk, Fontainebleau Hilton Hotel. No confirmations will be mailed.

Course Registration

Register early—enrollment is limited. List first, second, and third choices for each period. Also, indicate whether you wish to take the categorical course. Deadline for mail registration is March 26. All ticket orders will be filled by postmark. Course tickets *will not* be mailed. Tickets will be available on and after Saturday, April 25 (after 1 p.m.), at the ARRS registration desk in the Fontainebleau Hilton Hotel. There will be on-site registration for courses not already filled.

Hotel Registration

Reservations are handled by the ARRS Housing Bureau, Fontainebleau Hilton, Attn: Reservations, 4441 Collins Ave., Miami Beach, FL 33140. These must be received by March 26. Make check payable to Fontainebleau Hilton Hotel.

Fees

Meeting:

ARRS members and resident members	No fee
Nonmembers	\$100
Nonmember physicians in training (with verification)	25
Categorical course (all who attend)	75
Luncheon sessions/each	10
Golf tournament	65
Tennis tournaments	50
Local tours	11–40

Cancellations and Fee Refunds

Fees will be refunded only if cancellation is received by April 19. Send to American Roentgen Ray Society, 1891 Preston White Drive, Reston, VA 22091.

Air Transportation

Eastern Airlines will discount fares 60%. Information: (800) 468-7022 outside Florida and (800) 282-0244 within Florida. Mention ARRS number EZ4P5.

United Airlines is also offering discount fares. Call (800) 521-4041 (48 contiguous states) or (800) 722-5243, ext. 6608 (AL, HI). Mention ARRS number 7092H.

Associated Meeting

Society for Pediatric Radiology and European Society of Pediatric Radiology

The inaugural conjoint International Pediatric Radiology '87 meeting will meet May 30–June 4, 1987, at the Westin Hotel, Toronto, Ontario, Canada. Registration is limited to pediatric radiologists. For details contact: Donald R. Kirks, M.D., Secretary, Society for Pediatric Radiology, c/o Dept. of Radiology, Childrens Hospital Medical Center, Elland and Bethesda Aves., Cincinnati, OH 45229, (513) 559-4880. The 1988 SPR meeting will again be held in conjunction with the ARRS meeting.

Letters

Patient Education, Preventive Medicine, and the Radiologist

Diagnostic radiologists are frequently criticized (and more often than not envied) by clinical colleagues for their independence from direct patient care responsibilities. With exceptions, including interventional imaging, the nature of our daily work has traditionally been to provide insight into the causes of illnesses for referring physicians, who subsequently act upon the information. However, it has recently become apparent to me that members of our specialty can significantly influence an important aspect of our health care system: preventive medicine. The following remarks emphasize the point that the radiologist can contribute a great deal in this area.

Preventive medicine refers to the branch of medical science that deals with the avoidance of or prophylaxis against disease. Patient education constitutes a major component of preventive medicine. Unfortunately, the time pressures of many practicing physicians, as well as the stresses placed on house staff-in-training, do not allow for optimal communication of health-related information. For example, as a musculoskeletal radiologist in an academic medical center, I have been impressed by the number of patients who have little or no knowledge of the reasons for their referrals for specific diagnostic tests. This lack of knowledge is usually not caused by failure of the patient to listen or understand but rather by a harried physician who cannot or does not take the time to explain.

I believe that the diagnostic radiologist is in an ideal position to fill the patient-education void often left by the referring physician. Our work schedules tend to be somewhat less hectic than those of our clinical colleagues, and, even during busy times, we frequently can maintain a conversation with a patient during the performance of a procedure. It is usually possible to explain fully the reason for a diagnostic test before performing it, and to describe the preliminary findings and their significance if the patient requests this information. With this approach, I have found patients to be more cooperative during procedures and to be more satisfied and less skeptical after the procedure.

Extension of these concepts to preventive medicine is possible in situations in which the reason for a diagnostic test lies in some aspect of a patient's life-style that can be changed. As examples from my own subspecialty, the young woman with a mild hallux valgus deformity can be encouraged to abandon causative footwear, the aerobics class attendee with a meniscal tear can be directed to bicycling or swimming as a safer alternative, and the postmenopausal osteoporotic woman can be counseled regarding dietary calcium and estrogen supplementation. Use of the images obtained during the course of the examination as teaching tools can be extremely effective. For example, all previous attempts to convince a patient to stop smoking failed until I pointed out the differences between her own chest radiograph and that of a healthy nonsmoker of comparable age.

I believe that increased attention to patient education on the part of diagnostic radiologists can improve the quality of our entire health care system. Many medical malpractice suits undoubtedly result from public mistrust of our profession caused by a lack of understanding about its limitations and the general nature of our work. Of even greater importance, however, is the fact that the patient has a right to know the reasons for what we do and that his or her well-being is frequently as much in his or her control as in ours. As physicians, we must not only treat individuals in need, but also provide them with information concerning life-style and personal habits that may in the future help them avoid the need for our services. With some individual effort, the radiologist can contribute to this most important aspect of patient care in medicine.

David J. Sartoris
UCSD Medical Center
San Diego, CA 92103

Mammographic Grids and Breast Radiation

A recent article by Dershaw and Malik [1] examines the relationship between radiation dose and the use of stationary and moving grids for mammography. The authors conclude that the "mean gland dose to the breast was increased two to four times using either grid" and that "the mean increase in dose to the patient with both grids was 3.5 when compared with nongrid studies."

The radiation dangers of mammography are exceedingly small, particularly as regards the individual patient [2]. However, historically, and particularly in relation to mass screening, radiation has been an important issue in mammography. Therefore, Dershaw and Malik's finding that grids increase radiation dose by a factor of 3.5 is noteworthy and will probably come as a surprise to many mammographers. This negates any advantages of reduced radiation that film-screen techniques have over nongrid xeromammography (to my knowledge the potential advantages of grids for xeromammography, particularly in assessing microcalcifications, have not been assessed).

The findings of Dershaw and Malik may be slightly misleading to some readers. The authors used a faster film for grid examinations and kept the optical density of the grid and nongrid films the same by adjusting amperage rather than kilovoltage. This was presumably done in the light of the authors' previous finding that "an increase in kVp resulted in modest improvement in image contrast, whereas increasing mA with the grid in place resulted in a greater improvement in image contrast" [3]. However, from a practical standpoint it is probably desirable to partially offset the increased radiation required with grid examinations by an increase in kilovoltage. Indeed, I believe that most mammographers performing grid mammography do this, and to my knowledge all manufacturers of molybdenum target mammographic machines recommend an increase in 2 kVp for grid examinations. This results in a reduction of approximately 50% in the midbreast radiation dose with comparable film density.

Sickles and Weber [4], using the same films and screens as Dershaw and Malik, but with an increase of 1 kVp on grid examinations, found the midbreast "average dose using the grid was approximately 70% higher than that of the nongrid technique." Whether these marked differences in calculated breast dose relate to the 1 kVp or to other factors is unclear to me. Also, at least one manufacturer (CGR) has shown that, with other factors including kilovoltage held constant, the use of their grid resulted in only a doubling of breast radiation (V. Wentz, personal communication).

Grids represent a major improvement in mammography. I believe that they should be used routinely for screening mammography and perhaps all mammography [5], although this view is not shared by others [4, 6]. The work of Dershaw and Malik is an important contribution in this matter and I commend these authors. However, additional studies on grid mammography are needed to assess breast radiation and image quality with the use of variable kilovoltage.

Ferris M. Hall
Beth Israel Hospital
Boston, MA 02215

REFERENCES

1. Dershaw DD, Malik S. Stationary and moving mammography grids: comparative radiation dose. *AJR* 1986;147:491-492
2. Feig S. Assessment of the hypothetical risk from mammography and evaluation of the potential benefit. *Radiol Clin North Am* 1983;21:173-191
3. Dershaw DD, Masterson ME, Malik S, Cruz NM. Mammography using an ultrahighstrip-density, stationary, focused grid. *Radiology* 1985;156:541-544
4. Sickles EA, Weber WN. High-contrast mammography with a moving grid: assessment of clinical utility. *AJR* 1986;146:1137-1139
5. Hall FM. Mammography and grids (letter). *AJR* 1986;147:860-861
6. Sickles EA, Weber WN. Mammography and grids (reply). *AJR* 1986;147:861-862

Reply

The contribution of grid technique in mammography involves improved resolution of microcalcifications and soft-tissue masses. Alteration in radiographic technique when using grids, therefore, should be designed to maintain the improved image contrast for which the grid is being used. Alteration in our radiographic technique to maintain this image contrast was best achieved with stable kilovoltage and a prolongation of exposure time by approximately 2 sec, when an adjustment of either kilovoltage or amperage was studied. Alterations of both of these factors were not tested. Sickles and Weber increased the kilovoltage by 1 kV and the amperage per second by 1 sec in their study. A comparison of the diagnostic efficacy of these different techniques has not been performed and would be worthwhile. We have found (Dershaw et al.) that the sacrifice of improved image resolution to reduce mean glandular dose by maintaining stable amperage and only increasing kilovoltage when using grids is self-defeating.

Computation of the radiation dose to the breast done by Malik and me differed from that done by Sickles and Weber. The mean glandular dose, which we reported, is 1.47 times greater than the midbreast dose, which was reported by Sickles and Weber, when calculated for a 6-cm breast [1]. Since their grid technique resulted in a breast dose 1.7 times that of the nongrid technique, a 70% increase, the resultant mean glandular dose would be greater by a factor of 2.5, that is, 1.47×1.7 . This is somewhat less than the average increased dose by our technique but within our reported range of 2-4.

Finally, we cannot agree with Dr. Hall's recommendation that grids be used in all mammography. No evidence indicates an improved ability to diagnose breast disease in women with fatty or mildly glandular breasts with grid mammography, although breast irradiation is increased. The suggestion to seek a means to decrease radiation in some women while recommending a technique that will increase it in others without increased diagnostic efficacy cannot be accepted.

D. David Dershaw
Memorial Sloan Kettering Cancer Center
New York, NY 10021

REFERENCE

1. Hammerstein RG, Miller DW, White DR, Masterson M, Woodard HQ, Laughlin JS. Absorbed radiation dose in mammography. *Radiology* 1979;130:485-491

Vitamin A and DISH

In the October issue of *AJR*, Yagan and Karlins [1] called attention to the severe spinal cord injuries that occasionally result from trivial trauma in patients with diffuse idiopathic skeletal hyperostosis (DISH). Their observations are pertinent and serve to point out that DISH is not always a benign, incidental condition encountered on radiographs.

The second patient that Yagan and Karlins described was a 30-year-old man with extensive ossification of the anterior longitudinal ligament. Since DISH is primarily an affliction of elderly patients, I was struck by the extensive ossification in a person who was only 30 years old.

Naturally occurring [2] as well as synthetic forms [3] of vitamin A cause DISH-like changes when administered in high doses for prolonged periods. Is it possible that the individual in the second case was suffering from chronic hypervitaminosis A?

David R. Pennes
University of Michigan Medical Center
Ann Arbor, MI 48109

REFERENCES

1. Yagan R, Karlins N. Quadriplegia in diffuse idiopathic skeletal hyperostosis after minor trauma. *AJR* 1986;47:858-859
2. Gerber A, Raab AP, Sobel AE. Vitamin A poisoning in adults: with description of a case. *Am J Med* 1954;16:729-745
3. Pittsley RA, Yoder FW. Retinoid hyperostosis: skeletal toxicity associated with long-term administration of 13-cis-retinoic acid for refractory ichthyosis. *N Engl J Med* 1983;308:1012-1014

Reply

We appreciate Pennes's comments on the second patient in our report. We agree that skeletal changes resembling DISH can occur in hypervitaminosis A. It is unlikely, however, that our patient suffered from this condition. He was severely retarded and incapable of self-dosage with vitamin A or retinoids. To our knowledge, he was not receiving vitamin A or any retinoids from a physician. The patients in the literature cited by Pennes were all taking vitamin A for ichthyosis. Our patient did not have this disease nor were any of the cutaneous signs of hypervitaminosis A noted on physical examination. There was also no clinical evidence of increased intracranial pressure, another complication of vitamin A overdosage. The ossified anterior longitudinal ligaments in the cited cases were thinner than in our patient. For these reasons, we do not believe our second patient had hypervitaminosis A. Other conditions that mimic DISH, such as ankylosing spondylitis, spondylitic "variants," acromegaly, hypoparathyroidism, ochronosis, and fluorosis [1], were also excluded by the clinical history and radiographic findings.

The age of our patient (30 years) was less than the reported age range (48-85 years) in the literature [1]; however, in our practice, we have seen much younger patients with DISH, including the case in our report. Resnick and Niwayama state that the clinical and radiographic features of this condition may occur in patients younger than the reported age range. The radiographic findings in younger patients are usually not as advanced; however, we believe that these findings are part of a spectrum that is much wider than originally thought and that, in some young patients the disease may be quite

advanced. We believe that, although our patient is much younger than the reported age range, DISH is still a tenable diagnosis.

Rauf Yagan
Nathaniel Karlins
Case Western Reserve University
Cleveland, OH 44109

REFERENCE

1. Resnick D, Niwayama G. *Diagnosis of bone and joint disorders*. Philadelphia: Saunders, 1981;1416-1452

Auto Seat Restraint Soft-Tissue Injury

Since the advent of automobile seat restraint devices, it has become clear that although these devices save lives, a variety of skeletal and visceral injuries may result from their use. Such injuries have included Chance and other spine fractures [1], traumatic abdominal aortic aneurysms [2], duodenal transections [3], and others [4, 5]. We wish to point out an additional, previously unrecognized restraint device-related injury.

A 35-year-old woman with silicone breast implants was involved in a motor vehicle accident while restrained in a seat belt/shoulder harness device. Since she was the driver, the restraint crossed her abdomen and chest obliquely from the right hip to the left shoulder. Immediately after the motor vehicle accident, the patient experienced pain and tenderness in the left breast associated with a visible breast deformity. The mammogram (Fig. 1) showed gross deformity of the prosthesis with rupture of the silicone bag and extrusion of silicone into the axillary portion of the breast, findings that were confirmed at surgery. Although this woman undoubtedly escaped more serious injury by wearing her shoulder harness, the case serves to illustrate an additional soft-tissue injury to be added to the list of injuries related to automobile seat restraint devices.

David R. Pennes
William A. Phillips
University of Michigan Medical Center
Ann Arbor, MI 48109

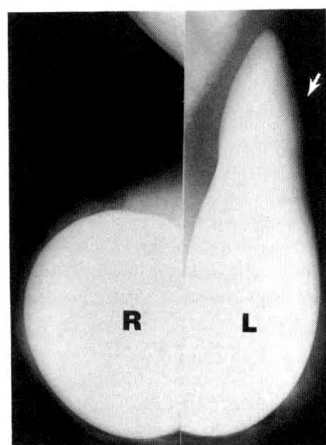


Fig. 1.—Oblique views of right (R) and left (L) breasts show rupture of left prosthesis and silicone extrusion into axillary tail (arrow).

REFERENCES

1. Smith WS, Kaufer H. Patterns and mechanisms of lumbar injuries associated with lap seat belts. *J Bone Joint Surg* 1969;51A:239-254
2. Matsubara J, Seko T, Ohta T, Shionoya S, Ban I. Traumatic aneurysm of the abdominal aorta with acute thrombosis of bilateral iliac arteries. *Arch Surg* 1983;118:1337-1339
3. Hudson I, Kavanagh TG. Duodenal transection and vertebral injury occurring in combination in a patient wearing a seat belt. *Injury* 1983;15:6-9
4. Mollitt DL, Ballantine TV, DeRosa GP. Jejuno-renal injury following traumatic hyperextension. *J Trauma* 1980;20:996-998
5. Kocke WM Jr, Meyer K. Splenic rupture due to improper placement of automobile seat belt. *JAMA* 1963;183:693

Reassessing the Role of Radiology in Hemoccult Screening

Feczko and Halpert [1] claim that double-contrast barium enema (DCBE) in their 98 patients has a "detection rate" of 93%. They have based this, however, on an assumption that no significant lesions were missed in the 78 patients who did not undergo colonoscopy. They present no collaborating evidence to support this assumption. Nor can the sensitivity of DCBE be properly determined from the 20 patients who underwent colonoscopy since radiographic lesions were often the indication for the second procedure. Numerous comparative studies have found colonoscopy to be about 12% more accurate for diagnosing polyps (from both a false-negative and false-positive standpoint) than DCBE. In a prospective study at Memorial Sloan-Kettering Cancer Center that compared DCBE, colonoscopy, and sigmoidoscopy in patients with fecal occult blood, the tumors in 30% of those found to have neoplasia would have gone undetected without colonoscopy [2]. In a recent study of patients with known colonic adenocarcinomas, DCBE missed synchronous cancers in 27% and polyps in 58% [3].

Additionally, in an examination of cost-effectiveness, the goal should be to find the approach that will minimize morbidity and mortality while keeping costs under control, not to determine which diagnostic test is cheaper in the short run. Feczko and Halpert, in their analysis, fail to consider the long-term costs of missing premalignant or early malignant lesions, and they ignore the fact that colonoscopy with polypectomy is therapeutic as well as diagnostic for colonic polyps.

Colonoscopy by an experienced examiner should be the initial diagnostic procedure in the asymptomatic patient with fecal occult blood by virtue of its superior diagnostic capabilities and therapeutic potential. While a barium enema may complement colonoscopy for evaluation of occult bleeding, it cannot replace colonoscopy. If polyps are found, they must be excised and synchronous cancers and polyps must be sought.

Michael L. Margolin
Lenox Hill Hospital
New York, NY 10021

REFERENCES

1. Feczko PJ, Halpert RD. Reassessing the role of radiology in hemoccult screening. *AJR* 1986;146:687-701
2. Strohlein JR, Goulston K, Hunt RH. Diagnostic approach to evaluating the cause of a positive fecal occult blood test. *Cancer* 1984;34:148-157
3. Thorson AG, Christensen MA, Davis SJ. The role of colonoscopy in the assessment of patients with colorectal cancer. *Dis Colon Rectum* 1986;29:306-311

Letters to the Editor must not be more than two double-spaced typewritten pages. One or two Figures may be included

News

Winter Congress in Medical Diagnostic Imaging

The sixth annual Winter Congress in Medical Diagnostic Imaging will be held Jan. 31–Feb. 7 in Cortina d'Ampezzo, Italy. Category 1 credit: 25 hr. Fee: \$435. Information: Winter Congress–Medical Seminars International, 21915 Roscoe Blvd., Ste. 222, Canoga Park, CA 91304; (818) 701-5143.

Radiology Imaging and Intervention

The Dept. of Radiology of the University of California, San Diego, School of Medicine will present the 67th annual UCSD Radiology Imaging and Intervention course Feb. 2–6 at the Hotel Intercontinental, San Diego, CA. The course will provide an update of current approaches to practical aspects of radiology. Category 1 credit: 21½ hr. Course directors: E. vanSonnenberg, G. R. Leopold, L. B. Talner, and G. Casola. Guest faculty: R. A. Castellino, J. F. Simeone. Fee: \$425; \$250: residents, fellows, nurses, and technologists. Information: R. Dawne Ryals, Ryals & Assoc., P.O. Box 920113, Norcross, GA 30092-0113; (404) 641-9773.

Winter Seminar in Medical Diagnostic Imaging

The sixth annual Winter Seminar in Medical Diagnostic Imaging will be held Feb. 7–11 in London, England. Category 1 credit: 15 hr (approximately). Fee: \$435. Information: Winter Seminar–Medical Seminars International, 21915 Roscoe Blvd., Ste. 222, Canoga Park, CA 91304; (818) 701-5143.

Neuroradiology and Head and Neck Radiology

The Depts. of Radiology and Otolaryngology and the Continuing Education Office, State University of New York, Health Science Center at Syracuse will hold its sixth annual comprehensive update on Neuroradiology and Head and Neck Radiology: CT and MR Imaging, Feb. 23–28 in Acapulco, Mexico. The course will explore imaging of the normal anatomy and disease of the brain, spine, and head and neck. The applications, merits, and limitations of both conventional and more recent techniques (including MR) will be examined. Program directors: E. D. Cacayorin and R. M. Kellman. Fee: \$500 (entire course); \$400 (neuroradiology); \$300 (head and neck radiology). Information: Betty Frost, Program Coordinator, Continuing Education Office, SUNY Health Science Center at Syracuse, 750 E. Adams St., Syracuse, NY 13210; (315) 473-4606.

Diagnostic Radiology Courses

The Dept. of Radiology, University of California, San Diego, School of Medicine will present three courses designed for physicians and allied health personnel: Neuroradiology Update, March 2–4; Magnetic Resonance Imaging, March 3–6; and MRI for Technologists—Symposium and Workshops, March 3–5. The courses, which will be held at the Hotel del Coronado, Coronado, CA, will highlight the physical basis of MR imaging and clinical applications, as well as preview anticipated future developments in MR technology. Program director: J. R. Hesselink. Guest faculty: D. G. Amaral, L. Atkins, M. Blumenfeld, W. G. Bradley, M. N. Brandt-Zawadzki, E. G. Grant, C. B. Higgins, H. Hricak, and C. Tauber. Category 1 credit: available. Fee (neuro-radiology update course): \$350; \$250: residents, fellows, nurses, and technologists. Fee (MRI course): \$400; \$250: residents, fellows, nurses, and technologists. Fee (combined course): \$425; \$325: residents, fellows, nurses, and technologists. The fee for the MRI for Technologists—Symposium and Workshops is \$250. Information: R. Dawne Ryals, Ryals & Assoc., P.O. Box 920113, Norcross, GA 30092-0113; (404) 641-9773.

Doppler for Radiologists

Yale University School of Medicine will sponsor a course in Doppler techniques for radiologists (carotid, abdominal, and pelvic, including obstetrics) March 16–19 at Yale University in New Haven, CT. The course will summarize recent progress in the application of Doppler techniques. Course director: Kenneth J. W. Taylor. Category 1 credit: 21 hr. Fee: \$375; \$300: sonographers and residents. Information: Janice Gore, Office of Graduate and Continuing Education, 333 Cedar St., New Haven, CT 06510; (203) 785-4578.

1987 European Workshop on MR in Medicine

The 1987 European Workshop on Magnetic Resonance in Medicine will be held March 25–27 at University College, London, England. The workshop includes a basic teaching course, a symposium on clinical spectroscopy, and a workshop on advanced imaging techniques. Category 1 credit: applied for. Fee: £30 (basic teaching course only); £50 (symposium on clinical spectroscopy only); £70 (entire workshop). Information: Conference Secretariat, Magnetic Resonance in Medicine 1987 (European Workshop), % Institute of Physical Sciences in Medicine, 47 Belgrave Sq., London SW1X 8QX; (01) 235-6111.

Skeletal Radiology at the Pointe

The Dept. of Diagnostic Radiology, Allegheny General Hospital, will present the fourth annual course on Skeletal Radiology March 28–April 2 at the Pointe Resort in Phoenix, AZ. The course will cover a variety of topics, including metabolic bone disease, skeletal/dental abnormalities, facet joint arthrograms, neoplasia, pediatric and developmental bone abnormalities, arthritis, infections, and trauma. In addition, there will be a minisymposium covering the multidisciplinary approach to abnormalities of the temporomandibular joint and facial fractures. Guest faculty: H. D. Curtain, R. G. Dussault, R. H. Freiburger, H. G. Jacobson, J. P. Lawson, L. W. Young. Category 1 credit: 20 hr. Fee: \$425; \$250: residents, fellows, and retirees. Information: Sandra Johnston, Dept. of Continuing Education, Allegheny General Hospital, 320 E. North Ave., Pittsburgh, PA 15212-9986; (412) 359-4952.

International Diagnostic Course: Skeletal Radiology

The European Association of Radiologists and the Johns Hopkins Radiological Alumni Association will sponsor the 19th International Diagnostic Course March 29–April 4 in Davos, Switzerland. The topic is "Skeletal Radiology" and the course will stress both classic and newer diagnostic imaging techniques. Other lectures and seminars will feature the anatomic and physiologic basis for radiologic-pathologic correlation and the diagnostic approach to specific musculoskeletal diseases. Category 1 credit: 40 hr/week attendance. Fee: \$350; \$250: residents. Information: B. G. Brogdon, USA Medical Center, Mobile, AL 36617, (205) 471-7868; or M. W. Donner, Johns Hopkins Hospital, Baltimore, MD 21205; (301) 955-5677.

Laser Angioplasty and Interventional Radiology

Tutorials in Laser Angioplasty and Interventional Radiology, sponsored by the Dept. of Radiology and Radiological Sciences at The Johns Hopkins School of Medicine, will be held March 30–April 1 at The Johns Hopkins Medical Institutions in Baltimore, MD. The course will include live demonstrations of techniques in biliary stenting, embolotherapy, and transluminal angioplasty. The Argon "Hot Tip" laser will also be demonstrated. Category 1 credit: 24 hr. Fee: \$400; \$200: residents, nurses, and technicians. Information: Program Coordinator, Office of Continuing Education, The Johns Hopkins Medical Institutions, Room 19 Turner, 720 Rutland Ave., Baltimore, MD 21205; (301) 955-3168.

Hyperthermia

The Depts. of Radiation Oncology and Nuclear Medicine of Hahnemann University and Thomas Jefferson University are organizing a conference on hyperthermia, "First Eastern Clinical Hyperthermia Symposium & Workshop," to be held April 1–3 at the Franklin Plaza Hotel in Philadelphia, PA. Program chairman: C. M. Mansfield. Information: M. Heinrich Seegenschmiedt, Registration Chairman, Dept. of Radiation Oncology and Nuclear Medicine, Hahnemann University, 230 N. Broad St., Mail Stop 200, Philadelphia, PA 19102-1192; (215) 448-8410.

Ultrasound Symposium

North Carolina Ultrasound Society's sixth annual Ultrasound Symposium will be held April 3–5, 1987, in Greensboro, NC. The symposium will consist of a 1-day physics course taught by Fred Kre-

makau followed by 2 days of lectures by well-known sonographers on the abdomen; obstetrics/gynecology; echocardiography, and duplex vascular, small parts, intercavitary, and pediatric ultrasound. Category 1 credit: 16 hr. Information: Sharon Hughes, Rt. 2, Box 196, Denton, NC 27239; (919) 748-4505.

The Johns Hopkins Medical Institutions Courses

The Johns Hopkins Medical Institutions, Dept. of Radiology and Radiological Science, Baltimore, MD, offers several courses in abdominal and obstetric ultrasound: Advanced Obstetrics and Gynecology, April 8–10. Category 1 credit: 24 hr. Fee: \$325. Basic Practicum, May 11–15 and November 16–20. Category 1 credit: 40 hr. Fee: \$460. Advanced Practicum in Ultrasound, December 7–11. Category 1 credit: 40 hr. Fee: \$460. Visiting Physicians, offered year-round for experience in the laboratory and participation in read-in sessions. By appointment only. Category 1 credit: 40 hr. Fee: \$460. Information: Joan Mosmiller, Dept. of Radiology, Johns Hopkins Hospital, Baltimore, MD 21205; (301) 955-8450.

Advances in MR Imaging

The Advances in Magnetic Resonance Imaging Seminar, sponsored by the Dept. of Radiology at the University of South Florida School of Medicine, will be held April 13–16 at the Buena Vista Palace, Lake Buena Vista, FL. The program will include lectures and panel discussions and will stress practical, clinical, and technical aspects of MR imaging. Program directors: R. Clark, F. R. Murtagh, and M. L. Silbiger. Category 1 credit: 22 hr. Fee: \$475; \$400: residents and fellows. Information: Charleen Krissman, 12901 N. 30th St., Tampa, FL 33612; (813) 974-2538.

Diseases and Imaging of the Spine

The 1987 Update on Diseases and Imaging of the Spine seminar, sponsored by the Dept. of Radiology at the University of South Florida College of Medicine, will be held April 17–18 at the Buena Vista Palace, Lake Buena Vista, FL. The program, which will include lectures and panel discussions, will stress the interrelationship of the various radiographic techniques that are available for evaluating the spine. Program directors: R. Clark, F. R. Murtagh, and M. L. Silbiger. Category 1 credit: 11 hr. Fee: \$240; \$175: residents and fellows. Information: Charleen Krissman, 12901 N. 30th St., Tampa, FL 33612; (813) 974-2538.

Nuclear Medicine 1987

A conference on current clinical practice and current future concepts in nuclear medicine, sponsored by Montefiore Medical Center and Albert Einstein College of Medicine, will be held April 27–30 at the Grand Hyatt Hotel, New York, NY. Category 1 credit: 23 hr. Fee: \$400; \$250: residents and technologists. Information: Mitchell H. Stromer, Albert Einstein College of Medicine, 1300 Morris Park Ave., Bronx, NY 10461; (212) 904-4180.

Diagnostic Ultrasound Conference and Post Conference Seminar

The Continuing Education Committee of the Los Angeles Radiological Society announces the 12th annual Spring Diagnostic Ultra-

sound Conference to be held May 1-3 and the seventh annual Post Conference Seminar to be held May 5-9. Both conferences will take place at the Century Plaza Hotel in Los Angeles, CA. Category 1 credit: 19½ hr. Fee for the Diagnostic Ultrasound Conference (3-day participation): \$325: regular registrant; \$300: LARS and ultrasound section members. Fee (2-day participation): \$275: regular registrant; \$250: LARS and ultrasound section members. Fee for the Post Conference Seminar: \$395; \$295: technologists. Information: Los Angeles Radiological Society, Attn: Diane L. Johnson, 5200 Century Blvd., Ste. 920, Los Angeles, CA 90045; (213) 642-0921.

Nuclear Medicine

The annual meeting of the Pittsburgh Chapter of the Society of Nuclear Medicine will be held May 1-3 in Pittsburgh, PA. The topics to be presented include gallium scintigraphy, lymphoscintigraphy, current trends in GI imaging, and updates in bone scintigraphy. Category 1 credit: available. Fees: \$55: full members; \$75: nonmembers; \$15: member technologists; \$35: nonmember technologists; \$15: students. Information: Gary G. Winzelberg, President, Pittsburgh Chapter, Society of Nuclear Medicine, 5230 Centre Ave., Pittsburgh, PA 15232; (412) 622-2284.

Radiology Review Course

The Mount Sinai Medical Center, Miami Beach, FL, and the University of Miami School of Medicine will sponsor a seminar to review all the major organ systems including the chest, cardiovascular system, abdomen, retroperitoneum, pelvis, musculoskeletal system, and central nervous system. The course will be held May 3-8 in Miami Beach, FL. Program directors: M. Viamonte and C. A. Poole. Category 1 credit: 44.5 hr. Fee: \$390. Information: Lucy R. Kelley, Radiology Seminars, P.O. Box 343762, Coral Gables, FL 33134; (305) 674-2681.

International Nijmegen Vascular Symposium: Angioplasty, Vascular Surgery, Combined Approach

The Fifth International Nijmegen Vascular Symposium will be held May 15-16 in Nijmegen, The Netherlands. Information: S. H. Skotnicki, Dept. of Thoracic and Cardiovascular Surgery, St. Radboud Hospital, P.O. Box 9101, 6500 HB Nijmegen, The Netherlands.

Congress on Ultrasonic Examination of the Breast

The fifth International Congress on the Ultrasonic Examination of the Breast will be held Oct. 3-5 in New Orleans, LA. The meeting is open to all clinicians and technologists interested in breast disease diagnosis. Proffered presentations are encouraged and will be reviewed after an abstract is submitted to Elizabeth Kelly-Fry, Dept. of Radiology, Wishard Memorial Hospital, 1001 W. 10th St., Indianapolis IN 46202; (317) 360-6131; telefax (317) 636-3198. Guest faculty: D. Amy, J. C. Bamer, J. Croll, B. J. Hackeloer, J. Jellins, T. Kobayashi, M. McSweeney, T. S. Reeve, J. Teubner, and T. Wagai. Category credit: available. Information: Catherine Cole-Beuglet, Dept. of Radiological Sciences, University of California Medical Center, Irvine, University Hospital, 101 City Dr. S., Orange, CA 92668.

Visiting Fellowship in MR Imaging

The Dept. of Radiology of the University of California, San Diego Medical Center/AMI Magnetic Resonance Institute is offering a 1- to 4-week visiting fellowship in Magnetic Resonance Imaging. The program includes 2 hr of lectures each day as well as daily interpretation sessions with the faculty. Program director: J. R. Hesselink. Category 1 credit: up to 34 hr. Fee (1 week): \$1000, (additional weeks): \$750/week. Information: R. Dawne Ryals, Ryals & Assoc., P.O. Box 920113, Norcross, GA 30092-0113; (404) 641-9773.

Election Results

The Canadian Association of Radiologists elected the following officers for the year 1986-1987: David B. Fraser, President; Edward L. Lansdown, Past President; Walter M. Little, President-Elect; David G. McGowan, Vice-President Oncology; W. James Knickerbocker, Honorary Treasurer; Robert G. Dussault, Honorary Secretary; Carl J. Zylak, Chairman of Council, Donald E. Newman, David G. Gray, and Jacques Sylvestre, Commissioners; Philip C. Urich, Chairman of Councillors; Alva Ekstrand Pentecost, Executive Director.

Meeting and Course Review

For reader convenience, a summary of upcoming meetings and courses is provided. Detailed listings are given in the *AJR* issues noted in parentheses.

UC San Diego Courses; Physicians Imaging Courses 1987, times arranged, San Diego, CA (Nov)

Delaware Valley MRI Society Meetings, monthly, Philadelphia, PA (Jan)

Clinical Ultrasound Fellowships, year-round, Vancouver, BC, Canada (Jan)

The Pacific Radiological Institute Courses, Feb.-April (weekly courses), Honolulu, HI (Dec)

UC San Francisco Courses; Diagnostic Radiology Seminars, Feb. 1-6, Aspen, CO; Feb. 22-27, Park City, UT; Diagnostic Imaging: March 16-21, Waiohai, Kauai, Hawaii (Oct)

Perspectives on Imaging Modalities, Feb. 2-6, Cancun, Mexico (Sept)

Palm Beach Magnetic Resonance Imaging Update, Feb. 8-11, West Palm Beach, FL (Dec)

Big Sky Radiology Conference, Feb. 8-13, Great Falls, MT (Oct)

Advanced Course in Diagnostic Imaging, Feb. 8-13, Singapore (Nov)

Gastrointestinal Radiologists' Meeting and Course, Feb. 8-13, Scottsdale, AZ (Aug)

University of Texas Continuing Medical Education, Basic Radiologic Health, Feb. 9-13; **Review of Radiation Calculations**, Feb. 16-18; **Advanced Radiologic Health**, May 11-15; **Radiation Safety Officer's Course**, May 18-22, San Antonio, TX (Sept)

International Continuing Medical Education Series: Clinical Update in Medicine & Surgery, Feb. 10-17, Feb. 17-24, Maui, HI; **Topic to be announced**, March 14-21, Banff, Canada; **Topic to be announced**, May 20-26, Japan; **Topic to be announced**, May 20-26, Bermuda; **Topic to be announced**, June, Ireland; **Topic to be announced**, July 24-30, Pebble Beach, CA; **Topic to be announced**, Aug., Gstaad, Switzerland (Oct)

Sun Valley Imaging, Feb. 14-21, Sun Valley, ID (Nov)

Intermountain Imaging Conference, Feb. 14-21, Snowmass, CO (Nov)

- Postgraduate Course in Diagnostic Imaging**, Feb. 14–21, Cancun, Mexico (Nov)
- Thoracic Imaging 1987**, Feb. 16–19, Orlando, FL (May)
- University of Arizona Postgraduate Practical Radiology Course**, Feb. 16–19, Loews Ventana Canyon Resort, AZ (Nov)
- Mammography: A Practical Approach**, Feb. 16–20, Aspen, CO (Nov)
- Sonomammography**, Feb. 16–20, Philadelphia, PA (Nov)
- Radiologic-Pathologic Concepts in Diagnosis**, Feb. 19–23, Lake Buena Vista, FL (Nov)
- Diagnostic Radiology and Nuclear Medicine**, Feb. 21–28, St. Thomas, U. S. Virgin Islands (Oct)
- Vail Winter Imaging Seminar III**, Feb. 21–28, Vail, CO (Dec)
- Medical Imaging Conference in the High Sierras**, Feb. 22–27, Lake Tahoe, NV (Nov)
- Masters Diagnostic Radiology Conference**, Feb. 22–27, Maui, HI (Nov)
- AFIP Neuroradiology Review Course**, Feb. 23, Bethesda, MD (Jan)
- Advanced Perinatal Ultrasound Seminar**, Feb. 26–28, Lake Buena Vista, FL (Aug)
- Society for Magnetic Resonance Imaging**, Feb. 28–March 4, San Antonio, TX (Oct)
- George Simon Award—The Fleischner Society**, deadline March 1 (Dec)
- Aspen Uroradiology Seminar**, March 1–4, Aspen, CO (Jan)
- Practical Radiology**, March 1–6, Vancouver, BC, Canada (Nov)
- Intermountain Imaging Conference—Extension**, March 1–7, Snowbird, UT (Nov)
- Sierra Radiology Conference**, March 2–6, Incline Village, NV (Jan)
- Winter Imaging at Stowe, VT**, March 2–6, Stowe, VT (Dec)
- Computed Body Tomography 1987—The Cutting Edge**, March 5–8, Orlando, FL (Nov)
- Diagnostic Imaging and Interventional Radiology**, March 8–13, Park City, UT (Dec)
- Skeletal Symposium**, March 9–16, Sun Valley, ID (Jan)
- Positron Emission Tomography and the Chemistry of Mental Illness**, March 12–13, Baltimore, MD (Dec)
- London Course in Whole Body CT**, March 15–19, Auchterarder, Perthshire, Scotland, UK (Nov)
- Diagnostic Radiology Conference on Imaging Modalities in Chest and Abdomen**, March 16–20, Maui, HI (Dec)
- Breast Disease Update IV Seminar**, March 18–22, Lake Buena Vista, FL (Jan)
- Pediatric Radiology**, March 19–21, Philadelphia, PA (Jan)
- Ultrasound at Vail**, March 22–28, Vail, CO (Nov)
- Diagnostic Angiography and Interventional Radiology**, March 23–26, San Diego, CA (Nov)
- Neuroradiology at Vail**, March 23–27, Vail, CO (Jan)
- Radiology and Early Colon Cancer Workshop**, March 30, Denver, CO (Nov)
- Federation of Western Societies of Neurological Science Meeting**, March 30–April 1, Coronado, CA (Dec)
- Society of Computed Tomography Meeting/Course**, March 30–April 3, 1987, San Diego, CA (Dec)
- Alexandria International Conference on Laryngeal Cancer**, April 1–2, Alexandria, Egypt (Sept)
- Intrauterine Diagnosis and Treatment: The New Frontier**, April 2–4, San Diego, CA (Nov)
- Differential Diagnosis in Radiology**, April 3–5, Ann Arbor, MI (Jan)
- Mammography Course**, April 6–9; May 18–21, Oct. 5–8, Nov. 2–5, Boston, MA (Jan)
- American Radium Society Meeting**, April 6–10, London (Aug)
- Annual Meeting, National Council on Radiation Protection and Measurements**, April 8–9, Bethesda, MD (Sept)
- Radiation Therapy Clinical Research Seminar**, April 23–25, Gainesville, FL (Dec)
- The Profession of Medical Physics**, April 29–May 1, Lake Tahoe, CA (Jan)
- Surgical Neuroangiography**, May 4–8, New York, NY (Jan)
- Echocardiography 1987**, May 14–16, Cambridge, MA (Jan)
- Fleischner Society Annual Symposium**, May 21–23, San Francisco, CA (July)
- 1987 Radiology Congress**, Lisbon, May 31–June 6 (Aug)
- Society of Nuclear Medicine Annual Meeting**, June 2–5, Toronto, Ontario, Canada (Dec)
- The American Board of Radiology Examinations**. Oral examinations: June 8–12, 1987; May 23–27, 1988; June 5–9, 1989, all at Louisville, KY. Written examinations: Oct. 8–9, 1987; Oct. 6–7, 1988; Oct. 5–6, 1989 (Dec)
- Euroson '87**, June 14–18, Helsinki, Finland (Sept)
- International Conference on Computer Assisted Radiology**, July 1–4, West Berlin (Feb. 1986)
- Sarcoidosis and Granulomatous Disorders**, Sept. 6–11, Milan, Italy (June)
- The Asian-Oceanian Congress of Radiology**, Sept. 21–25, Seoul, South Korea (Nov)

Classified Advertising

Positions Available

NEURORADIOLOGIST to join a 21-member private practice radiology group in Birmingham, AL. Board certification/board eligibility, MR experience/training essential. Send CV to R. M. Doughton, M.D., 1920 Huntington Rd., Birmingham, AL 35209. 2-3a

BOARD CERTIFIED RADIOLOGIST—Six-man radiology group seeks new associate with 6-12 month fellowship/experience in MRI. New 1.5 T unit soon to be operational. The group provides complete radiologic services in fully-equipped 500-bed hospital, and private out-patient office. Send CV to Eric R. Rosenberg, M.D., Dept. of Radiology, New Hanover Memorial Hospital, Wilmington, NC 28403. 2-4a

STAFF RADIOLOGISTS—The College of Physicians and Surgeons of Columbia University is searching for staff radiologists in our angiography division at the Instructor or Assistant/Associate Professor level. Salary and academic rank will be commensurate with experience and qualifications. Responsibilities for the Instructor level include patient care, teaching and supervising residents. Responsibilities for Assistant/Associate Professor level include all of the above plus research, as well as demonstrated academic ability. Requirements include board eligibility or certification in diagnostic radiology for Instructor level; board certification and at least 2 yr of cardiovascular and interventional radiology experience for Assistant/Associate Professor level. N.Y.S. medical license required; narcotics license desirable. Please send resume to David H. Baker, M.D., Dept. of Radiology, 622 West 168th St., New York, NY 10032. Columbia University is an affirmative action/equal opportunity employer. 2a

RADIOLOGIST—A board certified/board eligible radiologist with experience is needed to join the staff of the Alaska Native Medical Center, 170-bed referral facility for a state-wide system of Indian Health Service hospitals and clinics. Practice stimulating and challenging radiology in a relaxed and casual atmosphere. State-of-the-art in-house CT, sonography, and mammography. Send C.V. to C.J. Heitz, Jr., M.D., P.O. Box 7-741, Anchorage, AK 99510. EOE 2-7a

RADIOLOGIST for a thriving community on the beautiful Pacific northwest coast at Prince Rupert, B.C., gateway to Alaska. The 124-bed regional hospital serves Prince Rupert and the surrounding area. Total number of examinations per yr is 16,000. Candidates must have obtained LMCC status and should have a Fellowship in Radiology with experience in ultrasound. Salary and/or fee for service basis. Direct applications or inquiries to The Administrator, Prince Rupert Regional Hospital, 1305 Summit Ave., Prince Rupert, B.C., V8J 2A6, Canada. 2-5a

BC/BE RADIOLOGIST, RECENT GRADUATE, JULY 1987—Small New Hampshire hospital, nuclear medicine, CT, ultrasound. Near lakes, mountains, beaches, 100 mi to Boston. Early partnership. Reply Box 08, *AJR* (see address this section). 2ap

NEURORADIOLOGIST. Applications are being sought for an academically oriented neuroradiologist for a 612-bed teaching hospital. Position to start July 1987. Candidate should be board certified preferably with 2 yr of neuroradiology fellowship. Training in MR, CT, angiography, and myelography necessary. Individual will be the second neuroradiologist in an active, aggressive section. Private practice. Send current CV to Harvey L. Neiman, M.D., Chairman, Dept. of Radiology, The Western Pennsylvania Hospital, 4800 Friendship Ave., Pittsburgh, PA 15224. 12-2a

CHIEF, DEPARTMENT OF RADIOLOGY—350-bed community teaching hospital and major affiliate of Tufts Medical School, located in the western suburb of Boston, is seeking a board-certified radiologist to serve as Chief of Radiology. Full-time position administering a comprehensive Radiology Dept. including CT (head and body) scanning, nuclear medicine, and ultrasound. Must be conversant with all aspects of modern diagnostic imaging modalities. Solid experience providing clinical and administrative leadership required. Interested candidates should submit a CV to Mark Belsky, M.D., Chairman, Search Committee, C/O Jeffrey R. Kelly, Chief Operating Office, Newton-Wellesley Hospital, 2014 Washington St., Newton, MA 02162. An equal opportunity employer. 2a

FREE STANDING MRI FACILITY—The Johnstown Regional MRI Center Corporation, a 4-hospital joint venture, is seeking a board-certified radiologist with training, experience, and education background to direct and conduct the activities of a new free-standing regional MRI center, servicing a 6-county area (1.5 GE Signa System). Contact Isadore Suchman, Chairman, MRI Search Committee, Johnstown Regional MRI Center Corp., Ste. 303, 551 Main St., Johnstown, PA 15901. 2a

GENERAL RADIOLOGIST—The Dept. of Diagnostic Radiology at the University of Louisville School of Medicine is seeking a board-certified radiologist with interest and/or experience in gastrointestinal and chest radiology. Fine opportunity in a growing and busy dept. with excellent equipment. Contact Hollis A. Thomas, M.D., Acting Chairman, Dept. of Diagnostic Radiology, Humana Hospital University, 530 South Jackson St., Louisville, KY 40202. An equal opportunity/affirmative action employer. 2a

ULTRASOUND/CT/MRI. Opportunity for board-certified radiologist specializing in ultrasound, body CT, and body MRI to pursue academic career at The New York Hospital-Cornell Medical Center. Dept. provides state-of-the-art equipment, including Acuson ultrasound, GE 9800 CT, and GE Signa 1.5 Tesla MR. Wide variety of ultrasound examinations include abdominal, doppler, Ob-Gyn, small parts, and neonatal head. Prefer candidate with prior fellowship in sectional imaging or ultrasound. Responsibilities include clinical practice, teaching, and research. Please send CV to Elias Kazam, M.D., Dept. of Radiology, The New York Hospital-Cornell Medical Center, 525 East 68th St., New York, NY 10021. 1-2a

DIAGNOSTIC RADIOLOGIST—500-bed VA Medical Center located in Augusta, ME offers opportunity for a board-certified/eligible radiologist to perform all aspects of diagnostic radiology. Located in central Maine, VAMC Togus, is within 1 hr of mountains and ocean recreational opportunities. Apply to Chief of Staff, VA Medical and Regional Office Center, Togus, ME 04330, (207) 623-8411, ext. 368. 2a

RADIOLOGY INSTRUCTOR to assist candidate in preparation for Oral Radiology Boards. Candidate needs practice in formally discussing cases and answering board-type questions. Would like to meet on a weekly basis beginning early 1987. Fee negotiable. Please call (215) 342-4110 or (615) 359-7092 eves. 12-2a

DIAGNOSTIC RADIOLOGIST. Need aggressive associate to perform all aspects of diagnostic radiology in well-equipped hospital with large out-patient component in South Texas. MR training a plus but not essential. Excellent salary and early partnership available. For confidential consideration please submit CV to Box H70, *AJR* (see address this section). 11xa

ISRAEL, DIAGNOSTIC RADIOLOGY. Opportunities for 3-4 week or longer working vacations in a number of Israeli medical centers, on a volunteer basis. Positions varied, arrangements flexible. For information contact: Jonathan H. Fish, M.D., 1844 San Miguel Dr., #302, Walnut Creek, CA 94596; (415) 947-0560. 8xa

IMMEDIATE OPENING—BC/BE RADIOLOGIST to join 8-man group in South Bay area of northern CA. Hospital and private office practice. All diagnostic modalities including MRI. Send CV to Box M3, *AJR* (see address this section). 1-3ap

PEDIATRIC RADIOLOGIST. Large hospital-based group seeks associate with recent pediatric radiology fellowship training. Busy private practice group needs second pediatric radiologist for coverage of small pediatric hospital. Practice would include 25% pediatric and 75% adult work. All modalities including MRI. Board certification mandatory. Opportunity for partnership in well-established western Washington practice. Reply Box H74, *AJR* (see address this section). 11-6a

TWO YOUNG RADIOLOGISTS seek a third radiologist in expanding hospital-based practice near Canadian border in northern New York. All modalities available. Write P. Berman, HC 61 Box 454, Massena, NY 13662. 8-7a

BOARD CERTIFIED diagnostic radiologist. All diagnostic modalities except MR. MR installation planned in 1½ years. Busy in-patient and out-patient practice. Salary negotiable and early partnership available. Send CV to Box C23, *AJR* (see address this section). 6xa

Positions Desired

BOARD-CERTIFIED EXPERIENCED DIAGNOSTIC RADIOLOGIST will be available for part-time office or hospital radiology approximately May 1, 1987. Have expertise in CT, ultrasound, mammography, and nuclear medicine. Interested in Hartford or Tolland counties in CT. Times and months flexible. Reply Box 07, *AJR* (see address this section). 2b

PGY II RADIOLOGY POSITION sought for July 1, 1987 by quality American grad now engaged in medical internship at a major medical school affiliated with a New England teaching hospital. Reply Box M1, *AJR* (see address this section). 1-4bp

BOARD-CERTIFIED RADIOLOGIST, currently angiography and interventional fellow at major university center, seeks hospital or private practice position beginning July 1987. Reply Box M5, *AJR* (see address this section). 1-2b

Fellowship and Residencies

CARDIOPULMONARY RADIOLOGY FELLOWSHIP—The Dept. of Radiology of Thomas Jefferson University Hospital offers a fellowship in cardiopulmonary radiology. This innovative program provides intense training in pulmonary radiology under the guidance of a highly motivated staff in an academic university setting. It also includes experience in thoracic CT, percutaneous thoracic interventional procedures, cardiovascular MRI, cardiac angiography, and echocardiography. In close cooperation with the division of pulmonary medicine, an excellent background in the clinical and physiologic aspects of pulmonary disease will be provided. Applicants should be board certified or eligible. Contact Robert M. Steiner, M.D., Chief of Thoracic Radiology, Thomas Jefferson University Hospital, Philadelphia, PA 19107. 1-2c

VISITING ULTRASOUND FELLOWSHIPS, VANCOUVER, B.C. Year-round basis. Fellowships are 1-12 wk at the University of British Columbia, under Peter L. Cooperberg, M.D. Heavy ultrasound caseload, with Doppler and real-time techniques emphasized. Contact Ultrasound Dept., Vancouver General Hospital, 855 West 12th Ave., Vancouver, B.C., V5Z 1M9, Canada. 2c

A NEURORADIOLOGY FELLOWSHIP IS AVAILABLE at the University of Massachusetts Medical Center, a 350-bed teaching hospital, 35 mi from Boston. This fellowship provides in-depth training in all current aspects of clinical neuroradiology and head and neck radiology, including CT, angiography, myelography, polytomography, and plain film diagnosis. It also provides exposure to general and interventional angiography and participation in research and teaching. The fellow is closely supervised by full-time faculty members and increasing clinical responsibilities are given as the year progresses. Equipment consists of a high resolution CT scanner dedicated to neuroradiology, a GE 1.5 Tesla MRI scanner, state-of-the-art angiography and DSI suites, and Phillips polytomography unit, and R & F rooms (shared with general radiology). Please address all inquiries to Eugenio L. Suran, M.D., Director of Neuroradiology, Dept. of Radiology, University of Massachusetts Medical Center, Worcester, MA 01605. 2-3c

CARDIOVASCULAR/INTERVENTIONAL RADIOLOGY FELLOWSHIP—Thomas Jefferson University Hospital announces a new fellowship program combining training in cardiac, vascular, and interventional radiology. One- and two-year positions are available beginning July 1, 1987. The 1-yr program offers intensive clinical experience in general angiography, coronary angiography, and interventional procedures. The 2-yr program emphasizes additional experience in interventional techniques and cardiac imaging, and provides time for research. Applicants should be board certified or in the certification process. Contact David C. Levin, M.D., or Geoffrey A. Gardiner, Jr., M.D. at Dept. of Radiology, Thomas Jefferson University Hospital, Philadelphia, PA 19107. 1-3c

Tutorials/Courses

LONDON, ENGLAND—MAY 2-10, 1987. CME I Accred. International Faculty. Topics: CT, MR, and other imaging modalities. Fees: To Feb. 28, US\$395. After Mar. 1, US\$435. Information: Medical Seminars, 21915 Roscoe Blvd., Suite 222, Canoga Park, CA 91304. (818) 340-0580 X280. 1-4d

Other

RAD/TOMO ROOM FOR SALE. Fischer 660 ma, single phase, automatic exposure control, wall bucky. Still under warranty. 80% of cost. Contact Margaret M. Sanders, M.D., Dallas, TX (214) 661-7575. 1-2ep

MRI OVER-READING SERVICE. Backup interpretation of MR scans now available using state-of-the-art Raytel teleradiology equipment and regular phone lines. Service available from across-the-street to across-the-country from 1-month to 1-year. Competitive rates. Contact Murray A. Solomon, M.D., San Jose MRI Center, 361 South Monroe, San Jose, CA 95128. 1-6ep

REALIZE THE VALUE of your practice. A group of successful and well-qualified radiologists is interested in acquiring established radiology practices. Hospital contracts, clinics, and private office settings are desired. Opportunity for radiologists considering retirement or reduction in practice activities to capitalize on the value of the practice they have built up during their careers. Alleviate the problems of professional recruitment or administrative pressures. Practices considered throughout the country. Flexible purchase options with opportunity for continuing relationship arrangements. Write Box C49, AJR (see address this section). 6-5e

AJR Classified Advertising Information

Box Responses and Address for Ad Placement

Write Box _____, AJR, Suite 200, 2223 Avenida de la Playa, La Jolla, CA 92037; (619) 459-2229.

How to Place an Ad

AJR accepts classified advertising for Positions Available, Positions Desired, Fellowships and Residencies, and Tutorials/Courses. Ads are accepted by mail or telephone. Institutions should supply purchase orders.

Rates: \$6.00/line with a \$30 minimum charge. Box service is \$10 additional for each month the ad appears. There are discounts for multiple insertions: 10% for 2-3 insertions; 20% for 4 or more. To estimate lines, count all words and divide by 5.5.

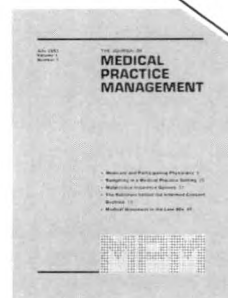
Billing: Ads may be prepaid or invoices will be sent after the ad appears.

Deadlines. About 3 weeks before the issue mails. AJR issues mail in the middle of the month preceding the cover date (e.g., July mails June 17). For specific deadlines, write or telephone the AJR editorial office.

Estimating Ad Charges

Line charge: divide total words by 5.5 and multiply by \$6.00	\$ _____
Multiple insertions? If so, multiply by number	x _____
Subtotal	\$ _____
Box response requested? If so, multiply number of months by \$10.00	+ _____
Subtotal	\$ _____
Discount applies to two or more insertions. Subtract 10% if ad appears 2-3 months, 20% if 4 months or more	- _____
Approximate advertising charge	\$ _____

Control the future of your practice



NEW!

The Journal of MEDICAL PRACTICE MANAGEMENT

Editor: Marcel Frenkel, MD, MBA

A new journal gives you the management skills you need to pull ahead

Right now you need information on some important topics that weren't covered in medical school. Topics that are having a profound impact on private practice and hospital-based physicians across the country.

Like competition from HMOs. Industrialization of medicine. The sheer number of physicians competing for your patients. Increasing costs.

You know the issues. What you need to know is the best way to face them so your practice will flourish in years to come.

And that's where **The Journal of Medical Practice Management** comes in.

Keep up with the issues that are changing your way of practice forever

The Journal of Medical Practice Management is a new quarterly publication that covers *your* concerns...issues affecting the way you practice now — and the way you'll practice in the future.

Four times a year, an expert editorial board headed by Dr. Marcel Frenkel brings you concise, readable coverage of today's issues and tomorrow's trends.

You'll find departments covering • office procedures and management • malpractice • marketing • manpower • computers • taxation • legal and legislative affairs • and health policy.

You'll also find pertinent features like the **Washington Report**, telling you what's up in the nation's capital and how it affects you...a **Letter from Abroad**, offering perspectives on how physicians are handling health care issues in other countries...and profiles of profit and not-for-profit health care delivery systems.

A multidisciplinary editorial board

Members of the editorial board for **The Journal of Medical Practice Management** have been carefully chosen for their knowledge of the management aspects of practicing medicine. These experts, many with experience in more than one field, give you the perspectives you need from medicine, law, management, government, and education.

You can control the future of your practice

The issues you can't afford to ignore are in **The Journal of Medical Practice Management**. It's a lot of information for a little money. And that's good business for you.

Reserve your charter subscription today!

Just return the attached coupon, or **call our FREE number**, 800-638-6423, from anywhere in the US except Alaska. In Maryland, call 528-4105 collect. **Quarterly**

Williams & Wilkins

428 East Preston Street
Baltimore, Maryland 21202

266 Fulham Road
London SW10 9EL England

YES, I want to control the future of my practice!

Please enter my subscription to **The Journal of Medical Practice Management** (quarterly)

☐ Individuals and Institutions \$40

All subscribers: add \$10 outside the U.S.

☐ Check enclosed ☐ Bill me

☐ MasterCard ☐ American Express ☐ VISA

Card # _____ Exp. date _____

Signature _____

Name _____

Address _____

City/State/Zip _____

Maryland residents add 5% sales tax. Subscriptions outside the US must be prepaid. All subscriptions must be paid in US dollars. Rates valid through April 30, 1988.

Please allow 8 weeks for delivery of your first issue, up to 16 weeks for surface delivery outside the US. Airmail rates available on request.

Williams & Wilkins

P.O. Box 23291
Baltimore, Maryland 21203

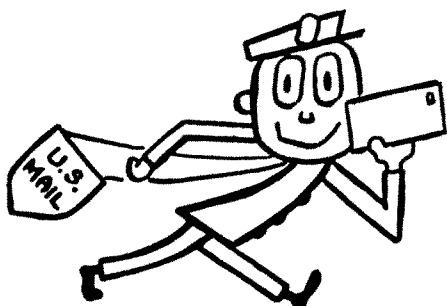
266 Fulham Road
London SW10 9EL England

MPMAD 95048 87

Help us to serve you better.....

If your mailing label does not contain your zip code, note it on the label and return it to us for correction.

Remember, your Zip Code provides faster, more direct delivery of your journals. Use it on all correspondence, too.



INDEX TO ADVERTISERS

Ackrad Laboratories, Inc.	A11
Adria Laboratories	A2
Aramco Services	A13
Eastman Kodak	A6, A7
E-Z-EM Company	Cover 2
Toshiba Medical Systems	A16, A17
Konica Medical Corporation ...	A11, A12, A13
Nuclear Associates	A26
Picker International	A8, A9, A10
Precise Optics/PME, Inc.	A12
Pyne Corporation	Cover 3
F. R. Squibb & Sons, Inc.	A19, A20, A21, A23, A24
S & S X-Ray	A14
Tecnomed USA	A18

We try to present an accurate index. Occasionally this may not be possible because of a last-minute change or an omission.

CARDIOVASCULAR RADIOLOGY

- 239 Cine MR imaging: potential for the evaluation of cardiovascular function. *Sechtem U, Pflugfelder PW, White RD, et al.*
- 247 Acute myocardial infarction: MR evaluation in 29 patients. *Fisher MR, McNamara MT, Higgins CB*
- 253 Aberrant right subclavian artery: further observations. *Proto AV, Cuthbert NW, Raider L*
- 259 Superior vena cava obstruction: a venographic classification. *Stanford W, Jolles H, Ell S, Chiu LC*
- 263 Occult pulmonary embolism: a common occurrence in deep venous thrombosis. *Dorfman GS, Cronan JJ, Tupper TB, Messersmith RN, Denny DF, Lee CH*
- 267 Case report. Primary angiosarcoma of the heart: CT characteristics. *Shin MS, Kirklin JK, Cain JB, Ho K-J*

GASTROINTESTINAL RADIOLOGY

- 269 Pictorial essay. Contrast pharyngography: the importance of phonation. *Rubesin SE, Jones B, Donner MW*
- 273 Patterns of recurrence of esophageal carcinoma after transhiatal esophagectomy and gastric interposition. *Becker CD, Barbier PA, Terrier F, Porcellini B*
- 279 Case report. Acute gastric dilatation: a rare cause of portal venous gas. *Radin DR, Rosen RS, Halls JM*
- 281 Natural history of the obstructed rabbit appendix: observations with radiography, sonography, and CT. *Dachman AH, Nichols JB, Patrick DH, Lichtenstein JE*
- 285 Case report. Ringlike rectal ulcers after biopsy or polypectomy. *Lev-Toaff AS, Levine MS, Laufer I, Herlinger H*

GENITOURINARY RADIOLOGY

- 287 MR evaluation of uterine anomalies. *Mintz MC, Thickman DJ, Gussman D, Kressel HY*
- 291 Sonography in the diagnosis of acute renal allograft rejection and cyclosporine nephrotoxicity. *Linskowski GD, Warvariv V, Filly RA, Vincenti F*
- 297 Needle puncture of cystic renal masses: a survey of the Society of Uroradiology. *Amis ES Jr, Cronan JJ, Pfister RC*
- 301 Interstitial emphysema associated with epidural anesthesia for extracorporeal shock-wave lithotripsy. *Roberts MC, Pollack HM, Banner MP, Castro AD, Van-Ardsalen KN*
- 305 Case report. Polyorchidism: evaluation by MR. *Baker LL, Hajek PC, Burkhard TK, Mattrey RF*

MUSCULOSKELETAL RADIOLOGY

- 307 MR imaging of the carpal tunnel: normal anatomy and preliminary findings in the carpal tunnel syndrome. *Middleton WD, Kneeland JB, Kellman GM, et al.*
- 317 MR imaging of osteogenic and Ewing's sarcoma. *Boyko OB, Cory DA, Cohen MD, Provisor A, Mirkin D, DeRosa GP*
- 323 Parosteal osteosarcoma: radiologic-pathologic correlation with emphasis on CT. *Lindell MM Jr, Shirkhoda A, Raymond AK, Murray JA, Harle TS*
- 329 Pictorial essay. Cystic masses of the knee: arthrographic and CT evaluation. *Lee KR, Cox GG, Neff JR, Arnett GR, Murphey MD*
- 335 CT patterns of facet fracture dislocations in the thoracolumbar region. *Manaster BJ, Osborn AG*
- 341 Diagnostic oncology case study. Bone scan-positive and radiograph- and CT-negative vertebral lesion in a woman with locally advanced breast cancer. *Mink JH, Weitz I, Kagan AR, Steckel RJ*
- 344 Technical note. Digital subtraction arthrography of the temporomandibular joint. *Jacobs JM, Manaster BJ*

PEDIATRIC AND FETAL RADIOLOGY

- 347 Chronic airway obstruction in children: evaluation with cine-CT. *Frey EE, Smith WL, Grandgeorge S, et al.*
- 353 Radiographic findings in children and young adults with Barrett's esophagus. *Yulish BS, Rothstein FC, Halpin TC Jr*

- 359 Sonographic analysis of the fetus with ureteropelvic junction obstruction. *Kleiner B, Callen PW, Filly RA*
- 364 Case report. Main-stem bronchial atresia: intrauterine sonographic diagnosis. *McAlister WH, Wright JR Jr, Crane JP*

INTERVENTIONAL RADIOLOGY

- 367 Risks of percutaneous transhepatic drainage in patients with cholangitis. *Lois JF, Gomes AS, Grace PA, Deutsch L-S, Pitt HA*
- 372 Case report. Common bile duct stone dissolution with methyl tertiary butyl ether: experience with three patients. *Teplick SK, Haskin PH, Goldstein RC, et al.*
- 375 Case report. Transcatheter recanalization of a chronically occluded saphenous aortocoronary bypass graft. *Marx M, Armstrong WT, Brent BN, Wack JP, Bernstein RM, Gregoratos G*
- 378 Case report. Transcatheter intracavitary fibrinolysis of infected extravascular hematomas. *Vogelzang RL, Tobin RS, Burstein S, Anschuetz SL, Marzano M, Kozlowski JM*

NEURORADIOLOGY

- 381 The MR appearance of syringomyelia: new observations. *Sherman JL, Barkovich AJ, Citrin CM*
- 393 Spontaneous dissection of the cervical internal carotid artery: correlation of arteriography, CT, and pathology. *Petro GR, Witwer GA, Cacayorin ED, et al.*

MAGNETIC RESONANCE

- 399 Magnetite albumin microspheres: a new MR contrast material. *Widder DJ, Greif WL, Widder KJ, Edelman RR, Brady TJ*
- 405 Use of standard gradients with compound oblique angulation for optimal quantitative MR flow imaging in oblique vessels. *Pettigrew RI, Dannels W*
- 411 Quantitative phase-flow MR imaging in dogs by using standard sequences: comparison with in vivo flowmeter measurements. *Pettigrew RI, Dannels W, Galloway JR, et al.*
- 415 Effects of MR imaging on murine natural killer cell cytotoxicity. *Prasad N, Lotzova E, Thornby JL, Made-well JE, Ford JJ, Bushong SC*
- 418 Technical note. Intensity correction in surface-coil MR imaging. *Axel L, Costantini J, Listerud J*

DIGITAL RADIOLOGY

- 421 Total digital radiology department: spatial resolution requirements. *Seeley GW, Fisher HD, Stempski MO, Borgstrom M, Bjelland J, Capp MP*
- 427 Commentary. Picture archiving and communication systems in Japan. *Huang HK, Mankovich NJ, Cho PS, Taira R, Stewart BK, Ho BK*

OTHER CONTENT

- 252 American Roentgen Ray Society Officers
- 258 Forthcoming articles
- 278 Books received
- 431 ARRS 1987 meeting invitation
- 433 ARRS section on instruction
- 443 ARRS scientific program
- 449 ARRS local activities
- 451 ARRS registration forms
- 454 ARRS airline discounts
- 455 ARRS meeting summary
- 456 Letters
- 459 News
- 463 Classified ads
- Book reviews 296, 300, 358, 392
- Memorials John H. Gilmore 410
Walter L. Kilby 430
- A3 Guidelines for authors
- S1 ARRS meeting packet (insert)

Acc.
18.9.87



AJR

American
Journal of
Roentgenology



March 1987

Serious side effects.

Pulling forward on the side straps of any of E-Z-EM's Pinnacle™ Adjust-A-Weight™ protective garments has a very noticeable effect—it gradually redistributes the weight of the garment from your shoulders to your back and hips. The amount that you pull determines how the weight is spread, and spreading the load makes you feel more comfortable all over.

Our patented design uses non-snag Velcro® brand fasteners for easy adjustment, and comes in a variety of styles for radiology, cath lab, and operating room use. They're available in your choice of fabric, color, and trim.

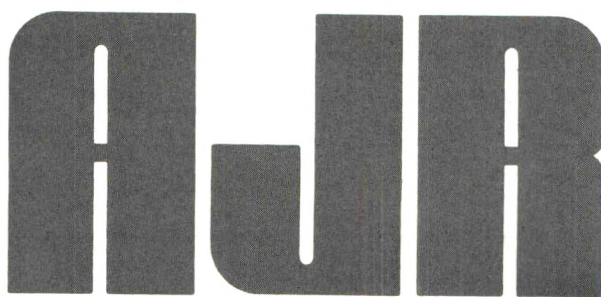
To find out why Pinnacle has become the industry standard for comfort, contact your local representative, or call E-Z-EM toll-free at 800-645-3052. In New York call 516-333-8230.

E-Z-EM
More than barium—
much more



E-Z-EM, Inc.
7 Portland Avenue
Westbury, NY 11590

Official Journal of the American Roentgen Ray Society



American Journal of Roentgenology
Diagnostic Imaging and Related Sciences

Editor-In-Chief Robert N. Berk, *San Diego, California*

Editor Emeritus Melvin M. Figley, *Seattle, Washington*

Associate Editors Alan J. Davidson, *Washington, District of Columbia*
Saskia von Waldenburg Hilton, *San Diego, California*
Juan M. Taveras, *Boston, Massachusetts*

Assistant Editors William L. Ashburn, *San Diego, California*
Charles C. Berry, *San Diego, California*
William G. Bradley Jr., *Pasadena, California*
Edward Buonocore, *Knoxville, Tennessee*
Peter L. Cooperberg, *Vancouver, British Columbia*
Peter Doubilet, *Boston, Massachusetts*
N. Reed Dunnick, *Durham, North Carolina*
Ronald G. Evens, *St. Louis, Missouri*
Henry I. Goldberg, *San Francisco, California*
William R. Hendee, *Chicago, Illinois*
John R. Hesselink, *San Diego, California*
Charles B. Higgins, *San Francisco, California*
Helen C. Redman, *Dallas, Texas*
Donald L. Resnick, *San Diego, California*
Stewart R. Reuter, *San Antonio, Texas*
Stuart S. Sagel, *St. Louis, Missouri*
Edward A. Sickles, *San Francisco, California*
Eric vanSonnenberg, *San Diego, California*

Editorial Staff: Gita S. Braude, *managing editor*; Elizabeth A. Whalen, *senior editor*; Linda Wood and Barbara Rose, *manuscript editors*; Nancy Rydbeck, *administrative assistant*; Sandra Wood, *administrative secretary*.

All business correspondence, including display (not classified) advertising, subscriptions, address changes, reprints, and permission requests should be addressed to Williams & Wilkins, 428 East Preston Street, Baltimore, MD 21202. Correspondence regarding editorial matters and classified advertising should be addressed to the editorial office, AJR, 2223 Avenida de la Playa, Suite 200, La Jolla, CA 92037. For manuscript submission, see Guidelines for Authors, next page. Undelivered or damaged copies replaced within 60 days of publication; 90 days for foreign subscribers. Allow 90 days for address changes. AJR AMERICAN JOURNAL OF ROENTGENOLOGY (ISSN 0361 803X) is published monthly by American Roentgen Ray Society, 428 E. Preston Street, Baltimore, MD 21202. Annual dues include \$50 for journal subscription. Second class postage paid at Baltimore, MD and at additional mailing offices. Postmaster send address changes (Form 3579) to Williams & Wilkins, 428 East Preston St., Baltimore, MD 21202. Subscription rates \$90 (\$120 foreign); institutions \$100 (\$130 foreign); in training \$25; single copy \$16 (\$19). Japanese Yen price is available from our sole agent USACO Corporation, 13-12, Shimbashi 1-Chôme, Minato-Ku, Tokyo 105, Japan, telephone 03-502-6471. Airmail rates furnished on request. Indexed by *Current Contents* and *Index Medicus*. Copyright © 1987 by American Roentgen Ray Society. 0361-803X/87\$2.00

Tecnomed USA

Mamex DC

MAMMOGRAPHIC
SYSTEM

In the beginning...

The original MAMEX DC

The Mamex DC is a complete mammographic system, consisting of a modern, efficient DC generator which virtually eliminates "ripple" and gives a higher resolution image with consistently higher subject contrast; a molybdenum anode x-ray tube; and a motorized compression system with floor remote control.

Standard features:

- ★ Compact DC generator with automatic exposure control.
Exposures can be made once every 30 seconds.
- ★ Stand designed for x-ray examination of the breast.
- ★ Hardened glass screen protects technician during exposure.
- ★ Floor remote compression control.
- ★ Phototiming detector position selector.
- ★ Field light.
- ★ Breast compression plate;
Biopsy compression plate;
Spot cone compression plate.
- ★ 18x24cm Kodak Min-R cassette with screen.
- ★ Film identification markers.
- ★ Automatic line voltage compensation.
- ★ .6x.6 stationary anode molybdenum x-ray tube with beryllium window.

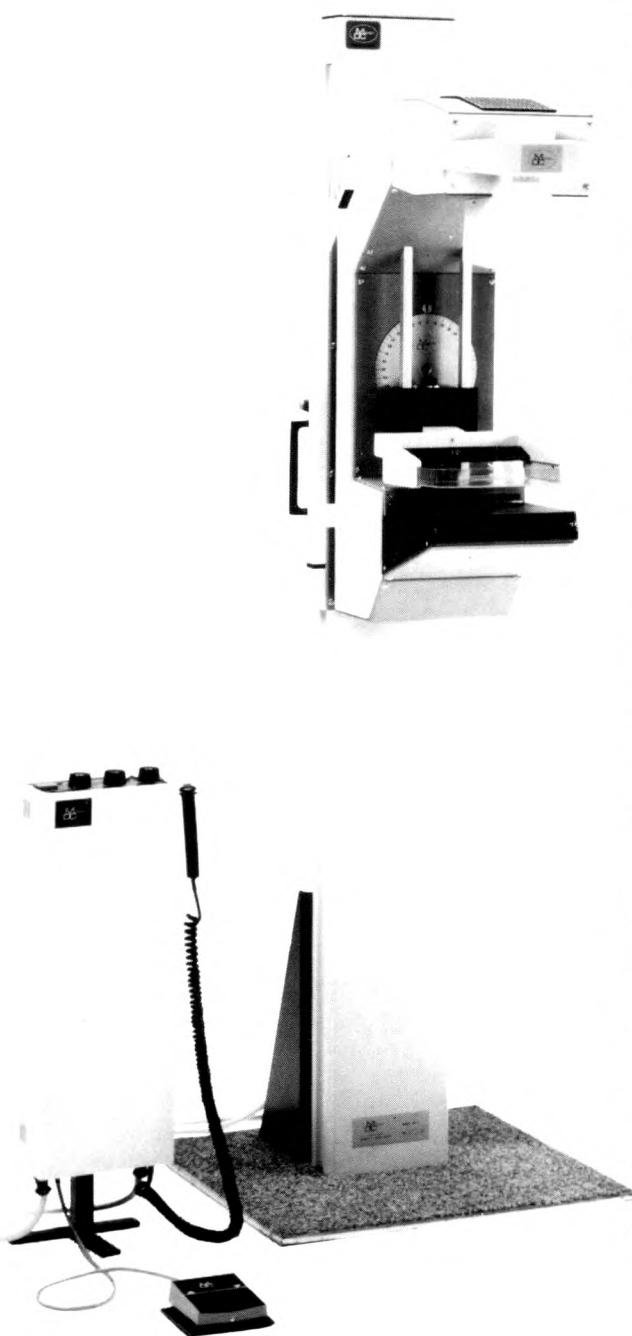
Options:

- ★ 200L 3.5:1 grid.
- ★ Carbon fiber cassette tunnel with grid pocket.
- ★ In-hospital wheel assembly (shown).
- ★ Van wheel assembly.

Mamex DC . . .

- ★ Five-year proven track record of performance and reliability;
- ★ Hundreds of satisfied physicians, clinics, and hospitals throughout the United States and internationally;
- ★ Full 12-month non-prorated warranty on the x-ray tube;
- ★ Average midbreast dosages, on a 2-film exam of a 6cm compressed breast, of .07R or less (as documented by the University of Michigan Breast Cancer Detection Center - Ingvar Andersson, M.D.)

. . . offers your facility the very best in diagnostic equipment available in today's marketplace.



Original MAMEX DC

CIRCLE 10 ON READER SERVICE CARD

AJR Guidelines for Authors

Address new and revised manuscripts, correspondence, and classified ads to the Editor:

AJR Editorial Office

2223 Avenida de la Playa, Suite 200

La Jolla, CA 92037 Telephone: (619) 459-2229

Inquiries regarding subscriptions, display advertising, reprints, or permission to republish AJR material should be addressed to the publisher:

The Williams & Wilkins Co.

428 E. Preston St.

Baltimore, MD 21202 Telephone: (301) 528-4133

The AJR publishes original contributions to the advancement of medical diagnosis and treatment. Submitted manuscripts should not contain previously published material and should not be under consideration for publication elsewhere. Papers dealing with neuroradiology should be addressed to: American Journal of Neuroradiology, Dept. of Radiology, Massachusetts General Hospital, Boston, MA 02114. At the discretion of the AJR Editor, AJNR articles that are of interest to the general reader may be republished in the AJR. Neuroradiologic papers sent to the AJR will be forwarded to the Editorial Office of the AJNR.

Manuscript decisions are based on peer review. Reviewers receive manuscripts without title pages to ensure an unbiased review. All accepted manuscripts are subject to editing. Statements made in the article, including changes made by the Editor or manuscript editor, are the responsibility of the author and not of the AJR or its publisher. Authors will be sent the edited manuscript, galley proof, and proofs of illustrations. If the corresponding author will be unavailable to review galleys, arrangements should be made for a coauthor or colleague to read and return the proof.

General Guidelines for Major Papers

Abstract. Clearly state (in 150 words or less) the purpose, methods, results, and conclusions of the study. Include actual data.

Introduction. Briefly describe the purpose of the investigation, including relevant background information.

Methods. Describe the research plan, the materials (or subjects), and the methods used, in that order. State in detail the confirmation of disease and control of subjectivity in observations.

Results. Present results in a clear, logical sequence. If tables are used, do not duplicate tabular data in text, but do describe important trends and points.

Discussion. Describe the limitations of the research plan, materials (or subjects), and methods, considering both the purpose and the outcome of the study. When results differ from those of previous investigators, explain the discrepancy.

AUTHOR'S CHECKLIST

For priority handling, please complete the following checklist, sign the copyright form on the reverse side of this page, and send in both with your manuscript.

_____ Two copies of the manuscript (the original and a photocopy) and two complete sets of figures are submitted.

_____ If appropriate, AJR Guidelines for case reports, technical notes, pictorial essays, or letters to the Editor have been followed.

_____ The manuscript, including references, figure legends, and tables, is typed double-spaced throughout on 8½ × 11 in. (21.6 × 27.9 cm) nonerasable paper. Right-hand margins are not justified.

_____ All manuscript pages are numbered consecutively without author identification.

_____ The manuscript is organized as follows: title page, blind title page (title only), abstract, introduction, methods, results, discussion, acknowledgments, references, tables, figure legends, and figures.

_____ Use of unfamiliar acronyms and abbreviations is kept to a minimum. When abbreviations are used they are written out at first mention, with the abbreviation following in parentheses.

_____ Metric measurements are used throughout, or the metric equivalent is given in parentheses.

_____ Names and locations (city and state only) of manufacturers are given for equipment and nongeneric drugs.

Title Page

_____ The following information is given: title of article; names and complete addresses (including zip code) of all authors; current addresses of authors who have moved since study; acknowledgment of grant or other assistance; and a current phone number for the corresponding author.

_____ Two copies of a blind title page are included giving only the title (omitting the authors' names) for use in the review process.

Abstract

_____ An abstract of approximately 150 words concisely states the purpose, methods, results, and conclusions of the study. Actual data are included.

_____ No abbreviations or reference citations are used in the abstract.

References

References (not to exceed 35) are typed double-spaced starting on a separate page and are **numbered consecutively in the order in which they appear in the text**. All references are cited in the text and are enclosed in brackets and typed on line with the text (not superscript). Unpublished data are not cited in the reference list, but are cited parenthetically in the text, for example, (Smith DJ, personal communication), (Smith DJ, unpublished data). This includes papers submitted, but not yet accepted, for publication. Inclusive page numbers (e.g., 333–335) are given for all references. Journal names are abbreviated according to *Index Medicus*. Style and punctuation of references follow the format illustrated in the following examples (all authors are listed when six or less; when seven or more authors, the first three are listed, followed by “et al.”):

Journal article
1. Long RS, Roe EW, Wu EU, et al. Membrane oxygenation: radiographic appearance. *AJR* 1986;146:1257–1260

Book
2. Smith LW, Cohen AR. *Pathology of tumors*, 6th ed. Baltimore: Williams & Wilkins, 1977:100–109

Chapter in a book
3. Breon AJ. Serum monitors of bone metastasis. In: Clark SA, ed. *Bone metastases*. Baltimore: Williams & Wilkins, 1983:165–180

Paper presented at a meeting
4. Lau FS, Kirk AN, Beck RA. MR imaging of the spine. Presented at the annual meeting of the American Roentgen Ray Society, Washington DC, April 1986

Tables

Each table is typed double-spaced on a separate page without vertical or horizontal rules; each has a short, descriptive title. Tables do not exceed two pages in length and contain at least four lines of data.

Tables are numbered in the order in which they are cited in the text. Abbreviations are defined in an explanatory note below each table. Tables are self-explanatory and do not duplicate data given in the text or figures. All arithmetic (percentages, totals, differences) has been double checked for accuracy, and tabular data agree with data given in the text.

Figures and Legends

Two complete sets of original figures are submitted unmounted in labeled envelopes. Figures are clean, unscratched, 5 × 7 in. (13 × 18 cm) glossy prints with white borders. A separate print is submitted for each figure *part*. Each figure is labeled on the back with the figure number and an arrow indicating “top.” Labeling is done on a gummed label and then affixed to the back of the print. (Never use ink on front or back of figures.) Author’s names are *not* written on the backs of figures. Only removable (rub-on) arrows and letters are used on the figures themselves. Symbols are not broken or cracked. Images are uniform in size and magnification. Line drawings are done in black ink on a white background and are of professional quality. (Only glossy prints, not originals or photocopies, are acceptable.) Written permission has been obtained for use of all previously published illustrations (and copies of permission letters are included), and an appropriate credit line is given in the legends. Legends are typed double-spaced, and figure numbers correspond with the order in which the figures are cited in the text.

Transfer of Copyright Agreement and Exclusive Publication Statement

Complete copyright to the article entitled: _____

is hereby transferred to the American Roentgen Ray Society (for United States government employees to the extent transferable), effective if and when the article is accepted for publication in the *American Journal of Roentgenology*. In the case of the authors who are officers or employees of the United States government, the American Roentgen Ray Society recognizes that works prepared by officers or employees of the United States government as part of their official government duties are in the public domain.

Authors reserve all proprietary rights other than copyright, such as patent rights and the right to use all or part of this article in future works of their own. The authors retain the right of replication, subject only to crediting the original source of publication and receiving written permission from the publisher.

Authors guarantee that this manuscript contains no matter that is libelous or otherwise unlawful, invades individual privacy, or infringes any proprietary rights.

Authors understand that they will receive no royalty or other compensation from the American Roentgen Ray Society.

Finally, the authors certify that none of the material in this manuscript has been published previously or is currently under consideration for publication elsewhere.

First author/date	Second author	Third author
_____	_____	_____
_____	_____	_____

This agreement must be signed by all authors in order for the manuscript to be published.

Guidelines for Case Reports

A case report is a brief description of a special case that provides a message that transcends the individual patient.

Format. There is no abstract. The introduction should be a short paragraph giving the general background and the specific interest of the case. No more than one case should be described in detail (similar ones can be mentioned briefly in the discussion). Emphasis should be on the radiologic aspects; clinical information must be limited to that necessary to provide a background for the radiology. The discussion should be succinct and should focus on the specific message and relevance of radiologic methods. A review of the literature is not appropriate.

Length. Maximum of five double-spaced, typewritten pages, including the references but not the title page or figure legends.

References. Maximum of eight.

Figures. Maximum of three or four, unless the text is shortened accordingly. Legends must not repeat the text.

Tables and Acknowledgments. Not appropriate in case reports.

Author's Checklist and Copyright Agreement. Submit both with the manuscript.

Guidelines for Technical Notes

A technical note is a brief description of a specific technique or procedure, modification of a technique, or equipment of interest to radiologists.

Format. No abstract, headings, or subheadings are required. If headings are used, they should be a combination of "Case Report," "Materials and Methods," "Results," and "Discussion." A brief one-paragraph introduction should be included to give the general background. Discussion should be limited to the specific message, including the uses of the technique or equipment. Literature reviews and lengthy case reports are not appropriate.

Length. Maximum of five double-spaced, typewritten pages, including the references but not the title page or figure legends.

References. Maximum of eight.

Figures. Maximum of two, unless the text is shortened accordingly.

Tables and Acknowledgments. Not appropriate in technical notes.

Author's Checklist and Copyright Agreement. Submit both with the manuscript.

Guidelines for Pictorial Essays

A "pictorial essay" is an article that conveys its message through illustrations and their legends. Unlike other *AJR* articles, which are based on original research, pictorial essays serve primarily as teaching tools, like exhibits at a scientific meeting. They are not encyclopedic book chapters. No abstract is necessary.

Length. Maximum of four double-spaced, typewritten pages, including the references but not the title page or figure legends.

References. Maximum of four.

Figures. Maximum of 30 figure parts. Number should be as few as necessary to convey the message of the paper.

Tables and Acknowledgments. Not appropriate in pictorial essays.

Author's Checklist and Copyright Agreement. Submit both with the manuscript.

Guidelines for Letters to the Editor and Replies

Letters to the Editor and Replies should offer objective and constructive criticism of published articles. Letters may also discuss matters of general interest to radiologists. Letters and replies are subject to editing and condensation. Authors will receive galley proof for correction and approval.

Format. All letters should be typed double-spaced on nonletterhead paper, with no greeting or salutation. Signature and affiliation should appear at the end of the letter. Titles for letters should be short and pertinent. The title for a reply is simply "Reply."

Length. Maximum of two double-spaced, typewritten pages, including references and figure legends.

References. Maximum of four.

Figures. Maximum of two.

Tables and Acknowledgments. Not appropriate in Letters to the Editor and Replies.

Author's Checklist and Copyright Release Form. Submit both with the manuscript.

Simply...the best



CT 9000 from GE... an uncomplicated system that's the best in its class

When you're buying a CT system to handle routine procedures, the last thing you want is unnecessary complexity. Complexity can compromise the economy you're looking for in such a system... it can raise your overhead, increase downtime, and slow down throughput.

That's why the CT 9000 from General Electric has become the best-selling system in its class: it's remarkably uncomplicated.

Simple installation: The entire computer system is housed in the operator's console. That means you

requirements. And the CT 9000 fits into a room as small as 20 x 20 feet... in most cases, it can be installed without renovation.

Uncomplicated operation: The CT 9000 incorporates advanced micro-electronic technology to streamline operation and enhance



operator efficiency. Operation is so easy that training can be completed in as little as one day. Routine protocols can be initiated with the touch of a button. And the unique AutoVoice synthesizer automatically relays proper breathing instructions to the patient, letting the operator concentrate on the procedure at hand. Because the CT 9000 system is so easy to use, most procedures can be completed faster...enhancing patient throughput even further.

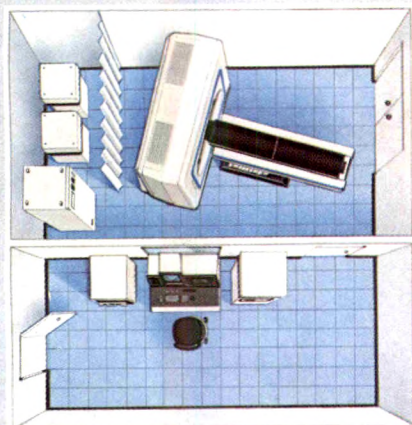
Uncommonly reliable: The CT 9000's modular electronics not only give you scan versatility, they also set a new standard in system reliability. You get consistently excellent performance, day after day, with minimum downtime and maximum throughput.

Financing made easy: GE offers a complete range of financing and lease plans that can be tailored to fit your budget and cash flow requirements. Our Super Saver lease plan, for example, offers a fixed lease rate as low as 4.8%* with no payments for the first 90 days of operation... that means your CT 9000 system will begin earning income for your facility immediately.

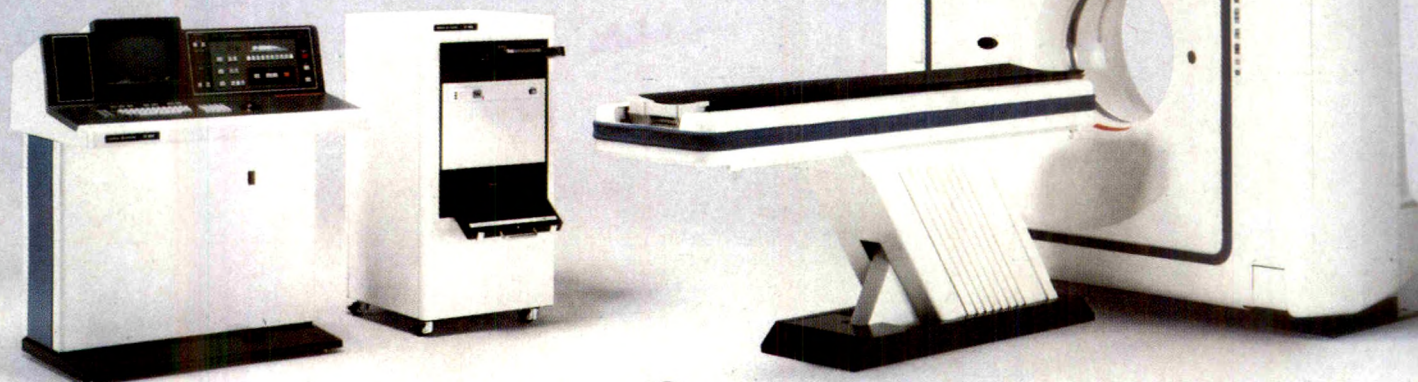
More information? Contact your General Electric sales representative, or call us and find out how the CT 9000 system can fit into your healthcare delivery plans.

800-433-5566 Ext. 5303

*Rate in effect for a limited time only. Some restrictions apply. Contact your GE sales representative for details.



don't need a separate computer room with special air conditioning



GENERAL  ELECTRIC

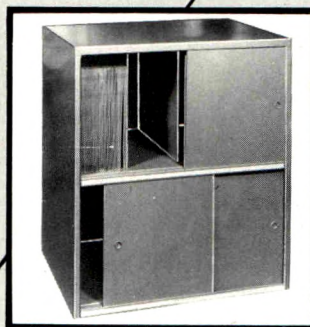
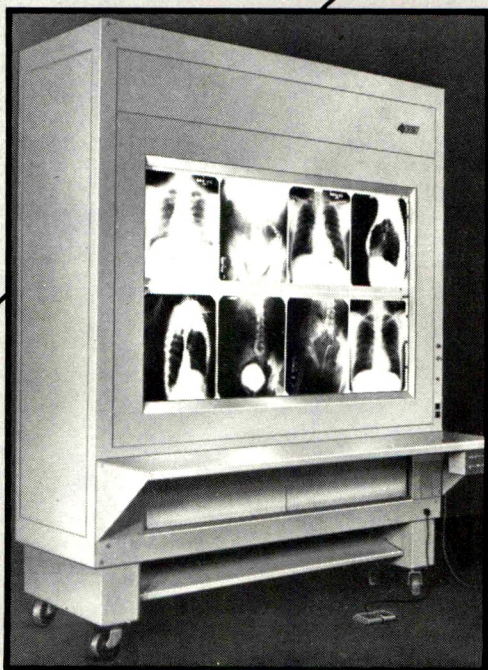
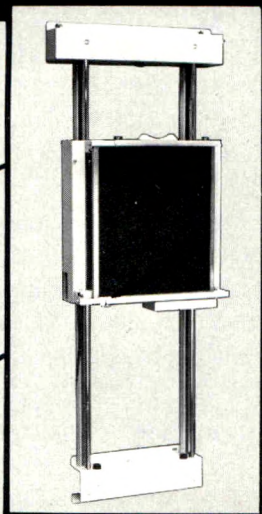
There are reasons
S.&S. X-RAY ACCESSORIES
 are preferred...



PROVEN the best in X-Ray Departments
 throughout the world

UNEQUALLED in design, construction and—quality

REPUTATION unmatched for RELIABILITY
 and PERFORMANCE



- Motorized Viewers
- Illuminators
- Transfer Cabinets
- File Cabinets
- Protective Panels
- Protective Aprons
- Wall Cassette Holders
- Dryers
- Safelights
- Dark Room Cabinets
- Storage Chests
- Loading Bins
- X-Ray Accessories

For more than 30 years, S. & S. has been meeting Radiologists' needs with a complete line of illuminators and accessories.

Contact S. & S. or your local x-ray dealer for additional information.

CIRCLE 9 ON READER SERVICE CARD

MANUFACTURED BY

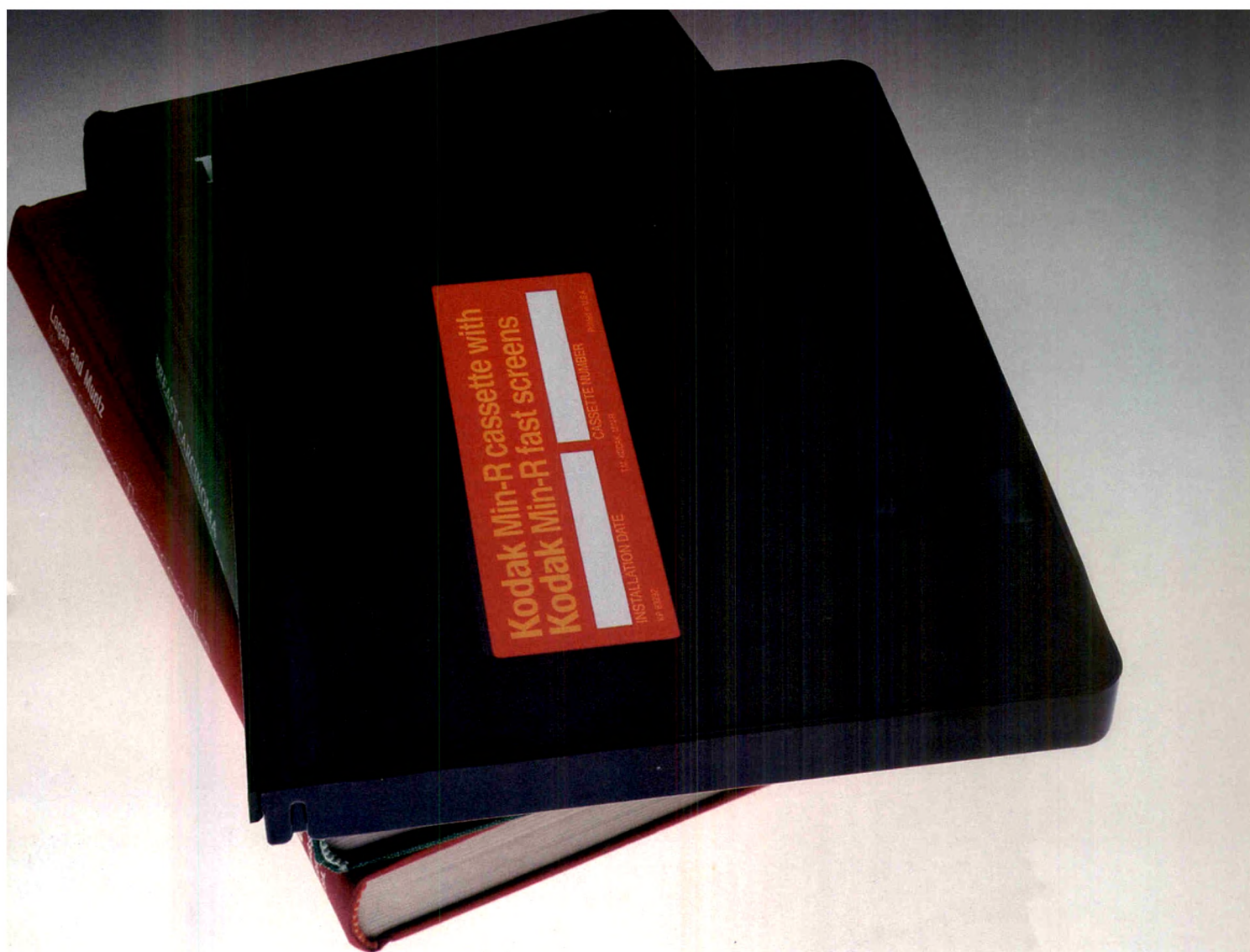
S. & S. X-RAY PRODUCTS INC.



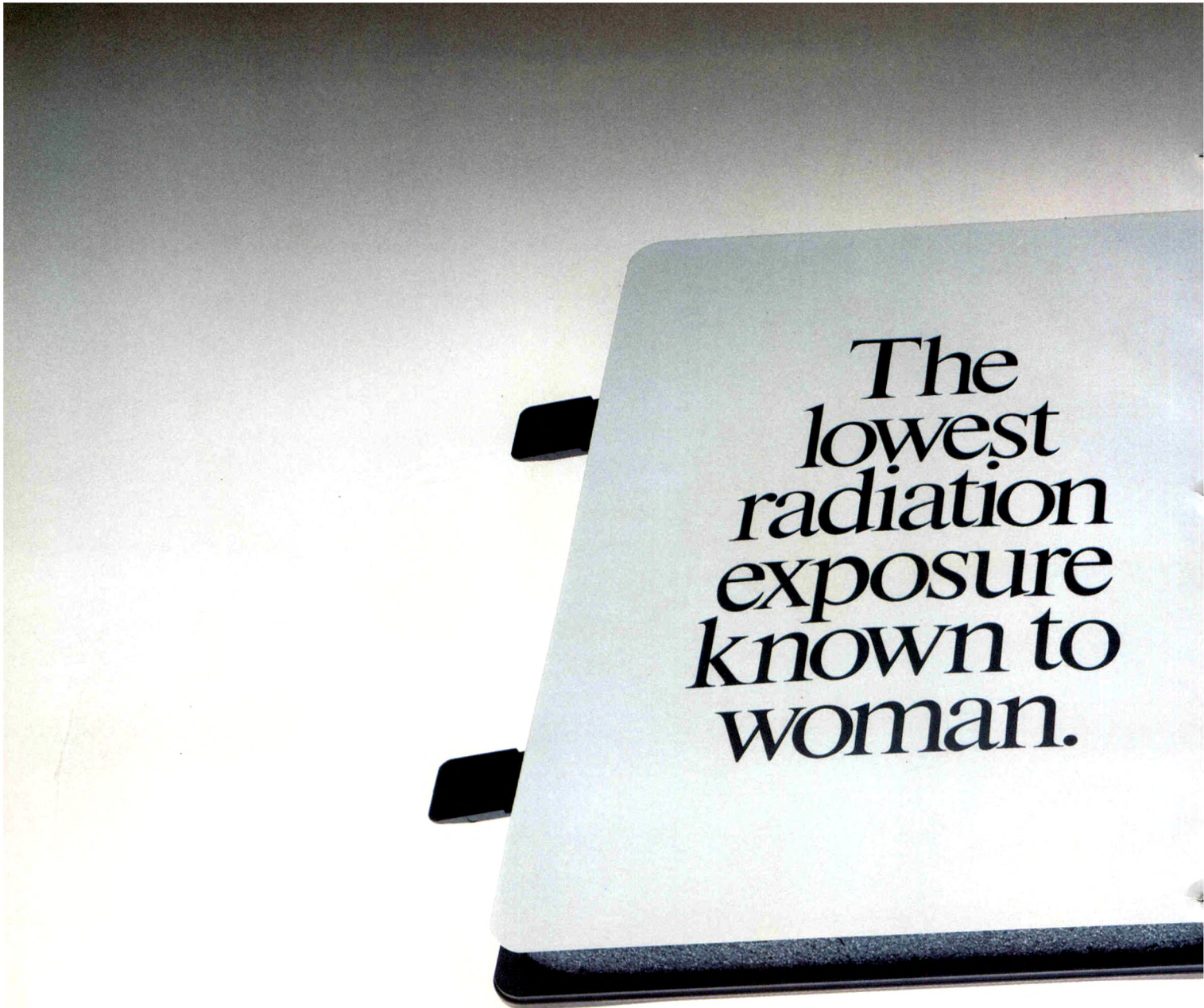
*The Complete Line of
 X-Ray Accessories
 (800)221-6634*

Telephone: (212) 852-6900

87-93 JAY STREET, BROOKLYN, N.Y. 11201



Kodak opens a new chapter
in screen-film mammography.



The
lowest
radiation
exposure
known to
woman.

New two-screen, double-emulsion film combination.

Introducing
**KODAK MIN-R Fast Screens and
KODAK T-MAT M Film**

For years, Kodak has been writing the book on mammographic imaging. Now a new chapter unfolds.

For the first time, you can use a two-screen,

double-emulsion film combination for mammography. A combination that Kodak has created specifically for mammographic applications.

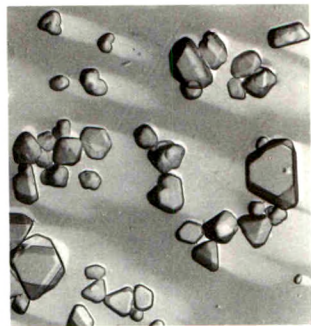
It's the new KODAK MIN-R Fast Screens and KODAK T-MAT M Film combination. And it's the fastest, high-quality, low-radiation-exposure mammographic imaging system in existence. It's so efficient, it reduces radiation exposure by 2.5x.

This technological breakthrough is the result of new screen-coating capabilities combined with Kodak's innovative T-Grain emulsion technology.

The proprietary new screens comprise a thin front screen and a conventional thickness mammographic back screen. These new screens are important elements that make possible the use of a double-emulsion film for mammography.

- **2.5x radiation reduction**
- **Sharp, high contrast images**
- **Ideal for grid and magnification**
- **Ideal for low output units**
- **Reduces imaging dust and dirt artifacts**

T-Grain emulsions are perhaps the biggest advance in silver halide imaging in 50 years. The new tablet-shaped silver halide grains used in KODAK T-MAT M Film capture more light, afford increased speed, and don't compromise image quality.



T-Grain emulsion technology is the basis for the new KODAK T-MAT M Film. The emulsions employ flat, tabular grains of silver halide (left) rather than the conventional pebble-shaped grains.

In addition, the T-MAT M Film has a magenta dye adsorbed onto the T-Grain crystals to absorb the green light emitted by the rare earth intensifying screens, reducing crossover without sacrificing system speed.

The double MIN-R Fast Screens and the T-MAT M Film are provided in low-absorbing KODAK MIN-R Cassettes or mounted in folders for use in vacuum devices. The result is a state-of-the-art system customized for mammography. A system that eliminates imaging dust and dirt artifacts, and provides an intimate screen-film contact to further maintain image sharpness. A system that can be used with grids to deliver the high-contrast image you need, while reducing radiation dose.

To open a new chapter in mammography for you and your patients, contact your Kodak technical sales representative.

New KODAK MIN-R Fast Screens and KODAK T-MAT M Film, the combination with a 2.5x radiation dose reduction.

Relative contrasts, speeds, and average glandular dose comparisons of Kodak films used with Kodak screens for mammography

Film	Contrast ¹	Relative Speed ²	Average Glandular Dose ³ (Rads)
KODAK Ortho M Film KODAK MIN-R Screen	2.85	100	0.05
KODAK T-MAT M Film KODAK MIN-R Fast Screens	3.05	250	0.02

Development—KODAK RP X-OMAT Processors using seasoned KODAK RP X-OMAT Chemicals or equivalent at recommended temperatures.

Contrast¹—Measured as the average gradient between densities 0.25 and 2.00 above gross fog.

Relative Speed²—Determined from matched density radiographs. KODAK Ortho M Film arbitrarily assigned a relative speed of 100.

Technique³—Based on average size breast, craniocaudal view, molybdenum target tube, 0.03 mm molybdenum filter, 28 kVp setting.

New KODAK MIN-R Fast Screens

The KODAK MIN-R Fast Screens incorporate phosphors which contain metals from the lanthanide series of “rare earth” elements. Using a molybdenum target x-ray tube with a beryllium window, 30 microns molybdenum filtration, and a 4 cm clear plastic breast test object, energy absorption by the screens is approximately 90 percent. The MIN-R Fast Screens are to be used in a KODAK MIN-R Cassette or suitable vacuum holder, with KODAK T-MAT M Film.

New KODAK T-MAT M Film

The new double-coated KODAK T-MAT M Film is a high-speed, high-contrast orthochromatic x-ray film specially designed for mammographic imaging. It incorporates light-sensitive dyes to absorb green light emitted by the intensifying screens and reduce image blur.

It is ideal for applications where high film speed is desired to reduce exposure times and radiation dose—for example, with the use of grids, small focal spots, and magnification techniques.

The KODAK MIN-R Cassette

The KODAK MIN-R Cassette provides fast, easy loading of films for the mammographic procedure. The all-plastic molded cassette provides intimate screen-film contact and low absorption. The tube-side panel of the cassette is thin, injection-molded polycarbonate, with low x-ray absorption. Combined with appropriate compression, the design of the MIN-R Cassette permits good visualization of soft-tissue information near the chest wall of the patient. MIN-R Cassettes can be supported with a holding device available on most dedicated mammography x-ray units.

Availability

KODAK T-MAT M Film

24 x 30 cm CAT No. 810 9456
18 x 24 cm CAT No. 809 6091
8 x 10 in. CAT No. 847 4975

KODAK MIN-R Fast Screens (in KODAK MIN-R Cassettes)

24 x 30 cm CAT No. 813 3332
18 x 24 cm CAT No. 810 1412

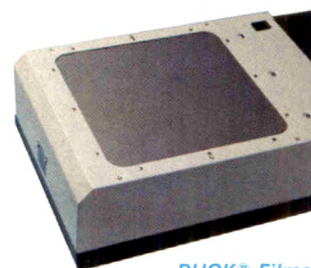
(in folder for vacuum devices)

8 x 10 in. CAT No. 847 6673



Kodak, X-Omat, Min-R, T-Grain, and T-Mat are trademarks.

ELEMA-SCHONANDER



*PUCK® Filmch
Model UD4...pos
for multi-directional
Model U4 for a.p. and*

Long useful life is built into every Elema-Schonander angiographic filmchanger system.

The two PUCK filmchanger systems shown below—still in frequent use—are but two of many examples of Elema-Schonander filmchanger systems, working dependably day after day, year after year, for ten...fifteen years or more.

- The same quality of engineering, material, workmanship and solid construction demonstrated in these two examples, characterizes

also today's generation of AOT and PUCK filmchangers.

- The long useful life and dependability of Elema-Schonander filmchanger systems translates directly into lower cost per examination. Together with excellent image quality, these and other Elema-Schonander advantages have been proven again and again over the years.

Elema-Schonander,
2360 North Palmer Drive
P.O. Box 94517
Schaumburg, IL 60195
Telephone (312) 397-5959



elema-schonander
CIRCLE 4 ON READER SERVICE

MG/5810-05 8

Examples of Elema-Schonander filmchanger systems in frequent use for

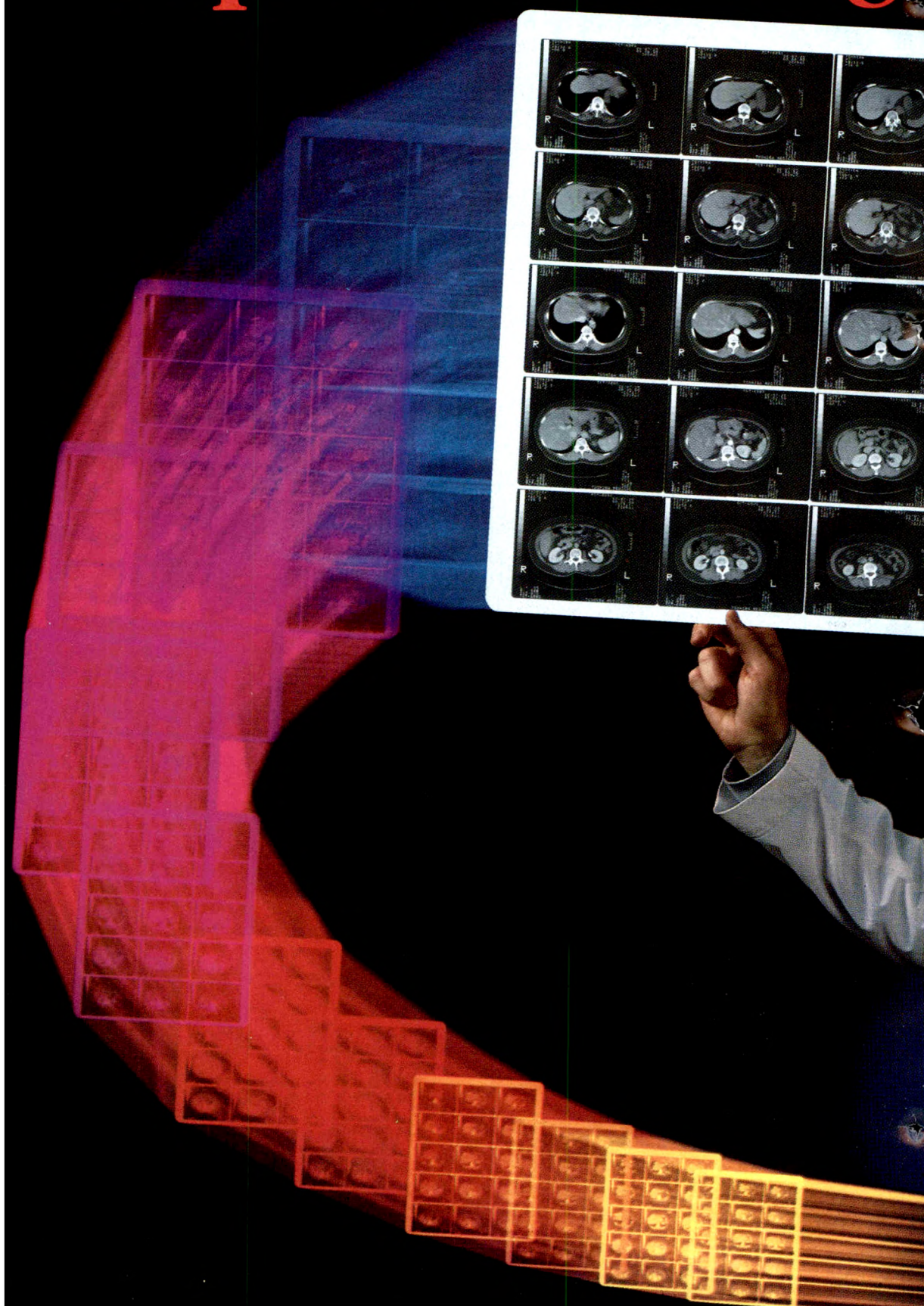
The Sabbatsberg Hospital, Stockholm, Sweden
PUCK U-35 system in service since 1970.



Kaiser Foundation Hospital, Los Angeles, CA
PUCK U-35 system in service since 1971.



Unparalleled image





quality. Time after time.

Toshiba's TCT-600 Series

Toshiba's TCT-600 Series Whole Body CT Scanners are just what you would expect from a world leader in diagnostic imaging: fast, flexible, and expandable. And that's just what you should ask for. But Toshiba's TCT-600 Series give you even more:

1. Image quality and performance second to none.
2. Reliability, flexibility, and easy "one-touch command" operations for high throughput.
3. System expandability for widening applications.

Ask for more. Ask for the image quality and level of performance you get with Toshiba. Time after time after time.

For more information about the TCT-600 Series Whole Body Scanners, call or write: Toshiba Medical Systems, 2441 Michelle Drive, Tustin, CA 92680. In California, call (714) 669-5419. Outside California, call toll-free (800) 421-1968. In Canada, call (416) 298-6100.

In Touch with Tomorrow

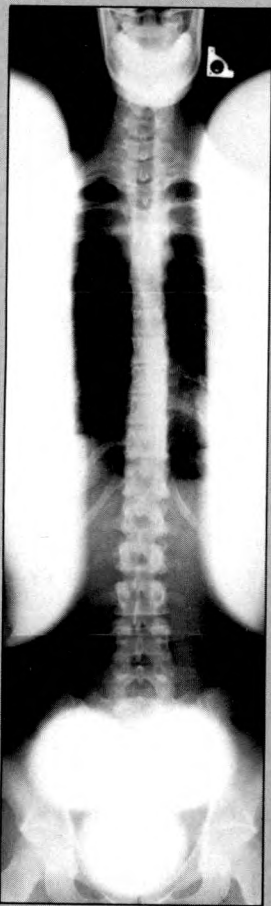


TOSHIBA

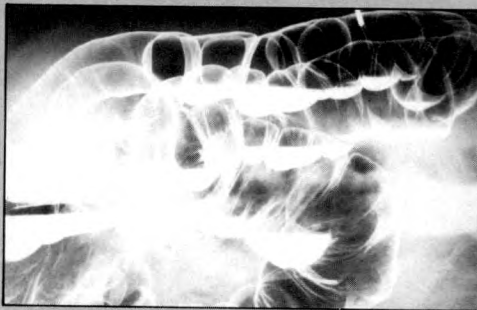
GLOBAL IMAGING SPECIALISTS

CIRCLE 19 ON READER SERVICE CARD

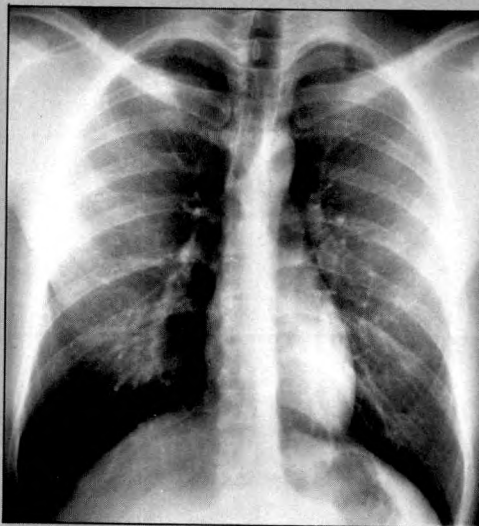
MORE DIAGNOSTIC DETAIL... LESS RADIATION EXPOSURE



FULL-SPINE. Full-spine scoliosis exam using compensation filters (as recommended by the FDA to reduce exposure). Note ideal density throughout the spinal column.



DECUBITUS. Right lateral decubitus radiograph with double contrast (barium and air). CLEAR-Pb Filter ends "image burn-out."

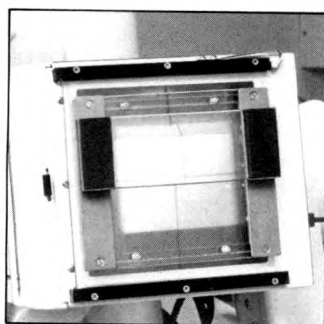


CHEST. Chest radiograph taken with CLEAR-Pb Chest Filter. Reveals all details of lungs and mediastinum.



LONG-LEG. Long-leg radiograph (weight-bearing) obtained with uniform-speed screens and a CLEAR-Pb Long-Leg filter. Note the even film density from hips to ankles.

Radiography Takes a Giant Step Forward with CLEAR-Pb® TRANSPARENT X-RAY COMPENSATION FILTERS



Magnetic mounting system allows instant adjustment of lightweight filter.

- Improve image quality by providing a more uniform film density.
- Reduce patient exposure by selectively attenuating the x-ray beam.
- Reduce the need for multiple exposures.
- Transparent lead-plastic filters never block the collimator light field.
- Easy to use; mount to any collimator.

Finally, there's an easy way to solve your imaging problems. With a CLEAR-Pb Filter you are assured of top-quality images the first time... every time. Over and under-penetration of the patient are eliminated, and important details are improved dramatically.

Try a CLEAR-Pb Filter. You will find one available for most routine exams. There's no easier or better way to obtain superb images... **GUARANTEED!**

***100% SATISFACTION GUARANTEED!** Buy a CLEAR-Pb Filter and use it for 30 days. If it doesn't meet your expectations, return it for full credit.

For details on our full line of
Image Compensators,
request Bulletin 361-C.

CIRCLE 16 ON READER SERVICE CARD

NUCLEAR ASSOCIATES



A Division of VICTOREEN, INC.
100 VOICE ROAD
CARLE PLACE, NY 11514-1593
(516) 741-6360
A Subsidiary of Sheller-Globe **SG**

© Victoreen, Inc.

THE BREAKTHROUGH IN IMAGE COMPENSATORS

Administration time	6 hours
Sugar	No
Alcohol	No
Sodium content	Low

Evac-Q-Kwik thoroughly cleans the colon. Patients arrive ready for X-ray. No staff time or extra prepping needed. One take is all—virtually every time. This means better work flow, cost containment and patient comfort.

Everything is in the kit, including easy-to-follow instructions. No mixing, no enemas, no alcohol, no sugar, low sodium... and low cost. Easy to use for better compliance.

Seeing is believing. Give Evac-Q-Kwik a trial.

There's more.

Take advantage of our service materials:

☐ Inservice film for nurses ☐ Multi-language instruction sheets ☐ Radiology work sheets ☐ "What to expect" booklet for patients. Ask your Adria Representative, or drop us a line. Adria Laboratories, Columbus, Ohio 43215.

Evac-Q-Kwik[®]

Clean colon, clear advantages.



Adria Laboratories
Columbus, OH 43215

YOU KNOW ALL ABOUT IMAGING NEGATIVES.



NOW, RAYTHEON OFFERS YOU SOME POSITIVES.

Take heart. Those imaging negatives you face every day may not be as overwhelming as they seem.

Dwindling budgets. Escalating costs. Runaway technology.

Problems, all. Negatives, all. Yet there is a way to cope. There is a way to convert those imaging negatives into positives.

Raytheon Medical Systems!

You demand quality imaging systems! Raytheon delivers. You demand prices that won't upset

your budget! Raytheon delivers. And you demand excellent imaging results! Again, Raytheon delivers.

Because Raytheon Medical Systems believes that quality starts with fundamentals. And because we are part of a 7-billion-dollar multinational company, we offer the fundamentals that are important to you: strength, capability, support.

Raytheon Medical Systems can provide the knowledge, the resources, and the insight required

to deliver the kind of imaging equipment you want.

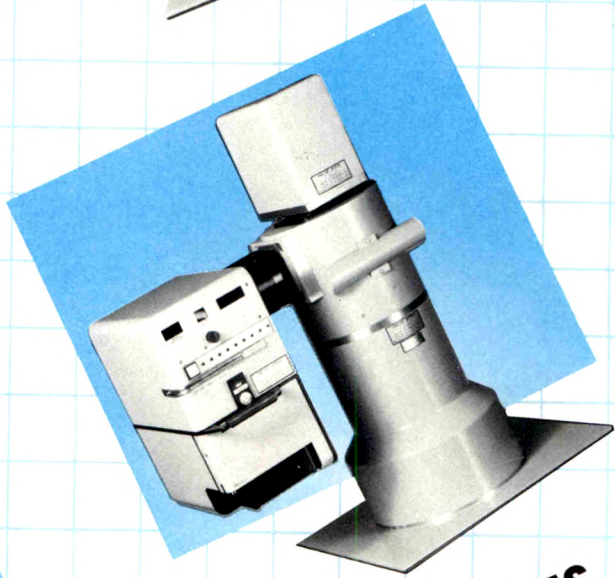
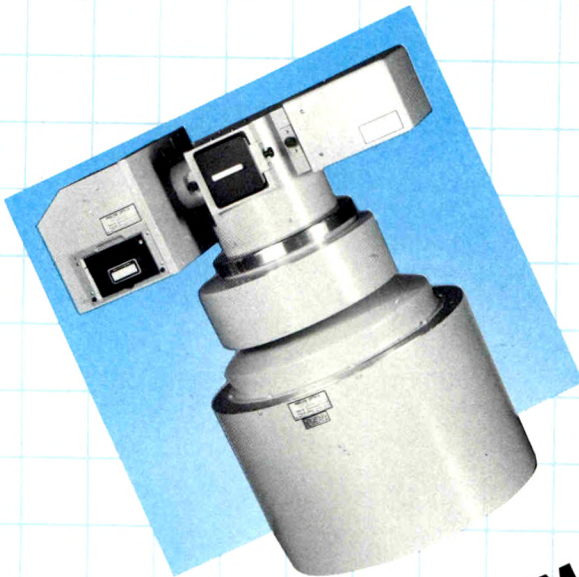
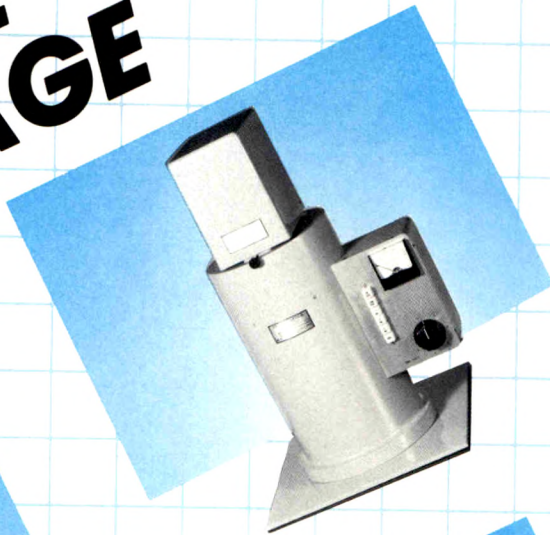
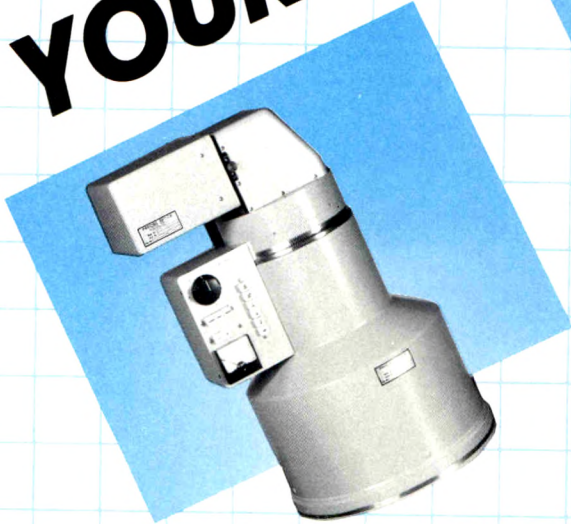
Raytheon Medical Systems. The one imaging company with the capabilities and the commitment that can change your negatives into positives.

Raytheon

MEDICAL SYSTEMS
2020 North Janice Avenue
Melrose Park, Illinois 60160
1-312-865-2600
1-800-323-2213

CIRCLE 20 ON READER SERVICE CARD

IMPROVE YOUR IMAGE



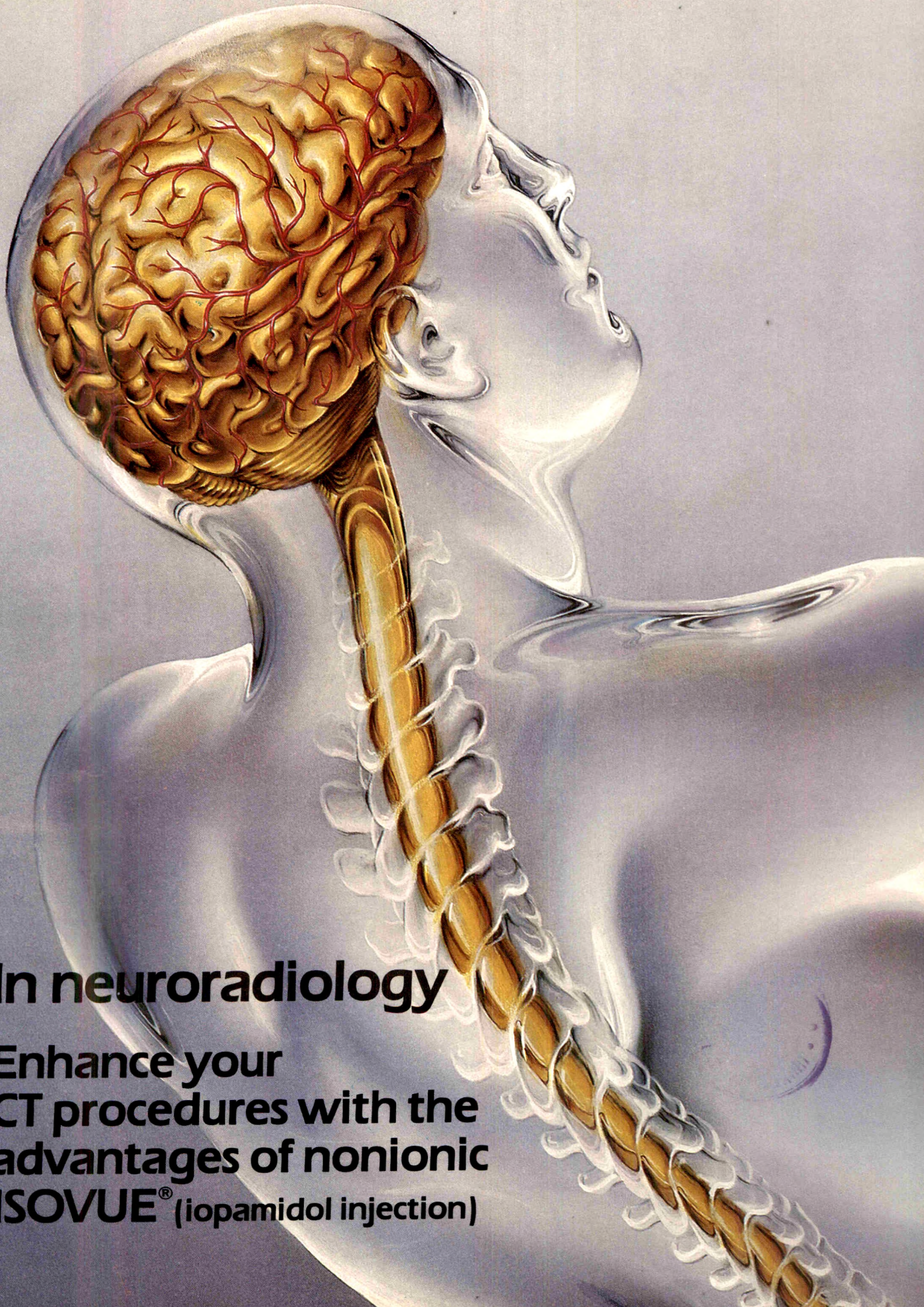
WITH PRECISE OPTICS IMAGE INTENSIFIER SYSTEMS

- The world's largest independent manufacturer of Image Intensifier Systems and components
- Over 30 years of experience in design and manufacture
- 6, 9, 12, and 16-Inch latest series image tubes for optimum performance
- 525/875/1023 line CCTV's, 6fps 100mm/105mm cameras

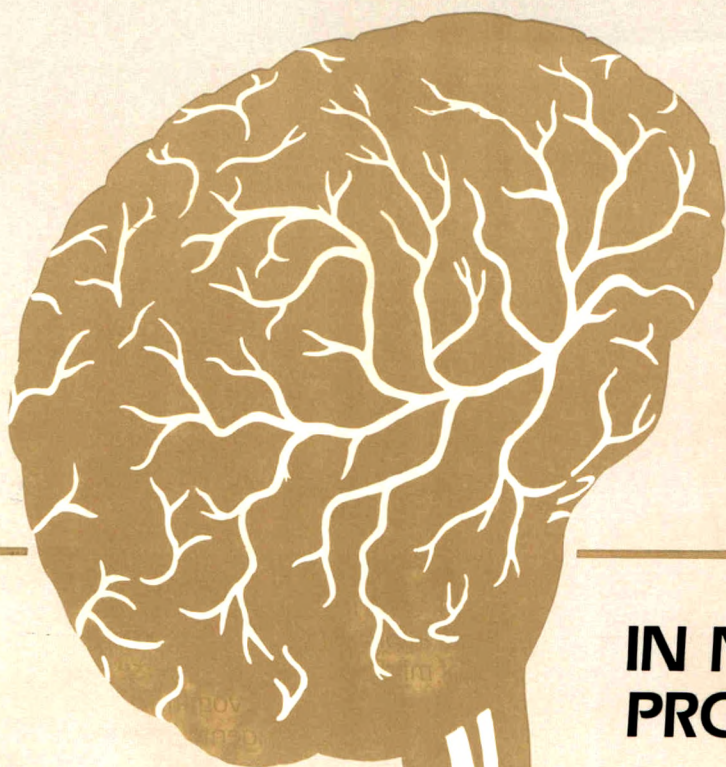
- Cost effective, versatile, reliable
- Compatible with new or existing x-ray equipment
- Extend the life of existing apparatus
- Worldwide dealer network

239 South Fehr Way
Bay Shore, New York 11706
Tel.: 516 242-6600
TWX: 510-227-9837
CIRCLE 6 ON READER SERVICE CARD

**precise
optics®**
PHOTO MEDIC
EQUIPMENT, INC.



In neuroradiology
Enhance your
CT procedures with the
advantages of nonionic
ISOVUE[®] (iopamidol injection)



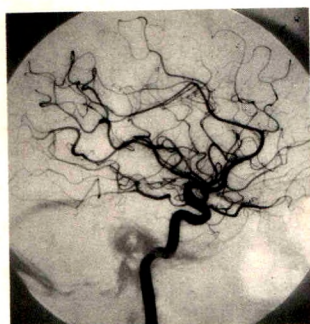
**IN NEURORADIOLOGY
PROCEDURES:**

**Use with
confidence
on both sides of
the blood-brain
barrier**

ISOVUE
iopamidol injection

ISOVUE-M
iopamidol injection

OUTSIDE
Intravascular
use



In clinical trials involving 1099 Isovue patients: approximately half the incidence of mild to moderate adverse reactions (e.g., pain, nausea, vomiting) seen with the ionic control agent* in all intravascular procedures combined.¹

INSIDE
Intrathecal
use



When Isovue-M was compared in a double-blind study to metrizamide in lumbar, thoracic, cervical, and total columnar myelography, the 370 patients given Isovue-M experienced less neurotoxicity (psycho-organic manifestations) and approximately half the incidence of observed adverse reactions.¹



An excellent choice
when contrast media
may cross the blood-brain
barrier unexpectedly

**The first "nonionic" indicated in
intravenous contrast enhanced CT.
Also indicated in CT cisternography
and ventriculography.**

As with all injectable contrast agents, the possibility of severe reactions should be borne in mind. See brief summary of prescribing information on last pages of this advertisement for CONTRAINDICATIONS, WARNINGS, PRECAUTIONS, and ADVERSE REACTIONS.

*Diatrizoate meglumine/diatrizoate sodium for most intravascular procedures; iothalamate meglumine for cerebral arteriography.

Enhance your CT procedures with the advantages of nonionic ISOVUE

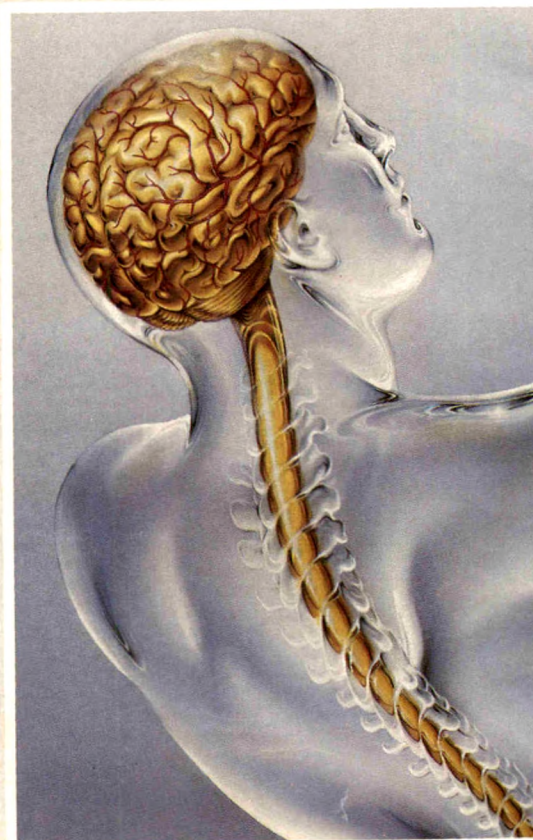
ISOVUE[®]-300
iopamidol injection 61%

For cerebral arteriography
and head and body CT

ISOVUE[®]-M 200
iopamidol injection 41%

ISOVUE[®]-M 300
iopamidol injection 61%

For myelography and CT cistern-
ography and ventriculography




Compared to conventional, ionic contrast media

- Nonionic and low osmolality.
- Increased confidence for the radiologist.
 - Improved patient comfort and cooperation.
 - Fewer mild to moderate adverse reactions: less pain, less nausea, less vomiting.
- Procedures go more efficiently with fewer disruptions.

As with all injectable contrast agents, the possibility of severe reactions should be borne in mind. See brief summary of prescribing information on next page for CONTRAINDICATIONS, WARNINGS, PRECAUTIONS, and ADVERSE REACTIONS.

References: 1. Data on file, Squibb Institute for Medical Research.

This product is under license from Bracco Industria Chimica, S.p.A.
U.S. Patent #4,001,323.

 **SQUIBB**[™]
Diagnostics 646-507

ISOVUE®-300
Iopamidol Injection 61%
ISOVUE®-370
Iopamidol Injection 76%
ISOVUE-M® 200
Iopamidol Injection 41%
ISOVUE-M® 300
Iopamidol Injection 61%

DESCRIPTION—ISOVUE and ISOVUE-M (iopamidol injection) are nonionic radiopaque contrast media for diagnostic use. The formulations are stable, aqueous, sterile, and nonpyrogenic solutions for intravascular and intrathecal administration, respectively. Each mL of ISOVUE-300 (iopamidol injection 61%) provides 612 mg iopamidol with 1 mg tromethamine and 0.39 mg edetate calcium disodium. The solution contains approximately 0.037 mg (0.002 mEq) sodium and 300 mg organically bound iodine per mL. Each mL of ISOVUE-370 (iopamidol injection 76%) provides 755 mg iopamidol with 1 mg tromethamine and 0.48 mg edetate calcium disodium. The solution contains approximately 0.046 mg (0.002 mEq) sodium and 370 mg organically bound iodine per mL. Each mL of ISOVUE-M 200 (iopamidol injection 41%) provides 408 mg iopamidol with 1 mg tromethamine and 0.26 mg edetate calcium disodium. The solution contains approximately 0.025 mg (0.001 mEq) sodium and 200 mg organically bound iodine per mL. Each mL of ISOVUE-M 300 (iopamidol injection 61%) provides 612 mg iopamidol with 1 mg tromethamine and 0.39 mg edetate calcium disodium. The solution contains approximately 0.037 mg (0.002 mEq) sodium and 300 mg organically bound iodine per mL. The pH of each solution has been adjusted to 6.5 to 7.5 with hydrochloric acid.

CONTRAINDICATIONS: ISOVUE (iopamidol injection)—None.

ISOVUE-M (iopamidol injection)—Intrathecal administration of corticosteroids with iopamidol is contraindicated. Because of overdosage considerations, immediate repeat myelography in the event of technical failure is contraindicated (see interval recommendation under DOSAGE AND ADMINISTRATION in the product package insert). Myelography should not be performed in the presence of significant local or systemic infection where bacteremia is likely.

WARNINGS: ISOVUE (iopamidol injection)—Use caution in patients with severely impaired renal function, combined renal and hepatic disease, or anuria, particularly when larger doses are administered. Radiopaque diagnostic contrast agents are potentially hazardous in patients with multiple myeloma or other paraproteinemia, particularly in those with therapeutically resistant anuria. It has been speculated that the combination of the contrast agent and dehydration may be causative of anuria in myelomatous patients. This risk is not a contraindication; however, special precautions are required. Contrast media may promote sickling in individuals who are homozygous for sickle cell disease when injected intravenously or intraarterially. Administration to patients known or suspected of having pheochromocytoma should be performed with extreme caution. If the possible benefits outweigh the considered risks, the procedures may be performed; however, the amount of the medium injected should be kept to an absolute minimum. Assess blood pressure throughout the procedure and measures for treatment of a hypertensive crisis should be available. Monitor such patients very closely. Use caution in patients with hyperthyroidism or with an autonomously functioning thyroid nodule because of risk of thyroid storm.

ISOVUE-M (iopamidol injection)—Carefully evaluate the need for myelographic examination. Administer with caution in patients with increased intracranial pressure or suspicion of intracranial tumor, abscess or hematoma, those with a history of convulsive disorder, severe cardiovascular disease, chronic alcoholism, or multiple sclerosis, and elderly patients. Particular attention must be given to state of hydration, concentration of medium, dose, and technique used in these patients. If frankly bloody cerebrospinal fluid is observed, the possible benefits of the examination should be considered in terms of risk to the patient. Patients on anticonvulsant medication should be maintained on this therapy. Direct intracisternal or ventricular administration for standard radiography (without computerized tomographic enhancement) is not recommended. Inadvertent intracranial entry of a large or concentrated bolus of agent, which increases the risk of neurotoxicity, can be prevented by careful patient management. Avoid rapid dispersion of the medium causing inadvertent rise to intracranial levels. If such entry of the medium occurs, prophylactic anticonvulsant treatment with diazepam or barbiturates orally for 24 to 48 hours should be considered. Use of medications that may lower the seizure threshold should be carefully evaluated. While the contributory role of such medications has not been established, these agents are often discontinued at least 48 hours before and for at least 24 hours following intrathecal use. Motor seizures have been reported after intrathecal use, however in several of the cases, higher than recommended doses were employed. Therefore *avoid*: deviations from recommended neuroradiologic procedure or patient management; use in patients with a history of epilepsy; overdosage; intracranial entry of a bolus or premature diffusion of a high concentration of the medium; failure to maintain head elevation during procedure, on stretcher, and in bed; excessive and active patient movement or staining.

PRECAUTIONS: General—Diagnostic procedures should be carried out under the direction of personnel with the prerequisite training and a thorough knowledge of the particular procedure to be performed. Appropriate facilities should be available for coping with any complications for emergency treatment of severe reaction to the agent itself. After parenteral administration, competent personnel and emergency facilities should be available for at least 30 to 60 minutes since severe delayed reactions may occur. Preparatory dehydration is dangerous and may contribute to acute renal failure in susceptible patients. *Patients should be well hydrated prior to and following administration.* Reactions to the medium, including serious, life-threatening, fatal, anaphylactoid or cardiovascular reactions, should always be considered (see ADVERSE REACTIONS in the product package insert). Patients at increased risk include those with a history of a previous reaction to a contrast medium, a known sensitivity to iodine per se, and those with a known clinical hypersensitivity (bronchial asthma, hay fever, and food allergies). Pretesting cannot be relied upon to predict severe reactions and may itself be hazardous for the patient. A thorough medical his-

tory with emphasis on allergy and hypersensitivity prior to the injection of any contrast medium may be more predictive and accurate than pretesting. Premedication with antihistamines or corticosteroids to avoid or minimize possible allergic reactions in such patients should be considered (see CONTRAINDICATIONS). If nondisposable equipment is used, scrupulous care should be taken to prevent residual contamination.

ISOVUE (iopamidol injection)—General anesthesia may be indicated in some procedures in selected patients; however, a higher incidence of adverse reactions has been reported in anesthetized patients, which may be attributable to the inability of the patient to identify untoward symptoms, or to the hypotensive effect of anesthesia which can reduce cardiac output and increase the duration of exposure to the agent. Even though the osmolality is low compared to diatrizoate or iohalamate based ionic agents of comparable iodine concentration, the potential transitory increase in the circulatory osmotic load in patients with congestive heart failure requires caution during injection. Observe these patients for several hours following the procedure. In angiographic procedures, be aware of the possibility of dislodging plaques or damaging or perforating the vessel wall during catheter manipulations and contrast medium injection. Test injections to ensure proper catheter placement are suggested.

The inhibitory effects of nonionic contrast media on mechanisms of hemostasis have been shown, *in vitro*, to be less than ionic contrast media at comparable concentrations. For this reason, standard angiographic procedures should always be followed: angiographic catheters should be flushed frequently, and prolonged contact of blood with contrast in syringes and catheters should be avoided.

Perform *selective coronary arteriography* only in those in whom the expected benefits outweigh the procedural risk. The inherent risks of *angiocardiology* in patients with chronic pulmonary emphysema must be weighed against the necessity for performing this procedure. *Angiography* should be avoided whenever possible in patients with homocystinuria, because of the risk of inducing thrombosis and embolism.

Drug Interactions: General—Other drugs should not be admixed with iopamidol (see CONTRAINDICATIONS, and DOSAGE AND ADMINISTRATION, Drug Incompatibilities).

ISOVUE (iopamidol injection)—Renal toxicity has been reported in a few patients with liver dysfunction who were given oral cholecystographic agents followed by intravascular contrast agents. Administration of intravascular agents should therefore be postponed in any patient with a known or suspected hepatic or biliary disorder who has recently received a cholecystographic contrast agent.

Drug/Laboratory Test Interactions—PBI and radioactive iodine uptake studies will not accurately reflect thyroid function for up to 16 days following administration, however T3 resin uptake and total or free thyroxine (T4) assays are not affected.

Carcinogenesis, Mutagenesis, Impairment of Fertility—In animal reproduction studies performed on rats, intravenously administered iopamidol did not induce adverse effects on fertility or general reproductive performance. In studies to determine mutagenic activity, iopamidol did not cause any increase in mutation rates.

Pregnancy Category B—No teratogenic effects attributable to iopamidol have been observed in teratology studies performed in animals. There are, however, no adequate and well controlled studies in pregnant women. It is not known whether iopamidol crosses the placental barrier or reaches fetal tissues. Because animal studies are not always predictive of human response, this drug should be used during pregnancy only if clearly needed. Radiologic procedures involve a certain risk related to the exposure of the fetus to ionizing radiation.

Labor and Delivery: ISOVUE (iopamidol injection)—It is not known whether use during labor or delivery has immediate or delayed adverse effects on the labor, the delivery or the newborn.

Nursing Mothers—It is not known whether iopamidol is excreted in human milk. Use caution when contrast media are administered to nursing women because of potential adverse reactions; consideration should be given to temporarily discontinuing nursing.

Pediatric Use—Safety and effectiveness in children have not been established.

ADVERSE REACTIONS: ISOVUE (iopamidol injection)—Usually mild to moderate, self-limited and transient. In angiocardiology (597 patients), the adverse reactions with an estimated incidence of one percent or higher are: hot flashes 3.4%; angina pectoris 3.0%; flushing 1.8%; bradycardia 1.3%; hypotension 1.0%; hives 1.0%. Intravascular injection is frequently associated with the sensation of warmth and pain, especially in peripheral arteriography; pain and warmth are less frequent and less severe with ISOVUE than with diatrizoate meglumine and diatrizoate sodium injection. The following table of incidence of reactions is based on clinical studies with ISOVUE in about 1835 patients:

System	Adverse Reactions Estimated Overall Incidence	
	>1%	≤1%
Cardiovascular	none	tachycardia hypotension hypertension myocardial ischemia circulatory collapse S-T segment depression bigeminy extrasystoles ventricular fibrillation angina pectoris bradycardia transient ischemic attack thrombophlebitis

(continued on next page)

Adverse Reactions (continued from previous page)		
System	>1%	Estimated Overall Incidence ≤ 1%
Nervous	pain (1.7%) burning sensation (1.4%)	vasovagal reaction tingling in arms grimace faintness
Digestive	nausea (1.2%)	vomiting anorexia
Respiratory	none	throat constriction dyspnea pulmonary edema
Skin and Appendages	none	rash urticaria pruritus flushing
Body as a Whole	hot flashes (1.5%)	headache fever chills excessive sweating back spasm
Special Senses	warmth (1.1%)	taste alterations warmth in throat/ arms/chest nasal congestion visual disturbances
Urogenital	none	urinary retention

Regardless of the agent employed, overall estimated incidence of serious adverse reactions is higher with *coronary arteriography* than with other procedures. Cardiac decompensation, serious arrhythmias, or myocardial ischemia or infarction may occur during *coronary arteriography* and *left ventriculography*. Following coronary and ventricular injections, certain electrocardiographic changes (increased QTc, increased R-R, T-wave amplitude) and certain hemodynamic changes (decreased systolic pressure) occurred less frequently with ISOVUE (iopamidol injection) than with diatrizoate meglumine and diatrizoate sodium injection; increased LVEDP occurred less frequently after ventricular iopamidol injections. In *aortography*, the risks of procedures also include injury to the aorta and neighboring organs, pleural puncture, renal damage including infarction and acute tubular necrosis with oliguria and anuria, accidental selective filling of the right renal artery during the translumbar procedure in the presence of preexisting renal disease, retroperitoneal hemorrhage from the translumbar approach, and spinal cord injury and pathology associated with the syndrome of transverse myelitis. Adverse effects reported in literature include arrhythmia, arterial spasms, hematuria, periorbital edema, involuntary leg movement, malaise, and triggering of deglutition; some of these may be procedural. Other reactions due to procedural hazards include hemorrhage or pseudoaneurysms at the puncture site, brachial plexus palsy following axillary artery injections, chest pain, myocardial infarction, and transient changes in hepatorenal chemistry tests; and rarely arterial thrombosis, displacement of arterial plaques, venous thrombosis, dissection of the coronary vessels and transient sinus arrest.

ISOVUE-M (iopamidol injection)—The most frequently reported following intrathecal administration are headache, nausea, vomiting, usually mild to moderate, and musculoskeletal pain. These usually occur 1 to 10 hours after injection, almost all occurring and ending within 24 hours. Backache, neck stiffness, numbness and paresthesias, leg or sciatic-type pain occurred less frequently. Transient alterations in vital signs may occur and should be assessed on an individual basis. The following table of incidence of reactions is based on clinical studies with ISOVUE-M in about 615 patients:

Adverse Reactions		
System	>1%	Estimated Overall Incidence ≤ 1%
Body as a Whole	headache (18.1%)	pyrexia muscle weakness hot flashes malaise fatigue weakness
Digestive	nausea (7.3%) vomiting (3.7%)	diarrhea heartburn
Musculoskeletal	back pain (2.3%) leg pain (1.4%) neck pain (1.1%)	leg cramps sciatica cervicobrachial irritation meningeal irritation radicular irritation, lumbosacral other musculoskeletal pain involuntary movement burning sensation
Cardiovascular	hypotension (1.1%)	tachycardia hypertension chest pain

(continued on next column)

Nervous	none	emotional stress dizziness paresthesia confusion hallucinations lightheadedness syncope numbness cold extremities
Urogenital	none	urinary retention
Respiratory	none	dyspnea
Skin and Appendages	none	rash
Miscellaneous	none	injection site pain

Other adverse effects reported in literature include facial neuralgia, tinnitus, and sweating. Major motor seizures have been reported in the clinical literature and since market introduction in the United States. Transitory EEG changes occur and usually take the form of slow wave activity. The following adverse reactions may occur because they have been reported with other nonionic contrast agents: cardiovascular (arrhythmias); aseptic meningitis syndrome; allergy or idiosyncrasy (chills, pruritus, nasal congestion, Guillain-Barre syndrome); CNS irritation (psycho-organic syndrome: mild and transitory perceptual aberrations such as depersonalization, anxiety, depression, hyperesthesia, disturbances in speech, sight, or hearing, and disorientation; in addition, hyperreflexia or areflexia, hypertonia or flaccidity, restlessness, tremor, echoacousia, echolalia, asterixis or dysphasia have occurred). Profound mental disturbances have rarely been reported (various forms and degrees of aphasia, mental confusion or disorientation); the onset is usually 8 to 10 hours and lasts for about 24 hours without aftereffects. However, occasionally they have been manifest as apprehension, agitation, or progressive withdrawal to the point of stupor, rarely accompanied by transitory hearing loss or other auditory symptoms and visual disturbances. Also reported: persistent cortical loss of vision in association with convulsions, and ventricular block, transitory weakness in the leg or ocular muscles, *peripheral neuropathies*, including sensory and/or motor or nerve root disturbances, myelitis, persistent leg muscle pain or weakness, or sixth nerve palsy, or cauda equina syndrome, muscle cramps, fasciculation or myoclonia, spinal convulsion, or spasticity.

General Adverse Reactions To Contrast Media—Reactions known to occur (mostly mild—moderate in degree) with parenteral administration of iodinated ionic contrast agents (see the listing below) are possible with any nonionic agent. Life-threatening reactions and fatalities, mostly of cardiovascular origin, have occurred. Reported incidences of death from administration of other iodinated contrast media range from 6.6 per 1 million (0.00066%) to 1 in 10,000 patients (0.01%). Most deaths occur during injection or 5 to 10 minutes later, the main feature being cardiac arrest with cardiovascular disease as the main aggravating factor with isolated reports of hypotensive collapse and shock (est. 0.005%). Experience with iopamidol suggests less discomfort (e.g., pain and/or warmth) with peripheral arteriography. Fever changes are noted in ventricular function after ventriculography and coronary arteriography. During intrathecal use, there is a lower incidence of electroencephalographic changes as well as neurotoxicity by virtue of the intrinsic properties of the iopamidol molecule. The reported incidence of adverse reactions to contrast media in patients with a history of allergy is twice that for the general population; patients with a history of previous reactions to a contrast medium are three times more susceptible. Although most reactions to intravascular contrast agents appear within 1-3 minutes after start of injection, delayed reactions may occur (see PRECAUTIONS, General). Adverse reactions reported with other intravascular contrast agents and therefore theoretically possible with iopamidol include: *Cardiovascular*: vasodilation, cerebral hematomas, petechiae, hemodynamic disturbances, sinus bradycardia, transient electrocardiographic abnormalities, ventricular fibrillation; *Nervous*: paresthesia, dizziness, convulsions, paralysis, coma; *Digestive*: nausea, vomiting, severe unilateral or bilateral swelling of the parotid and subparotid glands; *Respiratory*: increased cough, asthma, laryngeal edema, pulmonary edema, bronchospasm, rhinitis; *Skin and Appendages*: injection site pain usually due to extravasation and/or erythematous swelling, skin necrosis, urticaria; *Urogenital*: osmotic nephrosis of proximal tubular cells, renal failure, pain; *Special Senses*: bilateral ocular irritation; lacrimation; conjunctival chemosis, infection, and conjunctivitis, perversion of taste; *Other*: neutropenia, thrombophlebitis, flushing, pallor, weakness, severe retching and choking, wheezing, cramps, tremors, and sneezing.

OVERDOSAGE—Treatment is directed toward the support of all vital functions, and prompt institution of symptomatic therapy. In myelography, even use of a recommended dose can produce mental aberrations tantamount to overdosage, if incorrect management of the patient during or immediately following the procedure permits inadvertent early intracranial entry of a large portion of the medium. Treatment is directed toward the support of all vital functions, and prompt institution of symptomatic therapy.

HOW SUPPLIED—ISOVUE-300 (iopamidol injection 61%) and ISOVUE-370 (iopamidol injection 76%) are available in cartons of ten single dose vials, and ten 100 mL single dose bottles. ISOVUE-370 is also available in cartons of ten 150 mL and ten 200 mL single dose bottles. ISOVUE-M 200 (iopamidol injection 41%) and ISOVUE-M 300 (iopamidol injection 61%) are available in cartons of ten 20 mL and ten 15 mL single dose vials, respectively.

For full prescribing information consult package insert. (J3-652D/J3-653E)

Under license from Bracco Industria Chimica S.p.A. U.S. Patent #4,001,323

© 1987 E.R. Squibb & Sons, Inc., Princeton, NJ 646-507 Issued: Jan. 1987

CIRCLE 14 ON READER SERVICE CARD

Assessing fibrosarcoma of the lower extremity

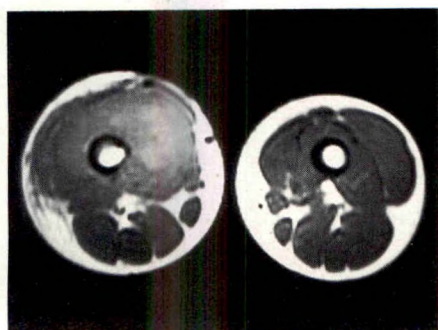


Fig. 1 Asymmetrical thighs with right bony cortical thinning and destruction evident. Abnormally low signal in right medullary cavity suggests additional bone involvement by tumor. (TR 600, TE 25)

Magnetic resonance (MR) imaging is becoming the preferred approach for diagnostic evaluation of patients with musculo-skeletal disease.

As demonstrated in these Signa system images, no other single modality can provide the same amount of comprehensive diagnostic information for tumor assessment in patients with soft tissue sarcomas of the extremities.

With its multiplanar imaging capability, the Signa system permits acquisition of critical data needed for limb salvage and extirpative procedures, as seen in the following case study.

Case study

A 22-year-old male presented to an orthopedic surgeon with progressive pain and swelling over the right thigh one year after surgical resection and radiation treatment for a fibrosarcoma.

A CT study showed recurrent tumor without bone involvement, and a radionuclide bone scan was normal.



Fig. 2 Disease clearly involves mid thigh both medially and laterally. Bone marrow involvement is obvious in at least two sites. (TR 1500, TE 75)

The patient was then referred to a Signa user for an MR exam. An axial image of the right thigh (Fig. 1) demonstrated a bulky mass involving both medial and lateral compartments. A coronal image (Fig. 2) revealed recurrent tumor and clear evidence of bone involvement. An additional axial image (Fig. 3) suggested patency of the vascular bundle of the thigh.

Based on this information, a right hip disarticulation was performed.

Tumor assessment

MR imaging established the extent of disease, suggested its proximal extension, and unquestionably demonstrated local extension of disease into the adjacent bone. Due to its multiplanar capabilities, magnetic resonance is a more efficient methodology for assessment of local tumor extent in patients with soft tissue sarcomas of the extremities.

Acknowledgement: Allan M. Haggar, M.D., George Schkudor, M.D., Jerry W. Froelich, M.D., Div. of Nuclear Magnetic Resonance Imaging, Dept. of Diagnostic Radiology, Henry Ford Hospital, Detroit, MI.

Signa... the MR reference point

For referring physicians of all specialties, Signa sites are the reference point for optimal image quality across the broadest range of applications.

The Signa system provides clinical flexibility and technological superiority to help assess tumor extent where no contour-deforming abnormalities are present in musculoskeletal disease.

To receive a detailed discussion of the case presented here, call General Electric at 1-800-624-5692 and request MR Clinical Symposium No. 7111. We will also be glad to provide a list of the Signa sites in your area.

CIRCLE 3 ON READER SERVICE CARD

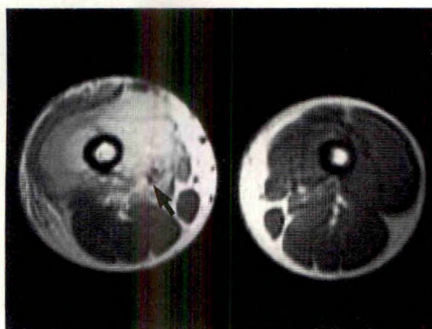


Fig. 3 Mass extends to posterior compartment. Normal flow void effects indicate vascular patency (arrow). (TR 2000, TE 30)





The Case For Quality

- Patient:** 60-year-old male with palpable abdominal mass.
- Diagnosis:** Abdominal aortic aneurysm.
- Treatment:** Surgical aorto-bifemoral bypass.
- Considerations:** Abdominal aortogram requires high contrast flow for maximum filling. Superior visualization of the aorta. Tail catheter must retain shape during injection for safe delivery of large contrast bolus.
- Catheter Selected:** 5 French Medi-tech High Flow pigtail catheter, 65 cm. One of the complete line of Flow Angiographic Catheters for routine and selective studies, combining advanced technology with strict clinical standards of quality and reliability.



Medi-tech, Incorporated
480 Pleasant Street
P.O. Box 7407
Watertown, Massachusetts 02272
(617) 923-1720 Telex 922-453

Ordering Information (800) 225-3238

CIRCLE 11 ON READER SERVICE CARD

© 1986 Medi-tech, Inc.

Radiograph courtesy of Michael E. Jay, M.D.,
Harvard Medical School

Aubrey O. Hampton Lecture

Subspecialization in Radiology: Response to a Need

Juan M. Taveras¹

This discussion comes at a time when many changes in medical care and medical practice are taking place, and these changes may well continue to occur for a number of years into the future. Rather than attempt to predict the final outcome, I shall limit my remarks to some of the historic developments that brought radiology to its present state regarding subspecialization and how the current changes may affect subspecialization in the future.

My career is entangled with the development of subspecialization in radiology. For that reason, a few comments related to the birth and growth of my own thinking in this area are included in this discussion without any intention of self-aggrandizement or claim of exclusivity in the development of subspecialization in radiology.

After completion of my training in general radiology at the Graduate Hospital of the University of Pennsylvania in Philadelphia in 1950, I accepted a position as an assistant attending radiologist at the Columbia Presbyterian Medical Center. I was lucky to be the first person exposed to a new program started by the chairman of radiology, Ross Golden, in which a junior staff appointee was able to spend 6 months in four different areas over a period of 2 years. Thus, I was assigned to pediatric radiology under John Caffey at Baby's Hospital, neuroradiology with Ernest Wood at the Neurological Institute, radiation therapy, and general radiology. After Dr. Wood accepted the position of chairman of the Department of Radiology at the University of North Carolina at Chapel Hill in 1952, I was asked to become head of neuroradiology at the Neurological Institute. For the next 3 years I was full-time radiologist at the Neurological Institute and became well

acquainted with all the problems involved in diagnosing diseases of the brain and spinal cord. It was obvious to me that I had learned tremendously over the preceding 3 years and that I was head and shoulders above general radiologists in dealing with radiology of the nervous system. Thus, when I was asked by Harold Jacox, the acting director of the Department of Radiology, to be in charge of the general radiology section at Presbyterian Hospital until the arrival of the newly appointed chairman, William B. Seaman, I accepted the challenge, provided that it was limited to 1 year and that I would be allowed to organize the department in my own way. As soon as I arrived there in 1955, I initiated a subspecialty approach that included establishing separate pulmonary, skeletal, and gastrointestinal radiology services. The Presbyterian Hospital can take credit for being the first hospital in the United States to have radiology organized along subspecialty lines.

Ten years later in 1965, I accepted the chairmanship of the Department of Radiology at Washington University School of Medicine and the directorship of the Mallinckrodt Institute of Radiology because I thought I had a message for the specialty of radiology in the United States. This message was the need to subspecialize, and I wanted an opportunity to develop a model to accommodate these ideas.

Development of Subspecialization in Medicine

Before the 19th century, medicine was a whole. All physicians did everything (with the exception of some surgical

Received July 14, 1986; accepted after revision October 3, 1986.

Presented as the 19th Aubrey O. Hampton Lecture at Massachusetts General Hospital, Boston, April 4, 1986.

¹ Department of Radiology, Massachusetts General Hospital, 32 Fruit St., Boston, MA 02114. Address reprint requests to J. M. Taveras.

procedures carried out, in the very early period, by trained "barbers").

In the 19th century, when scientific medicine really started, the following happened: (1) Pathology received increasing attention and clinical-pathologic correlation began in earnest. (2) Pasteur discovered pathologic organisms. (3) Antisepsis and asepsis were introduced. (4) Anesthesia was discovered and applied. (5) Laboratory diagnosis began. (6) X-rays were discovered.

In the first quarter of the 20th century, advances in medical knowledge and technology opened new approaches for diagnosis and treatment. These complexities created a need for specialization. In surgery, the subspecialties were ophthalmology, otolaryngology, neurosurgery, orthopedics, urology, plastic and reconstructive surgery, and obstetrics and gynecology. In medicine, they were neurology, psychiatry, and pediatrics.

The creation of boards to certify these specialists soon followed because of the needs to (1) determine who was qualified to carry out the specialized procedures, (2) define standards of training, and (3) grant the authority to various institutions to provide the training. The first board was in ophthalmology in 1917, followed by otolaryngology in 1924 and obstetrics and gynecology in 1930. The Board of Internal Medicine was established in 1936, and subspecialties in medicine began to develop shortly thereafter. Now there are 10 recognized subspecialties of medicine (Table 1).

Development of Subspecialization in Radiology

After the discovery of the roentgen ray in 1895, the first 30 or 35 years were an important period of development. General radiologists did their utmost to expand knowledge and to improve techniques. The first subspecialty of diagnostic radiology was neuroradiology. The first full-time neuroradiologist in the United States was Cornelius Dyke, who, during his radiology residency at the Peter Bent Brigham Hospital in Boston, Massachusetts, was exposed to Harvey Cushing's rich neurosurgical material. After completion of his residency, he became head of radiology at the Neurological Institute of

New York in 1929. His contributions are classic and numerous but, unfortunately, he died in 1943 at the young age of 42, at the height of his professional career. The second subspecialty of radiology was pediatric radiology. Dr. John Caffey, a pediatrician who became a pediatric radiologist, was a pioneer in this field. Radiation therapy was also emerging as a subspecialty. However, it was progressing more slowly than it should have if we consider how fundamentally different diagnostic and therapeutic radiology are. As was the case with the subspecialties in diagnostic radiology, radiation therapy could not develop its full potential until it was no longer dominated by general radiologists. This delay was unfortunate and greatly slowed the development of therapeutic radiology in the United States.

Diagnostic radiology received a tremendous boost beginning in the 1950s with the development of nuclear radiologic procedures, the introduction of the Seldinger technique for angiography, and progress in sonographic instrumentation [1-3]. During the decade of 1960-1970, great advances in angiography, nuclear medicine, and sonography took place. In addition, during that period Charles Dotter set the foundation for interventional radiology [4, 5].

In the decade of 1970-1980, the most important development was the revolutionary discovery of CT by Godfrey Hounsfield [6] in 1972. Shortly thereafter, the possibility of using MR to generate images was suggested by Lauterbur in New York, and positron emission tomography was described by Ter-Pogossian in St. Louis [7-9]. Thus, the 1970s can be regarded as the decade of imaging developments.

Now, in the 1980s, we are witnessing continued rapid progress in all of these areas, particularly in MR imaging as well as in consolidation of knowledge regarding sonography, CT, scintigraphy, and interventional procedures.

Loss of Cardiac Radiology and Nuclear Medicine to Radiology

Progress in technology, including methods for vascular catheterization and its increased use in the late 1950s, led to the development of the subspecialty of vascular radiology

TABLE 1: American Specialty and Subspecialty Boards and Year Accepted

Medicine	Pediatrics	Surgery
Internal medicine (1936)	Pediatrics (1933)	Ophthalmology (1917)
Cardiovascular diseases (1940)	Cardiology (1959)	Otolaryngology (1924)
Gastroenterology (1940)	Hematology/oncology (1973)	Obstetrics and gynecology (1930)
Pulmonary diseases (1940)	Nephrology (1973)	Colon-rectal surgery (proctology) (1934)
Allergy/immunology (1971)	Neonatal/perinatal medicine (1974)	Orthopedics (1935)
Endocrinology/metabolism (1972)	Endocrinology (1977)	Urology (1935)
Hematology (1972)	Pulmonary diseases (1984)	Surgery (1937)
Infectious disease (1972)	Critical care (1985)	Neurosurgery (1940)
Nephrology (1972)		Plastic surgery (1941)
		Thoracic surgery (1950)
Rheumatology (1972)		
Oncology (1973)		

(also called cardiovascular radiology). Starting then, a need for subspecialization in cardiac radiology and cardiac angiography existed, but unfortunately no effort was made to train radiologists in this area. Despite seminal advances made in the field by radiologists such as Steinberg, Dotter, and others [10-12], cardiologists took over cardiac radiology, because chiefs of radiology in academic institutions did not support postresidency training. Probably radiology will never recover any significant portion of this subspecialty.

The development of nuclear medicine required special effort and dedication. Early on, chairmen of departments of radiology failed to recognize the need or, in some cases, refused to accept responsibility for development of nuclear medicine facilities. The result was that internists and pathologists organized divisions of nuclear medicine. Later they applied considerable pressure to the specialty of radiology, which resulted in the radiologists agreeing to form a conjoint board, the American Board of Nuclear Medicine. The outcome was that radiology lost a significant portion of nuclear medicine and now controls only about two-thirds of nuclear medicine departments in the United States. Later, the American Board of Radiology created a special competence certificate in nuclear radiology. Radiology will not recover those nuclear medicine departments that are now functioning outside radiology departments.

Subspecialization Based on Specific Techniques

The rapid technological progress made in sonographic instrumentation led to the need to acquire special expertise in this area. I believe that sonography is an important tool for all radiologists and that all subspecialists should be trained to use it. Some, however, believe that sonography should be a separate subspecialty within radiology. I am opposed to any subspecialization based on an instrument. Nevertheless, individuals are needed who can coordinate the efforts of a department while, at the same time, permitting access and collaboration with the organ-oriented subspecialists.

Progress in interventional radiology has led to the need for further subspecialization. Organ orientation here is even more important in order to carry out research and to perform therapeutic procedures based on thorough knowledge of the anatomy, physiology, and pathology of the organ system involved.

The development of CT attracted immediate attention from all radiologists and provided another temptation for radiologists to subspecialize according to a specific procedure. MR presents the same dilemma. I believe, however, that in a manner similar to nuclear medicine, MR presents a variety of challenges, including the need for paramagnetic agents and the possibility of *in vivo* spectroscopy, which will require a large amount of research and development in the next 5-10 years. This will justify the dedication of some radiologists (as well as physicians and scientists from other fields) to MR in general. This specialization, however, should be coupled with the organ-system orientation by which organ-system specialists do clinical MR imaging in their respective areas of interest.

Subspecialization by Organ System

From the beginning, the American Board of Radiology examined candidates in subspecialty areas (bone, chest, gastrointestinal system, genitourinary system, and neuroradiology). This later was expanded more than once, so that now candidates are examined in nine subspecialties. Up until about 1970, if anyone was considered a subspecialist in radiology, he was asked to be an examiner in another organ system. For instance, I was asked to be an examiner in genitourinary radiology for 3 years, until 1970, when I indicated that I would not continue to be an examiner at the Board unless it was in neuroradiology. Now, subspecialists are usually asked to be examiners in their areas of special expertise.

I believe that subspecialization strictly following an organ-system approach is the only rational approach. The best example is neuroradiology. In most teaching hospitals in the United States, the neuroradiologist carries out all the noninvasive as well as the invasive procedures related to the nervous system. Because of the special knowledge of anatomy and pathology of the nervous system that is required, neuroangiography is also done by neuroradiologists. The subspecialties of gastrointestinal and genitourinary radiology should include the classic radiographic and fluoroscopic procedures, sonography, CT, and abdominal interventional procedures of various types but should exclude angiography.

The vascular system is an organ system and is well represented by a surgical specialty. The exception made for neuroradiology is usually sanctioned by vascular surgeons. Neurosurgeons perform all vascular procedures that involve the nervous system, often also including the vessels in the neck supplying the brain.

The organ-oriented, fully trained, subspecialized radiologist not only has special interpretive skills but also can safely perform all invasive diagnostic and interventional procedures in his subspecialty. He works closely with the clinical specialists who are involved with the same organ-system, creating the team approach that leads to improved patient care. This is not achieved by radiologists who are technique-oriented subspecialists.

Training Programs

Increasingly, residency training is being organized around the subspecialties. There is still a need for teachers who are general radiologists, but the resident will learn the most up-to-date information and technology, if taught by subspecialists throughout most of the training period. The exposure to subspecialists encourages residents to achieve a higher degree of expertise in each area of radiology and to seek fellowships after residency. The job market is becoming increasingly subspecialized and is forcing the young radiologist to seek subspecialty training.

To determine the present status of subspecialization in teaching hospitals in the United States and Canada, I conducted a survey of 92 university and 12 nonuniversity hospitals (Tables 2-4). Seventy-five university and 10 nonuniversity hospitals responded. Of these, 79 indicated that their depart-

TABLE 2: Subspecialization in Radiology Departments

Subspecialty	No. of Hospitals		No. with Staff		No. with Fellowship Training ^a	
	UH	Non-UH	Separate	Interchange	UH	Non-UH
Nuclear medicine	75	10	70	11 ^b	24	2
Neuroradiology	76	7	64	8 ^c	49	3
Pediatrics	62	2	49	11	16	1
Vascular	67	6	53	13	13	1
Chest	56	5	23	37	6	0
Cardiac	42	4	22	22	8	1
Skeletal	58	4	31	30	4	1
Gastrointestinal	54	7	26	35	3	0
Genitourinary	48	6	22	32	4	0
Abdominal (including GI, GU)	24	1	8	17	13	0
Diagnostic oncology and breast imaging	37	4	20	21	1	0
Breast imaging only	4					
Interventional ^d	59	4	44	15	17	0

Note.—UH = university hospital, GI = gastrointestinal, GU = genitourinary.

^a 33 institutions offer fellowships in CT/sonography, 21 in MR, and 19 in sonography only. Some do not offer fellowships. A total of 59 university hospitals and 9 nonuniversity hospitals offer some fellowship training.

^b Some are free-standing departments of nuclear medicine.

^c Some did not comment on staff interchange.

^d Some with angiography, some with GU, and some with sonography.

TABLE 3: Number of Hospitals with Recognized Subspecialties in Radiology

Year	UH	Non-UH	Year	UH	Non-UH
1956	1	0	1974	1	0
1963	1	0	1975	11	2
1965	3	0	1976	4	1
1968	3	0	1977	2	0
1969	1	0	1978	9	2
1970	11	0	1979	2	0
1971	2	1	1980	7	1
1972	2	1	1981	3	1
1973	1	0	1982	6	0
			1983	3	0

Note.—83 answers were received. Year = year recognized. UH = university hospital.

ment was divided into subspecialty areas, four indicated that it was not, and two did not answer the question. The years in which these departments recognized subspecialization are given in Table 3. The rate of this recognition accelerated after 1969.

Table 4 presents data concerning whether sonography, CT, MR, and interventional radiology are regarded as subspecialties by the hospitals queried. The reasons given for creation of a specific subspecialty area varied: Sometimes it was based on personal philosophy, but, more often, it was due to peculiarities within the department (e.g., the number of examinations, the need for economy, or simply the ease of organization).

The question as to which subspecialties work best was not answered completely, but the subspecialties given and the number of times that they were mentioned were neuroradiology, 53; pediatrics, 31; nuclear medicine, 22; vascular radiology, 15; and chest radiology, 14. The technical areas that worked best were CT/sonography, 14; sonography, 11; and interventional radiology, 15.

TABLE 4: Responses to Questionnaire on Non-Organ-System Subspecialization

Question	Answer		
	Yes	No	No Opinion
Do you believe CT is a subspecialty?	16	69	0
If you believe CT is a specialty is it:			
a. For ease of organization?	15	1	0
b. For economic or department reasons?	13	3	0
c. Because organ approach unnecessary?	9	7	0
d. Organ-system approach too expensive?	5	11	0
e. Not enough patients in each area in my department?	9	7	0
Is ultrasound a subspecialty?	45	38	2
Is MR a subspecialty?	29	54	2
Is nuclear medicine a subspecialty?	75	9	1
Is interventional radiology a separate subspecialty?	47	37	1
a. Should be done by organ-system specialists?	42	38	5
b. Should be attached to cardiovascular radiology?	36	47	2

Note.—85 hospitals responded. Answers were not separated for university and nonuniversity hospitals.

What Can We Expect in the Future?

At present at the Massachusetts General Hospital radiology department, we have relatively few general radiologists and many more subspecialists. As in internal medicine, the generalist in radiology has a real place. For instance, in an ambulatory setting or in an emergency room, use of general radiologists is more economical. However, tertiary referral hospitals require physicians who have an in-depth knowledge

in the various medical and surgical specialties. Also, in teaching hospitals where there is the responsibility to advance knowledge, subspecialists are necessary to do research, write papers and books, and deliver lectures at continuing education courses. Thus, in tertiary hospitals the tendency for subspecialization in radiology will accelerate in the future.

An important goal is to prevent erosion of radiology by specialists in other fields, such as urology, orthopedics, neurology, and cardiology. This can be achieved only if radiologists have thorough and up-to-date knowledge of all radiologic subspecialties. We certainly will not be able to maintain control by knowing less—relatively or absolutely.

In internal medicine departments, the divisions or sections (e.g., cardiology, pulmonary medicine, gastroenterology, nephrology) are virtually independent units, although a single chairman represents them in the hospital and medical school. In surgery, the divisions are even stronger and more independent, but most are still represented by a single chairman. In radiology, more interdependence exists among the various subspecialties, in part because of the costly equipment that must be shared, and I doubt that the independence of subspecialties will ever equal that of the subspecialties of medicine and surgery.

Radiologic knowledge continues to grow, and with it the expectations of the physicians and surgeons for whom we consult. They respect us as radiologic consultants only in proportion to the help they get from us, and in proportion to the extent that our knowledge and powers of observation surpass theirs. For instance, I believe that an abdominal surgeon may be perfectly happy to accept the opinion of the general radiologist regarding problems that his patient may have involving the brain or lungs, but I doubt that the neurosurgeon or the pulmonologist consulting on the case would be equally satisfied. The latter find themselves knowing as much as, and often more than, the general radiologist about the imaging studies in their specialty, and thus they seek the subspecialist radiologist for a more informed analysis.

The tendency in radiology today, and this is expected to increase in the future, is toward performing less invasive diagnostic procedures. This is a change from the 1960s when radiology was becoming progressively more invasive. The change occurred with the introduction of CT and improvements in sonographic instrumentation. Now MR will have a similar effect. The reduced invasiveness will make it easier for physicians from other specialties to claim sufficient knowledge in their own fields to undertake imaging interpretations on their own.

Thus, obstetrician-gynecologists claim sonographic expertise. Neurologists claim sufficient knowledge of anatomy and pathology of the brain to interpret the cross-sectional images of CT and MR and apply for hospital privileges or acquire their own instruments. Chest physicians claim the same and usually acquire X-ray units in their offices, and the latter practice is widespread among internists. However, the same groups would never attempt to carry out the invasive procedures such as angiography, which today are carried out less frequently than in the past.

Unfortunately, many radiologists are convinced that they,

and only they, are entitled to carry out and interpret these procedures because they or their departments own the equipment. This is a tenuous and nearly fallacious argument that will not survive. The only way that interpretation of diagnostic imaging procedures by nonradiologists can be effectively counteracted is through competence of the radiologists.

For several years, radiologists in private practice have affiliated themselves in radiologic groups, and these groups continue to grow. Ronald Evens (personal communication) believes that the number of these groups will decrease as their size increases. This will provide an opportunity for patients in community hospitals to benefit from subspecialization.

Strengthening subspecialization in radiology in the United States is necessary to improve the quality of radiologic care. Furthermore, it is the only way to prevent gradual penetration of the field by nonradiologists. Future advances in the field will not be provided by the general radiologist or by nonradiologists, but by the subspecialists. These are the ones who, because of their in-depth knowledge in specific areas, are capable of finding solutions to problems peculiar to individual organ systems.

I believe that the accelerated development of subspecialization in radiology that we have been witnessing in the last decade and a half is a *response to a need* and that it is important for all radiologists to support rather than impede this development. Until now radiology has not taken an official step to recognize subspecialties, but, as can be seen from the foregoing, it can be expected that the strong trend towards subspecialization will continue and will gain strength, thus commanding more attention from the certifying bodies.

REFERENCES

1. Moore GE. Use of radioactive di-iodofluorescein in the diagnosis and localization of brain tumors. *Science* 1948;107:569-571
2. Seldinger SI. Catheter replacement of needle in percutaneous arteriography, a new technique. *Acta Radiol* 1953;39:368-376
3. Leksell L. Echo-encephalography: detection of intracranial complications following head injury. *Acta Chir Scand* 1956;115:255-259
4. Dotter CT, Judkins MP. Transluminal treatment of arteriosclerotic obstruction: description of a new technique and a preliminary report of its application. *Circulation* 1964;30:654-670
5. Dotter CT, Judkins MD. Percutaneous transluminal treatment of arteriosclerotic obstruction. *Radiology* 1965;84:631-643
6. Hounsfield GN. Computerized transverse axial scanning (tomography). Part I. Description of system. *Br J Radiol* 1973;46:1016-1022
7. Ter-Pogossian MM, Phelps ME, Hoffman EJ, Mullan NA. A positron emission transaxial tomograph for nuclear imaging (PETT). *Radiology* 1975;114:89-98
8. Lauterbur PC. Image formation by induced local interactions: examples employing nuclear magnetic resonance. *Nature* 1973;242:190-191
9. Hinshaw WS, Bottomley PA, Holland GN. Radiographic thin-section imaging of the human wrist by nuclear magnetic resonance. *Nature* 1977;270:722-723
10. Robb GP, Steinberg I. Visualization of the chambers of the heart, the pulmonary circulation, and the great blood vessels in man: practical method. *AJR* 1939;53:432-438
11. Steinberg I, Dotter CT. The differentiation of mediastinal tumor and aneurysm: value of angiocardiology. *Brit J Radiol* 1949;22:567-572
12. Steinberg I, Dotter CT, Andrus W De W. Angiocardiology in thoracic surgery. *Surg Gynecol Obstet* 1950;90:45-59

Book Review

Atlas of Fetal Sectional Anatomy: With Ultrasound and Magnetic Resonance Imaging. By G. Isaacson, M. D. Mintz, and E. S. Crelin. New York: Springer-Verlag, 184 pp., 1986. \$87

Photographs and corresponding line drawings of fetal gross specimens illustrated in cross-section form the foundation of this atlas. MR and/or sonographic images accompany gross sections. Fetal specimens for gross section and MR images are from therapeutically or spontaneously aborted second and third trimester fetuses; sonographic images are from in utero studies. The work illustrates axial, sagittal, and/or coronal sections through the fetal head and neck, trunk, abdomen, pelvis, and extremities. Special sections on development of the brain, anatomy of the ductus venosus, and fetal heart are included. The book contains no text except for a technical description of the materials and methods employed in specimen fixation, photography, and image production.

Photographs of the gross fetal sections are black and white and are of excellent quality. A line drawing accompanies each gross section. Important anatomic structures are generously labeled on the line drawing, eliminating the distraction of applying labels to the photographs of gross specimens. MR images obtained at levels corresponding to gross fetal specimens are of generally good quality.

Sonographic images obtained from in utero studies accompany some of the gross fetal specimens, but their quality is inconsistent. The authors indicate that the text is intended to represent a comprehensive reference for normal fetal cross-sectional anatomy, correlated with in utero sonographic images. While the gross sections and line drawings are well photographed and labeled, sonographic correlation

represents the least useful aspect of this atlas. The work could be improved by inclusion of more correlative sonographic images.

Sectional anatomy of the fetal head and neck is shown on specimens of 20, 24, 30, and 38 weeks of gestation. All illustrations of the fetal thorax, abdomen, and pelvis are of 20-week fetuses. A section on development of the fetal brain attempts to address anatomic changes that are reflected in advancing gestational age. Gross specimens from 20-, 24-, 30-, and 38-week fetuses are presented; however, a broader spectrum of fetal specimens and a more detailed study of each gestational stage would improve the reader's understanding of fetal brain development. Similarly, readers desiring a comprehensive review of fetal heart anatomy will be disappointed by the limited sections available. References for fetal anatomy are not cited. The index is complete and useful for locating specific anatomic structures.

This book is directed to radiologists interested in imaging fetuses. The atlas does not take full advantage of the opportunity to show the spectrum and detail of fetal anatomy available with current sonographic equipment. Nonetheless, photographs of gross fetal sections are of excellent quality and sufficient in themselves to warrant use of this text as a reference by fetal imagers.

Donald A. Cubberley
University of Utah Sciences Center
Salt Lake City, UT 84132

Imaging in Acute Renal Infection in Children

John R. Sty¹
Robert G. Wells
Robert J. Starshak
Bruce A. Schroeder

Infection is the most common disease of the urinary tract in children, and various imaging techniques have been used to verify its presence and location. On retrospective analysis, 50 consecutive children with documented upper urinary tract infection had abnormal findings on renal cortical scintigraphy with ^{99m}Tc-glucoheptonate. The infection involved the renal poles only in 38 and the poles plus other renal cortical areas in eight. Four had abnormalities that spared the poles. Renal sonograms were abnormal in 32 of 50 children. Excretory urograms were abnormal in six of 23 children in whom they were obtained. Vesicoureteral reflux was found in 34 of 40 children in whom voiding cystourethrography was performed. These data show the high sensitivity of renal cortical scintigraphy with ^{99m}Tc-glucoheptonate in documenting upper urinary tract infection. The location of the abnormalities detected suggests that renal infections spread via an ascending mode and implies that intrarenal reflux is a major contributing factor.

Infection is the most common disease of the urinary tract in children, and the evaluation of such infections is the most common reason for imaging of the urinary tract. Uncomplicated acute renal infection does not require imaging for diagnosis if the clinical presentation and laboratory data are diagnostic. However, diagnostic difficulties occur because of the diverse manifestations in children of different ages: (1) obstructive uropathy and sepsis in neonates, (2) specific systemic manifestations in infants with vesicoureteral reflux, (3) cystitis in preschool children, (4) asymptomatic recurrent bacteriuria after an initial symptomatic infection in school-aged girls, and (5) frequency-dysuria syndrome in sexually active teenage girls [1].

Diagnostic evaluation of acute renal infection must be tailored to the existing signs and symptoms, with careful selection from the many techniques available. These include excretory urography, renal sonography, CT, and renal cortical scintigraphy with ^{99m}Tc-glucoheptonate.

We investigated the sensitivity of renal cortical scintigraphy with ^{99m}Tc-glucoheptonate in localizing acute renal infection and compared the results to those obtained from renal sonography, excretory urography, and CT.

Materials and Methods

A retrospective analysis of 50 consecutive children who had renal imaging for acute renal infection was performed at Children's Hospital of Wisconsin. All had systemic illness and had been hospitalized for management of their diseases. They had had symptoms for 2 to 5 days before the examinations. Renal cortical scintigrams and renal sonograms were obtained for all 50 patients. Additionally, CT scans were obtained for four and excretory urograms for 23. All comparative examinations were performed within a 48-hr period. The 16 boys and 34 girls ranged in age from 2 months to 16 years (median age, 3.5 years). None had obstructive uropathy or required surgery. Children with the clinical diagnosis of renal infection were not included if comparative imaging studies had not been performed.

Renal cortical scintigraphy was performed with ^{99m}Tc-glucoheptonate, 6 mCi/1.7m² (222 MBq/1.7m²), with a minimum dose of 2.0 mCi (74 MBq). The imaging sequence was 1, 2, 3,

Received April 22, 1986; accepted after revision September 15, 1986.

¹ All authors: Department of Radiology, Children's Hospital of Wisconsin, 1700 W. Wisconsin Ave., P.O. Box 1997, Milwaukee, WI 53201. Address reprint requests to J. R. Sty.

AJR 148:471-477, March 1987
0361-803X/87/1483-0471
© American Roentgen Ray Society

6, 9, 12 and 15 min. Two- to 4-hr delayed images were also obtained. Most delayed images included posterior oblique views in addition to the posterior image. Collimator selection was based on patient size. The scintillation cameras used for the examinations were Siemens LEM, Siemens 3700 ZLC, or a Siemens PhoGamma V; 500,000 counts were obtained on the delayed images.

Sonography was performed with an ATL Neurosector real-time imaging system. A 5.0-MHz transducer was used for most children and a 7.5-MHz transducer for infants. Excretory urography was performed with 2 ml/kg of 50% Hypaque (Winthrop-Breon, New York, NY). Radiographs were obtained of the upper abdomen at 2 min and of the entire abdomen at 8 min. In selected cases, coned or full abdominal oblique projections were obtained. Tomography was not performed. CT with either the GE 8800 or 9600 scanner consisted of continuous 10-mm sections acquired dynamically after bolus injection of 2 ml/kg of Renografin-60 (Squibb, Princeton, NJ).

Results

All 50 patients had positive findings on renal cortical scintigraphy and a discharge diagnosis of upper urinary tract infection. Typical scintigraphic abnormalities were polar photopenic defects in 38 children, scattered photopenic areas including the polar areas in eight, and abnormalities in areas other than the polar regions in four. The latter ranged from mildly decreased tracer accumulation to total tracer absence. The shape of the defect was variable. A few children had abnormalities on early imaging sequences that included poor function (delayed appearance of tracer) and subtle photon-deficient regions. Children in this group had the largest defects seen on delayed 2-hr images.

Sonographic findings were abnormal (diffuse, multifocal, or focal) in 32 of 50 children. These lesions were either hyper- or hypoechoic, with loss of cortical medullary definition. All children with abnormal sonograms had abnormal scintigrams. However, sonography showed no abnormalities in 18 children with clearly abnormal findings on renal cortical scintigraphy. Excretory urograms showed signs of renal infection in six of 23 children. All six had abnormal sonograms and scintigrams. All four children studied with CT had abnormal CT scans, sonograms, and scintigrams. Voiding cystography was performed on 40 children after the first diagnostic evaluation, 1 week to 4 months (average, 1 month) after the first infections. Thirty-four of these had vesicoureteral reflux.

Discussion

Urinary tract infection is defined as a bacterial infection of the renal parenchyma, bladder, or urethra, singly or in combination. The combination of renal parenchymal and pyelocaliceal inflammation is pyelonephritis. Distinguishing between upper and lower urinary tract infections on purely clinical grounds and, in some cases, determining that the infection is localized to the urinary tract can be difficult. Localization of infection within the urinary tract is important because of the potential for renal parenchymal damage that is associated with upper urinary tract disease.

Bacterial pyelonephritis may occur via an ascending route; that is, infection begins in the urinary bladder and ascends to

the kidney. Another route may be via the subepithelial lymphatic channels of the bladder and ureter and hence into the renal interstitium. Abnormal conditions such as neurogenic bladder, altered host resistance, and urinary tract obstruction may be either predisposing or pathogenetic factors in urinary tract infection. Hematogenous infection of the kidney is seen most commonly in the neonates.

Children of different ages have different diagnostic signs and symptoms. In neonates, urinary tract infections frequently cause nonspecific systemic illness. Bacteremia occurs in approximately 30–40% and can lead to life-threatening sepsis and meningitis. In patients 1 month to 2 years old, nonspecific systemic manifestations are still the preponderant findings; however, sepsis and severe illness are less common. Bacteremia is found in less than 20% in this age group [2–4].

In ambulatory patients younger than 2 years old who have fever only, urinary tract infection is a common cause. In one multicenter study, eight (7%) of 108 febrile girls and none of 85 febrile boys had urinary tract infection [5]. However, a study from an outpatient practice reported urinary tract infection in 19% of 156 children of all ages with fever. If abdominal pain was an added symptom, the percentage rose to 31 [6].

In preschool and school-age children, dysuria is a frequent symptom. Other associated findings include abdominal or flank pain, enuresis, fever, and foul-smelling urine. The systemic illness often seen in infants is unusual in this age group. Still, problems in diagnosis exist. Two-thirds or more of preschool and school-age children with symptoms of typical lower urinary tract infection may not have bacteriuria of more than 10^5 organisms/ml. Possible explanations for dysuria in this age group include vaginitis, urethritis, and urinary tract infections associated with low colony counts or due to difficult-to-culture urinary pathogens [7].

Invasive bladder washout and ureteral catheterization studies have demonstrated the presence of bacteria in the renal collecting systems of as many as 20% of children with urinary tract infection who have no clinical signs or symptoms of renal involvement. These children presumably are at risk for significant renal damage [8–10]. These data indicate the need for accurate noninvasive methods to determine if infections are localized to the upper or lower urinary tracts.

Information gained from the history and physical examination, laboratory studies, and radiologic imaging all can be used to determine localization of urinary tract infections. Laboratory methods include urinalysis, urine cultures, colony counts, chemical tests for detection of bacteria, and specific localizing studies.

Localizing studies with antibody-coated bacteria are valuable in adults but do not correlate accurately with upper urinary tract involvement in children [11, 12]. Serum levels of C-reactive protein correlate well with clinical, but not occult, renal infection. Assays for urine lactate dehydrogenase are difficult to perform, and the results may or may not correlate well with renal bacteriuria [13, 14]. Other tests, such as serum antibodies to Tamm-Horsfall protein and urine lactic acid levels, have been suggested for renal infection, but these need further evaluation [15, 16].

Excretory urography can be used to assess the morphology

of the urinary tract if renal function is adequate. It is often suboptimal in infants because the glomerular filtration rate is low in neonates and the kidneys are often obscured by overlying bowel gas.

Approximately 20 to 25% of patients with acute renal infection have suggestive findings on excretory urography. These findings include ileus or dilatation of the ureter, loss of visualization of a portion of renal outline, diffuse renal enlargement, a focal renal mass, diminished pyelogram, and an altered nephrogram (Fig. 1). The primary reason for performing excretory urography in children suspected of having an acute renal infection is to define abnormalities caused by previous urinary tract infection and to exclude hydronephrosis. The latter is best studied with renal sonography. Excretory urography can be used to evaluate renal cortical scarring and pelvocaliceal and ureteral anatomy, but it is often insensitive in detecting acute renal infection [17, 18]. In our group of patients, only 26% had urographic findings of acute infection.

Renal sonography is useful in complicated renal infections such as abscesses, pyonephrosis, and perinephric fluid collections. Technical improvements permit diagnosis of both focal and diffuse renal infection in many cases [19]. In our

study, six children had abnormal findings on both excretory urography and sonography. An additional 17 had abnormal findings on sonography but normal findings on urography.

Sonography is a sensitive imaging technique for identifying renal enlargement in diffuse renal infection; however, normal variation in renal size makes interpretation difficult. Reliable sonographic findings in diffuse infection include (1) decreased parenchymal echogenicity and increased renal sound transmission (Fig. 2), (2) minimal renal pelvis dilatation reflecting atony, (3) loss of normal cortical medullary differentiation, and (4) rarely, increased echogenicity.

Focal pyelonephritis or lobar nephronia is a localized infection without major suppuration that usually appears as a mass on sonography (Fig. 3). The borders of the mass are usually poorly defined, and there is focal loss of the regional cortical medullary differentiation. The abnormal focus can be relatively anechoic with low-level echoes or can be more echogenic than the kidney. If this process extends to the renal capsule, a bulge in the renal contour will be seen [20]. This abnormality could be misinterpreted as a neoplasm if the sonographic findings are not correlated with the clinical presentation.

CT offers a sensitive means of evaluating the renal paren-

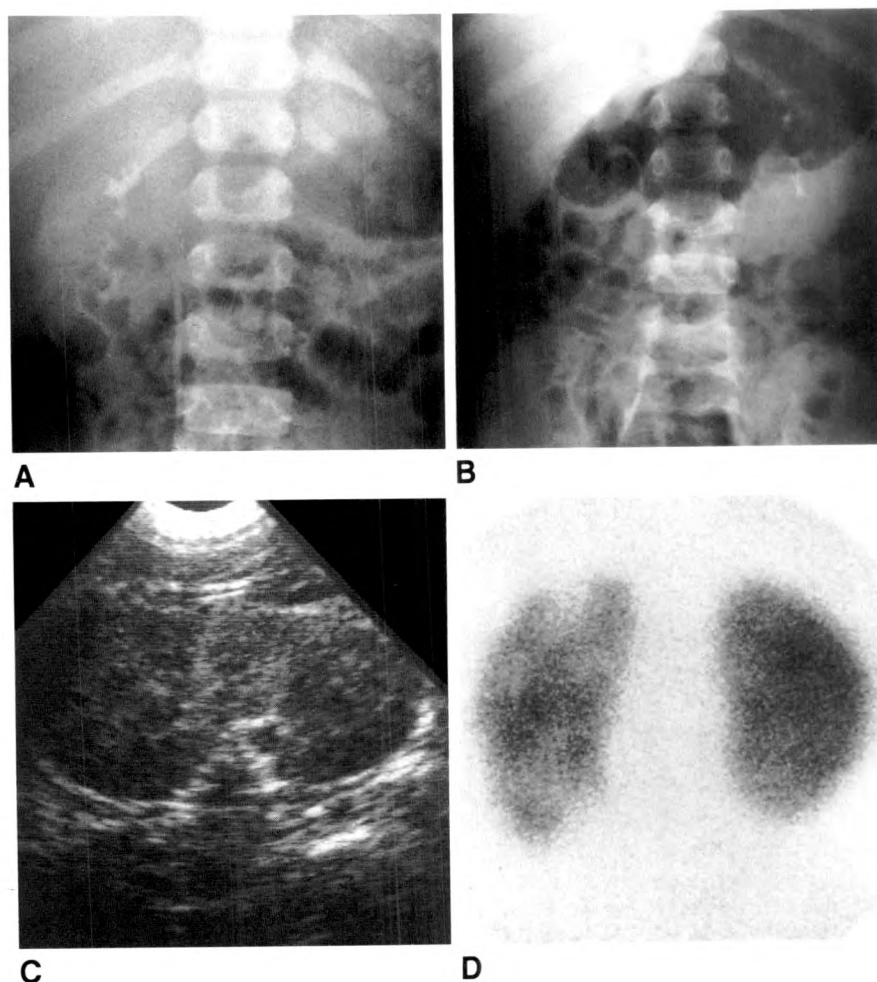


Fig. 1.—A, 2-min radiograph from excretory urogram of a 5-year-old boy with suspected upper urinary tract infection shows normal opacification of collecting system of right kidney and delayed opacification of pelvicaliceal system on left.

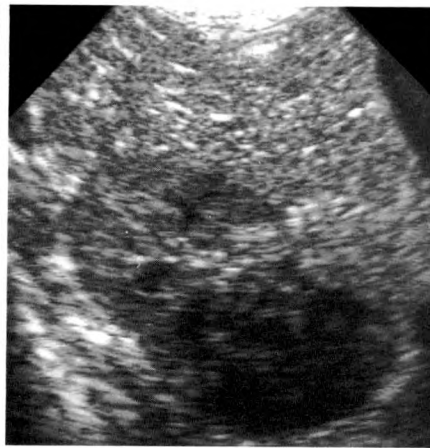
B, 8-min radiograph from excretory urogram shows pelvicaliceal system of both kidneys is opacified. Calices are sharp, but there is enlargement of lower pole of left kidney.

C, Coronal sonogram of left kidney performed the same day as excretory urogram shows diffuse enlargement of kidney with loss of usual cortical medullary differentiation. Kidney is more echogenic than normal.

D, Posterior image made 2 hr after IV injection of ^{99m}Tc -glucroheptonate shows multifocal photon-deficient areas throughout left kidney. Major abnormalities, however, are in upper and lower poles. Right kidney is normal.



A



B

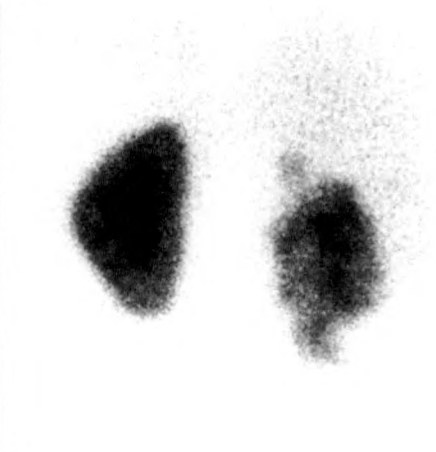
Fig. 2.—A and B, Longitudinal sonograms of right kidney of a 7-year-old boy with suspected upper urinary tract infection show hypoechoic regions in both upper and lower poles. Notice increased through-transmission of sound posterior to these hypoechoic lesions as compared with normal kidney.

C, Excretory urogram obtained that same day shows no abnormalities.

D, Posterior image obtained 2 hr after injection of ^{99m}Tc -glucoheptonate shows large photon-deficient areas in upper and lower poles of right kidney caused by focal renal infection. Abnormalities in midportion are less marked. Left kidney is normal.



C



D



A

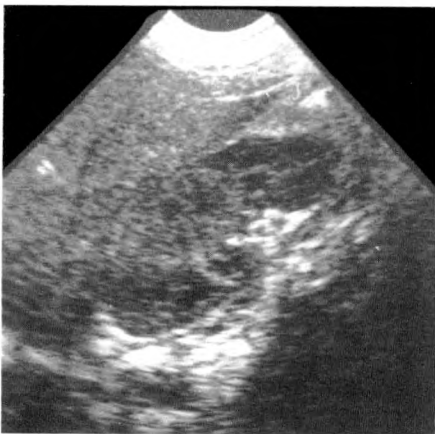


B

Fig. 3.—A and B, Supine and right posterior oblique films made 8 min after injection of contrast material in 18-month-old girl with suspected upper urinary tract infection are entirely normal.

C, Longitudinal sonogram of right kidney shows bulbous enlargement of upper pole with a marked increase in echogenicity.

D, Posterior image made 2 hr after IV injection of ^{99m}Tc -glucoheptonate shows focal abnormality in upper pole of right kidney. Left kidney is normal.



C



D

chyma in acute renal infection. Inflammatory edema and microabscesses cause easily detected alterations in tissue density. Hoffman et al. [21] noted radially oriented linear regions of decreased attenuation on postcontrast examinations, and Rauschkolb et al. [22] reported rounded or irregular lobar abnormalities in patients with renal infection. These regions appeared as low-density abnormalities on precontrast images and showed poor enhancement on the postcontrast images (Fig. 4). In diffuse renal infection, homogeneous enlargement of the affected kidney may be seen. The kidney may be normal by excretory urography, but segmental or diffuse regions of decreased attenuation with macrostriations may be detected by CT. A spectrum of changes from diffuse renal

enlargement to frank necrosis can be seen in renal infection, depending on the duration and extent of the insult [23–25]. An additional advantage of CT, one shared with renal sonography, is evaluation of the pararenal and retroperitoneal spaces.

Four children in our review were studied with CT because their clinical course suggested a renal abscess or pararenal extension of infection. Each of these four had abnormal scintigrams and sonograms. CT and renal sonography showed pararenal fluid in two. CT was not performed on children with uncomplicated renal infection; consequently, we could not adequately compare CT to the other techniques in this group of patients.

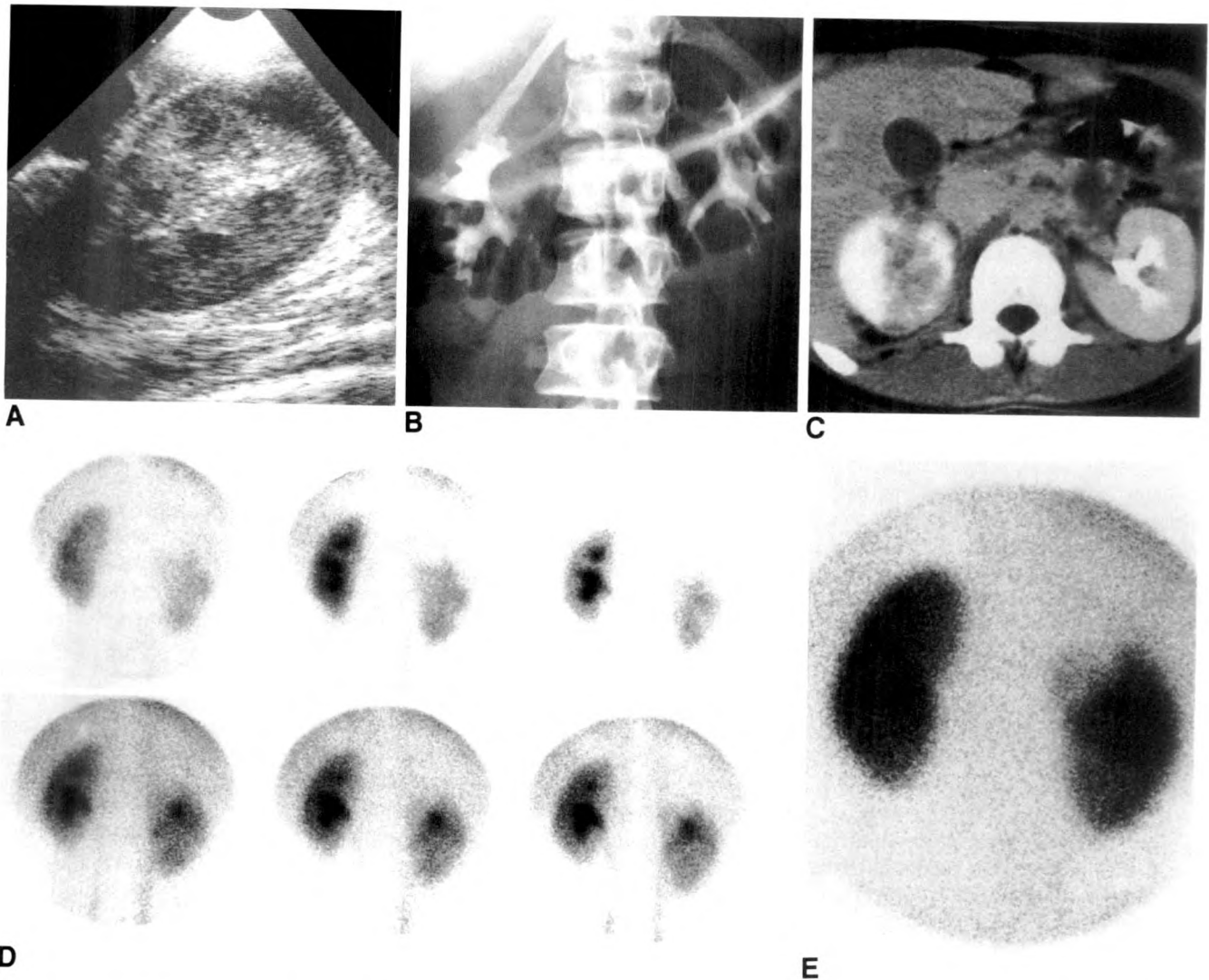


Fig. 4—A, Longitudinal sonogram of right kidney of 16-year-old girl with sepsis and right flank pain shows generalized enlargement of kidney with surrounding perinephric fluid. There are scattered areas of decreased echogenicity.

B, Right posterior oblique radiograph from excretory urogram performed the same day shows no abnormalities.

C, CT of abdomen shows mottled nephrogram in upper pole of right kidney. Renal parenchyma surrounding areas of decreased attenuation

shows increased attenuation possibly caused by tubular obstruction. Perinephric fluid collection is seen surrounding kidney.

D, Sequential 2-min images in posterior projection made after IV injection of ^{99m}Tc -glucoheptonate show delayed extraction of tracer by right kidney and a noticeable nonfunctioning area in upper pole of kidney. Left kidney is normal.

E, Posterior image obtained 2 hr later shows a large photon-deficient area in upper pole of right kidney.

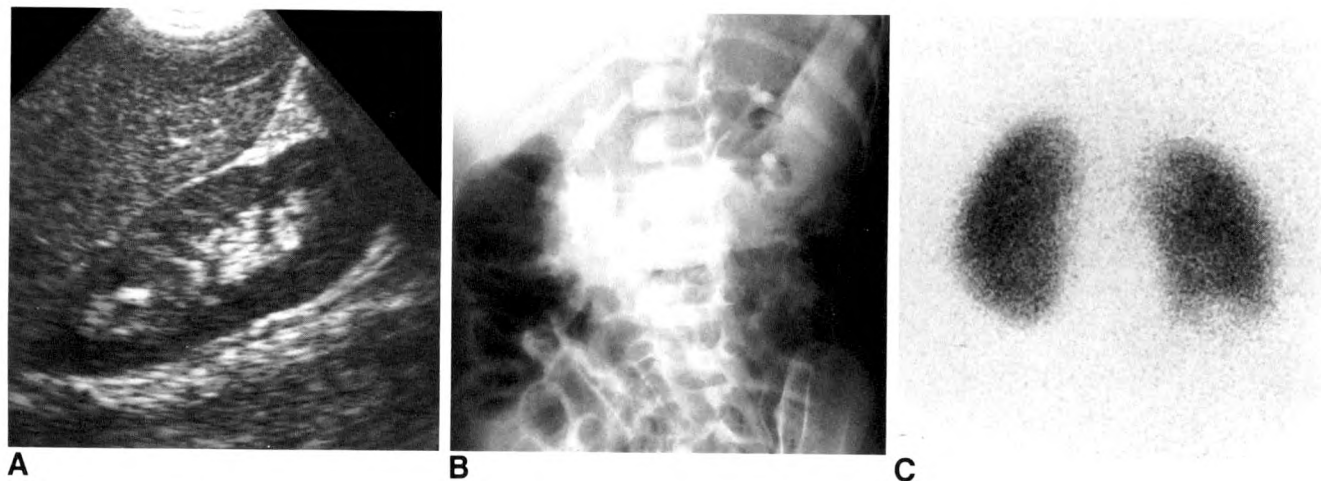


Fig. 5.—A, Longitudinal sonogram of right kidney of a 4-year-old girl with suspected urinary tract infection shows a duplex collecting system but is otherwise normal.

B, Right posterior oblique radiograph made 15 min after IV injection of contrast material shows bilateral duplication anomalies. Urogram is other-

wise normal.

C, Posterior image of kidneys made 2 hr after IV injection of ^{99m}Tc -glucuheptonate shows major photon-deficient area in lower pole of right kidney and a small photon-deficient area in medial aspect of upper pole. Left kidney is normal.

The advantages of renal cortical imaging agents include high-resolution images of the renal parenchyma, ready availability, and capability of quantifying renal cortical mass [26]. Renal cortical scintigraphy can be used to acquire qualitative information on renal perfusion and function. Delayed images obtained 2 hr after injection provide a functional cortical map of renal tubular mass. Glucoheptonate is preferable to dimer-caprotosuccinic acid when children are studied because it delivers a significantly lower radiation dose to the kidney.

Renal cortical scintigraphy has been useful in identifying both acute parenchymal inflammation and the scars of reflux nephropathy. Handmaker [27] found a relatively specific pattern in acute bacterial renal infection, a flare-shaped region of decreased renal activity radiating from the pelvicaliceal structures toward the periphery of the kidney [27]. In our patients the "flare sign" was uncommon. Most inflammatory lesions appeared as spherical masses.

Delayed images with glucuheptonate provide an image of the renal cortex because the radiopharmaceutical is retained by the proximal tubules [28, 29]. The cause of the scintigraphic defects associated with renal parenchymal infection is not clear. Hill and Clark [30] studied acute renal infection and its sequelae in a rabbit model and found marked cortical vasoconstriction in the areas of acute inflammation, with inflammatory cells obstructing the paratubular capillaries. Ischemia may play a role, although this probably occurs only with moderately severe disease. A more likely explanation is a metabolic alteration in the transport mechanism for the radiopharmaceutical across the tubular cell membranes.

In Handmaker's report [27], no patient with proven acute bacterial renal infection had normal findings on renal cortical scintigraphy. The work of Traisman et al. [31] differed somewhat; some of their patients with the discharge diagnosis of acute renal infection did not have normal renal cortical scans.

However, no cases were missed on renal cortical scintigraphy when findings on excretory urography or renal sonography were abnormal. Discrepancy in the absolute detection rate of acute renal infection can be explained by patient selection and timing of the examination. With available noninvasive testing, an accurate clinical diagnosis can be difficult, and only a presumptive diagnosis of acute renal infection can be made in some cases. No diagnostic "gold standard" is available with this disease.

An important observation in our review was the location of abnormalities found with renal cortical scintigraphy. These were located in the polar (either upper, lower, or both) regions in 44 of 50 children (Fig. 5). These photon-deficient cortical abnormalities were found (1) exclusively in the polar regions in 38, (2) in several locations that included the polar regions in eight, (3) in locations that spared the polar regions in four.

Vesicoureteral reflux was found in 34 (85%) of 40 children studied with voiding cystography. This prevalence of reflux exceeds the 30 to 50% commonly experienced in practice. The reason for this discrepancy was not apparent.

In summary, in children with upper urinary tract infection, findings on renal cortical scintigraphy are abnormal far more often than are findings on excretory urography or renal sonography.

REFERENCES

1. Durbin WA, Peter G. Management of urinary tract infections in infants and children. *Pediatr Infect Dis* 1984;3:564-574
2. Winberg J, Andersen HJ, Bergstrom T. Epidemiology of symptomatic urinary tract infection in childhood. *Acta Paediatr Scand [Suppl]* 1974;252:1-20
3. Bergstrom T, Larson H, Lincoln K. Studies of urinary tract infections in infancy and childhood. *J Pediatr* 1972;80:858-866
4. Randolph M, Morris K, Gould EB. The first urinary tract infection in the

- female infant. *J Pediatr* 1975;86:342-348
5. Roberts K, Charney E, Sweren RJ. Urinary tract infection in infants with unexplained fever: a collaborative study. *J Pediatr* 1983;103:864-867
 6. Leape L, McEachen W. Office urine cultures in pediatric practice. *Postgrad Med* 1974;56:177-182
 7. Etkin T, O'Shea J. Urinary tract infection in school-aged girls. *Pediatrics* 1978;62:844-846
 8. Hellerstein S, Duggan E, Welchert E, Grossmann H, Sharma P. Localization of the site of urinary tract infections with bladder washout test. *J Pediatr* 1981;98:201-206
 9. Lindberg U, Jodal U, Hanson LA. Asymptomatic bacteriuria in schoolgirls. IV. Difficulties of level diagnosis and the possible relation to the character of infecting bacteria. *Acta Paediatr Scand* 1975;64:574-580
 10. Hellerstein S, Duggan E, Welchert E. Serum C-reactive protein in the site of urinary tract infection. *J Pediatr* 1982;100:21-25
 11. Thomas V, Forland M. Antibody-coated bacteria in urinary tract infections. *Kidney Int* 1982;21:1-7
 12. Lorentz W, Resnick M. Comparison of urinary lactic dehydrogenase with antibody-coated bacteria in the urine sediment as a means of localizing the site of urinary tract infection. *Pediatrics* 1979;64:672-677
 13. Wientzen RL, McCracken GH Jr, Petruska ML, Swinson SG, Kaijser U, Hanson LA. Localization in therapy of urinary tract infections in childhood. *Pediatrics* 1979;63:467-474
 14. Duggan E, Hellerstein S, Mansour F, Welchert E. Urinary tract infection in girls: comparison of bladder washout localization technique with urinary LDH activity. *Pediatr Res* 1981;15:692-695
 15. Fasth A, Hanson LA, Jodal U, Peterson H. Autoantibodies to Tamm-Horsfall protein associated with urinary tract infection in girls. *J Pediatr* 1979;95:54-60
 16. Brook I, Belman B, Controni G. Lactic acid in urine of children with lower and upper urinary tract infection and renal obstruction. *Am J Clin Pathol* 1981;75:110-113
 17. Silver TM, Kass EG, Thornbury JR, Konnak JW, Wolfman MG. The radiologic spectrum of acute pyelonephritis in adults and adolescents. *Radiology* 1976;118:65-71
 18. Wicks JD, Thornbury JR. Acute renal infections in adults. *Radiol Clin North Am* 1979;17:245-260
 19. Fiegler W. Ultrasound in acute renal inflammatory lesions. *Eur J Radiol* 1983;3:354-357
 20. Edell SL, Bonavite JA. The sonographic appearance of acute pyelonephritis. *Radiology* 1979;132:683-685
 21. Hoffman EP, Mindelzun RE, Anderson RU. Computed tomography in acute pyelonephritis associated with diabetes. *Radiology* 1980;135:691-695
 22. Rauschkolb EN, Sandler CM, Patel S, Childs TL. Computed tomography of renal inflammatory disease. *J Comput Assist Tomogr* 1982;6:502-506
 23. Morehouse HT, Weiner SN, Hoffmann JC. Imaging in inflammatory disease of the kidney. *AJR* 1984;143:135-141
 24. Gold RP, McClennan BL, Rottenberg RR. CT appearance of acute inflammatory disease of the renal interstitium. *AJR* 1983;141:343-349
 25. Bankoff MS, Sarno RC, Mitcheson HD. Computed tomography in a differential diagnosis of pyelonephritis and renal infections. *Comput Tomogr* 1984;8:239-243
 26. Davies ER, Roberts M, Roylance J, et al. The renal scintigram in pyelonephritis. *Clin Radiol* 1972;23:370-376
 27. Handmaker H. Nuclear renal imaging in acute pyelonephritis. *Semin Nucl Med* 1982;12:246-253
 28. McRae J, Barry AC, Valk PE. Renal scintigraphy using Tc-stannous chloride gluconate. *Aust NZ J Med* 1971;1:291-296
 29. Boyd RE, Robson J, Hunt FC, Sorby PJ, Murray IP, McKay WJ. 99Tcm gluconate complexes for renal scintigraphy. *Br J Radiol* 1973;46:604-612
 30. Hill GS, Clark RL. A comparative angiographic, microangiographic, and histologic study of experimental pyelonephritis. *Invest Radiol* 1972;7:33-47
 31. Traisman ES, Conway JJ, Traisman HS, et al. Localization of urinary tract infection with 99mTc glucoheptonate scintigraphy. *Pediatr Radiol* 1986;16:403-406

Book Review



Cranial Computed Tomography in Infants and Children. By Eric N. Faerber. Philadelphia: Lippincott, 237 pp., 1986. \$39.95

The author's intent is to describe the basic physical principles of CT and the essential CT features of the major disease processes in the fields of pediatric neurology and neurosurgery. The basic physical principles includes the historical background, production of a CT scan, and techniques for cerebral CT scans. This section is well handled and is concise. The review of normal anatomy provides the bare essentials for understanding the head scan.

In the neonatal section, particular attention is given to the development of the brain, imaging of the neonatal brain, and conditions that include periventricular leukomalacia (infarction), intracranial hemorrhage, and periventricular hemorrhage. Other chapters describe congenital abnormalities, hydrocephalus, trauma, vascular disorders, CNS infection and immune deficiency disorders, tumors, metabolic and degenerative disorders.

This book is well-written and is easy to read. The line drawings

and copies of CT scans are excellent. They depict the particular anatomy or abnormality in a discernible manner. The bibliography for each entity is excellent and provides an excellent reference for quick retrieval of pertinent literature for researching a clinical problem.

The only unfavorable criticism is that some of the entities described are not illustrated. One hopes that this will be corrected in future editions. This book is a valuable addition to the library of any radiologist interpreting head scans of children. It should be available in the department library of institutions in which there is a radiology residency training program. Clinicians managing pediatric neurologic and neurosurgical problems will also find it useful.

Jack I. Eisenman
King/Drew Medical Center
Los Angeles, CA 90059

Urography and Voiding Cystourethrography:

Findings in Girls with Urinary Tract Infection

George S. Bisset III¹
Janet L. Strife
J. Scott Dunbar

The voiding cystourethrogram and excretory urogram have been considered essential parts of the evaluation of girls with urinary tract infections. To evaluate the usefulness of these procedures, 523 examinations in girls with urinary tract infections were reviewed retrospectively. The major finding on voiding cystourethrograms was vesicoureteral reflux, occurring in 36% of the children. Of the total group, 8% had excretory urographic evidence of parenchymal scarring. Higher grades of reflux were associated with an increase in parenchymal scarring. All urethras were normal, and only one paraureteral diverticulum was identified. Bladder emptying was incomplete in 46% of the patients. Ovarian radiation doses were measured with "low-dose" and standard systems. On the basis of this study, traditional approaches to the standard workup are questioned.

Urinary tract infections occur in approximately 1% of healthy girls [1], and associated vesicoureteral reflux has been reported to be present in 19–34% [2–4]. Bacteriuria and vesicoureteral reflux may cause renal scarring, with subsequent hypertension, and/or renal insufficiency. Although only a small percentage of children develop renal insufficiency secondary to chronic reflux and infection, the problem has been efficient identification and treatment of children at risk.

The traditional imaging approach includes a voiding cystourethrogram (VCUG) and an excretory urogram. Advances in sonography and other imaging techniques have resulted in reevaluation of this traditional approach. In an attempt to evaluate the findings and roles of voiding cystourethrography and excretory urography, radiographs of 523 girls with documented urinary tract infection were reviewed retrospectively.

Subjects and Methods

All VCUGs and excretory urograms were obtained between September 1978 and November 1984. To be included in the study group, girls had to be outpatients referred for evaluation of a urinary tract infection. Both studies had to be performed within 48 hr of each other. All patients with recognized congenital syndromes or chronic disease predisposing to urinary tract anomalies (e.g., meningomyelocele, polycystic kidneys) were excluded, and no studies were performed during acute infections.

Ages of the girls ranged from 1 month to 18 years (mean, 5.3 years). Fifty-four were less than 2 years old, 314 between 2 and 7, 132 between 7 and 12, and 23 more than 12.

The VCUG was performed by suspending the contrast material (17.2% meglumine iohalamate) in a bottle approximately 1 m above the child's pubic symphysis. Fluoroscopy was done intermittently during bladder filling; 105-mm spot films were obtained in both oblique projections to evaluate vesicoureteral anatomy. Films of the urethra and refluxing ureters were obtained during voiding and a spot film of the bladder was obtained at cessation of voiding. If the patient refluxed, a spot film of the affected kidney was also obtained. Very young or uncooperative children were studied while they were recumbent. Older children stood or sat on a radiolucent "potty" seat [5]. Excretory urography was performed by injecting 60% diatrizoate meglumine IV at a dose of 2 ml/kg (maximum dose, 100 ml).

The VCUG was interpreted before the excretory urogram. Each retrospective interpretation

Received January 8, 1986; accepted after revision September 23, 1986.

Presented at the annual meeting of the Society for Pediatric Radiology, Boston, April 1985.

¹ All authors: Departments of Radiology and Pediatrics, University of Cincinnati College of Medicine, Cincinnati OH 45267, and the Division of Radiology, The Children's Hospital Medical Center, Elland and Bethesda Avenues, Cincinnati, OH 45229. Address reprint requests to G. S. Bisset III, Division of Radiology, The Children's Hospital Medical Center, Elland and Bethesda Avenues, Cincinnati, OH 45229.

AJR 148:479–482, March 1987
0361–803X/87/1483–0479
© American Roentgen Ray Society

was performed independently by two of us, without knowledge of the first reading.

VCUGs were evaluated for bladder contour, urethral and vesicoureteral abnormalities, bladder emptying during voiding, and the presence of vesicoureteral reflux. Reflux was graded according to the International Classification [6]: I = ureter only. II = ureter, pelvis, and calices; no dilatation, normal caliceal fornices. III = mild or moderate dilatation and/or tortuosity of the ureter and mild or moderate dilatation of renal pelvis but no or slight blunting of the fornices. IV = moderate dilatation and/or tortuosity of ureter and moderate dilatation of renal pelvis and calices; complete obliteration of sharp angles of fornices but maintenance of papillary impressions. V = gross dilatation and tortuosity of ureter; gross distention of renal pelvis and calices; papillary impressions no longer visible.

If a child had bilateral vesicoureteral reflux, the side with the most severe reflux was used for the statistics. Assessment of bladder emptying was possible in 501 girls for whom films were obtained immediately after voiding or from the fluoroscopist's evaluation. Bladder emptying was graded as follows: no residual, small residual, or large residual.

Excretory urograms were evaluated for renal size, position, contour, parenchymal scarring, and other abnormalities. Radiologic criteria for scarring included blunting or clubbing of calices and loss of parenchyma, with or without indentation of the kidney surface [7].

We compared the ovarian radiation dose received during standard cystourethrography at "low-dose" and standard settings. Thermoluminescent chips were placed at the approximate position of the ovaries in phantoms, and typical fluoroscopic procedures were followed. Low-dose settings included a tube current of 0.2–0.4 mA and a tube voltage of 50–100 kVp. Spot films were 40-mA phototimed exposures. Standard fluoroscopy was done with a tube current of 0.2–0.5 mA and a tube voltage of 120 kVp, with 300 mA phototimed spot films.

Results

Of the 523 VCUGs, 329 (63%) were normal. Vesicoureteral reflux was seen in 188 (36%): 37 with grade I, 114 with grade II, 32 with grade III, five with grade IV, and none with grade V. The prevalence of renal parenchymal scarring relative to the grade of reflux is shown in Figure 1.

Bladder contour was normal in 518 girls (99%). Two girls had neurogenic bladders that were not recognized clinically, and five had isolated bladder diverticula.

Adequate radiographs to assess bladder emptying were available for 501 patients. Complete voiding during cystourethrography occurred in 273 (54%). In those 228 (46%) with incomplete voiding, a small residual was present in 145 (64%), and a large residual was seen in 83 (36%). The distribution of bladder residuals by age group is shown in Table 1.

Table 2 shows the relative occurrence of bladder emptying and reflux. Of the 501 girls in whom bladder functioning was assessed, 176 (35%) had vesicoureteral reflux. Of this group, 78 (44%) had no residual, 62 (35%) had a small residual, and 36 (20%) had a large residual. The grade of vesicoureteral reflux as related to the number of patients who had residual urine is presented in Table 3.

Vesicoureteral reflux occurred in 188 (36%) of the 523 girls. When those with reflux were evaluated by excretory urography, 128 (68%) had normal findings. A duplex kidney was seen in 27 (14%); duplication was complete in 20 and partial

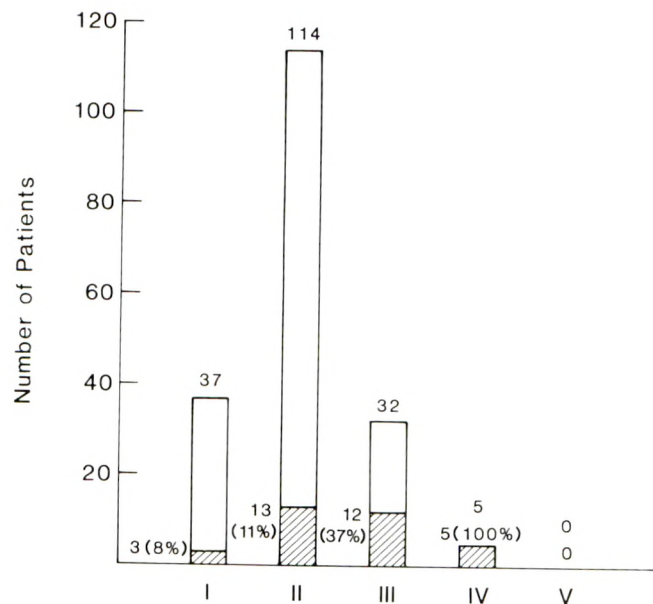


Fig. 1.—Distribution of vesicoureteral reflux by grade in 188 girls with urinary tract infections. Cross-hatched areas and numbers in parentheses are percentages with parenchymal scarring. Roman numerals indicate grade of reflux according to the International Classification (see text).

in seven. Renal parenchymal scarring was seen in 33 (18%), 10 of whom also had duplex systems. Miscellaneous findings included ectopic ureterocele (2), a nonfunctioning kidney (1), anatomically normal small kidneys (1), ureteropelvic striations [5], caliceal diverticula (1), megaureter (1), ureteropelvic junction obstruction (1), caliectasis without parenchymal scarring (2), and neurogenic bladder (1).

In the 329 girls with normal findings on VCUGs, excretory urographic studies were normal in 308 (94%). Duplex collecting systems were noted in 14 (4%); duplication was complete in four and partial in 10. Renal parenchymal scarring was detected in 10 children (3%), one of whom had complete duplication of the collecting system. Additional findings on excretory urograms in those children without vesicoureteral reflux included caliceal diverticula (4), caliectasis without demonstrable parenchymal scarring (1), ureteral striations (1), and right ureteropelvic junction obstruction (1). Table 4 compares the radiographic abnormalities (other than reflux) seen on excretory urograms and VCUGs.

Discussion

Our overall prevalence of vesicoureteral reflux (36%) in girls with urinary tract infection is comparable to that found by other authors [2, 4, 8, 9]. In our patients, and in those reported by others, the more severe grades of reflux had a higher association with renal parenchymal scarring [10, 11]. This association is well documented [6, 12–14], even though a direct causal relationship and the true prevalence of vesicoureteral reflux in a normal population is difficult to establish.

Smellie et al. [15] noted that renal scarring was found

TABLE 1: Age Distribution of Incomplete Voiding During VCUG in Girls with Urinary Tract Infections

Age (yr)	No. of Patients (%)
0-2	30/46 (65)
2-6	145/299 (48)
7-12	47/132 (36)
13-18	6/24 (25)
Overall	228/501 (46)

Note.—VCUG = voiding cystourethrography.

TABLE 2: Bladder Emptying and Vesicoureteral Reflux in Girls with Urinary Tract Infections

Bladder Emptying	No. of Patients (%)		
	Reflux	No Reflux	Total
Complete voiding	78 (29)	195 (71)	273 (54)
Incomplete voiding	98 (43)	130 (57)	228 (46)
Overall	176 (35)	325 (65)	501 (100)

TABLE 3: Grade of Vesicoureteral Reflux and Residual Urine in Girls with Urinary Tract Infections

Grade of Reflux	No. with Residual Urine (%)
I	14/36 (39)
II	68/116 (60)
III	15/22 (68)
IV	3/4 (75)
Overall	100/176 (56)

TABLE 4: Comparison of Radiographic Findings in Girls with Urinary Tract Infections

Abnormality	Excretory Urography	Voiding Cystourethrography
Duplex systems	41	15
Ureteropelvic striations	6	0
Caliceal diverticula	5	1
Ectopic ureterocele	2	2
Neurogenic bladder	2	2
Ureteropelvic junction obstruction	2	1
Megaureter	1	1
Small kidneys bilaterally	1	0

Note.—Does not include vesicoureteral reflux. Several abnormalities detected on excretory urograms were seen only occasionally on voiding cystourethrograms and often depended on reflux for their visibility. Abnormalities shown solely with voiding cystourethrography were reflux and bladder diverticula.

almost exclusively in children with reflux. We found that in the group of girls with grade III or IV reflux, 46% had some degree of parenchymal scarring, whereas in those with no reflux or grade I reflux, the incidence of renal parenchymal scarring was only 3%. Shah et al. [16] reported a 2% incidence of renal scarring in patients without reflux. Parenchymal

scars without demonstrable reflux suggest that (1) reflux has resolved, (2) scarring was caused by previous pyelonephritis without reflux, or (3) although present, reflux was undetected by voiding cystourethrography. Proponents of the "big bang" theory believe that if papillary morphology is abnormal, even transient vesicoureteral reflux during a urinary tract infection may result in early parenchymal damage with scarring, which progresses over a period of weeks to months, despite resolution of the reflux [17].

In our study, the prevalence of duplex systems in girls with reflux is higher than expected. At autopsy, Campbell [18] found a 0.7% incidence of duplication, with complete duplication in 0.2%. Nordmark [19] and Nation [20], on the basis of excretory urograms performed for urinary tract symptoms, found an incidence of 2-4%. The overall prevalence of 8% in our selected population with urinary tract infection may reflect the increased morbidity associated with this anomaly. This hypothesis is also supported by our findings that the prevalence of duplex systems in those with reflux (14%) was significantly higher than the prevalence in those without reflux (4%). The higher prevalence also may be partially caused by selection of girls only, as duplication anomalies of the ureters are twice as common in females as in males [21].

Assessment of bladder emptying or voiding capacity has been considered an important aspect of the voiding cystourethrogram. However, in our study, 48% of patients did not empty their bladders completely, and in the group 0-2 years old, 63% did not void completely. Does this indicate that incomplete voiding occurs routinely in nearly one-half of the patients, or does the "unnatural" state of voiding cystourethrography contribute to incomplete voiding? We think the latter may be true. The large percentage of patients who have incomplete voiding without significant vesicoureteral reflux or parenchymal scarring makes the finding of incomplete voiding useless. More recently, sonography has been used to assess residual urine, and many techniques, including volume computations, are now considered fairly reliable [22, 23].

All 523 girls had normal urethras. Although urethral abnormalities in girls are exceedingly rare, some radiologists still routinely obtain several urethral views during voiding cystourethrography. The results of this study suggest that a single spot film of the urethra is sufficient.

In comparing the ability to detect abnormalities (other than reflux) on VCUGs that are not seen on excretory urograms, we found that the only value of the VCUG was in diagnosing bladder diverticula or saccules (Table 4). The significance of finding a small bladder diverticulum in an otherwise normal patient is unclear. Usually there is no change in therapy unless the patient refluxes.

Evaluation of the vesicoureteral junction and the detection of secondary causes of reflux such as a paraureteral diverticulum have been considered important reasons for voiding cystourethrography. Only one girl in 523 had a paraureteral (Hutch) diverticulum that was associated with bilateral grade II reflux. The presence of reflux and a Hutch diverticulum is an indication for cystoscopy and possibly antireflux surgery in many institutions. Unfortunately, only VCUGs provide adequate anatomic detail for diagnosing a paraureteral diverticu-

lum giving rise to a refluxing ureter. However, it may not be appropriate to do VCUGs on all females with urinary tract infection to identify this rare lesion. Perhaps a reasonable approach is to obtain VCUGs only for girls whose reflux increases in severity or does not resolve with medical management.

Lastly, both the low-dose system and standard fluoroscopic studies used for voiding cystourethrography resulted in significantly higher radiation levels than those associated with radionuclide procedures [23], in which an average ovarian radiation exposure of 0.002–0.005 rad (0.02–0.05 mGy) per study has been calculated by several authors [24–27]. The average dose to the ovaries was 0.096 rad (0.96 mGy) per study with the low-dose settings and 0.208 rad (2.08 mGy) per VCUG with the standard settings. Thus, there is nearly a 100-fold difference in ovarian exposure when voiding cystourethrography is compared to radionuclide cystography.

REFERENCES

1. Kunin CM, Zacha E, Paquin AJ. Urinary tract infection in school children. I. Prevalence of bacteriuria and associated urologic findings. *N Engl J Med* 1962;266:1287–1296
2. Newcastle Asymptomatic Bacteriuria Research Group. Asymptomatic bacteriuria in school children in Newcastle-upon-Tyne. *Arch Dis Child* 1975;50:90–102
3. Lindberg U, Claesson I, Hanson LA, Jodal U. Asymptomatic bacteriuria in schoolgirls. VIII. Clinical course during a 3-year follow-up. *J Pediatr* 1978;92:194–199
4. Asscher AW, Fletcher EWL, Johnston HH, et al. Sequelae of covert bacteriuria in school girls: a four-year follow-up study. *Lancet* 1978;2:889–893
5. Nogrady BM, Dunbar JS. The technique of roentgen investigation of the urinary tract in infants and children. *Prog Pediatr Radiol* 1970;3:3–50
6. Report of the International Reflux Study Committee. Medical versus surgical treatment of primary vesicoureteral reflux. *Pediatrics* 1981;67:392–400
7. Hodson CJ. The radiological diagnosis of pyelonephritis. *Proc R Soc Med* 1959;52:669–672
8. Winberg J, Andersen HG, Bergstrom J, Jacobsson B, Larson H, Lincoln K. Epidemiology of symptomatic urinary tract infection in childhood. *Acta Paediatr Scand* [Suppl 252] 1974;1–20
9. Smellie JM. Medical aspects of urinary infection in children. *J R Coll Physicians Lond* 1967;1:189–193
10. MacGregor ME, Freeman P. Childhood urinary infection associated with vesico-ureteral reflux. *Q J Med* 1975;44:481–489
11. McLachlan MSF, Meller SJ, Verrier-Jones ER, et al. Urinary tract in schoolgirls with covert bacteriuria. *Arch Dis Child* 1975;50:253–258
12. Rolleston GL, Shannon FT, Utley WLF. Relationship of infantile vesicoureteral reflux to renal damage. *Br Med J* 1970;1:460–463
13. Scott JES, Stansfeld JM. Ureteric reflux and kidney scarring in children. *Arch Dis Child* 1968;43:468–478
14. Hodson CJ, Maling TMJ, McManamon PJ, Lewis MG. The pathogenesis of reflux nephropathy. *Br J Radiol* [Suppl 13] 1975:1–26
15. Smellie JM, Normand ICS, Katz G. Children with urinary tract infection: a comparison of those with and those without vesicoureteric reflux. *Kidney Int* 1981;20:717–722
16. Shah KJ, Robins DG, White RHR. Renal scarring and vesicoureteral reflux. *Arch Dis Child* 1978;53:210–217
17. Ransley PG, Risdon RA. The renal papilla, intrarenal reflux, and chronic pyelonephritis. In: Hodson J, Kincaid-Smith P, eds. *Reflux nephropathy*. New York: Masson, 1979:126–133
18. Campbell MF. Embryology and anomalies of the urogenital tract. In: Kelalis PP, King LR, eds. *Clinical pediatric urology*. Philadelphia: Saunders, 1951:159–353
19. Nordmark B. Double formation of the pelves of the kidneys and the ureters: embryology, occurrence and clinical significance. *Acta Radiol* 1948;30:267–278
20. Nation EF. Duplication of the kidney and ureter: a statistical study of 230 new cases. *J Urol* 1944;51:456–465
21. Kelalis PP. Renal pelvis and ureter. In: Kelalis PP, King LR, eds. *Clinical pediatric urology*. Philadelphia: Saunders, 1976:503–541
22. Beacock CJM, Roberts EE, Rees RWM, Buck AC. Ultrasound assessment of residual urine: a quantitative method. *Br J Urol* 1985;57:410–413
23. Ravichandran G, Fellows GJ. The accuracy of a hand-held real time ultrasound scanner for estimating bladder volume. *Br J Urol* 1983;55:25–27
24. Keriakes JG, Strife JL, Henry G, Modur T, Dunbar JS. Radiation dose in pediatric cystourethrography. Presented at the International Congress of Radiology, Honolulu, HI, July 1985
25. Conway JJ, King LR, Belman B, Thorson T. Detection of vesicoureteral reflux with radionuclide cystography: a comparison with roentgenographic cystography. *AJR* 1972;115:720–727
26. Blaufox MD, Gruskin A, Sandler P, Goldman H, Ogwo JE, Edelmann CM. Radionuclide scintigraphy for detection of vesicoureteral reflux in children. *J Pediatr* 1971;79:239–246
27. Dimitriou P, Fretzayas A, Nicolaidon P, Gritzal F, Kasfiki A, Karpathios T. Estimates of dose to the bladder during direct radionuclide cystography: concise communication. *J Nucl Med* 1984;25:792–795

Ureteral Dilatation in Children with Febrile Urinary Tract Infection or Bacteriuria

Mikael Hellström¹
 Ulf Jodal²
 Staffan Mårild²
 Björn Wettergren²

Little information is available on the relationship between urinary infection in children and infants, with or without vesicoureteral reflux, and dilatation of the urinary tract. The purpose of this study was to determine the effects of infection and reflux on the diameter of the ureter at excretory urography in children with acute, febrile urinary tract infections and in infants with bacteriuria found at screening. Standardized measurements of ureteral diameter were obtained for 79 children (2 months to 6 years old) with urinary tract infections and for 45 infants with bacteriuria. Patients with urinary tract obstruction or malformations were excluded. Seventy-one children with febrile urinary tract infection had ureteral visualization that allowed measurements. Ureteral diameter in this group was significantly wider than in a reference group, and 42 children (59%) had ureteral diameters that were more than 2 standard deviations above the normal mean. Ureteral diameter at excretory urography increased with increasing grades of reflux, but dilatation occurred also in the absence of reflux. Twenty-two of the 45 infants in the group with bacteriuria had sufficient ureteral visualization for measurements. The ureters in this group were wider than in the reference group, and eight infants had ureteral diameters that were more than 2 standard deviations above the normal mean. We conclude that ureteral dilatation is a common effect of acute urinary tract infection and bacteriuria in children.

Radiologic findings of acute urinary tract infection are usually scant or absent but may include delayed caliceal filling, diminished density of contrast, swelling of the affected kidney, or dilatation of the collecting system [1-6]. Dilatation of the collecting system thus may indicate infection, but it also may be a sign of vesicoureteral reflux or obstruction. Dilatation caused by infection often is referred to as nonobstructive, to indicate the absence of anatomic obstruction. However, animal studies [7, 8] suggest that the dilatation caused by infection may be associated with functional obstruction, since they found delayed excretion on scintigraphic examinations as well as increased intraureteral pressure after infection.

So far, series have been small in studies on the frequency and degree of ureteral involvement in children with urinary tract infection, and normal values for ureteral diameter at excretory urography have not been available until recently [9]. The aim of the present investigation is to study the effects of infection and reflux on the diameter of the ureter at excretory urography in children with febrile urinary tract infection and in infants with bacteriuria found at screening. Ureteral diameter was measured by a standardized method, and the results were compared to a previously established reference for normal ureteral diameter [9].

Material and Methods

Febrile Urinary Tract Infection

All consecutive cases of first-time febrile urinary tract infection in children 2 months to 6 years old diagnosed at the Children's Hospital in Göteborg from September 1979 to May

Received July 30, 1986; accepted after revision November 11, 1986.

This work was supported by grants from the Swedish Society of Medical Radiology, the Göteborg Medical Society and Agfa-Gevaert AB, Stockholm, Sweden.

¹ Department of Pediatric Radiology, Östra sjukhuset, University of Göteborg, S-416 85 Göteborg, Sweden. Address reprint requests to M. Hellström, Department of Pediatric Radiology, Barnkliniken, Östra sjukhuset, S-416 85 Göteborg, Sweden.

² Department of Pediatrics, Östra sjukhuset, University of Göteborg, S-416 85 Göteborg, Sweden.

AJR 148:483-486, March 1987

0361-803X/87/1483-0483

© American Roentgen Ray Society

1981 were reviewed. Criteria for inclusion in the study were fever (body temperature $\geq 38.5^\circ\text{C}$) and bacteriuria. Bacteriuria was diagnosed by suprapubic aspiration (≥ 1000 bacteria/ml of urine), by culturing the same organism from two urine-bag or midstream samples ($\geq 100,000/\text{ml}$), or by culturing organisms from one such sample that was positive on a nitrite test. No cases with duplication, obstruction, or neurogenic abnormalities of the urinary tract were included.

Seventy-nine children fulfilled the criteria; 20 were boys and 59 were girls; the median age was 0.8 years. The combination of bacteriuria, fever, elevated levels of C-reactive protein, and reduced renal concentrating capacity made acute pyelonephritis likely in most cases [10]. All children were treated for 10 days.

Excretory urography was performed an average of 6.4 days (range, 1–25) after the beginning of antibacterial treatment. All except one child underwent voiding cystourethrography.

Screening Bacteriuria

Screening for bacteriuria was performed in an unselected population of 3581 infants in Göteborg. Screening was performed at 2 weeks, 3 months, and 10 months of age. Ninety-four percent of the infants took part in at least one screening, and two-thirds took part in all three. Bag samples were used for the first culture of urine at each screening occasion, and growth in samples obtained by suprapubic aspiration (≥ 1000 bacteria/ml) was used for confirmation. Bacteriuria was diagnosed in 50 infants (36 boys and 14 girls). Fever or other symptoms were found in two infants only, who were treated accordingly. Levels of C-reactive protein were normal in all cases.

Excretory urography was performed in 49 of the 50 infants. Two patients were excluded because of obstruction and two because of duplication of the collecting system. The remaining 45 infants included 33 boys and 12 girls. Bacteriuria was detected at the 2-week screening in 23, at the 3-month screening in 14, and at the 10-month screening in eight. The mean interval between confirmation of bacteriuria at bladder aspiration and excretory urography was 24 days (range, 4–47). Forty-three infants underwent voiding cystourethrography in association with the excretory urography.

Preparation for excretory urography did not include fluid restriction, and the procedure was performed as described for the reference groups [9]. The ureter was evaluated according to the method of Hellström et al. [9]. Ureteral visualization was defined as the added length of the ureteral segments filled with contrast medium, in relation to the total length of the ureter, and was classified as (1) $<50\%$, (2) between 50% and 90%, or (3) $>90\%$. The widest point of the ureter was measured on films obtained without abdominal compression and was categorized as proximal, middle, or distal. Ureteral diameter was correlated with the length of a segment of the lumbar spine, the L1–L3 distance, defined as the distance between the upper border of the first to the lower border of the third lumbar vertebra. Bladder fullness was registered as nearly empty, moderately filled, or well filled.

The results were compared to a previously established reference for normal ureteral diameter that included 194 children [9].

Voiding cystourethrography was performed according to a stan-

dardized procedure [11] by using drip infusion from a standardized height, intermittent fluoroscopy, and 70-mm film for documentation. Vesicoureteral reflux was graded according to the international grading system [12].

All comparisons between patient and reference measurements were performed by using raw data from groups (patient or reference) who had the same L1–L3 distances. All analyses (except that for vesicoureteral reflux) used the diameter of the wider of the two ureters. Analysis of the effect of vesicoureteral reflux on ureteral diameter included measurements of the ureteral diameter, plus reflux grade of the affected side for patients with unilateral reflux. For the rest of the patients, the mean of right and left ureteral diameters and the mean of right and left reflux grades were used in each case. Ureters visualized $<50\%$ were excluded in all analyses of ureteral diameter.

Correlation between variables was determined by Pitman's test [13]. For the intraindividual comparison between right and left ureteral diameters, Fisher's test for paired comparisons was used [13]. The influence of L1–L3 distance was eliminated in comparisons of ureteral diameter by using Mantel's test [14]. A p -value less than .05 (two-sided test) was considered significant.

Results

Febrile Urinary Tract Infection

Levels of C-reactive protein were determined for all but one patient. Significant elevations occurred in all but five; the median value for the group was 100 mg/l (normal, <20). The renal concentrating capacity, determined by the DDAVP (synthetic vasopressin) test [15], was significantly reduced for the entire group; the median value was 2.29 standard deviations below the normal mean.

Eight (10%) of the 79 children with febrile urinary tract infection were excluded from the analyses of ureteral diameter because of poor filling ($<50\%$ visualization) of both ureters. The corresponding percentage in the reference group of normal children of similar size was 27%, indicating that there was better ureteral filling in the infected group ($p < .01$).

Thus, 71 children with febrile urinary tract infection had at least one ureter visualized $\geq 50\%$. Ureteral diameter in this group was wider than in the reference group with the same L1–L3 distance (Table 1), and the difference was highly significant ($p < .001$). When dilatation was defined as a ureteral diameter more than 2 standard deviations above the normal mean, 42 (59%) had at least one dilated ureter (Fig. 1). Such dilatation occurred unilaterally in 28 (18 on the right side and 10 on the left) and bilaterally in 14 children.

Separate analysis of the subgroup without vesicoureteral reflux (Table 1) showed significantly wider ureters than in the reference group ($p < .001$).

TABLE 1: Ureteral Diameter in Children with Febrile Urinary Tract Infection

	Patient Groups			Reference Group
	Entire Group	No VUR	VUR	
No. of Patients	71	49	22	981
L1–L3, mean (mm)	53.4	52.5	55.4	52.5
Diameter, mean \pm SD (mm)	6.5 \pm 1.9	6.1 \pm 1.7	7.4 \pm 2.1	4.7

Note.—All groups are children with at least one ureter visualized $\geq 50\%$ of its length. Diameters in the group [9] were measurements of the wider of two ureters (left or right). In the reference group estimated mean of ureteral diameter was determined by regression analysis, with mean and range of L1–L3 distance in the reference group [9] equal to that in the patient groups. VUR = vesicoureteral reflux.

Vesicoureteral reflux was diagnosed in 24 (31%) of the 78 children who had voiding cystourethrography performed. Reflux was seen in 36 renal units (11 with grade I, 19 with grade II, and six with grade III). Analysis of correlation between ureteral diameter at excretory urography and grade of reflux revealed a significant increase of ureteral diameter with increasing grades of reflux ($p < .001$).

The right ureter was significantly wider than the left one, with a mean difference of 0.6 mm. The widest point of the ureter was located most often (73%) in the middle part (i.e., just above the iliac vessel crossing at the pelvic brim) and less often in the proximal or distal part. These findings are in agreement with those of the reference group [9].

The degree of bladder fullness at excretory urography was similar to that in the reference group. However, in the five patients with well-filled bladders in the group with febrile urinary tract infection, dilatation was noted in eight of the 10 ureters.

Screening Bacteriuria

Visualization of the ureters in the group with screening bacteriuria was poorer than in the group with febrile urinary tract infection ($p < .001$) but the same as in a comparable group of normal children [9] ($p = .30$). Twenty-three (51%) of the 45 patients had $<50\%$ ureteral visualization bilaterally.

Twenty-two infants with screening bacteriuria had at least one ureter visualized $\geq 50\%$. Ureteral diameter in this group was significantly larger ($p < .01$) than in the normal group, even when refluxing individuals (two renal units with grade I reflux and five with grade II) were excluded ($p < .001$). Eight (36%) had unilateral (six) or bilateral (two) ureteral diameters that were more than 2 standard deviations above the normal mean (Fig. 2).

The degree of bladder fullness was similar to that in the normal standard. In the four infants with well-filled bladders, dilatation was noted in three of eight ureters.

The ureters were wider in the body size-matched group with febrile urinary tract infection than in the group with screening bacteriuria, but the difference was not significant ($p = .09$).

Discussion

The present study shows that ureteral dilatation is a common phenomenon in children with febrile urinary tract infection and that it also occurs, although to a lesser extent, in infants with bacteriuria found at screening. Ureteral dilatation may be mediated by several different mechanisms. A full bladder, even in the absence of infection, may cause dilatation of the upper urinary tract due to impaired drainage of the ureters [16, 17]. In the present study, increased bladder fullness could not be documented and therefore did not explain the ureteral dilatation.

Another important factor in ureteral dimensions is diuresis [18], which is influenced by the fluid intake before excretory urography and the osmotic effects of the contrast medium. There was no reason to believe that hydration in the patient groups differed from that in the reference group, and the contrast media used were similar in the two groups.

Vesicoureteral reflux also may have a widening effect on the ureters that is sometimes obvious at excretory urography [19]. In the present study reflux influenced the ureteral dimensions, but significant widening of the ureters also occurred without reflux, indicating that infection was responsible for the ureteral widening.

Experimental studies in animals and on isolated ureteral strips have shown that bacteria and bacterial endotoxin can impair peristalsis by affecting smooth-muscle function in the ureteral wall [20-23]. Marked ultrastructural changes also have been shown in animal ureters after experimentally induced pyelonephritis [24, 25]. The dilatation and the increased ureteral visualization found in the group with febrile urinary tract infection can be explained on the basis of these mech-

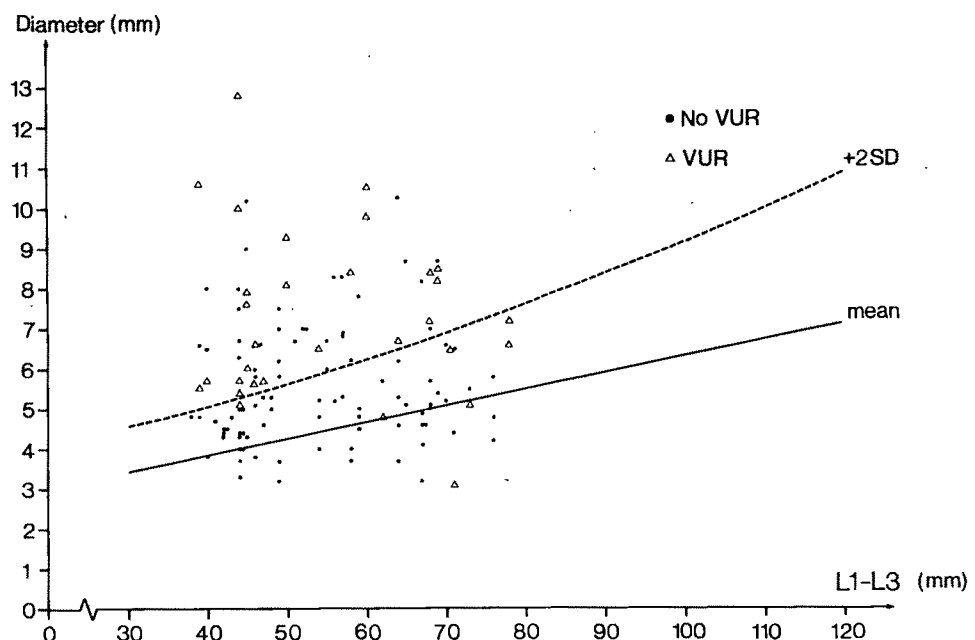


Fig. 1.—Ureteral diameters in 71 of 79 children with febrile urinary tract infection who had at least one ureter visualized $\geq 50\%$ of its length (123 ureters) compared to reference group [9] (mean and 2 standard deviations [SD] above the mean). VUR = vesicoureteral reflux.

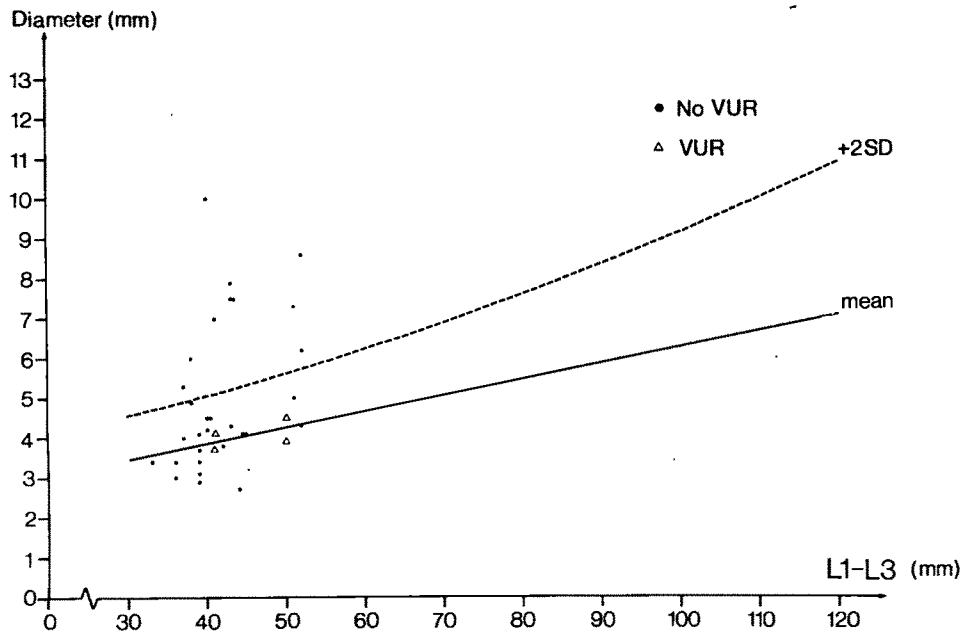


Fig. 2.—Ureteral diameters in 22 of 45 infants with screening bacteriuria who had at least one ureter visualized $\geq 50\%$ of its length (34 ureters) compared to reference group [9] (mean and 2 standard deviations [SD] above the mean). VUR = vesicoureteral reflux.

anisms, as laboratory results suggested the existence of bacteria or bacterial products in the kidney and ureter in most patients. It is more difficult to explain the ureteral widening in the group with bacteriuria found at screening, in which clinical and laboratory data did not suggest upper urinary tract involvement. Possibly, some of these patients had infection confined to the bladder and ureters without detectable involvement of the kidneys.

The clinical relevance of ureteral dilatation in children with urinary tract infection in the absence of manifest obstruction still is not clear. Its correlation to functional studies like renography and its relation to both bacterial adhesive properties and the development of renal damage are the subject of ongoing prospective studies.

ACKNOWLEDGMENT

Statistical analyses were performed by Anders Odén.

REFERENCES

- Little PJ, McPherson DR, de Wardener HE. The appearance of the intravenous pyelogram during and after acute pyelonephritis. *Lancet* 1965;1:1186-1188
- Shopfner CE. Nonobstructive hydronephrosis and hydroureter. *AJR* 1966;98:172-180
- Shopfner CE. Urinary tract pathology with sepsis. *AJR* 1970;108:632-640
- Welch TR, Nogrady BM, Outerbridge EW. Roentgenologic sequelae of neonatal septicemia and urinary tract infection. *AJR* 1973;118:28-38
- Kass EJ, Silver TM, Konnak JW, Thornbury JR, Wolfman MG. The urographic findings in acute pyelonephritis: non-obstructive hydronephrosis. *J Urol* 1976;116:544-546
- Silver TM, Kass EJ, Thornbury JR, Konnak JW, Wolfman MG. The radiological spectrum of acute pyelonephritis in adults and adolescents. *Radiology* 1976;118:65-71
- Roberts JA. Experimental pyelonephritis in the monkey. III. Pathophysiology of ureteral malfunction induced by bacteria. *Invest Urol* 1975;13:117-120
- Roberts JA, Domingue GJ. Experimental pyelonephritis in the monkey. II. The prognostic value of radionuclide evaluation of the urinary tract. *Invest Urol* 1975;12:374-380
- Hellström M, Hjälmås K, Jacobsson B, Jodal U, Odén A. Normal ureteral diameter in infancy and childhood. *Acta Radiol [Diagn]* (Stockh) 1985;26:433-439
- Jodal U, Lindberg U, Lincoln K. Level diagnosis of symptomatic urinary tract infections in childhood. *Acta Paediatr Scand* 1975;64:201-208
- Hellström M, Hjälmås K, Jacobsson B, Jodal U. Ureteral diameter in low-risk vesicoureteral reflux in infancy and childhood. *Acta Radiol [Diagn]* (Stockh) 1986;27:77-83
- IRSC (International Reflux Study in Children). International system of radiographic grading of vesicoureteric reflux. *Pediatr Radiol* 1985;15:105-109
- Bradley JW. *Distribution-free statistical tests*. London: Prentice-Hall, 1968:68-86
- Mantel N. Chi-square tests with one degree of freedom: extensions of the Mantel-Haenszel procedure. *J Am Statist Assoc* 1963;58:690-700
- Aronson AS, Svenningsen NW. DDAVP test for estimation of renal concentrating capacity in infants and children. *Arch Dis Child* 1974;49:654-659
- Berdon WE, Baker DH. The significance of a distended bladder in the interpretation of intravenous pyelograms obtained on patients with "hydronephrosis." *AJR* 1974;120:402-409
- Gill WB, Curtis GA. The influence of bladder fullness on upper urinary tract dimensions and renal excretory function. *J Urol* 1977;117:573-576
- Shapiro SR, Woerner S, Adelman RD, Palmer JM. Diabetes insipidus and hydronephrosis. *J Urol* 1978;119:715-719
- Hutch JA, Tanagho EA. Etiology of non-occlusive ureteral dilatation. *J Urol* 1965;93:177-184
- Grana L, Donnellan WL, Swenson O. Effects of gram-negative bacteria on ureteral structure and function. *J Urol* 1968;99:539-550
- Teague N, Boyarsky S. The effect of coliform bacilli upon ureteral peristalsis. *Invest Urol* 1968;5:423-426
- Teague N, Boyarsky S. Further effects of coliform bacteria on ureteral peristalsis. *J Urol* 1968;99:720-724
- King WW, Cox CE. Bacterial inhibition of ureteral smooth muscle contractility. I. The effect of common urinary pathogens and endotoxin in an in vitro system. *J Urol* 1972;108:700-705
- Fussell EN, Roberts JA. Chronic pyelonephritis: electron microscopic study. III. The ureter. *Invest Urol* 1979;17:108-119
- Fussell EN, Roberts JA. The ultrastructure of acute pyelonephritis in the monkey. *J Urol* 1984;133:179-183

Posttransplant Renal Artery Stenosis: Angiographic Study in 32 Children

Philip Stanley¹
 Mohammad Malekzadeh²
 Michael J. Diamant¹

Renal artery stenosis was identified in 32 children who either developed or had an exacerbation of hypertension after renal transplantation. One child developed renal artery stenosis in two sequential transplants. Renal artery stenosis occurred only in those patients who received transplants from cadavers. In 14 of the 15 patients with end-to-end renal artery anastomoses, the stenosis was at the anastomosis. In 14 of the 18 patients with end-to-side anastomoses, the stenosis was distal to the anastomosis.

Systemic hypertension after renal transplantation is not uncommon, occurring in at least 50% of recipients [1-3]. Many factors have been implicated as a cause, including acute tubular necrosis, rejection, steroids, hypercalcemia, retention of native kidneys, and intrinsic parenchymal disease of the graft [1-5]. However, the most important cause of sustained severe hypertension that begins after transplantation is transplant renal artery stenosis, a condition that is potentially correctable with surgery or angioplasty [1-4]. We describe our experience with 32 children who had severe systemic hypertension after renal transplantation and who were found to have renal artery stenosis on angiography.

Materials and Methods

Between January 1967 and May 1986, 343 children received 481 renal allografts at the Childrens Hospital of Los Angeles. Four hundred six transplants were from cadaveric donors and 75 were from live, related donors. Fifty-one patients who either developed or had an exacerbation of severe hypertension were investigated by arteriography. Thirty-two of the 51 patients were found to have renal artery stenosis and form the basis of this report. These 17 females and 15 males ranged in age from 6 months to 21 years at the time of arteriography.

Preangiographic preparation of the patients consisted of medical reduction of the diastolic blood pressure to below 100 mm/Hg. Hypertensive therapy (diazoxide 1-3 mg/kg IV bolus) and sublingual therapy (Nifedipine 5-10 mg) were given as necessary. Sedation was achieved by intramuscular injection of DPT (Demerol 25 mg, Phenergan 6.25 mg, and Thorazine 6.25 mg/ml) at a dose of 1 ml/10 kg to a maximum of 2 ml; this was supplemented by IV Valium in 1 mg aliquots as necessary. General anesthesia was not required. The femoral artery of the side of the renal graft was punctured in all patients. For the first 16 patients, end- and side-hole catheters were used; but over the past 4 years, a dilator has proved to be sufficient for the delivery of the contrast material. Initial intraarterial digital subtraction angiography with 30% Conray determined the optimal degree of obliquity for showing the anastomosis. This was followed by a film-changer series with 60% Conray. The filming rate was two frames/sec for 5 sec followed by one frame/sec for an additional 5 sec. Over the past year, the Conray has been replaced by low-osmolarity contrast agents (Iopamidol and Iohexol). The contrast dose per injection varied between 0.75 and 1 ml/kg (maximum 3 ml/kg). Overnight observation was routine.

Received July 16, 1986; accepted after revision September 23, 1986.

Presented at the annual meeting of the American Roentgen Ray Society, Washington, DC, April 1986.

¹ Department of Radiology, University of Southern California, and Childrens Hospital of Los Angeles, 4650 Sunset Blvd., Los Angeles, CA 90027. Address reprint requests to P. Stanley.

² Department of Pediatrics, Division of Nephrology, University of Southern California, and Childrens Hospital of Los Angeles, Los Angeles, CA 90027.

AJR 148:487-490, March 1987

0361-803X/87/1483-0487

© American Roentgen Ray Society

Results

Renal artery stenosis was demonstrated in 33 allografts in 32 patients. One patient developed renal artery stenosis in her first graft, which was subsequently lost. She also developed renal artery stenosis in her second graft.

None of the recipients of the 75 live, related donors developed renal artery stenosis. All 33 renal artery stenoses were from the 406 patients who received cadaveric transplants. The frequency of stenosis was 8% within the cadaver group and 6.9% overall. Of these 406 cadaver allografts, 40 were from young donors (2 years old or less) and 366 from donors 3 years old or more. Renal artery stenosis developed from 22 of 366 older donors and from 11 of 40 of the younger donors. Ten of the 11 grafts from young donors that later resulted in renal artery stenosis were transplanted into children more than 8 years old.

The degree of stenosis was classified as moderate if there was 50–70% narrowing, severe if 70–90%, and very severe if greater than 90%. The site of the stenosis correlated with the type of arterial anastomosis.

Of 15 patients with arterial anastomoses between the end of the donor renal artery and the end of the recipient hypogastric artery, the stenosis was at the anastomosis in 14. In two-thirds of patients the stenosis was tubular (Fig. 1) and in one-third it was discrete (Fig. 2). Nine patients had moderate stenosis, four severe, and two very severe. No poststenotic dilatation was present in this group of end-to-end anastomoses.

Of the 18 patients with arterial anastomoses between the end of the donor artery and the side wall of the recipient common or internal iliac artery, the stenosis was distal to the anastomosis in 14 patients and involved the anastomosis with distal extension in four. In nine of the 14 patients without involvement of the anastomosis, the maximum area of stenosis was within 5 mm of the anastomosis; in the other five, it was more distal. In 12 patients, the stenosis was tubular or a long taper; in six, it was discrete (Fig. 3). In one patient with

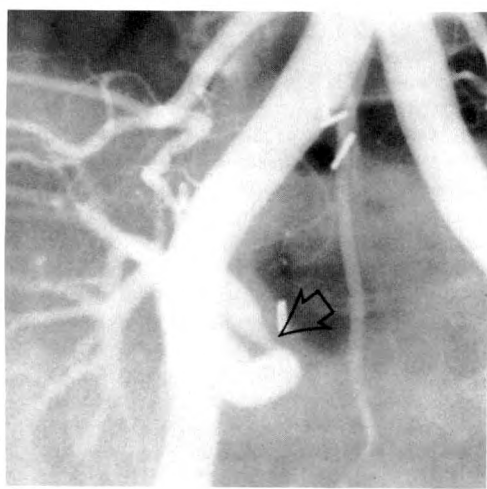
a long, tapered stenosis, discrete intimal ridging was present (Fig. 4). In two patients donor kidneys were supplied by two renal arteries. In one patient in whom both arteries were separately anastomosed end-to-side, a long tubular stenosis developed in the lower polar artery and a shorter stenosis in the more superior artery; both stenoses occurred distal to the anastomosis (Fig. 5). In the second patient in whom a cuff of donor aorta bearing both renal arteries was anastomosed to the recipient iliac artery, discrete stenosis developed in both donor arteries immediately beyond the anastomosis (Fig. 6). In one patient with end-to-side anastomosis, the stenosis was originally missed because of insufficient obliquity on the original arteriogram (Fig. 7). With end-to-side anastomosis, 10 patients had moderate stenosis, four severe, and four very severe.

Angiography was performed with only minor complications including small groin hematomas (six) and transient elevation of the creatinine level (three).

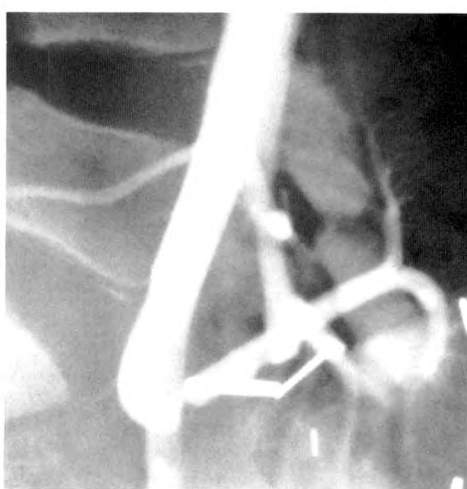
Discussion

The overall incidence of posttransplant renal artery stenosis in this series was 6.9%. Transplant renal artery stenosis unassociated with hypertension has been recorded in patients in whom posttransplant arteriography was routinely performed [6]. However, in our series, arteriography was performed only if the patients were severely hypertensive. All our patients had at least a 50% reduction in the diameter of the artery at the level of the stenosis, a degree regarded as significant by previous investigators [7–9].

Many factors acting either singly or in combination have been implicated in the etiology of posttransplant renal artery stenosis. In our series, only patients receiving a cadaver kidney developed renal artery stenosis; stenoses exclusively from cadaver donors were found in another series also [10]. Other investigators have commented on the higher incidence



1



2

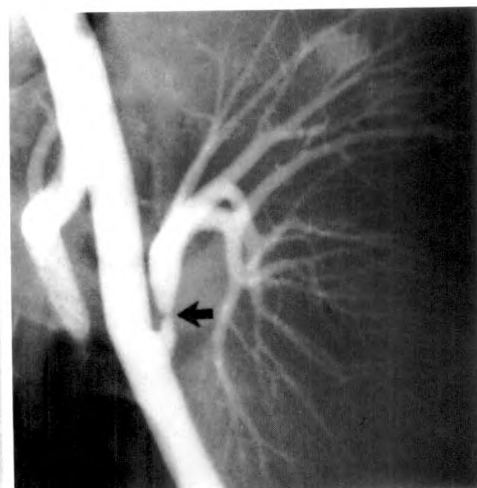
Fig. 1.—Long tubular stenosis (arrow) at level of anastomosis between donor artery and hypogastric.

Fig. 2.—Lateral view showing discrete severe stenosis at site of end-to-end anastomosis. Inferior ridge most probably results from intimal malalignment at time of original anastomosis.

Fig. 3.—Subtraction print of an oblique view of end-to-side anastomosis shows discrete stenosis distal to anastomosis with poststenotic dilatation.



3



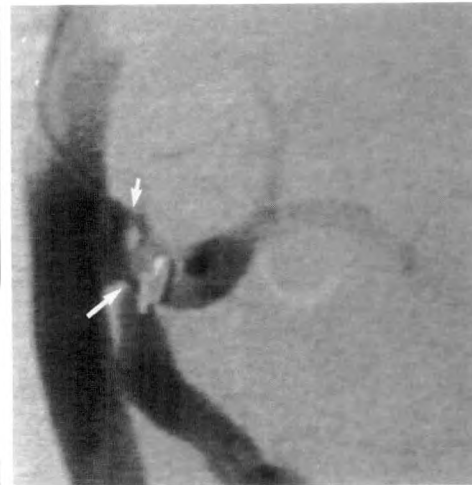
4

Fig. 4.—Oblique arteriogram shows tubular narrowing of most proximal part of donor artery with discrete ridge (arrow). Ridging may represent perfusion cannula damage or be from turbulence.

Fig. 5.—Oblique view of arteriogram shows separate donor arteries anastomosed end-to-side to recipient iliac artery. There is a long tubular narrowing of lower polar artery (solid arrows) and discrete narrowing of upper-pole artery immediately proximal to bifurcation (open arrow).

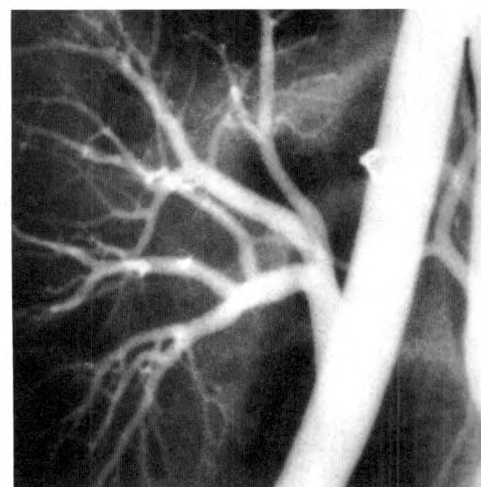


5

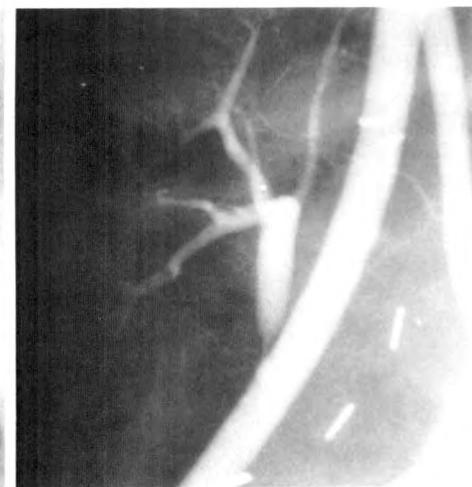


6

Fig. 6.—Intraarterial digital subtraction angiogram shows anastomosis of cuff of aorta bearing two donor arteries to side wall of external iliac artery. Both arteries have severe discrete stenosis (arrows) immediately distal to anastomosis with poststenotic dilatation.



A



B

Fig. 7.—A, Arteriogram shows apparent normal anastomosis. However, close inspection reveals probable stenosis obscured by overlying contrast-filled iliac artery.

B, Repeat film with more obliquity shows severe stenosis to better effect. In addition, there are angiographic features of chronic rejection.

of renal artery stenosis among cadaver donors [11, 12]. With live, related donors, there is usually a shorter warm ischemia time and better control of harvesting and perfusion; rejection is usually not so severe. Although there has been improvement in the harvesting of cadaver kidneys with aortic perfusion techniques, not all harvesting has been performed in this way, and some of the arterial injuries may be ascribed to harvesting. The donor artery may be damaged by stretching, by clamping, and by the perfusion cannula [13] along with stripping of the adventitia and vasovasorum in preparation for the anastomosis [5, 12, 14]. In some patients, immunofluorescence studies of the excised stenosis have implicated rejection [15]; this was not found in our series.

Previous authors have commented on the high rate of major arterial narrowing and occlusion after transplantation into very small infants [16, 17]. Our series emphasizes the problems of anastomoses between arteries of disparate size. When compared with older donors, the group of young donors (2 years old and younger) had a significantly higher incidence of recipient artery stenosis when transplanted into older children ($p < .001$).

Stenosis occurred predominantly at the anastomosis with end-to-end anastomosis, and beyond the anastomosis with end-to-side anastomosis. With end-to-end anastomoses, malalignment of the intima at the time of surgery and an unusually long donor renal artery (which may undergo torsion or kinking compounded by postoperative adhesions) have been implicated [5, 11, 13, 18].

Stenosis beyond an end-to-side anastomosis has been attributed in part to turbulence [12, 19]. Blood flow with an end-to-side anastomosis is not as efficient as with an end-to-end anastomosis [20]. The more acute the proximal angle between the donor and recipient arteries, the greater the loss of flow with subsequent distal turbulence. Also, it has been shown experimentally that moderate arterial kinking results in turbulence with intimal damage distal to the kinked segment [21].

It is essential that the correct radiologic projection be used to show the area of stenosis [22]. Previous investigators have recommended biplane techniques [23] or a steep lateral projection [24]. In one patient in this series, the stenosis was originally missed because the correct degree of obliquity was not used. Initial filming is now performed with intraarterial digital techniques. When the angle has been determined that best shows the stenosis, a final film-screen series is performed.

REFERENCES

1. Rao TKS, Gupta SK, Butt KMH, Kountz SL, Friedman EA. Relationship of renal transplantation to hypertension in end-stage renal failure. *Arch Intern Med* 1978;138:1236-1241
2. Waltzer WC, Turner S, Frohnert P, Rapaport FT. Etiology and pathogenesis of hypertension following renal transplantation. *Nephron* 1986;42:102-109
3. Curtis JJ. Hypertension: a common problem for kidney transplant patients. *Kidney* 1985;18:5-8
4. Malekzadeh MH, Brennan LP, Payne VG, Fine RN. Hypertension after renal transplantation in children. *J Pediatr* 1975;86:370-375
5. Smith RB, Cosimi AB, Lordon R, Thompson AL, Ehrlich RM. Diagnosis and management of arterial stenosis causing hypertension after successful renal transplantation. *J Urol* 1976;115:639-642
6. Howe HS, Woo KT, Tan LKA, Rauff A, Foong WC, Lim CH. A review of post-transplant renal artery stenosis in Singapore. *Singapore Med J* 1984;25:14-17
7. Jones BJ, Palmer FJ, Charlesworth JA, et al. Angiography in the diagnosis of renal allograft dysfunction. *J Urol* 1978;119:461-462
8. Pollini J, Guttman RD, Beaudoin JG, Morehouse DD, Klassen J, Knaack J. Late hypertension following renal allotransplantation. *Clin Nephrol* 1978;11:202-212
9. Hendriksson C, Nilsson AE, Thoren OK. Artery stenosis in renal transplantation. *Scand J Urol Nephrol [Suppl]* 1975;29:89-90
10. Rijkse JFWB, Koolen MI, Walaszewski JE, Terpstra JL, Vink M. Vascular complications in 400 consecutive renal allotransplants. *J Cardiovasc Surg (Torino)* 1982;23:91-98
11. Doyle TJ, McGregor WR, Fox PS, Maddison FE, Rodgers RE, Kauffman HM. Homotransplant renal artery stenosis. *Surgery* 1975;77:53-60
12. Lacombe M. Arterial stenosis complicating renal allotransplantation in man—a study of 38 cases. *Ann Surg* 1975;181:283-288
13. Ricotta JJ, Schaff HV, Williams GM, Rolley RT, Whelton PK, Harrington DM. Renal artery stenosis following transplantation: etiology, diagnosis, and prevention. *Surgery* 1978;84:595-602
14. Vidne B, Leapman SB, Butt KM, Kountz SL. Vascular complications in human renal transplantation. *Surgery* 1976;79:77-81
15. Kaufman JJ, Ehrlich RM, Dornfeld L. Immunologic considerations in renovascular hypertension. *J Urol* 1976;116:142-147
16. Trompeter RS, Bewick M, Haycock GB, Chantler C. Renal transplantation in very young children. *Lancet* 1983;1:373-375
17. Lum CT, Fryd DS, Polta TA, Najarian JS. Results of kidney transplantation in the young child. *Transplantation* 1982;34:167-171
18. Tilney NL, Rocha A, Strom TB, Kirkman RL. Renal artery stenosis in transplant patients. *Ann Surg* 1984;199:454-460
19. Morris PJ, Yadav RVS, Kincaid-Smith P, et al. Renal artery stenosis in renal transplantation. *Med J Aust* 1971;1:1255-1257
20. Szilagyi DE, Whitcomb JG, Schenker W, Waibel P. The laws of fluid flow and arterial grafting. *Surgery* 1960;47:55-73
21. Texon M, Imperato AM, Lord JW, Helsen M. Experimental production of arterial lesions. *Arch Intern Med* 1962;110:50-52
22. Raphael MJ, Steiner RE, Shackman R, Ware RG. Postoperative angiography in renal homotransplantation. *Br J Radiol* 1969;42:873-885
23. Rankin RS, Crummy AB, Belzer FO. Biplane arteriography for the evaluation of arterial stenosis in renal transplantation. *AJR* 1977;128:330-331
24. Kyaw MM. Ideal radiographic projection for renal transplant angiograms. *Radiology* 1973;107:275-278

Stones in the Urinary Bladder in Children and Young Adults

Robert L. Lebowitz¹
Blanca Vargas

Bladder stones were diagnosed in 22 children and young adults at The Children's Hospital, Boston, from 1969 to 1985. One half of the patients were less than 12 years old (mean, 11.9 years). One or more lithogenic factors were implicated in all but two. The most common causes were (1) the presence of an intravesical foreign body, (2) infection with *Proteus* (a urea-splitting organism), (3) exstrophy of the bladder, and (4) the presence of intestinal mucosa in the urinary tract. The radiologic features of the stones were not specific, and no special techniques were needed to identify them. Heightened awareness of patients at risk will lead to prompt diagnosis and treatment.

Stones in the urinary bladder have become unusual. The reason for their formation, such as the presence of an intravesical foreign body, is usually apparent, and often there is more than one cause. Bladder stones are typically discovered during urologic evaluation, either on radiographs or sonograms.

Materials and Methods

A review of the records of the Department of Radiology at The Children's Hospital, Boston, from 1969 to 1985 revealed 22 patients with a stone or stones in the urinary bladder. The clinical and radiologic findings were analyzed and stones were categorized according to number, size, shape, and radiographic density.

Results

Fourteen of the patients were female (1.7:1). The age of the patient at the time of diagnosis ranged from 9 months to 35 years (mean 11.9 years). Half were less than 12 years old. Most of the stones were found on radiographs made during periodic urinary tract screening, and most patients were asymptomatic. In only two was a stone suspected clinically.

All patients had some underlying congenital urinary tract abnormality. In a few it was minor (mild vesicoureteral reflux) (Fig. 1), but most had severe and complex anomalies and had undergone one or several reconstructive operations. The stones were considered to be idiopathic (primary lithiasis) in only two children. In all the other patients at least one lithogenic factor was recognized (secondary lithiasis); these included: (1) an intravesical foreign body, (2) infection with a urea-splitting organism (usually *Proteus* species), (3) intestine inserted into the urinary tract, such as augmentation of the bladder with bowel or an intestinal conduit or both, (4) exstrophy of the bladder, (5) hypercalciuria, and (6) stasis of urine.

In nine patients (41%), a single lithogenic factor was present, whereas in 12 (55%), there were two or more. Ten of these 12 (45%) were patients who had a foreign body in addition to either augmentation of the bladder with intestine, exstrophy of the bladder, or an ileal conduit. Two patients with multiple factors had a foreign body in addition to infection of the urinary tract with *Proteus* (9%).

Received October 7, 1986; accepted after revision November 14, 1986.

¹ Both authors: Department of Radiology, The Children's Hospital and Harvard Medical School, Boston, MA 02115. Address reprint requests to R. L. Lebowitz, Dept. of Radiology, The Children's Hospital, 300 Longwood Ave., Boston, MA 02115.

AJR 148:491-495, March 1987
0361-803X/87/1483-0491
© American Roentgen Ray Society



Fig. 1.—2½-year-old girl with urinary infection (*Escherichia coli*) and grade 2/5 right vesicoureteral reflux. Scout radiograph before voiding cystourethrogram shows stone. This patient is one of only two in whom no definite lithogenic factor was recognized.



Fig. 2.—Large, round bladder stone with pubic hair as nidus found during routine periodic study in a 19-year-old woman with neurogenic vesical dysfunction. A previous ileal conduit had been discontinued and she was performing clean intermittent self-catheterization.



Fig. 3.—16-year-old girl who has had turn-in of her exstrophied bladder and reconstruction of her bladder neck and urethra. A suprapubic tube was in her bladder for 2 weeks, 1 year before the discovery of this large, oval bladder stone on a routine, periodic study.

In 19 patients (86%) the stones were single, round or oval, and usually large (Figs. 2–4). The stone was occasionally enormous and filled the lumen of the bladder (Fig. 4C). Multiple stones were smaller, impinged on each other, and were faceted (Fig. 5). The stones were radiopaque in all patients, and were of homogeneous density in all but four. Three patients had laminated stones (Fig. 6). The remaining child had several stones during the period of this report, one of which had a central dense area surrounded by a less opaque margin (Fig. 4B). In all of the stones that were analyzed, there was an admixture of crystalline components. Thus, it was not possible to predict the exact composition of a stone on the basis of its radiographic appearance. The appearances on sonography were also nonspecific, showing only a strongly echogenic focus within the urine-filled bladder with acoustic shadowing (Fig. 7).

In addition to the stones in the bladder, three patients also had stones in extravescical locations within the genitourinary tract. One boy had stones in his genital ducts (abnormal seminal vesicles or vasa deferens), another had a stone in a urethral diverticulum, and one had a stone in his posterior urethra. This latter stone undoubtedly arose in his bladder (Fig. 8). A foreign body was identified as the nidus for stone formation in four patients: a stent catheter in one (Fig. 9), a Foley catheter in one (Fig. 10), and suture material in two. A pubic hair introduced into the bladder during clean intermittent self-catheterization (CIC) was thought to be the sole lithogenic factor in one patient (Fig. 6), but the method of removal of the stone (see following paragraph) precluded proving this.

In all, a routine periodic search for residual and/or recurrent stones was carried out after the stones were removed either by transurethral lithotripsy (all were crushed except one that was ultrasonically disrupted) or by means of suprapubic lithotomy. In nine (41%) the stones recurred and were discovered 1 to 2 years after removal of the original stone in all but

one. This child presented with a recurrent stone after only 2 months and had infection of his urine with *Proteus*. Recurrences were more frequent (seven of 14) (50%) when removal of the stone was accomplished by transurethral lithotripsy. When suprapubic lithotomy was performed, only two (28%) of seven patients had recurring stones. The stone was not removed in one patient in whom it was residing in an unused bladder.

Discussion

Bladder stones are common in dogs and cats [1]. In humans, bladder stones have been described since at least 4800 BC [2] and through the first third of this century they were common, particularly in children, in a large number of regions including the United States, England, and Western Europe [3]. During the last 40 years, however, the incidence of bladder stones in childhood in these countries has decreased strikingly and they are now primarily confined to a broad "belt" running from North Africa to India and Indonesia [4]. These primary or idiopathic calculi are likely related to nutritional deficiencies. Most bladder stones in children now seen in the United States are secondary calculi, as was the case in virtually all of the patients in this series. Whereas endemic or primary calculi of the bladder have been reported to be more common in males [2], the mainly secondary stones in this series were more common in females.

Among the lithogenic factors previously reported, stasis was the major cause [4]. In this series, however, significant stasis of urine was seen in only one patient. The role of infection in stone formation is linked specifically to the presence of urea-splitting organisms in the urine, especially *Proteus mirabilis* [5]. These bacteria have been shown to be deeply embedded in the stone, protected from the action of antibacterial agents (Fig. 11). This is of practical importance

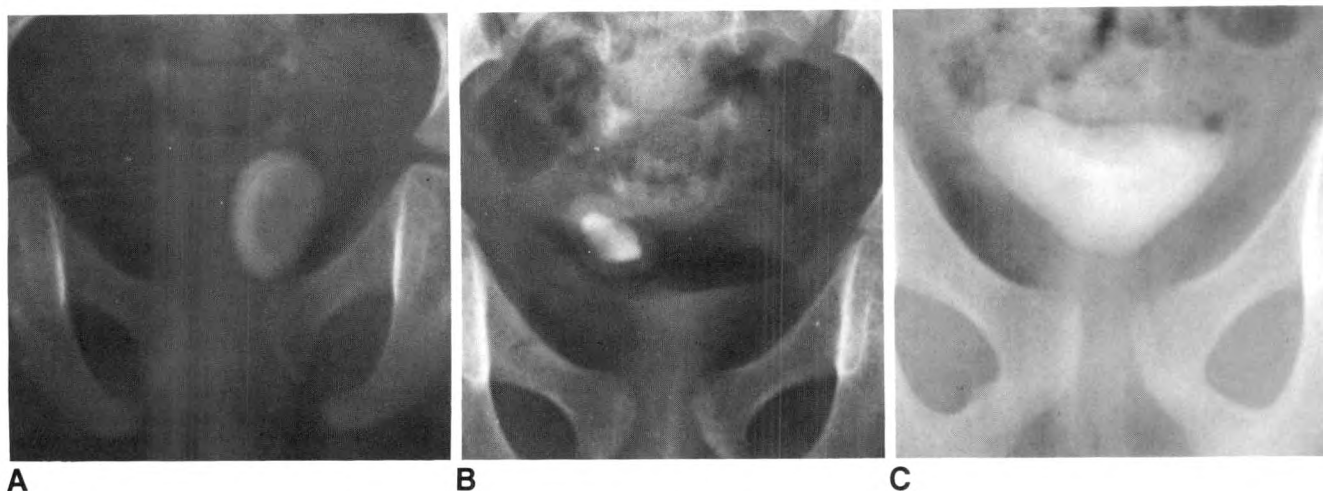


Fig. 4.—7-year-old girl with urogenital sinus anomaly. Her urine was infected with *Proteus*.

A, Large, oval bladder stone removed by transurethral litholapaxy.

B, 2 years later. Large bladder stone with dense center and less opaque margin also removed by transurethral litholapaxy.

C, 5 years later. Enormous bladder stone.



Fig. 5.—Previous ileal conduit. Turned-in bladder augmented with cecum. Multiple small-faceted stones formed on suture material. (Catheter in bladder before voiding cystourethrogram.)

Fig. 6.—15-year-old girl with sacral myelomeningocele and neurogenic vesical dysfunction who noticed that when she inserted her catheter it bumped into something solid. This large, laminated bladder stone with pubic hair as the nidus was discovered. She was one of only two patients in whom a stone was suspected from symptoms alone.

Fig. 7.—Sonogram reveals stone as strongly echogenic focus in bladder. Stone casts an acoustic shadow.

because even minute particles left at surgery represent foci of persistent infection that may result in recurrent stone formation (Fig. 4). This vicious cycle occurred in several patients, and in one of these a stone recurred only 2 months after transurethral lithotripsy. In three patients in this series, either infection with a urea-splitting species was the sole lithogenic factor or it was present in association with an intravesical foreign body.

Hypercalciuria in children is a well-known cause of urinary tract calculi [6]. In this series hypercalciuria was found to be the lithogenic factor in only one patient, and the metabolic

disorder was idiopathic. Associated nephrolithiasis was not found, but the bladder stone probably came from the kidney.

Encrustation of an intravesical foreign body by calcium salts is a well-known cause of bladder stones [4] and can be identified by an analysis of the nidus if the specimen is available. After transurethral lithotripsy, however, the stone is fragmented and this type of analysis is often not possible. Sutures [4], catheters, and pubic hair [7] (the latter introduced during CIC) (Figs. 2, 6, and 12) have all been shown to be the nidus for formation of a stone. All but one of our patients in whom CIC was related to bladder stones were female. The

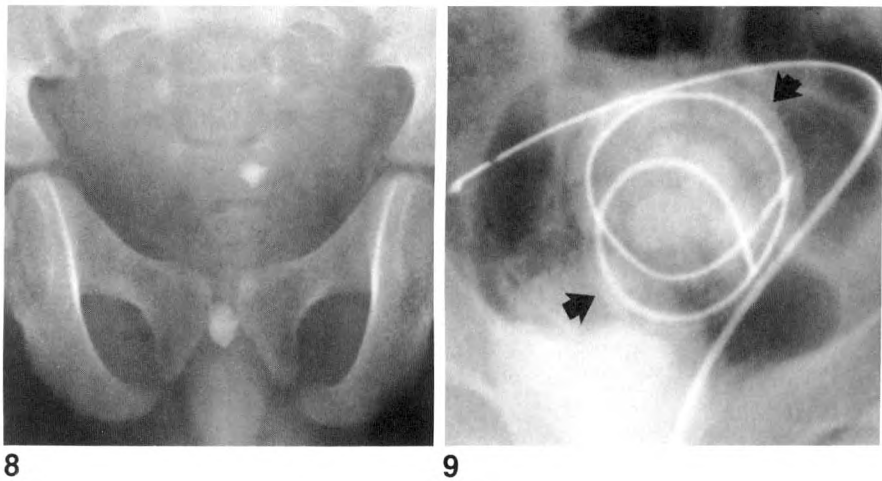


Fig. 8.—2½-year-old boy with idiopathic hypercalciuria and bilateral grade 2/5 reflux. There is one small stone in the bladder and another in the posterior urethra. The latter presumably formed in the bladder.

Fig. 9.—3-year-old boy 1 year after repair of hypospadias. Missing urethral stent (an infant feeding tube) is coiled in bladder. It was incorrectly presumed to have fallen out 1 year before, but actually served as a nidus for the formation of a faintly opaque stone (arrows). (Catheter in bladder before voiding cystourethrogram)

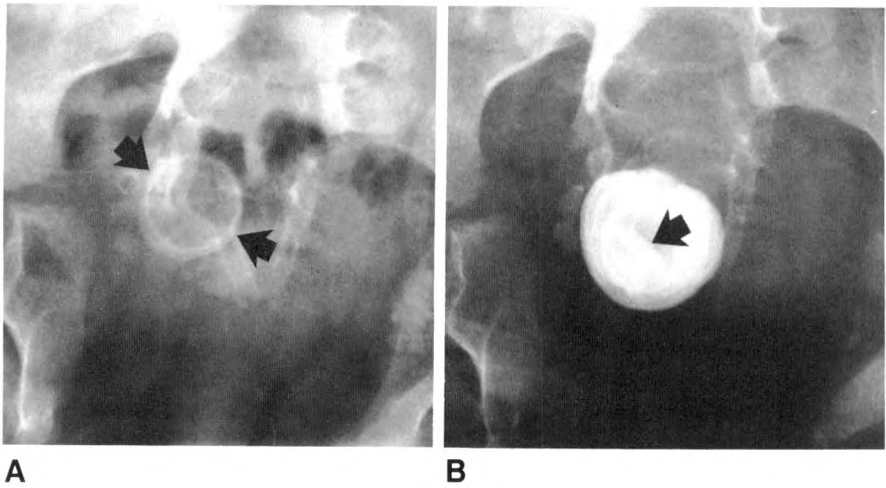


Fig. 10.—6-year-old girl with cloacal exstrophy has a turned-in bladder augmented with intestine and a reconstructed urethra. A Foley catheter was in place for 50 days.

A, Plain radiography just before removal of catheter. Faintly calcified cast of catheter not recognized (arrows). Catheter removed without difficulty.

B, 1 year later. Plain radiograph shows densely calcified, laminated cast of balloon of previous Foley catheter with cast of tip inside (arrow) and two small satellite stones.

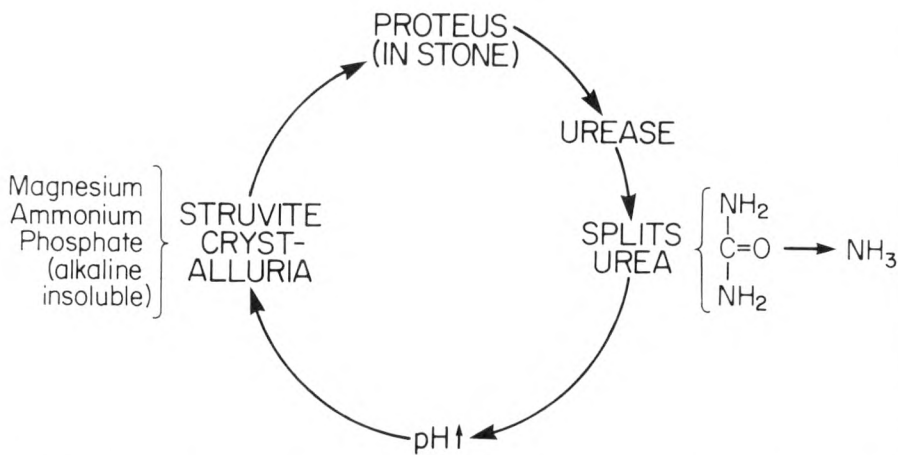


Fig. 11.—Diagram of interaction between *Proteus* and stone. *Proteus* in stone produces urease, which splits urea with production of ammonia. Urine becomes alkaline, and struvite becomes less soluble and precipitates. Stone becomes larger and bacteria less accessible to antibiotics.

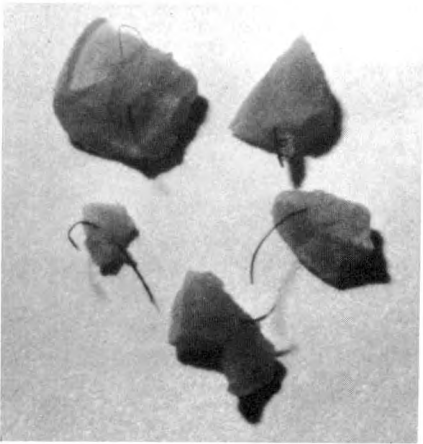


Fig. 12.—Solitary, densely opaque bladder stone was removed and then split into several fragments. Pubic hair(s) clearly visible. (Courtesy of S. Bauer.)

possibility of introducing pubic hair during self-catheterization is more likely in girls. The radiographic appearance of stones in patients performing CIC was different in this series (Figs. 2 and 6) than in those previously reported [7].

A definite association between ileal dysfunction (such as inflammatory bowel disease or removal of a portion of the terminal ileum from the fecal stream for use in the urinary tract) has been established [8-10]. The patients described here with ileal dysfunction had it because of a ileal loop, ileocecal loop, or ileocecal augmentation of the bladder.

Adenomucosa in the urinary tract probably plays a role in lithogenesis as well. It is assumed that the mucus produced provides a nidus for the formation of calculi. This occurs (1) when the bladder is augmented with intestine, (2) when bowel is used to bridge a ureteral gap (during "undiversion," for example), or (3) when there is exstrophy of the bladder and the bladder itself contains rests of bowel mucosa [11].

In the patients in this series, the most common presumptive cause for stone formation was the association of an intravesical foreign body with either augmentation of the bladder, exstrophy of the bladder, or ileal dysfunction; the second most common cause was an intravesical foreign body alone. Eighty-six percent of the patients had a long-standing intravesical foreign body either alone or in association with other lithogenic factors. When more than one factor was present, the individual role played by each is impossible to determine.

The detection of stones in the patients reported here was straightforward with plain radiographs or sonograms or both when the stones were searched for. Several stones were originally overlooked because they were not suspected and therefore were not looked for, or because the film did not include the inferior portion of the patient's pelvis, or because the bladder was empty during sonography and thus there was no "acoustic window."

The bladder stones were usually single, large, rounded, and of homogeneous calcific density and thus were evident on a plain radiograph. Excretion urography or cystography with a dilute contrast agent can confirm the diagnosis by showing the stone as an intravesical filling defect. Sonography was very helpful in confirming or detecting the bladder stones.

Uroradiologic follow-up after removal of the stone is rec-

ommended to detect recurrences, which were more common after procedures that fragmented the stone and washed out the fragments (transurethral lithotripsy) than after the stone was removed intact (suprapubic lithotomy).

A high index of suspicion for bladder stones helps to detect them without undue delay. Patients at risk include those with (1) long-standing intravesical foreign bodies such as catheters, (2) those with intestine incorporated in the urinary tract or with exstrophy of the bladder, and (3) those on CIC who are postpubertal (that is, who have pubic hair).

Periodic evaluation of patients at special risk for bladder stones should be done and should include sonography [12] and, when needed, a plain radiograph of the pelvis.

ACKNOWLEDGMENTS

Helen Lebowitz edited the manuscript. It was typed by Robert Davis, Ann Kotell, and Judith Cohen.

REFERENCES

1. Ettinger SJ. *Textbook of veterinary internal medicine*. Philadelphia: Saunders, 1975;1547-1555, 1568-1576
2. Van Reen R. Idiopathic urinary bladder stones of childhood. *Aust NZ J Surg* 1980;50:18-22
3. Shaw AB. The Norwich School of Lithotomy. *Med Hist* 1970;14:221-259
4. Banner MP, Pollack HM. Radiologic evaluation of urinary calculi. In: Roth RA, Finlayson B, eds. *Stones: clinical management of urolithiasis*. Baltimore: Williams & Wilkins, 1983:146-152
5. Stamey TA. *Pathogenesis and treatment of urinary tract infections*. Baltimore: Williams & Wilkins, 1980:430-474
6. Roy S, Stapleton FB, Noe HN, Jerkins G. Hematuria preceding renal calculus formation in children with hypercalciuria. *J Pediatr* 1981;99:712-715
7. Amendola MA, Sonda LP, Diokno AC, Vidyasagar M. Bladder calculi complicating intermittent clean catheterization. *AJR* 1983;141:751-753
8. Kirks DR. Lithiasis due to interruption of the enterohepatic circulation of bile salts. *AJR* 1979;133:383-388
9. Chikos PM, McDonald GB. Regional enteritis complicated by nephrocalcinosis and nephrolithiasis. *Radiology* 1976;127:75-78
10. Hoffman AF, Thomas PJ, Smith LH, McCall JT. Pathogenesis of secondary hyperoxaluria in patients with ileal resection and diarrhea. *Gastroenterology* 1974;66:1114-1122
11. White P, Lebowitz RL. Exstrophy of the bladder. *Radiol Clin North Am* 1977;15:93-107
12. Rosenfield AJ, Taylor KJW, Weiss RM. Ultrasound evaluation of bladder calculi. *J Urol* 1979;121:119-120

Books Received

Receipt of books is acknowledged as a courtesy to the sender. Books that appear of sufficient interest will be reviewed as space permits.

- Digital Radiography: Selected Topics.** Edited by James G. Ker-eiakes, Stephen R. Thomas, and Colin G. Orton. New York: Plenum, 193 pp., 1986. \$39.50
- Two-Dimensional Real-Time Ultrasonic Imaging of the Heart.** Edited by Emilio R. Giuliani. Boston: Nijhoff, 423 pp., 1986. \$92.50
- NMR in Living Systems.** Edited by T. Axenrod and G. Ceccarelli. Dordrecht, The Netherlands: Reidel, 410 pp., 1986. \$64
- Environmental Health Criteria 55: Ethylene Oxide.** By the World Health Organization. Geneva: World Health Organization, 79 pp., 1986. Swiss Fr/9
- Biological Effects and Exposure Criteria for Radiofrequency Electromagnetic Fields.** NCRP Report. Bethesda, MD: NCRP, 382 pp., 1986.
- Index for Radiological Diagnoses, 3rd ed.** By the American College of Radiology. Reston, VA: American College of Radiology, 170 pp., 1986.
- Atlas Illustré des Indications Classiques et Nouvelles de l'Échographie.** By Rodolphe Gombergh. France: Polaroid, 559 pp., 1985.
- Atoms, Radiation, and Radiation Protection.** By James E. Turner. New York: Pergamon, 324 pp., 1986.
- Neurology.** Edited by K. Poech, H.-J. Freund, and H. Ganshirt. New York: Springer-Verlag, 497 pp., 1986. \$146.50
- NCI Monographs.** Edited by Robert E. Wittes. Bethesda, MD: National Institutes of Health, 165 pp., 1986. \$8.50
- Clinical Applications of Continuous Infusion Chemotherapy and Concomitant Radiation Therapy.** Edited by C. Julian Rosenthal and Marvin Rotman. New York: Plenum, 248 pp., 1986.
- Physician's Guide to Cancer Care Complications.** Edited by John Laszlo. New York: Dekker, 345 pp., 1986.
- Cardiac Doppler Diagnosis, vol. II.** Edited by Merrill P. Spencer. Boston: Nijhoff, 244 pp., 1986.
- Ultrasound Diagnosis in Obstetrics and Gynecology.** Edited by B. K. Wittmann. New York: Springer-Verlag, 495 pp., 1986.
- Diagnostic Nuclear Medicine: Patient Studies.** By Henry N. Wagner, Julia W. Buchanan, and Danelo Expinola-Vassallo. Chicago: Year Book Medical, 430 pp., 1986
- Computed Tomography of the Gastrointestinal Tract.** Edited by Morton A. Meyers. New York: Springer-Verlag, 1986.
- Cardiac Imaging: New Technologies and Clinical Applications.** Edited by Morris N. Kotler and Robert M. Steiner. Philadelphia: Davis, 454 pp., 1986. \$85
- Polypoid Disease of the Colon: Emphasis on Radiologic Evaluation.** Edited by David J. Ott and Wallace C. Wu. Baltimore, MD: Urban & Schwarzenberg, 1986.
- Multiplanar CT of the Spine.** By Stephen L. G. Rothman and William V. Glenn, Jr. Baltimore, MD: University Park Press, 520 pp., 1986. \$125
- 1986 Year Book of Nuclear Medicine.** Edited by Paul B. Hoffer. Chicago: Year Book Medical, 1986.
- Gastrointestinal Angiography.** Edited by Dean Manke. Philadelphia: Saunders, 1986. \$47.95
- Cranial Computed Tomography in Infants and Children.** By Eric N. Faerber. Philadelphia: Lippincott, 237 pp., 1986. \$39.59
- Urologic Pathology.** By Robert O. Petersen. Philadelphia: Lippincott, 762 pp., 1986. \$87.50
- Notes on Radiological Diagnosis.** By Lawrence S. W. Lau and John F. De Camp. Philadelphia: Saunders, 204 pp., 1986. \$24.95
- Amphetamines and pH-shift Agents for Brain Imaging.** Edited by H. J. Biersack and C. Winkler. Berlin: de Gruyter, 186 pp., 1986. \$67.65
- Nuclear Techniques in Diagnostic Medicine.** Edited by P. P. Van Rijk. The Hague, The Netherlands: Nijhoff, 527 pp., 1986. \$156
- The Complete Review of Radiography.** By Kathryn M. Marzano and Pauline D. Lyons. New York: Wiley, 252 pp., 1986. \$19.50
- Orthopedic Radiology.** By Barbara N. W. Weissman and Clement B. Sledge. Philadelphia: Saunders, 679 pp., 1986. \$75
- Normal Variants and Pitfalls in Imaging.** By James B. Vogler, Clyde A. Helms, and Peter W. Callen. Philadelphia: Saunders, 698 pp., 1986. \$95
- Quantitative Obstetrical Ultrasonography.** By R. L. Deter, R. B. Harrist, J. C. Birnholz, and F. P. Hadlock. New York: Wiley, 377 pp., 1986. \$45
- Cancer of the Stomach.** Edited by Paul E. Preece, Alfred Cuschieri, and James M. Wellwood. Orlando, FL: Grune & Stratton, 311 pp., 1986. \$44.50
- Physical Techniques in Clinical Hyperthermia.** Edited by Jeffrey W. Hand and James R. James. New York: Wiley, 558 pp., 1986. \$115
- Radioactive Waste.** NCRP Report. Bethesda, MD: NCRP, 289 pp., 1986.
- Guide to the Ultrasound Examination of the Abdomen.** By M. Leon Skolnick. New York: Springer-Verlag, 240 pp., 1986. \$51
- Pediatric Imaging Doppler Ultrasound of the Chest: Extracardiac Diagnosis.** By James C. Huhta. Philadelphia: Lea & Febiger, 225 pp., 1986. \$42.50
- Radiotherapy in Clinical Practice.** Edited by H. F. Hope-Stone. Boston: Butterworth, 454 pp., 1986. \$115
- The Radiologic Clinics of North America. Vascular Imaging: Angiography and the New Modalities.** Edited by Harvey A. Koolpe. Philadelphia: Saunders, 525 pp., 1986.
- Ultrasound Annual 1986.** Edited by Roger C. Sanders and Michael C. Hill. New York: Raven, 279 pp., 1986. \$79
- Manual of Radiographic Technique.** By P. E. S. Palmer, K. Holm, and E. Lehtinen. Geneva: World Health Organization, 256 pp., 1986. \$15
- Cardiovascular Procedures.** Diagnostic Techniques and Therapeutic Procedures. By Ara G. Tilkian and Elaine Kiess Daily. St. Louis: Mosby, 521 pp., 1986.
- Diagnostic Imaging in Surgery.** By Ronald L. Eisenberg. New York: McGraw-Hill, 834 pp., 1987. \$135
- An Insider's Guide for Medical Authors & Editors.** By Peter Morgan. Philadelphia: ISI Press, 110 pp., 1986. \$14.95
- Cerebral Ischaemia.** Edited by Jacques Bories. Berlin: Springer-Verlag, 150 pp., 1986. German marks/128
- Cisternographic Anatomy of the Posterior Cranial Fossa.** By R. G. M. de Slegte, J. Valk, A. H. M. Lohman, and F. W. Zonneveld. The Netherlands: Van Gorcum, 170 pp., 1986.
- Computed Tomography of the Cranial Skeleton (Face and Skull).** By Marcelle Megret. New York: Springer-Verlag, 168 pp., 1986. \$22

The Duplex Collecting System in Girls with Urinary Tract Infection: Prevalence and Significance

George S. Bisset III¹
Janet L. Strife

The association between vesicoureteral reflux, parenchymal scarring, and urinary tract infection in children with nonduplicated collecting systems is well known, but similar data for children with duplex systems are sparse. The purpose of this study was to determine the prevalence of duplex anomalies in girls with a history of urinary tract infection and to compare the prevalence of associated reflux and parenchymal scarring to that found in girls with nonduplex systems. Voiding cystourethrograms and excretory urograms of 560 girls referred for evaluation of urinary tract infections were reviewed retrospectively. Duplex collecting systems (complete and partial) were found in 8%. Vesicoureteral reflux was seen in 69% of complete duplex systems and in 22% of partial duplex systems. Parenchymal scarring was evident in 17% of those girls with complete duplication and in 6% of those with incomplete duplication. The statistics for girls with partial duplication were very similar to those for girls with urinary tract infection and nonduplex systems. These data indicated that girls with partial duplex systems clinically appear similar to those girls with anatomically normal systems. Girls with complete duplex systems had a higher prevalence of vesicoureteral reflux and associated anomalies, indicating a need for closer follow-up and/or surgical intervention.

A duplex collecting system is the most common malformation of the urinary tract [1], and vesicoureteral reflux is the most common abnormality associated with it. Although the association between urinary tract infection, vesicoureteral reflux, and parenchymal scarring in a nonduplicated collecting system is well known [2], little has been written about the prevalence and distribution of vesicoureteral reflux and parenchymal scarring in duplicated systems.

We retrospectively evaluated the voiding cystourethrograms and excretory urograms of girls with a history of urinary tract infection who had duplex systems. This subgroup of patients with duplicated systems was compared to girls with nonduplex systems.

The purposes of this study were to evaluate (1) the prevalence of duplication anomalies, (2) the prevalence and distribution of vesicoureteral reflux, (3) the correlation of vesicoureteral reflux with parenchymal scarring, and (4) the short-term natural history of girls with these anomalies.

Materials and Methods

Definitions of the entities to be described have been established by The Committee on Terminology, Nomenclature, and Classification, Section on Urology, American Academy of Pediatrics [3]. A duplex kidney is defined as any kidney with two pelvicaliceal systems. Partial duplication includes those duplex kidneys with single ureters or with bifid ureters that join before emptying into the bladder. Complete duplication means duplex kidneys with two ureters that empty separately into the genital or urinary tract. Children with simple bifid renal pelves only were excluded from the study.

Voiding cystourethrograms and excretory urograms of 560 randomly selected outpatient girls referred for evaluation of urinary tract infection were reviewed. Routine films of the

Received September 8, 1986; accepted after revision November 11, 1986.

Presented at the annual meeting of the Society for Pediatric Radiology, Washington, DC, April 1986.

¹ Both authors: Departments of Radiology and Pediatrics, University of Cincinnati College of Medicine, Cincinnati, OH 45267, and the Division of Radiology, The Children's Hospital Medical Center, Elland and Bethesda Avenues, Cincinnati, OH 45229. Address reprint requests to G. S. Bisset III, Division of Radiology, The Children's Hospital Medical Center, Elland and Bethesda Avenues, Cincinnati, OH 45229.

AJR 148:497-500, March 1987
0361-803X/87/1483-0497

© American Roentgen Ray Society

bladder obtained during voiding cystourethrography included an anteroposterior and both oblique views and a film taken after voiding. Additional views of the kidney were taken when reflux occurred. The voiding cystourethrograms were obtained within 24 hr of the excretory urograms. Criteria for selection and examination techniques have been reported [4].

Both the voiding cystourethrogram and excretory urogram were used to categorize patients as having either partial or complete duplication. It was, at times, impossible to determine if the ureters joined within the bladder wall, even with adequate spot films and fluoroscopy. For purposes of categorization, if two ureters could not be clearly recognized as entering separately into the bladder, the system was classified as partial duplication (Fig. 1). None of the patients had cystoscopy, and therefore some girls who are classified as having complete duplication may, indeed, have partial duplication. Vesicoureteral reflux was classified according to the International Classification [5].

Excretory urograms were evaluated for renal size, position, contour, and parenchymal scarring. The radiologic criteria for scarring included blunting or clubbing of calices and loss of parenchyma, with or without indentation of the kidney surface [6].

The age of the patients ranged from 1 month to 15 years (mean, 5.2 years). All studies were performed between April 1978 and March 1986.

Results

A total of 44 girls were included in the study group. There were 54 duplex systems and 34 normal systems.

Complete Duplication

Complete duplication was seen in 36 kidneys in 26 patients. It was right-sided in 14 kidneys (39%) and left-sided in 22 (61%). In 31 of 36 kidneys, the collecting system in the lower pole was larger than the system in the upper pole. In the remaining five kidneys, both poles were of equal size. The corresponding parenchymal size correlated closely with the number of calices unless scarring was present.



Fig. 1.—Excretory urogram shows two ureters entering bladder on right side and one entering on left. A voiding cystourethrogram showed vesicoureteral reflux into both right ureters.

Vesicoureteral reflux was seen in 25 (69%) of the 36 complete duplex systems. It occurred most commonly into the lower pole moiety (72%). Voiding cystourethrograms showed reflux into both poles in 20% and into the upper pole exclusively in 8%.

Renal parenchymal scarring was noted in 6 (17%) of 36 of those kidneys with complete duplication. Each of these renal systems showed vesicoureteral reflux on the voiding cystourethrogram. Five of six kidneys had grade II–IV vesicoureteral reflux into the lower poles; the remaining kidney had grade II reflux into the upper pole. For comparison, three (9%) of 34 nonduplicated systems had parenchymal scars. The prevalence of vesicoureteral reflux in the contralateral non-duplex systems was 26% (9/34).

Partial Duplication

Of 18 kidneys with partial duplication, 10 (56%) were right-sided and eight (44%) were left-sided. The lower-pole collecting system was the largest of the two duplicated segments in 13 systems, the upper-pole system was largest in one, and the two poles were approximately equal in size in four.

Vesicoureteral reflux was present in four (22%) of 18 kidneys with partial duplication. In every case, vesicoureteral reflux occurred into both poles. Two patients had grade II vesicoureteral reflux, one had grade III, and one had grade IV. Only one girl with partial duplication (the previously mentioned patient with grade IV vesicoureteral reflux) had parenchymal scarring.

Follow-up Studies

Of the 44 patients evaluated, 15 girls (with a total of 20 duplex systems) had follow-up voiding cystourethrographic studies from 1 to 4 years after the first study. Of the 16 complete duplex systems, four showed no vesicoureteral reflux at any time, and four patients had surgical intervention between examinations. In the remaining eight systems, no change was seen in two, three showed improvement in grade of reflux, two showed complete resolution of vesicoureteral reflux, and one patient who had had no vesicoureteral reflux in the first study had developed grade II reflux on follow-up examination.

In the four girls with partially duplicated systems who were followed up, two patients had had surgery (one had a ureteroneocystostomy, and the other had repair of ureteropelvic junction obstruction of the lower pole), and two had improvement or resolution of the vesicoureteral reflux.

In the entire group of girls with duplex systems, associated urinary tract anomalies were present in 16%. These anomalies are shown in Table 1.

Discussion

Duplex anomalies of the urinary tract are a common finding in girls with urinary tract infection. In our study the duplex anomaly occurred in one of 12 patients (8% of total group with urinary tract infections). Complete duplication occurs in 5% of girls with urinary tract infection, and partial duplication

TABLE 1: Associated Anomalies in Girls with Duplex Collecting Systems

Anomaly	No. of Patients
Ureterocele	2
Malrotation	2
Ureteropelvic junction obstruction	2
Bladder diverticulum	1

occurs in 3%. This incidence of partial duplication may be somewhat higher if patients with bifid renal pelves are included. The total prevalence of 8% in our selected population is higher than the incidence of 0.7% noted by Campbell [7] in a large autopsy series of males and females. Nordmark [1] and Nation [8] found an incidence of duplication of 2–4% in a large group of male and female patients who underwent excretory urography for urinary tract symptoms. Our higher prevalence may reflect our selection of girls only. Duplication anomalies of the ureters are two to five times more common in females than in males [9–11].

Embryologically, the collecting tubules, the calices, and the pelvis are formed from the ureteric bud. When there is premature division of the ureteric bud or a double ureteric bud, two separate collecting systems may be formed within the kidney with development of two separate renal pelves. There may be a complete double ureter, or the ureters may join anywhere along their course before entrance into the bladder. The upper renal pelvis usually is the smaller of the two and may consist of one or two groups of calices, whereas the lower renal pelvis may appear to represent an entire renal collecting system or only the middle and lower caliceal systems. In most of our patients, the lower collecting system was larger and had more calices than the upper pole. When there is a disproportion between the renal parenchymal size and the number of calices, renal scarring may be present. Mackie and Stephens [12] have suggested that the caliceal changes associated with reflux may not be the result of reflux or infection. They speculated that a thin cortex may reflect abnormal renal development that is associated with, but not the result of, reflux.

Vesicoureteral reflux is the most common problem associated with duplicated systems. Our data indicate that in those girls with complete duplication and urinary tract infection, vesicoureteral reflux is more likely present than not; it occurred in 69%. Fehrenbaker et al. [2] noted a 72% incidence of vesicoureteral reflux in children (boys and girls) with complete ureteral duplication and urinary tract infection. In a study of adults with complete duplex systems, Ambrose and Nicolson [10] found that 50% of ureterovesical junctions were incompetent.

Vesicoureteral reflux occurred most commonly (72%) into the lower pole. This compares with an occurrence of 88% reported by Fehrenbaker et al. [2]. These percentages reflect the importance of the Weigert-Meyer rule, which states that when the distal ureters are separate, the ureter leading to the lower system inserts more superiorly and laterally into the bladder. Because of this development, the distal, lower-pole

ureter enters the bladder at a shallower angle and tends to have a short intramural course. This insertion anomaly, then, may result in vesicoureteral reflux.

There appears to be a discrepancy between the prevalence of parenchymal scarring found in our study group and that reported in other studies. We noted a 17% prevalence in girls with complete duplex systems. Every patient with scarring had vesicoureteral reflux. Fehrenbaker et al. [2] detected cortical atrophy of various degrees in every patient with vesicoureteral reflux into a lower-pole duplication. They stated that reflux into these systems is, therefore, an indication for surgery. Ambrose and Nicolson [10] observed similar changes of chronic pyelonephritis in the renal parenchyma drained by every refluxing ureter. In an autopsy series of adult patients with complete duplication Nation [8] found a 16% incidence of associated renal disease, and he found a 50% incidence of renal disease in clinical cases.

When compared with these cited articles, which were published between 1944 and 1972, our much lower prevalence of renal parenchymal disease is significant. One possible explanation is earlier detection and improved therapy of urinary tract infection. The prevalence of scarring, however, remains slightly higher than the 10% incidence in girls with urinary tract infection reported by Claesson and Lindberg [13]. This 17% prevalence is also higher than that noted in our series with nonduplex morphology in which the prevalence of scarring was 7% [4]. Another factor may be our selection of girls only because, as mentioned before, anatomic anomalies are more common in females than in males. Selection of a younger age group may also be a factor; renal parenchymal disease may not manifest itself until later years.

Associated urinary tract anomalies occurred in 17% of children with complete duplication. Nation [8] noted that 12% of male and female patients with complete duplication had associated renal anomalies.

In girls with partial duplication, the prevalence of vesicoureteral reflux was similar to that in girls with nonduplicated ureters. This is not surprising; embryologically, a single ureteral bud arises from the Wolffian duct and bifurcates before reaching the nephrogenic mass, resulting in a normal intramural distal ureter [1].

The prevalence of parenchymal scarring (6%) in this group of girls with partially duplicated systems also compares favorably with the 7% prevalence found in girls with urinary tract infections and nonduplex systems [4]. Associated urinary tract anomalies also were rare in this group, approaching the incidence of anomalies in the anatomically normal patients.

Because only a limited number of girls had follow-up studies, it is difficult to make conclusions about resolution of the vesicoureteral reflux or progression of renal parenchymal scarring. Certainly, some cases of resolution of vesicoureteral reflux in completely and partially duplicated systems were documented. This contradicts the idea that the anatomic defect associated with complete duplication precludes resolution of vesicoureteral reflux [2, 10]. Filly et al. [14] have reported caliceal clubbing and parenchymal scarring in females with cystoscopically proven abnormal ureteral orifices and no evidence of reflux on voiding cystourethrography. This most likely indicates previous vesicoureteral reflux that has

resolved. Kaplan et al. [15] reported a 22% incidence of resolution of vesicoureteral reflux in patients with complete duplex systems who were followed medically.

Only one girl whose reflux was being managed medically developed new parenchymal scarring. This was the youngest patient in the study group; she was 1 month old at the time of the first investigation. Although the first excretory urogram was only of fair quality, we did not believe there was any significant parenchymal scarring. On follow-up examination 2 years later, there was parenchymal loss in the left lower pole associated with grade III reflux into a complete duplex system.

Conclusions

Patients with partial duplication have a similar prevalence of reflux, parenchymal scarring, and associated urinary tract anomalies as girls with urinary tract infections and nonduplex systems.

Duplex anomalies in girls with urinary tract infection occurred in 8% of patients in this series. In those with complete duplication, vesicoureteral reflux is common, and the prevalence of parenchymal scarring is increased slightly compared to that found in girls with nonduplicated or partially duplicated systems. In some of these patients, vesicoureteral reflux may resolve, and progressive parenchymal scarring is unusual. Associated urinary tract anomalies are relatively common. Therefore, although these findings merit follow-up examinations, early surgical correction of uncomplicated vesicoureteral reflux in complete duplex systems appears unwarranted.

REFERENCES

1. Nordmark B. Double formations of the pelves of the kidneys and the ureters: embryology, occurrence and clinical significance. *Acta Radiol* 1948;30:276-278
2. Fehrenbaker LG, Kelalis PP, Stickler GB. Vesicoureteral reflux and ureteral duplication in children. *J Urol* 1972;107:862-864
3. Glassberg KI, Braren V, Duckett JW, et al. (Committee on Terminology, Nomenclature and Classification, Section on Urology, American Academy of Pediatrics). Suggested terminology for duplex systems, ectopic ureters and ureteroceles. *J Urol* 1984;132:1153-1154
4. Bisset GS III, Strife JL, Dunbar JS. Urography and voiding cystourethrography: findings in girls with urinary tract infection. *AJR* 1987;148:479-482
5. Report of the International Reflux Study Committee. Medical versus surgical treatment of primary vesicoureteral reflux. *Pediatrics* 1981;67:392-400
6. Hodson CJ. The radiological diagnosis of pyelonephritis. *Proc R Soc Med* 1959;52:669-672
7. Campbell MF. Embryology and anomalies of the urogenital tract. In: Kelalis PP, King LR, eds. *Clinical pediatric urology*. Philadelphia: Saunders, 1951:159-353
8. Nation EF. Duplication of the kidney and ureter: a statistical study of 230 new cases. *J Urol* 1944;51:456-465
9. Kelalis PP. Renal pelvis and ureter. In: Kelalis PP, King LR, eds. *Clinical pediatric urology*. Philadelphia: Saunders, 1951:503-541
10. Ambrose SS, Nicolson WP. Ureteral reflux in duplicated ureters. *J Urol* 1964;92:439-444
11. Lenaghan D. Bifid ureters in children: an anatomical, physiological and clinical study. *J Urol* 1962;87:808-817
12. Mackie GG, Stephens FD. Duplex kidneys: a correlation of renal dysplasia with position of the ureteral orifice. *J Urol* 1975;114:274-280
13. Claesson I, Lindberg U. Asymptomatic bacteriuria in schoolgirls. *Pediatr Radiol* 1977;123:179-183
14. Filly RA, Friedland GW, Govan DE, Fair WR. Urinary tract infections in children. *West J Med* 1974;121:374-381
15. Kaplan WE, Nasrallah P, King LR. Reflux in complete duplication in children. *J Urol* 1978;120:220-222

Pulmonary Vascular Obstruction in Severe ARDS: Angiographic Alterations after IV Fibrinolytic Therapy

Reginald Greene¹
 Stuart Lind²
 Hans Jantsch¹
 Roger Wilson³
 Karen Lynch³
 Rosemary Jones⁴
 Angelina Carvalho⁵
 Lynne Reid⁴
 Arthur C. Waltman¹
 Warren Zapol³

IV streptokinase was infused to test the potential reversibility of adult respiratory distress syndrome (ARDS) associated pulmonary vascular thrombosis in five patients suffering from severe ARDS with elevated mean pulmonary artery pressure, increased pulmonary vascular resistance, and angiographically documented pulmonary vascular thrombosis. At 48 hr there was clearance of obstructions in arteries larger than 1 mm in diameter in all patients, increased filling of the microvasculature and small arteries <1 mm in diameter in four patients, a fall in pulmonary vascular resistance in all patients, a rise in cardiac output in four patients, improved oxygenation (PA_{O_2}/FI_{O_2}) in three patients, and variable changes in shunt fraction and ventilator pressures. Expressed as a mean fraction of the preinfusion controls, the postinfusion physiologic values were pulmonary artery pressure = 0.89 mm Hg, pulmonary vascular resistance = 0.68 mm Hg \times min/L, cardiac output = 1.36 L/min, central venous pressure = 0.77 cm H₂O, pulmonary capillary wedge pressure = 0.92 mm Hg, PA_{O_2}/FI_{O_2} = 1.08, and shunt fraction = 0.95. Follow-up angiography showed no evidence of reocclusion. Postmortem studies of the three nonsurvivors confirmed recanalization of thrombosed pulmonary arteries. One documented bleeding episode occurred.

We conclude that fibrinolytic infusion can lyse thrombi and possibly improve hemodynamics and oxygenation in ARDS-associated pulmonary vascular thrombosis.

Obstruction of the pulmonary arterial tree secondary to widespread pulmonary vascular thrombosis (PVT) is a consistent feature of severe adult respiratory distress syndrome (ARDS) of diverse etiology [1-8]. Angiographic studies have confirmed that PVT occurs early, persists during fatal cases, and predicts >90% mortality [3]. PVT impairs gas exchange, increases pulmonary vascular resistance, induces right ventricular dysfunction, adds to the mortality risk, and increases damage to lung by promoting ischemic lung necrosis and increasing extravascular fluid leakage [9-12]. Multiple factors associated with ARDS induce in situ thrombosis, damage endothelium, destroy microvasculature, activate the blood coagulation system, and impede the action of intrinsic fibrinolysis [6, 7, 13-16]. We studied the possibility that IV fibrinolytic infusion might relieve thrombosis and prevent the injurious consequences of obstruction in a highly selected group of patients with ARDS and PVT.

Subjects and Methods

Between March 1982 and June 1986, severe ARDS-associated PVT was evaluated with angiography and clinical assessment in five patients immediately before starting fibrinolytic infusion and 48 hr after initiating therapy. The patients were selected from a group of about 200 who were admitted to the Respiratory Intensive Care Unit of the Massachusetts General Hospital during the study period for treatment of severe acute respiratory failure. Each patient met entry criteria (approved by a hospital subcommittee on human studies) that were designed to identify a >90% mortality risk [3].

Severe acute respiratory failure was characterized by increased shunt fraction [17, 18],

Received May 27, 1986; accepted after revision October 14, 1986.

Presented at the annual meeting of the American Roentgen Ray Society, Washington, DC, April 1986.

This work was supported by grant HL 23591 from the Specialized Center of Research in Adult Respiratory Failure.

¹ Department of Radiology, Massachusetts General Hospital, Boston, MA 02114. Address reprint requests to R. Greene.

² Department of Medicine, Massachusetts General Hospital, Boston, MA 02114.

³ Department of Anesthesia, Massachusetts General Hospital, Boston, MA 02114.

⁴ Department of Pathology, Children's Hospital Medical Center and Harvard Medical School, Boston, MA 02115.

⁵ Department of Medicine, Veterans Administration Hospital and Brown University, Providence, RI 02912.

AJR 148:501-508, March 1987
 0361-803X/87/1483-0501
 © American Roentgen Ray Society

decreased compliance, and diffuse radiographic lung opacification. Patients required fractional inspired oxygen concentrations (FI_{O_2}) of 1.0 for at least 8 hr or FI_{O_2} of 0.6 or more for at least 48 hr, with positive end-expiratory pressure (PEEP) of at least 5 cm H_2O . The shunt fraction for oxygen—that is, the proportion of cardiac output that passed to the left atrium without becoming oxygenated—was about 0.2 or more during mechanical ventilation with an FI_{O_2} and a PEEP of at least 5 cm H_2O . Mean pulmonary artery pressure (PAP) was >25 mm Hg due to increased pulmonary vascular resistance (PVR), that is, PVR was at least 2.0 mm Hg \times min/L when cardiac output was in the normal range and systemic hypoxemia was absent.

Informed consent was obtained from family members after full discussion of the alternatives, risks, and possible benefits, and after confirming that there were no contraindications to fibrinolytic therapy, such as absence of thrombocytopenia ($<50,000/mm^3$), recent intracranial injury, or suspected internal bleeding after trauma. Streptokinase (Hoechst-Roussel Pharmaceutical, Somerville, NJ) was administered with a constant-volume infusion pump into a central venous catheter. A loading dose of 250,000 units, followed by hourly cycles of 100,000 units, was delivered over 20-min intervals during each hour. Lytic and anticoagulant effects were monitored with partial thromboplastin time, fibrinogen concentration, thrombin time, and titers of fibrinogen degradation products [19]. The lytic state was assessed every 4 hr by documenting a thrombin time that was at least twice the control value. Fibrinolytic infusion was interrupted if significant bleeding occurred. Because of the short half-life of streptokinase activity, reversal of thrombolytic effect was expected to occur within 30 min of drug discontinuation [20, 21].

Hemodynamic measurements were obtained with indwelling balloon-tipped pulmonary artery catheters (for example, 93-118 7-French, Edwards Laboratories, Santa Ana, CA) while the patients were in a supine position. Vascular pressures were measured with Statham P-27 Db transducers (Statham Instruments, Hato Rey, PR) at end-tidal expiration. Atmospheric pressure at the midaxillary line was used as a zero reference point. PVR was calculated by dividing the PAP and pulmonary capillary wedge pressure difference by the cardiac output as determined in triplicate by thermodilution [9]. Ven-

tilator and gas exchange data included PEEP; peak inspiratory pressure (PIP); FI_{O_2} ; arterial blood gas analysis for pH, carbon dioxide, and oxygen (PA_{O_2}); and mixed venous blood gas tensions. Shunt effect was calculated according to a standard formula [17, 18].

Bedside balloon occlusion pulmonary angiography was performed as soon as possible after catheter placement with the indwelling hemodynamic-monitoring catheters [3]. Angiography was performed by inflating the balloon, confirming wedge position with a pressure tracing, and making a mechanical injection (Model 2500, OMP Laboratories, Killingworth, CT) of 20 ml of contrast medium (diatrizoate meglucamine and diatrizoate sodium, Renografin-60, Squibb) at 1 ml/sec through the port distal to the occluding balloon. Arterial, microvascular, and venous rami of one or more pulmonary segments were imaged on a single radiograph (Kodak RP film, X-omatic regular intensifying screen) exposed at the end of injection with a conventional mobile radiographic unit (nominal focal spot size of 1 mm). Typical radiographic factors (76 kVp, 10 mAs, and 115-cm film-focus distance) provide good detail of vessels down to 0.5-mm diameter. When possible, the respirator cycle was momentarily interrupted at end-tidal expiration to prevent respiratory motion during the radiographic exposure. At the end of angiography the balloon occlusion was reconfirmed with a pressure tracing, the balloon was deflated, and the catheter was flushed with normal saline. Angiograms were evaluated for PVT by demonstrating multiple filling defects in pulmonary arteries of at least 1 mm in diameter. Decreased capacitance of the microvasculature was assessed by noting (1) incomplete filling of small pulmonary arteries, that is, <1 mm in diameter, and (2) reduced background density of contrast medium in the pulmonary tissue.

The distribution and density of radiographic consolidation was scored in each of six lung zones according to an arbitrary four-point scale. Zero indicated no consolidation, one indicated faint peribronchovascular haziness, two indicated incomplete consolidation with partial obliteration of the bronchovascular outlines, and three indicated complete consolidation of the lung zone with total obliteration of the bronchovascular outlines. The angiographic and radiographic findings were determined by consensus. Mean data are expressed with standard error of the mean (SEM).

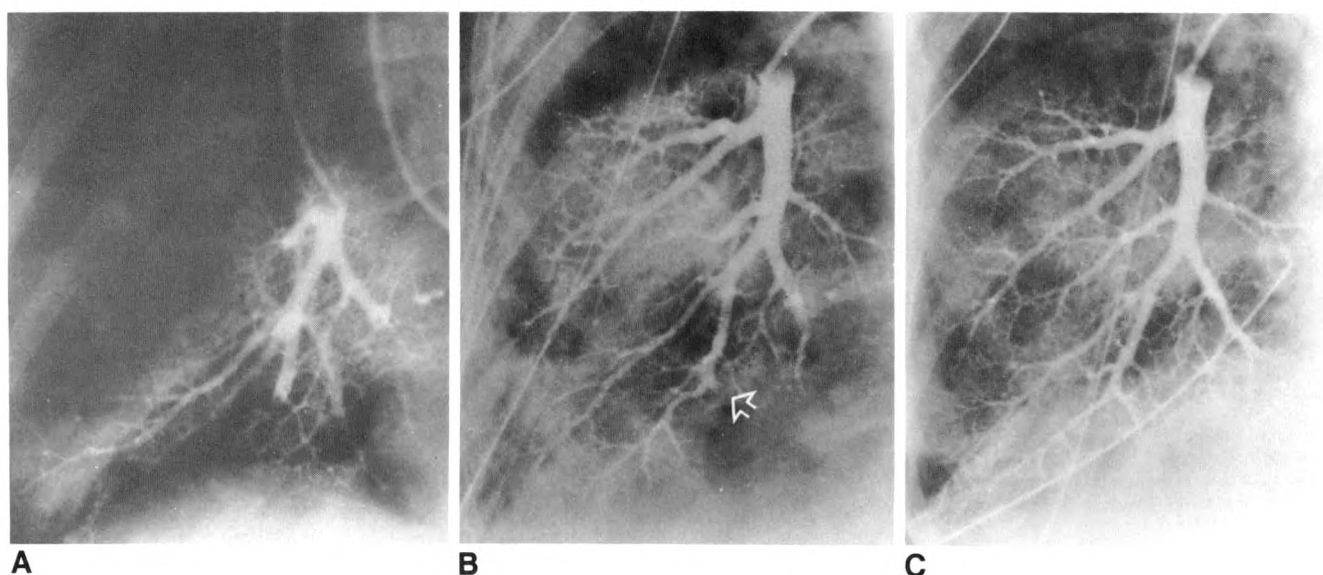


Fig. 1.—Case 4.

A, Balloon occlusion pulmonary angiogram of right lower lobe before IV streptokinase infusion shows multiple filling defects in large arteries, irregular filling of small arteries, and markedly decreased density of contrast medium in pulmonary tissue background.

B, 48 hr after start of infusion there is marked clearing of obstructions and an increase in background density of contrast medium. Occlusion of single subsegmental artery (arrow) persisted.

C, After completion of 96 hourly cycles of infusion further clearing of obstructions is evident.

Results

Angiographic and Radiographic Findings

With the exception of an unexplained increase of radiographic lung consolidation in a single lung zone of one patient, there was no change in radiographic consolidation at 48 hr. The mean density of lung consolidation per lung zone was 2.75 (0.32 SEM) at zero hr versus 2.54 (0.57 SEM) at 48 hr.

At 48 hr there was angiographic evidence of clearing of PVT. Pulmonary artery filling defects in arteries at least 1 mm in diameter were decreased in all patients (Fig. 1). The filling of small arteries and the background density of contrast medium in the pulmonary tissue increased in four patients (Fig. 2). Angiographic abnormalities that persisted in the small arteries and microvasculature of one patient after complete clearing of filling defects in arteries at least 1 mm in diameter were attributed to fibrosis that was documented post mortem

(Fig. 3). Late follow-up studies in four of the patients each showed no evidence of rethrombosis 1, 3, 1, and 47 days, respectively, after cessation of infusion.

Clinical Findings

Pertinent information is summarized in Table 1.

Hemodynamics.—At 48 hr PVR was lower than preinfusion levels in all patients (Fig. 4). Postinfusion cardiac output was higher in four and unchanged in one patient. Central venous pressure fell in four patients and was unchanged in another. Expressed as a mean fraction of preinfusion controls, PVR = 0.68 mm Hg \times min/L, PAP = 0.89 mm Hg, cardiac output = 1.36 L/min, pulmonary capillary wedge pressure = 0.92 mm Hg, and central venous pressure = 0.77 cm H₂O.

Gas Exchange.—Oxygenation, expressed as a fraction of FI_{O₂ to correct for difference in inspired oxygen concentration,}

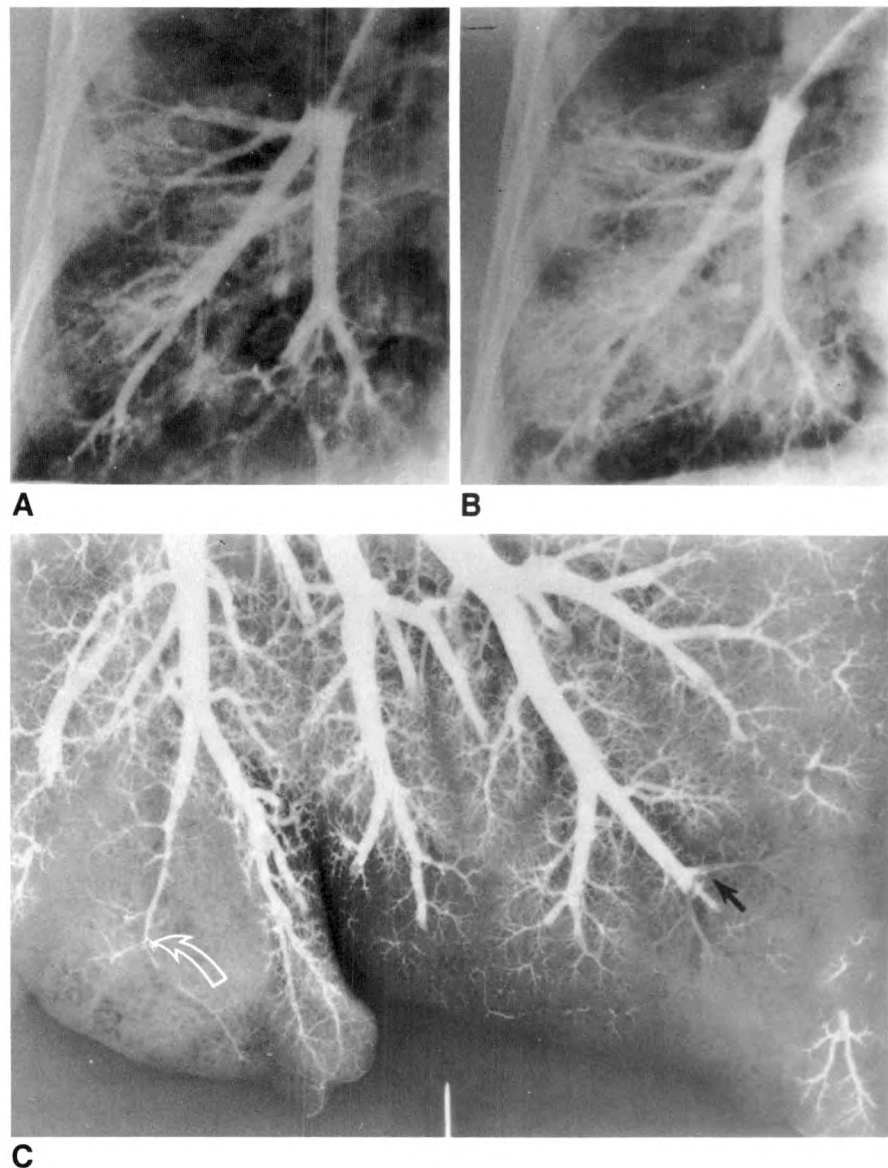


Fig. 2.—Case 3.

A, Balloon occlusion angiogram of right lower lobe before infusion. Multiple filling defects in large arteries, irregular filling of small arteries, and decreased density of contrast medium in pulmonary tissue background.

B, 48 hr after initiating infusion there is partial clearing of obstructions and an increase in background density of contrast medium.

C, Barium sulfate injection into pulmonary artery post mortem shows residual intraluminal filling defects corresponding to antemortem fibrin thrombosis (solid arrow), irregular vascular narrowing suggesting recanalization of thrombosed vessel (open arrow), an oligemia of lung distal to obstructions. A 500- μ m-diameter calibrating marker is at bottom.

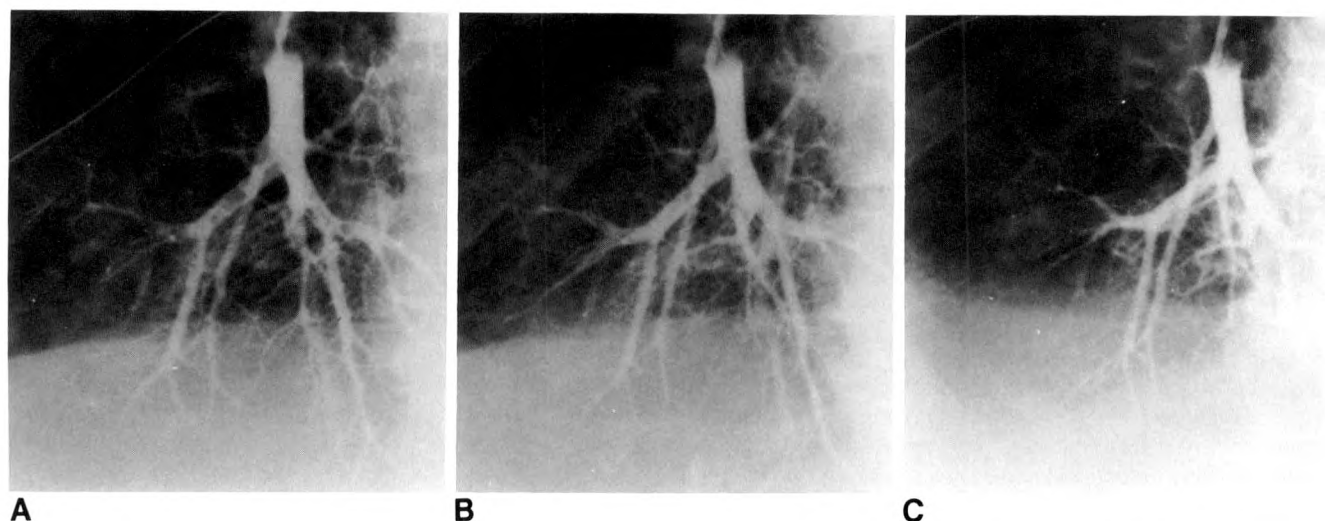


Fig. 3.—Case 1.

A, Balloon occlusion pulmonary angiogram of right lower lobe before infusion shows multiple intraluminal filling defects in large arteries, irregular stringlike narrowing of small arteries, and decreased density of contrast medium in pulmonary tissue background.

B, At 48 hr there is partial clearing of obstructions in large arteries.

C, Complete clearing of intraluminal defects in large arteries is evident 1 day after completing infusion, but there is persistent narrowing of small arteries and a continued decrease in background density of contrast medium.

TABLE 1: Clinical Summary in Adult Respiratory Distress Syndrome

Case No.	Age	Gender	Diagnosis	Duration (days)	Infusion (hr)	Rethrombosis	Survival	Clearance of Defects	
								≥1 mm diam	<1 mm diam
1	76	M	Pneumonia	1.3	33	No	No	Yes	No
2	47	F	Fibrosis	3	46	No	No	Yes	Yes
3	31	F	Overdose	12	59	No	No	Yes	Yes
4	57	F	Sepsis	10	96	No	Yes	Yes	Yes
5	27	F	Aspiration	10	32	No data	Yes	Yes	Yes

Note.—In all patients the respiratory distress was severe. diam = diameter.

tion, was improved in three patients, fell in one, and was unchanged in another (Fig. 5). Shunt fraction increased in three patients, fell in one, and was unchanged in another (Fig. 5). Expressed as mean fractions of control values, PA_{O_2}/FI_{O_2} and shunt fraction were 1.08 and 0.95, respectively.

Ventilation.—Alterations in PIP, PEEP, tidal volume, and FI_{O_2} at 48 hr were variable, reflecting changes in clinical requirements for mechanical ventilation (Fig. 6). In two patients PIP increased despite unchanged or lowered levels of PEEP. Expressed as mean fractions of control values, PIP and PEEP were 1.10 and 0.96, respectively.

Hematology.—Data are summarized in Table 2. All patients had elevated titers for fibrinogen degradation products before infusion and at 48 hr. One patient who was marginally thrombocytopenic before the start of streptokinase infusion ($67,000/mm^3$) experienced a bleeding episode requiring blood product replacement and interruption of infusion. The bleeding, which was attributed to a markedly depressed fibrinogen level (<100 mg/dl), promptly ceased on discontinuation of infusion and administration of fresh, frozen plasma. An occult

bleeding episode may have occurred in another patient (case 5) who had a single abnormal hematocrit value but no overt signs of bleeding. The infusion was discontinued, two units of plasma were administered, and the subsequent clinical course was uneventful. One bleeding episode unrelated to streptokinase infusion occurred in another patient during interval heparin infusion (case 2).

Postmortem studies.—Widespread recanalization of thrombosed large and small pulmonary arteries and diffuse lung damage consistent with ARDS were found in each of the three nonsurvivors (Fig. 2). No residual pulmonary artery thrombus was found in one patient (case 1). Thrombus was absent from the main pulmonary arteries, right heart, vena cava, and systemic veins in all patients.

Discussion

The major finding in this study was the consistent demonstration that macroscopic PVT could be lysed in patients with severe ARDS. Forty-eight hr after initiating fibrinolytic infusion

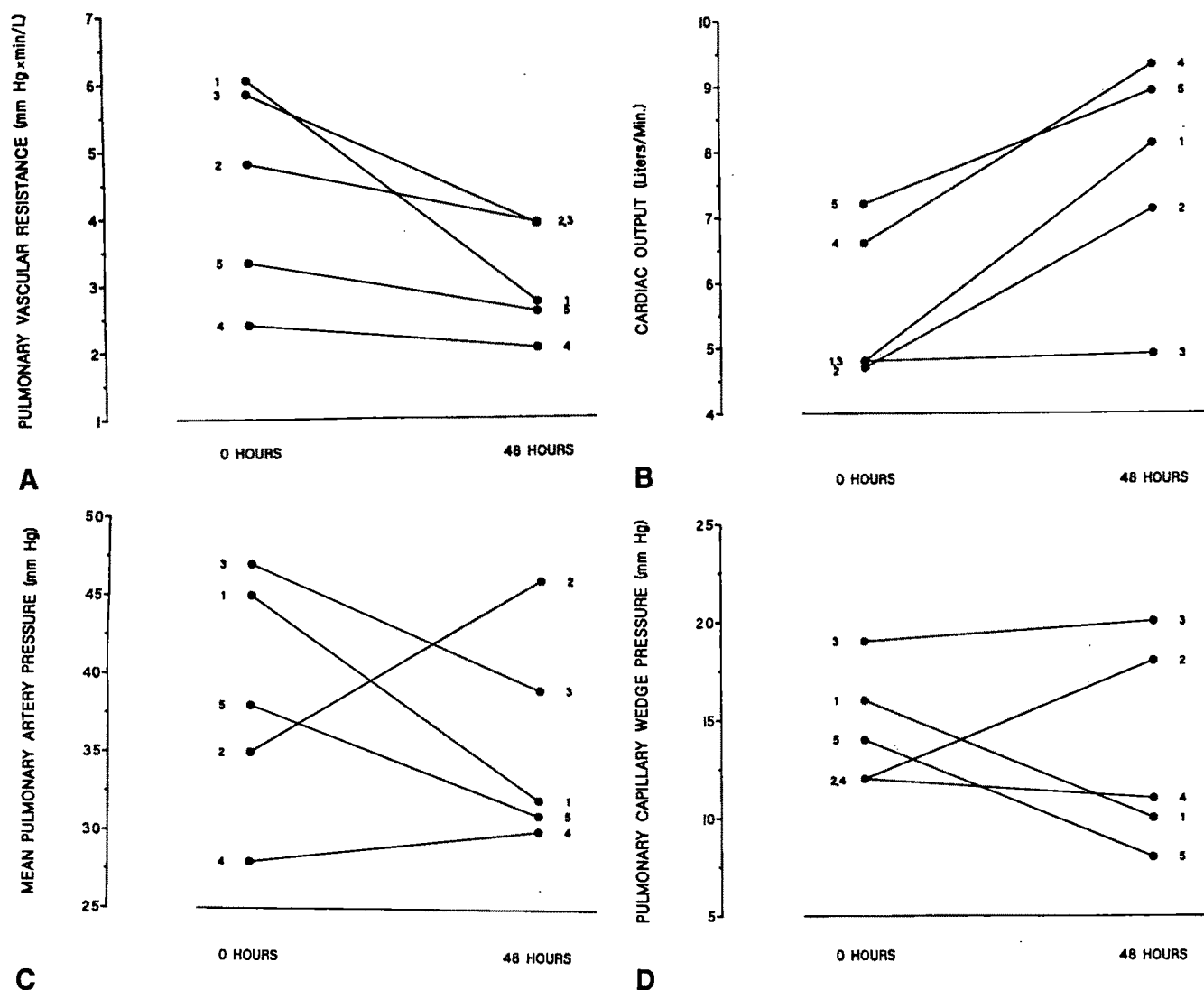


Fig. 4.—Individual hemodynamic data before infusion (0 hr) and 48 hr after initiating streptokinase infusion are compared. Pulmonary vascular resistance (A), cardiac output (B), mean pulmonary artery pressure (C),

and pulmonary capillary wedge pressure (D). Individual case numbers are indicated.

we found angiographic evidence of clearing of PVT in large arteries in all patients. Our second major finding was that lysis is usually followed by increased capacitance of the microvasculature. The lysis of obstructions in large arteries in four of our patients was followed by angiographic evidence of reperfusion of microvasculature and by clinical signs of corresponding improvement in pulmonary hemodynamics. This supports our conclusion that the capacitance of the microcirculation increased 48 hr after initiating fibrinolytic therapy. We do not believe that thrombolysis occurred spontaneously because we previously found that untreated PVT tends to persist during ARDS. Of 18 patients with ARDS previously studied by us with serial angiography, only two had documented filling defects that might have diminished spontaneously.

We do not ascribe the PVT in our patients to embolization

from distant venous sources. Negative postmortem examinations of pelvic and lower extremity veins in the three nonsurvivors and a negative noninvasive study of lower extremity veins in one of the survivors argue against an embolic etiology.

Although our angiographic studies were restricted in scope, we know that PVT was not limited to single lung segments. At some point during each study there was documentation of obstruction in more than one segment or lobe. We also know from postmortem studies of the three nonsurvivors that there was widespread recanalization of thrombosed pulmonary arteries. We have previously found that arteriographic demonstration of PVT in patients with severe ARDS is consistently associated with widespread fibrin thrombosis of pulmonary arteries [2-5]. We obtained our angiograms as soon as

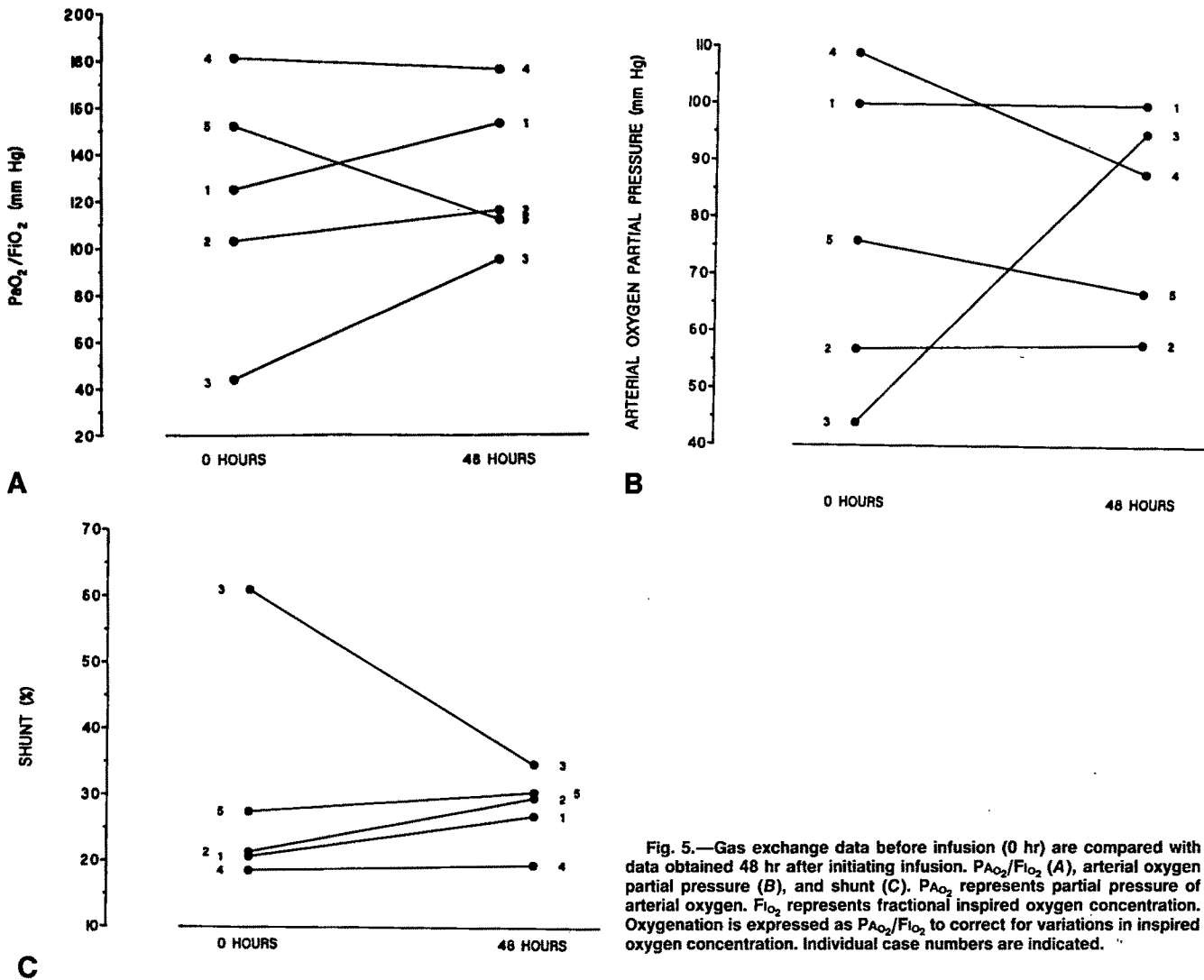


Fig. 5.—Gas exchange data before infusion (0 hr) are compared with data obtained 48 hr after initiating infusion. PA_{O_2}/FI_{O_2} (A), arterial oxygen partial pressure (B), and shunt (C). PA_{O_2} represents partial pressure of arterial oxygen. FI_{O_2} represents fractional inspired oxygen concentration. Oxygenation is expressed as PA_{O_2}/FI_{O_2} to correct for variations in inspired oxygen concentration. Individual case numbers are indicated.

possible after insertion of pulmonary artery lines to minimize the potentially confounding effect of catheter-induced clot [22].

Because of its unique pathogenesis, we expected to find that ARDS-associated PVT was relatively resistant to fibrinolytic therapy. Unlike conventional pulmonary thromboembolism, ARDS is associated with several factors that promote in situ thrombosis and resist thrombolysis: inflammatory denudation of the microvascular endothelium, reduced small-vessel "run-off" secondary to microvascular obstruction, inhibition of intrinsic fibrinolysis, platelet aggregation, local fibrin deposition, vasoconstriction, and vascular compression secondary to parenchymal consolidation [12–15, 23–29]. We were encouraged by the responsiveness of PVT to fibrinolytic infusion despite the significant delays in initiating fibrinolytic infusion in some of our patients with ARDS. Thrombi consistently cleared at 48 hr and did not recur up to 47 days later. The small size of our study group and the occasional delays in initiating fibrinolytic therapy resulted from contraindications to

streptokinase therapy, delays in interhospital transfer, and failure to promptly recognize PVT.

The angiographic findings in one of our patients suggest that fibrinolytic infusion may have limited effectiveness in severely damaged regions of lung. In case 4 we found persistent obstruction of a subsegmental artery that fed a zone of oligemia and appeared to be the source of a recurrent bronchopleural fistula (Fig. 1B). Severe local damage or obliteration of the microvasculature may have prevented reperfusion.

Because our patients were treated with several techniques simultaneously, it is not possible to ascribe all of the observed functional alterations to any single treatment. However, we observed several interesting results that suggest that fibrinolytic infusion produced beneficial results. The decreased PVR and/or increased cardiac output or lower PAP in all our patients indicate a consistent increase in vascular cross section and confirm our angiographic findings at 48 hr. Our clinical data exclude the possibility that the observed increase in vascular cross section was the result of positive cardiac

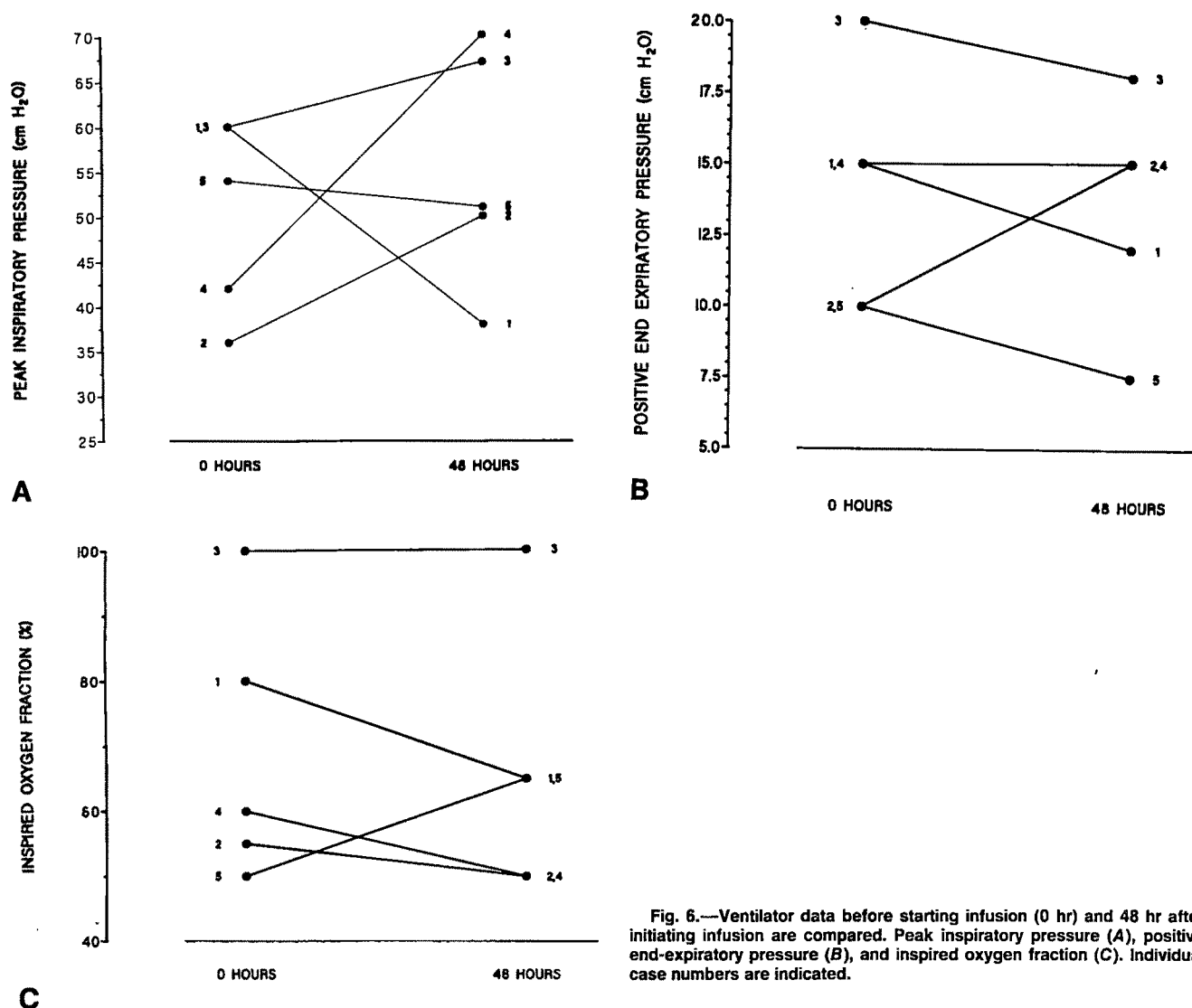


Fig. 6.—Ventilator data before starting infusion (0 hr) and 48 hr after initiating infusion are compared. Peak inspiratory pressure (A), positive end-expiratory pressure (B), and inspired oxygen fraction (C). Individual case numbers are indicated.

TABLE 2: Hematology Before and After Initiating Streptokinase

Hematologic Parameter	Mean (SEM)	
	0 hr	48 hr
WBCs ($\times 1000/\text{mm}^3$)	19.1 (3.9)	18.2 (7.1)
Hematocrit (%)	31.8 (1.6)	32.2 (1.9)
Platelets ($\times 1000/\text{mm}^3$)	240 (60)	250 (60)
Fibrinogen (g/dl)	0.39 (0.07)	0.31 (0.06)
Partial thromboplastin time (sec)	31.1 (2.9)	38.9 (5.9)

inotropic drugs, pulmonary vasodilators, increased right ventricular preload, or reduced PEEP. It is unlikely that the slightly decreased blood viscosity associated with lower fibrinogen levels could explain the observed hemodynamic changes at 48 hr. We hypothesize that the increased pulmonary vascular cross section (and the resulting decrease in right ventricular

afterload) may have permitted the higher observed levels of cardiac output at 48 hr.

Thrombolysis can impair oxygenation if it increases shunt flow through consolidated, unventilated lung. However, our data did not show a consistent increase in shunt fraction at roughly comparable levels of PEEP. The shunt fraction rose in three patients but fell greatly in one and was unchanged in another. We believe that streptokinase infusion is most likely to recanalize the vasculature of less severely damaged regions of the lung that possess an intact microvasculature capable of carrying out gas exchange. To support this view we found that oxygenation improved in three of our patients.

Irregular reperfusion induced by streptokinase can lead to "reperfusion injury," that is, increased permeability edema, but we found little evidence that it actually occurred [30]. In two patients we did observe an increase in PIP that could not be accounted for by an increase in PEEP. In one of these patients there was a transient unexplained increase in radiographic consolidation at 48 hr. However, it was not clear

whether the radiographic and ventilator changes were from progressive lung damage, reperfusion injury, or other complicating conditions. We did not observe the increase in shunt fraction that we would have expected to find had reperfusion injury actually occurred in this patient.

Fibrinolytic infusion can induce life-threatening hemorrhage requiring blood replacement and discontinuation of therapy [20-24]. The one bleeding episode was documented during streptokinase infusion could have been avoided if hypofibrinogenemia had been recognized and treated at an earlier stage. It is noteworthy that a bleeding episode occurred during interval heparin infusion, and that streptokinase was administered without untoward effect in two of our patients within 30 and 48 hr of major surgery.

From this pilot experience we conclude that fibrinolytic infusion reduces ARDS-associated PVT. Our data further suggest that pulmonary vascular cross section can be increased and oxygenation may be improved 48 hr after initiation of infusion. Despite our promising results, proof of the ultimate clinical efficacy of fibrinolytic infusion in ARDS-associated PVT must await the results of further study.

ACKNOWLEDGMENTS

We thank Deborah Quinn, the nursing staff of the Respiratory Intensive Care Unit, and the radiologic technologists of Massachusetts General Hospital for their assistance in carrying out this clinical study.

REFERENCES

1. Zapol WM, Snider MT. Pulmonary hypertension in severe acute respiratory failure. *N Engl J Med* 1977;296:476-480
2. Zapol WM, Kobayashi K, Snider MT, Greene R, Laver MB. Vascular obstruction causes pulmonary hypertension in severe acute respiratory failure. *Chest* 1977;71[suppl]:306-307
3. Greene R, Zapol WM, Snider MT, et al. Early bedside detection of pulmonary vascular occlusion during acute respiratory failure. *Am Rev Respir Dis* 1981;124:593-601
4. Snow RL, Davies P, Pontoppian H, Zapol WM, Reid L. Pulmonary vascular remodelling in adult respiratory distress syndrome. *Am Rev Respir Dis* 1982;126:887-892
5. Tomashefski JF, Davies P, Boggis C, Greene R, Zapol WM, Reid LM. The pulmonary vascular lesions of the adult respiratory distress syndrome. *Am J Pathol* 1983;112:112-126
6. Blaisdell FW. Pathophysiology of the respiratory distress syndrome. *Arch Surg* 1974;108:44-49
7. Saldeen T. Trends in microvascular research: the microembolism syndrome. *Microvasc Res* 1976;11:227-259
8. Hill JD, Ratliff JL, Parrott JCW, et al. Pulmonary pathology in acute respiratory insufficiency: lung biopsy as a diagnostic tool. *J Thorac Cardiovasc Surg* 1976;71:64-72
9. Martyn JA, Snider MT, Szyfelbein SK, Burke JF, Laver MB. Right ventricular dysfunction in acute thermal injury. *Ann Surg* 1980;191:330-335
10. Sibbald WJ, Driedger AA, Meyers ML, Short A, Wells GA. Biventricular function in the adult respiratory distress syndrome. Hemodynamic and radionuclide assessment with special emphasis on right ventricular function. *Chest* 1983;84(2):126-134
11. Laver MB, Strauss HW, Pohost GM. Right and left ventricular geometry: adjustments during acute respiratory failure. *Crit Care Med* 1979;7(12):509-519
12. McCord JM. Oxygen-derived free radicals in postischemic tissue injury. *N Engl J Med* 1985;312:159-163
13. Carvalho ACA, Bellman SM, Saullo VJ, Quinn D, Zapol WM. Altered factor VIII in acute respiratory failure. *N Engl J Med* 1982;307:1113-1120
14. Lindquist O, Rammer L, Saldeen T. Pulmonary insufficiency, microembolism and fibrinolysis inhibition in post-traumatic autopsy material. *Acta Chir Scand* 1972;138:545-549
15. Olsson P, Swedenborg S, Lindquist O. Effects of slow defibrination on the canine lung. *J Trauma* 1974;14:325-329
16. Bo G, Hognestad J, Vaage J. The role of blood platelets in pulmonary responses to microemboli with barium sulphate. *Acta Physiol Scand* 1974;90:244-251
17. Snider MT, Zapol WM. Assessment of pulmonary oxygenation during venoarterial bypass with aortic root return. In: Zapol WM, Qvist J, eds. *Artificial lungs for acute respiratory failure*. New York: Academic Press, 1976:251-274
18. Kelman GR. Digital computer subroutine for conversion of oxygen tension into saturation. *J Appl Physiol* 1966;21:1375-1376
19. Carvalho ACA, Ellman LL, Colman RW. A comparison of the staphylococcal clumping test and an agglutination test for detection of fibrinogen degradation products. *Am J Clin Pathol* 1974;62:107-112
20. Urokinase-streptokinase embolism trial. *JAMA* 1974;229:1606-1613
21. Bell WR, Meek AG. Current concepts: guidelines for the use of thrombolytic agents. *N Engl J Med* 1979;301:1266-1270
22. Hoar PF, Stone SG, Wicks AE, Edie RN, Scholes JV. Thrombogenesis associated with Swan-Ganz catheters. *Anesthesiology* 1978;48:445-447
23. Frattantoni JC, Ness P, Simon TL. Thrombolytic therapy. *N Engl J Med* 1975;293:1073-1078
24. Sharma CVRK, Burleson VA, Sasahara AA. Effect of thrombolytic therapy on pulmonary capillary blood volume in patients with pulmonary embolism. *N Engl J Med* 1980;303:843-845
25. Sharma GVRK, Cella G, Parisi AF, Sasahara AA. Thrombolytic therapy. *N Engl J Med* 1982;306:1268-1276
26. Costantini C, Corday E, Lang TW, et al. Revascularization after 3 hours of coronary arterial occlusion: effects on regional cardiac metabolic function and infarct size. *Am J Cardiol* 1975;36:368-384
27. Rentrop P, Blanke H, Karsch KR, Kaiser H, Kosterling H, Leitz K. Selective intracoronary thrombolysis in acute myocardial infarction and unstable angina pectoris. *Circulation* 1981;63:307-317
28. Ganz W, Buchbinder N, Marcus H, et al. Intracoronary thrombolysis in evolving myocardial infarction. *Am Heart J* 1981;101:4-13
29. Ganz W, Geft I, Shah PK, et al. Intravenous streptokinase in evolving acute myocardial infarction. *Am J Cardiol* 1984;53:1209-1220
30. Ohkuda K, Nakaharak, Weidner WJ, Binder A, Staub NC. Lung fluid exchange after uneven pulmonary artery obstruction in sheep. *Circ Res* 1978;42:152-161

CT Assessment of Silicosis in Exposed Workers

R. Bégin¹
D. Bergeron
L. Samson
M. Boctor
A. Cantin

For evaluation of the clinical usefulness of CT of the thorax in workers exposed to silica, 58 workers with long-term exposure to silica in the granite and foundry industries of the Eastern Townships of Quebec were examined. CT scans were compared with standard posteroanterior chest radiographs by using the International Labour Office 1980 grading system for silicosis. Six areas of the lung in each patient were assessed by both techniques for profusion (number) of opacities (small nodules), coalescence, and the presence of large opacities. CT scans and chest radiographs yielded similar average scores for detection of opacities. CT identified significantly more coalescence and large opacities in patients with simple silicosis. In patients with complicated silicosis, CT results were comparable with those of chest radiographs. CT of the thorax in workers exposed to silica does not identify more patients with minimal parenchymal disease, but it does detect earlier changes of coalescence.

In the investigation of pleuropulmonary disease, CT of the thorax often yields information not available by other methods [1-4]. It is a valuable tool for the study of mediastinal, chest wall, and pleural conditions as well as pulmonary parenchymal abnormalities, such as solitary nodules and metastases.

In the study of interstitial lung diseases, the distribution of the disease as seen on CT can help differentiate various diseases [5-9]. With regard to the pneumoconioses, Katz and Kreel [6] reported using CT for the early detection of asbestosis, and we have reported an analysis of CT and chest radiography for evaluation of long-term asbestos workers [10]. We found CT as sensitive as chest radiographs for detection of parenchymal disease but more sensitive for identification of pleural disease. We currently use CT in asbestos workers to differentiate pleural and parenchymal diseases, a major issue in cases settled by the Quebec Workman Compensation Board for occupational lung disease.

To determine the usefulness of CT in workers exposed to silica, we studied the CT scans from 58 long-term silica-exposed workers in the granite and foundry industries of the Eastern Townships of Quebec. These workers were examined concomitantly by standard clinical, radiographic, and pulmonary function tests.

Subjects and Methods

Patients

The average age of the 58 workers included in the study was 59 ± 2 years (range, 35-71 years). All had been exposed to silica dust in the granite or foundry industries of the Eastern Townships of Quebec for an average of 30 years (range, 14-40 years). Ninety percent were either current or former cigarette smokers, and they had smoked, on the average, 25 ± 3 pack-years.

Clinical Evaluations

All patients had a history taken and underwent physical examination with emphasis on the detection of abnormalities suggesting silicosis. A questionnaire designed to elicit respiratory

Received February 27, 1986; accepted after revision October 6, 1986.

This work was supported in part by Institut de Recherche en Santé et Sécurité au Travail du Québec.

¹All authors: Centre Hospitalier Universitaire, Université de Sherbrooke, Sherbrooke, Québec, Canada J1H 5N4. Address reprint requests to R. Bégin.

AJR 148:509-514, March 1987
0361-803X/87/1483-0509
© American Roentgen Ray Society

symptoms and factors associated with chronic obstructive pulmonary disease, lifetime smoking habits, and occupational history was administered. Silica exposure time for each worker was computed as the number of years of employment in a silica-dust work environment. Dyspnea was graded according to the method of Crofton and Douglas [11].

Chest Radiographs

Standard high-kilovoltage posteroanterior, lateral, and oblique films were obtained at maximal inspiration. The radiograph was graded for number of small opacities by three observers according to the International Labour Organization (ILO) 1980 classification [12].

The profusion (number) of opacities was scored by using the ILO grading system based on the viewers' assessment of the concentration of opacities compared with standard radiographs provided by the ILO. This classification recognizes the existence of a continuum of change, from no opacity to the most advanced category. The scores were converted to a linear scale of 0 to 10 (12 categories) as follows: ILO grade 0/- (clearly normal) and grade 0/0 (normal after close examination) = 0 on the linear scale; 0/1 = 1; 1/0 = 2; 1/1 = 3; 1/2 = 4; 2/1 = 5; 2/2 = 6; 2/3 = 7; 3/2 = 8; 3/3 = 9; 3/4 = 10.

In the ILO classification, in order to group patients with similar disease, four categories are defined on the basis of these same profusion scores: category 0 = profusion scores 0/-, 0/0, and 0/1; category 1 = profusion scores 1/0, 1/1, and 1/2; category 2 = profusion scores 2/1, 2/2, and 2/3; category 3 = profusion scores 3/2, 3/3, and 3/4. We will be referring to these four categories in the rest of this paper.

The profusion of opacities was recorded separately in the six areas of the lung to yield a total score of parenchymal opacities (number \times areas), in addition to the usual ILO global score of profusion (one grade per radiograph) and category classification.

Grouping of opacities or confluence is classified as coalescence when the confluence is smaller than 10 mm in diameter and as large opacities when greater than 10 mm in diameter: category A = an opacity having a greatest diameter exceeding 10 mm, up to (and including) 50 mm, or several opacities each greater than 10 mm, the sum of whose greatest diameters does not exceed 50 mm; category B = one or more opacities larger or more numerous than those in category A, whose combined area does not exceed the equivalent of the right upper lung field ($\frac{1}{3}$ of lung height); category C = one or more opacities whose combined area exceeds the equivalent of the right upper lung field.

CT of the Thorax

All CT examinations were performed on a General Electric Model 8800 scanner (Canadian General Electric, Co., Montréal, Québec, Canada). For each patient, 10 slices of 1-cm thickness were obtained with wide windows and 10 were obtained with narrow windows for adequate assessment of pulmonary, chest wall, and pleural changes. All scans were obtained without contrast medium, in the prone position, during a 9.4-sec breath-holding procedure at near-functional residual capacity. The profusion of pulmonary opacities as evaluated by CT was graded by using the same basic principles as the ILO 1980 system for grading pulmonary disease on chest radiographs. CT scans were obtained within 48-72 hr of the plain chest radiographs.

Diagnosis of Silicosis

The diagnosis of silicosis [13] was based on both a history of prolonged exposure to silica-containing dust and a chest radiograph showing changes consistent with silicosis in category 1 or higher, according to the ILO 1980 classification [12].

Statistical Analysis

All results are expressed as the mean \pm standard error of measurement. The data were tested by the Student's *t* test or Mann-Whitney *U* test for differences between groups, by the Wilcoxon matched-pairs signed-rank test for differences between radiologic

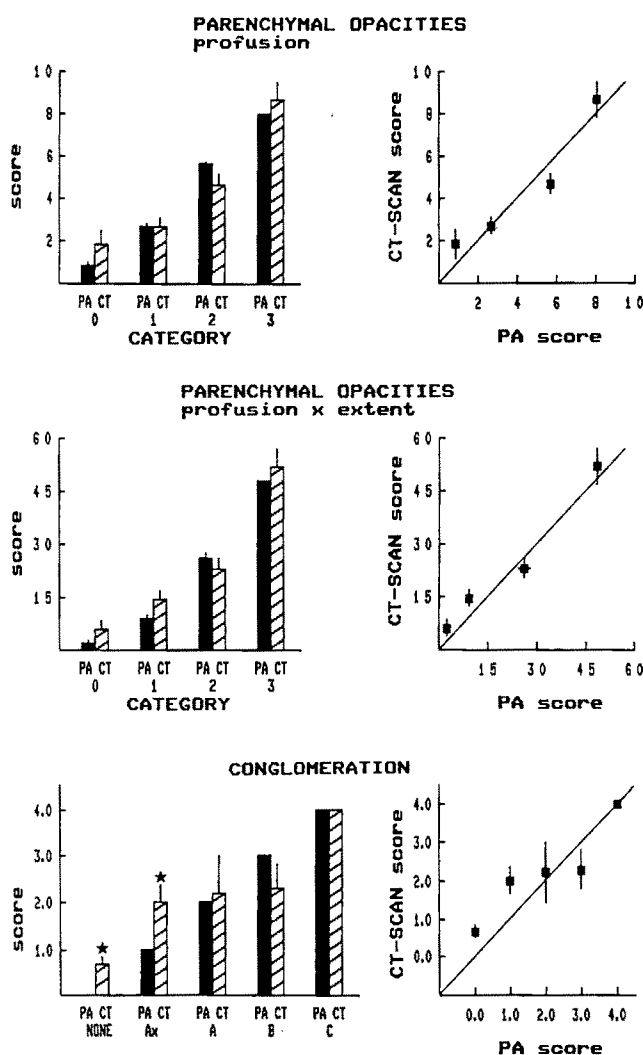


Fig. 1.—Analysis of pulmonary parenchymal changes as scored on each posteroanterior chest radiograph (PA score) and CT for profusion of parenchymal nodules, profusion \times extent, and conglomeration. Left upper and middle panels are bar diagrams for PA or CT in categories 0-3; left lower panel is bar diagram for severity of conglomeration from none to category C. Groups are based on ILO 1980 classification of lung radiographs [12]. Right panels are correlation diagrams of CT with PA chest radiographs for same data. A star indicates $p < .001$ between scores obtained by two techniques in each patient group. See text for further explanation.

methods, and by Spearman's correlation procedure when appropriate [14, 15].

Results

On the basis of chest radiographs, six of the 58 patients studied did not have silicosis (ILO category 0). Of the 52 patients who were recognized as having silicosis, 30 had simple silicosis (small opacities) without coalescence of opacities or large opacities, and 22 had radiographically complicated silicosis (13 patients had silicosis with coalescence, and nine patients had silicosis with large pulmonary opacities).

Comparative analysis of chest radiographs and CT scores of parenchymal opacities and conglomeration documented significant differences between the two techniques (Fig. 1). For the whole group, the average scores of profusion were 4.04 ± 0.28 for radiographs and 3.78 ± 0.36 for CT ($p > .05$). The scores for conglomeration were 1.07 ± 0.19 for radiographs and 1.50 ± 0.19 for CT ($p < .001$). In assessment of profusion of parenchymal opacities, an overall good correlation was found between CT and radiographic scores for opacities ($r = .54$, $p < .001$, Spearman's correlation). However, this correlation was not as high as could be expected, largely because there were six patients in category 0 by radiograph and 12 by CT scan, which means that six subjects in category 1 by radiograph had no detectable change on CT scan (Fig. 2).

In the evaluation of conglomeration of small opacities (Fig. 1, lower panels), an overall good correlation also was found ($r = .71$, $p < .001$), but CT identified a significantly larger number of patients with conglomeration ($n = 33$) than did radiography ($n = 23$) ($p < .001$). This finding is clearly seen in the numbers of patients with large opacities in category A by radiograph ($n = 5$) vs CT scan ($n = 11$). Of the 30 patients with silicosis whose radiographs were classified as being without conglomeration or large opacities, 10 were found to have conglomeration and/or large opacity on CT. Analysis of 10 silicotic patients with conglomeration on CT compared with the 20 without conglomeration confirmed the presence of lung-function changes that were consistent with changes found in cases of more advanced disease. Of the 22 patients with radiographically complicated silicosis, six were in category 1, 13 in category 2, and three in category 3. Of the 33 patients with complicated silicosis on CT, 16 were in category 1, 12 in category 2, and five in category 3. Of the 10 patients with complicated silicosis on CT without conglomeration on radiograph, eight were in category 1 and two in category 2.

Figure 2 presents a radiograph and CT scans in which small opacities are better appreciated on the radiograph. Figures 3 and 4 contain radiographs and CT scans in which small opacities and conglomerations were scored similarly by both techniques. Figure 5 shows conglomerations on CT scan not clearly detected on the chest radiograph. With the additional

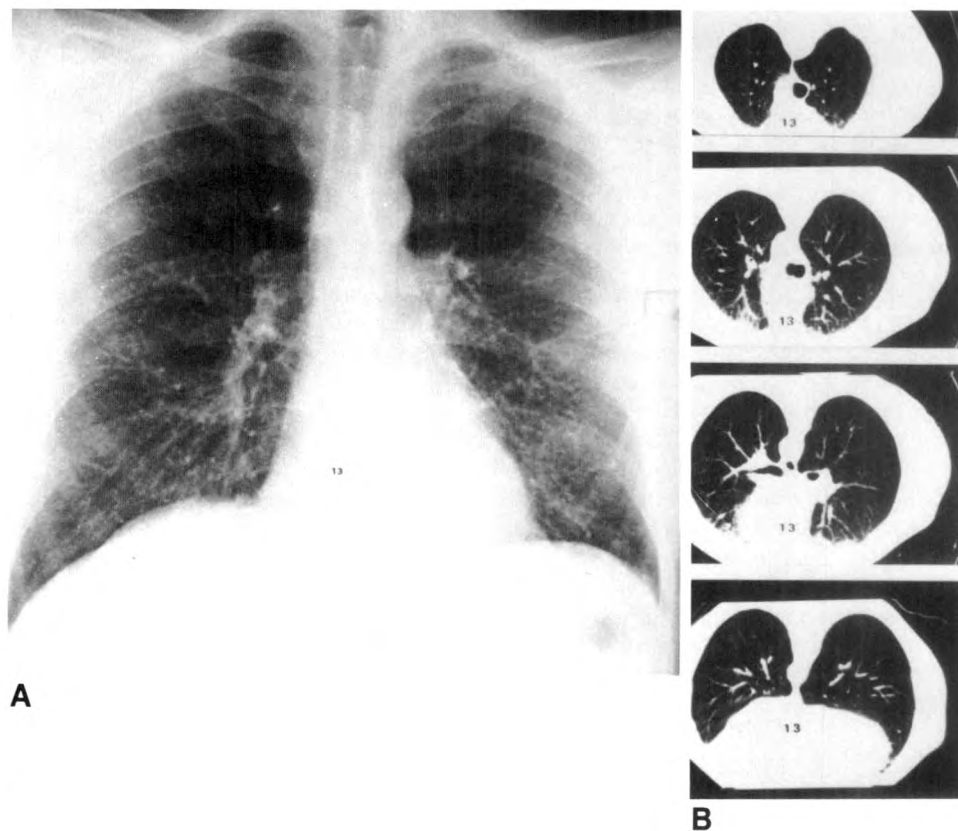


Fig. 2.—Chest radiograph (A) and CT scans (B) of patient with simple silicosis. Opacities are evident on plain radiograph but are not seen on CT scan.

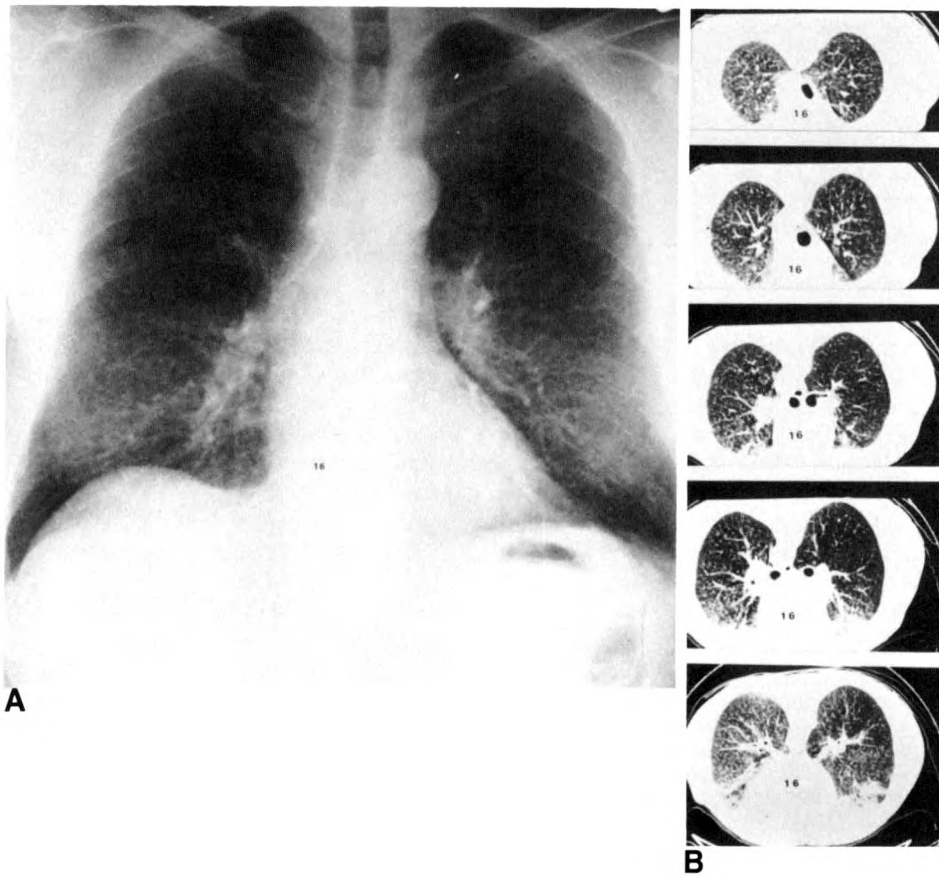


Fig. 3.—Chest radiograph (A) and CT scans (B) in patient with simple silicosis. The findings are similar in both methods. The opacities are distributed more evenly throughout the lungs than in Fig. 2.

use of lateral and oblique films, three of 10 cases showed conglomeration on radiographs.

Discussion

This study of 58 long-term silica-exposed workers found that CT of the thorax is not superior to the standard chest radiograph for early detection of small opacities in workers exposed to silica. However, it provides significant additional information on the stage of the disease in approximately 33% of the patients with simple silicosis on chest radiograph (Fig. 1). The superiority of the plain chest radiograph over CT is documented in the early detection of silicosis: six of the subjects with category 1 silicosis were classified as category 0 by CT (Fig. 2). This difference is not unexpected because the plain chest radiograph is an image that takes advantage of the superimposition of several small lesions across the chest, whereas the CT focuses on thin slices, which reduces the effect of superimposition of lesions [9]. When the nodular lesions of silicosis are sufficiently dense, chest radiographs and CT image them equally well (Figs. 3 and 4).

CT detects coalescence or large opacities as well as radiography does (Fig. 4). However, in the presence of simple silicosis (category 1, 2, or 3) without coalescence or large opacities on plain chest radiograph, CT of the thorax revealed

conglomerations in 10 of 30 cases (Fig. 5), 70% of which could not be seen with the addition of lateral and oblique chest films. This additional information is particularly important because it identifies the presence of a complicated disease that could be either early coalescence of silicotic nodules, tuberculosis, or other lung process, such as lung tumor, a common finding in patients of this age group (i.e., 35 to 71 years). Because these early conglomerations of silicotic nodules do not have the well-described typical appearance of large opacities (Fig. 4) (fibrous masses surrounded by emphysematous areas of lung tissue), it is impossible to establish with certainty the specific nature of these early conglomerations on radiographic or CT image patterns. Of the 10 cases identified by CT scan in this study, the conglomerations were tuberculous lesions in two cases (20%), malignant neoplastic lesion in one (10%), and silicotic coalescence in seven (70%) (Fig. 5). Early recognition of coalescence of silicotic lesions is important because such coalescence constitutes replacement of normally aerated lung tissue by a functionless mass of fibrous tissue [16], is associated with the appearance of respiratory symptoms, and leads to deterioration of lung function [17]. This complicated form of silicosis also has a poorer prognosis than simple silicosis [18].

Thus, in the evaluation of silica-exposed workers, CT of the thorax is primarily useful in patients with simple silicosis identified on plain chest films. Conglomerations are identified

Fig. 4.—Chest radiograph (A) and CT scans (B) of patient with complicated silicosis. Large conglomerations surrounded by the emphysematous changes are evident. Although conglomeration is diagnosed as such by both methods, CT identifies more areas of coalescence.

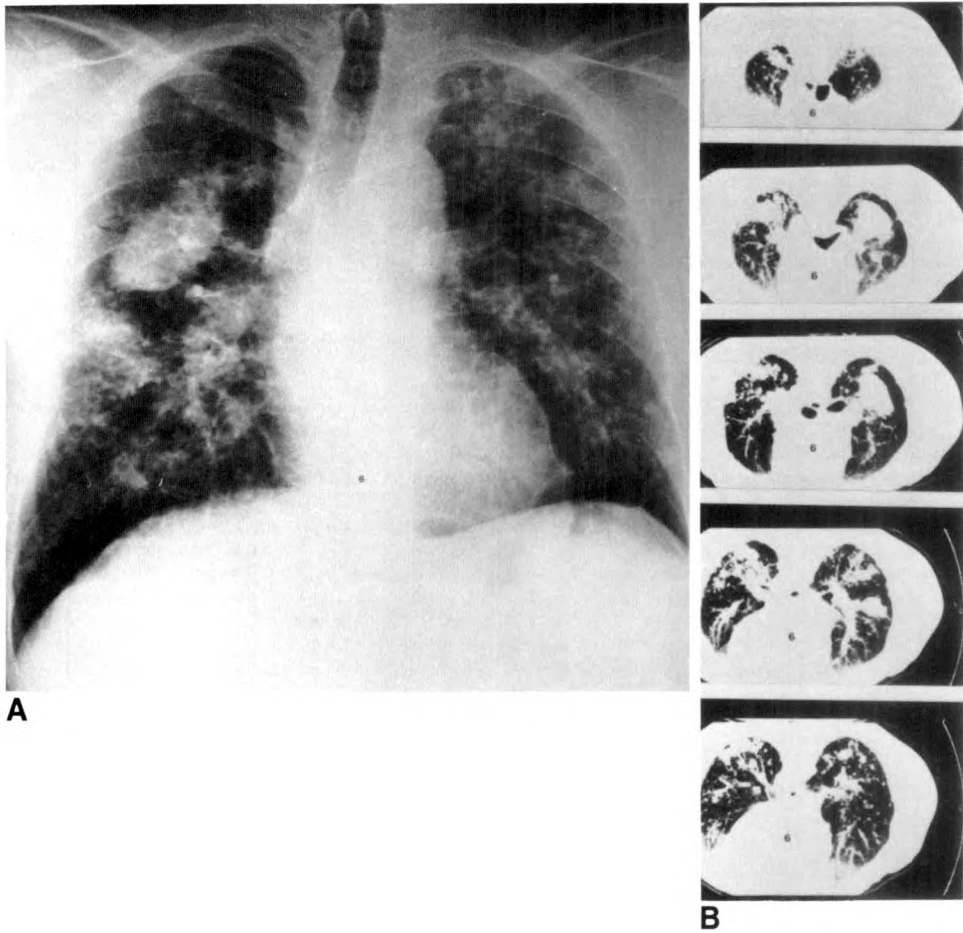
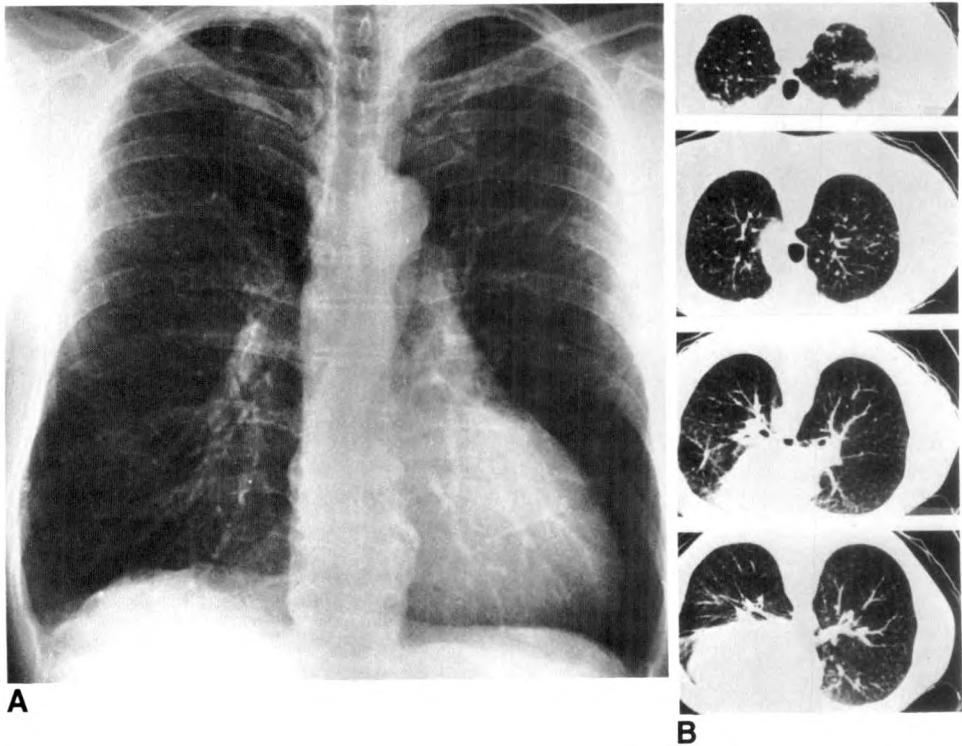


Fig. 5.—Chest radiograph (A) and CT scans (B) of patient with nodular silicosis. The abnormalities are seen equally well on chest radiograph and CT scans, but an upper-lobe conglomeration can be appreciated only on CT.



in 33% of such cases. Because identification of such masses is important in the staging of diseases that are potentially treatable (tuberculosis and lung cancer), we believe that additional information gained by CT justifies the added cost of the procedure once simple silicosis has been identified.

REFERENCES

1. Kreel L. Computed tomography of the lung and pleura. *Semin Roentgenol* 1978;13:213-225
2. Jost RG, Sagel SS, Stanley RJ, Levitt RG. Computed tomography of the thorax. *Radiology* 1978;126:125-136
3. Pugatch RD, Faling LJ. Computed tomography of the thorax: a status report. *Chest* 1981;80:618-626
4. Brown LR, Muhm JR. Computed tomography of the thorax. Current perspectives. *Chest* 1983;83:806-813
5. Kreel L. Computer tomography in the evaluation of pulmonary asbestosis: preliminary experiences with the EMI general purpose scanner. *Acta Radiol [Diagn] (Stockh)* 1976;17:405-412
6. Katz D, Kreel L. Computed tomography in pulmonary asbestosis. *Clin Radiol* 1979;30:207-213
7. Kreel L. Computed tomography of interstitial pulmonary disease. *J Comput Assist Tomogr* 1982;6:181-199
8. Naidich DP, Zerhouni EA, Siegelman SS. *Computed tomography of the thorax*. New York: Raven, 1984:219-230
9. Bergin CJ, Müller NL. CT in the diagnosis of interstitial lung disease. *AJR* 1985;145:505-510
10. Bégin R, Boctor M, Bergeron D, et al. Radiographic assessment of pleuropulmonary disease in asbestos workers: postero-anterior, four view films and computed tomograms of the thorax. *Br J Indust Med* 1984;41:373-383
11. Crofton J, Douglas A. *Respiratory diseases*. Oxford: Blackwell, 1969:51
12. International Labour Office/University of Cincinnati. *International classification of radiographs of pneumoconiosis 1980*, No. 22 revised, Occupational safety and health series. Geneva: International Labour Office, 1980
13. Task force on occupational respiratory disease. *Health and welfare canada*. Ottawa: Canadian government, 1979:35-48
14. Snedecor GW, Cochran WC. *Statistical methods*. Ames, IO: Iowa State Univ. Press, 1967
15. Siegel S. *Non parametric statistics*. New York: McGraw-Hill, 1956:195-240
16. Becklake MR. Pneumoconiosis. In: *Handbook of physiology*, sect. 3. *Respiration*, vol. 2. Washington, DC: American Physiological Society, 1964:1601-1614
17. Fraser RG, Paré JAP. Silicosis. In: *Diagnosis of diseases of the chest*, vol. 3. Philadelphia: Saunders, 1979:1484-1502
18. Parkes WR. Diseases due to free silica. In: *Occupational lung disorders*, 2nd ed. London: Butterworth, 1982:134-158

Mediastinal Imaging in Myasthenia Gravis: Correlation of Chest Radiography, CT, MR, and Surgical Findings

Poonam Batra¹
Christian Herrmann, Jr.²
Donald Mulder³

Chest radiographs and CT and MR images of the mediastinum were studied in 16 patients with myasthenia gravis who underwent thymectomy (two with a final diagnosis of thymoma, seven with hyperplasia, and seven with a normal thymus). The anterior mediastinum was analyzed on imaging studies for thymic morphology and the presence of mass lesions, and the findings were then correlated with the results of surgical resection and pathologic examination. The chest radiographs detected an anterior mediastinal mass in two patients consistent with thymoma on subsequent CT and MR examinations. Chest radiographs in the other 14 patients were normal. In seven patients with a final diagnosis of thymic hyperplasia, both CT and MR demonstrated normal thymic morphology in five, an enlarged thymus in one, and a small thymus in one that was easily identified on CT but was difficult to define on MR. In the other seven patients with a normal thymus on pathologic examination, both CT and MR showed an involuted thymus in four, a normal thymus in two, and an enlarged thymus in one. While both CT and MR were superior to chest radiography for studying the thymus, CT provided better spatial resolution and thymic definition in a much shorter scanning time than MR did.

This study suggests that CT should remain the procedure of choice when further imaging of the thymus is needed after the initial chest radiographs in patients with myasthenia gravis.

The radiologic detection of a thymoma is clinically important in patients with myasthenia gravis. Thymectomy is generally recommended, and potentially invasive tumors can often be excised while they are still in a preinvasive state. Removal of adjacent thymic tissue along with the thymoma is sometimes followed by improvement or remission in myasthenia gravis [1]. Routine chest radiography, conventional tomography, fluoroscopy [2], and CT [3-5] have all been used to detect and localize thymomas. In the present study, we performed MR imaging of the mediastinum to evaluate the utility of this technique and to compare it with chest radiography and CT for evaluating thymic morphology preoperatively in myasthenia gravis patients.

Materials and Methods

The study group consisted of 16 patients with a confirmed diagnosis of myasthenia gravis who had had chest radiographs, CT scans, and MR images within 1 month before surgery and who had undergone thymectomy; histologic and surgical reports were available for all patients. Seven men and nine women aged 11-69 years (mean, 39.3 years) were evaluated.

All patients underwent phototimed high-kilovoltage (130-150 kVp) posteroanterior and lateral chest radiography. CT scans were obtained at our institution on a Siemens Somatom DR 3 machine in 10 patients and on a GE 9800 machine in three. In the other three patients, CT scans were obtained at their referring institutions. All scans were obtained at 1-cm intervals from the lung apex to the diaphragm; IV contrast material was used in 12 of the 16 examinations.

MR scans were obtained with a 0.3-T permanent magnet imaging system (Fonar Beta 3000). All imaging was performed during quiet breathing with the patient supine. Multisection

Received July 30, 1986; accepted after revision November 5, 1986.

¹ Department of Radiological Sciences, UCLA School of Medicine, Los Angeles, CA 90024. Address reprint requests to P. Batra.

² Department of Neurology, UCLA School of Medicine, Los Angeles, CA 90024.

³ Department of Thoracic Surgery, UCLA School of Medicine, Los Angeles, CA 90024.

AJR 148:515-519, March 1987

0361-803X/87/1483-0515

© American Roentgen Ray Society

spin-echo (SE) images in the axial plane were obtained in all cases using a 28-msec echo time (TE) and a 500-msec repetition time (TR). Four averages and a 256×256 matrix were usually used for each image, and the section thickness was 9 mm with 12-mm separations between the centers of adjacent slices. Seven simultaneous sections were obtained in each sequence over a period of 8½ min. Nine scans were also obtained in the sagittal plane using the same SE 500/28 sequence. While respiratory gating was not used in any of the 16 patients, cardiac gating was used in three. T2-weighted images, usually with a TE of 56 msec and a TR of 1500–2000 msec, were also obtained in nine of the 16 patients. Eight of these scans were in the axial plane and one in the coronal.

Before surgery the chest radiographs, CT scans, and MR images were reviewed with special attention to the anterior mediastinum and the thymus and with the knowledge that the patients had myasthenia gravis. Thymic morphology was analyzed for the visibility of each lobe: shape (triangular, round, ovoid, or quadrilateral); lateral contours (concave, straight, convex, or multilobular); density (CT) or signal intensity (MR); and homogeneity of thymic tissue. On CT and MR images patients were described as having (1) a focal mass, (2) an enlarged thymus, (3) a normal thymus, or (4) an involuted thymus. The term focal mass indicated a radiologic diagnosis of thymoma. In these patients there was a rounded or lobulated mass with an observed density on CT or a signal intensity on MR that was similar to muscle and that produced a focal bulge in the adjacent pleural surface. In patients judged to have an enlarged thymus the thymus was thicker and/or larger than expected for the patient's age. The density or signal intensity of the thymus in these patients was similar to muscle, with little or no visible fat in the thymus and without any focal contour abnormality. This category was believed to be applicable to a large normal thymus, to a hyperplastic thymus, or possibly to a small thymoma. The radiologic category of normal thymus referred to a thymus with a density (or signal intensity) comparable to that of combined muscle and fat and with no evidence of gross enlargement or discrete mass. Patients who were judged to have an involuted thymus had a thymic density or signal intensity that was consistent with a predominance of fat. Thymic thickness, which is the widest dimension of each lobe perpendicular to the long axis of the thymus [6], was also measured in patients with an enlarged or normal thymus. Tissue diagnoses were based on the final gross and microscopic pathologic reports on specimens removed at surgery.

Results

On CT and MR examinations visible thymic tissue was confined to the superior and anterior mediastinum in all patients. There was a focal bulge in the lateral mediastinal contour in two of the 16 patients who were diagnosed as having an anterior mediastinal mass on chest radiographs. In the other 14 patients with negative chest radiographs, the lateral mediastinal contour was concave in nine, straight in one, and had a smooth gentle convexity to the left in four. Frequently, the left thymic lobe was predominant, appeared oval, and projected adjacent to the aortic arch. On T1-weighted MR images, the signal intensity of thymic tissue was less than that of the surrounding fat in all patients. In one patient a small thymus that was seen on CT was poorly seen on MR. In nine patients with T2-weighted images, the signal intensity of the thymic tissue increased and approached that of fat in seven patients, while the thymic signal intensity increased only minimally in two patients. On the basis of CT and MR findings, two of the 16 patients were judged to have a focal mass, two an enlarged thymus, eight a normal thymus, and four an involuted thymus. On thymectomy two patients proved to have thymoma, seven hyperplasia, and seven a normal thymus.

In both of the patients with histologically proved thymomas, chest radiographs, CT scans, and MR images accurately diagnosed focal masses in the thymus. One of these was an invasive thymoma in which tumoral calcification was seen only by CT. In retrospect, CT and probably MR showed tissue strands extending from the left margin of the tumor into the pulmonary parenchyma. MR distinguished the tumor mass from the mediastinal vessels more easily than unenhanced CT in this patient (Fig. 1). The encapsulated thymoma was particularly well seen on the sagittal MR image (SE 500/28) (Fig. 2).

The posteroanterior and lateral chest radiographs were normal in all seven patients with thymic hyperplasia. In five of these patients both the CT and MR scans indicated normal

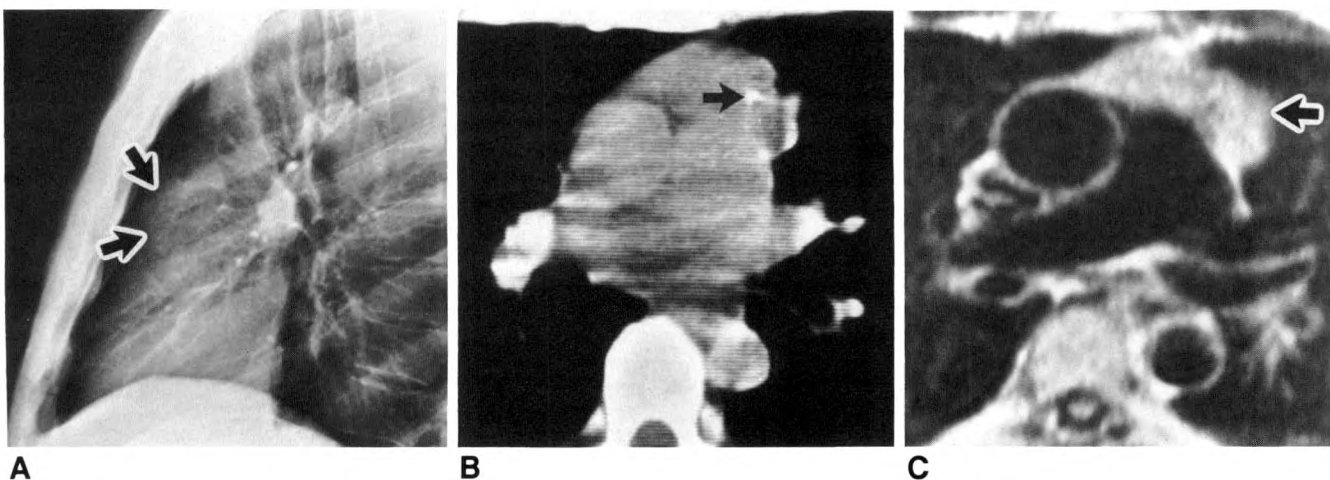


Fig. 1.—Case 1: Invasive thymoma in 52-year-old man with myasthenia gravis.

A, Lateral chest radiograph shows anterior mediastinal mass (arrows).

B, CT scan shows calcification within mass (arrow).

C, Axial T1-weighted SE 500/28 image. Thymoma appears as lobulated mass of intermediate signal intensity (arrow). Calcification is not identified.

Fig. 2.—Case 2: Encapsulated thymoma in 69-year-old woman with myasthenia gravis.

A, Postenhancement CT scan shows anterior mediastinal mass (arrow).

B, Axial T1-weighted SE 500/28 image shows intermediate-signal-intensity mass (arrow) and focal mediastinal bulge (arrowhead).

C, Axial T2-weighted SE 1500/56 image shows heterogeneity and marked increase in signal intensity from mass (arrow).

D, Sagittal T1-weighted SE 500/28 image shows entire mass (arrow).

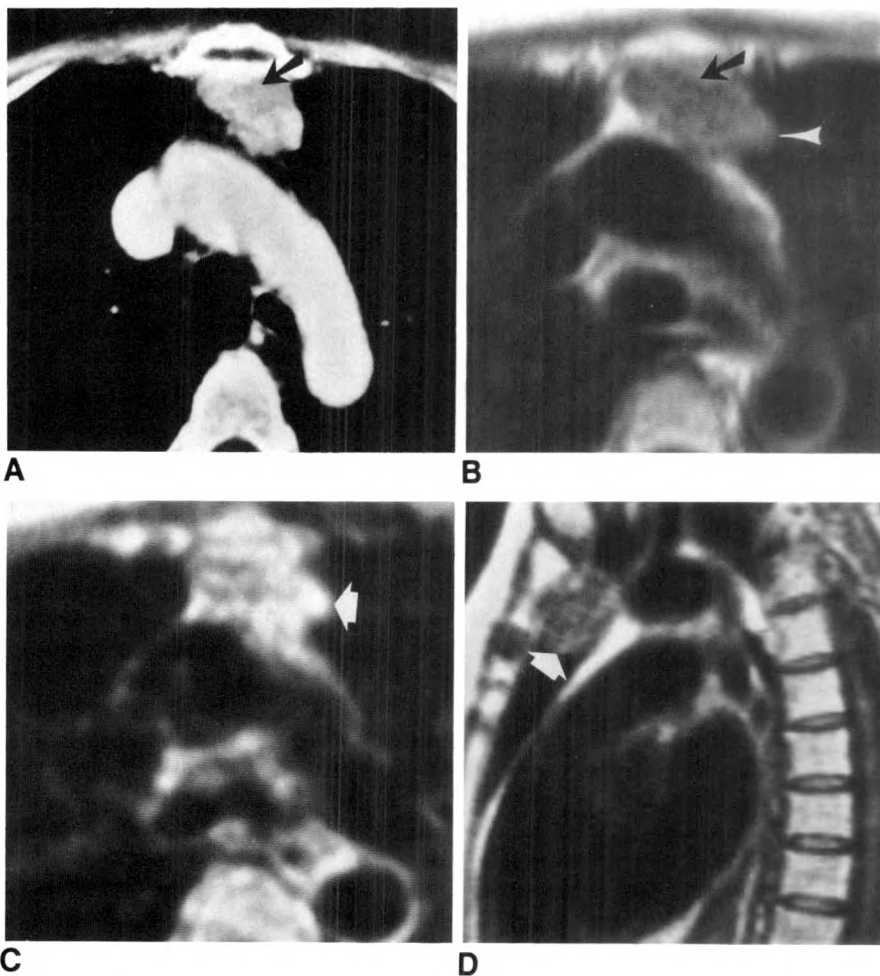
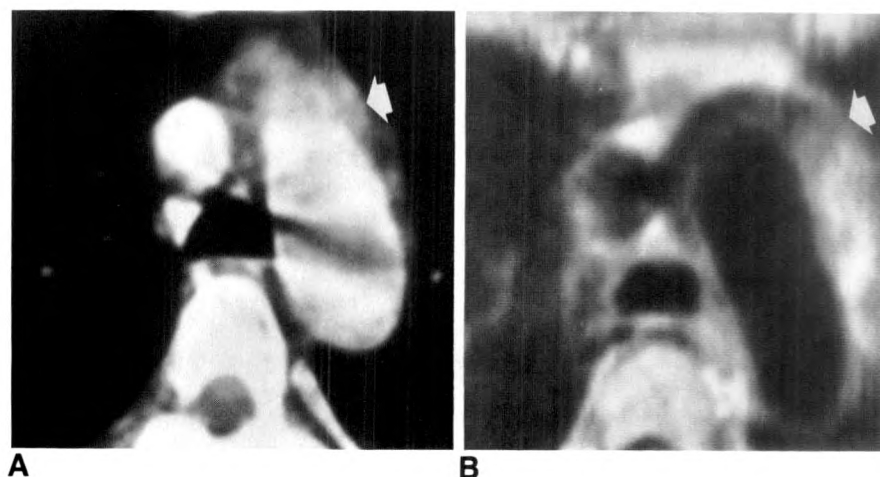


Fig. 3.—Case 3: Thymic hyperplasia in 44-year-old woman with myasthenia gravis with normal thymus on CT and MR.

A, CT scan shows thymus infiltrated by fat anterior and lateral to arch of aorta (arrow).

B, Axial T1-weighted SE 500/28 image distinguishes intermediate signal intensity of thymus from bright signal intensity of fat (arrow).



thymic morphology (Fig. 3). Both lobes of the thymus were visible in three of the five patients; the right lobe only was visible in the fourth patient and the left lobe only in the fifth patient. The thymic thickness, as measured from axial images, ranged from 3 to 9 mm by CT (mean, 5.7 mm) and from 3 to

19.5 mm by MR (mean, 8.2 mm). In one of the seven patients with proved hyperplasia, the thickness of the right and left lobes (14.0 and 17.5 mm on CT, 12.0 and 24.0 mm on MR) was considered to be enlarged for the patient's age of 11 years. In one other patient, while the thickness of the thymus

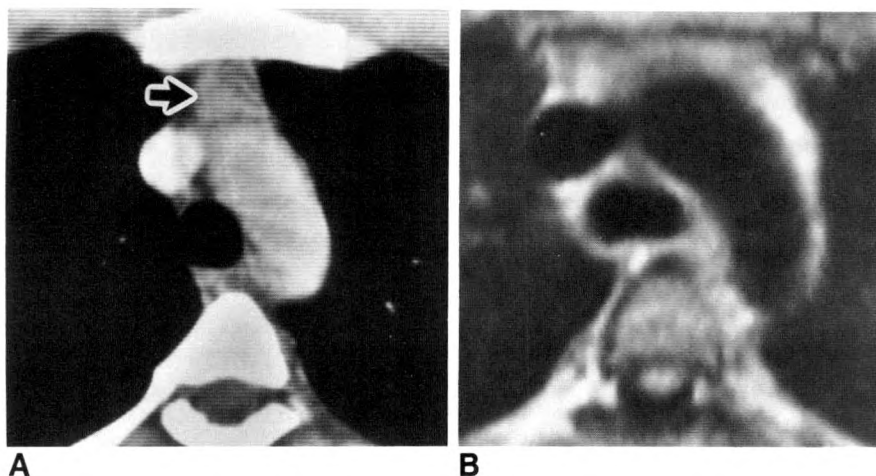


Fig. 4.—Case 9: Thymic hyperplasia in 24-year-old woman with myasthenia gravis in whom CT was considered better than MR for defining thymus.

A, CT scan shows 1.2- by 0.9-cm residual thymus anterior to arch of aorta (arrow).

B, Axial T1-weighted SE 500/28 image slightly caudad to A. Residual thymus is difficult to define.

(9 mm) on CT was judged to be normal for the patient's age of 24 years, the thymus was poorly seen on MR (Fig. 4).

In the seven patients with a histologically normal thymus, all of the preoperative chest radiographs were normal. In four of these patients both CT and MR showed an involuted thymus, and in two of these patients both CT and MR were consistent with a normal thymus. In the other patient, although the thymic lobe thickness of 10 mm on CT and 15 mm on MR was normal for the patient's age of 35 years, the overall size of the thymus appeared large on both CT and MR examinations.

Discussion

Chest radiographs and CT and MR images accurately detected two surgically confirmed thymomas. However, tumoral calcification seen on CT in one of these patients (with an invasive lesion) was not identified on MR. The identification of calcification in a mediastinal mass may be useful in considering a differential diagnosis. The thymomas appeared on CT and MR as oval or lobulated masses with a density or signal intensity (on T1-weighted images) similar to that of muscle. The signal intensity of the tumors increased and approached that of fat on T2-weighted images. Webb et al. [7] reported mediastinal masses other than thymomas to be less intense than surrounding fat when a short TR was used. This suggests that the T1 of mediastinal masses including our thymomas is longer than that of fat. Similarly, in the series of Webb et al. [7], the signal intensity of masses increased relative to fat when the TR value was increased, with a resulting decrease in the contrast between mass and surrounding fat. In our series the benign encapsulated thymoma was especially well seen on sagittal MR images. We added the sagittal projection for MR imaging in nine patients because it is analogous to lateral tomograms of the anterior mediastinum, which have traditionally been used to identify thymo-

mas [2]. Ross et al. [8] also reported a thymoma as being well defined on sagittal MR images.

Thymic hyperplasia is a histologic diagnosis based on a microscopic finding of hyperplastic thymic germinal centers. The thymus itself may or may not actually be enlarged. In our series of 16 patients with myasthenia gravis, histologic diagnosis revealed hyperplasia in seven (44%) of 16, a normal thymus in seven (44%), and a thymoma in two (12%). Both lobes of the thymus were visible on CT and MR in four of the seven patients with thymic hyperplasia. The thickness of the thymic lobes was considered to be normal for the patient's age in six of seven patients with thymic hyperplasia. However, their thymic lobes were thicker than in five of seven patients who were proved to have a normal thymus at surgery. No patient with an involuted thymus on imaging studies was found to have thymic hyperplasia on histologic examination. Baron et al. [9] reported diffuse enlargement and an increased thymic thickness on CT in three of five myasthenia gravis patients with a pathologic diagnosis of thymic hyperplasia. In two of their patients with thymic hyperplasia, however, the thymus was of normal size and shape. Similarly, six of our myasthenia gravis patients with thymic hyperplasia were considered to have a normal thymus for their age on MR and CT. Another of our patients, a 35-year-old man with an apparently enlarged thymus on CT and MR, was found to have a normal thymus at surgery.

In one of our patients with thymic hyperplasia a small thymus (1.2 × 0.9 cm) was shown on CT but was difficult to define on the SE 500/28 image sequence. A T2-weighted image was not obtained in this case. The surgical specimen weighed 32 g. Another patient whose thymus was clearly visible on MR had a normal thymus at surgery that weighed only 22 g. This may be explained by the fact that in the patient with hyperplasia the thymus contained more adipose tissue than glandular tissue, while in the latter patient the thymus consisted predominantly of glandular tissue. Therefore, distinguishing a small thymus of intermediate signal intensity on a T1-weighted image from the bright signal of surrounding fat

may not be possible, because partial-volume averaging and the prolonged scanning time result in motion degradation of the image.

All of our patients who proved to have a normal thymus were over the age of 30. Their thymus was visible on CT as well as on MR and often appeared thicker on MR images than on CT scans. These results confirm the findings of de Geer et al. [10] for the MR appearance of a normal thymus.

In conclusion, MR examination of the thymus added no clinically important information to results obtained with CT in our series of 16 myasthenia gravis patients who had thymoma, thymic hyperplasia, and a normal or involuted thymus. Because of better spatial resolution and a much shorter scanning time, CT remains the procedure of choice for imaging the mediastinum in these patients after standard chest radiography.

ACKNOWLEDGMENTS

We thank Richard Steckel for reviewing the manuscript and Melody Duran for assistance in manuscript preparation.

REFERENCES

1. Mulder DG, Herrmann C, Keesey J, Edwards H. Thymectomy for myasthenia gravis. *Am J Surg* 1983;146:61-66
2. Brown LR, Muhm RJ, Gray JE. Radiographic detection of thymoma. *AJR* 1980;134:1181-1188
3. Fon GT, Bein ME, Mancuso AA, Keesey JC, Lupetin AR, Wong WS. Computed tomography of the anterior mediastinum in myasthenia gravis. *Radiology* 1982;142:135-141
4. Brown LR, Muhm JR, Sheedy PF, Unni KK, Bernata PE, Herrmann RC. The value of computed tomography in myasthenia gravis. *AJR* 1983;140:31-35
5. Moore AV, Korobkin M, Powers B, et al. Thymoma detection by mediastinal CT: patients with myasthenia gravis. *AJR* 1982;138:217-222
6. Baron RL, Lee JKT, Sagel SS, Peterson RR. Computed tomography of the normal thymus. *Radiology* 1982;142:121-125
7. Webb WR, Gamsu G, Stark DD, Moon KL, Moore EH. Evaluation of magnetic resonance sequences in imaging mediastinal tumors. *AJR* 1984;143:723-727
8. Ross JS, O'Donovan PB, Novoa R, et al. Magnetic resonance of the chest: initial experience with imaging and in vivo T1 and T2 calculations. *Radiology* 1984;152:95-101
9. Baron RL, Lee JKT, Sagel SS, Levitt RG. Computed tomography of the abnormal thymus. *Radiology* 1982;142:127-134
10. de Geer G, Webb WR, Gamsu G. Normal thymus: assessment with MR and CT. *Radiology* 1986;158:313-317

Book Review

Nuclear Cardiac Imaging: Principles and Applications. By A. S. Iskandrian. Philadelphia: F. A. Davis, 552 pp., 1987. \$75

This book, intended for trainees and clinicians in cardiology, internal medicine, nuclear medicine, and radiology, avoids the incoherence so often associated with multiauthored books. Although written by a distinguished practitioner, the book nonetheless starts with inappropriate basics. While I would accept cardiac physiology or clinical cardiology as an appropriate introduction to nuclear cardiac imaging, I do not see the particular benefit of a cursory review of laboratory organization, instrumentation and imaging, radiopharmaceuticals, and dosimetry given in chapters 1–3. A few examples will illustrate the superficiality of this introduction: in the laboratory section, scintillation cameras are defined as either Anger Cameras (single-crystal cameras) or Baird Atomic, a tradename for a multiple-crystal camera. In the same chapter, a reporting form is suggested for rest (T1-201) myocardial imaging and stress myocardial imaging, but not for the combination of both. A single paragraph covers basic physics. Nuclear notation is reduced to a definition of isotope, isobar, isotone, and isomer. A brief discussion of photoelectric interaction, Compton scatter, and pair formation is followed by a discussion of the attenuation of high-energy [sic] photon beams as a separate phenomenon, without reference to scatter. Spatial resolution is defined in terms of the point-spread function, but not the modulation transfer function. The author also includes the now almost obligatory list of the components of a digital computer, as well as octal and hexadecimal

notations. The references in chapter 2 do not seem to have been perused by the author, but rather seem to be quoted derivatively; for example, in the description of the interpolative background subtraction, the weighting is misquoted and the reference is incomplete although it is given correctly a few chapters later. But once the author leaves this totally unnecessary introduction, he finds his pace with a vengeance. The chapter on exercise testing is wonderful, and the next one (chapter 5) on myocardial imaging and ventriculography (technical considerations and interpretation) is thorough and richly referenced. All subsequent chapters are equally good, clear, complete, and lavishly and beautifully illustrated. Tables are used abundantly and to great advantage to report on the experience of others.

It is worth reading past the first pages: the rewards are plentiful. No nuclear medicine physician should be without this book—and each should offer it to his or her referring cardiologist.

Students should keep it as a reference book, or convince their school library to purchase a copy. I will keep it at home, far away from the roving eyes of my residents, for fear of losing it.

Michael L. Goris
Stanford University School of Medicine
Stanford, CA 94305

Case Report

Mediastinal Paraganglioma: Radiologic Evaluation of an Unusual Vascular Tumor

Elizabeth A. Drucker,¹ Theresa C. McCloud,¹ Carolyn G. Dedrick,² Alan D. Hilgenberg,³ Stuart C. Geller,¹ and Jo-Anne O. Shepard¹

Paragangliomas are vascular tumors derived from neuroectodermal cells associated with ganglion cells of the autonomic nervous system. Their occurrence in the mediastinum is extremely rare. Such lesions are usually discovered on incidental chest radiographs of asymptomatic individuals. Although the radiographic features of these tumors have previously been reported [1-6], we wish to present a case in which angiography was important in both diagnosis and preoperative management.

Case Report

A 30-year-old man was found to have a left posterior mediastinal mass during routine chest radiography 6 years before admission. He refused surgery at that time. Eight months before admission, he experienced intermittent, sharp left anterior chest pain radiating to the back and a productive cough. A chest radiograph again showed the mass, which had doubled in diameter since the previous examination (Fig. 1A). A barium esophagram showed that the lesion was extrinsic to the esophagus and displaced it anteriorly. Conventional and computed tomography performed at another institution confirmed the presence of a noncalcified mass of soft-tissue density, extending from the pulmonary veins to the carina, displacing the left mainstem bronchus anteriorly. The preoperative diagnosis was intercostal neurofibroma or bronchogenic cyst. Exploratory thoracotomy identified a fleshy mass in the posterior mediastinum lateral to the aorta, measuring 6.5 × 7.5 × 1.1 cm. During the preliminary dissection, profuse hemorrhage occurred. Complete resection was consequently deferred until the vascular supply of the tumor could be defined.

Selective arteriography showed a markedly hypervascular mass supplied primarily by dilated sixth and seventh left intercostal arteries (Fig. 1B). The mass produced extrinsic compression of the left side of the descending aorta. Four days later, successful preoperative embolization of these intercostal arteries was performed with steel-coil occlusion devices. This was followed by a second surgical procedure. However, because of extension of the mass into the posterior intercostal musculature, resection was incomplete. At autopsy, the tumor proved to be a paraganglioma.

Discussion

Mediastinal paragangliomas are derived from neuroectodermal cells, which occur in two major clusters: aorticopulmonary (in the region of the aortic arch) and aorticosympathetic (in the posterior mediastinum). These tumors are quite rare, accounting for less than 0.3% in a large series of over 1000 mediastinal masses [7].

No age or sex predilection has been reported in patients with mediastinal paragangliomas [1-3]. Patients may be asymptomatic; however, dyspnea, hemoptysis, neurologic symptoms, or occasionally superior vena cava syndrome may occur if the lesion reaches a size sufficient to compress contiguous structures [1, 3, 4].

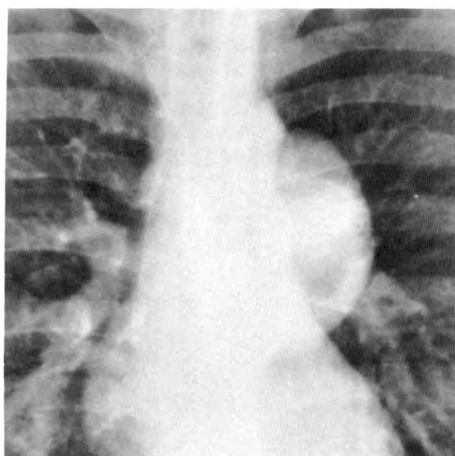
The plain-film characteristics of mediastinal paragangliomas are nonspecific. CT may be extremely valuable in the diagnosis of these lesions [5]. CT features include a mass of soft-tissue density in characteristic locations, either the aortico-

Received July 10, 1985; accepted after revision September 24, 1986.

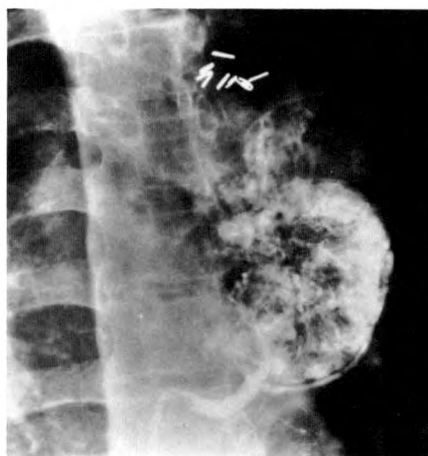
¹ Department of Radiology, Massachusetts General Hospital, Boston, MA 02114. Address reprint requests to T. C. McCloud.

² Department of Radiology, Lahey Clinic Medical Center, Burlington, MA 01805.

³ Department of Surgery, Massachusetts General Hospital, Boston, MA 02114.



A



B

Fig. 1.—30-year-old man with intermittent left anterior chest pain.
A, Frontal chest radiograph revealing a left posterior mediastinal mass.
B, Selective seventh left intercostal arteriogram showing the markedly hypervascular mass.
(Courtesy of A. J. Greenfield. Reprinted with permission.)

pulmonary window or the posterior mediastinum. Dynamic scanning during bolus injection of contrast material shows extreme vascularity, allowing for a more specific diagnosis (Fig. 2). The diagnostic possibilities based on these CT findings are limited to three entities. They are Castleman's disease (angiofollicular lymph node hyperplasia), hemangioma, and mediastinal goiter, all of which are extremely vascular.

Preoperative angiography is often helpful in defining the vascular supply and determining the resectability of mediastinal paragangliomas [2, 5, 6]. The angiographic features of these lesions include hypervascularity, multiple feeding vessels, and homogeneous capillary blush (Fig. 1B).

If the major feeding arteries are hypertrophied, transcatheter vascular embolization can be performed preoperatively in order to lessen intraoperative hemorrhage. Although the literature has not previously described preoperative embolization of paragangliomas, there is an example of successful embolization in a case of mediastinal Castleman's disease [8]. We found this procedure to be particularly useful as an adjunct to surgical management of an extremely hypervascular paraganglioma. Surgery is curative if the lesion is removed in its entirety [4].

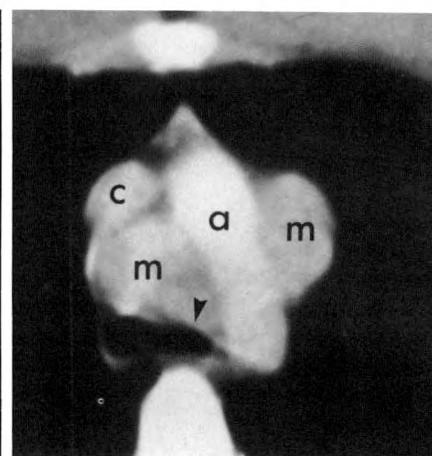


Fig. 2.—26-year-old man with increasing cough and wheezing. Contrast-enhanced CT showing an inhomogeneous, hypervascular, enhancing mediastinal mass (m) with its center on the aorticopulmonary region. Posterior displacement and narrowing of carina and left main bronchus (arrowhead). a = aorta; c = superior vena cava. An aortogram confirmed hypervascularity of mass.

REFERENCES

1. Haber S. Retroperitoneal and mediastinal chemodectoma: report of a case and review of the literature. *AJR* 1964;92:1029-1041
2. Lacquet LK, Moulijn AC, Jongerios CM, Umburg M, Rensing JB. Intrathoracic chemodectoma with multiple localizations. *Thorax* 1977;32:203-209
3. Olson JL, Salyer WR. Mediastinal paragangliomas (aortic body tumor). *Cancer* 1978;41:2405-2412
4. Lack EE, Stillinger RA, Colvin DB, Groves RM, Burnette DG. Aorticopulmonary paraganglioma: report of a case with ultrastructural study and review of the literature. *Cancer* 1979;43:269-278
5. Ogawa J, Inoue H, Koide S, Kawada S, Shohtsu A, Hata J. Functioning paraganglioma in the posterior mediastinum. *Ann Thorac Surg* 1982;33:507-510
6. D'Altorio RA, Rishi US, Bhagwanani DG. Arteriographic findings in mediastinal chemodectoma. *J Thorac Cardiovasc Surg* 1974;67:963-965
7. Wychulis AR, Payne WS, Clagett OT, Woolner LB. Surgical treatment of mediastinal tumors: a 40 year experience. *J Thorac Cardiovasc Surg* 1971;62:379-392
8. Walter JF, Rottenberg RW, Cannon WB, Sheridan LA, Pizzimenti J, Orr JT. Giant mediastinal lymph node hyperplasia (Castleman's disease): angiographic and clinical features. *AJR* 1978;130:447-450

Case Report

Pleural Endometriosis: CT and Sonographic Findings

Jung-Gi Im,^{1,2} Heung Sik Kang,¹ Byung Ihn Choi,¹ Jae Hyung Park,¹ Man Chung Han,¹ and Chu-Wan Kim¹

Pleural endometriosis is a rare condition caused by transdiaphragmatic extension of uterine endometrial tissue to the pleura or hematogenous implantation of endometrial cells in the lung [1, 2]. We present a case of pleural endometriosis that shows classic transdiaphragmatic extension of endometrioma through defects in the diaphragm. CT and sonography showed masses in the pleural and peritoneal cavity and defects in the right diaphragm.

Case Report

A 38-year-old woman was admitted because of dyspnea and right chest pain of 2 weeks' duration. There was a history of dysmenorrhea and infertility. Ten months before admission, laparoscopy revealed extensive pelvic endometriosis. For 5 months prior to admission, the patient complained of intermittent mild right chest pain, especially during menstruation.

Initial chest radiographs obtained at the time of admission showed

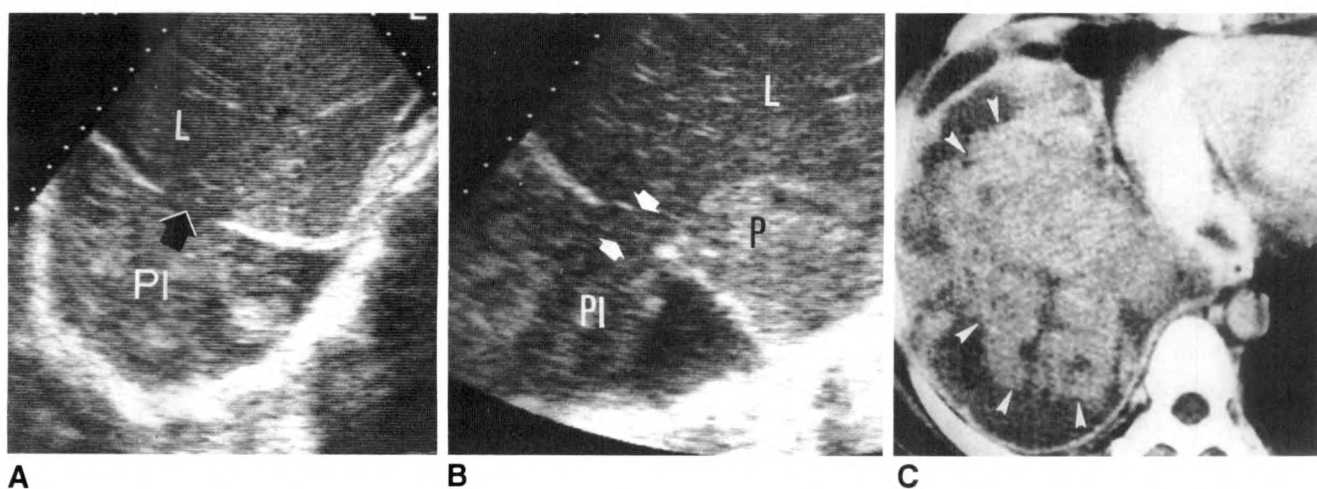


Fig. 1.—Radiologic findings on admission.

A, Right subcostal transverse sonogram shows abrupt disruption of diaphragm (arrow). L = liver. Note nodular echogenic endometrial tissue and fluid in pleural space (PI).

B, Right subcostal longitudinal sonogram shows diaphragmatic defect (arrows), as well as mixed echogenic materials of endometrial tissue in both pleural (PI) and peritoneal (P) space behind liver (L).

C, Postcontrast CT scan shows multilobulated, slightly enhancing mass (arrowheads) with surrounding fluid density in right pleural space.

Received July 16, 1986; accepted after revision September 19, 1986.

¹ Department of Radiology, College of Medicine, Seoul National University, 28 Yeongun-Dong, Chongro-Ku, Seoul 110, Korea.

² Present address: University of California, San Francisco, School of Medicine, c/o Gordon Gamsu, Department of Radiology, C-309, 505 Parnassus Ave., San Francisco, CA 94143-0628. Address reprint requests to J.-G. Im.

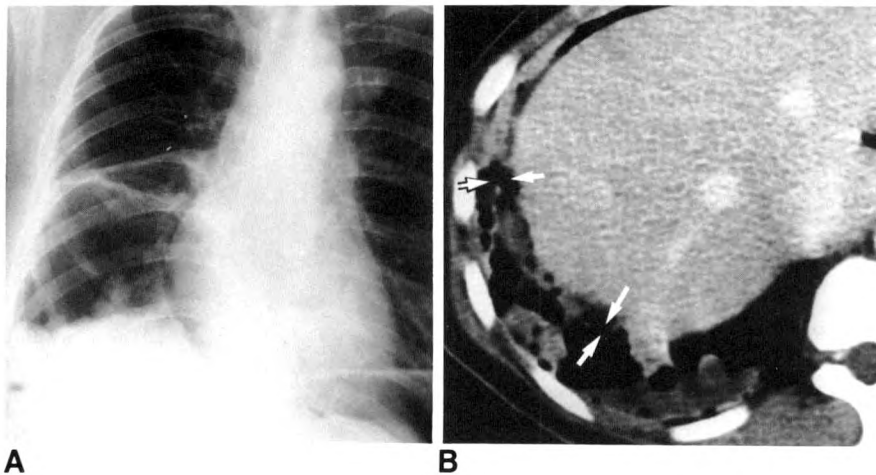


Fig. 2.—Radiologic findings 2 months after bilateral salpingo-oophorectomy. Plain chest radiograph (A) and CT scan (B).

A, Chest radiograph showing right localized pneumothorax and pneumoperitoneum. Multiple nodular densities can be seen in supradiaphragmatic area.

B, CT scan shows diaphragmatic defects (arrows) revealed by contrast of air in both peritoneal and pleural spaces. There are residual nodules of endometrioma and pleural fluid.

a pleural effusion. Diagnostic thoracentesis produced a thick, old, bloodlike aspirate without any microorganisms.

Sonography of the upper abdomen and chest showed numerous defects 0.5 to 3 cm in diameter in the posterolateral portion of right hemidiaphragm. A large amount of echogenic fluid was present in the right pleural space and in the peritoneal space posterior to liver (Figs. 1A and 1B). A CT scan of the chest showed a lobulated soft-tissue mass mixed with fluid in the right pleural space (Fig. 1C).

Transthoracic needle aspiration biopsy of the pleural mass revealed sheets of glandular epithelial cells with hemorrhagic background consistent with endometrial tissue. Biopsy of a right supraclavicular lymph node showed endometriosis.

A laparotomy disclosed 800 ml of bloody fluid with old clots in the peritoneal cavity. Bilateral salpingo-oophorectomy and hysterectomy were performed, and pathologic examination revealed multifocal endometriosis of both adnexa, the omentum, the intestinal walls, and the outer surface of the uterus. Subsequently, the dyspnea and chest pain improved slowly without any treatment of the pleural lesion.

A chest radiograph made 2 months later showed right-sided pneumothorax and pneumoperitoneum (Fig. 2A). A follow-up CT scan revealed multiple right diaphragmatic defects shown by air in both the pleural and peritoneal cavity (Fig. 2B). Multiple aggregated nodular densities in the right pleura and in the peritoneum suggested that there was remaining endometrial tissue with hematoma.

Discussion

Since the first description of pleural endometriosis by Swarz in 1938 [1], 87 cases of pleural and pulmonary endometriosis have been reported in the English-language literature [1]. Pleural endometriosis causes catamenial pneumothorax or

hemothorax. Most of the reported cases have the latter (64 cases) [1–4]. Ten cases have been reported with hemothorax similar to the case reported here [1, 5, 6].

Pleural endometriosis most often occurs in the right chest (95%) and is the result of migration of endometrial tissue from the pelvis [2]. Our case shows the classic route of spread through defects in the right diaphragm.

Disruption of right diaphragmatic echoes on sonography has been regarded as a sign of diaphragmatic disease including direct tumor invasion, metastatic implants, diaphragmatic rupture, and congenital defect [7, 8].

REFERENCES

1. Karpel JP, Appel D, Merav A. Pulmonary endometriosis. *Lung* 1985;163:151–159
2. Foster DC, Stern JL, Buscema J, Rock JA, Woodruff JD. Pleural and parenchymal pulmonary endometriosis. *Obstet Gynecol* 1981;58:552–556
3. Slasky BS, Siewers RD, Lecky JW, Zajko A, Burkholder JA. Catamenial pneumothorax: the roles of diaphragmatic defects and endometriosis. *AJR* 1982;138:639–643
4. Rossi NP, Goplerud CP. Recurrent catamenial pneumothorax. *Arch Surg* 1974;109:173–176
5. Hegeghan MA, Teixidor HS. Pleuroperitoneal endometriosis. *AJR* 1979;133:727–733
6. Wilkins SB, Thomson JB, Tyras DH. Hemothorax associated with endometriosis. *J Thorac Cardiovasc Surg* 1985;89:636–638
7. Worthen NJ, Worthen WF. Disruption of diaphragmatic echoes: a sonographic sign of diaphragmatic disease. *J Clin Ultrasound* 1982;10:43–45
8. Merten DF, Bowie JD, Kirks DR, Grossman H. Anteromedial diaphragmatic defects in infancy: current approaches to diagnostic imaging. *Radiology* 1982;142:361–365

Mammographic Density and Physical Assessment of the Breast



Cynthia A. Swann^{1,2}
 Daniel B. Kopans¹
 Kathleen A. McCarthy¹
 George White¹
 Deborah A. Hall¹

We studied the relationship between the radiographic density of the breast as measured by parenchymal pattern vs age, breast size, thickness after compression, and compressibility. Two hundred consecutive women were evaluated. None of the three parameters or the patient's age correlated with the degree of radiographic density. Although more older women had lucent parenchyma, 37% of women more than 50 years of age had dense patterns. Thus, these factors cannot be used to predict radiographic density. Phototiming is required to maintain image quality, and only a test exposure can accurately predict breast density.

The importance of parenchymal pattern as a risk factor for the development of breast cancer continues to be controversial. More basic, however, is the lack of information on the underlying determinants of these patterns. Although histologic correlates of parenchymal patterns have been suggested [1], the reasons for variations in parenchymal pattern and for the overall radiographic density of the breast have not been elucidated completely.

Mammographic technique is important in the detection of early-stage lesions. Sickles and Weber [2] have suggested that grids improve the detection of lesions in breasts that cannot be compressed to less than 6 cm in thickness, and they have emphasized the importance of using scatter-reduction grids for the radiographically dense breast. The ability to predict parenchymal patterns or, more simply, the radiographic density of the breast from measurable physical parameters would greatly facilitate the choice of optimal exposure factors.

It is commonly believed that physical characteristics of the breast such as size and firmness can be equated with radiographic density. Intuitively, firm breasts might be expected to be radiographically dense and large, soft breasts to be radiolucent. Such a relationship, if true, would help predict parenchymal density and permit choice of the best mammographic technique. We therefore undertook a study to determine if clinical assessment of simple physical characteristics of the breast could be used to predict the degree of radiographic density.

Materials and Methods

The study group consisted of 200 women who came to the Breast Imaging section of the Department of Radiology at the Massachusetts General Hospital for routine screening or diagnostic evaluation. Their ages ranged from 26 to 86 years. All studies were performed with a Thomson-CGR (Columbia, MD) 500-T mammographic unit with a 0.3-mm focal spot and a source-to-image distance of 65 cm. All studies were phototimed and were performed with an oscillating grid. In addition to age, three parameters were recorded before mammography for each patient: breast compressibility (or firmness), size, and thickness.

The technologist made a subjective assessment of breast firmness by grading the amount of force required to compress the breast in the craniocaudal projection. We assumed that both breasts were the same and recorded data from one side only. Firmness was categorized as easy to compress, moderately compressible (average), or difficult to compress. Because

Received September 19, 1986; accepted after revision November 4, 1986.

¹ Department of Radiology, Massachusetts General Hospital; Massachusetts General Hospital Cancer Center, and Harvard Medical School, Boston, MA 02114.

² Present address: Department of Radiology, Holy Cross Hospital of Silver Spring, Silver Spring, MD 20910. Address reprint requests to C. A. Swann.

AJR 148:525-526, March 1987
 0361-803X/87/1483-0525
 © American Roentgen Ray Society

absolute measurement of breast size is difficult, bra cup size was used for simplicity and objectivity. The thickness of the breast while compressed in the craniocaudal projection was the distance between the upper and lower compression plates.

A radiologist assessed the parenchymal patterns on the radiographs without knowledge of the breast's compressibility, size, or thickness. Mammographic patterns were grouped into those that appeared primarily dense or fibroglandular (P2/DY in Wolfe's classification [1]) and those that were primarily lucent or fat-containing (N1/P1) in Wolfe's classification [1].

Results

Table 1 summarizes the relationship of breast size to radiographic density. Approximately one-half of the smallest breasts were radiographically lucent, and one-half were radiographically dense. Very large breasts often had lucent parenchymal patterns, but 30% of the largest breasts had dense mammary parenchyma. Thus, size is not a good indicator of radiographic density.

Table 2 compares radiographic density and breast compressibility. The majority of patients who were categorized as difficult to compress had radiolucent parenchymal patterns. Nevertheless, 38% of these women had radiographically dense breasts. Among women whose breasts were easily compressed, the percentages of those with lucent patterns and those with dense patterns were almost equal. The remaining women, who were categorized as average on compression, also had an almost equal chance of having radiographically lucent or dense breasts.

Table 3 compares parenchymal patterns and the objective measurement of compressed breast thickness in the craniocaudal view. Although there was a slight tendency for breasts that were relatively thick on compression to be more radiolu-

TABLE 1: Bra Cup Size vs Mammographic Density

Size	Lucent (N1/P1)	Dense (P2/DY)	Total
A	13 (46)	15 (54)	28
B	45 (52)	42 (48)	87
C	32 (55)	26 (45)	58
D or larger	19 (70)	8 (30)	27

Note.—N1/P1 and P2/DY are Wolfe's classifications [1]. Numbers are numbers of patients; numbers in parentheses are percentages.

TABLE 2: Compressibility of the Breast vs Mammographic Density

Firmness	Lucent (N1/P1)	Dense (P2/DY)	Total
Hard to compress	28 (62)	17 (38)	45
Average	46 (51)	45 (49)	91
Easy to compress	35 (55)	29 (45)	64

Note.—N1/P1 and P2/DY are Wolfe's classifications [1]. Numbers are numbers of patients; numbers in parentheses are percentages.

TABLE 3: Compressed Breast Thickness vs Mammographic Density

Breast Thickness (cm)	Lucent (N1/P1)	Dense (DY/P2)	Total
2	4 (44)	5 (56)	9
3	14 (44)	18 (56)	32
4	28 (65)	15 (35)	43
5	34 (51)	33 (49)	67
6	18 (60)	12 (40)	30
7	11 (58)	8 (42)	19
Total patterns	109	91	200

Note.—N1/P1 and DY/P2 are Wolfe's classifications [1]. Numbers are numbers of patients; numbers in parentheses are percentages.

cent, this tendency was insufficient to correctly predict radiographic density.

Radiographic density also was evaluated relative to patient age. Although more older women had lucent parenchyma, 37% of women more than 50 years old had dense parenchymal patterns.

Discussion

The paucity of information on factors that contribute to breast parenchymal patterns is surprising. We have shown previously that parenchymal patterns are related, in part, to the patient's body size and weight [3]. Short, heavy women tend to have more breast fat, and tall, thin women tend to have radiographically dense breasts, but even this is not a precise relationship. The determinants of parenchymal patterns are probably multifactorial, related to genetics, age, parity, hormonal status, and body habitus.

We conclude that intuitive predictions of mammographic density are correct only by chance. The three parameters of breast compressibility, size, and thickness cannot accurately predict radiographic density. Age is also an insufficient predictor. In our study, 37% of women more than 50 years old had dense patterns. We believe that a technologist cannot correctly predict the parenchymal density of the patient's breast using these characteristics. Thus, phototiming must be relied on to provide optimal radiographs. Additionally, unless grids are used for all mammograms, a test exposure must be performed to determine the radiographic density of the breast and the need for grid technique.

REFERENCES

1. Wellings SR, Wolfe JN. Correlative studies of the histological and radiological appearance of the breast parenchyma. *Radiology* 1978;129:299-306
2. Sickles EA, Weber WN. High contrast mammography with a moving grid: assessment of clinical utility. *AJR* 1986;146:1137-1139
3. Brisson J, Morrison AS, Kopans DB, et al. Height, weight, mammographic features of breast tissue and breast cancer risk. *Am J Epidemiol* 1984;119(3):371-381

Efficacy of Thyroid Scintigraphy in the Diagnosis of Intrathoracic Goiter

Hee-Myung Park¹
Robert D. Tarver
Aslam R. Siddiqui
Donald S. Schauwecker
Henry N. Wellman

For evaluation of the usefulness of thyroid scintigraphy in the diagnosis of intrathoracic goiter, we analyzed the results of radionuclide thyroid scintigraphy in 54 consecutive cases with suspected upper mediastinal masses. Intrathoracic goiters were found in 42. The sensitivity, specificity, and accuracy of the scintigraphy for intrathoracic goiter were 93% (39/42), 100% (12/12), and 94% (51/54), respectively. Scintigraphic morphology, scanning technique, and pitfalls are discussed. The results show that most intrathoracic goiters do have thyroid function and that radioiodine scintigraphy is a definitive and cost-effective diagnostic procedure for this disease.

Intrathoracic goiter (retrosternal goiter, substernal goiter) is a major diagnostic consideration in the evaluation of upper anterior mediastinal masses. A positive result on radioiodine scintigraphy confirms the diagnosis. There is, however, little published data on the sensitivity, specificity, and accuracy of thyroid scintigraphy as a diagnostic test for intrathoracic goiters. Some authors [1, 2] have indicated that thyroid scintigraphy often is not helpful. To evaluate this further, we examined thyroid function; the morphology and relative activity of the cervical vs. the intrathoracic part of the goiters; and the efficacy and pitfalls of thyroid scintigraphy.

Materials and Methods

We reviewed the records of 54 consecutive patients with suspected upper mediastinal masses seen on chest radiographs or CT scans who had radionuclide thyroid scans between 1972 and 1985. There were 32 women and 22 men. The age range was 26 to 87 years (mean, 66). The radionuclides and dosages used were iodine-131, 50–100 μ Ci (1.9–3.7 MBq) in 26 patients; iodine-123, 250–400 μ Ci (9.3–14.8 MBq) in 26 patients; and ^{99m}Tc-pertechnetate, 5 mCi (185 MBq) in two patients. Imaging was performed by using a rectilinear scanner (25 patients); a scintillation camera (17 patients), or both (12 patients). The 24-hr thyroidal radioiodine uptake was determined in 47 of 54 patients. For pinhole images, 20,000 to 50,000 counts were obtained, depending on the 24-hr thyroidal uptake. For ^{99m}Tc-pertechnetate, 100,000 counts were obtained. For the rectilinear scanning, the minimum count density was 800/cm². Thyroid function tests (including serum T₄ (radioimmunoassay), T₃ uptake, free T₄ index, serum T₃ (radioimmunoassay), and serum levels of thyroid-stimulating hormone) were obtained in 30 of the 54 patients. Chest CT was performed in 20 patients. The diagnosis of intrathoracic goiter was made when there was a definite concentration of radioiodine in the suspected mass. In seven of 12 patients who showed no uptake in the mass, the final diagnoses were based on surgical findings. In the remaining five, the CT either did not show a mass lesion or showed that the mass was tortuous great vessels. The final diagnoses of the 54 patients were intrathoracic goiters in 42, tortuous great vessels in two, metastatic lung cancer in three, thymoma in one, and no mass lesion in six.

Results

Of the 42 patients who had intrathoracic goiters, 29 were euthyroid with a mean serum T₄ of 8.8 μ g/dl (normal, 4.5–11.5). Hyperthyroidism was present in four

Received July 28, 1986; accepted after revision September 22, 1986.

¹ All authors: Division of Nuclear Medicine, Department of Radiology, School of Medicine, Indiana University, Indianapolis, IN 46202. Address reprint requests to H. M. Park, Clinical Service, Nuclear Medicine, Indiana University Hospital, 926 W. Michigan St., Indianapolis, IN 46223.

AJR 148:527–529, March 1987
0361–803X/87/1483–0527
© American Roentgen Ray Society

patients: three had toxic multinodular goiters, and one had a toxic autonomous hot nodule. Two patients were hypothyroid. Thyroid function was not determined in eight patients.

Scintigraphic morphology revealed that the intrathoracic goiter was due to extension of the right lobe in 18 (43%) of 42 patients, extension of the left lobe in 10 (24%), and extension of both lobes or the isthmus in 14 (33%) (Fig. 1). A relatively clear demarcation between the cervical thyroid and the intrathoracic part was seen in two (5%) of 42 patients (Fig. 2). We did not encounter any ectopic intrathoracic goiters [3, 4]. Uptake of radionuclide by the intrathoracic part was equal to that of the cervical gland in 18 (43%), greater in three (7%), and less in 21 (50%) of the 42 patients (Fig. 3). Those with less intrathoracic uptake included nine patients who had solitary intrathoracic cold nodules.

Superior vena cava syndrome due to an intrathoracic goiter [5, 6] was seen in only one patient. The effect of parallax error of pinhole collimator [7] (Fig. 4) was observed in eight (40%) of 20 patients who had pinhole scintigraphy.

The overall sensitivity of thyroid scintigraphy for the diagnosis of intrathoracic goiter was 93% (39/42). The specificity was 100% (12/12), and the accuracy was 94% (51/54). Scintigraphic findings were false negative for three patients. One, with a multinodular goiter with a 24-hr uptake of iodine-131 of only 6%, had posterior mediastinal extension that was mostly nonfunctioning. Another patient had a large cyst completely replacing the intrathoracic thyroid. The third patient had a diffuse goiter with posterior mediastinal extension that was missed completely because of a parallax error of pinhole scintigraphy.

Discussion

The definition of intrathoracic goiter varies considerably, and there are no uniformly accepted criteria [8]. We defined intrathoracic goiter as a thyroid gland that extends caudally into the mediastinum, below the level of the suprasternal notch. The prevalence of intrathoracic goiters varies from 0.2% to 15% of thyroidectomies [9]. Intrathoracic goiter, however, is the most common cause of anterior upper mediastinal masses in adults [10].

Pathologically, intrathoracic goiter is an extension of the cervical thyroid in most cases. Because iodine is trapped by thyroid tissue, scintigraphy with radioiodine should be an excellent confirmatory test. Without supporting data, some authors have made misleading statements, such as "many retrosternal goiters are not hormonally active and scintiscan is often unremarkable" [1], or "these lesions are seldom functioning" [2]. These statements stem from a series of misinterpretations or generalizations of remarks of other authors [11, 12]. Our study certainly indicates that most intrathoracic goiters can be diagnosed by thyroid scintigraphy. Our finding of a sensitivity of 93% agrees with that of Irwin et al. [13], who found that all of their 24 patients with mediastinal goiter had positive results on iodine-131 scans preoperatively.

We have noticed that parallax error [7] is a common prob-

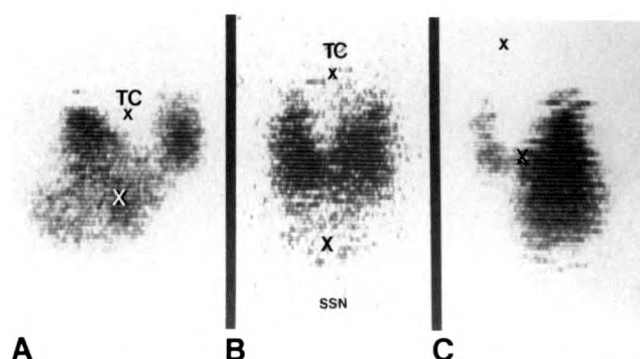


Fig. 1.—Radioiodine-131 thyroid scintigrams show three examples of intrathoracic goiters. Lower markers (X's) indicate suprasternal notch (SSN); upper markers, thyroid cartilage (TC).

- A, Goiter due to extension of right lobe.
- B, Goiter due to extension of both lobes or isthmus.
- C, Goiter due to extension of left lobe.

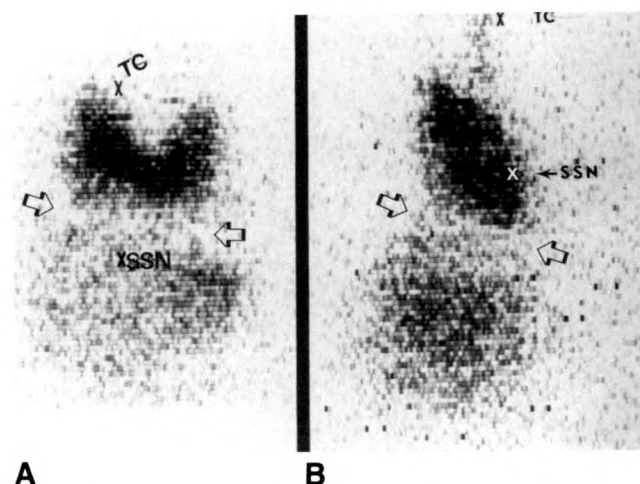


Fig. 2.—Radioiodine thyroid scintigrams show discontinuity of intrathoracic part from cervical gland in two patients. Note relatively clear band (open arrows) between the two parts. Lower markers (X's) indicate suprasternal notch (SSN); upper markers, thyroid cartilage (TC).

- A, With iodine-123.
- B, With iodine-131. Patient had a left lobectomy for a goiter several years before this scintigram.

lem in pinhole scintigraphy. It causes deeply located thyroid tissue caudal to the suprasternal notch to appear cephalad to the notch on the image. Because of their deeper location, posterior mediastinal goiters are affected even more. This parallax error can be avoided by (1) using a parallel-hole collimator, (2) placing the pinhole perpendicular to the suprasternal notch, or (3) using a rectilinear scanner. Another important consideration is placing the patient's head in the same position as that used for chest radiography.

Concern that the attenuation of photons by the overlying bone may limit the usefulness of thyroid scintigraphy [14] might have been valid in the 1960s when iodine-125 (27 keV) was used as a scanning agent. The photon energies of currently used radionuclides, iodine-131 (364 keV), iodine-

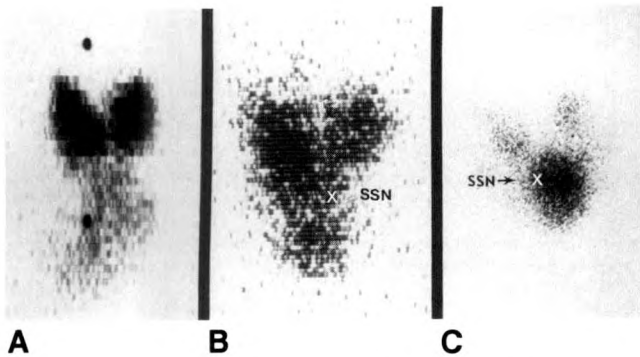


Fig. 3.—Radioiodine thyroid scintigrams show three functional variations of intrathoracic part of thyroid.

A, Uptake of iodine-131 by intrathoracic part is less than uptake by cervical gland.

B, Uptake of iodine-131 by intrathoracic part is equal to uptake by cervical gland. X shows suprasternal notch (SSN).

C, Uptake of iodine-123 by intrathoracic part is greater than uptake by cervical gland. X shows suprasternal notch (SSN).

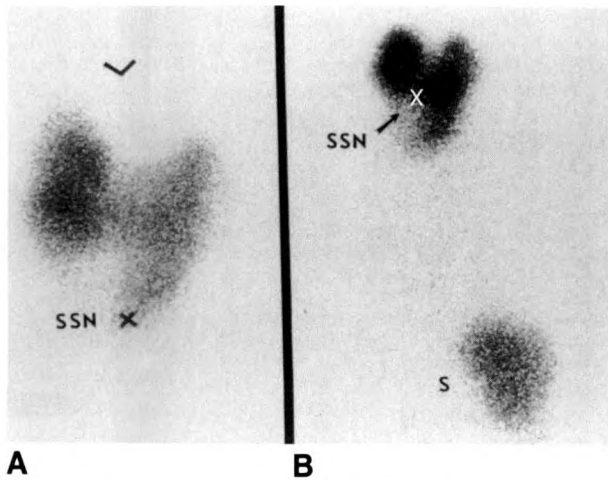


Fig. 4.—Parallax error of pinhole scintigraphy. X shows suprasternal notch (SSN).

A, Lower margin of intrathoracic goiter appears at level of suprasternal notch because of parallax, an inherent error of pinhole collimator.

B, Image obtained by using a large-field-of-view camera with a straight-bore collimator correctly reveals degree of intrathoracic extension. Activity in left upper abdomen represents iodine-131 in stomach (S).

^{123}I (160 keV) and technetium-99m (140 keV), are much higher than that of iodine-125 and can easily penetrate the bones. We have found that the percentage of attenuation of ^{131}I , ^{123}I , and $^{99\text{m}}\text{Tc}$ photons by a fresh adult cadaver sternum were 9%, 21%, and 22%, respectively. This degree of attenuation caused little discernible effect on scintigraphs.

When an intrathoracic goiter is shown by radioiodine scin-

tigraphy, usually no further diagnostic evaluation is necessary unless the imaged goiter is smaller than the mass seen on chest radiograph. Although not as specific as radioiodine scintigraphy [14], CT and MR imaging studies can provide additional and/or better anatomic information [15, 16]. The cost of the CT or MR, however, is much greater than that of scintigraphy. In our city, the cost of CT of the thorax with and without contrast is up to five times more than the cost of radioiodine scintigraphy, and the cost of MR is up to 10 times more.

We conclude that most intrathoracic goiters do have thyroid function and that radioiodine scintigraphy is a definitive and cost-effective means for their diagnosis. We recommend that radioiodine scintigraphy be the first study in the further evaluation of an anterior upper mediastinal mass seen on chest radiographs.

ACKNOWLEDGMENT

We extend our appreciation to James Ellis for his advice and to Katie Natalie for her expert secretarial assistance.

REFERENCES

- Wright FW. *The radiological diagnosis of lung and mediastinal tumours*. London: Butterworth, 1973: 91
- Fraser RG, Pare JAP. *Diagnosis of diseases of the chest*, 2nd ed., vol 3. Philadelphia: Saunders, 1979:1823-2029
- Kaplan WD, Watnick M, Holman BL. Scintigraphic identification of complete thoracic goiter with normal appearing cervical thyroid: a case report. *J Can Assoc Radiol* 1974;25:193-195
- Fogelfeld L, Rubinstein U, Bar-on J, Feigl D. Severe thyrotoxicosis caused by an ectopic intrathoracic goiter. *Clin Nucl Med* 1986;11:20-23
- Ng AC, Brown DL, Taylor SD. Superior vena cava syndrome caused by intrathoracic goiter. *J Indiana State Med Assoc* 1979;72:192
- Aasted A, Bertelsen S. Superior vena caval syndrome in benign mediastinal goitre. *Acta Chir Scand* 1981;147:405-408
- McKittrick WL, Park HM, Kosegi JE. Parallax error in pinhole thyroid scintigraphy: a critical consideration in the evaluation of substernal goiters. *J Nucl Med* 1985;26:418-420
- McCort JJ. Intrathoracic goiter, its incidence, symptomatology, and roentgen diagnosis. *Radiology* 1979;53:227-239
- Lamke LO, Bergdahl L, Lamke B. Intrathoracic goitre: a review of 29 cases. *Acta Chir Scand* 1979;145:83-86
- Maier HC, Schwartz SI. Superior mediastinal lesions. In: Schwartz SI, ed. *Principles of surgery*. New York: McGraw Hill, 1974:664-665
- Rietz KA, Werner B. Intrathoracic goiter. *Acta Chir Scand* 1960;119:379-388
- King ER, Henkelmann MC. Tumor localization with radioisotopes. *South Med J* 1951;50:1096-1106
- Irwin RS, Braman SS, Arvanitidis AN, Hamolsky MW. I-131 thyroid scanning in preoperative diagnosis of mediastinal goiter. *Ann Intern Med* 1978;89:73-74
- Morris UL, Colletti PM, Ralls PW, et al. Case report: CT demonstration of intrathoracic thyroid tissue. *J Comput Assist Tomogr* 1982;6:821-824
- Bashist B, Ellis K, Gold RP. Computed tomography of intrathoracic goiters. *AJR* 1983;140:455-460
- Sandler MP, Patton JA, Sacks GA, Shaff MI, Kulkarni MV, Partain CL. Evaluation of intrathoracic goiter with I-123 scintigraphy and nuclear magnetic resonance imaging: case report. *J Nucl Med* 1984;25:874-876

Forthcoming Articles

CHEST RADIOLOGY

- MR imaging of the aortic root and proximal coronary arteries.** *Paulin S, von Schulthess GK, Fossel E, Krayenbuehl HP*
- Right atrioventricular valve atresia: anatomic evaluation with MR imaging.** *Fletcher BD, Jacobstein MD, Abramowsky CR, Anderson RH*
- Pulmonary vascular obstruction in severe ARDS: angiographic alterations, after IV fibrinolytic therapy.** *Greene R, Lind S, Jantsch H, et al.*
- The accuracy of detecting pleural effusions on supine radiographs.** *Ruskin JA, Gurney JW, Thorsen MK, Goodman LR*
- Value of thoracic CT in detecting occult disease in critically ill patients.** *Mirvis SE, Tobin KD, Kostrubiak I, Belzberg H*
- Mediastinal imaging in myasthenia gravis: correlation of radiographs, CT, MR, and surgical findings.** *Batra P, Herrmann C Jr, Mulder D*
- Radiologic and pathologic abnormalities of the trachea in older patients with cystic fibrosis.** *Griscom NT, Vawter GF, Stigol LC*
- Early radiographic signs of tracheal rupture.** *Rollins RJ, Tocino I*
- The radiographic distinction between pericardial and myocardial calcification.** *MacGregor JH, Chen JTT, Chiles C, Kier R, Godwin JD, Ravin CE*
- Case report. Tension pneumopericardium: an unusual manifestation of invasive pulmonary aspergillosis.** *Müller NL, Miller RR, Ostrow DN, Nelems B, Vickers LM*

BREAST RADIOLOGY

- Breast localization device for occult lesions: utility in 75 patients.** *Parekh NJ, Wolfe JN*

GASTROINTESTINAL RADIOLOGY

- MR imaging in the diagnosis of pancreatic disease.** *Tscholakoff D, Hricak H, Thoeni R, Winkler ML, Margulis AR*
- MR imaging of hepatic focal nodular hyperplasia: characterization and distinction from primary malignant hepatic tumors.** *Mattison GR, Glazer GM, Quint LE, Francis IR, Bree RL, Ensminger WD*
- Nodular regenerative hyperplasia of the liver: clinical and radiologic observations.** *Dachman AH, Ros PR, Goodman ZD, Olmsted WW, Ishak KG*
- The mistaken or indeterminate CT diagnosis of hepatic metastases: the value of sonography.** *Brick SH, Hill MC, Lande IM*
- Radiologic findings in xanthogranulomatous cholecystitis.** *Hanada K, Nakata H, Nakayama T, et al.*
- Medication-induced esophagitis: diagnosis by double-contrast esophagography.** *Bova JG, Dutton N, Goldstein HM, Hoberman LJ*
- Indium-111 leukocyte imaging in appendicitis.** *Navarro DA, Weber PM, Kang IY, dos Remedios LV, Jasko IA, Sawicki JE*
- Diverticulitis of the right colon: CT observations.** *Scatarige JC, Fishman EK, Christ DW, Cameron JL, Siegelman SS*

INTERVENTIONAL RADIOLOGY

- Silicone biliary stents.** *Iaccarino V, Niola R, Porta E*
- Case report. Use of angioplasty balloons in the percutaneous management of biliary calculi: tandem balloon method.** *Saeed M, Newman GE, Dunnick NR*
- Case report. Percutaneous decompression of cecal volvulus.** *Patel D, Ansari E, Berman MD*

GENITOURINARY RADIOLOGY

- Diagnosis and staging of renal cell carcinoma: a comparison of MR imaging and CT.** *Fein AB, Lee JKT, Balfe DM, Heiken JP, Ling D, Glazer HS, McClennan BL*
- Spontaneous subcapsular and perinephric hemorrhage in end-stage kidney disease: clinical and CT findings.** *Levine E, Grantham JJ, MacDougall ML*
- Evaluation of renal transplant rejection by duplex Doppler examination: value of the resistive index.** *Rifkin MD, Needleman L, Pasto ME, et al.*
- Case report. Spontaneous renal hemorrhage due to cyst rupture: CT findings.** *Davis JM III, McLaughlin AP*
- Sonographic findings in adenomyosis of the uterus.** *Bohlman ME, Ensor RE, Sanders RC*

MUSCULOSKELETAL RADIOLOGY

- Pictorial essay. Radiographic spectrum of osteogenic sarcoma.** *Kumar R, David R, Madewell JE, Lindell MM Jr*
- Periostitis in hypertrophic osteoarthropathy: relationship to disease duration.** *Pineda CJ, Martinez-Lavin M, Goobar JE, Sartoris DJ, Clopton P, Resnick D*
- Patterns of paravertebral ossification in the prehistoric saber-toothed cat.** *Bjorkengren AG, Sartoris DJ, Shermis S, Resnick D*
- Case report. Popliteal vein thrombosis and popliteal artery pseudoaneurysm complicating osteochondroma of the femur.** *Lizama VA, Zerbini MA, Gagliardi RA, Howell L*

NEURORADIOLOGY

- MR imaging of the cervical spine: neurovascular anatomy.** *Flannigan BD, Lufkin RB, McGlade C, Winter J, Batzdorf U, Wilson G, Rauschnig W, Bradley WG Jr*
- MR imaging of intracranial tuberos sclerososis.** *McMurdo SK Jr, Moore SG, Brant-Zawadzki M, Berg BO, Koch T, Newton TH, Edwards MSB*
- MR imaging of pituitary adenoma: CT, clinical, and surgical correlation.** *Davis PC, Hoffman JC Jr, Spencer T, Tindall GT, Braun IF*
- Surface-coil MR of orbital pseudotumor.** *Atlas SW, Grossman RI, Savino PJ, Sergott RC, Schatz NJ, Bosley TM, Hackney DB, Goldberg HI, Bilaniuk LT, Zimmerman RA*

MAGNETIC RESONANCE

- Use of MR imaging in an outpatient MR center.** *Peddecord KM, Janon EA, Robins JM*
- High-field MR imaging of extracranial hematomas.** *Rubin MI, Gomori JM, Grossman RI, Geffer WB, Kressel HY*

VASCULAR RADIOLOGY

- Detection of prosthetic vascular complications: comparison of CT and angiography.** *Vogelzang RL, Limpert JD, Yao JST*

OPINION

- "Cost-effective": a trendy, often misused term.** *Doubilet PM*

Primary Adrenocortical Carcinoma:

CT Evaluation with Clinical Correlation



Elliot K. Fishman¹
 Beth M. Deutch¹
 David S. Hartman²
 Stanford M. Goldman^{1,3}
 Elias A. Zerhouni¹
 Stanley S. Siegelman¹

Clinical histories and CT findings were reviewed in 38 patients with primary adrenocortical carcinomas. The primary tumors exhibited central areas of low attenuation representing tumor necrosis ($n = 26$), irregular contrast enhancement ($n = 16$), detectable calcification ($n = 9$), and a thin, capsulelike rim surrounding the tumor ($n = 7$). Tumors metastasized to liver ($n = 9$), lung ($n = 5$), and lymph nodes ($n = 5$). In eight of nine cases of liver metastasis the primary tumor arose in the left adrenal gland. Evidence of endocrinopathy was present in each of nine patients with lesions 6 cm or less in diameter, but in only two of seven adults with lesions exceeding 15 cm in diameter. We conclude that, contrary to established concepts, adrenocortical carcinoma may present as a smooth, homogeneous, functioning mass 6 cm or less in diameter on CT.

The size of an adrenal mass as an indicator of malignancy or benignancy has been the subject of controversy [1, 2]. It is generally held that tumors in the range of 10–15 cm in diameter, in asymptomatic patients, and associated with hormone production, regardless of size, are likely to be malignant and are properly managed by excision [3]. On the other hand, some studies have suggested that adrenal masses under 5 cm in diameter that are not associated with symptoms should be treated conservatively [1, 2]. Still others have expressed concern about the malignant potential of any adrenal mass. This study assesses the relationship between tumor size, hormonal activity, and CT findings in 38 patients with primary adrenal cortical carcinoma.

Received July 14, 1986; accepted after revision September 26, 1986.

The opinions or assertions contained herein are the private views of the authors and are not to be construed as official or as reflecting the view of the Department of the Navy or the Department of Defense.

Presented at the annual meeting of the American Roentgen Ray Society, Washington, DC, April 1986.

¹ Department of Radiology, Johns Hopkins University School of Medicine, 600 N. Wolfe St., Baltimore, MD 21205. Address reprint requests to E. K. Fishman.

² Department of Radiologic Pathology, Armed Forces Institute of Pathology, Washington, DC 20300, and Department of Radiology, Uniformed Services University of the Health Sciences, Bethesda, MA 20814.

³ Department of Radiology, Francis Scott Key Medical Center, Baltimore, MD 21205.

AJR 148:531–535, March 1987
 0361–803X/87/1483–0531

© American Roentgen Ray Society

Materials and Methods

A computer search of the files of the Johns Hopkins Oncology Center and the Armed Forces Institute of Pathology (AFIP) identified all cases of primary adrenal cortical carcinoma accessioned between January 1978 and September 1985. Nine cases from The Johns Hopkins Hospital and 29 cases from the AFIP were found in which a CT scan had been obtained at the time of initial clinical presentation. All CT scans were reviewed to determine lesion size, appearance both before and after contrast enhancement, presence of calcification, extent of metastases, and presence of a "capsulelike rim." Available plain films, sonograms, and nuclear medicine studies were also reviewed in all patients to determine the extent of metastatic disease. The patients' charts and/or clinical records were reviewed to determine the clinical presentation in each case.

Patients scanned at Johns Hopkins Hospital were examined on either a Pfizer/AS&E 0500 or a Siemens Somatom DR-3. Scanning parameters were 10 sec, 20 mAs, 125 kVp, and 5- or 10-mm collimation; or 3 sec, 230 mAs, 125 kVp, and 4- or 8-mm collimation, respectively. Patients were examined after administration of 720 ml of oral Hypaque (3% solution) over a 90-min period before the study. All patients were examined both before and after a bolus administration of 50–100 ml of 60% Hypaque. Scans were obtained at 1- to 1.5-cm intervals from the diaphragm to the symphysis with additional scans (4-mm intervals) through the adrenal glands.

In those cases with material submitted to the AFIP, various scanners were used with techniques differing from institution to institution. In all cases, tissue proof of diagnosis was

obtained. All images were reviewed by three of the authors and were correlated with the available pathologic specimens.

Results

The patients' ages ranged from 8 months to 79 years (mean, 39 years). Seventeen of the patients were men and 21 were women. Thirty-four were white, three were black, and one was Hispanic.

The tumor originated in the left adrenal gland in 21 cases and in the right adrenal gland in 17; no tumors were bilateral. Tumor size varied from 3 to 25 cm and all tumors were readily visible on CT (Table 1). In the group of seven patients under 15 years of age, the smallest tumor was 3.5 cm in diameter (Fig. 1) and the largest measured 20 cm. The average tumor diameter in this population was 9 cm. Of the 31 patients 15 years of age or older, the smallest lesion was 3 cm in diameter (Fig. 2) and the largest was 25 cm. The mean tumor diameter in this age group was 11.5 cm.

Unenhanced CT studies revealed an inhomogeneous but well-defined oblong, spherical, or lobulated mass in the area of the adrenal gland. Posterior compression of the ipsilateral kidney was common, as was anterior displacement of the stomach and pancreas in those left-sided lesions in which the diameter of the mass exceeded 8 cm. Areas of low density, proven by pathologic correlation to be tumor necrosis, were recognized in 26 cases and were usually centrally located (Fig. 3). The CT studies of the six lesions 5 cm or less in diameter demonstrated homogeneous masses of attenuation similar to muscle without evidence of central or peripheral necrosis. Tumors greater than 6 cm in diameter invariably

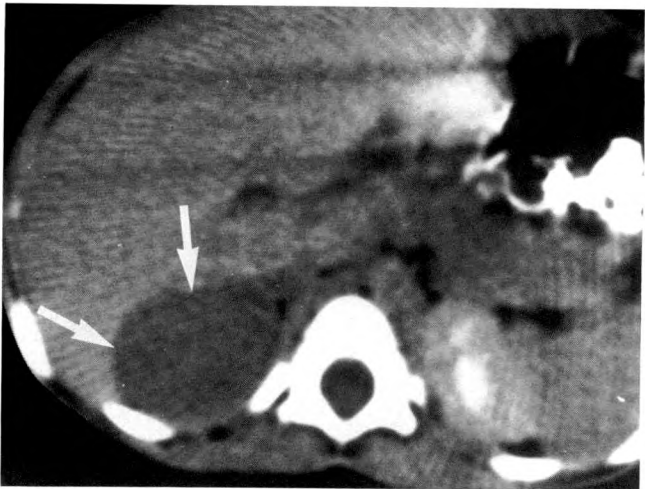


Fig. 1.—8-month-old girl with history of virilization syndrome has 3.5-cm right adrenal mass (arrows). Mass is homogeneous and of low attenuation.

exhibited some degree of inhomogeneity or central necrosis. Tumor calcifications, including microcalcifications ($n = 6$) and dense accretions of calcium ($n = 3$), were present in nine cases (Fig. 3). In two cases the contralateral adrenal glands appeared atrophic. In both of these cases the primary tumor was hormonally active. The other contralateral glands were normal in size, shape, and configuration.

After IV contrast enhancement via either a bolus or infusion technique, inhomogeneous enhancement of the tumor was noted with an increase in attenuation of the more peripheral portions of the tumor and relatively little enhancement in the central low-density portion. In seven cases with contrast enhancement a thin, capsulelike rim was demonstrated around the tumor (Fig. 4). These capsules were continuous, and distinct from both high-density tumor tissue and surrounding organs. They were seen in both small and large tumors. There was minimal central enhancement of those tumors that appeared to be homogeneous on unenhanced studies.

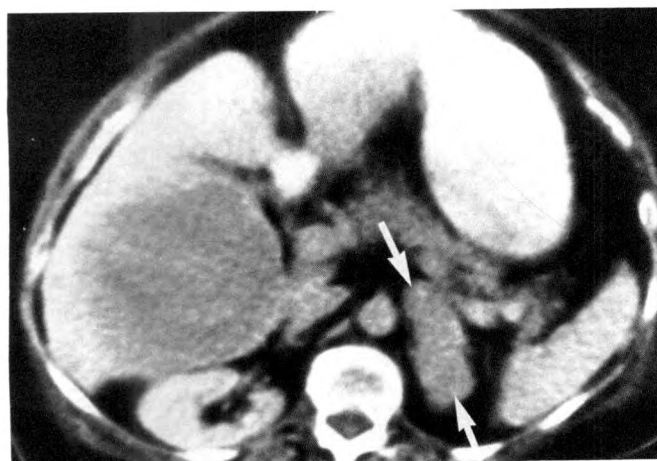
At the time of initial examination, tumor dissemination was seen in 21 cases, nine of which had hepatic metastases (Figs. 1 and 3). Of these nine cases, eight originated from left adrenal tumors. One right adrenal tumor directly invaded the liver. Five tumors had metastasized to the lungs and five to the lymph nodes: paraaortic (four), pararenal (one), and subcrural (one). Two tumors directly invaded the ipsilateral renal pelvis, and one left adrenal tumor was metastatic to the contralateral right renal pelvis. Three other tumors extended to adjacent Gerota's fascia and the paraadrenal soft tissues. A thrombus in the inferior vena cava was visible in one case and was confirmed at surgery and by pathology studies to represent direct tumor extension. Three other cases were found to have left renal vein involvement; however, only one of these was shown by CT.

Endocrine dysfunction was present in 21 patients and included Cushing's syndrome (12); precocious puberty

TABLE 1: Size of Adrenal Tumor and Relationship to Clinical Presentation in Primary Adrenocortical Carcinoma

Group: Characteristic	No. of Tumors by Size (in cm)			
	0-6	>6-12	>12-14	≥15
Adults:				
Total	5	12	6	7
Hormonally active	5	6	3	2
Cushing's syndrome	3	6	2	0
Mixed	0	0	0	0
Evidence of metastasis (location):				
Liver	2	2	2	2
Lung	0	4	0	1
Nodes	1	1	1	1
Children:				
Total	4	1	0	2
Hormonally active	4	1	0	2
Cushing's syndrome	1	0	0	0
Adrenogenital syndrome	2	0	0	0
Precocious puberty	1	1	0	1
Mixed	1	0	0	0
Evidence of metastasis (location):				
Liver	0	1	0	0
Lung	0	0	0	0
Nodes	0	0	0	1

Note.—Adults were older than 15 years of age; children were 15 years of age or younger.



A

Fig. 2.—64-year-old woman with history of ulcerative colitis treated with prednisone. Patient developed recent onset of weakness and ankle swelling.

A, 3-cm left adrenal carcinoma (arrows). Notice large metastatic lesion



B

in liver.

B, Gross specimen of adrenal mass (arrows) in relation to vascular structures. Adrenal vein is distended with tumor thrombus. No renal vein involvement is noted.



Fig. 3.—23-year-old woman with history of generalized weakness, hypertension, and cushingoid features. Left adrenal carcinoma measures 13 cm. Note dense calcification within mass (long arrows). Liver metastases also seen (short arrow).

(three); adrenogenital syndrome (two); mixed syndrome (one); and/or the complaints of weight gain, hirsutism, amenorrhea, or recent onset of hypertension in a young patient. In a number of patients, several of these clinical symptoms were present simultaneously. Sixteen patients presented with pain and an abdominal or flank mass. Three patients complained of long-standing fatigue and malaise, while one patient presented with a fever of unknown origin.

In several of the cases with symptoms caused by hormone production of the tumor, the clinical symptoms preceded the diagnosis by several years. In one case, the patient presented with mediastinal widening on routine chest studies, at which time excessive fat in the mediastinum was seen on a chest CT scan. Two years later, when he reappeared with fatigue

and malaise, the patient was found to have a 4-cm adrenal cancer and hepatic metastases.

The study included a group of small adrenal neoplasms: Nine lesions were 6 cm or less in diameter; six of these were 5 cm or less in diameter. All were well defined, sharply outlined, and nonadherent to adjacent tissues. Seven were homogeneous; two (5–6 cm in diameter) had central areas of lower attenuation. Two of these tumors had metastasized to the liver; in a third case, there was evidence of enlarged paraaortic and subcrural lymph nodes on CT.

There was an inverse relationship between tumor size and endocrine function (Table 1). All nine patients with lesions 6 cm or less in diameter had symptoms of hormone overproduction, whereas only four of nine patients with lesions 15 cm or greater had endocrinopathy.

Discussion

While primary adrenocortical carcinoma is a very rare cancer [4], the incidence of benign, nonfunctioning adrenal adenoma is estimated at 2–8% of the general population [5, 6]. As such, an adrenal lesion imaged by CT is much more likely to be a benign adenoma or an adrenal metastasis than to be a primary carcinoma. Nonetheless, the distinction is an important one since adrenocortical carcinoma has a median survival of only 6 months if left untreated, but is potentially curable by surgery if detected early [7].

Several adrenal lesions have CT findings that permit an accurate pathologic diagnosis. Cysts and myelolipomas are discernible by their respective water and fat attenuation values on CT [8–11]. When adrenal hemorrhage is suspected clinically by an appropriate history of trauma, meningococemia, anticoagulation, or other bleeding diatheses, it can be confirmed by CT studies showing increased attenuation [12]. Adrenal hyperplasia classically leads to glandular en-

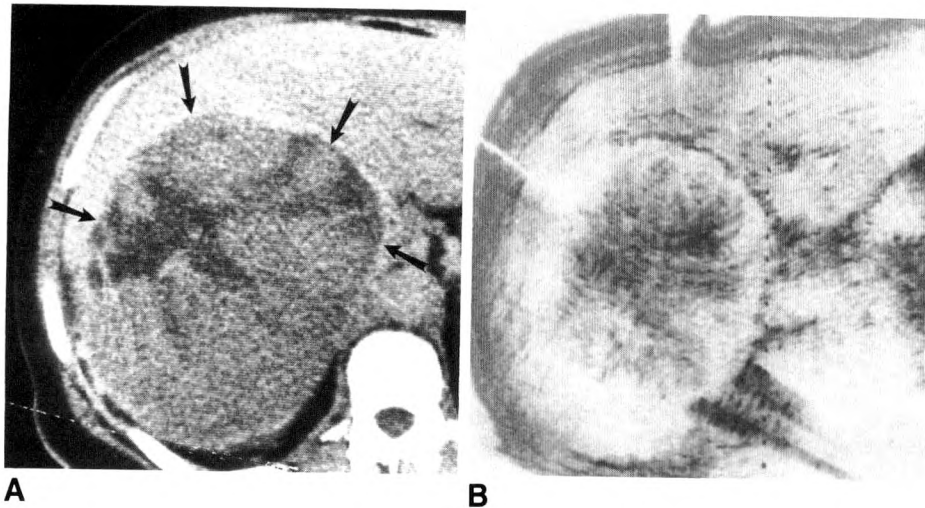


Fig. 4.—51-year-old woman with history of hirsutism and right upper quadrant mass.

A, 15-cm right adrenal carcinoma is clearly seen within "capsule" (arrows).

B, Sonogram of adrenal mass shows echogenic rim corresponding to enhancing capsule on CT scan.

largement with maintenance of the Y-shaped configuration of the adrenal glands and occasional minimal diffuse nodularity [11, 13]. The consideration of metastasis becomes paramount when bilateral, homogeneous adrenal lesions are discernible, when there is evidence of other metastases, or when the patient is known to have a primary neoplasm elsewhere.

Distinguishing the very common benign adrenal adenomas from adrenocortical carcinoma may be difficult, even when tissue is available for examination. Diagnosis in these cases has rested largely on the pattern of growth, behavior, and size of the lesion, that is, the larger the lesion, the more need for concern. Mitnick et al. [2] monitored a series of patients for 1 year in whom small, nonfunctional adrenal lesions were found incidentally, and recommended CT criteria for establishing benignancy of adrenal lesions: Tumors with a smooth contour, a well-defined margin, no growth on serial CT scans over 1 year, and a diameter less than 5 cm need not be followed further for possible malignancy. Previous studies of primary adrenocortical carcinoma lend support to these criteria, in that all have reported the carcinomas to be large at presentation [1, 3, 10]. Dunnick et al. [3] reported eight cases in 1982: The smallest tumor in the study measured 9 cm and the median size was 12 cm. Adrenocortical carcinomas 20 cm or larger have often been reported, whereas there has been only a single case report of a carcinoma less than 3 cm.

In addition to size, several CT characteristics have been proposed as typical of primary adrenocortical carcinoma. Dunnick et al. [3] reported central diminished attenuation, representing central tumor necrosis, and irregular contrast enhancement in all eight of their cases; three had tumor calcifications. Similarly, we identified central necrosis in 26 cases and tumor calcification in nine. As Dunnick et al. [3] noted, these findings have also been seen in pheochromocytomas and large metastases [3]. In addition, Mitnick et al. [2] reported centrally diminished attenuation in three benign, nonfunctioning adrenal adenomas smaller than 5 cm. Review of the pathology reports in two of these cases revealed

hemorrhagic necrosis in one and hyalinization in the other. Furthermore, two adenomas contained calcifications seen on CT. Thus, calcification and decreased central attenuation can be identified in both benign and malignant processes and are of little help in making the differential diagnosis.

A new finding identified in seven of our cases was a thin, enhancing, capsulelike rim surrounding the neoplasms (Fig. 4). This may add to the specificity of CT diagnosis. All seven "capsules" were continuous, smooth, and nonadherent to adjacent structures. The capsule was present in both small and large tumors of 3.5–15 cm, suggesting that it is not simply a rim of adjacent tissue compressed by a large, expanding tumor mass. Furthermore, all seven capsules enhanced with IV contrast material, suggesting that they represent well-vascularized portions of the tumor. There have been no reports in the literature of this finding in either benign adrenal adenomas or metastases. In several cases that had the capsule, no normal compressed adrenal gland was present on pathologic examination of the specimen. Rather, the enhancing rim was part of the tumor. The cause of the enhancement is not known.

Both small and large tumors showed a predilection for metastasizing to liver; furthermore, of our nine cases with hepatic metastases, eight had originated from left-sided tumors. The only right-sided tumor with hepatic metastases abutted on the liver and most likely spread by direct contiguity to hepatic portal vessels. From this location nests of tumor cells presumably "embolized" to more distant liver sites. One could speculate that the liver metastases of purely left-sided origin arrived via adrenal-splenic collateral circulation to the portal vein. Adrenal-splenic circulation may become particularly significant in the setting of tumor thrombosis in the renal vein, and has been described in renal cell carcinoma [14].

Distinguishing malignant from benign adrenal lesions is difficult because no single criterion is specific. Central necrosis and tumor calcification are seen in a variety of lesions, including small benign adenomas. Adrenocortical carcinomas may

be functional or silent. They may be large, or, as in our study, less than 5 cm in diameter, a size previously believed to be safe for nonsurgical follow-up. They may have irregular margins and shapes but may also be smooth, well-defined spheres, especially when small. The only definite criterion for malignancy is the presence of metastases. Certainly a 20-cm irregular, centrally necrotic, partially calcified adrenal mass merits adrenal suspicion of malignancy, just as a 3-cm, non-functional, homogeneous, well-circumscribed adrenal lesion will most likely be benign. Earlier diagnosis might be achieved by closer examination of adrenal glands in patients with even vague endocrine complaints. When a small adrenal lesion is found in this setting, suspicion of malignancy should warrant prompt removal of the lesion. Both unenhanced and IV contrast enhancement studies should be performed to better delineate central necrosis, tumor capsule, venous extension, and hepatic metastases.

REFERENCES

1. Glazer HS, Weyman PJ, Sagel SS, Levitt RG, McClennan BL. Nonfunctioning adrenal masses: incidental discovery on CT. *AJR* **1982**;139:81-85
2. Mitnick JS, Bosniak MA, Megibow AJ, Naidich DP. Non-functioning adrenal adenomas discovered incidentally on CT. *Radiology* **1983**;148:495-499
3. Dunnick NR, Heaston D, Halvorsen R, Moore AV, Korobkin M. CT appearance of adrenal cortical carcinoma. *J Comput Assist Tomogr* **1982**;6(5):978-982
4. King DR, Lack EE. Adrenal cortical carcinoma: a clinical pathologic study of 49 cases. *Cancer* **1979**;44:239-244
5. Sommers SC. Adrenal glands. In: Anderson WAD, Kissane JM, eds. *Pathology*, vol 27. St Louis: Mosby, **1977**:1658-1679
6. Commons RR, Callaway CP. Adenomas of the adrenal cortex. *Arch Intern Med* **1948**;81:37-41
7. Daneman A, Chan HS, Martin J. Adrenal carcinoma and adenoma in children: a review of 17 patients. *Pediatr Radiol* **1983**;13(1):11-18
8. Behan M, Martin EC, Moeche EC, Kazam E. Myelolipoma of the adrenal: 2. Cases with ultrasound and CT findings. *AJR* **1977**;129:993-996
9. Kleinhaus U, Ensel A, Adler O. Computed tomography in the diagnosis of adrenal pathology. *Isr J Med Sci* **1983**;19(6):524-529
10. Hattery RR, Sheedy PF II, Stephens DH, van Heerden JA. Computed tomography of the adrenal gland. *Semin Roentgenol* **1981**;16(4):290-300
11. Hauser H, Battikha JG, Wettstein P. Pathology of the adrenal glands. Common and uncommon findings in computed tomography. *Eur J Radiol* **1981**;1(3):215-226
12. Eghari M, McLoughlin MJ, Rosen IE, et al. The role of computed tomography of the adrenal glands. *J Comput Assist Tomogr* **1980**;4:71-77
13. Harrison JH, Mahoney EM, Bennet AH. Tumors of the adrenal cortex. *Cancer* **1973**;32:1227-1235
14. Saitoh H. Distant metastasis of renal adenocarcinoma in patients with tumor thrombus in the renal vein and/or vena cava. *J Urol* **1982**;127:652-653

Book Review

Guide to the Ultrasound Examination of the Abdomen. By M. Leon Skolnick. New York: Springer-Verlag, 240 pp., 1986. \$51

This book covers ultrasound of the abdomen in an outline form. It is logical and organized by body organs. The ultrasonic abnormality is first described and then the possible causes are presented. There is a moderate amount of repetition, but the book is intended to help the user with technical problems or for further study of the ultrasonic findings. Line drawings (instead of illustrations) do not include all disease processes.

Chapters cover abscess search, ascites search, biliary tract, fine-needle aspiration biopsy, native kidney, kidney transplant, liver, painful or tender regions, palpable masses, pancreas, female pelvis, male

pelvis, retroperitoneum, and spleen. Obstetrics are not included. Although the text is detailed for a workbook, it is not meant to be a complete reference. It is accurate, with a good style for its purpose.

I recommend this book for the radiologist, especially the beginner, or as a workbook for anyone evaluating a difficult case. It should be helpful for the technologist and a useful addition to most radiology libraries.

Harris Nemark III
1424 Brinkley Avenue
Los Angeles, CA 90049

CT Evaluation of Crohn's Disease: Effect on Patient Management



Elliot K. Fishman¹
Edward J. Wolf²
Bronwyn Jones¹
Theodore M. Bayless²
Stanley S. Siegelman¹

CT scans from 80 consecutive patients with clinically symptomatic Crohn's disease were reviewed retrospectively to determine the effect of CT diagnosis on patient management. The initial clinical impression and any subsequent change in patient management because of the CT findings were noted. In 22 (28%) of the 80 patients, significant previously unsuspected findings led to a change in medical or surgical management. These included 12 patients with fistulae, four with abscess, two with avascular necrosis of the femoral head, two with sacral osteomyelitis, and single cases of pelvic inflammatory disease and femoral vein thrombosis.

Although CT has been shown to be of limited value in the patient with generalized abdominal pain [1], it has proven to be extremely useful when disease is found clinically to be localized to a specific quadrant of the abdomen [2-5]. The CT findings in Crohn's disease have been reported. Previous studies have stressed that, although CT may not be the ideal initial study when Crohn's disease is suspected, it can play an important role in the detection and evaluation of potential complications [6-9]. However, no previous study has evaluated the role of routine CT scanning in determining management in patients with Crohn's disease. With this goal in mind, the records of 100 consecutive patients with Crohn's disease were reviewed retrospectively, and any change in management brought about by the CT findings was noted.

Materials and Methods

One hundred consecutive patients referred for CT scans with a history of Crohn's disease were reviewed; patients in the immediate postoperative period were not included. Of the 100 patients reviewed, clinical follow-up was insufficient in 20 because of inadequate follow-up or unavailability of medical records; these 20 patients were excluded from the study.

All CT scans were reviewed by a radiologist with knowledge of the clinical problems as given on the requisition. The patients' charts were reviewed to determine what the diagnoses and projected treatment plans were prior to CT, as well as to determine what the subsequent management of the patient was. Direct consultation with the patient's personal physician was done when the medical records or charts were incomplete or inconclusive. To be considered to have a significant impact on patient management, the results of the CT studies must have led to a change in medical therapy, a change from medical treatment to surgery, or a reversal of a decision to operate.

Scanning was performed on either a Siemens DR-3 or Pfizer/AS&E 0500 scanner, usually the former. Scanning techniques were 5 sec, 450 mAs, 125 kVp, and 4-mm collimation or 10 sec, 230 mAs, 125 kVp, and 5- or 10-mm collimation, respectively. Scans were obtained at 1.5-cm sequential intervals from the diaphragm to the lower perineum with additional scans obtained as necessary. All patients were given 1000 ml of oral contrast material over a 2-3 hr period before the examination, with another 250 ml of oral contrast medium immediately before the study. Rectal contrast material consisting of 150 ml of 2% Hypaque was routinely administered through a 24-French catheter. IV contrast material consisting of a 100-ml drip infusion of Hypaque-60 was used routinely.

Received July 28, 1986; accepted after revision September 26, 1986.

¹ Russell H. Morgan Department of Radiology and Radiological Science, The Johns Hopkins Medical Institutions, 600 N. Wolfe St., Baltimore, MD 21205. Address reprint requests to E. K. Fishman.

² Meyerhoff Digestive Disease-Inflammatory Bowel Disease Center, The Johns Hopkins Medical Institutions, Baltimore, MD 21205.

AJR 148:537-540, March 1987
0361-803X/87/1483-0537
© American Roentgen Ray Society

The most common reason for performing the CT study (35/80) was to rule out abscess. Other reasons for performing CT were: (1) to evaluate suspected fistula (12 patients), increasing abdominal pain (eight patients), or suspected abdominal mass (seven patients); (2) to define the extent of Crohn's disease (seven patients); and (3) to evaluate the cause of suspected small-bowel obstruction, to exclude neoplasm, or to define an abnormality seen on another radiographic examination (11 patients).

Results

In 22 patients (28%), significant unsuspected findings were detected that led to a change in medical or surgical management. These consisted of 12 patients with fistulae, four with an abscess, two each with avascular necrosis of the femoral head and sacral osteomyelitis, and single cases each of pelvic inflammatory disease and femoral vein thrombosis. In another 13 patients, CT demonstrated unsuspected findings that did not alter the clinical management and were therefore not considered in this context to be significant. These included gallstones (four patients), fatty infiltration of the liver (four patients), and ovarian cyst (five patients).

Abscesses

Of the 35 patients evaluated to rule out abscess, abscess was confirmed in eight (23%). Other radiologic studies had suggested or identified an abscess in only three of these eight patients. Location was perirectal (three), left lower quadrant (two), right lower quadrant (one), cul de sac (one), and anterior (one) and superior (one) to the bladder.

In the other 45 patients, CT detected an unsuspected abscess in four (9%); all of these were subsequently confirmed by surgery. They were located in the pelvis involving the bladder wall, above the dome of the bladder, in the left psoas muscle, and in the left lower quadrant near the junction of the sigmoid and descending colon (Figs. 1 and 2). In five

(6%) of the 80 patients in whom other radiologic studies had suggested abscess, CT excluded this diagnosis. On the basis of CT results, these patients were treated with an increased steroid regimen and improved clinically (Fig. 3).

Fistula

In 12 patients evaluated to determine the presence or extent of a suspected fistula, a fistula was confirmed in 10, with more than one fistula in five. Fistulae were enterovesical (five), enterocutaneous (three), perirectal/perianal (four), rectovaginal (one), to levator muscle (one), and to sacrum (one) (Fig. 4). The fistulae were seen as defined tracts usually opacified with contrast material extending between adjacent bowel loops, from bowel to the subcutaneous tissues, or to adjacent muscle or skeletal structures.

In another 12 patients, CT demonstrated a fistula previously unsuspected on physical examination or from other radiographic studies. These fistulae included perirectal (four); enteroenteric (three); and a single case each of enterovesical, ischiorectal, enterocutaneous, rectovaginal, and bowel to sacrum (Figs. 5 and 6).

Skeletal Findings

In four patients, unsuspected skeletal abnormalities were found that proved to be the basis for the presenting symptoms. Two patients had avascular necrosis of the femoral heads and two, osteomyelitis of the sacrum that required surgical intervention. In one of the patients, a barium enema had demonstrated widening of the presacral space suggesting a presacral abscess. CT excluded an abscess by demonstrating that the widening was caused by extensive presacral fat and also demonstrated previously unsuspected bilateral avascular necrosis.

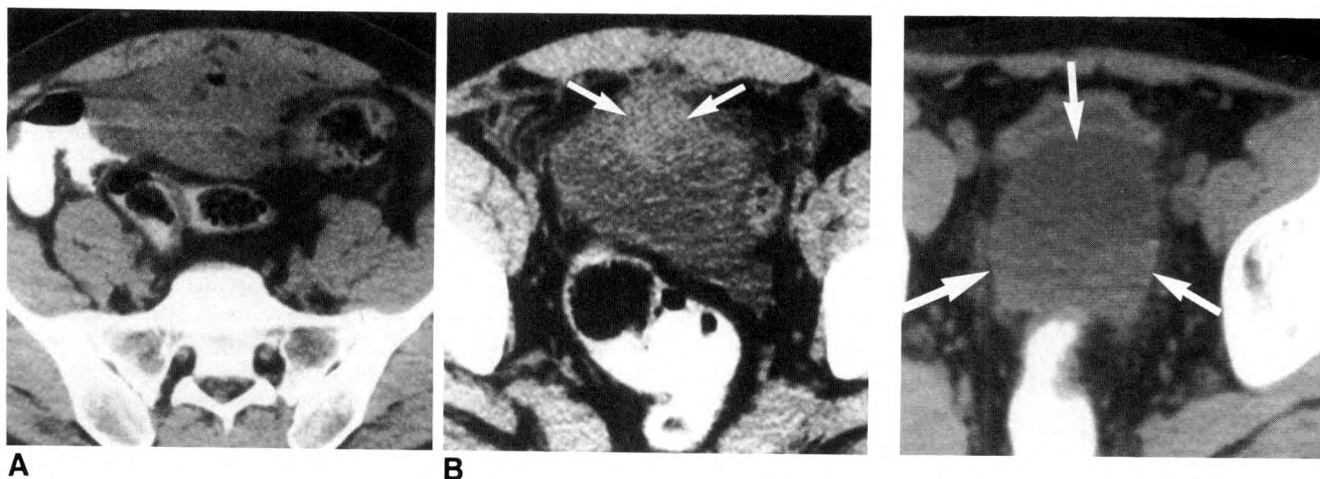


Fig. 1.—38-year-old man presenting with dysuria. Cystoscopy was negative. Small-bowel series showed thickening of small bowel without a fistula. CT shows abscess beneath anterior abdominal wall (arrows) extending to dome of bladder. At surgery a fistula was found into bladder wall but not into bladder. About 0.5 m of small bowel was resected but bladder was not.

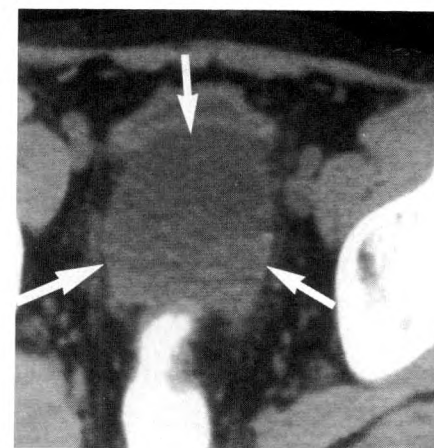


Fig. 2.—22-year-old man with increasing abdominal pain and fever. Barium enema and upper gastrointestinal series demonstrated abnormal bowel but no evidence of abscess. CT shows abscess above prostate and bladder (arrows). Treatment was conservative with antibiotics; subsequent CT scans showed resolution of abscess.

Fig. 3.—History of Crohn's disease with ileocecal anastomosis and increasing right groin pain. Barium enema showed thickened sigmoid colon and possible presacral abscess. CT shows increase in presacral space because of excessive fat deposition. Bilateral avascular necrosis is seen as cause of pelvic pain. A right total hip replacement was performed later. Retrospective review of plain radiographs documented early avascular necrosis of femoral heads.

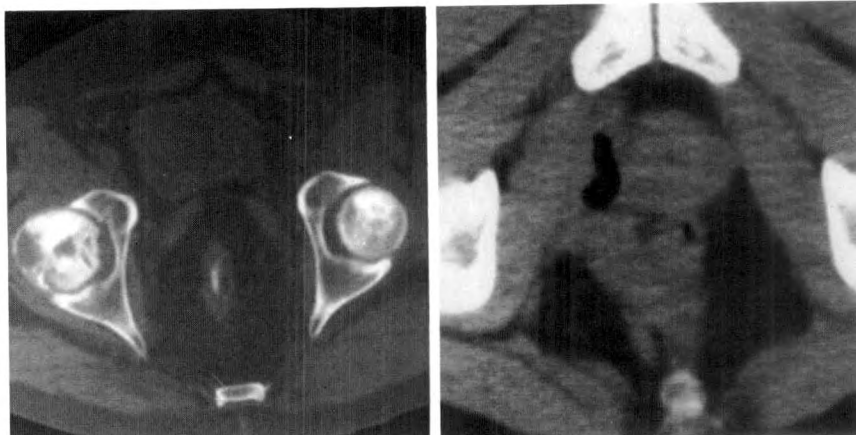
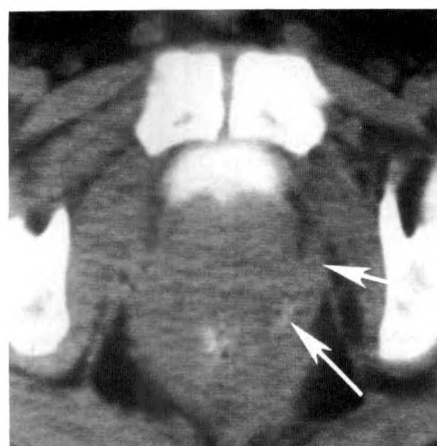
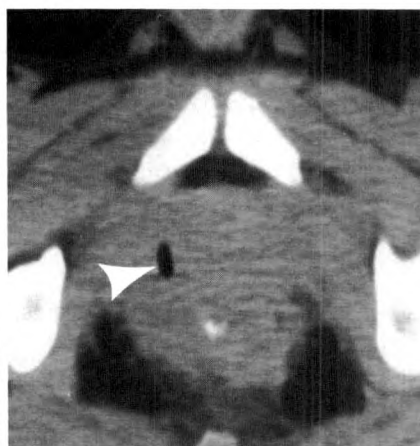


Fig. 4.—28-year-old man with pelvic pain. Clinical impression was of possible pelvic abscess. CT shows periprostatic abscess with perirectal fistula on right side. Medical therapy was stopped and surgery was performed with drainage of periprostatic abscess.



A



B

Fig. 5.—24-year-old man with history of Crohn's disease suspected to have abscess. CT shows evidence of marked inflammation of rectum with perirectal fistulae (arrows). Fistula extends into prostate bed (arrowhead).

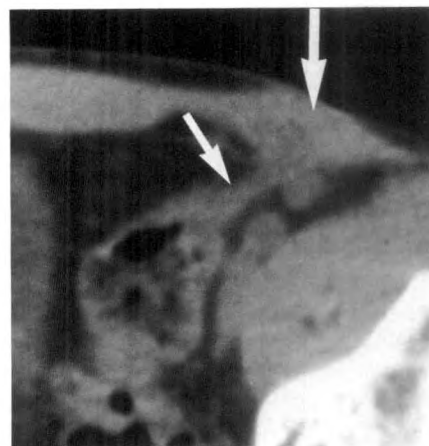


Fig. 6.—25-year-old man with abdominal pain and palpable area of fullness in left lower quadrant. Clinical impression was possible enterocutaneous fistula. Barium enema and upper gastrointestinal small-bowel follow-through did not show fistula. CT shows fistula from sigmoid colon into anterior abdominal wall with inflammatory mass present (arrows).

Pelvic Inflammatory Disease

In one patient, unsuspected pelvic inflammatory disease was found with inflammation and enlargement of both ovaries. Previous sonograms suggested a pelvic abscess, which was not confirmed on CT.

Femoral Vein Thrombosis

Unsuspected femoral vein thrombosis was detected in one patient who presented with vague abdominal pain and no localizing signs. Anticoagulants were given with resolution of clinical symptoms.

Discussion

Clinical management of the patient with Crohn's disease can be extremely problematic. These patients are prone to develop complications from the primary disease as well as

from the medical or surgical therapy. In addition, there may be psychological overtones such that the physical complaints may be considered psychosomatic. Also, when a definite complication is found the decision must be made whether to maintain or modify medical therapy or to opt for surgical intervention.

Double-contrast barium studies of the upper and lower gastrointestinal tract have long been the standard diagnostic procedures for evaluation of inflammatory bowel disease [10–12]. A carefully performed double-contrast examination undoubtedly detects subtle disease, particularly mucosal involvement including aphthous ulcers [13]. Fistulae can also be seen. Extraluminal abscess usually cannot be defined fully, but rather only inferred by secondary signs such as spiculation of the bowel wall, separation of bowel loops, and mass effect [14]. The full extent of disease, however, may be underestimated by contrast studies since involvement of the mesentery, ischiorectal fossa, and solid viscera cannot be evaluated

well. Contrast studies may show separation of bowel loops and the question remains: Are the bowel loops separated merely because of wall thickening or is there a complication such as fistulous tracts or an interloop abscess [15]?

CT scans have several distinct advantages over routine contrast studies in the evaluation of the extraluminal components of disease. CT not only clearly defines the full extent of bowel-wall thickening, the cause of separation of bowel loops, and the mesenteric component of the disease process [6], but directly shows the extraluminal process.

CT can be particularly helpful in the evaluation of mesenteric disease in the patient with inflammatory bowel disease. In Crohn's disease, several mesenteric abnormalities may be seen, including mesenteric thickening with an increase in mesenteric density, mesenteric inflammation with edema of the mesentery, or mesenteric adenopathy [6].

An abscess requiring surgical intervention can be shown directly with CT. CT has proven to be superior to sonography in the evaluation of abscesses, as abscesses can be interloop, in the mesentery, or in the perirectal zones, which are areas less accessible to the sonographic probe. In many cases CT can be used for direction of drainage of these abscesses, thereby circumventing the need for surgical intervention [16].

Barium studies often adequately determine the presence of fistulae. The full extent of the fistulous tract may, however, be more clearly defined by CT, especially when the fistulae are in the perirectal area. Perirectal fistulae can be difficult to evaluate on clinical examination and routine contrast studies. Physical examination may be painful or even impossible because of extreme rectal tenderness. Barium enema may fail because of inability to insert the rectal catheter or incontinence. Small fistulas may go undetected on contrast studies because of nonfilling or spasm. CT is able to detect a fistula in the perirectal area and ischiorectal fossa in the range of 2–5 mm. The high detection rate is because the ischiorectal fossa normally consists of fat. The most subtle changes in fat density from even small tracts extending into the ischiorectal zones can be detected with a high degree of accuracy and specificity. In addition, perirectal fistulas can be evaluated for possible extension into adjacent organs, including prostate and vagina. CT allows definition of the full extent of the fistulous tract and its involvement of adjacent organs, particularly the musculoskeletal structures. For example, in our group of patients, two had unsuspected sacral osteomyelitis not evident on plain films or contrast studies, but clearly defined by CT as a fistulous tract with an associated mass involving the anterior sacral segments. CT not only made the diagnosis but also aided in subsequent surgical planning. Two others had avascular necrosis of the femoral head, a process for which CT is clearly superior to plain films [17].

An enterovesical fistula can be detected accurately with CT scanning [18, 19], whereas other imaging techniques, including cystoscopy, contrast studies, and excretory urograms, have a detection rate of much less than 50%. We previously reported our experience showing that CT can detect over 90% of surgically proven enterovesical fistulae. In that series of 26 patients with enterovesical fistula, the fistula was defined only by CT in six [19].

While we would not suggest that CT can approach the diagnostic accuracy of an air-contrast examination for mucosal disease, CT can be extremely helpful in the evaluation of the patient with Crohn's disease, allowing further evaluation of the extent of bowel disease and also an assessment of mesenteric disease; and it may provide additional information about fistulous tracts. In a single examination, the full extent of disease can be determined in a rapid, noninvasive fashion. Subsequent management decisions can be made quickly on the basis of CT data. In addition, CT is not an organ-specific study, simply evaluating the bowel or the extracolonic component of disease. Rather, on a single examination, the entire abdomen and pelvis are evaluated, allowing detection of serendipitous findings that are often of high clinical significance. For instance, skeletal manifestations producing clinical symptoms thought to be from intrinsic bowel disease were seen in four patients in our present study.

REFERENCES

1. Benson M, Bree RL, Schwab RE, Quimette M. Computed tomographic studies of the painful abdomen. *Radiology* 1985;155:443–444
2. Wittenberg J, Fineberg HV, Ferruci Jr JT, et al. Clinical efficacy of computed body tomography. *AJR* 1980;134:1111–1120
3. Scatarige JC, Yousem DM, Fishman EK, Jones B, Siegelman SS. CT abnormalities in right lower quadrant inflammatory disease: review of 26 adults. *Gastrointest Radiol* (in press)
4. Feldberg M AM, Hendriks MJ, van Waes PFGM. Computed tomography in complicated acute appendicitis. *Gastrointest Radiol* 1985;10:289–295
5. Hulnick DH, Megibow AJ, Balthazar E, Naidich DP, Bosniak MA. Computed tomography in the evaluation of diverticulitis. *Radiology* 1984;152:491–495
6. Goldberg HI, Gore RM, Margulis AR, Moss AA, Baker EL. Computed tomography in the evaluation of Crohn's disease. *AJR* 1983;140:277–282
7. Berliner L, Redmond P, Purov E, Megna D, Sottile V. Computed tomography in Crohn's disease. *Am J Gastroenterol* 1982;77:548–553
8. Gore RM, Mann CS, Kirby DF, Vogelzang RL, Neiman HL. CT findings in ulcerative, granulomatous and indeterminate colitis. *AJR* 1984;143:279–284
9. Kerber GW, Greenberg M, Rubin JM. Computed tomography evaluation of local and extraintestinal complications of Crohn's disease. *Gastrointest Radiol* 1984;9:143–148
10. Marshak R, Lindner AE. *Regional enteritis: differential diagnosis in radiology of the small intestine*. Philadelphia: Saunders, 1976:235–245
11. Bertram CI, Laufer I. Inflammatory bowel disease. In: Laufer I, ed. *Double contrast gastrointestinal radiology with endoscopic correlation*. Philadelphia: Saunders, 1979:601–688
12. Laufer I, Costopoulos L. Early lesions of Crohn's disease. *AJR* 1978;130:307–311
13. Williams JH, Stephens D, Carlson H. Double contrast radiology: colonic inflammatory disease. *AJR* 1981;137:315–322
14. Scanlon MH, Blumberg ML, Ostrum BJ. Computed tomographic recognition of gastrointestinal pathology. *Radiographics* 1983;3(2):201–227
15. Yeh HC, Rabinowitz JG. Granulomatous enterocolitis: findings by ultrasonography and computed tomography. *Radiology* 1983;149:253–259
16. Haaga JR, Weinstein AJ. CT-guided percutaneous aspiration and drainage of abscesses. *AJR* 1980;135:1187–1194
17. Magid D, Fishman EK, Scott WW Jr, et al. Computed tomography with multiplanar reconstruction in the assessment of avascular necrosis of the femoral head. *Radiology* 1985;157:751–756
18. Goldman SM, Fishman EK, Gatewood OMB, Jones B, Siegelman SS. CT in the diagnosis of enterovesical fistulae. *AJR* 1985;144:1229–1233
19. Saar MG, Fishman EK, Goldman SM, Siegelman SS, Cameron JL. Enterovesical fistula: a new and highly sensitive method of diagnosis—computed axial tomography. *Surg Gynecol Obstet* (in press)

Diagnosis of Acute Colonic Diverticulitis: Comparison of Barium Enema and CT

C. Daniel Johnson^{1,2}
 Mark E. Baker¹
 Reed P. Rice¹
 Paul Silverman^{1,3}
 William M. Thompson^{1,4}

The contrast enema and CT studies in 102 patients with a clinical diagnosis (41%) or surgically confirmed (59%) diagnosis of colonic diverticulitis were reviewed retrospectively to determine the sensitivity of the two techniques. Combined results from all patients showed that the contrast enema was correct in 77% of patients. The contrast enema was falsely negative in 15% and was indeterminate in 7%. The CT examination was diagnostic in 41%, consistent with the diagnosis of diverticulitis in 38%, and falsely negative in 21% of patients. Both CT and contrast enemas were more accurate in patients with severe disease requiring surgery. No complications occurred from 109 enemas performed. Patient management was altered in only one patient as a result of the additional information provided by CT. The contrast enema should remain the initial and routine examination for the evaluation of patients with suspected diverticulitis. CT should be reserved for patients who are unable to have an adequate contrast enema, those with suspected distant or diffuse abdominal abscess, those who are unresponsive to medical therapy, and those who are candidates for percutaneous drainage.

Acute diverticulitis is a common cause of acute abdominal symptoms. Often the clinical diagnosis is obvious and treatment is implemented without radiologic confirmation. Bowel rest and antibiotics constitute the major components of therapy. Radiographic evaluation of diverticulitis is indicated to confirm an uncertain clinical diagnosis, to exclude carcinoma, to evaluate for a suspected fistula, or to determine the extent of disease in acutely ill patients. The contrast enema examination has been the traditional method of imaging the colon in patients with suspected diverticulitis. Recently, CT has been advocated as the initial imaging technique in the evaluation of patients with signs and symptoms of diverticulitis because of the superior definition of bowel-wall thickness and the extent of extraluminal disease [1-3]. Our study was performed to assess the sensitivity of contrast enemas and CT to detect clinically suspected or surgically proven diverticulitis [4]. In particular, an assessment was made to determine if the contrast enema and/or CT provided diagnostic rather than suggestive information, and if the additional information regarding the extent of extraluminal disease obtained by CT changed management when both examinations were performed.

Materials and Methods

The medical records and radiographs of 102 patients with a clinical (42 patients) or surgical (60 patients) discharge diagnosis of diverticulitis from January 1979 through February 1986 were reviewed retrospectively. Patients were gathered from the Duke University Hospital diagnosis registry, and consecutive records were reviewed. There were 59 men and 43 women aged 30-84 years. The site of diverticulitis was the sigmoid or descending colon in all patients. The clinical diagnosis of diverticulitis was based on the discharge diagnosis of the primary care physician. In an effort to further substantiate the clinical diagnosis, we required patients to have at least two of three criteria: abdominal pain, fever ($\geq 38^{\circ}\text{C}$), and an elevated WBC ($\geq 10,000/\text{mm}^3$). In 42 (41%) of the 102 patients, the diagnosis of diverticulitis

Received June 9, 1986; accepted after revision September 24, 1986.

¹ Department of Diagnostic Radiology, Duke University Medical Center, and Durham Veterans Administration Medical Center, Durham, NC 27710.

² Present address: Department of Diagnostic Radiology, Mayo Clinic, Rochester, MN 55905. Address reprint requests to C. D. Johnson.

³ Present address: Department of Radiology, Alexandria Hospital, Alexandria, VA 22310.

⁴ Present address: Department of Radiology, University of Minnesota Hospital and Clinics, Minneapolis, MN 55455.

AJR 148:541-546, March 1987
 0361-803X/87/1483-0541
 © American Roentgen Ray Society

was made in this fashion.

Sixty patients (59%) had surgical confirmation of the diagnosis of diverticulitis. In 53 patients pathologic study of the surgical specimen confirmed the diagnosis. The other seven patients were found to have large inflammatory masses at surgery that were not resected. These patients initially received diverting colostomies before resection and pathologic examination.

Sixty-three patients (62%) had only a contrast enema, 11 patients (11%) only a CT examination, and 28 patients (27%) both CT and a contrast enema study during an acute episode of diverticulitis.

Contrast enemas were performed with barium unless the patient had clinical evidence of generalized peritonitis. In these cases a water-soluble contrast agent was used. Glucagon was administered occasionally at the discretion of the radiologist. The diagnosis of diverticulitis was made on the basis of at least two of the following criteria: localized contrast extravasation, marked and distorted colonic fold thickening, localized mass effect, and mucosal tethering. Studies were considered indeterminate if we could not differentiate between diverticulitis and cancer. All contrast enema films were reviewed and the findings categorized by one author. If the retrospective diagnosis differed from the original radiologic diagnosis, the films were reviewed by two examiners and a final diagnosis was agreed upon.

CT was performed with either a GE 8800 or GE 9800 scanner in all but three cases. Sections through the abdomen were 10 mm thick at 10-mm intervals in 30 patients (71%) and 10 mm thick at 20-mm intervals in the other 12 patients. Unless contraindicated IV contrast material was routinely administered. Oral contrast material was used in all cases. One hundred to 300 ml of water-soluble contrast was administered through the rectum without complication in 18 (43%) of 42 CT examinations.

All CT studies were reviewed retrospectively by two reviewers and were categorized as either positive or negative. Positive CT scans were further subdivided into consistent with or diagnostic of diverticulitis. Scans were considered consistent with but nondiagnostic of diverticulitis if bowel-wall thickening (≥ 4 mm) and/or mesenteric or fascial soft-tissue stranding was present. CT examinations were considered diagnostic if any of the previously mentioned criteria were present in addition to an abnormal adjacent pericolic fluid or gas collection, indicating abscess. Twenty-four CT examinations (80%) were performed within 1 week and six CT studies within 12–17 days of the contrast enema. One patient was examined 2 months apart, but had diagnostic findings by both studies.

Patients having both studies (28) were evaluated to determine if management was altered as a result of the additional information provided by CT. Criteria for altered patient management included major therapy change (for example, surgery performed rather than planned medical therapy) and altered or additional medical/surgical therapy (for example, a different operation performed than that planned or additional medical consultation required).

The records of patients having an enema, for either the contrast enema or CT, were reviewed to assess for complications during acute diverticulitis.

Results

Contrast Enema Only

Sixty-three patients had only a contrast enema examination; of these 34 (54%) patients were diagnosed surgically, while 29 (46%) were diagnosed clinically. Thirty (88%) of 34 surgically proven abscesses were correctly diagnosed by contrast enemas. The contrast enemas in the other four (12%) were judged as having indeterminate findings: two with com-

plete colonic obstruction, one with a region of mucosal irregularity making differentiation from a primary carcinoma difficult, and one with a large rectovaginal fistula that prevented adequate filling and evaluation of the affected proximal colon. There were no false-negative contrast enemas in this group (Table 1).

The contrast enema was correct in 17 (59%) of 29 patients with diverticulitis diagnosed on clinical grounds. Twelve (41%) of 29 studies were false negatives, with demonstration of uncomplicated diverticulosis or a normal colon.

The contrast enema diagnosis was correct in 47 (75%) of 63 patients in whom the diagnosis was established by either surgical or clinical grounds. Twelve (19%) of 63 studies were negative, all from the group diagnosed clinically. Four (6%) of 63 studies were indeterminate, all requiring eventual surgery.

CT Only

Eleven patients had only a CT examination. Of these, eight (73%) were diagnosed surgically, while the other three (27%) were diagnosed clinically.

Three (37%) of eight patients with surgically proven disease had diagnostic CT studies. Two (25%) had CT findings consistent with but nondiagnostic of diverticulitis. When these categories were combined, CT was "correct" in five (63%) of eight patients. Three (37%) of eight patients had false-negative CT findings (diverticulosis or normal colon) (Table 2).

No CT studies were diagnostic in patients diagnosed clinically. Two (67%) of three patients had CT studies consistent

TABLE 1: Contrast Enema Alone in the Diagnosis of Acute Colonic Diverticulitis

Contrast Enema Diagnosis	No. of Patients (%)		
	Surgical	Clinical	Combined
Correct	30 (38)	17 (59)	47 (75)
Negative	0	12 (41)	12 (19)
Indeterminate	4 (12)	0	4 (6)
Total	34	29	63

TABLE 2: CT Alone in the Diagnosis of Acute Colonic Diverticulitis

CT Diagnosis	No. of Patients (%)		
	Surgical	Clinical	Combined
"Correct":			
Diagnostic of diverticulitis	3 (38)	0	3 (27)
Consistent with diverticulitis	2 (25)	2 (67)	4 (36)
Subtotal	5 (63)	2 (67)	7 (63)
Negative	3 (37)	1 (33)	4 (36)
Total	8	3	11

Note.—Scans were considered consistent with but nondiagnostic of diverticulitis if bowel-wall thickening (≥ 4 mm) and/or mesenteric or fascial soft-tissue stranding was present. Scans were considered diagnostic if any of these criteria were present in addition to an abnormal adjacent pericolic fluid or gas collection, indicating abscess.

with but nondiagnostic of diverticulitis. One error occurred in this group in which only diverticulosis was detected.

Combined results (clinical and surgical diagnosis) showed diagnostic CT findings in three (27%) of 11 patients and consistent but nondiagnostic findings in four (36%) of 11. CT was correct overall in seven (63%) of 11 patients. Four (36%) of 11 studies were false negatives, all but one surgically proven.

Both CT and Contrast Enema

Twenty-eight patients had both contrast enema and CT studies. Eighteen (64%) were surgically proven, while 10 (36%) were diagnosed clinically (Table 3).

Surgically proven diverticulitis was correctly diagnosed by the contrast enema in 15 (83%) of 18 patients (Fig. 1A). One (5%) of 18 examinations was false negative (Fig. 2A), while two (11%) of 18 were indeterminate—one because of complete sigmoid obstruction and the other with mucosal changes suggesting carcinoma (Fig. 3A).

Only 10 (56%) of 18 CT examinations were diagnostic in patients with surgically proven diverticulitis (Fig. 1B). In seven (39%) of 18 patients with surgical disease CT was consistent with but nondiagnostic of diverticulitis (Fig. 3B). Combined, 17 (95%) of 18 CT examinations were "correct." One (5%) of the 18 CT studies was false negative (Fig. 2B).

In the group of 10 patients with clinically diagnosed diverticulitis, the contrast enema was correct in eight (80%). One contrast enema study was negative, and the other indeterminate because of a large rectovaginal fistula that prevented adequate filling of the colon. Three (30%) of 10 clinically confirmed CT studies were diagnostic, while four (40%) of 10 were consistent with but nondiagnostic of diverticulitis. CT studies were correct overall in seven (70%) of 10 patients. Three (30%) of 10 CT studies were errors.

Combined results from diagnoses made clinically and surgically show correct diagnoses in 23 (82%) of 28 contrast enema studies. Two (7%) of 28 contrast enemas were negative and three (11%) were indeterminate. Only 13 (47%) of 28

TABLE 3: Contrast Enema and CT in the Diagnosis of Acute Colonic Diverticulitis in Patients Undergoing Both Studies

Diagnosis	Type of Confirmation/No. of Patients (%)		
	Surgical	Clinical	Combined
Contrast enema:			
Correct	15 (83)	8 (80)	23 (82)
Negative	1 (5)	1 (10)	2 (7)
Indeterminate	2 (11)	1 (10)	3 (11)
Total	18	10	28
CT:			
"Correct":			
Diagnostic of diverticulitis	10 (56)	3 (30)	13 (47)
Consistent with diverticulitis	7 (39)	4 (40)	11 (39)
Subtotal	17 (96)	7 (70)	24 (86)
Negative	1 (5)	3 (30)	4 (14)
Total	18	10	28

patients had diagnostic CT findings, with 11 (39%) of 28 consistent with but nondiagnostic. CT was correct overall in 24 (86%) of 28 patients. Four (14%) of 28 patients had false-negative CT studies. Two of these four patients had diagnostic contrast enema studies (Fig. 4). In no indeterminate or negative contrast enema studies were CT findings diagnostic. The differences in sensitivity between the two imaging techniques were not significant.

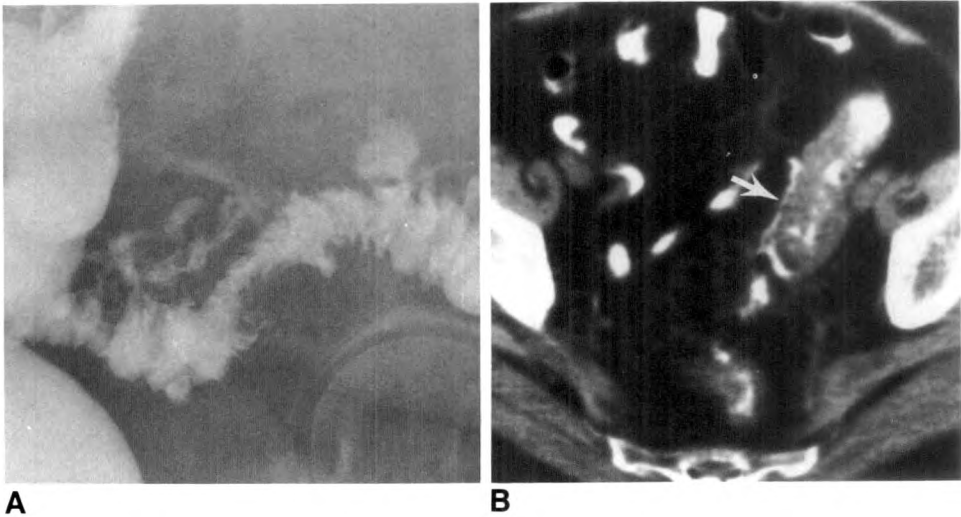
All Patients

A total of 102 patients had either CT, a contrast enema, or both examinations (Table 4). Forty-five (87%) of 52 patients with surgically proven disease had correct contrast enemas. One (2%) of 52 patients had a false-negative contrast enema, while six (11%) had indeterminate findings. Diagnostic CT studies were found in 13 (50%) of 26 patients, and nine (35%) had consistent but nondiagnostic findings. CT results were

Fig. 1.—Diagnostic contrast enema/CT.

A, Diagnostic changes of diverticulitis by contrast enema. Localized contrast extravasation, narrowing of bowel lumen, mass effect, and thickened folds.

B, Diagnostic CT in same patient. Thickened sigmoid wall, pericolic contrast extravasation (arrow), and soft-tissue stranding in adjacent mesentery.



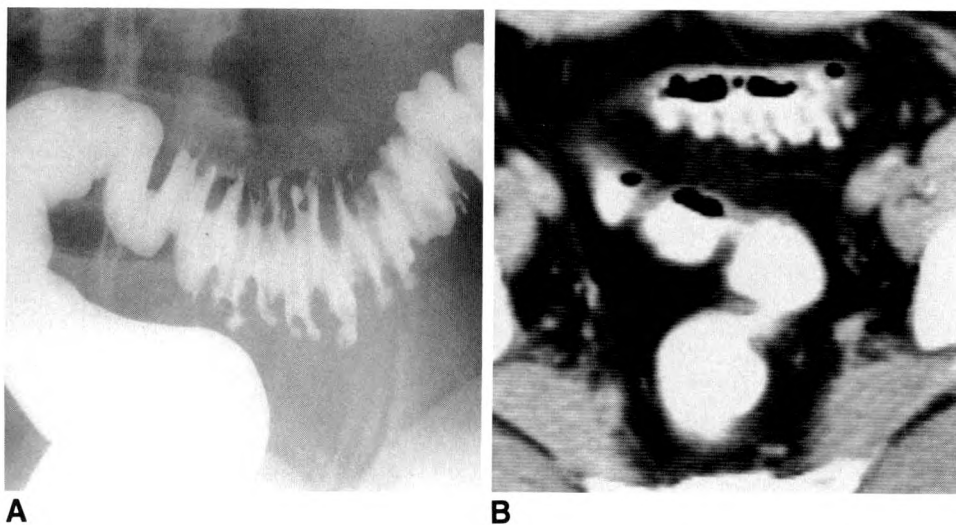


Fig. 2.—False-negative contrast enema/CT.

A, Contrast enema. Diverticulosis with prominent muscular hypertrophy. No evidence for pericolic inflammatory process.

B, CT scan in same patient. Diverticulosis with normal bowel-wall thickness and pericolic fat. Pathologically, focal diverticulitis was present.

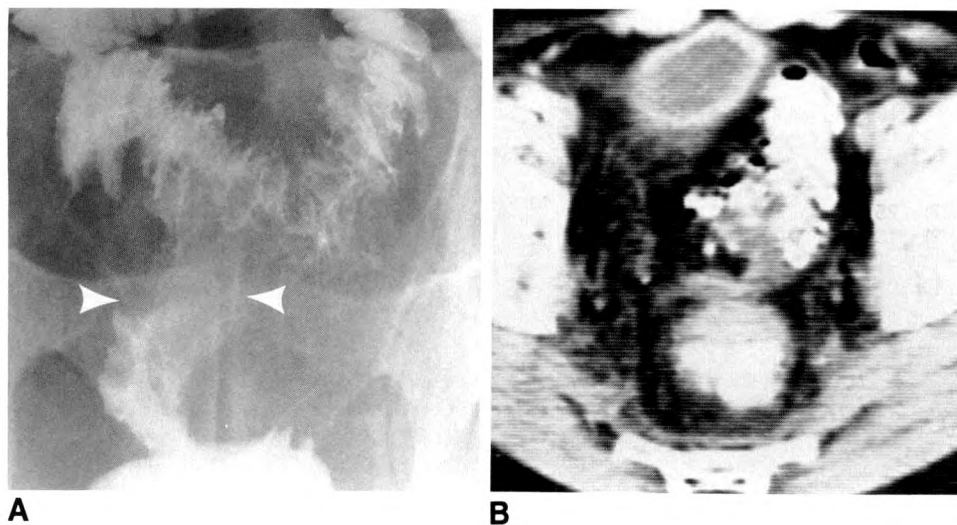


Fig. 3.—Indeterminate contrast enema/CT.

A, Contrast enema. Thickened sigmoid folds, with region in rectosigmoid (arrowheads) suggestive of cancer.

B, CT scan in same patient. Thickened colonic wall, mesenteric soft-tissue stranding, and diverticulosis. Exact course of bowel lumen is uncertain. These findings were also consistent with carcinoma. Pathologically, perforated diverticulitis found.

correct overall in 22 (85%) of 26 patients. Four (15%) of 26 patients had false-negative CT studies.

Clinically diagnosed diverticulitis was correctly detected in 25 (64%) of 39 contrast enemas. Thirteen (33%) of 39 examinations were falsely negative, and one patient had an indeterminate contrast enema study. Three (23%) of 13 clinically confirmed CT studies were diagnostic. Consistent but nondiagnostic findings were present in six (46%) of 13, with nine (69%) of 13 studies were correct overall. There were four (31%) false-negative CT studies.

Total combined results found 70 (77%) of 91 contrast enemas to be correct. Fourteen (15%) of 91 were false negatives, all but one of these from the group diagnosed clinically. Seven (8%) of 91 contrast enema studies were indeterminate, all but one from the surgically treated group. Diagnostic CT studies were present in 16 (41%) of 39 patients, with consistent findings in 15 (38%). "Correct" overall CT results were found in 31 (79%) of 39 patients. Eight (21%)

of 39 patients had false-negative CT scans that were equally distributed between the surgical and clinically diagnosed groups.

CT findings changed or significantly contributed to patient management in only one patient. This patient had characteristic changes of diverticulitis by both examinations, but CT noted a fluid collection adjacent to the sacrum—raising the possibility of osteomyelitis, which prompted surgical exploration of this area. No osteomyelitis was present.

There were no complications from 109 enemas administered for either the 91 contrast enemas or the 18 CT examinations.

Discussion

Acute diverticulitis is a common disease, occurring in up to 30% of patients with diverticulosis [5]. Patients with characteristic signs and symptoms are often treated successfully

Fig. 4.—Diagnostic contrast enema, negative CT.

A, Contrast enema shows diverticulosis and narrowed sigmoid lumen with thickened and tethered folds, considered diagnostic of diverticulitis.

B, CT shows diverticulosis and only minimal stranding in adjacent mesentery. Bowel-wall thickening cannot be assessed well without more intraluminal contrast. This study was judged negative for diverticulitis.

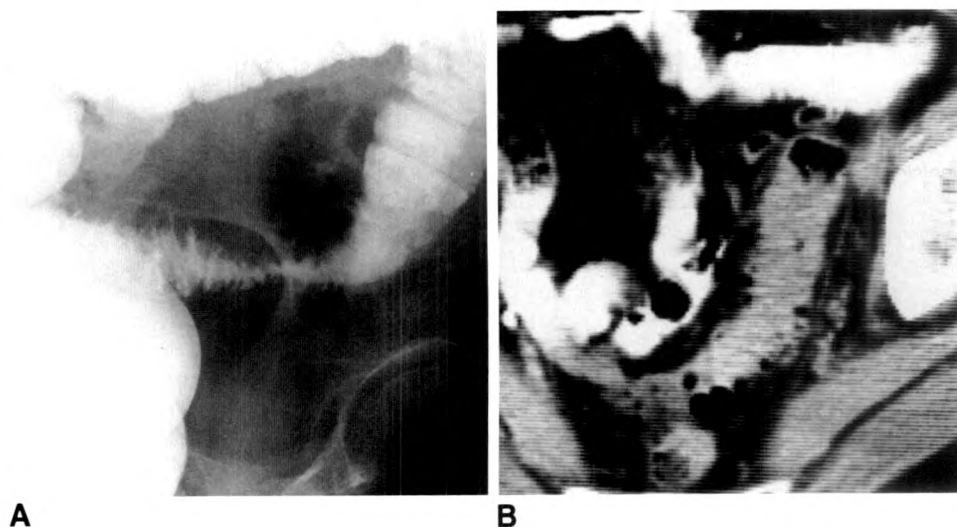


TABLE 4: Combined Contrast Enema and CT in the Diagnosis of Acute Colonic Diverticulitis

Diagnosis	Type of Confirmation/No. of Patients (%)		
	Surgical	Clinical	Combined
Contrast enema:			
Correct	45 (87)	25 (64)	70 (77)
Negative	1 (2)	13 (33)	14 (15)
Indeterminate	6 (11)	1 (3)	7 (8)
Total	52	39	91
CT:			
"Correct":			
Diagnostic of diverticulitis	13 (50)	3 (23)	16 (41)
Consistent with diverticulitis	9 (35)	6 (46)	15 (38)
Subtotal	22 (85)	9 (69)	31 (79)
Negative	4 (15)	4 (31)	8 (21)
Total	26	13	39

with conservative therapy and require no imaging studies. Radiographic evaluation is indicated in patients with an uncertain diagnosis or suspected fistulae and in patients unresponsive to medical therapy. Traditionally, the contrast enema has been the primary and initial imaging technique for diagnosing diverticulitis. CT has recently been shown to successfully detect diverticulitis [1-3]. One recent study recommended that CT should be the initial and routine imaging procedure in all patients with signs and symptoms suspicious for diverticulitis as a result of CT's ability to better define the extraluminal extent of disease [1].

In this study we attempted to determine whether a contrast enema or CT is best for initial evaluation of diverticulitis. Because patients with severe diverticulitis may require a different type of imaging than those with mild disease, we made the assumption that clinically diagnosed diverticulitis that was conservatively treated represented mild to moderate

disease, while diverticulitis requiring surgery represented severe disease. The ability of CT and contrast enemas to diagnose diverticulitis was assessed in both of these groups. In addition, we attempted to determine if the additional information provided by CT alters patient management.

Both CT and contrast enemas are reasonable, reliable methods for detecting diverticulitis. Both are more sensitive in patients with severe disease (those requiring surgical treatment) than in patients with mild disease (those diagnosed clinically). If strict diagnostic criteria are applied to CT (a pericolic abscess or gas collection), a contrast enema is more sensitive than CT. Overall, CT had diagnostic studies in only 41% of patients compared with 77% by contrast enema (Table 4). Contrast enema is also more specific than CT in the diagnosis of diverticulitis, since the consistent with but nondiagnostic results (bowel-wall thickening and mesenteric and/or fascial stranding) found in 38% of CT studies can be caused by a variety of conditions, most importantly carcinoma. Only seven (8%) of 91 contrast enema examinations were indeterminate, 2% because of the possibility of an underlying carcinoma.

Neither a negative CT nor a negative contrast enema excludes the diagnosis of diverticulitis. Eight (21%) of 39 patients had false-negative CT examinations, half of these requiring surgical treatment. Fourteen (15%) of 91 contrast enema examinations also were in error. All but one of these false-negative contrast enemas were associated with mild diverticular disease not requiring surgery (Table 4). This discrepancy may be explained by the possibility of selection bias, for patients with mild disease may have been more likely to have had contrast enema than a CT study. Interestingly, among the four errors made by CT in the group of patients that had both studies, the contrast enema was diagnostic in two (Fig. 4). The exact cause of these false-negative studies is not known, but it most likely resulted from minimal disease at the time of the examination. CT was not diagnostic in any of the five contrast enema studies classified as indeterminate or as negative.

While CT can better portray the extraluminal extent of disease, it provided significant information altering therapy in only one of 28 patients. In our hospital, radiologic evaluation of diverticulitis is indicated primarily for diagnostic purposes. Decisions regarding therapy (for example, surgical vs medical management) are nearly always based on the clinical course of the patient, rather than radiographic findings. It is for this reason that in only one of 31 patients did the additional information provided by CT alter management. In this patient, surgery was already planned, but more careful exploration of the pelvis was performed to exclude osteomyelitis from an abscess adjacent to the sacrum. Our results differ from those reported by Hulnick et al. [1], who report a higher percentage of patients treated surgically (81%) and a higher incidence of distant unsuspected abscesses (12%). This discrepancy may be due to differences between the two patient populations, with more severe disease among Hulnick's patients.

No complications occurred in any patient as a result of an enema given with a contrast enema or CT. Nearly all of our patients were examined during the acute phase, with enemas given in conjunction with 43% of CT examinations. Contrast enemas in the presence of acute diverticulitis are not contraindicated. Rectal contrast material is commonly useful during the CT examination to better define sigmoid lumen, bowel-wall thickness, and the relationship of rectosigmoid to adjacent structures. If rectal contrast material had been administered to all 39 patients undergoing CT, the CT results might have been better.

A contrast enema without preparation can be performed

more quickly and is generally less expensive than a CT examination, which requires good opacification of the entire gastrointestinal lumen.

There are indications for using CT in preference to the contrast enema, particularly if a large abdominal abscess is strongly suspected, if a patient is refractory to medical therapy, or if a patient is a candidate for percutaneous drainage of the diverticular abscess [6]. Rarely, patients with large fistulous tracts, which usually involve the bladder or vagina, may be more easily imaged by CT, because it may be impossible for a contrast enema to fill the affected segment in the more proximal colon. A contrast enema will often be needed later to better define the site and size of the fistula.

REFERENCES

1. Hulnick DH, Megibow AJ, Balthazar EJ, Naidich DP, Bosniak MA. Computed tomography in the evaluation of diverticulitis. *Radiology* 1984;152:491-495
2. Feldberg MAM, Hendriks MJ, van Waes PFGM. Role of CT in diagnosis and management of complications of diverticular disease. *Gastrointest Radiol* 1985;10:370-377
3. Pillari G, Greenspan B, Vernace FM, Rosenblum G. Computed tomography of diverticulitis. *Gastrointest Radiol* 1984;9:263-268
4. Hall FM. Computed tomography in the evaluation of diverticulitis (letter). *Radiology* 1985;154:835
5. Asch MJ, Markowitz AM. Diverticulitis coli: a surgical appraisal. *Surgery* 1967;62:239-247
6. Saini S, Mueller PR, Wittenberg J, Butch RJ, Rodkey GV, Welch CE. Percutaneous drainage of diverticular abscess: an adjunct to surgical therapy. *Arch Surg* 1986;121:475-478

Technical Note

Efficacy of an Intracassette Filter for Improved Pneumocolon Decubitus Radiographs

David L. Olson,¹ Wylie J. Dodds, Edward T. Stewart, and George F. Unger

Decubitus radiographs are important in air-contrast barium enemas [1-5]. Uneven exposure of the film, however, often interferes with the diagnostic quality of the image. Because of uneven beam attenuation, the upper portion of the film is often overexposed when compared with the lower portion. In this study we evaluated the efficacy of an intracassette filter for improving the quality of decubitus radiographs obtained during the pneumocolon examination.

Subjects and Methods

We evaluated 45 consecutive decubitus examinations on 33 unselected patients who were undergoing pneumocolon examinations. Both a filtered and an unfiltered radiograph were obtained for the right and left decubitus examinations. Filtered radiographs were obtained by using a 14 × 17 in. (35.6 × 43.2 cm) LEED filter (Czarnecki Associates, Inc., Milwaukee, WI) made of a plastic sheet coated with a light-absorbing dye. The filter was placed between the X-ray film (Kodak XRP-1) and the cassette screen (DuPont Hi Plus). Care was taken not to move the patient between comparison exposures. All examinations were done with a ceiling-mounted X-ray tube with a focal spot of 2 mm. In all cases we used 8-to-1 grid cassettes supported by a film holder, a tube-to-skin distance of 40 in. (101.6 cm), and 120-keV technique. The amperage was selected according to the patient's anteroposterior diameter when the patient was in the decubitus position. The amperage for the filtered radiographs was generally 20% higher than for the unfiltered radiographs. Ten of the 45 examinations were not included in the final evaluation because we judged that they did not represent a satisfactory comparison because of grid cutoff, poor centering, gross underexposure, or gross overexposure of one or both films.

The decubitus radiographs were subjected to blind analysis by two

experienced gastrointestinal radiologists. Each observer evaluated the series of radiographs in two separate surveys. In survey 1, the filtered and unfiltered right and left decubitus films were mixed randomly and evaluated individually. The image quality of the right and left colon on each radiograph was graded independently and scored for exposure quality as follows: markedly underexposed (-2), slightly underexposed (-1), optimally exposed (0), slightly overexposed (+1), markedly overexposed (+2). In survey 2, the observers compared directly the image quality of the filtered and unfiltered radiographs from the same patient. For each decubitus pair, the observer was asked to judge, for the right-colon, left-colon, and overall radiographs, whether one radiograph was superior to the other. Statistical evaluation was done by chi-square analysis.

Results

A total of 35 decubitus pairs (70 radiographs) from 28 patients were evaluated. There were 21 right decubitus pairs (right side down) and 14 left decubitus pairs (left side down). Only the last seven patients examined had both right and left decubitus radiographs taken. Six patients had a small body habitus (anteroposterior diameter, 15-25 cm), 12 had a medium habitus (anteroposterior diameter, 26-30 cm), and 10 had a large habitus (anteroposterior diameter ≥31 cm).

Analysis of the film scores for survey 1 indicated minimal observer error. For 74% of the 70 films, perfect agreement existed between the scores of the two observers. In 25% of comparisons, interobserver scoring variations differed by only one grade on the scoring scale. In the remaining 1%, the interobserver scoring error was greater than one grade. Because of the modest interobserver scoring error, the scores for both observers were combined.

Received August 18, 1986; accepted after revision September 26, 1986.

¹ All authors: Departments of Radiology, Clement J. Zablocki Veterans Administration Medical Center, Milwaukee, WI 53295, and the Medical College of Wisconsin, Milwaukee, WI 53226. Address reprint requests to D. L. Olson, Medical College of Wisconsin, Department of Radiology, Clement J. Zablocki Veterans Administration Medical Center, 5000 W. National Ave., Milwaukee, WI 53295.

AJR 148:547-549, March 1987 0361-803X/87/1483-0547 © American Roentgen Ray Society

Figure 1A shows the results of survey 1 for the 21 right decubitus pairs. A bell-shaped distribution of film exposure was found for the dependent right colon. The majority of both the filtered radiographs (74%) and unfiltered radiographs (62%) were optimally exposed. For these same radiographs, however, there was a substantial difference in exposure quality between the filtered and unfiltered radiographs of the nondependent left colon. Exposure scores for the filtered radiographs of the left colon had a bell-shaped distribution, whereas the scores for unfiltered radiographs were skewed significantly toward overexposure ($p < .01$). The reverse of these differences was seen for the 14 left decubitus pairs (Fig. 1B). On the left decubitus views, scores for the dependent left colon showed a bell-shaped distribution. The majority of both the filtered (64%) and unfiltered (61%) radiographs were optimally exposed. For the nondependent right colon,

however, scores for the filtered radiographs had a bell-shaped distribution, but scores for the unfiltered radiographs were skewed significantly toward overexposure ($p < .01$).

A typical example from survey 2 is shown in Fig. 2. When the filtered and unfiltered radiographs for each decubitus pair were compared directly with each other, the findings were similar to those of survey 1 (Fig. 1C). The exposure of the filtered radiograph for the nondependent colon was preferred 86% of the time for the left decubitus and 76% of the time for the right decubitus ($p < .01$). The observers did not indicate any preference between filtered and unfiltered films for the dependent colon 77% of the time for the left decubitus and 74% of the time for the right decubitus. Overall, the radiologists preferred the filtered over the unfiltered film 86% of the time for the left decubitus and 81% of the time for the right decubitus ($p < .01$).

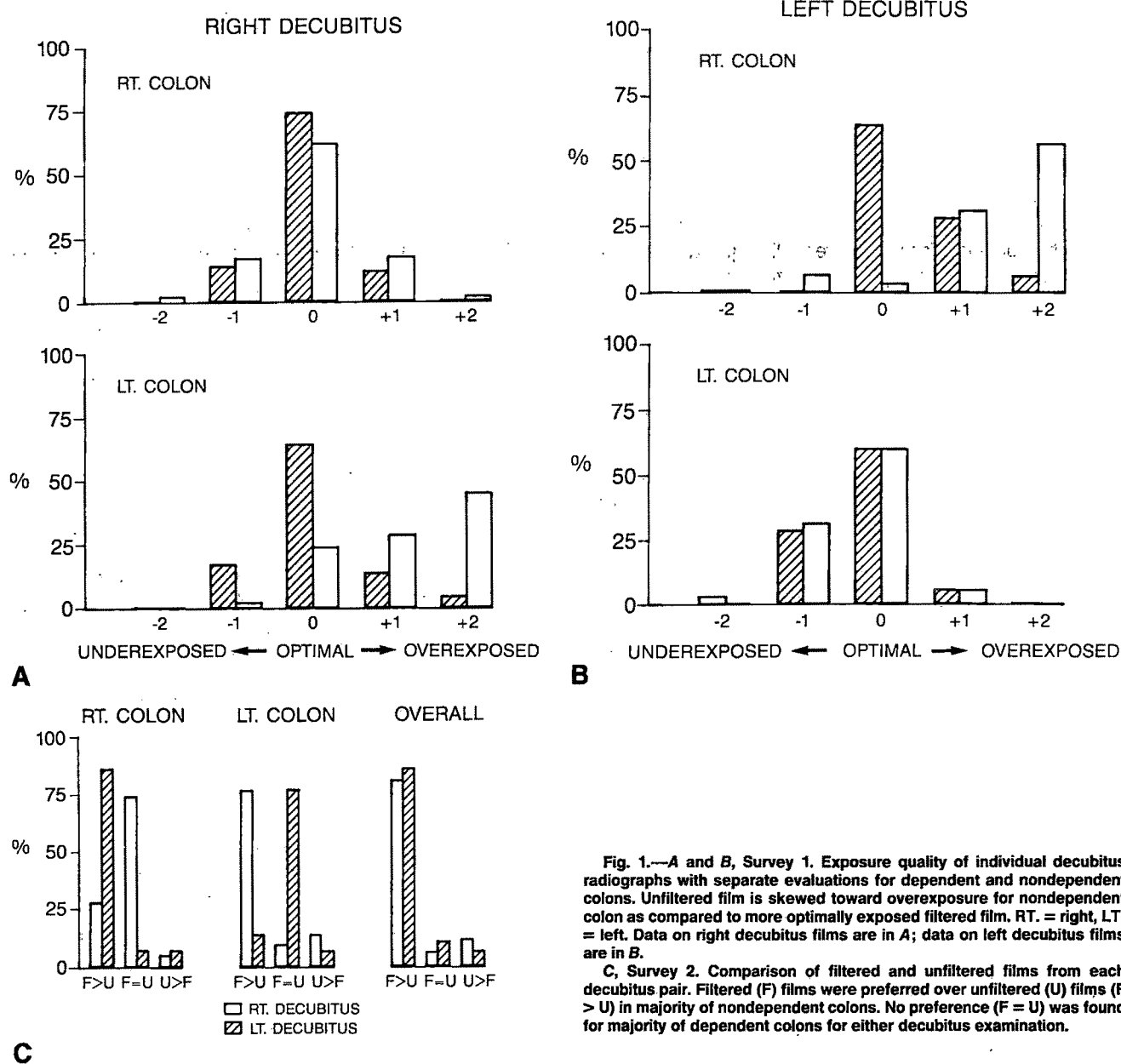


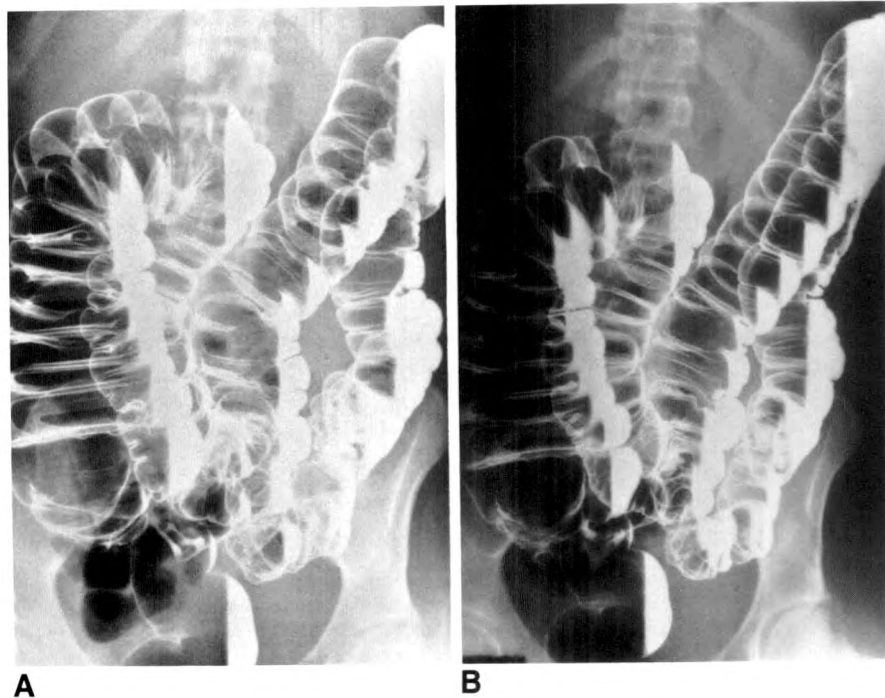
Fig. 1.—A and B, Survey 1. Exposure quality of individual decubitus radiographs with separate evaluations for dependent and nondependent colons. Unfiltered film is skewed toward overexposure for nondependent colon as compared to more optimally exposed filtered film. RT. = right, LT. = left. Data on right decubitus films are in A; data on left decubitus films are in B.

C, Survey 2. Comparison of filtered and unfiltered films from each decubitus pair. Filtered (F) films were preferred over unfiltered (U) films (F > U) in majority of nondependent colons. No preference (F = U) was found for majority of dependent colons for either decubitus examination.

Fig. 2.—Comparison of typical left decubitus radiographs taken with and without an intracassette filter.

A, Filtered radiograph. Right colon is optimally exposed.

B, Unfiltered radiograph. Right colon is moderately overexposed.



Discussion

The usefulness of the double-contrast method for evaluation of the colon is widely accepted. High-quality lateral decubitus views are an integral part of the pneumocolon examination. Technical difficulties, however, often undermine optimal, uniform exposure of decubitus radiographs. Potential problems for obtaining high-quality decubitus radiographs include improper patient or film centering, grid cutoff, and poor exposure technique.

Good centering techniques can be readily taught to technologists. Cassette holders are useful for keeping the film perpendicular to the X-ray beam, thereby eliminating grid cutoff when combined with proper centering [2]. Measurement of the anteroposterior diameter of the patient while the patient is in the decubitus position, after administration of barium and air, and use of this measurement to determine X-ray technique helps achieve optimal film exposure.

An additional problem is nonuniformity in the exposure quality across the film. In the decubitus position, colonic contents shift to the dependent side, and gas rises to the nondependent segment of colon. The net result is a greater amount of soft tissue on the dependent side of the patient. The decubitus radiograph commonly is overexposed on the nondependent side and/or underexposed on the dependent side. Aluminum wedges or lead-impregnated Plexiglas compensation filters, attached to the X-ray collimators, have been used to alleviate this problem [2–4]. An advantage to the collimator-attached filters is a slight reduction in patient radiation dose, at the price of some increased tube loading [4]. A disadvantage is that an extra step is required to attach and remove the filter for each decubitus examination.

The filter evaluated in this study is unique because it is incorporated into the film cassette. The intracassette filter, situated between the X-ray film and screen, functions by absorbing light photons emitted by the screen. The absorption

gradient across the filter results in greatest absorption on the nondependent side of the decubitus radiograph. This type of filter is easy to use and can be placed permanently into any standard X-ray cassette. The only requirement is that the cassette be used with the appropriate side up. This is accomplished by clearly labeling the outside of the cassette. A slight disadvantage is the fact that adequate X-ray exposure requires a slight increase in the radiographic dose of about 20%. However, this disadvantage is offset by a decrease in the need for repeat radiographs due to suboptimal exposure of the first radiograph. In our department, we have managed comfortably with two intracassette filters for each fluoroscopy room used for barium enemas.

Optimal film exposure is fundamental to high-quality diagnostic radiology. Carcinomas missed during air-contrast barium enemas, in some instances, may be missed because of incorrect exposure of lateral decubitus radiographs [5]. Our findings validate the efficacy of an intracassette filter in obtaining optimally exposed decubitus radiographs during the pneumocolon examination. Whether these improved radiographs ensure any significant improvement in diagnostic accuracy remains to be determined, but such a result seems likely.

REFERENCES

- Peterson GH, Miller RE. The barium enema: a reassessment looking toward perfection. *Radiology* 1978;128:315–320
- DeLacey G, Wignall B, Ambrose J, Baylis K, Bridges C. The double contrast barium enema: improvements to lateral decubitus views including the use of a wedge filter. *Clin Radiol* 1978;29:197–199
- Miller RE. Simple apparatus for decubitus films with horizontal beam. *Radiology* 1970;97:682–683
- Feczko PJ, Haggard AM, Ranch PL, Halpert RI, Simms SM. Compensation filtration for decubitus radiography during double-contrast barium enema examinations. *Radiology* 1983;149:848–850
- Kelvin FM, Gardiner R, Vas W, Stevenson GA. Colorectal carcinoma missed on double contrast barium enema study. *AJR* 1981;137:307–313

Book Review

Ultrasound-Guided Biopsy and Drainage. By Rainer Ch. Otto and Josef Wellauer. Berlin: Springer-Verlag, 160 pp., 1986.

This concise, well-organized, and timely book presents an excellent review of the techniques of percutaneous ultrasound-guided biopsy and drainage. The text is well-written and practically oriented. The translation is very good.

After a short introductory chapter, the authors divide the book into three major parts: principles and technique, results; and practical aspects of biopsy and drainage, including indications and risks. They present their own large experience with percutaneous techniques and provide much useful information regarding methods and approach. The text, which is well-illustrated, includes photographs and line drawings of the various needles used today, drawings demonstrating the use of different transducers and needles, and photographs of gross and histologic specimens, as well as sonograms and

radiographs. The graphic line drawings were especially helpful to this reviewer when learning how to use a particular biopsy needle that was described in this book.

The book is complete in its discussion, including relevant sections regarding processing of the specimens obtained and indications and complications of each specific procedure. It is easy to use both as a reference text to answer questions about specific techniques and as a general guide to be read from cover to cover. I highly recommend it for anyone who is involved with percutaneous biopsy and drainage.

Beverly A. Spirt
State University of New York Health Science Center
Syracuse, NY 13210

Pictorial Essay

Sonography in Patients with a Possible Pancreatic Mass Shown on CT

Mark J. Ormson,¹ J. William Charboneau, and David H. Stephens

During the past decade, pancreatic imaging has advanced rapidly as indirect methods have been supplanted by direct methods. CT and sonography allow direct imaging of pancreatic tissue, and ERCP can display the ductal pattern. Because sonography and CT are noninvasive, they have become the primary imaging methods for the detection of pancreatic masses. Their success rate in detecting pancreatic carcinomas has continued to improve with advances in equipment, scanning techniques, and interpretive skills [1-5]. When either sonography or CT fails to establish the presence or absence of a mass, ERCP is often used next [6, 7].

Although it is recognized that CT is useful for evaluating the pancreas when visualization of the gland by sonography is incomplete, the use of sonography to resolve inconclusive findings on CT has had little emphasis [8, 9]. We report a retrospective review of 27 patients in whom a pancreatic mass could not be confidently confirmed or excluded on CT. In these cases, the complementary use of sonography, with its ability to detect changes of parenchymal echotexture, was instrumental in confirming or excluding a lesion.

Materials and Methods

The 27 cases selected for review had been evaluated at our institution within the past 3 years. These cases are representative of our imaging approach in patients with a possible pancreatic mass on CT. These cases were selected to demonstrate the role of sonography in this patient group and are not intended for statistical purposes. In these cases, the presence of a pancreatic mass was questioned

on CT, but the CT findings were considered to be inconclusive. Consequently, sonography was performed for further evaluation. This group of patients included 16 women and nine men aged 24-76 years (mean, 53 years). Major clinical symptoms included abdominal pain of more than 1 month's duration in 23 patients, weight loss in 10, and jaundice in two. Biochemical changes included an increased alkaline phosphatase value in six patients, increased aspartate aminotransferase in three, increased total and direct bilirubin in two, and increased serum amylase in two.

For 21 of the 27 patients, CT scans had been obtained at our institution. Ten patients had been referred to us for further evaluation of a presumed pancreatic mass on the basis of CT performed elsewhere (all outside CT scans were reviewed by us; we repeated the CT studies in four of these 10 cases). All CT scans were obtained on current-generation scanners and, with the exception of one patient, IV contrast medium was used.

All 27 patients underwent pancreatic sonography at our institution. In 25, a real-time examination was performed in both the supine and sitting positions and both before and after the patient drank about 700 ml of water to provide an acoustic window to the pancreas. Two patients underwent only gray-scale sonography.

All patients with a positive pancreatic sonogram underwent surgery, so pathologic identification of the lesion was available. All patients with negative pancreatic sonograms have had clinical follow-up of 9 months to 3 years.

Results

In 16 of the 27 cases, results of sonography were normal. In these patients, a mass was questioned on CT in the head

Received April 16, 1986; accepted after revision October 7, 1986.

Presented at the annual meeting of the Society of Gastrointestinal Radiologists, Acapulco, Mexico, January 1986.

¹ All authors: Department of Diagnostic Radiology, Mayo Clinic and Mayo Foundation, Rochester, MN 55905. Address reprint requests to J. W. Charboneau.

of the pancreas in 13 and in the tail in three. In these 16 cases, sonography revealed normal pancreatic echotexture throughout the pancreas, including the region of concern (Figs. 1 and 2). On clinical follow-up, all 16 patients were alive and had no clinical evidence of pancreatic disease. For seven of these patients the follow-up was more than 24 months; it was 12–24 months for three and 9–12 months for six.

Sonography revealed a focal hypoechoic solid lesion in the other 11 patients who had CT scans in which a pancreatic mass was questioned (Figs. 3–7). Pathologic confirmation at surgery revealed a pancreatic adenocarcinoma in seven of these cases and chronic focal pancreatitis in four. In these cases, sonography was unable to differentiate between pancreatic carcinoma and chronic focal pancreatitis because findings indicative of carcinoma, such as hepatic metastasis or regional adenopathy, were not present. The four inflammatory lesions (Fig. 4) all were within the pancreatic head; three were completely resected and one was diagnosed by multiple biopsies at laparotomy. Of the seven adenocarcinomas, four were within the pancreatic head (Fig. 3), two were in the body

(Figs. 5 and 6), and one was in the tail (Fig. 7). Even though there were no signs of unresectability by CT and sonography, four of the seven carcinomas were found to be unresectable at surgery.

A common indication for sonography (16 of 27 cases) was the CT finding of fullness of the pancreatic head unaccompanied by a low-density area or secondary signs of tumor (Figs. 1 and 2). In another five cases there was dilatation of the common bile duct or of the pancreatic duct to the region of the pancreatic head (or both), but no definite mass was apparent on CT (Figs. 3 and 4). In eight of these 21 cases, sonography confirmed the presence of a solid hypoechoic lesion within the pancreatic head, but it was not possible to distinguish between pancreatic carcinoma and chronic focal pancreatitis (Figs. 3 and 4) [10]. In the 13 other cases, the pancreas had a normal sonographic appearance.

Although most diagnostic challenges involved the pancreatic head (21 cases), sonography was also useful in evaluating a possible lesion in the body or tail of the pancreas in six cases (Figs. 5–7).

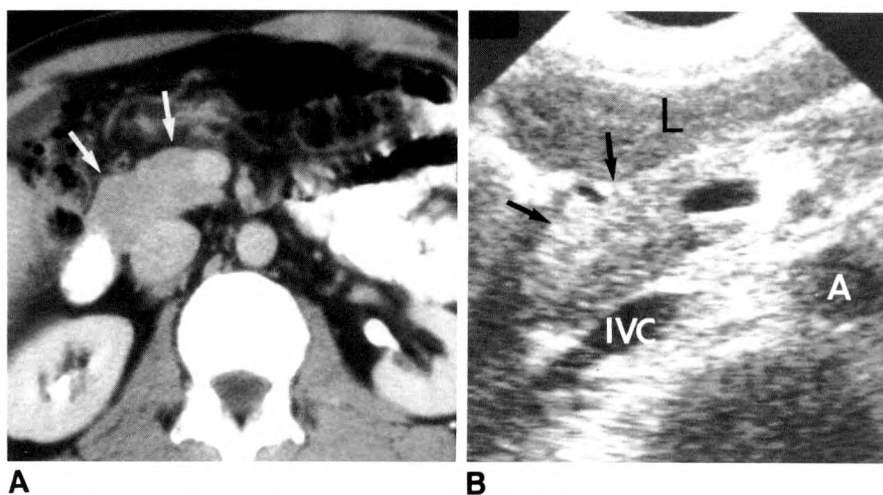


Fig. 1.—55-year-old man had suspected mass in head of pancreas on CT at another hospital.

A, Repeat CT shows prominent pancreatic head (arrows).

B, Transverse sonogram reveals normal pancreatic echotexture (arrows) and prominent but normal pancreatic head. L = left lobe of liver; A = aorta; IVC = inferior vena cava. No evidence of pancreatic disease on clinical follow-up (12 months).

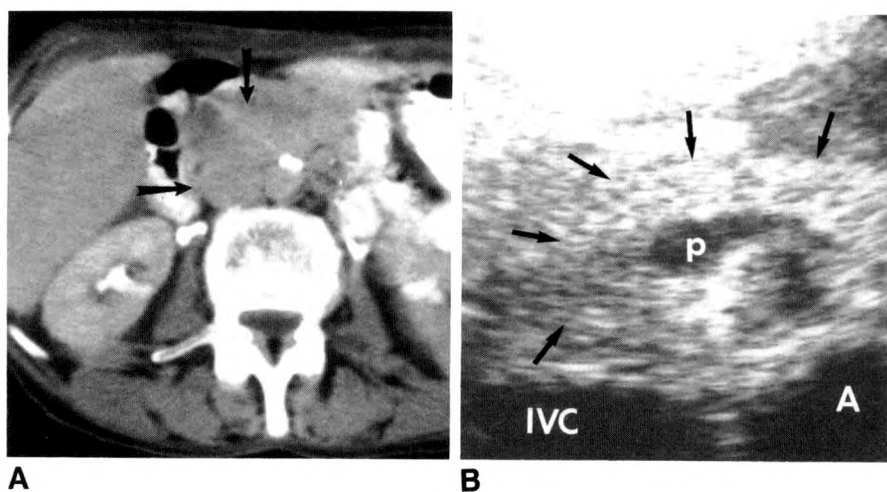


Fig. 2.—Abdominal pain in 75-year-old woman.

A, Question of mass in head of pancreas on CT (arrows). Paucity of retroperitoneal fat makes evaluation of pancreatic head difficult.

B, Transverse sonogram shows normal pancreatic size and echotexture (arrows). A = aorta; IVC = inferior vena cava; p = confluence of splenic and portal veins. No evidence of pancreatic disease on clinical follow-up (36 months).

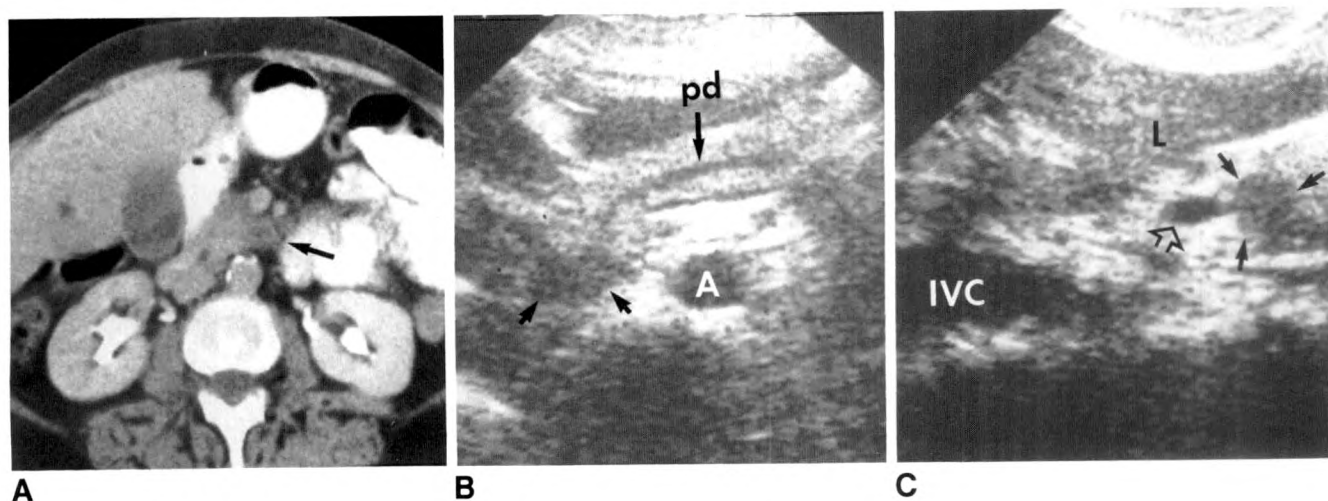


Fig. 3.—62-year-old woman with abdominal pain for 2 months and jaundice for 1 week.

A, CT shows dilated bile and pancreatic ducts (the latter were seen on higher CT slices) to level of slightly enlarged and hypodense uncinate process (arrow) where mass is suspected. Transverse (B) and longitudinal (C) sonograms confirm presence of 2-cm solid, hypoechoic mass (solid arrows) in uncinate region of head of pancreas causing dilatation of pancreatic duct. L = left lobe of liver; IVC = inferior vena cava; A = aorta; pd = pancreatic duct. At surgery, an unresectable adenocarcinoma adherent to portal vein (open arrow) was found.

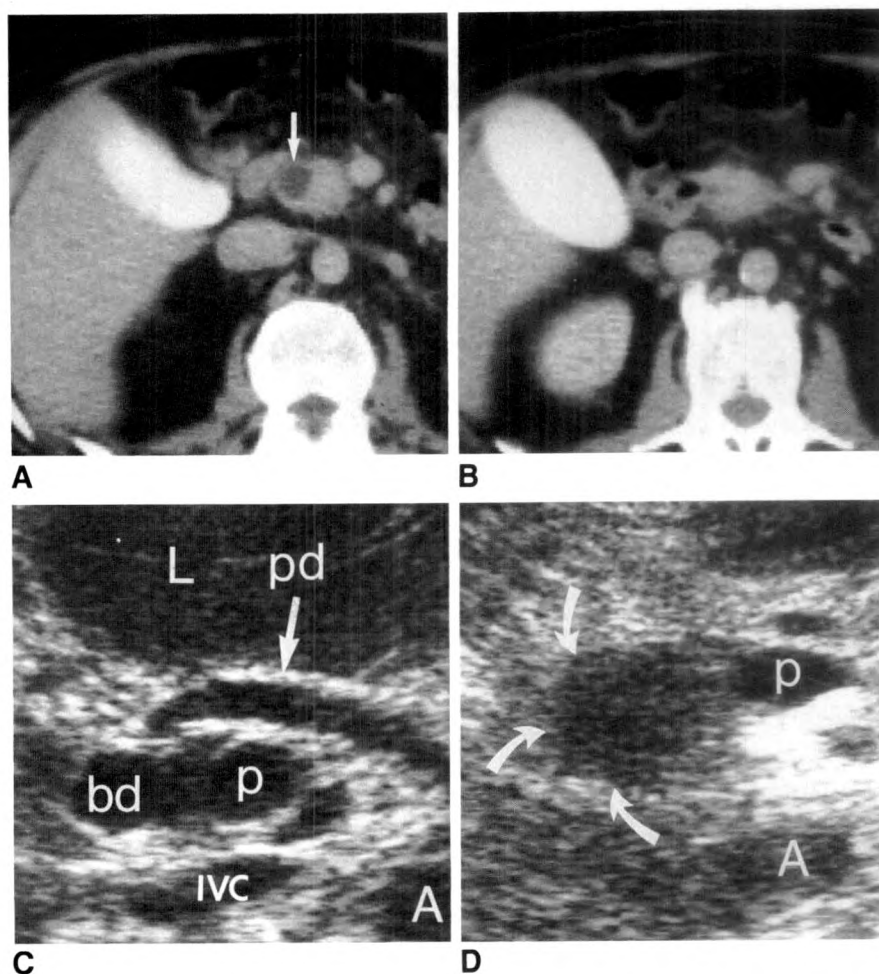


Fig. 4.—71-year-old man with abdominal pain.

A and B, CT reveals dilated common bile duct (arrow) to level of pancreatic head (A), but no cause of obstruction was apparent (B).

C and D, Close-up transverse sonograms corresponding to A and B, respectively, show dilatation of pancreatic duct (pd) and distal common bile duct (bd). At lower level (D), small focal hypoechoic solid mass (curved arrows) causes duct dilatation. L = left lobe of liver; A = aorta; IVC = inferior vena cava; p = portal vein. Focus of chronic pancreatitis was resected.

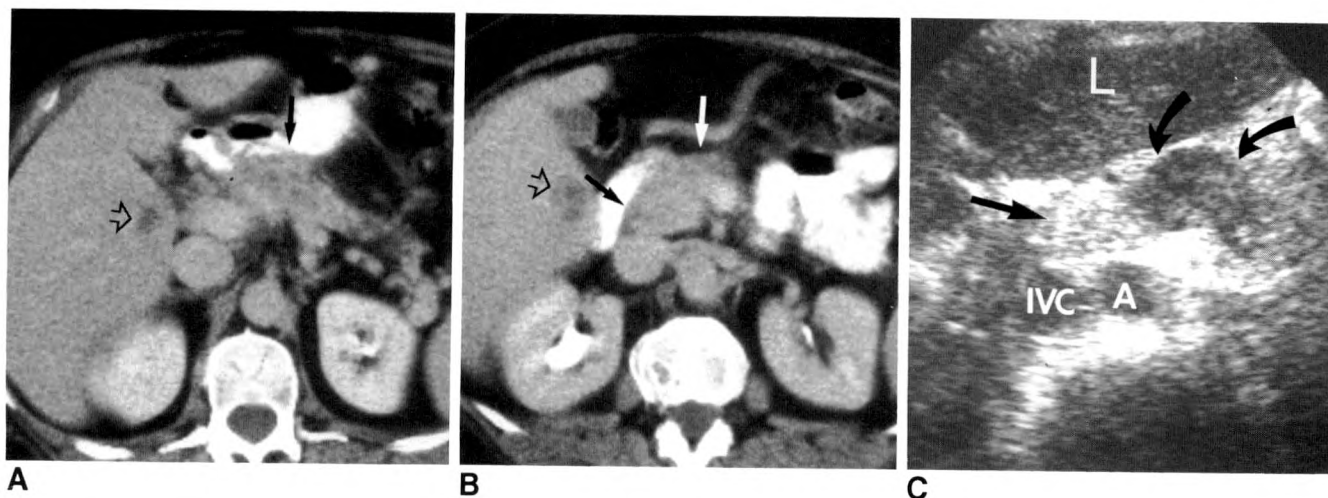


Fig. 5.—58-year-old woman with abdominal pain.

A and B, CT shows areas of low density and mild enlargement involving pancreatic head and body (solid arrows). There is also atrophy of pancreatic tail and low-density lesion in liver (open arrow).

C, Transverse sonogram depicts hypoechoic solid mass involving pancreatic body (curved arrows); pancreatic head has normal echotexture (straight arrow). L = left lobe of liver; A = aorta; IVC = inferior vena cava. At surgery, unresectable adenocarcinoma of pancreatic body and normal pancreatic head were identified; low-density lesion in liver was a cyst.

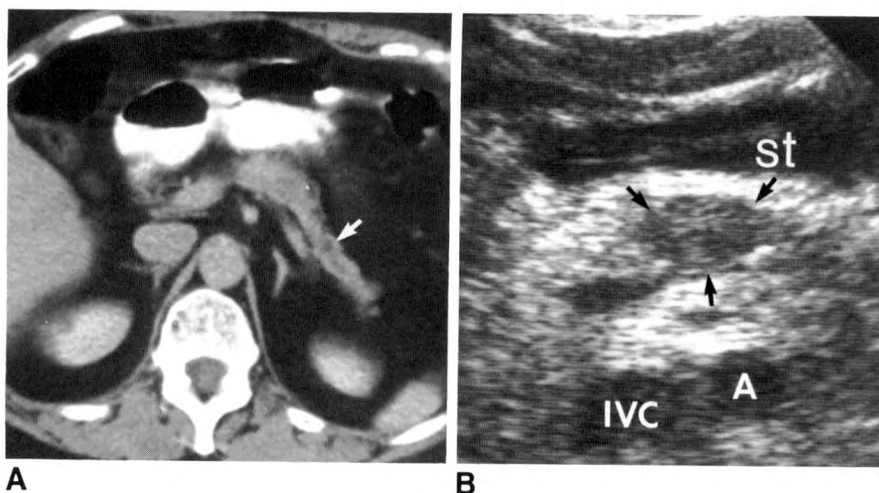


Fig. 6.—70-year-old woman with abdominal pain.

A, CT shows dilatation of distal pancreatic duct (arrow) and atrophy of pancreatic tail, suggesting obstructing lesion in pancreatic body.

B, Transverse sonogram reveals small hypoechoic solid mass within pancreatic body (arrows). st = stomach; A = aorta; IVC = inferior vena cava. A 2.5-cm pancreatic adenocarcinoma was resected.

ERCP examinations were attempted in five patients and were successful in four. The findings in all four successful ERCP examinations agreed with the sonographic findings.

Discussion

CT is usually reliable in detecting or excluding a pancreatic mass [1, 3]. However, in some cases the normal variations in size or shape of the pancreas may simulate a mass on CT. In other cases, CT findings may be indeterminate when a pancreatic mass is present. To resolve these difficult cases, various complementary but invasive methods such as ERCP, transhepatic cholangiography, angiography, percutaneous biopsy, and surgical exploration may be used. As an alternative

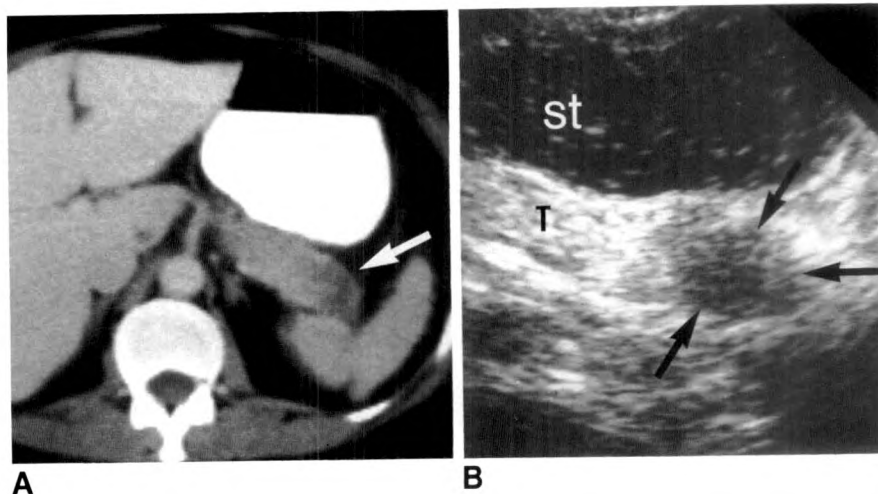
imaging procedure, sonography is readily available, noninvasive, relatively inexpensive, and highly sensitive to parenchymal changes in echotexture. The ability of sonography to detect changes in pancreatic echotexture has enabled detection of intrapancreatic tumors that do not distort the size or shape of the pancreas [2].

Because both CT and sonography usually are reliable in detecting pancreatic masses, either is used as the first imaging test at our institution when there is clinical suspicion of a pancreatic mass. Our experience has been that CT and sonography may offer complementary information in the evaluation of suspected pancreatic masses. In the subgroup of patients in whom the CT findings are inconclusive for a pancreatic mass, sonography is often valuable in excluding or confirming a mass. Because, with careful scanning tech-

Fig. 7.—61-year-old woman with abdominal pain.

A, CT shows subtle low-density mass in tail of pancreas (arrow) adjacent to splenic hilum.

B, Transverse sonogram of tail of pancreas (T) through water-filled stomach (st) confirms hypoechoic solid mass in distal tail of pancreas (arrows). A 4-cm pancreatic adenocarcinoma was resected.



nique, sonography allows visualization of the pancreas in about 85% of patients [2, 7], it will confirm or exclude a pancreatic lesion in most, but not all, cases. When a question of pancreatic mass on CT cannot be resolved by sonography, then a more invasive procedure such as an ERCP or percutaneous CT-guided biopsy might be appropriate.

REFERENCES

1. Foley WD, Stewart ET, Lawson TL, et al. Computed tomography, ultrasonography, and endoscopic retrograde cholangiopancreatography in the diagnosis of pancreatic disease: a comparative study. *Gastrointest Radiol* 1980;5:29-35
2. Taylor KJW, Buchin PJ, Viscomi GN, Rosenfield AT. Ultrasonographic scanning of the pancreas: prospective study of clinical results. *Radiology* 1981;138:211-213
3. Hessel SJ, Siegelman SS, McNeil BJ, et al. A prospective evaluation of computed tomography and ultrasound of the pancreas. *Radiology* 1982;143:129-133
4. Ward EM, Stephens DH, Sheedy PF. Computed tomographic characteristics of pancreatic carcinoma: an analysis of 100 cases. *Radiographics* 1983;3:547-565
5. Freeny PC, Lawson TL. *Radiology of the pancreas*. New York: Springer-Verlag, 1982
6. Moss AA, Federle M, Shapiro HA, et al. The combined use of computed tomography and endoscopic retrograde cholangiopancreatography in the assessment of suspected pancreatic neoplasm: a blind clinical evaluation. *Radiology* 1980;134:159-163
7. Cotton PB, Lees WR, Vallon AG, Cottone M, Croker JR, Chapman M. Gray-scale ultrasonography and endoscopic pancreatography in pancreatic diagnosis. *Radiology* 1980;134:453-459
8. Levitt RG, Geisse GG, Sagel SS, et al. Complementary use of ultrasound and computed tomography in studies of the pancreas and kidney. *Radiology* 1978;126:149-152
9. Ferrucci JT, Wittenberg J. A comprehensive approach for diagnosing pancreatic disease. *Radiology* 1980;136:255-256
10. Neff CC, Simeone JF, Wittenberg J, Mueller PR, Ferrucci JT Jr. Inflammatory pancreatic masses: problems in differentiating focal pancreatitis from carcinoma. *Radiology* 1984;150:35-38

American Roentgen Ray Society: Officers, Committees, and Meeting Information

Officers

President: Jerome F. Wiot
President-elect: Raymond A. Gagliardi
1st Vice-president: Lee F. Rogers
2nd Vice-president: Gerald D. Dodd
Secretary: Glen W. Hartman
Treasurer: Ronald G. Evens

Executive Council: E. Gedgaudas, J. F. Wiot, L. F. Rogers, R. A. Gagliardi, R. G. Evens, R. N. Berk, F. L. Angell, J. E. Madewell, M. P. Capp, G. W. Hartman, B. G. Brogdon, G. A. Kling, H. C. Carlson, A. K. Poznanski, A. E. James, Jr., J. A. Kirkpatrick, Jr., G. R. Leopold, G. D. Dodd, J. T. Ferrucci, Jr., R. H. Troupin, chairman

Committees 1986-1987

Editorial Policy: S. S. Sagel, W. J. Casarella, J. T. Ferrucci, Jr., N. C. Whitley, S. Hilton, A. J. Davidson, J. M. Taveras, R. N. Berk, M. P. Capp, chairman

Education and Research: C. E. Putman, A. R. Margulis, J. R. Thornbury, R. A. McLeod, J. T. Ferrucci, Jr., ex officio, B. G. Brogdon, chairman

Finance and Budget: B. P. Wood, L. R. James, J. A. Kirkpatrick, Jr., A. E. James, F. L. Angell, chairman

Instruction Courses: R. A. McLeod, associate chairman, J. T. Ferrucci, Jr., chairman

Program: J. Wiot, G. W. Hartman, J. A. Kirkpatrick, Jr., R. H. Troupin, M. P. Capp, J. E. Madewell, B. G. Brogdon, J. T. Ferrucci, Jr., G. A. Kling, G. G. Ghahremani, M. Viamonte, R. A. Gagliardi, chairman

Publications: W. J. Casarella, J. T. Ferrucci, Jr., S. S. Sagel, N. C. Whitley, M. P. Capp, chairman

Scientific Exhibits: S. G. Kirchner, A. V. Proto, S. M. Goldman, J. E. Madewell, chairman

Nominating: W. J. Casarella, H. C. Carlson, A. E. James, chairman

Representatives to Other Organizations

American Board of Radiology: E. C. Klatte, R. W. McConnell, L. F. Rogers

American College of Radiology: J. L. Gwinn, G. A. Kling, G. W. Hartman, J. M. Dennis, E. J. Ferris, J. E. Madewell

American Medical Association House of Delegates: S. F. Ochsner, K. C. Krabbenhoft, alternate

American National Standards Institute: M. Haskin

National Council on Radiation Protection and Measurements: E. L. Saenger, H. L. Friedell

Meetings, Membership, Business Information

Annual Meetings: April 26-May 1, 1987, Fontainebleau-Hilton, Miami Beach; May 8-13, 1988, Hilton, San Francisco; May 7-13, 1989, Hilton, New Orleans.

Director Annual Meeting: George A. Kling, Harper Hospital, Detroit, MI 48201; (313) 745-8401.

ARRS Membership: Rosalind H. Troupin, Dept. of Radiology, Hospital of University of Pennsylvania, 3400 Spruce St., Philadelphia, PA 19104. The ARRS has two membership categories: active and in-training. For active membership, applicants must practice radiology in the U.S. or Canada. Each must have graduated in good standing from an approved medical school or hold an advanced degree in a physical, chemical, or biological science and be certified by the American Board of Radiology, the Royal College of Physicians and Surgeons of Canada, or otherwise adequately document training and credentials. A member-in-training must be in a radiology residency, a postresidency fellowship program, or a postgraduate student in an allied science. Status must be verified by the program director. For consideration during the 1987 ARRS meeting, completed applications must be received by Dr. Troupin no later than Feb. 1, 1987.

Business Office: Paul Fullagar, administrative director, American Roentgen Ray Society, 1891 Preston White Dr., Reston, VA 22091; (703) 648-8900.

Technical Note

Daytime Constancy of Bile Duct Diameter

Vassilios Raptopoulos,¹ Edward H. Smith, Andrew Karellas, Dianne K. Miranda, and Cynthia A. Tefft

We measured the diameter of the common bile duct sonographically in 20 volunteers on five occasions between 8 a.m. and 5 p.m. on one day to determine if it varied during the day in normal subjects. To our knowledge, the presence or absence of such variation has not been determined before.

Subjects and Methods

The study group included 12 women and eight men. Their age range was 21 to 49 years (mean = 31, standard deviation = 9). Criteria for participation in the study included good general health, no history of dyspeptic symptoms, and the presence of a normal gallbladder on sonography. No special diet was prescribed, and informed consent was obtained.

Dynamic (real-time) equipment (ATL MK3001, ATL, Inc., Fairlawn, NJ) was used. Its calibration was monitored daily with an ULTRACAL phantom (Ultra-Cal Inc., Monrovia, CA). Subjects were examined in the right anterior oblique position, and sagittal images of the extrahepatic bile duct just anterior to the portal vein were obtained. The anteroposterior internal diameter of the duct was measured at the level of the hepatic artery. This location was chosen because it is considered the most accurately reproducible measurement of the extrahepatic bile ducts [1, 2].

Examinations were performed by one of two experienced sonographic technologists and a radiologist. Measurements were made with an electronic caliper, and the image was recorded on hard copy. The duct diameter recorded for each examination was the mean of three separate measurements. The study was done five times during the course of a working day: before breakfast after an overnight fast; 30 min after breakfast; before lunch at approximately noon; 30 min after lunch; and at the end of the working day, at approximately 5 p.m. (Fig. 1).

For each of the five studies, mean duct diameter was calculated, and statistical analysis of variance was determined by using the F-distribution test. The smallest and largest duct dimensions obtained irrespective of the time of day were recorded also for each of the 20 subjects. A statistical analysis of the difference in these two means was made by using the t-distribution test applied to a paired comparison.

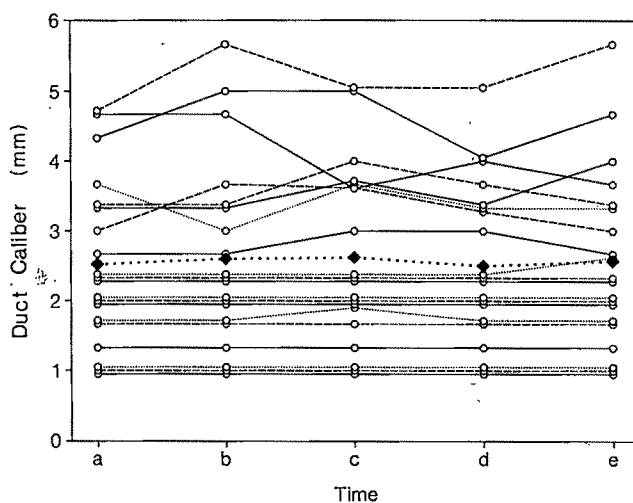


Fig. 1.—Common hepatic duct diameters in 20 volunteers determined on five occasions during course of a day. Each duct diameter is the mean of three measurements. Solid diamonds are overall mean. No significant change is evident for any subject or for the mean of all of them. a = before breakfast; b = 30 min after breakfast; c = before lunch; d = 30 min after lunch; e = end of working day.

Received July 14, 1986; accepted October 10, 1986.

¹ All authors: Department of Radiology, University of Massachusetts Medical Center, 55 Lake Ave. N., Worcester, MA 01605. Address reprint requests to V. Raptopoulos.

AJR 148:557-558, March 1987 0361-803X/87/1483-0557 © American Roentgen Ray Society

An effort was made to determine the duct size in each subject without regard for previous measurements in that subject. However, recollection of duct diameter from one study to another could have biased the results. This was partially avoided by recording each measurement on hard copy images, by randomly interchanging the technologists, and by having the radiologist make random remeasurements.

Results

In the 20 normal subjects, the caliber of the common hepatic duct ranged from 1 to 6 mm (Fig. 1). The mean duct diameter of all of the ducts was 2.52 mm before breakfast, 2.60 mm after breakfast, 2.62 mm before lunch, 2.50 mm after lunch, and 2.57 mm at the end of the working day. The F-distribution test showed that the differences in diameter were not statistically significant. Irrespective of the time of day that the measurements were made, the mean of the smallest duct dimensions of all subjects was 2.38 mm, and that of the largest was 2.75 mm. A t-distribution test applied to a paired comparison showed that the difference in these two means was not statistically significant.

Discussion

Sonography is the preferred technique for assessment of bile-duct size because it is accurate and free of variables that influence duct diameter during cholangiography, such as the

volume of contrast material used and pressure of injection [1, 3]. Furthermore, sonography may safely be performed repeatedly, providing means for assessing dynamic physiologic or pathologic changes in duct size [1-5].

Our results show that in normal subjects the bile-duct diameter remains constant during the day. Thus, during cholestasis associated with meals, there is adequate relaxation of the sphincter of Oddi to compensate for the increased flow of bile.

ACKNOWLEDGMENT

We are grateful to Ellen Hubbell and Donna Beshai for administrative assistance and Donald Engstrom for preparing the graph.

REFERENCES

1. Baron RL, Stanley RJ, Lee JKT, et al. A prospective comparison of the evaluation of biliary obstruction using computed tomography and ultrasonography. *Radiology* 1982;145:91-98
2. Mueller PR, Simeone JF. New concepts in biliary ultrasound. *Semin Ultrasound* 1984;5:333-348
3. Mueller PR, Ferrucci JT Jr, Simeone JF, et al. Postcholecystectomy bile duct dilatation: myth or reality? *AJR* 1981;136:355-358
4. Raptopoulos V, Fabian TM, Silva W, et al. The effect of time and cholecystectomy on experimental biliary tree dilatation: a multi-imaging evaluation. *Invest Radiol* 1985;20:276-286
5. Raptopoulos V, Smith EH, Cummings T, Silva W, Karellas A. Bile-duct dilatation after laparotomy: a potential effect of intestinal hypomotility. *AJR* 1986;147:729-731

High-Resolution MR Imaging of the Normal Rotator Cuff

William D. Middleton¹
 J. Bruce Kneeland¹
 Guillermo F. Carrera¹
 James D. Cates^{1,2}
 Gary M. Kellman^{1,3}
 Nicholas G. Campagna⁴
 Andrzej Jesmanowicz¹
 Wojciech Froncisz^{1,5}
 James S. Hyde¹

The shoulders of six normal volunteers were imaged with high-resolution MR in the axial, sagittal, and coronal planes. An angled pair of counter-rotating current loop-gap resonators designed specifically for the shoulder was used as a local coil. All images were compared with corresponding cryomicrotome sections from cadaver shoulders. The rotator cuff was analyzed in detail. It appeared as a complex, heterogeneous band of tissue superficial to the humeral head. The areas of low signal intensity corresponded to the central tendons of the four rotator cuff muscles. These tendons could be distinguished from each other as well as from the intervening components of the cuff, which have a moderate intensity. We concluded that MR is capable of imaging the normal rotator cuff and of separating the various components. This may allow for improved precision in the diagnosis of rotator cuff disorders.

The rotator cuff consists of four muscles that originate from the scapula and insert on the tuberosities of the humeral head. These muscles fuse as they cross the glenohumeral joint, and together they form a musculotendinous hood that provides strength and dynamic stability to the joint.

Later in life, degenerative changes in the cuff predispose to rotator cuff tears. Traditionally, arthrography has been required for radiologic confirmation of a clinically suspected tear. More recently CT [1, 2] and sonography [3–6] have been used to image the shoulder. MR is another means of imaging the shoulder. While the MR anatomy of the normal shoulder has been described in general [7–9], a detailed analysis of the MR appearance of the rotator cuff has not been performed. This lack of understanding of the MR anatomy of the normal rotator cuff limited our initial attempts at diagnosing rotator cuff tears [10]. Therefore, this study was performed to correlate MR images of the rotator cuff with anatomic sections and thereby determine the structures responsible for the complex appearance on MR.

Materials and Methods

All imaging was performed on a GE Signa system that operated at 1.5 T. After considerable experimentation, it was concluded that a 3-in. (8-cm) tandem-angled pair of counter-rotating current loop-gap resonators offered the best combination of high signal-to-noise ratio and uniformity of the region of sensitivity of the coil over the anatomic region of interest. These coils have been investigated at length, and the results have been presented in previous publications [10, 11].

Six normal volunteers (four men, two women) were imaged. The volunteers were all young (ages 25–33) and had no signs or symptoms referable to the shoulder.

Imaging data were acquired with a two-dimensional Fourier transform multisection technique by using either a 128 × 256 or a 256 × 256 matrix, a 16-cm field of view, and 3-mm-thick sections obtained in either a contiguous mode or with a 1.5-mm gap. Two excitations were used in all cases. Images of the volunteers were obtained in coronal, sagittal, and axial planes. Coronal and axial images were obtained by using a method of off-center field-of-view

Received August 4, 1986; accepted after revision September 24, 1986.

This work was supported by NIH grants RR01008, CA 41464-01, and AM 33667 and by a grant from General Electric Medical Systems.

¹Department of Radiology, Medical College of Wisconsin, Milwaukee, WI 53226. Address reprint requests to W. D. Middleton, Department of Radiology, Milwaukee County Medical Complex, 8700 W. Wisconsin Ave., Milwaukee, WI 53226.

²Present address: Department of Radiology, Tampa General Hospital, Tampa, FL 33606.

³Present address: Department of Radiology, Western Pennsylvania Hospital, Pittsburgh, PA 15224.

⁴General Electric Medical Systems, Milwaukee, WI 53201.

⁵On leave from the Department of Biophysics, Jagiellonian University, Krakow, Poland.

AJR 148:559–564, March 1987
 0361–803X/87/1483–0559
 © American Roentgen Ray Society

data acquisition described in a previous publication [10]. Relatively T1-weighted (TR = 500–600 msec, TE = 20–25 msec), proton-density-weighted (TR = 2000–2500 msec, TE = 20–25 msec), and T2-weighted (TR = 2000–2500 msec, TE = 60–80 msec) spin-echo pulse sequences were obtained for the coronal and sagittal sections and T1-weighted sequences for the axial sections. For the imaging studies, the subjects were supine with the arm held comfortably in neutral rotation.

Anatomic sections of five shoulders were obtained (two each in coronal and sagittal planes and one in an axial plane) with a cryomicrotome (LKB 2250, Gaithersburg, MD). Blocks of tissue were frozen and placed on the stage of the cryomicrotome. As each millimeter of tissue was removed, a photograph was taken of the surface. The photographs and MR images were then compared.

Results

The normal anatomy of the soft-tissue structures of the shoulder was best displayed on relatively T1-weighted pulse sequences by using a 256 × 256 matrix. Figures 1–3 are sagittal, coronal, and axial MR images obtained by using a repetition time (TR) of 600 msec and an echo delay time (TE) of 25 msec. The corresponding anatomic sections are shown for comparison.

With this pulse sequence, fat and bone marrow appeared white because of their short T1 relaxation times. Cortical bone, fibrocartilage, tendons, ligaments, and fascial structures showed essentially no signal owing to their comparative lack of mobile protons. Muscles and hyaline cartilage displayed intermediate signal intensities.

Most of the normal MR anatomy of the shoulder was relatively straightforward and easily obtained through careful study of standard anatomy texts [12]. The bony structures were well displayed and provided valuable landmarks for identification of the various soft-tissue structures of the shoulder. The deltoid was the most prominent muscular structure of the shoulder. It was readily identified in all planes and could be separated from the four muscles of the rotator cuff without difficulty. Its multiple separate tendons were quite apparent, particularly on sagittal sections just lateral to the acromion process (Fig. 2E).

Fat in the interspace between the deltoid muscle and the rotator cuff allowed for clear separation of these two structures. On the anatomic sections, the subacromial/subdeltoid bursa and the coracoacromial ligament were identified in this space. On sagittal MR images, the coracoacromial ligament was visualized forming an arch over the anterior aspect of the rotator cuff between the acromion and coracoid (Figs. 2A and 2B). Portions of the subacromial/subdeltoid bursa were occasionally imaged with MR.

The rotator cuff itself was well seen on MR, particularly in the coronal and sagittal planes. Because of the different signal intensities of the various components of the rotator cuff, a complex MR appearance resulted. Identification of the separate components of the rotator cuff required careful correlation with the anatomic sections and was best understood by considering the four muscles that comprise the cuff separately.

The subscapularis muscle is a triangular muscle with multiple tendons arising from the anterior aspect of the body of the scapula. Its tendons were best displayed on coronal

Key to Abbreviations Used in Figures

Small white arrow	supraspinatus tendon
Large white arrow	teres minor tendon
Arrowheads	infraspinatus tendons
Open arrows	subscapularis tendons
Curved white arrow	biceps tendon
Black arrows	glenoid labrum
Curved black arrow	coracoacromial ligament
Black arrowheads	subacromial/subdeltoid bursa
A	acromion
C	coracoid
CC	coracoclavicular ligament
CL	clavicle
D	deltoid
G	glenoid
H	humeral head
IS	infraspinatus muscle
S	subscapularis muscle and tendon
SS	supraspinatus muscle
TM	teres minor muscle

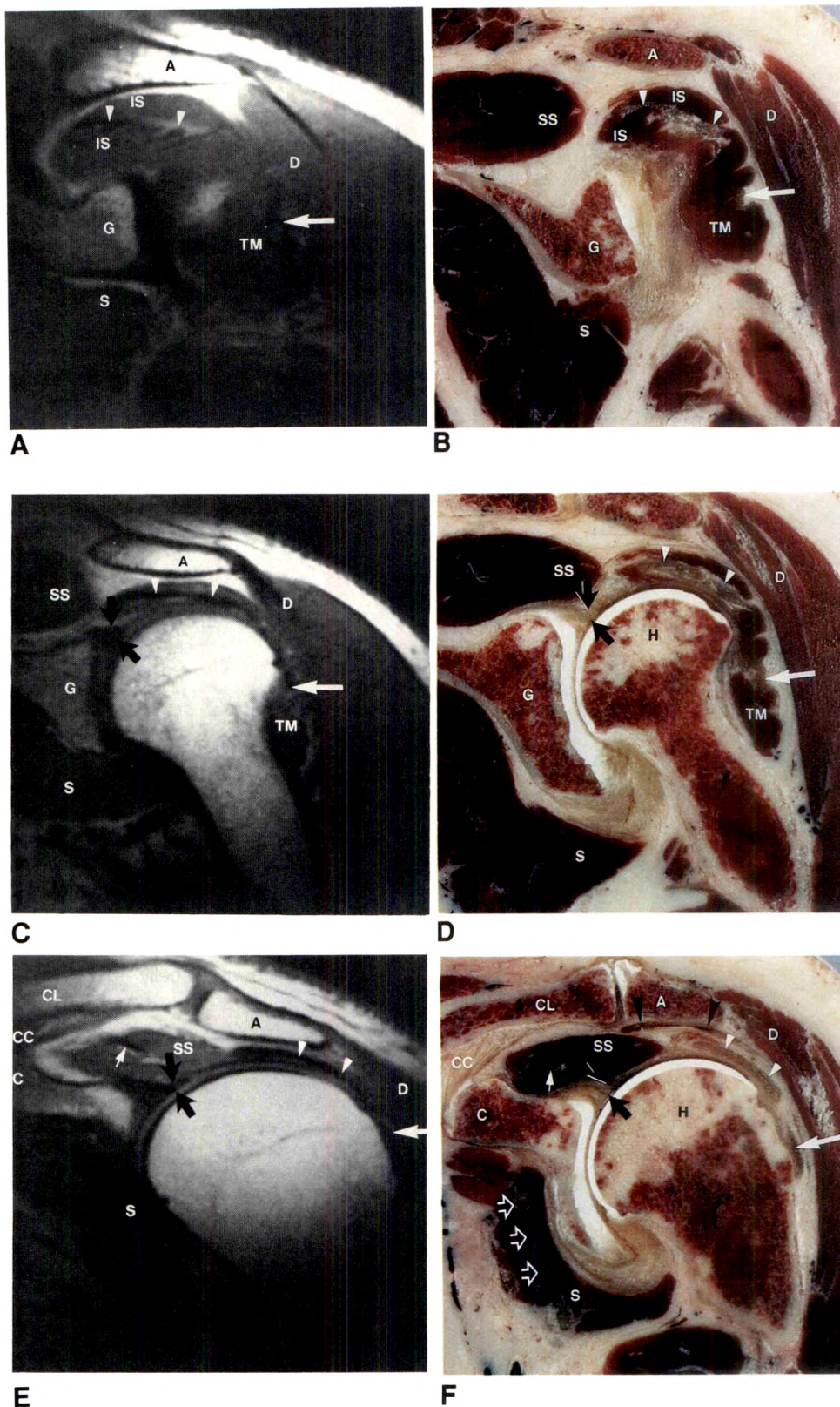
anatomic sections (Fig. 1F). Because the medial portions of the subscapularis were generally out of the field of sensitivity of the coil, the multiple tendons were not well seen on MR images until they converged and fused into a broad tendon that crossed the anterior aspect of the glenohumeral joint and inserted into the lesser tuberosity. On sagittal and axial images, the tendon of the subscapularis was seen anterior to the humeral head just medial to its insertion on the lesser tuberosity (Figs. 2A, 2B, 3C, and 3D).

The supraspinatus muscle arises from the supraspinous fossa of the scapula and crosses the glenohumeral joint superiorly to insert on the anterior aspect of the greater tuberosity. On both sagittal anatomic sections and MR images, the supraspinatus appeared to be arranged with a single central tendon. As the muscle was followed laterally in sequential sagittal section, the central tendon gradually assumed a more anterior position relative to the bulk of the muscle belly (Figs. 2A and 2B). Axial images through the supraspinatus also showed the relationship of the central tendon to the muscle belly well (Figs. 3A and 3B). On the most lateral sagittal sections, the tendon thinned and elongated in an anteroposterior direction (Figs. 2C and 2D). It also began to blend with the intervening components of the cuff, becoming progressively more difficult to identify as a discrete structure on both the anatomic sections and the MR images (Figs. 2E and 2F).

The infraspinatus muscle arises from the posterior surface of the scapula inferior to the scapular spine. It crosses the glenohumeral joint posterior to the supraspinatus to insert onto the lateral aspect of the greater tuberosity. Its muscle belly was easily separated from the supraspinatus muscle medially by fat in the subacromial space. This separation was evident in both sagittal and coronal planes (Figs. 1A–F, 2A, and 2B). As the two muscles extend laterally and anteriorly, the fat separating them decreased progressively and eventually disappeared. A small interdigitation of fat could be seen between the superficial surfaces of the two muscles on sections through the more distal cuff; however, this also disappeared on the most anterior and lateral sections.

The multiple tendons of the infraspinatus were well seen

Fig. 1.—Coronal MR images (TR = 600, TE = 25) and corresponding anatomic sections through posterior glenoid (A, B), posterior humeral head (C, D), and midhumeral head (E, F). These sections demonstrate the ability of MR to separate the tendon of the infraspinatus (white arrowheads) from the supraspinatus muscle (SS) and its central tendon (small white arrow). The subacromial/subdeltoid bursa is seen on the anatomic sections (black arrowheads) but not on the MR images. See Key to Abbreviations.



on sagittal sections from the medial aspect of the humeral head (Figs. 2A and 2B). The tendons could be followed laterally where they converged to form a single flattened tendon (Figs. 2C and 2D). On coronal images the multitendi-

nous nature of the infraspinatus was manifest as clefts within the distal tendon. Unlike the supraspinatus, the distal portion of the central tendon of the infraspinatus remained discrete and easily separable from the intervening components of the

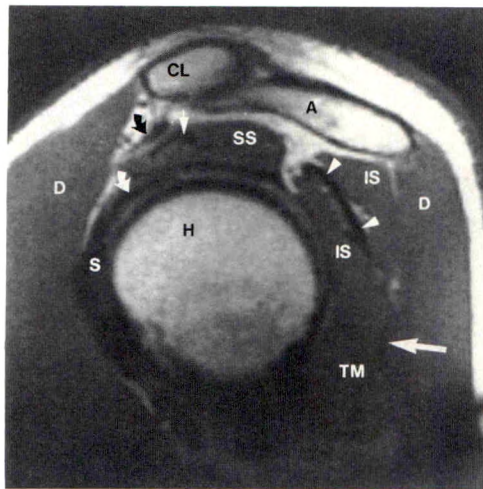
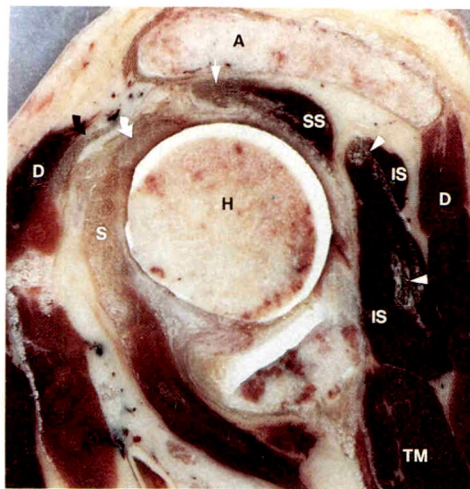
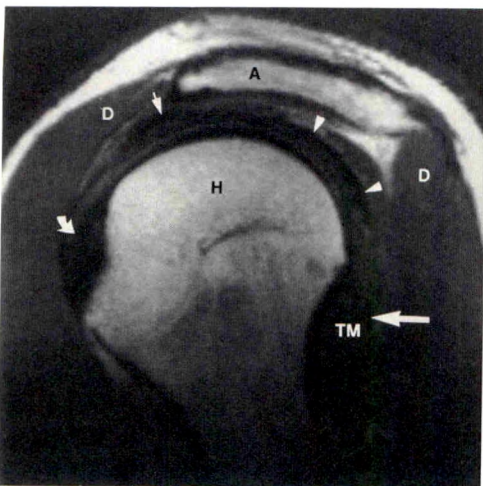
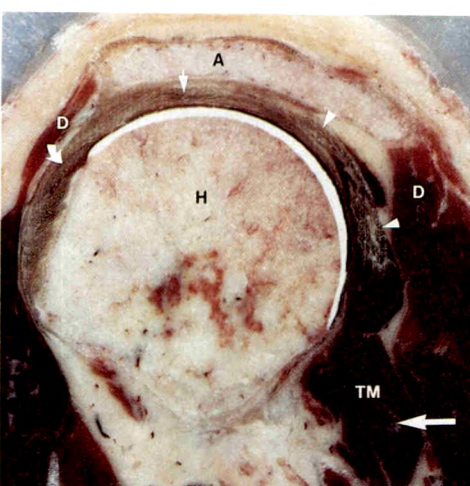
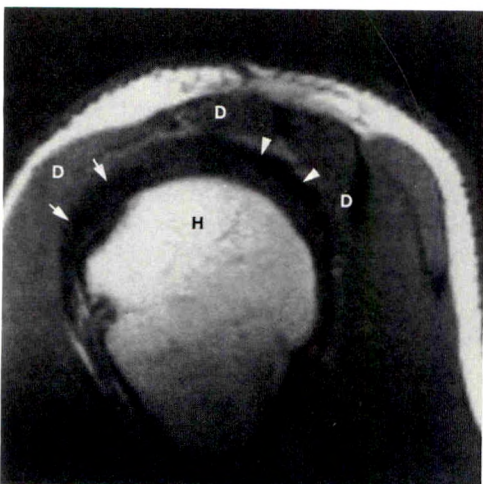
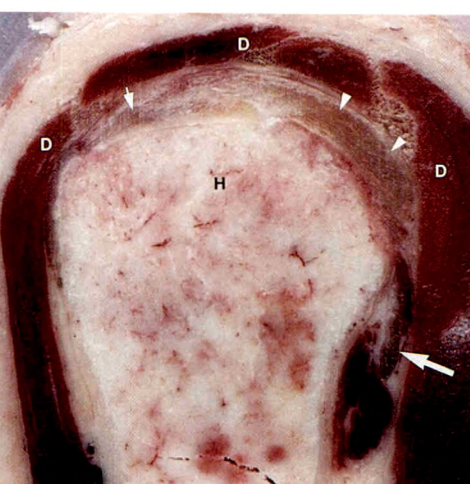
**A****B****C****D****E****F**

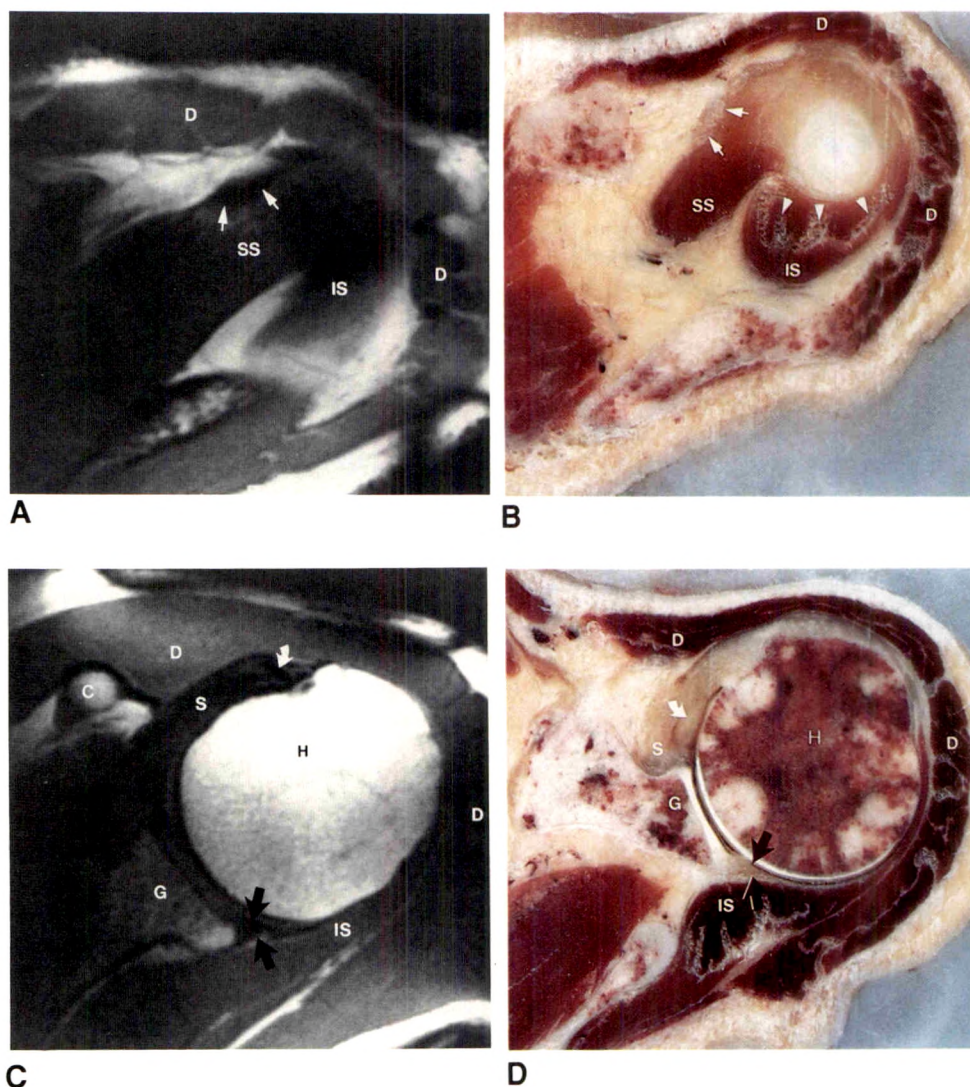
Fig. 2.—Sagittal MR images (TR = 600, TE = 25) and corresponding anatomic sections through the medial (A, B), middle (C, D), and lateral (E, F) humeral head. See Key to Abbreviations on page 560.

cuff. It formed the most prominent tendinous structure within the rotator cuff.

The teres minor is a small muscle that arises from the inferior aspect of the infraspinatus fossa. It is intimately as-

sociated with or fused with the infraspinatus muscle [13]. Because its medial aspect is located inferiorly, this portion of the muscle was out of the range of sensitivity of the 3-in. (8-cm) angled pair coil. As it extended superiorly and laterally,

Fig. 3.—Axial MR images (TR = 600, TE = 25) and corresponding anatomic sections through the subacromial space (A, B) and midhumeral head (C, D). White arrows = supraspinatus tendon. See Key to Abbreviations on page 560.



its muscle and central tendon moved into the coils range of sensitivity and could be imaged (Figs. 1A–F and 2A–F). The most lateral aspect of the muscle wraps around the humeral head and could be seen inserting into the most inferior portion of the greater tuberosity (Figs. 1E and 1F).

The tendon of the long head of the biceps muscle has an intraarticular portion that runs between the supraspinatus and the subscapularis from the biceps tendon groove to the superior aspect of the glenoid labrum. On sagittal MR images it was identified routinely (Figs. 2A–D). The intraarticular portion of the biceps tendon was seen within the biceps tendon groove in all planes.

Discussion

In the past, radiologic evaluation of the soft tissues of the shoulder, in particular the rotator cuff, has relied on conventional radiography and shoulder arthrography. Recently there has been a great deal of research directed at cross-sectional imaging of the shoulder. Sonography has emerged as an effective means of imaging the rotator cuff and biceps tendon

[3–6], and postarthrography CT has proved valuable in evaluating the glenoid labrum and the joint capsule [1, 2]. MR imaging would seem to be another potential means of evaluating the soft tissues of the shoulder [7–9]. In fact, because of its inherently high contrast resolution and multiplanar imaging capability, it is reasonable to assume that MR imaging might have advantages over the other cross-sectional techniques.

Huber et al. [7] have previously imaged the shoulder of one volunteer and documented that MR can show almost all of the normal anatomy previously described on sonography and CT. Kieft et al. [8] and Seeger et al. [9] have expanded this work by looking at larger series of volunteers and comparing the MR images with anatomic sections. However, none of these studies have analyzed the MR appearance of the rotator cuff in detail. On the basis of the results of previous imaging studies [14, 15] one might expect the rotator cuff to appear as a homogeneous structure on MR images. However, high-resolution MR imaging reveals a great deal of internal complexity to the rotator cuff that is not resolvable with CT or sonography. This complexity caused difficulties in interpreta-

tion of images from an earlier study designed to detect rotator cuff tears [10] and prompted the current study.

In this study, MR images of the shoulder were carefully compared with corresponding anatomic sections. The areas of absent signal in the rotator cuff corresponded to the central tendons of the four contributing muscles. These tendons could be separated from each other as well as from the intervening components of the cuff. The ability to separate the four tendons is in marked contrast to sonography, on which the tendons merge together into a layer of homogeneous echogenicity.

This improved anatomic detail that can be achieved with MR is both a disadvantage and an advantage. Because of the complexity of the rotator cuff, a thorough knowledge of the normal anatomy will be necessary to distinguish the normal from the abnormal. However, MR offers a real possibility of localizing and quantifying abnormalities of the cuff with improved precision. If this can be proved with further investigation, MR imaging may become important in the evaluation of patients with rotator-cuff abnormalities.

REFERENCES

1. Shuman WP, Kilcoyne RF, Matsen FA, Rogers JV, Mack LA. Double contrast computed tomography of the glenoid labrum. *AJR* 1983;141:581-584
2. Deutch AL, Resnick D, Mink J, et al. Computed and conventional arthro-tomography of the glenohumeral joint: normal anatomy and clinical experience. *Radiology* 1984;153:603-609
3. Crass JR, Craig EV, Thompson RC, Fienberg SB. Ultrasonography of the rotator cuff: surgical correlation. *J Clin Ultrasound* 1984;12:487-492
4. Mack LA, Matsen FA, Kilcoyne RF, Davies PK, Sickler ME. Ultrasound evaluation of the rotator cuff. *Radiology* 1985;157:205-209
5. Middleton WD, Edelstein G, Reinus WR, Melson GL, Totty WG, Murphy WA. Sonographic detection of rotator cuff tears. *AJR* 1985;144:349-353
6. Middleton WD, Reinus WR, Totty WG, Melson GL, Murphy WA. Ultrasonographic evaluation of the rotator cuff and biceps tendon. *J Bone Joint Surg [Am]* 1986;68:440-450
7. Huber DJ, Sauter R, Mueller E, Requardt H, Weber H. MR imaging of the normal shoulder. *Radiology* 1986;158:405-408
8. Kieft GJ, Bloem JL, Oberman WR, Verbout AJ, Rozing PM, Doornbos J. Normal shoulder: MR imaging. *Radiology* 1986;159:741-745
9. Seeger LL, Bassett LW, Kahmann RD, Kay SP, Ellman H, Ruszkowski JT. Magnetic resonance imaging of the shoulder: evaluation of normal anatomy using high resolution multiplanar scanning with a dedicated surface coil. Presented at the Annual Meeting of the American Roentgen Ray Society, Washington, DC, April 1986
10. Kneeland JB, Carrera GF, Middleton WD, et al. Rotator cuff tears: preliminary application of high resolution MR imaging with counter rotating current loop-gap resonators. *Radiology* 1986;160:695-699
11. Kneeland JB, Jesmanowicz A, Froncisz W, Grist TM, Hyde JS. High resolution MRI using loop gap resonators. Work in progress. *Radiology* 1986;158:247-250
12. Warwick R, Williams PL, eds. *Gray's anatomy*, 34 ed. Philadelphia: Saunders, 1973:538-540
13. Gardner E, Gray DJ, O'Rahilly R, eds. *Anatomy: a regional study of human structure*, 4th ed. Philadelphia: Saunders, 1975:108
14. Middleton WD, Reinus WR, Edelstein G, Melson GL, Murphy WA. Ultrasonography of the rotator cuff: technique and normal anatomy. *J Ultrasound Med* 1984;3:549-551
15. Beltran J, Gray LA, Bools JC, Zuelzer W, Weis LD, Unverferth LJ. Rotator cuff lesions of the shoulder: evaluation by direct sagittal CT arthrography. *Radiology* 1986;160:161-165

Lumbar Hernia: Diagnosis by CT

Mark E. Baker¹
John L. Weinerth²
Rudy T. Andriani²
Richard H. Cohan¹
N. Reed Dunnick¹

Lumbar hernias occur in the region of the flank bounded by the 12th rib, the iliac crest, and the erector spinae and external oblique muscles. We present the CT findings of seven lumbar hernias: six traumatic (four secondary to postoperative flank incisions, one secondary to an iliac bone-graft donor site, one secondary to nonunion of an iliac fracture) and one spontaneous. Because CT portrays the anatomic relationships in this region so well, it may be the only radiographic procedure necessary to make the diagnosis of a lumbar hernia. Furthermore, it can be helpful in the assessment of symptomatic patients after flank incision, to differentiate postincisional muscular weakness and intercostal neuralgia from a lumbar hernia.

Lumbar hernias occur in the flank and are most often acquired (spontaneous, posttraumatic, or postoperative) rather than congenital [1, 2]. Symptoms are absent, variable, or confusing because postincisional neuralgia may be indistinguishable from pain caused by a lumbar hernia. A flank bulge may be detectable, but the clinical diagnosis can be very difficult in obese and postoperative patients.

Whereas the diagnosis of other hernias has been discussed in the literature, to our knowledge only three reports of the CT diagnosis of lumbar hernias exist, one spontaneous and two secondary to iliac bone-graft donor sites [3-5]. We present the CT findings of seven patients with lumbar hernias diagnosed by CT. We report the normal anatomy of this region on CT (Figs. 1 and 2), the ease of CT diagnosis of these lesions, and the value of CT in a patient with a suspected lumbar hernia, especially those due to flank incision.

Materials and Methods

Over a 15-month period, lumbar hernias were detected with CT in seven patients. The mean age was 58 years (range 30-76); five were women and two were men. Of these, four were asymptomatic (one spontaneous, one after flank incision, one after iliac bone-graft harvest, one with a nonunion of an iliac fracture). Only the patient who had a flank incision had a detectable flank bulge. The three symptomatic patients had all had flank incisions, two 7 months and one 4 years earlier. All of these patients had postincisional flank/intercostal protrusions and pain; hernia could not be distinguished from postsurgical muscular weakness. All three symptomatic patients had surgical repair. After repair, all three patients were asymptomatic. Intercostal pain recurred in one patient 7 months after repair. A repeat CT showed no hernia, and intercostal nerve ablation relieved his symptoms.

In addition to these symptomatic patients, a patient who had had a flank incision six months before was studied to exclude a lumbar hernia. No hernia was found and the patient was successfully treated with an intercostal nerve block.

Results

All seven lumbar hernias detected on CT were on the left. All contained extra-peritoneal fat and five of the seven contained bowel (splenic flexure, descending

Received July 21, 1986; accepted after revision September 22, 1986.

¹ Department of Radiology, Duke University Medical Center, Box 3808, Durham, NC 27710. Address reprint requests to M. E. Baker.

² Department of Urology, Duke University Medical Center, Durham, NC 27710.

AJR 148:565-567, March 1987
0361-803X/87/1483-0565
© American Roentgen Ray Society

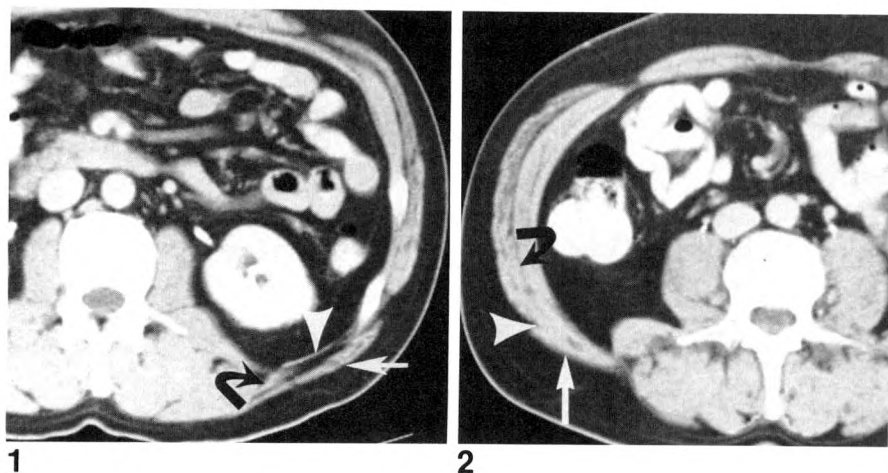


Fig. 1.—CT through base of superior lumbar triangle in normal patient showing latissimus dorsi muscle (arrow), serratus posterior inferior muscle (curved arrow), and thoracolumbar fascia (arrowhead).

Fig. 2.—CT through inferior lumbar triangle in normal patient showing inferior triangle region (arrowhead), latissimus dorsi muscle (arrow), and external oblique muscle (curved arrow).

colon, or sigmoid colon). The remaining two showed bowel close to the hernia ring. The one spontaneous hernia was located superiorly in the superior triangle of Grynfeltt-Lesshaft (Fig. 3). All four of the postincisional hernias showed disruption of normal muscle layers. In two of these only the external oblique muscles were intact (Fig. 4). In a high postincisional hernia there was disruption of the intercostal muscles (Fig. 5). In the remaining patient it was difficult to determine whether the thin linear opacity represented fascia or muscle. CT showed all muscular layers intact in the symptomatic postincisional patient and in the patient studied after hernia repair. In the patient where nonunion of an iliac bone fracture created a pseudoarthrosis, only extraperitoneal fat had herniated through the ring (Fig. 6). Nonetheless, sigmoid colon was close to the ring. Symptomatic postincisional hernias could not be distinguished from the asymptomatic ones on the basis of appearance or hernia contents.

Discussion

The lumbar region is an area defined superiorly by the 12th rib, inferiorly by the iliac crest, medially by the erector spinae muscle group, and laterally by the posterior border of the external oblique muscle as it extends from the 12th rib to the iliac crest [1, 2]. Defects in the lumbar musculature/aponeurosis may occur anywhere in this region and may be congenital, spontaneous, or traumatic. Congenital hernias are rare, are usually seen in infants, and are thought to represent arrested or abnormal musculoskeletal development [6]. Spontaneous hernias represent approximately 50% of all lumbar hernias and most frequently occur in the superior triangle of Grynfeltt-Lesshaft inferior to the 12th rib and the inferior lumbar triangle of Petit just cephalad to the iliac crest [7]. Traumatic lumbar hernias represent approximately 25% of all cases and are caused by postoperative flank incisions as well as nonoperative factors including crushing or penetrating injuries, falls, or postinflammatory states [1, 2]. Both spontaneous and traumatic types show a predilection for the left

side, are more common in men, and are most common in patients between ages 50 and 70. These hernias can occur anywhere along the lumbar region but depend on the site of trauma or incision.

The most common presentation of a patient with a lumbar hernia is discomfort or a dragging sensation in the flank. In those patients who have had lumbar incision, either intercostal/flank pain or a physical bulge may be due to neuralgia, muscular weakness secondary to intercostal nerve injury, or a hernia due to inadequate closure or muscular/fascial diastasis [8]. Clinically, the distinction is difficult. Because therapy for these entities is radically different, differentiation is essential. The differential diagnosis of flank pain or a bulge in a nonsurgical patient includes lipoma, fibroma, or other soft-tissue tumor. A hematoma or an abscess may mimic a lumbar hernia as well. In the past, authors have suggested radiographs of the lumbar spine as well as upper and lower intestinal barium examinations for the diagnosis of this abnormality [1, 2]. Diagnosis of this kind depends on herniation of bowel through the defect, however, and this is not always present. CT has been used in the past in the diagnosis of inguinal, obturator, diaphragmatic, and Spigelian hernias [9–12]. CT is able to delineate muscular and fascial layers, a defect in one or more of these layers, and the presence of herniated fat and/or viscera. In all cases of lumbar hernias, there may be vast differences in the amount of tissue within the hernial sac. They may contain only extraperitoneal fat, extraperitoneal fat plus kidney or colon, as well as intraperitoneal structures (most commonly small bowel). When muscular layers are intact, CT is the only radiographic method necessary for diagnosis. When hernias do exist, CT can show which fascial or muscular layers are involved and the content of the hernial sac. A normal CT of this region in a symptomatic patient enables the physician to confidently exclude a lumbar hernia and guide therapy away from dealing with a structural abnormality. This is especially important in symptomatic, postincisional patients. When pain is present and no hernia exists, intercostal nerve block often eliminates pain and obviates exploratory surgery to exclude a hernia.

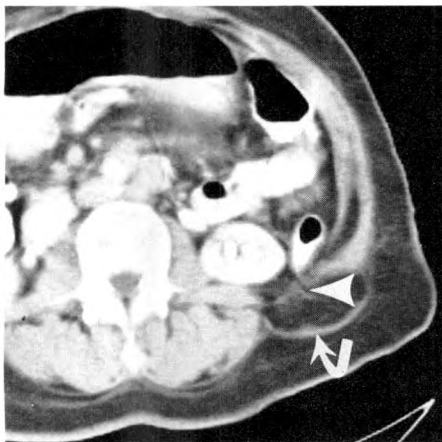
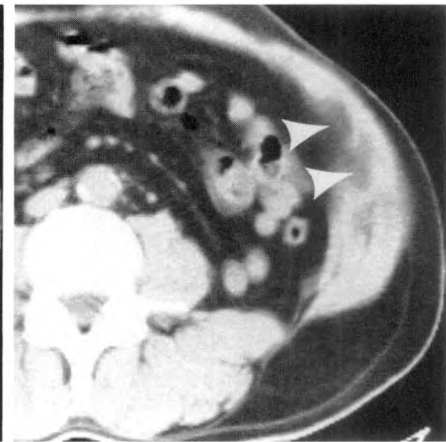


Fig. 3.—CT showing spontaneous lumbar hernia in superior triangle with thinned latissimus dorsi muscle (curved arrow) and disrupted thoracolumbar fascia (arrowhead). Hernia contains extraperitoneal fat.



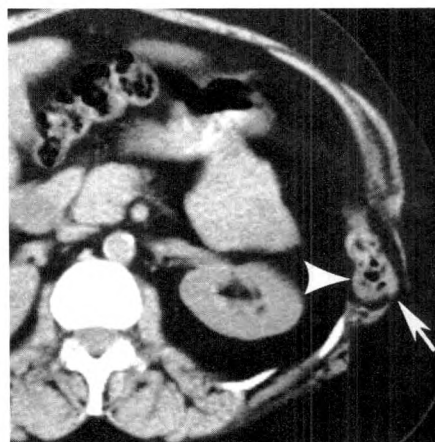
A



B

Fig. 4.—CT showing postincisional lumbar hernia.
A, External oblique muscle (arrow) is thinned superiorly.
B, Inferior scan shows anterior disruption of transversus abdominis and internal oblique muscles (arrowheads).

Fig. 5.—CT showing high, postincisional lumbar hernia. Intercostal muscle (arrow) is disrupted. Bowel (arrowhead) is within hernia.



5



6

Fig. 6.—CT shows lumbar hernia that occurred after nonunion of iliac fracture. Thoracolumbar fascia (arrowheads) is thinned and bulging. Hernia contains extraperitoneal fat.

REFERENCES

- Swartz WT. Lumbar hernia. In: Nyhus LM, Condon RE, eds. *Hernia*, 2nd ed. Philadelphia: Lippincott, 1978:409-426.
- Ponka JL. Lumbar hernias. In: Ponka JL. *Hernias of the abdominal wall*. Philadelphia: Saunders, 1980:465-477.
- Wang JH. Lumbar hernia simulating an adrenal pseudotumor: case report, a CT diagnosis. *Tawain I Hsueh Hui Tsa Chih* 1983;82:795-799.
- Ramirez H, Bennett WF, Peters V. CT diagnosis of hernia through iliac bone-graft donor site. *J Comput Assist Tomogr* 1985;9:411-412.
- Kane VG, Silverstein GS. CT demonstration of hernia through an iliac crest defect. *J Comput Assist Tomogr* 1986;10:432-434.
- Thorek M. Lumbar hernia. *J Int Coll Surg* 1950;14:367-393.
- Ferner H, Staubesand J, eds. *Sobotta atlas of human anatomy*, vol. 2, 18th ed. Baltimore: Urban & Schwarzenberg, 1983:225, 224.
- Ward JN, Lavengood RW, Subramanian AP, Draper JW. Lumbar approaches to kidney: complications associated with procedure. *Urology* 1974;3:163-167.
- Widlus DM. Inguinal hernia: CT appearance after injection therapy. *Radiology* 1984;151:156.
- Cubillo E. Obturator hernia diagnosed by computed tomography. *AJR* 1983;140:735-736.
- Gale ME. Bochdalek hernia: prevalence and CT characteristics. *Radiology* 1985;156:449-452.
- Papierniak KJ, Wittenstein B, Bartizal JF, Wielgolewski JW, Love L. Diagnosis of Spigelian hernia by computed tomography. *Arch Surg* 1983;118:109-110.

Book Review

Bone Tumors: General Aspects and Data on 8,542 Cases, 4th ed. By David C. Dahlin and Krishnan K. Unni. Springfield, IL: Thomas, 522 pp., 1986. \$82

The fourth edition of this well-known textbook on bone tumors is an updated and expanded version of the previous volume, containing 2321 new case studies. The current total of 8542 patients with osseous neoplasms evaluated at the Mayo Clinic constitutes a comprehensive overview of both benign and malignant lesions. Enhanced diagnostic insight is provided by the inclusion of data from over 15,000 new consultation cases. The text uses accepted classifications to categorize each tumor on the basis of its matrix and/or cytologic characteristics. The discussion of each lesion includes information concerning basic clinical features, radiology, gross pathology, histopathology, prognosis, principles of treatment, and follow-up. As in previous editions, the expertise and reputations of the authors are reflected in the superior clarity and organization of the subject matter presented.

Although each tumor is generally discussed in a separate chapter, subdivision into hematopoietic, osteogenic, chondrogenic, fibrogenic, vascular, neurogenic, lipogenic, histiocytic, notochordal, and unknown-origin types is made. Basic information is conveyed via a readily comprehended tabular format, and includes age, sex, and site of involvement. The book is exceptionally well illustrated and features over 700 clinical, pathologic, and diagnostic imaging photographs in black and white. In selected instances, evaluation of the lesion in question by CT and MR imaging is considered.

A notable positive aspect of the book is its exhaustive content, which includes an in-depth chapter devoted to metastatic lesions. Over 20 nonneoplastic conditions manifesting clinical and radiographic features that resemble those of osseous tumors are also discussed. Furthermore, the final chapter of the book is devoted to odontogenic neoplasms and includes a standard classification as well as detailed diagnostic information. The extensive updated reference lists feature numerous new pertinent bibliographic citations, as com-

pared with the third edition. A comprehensive index provides ready access to both cited authors and specific topics covered.

The only significant negative aspect of the book is its absence of color photographs, which would greatly enhance presentation of clinical and pathologic illustrations. As compared to the exhaustive four-volume text by D. Wilner, *Radiology of Bone Tumors and Allied Disorders*, the work is more limited in scope and less well illustrated, although infinitely more readable. The style of the book resembles that of H.L. Jaffe's classic text, *Tumors and Tumorous Conditions of the Bones and Joints*, although the newer book contains far more contemporary information. The quality and number of radiographic images are superior to those of *Bone Tumors: Diagnosis, Treatment, and Prognosis* by A. G. Huvos, although the text material is less comprehensive.

Having been introduced to the earlier editions of this outstanding text as a resident by one of my mentors in osteoradiology, I can unquestionably testify to its utility as a teaching tool for radiologists-in-training. Furthermore, an appropriate balance of information concerning the clinical, pathologic, and diagnostic imaging aspects of osseous neoplasms renders the book equally beneficial to radiologists, pathologists, and orthopedic surgeons seeking familiarity with concepts outside their fields of expertise. The volume is well worth its moderate cost and would definitely be a worthwhile addition to any diagnostic radiology library, in either an academic or private-practice setting. Dahlin and Unni are to be commended for succeeding at a difficult task: improving significantly on a work that was already known and respected as one of the foremost publications on the subject.

David J. Sartoris
University of California, San Diego, Medical Center
San Diego, CA 92103

Direct Radiographic Magnification with Computed Radiography

Yoshihisa Nakano¹
 Tetsurou Hiraoka
 Kaori Togashi
 Kazumasa Nishimura
 Kyo Itoh
 Ichiro Fujisawa
 Tadashi Sagoh
 Shunsuke Minami
 Harumi Itoh
 Kânji Torizuka

Computed radiography was combined with a 0.1-mm microfocus radiographic tube to obtain radiographic magnification of $\times 3$ to $\times 5$. Gray-scale image processing compensated for the loss of radiographic contrast associated with the high-kilovoltage, short-exposure technique. The high-pass spatial frequency filtering capability of the computed radiography resulted in enhanced edges and increased displayed latitude. The improved image quality obtained by magnification computed radiography allowed delineation of subtle abnormalities and small anatomic structures not apparent on conventional screen-film contact or magnification radiographs.

We combined computed radiography (FCR101, Fuji, Tokyo) with a 0.1-mm microfocus radiographic tube to obtain direct radiographic magnifications and applied the technique not only to the peripheral skeleton but also to the central skeleton, chest, or gastrointestinal tract, sites in which the technique is not commonly employed. We describe a technique for generating radiographic magnification directly by using computed radiography and assess its use in showing various normal and pathologic structures.

Materials and Methods

The computed radiographic system has been described in detail previously [1]. Image format, sampling raster, laser spot size, and the gray levels of the image reader are 30×25 cm, 10 pixels/mm, 100 μ m, and 8 bits; those of the image recorder are 20×17 cm, 10 pixels/mm, 120 μ m, and 10 bits, respectively.

A lead bar pattern with a range of 0.5 to 10 line pairs/mm (type 1, no. 31667, Emil Funk Optik Foto, Erlangen, West Germany) was used to test resolving power at the various computed radiography magnifications. We used a microfocus tube with a nominal focal spot size of 0.1 mm (Toshiba DRX-8316 HD, Tokyo, Japan). A contact radiograph of the test pattern with a conventional medium-speed screen-film combination (calcium tungstate screen, Kyokko LT II; Fuji RX film) was also made for comparison. The results were expressed in terms of the square-wave response function [2], permitting convenient comparison between the various magnifications and the medium-speed film-screen combination.

During the past year 116 patients were examined by using direct magnification by computed radiography. These included studies of bones and soft tissues, lungs, and gastrointestinal tract. Images were enhanced by mathematical, computer-assisted manipulations. The types of digital processing available were contrast enhancement that used output transformation (Fig. 1) and high-pass frequency filtering that used a nonlinear unsharp masking technique [3] (Fig. 2). Microfocus tubes with nominal focal spot sizes of 0.1 mm (Siemens OPTI 110/12/50/HSG, Iselin, NJ; Toshiba DRX-8316 HD) and 0.2 mm (Shimazu 0.2/1U14YBE, Kyoto, Japan) were used for magnification in the clinical study.

Data on magnification technique and typical exposure conditions are given in Table 1.

Results

Square-wave response functions for computed radiographic images with magnification of $\times 1$ to $\times 5$ are shown in Figure 3. The square-wave response function

Received June 30, 1986; accepted after revision October 7, 1986.

¹ All authors: Department of Radiology and Nuclear Medicine, Kyoto University Medical School, Sakyo-ku, Kyoto 606, Japan. Address reprint requests to Y. Nakano.

AJR 148:569-573, March 1987
 0361-803X/87/1483-0569
 © American Roentgen Ray Society

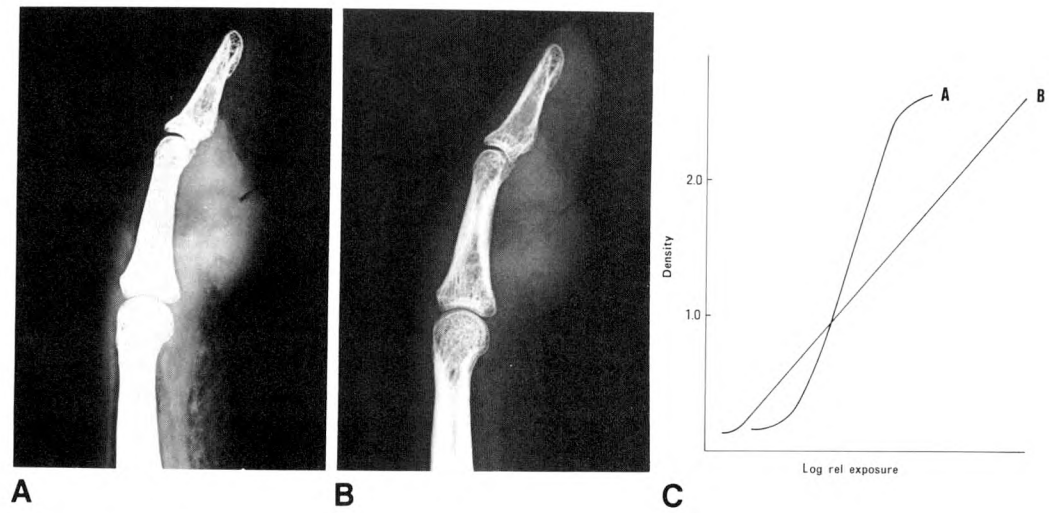


Fig. 1.—Effect of contrast enhancement that uses intensity transformation. Computed radiographic magnification image ($\times 3$) of epiphyseal sarcoma is displayed with different transformation curves for soft tissue (A) and bone (B) from same image data. The radiographic technical factors were 40 kVp, 10 mAs, and 90 cm focus-film distance with 0.1-mm focal spot size. Entrance skin exposure was 1.0 R (25.8 mC/kg).
C, Diagram of intensity transformation curve used to generate images A and B.

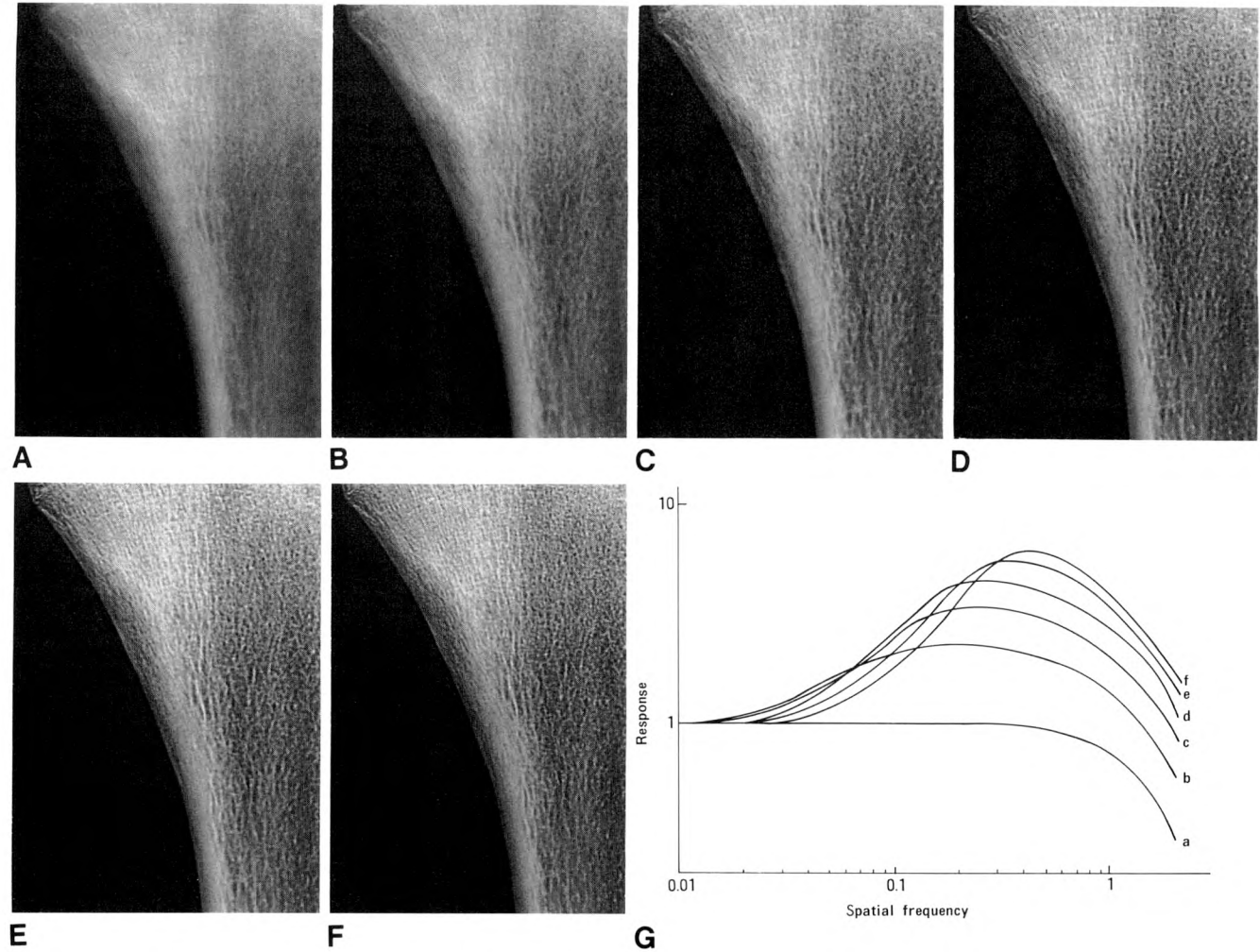


Fig. 2.—Effect of spatial frequency filtering with unsharp masking (A–F). Magnification ($\times 3$) of intracortical osteoid osteoma is displayed with different spatial frequency filters. The radiographic technical factors were 90 kVp, 20 mAs, and 150 cm focus-film distance with 1.0-mm focal spot size. Entrance skin exposure was 0.8 R (20.6 mC/kg).
A–C, Radiolucency of lesion is easily recognized with low-pass spatial frequency filter.
D–F, Fine trabecular pattern is accentuated in high-pass filter.
G, Diagram of frequency representations used to generate images A to F.

TABLE 1: Typical Radiographic Technical Factors for Computed Radiography Magnification

Site	Focal Spot (mm)	Magnification	kVp	mA	sec	FFD ^a (cm)	Entrance Skin Dose in R (mC/kg in parentheses)
Bones	0.1	×3–×5	60–100	30	1–5	145	0.6–6.2 (15.5–160)
Lungs	0.1	×4	90	50	0.3	135	1.5 (38.7)
Upper gastrointestinal tract	0.1	×3	102	60	0.1	90–115	0.6–1.6 (15.5–41.3)
Soft tissues and extremities	0.2	×3	40–50	20	0.5–1	90	0.2–1.0 (5.16–25.8)

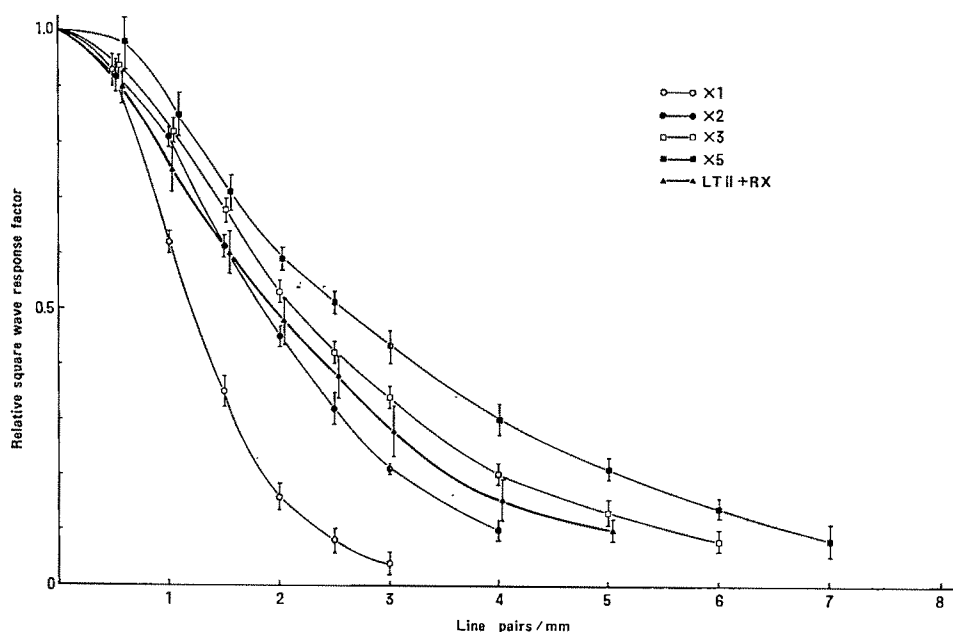
^a FFD: Focus-film distance.

Fig. 3.—Square-wave response factor obtained from various magnifications by using computed radiography (×1–×3, ×5) and from contact radiograph by using conventional screen-film system (LT II + RX).

for the contact exposure technique that uses a medium-speed screen-film combination is also shown for comparison. The resolution of the computed radiography system can be made to approach that of film-screen systems by using magnification techniques of ×2 magnification or higher.

Most computed radiographic magnification images obtained during the period of this study were of diagnostic quality. The fine spatial resolution and image enhancement afforded by computed radiographic magnification permit the definition of small anatomic structures and subtle abnormalities not apparent on contact radiographs. The trabecular deterioration (Fig. 4) of the skeleton in the part of the body with increased thickness, the thickening of the peripheral small bronchus (Fig. 5), and micromucosal pattern of the gastrointestinal tract were clearly visible.

In the conventional film-screen system, excessive variations in transmitted X-ray intensity create serious problems. When the exposure range exceeds the latitude of the film, information contained at the extremes of the characteristic curve of the film is difficult to see. The rugal pattern of the duodenal bulb and gastric antrum was not clearly shown by the film-screen system (Fig. 6A), but with edge enhancement that used a high-pass filter, areae gastricae and duodenal villi became more visible (Fig. 6B). The use of high-kilovoltage

techniques decreases the exposure time but results in a loss of contrast (Fig. 7A). Edge enhancement that uses a high-pass filter improved visibility of trabecular detail (Fig. 7B), which was not clearly seen on film-screen magnification. The computed radiographic image reproduction range is much wider and more flexible, and image processing offers the choice of variable image characteristics optimized for specific diagnostic tasks.

Discussion

The advantages of computed radiography are (1) increased visualization of tissues of various density as a result of the wide latitude of the detector system, (2) improved image quality by image enhancement, such as spatial filtering and gray-scale image processing, and (3) the elimination—by using the automatic image processing capabilities—of repeats due to exposure error.

The potential disadvantages of computed radiography include (1) the somewhat reduced spatial resolution relative to the film, which can be attributed to the use of a 0.1-mm sampling aperture for digitizing the computed radiography image, (2) the cost of the equipment, and (3) the limited throughput.

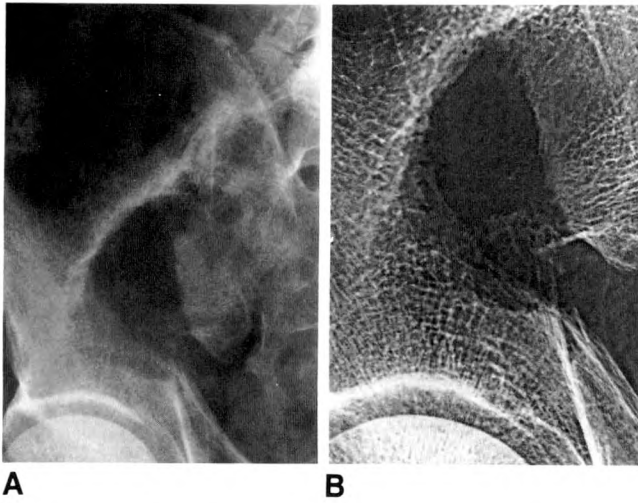


Fig. 4.—Metastatic tumor of the pelvis.

A, Optical magnification of conventional contact radiograph. Exposure settings were 75 kVp, 45 mAs, 120 cm focus-film distance with a grid of 8:1, 34 lines/cm. Entrance skin exposure was 420 mR (10.8 mC/kg).

B, Computed radiographic magnification ($\times 4.5$). Exposure settings were 90 kVp, 60 mAs, and 150 cm focus-film distance. Entrance skin exposure was 2.8 R (72.2 mC/kg). Despite higher magnification, enhancement of higher spatial frequencies allowed trabeculae to be seen in detail.

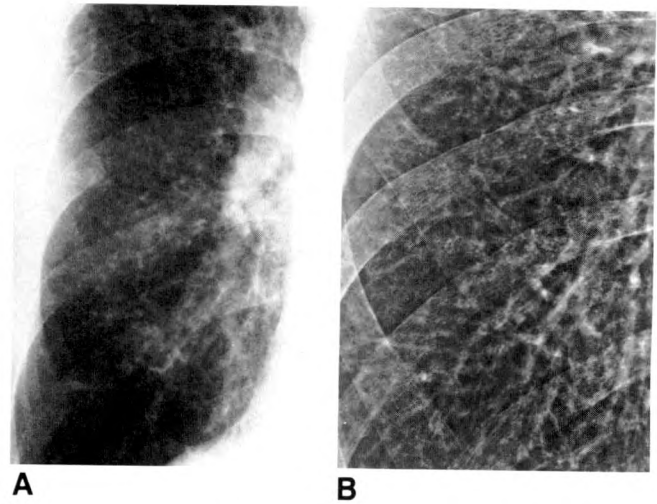


Fig. 5.—Chronic bronchitis.

A, Optical magnification of contact radiograph. Exposure settings were 120 kVp, 8 mAs, and 180 cm focus-film distance with a grid of 10:1, 40 lines/cm. Entrance skin exposure was 70 mR (1.8 mC/kg).

B, Computed radiographic magnification ($\times 4$). Exposure settings were 90 kVp, 30 mAs, and 150 cm focus-film distance. Entrance skin exposure was 1.5 R (38.7 mC/kg).

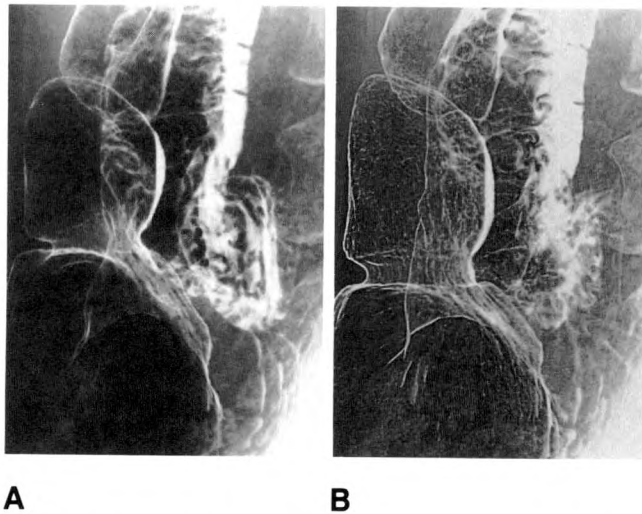


Fig. 6.—Comparison of film-screen (A) and computed radiographic (B) magnification images ($\times 3$) of air-barium double-contrast study of the stomach and duodenum. Exposure settings were 102 kVp, 6.4 mAs, 115 cm focus-film distance. Entrance skin exposure was 1.5 R (38.7 mC/kg). Exposure settings and entrance skin exposure were the same in both systems.

The direct magnification technique overcomes the problem of reduced spatial resolution in the computed radiography system but has significant drawbacks in clinical practice.

For use of magnification factors of greater than approximately $\times 2$ to match the film-screen system, small focal spots must be used, with the attendant problem of limited tube-loading capability, which causes several technical difficulties. The determinations of optimum magnification ratio and radiographic factor is the most difficult part of the procedure.

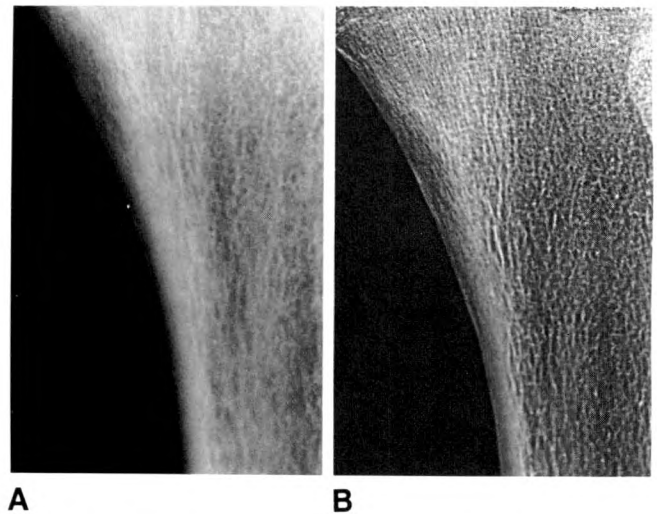


Fig. 7.—Comparison of conventional film-screen (A) and computed radiographic (B) magnification of osteoid osteoma. Same case as in Fig. 2. Exposure settings and entrance skin exposure were the same in both systems (see legend for Fig. 2).

The magnification ratio is determined by the thickness of the body and the movement of the organ. For a stationary organ, for which the exposure time may be fairly long, a higher magnification ratio of $\times 4$ to $\times 5$ to increase spatial resolution or a lower kilovoltage for better image contrast may be selected. However, moving organs, such as those of the gastrointestinal tract, require shorter exposures, and either magnification must be reduced to between $\times 2.5$ and $\times 3$ or a higher kilovoltage must be used to reduce motion unsharpness. Thus, the technique necessarily represents a compromise between spatial resolution, contrast, and sharpness.

The computed radiography system makes the selection of radiographic factors very simple. Fixed focus-film distance, maximum amperage, and highest kilovoltage are used, and exposure times are varied according to the thickness of the object. Degrees of over- or underexposure that would result in totally nondiagnostic conventional radiographs produce readable images with computed radiography. Moreover, the computed radiography system can be used to analyze the image exposure distribution, and this information can be used to achieve a constant optical density independent of technique. Normal film density can be obtained over an extremely wide range of doses since the receptor plate has a dynamic range of approximately 1:10,000.

The effect of motion can be minimized by reducing exposure times and using high-kilovoltage settings. Although images obtained by using high-kilovoltage settings result in less object contrast, they are acceptable because of the ability to enhance the contrast in computed radiography. However, overenhancement causes noisy images, and attempts to reduce the noise result in an increase in the required radiation dose, with a consequent overloading of the microfocus tube. Thus, although the potential for this type of improvement is limited, the technique does make possible the use of exposure conditions that the microfocus tube, with its limited dosages, is not normally capable of handling.

Other disadvantages that computed radiography cannot overcome in magnification radiography are the limited field of

view and increased radiation dose. The dosage that we used in the computed radiography magnification was from 50% to 100% of that used in the conventional medium-speed film-screen combination. However, because the patient's body surface comes closer to the X-ray tube, skin exposure increases. At the present stage of development, the speed of the imaging plate leaves much to be desired. It is always desirable to minimize patient exposure. Subjects should be selected after their clinical histories have been analyzed and tentative diagnoses have been made.

We conclude that $\times 3$ to $\times 5$ magnification with computed radiography and a microfocus tube is clinically feasible in abdominal, chest, or skeletal radiography, because the technical difficulties caused by a relatively low generator capacity due to the inherent tube limitations in magnification radiography are outweighed by the advantages of computed radiography. The usefulness of the latter in clinical practice has yet, however, to be established.

REFERENCES

1. Sonoda M, Takano M, Miyahara J, Kato H. Computed radiography: utilizing scanning laser stimulated luminescence. *Radiology* 1983;148:833-838
2. Lubberts G. Some aspects of the square wave response function of radiographic screen-film systems. *AJR* 1969; 106:650-654
3. Ishida M, Kato, H, Doi, K, Frank PH. Development of a new digital radiographic image processing system. *Proc SPIE* 1982;347:42-48

Case Report

CT Diagnosis of Synovial Chondromatosis of the Temporomandibular Joint

Lawrence G. Manco¹ and Dean M. DeLuke²

Synovial chondromatosis is a rare monoarticular arthropathy of unknown origin [1, 2]. Although it more commonly involves the knee, elbow, and hip, it may occur in the temporomandibular joint (TMJ), producing signs and symptoms similar to an internal derangement of the TMJ meniscus. The purpose of this report is to present the CT characteristics of TMJ synovial chondromatosis, focusing on those features that suggest the correct diagnosis.

Case Report

A 56-year-old woman presented with left TMJ pain and preauricular swelling. She had a long history of left TMJ discomfort, episodic preauricular swelling, and limitation of jaw opening. There was no history of trauma or systemic arthritis.

Physical examination revealed a slightly tender, firm, left preauricular mass contiguous with the left condylar head. Although no true clicking or popping was present, joint crepitus was detected. Plain radiographs showed some irregularity of the left condylar head, which was considered consistent with degenerative joint disease. High-resolution CT of the left TMJ in the direct sagittal plane showed several small, high-density, intraarticular, loose bodies associated with joint effusion and left condylar head erosions (Fig. 1A). One of the larger loose bodies appeared caught within a substantial erosion in the posterior surface of the condylar head (Fig. 1B). Direct coronal images clearly defined the medial and lateral margins of the dilated joint capsule, identifying loose bodies within the far medial joint space (Fig. 2A). A large, medial, condylar head erosion showed more clearly with bone windows than with conventional soft-tissue windows (Fig. 2B). These findings were highly suggestive of synovial chondromatosis.

The left TMJ was explored and found to contain hyperplastic synovium, numerous small, cartilaginous, loose bodies, and several

condylar head erosions, consistent with the preoperative diagnosis of synovial chondromatosis. This was confirmed by pathologic examination.

Discussion

Synovial chondromatosis (osteochondromatosis) is commonly described as a chronic monoarticular arthropathy secondary to synovial metaplasia, usually affecting young adults [1, 2]. The abnormal synovium produces numerous hyaline cartilage nodules that become intraarticular loose bodies, which can cause crepitus, swelling, painful clicking, and occasional joint locking [1, 2]. In some cases, the cartilaginous nodules become partially mineralized, containing a central area of endochondral bone formation. If sufficiently mineralized, they may be detected by plain radiography as multiple juxtaarticular radiodensities of varying size and shape [2]. The involved joint space may also become widened, and articular erosions can develop, eventually leading to secondary osteoarthritis.

CT is now being used with great success to evaluate TMJ disorders [3, 4]. TMJ meniscus displacements and degenerative joint disease are now routinely identified with respective accuracies exceeding 87% and 95% [3]. However, the clinical signs and symptoms of anterior TMJ meniscus displacement, with or without degenerative disease, clearly overlap those of synovial chondromatosis. Both conditions may present with chronic joint pain, crepitus, grinding, limitation of motion, and locking [1, 3]. Because the treatment of a TMJ meniscus abnormality differs completely from that of synovial chondro-

Received July 30, 1986; accepted after revision September 22, 1986.

¹ Department of Medical Imaging, Memorial Hospital, 600 Northern Blvd., Albany, NY 12204. Address reprint to L. G. Manco.

² Department of Oral Surgery, St. Clare's Hospital, 600 McClellan St., Schenectady, NY 12304.

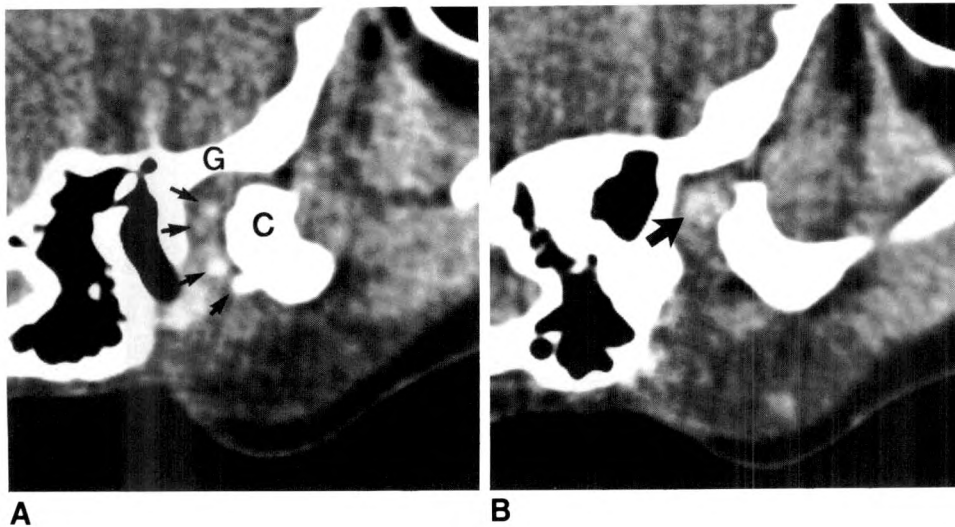


Fig. 1. A, Direct sagittal CT scan in closed position shows several intra-articular, high-density, loose bodies (arrows) projecting into widened joint space. Condylar head (C) is displaced anteriorly to its normal point of articulation with glenoid fossa (G). Condylar head is mildly irregular and angulated. These findings strongly suggest synovial chondromatosis.

B, Direct sagittal scan more medial than A shows large, loose body (arrow) associated with substantial erosion in posterior condylar head. Loose body holds condylar head anterior to its normal closed position and widens joint space. Although clearly seen with direct sagittal CT, this loose body was not visualized by conventional radiography.

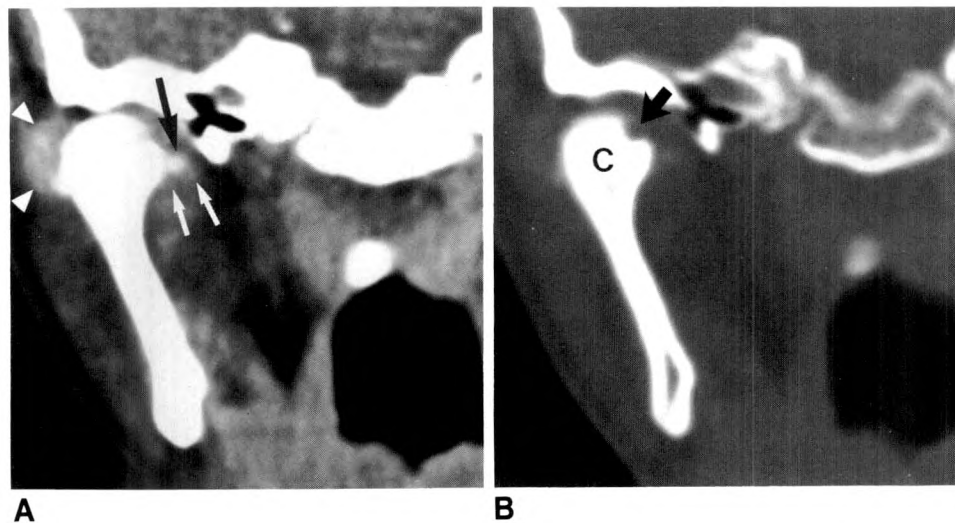


Fig. 2. A, Direct coronal CT scan identifies medial (white arrows) and lateral (white arrowheads) margins of dilated joint space. Loose body is seen within far medial joint space (black arrow) adjacent to medial condylar-head erosion.

B, Condylar-head erosion (arrow) is seen more easily by using bone windows. Condylar head (C) provides reference.

matosis, it is important that the correct diagnosis be made [4-8].

In this case, by using direct sagittal and coronal CT techniques, synovial chondromatosis presented as numerous, high-density foci within a definable dilated joint capsule. The joint space was enlarged, and well-defined bony erosions secondary to loose bodies were easily identified. Direct coronal imaging was particularly valuable for identifying the medial and lateral margins of the dilated joint capsule.

Synovial chondromatosis of the TMJ is an unusual but well-recognized entity; its pathophysiology has been described [6-8]. Unlike other diarthrodial joints, the TMJ articular surfaces are composed entirely of fibrocartilage [8]. The presence of hyaline cartilage within this joint is abnormal and can only occur through a metaplastic or neoplastic process. Approximately 65% of patients having synovial chondromatosis of more commonly involved joints such as the knee and hip are men; but of the 30 cases reported, 75% of patients with

TMJ synovial chondromatosis are women [8]. This striking difference in gender parallels the overall pattern of TMJ internal derangements and pain syndromes in which approximately 85% of patients are women [3].

The inherent high-contrast resolution of CT is at its best when direct sagittal or coronal imaging is performed. Axial imaging with reconstruction into these planes is severely degraded by patient motion and does not have the high-quality bone detail or spatial resolution of direct imaging techniques [3]. The failure of plain radiography to visualize the partially calcified loose bodies so easily seen with CT in this case underscores the value of direct orthogonal CT imaging.

Synovial chondromatosis is an uncommon arthropathy, but one that should be considered in the differential diagnosis of TMJ-pain syndromes. Because its clinical presentation closely parallels that of TMJ meniscus displacement and degenerative joint disease, its radiologic recognition is extremely im-

portant. In many institutions, CT has become the noninvasive method of choice for TMJ imaging. Direct sagittal and coronal CT techniques are well suited for detecting synovial chondromatosis, in addition to excluding more common TMJ abnormalities. CT delineates fine anatomic detail not seen with conventional radiography and can provide the correct preoperative diagnosis noninvasively.

REFERENCES

1. Madewell JE, Sweet DE. Tumors and tumor-like lesions in or about joints. In: Resnick D, Niwayama G, eds. *Diagnosis of bone and joint disorders*. Philadelphia: Saunders, 1981 : 2690-2751
2. Wilner D. Tumors of synovial joints, bursae, and tendon sheaths. In: *Radiology of bone tumors and allied disorders*. Philadelphia: Saunders, 1982 : 3911-3988
3. Manco LG, Messing SG, Busino LJ, Fasulo CP, Sordill WC. Internal derangements of the temporomandibular joint evaluated with direct sagittal CT: a prospective study. *Radiology* 1985;157 : 407-412
4. Manco LG, Messing SG. Splint therapy evaluation with direct sagittal computed tomography. *Oral Surg* 1986;61 : 5-11
5. Dolwick MF. Surgical management. In: Helms CA, Katzberg RW, Dolwick MF, eds. *Internal derangements of the temporomandibular joint*. San Francisco: Radiology Research and Education Foundation, 1983 : 167-191
6. Ronald JB, Keller EE, Weiland LH. Synovial chondromatosis of the temporomandibular joint. *J Oral Surg* 1978;36 : 13-19
7. Blankestijn J, Panders AK, Vermey A, Scherpbier AJ. Synovial chondromatosis of the temporomandibular joint: report of three cases and review of the literature. *Cancer* 1985;55 : 479-485
8. Rosen PS, Pritzker KP, Greenbaum J, Holgate RC, Noyek AM. Synovial chondromatosis affecting the temporomandibular joint. *Arthritis Rheum* 1977;20 : 736-740

Case Report

Superficial Fascial Calcification in Epidermolysis Bullosa

David M. Panicek¹ and Susan H. Leeson

Epidermolysis bullosa is a rare hereditary condition characterized by the appearance of cutaneous and mucosal blistering after trauma to the skin [1]. To date, reported radiographic manifestations include wedging of terminal phalangeal tufts, soft-tissue calcification adjacent to the terminal tufts of digits, overtubulation of long-bone shafts, erosion of teeth, esophageal bullae and strictures, pyloric atresia, subglottic narrowing, chronic vaginal urinary reflux, and urinary retention [2-5]. We report a patient with epidermolysis bullosa whose abdominal CT scan showed marked thickening and calcification restricted to the superficial fascia.

Case Report

A 40-year-old woman was brought to the emergency room after she had sustained blunt abdominal trauma in a motor vehicle accident. Since infancy she had developed several skin bullae whenever she had minor trauma, and when she was 25 years old, dystrophic epidermolysis bullosa, dominant type, was diagnosed on the basis of a skin biopsy. The disease had affected her eyes, ears, throat, teeth, esophagus, and bladder. She had had several hospital admissions for wound care and treatment of related sepsis.

In the emergency room, she complained of lower abdominal pain and was bleeding from a blistered leg wound. Because of the presence of several skin lesions and her known susceptibility to further blistering, only a very limited physical examination was performed. An abdominal radiograph (Fig. 1A) showed several small, rounded, soft-tissue calcifications lateral to the pelvis bilaterally and extending from the superior iliac crests to the hips. An abdominal CT scan showed no evidence of internal injury. However, several small, rounded calcific deposits were noted in the thickened superficial

fascia lateral to the pelvis bilaterally (Fig. 1B). Several areas of skin thickening were evident also. The patient was discharged after treatment of the leg wound.

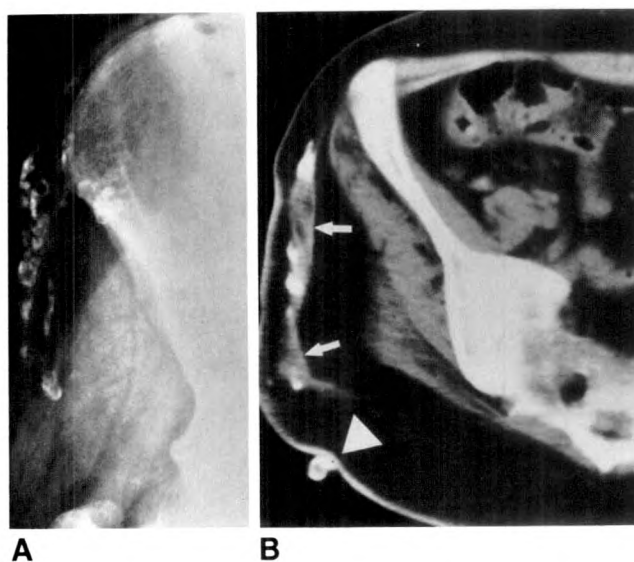


Fig. 1.—A, Radiograph of pelvis shows small rounded soft-tissue calcifications with a linear distribution lateral to pelvis.

B, CT scan shows calcifications aligned in thickened superficial fascia (arrows). Note overlying skin thickening on right. IV tubing is present external to patient (arrowhead).

Received June 23, 1986; accepted after revision August 20, 1986.

¹ Both authors: Department of Radiology, State University of New York Health Science Center at Syracuse, 750 E. Adams St., Syracuse, NY 13210. Address reprint requests to D. M. Panicek.

AJR 148:577-578, March 1987 0361-803X/87/1483-0577 © American Roentgen Ray Society

Discussion

Patients with epidermolysis bullosa can be classified into five types on the basis of genetics, histology, and clinical course [1]. The amount of trauma required to cause bullous changes varies widely, even within a given type. In those patients who react to mild skin irritation, the palpation associated with physical examination can start severe skin changes. Although CT scanning should not be considered equivalent to a well-performed physical examination, it can yield important information without the risk associated with palpating the skin.

The soft-tissue calcification in this patient is restricted to the thickened superficial fascia, which is a fibrous connective-tissue layer located within the subcutaneous adipose tissue [6]. This precise localization differentiates the calcifications from injection granulomas, which are more random in depth and usually located in the posterolateral aspect of the buttock.

Other differential considerations include hypercalcemic states, dermatomyositis, idiopathic calcinosis, Ehlers-Danlos

syndrome, and scleroderma [7], all of which bear no clinical resemblance to epidermolysis bullosa.

The cause of the calcifications in this patient is unknown.

REFERENCES

1. Carter DM, O'Keefe EJ. Hereditary cutaneous disorders. In: Moschella SL, Hurley HJ, eds. *Dermatology*, 2nd ed. Philadelphia: Saunders, 1985:1200-1206
2. Alpert M. Roentgen manifestations of epidermolysis bullosa. *AJR* 1957;78:66-72
3. Shackelford GD, Bauer EA, Graviss ER, McAlister WH. Upper airway and external genital involvement in epidermolysis bullosa dystrophica. *Radiology* 1982;143:429-432
4. Tishler JM, Han SY, Helman CA. Esophageal involvement in epidermolysis bullosa dystrophica. *AJR* 1983;141:1283-1286
5. Bull MJ, Norins AL, Weaver DD, Weber T, Mitchell M. Epidermolysis bullosa-pyloric atresia: an autosomal recessive syndrome. *Am J Dis Child* 1983;137:449-451
6. Congdon ED, Edson J, Yanitelli S. Gross structure of the subcutaneous layer of the anterior and lateral trunk in the male. *Am J Anat* 1946;79:399-429
7. Resnick D, Niwayama G. Soft tissues. In: Resnick D, Niwayama G, eds. *Diagnosis of bone and joint disorders*. Philadelphia: Saunders, 1981:3146-3147

MR Imaging and Spectroscopy in Clinical and Experimental Cerebral Ischemia: A Review

Michael Brant-Zawadzki^{1,2}
Philip Weinstein³
Henry Bartkowski³
Michael Moseley¹

The superior sensitivity of MR imaging to changes in brain water caused by various insults is well established [1-6]. Because detectable alteration of brain-water content may start within the first hours after an ischemic insult [7, 8], MR imaging promises to be a unique tool in the experimental and clinical approach to cerebral infarction. MR spectroscopy offers a noninvasive method for observing the fundamental metabolic processes of cell function. Phosphorus-31 (P-31) MR spectroscopy can elucidate the accumulation and depletion of molecules that act as the energy storage substrates of the cell and their breakdown products. The pH within the tissue of interest can be calculated. Hydrogen MR spectroscopy can detect lactate accumulation when ischemia forces a shift from aerobic to anaerobic glycolysis. More sophisticated metabolic pathways are also accessible to MR spectroscopy. Because MR imaging and MR spectroscopy can be done with the same instrument in a single experimental model or in a human patient, MR offers a unique methodology for investigating acute (potentially reversible) ischemia, its evolution, and the effect of various therapeutic interventions on its prognosis.

The purpose of this review is to summarize the initial experience with MR imaging in the clinical setting of cerebral ischemia and to introduce the reader to the potential future application of combined MR imaging/spectroscopy in this disease process by discussing clinically relevant experimental models. A brief overview of the basic principles of MR spectroscopy is included. A broad understanding of the pathophysiology of ischemia is vital to the task at hand and is a good starting point for subsequent discussion.

Cerebral Ischemia: Pathophysiology

It should be emphasized at the start that a dissociation between the pathophysiology of ischemia and its clinical expression often occurs. That is, even when permanent tissue damage (i.e., infarction) occurs, the clinical neurologic deficit may be either nonexistent, transient, or permanent to varying degrees. Therefore, strict adherence to proper terminology is important in any discussion of ischemic phenomena.

Cerebral ischemia results when either general or focal reduction of blood flow to the brain occurs. If such reduction of flow is of sufficient magnitude and duration, irreversible cellular changes leading to cell death ensue. Hypoxia and hypoglycemia may produce similar effects despite intact cerebral perfusion, but these specific insults are beyond the scope of the current discussion and, as such, will not be considered.

Global reduction of cerebral blood flow generally results from extracranial events, such as significant loss in cardiac output due to muscle damage, arrhythmia, massive central vessel thrombosis, or diffuse occlusive disease in the carotid and vertebrobasilar system. If perfusion is lowered diffusely, compensatory collateral pathways are themselves affected and unavailable. Most often, however, cerebral

This article appears in the January/February 1987 issue of *AJNR* and the March 1987 issue of *AJR*.

Received June 16, 1986; accepted after revision August 4, 1986.

¹Department of Radiology, University of California, San Francisco, CA 94143.

²Present address: Newport Harbor Radiology Associates, 355 Placentia, Suite 207, Newport Beach, CA 92663. Address reprint requests to M. Brant-Zawadzki.

³Department of Neurosurgery, University of California, San Francisco, CA 94143.

AJR 148:579-588, March 1987

0361-803X/87/1483-0579

© American Roentgen Ray Society

ischemia is a regional event in the distribution of one of the three major vascular territories and is due to a combination of factors, including the efficiency of the heart's pumping action in providing flow, the state of the vessels delivering it, and the character of the circulating medium (i.e., blood-oxygen carrying capacity, viscosity, coagulability). Most cerebral infarctions are due to coexisting changes in several of these factors.

Once regional cerebral blood flow (rCBF) drops below a critical threshold (10–20 cc/100g/min), a number of biochemical alterations are triggered in the ischemic tissue. The subsequent rapid shifts in electrolyte and water concentrations between the intra- and extracellular compartments have been investigated in a number of elegant experimental models [7–13]. The brain normally extracts 50% of the oxygen and 10% of the glucose available from blood for energy production. With ischemia, therefore, there is initially a relative lack of oxygen but not glucose, and the reduced energy production from oxidative phosphorylation can for a time be counteracted by increased glycolysis. However, the progressive loss of oxygen necessitates anaerobic glycolysis, which yields much less adenosine triphosphate (ATP) and produces increasing amounts of lactic acid. Any residual flow delivers only a limited amount of oxygen, given the tissue needs, but sufficient glucose. This tissue hyperglycemia raises tissue osmolality, fuels the lactic acid production, and depletes the ATP available for maintaining electrolyte hemostasis within the cell. Release of ions from intracellular binding sites occurs, the Na/K pump (fueled by ATP) fails, extracellular Na goes into the cells, K leaks out. Of interest, sodium and water fluxes parallel each other in the first few hours [9]. Water begins to accumulate within the cell due to the osmotic gradient caused by the increased lactate and sodium levels. Phospholipid catabolism occurs during early ischemia, leading to free fatty acid accumulation. The free fatty acids increase tissue osmolality further, more water shifts from the capillary space into the affected tissues, and the local acidosis (lactic and fatty acids) destroys mitochondria. All this occurs within the first 30 min of ischemia. Further progression of these events leads to extensive damage to mitochondrial and cytoplasmic membranes as well as to those of vascular endothelium. By 6 hr, the blood-brain barrier (BBB) begins to break down, with subsequent leakage of water and protein from the intravascular compartment. The above-described mechanisms yield early intracellular (cytotoxic) edema on the basis of redistribution of water from the microcapillary and extracellular-to-intracellular spaces, but some (approximately 3%) overall increase in total water is seen within the first hour or so. When flow drops to zero, the lack of continued vascular supply precludes any further increase in water within the tissue as a whole. Conversely, reperfusion of severely ischemic tissue, either by the native routes or via established (as often happens in vivo) collaterals, may significantly aggravate the degree of edema formation, especially of the extracellular space. The degree of this type of edema formation (vasogenic) is dependent somewhat on persistent perfusion of the region. The resulting mass effect may compromise the microcirculation, including that in the zone just adjacent to

the severely ischemic region, and this border zone (penumbra) may itself progress to irreversible ischemia. Because reperfusion can reverse ischemia within the first 30 min of onset but may aggravate the situation if instituted later, the value and timing of such therapy is controversial.

Given the above sequence of events, the factors that will most affect the MR images relate to the initially slight increase in overall tissue-water content associated with early cytotoxic edema, followed by the more massive water accumulation of the vasogenic phase. The degree of protein leakage associated with this latter phase may modify the initial prolongation of T1 and T2 relaxation effects, and will correlate with the degree of enhancement produced by paramagnetic agents, themselves large proteinaceous molecules.

The more basic mechanisms of early ischemia, easily amenable to study with MR spectroscopy, include the acute depletion of ATP, accumulation of inorganic phosphates, lactic acid production, and calculation of tissue pH. It may eventually be possible to monitor levels of certain fatty acids and even track glucose utilization in certain experimental models of brain ischemia.

The further pathologic evolution of acute ischemia is also important to understand for imaging purposes. The edematous mass effect of infarction is greatest in the first week, but it should be resolving by the third week. Petechial hemorrhage occurs in up to 40% of cases, usually in the second week, and is most often clinically occult [14]. The residual tissue will become atrophied, soft (due to fewer cellular elements and greater water content), and will show gliosis. If hemorrhage accompanied the infarct, hemosiderin staining may be evident in the residual tissue. Frankly cystic foci may be seen after small infarcts and, rarely, dystrophic calcification of infarcted brain may occur.

Given this brief overview of the pathophysiology of acute cerebral ischemia and its evolution, manifestations of this process on clinical and experimental MR studies can now be better understood.

MR Imaging of Cerebral Ischemia

The major advantage of proton MR imaging in evaluating cerebral ischemia is this technique's superior sensitivity to the insult. This should not be surprising given the fact that water accumulates within the first hours of the onset of cerebral ischemia, and each water molecule has two hydrogen nuclei that provide the MR signal. Not surprisingly, most clinical studies document the improved ability to detect infarction with MR as compared with CT [15–23]. Indeed, experimental models of cerebral infarction have shown that MR can detect the changes associated with ischemia in the first 2 hr after vascular occlusion [24, 25]. In our own laboratory, cats with middle cerebral artery occlusion (MCA-O) showed changes consistent with ischemia within the first hour in two of five instances. Ischemia beyond 6 hr in duration was routinely demonstrated [26].

As expected from the pathophysiologic events described, the T1 and T2 relaxation parameters that are responsible for signal-intensity alterations are both prolonged. In fact, experimental evidence suggests that T1 and T2 prolongation is greatest in the earliest stages of ischemia, when bulk water accumulates, and before opening of the BBB to macromolecules. At this early time, low intensity should

be seen on T1-weighted images, and high intensity on T2-weighted ones. The latter prove more sensitive to infarction, because some T2 effect is impossible to avoid on T1-weighted sequences [1] (Figs. 1 and 2). An influx of protein into the edematous region serves to decrease somewhat the abnormally prolonged T1 and T2 relaxation values [26] and, in turn, may modify the imaged signal intensity. It has been suggested that sodium MR imaging might offer unique advantages in the evaluation of infarction given the early accumulation of sodium in ischemic tissue [27]. However, because water and sodium shifts parallel each other in acute ischemia, and proton MR imaging is so sensitive, the clinical value of sodium MR imaging in this setting seems limited.

The great sensitivity of MR imaging to acute ischemia both in the experimental and clinical experience suggests that reversible, transient alterations might be detectable. Such reversibility of acute ischemia has been documented in an experimental model providing that reperfusion of the ischemic region occurs before the onset of

permanent damage [7]. Clinical experience has shown reversibility of MR imaging changes thought to be due to ischemia in patients with vasculitis secondary to systemic lupus erythematosus [21].

Contrast enhancement with paramagnetic Gd-DTPA depends on development of BBB breakdown [28]. Enhancement with this contrast agent was seen first at 16–18 hr (rate of accumulation) in our experimental model [29]. Of note, the wash-in of contrast in this same model was greatest in the first 24–72 hr. At a later stage, when a significant amount of vasogenic edema was present in the infarcted brain, the wash-in of contrast was slow. This slow inflow correlated with the greatest phase of edema and mass effect. Presumably, microvascular compromise due to that mass effect precluded rapid inflow of contrast agent (and, by extension, of blood nutrients).

The ability of MR imaging to separate acute hemorrhage from edema has been suboptimal within the first few days of a clinically manifest cerebrovascular accident. Both infarction and hemorrhage tended to show a high signal on T2-weighted images, with variably low to isointense signal on T1-weighted images (Fig. 3). More recently, preferential T2 shortening has been shown in acute hemorrhage, especially noticeable at high fields [30]. Such T2 shortening is especially evident in high-field images as a focus of low signal intensity in acute hemorrhagic foci on T2-weighted images (Fig. 4). Further experience with acute hemorrhage at various field strengths is necessary to convincingly prove that MR imaging can distinguish acute hemorrhage and ischemia in all instances.

On the other hand, subacute hemorrhage within infarction is sensitively documented by MR imaging. Many bland infarcts have at least some microscopic and CT evidence of petechial hemorrhage if looked for [14]. It is likely, that given the paramagnetic effects of methemoglobin, such small foci of hemorrhage may be more sensitively detected with MR imaging (Fig. 5). Because the controversy regarding anticoagulation of patients with recent infarction continues [31], such improved sensitivity of MR imaging may add fuel to the discussion.

Other limitations of MR imaging in the evaluation of cerebral ischemia exist. Because the gray matter has a significantly greater water content than the white matter, small infarcts within the cortical mantle may be difficult to identify in the early stages. This is especially true when the slice thickness and image matrix are coarse, and

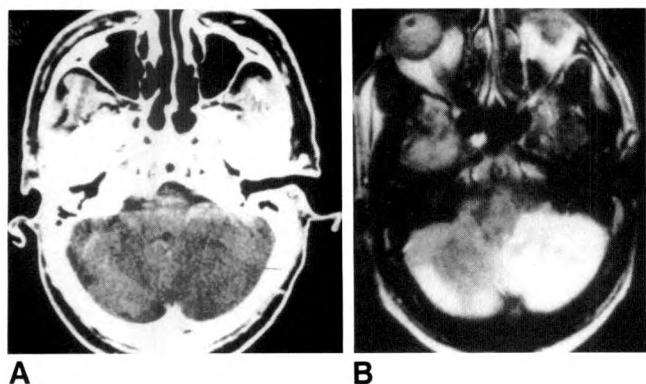


Fig. 1.—Cerebellar infarction, 16 hr.
A, CT scan shows equivocal low density in left cerebellar hemisphere; study degraded by streak artifact.
B, T2-weighted (SE 2000/60) 0.35-T MR image shows abnormally high signal throughout left cerebellar hemisphere as well as in periphery of right cerebellar hemisphere.

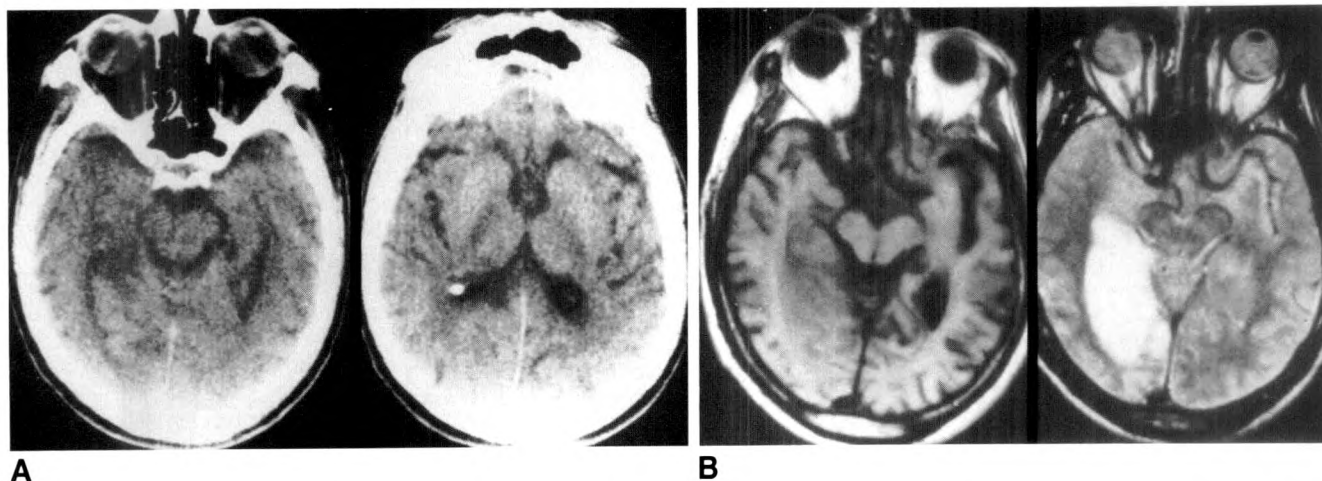


Fig. 2.—Acute onset of left homonymous hemianopsia and weakness 12 hr before imaging.
A, CT study shows vague foci of low density in distribution of right posterior cerebellar artery on two adjacent sections.

B, T1-weighted (SE 500/30) and T2-weighted (SE 2000/60) 0.35-T images (left and right, respectively) from MR scan done just after CT at same level. Note superior depiction of large infarcted region with T2-weighted study.

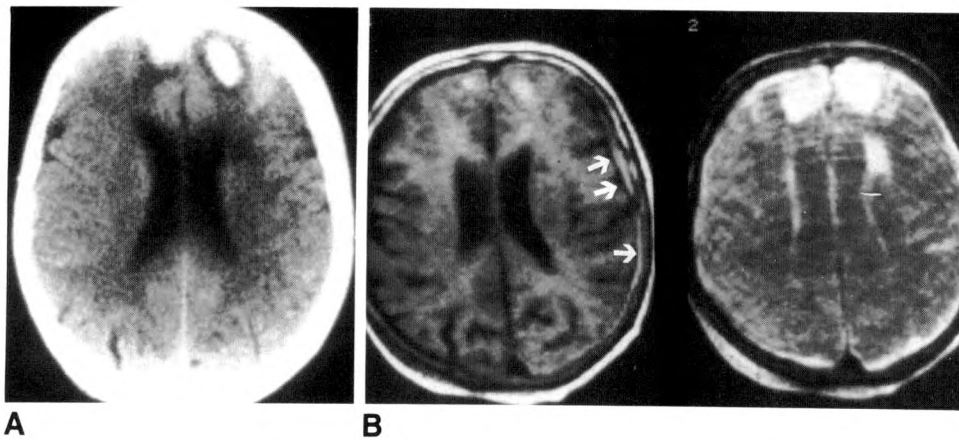


Fig. 3.—Acute bifrontal hematomas (8 hr); old left caudate infarct.

A, CT scan shows the two hematomas as high-density foci.

B, T1-weighted (SE 500/30) and T2-weighted (SE 2000/60) 0.35-T images (left and right, respectively) obtained just after the CT. Note that intensity of left subdural hematoma (arrows) matches that of white matter with SE 500/30, so that focal bifrontal hematomas are not distinguishable. With SE 2000/60, these hematomas show high signal, but one matching that of caudate infarct.

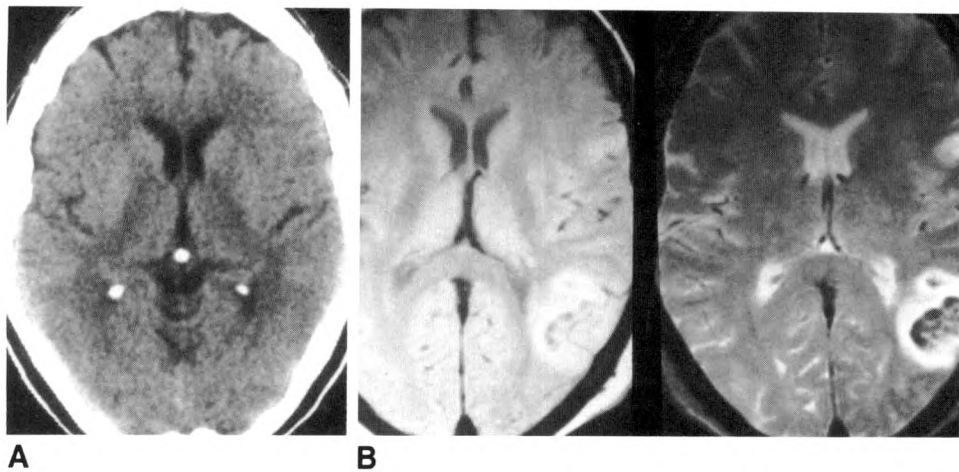


Fig. 4.—Acute infarct with secondary hemorrhage.

A, CT scans at 8-hr after onset of aphasia is negative.

B, Two echoes of a T2-weighted (SE 2000/40, 80) sequence done on a 1.5-T unit at day 1 when patient was still aphasic but excessively anticoagulated show preferential T2 shortening (low signal) within left temporal infarct. Clinical course was that of typical cerebral infarct.

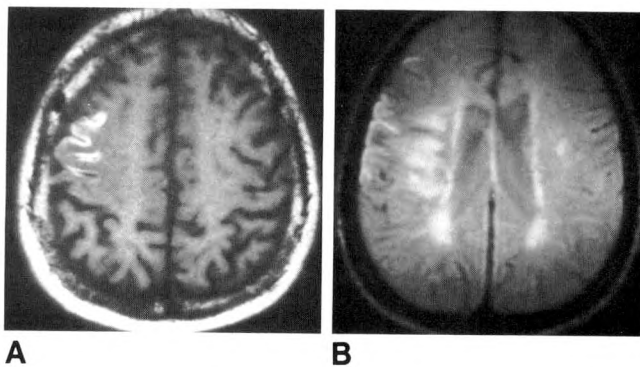


Fig. 5.—Subacute infarct with hemorrhage.

A, Gyriform pattern of high signal intensity is seen on this T1-weighted (PS 600/25) image in a patient with right hemispheric infarction.

B, More extensive abnormality due to edema is seen on T2-weighted, 1.5-T images (SE 2000/80) in infarcted region.

partial-volume artifact becomes a problem. Also difficult for MR imaging is the phenomenon of luxury perfusion. This refers to the presence of arteriovenous shunting of blood in the peripheral zone of infarction, shown by angiography or contrast-enhanced CT as a

cortical blush. MR imaging has difficulty depicting flow in the capillary space. The normal intravascular volume represents only 4–7% of the overall brain volume. Therefore, the flow within the capillary space, or its absence, contributes little overall signal on routine MR imaging within any given volume of interest. Indeed, even when paramagnetic contrast agents are injected, the capillary space does not visibly enhance [32]. Therefore, unlike CT, where enhancement can be due to either intravascular contrast or its extravasation through a broken BBB, contrast enhancement in MR imaging does not appear within the vascular space on the arterial side of the circulation under normal circumstances, and the vascular blush of luxury perfusion will likely be missed on MR imaging despite use of intravenous Gd-DTPA.

The sensitivity of MR imaging to the edema produced by infarction is of tremendous value in assessing the acute stages of the process, when the clinical picture is consistent with the MR imaging appearance. However, most pathologic processes in the brain can produce edema. Therefore, if the clinical history is nonspecific, and/or the pattern of distribution of edema is not typical for that of infarction, the diagnosis may be difficult to ascertain (Fig. 6).

Atypical location for infarction may occur with ischemia due to causes other than the typical embolic phenomena seen in atherosclerotic disease. For example, vasculitides produce ischemia in the multifocal distribution of the small arterioles at the gray-white junction, whereas a spasm due to subarachnoid hemorrhage and other causes of global hyperperfusion tend to affect the watershed regions most

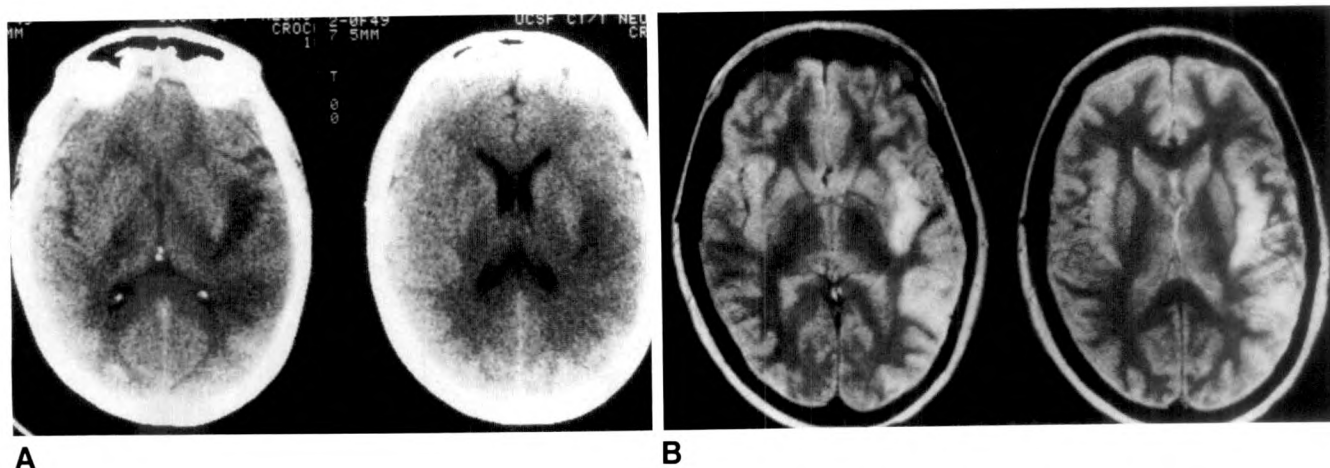


Fig. 6.—Suspected brain tumor in middle-aged woman with 2-week history of confusion.

A, CT at two adjacent levels shows well-circumscribed, low density in sylvian region, with subtle mass effect.

B, MR (SE 2000/60) 0.35-T image at corresponding levels shows high signal in abnormal region consistent with increased water content. The nonspecific history and persistence of abnormal CT findings prompted biopsy for suspected neoplasm. A subacute infarct was seen histologically.

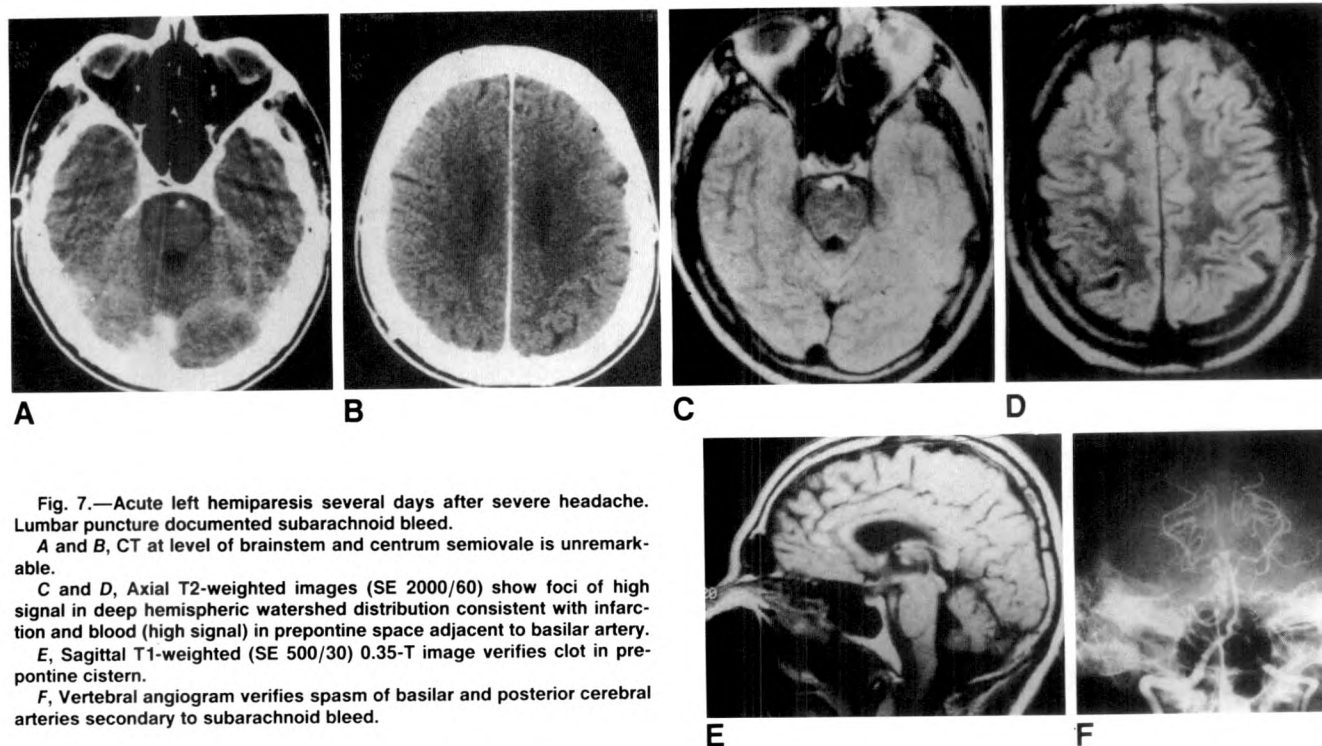


Fig. 7.—Acute left hemiparesis several days after severe headache. Lumbar puncture documented subarachnoid bleed.

A and B, CT at level of brainstem and centrum semiovale is unremarkable.

C and D, Axial T2-weighted images (SE 2000/60) show foci of high signal in deep hemispheric watershed distribution consistent with infarction and blood (high signal) in prefrontal space adjacent to basilar artery.

E, Sagittal T1-weighted (SE 500/30) 0.35-T image verifies clot in prefrontal cistern.

F, Vertebral angiogram verifies spasm of basilar and posterior cerebral arteries secondary to subarachnoid bleed.

typically (Fig. 7). In questionable cases of appearance or distribution, it is best to wait for the temporal evolution of acute infarction to manifest itself. For example, if 3 or 4 weeks go by and the lesion in question is not diminishing in its mass effect, and certainly if it is enlarging, another process must be sought as the explanation for the MR imaging abnormality.

Old infarcts may show regions of focal cystic change in the brain, exhibiting marked prolongation of T1 and T2 relaxation values. In

such cases, the structure affected is generally atrophic. However, not all old infarcts are cystic. In fact, chronic ischemic foci may simply show areas of focal encephalomalacia: loose stroma in the brain with increased water content, and associated gliosis. Such lesions are quite typical of the population over age 65. Autopsy studies show that small infarcts in the deep portions of the brain are the commonest finding at autopsy in otherwise normal patients [33, 34]. MR imaging reflects this fact in that 20–30% of patients over age 65 show

multifocal regions of high signal intensity on T2-weighted images consistent with edema and/or demyelination [35].

The pathophysiology of the aging brain helps shed some light on the possible etiologies behind these deep, patchy white-matter lesions. In the normal adult, the perfusion to the cortical mantle is threefold that to the deep hemispheric white matter, the latter being dependent on relatively sparse, long, and thin perforating vessels. With aging, cerebral blood flow diminishes diffusely [36–38]. Therefore, the effects of the diminished cerebral perfusion with advancing age are probably first felt in the deep hemispheric portions, given the relative lower flow to this region to begin with. It is not too far fetched to suppose that with superimposed hypotensive episodes, perhaps some degree of extracranial cerebrovascular occlusive disease, or intracranial small-vessel disease, the threshold for ischemic change in the deep hemispheric white matter is reached. It is also not surprising that most of these infarcts are silent. Even large, vascular distribution infarctions may occasionally produce no or minimal symptomatology. Transient ischemic attacks are, by definition, reversible clinical events. But their pathologic counterpart may be permanent [39]. Therefore, the high frequency of high-signal abnormalities on T2-weighted MR images in the deep hemisphere in the brains of asymptomatic, normal elderly people may well represent diffuse ischemic change. Such abnormalities have anecdotally shown an association with cerebrovascular disease risk factors, and even dementia [40]. Because multiinfarct dementia is the second commonest cause of cognitive loss in the elderly, the impact of MR imaging on investigations of the aging brain should be significant.

In summary, then, the major strength of MR imaging in evaluating cerebral ischemia is in the sensitivity that it provides for detecting the disease process. This advantage must be tempered by the realization that edema is a nonspecific event related to various insults affecting the brain, as well as the still uncertain ability of MR imaging, at least at the lower field strengths, to separate acute hemorrhagic from acute ischemic events. The superior sensitivity of MR imaging should help in investigations aimed at evaluating various forms of intervention in acute ischemia. Whether reperfusion, antiedema agents, or calcium channel blocking agents (which affect the early electrolyte shifts in acute ischemia) can ameliorate some of the damage caused by ischemia remains to be seen. Because some of these acute changes are at a fundamental level of biochemistry, proton MR imaging may be insufficient to explore the numerous variables. For this reason, the potential offered by MR spectroscopy in cerebral ischemia research and possibly in clinical settings is worth discussing, at least briefly.

MR Spectroscopy in Cerebral Ischemia

Before launching into some of the early experience in this area, let us briefly review the basic principles of MR spectroscopy in a simplistic fashion.

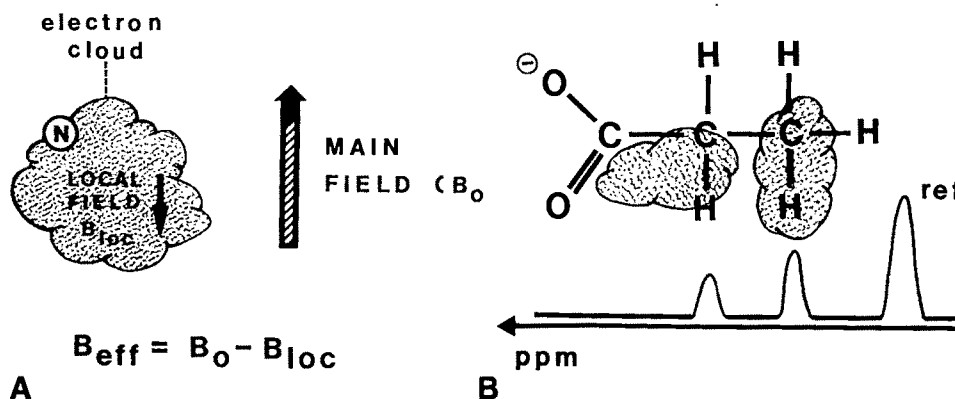
MR imaging and spectroscopy share the same fundamental principles and instrumentation, leading to the eventuality that both techniques can be done in the same machine. In essence, MR imaging is a sophisticated adaptation of MR spectroscopy. One major difference in the data acquisition process distinguishes the two techniques. In MR imaging, the operator changes the homogeneity of the external magnetic field in a predetermined pattern in order to produce a change in the resonant frequency of the nuclear signal being sampled, that change providing spatial localization for the particular nucleus. On the other hand, MR spectroscopy requires a homogeneous external magnetic field in the region of interest. Any deviation from the expected resonant frequency for a nucleus must reflect microenvironmental magnetic field gradients induced by the chemistry of the tissue (Fig. 8). These local gradients are of a much smaller order of magnitude than the predetermined gradient produced in MR imaging. The local gradients result mostly from the groupings of electrons (electron clouds) around the target nuclei within the molecule in which these nuclei reside. As a result, each particular nucleus sees a slightly different magnetic field and resonates with the frequency reflecting that locally altered magnetic field, and not the frequency with which the nucleus would resonate were the external field totally homogeneous and not influenced by the local microenvironment. By measuring this change in resonant frequency from the ideal, we can determine the type of molecule the nucleus is in, and even the various positions of the given nucleus within the same molecule, because the electron clouds will vary in configuration and effect from place to place.

For example, with phosphorus (P-31) MR spectroscopy, one can identify different resonant frequencies from the various terminal phosphorus nuclei in ATP. The separation of ATP from other phosphorus-containing molecules—such as phosphocreatine, inorganic phosphate moieties, phosphodiesterase, and so on—is easily accomplished. MR spectroscopy can be performed with attention to nuclei other than phosphorus, and hydrogen is a good candidate for spectroscopy as well as imaging. Hydrogen (H-1) spectroscopy can allow the detection of lactate, an important product of anaerobic glycolysis. Other nuclei—such as carbon-13, fluorine-19, sodium-23, and so

Fig. 8.—Schematic representation of the chemical shift principle: see text.

A, The nucleus (N) should resonate at a frequency set by the homogeneous external magnetic field B_0 . The presence of local tissue magnetic field due to imaging electrons (B_{loc}) produces a slightly different effective field seen by the nucleus; this causes a slight alteration of the resonant frequency from that expected in B_0 alone.

B, An illustrative molecule examined with hydrogen spectroscopy. Despite identical external field (B_0), each hydrogen nucleus resonates with a slightly different frequency from that of the reference, due to distinct configurations of the electron cloud produced by the molecule's configuration. The change in frequency is expressed as a ratio—parts per million (ppm).



on—can also be used for spectroscopy. However, in terms of cerebral ischemia, P-31 and H-1 spectroscopy have been the two nuclei with which MR spectroscopy has been done in the initial stages of evaluating in vivo spectroscopy of cerebral ischemia.

Most experience in this area has been derived from well-controlled studies of global cerebral hypoxia [41–43]. Basically, P-31 spectroscopy shows the depletion of high-energy phosphates (ATP and phosphocreatine) with progressive global hypoxia, accumulation of inorganic phosphates, and a lowered pH due to acidosis in the ischemic tissue. Lactic acid accumulation has been documented with progressive ischemia using H-1 spectroscopy.

Because most clinical cerebral ischemic lesions are focal rather than global, we have begun evaluating MR spectroscopy and imaging in a single instrument using both hemispheric and regional cerebral infarction models. What we have noted is dissociation between the information provided by the imaging and spectroscopy techniques, as well as their relationship to the clinical state of the animal.

For example, we have evaluated infarction in the mongrel dog

brain. By surgical occlusion of all six vessels leading to one hemisphere, a global hemispheric infarct can be produced. This is seen on T2-weighted MR imaging 24 hr after the injury as a panhemispheric region of high signal intensity consistent with edema (Fig. 9). The midline shift accompanies the finding. Spectroscopy obtained at the same time shows a single large inorganic phosphate peak that is consistent with total devitalization of the organ (Fig. 10).

On the other hand, surgical occlusion of only three vessels allows more regional ischemia to occur, with preservation of collateral perfusion. In such a model, the initial spectra are more ominous than the MR images (Fig. 11). The imaging shows only slight suggestion of high signal intensity in the affected hemisphere (Fig. 12) whereas the spectra already show marked depletion of the high-energy phosphates and a shift of inorganic phosphate indicating lowered pH in the first hours of infarction. Lactate levels were studied with hydrogen MR spectroscopy at the same time the phosphorus spectra were obtained, and showed accumulation in concert with the decreased high-energy phosphate levels.

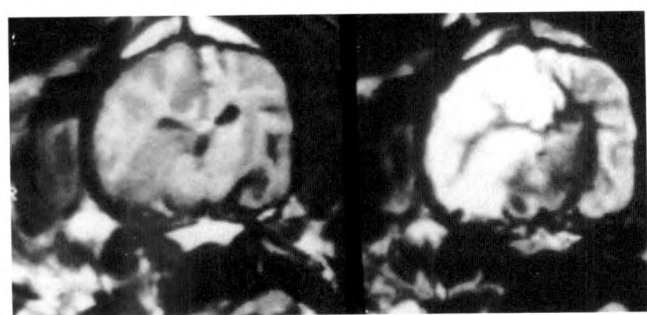


Fig. 9.—Experimental global hemispheric infarct in dog—24 hr.T1-weighted (left) and T2-weighted (right) images shows midline shift and high signal on T2-weighted image throughout right hemisphere.

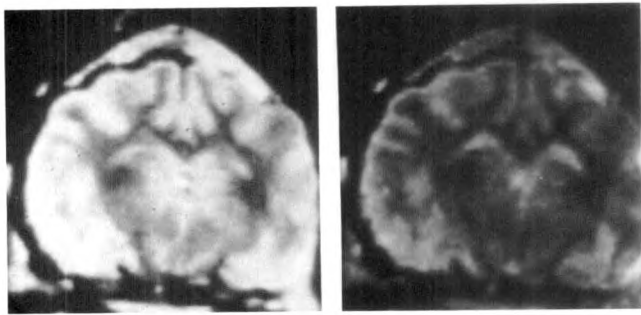


Fig. 11.—Regional cerebral infarct in dog with collateral perfusion—5 hr. T2-weighted images (SE 2000/30, 60) show equivocal changes only.

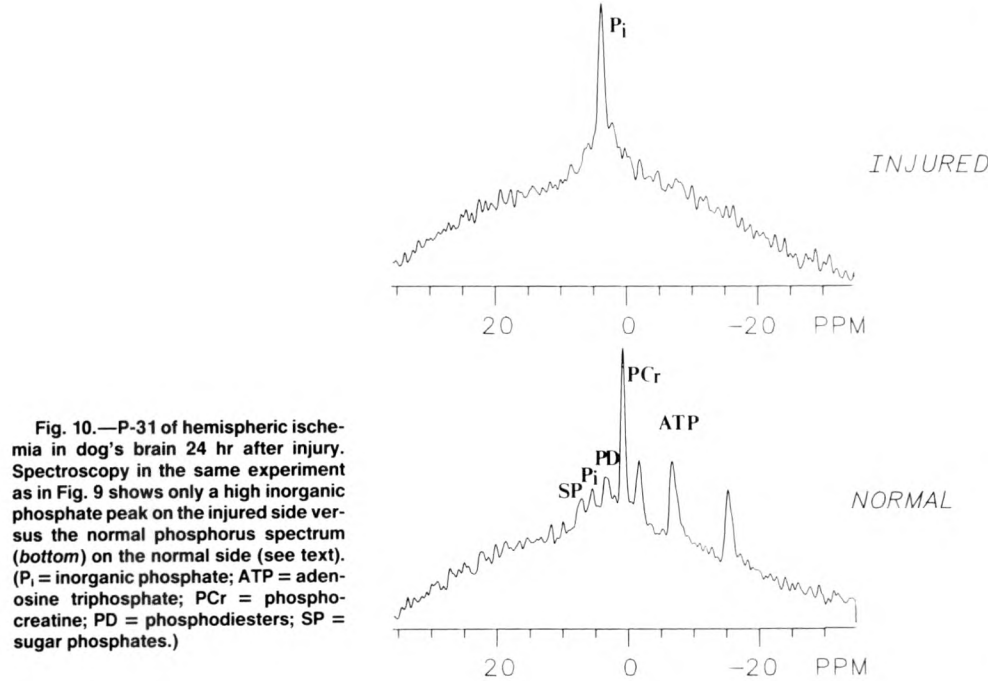


Fig. 10.—P-31 of hemispheric ischemia in dog's brain 24 hr after injury. Spectroscopy in the same experiment as in Fig. 9 shows only a high inorganic phosphate peak on the injured side versus the normal phosphorus spectrum (bottom) on the normal side (see text). (Pi = inorganic phosphate; ATP = adenosine triphosphate; PCr = phosphocreatine; PD = phosphodiester; SP = sugar phosphates.)

BETH	004
MM	18JUL85
24 HOUR ISCHEMIA NORMAL SIDE	
PREPULSE P2=90 P5=30 D12 1U OP1	
P2	= 110.00 USEC
P5	= 36.60 USEC
D5	= 2.00 SEC
D12	= 0.00 USEC
NA	= 128
SIZE	= 4096
ADC	= 12
AI	= 2
RG	= 40
SW	= +/- 3012.04 HZ
DW	= 166 USEC
DE/DW	= 80
AT	= 339.97 MSEC
F2	= 500.058852
OF	= 288.26
SF	= 34.631002
PA	= 290.7
PB	= 12.2
LOCK	= 4.80
OBS HI PWR	= 63
OBS LO PWR	= 200
DEC PWR	= 0
DEC SCHEME	= 4
SCALE	= 245.31 HZ/CM
	= 7.0837 PPM/CM
FROM	35.84
TO	-34.90 PPM

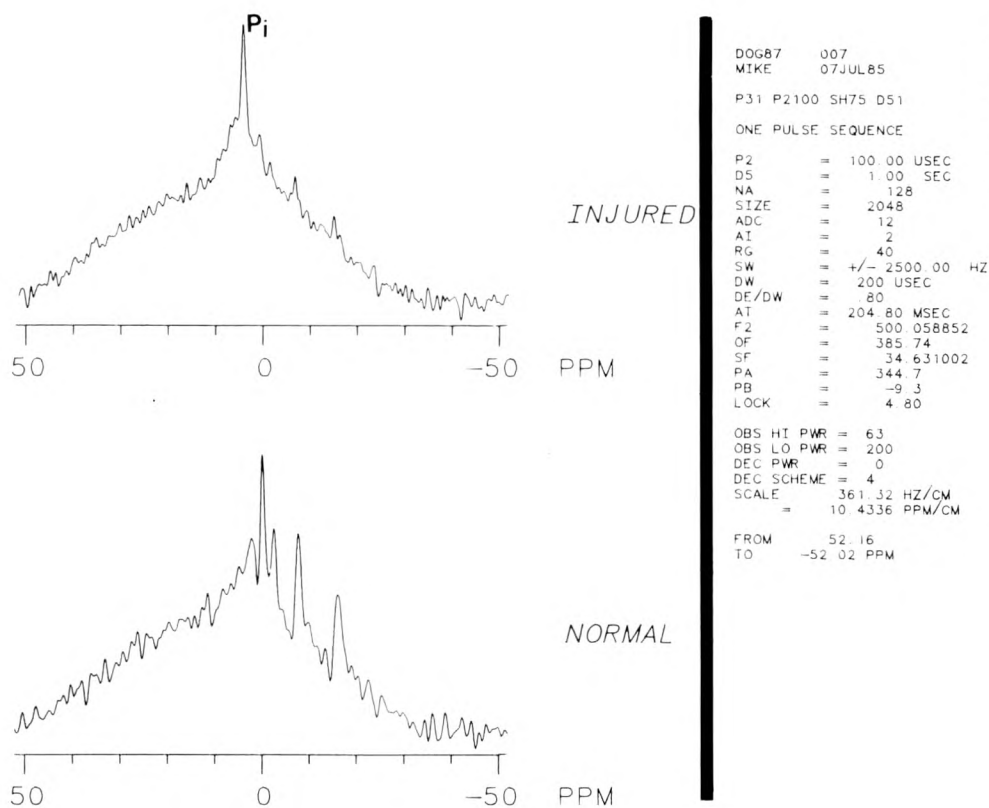


Fig. 12.—P-31 of unilateral ischemia in dog's brain 5 hr after occlusion. Spectroscopy in same experiment as in Fig. 11 shows depletion of high-energy phosphates and elevation with shift of inorganic phosphate peak in abnormal hemisphere (top) when compared with normal side (bottom).

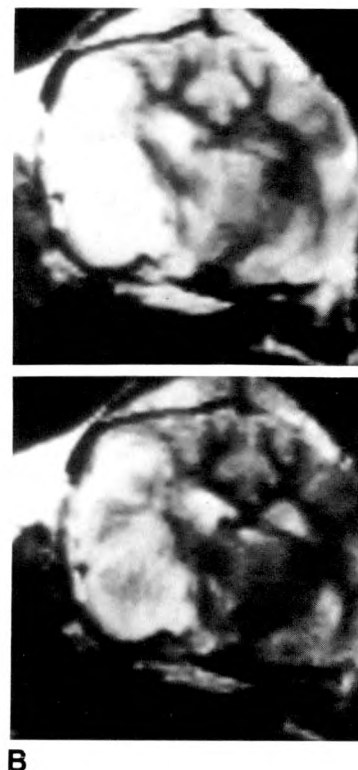
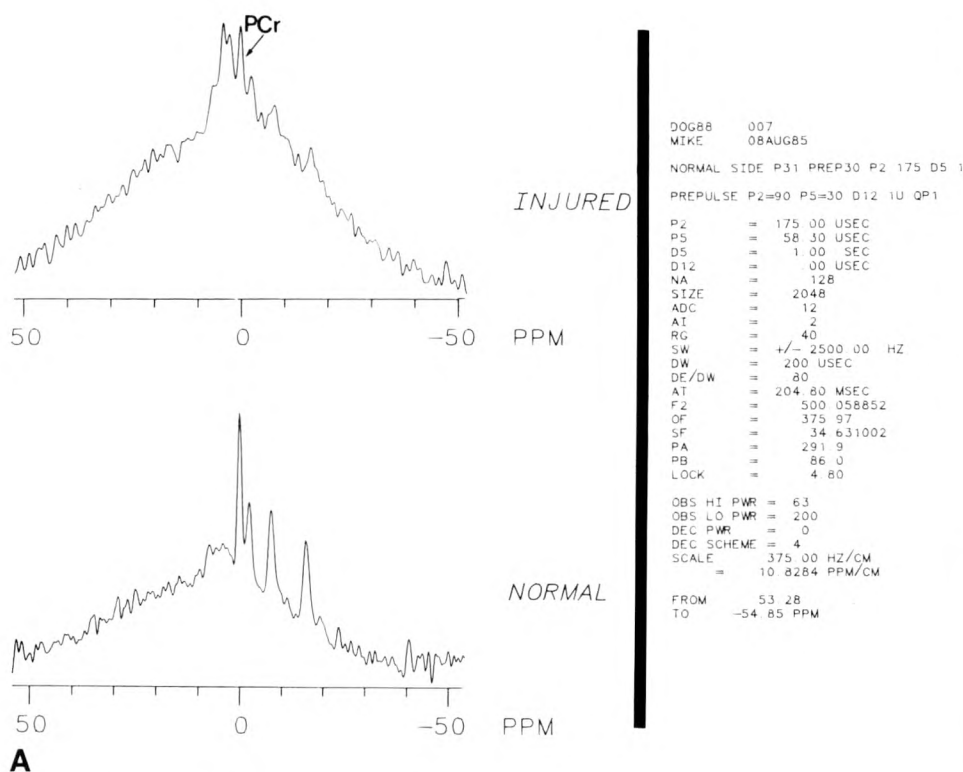


Fig. 13.—Imaging and spectroscopy repeated in same animal as in Figs. 11 and 12 at 30 hr.
 A, P-31 of unilateral ischemia in dog's brain 30 hr after occlusion. Spectra from abnormal side (top) are more normal in appearance when compared with study 24 hr earlier—compare with Fig. 12 (see text).
 B, T2-weighted images (SE 2000/30, 60) now show large area of high signal due to infarction.

This same animal was studied 25 hr later. The MR images became much more abnormal (Fig. 13); however, the spectra were returning toward normal. In fact, clinically, the animal appeared somewhat improved at this time. Nevertheless, death ensued several hours later. Such data can be interpreted in several ways. Clearly, in the initial phases of ischemia, the spectroscopy appeared more sensitive than imaging in this particular experiment. Subsequently, the images suggested a more ominous insult than one that would correspond to the now resolving spectra. Two possibilities may explain this phenomenon. On the one hand, MR spectroscopy may reflect the improving picture of the animal neurologically. More likely, however, is the fact that with maintained collateral perfusion over the 25-hr interval between the first and second study, the abnormal tissues have been totally devitalized and the abnormal metabolites have been washed out through collateral perfusion. Left behind are the remnant, viable cells with normal metabolism detected by spectroscopy. The progressive edema occurring through the sites of BBB breakdown, driven by the collateral perfusion to the region, eventually causes further ischemia and subsequently sufficient mass effect to produce the animal's death.

This early anecdotal experience points out that a great deal still needs to be learned about MR spectroscopy and imaging in combination. Specifically, the biggest current hurdle is obtaining spectra from a localized, small region of interest. Until this is available, there is always the probability that partial-volume effects of spectra from normal as well as abnormal tissue will be obtained. Nevertheless, the potential of spectroscopy in evaluating acute intervention and therapy in the early stages of ischemia—or possibly subclinical, potentially reversible, chronic ischemia—is clear. It is this hope that drives the further development of combined MR imaging and spectroscopy to its logical extent.

REFERENCES

- Brant-Zawadzki M, Norman D, Newton TH, et al. Magnetic resonance of the brain: the optimal screening technique. *Radiology* 1984;152:71-77
- Bradley WG, Waluch V, Yadley RA, Wycoff RR. Comparison of CT and MR in 400 patients with suspected disease of the brain and cervical spinal cord. *Radiology* 1979;152:695-702
- Bydder GM, Steiner RE, Young IR, et al. Clinical NMR imaging of the brain: 140 cases. *AJNR* 1982;3:459-480
- Brant-Zawadzki M, Badami JP, Mills CM, Norman D, Newton TH. Primary intracranial tumor imaging: a comparison of magnetic resonance and CT. *Radiology* 1984;150:435-440
- Naruse S, Horikawa Y, Tanaka C, Hirakawa K, Nishikawa H, Yoshizaki K. Proton nuclear magnetic resonance studies on brain edema. *J Neurosurg* 1982;56:747-752
- Brant-Zawadzki M, Bartkowski HM, Ortendahl DA, et al. NMR in experimental and clinical cerebral edema. *Noninvasive Med Imag* 1984;1:43-47
- Bell BA, Symon L, Branston NM. CBF and time thresholds for the formation of ischemic cerebral edema, and effect of reperfusion in baboons. *J Neurosurg* 1985;62:31-41
- Iannotti F, Hoff JT, Schielke GP. Brain tissue pressure in focal cerebral ischemia. *J Neurosurg* 1985;62:83-89
- Gotoh O, Asano T, Koide T, Takakura K. Ischemic brain edema following occlusion of the middle cerebral artery in the rat. I: The time courses of the brain water, sodium and potassium contents and blood-brain barrier permeability to ^{125}I -Albumin. *Stroke* 1985;16(1):101-109
- Hossmann K-A, Schuier FJ. Experimental brain infarcts in cats. I. Pathophysiological observations. *Stroke* 1980;11(6):583-592
- Schuier FJ, Hossmann K-A. Experimental brain infarcts in cats. II. Ischemic brain edema. *Stroke* 1980;11(6):593-601
- Marcy VR, Welsh FA. Correlation between cerebral blood flow and ATP content following tourniquet-induced ischemia in cat brain. *J Cereb Blood Flow Metab* 1984;4:362-367
- Welsh FA. Review regional evaluation of ischemic metabolic alterations. *J Cereb Blood Flow Metab* 1984;4:309-316
- Horning CR, Dorndorf W, Agnoli AL. Hemorrhagic cerebral infarction: a progressive study. *Stroke* 1986;17:179-184
- Bryan RN, Willcott MR, Schneiders NJ, Ford JJ, Derman HS. Nuclear magnetic resonance evaluation of stroke: a preliminary report. *Radiology* 1983;149:189-192
- Sipponen JT. Uses of techniques: visualization of brain infarction with nuclear magnetic resonance imaging. *Neuroradiology* 1984;26:387-391
- Kistler JP, Buonanno FS, DeWitt LD, Davis KR, Brady TJ, Fisher CM. Vertebral-basilar posterior cerebral territory stroke—delineation by proton nuclear magnetic resonance imaging. *Stroke* 1984;15(3):417-426
- Pykett IL, Buonanno FS, Brady TJ, Kistler JP. True three-dimensional nuclear magnetic resonance neuro-imaging in ischemic stroke: correlation of NMR, x-ray CT and pathology. *Stroke* 1983;14(2):173-177
- Sipponen JT, Kaste M, Ketonen L, Sepponen RE, Kätevuo K, Sivula A. Serial nuclear magnetic resonance (NMR) imaging in patients with cerebral infarction. *J Comput Assist Tomogr* 1983;7(4):585-589
- Brant-Zawadzki M, Solomon M, Newton TH, Weinstein P, Schmidley J, Norman D. Basic principles of magnetic resonance imaging in cerebral ischemia and initial clinical experience. *Neuroradiology* 1985;27(6):517-520
- Aisen AM, Gabrielsen TO, McCune WJ. MR imaging of systemic lupus erythematosus involving the brain. *AJNR* 1985;6:197-201
- Vermess M, Bernstein RM, Bydder GM, Steiner RE, Young IR, Hughes GRV. Nuclear magnetic resonance (NMR) imaging of the brain in systemic lupus erythematosus. *J Comput Assist Tomogr* 1983;7(3):461-467
- Swanson RA, Schmidley JW. Amnesic syndrome and vertical gaze palsy: early detection of bilateral thalamic infarction by CT and NMR. *Stroke* 1985;16(5):823-827
- Buonanno FS, Pykett IL, Brady TJ, et al. Proton NMR imaging in experimental ischemic infarction. *Stroke* 1983;14(2):178-184
- Spetzler RF, Zabramski JM, Kaufman B, Yeung HN. Acute NMR changes during MCA occlusion: a preliminary study in primates. *Stroke* 1983;14(2):185-190
- Brant-Zawadzki M, Pereira B, Weinstein P, et al. MR imaging of acute experimental ischemia in cats. *AJNR* 1986;7:7-11
- Hilal SK, Maudsley AA, Simon HE, et al. In vivo NMR imaging of tissue sodium in the intact cat before and after acute cerebral stroke. *AJNR* 1983;4:245-249
- Carr DH, Brown J, Bydder GM, et al. Gadolinium-DTPA as a contrast agent in MRI: initial clinical experience in 20 patients. *AJR* 1984;143:215-224
- McNamara MT, Brant-Zawadzki M, Berry I, et al. Acute experimental cerebral ischemia: MRI enhancement using Gd-DTPA. *Radiology* 1986;158:701-704
- Gomori JM, Grossman RI, Goldberg HI, Zimmerman RA, Bilaniuk LT. Intracranial hematomas: imaging by high-field MR. *Radiology* 1985;157:87-93
- Hart RG, Lockwood KI, Hakim AM, et al. Immediate anticoagulation of embolic stroke: brain hemorrhage and management options. *Stroke* 1984;15(5):779-789
- Brant-Zawadzki M, Berry I, Osaki L, Brasch R, Murovic J, Norman D. Gd-DTPA in clinical MR of the brain: I. Intraaxial lesions. *AJNR* 1986;7:781-788
- Wisniewski HM, Terry RD. Morphology of the aging brain, human

- and animal. In: Ford DE, ed. *Neurobiological aspects of maturation and aging. Progress in Brain Research Series*, vol. 40. New York: Elsevier, 1973:253-265
34. Peress NS, Kane WC, Aronson SM. Central nervous system findings in a tenth decade autopsy population. In: Ford DE, ed. *Neurobiological aspects of maturation and aging. Progress in Brain Research Series*, vol. 40. New York: Elsevier, 1973:482-483
35. Bradley WG, Waluch V, Brant-Zawadzki M, Yadley RA, Wycoff RR. Patchy, periventricular white matter lesions in the elderly: a common observation during NMR imaging. *Noninvasive Med Imag* 1984;1:35-41
36. Melamed E, Lavy S, Bentin S, Cooper YR, Rinot Y. Reduction in regional cerebral blood flow during normal aging in man. *Stroke* 1980;11(1):31-36
37. Shaw TG, Mortel KF, Meyer JS, Rogers RL, Hardenberg J, Cutaia MM. Cerebral blood flow changes in benign aging and cerebrovascular disease. *Neurology* 1984;34:855-862
38. Naritomi H, Meyer JS, Sakai F, Yamaguchi F, Shaw T. Effects of advancing age on regional cerebral blood flow. *Arch Neurol* 1979;36:410-416
39. Humphrey PRD, Marshall J. Transient ischemic attacks and strokes with recovery prognosis and investigation. *Stroke* 1981;12(6):765-769
40. Brant-Zawadzki M, Fein G, Van Dyke C, Kiernan R, Davenport L, deGroot J. Magnetic resonance imaging of the aging brain: patchy white matter lesions and dementia. *AJNR* 1985;6:675-682
41. Radda GK, Bore PJ, Rajagopalan B. Clinical aspects of P-31 NMR spectroscopy. *Br Med Bull* 1984;40:155-159
42. Chance B. Studies of exercise performance, vascular disease, and genetic disease. In: James TL, Margulis AR, eds. *Biomedical Magnetic Resonance*. San Francisco: Radiology Research and Education Foundation, 1984
43. Horikawa Y, Naruse S, Tanaka C, et al. In vivo ³¹P NMR studies on experimental cerebral infarction using topical magnetic resonance. *Mag Res Med* 1984;1(2):169-171

MR Imaging of the Intratemporal Facial Nerve by Using Surface Coils



L. Teresi¹
 R. Lufkin¹
 D. Wortham²
 B. Flannigan¹
 M. Reicher¹
 V. Halbach¹
 J. Bentson¹
 G. Wilson¹
 P. Ward²
 W. Hanafee¹

MR images of the intratemporal portion of the facial nerve were obtained with surface coils using a 0.3-T permanent magnet whole-body imaging system. Various 2DFT spin-echo pulse sequences were used to produce 5-mm thick sections with 0.5-mm pixels on a 512 × 512 acquisition matrix. The MR images from normal volunteers were correlated with cryosection specimens of three fresh human cadavers. The seventh nerve was followed in the internal auditory and fallopian canal and through temporal bone to the stylomastoid foramen. The entire labyrinthine, tympanic, and mastoid portions, as well as the geniculate ganglion, could be shown with appropriate scan planes. MR produces excellent images of the facial nerve with high-contrast resolution. Unlike CT, no beam-hardening artifact from the temporal bone is apparent. MR should be a sensitive study for the evaluation of intratemporal facial nerve disease.

The facial nerve has the longest course within bone of any nerve, and is the most frequently paralyzed nerve in the human body. CT with intravenous contrast, intrathecal air, or metrizamide contrast; plain X-rays; and, in some cases, angiography have been used to image a variety of diseases in the facial nerve with varying degrees of success [1-9].

MR has advantages over many of these older techniques in that it is noninvasive and has excellent soft-tissue contrast resolution in a variety of scanning planes [10-13]. With the use of specialized high-performance RF coils, thin sections and spatial resolution approaching that of CT scanning may be achieved. Unlike CT, no beam-hardening artifact from bone is evident. In addition, variations in pulse sequences may be used to optimize contrast resolution for regions of normal anatomy and pathology. This study evaluates MR of the normal intratemporal facial nerve.

Subjects and Methods

Fifteen examinations of the temporal bone were performed on normal volunteers or patients with no evidence of temporal bone disease with a 0.3-T permanent magnet MR system (Fonar B-3000, Melville, NY). Most of the examinations were conducted to test the RF coils or to study extracranial disease without involvement of the temporal bone. The normal MR images were correlated with cryosection specimens of fresh human cadavers. The seventh nerve was followed through the temporal bone. The entire labyrinthine, tympanic, and mastoid portions, as well as the geniculate ganglion, were shown.

MR images were acquired with a multislice 2DFT spin-echo pulse sequence. Planar surface coils (Fig. 1), used to improve the signal-to-noise performance of the system, permitted the use of steeper magnetic field gradients to decrease the pixel size from 1 × 1 mm to 0.5 × 0.5 mm [14]. Four-mm-thick sections were acquired every 7 mm on a 256 × 256 matrix and interpolated to a 512 × 512 display. A short spin-echo technique was used for most of the scans, with a repetition time (TR) of 500 msec and an echo time (TE) of 28 msec (SE/500/28). This relatively T1-weighted image maximized the visibility of the seventh nerve as it crossed the subarachnoid space surrounding the brainstem and passed through the temporal bone.

This article appears in the January/February 1987 issue of *AJNR* and the March 1987 issue of *AJR*.

Received February 20, 1986; accepted after revision June 10, 1986.

Presented at the annual meeting of the American Society of Neuroradiology, San Diego, January 1986.

This work was supported by PHS grant number 1K08 CA 00979-01, awarded by the National Cancer Institute, DHHS.

¹Department of Radiological Sciences, UCLA Medical Center, Los Angeles, CA 90024. Address reprint requests to R. B. Lufkin.

²Department of Head and Neck Surgery, UCLA Medical Center, Los Angeles, CA 90024.

AJR 148:589-594, March 1987

0361-803X/87/1483-0589

© American Roentgen Ray Society

A single-slice scout image obtained in 1 min and 51 sec was often used for localization of the nerve. Subsequent scans through the nerve were positioned with cursors from the scout image. A rapid sagittal view provided a scout for axial images through the internal

auditory canal (Fig. 2A). One of the axial images through the descending facial nerve served as a scout for later sagittal images through this structure (Fig. 2B). By using these two scan planes, we could study the entire intratemporal course of the facial nerve.

Occasionally, a second interleaved sequence was obtained by electronically offsetting the next slice series by 2.5 mm to produce overlapping sections. This allowed visualization of planes of tissue missed between slices of the first sequence.

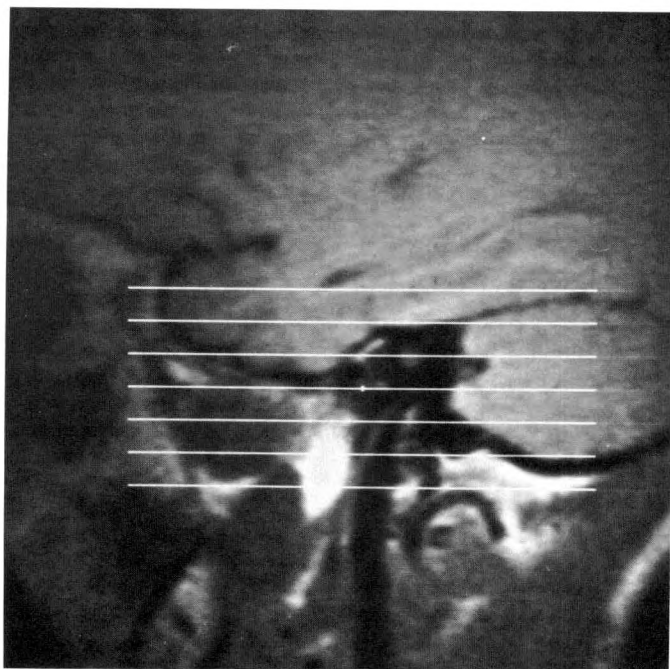
A cryomicrotome freezing sectioning technique described by Rauschnig et al. [15] and Holliday et al. [16] was used to better define the normal anatomy of the intratemporal facial nerve. The MR sections from volunteers were compared with matched whole-organ



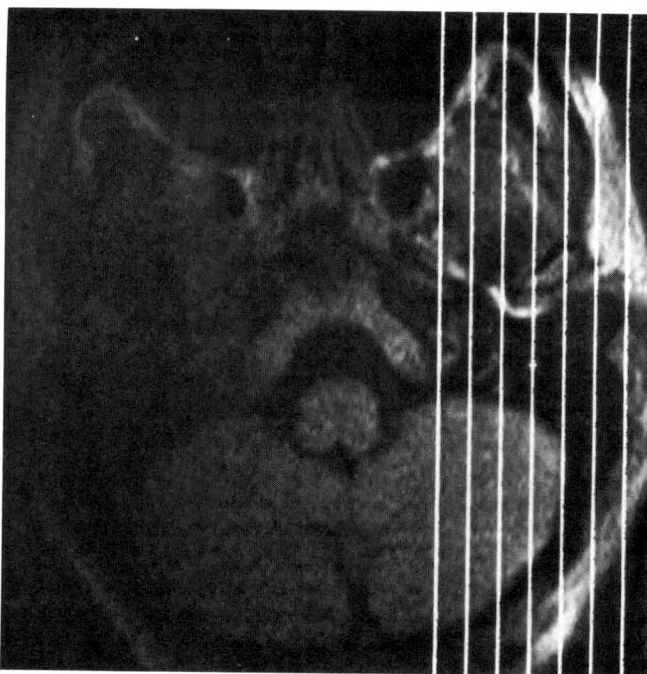
Fig. 1.—14-cm planar surface coil is positioned over temporal bone for facial nerve studies.

Key for Figures 3-5

1. Facial nerve: meatal portion
2. Facial nerve: labyrinthine portion
3. Facial nerve: geniculate ganglion
4. Facial nerve: tympanic (horizontal) portion
5. Facial nerve: mastoid (vertical) portion
6. Facial nerve: intraparotid portion
7. Vestibular nerve(s)
8. Cochlear nerve
9. CN IX-XI
10. Basal turn of cochlea
11. Cochlear aqueduct
12. Vestibule
13. Horizontal semicircular canal
14. Posterior semicircular canal
15. Carotid artery
16. Jugular vein
17. Sigmoid sinus
18. Internal auditory canal
19. External auditory canal
20. Mastoid air cells
21. Stapes



A



B

Fig. 2.—Scout views with cursors placed to localize facial nerve.

A, Sagittal scout view is used to position subsequent axial sections through level of internal auditory canal.

B, Axial scout view allows accurate positioning of sagittal images through vertical (mastoid) portion of facial nerve.

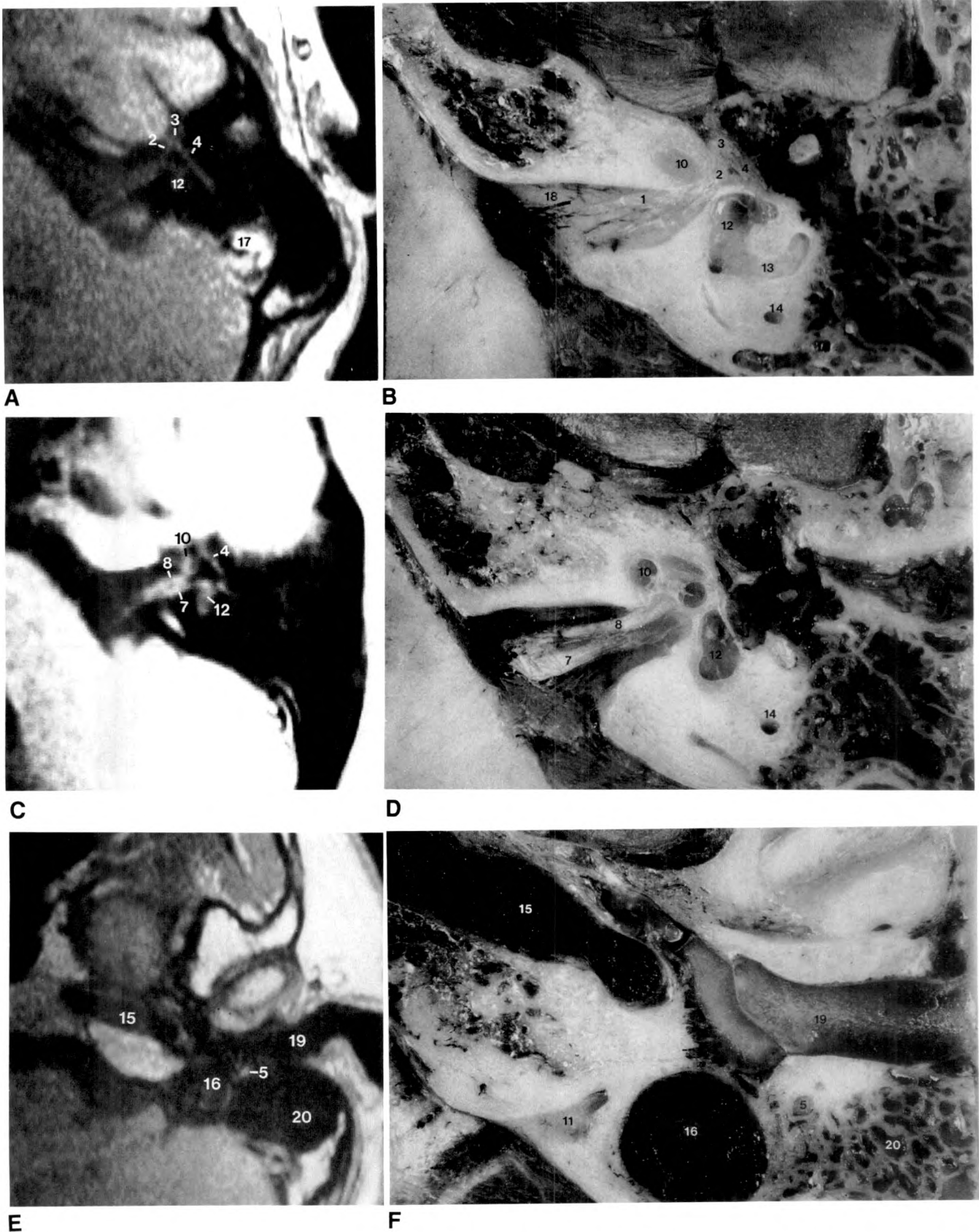


Fig. 3.—Axial MR and cryosections.
A and B, Level of superior aspect of internal auditory meatus.

C and D, Level of inferior aspect of internal auditory meatus.
E and F, Level of external auditory canal.

sections obtained from three cadavers. The specimens were first prepared by arterial injection of a pigmented barium compound to permit identification of arteries and veins. To preserve undistorted topographic anatomy, the soft tissues to be examined were frozen in situ before blood or other fluids from the region of interest were drained.

The frozen specimens were transferred to a horizontal-sectioning, heavy-duty sledge cryomicrotome (LKB 2250, Broma, Sweden). Inside the cabinetlike freezing compartment of the cryomicrotome the specimens were mounted on a bed that weighed approximately 400 pounds, which prevented vibrations and ensured an even shaving slice. The microtome knife sectioned the specimens at predetermined thicknesses varying from 5 to 50 μ m.

At intervals, when photography was desired, the surface of the specimen was gently rubbed with a warm cloth soaked in ethylene glycol to produce a frost-free surface. Photographs of representative gross sections were then compared with the respective normal MR sections in the volunteer.

Results

Figures 3 through 5 present anatomic correlations of cadaver cryosections and MR images of the normal intratemporal facial nerve. Axial, sagittal, and coronal scan planes are presented.

Upon leaving the brainstem at the inferior border of the pons, the facial nerve (1) enters the porus of the internal acoustic meatus accompanied by the nervus intermedius, the cochlear (8) and vestibular (7) divisions of the vestibulocochlear nerve, and the internal auditory artery and vein (Fig. 3). The seventh nerve occupies a position anterior to the superior vestibular nerve and cephalad to the cochlear nerve. These structures can be routinely identified on a sagittal view through the internal auditory canal. The sagittal view also serves as a convenient "scout" projection to assure accurate placement of axial scans (Fig. 2A). Although currently not a

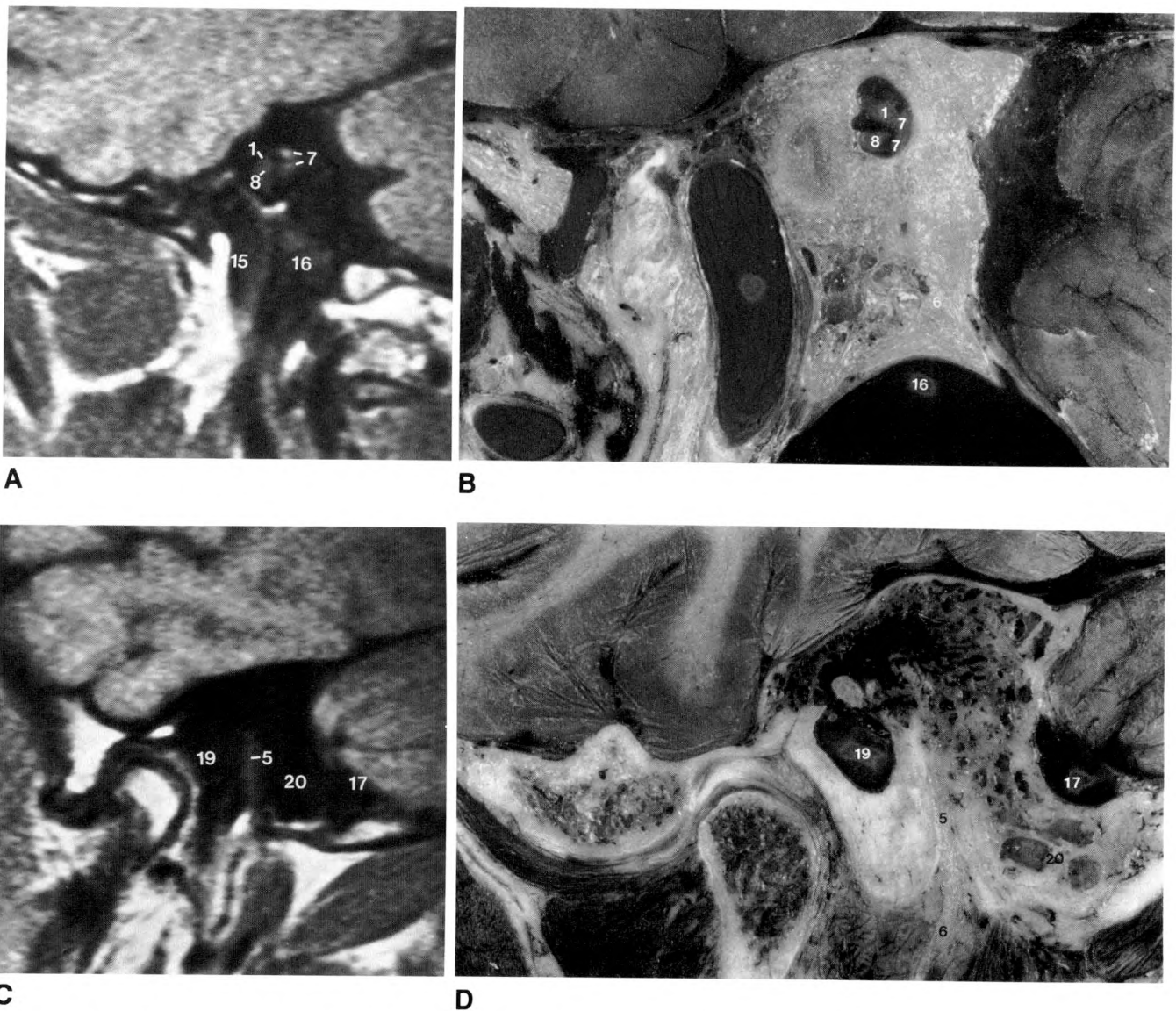


Fig. 4.—Sagittal MR images and cryosections.

A and B, Level of internal auditory canal. C and D, Level of vertical portion of facial nerve.

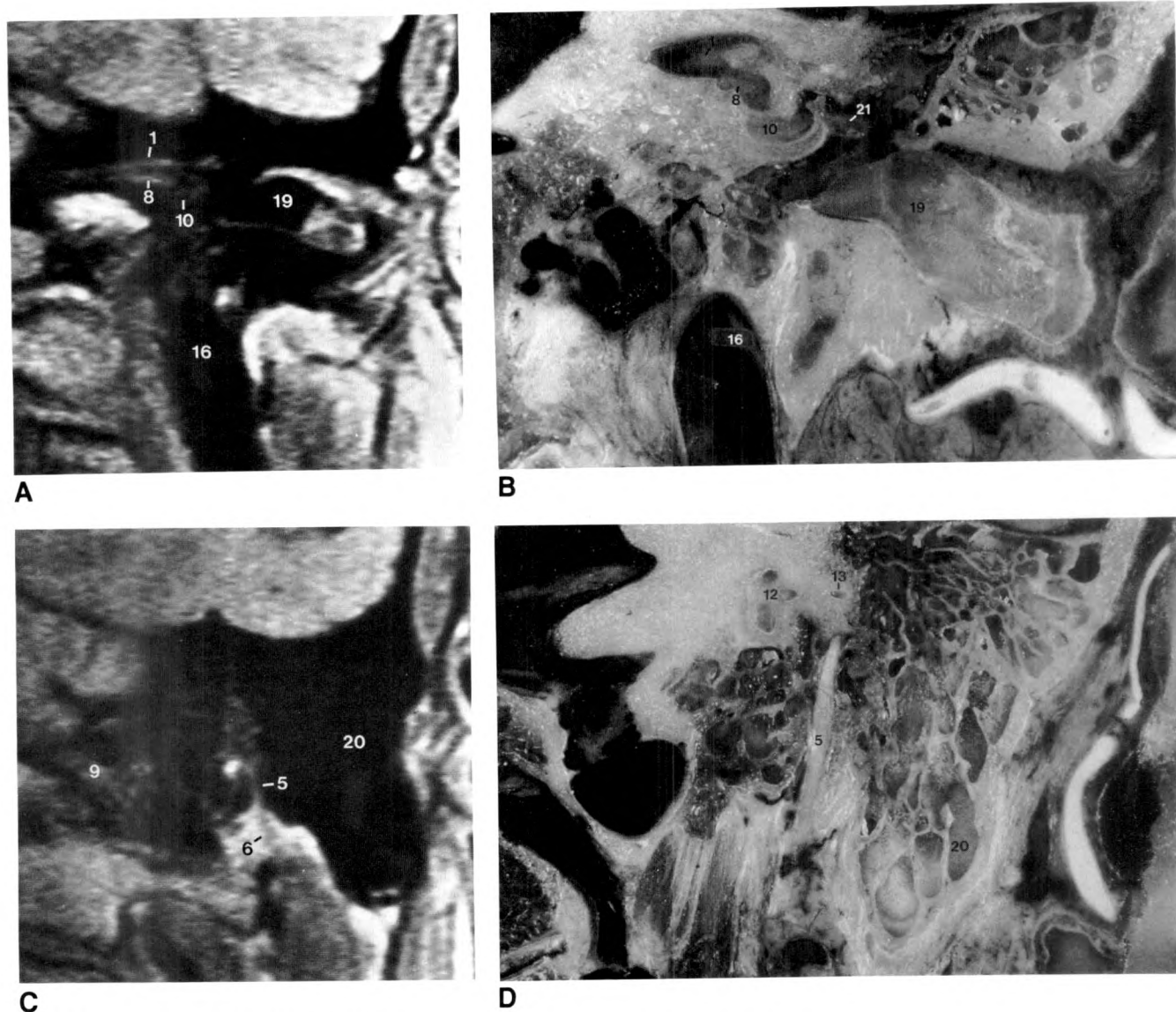


Fig. 5.—Coronal MR images and cryosections.

A and B, Level of internal auditory canal. C and D, Level of vertical portion of facial nerve.

consistent finding on all normal studies, separation of nerves in the internal auditory canal in the axial plane is not unusual (Fig. 3).

The facial nerve exits the internal auditory meatus cephalad to the transverse crest and anterior to a vertical bony landmark, unknown to anatomists but known to surgeons as "Bill's bar." The location of this dense cortical bone is marked by a corresponding region of signal void. At this point, the facial nerve enters the fallopian (or facial nerve) canal, which is roughly 30 mm long and is divided into labyrinthine, tympanic, and mastoid sections. In the labyrinthine portion, the nerve (2) passes anteriorly around the basal turn of the cochlea and expands to form the geniculate ganglion (3). The greater superficial petrosal nerve branches from the main facial nerve at this ganglion, and can occasionally be seen as a high-signal linear structure coursing from the geniculate

ganglion to the pterygopalatine fossa.

The tympanic or horizontal portion of the facial nerve (4) begins at the geniculate ganglion where the facial nerve makes an abrupt posterior bend to form its anterior genu. It then courses posteriorly, cephalad to the oval window and caudal to the prominence of the horizontal semicircular canal. Because they travel roughly parallel to the lateral semicircular canal, the labyrinthine and tympanic portions of the facial nerve are best evaluated in the axial projection (Fig. 3).

The facial nerve then curves gently downward to its mastoid or vertical portion (5) (Fig. 5). As it descends toward the stylomastoid foramen, the nerve passes lateral to the sinus tympani and stapedius muscle. The nerve to the stapedius muscle and the chorda tympani are two important branches that both originate in the mastoid portion of the facial nerve. Because of small size and proximity to other high-signal

structures, neither branch is routinely identified with present MR techniques. The vertical portion of the facial nerve is identified on axial sections; however, to visualize the entire course of this structure, either sagittal or coronal scans must be obtained. We routinely use the sagittal projection for this purpose because it also provides useful information about the parotid bed. In either case, because of the small size of the nerve, accurate alignment of the MR plane with the nerve using a scout view is essential.

Discussion

The complex course of the facial nerve in the temporal bone may be more fully understood if one considers the embryology of the region. The muscles of facial expression originate from the second branchial arch, and therefore, the facial nerve is known as the nerve of the second arch [17].

Nerves of the branchial arches descend into the arch posterior to the cartilage and then turn anterolaterally to reach the front of the arch. The stapes and styloid processes are both derivatives of second-arch cartilage. This explains why, in the adult, the facial nerve moves posteriorly to descend posterior to both the stapes and styloid processes before turning anterolaterally to reach the facial muscles beyond the stylomastoid foramen.

Each arch also receives a nerve branch from the arch caudal to it. Known as pretrematic, these branches course over and anterior to the adjacent branchial cleft (or trema), which separates the two branchial arches. The pretrematic branch of the first arch, the chorda tympani, leaves the facial nerve to arch over the tympanic cavity to join the lingual division of the mandibular nerve (nerve of the first arch).

The entire course of the facial nerve within the temporal bone may be identified with appropriately positioned surface-coil MR images. MR should be a valuable technique in identifying disease of the facial nerve that results in morphologic alterations.

The superior soft-tissue contrast resolution of MR imaging compared with CT scanning or other imaging techniques has been well documented. This is especially true with the detection of edema and other subtle alterations in nervous tissue without gross morphologic distortion. MR may someday be useful for evaluating patients with facial palsy, including those with idiopathic or Bell's palsy, who show no morphologic alteration in the facial nerve. Current imaging techniques have little to offer this group other than to exclude other causes of the disease.

ACKNOWLEDGMENTS

We thank Wolfgang Rauschnig and John Robert for assistance with cryosectioning, and Melody Duran and Julien Keesing for assistance with manuscript preparation.

REFERENCES

1. Steele JR, Hoffman JC. Brainstem evaluation with CT cisternography. *AJNR* 1980;1:521-526
2. Glanz S, Geehr RB, Duncan CC, et al. Metrizamide-enhanced CT for evaluation of brainstem tumors. *AJNR* 1980;1:31-34
3. Maward ME, Silver AJ, Hilal SK, Ganti SR. Computed tomography of the brainstem with intrathecal metrizamide. Part 1: the normal brainstem. *AJNR* 1983;4:1-11
4. Maward ME, Silver AJ, Hilal SK, Ganti SR. Computed tomography of the brainstem with intrathecal metrizamide. Part II: lesions in and around the brainstem. *AJNR* 1983;4:13-19
5. Johnson DW. Air cisternography of the cerebellopontine angle using high resolution computed tomography. *Radiology* 1984;151:401-403
6. Chakeres DW, Kapila A. Brainstem and related structures: normal CT anatomy using direct longitudinal scanning with metrizamide cisternography. *Radiology* 1983;149:709-715
7. Disbro M, Harnsberger HR, Osborn AG. Peripheral facial nerve dysfunction: CT evaluation. *Radiology* 1985;155:659-663
8. Harnsberger HR, Dillon WP. Major motor atrophic patterns in the face and neck: CT evaluation. *Radiology* 1985;155:665-670
9. Curtin H, Wolfe P, Snyderman N. The facial nerve between the stylomastoid foramen and the parotid: computed tomographic imaging. *Radiology* 1983;149:165-169
10. Daniels DL, Schenck J, Foster T, et al. Surface coil magnetic resonance imaging of the internal auditory canal. *AJNR* 1985;6:487-490
11. Daniels DL, Herfkens R, Koehler RP, et al. Magnetic resonance imaging of the internal auditory canal. *Radiology* 1984;151:105-108
12. Han JS, Bonstelle CT, Benson JE, et al. Magnetic resonance imaging in the evaluation of the brainstem. *Radiology* 1984;150:705-712
13. Flannigan BD, Bradley WG Jr, Mazziotto J, et al. Magnetic resonance imaging of the brainstem: normal structure and basic function. *Radiology* 1985;154:375-383
14. Lufkin R, Votruba J, Reicher M, Bassett L, Smith D, Hanafee W. Solenoid surface coils in MRI. *AJR* 1986;146:409-412
15. Rauschnig W, Bergstrom K, Pech P. Correlative craniospinal anatomy studies by computed tomography and cryomicrotomy. *J Comput Asst Tomogr* 1983;7:9-13
16. Holliday J, Saxon R, Lufkin R, et al. Anatomic correlation of magnetic resonance images with cadaver cryosections. *Radiographics* 1985;5(6):887-921
17. Last RJ. *Anatomy: regional and applied*. New York: Churchill Livingstone, 1978

The Utility of MR in Planning the Radiation Therapy of Oligodendroglioma

William P. Shuman¹
 Brian R. Griffin²
 David R. Haynor¹
 David C. Jones²
 J. Steve Johnson²
 Laurence D. Cromwell¹
 George E. Laramore²

Newer methods of radiation therapy for treating oligodendroglioma after surgical resection have produced promising results using high doses of radiation. However, these doses are close to those that cause necrosis of normal brain, making the accurate spatial localization of tissue at risk for containing tumor cells more important. Because MR imaging is superior to CT in detecting some types of intracranial disease, nine patients with oligodendroglioma were studied with both MR and CT. Results were compared with surgical findings. In six cases, MR identified some tumor volume found during surgery that was not detected by CT. In addition, the interface between abnormality (tumor plus edema) and normality was depicted much more clearly by MR than by CT in most cases. Such superior depiction of the margins of abnormality is important for radiation therapy planning because of the known tendency of oligodendroglioma to infiltrate adjacent edema, making all areas of abnormality potential tumor-bearing tissue. Finally, MR showed normal brain tissue in areas considered suspicious by CT, because they were not well seen on CT in several patients. In these cases of low-grade oligodendroglioma, MR was believed to be superior to CT in providing information needed for radiation therapy planning because of its ability to distinguish tumor and adjacent edema (considered tissue at risk for containing microscopic tumor) from contiguous normal brain.

Radiation therapy for oligodendroglioma after surgery may result in improved survival rates compared with surgery alone [1, 2]. However, radiation doses close to those resulting in necrosis of normal brain are required for long-term control of oligodendroglioma [1, 3, 4]. Such high doses require accurate localization of radiation to a volume that contains all bulk tumor as well as tissue potentially infiltrated with tumor and that contains as little normal brain as possible.

Oligodendroglioma is known to have a propensity for microscopically infiltrating adjacent edematous brain tissue [5]. For this reason, all areas identified by an imaging method as abnormal, including edema, are potential tumor-bearing regions. Accurate localization of this potential tumor-bearing tissue for planning radiation therapy for oligodendroglioma is a difficult problem because margins of abnormality (consisting of tumor plus edema) may be poorly demarcated from normal brain on CT studies [6]. Such poor definition of borders on CT introduces uncertainty into the radiation therapy planning process and may result in inclusion of some volume of normal-appearing brain in the treatment fields inadvertently or deliberately to ensure that all tissue at risk is treated.

MR imaging has been shown to be better than CT in detecting some types of intracranial disease [7, 8]. This superior detectability and demarcation of abnormality seemed particularly evident with the lower grades of glioma. For this reason, we studied nine consecutive cases of oligodendroglioma imaged with both CT and MR. Imaging results were correlated with surgical findings, and the utility of information provided by CT for planning the radiation therapy for this tumor was compared with that provided by MR.

This article appears in the January/February 1987 issue of *AJNR* and the March 1987 issue of *AJR*.

Received February 13, 1986; accepted after revision June 4, 1986.

¹Department of Radiology SB-05, University of Washington, Seattle, WA 98195. Address reprint requests to W. P. Shuman.

²Department of Radiation Oncology, University of Washington, Seattle, WA 98195.

AJR 148:595-600, March 1987
 0361-803X/87/1483-0595
 © American Roentgen Ray Society

Subjects and Methods

CT was performed on a GE 9800 or a Picker 1200 scanner with and/or without contrast enhancement. Technical factors included 120 kVp, variable mA, head calibration size, 2 sec scan time, and contiguous 10-mm-thick slices. MR studies were performed on a Picker 0.15 T resistive system. Spin-echo sequences weighted for T2 were performed in all studies, and a 60 msec echo time (TE) and 1000, 1500, or 2000 msec repetition time (TR) were used. In addition, T1-weighted spin-echo sequences (TE 40/TR 600) were performed in eight studies. Slice thickness was 10 mm with 2 mm between slices; studies were performed multislice, single echo. Transverse, sagittal, and coronal images were obtained on all patients.

Temporally matched (within 72 hr) pairs of CT and MR studies were reviewed by five of the authors. Potential tumor volume as defined by areas of abnormality (representing tumor plus edema) was determined for each test. Pairs of CT and MR studies were compared for regions of abnormality detected by one method and not the other. The same pairs were also compared for relative definition (clarity) of borders between areas of abnormality and normal-appearing brain (Figs. 1 and 2). Definitions of three sets of borders (the craniocaudal, the anteroposterior, and the right and left lateral) of each region of abnormality were subjectively scored by consensus among the five reviewers: 0 = borders not defined, 1 = borders poorly defined, 2 = borders moderately well defined, 3 = borders well defined. Thus,

there were three scores for each region of abnormality on each study. In addition to temporally matched CT and MR studies, CT studies that were not temporally matchable to an MR study were also reviewed and scored. This was done to increase the size of the CT sample and to look for consistency in the scores between matched and unmatched CT studies.

Eight of the patients had subtotal surgical resection of tumor before radiation therapy; one patient had four biopsies in the region of tumor and no resection. Pathologic specimens and slides were reviewed by a neuropathologist. Pathologic diagnosis was low-grade oligodendroglioma in seven cases and predominant low-grade oligodendroglioma with some scattered elements of low-grade astrocytoma in two cases. The patients consisted of six women and three men, ranging in age from 25–52 years.

Confirmation of tumor extent was based first on written surgical reports of tumor location, tumor volume resected, and tumor volume left behind after resection. Second, operative findings were compared with tumor location on CT and MR studies by the operating surgeon in conference with radiologists and radiation therapists within several days of surgery in each case. Regions of discrepancy between the imaging techniques were reviewed by the surgeon in light of findings at surgery, including histologic findings along the margins of excised tumor, results of biopsies of residual suspect regions after as much tumor bulk as possible had been resected, and visual inspection of the operative cavity before closing.

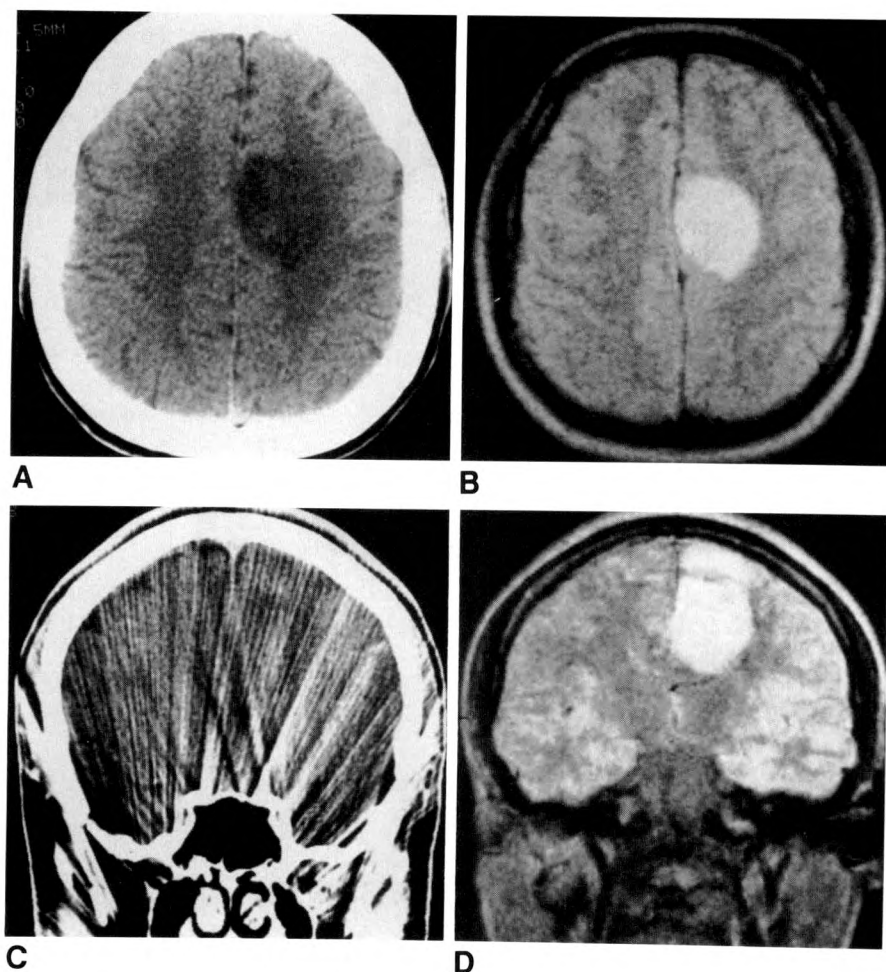


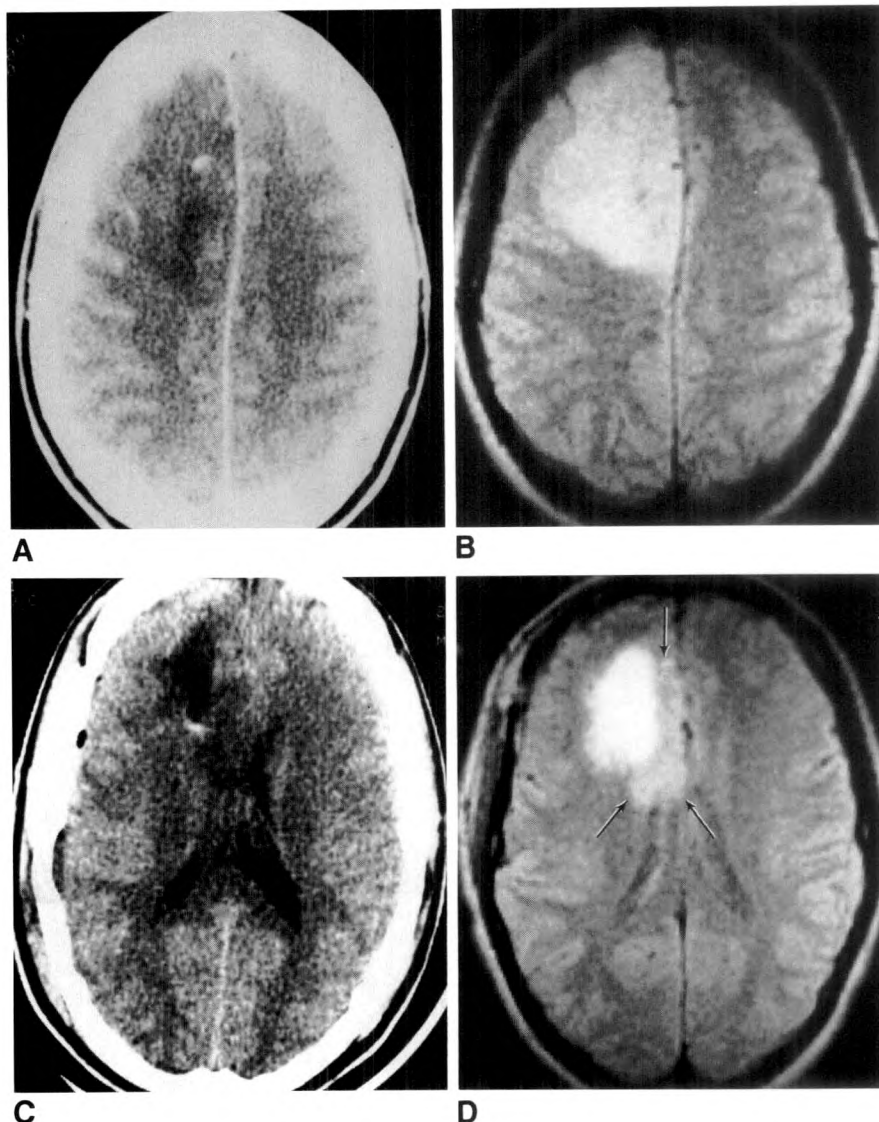
Fig. 1.—A, CT of oligodendroglioma. Poor definition of lateral border of lesion.
B, MR. Borders are well defined.
C, Coronal CT. Artifact from dental amalgam obscures most information.
D, Coronal MR. Craniocaudal extent of lesion is well defined.

Fig. 2.—A, Preoperative CT of oligodendroglioma. Calcification identified but borders poorly defined.

B, Preoperative MR. Border definition is better than on CT.

C, Postoperative CT after subtotal resection. Surgical defect seen, but borders of abnormality difficult to identify.

D, Postoperative MR. Operatively confirmed residual tumor identified (arrows).



Radiation therapy planning was performed on an AECL simulator to design therapy portals. Dosimetry was computer calculated and displayed using CT-generated cranial outlines. Portals and dosimetry were designed to treat all areas of abnormality detected by CT or MR with a generous margin for the initial 4500 to 5000 rad (45–50 Gy) over 5–5½ weeks; subsequent field reduction to only the area of abnormality plus a small margin was used for the boost dose over 1–1½ weeks to a total of 5500–6000 rad (55–60 Gy). Treatment was delivered on Varian linear accelerators with peak photon energies of 6, 15, or 24 MeV.

Results

Oligodendroglioma-associated abnormality ranged in size from $3.5 \times 3.0 \times 3.0$ cm to $12 \times 7 \times 5$ cm. Six lesions showed calcification on CT and three did not. Calcification, evident on MR images in two cases, appeared as a focal signal void. Two lesions had definite cystic areas on both CT

and MR. All lesions had some apparent associated brain edema, although neither CT nor MR was consistently able to separate tumor from adjacent edema.

Twenty-five CT and 11 MR studies were performed and evaluated on the nine patients. Of the CT studies, 16 were performed with IV contrast material, seven without contrast material, and two both without and with contrast material. There were 11 pairs of temporally matched CT and MR studies in the nine patients; seven patients had one MR and one CT study each, while two patients had two MR studies and two CT studies each. Of the temporally matched CT studies, two were performed with and without contrast material, eight with, and one without. In addition, 14 CT studies were not temporally matched to an MR study.

Subjective border definition (clarity) scores assigned to the three sets of borders for each area of abnormality are presented in Table 1. Note that scores from CT studies with no temporally matched MR study were similar to CT studies with

TABLE 1: Subjective Scores Assigned to Lesion Borders in Oligodendroglioma

Score	No. of Lesion Borders by Score			Total
	CT Studies		MR Studies Matched to CT	
	Unmatched	Matched to MR		
0	5	8	0	13
1	33	21	1	55
2	4	2	9	15
3	0	2	23	25
Total	42	33	33	108

Note.—0 = borders not defined; 1 = borders poorly defined; 2 = borders moderately defined; 3 = borders well defined.

temporally matched MR studies, indicating some degree of consistency between these two groups. In general, there were more CT scores than MR scores in the lower two categories, and more MR scores than CT scores in the higher two categories, indicating that border definition between abnormality and normality was generally better with MR than with CT. In particular, significantly more MR studies had scores of 3 ($n = 23$) than did CT studies ($n = 2$). When individual lesion-border scores were compared on temporally matched CT and MR studies, CT had better border definition in none, MR had better border definition in 29, and the border definition was equal in four.

In each of the nine patients, MR was the primary method used for planning radiation therapy for one or more of five reasons. First, MR identified some operatively and histologically confirmed volume of tissue containing oligodendroglioma that was not seen by CT in six patients (Figs. 2C and 2D). This tumor volume seen only by MR often was a tongue or knob projecting away from the main tumor mass. It was appreciated on MR because of that technique's superior ability to evaluate the posterior fossa (two cases), the superior soft-tissue contrast of MR (four cases), the better definition provided by MR because of the multiple planes of image display (two cases), or various combinations of these reasons. Second, MR showed clearly superior border definition between abnormality and normal-appearing brain in six patients. Third, MR showed abnormality in two cases that was not seen on CT nor was it histologically confirmed to be tumor, but it was presumed to be tumor on the basis of MR and operative appearance (the tissue in question was not biopsied but was observed by the surgeon). Fourth, MR showed abnormality not surgically confirmed but presumed to be edema at risk for microscopic infiltration from adjacent tumor and not seen on CT in four cases. Fifth, superior border definition on MR allowed exclusion of normal-appearing tissue from the radiation field that otherwise would have been treated because of poor definition on CT in three patients (one in the posterior fossa, two involving tumor adjacent to but not crossing the falx) (Fig. 3).

Radiation therapists changed their therapy plans as a result of this MR information. These changes included making the field larger and shifting the field position in three patients;

making the field larger, shifting the field position, and adding additional fields in two patients; making the field smaller and adding additional fields in two patients; and adding additional fields only or shifting the fields only in one patient each.

Discussion

Oligodendroglioma is a relatively rare, usually slow-growing low-grade glioma that has a tendency to infiltrate microscopically adjacent edematous brain [9, 10]. The treatment of choice for oligodendroglioma is radical excision of all tumor [1, 10, 11]. However, complete surgical excision of all tumor cells often is not possible because of microscopic infiltration of tumor into surrounding edematous brain tissue [9].

The role of postoperative radiation therapy for the treatment of residual tumor mass or residual microscopic tumor in edematous brain has been controversial [1, 2, 11]. Reports of series, including some patients treated with a low-dose orthovoltage technique, have shown no improved survival from the addition of postoperative radiation therapy [11]. By contrast, series with patients treated by megavoltage technique to high doses of 5000–6000 rad (50–60 Gy) report improved long-term survival with postoperative radiation [1, 2, 12, 13]. For example, Chin et al. [1] reported a 5-year survival of 100% in 24 patients treated in this fashion.

Newer high-dose treatment techniques require precise localization of tissue at risk for containing tumor cells because therapeutic doses of 5000–6000 rad (50–60 Gy) are close to those that may cause necrosis of normal brain, 5500–6000 rad (55–60 Gy) [2, 4]. The chance of radionecrosis of normal brain is related to the size of the volume of normal brain treated as well as to the dose [4]. This potential morbidity makes it important to exclude as much normal brain as possible from the treatment volume, while the tendency of oligodendroglioma to infiltrate adjacent edema makes it important to treat all areas of detectable abnormality, because these areas are potential tumor-bearing tissue.

If an imaging technique can depict the border between abnormality (tumor plus edema) and normal brain with a well-defined margin, the task of localizing radiation therapy to the abnormal region is easier and may be more precise. Separating tumor from edema is less important to the radiation therapist than separating normal brain from adjacent detectable abnormality (tumor *plus* edema), since potentially all areas of contiguous abnormality around oligodendroglioma are microscopically infiltrated with tumor.

CT has been shown to be quite sensitive to the presence of oligodendroglioma [6]. However, because of the characteristic low-grade histology of oligodendroglioma, CT often does poorly in defining the interface between tumor-associated abnormality and normal brain structures [14, 15]. MR is known to have soft-tissue contrast superior to that of CT in cerebral tissues [16]. MR's superior detection capability over CT has been demonstrated previously with the plaques of multiple sclerosis [7, 8, 17] as well as with other types of disease. The multiplanar display format of MR can also be helpful in displaying clearly all margins of abnormality, which may result in an improved understanding of the relationships

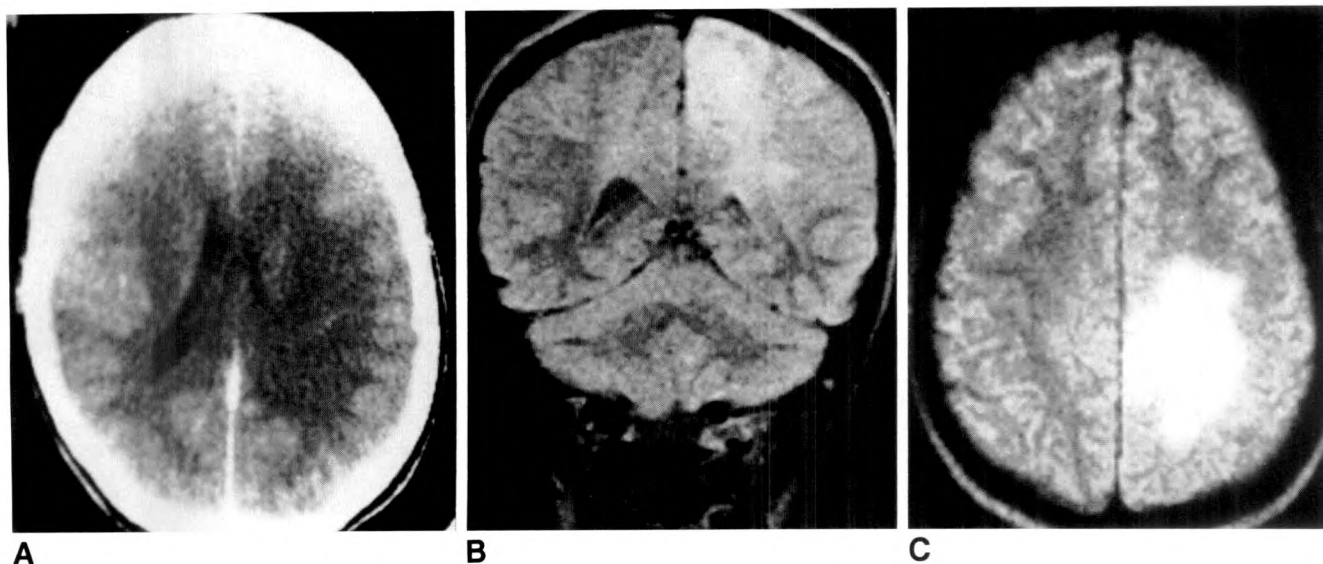


Fig. 3.—A, CT shows poorly defined area of low attenuation. Whether tumor crosses midline is uncertain.
B, MR clearly shows tumor does not cross midline (confirmed at surgery).
C, Axial MR.

between tumor and surrounding normal tissue [18]. In particular, we noted that margins of abnormality associated with tumors of low-grade histology were defined much better with MR than with CT, especially oligodendroglioma. The discrepancy between imaging techniques may not be as great for higher-grade gliomas, but that remains to be documented. While MR studies provided superior border definition in many cases, no MR findings were considered specific for oligodendroglioma. The amount of associated edema was not unique for low-grade tumor nor were the intensity differences with surrounding brain. In the future, the use of contrast material such as gadolinium may improve the specificity of MR for tumor grade.

In all nine cases in our report, both CT and MR detected regions of abnormality. However, MR subjectively provided better border definition between abnormality and normal-appearing brain tissue. When compared with surgical results, MR found some tumor volume not detected by CT in six of nine cases. In addition, MR found edema at risk for tumor infiltration that was missed by CT in four cases, and it showed normal-appearing brain tissue that was not well defined by CT and thus considered suspicious on the basis of CT findings alone. For various combinations of these reasons, MR was the primary technique used for identifying potential tumor-bearing tissue and separating it from normal brain for therapy-planning purposes in all of these cases. MR studies resulted in changes in therapy portal size, location, and number of fields. MR information was believed to be particularly helpful in designing the smaller therapy portals for the final boost dose.

This report does not attempt to assess improvement in response or cure rates for oligodendroglioma resulting from the use of MR. It does attempt to compare the value of information available from MR with that available from CT for

purposes of planning radiation therapy and for verifying as much as possible the validity of that information on the basis of surgical findings in these low-grade tumors. It should be cautioned that gliomas of histologically higher grades may produce different results. However, our limited series suggests that, in cases of low-grade oligodendroglioma, MR may provide more useful information than CT and may become a necessary procedure for planning the postoperative radiation therapy of this tumor.

ACKNOWLEDGMENT

We thank the MR technical staff and First Hill Diagnostic Imaging, Inc., for support.

REFERENCES

1. Chin HW, Hazel JJ, Kim TH, Webster JH. Oligodendrogliomas. 1. A clinical study of oligodendrogliomas. *Cancer* **1980**;45:1458-1466
2. Sheline GE. Radiation therapy of brain tumors. *Cancer* **1977**;39:873-881
3. Sheline GE, Wara WM, Smith V. Therapeutic irradiation and brain injury. *Int J Radiat Oncol Biol Phys* **1980**;6:1215-1228
4. Marks JE, Baglan RJ, Prasad SC, Blank WF. Cerebral radionecrosis: incidence and risk in relation to dose, time, fractionation, and volume. *Int J Radiat Oncol Biol Phys* **1981**;7:243-252
5. Daumas-Duport C, Meder JF, Mon Saigne V, Missir O, Aubin ML, Szikla G. Cerebral gliomas: malignancy, limits, and spatial configuration. *J Neuroradiol* **1983**;10:51-80
6. Vonofakos D, Marcu H, Hacker H. Oligodendrogliomas: CT patterns with emphasis on features indicating malignancy. *J Comput Assist Tomogr* **1979**;3:783-788
7. Brant-Zawadzki M, Davis PL, Crooks LE, et al. NMR demonstration of cerebral abnormalities: comparison with CT. *AJNR*

- 1983;4:117-124, *AJR* 1983;140:847-854
8. Lukes SA, Crooks LE, Aminoff MJ, et al. Nuclear magnetic imaging in multiple sclerosis. *Ann Neurol* 1983;13:592-601
 9. Sheline GE, Boldrey E, Karlsberg P, Phillips TL. Therapeutic considerations in tumors affecting the central nervous system: oligodendrogliomas. *Radiology* 1964;82:84-89
 10. Bloom HJG. Intracranial tumors: response and resistance to therapeutic endeavors, 1970-1980. *Int J Radiat Oncol Biol Phys* 1982;8:1083-1113
 11. Reedy DP, Bay JW, Hahn JF. Role of radiation therapy in the treatment of cerebral oligodendroglioma: an analysis of 57 cases and a literature review. *Neurosurgery* 1983;13:499-503
 12. Walker MD, Strike TA, Sheline GE. An analysis of dose-effect relationship in the radiotherapy of malignant gliomas. *Int J Radiat Oncol Biol Phys* 1979;5:1725-1731
 13. Mork SJ, Lindegaard KF, Halvorsen TB, et al. Oligodendroglioma: incidence and biological behavior in a defined population. *J Neurosurg* 1985;63:881-889
 14. Lilja A, Bergstrom K, Spannare B, Olsson Y. Reliability of computed tomography in assessing histopathological features of malignant supratentorial gliomas. *J Comput Assist Tomogr* 1981;5:625-636
 15. Silverman C, Marks JE. Prognostic significance of contrast enhancement in low-grade astrocytomas of the adult cerebrum. *Radiology* 1981;139:211-213
 16. Margulis AR, Crooks LE, Kaufman L. Present clinical status of magnetic resonance imaging. In: James TL, Margulis AR, eds. *Biomedical magnetic resonance*. San Francisco: Radiology Research and Education Foundation, 1984:301-308
 17. Young IR, Hall AS, Pallis CA, Bydder GM, Legg NJ, Steiner RE. Nuclear magnetic imaging of the brain in multiple sclerosis. *Lancet* 1981;2:1063-1066
 18. Shuman WP, Griffin BR, Haynor DR, et al. MR imaging in radiation therapy planning. *Radiology* 1985;156:143-147

Direct Oblique Sagittal CT of Orbital Wall Fractures



James B. Ball, Jr.¹

Direct oblique sagittal CT was used to evaluate trauma to 77 orbits. Sixty-seven orbital wall fractures with intact orbital rims (36 floor, 22 medial wall, nine roof) were identified in 47 orbits. Since persistent diplopia and/or enophthalmos may warrant surgical repair of orbital floor fractures, optimal imaging should include an evaluation of extraocular muscle status, the nature and amount of displaced orbital contents, and an accurate definition of fracture margins. For orbital floor fractures, a combination of the direct oblique sagittal and direct coronal projections optimally displayed all fracture margins, the fracture's relationship to the inferior orbital rim and medial orbital wall, and the amount of displacement into the maxillary sinus. Inferior rectus muscle status with 36 floor fractures was best seen on the direct oblique sagittal projection in 30 fractures (83.3%) and was equally well seen on sagittal and coronal projections in two fractures (5.5%). Floor fractures were missed on 100% of axial, 5.5% of sagittal, and 0% of coronal projections. Since the direct oblique sagittal projection complements the direct coronal projection in evaluating orbital floor fractures, it should not be performed alone. A technical approach to the CT evaluation of orbital wall fractures is presented.

Fracture of the orbital floor was first described in 1844 [1], and a case of traumatic enophthalmos was reported 45 years later [2]. The term "blow-out fracture" of the orbital floor was coined by Smith and Regan [3]. Orbital floor blow-out fractures are the third most common fracture of the middle third of the face [4]. The reported incidence of medial orbital wall fractures in association with orbital floor fractures is 5–71%, while isolated medial orbital wall fractures are said to be uncommon [5, 6]. Fractures of the orbital roof are unusual, normally occurring into the floor of the frontal sinus [7].

The use of both axial and coronal CT projections is well established. Our technique for obtaining direct sagittal images of the cranium and face was recently described [8].

The purpose of this study is to assess the usefulness of direct oblique sagittal CT of the orbit in evaluating orbital wall fractures and to determine the optimal CT technique for evaluating suspected orbital wall fractures.

Materials and Methods

During an 18-month period, 74 patients were referred for CT to evaluate the presence and extent of orbital trauma. In three patients evaluation of both orbits was requested, for a total of 77 orbits (36 left, 41 right). There were 20 women and 54 men, ranging in age from 16 to 64 years (mean, 31.9).

CT examinations of all 74 patients were performed on a GE 9800 scanner. All 77 orbits were evaluated in the oblique sagittal plane using a technique previously described [8]; three examinations used contiguous 5-mm slices and the rest used contiguous 3-mm slices. Seventy-three orbits were also evaluated in the coronal plane; six examinations used contiguous 3-mm slices and the rest used contiguous 5-mm slices. Six orbits were examined in the axial plane; two examinations used contiguous 5-mm slices and four examinations

This article appears in the January/February 1987 issue of *AJNR* and the March 1987 issue of *AJR*.

Received January 22, 1986; accepted after revision May 27, 1986.

Presented at the annual meeting of the American Society of Neuroradiology, San Diego, January 1986.

¹ Department of Radiology, Division of Neuroradiology, University of Cincinnati Medical Center and University Hospitals, Cincinnati, OH 45267-0742. Present address: Florida Hospital, 601 E. Rollins, Orlando, FL 32803. Address reprint requests to J. B. Ball.

AJR 148:601–608, March 1987
0361–803X/87/1483–0601
© American Roentgen Ray Society

used contiguous 3-mm slices. Seventy-one orbits were evaluated in both sagittal and coronal planes. Four orbits were evaluated in both sagittal and axial planes. Two orbits were evaluated in all three planes.

When available, a retrospective review was made of the patient's chart for clinical data. All CT examinations were reviewed retrospectively.

To assess the relative radiation dose to the lens using these three CT planes, a tissue-equivalent head phantom was scanned with thermoluminescent dosimeters (TLDs) placed on the lens. For each of the three planes (axial, coronal, sagittal), two slice widths were used (contiguous 3-mm and contiguous 5-mm) for a total of six techniques. In the coronal technique, the neck was hyperextended. Eight slices per technique were used to scan through the lens. Technical factors were: 120 kV, 200 mA, 3 sec. A scout view preceded each technique (120 kV, 100 mA). Six TLDs per technique were used and these results were averaged. A background determination was made from four TLDs.

Results

Clinical data are available for 64 orbits. Two patients had exophthalmos, both with floor fractures. Four patients had enophthalmos, three with floor fractures and one with a tripod fracture. Thirteen patients had diplopia, six with floor fractures, three with a tripod fracture, one with a roof fracture, and three with no visible fracture. Sixteen patients had limitation of eye movement, 12 with floor fractures, two with a tripod fracture, one with a roof fracture, and one with both a tripod and roof fracture.

Sixty-seven orbital wall fractures were identified in 47 orbits. Thirty-six (54%) involved the orbital floor, 22 (33%) involved the medial orbital wall, and nine (13%) involved the orbital roof. Twenty-seven (57%) of the 47 orbits had only one wall fractured.

For the 36 orbital floor fractures, distance from the inferior orbital rim to the fracture site (average 7.8 mm, range 2–22 mm) and depth of fracture (average 19.5 mm, range 2–30 mm) were measured on sagittal images; width of fracture (average 16.2 mm, range 5–30 mm) was measured on coronal images; and inferior displacement of fracture fragments (average 6.3 mm, range 0–11 mm) was measured on whichever projection showed the greatest displacement. Thickening and/or displacement of the muscle toward the fracture site was seen with the inferior rectus muscle in 22 (61%) and with the medial rectus muscle in seven (19%). Thickened muscles represent edema and/or hemorrhage. Entrapment by bony fragments was not identified.

The projection best demonstrating the pathologic findings associated with 36 orbital floor fractures is shown in Table 1. While inferior rectus muscle status was best determined on the sagittal projection, muscle thickening was frequently easier to appreciate on the coronal projection where the opposite inferior rectus muscle was available for comparison.

Two (5.5%) of the 36 floor fractures were not identified in the sagittal plane. Neither of the two floor fractures scanned in the axial plane was identified in this plane. All 34 floor fractures scanned in the coronal plane were identified in this plane.

Other fractures identified included 12 zygomaticomaxillary (tripod), 10 anterior maxillary sinus wall, and five inferior orbital rim/anterior maxillary sinus wall. Twelve orbits demonstrated no fracture. Associated with the nine orbital roof fractures were one frontal lobe hematoma, one squamous frontal epidural hematoma, one subfrontal epidural hematoma, one superior rectus muscle impingement, and one greater sphenoid wing fracture.

Radiation dose to the lens as determined by phantom scanning with TLDs is shown in Table 2. Radiation dose to the four control TLD chips was negligible.

Discussion

The term "blow-out fracture" [3] is best reserved for orbital wall fractures with intact adjacent orbital rims. Sixty-seven orbital wall blow-out fractures occurred in 47 of 77 orbits studied for orbit trauma, including 36 orbital floor, 22 medial orbital wall, and nine orbital roof fractures.

There are two proposed mechanisms for the production of orbital wall blow-out fractures. The most commonly accepted mechanism is a sudden increase in intraorbital hydraulic pressure due to force delivered to the anterior globe by an object

TABLE 2: Radiation Dose to the Lens with Thermoluminescent Dosimeters

Projection	Slice Width (mm)	Average Dose (rad)
Sagittal	3	2.62
Sagittal	5	2.52
Axial	3	4.50
Axial	5	4.04
Coronal	3	5.99
Coronal	5	5.87

TABLE 1: Projection(s) Best Demonstrating CT Findings in Orbital Floor Fractures

Finding	No. of Fractures (%) (n = 36)				
	Not Involved	Sagittal and Coronal Equivalent	Sagittal	Coronal	Axial
Floor fracture	0	21 (58)	7 (19)	8 (22)	0
Contiguous medial wall involvement	27 (75)	1 (3)	1 (3)	6 (17)	1 (3)
Inferior rectus muscle status	0	2 (6)	30 (83)	4 (11)	0
Medial rectus muscle status	0	0	0	34 (94)	2 (6)

larger than the orbital rim, resulting in decompression of the orbit contents through the weakest portion of the orbital wall [9]. This mechanism would explain blow-out fractures of the orbital floor, medial wall, and roof. A second proposed mechanism for orbital floor blow-out fractures is floor buckling due to a force applied to the inferior orbital rim [10].

The need for and timing of surgical treatment of orbital floor fractures is controversial [3, 11, 12]. Most would agree that elective surgical treatment is best reserved for patients with persistent diplopia and/or enophthalmos [11]. Surgical treatment for medial orbital wall fractures is less common, and the same considerations of diplopia and enophthalmos apply. Surgical treatment of orbital roof fractures is usually dictated by other complications [13].

Since the sagittal plane is poor for evaluating medial orbital wall fractures, only orbital floor and roof fractures are discussed.

Orbital Floor Blow-out Fractures

Clinical findings with orbital floor fractures include periorbital ecchymosis, infraorbital hypesthesia, depression of the globe, exophthalmos, enophthalmos, decreased or absent extraocular muscle movement, and vertical diplopia [9, 14]. The most important late complications of missed orbital floor fractures are diplopia and enophthalmos [15].

Diplopia is common and usually resolves [11]. It may result from edema, hemorrhage, or damage to the nerve supply of the inferior rectus muscle. Diplopia from decreased mobility of the inferior rectus muscle may also occur by two other mechanisms [16]. Incarceration of the inferior rectus muscle by fracture fragments is a rare cause of diplopia and was not identified in this study. A more common cause is a restriction of inferior rectus muscle movement associated with herniation of the posterior inferior orbital fat pad through the fracture site into the upper maxillary sinus (Fig. 1). The posterior inferior orbital fat pad, lying between the orbital floor periosteum and the inferior rectus and inferior oblique muscles, has

numerous fibrous connective tissue strands between the periosteum and the extraocular muscle sheaths. This is a vascular area with a large venular network draining into the inferior ophthalmic vein. Displacement of the posterior inferior orbital fat pad inferiorly with associated hemorrhage and edema within the fat pad causes increased tension on the fibrous strands between the floor periosteum and the inferior rectus muscle, resulting in a limitation of mobility [11, 12, 16]. Fibrosis within this "inferior rectus motility apparatus" may cause persistent diplopia after resolution of hemorrhage and edema [12]. Another proposed mechanism for chronic decreased mobility of the inferior rectus muscle after a relatively nondisplaced fracture is Volkmann's ischemic contracture [17]. Displacement of the globe below the visual axis will also result in diplopia [9, 18].

Enophthalmos may occur early or late [19]. Early enophthalmos is usually caused by disruption of the orbital floor periosteum with herniation of orbital contents into the maxillary sinus (Fig. 1) or displacement of the orbital floor inferiorly resulting in an increase in intraorbital volume despite an intact periosteum (Fig. 2). Late enophthalmos may result from orbital fat atrophy and/or fibrotic contraction of extraocular muscles due to injury. The incidence of enophthalmos is 8–54% within weeks to months after injury [20]. Enophthalmos may be masked early because of traumatic hemorrhage and edema [15, 19]. A large fracture volume may suggest the need for early surgical repair to prevent enophthalmos [21]. A positive correlation of fracture area with enophthalmos has been reported.

CT can evaluate both bony and soft-tissue components of the orbit. Its optimal use depends on an understanding of the pertinent anatomy of the orbital floor and adjacent soft-tissue structures. The orbits are roughly conical with their long axes diverging about 45° from the midsagittal plane. The long axes of the optic nerve and inferior rectus muscle deviate about 30–35° from the midsagittal plane.

The orbital floor slopes downward from posterior to anterior and from medial to lateral (Fig. 3), with an undulating contour



Fig. 1.—Floor fracture and acute enophthalmos explained on direct oblique sagittal projection by herniation of posterior inferior orbital fat pad (small arrows) into maxillary sinus associated with thickening and displacement of inferior rectus muscle (large arrow). Note optimal longitudinal imaging of inferior rectus muscle.

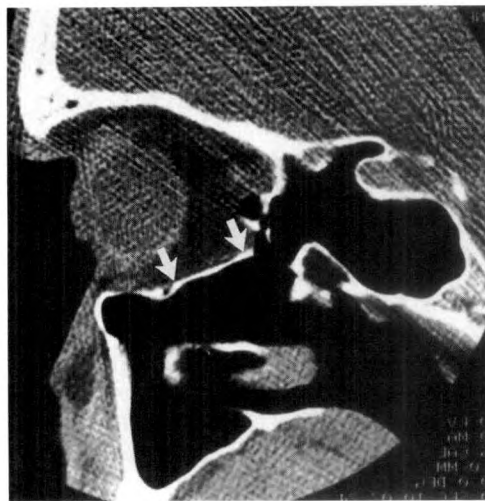


Fig. 2.—Floor fracture and acute enophthalmos caused by inferior displacement of orbital floor (arrows) with resultant increase in intraorbital volume.

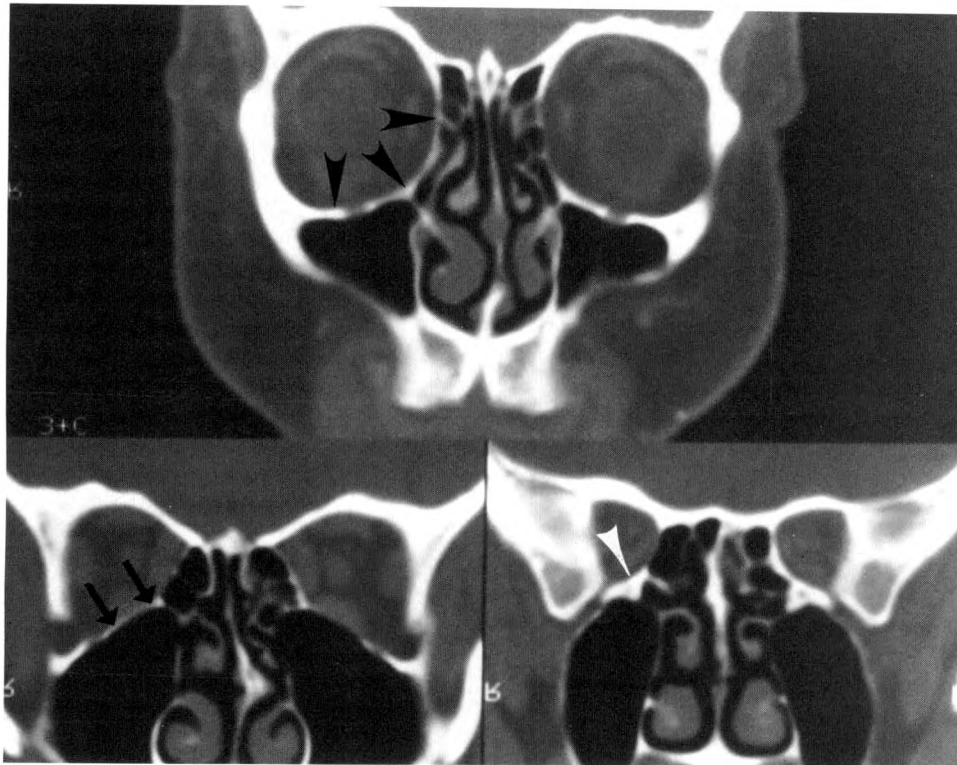


Fig. 3.—Curving junction of orbital medial wall and floor with downward sloping of floor just posterior to orbital rim (black arrowheads), about halfway between orbital rim and apex (arrows), and just anterior to apex (white arrowhead).

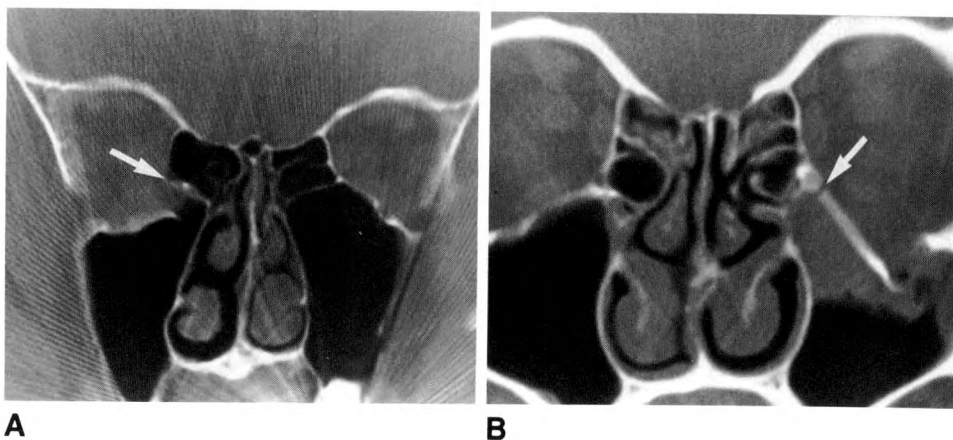


Fig. 4.—Different patients with medial margin of floor fracture at or near maxillary-ethmoid plate (arrows), hinged laterally (A) and medially (B).

that is superiorly convex posteromedially. The thinnest portion of the orbital floor is the floor of the infraorbital groove posteriorly. The next thinnest portion is medial to the infraorbital groove just anterior to the inferior orbital fissure. This is the most common site of orbital floor fracture. The thickest portion of the orbital floor lies lateral to the infraorbital groove and anterior to the inferior orbital fissure [22]. The orbital floor has no well-defined boundaries, forming a curving junction with the medial orbital wall (Fig. 3). It is generally defined by the limits of the maxillary sinus roof, and thus a fracture crossing the maxillary-ethmoid plate also involves the contiguous medial orbital wall. Of the 27 orbital floor fractures that

did not involve the contiguous medial orbital wall, most had a medial margin at or near the maxillary-ethmoid plate (Fig. 4).

Depending on patient positioning and gantry angle, axial CT is nearly parallel to the orbital floor and is thus a poor method for evaluating orbital floor fractures. Both orbital floor fractures scanned in the axial plane in this study were missed with contiguous 3-mm images on this projection. The only advantage of axial CT is the ease of patient positioning. While thin-section axial CT with computer reformations has been advocated [16], the resulting spatial resolution is inferior to that of direct coronal or sagittal CT.

Since direct coronal CT is nearly perpendicular to all four

orbital walls, it is the best projection for evaluating trauma to the middle third of the face and orbits. No orbital floor fracture was missed on the coronal projection in 34 cases in this study. It is the best projection for evaluating the medial and lateral extent of floor fractures and for assessing inferior rectus muscle size since comparison with the contralateral side is possible (Fig. 5A). However, the anterior and posterior limits of the fracture are not optimally demonstrated in the coronal plane, and coronal images are not optimal for evaluating displacement of the inferior rectus muscle (Fig. 6) because of poor definition of muscle kinks [16].

With the patient supine and the neck hyperextended it is rare that the gantry can be tilted enough to make the coronal plane directly perpendicular to the orbital floor. An alternative method of patient positioning is supine with the neck hyperflexed [23]. In most patients this will allow the coronal plane to be directly perpendicular to the orbital floor, and thus it is probably the preferred method for performing direct coronal CT of the orbital floor. There is some increase in image noise and decrease in lens radiation dose because of inclusion of parts of the neck and shoulders in the scanning plane.

I agree with the suggestion of Hammerschlag et al. [16] that oblique sagittal sections be obtained through the plane of the inferior rectus muscle for optimal evaluation of orbital floor fractures. Their method, however, was to perform axial CT with computer reformations. Our method of obtaining direct oblique sagittal CT images of the orbital floor [8] results in superior spatial resolution. For scanning the orbit with this technique, the orbit of interest is placed away from the positioning block and the patient's head turned about 30° toward the positioning block (Fig. 7A) so that the scanning plane is parallel to the course of the optic nerve and inferior rectus muscle. Using the lateral scout view, a gantry angle is chosen that does not pass directly through the vertical plane of the orbit, but rather runs slightly superolateral to inferomedial so that the scan plane is more nearly perpendicular to the laterally sloping orbital floor (Fig. 7B).

The main advantage of this direct oblique sagittal plane is longitudinal imaging of the inferior rectus muscle in one or two CT sections so that the course of the inferior rectus muscle is better appreciated (Figs. 1 and 6B). In our study, inferior rectus muscle status was demonstrated best on the

Fig. 5.—Floor fracture with contiguous medial-wall involvement best evaluated with combination of coronal (A) and direct oblique sagittal (B) projections. This combination accurately defines all fracture margins (open arrows). Coronal projection is best for demonstrating medial-wall involvement and is perpendicular to long axes of medial (small white arrow) and inferior (large white arrow) rectus muscles, allowing size comparison with contralateral side.

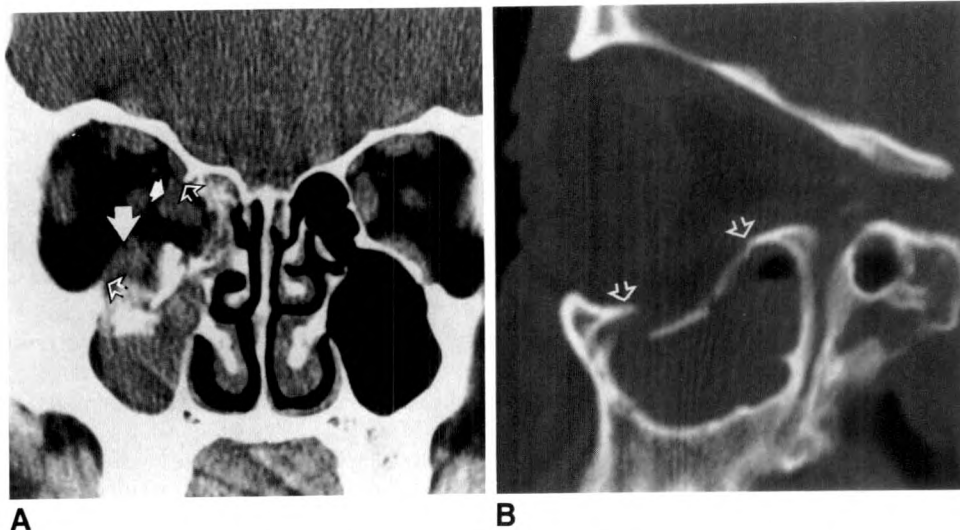
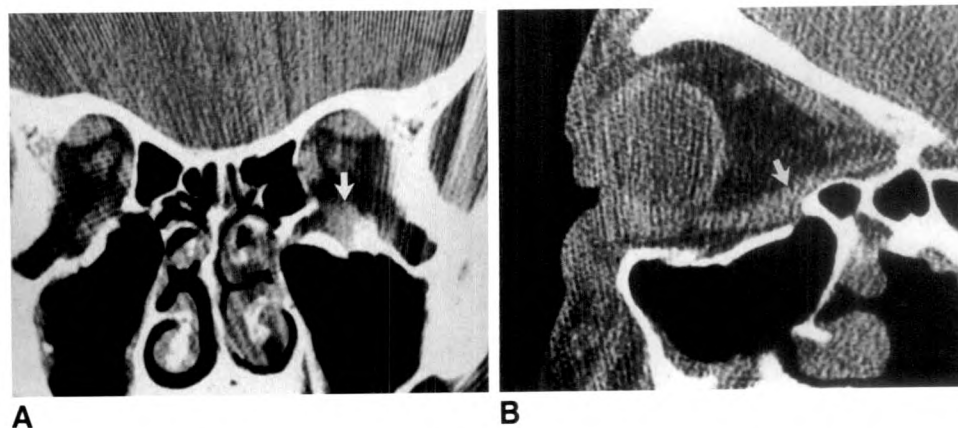


Fig. 6.—Floor fracture with inferior rectus muscle status best demonstrated on direct oblique sagittal projection. While coronal projection (A) demonstrates thickening and some displacement of inferior rectus muscle (arrow), exact relationship to fracture site is uncertain. Direct oblique sagittal projection (B) allows optimal longitudinal imaging of inferior rectus muscle (arrow), demonstrating relationship to posterior fracture margin.



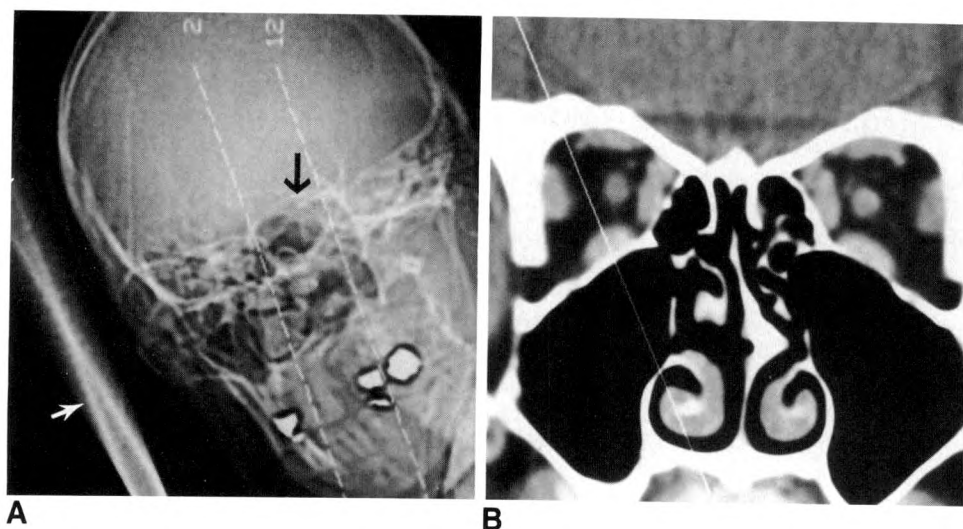


Fig. 7.—A and B, Direct oblique sagittal technique: Patient prone on scanner table (not shown) with neck flexed laterally and head placed against surface of positioning block (white arrow) so that orbit of interest (black arrow) is away from positioning block. Head turned about 30° toward positioning block so that scan plane is parallel to long axis of orbit of interest and inferior rectus muscle. Gantry angled so that scan plane is perpendicular to downward-sloping orbit floor (white lines), not parallel to vertical plane of orbit.

sagittal projection in 83% of floor fractures, and the sagittal and coronal projections were equivalent in 6%. The precise relationship of the anterior fracture margin to the inferior orbital rim as well as to the anterior and posterior margins of the floor fracture are also best determined with the direct oblique sagittal plane (Fig. 5B).

Disadvantages of the direct oblique sagittal technique include difficulty in patient positioning, requiring better technical assistance; suboptimal evaluation of involvement of the medial orbital wall, either contiguously or with a separate blow-out fracture; and no demonstration of the contralateral orbit, and thus suboptimal evaluation of other midface fractures. As with the coronal plane, artifacts from dental fillings can be a problem.

Direct oblique sagittal CT should be a supplement to, not a replacement for, the direct coronal projection. Two (5.5%) of 36 orbital floor blow-out fractures in our study were not identified on the direct oblique sagittal projection. Although the orbital floor was not clearly normal in either case, a definite fracture was not identified. These were small, relatively non-displaced fractures.

The optimal CT technique for evaluating orbital floor blow-out fractures includes two projections: the direct coronal projection with the patient supine and neck hyperflexed and the direct oblique sagittal projection (Figs. 5 and 6).

Orbital Roof Fractures

The clinical setting in which orbital roof fractures occur is often different from that of orbital medial wall or floor fractures in that more significant trauma has usually occurred resulting in multiple and complex facial fractures. While diplopia and enophthalmos may occur, other more immediate clinical problems may take precedence.

Orbital roof fractures may result in ocular complications; structural deformity of the orbit; enophthalmos; extraocular

muscle imbalance from superior rectus dysfunction; blepharoptosis from levator palpebrae injury; or intracranial complications including cerebrospinal fluid rhinorrhea, dural fistula, intracranial gas associated with dural tear, and meningitis [13].

Restriction of upward gaze caused by involvement of the superior rectus muscle results from mechanical impingement rather than entrapment [13]. In the presence of orbital floor fracture, the inability to elevate the globe may be from superior rectus injury accompanying associated orbital roof fracture [14] (Fig. 8).

As with orbital floor and medial wall fractures, evaluation of orbital soft-tissue structures is best performed with CT. CT is also suited to evaluation of the acute intracranial complications that often accompany orbital roof fractures. Three of our nine patients with orbital roof fractures had unsuspected intracranial hematomas, one intracerebral and two extracerebral (Fig. 9).

The direct coronal CT projection with the patient supine and neck hyperextended is nearly perpendicular to the orbital roof and is the best projection for evaluating orbital roof fractures (Fig. 9). It will also allow evaluation of the supra-adjacent cranial compartment and may lead to detection of unsuspected hematomas. As with evaluation of the medial and inferior rectus muscles, the superior rectus muscle can be easily evaluated but is not optimally displayed in the coronal plane.

Direct oblique sagittal CT is the best method for evaluating the status of the superior rectus muscle (Fig. 8), which deviates from the midsagittal plane of the head in the same manner as the optic nerve and inferior rectus muscle. Because of the multiple convolutions of the orbital roof and increased image noise from scanning through the patient's neck and shoulder, small, relatively nondisplaced fractures are not easily seen on the sagittal projection.

The optimal CT technique for evaluating orbital roof fractures includes two projections, the direct coronal projection

Fig. 8.—Direct oblique sagittal projection is optimal for evaluation of superior and inferior rectus muscles. Patient with limitation of eye movement on upward gaze after trauma.

A, Bone settings demonstrate floor fracture (arrowheads) and roof fracture with rotated fragment (arrow).

B, Soft-tissue settings demonstrate nondisplaced inferior rectus muscle (white arrow) with some fat herniation into maxillary sinus (black arrow) associated with floor fracture. Eye movement is limited, however, because of impingement of roof-fracture fragment on superior rectus muscle complex (open arrow).

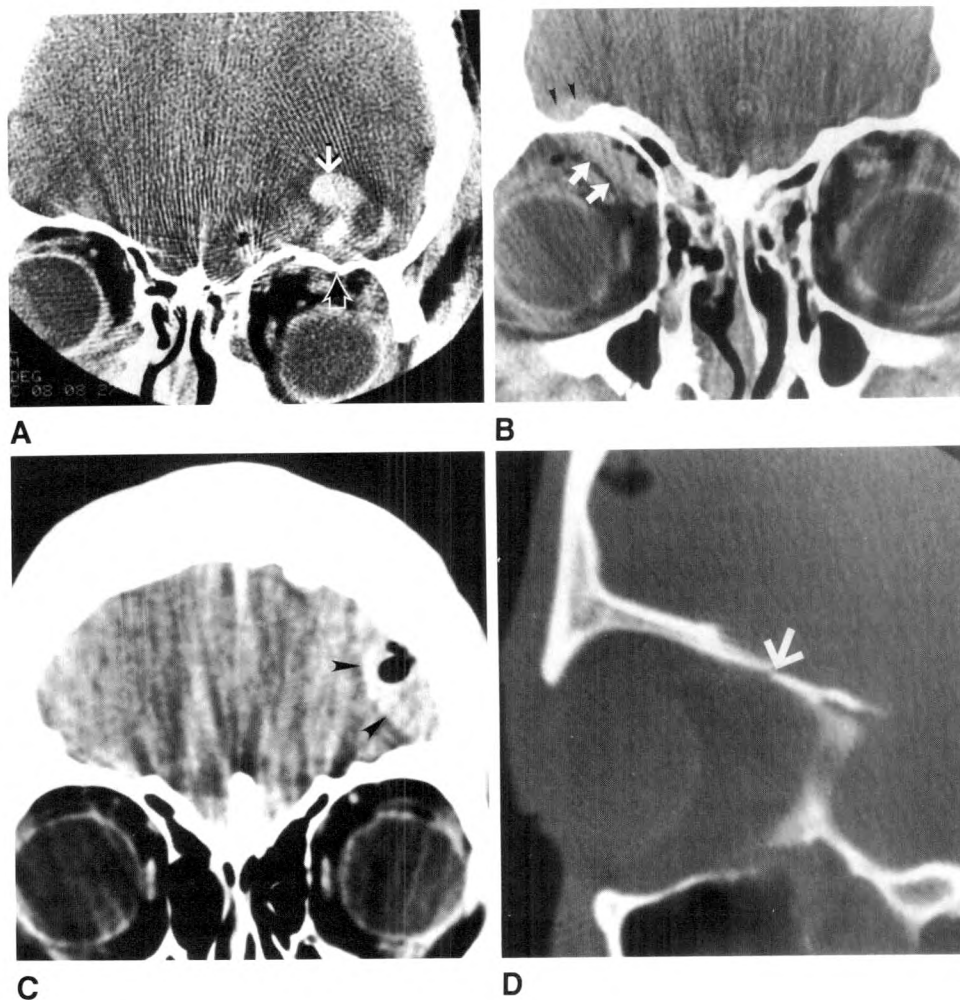
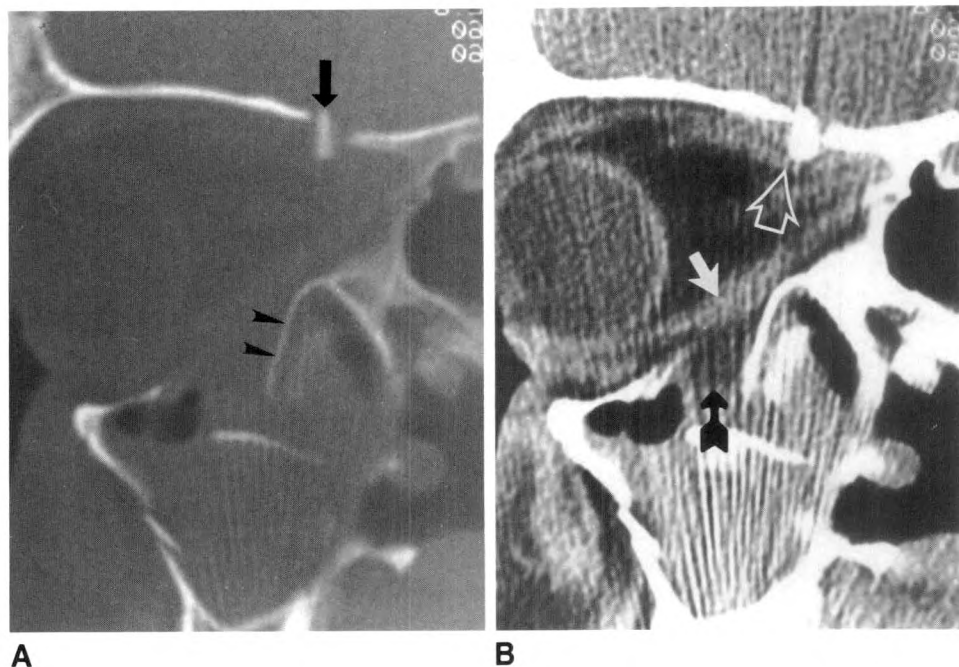


Fig. 9.—Intracranial hematomas associated with orbital roof fractures.

A, patient with intracerebral hematoma (closed arrow) associated with roof fracture (open arrow).

B, Patient with subfrontal epidural hematoma (arrowheads) as well as intraorbital hematoma (arrows) associated with orbital roof fracture (not shown).

C and D, Patient with gas-containing epidural hematoma (arrowheads) associated with roof fracture (arrow).

with the patient supine and neck hyperextended (Fig. 9A) and the direct oblique sagittal projection (Fig. 8).

Radiation Considerations

The greatest radiation dose to the lens in our phantom determinations (Table 2) was with the coronal hyperextended projection, because there is little other body tissue in the scanning plane. In practice it is not always necessary to scan directly through the lens while including the entire orbital floor. Using the hyperflexed neck technique will also decrease lens radiation dose because of inclusion of the neck and shoulders in the scanning plane. For the same reason (inclusion of neck and shoulders in the scanning plane), the least lens radiation dose in our phantom determinations was with the sagittal projection. The increased dose with thinner slices was minimal. The small additional lens radiation exposure from using the sagittal projection should not deter its use, especially when combined with the coronal projection with neck hyperflexed and the lens excluded from the coronal scans.

In conclusion, direct oblique sagittal CT is easily performed and is complementary to the direct coronal projection for the evaluation of orbital floor and roof fractures. It should not be performed alone.

Optimal evaluation of the orbital floor includes the direct coronal projection with the patient supine and neck hyperflexed and the direct oblique sagittal projection. Optimal evaluation of the orbital roof includes the direct coronal projection with the patient supine and neck hyperextended and the direct oblique sagittal projection.

If only one CT projection is to be used, the direct coronal projection is best. If two CT projections are to be used, a consideration of the frequency distribution of orbital wall fractures should dictate the examination sequence. In addition to being thinner, the floor and medial wall are closer to the central axis of the orbit than the roof and lateral wall and are more often fractured by compression of orbital contents, the probable mechanism of orbital wall blow-out fractures [22]. With this in mind, the initial CT projection should be direct coronal with the patient supine and neck hyperflexed. If an orbital floor fracture is present, the direct oblique sagittal projection can then be obtained. If a medial wall fracture is present, the axial projection can then be obtained. If the orbital floor and medial wall are both involved with fracture, the subsequent projection(s) should be selected on the basis of the need to further evaluate the inferior (direct oblique sagittal projection) or medial (axial projection) rectus muscles. If an orbital roof fracture is present, the direct oblique sagittal projection may be considered for further evaluation. Axial head CT may be prudent to evaluate possible associated intracranial injury.

ACKNOWLEDGMENTS

I thank Robert E. Staton, Judith E. Simon, and Barbara Laxton for help with data collection, and Susan Whisenhunt for text preparation.

REFERENCES

1. Mackenzie W. Traite pratique des maladies des yeux. *Trad Laugier Richelot* (Paris) 1844;7
2. Lang W. Injuries and disease of the orbit. *Trans Ophthalmol Soc UK* 1889;9:41-45
3. Smith B, Regan WF Jr. Blow-out fracture of the orbit. *Am J Ophthalmol* 1957;44:733-739
4. Noyek AM, Kassel EE, Wortzman G, Jazrawy H, Greyson ND, Zizmor J. Contemporary radiologic evaluation in maxillofacial trauma. *Otolaryngol Clin North Am* 1983;16:473-508
5. Johnson DH Jr. CT of maxillofacial trauma. *Radiol Clin North Am* 1984;22:131-144
6. Mirsky RG, Saunders RA. A case of isolated medial wall fracture with medial rectus entrapment following seemingly trivial trauma. *J Pediatr Ophthalmol Strabismus* 1979;16:287-290
7. Curtin HD, Wolfe P, Schramm V. Orbital roof blow-out fractures. *AJNR* 1982;3:531-534, *AJR* 1982;139:969-972
8. Ball JB Jr, Towbin RB, Staton RE, Cowdrey KE. Direct sagittal computed tomography of the head. *Radiology* 1985;155:822
9. Converse JM, Smith B. Enophthalmos and diplopia in fractures of the orbital floor. *Br J Plastic Surg* 1957;9:265-274
10. Fujino T. Experimental "blowout" fracture of the orbit. *Plast Reconstr Surg* 1974;54:81-82
11. Putterman AM, Stevens T, Urist MJ. Nonsurgical management of blow-out fractures of the orbital floor. *Am J Ophthalmol* 1974;77:232-239
12. Koornneef L. Current concepts on the management of orbital blow-out fractures. *Ann Plast Surg* 1982;9:185-200
13. McLachlan DL, Flanagan JC, Shannon GM. Complications of orbital roof fractures. *Ophthalmology* 1982;89:1274-1278
14. Cramer LM, Tooze FM, Lerman S. Blowout fractures of the orbit. *Br J Plast Surg* 1965;18:171-179
15. Gould HR, Titus CO. Internal orbital fractures: the value of laminagraphy in diagnosis. *AJR* 1966;97:618-623
16. Hammerschlag SB, Hughes S, O'Reilly GV, Naheedy MH, Rumbaugh CL. Blow-out fractures of the orbit: a comparison of computed tomography and conventional radiography with anatomical correlation. *Radiology* 1982;143:487-492
17. Smith B, Lisman RD, Simonton J, Della Rocca R. Volkmann's contracture of the extraocular muscles following blowout fracture. *Plast Reconstr Surg* 1984;74:200-216
18. Berkowitz RA, Putterman AM, Patel DB. Prolapse of the globe into the maxillary sinus after orbital floor fracture. *Am J Ophthalmol* 1981;91:253-257
19. Smith B, Nightingale JD. Fractures of the orbit: blowout and nasoorbital fractures. *Int Ophthalmol Clin* 1978;18:137-147
20. Stasior OG, Roen JL. Traumatic enophthalmos. *Ophthalmology* 1982;89:1267-1273
21. Hawes MJ, Dortzbach RK. Surgery on orbital floor fractures: influence of time of repair and fracture size. *Ophthalmology* 1983;90:1066-1070
22. Jones DEP, Evans JNG. "Blow-out" fractures of the orbit: an investigation into their anatomical basis. *J Laryngol Otol* 1967;81:1109-1120
23. Yamamoto Y, Sakurai M, Asari S. Towne (half-axial) and semi-sagittal computed tomography in the evaluation of blow-out fractures of the orbit. *J Comput Assist Tomogr* 1983;7:306-309

The "Fat" C2: A Sign of Fracture

Wendy R. K. Smoker^{1,2}
Kenneth D. Dolan

Rotational and lateral bending injuries may cause oblique fractures of the centrum (body) of the second cervical vertebra below the odontoid and plane of the superior articular facets. These fractures are often obscure because the fracture lines are frequently not perpendicular to the plane of the radiograph on either anteroposterior or lateral views. The fracture fragments may shift in relation to one another, causing the body of C2 to appear enlarged or "fat" in relation to C3. We discuss the basis of the "fat" C2 sign and illustrate a variety of fractures that can produce this change.

Because they are so uncommon, C2 body fractures have received little attention in the literature. In a recent review of 107 axis fractures encountered over a period of 8 years, Hadley et al. [1] identified only eight (7.5%) fractures of the body of the axis. The purpose of the present study is to draw attention to the fact that enlargement of the C2 centrum on plain lateral radiographs may be the only indication of an unstable axis injury.

The "Fat" C2

Vertical fractures in the coronal plane with little oblique component but with fragment displacement facilitate our understanding of the "fat" C2 sign (Fig. 1). The fracture lines are clearly visible, and there is interruption of both the anterior and posterior tangent lines.

If the fracture courses obliquely through the body of the axis, the fracture lines (fragment separation) may not be visible on lateral radiographs. Displacement of the fracture fragments, however, will cause the body of C2 to appear fat in relation to C3. The enlargement of C2 may be rather obvious (Fig. 2) or it may be extremely subtle (Fig. 3). Although only the anterior or posterior tangent line may be interrupted, most commonly both lines are affected. Predominant anterior tangent-line interruption indicates a primary hyperflexion injury (Fig. 4), while predominant posterior tangent-line interruption is indicative of a hyperextension injury (Fig. 5). Interruption of both lines may be secondary to a combined hyperflexion-hyperextension injury (Figs. 6 and 7).

Discussion

We have found that the centrum of the C2 vertebrae in males may differ from that in females. In males, the anteroposterior dimension is often greater than the vertical dimension, producing a rectangular configuration. (The superior margin of the centrum is considered to be at the plane of the superior articular facets.) In females, the anteroposterior and vertical dimensions may be almost equal, producing a square configuration. Normally, lines drawn tangent to the anterior and posterior surfaces of C3 fall tangent to the anterior and posterior surfaces of C2 (Fig. 8) [2].

"Complex" fractures involving the body of the axis may result from a combination of forces during injury. Rotation-extension, rotation-flexion, right or left lateral bending with flexion and/or extension, and long-axis force applications produce

This article appears in the January/February 1987 issue of *AJNR* and the March 1987 issue of *AJR*.

Received March 12, 1986; accepted after revision June 10, 1986.

¹ Both authors: Department of Radiology, University of Iowa Hospitals and Clinics, Iowa City, IA 52242.

² Present address: Department of Radiology, University of Utah School of Medicine, 50 North Medical Drive, Salt Lake City, UT 84132. Address reprint requests to W. R. K. Smoker.

AJR 148:609-614, March 1987
0361-803X/87/1483-0609
© American Roentgen Ray Society

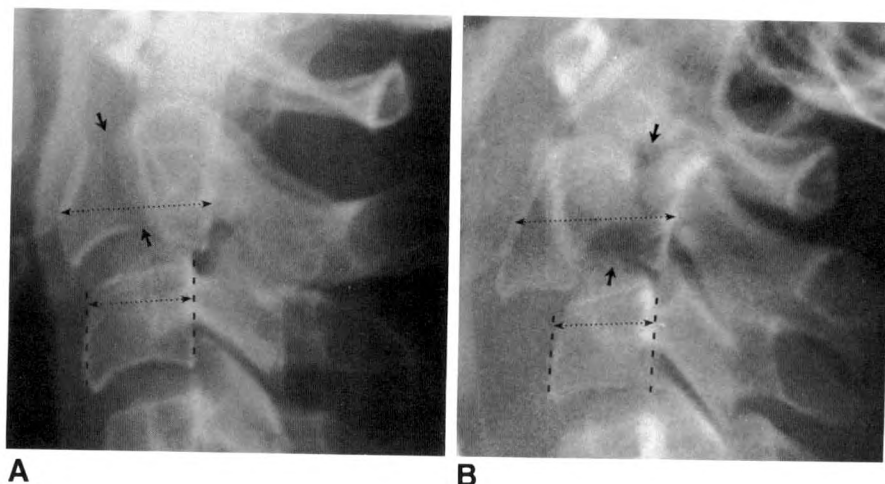


Fig. 1.—Fat C2 in two patients (A and B, respectively) resulting from obvious vertical oblique fractures (arrows). Both anterior and posterior tangent lines are interrupted. Anteroposterior dimensions of C2 are much greater than those of C3.

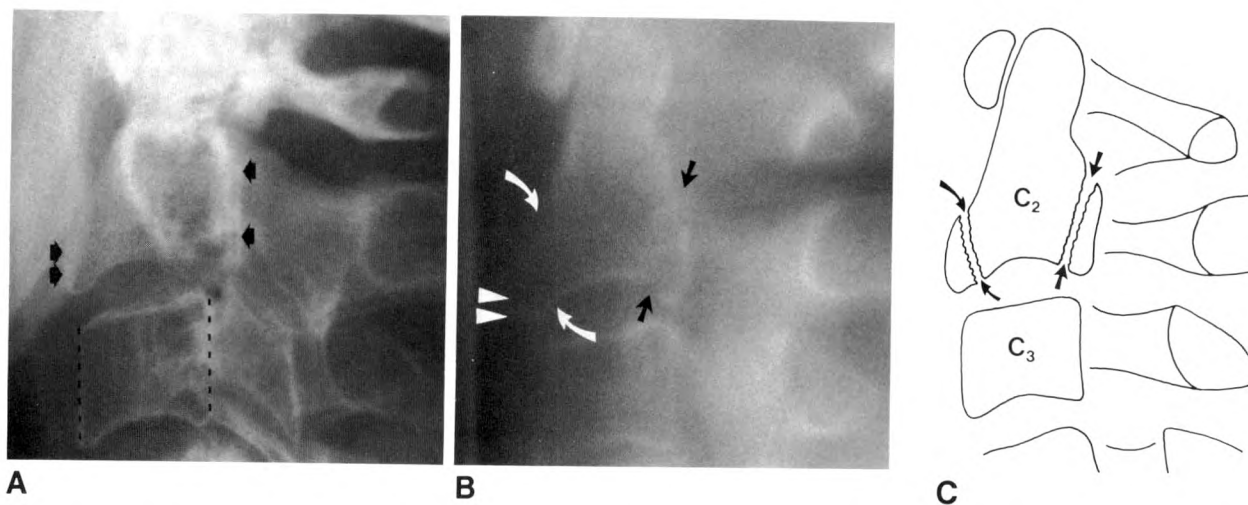


Fig. 2.—A, Lateral radiograph—obvious fat C2 resulting from compound oblique fracture. Fracture line is not clearly visible. Midsagittal tomogram (B) and line diagram (C) demonstrate anterior (curved arrows) and posterior (straight arrows) extent of fracture. Parasagittal tomograms (not illus-

trated) revealed a vertical oblique fracture extending through left foramen transversarium and a horizontal oblique fracture extending across right neural arch.

complex obliquity of the fracture planes as they extend through the body of the axis. This may lead to separation of the axis body into two or more fracture fragments. Anterior tangent-line interruption occurs when a fracture fragment is displaced anteriorly, whereas posterior fragment displacement will result in interruption of the posterior tangent line. A "bursting" type of fracture, or a combined hyperflexion-hyperextension injury, may produce anterior shift of one fragment and posterior shift of the other fragment, resulting in simultaneous anterior and posterior tangent-line interruption. This pattern of tangent-line displacement is the type we have encountered most commonly. Similarly, Davis et al. [3] found combination anterior and posterior ligamentous disruption to be most common in autopsy series. In all three conditions, the anteroposterior diameter of the axis vertebral body, as seen on plain radiographs, will be larger than the anteropos-

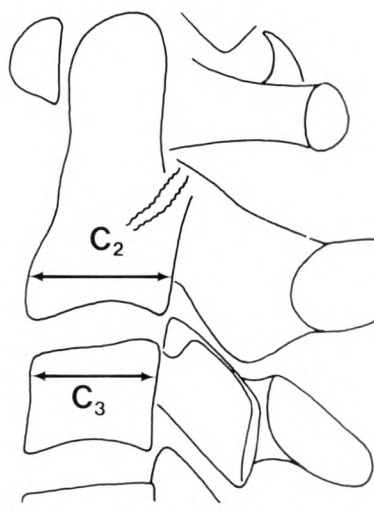
terior diameter of the subjacent normal C3 vertebral body; hence, the fat C2 as a term suggesting a complex fracture involving the axis. The horizontal shift in fragment position results in an increased anteroposterior diameter of the centrum axis on plain lateral radiographs.

We have illustrated with complex-motion tomography the very oblique direction of the fracture planes in these rare injuries. This obliquity is such that the actual separation of bone is in neither the coronal nor the lateral plane so that the associated separation one customarily expects to see with a fracture is not evident on plain frontal or lateral radiographs.

CT may be helpful for further evaluation of "complex" axis fractures [4, 5]. If the fracture plane is predominantly coronal, the principal fracture fragments will be separated in an anteroposterior direction and one may see the anterior and posterior fragment displacement that interrupted the appropriate



A



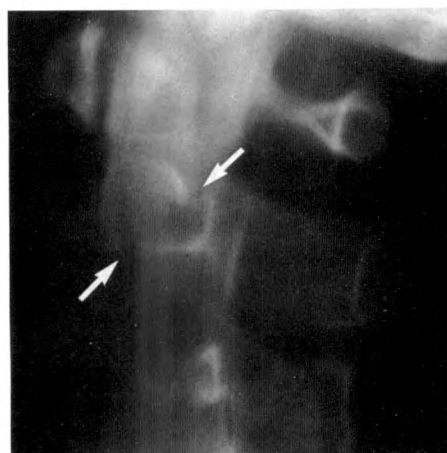
B

Fig. 3—Lateral radiograph (A) and line diagram (B) reveal subtle increase in anteroposterior diameter of C2. Both anterior and posterior tangent lines are interrupted.

C, Left parasagittal tomogram.

D, Midsagittal tomogram.

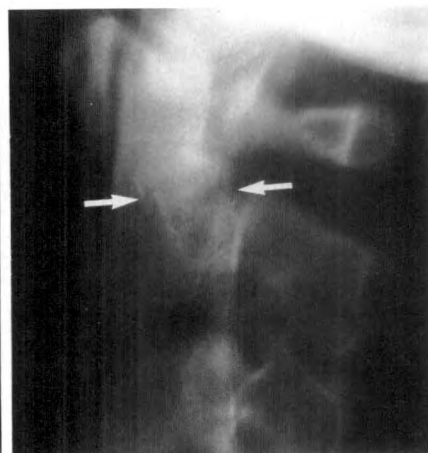
E, Right parasagittal tomogram. Note change in position of compound oblique fracture as it crosses from left to right (arrows).



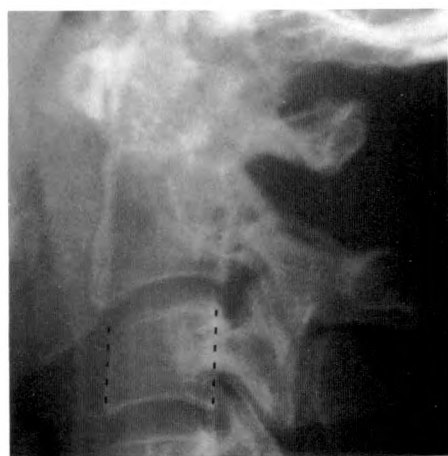
C



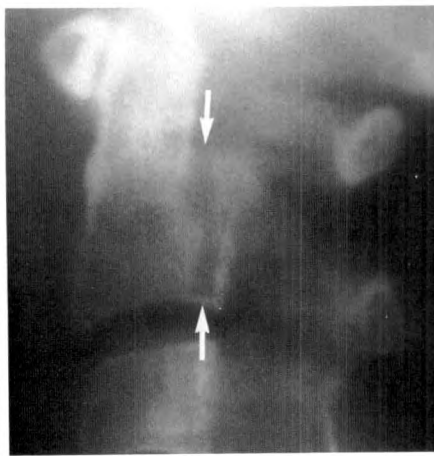
D



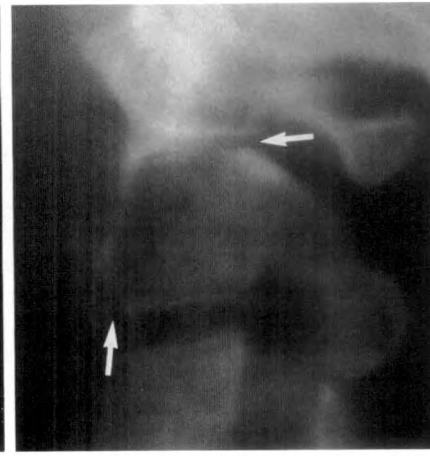
E



A



B



C

Fig. 4.—A, Lateral radiograph—predominant interruption of anterior tangent line produces a fat C2. Fracture line is not visible.

B, Midsagittal tomogram reveals posterior component of vertical oblique fracture (arrows).

C, Right parasagittal tomogram shows anterior component of same fracture (arrows). Left half of C2 and odontoid process have been displaced anteriorly, producing a fat C2.

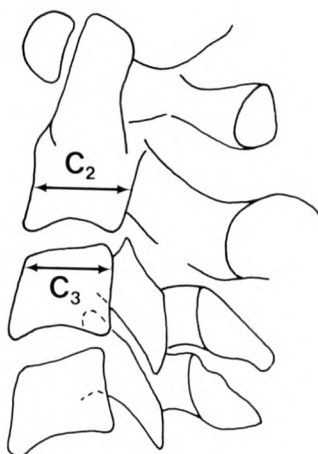
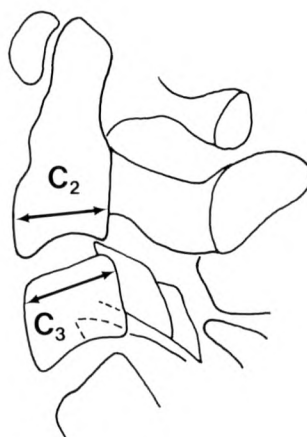
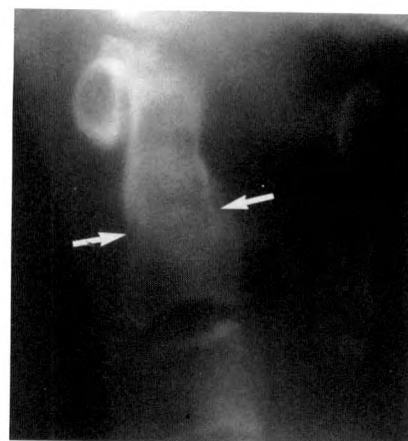
**A****B****C****D****E**

Fig. 5.—Lateral radiograph (A) and line diagram (B)— isolated posterior tangent line interruption without visualization of fracture. Previous normal lateral radiograph (C) and line diagram (D) for comparison. Midsagittal tomogram (E) shows horizontal fracture of axis body below odontoid (arrows).

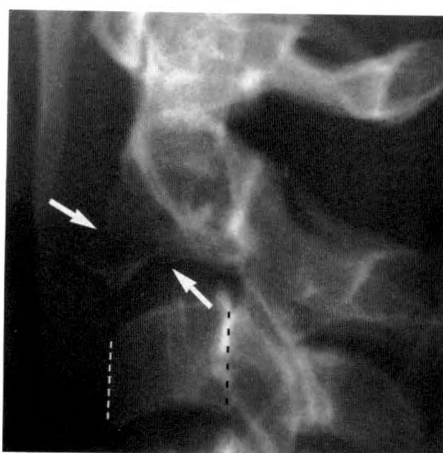
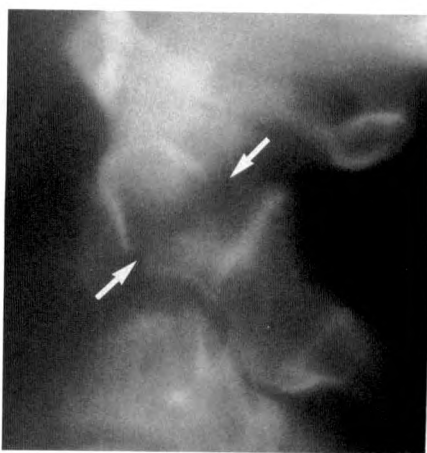
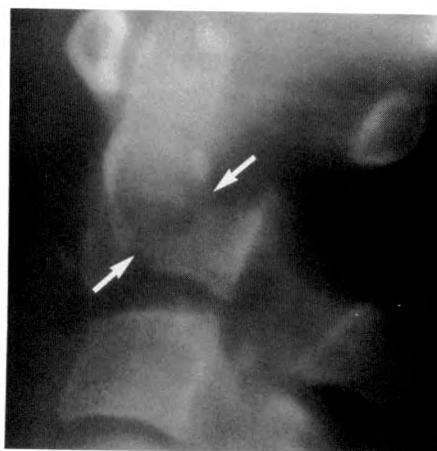
**A****B****C**

Fig. 6.—A, Lateral radiograph—a small anterior avulsion fracture is identified (arrows) that does not explain tangent line interruption and fat C2 appearance. Left parasagittal (B) and midsagittal (C) tomograms show C2 body fracture (arrows).

tangent lines on plain radiographs (Fig. 7). If, however, the fracture plane is largely in the horizontal axis, it may be extremely difficult to see the fracture on CT unless high-quality sagittal or coronal reconstructed images are obtained.

Patients with cervical spine injuries are often in pain and, in our experience, frequently move during scanning, making reconstructed images difficult to obtain. We have found that sagittal polytomography can be performed in less than half

Fig. 7.—Lateral radiograph (A) and line diagram (B) reveal sizable anterior avulsion fracture (arrow) and a fat C2. Axial CT cuts (C and D) demonstrate oblique and vertical components of axis fracture (arrowheads). (Reprinted with permission from [8]).

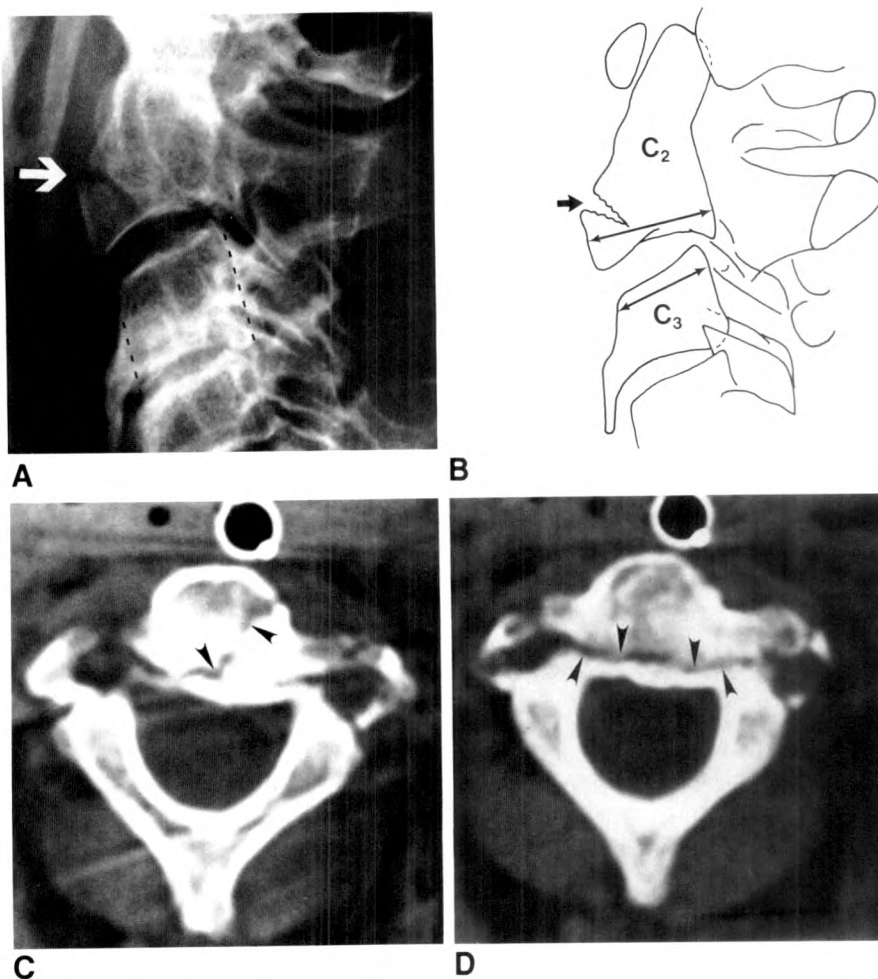
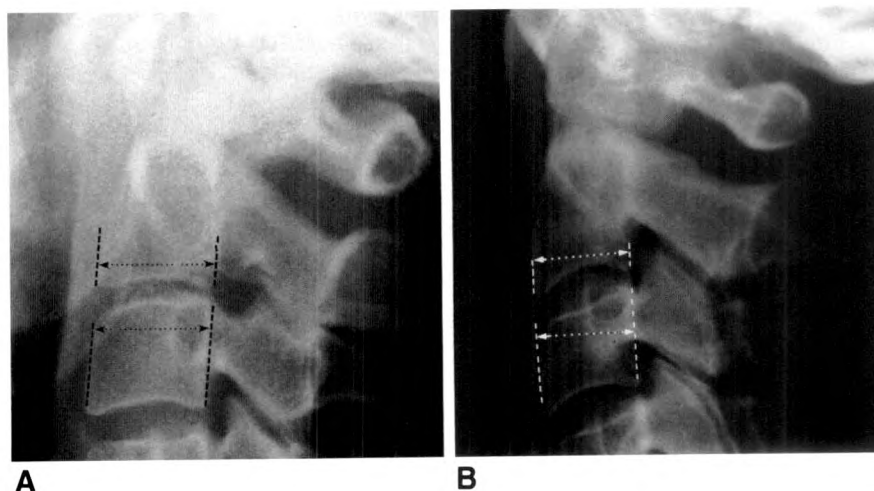


Fig. 8.—Normal male (A) and female (B). Lines drawn tangent to anterior and posterior surfaces of C3 fall tangent to anterior and posterior surfaces of C2. Anteroposterior dimensions of C2 and C3 are the same.



the time required to obtain thin overlapping axial CT cuts necessary for high-quality sagittal CT reconstructions. Depending on the condition of the patient and the findings on sagittal polytomography, coronal polytomograms may additionally be obtained.

MR imaging may be helpful for evaluating patients with

complex-angle axis fractures [6, 7]. The vertebral marrow, spinal cord, size and shape of the spinal canal, and adjacent soft-tissue structures may all be directly imaged in multiple planes without patient manipulation (Fig. 9). The presence or absence of subarachnoid space or spinal cord compression by a posteriorly displaced fracture fragment or an associated

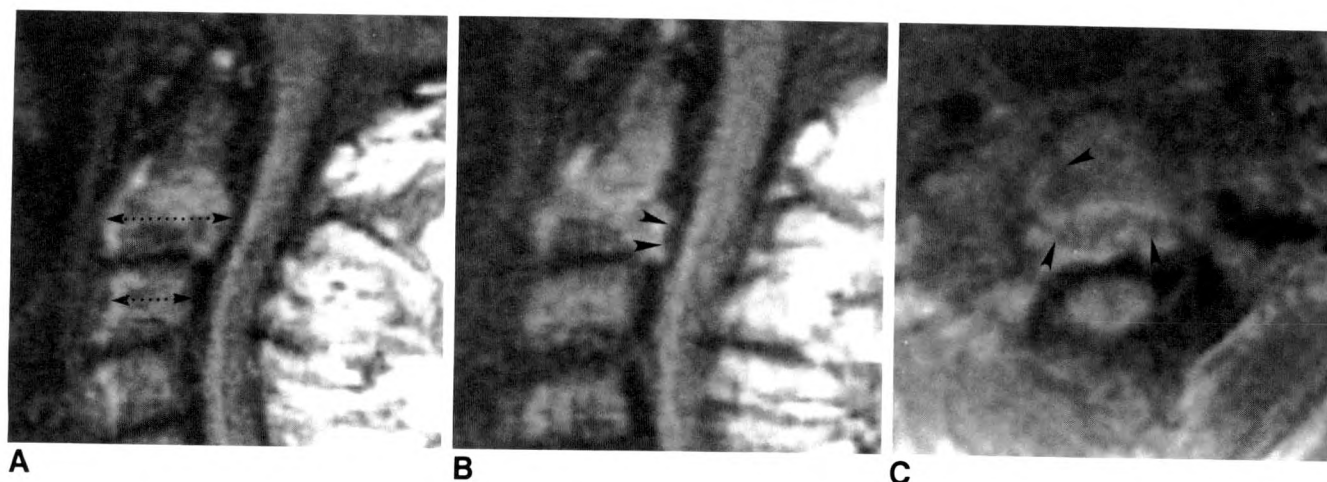


Fig. 9.—A, Midsagittal T1-weighted MR scan shows a fat C2. In midline, expansion of C2 is noted to be both anterior and posterior. B, Right parasagittal MR scan—right portion of fragment is displaced more posteriorly (arrowheads). No significant cord compression is identified, although ventral subarachnoid space is compromised. C, Axial T1-weighted MR scan shows components of fracture (arrowheads).

epidural hematoma is easily assessed without the necessity of intrathecal contrast material. For optimal evaluation, T1- and T2-weighted images in both the sagittal and transverse planes are recommended. The T1-weighted images better delineate the presence of spinal cord compression. In the absence of cord compression, we have found compromise of the subarachnoid space more accurately depicted on the T2-weighted images.

The main purpose of the fat C2 sign is to provide an easily recognizable sign of axis injury when the geometric complexity of an oblique fracture makes recognition by means of fracture-line separation difficult. The main implication of a fat C2, identified on plain radiographs, is that an unstable fracture with fragment displacement is present and that further imaging assessment is necessary to evaluate the effect of the fracture on the adjacent spinal cord and meningeal structures.

We have illustrated a variety of axis centrum (body) fractures that can produce anteroposterior displacement of the fracture fragments and lead to apparent "enlargement" of the axis vertebral body on plain radiographs. The fat C2 sign should be a helpful radiographic means for identifying these injuries.

ACKNOWLEDGMENTS

Our thanks to William D. Keyes for the MR in Case 9, to Mark N.

Hadley for the material in Case 7, to Janice Widmer for her excellent secretarial assistance, and to Steve Moon for his photographic expertise.

REFERENCES

1. Hadley MN, Browner C, Sonntag VKH. Axis fractures: a comprehensive review of management and treatment in 107 cases. *Neurosurgery* 1985;17:281-290
2. Gerlock AJ, Kirchner SG, Heller RM, Kaye JJ. *The cervical spine in trauma*. Philadelphia: Saunders, 1978;6-7
3. Davis D, Bohlman H, Walker EA, Fisher R, Robinson R. The pathological findings in fatal craniocervical injuries. *J Neurosurg* 1971;34:603-613
4. Steppe R, Bellemans M, Boven F, DeSmedt E. The value of computed tomographic scanning in elusive fractures of the cervical spine. *Skeletal Radiol* 1981;6:175-178
5. Baumgarten M, Mouradian W, Boger D, Watkins R. Computed axial tomography in C1-C2 trauma. *Spine* 1985;10:187-192
6. Han JS, Benson JE, Yoon YS. Magnetic resonance imaging in the spinal column and craniovertebral junction. *Radiol Clin North Am* 1984;22:805-827
7. Modic MT, Weinstein MA, Pavlicek W, et al. Nuclear magnetic resonance imaging of the spine. *Radiology* 1983;148:757-762
8. Hadley MN, Browner C, Sonntag VKH. Miscellaneous fractures of the second cervical vertebra. *BNJ Quart* 1985;1:34-39

Case Report

Traumatic Pneumorrhachis

Ronald G. Newbold,¹ M. David Wiener, James B. Vogler III, and Salutaris Martinez

Although pneumocephalus is a well-recognized complication of skull fracture, extracranial air collections previously have been reported only within the subaponeurotic space of the scalp, the subgaleal aerocele [1]. A case of cervical pneumorrhachis (air within the spinal canal) secondary to basilar skull fracture is presented.

Case Report

A 24-year-old man was found lying next to his automobile; apparently, he had been involved in a motor vehicle accident. He was awake and hemodynamically stable. Clinical evidence indicated extensive facial trauma. A chest radiograph showed several rib fractures; a subsequent aortogram was normal. A lateral cervical spine radiograph showed air within the spinal canal (Fig. 1). Skull radiographs were not obtained. Cranial CT showed extensive bilateral comminuted facial fractures, comminuted sphenoid sinus and basioccipital fractures, and bilateral temporoparietal fractures. In addition, pneumocephalus with air/fluid levels in multiple paranasal sinus was seen (Fig. 2).

The patient underwent incision and drainage of a depressed left parietal fracture and surgical fixation of a mandibular fracture. His hospital course was complicated by meningitis and persistent CSF rhinorrhea requiring transsphenoidal patch repair of the leak. The patient was still alive after a 2-month hospitalization.

Discussion

Air contained within the spinal canal is termed pneumorrhachis. Although not previously reported, traumatic pneumocephalus can cause pneumorrhachis.

The term pneumocephalus was first used in 1852 to describe spontaneous accumulation of extracranial air secondary to changes in the mastoid cells. Intracranial air was first described at autopsy by Chiari in 1884. Traumatic pneumocephalus was recognized later in 1913, by skull radiography in a man struck by a trolley car [2]. Trauma now accounts for most cases of pneumocephalus (74%). Other causes include neoplasms (13%), infections (9%), and previous surgery (4%). Although less than 3% of all skull fractures are associated with pneumocephalus, approximately 8% of fractures of the paranasal sinuses result in this condition [3]. Along with air/fluid levels in or opacification of the sphenoid sinus, pneumocephalus is an important secondary sign of basilar skull fracture on skull radiographs.

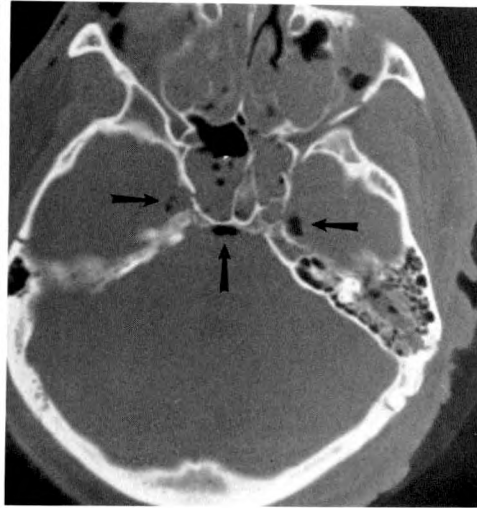
Pneumocephalus is classified as either intra- or extracranial. Intracranial pneumocephalus is further subdivided into extradural, subdural, subarachnoid, intracerebral, and intraventricular [1]. Subdural and subarachnoid collections are most common. Extracranial pneumocephalus previously has been reported only within the subaponeurotic space of the scalp, the subgaleal aerocele [1]. It results from fracture of the mastoid air cells or, less commonly, frontal sinuses [3].

Traumatic pneumorrhachis results from fracture of an air-containing cranial cavity with an associated dural tear thus allowing communication with the subarachnoid space. Its presence implies an open injury with an accompanying 25% risk of meningitis and a 16% mortality rate [4]. In our case, pneumorrhachis was the initial radiographic indication of basilar skull fracture. We therefore suggest that pneumorrhachis, like pneumocephalus, be recognized as a secondary sign of

¹ All authors: Department of Radiology, Duke University Medical Center, Durham, NC 27710. Address reprint requests to J. B. Vogler III.



1



2

Fig. 1.—Lateral cervical spine radiograph shows air within spinal canal.

Fig. 2.—Cranial CT scan shows comminuted sphenoid sinus fracture with surrounding pneumocephalus (arrows).

basilar skull fracture on lateral cervical spine radiographs. Discovery of pneumorrhachis should prompt further investigation with cranial CT to define the extent of injury.

REFERENCES

1. Jones HM. Cranial pneumatocele. *Proc R Soc Med* 1970;63:257-262
2. Markham JW. The clinical features of pneumocephalus based upon a survey of 284 cases with report of 11 additional cases. *Acta Neurochir (Wein)* 1967;16:1-78
3. Rogers LF. *Radiology of skeletal trauma*. New York: Churchill Livingstone, 1982:221-223
4. North JW. On the importance of intracranial air. *Br J Surg* 1971;58:826-829

Technical Note

Direct Percutaneous Ureterolithotomy

Tony P. Smith,¹ David W. Hunter,¹ John C. Hulbert,² Michael D. Darcy,¹ Wilfrido R. Castaneda-Zuniga,¹ and Kurt Amplatz¹

Although percutaneous removal of ureteral calculi via a nephrostomy tract has been successful [1, 2], stones occasionally become impacted or even extruded during the attempt [3]. In such a case, an alternative to open surgical ureterolithotomy might be a percutaneous ureterolithotomy done directly via the flank.

Case Report

An 88-year-old woman had a large, partially obstructing, upper ureteral calculus that had resulted in several episodes of urosepsis. After the infection was well controlled with conventional nephrostomy drainage and 6 days of antibiotic therapy, conventional percutaneous removal was attempted. During the attempt, the stone became impacted in the previously normal ureteral wall, and the procedure was halted with the unreachable stone protruding partially inside and partially outside the tortuous and edematous ureter. A follow-up nephrostogram showed complete obstruction at the site of the stone.

At the time of the second attempt, a safety wire could be advanced past the stone to the bladder, but the stone could still not be removed even with the flexible nephroscope (Figs. 1, 2A). By using the stone as a radiographic target, a direct puncture through the left flank was made with an 18-gauge needle. The needle tip was deflected off the stone into the adjacent ureter. A 0.035-in. (0.089 cm) floppy guidewire was passed into the ureter, where it was grasped with the flexible scope and brought out at the original nephrostomy site (Fig. 2B). Over the resulting through-and-through wire (Fig. 2C), the tract was easily dilated to 30 French, and a working sheath with a 34-French outer diameter was placed with its tip just outside the opening into the side of the ureter. Nephroscopic lithotripsy was used to completely remove the stone (Fig. 2D). A 5-French catheter was left outside the ureter in the flank for drainage. A 14-French internal-

external stent was placed over the original safety wire with side holes in the renal pelvis and bladder. The 5-French catheter was removed 48 hr later after only scant drainage had ceased. The patient was discharged after 72 hr. The 14-French catheter was removed 1 month

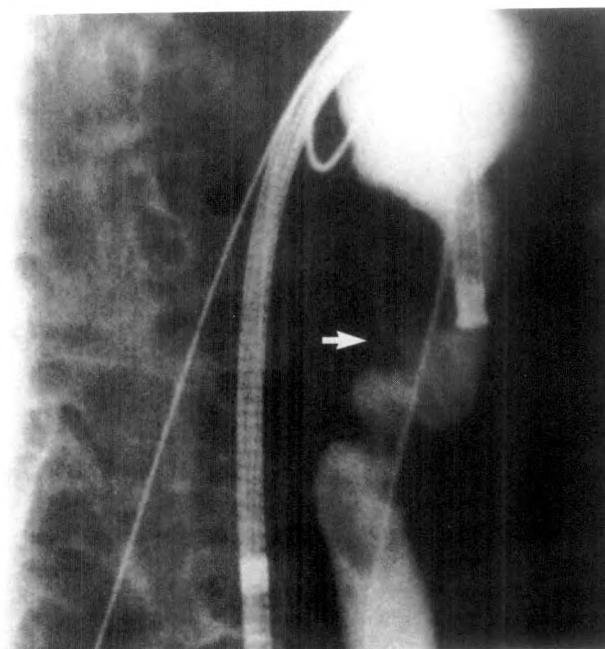


Fig. 1.—Nephrostogram shows flexible nephroscope placed via nephrostomy site to level of stone (arrow) and a guidewire placed from nephrostomy site to bladder via the ureter.

Received July 1, 1986; accepted after revision September 25, 1986.

¹ Department of Radiology, University of Minnesota Hospital, Minneapolis, MN 55455. Address reprint requests to K. Amplatz, Department of Radiology, University of Minnesota Hospital and Clinic, Harvard St. at East River Rd., Box 292 UMHC, Minneapolis, MN 55455.

² Department of Urology, University of Minnesota Hospital, Minneapolis, MN 55455.

AJR 148:617-619, March 1987 0361-803X/87/1483-0617 © American Roentgen Ray Society

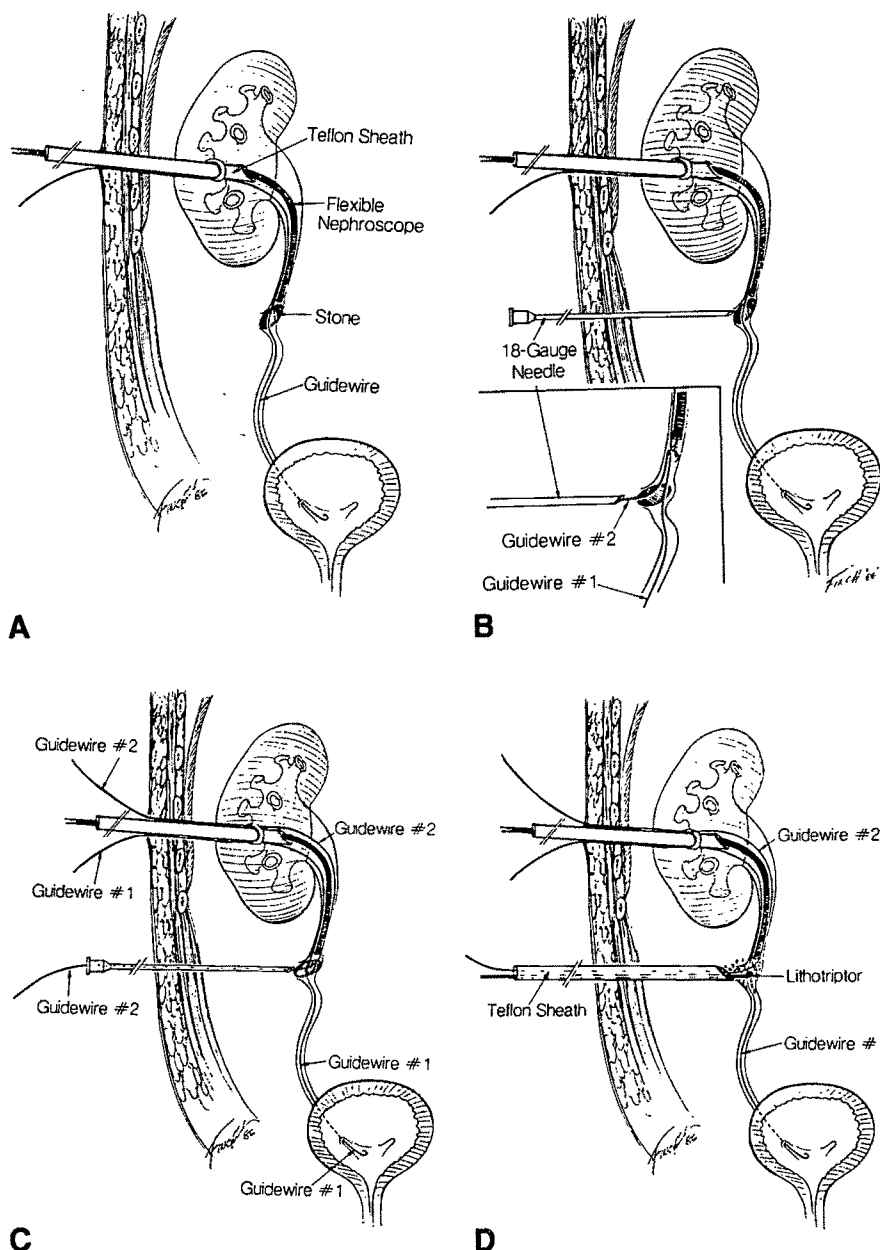


Fig. 2—A, Teflon working sheath is inserted via nephrostomy site for placement of flexible nephroscope to level of stone from above.

B, 18-gauge needle is placed onto stone. Inset shows grasping of wire via flexible scope to pull wire through nephrostomy site, resulting in a through-and-through working wire.

C, Through-and-through wire is placed past stone via 18-gauge needle.

D, Lithotripter is placed via a working sheath for disintegration of stone.

later after a follow-up nephrostogram showed a normal ureter, and the patient has been doing well on subsequent visits.

Discussion

The direct percutaneous retroperitoneal approach has been used in laboratory animals for ureteral manipulations [4]. A single case of percutaneous ureterolithotomy has been described [5], but a direct transretroperitoneal ureteral puncture for stone removal has not.

Direct ureteral puncture was aided significantly in this case by the previous nephrostomy through which contrast material could be injected to opacify the ureter (Fig. 1). A nephroscope could then be inserted for direct visualization of the needle tip to confirm its location (Fig. 2B) and grasp the guidewire as

the guidewire emerged from the needle tip (Fig. 2B inset) to form a through-and-through wire (Fig. 2C). Direct visualization by endoscopy coupled with fluoroscopy allowed tract dilatation to be carried up to, but not into, the ureter. A 5-French catheter was placed over the through-and-through wire to prevent laceration of the ureter by any inadvertent sawing motions of the bare guidewire against the ureteral wall at the entry site. No catheter larger than 8-French was ever placed through the ureterotomy, which meant that the size of the ureteral opening was limited to that created by the 9-French tip of the lithotripsy probe. Given the known ability of the perforated urinary tract to heal [6], it is not surprising that a puncture of this size can be made into the ureter without complication.

A number of possible complications were considered before the procedure was performed. Anatomic landmarks were carefully studied to prevent perforation or laceration of bowel and aorta. A working sheath was used to prevent collection of the intraprocedural flush fluid in the retroperitoneum, and a drainage catheter was used to prevent postprocedural formation of a urinoma. The lithotripter was used instead of graspers to prevent ureteral avulsion. The procedure could be attempted only after a safety wire was placed down the ureter past the stone. Such a wire was essential to preserve the integrity of the ureter so that an internal-external ureteral stent could be placed across the ureterotomy at the end of the procedure. The stent allowed the ureter to heal without leakage or formation of a stricture.

This case illustrates the potential of interventional and endourological procedures and shows that standard nephrostomy skills can be applied to direct ureteral access. Although clinical indications for such an approach to impacted and partially extruded ureteral stones are limited, the technique is

an alternative to standard surgical ureterolithotomy in selected cases.

REFERENCES

1. Reddy PK, Hulbert JC, Lange PH, et al. Percutaneous removal of renal and ureteral calculi: experience with 400 cases. *J Urol* 1985;134:662-665
2. Hunter DW, Castaneda-Zuniga WR, Young AT, et al. Percutaneous removal of ureteral calculi: clinical and experimental results. *Radiology* 1985;156:341-348
3. Verstandig AG, Banner MD, Arsdalen KN, Pollack HM. Upper urinary tract calculi: extrusion into perinephric and periureteric tissues during percutaneous management. *Radiology* 1986;158:215-218
4. Lund G, Rysavy JA, Hunter DW, Castaneda-Zuniga WR, Amplatz K. Percutaneous occlusion of the ureter: a new approach for relief of urinary tract fistulae. *Semin Intervent Radiol* 1984;1:92-93
5. Clayman RV, Preminger GM, Franklin JF, Curry T, Peters PC. Percutaneous ureterolithotomy. *J Urol* 1985;133:671-673
6. Brannen GE, Bush WH, Correa RJ, Gibbons RP, Elder JS. Kidney stone removal: percutaneous versus surgical lithotomy. *J Urol* 1985;133:6-12

1987 ARRS Meeting Summary, April 26–May 1, Miami Beach, FL

A comprehensive description of the meeting, including the scientific program, Categorical Course in Gastrointestinal Radiology, and instructional courses, appears in this issue of the *AJR*. A special loose insert on the meeting also accompanies this issue. Meeting and registration forms will be found in the February and March issues. These may be photocopied.

Accreditation

All courses and scientific sessions carry AMA Category I credit on an hour-for-hour basis.

Meeting Format

Scientific Program. Sessions will be grouped in parallel sessions, Monday–Thursday. A total of 189 scientific papers will be presented in 18 sessions. In addition, on Wednesday, April 29, the morning session will feature award papers and the Caldwell Lecture, which will be delivered by M. Paul Capp of the Arizona Health Sciences Center, Tucson, AZ. On Friday, there will be a special symposium on genitourinary imaging.

Categorical Course in Gastrointestinal Radiology. This 14-hr course will be Sunday–Thursday. Registrants may enroll in other courses as well.

Luncheon Sessions. Registrants may enroll in special luncheon sessions, Monday–Thursday. A box lunch will be provided.

Exhibits

Scientific Exhibits and Case of the Day Presentations will be Monday–Thursday, April 27–30.

Commercial Exhibits will be open daily, Monday–Thursday.

Local Activities

General Reception. Tuesday evening, April 28, for all registrants.

Golf Tournament. Monday, April 27, Turnberry Isle Country Club, North Miami Beach, FL. Transportation leaves the hotel at 11 a.m.; shotgun start at 1 p.m.

Men's and Women's Tennis Tournaments. Monday, April 27, Turnberry Isle Country Club, North Miami Beach, FL. Transportation leaves the hotel at 11 a.m.

Local Tours. Sunday, April 26, 6–10 p.m., Dinner Cruise and Show Aboard the Yacht THE SPIRIT; Monday, April 27, 9 a.m.–1 p.m., Tour of Miami and Bal Harbour Shopping Tour; Tuesday, April 28, 9 a.m.–4 p.m., Parrott Jungle and Seaquarium; Wednesday, April 29, 9 a.m.–1 p.m., Villa Vizcaya Tour; Thursday, April 30, 9 a.m.–1 p.m., Metro Zoo; 6:30–11:30 p.m., Les Violins Supper Club; Friday, May 1, 9–11 a.m., Tour of Miami Beach. No refunds after April 15 (March 20 for SPIRIT cruise).

Meeting Registration

Preregistration will be accepted until March 26. There will be on-site registration. Official badges and program books will be available at the registration desk, Fontainebleau Hilton Hotel. No confirmations will be mailed.

Course Registration

Register early—enrollment is limited. List first, second, and third choices for each period. Also, indicate whether you wish to take the categorical course. Deadline for mail registration is March 26. All ticket orders will be filled by postmark. Course tickets *will not* be mailed. Tickets will be available on and after Saturday, April 25 (after 1 p.m.), at the ARRS registration desk in the Fontainebleau Hilton Hotel. There will be on-site registration for courses not already filled.

Hotel Registration

Reservations are handled by the ARRS Housing Bureau, Fontainebleau Hilton, Attn: Reservations, 4441 Collins Ave., Miami Beach, FL 33140. These must be received by March 26. Make check payable to Fontainebleau Hilton Hotel.

Fees

Meeting:

ARRS members and resident members	No fee
Nonmembers	\$100
Nonmember physicians in training (with verification)	25
Categorical course (all who attend)	75
Luncheon sessions/each	10
Golf tournament	65
Tennis tournaments	50
Local tours	11–40

Cancellations and Fee Refunds

Fees will be refunded only if cancellation is received by April 19. Send to American Roentgen Ray Society, 1891 Preston White Drive, Reston, VA 22091.

Air Transportation

Eastern Airlines will discount fares 60%. Information: (800) 468-7022 outside Florida and (800) 282-0244 within Florida. Mention ARRS number EZ4P5.

United Airlines is also offering discount fares. Call (800) 521-4041 (48 contiguous states) or (800) 722-5243, ext. 6608 (AL, HI). Mention ARRS number 7092H.

Associated Meeting

Society for Pediatric Radiology and European Society of Pediatric Radiology

The inaugural conjoint International Pediatric Radiology '87 meeting will meet May 30–June 4, 1987, at the Westin Hotel, Toronto, Ontario, Canada. Registration is limited to pediatric radiologists. For details contact: Donald R. Kirks, M.D., Secretary, Society for Pediatric Radiology, c/o Dept. of Radiology, Childrens Hospital Medical Center, Elland and Bethesda Aves., Cincinnati, OH 45229, (513) 559-4880.

The 1988 SPR meeting will be held the weekend preceding the ARRS meeting.

Technical Note

Translumbar Inferior Vena Cava Hickman Catheter Placement for Total Parenteral Nutrition

Donald F. Denny, Jr.,¹ Gary S. Dorfman,² Lee H. Greenwood,¹ Nina R. Horowitz,³ and Steven S. Morse¹

Permanent total parenteral nutrition (TPN) via an indwelling, Silastic, central venous catheter is in wide use for patients with short-bowel syndrome or malabsorption. Standard vascular access has been via the jugular or subclavian veins with the catheter tip placed in the superior vena cava or right atrium. Unfortunately, the combination of the indwelling foreign body and the hyperosmolar TPN solution often results in thrombosis and sclerosis of the access veins, requiring a new catheter in a different position [1]. With time, all standard access routes may become occluded. Alternate routes such as the inferior epigastric vein and the saphenous vein are useful in children [2]. Arteriovenous fistulas have had mixed results [1, 3]. Direct central venous cannulation via open thoracotomy is limited by the complexity and risk of the surgery [4]. In this report we describe a technique for placement of a Hickman catheter (Evermed, Medina, WA) by percutaneous translumbar inferior vena cava (IVC) cannulation.

Subjects and Methods

The procedure was performed on two patients requiring home TPN for short-bowel syndrome. Each patient had occluded both jugular and subclavian veins from previous catheters and had superior vena cava (SVC) thrombosis. The clinical details of one patient have been previously described [5].

Preoperative evaluation included prothrombin time, partial thromboplastin time, platelet count, and hematocrit. An inferior vena cogram was performed to rule out anatomic variation and to confirm patency. A catheter may be left in the IVC as an aid to translumbar

needle placement.

The technique for translumbar IVC cannulation is analogous to that of translumbar arteriography [6]. With the patient prone, a point on the skin just cephalad to the right iliac crest and approximately 10 cm lateral to the midline is marked. The desired entry point into the IVC is below the renal veins. The third lumbar vertebral body (L3) is marked under fluoroscopy. After infiltration of the skin and subcutaneous tissues with lidocaine 1%, an 18-gauge Teflon sheath over a 19-gauge stylet needle (Becton Dickinson, Rutherford, NJ) is advanced under fluoroscopy in an oblique path at approximately a 45° angle until it hits L3. Then, by redirecting the needle at slightly increasing angles, the needle tip is "marched" anteriorly across the vertebral body into the IVC. When the needle tip is seen to project in front of L3 in the expected position of the IVC, the stylet is removed and a syringe is attached to the needle. By advancing or withdrawing the needle while maintaining negative pressure on the syringe, the IVC lumen will be found. Sometimes, a distinct "pop" will be felt as the needle enters the IVC. Once in the lumen the needle is removed leaving the 18-gauge sheath in place.

An 0.038-inch (0.097-cm), 3 mm, J guidewire is advanced through the sheath to the level of the diaphragm. The tract is dilated with 7-French and 9-French vascular dilators. A 10-French, 20-cm-long, peel-away sheath is then placed, and the guidewire is removed. The dilator in the sheath assembly is left in place and connected to an IV infusion to prevent thrombus formation. Next, the surgeon makes an incision below the right breast and another at the catheter entry point. A single-lumen, 9.5-French Hickman catheter is tunneled subcutaneously from the anterior incision to the sheath. A lateral counterincision may be necessary. After tunneling, the catheter is cut to the desired length. The dilator is then removed from the sheath and the catheter is advanced into the IVC to the level of the hepatic veins.

Received July 28, 1986; accepted after revision October 7, 1986.

¹ Department of Diagnostic Radiology, Yale University School of Medicine, P.O. Box 3333, New Haven, CT 06510. Address reprint requests to D. F. Denny.

² Department of Diagnostic Radiology, Rhode Island Hospital, Providence, RI 02902.

³ Department of Surgery, Yale University School of Medicine, New Haven, CT 06510.

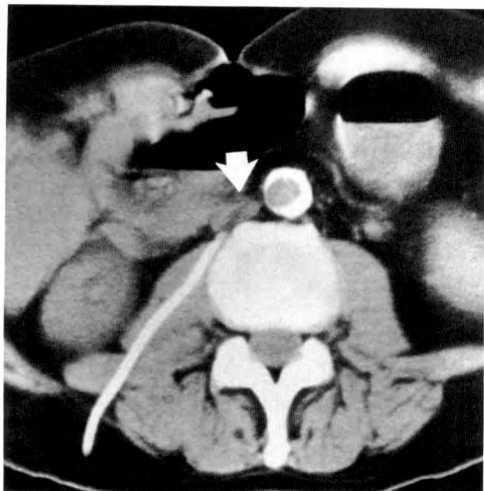


Fig. 1.—CT scan. Catheter passes through psoas muscle between spine and kidney, entering inferior vena cava (IVC) (arrow). Note absence of hematoma around IVC or in psoas muscle.

Finally, the sheath is peeled away, and the incisions are closed. An abdominal radiograph is performed to document location. TPN may be started immediately.

Results

Catheter placement was successful and uncomplicated in both patients. CT scans were performed on both patients on the second postoperative day; there was no evidence of retroperitoneal hematoma or other abnormality (Fig. 1).

Inferior vena cavogram performed on one patient 1 month postoperatively showed no caval thrombosis. This patient died of other causes 12 months later; at autopsy the IVC was patent and free of thrombus. The second patient is alive and well with a functioning catheter 10 months after the procedure.

Discussion

Home TPN has proven to be life saving for many patients who cannot be fed enterally. However, only the largest veins in the body are able to tolerate infusion of TPN solutions. With time, all standard access routes may become occluded, and alternative access paths are limited. Cannulation of the saphenous vein risks thrombosis in the veins of the leg, pelvis, and IVC [7]. Thoracotomy and direct cannulation of the azygous vein, superior vena cava [8], or right atrium [4] are more

invasive and potentially risky in these nutritionally compromised patients. Arteriovenous fistulas, as first reported by Broviac et al. [1], were unsuccessful. A subsequent report by Baird et al. [3] was more promising; however, many of their patients only used their fistulas intermittently.

Translumbar IVC cannulation offers direct, nonoperative access to the largest vein in the body. We believe the risk of thrombosis is minimal because of the high flow within the IVC. This not only prevents thrombus formation on the catheter but also dilutes the highly concentrated, sclerotic TPN solutions. Risk of retroperitoneal hemorrhage is minimal because of the low IVC pressure. The approach route avoids jeopardizing any major organs and is analogous to the traditional access for translumbar arteriography.

The Hickman catheter is thick walled, so that kinking or compression due to the subcutaneous position in the back has not been a problem. The catheter port is anterior, in a convenient position for the patient to self-administer TPN solution. The soft, floppy nature of the catheter and its inability to be passed over a guidewire require placement through a sheath. We find a peel-away sheath to be ideal because it can be readily passed through the thick tissues of the back and can be easily removed once the catheter has been positioned.

Our experience with translumbar IVC placement of a Silastic TPN catheter suggests that it is an effective alternative in selected patients who have lost all standard venous access routes. The technique is a straightforward extension of translumbar arteriography, a procedure with which angiographer is already familiar.

REFERENCES

1. Broviac JW, Cole JJ, Scribner BH. A silicone rubber atrial catheter for prolonged parenteral alimentation. *Surg Gynecol Obstet* 1973;136:602-606
2. Fonkalsrud EW, Berquist WE, Burke M, Ament ME. Long-term hyperalimentation in children through saphenous central vein catheterization. *Am J Surg* 1982;143:209-211
3. Baird RM, Rae AI, Chan-Yan C. Long-term parenteral nutrition with arteriovenous fistula. *Am J Surg* 1980;139:637-640
4. Oram-Smith JC, Mullen JL, Harken AH, Fitts WT. Direct right atrial catheterization for total parenteral nutrition. *Surgery* 1978;83:274-276
5. Kenney PR, Dorfman GS, Denny DF. Percutaneous inferior vena cava cannulation for long-term parenteral nutrition. *Surgery* 1985;97:602-605
6. Lipchik EO, Rogoff SM. Abdominal aortography: translumbar, femoral, and axillary artery catheterization techniques. In: Abrams HL, ed. *Abrams Angiography*. Boston: Little, Brown, 1983:1032
7. Fonkalsrud EW, Ament ME, Berquist WE, Burke M. Occlusion of the vena cava in infants receiving central venous hyperalimentation. *Surg Gynecol Obstet* 1982;154:189-192
8. Malt RA, Kempster M. Direct azygous vein and superior vena cava cannulation for parenteral nutrition. *J Parenter Enter Nutr* 1983;7:580-581

Technical Note

Aspiration Biopsy of Superficial Lesions: Ultrasonic Guidance with a Linear-Array Probe

Giorgio Rizzatto,¹ Luigi Solbiati,² Fausto Croce,² and Lorenzo E. Derchi³

With the introduction of small-parts scanners with 7.5- and 10-MHz transducers, nonpalpable lesions of superficial structures are being detected in increasing numbers [1]. These lesions may often require cytologic evaluation by fine-needle aspiration biopsy (FNAB), which is necessarily performed under instrumental guidance. Because currently available high-frequency probes are not ideally suited for the biopsy procedure, we evaluated the use of a linear-array intraoperative biopsy probe for guiding FNAB of superficial lesions.

Subjects and Methods

Ultrasonically guided FNAB of nonpalpable superficial lesions was performed in 68 patients over a period of 15 months. Sites and dimensions of the targets are listed in Table 1. The superficial masses had been detected previously with small-parts scanners equipped with either a 7.5- or a 10-MHz transducer.

Each biopsy was guided by a 5-MHz linear-array probe (Hitachi, Chiyoda-ku, Tokyo, Japan) designed for intraoperative use. Each probe had a central open canal to introduce and guide the needle (Fig. 1). The probe has 50 groups of active elements and an effective field of view of 35 mm. Its acoustic properties had been evaluated in phantoms and found to be suitable for clinical use in FNAB of superficial structures. Because of the acoustic shadow generated by the central canal, we found that needle-tip visibility was increased when, with the needle inserted, the probe was given a slight lateral inclination. This maneuver was facilitated by both the relatively large canal (1.8 mm) and the small size of the probe (19.5 mm). Needle-tip visibility also was increased by turning off the dynamic focusing.

FNAB of breast lesions was performed with three different types of needles: 20-gauge short needles (3.7 cm long) without stylet, 20-gauge spinal needles (6 or 9 cm long), and 20- or 21-gauge cutting needles (6 cm long). Most nodules (65%) were aspirated with a single pass of the needle. Thyroid, parathyroid, and soft-tissue lesions were punctured using 22-gauge needles, either short (3.7 cm) needles without stylet or 9.5-cm spinal needles. Two passes were performed routinely in each nodule.

Results

Ultrasonic guidance of FNAB with the intraoperative biopsy probe proved successful in 66 (97%) of 68 cases, providing an adequate sample for cytologic examination. In only two of the 68 patients the procedure had to be repeated because the first aspiration yielded insufficient material; after the second attempt, a cytologic diagnosis was obtained in these two patients as well.

The needle tip was clearly visible in 52 (76%) of 68 cases (Fig. 2). In the remaining 16 patients the position of the needle could be monitored by observing slight tissue displacement at the sides of the central acoustic shadow due to the needle penetration.

Thyroid nodules were diagnosed cytologically as nodular goiters (10), follicular adenomas (two), nonfollicular adenomas (two), and papillary carcinomas (five). Parathyroid lesions were benign in 12 cases (either hyperplasias or adenomas, indistinguishable cytologically) and malignant in one case. The

Received March 13, 1986; accepted after revision September 25, 1986.

Presented at the AIUM/SDMS Annual Convention, Dallas, TX, October 1985.

¹ Servizio di Radiologia, Ospedale, 34170-Gorizia, Italy. Address reprint requests to G. Rizzatto, P.O. Box 27, 34170-Gorizia, Italy.

² Servizio di Radiologia, Ospedale, 21052-Busto Arsizio (Va), Italy.

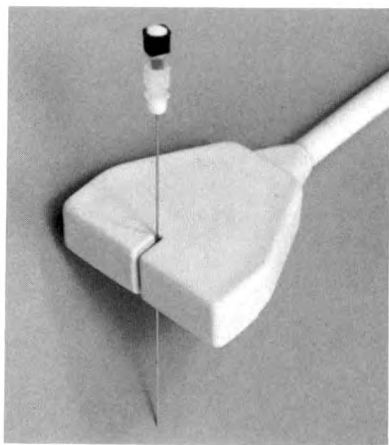
³ Istituto di Radiologia, Università, 16132-Genova, Italy.

TABLE 1. Ranges of Target Dimensions and Their Depth from the Skin Measured at Midpoint

Dimension	Thyroid (n = 19)	Parathyroid (n = 15)	Breast ^a (n = 32)	Soft Tissues (n = 2)
Maximum diameter	5–22 (12)	5–19 (10)	5–30 (15)	19–25 (22)
Anteroposterior diameter	4–17 (10)	5–16 (8)	5–15 (8)	15–16 (15)
Depth from skin	11–32 (20)	14–31 (24)	7–31 (14)	27–41 (34)

Note.—All dimensions are in millimeters. Numbers in parentheses are averages.
^a Distance from the thoracic wall was 0–12 mm (average, 3.9 mm); in 13 patients it was less than 3 mm.

Fig. 1.—Intraoperative biopsy probe with a 9-cm, 20-gauge spinal needle inserted into the open central canal.



final cytologic diagnoses of breast lesions included the following: cysts (nine: four simple, two with inflammatory changes, and three hemorrhagic), chronic galactoceles (three), fibroadenomas (seven), dysplastic areas (nine), and malignancies (four). Biopsy of the thigh in two cases showed local recurrences of liposarcoma.

In the remaining two of the 68 cases biopsied (subsequently proved to be parathyroid hyperplasias), only blood was aspirated, preventing cytologic evaluation; no thyroid cells were present in the cytologic specimens. In both the cases the needle tip was visible inside the lesion. No complications were encountered in our group of cases, and the whole procedure proved to be simple and rapid.

Discussion

Blind FNAB of superficial, palpable lesions has been employed successfully for over 25 years. More recently introduced imaging methods to guide needle penetration (fluoroscopy, sonography, CT) have allowed sampling of more deeply located targets but have not significantly affected the biopsy approach to superficial structures, in which the needle is usually directed into the mass with the aid of simple palpation.

In recent years the increasing use of small-parts scanners has resulted in situations in which superficial lesions may not be palpable yet may require cytologic assessment by FNAB. In these cases, instrumental guidance of FNAB is mandatory, not only to locate the target but also to protect vascular and neural structures, which, especially in the neck, may lie in close proximity to the mass. Currently available small-parts

scanners cannot easily be converted for biopsy use; they are sector scanners that can only be fitted with a lateral adaptor and, therefore, require angled needle passes. In fact, the more superficial the target, the wider the angle between the ultrasonic beam and the needle path, so that relatively large portions of normal tissues have to be crossed before the mass is reached. This means that longer needles must be employed, increasing the risk of needle deviations and thus preventing adequate real-time monitoring of the puncture.

High-frequency ultrasonic beams of small-parts scanners are in fact well focused and have a high lateral resolution. Even minimal deviations may shift the needle axis away from the ultrasonic beam. Furthermore, most small-parts scanners have relatively large dimensions because of the included water-path, making them difficult to use in some anatomic regions and allowing only very angled punctures.

Because of all these problems most investigators routinely use small-parts scanners only to measure the depth of the target and to localize it on the skin, then performing a blind biopsy [2–5]. Owing to these considerations, the coaxial, perpendicular approach is likely to be preferable to the lateral method; such an approach commonly is provided by linear-array biopsy probes, which generally are designed for abdominal use, having low frequencies and large dimensions. To our knowledge, the only currently available linear-array biopsy probes with sufficiently high frequency are those designed for intraoperative use, such as the model tested in this study. In our experience, the acoustic shadow generated by the central canal did not prove to be a major draw-back. In a high percentage of cases (76%) the needle tip was easily recognized by giving a slight lateral inclination to the probe, so that the needle tip could enter the ultrasonic beam. When the needle could not be identified, it was known to lie in the acoustic shadow and, therefore, it followed the direction of the biopsy canal. A faint tissue movement at the sides of the needle suggested its presence and penetration. In these cases, we usually measured the depth of the lesion and performed a second pass with a needle stop to prevent overpenetration. Other advantages of the probe that we used (small dimensions, limited thickness, open central canal, and relatively high frequency) allowed us to hit even small targets with relative ease, always using short needles and making only one or two passes. This reduced the risk of adverse reactions.

Sixty-six lesions (97%) were biopsied accurately. The needle position was correct also in the remaining two cases of parathyroid nodules, but only blood cells were aspirated;

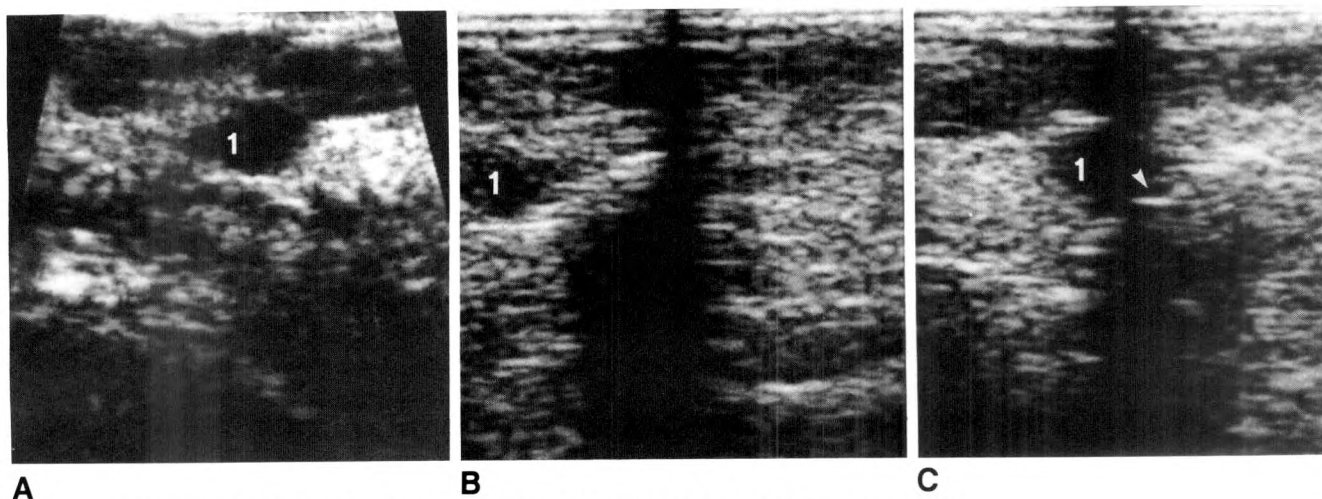


Fig. 2.—Sonograms of the breast showing a 1×0.6 cm hypoechoic nodule due to medullary carcinoma (1).
 A, small-parts scan, 7.5 MHz.
 B, Scan with biopsy probe in place, 5 MHz.
 C, Scan shows good visualization of the needle tip (arrowhead).

although parathyroid tissue may be highly vascularized and no thyroid cells were found, the cytologic material was considered inadequate.

The characteristics of the intraoperative biopsy probe make it particularly suitable for guiding FNAB in the neck and breast. In the neck, the small dimensions of the region, the depth of some lesions, and the proximity of large blood vessels and nerves pose difficulties that can be resolved with the intraoperative probe if suitable scan planes are chosen. Breast tissue is typically soft and quite deformable, especially in large breasts and in those with fatty involution. The perpendicular approach and the use of short needles reduce the possibilities of needle deviation, target mobility, and puncture of the thoracic wall. In addition to guiding biopsy needles, we could easily perform needle-hookwire localization of breast lesions that required surgery. The accuracy of this guidance system has also allowed us to inject ethanol into a few hyperplastic parathyroid glands to obtain a reduction in size [6].

We have successfully used FNAB under coaxial guidance in other superficial lesions: upper mediastinal and pleural tumors, lymph nodes, small soft-tissue masses, and fluid

collections. We anticipate an increasing use of ultrasonic guidance in interventional radiology involving superficial structures. Its applications will be facilitated by the development of smaller biopsy probes with high-frequency transducers.

REFERENCES

1. Carroll BA. Asymptomatic thyroid nodule: incidental sonographic detection. *AJR* **1982**;133:499-501
2. Kopans DB, Meyers JE, Lindfors KK, Bucchianeri SS. Breast sonography to guide cyst aspiration and wire localization of occult solid lesions. *AJR* **1984**;143:489-492
3. Laing FC, Jeffrey RB, Minagi H. Ultrasound localization of occult breast lesions. *Radiology* **1984**;151:795-796
4. Weber WN, Sickles EA, Callen PW, Filly RA. Nonpalpable breast lesion localization: limited efficacy of sonography. *Radiology* **1985**;155:783-784
5. Gooding GAW, Clark OH, Stark DD, Moss AA, Montgomery CK. Parathyroid aspiration biopsy under ultrasound guidance in the postoperative hyperparathyroid patient. *Radiology* **1985**;155:193-196
6. Solbiati L, Giangrande A, De Pra L, Bellotti E, Cantù P, Ravetto C. Percutaneous ethanol injection of parathyroid tumors under US guidance: treatment for secondary hyperparathyroidism. *Radiology* **1985**;155:607-610

Technical Note

Hepatic Embolization Through Periportal Collaterals: Balloon Occlusion Technique

Hironobu Nakamura,¹ Tsutomu Hashimoto,¹ Hiromichi Oi,² and Satoshi Sawada³

Occlusion or severe stenosis of the proper hepatic artery may occur after transcatheter hepatic artery embolization or intimal injury due to hepatic artery catheterization. In such cases, multiple collaterals develop from the gastroduodenal artery and pancreaticoduodenal arcades, which carry blood toward the liver [1, 2], making the next hepatic embolization difficult [3, 4]. Using the balloon occlusion technique, we performed embolization from the common hepatic artery through periportal collaterals.

Materials and Methods

In four patients with hepatocellular carcinoma (three men and one woman, ranging in age from 56 to 60 years), occlusion or severe stenosis of the proper hepatic artery was followed by the development of extrahepatic collaterals that made catheterization difficult. Three of these patients had undergone two to three hepatic artery embolization procedures earlier, whereas the remaining patient had had an intimal injury during catheterization. In the previous embolizations, either 20 mg of mitomycin C (Kyowa Hakko Kogyo, Tokyo, Japan) or 60 mg of doxorubicin hydrochloride (Adriamycin, Adria Laboratories, Dublin, OH) and 1–3 mm of gelatin sponge (Gelfoam) (Upjohn, Kalamazoo, MI) particles were used. The interval between the first embolization and collateral embolization was 13 to 26

A 7-French cobra-type, torque-controlled balloon catheter (Cordis, Miami, FL) was used. The procedure is performed as follows. The



Fig. 1.—Diagram of hemodynamic change from balloon occlusion of common hepatic artery when proper hepatic artery is obstructed. Blood flow in pancreaticoduodenal arcades, gastroduodenal artery, and periportal collaterals is toward liver (arrows).

balloon catheter is inserted into the common hepatic artery, and the balloon is inflated to obstruct the blood flow in the vessel. Blood in the superior mesenteric artery, therefore, flows through the pancreaticoduodenal arcades and gastroduodenal artery and, via collaterals in the periportal route, into the intrahepatic arteries (Fig. 1). Consequently, the embolic materials injected into the common hepatic artery distal to the balloon flow through the hepatic arteries only and do not enter the arteries of the stomach, duodenum, or pancreas. Hepatic embolization is thus made feasible, although fluoroscopic monitoring is required. For embolization, an iodized oil (Lipiodol, André-Gelbe, France) and an antitumor agent mixture and Gelfoam particles (less than 1 mm) are used. After this collateral embolization, follow-up CT and alpha-fetoprotein determinations showed some therapeutic effect in all four cases. Two cases are described here.

Received June 2, 1986; accepted after revision September 24, 1986.

¹ Department of Radiology, Research Institute for Microbial Diseases, Osaka University, 3-1, Yamadaoka, Suita, Osaka 565, Japan. Address reprint requests to

² Department of Radiology, Osaka Teishin Hospital, Osaka 543, Japan.

³ Department of Radiology, Kansai Medical School, Moriguchi 432, Japan.

AJR 148:626–628, March 1987 0361–803X/87/1483–0626 © American Roentgen Ray Society

Representative Cases

Case 1

A 56-year-old man was found by liver scintigram and CT scan to have a hepatic tumor during follow-up of liver cirrhosis. Hepatic angiography was first performed in 1983, and multiple hepatomas were discovered in the anterior segment of the right lobe. Because of cirrhosis, hepatic resection was not performed but, instead, hepatic artery embolization was done using Adriamycin, 60 mg, and Gelfoam. During the subsequent 2 years and 2 months, two additional hepatic embolizations were performed, and in 1985 a fourth embolization was attempted. The proper hepatic artery showed severe stenosis with collaterals arising from the posterior superior pancreaticoduodenal artery (Fig. 2A). Because selective catheterization into this collateral was impossible, a mixture of 60 mg of Adriamycin and 10 ml of Lipiodol was infused into the common hepatic artery while the vessel was occluded with the balloon. The Lipiodol that entered the gastroduodenal artery and right gastric artery was forced back, and

most of it entered the liver from the posterior superior pancreaticoduodenal artery through the collateral (Fig. 2B). Nine months later, another, similar collateral embolization was carried out. The patient is still alive more than 2 years and 8 months later.

Case 2

A 60-year-old woman was discovered to have a hepatoma in the right lobe of the liver with an increase in alpha-fetoprotein. In March 1984, transcatheter embolization was performed by using Gelfoam and 20 mg of mitomycin. The embolization resulted in a decrease in alpha-fetoprotein, but when the alpha-fetoprotein increased again after 6 months, a second embolization procedure was attempted 9 months later. During catheterization, however, intimal dissection occurred at the origin of the proper hepatic artery, and the procedure was discontinued. Two months later, angiography showed that the proper hepatic artery was completely occluded. Several collaterals had developed in the periportal route (Fig. 3A). Therefore, by use of

Fig. 2.—A, After three embolizations of a hepatoma in right hepatic lobe, proper hepatic artery is narrowed and collaterals (arrows) are present.

B, Lipiodol flows to intrahepatic arteries via collaterals during balloon occlusion of common hepatic artery. No flow occurs to gastroduodenal, right gastric, and pancreatic arteries.

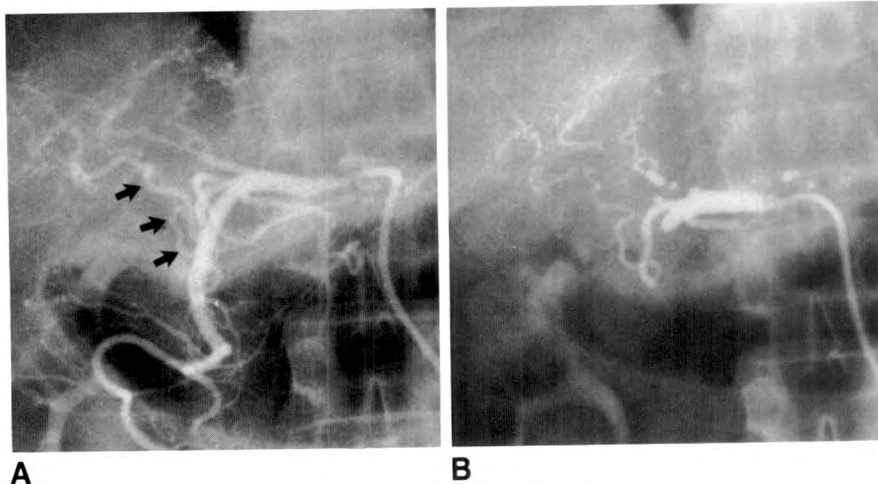
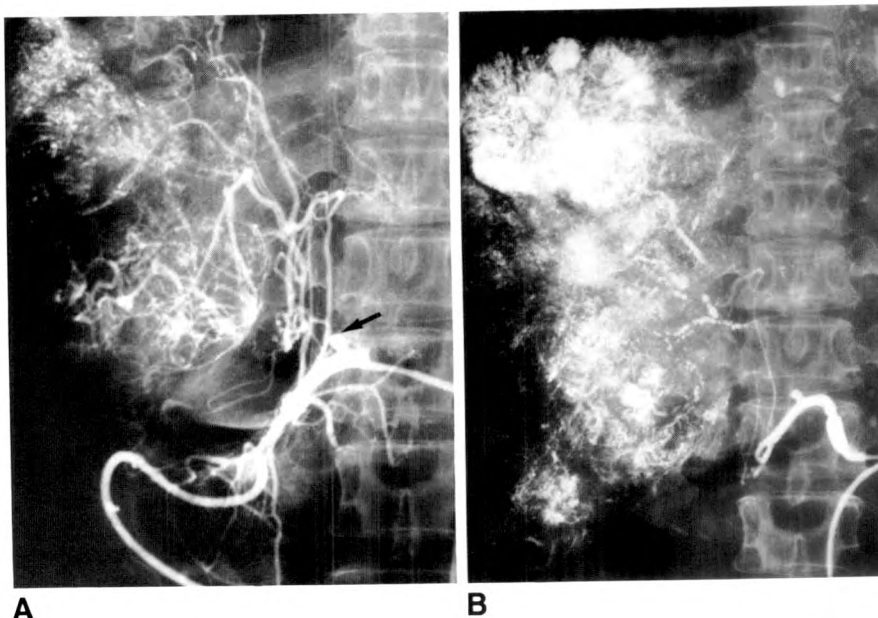


Fig. 3.—A, Common hepatic arteriogram in patient with large hepatoma. Proper hepatic artery is completely occluded (arrow) by last catheterization, with development of periportal collaterals.

B, Lipiodol accumulates in hepatoma during collateral embolization with balloon. No branches other than periportal collaterals are opacified.



a balloon catheter, 20 mg of mitomycin C and 10 ml of Lipiodol were infused via the common hepatic artery. Because alpha-fetoprotein decreased only slightly, a second collateral embolization was performed 2 months later, with 20 mg of mitomycin C, 25 ml of Lipiodol, and Gelfoam (Fig. 3B). This procedure resulted in a decrease in alpha-fetoprotein, but hepatic failure occurred, probably from the embolization damage. The patient died 40 days after the last embolization.

Discussion

Repeated hepatic artery embolizations are an effective treatment of malignant hepatic tumors [4-7]. However, stenosis or occlusion of the proper hepatic artery may occur and interfere with the procedure. Multiple collaterals in the periportal route develop from the gastroduodenal artery and pancreaticoduodenal arcades, preventing further embolization. In such cases, we attempt hepatic embolization from the common hepatic artery distal to the balloon via the collaterals using the balloon catheter embolization technique that we have reported previously [8]. We found that as hemodynamic change occurred in the pancreaticoduodenal arcades and their surrounding regions, the embolic materials could be efficiently infused into the intrahepatic arteries. Collateral embolization can give almost the same effect as an ordinary hepatic embolization. No complications in the gastroduodenal and pancreatic regions occurred in any of the four cases in which collateral embolization was attempted.

Collateral embolization with the balloon catheter is, therefore, effective therapy in cases of hepatoma, in which periportal route collaterals have developed that prevent selective catheterization. Moreover, in cases in which a similar problem occurs when hepatic-artery-infusion chemotherapy is repeated, this method permits continuation of the infusion therapy as long as a balloon catheter can be inserted.

REFERENCES

1. Ohishi H, Ohue S, Katsuragi M, et al. Angiographic demonstration of the collateral circulation to the liver after arterial embolization of hepatocellular carcinoma. *Rinsho Hoshasen (Jpn J Clin Radiol)* 1982;27:1235-1241
2. Charnsangavej C, Chuang VP, Wallace S, Soo CS, Bowers T. Angiographic classification of hepatic arterial collaterals. *Radiology* 1982;144:485-494
3. Ohtomo K, Furui S, Yoshikawa K, et al. Extrahepatic collaterals in the postembolization cases of hepatocellular carcinoma. *Rinsho Hoshasen (Jpn J Clin Radiol)* 1983;28:763-766
4. Soo CS, Chuang VP, Wallace S, Charnsangavej C, Carrasco H. Treatment of hepatic neoplasm through extrahepatic collaterals. *Radiology* 1983;147:45-49
5. Chuang VP, Wallace S. Hepatic artery embolization in the treatment of hepatic neoplasms. *Radiology* 1981;140:51-58
6. Nakamura H, Tanaka T, Hori S, et al. Transcatheter embolization of hepatocellular carcinoma: assessment of efficacy in cases of resection following embolization. *Radiology* 1983;147:401-405
7. Matsuo N, Katsuragi M, Yoshioka T, et al. Collateral embolization after hepatic artery embolization to the hepatocellular carcinoma. *J Jpn Coll Angiol* 1985;25:365-372
8. Nakamura H, Tanaka M, Oi H. Hepatic embolization from the common hepatic artery using balloon occlusion technique. *AJR* 1985;145:115-116

Two-Second MR Images: Comparison with Spin-Echo Images in 29 Patients

Joseph A. Utz^{1,2}
Robert J. Herfkens¹
C. Daniel Johnson¹
Ann Shimakawa³
Norbert Pelc³
Gary Glover³
G. Allan Johnson¹
Charles E. Spritzer¹

MR images can be obtained with a 2-sec scan time when an extremely short repetition rate (22 msec), limited flip angle (30°), and gradient refocused echoes are used. Comparison of 415 such images obtained in 29 patients with routine T1-weighted (TR 500, TE 25) and T2-weighted (TR 2000, TE 80) images showed that images free of respiratory artifacts could be obtained in all patients. Although abdominal organs were well seen with 2-sec scan time, overall evaluation of these organs was better on routine T1-weighted images. Vascular structures, however, were seen as well or better on the 2-sec images in 60% of cases. The images were extremely sensitive to field nonhomogeneity, and metallic artifact was exaggerated in five patients with surgical clips. Two-sec MR images provide a rapid method of localizing abdominal organs for further evaluation. The sensitivity to blood flow may assist in the assessment of vascular patency.

MR imaging is a rapidly growing technology with an ever-increasing role in diagnostic radiology. Contrast resolution is superior to CT, and spatial resolution, especially since the introduction of surface coils, is approaching that of CT. The examination is, however, currently limited by prolonged imaging times, which average 4–17 min for examinations with repetition rates of 500–2000 msec, with 128 or 256 matrix sizes and two to four excitations. This disadvantage is somewhat lessened by multislice imaging techniques. Motion artifacts may, however, present a problem, and the time required to add or repeat a single slice is inconvenient.

Several techniques have been suggested to shorten imaging time [1–5]. One such technique uses an extremely short repetition rate, a limited flip angle, and gradient-refocused echo to decrease overall imaging time [6]. One variation of this sequence is gradient-recalled acquisition in a steady-state mode (GRASS) imaging. This report describes our initial experience with this technique as applied to a 1.5-T MR system (General Electric Signa System, Milwaukee, WI).

Materials and Methods

Four hundred fifteen GRASS images were obtained in 29 patients between October 31 and December 9, 1985. Four hundred five abdominal images were obtained in 28 patients and 10 pelvic images were obtained in one patient. In addition to the GRASS images, routine spin-echo transaxial images were obtained in all patients with repetition time (TR) 500, echo delay time (TE) 20/25 and TR 2000, TE 40/80 msec. Gradient-refocused images were obtained at 1-cm intervals with TR 22 msec, a flip angle of 30°, and a gradient reversal echo at 8–12 msec. Total time per image was 2.7 sec, and all GRASS images were obtained in suspended respiration.

The GRASS images were directly compared with the standard transaxial images by radiologists experienced in MR imaging. Each patient's T1-weighted images were used as a standard by which that patient's GRASS images were compared. The routine images and GRASS images of the same patient of the same area were termed an image set. The visibility of abdominal organs and the ability to assess vascularity on the GRASS images were graded

Received May 27, 1986; accepted after revision October 2, 1986.

The opinions and assertions contained herein are the private views of the authors and are not to be construed as official or as reflecting the views of the Department of the Army or the Department of Defense.

Presented in part at the annual meeting of the Society of Magnetic Resonance Imaging, Philadelphia, March 1986.

¹Department of Radiology, Duke University Medical Center, Durham, NC 27710.

²Department of Radiology, Walter Reed Army Medical Center, Washington, DC 20307. Address reprint requests to J. A. Utz.

³Medical Systems Group, General Electric Co., Milwaukee, WI 53201.

AJR 148:629–633, March 1987

0361–803X/87/1483–0629

© American Roentgen Ray Society

as inferior to, equal to, or superior to the routine images of the same image set. The presence of artifacts (respiratory artifact, motion artifact, metallic artifact) was noted, and when present, the effects of this artifact on the routine images and GRASS images were compared.

To help eliminate bias, a third observer evaluated the GRASS images and T1-weighted images independently in a blinded manner and graded each of the organs and vessels on a four-point scale: (1) nonvisualization, (2) probable but poor, (3) definite visualization, and (4) extremely good visualization. Average scores for each of the organs and vessels were calculated.

Results

The regions of the liver, spleen, pancreas, adrenal glands, and kidneys were included on 22, 20, 20, 19, and 18 image sets, respectively. The liver was equally well seen on both T1 and GRASS images in 64% of cases, better seen on T1 images in 27%, and better seen on GRASS images in 9% of image sets. The spleen, pancreas, kidney, and adrenal glands were better evaluated on the routine T1-weighted images in 70%, 75%, 94%, and 89% of image sets, respectively. Pulsatile artifact from the aorta markedly compromised evaluation of the pancreas, while the 1-cm slice thickness was suboptimal for examination of the adrenal glands.

Each of the abdominal vessels was evaluated on 25 image sets (Table 1). The aorta was well seen on all images, although pulsatile artifact in the phase-encoding direction was pronounced and compromised visualization of the celiac axis in 14 of 16 sets in which this area was included. Venous structures were, however, as well seen (48%) or better seen (19%) on the GRASS images.

Five patients with metallic surgical clips were imaged, and in each patient the area of signal loss due to the metallic clip was larger on the GRASS images.

Average scores for each of the organs and vessels for the T1 and GRASS images are shown in Table 2.

Discussion

Many attempts have been made to decrease MR imaging time. The GRASS technique has an extremely short TR (21–

TABLE 2: Scores of T1 and GRASS for Imaging Various Anatomic Areas

Abdominal Area	Score	
	T1 Image	GRASS Image
Liver	3.1	2.3
Spleen	3.4	3.0
Pancreas	2.6	2.5
Kidney	3.1	2.9
Adrenals	2.8	2.0
Hepatic veins	2.7	3.0
Portal vein	2.9	3.0
Splenic vein	2.5	2.8
Inferior vena cava	3.2	3.6
Celiac artery	2.2	1.8
Left renal vein	3.2	2.5
Right renal vein	2.5	3.0

Note.—Images were evaluated in a blinded manner and each anatomic area was graded: 1 = nonvisualization; 2 = probable but poor visualization; 3 = definite visualization; 4 = good visualization. The number reported for each area is the numeric average of all the images evaluated. GRASS = gradient-recalled acquisition in a steady-state mode.

40 msec), a limited flip angle, and a gradient-refocused echo to decrease imaging time. This technique has the advantage of producing diagnostic images in markedly reduced imaging times of about 2 sec/image. Since the spin-warp technique and two-dimensional Fourier transform data analysis are preserved, a matrix size of 128 × 256 is available, and image reconstruction time per slice is the same as that for routine spin-echo sequences. The signal intensity for GRASS images is described by the equation, $S = ([1 - E_1] \sin \beta \text{ Mo}) / (1 - E_1 E_2 - \cos \beta [E_1 - E_2])$, where $E_1 = e^{-TR/T_1}$, $E_2 = e^{-TE/T_2}$, β = flip angle, Mo = spin density, T_1 = longitudinal relaxation time, and T_{2M} = measured transverse relaxation time [7]. The measured transverse relaxation time is dependent on both nuclear interactions and field inhomogeneity and is given by the equation, $1/T_{2M} = (1/T_{2N}) + (1/T_2^*)$, where T_{2N} = transverse relaxation time due to nuclear interactions and T_2^* = transverse relaxation time due to field inhomogeneity.

From the above equations it is apparent that the precise signal characteristics of the GRASS images is a complex interrelationship of TR, TE, T1, T2, Mo, and flip angle.

Although the explanation of the signal characteristics of tissue on GRASS images is complex, anatomic resolution is equivalent to routine spin-echo images with a 128 × 256 matrix size. The markedly shortened acquisition time is a distinct advantage since all images can be obtained in suspended respiration, thus eliminating respiratory artifacts (Fig. 1). Overall, the liver was well seen on the GRASS images probably because of the absence of respiratory motion. A flow-compensated version of the GRASS imaging sequence was not available for this evaluation. As a consequence of this, the pulsatile motion of the aorta caused ghost artifacts in the phase-encoding direction that compromised the evaluation of the pancreas.

Vessels were well seen on GRASS images as areas of an absolute increase in signal intensity. Of the 111 veins analyzed, 19% were better seen on GRASS images than on routine images and 48% were seen equally well on both sequences. This sensitivity to blood flow was most valuable

TABLE 1: Direct Comparison of Vascular Visualization on T1 and GRASS Images

Vessel	Visualization of Vessel (n = 25)		
	Better on T1 Images	Equal on Both Images	Better on GRASS Images
Hepatic vein	8	6	3
Portal vein	8	9	6
Splenic vein	11	7	3
Inferior vena cava	3	14	8
Left renal vein	5	9	0
Right renal vein	2	8	1
Celiac axis	14	2	0

Note.—Twenty-five image sets were evaluated. The number in each column indicates the number of image sets in each category for the vessel indicated. For example, the hepatic veins were better seen on GRASS (gradient-recalled acquisition in a steady-state mode) images in three of the 25 image sets evaluated, and this area was not included in eight image sets.

Fig. 1.—Colon carcinoma.

A, TR 500, TE 20, two excitations. Respiratory artifact degrades visualization of liver and obscures liver metastasis.

B, GRASS image in suspended respiration shows metastasis (arrow) in posterior aspect of right lobe of liver.

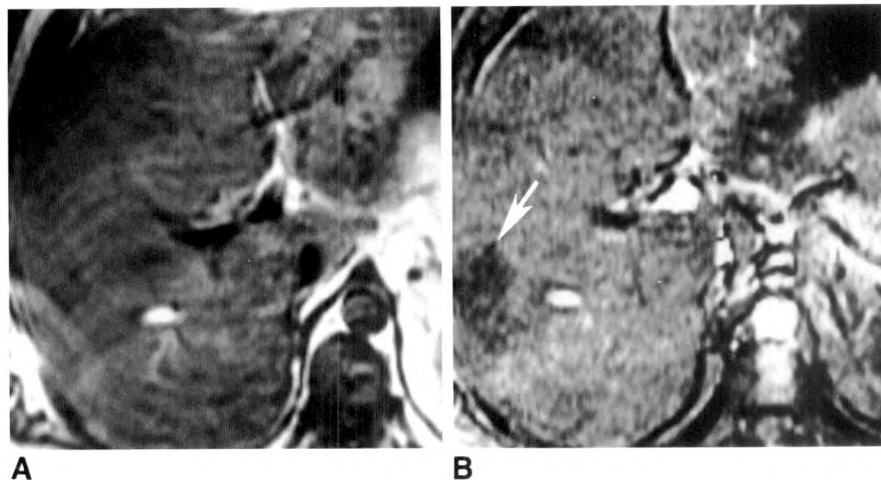
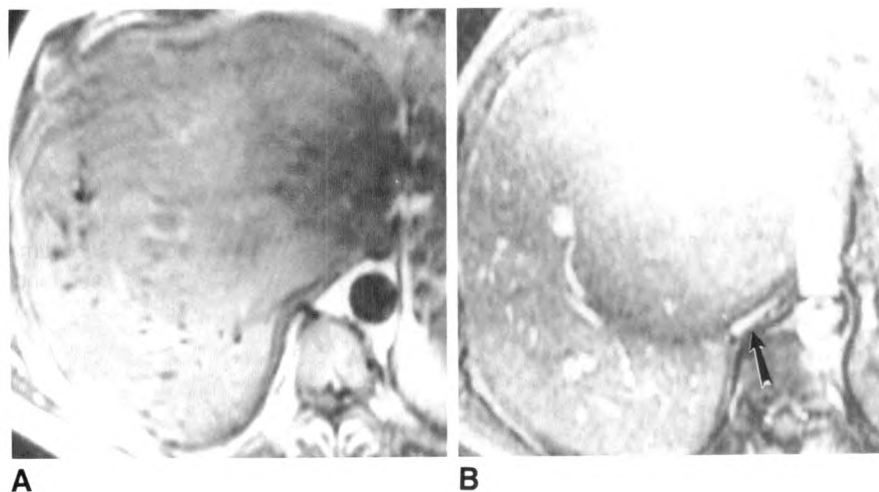


Fig. 2.—Large fibrosarcoma of liver with marked compression of inferior vena cava.

A, TR 500, TE 20 image shows poor visualization of inferior vena cava. Hepatic mass is not well seen.

B, GRASS image. Increased signal from inferior vena cava (arrow) caused by flowing blood, verifying vascular patency. Absence of respiratory artifact and displacement of hepatic vessels by liver mass are also evident.



in those instances in which a vessel was compressed and the question of patency was raised (Fig. 2). Increased signal within a vessel on the GRASS images suggests vascular patency. Vascular occlusion can be determined by an absence of this increased signal intensity (Fig. 3). The reason for the better visibility of venous vasculature on GRASS images is uncertain. It may be that the Valsalva maneuver performed during suspended respiration results in distension of the venous structures, or perhaps the flow of saturated blood into the single-slice images results in an area of increased signal, which is more easily appreciated than a small area of decreased signal intensity. A third reason for flow sensitivity may be that a gradient-refocused echo refocuses all spins tagged with the initial slice-selective RF pulse, thus limiting time-of-flight decreases in signal intensity. As a result of this increased sensitivity to blood flow, vascularity is often well portrayed on the GRASS images (Fig. 2). This sensitivity to flow has yet to be fully explored.

The shorter imaging time of the GRASS technique also provides a quick way to localize an area for further study,

such as the adrenal glands or the renal veins, or for verifying abnormalities in an orthogonal plane (Fig. 4). The ability to obtain images in the three orthogonal planes is often neglected because of the prolonged imaging times required to obtain that orthogonal view. Two-sec GRASS images may make imaging in several planes a practical clinical reality.

The GRASS images were more sensitive to field inhomogeneity and metallic clip artifacts than spin-echo images were (Fig. 5). Routine spin-echo images compensate for local inhomogeneities with the 180° RF pulse, while the GRASS images, which use a gradient-refocused acquisition, do not correct for inhomogeneities.

In conclusion, GRASS imaging is an effective technique that produces diagnostic images with minimal imaging time, providing a quick localizing view as well as a rapid means of obtaining three-dimensional anatomy. The images are sensitive to blood flow, and the assessment of vascular patency is a potential application. Since an entire organ such as the liver can be imaged in less than 30 sec, GRASS images are a useful addition to routine MR examinations.

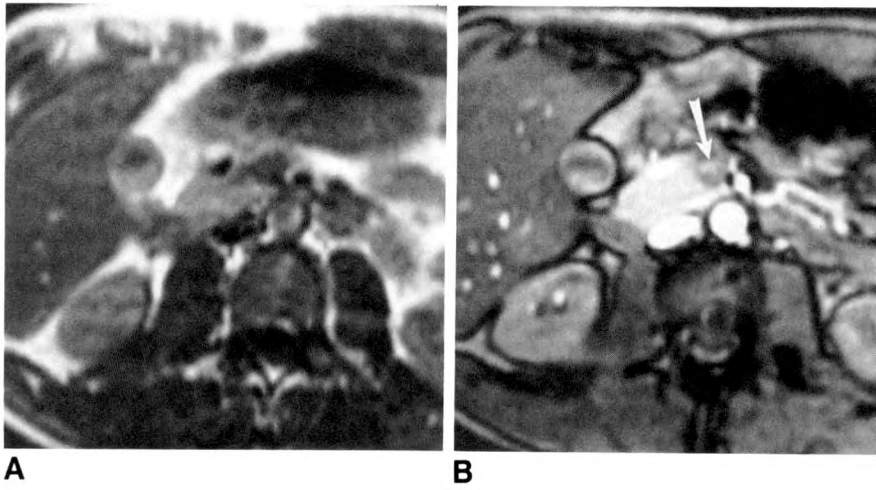


Fig. 3.—Superior mesenteric vein occlusion.
A, TR 500, TE 20 image. Poor visualization of superior mesenteric vein.
B, GRASS image shows absence of increased signal in superior mesenteric vein caused by thrombosis (arrow).

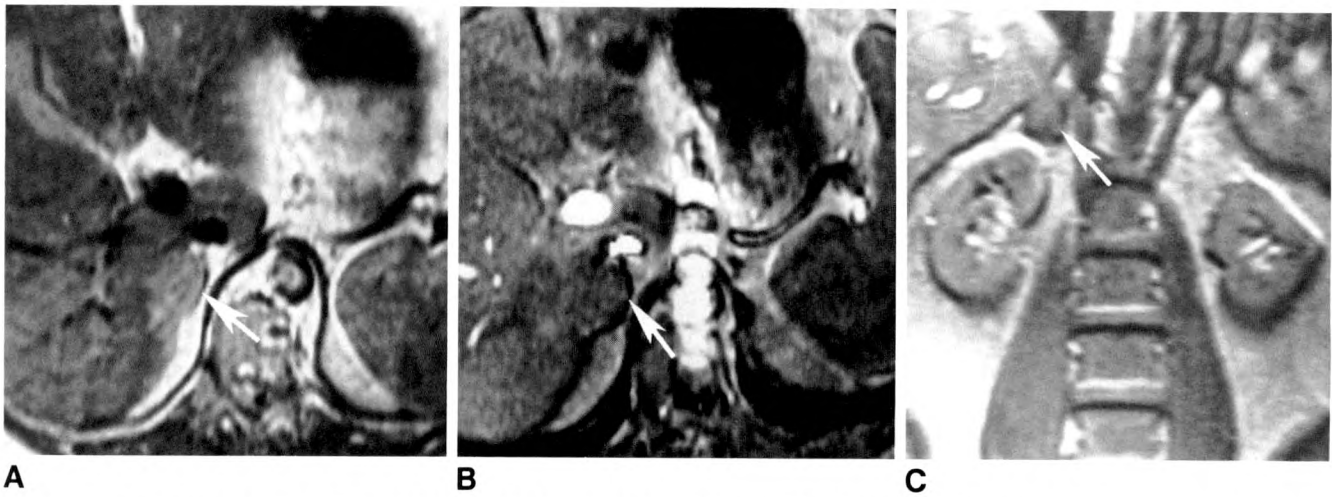


Fig. 4.—Right adrenal adenoma (arrows) on TR 2000, TE 40 (**A**), GRASS (**B**), and coronal GRASS (**C**) images. Adenoma is well seen on both transaxial images. Coronal GRASS image defines relationship of mass to

kidney and liver in 2 sec. Similar spin-echo image would require several minutes. Absence of flow-compensating pulse results in ghost images from aorta in phase-encoding direction.

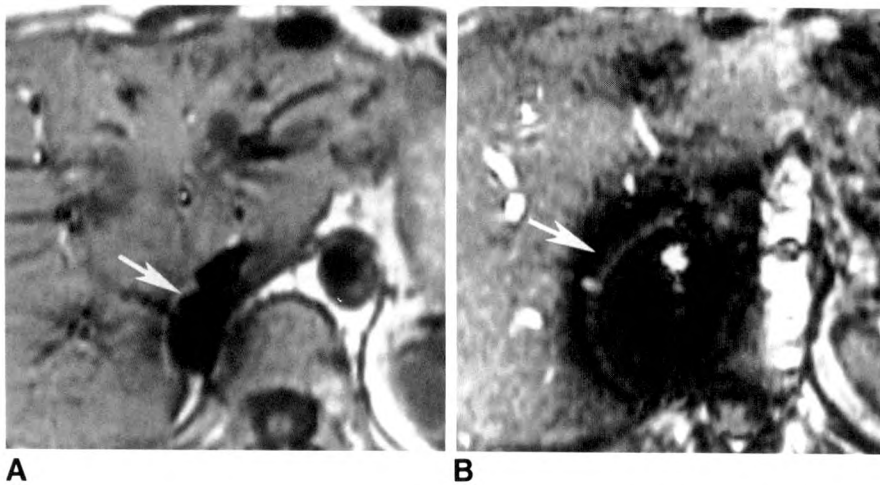


Fig. 5.—Metallic clips in the liver.
A, TR 500, TE 20 image shows clips (arrow).
B, 2-sec GRASS image shows exaggeration of size of clip artifact (arrow).

ACKNOWLEDGMENTS

The authors thank Rose Boyd, Cindy Picco-Hervey, Bobby Burns, Pamela Collins, Wandra Davis, Lucy Upchurch, and Marilyn Burkman for their valued assistance on this project.

REFERENCES

1. Ahn CB, Rew CY, Kim JH, Nalcioğlu O, Cho ZH. A new high speed spiral-scan echo planar (SEPI) NMR imaging (abstr). Presented at the annual meeting of the Society of Magnetic Resonance Imaging in Medicine, London, August 1985
2. Haacke EM, Bearden FH, Clayton JR. Implementation of low frequency hybrid fast scan imaging (abstr). Presented at the annual meeting of the Society of Magnetic Resonance Imaging in Medicine, London, August 1985
3. Haase A, Frahm J, Matthaei D, Hanicke W, Merboldt KD. Rapid images and NMR movies (abstr). Presented at the annual meeting of the Society of Magnetic Resonance Imaging in Medicine, London, August 1985
4. Mezrich R, Axel L, Dougherty L, Kressel H. Strip-scan: a method for faster NMR imaging (abstr). Presented at the annual meeting of the Society of Magnetic Resonance Imaging in Medicine, London, August 1985
5. Haacke EM, Bearden FH, Clayton JR, Ling NR. Reduction of MR imaging time by the hybrid fast-scan technique: *Radiology* 1986;158:521-529
6. VanDer Meulen P, Groen JP, Cuppen JJM. Very fast MR imaging by field echoes and small angle excitation. *Magnetic Resonance Imag* 1985;3:297-299
7. Mansfield P, Morris PG. Generalized RF pulses. In: Waugh JS, ed. *NMR imaging in biomedicine*. London: Academic, 1982[Suppl 2]:75-77

Technical Note

Phase-Offset Technique to Distinguish Slow Blood Flow and Thrombus on MR Images

Robert E. Dinsmore,¹ Van Wedeen,¹ Bruce Rosen,¹ Gary L. Wismer,¹ Stephen W. Miller,¹ and Thomas J. Brady^{1,2}

ECG-gated MR imaging has been shown to be a promising new method for the study of cardiovascular disease. Since little or no signal is received from rapidly flowing blood, there is excellent inherent contrast between cardiovascular cavities and walls without the need for introduction of contrast material. However, slowly flowing blood generates signal in the aorta in diastole and may produce intracardiac signal throughout the cardiac cycle under some conditions [1]. As a result, slow flow may be difficult to distinguish from thrombus. Techniques for making this distinction have depended on changes in relative signal intensity between first- and second-echo images [2] or between images in systole and diastole [3]. This report describes the use of a phase-offset technique [4] that is independent of relative signal intensity to distinguish between slowly flowing blood and thrombus in three patients with saccular thoracic aortic aneurysms.

Subjects and Methods

Three patients, ages 40, 64, and 76 years, were studied. One had undergone repair of coarctation of the aorta 20 years earlier and had developed a saccular false aneurysm in the aortic arch at the site of graft anastomosis. The other two presented with slowly enlarging descending thoracic aortic aneurysms. Two also had selective aortography, and the third had CT of the aorta.

MR images of the aorta were acquired with a whole-body superconducting magnet system (Technicare, Solon, OH) with a magnetic field strength of 0.6 T, by using spin-echo pulse sequences with echo delays of 30 msec. Single or multiple images were acquired with 1.0-

cm slice thickness. Images were acquired both in a short-axis projection, by using an image plane transverse to the thorax, and in a long-axis plane by using a technique that we have described previously [5, 6]. ECG synchronization was accomplished by use of a telemetry system with three standard electrodes on the extremities with non-magnetic lead wires.

After the images had been obtained, the data were evaluated by a phase-display method described by Wedeen et al. [4]. This method superimposes on the previously acquired image data a linear phase shift, which appears as a series of "zebra" stripes on images that display the real component of transverse magnetization (so-called "phase-reconstructed" images) rather than the absolute magnitude of the signal. Phase-reconstructed images thereby provide an image of phase differences induced by motion of blood through the imaging (frequency-encoding) gradient. The stripes remain straight within stationary objects, but show a local shift in the direction of motion in the presence of moving protons such as blood in the aorta. The degree of shift of the phase stripes is proportional to the flow velocity; higher flow velocities lead to greater displacement of the phase stripes relative to adjacent stationary structures.

Results

In each case areas of increased signal intensity within the aortic aneurysm persisted throughout the cardiac cycle. In two aneurysms, there was no deflection of the phase stripes through the parts that were found to be thrombosed by CT or aortography, while the nonthrombosed part of the aneurysm showed deflection of the phase stripes in the direction of flow (Fig. 1). In the third case, there was deflection of the

Received July 7, 1986; accepted after revision September 24, 1986.

¹ Department of Radiology, Massachusetts General Hospital, Boston, MA 02114. Address reprint requests to R. E. Dinsmore.

² T. J. Brady is supported by U.S. Public Health Service grant number 5 KO4 CA-00848-02 awarded by the National Cancer Institute.

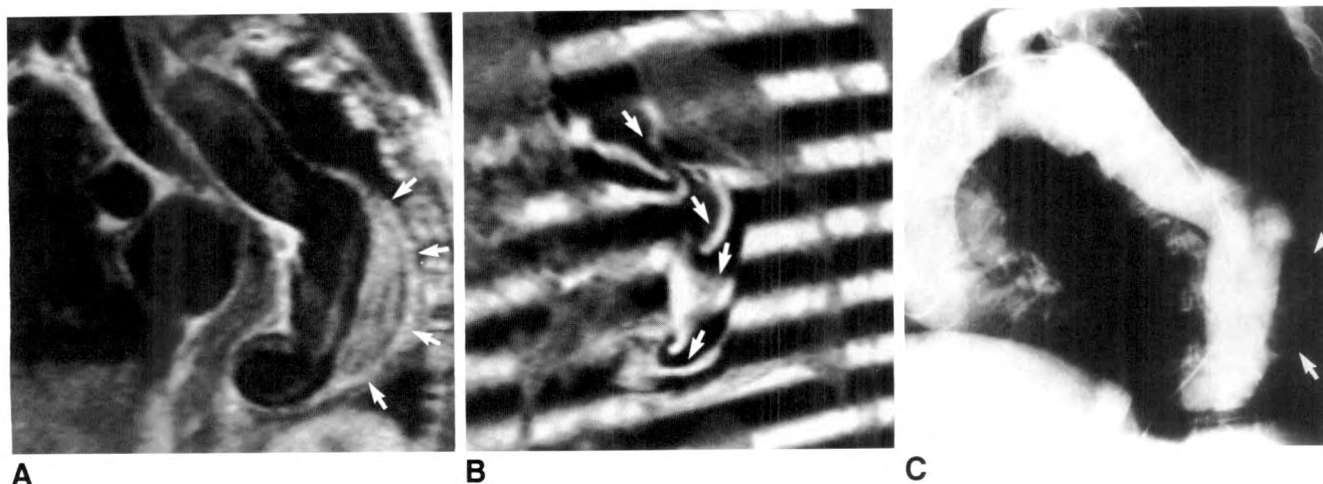


Fig. 1.—A, MR image in long axis showing detail of descending thoracic aortic aneurysm in systole. Note intraluminal signal throughout aorta, though most intense in periphery of aneurysm (arrows).

B, Phase-shift image in diastole showing no deflection of phase stripes in periphery of aneurysm, and antegrade deflection in a central channel indicating flowing blood (arrows).

C, Thoracic aortogram confirming presence of peripheral thrombus (arrows) and central open channel.

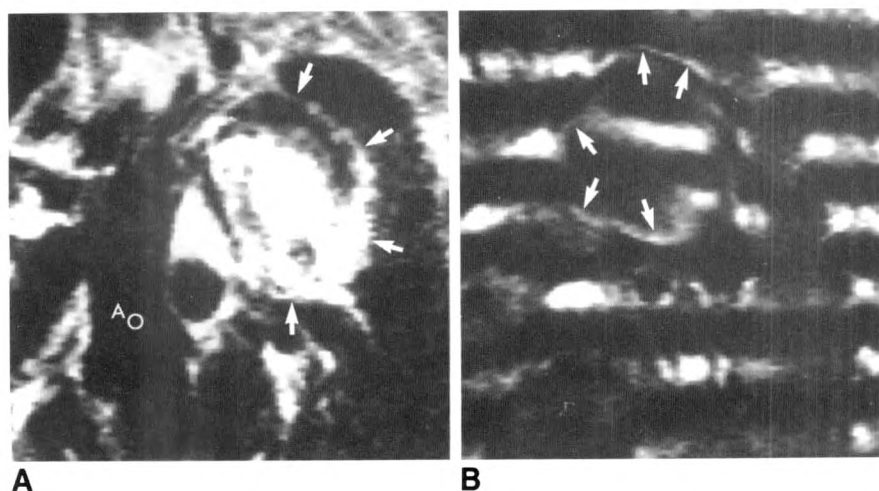


Fig. 2.—A, MR image of long axis of aortic arch in systole showing intense signal in a large saccular aneurysm (arrows). AO = ascending aorta. B, Phase-shift image showing deflection of phase stripes in aneurysm (arrows) with a chaotic pattern, indicating that signal arose in slowly flowing blood.

phase stripes throughout the aneurysm indicating slowly moving blood, with a chaotic pattern suggesting turbulence (Fig. 2). The absence of thrombus in this aneurysm was confirmed by aortography.

Discussion

With a double spin-echo technique, areas of slow flow show a relative increase in intensity on the second-echo images, whereas thrombus shows a decrease in relative intensity [2]. With this method, Higgins et al. [7] found that it was usually, but not always, possible to discriminate intracardiac stasis from thrombus. Glazer et al. [8] found a decrease in relative signal intensity on the second-echo image in the thrombosed lumens of two of three patients with dissecting aneurysm; however, the third patient showed an increase in signal intensity. While the reason for discrepancies in individual cases may not be clear, relative MR signal intensity is

affected by a number of factors apart from echo-delay time (TE) and blood flow velocity. Some, such as proton density, T1 and T2 of substances imaged, and RF inhomogeneity are not likely sources of error in this instance. Others, such as partial volume averaging and, in particular, subject motion during image acquisition, could cause significant error. Geisinger et al. [3] used the difference in signal intensity between diastole and systole to aid in differentiation of slow flow from thrombus in the false channel of dissecting aneurysms. However, they observed that mural thrombus tended to appear larger on MR images than on CT images and suggested that signal may arise from slowly flowing blood adjacent to the thrombus, even in systole.

Wedeen et al. [4] have shown that conventional spin-echo Fourier transform image acquisitions encode the component of flow velocity that lies within the image plane parallel to the frequency-encoding gradient. Therefore, signal within the aorta on long-axis images can be analyzed by the phase-

display imaging technique if frequency-encoding gradient is parallel to the long axis of the body, yielding both velocity and direction of flow data that are independent of relative signal intensity. The cases described in this paper suggest that phase-display imaging may provide a rigorous method of distinguishing between signal arising from a condition of no flow (e.g., thrombus) and signal due to slow or turbulent flow. In addition, because this technique involves phase reconstructions of previously required data sets, no additional imaging time is required for the MR study.

REFERENCES

1. von Schulthess GK, Fisher M, Crooks LE, Higgins CB. Gated MR imaging of the heart: intracardiac signals in patients and healthy subjects. *Radiology* 1985;156:125-132
2. Amparo EG, Higgins CB, Hoddick W, et al. Magnetic resonance imaging of aortic disease: preliminary results. *AJR* 1984;143:1203-1209
3. Geisinger MA, Risius B, O'Donnell JA, et al. Thoracic aortic dissections: magnetic resonance imaging. *Radiology* 1985;155:407-412
4. Wedeen VJ, Rosen BR, Chesler D, Brady TJ. MR velocity imaging by phase display. *J Comput Assist Tomogr* 1985;9(3):530-536
5. Dinsmore RE, Wismer GL, Levine RA, Okada RD, Brady TJ. Magnetic resonance imaging of the heart: positioning and gradient angle selection for optimal imaging planes. *AJR* 1984;143:1135-1142
6. Dinsmore RE, Liberthson RR, Wismer GL, et al. Magnetic resonance imaging of thoracic aortic aneurysms: comparison with other imaging methods. *AJR* 1986;146:309-314
7. Higgins CB, Byrd BF, McNamara MT, et al. Magnetic resonance imaging of the heart: a review of the experience in 172 subjects. *Radiology* 1985;155:671-679
8. Glazer HS, Gutierrez FR, Levitt RG, Lee JKT, Murphy WA. The thoracic aorta studied by MR imaging. *Radiology* 1985;157:149-155

ARRS Case of the Day



In keeping with tradition, a Case of the Day exhibit will be shown at the forthcoming annual meeting of the American Roentgen Ray Society to be held in Miami Beach, FL, April 26–May 1, 1987. Each day a new set of interesting cases will be placed on exhibit and the “answers” to the preceding day’s cases will be revealed. The cases presented will be in four general categories: “Abdominal,” “Chest,” “Neuroradiology,” and “Musculoskeletal.”

Readers of *AJR* can see the cases as they will appear in the exhibit. The current issue of *AJR* contains the “unknown” cases; the answers to these cases will appear in the May issue. If you can attend the meeting in person, visit the exhibit; otherwise follow along on these pages.

The cases used in the Case of the Day are taken from the files of the Department of Radiology at the University of Minnesota Hospital, and the VA Medical Center in Minneapolis, MN. All of the authors are members of the faculty of the University of Minnesota Department of Radiology.

Marvin E. Goldberg
Department of Radiology
University of Minnesota
Minneapolis, MN 55455

Chest Case of the Day

Jeffrey R. Crass,¹ Janis G. Letourneau, Deborah L. Day, and Marvin E. Goldberg

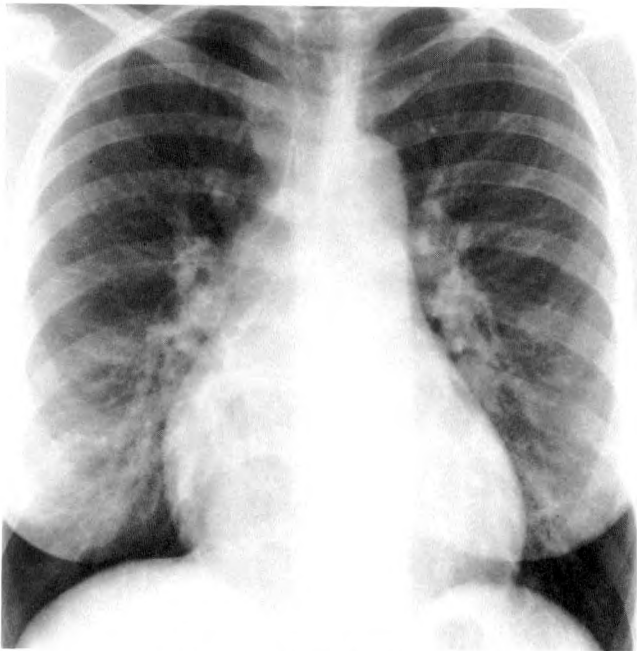


Fig. 1.—Case 1: 23-year-old woman presented with heart murmur, decreased exercise tolerance, and chronic right leg swelling. Posteroanterior chest radiograph.



Fig. 2.—Case 2: Middle-aged man with a history of cardiac arrhythmias developed symptoms of respiratory insufficiency. Posteroanterior chest radiograph.

¹ All authors: Department of Radiology, University of Minnesota, Box 292 UMHC, 420 Delaware St. S.E., Minneapolis, MN 55455. Cases 1–4 prepared by J. R. Crass et al. M. E. Goldberg is coordinator of the Case of the Day series.

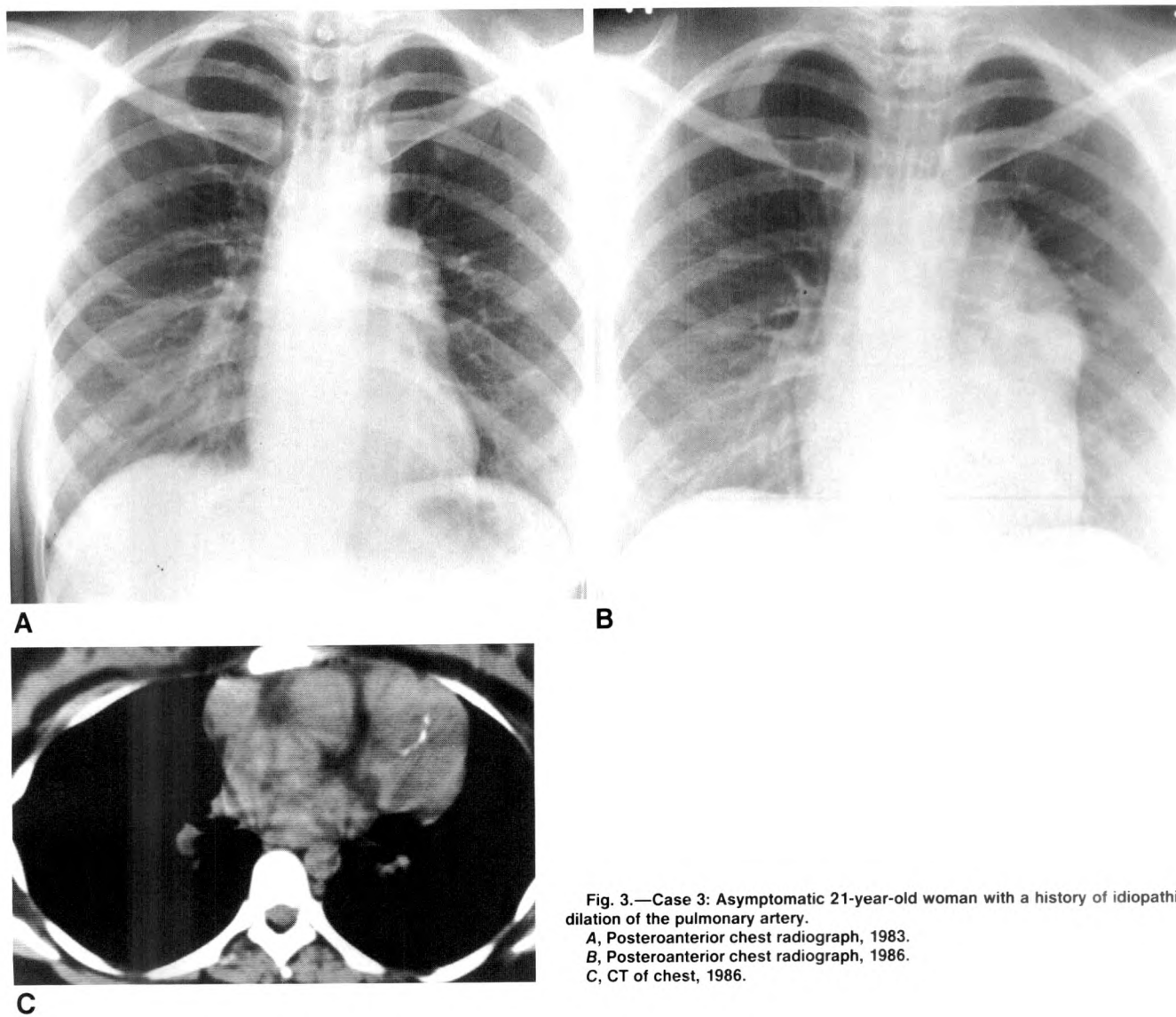


Fig. 3.—Case 3: Asymptomatic 21-year-old woman with a history of idiopathic dilation of the pulmonary artery.
 A, Posteroanterior chest radiograph, 1983.
 B, Posteroanterior chest radiograph, 1986.
 C, CT of chest, 1986.

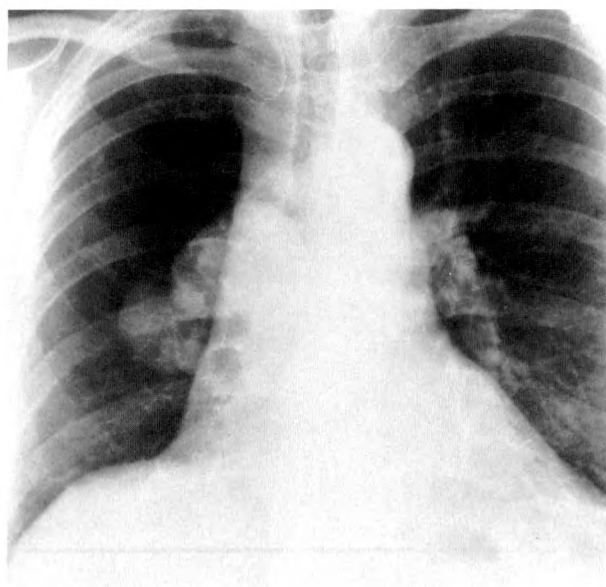
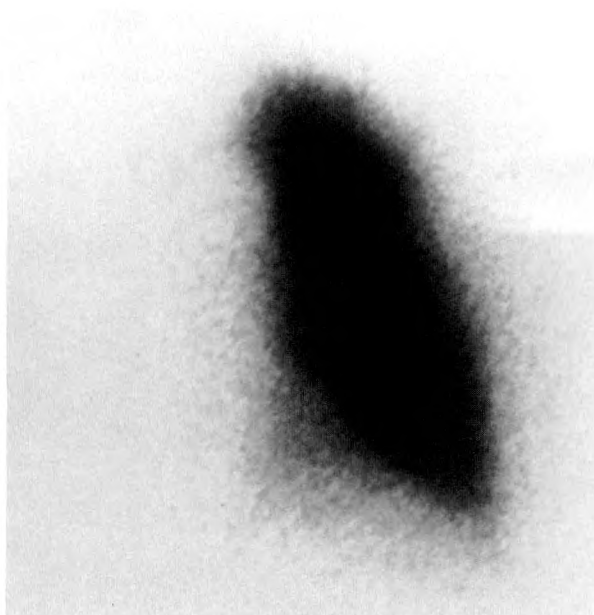
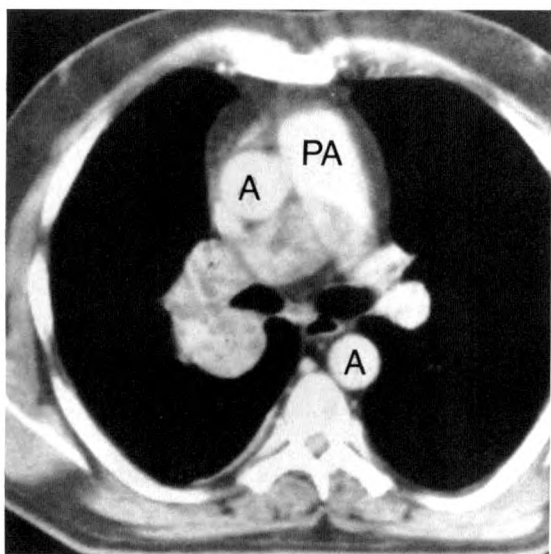
**A****B****C**

Fig. 4.—Case 4: 50-year-old man presented with decreased exercise tolerance and chest discomfort.

A, Posteroanterior chest radiograph.

B, Perfusion lung scan.

C, Chest CT with IV contrast material. A = aorta; PA = pulmonary artery.

Abdominal Case of the Day

Janis G. Letourneau,¹ Deborah L. Day, Jeffrey R. Crass, Marvin E. Goldberg, and Gordon Drake

Fig. 1.—Case 1: This 56-year-old man complained of nausea, vomiting, and early satiety. He underwent a cholecystojejunostomy 8 years earlier for jaundice secondary to biliary obstruction.

A, Venous phase, selective superior mesenteric angiogram, 1978.

B, Transaxial CT of midabdomen, 1983.

C, Lateral view, upper gastrointestinal series, 1985.

D, Transaxial CT of midabdomen, 1985.

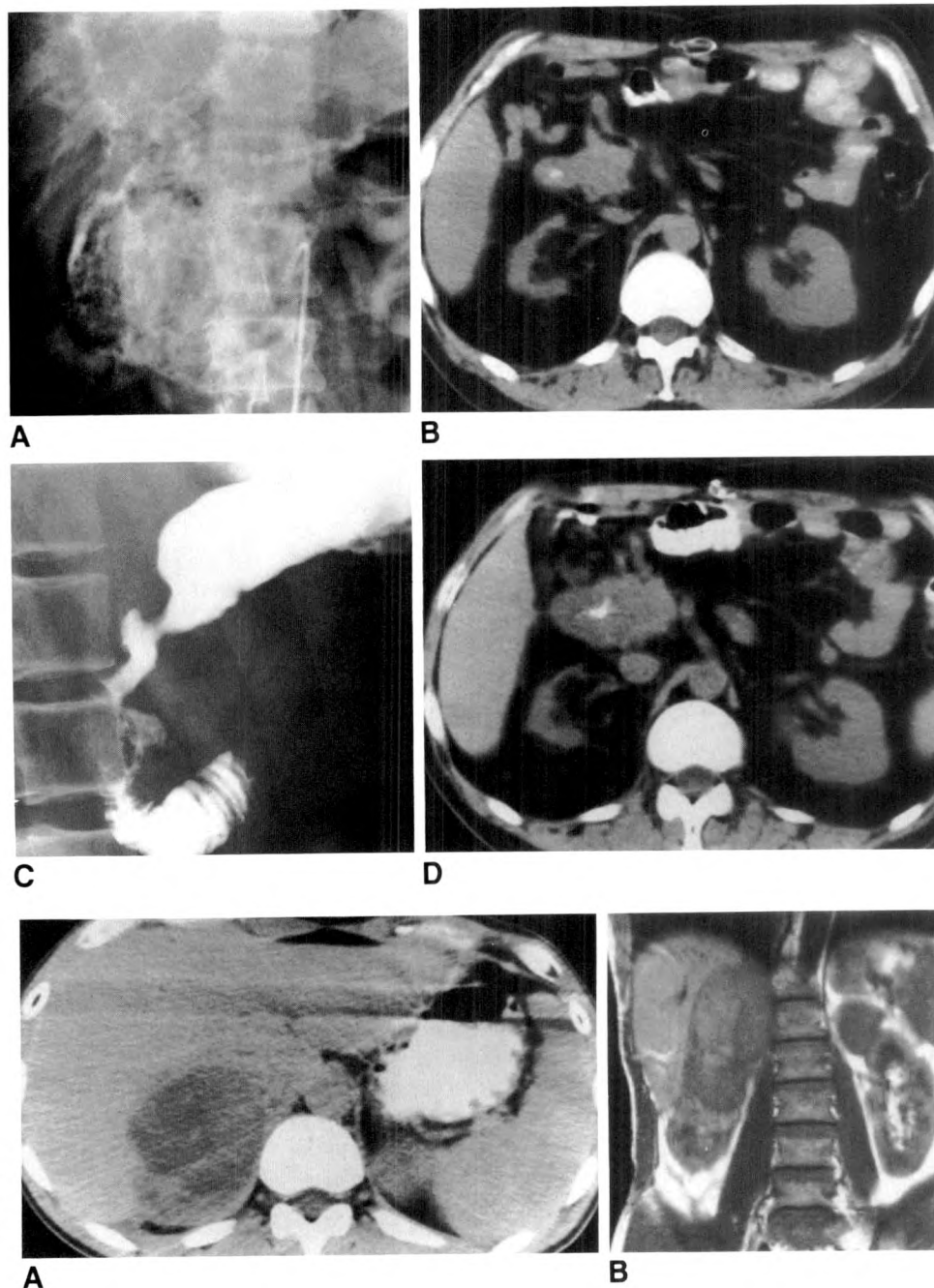
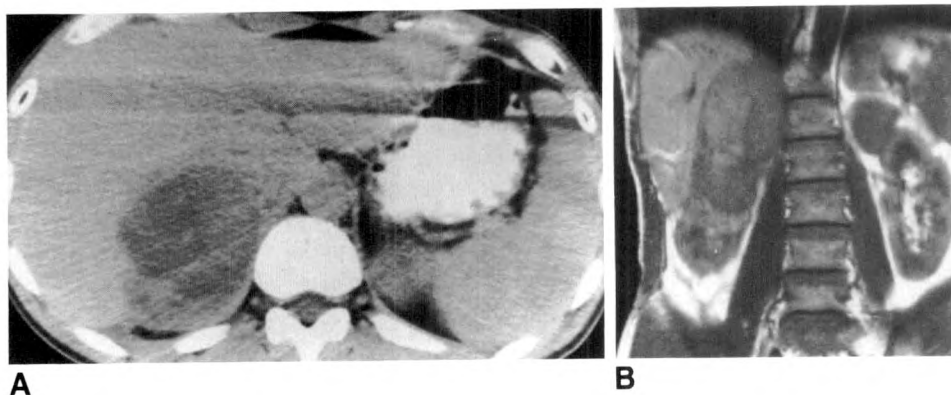


Fig. 2.—Case 2: This previously healthy 50-year-old man presented with weight loss and fatigue.

A, Transaxial CT of upper abdomen.

B, Coronal T1-weighted MR image of abdomen.



¹ All authors: Department of Radiology, University of Minnesota, Box 292 UMHC, 420 Delaware St. S.E., Minneapolis, MN 55455. Cases 1, 2, and 4 prepared by J. G. Letourneau, D. L. Day, J. R. Crass, and M. E. Goldberg. Case 3 prepared by D. L. Day, J. G. Letourneau, J. R. Crass, M. E. Goldberg, and G. Drake. M. E. Goldberg is coordinator of the Case of the Day series.

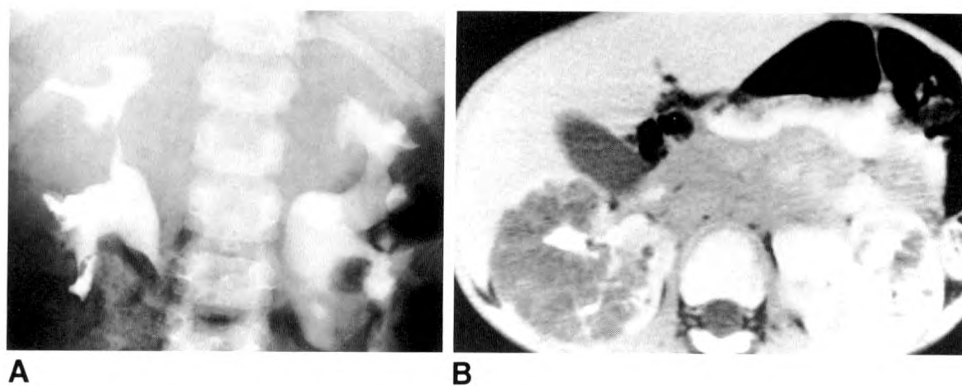


Fig. 3.—Case 3: Healthy 5-year-old boy was found to be hypertensive during prekindergarten physical examination. He had no family history of hypertension or renal disease. Renal and hepatic laboratory studies were normal.
A, Retrograde pyelogram.
B, Upper abdominal CT scan.

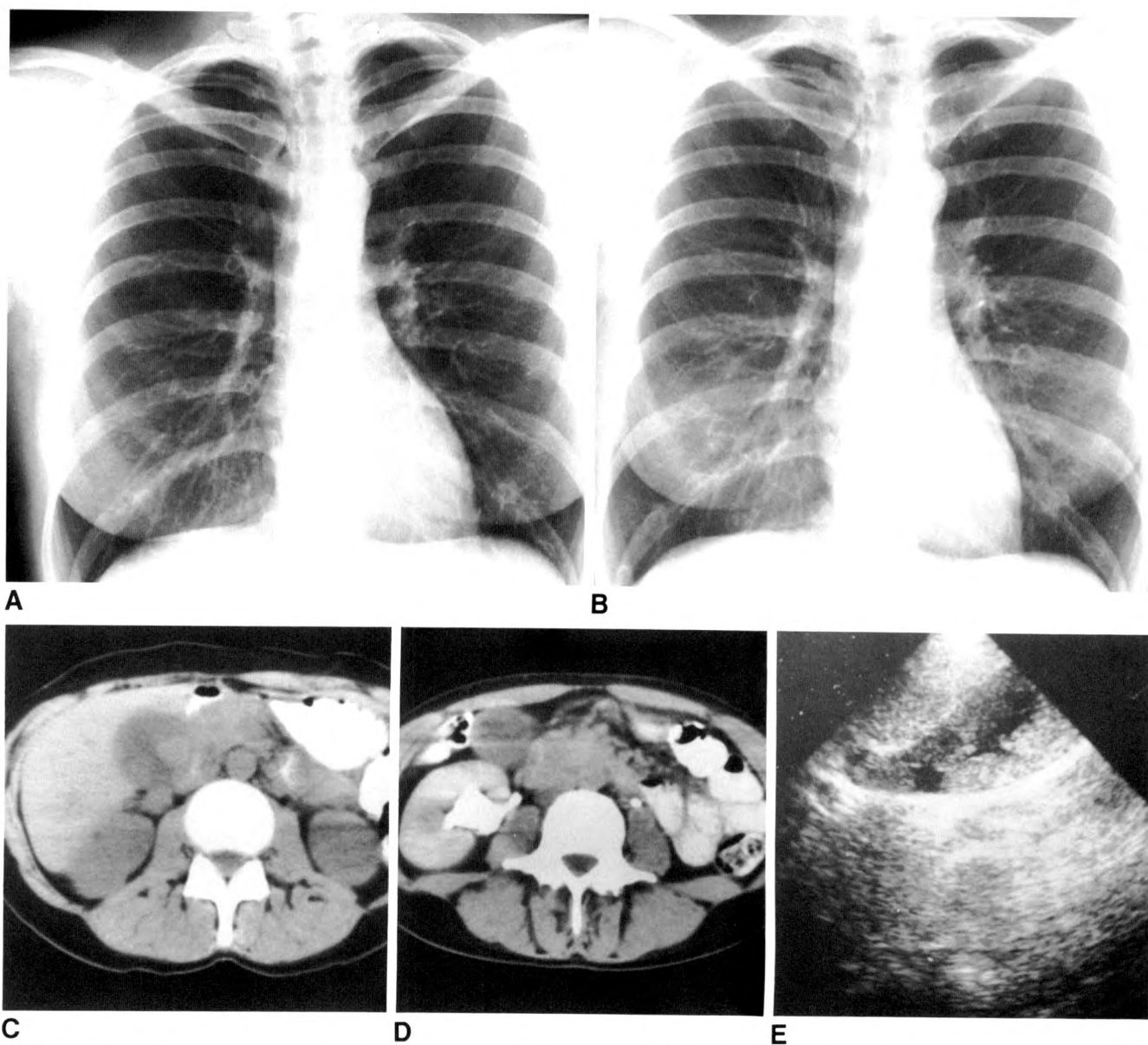


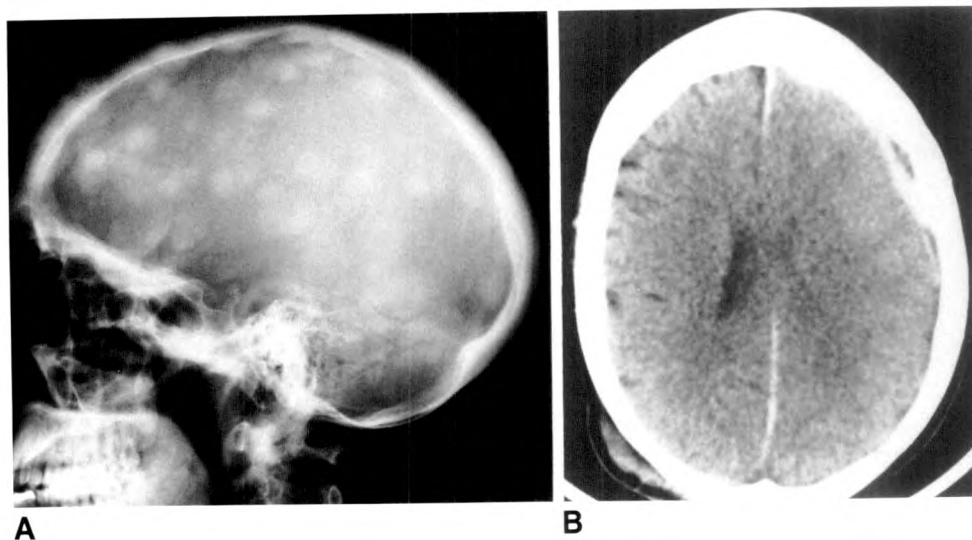
Fig. 4.—Case 4: This 38-year-old woman was referred for progressive dyspnea. She complained of vague right upper quadrant abdominal pain. Physical examination of chest and abdomen was remarkable only for diffuse wheezing. A, Posteroanterior chest, 1985. B, Posteroanterior chest at time of admission, 1986. C, Transaxial CT of upper abdomen, 4 days after admission. D, Transaxial CT of midabdomen, 4 days after admission. E, Sonogram of gallbladder, 5 days after admission.

Musculoskeletal Case of the Day

Deborah L. Day,¹ Janis G. Letourneau, Jeffrey R. Crass, Marvin E. Goldberg, and Gordon Drake

Fig. 1.—Case 1: This chronically ill young man had a seizure, fell, and hit his head.

A, Lateral skull.
B, Head CT.



¹ All authors: Department of Radiology, University of Minnesota, Box 292 UMHC, 420 Delaware St. S.E., Minneapolis, MN 55455. Individual cases prepared by D. L. Day, J. G. Letourneau, J. R. Crass, M. E. Goldberg, and G. Drake (cases 1 and 4); J. G. Letourneau, D. L. Day, J. R. Crass, and M. E. Goldberg (case 2); G. Drake, D. L. Day, J. G. Letourneau, J. R. Crass, M. E. Goldberg (case 3). M. E. Goldberg is coordinator of the Case of the Day series.

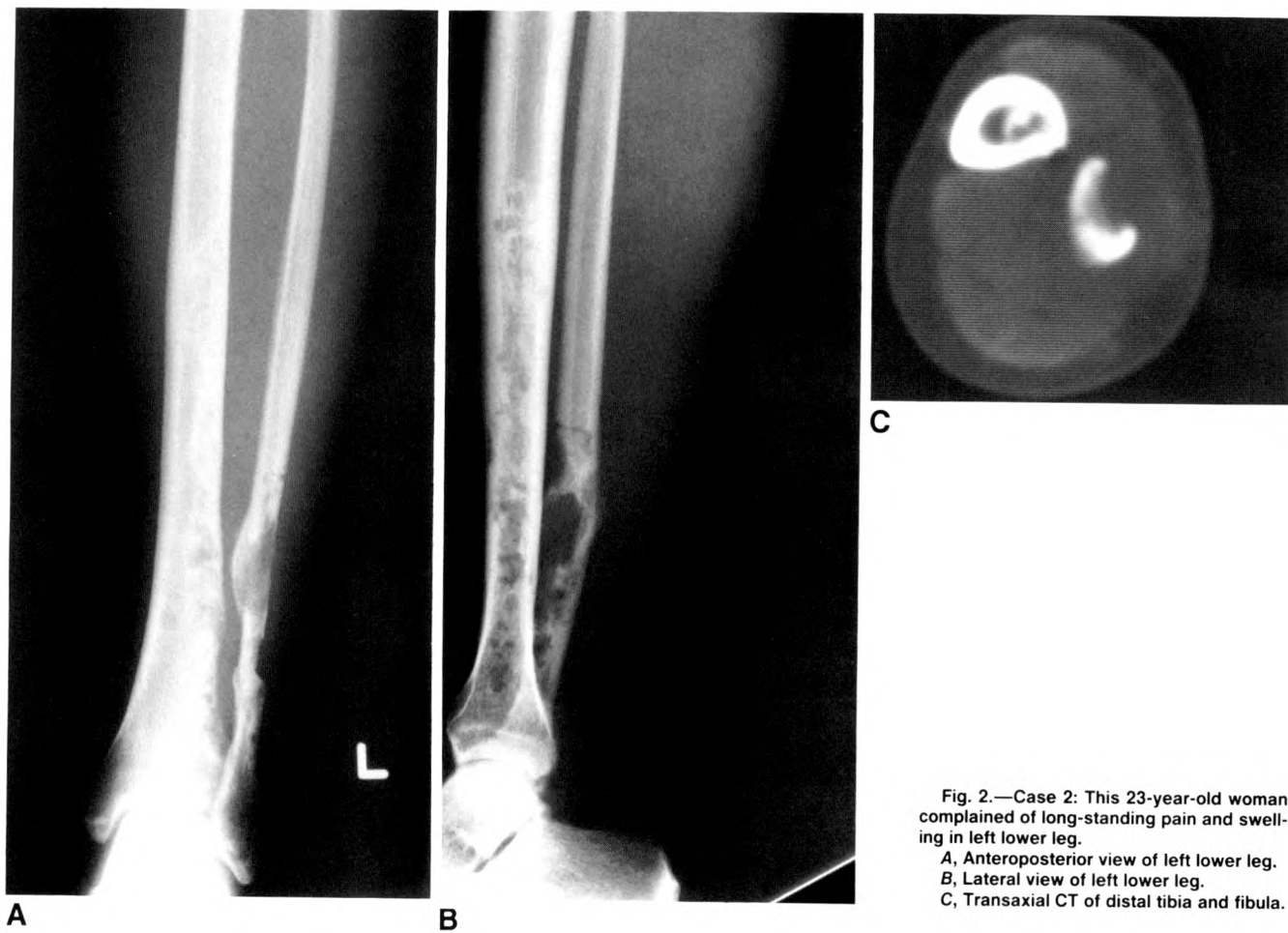


Fig. 2.—Case 2: This 23-year-old woman complained of long-standing pain and swelling in left lower leg.
A, Anteroposterior view of left lower leg.
B, Lateral view of left lower leg.
C, Transaxial CT of distal tibia and fibula.



A



B



C



D

Fig. 3.—Case 3: This 9-year-old boy had an hepatic embryonal cell sarcoma completely resected. Metastatic evaluation at that time was negative. 5 months after resection, before a course of chemotherapy was begun, an isolated sacral “hot” spot was found on radionuclide bone scan. There was no other evidence of metastatic disease.

A, Upper abdominal CT scan.

B, Posterior view, ^{99m}Tc -diphosphonate bone scan.

C, Anteroposterior lumbosacral spine.

D, Pelvic CT with bone window setting.



A



B



C

Fig. 4.—Case 4: This 7-year-old boy had bilateral enucleations at age 2 years for bilateral retinoblastoma. A recurrence in the right orbit 1 year later had been treated with a radical resection. Patient now presents with a 2-week history of left lower leg pain and swelling.

A, Anteroposterior view of skull.

B, CT scan through orbits.

C, Anteroposterior view of left lower leg.

Neuroradiology Case of the Day

Robert E. McGeachie,¹ William J. Ford, Mary Jo Nelson, and Dean Elias

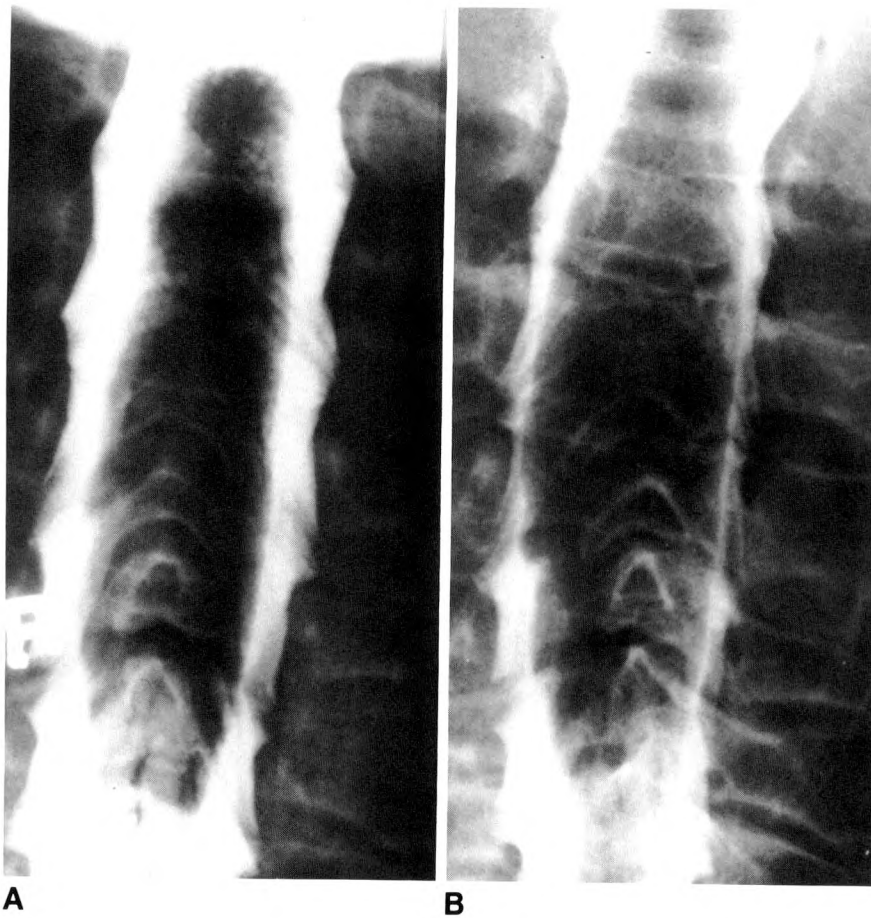


Fig. 1.—Case 1: 72-year-old previously healthy man with recent onset of neck pain, weakness and numbness of the arms, and difficulty walking.

A, Cervical myelogram (lateral view confirmed intramedullary location).

B, Repeat study 24 hr later.

¹ All authors: Department of Radiology, University of Minnesota, Box 292 UMHC, 420 Delaware St. S.E., Minneapolis, MN 55455. Cases 1, 3, and 4 prepared by R. E. McGeachie, W. J. Ford, and M. J. Nelson. Case 2 prepared by R. E. McGeachie, W. J. Ford, M. J. Nelson, and D. Elias. M. E. Goldberg is coordinator of the Case of the Day series.

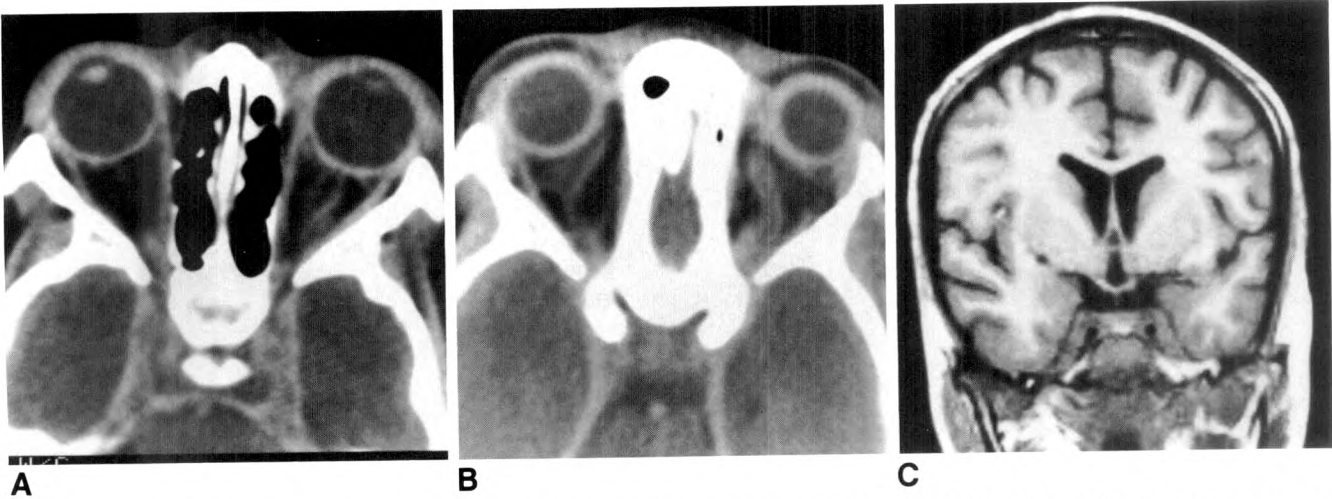


Fig. 2.—Case 2: 6-year-old girl with recent onset of periorbital swelling and proptosis. A, B, CT scans of orbits and parasellar region with IV contrast material. C, Coronal MR image (TR = 500 msec, TE = 17 msec).

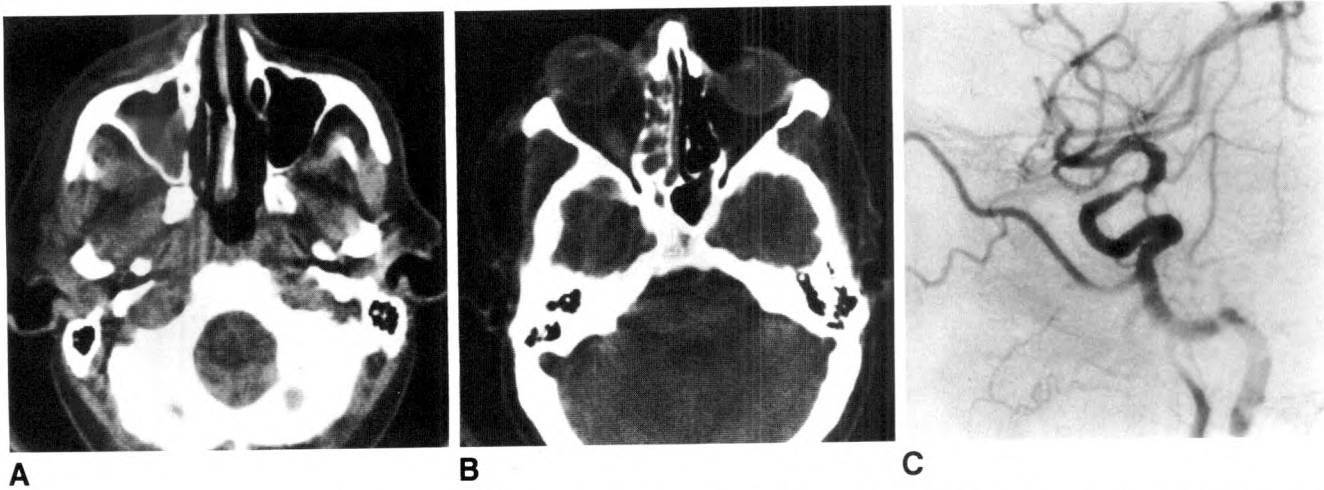


Fig. 3.—Case 3: 53-year-old man with 3-day history of facial pain and right proptosis progressing to lethargy and left hemiparesis. A, CT scan, maxillary sinus level. B, CT scan of orbits. C, Lateral view, right common carotid angiogram.

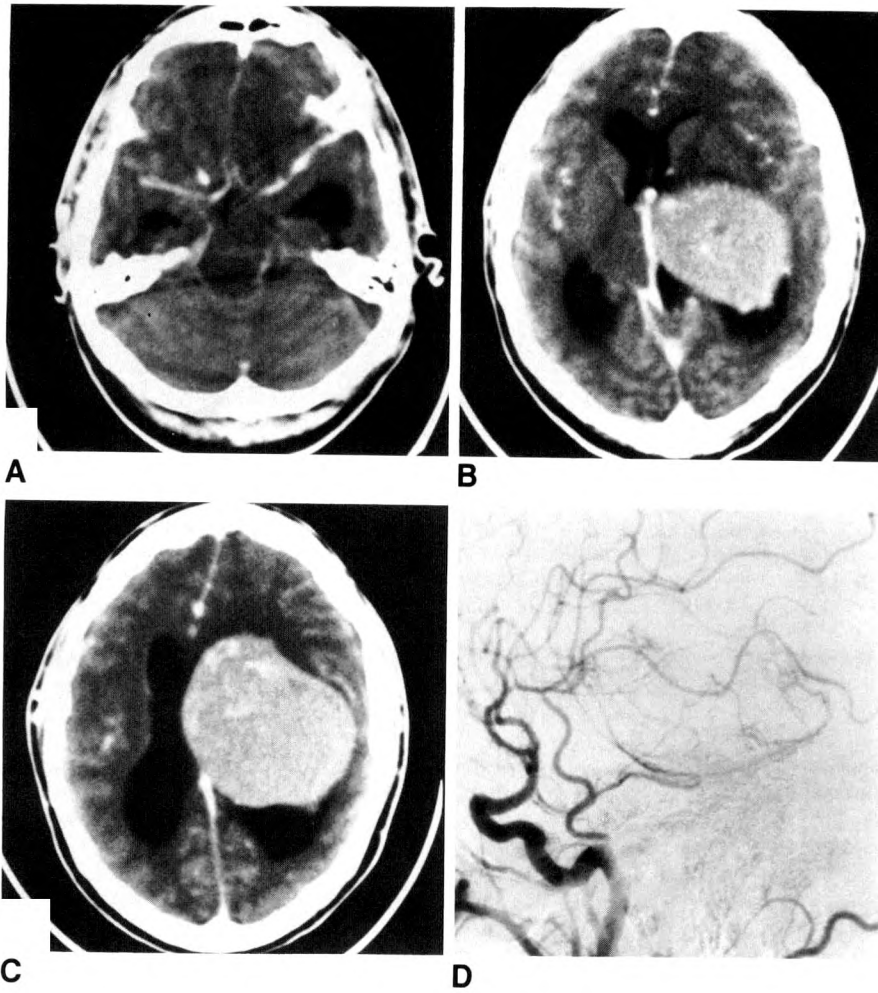


Fig. 4.—Case 4: 23-year-old man with onset of right hemiparesis and hemianesthesia, visual field cut, and behavior change.

A–C, CT scans of brain with IV contrast material.

D, Lateral view, left common carotid angiogram.

Letters

MRI of the Normal Pericardium

In the article by Sechtem et al. [1] it is unclear how the authors were able to get measurements of pericardial thickness to 0.1 mm when the pixel size is 1.7 mm. The authors state that "visual discrimination of gray-scale differences can discern points less than 1-pixel size apart."

This implies that by using subjective visual interpolation, the authors are able to increase spatial frequency resolution of the MR image by a factor of more than 10. Was this empirically possible—that is, were there tests of reproducibility between and within observers for this measurement? Even if it was reproducible, extrapolating the observation to inferences of pericardial thickness involves assumptions of linearity of MR signal, angle independence of the plane of section relative to the pericardium, the position invariance of the MR signal, and spatial frequency filtering of the reconstruction algorithm.

If the technique of measurement was indeed available to improve the spatial resolution a factor of 10 over pixel size, it would have tremendous applications in vascular imaging.

Andrew Yang
Johns Hopkins Hospital
Baltimore, MD 21205

REFERENCE

1. Sechtem U, Tscholakoff D, Higgins CB. MRI of the normal pericardium. *AJR* 1986;147:239–244

Reply

We appreciate the interest of Dr. Yang in our work. However, the fact that the reported means and standard deviations were fractions of the pixel size does not reflect that measurements were made to 0.1 mm, as concluded by Dr. Yang.

Figure 1 shows the effects of image postprocessing performed by the imager that was used in our study. In the left upper corner the border between air and chest wall was magnified by a factor of 10 and is displayed in the so-called pixel mode. The panel in the right upper corner shows the same aspect of the chest wall in the interpolated display. When magnified 100-fold, the pixel mode shows homogeneous intensity throughout the pixels (lower left panel). In contrast, the interpolation algorithm divides the original homogeneous pixel intensity into several different shades of gray (lower right panel), taking into account the different signal intensities of the neighboring pixels. The gray pixel in the center of the left lower panel is highlighted

by a white box in the interpolated display. Therefore, intensity differences that were less than 1.7-mm apart could be measured. As mentioned in the paper, it was possible to identify a pericardial line of a minimal width of 0.8 mm, which corresponded to half the pixel size.

Our paper was not intended to provide precise measurements of changes in thickness of the pericardium during the cardiac cycle when such measurements may be in the submillimeter range. We were impressed by the actual width of the pericardial line that is clearly thicker than the pericardium itself, which is an anatomic structure of less than 0.8-mm thickness. Trying to find an explanation for this unexpected thickness, we quantitatively followed variations of the thickness of the pericardial line over the cardiac cycle. To express this visual change in the thickness of the pericardial line during the cardiac cycle, we attempted to measure the structure at various phases. For this purpose it was useful to take advantage of the improved spatial discrimination provided by the interpolation process. Our measurements supported the visual findings that the pericardial line varies in thickness during the cardiac cycle. This

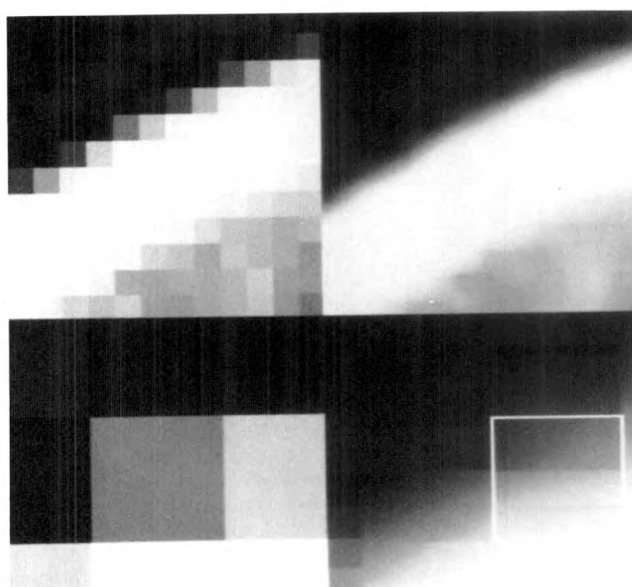


Fig. 1.—Effects of image postprocessing of normal pericardium.

suggests that normal pericardial fluid, as well as the pericardium, contribute to the thickness of the pericardial line.

We caution the author of this letter against making the assumption that the technique of measurements "improve(s) spatial resolution by a factor of 10 over pixel size." Our observations indicate only that a change in thickness of the pericardial line of less than 1 mm can be observed on gated MR images.

Udo Sechtem

University of California, San Francisco, School of Medicine
San Francisco, CA 94143

Bizarre Parosteal Osteochondromatous Proliferation vs. Benign Florid Reactive Periostitis

In the March 1985 issue of *AJR*, Porter et al. [1] presented a case that they call florid reactive periostitis (FRP) of the phalanges. In our opinion, however, their case has all the radiologic and histologic features of a different but distinctive entity, which is bizarre parosteal osteochondromatous proliferation (BPOP). This lesion has been well described in the pathologic and orthopedic literature [2, 3] and will be reported by us in the radiologic literature soon [4]. As in FRP, BPOP occurs most commonly in small bones of the hands and feet. FRP usually presents with a laminated or mature periosteal reaction, juxtacortical soft-tissue calcification, and minimal periosteal elevation, and without distortion of the underlying cortex [5, 6]. BPOP, however, is a well-defined pedunculated or sessile tumor, ranging from 0.4 to 3.0 cm in diameter that, characteristically, arises directly from the cortical surface of the underlying bone without disturbing the native architecture or alternating the surrounding cortex. These features are well demonstrated in Figure 1B of the paper of Porter et al. Both FRP and BPOP have a high tendency to recur.

Histologically, BPOP is characterized by irregular bone-cartilage interfaces and active-appearing fibrous tissue. This cluster of findings is evident in Figure 2 of the paper by Porter et al. FRP tends to have more bone formation, and it may have a greater degree of organization and maturation than BPOP. Admittedly, FRP and BPOP can have some histologic overlap since there is only a limited number of images that can be produced by reactive bone, cartilage, and fibrous tissue. Nonetheless, the microscopic conger of tissues coupled with the radiograph from the patient of Porter et al. makes BPOP a more likely diagnosis than FRP.

We believe, therefore, that the case described by Porter et al. is in reality bizarre parosteal osteochondromatous proliferation and not florid reactive periostitis.

Eduard E. de Lange

Thomas L. Pope, Jr.

Robert E. Fechner

Theodore E. Keats

University of Virginia Medical Center
Charlottesville, VA 22908

REFERENCES

- Porter AR, Tristan TA, Rudy FR, Eshbach TB. Florid reactive periostitis of the phalanges. *AJR* 1985;144:617-618
- Nora FE, Dahlin DC, Beabout JW. Bizarre parosteal osteochondromatous proliferations of the hands and feet. *Am J Surg Pathol* 1983;7:245-250
- Davies CWT. Bizarre parosteal osteochondromatous proliferation in the hand. *J Bone Joint Surg* 1985;76A:648-650
- de Lange EE, Pope TL Jr, Fechner RE, Keats TE. Bizarre parosteal osteochondromatous proliferation of the foot. *Skel Radiol* (in press)
- Spjut HJ, Dorfman HD. Florid reactive periostitis of the tubular bones of the hands and feet, A benign lesion which may simulate osteosarcoma. *Am J Surg Pathol* 1981;5:423-433

- Holmes WS, Pope TL, de Lange EE, Fechner RE, McDowell CL, Keats TE. Benign florid reactive periostitis of the phalanges. *Skeletal Radiol* (in press)

Reply

The description of BPOP by Davies was published concurrently or after the description of our case. In our search of the literature, December 1982-January 1983, we missed the work by Nora et al. because it had not been published. We did not submit our report immediately since we desired further follow-up on this patient. Such follow-up was not achieved, so the paper was submitted in March 1984.

We did have Howard D. Dorfman (author of reference 5 of the preceding letter) review the material and he agreed with the diagnosis of reactive periostitis.

There are "lumpers" and "splitters" and since I am of the latter persuasion, and in view of more recent material, a diagnosis of BPOP radiographically may be appropriate.

The discordance between histologic diagnosis and radiologic appearance of a bone lesion is well known, and the overlap between FRP and BPOP histologically is probable, as de Lange et al. mention. Radiographically, we initially thought this was an osteoma or an osteochondroma, as well. We look forward to the publication of reference 6 so that these lesions may be accurately defined radiologically.

Theodore A. Tristan

Polyclinic Medical Center
Harrisburg, PA 17110

Language of Certainty

In his editorial entitled "Language of Certainty" [1] on how to conclude reports of radiologic examinations, Marvin L. Daves chooses the term "impression" as optimal. He discards the term "diagnosis" as an appropriate conclusion, apparently believing that this term is beyond the domain of the radiologist. Instead, he asserts that the "diagnosis" is the responsibility of the clinician, and also that it connotes more commitment or certainty than is justifiable for a radiologic report.

American medicine in general is struggling with certainty today. Our preoccupation with certainty (or more accurately, our discomfort with even small increments of *uncertainty*) is a principal cause of over-testing and the added health costs it generates. I postulate that diagnoses, even those of pathologists, and certainly those of referring clinicians, do not invariably represent fixed certitudes or absolute truth. Instead, they imply a *range* of certainty.

I am a diagnostic radiologist, certified by the American Board of Radiology in diagnostic radiology. I work in the Department of Diagnostic Radiology. I make radiologic *diagnoses* daily. And, like the diagnoses of my clinical colleagues, many of mine are correct, some are near the truth, and some are totally wrong. But they are diagnoses all the same.

Those who prefer the term "impression" for the reasons cited by Daves or for other reasons should continue to take comfort in it. They should not, however, urge this term on others.

Reiley Kidd

The Mason Clinic
Seattle, WA 98111-0900

REFERENCE

- Daves ML. Language of Certainty. *AJR* 1986;147:209-210.

Reply

My comments were made in defense of "impression," which Orrison et al. [1] had impugned as too "vague, subjective, and unreliable" for the conclusion of an imaging report. I wrote in defense of a common practice. It is Orrison, Nord, Kinard, and Juhl who urge a term on others, namely "reading."

I work in the Diagnostic Division of The Department of Radiology, University of Colorado, but at Boulder Community Hospital I work in the Imaging Department. Regardless of the name, I agree with Dr. Kidd that the major function of these units is diagnosis and that in most of the world of medicine we imagers are *the* diagnosticians. However, for a practical matter, as a heading for the end of my reports I find "diagnosis" too confining. With "impression" I can offer a diagnosis, suggest a differential, or render an opinion.

Marvin L. Daves
University of Colorado
Medical School and Hospital
Denver, CO 80262

REFERENCE

1. Orrison WW, Nord TE, Kinard RE, Juhl JH. The language of certainty: proper terminology for the ending of the radiologic report. *AJR* 1985;145:1093-1095

Fibromuscular Dysplasia vs Catheter-Induced Renal Artery Spasm

The October 1986 issue of *AJR* presents a case [1] of what the authors believe was "reversible" fibromuscular dysplasia of the right renal artery, which was shown to have disappeared some years later. They propose that the abnormality was somehow "reversed" by medical antihypertensive therapy, the first such case to be reported. Their illustration shows a catheter inserted deeply into the right renal artery, with two or three constrictions around the renal artery at its bifurcation.

In my opinion, the patient has catheter-induced renal artery spasm rather than fibromuscular dysplasia. True concentric narrowing due to fibromuscular dysplasia has dilated segments of renal artery between the constrictions. Fibromuscular dysplasia also most commonly involves the main renal artery, not the bifurcation. Their diagnosis of renovascular hypertension is not supported by the laboratory findings because there is no significant elevation of renal vein renin on the right side as compared with the left side.

Fortunately, the patient refused surgery.

Terence W. McGrath
Kaiser Permanente Medical Center
Oakland, CA 94611

REFERENCE

1. Nemcek AA, Holmburg CE. Reversible renal fibromuscular dysplasia. *AJR* 1986;147:737-738

Reply

The initial angiogram performed in this patient was a flush abdominal aortogram during which there was no catheter manipulation of the right renal artery. It shows narrowing in the renal artery, so the finding was not due to catheter-induced spasm.

The location of the lesion is not critical. Numerous standard texts describe the various types of fibromuscular dysplasia as being in the main and/or branch vessels of the renal artery, and not all types show aneurysmal dilatation between the stenotic areas [1].

While the ratio of abnormal kidney renin to normal kidney renin should ideally be 1.5 to 1.0 or higher before interventional procedures, it is well known that some cases with a lower ratio may still respond satisfactorily [2]. Furthermore, the renin values selectively obtained were 3 to 5 times our laboratory normals. Such high values are not usually seen in essential hypertension.

The clinical evidence for renovascular hypertension is overwhelming. This patient is a young normotensive woman who developed hypertension under observation after an initial normal IV urogram. After 4 years of usually adequate therapy, the IV urogram became abnormal, the hypertension was not controlled, other causes of hypertension were excluded, markedly elevated renins were found, and an abnormal right renal artery was seen.

I agree that it was fortunate the patient refused surgery.

Albert A. Nemcek
Community Memorial Hospital
Menomonee Falls, WI 53051

REFERENCES

1. Sos TA. Renal vascular hypertension, Part C. In: Castaneda-Zuniga WR, ed. *Transluminal angioplasty*. New York: Thieme-Stratton, 1983:70
2. Kadar S. Renin determination in the management of renal vascular hypertension. In: Athanasoulis CA, Pfister RC, Greene RE, Roberson GH, eds. *Interventional radiology*. Philadelphia: Saunders, 1982:308

Heating Lidocaine Appears to Prevent Painful Injection

Approximately 9 months ago we began heating lidocaine hydrochloride to approximately 43°C (110°F) before infiltrative injection for local anesthesia in arthrography, angiography, and all interventional procedures. Previously, almost all patients complained of an uncomfortable burning sensation with local anesthesia. Now, patients rarely complain about the injection because they experience minimal or no burning sensation. I confirmed both the burning sensation of the nonheated lidocaine and the absence of pain with the heated lidocaine by infiltrative injections in my lumbar region on separate occasions.

Personal contact with the manufacturer of lidocaine, Elkins-Sinn, Inc. (Cherry Hill, NJ) revealed that heating of lidocaine causes no chemical denaturation. Neither Elkins-Sinn, Inc., nor I could find any previous mention of this relationship of heating lidocaine with the absence of pain in the medical, surgical, or radiologic literature.

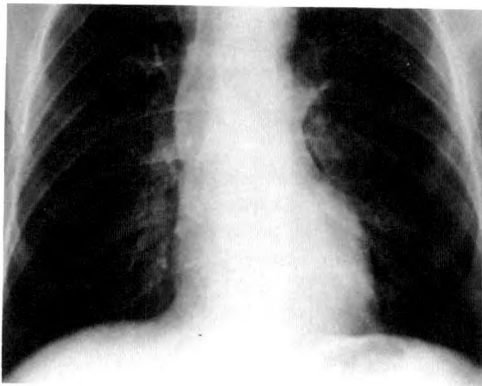
In our department, we now simply place the day's vials of lidocaine in a bath of water in a baby-food warmer, which keeps them at a constant temperature of 43°C (110°F). There is a significant absence of the painful injection we have all experienced in the past and an absence of hesitancy for future injections.

No prolonged or double-blind study was carried out because of the obvious difference in patient response. We suggest that your readers try this in their practice and determine its usefulness and patient acceptance.

Lawrence I. Finkel
David J. Berg
Phoenix General Hospital
Phoenix, AZ 85015

The Reverse Lordotic View for Visualization of the Lung Bases

Evaluation of the posterior lung bases with plain film chest radiography is sometimes difficult. Various special views, such as an overpenetrated anteroposterior (AP) view centered at the diaphragm



A
Fig. 1.—A, Posteroanterior view of chest. B, Lateral view of chest.

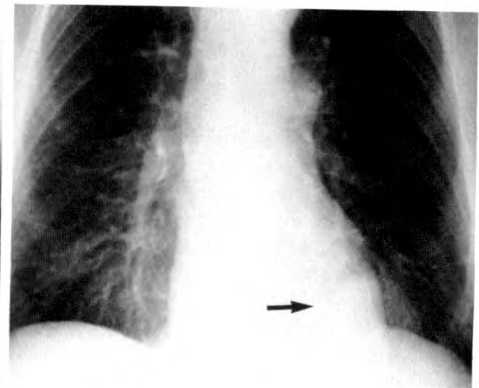


Fig. 2.—“Reverse lordotic” anteroposterior view showing a mass (arrow) in left lung base.

and oblique views are helpful. Another simple view is suggested to assist with plain film evaluation of this area.

A tangential view of the posterior aspect of the diaphragm will improve demonstration of the posterior lung bases. With the patient upright (sitting or standing), an AP view of the chest with caudal angulation of the beam is obtained. A posteroanterior (PA) view with cephalic beam angulation with the patient prone can also be used, but will increase magnification of structures located posteriorly. The degree of angulation can be adjusted for each patient on the basis of the appearance of their diaphragm on a lateral chest view. This view is not described in common radiographic positioning texts [1, 2].

Figure 1 is a PA examination of the chest, which appears normal. The corresponding lateral view shows a vague density in one of the posterior costophrenic angles. A 30° “reverse lordotic” view (Fig. 2) shows a 4-cm mass in the left lower lobe.

Jerome J. Gehl
Bloomington Radiology, S.C.
Bloomington, IL 61701

Lisa A. Johnson
St. Joseph's Hospital Medical Center
Bloomington, IL 61701

REFERENCES

1. Ballinger PW. *Merrill's atlas of radiographic positions and radiologic procedures*, 6th ed. St. Louis: Mosby, 1986
2. Bontrager KL, Anthony BT. *Textbook of radiographic positioning and related anatomy*. Blauvelt, NY: Multimedia, 1982

A Clinical Year for Radiology Trainees: Necessary or Detrimental?

During recent years, the academic radiology community has increasingly favored the requirement of a clinical internship for aspiring trainees in diagnostic radiology, which has resulted in a declining number of available PGY-1 positions in the field. While a clinical year most certainly provides the radiology resident with enhanced understanding of problems related to direct patient care and the ability to communicate more effectively with physicians in other disciplines, it may also have negative consequences. Foremost among these is the serious threat of diminishing the idealism and initiative of the typical

4th-year medical student. It is appropriate to question whether the knowledge to be gained from a clinical year is worth the potential losses.

The clinical internship is traditionally looked upon as the most difficult year of medical training, and frequently becomes inconsistent with our stated objectives as physicians: to care for the sick or disabled to the best of our abilities and, above all, to do no harm. The overworked, depressed intern deprived of regular sleep, meals, and exercise is obviously incapable of functioning optimally, and also more prone to errors that may adversely affect his or her patients. Unfortunately, the net result (usually temporary; occasionally permanent) of a year of such treatment may include loss of extracurricular interests, breakup of a relationship, bitterness toward the field, and diminished self-motivation, as well as personal enthusiasm, in future work.

As a member of the Resident Selection Committee in a respected academic radiology department, I have recently had the good fortune to meet with many of the country's finest medical students aspiring to pursue a career in diagnostic imaging. The quality of the current applicant pool is staggering; the average individual is exceptionally bright, self-disciplined, capable of independent thought, sincere in aspirations, and capable of positive personal interaction. Yet, after talking with these gifted people, it is clear that among their greatest assets are personal enthusiasm, energy, and self-motivation.

While a 4th-year medical student, I was fortunate to be counseled by a radiology residency program chairman who shared these attitudes. As a result, my postgraduate training included 3 years of practical radiology and 1 year of full-time research, as opposed to a clinical internship. The elective year provided a unique opportunity to solidify my interests in an academic career through enhancement of teaching, investigative writing, and scientific presentation skills. Most importantly, the inherent enthusiasm of every graduating medical student is still fresh with and works for me in every professional activity.

The arguments for a required clinical year as part of training in diagnostic radiology are relatively weak by comparison. Provided an applicant has had broad and extensive clinical experience at the subintern level while a medical student, he or she should possess adequate understanding of problems related to direct patient care, as well as the tools needed for effective communication with referring physicians. A further disincentive for a required year of indirectly related activities is the increasing demand for diagnostic imaging

services, which has made the job of the trainee in radiology progressively more difficult both physically and mentally. The average radiology resident, today, has the added stress created by the exponentially increasing body of knowledge he or she must learn. The 4-year residency requirement is a response to this demand.

I believe that a careful reexamination of the pros and cons of a clinical internship for trainees in radiology is warranted. As a compro-

mise, perhaps postgraduate clinical training could be limited to 6 months, or major academic programs could create less demanding clinical PGY-1 positions that would allow for early integration of activities in radiology.

David J. Sartoris
UCSD Medical Center
San Diego, CA 92103

Letters are published at the discretion of the Editor and are subject to editing.

Letters to the Editor must not be more than two *double-spaced* typewritten pages. One or two figures may be included. See Author Guidelines for letters, page A5.

Letters concerning a paper published in AJR will be sent to the authors of the paper for a reply to be published in the same issue. Opinions expressed in the Letters to the Editor do not necessarily reflect the opinions of the Editor.

Abstracts

Heart

Calculation of aortic valve area by Doppler echocardiography: a direct application of the continuity equation. Richards KL, Cannon SR, Miller JF, et al. (Division of Cardiology, Veterans Administration Hospital, San Antonio, TX 78284). *Circulation* 73:964-969, May 1986

The continuity equation suggests that a ratio of velocities at two different cardiac valves is inversely proportional to the ratio of cross-sectional areas of the valves. To determine whether a ratio of mitral/aortic valve orifice velocities is useful in determining aortic valve areas in patients with aortic stenosis, 10 control subjects and 22 patients with predominant aortic stenosis were examined by Doppler echocardiography. The ratio of mean diastolic mitral velocity to mean systolic aortic velocity (V_m/V_a), and the ratio of mitral diastolic velocity-time integral to aortic systolic velocity-time integral (VT_m/VT_a) were determined from Doppler spectral recordings. Aortic valve area determined at catheterization by the Gorlin equation was the standard of reference. High-quality Doppler recordings were obtained in 30 of 32 subjects (94%). Catheterization documented valve areas of 0.5 to 2.6 cm² (mean 1.1). There was good correlation between Doppler-determined V_m/V_a and Gorlin valve area ($r = .90$, $SEE = 0.23$ cm²); a better correlation was noted between VT_m/VT_a and Gorlin valve area ($r = .93$, $SEE = 0.18$ cm²). The data showed the usefulness of Doppler alone in the determination of aortic valve area in adults with absent or mild aortic or mitral regurgitation and no mitral stenosis. Although the use of mean velocity and velocity-time integral ratios requires accurate measurement of mitral and aortic velocities, it does not require squaring of these velocities or measurement of cross-sectional area of flow.

Author Abstract

Muscles and Skeleton

Rheumatoid arthritis of the thoracic and lumbar spine. Heyweek A, Meyers O (Princess Alice Orthopaedic Hospital, White Road, Retreat, Cape Town 7945, South Africa). *J Bone Joint Surg [Br]* 68-B:362-368, 1986

The authors report seven cases, four with histologic proof, of seropositive rheumatoid arthritis in whom involvement of the thoracic and lumbar vertebrae occurred. All patients had proven rheumatoid arthritis with vertebral involvement and are not to be confused with ankylosing spondylitis. The findings included ill-defined, blurred, and eroded margins of the vertebral end-plates in the thoracic and lumbar spine. The facet joints were ill-defined and eroded. The presence of osteophytes as a degenerative process does not negate the diagnosis of rheumatoid spondylitis if the other findings are present. The authors

propose a hypothesis that the synovitis probably starts in the apophyseal joints, slowly eroding cartilage and subchondral bone in exactly the same way as it does in peripheral joints. Erosion of the facet joints produces anteroposterior and lateral instability. Rheumatoid discitis probably starts at the discovertebral junction as an enthesopathy. Inflammatory degradation of collagen at the junction between the disc and the vertebral end-plate leads to loss of disc substance and invasive erosions of the end-plates. In the thoracic area, the costovertebral joints are also involved. Nerve-root compression can occur from instability. The authors conclude that thoracic and lumbar rheumatoid spondylitis is far more common than the sparse reports the literature would lead one to believe.

Ray F. Kilcoyne

Evaluation of Gaucher Disease Using Magnetic Resonance Imaging. Rosenthal D, Scott J, Barranger J, et al. (Massachusetts General Hospital, Dept. of Radiology, Boston, MA 02114). *J Bone Joint Surg [Am]* 68-A:802-808, 1986

MR imaging was used to study the skeletal involvement in a series of 24 patients with Gaucher's disease. Radiographic findings previously described in this disease include: (1) infarction of the bone and bone marrow, (2) focal replacement of marrow by infiltration of Gaucher cells, and (3) generalized osteopenia. Because MR is highly sensitive in detecting disorders of the bone marrow, the authors investigated the potential for assessing abnormal marrow in patients with Gaucher's disease. A series of spin-echo images were obtained with sequences that emphasized T1 or T2 weighting. In all patients, the normal high intensity of marrow fat was replaced in some areas by a very low signal intensity, either patchy or widespread. The spine was always affected. The metaphyses of the long bones were usually affected, but the epiphyses were often spared. Areas of nonhomogeneous decreased signal within epiphyseal portions of bone were thought to represent osteonecrosis. Bones closer to the axial skeleton tended to have more involvement than more distal sites. Involvement of the epiphyses of the long bones appeared to correlate with the presence of avascular necrosis. It is apparent that the skeletal alterations of Gaucher's disease are more extensive than would be expected from either plain radiography or CT.

Ray F. Kilcoyne

A Comparative Study of the Tolerance of Skeletal Muscle to Ischemia. Heppenstall RB, Scott R, Sapega A, Park YS, Chance B (Hospital of the University of Pennsylvania, 3400 Spruce St., Philadelphia, PA 19104). *J Bone Joint Surg [Am]* 68-A:820-828, 1986

The tolerance of skeletal muscle to tourniquet application (ischemia) and to acute compartment syndrome (ischemia and pressure) was compared. During both the ischemic period and a 2-hr recovery

period immediately after, the mean intracellular pH and levels of adenosine triphosphate and phosphocreatine of the muscles of the anterolateral compartment were monitored by phosphorus nuclear MR spectroscopy. During ischemia, the cellular levels of phosphocreatine decreased at an identical rate in both the acute and chronic compartment syndrome groups. In contrast, the levels of the adenosine triphosphate diminished rapidly in the animals with the compartment syndrome, but remained unchanged in the tourniquet group. In the tourniquet group, the phosphocreatine, adenosine, and pH were all normal within 15 min after the release of the tourniquet, but these values remained depressed even 2 hr after fasciotomy in the group with compartment syndrome. Elevated tissue pressure appears to act synergistically with ischemia to produce more severe cellular damage than does ischemia alone. The clinical relevance of the study is that established concepts regarding the tolerance of skeletal muscle to ischemia are based on tourniquet studies alone and do not take into account the additional cellular damage produced by acute high-pressure compartment syndrome.

Ray F. Kilcoyne

Excessive retroversion of the glenoid cavity: A cause of non-traumatic posterior instability of the shoulder. By Brewer BJ, Wubben RC, Carrera GF (Medical College of Wisconsin, Milwaukee County Medical Complex, 8700 W. Wisconsin Ave., Milwaukee, WI 53226). *J Bone Joint Surg* 68A:724-731, 1986

Excessive retroversion of the glenoid cavity is a developmental deformity and is considered the primary cause of posterior instability of the shoulder. A surgical technique that employs a posterior opening-wedge osteotomy of the scapula neck to correct the defect and the instability is described. Seventeen shoulders in 10 adolescents were evaluated for nontraumatic posterior instability. Each patient had significant disability in throwing a ball, swimming, arm-blocking in football, or bench-pressing weights. Radiographically the glenohumeral index was measured by comparing the maximum transverse diameter of the articular surface of the glenoid with the maximally transverse diameter of the humeral head. Small glenoid fossae are considered to predispose to instability of the shoulder joint. Measurements were made from either axillary radiographs or CT. The retroversion of the head of the humerus is expressed in degrees as determined on a single axial radiograph of the humerus made with the central ray passing down through the shoulder to the elbow resting on the plane of the cassette. The retroversion of the humeral head was readily measured in reference to the humeral shaft and condyles on this radiograph. Glenoid tilt is measured on an axillary radiograph made with the arm abducted, flexed, and neutrally rotated. Most of the patients had excessive glenoid retroversion, averaging 10°. Of five patients who had surgical correction of the glenoid retroversion four had an excellent functional result. One shoulder became unstable shortly after the operation and a revision was necessary.

Ray F. Kilcoyne

Magnetic resonance imaging and discography in the diagnosis of disc degeneration. Gibson M, Buckley R, Mawhinney R, Mulholland R, Worthington B (Harlow Wood Orthopaedic Hospital, Near Mansfield, Nottinghamshire NG18 4th, England). *J Bone Joint Surg* 68-B:369-373, 1986

The lumbar spines of 22 patients were examined for disc degeneration by MR and discography. A total of 50 intervertebral discs were studied by both methods. TR 2000/TE 80 msec were obtained on a 0.15-T resistive-magnet machine. In 44 of the 50 discs studied, both techniques were in complete agreement. In three of the other studies the discograms were initially reported to be normal, but on reexamination minor lateral fissuring was found. In a fourth case, the MR scan was reported as normal but, in retrospect, was probably abnormal. Faulty needle placement for discography produced inaccurate results in two cases. MR has several major advantages over discography: it is noninvasive, nonpainful, simple to perform and

interpret, and able to visualize many lumbar disc levels at once. Also, it uses no ionizing radiation.

Ray F. Kilcoyne

A dynamic classification of Paget's disease. Lander P, Hadjipavlou (The Sir Mortimer B. Davis-Jewish General Hospital, 3755 Cote St. Catherine Rd., Montreal, Quebec, Canada H3T 1E2). *J Bone Joint Surg [Br]* 68-B:431-438, 1986

A new classification of Paget's disease is proposed, incorporating both the radiographic phases of bone remodeling and the scintigraphic findings. Bone scans are a sensitive guide to the activity of Paget's disease. The authors classify the disease by linking three classic radiologic phases with the bone-scan appearance. The osteolytic phase, the mixed phase, and the osteoblastic phase have an increase in bone blood-flow and in bone-scan activity, but the osteosclerotic phase has decreased activity. Modeling in Paget's disease may lead to bone expansion or contraction by the change in diameter or thickness of the cortical bone. Comparisons were made with normal bone at an equivalent location. Biopsies were used to confirm the diagnosis in 15 patients in whom the radiologic diagnosis was not clear. In all, 112 patients with symptoms of Paget's disease were studied by radiographs and bone scans. The type of modeling known as bone expansion is considered to be a cardinal sign of Paget's disease. However, 27% of the abnormal bones in the current study showed no modeling deformities of expansion or contraction. Although bone scans are a recognized noninvasive method of assessing bone turnover, 4.7% of the current bone lesions were in the osteosclerotic phase and had a normal or diminished bone scan. Patients with bone pain that persists during medical therapy should have serial radiographs as well as bone scans and biochemical studies to detect such complications as advancement of an osteolytic front, osteopenia, stress fracture, malignant transformation, or metastatic disease.

Ray F. Kilcoyne

Pediatric Radiology

Ultrasonography in the radiologic evaluation of children with urinary tract infection. Alon U, Perry M, Davidai G, Berant M (Section of Pediatric Nephrology, Dept. of Pediatrics, Ramban Medical Center, Haifa 35254, Israel). *Pediatrics* 78:58-64, July 1986

Over a 10-month period, 81 children with urinary tract infections aged 2 weeks to 12 years were prospectively studied by renal sonography, excretory urography, and voiding cystourethrography. In 52 children no abnormality was found. Of the 29 cases with abnormal urinary tracts, 18 had vesicoureteral reflux, 11 had hydronephrosis, and six had partial or complete duplication. Renal sonography and excretory urography correlated in 90%. Of the remaining eight patients, seven had negative sonography, but voiding cystourethrography and/or excretory urography showed vesicoureteral reflux (three patients), duplex collecting system (three patients), and calyceal cyst (one patient). Sonography was the only technique to diagnose the cystic nature of a kidney. The authors suggest that renal sonography can effectively replace excretory urography as a screening procedure of the upper urinary tract. Excretory urography is indicated whenever sonography or voiding cystourethrography is abnormal. They propose an algorithm for the radiologic evaluation of urinary tract infection. Outpatients should begin with a voiding cystourethrography; if results are normal, sonography is performed. If no abnormality is found, nothing further is done. If voiding cystourethrography is abnormal, excretory urography and not sonography is performed. If sonography is abnormal, excretory urography is performed. Inpatients are initially examined with sonography; if results are normal, voiding cystourethrography is done. If voiding cystourethrography is also normal, no other study is required. If voiding cystourethrography or sonography is abnormal, excretory urography is indicated.

Richard Towbin

Gastrointestinal System

Evaluation of focal hepatic masses: a comparative study of MRI and CT. Glazer GM, Aisen AM, Francis IR, Gross BH, Gyves JW, Ensminger WD (Dept. of Radiology—Box 13, University of Michigan Medical School, Ann Arbor, MI 48109). *Gastrointest Radiol* 11:263–268, 1986

Comparison of 0.35-T superconducting-magnet MR to CT was undertaken in 30 patients suspected of having hepatic lesions. In 27 patients with focal lesions, both techniques detected abnormalities in 26 patients. Liver lesions were equally well demonstrated by both MR and CT in 15 patients, better demonstrated by CT in 11, and better demonstrated by MR in one. Small lesions of less than 2-cm diameter were much better demonstrated with CT than MR. Extra-hepatic disease was detected by CT in five patients. MR identified these abnormalities in two of these five patients. The authors conclude that with the technology available to them, CT is more useful than nongated spin-echo MR in the evaluation of suspected hepatic masses.

Charles A. Rohrmann, Jr.

Cytomegalovirus colitis in acquired immune deficiency syndrome: radiologic spectrum. Frager DH, Frager JD, Wolf EL, et al. (Dept. of Radiology, Montefiore Medical Center, 111 E. 210th St., Bronx, NY 10467). *Gastrointest Radiol* 11:241–246, 1986

The incidence of cytomegalovirus infection as a gastrointestinal opportunistic pathogen in patients with immunodeficiency is increasing. Six cases of cytomegalovirus colitis in patients with AIDS are presented. The radiographic findings are nonspecific and usually mimic the findings of ulcerative colitis (diffuse form) or granulomatous colitis (focal ulceration). One patient showed involvement of the terminal ileum. Nonspecific edema was present in two cases. In one patient, right colon nodularity due to pseudomembranes was shown and in another, large flat ulcerations were identified. Endoscopic biopsy is needed to establish precise diagnosis by demonstration of cytomegalovirus inclusion bodies in endothelial cells.

Charles A. Rohrmann, Jr.

Radiology of colonic interposition and its associated complications. Christensen LR, Shapir J (Dept. of Radiology, Memorial Hospital, 3501 Johnson, Hollywood, FL 33021). *Gastrointest Radiol* 11:233–240, 1986

Of 81 patients who underwent colonic interposition, 50 had a preoperative diagnosis of benign disease and 31 had malignancies. Complications were divided into early (within 30 days of surgery) and late (more than 30 days after surgery). All patients had initial early radiographic studies approximately 1 week postoperatively. Combined examinations with initial use of water-soluble contrast material followed by barium contrast media were used. Early findings included

anastomotic narrowing (18 patients), anastomotic leak (13), aspiration (11), and ischemic necrosis (three). Late findings included aspiration (nine patients), anastomotic strictures (eight), gastric stasis (six), anastomotic ulcers (four), and gastrocolic reflux (three). The authors suggest that oral feedings should not be started until a contrast examination is performed to rule out an anastomotic leak. Although water-soluble contrast medium has been suggested in the past, the authors suggest that the high incidence of aspiration in the early postoperative period is an indication for the use of dilute barium instead of water-soluble contrast material. Only in patients in which a distal anastomotic leak is suspected should diatrizoate be used to protect against intraperitoneal barium contamination.

Charles A. Rohrmann, Jr.

Focal esophageal candidiasis in acquired immunodeficiency syndrome (AIDS). Farman J, Tavitian A, Rosenthal LE, Schwartz GE, Raufman J-P (Box 1215, Downstate Medical Center, 450 Clarkson Ave., Brooklyn, NY 11203). *Gastrointest Radiol* 11:213–217, 1986

Of 25 patients with AIDS and esophageal candidiasis studied radiographically, four presented with localized involvement of the esophagus. In contrast to the typical findings in esophageal candidiasis, these patients showed large (greater than 4 cm) fixed ulcerating masses of the esophagus (three patients) or localized irregular stricture (one patient). The endoscopic examination showed diffuse superficial involvement of the entire esophagus in addition to the focal defects. The authors report being limited to the use of single contrast esophagography in 75% of the patients because of severe odynophagia. Superficial disease may be underestimated with single contrast examinations. The authors refer to their unpublished data as indicating that if oral candidiasis is present in a patient with radiographic findings of esophagitis, the esophageal lesion is due to the same organism. Endoscopy is not necessary to confirm the diagnosis.

Charles A. Rohrmann, Jr.

Genitourinary System

CT and sonographic demonstration of perirenal and renal changes following extra-corporeal lithotripsy (in German). Grote R, Dohring W, Aeikens B. (Med. Hochschule Hannover Abt. Diagn. Radiologie I, PF 610180, D-3000 Hannover 61, Germany). *Fortschr Roentgenstr* 144:434–439, 1986

CT was performed on 42 patients and sonography on 24 patients, before and after lithotripsy. In 37 patients, the postlithotripsy CT showed perirenal and subcapsular streaks of increased density believed to represent areas of hemorrhage. The extent of these findings was related to the number of shock waves administered. Except for two sizeable perirenal hematomas, no corresponding findings were shown by sonography.

Peter F. Winter

News

Quantitative Thallium Myocardial Tomography

The Radiology Dept., Emory University School of Medicine, will sponsor a program for cardiologists, radiologists, and nuclear medicine physicians to familiarize them with the basic principles and the clinical utility of quantitative thallium tomography. Dates are: March 16-17, April 6-7, and May 18-19. Information: Continuing Medical Education, Emory University School of Medicine, 1440 Clifton Road, N.E., 110 WHSCAB, Atlanta, GA 30322; (404) 727-5695.

Ultrasound 1987

The 12th annual postgraduate course offered by the Radiology Dept., Brigham and Women's Hospital and Harvard Medical School will be held April 7-19. A special feature is a Basics of Ultrasound Day, April 7. Category 1 credit: 36 hr. Fee: \$495: physicians; \$325: residents, fellows, RTs; \$100 for Special Day course. Peter M. Doubilet, program director. Information: Dept. of Continuing Education, Harvard Medical School, 25 Shattuck St., Boston, MA 02115; (617) 732-1525.

San Diego Residents' Radiology Review Course

The Radiology Dept. of the University of California, San Diego, School of Medicine will present the 7th Annual San Diego Residents' Radiology Review Course April 19-24, at the Town and Country Hotel, San Diego, CA. Category 1 credit: 39 hr. Fee: \$395. Folke J. Brahme and Saskia v.W. Hilton, course directors. Information: R. Dawne Ryals & Associates, P.O. Box 920113, Norcross, GA 30092-0113; (404) 641-9773.

Clinical Nuclear Medicine 1987

Harvard Medical School and the Joint Program in Nuclear Medicine at the Beth Israel Hospital, the Brigham and Women's Hospital, the Children's Hospital, and the Dana-Farber Cancer Institute will sponsor the 11th annual postgraduate course in clinical nuclear medicine on April 20-23. Category 1 credit: 24 hr. Fee: \$450: physicians; \$325: residents, fellows, RTs. William D. Kaplan, program director. Information: Dept. of Continuing Education, Harvard Medical School, 24 Shattuck St., Boston, MA 02115; (617) 732-1525.

1987 Neuroradiology Review Course

Loyola University of Chicago, Depts. of Radiology and Continuing Medical Education, will hold its 1987 neuroradiology review course

May 2-3, at the Chicago Marriott Hotel/Oak Brook, Oak Brook, IL. It is designed as a review for a better understanding of neuroradiology and new modalities for general radiologists, neuroradiologists, neurosurgeons, and residents. Category 1 credit: 16 hr. Fee: \$170: physicians; \$100: residents. Information: Linda K. Gunzburger, Ph.D., Director of Educational Research and Development, Loyola University Stritch School of Medicine, 2160 S. First Ave., Maywood, IL 60153; (312) 531-3237.

Refresher Course in Diagnostic Roentgenology

The Radiology Dept. of the University of Cincinnati College of Medicine will offer a newly revised refresher course in diagnostic roentgenology May 4-8. Reviews will include: chest, GI, GU, bone, nuclear medicine, cardiac ultrasound, pediatrics, and neuroradiology. Category 1 credit will be available. Fee: \$350. Information: Dr. Harold B. Spitz, Dept. of Radiology, University Hospital, 234 Goodman St., Mail Location 742, Cincinnati, OH 45267.

Cardiovascular and Interventional Radiology and New Imaging Modalities

A joint meeting of the European and American Societies of Cardiovascular and Interventional Radiology will be held May 25-29, in Porto Cervo (Emerald Coast), Sardinia, Italy. Cardiovascular and interventional radiology and new imaging modalities will be covered. Information and brochure: Society of Cardiovascular & Interventional Radiology, P.O. Box 44113, Pittsburgh, PA 15205; (412) 921-2636; or Plinio Rossi, M.D., 2a Cattedra di Radiologia, Policlinico Umberto 1, 00161 Rome, Italy; telephone: 06/4955602.

International Congress on Medical Ethics

Beth Israel Medical Center in New York will host the 2nd International Congress on Ethics in Medicine at the Vista International Hotel, New York City, June 9-12. The congress is sponsored by Beth Israel Medical Center, Ben-Gurion University of the Negev (Israel), and the Karolinska Institute of Sweden. Leading experts from around the world will confront the complex ethical issues associated with the dramatic advances in medical technology. Category 1 credit will be available. Information: Beth Israel Medical Center, First Ave. at 16th St., New York, NY 10003; (212) 420-2069.

Interventional Radiology

The Dept. of Radiology and Office of Continuing Medical Education of the University of Minnesota Medical School will present an Inter-

ventional Radiology continuation course at the Radisson University Hotel, Minneapolis, MN, June 11–13. The course will include lectures, live cases, and laboratories. Information: Continuing Medical Education, Box 202 UMHC, 420 Delaware St. S.E., Minneapolis, MN 55455; (612) 626-5525.

Masters International Diagnostic Radiology Conference, Paris, France

The 2nd Annual Masters International Diagnostic Radiology Conference will be held August 23–28 at the Hotel Inter-Continental, Paris, France. The comprehensive course emphasizes lectures and discussions in chest, skeletal, gastrointestinal, pediatric, and interventional radiology, as well as MR imaging, CT, and ultrasound. Guest faculty: B. Felson, H. Hricak, A. E. James, Jr., A. Margulis, M. Reeder, F. Brunelle, J. Moret, W. Wenz, and E. Zeitler. Category 1 credit: 25 hr. Fee: \$545: physicians; \$395: residents, fellows, U. S. military. Information: Maurice M. Reeder, M.D., Chairman, Dept. of Radiology, University of Hawaii School of Medicine, 1356 Lusitana St., Room 502, Honolulu, HI 96813; (808) 531-6471.

Radiology in Yorkshire

The University of Connecticut and the Bradford Royal Infirmary, England, will sponsor Radiology in Yorkshire on Sept. 13–20, at Harrogate, Yorkshire, England. Topics will include: interventional radiology; ultrasound of the abdomen including Doppler studies; MR imaging of the head, spine, and body; obstetric and neonatal ultrasound; oncologic radiology; CT of the chest and abdomen; and mammography. Category 1 credit: 35 hr. Fee: \$550 before April 1, \$600 thereafter: physicians, \$350 and \$400: residents. Information: D. Beatty Crawford, M.D., Program Director, Department of Radiology, University of Connecticut Health Center, Farmington, CT 06032; (203) 674-3322.

International Workshop on Bone and Soft Tissue Densitometry

The Dept. of Diagnostic Radiology, University of Manchester, Manchester, England, will sponsor the 6th International Workshop on Bone and Soft Tissue Densitometry at the Palace Hotel, Buxton, Derbyshire, UK, on Sept. 22–25. Information: Dr. J. E. Adams, Senior Lecturer, Dept. of Diagnostic Radiology, Stopford Building, Oxford Rd., Manchester M13 9PT, UK.

Society Elects Officers

The American Society for Therapeutic Radiology and Oncology elected the following officers at its annual meeting: Robert W. Edland, President; Lawrence Davis, President-Elect; James Cox, Chairman of the Board of Directors; Morris J. Wizenberg, Secretary; Robert Goodman, Treasurer; Theodore L. Phillips, Past Chairman of the Board of Directors; Stanley Order and Lester Peters, Members-at-Large.

Meeting and Course Review

For reader convenience, a summary of upcoming meetings and courses is provided. Detailed listings are given in the *AJR* issues noted in parentheses.

UC San Diego Courses; Physicians Imaging Courses 1987, times arranged, San Diego, CA (Nov)

UC San Diego Visiting Fellowships in MR Imaging, times arranged, San Diego, CA (Feb)

The Pacific Radiological Institute Courses, Honolulu, HI (weekly courses) Feb.–April (Dec)

Society for Magnetic Resonance Imaging, Feb. 28– March 4, San Antonio, TX (Oct)

Aspen Uroradiology Seminar, March 1–4, Aspen, CO (Jan)

Practical Radiology, March 1–6, Vancouver, BC, Canada (Nov)

Intermountain Imaging Conference-Extension, March 1–7, Snowbird, UT (Nov)

Diagnostic Radiology Courses, Update, March 2–4; **MR Imaging**, March 3–6; and **MR Imaging for Technologists**, March 3–5, Coronado, CA (Feb)

Sierra Radiology Conference, March 2–6, Incline Village, NV (Jan)

Winter Imaging at Stowe, VT, March 2–6, Stowe, VT (Dec)

Computed Body Tomography 1987—The Cutting Edge, March 5–8, Orlando, FL (Nov)

Diagnostic Imaging and Interventional Radiology, March 8–13, Park City, UT (Dec)

Skeletal Symposium March 9–16, Sun Valley, ID (Jan)

Positron Emission Tomography and the Chemistry of Mental Illness, March 12–13, Baltimore, MD (Dec)

International Continuing Medical Education Series: Topic to be announced, March 14–21, Banff, Canada; **Topic to be announced**, May 20–26, Bermuda; **Topic to be announced**, June, Ireland; **Topic to be announced**, July 24–30, Pebble Beach, CA; **Topic to be announced**, Aug., Gstaad, Switzerland (Oct)

London Course in Whole Body CT, March 15–19, Auchterarder, Perthshire, Scotland, UK (Nov)

Doppler for Radiologists, March 16–19, New Haven, CT (Feb)

Diagnostic Radiology Conference on Imaging Modalities in Chest and Abdomen, March 16–20, Maui, HI (Dec)

UC San Francisco Courses; Diagnostic Imaging, March 16–21, Waiohai, Kauai, HI (Oct)

Breast Disease Update IV Seminar, March 18–22, Lake Buena Vista, FL (Jan)

Pediatric Radiology, March 19–21, Philadelphia, PA (Jan)

Ultrasound at Vail, March 22–28, Vail, CO (Nov)

Diagnostic Angiography and Interventional Radiology, March 23–26, San Diego, CA (Nov)

1987 European Workshop on MR in Medicine, March 25–27, London, England (Feb)

Skeletal Radiology at the Pointe, March 28–April 2, Phoenix, AZ (Feb)

International Diagnostic Course: Skeletal Radiology, March 29–April 4, Davos, Switzerland (Feb)

Radiology and Early Colon Cancer Workshop, March 30, Denver, CO (Nov)

Federation of Western Societies of Neurological Science Meeting, March 30–April 1, Coronado, CA (Dec)

Laser Angioplasty and Interventional Radiology, March 30–April 1, Baltimore, MD (Feb)

Society of Computed Tomography Meeting/Course, March 30–April 3, San Diego, CA (Dec)

Alexandria International Conference on Laryngeal Cancer, April 1–2, Alexandria, Egypt (Sept)

Hyperthermia, April 1–3, Philadelphia (Feb)

Intrauterine Diagnosis and Treatment: the New Frontier, April 2–4, San Diego, CA (Nov)

Ultrasound Symposium, April 3–5, Greensboro, NC (Feb)

Differential Diagnosis and Treatment: The New Frontier, April 3–5, Ann Arbor, MI (Jan)

Mammography Courses, April 6–9, May 18–21, Oct. 5–8, Nov. 2–5, Boston, MA (Jan)

American Radium Society Meeting, April 6–10, London (Aug)
Annual Meeting, National Council on Radiation Protection and Measurements, April 8–9, Bethesda, MD (Sept)
The Johns Hopkins Medical Institutions Courses in Abdominal and Obstetric Ultrasound: Advanced Obstetrics and Gynecology, April 8–10; **Basic Practicum**, May 11–15 and Nov. 16–20; **Advanced Practicum in Ultrasound**, Dec. 7–11, Baltimore, MD (Feb)
Advances in MR Imaging, April 13–16, Lake Buena Vista, FL (Feb)
Diseases and Imaging of the Spine, April 17–18, Lake Buena Vista, FL (Feb)
Radiation Therapy Clinical Research Seminar, April 23–25, Gainesville, FL (Dec)
Nuclear Medicine 1987, April 27–30, New York, NY (Feb)
The Profession of Medical Physics, April 29–May 1, Lake Tahoe, CA (Jan)
Diagnostic Ultrasound Conference and Post Conference Seminar, May 1–3; May 5–9, Los Angeles, CA (Feb)
Nuclear Medicine, May 3, Pittsburgh, PA (Feb)
Radiology Review Course, May 3–5, Miami Beach, FL (Feb)
Surgical Neuroangiography, May 4–8, New York, NY (Jan)
University of Texas Continuing Medical Education, Advanced Radiologic Health, May 11–15; **Radiation Safety Officer's Course**, May 18–22, San Antonio, TX (Sept)

Echocardiography 1987, May 14–16, Cambridge, MA (Jan)
International Nijmegen Vascular Symposium: Angioplasty, Vascular Surgery, Combined Approach, May 15–16, Nijmegen, The Netherlands (Feb)
Fleischner Society Annual Symposium, May 21–23, San Francisco, CA (July)
1987 Radiology Congress, Lisbon, May 31–June 6 (Aug)
Society of Nuclear Medicine Annual Meeting, June 2–5, Toronto, Ontario, Canada (Dec)
The American Board of Radiology Examinations. Oral Examinations: June 8–12, 1987; May 23–27, 1988; June 5–9, 1989, all at Louisville, KY. **Written examinations**: Oct. 8–9, 1987; Oct. 6–7, 1988; Oct. 5–6, 1989 (Dec)
Euroson '87, June 14–18, Helsinki, Finland (Sept)
International Conference on Computer Assisted Radiology, July 1–4, West Berlin (Feb 1986)
Sarcoidosis and Granulomatous Disorders, Sept. 6–11, Milan (June)
The Asian-Oceanian Congress of Radiology, Sept. 21–25, Seoul, South Korea (Nov)
Congress on Ultrasonic Examination of the Breast, Oct. 3–5, New Orleans, LA (Feb)
Erratum

Erratum

In the article "Subcortical arteriosclerotic encephalopathy: CT spectrum and pathologic correlation" by Lotz, Ballinger, and Quisling that appeared in the December 1986 issue of *AJR* (*AJR* 1986;147:1209–1214), an error was made in the caption to Figure 6 (page 1213). The caption title should read "Transepndymal resorption of cerebrospinal fluid," not "Transepndymal resorption of subcortical arteriosclerotic encephalopathy." *AJR* apologizes for this error.

Meeting and Local Activities Registration Form: ARRS 87th Annual Meeting, April 26-May 1, Miami Beach, FL

If you plan to attend, please complete this form. Official badges and program booklets will be available at the ARRS Registration Desk, Fontainebleau Hilton. There will be no confirmations before the meeting. Preregistration by mail will be accepted until March 26. On site registration will be available.

Make all checks payable to: American Roentgen Ray Society

Mail to: American Roentgen Ray Society
1891 Preston White Drive
Reston, VA 22091

Please type or print:

Last Name First Name or Initials

Street

City State ZIP Code

Check here if you wish a program of events for accompanying persons. Indicate the address to which this is to be sent.

Name (Accompanying person's name to be printed on badge)

Street

City State ZIP Code

- Check those desired: Registration fee:
Member ARRS None
Guest \$100
Physician in training (please fill where indicated below) \$25
Course faculty, scientific paper author, scientific exhibitor None
ACR luncheon course, Monday, April 27 \$10
ACR luncheon course, Tuesday, April 28 \$10
ACR luncheon course, Wednesday, April 29 \$10
ACR luncheon course, Thursday, April 30 \$10
Categorical course on gastrointestinal radiology. Categorical course registrants may also register for other instructional courses. \$75

Total enclosed

Section on Instruction

Please register early for Instruction Courses. Attendance is limited. List first, second, and third choices for each period by course number. Ticket orders are filled according to postmark. ARRS members, nonmembers, and those in radiology training may take all courses without charge except the Categorical Course on Gastrointestinal Radiology. For the categorical course, all must pay \$75. All who wish to attend courses must complete this section. Residents and nonmembers must pay the meeting registration fee.

Course tickets will be available at the ARRS Registration Desk of the Section on Instruction at the Fontainebleau Hilton on and after Saturday, April 25, at 1 p.m.

Complete section at right for courses other than the categorical course. Be sure to fill out second and third choices for each period.

First Choice Second Choice Third Choice
Monday
Tuesday
Wednesday
Thursday
Friday Check if you wish to attend the Genitourinary Symposium (only course offered this day)
For Physicians in Training:
is in training in my department
Department Chief
Institution Date

Local Activities

No refunds after April 15
Exception: Dinner Cruise on Sunday: no refunds after March 20

Sunday, April 26, 6:00–10:00 p.m., Dinner Cruise and Show aboard the Yacht THE SPIRIT (cruises up the Intracoastal Waterway to Fort Lauderdale; bus departs from Hotel at 6:00 p.m. No refunds on this tour after March 20. _____ tickets @ \$30 \$ _____

Monday, April 27, 9:00 a.m.–1:00 p.m., Tour of Miami and shopping tour to Bal Harbour _____ tickets @ \$12 \$ _____

Tuesday, April 28, 9:00 a.m.–4:00 p.m., Parrot Jungle and Seaquarium (Box lunch will be served.) _____ tickets @ \$40 \$ _____

Wednesday, April 29, 9:00 a.m.–1:00 p.m., Villa Vizcaya Boat Tour (Deering Estate) _____ tickets @ \$30 \$ _____

Thursday, April 30, 9:00 a.m.–1:00 p.m., Metro Zoo _____ tickets @ \$15 \$ _____

Thursday, April 30, 6:30–11:30 p.m., Dinner and Show at Les Violins Supper Club (Latin Extravaganza) _____ tickets @ \$30 \$ _____

Friday, May 1, 9:00 a.m.–11:00 a.m., Tour of Miami Beach _____ tickets @ \$11 \$ _____

Preregistration is required.

Annual ARRS Golf Tournament, Monday, April 27, 11 a.m.

The tournament will be at the Turnberry Isle Country Club, North Miami Beach, FL. Transportation, luncheon, greens fee, cart, and prizes are included in the \$65 fee. Preregistration is important.

Name: _____ Telephone: _____

Address: _____

Hotel: _____ Handicap (if any): _____

My foursome includes (list handicaps): _____

_____ tickets @ \$65 \$ _____

Men’s and Women’s Tennis Tournaments, Monday, April 27, 11 a.m.

The tournaments will be at the Turnberry Isle Country Club, North Miami Beach, FL. Tennis attire is required. Fee of \$50 includes transportation, luncheon, court fees, and prizes.

Name: _____ Telephone: _____

Address: _____

_____ tickets @ \$50 \$ _____

(OVER)

May be photocopied

Deadline: March 26

Hotel Registration Form: ARRS 87th Annual Meeting, April 26–May 1, 1987, Fontainebleau Hilton, Miami Beach, FL

Mail to:

ARRS Housing Bureau
Fontainebleau Hilton
Attention: Reservations
4441 Collins Ave.
Miami Beach, FL 33140

(PLEASE MAKE CHECKS PAYABLE TO THE FONTAINEBLEAU HILTON HOTEL—NOT TO THE ARRS)

Individual guest name _____

Address _____

City & State _____ ZIP _____

Arrival date/time _____ Departure date/time _____

Individual requesting reservation _____

Address _____

City & State _____ ZIP _____

Deposit amount: _____

Please forward with your reservation a deposit of one night's room rate to be applied to the last night of your scheduled stay, or provide credit card information to guarantee your reservation. The hotel accepts American Express, Diners Club, Carte Blanche, and Hilton credit cards. The deposit will hold your room until 6 a.m. of the morning following your scheduled arrival date. In the event of an early departure, the deposit is nonrefundable unless the hotel is notified prior to or at the time of check-in. Cancellation notice of 14 days is required for a deposit refund.

Check accommodations desired

Room Category	Rate
Single	— \$115
Double	— \$115
1-bedroom suite	— \$325–450
2-bedroom suite	— \$450–600

Important Information:

1. Reservations must be received by the Fontainebleau Hilton/ARRS Housing Bureau no later than March 26 to be assured of written confirmed accommodation. Reservations after that time are subject to availability. We urge you to make your reservations promptly.
2. Written confirmation of your reservation will be sent to you by the hotel.
3. To change or cancel reservations, please call either Hilton Reservations Service at 1-800-HILTONS or the hotel directly at (305) 538-2000.
4. If you plan to share a room, please send in only one housing form. Be sure to list all names of occupants of rooms. Assignment is delayed until complete information is received.
5. Check-in is after 3 p.m., or earlier if the room is available. Check-out time is 11 a.m.

Classified Advertising

Positions Available

BOARD-CERTIFIED/BOARD-ELIGIBLE DIAGNOSTIC RADIOLOGIST needed for affiliated VA Medical Center with expansive programs in education and research. Academically oriented individual with training in CT and vascular radiology preferred. Equal opportunity employer. Contact J. Kalus, M.D. at (806) 355-9703. 3a

BOARD-CERTIFIED RADIOLOGIST with private practice experience to join solo Pacific Northwest office radiologist. Three years graduated salary; then buy in. Extensive orthopaedic and mammographic background mandatory. CT, nuclear medicine and hands-on ultrasound experience/training necessary. Reply including salary, complete training, background, and availability to Box P20, *AJR* (see address this section). 3a

BOARD-CERTIFIED DIAGNOSTIC RADIOLOGIST to join 8-man hospital-based group. Expertise in MRI and interventional radiology required. Fellowship training preferred. Send CV to W. Dittman, M.D., 7515 Greenville Ave., Ste. 710, Dallas, TX 75231. 3-6ap

PART-TIME ASSOCIATE REQUIRED, with possibility of full-time in future for progressive radiology group in Southeast, covering three hospitals. All modalities except MR, which is expected in 1987. Send reply to Box P22, *AJR* (see address this section). 3-6a

CENTRAL WASHINGTON STATE MULTI-SPECIALTY GROUP seeks second BC/BE general radiologist. Hospital and clinic practice with ultrasound, nuclear medicine, and mammography. Young, high-quality group of physicians. Beautiful four-season town of 25,000 with abundant recreational opportunities. Please submit CV to Michael Graham, M.D., 840 Hill Ave., Moses Lake, WA 98837, (509) 765-0216. 3-5a

NEURORADIOLOGIST-MRI TRAINED to join a group of four radiologists in a Brown University affiliated hospital. Reply to W. Colaiace, M.D., Roger Williams General Hospital, 825 Chalkstone Ave., Providence, RI 02908, (401) 456-2204. 3-5a

BOARD-CERTIFIED, DIAGNOSTIC RADIOLOGIST to join 40-doctor multi-specialty clinic in south central Minnesota. Located in All-American University city. Outstanding educational, cultural, and recreational activities. Send CV and reply to Box P26, *AJR* (see address this section). 3ap

BC/BE DIAGNOSTIC RADIOLOGIST—Unexpected vacancy July 1, 1987 in expanding 35-man multi-specialty clinic in beautiful Northwest. Seek third radiologist for general radiology, mammography, ultrasound, and CT. Special training in ultrasound and CT desirable. Send CV to M.L. Eaton, M.D., TAF-C13, Spokane, WA 99220. 3-5a

DIAGNOSTIC RADIOLOGIST—IMMEDIATE VACANCY in well-established, hospital-based group in Southwest metropolitan area. Seeking associate well-trained or experienced in general diagnostic radiology, including ultrasound and mammography, to service outpatient office during regular weekly hours. Rapidly growing area with superior climate and outdoor recreational activities. Seeking a motivated physician to develop this segment of already established, quality practice. Send CV to Diana Welch, Radiology Associates, 4001 Indian School NE, Ste. 300, Albuquerque, NM 87110. 3-4a

BOARD CERTIFIED RADIOLOGIST—Six-man radiology group seeks new associate with 6-12 month fellowship/experience in MRI. New 1.5 T unit soon to be operational. The group provides complete radiologic services in fully-equipped 500-bed hospital, and private outpatient office. Send CV to Eric R. Rosenberg, M.D., Dept. of Radiology, New Hanover Memorial Hospital, Wilmington, NC 28403. 2-4a

GENERAL DIAGNOSTIC RADIOLOGIST—Outstanding practice opportunity for qualified individual in Fargo, ND. Multi-specialty group practice of 200+ in tri-college community of 130,000. Will join 13 in established departments in clinic and 400+-bed hospital. Subspecialty training in ultrasound, MRI, and/or nuclear medicine desirable. Respond with CV in confidence to Charles Anderson, M.D., Box 2067, Fargo, ND 58123. 3-4ap

MCGUIRE CLINIC, A MULTI-SPECIALTY GROUP in central Virginia seeks general radiologist to join a four-man radiology dept. Practice includes both hospital and outpatient setting. Applicant must be experienced in mammography, ultrasound, CT, MRI, nuclear medicine, angiography, and interventional radiology. Competitive salary and excellent benefits available. Work towards stockholder status in professional corporation. For further information, please contact William Proctor, M.D., Chairman of the Dept. of Radiology at (804) 346-1741 or Hilton R. Almond, M.D., Medical Director, McGuire Clinic, Inc. at (804) 346-1502. 3-5a

DIAGNOSTIC RADIOLOGIST position available in our 9-person group 10 min. from San Francisco. Desire fellowship training in angiography, chest, or MRI. Fully-equipped hospital-based HMO practice. CV to Terence W. McGrath, M.D., Kaiser Permanente Center, 280 W. MacArthur Blvd., Oakland, CA 94611. 3-5ap

BETH-ISRAEL HOSPITAL/HARVARD MEDICAL SCHOOL—The Dept. of Radiology at the Beth Israel Hospital in Boston is seeking a radiologist with broad experience in general radiology for a July 1, 1987 opening. Expertise in ultrasound, CT, mammography, and/or angiography is desirable. The hospital is a 460-bed voluntary teaching hospital affiliated with the Harvard Medical School. Candidates should meet the requirements for faculty appointment. Please send inquiries with a CV to Sven Paulin, M.D., Radiologist-in-Chief, Beth Israel Hospital, 330 Brookline Ave., Boston, MA 02215. The hospital is an affirmative action/equal opportunity employer. Minorities and female candidates are encouraged. 3-4a

NEW YORK CITY SUBURBAN PRACTICE seeks board-certified radiologist. Hands-on ultrasound skills essential. Solid imaging knowledge. Personality counts. High pay with early partnership for special individual. CV to Box 18, Meacham Station, Elmont, NY 11003. 3-4a

NUCLEAR MEDICINE—AVAILABLE SEPT. 1987, full-time position in Palo Alto VA Hospital, affiliated with Stanford University School of Medicine, carrying university appointment as Assistant Professor. Prerequisites include certification by American Board of Nuclear Medicine, broad clinical expertise, evidence of teaching ability, research training and productivity, and focused research interest. Unit is in new quarters and is equipped with most modern equipment, including PET scanner. Stanford University is committed to increasing representation of women and members of minority groups on its faculty and particularly encourages applications from such candidates. Provide complete CV, names and addresses of references, and statement of interests in first letter to Joseph P. Kriss, M.D., Division of Nuclear Medicine, Stanford University Medical Center, Stanford, CA 94305. 3a

DIAGNOSTIC RADIOLOGIST. Need aggressive associate to perform all aspects of diagnostic radiology in well-equipped hospital with large outpatient component in South Texas. MR training a plus but not essential. Excellent salary and early partnership available. For confidential consideration please submit CV to Box H70, *AJR* (see address this section). 11xa

DIAGNOSTIC RADIOLOGIST with special experience and/or training in chest radiology is being sought for St. Lukes-Roosevelt Hospital Center, a 1315-bed voluntary-university hospital of Columbia University College of Physicians and Surgeons, New York City. Strong interest in clinical teaching and research as well as in patient care required. Excellent remuneration. Please send inquiries with CV to Ronald C. Ablow, M.D., Radiology Dept., St. Lukes-Roosevelt Hospital Center, Amsterdam Ave. & 114th St., New York, NY 10025. Equal opportunity employer. 3-4a

DIAGNOSTIC RADIOLOGIST—Radiologist seeks board-eligible/board-certified partner to join a group practice in a 175-bed general hospital in northern Michigan. Our recently renovated radiology dept. includes an angiography suite, a Phillips real-time ultrasound unit, a Siemens ZLC gamma camera with computer, and a new dedicated Phillips mammography unit. A Siemens DRH CT scanner is currently being installed. We are a regional referral center with a service population of approximately 100,000. The town is located on the shore of Lake Huron and offers excellent sailing, fishing, hunting, and cross-country skiing; a great location for those who enjoy small town life and the scenic beauty of a 4-season climate in the pristine north. Send CV to Box P30, *AJR* (see address this section). 3-5a

RADIOLOGIST—A board certified/board eligible radiologist with experience is needed to join the staff of the Alaska Native Medical Center, 170-bed referral facility for a state-wide system of Indian Health Service hospitals and clinics. Practice stimulating and challenging radiology in a relaxed and casual atmosphere. State-of-the-art in-house CT, sonography, and mammography. Send CV to C.J. Heitz, Jr., M.D., P.O. Box 7-741, Anchorage, AK 99510. EOE 2-7a

RADIOLOGIST for a thriving community on the beautiful Pacific northwest coast at Prince Rupert, B.C., gateway to Alaska. The 124-bed regional hospital serves Prince Rupert and the surrounding area. Total number of examinations per yr is 16,000. Candidates must have obtained LMCC status and should have a Fellowship in Radiology with experience in ultrasound. Salary and/or fee for service basis. Direct applications or inquiries to The Administrator, Prince Rupert Regional Hospital, 1305 Summit Ave., Prince Rupert, B.C., V8J 2A6, Canada. 2-5a

ISRAEL, DIAGNOSTIC RADIOLOGY. Opportunities for 3-4 week or longer working vacations in a number of Israeli medical centers, on a volunteer basis. Positions varied, arrangements flexible. For information contact: Jonathan H. Fish, M.D., 1844 San Miguel Dr., #302, Walnut Creek, CA 94596; (415) 947-0560. 8xa

RADIOLOGY INSTRUCTOR to assist candidate in preparation for Oral Radiology Boards. Candidate needs practice in formally discussing cases and answering board-type questions. Would like to meet on a weekly basis beginning early 1987. Fee negotiable. Please call (215) 342-4110 or (615) 359-7092 eves. 12-3a

CHIEF, DIVISION OF VASCULAR AND INTERVENTIONAL RADIOLOGY—The Dept. of Diagnostic Radiology of William Beaumont Hospital, a major tertiary care and academic institution in Michigan, is seeking a candidate to direct the Division of Vascular Interventional Radiology. Candidates must be board certified in diagnostic radiology and have significant academic achievements. Income is negotiable and competitive. Send CV to Jalil Farah, M.D., Director, Diagnostic Radiology, William Beaumont Hospital, 3601 West 13 Mile Rd., Royal Oak, MI 48072. 3-5a

IMMEDIATE OPENING—BC/BE RADIOLOGIST to join 8-man group in South Bay area of northern CA. Hospital and private office practice. All diagnostic modalities including MRI. Send CV to Box M3, *AJR* (see address this section). 1-3ap

CHAIRMAN, DIAGNOSTIC RADIOLOGY—Applications are invited for the position of Chairperson, Dept. of Diagnostic Radiology, University of Louisville School of Medicine. The program has extensive clinical facilities and educational programs at undergraduate and residency levels. There is an excellent diagnostic radiology facility. Responsibilities of the position include clinical service, teaching, research, and departmental administration. The applicant should have proven ability in these areas. Qualified candidates should submit CV to Joel Kupersmith, M.D., Chairperson, Search Committee, Chief, Cardiovascular Division, University of Louisville School of Medicine, Louisville, KY 40292. The University of Louisville is an equal employment/affirmative action employer. 3a

RADIOLOGIST—Expanding western Massachusetts staff model health maintenance organization seeks a fourth, full-time certified radiologist. Our multi-specialty group practice employs 68 full-time positions and provides care for a growing membership of over 65,000 from modern, suburban facilities. Annual case load of 31,000. State-of-the-art ultrasound and mammography used. Attractive pioneer valley location with fine educational, cultural, and recreational opportunities. Excellent salary and comprehensive benefit program. Please send CV to John Collins, M.D., Medical Director, Medical West Community Health Plan, Inc., 444 Montgomery Street, Chicopee, MA 01020. An affirmative action/equal opportunity employer. 3-4a

MAMMOGRAPHY AND GENERAL ULTRASOUND—SEATTLE. Board-certified or eligible. 4 offices. Send CV to Irwin Schiller, D.O., Breast Diagnostic Center, 411 Strander Blvd., #303, Seattle, WA 98188. 3ap

NEURORADIOLOGIST to join a 21-member private practice radiology group in Birmingham, AL. Board certification/board eligibility, MR experience/training essential. Send CV to R. M. Doughton, M.D., 1920 Huntington Rd., Birmingham, AL 35209. 2-3a

PEDIATRIC RADIOLOGIST. Large hospital-based group seeks associate with recent pediatric radiology fellowship training. Busy private practice group needs second pediatric radiologist for coverage of small pediatric hospital. Practice would include 25% pediatric and 75% adult work. All modalities including MRI. Board certification mandatory. Opportunity for partnership in well-established western Washington practice. Reply Box H74, *AJR* (see address this section). 11-6a

TWO YOUNG RADIOLOGISTS seek a third radiologist in expanding hospital-based practice near Canadian border in northern New York. All modalities available. Write P. Berman, HC 61 Box 454, Massena, NY 13662. 8-7a

Positions Desired

IVY-LEAGUE TRAINED GROUP, all with fellowships, desire 6 to take over radiology dept. of small to medium-sized hospital, preferably in Northeast corridor, all modalities including MRI and interventional radiology. Reply Box P24, *AJR* (see address this section). 3b

BOARD-CERTIFIED RADIOLOGIST-52, all modalities. Administrative and academic background. Write Box P28, *AJR* (see address this section). 3bp

PGY II RADIOLOGY POSITION sought for July 1, 1987 by quality American grad now engaged in medical internship at a major medical school affiliated with a New England teaching hospital. Reply Box M1, *AJR* (see address this section). 1-4bp

Fellowship and Residencies

A NEURORADIOLOGY FELLOWSHIP at the University of Massachusetts Medical Center, a 350-bed teaching hospital, 35 mi from Boston. This fellowship provides in-depth training in all current aspects of clinical neuroradiology and head and neck radiology, including CT, angiography, myelography, polytomography, and plain film diagnosis. It also provides exposure to general and interventional angiography and participation in research and teaching. The fellow is closely supervised by full-time faculty members and increasing clinical responsibilities are given as the year progresses. Equipment consists of a high resolution CT scanner dedicated to neuroradiology, a GE 1.5 Tesla MRI scanner, state-of-the-art angiography and DSI suites, and Phillips polytomography unit, and R & F rooms (shared with general radiology). Please address all inquiries to Eugenio L. Suran, M.D., Director of Neuroradiology, Dept. of Radiology, University of Massachusetts Medical Center, Worcester, MA 01605. 2-3c

CARDIOVASCULAR/INTERVENTIONAL RADIOLOGY FELLOWSHIP—Thomas Jefferson University Hospital announces a new fellowship program combining training in cardiac, vascular, and interventional radiology. One- and two-year positions are available beginning July 1, 1987. The 1-yr program offers intensive clinical experience in general angiography, coronary angiography, and interventional procedures. The 2-yr program emphasizes additional experience in interventional techniques and cardiac imaging, and provides time for research. Applicants should be board certified or in the certification process. Contact David C. Levin, M.D., or Geoffrey A. Gardiner, Jr., M.D. at Dept. of Radiology, Thomas Jefferson University Hospital, Philadelphia, PA 19107. 1-3c

Tutorials/Courses

LONDON—PARIS FALL ULTRASOUND. Attend one or both, September 19-27, 1987, CME I accreditation. For registration and information contact Medical Seminars International, 21915 Roscoe Blvd., Ste. 222, Canoga Park, CA 91304, (818) 340-0580 ext. 280. 3-8d

ALASKA 87—CRUISE THE INLAND PASSAGE. Dr. Thomas Berquist, Mayo Clinic, Diagnostic Imaging, CME I. For information contact Medical Seminars International, 21915 Roscoe Blvd., Ste. 222, Canoga Park, CA 91304, (818) 340-0580 ext. 280. 3-6d

LONDON, ENGLAND—MAY 2-10, 1987. CME I Accred. International Faculty. Topics: CT, MR, and other imaging modalities. Fees: To Feb. 28, US\$395. After Mar. 1, US\$435. Information: Medical Seminars, 21915 Roscoe Blvd., Suite 222, Canoga Park, CA 91304. (818) 340-0580 X280. 1-4d

Other

SUNBELT INVESTMENT OPPORTUNITY. Established radiology office on health campus. Retiring radiologist will introduce. High gross receipts. No nights or weekends. TV suite (2) and new ultrasound. 3e

REALIZE THE VALUE of your practice. A group of successful and well-qualified radiologists is interested in acquiring established radiology practices. Hospital contracts, clinics, and private office settings are desired. Opportunity for radiologists considering retirement or reduction in practice activities to capitalize on the value of the practice they have built up during their careers. Alleviate the problems of professional recruitment or administrative pressures. Practices considered throughout the country. Flexible purchase options with opportunity for continuing relationship arrangements. Write Box C49, *AJR* (see address this section). 6-5e

MRI OVER-READING SERVICE. Backup interpretation of MR scans now available using state-of-the-art Raytel teleradiology equipment and regular phone lines. Service available from across-the-street to across-the-country from 1-month to 1-year. Competitive rates. Contact Murray A. Solomon, M.D., San Jose MRI Center, 361 South Monroe, San Jose, CA 95128. 1-6ep

AJR Classified Advertising Information

Box Responses and Address for Ad Placement

Write Box _____, *AJR*, Suite 200, 2223 Avenida de la Playa, La Jolla, CA 92037; (619) 459-2229.

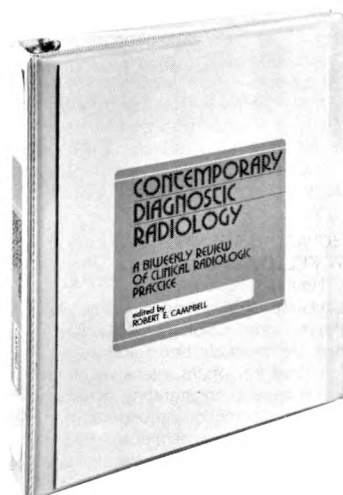
You learn from your experience with **CONTEMPORARY DIAGNOSTIC RADIOLOGY**

Editor: **Robert E. Campbell, M.D.**

A Biweekly Review of Clinical Radiologic Practice—26 issues a year!

One of your toughest jobs is keeping up with the many new developments that affect radiology. That's why you want **Contemporary Diagnostic Radiology**... an effective and convenient way to perfect your skills and maintain your professional status.

Contemporary Diagnostic Radiology is designed as a continuing education program that lets you work at your own pace. Every two weeks you'll receive an issue that covers a single topic or procedure in detail. Read the information and study the clearly reproduced radiographs—and then, if you choose, respond to a comprehensive examination in the strictest confidence. You set the pace. Each biweekly lesson brings you pertinent review of the basics in bone radiology... gastrointestinal radiology... pediatric radiology... genitourinary radiology... MR imaging... and all of the topics you want to know more about.



Contemporary Diagnostic Radiology works two ways. You may choose to subscribe to the non-scoring version, receiving every issue as an important element of your professional reading. The scoring version, however, supplements your reading and computer-coded examinations with confidential result responses, making you eligible for Continuing Medical Education credits co-sponsored by the University of Pennsylvania School of Medicine.

"As an organization for continuing medical education, the University of Pennsylvania School of Medicine designates this continuing medical education activity as meeting the criteria for 1 credit hour per bi-weekly issue in Category I for Educational Materials for the Physician's Recognition Award of the American Medical Association provided it has been completed according to instructions."

You can begin this ongoing program today. **Contemporary Diagnostic Radiology** is a year-round program, so you can join at any time. To begin your lessons, just fill out the enclosed card and return it to us. Or call **FREE** 1-800-638-6423 (except from Alaska). In Maryland call **COLLECT** 528-4105. You'll find that **Contemporary Diagnostic Radiology** is the most efficient and inexpensive way to keep up with your dynamic field.

Williams & Wilkins

P.O. Box 23291
Baltimore, Maryland 21203



266 Fulham Road
London SW10 9EL England

clip & mail

CONTEMPORARY DIAGNOSTIC RADIOLOGY

☐ **Yes!** I want to keep pace in my field! Begin my 26-issue subscription:

- ☐ Send me the scoring version (\$220)
- ☐ Send me the non-scoring version (\$180)
- ☐ Send me the resident non-scoring version (\$160)
(add \$35 for optional air mail delivery outside the U.S.)
- ☐ new subscription
- ☐ renewal

name _____

address _____

city/state/zip _____

payment options

- ☐ payment enclosed
- ☐ American Express

☐ bill me

☐ MasterCard

☐ VISA

printed in USA

card # _____

expiration date _____

signature/P.O. # _____

Maryland residents add 5% sales tax. Subscriptions outside the U.S. must be prepaid in U.S. dollars only. Rates subject to change without notice. Please allow 8 weeks for delivery of your first issue, up to 16 weeks for surface delivery outside the U.S. Optional airmail rates add \$35 per subscription.

Residents are eligible for the special in-training rate for up to three years. When requesting this rate, please include training status and institution.



Don't forget: you can order with a **FREE** phone call at 1-800-638-6423 (except from Alaska). In Maryland, call collect 528-4105.

Williams & Wilkins

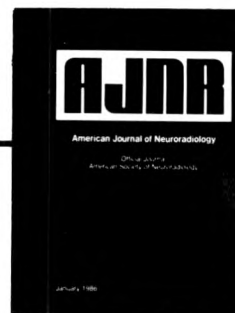
P.O. Box 23291
Baltimore, Maryland 21203

266 Fulham Road
London SW10 9EL England

CDRAD 95191 87

Increase your expertise in evaluating CNS lesions

AJNR American Journal of Neuroradiology



Editor: **Juan M. Taveras, MD**, Harvard Medical School; MGH

Outstanding clinical papers on every aspect of CNS imaging, including spinal diagnosis...informed coverage of head and neck radiology...clear, readable CTs, angiographs, MR imaging and ultrasound studies. These are the features you demand of a quality professional journal. You'll find them in every issue of **AJNR: American Journal of Neuroradiology**.

As you are called upon to perform and interpret more and more sophisticated diagnostic tests — from myelography to CT to newborn ultrasound studies — you need a comprehensive, reliable journal that can keep you abreast of all the latest developments. Each bimonthly issue of **AJNR** brings you timely, clinically pertinent information, as well as important clinical research presented with an eye toward immediate practical application.

Here are just a few of the many excellent articles from the November/December 1986 issue:

The MR Appearance of Syringomyelia: New Observations. *Sherman, et al.*

Cranial MR in Spinal Cord MS: Diagnosing Patients with Isolated Spinal Cord Symptoms. *Edwards, et al.*

Time-Dependent Changes in Image Contrast in Brain Tumors After Gadolinium-DTPA. *Schörner, et al.*

Physiology of the CSF Flow-Void Sign: Modification by Cardiac Gating. *Citrin, et al.*

Percutaneous Laser Catheter Recanalization of Carotid Arteries in Seven Cadavers and One Patient. *Choy, et al.*

Focal Necrosis of the White Matter (Periventricular Leukomalacia): Sonographic, Pathologic, and Electroencephalographic Features. *Bejar, et al.*


If you can benefit from articles like these, then you should be a regular reader of **AJNR**. Use the attached coupon to subscribe today.

Bimonthly

Personal \$100/yr **Institutions** \$120/yr

In-training \$65/yr (add \$20.00 outside the US)

ORDER FREE BY PHONE. Just call

 1-800-638-6423 from anywhere in the US except AK. Maryland residents, call 528-4105 collect.

Williams & Wilkins

P.O. Box 23291 Baltimore, Maryland 21203

266 Fulham Road London SW10 9EL England



Subscribe to AJNR for 3 years and SAVE

Avoid future rate increases and ensure uninterrupted service by placing a multi-year subscription at current rates.

☐ New subscription ☐ Renewal

☐ 3 yrs ☐ 2 yrs ☐ 1 yr

☐ **Personal** \$100 ☐ **Institutions** \$120 ☐ **In-training** \$65
(add \$20.00 outside the US)

☐ Also send me the **1987 Bound Volume** at \$45.00 (\$50.00 outside the US). \$2.00 discount for orders placed before October 1, 1986, and for pre-paid orders. I understand that the bound volume is *in addition* to my regular subscription and is available only to subscribers. (To be shipped in early 1988. Sorry, bound volumes for years prior to 1987 are not available.) *All bound volume orders must be received by December 31, 1987.*

☐ Check enclosed ☐ Bill me
☐ VISA ☐ MasterCard ☐ American Express

card #

exp.

signature/P.O. #

printed in USA

Name

Address

City/State/Zip

MD residents, please add 5% sales tax. Subscription orders from outside the US must be prepaid in US dollars only.

Residents, Fellows, Interns, and Students: when applying for the in-training rate, available for 3 years, please specify name of institution and training status. Rates valid through October 31, 1987.

Please allow 8 weeks for order processing and delivery of your first issue. Surface mail delivery to countries outside the US may take up to 16 weeks. Airmail rates available upon request.

Williams & Wilkins

P.O. Box 23291

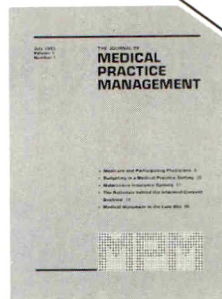
Baltimore, Maryland 21203

266 Fulham Road
London SW10 9EL
England



AJNRAD 94625 87

Control the future of your practice



NEW!

The Journal of MEDICAL PRACTICE MANAGEMENT

Editor: Marcel Frenkel, MD, MBA

A new journal gives you the management skills you need to pull ahead

Right now you need information on some important topics that weren't covered in medical school. Topics that are having a profound impact on private practice and hospital-based physicians across the country.

Like competition from HMOs. Industrialization of medicine. The sheer number of physicians competing for your patients. Increasing costs.

You know the issues. What you need to know is the best way to face them so your practice will flourish in years to come.

And that's where **The Journal of Medical Practice Management** comes in.

Keep up with the issues that are changing your way of practice forever

The Journal of Medical Practice Management is a new quarterly publication that covers your concerns...issues affecting the way you practice now — and the way you'll practice in the future.

Four times a year, an expert editorial board headed by Dr. Marcel Frenkel brings you concise, readable coverage of today's issues and tomorrow's trends.

You'll find departments covering • office procedures and management • malpractice • marketing • manpower • computers • taxation • legal and legislative affairs • and health policy.

You'll also find pertinent features like the **Washington Report**, telling you what's up in the nation's capital and how it affects you...a **Letter from Abroad**, offering perspectives on how physicians are handling health care issues in other countries...and profiles of profit and not-for-profit health care delivery systems.

A multidisciplinary editorial board

Members of the editorial board for **The Journal of Medical Practice Management** have been carefully chosen for their knowledge of the management aspects of practicing medicine. These experts, many with experience in more than one field, give you the perspectives you need from medicine, law, management, government, and education.

You can control the future of your practice

The issues you can't afford to ignore are in **The Journal of Medical Practice Management**. It's a lot of information for a little money. And that's good business for you.

Reserve your charter subscription today!

Just return the attached coupon, or call our **FREE number**, 800-638-6423, from anywhere in the US except Alaska. In Maryland, call 528-4105 collect. **Quarterly**

Williams & Wilkins

428 East Preston Street
Baltimore, Maryland 21202

266 Fulham Road
London SW10 9EL England

YES, I want to control the future of my practice!

Please enter my subscription to **The Journal of Medical Practice Management** (quarterly)

☐ Individuals and Institutions \$40

All subscribers: add \$10 outside the U.S.

☐ Check enclosed ☐ Bill me

☐ MasterCard ☐ American Express ☐ VISA

Card # _____ Exp. date _____

Signature _____

Name _____

Address _____

City/State/Zip _____

Maryland residents add 5% sales tax. Subscriptions outside the US must be prepaid. All subscriptions must be paid in US dollars. Rates valid through April 30, 1988.

Please allow 8 weeks for delivery of your first issue, up to 16 weeks for surface delivery outside the US. Airmail rates available on request.

Williams & Wilkins

P.O. Box 23291
Baltimore, Maryland 21203

266 Fulham Road
London SW10 9EL England

MPMAD 95048 87

RADIOLOGY/NUCLEAR MEDICINE

Excellent opportunity for radiologist with specialty training in nuclear medicine to develop and expand the nuclear medicine department within Kaiser-Permanente. Experience in the area of cardiac nuclear medicine is a plus.

Practice located in midtown location within 10 minutes of downtown Denver. Hospitals within walking distance. Established group practice HMO with excellent benefits including fully paid professional liability insurance.

For additional information, please contact:

Toby P. Cole, M.D., Executive Medical Director, Colorado Permanente Medical Group, P.C., 2045 Franklin Street, 11th Floor, Denver, Colorado 80205 (303) 861-3262. EOE

Help us to serve you better.....



**USE
YOUR
ZIP
CODE**

**Remember, your zip code
provides faster, more direct
delivery of your journals.
Use it on all correspondence,
too.**

INDEX TO ADVI

Adria Laboratories

Colorado Permanente

Eastman Kodak

Elema Schonander, Inc.

E-Z-EM Company

General Electric

Medi-Tech

Nuclear Associates

Precise Optics/PME, Inc.

Pyne Corporation

Raytheon Medical Systems ...

Squibb A21, A22, A23

S & S X-Ray

Tecnomed USA

Toshiba Medical Systems ...

We try to present an accurate index. Occasional omissions may be possible because of a last-minute change.



From the beginning to manufacture the most consistent medical x-ray films in the world was apparent. Quality was produced with every sheet. That's why Fuji designed what remains today the most sophisticated medical x-ray film factory. Exclusive Fuji technologies—such as helical emulsion drying—have elevated the consistent performance of photographic film to a new plateau. The result: From sheet-to-sheet, Fuji produces a more consistent quality than FUJI. NO ONE!

The point is—If you're not getting this kind of consistency from your current film, you are wasting hundreds of dollars.

Let Fuji show your radiology department the difference between consistent and **UNCOMMONLY CONSISTENT**. Call your local Fuji Representative, or 800-431-1850.



**FUJI QUALITY...
UNCOMMONLY
CONSISTENT.**



I&I Imaging & Information

FUJI MEDICAL SYSTEMS, U.S.A.,
90 Viaduct Road, P.O. Box 4960, Stamford, CT 06907

CIRCLE 7 ON READER SERVICE CARD

SPECIAL ARTICLE

- 465 Aubrey O. Hampton lecture. Subspecialization in radiology: response to a need. *Taveras JM*

PEDIATRIC URORADIOLOGY

- 471 Imaging in acute renal infection in children. *Sty JR, Wells RG, Starshak RJ, Schroeder BA*
 479 Urography and voiding cystourethrography: findings in girls with urinary tract infection. *Bisset GS III, Strife JL, Dunbar JS*
 483 Ureteral dilation in children with febrile urinary tract infection or bacteriuria. *Hellström M, Jodal U, Mårild S, Wettergren B*
 487 Posttransplant renal artery stenosis: angiographic study in 32 children. *Stanley P, Malekzadeh M, Diamant MJ*
 491 Stones in the urinary bladder in children and young adults. *Lebowitz RL, Vargas B*
 497 The duplex collecting system in girls with urinary tract infection: prevalence and significance. *Bissett GS III, Strife JL*

CHEST RADIOLOGY

- 501 Pulmonary vascular obstruction in severe ARDS: angiographic alterations after IV fibrinolytic therapy. *Greene R, Lind S, Jantsch H, et al.*
 509 CT assessment of silicosis in exposed workers. *Bégin R, Bergeron D, Samson L, Boctor M, Cantin A*
 515 Mediastinal imaging in myasthenia gravis: correlation of chest radiography, CT, MR, and surgical findings. *Batra P, Herrmann C Jr, Mulder D*
 521 Case report. Mediastinal paraganglioma: radiologic evaluation of an unusual vascular tumor. *Drucker EA, McLoud TC, Dedrick CG, Hilgenberg AD, Geller SC, Shepard JO*
 523 Case report. Pleural endometriosis with diaphragmatic defects: CT and sonographic findings. *Im J-G, Kang HS, Choi BI, Park JH, Han MC, Kim C-W*

BREAST RADIOLOGY

- 525 Mammographic density and physical assessment of the breast. *Swann CA, Kopans DB, McCarthy KA, White G, Hall DA*

ENDOCRINE RADIOLOGY

- 527 Efficacy of thyroid scintigraphy in the diagnosis of intrathoracic goiter. *Park H-M, Tarver RD, Siddiqui AR, Schauwecker DS, Wellman HN*
 531 Primary adrenocortical carcinoma: CT evaluation with clinical correlation. *Fishman EK, Deutch BM, Hartman DS, Goldman SM, Zerhouni EA, Siegelman SS*

GASTROINTESTINAL RADIOLOGY

- 537 CT evaluation of Crohn's disease: effect on patient management. *Fishman EK, Wolf EJ, Jones B, Bayless TM, Siegelman SS*
 541 Diagnosis of acute colonic diverticulitis: comparison of barium enema and CT. *Johnson CD, Baker ME, Rice RP, Silverman P, Thompson WM*
 547 Technical note. Efficacy of an intracassette filter for improved pneumocolon decubitus radiographs. *Olson DL, Dodds WJ, Stewart ET, Unger GF*
 551 Pictorial essay. Sonography in patients with a possible pancreatic mass shown on CT. *Ormsen MJ, Charbonneau JW, Stephens DH*
 557 Technical note. Daytime constancy of bile duct diameter. *Raptopoulos V, Smith EH, Karellas A, Miranda DK, Tefft CA*

MUSCULOSKELETAL RADIOLOGY

- 559 High-resolution MR imaging of the normal rotator cuff. *Middleton WD, Kneeland JB, Carrera GF, et al.*
 565 Lumbar hernia: diagnosis by CT. *Baker ME, Weinerth JL, Andriani RT, Cohan RH, Dunnick NR*

- 569 Direct radiographic magnification with computed radiography. *Nakano Y, Hiraoka T, Togashi K, et al.*
 574 Case report. CT diagnosis of synovial chondromatosis of temporomandibular joint. *Manco LG, DeLuke DM*
 577 Case report. Superficial fascial calcification in epidermolysis bullosa. *Panicek DM, Leeson SH*

NEURORADIOLOGY

- 579 MR imaging and spectroscopy in clinical and experimental cerebral ischemia: a review. *Brant-Zawadzki M, Weinstein P, Bartowski H, Moseley M*
 589 MR imaging of the intratemporal facial nerve by using surface coils. *Teresi L, Lufkin R, Wortham D, et al.*
 595 The utility of MR in planning the radiation therapy of oligodendroglioma. *Shuman WP, Griffin BR, Haynor DR, et al.*
 601 Direct oblique sagittal CT of orbital wall fractures. *Ball JB Jr*
 609 The "fat" C2: a sign of fracture. *Smoker WRK, Dolan KD*
 615 Case report. Traumatic pneumorrhachis. *Newbold RG, Wiener MD, Vogler JB III, Martinez S*

INTERVENTIONAL RADIOLOGY

- 617 Technical note. Direct percutaneous ureterolithotomy. *Smith TP, Hunter DW, Hulbert JC, Darcy MD, Castaneda-Zuniga WR, Amplatz K*
 621 Technical note. Translumbar inferior vena cava Hickman catheter placement for total parenteral nutrition. *Denny DF Jr, Dorfman GS, Greenwood LH, Horowitz NR, Morse SS*
 623 Technical note. Aspiration biopsy of superficial lesions: ultrasonic guidance with a linear-array probe. *Rizzatto G, Solbiati L, Croce F, Derchi LE*
 626 Technical note. Hepatic embolization through periportal collaterals: balloon occlusion technique. *Nakamura H, Hashimoto T, Oi H, Sawada S*

MAGNETIC RESONANCE IMAGING

- 629 Two-second MR images: comparison with spin-echo images in 29 patients. *Utz JA, Herfkens RJ, Johnson CD, et al.*
 634 Technical note. Phase-offset technique to distinguish slow blood flow and thrombus on MR images. *Dinsmore RE, Wedeen V, Rosen B, Wisner GL, Miller SW, Brady TJ*

ARRS ANNUAL MEETING CASE OF THE DAY

- 637 Introduction. *Goldberg ME*
 638 Chest case of the day. *Crass JR, Letourneau JG, Day DL, Goldberg ME*
 641 Abdominal case of the day. *Letourneau JG, Day DL, Crass JR, Goldberg ME, Drake G*
 643 Musculoskeletal case of the day. *Day DL, Letourneau JG, Crass JR, Goldberg ME, Drake G*
 646 Neuroradiology case of the day. *McGeachie RE, Ford WJ, Nelson MJ, Elias D*

OTHER CONTENT

- 496 Books received
 530 Forthcoming articles
 556 American Roentgen Ray Society officers and information
 620 ARRS 1987 meeting summary
 649 Letters
 654 Abstracts
 657 News
 659 Erratum
 660 ARRS 1987 meeting registration forms
 663 Classified ads
 Book reviews 470, 478, 520, 536, 550, 568
 A3 Guidelines for authors